LINAC 2004

XXII International Linear Accelerator Conference

Lübeck, Germany, August 16 - 20, 2004

Chairman's Foreword

The 22nd International Linac Conference was held in the Musik- und Kongresshalle (MuK) Lübeck, Germany, from the August 16th-20th, 2004. The conference was jointly hosted by the Deutsches Elektronen-Synchrotron (DESY) in Hamburg and the Gesellschaft für Schwerionenforschung (GSI) in Darmstadt. From around the world came 286 physicist and engineers from some 61 institutes and 27 industrial companies to participate in the conference. We had 13 industrial exhibits, which we conveniently located around the poster forum in the MuK. Many of you took the opportunity to visit the VUV FEL linac at DESY on the Friday afternoon.

At the beginning of the conference we had opening addresses by honorary guests: Dr. Hermann Schunck, Director in the Federal Ministry for Education and Research; Dr. Hellmut Koerner, State Secretary in the Ministry for Education, Science, Research and Culture of Schleswig Holstein; Mr. Thorsten Geissler, Senator of the Interior of Lübeck; and Prof. Dr. Alfred Xaver Trautwein, Rector of the University of Lübeck. All of them stressed the importance of accelerators for the progress of science and especially supported the new European projects located in Germany: FAIR and the XFEL.

Following the time-honoured tradition of the Linac Conference, the programme was arranged in a sequence of plenary sessions in the mornings, followed by poster sessions in three of the afternoons (including the so-called 'oral-poster' presentations). This year's Programme Committee, chaired by Norbert Angert from GSI, had the job of reducing the many proposals for invited talks to the 45 that eventually formed the morning sessions. In addition to the invited orals, we had 249 poster presentations, of which 36 were selected for five-minute oral-poster presentations.

In many ways the International Linac Conference is unique: the traditions of being by invitation only, of being accommodated in a single hotel, and having no parallel sessions have always been intended to promote intense and positive discussion between the experts in the field of linear accelerators. I hope that we successfully continued these traditions in Lübeck.

Besides the excellent scientific program of the conference, I like to think that our hospitality helped make the conference a memorable one. Set in the beautiful Hanseatic city of Lübeck, we arranged several social events to help you relax and enjoy the surroundings. We started with a cocktail reception on the Sunday at the Petri-Kirche (one of Lübeck's many famous and beautiful historical churches). While we wined and dined, we were entertained by a solo saxophone player, and a mixed choir. Wednesday afternoon we had the official conference 'outing', which - by tradition - had a slightly sporting element, with a 12km hike through the beautiful countryside around the Ratzeburger lake, with several of you taking advantage of the good weather to go

swimming. We closed our day with an open-air dinner on the shores of the Küchensee (Kitchen Lake). On Thursday evening we had a fine banquet in the rustic nautical setting of 'Schuppen 9' in Lübeck harbour, accompanied by a jazz-swing combo, featuring one of our own (Reinhard Brinkmann) on the piano.

On the following Friday morning plenary session, a little bit of history was made: Norbert Holtkamp gave a short (unscheduled) presentation announcing the conclusions of the Linear Collider International Technology Recommendation Panel (ITRP). The Panel had spent the best part of the last eight months reviewing both the X-band and superconducting L-band proposals, eventually selecting the latter to be recommended for the International Linear Collider (ILC). It seems only fitting that such an important decision by the world community should be made public at the International Linac Conference.

A successful conference is the sum of many important parts. I'd like to take the opportunity to say a big thank you to all the various committees that have worked hard to make this conference a success. I'm sure you will join me in sending a particular big thanks to the local organising committee, the secretaries and the numerous technical people who made the whole thing happen. A conference is only as good as the people that attend and the standard of the work that is presented; we like to think that the 22nd International Linac Conference was a very good conference indeed, and I would like to thank you - the participants - for making it so.

Dieter Trines
XXII International Linac Conference Chair

Contents

Conference Chair

D. Trines (Chair)	DESY, Hamburg

International Organizing Committee

J. Alessi	BNL, Upton N.Y.
N. Angert	GSI, Darmstadt
S. Chattopadhyay	JLAB, Newport News
Y. Cho	ANL, Argonne
M. Fazio	LANL, Los Alamos
G. Fortuna	INFN-LNL, Legnaro
T. Garvey	LAL-Orsay, Orsay-Cedex
R.L. Gluckstern	Univ. Maryland, College Park
H.D. Haseroth	CERN, Geneva
N. Holtkamp	ORNL, Oak Ridge
H. Klein	Goethe-Univ. , Frankfurt
A. Kolomiets	ITEP, Moscow
L. Kravchuk	INR, Moscow
G.A. Loew	SLAC, Stanford
G.E. McMichael	ANL, Argonne
A. Mosnier	CEA-Saclay, Gif-sur-Yvette
W. Namkung	POSTECH, Pohang
A. Noda	Univ. Kyoto
R. Ruth	SLAC, Stanford
C.W. Schmidt	FNAL, Batavia
P. Schmor	TRIUMF, Vancouver
S.O. Schriber	Michigan State University
Ch. Sinclair	Univ. Cornell
D.F. Sutter	US DOE, Washington
D. Trines (Chair)	DESY, Hamburg
S.H. Wang	IHEP, Beijing
H. Weise	DESY, Hamburg
Y. Yamazaki	JAERI, Tokai
S. Yu	LBNL, Berkeley

Local Organizing Committee

W. Barth	GSI, Darmstadt
S. Bergelt-Brückner	GSI, Darmstadt
P. Castro	DESY, Hamburg
W. Decking	DESY, Hamburg
K. Flöttmann	DESY, Hamburg
C. Germer	DESY, Hamburg
C. Kluth	DESY, Hamburg
K. Lando	DESY, Hamburg
T. Limberg	DESY, Hamburg
M. Marx	DESY, Hamburg
S. Mette	DESY, Hamburg
I. Nikodem	DESY, Hamburg
Ch. Oevermann	DESY, Hamburg
D. Ramert	DESY, Hamburg
R. Roude	DESY, Hamburg
V. Schaa	GSI, Darmstadt
W. Stork	GSI, Darmstadt
N. Walker	DESY, Hamburg
H. Weise (Chair)	DESY, Hamburg

Program Committee

N. Angert (Chair)	GSI, Darmstadt
W. Barth	GSI, Darmstadt
R. Brinkmann	DESY, Hamburg
Y. Cho	ANL, Argonne
G. Dutto	TRIUMF, Vancouver
G. Fortuna	INFN-LNL, Legnaro
T. Garvey	LAL-Orsay, Orsay-Cedex
H.D. Haseroth	CERN, Geneva
N. Holtkamp	ORNL, Oak Ridge
A. Kolomiets	ITEP, Moscow
E. McCrory	FNAL, Batavia
G.E. McMichael	ANL, Argonne
A. Mosnier	CEA-Saclay, Gif-sur-Yvette
W. Namkung	POSTECH, Pohang
O. Napoly	CEA-Saclay, Gif-sur-Yvette
G. Neil	JLAB, Newport News
M. Poole	DL, Daresbury
D. Raparia	BNL, Upton, N.Y.
T. Raubenheimer	SLAC, Stanford
R. Ruth	SLAC, Stanford
A. Schempp	Goethe-Univ. , Frankfurt
S.O. Schriber	Michigan State Univ.
K. Shepard	ANL, Argonne
T. Shintake	SPring8, Harima
D.F. Sutter	US Department of Energy, Washington
D. Trines	DESY, Hamburg
H. Weise	DESY, Hamburg
M. White	ORNL, Oak Ridge
Y. Yamazaki	JAERI, Tokai
M. Yoshioka	KEK, Tsukuba
S. Yu	LBNL, Berkeley

Monday, August 16, 2004

09:00 – 09:30 **Welcome Addresses**
Dr. Hermann Schunck
(Ministerial Director, Federal Ministry for Education and Research)
Dr. Hellmut Körner
(State Secretary, Ministry for Education, Science Research and Culture for Schleswig-Holstein)
Mr. Thorsten Geissler
(Senator of the Interior of Lübeck)
Prof. Dr. Alfred Xaver Trautwein
(Rector of the University of Lübeck)

09:30 – 10:30 **MO1 — Monday Morning Session**
Session Chair: D. Trines (DESY, Hamburg)

MO101 **Advanced Analysis in Nanospace: Research with the XFEL**
H. Dosch (MPI, Stuttgart)

MO102 **Accelerator Layout of the XFEL**
R. Brinkmann (DESY, Hamburg)

10:30 – 11:00 **Coffee Break**

11:00 – 12:20 **MO2 — Monday Late Morning Session**
Session Chair: H. Haseroth (CERN, Geneva)

MO201 **Linac Coherent Light Source (LCLS) – Accelerator System Overview**
P. Krejcik, Z. Huang, J. Wu (SLAC, Menlo Park, California) P. Emma (SLAC/ARDA, Menlo Park, California)

MO202 **High-Intensity, High Charge-State Heavy Ion Sources**
J. Alessi (BNL, Upton, Long Island, New York)

MO203 **Non-Interfering Beam Diagnostic Developments**
A. Peters, P. Forck (GSI, Darmstadt)

MO204 **Status of REX-ISOLDE**
O.K. Kester, S. Emhofer, D. Habs, M. Pasini, K. Rudolph (LMU, Garching) F. Ames, P. Butler, P. Delahaye, M. Lindroos, T. Sieber, F.J.C. Wenander (CERN, Geneva) R. Repnow, H. Scheit, D. Schwalm, R. von Hahn (MPI-K, Heidelberg)

12:20 – 13:40 **Lunch**

13:40 – 14:30 **MO3 — Monday Early Afternoon Session**
Session Chair: Y. Cho (ANL, Argonne, Illinois)

MO301 **SPIRAL2 at GANIL**
M.-H. Moscatello (GANIL, Caen)

MO302 **Development of Superconducting and Room Temperature CH-Structures**
H. Podlech, H. Deitinghoff, H. Klein, H. Liebermann, U. Ratzinger, A.C. Sauer, R. Tiede (IAP, Frankfurt-am-Main) Z. Li (IMP, Lanzhou)

14:30 – 15:30 **MO4 — Oral Poster Presentation**
5 min each

MOP06 **A Dedicated 70 MeV Proton Linac for the Antiproton Physics Program of the Future Facility for Ion and Antiproton Research at Darmstadt**
L. Groening, W. Barth, L. Dahl, R. Hollinger, P.S. Spädtke, S. Yaramishev (GSI, Darmstadt) B.H. Hofmann, Z. Li, U. Ratzinger, A. Schempp, R. Tiede (IAP, Frankfurt-am-Main)

MOP08 **Investigation of the Beam Matching to the GSI-Alvarez DTL under Space Charge Conditions**
S. Yaramishev, W. Barth, L. Dahl, L. Groening, S. Richter (GSI, Darmstadt)

MOP09 **Status of the 7 MeV/u, 217 MHz Injector Linac for the Heidelberg Cancer Therapy Facility**
B. Schlitt, G. Hutter, F. Klos, C. Muehle, W. Vinzenz (GSI, Darmstadt) A. Bechtold, U. Ratzinger, A. Schempp (IAP, Frankfurt-am-Main) Y.R. Lu (PKU/IHIP, Beijing)

MOP21 **The Pre-Injector Linac for the Diamond Light Source**
C. Christou, V. Kempson (DIAMOND, Chilton, Didcot, Oxon) K. Dunkel, C. Piel (ACCEL, Bergisch Gladbach)

MOP34 **Injector Linac Upgrade for the BEPCII Project**
S.H. Wang (IHEP Beijing, Beijing)

MOP37 **Optimization of Positron Capture in NLC**
Y.K. Batygin (SLAC, Stanford)

MOP44 **Electron-Cloud Effects in the Positron Linacs of Future Linear Colliders**
D. Schulte, F. Zimmermann (CERN, Geneva) K. Oide (KEK, Ibaraki)

MOP49 **Status And Operating Experience of The TTF Coupler**
W.-D. Möller (DESY, Hamburg)

MOP72 **RF Breakdown in Accelerator Structures: From Plasma Spots to Surface Melting**
P.B. Wilson (SLAC, Menlo Park, California)

MOP74 **Recent Results of the 2.45 GHz ECR Source to Produce H^- Ions at CEA/Saclay**
R. Gobin, K.B. Benmeziane, O. Delferriere, R.F. Ferdinand, A. France, F.H. Harrault (CEA/DAPNIA-SACM, Gif-sur-Yvette Cedex) A.G. Girard (CEA DSM Grenoble, Grenoble)

MOP79 **Design of a Monochromatic X-Ray Thomson Source at SPARC**
L. Serafini (INFN Milano, Milano)

MOP86 **Cold Test Results of the ISAC-II Medium Beta High Gradient Cryomodule**
R.E. Laxdal, I. Bylinskii, G.S. Clark, K. Fong, A.K. Mitra, R. L. Poirier, B. Rawnsley, T.R. Ries, I. Sekatchev, G. Stanford, V. Zvyagintsev (TRIUMF, Vancouver)

15:30 – 17:30 **MOP — Monday Poster Session**

MOP01 **Beam Intensity Adjustment in the RIA Driver Linac**
P.N. Ostroumov, J.A. Nolen, I. Sharamentov (ANL/Phys, Argonne, Illinois) A.V. Novikov-Borodin (RAS/INR, Moscow)

MOP02 **Design of the Matching Beamline Between an EBIS and RFQ**
J. Alessi, E. Beebe, J.R. John, A.K. Kponou, A.I. Pikin, D. Raparia (BNL, Upton, Long Island, New York)

MOP03 **Proposal for Reduction of Transverse Emittance of BNL 200 MeV Linac**
J. Alessi, D. Raparia, W.-T. Weng (BNL, Upton, Long Island, New York)

MOP04 **Fermilab Drift Tube Linac Revisited**
M. Popovic, L. Allen (FNAL, Batavia, Illinois)

MOP05 **The HITRAP-Decelerator for Heavy Highly-Charged Ions**
L. Dahl, W. Barth, T. Beier (GSI, Darmstadt) C. A. Kitegi, U. Ratzinger, A. Schempp (IAP, Frankfurt-am-Main)

MOP06 **A Dedicated 70 MeV Proton Linac for the Antiproton Physics Program of the Future Facility for Ion and Antiproton Research at Darmstadt**
L. Groening, W. Barth, L. Dahl, R. Hollinger, P.S. Spädtke, S. Yaramishev (GSI, Darmstadt) B.H. Hofmann, Z. Li, U. Ratzinger, A. Schempp, R. Tiede (IAP, Frankfurt-am-Main)

MOP07 **High Current Beam Transport to SIS18**
S. Richter, W. Barth, L. Dahl, J. Glatz, L. Groening, S. Yaramishev (GSI, Darmstadt)

MOP08 **Investigation of the Beam Matching to the GSI-Alvarez DTL under Space Charge Conditions**
S. Yaramishev, W. Barth, L. Dahl, L. Groening, S. Richter (GSI, Darmstadt)

MOP09 **Status of the 7 MeV/u, 217 MHz Injector Linac for the Heidelberg Cancer Therapy Facility**
B. Schlitt, G. Hutter, F. Klos, C. Muehle, W. Vinzenz (GSI, Darmstadt) A. Bechtold, U. Ratzinger, A. Schempp (IAP, Frankfurt-am-Main) Y.R. Lu (PKU/IHIP, Beijing)

MOP10 **The IH Cavity for HITRAP**
C. A. Kitegi, U. Ratzinger (IAP, Frankfurt-am-Main) S. Minaev (ITEP, Moscow)

MOP11 **RF Model Measurements and Numerical Simulations for the 20 MV IH-DTL Cavity of the Heidelberg Cancer Therapy Facility**
Y.R. Lu, Y.R. Lu, B. Schlitt (GSI, Darmstadt) S. Minaev (ITEP, Moscow) U. Ratzinger, R. Tiede (IAP, Frankfurt-am-Main)

MOP12 **KONUS Beam Dynamics Design of a 70 mA, 70 MeV Proton CH-DTL for GSI-SIS12**
R. Tiede, G. Clemente, H. Podlech, U. Ratzinger (IAP, Frankfurt-am-Main) W. Barth, L. Groening (GSI, Darmstadt) Z. Li (IMP, Lanzhou) S. Minaev (ITEP, Moscow)

MOP13 **Status of A Tuner Development for A 352 MHz Superconducting CH-Cavity**
A.C. Sauer, H. Deitinghoff, H. Klein, H. Liebermann, H. Podlech, U. Ratzinger, R. Tiede (IAP, Frankfurt-am-Main)

MOP14 **Development of Intense Beam Proton Linac in China**
S. Fu, S.X. Fang, H. Ouyang, S. Zhao (IHEP Beijing, Beijing) B. Cui, X. Guan (CIAE, Beijing)

MOP15 **TRASCO-RFQ as Injector for the SPES-1 Project**
P. Posocco, M. Comunian, A. Pisent (INFN/LNL, Legnaro, Padova) E.F. Fagotti (INFN Milano, Milano)

MOP16 **The TRASCO-SPES RFQ**
A. Pisent, M. Comunian, J. E. Esposito, A. Palmieri (INFN/LNL, Legnaro, Padova) E.F. Fagotti (INFN Milano, Milano) G. Lamanna (INFN-Bari, Bari) M. S. Mathot (CERN, Geneva)

MOP17 **Design of the SPES-1 LEBT**
E.F. Fagotti (INFN Milano, Milano) M. Comunian, A. Pisent (INFN/LNL, Legnaro, Padova)

MOP18 **Cold-Model Tests and Fabrication Status for J-PARC ACS**
H. Ao, H.A. Akikawa (JAERI/LINAC, Ibaraki-ken) K. Hasegawa, A. Ueno (JAERI, Ibaraki-ken) N. Hayashizaki (TIT, Tokyo) M. Ikegami, S. Noguchi (KEK, Ibaraki) V.V. Paramonov (RAS/INR, Moscow) Y. Yamazaki (J-PARC, Ibaraki-ken)

MOP19 **Particle Distributions at the Exit of the J-PARC RFQ**
Y. Kondo, A. Ueno (JAERI, Ibaraki-ken) K.I. Ikegami, M. Ikegami (KEK, Ibaraki)

MOP20 **Design of the R.T. CH-Cavity and Perspectives for a New GSI Proton Linac**
Z. Li (IMP, Lanzhou) W. Barth, L. Groening (GSI, Darmstadt) H. Podlech, U. Ratzinger, R. Tiede (IAP, Frankfurt-am-Main)

MOP21 **The Pre-Injector Linac for the Diamond Light Source**
C. Christou, V. Kempson (DIAMOND, Chilton, Didcot, Oxon) K. Dunkel, C. Piel (ACCEL, Bergisch Gladbach)

MOP22 **Status of the Dragon-I Linear Induction Accelerator**
J. Deng, N. Chen, S. Chen, G. Dai, Z. Dai, B. Ding, Q. Lai, H. Li, J. Li, X. Liu, J. Shi, H. Wang, L. Wen, Y. Xie, A. Yang, G. Yang, K. Zhang, L. Zhang, W. Zhang (CAEP/IFP, Mainyang, Sichuan)

MOP23 **Electron Beam Properties of the FNPL Photoinjector**
K. Desler (FNAL, Batavia, Illinois)

MOP24 **Using a Solid State Switch for a 60kV Bouncer to Control Energy Spread during the Beam Pulse**
L. Donley, J.C. Dooling, G.E. McMichael, V. F. Stipp (ANL, Argonne, Illinois)

MOP25 **The LEBRA 125MeV Electron Linac for FEL And PXR Generation**
K. Hayakawa, Y. Hayakawa, K. Ishiwata, K. Kanno, K. Nakao, T. Sakai, I. Sato, T. Tanaka (LEBRA, Funabashi) K. Yokoyama (KEK, Ibaraki)

MOP26 **ERLP Gun Commissioning Beamline Design**
D.J. Holder, C.K.M. Gerth, F.E. Hannon (CCLRC/DL/ASTeC, Daresbury, Warrington, Cheshire) R.J. Smith (CLRC, Daresbury, Warrington, Cheshire)

MOP27 **The Commssioning of X-Band SW Accelerator Guide**
Q. Jin, B. Chen, Y. Lin, B. Sun, X. Sun, X. Tao, D. Tong, Y. Zou (TSINGHUA, Beijing)

MOP28 **A Study of Dipole Higher-Band Wakefields in X-Band Accelerating Structures for the GLC/NLC**
R.M. Jones (SLAC/ARDA, Menlo Park, California)

MOP29 **The RHIC Electron Cooler**
J. Kewisch, I. Ben-Zvi, X.Y. Chang, V. Litvinenko, C. Montag, V. Yakimenko (BNL, Upton, Long Island, New York)

MOP30 **Linear Accelerator LINAC-800 of the DELSY Project**
V.V. Kobets, N. Balalykin, I.N. Meshkov, I.A. Seleznev, G. Shirkov (JINR, Dubna, Moscow Region)

MOP31 **Development of C-band Accelerator Unit for Super KEKB**
S. Ohsawa, K. Kakihara, T. Kamitani, T. Oogoe, T.S. Sugimura (KEK, Ibaraki)

MOP32 **Acceleration Results from a Four-Cell S-Band PWT Linac Structure**
K. K. Pant, B. Biswas, U. Kale, V. Kodiarasan, S. Krishnagopal, A. Kumar, V. Kumar, S.L. Kumawat, P. Nerpagar (CAT, Indore) R. Parkar (CAT, Indore M.P.)

MOP33 **A Flat Beam Electron Source for the TESLA Linear Collider**
P. Piot (FNAL, Batavia, Illinois)

MOP34 **Injector Linac Upgrade for the BEPCII Project**
S.H. Wang (IHEP Beijing, Beijing)

MOP35 **The Research of a SW Accelerating Structure with Small Beam Spot**
X. Yang (CAEP/IAP, Mianyang, Sichuan)

MOP36 **Preliminary Study on HOM-Based Beam Alignment in the TESLA Test Facility**
N. Baboi, H. Schlarb (DESY, Hamburg) O. Napoly (CEA/DSM/DAPNIA, Gif-sur-Yvette) R. Paparella (CEA/DAPNIA-SACM, Gif-sur-Yvette Cedex)

MOP37 **Optimization of Positron Capture in NLC**
Y.K. Batygin (SLAC, Stanford)

MOP38 **Background from Undulator in a Proposed Experiment with Polarized Positrons**
Y.K. Batygin (SLAC, Stanford)

MOP39 **Positron Transmission and Polarization in E-166 Experiment**
Y.K. Batygin (SLAC, Stanford)

MOP40 **A Study Of Coupler-Trapped Modes In X-Band Linacs for the GLC/NLC**
R.M. Jones, V.A. Dolgashev (SLAC/ARDA, Menlo Park, California) Z. Li (SLAC, Menlo Park, California) J.W. Wang (SLAC/ARDB, Menlo Park, California)

MOP41 **Emittance-Imposed Alignment and Frequency Tolerances for the TESLA Collider**
N. Baboi (DESY, Hamburg) R.M. Jones (SLAC/ARDA, Menlo Park, California)

MOP42 **Linac Alignment and Frequency Tolerances from the Perspective of Contained Emittances for the GLC/NLC**
R.M. Jones (SLAC/ARDA, Menlo Park, California)

MOP43 **The Impact of Longitudinal Drive Beam Jitter on the CLIC Luminosity**
D. Schulte, E. J. N. Wilson, F. Zimmermann (CERN, Geneva)

MOP44 **Electron-Cloud Effects in the Positron Linacs of Future Linear Colliders**
D. Schulte, F. Zimmermann (CERN, Geneva) K. Oide (KEK, Ibaraki)

MOP45 **A Potential Signal for Luminosity Optimisation in CLIC**
D. Schulte (CERN, Geneva)

MOP46 **Experimental Investigation of the Longitudinal Beam Dynamics using a Two-Macroparticle Bunch Technique**
R. Tikhoplav (Rochester University Physics and Astronomy Department, Rochester, New York) N. Barov (Northern Illinois University Department of Physics, DeKalb, Illinois) P. Piot (FNAL, Batavia, Illinois)

MOP47 **Limiting Effects in the Round-To-Flat Beam Transformation**
Y.-E. Sun (Fermilab, Batavia, Illinois) K.-J. Kim (Chicago University Department of Physics, Chicago, Illinois) P. Piot (FNAL, Batavia, Illinois)

MOP48 **Gamma and X-rays Production for Experiments at ELSA Facility**
J. Lemaire (CEA/DAM, Bruyères-le-Châtel)

MOP49 **Status And Operating Experience of The TTF Coupler**
W.-D. Möller (DESY, Hamburg)

MOP50 **Muon Test Area at Fernilab**
M. Popovic (FNAL, Batavia, Illinois)

MOP61 **Automated Beam Steering and Shaping Using Optimal Control Theory and Extremum Seeking**
C.K.A. Allen (LANL, Los Alamos, New Mexico) C. Chu, J. Galambos, T.A.P. Pelaia, A. Shishlo (ORNL/SNS, Oak Ridge, Tennessee) M.K. Krstic (UCSD, La Jolla, California)

MOP62 **Single Bunch Energy Spread in BTW Accelerating Structures at ELETTRA**
G. D'Auria (Sincrotrone Trieste S.C.p.A., Basovizza, Trieste)

MOP63 **Numerical Calculation of Coupling Impedances in Kicker Modules for Non-Relativistic Particle Beams**
B. Doliwa, T. Weiland (TU Darmstadt, Darmstadt)

MOP64 **A Circuit Model of the Wire Measurement of Impedance of an X-Band Accelerating Structure**
R.M. Jones (SLAC/ARDA, Menlo Park, California) N. Baboi (DESY, Hamburg) N.M. Kroll (UCSD, La Jolla, California)

MOP65 **Simple Theory of Thermal Fatigue Caused by RF Pulse Heating**
S. Kuzikov (IAP, Nizhniy Novgorod)

MOP66 **Calculation of RF Properties of the Third Harmonic Cavity**
K. Rothemund, H.-W. Glock, D. Hecht, U. van Rienen (Rostock University Faculty of Engineering, Rostock)

MOP67 **TTF RF Power Coupler Thermal Calculations**
D. Kostin, M. Dohlus, W.-D. Möller (DESY, Hamburg)

MOP68 **Ribbon Ion Beam Dynamics in Undulator Linear Accelerator.**
E.S. Masunov, S.M. Polozov (MEPhI, Moscow)

MOP69 **RF Control Modelling Issues for Future Superconducting Accelerators**
A.H. Hofler (TJNAF, Newport News, Virginia) A. Brandt, S. Simrock (DESY, Hamburg) T. Czarski (WUT, Warsaw) J. R. Delayen (Jefferson Lab, Newport News, Virginia) T. Matsumoto (KEK, Ibaraki)

MOP70 **A Pass Band Performance Simulation Code of Accelerating Cavities**
X. Tao, D. Tong (TSINGHUA, Beijing)

MOP71 **Advanced Beam-Dynamics Simulation Tools for RIA**
T. Wangler, R. Garnett (LANL, Los Alamos, New Mexico) N. Aseev, P.N. Ostroumov (ANL/Phys, Argonne, Illinois) R. Crandall (TechSource, Santa Fe, NM) D. Gorelov, R.C. York (NSCL, East Lansing, Michigan) J. Qiang, R. Ryne (LBNL, Berkeley, California)

MOP72 **RF Breakdown in Accelerator Structures: From Plasma Spots to Surface Melting**
P.B. Wilson (SLAC, Menlo Park, California)

MOP73 **Development of a Permanent Magnet ECR Source to Produce a 5 mA Deuteron Beam at CEA/Saclay**
R. Gobin, D.D.M. De Menezes, O. Delferriere, R.F. Ferdinand, A. France, F.H. Harrault (CEA/DAPNIA-SACM, Gif-sur-Yvette Cedex) P.-Y. Beauvais (CEA/DSM/DAPNIA, Gif-sur-Yvette) P.L. Lehérissier, J.Y.P. Pacquet (GANIL, Caen)

MOP74 **Recent Results of the 2.45 GHz ECR Source to Produce H^- Ions at CEA/Saclay**
R. Gobin, K.B. Benmeziane, O. Delferriere, R.F. Ferdinand, A. France, F.H. Harrault (CEA/DAPNIA-SACM, Gif-sur-Yvette Cedex) A.G. Girard (CEA DSM Grenoble, Grenoble)

MOP75 **Hminus Distribution in the HERA RF-Volume Source**
J. Peters (DESY, Hamburg)

MOP76 **Ultra-High-Vacuum Problem for a 200 keV Polarized Electron Gun with an NEA-GaAs Photocathode**
T. Nakanishi (DOP Nagoya, Nagoya)

MOP77 **Design Parameters of the Normal Conducting Cavity for the PITZ-2 Test Stand**
V.V. Paramonov, N.I. Brusova, A.S. Kovalishin, A.I. Kvasha, A. Menshov, O.D. Pronin, A.K. Skasyrskaya, A.A. Stepanov (RAS/INR, Moscow) A. Donat, M. Krasilnikov, A. Oppelt, F. Stephan (DESY Zeuthen, Zeuthen)

MOP79 **Design of a Monochromatic X-Ray Thomson Source at SPARC**
L. Serafini (INFN Milano, Milano)

MOP80 **Development of Adaptive Feedback Control System of Both Spatial and Temporal Beam Shaping for UV-Laser Light Source for RF Gun**
H. Tomizawa, T. Asaka, H. D. Dewa, H. Hanaki, T. Kobayashi, A. Mizuno, S. S. Suzuki, T. T. Taniuchi, K. Yanagida (JASRI-SPring-8, Hyogo)

MOP81 **Analysis of the Qualification-Tests Performance of the Superconducting Cavities for the SNS Linac**
J. R. Delayen, J. Mammosser, O. Ozelis (Jefferson Lab, Newport News, Virginia)

MOP82 **Fermilab SRF Cavity and Infrastructure R&D**
N. Khabiboulline, L. Bellantoni, T. Berenc, C. Boffo, H. Edwards, H. Foley, D. Mitchell, A. Rowe, I. Terechkine (FNAL, Batavia, Illinois) N. Solyak (Fermilab, Batavia, Illinois)

MOP83 **Prototype Cryomodule for SCRF Cavities of 100 MeV Proton Linac**
P. Khare (CAT, Indore M.P.) M.G. Karmarkar, P.K. Kush (CAT, Indore)

MOP84 **First Cryogenic Tests with JLab's new Upgrade Cavities***
P. Kneisel, G. Ciovati, G. Myneni, G. Wu (Jefferson Lab, Newport News, Virginia) J. Halbritter (FZ Karlsruhe, Karlsruhe) J. Sekutowicz (DESY, Hamburg)

MOP85 **Influence of Ta Content in High Purity Niobium on Cavity Performance: Preliminary Results***
P. Kneisel, G. Myneni (Jefferson Lab, Newport News, Virginia) T. Carneiro (RMC, Bridgeville) M. Imagumbai (CBMM, Tokyo) Chr. Klinkenberg (NPC, Düsseldorf) D. Proch, W. Singer, X. Singer (DESY, Hamburg)

MOP86 **Cold Test Results of the ISAC-II Medium Beta High Gradient Cryomodule**
R.E. Laxdal, I. Bylinskii, G.S. Clark, K. Fong, A.K. Mitra, R. L. Poirier, B. Rawnsley, T.R. Ries, I. Sekatchev, G. Stanford, V. Zvyagintsev (TRIUMF, Vancouver)

MOP87 **Conceptual Layout of the European X-FEL Linac Cryogenic Supply**
B. Petersen (DESY, Hamburg)

MOP88 **RF Coupler Design for the TRIUMF ISAC-II Superconducting Quarter Wave Resonators**
R. L. Poirier, K. Fong, P. Harmer, R.E. Laxdal, A.K. Mitra, I. Sekatchev, B. Waraich, V. Zvyagintsev (TRIUMF, Vancouver)

MOP89 **A Wire Position Monitor System for the ISAC-II Cryomodule Components Alignment**
B. Rawnsley, I. Bylinskii, G. Dutto, K. Fong, R.E. Laxdal (TRIUMF, Vancouver) D. Giove (INFN/LASA, Segrate (MI))

MOP90 **Superconducting Linac Cryostat for RIA**
K.W. Shepard, J.D. Fuerst (ANL/Phys, Argonne, Illinois)

MOP92 **Simulation of the RF Coupler for TRIUMF ISAC-II Superconducting Quarter Wave Resonators**
V. Zvyagintsev (TRIUMF, Vancouver)

Tuesday, August 17, 2004

08:30 – 10:30 **TU1 — Tuesday Morning Session**
Session Chair: W. Namkung (PAL, Pohang)

TU101 **Engineering and Building RF Structures - The Works**
D. Schrage (LANL, Los Alamos, New Mexico)

TU102 **Survey of Advanced Accelerator Concepts**
C.J. Joshi (UCLA, Los Angeles, California)

TU103 **Development of the UNILAC Towards a Megawatt Beam Injector**
W. Barth, L. Dahl, J. Glatz, L. Groening, S. Richter, S. Yaramishev (GSI, Darmstadt)

TU104 **Developments and Future Plans at ISAC/TRIUMF**
P. Schmor (TRIUMF, Vancouver)

10:30 – 11:00 **Coffee Break**

11:00 – 12:20 **TU2 — Tuesday Late Morning Session**
Session Chair: Y. Yamazaki (J-PARC, Ibaraki-ken)

TU201 **The KEK C-Band RF System for a Linear Collider**
H. Matsumoto (KEK, Ibaraki)

TU202 **Low Emittance 500 kV Thermionic Electron Gun**
K. Togawa, H. Baba, T. Inagaki, K. Onoe, T. Shintake, T. Tanaka (RIKEN Spring-8 Harima, Hyogo) H. Matsumoto (KEK, Ibaraki)

TU203 **High Pressure, High Gradient Cavities for Muon Cooling**
R. P. Johnson, M. Popovic (FNAL, Batavia, Illinois) C. M. Ankenbrandt, A. Moretti (Fermilab, Batavia, Illinois) D. M. Kaplan, K. Yonehara (IIT, Chicago, Illinois)

TU204 **Dark Current and the Effect of High Solenoidal Magnetic Fields on Breakdown Voltages of High Vacuum 805 MHz Cavities**
A. Moretti, A.D. Bross, S. Geer, Z. Qian (Fermilab, Batavia, Illinois) D.M. Errede (University of Illinois at Urbana-Champaign Physics, Urbana, Illinois) D. Li (LBNL/AFR, Berkeley, California) J. Norem (ANL, Argonne, Illinois) R.A. Rimmer (Jefferson Lab, Newport News, Virginia) Y. Torun (IIT, Chicago, Illinois) M.S. Zisman (LBNL, Berkeley, California)

12:20 – 13:40 **Lunch**

13:40 – 14:30 **TU3 — Tuesday Early Afternoon Session**
Session Chair: T. Garvey (LAL, Orsay)

TU301 **High Power CW Superconducting Linacs for EURISOL and XADS**
J.-L. Biarrotte (IPN, Orsay)

TU302 **Future Developments in Electron Linac Diagnostics**
M.C. Ross (SLAC/NLC, Menlo Park, California)

14:30 – 15:30 **TU4 — Oral Poster Presentation**
5 min each

TUP01 **RFQ Drift-Tube Proton Linacs in IHEP**
Y. Budanov, O.K. Belyaev, A.P. Maltsev, I.G. Maltsev, V.B. Stepanov, S.A. Strekalovskyh, V.A. Teplyakov (IHEP Protvino, Protvino, Moscow Region)

TUP04 **The SPL Front End: A 3 MeV H^- Test Stand at CERN**
R. Garoby, L. Bruno, F. Caspers, J. Genest, K. Hanke, M. Hori, A.M. Lombardi, M. Magistris, A. Millich, M. Paoluzzi, C.R. Rossi, M. Silari, M. Vretenar (CERN, Geneva) P. Ausset (IPN, Orsay) P.-Y. Beauvais (CEA/DSM/DAPNIA, Gif-sur-Yvette)

TUP05 **Beam Dynamics for a new 160 MeV H^- Linac at CERN (LINAC4)**
F. Gerigk (CCLRC/RAL/ASTeC, Chilton, Didcot, Oxon) E. Benedico Mora, A.M. Lombardi, E.Zh. Sargsyan, M. Vretenar (CERN, Geneva)

TUP22 **A Simulation Study on Chopper Transient Effects in J-PARC Linac**
M. Ikegami (KEK, Ibaraki) Y. Kondo, T. Ohkawa, A. Ueno (JAERI, Ibaraki-ken)

TUP27 **Acceleration of Several Charge States of Lead Ion in CERN LINAC3**
V.C. Coco, J.A.C. Chamings, A.M. Lombardi, E.Zh. Sargsyan, R. Scrivens (CERN, Geneva)

TUP29 **Proton Beam Dynamics Simulation of the SARAF Linac**
A. Shor, D. Berkovits, G. Feinberg, S. Halfon (SOREQ, Yavne)

TUP41 **Multi-Bunch Beam Dynamics Studies in the TESLA XFEL**
N. Baboi (DESY, Hamburg)

TUP43 **The Superconducting CW Driver Linac for the BESSY-FEL User Facility**
J. Knobloch, M. Abo-Bakr, W. Anders, F. Marhauser, A. Neumann, M.S. Schuster (BESSY GmbH, Berlin) A.K. Annett, C.H. Haberstroh, H.Q. Quack (TU Dresden, Dresden) Y.X. Xiang (GSI, Darmstadt)

TUP47 **The Photo Injector Test Facility at DESY Zeuthen: Results of the First Phase**
A. Oppelt, K. Abrahamyan, I. Bohnet, J. Bähr, U. Gensch, H.-J. Grabosch, J.H. Han, M. Krasilnikov, D. Lipka, V. Miltchev, B. Petrosyan, L. Staykov, F. Stephan (DESY Zeuthen, Zeuthen) W. Ackermann, W.F.O. Müller, S. Setzer, T. Weiland (TU Darmstadt, Darmstadt) J.-P. Carneiro, K. Flöttmann, S. Schreiber (DESY, Hamburg) E. Jaeschke, D. Krämer, D. Richter, M. von Hartrott (BESSY GmbH, Berlin) P. Michelato, C. Pagani, D.S. Sertore (INFN/LASA, Segrate (MI)) J. Rossbach (Uni HH, Hamburg) W. Sandner, I. Will (MBI, Berlin) I. Tsakov (INRNE, Sofia)

TUP63 **The First Results of Bunch Shape Measurements in SNS Linac**
A. Feschenko, A. Gaidash, Yu. Kisselev, L.V. Kravchuk, A. Liyu, A. Menshov, A.N. Mirzojan (RAS/INR, Moscow) S. Assadi, W. Blokland, S. Henderson, E.P. Tanke (ORNL/SNS, Oak Ridge, Tennessee) D.-O. Jeon (ORNL, Oak Ridge)

TUP81 **A Super-Strong Permanent Magnet Quadrupole with Variable Strength**
Y. Iwashita, T. Mihara (Kyoto ICR, Kyoto) A. Evgeny, M. Kumada (NIRS, Chiba-shi) C. M. Spencer (SLAC, Menlo Park, California) E. Sugiyama (NEOMAX, Osaka)

TUP88 **CLIC Magnet Stabilization Studies**
S. Redaelli, R.W. Assmann, W. Coosemans, G. Guignard, D. Schulte, I. Wilson, F. Zimmermann (CERN, Geneva)

15:30 – 17:30 **TUP — Tuesday Poster Session**

TUP01 **RFQ Drift-Tube Proton Linacs in IHEP**
Y. Budanov, O.K. Belyaev, A.P. Maltsev, I.G. Maltsev, V.B. Stepanov, S.A. Strekalovskyh, V.A. Teplyakov (IHEP Protvino, Protvino, Moscow Region)

TUP02 **Development of a 352 MHz Cell-Coupled Drift Tube Linac Prototype**
M. Vretenar, Y. Cuvet, J. Genest, C. Völlinger (CERN, Geneva) F. Gerigk (CCLRC/RAL/ASTeC, Chilton, Didcot, Oxon)

TUP03 **Design of The LINAC4, A New Injector for The CERN Booster**
M. Vretenar, R. Garoby, K. Hanke, A.M. Lombardi, C.R. Rossi (CERN, Geneva) F. Gerigk (CCLRC/RAL/ASTeC, Chilton, Didcot, Oxon)

TUP04 **The SPL Front End: A 3 MeV H^- Test Stand at CERN**
R. Garoby, L. Bruno, F. Caspers, J. Genest, K. Hanke, M. Hori, A.M. Lombardi, M. Magistris, A. Millich, M. Paoluzzi, C.R. Rossi, M. Silari, M. Vretenar (CERN, Geneva) P. Ausset (IPN, Orsay) P.-Y. Beauvais (CEA/DSM/DAPNIA, Gif-sur-Yvette)

TUP05 **Beam Dynamics for a new 160 MeV H^- Linac at CERN (LINAC4)**
F. Gerigk (CCLRC/RAL/ASTeC, Chilton, Didcot, Oxon) E. Benedico Mora, A.M. Lombardi, E.Zh. Sargsyan, M. Vretenar (CERN, Geneva)

TUP06 **Results of the High-Power Conditioning and the First Beam Acceleration of the DTL-1 for J-PARC**
F. Naito, S. A. Anami, J.C. Chiba, Y.F. Fukui, K. Furukawa, Z. Igarashi, K.I. Ikegami, M. Ikegami, E. Kadokura, N. Kamikubota, T. Kato, M.K. Kawamura, H. Kobayashi, C.K. Kubota, E.T. Takasaki, H.T. Tanaka, S. Yamaguchi, K.Y. Yoshino (KEK, Ibaraki) K. Hasegawa, Y. Kondo, A. Ueno (JAERI, Ibaraki-ken) T.I. Itou, Y. Yamazaki (JAERI/LINAC, Ibaraki-ken) T. Kobayashi (J-PARC, Ibaraki-ken)

TUP07 **A Linac-to-Booster Injection Line for Transverse Matching and Correlated Injection Painting**
R. Garnett, L. Rybarcyk (LANL, Los Alamos, New Mexico)

TUP08 **Carbon Ion Injector Linac for a Heavy Ion Medical Synchrotron**
D.A. Swenson (LLC, Albuquerque, New Mexico)

TUP09 **The Heidelberg High Current Injector: a Versatile Injector for Storage Ring Experiments**
R. von Hahn, M. Grieser, R. Repnow, D. Schwalm, C.P.W. Welsch (MPI-K, Heidelberg)

TUP10 **Design of a Deuteron RFQ for Neutron Generation**
Z.Y. Guo, J. Chen, J. Fang, Y.R. Lu, C. Zhang, K. Zhu (PKU/IHIP, Beijing) A. Schempp (IAP, Frankfurt-am-Main)

TUP11 **High Current RFQ Using Laser Ion Source**
M. Okamura, R.A. Jameson (RIKEN, Saitama) T. H. Hattori, N. Hayashizaki, K. Yamamoto (TIT, Tokyo) H. Kashiwagi (JAERI/ARTC, Gunma-ken)

TUP12 **Installation of the Spallation Neutron Source Warm Linac**
G. Johnson, C. Deibele (ORNL, Oak Ridge) N.K. Bultman, J. Stovall (LANL, Los Alamos, New Mexico) J. Error, P. Gibson, P. Ladd (ORNL/SNS, Oak Ridge, Tennessee)

TUP13 **Test and First Experiments with the new REX-ISOLDE 200 MHz IH-Structure**
T. Sieber (CERN, Geneva) D. Habs, O.K. Kester (LMU, Garching)

TUP14 **Status of the RFI Linac Prototype**
D.A. Swenson, W.J. Starling (LLC, Albuquerque, New Mexico)

TUP15 **Space Charge Compensation in Low Energy Proton Beams**
A.B. Ismail, U.D. Uriot (CEA/DSM/DAPNIA, Gif-sur-Yvette) R. Duperrier (CEA/DAPNIA-SACM, Gif-sur-Yvette Cedex) N. Pichoff (CEA/DAM, Bruyères-le-Châtel)

TUP16 **Investigation on Beam Dynamics Design of High-Intensity RFQs**
C. Zhang, A. Schempp (IAP, Frankfurt-am-Main) Z.Y. Guo (PKU/IHIP, Beijing)

TUP18 **Beam Dynamics Issues of SPES-1 Linac**
E.F. Fagotti (INFN Milano, Milano) G. Bisoffi, M. Comunian, A. Facco, A. Palmieri, A. Pisent (INFN/LNL, Legnaro, Padova)

TUP19 **Characterization of Beam Parameter and Halo for a High Intensity RFQ Output under Different Current Regimes**
E.F. Fagotti (INFN Milano, Milano) M. Comunian, A. Palmieri, A. Pisent (INFN/LNL, Legnaro, Padova)

TUP20 **Some Relevant Aspects in the Design and Construction of a 30-62 MeV Linac Booster for Proton Therapy**
V.G. Vaccaro (Naples University Federico II Mathematical, Physical and Natural Sciences Faculty Physical Sciences Department, Napoli) A. D'Elia (Naples University Federico II, Napoli) D. Davino (Universita' degli Studi del Sannio, Benevento) S. Falco (New Affiliation Request Pending) M.R. Masullo (INFN-Napoli, Napoli)

TUP21 **Beam Dynamics Design of J-PARC Linac High Energy Section**
M. Ikegami, T. Kato (KEK, Ibaraki) H. Ao, Y. Yamazaki (JAERI/LINAC, Ibaraki-ken) K. Hasegawa, T. Ohkawa, A. Ueno (JAERI, Ibaraki-ken) N. Hayashizaki (TIT, Tokyo) V.V. Paramonov (RAS/INR, Moscow)

TUP22 **A Simulation Study on Chopper Transient Effects in J-PARC Linac**
M. Ikegami (KEK, Ibaraki) Y. Kondo, T. Ohkawa, A. Ueno (JAERI, Ibaraki-ken)

TUP23 **A Simulation Study on Error Effects in J-PARC Linac**
M. Ikegami (KEK, Ibaraki) Y. Kondo, T. Ohkawa, A. Ueno (JAERI, Ibaraki-ken)

TUP26 **Alternating Phase Focusing in Low-Velocity Heavy-Ion Superconducting Linac**
P.N. Ostroumov (ANL/Phys, Argonne, Illinois) A. Kolomiets (ITEP, Moscow) E.S. Masunov (MEPhI, Moscow)

TUP27 **Acceleration of Several Charge States of Lead Ion in CERN LINAC3**
V.C. Coco, J.A.C. Chamings, A.M. Lombardi, E.Zh. Sargsyan, R. Scrivens (CERN, Geneva)

TUP28 **Post Accelerator Design for the RIA Facility**
S.O. Schriber (NSCL, East Lansing, Michigan) R. Crandall (TechSource, Santa Fe, NM) R. Garnett (LANL, Los Alamos, New Mexico) T. Wangler (LANL/LANSCE, Los Alamos, New Mexico)

TUP29 **Proton Beam Dynamics Simulation of the SARAF Linac**
A. Shor, D. Berkovits, G. Feinberg, S. Halfon (SOREQ, Yavne)

TUP41 **Multi-Bunch Beam Dynamics Studies in the TESLA XFEL**
N. Baboi (DESY, Hamburg)

TUP42 **Beam Optics Studies for the TESLA Test Facility Linac**
P. Castro, V. Balandin, N. Golubeva (DESY, Hamburg)

TUP43 **The Superconducting CW Driver Linac for the BESSY-FEL User Facility**
J. Knobloch, M. Abo-Bakr, W. Anders, F. Marhauser, A. Neumann, M.S. Schuster (BESSY GmbH, Berlin) A.K. Annett, C.H. Haberstroh, H.Q. Quack (TU Dresden, Dresden) Y.X. Xiang (GSI, Darmstadt)

TUP44 **Linac Upgrades for FERMI@ELETTRA**
G. D'Auria (Sincrotrone Trieste S.C.p.A., Basovizza, Trieste)

TUP45 **Extended Parametric Evaluation for 1 Å FEL - Emittance and Current Requirements**
M. Pedrozzi, M. Dehler, G. Ingold, J.-Y. Raguin, L. Rivkin, A. Wrulich (PSI, Villigen)

TUP46 **Development of a New Control System for the S-DALINAC**
M. Brunken, H.-D. Gräf, M. Hertling, A. Karnaukhov, O. Patalakha, M. Platz, A. Richter, O. Titze, B. Truckses (TU Darmstadt, Darmstadt)

TUP47 **The Photo Injector Test Facility at DESY Zeuthen: Results of the First Phase**
A. Oppelt, K. Abrahamyan, I. Bohnet, J. Bähr, U. Gensch, H.-J. Grabosch, J.H. Han, M. Krasilnikov, D. Lipka, V. Miltchev, B. Petrosyan, L. Staykov, F. Stephan (DESY Zeuthen, Zeuthen) W. Ackermann, W.F.O. Müller, S. Setzer, T. Weiland (TU Darmstadt, Darmstadt) J.-P. Carneiro, K. Flöttmann, S. Schreiber (DESY, Hamburg) E. Jaeschke, D. Krämer, D. Richter, M. von Hartrott (BESSY GmbH, Berlin) P. Michelato, C. Pagani, D.S. Sertore (INFN/LASA, Segrate (MI)) J. Rossbach (Uni HH, Hamburg) W. Sandner, I. Will (MBI, Berlin) I. Tsakov (INRNE, Sofia)

TUP48 **Progress Report on the Flat Beam Experiment at the Fermilab/Nicadd Photoinjector Laboratory**
Y.-E. Sun (Chicago University Department of Physics, Chicago, Illinois) N. Barov (Northern Illinois University Department of Physics, DeKalb, Illinois) K. Desler (DESY, Hamburg) H. Edwards, P. Piot (FNAL, Batavia, Illinois) S. Lidia (LBNL/AFR, Berkeley, California) R. Tikhoplav (Rochester University Physics and Astronomy Department, Rochester, New York)

TUP49 **Simulations of the Ion-Hose Instability for DARHT-II Long-Pulse Experiments**
K. C. D. Chan, C. Ekdahl (LANL, Los Alamos, New Mexico) C. Genoni, P. Hughes (MRC, Albuquerque, NM)

TUP50 **Cumulative Beam Breakup with Time-Dependent Parameters**
J. R. Delayen (Jefferson Lab, Newport News, Virginia)

TUP52 **Methods for Measuring and Controlling Beam Breakup in High Current ERLs**
C. Tennant, E. Pozdeyev, H. Wang, G. Wu (Jefferson Lab, Newport News, Virginia) S. Simrock (DESY, Hamburg)

TUP53 **Temporal Profile of the LCLS Photocathode Ultraviolet Drive Laser Tolerated by the Microbunching Instability**
J. Wu, Z. Huang (SLAC, Menlo Park, California) M. Borland (ANL, Argonne, Illinois) P. Emma (SLAC/ARDA, Menlo Park, California) C. Limborg (SLAC/SSRL, Menlo Park, California)

TUP54 **Resistive Wake Effects in Final Beam Delivery Systems**
J. Wu (SLAC, Menlo Park, California) J. R. Delayen (Jefferson Lab, Newport News, Virginia) T.O. Raubenheimer (SLAC/NLC, Menlo Park, California) J.-M. Wang (BNL/NSLS, Upton, Long Island, New York)

TUP55 **Luminosity Loss due to Beam-Beam Instability**
J. Wu, A. Chao (SLAC, Menlo Park, California) T.O. Raubenheimer (SLAC/NLC, Menlo Park, California) C.K. Sramek (WRC, Houston, TX)

TUP56 **Simulation of RF Breakdowns Effects on NLC Beam**
V.A. Dolgashev (SLAC/ARDB, Menlo Park, California) T.O. Raubenheimer (SLAC/NLC, Menlo Park, California)

TUP57 **On Injector Optimization for the European XFEL Project**
Y. Kim, K. Flöttmann, T. Limberg (DESY, Hamburg)

TUP58 **Start-To-End Simulation with Two Bunch Compressor Stages for European XFEL Project**
Y. Kim, M. Dohlus, K. Flöttmann, T. Limberg (DESY, Hamburg)

TUP59 **Extraction of High Charged Electron Bunch from the ELSA RF Injector - Comparison Between Simulation and Experiment**
J. Lemaire, P. Balleyguier, A. Binet, J.M. Lagniel, V. Le Flanchec, N. Pichoff (CEA/DAM, Bruyères-le-Châtel) R. Bailly-Salins, M. Millerioux (CEA/DIF/DPTA/SP2A, Bruyeres-le-Chatel)

TUP61 **Beam Analysis Using the IPNS Linac ESEM**
J.C. Dooling, F. R. Brumwell, L. Donley, G.E. McMichael, V. F. Stipp (ANL, Argonne, Illinois)

TUP62 **The Isotope Production Facility Harp Electronics Package - High-Speed Data Acquisition And Processing On One VME Board**
R. Merl (LANL, Los Alamos, New Mexico)

TUP63 **The First Results of Bunch Shape Measurements in SNS Linac**
A. Feschenko, A. Gaidash, Yu. Kisselev, L.V. Kravchuk, A. Liyu, A. Menshov, A.N. Mirzojan (RAS/INR, Moscow) S. Assadi, W. Blokland, S. Henderson, E.P. Tanke (ORNL/SNS, Oak Ridge, Tennessee) D.-O. Jeon (ORNL, Oak Ridge)

TUP64 **Bunch Length Measurements at LEBRA**
K. Yokoyama (KEK, Ibaraki) K. Hayakawa, Y. Hayakawa, K. Nakao, I. Sato, T. Tanaka (LEBRA, Funabashi)

TUP65 **RF Tuning Schemes for J-PARC DTL and SDTL**
M. Ikegami (KEK, Ibaraki) Y. Kondo, A. Ueno (JAERI, Ibaraki-ken)

TUP66 **An Alternate Scheme for J-PARC SDTL Tuning**
M. Ikegami (KEK, Ibaraki) Y. Kondo, A. Ueno (JAERI, Ibaraki-ken)

TUP67 **Beam-Based Alignment Measurements of the LANSCE Linac**
R.C. McCrady, L. Rybarcyk (LANL, Los Alamos, New Mexico)

TUP68 **The LANSCE Low Momentum Beam Monitor**
R. Merl (LANL, Los Alamos, New Mexico)

TUP87 **Technologies of The Peripheral Equipments of The J-PARC DTL1 for the Beam Test**
K.Y. Yoshino, Y.F. Fukui, E. Kadokura, T. Kato, C.K. Kubota, F. Naito, E.T. Takasaki, H.T. Tanaka (KEK, Ibaraki) T.I. Itou (JAERI/LINAC, Ibaraki-ken)

TUP88 **CLIC Magnet Stabilization Studies**
S. Redaelli, R.W. Assmann, W. Coosemans, G. Guignard, D. Schulte, I. Wilson, F. Zimmermann (CERN, Geneva)

TUP89 **Static Absolute Force Measurement for Preload Piezoelements Used for Active Lorentz Force Detuning System**
S. P. M. Sekalski, S. Simrock (DESY, Hamburg) A. Bosotti (INFN/LASA, Segrate (MI)) M. Fouaidy (IPN, Orsay) A. Napieralski (TUL, Lodz) R. Paparella (INFN Milano, Milano)

TUP90 **Improvements of RF Characteristics in the SDTL of the J-PARC Proton LINAC**
S. Wang, S. Fu (IHEP Beijing, Beijing) T. Kato (KEK, Ibaraki) V.V. Paramonov (RAS/INR, Moscow)

TUP91 **Compact Electron-Linac Design Concept for a Gamma Ray Source**
K. C. D. Chan, B.E. Carlsten, G. Dale, R. Garnett, C. Kirbie, F.L. Krawczyk, S.J. Russell, T. Wangler (LANL, Los Alamos, New Mexico) E. Wright (CPI, Palo Alto, California)

TUP92 **Study of 3D-fields in RF Crossed Lens**
G. Kropachev, A.I. Balabin, V. Pershin (ITEP, Moscow)

TUP93 **Results of A 3D-EM-Code Comparison on Our TRISPAL Cavity Benchmark**
P. Balleyguier, J. Lemaire (CEA/DAM, Bruyères-le-Châtel)

TUP94 **Parallel Particle in Cell Computation of an Electron Gun with GdfidL**
W. Bruns (TU Berlin TET, Berlin)

TUP95 **Evaluation of Magnetic Field Enhancement Along a Boundary**
Y. Iwashita (Kyoto ICR, Kyoto) T. Higo (KEK, Ibaraki)

TUP96 **Mechanical Stability Simulations on a Quarter Wave Resonator for the SPIRAL II Project**
H. Saugnac, S. B. Blivet, G. Olry (IPN, Orsay)

TUP97 **Some Estimations for Correlation Between the RF Cavity Surface Temperature and Electrical Breakdown Possibility**
V.V. Paramonov (RAS/INR, Moscow)

TUP98 **The Finite State Machine for Klystron Operation for TESLA and the European X-FEL Linear Accelerator**
W. Cichalewski, B. Koseda (TUL, Lodz) F.-R. Kaiser, S. Simrock (DESY, Hamburg)

Wednesday, August 18, 2004

08:30 – 10:30 **WE1 — Wednesday Morning Session**
Session Chair: M. White (ANL, Argonne, Illinois)

WE101 **Gradient Limitations for High-Frequency Accelerators**
S. Doebert (SLAC, Stanford)

WE102 **State of the Art SRF Cavity Performance**
L. Lilje (DESY, Hamburg)

WE103 **State of the Art in RF Control**
S. Simrock (DESY, Hamburg)

WE104 **State of the Art Electron Bunch Compression**
P. Piot (FNAL, Batavia, Illinois)

10:30 – 11:00 **Coffee Break**

11:00 – 12:20 **WE2 — Wednesday Late Morning Session**
Session Chair: M. Poole (CCLRC/DL/ASTeC, Daresbury, Warrington, Cheshire)

WE201 **Results from the Initial Operations of the SNS Front End and DT Linac**
V. Aleksandrov (ORNL/SNS, Oak Ridge, Tennessee)

WE202 **Recent Results in the Field of High Intensity CW Linac Development for RIB Production**
A. Pisent (INFN/LNL, Legnaro, Padova)

WE203 **Challenges of Linac Driven Light Sources**
C. Bocchetta (ELETTRA, Basovizza, Trieste)

WE204 **PAL Linac Upgrade for a 1-3 Å XFEL**
J-O. Oh (POSTECH, Pohang) Y. Kim (DESY, Hamburg) W. Namkung (POSTECH, Pohang, Kyungbuk)

WE205 **KEKB Injector Linac and Upgrade for Super-KEKB**
S. Michizono (KEK, Ibaraki)

12:40 – 21:00 Lunch and Outing

Thursday, August 19, 2004

08:30 – 10:30 **TH1 — Thursday Morning Session**
Session Chair: S.O. Schriber (NSCL, East Lansing, Michigan)

TH101 **Status of the J-PARC Linac, Initial Results and Upgrade Plan**
Y. Yamazaki (JAERI/LINAC, Ibaraki-ken)

TH102 **Overview of High Intensity Linac Programs in Europe**
M. Vretenar, R. Garoby (CERN, Geneva)

TH103 **Workshop on High Gradient RF at Argonne Oct 7 - 9 2003**
J. Norem (ANL, Argonne, Illinois)

TH104 **Industrial RF Linac Experiences and Laboratory Interactions**
M. Peiniger (ACCEL, Bergisch Gladbach)

10:30 – 11:00 **Coffee Break**

11:00 – 12:20 **TH2 — Thursday Late Morning Session**
Session Chair: L.V. Kravchuk (RAS/INR, Moscow)

TH201 **IOT RF Power Sources for Pulsed and CW Linacs**
H.P. Bohlen (CPI, Palo Alto, California)

TH202 **Review of Fast Beam Chopping**
F. Caspers (CERN, Geneva)

TH203 **High Power Targets**
H. Kirk (BNL, Upton, Long Island, New York)

TH204 **End-to-End Beam Dynamics Simulations for the ANL-RIA Driver Linac**
P.N. Ostroumov (ANL/Phys, Argonne, Illinois)

12:20 – 13:40 **Lunch**

13:40 – 14:30 **TH3 — Thursday Early Afternoon Session**
Session Chair: H. Weise (DESY, Hamburg)

TH301 **Intermediate-Velocity Superconducting Accelerating Structures**
J. R. Delayen (Jefferson Lab, Newport News, Virginia)

TH302 **End-to-End Beam Dynamics Simulations for the MSU-RIA Driver Linac**
X. Wu (NSCL, East Lansing, Michigan)

14:30 – 15:30 **TH4 — Oral Poster Presentation**

THP04 **Fabrication of Superconducting Cavities for SNS**
M. Pekeler, S. Bauer, J. Schwellenbach, M. Tradt, H. Vogel, P. vom Stein (ACCEL, Bergisch Gladbach)

THP06 **Cold Tests of a Superconducting Co-Axial Half-Wave Cavity for RIA**
M. Kelly (ANL, Argonne, Illinois) J.D. Fuerst, M. Kedzie, K.W. Shepard (ANL/Phys, Argonne, Illinois)

THP17 **Progress in the Development of the TOP Linac**
L. Picardi, C. Ronsivalle (ENEA C.R. Frascati, Frascati (Roma)) S.F. Frullani (ISS, Rome)

THP27 **Ultra Low Emittance Electron Gun Project for FEL Application**
R. Ganter, M. Dehler, J. Gobrecht, C. Gough, G. Ingold, S. Leemann, M. Paraliev, M. Pedrozzi, J.-Y. Raguin, L. Rivkin, V. Schlott, A. Streun, A. Wrulich (PSI, Villigen) A. Candel, K. Li (ETH, Zürich)

THP28 **Multi-Mode SLED-II Pulse Compressors**
S. Kuzikov, Y.Y. Danilov, G. G. Denisov, V. G. Paveliev, D. Yu. Shegol'kov, A. A. Vikharev (IAP, Nizhniy Novgorod)

THP34 **A High-Power Test of an X-Band Molybdenum-Iris Structure**
W. Wuensch, A. Grudiev, T. Heikkinen, I. Syratchev, T. Taborelli, I. Wilson (CERN, Geneva) C. Adolphsen (SLAC/NLC, Menlo Park, California) S. Doebert (SLAC, Stanford)

THP35 **Development of a Non-Magnetic Inertial Sensor for Vibration Stabilization in a Linear Collider.**
J. Frisch, L. Hendrickson, T. Markiewicz, A. Seryi (SLAC, Menlo Park, California) D. Eric, T. Himel (SLAC/NLC, Menlo Park, California) R. Partridge (SLAC, Stanford)

THP47 **The RF-System for A High Current RFQ at IHEP**
Z. Zhang, J. Li, J. Qiao, X. Xu (IHEP Beijing, Beijing)

THP55 **Electromagnetic Design of New RF Power Couplers for the S-DALINAC**
M. Kunze, M. Brunken, H.-D. Gräf, W.F.O. Müller, A. Richter, T. Weiland (TU Darmstadt, Darmstadt)

THP66 **Measurement and Control of Microphonics in High Loaded-Q Superconducting RF Cavities**
T.L. Grimm, W. Hartung, T. Kandil, H. Khalil, J. Popielarski, J. Vincent, R.C. York (NSCL, East Lansing, Michigan)

THP73 **8 GeV Superconducting Linac for Muon Acceleration**
M. Popovic (FNAL, Batavia, Illinois)

THP82 **Experiences in Fabrication and Testing the Prototype of the 4.90 GHz Accelerating Sections for MAMI C**
A. Jankowiak, H. Euteneuer, S.S. Schumann, O.T. Tchoubarov (IKP, Mainz)

15:30 – 17:30 **THP — Thursday Poster Session**

THP01 **Implementation of Mathematical Optimization for RFQ Linac Designing**
A.P. Durkin, I.V. Shumakov, S. Vinogradov (MRTI RAS, Moscow) A. Ovsyannikov (St. Petersburg State University Applied Mathematics & Control Processes Faculty, St. Petersburg) D.A. Ovsyannikov (St. Petersburg State University Institute of Computational Mathematics & Control Processes, St. Petersburg)

THP02 **Perturbation Analysis and Monte-Carlo Simulation for Beam Dynamic Investigation in Linear Accelerator**
A.P. Durkin, I.V. Shumakov, S. Vinogradov (MRTI RAS, Moscow)

THP03 **Design Improvement of the 80.5 MHz RFQ for RIA Driver Linac**
Q. Zhao, V. Andreev, M. Doleans, D. Gorelov, T.L. Grimm, W. Hartung, F. Marti, S.O. Schriber, X. Wu, R.C. York (NSCL, East Lansing, Michigan)

THP04 **Fabrication of Superconducting Cavities for SNS**
M. Pekeler, S. Bauer, J. Schwellenbach, M. Tradt, H. Vogel, P. vom Stein (ACCEL, Bergisch Gladbach)

THP05 **Superconducting β=0.15 Quarter-Wave Cavity for RIA**
M. Kelly (ANL, Argonne, Illinois) Z.A. Conway, J.D. Fuerst, M. Kedzie, K.W. Shepard (ANL/Phys, Argonne, Illinois)

THP06 **Cold Tests of a Superconducting Co-Axial Half-Wave Cavity for RIA**
M. Kelly (ANL, Argonne, Illinois) J.D. Fuerst, M. Kedzie, K.W. Shepard (ANL/Phys, Argonne, Illinois)

THP07 **Performances Improvement for the French Multicell Superconducting Cavity Prototype Dedicated to Proton LINAC Projects.**
B. Visentin, D. Braud, J.P. Charrier, Y. Gasser, J.P. Poupeau, D. Roudier, P. Sahuquet (CEA/DSM/DAPNIA, Gif-sur-Yvette) S. Bousson, H. Saugnac, P. Szott (IPN, Orsay)

THP08 **The Frankfurt Funneling Experiment**
A. Schempp, U.B. Bartz, N. Müller, J. Thibus, H. Zimmermann (IAP, Frankfurt-am-Main)

THP09 **Beam Test of a RFQ-Drifttube-Combination**
A. Schempp, A. Bechtold, M.O. Otto, E. Vassilakis (IAP, Frankfurt-am-Main) B. Schlitt (GSI, Darmstadt)

THP10 **Tuner Design for High Power 4-Rod-RFQs**
A. Schempp, L.B. Brendel, B.H. Hofmann, H. Liebermann (IAP, Frankfurt-am-Main)

THP11 **Design of A 350 MHz-Proton-RFQ for GSI**
A. Schempp, L.B. Brendel, B.H. Hofmann (IAP, Frankfurt-am-Main)

THP12 **Superconducting RFQs in the PIAVE Injector**
G. Bisoffi, G. Bassato, G. Bezzon, S. Canella, F. Chiurlotto, A. Lombardi, A.M. Porcellato, S. Stark (INFN/LNL, Legnaro, Padova)

THP13 **Construction of a 161 MHz, β=0.16 Superconducting Quarter Wave Resonator with Steering Correction for RIA**
A. Facco (INFN/LNL, Legnaro, Padova) C. Compton, T.L. Grimm, W. Hartung, F. Marti, R.C. York (NSCL, East Lansing, Michigan) V. Zvyagintsev (TRIUMF, Vancouver)

THP14 **High Beta Cavity Optimization for ISAC-II**
R.E. Laxdal, V. Zvyagintsev (TRIUMF, Vancouver) Z.H. Peng (CIAE, Beijing)

THP15 **Spoke-loaded SC Cavities for the RIA Driver Linac**
K.W. Shepard, J.D. Fuerst, M. Kedzie, M. Kelly (ANL/Phys, Argonne, Illinois) E. Peterson, J. Rathke, T. Schultheiss (AES, Medford)

THP16 **Engineering and Cryogenic Testing of the ISAC-II Medium Beta Cryomodule**
G. Stanford, I. Bylinskii, R.E. Laxdal, C. Marshall, B. Rawnsley, T.R. Ries, I. Sekatchev (TRIUMF, Vancouver)

THP17 **Progress in the Development of the TOP Linac**
L. Picardi, C. Ronsivalle (ENEA C.R. Frascati, Frascati (Roma)) S.F. Frullani (ISS, Rome)

THP18 **The Acceleration Test of the APF-IH-LINAC**
K. Yamamoto, M. Okamura (RIKEN, Saitama) S. Yamada (NIRS, Chiba-shi)

THP21 **Calculation of Electron Beam Dynamics of LUE-200 Accelerator**
A.P. Sumbaev, V. Alexandrov, N.Y. Kazarinov, F.V. Shevtsov (JINR, Dubna, Moscow Region)

THP22 **3D Beam Dynamics Simulation in Undulator Linac**
E.S. Masunov, S.M. Polozov (MEPhI, Moscow)

THP23 **A Molybdenum-Titanium Paired Electrode Used for a High Gradient DC Gun to Minimize Field Emission Dark Currents**
T. Nakanishi (DOP Nagoya, Nagoya)

THP24 **Highly Polarized Electrons from GaAs-GaAsP Strained Layer Superlattice Photocathodes**
T. Nakanishi (DOP Nagoya, Nagoya)

THP25 **Development of Field-Emission Electron Guns from Carbon Nanotubes**
Y. Hozumi (GUAS/AS, Ibaraki) M. Ikeda, S. Ohsawa, T.S. Sugimura (KEK, Ibaraki)

THP26 **Comparison of 2 Cathode Geometries for High Current (2 kA) Diodes**
N. Pichoff (CEA/DAM, Bruyères-le-Châtel) F. Bombardier, M. Caron, E. Merle, C. Noel, O. Pierret, R. Rosol, C. Vermare (CEA, Pontfaverger-Moronvilliers) D.C. Moir (LANL, Los Alamos, New Mexico) A. Piquemal (CEA/PTN, Bruyères-le-Châtel)

THP27 **Ultra Low Emittance Electron Gun Project for FEL Application**
R. Ganter, M. Dehler, J. Gobrecht, C. Gough, G. Ingold, S. Leemann, M. Paraliev, M. Pedrozzi, J.-Y. Raguin, L. Rivkin, V. Schlott, A. Streun, A. Wrulich (PSI, Villigen) A. Candel, K. Li (ETH, Zürich)

THP28 **Multi-Mode SLED-II Pulse Compressors**
S. Kuzikov, Y.Y. Danilov, G. G. Denisov, V. G. Paveliev, D. Yu. Shegol'kov, A. A. Vikharev (IAP, Nizhniy Novgorod)

THP29 **Development of C-band Accelerating Section for SuperKEKB**
T. Kamitani, M. Ikeda, K. Kakihara, S. Ohsawa, T. Oogoe, T.S. Sugimura, K. Yokoyama (KEK, Ibaraki)

THP30 **Production of S-band Accelerating Structures**
C. Piel, K. Dunkel, H. Vogel, P. vom Stein (ACCEL, Bergisch Gladbach)

THP31 **A Four-Cell Periodically HOM-Damped RF Cavity for High Beam Current Accelerators**
G. Wu, R.A. Rimmer, H. Wang (Jefferson Lab, Newport News, Virginia) J. Sekutowicz (DESY, Hamburg) A. Sun (ORNL/SNS, Oak Ridge, Tennessee)

THP32 **New Accelerating Modules RF Test at TTF**
D. Kostin (DESY, Hamburg)

THP33 **Progress toward NLC/GLC Prototype Accelerator Structures**
J.W. Wang, G.B. Bowden, V.A. Dolgashev, R.M. Jones, J. Lewandowski, C.D. Nantista, S.G. Tantawi (SLAC/ARDA, Menlo Park, California) C. Adolphsen, D.L. Burke, J. Cornuelle, S. Doebert (SLAC/NLC, Menlo Park, California) T. Arkan, C. Boffo, H. Carter, N. Khabiboulline (FNAL, Batavia, Illinois) D. Finley, I. Gonin, S. Mishra, G. Romanov, N. Solyak (Fermilab, Batavia, Illinois) Y. Higashi, T. Higo, T. Kumi, Y. Morozumi, N. Toge, K. Ueno (KEK, Ibaraki) Z. Li, R. Miller, R.D. Ruth, P.B. Wilson (SLAC, Menlo Park, California) C. Pearson (SLAC, Stanford)

THP34 **A High-Power Test of an X-Band Molybdenum-Iris Structure**
W. Wuensch, A. Grudiev, T. Heikkinen, I. Syratchev, T. Taborelli, I. Wilson (CERN, Geneva) C. Adolphsen (SLAC/NLC, Menlo Park, California) S. Doebert (SLAC, Stanford)

THP35 **Development of a Non-Magnetic Inertial Sensor for Vibration Stabilization in a Linear Collider.**
J. Frisch, L. Hendrickson, T. Markiewicz, A. Seryi (SLAC, Menlo Park, California) D. Eric, T. Himel (SLAC/NLC, Menlo Park, California) R. Partridge (SLAC, Stanford)

THP36 **Vibration Stabilization of a Mechanical Model of a X-Band Linear Collider Final Focus Magnet**
J. Frisch, L. Hendrickson, T. Markiewicz, A. Seryi (SLAC, Menlo Park, California) E. Eric, L. Eriksson, T. Himel (SLAC/NLC, Menlo Park, California) R. Partridge (SLAC, Stanford)

THP37 **Approaches to Beam Stabilization in X-Band Linear Colliders**
J. Frisch, L. Hendrickson, T. Markiewicz, A. Seryi (SLAC, Menlo Park, California) P. Burrows, S. Molloy, G. White (Queen Mary University of London Physics Department, London) C. Perry (OXFORDphysics, Oxford, Oxon) T.O. Raubenheimer, T. Thomas (SLAC/NLC, Menlo Park, California)

THP38 **High Precision Survey and Alignment of Large Linear Accelerators**
J. Prenting, M. Schlösser (DESY, Hamburg) J. Green, G. Grzelak, A. Mitra, A. Reichold (OXFORDphysics, Oxford, Oxon) A. Herty (CERN, Geneva)

THP39 **Operation of a 1.3 GHz, 10 MW Multiple Beam Klystron**
H.P. Bohlen, E. Wright (CPI, Palo Alto, California) A. Balkcum, M. Cattelino, L. Cox, M. Cusick, S. Forrest, F. Friedlander, A. Staprans, L. Zitelli (CPI, Palo Alto) K. Eppley (SAIC, Boston)

THP41 **Development of High RF Power Delivery System for 1300 MHz Superconducting Cavities of Cornell ERL Injector**
S.A. Belomestnykh, M. Liepe, H. Padamsee, V. Veshcherevich (LEPP, Ithaca, New York) N.P. Sobenin (MEPhI, Moscow)

THP42 **NLC Hybrid Solid State Induction Modulator**
R. Cassel, M.N. Nguyen, G.C. Pappas, J.E. deLamare (SLAC, Stanford) C. Brooksby, E. Cook (LLNL, Livermore)

THP43 **Reduction of RF Power Loss Caused by Skin Effect**
Y. Iwashita (Kyoto ICR, Kyoto)

THP44 **The Design and Performance of the Spallation Neutron Source Low-Level RF Control System**
M. Champion (ORNL/SNS, Oak Ridge, Tennessee) A. Ratti (LBNL, Berkeley, California)

THP45 **The Toshiba E3736 Multi Beam Klystron**
A. Yano, S. Miyake (TETD, Saitama) Y.H. Chin (KEK, Ibaraki) S. Kazakov (IHEP Protvino, Protvino, Moscow Region) A.V. Larionov, V.E. Teryaev (BINP SB RAS, Protvino, Moscow Region)

THP46 **Cable Insulation Breakdowns in the Modulator with a Switch Mode High Voltage Power Supply**
A. Cours (ANL, Argonne, Illinois)

THP47 **The RF-System for A High Current RFQ at IHEP**
Z. Zhang, J. Li, J. Qiao, X. Xu (IHEP Beijing, Beijing)

THP48 **A High-Resolution S-band Down-Converting Digital Phase Detector for SASE FEL Use**
A.E. Grelick, N.D. Arnold (ANL/APS, Argonne, Illinois) J. Carwardine, A. Nassiri, T. Smith (ANL, Argonne, Illinois)

THP49 **The RF-Station Interlock for the European X-ray laser**
T. Grevsmühl, S. Choroba, Ph. Duval, O. Hensler, F.-R. Kaiser, S. Simrock (DESY, Hamburg) H. Leich, RW. Wenndorff (DESY Zeuthen, Zeuthen)

THP50 **The CEBAF RF Separator System Upgrade**
C. Hovater, M.A. Augustine, M.W. Mark, R. Nelson, R.A. Terrel (TJNAF, Newport News, Virginia)

THP51 **Tuning of External Q And Phase for The Cavities of A Superconducting Linear Accelerator**
V.V. Katalev, S. Choroba (DESY, Hamburg)

THP52 **RF Reference Distribution System for J-PARC Linac**
T. Kobayashi, E. Chishiro (JAERI, Ibaraki-ken) S. A. Anami, S. Michizono, S. Yamaguchi (KEK, Ibaraki)

THP53 **Quasi-Optical Components for Future Linear Colliders**
S. Kuzikov, Y.Y. Danilov, G. G. Denisov, V. I. Malygin, V. G. Paveliev, M. I. Petelin, D. Yu. Shegol'kov, M. Yu. Shmelyov (IAP, Nizhniy Novgorod) J.L. Hirshfield (Omega-P, Inc., New Haven, Connecticut) F. Mirizzi (ENEA C.R. Frascati, Frascati (Roma))

THP54 **MMF DTL RF System Upgrade**
A.I. Kvasha (RAS/INR, Moscow)

THP55 **Electromagnetic Design of New RF Power Couplers for the S-DALINAC**
M. Kunze, M. Brunken, H.-D. Gräf, W.F.O. Müller, A. Richter, T. Weiland (TU Darmstadt, Darmstadt)

THP56 **Control of Low Level RF System for J-Parc Linac**
S. Michizono, S. A. Anami, E. Kadokura, S. Yamaguchi (KEK, Ibaraki) E. Chishiro, H. Suzuki (JAERI, Ibaraki-ken)

THP57 **Digital Feedback System for J-Parc Linac RF Source**
S. Michizono, S. A. Anami, S. Yamaguchi (KEK, Ibaraki) T. Kobayashi (J-PARC, Ibaraki-ken)

THP58 **Development of C-band High-Power Mix-Mode RF Window**
S. Michizono, S. Fukuda, T. Matsumoto, K. Nakao, T. Takenaka (KEK, Ibaraki) K. Yoshida (MELCO, Hyogo)

THP59 **Low Level RF Including a Sophisticated Phase Control System for CTF3**
J. Mourier, R. Bossart, J. Nonglaton, I. Syratchev, L. Tanner (CERN, Geneva)

THP60 **High-Power RF Distribution System for the 8-Pack Project**
C.D. Nantista (SLAC/ARDB, Menlo Park, California) D.P.A. Atkinson (LLNL, Livermore) J.Q.C. Chan (SLAC/NLC, Menlo Park, California) S.Y.K. Kazakov (KEK, Ibaraki) D.C. Schultz (SLAC, Menlo Park, California) S.G. Tantawi (SLAC/ARDA, Menlo Park, California)

THP61 **SKIP - A Pulse Compressor for SuperKEKB Injector**
T.S. Sugimura, K. Kakihara, T. Kamitani, S. Ohsawa (KEK, Ibaraki)

THP62 **An All-Solid State 55 kV Hard FET Modulator for Electron Gun of a 10MeV, 10kW Industrial LINAC**
P. Shrivastava, J. Mulchandani (CAT, Indore M.P.)

THP63 **Design and Development of a Long Pulse High Average Power Pulse Modulator for a Multi Beam Klystron for 10MeV, 10kW LINAC for Food Irradiation**
P. Shrivastava, P.R. Hannurkar, J. Mulchandani (CAT, Indore M.P.)

THP64 **Waveguide Stub Tuner Analysis for CEBAF Machine Application**
H. Wang (Jefferson Lab, Newport News, Virginia) M. Tiefenback (TJNAF, Newport News, Virginia)

THP65 **Tuning the Spallation Neutron Source Warm Linac RF Structures***
C. Deibele, G. Johnson (ORNL, Oak Ridge) J. Billen, N.K. Bultman, J. Stovall (LANL, Los Alamos, New Mexico) J. Error, P. Gibson (ORNL/SNS, Oak Ridge, Tennessee) J. Manolitsas, D. Trompetter (ACCEL, Bergisch Gladbach) A. Vasyuchenko (RAS/INR, Moscow) L. Young (Tech-Source, Santa Fe, NM)

THP66 **Measurement and Control of Microphonics in High Loaded-Q Superconducting RF Cavities**
T.L. Grimm, W. Hartung, T. Kandil, H. Khalil, J. Popielarski, J. Vincent, R.C. York (NSCL, East Lansing, Michigan)

THP67 **Single-Cell High Gradient Tests**
V.A. Dolgashev (SLAC/ARDB, Menlo Park, California) Y. Higashi, T. Higo (KEK, Ibaraki) C.D. Nantista, S.G. Tantawi (SLAC/ARDA, Menlo Park, California)

THP68 **The Simulation Calculations And Dielectric Characteristics Investigation of a Hybrid Dielectric-Iris-Loaded Travelling Accelerating Structure**
C.-F. Wu (USTC/NSRL, Hefei, Anhui)

THP69 **The Tuning Study of the Coupled Loaded Cavities for the RF Chopper System of J-PARC**
S. Wang, S. Fu (IHEP Beijing, Beijing) T. Kato (KEK, Ibaraki)

THP70 **Experimental Study of an 805 MHz Cryomodule for the Rare Isotope Accelerator**
T.L. Grimm, S. Bricker, C. Compton, W. Hartung, M. Johnson, F. Marti, R.C. York (NSCL, East Lansing, Michigan) G. Ciovati, P. Kneisel (Jefferson Lab, Newport News, Virginia)

THP71 **First Experience with Dry-Ice Cleaning on SRF Cavities**
D. Reschke, A. Brinkmann (DESY, Hamburg) G. Müller (BUW, Wuppertal) D. Werner (IPA, Stuttgart)

THP72 **A Newly Designed and Optimized CLIC Main Linac Accelerating Structure**
A. Grudiev, W. Wuensch (CERN, Geneva)

THP73 **8 GeV Superconducting Linac for Muon Acceleration**
M. Popovic (FNAL, Batavia, Illinois)

THP74 **Laser Produced Ions as an Injection Beam for Cancer Therapy Facility**
A. Noda, Y. Iwashita, S. Nakamura, T. Shirai (Kyoto ICR, Kyoto) H. Daido (JAERI APRC, Ibaraki-ken) A. Fukumi, Z. Li, K. Matsukado (NIRS, Chiba-shi)

THP75 **A Superconducting Accelerating Structure with a Gradient Two Times Higher Than the TESLA Structures**
P. V. Avrakhov, V.E. Balakin (PTC LPI, Protvino, Moscow Region)

THP81 **Tuning of Reentrant Cavities by Deflection using Radial and Circumferential Stiffening Options**
V. Jain (CAT, Indore M.P.) M.G. Karmarkar (CAT, Indore)

THP82 **Experiences in Fabrication and Testing the Prototype of the 4.90 GHz Accelerating Sections for MAMI C**
A. Jankowiak, H. Euteneuer, S.S. Schumann, O.T. Tchoubarov (IKP, Mainz)

THP83 **Measurements of High Order Modes in High Phase Advance Damped Detuned Accelerating Structure for NLC**
N. Khabiboulline (FNAL, Batavia, Illinois) G. Romanov (Fermilab, Batavia, Illinois)

THP84 **Design of a 300 GHz Broadband Coupler and RF-Structure**
F.L. Krawczyk, F.E. Sigler (LANL/LANSCE, Los Alamos, New Mexico) B.E. Carlsten, L.M. Earley (LANL, Los Alamos, New Mexico) J.M. Potter (JP Accelerator Works, Inc., 2245, Los Alamos, NM) M.E. Schulze (GA, Los Alamos)

THP85 **Test Results of the 3.9 GHz Superconducting Accelerating Cavity at Fermilab.**
N. Solyak (Fermilab, Batavia, Illinois) L. Bellantoni, T. Berenc, H. Edwards, M.F. Foley, N. Khabiboulline, D. Mitchell (FNAL, Batavia, Illinois)

THP86 **Low Power Measurements on a Finger Drift Tube Linac**
K.-U. Kühnel, A. Schempp (IAP, Frankfurt-am-Main) C.P.W. Welsch (MPI-K, Heidelberg)

THP87 **Accelerator Structure Microwave Measurement at SLAC**
J. Lewandowski, G.B. Bowden, J.W. Wang (SLAC/ARDA, Menlo Park, California) R. Miller (SLAC, Menlo Park, California)

THP88 **Longitudinal Bunch Shape Monitor Using the Beam Chopper of J-PARC**
F. Naito (KEK, Ibaraki)

THP89	**Measured RF Properties of The DTL for J-PARC** H.T. Tanaka, T. Kato, F. Naito, E.T. Takasaki (KEK, Ibaraki) T.I. Itou (JAERI/LINAC, Ibaraki-ken) T.M. Morishita (JAERI, Ibaraki-ken)
THP90	**The Technique for the Numerical Tolerances Estimation in the Construction of Compensated Accelerating Structures** V.V. Paramonov, A.K. Skasyrskaya (RAS/INR, Moscow)
THP92	**Tuner Effect on the Field Flatness of SNS Superconducting RF Cavity** A. Sun (ORNL/SNS, Oak Ridge, Tennessee) H. Wang, G. Wu (Jefferson Lab, Newport News, Virginia)
THP93	**A 3D Self-Consistent, Analytical Model for Longitudinal Plasma Oscillation in a Relativistic Electron Beam** G. Geloni, E. Saldin, E. Schneidmiller, M.V. Yurkov (DESY, Hamburg)
THP94	**Cold Tests of a 160 MHz Half-Wave Resonator** R. Stassen, R. Maier, R. Tölle (FZJ/IKP, Jülich) R. Eichhorn, F. M. Esser, B. Laatsch, G. Schug (FZJ, Jülich)
THP95	**Electro Polishing of Niobium Cavities at DESY** S. Matheisen, L. Lilje, H. Morales, B. Petersen, M. Schmoekel, N. Steinhau-Kühl (DESY, Hamburg)

19:00 – The conference dinner will be held in the Lübeck Harbor at “Schuppen 9”,
Aperitifs by the waterside from 19:00 on

Friday, August 20, 2004

08:30 – 10:30 **FR1 — Friday Morning Session**
Session Chair: S.H. Wang (IHEP Beijing, Beijing)

FR101	**Overview of Linear Collider Test Facilities and Results** H. Hayano (KEK, Ibaraki)
FR102	**Muon Ionization Cooling Experiment** M.S. Zisman (LBNL, Berkeley, California)
FR103	**Status of the SNS Linac: An Overview** N. Holtkamp (ORNL, Oak Ridge)
FR104	**Overview on High-Brightness Electron Guns** J.W. Lewellen (ANL, Argonne, Illinois)

10:30 – 11:00 **Coffee Break**

11:00 – 12:30 **FR2 — Friday Late Morning Session**
Session Chair: N. Angert (GSI, Darmstadt)

FR201	**Accelerator Control and Global Networks - State of the Art** D.P. Gurd (ORNL, Oak Ridge)
FR202	**Status of High-Power Tests of the Dual Mode SLED-II System for an X-Band Linear Collider** S.G. Tantawi (SLAC/ARDA, Menlo Park, California)
FR203	**The Science of Radioactive Ion Beams** B. Sherrill (NSCL, East Lansing, Michigan)
FR204	**The Physics Perspective at the Future Accelerator Facility FAIR** J. Stroth (GSI, Darmstadt)

12:30 – 13:00 **Closing Remarks**
13:00 – 15:00 **Bus Transfers**
15:00 – 17:00 **Laboratory Tour DESY**

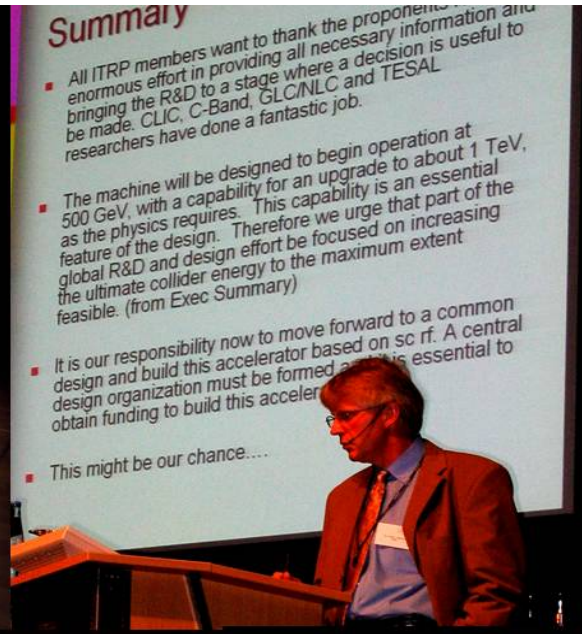
Summary
All ITRP members want to thank the proponents and
enormous effort in providing all necessary information and
bringing the R&D to a stage where a decision is useful to
be made. CLIC, C-Band, GLC/NLC and TESAL
researchers have done a fantastic job.
The machine will be designed to begin operation at
500 GeV, with a capability for an upgrade to about 1 TeV,
as the physics requires. This capability is an essential
feature of the design. Therefore we urge that part of the
global R&D and design effort be focused on increasing
the ultimate collider energy to the maximum extent
feasible. (from Exec Summary)
It is our responsibility now to move forward to a common
design and build this accelerator based on sc rf. A central
design organization must be formed and it is essential to
obtain funding to build this accelerator
This might be our chance....


GLOBES


LINAC2004
LÜBECK

Advanced Analysis in Nanospace: Research with the XFEL

H. Dosch, MPI, Stuttgart

Abstract

Little happens in industrialised countries without the use of high-tech materials which are the building blocks of all modern technologies ranging from information, communication, health, energy and environment to transport. In the last decades the development of novel materials has progressed at a breathtaking rate. This has become possible through our microscopic insight into the atomistic structure of condensed matter which finally enabled us to assemble new material systems atom-by-atom. These days, we are facing a revolution in the investigation of nanospace: Through new concepts in accelerator physics, electrons can be forced to emit short-pulsed x-ray laser radiation. Such a futuristic European x-ray free electron laser (XFEL) laboratory is currently being constructed and will allow mankind to finally get holographic snapshots of the motion of atoms and electrons in materials. Ultimate insights into matter, as the realtime-observation of the formation and the breaking of molecular bonds, sound like science fiction, but could become reality in less than a decade, if Europe embarks today into this bold adventure which will lead us into unexplored dimensions of nanospace.

NO SUBMISSION RECEIVED

ACCELERATOR LAYOUT OF THE XFEL

R. Brinkmann, Deutsches Elektronen-Synchrotron, Hamburg, Germany
for the XFEL Group

Abstract

The X-ray Free Electron Laser XFEL is a 4th generation synchrotron radiation facility based on the SASE FEL concept and the superconducting TESLA technology for the linear accelerator. In February 2003 the German government decided that the XFEL should be realised as a European project and located at DESY/Hamburg. The Ministry for Education and Research also announced that Germany is prepared to cover half of the investment and personnel costs of the project. This paper gives an overview of the overall layout and parameters of the facility, with emphasis on the accelerator design, technology and physics.

INTRODUCTION

X-rays have played for many decades a crucial role in the study of structural and electronic properties of matter on an atomic scale. With the ultra-high brilliant and sub-100 fs pulse length coherent radiation achievable with free electron laser X-ray sources the research in this field will enter a new era [1]. It will become possible to take holographic snapshots with atomic resolution in space and time resolution on the scale of chemical bond formation and breaking. Linear accelerator driven FELs using the principle of self-amplified spontaneous emission (SASE) [2] appear to be the most promising approach to produce this radiation with unprecedented quality in the Å-wavelength regime. The first facility of this type, using part of the existing SLAC linac, was proposed at Stanford and is now under construction [3,4]. The XFEL was originally proposed as integral part of the TESLA project together with a 500 – 800 GeV e+e- Linear Collider based on superconducting RF (SRF) technology [5]. In a later update [6], the proposal was modified such as to build the XFEL with its own, separate linac for the benefit of flexibility regarding construction, commissioning and operation of the facility, maintaining the SRF technology identical to the collider linac and a common experimental site 16km northwest from the DESY site in Hamburg. The German government decision in 2003 to go ahead with the XFEL as a European project and to postpone the decision on the collider led to a revision of the site, with synergy arguments for a common site no longer in effect. The new site layout, sketched in Fig. 1, has the XFEL linac starting on the DESY site, permitting to make optimum use of existing infrastructure, and the user facility in a rural area about 3km west-northwest from DESY. The legal procedure to obtain permission for construction is in preparation and expected to be completed by end of 2005.

The project organisation at the European level is ongoing. A steering committee and two working groups, on scientific-technical and administrative-financial issues, have been established early in 2004, with members from all European countries which are interested in participating in the project. The main task of these groups is to prepare the documents required for the technical definition and organisational structure of the project by 2005. The final decision to move into the construction phase is expected for 2006. The construction time until beam operation will be 6 years. The total project cost is estimated at 684 M€ (year 2000 price level), of which Germany will cover 50%.

Figure 1: Sketch of the XFEL site near DESY.

The electron beam quality and stability required by the SASE process presents considerable challenges to the linear accelerator community. SASE test facilities in the visible and ultra-violet wavelength range were built and operated during the last years [7]. The results have demonstrated the viability of the challenging accelerator subsystems and the good understanding of the SASE process. In particular the successful operation of the TESLA Test Facility (TTF) linac and FEL at DESY provides a firm basis for the XFEL, regarding the SRF technology, beam dynamics and the FEL process [8] and the conduction of user experiments [9]. In its 2nd phase, just about to start, operation of the VUVFEL, designed for FEL radiation down to 6nm wavelength, will continue to deliver a vast amount of experience as a pilot facility for the future project [10].

OVERALL LAYOUT AND PARAMETERS

The XFEL is laid out as a multi-user facility. In its 1st stage, it will have 5 undulator beamlines, 3 of which are SASE-FELs (two for the Å wavelength regime, one for softer X-rays), the other two for hard X-ray spontaneous radiation. Initially, 10 experimental stations are foreseen. The underground experimental hall has a floor space of $50\times90m^2$ and more stations can be added later. The site allows to extend the user facility for more beam lines in a later stage (see Figure 2).

The undulator sections have a maximum total length of 250m. Variable gap (min. 10mm) type 5m long undulator segments are foreseen, which not only permits to independently adjust the photon energy within certain limits, but also facilitates the precise steering of the electron beam for optimum overlap with the photon beam [11].

Table 1: XFEL Design Parameters

Performance Goals for the Electron Beam	
Beam Energy	10 - 20 GeV
Emittance (norm.)	1.4 mrad × mm
Bunch Charge	1 nC
Bunch Length	80 fs
Energy spread (uncorrel.)	<2.5 MeV rms
Main Linac	
Acc. Gradient @ 20 GeV	23 MV/m
Linac Length	approx. 1.5 km
Inst. Accelerator Modules	116
Installed Klystrons	29
Beam Current (max)	5 mA
Beam Pulse Length	0.65 ms
# Bunches p. Pulse (max)	3250
Bunch Spacing (min)	200 ns
Repetition Rate	10 Hz
Max. Avg. Beam Power	650 kW
Performance Goals for SASE FEL Radiation	
photon energy	15 – 0.2 keV
wavelength	0.08 – 6.4 nm
peak power	24 – 135 GW
average power	66 – 800 W
number photon per pulse	$1.1 – 430 \times 10^{12}$
peak brillance	$5.4 – 0.06 \times 10^{33}$ *
average brillance	$1.6 – 0.03 \times 10^{25}$ *
* in units of photons / (s mrad^2 mm^2 0.1% b.w.)	

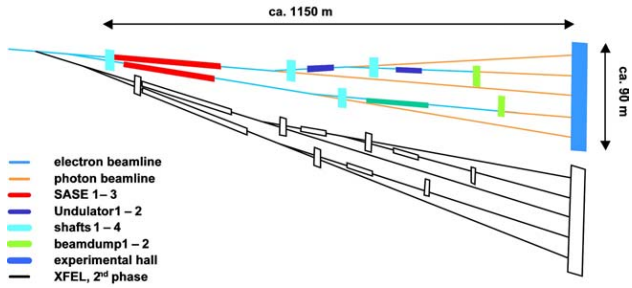

Figure 2: The 1st stage user beamline layout (coloured) and the possible extension.

An overview of the main XFEL parameters is given in Table 1. The undulator parameters have been optimised for one Å wavelength at a beam energy of 17.5 GeV. This implies that at the nominal maximum beam energy from the linac of 20GeV at 23MV/m accelerating gradient, the ^{57}Fe line at 0.08nm, of interest for certain experiments, will be accessible. Furthermore, the expected higher performance of the superconducting cavities (see below) will permit to operate at even shorter wavelength, provided that the electron beam quality can also be further improved to guarantee saturation in the SASE FEL process.

The basic accelerator layout is sketched in Figure 3. The main linac uses 116 12m long accelerator modules with 8 superconducting cavities each, grouped in 29 RF stations. Twelve spare modules, i.e. three RF stations, are included in the design in order to guarantee the overall availability of the accelerator in case of failures. The linac is housed in a tunnel (Figure 4) 15 – 30m underground. The klystrons are in the tunnel and connected to the modulators in an easily accessible surface building on the DESY site by 10kV pulse cables.

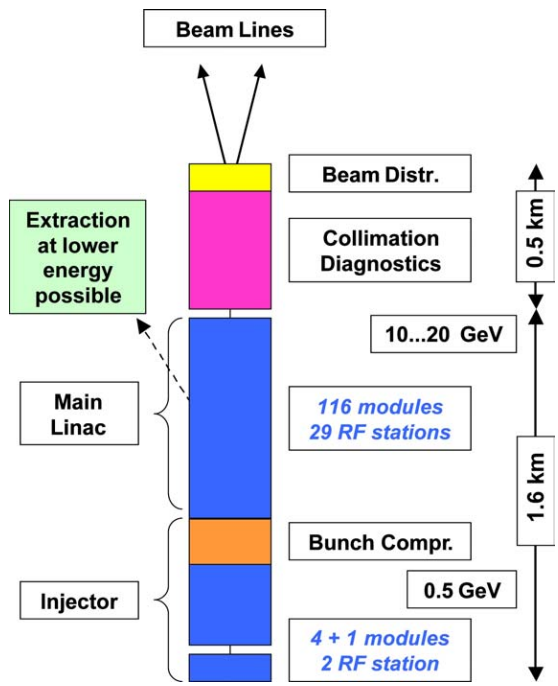

Figure 3: Basic Layout of the XFEL Accelerator.

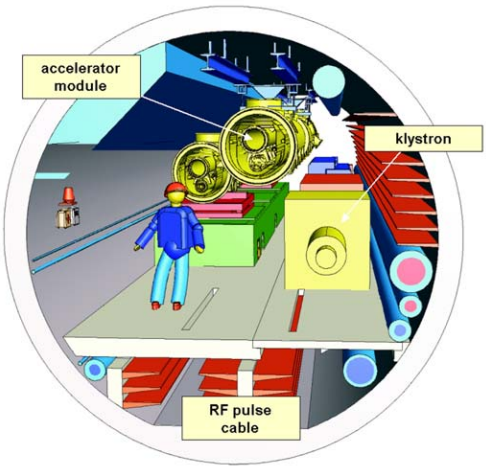

Figure 4: 3-d drawing of the 5.2m diameter main linac tunnel. The accelerator modules will be suspended from the ceiling.

The required klystron power per station is 4.8MW, well below the maximum power of 10MW of the multi-beam klystrons developed in industry for the TESLA project. This will not only cover the power needs for the above mentioned operation at higher energies, but also allow to operate the linac at higher repetition rates (and duty cycles) at lower energy (the main limitation then being the *average* power of the RF system).

In contrast to conventional linacs, with the superconducting accelerator technology even a continuous wave (CW, 100% duty cycle) operation of the linac is conceivable, although only at reduced energy/accelerating gradient in order to avoid excessive cryogenic load into the Helium at 2K. Such an option is not viewed as being part of the initial stage of the facility, but could become attractive if lower-emittance, high duty cycle beam sources become available [12], possibly in combination with advanced FEL concepts. We estimate that with a gradient of 7 – 8 MV/m (~7 GeV beam energy) this mode of operation would be compatible with the foreseen cryogenic plant [13]. A list of preliminary CW-parameters is shown in Table 2. A 2nd , low-power-CW RF system would have to be added, with IOT devices [14] being possible candidates as power source.

Table 2: Preliminary parameters for a possible future CW operation mode of the linac

Beam energy [GeV]	6.5 – 7.5
Acc gradient [MV/m]	7 – 8
Beam current [mA]	0.18
Bunch spacing [μs]	5.5
RF power / module [kW] (incl. regulation overhead)	~20 – 30
Dynamic cryo load 2K [kW]	~2.4 – 3.2

SRF LINAC TECHNOLOGY

The XFEL linac is based entirely on the technology which was over the past years developed by the TESLA collaboration as the most essential part of the R&D programme towards a superconducting linear collider. The successful completion of the 1st phase of the TESLA Test Facility (TTF) has demonstrated that superconducting 9-cell Nb cavities can be reliably produced with the XFEL design performance of 23MV/m. Stable beam acceleration at (or near) this gradient was also demonstrated with complete 12m long accelerator modules, containing 8 cavities each, in the TTF linac [15]. The latest generation accelerator module #5, now installed in the upgraded phase-2 TTF/VUV-FEL (Figure 5), performed in RF tests at a gradient of 25MV/m for all cavities simultaneously (higher for 6 out of 8 in single cavity RF tests) [16]. Several 10MW multi-beam klystrons have been built by industry in France and operated at TTF at design specs. Prototypes from additional vendors are under development [17,18]. Industrialisation of all linac components is one of the crucial tasks on the way towards construction of the machine.

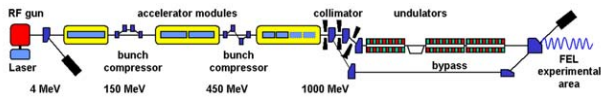

Figure 5: TTF-II and VUV-FEL layout.

The continuing TESLA SRF R&D programme has by now delivered state-of-the-art cavities with a performance well exceeding the XFEL baseline requirements. With the electropolishing (EP) method to improve the Nb surface quality, pioneered at KEK, five 9-cell cavities were tested at gradients of 35 – 40MV/m [19], see Figure 6. One cavity was installed in the first module of the TTF linac and the gradient of 35MV/m previously obtained on the test stand was reproduced in a measurement with beam. The SRF linac for the XFEL will be built with the EP technique and these recent results clearly justify the expectation that the machine will be able to provide the above mentioned flexibility to operate at higher energies without the need to extend the linac length.

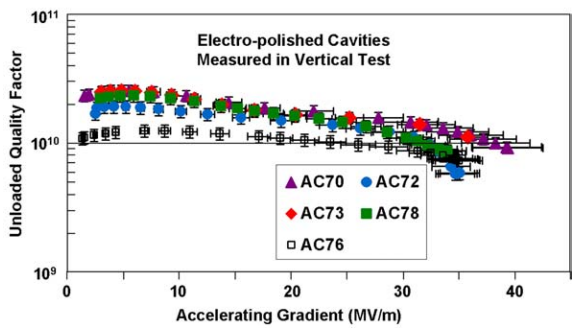

Figure 6: Recent test results for electro-polished TESLA cavities.

INJECTOR AND BUNCH COMPRESSOR

To optimise availability, there are two parallel injectors to produce and accelerate the electron beam before combining the beam lines at roughly 100 MeV. The injector tunnels are shielded from each other, such that maintenance, repair or modifications of one of them is possible while continuing to operate the facility with the other. A short accelerator section at the 3rd harmonic RF frequency is then used for the linearisation of longitudinal phase space. This section is followed by a booster linac increasing the energy to 500 MeV. At this energy the electron bunches are compressed by about a factor of 100 down to $\sigma_z \cong 22\mu m$, corresponding to approx. 5 kA peak current for 1nC charge. A detailed description of this process is given in Ref. [20]. Operation in this extremely short bunch length regime presents considerable technical and beam dynamics challenges, for a recent overview of this subject, see ref. [21].

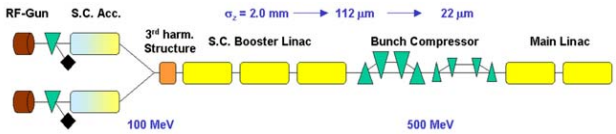

Figure 7: XFEL Injector Layout.

Simulation results for the photocathode RF gun indicate that an rms normalised emittance of 0.9mm×mrad is achievable (see ref. [22] for a recent update). The R&D for low-emittance electron beam sources has been performed within the TESLA collaboration and is supported by the EU Framework Programme 6. Beam tests of the latest version of the RF gun have been done at the PITZ test stand at DESY-Zeuthen [23], yielding a normalised emittance of 1.7mm×mrad. Further improvements are expected by increasing the accelerating field on the cathode from 40 to 60MV/m and optimising the homogeneity of the laser beam profile. The gun previously tested at PITZ is now installed at the VUV-FEL and commissioning with beam has started [24].

The bunch compressor has in comparison to the earlier version [6] been simplified by going from a 3-stage to a single stage layout. This approach turned out to be more robust against the potential problem of the micro-bunching instability. The latter can lead to a strong amplification of initially small modulations in the longitudinal bunch charge distribution by coherent synchrotron radiation (CSR) and space charge effects, unless the uncorrelated energy spread is intentionally increased by 'heating' with a laser [25,26]. The effect of CSR on the beam emittance is in the present layout strongly reduced by splitting up the magnetic chicane of the compressor into a first section with large momentum compaction (transfer matrix element R_{56}) and a second one with small R_{56}. The weak bends in the second section avoid excessive CSR at a position where the bunch becomes shortest. The residual emittance growth obtained from extensive beam dynamics simulations is of the order of 10%, well within the 50% total budget for emittance dilution from the source to the undulators. Further dilution in the downstream main linac is small as a result of very weak wakefields in the TESLA accelerating structures, so that the overall design includes a reasonable safety margin regarding the beam emittance requirements.

The large bunch compression ratio is inevitably connected with tight tolerances on timing, RF phases and amplitude of the gun and the booster section. The effects of jitter in these and other parameters on the FEL photon beam properties have been studied in a model calculations [27]. Even with tight assumptions of 0.05°, 0.02% and 0.1ps in RF phase, amplitude and gun timing jitter (rms) respectively, the fluctuations of photon pulse length and saturation power are not negligible and efficient photon diagnostics are likely required to monitor the beam and correlate variations with experimental data. An advantage of the SRF concept is the possibility to stabilise the RF parameters within a pulse by feedback. An alternative layout with 2 compressor stages is being investigated [28] to asses whether potential advantages regarding jitter tolerances would justify such a 2nd stage.

BEAM DISTRIBUTION

The XFEL linac can accelerate more than 3,000 bunches per RF pulse, serious beam dynamics problems related to higher order modes in the cavities are not expected [29]. User requirements regarding beam time structure will vary over a large range, from single or few bunches to partial or full trains per RF pulse. Generation of such patterns is possible at the source, at the end of the linac or by a combination of both. From the point of view of maximum flexibility a system using programmable fast kickers appears to be the optimum solution. Beam loading conditions in the linac could be quasi static, i.e. the same from pulse to pulse, and bunches could be distributed to different beam lines according to the needs of the respective experiments. The required switching devices are demanding, though, regarding jitter tolerances and reliability. The developments in this direction profit from the R&D work for the linear collider damping ring kickers which have more or less similar requirements. Recently, a very stable kicker pulser was developed at BESSY [30], which appears promising and will be further investigated in the future. In addition to switching the electron beam, it is also possible to switch the FEL process on and off by phase shifters, such that different photon pulse time structures can be generated in a beam line with a sequence of several undulators [31].

The beam transport lattice from the end of the linac to the undulators includes sections for diagnostics and collimation to protect the undulators from potentially large amplitude halo or mis-steered beam. A large momentum acceptance is foreseen so that energy modulation with a bunch train by up to 3% is possible. The lattice layout and the civil construction in the beam distribution region for the 1st phase of the user facility will also already take into account the possibility of later adding more beamlines.

Among the options to add features to the range of possible photon beam properties, very short pulses in the sub-fs regime appear very attractive for certain classes of experiments and could be generated by modulating the energy distribution in the bunch with a very fast laser just upstream from the SASE undulators [32,33].

CONCLUSION

The 20 GeV s.c. linac based on the technology developed by the TESLA collaboration and successfully demonstrated at TTF / VUV-FEL is an ideal driver for the X-ray Free Electron Laser facility, offering a broad range of operating parameters in its baseline design and a considerable potential for future upgrades and options.

With the R&D work progressing towards industrial production of major components and the preparations for the site and the legal procedure (plan approval procedure) well under way, we should be ready to go into the construction phase in ~2 years from now.

REFERENCES

[1] H. Dosch, "Advanced Analysis in Nanospace: Research with the XFEL", this conference, MO101.

[2] Ya. S. Derbenev, A. M. Kondratenko and E. L. Saldin, Nucl. Instr. Meth. 193(1982)415.

[3] „LCLS Conceptual Design Report", SLAC-R-593, April 2002; http://www-ssrl.slac.stanford.edu/lcls/cdr

[4] P. Krejcik et al., "Linac Coherent Light Source (LCLS) – Accelerator System Overview", this conference, MO201.

[5] F. Richard et al. (eds.), "TESLA Technical Design Report", DESY 2001-011, March 2001; http://tesla.desy.de

[6] R. Brinkmann et al. (eds.), "Supplement to the TESLA XFEL TDR", DESY 2002-167, October 2002; http://xfel.desy.de

[7] P. Castro, "Steps towards sources Bases on Linac-Driven Free-Electron Lasers", PAC 2003, Portland, May 2003, p. 198.

[8] M. Dohlus et al., "Start-to-End Simulations of SASE FEL at the TESLA Test Facility, Phase 1", submitted and in press, Nucl.Instr. and Methods A.

[9] H. Wabnitz et al., "Multiple ionization of atom clusters by intense soft X-rays from a free-electron laser", Nature Vol. 420, pp 482-485, Dec.2002.

[10] J. Rossbach, "The VUV-FEL as a Pilot Facility for the XFEL", presented at the XFEL STI Round Table Meeting, DESY, June 22-24; http://xfel.desy.de/content/e761/e830/index.html

[11] M. Tischer et al., Nucl. Instr. Meth. A483(2002)418.

[12] M. Ferrario, J.Sekutowicz and J. Rosenzweig, "An Ultra-High Brightness, High Duty Factor, Superconducting RF Photoinjector", EPAC2004, Lucerne, MOPKF043.

[13] B. Petersen, "Conceptual Layout of the European XFEL Linac Cryogenic Supply", this conference, MOP87.

[14] H. P. Bohlen, "IOT RF Power Sources for Pulsed and CW Linacs", this conference, TH201.

[15] H. Weise, "Superconducting RF Structures – Test Facilities and Results", Proc. PAC 2003, Portland, May 2003, p. 673.

[16] D. Kostin, "New Accelerating Modules RF Tests at TTF", this conference, THP32.

[17] H. P. Bohlen et al., "Operation of a 1.3GHz 10MW Multiple Beam Klystron", this conference, THP39.

[18] A. Yano et al., "The Toshiba E3736 Multi Beam Klystron", this conference, THP49.

[19] L. Lilje et al., "Achievement of 35MV/m in the TESLA Superconducting Cavities Using Electropolishing as a Surface Treatment", EPAC2004, Lucerne, WEOACH03.

[20] Y. Kim et al., "Injector And Bunch Compressor for the European XFEL", EPAC2004, Lucerne, MOPKF018.

[21] P. Emma et al., "Emittance Control for Very Short Bunches", EPAC2004, Lucerne, WEYLH01.

[22] Y. Kim, K. Flöttman and T. Limberg, "On Injector Optimisation for the European XFEL", this conference, TUP57.

[23] A. Oppelt et al., "The Photo Injector Test Facility at Zeuthen: Results of the First Phase", this conference, TUP47.

[24] S. Schreiber and K. Flöttmann, "Commissioning of the VUV-FEL Injector at TTF", EPAC2004, Lucerne, MOPKF022.

[25] E. Saldin et al., DESY-TESLA-FEL-2003-02, May 2003.

[26] Z. Huang et al., "Suppression of Microbunching Instability in the Linac Coherent Light Source", EPAC2004, Lucerne, WEPLT156.

[27] Y. Kim et al., "Start-to-end Simulations on Jitter and Error Tolerances in the European XFEL Project", EPAC2004, Lucerne, MOPKF016.

[28] Y. Kim et al., "Start-to-end Simulations with Two Bunch Compressor Stages for European XFEL Project", this conference, TUP58.

[29] N. Baboi, "Multi-Bunch Beam Dynamics Studies in the TESLA XFEL", this conference, TUP57.

[30] J. Feikes, O. Dressler and J. Kuszynski, "A Highly Stable Kicker Pulser System for the BESSY FEL Project", EPAC2004, Lucerne, WEPKF026.

[31] E. L. Saldin, E. A. Schneidmiller and M. V. Yurkov, DESY-TESLA-FEL-2004-02, May 2004.

[32] A. Zholents, W. Fawley, "Towards Attosecond X-ray Pulses from the FEL", EPAC2004, Lucerne, MOPKF072.

[33] E. L. Saldin, E. A. Schneidmiller and M. V. Yurkov, DESY-04-045, March 2004.

Linac Coherent Light Source (LCLS) Accelerator System Overview

P. Krejcik, Z. Huang, J. Wu, SLAC, Menlo Park, California;
P. Emma, SLAC/ARDA, Menlo Park, California

Abstract

The Linac Coherent Light Source (LCLS) will be the world's first x-ray free-electron laser (FEL). Pulses of LCLS x-ray FEL will be several orders of magnitude brighter and shorter than most existing sources. These characteristics will enable frontier new science in several areas. To ensure the vitality of FEL lasing, it is critical to preserve the high quality of the electron beam during the acceleration and compression. We will give an overview of the LCLS accelerator system. We will address design essentials and technique challenges to satisfy the FEL requirements. We will report studies on the microbunching instability suppression via a Laser-Heater. The studies clearly prove the necessary of adding the Laser-Heater and show how effectively this Laser-Heater suppresses the instability by enhancing the Landau damping. We will report how to minimize the sensitivity of the final energy spread and the peak current to various system jitters. To minimize this sensitivity, a feedback system is required together with other diagnostics. With all these considerations, full start-to-end simulations show saturation at 1.5 , though the LCLS is expected to be a very challenging machine.

NO SUBMISSION RECEIVED

HIGH-INTENSITY, HIGH CHARGE-STATE HEAVY ION SOURCES*

J. G. Alessi
Brookhaven National Laboratory, Upton, NY 11973, USA

Abstract

There are many accelerator applications for high intensity heavy ion sources, with recent needs including dc beams for RIA, and pulsed beams for injection into synchrotrons such as RHIC and LHC. The present status of sources producing high currents of high charge state heavy ions is reviewed. These sources include ECR, EBIS, and Laser ion sources. Benefits and limitations for these type sources are described. Possible future improvements in these sources are also mentioned.

INTRODUCTION

In heavy ion preinjectors, the choice of charge state, (or minimum charge-to-mass ratio), to be designed for, is an important consideration. Higher Q/M from an ion source makes the downstream accelerators more compact and less costly, but generally there is a tradeoff between intensity and charge state from a source, which may or may not be acceptable. If one can select a charge state high enough to eliminate one or more subsequent stripping stages, however, this lower initial intensity may result in equal or higher final intensities.

Examples of future applications which are pushing requirements for high intensity, high charge state heavy ion sources include the following:

- At Brookhaven, a new heavy ion preinjector is planned as a simpler, more modern replacement for the two Tandem Van de Graaff accelerators which are presently used for the heavy ion program at RHIC. As an example, ion source requirements for Au ions include the following a.) charge state 32+, to eliminate the need for stripping before injection into the Booster synchrotron; b.) pulse width ~ 10 µs, to allow simple single turn injection into the Booster; c.) Au^{32+} current from the source of 1.7 emA, in order to deliver the required intensity of 3 x 10^9 ions/pulse to the Booster; d.) 5 Hz repetition rate. In addition, in order to support simultaneously the beam requirements for the NASA Space Radiation Laboratory (NSRL), the ion source must be able to deliver to Booster a second beam species, with pulses interleaved with the RHIC beam pulses, *switching species at the 5 Hz repetition rate*. Examples of the beams required for NSRL include He^{2+}, C^{6+}, O^{8+}, Si^{14+}, Ti^{18+}, Fe^{21+}, and Cu^{22+}, all at currents of 2-3 emA, and pulse widths of ~ 10 µs. As will be discussed below, an Electron Beam Ion Source (EBIS), similar to that which has been developed at Brookhaven [1], can meet these requirements.
- Driver accelerators for rare ion production, such as the Rare Ion Accelerator (RIA), require dc beams of essentially any ion species. Examples of required beams and intensities for RIA are 230 eµA of $U^{28+, 29+}$, 280 eµA of $Pb^{25+,26+}$, 220 eµA of Xe^{18+}, 350 eµA of Ni^{12+}, 230 eµA of Ar^{8+} [2]. In applications such as this, which require high current dc beams, the ECR ion source is essentially the only option. Present state-of-the-art ECRs can exceed RIA requirements for gaseous beams, and are close to meeting the requirements for the more difficult beams produced from solids.
- At CERN, LHC requirements for heavy ions depend on the acceleration scheme used. While initial operation is with Pb ions, ions such as He, O, Ar, Kr, and In have also been requested [3]. The baseline plan for Pb ions requires an upgraded ECR producing > 200 eµA of Pb^{27+}, in 200 µs pulses, at 5 Hz. This scheme also requires the use of LEIR for ion storage and cooling. In an alternative scheme, one could avoid the use of LEIR if one would produce directly from the source ~ 5 emA of Pb^{25+}, in 5.5 µs pulses, at 1 Hz. A laser ion source (LIS) was being developed for this option [4], and an EBIS with a reasonable scaling from Brookhaven parameters could also be considered. A third option, also not needing LEIR, would be to produce ions in a charge state which would also eliminate a stripping stage. In this case, one would need 2-3 emA of Pb^{54+} ions, in 5.5 µs pulses at 1 Hz. Parameters for an EBIS meeting these requirements were presented in [5].

ION SOURCE CONSIDERATIONS

As seen from the above examples, source requirements can depend strongly on the application. Some important considerations are common to almost all accelerator applications, such as source lifetime, reliability, stability (both pulse-to-pulse and long term), magnitude of current fluctuations (noise), and beam emittance. Other aspects have varying importance depending on the application. For instance, the ease and speed of changing species is important for RHIC, but nearly irrelevant for the other applications. Some applications have less flexibility than others regarding the choice of beam species, so sources favoring ions coming either from gases (ECR) or solids (LIS), may be at a disadvantage. Finally, for these high current applications, the charge state distribution of ions coming from the source can be an important

*Work performed under Contract Number DE-AC02-98CH10886 with the auspices of the US Department of Energy.

consideration, because the extraction and initial transport has to be designed to handle space charge from the total extracted current, which can be anywhere from a few times to a hundred times larger than the current in the desired charge state, depending on the ion source, charge state, etc.

The sources described in the following sections have characteristics which are favorable for the production of high charge state ions. To produce high charge state ions, one needs high energy electrons in the source. A high density of these high energy electrons is required to produce the desired intensity and charge state. The ions must stay in the electron beam or plasma long enough to reach the desired charge state through stepwise ionization. Also, it is desirable to keep the background pressure as low as possible to minimize the recombination of ions. In the EBIS, one can control precisely and independently these parameters, while in ECR sources these parameters are coupled quite a bit, and the LIS offers the least control over them independently.

EBIS SOURCE

Principle of Operation

In an EBIS source, a high current electron beam is produced on one end, compressed to high current density as it passes through a long magnetic solenoid, and is then decelerated and stopped in an electron collector on the other end of the solenoid. Gas can be fed into the solenoid region, or singly charged ions injected into the solenoid from an external source through the collector end, to feed the trap with the desired beam species. Electrostatic potentials are applied to cylindrical electrodes in the solenoid bore to trap ions axially, while the space charge of the electron beam provides radial trapping of the ions. These trapped ions undergo stepwise ionization by the electron beam; the longer they are held in the trap, the higher the charge state of the ions. When the desired charge state is at the peak of the charge state distribution, the electrostatic barrier is dropped from the collector end, and ions exit the trap and are extracted through an aperture on the axis of the electron collector. The total number of charges extracted is limited by the loss of radial confinement when the space charge of the electron beam is fully neutralized, and this extracted ion charge can be 50-75% of the total electron charge in the trap. Therefore, the extracted ion current can be accurately predicted for an EBIS, based on the easily calculable electron charge in the trap region – determined by the electron current, electron beam velocity, and trap length.

As a result of this ion production process, the EBIS has the unique feature that the total extracted charge per pulse is nearly independent of ion species or charge state (except at the very high charge states)! In addition, because one can control how one drops the barrier voltage (or puts a small accelerating gradient within the trap electrodes), one can control the pulse width of the extracted ion beam, and therefore short pulses of high current are possible, making it well suited for few-turn synchrotron injection.

Performance

Recent advances in the standard EBIS have been achieved at Brookhaven, where a prototype of the EBIS required for RHIC has been developed [1]. This EBIS has been operated with a 10 A electron beam current, and a 0.7 m long trap. Experiments have mainly concentrated on performance with Au beams, with > 50nC of charge per pulse being extracted. A current of ~550 µA of Au^{32+} has been produced in ~ 15 µs pulses. A scaling up of the trap length to 1.5 m is planned to get a factor of 2 increase in ion current, thus meeting the RHIC requirements.

Features; Advantages

- Easily produces the highest charge states of the three type sources
- Produces a narrow charge state distribution; typically 20% of the total current is in the desired charge state
- Produces beams of any species; intensity is independent of species; can switch species pulse-to-pulse
- One can control the pulse width (produces a fixed charge/pulse)

Technological Aspects of the Source

- Electron gun (BNL EBIS uses 10A electron beam)
- Electron collector (BNL design for 15A * 15 kV = 225 kW)
- Superconducting solenoid (5T, 8" bore, 2 m long will be required for the RHIC EBIS)
- Auxiliary ion sources used for external injection of 10's of µA of singly charged ions; multiple sources feeding the trap for fast switching of species.
- Ultrahigh vacuum (10^{-9} to 10^{-10} Torr)
- Modern control system makes operation stable, reproducible, and increases flexibility. Makes control of many EBIS parameters in a complex cycle easy.

Potential Issues

- Possibility of instabilities at high electron beam currents. (Not observed at BNL, up to 10A).
- Not much operating experience at high currents.
- Energy spread of fast-extracted ions

ECR SOURCE

Principle of Operation

The ECR plasma chamber is placed in an axial magnetic mirror field configuration, produced by two

solenoid coils, and a radial cusp magnetic field produced by a sextupole magnet. The superposition of these fields produces a minimum-B configuration in the center. Gas for the species of interest, or alternatively a buffer gas, is fed in to the chamber. Plasma is produced via the injection of microwave power into the chamber, and is confined due to the confinement of plasma electrons in the magnetic field configuration. For a given microwave frequency, the magnetic fields are chosen such that there is a surface within the chamber where the electron-cyclotron resonance condition is satisfied. Electrons in this region are resonantly heated to high electron temperatures, necessary for the high charge state ion production in the plasma, which then occurs predominantly via stepwise ionization. Ion current can be increased with increasing rf power, and by increasing the rf frequency/magnetic field combination. When the beam of interest can not be produced from a gas, the options are the heating/sputtering of solid material inserted into the plasma, using metal in vapor released from volatile compounds, or the use of a very high temperature oven.

In pulsed operation, one sometimes measures an enhanced intensity of extracted high charge state ions right after the rf power is turned off, called the "afterglow" mode. This enhancement is explained by the increase in the rate of electron loss when rf power is turned off, causing ions, confined by the electron space charge, to exit the plasma more quickly as well.

A recent review of the physics of ECR's has been presented in [6].

Performance

The superconducting ECR VENUS is being developed at LBL as a demonstration of a source which will meet RIA requirements, and there are also very active developments at many other labs worldwide. Only a few examples of high current ECR performance, pulsed and dc, are given in Table 1. Further details for various sources can be found in [7].

Table 1: Some examples of ECR performance

	Ion	Q	I (eμA)	Width (μs)
CERN, 14.5 GHz [3]	Pb	27	120	~200
PHOENIX, 28 GHz [8]	Pb	27	~550	~200
SERSE, 28 GHz [9]	Xe	25	500	>200
SERSE, 28 GHz [9]	Xe	27	~100	dc
LBL VENUS 28 GHz [10, 11]	Xe	27	120	dc
CEA-GTS 18 GHz [12]	Xe	27	168	dc
LBL VENUS 28 GHz [10, 11]	Bi	27	220	dc
RIKEN 18 GHz [13]	Xe	20	300	dc

While, as mentioned above, for EBIS the output current is almost independent of species or charge state, for the ECR there are strong dependencies on both, and going up by one or two charge states can sometime result in a factor of 2 drop in intensity. A schematic representation of the charge state dependence for both type sources is illustrated in Fig. 1.

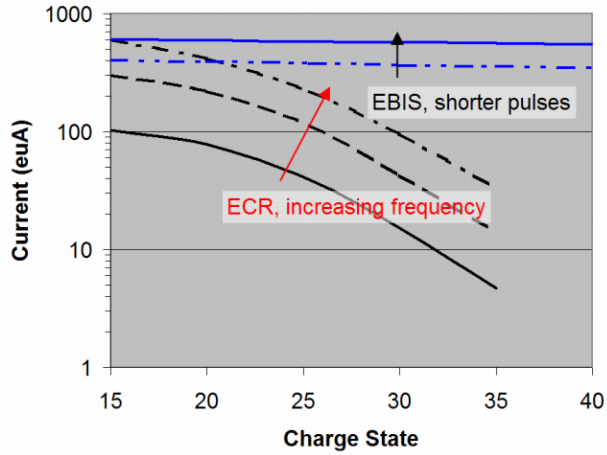

Figure 1: Illustration of approximate charge state dependence for ECR and EBIS, for species such as Xe.

Features; Advantages

- Essentially the only choice for high current, high charge state, dc applications
- Reliable; many operating ECRs, a lot of experience

Technological Aspects of the Source

- Superconducting magnets (both solenoids and hexapoles). VENUS, operating at LBL at 28 GHz, has 4 T injection field and 2 T hexapole at plasma chamber.
- RF power source – for example, 28 GHz gyrotron, at 10-15 kW; plus sometimes multiple frequencies used, requiring multiple rf sources.
- High temperature oven may be used for metal ion production.

Potential Issues

- Broad charge state distribution, so one has to extract & transport a high total current
- Performance depends on species, favoring gases and low melting point solids
- "Memory" effects in the plasma chamber can lead to slow ion species switching times.

LASER ION SOURCE

Principle of Operation

A simplified picture of the process of high charge state ion production in a laser ion source is the following. A short pulsed, high power laser beam is focused to a small spot on a solid target containing the desired beam species. Evaporation of target material occurs, and electrons in the gas absorb laser energy via inverse Bremstrahlung, causing their energy to increase. A plasma forms, and rapidly expands normal

to the target. Plasma ions are stepwise ionized to high charge states.

The electron temperature increases with laser power density and wavelength, which is advantageous for the production of high charge states. More details on the design choices for a LIS can be found in [14]. Results of an experimental comparison of several different laser types was presented in [15]. A CO_2 laser is still the best choice for the production of highly charged ions.

Performance

There has been an ongoing collaboration between CERN, ITEP-Moscow, and TRINITI-Troitsk on the development of the LIS for LHC, an application mentioned in the introduction. The most recent step has been the development of a 100 J, 15-30 ns CO_2 laser operating in the master oscillator-power amplifier configuration, and the testing of a source using this laser. The laser is designed to operate at the required repetition rate of 1 Hz. With this laser, they have produced a few emA's peak current of Pb^{27+}, with a pulse width of several microseconds, and extracted these ions at 105 kV [4]. The total extracted current was ~ 20 emA, and the charge state distribution was quite a bit narrower than previous results for Ta using a 30 J laser. Since the LIS produces higher currents and shorter pulses than the ECR, if it were included in Fig. 1, it would be at higher current but with a falloff with charge state similar to the ECR.

Unfortunately, the lifetime of the source at 1 Hz operation is so far only on the order of hours, and improvements are needed in several areas in order to achieve at least a minimum acceptable lifetime of ~ 2 weeks. Since the baseline for LHC is now an ECR, the first use of this LIS is now redirected to a new high current injector for the ITEP Terawatt Accumulator (TWAC) project.

Features; Advantages

- Produces high currents, short pulses

Technological Aspects of the Source

- High power laser – 100 J, CO_2, 15-30 ns pulse
- Laser beam optics
- Targets – 3 x 10^{13} W/cm^2 on the target

Potential Issues

- Laser reliability
- Achieving the desired repetition rate of the laser
- Pulse-to-pulse beam current fluctuations
- Target erosion; coating of optics by evaporated target material
- Species approximately limited to solid targets (high melting point solids are best).

FUTURE DEVELOPMENTS

Improvements continue to be made in all three type sources. EBISs are going to higher intensities via higher electron beam currents and longer trap lengths. ECRs continue to move to higher frequencies and higher magnetic fields. For the LIS, developments are aimed more at reliability and lifetime. However, there are more extreme variations on these type sources which are also being developed.

At Dubna, rather than dumping the electron beam after a single pass through the trap region of an EBIS, the electron collector was replaced with a repeller electrode, using a geometry which was very symmetric to the electron gun side. With this negatively biased electrode, electrons reflect/oscillate repeatedly through the trap, raising the effective electron current in the trap by forming what is called a "string" [16]. This Reflex EBIS was used at JINR on the Nucleotron in June '02 and June '03 runs to produce N^{6+} (300 eμA), N^{7+} (350 eμA), Ar^{16+} (200 eμA), and Fe^{24+} (150 eμA) [17]. Beam pulse width was ~8 μs, for single turn injection into the ring. The outstanding feature here was that this was achieved with *only 5-6.5 mA electron current*! This represented an effective 50-times reflection of electrons through the trap, and therefore an electron beam with only 2% of the beam power that would have been required in the normal EBIS mode. The effective electron current density in the trap was 150-200 A/cm^2. They report good stability over the 4 weeks of running for this Reflex EBIS. A step even beyond this is the Tubular EBIS, also being developed at Dubna [18]. Here, the attempt is being made to increase the effective electron beam current even further by establishing a reflex mode of operation of an electron beam in a somewhat complicated geometry, but which essentially fills the space between two coaxial cylinders running the length of the trap (a "tubular" geometry).

The ECLISSE project is a coupling of a LIS and an ECR, where one hopes to enhance with the ECR the charge states coming from the LIS [19].

CONCLUSION

While all performance goals have not yet been demonstrated for high charge state heavy ion sources which would fulfill RHIC, LHC and RIA requirements, solutions for all three applications seem to be well within reach. One important aspect not covered in this paper is the fact that as intensity from these sources steadily increases, the transport of these beams, for matching into an RFQ, for example, is becoming more difficult, due to space charge.

The sources described above have differing characteristics, so depending on the application, frequently one will be a better fit than another. The ECR is clearly the choice for RIA, which requires dc beams. However, for RHIC, where one requires high currents in short pulses, plus any ions species and fast switching, the EBIS is an excellent match. For LHC,

all 3 source types would seem to be candidates, but constraints in the schedule result in the ECR being the best choice at present.

REFERENCES

[1] J.G. Alessi, E. Beebe, D. Graham, A. Kponou, A. Pikin, K. Prelec, J. Ritter, V. Zajic, Proc. PAC 2003, p. 89.

[2] J.A. Nolen, Proc. Linac 2002, p. 29.

[3] C.E. Hill, D. Küchler, H. Kugler, R. Scrivens, Proc. Linac 2002, p. 148.

[4] A. Balabaev, S. Kondrashev, K. Konukov, A. Lozhkin, B. Sharkov, A. Shumshurov, A. Charushin, K. Makarov, Yu. Satov, Yu. Smakovskii O. Camut, J. Chamings, H. Kugler, and R. Scrivens, Rev. Sci. Instrum. 75 (2004) 1572.

[5] E. Beebe, J. Alessi, A. Kponou, A. Pikin, K. Prelec, Proc. EPAC 2003, p. 281.

[6] A. Girard, D. Hitz, G. Melin, K. Serebrennikov, Rev. Sci. Instrum. 75 (2004) 1381.

[7] S. Gammino, G. Ciavola, L. Celona, L. Andò, D. Hitz, A. Girard, G. Melin, Proc. PAC 2003, p. 81.

[8] P. Sortais, J.-L. Bouly, J.-C. Curdy, T. Lamy, P. Sole, T. Thuillier, J.-L. Vieux-Rochaz, D. Voulot, Rev. Sci. Instrum. 75 (2004) 1610.

[9] S. Gammino, G. Ciavola, L. Celona, D. Hitz, A. Girard, G. Melin, Rev. Sci. Instrum. 72 (2001) 4090.

[10] C.M. Lyneis, D. Leitner, S.R. Abbott, R.D. Dwinell, M. Leitner, C.S. Silver, C. Taylor, Rev. Sci. Instrum. 75 (2004) 1389.

[11] D. Leitner, private communication.

[12] D. Hitz, A. Girard, K. Serebrennikov, G. Melin, D. Cormier, J.M. Mathonnet, J. Chartier, L. Sun, J. P. Briand, M. Benhachoum, Rev. Sci. Instrum. 75 (2004) 1403.

[13] T. Nakagawa, T. Aihara, Y. Higurashi, M. Kidera, M. Kase, Y. Yano, I. Arai, H. Arai, M. Imanaka, S. M. Lee, G. Arzumanyan, G. Shirkov, Rev. Sci. Instrum. 75 (2004) 1394.

[14] B. Yu. Sharkov, S. A. Kondrashev, Proc. EPAC 1996, p. 1550.

[15] P. Fournier, H. Haseroth, H. Kugler, N. Lisi, R. Scrivens, F. Varela Rodriguez, P. Di Lazzaro, F. Flora, S. Duesterer, R. Sauerbrey, H. Schillinger, W. Theobald, L. Veisz, J. W. G. Tisch and R. A. Smith, Rev. Sci. Instrum. 71 (2000) 1405.

[16] E. D. Donets, Rev. Sci. Instrum. 71 (2000) 810.

[17] E.D. Donets, D.E. Donets, E.E. Donets, V.V. Salnikov, V.B. Shutov, S.V. Gudkov, Yu.A. Tumanova, and V.P. Vadeev, Rev. Sci. Instrum. 75 (2004) 1543.

[18] E.D. Donets, E.E. Donets, R. Becker, L. Liljeby, K.-G. Rensfelt, E.N. Beebe, and A.I. Pikin, Rev. Sci. Instrum. 75 (2004) 1566.

[19] S. Gammino, L. Andò, L. Celona, G. Ciavola, L. Torrisi, J. Krasa, L. Laska, M. Pfeifer, K. Rohlena, B. Badziak, P. Parys, J. Wolowski, E. Woryna, G. Shirkov, Proc. EPAC 2002, p. 1709.

NON-INTERFERING BEAM DIAGNOSTIC DEVELOPMENTS

A. Peters, P. Forck, GSI, Darmstadt, Germany

Abstract

New high power proton and heavy ion LINAC projects are a big challenge for beam diagnostic developments. Due to the high inherent beam power mostly all destructive measurement techniques are not applicable. Thus a lot of beam diagnostic developments are under way from enhancements of well-known systems like current transformers to new designs for profile or bunch length measurements using e.g. the interaction of the high power beams with the residual gas in the LINACs. The latest progress in this field will be reviewed with descriptions of some remarkable solutions.

INTRODUCTION

The development of new high power proton/ion LINACs is still going on. The aims of such new accelerators are highest beam pulse or D.C. currents and highest brilliances. The demands for new beam diagnostic devices are as follows:

- As much as possible the devices shall work non-interfering to measure even beams of highest power which destroy every material put into the beam line.
- The length of diagnostics mechanics in beam direction shall be as small as possible to have nearly 100 % space for accelerating and focusing elements, which is necessary because of the high space charge forces.

All these parameters together are very challenging, but those developing beam diagnostic equipment can profit from the following trends in the industry:

- A huge market of remote controllable devices has grown, which can be used as parts of diagnostic systems without modifications.
- Digital data treatment methods and devices like FPGAs and DSPs have become cheap and their capabilities are growing fast.
- A special industry segment, the vision systems, shows these trends exemplarily. Digital cameras with fast speeds and/or high resolution are capable to send their image data without any loss directly digital to the user [1].

This overview will report about some examples following the above mentioned tendencies – the focus is glanced at the latest developments in the field of transformers, optical profile measurement devices and a nonintersecting bunch length measuring techniques.

NEW TRANSFORMER APPLICATIONS

BNL Developments for SNS

An interesting example for the use of digital data treatment in connection with a well-known transformer technique was developed by M. Kesselman et al. for the SNS facility [2]. The time structures of the beams range from sub-µs bunches to 1 ms long macro-pulses.

Figure 1: SNS transformer for the DTL section.

To realize only one current measurement device which is capable to observe these different beams with a rise time of about 1 ns and a droop of 0.1 %/ms is normally not possible: an extremely large and expensive core of a (passive) transformer would meet the low droop but not the necessary rise time. In addition, the required space for such a device is not given in a linac. An active-passive transformer would have the same problems, only the size would shrink. To meet both requirements a digital compensation scheme was developed to use a commercial available Fast Current Transformer [3], see Fig. 1 and 2.

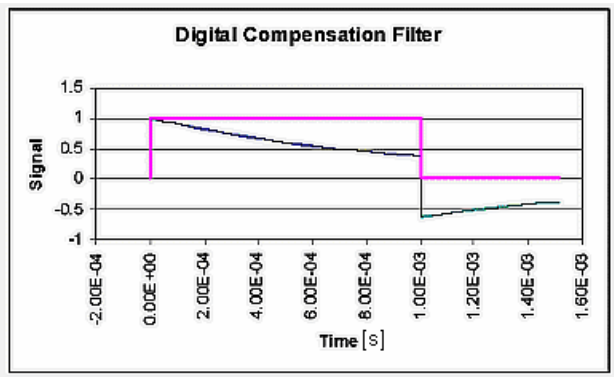

Figure 2: Compensation of an ideal exponentially decaying transformer output signal (blue drooping trace) with a 1ms time constant compensated by an IIR filter that introduces a 1s time constant instead of the 1ms time constant (squared-up magenta trace).

The reconstruction of the original current pulse is based on using an IIR (infinite impulse response) filter. The realization shows that the transformer time constant has to be known with high accuracy that could only be achieved by implementing an online calibration procedure [4]. The IIR filter can easily be realized in a field programmable

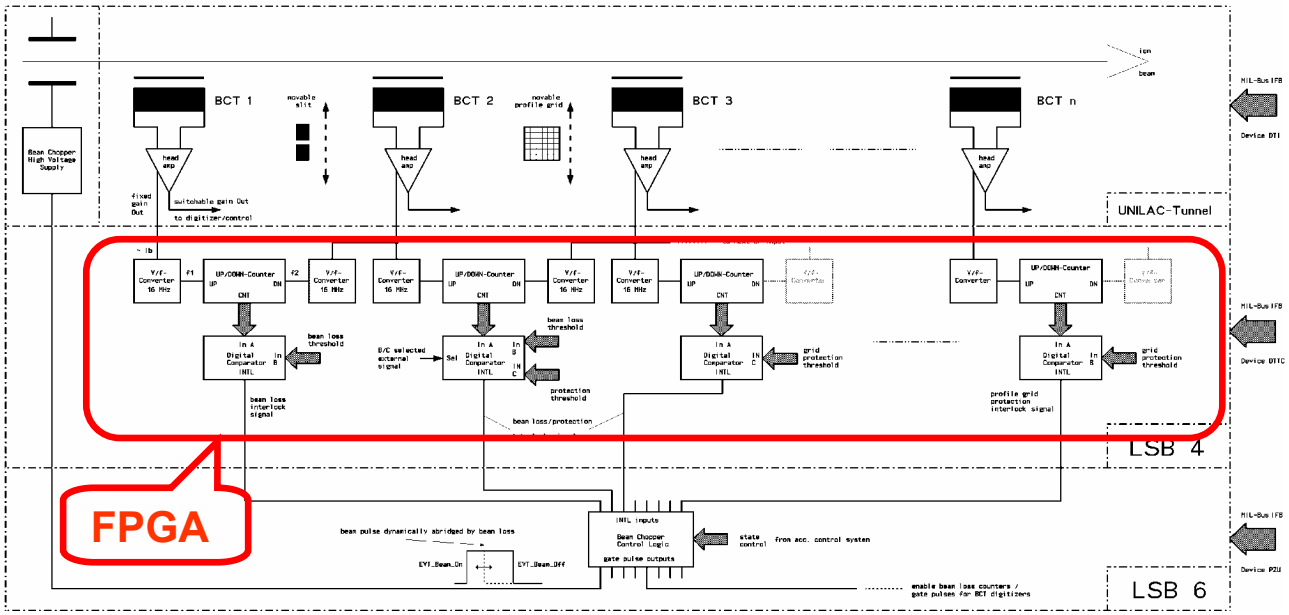

Figure 3: Scheme of the online transmission control electronics at GSI.

gate array (FPGA) or digital signal processor (DSP) and can run at real time if required. The present version is successfully running offline on a PC under LabVIEW.

GSI Transmission Control Electronics

A complex system was built up at GSI to protect the machine against destruction [5], see Fig 3. It consists of a couple of transformers along the LINAC and the transfer line to the following synchrotron each having a pre-amplifier directly attached and a high-dynamic voltage-to-frequency converter outside the tunnel, which is also used for the digitisation of the macro-pulse currents. The simple idea now is to use an up-down counter for each pair of consecutive transformers with a digital comparator which can handle several thresholds in parallel for multiple functions: transmission control (beam loss control), protection control for slits and SEM profile grids. The implementation of the electronics is done in FPGAs, working with a pulse repetition rate of 50 Hz. Protection and loss control are done online by actively chopping the beam on the low energy side. The digital approach has a very high dynamics and beam pulses from 10 µs to 8 ms can be handled without gain range switching. The reaction time of some µs is dominated by cable delays in the moment. Because the principles are simple and very reliable, no further machine destructions are observed after the installation.

TRANSVERSE PROFILE MEASUREMENTS USING BEAM INDUCED FLUORESCENCE

The profile of a proton or ion beam can be determined by observing the beam induced fluorescence (BIF) emitted by the residual gas molecules. In most cases N_2 dominates the residual gas composition. Due to the electronic stopping power the molecules are ionized. The fluorescence in the wavelength range 390 nm < λ < 470 nm is generated by a transition band to the N_2^+ electronic ground state, having a lifetime of about 60 ns [6]. The low amounts of photons have to be amplified using an image intensifier. This commercially available device consists of a photo cathode to transform the photons into electrons, which are than amplified by a spatial resolving MCP electron multiplier. It is followed by a phosphor screen to create again photons, which are finally monitored by a CCD camera.

Developments at LANL

During the 90ies first developments exploring the above mentioned technique were done at LANL by D. P. Sandoval, J.D. Gilpatrick et al [7,8]. Mostly commercial devices were used for the measurement set-up:

- CCD camera based on a Kodak DCS 420m chip
- DEP image intensifier, variable gain from 1 to 4000
- Lens system: Computar f/1.8, remote controlled
- N2 gas injection system with Maxtek piezoelectric valve and a Balzers backpressure control system

Series of comparative measurements with a wire scanner (WS) were performed using the following beam conditions: a some MeV proton beam of 100 mA, 1 to 10 ms pulse length, 6 Hz repetition rate, 6-7 averages per picture, see an example in Fig. 4. The profile measurement data agree within < 10% with those of the wire scanner, while the BIF profiles show always a slight broadening, maybe caused by the movement of the ionized N_2^+-particles due to space charge effect in the lifetime (60 ns) of the excited state.

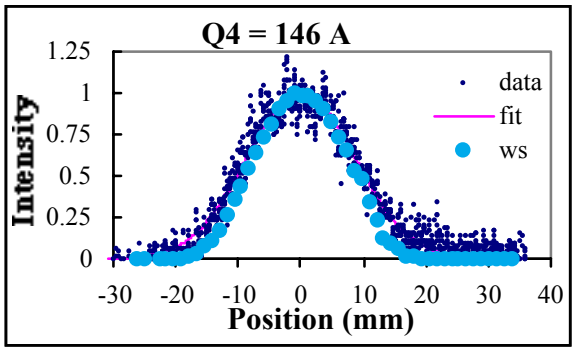

Figure 4: BIF example measurement at LANL in comparison with a measurement of a wire scanner (WS).

Investigations at Orsay

P. Ausset et al made intense investigations on the BIF method using a 95 keV, 100 mA proton beam in a low energy beam transport line between the ECR ion source and the following RFQ [9]. The measurement system was based on a set-up similar to LANL, but using an intensified 16 bit CCD camera instead. The measured profiles have the same geometrical shape for all gases (N_2, Ne, Ar, Kr, Xe in addition to the residual gas) at the same pressure, see Fig. 5 for a comparison.

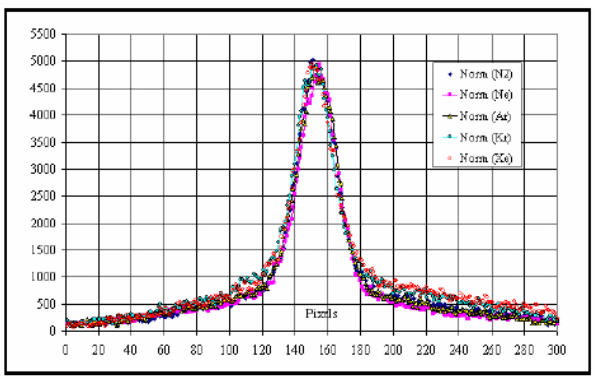

Figure 5: Normalised Profiles measured in the LEBT section of the IPHI project at Orsay.

BIF System Development at GSI

The GSI UNILAC is a pulsed heavy ion LINAC with a macro pulse length of about 100 µs to fill the proceeding synchrotron. The beam profile should be monitored within a single macro pulse. Therefore the use of a long integration time for an improved signal-to-noise ratio is impossible. Due to the low amount of emitted photons during the 100 µs integration time, a large amplification of 10^6 is required by using a double MCP inside the image intensifier [10]. The whole set-up is shown in Fig. 6. A raw image is displayed in Fig. 7 together with the transverse profile as yielded from the projection along the beam path [11]. Each of the light spots on the raw image is created by a single photon.

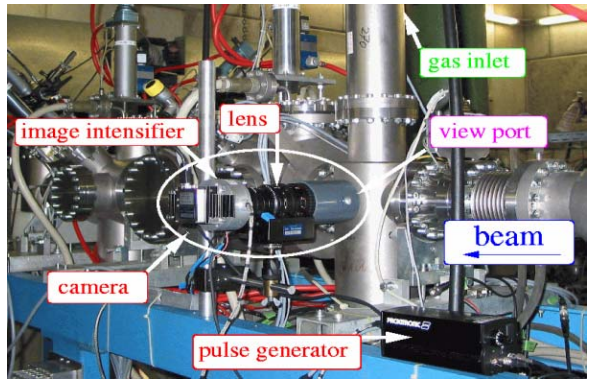

Figure 6: Measurement set-up in the experimental hall after the UNILAC at GSI.

Due to the statistical nature of the signal generation, the data quality can be enhanced by data binning of the individual projections or by summing up several images. The resolution of 300 µm/pixel is sufficient for the displayed parameters. A higher resolution can be reached by varying the distance between the beam pass and camera or by a proper choice of the optics, making this method very flexible. By using a regulated gas valve the pressure could be locally (within ~1 m) raised up to 10^{-4} mbar. No measurable influence on the ion beam delivered to the GSI synchrotron was detected. The correspondence of the measured profile to other methods is excellent.

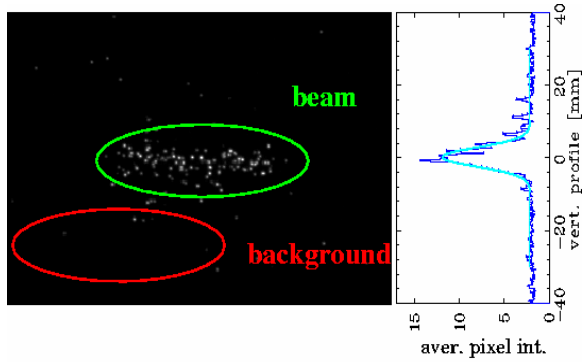

Figure 7: Image of a 200 µs U^{28+} beam with I=700 µA recorded during one UNILAC macro-pulse with a vacuum pressure of about 10^{-5}mbar. The two dimensional image from the intensifier (left) and the projection for the vertical beam profile (right) is shown.

An advanced application for the residual fluorescence measurement is the determination of a possible variation of the beam profile during the macro pulse, as shown in Fig. 8. The fast switching of the voltage between the photo cathode and the MCP within 100 ns can be used to restrict the exposure time. For the case of Fig. 8 one image of 40 µs exposure time is recorded and the measurement is repeated with 8 different trigger delays. This type of measurement is not possible with an intersecting SEM-grid due to the risk of wire melting by the large beam power.

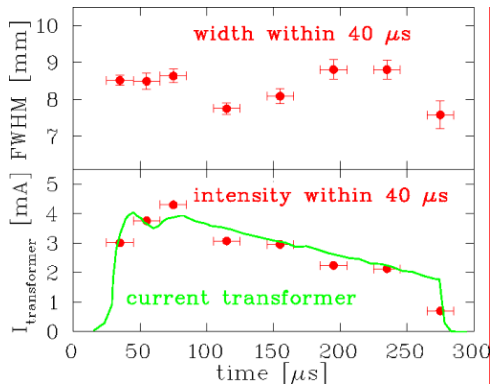

Figure 8: The measurement of the width variation during a macro pulse is shown. The lower graph shows the normalized image intensity together with the measured beam current.

At the GSI test set-up an 8 bit Basler 301f CCD camera with a maximum of 80 frames per second at 658 x 494 pixels was chosen. The CCD signals are directly digital-converted at the camera head and transferred using Firewire IEE1394a protocol [12]. Compared to an analog video link, no degradation of the signal due to long cables occurs. At the moment the Firewire bus standard allows a maximum data rate of 400 Mb/s which equals to 100 frames per second at VGA resolution. The variable bus architecture with up to 63 nodes is well suited for the distributed diagnostic installations in the various beam lines. The maximum cable length for electrical transmission is 20 m. For the long distances between the diagnostics and the control room fiber optic cables driven by opto-couplers are used.

The data are transferred to a Windows PC via a standard PCI interface. The analysing software is written in LabVIEW, serving as a modern software tool with embedded image processing macros. The Firewire driver from the commercial package IMAQ-Vision is used for data acquisition and analysis. It also allows controlling various camera functions like exposure time, electronic gain and triggering. With minor modifications, the same software can be installed on a recent available real-time platform with LabVIEW-RT as the basic operating system. The data acquisition and the first step of data analysis can than be treated locally. It is linked via standard Ethernet to a PC or workstation, where further analysis and archiving is performed.

LONGITUDINAL PROFILE MEASUREMENTS

The determination of the longitudinal density distribution of a bunched beam is an important issue because it is required for an optimal matching between different LINAC-modules as well as for the comparison with numerical calculations taking space charge effects into account. The bunch structure cannot be determined by capacitive pick-ups for non-relativistic beam velocities due to a faster propagation of the electric field. Thus, at most LINACs an intersecting method is used with the help of secondary electrons emitted from a wire crossing the beam [13,14]. The wire is biased with about -10 kV to pull the secondary electrons toward a slit outside the beam path. An rf-deflector follows, where the electrons are modulated in transverse direction by an electric rf-field. The deflection angle depends on their relative phases, i.e. the device transforms the time information into a spatial difference.

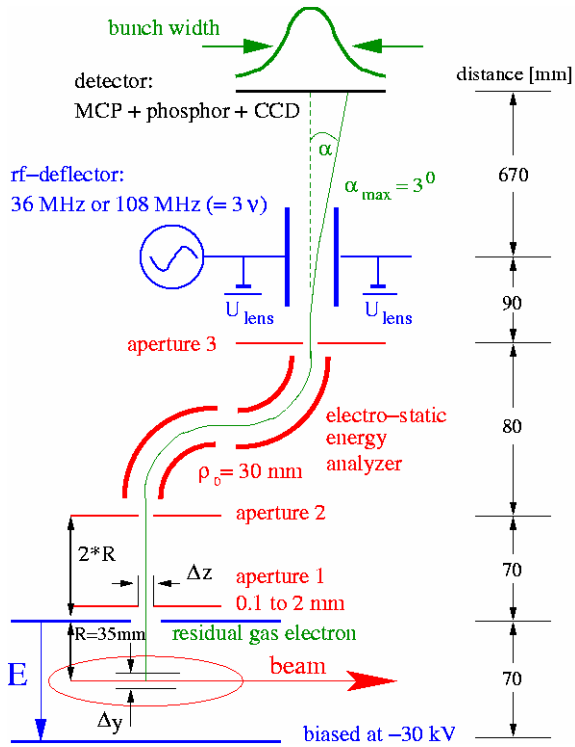

Figure 9: Schematic sketch of the GSI bunch shape monitor.

An adoption to a non-intersecting approach has recently tested at GSI [15]. Here the time spectroscopy of secondary electrons created by atomic collisions between the beam ions and the residual gas molecules is performed. In Fig. 9 the general principle is shown. The secondary electrons are accelerated by a homogeneous electrical field of 420 V/mm formed by 160 x 60 mm^2 electrodes outside of the beam pass, as usually used for residual gas profile monitors. To restrict the source region for the secondary electrons, an aperture system is used with remotely controlled opening. These apertures serve also as entrance and exit slits for an electro-static energy analyzer in a point-to-point focusing mode. In connection with the apertures, the source volume is only about 0.2 mm in ion beam direction and in the direction of the external E-field. This is comparable to the wire thickness in the standard wire application. The time-to-spatial transformation is performed with the same type rf-deflector as mentioned above [14]. We use either a device on the ground rf-frequency of 36 MHz or on the third harmonics of 108 MHz. The latter one offers a higher resolution, but the measurable bunch length is restricted to about a phase 20° of the ground rf, i.e. to about 1.5 ns.

The deflectors are built as λ/4 resonators and a power input of about 10 W is sufficient for the required transverse deflection. After a flight length of 670 mm the single electrons are amplified by a Chevron MCP-phosphor combination and monitored by a digital CCD camera.

Systematic test measurements with this new device were performed at 11.4 MeV/u for several ion beams. A typical raw image of the bunch as seen by the CCD camera is shown in Fig. 10. The deflection with a frequency of 108 MHz is displayed horizontally. The projection of the light intensity on this axis gives the bunch shape. This measurement proves the general functionality of this novel device, where short bunches of σ = 125 ps had been monitored. It is required to subtract a homogeneous distributed background. This is probably due to X-rays from secondary electrons accelerated by the electric field and hitting the stainless steel plate of the electric field box. A 5 mm thick steel shielding behind the energy analyzer will be installed in the near future to absorb these X-rays (maximum energy 30 keV), thus leading to a strong background reduction by a factor of at least 100. After this modification, a nearly background-free measurement is expected, which will allow single macro-pulse monitoring. The displayed measurement had been performed with a low current 60 µA Au^{25+} beam. If the amount of secondary electrons does not result in a sufficient statistics, the vacuum pressure can be raised by a regulated gas inlet system. It has been proved, that a local pressure bump up to 10^{-4} mbar in the transfer lines does not influence the beam properties. Due to the statistical nature, averaging also improves the signal-to-noise ratio leading to a large dynamic range.

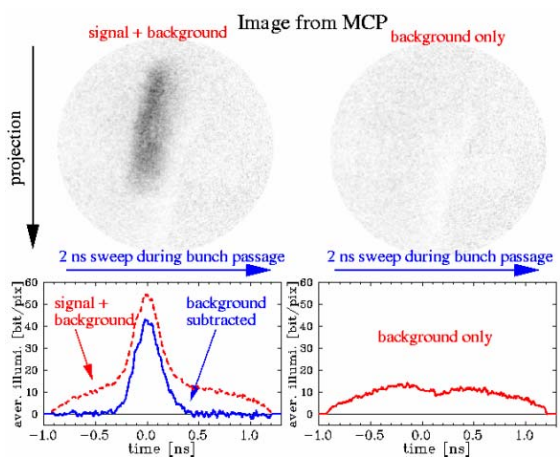

Figure 10: Typical image (inverted colour) from the MCP for a 60 µA Au^{25+} beam averaged over 16 macro-pulses with 1 ms. The background is displayed on the right.

The longitudinal emittance can be estimated by varying the voltage amplitude of a buncher cavity and measuring the bunch width. This corresponds to the quadruple variation for the transverse case. The orientation and absolute value of the emittance is yielded by fitting a parabola through the square of the bunch width. This is shown in Fig. 11. For a high current, 2 mA Ni^{14+} beam only 4 macro-pulses of 0.2 ms duration were averaged. Due to the nature of the fitting procedure, the error is relatively large, but it offers a simple method of emittance estimation.

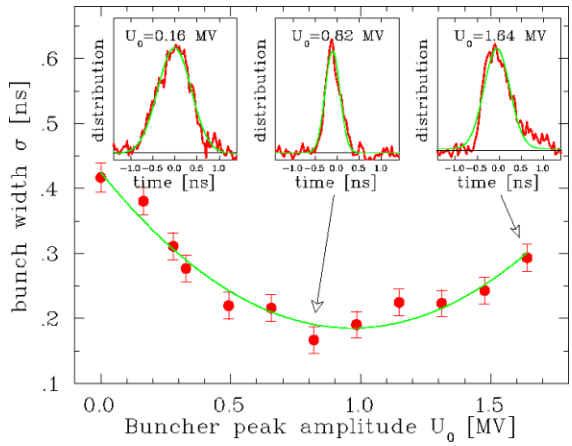

Figure 11: Measurement of the bunch width (one standard deviation) as a function of the buncher voltage 31 m upstream to the detector performed with a 2 mA Ni^{14+} beam.

The trajectories of the secondary electrons are influenced by the space charge of the high intensity beam. This influence is larger as for the wire based method, because in the latter case the electric field is much stronger close to the biased wire as compared to the homogeneous field of the non-interfering method. A numerical analysis is required to estimate the beam current and bunch length, where the electron trajectories are deformed significantly, resulting in a misleading signal reading. For the high current operation at the UNILAC, the influence is tolerable, as the calculations reported in [15] have shown.

REFERENCES

[1] A.Peters et al., DIPAC 2001, Grenoble, p. 123
[2] M.Kesselman, PAC 2001, Chicago, p. 2323
[3] www.bergoz.com
[4] M.Kesselman, NIM A, 2004, in press
[5] H. Reeg, GSI, priv. comm.
[6] R.H. Hughes et al., Phys. Rev. 123, 2048 (1961).
[7] D.P.Sandoval et al., BIW 1994, AIP 319, p. 273
[8] J.D. Gilpatrick, LHC Emittance and Profile-Measurement Workshop, CERN, July 2000
[9] P. Ausset et al., EPAC 2002, p. 1840 (2002)
[10] www.proxitronic.de
[11] P.Forck, A.Bank, EPAC 2002, Paris, p.1885 and DIPAC 2003, Mainz, p. 137
[12] D. Anderson, FireWire architecture: 1394a, www.mindsharing.com, Addison-Wesley, 1999
[13] A.Feschenko, PAC 2001, Chicago, p. 517 and references therein
[14] N.Y. Vinogradov et al., NIM A 526, p. 206, 2004
[15] P.Forck et al., EPAC 2004, Lucerne, to be published

STATUS OF REX-ISOLDE*

O. Kester#, D. Habs, S. Emhofer, K. Rudolph, LMU München, 85748 Garching, Germany
T. Sieber, F. Wenander, F. Ames, P. Delahaye, M. Lindroos, P. Butler, CERN, Geneva, Switzerland
R. von Hahn, H. Scheit, R. Repnow, D. Schwalm, MPI-K, Heidelberg, Germany
and the REX-ISOLDE collaboration

Abstract

After commissioning of the radioactive beam experiment at ISOLDE (REX-ISOLDE) and the ν-Detector array MINIBALL first series of physics experiments have been performed in 2002 and 2003. The REX-ISOLDE charge state breeder adjusts the charge-to-mass ratio of isotopes from the whole nuclear chart to the LINAC requirements. A variety of isotopes from different mass regions of the nuclear chart have been charge bred with REXEBIS [1] to the required A/q < 4.5. A variety of tests with REXTRAP, REXEBIS and the LINAC structures have been done, in order to study the beam parameters, transmission efficiency and upgrade options. The LINAC now consists of six resonators and one re-buncher cavity. The beam energy, which can be delivered towards the target areas, can be varied between 0.8 and 2.2. An additional boost to 3 MeV/u is now possible because of the upgrade with a 202.56 MHz IH-cavity developed for the MAFF project. In addition beams from the RFQ at 0.3 MeV/u have been used for solid state physics experiments. The present status of the projects and the commissioning measurements will be presented.

INTRODUCTION

Radioactive ion beam (RIB) facilities give rich opportunities for nuclear structure research as well as for nuclear astrophysics and applied physics. RIB facilities drive the increasing understanding of the evolution of nuclear structure and the growing wealth of nuclear structure data. As yet only relatively small part of the nuclear landscape has been explored, especially on the neutron-rich side where the limit of stable nuclei is only known for the lightest elements. The European nuclear physics community, represented by NuPECC, has identified the need for a second generation of Radioactive Ion Beam (RIB) facilities in Europe. The design of such a second generation RIB facility, based on the ISOL technique, has been investigated, under the auspices of the EU Fifth Framework as the RTD proposal EURISOL [2]. Therefore huge effort is spent on extrapolation from running RIB facilities and present techniques towards those new intense ISOL facilities like EURISOL or RIA [3]. Running ISOL facilities in Europe that provide post accelerated RIBs for nuclear physics experiments are ARENAS (Leuven), ISOLDE (CERN) and SPIRAL (GANIL). Preparation work for future facilities is carried out by those facilities, which is important for the EURISOL design study.

*supported by BMBF under contract number 06 ML 185, 06 ML 186 I and 06 ML 188.
#oliver.kester@physik.uni-muenchen.de

The Radioactive Beam Experiment at ISOLDE, REX-ISOLDE, delivers post accelerated beams of exotic isotopes for nuclear physics research and it has been the dominant experiment in the past two ISOLDE running periods [4]. REX-ISOLDE profits from the vast experience of ISOLDE in production of radioactive beams of more than 600 isotopes from 72 elements. In addition the resonant ionisation laser ion source (RILIS) can provide beams with high selectivity, even isomeric beams. Since end of 2001 the LINAC provides radioactive beams from the ISOLDE online separators with energies of 2.2 MeV/u towards two target stations. One target station is used for the efficient ν-ray MINIBALL array [5] and the other target station is dedicated for smaller experimental set-ups. In order to make the full variety of beams from ISOLDE available for nuclear physics experiments the method of charge breeding of the singly charged radioactive ions has been employed [1]. Hence the concept of REX-ISOLDE is based on a large Penning trap which accumulates the radioactive ions from the ISOLDE mass separators and allows phase space cooling of the RIBs. The prepared ions are then injected into an Electron Beam Ion Source (EBIS), which raises the charge state of the radioactive ion to an A/q < 4.5. The extracted highly charged ions are charge state selected with subsequent acceleration in a short LINAC

THE LOW ENERGY SYSTEM

The low energy part of REX-ISOLDE has several tasks. The low energy part transports the 60 keV beam from the ISOLDE main beam line towards the accelerator and prepares the ion beam for injection into the LINAC. The size of the post-accelerator needed to bring the unstable nuclei to the energies required to study nuclear reactions depends linear on the charge state of the radioactive ions. The capability to raise the charge state of the radioactive ions before injection into an accelerator leads to an enormous reduction of construction and running costs of the accelerator and of the infrastructure. In addition it allows in principle to accelerate ions from all regions of the nuclear chart to the same energy per mass unit.

The principal scheme of the charge multiplication (charge breeding) in case of REX-ISOLDE is shown in fig.1. An EBIS delivers high charge states and is employed as breeder for the radioactive isotopes at REX-ISOLDE. The ISOLDE beam can not be injected into the Electron Beam Ion Source (EBIS) with high efficiency without any beam preparation, because of the small

transverse acceptance of the electron beam confining the injected ions. Thus an beam emittance cooler was required for beam preparation at REX-ISOLDE. A large Penning trap, the REXTRAP [6], was therefore installed in front of the REXEBIS. It accumulates, bunches and phase space cools the continuous ISOL-beam within 10-20 ms the beam from ISOLDE. Bunches of 10 σs length and transverse emittance of 10 mm·mrad for 80% at 30 keV are extracted from the trap. A considerably higher injection and trapping efficiency into the EBIS is obtained compared with beam emittances up to 30 mm·mrad (at 60 kV) from the ISOLDE target ion source. The extracted pulse is transferred to the EBIS via a transport line, and because of the buffer gas pressure (~10^{-3} mbar of Ne or Ar), several stages of differential pumping have to be inserted into the transport line to ensure a high vacuum inside the EBIS.

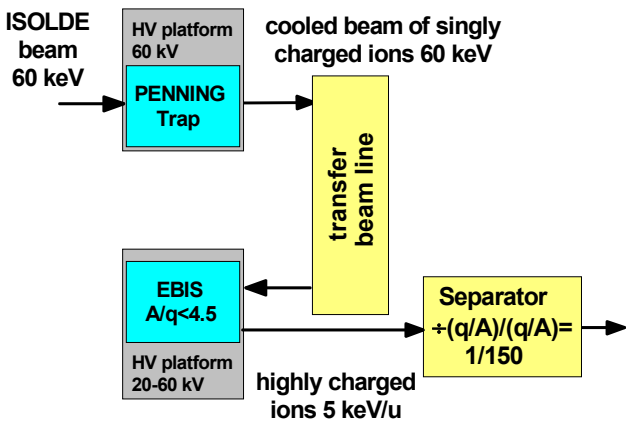

Figure 1: Schematics of the REX-ISOLDE low energy system.

The operation parameters of REXTRAP and REXEBIS are summarized in table 1. An offline ion source for injection of stable alkaline isotopes into REXTRAP is available for tuning of the low energy system of REX-ISOLDE. All elements except for He can be handled by the trap with transmission efficiencies up to 45%. Space charge effects start occurring for more than 10^5 ions per pulse, with an efficiency decrease and emittance increase [7]. At present the Penning trap-EBIS concept has a limited ion throughput of ~10^8 ions/s. Because of the pulsed beam injection into the EBIS, its platform-potential can be ramped between injection and extraction and thereby the potential of the ISOL production part is decoupled from the injection. In addition the injection energy into the RFQ can be adjusted according to the chosen A/q-value. Within the past running periods of ISOLDE, a variety of nuclides has been charge bred, as shown in table 2. Stable ions have been used for pilot beams to tune the accelerator and to test the breeding capabilities of the REX-ISOLDE charge state breeder. High currents of several nA of He^+ from the EBIS were used for intensive studies of the beam dynamics of the accelerator structures.

Table 1: Operation parameter of REXTRAP and REXEBIS

REXTRAP	
magnetic field	3 T
buffer gas pressure	10^{-2}-10^{-4} mbar
cycle time	10-20 ms
trap length	0.9 m
mass resolution	~ 300
REXEBIS	
magnetic field	2 T
electron current	200-300 mA
electron beam energy	4-5 keV
confinement length	0.8 m
max. current density	150-200 A/cm^2

To prepare for the energy upgrade of the LINAC, heavier elements have been charge bred in REXEBIS, because with the energy upgrade experiments with heavier isotopes become possible. With Caesium the charge state 32 could be produced as the maximum of the charge distribution using an extended breeding time of 160 ms. Radioactive ions from $^{9}Li^{2+}$ to $^{156}Eu^{28+}$, have been delivered to experiments at MINIBALL and the second beam line. In addition $^{138}Ba^{26+}$ and $^{153}Sm^{28+}$ have been produced using breeding times of 18 ms and 38 ms respectively. The Samarium and Europium ions (A/q = 5.46) have been accelerated in the RFQ for ion implantation into Silicon Carbide as radiotracers.

Table 2: Isotopes that have been charge bred in the REX-ISOLDE charge state breeder

Stable	Radioactive
$^{7}Li^{2+}$	$^{9}Li^{2+}$, $^{11}Li^{3+}$
$^{23}Na^{7+}$	$^{24\text{-}29}Na^{7+}$
$^{27}Al^{8+}$	
$^{24}Mg^{8+}$	$^{30}Mg^{8+}$
$^{39}K^{10+}$	
	$^{74,76}Zn^{18+}$
$^{84}Kr^{20+}$	$^{88}Kr^{21+}$
$^{133}Cs^{32+}$	
$^{138}Ba^{26+}$	
	$^{153}Sm^{28+}$
	$^{156}Eu^{28+}$

The efficiency of the breeding system of interest is the ratio between the number of ions injected into the RFQ and the number of ions injected into the Penning trap. The trap efficiency does not exceed 50% and is somehow the bottleneck of the system. For high intensities (>10^5 ions/s) the efficiency drops down to 4%, dependent on the species and the intensity. Therefore the rotating wall cooling method [8] is under study to be applied for REXTRAP. The transmission from trap to EBIS is about 90%. The mass separator transmission is about 80%. The maximum ratio of ions in one charge state for light ions, if no charge state at shell closure is selected, is about 30%. This should give 20% efficiency in one charge state. Until now the efficiency after the trap to the analyser

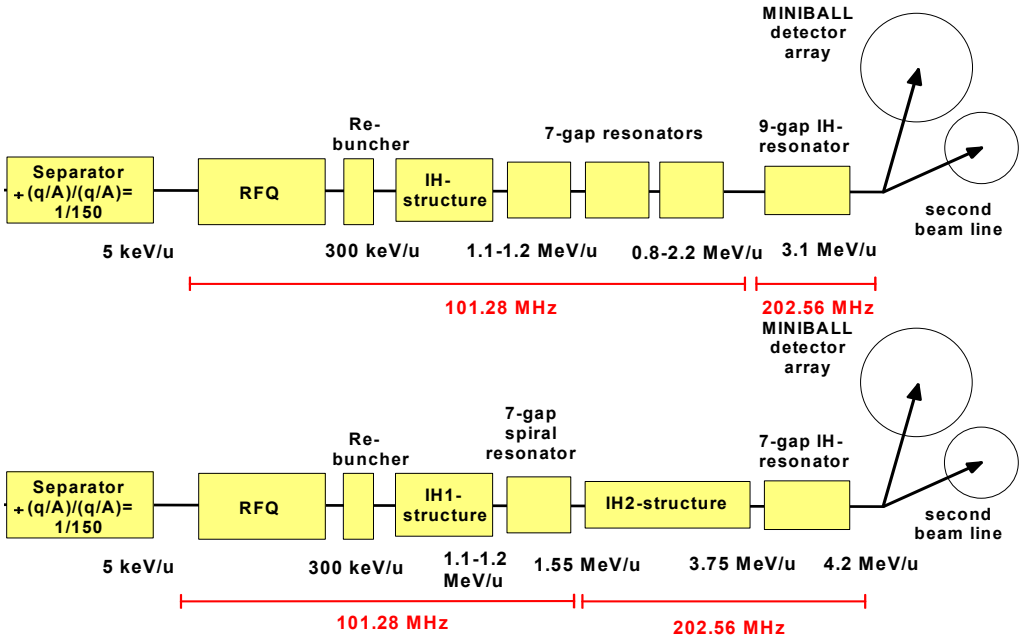

Figure 2: Schematic of the present REX-ISOLDE LINAC structure (upper panel) and of the planned upgrade to energies above 4 MeV/u (lower panel).

magnet is 5-10%. At higher intensities the efficiency can drop to as low as 2% due to space charge effects in REXTRAP. To this value the trap efficiency of ~45% should be included. Thus the injection and trapping efficiency in REXEBIS is only 30-50%. The injection efficiency can be improved by using a partially compensated electron beam as Coulomb target [9], which will be explored in the EURONS project within the EU 6th framework programme. However the charge state breeder is a major component for the success of the REX-ISOLDE experimental programme.

THE REX-ISOLDE LINAC

The linear accelerator of REX-ISOLDE is composed of modern ion accelerator structures. A 4-rod RFQ and an IH-DTL accelerate the ions to an intermediate energy of 1.2 MeV/u where they are further accelerated or decelerated by three 7-gap resonators of the split ring type. All structures operate at 101.28 MHz, which is half of the CERN proton LINAC frequency. One 202.56 MHz IH-cavity with nine gaps has been added in order to boost the energy to 3 MeV/u. The cavity is shown in fig.3. The maximum duty cycle of the cavities is 10%, the typical duty factor at operation is 5%. The maximum A/q of the ions can be 4.5. The linac composition is sketched in Fig.2. The actual beam and rf parameter of the structures are summarized in table 3. The acceptance of the cavities is calculated for 95% transmission.

The macrostructure of the accelerated ions have a typical bunch width of 15-50 σs, whereby a slower EBIS extraction (500 σs) is possible, but not yet in use. The time span between the macro pulses is 20 ms for the light ions with A < 50 and 40-100 ms for heavier ions. The beam quality in front of the linac has been analysed via emittance measurements close to the mass slit of the separator. The LINAC tune has been examined via energy spectra taken from each cavity.

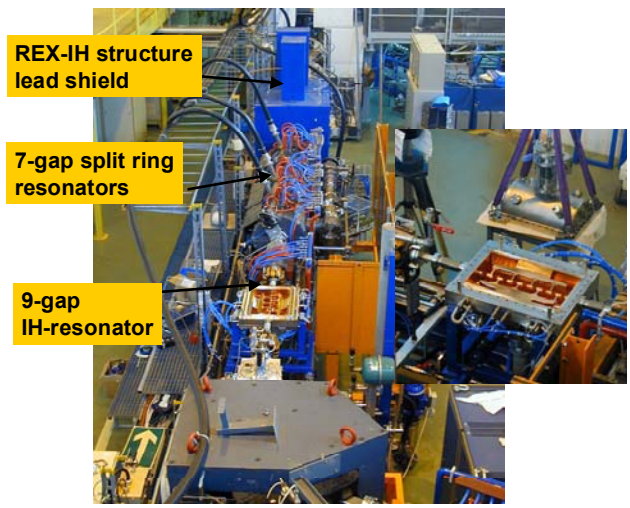

Figure 3: Picture of the REX-ISOLDE LINAC in its present set-up including the 9-gap IH-structure.

Two EBIS operation modes have been tested, one with highly charged ions from residual gas and one using He-ions to reach higher beam currents needed for emittance measurements of the linac at higher energies. The geometrical emittance of the REXEBIS has been measured as ~10 mm·mrad (95%) for highly charged ions at 20 kV extraction voltage, which corresponds to 5 keV/u. The value of the emittance is dependent on the ion neutralization of the electron beam and on the ion species, especially the mass. Fig. 4 shows emittance measurements of the EBIS beam behind the A/q-separator mass slit for different degrees of compensation and for different ion species. For emittance measurements of the

LINAC beam, a beam intensity of several nA was required. Therefore He-gas has been injected into the EBIS and the electron beam has been neutralized. For such increased compensation level with low charged ions like He^+, the emittance amounts to 35-70 mm·mrad (0.11-0.23 mm mrad normalized). For operation with radioactive beam the emittance correspond to the measured EBIS emittance of 10 mm mrad.

Table 3: Measured beam parameter of the REX-ISOLDE LINAC structures

	RFQ	Buncher	IH	7-gap	9-gap IH
f_{inject}# [MeV/u]#	0.005	0.3	0.3	1.1-1.2	2.25
η_{inject}#	0.0033	0.0254	0.0254	0.049-0.051	0.069
f_{exit}# [MeV/u]#	0.3	0.3	1.1-1.2	0.85-2.3	2.9-3.0
$\eta_{extract}$#	0.0254	0.0254	0.049-0.051	0.043-0.07	0.079
$\zeta_{xx'}$, ζ^n [mmmrad]	200 (0.66)	---	25.3 (0.643)	40 (2)	20 (1.4)
$\zeta_{yy'}$, ζ^n [mmmrad]	200 (0.66)	---	25 (0.636)	52 (2.55)	20 (1.4)
Q	3400	3500	16200	5370	10100
R_p, Z_{eff} kT m, MT /m	146	20	215	60	165

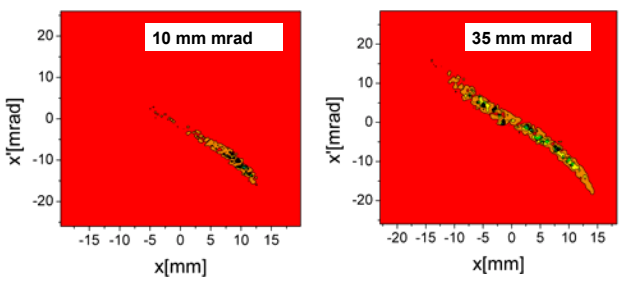

Figure 4: Right: Typical EBIS emittances of 10 ϕ mm mrad for highly charged ions from REXEBIS. Left: The electron beam has been neutralized with light ions (He).

The past two running periods commissioning measurements have been carried out with the LINAC structures in order to improve the beam quality especially the energy spread of the beam [10]. The commissioning measurements comprise scans of the beam energy spread and emittance measurements of the different structures. Due to the very low intensities from the REXEBIS, bunch length measurements could not be performed so far. Therefore the longitudinal emittance of the beam from the different cavities has been calculated and the energy spreads have been determined. The phases have been adjusted in two steps. First the beam energy has been maximized for given amplitude, to define the 0°-synchronous phase. Then the required phase according to the design calculations has been set and the energy spectrum has been measured and compared with calculated values. The energy measurements of the IH-structure have been presented in [10]. As an example of additional energy measurement the beam energy spectrum from the first 7-gap resonator at 1.55 MeV/u is shown in fig.5. The beam energy spreads of all cavities are summarized in table 4 for the settings of the 2.9 MeV/u accelerator tune. The measured values are in good agreement to the design values of the simulation calculation. The discrepancy results mainly from the tune of the re-buncher cavity.

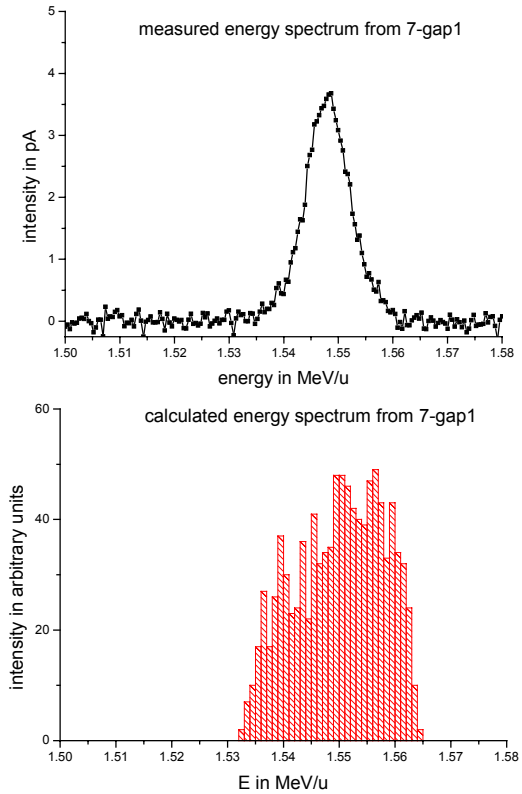

Figure 5: Comparison of the measured and calculated energy-spectra of the first 7-gap resonator.

Table 4: Measured and calculated energy spread of the beam from the different LINAC structures. The phase are adjusted for 2.9 MeV/u final energy

	phase	E-spread calculated [%]	E-spread measured [%]
RFQ	--	±1.5	±1.4
Buncher#	-90°	±3.2	±3.0
IH#	0°	±1.0	±0.85
>-gap1#	-20°	±1.1	±0.75
>-gap2	-20°	±0.8	±0.7
>-gap3	-20°	±0.7	±0.65
9-gap IH	0°	±0.5	±0.65

In addition transverse emittances from different cavities of the front part of the REX-ISOLDE LINAC have been determined in order to evaluate the transverse emittance growth. In fig.6 the emittance of the IH-structure is shown. The injected normalized emittance has been 0.26

mm mrad and 0.2 mm mrad respectively. The normalized emittance from the IH-structure is 0.29 and 0.21 mm mrad respectively. Thus an emittance growth of about 10% occurs in the IH-cavity. The difficulties of the emittance measurements are the very low beam intensity of about 1nA, which is the limit of the Munich emittance meter. In addition the angular resolution has been only 0.5 mrad, which put large error bars on the measured values of 20%, which is in the range of the emittance growth.

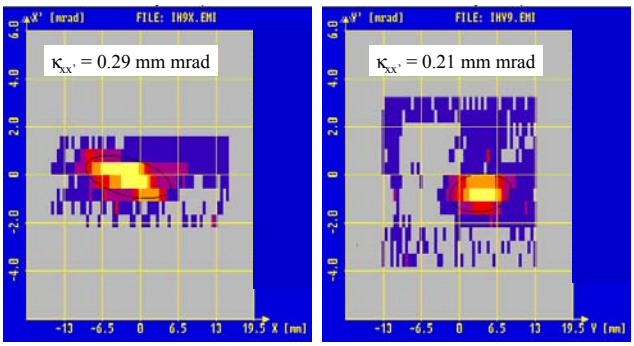

Figure 6: Normalized emittances from the IH-structure. A 1nA He^+-beam has been used for the measurements.

The emittances of the IH-structures and the 7-gap split-ring structures cavities will be measured before the next shut down period, with higher angular resolution. However the beam measurements reveal the proper tune of the LINAC for energies above 2.2 MeV/u and a small emittance growth so far, which corresponds to the small spot size at the MINBALL target position.

FURTHER UPGRADE PLANS

To use the full range of isotopes from ISOLDE for nuclear physics experiments with Coulomb excitation and transfer reactions, higher beam energies are required. An increased energy of 3 MeV/u allows studies of nuclear reactions up to mass A=85 on deuterium targets. An even higher beam energy above 4 MeV/u would be suitable up to mass A=145. Therefore a study of a further energy upgrade of the REX-ISOLDE LINAC has been launched. A major change of the LINAC structure will be required in order to reach energies of approximately 4.2 MeV/u and beyond. The proposed structure is sketched in fig.2. Thus two of the 7-gap spiral resonators with 101.28 MHz resonance frequency have to be replaced by a 1.5 m IH-cavity with 202.56 MHz resonance frequency to boost the energy to required region of 3.75 MeV/u. Then a 7-gap IH-resonator of the MAFF type cavity can be used to accelerate to final energies above 4 MeV/u.

The first 7-gap split ring structure will be used to prepare the beam for injection into the 28 gap 202.56 MHz IH-structure. The synchronous phase of the 7-gap resonator will be adjusted to -20^o, which allows a exit energy of 1.53 MeV/u and a phase spread of $\pm 10^o$ at the entrance of the 202.56 MHz structure. The cavity will boost the energy to 3.75 MeV/u which requires 10.14 MV effective acceleration voltage for ions with A/q = 4.5. With an effective shunt impedance of 180 MT/m, which is feasible for such cavities, an rf-power of 380 kW would be require. Results from beam dynamics calculation with LORASR are shown in fig. 7 concerning the development of the longitudinal phase space. A phase spread of $\pm 8^o$ and an energy spread of ±0.6% and a small emittance growth of 10% will be expected for the 3.75 MeV/u beam. The beam energy can be varied in the range of ±0.5 MeV/u via the 202.56 MHz 7-gap resonator of the MAFF type, which presently serves as 9-gap booster cavity at REX-ISOLDE.

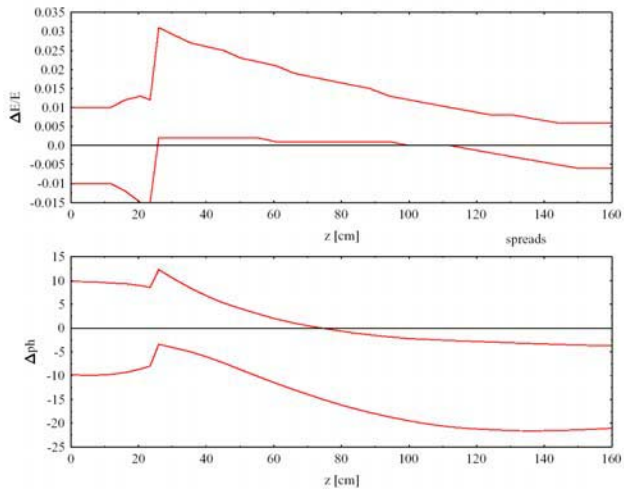

Figure 7: Development of phase and energy spread in the 28 gap 202.56 MHz IH-cavity for the energy upgrade above 4 MeV/u.

REFERENCES

[1] F. Wenander, Proc. of the RNB6, ANL, Chicago, USA, Sept. 2003, accepted for publication in Nucl. Phys. A
[2] http://www.ganil.fr/eurisol/index.html
[3] RIA white paper: http://www.sc.doe.gov/production/henp/np/projects/docs/ria-whitepaper-2000.pdf
[4] O. Kester and D. Habs, Nuclear Physics News 13, No.3 (2003) p.25
[5] J. Eberth et al., Prog. in Part. and Nucl. Phys. 48 (2001) 389.
[6] P. Schmidt, Nucl. Phys. A701, (2002) 550c
[7] F. Ames et al., Hyperfine Int. 132 (2001) 469-472
[8] K. Reisinger, "Emittance measurements on the sideband cooling technique and introduction of the rotating wall cooling technique at REXTRAP", Diploma thesis, TU München, July 2002
[9] R. Becker and O. Kester, "The EBIS/T as a Coulomb Target for Ions", EBIS/T 2004, Tokyo, Japan, 2004, to be published in AIP conference proceedings.
[10] S. Emhofer et al., "Commissioning results of the REX-ISOLDE LINAC", PAC'2003, Portland, Oregon, USA, May 2003, p.2872
[11] O. Kester et al., "An energy upgrade of the REX-ISOLDE LINAC", PAC'2003, Portland, Oregon, USA, May 2003, p.2869

SPIRAL2 AT GANIL

M.-H. Moscatello for the Spiral2 Project Group, GANIL-CEA/CNRS, Caen, FRANCE

ABSTRACT

The SPIRAL2 project has been under detailed design study since beginning of 2003. The aim of this facility is to produce rare ion beams, using a Uranium carbide target fission process, based on a fission rate of 10^{13} to 10^{14} fissions/s.

The driver accelerator accelerates a 5 mA deuteron beam up to 20 MeV/u, impinging on a carbon converter to produce the neutrons necessary to the fission process. It has also to accelerate q/A=1/3 heavy ions, to energies between 0.75 and 14.5 MeV/A for different types of nuclear and non-nuclear physics experiments.

The accelerator is based on a RFQ followed by an independently phased superconducting cavity linac with warm focusing sections.

This paper presents the reference design chosen for the SPIRAL2 driver accelerator, and gives the design status of the different components: Sources, RFQ, Superconducting linac, RF Systems, Cryogenics, Mechanical layout.

INTRODUCTION

The Spiral2 project is originally based on the LINAG1 conceptual design [1], that proposed a facility aiming at delivering high intensity radioactive beams produced by different methods (fission of uranium target via a carbon converter, direct target irradiation), as well as high intensity stable ion beams.

Since the creation of the Spiral2 project group at the beginning of 2003, many detailed studies have been undertaken [2], and have led now to new solutions and technical choices for the accelerator design as well as for the target ion source system and radioactive beam transport lines.

SPIRAL2 GENERAL LAYOUT

The facility consists of a linac driver able to accelerate a 5mA deuteron beam up to 20A.MeV as well as light ion (q/A=1/3), 1mA beams up to 14.5 A.MeV. The deuteron beam impinges on a carbon converter to produce neutrons, used then in the fission process of a uranium carbide for the production of radioactive ion beams (RIB). Theses fission products, extracted from a source, are transported towards a charge breeder, and accelerated by the existing CIME cyclotron to maximum energies between 5 and 10 A.MeV, according to the ion q/A ratio. The stable ion beams can be used also for the production of RIBS on different target types, or sent directly towards an experimental cave, for nuclear physics experiments. Fig.1 shows a schematic layout of the planned facility.

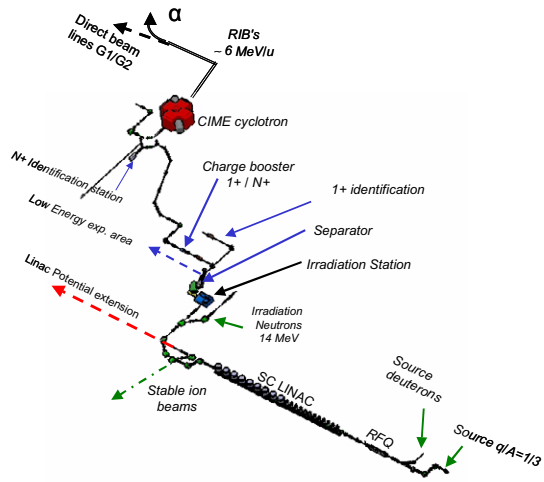

Figure 1: Spiral2 facility schematic layout

THE LINAC ACCELERATOR

Linac Main Specifications and Parameters

The accelerator has been designed with the following main specifications:

- CW accelerator.
- 0.15–5 mA of, 40-MeV deuterons.
- Up to 1 mA (Argon) for q/A=1/3 ions, 14.5 MeV/u.
- Two ion sources, one for the deuterons, the other one for the ions q/A=1/3.
- Normal conducting RFQ injector designed for both D^+ and q/A=1/3 ions.
- Optimisation of the accelerator for 1mA q/A=1/3 ion beams, with the capability of accelerating a 5 mA deuteron beam to the required energy.
- Possibility for the SC linac to accelerate ion beams of q/A=1/6 (up to 1 mA) in the future, and to be extended towards higher energies.
- Maximum energy gain for each kind of ion, which implies independently phased cavities.

A principle layout of the accelerator is presented in fig.2.

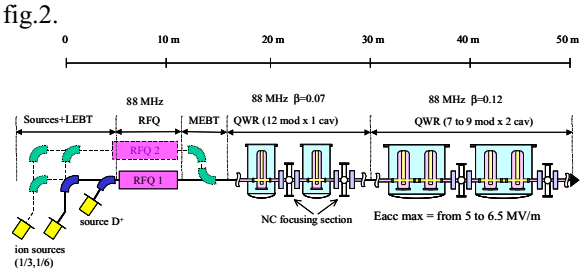

Figure 2: Principle layout of the accelerator

Detailed beam dynamics studies have led to the final frequency choice of 88.05 MHz for the whole

accelerator, and 2 beta QWR families for the superconducting linac: β=0.07 and β=0.12, for the following reasons:

- The RFQ and QWR beam apertures are larger, and lead thus to a higher acceptance.
- In the superconducting linac, the cavity number is highly reduced in the high beta family, compared to a 176 MHz solution, thanks to an approximately twice longer accelerating gap.
- concerning the RFQ, even if the cavity is bigger, the thermal problems and power consumption are minimized.

Beam Dynamics

Beam dynamics calculation have been performed with several different multi-particle codes, including beam space charge [3], and have led to an almost frozen design:

- A Low Energy Beam Transport (LEBT) line which allows to inject D^+ and q/A=1/3 ions from 2 different sources inside the RFQ.
- A RFQ that bunches and accelerates beams up to 0.75 A.MeV.
- A Medium Energy Beam Transport (MEBT) line that allows the insertion of a q/A=1/6 injector for a possible upgrade, as well as a possible high frequency chopper (for physics needs).
- A superconducting linac with minimum technical risks (warm conducting sections, short cryostats, numerous diagnostics).
- A High Energy Beam Transport (HEBT) line that distributes beams towards the production caves (with a uniformisation of the beam density), as well as towards stable ion experimental areas.

Emittances considered for all the calculations are:

- $\varepsilon_{rms,norm}$=0.4 π.mm.mrad for q/A=1/3
- $\varepsilon_{rms,norm}$=0.2 π.mm.mrad for D^+ beams

These values should ensure a rather large acceptance compared to beam emittance that have been measured with D^+ and ion beams up to now.

Start-to-end simulations of the whole linac have been performed [4], considering a Gaussian distribution truncated at 4σ at the source extraction (fig.3).

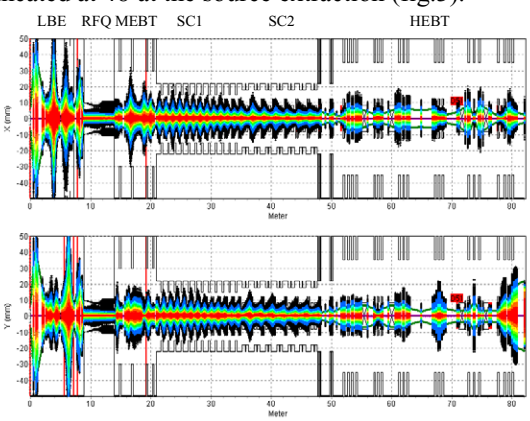

Figure 3. Start-to-end simulation with a 5mA, 0.2 π.mm.mrad, D^+ beam, without errors

Statistic error have then been introduced in the start-to-end simulations. The following static error values have been considered for the various accelerator components:

- RFQ: ±0.05mm for machining defects, and ±0.1 mm for segment positioning in various directions.
- Magnets: ±0.1mm for positioning and around 0.05° for rotations, ±1% for gradients.
- Superconducting cavities: ±1mm for positioning and ±0.3° for rotations, ±1° for field phase and ±1% for field amplitude.

They are corrected with various steerers, and using various beam profile and beam position monitors. Some dynamics errors, that cannot be corrected, have also been considered. The QWR steering effect is not compensated, neither with the cavity shape, nor with a cavity vertical displacement, but is just corrected by magnetic steerers.

The losses can be concentrated in localised points inside the LEBT and MEBT, with the use of scrappers that cut a few percent of beam, as presented on fig.4.

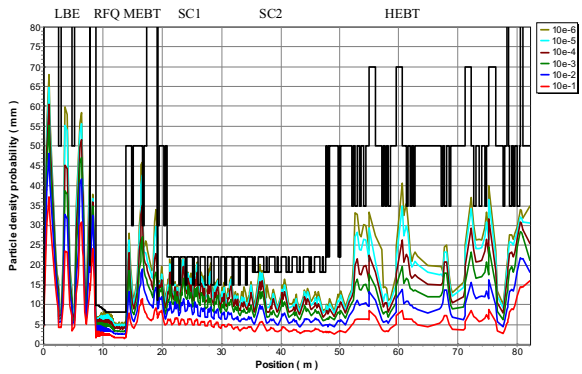

Figure 4: Loss distribution along the accelerator with a 100% error combination for D^+ beam

The next step will consist in performing these calculations with measured beam distributions and emittances, for both D^+ and q/A=1/3.

Calculations have also been performed with a faulty cavity, and show that beams can be accelerated with good characteristics, wherever it is situated.

Deuteron and Ion Sources

The deuteron source under study is of SILHI type, running at 2.45GHz and including a modified magnetic structure, with permanent magnets [5]. The 5mA beam is extracted at a 40kV voltage, and must fit an rms normalized emittance lower than 0.2 π.mm.mrad. Some preliminary emittance measurements have been performed, showing that the source should be well inside the emittance requirements (fig.4).

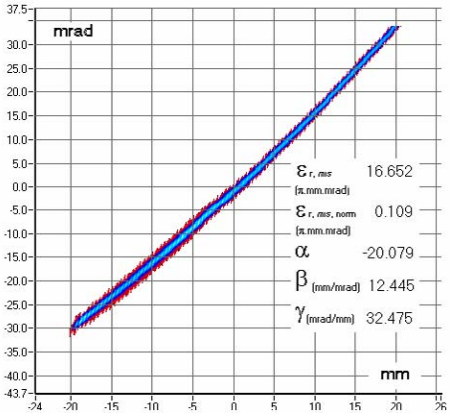

Figure 4: 4.2mA deuteron beam measured emittance with SILHI like source

The q/A=1/3 ion source under study is a A-Phoenix type, running at 28 GHz and using high remanence magnet as well as high temperature superconducting (HTC) coils for the magnetic structure [6].
Preliminary emittance measurements have been performed on the existing 28GHz PHOENIX source, with a 1mA $^{16}O^{6+}$ beam, extracted at 60kV (fig.5).

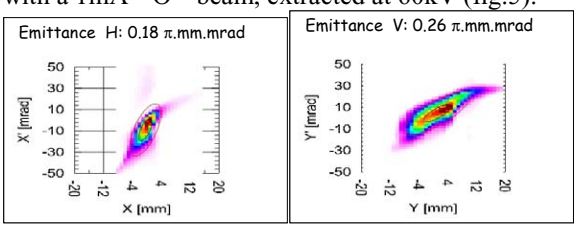

Figure 5: Emmitance measurements on the LPSC PHOENIX source 1mA $^{16}O^{6+}$ beam

The next step will be to perform emittance measurements with a 1mA $^{36}Ar^{12+}$ beam, with a preliminary version of the A-PHOENIX source, in the next weeks.

RFQ

Preliminary studies were performed for different types of cavities (4-vanes, 4-rods, skirt-RFQ,…), and the final choice has been made in favour of a 4-vane structure, without any brazing and based on a mechanical assembly [7]. The main parameters of this RFQ are presented in Table 1.

Table 1: RFQ main parameters

Parameter	*Value*
Length	5.077m
Mean aperture R_0	8.1 – 10.0 mm
Vane voltage	100 – 113 kV
Modulation	1 – 1.99
Input rms emittance (π.mm.mrad)	0.2 (D^+) / 0.4 (1/3)
Transverse emittance growth	0
Peak electric field	1.65 kp
Transmission w/o errors	>99.9%
Transmission with errors	99.87%
Input energy	20 keV/u
Output energy	0.75 MeV/u

A 1meter prototype module has been built (fig.6), and will be tested at full power in INFN-LNS (Catania) at the beginning of September, before the final design of the complete RFQ.

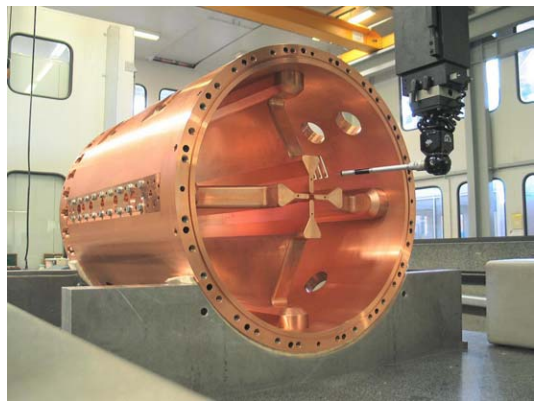

Figure 6: RFQ prototype 1 meter module

Superconducting Linac

Several designs have been initially studied, with beam dynamics and RF considerations, assuming a 1 frequency (88 MHz) or 2 frequency linac (88 and 176 MHz), QWR and HWR for the different cavity families, superconducting solenoids or normal conducting quadrupoles for beam focusing, long or short cryostats. The final design has been frozen with the following parameters:

- 1 frequency machine: 88.05 MHz
- 2 β QWR families: 0.07 and 0.12, with a transition β of 0.11.
- normal conducting Qpoles for focusing
- short cryostats: 1 per cavity in the low beta part, and 1 for 2 cavities in the high beta part.

It appears to be safer from a technological point of view (simpler cryostats and alignments) and from the beam tuning point of view (one diagnostic box every cryostat), the acceptance, even if lower, being increased in the high beta family by a larger aperture of the cavity beam drift tubes. The beam dynamics calculations showed it was not necessary to tilt the accelerating gap walls in order to compensate the steering effect of the QWRs: it is corrected by the steerers placed inside the quadrupoles.
The QWRs have been designed in order to reach accelerating fields of 6.5MV/m in operation [8,9]. In the low beta family, among the 12 necessary cavities, only the 3 last cavities are tuned at the maximum accelerating field (for longitudinal phase advance reasons), and in the high beta part of the linac, beyond the 7 cryomodules, each of them containing 2 cavities, 2 spare cryomodules are planned to be installed if necessary (which would allow a maximum accelerating field of 5MV/m in that case).
The main parameters of the 2 β cavities are summarized in table 2.

Table 2: main parameters of the 2 QWRs

Optimal β	0.070	0.12
E_{peak}/E_{acc}	5.00	5.54
B_{peak}/E_{acc} (mT/MV/m)	8.75	10.1
R_s/Q (Ω)	632	520
Quality factor Q_0	$2.2\ 10^9$	$1.7.10^9$
Cavity losses (@ E_{acc}=6,5 MV/m) (W)	1.75	8.2
Gasket losses (@ E_{acc}=6,5 MV/m) (mW)	26	-

The expected accelerating field in operation (6.5 MV/m) relies on: the choice of a high quality Niobium RRR250, a high quality electron beam welding, a high quality chemical etching and high pressure rinsing with high purity water. Two prototypes are under construction, one for each type of cavity, and the tests should be performed in November 2004 (fig.7).

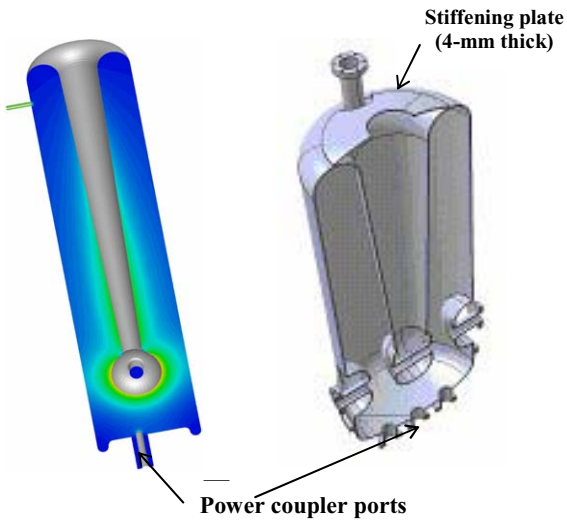

Figure 7: views of low beta (0.07) and high beta (0.12) SC linac QWR

The power coupler is under design [9], and is planned to be the same for both cavities, except the antenna penetration length. The beam load ranges from 1 kW to 13 kW, depending on the cavity position and beam intensity. Two types of ceramic windows are under design, disc and cylinder, and both prototypes are about to be constructed and will be tested at the beginning of 2005. The model with a ceramic disc window is presented in fig. 8.

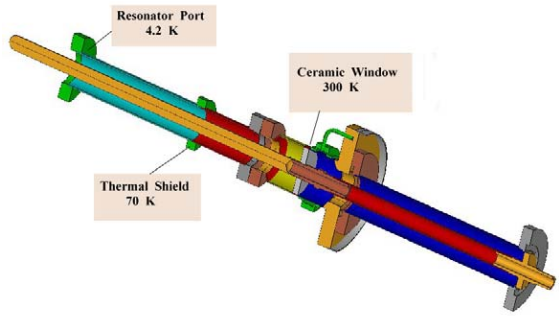

Figure 8: power coupler with ceramic disk window

For the cryostats, the choice was made to have small and simple cryostats (1 or 2 cavities), for technological and maintenance reasons. Besides, the use of tricky superconducting solenoids is avoided. The low beta family cryostat contains 1 cavity, and is box-shaped, with one door on each side for easy access, while the high beta family cryostat contains 2 cavities. For both types, the tube extremities are as short as possible, as well as the 70-4 K transitions and corresponding bellows, for beam dynamics reasons.
The warm sections, including 2 quadrupoles and 1 diagnostic box, are mechanically optimized to have very short longitudinal dimensions, as presented in fig. 9.

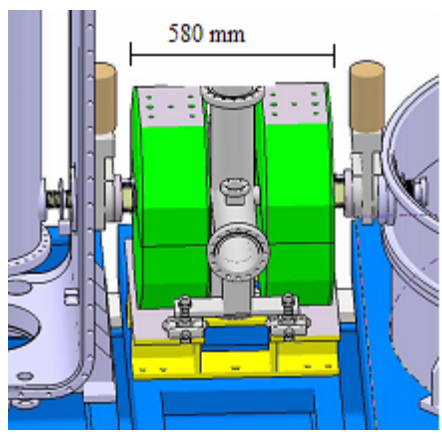

Figure 9: View of the SC linac warm section, including 2 quadrupoles and 1 diagnostic box

RF System

For the superconducting cavities, the choice of solid state technology has been made, for high reliability and ease of maintenance reasons [10]. The power required by the different cavities is mainly dominated by the beam loading, it will range from 1 to 13 kW. In the 88 MHz range (FM band), amplifiers around 30kW are now commercially available, the only difference between the FM broadcast applications and accelerator concerns the high voltage standing-wave ratio that is needed for superconducting cavity operation, and that requires the use of circulators.

For the RFQ cavity, a total power of 180 to 200kW has to be available at the amplifier exit: 150kW are required for the ion operation voltages (beam loading of a few kW), and 70kW are required for the deuteron operation voltage (beam loading around 7,5kW). The presently chosen solution is a set of 4 amplifiers, 50kW each, with circulators to eliminate coupling and oscillation risks; moreover, the cost of solid state amplifiers decreasing with time, it might be considered to use the solid state technology for the RFQ amplifier.

The Low Level RF system will be based on a digital solution, in order to fit the requirements of all the cavity types, RFQ, SC linac and normal conducting bunchers in the MEBT. Preliminary calculations show that a slow chopper can be used to tune the whole accelerator with a low mean intensity and the nominal peak intensity.

Cryogenics

The cryogenics system has been designed with a liquefier of 900W power at 4K (calculated required power at 4K: 570W), 2000W power at 60-80K (calculated: 1600W), and that must supply 10l/h for other uses (RF tests, various experiments).

The liquid helium will be produced from 1 (or 2) cold box(es) and stored in a 3000 litre tank. The helium gaz will be stored in three 15 bar tanks (fig.10).

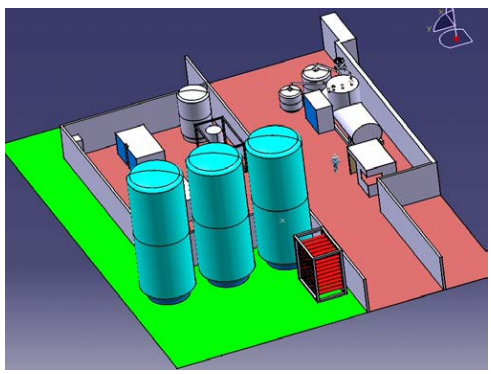

Figure 10: View of SPIRAL2 cryogenic plant

Mechanical Llayout

The mechanical layout of the whole accelerator is under detailed design, and must take into account the strong longitudinal dimension constraints in the LEBT, MEBT and superconducting linac. Once the cryomodules, that contain only one or two resonators, are aligned onto the mechanical frame, their positions can be further adjusted in order to precisely re-align the resonators according to beam trajectory measurements (fig.11).

CONCLUSION

The detailed study of the Spiral2 driver accelerator is almost completed. After the different prototype test results, that should occur around the end of 2004, the various designs will be frozen, in order to launch the calls for tender of the various components as soon as the decision on the project construction is taken.

REFERENCES

[1] W.Mittig et al, "LINAG Phase1", Ganil internal report, June 2002, http://www.ganil.fr/research/sp/reports

[2] A.Mosnier for the Spiral2 project team, "SPIRAL2: a high intensity deuteron and ion linear accelerator for exotic beam production", PAC 2003, Portland, USA, May 2003, p.595

[3] R.Duperrier et al, "Beam dynamic development for the SPIRAL2 project- Intermediate report", SPIRAL2 internal report, January 2004, http://www.edms.in2p3.f.

[4] R.Duperrier et al, "Status report on the beam dynamics developments for the SPIRAL2 project", EPAC 2004, Luzern, Switzerland, July 2004.

[5] R.Gobin et al, "Development of a permanent magnet ECR source to produce a 5mA deuteron beam at CEA/Saclay", LINAC2004, Lübeck, Germany, August 2004.

[6] T.Thuillier et al, "Advanced magnetic calculations for high magnetic field compact ion source", Rev. Sci. Instrum., Vol. 75, 5 (2004) .

[7] R.Ferdinand et al, "SPIRAL2 RFQ design", EPAC 2004, Luzern, Switzerland, July 2004

[8] P.-E. Bernaudin et al, "Design of a low-beta, quarter-wave resonator and its cryomodule for the SPIRAL2 project", EPAC 2004, Luzern Switzerland, July 2004.

[9] T.Junquera et al, "High intensity linac driver for the SPIRAL2 project: design of superconducting 88 MHz quarter-wave resonators, power couplers and cryomodules", EPAC 2004, Luzern, Switzerland, July 2004.

[10] M.Di Giacomo et al, "Preliminary design of the RF systems for the SPIRAL2 linac", EPAC 2004, Luzern, Switzerland, July 2004.

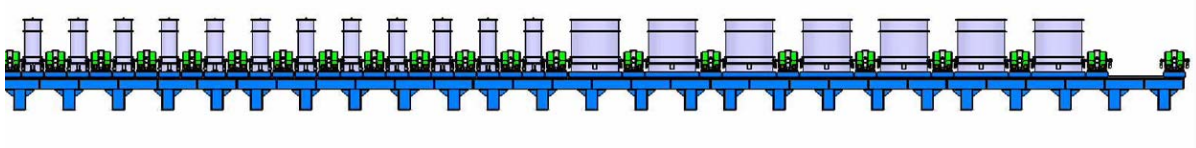

Figure 11: Superconducting linac layout

DEVELOPMENT OF ROOM TEMPERATURE AND SUPERCONDUCTING CH-STRUCTURES

H. Podlech
IAP, Universität Frankfurt/Main, Germany

Abstract

In the last decades several types of H-mode cavities have been developed for a wide range of applications. Several drift tube cavities (IH-structure) are in routine operation [1][2]. At the IAP (University of Frankfurt, Germany) a new type of H-mode cavity, the Cross-Bar-H-mode or CH-structure is presently under development. This multicell drift tube cavity is operated in the $H_{21(0)}$-mode. The CH-structure is an excellent candidate for high power proton accelerators in the energy range from 3 to 100 MeV. We present the status of the room temperature (r.t.) CH-cavity development for a dedicated 70 MeV proton injector for the international accelerator facility FAIR at GSI [3]. Due to its mechanical rigidity this cavity can be realized not only for room temperature but also for superconducting (s.c.) operation. To prove the very promising properties of superconducting CH-structures obtained by simulations, a 352 MHz prototype CH-cavity has been designed. Presently, this cavity is in the final stage of production. We present recent results of the s.c. cavity development and different applications which could take advantage of the s.c. CH-structure (XADS, IFMIF, cw-linac for the production of superheavy elements).

INTRODUCTION

A common property of all H-mode cavities is the high shunt impedance and the uniform power loss distribution which simplifies the cooling, especially at higher duty factors or cw operation . Figure 1 shows the effective shunt impedance as function of the particle velocity for different kinds of drift tube cavities. The well known IH-structure ($TE_{11(0)}$-mode) has no competitor in the low β-range from 0.01 to 0.1. The main reason for the high shunt impedance is the low capacitive load by using slim drift tubes without transverse focusing elements inside the tubes. Very high accelerating gradients up to 10.7 MV/m have been achieved in pulsed operation [1], and cw operation has been realized successfully, too [4][5]. Limitation of IH-structures are the lack of mechanical stability for s.c. operation and the upper operation frequency of about 300 MHz. Above this frequency the tank diameter becomes unreasonable small.
The CH-structure which is operated in the $H_{21(0)}$-mode has a larger diameter for a given frequency compared with the IH-structure. Cavities with frequencies from 150 to 800 MHz can be realized. This means that the CH-structure fits well to the popular frequency of proton drivers at around 350 MHz.
Unlike cavities with only two gaps as half wave or spoke resonators which cover typically a broad velocity range, the CH-structure is a multi cell cavity with a fixed velocity profile. Therefore this cavity has a constant high transit time factor larger than 0.8. Additionally, the KONUS beam dynamics (Kombinierte Null Grad Struktur) [1] is used to optimise the individual cavity cells. Due to the reduced transverse rf defocusing, long lens free sections can be realized even at high beam currents. This results in very high real estate gradients

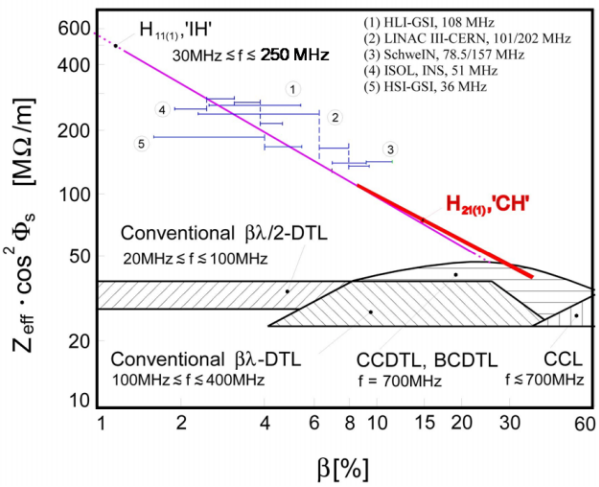

Figure 1: Effective shunt impedance as function of β for different rf structures. The horizontal blue bars represent existing IH-structures and the red line is the expected shunt impedance of the designated CH-proton linac for FAIR/GSI.

R.T. CAVITY DEVELOPMENT FOR THE GSI PROTON-INJECTOR

The existing Unilac at GSI is a fixed velocity heavy ion linac and can fill the synchrotron SIS12 only to about a few percent of the space charge limit for protons [1]. For the physics program, especially for the antiproton producton at FAIR, it is required to increase the proton current by a factor of 70 compared with the present capabilities. This can only be fulfilled by a dedicated proton injector. The key parameters are the final energy of 70 MeV, the neccessary peak current of 70 mA and the rf frequency of 352 MHz.
A combination of a 4-rod-RFQ [6] and of a CH-linac consisting of 11 r.t. CH-cavities is planned [7]. The design goal

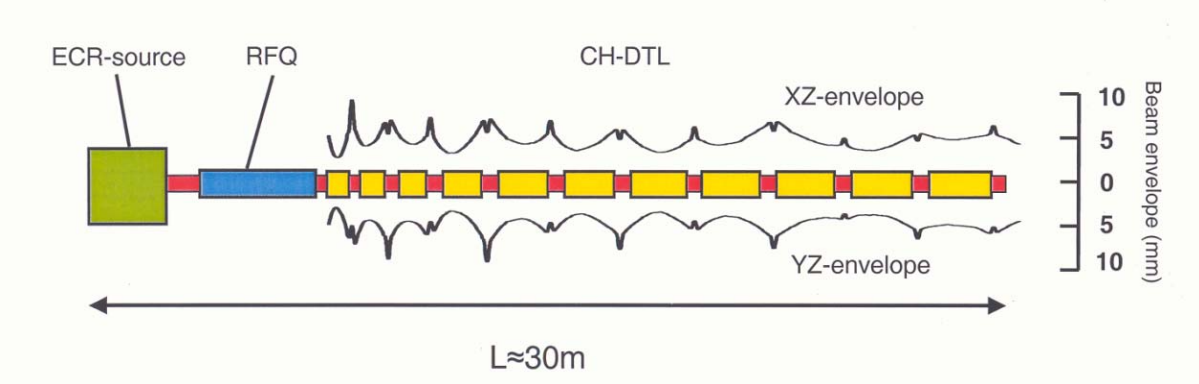

Figure 2: Principal layout of the FAIR proton linac with an ECR-source, a 4-rod-RFQ and 11 r.t. CH-cavities.

is to realize a proton injector which is efficient with respect to capital costs, maintainance and rf power consumption. Figure 2 shows a scheme of the the proposed proton linac. Additionally, the 99% beam envelopes derived from multi particle simulations are plotted along the CH-DTL [8]. The LEP klystrons will be used as rf drivers for all cavities including the RFQ. The maximum pulsed power per cavity varies between 500 and 1100 kW with beam loading [7].
The main concern regarding the cavity rf design was to maximise the shunt impedance by lowering the capacitive load without loosing mechanical stability. Therefore thin slices with only one accelerating cell have been optimised using Microwave Studio [9]. The effective shunt impedance $Z_{eff} = Z_0 T^2$ ranges from 100 to 45 MΩ/m [7] which are competitive values compared with conventional rf structures like the Alvarez-DTL. Fig. 3 shows a design

Table 1: Main parameter of the FAIR proton injector (CH-DTL)

Frequency	352 MHz
rf pulse length	1 ms
Repetiton rate	5 Hz
Macro pulse length	100 μs
Current (design/operation)	90/70 mA
Energy range	3-70 MeV
Nr. of CH-cavities	11
Length	22 m
Single tank length	0.6-2.2 m
Accelerating gradient	6.3-2.7 MV/m
Nr. of gaps/cavity	12-17
Effective shunt impedance	100-45 MΩ/m
rf power per cavity	600-1100 kW

study of the r.t. CH-structure for the FAIR proton injector. Each stem is cooled by water. ANSYS-simulations [10] have been performed to determine the mechanical stress and the deformation of the drift tubes under pressure due to thermally induced variations of the stem length. These results are in good agreement with experimental tests.

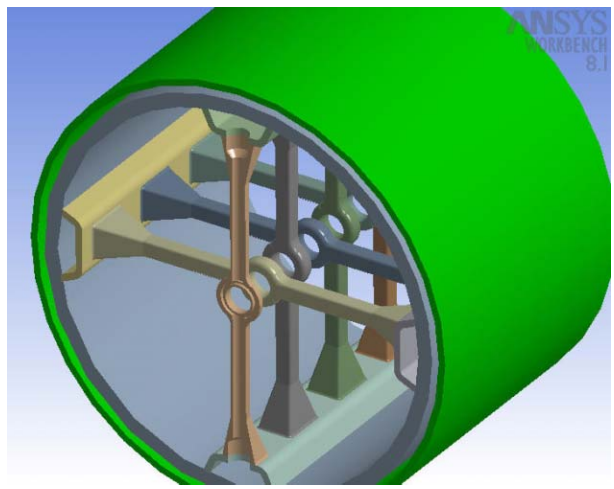

Figure 3: Three-dimensional view of the first CH-cavity for the FAIR proton linac.

SUPERCONDUCTING CH-CAVITIES

For accelerators operated with high duty cycles or even cw it is often advantageous to use superconducting cavities to reduce the overall power consumption. Additonally, s.c. cavities can have much larger apertures than r.t. cavities. This reduces particle losses and activation which is especially important if the linac should be a hands-on maintainance system.
For higher beam energies above around 100 AMeV s.c. elliptical cavities seem to be the best choice. These very efficient s.c. rf structures provide high gradients and a large voltage gain per cavity. Different projects will use or consider elliptical cavities [11][12][13].
In the case of s.c. low and medium β-cavities the situation is not as clear as for the high energy part. Many different cavities for ion and proton acceleration have been developed since the late 1960's. Even after the development of half wave and spoke resonators which have demonstrated very high gradients in recent tests [14][15] there is still a lack of efficient s.c. low and medium β cavities with frequencies of around 350 MHz whereas "efficient" means

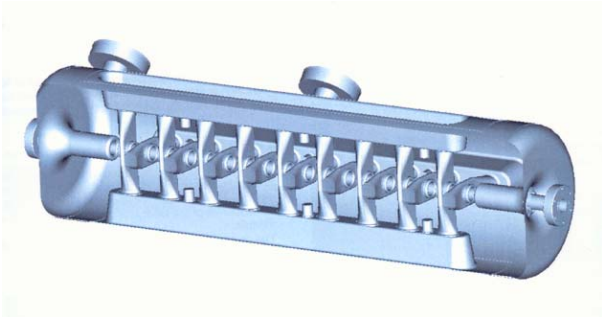

Figure 4: The superconducting CH-prototype.

high real estate gradient and large voltage gain per cavity. If energy variability is not an issue as for fixed velocity driver accelerators it is very reasonable to use multi cell cavities. If reliability is an issue it is clear that a multi cell cavity has to be designed very carefully with enough safety margin. This is in particular true for the peak fields.
The CH-structure will be the first s.c. multi cell cavity for the low and medium energy range. Due to the crossed stem

Figure 5: Some of the niobium parts of the s.c. CH-cavity which is in the final stage of production.

construction this cavity has a very high mechanical rigidity which is needed for superconducting operation. The CH-structure has some common features with the multi-spoke resonator. But the CH-structure uses girders to connect the stems which decreases the transverse dimensions of the cavity and results in lower magnetic peak fields. The use of the KONUS beam dynamics increases the number of possible acceleration cells without transverse focusing. Together with a velocity profile this leads to high real estate gradients between 3 and 4 MV/m which is much higher than in typical low β 350 MHz spoke cavities running with higher nominal gradients.

To prove the promising properties of s.c. CH-structures a 352 MHz β=0.1 CH-cavity with 19 gaps has been designed (see. fig.4) [16]. Table 2 summarises the main parameters of the CH-prototype cavity. The electric peak

Table 2: Parameters of the superconducting CH-cavity prototype

f	MHz	352
β		0.1
length	cm	104.8
diameter	cm	28
number of gaps		19
R_a/Q_0	Ω	3220
G	Ω	56
$(R_a/Q_0) \cdot G$	Ω^2	180000
E_p/E_a		6.59
B_p/E_a	mT/(MV/m)	7.29
E_p @ E_a=3.2 MV/m	MV/m	21
B_p @ E_a=3.2 MV/m	mT	23.3
W	mJ/(MV/m)^2	155
W @ E_a=3.2 MV/m	J	1.58
Q_0 (BCS, 4.2K)		$1.5 \cdot 10^9$
Q_0 (R_s=140 nΩ)		$4 \cdot 10^8$
P @ E_a=3.2 MV/m	W	9
material		bulk niobium
RRR		250
sheet thickness	mm	2-3

fields in CH-structures are higher compared with half wave or spoke resonators whereas the magnetic peak fields are lower. The ratio E_p/E_a is 6.59 and B_p/E_a is 7.29 mT/(MV/m) in the case of the CH-prototype cavity. This means that this cavity will be limited most likely by field emission. A gradient E_a=3.2 MV/m leads to an electric peak field of 21 MV/m and to a magnetic peak field of 23 mT. With an assumed intrinsic Q-value of $3.7 \cdot 10^8$ (R_s=140 nΩ) an rf power of 9 W is required to reach the gradient of 3.2 MV/m and the effective voltage gain of 3.4 MV, respectively. After a study had shown the technical feasibility of producing s.c. CH-structures the fabrication of this prototype cavity has been started in 2003 by the company ACCEL (Bergisch-Gladbach, Germany). The

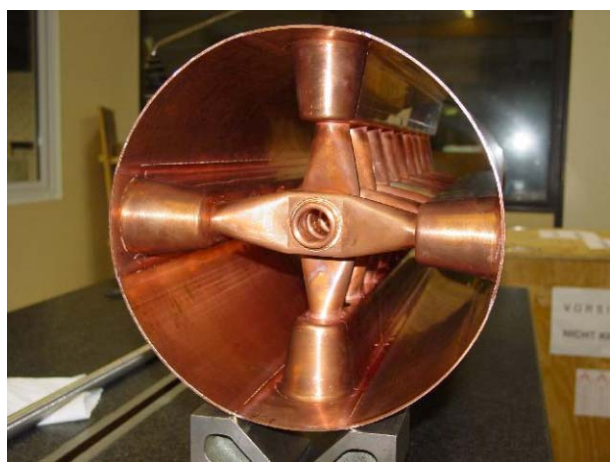

Figure 6: The full scale CH-prototype in copper.

cavity parts are produced with 2-3 mm thick high RRR bulk niobium sheets by deep drawing and spinning. Because of the very complex geometry many procedures of the production had to be developed first. Each production step has been performed in copper including the electron beam welding. Then the same step has been performed with niobium. Presently the niobium cavity is in the final stage of production (fig.5) whereas the copper version is already finished (see fig.6). The CH-prototype cavity will then be chemically treated with Buffered Chemical Polishing (BCP) and High Pressure Rinsing (HPR).

To test superconducting cavities at the IAP in Frankfurt, a cryogenic laboratory has been established recently. The laboratory has been equipped with a 3 m long vertical cryostat, a magnetic shielding (shielding factor 30), two transport dewars for LHe, a class 100 laminar flow box and the necessary rf equipment including the control system. The cryogenic laboratory has been already put into operation. Cold tests of a 176 MHz half wave resonator built by ACCEL have started and the cavity has been operated in a phase locked loop mode.

There are different possibilities to couple rf power to a s.c. CH-cavity. To study different coupling methods MWS simulations have been performed [17]. For the first cryo tests it is foreseen to couple electrically with a coaxial coupler through the girder (see. fig. 7). The simulations of the external Q-value could be reproduced by measurements very well (see. fig. 8).

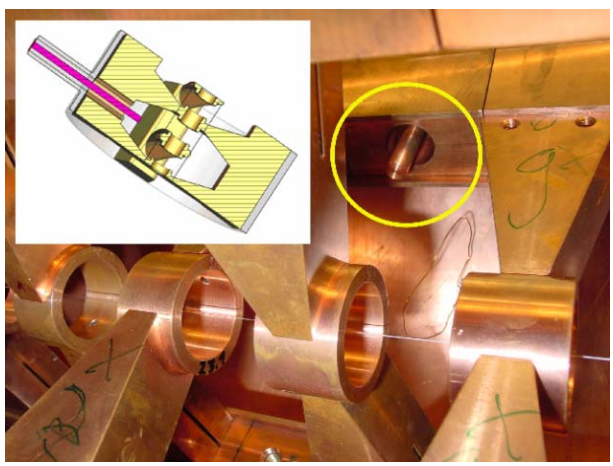

Figure 7: It is planned to couple with a coaxial coupler (yellow circle) through the girder to the electric field.

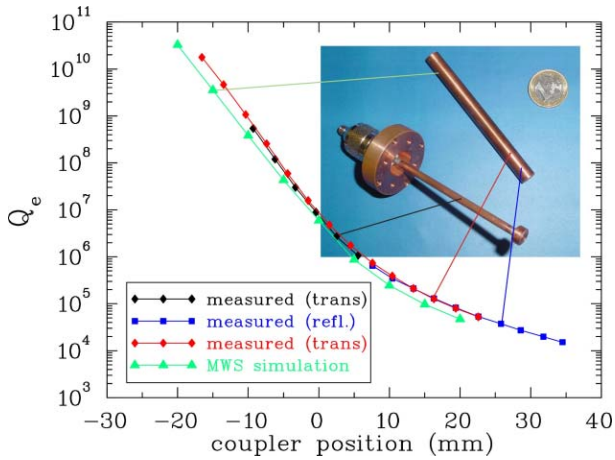

Figure 8: Different capacitive couplers have been used for model measurements. It could be demonstrated that sufficient coupling ($Q_e \approx 2 \cdot 10^8$) can be provided. A positive position means that the coupler protrudes from the girder.

APPLICATIONS OF S.C. CH-STRUCTURES

XADS

XADS (**E**xperimental **A**ccelerator **D**riven **S**ystem) is a nuclear waste transmutation project [18]. A superconducting driver linac delivers a cw 10 mA, 600 MeV proton beam to a subcritical core with a liquid metal spallation target. The main concern of this linac is the reliability because only a few beam trips (t>1 s) per year are allowed. Therefore it is considered to build two identical injectors up to an energy of about 35 MeV. Above this energy the linac is expected to be more robust against parameter deviations. Superconducting CH-structures could be used for the injector part from the RFQ energy (5 MeV) to the transition energy. This would reduce the number of cavities significantly compared with the use of 2-gap spoke resonators. In particular, the real estate gradient of low energy 2-gap spokes is very small because of a short cell length, long drift sections, a small number of cavities per focusing lattice and partially low transit time factors. Table 3 shows a comparison between a CH-linac and a spoke linac based on β=0.15 spoke cavities in the low energy range from 5 to 18 MeV [19].

Table 3: Comparison of a CH-linac and a 2-gap spoke linac for XADS in the energy range from 5 to 18 MeV [19]

parameter	CH-linac	spoke linac
number of cavities	4	30
β	0.1-0.2	0.15
gradient at β_{opt}	3 MV/m	6.3 MV/m
gradient (cavity length)	3 MV/m	2.5 MV/m
real estate gradient	1.62 MV/m	0.33 MV/m
energy gain per cavity	3-3.5 MeV	0.16-0.42 MeV
E_p at design gradient	19.5 MV	25 MV
B_p at design gradient	22 mT	50 mT
total length (m)	8	40

IFMIF

The **IFMIF** project (**I**nternational **F**usion **M**aterial **I**rradiation **F**acility) is planned as a high flux source of fast neutrons to develop appropriate wall materials for future fusion reactors [20]. The facility has to provide a 250 mA, 40 MeV, 10 MW deuteron beam accelerated by two 175 MHz linacs to a liquid Li target. In the reference design, a r.t. Alvarez-DTL is foreseen [20]. But because of the required cw operation it is attractive to use superconducting cavities to reduce the overall plug power and to avoid thermal problems in the r.t. Alvarez-type drift tube structures. At the IAP a linac for IFMIF has been proposed consisting of a r.t. IH-structure followed by a chain of 7 s.c. CH-structures [21].

CW Linac for Production of Superheavy Elements

At GSI and IAP a new linac for A/q=7 has been proposed for the production of superheavy elements [22]. Up to an energy of 1.4 AMeV the linac would consist of an ECR-source, a 4-rod-RFQ and an IH-structure. Due to the high duty cycle (cw) superconducting operation of the following cavities is advantageous. Therefore 8-10 s.c. CH-structures are foreseen to accelerate the beam up to an energy of 7.5 AMeV. The final energy would be continiously varied by using several s.c. 2-gap half wave resonatos.

CONCLUSIONS AND OUTLOOK

The CH-structure is a new multi cell drift tube cavity with promising properties. It can be applied in room temperature as well as in superconducting linacs for the acceleration of protons and ions in the low and medium energy range. A high current proton linac for FAIR at GSI consisting of r.t. CH-structures is presently under development. A protoype cavity will be built and tested with high power.
Several future projects as IFMIF or XADS could take advantage of s.c. CH-cavities. A s.c. prototype cavity is in the final stage of production and will be tested this year. The development of a mechanical tuner for the CH-structure and a structural analysis using ANSYS has started.

ACKNOWLEDGEMENT

The author would like to thank U. Ratzinger, H. Klein, H. Deitinghoff, the members of the Linac group, and the technical staff of the IAP.
This work has been supported by GSI, BMBF contr. No. 06F134I. and EU contr. No. EFDA/99-507ERB5005 CT990061. We acknowledge also the support of the European Community-Research Infrastructure Activity under the FP6 "Structuring the European Research Area" program (CARE, contract number RII3-CT-2003-506395)

REFERENCES

[1] U. Ratzinger, Habilitationsschrift, Universität Frankfurt, 1998

[2] U. Ratzinger, The New High Current Ion Accelerator at GSI and Perspectives for Linac Design Based on H-Mode Cavities, Proceedings of the EPAC 2000, p.98, Vienna, Austria

[3] W. Henning, The Future GSI Facility: Beams of Ions and Antiprotons, Proceedings of the PAC 2003, p.16, Portland, OR; USA

[4] E. Nolte et. al., The Munich Heavy Ion Post Accelerator, Nucl. Instr. and Meth. 1979, vol.158, p.311

[5] R. Laxdal et al., Beam commissioning and first operation of the ISAC DTL at TRIUMF, Proceedings of the PAC 2001, p3942, Chicago, IL, USA

[6] A. Schempp et al., Design of a 352 MHz Proton-RFQ for GSI, these Proceedings

[7] Z. Li et al., Design of the r.t. CH-Cavity and Perspectives for a New GSI Proton Linac, these Proceedings

[8] R. Tiede et al., KONUS Beam Dynamics Design of a 70 mA, 70 MeV Proton CH-DTL for SIS at GSI, these Proceedings

[9] http://www.cst.com

[10] http://www.ansys.com

[11] M. White, The Spallation Neutron Source (SNS), Proceedings of the LINAC 2002, p.1, Gyeongju, Korea

[12] J.A. Nolen, The U.S. Rare Isotope Accelerator Project, Proceedings of the LINAC 2002, p.29, Gyeongju, Korea

[13] J-L. Biarrotte, High Intensity Driver Accelerators for EURISOL, Proceedings of the EPAC 2002, p.1007, Paris, France

[14] G. Olry et al., Recent Developments on Superconducting β=0.15 and β=0.35 Spoke Cavities at IPN for Low and Medium Energy Sections of Proton Linear Accelerators, Proceedings of the EPAC 2004, Lucerne, Switzerland

[15] T. Tajima et al., Test Results of the LANL 350 MHz, β=0.175, 2-Gap Spoke Resonator, Proceedings of the LINAC 2002, p.228, Gyeongju, Korea

[16] H. Liebermann et al., Design of a Superconducting CH-Cavity for Low- and Medium Beta Ion and Proton Acceleration, Proceedings of the PAC 2003, p.2820, Portland, OR; USA

[17] H. Liebermann et al., Status of the Coupler Development for the 352 MHz Superconducting CH-Cavity, these Proceedings

[18] "A European Roadmap for Developing Accelerator Driven Systems (ADS) for Nuclear Waste Incineration", April 2001, ENEA, Italy

[19] J.-L. Biarrotte et. al., High Intensity Proton SC Linac Using Spoke Cavities, Proceedings of the EPAC 2002, p.1010, Paris, France

[20] IFMIF Conceptual Design Report

[21] A. Sauer et al., Beam Dynamics Design of a Superconducting 175 MHz CH-Linac for IFMIF, Proceedings of the EPAC 2002, p.1404, Paris, France

[22] R. Eichhorn, RF Structures for Linear Acceleration of Radioactive Beams, Proceedings of the PAC 2001, p.495, Chicago, IL, USA

BEAM INTENSITY ADJUSTMENT IN THE RIA DRIVER LINAC*

P. N. Ostroumov#, J.A. Nolen, S.I. Sharamentov, ANL, 9700 S. Cass Avenue, Argonne, IL, 60439
A.V. Novikov-Borodin, INR, Moscow 117312, Russia

Abstract

The Rare Isotope Accelerator Facility currently being designed in the U.S. will use both heavy ion and light ion beams to produce radionuclides via the fragmentation and spallation reactions, respectively. Driver beam power of up to 400 kW will be available so that beam sharing between target stations is a viable option to increase the number of simultaneous users. Using a combination of rf-sweepers and DC magnets the driver beams can be delivered to up to four targets simultaneously. With simultaneous beam delivery to more than one target independent adjustment of the relative beam intensities is essential. To enable such intensity adjustment we propose to use a fast chopper in the Medium Energy Beam Transport (MEBT) section. Several design options for the fast chopper are discussed. The MEBT beam optics is being designed to accommodate and match the chopper technical specifications.

BEAM SWITCHYARD

A preliminary design for a driver linac switchyard has been discussed in the recent RIA Facility Workshop [1]. The proposed switchyard will deliver beams to four production targets. The design of the switchyard for the driver beams of RIA is a complex problem due to the following features: 1) Sharing beams of various ion species accelerated over a wide range of energies; 2) Delivery of beams to four target stations simultaneously; 3) Providing high quality beam optics with higher order corrections for multiple charge state beams. The accelerated beam in the RIA driver can be distributed to four targets simultaneously using rf sweepers. A low frequency rf sweeper is appropriate for the deflection of heavy ion beams and the delivery to two or more targets simultaneously. The deflector design is based on an H-type rf cavity. The fundamental frequency of the bunch sequence is determined by the multiharmonic buncher at the front-end of the driver linac. In the two-charge state injector mode all four harmonics are applied and the bunch repetition rate will be 57.5 MHz. In the single charge state injector mode only three harmonics of the multi-harmonic buncher will be used and the bunch repetition rate is still 57.5 MHz. Therefore the rf sweeper can operate at 86.25 MHz to split the beam intensity 50/50 to two directions. The length of the rf sweeper's electrode is chosen to provide a phase slippage of 180° inside the cavity for uranium beams. This condition eliminates any effect of fringing fields on uranium beams but produces negligible momentum spread for lighter ions because of their higher velocity and shorter time-of-flight. A room temperature rf cavity operating at 86.25 MHz can provide a maximum electric field on the surface of ~18 MV/m in cw mode. We have conservatively designed for a maximum electric field of ~7.2 MV/m between the electrodes. The main parameters of the rf sweeper are shown in Table 1. Two such sweepers are used in series. The rf sweeper is followed by two DC septum magnets.

Table 1: Basic parameters of the rf deflector for the RIA switchyard

Maximum electric field between the plates	7.2 MV/m
Effective length	1.2 m
Deflecting angle	± 3 mrad
Aperture	3.0 cm
Tank diameter	68 cm
Required rf power according to the MWS Studio	25 kW

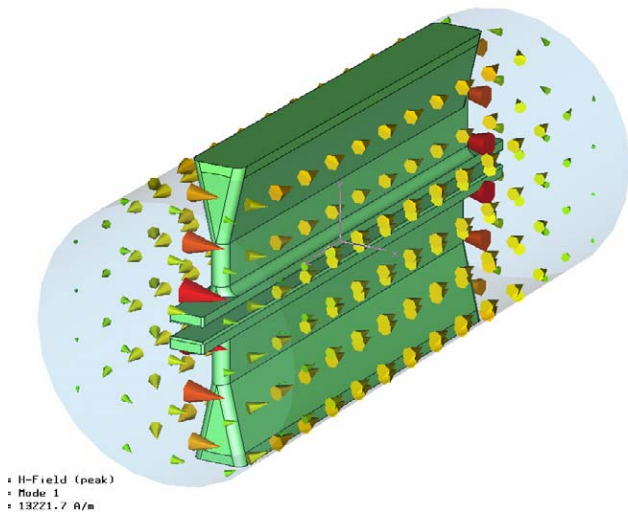

Figure 1: MWS design of the 86 MHz rf sweeper.

BEAM INTENSITY ADJUSTMENT

The switchyard will deliver beams to 4 targets simultaneously. Using rf sweepers beam microbunches will be alternatively sent to different targets. In this mode, all targets will receive equally distributed beam power. For most experiments it is desirable to have adjustable level of beam intensity on the targets. This problem can be solved by using a chopper which could remove any fraction of the beam. The chopper can be made as a device with a deflecting electric field and should be located in the MEBT to minimize the required voltage as well as to reduce the power on the beam dump. The

* This work was supported by the U.S. Department of Energy, Office of Nuclear Physics, under Contract No. W-31-109-ENG-38.
#ostroumov@phy.anl.gov

MEBT will transport 200 keV/u beams of any ion with charge-to-mass ratio in the range $28/238 \leq q/A \leq 1$. Due to the low energy of ions in the MEBT, the utilization of the deflected beam power is straightforward. The total beam power does not exceed 100 kW. In the most extreme case, about 75% of this power should be dumped. To absorb and remove this power, water-cooled slits must be provided.

BEAM INTENSITY ADJUSTMENT OF DUAL CHARGE STATE BEAMS

The baseline design of the RIA driver linac calls for the extraction and the acceleration of dual charge state beams with masses from 180 to 238 to the location of the first stripper [2]. The intensity adjustment of two-charge state heavy-ion beams extracted from the ion source does not require any additional equipment. The LEBT section between the ECR source and multi-harmonic buncher is designed as an achromatic system. The horizontal position of the beam depends on the charge state at high dispersion area which reaches its maximum in the mid-plane between the magnets [2]. At this location, beams of different charge state are completely separated in space and the intensity of each beam can be adjusted by the slits. The front-end of the driver is designed such that the same ion species with different charge states are accelerated in alternative buckets of the RFQ [2], therefore the rf sweeper will automatically produce two beams of different intensities.

CHOPPER CHOICE

Two basic options have been considered for the intensity adjustment in the RIA driver linac: 1) A fast chopper with high repetition rate (57.5/2 MHz) of deflecting voltage pulses; 2) A combination of low repetition rate fast chopper and rf chopper.

Fast Chopper

The arbitrary adjustment of the intensity of three beams delivered to 3 of the 4 targets can be performed in the MEBT using the fast chopper, similar to the ATLAS chopper [3]. In this mode of operation, one of the targets will receive 25% of maximum available intensity while the other three will receive any fraction between 0 and 25% of the full intensity. The available space for the chopper location in the MEBT is restricted to ~50 cm and it is defined by the beam matching requirements in the 6D phase space. The most challenging chopper parameters are those for the uranium beam (see Table 2, Regime A). As is seen, the voltage requirement is similar to the SNS chopper [4], however, the repetition rate is significantly higher. Therefore the SNS-type voltage switcher is not directly suitable for our application. Higher repetition rate of 12 MHz is provided in the ATLAS chopper [3] but the voltage ~0.8 kV is too low for the RIA application.

A traditional solution for the fast chopper includes two main devices: a) a voltage modulator with nanosecond rise- and fall-time and b) a traveling wave structure to synchronize the voltage pulse propagation to the beam velocity. The modulator power is determined by the required deflecting voltage and impedance of the traveling wave structure. To minimize the power requirements of the voltage modulator, high shunt impedance (~300 Ω or higher) is required. Even if the high impedance is provided, the frequency of the modulator is still high and not available commercially. In addition, high shunt impedance reduces effective deflecting voltage.

To reduce the required power significantly, we are considering series of solid-state or vacuum tube switchers operating at an individual capacitance of ~10 pF instead of a traveling wave structure. About 15 modulators can be triggered with appropriate delay to match the beam velocity. Further detailed engineering studies and prototyping are under-way.

If it is proven, the fast chopper operating at 28.75 MHz repetition rate can be easily implemented into the MEBT and simplifies the overall MEBT equipment compared to the option described below.

Table 2: Basic parameters of the chopper

	Regime A	Regime B
Beam velocity	0.02c	0.02c
q/A	28/238	28/238
Length	60 cm	60 cm
Voltage	±1.8 kV	±1.8 kV
Pulse rise/fall time	12 nsec	12 nsec
Pulse length	5-40 nsec	2 μsec
Repetition rate	28.75 MHz	0.25 MHz
Duty cycle	Up to 75 %	25 %

Beam Intensity Adjustment using a Combination of a Fast and an RF Chopper

Both ISOL and fragmentation targets tolerate ~0.25 MHz beam intensity modulation. An rf chopper can be used to adjust number of bunches within ~2 μsec length of beam burst that will reduce the beam intensity. However, to avoid not fully deflected bunches during the rise- and fall-time of the rf chopper, ~2 μsec "gaps" in the beam structure are required. These "gaps" can be produced by a fast chopper which will operate at 0.25 MHz repetition rate (see Regime B in Table 2). Such a chopper is entirely technically feasible. The beam structure downstream of the fast chopper is shown in Fig. 2.

For the actual beam intensity reduction within every ~2 μsec beam burst a dual frequency rf chopper, similar to the device developed at TRIUMF [5] can be used. In this chopper an rf voltage is applied to the deflecting plates. One of the plates have to be biased by a dc voltage $V_{dc}=V_{rf}$, where V_{rf} is the amplitude of the rf voltage. To transport the beam through the chopper without any deflection, the rf chopper should operate at 57.5 MHz in order to compensate for the dc voltage (see Fig. 3a).

Operating at 28.75 MHz the rf chopper will deflect and remove every other bunch (see Fig. 3b). As was indicated

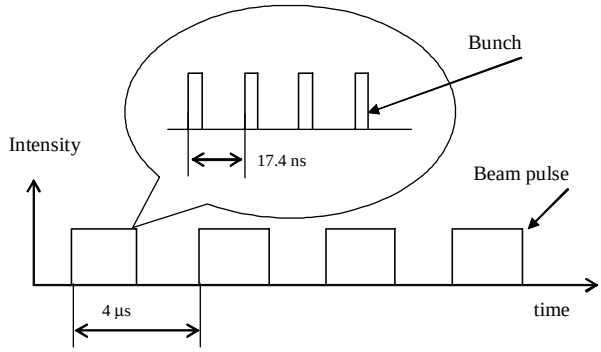

Figure 2: Beam structure downstream of the fast chopper.

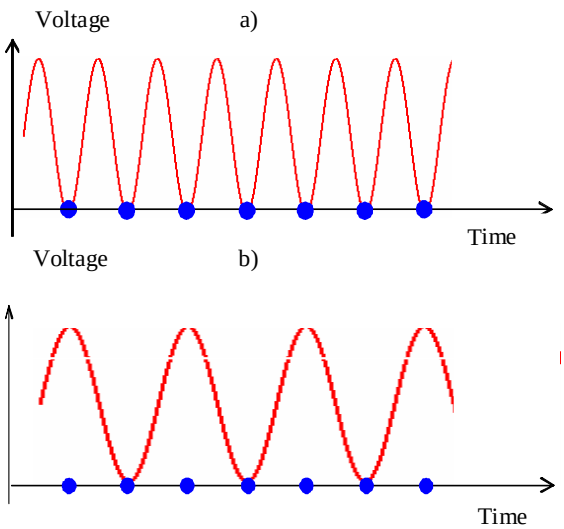

Figure 3: Dual frequency rf chopper with biased plates.

in ref [5], the cosine-wave rf chopper introduces negligible distortion to the beam emittances. To provide beam intensity adjustment to 4 targets an additional dual frequency chopper operating at 28.75 and 14.375 MHz is needed. Two rf choppers and one fast chopper will require ~50 cm space each. Although this design is technically feasible, it significantly complicates the MEBT. Each 50 cm space for the chopper should be supplied by a focusing triplet or a SC solenoid and an rf rebuncher.

MEBT DESIGN

The MEBT matches two-charge state beam to the 6D acceptance of the SRF linac. The MEBT must contain: 1) focusing elements; 2) rebunchers; 3) beam diagnostics tools; 4) steering magnets for simultaneous correction of gravity centers of the two-charge state beams; 5) One or more choppers.

Several options of the MEBT have been studied: focusing by doublets, triplets and solenoids. It was shown that the focusing by SC solenoids is the best system for the transport of two-charge state beams. The solenoidal channel is less sensitive to the charge state and does not introduce additional mismatch of the two-charge state beam. The beam exiting the RFQ is matched to the axial-symmetric channel by three strong electromagnet quadrupoles. The MEBT has been designed by the code TRACE-3D and verified by the code TRACK. Fig. 4 shows transverse envelopes of the deflected and undeflected dual charge-state uranium beam along the MEBT for the case of a single fast chopper.

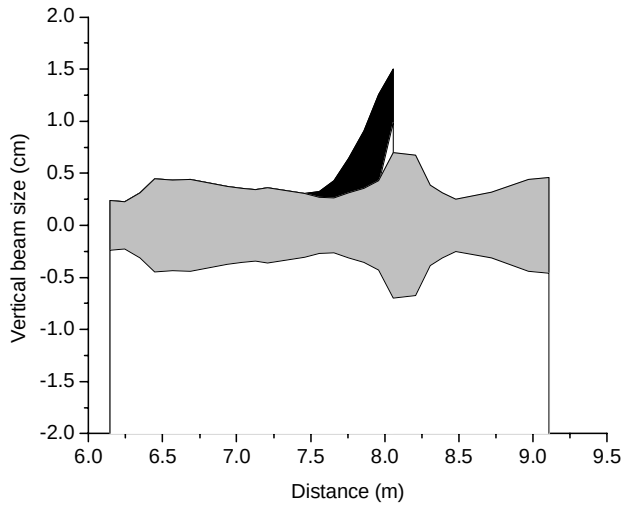

Figure 4: Envelopes of undeflected (gray area) and deflected (black area) beams in the vertical plane along the MEBT. The elements of the MEBT include triplet, SC solenoid, rebuncher, SC solenoid, fast chopper, triplet with slits, rebuncher, and SC solenoid.

CONCLUSION

Several possible solutions for the independent beam power adjustment on four RIA targets are discussed. The most technically feasible solution is a combination of a fast chopper and an rf choppers. However, this solution complicates and increases the MEBT cost by adding more rebunchers and focusing elements. If tested, the fast chopper operating at 28.75 MHz repetition rate can be easily implemented into the MEBT and will keep the overall MEBT equipment simple. However, a significant effort for R&D and prototyping of the fast chopper is required.

REFERENCES

[1] P.N.Ostroumov and J. Nolen. Variable Intensity Mode for the RIA Driver Linac. – RIA Facility Workshop, ANL, USA, March 9-13, 2004.
[2] A. A. Kolomiets, et al, Proc. of the PAC2003, Portland, OR, May 12-16, 2003, p. 2876.
[3] R.C. Pardo et al. Pramana – J. Phys., Vol. 59, No. 6, December 2002, p. 989.
[4] R. Hardekopf, et al. Proc. of the PAC-2003, p. 1661.
[5] R. E. Laxdal, et al., Proc. of the LINAC 2002, p. 407.

PROPOSAL FOR REDUCTION OF TRANSVERSE EMITTANCE OF BNL 200 MEV LINAC*

D. Raparia, J. Alessi, J. Beebe Wang, W. T. Weng, Collider-Accelerator Department,
Brookhaven National Laboratory, Upton, New York 11973, USA

Abstract

BNL has a plan to upgrade the AGS proton beam from the current 0.14 MW to higher than 1.0 MW and beyond for a neutrino facility which consists of two major subsystems. First is a 1.45 GeV superconducting linac (SCL) to replace the Booster as injector for the AGS. Second is the performance upgrade for the AGS itself for the higher intensity and repetition rate. For high intensity proton accelerators, such as the upgraded AGS, there are very stringent limitations on uncontrolled beam losses. A direct effect of increased linac beam emittance is the halo/tail generation in the circulating beam. Studies show the estimated halo/tail generation in the beam for the present normalized RMS emittance of the linac beam is unacceptable. To reduce the transverse emittance of the 200 MeV linac, the existing radio frequency quadrupole linac (RFQ) has to be relocated closer to drift tube linac (DTL) tank 1 to meet the emittance requirement for AGS injection with low loss. This paper will present the various options of matching between RFQ and DTL, and chopping options in the low energy beam transport (LEBT).

INTRODUCTION

We have examined possible upgrades to the AGS complex that would meet the requirements of the proton beam for a 1.0 MW neutrino superbeam facility [1]. We are proposing to upgrade the existing 200 MeV linac to 400 MeV using the Fermilab style CCL, followed by a superconducting linac to an energy of 1.45 GeV for direct H^- injection into the AGS [1].

The requirements of the proton beam for the super neutrino beam are summarized in Table 1. Since the present number of protons per fill is already close to the required number, the upgrade focuses on increasing the repetition rate and reducing beam losses (to avoid excessive shielding requirements and to keep activation of the machine components to a workable level). It is also important to preserve all the present capabilities of the AGS, in particular its role as injector to RHIC. Present injection into the AGS requires the accumulation of four Booster loads in the AGS, which takes about 0.6 sec, and is therefore not suited for high average beam power operation.

Table 1: AGS Proton Driver Parameters

Total beam power	1 MW
Beam energy	28 GeV
Average beam current	42 μA
Cycle time	400 msec
Number of protons per fill	0.9×10^{14}
Number of bunches per fill	24
Protons per bunch	0.4×10^{13}
Injection turns	230
Repetition rate	2.5 Hz
Pulse length	0.72 msec
Chopping rate	0.75
Linac average/peak current	20 / 30 mA

To reduce the injection time to about 1 msec, the Booster will be replaced by a 1.45 GeV linac. The injection linac consists of the existing warm linac of 200 MeV upgraded to 400 MeV and a new superconducting linac to 1.45 GeV. The multi-turn injection from a source of 28 mA and 720 μsec pulse width is sufficient to accumulate 0.9×10^{14} particle per pulse in the AGS. The minimum ramp time of the AGS to full energy is presently 0.5 sec. This must be reduced to 0.2 sec to reach the required repetition rate of 2.5 Hz to deliver the required 1 MW beam to the target.

HALO/TAIL GENERATION VS. LINAC EMITTANCE

For high intensity proton accelerators, such as the upgraded AGS, there are very stringent limitations on uncontrolled beam losses. We have examined the emittance growth and uncontrolled beam losses as a function of linac emittance by computer simulations.

All of the physical quantities used in the simulations (Table 1 and 2) are chosen according to the design specifications. Correlated painting is chosen for injection into AGS, considering the available aperture at injection and beam halo/tail control. The average stripping foil thickness is assumed to be 300 $\mu g/cm^2$. In order to separate the effects of linac emittance from the other issues, the effects of space charge and magnet errors are not included in this study.

A direct effect of linac beam emittance is the halo/tail generation in the circulating beam. Figure 2 shows the estimated halo/tail generation in the AGS beam as a function of normalized RMS emittance of linac beam.
Here, the halo/tail generation is defined as the ratio of the number of particles with emittance larger than the designed acceptance of 49π mm-mrad to the total number of particles in the circulating beam.

* Work performed under the auspices of the US Department of Energy
** E-mail raparia@bnl.gov

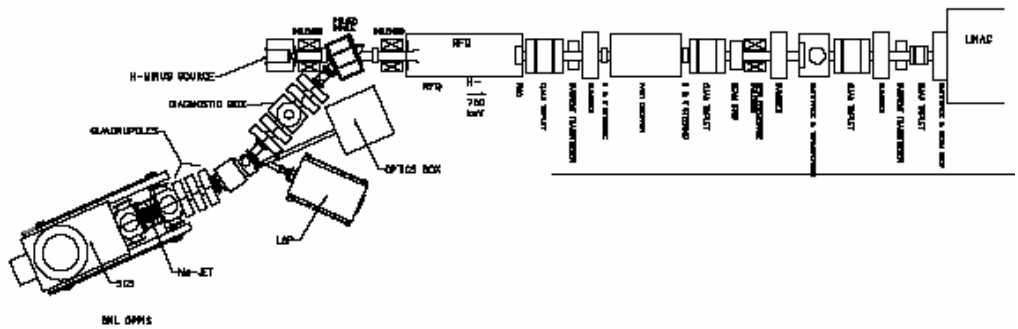

Figure 3: Layout of the MEBT

Table 2: Simulation parameters

Horizontal beta at the injection	28.0 m
Vertical beta at the injection	8.0 m
Horizontal emittance of injected beam	2π mm-mrad
Vertical emittance of injected beam	2π mm-mrad
Horizontal beam size at injection, σ_x	5.2293 mm
Vertical beam size at injection, σ_y	2.7952 mm
Horizontal Foil size (2.5 σ_x)	13.0731 mm
Vertical foil size (2.5 σ_y)	6.9878 mm

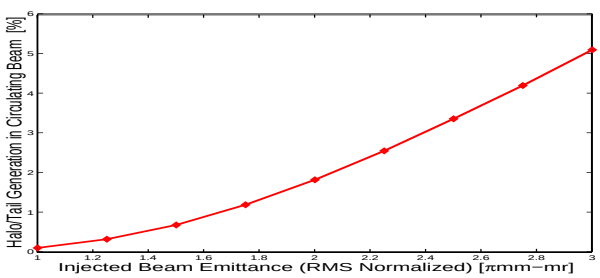

Figure 2: The estimated halo/tail generation in the circulating beam as functions of normalized RMS emittance of injected beam.

PRESENT MEBT

The source of the emittance growth in our linac lies in the medium energy beam transport (MEBT). The 7 meters long MEBT includes 10 quadrupoles and 3 bunchers for beam matching into the linac and a fast beam chopper which allow beam chopping with ~10 ns rise and fall time. Figure 3 shows the layout of the line.

The present configuration of the MEBT is the result of having to meet several requirements imposed on the line, like providing an approximate 1 m long drift space for a fast chopper, a 1 meter long drift for a dipole for beam injection from the old polarized ion source, a movable beam dump, diagnostics box etc. This configuration results in a lattice mismatch in both transverse as well as longitudinal direction. The RFQ ($\beta\lambda$~ 6cm) and DTL ($\beta\lambda$ = 6 cm) both have a FODO lattice (period length 6-12 cm) but in between, the MEBT has a triplet configuration to provide long drift spaces for fast and slow choppers and dipoles. Similarly in the longitudinal direction the focusing period in the RFQ and DTL is much smaller than the unevenly spaced bunchers in the MEBT, and the resulting beam is debunched by the time it enter the DTL. Figure 4 shows the longitudinal phase space at end of RFQ, 1st, 2nd, 3rd buncher, entrance of the DTL and after cell 20 in DTL Tank 1.

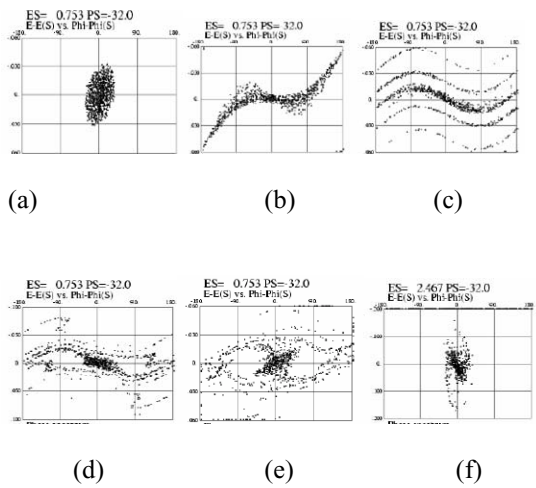

Figure 4: Longitudinal phase space plots (a) at end of RFQ, (b) after buncher 1, (c) after buncher 2, (d) after buncher 3, (e) at entrance of DTL and (f) at DTL cell 20.

It is clear from figure 4, beam is debunched at the entrance of the DTL, which results in beam loss (~ 40 %) and transverse emittance growth of 450-500% .

OPTIONS FOR MEBT

We have studied following MEBT configurations to reduce the transverse emittance: (1) adding a 4th

buncher after the fast chopper, (2) bring the RFQ close to the DTL, only providing space for a gate valve, and (3) a short (0.5m) MEBT with 3 quadrupoles and two bunchers.

Adding a 4th buncher after the chopper improve the transmission to ~ 75% and reduces emittance growth to 60-70%. Bringing the RFQ right against the DTL increases the transmission to 100% and reduces the emittance growth to 40-65%, since the beam is still bunched but mismatched to the DTL. The short MEBT provides enough degrees of freedom to match into the DTL in all three planes. The resulting emittance growth is only 0-20% in the transverse plane but ~75% in the longitudinal plane. The emittance growth in the longitudinal plane is due to the inherent mismatch between DTL Tanks. This mismatch is due to the fact that there is 0.6 – 1meter drift space between the tanks which causes discontinuities in the longitudinal focusing pattern. In the modern linacs, these discontinuities are compensated by shifting the synchronous phase of the first and last few cells in each tank [2]. Table III shows the result of PARMILA simulations for these options.

Table 3: MEBT upgrade options, emittance at source 0.4 π mm mrad (rms,nor)

Configuration	Transmission	RMS emit growth (x, y, z) %
(A)Present	~60%	450, 500, 350
(A) +4th B	79%	56, 70, 170
RFQ +DTL	100%	64, 40, 64
Short MEBT	100%	16, 0, 74

Our choice is the short MEBT, which provides enough degrees of freedom to match in all three planes. The choice of this MEBT forces the chopping to be done before the RFQ in the low energy beam transport (LEBT).

LOW ENERGY BEAM TRANSPORT

Previous experience at BNL has shown that due to space charge, the chopper in the magnetic LEBT would not work [3]. We are now considering an all electrostatic LEBT with einzel lenses and a 90 degree electrostatic spherical deflector to merge the H^- polarized beam into the RFQ. An electrostatic field can be used to deflect/reflect the H^- ions. The SNS LEBT uses an electrostatic chopper in deflection mode in the LEBT with a rise time of 50 ns [4]. We need to decrease the rise and fall times to 10 ns or better. At 35 keV, H^- ions travel about 2.5 cm in 10 ns. This implies the deflecting/reflecting field should be confined to 2.5 cm. Figure 5 shows the conceptual design of the chopping with einzel lenses in decelerating mode with (a) reflecting field on and (b) reflecting off. The required voltage for the reflecting mode is about 37 kV and for transmission mode is about 32 kV.

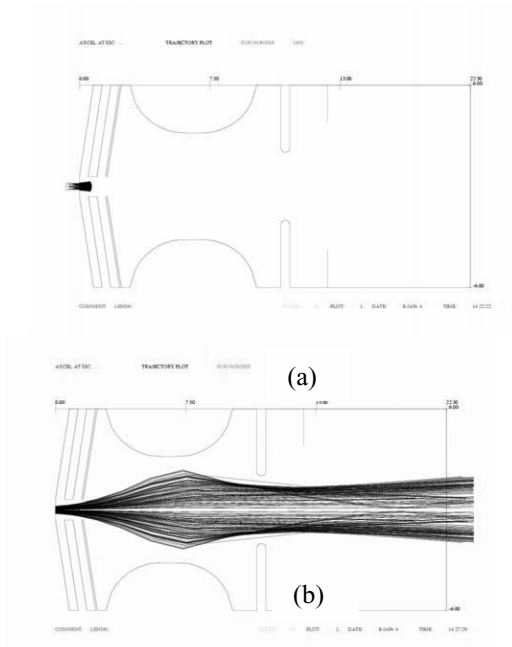

Figure 5: Conceptual design of chopper with einzel lens in decelerating mode with (a) reflecting field on and (b) reflecting field off.

H^- polarized beam will merge into the LEBT using a 90 degree spherical deflector and will able to maintain the desired polarization direction. Initial simulation has shown that rms emittance growth for polarized beam is less than 20% and for the high intensity H^- beam is about 30%. Some R&D effort is needed to realize the 10 ns rise time for this chopping and spherical deflector scheme.

CONCLUSIONS

Simulation studies have shown that the transverse emittance of the 200 MeV BNL linac could be reduced to achieve acceptable losses for 1MW AGS operation. R&D efforts are needed to realize chopping with a rise time of 10 ns in all electrostatic LEBT.

REFERENCES

[1] W.T. Weng and D. Raparia (editor), "The AGS-Based Super Neutrino Beam Facility, Conceptual Design Report", to be published.

[2] K. R. Crandall and D. Raparia, "Reducing the field perturbation produced by shifted gaps in a drift-tube linac", 1992 Linear Accelerator Conference, Ottawa, Canada, AECL-10728, pp504, August 1992.

[3] J. Alessi, et al., 'The BNL 200 MeV H^- Linac Performance and Upgrade", 1990 Linear Accelerator Conference, Albuquerque, NM, pp 774, September 1990

[4] J. W. Staples et al., "The SNS Four-Phase LEBT Chopper", 1999 Particle Accelerator Conference, New York, pp 1963, 1999.

THE HITRAP-DECELERATOR FOR HEAVY HIGHLY-CHARGED IONS

L. Dahl*, W. Barth, Th. Beier, W. Vinzenz
Gesellschaft für Schwerionenforschung, D-64291 Darmstadt, Germany

C. Kitegi, U. Ratzinger, A. Schempp
J.W. Goethe-University, D-60054 Frankfurt a.M., Germany

Abstract

The GSI accelerator facility provides highly-charged ions up to U^{92+} by stripping the ions at 400 MeV/u in the transfer line from the SIS18 (Heavy Ion Synchrotron) to the ESR (Experimental Storage Ring). The ESR provides high quality beams by means of stochastic cooling and electron cooling. Deceleration down to 4 MeV/u was already successfully demonstrated. After suitable rebunching, further deceleration down to 6 keV/u, necessary for the capture of the ions by a penning trap, is done by IH/RFQ-structures. All cavities are operated at 108 MHz. Recently the HITRAP-project (Heavy Ion Trap), described in a Technical Design Report, was approved. The layout of the decelerator and the beam dynamics in different sections are reported.

INTRODUCTION

Up to now, GSI is the world´s only facility (Fig. 1) which provides heavy highly-charged ions up to U^{92+} for atomic-physics experiments. The high energy, necessary for stripping the ions up to bare nuclei, is obtained by a first acceleration stage of Uranium to 11.4 MeV/u in the UNILAC. Through a transfer line the SIS18 is fed with single macro pulses of 100 µs length which are accelerated up to 400 MeV/u. After extraction and during the transfer to the ESR finally a foil stripper enables a high yield of U^{92+}-ions.

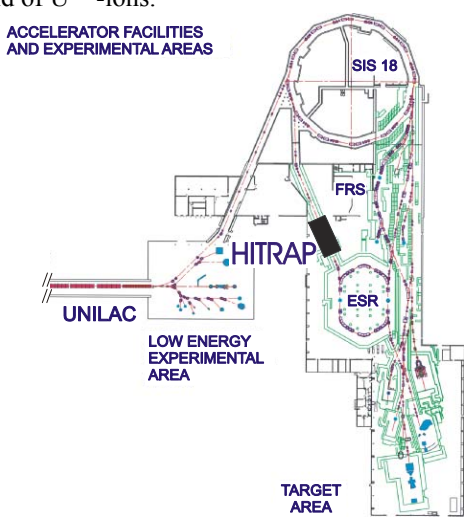

Figure 1: GSI accelerator facility and location of the HITRAP facility.

*L.Dahl@gsi.de

In a multi-stage process the ESR decelerates the U^{92+}-beam down to 4 MeV/u and extracts it to the HITRAP-linear decelerator, described in a Technical Design Report [1]. This decelerator reduces the energy of the heavy highly-charged ions from 4 MeV/u down to 6 keV/u. After ejection from the ESR, the beam will be rebunched by a λ/4-resonator. In a subsequent step an IH-type structure will decelerate the beam from 4 MeV/u to 0.5 MeV/u. Another rebuncher tank of spiral-type will prepare the beam longitudinally for the second deceleration down to 6 keV/u by an RFQ-structure. With this energy the highly-charged ions can be captured in a cylindrical Penning trap and be cooled further by electron and resistive cooling to cryogenic temperatures. The cold ions can be extracted again and transported to the final experiments.

PRODUCTION OF BARE NUCLEI

To provide highly-charged ions up to U^{92+}, which is the design ion for the HITRAP facility, the beam has to pass through three stripping processes. After the U^{4+}-ions are generated either in a high current MEVVA ion source or in a PIG ion source they are accelerated to 1.4 MeV/u by the HSI (High Current Injector) [2] of the UNILAC. Subsequently, a nitrogen gas jet stripper increases the charge state from 4+ to 28+ as the equilibrium charge state, which is needed for acceleration in the Alvarez main accelerator. The fraction of U^{28+} particles amounts to 12 %.

At 11.4 MeV/u a foil stripper, located in the transfer beam line to the SIS18, increases the charge state to 73+ using carbon foils of 600 µg/cm². Again, by the loss of neighbouring charge states only 15 % of the uranium particles remain for injection of 100 µs macro beam pulses into the SIS18 for acceleration to 400 MeV/u. Finally, a copper sheet of 40 mg/cm², located in the beam transfer line between SIS18 extraction and ESR injection strips about 30 % of the uranium ions at the energy of 400 MeV/u to bare nuclei.

The ESR [3] was designed for the deceleration of ions to a minimum energy of 3 MeV/u. Machine experiments have successfully demonstrated the feasibility of U^{92+}-beam deceleration. At 5 MeV/u a U^{92+}-beam intensity of $1 \cdot 10^6$ particles per cycle was achieved and $2 \cdot 10^5$ particles at 3 MeV/u. The corresponding momentum spread was $dp/p = 2.4 \cdot 10^{-4}$ and $dp/p = 1 \cdot 10^{-4}$, detected by Schottky diagnostics. Due to electron cooling the normalized transverse emittances were measured with

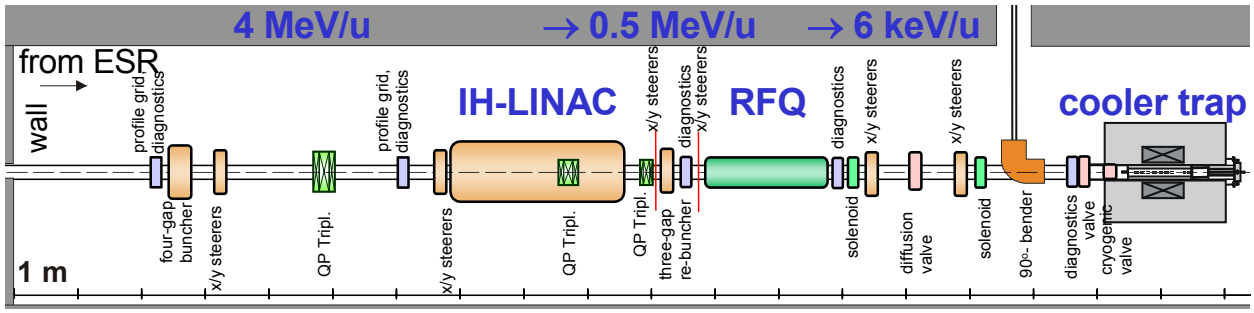

Figure 2: Outline of HITRAP in the re-injection channel between ESR and SIS18.

$\varepsilon_{x,y} = 0.093\ \pi$ mm mrad at 5 MeV/u only and $\varepsilon_{x,y} = 0.06\ \pi$ mm mrad at 3 MeV/u. The measured data are summarized in table 1.

For reliable operation of the ESR, the energy of 4 MeV/u was chosen as design input energy of the HITRAP-decelerator.

THE HITRAP LINEAR DECELERATOR

The experimentally defined beam parameters in the ESR extraction system are the basis for the HITRAP decelerator design. The task is the deceleration of the design ion U^{92+} down to 6 keV/u. Fig. 2 shows schematically the layout of the machine. It will be located in the re-injection channel from the ESR to the SIS18 (see Fig.1). The operating frequency for all structures is 108 MHz, except for the optionally foreseen second harmonic buncher. Table 1 gives an overview of the beam parameters along the HITRAP decelerator.

Table 1: Beam parameters along the HITRAP decelerator

HITRAP Section	Energy [MeV/u]	ΔT/T	$\varepsilon_{x,n}$ (= $\varepsilon_{y,n}$) [π·mm· mrad]	ε_x (=ε_y) [π·mm·mrad]	total Transmission	particles/ spill
ESR	5.0	$4.8 \cdot 10^{-4}$	0.093	0.9		$1 \cdot 10^6$ measured
	4.0		0.1	1.0	100%	$(6 \cdot 10^5)$ estimated
	3.0	$2 \cdot 10^{-4}$	0.06	0.7		$2 \cdot 10^5$ measured
Entrance Prebuncher	4.0	$4.8 \cdot 10^{-4}$	0.2	2.2	100 %	$6 \cdot 10^5$
Entrance IH	4.0	$\pm 1.3 \cdot 10^{-2}$	0.2	2.2	28 %	$1.7 \cdot 10^5$
Exit IH / Entr. RFQ	0.5	$\pm 2 \cdot 10^{-2}$	0.24	7.3	28 %	$1.7 \cdot 10^5$
Exit RFQ	0.006	$\pm 7 \cdot 10^{-2}$	0.37	100	26 %	$1.5 \cdot 10^5$
LEBT, entrance of trap	0.006	$\pm 7 \cdot 10^{-2}$	0.37	100	21 %	$1.2 \cdot 10^5$

First, a four-gap bunching cavity of quarter-wave coaxial line type with an applied effective voltage of 216 kV focuses the beam longitudinally into the IH-type decelerator in a distance of 4 m. This buncher type requests an RF power of only 2 kW. The transverse beam matching to the IH-structure is performed by magnetic quadrupoles.

The IH-structure [4] is designed with only one inner magnetic triplet. The power consumption is below 200 kW, determined by the available RF-amplifiers. For the deceleration of bare Uranium ions from 4 MeV/u down to 0.5 MeV/u a total effective RF voltage of 11.35 MV is applied over 25 gaps in a tank of the length of 2.7 m. Pointing instability of the beam extracted from the ESR has already been investigated. A beam displacement at the entrance of the IH-structure of up to ±1.5 mm does not cause particle losses in the structure. A safety margin of a factor of 2 is considered in the emittance value of 0.2 π mm mrad. Fig. 3 shows the transverse beam envelope from the ESR extraction to the RFQ entrance.

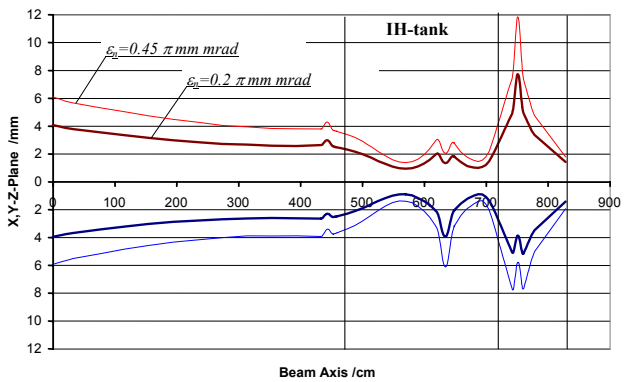

Figure 3: Transverse 98%-beam envelopes for two different emittances. The emittance of 0.45 π mm mrad refers to the acceptance of the IH-structure.

The rebuncher between the IH-structure and the RFQ has to provide a longitudinal focus at the RFQ entrance at 0.5 MeV/u. An existing spiral loaded cavity, equipped with a three-gap electrode structure with a total length of $5 \bullet \beta\lambda/2$, consumes a power below 2 kW.

Finally, a 4-rod RFQ decelerates the beam down to 6 keV/u. The low mass to charge ratio of $m/q \leq 3$ prevents any RF power problem and allows for a compact tank of 1.9 m length. The maximum electrode voltage is 70 kV, the power consumption amounts to 80 kW, fitting to an available RF-amplifier.

The low energy beam transport system (LEBT) (Fig. 4) matches the transverse beam parameters at the RFQ exit onto the required focus at the ion trap entrance. The normalized emittance of $\varepsilon_{x,y} = 0.55\ \pi$ mm mrad includes a safety margin of 50 %. Horizontal and vertical emittances have the same orientations. This permits the use of solenoid magnets. The expected beam energy spread of $\Delta T/T = \pm 7$ % causes a beam halo. Further optimization studies may reduce the energy spread at the exit of the RFQ.

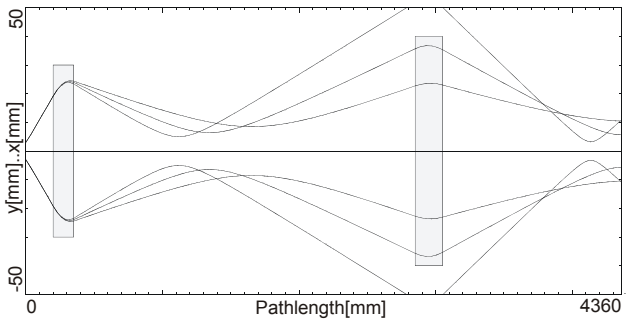

Figure 4: Beam envelopes of the LEBT section for a normalized emittance of $\varepsilon_{x,y,n} = 0.55\ \pi$ mm mrad and energy deviations of ±7 %.

As shown in Table 1, the overall transmission amounts to only 21 % of the particles extracted from the ESR. A gain of factor of two can be achieved by an optional additional second harmonic buncher installed between the first rebuncher and the IH-cavity.

As the ESR ultra-high vacuum system as well as the ion trap runs at a base pressure in the low 10^{-9} Pa region, differential pumping sections have to be integrated into the beam transport line in front of the decelerator and in front of the ion trap. The vacuum of the decelerator itself is planned to be in the low 10^{-5} Pa region.

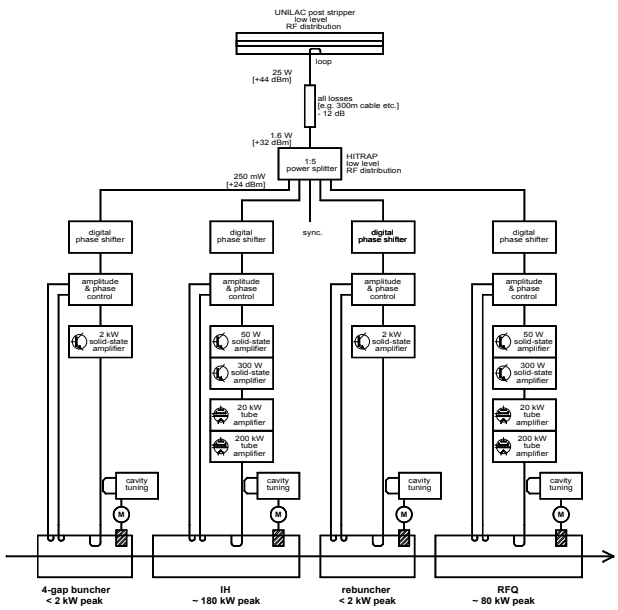

Figure 5: HITRAP RF-system with cavity tuning

Plans are to use two available 30-year-old 200 kW tube amplifiers for the RF-supply. To match the present state of the art they have been upgraded by programmable controls and new amplitude and phase controls. One available power supply can serve for both amplifier chains. To feed the two bunchers, two 2 kW solid-state amplifiers have to be purchased.

The total costs for the HITRAP-facility willl amount to a sum of 4.69 M€. Table 2 summarizes the costs for each component. Due to available equipment the actual costs are only 2.86 M€.

Table 2: Total costs of the HITRAP facility

Investment, equipment, construction (cf. chapter/section)	**Costs[k€]**	**Savings[k€]**
IH structure and bunchers	486	Rebuncher
RFQ cavity	197	
RF supplies	405	1,655
Cooler trap, including 90° bender and valves	306	
Magnets and steerers	80	75
Power supplies for magnets and steerers	319	98
Beam diagnostics	185	
Controls	111	
Vacuum	479	
Civil engineering	103	
Media supply	108	
Safety	81	
Total sum:	**2,860**	**1,828**

OUTLOOK

The HITRAP-project has already been approved but not yet funded. The facility is envisaged to be ready for operation within 30 months after the start of the project in January 2005. Elaborative work was invested in a technical design report taking into consideration all physical, technical, financial, and manpower aspects. In particular, possibilities to save money by the use of existing equipment were taken into account, covering 40 % of the total costs. The two main decelerator structures, the IH-cavity and a 4-rod RFQ, as well as the rebuncher cavities are beeing designed by the Institute of Applied Physics of the University of Frankfurt.

The new HITRAP facility will be the first ever set-up to abundantly provide ions of selected charge states up to U^{92+} at cryogenic temperatures in the laboratory frame, thus allowing to investigate them in a trap or for low energy collision experiments with surfaces or other atoms, ions, and molecules. Experiments of this kind have been impossible up to now.

After successful operation at the ESR and the final shut-down of this storage ring, the HITRAP set-up will be an integral part of the GSI future facility FAIR [5] at a new location behind the NESR (New Experimental Storage Ring). The major areas of investigations with HITRAP will be extended to antiprotons.

REFERENCES

[1] Th. Beier, et al., HITRAP Technical Design Report, GSI Darmstadt, Germany, Oct. 2003

[2] W. Barth, et al., Development of the UNILAC towards a Megawatt Beam Injector, these proceedings

[3] M. Steck, et al., Improved Performance of the Heavy Ion Storage Ring ESR, EPAC, Luzern, Switzerland, 2004

[4] U. Ratzinger, et al., The IH Cavity for HITRAP, these proceedings

[5] An International Accelerator Facility for Beams of Ions and Antiprotons (FAIR), GSI Darmstadt, Germany, Nov. 2001

A DEDICATED 70 MEV PROTON LINAC FOR THE ANTIPROTON PHYSICS PROGRAM OF THE FUTURE FACILITY FOR ANTIPROTON AND ION RESEARCH (FAIR) AT DARMSTADT

L. Groening, W. Barth, L. Dahl, R. Hollinger, P. Spädtke, W. Vinzenz, S. Yaramishev*, GSI, Darmstadt, Germany
B. Hofmann, Z. Li, U. Ratzinger, A. Schempp, R Tiede, Johann Wolfgang Goethe University, Frankfurt a.M., Germany

Abstract

The antiproton physics program of the proposed International Accelerator Facility at Darmstadt is based on a rate of $7{\cdot}10^{10}$ cooled antiprotons per hour. To provide the primary proton intensities a proton linac is planned, which will be operated independently from the existing UNILAC for heavy ions. The proposed linac comprises a proton source, a RFQ, and a DTL. Its operation frequency of 352 MHz allows for an efficient acceleration to up to 70 MeV using normal conducting Crossed-bar H-cavities. These CH-cavities show high shunt impedances as known from IH-structures, but allow for much higher relative particle velocities of up to 50 %. The beam pulses with a length of at least 25 µs, a current of 70 mA, and total normalized transverse emittances of 2.8 µm will allow to fill the existing synchrotron SIS within one multi-turn-injection up to its space charge limit of $7{\cdot}10^{12}$ protons. The maximum SIS ramping rate limits the applied proton linac repetition rate to 4 Hz. This paper gives an overview of the proposed proton linac. The status of the design including beam dynamic studies will be reported. We acknowledge the support of the European Community-Research Infrastructure Activity under the FP6 "Structuring the European Research Area" programme (CARE, contract number RII3-CT-2003-506395).

INTRODUCTION

A new international Facility for Antiproton and Ion Research (FAIR) is projected at GSI in Darmstadt [1], for which the existing UNILAC and the synchrotron will serve as injectors. Beside radioactive ion research a major part of the experimental program is dedicated to pbar physics (Fig. 1). The need at FAIR sums up to $7{\cdot}10^{10}$ cooled pbar/h. Taking into account the pbar production and cooling rate this is equivalent to $2{\cdot}10^{16}$ primary protons/h to be provided by a chain of accelerators comprising an injector linac and two synchrotrons. The achievable primary proton rate is limited by the repetition rate and by the space charge limit (SCL) of the first synchrotron SIS12 (4 Hz). The scaling of its SCL with $\beta^2\gamma^3$ in connection with the cycle times of the two synchrotrons requires an injector providing protons of at least 18 MeV. The SIS12 is filled during one injection pulse by horizontal multi-turn injection (MTI). To reach the SCL, the beam brilliance B_n provided by the injector linac must be above a minimum value, which depends on the specific parameters of the MTI [2]:

$$B_n \equiv \frac{I}{\beta\gamma\varepsilon_x} \geq 63.6\frac{\text{mA}}{\mu\text{m}}\cdot\frac{(\beta\gamma)^2}{\eta_{MTI}} \equiv B_{n,\min}\ , \quad (1)$$

where I is the proton beam current, ε_x is the total horizontal emittance, and η_{MTI} is the efficiency of the

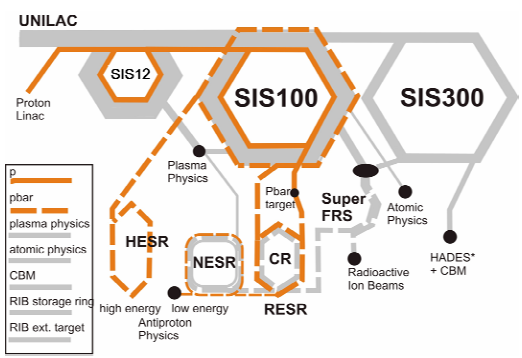

Figure 1: Schematic overview of the accelerator chain to provide cooled antiprotons at FAIR.

*on leave from ITEP, Moscow, Russia

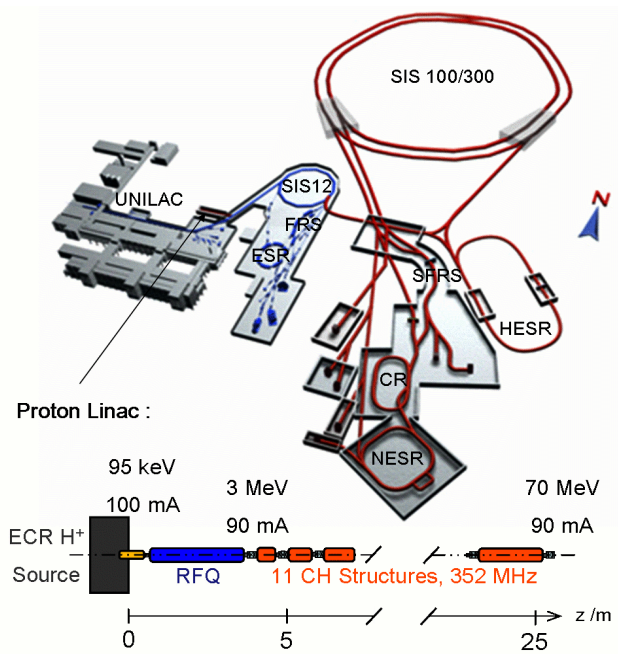

Figure 2: Schematic overview of the new proton injector linac and its implementation into FAIR. The quoted proton currents include safety margins.

MTI. Although the existing UNILAC [3] provides ions from protons to uranium, its design is optimized for heavy ion operation. It could provide a proton beam of 18 MeV with currents of 0.25 mA and a normalized emittance of 1 µm. However, the resulting brilliance is at least one order of magnitude below $B_{n,\min}$, which even increases with higher energies (Eq. 1). Accordingly, a dedicated proton injector linac (Fig. 2) is projected within FAIR which will be operated independently from the existing UNILAC. Table 1 summarizes its design parameters.

The required primary proton rate can be achieved using an injector of 18 MeV. In this case the pbar cooling time is equal to the cycle time for primary proton delivery and the accelerator chain would be fully stretched with pbar production. Higher injection energies increase the SCL of SIS12 hence reducing the number of required SIS12 cycles. Accordingly, the primary proton cycle is shortened thus disengaging capacity for cycles providing other ion species. For a multi-ion facility like FAIR the choice of the proton injector energy is a trade-off between efficient use of cycle times and linac economics.

The injection energy of 70 MeV was considered as an adequate compromise. It results in a pbar duty cycle of 40 % and still allows for linac operation at one single rf-frequency. The output current was set to 70 mA, which imposes challenging but attainable currents on the front-end system. The total normalized transverse design emittances were set to 2.8 µm. Assuming a multi-turn efficiency η_{MTI} of 60 %, the corresponding brilliance B_n amounts to 25 mA/µm leaving a comfortable margin with respect to the required value of $B_{n,\min}$ = 16 mA/µm.

Table 1: Parameters of the FAIR proton linac design.

Source	H+, ECR, 95 keV, 110 mA
LEBT (2-solenoid foc.)	95 keV, 100 mA, 0.3 µm*
RFQ (4-rod / 4-windows)	3 MeV, 90 mA, 0.4 µm* *(norm., rms)
DTL (352 MHz, rt) current emittance rel. momentum spread rf pulse max. beam pulse max. repetition rate	11 CH-structures, 70 MeV 90 mA (design) 70 mA (operation) 2.8 µm** $\pm 5 \cdot 10^{-4}$ 250 µs 25 - 100 µs 5 Hz **(norm., tot)
Overall linac length	≈ 30 m

FRONT-END SYSTEM

An ECR type proton source seems the best choice with respect to long-time reliability and the required time for source maintenance. The ECR design proton current was set to 110 mA to be delivered at pulses of 1 ms length at 5 Hz. The LEBT design is based on 2-solenoid focusing to provide at least 100 mA of protons for the injection into the subsequent RFQ. This focusing scheme will also assure the separation of protons from H_2^+ and H_3^+ ions. At CEA/Saclay the SILHI source & LEBT set-up [4] is under operation which fits well to our requirements with respect to the design beam parameters.

Accordingly, the input beam parameters of the RFQ are chosen in agreement with the output parameters at the LEBT demonstrated experimentally at SILHI. Joint measurements on various beam parameters are planned at CEA/Saclay for the beginning of 2005 in order to optimize the matching into the RFQ. Based on former measurements performed at cw-operation of SILHI, the design input current and transverse emittances for the RFQ are chosen as 100 mA and 0.3 µm (norm., rms), respectively. These parameters allow for at least 90 mA and less than 0.4 µm at the RFQ output. Conceptual RFQ designs are currently under development for two different RFQ types simultaneously (Fig. 3): at the University of Frankfurt a RFQ of 4-rod type is proposed [5] while at ITEP/Moscow the layout of a 4-windows RFQ is under investigation.

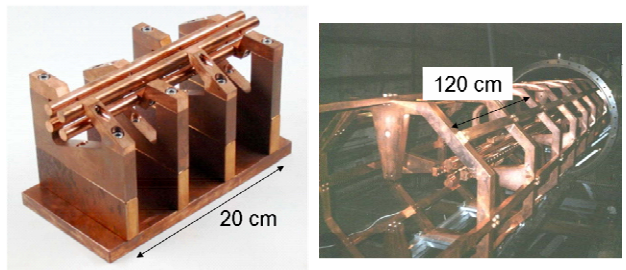

Figure 3: Part of a model for a 4-rod RFQ at 352 MHz (left) [5] and a prototype of a 4-windows RFQ at 27 MHz [6] (right).

The 4-rod type is successfully in use at several proton linacs and the University of Frankfurt acquired a huge experience in 4-rod RFQ design and construction, which is less arduous with respect to 4-vane types and its costs are significantly lower. However, 4-rod RFQs inhabit an intrinsic magnetic dipole field component due to the asymmetric installation of their stems, which can be compensated partially. We foresee the construction of a cold model to optimize the rf-field quality.

4-vane RFQs in turn offer higher field quality and an increased mechanical stability. This type is commonly in use at recent high intensity proton linacs operating at frequencies higher then 300 MHz. However, these features come along with a more complicated implementation of cooling and with increased overall costs with respect to a 4-rod RFQ. The 4-windows type RFQs developed at ITEP/Moscow [6] promise to merge the advantages of the 4-rod and of the 4-vane types, i.e. high field quality at moderate costs. A 4-windows RFQ is foreseen to be used within the RIA project [7] and is also an interesting option for the FAIR proton linac. On the other hand both types considered (4-rod & 4-windows) had not been built at a frequency of 352 MHz yet. Design studies are done for both types and the decision on the final design of the FAIR proton linac RFQ is scheduled for spring of 2005.

MAIN LINAC

In order to reduce the overall linac costs, the main objective of the linac design is to maximize the acceleration efficiency. At heavy ion linacs very high effective shunt impedances were achieved using Interdigital H-mode (IH) structures in combination with the KONUS beam dynamics [8]. There is a high interest to extend the successfully demonstrated features of IH-structures to light ion linacs, i.e. to higher particle velocities of up to β=0.5. Accordingly, Crossed-bar H-mode (CH) structures (Fig. 4) are presently under development at the University of Frankfurt [9]. They are operated in the H_{210}-mode and the installation of the stems result in an even higher mechanical stability with respect to IH-structures.

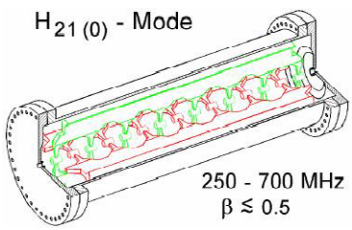

Figure 4: Sketch of a Crossed-bar H-structure (CH) presently under development at the University of Frankfurt [8].

The FAIR proton linac output energy of 70 MeV can be reached with 11 independent CH-tanks operated at one single rf frequency of 352 MHz, which developed to a common operating frequency of the low energy part of projected high current proton linacs in Europe. With the CH-structures velocity dependent effective shunt impedances ranging from 45 MΩ/m to 100 MΩ/m seem attainable corresponding to a total rf power of up to 1.3 MW per cavity including beam loading of up to 0.5 MW at 70 mA. The rf pulse length will be 250 µs at 5 Hz resulting in a rf duty cycle being very close to the present layout of Linac4 at CERN [10]. Since both linacs will operate at 352 MHz, a joint CERN/GSI development and commissioning program on pulsed klystron power supplies at 352 MHz was initiated. It implies systematic testing of the CH-structures at GSI in 2006. A study on mechanical structure design including investigations on tolerable deformations is under progress as well.

Multi-particle simulations on the CH-DTL KONUS beam dynamics were done [11] for different layouts of the beam optics at the DTL entrance. Figure 5 shows the beam envelopes along the section. The RFQ-DTL matching section can be designed very compact if the matching quadrupoles will be integrated into the first cavity. Alternatively, a dedicated matching section before the DTL offers increased flexibility for the operation of the linac and will simplify the design of the first cavity. Both options are presently under investigation and show full transmission of a 70 mA input beam with an emittance of 0.3 µm from the RFQ. The emittance growth

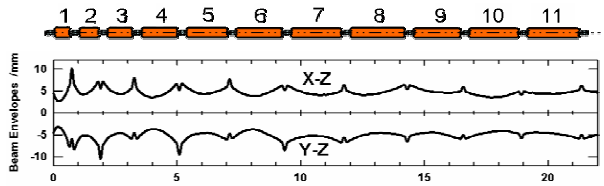

Figure 5: Transverse beam envelopes along the CH-DTL according to multi-particle simulations [11].

is sufficiently small in order to attain the design emittances at the injection into the SIS12. However, it is foreseen to achieve a design which also copes with a DTL input current of 90 mA.

SUMMARY

The requirements of the FAIR project on primary proton intensities can be met with a new dedicated injector linac providing 70 mA of protons at 70 MeV. The use of CH-structures allows for high effective shunt impedances and thus for a compact 352 MHz linac. The design of the RFQ and of the DTL section is in progress. Recent simulations on beam dynamics show that all requirements on beam quality can be fulfilled. The design of the front-end including the RFQ is planned to be completed in 2005 and CH-structure testing will start in 2006. A TDR is scheduled for 2007 followed by the beginning of civil construction.

REFERENCES

[1] *An International Accelerator Facility for Beams of Ions and Antiprotons*, Conceptual Design Report, GSI, p. 503, (2001).

[2] L. Groening, *Beam currents and emittances of the front-end of the GSI proton linac and of other facilities*, UNILAC-Arbeitsnotiz, (2003).

[3] W. Barth et al., *Development of the UNILAC towards Megawatt Beams,* these proceedings.

[4] R. Gobin et al., *Saclay High Intensity Light Ion Source Status*, Proc. of EPAC2002, p. 1712, Paris, (2002).

[5] A. Schempp et al., *Design of a 352 MHz Proton RFQ for GSI*, these procedeedings.

[6] D. Kashinsky et al., *Commissioning of ITEP 27 MHz Heavy Ion RFQ*, Proc. of EPAC2002, p. 854, Vienna, (2002).

[7] P. N. Ostroumov et al., *Design of 57.5 MHz cw RFQ for medium energy heavy ion superconducting linac*, Phys. Rev. ST Accel. Beams 5, 060101, (2002).

[8] U. Ratzinger et al., *Status of the HIIF RF Linac Study Based on H-Mode Cavities*, NIM A 415, p. 229, (1998).

[9] Z. Li, *Design of the R.T. CH-Cavity and Perspectives for a New GSI Proton Linac*, these proceedings.

[10] R. Garoby et al., *Design of the Linac4, a New Injector for the CERN Booster*, these proceedings.

[11] R. Tiede et al., *KONUS Beam Dynamics Design of a 70 mA, 70 MeV Proton CH-DTL for SIS12 at GSI*, these proceedings.

HIGH CURRENT BEAM TRANSPORT TO SIS18

S. Richter[#], W. Barth, L. Dahl, J. Glatz, L. Groening, S. Yaramishev[1],
Gesellschaft für Schwerionenforschung, D-64291 Darmstadt, Germany

Abstract

The optimized transversal and longitudinal matching of space charged dominated ion beams to the heavy ion synchrotron SIS18 is essential for minimizing injection losses. This paper focuses on the beam dynamics in the transfer line (TK) from the post-stripper accelerator of the Unilac to the SIS18. Transverse beam emittance measurements at different positions along the TK were done. In particular, the different foil stripping modes were investigated. A longitudinal emittance measurement set-up was commissioned at the entry to the TK. It is used extensively to tune all the rebunchers along the Unilac. In addition, a test bench is in use for measurements of longitudinal bunch profiles, enabling the monitoring of the final debunching to SIS18. Multi particle simulations by means of PARMILA allow a detailed analysis of experimental results for different ion currents.

INTRODUCTION

For the FAIR project the Unilac and SIS18 combination is foreseen to serve as an injector for the SIS100 [1]. To gain the envisaged intensities, up to 10^{12} U^{28+} particles/s must be injected from the Unilac into the synchrotron. To reach this number, different measures must be undertaken to achieve this goal.

Since the successful commissioning of the Unilac High Current Injector (HSI) the particle numbers for the heaviest ions have steadily increased due to constant machine improvement [2].

The high current within the 100 µs pulses offered by the HSI/poststripper accelerators must be transported via the 130 m transfer line (TK) to SIS18. The TK is divided into nine sections (TK1-TK9). A foil stripper in section three allows stripping to higher charge states for SIS18 injection, the charge state analysis is done by using dipole magnets in section 4; the beam is inserted during 20 turns. Typically the ions are stripped at a foil stripper in the TK for SIS18 operation. The ion beam may either be kicked, or in order to reduce the thermal stress, be swept over the foil. For the design ion uranium the charge state equilibrium changes from U^{28+} to U^{73+}. The beam can be manipulated longitudinally after the poststripper by two bunchers.

Table 1: Beam parameters required for SIS18 injection at 11.4 MeV/u.

$\varepsilon_{n,x}$ [mm mrad]	0.8
$\varepsilon_{n,y}$ [mm mrad]	2.5
$\Delta W/W$	$\pm 2 \cdot 10^{-3}$

[#] S.Richter@gsi.de
[1] on leave from ITEP, Moscow, Russia

For an optimum SIS injection both the transversal and longitudinal matching conditions have to be met (see table 1).

Until the end of 2003 the only available longitudinal diagnosis in the Unilac were the phase probe signals, and after a successful injection into SIS18 the Schottky analysis of the circulating beam on the injection plateau.

The TK is currently equipped with two transverse emittance measurement devices and one longitudinal emittance measurement device which was recently commissioned.

PARMILA SIMULATIONS

The multi particle simulations indicate different regions where further experimental investigations should be carried out and additional beam diagnosis elements should be installed. A full description of the beam transport line from the Alvarez accelerator section to the SIS18 injection point at the end of the transfer channel was compiled for PARMILA simulations [3]. After the Alvarez a single gap resonator is used as a rebuncher.

As an outcome of the simulations, the region after the foil stripper is identified as a beam transport line where strong space charge influences are expected. This is due to the approx. 25 m drift of the not yet analyzed multi-charge beam to the charge state separator. Thus, a comparison between the theoretically determined emittances at the exit of the Alvarez section, the stripper section and before SIS injection (see Fig. 1) can be performed. The installed beam diagnostic elements allow a comparison of simulations and measurement.

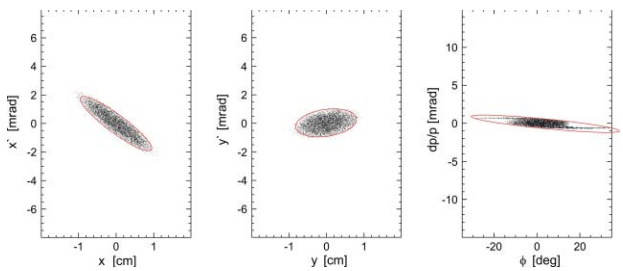

Figure 1: Calculated transversal and longitudinal emittances at the end of the TK.

TRANSVERSE EMITTANCE MEASUREMENTS

Machine development strongly focused on the systematic investigation of emittance growth along the whole Unilac. The results from the last campaigns during 2003 and 2004 are presented here [4]. Two ion species – uranium and argon - delivered by the HSI were investigated. The uranium beam was produced in a MEVVA ion source, whereas argon beam was delivered

by the MUCIS. The transverse emittance measurements were carried out behind the Alvarez exit, the foil stripper where the two different modes (kicked - TK5-Ki - and sweeped - TK5-Sw) were analyzed, and in TK8 (for sweeper mode) before the SIS18 injection.

To determine the emittance growth due to the space charge effects, measurements were done with full and reduced intensity. The attenuation was done by reducing the gas stripper pressure behind the HSI. This method ensures that there is no influence on the emittance size before the Alvarez entrance. The conditions for the beam envelope at the TK-foil-stripper are a waist in the horizontal plane and a broad beam in the vertical one.

In high current uranium operation the kicker mode cannot be used as the foil would be destroyed due to the thermal stress, no measurement was performed in the TK8 region.

The 90 % normalized emittances for low and high current argon and of uranium beams respectively are shown in Fig. 2. The upper part displays the results for the horizontal plane and those for the vertical plane are shown in the lower part.

For comparison the green line indicates the acceptance of the SIS18.

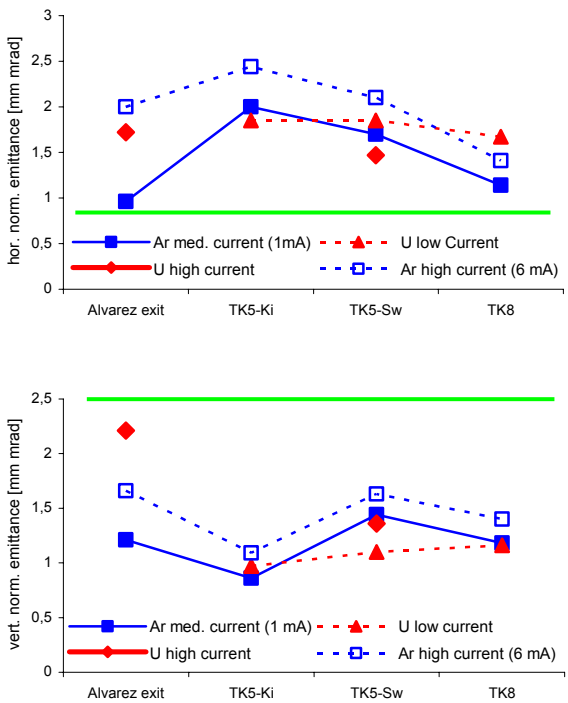

Figure 2: 90 % normalized transverse emittances along the TK. All measurements were performed at an energy of 11.4 MeV/u. Intensities are given for Alvarez exit.

For the horizontal plane an emittance growth is visible between the Alvarez exit and stripping region, whereas a slight size reduction in the vertical plane is detected. This observation can be explained by the strong space charge forces after the foil stripper, where the separation has not yet taken place. Thus a strong coupling between the horizontal and vertical phase space is established.

If the emittances for the two argon intensities are compared a much stronger influence of the space charge forces can be detected for the 6 mA case.

The emittance decrease in TK8 is explained by losses between TK5 and TK8.

LONGITUDINAL EMITTANCE MEASUREMENTS

Next to the transverse emittances the knowledge and tuning of the longitudinal beam parameters is crucial for an optimisation of the matching to the SIS. The phase probe signals have proved not to deliver sufficient information to tune the two bunchers after the Alvarez exit. To gain the necessary information at the entrance of the TK, a longitudinal emittance measurement was installed at the end of 2003.

The schematic layout of the configuration is shown in fig. 3.

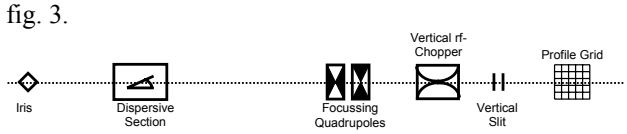

Figure 3: Schematic layout of the longitudinal emittance measurement. For explanation see text.

The insertion region in the transfer channel with its three dipole magnets provides the dispersion needed to monitor the energy spread of the beam. To get a sufficiently small focus in the transversal analysis plane, a rhomb aperture with a typical radius of 1 mm transversally trims the beam which then drifts through the dispersive section and is focussed with a quadrupole doublet. To gain information about the phase distribution a 108 MHz rf-chopper was installed behind the third dipole at the beginning of the focussing drift section. The chopper is used to deflect the beam vertically, corresponding to its phase dispersion.

Simulations (see Fig. 4) for the theoretically achievable resolution ($\Delta p/p = 2.7 \cdot 10^{-4}$, phase dispersion 1°) were done with MIRKO [5] and could be confirmed during the commissioning of the device.

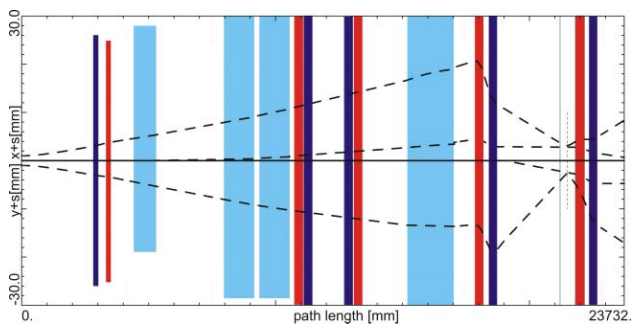

Figure 4: Theoretical simulation of transversal beam envelopes for longitudinal emittance measurement. (Colour scheme red/dark blue: focussing/defocussing

quadrupole, light blue: dipole, dotted line: envelope in x and y)

The analysis of the horizontal plane of the profile grid gives the information about the momentum spread, bunch length, and orientation of the longitudinal phase ellipse. So far only one measurement of the ellipse was possible, but the calibration of rf-chopper amplitude has not been done yet, so that a full evaluation of the emittance size could not be performed.

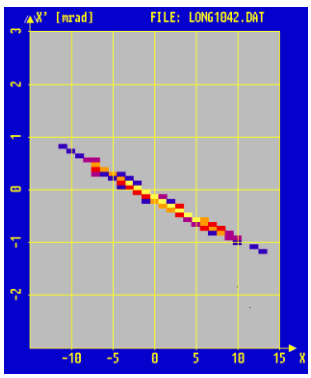

Figure 5: Result of a longitudinal emittance measurement.

Thus Fig. 5 shows in arbitrary units the phase width on the abscissa and the momentum spread on the ordinate. The theoretical limit for the resolution could not be reached in that case, as the opening diameter of the iris was 2 mm. Thus more than one wire on the profile grid was hit. To transform the measured data into values to determine the emittance size, the calibration of the buncher has still to be done.

First commissioning experiments promised that even without measuring the full emittance, this measurement device is a very helpful tool to set up the rebuncher correctly. The information gained at this point (after the first rebuncher) can be used to be fed into a simulation that gives the correct setting for the second buncher.

A viewing screen is planned to substitute the profile grid, to have an instantaneous picture of the longitudinal emittance and to tune online the beam properties with the rebuncher after the Alvarez exit.

LONGITUDINAL BUNCH PROFILE MEASUREMENT

To gain further longitudinal information just before the injection into SIS18 a bunch shape measurement [6,7] will be installed in the TK8 region. This detector is capable of determining non-destructively the bunch structure in the range of 0.1 to 5 ns as it uses the time spectra of secondary electrons created by residual gas interaction. The time spectrum is transformed into a spatial separation by an rf-deflector driven by the main acceleration frequency. A multi-channel plate equipped with a phosphor screen is observed by a CCD camera. The achievable time resolution is 50 ps, which corresponds to 2° for the 108 MHz acceleration frequency.

To reconstruct the longitudinal emittance, the voltage amplitude of the buncher cavity is varied and the bunch length is measured correspondingly. A parabola is fitted through the square of the bunch width and gives then an estimate for the emittance.

First successful test measurements in the Experimental Hall of the Unilac were performed for different ion beams at 11.4 MeV/u.

CONCLUSION AND OUTLOOK

The multi particle simulations indicate the critical regions for the beam transport in the transfer line to SIS18. These regions are already or will be equipped in the near future with additional beam diagnosis devices. To overcome the strong space charge forces after the foil stripper, a new compact charge state separator [8] with the separation directly behind the foil is foreseen.

The determination of the transverse beam emittances along the TK is sufficient. The measured transversal normalized emittances for space charge dominated beams are in the region of 1.5 mm·mrad for both planes. For zero current beams the emittances fit very well to the SIS18 acceptance.

To obtain full benefit from the transversal and longitudinal emittance measurement devices, a concept for an operating instruction will be developed. The transverse emittance measurements are applied to an online MIRKO simulation of the TK (after the foil-stripper) which should allow a good matching to the required parameters for SIS18 injection. The longitudinal properties of the beam will be tuned independently of the Schottky diagnosis in the SIS18, by especially setting up the beam line automatically for the measurement of the longitudinal emittance at the entrance of the transfer line. The result of this measurement will then be used to tune the second buncher.

There is strong expectation to improve significantly the matching to SIS18 and prepare the Unilac operation for the FAIR facility.

REFERENCES

[1] An International Accelerator Facility for Beams of Ions and Antiprotons, Concept. Design Report, GSI, 2001

[2] W. Barth, et. al., Development of the UNILAC Towards a Megawatt Beam Injector, these proceedings

[3] L. Groening, private communication

[4] W. Barth, et. al., GSI-ann. rep., p 207 (2003)

[5] B. Franzcak, MIRKO - An Interactive Program for Beam Lines and Synchrotrons, Europhysics Conf. on Computing in Acc. Design and Operation, Berlin (1983)

[6] P. Forck, et. al., A Novel Device for Non-intersecting Bunch Shape Measurement at the High Current GSI-Linac, Proc. of the EPAC-04, Lucerne, (2004)

[7] A. Peters, P. Forck, Non-Interfering Beam Diagnostic Developments, these proceedings

[8] J. Glatz, B. Langenbeck, The High current Charge Stripper, Conf. on Magnet Technology, IEEE Transaction on Magnetics (2000)

INVESTIGATION OF THE BEAM MATCHING TO THE GSI-ALVAREZ DTL UNDER SPACE CHARGE CONDITIONS

S. Yaramishev[1,2], W. Barth, L. Dahl, L. Groening, S. Richter
Gesellschaft für Schwerionenforschung, D-64291 Darmstadt, Germany

Abstract

The main part of the UNILAC consists of the 36 MHz high current RFQ/IH-injector, a gas stripper at an energy of 1.4 MeV/u and a 108 MHz Alvarez poststripper, accelerating ions up to 11.4 MeV/u. The design beam current for U^{28+} is 12.6 emA at full energy. After the stripping process the electrical beam current is increased by a factor of 7 for uranium. This leads to a significant beam emittance growth during the transport through the charge state separator and the matching section to the Alvarez DTL. This paper reports results of numerical studies and beam experiments focused on the matching of the high intensity beams to the Alvarez for different ion species. Possible improvements of the transverse focusing in the Alvarez linac are discussed and the total impact to the beam quality at the synchrotron injection is evaluated.

GSI UNILAC

The UNILAC [1] is designed to accelerate all ion species with mass over charge ratios of up to 8.5 and to fill the heavy ion synchrotron SIS up to its space charge limit. The main part of the UNILAC consists of the 36 MHz high current injector (HSI), a gas stripper section at energy of 1.4 MeV/u and a 108 MHz Alvarez type poststripper, accelerating ions up to 11.4 MeV/u (Fig.1).

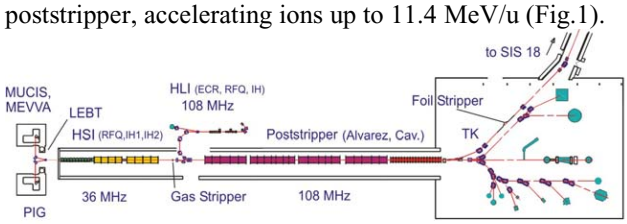

Figure 1: Schematic overview of the GSI UNILAC.

The prestripper section HSI [2] consists of two ion source terminals (PIG and MUCIS/MEVVA), the Low Energy Beam Transport (LEBT), a Radio Frequency Quadrupole accelerator (RFQ), a short matching section (superlens), and two IH (Interdigital H-structure) tanks.

The HSI has been in routine operation since 1999 and has achieved the design intensities for light and medium ions with a significant surplus of the primary beam current coming from the ion source. For heavy ions the achieved beam intensities behind HSI are about factor of two lower than the design values. Several measures were proposed and partially realized for the increase of the beam current and brilliance at the entrance of the synchrotron SIS 18 [3].

[1] S.Yaramishev@gsi.de
[2] On leave from ITEP, Moscow, Russia.

GAS STRIPPER SECTION

In the UNILAC gas stripper section [4] the charge states of incoming ions at energy of 1.4 Mev/u with a charge to mass ratio of $A/q \leq 65$ are increased by stripping in a nitrogen gas jet to allow for further acceleration at $A/q \leq 8.5$. The design U^{4+} beam current of 15 emA rises up to 7 times during stripping. The U^{28+} ions with design beam current of up to 12.6 emA have to be separated entirely from the neighbouring charge states.

Space charge parameter (SCP), calculated from the results of the uranium beam dynamics simulation in the UNILAC, is shown on Fig.2. As can be seen, the SCP is the highest in the stripper area, but it decreases rapidly with particle separation. Another significant peak at the entrance of the 1st Alvarez tank appears due to the small size of the beam in all three dimensions, as required for the beam matching.

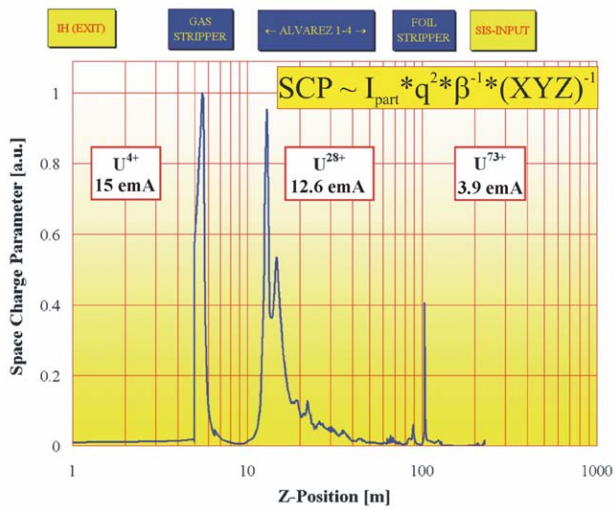

Figure 2: Space charge parameter along UNILAC.

Therefore the separation of the required ion species and the beam matching to the DTL structure are taking place under extremely high space charge influence.

A special optimization procedure, described below in detail, was proposed for the beam matching to the DTL and successfully implemented during machine experiments. It must be pointed out that the recently described procedure does not take into account the defocusing space charge forces. Nevertheless, for the maximum achieved beam current behind the stripper section for the U^{28+} (4 emA), the proposed method was implemented and transmission through the whole Alvarez section up to 100% was reached.

However, the design beam current behind the stripper section is about factor of three higher (12.6 emA for

U^{28+}). The FAIR project [5] requires a uranium beam current even up to 15 emA. For these cases a much more complicated matching which also depends on the longitudinal structure of the beam is necessary.

The postaccelerator performance can also be improved by the optimization of the quadrupole settings in Alvarez DTL. It is most important in the 1st Alvarez tank [7], where increasing of the quadrupole strength leads to the higher phase advance of the focusing channel.

Due to the high mass to charge ratio of $^{238}U^{28+}$ ions, the maximum zero current phase advance σ_0 in the 1st Alvarez DTL is limited to 45° by the quadrupole power supplies. For a $^{40}Ar^{10+}$ beam mass to charge ratio is less, which allows the experimental study of the phase advance influence to the beam quality in the Alvarez accelerator. The space charge effects can be scaled from argon beam to uranium. To satisfy the requirements of the FAIR project, the intensities of Ar^{10+} beams up to 11 emA have been studied experimentally.

Accordingly, systematic numerical studies have already been started in collaboration with the several institutions over the world.

Matching Section

After the separation of the U^{28+} ions the beam must be matched to the periodic solution of the beta function of the 1st Alvarez DTL. The 6-D matching of the beam is carried out by a system consisting of the 36 MHz rebuncher, the quadrupole doublet, the quadrupole triplet and the 108 MHz rebuncher (Fig.3).

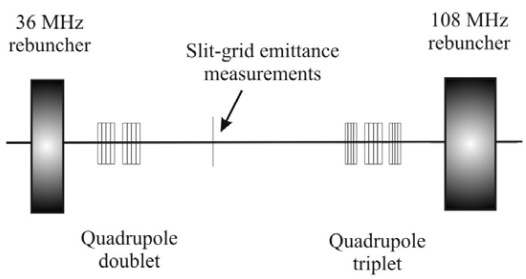

Figure 3: Matching section to the 1st Alvarez DTL.

Usually empirical matching can be done by a variation of the quadrupole settings preceding the DTL until a sufficient transmission through the Alvarez section of more than 90% is achieved. In order to increase the transmission close to 100%, a systematic matching procedure was proposed and realized during machine experiments. The method includes calculations of beam dynamics by means of MAD8 code in matching line to the 1st Alvarez tank and is based on the beam emittance measurements.

Emittance Measurements

The transverse phase space distribution (Fig.4) in front of the DTL is measured in both directions with a slit-grid device placed between quadrupole doublet and triplet (Fig.3). From the obtained data the beam Twiss parameters are extracted.

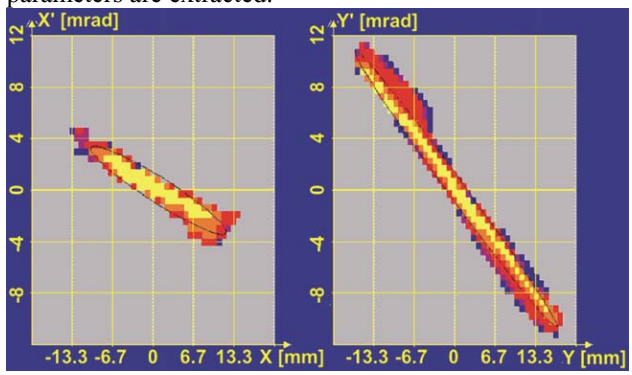

Figure 4: Data of emittance measurements at the matching section for 4 emA U^{28+} beam. Level of intensity is shown by the colour scale.

Optimization Procedure

Knowing the settings of the quadrupoles in the matching section, the measured Twiss parameters are transformed back to the entry of the matching section. The obtained Twiss parameters are used for the calculation of the horizontal and vertical beta-functions of the beam in the matching section and first cells of the 1st Alvarez tank (upper graph of Fig.5).

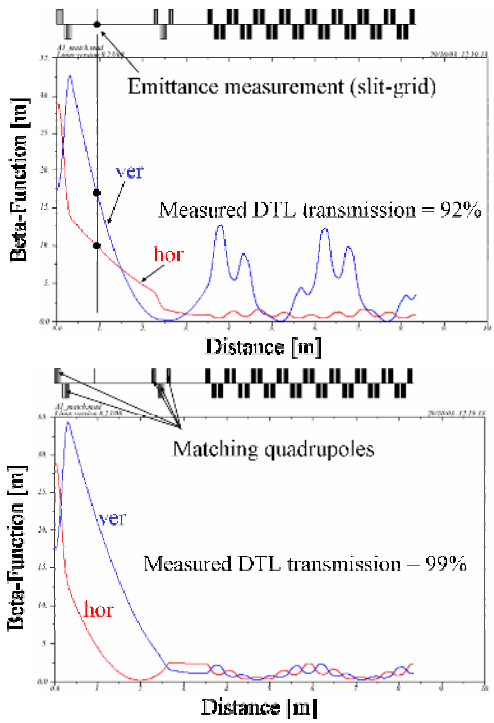

Figure 5: Horizontal and vertical beta-functions in the matching section and first cells of the 1st Alvarez tank with quadrupole setting before (upper graph) and after (lower graph) optimization.

In general the beam is mismatched with the DTL resulting in large beta function oscillations along the whole Alvarez accelerator, which may cause transmission losses and emittance growth.

Using the quadrupole settings in the first cells of the DTL the periodic solution for the 1st Alvarez tank is calculated. To match the periodic DTL solution, a fitting routine involving the five matching quadrupoles is applied. The optimized quadrupole settings provide the Twiss parameters, which are better matched to the DTL.

Applying these strengths the losses along the Alvarez section were reduced from 8% to less than 1%, being the resolution of the transmission measurement.

MULTI-PARTICLE BEAM DYNAMICS SIMULATIONS

Transmission in A1-A4 tanks as a function of beam current was measured during experiments by changing the gas pressure in the stripper and also was simulated by means of the DYNAMION code [6]. The measured transmission was about 90% and the simulated one is about 97% in range of beam current up to 4 mA of U^{28+} beam. The DYNAMION simulations were done from the position of the emittance measurements. The transversal input distribution of the particles was generated from the experimental data. The number of multi-particles in each bin is proportional to the measured beam intensity. The longitudinal distribution was obtained from the beam dynamics simulations in the IH tanks and stripper section with the codes LORASR and PARMTRA (Fig.6).

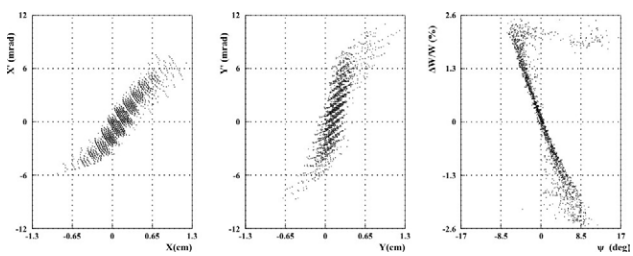

Figure 6: The particle distribution at the entrance of the 1st Alvarez tank simulated with the DYNAMION code from the position of emittance measurements.

The DYNAMION simulations of the beam dynamics in the 1st Alvarez tank show high transmission, but also oscillation of transverse beam envelopes and remarkable emittance growth, which leads to the particle losses in the following part of the UNILAC.

OPTIMIZATION OF THE DTL

The procedure, described above, was implemented to the matching of 6 emA argon beam (corresponding to a 12.6 emA uranium beam) to the 1st Alvarez tank with different values of the phase advance σ_0.

The transmission rises with the increasing of the phase advance up to 50° and then comes to the saturation level. Measurements of the beam emittance have been done with a slit-grid device behind the whole Alvarez section. The beam brilliance in dependence of the phase advance in the 1st Alvarez tank is shown in Fig.7. As can be seen, a phase advance σ_0>50° is required to increase the beam brilliance.

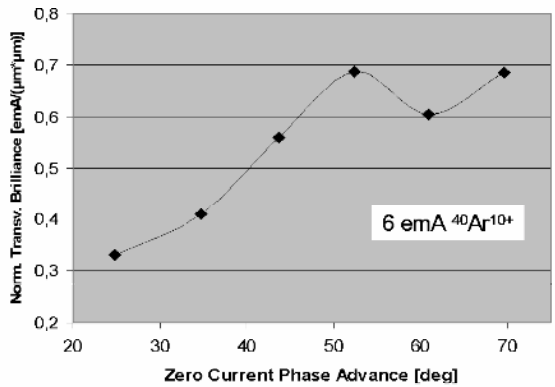

Figure 7: Brilliance of an Ar^{10+} beam behind the Alvarez section as a function of the transverse phase advance σ_0.

CONCLUSION

An efficient method for beam matching to the Alvarez section of the UNILAC was proposed and successfully realized for the beams with medium intensities. The matching of the required for FAIR space charge dominated beam needs more complicated procedures. Numerical studies of the problem have already been started. It is shown that the beam brilliance behind the Alvarez accelerator can be improved. The plans are to upgrade part of the power supplies for the quadrupoles of the 1st Alvarez tank, resulting in a higher phase advance σ_0 for the uranium case. These measures should lead to higher transmission, less emittance growth in the DTL and a significantly improved quality of the beam injected into the synchrotron. We acknowledge the support of the European Community-Research Infrastructure Activity under the FP6 “Structuring the European Research Area” programme (CARE, contract number RII3-CT-2003-506395) and under INTAS project 03-54-3543.

REFERENCES

[1] W. Barth et al., Development of the UNILAC towards a Megawatt Beam Injector// these proceedings.

[2] W. Barth et al., Commissioning of the 1.4 MeV/u High Current Heavy Ion Linac at GSI// Proc. LINAC-2000, Monterey, USA, 2000.

[3] W. Barth et al., Achievements of the High Current Beam Performance of the GSI UNILAC// EPAC-04, Lucerne, 2004.

[4] W. Barth et al., The New Gas Stripper and Charge State Separator of the GSI High Current Injector// Proc. LINAC-2000, Monterey, USA, 2000.

[5] W. Henning, An International Accelerator Facility for Research with Ions and Antiprotons// EPAC-04, Lucerne, 2004.

[6] A. Kolomiets et al., DYNAMION - The Code for Beam Dynamics Simulation in High Current Ion Linac// Proc. EPAC-98, Stockholm, Sweden, 1998.

[7] L. Groening et al., Measurements and Simulations on the Beam Brilliance in the Universal Linear Accelerator UNILAC at GSI// Proc. LINAC-02, Kuongjui, Korea, 2002.

STATUS OF THE 7 MeV/u, 217 MHz INJECTOR LINAC FOR THE HEIDELBERG CANCER THERAPY FACILITY

B. Schlitt, K. Dermati, G. Hutter, F. Klos, C. Muehle, W. Vinzenz, C. Will, O. Zurkan
GSI, Darmstadt, Germany
A. Bechtold, Y.R. Lu, U. Ratzinger, A. Schempp, IAP, Frankfurt am Main, Germany

Abstract

A clinical synchrotron facility designed by GSI for cancer therapy using energetic proton and ion beams (C, He and O) is under construction and will be installed at the university hospital in Heidelberg, Germany, starting in 2005. The status of the ECR ion source systems, the beam line components, the 400 keV/u RFQ and the 20 MV IH cavity as well as the linac RF system is reported. The production of most of the components is in progress. First devices have been delivered to GSI already. The RF cavities of the injector linac have been designed in close cooperation between GSI and IAP. A beam test stand for the RFQ using proton beams is presently being set up at the IAP. Two prototype magnets of the linac quadrupole magnets have been built at GSI and have been tested successfully. An 1.4 MW, 217 MHz cavity amplifier has been delivered by BERTRONIX recently. A test bench for this system has been installed at GSI including a 120 kW driver amplifier.

INTRODUCTION

A dedicated clinical Heavy Ion CAncer Therapy facility (HICAT) has been designed at GSI and will be built at the university hospital in Heidelberg, Germany [1][2]. The accelerator chain is designed to accelerate low-LET (linear energy transfer) ions (p, He) as well as high-LET ions (C, O) to cover the specific medical requirements. It consists of two ECR ion sources, a 7 MeV/u injector linac and a compact 6.5 Tm synchrotron to accelerate the ions to final energies of 48 – 430 MeV/u. Three treatment stations (two fixed horizontal beam lines and one isocentric ion gantry) as well as a quality assurance place for R&D activities are planned. The facility is designed to treat more than 1000 patients per year using the intensity controlled rasterscan method, which has been developed at GSI and has been successfully applied with carbon ion beams to about 230 patients since more than six years within the GSI therapy project [3]. The requested maximum beam intensities at the treatment places are 1×10^9 $^{12}C^{6+}$ ions/spill and 4×10^{10} protons/spill. Only active and no passive beam manipulating systems are planned.

The layout of the injector linac is presented in Fig. 1 [4][5], major linac parameters are listed in Table 1. The low energy beam transport lines (LEBT) consist of two independent spectrometer lines and allow for a fast selection between two different ion species by a switching magnet. DC operation is planned for the ion sources. A short beam pulse with a length of up to about 300 µs will be formed by a macropulse chopper. The RF linac consists of an 1.4 m long four-rod type RFQ for acceleration of the ions to 400 keV/u [6][7], a very compact intertank matching section [4] and a 3.8 m long 20 MV IH-type drift tube cavity [4][5][8][9]. The remaining electrons of the ions will be stripped off for all ion species in a thin stripper foil behind of the linac.

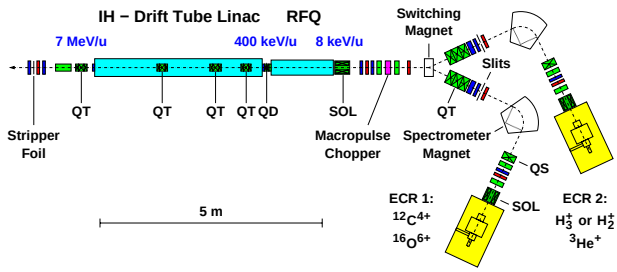

Figure 1: Schematic drawing of the injector linac. SOL ≡ solenoid magnet; QS, QD, QT ≡ magnetic quadrupole singlet, doublet, triplet.

Table 1: Selection of major linac parameters.

Ion species (from ion sources) and required ion source currents	$^{12}C^{4+}$: 130 µA H_3^+: 440 µA $^{16}O^{6+}$: 100 µA $^3He^+$: 320 µA
Ion mass-to-charge ratio	$A/q \leq 3$
Final beam energy	7 MeV/u
Operating frequency	216.816 MHz
RF pulse length	≤ 500 µs @ PRR ≤ 10 Hz

GENERAL STATUS

The components for the complete HICAT facility like vacuum chambers, magnets, power supplies, the RF systems and the accelerator control system have been ordered from industry in 2003. Most of the manufacturing drawings are completed and the production of the components is in progress. The first solenoid magnet for the LEBT has been delivered by SIGMAPHI to GSI last week.

Two complete 14.5 GHz SUPERNANOGAN ECR ion source systems have been ordered from PANTECHNIK [10]. Major components of the ion sources are fabricated and assembled already. Factory acceptance tests are planned for the fourth quarter of this year.

An overview of the beam diagnostics devices for the complete HICAT facility is given in Ref. [11]. The mechanical parts such as detector housings, stepping motor and pneumatic drives are produced or integrated by GSI whereas for the software and the electronic devices industrial solutions are preferred. The production of first

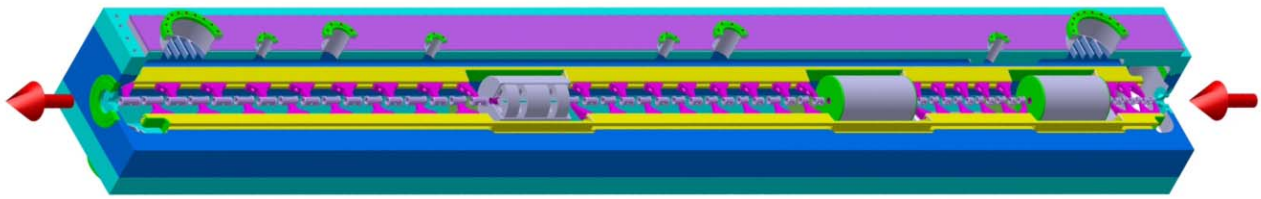

Figure 2: Design of the 20 MV IH cavity. The arrows mark the beam direction. In the drawing, the cavity is rotated around the beam axis for better visualisation. The view is diagonal from the top. In reality the small drift tubes mounted along the two opposing girders will be arranged in the horizontal plane. The three large drift tubes contain the magnetic quadrupole triplet lenses. The length of the cavity is about 3.77 m, the outer width of the center frame is 400 mm.

components at GSI has started in 2003, e.g. first SEM-grids for the LEBT have been produced already [11].

The excavation activities for the accelerator building in Heidelberg started in November 2003 and the cornerstone ceremony was held in May 2004. The work on the concrete ground plate and on the walls for the second underground floor is in progress. The beginning of the installation of the first accelerator components in Heidelberg is scheduled for the first half of 2005. A step-by-step commissioning of the accelerator facility and the treatment places is planned. First patient treatment is planned for 2006 / 2007.

RFQ

For longitudinal focusing of the ion bunches before injection of the ions into the IH structure, a drift tube set-up is integrated into the RFQ tank instead of using a separate rebunching cavity in the intertank section [6][7]. Major RFQ components like electrodes, stems, base plate and the tank have been fabricated by industry. Assembly and alignment of all components have been performed at the IAP. Basic RF properties have been measured [6][7]: The measured quality factor amounts to about 2500, the R_p value is about 30 kΩ. For the electrode design voltage of 70 kV, a power consumption of 165 kW is estimated. The total voltage along the two bunching gaps will be up to 140 kV for an electrode voltage of 70 kV.

Futhermore, a beam test stand has been set up at the IAP. First beam measurements behind the duoplasmatron ion source have been performed successfully as well as RF conditioning of the RFQ tank at 50 W continuous RF power [12]. Commissioning of the RFQ with proton beam is scheduled for September 2004.

IH CAVITY

The RF tuning of an 1:2 scaled cold model [4] of the IH structure has been completed successfully [8][9]. Microwave Studio simulations of the model and the power cavity have been also performed at the IAP [8][9].

The IH power cavity (Fig. 2) consists of three main parts: the center frame carrying 52 small drift tubes and the lower and upper half shells. Three magnetic quadrupole triplet lenses will be mounted in the lower half shell. The inner dimensions of the 217 MHz cavity are 260 mm in width and about 340 mm in height (see also Ref. [8]). The half shells as well as the center frame are fabricated by milling from massive mild steel blocks. The manufacturing of the IH tank is in progress at PINK GmbH Vakuumtechnik, Wertheim, Germany [13]. The completion of the tank is expected for November 2004. The small drift tubes including the stems are milled from small copper blocks and have been fabricated already also at PINK GmbH Vakuumtechnik. They have been additionally copper-plated at GSI.

LINAC QUADRUPOLE MAGNETS

A set of four magnetic quadrupole triplet lenses (three integrated into the IH cavity and one subsequent to the IH tank) as well as a quadrupole doublet in the intertank section between the RFQ and the IH tank are required. Due to the small inner diameter of the IH tank, a new compact quadrupole magnet design has been developed at GSI [4][14]. Five magnet types with different lengths but with identical cross section have been designed. Some key parameters are listed in Table 2.

Table 2: Selection of key parameters of the linac quadrupole magnets. The maximum field levels are given for the design ion ($^{12}C^{4+}$). For further details see Ref. [14].

Yoke outer diameter	130	mm
Yoke lengths	42 / 49 / 67 / 81 / 97	mm
Yoke material	VACOFLUX 50	
Magnet aperture diameter	20	mm
Number of turns per pole	5	
Excitation currents	≤ 1050	A
Field gradients B'	≤ 110	T/m

Figure 3: Prototype quadrupole doublet built at GSI [14]. The yoke lengths are 42 mm and 81 mm. The distance between the yokes of the two magnets is 27 mm only.

Two prototype magnets of the most excited quadrupoles (42 mm and 81 mm yoke length) have been built at the GSI workshops (Fig. 3) [14]. Different measurements have been performed at GSI [14]. The measured field gradients B' as well as the integrated gradients $B' \times L_{\mathrm{eff}}$ are shown in Fig. 4 for the quadrupole with 81 mm yoke length. The curves are linear up to about 800 A. With higher currents, increasing saturation effects are observed. The vertical lines at around 800 A and 900 A represent approximately the expected minimum and maximum operational values. They are close to the border of the linear region.

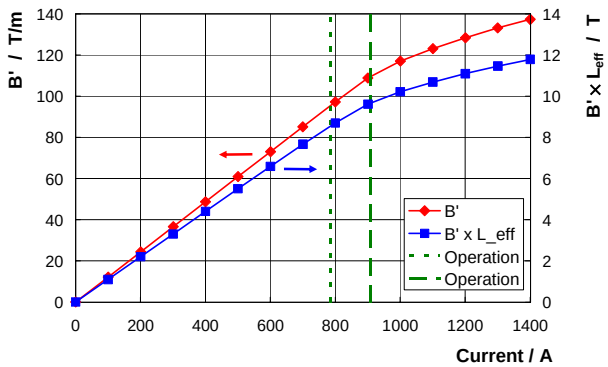

Figure 4: Measured field gradients (upper curve) and integrated gradients (lower curve) for the prototype magnet with a yoke length of 81 mm.

Production of the final linac quadrupole magnets including integration into the water-cooled drift tube housings for the internal triplet lenses is in progress at DANFYSIK. The yokes of the magnets are fabricated already. Delivery of the completed magnet units to GSI is scheduled for January 2005. Afterwards, the triplet lenses will be copper-plated at GSI and will be integrated into the IH tank.

RF SYSTEM

The linac RF system [4] covering three amplifier chains for 4 kW, 200 kW and 1.4 MW is under construction at THALES Broadcast & Multimedia AG in Turgi, Switzerland. The cavity amplifier for the 1.4 MW final stage for the IH cavity has been manufactured already at BERTRONIX Electronic GmbH, Munich, Germany [4] and has been delivered to GSI recently (Fig. 5). The stage can be equipped either with a TH 526 B tetrode from THALES Electron Devices or with an EIMAC 8973 from CPI using an adapter set. For high power tests of the BERTRONIX stage, an existing amplifier set-up at GSI has been modified to be used as a driver for the 1.4 MW stage. A commercial 4 kW transistorized amplifier from THALES B&M is used as the first stage of the driver amplifier. For the second stage, a THALES TH 18527 C cavity equipped with a THALES TH 571 B tetrode has been integrated into an existing GSI amplifier. A pulse power of 120 kW has been produced successfully at GSI with this driver set-up. High power commissioning of the 1.4 MW BERTRONIX stage is scheduled for September 2004. It is planned to use this set-up including the BERTRONIX stage also for high power tests of the RFQ up to 200 kW pulse power.

Figure 5: View on the 1.4 MW final stage cavity amplifier after delivery to GSI. The outer diameter of the system is 980 mm, the total height 2595 mm. (Photo by G. Otto, GSI; published with great acknowledgements to Dr. Klaus Berdermann, BERTRONIX Electronic GmbH, Munich, Germany.)

REFERENCES

[1] H. Eickhoff et al., in: *Proc. PAC 2003, Portland*, p. 694, and references therein.
[2] H. Eickhoff, Th. Haberer, B. Schlitt and U. Weinrich, in: *Proc. EPAC 2004, Lucerne*, in print.
[3] H. Eickhoff et al., in: *Proc. PAC 97, Vancouver*, p. 3801.
[4] B. Schlitt et al., in: *Proc. LINAC 2002, Gyeongju*, p. 781.
[5] B. Schlitt, A. Bechtold, U. Ratzinger and A. Schempp, in: *Proc. Linac 2000, Monterey*, p. 226.
[6] A. Bechtold, U. Ratzinger, A. Schempp and B. Schlitt, in: *Proc. PAC 2003, Portland*, p. 1062, and references therein.
[7] A. Bechtold, PhD thesis, Johann Wolfgang Goethe-University, Frankfurt am Main, 2003.
[8] Y.R. Lu, U. Ratzinger, R. Tiede, B. Schlitt and S. Minaev, contribution MOP11, this conference.
[9] Y.R. Lu, PhD thesis, Johann Wolfgang Goethe-University, Frankfurt am Main, in preparation.
[10] http://www.pantechnik.net/
[11] M. Schwickert and A. Peters, in: *Proc. EPAC 2004, Lucerne*, in print.
[12] A. Bechtold et al., in: *Proc. EPAC 2004, Lucerne*, in print.
[13] http://www.pink.de/
[14] C. Muehle, B. Langenbeck, A. Kalimov, F. Klos, G. Moritz and B. Schlitt, IEEE Trans. on Applied Superconductivity **14**, No. 2, July 2004, in print.

THE IH CAVITY FOR HITRAP

C. Kitegi, U. Ratzinger, IAP, University Frankfurt/Main, Germany
S. Minaev, ITEP, Moscow, Russia

Abstract

RFQs are already successfully used to decelerate ions and to match them to ion traps. Within the Heavy Ions TRAP project HITRAP at GSI a combination of an IH drift tube cavity operating at the $H_{11(0)}$ mode and a 4-rod RFQ is proposed to decelerate the 1 µs long heavy ion bunches (up to U^{92+}) from 4 A·MeV to 6 A keV after storage ring extraction. The transition energy from the IH into the RFQ is 0.5AmeV. The operating frequency is 108.408 MHz. The A/q range of the linac is up to 3.

A 4-gap quarter wave resonator working at 108.408MHz provides the micro bunch structure for the IH. The transmission mainly defined by the buncher is about 30%. An alternative 2nd harmonic bunching section, which allows higher transmission and/or smaller longitudinal emittance, will be discussed.

By applying the KONUS dynamics, the 2.7 meter long IH cavity will perform a high efficient deceleration by up 10.5 MV with 200kW rf power. The beam dynamics performed with the LORASR simulation code will be shown. It is aimed to reach an effective shunt impedance around 220MΩ/m for the IH cavity.

IH CAVITY

General Parameters

The HITRAP decelerator will enlarge the variety of decelerated ion beams to Highly Charged Ions up to U^{92+}. The decelerator linac will be installed in the re-injection beam line between ESR and synchrotron SIS. The decelerator is designed for a A/q range up to 3. The HCI are extracted from the ESR at 4 AMeV in a 1 µs long cooled bunch [1]. As for such an A/q range the input energy is too high for an efficient RFQ solution, an IH cavity is proposed to decelerate to an intermediate energy of 0.5 AMeV. A 4-rod RFQ performs the deceleration down to 6AkeV. The chosen intermediate energy allows for a design of an IH tank with one internal lens. Only the IH cavity will be discussed in this paper. The succeeding RFQ will be of the 4-rod type and is designed at IAP as well. The needed repetition time is approximately 10 seconds at a low duty cycle of 0.15%. Intermediate rf pulses may be needed to keep the linac in resonance.

Table1: General IH parameters

	IH LINAC	
	input	output
W [A.MeV]	4	0.5
β	0.0924	0.0328
frequency in MHz	108.408	
duty factor	0.15%	

Beam Dynamics

IH drift tube linacs using the KONUS beam dynamics concept [2] (KOmbinierte NUll grad struktur) are used as injectors for the Alvarez section of UNILAC. The same beam dynamics concept can be applied for beam deceleration.

Within the KONUS scheme particle bunches are decelerated in successive gaps with 180° synchronous phase in order to reduce the transverse defocusing effect. This allows the use of slim drift tubes without any optical element. Consequently the decelerating H mode cavity using the Konus dynamics is composed by:

-One main decelerating section with 180° synchronous phase.

-One quadrupole triplet to focus the beam.

-One short section with positive synchronous phase, typically 215° to focus longitudinally and match the beam.

Due to the rf buncher ahead of the cavity, the micro-bunch is convergent in the first gaps of the IH. To avoid over focusing, which could lead to beam instability, the 145° synchronous phase is used in the first gaps to "defocus" the bunch.

Deceleration of 10.5MV is then achieved within the 2.7m long IH cavity; Figure 2 shows the 98% transverse envelopes in the cavity calculated with LORASR, which is an adequate code to study the KONUS dynamics. As the beam is cooled in the ESR, transverse emittances are very small. The beam radius in the IH tank is less than 4mm.

Figure 3 shows the longitudinal output emittance obtained for an arbitrary reference input emittance. For such emittance the beam dynamics is rather safe as the acceptance of the IH is twice.

The simulations of the matching section were performed in order to match micro bunches into this emittance.

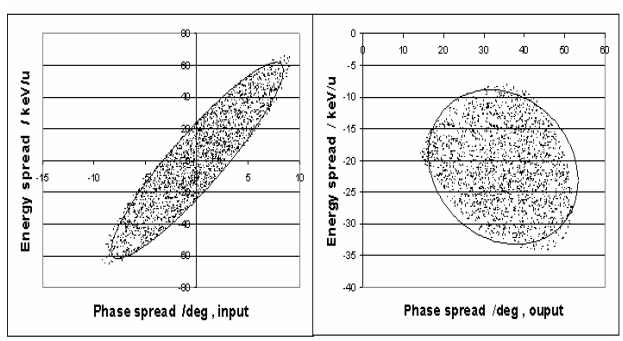

Figure 1: 98% input (left) and output (right) longitudinal emittance.

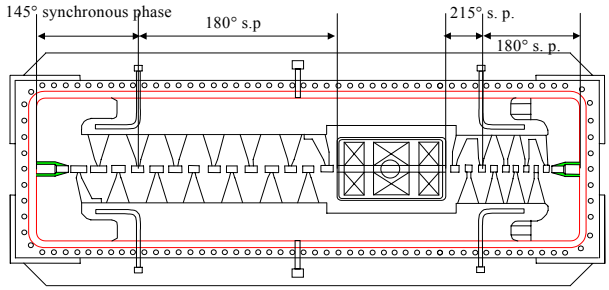

Figure 2: Schematic drawing of the IH cavity design with one internal lens.

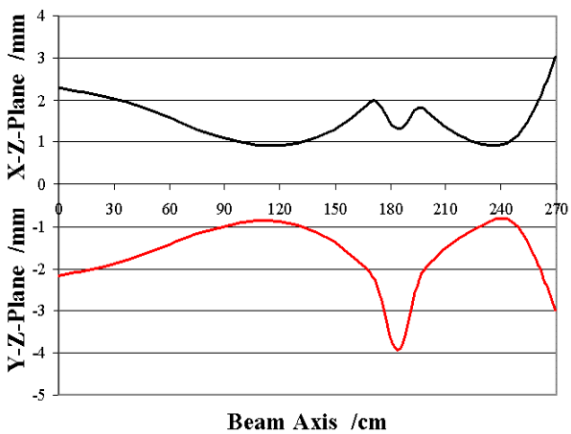

Figure 3: 98% transverse beam envelopes along the IH tank.

Cavity Design

The IH tank rf power supply is already available at GSI. This is a transmitter with rf power levels up to 200 kW. To reach the 10.5MV deceleration, the expected effective shunt impedance is 220MΩ/m for an estimated 180kW rf power loss. Since HLI operates at the same frequency with very high shunt impedance, the HITRAP IH cross-section geometry is intended to be similar. The small transverse dimension of the beam (<6 mm) allows the use of small drift tube aperture diameter (12-10mm).

As no model cavity is planned, the electromagnetic simulation of the cavity performed with Microwave Studio simulation will be an important issue. Table 2 lists the main cavity parameters.

Table 2: Cavity and beam parameters

W [A.MeV] input /output	4/ 0.5
A/q	3
input/output normalised transverse emittance [mm.mrad]	0.18 / 0.25
input/output normalised longitudinal emittance [AkeV/ns]	5.2/ 5.7
frequency in MHz	108.408
U_0 [MV]	10.5
Z_0 in [MΩ/m]	305
aperture radius [mm]	6 - 5
number of cells	25
L [m]	2.70
P[kW]	180

MATCHING SECTION

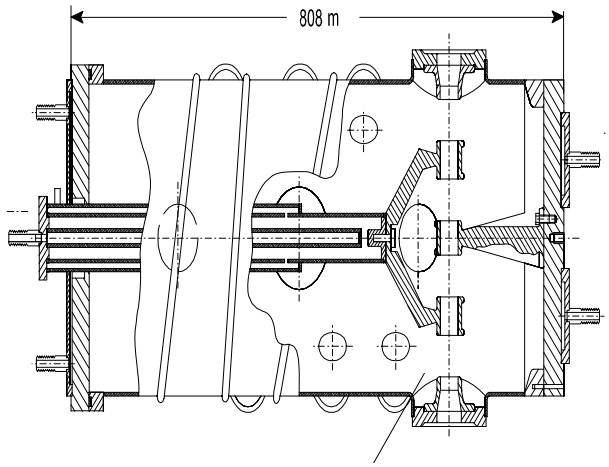

Figure 4: 108.408 MHz Quarter wave resonator at 4 AMeV.

First Harmonic Drift Buncher

A first matching section is needed to match the 1µs macro pulse from the ESR into the emittance shown in figure 3. A first matching section consisting in a one harmonic buncher and in one quadrupole triplet was considered. This option allows the most compact decelerator design but reduces the decelerator beam transmission to about 28%.

The buncher used is a 108.408 MHz 4-gap quarter wave resonator and is located 4 meters ahead the IH tank [2]. The quadrupole triplet provides the transverse matching. Only the use of multiple harmonic bunching can increase the bunching efficiency and/or can reduce the S-shape of the longitudinal emittance. As a Double Drift Buncher DDB is easier to drive and is more flexible than one cavity with several harmonics, only the DDB solution was considered.

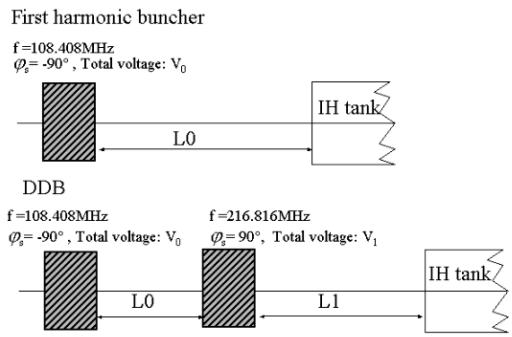

Figure 5: Scheme of first harmonic buncher and DDB.

Double Drift Buncher

The double drift buncher consists of two bunchers separated in space, independently driven and phase locked together [3]. The second buncher is driven at twice the frequency of the first one. The bunching efficiency for such a DDB is better than what is expected for a single buncher driven with three harmonics.

According to the available space and for beam stability reasons (phase and energy deviation) the matching section length, i.e. the distance between the first buncher and the

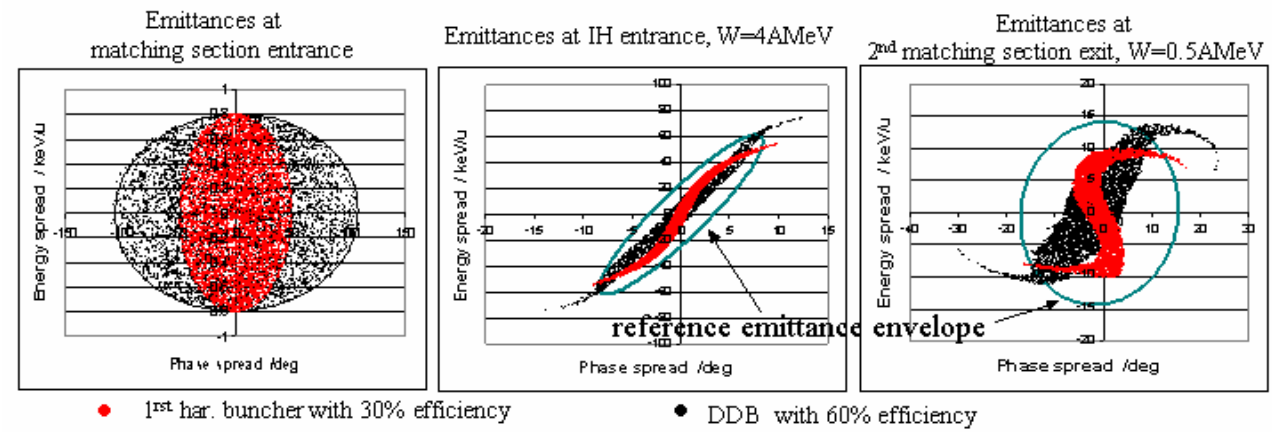

Figure 6: Longitudinal emittance at different locations for the both buncher designs. The envelope of the 98% reference emittance at the IH entrance (middle) and at the exit (right) of the RFQ matching section is plotted.

cavity shouldn't exceed 8m. Furthermore, at the IH entrance the energy spread of the bunched beam should be kept within ±60AkeV. These two parameters give the maximum voltage achievable in the two bunchers. For a conventional DDB, a bunching efficiency of around 80% is achievable. Nevertheless to get such high efficiency with smaller energy spread than 60AkeV, the total length needed is higher than the upper limit.

By reducing the efficiency to 60%, the bunched beam matches the IH longitudinal input emittance plotted in figure 1 with a reduced S-shape. The matching section length is then 7.5 m. Transverse beam envelopes for both matcher designs are shown in figure 7. The settings of the both bunchers are listed in table 4. The simulation also includes the RFQ matching section consisting in one spiral resonator and one quadrupole triplet [1].

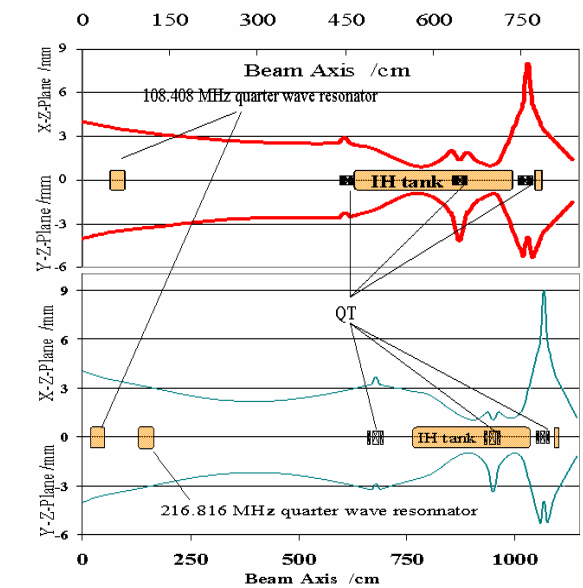

Figure 7: 98% transverse beams envelope for a first harmonic buncher (upper plot) and for the double drift buncher design (lower plot).

Table 3: 98% transverse and longitudinal emittance, the input corresponds to the entrance of the buncher ahead of the IH cavity and the output to the exit of the RFQ matching section

	First har.	DDB	Ref
ε_x (98%,norm) in mm.mrad input/output	0.21/0.29	0.21/0.29	0.17/0.27
ε_y (98%,norm)in mm.mrad input/output	0.21/0.30	0.21/0.27	0.17/0.26
ε_{long} (98%,norm) in AkeV/ns input /output	1/5.79	2.2/7.0	5.23/5.95

Table 4: First harmonic buncher and DDB main parameters

First harmonic buncher	
frequency in MHz	108.408
V0	255
L0	4
Zeff/ MΩ /m	80
Prf	<2kW
bunching efficiency	< 30%

DDB		
frequency in MHz	108.408	216.816
V0 / V1 in kV	256	78.5
L0 / L1 in m	0.8	5.95
Zeff/ MΩ /m	80	57
Prf	<2kW	
bunching efficiency	60%	

SUMMARY AND OUTLOOK

A double drift buncher increases the transmission; nevertheless the high theoretical bunching efficiency couldn't be reached. The fast extraction of the 4 AMeV beam from the ESR is planned to be tested in September 2004. The stability of the extracted beam should be checked with respect to the transverse beam stability.

REFERENCES

[1] *HITRAP technical design report,* GSI-10/2004.
[2] U. Ratzinger, Habilitationsschrift, Frankfurt University, July 1998, Germany.
[3] V.S Pandit, optimisation of the parameters of an ion beam buncher, NIM A276 1989

THE COMPACT 20 MV IH-DTL FOR THE HEIDELBERG THERAPY FACILITY

Y.R. Lu[*,#,§], S. Minaev[*,$], U. Ratzinger[*], B. Schlitt[#], R. Tiede[*]
[*]IAP, Universität Frankfurt/Main, Germany
[#]Gesellschaft für Schwerionenforschung mbH, Darmstadt, Germany
[§]Institute of Heavy Ion Physics, Peking University, P.R.China
[$]Institute of Theoretical and Experimental Physics, Moscow, Russia

Abstract

A clinical facility for cancer therapy using energetic proton and ion beams (C, He and O) is under construction and will be installed at the Radiologische Universitaetsklinik in Heidelberg, Germany, starting in 2005. It consists of two ECR ion sources, a 7 AMeV linac injector and a 6.5 Tm synchrotron to accelerate the ions to final energies of 50-430 AMeV[1-3]. The linac is the combination of a 400 AkeV RFQ and a 20MV IH-DTL operating at 216.8MHz. The accelerator project is coordinated by GSI; IAP is responsible for the Linac cavities in cooperation with GSI. The different RF tuning concepts and tuning results for a 1:2 scaled IH-DTL model cavity are presented. Microwave Studio simulations have been carried out for the model and for the real power cavity. Results from the model measurements and the field simulations agree very well also for the higher order modes. The beam matching from the RFQ to the IH-DTL was optimised. The IH drift tube array was matched with the gap voltage distribution resulting from RF model measurements. Simulated RFQ output particle distributions were used in the final beam dynamics investigations along the IH cavity.

INTRODUCTION

By comparing cancer therapy with proton and carbon beams, one important aspect next to the medical efficiency is the treatment costs per patient. Since 1997 a very compact and efficient 7 AMeV C^{4+} linac has been developed. The status of the whole injector including ECR ion sources, linac, RF power system, and quadruple magnets will be discussed in another paper in this conference [4]. The beam matching from the RFQ to the IH-DTL ,the improved beam dynamics simulations with the software LORASR along the IH cavity as well as the RF tuning of the 1:2 scaled RF model cavity and accompanying simulations with Microwave Studio will be discussed in these proceedings.

KONUS BEAM DYNAMICS

The IH-DTL consists of four KONUS sections with a total of 56 gaps, and with three magnetic quadruple triplets, which are housed in one cavity with 3.77m in length and 0.32m equivalent cavity diameter. The beam dynamics simulations have been optimised with the code LORASR [5] for the beam matching from the RFQ exit to the IH-DTL with new geometry [6] and real particle distributions at the RFQ exit as calculated with the PARMTEQ code. The effective gap voltage distributions and real drift tube parameters are adapted from the results of the cold RF model cavity tuning measurements. RFQ internal buncher[7] effective voltage has been optimised to get normalized emittance growth factors as low as 1.18 in x-x', 1.05 in y-y' and 1.23 in w-z plane, respectively (Figure1). Figure 2 shows IH-DTL output particle distributions at the synchrotron injection point. The exit ellipses contain 95% of the particles. The transversal 98% envelopses up to the stripper foil are shown in Figure 3.

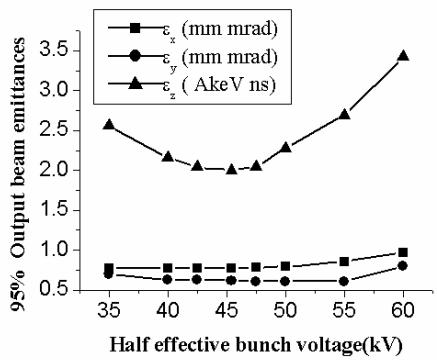

Figure 1: Output emittance at the stripper foil vs. the effective voltage of the RFQ internal 2 gap buncher.

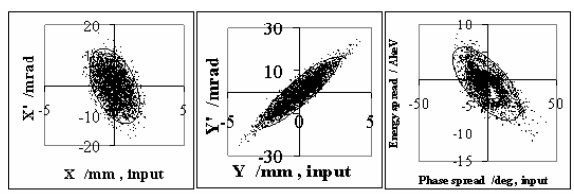

$\varepsilon_{n,x}$=0.58, $\varepsilon_{n,y}$=0.58 mm mrad, $\varepsilon_{n,z}$=1.57 AkeVns
ε_{xrms}=0.11, ε_{yrms}=0.11 mm mrad, ε_{zrms}=0.25 AkeVns

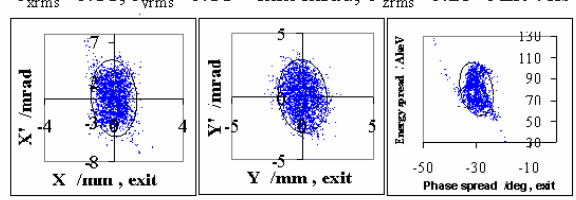

$\varepsilon_{n,x}$=0.77, $\varepsilon_{n,y}$=0.62 mm mrad, $\varepsilon_{n,z}$=2.00 AkeVns
ε_{xrms}=0.13, ε_{yrms}=0.12 mm mrad, ε_{zrms}=0.31 AkeVns

Figure 2: Particle distributions at the RFQ exit and at the stripper foil behind of the IH-DTL ,normalized as well as rms emittance values.

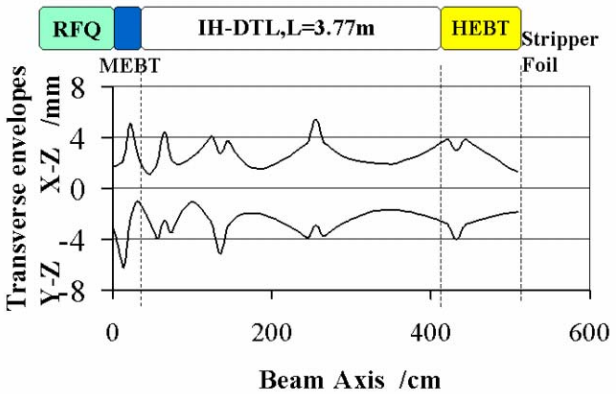

Figure 3: Transversal 98% beam envelopes Aperture in radius ranging from 6.0 to 10mm.

RF MODEL MEASUREMENTS

An IH-DTL 1:2 scaled model cavity was ready for measurements in Summer 2002. Four main tuning methods were applied to get the designed electric field distributions along the beam axis[8]. Figure4 shows the 3 out of 4 KONUS sections of the model cavity and its tuning concepts. Modification of the drift tube to periodic length-ratio along the tank is the traditional tuning concept to get a flat electric field distribution. Because of the extreme output/input energy ratio of 17.5 and of the cavity length to diameter-ratio of about 12, volume tuners are additionally needed to reduce locally the cavity cross sectional area, therefore to decrease the local inductance or to enhance the resonance frequency at the first and the second sections and to make the field in the last two sections larger. Undercut tuning is the most sensitive tuning at the end sections and with respect to the voltage balance along the structure. Lens coupling is an important tool to stabilize the operation mode and to change the coupling between neighbouring sections. After the tuning process, the measured resulting electric field, the difference of effective gap voltage distributions from the designed values in percent demonstrated the tunability of such a long structure (Figure 5). The finally needed level of agreement with the design distribution will be reached for the real cavity after a more careful tuning procedure.

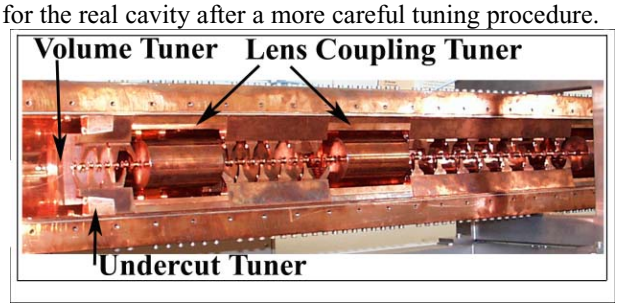

Figure 4: 1:2 IH model cavity and its tuning concepts.

The plunger with 30mm length and 74mm width in section 3 can lower the operating frequency by 1MHz, that is 0.23% of the frequency when it is moved in by 30mm depth. Figure 6 shows plunger tuning ability and its influence on the voltage distribution between the 4 sections. Because of that, the plunger range should be limited to about 15mm.

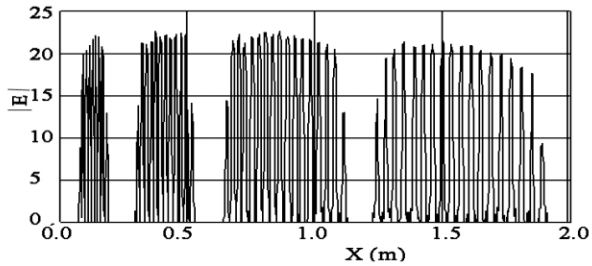

Figure 5a: Measured field distribution

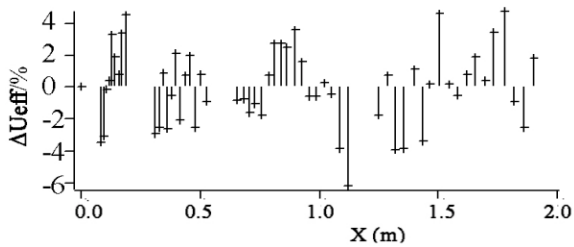

Figure 5b: Corresponding effective gap voltage difference between design and measurement.

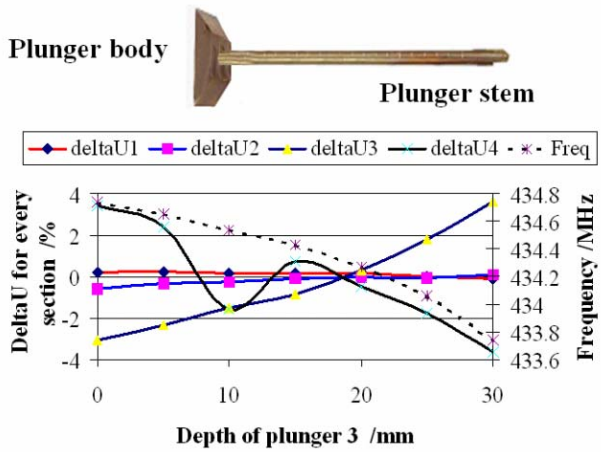

Figure 6: The detuning effect of plunger 3 on the voltage distribution of the 4 individual KONUS sections.

MICROWAVE STUDIO SIMULATION

In order to get higher simulated accuracy with limited mesh density and PC resources (Intel® Xeo 2.4GHz with 2.096GRAM), the asymmetric supporting stem of each triplet lens (Figure 7) is replaced by the mirror symmetric supporting cylinder. Figure 7 demonstrates this symmetrization, the RF current indicates the correct mode H_{110}, no or very low current is passing along the triplet stems, both geometries have the same local frequency. After the symmetrization, only one half of the cavity volume (upper or lower half in Figure 7) needs to be simulated by MWS, the minimum mesh size is 1mm, and the biggest mesh size is 6.0mm, there are a total 2.3million mesh points for the 1:2 scaled cavity simulation. The simulation takes about 12hours by the above-specified PC. Figure 8 shows the simulated and measured H_{110} mode electric field distributions of the 1:2 scaled IH model cavity. Figure 9 presents the simulated

H_{111} mode field distribution; it fits the IH model cavity measurements, as well as other higher order modes measurements and simulations [8]. The frequency separation from the fundamental mode H_{110} is 2.8MHz from the model measurement, this corresponds to about 201 half widths in units of the fundamental resonance.

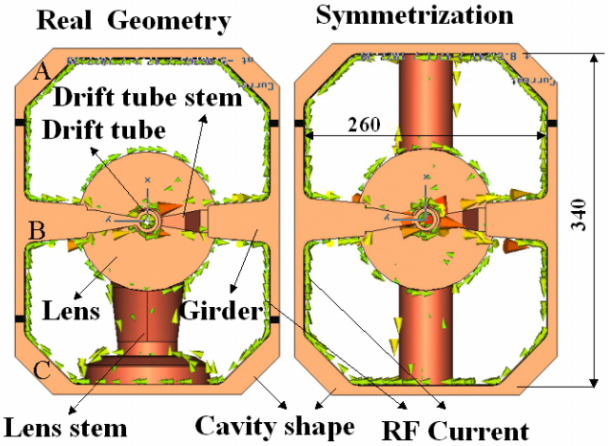

Figure 7: Symmetrization of the IH cavity at the magnetic lenses. Real IH cavity geometry consists of upper and lower half shells (A and C), central frame (B).

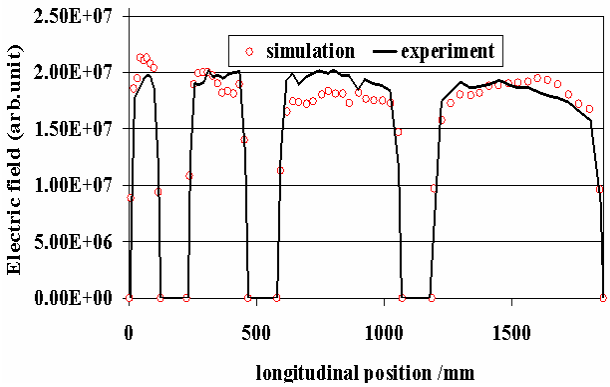

Figure 8: Simulated and measured the H_{110} mode electric field distribution for the 1:2 scaled model cavity.

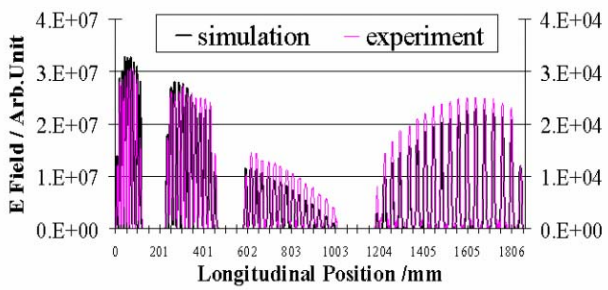

Figure 9: Simulated and measured electric field for H_{111} mode on the model cavity.

The simulation of the 1:2 scaled real power cavity is helpful to verify the real geometry design and to predict the RF performance of the cavity, such as quality factor, power dissipation, shunt impedance and so on. The electric field distribution is similar with that of model cavity that was shown in Figure 8. Figure 10 indicates the magnetic intensity H_z near by the cavity wall. After scaling to the real size of the IH cavity, the predicted main parameters for the IH cavity are listed in the table 1.

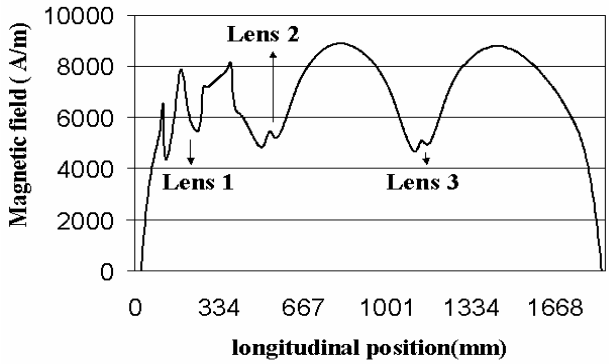

Figure 10: Magnetic field distribution H_z near by real cavity wall.

Table 1: Main parameters of the IH cavity

Accelerated ions	Proton, C^{4+},He^{2+}
Gap number	56
Input energy /AkeV	400
Output energy /AMeV	7
Equivalent diameter /m	0.32
Tank length /m	3.77
Quality factor	15600
Frequency /MHz	216.8
Averaged eff. Voltage gain [MV/m]	5.25
Shunt impedance Z_0 [MΩ/m]	200.3
Shunt impedance Z_{eff} [MΩ/m]	153.0
RF power dissipation (kW)	755

CONCLUSIONS

The KONUS beam dynamics for the 20MV IH-DTL with LORASR code has been optimised for the real PARMTEQ output particle distribution of the RFQ with respect to a low emittance at the stripper foil behind the IH-DTL. The RF tuning investigations on the IH model cavity resulted in a uniform electric field distribution and allowed to design the final IH power cavity. The Microwave Studio simulation of the IH model cavity fits well with the RF model measurements. Fine measurements on the power cavity are scheduled for September 2004.

REFERENCES

[1] GSI, University Klinik Heidelberg, DKFZ, Proposal of a dedicated ion beam facility for cancer therapy.
[2] B.Schlitt, et al., Proceedings of LINAC 2002, Gyeongju,Korea, p.781-783.
[3] H.Eickhoff, et al, Proceedings of PAC2003,Portland, p.694-698.
[4] B.Schlitt, et al., MOP09,LINAC2004
[5] U.Ratzinger,in :Proc. IEEE Part. Accel. Conf., San Francisco,1991,p.567
[6] B.Schlitt, U.Ratzinger, Proceedings of EPAC98, Stockholm,June,1998, p.2377-2379
[7] A.Bechtold, U.Ratzinger, A.Schempp, et al, Proceedings of PAC2003, Portland
[8] Y.Lu, et al, Internal report, IAP-ACCC-270103,-100603 and 010304, Frankfurt University

KONUS BEAM DYNAMICS DESIGN OF A 70 mA, 70 MeV PROTON CH-DTL FOR GSI-SIS12*

R. Tiede, G. Clemente, H. Podlech, U. Ratzinger, IAP, University of Frankfurt/Main, Germany,
W. Barth, L. Groening, GSI, Darmstadt, Germany,
Z. Li, IMP, Lanzhou, China, S. Minaev, ITEP, Moscow, Russia

Abstract

The future scientific program at GSI needs a dedicated proton injector into the synchrotron SIS, in order to increase the proton intensity of the existing UNILAC/SIS12 combination by a factor of 70, resulting in $7x10^{12}$ protons in the synchrotron. A compact and efficient 352 MHz RFQ - CH-DTL combination based on novel structure developments for RFQ and DTL was worked out. For DTL's operated in an H-mode like CH-cavities (H210-mode), the shunt impedance is optimized by use of the KONUS beam dynamics. Beam dynamics simulation results of the CH-DTL section, covering the energy range from 3 to 70 MeV, with emphasis on the low energy front end are presented. Optimization aims are the reduction of emittance growth, of beam losses and of capital costs, by making use of the high acceleration gradients and shunt impedance values provided by the Crossbar H-Type (CH) structure. In addition, the beam dynamics design of the overall DTL layout has to be matched to the power limits of the available 352 MHz power klystrons. The aim is to power each cavity by one klystron with a peak rf power of around 1 MW.

DESIGN CRITERIA AND PARAMETERS

KONUS Beam Dynamics and H-Mode Cavities

First investigations on proton beam acceleration with a CH-DTL were presented in ref. [1].

For the proposed GSI Proton Injector the KONUS beam dynamics ("Kombinierte Null Grad Struktur" – Combined 0° Structure [2]), together with the use of H-mode structures ("Crossbar H-Type" - CH) are foreseen for the energy range from 3 to 70 MeV. The advantages of this concept are:

- High accel. gradients (up to 6 MV/m) due to the high shunt impedance of the CH-DTL and the KONUS beam dynamics concept ("slim" drift tubes without integrated quadrupole lenses housed in each multi-cell cavity).
- Simplified construction, maintenance and reduced number of components.
- Reduction of project costs and overall linac size.

Design Parameters

Compared with the initial layout presented in ref. [3] the following modifications were necessary, leading to an updated overall linac design:

- The optimum RFQ-DTL transition energy was investigated and finally fixed at 3 MeV. This opens the option to realize the RFQ as 352 MHz 4 rod-RFQ in one cavity [4].
- The linac output energy has been increased and fixed at 70 MeV.
- The design current has been increased from 50 to 90 mA (safety factor included): for operation a maximum linac output current of 70 mA is specified.
- The operating rf frequency of 352 MHz along the whole linac has been fixed now.

The latter decision was motivated by the manifold offer of rf hardware (power klystrons) at that frequency. The exit energy and beam current were chosen with regard to a 10 – 15 turn injection scheme into the horizontal acceptance (150 π mm mrad) of SIS.

Table 1 summarizes the CH-DTL relevant Proton Linac beam parameters:

Table 1: Basic beam parameters specified for the Proton CH-DTL section

General	
rf frequency	352 MHz
macro pulse length	0.1 ms
rep. rate	5 Hz
macro pulse current at linac exit	90 mA (design current; 70 mA spec. for operation)
RFQ exit	
beam energy	3 MeV
transverse beam emittance (norm.)	1.5 mm mrad
CH-DTL exit	
beam energy	70 MeV
transverse beam emittance (norm.)	2.8 mm mrad
beam momentum spread	$\pm 5x10^{-4}$

Design Criteria and Restrictions

For the design of the 3-70 MeV CH-DTL section some constraints had to be taken into account:

- The choice of the RFQ-DTL transition energy is a trade-off between an adequate maximum output energy of the RFQ and the minimum input energy acceptable for the DTL. Covering a larger energy range by the RFQ reduces the acceleration efficiency and can lead to problems with respect to tank length, flatness and coupling between structure cells. In the DTL short period lengths

*Work supported by the EU (CARE, cont. no. RII3-CT-2003-506395), BMBF, contr. no. 06F134I

lead to construction problems. Different layouts with DTL input energies from 2.5 to 4 MeV were investigated; finally 3 MeV were chosen as a good compromise at the specified beam intensity. In addition, the 3 MeV MEBT section has to be carefully designed at that low transition energy.

- For matching to commercial klystrons (352 MHz, 1.3 MW), the maximum total power consumption per cavity (rf + beam power) should not exceed 1.1 MW. Thus cavity shunt impedances have to be carefully optimized for the whole 3-70 MeV energy range. Effective shunt impedances ranging from about 100 MΩ/m at injection energy down to 40 MΩ/m at the linac exit seem feasible [5].
  To keep below the 1.1 MW rf power and according to the achievable shunt impedance, parameters like the max. cavity length, number of gaps and acceleration gradient have to be adapted (especially towards the high energy end) and are not solely defined by the KONUS beam dynamics.

BEAM DYNAMICS DESIGN OF A 4-70 MeV CH-DTL SECTION

The beam dynamics design of the CH-DTL is still under development. Different schemes have been worked out for different injection energies and beam currents.

The results presented in Figures 1 and 2 show one intermediate step achieved for an input energy of 4 MeV and a beam current of 70 mA. Calculations were performed by using RFQ output distribution data (the "core" out of 20000 particles was used).

The final layout will basically depend on the DTL frontend design (MEBT and first CH-DTL tank, see next chapter).

Nevertheless these intermediate results give a realistic view on the expected CH-DTL layout parameters, e.g. overall length, number of tanks, acceleration gradients, quadrupole lens strengths. Furthermore it is shown that the beam requirements at the linac exit, as mentioned in Table 1, can be achieved.

The parameters of the CH-DTL section design presented here are summarized in Table 2, together with the resulting beam parameters.

Table 2: Proton Linac CH-DTL structure parameters (4-70 MeV, 70 mA intermediate design)

Cavity parameters		
total CH-DTL section length	21 m	
cavity lengths	0.6 – 2.2 m	
number of gaps	12 - 17	
accel. gradient	6.3 – 2.7 MV/m	
total rf input power	500 – 1100 kW	
Beam parameters	**Input**	**Exit**
ε_{tr} (99%,norm.)	1.5	1.9 mm mrad
ε_{tr} (rms)	0.31	0.35 mm mrad
ε_{long} (99%)	0.2	0.45 MeV deg
ε_{long} (rms)	0.044	0.075 MeV deg
transmission	100 %	

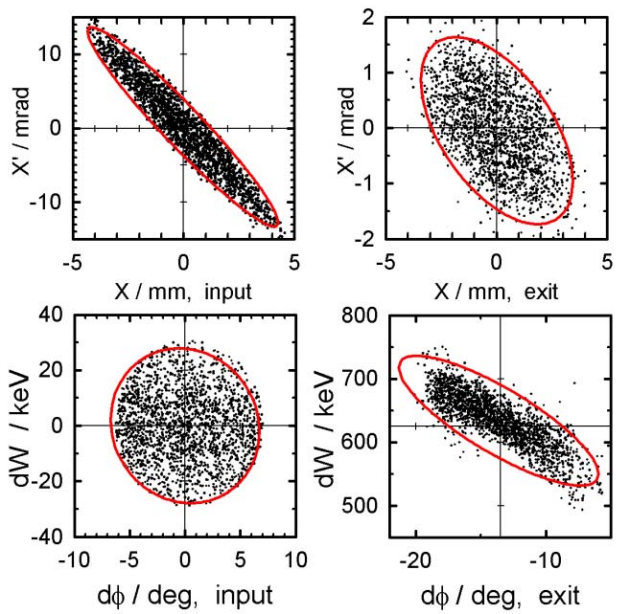

Figure 2: Transverse and long. particle distributions at entrance and exit of the CH-DTL section.

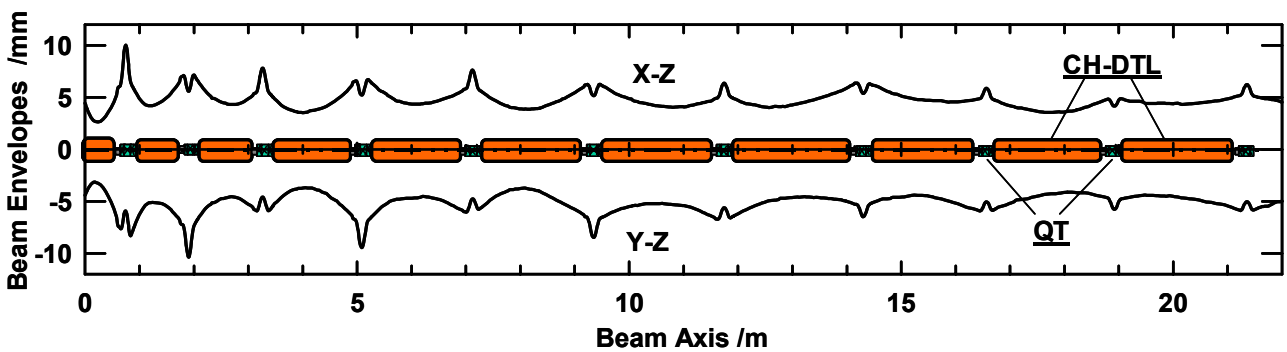

Figure 1: Schematic layout of the proposed GSI Proton Linac CH-DTL section, together with calculated transverse 99% beam envelopes (CH-DTL : Crossbar H-type Structure ; QT : magnetic quadrupole triplet lens).

BEAM DYNAMICS DESIGN OF THE MEBT AND CH-DTL FRONTEND

Compared to the initial design of the overall (up to 70 mA) CH-DTL section presented in the previous chapter, the DTL frontend including the beam transport section behind of the RFQ had to be carefully redesigned with respect to the following issues:

- A transition energy of 3 MeV was chosen as mentioned before. In this case the period lengths are quite short (34 mm at 3 MeV) and transverse focusing is necessary after about 10 periods. The question is then, whether internal quadrupole lenses are needed in the first CH-DTL tank or not. Several layouts were investigated, and finally a solution without internal lenses was favoured. This makes the CH cavity construction simpler and gives more flexibility for matching the beam out of the RFQ. Additionally, a 2 gap rebuncher is foreseen for longitudinal matching.
- The design current was set to 90 mA out of the RFQ (and for the CH-DTL section as well), which implies a complete redesign of the 3-70 MeV CH-DTL section. However, 70 mA have to be provided at SIS injection in operation, which gives a safety factor.

The status of the CH-DTL frontend design is summarized in Figures 3 and 4 and in Table 3.

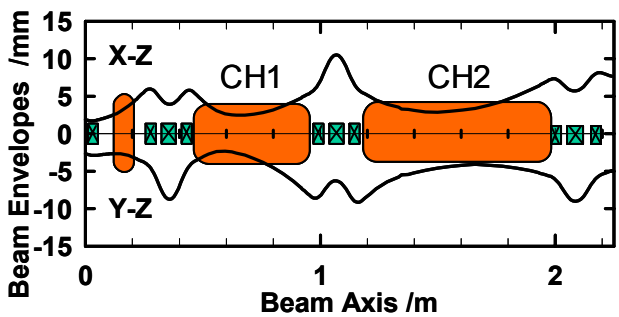

Figure 3: Scheme of the MEBT section and the first CH-DTL tanks, together with transverse beam envelopes.

Table 3: 10 MeV CH-DTL frontend parameters

Cavity parameters		
energy range	3 - 10.4 MeV	
beam current	90 mA	
total length	1.9 m (exit tank 2)	
max. on axis field	17 MV/m	
Beam parameters	**Input**	**Exit**
ε_{tr} (97%,norm.)	1.5	2.5 mm mrad
ε_{tr} (rms)	0.32	0.42 mm mrad
ε_{long} (97%)	0.3	0.56 MeV deg
ε_{long} (rms)	0.070	0.097 MeV deg

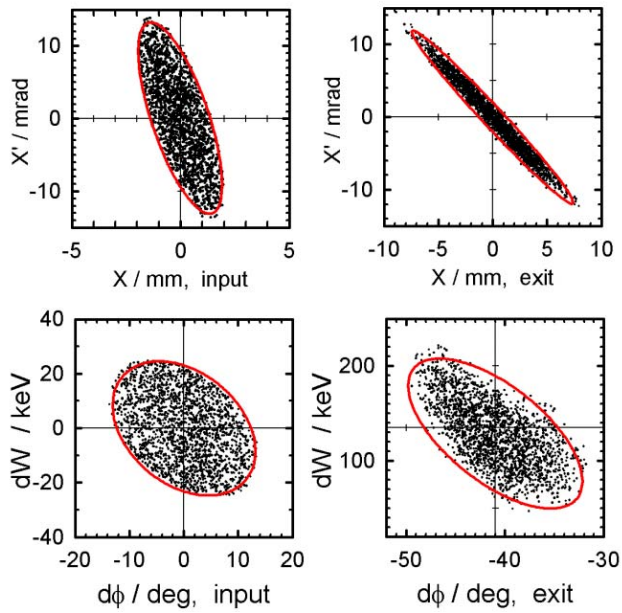

Figure 4: Transverse and long. particle distributions at RFQ exit and after second CH-DTL tank.

CONCLUSIONS

Beam acceleration by 12 to 17 cell CH-cavities and with intertank sections forming a quadrupole triplet channel seem well suited for high current proton beams. The design work is progressing, with special emphasis put on the RFQ-DTL transition.

The beam dynamics design goes hand in hand with the CH cavity development [5]. As a short term objective, a design report of the Proton Linac CH-DTL section is scheduled for the end of 2004.

ACKNOWLEDGEMENT

The IAP and GSI staffs like to thank our co-authors Z.Li and S.Minaev for their fruitful contributions to the work presented here. Both joined these activities during their stay at IAP and GSI, respectively and we appreciate them as valuable and pleasant partners.

REFERENCES

[1] U. Ratzinger, "The New High Current Ion Accelerator at GSI and Perspectives for Linac Design Based on H-Mode Cavities", Proc. of the 2000 EPAC Conf., Vienna, pp. 98-102.

[2] U. Ratzinger and R. Tiede, "Status of the HIIF RF linac study based on H-mode cavities", Nucl. Instr. and Meth. in Phys. Res. A 415 (1998), pp. 229-235.

[3] "An International Accelerator Facility for Beams of Ions and Antiprotons". GSI Conceptual Design Report 2002, pp. 515-517.

[4] A. Schempp et al., "Design of A 350 MHz-Proton-RFQ for GSI", these proceedings.

[5] Z. Li et al., "Design of the R.T. CH-Cavity and Perspectives for a New GSI Proton Linac", these proceedings.

DEVELOPMENT OF INTENSE BEAM PROTON LINAC IN CHINA

S.N.Fu[1], X.L.Guan[2], H.F.Ouyang[1], S.C.Zhao[1], B.Q.Cui[2], Z.Y.Guo[3], J.X.Fang[3], S.X.Fang[1]
[1]IHEP, Institute of High Energy Physics, P.O.Box 918, Beijing 100039, China
[2]CIAE, China Institute of Atomic Energy, Beijing 102413, China
[3]IHIP, Institute of Heavy Ion Physics, Peking University, Beijing 100871, China

Abstract

Study on intense beam proton linac was started about four years ago in a national program for the basic research on ADS in China. This ADS program is meant for the future development of the clean nuclear power generation. Another important application of HPPA for Chinese Spallation Neutron Source was also proposed recently in China, and it is now financially supported by Chinese Academy of Sciences. In this paper, the research progress on intense beam proton linac in these two application fields will be outlined including the test result of a high-current ECR proton source, construction status of a 3.5MeV RFQ accelerator, medium-β superconducting cavity test and the design of a DTL linac.

INTRODUCTION

Shortage of electricity supply is becoming a bottleneck for the rapid economy growth in China. However, fossil energy resources in the newly-increased power supply must be reduced for the environment protection (at present, coal contributes about 70% electricity). Nuclear power must play a more important role, especially, in the eastern part of China. So, there is a rapid development of nuclear power plant in China: 25 new nuclear power stations are going to be built within next 15 years. It means the electricity from nuclear power will increase from 3.8% to 9% of the total electricity supply in China.

Accelerator Driven Subcritical system (ADS) is recognized as one of the best options of fission nuclear power source. A basic research program of ADS[1] was lunched in 2000 under the support of the Ministry of Science and Technology, China. In this program, we have studied some key technologies of an intense beam proton linac, including construction of an ECR proton source and a pulsed beam RFQ accelerator. Chinese Academy of Sciences also gave a support to the linac research in the field of medium-β superconducting cavity. Institute of High Energy Physics, China Institute of Atomic Energy and Institute of Heavy Ion Physics of Peking University jointly conduct the researches.Chinese Spallation Neutron Source (CSNS) is a multidiscipline platform, as a complementary to synchrotron radiation (SR) facility. China will soon have 3 SR facilities in the mainland, but no spallation neutron source at all. There is a common sense among Chinese scientists that China should build a spallation neutron source as soon as possible, and it should rank in the world-class but within the limitation of financial capability of China, as a developing country. A preliminary research program for CSNS with a small budget was lunched in 2002 under the support of CAS. Institute of Physics and Institute of High Energy Physics undertook this task. A physics design and R&D prototyping program has been proposed and is now waiting for the ratification of our government. In comparison with ADS, CSNS is a near-term program with relatively mature technology.

In this paper, we will present our research progress in intense beam proton linac, including the test result of a high-current ECR proton source, construction status of a 3.5MeV RFQ accelerator, medium-β superconducting cavity test and the design of a DTL linac.

THE ECR PROTON SOURCE[2]

An ECR proton source and LEBT have been built at CIAE as the injector of the RFQ. Fig.1 shows the source and its major performance parameters. Our great efforts were made on the reliability and stability of the source operation. We have overcome the problems associated with the breakdown of the RF input ceramic window resulted from the electron back strike. The electrodes have been optimized for minimum spark rate. At present a high reliability of 99.9% is achieved during an 120 hours continuous operation.

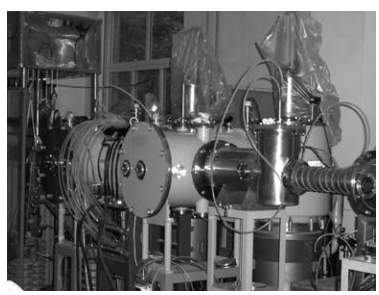

E(KeV)	75
I(mA)	70
f_{RF}(GHz)	2.45
P_{RF}(kw)	1
$E_{n,rms}$ (π mm-mrad)	0.13
H^+ Ratio	80%
Raliability	99%

Figure 1: The ECR source and its major parameters.

DEVELOPMENT OF THE RFQ[3-4]

The major parameters of the RFQ are listed in Table 1. It is separated into two segments and each segment consists of two technological modules. On each module there are 16 tuners distributed on the 4 quadrants for frequency and field tuning. Dipole stabilizer rods on both

the end plates and the coupling plate are applied. There are 20 cooling channels on the cavity body in each module. Four vane-wall pieces are brazed to form a cavity for both RF and vacuum seals.

Table 1: RFQ major parameters

Input Energy	75keV
Output Energy	3.5MeV
Peak Current	50mA
Structure Type	4 vane
Duty Factor	6%
RF Frequency	352.2MHz
Maximum E_s	33MV/m
Total Power	630kW
Total Length	4.75 m

Short RFQ Model

As the high accuracy fabrication of the RFQ cavity is a rather tough issue for us, we started with some technological models before the manufacture of the formal cavity. A short OFEC copper RFQ section of 0.42m long was fabricated with fine machining, as shown in Fig.2. There are two major purposes to make this model: one is to test the high-accuracy machining and another is to verify the brazing deformation. The machining tolerance reaches $\pm 20\,\mu$m on the vane tip and cavity wall measured with a CMM.

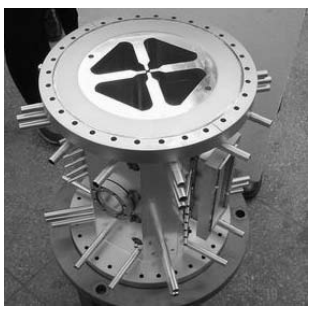

Figure 2: A Short RFQ technological model after final braze.

We measured the resonant modes and field distribution without any tuning in each brazing step. The measurement results indicate that there is a little frequency down-shift after the first brazing, which forms the cavity, but a little up-shift after the second brazing, which brazes all flanges and pipes, as listed in Tab.2. Field analysis indicates a dipole components of 3% exist in 1-3 quadrant after the final brazing.

Table 2: Operating frequency shift between brazing steps and comparison with the simulation.

Brazing Step	f_Q(MHz)	δf_Q(MHz)
Before 1st brazing	351.232	
After 1st brazing	350.955	-0.277
After 2nd brazing	351.119	+0.164
Simulation by code	351.345	-0.226

Full-Size RFQ Model

Another technological model is a full-length brazing test cavity. This cavity contains all of the flange ports in order to verify the furnace temperature's evenness in both radial and vertical directions. The stainless steel flange was first brazed with copper neck for the tuner port, or with the vacuum grid copper body. All of these flanges were then brazed onto the cavity after the four vane pieces had been brazed together. In Fig. 3 the up-left are the flanges of tuner port, the down-left is the vacuum grid body with the cooling-water channel covers, and the right is the 1.2 meter long brazing test model after the final brazing. Vacuum leak check demonstrates all of the brazing is vacuum tight. The leakage rate is 1.9×10^{-9} Torr l/s. The success of this model validates the design of the filler slot distribution, the machining accuracy of the brazing surface, the proper and balanced press force in the assembly of the four vanes, as well as the adequate control of the brazing temperature.

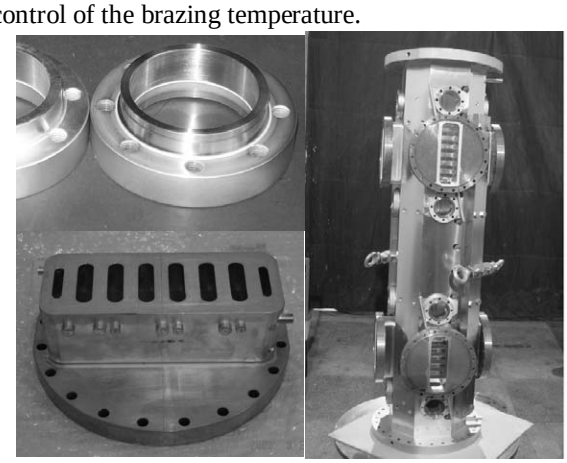

Figure 3: The 1.2m long full size model for brazing test with tuner and vacuum flanges.

After the success of the model cavities, the formal RFQ cavity is now under final-fine machining. It is expected all the modules will be manufactured in early next year.

RF Power Source

The RF power source for the RFQ, which was transferred from CERN, has been installed at IHEP. It was a CW RF power source of 352.2MHz/1.2MW, decommissioned from LEPII. The TH2098 klystron, modulator, HV power supply, Y-junction circulator, RF control system, dummy loads and water-cooling system have been connected. The modulator from CERN worked in ramping mode for LEPII. To adapt to our RFQ's square pulse mode at various duty factors, some necessary modifications of the modulator have been made.

The klystron is now in the process of high power conditioning. The 403kW output power in pulse mode has been delivered to the dummy loads. More details about the work on the source is presented in this conference[4].

Study on the Dipole Stabilizer Rods

IHIP has built a full-size module jointly with IHEP before the manufacture of the accelerator cavity[6]. There are vane undercuts of about 46mm long at each end of the module. Four dipole stabilization rods with variable insertion length are mounted on one end plate of the cavity. When we inserted rods into 1 and 3 quadrants only, the 1-3 dipole mode has no response to the rods. Instead, 2-4 dipole mode shifts, as shown in Fig. 4. This result agrees with 3D simulation, which reveals that the additional capacitance existing between the rods and the vanes decreases the frequency of the 2-4 dipole mode. The 1-3 rods insertion with a proper length can also reduce the 2-4 dipole field component in an asymmetrical cavity, but it can not decrease the tilt of the dipole field. And it does not correspond to the smallest dipole component if the two dipole-mode frequencies become the closest due to the rods insertion.

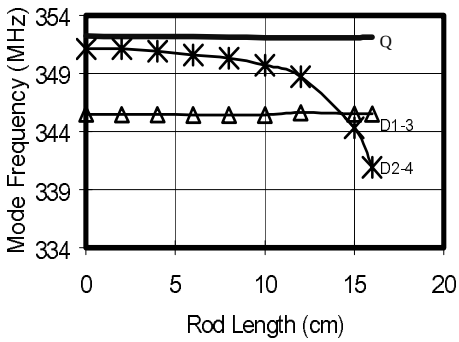

Figure 4: Two rods are inserted into 1 and 3 quadrants, resulting in the frequency shift of 2-4 dipole mode, but no effect on 1-3 dipole and quadrupole mode.

SUPERCONDUCTING CAVITY

The technology of medium-β superconducting RF cavity has been studied for the medium energy section of 1GeV proton linac for ADS. A superconducting single ellipsoid cell of 1.3GHz at β =0.45 was manufactured jointly with KEK. The measured Q_0 versus E_{sp} is plotted in Fig. 5.

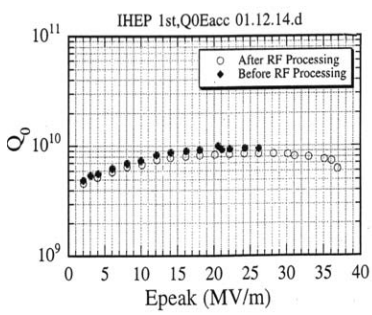

Figure 5: Measured Q_0 of the cell of 1.3GHz at β =0.45 with designed E_{sp}/E_{acc}=5.13.

Recently IHEP has set up an RF superconducting laboratory for the RF cell processing and measurement. A cryostat for 1.3GHz cavity has been built for vertical measurement at the working temperature of 1.5~4.2K.

LINAC DESIGN FOR CSNS

100kW CSNS uses a 70MeV H^- linac as an injector of a rapid-cycling synchrotron of 1.6GeV at a repetition rate of 25Hz. It consists of a H^- ion source, an RFQ and a conventional DTL. The RFQ described in section 3 can not be directly utilized for ADS linac because it is a pulsed machine, but it can be used in the CSNS. The following DTL linac is designed at the same RF frequency as the RFQ. The upgrade program of CSNS will raise its power to 200kW and the DTL energy will be 130MeV. The DTL consists of 8 tanks with the first half for 70MeV. Beam dynamic design was conducted with PARMILA code. The beam profile is shown in Fig.6 with a FODO lattice for transversal focusing.

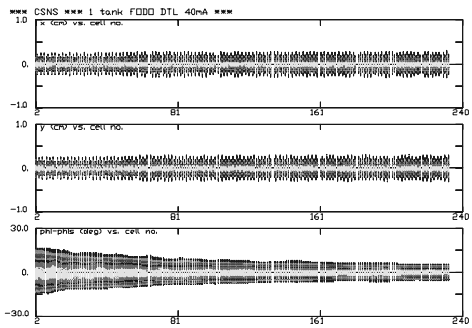

Figure 6: The beam profile in the 130MeV DTL.

ACKNOWLEDGEMENTS

The authors thank all the members of the ADS team and CSNS team for their great efforts in the study. We are very grateful to Dr. K.Hubner, Dr. H.Frischholz and their colleagues at CERN for their kind help in RF power source. The delightful collaboration with Dr. A.Pisent, Dr. G.Lamanna, Dr. M.Comunian and Dr. A.Palmieri of LNL, INFN is sincerely acknowledged. We would like to send many thanks to Dr.B.H.Choi and Dr.Y.S.Cho of KAERI for their friendly cooperation. The indispensable support in the superconducting cavity study from Dr.K.Saito of KEK is highly appreciated.

REFERENCES

[1] S.X.Fang, Current Status of ADS R&D in China, http://www.kaeri.re.kr/npet/WS-9/KOMAC/main.htm
[2] Baoqun Cui et al, Rev. of Sci. Instru., Vol.75(5), 2004, p.1457.
[3] Shinian Fu, et al., Proc. of LINAC'02, p.154.
[4] Xialing Guan, et al., Proc. of 4th Inter. Workshop on the Utilization and Reliability of High Power Proton Accelerators, KAERI, Daejeon, May 16-19,2004.
[5] Zhang Zonghua, et. al., on this conference THP-47.
[6] J.X.Fang, et al., Proc. of LINAC'02, p.335.

TRASCO-RFQ AS INJECTOR FOR THE SPES-1 PROJECT

P. A. Posocco, M. Comunian, E. Fagotti†, A. Pisent,
INFN - Laboratori Nazionali di Legnaro (LNL), Legnaro, Italy
†Università degli Studi di Milano, Milano, Italy

Abstract

The funded first phase of SPES foresees the realization at LNL of a facility able, on one hand, to accelerate a 10 mA protons beam up to 20 MeV for nuclear studies and, on the other hand, to accelerate a 30 mA protons beam up to 5 MeV for BNCT and preliminary ADS studies. In this two-way facility, the TRASCO RFQ will operate in two different current regimes. Moreover a specific MEBT has to be designed able to match the beam to the following superconducting linac and to deliver a beam with the correct characteristics to the neutron production target for the BNCT studies.

INTRODUCTION

The first phase of SPES facility (see Fig. 1) will produce a CW proton beam at 20 MeV 10 mA for nuclear studies and at 5 MeV 30 mA for BNCT (Boron Neutron Capture Therapy) studies [1]. The accelerator chain comprises the proton source TRIPS developed at LNS, a low energy beam transport (LEBT) [2] and the 352 MHz TRASCO RFQ [3], which can handle a beam up to 50 mA of current and 5 MeV of energy. After the RFQ a MEBT is necessary to inject the beam to the following superconducting linac [4] and to switch the line when the BNCT facility is operated.

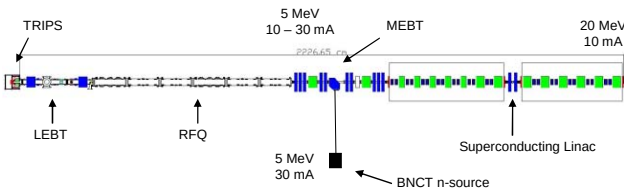

Figure 1: The SPES-1 project.

MEBT DESIGN

The MEBT lattice matches the 10 mA beam from the RFQ through 5 normal-conducting magnetic doublets and 2 longitudinal focusing 3-gap buncher into the first period of the superconducting linac and, at the same time, it should bend the 30 mA beam out of the linac direction for the BNCT studies. As shown in Fig. 2, the line to the BNCT target starts almost from the centre of the MEBT with a 90° degree bend (200 mm radius), for which a free length of 600 mm has been left: this choice is made in order to have a very short MEBT ensuring a high beam quality to the linac and, at the same time, to restrict the interferences between the BNCT facility and the RFQ-linac building.

The lattice of the BNCT line doesn't include any longitudinal focusing system because the BNCT target [5] requires a well defined transverse distribution and prefers a non bunched beam. Differently from the linac case, for which the requirements are on the 6 Twiss parameters, the focusing condition for the BNCT target is described by the transverse spot dimensions and by the condition of a very small dispersion to reduce error on beam position. These requirements are obtained with a simple combination of 4 normal-conducting doublets before the 4.5 m long drift to the collimator of the target (the drift is necessary for the radiation shielding walls and for the remote handling of the neutron converter).

Table 1: MEBT characteristics (line to BNCT from the dipole to the last doublet).

Line to		**Linac** (10 mA)		**BNCT** (30 mA)	
Total length (m)		3.15		5.9	
No. Doublets		5		4	
Length (mm)		100-70-100		150-100-150	
Bore radius (mm)		20		50	
Max env. (mm)		7.5		20	
Max gradient (T/m)		25		10	
		In	*Out*	*In*	*Out*
$\varepsilon_{n,RMS}$	x (mm.mrad)	0.204	0.208	0.217	0.709
	y (mm.mrad)	0.201	0.204	0.212	0.215
*ΔE/E	z (deg.MeV)	0.253	0.240	*0.83%	*1.9%

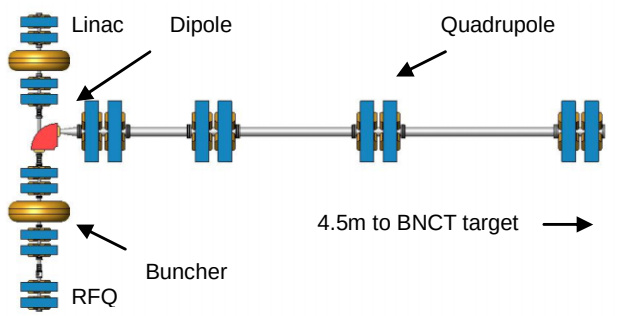

Figure 2: MEBT and BNCT line overview.

THE LINE TO THE LINAC

The choice of having 2 current regimes and the need for a dedicated line to the BNCT facility forces the shared part of the lattice to be flexible: this requirement is obtained with the use of normal conducting doublets (see Tab. 1) with independent power supply for each magnet.

The MEBT can be ideally divided in 2 parts, before and after the dipole, where the second one is specific designed to match the beam into the linac. More in details:

- the first doublet, also required in order to place the RFQ vacuum valve and some diagnostics in the following drift, should reduce the RMS differences

between the two types of beam (10 mA and 30 mA) at the RFQ out;

- the second doublet let the beam to have a waist at the first buncher (where the bore radius is 15 mm instead of the 20 mm of the MEBT pipe);
- the third doublet should help the beam to be controlled in the long middle drift (10 mA) and to be injected in the right way in the dipole (30 mA);
- the last two doublets should keep the envelope small inside the second buncher and are used to find the match to the first period of the linac.

Table 2: Cavity characteristics.

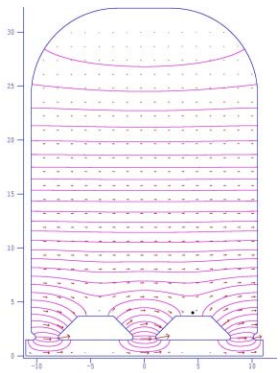

Inner length	220 mm
Inner radius	322 mm
Bore	15 mm
Mode	TM_{010}
Frequency	352 MHz
E_0	1 MV/m
E_{max} / E_0	7.76
TTF	0.715
Power loss	6.1 kW
Q	36000
Z_S	39.7 MΩ/m

The 2 bunchers are used to find the longitudinal focusing condition with a quite low longitudinal electric field (E_0TL<0.16 MV) and a preliminary study on the cavity design with Poisson Superfish (see Tab. 2) shows that a solution may be a normal-conducting 352 MHz 3-gap cavity that operates at the synchronous phase of -90 degree. The use of only 2 longitudinal focusing elements is not a problem for the matching capability because of the long drift in between, but is a constraint to the total length of the line if we want to limit the phase envelope in the linear zone.

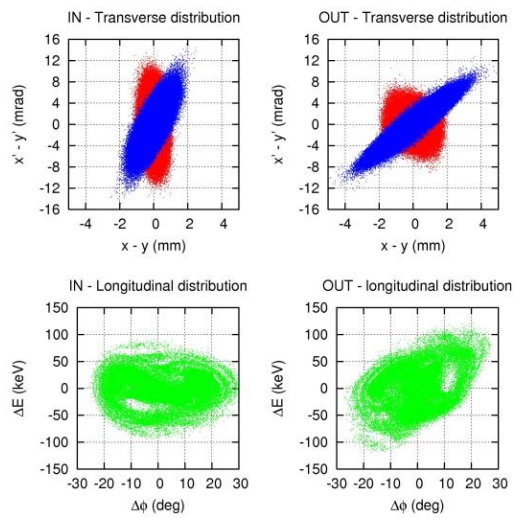

Figure 3: 10 mA in and output phase space distributions, x-x' plane in blue and y-y' in red.

First step of the simulation work of the line was performed with Trace 3-D [6] and Parmila [7] using a uniform distribution with the RMS parameter of the RFQ output (obtained accelerating a 4D waterbag with 100k macroparticles trough the RFQ). Afterwards we transported directly the RFQ out distribution (see Fig. 4) through the line and we monitored envelopes, emittances and halo. After a deeper optimization we obtained:

- a bore over RMS ratio greater than 9 inside the buncher and greater than 10 elsewhere (as shown in Fig. 3, the RMS envelope is less then 2 mm);
- the transverse RMS emittances growth contained in 2% of the entrance value;
- a redistribution of the longitudinal plane that reduces the RMS emittance of 5.5%.
- negligible transverse beam halo increase.

A preliminary error study shows no beam losses up to 0.5 mm of uniformly random off axis displacement of the line magnets.

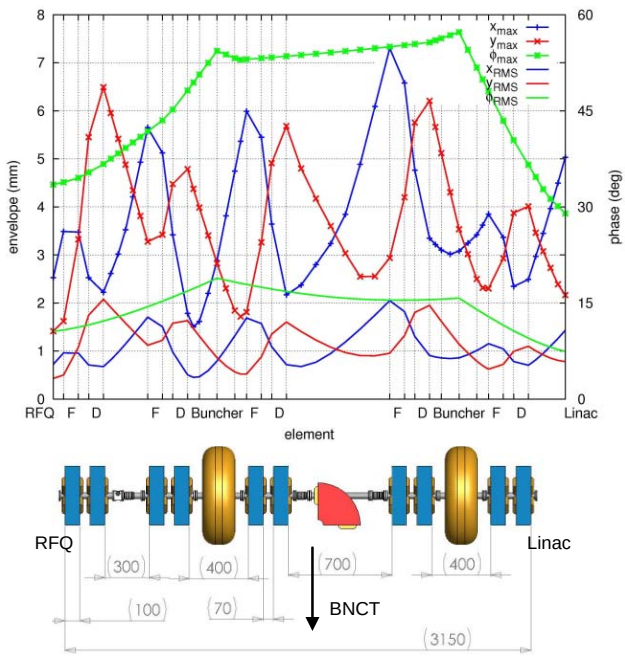

Figure 4: The beam envelopes (RMS and max) and some line specifications in mm.

THE LINE TO THE BNCT TARGET

The beam full current beam to BNCT has to reach the high power (150 kW) Be target for neutron production under development at the Efremov Institute [5]. Due to the limitation on the power density on the target, the beam has to arrive with a large spot and a well determined distribution. Since the transverse envelopes in the shared part is less the 10 mm and we need a half width spot on target of about 60 mm, the line to BNCT has to have a waist and a large magnification. Therefore we chose a bore radius of 50 mm for the line before the final drift (where the envelopes reach 20 mm) and of 100 mm for the last part where there are no more magnets (see Fig. 5).

Concerning the longitudinal phase space, the target accepts a debunched beam with the given energy spread.

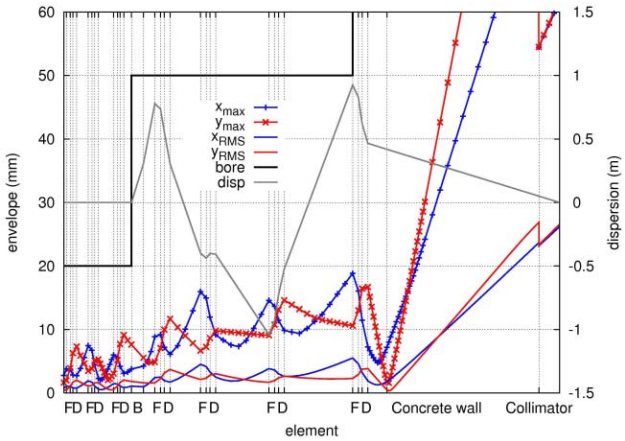

Figure 5: The envelopes and the dispersion function for the line to BNCT.

To avoid that the energy distribution of the beam contributes to the horizontal profile at the target, the energy dispersion is annulled on the target. As shown in Fig. 5, we get a very low dispersion angle (-92 mrad) and a small dispersion envelope, ensuring that even for out of nominal energy beam the probability of undesired beam loss along the pipe due to dispersion is very low.

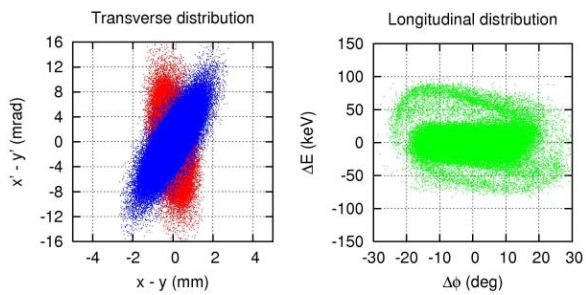

Figure 6: 30 mA RFQ output phase space distributions, x-x' plane in blue and y-y' in red.

Simulating the line with the RFQ output distribution (see Fig. 6) as input, we optimized the choice of the last two quadrupoles strength and the squared target collimator width (100.9 mm) in order to have a beam spot with axial symmetry, with a maximum width of 62 mm and a RMS radius of 26.5 mm. The resulting beam loss on the cooled collimator is evaluated in 8 kW and the losses in the meter before (already in the shielded zone) are contained in 0.5 kW.

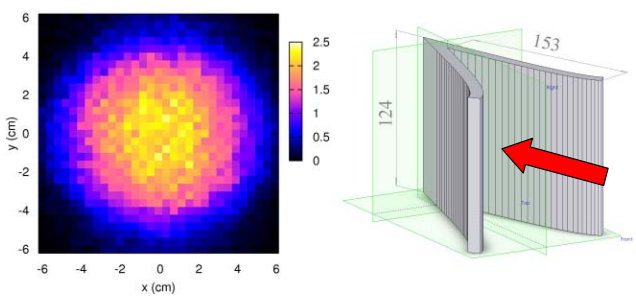

Figure 7: At left density power distribution (kW/cm^2) at the target on a plane perpendicular to the line, at right Beryllium converter profile (units are in mm).

As shown in Fig. 7, the maximum of the density power distribution on a plane perpendicular to the line reaches 2.5 kW/cm^2: that is the reason of the Beryllium converter profile. This design is optimized in order to keep the maximum density power of this beam below 700 Watt/cm^2 and depending on a technical choice for the orientation of the cooling channels could be used whether horizontal or vertical (see Fig. 8).

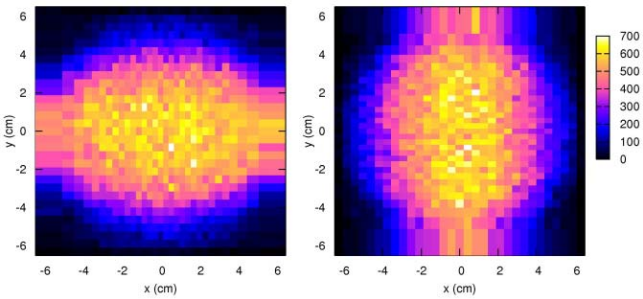

Figure 8: Density power distribution (Watt/cm^2) on the Beryllium converter surface: left with vertical and right with horizontal cooling channels.

A preliminary error study shows furthermore that we are working in a stable region in terms of the maximum of the density power distribution on the converter when we vary the last doublet strength up to 0.5%.

CONCLUSIONS

The MEBT structure can find the match requirements of the SPES-1 actual linac and it is able to work well with 5 mA of beam current as well, without degrading the quality of the beam in terms of emittance and halo.

The line to BNCT is able to reach the required target parameters with low losses, but may be modified following the technological improvements of the target and after a deeper study on halo growth (responsible of the last meter beam losses).

REFERENCES

[1] A. Bracco, A. Pisent, "SPES-Technical Design for an Advanced Exotic Ion Beam Facility at LNL", LNL-INFN, (REP) 181/02, June 2002;

[2] E. Fagotti, M. Comunian, A. Pisent, "Design of the SPES-1 LEBT", this conference;

[3] A. Pisent et al, "TRASCO RFQ", Proc. Of the XX Int. Linac Conf., Monterey, California, August 21-25, 2000;

[4] E. Fagotti et al, "Beam dynamics issues of SPES-1 linac", this conference;

[5] A. Makhankov et al, "An Accelerator-based Thermal Neutron Source for BNCT Application", 593-THPLT111 , EPAC 2004;

[6] K. R. Crandall, D. P. Rusthoi, "Trace 3-D", Los Alamos National Laboratory report LA-UR-97-886 (revision January 29, 2004);

[7] H. Takeda, J. H. Billen, "Parmila", Los Alamos National Laboratory report LA-UR-98-4478 (revision January 10, 2004).

THE TRASCO-SPES RFQ

A. Pisent, M.Comunian, A. Palmieri INFN/LNL, Legnaro, Padova, Italy
E. Fagotti, Università degli Studi di Milano, Milano, Italy - INFN/LNL, Legnaro, Padova, Italy
G.V. Lamanna, CINEL Strumenti Scientifici, Vigonza (PD), Italy
S. Mathot, CERN, Geneva Switzerland

Abstract

A high intensity RFQ is under construction at LNL. Developed within TRASCO research program, the Italian feasibility study an ADS (Accelerator Driven System), it will be employed as the first accelerating element of SPES facility, the ISOL project of LNL. The RFQ operates at the frequency of 352 MHz in CW mode. It delivers a proton current up to 30 mA and consists of six brazed segments whose length is 1.2 m. In this article the results obtained from the construction of a 20 cm "technological model", aimed at testing the construction procedure of the final structure, will be discussed. Finally we will report about the machining and the outcomes obtained after RF testing of the first two segments built up to now.

INTRODUCTION

The high intensity RFQ under construction at LNL, developed within TRASCO project [1] for ADS application, will be used as the front-end of a new generation ISOL facility for the production of exotic beams (SPES project [2]). The 5 MeV beam of the RFQ will also be used for the production of the neutrons necessary for the BNCT (Boron Neutron Capture Therapy); the first studies will be devoted to the application of this therapy for the treatment of skin melanoma. The construction of both this facility and a 20MeV, 10 mA superconducting proton linac (SPES-1) has been funded and is starting. In Table 1 the main RFQ parameters are listed.

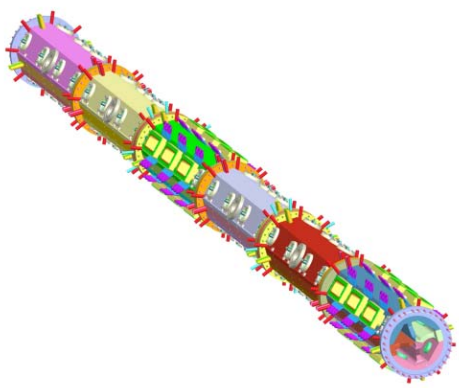

Figure 1: Layout of the TRASCO-SPES RFQ

CONSTRUCTION PROCEDURE

The RFQ consists of three modules 2.4 meters long resonantly coupled via two coupling cells in order to reduce sensitivity to machining errors. Each module consists of two 1.2 meters long segments, which are the basic construction units (Figure 1). Each segment, built in OFE copper, is made of four main parts (A, B, C, and D in Figure 2). The head flanges between segments and the rectangular vacuum flanges are made of SS (LN316). To reduce the number of brazing joints, the longitudinal cooling passages are deep-hole drilled from one side and closed with brazed plugs on the flat surfaces of the RFQ segment (opposite to the coupling or end cells). Moreover, the vacuum grids with their cooling channels are directly machined on the copper bulk.

Table 1: Main RFQ parameters

Energy Range	0.08-5	MeV
Frequency	352.2	MHz
Proton current	30	mA
Duty cycle	100	%
Emittance T RMS in/out	0.20/0.21	mm mrad norm.
Emittance L RMS	0.19	MeV deg
RFQ length	7.13	m (8.4 λ)
Intervane voltage	68	kV (1.8 Kilp.)
Transmission	95	%
Q (80% of Superfish result)	8000	
Beam Loading	0.148	MW
RF Power	0.726	MW

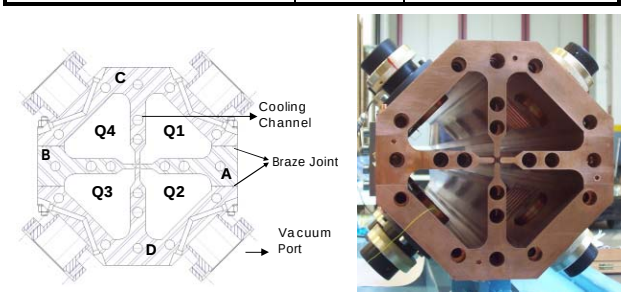

Figure 2: Transverse section of the RFQ with the indication of quadrants and pieces to be brazed.

Two brazing steps occur. In the first the four main parts are brazed in horizontal position in a horizontal vacuum furnace, as well as the OFE plugs for the cooling channels. The brazing alloy is B-Ag68CuPd-807/810 (according to ISO 3677) and the brazing temperature is 820^{O}C. After first brazing, the seat for the head flanges and the flat end surfaces (where the cooling channel plugs are located) are machined. In the second brazing cycle the head SS flanges, the inlet and outlet cooling water SS tubes and the SS flanges for vacuum ports or couplers are brazed in vertical position in a vertical vacuum furnace. The brazing alloy is B-Ag72Cu-780 (according to ISO 3677) and the brazing temperature is 790^{O}C.

RF and mechanical measurements allow to check the correctness of each step. The whole machining of the cavity is made by CINEL Strumenti Scientifici at Vigonza (PD), Italy, and the vacuum brazing as well as the copper heat treatment are made at CERN.

THE 20 CM TECHNOLOGICAL MODEL

The construction procedure above explained in its essentials has been checked with the construction of the so-called "20 cm technological model" (Figure 3). It is a 22 cm long RFQ, without modulation, onto which a vacuum, a tuner and a power coupler port and one cooling channel of each kind have been built. The RFQ copper test structure is coupled to an end plug (FMEC in the following) in order to get the proper boundary conditions for the quadrupole mode at the nominal frequency. The design of the whole structure has been accomplished by means of MAFIA and HFSS codes.

The results of the RF measurements are reported in Table 2

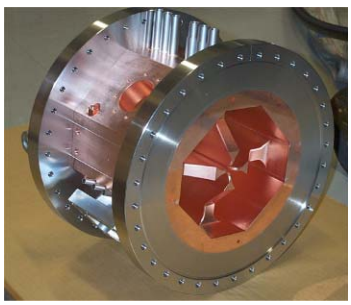

Figure 3: The 20 cm technological model after brazing

Table 2: Results of measurements of the copper test model ("H" is for HFSS, "M" is for MAFIA)

	Before 1st brazing	After 1st brazing	After 2nd brazing	Simulations
Q_0	5504	6590	5936	7044 (M) 7742 (H)
f_q (MHz)	349.312	349.328	349.602	348.63 (M) 350.70 (H)
f_{d1}(MHz)	366.66	367.056	367.441	368.07 (M) 371.11 (H)
f_{d2}(MHz)	369.31	369.141	369.002	368.20 (M) 371.35 (H)

The leak test was successful (leak rate=$5\cdot10^{-10}$ torr·liter/sec). The cooling channels, after being leak tested are being tested in a closed water circuit to check the corrosion due to water cavitation. One of the slug tuners has been built and tested. In particular the vacuum seal (Viton® O-ring) and the RF seal between tuner and RFQ surface have been successfully tested on the 20 cm RFQ. The calibration of the pick-up (V_{pu} vs. $V_{intravane}$) was tested by feeding the cavity with a known power through a loop in critical coupling conditions; the measured $V_{pu}/V_{intravane}$ agrees with calculation within 20%.

THE FIRST RFQ SEGMENT

After machining, the first segment of the RFQ was assembled in CINEL for preliminary RF measurements. In addition to the usual RF measurements it was decided to perform a "pre-tuning" of the structure, whose goal is to have an overall field variation $|\Delta u_q(z)|+|u_{d1}(z)|+|u_{d2}(z)|<0.05$, "q" being the quadrupole component and "d1" and "d2" being the dipoles Q1-Q3 and Q2-Q4 (See Figure 2) components respectively, aimed at checking the effectiveness of the tuning algorithm [3]. The components, extracted from bead-pull measurements in the four RFQ quadrants, are normalized in such a way that:

$$\frac{1}{L}\int_0^L \left(u_q(z)^2+u_{d1}(z)^2+u_{d2}(z)^2\right)dz=1$$

This procedure has been repeated before and after 1st brazing and after 2nd brazing. For such purpose a set of temporary brass "dummy tuners" has been employed. The tuners are in number of 4 per each quadrant and are initially set to 4.62 mm penetration. One tuner per quadrant is equipped with a loop for proper excitation of quadrupole and dipole modes. The RFQ segment has been equipped with the FMEC at the high-energy end. All measurements have been done with an Agilent 8753 ES Vector Network Analyzer.

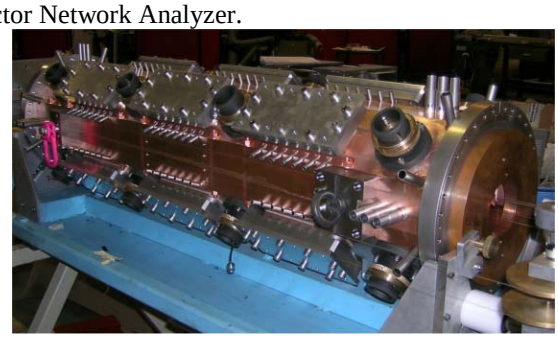

Figure 4: The first RFQ segment after 2nd brazing

After electrodes mechanical alignment with initial tuner settings, a quadrupole frequency f_q=350.698 MHz, dipole frequencies f_{d1}=346.493 MHz, f_{d2}=346.093 MHz and an unloaded Q=4500 have been measured. After moving the pieces A and B towards the external of 30 μm and 50 μm respectively the values of f_q=351.416 MHz, dipole frequencies f_{d1}=347.324 MHz, f_{d2}=346.666 MHz and an unloaded Q=4800 have been measured. Then the pre-braze measurements have been done at CERN. The frequency variation due to the 1st brazing is Δf_q^{0-1} =74 kHz, and the frequency variation between 1st and 2nd brazing is Δf_q^{1-2} =360 kHz. The Q_0 has increased to 5600 after 1st brazing and to 5700 after 2nd brazing. Such values, about 30% lower than the specifications, are supposed to be due to the presence of brass tuners and to

the end plugs. As for the field measurement results, in Figure 5 the behaviour of the quadrupole and dipole components is reported before and after 1st brazing.

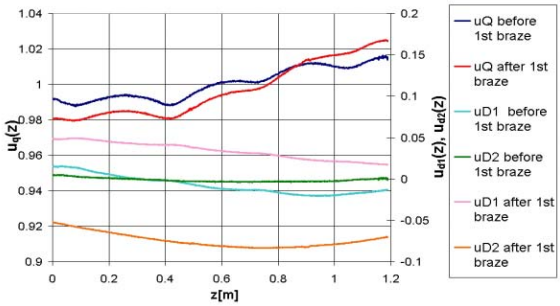

Figure 5: Field variation before and after 1st braze

In Figure 6 the same curve before and after 2nd brazing is shown.

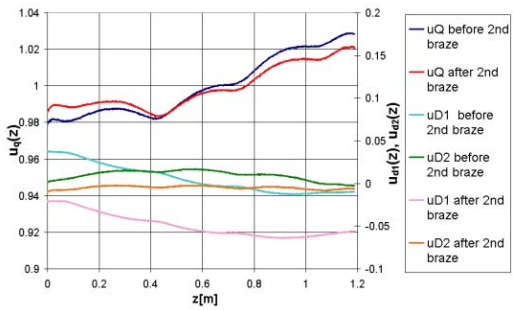

Figure 6: Field variation before and after 2nd braze.

The quadrupole mode keeps almost unchanged after each brazing step, while the dipole modes are a little bit mixed up.

Finally, the effectiveness of the tuning algorithm is shown by comparing the field variation before and after tuning (Figure 7) after the 2nd brazing. The field variation is lower than 1.5 % for any z, well below the "pre-tuning" specifications, and the dipole component content is about 1% of the total.

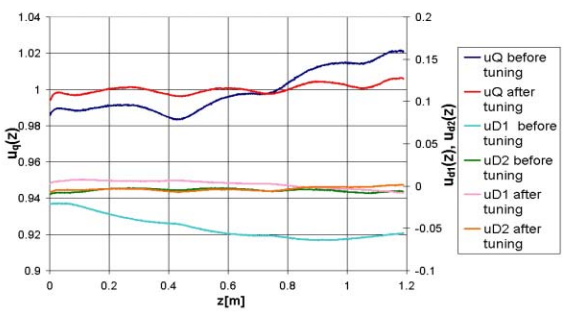

Figure 7: Effect of tuning upon field variation.

These results demonstrate the validity of the construction procedure and the attainment of the mechanical tolerances. It has to be added that a major vacuum leak has been found in the vacuum flange region. This has been the consequence of an unadapted mechanical tolerance of the flange and mounting fixture in the horizontal furnace. Therefore, the retained procedure is to braze the vacuum flanges also in vertical position (as described above) with a more complete fixture non usable in the horizontal furnace. A new flange design has been also adopted.

A repairing brazing cycle for the first segment will be performed soon. The leak tests of the main brazing joints, of the cooling channels and head flanges have been successful.

THE SECOND RFQ SEGMENT

The second RFQ segment has undergone the same alignment and RF measurement procedure as the first. Some extra regulations were made available: the pieces A and B have been constructed 80 µm thicker than nominal dimensions on both sides, to allow adjustment of the quadrupole frequency and dipole frequencies spacing. Flush copper plugs have been applied to the coupler ports. After electrodes mechanical alignment with initial tuner settings a quadrupole frequency f_q=353.200 MHz, dipole frequencies f_{d1}=347.881 MHz, f_{d2}=346.413 MHz and an unloaded Q=4400 have been measured. After removing 70 out of 80 µm thickness and moving A and B pieces towards the external of 20 µm the values of f_q=352.195 MHz, dipole frequencies f_{d1}=346.272 MHz, f_{d2}=346.113 MHz and an unloaded Q=4400 has have been measured.

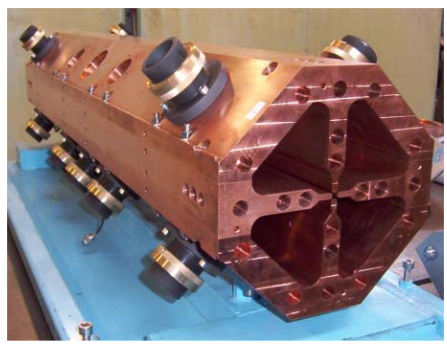

Figure 8: The 2nd RFQ segment.

The second segment has been brazed at CERN and is being delivered to Italy for machining and post 1st braze measurements.

ACKNOWLEDGMENTS

The authors wish to thank Enzo Bissiato (INFN-LNL) and Michele Franco (INFN-Bari) for their help during the operations of assembling RFQ and measurement setup, Fabio Scarpa (INFN-LNL) for his help in setting up the pick-up calibration measurements and Augusto Lombardi (INFN-LNL) for useful comments.

REFERENCES

[1] INFN-TC-00-23 21
[2] LNL-INFN(REP) 181-02.
[3] G.V. Lamanna et al. EPAC 2002, Paris, France page 924.

DESIGN OF THE SPES-1 LEBT

E. Fagotti*, Universita' degli studi di Milano, Milano, Italy - INFN/LNL, Legnaro, Padova, Italy
M. Comunian, A. Pisent, INFN/LNL, Legnaro, Padova, Italy

Abstract

The low-energy-beam transport (LEBT) system for the SPES-1 accelerator transports the beam at 80 keV and 30 mA from the ion-source TRIPS [1] to the TRASCO RFQ entrance. A second mode of operation corresponding to 10 mA current is also foreseen. The code PARMELA [2] performed these simulations of the beam transport through the LEBT. This code is used to transport H+ and H2+ in the electrostatic fields of the ion-source extraction, in the magnetic fields of both the source and the solenoid lenses and under space charge and neutralization influence.

INTRODUCTION

AXCEL code [3] is used to derive a first estimation of the radius of curvature r_p of the plasma boundary in the ion-source-extraction aperture. Beam is then generated on a spherical cathode with radius r_p and accelerated through the electrostatic fields of the ion source's accelerating column. Then beam goes through the LEBT (see Fig. 1), which has two magnetic solenoids and arrives at RFQ input after passing some collimators and an electrons trap. PARMELA code has been chosen for simulation because it allows transporting three different ion types in the electrostatic and magneto-static fields generated with SUPERFISH code [4]. This is a very interesting feature that allows simulating neutralization of H^+ and H_2^+ beams extracted from TRIPS source.

EXTRACTION AND NEUTRALIZATION

Being a t-code, PARMELA is able to simulate transient effects. A consequence is that simulation starts with no beam at all [5]. This means that a long enough stream of H^+ and H_2^+ ions must be injected to avoid head and tail effects due to the finite longitudinal dimension of the beam as shown in Fig. 2. Moreover time moves faster for H_2^+ ions in order to compensate the lower velocity and minimize simulation time.

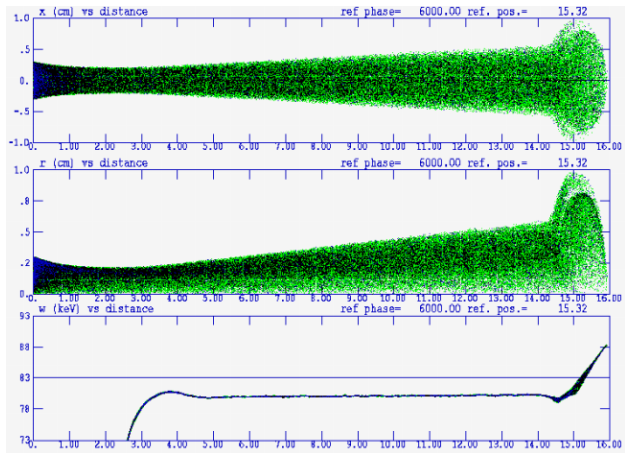

Figure 2: Head effect in beam generation. Cause to this effect, only central part of the beam enters the calculation.

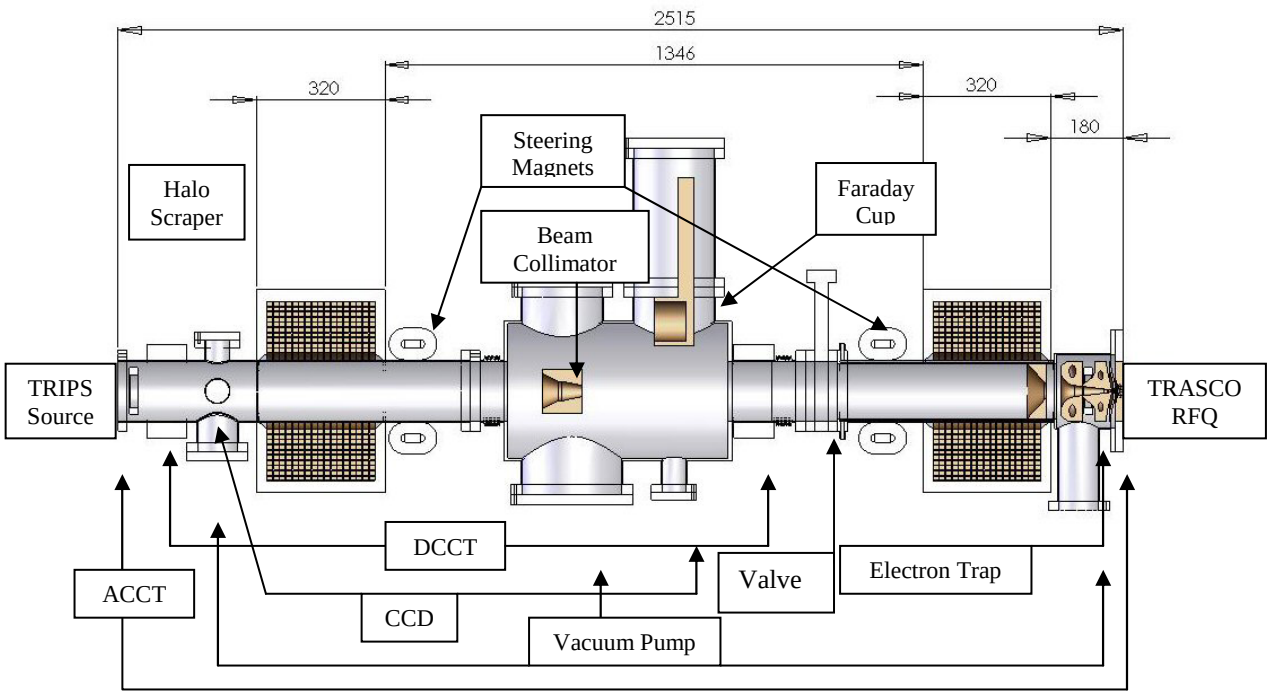

Figure 1: LEBT design. The location of five Bergoz dc and ac current transformers and two video camera diagnostics are indicated.

*Enrico.Fagotti@lnl.infn.it

At the beginning, H^+, H_2^+ ions extracted from the source and e^- generated by residual gas ionization move in the electrostatic fields of the column and in the residual magnetic field generated by the source solenoids. This transport allows finding the point where neutralization rises, that is the point where electrons are stopped by negative electrode (see Fig. 3). At this point electrons are suppressed and compensation of 95 % is assumed. An important feature to be noted is that the outer part of the beam is strongly focused by electrostatic fields. This over-focalization in conjunction with the presence of high axial residual magnetic field (950 G) creates a dropping in the beam density near the axis as shown in Fig. 4. This drop has to be minimized reducing the residual magnetic field because the evolution of such density perturbation may excite many possible modes of oscillation, some of which may become unstable or resonate with machine structure.

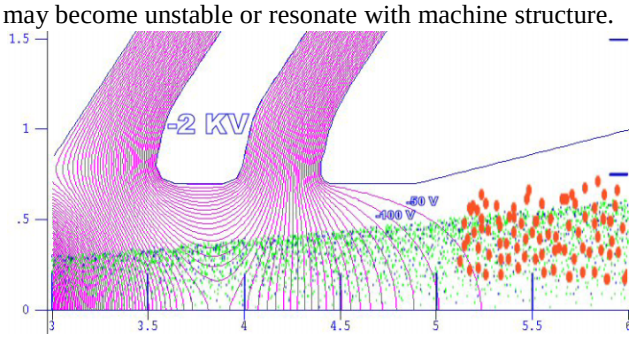

Figure 3: The negative electrode suppresses the electron current flowing towards extractor electrode at 80 KV.

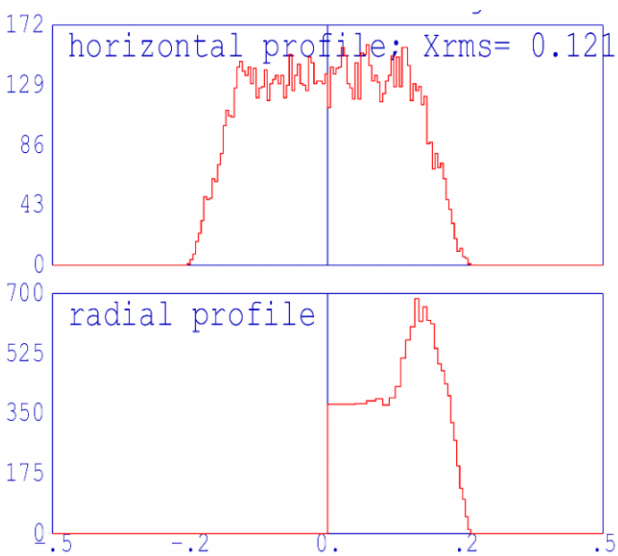

Figure 4: Horizontal and radial profile at 4.36 cm from plasma extraction hole.

SPES LEBT SIMULATION

Beam is modelled through the whole LEBT. At the exit of extraction column, the extreme part of beam envelope is constituted by particles that experienced non linear forces in extraction process. These particles are eliminated by a halo scraper after 41 cm from extraction and before they are refocused in the beam core by the first solenoid lens. This scraper is not cooled because it cuts only a very small beam fraction. This is not the case of the collimator between the two lenses that operates the ultimate current selection. With this collimator it is possible to operate a light cut leaving 33 mA protons current or a heavier one with 11 mA protons left. A collimation chain in front of RFQ entrance completes the modelling process. It is used to increase proton fraction at values greater than 99 %.

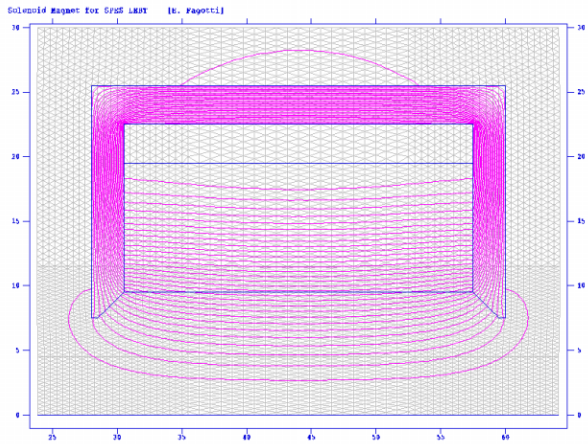

Figure 5: POISSON-calculated solenoid fields.

PARMELA simulations show that two crucial points for good beam transmission are the line neutralization and the solenoids non-linear effects. Recent neutralization measurements on TRASCO-SPES provisional line at LNS, demonstrate that electrons generated when part of the beam hit the pipe are sufficient to create good compensation even without gas injection [6]. This is a very important result because one of the main disadvantages of using gas injection to increase neutralization is the loss in proton transmission due to bad vacuum. So beam dynamics and pipe aperture have been optimized to have a selective loss of the H_2^+ ions through the line. If compensation will be not sufficient, it has been considered the possibility to put some hot cathodes to generate electrons [7].

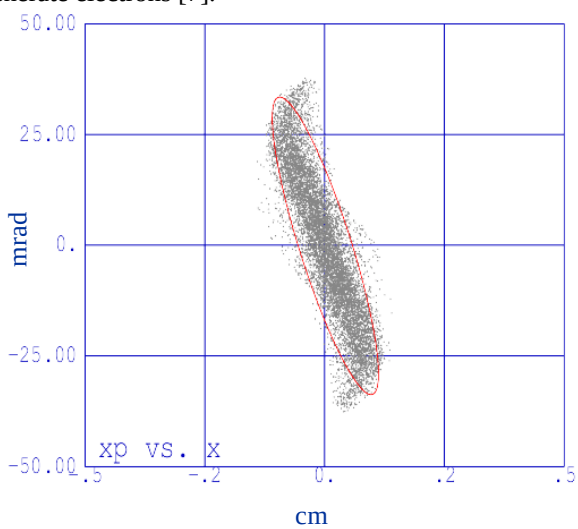

Figure 6: PARMELA-calculated RFQ input.

As regard non linear effects, simulations show that rms emittance is very sensitive to beam dimensions in the solenoids field. This non linear effect is even more dangerous if concurrent with neutralization loss at RFQ port. Ions with great radius experience a stronger focalization than other particles and penetrate in the beam core creating a pick in the density distribution when beam recover its full space charge. In this way, effect of space charge force becomes strongly non linear and contribute to emittance increase. To minimize this effect a new design of magnets has been developed (Fig. 5). Phase-space of the RFQ match point is shown in Fig. 6. With these improvements, rms normalized emittance at match point is reduced to 0.08 mm-mrad.

ELECTRON TRAP

As just said, to maximize proton fraction, a collimator is needed just before RFQ entrance. Collimation process needs some care because of the high power density of the beam in that location. For example, considering all the contaminant ions incident perpendicularly to a 5 mm bore radius collimator, it is simple to find power density values as high as 2 kW/cm^2 [8]. This number raise to 10 kW/cm^2 if we suppose that even the proton beam can intercept collimator. A particular device has being developed to solve this problem and at the same time to prevent electrons from entering RFQ. This device has been optimized to accept up to 20% of the total beam power. In Fig. 7 a schematic design is presented, while in Fig. 8 details of ANSYS thermal simulation are shown. Electrons generated by residual gas ionization have very little energy and it is sufficient to set a -1.5 kV potential on the device central electrode to stop them. Voltage used for trap is much higher than maximum electrons energy for two reasons. On one hand the electrode is at 8 mm distance from beam axis and we need more potential to have an effective field on axis; on the other hand, when electrons are stopped, the beam is completely un-neutralized and the space-charge effect is so high that it tends to attract electrons on the other side of the trap. With the nominal potential, electrons are stopped about 2.5 cm from the RFQ match point.

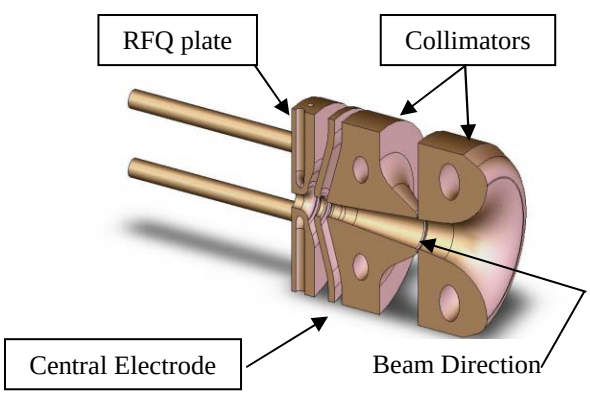

Figure 7: Beam collimator-electron trap device design. The two bars are RFQ stabilization bars.

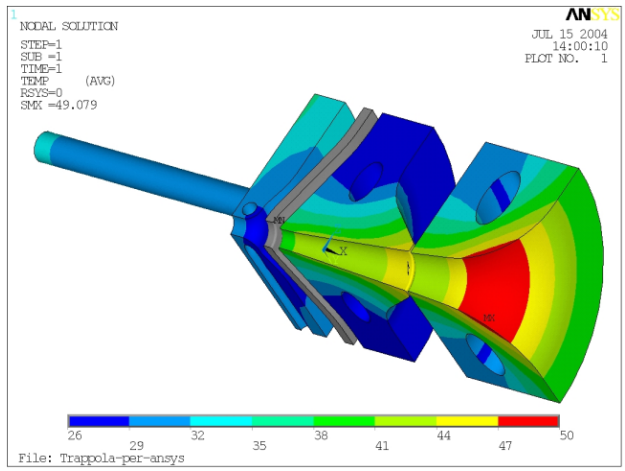

Figure 8: Thermal Analysis of one quarter of electron trap near RFQ port. No beam reaches high voltage electrode, because it is completely shielded by collimator.

CONCLUSIONS

PARMELA validate the old LEBT design defined using PARMTEQM code [9] and gives important information on beam distribution and compensation. Utilization of SUPERFISH simulated solenoids fields instead of hard edge approximation, allows investigation of emittance increase due to field aberration. This procedure results a powerful tool to find optimum magnets design.

REFERENCES

[1] L. Celona, G. Ciavola, S. Gammino, R. Gobin, R. Ferdinand, Rev. Sci. Instrum. 71 (2), (2000), 771.

[2] L. M. Young, J. H. Billen, "PARMELA Version 3" Los Alamos National Laboratory report LA-UR-96-1835 (revision June 8, 2004).

[3] P. Spädtke, "AXCEL Version 3.43", INP, Wiesbaden, October 1998.

[4] J. H. Billen, L. M. Young, "POISSON SUPERFISH," Los Alamos National Laboratory report LA-UR-96-1834 (revision January 29, 2004).

[5] L. Young, "Simulation of the LEDA LEBT with H^+, H_2^+, and e^- particles" PAC'97, Vancouver, May 1997, p. 2749.

[6] G. Ciavola et al., "The TRASCO high current proton source and its LEBT" LINAC'02, Kyongju, Korea, August 2002.

[7] M. D. Gabovich, I. A. Soloshenko, A. A. Ovcharenko, Ukrainskii Fizicheskii Zhurnal, Vol. 16, n. 5, 812-816, (1971).

[8] E. Fagotti, "Thermal analyses of electron trap", LNL internal report.

[9] K. R. Crandall, T. P. Wangler, et al. "RFQ Design Codes" Los Alamos National Laboratory report LA-UR-96-1836 (revision November 17, 2001).

COLD-MODEL TESTS AND FABRICATION STATUS FOR J-PARC ACS

H. Ao#, H. Akikawa, A. Ueno, K. Hasegawa, Y. Yamazaki, JAERI, Tokai, Ibaraki, 319-1195, Japan

M. Ikegami, S. Noguchi KEK, Tsukuba, Ibaraki, 305-0801, Japan

N. Hayashizaki, TIT, Meguro, Tokyo, 152-8550, Japan

V. Paramonov, INR RAS, Russia

Abstract

The J-PARC (Japan Proton Accelerator Research Complex) LINAC will be commissioned with energy of 181-MeV using 50-keV ion source, 3-MeV RFQ, 50-MeV DTL and 181-MeV SDTL (Separated DTL) on September 2006. It is planed to be upgraded by using a 400-MeV ACS (Annular Coupled Structure), which is a high-beta structure most suitable for the J-PARC, in a few years from the commissioning. The first ACS type cavity, which will be used as the first buncher between the SDTL and the ACS, is under fabrication. Detailed design and tuning procedure of ACS cavities has been studied with RF simulation analysis and cold-model measurements. The results of cold-model measurements, fabrication status, and related development items are described in this paper.

INTRODUCTION

An Annular Coupled Structure (ACS) has been developed for upgrade of a J-PARC linac from 180 MeV to 400 MeV. An operation frequency is 972 MHz.[1]

An ACS-type buncher cavity has been fabricated from Apr.2002. This cavity consists of two 5-cell ACS accelerating cavities and a bridge cavity, which will be installed to a matching section from the SDTL to the ACS as the first cavity of two buncher cavities. It is the first fabrication of an ACS-type cavity for the J-PARC linac. It will be finished at the end of FY2004.

For the study of tuning procedure and RF measurement, we machined some aluminium and OFC intermediate cells that were designed for a periodical symmetry part. RF measurement procedure, tools, and frequency tuning process have been improved with these test cells.

10-cell half-scale aluminum models (beta=0.7114) were also fabricated in FY2003. Intermediate cells and end-cells were tuned for an operating frequency, and then total properties and end-cell effects were measured with this model.

This paper reports a fabrication status and measurement results.

BUNCHER CAVITY

Intermediate Cell

Trial machining and RF measurement for the buncher cavity has been developed. [2,3,4,5]. The frequency has to be adjusted to an operating one by final machining with RF measurement. Because a cavity design based on a 2D and 3D electromagnetic analysis has some errors, and machining process also has certain errors.

In FY2004, we tried final frequency tuning process and measured a frequency correction factor (amount of cutting versus a frequency shift) for frequency tuning regions.

An accelerating mode and a coupling mode have to be considered for the ACS cavity. In the accelerating cell, outer diameter of the cell has a tuning margin, and in the coupling cell, a ledge part has a tuning margin. Figure 1 shows the tuning parts for each cell and the frequency correction factor.

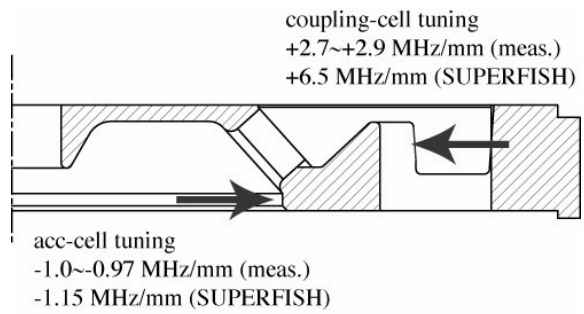

Figure 1: Tuning part and frequency shift.

About the accelerating cell, we consider that expanded volume of an electromagnetic field through a coupling slot makes the frequency shift of the accelerating cell smaller than the SUPERFISH analysis. About the coupling cell, eight vacuum ports cut the tuning ledge part, so that the frequency shift is smaller than the analysis. These results suggest the initial amount of cutting in frequency tuning procedure.

We also added a 5 mm vertical straight at bottom of the ledge part to make it easy for 3D profile measurement after machining.

The test brazing with these cells is planned to confirm a frequency shift before and after brazing.

The cell dimensions of the buncher cavity are almost fixed except for minor corrections required the mechanical restriction. Test cavities for an end-cell and bridge cavity were not fabricated, so that we design and correct dimensions based on a 2D and 3D electromagnetic analysis and the measurement of an half-scale aluminum model.

#aohi@linac.tokai.jaeri.go.jp

Module Design

The bridge cavity was located above a drift space between two ACS cavities in a previous ACS module developed in KEK. A quadruple magnet, beam monitors and a vacuum valve are installed in this space of an accelerating ACS module. The bridge cavity of this buncher moved to under a drift space as same as an accelerating ACS module fabricated in the next fiscal year, because of easy access for a magnet, alignment and maintenances. For this change, three frequency tuners have to be installed under the bridge cavity. Detailed arrangement about a bridge cavity, a wave-guide, cooling pipes, vacuum ports and pumps is in progress.

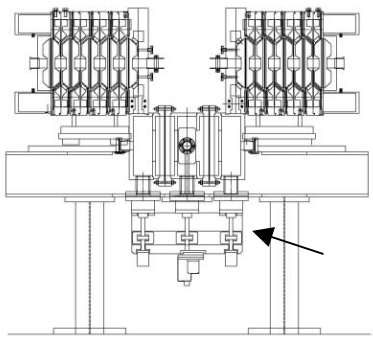

Figure 2: Buncher module (5+5-cell).

Alignment bases are attached on the upper side of ACS cavities. These bases have a common design for J-PARC accelerators; it is convenient to use and design an attachment for surveying instruments. These bases have to be mounted on the cavity after the final brazing, so that it is important to keep or confirm a relative position between the base and the beam-line of the cavity. This assembling procedure is considered with other module designs.

ICF Frange

The two ACS cavities are connected to the bridge cavity with a double edges conflat flange (ICF356) at a coupling cell of the bridge cavity. An inner edge keeps RF-contact and it has four slits for evacuation. This flange made of stainless steel is brazed to a cupper cavity, so that it should be strong for a thermal process. A pair of these flanges was fabricated to test for vacuum leak after the thermal process.

This result showed no vacuum leak and reliable properties. In detail observation, the inner edge looked lean slightly at a slit region, therefore these slits were changed to evacuation holes drilled at inner part of a flange.

TUNING OF ALUMINUM MODEL

High-Beta Aluminium Model

From the last of FY2003, we fabricated the 10-cell aluminium model of the ACS cavity for a high-beta region (beta = 0.7114). This model is half scale of 972 MHz ACS cavities, thus an operating frequency is 1944 MHz. The purposes of this model are check of an RF design and confirmation of tuning procedure for the buncher fabrication. RF tuning, measurement and related equipment design are not easy on a paper simulation, so that we plan and improve these procedure based on these results.

Tuning of Intermediate Cells

Accelerating and coupling mode frequencies of the intermediate cell are measured with short plates for each boundary condition. The coupling cell has second nearest coupling through vacuum ports, therefore the coupling mode frequency was measured in various cells from one to four. The frequency at infinity cell was estimated with the fitting curve of the measurement data.

The two accelerating cells (four half cells) were tuned, and then finial dimensions for other cells were fixed considering a correction based on 3D profile measurement results for a sensitive region such as a radius of nose cone and an accelerating gap length.

About a coupling cell, we planed that six cells (12 half cells) were tuned. Correction machining around an outer diameter in the coupling cell caused a slight deformation of an RF contact plane. Thus, the contact plane lost flatness. The measured frequency depends on a stacking torque strongly. As a result, repeatability of RF measurement could not be kept.

This deformation could be observed only scanning with a micron-order dial gauge on a NC lathe. At first, 3D profile measurement showed no deformations, because a probe could not pick up the small deformation. However, this problem solved with a careful check of a contact plane after machining and re-polish to keep flatness if needed.

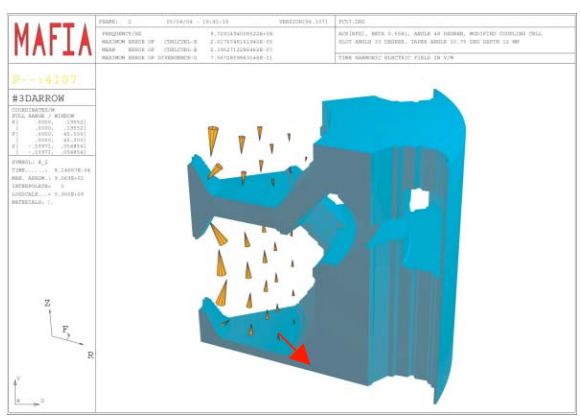

Figure 3: End cell tuning.

Tuning of End-Cells

The frequency of an end accelerating cell is higher than intermediate one if it keeps the same dimensions of the intermediate cell, because the cell do not have a slot. Frequency was adjusted by extending a volume of an accelerating cell. The example of analysis by a MAFIA is shown in Fig. 3. The gap length and nose cone dimensions were not changed. In this analysis, only the frequency was tuned. A measurement of an electric field distribution with these models is prepared using these models.

Multi-Cell Measurement

The dispersion curve of the accelerating cells and the coupling cells were measured up to 9-cell in a factory after frequency tuning. Figure 4 and 5 show the dispersion measurement result at a 9-cell and a 3-cell set up respectively.

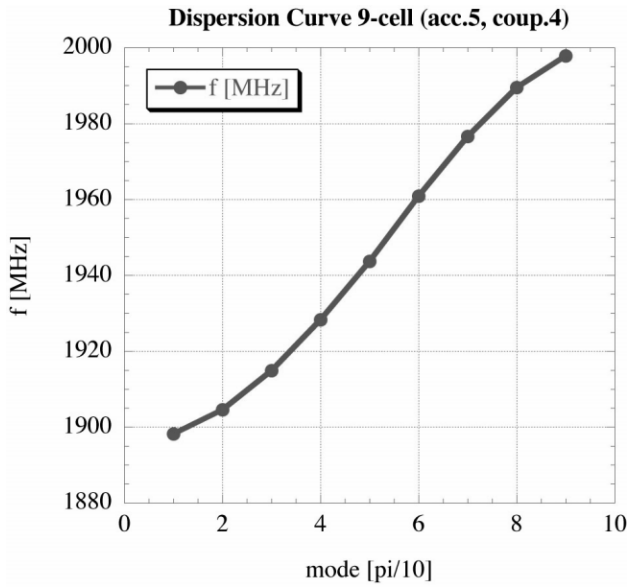

Figure 4: Dispersion curve of 9-cell.

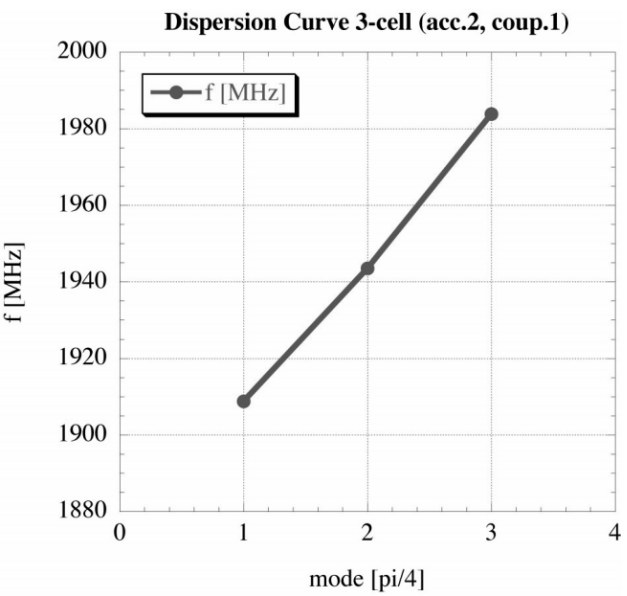

Figure 5: Dispersion curve of 3-cell.

The result of 3-cell measurement shows that the frequency of the coupling mode is slightly higher than accelerating one. This is because that a coupling cell has electric (short) conditions at both end sides in a 3-cell set up, and it was not equal to periodic (magnetic) boundary conditions. Only the both end coupling cell were not periodic conditions in 9-cell measurement. Although the frequency has been adjusted to the range of about 1944± 1MHz as the intermediate cell, the boundary conditions of an end cell, which has an irregular boundary, has not been compensated correctly. Therefore, the coupling mode frequency of the 9-cell measurement is averaged as whole cells.

On the process of coupling cell tuning, the end cell of the coupling cell was not distinguished clearly and adjusted. We are going to correct the frequency of the end cell to optimize a total frequency. The effect of boundary conditions for the each end coupling cells will be tuned correctly for the buncher cavity.

SUMMARY

The studies required for the fabrication of the buncher cavity, especially about the intermediate cell, have been performed for a long time. Consequently, the development of adjustment machining for the frequency tuning has been finished with the trial fabrication of real scale cells.

The end cell design and tuning process were confirmed based on measurement of the half scale aluminum model. These results will be reflected in the buncher design.

However, about the tuning procedure of the bridge cavity and vacuum properties are not discussed in this paper. Although these designs have been finished partly, we have still many items to be studied. These items have to be followed up in the process of buncher cavity fabrication. The high power test used this buncher module is planed for a next step.

REFERENCES

[1] V. V. Paromonov, "The Annular Coupled Structure Optimization for JAERI/KEK Joint Project for High Intensity Proton Accelerators", KEK Report 2001-14(2001)

[2] H. Ao et al. "R&D Status of the Annular Coupled Structure Linac for the JAERI/KEK Joint Project", Proc. of the 2002 Linac Conf., August 2002

[3] N. Hayashizaki et al. "Power-Handring Capability of the Annuler Coupled Structure Linac for the JAERI/KEK Joint Project", Proc. of the 2002 Linac Conf., August 2002

[4] N. Hayashizaki et al. "Structure Design of the Annuler Coupled Structure Linac for the JAERI/KEK Joint Project", Proc. of the 2002 Linac Conf., August 2002

[5] H. Ao et al. "Cold-model Tests of an Annular Coupled Structure for upgrade of a J-PARC Linac", Proc. of the 2003 Particle Accelerator Conf., May 2003

PARTICLE DISTRIBUTIONS AT THE EXIT OF THE J-PARC RFQ

Yasuhiro Kondo*, Akira Ueno, JAERI, Tokai, Ibaraki 319-1195, Japan
Masanori Ikegami, Kiyoshi Ikegami, KEK, Tsukuba, Ibaraki 305-0801, Japan

Abstract

A 3.115m long, 324MHz, 3MeV radio-frequency quadrupole (RFQ) linac is used as the first RF accelerator of the J-PARC linac. We have performed RFQ simulations to provide a particle distribution for an end-to-end (from the RFQ entrance to the injection point of the rapid cycling synchrotron (RCS)) simulation of the J-PARC linac. Two simulation codes, PARMTEQM and TOUTATIS are used for the RFQ simulations. The simulated emittances show good agreements with the ones measured at the exit of the medium energy beam transport (MEBT).

INTRODUCTION

Beam characteristics of the J-PARC linac are being discussed in detail by performing the end-to-end simulation, as described in separate papers [1][2][3]. The results of the simulation strongly depend on the initial particle distribution, therefore, "realistic" distribution should be adopted. The commissioning of the front-end part (from an ion source(IS) to the MEBT) of the J-PARC linac was done at KEK by February 2003 [4][5]. In this paper, we perform the RFQ simulations using a distribution based on measurement at the low energy beam transport (LEBT). Obtained distributions at the RFQ exit are transported to the MEBT exit. Simulation results are compared with the measurement at the MEBT exit to confirm the validity as an initial distribution for the J-PARC-linac end-to-end simulation.

PARTICLE DISTRIBUTION AT THE RFQ ENTRANCE

We assume following particle distribution at the RFQ entrance; A Gaussian distribution in the x-x' and y-y' planes (truncated at 4σ), the energy is 50keV with no spread and the phase is uniform. The width of the Gaussian is decided based on the measured distribution obtained with emittance monitors at the LEBT. Figure1 shows the measured distribution at the LEBT and the distribution used for the RFQ simulations. Since the LEBT emittance monitors are located between two solenoid magnets of the LEBT, neutral particles, such as H^0, are included in the measurement. Therefore, we regard the tails of the measured emittances as a background. The injection beam parameters used for the RFQ simulations are summarized in Table 1. The beam current is a measured value at the LEBT.

* yasuhiro.kondo@j-parc.jp

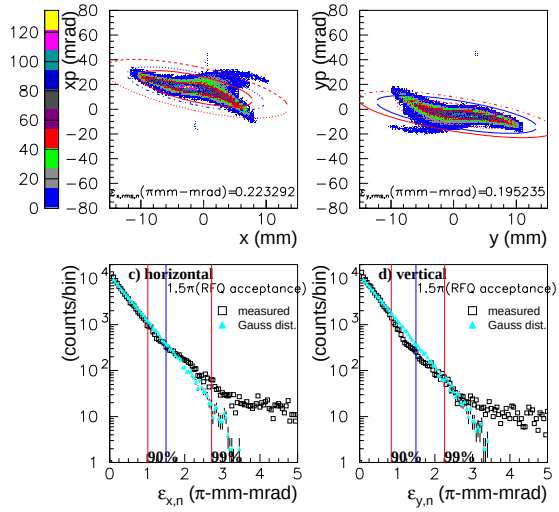

Figure 1: Measured emittances of the LEBT. The left-top and right-top show the phase space plots in the x-x' and y-y' planes, respectively. The ellipses are 90%, 1.5π mm·mrad (design acceptance of the RFQ) and 99% emittances. The bottom figures represent the beam current in the slices of the ellipses. The beam current is normalized to 100000. Open squares show the experimental result and closed triangles represent the distribution used for the simulation.

Table 1: Injection beam parameters used for the RFQ simulations

Parameters	values
Beam current	32 mA
Number of particles	100000
α_t	2.23
β_t	0.112 mm/mrad
ϵ_t(rms, normalized)	0.217π mm·mrad
Distribution(x-x', y-y')	Gaussian (truncated at 4 σ)
(phase)	Uniform
(energy)	50keV, no spread

SIMULATION RESULTS AT THE RFQ EXIT

We use two simulation codes, PARMTEQM[6] and TOUTATIS[7] for the RFQ simulations. Table 2 shows emittances and Twiss parameters at the RFQ exit obtained with use of the distribution described in the previous section. The rms emittances are not significantly different be-

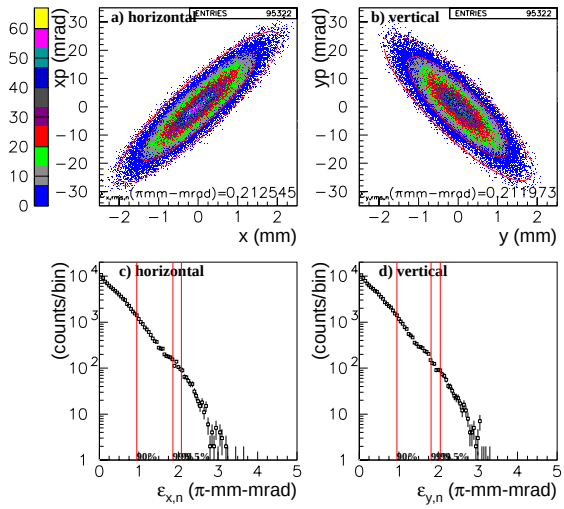

Figure 2: Particle distribution at the exit of the RFQ obtained with PARMTEQM.

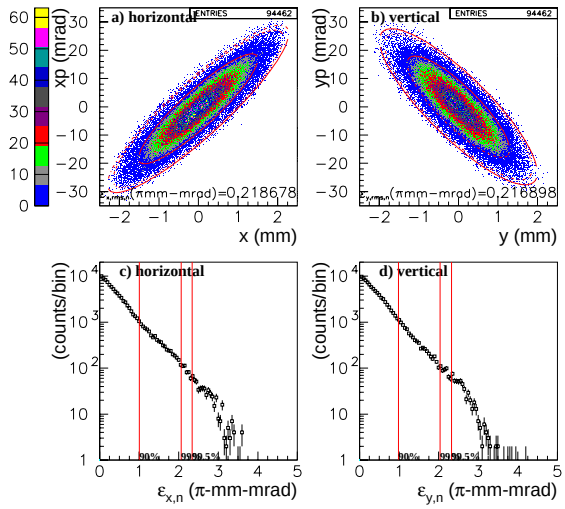

Figure 3: Particle distribution at the exit of the RFQ obtained with TOUTATIS.

tween the results of the two codes, but the 99.5% emittances of the TOUTATIS results are larger than those of the PARMTEQM results. Figures 2 and 3 are transverse distributions obtained with PARMTEQM and TOUTATIS, respectively.

Table 2: Simulation results at the RFQ exit. PQM and TTS mean PARMTEQM and TOUTATIS, respectively

Parameters	PQM	TTS
Transmission (%)	95.3	94.5
α_x	-2.11	-2.09
β_x (mm/mrad)	0.180	0.179
ϵ_x (π mm·mrad, rms, n)	0.213	0.219
ϵ_x (π mm·mrad, 99.5%, n)	2.08	2.33
α_y	1.63	1.60
β_y (mm/mrad)	0.138	0.136
ϵ_y (π mm·mrad, rms, n)	0.212	0.217
ϵ_y (π mm·mrad, 99.5%, n)	2.05	2.33
α_z	-0.123	0.0755
β_z (deg/MeV)	751	668
ϵ_z (π deg·MeV, rms)	0.0914	0.0957

Figure 4 represents the vane voltage dependence of the transmission of the RFQ. Both the simulation results and measured values are shown. Closed circles in the Figure 4 represent the experimental data of the measurement II in reference[4], and closed squares are the experimental data after the pre-chopper cavity installation into the LEBT, this decreased the transmission of the RFQ. This figure shows that the TOUTATIS result is closer to the measurement than PARMTEQM result, but the difference is not significant.

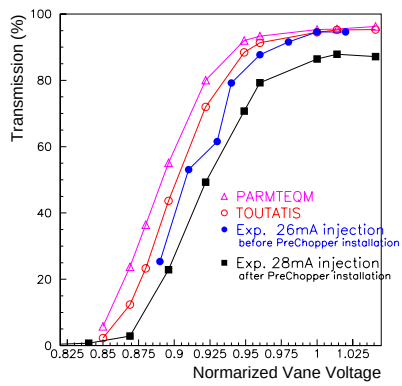

Figure 4: Measured and simulated transmission of the RFQ as functions of the vane voltage.

COMPARISON WITH THE EXPERIMENTAL RESULTS AT THE MEBT EXIT

With the simulated distributions obtained in the previous section, we compare the MEBT simulation results with the experimental data at the MEBT exit. For the MEBT simulation, we use PARMILA[8] with 2-D space charge, and took the fringing fields of the Q-magnets into account by the method described in [5]. In Table 3, the results using the distributions at the RFQ exit obtained with PARMTEQM and TOUTATIS are shown. The experimental data are also presented. The experimental data are results of the measurement I in [4]. The beam current was 29mA. Figures 5, 6 and 7 are measured distribution and simulated ones using PARMTEQM and TOUTATIS, respectively. Both the simulation results reasonably agree with the experimental data in the rms and 90% emittances.

Table 3: Measured and simulated results at the MEBT exit

Parameters	Exp.	PQM	TTS
α_x	-3.13	-3.70	-3.67
β_x (mm/mrad)	1.79	2.70	2.71
ϵ_x (π mm·mrad, rms, n)	0.252	0.244	0.259
ϵ_x (π mm·mrad, 90%, n)	1.17	1.10	1.20
α_y	-1.72	-1.40	-1.31
β_y (mm/mrad)	1.00	1.20	1.14
ϵ_y (π mm·mrad, rms, n)	0.214	0.234	0.250
ϵ_y (π mm·mrad, 90%, n)	0.971	1.04	1.09

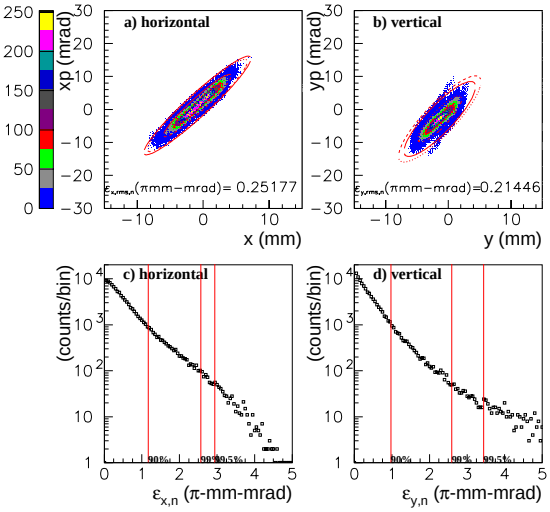

Figure 5: Measured emittances at the MEBT exit.

CONCLUSION

Starting with the distribution based on the measured distribution at the LEBT, we have performed the RFQ and MEBT simulations. For the RFQ simulations, PARMTEQM and TOUTATIS are used. In the rms emittances, there is no significant discrepancy between the results of the two codes, however, the tails of the emittances of the TOUTATIS result are about 10% larger than those of the PARMTEQM results. The MEBT simulation with these distributions well reproduce the experimental results at the MEBT exit in rms and 90% emittances. This shows that the simulated distributions at the RFQ exit are realistic enough to use the simulation of the J-PARC linac.

REFERENCES

[1] M. Ikegami et. al., "A Simulation Study on Error Effects in J-PARC Linac", in these proceedings.

[2] M. Ikegami et. al., "A Simulation Study on Chopper Transient Effects in J-PARC Linac", in these proceedings.

[3] M. Ikegami et. al., "An Alternative scheme for J-PARC SDTL Tuning", in these proceedings.

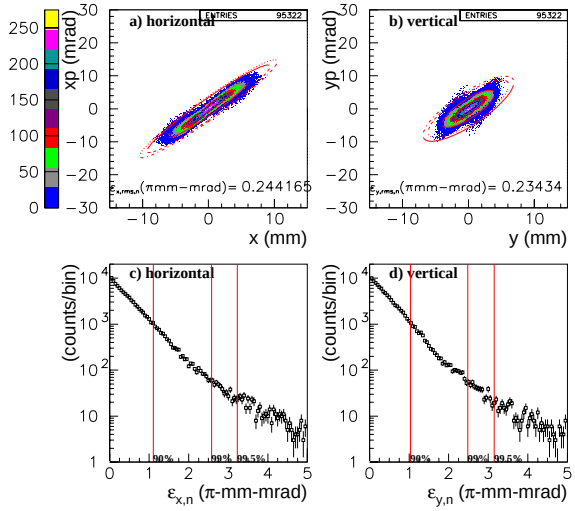

Figure 6: Simulation result at the MEBT exit using with the distribution obtained with PARMTEQM.

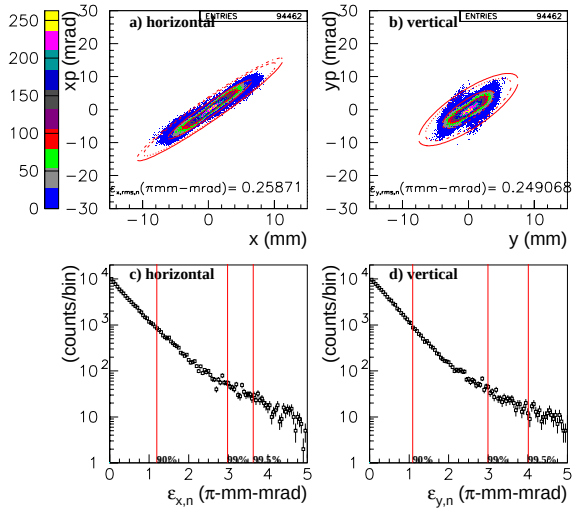

Figure 7: Simulation result at the MEBT exit using with the distribution obtained with TOUTATIS.

[4] M. Ikegami et. al., "Beam Commissioning of the J-PARC Linac Medium Energy Beam Transport at KEK", PAC,03, Portland, May 2003.

[5] A. Ueno et. al., "Beam Test of a Front-end System for the JAERI-KEK Joint (JKJ) Project", LINAC,02, Gyeongiu, August 2002.

[6] K. R. Crandall et. al., "RFQ Design Codes", LA-UR-96-1836.

[7] R. Duperrier, "TOUTATIS, a radio frequency quadrupole code", Phys. Rev. Specials, Topics Accelerator and beams, December 2000.

[8] H. Takeda, Parmila, LA-UR-98-4478.

DESIGN OF THE R.T. CH-CAVITY AND PERSPECTIVES FOR A NEW GSI PROTON LINAC*

Zhihui Li, IMP, Lanzhou, China
R. Tiede, U. Ratzinger, H. Podlech, G.Clemente, IAP, Universitaet Frankfurt/Main, Germany
K.Dermati, Winfried Barth, Lars Groening, GSI, Darmstadt, Germany

Abstract

The CH-Structure has been studied at the IAP Frankfurt and at GSI for several years. Compared with the IH structure (110-mode), the CH structure (210-mode) can operate at higher frequencies (150 - 700 MHz) and can accelerate ions to higher energies (up to 150 AMeV). Detailed Microwave Studio (MWS) simulations were performed for this structure. Since a multi-gap cavity can be approximated as a quasi-periodic structure, it is possible to analyse one βλ/2-cell at an energy corresponding to the cavity centre. A reduced copper conductivity of 85% was adopted in effective shunt impedance calculations. Geometry variations with respect to RF frequency and shunt impedance can be performed rapidly by that method in the first stage of optimization. Using the transit time factor calculated by the beam dynamics simulation code LORASR, effective shunt impedances from 100 MΩ/m down to 45 MΩ/m were obtained for the energy range from 6MeV to 66 MeV by this method. The RF frequency was 352 MHz. A systematic analysis of the influence of the cell number in long CH-cavities on the effective shunt impedance is presented. Actually, a 70 MeV, 70 mA, 352 MHz proton linac design for GSI Darmstadt is developed. About 12 CH-cavities will cover the energy range from 3 MeV up to the final energy, the DTL total length will be around 22m.

INTRODUCTION

The Interdigital H-type (IH) structure is well known for its high shunt impedance at low beta values. It is successfully used as front part for ion linacs like the Unilac at GSI [1] or the CERN Linac3 [2] and for rare isotope acceleration. Since a couple of years, a new type of H-structure was proposed and studied at IAP, Frankfurt and GSI, Darmstadt, that is the Cross Bar H-type (CH) structure. Compared with the IH-structure, the CH-structure is providing new features. Working in the H_{21} mode, the transverse cavity dimensions are significantly larger than that of the IH-cavity at a given frequency and velocity profile, thus it can work at higher frequencies up to around 700 MHz. This allows to close the velocity gap with respect to attractive structures at the low energy end of Coupled Cavity Linacs CCL. It can be designed for operation at about 350 MHz in the first section and at 700 MHz in the high-energy section up to about 150 AMeV. Furthermore, the CH cavity exceeds by far the mechanical rigidity of the IH cavity. This opens the possibility to develop superconducting multi-cell cavities as well [3].

A set of formulas based on a simple field model was derived for H-type structures to describe the main RF parameters as a function of the geometrical dimensions. A normal conducting 70 MeV, 70 mA proton injector based on a 3 Mev RFQ followed by a CH-DTL is designed for the future FAIR facility at GSI. The beam dynamics [4] and the cavity design are studied in parallel. The construction of a model cavity will start this year.

In the following sections we present the results got from cavity simulations for room temperature CH structures, the emphasis is put on the effective shunt impedance.

SIMULATION METHOD

In general a high level of accuracy is needed in the simulation of multi-cell cavities to achieve relevant results and in particular with respect to the cell voltage distribution. However, many important aspects can be investigated already with single cell calculations, which are very fast and reliable. In case of a quasi-periodic H-structure the following strategy was applied:

- For every cavity a single cell optimisation with respect to shunt impedance was performed for the relevant beam velocity at the tank mid plane.
- The capabilities of these geometries with respect to mechanical stability, cooling etc. were checked.
- Simulation of multi-cell cavities with steadily increasing cell numbers. Investigation the dependence of the main parameters on the cell number.

GEOMETRY OPTIMIZATION

The geometry optimization has been done for a sequence of discrete energies from 3 MeV up to 70 MeV. Figure 1(a) schematically shows the 50 MeV cavity cell used in MWS simulations. Figure 1(b) shows a design alternative with a drift tube geometry relevant for tank 1. The main difference is the central ring around the drift tube similar to the superconducting version [3].

For the real multi-cell cavity, the transverse geometries are kept unchanged, but in longitudinal direction, the period length will change with the velocity profile of the beam. In the investigation of the dependence of the RF parameters on the cell number, however, a constant periodic length along the cavity is used. The zero-mode can be achieved by a simple end cell geometry like shown in fig. 2.

In order to test the validity of the cell-cavity approximation, we calculate the CERN Linac3, tank3 that

*Work supported by the GSI, BMBF, contr. no. 06F134I and EU contr. nr. RII3-CT-2003-506395

is a 30-gap IH cavity with this method. The results are listed in table 1. From table 1 we can see that the measured effective shunt impedance is about 85% of the calculated one and the error in frequency is about 2%.

From this comparison resulted the reduction mentioned above to 85% in the estimated shunt impedance values from single cell MWS simulations. The factor includes the reduced efficiency at the cavity ends. It is assumed that the effects are comparable for IH- and CH-cavities.

Table 1: Cell cavity calculation results and measurement results for CERN Linac3 Tank3

	Measurement	Calculation
Frequency (MHz)	202.56	198.45
Q factor	15000	17225
$Z_{eff.}$ (M Ω /m)	150	184

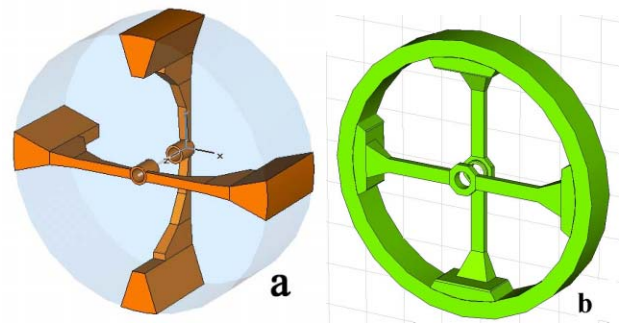

Figure 1: (a) A 50 MeV cell cavity, (b) multi cell design for low beam energies.

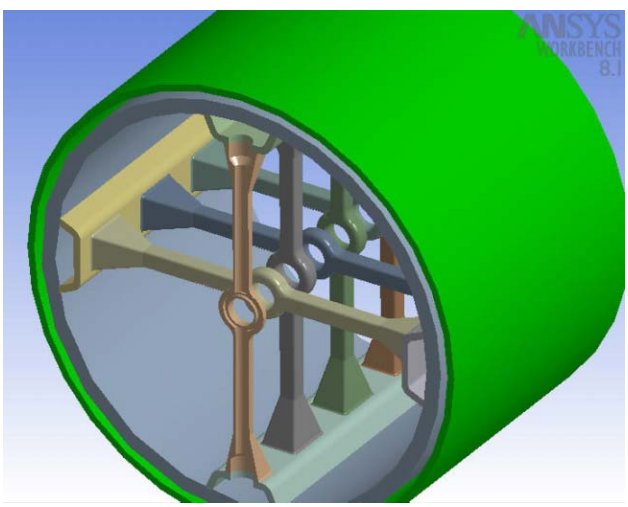

Figure 2: Mechanical design study of a CH-cavity at 3 MeV beam energy with directly water cooled stems.

SINGLE CELL SIMULATION RESULTS

The shunt impedance is one of the most important parameters for a room temperature linac. In our calculation, the effective shunt impedance is calculated by the following formula,

$$R_{shunt} = \frac{V^2}{\overline{P}^2 L} T^2 . \quad (1)$$

V is the peak value of the gap voltage, $\overline{P}$ is the average rf loss of the cavity, resulting from MWS simulations and corrected by the 85% conductivity value. L is the total tank length and T is the transit time factor calculated by the beam dynamics simulation code LORASR.

The effective shunt impedance and the radius of the tank as a function of the energy are shown in Figure 3. The effective shunt impedance changes from 100 MΩ/m down to about 43 MΩ/m while the energy XXXX from 6 MeV to 66 MeV. The tank radius changes from 165 mm up to 216 mm. The inner and outer drift tube diameters are 20 mm and 27 mm respectively.

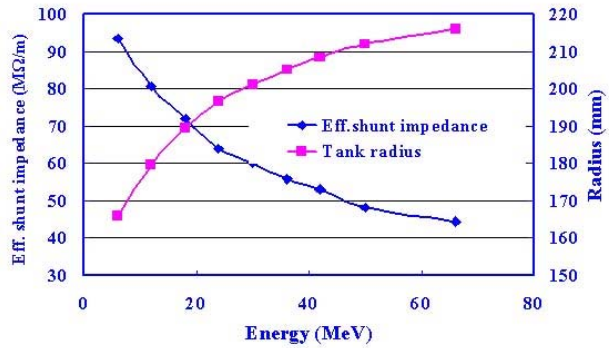

Figure 3: The effective shunt impedance and tank radius as a function of the beam energy.

DEPENDANCE OF RF PARAMETERS ON CELL NUMBERS

The cavity cell with magnetic boundary conditions is equivalent to an infinite long multi cell cavity, but ???

In the following we will investigate the dependence of the RF parameters on the cell number. The multi-cell cavity is constructed by the 50 MeV cell cavity. As figure 2 shows, all cells are the same with the exception of the end cells.

Resonance Frequency

The resonance frequency for cavities with different cell numbers is shown in figure 4. The horizontal pink line is the result from the cavity cell simulation. With increasing cell number, the frequency is approaching the simulation result. For a cavity with 12 cells, the difference is less then 1%. That means for cavities with more than 12 cells, the cell approximation method is rather valid for resonance frequency calculations.

Effective Shunt Impedance

The effective shunt impedances for cavities with different cell numbers are plotted in figure 5. The red dashed represents the effective shunt impedances obtained from cavity cell simulations and equal to the corresponding dot in figure 3. As mentioned before the cavity cell with magnetic boundary is equivalent to a cavity with infinite cells. The effective shunt impedance

of multi cell cavity will approach to this line as cell number increasing, just as the red line in figure 5 shows. For a cavity with 16 cells, the difference is less than 3 MΩ/m. From figure 5 we can conclude that we can use the 90% of the cell cavity simulation results to approximate that of the multi cell cavity in beam dynamics design.

In figure 5 we also plotted the effective shunt impedance with different apertures. We can see, the effective shunt impedance for cavities with 20 mm aperture diameter is about 3 MΩ/m larger than that for cavities with 25 mm diameter. But even for cavities with 25 mm aperture, the effective shunt impedance is larger than 40 MΩ/m for cavities with more than 8 cells at 50 MeV.

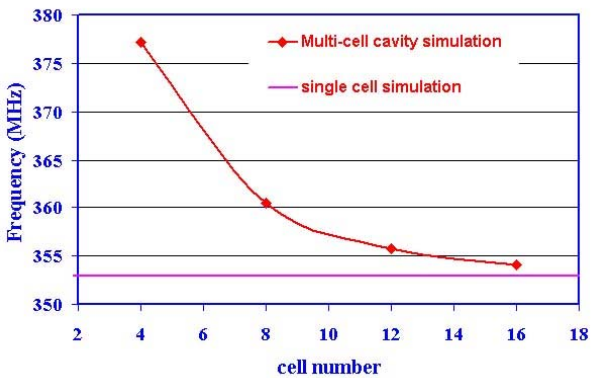

Figure 4: The frequency as a function of the cell numbers.

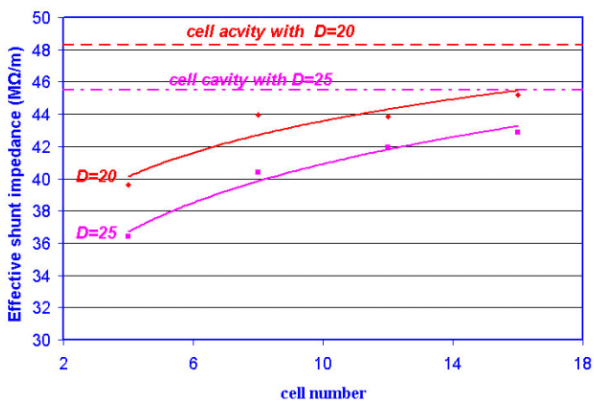

Figure 5: The effective shunt impedance as a function of the cell numbers.

GSI NEW PROTON LINAC

The future scientific program in GSI needs a dedicated proton linac. The frequency of the Linac is decided as 352 MHz since the existence of the klystron has the same frequency. This frequency is just within the range of the CH structure. Together with the KONUS beam dynamics, the DTL section is designed with the cell simulation results. The main cavity parameters are listed in table 2.

Table 2: Proton DTL structure parameters

Energy range	3 - 70 MeV
Beam current	70 mA
Total DTL length	21 m
Single tank length	0.6 - 2.2 m
Number of gaps	12 – 17
Accel. gradient	6.3 – 2.7 MV/m
Effective shunt impedance	100 – 45 MΩ/m
Rf power per tank	500 – 1100 kW
Minimum aperture diam.	20 mm

CONCLUSIONS

From the analysis above, we can draw the following conclusions:

- The cavity cell is an effective and efficient way for cavity optimization. The effective shunt impedance of the 352 MHz CH-cavity got from cavity cell simulation is from 100 MΩ/m down to 45 MΩ/m for the energy range from 6 MeV to 66 MeV.
- Considering the limited cell number of the real cavity, we can use 90% cell cavity simulation effective shunt impedance in design, and the error for frequency is about 1% for simple cavities.

ACKNOWLEDGEMENTS

We like to appreciate the close and fruitful collaboration between IAP and GSI. One of the authors (Z. Li) wants to thank GSI and CAS for providing financial support and Dr. N. Angert especially, for giving a lot of kind help during the stay in Germany.

REFERENCES

[1] U.Ratzinger, Nucl. Instr. And Meth. A464(2001), p.636
[2] H.Haseroth, proc. of the 1996 LINAC Conf., Geneva, CERN 96-07, p.283
[3] H. Podlech, these proceedings
[4] R.Tiede et. Al., these proceedings

THE PRE-INJECTOR LINAC FOR THE DIAMOND LIGHT SOURCE

C. Christou*, V. Kempson, Diamond Light Source, Rutherford Appleton Laboratory, Chilton, Didcot, Oxfordshire OX11 0QX, UK
K. Dunkel, C. Piel, Accel Instruments GmbH, Bergisch-Gladbach, Germany.

Abstract

The Diamond Light Source (DLS) is a new medium-energy high brightness synchrotron light facility which is under construction on the Rutherford Appleton Laboratory site in the U.K [1]. The accelerator facility can be divided into three major components; a 3 GeV 561 m circumference storage ring, a 158.4 m circumference full-energy booster synchrotron and a 100 MeV pre-injector linac. This paper describes the linac design and plans for operation.

LINAC PARAMETERS

The DLS linac generates an electron beam suitable for injection through the linac-to-booster transfer line (LTB) into the booster synchrotron. The Diamond master oscillator frequency is 499.654 MHz† and linac operation is synchronised to this at 2.997924 GHz‡. Two modes of operation are planned; short-pulse mode, in which a single electron bunch is injected into one booster RF bucket, and long-pulse mode in which a train of single bunches is injected into the booster at an operational frequency of 500 MHz.

Table 1: Linac parameters

Parameter	Short-pulse mode	Long-pulse mode
Energy	100 MeV	100 MeV
Pulse-to-pulse energy variation	0.25% rms	0.25% rms
Relative energy spread	0.25% rms, ±1.5% full spread	0.25% rms, ±1.5% full spread
Repetition rate	Single shot to 5 Hz	Single shot to 5 Hz
Normalised emittance (1σ)	50 π mm mrad in each transverse plane	50 π mm mrad in each transverse plane
Pulse duration	1 ns	300 ns to 1000 ns
Output charge	50 pC to 1.5 nC	50 pC to 3 nC
Pulse purity	1% of total charge	-

The linac will be capable of performing continuous top-up injection in both short-pulse and long-pulse modes. During top-up, 1-5 Hz repetitive operation in both modes will be maintained for 1-10 seconds, and repeated every 1-5 minutes, or single pulses (or pulse trains in long-pulse mode) will be repeated every 10-300 seconds.

LINAC COMPONENTS

The linac is supplied by ACCEL Instruments GmbH under a turn-key contract, with Diamond Light Source Ltd. providing linac beam diagnostics, control system hardware and standard vacuum components. The design chosen for the DLS linac is very similar to that operating at the Swiss Light Source (SLS) [2, 3], also supplied by ACCEL Instruments.

Electron gun

The electron gun assembly contains an EIMAC YU 171 thermionic dispenser cathode with integrated heater and grid. Cathode lifetime is estimated to be several thousand hours. The gun pulser contains two independent driving circuits, a 1 ns fwhm pulser driving the cathode for short-pulse operation, and a 500 MHz sine-wave driver modulating the cathode. Separation of the two driving circuits avoids the excitation of the cathode-grid resonance by the 500 MHz Fourier component of the short-pulse waveform. The electron gun is maintained at -90 kV relative to earth.

Bunching system

The linac buncher will consist of the following components:

- Subharmonic pre-buncher (SHPB): one copper single-cell 500 MHz standing-wave cavity
- Primary bunching unit (PBU): one copper four-cell constant-impedance travelling-wave structure operating in 2π/3 mode at 3 GHz
- Final bunching unit (FBU): one copper sixteen-cell constant-impedance travelling wave structure operating in 8π/9 mode at 3 GHz

The SHPB acts to velocity modulate the non-relativistic electron beam emerging from the gun, compressing the pulse before it passes into the PBU. In the PBU, the beam is given a 3 GHz S-band structure, and then this S-band beam is accelerated to a relativistic level in the FBU, and the S-band bunches are further compressed. Phase velocities in the bunching units are 0.6 c in the PBU and 0.95 c in the FBU.

A laminar flow tent will be used for SHPB installation to minimise the possibility of multipactoring during linac operation. Use of a driving amplifier with a higher duty

*chris.christou@diamond.ac.uk
†Rounded to 500 MHz for the remainder of this document
‡Rounded to 3 GHz for the remainder of this document

cycle than that used at the SLS is expected to reduce conditioning time during commissioning.

Accelerating structures

Two identical accelerating structures of the DESY S-Band Linear Collider Type II design [4] will be used to accelerate the bunched beam up to the final energy. They are both constant-gradient copper structures operating in $2\pi/3$ mode at 3 GHz.

Table 2: Accelerating structure parameters

Parameter	Value	Unit
Length	5.2	m
Number of cells	156	
Group velocity	0.02	c
Phase velocity	1	c
Filling time	740	ns
Shunt impedance	51	MΩ/m
Operating temperature	40	°C

RF system

The high-power RF system is driven by two 3 GHz modulator units, each with one Thales TH2100 klystron. This klystron is rated at 35 MW peak pulsed power and is driven by a 350 W pulsed preamplifier and a thyratron-switched LC line-type pulse-forming network. The first modulator-klystron unit drives the PBU, the FBU and the first accelerating structure, and the second modulator-klystron drives the second accelerating structure. The accelerating structures are designed to give 50 MeV beam acceleration for input power of 19 MW. Power is transmitted to the accelerating and bunching structures through SF_6-pressurised waveguide. The interface between the SF_6-pressurised region and the linac vacuum envelope is a vertical ceramic window. The 500 MHz master oscillator signal is used to drive the electron gun and the SHPB, and to ensure synchronisation of the high-power RF with the Diamond booster and storage ring.

Additional components

In order to compensate for RF defocusing and space-charge blow-up of the beam, 31 solenoids are required in the low-energy region of electron beam for energies up to 10 MeV. One solenoid is mounted at the electron gun and 30 are in the low-energy region around the bunchers and at the beginning of the first accelerating structure. In the 50 MeV drift section between the two accelerating structures, a quadrupole triplet is used to match the output of the first structure into the second structure. Alignment correction of the beam will be carried out by steerers mounted at different positions along the linac. Two different types of steerer are used, a Helmholtz type for use within solenoids, and an iron-cored type for use outside the solenoids.

Linac vacuum will be maintained at 10^{-8} mBar by a Gamma Vacuum 500T 500 l/s ion pump mounted at the gun, a 150T 150 l/s ion pump on the SHPB and six 100T 100 l/s ion pumps along the linac assembly. Evacuated waveguide on the linac-side of the ceramic windows leading to the PBU, the FBU and the two accelerating structures are pumped independently by one 100T 100 l/s ion pump each. The electron gun and SHPB will be protected against downstream leaks by a VAT series 75 fast-closing valve system mounted at the entrance to the second accelerating structure.

DIAGNOSTICS AND COMMISSIONING

Installation of the linac will begin in October 2004, and the large accelerating and bunching structures will be shipped to DLS in January 2005. Commissioning of the linac will take place before summer 2005. Commissioning and acceptance of the linac will require partial construction of the LTB, and supply of diagnostics by DLS.

The LTB extends 25.6 m from the end of the linac to the booster injection point and includes two 15° dipole bends and eight quadrupoles. Linac and LTB diagnostics are listed in table 3 and shown in figure 1. Temporal structure of the beam will be measured by wall current monitors in the linac at the gun exit, and in the LTB before the first dipole. Emittance will be measured by analysis of the image recorded on an OTR screen after a quadrupole doublet at the beginning of the LTB. Energy measurements will be made on an OTR screen in a dispersive length of the LTB between the two dipoles. Faraday cups and integrating current transformers will be used to measure beam charge. YAG screens, OTR screens and beam position monitors will used to check beam alignment. Linac diagnostics have been manufactured to SLS designs [5]. LTB diagnostics include a new beam position monitor system, a Bergoz integrating current transformer and a novel design of Faraday cup in the beam stops [6]. The two dipoles in the LTB are fitted with synchrotron radiation ports to retain the option of using optical diagnostics in the LTB.

Table 3: Linac and LTB diagnostics

Diagnostic	Linac	LTB
Wall current monitor	1	1
Faraday cup	2	2
YAG screen	4	2
OTR screen	1	4
Beam position monitor	-	7
Integrating current transformer	-	3
Synchrotron radiation port	-	2

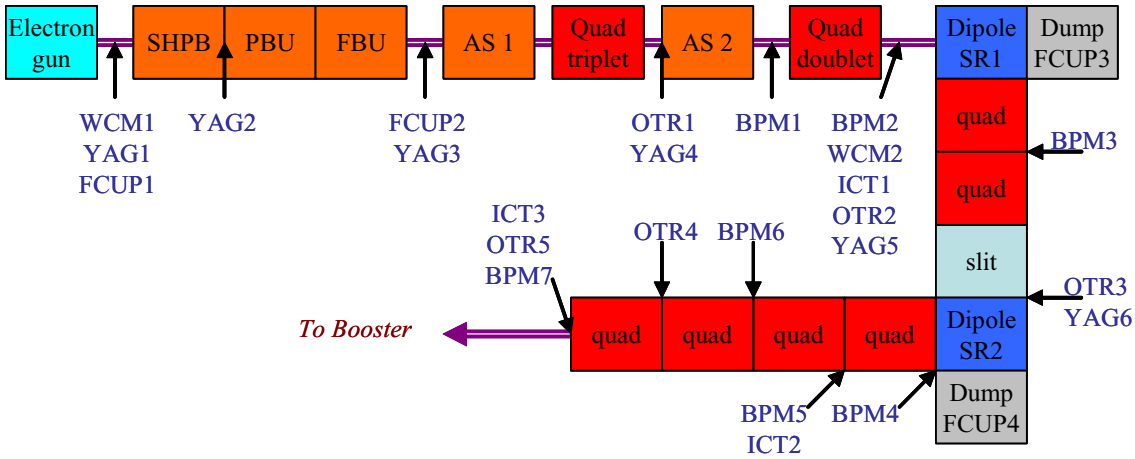

Figure 1: Schematic of linac and LTB showing principal components and locations of all diagnostics.

MODELLING OF LINAC AND LTB

The behaviour of the linac and LTB has been modelled using the electron-linac particle-dynamics code PARMELA. Modelling is valuable for commissioning the linac, beam-steering through the LTB, in regular operation and for gaining an understanding of the physical processes taking place. Figure 2 illustrates the bunching of the beam in single pulse mode, and shows the temporal structure expected at the exit of the gun, at the input to the first accelerating structure (AS1 in), and at WCM2 in the LTB before the first dipole: the broad gun pulse is bunched into S-band buckets by the PBU and this structure is maintained through the linac and LTB to the booster injection.

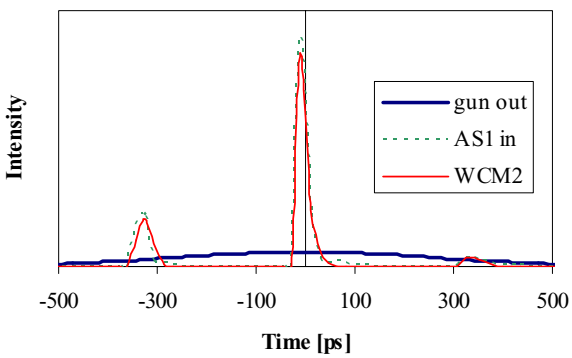

Figure 2: Bunching of the beam in short-pulse mode.

A summary of a PARMELA energy spectrum analysis is shown in figure 3. The beam is accelerated to around 5 MeV by the bunching units and then beyond the minimum booster acceptance energy of 100 MeV by the two accelerating structures. With the linac parameter settings chosen for this simulation there is a tail visible in the spectrum recorded at the OTR before the first dipole (OTR2), although the dispersive effects of the two dipoles remove this tail before the beam passes OTR5 at the end of the LTB. One of the goals of linac commissioning is to minimise the tail in the energy spectrum. The tail in the energy spectrum is a particular issue in relatively high charge long-pulse mode when beam loading in the accelerating structures reduces the field seen by electrons at the tail of the bunch train. To compensate for this effect, an energy defining slit will be used between the two LTB dipoles. Figure 3 also illustrates the expected transfer of around 50% of the beam in the required narrow energy window above 100 MeV from linac exit to booster injection.

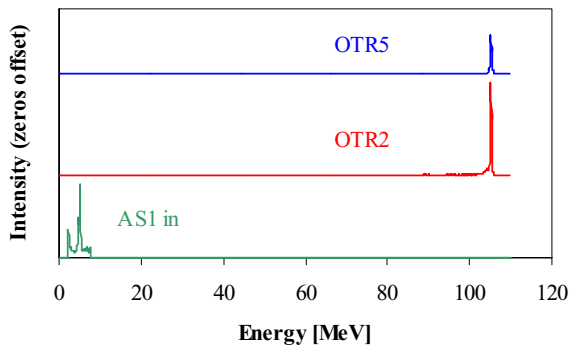

Figure 3: Energy spectrum in linac and LTB.

REFERENCES

[1] R. P. Walker, “Progress with the Diamond Light Source”, EPAC’04, Lucerne, July 2004.

[2] M. Peiniger et al., “A 100 MeV injector linac for the Swiss Light Source supplied by industry”, PAC’99 p 3510, New York, 1999.

[3] M. Pedrozzi et al., “Commissioning of the SLS-linac”, EPAC 2000, p 851, Vienna, 2000.

[4] R. Brinkmann et al., “Conceptual design report of a 500 GeV e^+e^- linear collider with integrated x-ray laser facility”, DESY 1997-048.

[5] V. Schlott et al., “SLS linac and transfer line diagnostics”, in PSI Scientific Report 1999, volume VII.

[6] G. Rehm et al., “Beam diagnostics systems for the Diamond Light Source”, EPAC’04, Lucerne, July 2004.

USING A SOLID STATE SWITCH FOR A 60KV BOUNCER TO CONTROL ENERGY SPREAD DURING THE BEAM PULSE *

L. Donley, J.C. Dooling, G.E. McMichael and V. F. Stipp, ANL, Argonne, Illinois, 60439

Abstract

The beam injected into the IPNS Linac is from a column utilizing a Cockcroft-Walton voltage source. The accelerating column consists of a single high gradient gap. To lessen the likelihood of gap voltage breakdown we pulse ("bounce") the column voltage up during the beam pulse allowing the column DC voltage to be lower. The accelerating voltage is supplied through a 5 MΩ resistor and has only small capacitance to hold the voltage constant during the beam pulse. A capacitor is connected between the high voltage end of the column and the bouncer pulse generator. The bouncer pulse increases the column voltage to the proper level just microseconds before the beam pulse. A slope on the top of the bouncer pulse allows for correction to be added, compensating for the voltage droop that results from beam loading. The bouncer that has served this purpose in the past utilized a tube amplifier. In searching for a suitable replacement system it was decided that the system should be able to deliver a 60 kV pulse and the slope on the top of the pulse could be controlled by an RC rise. A solid state switch was purchased for this application. Switch protection and other design decisions will be discussed

INTRODUCTION

The Intense pulsed Neutron Source (IPNS) injector linac[1] delivers 70 to 80 microsecond long pulses of 50 MeV H- particles to the 450 MeV synchrotron. The H- ion source is capable of delivering about 1.6×10^{13} particles per pulse at a 30 Hz rate. The linac is designed for a 750 keV input beam, but can operate at a reduced efficiency with input beams as low as 700 keV[2].

Column arc rate is acceptable if the DC voltage is below 700 kV. Our present operating energy is 730 keV out of the column. The DC voltage is operated at 690 kV, the extractor is 20 kV and the bouncer makes up the remaining 20 kV. The bouncer coupling network couples 50% of the supplied pulse so this requires that the bouncer supply a 40 kV pulse to the coupling network. The old bouncer meets these requirements but the tubes are no longer manufactured. Recent plans to upgrade the synchrotron by adding a third rf cavity may require more charge per pulse out of the linac, leading to a need to improve linac transmission efficiency. Furthermore, calculations indicate that much better control of linac output longitudinal emittance is possible if injection is at the design 750 keV. This could improve capture and lower losses in the synchrotron independent of the new rf cavity. Column redesign was a possibility but had no guarantee of success and would have required a long downtime for the modifications and commissioning. However improving the capability of the bouncer added little additional risk and could be incrementally tested during our regular machine research periods. To replace our present bouncer, the new bouncer would need to run at 40 kV; to meet future plans a 60kV bouncer and 700kV DC will provide a 750keV beam from the column.

Ideally, the bouncer should rapidly increase and decrease the column voltage in time for the beam pulse, and should compensate for the beam loading voltage droop of the Cockcroft-Walton during the pulse. This led to the following specifications:

1 Operate at 30Hz
2 Output up to 60 kV
3 Rise time ≈100 μs
4 Top slope of 5 0 V/μs
5 Top width of 90 μs
6 Fall time ≈ 1 ms
7 Survive in an environment where 700 kV pulses at several amperes are frequently generated.

DESIGN

Recent advances in semiconductor technology have made available fast high-voltage solid-state switches that can be cascaded to provide current and voltage capabilities unreachable only a few years ago. We now use these devices for our 20 kV extractor as well as for the bouncer. Figure 1 shows the 60 kV switch that we purchased from Diversified Technologies, Inc.

Figure 1: 60Kv 20A-50A switch as installed at the base of the IPNS ion source.

This switch has 6 plates assembled on a fiberglass channel and a control box with leads ready for connection

*This work is supported by the US DOE under contract no. W-31-109-ENG-38.

to the insulated trigger wire. The plates contain multiple insulated gate bipolar transistors. The plates can be stacked to make switches with a wide range of current and voltage capabilities. [3] This switch is capable of handling 25A at 60 kV for a pulse ≤ 500 µs. With switch turn on and off times much faster than 100ns, this switch is much faster than is required for our application. It is controlled by an optically-coupled pulse to turn the switch on and off. This is ideal for operation in an electrically noisy environment.

To design the bouncer, the load needed to be characterized. This was done by measuring the voltage, current and rise time from the tube circuit. It was determined that a large part of the load was the stray capacitance of the source enclosure to ground. The bouncer was built with sufficiently low impedance that rise time would not be significantly effected by this capacitance. Rise time would be controlled by components chosen to achieve the desired rise and slope on the top of the pulse. Components R1, R2, and C1 in the figure 2 accomplish this task.

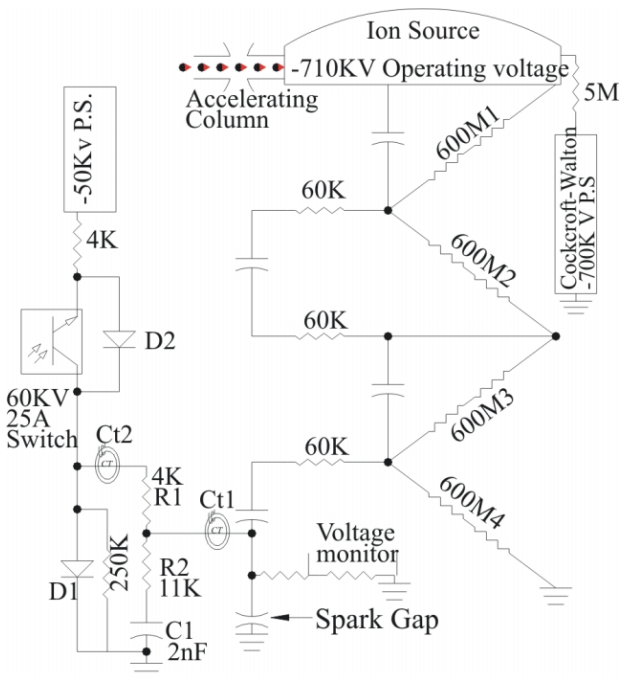

Figure 2: Block diagram of bouncer and coupling network.

BUILDING AND TESTING

The system was built and tested using a -50kV power supply that is the spare for another system. After more than 160 hours of trouble free operation connected to a test load, the bouncer was connected to the source coupling network. With the 700kV power supply turned off, a voltage monitor was connected to the source enclosure. The pulse amplitude and slope at beam time was compared to data taken on the tube bouncer. By changing the value of R1 and R2, the rise and pulse slope could be adjusted over the desired range. The output is shown in figure 3 for R1 and R2 at the values that were chosen for operations.

After the 700kV power supply was energized, it was observed that on most occurrences of a column spark the current was limited to 4 amperes by the three 60kΩ resistors. After C1 became charged, the entire current passed through R1 and D1 to ground. The purpose of D1 was to shunt this current to ground, preventing over-voltage from developing across the solid state switch.

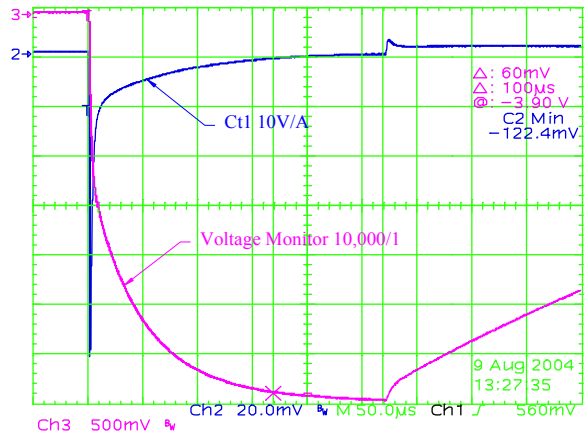

Figure 3: Scope trace of voltage monitor and Ct1.

OPERATIONS AND IMPROVEMENTS

After the system was in operation for several days, diode D1 failed. Although the failed diode could handle more current than the 4 amperes that should be the maximum current in the diode, a higher current capacity diode was used as a replacement. While investigating why D1 failed, it was noticed that on about 1% of the times the column sparked, the current on the two current toroids Ct1 and Ct2 was higher than the 4 amperes that was expected. After studying scope traces of Ct1, Ct2, and the voltage monitor, it was decided that something in the bouncer coupling network was occasionally breaking down when the column arced. Study of the bouncer network revealed that the transient voltages associated with the arc are not equally distributed across the four 600MΩ resistors. Most of the transient appears across 600M2 while 600M1 and 600M3 have no voltage across them. If 600M2 were to arc over that would leave only one 60kΩ resistor to control the current. The Ct1 reading was close to what would be expected if this happened. Diode D1 would most likely not be damaged by this current pulse, although the R1 voltage was observed to be over 3 times the manufactures maximum voltage rating. It was observed on a few pulses that the current in Ct2 was over 80 amperes. On these high current observations the voltage on the voltage monitor would increase for about 30µs to a voltage of about 60kV, then drop as the current

increased at Ct2. Our conclusion was that R1 was arcing over. That would place nearly all of the voltage on C1 across R2 and cause it to arc over. The diminished impedance of R1 and R2 would do little to control the current as C1 discharged through R1, R2, Ct2, and D1. A more robust resistor was installed for R1, and over several weeks of operations the current in Ct2 was not observed to be higher than would be expected if 600M2 arced over. The 600M2 was then relocated as shown in figure 4. This should reduce the transient voltage across 600M2 when the column arcs, such that 600M2 should not arc over.

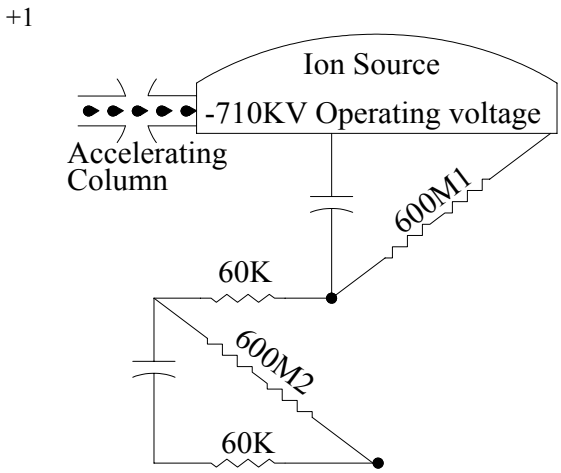

Figure 4: Modified diagram with 600M2 moved to lessen the likelihood it would arc over.

CONCLUSIONS

Tube circuits are no longer the only choice for applications that require fast switches that will operate in the tens of kilovolts range. Switches need to be protected from both over-current and over-voltage. Commercial switches have over-current trip protection built into them but require time to work. Switch loads need to either provide high enough impedance to limit current or limit the current rise so the switch's built in over-current circuit has time to protect the switch.

REFRENCES

[1] V. Stipp, et al, Proc. 18th LINAC Conference, CERN, Geneva, Switzerland, August 1996, p. 74
[2] J. C. Dooling et al., Proc. 19th LINAC Conference, Gyeongju, Korea August 2002, p. 439
[3] Dr. Marcel, et al,Proc. 23 Power Modulator Symposium, Rancho Mirage, Ca June 1998, p. 160

THE LEBRA 125 MEV ELECTRON LINAC FOR FEL AND PXR GENERATION

K.Hayakawa#, T.Tanaka, Y.Hayakawa, K.Yokoyama*, I.Sato,
LEBRA, Nihon University, Funabashi, Japan
K.Kanno, K.Nakao, K.Ishiwata and T.Sakai,
Graduate School of Science and Technology Nihon University, Funabashi, Japan

Abstract

A 125MeV electron linac has been constructed at Laboratory for Electron Beam Research and Application (LEBRA) in Nihon University for Free Electron Laser (FEL) and Parametric X-ray (PXR)[1] generation. Electron bunches of 3 - 4 psec width formed at the injector are compressed to within 1 psec during passing through the magnetic bunching system. Peak current of the electron beam injected to the FEL system is expected to be about 50 A. FEL lasing has been achieved at the wavelength range from 0.9 to 6 μm. Estimated peak power of the extracted FEL light pulse is about 4 MW. Applied researches using the FEL started last autumn. Preliminary experiment for the PXR generation has been proceeded. First light of the PXR is observed at April in this year.

INTRODUCTION

The specifications of the electron linac are listed in Table 1. The beam injection system and the regular accelerator sections of the linac were moved from KEK Photon Factory positron injector linac as a part of collaboration on development of a high quality electron linac. Schematic layout of the accelerating structures and RF system are shown in Fig.1.

FEL beam line has been installed to feed near infrared laser for application users [2]. To improve FEL gain, magnetic bunch compressor has been adopted.

To generate monochromatic X-ray, PXR beam line has been installed next to FEL beam line. Several interesting results are obtained.

LINAC

The electron linac has a conventional configuration. It consists of a DC electron gun with a dispenser cathode, a prebuncher which is a 7-cell travelling wave structure, a buncher which is a 21-cell travelling wave structure and three 4-m long normal accelerator sections.

Table 1:Specifications for LEBRA 125MeV linac.

Accelerating rf frequency	2856	MHz
Klystron peak output rf Power	30	MW
Number of klystrons	2	
Electron energy	30~125	MeV
Energy spread (FWHM)	0.5~1	%
Macropulse beam current	200	mA
Macropulse duration	20	μsec
Repletion rate	12.5	Hz

RF System

Two klystrons feed rf power of approximately 20MW peak and 20μsec pulse duration each to accelerating structures. Phase of the rf fed to each component is controlled independently.

Output RF phase of the solid state RF amplifier and the klystron drifts with a room temperature variation. Since RF amplifier is operated in pulse mode, RF phase change

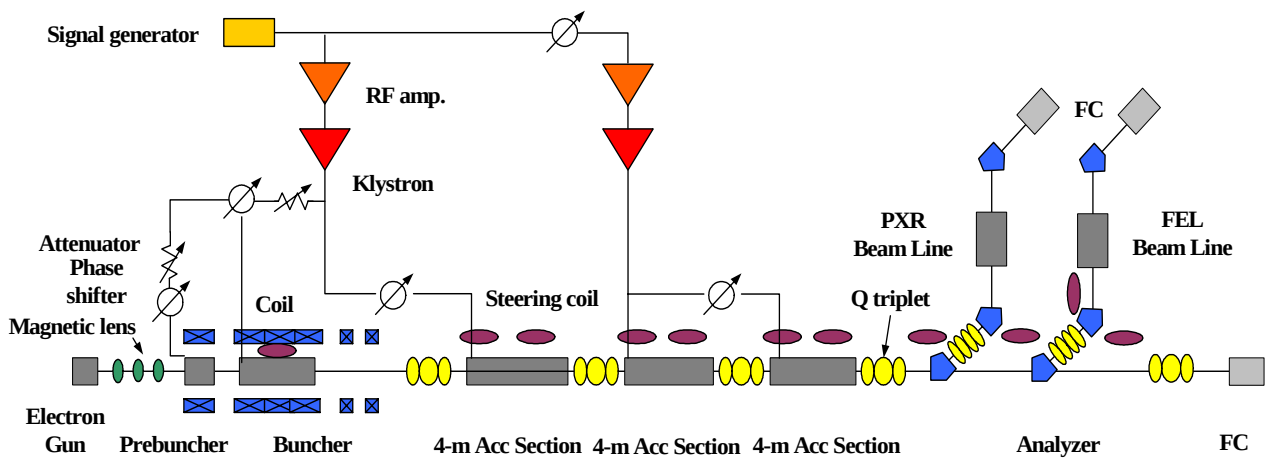

Figure1: Schematic layout of the LEBRA linac and the FEL and the PXR beam line.

#hayakawa@lebra.nihon-u.ac.jp
*Present affiliation: KEK, Tsukuba, Japan

during the pulse duration. Phase drift is compensated by using a slow feedback circuit and feed forward compensation is adopted for phase deviation during the pulse duration. Both feedback and feed forward signals are combined and fed to the fast phase shifter installed just upstream of the RF amplifier. Phase stability is achieved within 0.5 degree both long term and during the pulse duration [3].

Magnetic Bunch Compression

Last two accelerator sections are connected to the second klystron as shown in Fig.1. Accelerating phase of the third accelerator section is controlled independently of the second one using a phase shifter attached in the RF feed line of the third accelerator section. Then, the electron beam can be accelerated to same energy by various combination of the phase. Accelerating energy E without beam loading term in this section is described as follow.

$$E = E_0\left(\cos(\phi) + \cos(\phi + \Delta\phi)\right)$$
$$= 2E_0 \cos(\phi + \frac{\Delta\phi}{2})\cos\Delta\phi \quad .$$

Where E_0 is the maximum accelerating energy for each accelerator section, ϕ is the accelerating phase of the second accelerator section dependent on the klystron output phase and $\Delta\phi$ is the relative phase between the second and the third accelerator sections. Electron energy within a bunch is transformed in the first order approximation as

$$\delta E = \delta E_0 + \frac{\partial E}{\partial \phi}\delta\phi_0$$
$$= \delta E_0 - 2E_0 \sin(\phi + \frac{\Delta\phi}{2})\cos(\Delta\phi)\delta\phi_0$$

where $\delta\phi$ and δE are phase and energy relative to the central position and mean energy of the bunch. Suffix 0 of these variables means initial value. Even if the combination of the phase that gives the same energy, the effect on the energy distribution is different. Therefore we can handle the distribution of the electrons in the longitudinal phase space. Injection beam line to the FEL is a 90 degrees achromatic bending system as a momentum analyzer. It consists of two 45 degrees bending magnets, four quadrupole magnets and a momentum slit. In the case of achromatic bending, relative phase $\delta\phi$ is transformed as

$$\delta\phi = \delta\phi_0 + 2\rho(\theta - \sin\theta)\frac{2\pi}{\lambda}\frac{\delta E}{E_{total}} .$$

where ρ and θ are a orbital radius and bending angle of the bending magnets, λ is a wavelength of the accelerating RF in free space and E_{total} is an electron mean energy at the exit of the linac. If we select proper phase combination, which brings the required accelerating energy, bunch compression mechanism will be realized. By the bunch compression, about 3 psec of the bunch length at the exit of the linac becomes 1 psec at the entrance of the undulator[4]. Peak current of the electron beam also increases about three times. In the present operation condition, the peak current is estimated about 30 A. And it will be increased to 50 A or more in near future.

FEL

The undulator consists of a planar Halbach type permanent magnet, where the electron beam is wiggled in the vertical plain. The specifications of the FEL system are listed in Table 2. At the beginning of the FEL experiments, dielectric or Au coated quart based mirrors were used. Because of the poor thermal conductance of the quart, coated material was frequently damaged according to increasing the optical power at lasing. To avoid these kinds of trouble, cupper based silver coated mirrors are used. Optical power is extracted through the small hall excavated at the mirror center. Laser light beam extracted from the optical cavity is parallelised using beam expander that consists of spheroidal and parabolic mirrors and transmitted to the experimental rooms through the vacuum ducts.

Lasing of the LEBRA FEL has been achieved from 0.9 to 6 μm of wavelength. Typical FEL signal detected using an InSb photo detector, which indicate macro pulse structure is shown Fig. 3. Duration of the electron beam pulse is about 18 μsec, FEL is saturated after 8 μsec from start of the electron beam pulse and continued about 10 μsec. Output FEL energy per macro pulse is dependent on wavelength and beam current. Maximum power is

Table 2: Parameters for LEBRA infrared FEL system

Resonator length, L	6.718	m
Rayleigh range	1.467	m
Coupling hall	0.3	mm
Undulator period	48	mm
Undulator length	2.4	m
Number of periods	50	
Maximum K (rms)	1.35	

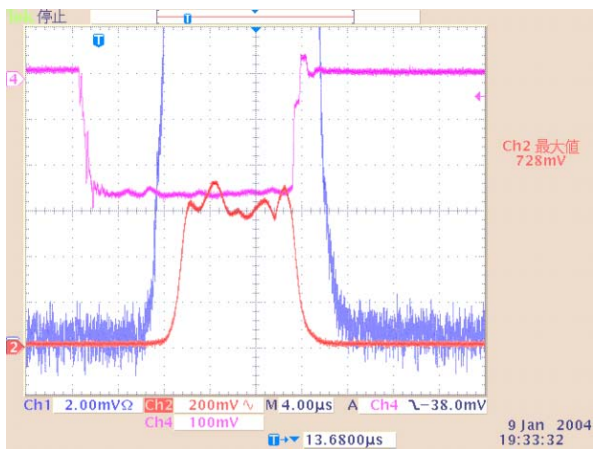

Figure 2: Typical waveform of the electron beam (upper trace) and FEL (lower trace).

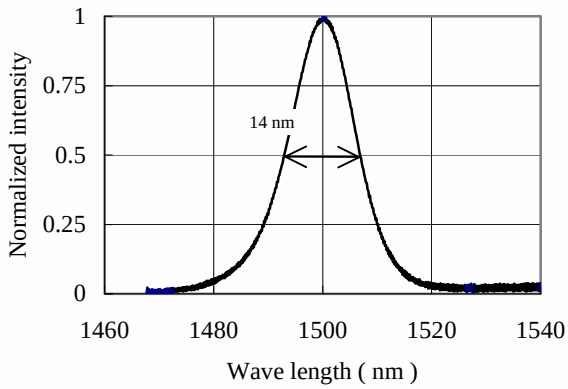

Figure 3: Spectrum of the FEL. Spectral width is about 14 nm.

accomplished wavelength of from 2 to 3 μm. Maximum energy per macro pulse obtained until now is 30 mJ.

Spectra were measured at up to wavelength of 1500nm by means of a monochrometor and an InGaAs photo diode array. Typical one is shown in Fig. 3. Spectral width is about 14 nm (FWHM) at mean wavelength of 1500 nm. Assuming Gaussian shape wave packet, about 70 μm (FWHM) of optical pulse length is deduced from inverse Fourier transformation from the spectrum. This value agrees well with what was obtained from the autocorrelation experiment[4]. If maximum energy of 30mJ per macro pulse of 10μsec converts simply, peak power is about 4 MW

Experiments of applied researchers started at last autumn.

PXR

The PXR beam line is installed parallel to the FEL beam line as shown in Fig. 1. The PXR system consists of two silicon single crystals. One of them is the radiator for PXR and another one is a reflector for X-rays. The reflector is movable parallel to the electron beam axis in order to extract X-rays with any defined wavelength through the fixed output port[5].

First light of the PXR was observed at April 14, this year. X-rays signal was detected by means of ionization chamber set at the output port. X-rays energy range in present setup is from 5 to 20keV. In principle, PXR has the spatial distribution with the energy gradient in the reflection plain. From the preliminary measurement, relation between X-ray direction and energy at incident electron energy of 100MeV is 0.7%/mrad. A photograph in which the Br-Kα absorption edge is seen as the boundary of light and darkness is taken by direct exposure at output port with the Polaroid film shown in Fig. 5. XAFS appears in the photograph but cannot be seen clearly in this figure.

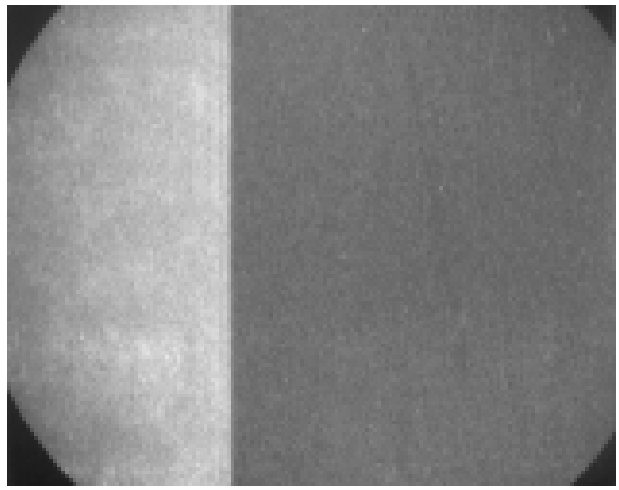

Figure 4: A photograph in which the Br-Kα absorption edge (13.5keV)is seen as the boundary of light and darkness.

REFERENCES

[1] A.V.Shchagin and X.K.Maruyama, Accelerator-Based Atomic Physics Techniques and Applications, S.M.Shafroth and J.C.Austin, Eds, New York: American Institute of Physics, 1997,ch9 pp 279-307

[2] T.Tanaka, I.Sato, K.Hayakawa, Y.Hayakawa and K.Sato,“Status of Infrared Free Electron Laser at Nihon University”, Jpn. J. Appl. Phys. 41(2002)Suppl. 41-1,pp.34-40

[3] K.Yokoyama, et al. “Suppression of Energy Fluctuation for the Free Electron Laser at LEBRA,” Jpn. J. Appl. Phys. 41(2002)4758

[4] K.Yokoyama, et al. “Bunch Length Measurements at LEBRA”, proceedings of this conference.

[5] Y.Hayakawa, “Simulations to the project of a PXR based X-ray source composed of an electron linac and a double-crystal system”, to be published.

ERLP GUN COMMISSIONING BEAMLINE DESIGN

D.J. Holder, C. Gerth, F.E. Hannon and R.J. Smith,

ASTeC, Daresbury Laboratory, Warrington, WA4 4AD, UK

Abstract

The 4GLS project is a novel next-generation solution for a UK national light source. It is based on an energy recovery linac (ERL) operating at high average beam currents up to 100mA and with compression schemes producing pulses in the 10-100 fs range. This challenging accelerator technology, new to Europe, necessitates a significant R&D programme and a major part of this is a low-energy prototype, the ERLP, which is currently under construction at Daresbury Laboratory, in the north-west of England. The first components of ERLP to be built will be the DC photocathode gun and low-energy beam transport and diagnostics. The gun will initially be operated with a diagnostic beamline in order to measure the properties of the high-brightness beams generated as fully as possible. This will allow comparison of its performance with the results of multi-particle tracking codes, prior to its integration into the ERLP machine. The diagnostic beamline will include diagnostics for measuring the transverse and longitudinal properties of the electron beam.

This paper will describe the design of this diagnostic beamline and demonstrate through simulation, the expected characteristics and performance achievable from this system.

INTRODUCTION

The ERLP uses a replica of the DC photocathode gun used in the IR Demo and Upgrade FELs at Thomas Jefferson National Accelerator Facility (J-Lab), which has already been producing high-brightness, high average-current electron beams [1]. The gun is currently being built at Daresbury Laboratory, and will be operated with a negative affinity GaAs photocathode which will be illuminated with a mode-locked Nd:YVO_4 laser with an oscillator frequency of 81.25MHz. The 350keV electron beam from the gun is transported via a normal conducting buncher cavity and accelerated by a superconducting booster to 8.35 MeV before entering the recirculating section. The fundamental frequency of both the buncher and the booster is 1.3GHz, and are based on ELBE designs [2]. A second superconducting linac module accelerates the beam to 35 MeV before it is then redirected back to the linac (for energy recovery) by the return transport line. The return path incorporates a FEL based on a permanent magnet wiggler (previously used in the Jefferson Laboratory IR-Demo machine) and two dipole chicanes. The layout of ERLP is illustrated in Fig. 1.

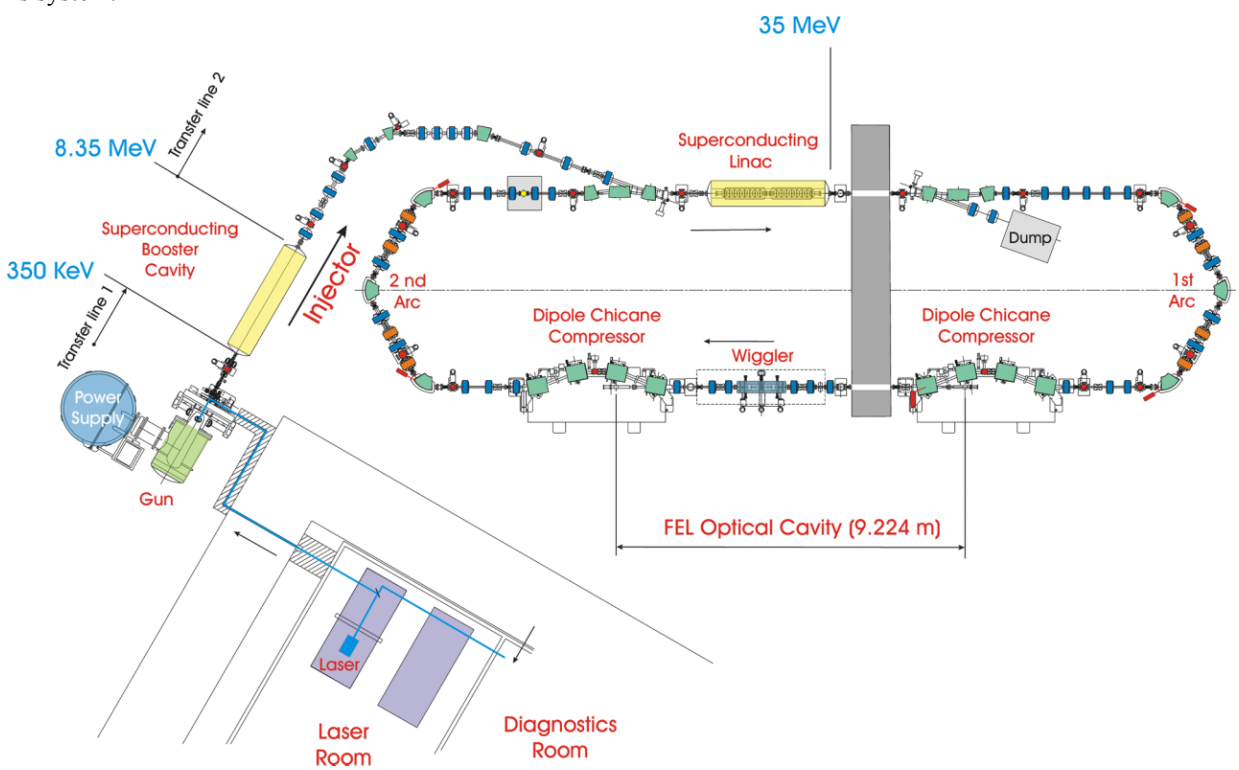

Figure 1: ERLP Layout.

PURPOSE OF MEASUREMENTS

The aim is to commission the gun prior to the construction of the rest of the machine. This will demonstrate that the gun meets its performance specifications and can work reliably, and to investigate the transverse and longitudinal properties of the beam produced. Comparing the measurements with computer simulations will validate the codes used to model this high charge and low energy regime. Due to the strong space charge forces at low beam energies, the injector layout can only be modelled properly with multi-particle tracking codes that include space charge effects, for example ASTRA and Parmela.

In order to make these measurements a dedicated diagnostic beamline has been designed and is currently being procured.

Overall Philosophy

The design of the diagnostic beam line described here has been constrained by the placing of the gun, solenoids and buncher cavity in the positions that are broadly optimum for the electron beam properties required for the ultimate operation of the ERLP. The commissioning of the gun is planned to take place in two phases: in phase one multiple diagnostics are positioned in place of the buncher cavity in order to study the beam parameters at this position, as this is the minimum aperture in the injector. For phase two the diagnostic is removed to make space for the buncher, and moved to make similar measurements at the proposed position of the centre of the first cell of the superconducting booster cavity. There are two advantages to this strategy:

- The disruption required in converting the diagnostic beam line into the ERLP injector is minimised.
- Most of the diagnostics can be left in place during subsequent operation of the ERLP for continued study of the performance of this part of the machine.

A large-bore solenoid directly follows the gun vacuum chamber, which includes horizontal and vertical steering coils, and a RF-shielded gate valve. Immediately after the valve is the light box, a device that directs incident laser light onto the photocathode and removes light reflected from the wafer into a beam dump. The light box is followed by some bellows and a BPM.

From this point onwards, the configurations for phase one gun commissioning, phase two gun commissioning and ERLP operation are different.

Beam Properties to be Measured

The measurements required to characterise the electron beam from the gun are:

- Electron beam position.
- Total charge in the pulse train.
- Pulse train length and charge stability within train.
- Electron beam energy and energy spread.
- Transverse beam profile.
- The electron beam transverse emittance.
- Longitudinal bunch shape.
- Longitudinal emittance.

Phased Measurements

In phase one of the gun commissioning a screen viewer follows the BPM and replaces the buncher. The layout of the diagnostic beam line in at this point is shown in Fig. 2. For phase two, the first slits/pepper pot/viewer unit (A) is removed to make space for the buncher cavity. This diagnostic is then added between the analyser magnet and viewer (C) in the straight-on path to study the beam properties at the envisaged position of the 1st cell of the booster cavity.

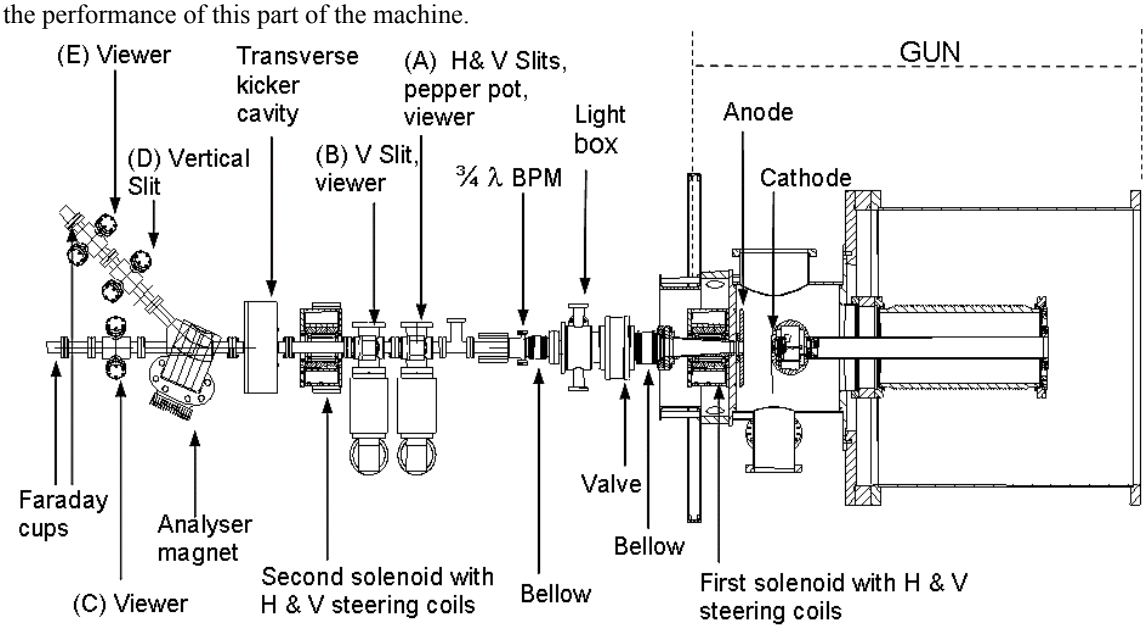

Figure 2: Phase One Diagnostic Layout.

DIAGNOSTIC MEASUREMENTS

Electron Beam Position

Phases 1 & 2: The ¾ λ BPM, all viewers and the Faraday cups can be used to position the electron beam and thread it through the diagnostic beamline. Using BPM readings to provide a cross-check with viewer measurements will improve accuracy.

Total Charge in the Pulse Train

Phases 1 & 2: Faraday cups are used to measure the charge produced for various cathode-laser powers and pulse durations (giving an estimation of quantum efficiency and electron losses).

Pulse Train Length and Charge Stability Within Train

Phase 1 & 2: The ¾ λ BPM and the Faraday cups can be used to study the stability of the laser and cathode response.

Electron Beam Energy and Energy Spread

Phases 1 & 2: Viewers (B & C) are used for setting up the analyser magnet, as the beam must be centred in the magnet for an accurate measurement. The vertical slit (B), analyser magnet and viewer (E) are used to measure the energy and energy spread.

Electron Beam Size

Phase 1: Viewers (A, B & C) are used to measure the evolution of beam size for comparison with simulation codes, and map the beam size at the location of the buncher for various parameter settings (e.g. beam energy, bunch charge, spot size at the cathode and solenoid field strength).

Phase 2: The same measurements that are taken in phase one are made at the position of the centre of the first cell of the booster.

Electron Beam Transverse Emittance:

Phase 1: Method 1 - The pepper pot and viewer B or method 2 - the slits (A or B) and viewers (B or C respectively) are used to measure the transverse emittance at the position of the buncher and unit B.

Phase 2: The transverse emittance at the position of the centre of the first cell of the booster is measured using the pepper pot and viewer (C).

Longitudinal Bunch Shape

Phases 1 & 2: The transverse kicker cavity and viewer (C) are used to measure the bunch shape dependence on the initial laser pulse length, beam energy, bunch charge (and buncher cavity gradient in phase two).

Longitudinal Emittance

Phases 1 & 2: Combining the results from the electron beam energy, energy spread and the longitudinal bunch shape measurements, the longitudinal emittance can be estimated.

MODELLING

The dimensions of the electron bunch at the cathode are mainly dependent on the laser and cathode material used. With a GaAs cathode, the electron bunch is longer than the laser pulse due to the emission process in this material [3]. The response behaviour of GaAs is difficult to predict and there is limited experimental data available. For modelling the longitudinal profile of the bunch has been assumed to be Gaussian, with an RMS length of 20ps. Transversely a near flat-top profile should be achievable from the laser, and a beam diameter of 4mm (1mm RMS) was used for the model. Table 1 shows a summary of the operating parameters. The evolution of the beam has been modelled for the injector to the end of the superconducting booster cavity [4].

The characteristics of the beam at the central position of the buncher cavity and first accelerating cell are summarised in Table 2.

Table 1: Injector parameters used for ASTRA modelling

Parameter	**Unit**	
Laser spot size	mm	4
Laser pulse length	ps	20
Bunch charge	pC	80
Gun voltage	kV	350
1st solenoid	G	300
Buncher	MV/m	1.7
Phase	deg	90
2nd Solenoid	G	210

Table 2: Summary of ASTRA modelling results

Characteristic	**Unit**	**Buncher Cavity**	**First Cell**
Transverse beam size (RMS)	mm	3.4	1.8
Normalised transverse emittance (RMS)	μm	1.6	3.1
Bunch length (RMS)	mm	6.7	3
Longitudinal emittance (RMS)	keV mm	3.7	1.7

REFERENCES

[1] Yunn, B.C.: "Physics of Jlab FEL Injector", PAC, 1999, pp 2453-5.

[2] Buchner, A. *et al*: "The ELBE Project at Dresden Rossendorf", EPAC, 2000.

[3] Hartmann, P. *et al*: "A diffusion model for picosecond electron bunches from negative electron affinity GaAs photocathodes", J. Appl. Phys. 86 (1999), p 2245.

[4] Gerth, C., Hannon, F.E.:" Injector Design for the 4GLS Energy Recovery Linac Prototype", EPAC, 2004.

COMMISSIONING OF A 6 MEV X-BAND SW ACCELERATING GUIDE

Qingxiu Jin, Dechun Tong, Yuzheng Lin, Xiang Sun, Xaokui Tao, Jingqing Sun, Xiuming Duan
Department of Engineering Physics, Tsinghua University Beijing 100084, P.R.China
Bingyi Chen, Baoyu Sun, Yang Zou, Yaozeng Li,
Beijing Institute of Electronics & Vacuum Technology, Beijing 100016, P.R.China

Abstract

A 6 MeV, X-band on axis-coupled SW electron linear accelerating guide was developed in Accelerator Laboratory of Tsinghua University. It can be suitable for portable radiotherapy and radiography. The design, manufacture and high power test of the guide are given in this paper.

The length of the guide is 47cm long. It includes a 38cm long accelerating structure, a Pierce electron gun and a target. A 1.5MW pulsed magnetron at 9300MHz is served as its RF power source.

This paper presents the design performance characteristics of the guide and the results of the high-power tests.

INTRODUCTION

New generation portable electron linear accelerator requires small size, less weight and reliable. X-band electron linac can meet these requirements. In order to reduce side and weight of accelerator, in general, magnetron is adopted as microwave power source for X-band linac. The X-band accelerating structure has been studying by Tsinghua University since 1990. For developing X-band linac, we pushed Beijing Institute of Electron & Vacuum Technology to develop a 1MW, X-band magnetron. Using the magnetron, as RF power source a 2.5MeV X-band SW linac was made and successfully was applied to the large container inspection system produced by NUCTECH Company Limited in 1998. For the need of new radiotherapy techniques and radiography, a 6MeV, X-band on axis-coupled SW accelerating guide which operated in the $\pi/2$ mode has been developed by Accelerator Laboratory of Tsinghua University. Using a 1.5MW X-band magnetron was supplied by E2V Technologies Limited, England, the guide of the high-power test has been completed.

GENERAL DESCRIPTION

The geometry of the accelerating structure is a 38cm long, which consists of 49 cavities concluding 9 cavities of buncher. Main parameters of accelerating structure are as following the beam energy being 6MeV, while the pulse beam currents being 50mA.

The microwave power source is an X-band 1.5MW magnetron at 9.3GHz.

The accelerating structure can be used in two modes: electron and X-ray generation. To obtain small size and less weight of the structure, the phase-focusing technique was used without any external magnetic focusing device. As a result, the beam spot size of the accelerating structure is less than 1.5mm in diameters. The accelerating structure characteristics are listed in table 1[1].

Table 1: Accelerating Structure parameter Characteristics

Length	38cm
Beam Energy	6MeV
Beam Current Peak	50mA
Spot Size	<1.5mm
Frequency	9300MHz
RF Peak Power	1.5MW
Input Coupling	1.36
Shunt Impedance	143MΩ/m
Injection Voltage	~ 15KV
Q_0	9000
Q_L	6800
Coupling coefficient K	22%

Figure 1 shows a photograph of the 6MeV SW accelerating guide after brazing. Due to excellence brazing technology, it did not need further tuning after brazing.

Figure 1: The accelerating guide after brazing.

Figure 2: MG6005 magnetron.

Figure 2 shows the MG6005 1.5MW magnetron, which was supplied by E2V Technologies Limited, England.

HIGH-POWER TESTS

Commissioning of the guide was completed in Accelerator Laboratory of Tsinghua University under the full peak power. The test condition is listed in table 2.

Table 2: High-power test conditions

Parameter	Value
Operating frequency	9302.7MHz
Operating temperature	18℃
RF power at guide entrance	1.32MW
Pulsed width of magnetron current (at 50% power level)	3.3μs
RF power envelop width (at 50% power level)	3.3μs
Duty cycle	0.0264%
Vacuum pressure	3×10^{-8} torr

Figure 3 and Figure 4 show the current waveform of magnetron and reflected power waveform while the accelerating guide is under resonance respectively.

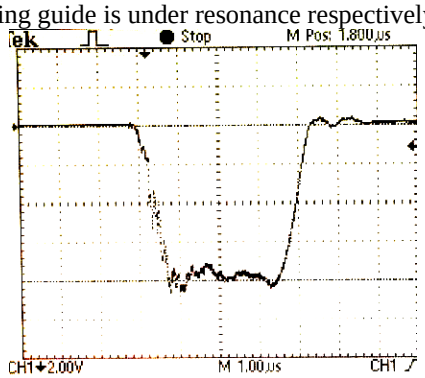

Figure 3: Waveform, Magnetron Current.

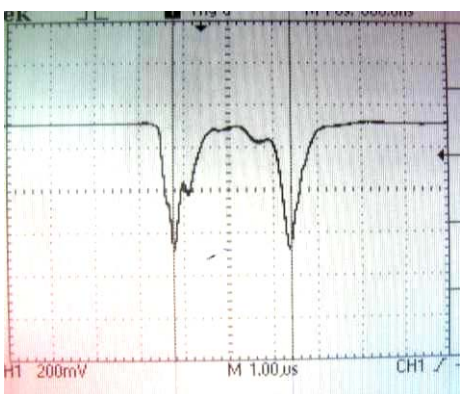

Figure 4: Waveform, reflected power at accelerator Guide resonance.

When an emission electron beam current from the electron gun is 90mA, and the injection voltage 15.4KV, the accelerated beam current and the X-ray radiation intensity was measured, which is 11.35μA, and 122.5R/min at meter respectively. At that time, in the accelerating guide entry, the peak power is 1.32MW.

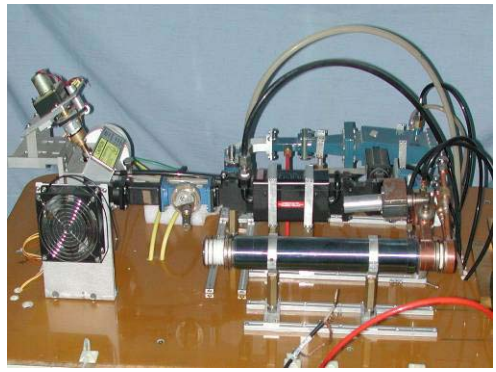

Figure 5: RF system facility.

The electron beam energy was measured with the penetrating range method. Figure 6 shows the measured curve.

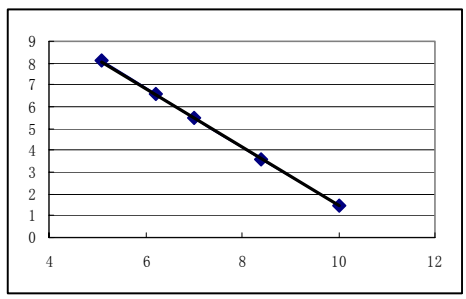

Figure 6: The penetrating range of electron beam.

With the curve, the electron energy we was calculated by the following formula:

$$W_e = W_{eo} + dW_e$$

Where $W_{eo} = \dfrac{(d\times\rho)+0.094}{0.526}$, d being penetrating range of electron, $\rho = 2.8$ being the density of alloy-aluminium, $dW_e = \dfrac{13\times W_{eo}{}^2}{(800-13W_{eo})}$ is a revised value of electron energy. From the experimental value of the penetrating range, the electron energy is equal to 6.09MeV.

The spot size is measured with a sandwich method. The magnitude of the spot size is less than 1.3mm in diameter.

CONCLUSION

The high-power tests of the accelerating guide have been completed. According to our experience and estimation, if the input power at accelerating guide entrance can reached a 1.5MW peak power, and a 1.1KW average power, X-ray dose rate should be more than 300R/min at 1 meter.

In the future, the follows works will be considered:

1. Further optimizations on accelerating structure.
2. Investigation and experiments under the condition of 1.8MW/1.1kW.
3. Less microwave power loss transmission system

4. Adopt triode electron gun for more easily controlling the injecting beam current.

The authors express their acknowledgments to E2V Technologies Limited, England for supplying us magnetron without any pay back.

REFERENCES

[1] Sun Xiang, “The Study Nonlinear RF Field Effects on the Beam Dynamics and X-band On-axis Accelerating Structure” Dissertation Submitted to Tsinghua University in partial fulfilment of the Requirement for the Degree of Doctor of Engineering.

[2] Sun Xiang, et al, “Development of a Portable X-Band Linac Structure” The China-Japan Joint Symposium on Accelerator for Nuclear Science and Their Applications.

[3] Schonberg RG, Deruyter H, Fowekes WR, et al. “Portable X-BAND, Linear Accelerator System” IEEE Transactions, 1985,32(5):3234.

[4] E. Tanabe, et al “An Standing Wave Linear Accelerator Structure” 1986 Linear Accelerator Conference Proceedings, Stanford, A USA,pp,455-457 1986.

[5] Schonberg Research Corporation, “Status Low Energy (10MeV Range) X-Band Linacs Developed Worldwide.

A STUDY OF HIGHER-BAND DIPOLE WAKEFIELDS IN X-BAND ACCELERATING STRUCTURES FOR THE G/NLC

R.M. Jones†, SLAC, Stanford, CA 94309, USA

Abstract

The X-band linacs for the G/NLC (Global/Next Linear Collider) [1] have evolved from the DDS (Damped Detuned Structure) [2] series. The present accelerating structures are 60 cm in length and incorporate damping and detuning of the dipole modes which comprise the wakefield. In order to adequately damp the wakefield, frequencies of adjacent structures are interleaved. Limited analysis has been done previously on the higher order dipole bands. Here, we calculate the contribution of higher order bands of interleaved structures to the wakefield. Beam dynamics issues are also studied.

INTRODUCTION

In the operation of the X-band linacs of the G/NLC, wakefields left behind a train of charged bunches can disrupt particles within bunches and can cause severe emittance dilution. For this reason the wakefield is damped by detuning the cell frequencies and by coupling out a portion of the wake to four manifolds that surround the accelerator structure [3].

All previous analyses of the interleaved wakefields for the G/NLC accelerating structures have been exclusively concerned with the 1st dipole band [4]. Herein, this is extended to higher order bands using a mode matching code *Smart2D* [5]. This is applied to the accelerating structure H60VG3 which consists of 55 cells and has an initial fundamental group velocity of 0.03c. Prior to applying the mode matching method we require the geometrical parameters of each cell. The method used to obtain the cell geometry is discussed in [6].

The detailed geometry of the cells is not taken into account with the mode matching method (the curvature of the irises for example is approximated by sharp transitions). However, previous analysis [7] of higher order modes has indicated that making these approximations in the geometry have a small effect on the synchronous frequencies and kick factors [8].

The following section presents the results of calculations on the dipole wakefield for interleaved and non-interleaved accelerating structures. Beam dynamics issues are discussed in the final main section.

TRANSVERSE WAKEFIELDS

Single Structure Wakefield

Smart2D is used to calculate the beam impedance of H60VG3 and the results are presented in Fig. 1. The 1st band is the dominant one. Significant impedances are also located in the 3rd and 6th bands. The kick factor is calculated from the beam impedance by the expanding the impedance into a summation of Lorentzian functions over all modes. A single Lorentzian for the nth mode is:

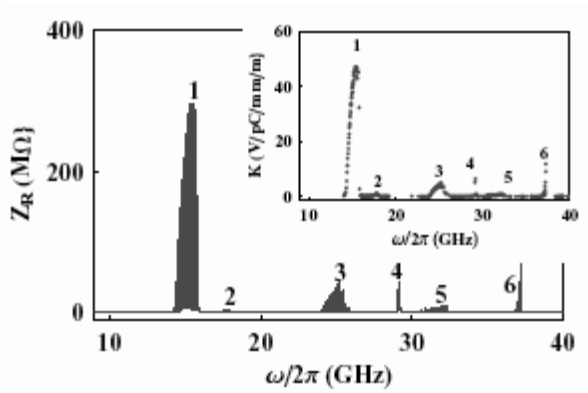

Figure 1: Real part of the beam impedance (Z_R). Kick factors (K) versus synchronous frequencies are shown inset. The approximate band locations are numbered.

$$L_n(\omega) = \frac{2Q_n}{\pi\omega_n}\frac{K_n}{1+4Q_n^2\left(\omega/\omega_n - 1\right)^2}. \qquad (1)$$

Here $\omega_n/2\pi$ is the resonant frequency of a mode with a quality factor Q_n and loss factor $K_n = \int_{-\infty}^{\infty} L(\omega)\,d\omega$. The kick factor is given in terms of the loss factor by $K_n = K_n c/\omega_n r_{off}^2 P$, where P is the period of a cell, and r_{off} the offset of the particle from the axis. Kick factors that result from this fitting procedure are shown inset to Fig. 1. The envelope of the long-range transverse wakefield is calculated from the absolute value of the modal sum:

$$\hat{W}(s) = 2\left|\sum_{n=1}^{N} K_n e^{i\omega_n s/c} e^{-\omega_n s/2Q_n c}\right| \qquad (2)$$

Various components of this wakefield are illustrated in Fig 2. We impose a Q of 700 for the first dipole band and 4000 for all subsequent bands. The optimized first-band wake is also shown in Fig 2 A (for the sake of clarity the wake at the location of the bunch is not shown in this case). This wake has been calculated with the spectral function method [9] which directly incorporates manifold-cell coupling (eliminating the need for an *a posteriori* imposition of a damping Q). Up until the first 20 m or so both wakes are quantitatively similar. However, the 1st band wake calculated with *Smart2D* is significantly larger for the 1st trailing bunch where it is more than 2 V/pC/mm/m. For both calculations in Fig. 2 A the wakefield is larger than 1 V/pC/mm/m in the neighborhood of 10 m and this will readily drive the beam into an unstable BBU mode [10]. In order to prevent this we interleave the frequencies of neighboring accelerator structures.

† Supported by the Department of Energy, grant number DE-AC03-76SF00515

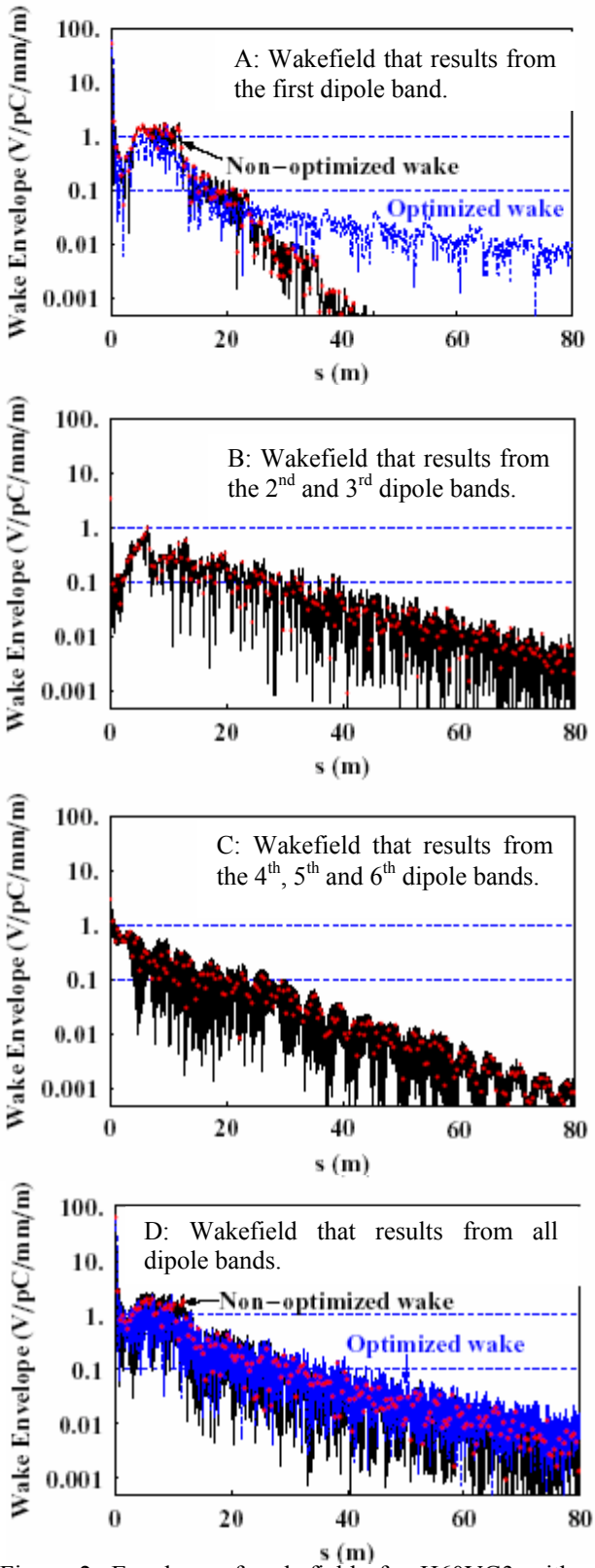

Figure 2: Envelope of wakefields for H60VG3 without any interleaving of the cell frequencies of accelerator structures. The red dots indicate the location of each bunch (spaced 42 cm from their immediate neighbours). The solid black curve corresponds to the wakefield calculated with *Smart2D* and the dashed blue curve is calculated with the spectral function method.

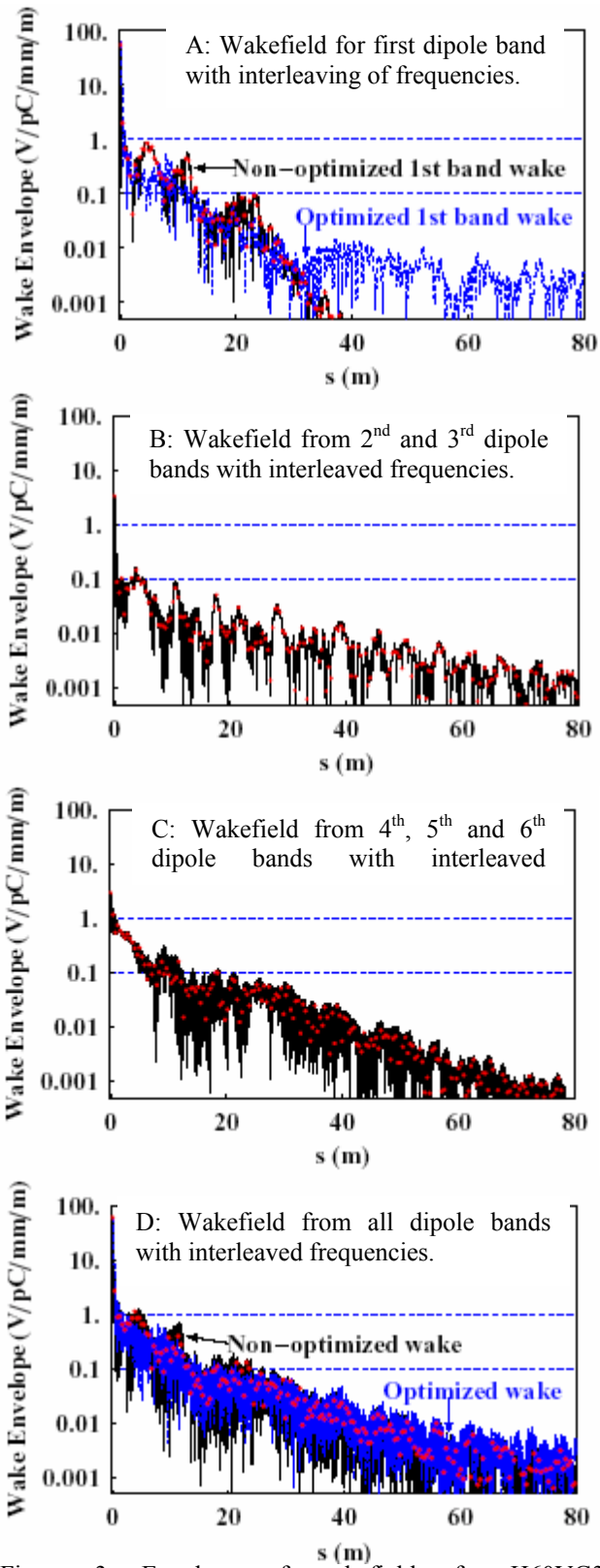

Figure 3: Envelope of wakefields for H60VG3 demonstrating the wake fall-off that occurs due to interleaving of the frequencies of accelerator structures. Here we use 3-fold interleaving of the frequencies of neighbouring structures. The interleaving is affected by changing both iris radius by ± 15 μm and the iris thickness by ± 40 μm.

Interleaved Structure Wakefield

In order to force the wakefield to continue to decay we fill-in frequencies between mode frequencies. This is achieved by shifting the frequencies of neighbouring accelerator structures such that the frequencies effectively become interleaved. For the first dipole band this is affected by systematically increasing (or decreasing) the iris radius and by changing the iris thickness for the higher order bands. In our simulation we considered 3-fold interleaving. The results of this simulation are shown in Fig 3, where they are shown side-by-side with their non-interleaved counterparts (Fig. 2). Clearly, interleaving improves the decay of the wakefield of all bands. In particular, the wakefield of the first band is now below 1 V/pC/mm/m for all bunch locations apart from the first trailing bunch. The first trailing bunch is important with regard to determining the progress of the beam down the linac and in the case of the wakefield calculated with *Smart2D* the wake for the first trailing bunch is above 2 V/pC/mm/m. This will readily drive the beam into an unstable BBU [10] regime and for this reason we will utilize the 4-fold optimized wake calculated with the spectral function and add higher bands calculated with *Smart2D*. In reality an optimized linac will be used in the final G/NLC design.

BEAM DYNAMICS

The sum wakefield [11] provides an indication as to whether BBU will occur. We evaluate the RMS of the sum wakefield in Fig. 4 for small changes in the bunch

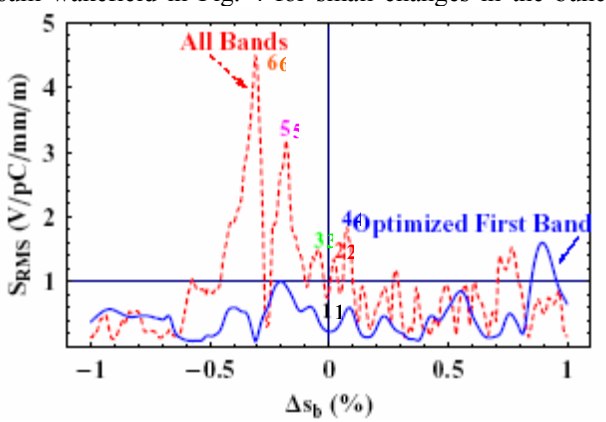

Figure 4: RMS of the sum wakefield (S_{RMS}) versus the percentage change in the bunch spacing from the nominal value. The optimized first band is illustrated by the solid blue line. S_{RMS} for the first (optimized) band and all additional higher order band components up until the 6th band is indicated by the dashed red line. Peak values used in tracking simulations are numbered 2 to 6.

spacing for both single and multi-band wakefields. A small change in the bunch spacing represents a systematic change in all cell frequencies and in effect it models systematic errors that are liable to occur in fabricating several tens of thousands of accelerating structures. However, in practice, we would expect errors of less than 15 MHz and this limits the percentage bunch deviation to

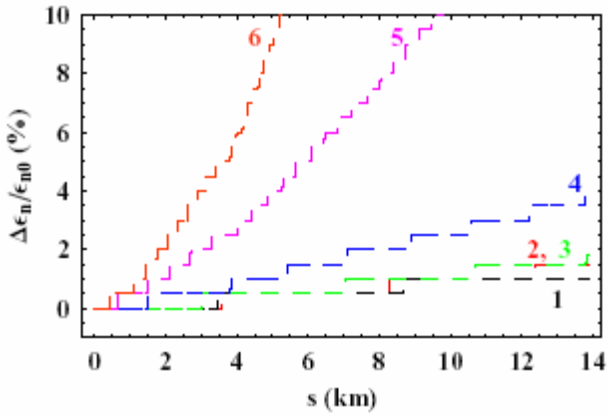

Figure 5: Percentage emittance dilution from the injected emittance of 20 nm.rads versus the distance down the linac for various fractional deviations in the nominal bunch spacing for a beam subjected to the interleaved wakefields. Curve 1 is for the nominal bunch spacing and curves 2 to 6 correspond to the peaks in S_{RMS} indicated on the dashed curve in Fig. 4.

~ ± 0.1%. In this region there are 4 peak values in the multi-band S_{RMS}

The emittance of the beam is monitored as proceeds down the complete linac for the peak values in S_{RMS} indicated on the curve in Fig. 4. The results of this tracking simulation for a beam initially offset by 1 μm from the axis of the accelerator structure are illustrated in Fig. 5. Provided the change in the bunch spacing is confined to 0.1% then we are limited to curves 1 to 4 where no more than 4% emittance occurs. For larger peaks located in the neighborhood of 4 and 5 in Fig. 4 the emittance grows quadratically along the linac and at the end reaches a maximum value of 18 % and 56 % respectively. However, errors in fabricating the structures are not expected to be this large and thus emittance dilution will be kept below 4%.

In conclusion, the beam emittance will not be diluted appreciably provided the frequencies of the 1st though 6th dipole bands are interleaved.

ACKNOWLEDGEMENTS

This work has benefited greatly from stimulating discussions in the weekly structures meetings at SLAC. I am grateful for the advice provided on the use of the code *Smart2D* by V.A. Dolgashev.

REFERENCES

[1] ILC/TRC 2nd Report, SLAC-R-606, 2003.
[2] R.M. Jones *et al.*, PAC97, SLAC-PUB-7537, 1997.
[3] R.M. Jones *et al.*, PAC99, SLAC-PUB-8103, 1999.
[4] R.M. Jones *et al.*, PAC03, SLAC-PUB-9868, 2003.
[5] V.A. Dolgashev, ICAP98, Monterey, CA, 1998.
[6] R.M. Jones *et al.*, EPAC04, SLAC-PUB-10557, 2004.
[7] Adolphsen *et al.*, LINAC00, SLAC-PUB-8604, 2000.
[8] P.B. Wilson, SLAC-PUB-4547, 1989.
[9] R.M. Jones *et al.*, LINAC96, SLAC-PUB-7287, 1996.
[10] K. Yokoya, DESY Report 86-084,1986.
[11] R.M Jones *et al.*, PAC 99, SLAC-PUB-8101, 1999.

RHIC Electron Cooler *

J. Kewisch, I. Ben-Zvi, X.Y. Chang, V. Litvinenko, C. Montag,
R. Calaga, A. Jain, V. Yakimenko,
Brookhaven National Laboratory, Upton, NY 11973, USA

Abstract

Electron cooling has been applied in many accelerators. All of them operate at low energies where cooling times are short. Electron cooling is now considered for RHIC where gold ions are stored at 100 GeV/u. The corresponding electron energy is 55 MeV. This energy cannot be reached with a DC source like a Fermilab's pelletron. The cooling time is proportional to the square of the energy. In order to have a cooling time of of less than one hour it is necessary to maintain a transverse normalized emittance of 50 mm mrad and an energy spread with a charge of 20 nC per bunch. Such beam quality cannot be achieved with a storage ring. Only a Photocathode Energy Recovery LINAC (PERL) promises success [1].

A special super-conducting cavity was developed for the RHIC electron cooler. It is optimized for high current operation and uses ferrite beam pipes outside the cryostat for higher order mode damping. First simulations with the TBBU computer code [2] show a beam breakup threshold of 3 Amperes.

A strong longitudinal field in the cooling section enhances the cooling process. A solenoid magnet with a field of 1Tesla and a field error of less than is being developed. For a minimum transverse temperature inside the solenoid it is necessary to have a "magnetized beam", i.e. a beam from a cathode immersed in a longitudinal magnetic field. The usual emittance compensation scheme needed to be adapted so that the magnetization does not lead to strong emittance growth.

The RF gun is super-conducting, providing high accelerating fields to minimize the effects of space charge. A cathode insert with a diamond window uses secondary electrons to produce the high charge and avoids a breakdown of superconductivity through surface contamination by the cathode material and the magnetic field required for the magnetization.

Finally, the bunch is lengthened and the energy spread in the cooling section is reduced by bunch rotation in the longitudinal phase space. This also reduces the space charge effect between electrons and ions. The original bunch length must be restored by a second rotation before deceleration and energy recovery.

INTRODUCTION

Electron cooling has been known for many years and is practiced in many machines around the world. The physics of cooling takes place in the reference frame of the ions (and electrons) bunch, which is independent of the energy of the machine. However, there are a number of differences between this electron cooler and any other built so far:

- The RHIC cooler will be by far the highest energy cooler, requiring electron energy of over 50 MeV as compared to the few hundred KeV of any previously built cooler (the only exception is the recycler cooler of FNAL, which is under construction and will have 4.3 MeV electron energy).
- The RHIC cooler is the only machine planned for cooling with bunched electron beams.
- The RHIC II will be the first instance of a directly cooled collider.
- The RHIC cooler will operate with electrons that are much "hotter" than in previous coolers.
- The RHIC cooler will use a very long, high-field, ultra-high precision solenoid.

The electron beam technology of this cooler will be different than any other, requiring high-energy, high-current and low-emittance (temperature) electron beams. In order to reach the goals R&D is taken along the following fronts:

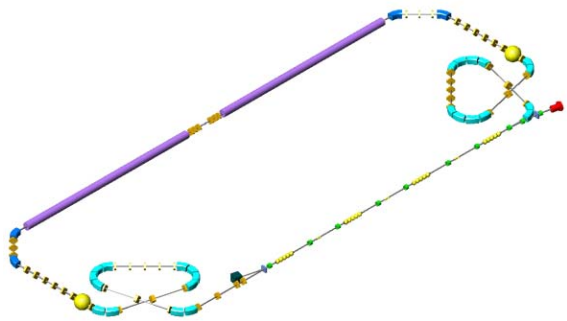

Figure 1: Electron bunches are produced in the gun and accelerated in the super-conducting linac. A beam-transport loop stretches the bunch length and a debunching cavity reduces the energy spread before the electrons are merged with the ion beams. A strong solenoid must be installed in the cooling section to enhance the cooling effect [10]. The electron bunches are then shortened by a combination of a second cavity / transport loop, and then decelerated in the linac before they are dumped. The start of operation is planned for January 2010.

* Work performed under the auspices of the U.S. Department of Energy

ELECTRON SOURCE

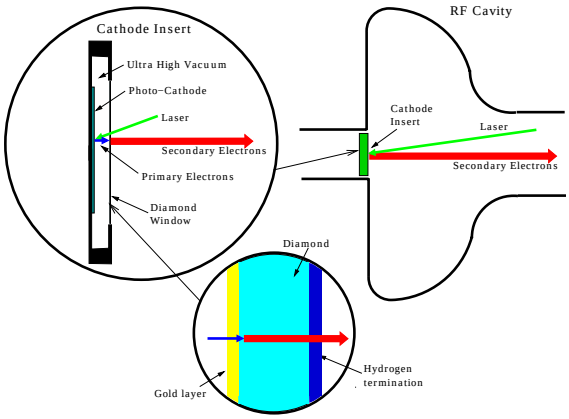

Figure 2: Schematic diagram of a secondary emission enhanced photoinjector. Please note that the figure is not to scale. The figure on top right shows the cathode insert in the gun cavity. The figure on top-left is a magnified view of the cathode insert. The gap between the diamond window and the photocathode is typically some fraction of a millimeter. The bottom figure is a blow-up of the diamond, showing (very schematically) a gold coating on the photocathode side of the diamond and hydrogen termination of the diamond's dangling bonds on the gun side of the diamond. The gold is very thin, about 10 nm or less, while the diamond may be as much as 10 microns thick, while the hydrogen is a monolayer.

An electron source based on a 703.75 MHz laser-photocathode RF gun (photo injector) must be developed. This research may be broken down to the following R&D components:

- High quantum-efficiency, long-lived photocathode. Fig. 2 shows the principle of a secondary emission enhanced photoinjector [3]. The secondary emission is produced in a diamond window which also shield the superconductive gun cavity from the photo-cathode material and the photo-cathode material from the cavity vacuum.
- High average-power, 9.4 MHz repetition frequency laser.
- A high electric field, CW operation RF gun.

ACCELERATING CAVITY

A five cell superconductive cavity (shown in Fig. 3) was developed which is optimized for high current operation. The large bore (17 cm iris radius, 24 cm beam pipe) allows HOMs to be damped in ferrite absorbers outside the cryostat. Fig. 4 shows the result of TDBBU calculations. The higher order modes differ in frequency from cavity to cavity due to manufacturing tolerances. A higher frequency spread allows higher beam current. The breakup current is above requirements.

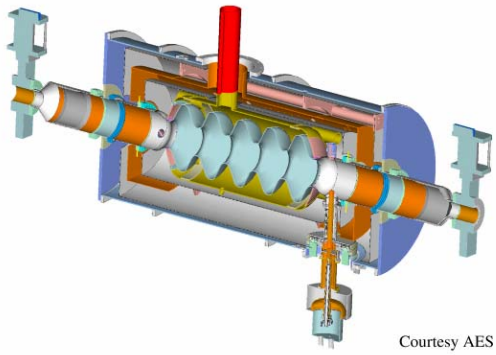

Figure 3: Superconductive cavity for high current operation.

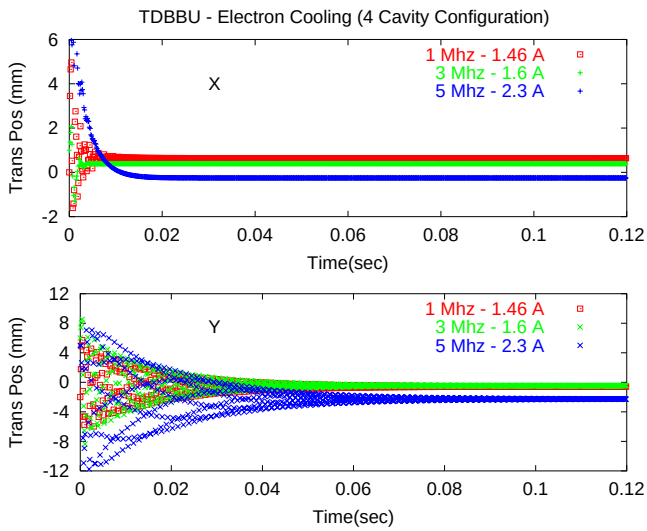

Figure 4: Beam breakup calculations with TDBBU.

ENERGY RECOVERY LINAC TEST FACILITY

In order to verify the energy recovery and beam breakup thresholds an energy recovery linac with a single cavity and variable optics will be build. The layout is shown in fig. 5. Injection energy will be 3-5 Mev, the maximum beam energy 15-20 MeV. Average beam current will be up to 200 mA, We expect a current recovery efficiency $>$ 99.95%. The ERL will operate in two modes: The high charge mode with a Bunch repetition rate 9.4 MHz, Charge per bunch $>=$ 10 nC, Normalized emittance $\tilde{3}$0 mm mrad. The low charge mode with a Bunch repetition rate 9.4-700 MHz, Charge per bunch 0.3-1 nC, Normalized emittance $\tilde{1}$-3 mm mrad. Start of installation in September 06, commissioning in March 07.

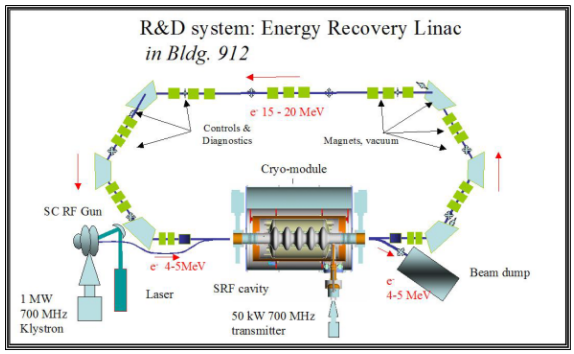

Figure 5: Energy recovery linac test facility.

COOLING SOLENOID

The friction force is proportional to $\frac{v_{ion}^2}{(v_{ion}^2+v_{longitudinal}^2+v_{tranverse}^2)^{3/2}}$ where $v_{tranverse}^2$ for a magnetized beam is given by the transverse field components of the solenoid. The relative field error must be less than $8 \cdot 10^{-6}$. The transverse field is measured using a magnetic mirror and corrected with dipole corrector.

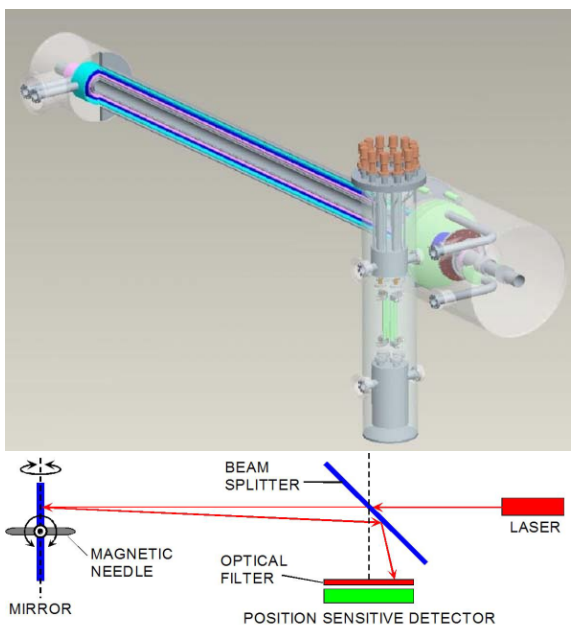

Figure 6: Cooling solenoid and field measuring setup.

BEAM DYNAMICS AT LOW ENERGIES

The fringe field of the cooling solenoid causes a rotation of the beam around the longitudinal axis. In order to minimize the transverse temperature of the electrons inside the solenoid they should enter the solenoid with the opposite rotation. Such beam can only be created through a magnetic field on the cathode and is therfore called a "magnetized" beam.

Traditional emittance compensation uses the space charge force to align the phase ellipses for different longitudinal slices of the bunch. The Bunch is then accelerated so that space charge forces can be neglected . For a magnetized beam Busch's Theorem must be taken into consideration. The rotation speed of a slice depends on its radius:

$$r^2\theta' + r^2\frac{e}{m_e\gamma\beta c}B = r_o^2\frac{e}{m_e\gamma\beta c}B_o$$

Therefore, in addition to the phase advance, the relative change of radius must be made equal for all longitudinal slices. Fig. 7 illustrates the effect of a radius change caused by space charge effects. On the cathode all slices have the same radius. As the bunch traverses the gun cavity the radii of the center slices increases more than those of the head and tail slices. In a frame that rotates with the average rotation of the bunch slices with larger radius rotate clockwise, slices with smaller radius rotate counterclockwise.

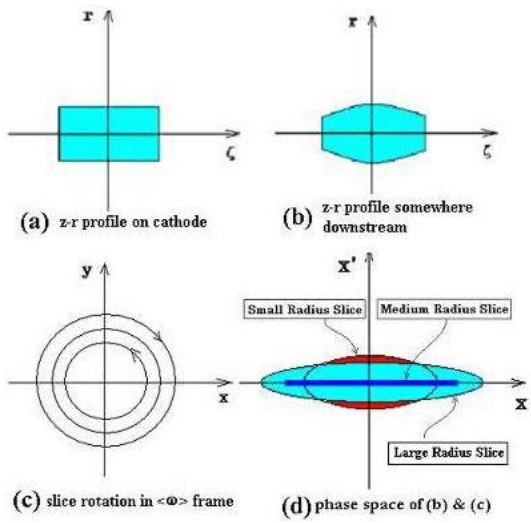

Figure 7: Emittance compensation for a magnetized beam.

CONCLUSION

The RHIC electron cooler is a challenging project. The limits of existing technology are pushed by orders of magnitude. R&D is in progress on many fronts to reach this goal.

REFERENCES

[1] J. Kewisch, X. Y. Chang, D. Wang, C. Montag, I. Ben-Zvi: "Layout and Optics for the RHIC Electron Cooler", PAC 2003

[2] G. A. Krafft, J. J. Bisognano: CEBAF PR-87-008

[3] I. Ben-Zvi, X. Y. Chang, P. D. Johnson, J. Kewisch, T. S. Rao: "Secondary Emission Enhanced Photoinjector ",C-A/AP/#149

LINEAR ACCELERATOR LINAC-800 OF THE DELSY PROJECT

V.V. Kobets, N.I. Balalykin, I.N. Meshkov, I.A. Seleznev, G.D. Shirkov,
JINR, Moscow region, 141980, Dubna, Russia

Abstract

In the report the modernization of electron linear accelerator MEA (Medium Energy Accelerator) is discussed. The goal of the work is to create on the base of MEA a complex of free electron lasers overlaying a range of radiation waves from infrared to ultraviolet. Status of the work is reported.

THE DELSY PROJECT

The DELSY (Dubna Electron Synchrotron) project is being under development at the JINR, Dubna, Russia [1]. It is based on an accelerator facility presented to JINR by the NIKHEF, Amsterdam. The construction of the DELSY facility will proceed in three phases. Phase I will be accomplished with the construction of a complex of FEL covering continuously the spectrum from far infrared down to ultraviolet [2]. Phase II will be accomplished with commissioning of the storage ring DELSY. The optics of the DELSY storage ring is characterized by its 2-fold symmetry, low horizontal emittance (11.4 nm), low-beta section at the wiggler location and section for miniundulator. Synchrotron radiation from the dipole magnets with critical photon energy up to 1.16 keV has rather high intensity in both ultraviolet and infrared regions. This radiation can be used in photoelectron microscopy, time-resolved fluorescent studies of biological objects, in absorption spectroscopy, metrology and photometry. Hard X-ray radiation from wiggler can be used for researches on VUV luminescence of crystal and pumping of VUV-lasers, time-resolved Moessbauer spectroscopy, EXAFS spectroscopy, DANES, DAFS. Phase III of the project is construction of an X-ray FEL. Recent studies have shown that the DELSY complex has a reliable potential for upgrading into a fourth-generation SR light source.

Phase I

Phase I will be accomplished with the construction of a complex of free electron lasers covering continuously the spectrum from far infrared down to ultraviolet (of about 150 nm). The far-infrared coherent source will cover continuously the submillimeter wavelength range. Realization of this phase will not require a significant modification of the JINR infrastructure. In Table 1 we present a summary of the radiation properties from coherent radiation sources being planned to build in Phase I. Notations G1-G4 refer to the FEL oscillators, and FIR stands for the far-infrared coherent source.

ACCELERATOR LINAC-800

The electron beam with necessary parameters for the Free Electron Laser will be generated with the electron linac, which is a modified version of the Medium Energy Accelerator (MEA) transferred to JINR from NIKHEF[3]. The energy of electrons at the linac exit is 800 MeV and peak current of 30-60 A, with subharmonic buncher of the frequency of 476 MHz, a buncher at the frequency of 2856 MHz and 24 acceleration sections, which are combined in 14 acceleration stations (A00 – A13).

Table 1: Summary of radiation properties from coherent radiation sources in Phase I.

	FIR	G1	G2	G3	G4
Radiation wavelength, [μm]	150-1000	20-150	50-30	1-6	0.15-1.2
Peak output power, [MW]	10-100	1-5	1-5	3-15	10-20
Micropulse energy, [μJ]	500	50-200	25-100	25-100	50-100
Micropulse duration (FWHM),[ps]	5-10	10-30	10	10	3-5
Spectrum bandwidth (FWHM),[%]		0.2-0.4	0.6	0.6	0.6
Micropulse repetition rate, [MHz]			19.8/ 39.7/ 59.5		
Macropulse duration, [μs]			5-10		
Repetition rate, [Hz]			1-100		
Average output power (max.), [W]	10-50		0.2-1		

To operate FEL, one needs an injector with a special subharmonic prebuncher. Such an injector has to be developed at JINR.

MEA Injector

To start the linac operation and test its condition, we plan to use the MEA injector consisting of an electron gun, chopper, prebuncher and buncher [4].

The electron gun (Table 2) has a dispenser thermocathode with the diameter of 8 mm. Its heater current is 15 A at the heater filament voltage of 12 V. The cathode lifetime is of the order of 20 thousand hours. The gun optics elements contain Pirce electrode at the cathode potential, control electrode and acceleration tube, which has 15 diaphragms forming homogeneous acceleration field. Linear potential distribution along the tube is provided with the divider, the voltage between two

neighbour diaphragms is of the order of 30 kV. One can "close" the gun by applying the voltage of –150 V between the cathode and control electrode. The gun is operated in a pulsed mode by applying voltage pulses of +6 kV amplitude between the cathode and control electrode.

Table 2: The electron gun parameters

Scheme	Triode
Type of cathode: Diameter, [mm] Heater: voltage, [V] current, [A]	Dispenser 8 0-12 0-15
Electron energy, [keV]	400
Peak current, [A]	0.45
Cathode current stability	$1.5 \cdot 10^{-3}$
Beam diameter, [mm]	1.5
Normalized emittance (1σ), [π·mm·mrad]	8

Buncher

The MEA buncher system (Table 3) contains three elements, and the first of them is the chopper. It is a deflector cavity of S-band type with collimator. The peak RF power consumed by the chopper is of 3 kW.

Table 3: The buncher system

Chopper	Scheme	RF-cavity (TM_{110})
	Frequency, [MHz]	2856
	Amplitude of transverse deflection, [mm]	16
	Drift space Length, [cm]	50
	Quality factor (unloaded)	4000
	Transmission efficiency, %	20
	Peak RF power input,[kW]	3.0
Prebuncher	Scheme	RF-cavity (TM_{010})
	Frequency, [MHz]	2856
	Mode	2π/3
	Peak electric field at the gap center, [kV/cm]	10.3
	Bunch phase length at the prebuncher exit: at 10 mA current at 20 mA current	 6° 10°
	Distance between chopper collimator and the buncher entrance, [cm]	98.7
	Distance between prebuncher exit and the buncher entrance, [cm]	132.7
Buncher	Frequency, [MHz]	2856
	Mode	2π/3
	Number of cavities	38
	Shunt impedance, [MΩ/m]	51.2 – 55.1
	Length at 24° C, cm]	127.77
	Bunch phase length at the buncher exit: at 10 mA current at 20 mA current	 ≤ 1° ≤ 2°
	Electron energy, [MeV]	6

The prebuncher cavity is installed just after the chopper cavity. It is fed with RF of 2 kW power from klystron of the first acceleration section through attenuator and phase shifter.

The buncher is actually the short acceleration section of the accelerator structure. The bunch phase length at the buncher exit is of 6°. Its structure is supplied with RF power of 2 MW from the first klystron. The RF power is transmitted from the buncher exit through phase shifter to the first acceleration section.

Acceleration Sections

The MEA linac contains acceleration waveguide sections of six types. They are similar in mechanical features, but differ in RF-parameters (Table 4). Each section contains eleven uniform 2π/3-mode segments. The numbering of the sections is done with the alphanumeric identifiers, in which first letter symbol (A or B) means the way of RF-feeder connection to the section: symbol A indicates that the feeder is connected to the top of the section, the symbol B – to the bottom. The last symbols (one or two) mean the type of the section.

Table 4: The parameters of acceleration sections

Type of section	Short	Long
Number of sections	3	18
Number of cells per sections	105	210
Section length, [m]	3.673	7.346
Frequency, [MHz]	2856	
Traveling-wave mode	2π/3	
Acceleration gradient, [MeV/m]	5	
Filling time, [μs]	1.3	
Beam load, [MeV/mA]	2.6	
Shunt impedance, [MΩm]	56.5 - 48	
Aperture: diameter, [mm] thickness, [mm]	32 5.84	

Besides, double letter symbol AA or BB indicates the short section, single letter A, B, C, D – a long section. The short sections have the length of 3.6 m, they are immersed in constant solenoidal magnetic field of the order of 500 Gauss. The long sections of the length of 7.35 m have no magnetic field. All the acceleration sections are combined in acceleration stations that comprise an RF-power source (klystrons with modulators), waveguide, acceleration section and drift section. The drift section is used as a place of disposition of beam diagnostic devices (monitoring of the electron energy, beam current, size, position and emittance).

FEL INJECTOR

Generation of an electron beam with the parameters suitable for feeding of FEL requires significant upgrade of the linac injector. The requirements to the FEL electron beam listed in Table 5 can be satisfied using a subharmonic bunch compressor (SBH) described in Ref.

[5]. It contains in our case (Figure 1) an electron gun, a cavity operating at subharmonic frequency, a drift section and the first acceleration section of the linac.

Table 5: Parameters of electron beam after injection and acceleration in the first linac section

Energy, [MeV]	7
Peak current, [A]	60
Micropulse duration, [ps]	20
Normalized emittance, [mm·mrad]	$\leq 30\pi$
Electron energy spread, [%]	< 3

The electron gun has a modulation grid, which provides generation of short electron bunches with the duration of 0.5 ns. The electrons emitted from the dispenser thermocathode are accelerated in the electric field of the

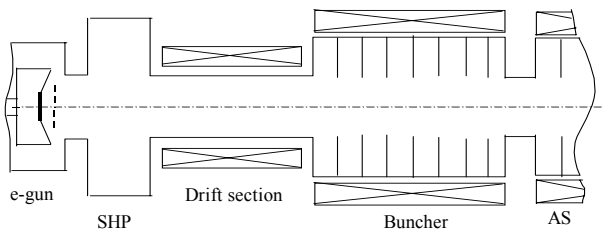

Figure 1: Injector layout.

gun electrodes up to energy of the order of 400 keV and are formed in the injector elements – prebuncher, drift section and acceleration section.

The electron bunch dynamics in the injector can be described as follows. Electron bunches have at the gun exit the length of

$$L_{gun} = \beta_{gun} c \tau_0,$$

where β_{gun} is the ratio of the electron velocity to light speed, τ_0,- the gun micropulse duration. Crossing the SHP cavity, the electron get additional energy

$$\Delta\varepsilon = eV_0 \cdot \sin\Omega t,$$

where V_0 and Ω are the amplitude and frequency of SNP "voltage" ($V_0 = E_{SHP} \cdot L_{SHP}$). We choose $\Omega = \omega_0/6$ and τ_0, equal to one quarter of SHP field oscillation:

$$\tau_0 = 1/4(2\pi/\Omega) = 3\pi/\omega_0 \approx 0{,}5 \text{ ns}.$$

If we inject electrons into the SHP cavity as it is shown in Figure 2 the maximal and minimal electron energy values are equal to:

$$E_{max} = e(V_{gun} + V_0) = 400 \text{ keV},$$
$$E_{min} = eV_{gun} = 350 \text{ keV}.$$

The electron gun delivers the pulse that enters SHP cavity at the phase of zero cavity field. Therefore, after SHP cavity passing the "head" of the beam contains slow electrons with minimal electron energy E_{min}, and the beam tail move faster in the drift section than the head. As a result, the bunch gets compressed. At the drift section exit we have:

$$I_0 = c\tau_{gun}\beta_{max} - L_0(\beta_{max}/\beta_{min} - 1) = 14.5 \text{ mm}.$$

The first linac section has a structure which corresponds to the stable electron velocity $\beta = 0.825$ ($\varepsilon = 400$ keV).

The phase oscillation frequency is very low at chosen parameters (of the order of a few MHz). One can show

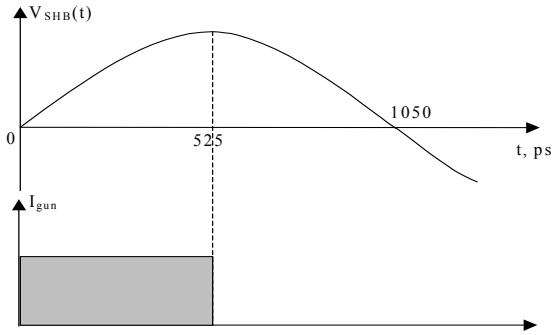

Figure 2: The time dependence of the acceleration voltage of subharmonic prebuncher and electron beam pulse at the gun exit.

that the bunch length at the exit of the section is given by the following formula:

$$l_{final} = l_0 - \gamma^3_{max} \cdot (\beta_{max} - \beta_{min})/\alpha \times (1 - A/(1+A)^{1/2}) - 1/4\alpha \times (2\pi l_0/\lambda)^2 \times 1/(1+A)^{1/2}$$

$\alpha = eE_0/mc^2$, $A = \beta_{min}\gamma_{min}$, $\gamma_{min,max} = (1 - \beta^2_{min,max})^{-1/2}$, E_0 – the acceleration field amplitude in the first linac section. The results of the estimates give us the final value of the electron bunch length:

$$l_{final} = 5.3 \text{ mm}.$$

The bunch compaction factor and peak electron current are equal to:

$$k = l_{final}/l_{gun} = 23,$$
$$I_{final} = kI_{gun} = 100 \text{ A}.$$

Three first linac sections have focusing solenoids with magnetic field of 500 G. In the FEL injector the most critical position for beam space charge influence is the exit part of the drift section and the entrance part of the first linac section. There $I_{peak} \approx 36$ A. The value of the solenoid magnetic field has to exceed the level of so-called Brillouin field.

$$B_{Brillouin} \approx 500 \text{ G}.$$

Keeping in mind future development of the injector, we have chosen maximum value of drift section magnetic field equal to 1 kG.

REFERENCES

[1] V.A. Arkhipov, V.K. Antropov, N.I. Balalykin et al., NIM A 470 (2001) 1;
[2] G. Arzumanian, N. Balalykin, V. Kobets et al., Konceptual Design Report, Dubna, 2001;
[3] F.B. Kroes, Electron Linac MEA, Compedium of Scientific Linacs, LINAC'96, 1996;
[4] F.B. Kroes et al., Improvement of the 400 kV Linac Electron Source of AMPS, Proc.of EPAC'92, p.1032;
[5] T. Tomimasu, Y. Morii, E. Oshita et al., NIM A 407 (1998) 370

DEVELOPMENT OF A C-BAND ACCELERATING MODULE FOR SUPERKEKB

S. Ohsawa, T. Kamitani, T. Sugimura, K. Kakihara, M. Ikeda, T. Oogoe,

S. Yamaguchi, and K. Yokoyama

High Energy Accelerator Research Organization, KEK, 1-1, Oho, Tsukuba, Ibaraki, Japan

Abstract

A C-band accelerating module has been constructed in KEKB/PF linac, and beam acceleration tests have been performed during 10-month operation. The purpose is to investigate C-band feasibility and stability of acceleration in the region beyond 40MV/m. The C-band accelerating module is expected to be promising for accelerating positrons up to 8GeV instead of 3.5GeV for both of the present KEK B-factory and SuperKEKB project in order to upgrade the luminosity. Last summer a 1m-long C-band accelerating section installed in the KEKB/PF linac. Accelerating field corresponding to 41 MV/m was successfully achieved in October in a beam test. Present status of C-band accelerator development is reported.

INTRODUCTION

The KEK-B factory is making highest luminosities ($>1.3\times10^{34}$ $cm^{-1}s^{-1}$) in the world, where 3.5-GeV electrons and 8-GeV positrons are colliding. Toward higher luminosities a future project SuperKEKB is under consideration, of which target luminosities arise in the order of 1-5 $\times10^{35}$ $cm^{-1}s^{-1}$ [1]. In order to put into practice such a high goal, requirements to the injector linac should inevitably become severe for all values such as beam intensities, energies and emittances etc., as are listed in table 1. Some schemes of linac upgrade have been considered what should be improved to meet the requirements as well as possibility and feasibility, and consideration is still going on.

Table 1: Upgrade requirements

		KEKB	SuperKEKB
Beam energy	e+	3.5 GeV	8.0 GeV
	e-	8.0 GeV	3.5 GeV
Stored current	e+	2.6 A	4.1 A
	e-	1.1 A	9.4 A
Linac beam	e+	0.6 nC x 2	1.2 nC x 2
	e-	1.0 nC x 1	2.5 nC x 2
Smaller emittance to fit IR&C-band structure aperture			
Faster e+/e- mode switching for continuous injection			

Among the requirements, there has been a subject useful not only SuperKEKB but also for the KEKB. It is a plan to exchange energies of electrons and positrons: positrons become 8GeV instead of 3.5GeV, and electrons become 3.5GeV from 8GeV. The purpose is to avoid positron instability in the ring due to electron cloud, of which influence depends on the positron energy: higher the energy, smaller the effect. Therefore 8GeV positrons would be useful and desirable also for the KEKB instead of the present energy 3.5GeV. The requirement and importance of the beam seem to be growing, especially so under the present status in which beam intensities are still kept rising in both KEKB rings to increase luminosity.

Then exchange of energies would be more urgent issue that should be realized quickly, if possible, before the SuperKEKB project starts. It would have an important role to escape the influence of the electron cloud effect on positrons. Our strategy to get 8GeV positrons is basically simple [2].

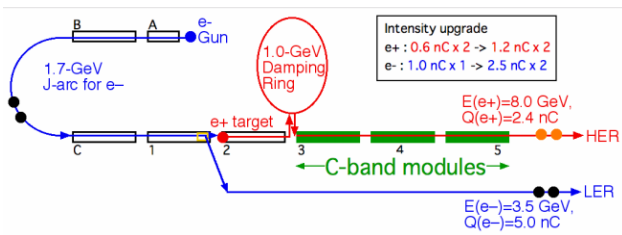

Figure 1: Layout of an upgrade scheme of the KEKB/PF linac

Presently positrons are produced at a production target which is installed halfway of the KEKB/PF linac, as is shown in Fig.1, and then accelerated up to 3.5 GeV in the following half of the linac. The most simple and feasible way to get 8-GeV positrons would be increasing the accelerating fields in the second half of the linac. This scheme is direct method and does not request any new buildings; however, the accelerating field strengths should be increased double from the present value of 21MV/m to 42 MV/m. How can we realise such a high accelerating field, that is the question to be solved. It is obvious that such a high field could not be obtained without increasing

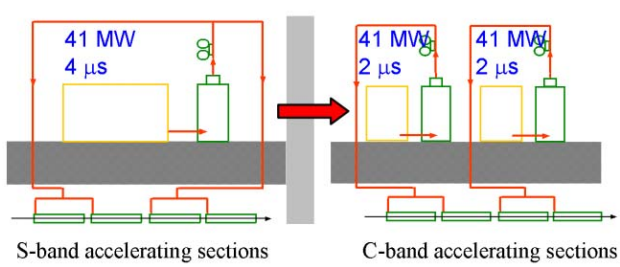

Figure 2: Layouts are showing how to replace accelerating modules from S-band to C-band.

satoshi.ohsawa@kek.jp

the accelerating frequency of S-band. Otherwise RF power of four times higher than the present value 41MW would be necessary. That would be impossible due to lack of powers of electricity and cooling water, and lack of space for the extra klystrons and modulators in the klystron gallery.

The only way we can take seems to be introducing a higher accelerating frequency instead of S-band. From the practical points of view, the frequency was automatically decided on C-band (5712MHz), of which accelerating structures could be expected to give apertures large enough for accelerating positrons with large emittances, at least, at high energy region. Furthermore a C-band klystron has been fortunately already developed, and is commercially available.

In order to achieve the average accelerating field of 42MV/m, it is not enough merely to replace accelerating structures to C-band ones, but also necessary to double the RF powers for each accelerating section This means that one accelerating module with a S-band klystron should be replaced, for instance as is shown in Fig. 2, with two C-band modules, each of which has a C-band klystron.

Outline of our energy upgrade is shown in Table 2: in the second half of the linac after the positron production target, most of the S-band Accelerating modules should be replaced by C-band ones, except for the beginning part following the target, where the positron beam emittance is still so large that the beam size is not small enough for accelerating in the C-band structures.

Table 2: Energy upgrade scheme with C-band accelerating sections

	S-band section	C-band section	e+ energy gain
Acc. field	21 MV/m	42 MV/m	-
Present	231 m	0	4.8 GeV
upgrade	46 m	185 m	8.0 GeV

DEVELOPMENT OF C-BAND MODULE

We decided in 2002 to start investigation of C-band accelerating structures how would be operational stability and reliability at accelerating fields as high as 42MV/m for both of KEKB and SuperKEKB. We started developing from April 2002 a C-band accelerating module to fine difficulties, if any, as quick as possible.

Although almost of all elements necessary for the C-band module should had been designed from the beginning except for the klystron, until July 2003 minimum elements, such as those listed in Table 3, had been prepared for making an acceleration test except for an RF pulse compressor [3]. Then after confirming high power performances in the test stand, we installed them in the KEKB/PF linac at the #44 unit where was empty and ready for C-band. The relevant main items that have been developed for C-band are listed in Table 3 with maximum values achieved in high power test operations. Most of the values exceeded successfully specifications.

Table 3: C-band R&D main items and maximum values achieved in test operations.

Klystron E3746	43MW, 2μs, 50pps
Compact Modulator (1/3size)	45kV, 2μs, 50pps
Sub-booster	400W, 2μs, 50pps
RF window	300MW, 2μs, 50pps
Accelerating section	41MV/m, 0.5μs, 50pps
Dummy load	100MW, 0.5μs, 50pps
3-dB hybrid power divider	200MW, 0.5μs, 50pps
Wave guide flange	200MW, 0.5μs, 50pps
Pulse compressor, SKIP	200MW, 0.5μs, 50pps

Accelerating Section

A first prototype accelerating section of C-band was designed basically as a half size of the present 2-meter long S-band section that is used in the KEKB/PF linac [4]. Therefore it is 1m long with a quasi-constant field gradient. By comparing with S-band values, we could determine with confidence precise sizes of each cavity from a few test cavities

After RF processing of totally 300 hours, which was performed at the test stand with 0.5 μs RF pulses, the acceleration field reached to the level of 41.8 MV/m. Then the C-band accelerating section had been installed in the KEKB/PF linac in September 2003. RF power from a C-band klystron fed into a single 1m-long section during the first 10-month operation without a pulse compressor, which was still under investigation last year, but installed recently August 2004 [5].

After the 10-month operation at 50 pps with 0.5 μs RF, we opened and directly observed the couplers and aperture disks August 2004, and found that the input-coupler iris was discoloured at peripherals and there were many discharge spots especially at the aperture corner of the first disk. This observation is consistent with other measurements such as analyses using the reflection and transmission waves or acoustic sensors. It is obvious that the iris is the main source of discharges. In the second prototype accelerating section, the coupler structure will be changed so that it will have a thicker and wider iris without sharp edges in order to avoid discharge due to RF heating.

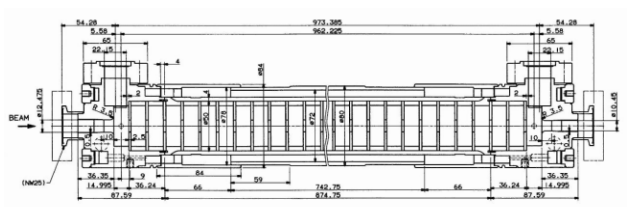

Figure 3: The first prototype 1m-long C-band accelerating structure.

Dummy Load

A dummy load was developed for C-band based on the S-band one which is used in the KEKB/PF linac. The dummy load that consists of 13 pairs of SiC buttons have been tested up to 100 MW peak and 2 kW average powers.

Figure 4: Photograph of a dummy load for C-band.

First Acceleration Test

During 10-month operation, the accelerating field strengths of the C-band section have been measured by analysing beam-energy gains as a function of the accelerating phase. A field gradient of 41.2 MV/m was achieved with the klystron output power of 43.8MW, which was almost our goal.

Figure 5: The first prototype 1m-long accelerating section installed in the beam line of the KEKB/PF linac.

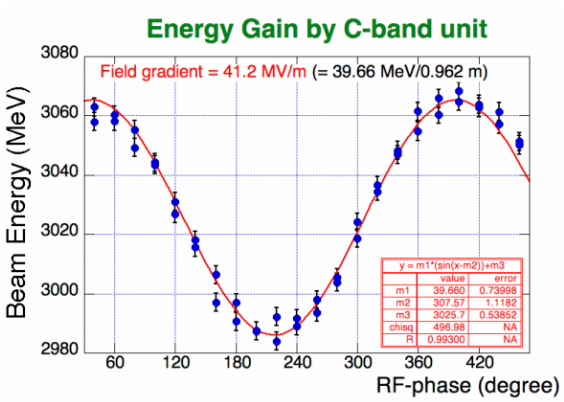

Figure 6: A result of beam acceleration.

Pulse Compressor（SKIP）

We have manufactured this year a C-band pulse compressor "SKIP", which stands for SuperKEKB Injector Pulse Compressor. After 170-hour RF processing, the peak output power attained 200 MW at a repetition rate of 50 pps for 43 MW input. SKIP has been installed in the C-band module in the linac for long time operation with beam acceleration.

Although SLED-type RF pulse compressors are used in the KEKB/PF linac, we adopted a different mode cavity for the C-band pulse compressor [5]. That is TE_{038}-mode used in the LIPS [6], because a Q factor much higher than100,000 is necessary to achieve the same field-multiplication factor as the S-band pulse compressors. This requirement comes from a difference of RF pulse lengths: C-band RF pulses have a half-length of the S-band. Although SKIP has many more nodes in the cavities than SLED, the C-band wavelength is half of S-band one. Therefore Mechanical sizes of SKIP become about the same as the S-band SLED.

Table 4: Comparison between KEKB-SLED and C-band SKIP

	KEKB-SLED	C-band SKIP
Frequency	2856 MHz	5712 MHz
RF pulse length	4.0 μs	2.0 μs
Resonance mode	TE_{015}	TE_{038}
Length	33.59 cm	30.72 cm
Cavity diameter	20.51 cm	23.28 cm
Q value (Q_o)	90,000	130,000
Coupling	6.4	6.6

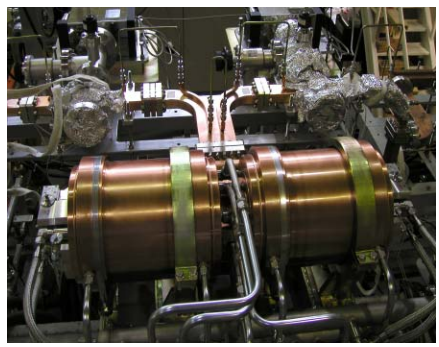

Figure 7: Photograph of SKIP at test stand.

ACKNOWLEDGEMENT

The authors would like to give their sincere thanks to all staff members of KEKB/PF linac and Mitsubishi Heavy Industries, LTD for their powerful cooperation.

REFERENCES

[1] J. W. Flanagan, Y. Ohnishi, et al., Letter of Intent for KEK Super B Factory, Part III: Accelerator Design, KEK Report 04-4
[2] T. Kamitani, EPAC2002, Paris, p.1088.
[3] S. Michizono, et al., "KEKB Injector Linac and Upgrade for SuperKEKB", this conference.
[4] T. Kamitani, et al., "Development of C-band accelerating section for SuperKEKB", this conference.
[5] T. Sugimura, et al., "SKIP- a Pulse Compressor for SuperKEKB ", this conference.
[6] A. Fiebig, et al., CERN/PS 87-45(RF) March, 1987.

INJECTOR LINAC UPGRADE FOR THE BEPCII PROJECT

Shu-Hong Wang† for BEPCII-Linac Group
Institute of High Energy Physics, IHEP, Beijing, P. O. Box 918, 100039, China

Abstract

BEPCII- an upgrade project of Beijing Electron Positron Collider (BEPC) is a factory type of e+e- collider. It requires its injector linac to have a higher beam energy (1.89 GeV) for on-energy injection and a higher beam current (40 mA e+ beam) for a higher injection rate (≥50 mA/min.). The low beam emittance (1.6πmm-mrad for e+ beam, and 0.2πmm-mrad for 300 mA e- beam) and low beam energy spread (±0.5%) are also required to meet the storage ring acceptance [1]. Hence the original BEPC injector linac must be upgraded to have a new electron gun with its complete tuning system, a new positron source with a flux concentrator, a new RF power system with its phasing loops and a new beam tuning system with orbit correction and optics tuning devices. These new components have been designed, fabricated, tested and now being installed in their final positions, which are described in this paper. The beam commissioning is expected to start from October of 2004.

INTRODUCTION

BEPCII is an upgrade project of Beijing Electron Positron Collider with a high luminosity of $1\times10^{33}\,cm^{-2}s^{-1}$ in the Tau-Charm energy region (2-5 GeV) in the centre of mass. The full energy injection with a high injection rate of > 50 mA/min (ten times of present value) for the e+ beam requires the original BEPC injector linac to be upgraded with its higher performances as listed in the Table 1.

Table 1: Beam Parameters of the BEPCII-Linac

	Unit	e- beam	e+ beam
Beam Energy	GeV	1.89	1.89
Beam Current	mA	~ 40	~ 300
Beam emittance	πmm-mrad	1.60	0.20
Energy spread	%	0.50	0.50
Injection rate	mA / min	> 50	> 300
Pulse repet. rate	Hz	50	50
Beam pulse length	ns	1.0	1.0

To meet these specifications, we need a new electron gun with its complete tuning system, a new positron source with a flux concentrator, a new RF power system with its phasing loop and a beam tuning system with the orbit correction and optics tuning. These new components have been designed, fabricated and now being installed in their final positions.

ELECTRON GUN SYSTEM

In order to increase the positron current as well as the injection rate, a new electron gun that can emit higher current is needed. A thermionic triode gun with a cathode-grid assembly of Y796 is employed with the gun beam parameters of 10 A, 1 ns, 10 nC, 150-200 keV and 50 Hz. The computed province is 0.22 μP. At the end port the beam radius is about 6.0 mm, and the emittance is 17.6 mm·mrad. The beam trajectories present that the current density is relatively uniform, which indicate a good beam performance. A Kentech pulser is employed which can be operated at 1ns of either one pulse or two pulses separated by about 56 ns for the two-bunch operation. Between the gun exit and the prebuncher, there are two focusing lens, two steering coils and two BPMs, and a profile monitor for having a well beam alignment and tuning, as shown in the Figure 1.

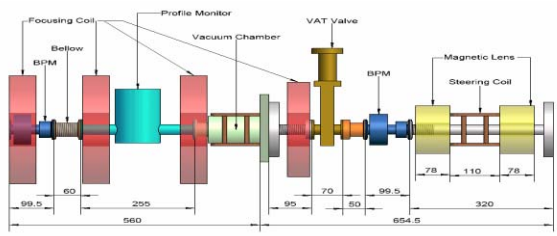

Figure 1: Components downstream the electron gun.

POSITRON SOURCE SYSTEM

A 250 MeV and 6 A primary electron beam at the e+ production target is designed. To have a maximum e+ yield, a tungsten target thickness is optimized at 8 mm and a primary e- beam spot size of 1.0 - 1.5 mm on the target is expected by the beam modeling. A flux concentrator (FC) of 10 cm long is employed to provide a maximum transverse acceptance of 0.31π (MeV/c)-cm, which provides the pulsed longitudinal magnet field of 5.3 T and 0.5 T at the input and output of the FC, respectively, with a 12 kA pulsed power supply. In the downstream FC, there is a 7.5 m long, 0.5 T, DC-solenoid to further focus the e+ beam and matches the beam into the downstream quadrupole focusing system. In addition to the available 15 triplet quads, 24 big aperture quads installed on the downstream accelerating structures will be employed to strongly focus the large emittance e+ beam. In order to bunch the beam longitudinally, the e+ beam is decelerated in the first 1 m of the structure just downstream the FC, and then to be soon accelerated with a high gradient so that the most of the positrons are bunched into a phase spread of $\pm5^0$ at the DC solenoid exit with the positron yield of 4.3%(e+/e-.GeV)[2]. The 8 accelerating structures of 3 meters long each in the e+ production system will be replaced by the new ones in order to have high stability and reliability in high gradient

† wangsh@sun.ihep.ac.cn

operation since some of these structures were a little damaged in the past operation.

All the components of the new positron source have been fabricated, inspected, pre-assembled and vacuum tested. A 12 kA pulsed power supply has been built and been operated with the existing e+ converter. It works well as expected. The flux concentrator has its inductance of 0.95μH, and a measured mechanic resonance frequency of 37 Hz as simulation predicted. The magnetic fields of the FC and DC solenoid have been well measured. The following pictures show the FC and the positron converter chamber.

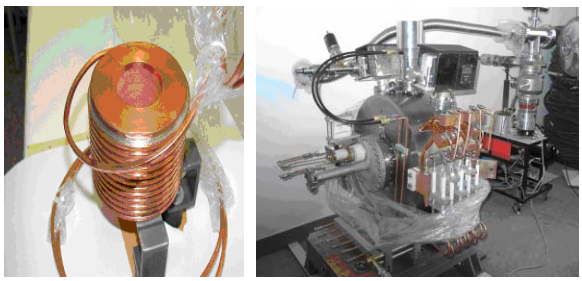

Figure 2: FC (left) and Positron converter chamber (right).

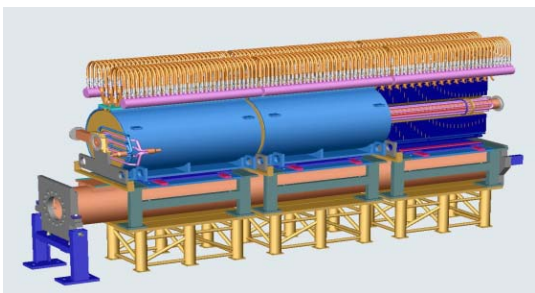

Figure 3: Positron focusing and accelerating system.

RF POWER SUPPLY SYSTEM

There are 16 klystron units in the linac. Downstream the positron target, there are 12 regular acceleration sections i.e. one klystron drives 4 SLAC type acceleration structure with a SLED. To increase the e+ energy from present 1.3 GeV to 1.89 GeV and to increase the primary e- beam energy for a higher e+ yield, the RF power system must to be upgrade to have higher power output and higher stability. 50 MW klystrons are needed to replace the original 30 MW HK-1 klystrons. All the 16 modulators will be rebuilt for 50 pps, 360 A beam current and 320 kV beam voltage with a target stability of ±0.1% provided by a De-Qing system. The pulse waveform of the new modulator is as shown in Figure 4. In the total 16 klystrons, there are two TH-2128C (45 MW), two SLAC-5045 (65 MW) and twelve E-3730A (50 MW). A new klystron test stand has been built, and two new klystrons /modulators have been put into operation already.

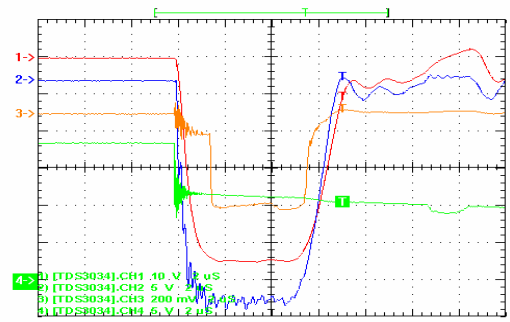

Figure 4: The modulator's pulse waveform 1) Beam voltage, 2) Beam current, 3) RF output.

PHASE CONTROL SYSTEM

A phase control system is being developed with the following measures. The maximum energy method is adopt to define the optimum phase, which appears preferable to the beam loading and beam induced methods.

A PAD system of I/Q demodulator type is used to monitor the phase with accuracy of 0.2^{o} and amplitude. The new IϕA. units have been developed with its minimum insertion loss of 2 dB, maximum decay of 20 dB and phasing range of > 360^{o}. A reference line of the phase stabilized co-axial type is used for its easy maintenance and cheaper than the optical type. The existing co-axial driving line can be further used by controlling the cooling water temperature within $\pm 0.1^{o}$C.

A master oscillator with high stability of phase and output power is demanded. To have the effective phasing system development, many measured data have been taken in the existing RF system, including the phase variation with the temperature, with the EM noise, etc. A prototype of the phase control system was made for the 1st RF unit, and a very good experimental result of this control unit has been obtained with the phase control within $\pm 2^{o}$ as shown in the Figure 5. The Figures 6 shows the BEPCII-Linac phasing system and its constitutions.

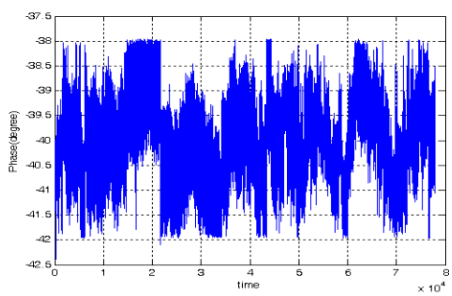

Figure 5: Phase control result with the prototype unit.

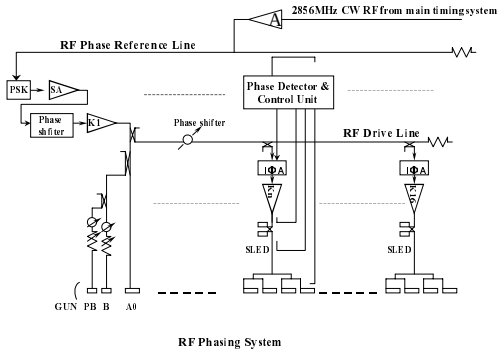

Figure 6: RF Phasing System.

BEAM MODELING

Positron beam simulations. With TRASPORT, EGS4, PARMELA and LIAR codes, the e+ beam performance at the production target and transportation in the linac are simulated. Table 2 shows that about 40 mA e+ with specified emittance and energy spread is expected. The 24 large aperture quads "riding" on the acceleration structures are needed to improve the transmission for the larger emittance positrons out of focusing solenoid. Beam initial offset of 0.3 mm, and 0.2 mm misalignment of the RF structures and quads are taken into account The orbit correction provided by 19 Strip-line BPMs and 19 sets of correctors is needed to meet the design goal of the beam performance.

Table 2: Simulation results for the e+ beam

Posit.	Ener. (MeV)	Curr. (mA)	Emitt. (m.rad)	ΔE/E (%)	Phase Spr. (o)	e^+ Yield (e^+/e^- .GeV)
Target	1 -14	80	3.08E-3	---	---	5.58%
Solen. exit	89.45	53	29.2E-6	±8.6	±16	3.67%
Linac -end	1890	42	1.42E-6	±0.5	±5.0	2.92%

Electron beam simulations. With EGUN, TRANSPORT, PARMELA and LIAR codes, the electron beam performances are simulated and are listed in Table 3 and Table 4. The 1.89GeV electron beam with small emittance and energy spread is not a problem, but the primary electron beam size on the converter target is an important issue because it's very sensitive to the positron yield. A beam size of less than 1.5 mm is expected, and the confinement mainly comes from the quads chromaticity due to the low energy (250 MeV) and large energy spread caused by the bunching. The other contributions come from the dispersive and wakefield effects due to the initial beam offset and machine misalignments. The orbit correction is needed to meet the design goal of the beam performance.

Table 3: Simulation results for the e- beam

Position	Energy (MeV)	Curr. (A)	Emitt. (m-rad)	ΔE/E (%)	Phase Spread (o)
Gun exit	0.150	1.5	42.5E-6	---	±180
Pre-injector	39	1.0	4.14 E-6	±1.5%	±5
Linac -end	1890	0.6	0.18 E-6	±0.5 %	±5

Table 4: Simulation results for the primary e- beam at the target

Position	Energy (MeV)	Current (A)	Emittance (m-rad)	Beam radius (mm)
Gun exit	0.150	10.0	17.1E-6	6.5
Pre-injector	40	6.5	2.79E-6	3.4
On target	1890	6.0	0.75 E-6	1.5

SUMMARY

1) A new electron gun, a new positron source, a new RF power system with phasing loops, 8 new acceleration sections and some modified RF components for the BEPCII injector linac upgrade are designed, fabricated, tested and being installed in their final positions. A new electron and positron beam from this linac is expected by this fall.

2) By controlling the phasing error within $\pm 2^0$, Quads /BPM/structure's alignment error within ±0.2 mm, and modulator's voltage jitter within ±0.1%, the beam performance at the linac exit can meet the design goal with the aid of orbit correction system[3].

REFERENCES

[1] G.X. Pei et al., Design Report of the BEPCII Injector Linac, IHEP-BEPCII-SB-03-02, November 2003.
[2] W.P. Gou, The Physical Design of the BEPCII Positron Source, IHEP, April 2001.
[3] S.H. Wang, P.D. Gu, et al, High Energy Phys.and Nucl. Phys., 2003, **27** (2):173.

THE RESEARCH OF A NOVEL SW ACCELERATING STRUCTURE WITH SMALL BEAM SPOT

Xingfan Yang, Zhou Xu, Xiao Jin, Ming Li, Hao Chen, Yanan Chen, Heping Lu

CAEP,P.R.China

Abstract

A new kind of on-axis coupled biperiodic standing-wave (SW) accelerating structure has been built for a 9MeV accelerator. The research progress was introduced in this paper; it includes the choice of the accelerating structure, the analysis of electron beam dynamics, the tuning of the cavity, the measurement of the accelerating tube and the powered test. The small beam spot is the most interesting feature of this accelerating structure, the diameter of the beam spot is 1.4mm.This accelerator has been used for the x photons generation and the x-ray dose rate is about 3400rad/min/m.

INTRODUCTION

The high energy industrial computed tomography (ICT) which uses accelerator as the driving source has important applications in the fields of aerospace, non-destructive inspection, precise machining etc, the result of the ICT was determined by the performance of the accelerator which used for the generation of x photons, so the accelerating structure with small beam spot is the key of obtaining high space solution and density solution. Usually in order to increasing the transit-time factor and so the effective shunt impedance, nose cone was set in the accelerating cells[1], but the transverse electric field was increased at the same time, so in order to decreasing the beam spot ,we attempt to take out of the nose of the accelerating cell .

DESIGN OF THE ACCELERATING STRUCTURE

This accelerating structure was an on-axis coupled biperiodic SW structure and was made of 11 accelerating cells and 10 coupling cells, illustrated in Figure 1.

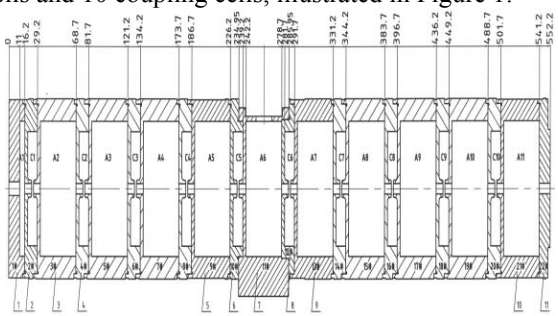

Figure 1: The accelerating tube

There are no nose cones in the accelerating cells and in order to making the electric field cutting off, the nose cones were set in the coupling cell. Adjacent cells are coupled magnetically, through slots cut in the outer walls and so the accelerating structure is a resonant system. In order to decreasing the secondary coupling. The SUPERFISH code was used in the design and optimised of the cavity; the distribution, the stored energy and the power dissipation of the wall were calculated. The electric field in the cells were illustrated in Figure 2 and electric field on the axis was illustrated in Figure 3.

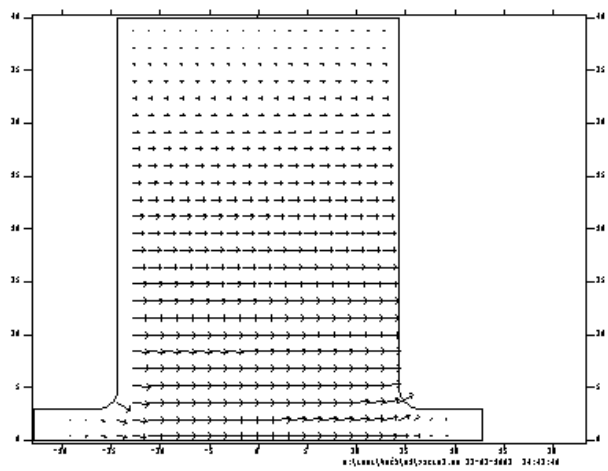

Figure 2: The electric field in the cell

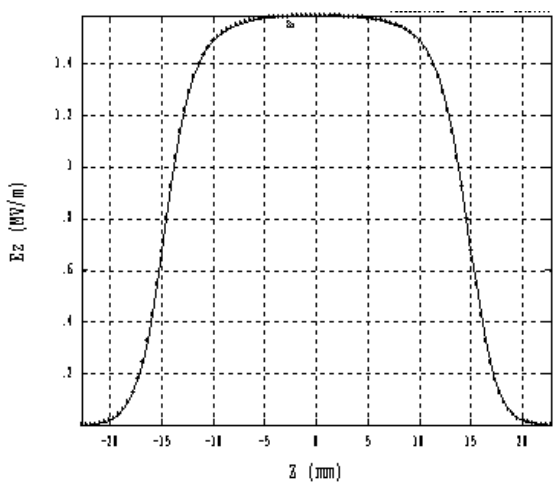

Figure 3: The on-axis electric field

There are no nose cone in the accelerating cells, this makes the longitudinal electric field much smooth, and

the transverse electric field was depressed, so the transverse defocusing forces is small, it contributes to obtain a small beam spot. The GPT code was used to analysis the behavior of the electron beam in the accelerating tube and several designs were check in order to get an small beam spot. It can getting a better transverse focusing by adjusting the ration of electric field in the first cell and the second cell, when optimising the ratio of the electric field to 1：2.3：2.5, the small beam spot was obtained, the diameter of the beam spot is about 1.0mm(FWHM) at the end of the accelerating tube without the external focusing, and it satisfied our need. Figure 4 shows the electrons trajectory. Figure 5 shows the electrons transverse distribution on the target. Figure 6 shows the electrons distribution at the exit of the accelerating tube.

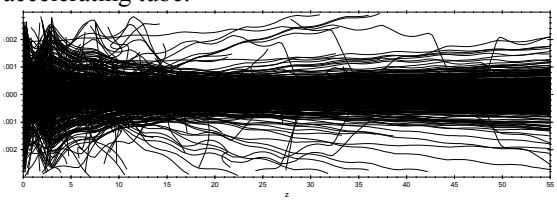

Figure 4: The trajectory of electrons

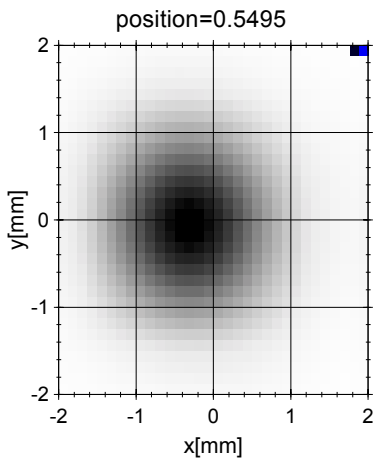

Figure 5: The transverse distribution of electrons

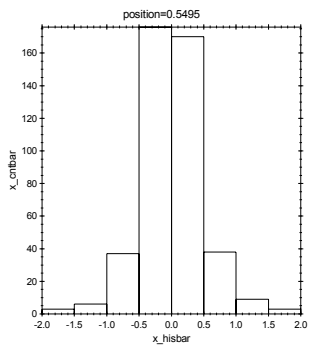

Figure 6: The relation of electrons and beam spot

THE TUNING OF THE ACCELERATING STRUCTURE

The vector net analyzer was used to measure the resonant frequency, the quality factor, and the electric field distribution. The tuning of the accelerating tube was finished by regulating the resonant frequency of each cell in the chain carefully. The adjacent coupling constant was calculated, it is about 1.8%. The secondary coupling factor was depressed by optimising arranged the cell. The jointing and cool measurement were done. The frequency of the π/2 mode is 2856MHz, the coupling factor of microwave source-to-accelerating tube is 1.3. Dispersion relation of the accelerating structure was illustrated in Figure7. The ratio of the electric field illustrated in Figure8 adjusts to 1：2.3：2.5 to satisfy the simulation condition. Figure9 is the jointed accelerating tube.

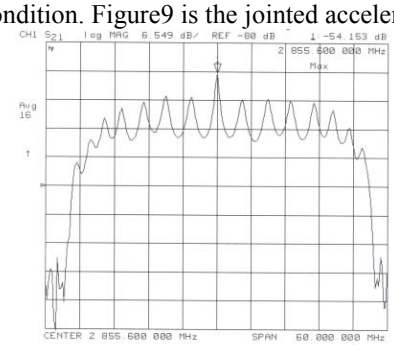

Figure 7: The dispersion relation of the tube

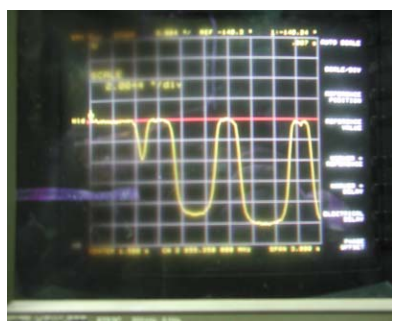

Figure 8: The electric field of the first three cells

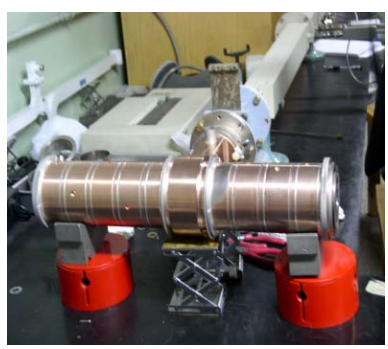

Figure 9: The accelerating tube

THE EXPERIMENT OF THE ACCELERATOR

The conditions of the accelerator experiment are: microwave power is about 7.5MW,the injected current from the electron gun is 500mA and the electron energy is 20keV. The energy of the electron at the end of the accelerating tube is 9MeV. The beam spot was measured carefully; the diameter of the beam spot is about 1.4mm(FWHM). This accelerator has been used for the x photons generation and the x-ray dose rate is about 3400rad/min/m. The 3D CT space solution is 2.5line pairs/mm, density solution is about 5‰.

SUMMARY

We use no-nose cone cells as accelerating structure, this makes the longitudinal electric field much flat, and the transverse electric field was depressed, so the transverse defocusing forces is small, it is one way of obtaining small beam spot.

REFERENCES

[1] T.P.Wangler,Principles of RF Linear Accelerators,1998

PRELIMINARY STUDY ON HOM-BASED BEAM ALIGNMENT IN THE TESLA TEST FACILITY

N. Baboi, G. Kreps, M. Wendt, DESY, Hamburg
G. Devanz, O. Napoly, R.G. Paparella, CEA/Saclay, DSM/DAPNIA, Gif-sur-Yvette

Abstract

The interaction of the beam with the higher order modes (HOM) in the TESLA cavities has been studied in the past at the TESLA Test Facility (TTF) in order to determine whether the modes with the highest loss factor are sufficiently damped. The same modes can be used actively for beam alignment. At TTF2 a first study on the beam alignment based on the HOM signals has been made in the first cryo-module, containing 8 accelerating cavities. Four modes with highest R/Q in the first two cavities have been monitored. One bunch has been usually used. The cavity center could be found for each of the modes. The results are presented in this paper.

INTRODUCTION

The TESLA Test Facility – phase 2 (TTF2) [1] at DESY is equipped with various monitors: beam position monitors, beam loss monitors, screens, wire scanner etc. However difficulties have been encountered to align the beam over long sections of the linac constituted by the cryo-modules. These contain eight 9-cell superconducting accelerating cavities, which are cooled together to about 2K. Each cavity is about 1 m long. Beam alignment in the cavities is important in order to avoid transverse kicks on the beam from higher-order modes (HOM), which may lead both to a single-bunch deformation and to beam break-up along the bunch train.

These monitor-free long sections can be filled by the signals from the HOM couplers. Such couplers are placed at either side of each cavity in order to extract energy from the fields excited by charged particles and hence damp the higher-order modes. In the past, signals from the HOM couplers have been used to study the modes, and to find out if the damping is sufficient for the dipole modes with high R/Q, i.e. good coupling to an off-axis beam [2]. The same HOM signals can be used to monitor the offset of the beam with respect to the cavity axis [3], since their amplitude is proportional to it. To improve the alignment tolerances for both the collider and the FEL applications of TTF superconducting modules, this beam-based method should achieve a positioning resolution significantly better than 500 µm obtained by the cavity mechanical alignments.

First studies on the possibility to align the beam in the cavities have been made. The amplitude of the fields excited by the beam at several resonances in the first two cavities of the first TTF module has been measured as a function of the beam position. In this paper the measurements are described and the results are discussed.

THE METHOD

Setup

Fig. 1 shows schematically the first part of the TTF2 injector in the first phase of commissioning. A gun accelerates the electrons emitted by a photo-cathode to 4.5 MeV. A horizontal and a vertical steerer can deflect the beam, correcting for possible errors in the transverse and angular alignment of the gun. Eight cavities in module ACC1 accelerate the beam with a gradient of 12 MV/m.

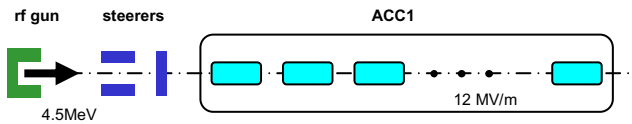

Figure 1: Schematic view of the alignment setup

The frequency spectrum of the wake fields excited by the beam is monitored with a spectrum analyzer. The spectrum of each cavity consists of resonant modes grouped in passbands by the type of the mode. There are 9 modes in each passband, and for the case of dipole modes there are 2 polarizations for each mode.

Fig. 2 shows such a spectrum for one mode of the first dipole passband of the first cavity. The two polarizations can be distinguished and their quality factors Q, of about $9.3 \cdot 10^3$ and $2.4 \cdot 10^4$, have been measured a priori with a network analyzer. This mode is one with highest R/Q. Four modes with highest R/Q have been used. Their frequencies and R/Q as predicted from simulations for an ideal TESLA cavity are shown in Table 1.

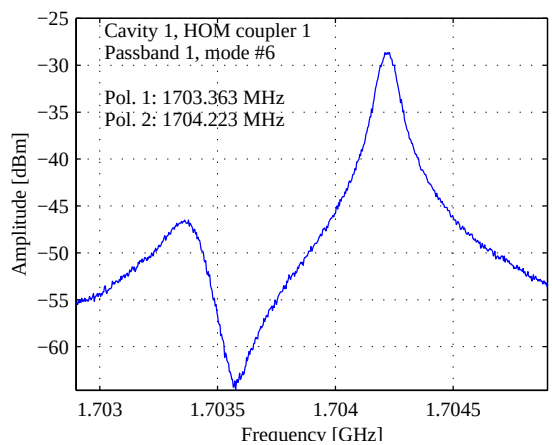

Figure 2: Mode #6 of the first dipole passband in cavity 1 of ACC1

Table 1: Dipole modes with highest R/Q used for beam monitoring as predicted by simulations

Dipole passband	Mode #	Frequency (simulation) [MHz]	R/Q [MΩ/m^2]
1 (TE-like)	6	1713.7	11.21
	7	1738.3	15.51
2 (TM-like)	4	1864.7	6.54
	5	1872.7	8.69

Principle

By the help of the horizontal and vertical steerers, the beam position in the cavity studied could be varied. The beam position with respect to the case of un-deflected beam (i.e. all steerers between the gun and the module are off) was calculated based on the steerer calibration and the transfer matrix from the steerer to the middle of the cavity. Notice that the effect of the beam angle with respect to the cavity axis was ignored in this experiment. It will be further studied and our analysis refined when two additional steerers are installed in the TTF2 injector.

A simple method to find the axis of a mode in a cavity is to monitor the integral power of a mode as a function of the 2D position of the beam. The spectrum analyzer provides a convenient filter, with variable bandwidth, but especially with variable frequency. Since the spectra take a long time to record, due to the low repetition frequency of the beam of 1 Hz, one can monitor the signal amplitude in time domain. A faster method is described below and has been adopted for our first measurements.

Each polarization of a dipole mode has a transverse symmetry axis. When the beam is somewhere on this axis, that particular polarization is not excited, and transverse deflections along this axis will not be seen. In this case the corresponding peak in Fig. 2 will disappear. In exchange, when moving the beam on the perpendicular direction, the amplitude of the HOM peak will change linearly with the beam offset with respect to the mode axis. In this way one can use one polarization to monitor movement in one direction and the other for the orthogonal direction.

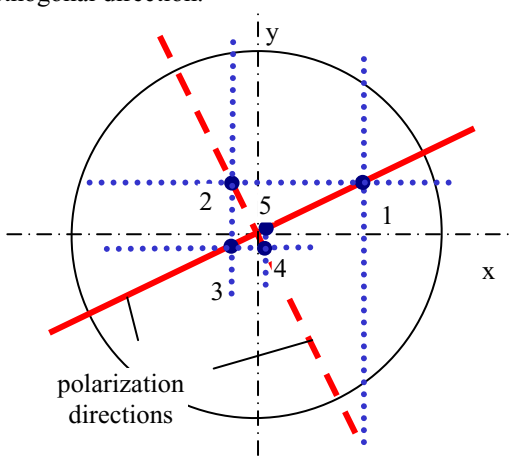

Figure 3: Alternate horizontal and vertical beam position scans for a mode with oblique polarization axes.

In reality the two polarizations have an arbitrary axis, randomly oriented with respect to the horizontal plane. When steering the beam position in the horizontal and vertical planes we have chosen the modes responding best to changes in each plane. Then we have made one scan say in the horizontal plane with one polarization until we found a point on the symmetry axis of the mode, followed by another scan in the vertical plane monitoring the other polarization until finding the minimum. Then by iterating alternate scans one approaches the electrical center of the mode, as illustrated in Fig. 3.

MEASUREMENTS AND RESULTS

The time domain signals for one scan in the horizontal plane for the second polarization of mode #6 (second peak in Fig. 2) of the first passband of cavity 1 are shown in Fig. 4. A filter bandwidth of 300 kHz was used. The vertical position of the beam was 0.45 mm, with respect to the un-deflected position. One bunch per beam, of about 1 nC, was used.

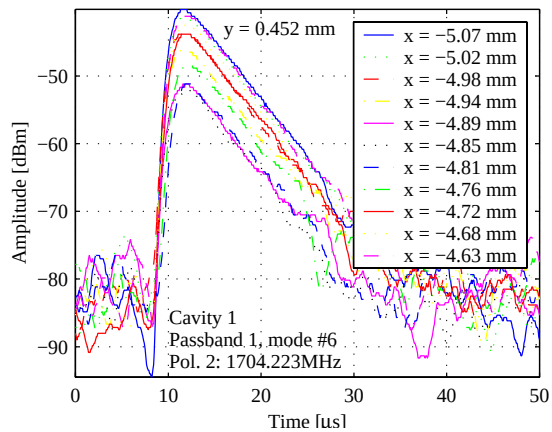

Figure 4: Time domain signals for the first polarization of the 6th mode of the 1st dipole band of the first cavity.

The HOM signal builds up rapidly after the bunch passes the cavity, at about 8 μs in the plot. Then the amplitude of the signal decays with a rate given by the quality factor of the mode. The variation of the signal amplitude with the beam position can be observed. The signal is minimized when the beam is on the axis of the mode. The amplitude is not zero in this case because of contributions from the other polarization and probably of an angle in the beam trajectory.

The amplitude of the signal in linear scale as a function of the beam position is presented in Fig. 5. Several scans have been made in the horizontal and vertical planes using alternatively the two polarizations. The beam position for minimum HOM amplitude is determined and its value is then used for the next scan. In the plots, the data is fitted by straight lines and the values inferred from the fits slightly deviate from the values determined during the measurements without using a fit. Note that for this mode four scans were sufficient to find the cavity axis. This was the case for all 4 modes measured in cavity 1, while for cavity 2 in general more scans were necessary. This can be explained by the fact that, for the modes studied in cavity 1 the polarization axes are close to horizontal and vertical, as corroborated by the observation

that the two resonance peaks shown in Fig. 1 are well decoupled when large horizontal and vertical beam offsets are imposed. This is not the case for the modes of cavity 2 where the polarization axes are oblique and more scans are therefore needed to converge towards the mode center. We believe that this difference between the two cavities is due to deformations in the cavity.

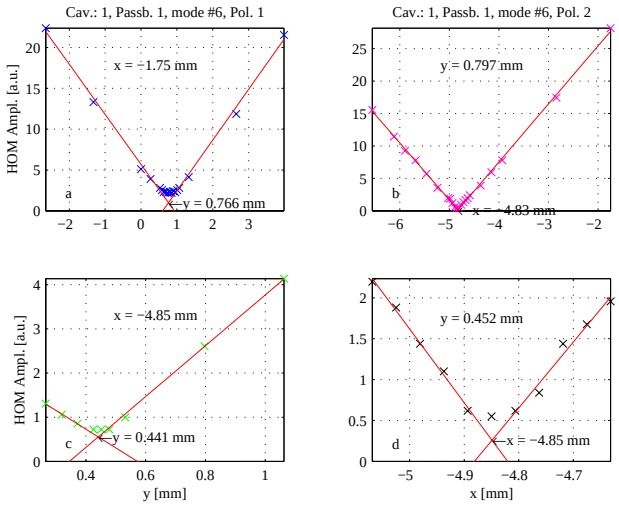

Figure 5: HOM signal amplitudes for each polarization of mode #6 of the first passband of cavity 1 as a function of the beam position.

It is remarkable that if the steerers between the gun and the module are switched off, the beam has a large horizontal offset in cavity 1. This seems to show that there is either a large offset of this cavity with respect to the gun axis, or that the gun components are not well aligned, shooting the beam at a rather large angle. This fact will be further analyzed in the next TTF2 run.

Beam position resolution and HOM centers

In the central regions of the scans, steps of about 50 µm in horizontal and vertical beam displacements have been used for both cavities and all modes. With a HOM amplitude signal resolution of 1 dBm, the effect of these steps could be clearly observed even at the minimum as illustrated in Fig. 4. Such a resolution on the beam position is also inferred from the fit accuracy and by comparing the center positions given by the minimum of the signal or by the fitting procedure.

However, the electric centers of the dipole modes do not coincide with such a fine resolution since they are essentially set by the relative cell to cell displacements and by their field distributions in the cavity. Fig. 6 compares the relative positions of the 9 cell geometric centers with the electric centers of the 4 dipole modes, by arbitrarily superposing their two barycenters. The mode centers differ by 100 µm or less in both planes. Clearly more experimental data as well as theoretical investigations of the electromagnetic properties of cavities with realistic geometries and cell eccentricities are needed.

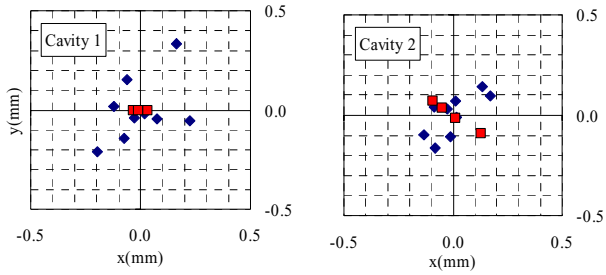

Figure 6: Relative positions of the 9 cell centers (blue diamonds) and of the 4 dipole mode centers (red squares).

CONCLUSIONS

The preliminary measurements presented in this paper show that by monitoring the HOM signal amplitude for two polarizations of a dipole mode, one can measure the electrical center of the modes with a resolution of 50 µm. Due to cavity deformations, the main dipole modes have different electrical centers which differ by about 100 µm in most cases. This method provides a way to align the beam with respect to each accelerating cavity with a resolution much better than the 500 µm accuracy of the cavity mechanical alignment in the cryo-modules. In the case of a cryo-module, one could align the beam through the middle of the first and the last cavities, or define an axis of the module based on the information about the cavity alignment in the module, which can be obtained also from these measurements.

Although the procedure described here, based on moving the beam, is lengthy, this would be necessary only at the beginning. Then one can calibrate the HOM signal, so that one can have a direct indication of the beam position. Alternatives to this method will also be studied in the future. One is to use 2D scans with the total power of both polarizations of a mode, or even use the total power at the HOM couplers.

Acknowledgements

We would like to thank all the TTF2 operators and coordinators for their participation in the measurements. In particular we would like to thank P. Castro for his help in analyzing the data, and the effort to prepare future measurements. We also would like to thank J. Sekutowicz and M. Dohlus for many useful discussions.

REFERENCES

[1] B. Faatz for the FEL team, " The SASE FEL at the TESLA Test Facility as User Facility", FEL 2002 Proceedings, Argonne, 2002

[2] Ch. Magne et al., "Measurement with Beam of the Deflecting Higher Order Modes in the TTF Superconducting Cavities", PAC 2001 Proceedings, p. 3771, Chicago, 2001

[3] G. Devanz et al, "HOM Beam Coupling Measurements at the TESLA Test Facility (TTF)", EPAC 2002 Proceedings, p. 230, Paris, 2002

OPTIMIZATION OF POSITRON CAPTURE IN NLC*

Yuri K. Batygin, SLAC, Stanford, CA 94309, USA

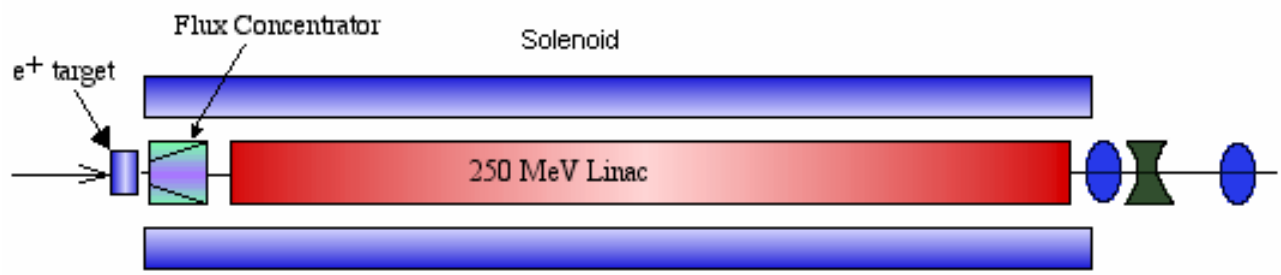

Figure 1: Layout of the NLC positron injector.

Abstract

In the Next Linear Collider design [1], the positron capture system includes a positron production target, followed by a short solenoid with a strong magnetic field (flux concentrator), a 250 MeV linac with solenoidal focusing, a 1.73 GeV linac with quadrupole focusing and an energy compressor system before injection into the positron pre-damping ring (see Fig. 1 for initial part of collector). Two schemes for positron production have been studied: (i) a conventional approach with a 6.2 GeV electron beam interacting with a high-Z target and (ii) polarized positron production using polarized photons generated in a helical undulator by a 150 GeV electron beam which then interact with a positron production target. The capture system has been optimized to insure high positron yield into the 6-dimensional acceptance of the pre-damping ring. As a result of these optimization studies, the positron yield in the conventional scheme has been increased from 1.0 to at least 1.5 and captuire for the polarized positron scheme from 0.25 to 0.30 while maintaining 60% positron polarization.

POSITRON YIELD, CAPTURE AND POLARIZATION

Generated positron beam is characterized by large value of beam emittance and wide energy spread (see Fig. 2). At the time of injection into the pre-damping ring, positron capture is restricted by the acceptance of the pre-damping ring. It is convenient to select an energy-invariant 6-dimensional phase space volume and compare positron capture within this volume at different stages of the injector. To provide positrons injection into the pre-damping ring, the normalized positron beam emittance is selected to be $\varepsilon_x, \varepsilon_y \le 0.03$ π m rad and the energy spread $\Delta E/E = \pm 1\%$ at the injection energy of 1.98 GeV (see Fig. 3).

For analysis, we use several criteria, which characterize efficiency of positron collection. Positron capture is a ratio of the number of positrons within invariant 6-dimensional volume, N_{e+}, to the number of positrons generated after the positron production target, $N_{e+,target}$. Positron yield is defined as a ratio of accepted positrons into the pre-damping ring at the energy of 1.98 GeV to the number of incident electrons, N_{e-}, or to the number of incident photons, N_γ, interacting with the target. Longitudinal polarization of a positron beam, $\langle P_z \rangle = \langle S_z P \rangle$, is an average of the product of the longitudinal component of positron spin vector, S_z, and the value of positron polarization, P, over all positrons.

Table 1 illustrates dependence of positron yield in the conventional production scheme with respect to different values of 6-dimensional acceptance of the pre-damping ring.

Table 1: Positron yield at 1.98 GeV as a function of 6D acceptance.

6-D phase space	$\varepsilon_x, \varepsilon_y$ <0.03 π m rad, $\Delta E/E$ =2%	$\varepsilon_x, \varepsilon_y$ <0.045 π m rad, $\Delta E/E$ =2%	$\varepsilon_x, \varepsilon_y$ <0.06 π m rad, $\Delta E/E$ =2%	$\varepsilon_x, \varepsilon_y$ <0.03 π m rad, $\Delta E/E$ =4%	$\varepsilon_x, \varepsilon_y$ <0.045 π m rad, $\Delta E/E$ =4%	$\varepsilon_x, \varepsilon_y$ <0.06 π m rad, $\Delta E/E$ =4%
Positron yield	1.01	1.26	1.36	1.25	1.55	1.69

*Work supported by the Department of Energy Contract No. DE-AC03-76SF00515

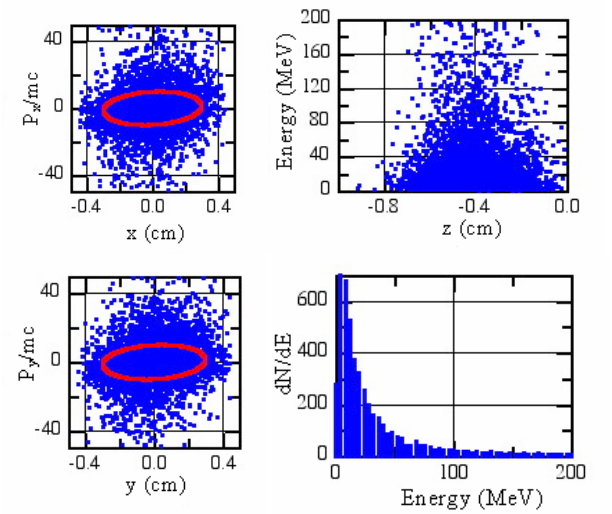

Figure 2: (Blue) initial distribution of positrons generated by a 6.2 GeV electron beam after interaction with a 4.5 RL W-Re target; (Red) area of 0.03 π m rad.

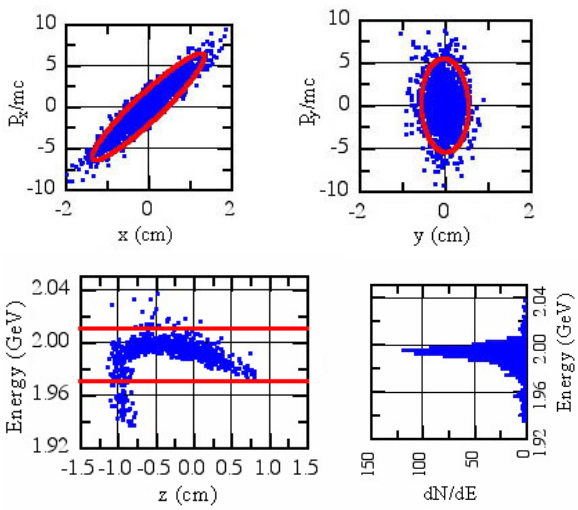

Figure 3: (Blue) distribution of positrons at 1.98 GeV; (Red) emittance area of 0.03 π m rad and ΔE/E=2%.

POSITRON TRANSMISSION TROUGH FLUX CONCENTRATOR

According to the design, the positron production target is surrounded by a tapered solenoidal magnetic field of B_t = 1.2 Tesla followed by a strong magnetic field of flux concentrator with a total peak field of B_{FC} = 6.4 Tesla. The sharp change in the magnetic field at the injection is a barrier for low-energy positrons. Fig. 4 illustrates the magnetic field profile of the flux concentrator and distribution of positrons after injection into flux concentrator. Fig. 4 features high-energy positrons which passed through the field and low-energy positrons reflected from the field. The barrier for low-energy positrons can be removed if the positron production target is placed inside a strong magnetic field

Table 2: Positron capture after the flux concentrator (FC) and after acceleration up to 250 MeV as function of FC magnetic field configuration

B_z at target, Tesla	FC field $B_z(z)$, Tesla	Aperture along FC, cm	Capture after FC	Capture at 250 MeV
1.2	6.4…0.5	0.5…2	0.29	0.24
6.4	6.4	0.5…2	0.42	0.09
6.4	6.4	2	0.42	0.09
6.4	6.4…0.5	0.5…2	0.39	0.33

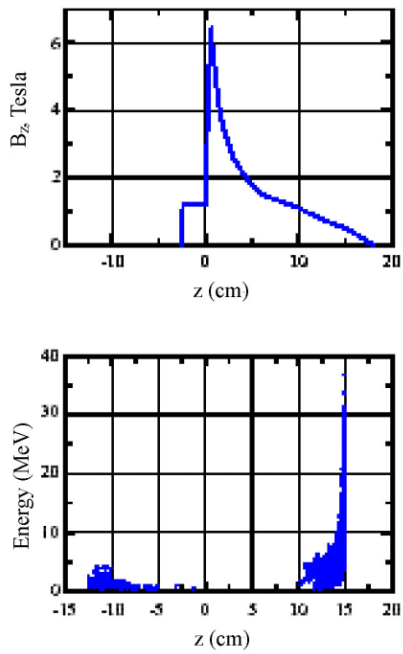

Figure 4: (Top) magnetic field profile in flux concentrator; (Bottom) distribution of positrons from 10.7 MeV γ-flux after injection into flux concentrator.

of flux concentrator [2]. Table 2 contains results of a simulation of positron capture at different configurations of the magnetic field of the flux concentrator. Moving the target inside strong magnetic field increases positron capture by a factor of 1.37 (compare the first and the last lines in Table 2). Utilizing a flux concentrator with a constant magnetic field of 6.4 Tesla results in better transmission of positrons through the magnet. However, because of the mismatching of the constant field of 6.4 Tesla with the 0.5 Tesla focusing field of the 250 MeV linac, transmission of accelerated positrons in this case drops seriously.

DECELERATION OF POSITRONS

After the flux concentrator, positron distribution has a tail created by low-energy positrons (see right side distribution of positrons in Fig. 4). An effective method of increasing of positron capture was proposed in Ref. [3]. It is based on the fact, that this specific positron distribution is close to the shape of longitudinal phase-

Table 3: Positron yield with respect to incident γ – flux

Energy of 1st harm. cutoff, MeV	Yield at the target	Capture at 1,9 GeV	Yield at 1.9 GeV
10.7	0.029	0.20	5.8×10^{-3}
30	0.11	0.058	6.4×10^{-3}
60	0.17	0.026	4.4×10^{-3}

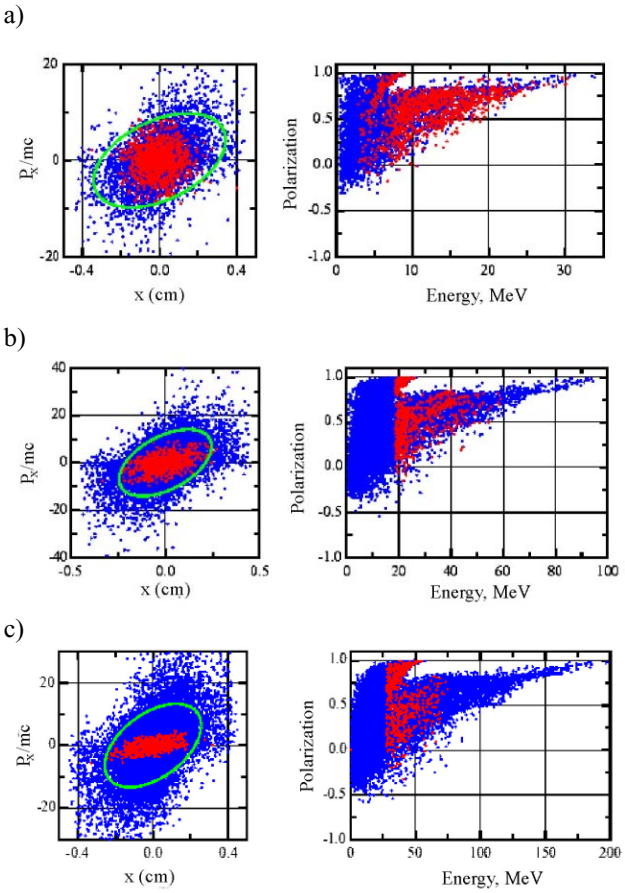

Figure 5: (Blue) initial distribution of polarized positrons, generated by: (a) 10.7 MeV γ-flux, (b) 30 MeV γ-flux, (c) 60 MeV γ-flux, (red) positrons accepted at 1.98 GeV, (green) area of 0.03 π m rad.

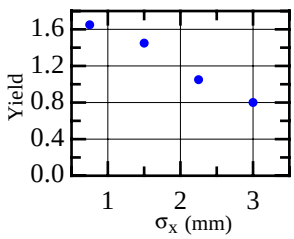

Figure 6: Positron yield vs. transverse electron bunch size (bunch length τ = 4 ps, target Hg, 4 RL).

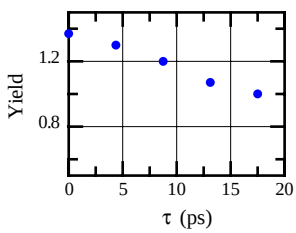

Figure 7: Positron yield vs. bunch length (σ_x=1.6mm, target W-Re, 4.5 RL).

space orbits of linac. Particles, originally placed along the phase-space trajectory, will remain at the trajectory. As shown in Ref. [3], particles, after deceleration, will be compressed and accelerated as a short bunch with better transmission efficiency.

Simulations indicate that this process of beam bunching is accompanied with an increase of transverse emittance of a beam. As a result, the total number of positrons accepted at 1.98 GeV within the normalized emittance of ε_x, $\varepsilon_y \le 0.03$ π m rad and the energy spread of $\Delta E/E = 2\%$, remains the same. However, if transverse acceptance is allowed to be increased by 0.06 π rad, the number of accepted positrons due to deceleration-bunching increases by a factor of 1.13.

POSITRON YIELD AS A FUNCTION OF ENERGY OF POLARIZED γ-FLUX

Fig. 5 and Table 3 contain results of capture of polarized positrons created by the K=1, helical undulator spectrum with first harmonic cutoff energies of 10.7 MeV, 30 MeV and 60 MeV. With an increase of energy of γ-flux, positron yield at the target increases. However, increase of the energy of incoming photons results in wider energy spectrum of outgoing positrons. From Fig. 5 it follows that the distribution of positron polarization as a function of energy remains qualitatively the same, but is scaled to a wider energy interval. As a result, positron capture drops with increase of energy of γ-flux. Positron yield at 1.9 GeV (last column in Table 3) is a product of that at the target (2nd column) and of the value of capture (3rd column). As a result, the positron yield has a maximum at the energy of γ -flux of 30 MeV while the final beam polarization is 60%.

POSITRON YIELD AS A FUNCTION OF INCIDENT ELECTRON BUNCH SIZES

Reduction of sizes of the incident electron beam results in a decrease of generated positron beam emittance in the conventional positron production scheme. Nominal value of a transverse electron beam size is $\sigma_x = 1.6$ mm and that of a bunch length is $\tau = 17$ ps. Incident electron bunch can be made more compact by utilizing traditional compression scheme. Figs. 6, 7 indicate that positron yield can be increased by a factor of 1.37 using electron bunch with smaller sizes.

REFERENCES

[1] Zeroth-Order Design Report for the Next Linear Collider, SLAC Report 474 (1996).

[2] V.Belov et al., Proceedings of the 2001 Particle Accelerator Conference, Editors P.Lucas, S.Webber (2001), p. 1505.

[3] B.Aune, R.H.Miller, Proceedings of the 1979 Linear Accelerator Conference, Edited by R.L.Witkover, BNL 51134 (1979), p. 440.

BACKGROUND FROM UNDULATOR IN THE PROPOSED EXPERIMENT WITH POLARIZED POSITRONS*

Yuri K. Batygin, SLAC, Stanford, CA 94309, USA

Abstract

In the proposed E-166 experiment [1], 50 GeV electrons pass through helical undulator, and produce circularly polarized photons, which interact with a tungsten target and generate longitudinally polarized positrons. The background is an issue for a considered experiment. GEANT3 simulations were performed to model production of secondary particles from high-energy electrons hitting an undulator. The energy density of generated photons at the target was analysed. Results of the simulations are presented and discussed.

INTRODUCTION

E-166 is the proposed experiment for the verification of polarized positron production for the Next Linear Collider [1]. According to the original suggestion of Ref. [2], high-energy electrons pass through a helical undulator and produce circularly polarized photons, which after interaction with tungsten target, generate longitudinally polarized positrons. In the E-166 experiment (see Fig. 1), the 50 GeV electron beam propagates inside 1 m long undulator followed by a drift space of 35 m. Polarized positrons generated in an undulator are analyzed by Si-W calorimeter which is placed along the axis. Polarized positrons are analyzed by a Cs-I calorimeter after reconversion of positrons to photons at the second target shifted by 45 cm from the axis. In this paper we discuss the effect of background particles generated by primary high-energy electrons hitting undulator tube.

SIMULATION SET-UP

Fig. 2 illustrates the simulation set-up of the Final Focus Test Beam (FFTB) line of SLAC linac. Beamline includes undulator (1), quadrupole magnet (2), bending magnets (3) and lead shields (4), (5). The undulator was substituted by a thin iron tube with length of 1 m and internal diameter of 0.88 mm. To prevent background, in front of the undulator a tungsten collimator with the length of 30 RL (10.5 cm) is used. Simulations were performed for two cases: illumination of the internal part of the undulator and illumination of collimator by halo electrons.

To define divergence of halo electrons, let us take into account that normalized rms beam emittance in FFTB line is $\gamma\varepsilon = 3\text{x}10^{-5}\ \pi$ m rad, and rms beam size is $\sigma = 40\cdot10^{-6}$ m. Therefore, rms beam divergence for beam energy of $\gamma = 10^5$ is

$$\left(\frac{dx}{dz}\right)_{rms} = \frac{\varepsilon}{\sigma} = 7.5\cdot10^{-6}. \quad (1)$$

The internal undulator radius is approximately 10 times larger than the rms beam size. As soon as halo electrons are distributed in a phase space within a 10 times larger ellipse than the beam core, the divergence of the halo electrons was selected to be

$$\left(\frac{dx}{dz}\right)_{halo} = 10\cdot\left(\frac{dx}{dz}\right)_{rms} = 7.5\cdot10^{-5}. \quad (2)$$

The generated secondary particles were collected and analyzed at the distance of 35 m from undulator.

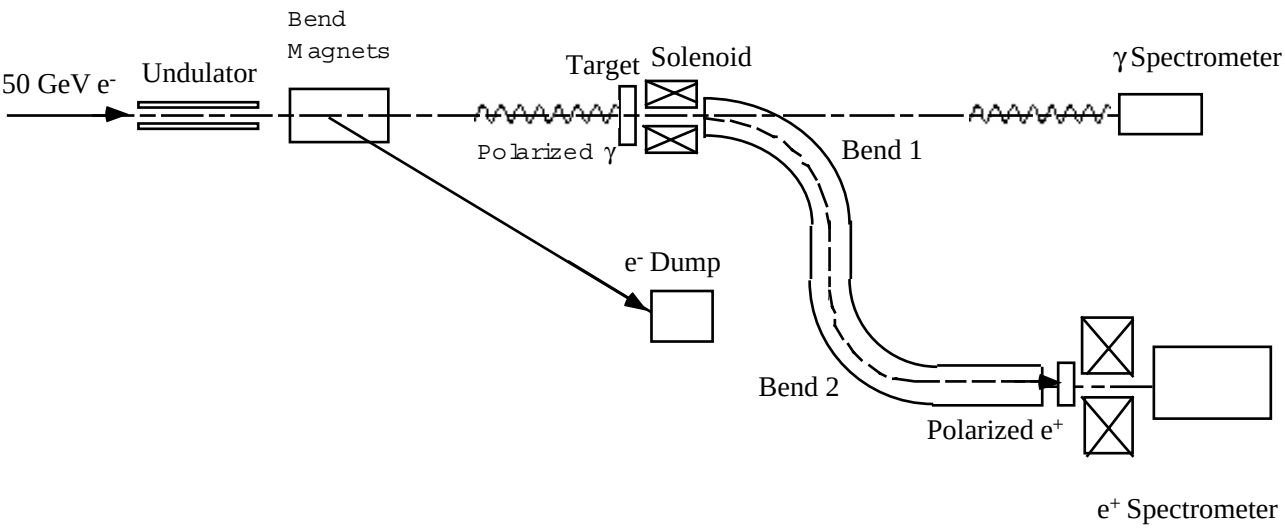

Figure 1: Layout of experiment.

*Work is supported by Department of Energy under Contract No. DE-AC03-76SF00515

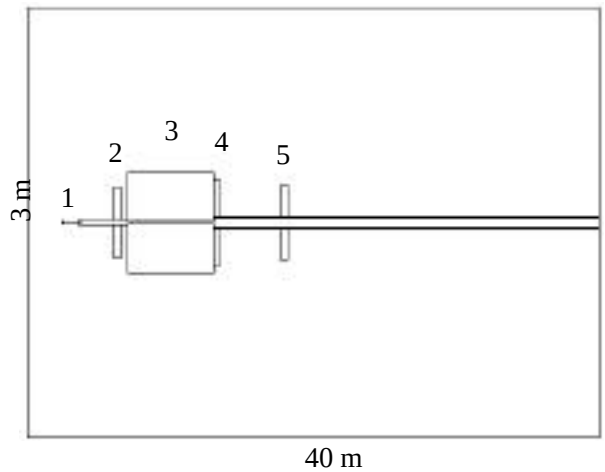

Figure 2: Simulation set-up: 1 –undulator, 2- quadrupole, 3- bending magnets, 4, 5- lead shield.

(a)

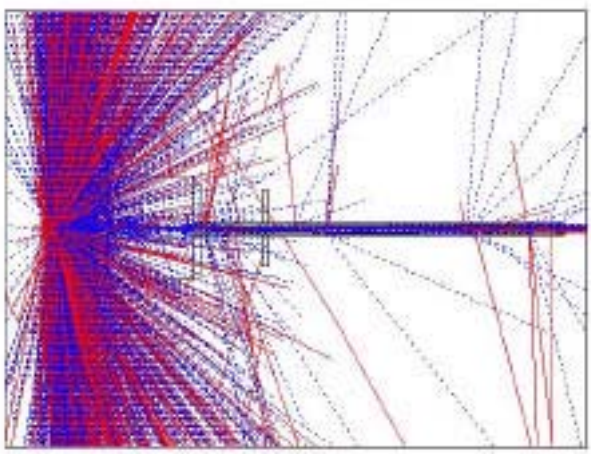

(b)

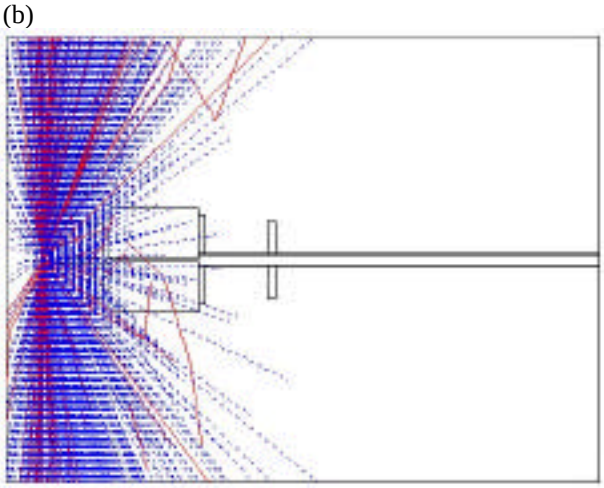

Figure 3: (a) Background from electrons hitting internal part of the undulator, (b) background from electrons hitting the collimator: blue – photons, red - electrons and positrons.

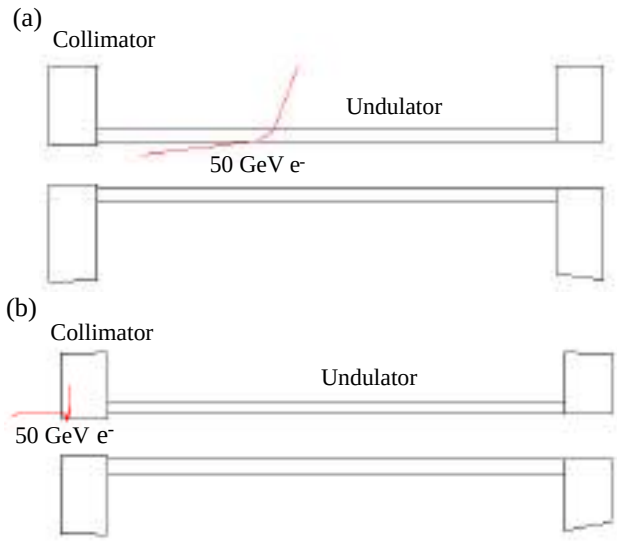

Figure 4: High energy electron hitting (a) internal part of undulator, (b) collimator.

BACKGROUND TREATMENT

Figs. 3, 4 illustrate illumination of the undulator by a single 50 GeV electron and the resulted background. Generated secondary particles contain mostly photons. Figs. 5, 6 illustrate energy density of photons, dE/dS, at the distance of 35 m from the undulator as a function of radial displacement:

$$\frac{dE}{dS}(r) = \frac{\sum_{i=1}^{N} E_i}{2\pi r dr}, \qquad (3)$$

where E_i is an energy of an individual photon. The results are normalized by a single primary electron. From simulations, it follows that each primary electron hitting the internal part of the undulator generates around 22 photons, 2.4 electrons and 1.7 positrons which eventually reach the target area at the distance of 35 m. The distribution of photons has a peak at the axis (see Fig. 5a) and drops quickly with the radius (see Fig. 5b). Specific concern are photons within radial displacement of $r < 0.15$ cm which can affect Si-W detector, providing background noise. The average value of the energy of those photons is 0.2 GeV per primary electron.

To prevent background generation, a collimator in front of undulateor is used (see Fig. 4b). The internal diameter of the collimator of 0.73 mm was selected to be smaller than that of the undulator to ensure that halo electrons with divergence of 10^{-4} will not hit the internal part of the undulator. The results of the simulations are presented in Fig. 6. While the general shape of the background distribution as a function of the radius is close to that as in the case of background from the undulator, the level of background reduced by three orders of magnitude.

COULOMB ELASTIC SCATTTERING ON RESIDUAL GAS IN UNDULATOR

Because of the small diameter of the undulator, the vacuum in the undulator is supposed to be around 1 mTorr, which might be a reason for elastic scattering of primary electrons on residual gas in the undulator. To estimate the fraction of scattered electrons in the undulator, consider the cross section of elastic Coulomb scattering given by the Rutherford formula:

$$d\sigma(\theta) = \left(\frac{Z\, r_e}{\gamma\beta^2}\right)^2 \frac{d\Omega}{4\left(\sin\frac{\theta}{2}\right)^4}, \qquad (4)$$

where r_e is the classical radius of the electron, Z is the charge of residual gas atoms, $d\Omega = 2\pi \sin\theta\, d\theta$ is the cone angle. The number of particles per volume, n, is given by the perfect gas equation:

$$n = \frac{N_A\, P}{R\, T}, \qquad (5)$$

where $N_A = 6 \times 10^{23}\ mol^{-1}$ is the Avogadro's number, $R = 8.31\ J\, mol^{-1} K^{-1}$ is the ideal gas constant, P is the gas pressure (in Pa), and T is the absolute temperature. After passing through the gas of the length L, the fraction of particles scattered within the angle interval of $[\theta, \theta + d\theta]$ is

$$\frac{dN_\theta}{N} = n\, L\, d\sigma(\theta). \qquad (6)$$

The probability of scattering of the particles within the angle interval $[\theta_{min}, \theta_{max}]$ is obtained via integration of Eq. (6)

$$P_\theta = \int_{\theta_{min}}^{\theta_{max}} \frac{dN(\theta)}{N} = 4\pi n L \left(\frac{Z\, r_e}{\gamma\beta^2}\right)^2 \left(\frac{1}{\theta_{min}^2} - \frac{1}{\theta_{max}^2}\right). \qquad (7)$$

For $\theta_{max} >> \theta_{min}$ the second term in Eq. (7) can be neglected. Finally, for the electron beam propagating in gas

$$P_\theta = \frac{4\pi n L}{\theta_{min}^2} \left(\frac{Z\, r_e}{\gamma\beta^2}\right)^2. \qquad (8)$$

The value of θ_{min} can be estimated as a ratio of aperture of the undulator, R, to the length of the undulator, L:

$$\theta_{min} = \frac{R}{L} = 0.44 \times 10^{-3}. \qquad (9)$$

Taking the E-166 parameters Z = 7, $\gamma = 10^5$, $n = 3.2 \times 10^{-19}\ m^{-3}$ (corresponds to pressure of 1 mTorr), the probability of a near-axis electron to be scattered for an angle sufficient to hit the undulator tube is

$$P_\theta = 0.79 \times 10^{-10}. \qquad (10)$$

As far as the number of electrons per bunch in FFTB is 1×10^{10}, it is around 1 electron per bunch to hit the undulator tube due to the elastic Coulomb scattering.

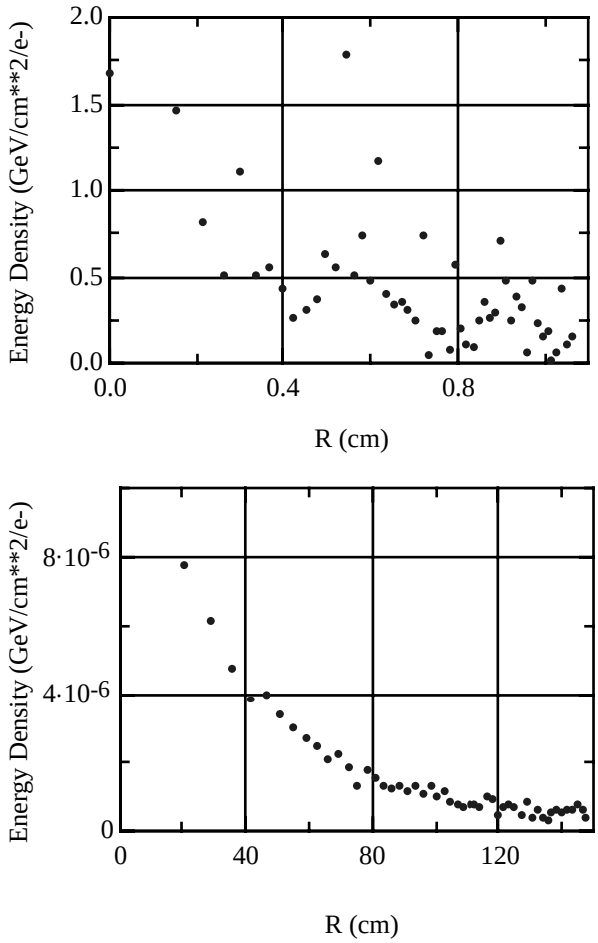

Figure 5: Photon background density from 50 GeV electron hitting internal part of undulator: (a) near axis, (b) far from axis.

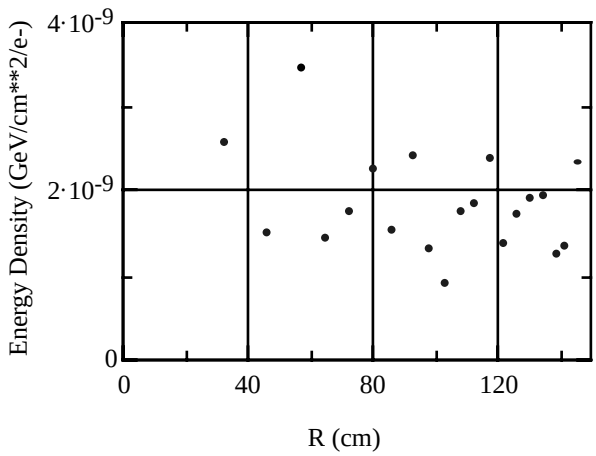

Figure 6: Photon background from 50 GeV electron hitting collimator.

REFERENCES

[1] "Undulator-based production of polarized positrons. A proposal for the 50-GeV beam in the FFTB", SLAC-NT-04-018, (20004), 67 pp.

[2] V.E.Balakin and A.A.Mikhailichenko, Preprint BINP 79-85 (1979).

POSITRON TRANSMISSION AND POLARIZATION IN E-166 EXPERIMENT*

Yuri K. Batygin, SLAC, Stanford, CA 94309, USA

Abstract

The proposed experiment E-166 at SLAC is designed to demonstrate the possibility of producing longitudinally polarized positrons from circularly polarized photons. The experimental set-up utilizes a low emittance 50 GeV electron beam passing through a helical undulator in the Final Focus Test Beam line of the SLAC accelerator. Circularly polarized photons generated by the electron beam in the undulator hit a target and produce electron-positron pairs. The purpose of the post-target spectrometer is to select the positron beam and to deliver it to a polarimeter, keeping the positron beam polarization as high as possible. The paper analyzes the positron transmission and polarization in the E-166 spectrometer both numerically and analytically. The value of positron transmission has a maximum of 5% for positron energy of 7 MeV, while positron polarization is around 80%.

INTRODUCTION

The polarized positron production experiment E-166 uses a strongly collimated 50 GeV electron beam to generate circularly polarized photons in a helical undulator. Photons, after interaction with a target, create polarized positrons. The layout and general description of experiment are given in Ref. [1]. The purpose of a spectrometer is to select the positron beam after the target from electron and photon beams and to deliver positrons to a reconversion target, keeping beam polarization as high as possible.

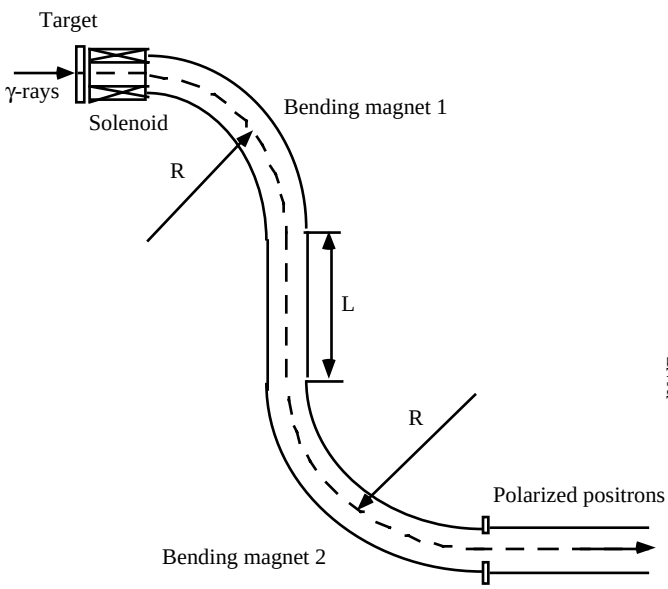

Figure 1: Layout of spectrometer.

Table 1: Parameters of spectrometer

Positron beam energy	0..10 MeV
Bending radius, R	12.5 cm
Bending angle, θ	90°
Drift space, L	20 cm
Positron transmission	5%
Positron polarization	80 %

POLARIZED POSITRON DISTRIBUTION AFTER TARGET

The initial distribution of positrons produced by circularly polarized photons was calculated by J.C.Sheppard using the program EGS4, modified for polarized positrons [2, 3]. Positron distribution after the target is presented in Fig. 2. The distribution is characterized by a large emittance of the positron beam and a large energy spread. The correlation between energy, polarization, and transverse momentum spread is illustrated by partial distributions presented in Figs. 3 – 5. Low energy positrons are less polarized and more transversely divergent, while high-energy positrons are strongly polarized and less divergent. The energy spectrum peaks near the low-energy end of the distribution.

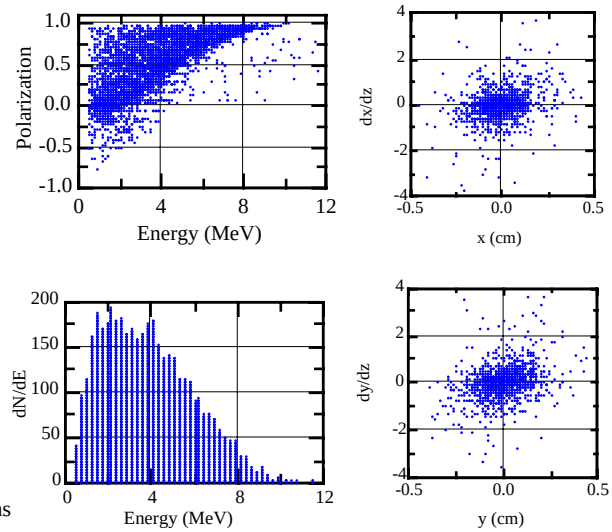

Figure 2: Initial distribution of positrons.

*Work is supported by Department of Energy under Contract No. DE-AC03-76SF00515

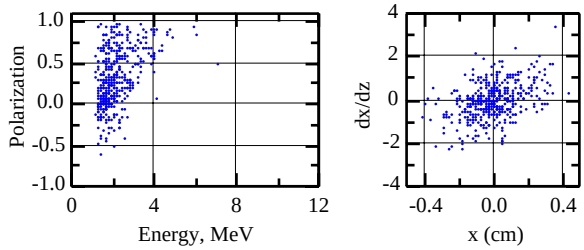

Figure 3: Fraction of initial positron distribution with average energy of $\bar{E}$ = 1.9 MeV, and $\Delta E/\bar{E} = \pm 0.15$.

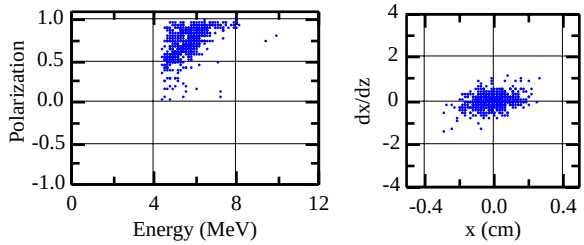

Figure 4: Fraction of initial positron distribution with average energy of $\bar{E}$ = 5.3 MeV, and $\Delta E/\bar{E} = \pm 0.15$.

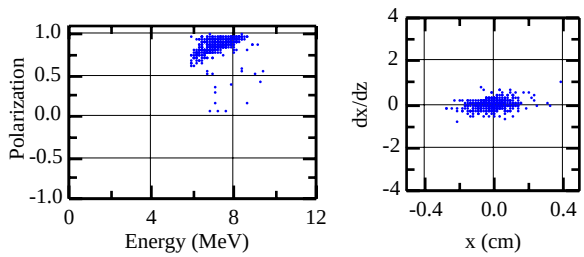

Figure 5: Fraction of initial positron distribution with average energy of $\bar{E}$ = 7.5 MeV, and $\Delta E/\bar{E} = \pm 0.15$.

SPECTROMETER WITH DOUBLE 90° MAGNETS

In the proposed experiment E-166, the spectrometer has to shift the beam from an original accelerator axis at the distance of 45 cm to separate the positron beam from a photon beam and an electron beam coming out from the target. The simple and cost-effective solution is to utilize two 90^0 magnets providing a point-to point transformation of the beam (see Fig. 6). The spectrometer includes a focusing solenoid and two 90° bending magnets separated by a drift space of L = 20 cm.

From the first order matrix analysis, the horizontal displacement of the particle after the first bend and drift is given by:

$$x = -\frac{L}{R} x_o + R x_o' + (R + L)\frac{\Delta p}{p_o}. \qquad (1)$$

The maximum deviation from the axis is equal to the radial aperture, a_x = 5 cm. Maximum radial displacement is $x_{o,\,max} = a_x R/L = 3.125$ cm and maximum divergence is $x'_{o,\,max} = a_x/R = 0.4$. Therefore, horizontal acceptance of the channel, ε_x, is defined as:

$$\varepsilon_x = \pi\, x_{o,\,max}\, x'_{o,\,max} = 1.25\,\pi \text{ cm rad}. \qquad (2)$$

The maximum energy spread is found from Eq. (1) as:

$$\left(\frac{\Delta p}{p_o}\right)_{max} = \frac{a}{R + L} = 0.15\,. \qquad (3)$$

In the vertical direction, particle motion is unaffected except edge defocusing at the entrance and exit of the bending magnets. The maximum vertical slope of particle trajectory including edge defocusing is $y'_{o,\,max} = 0.027$, and maximum initial vertical displacement of the positrons is $y_{o,max} = 0.9$ cm. Therefore, vertical acceptance is

$$\varepsilon_y = \pi\, y_{o,\,max}\, y'_{o,\,max} = 0.024\,\pi \text{ cm rad}. \qquad (4)$$

Applying above constraints to the initial positron distribution, it was found that the value of positron transmission efficiency has a maximum of $\Delta N/N = 10^{-2}$ for particle energy of 6 MeV.

An additional feature of the double 90° magnets design is absence of the depolarization of positrons. Spin precession of positrons with the anomalous magnetic moment G = 0.001159652 in a 90° bending magnet is:

$$\varphi = \theta\gamma\, G = 90^o \text{ x } 20 \text{ x } 0.00116 = 2^o. \qquad (5)$$

However, spin rotation in the first bending magnet is compensated by the second magnet.

Transmission efficiency in the spectrometer is improved by inserting a solenoid between the positron production target and the bending magnets. The focusing properties of the solenoid lens are characterized by the focal length of the lens, f, defined as

$$\frac{1}{f} = \left(\frac{e}{2p_z}\right)^2 \int_{-d}^{d} B_z^2\, dz. \qquad (6)$$

where B_z is the longitudinal on-axis component of the magnetic field of the solenoid. As far as positron momentum $p_z = eBR$, where B is the bending field, there is a linear relationship between the values of B and B_z to provide optimal focusing of particles along the beamline. An increase of the bending field, to provide transmission of positrons with larger energy, requires a proportional increase of the solenoid field.

RESULTS OF SIMULATION

The proposed spectrometer is characterized by large values of x/R ~ 0.4 and momentum deviation $\Delta p/p \sim 0.15$. The linear model based on matrix multiplication is not sufficient to provide accurate estimations of positron dynamics in the spectrometer. For calculation, the code BEAMPATH was used. Particle tracking was accompanied with integration of the Thomas-BMT equation, describing the precession of the spin vector $\vec{S}$:

$$\frac{d\vec{S}}{dt} = \frac{e\vec{S}}{m\gamma} \times [(1+G\gamma)\vec{B}_{\perp} + (1+G)\vec{B}_{II} + (G\gamma + \frac{\gamma}{1+\gamma})\frac{\vec{E}\times\vec{\beta}}{c}], \quad (7)$$

where $\vec{E}$ is the electrical field, and $\vec{B}_{\perp}$ and $\vec{B}_{II}$ are components of the magnetic field perpendicular and parallel to particle velocity. Initially, the spin vector of each positron is pointed along the momentum vector. During beam transport, the spin vector precesses. We define the longitudinal polarization as an average of the product of the longitudinal component S_z and the value of polarization, P, summed over all positrons:

$$<P_z> = \frac{1}{N}\sum_{i=1}^{N} S_z^{(i)} P^{(i)} . \quad (8)$$

The initial value of longitudinal polarization is $<P_z>$ = 0.41. After removing low-energy positrons in the spectrometer, the polarization of the final beam can reach the value of 0.8.

Particle trajectories in the proposed system are presented in Fig. 7. Fig. 8 contains transmission and polarization of positrons in the proposed spectrometer as a function of particle energy. The appearance of the positron transmission maximum is explained by the fact that low energy positrons are strongly divergent and only a small fraction of positrons is within the transverse acceptance of the spectrometer. With increasing energy, the positron beam becomes less divergent, but the number of positrons drops.

At the entrance and at the exit of the magnet, the slope of the particle trajectory is changed because of the pole angle α, according to the linear matrix transformation $\Delta x' = (x/R)tg\alpha$, $\Delta y' = -(y/R)tg(\alpha-\psi)$, where the correction angle ψ is given by

$$\psi = K_1 (\frac{g}{R}) (\frac{1+\sin^2\alpha}{\cos\alpha}) [\, 1 - K_1 K_2 (\frac{g}{R}) tg\alpha], \quad (9)$$

where g is the gap of the magnet and coefficients K_1, K_2 are defined by pole geometry. For α = 0, the value of angle ψ = 16°. Selecting α = 16° (horizontal edge defocusing), the value of the correction angle in this case, according to Eq. (9) is ψ = 11.5° and the total effect in vertical direction is focusing $\alpha - \psi$ =4.5°. Fig. 9 illustrates positron transmission as a function of pole face rotation angle. The value of transmission efficiency has a maximum around α = 16°.

Fig. 10 illustrates transmission efficiency as a function of field index.

$$n = -[\frac{R}{B}\frac{\partial B}{\partial x}]_{x=0,\, y=0} . \quad (10)$$

Positron transmission efficiency has a maximum at the value of n = 0.4. In this case focusing properties of the bending magnets are approximately equal each other in both directions. This value of field index was selected for final design.

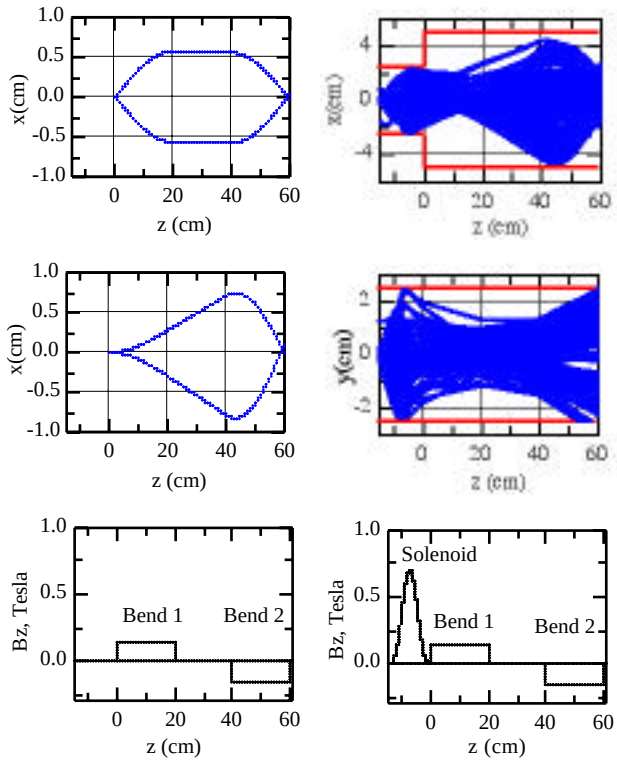

Figure 6: Particle trajectories in spectrometer: (up) dx/dz = ± 0.05, (bottom) Δp/p=±0.02.

Figure 7: Particle trajectories in the spectrometer.

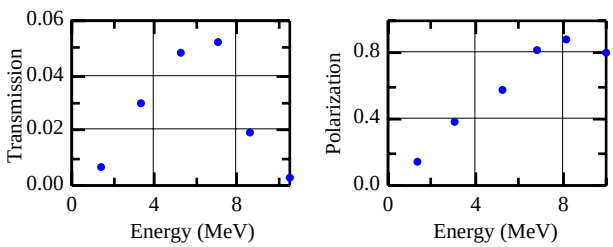

Figure 8: Positron transmission and polarization as functions of energy.

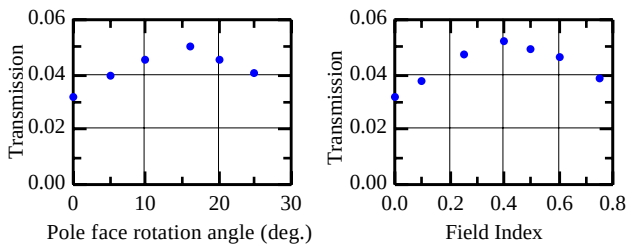

Figure 9: Positron transmission as a function of pole face rotation angle.

Figure 10: Positron transmission as a function of field index.

REFERENCES

[1] "Undulator-based production of polarized positrons. A proposal for the 50-GeV beam in the FFTB", SLAC-NT-04-018, (20004), 67 pp.

[2] W.Nelson, H.Hirayama and D.Rogers, "The EGS4 Code System", SLAC-Report-265 (1985).

[3] K.Flottmann, Ph.D. Thesis, DESY-93-161A (1993).

A STUDY OF COUPLER-TRAPPED MODES IN X-BAND LINACS FOR THE GLC/NLC†

R.M. Jones, V.A. Dolgashev, Z. Li, J.W. Wang, SLAC

Abstract

Each of the X-band accelerating structures for the GLC/NLC (Global Linear Collider/Next Linear Collider) consists of 55 cells which accelerate a train of charged bunches. The cells are carefully designed to ensure that the transverse wakefield left behind each bunch does not disrupt the trailing bunches, but some modes are trapped in the region of the coupler cells. These modes can give rise to severe emittance dilution if care is not taken to avoid a region of resonant growth in the emittance. Here, we present results on simulations, cold test experimental measurements and beam dynamics simulations arising as a consequence of modes trapped in the coupler. The region in which trapped modes have little influence on the beam is delineated.

INTRODUCTION

In the design of a next generation linear collider operating at room temperature there are two main issues that must be faced: firstly, operating at high gradients with minimal electrical breakdowns and secondly, damping the wakefield that the charged bunches leave behind such that disruptive Beam Break Up (BBU) instabilities do not develop. Means of controlling electrical breakdown is under intensive investigation at SLAC [1] and is not the subject of this paper.

Here we study the second major issue, namely, wakefield effects. The short range, or intra-bunch, wakefield affects particles within a given bunch and it is proportional to $a^{-3.8}$ (where a is the average iris radius of the accelerator structure). An $a/\lambda \sim 0.17$ (where λ is the free-space wave number at the accelerating frequency) gives rise to manageable short-range wakefields and this is the number used in several designs for the GLC/NLC. The long-range wakefield affects trailing bunches and it falls by almost two orders of magnitude by the time of the first trailing bunch (separated from its neighbor by 1.4 ns). This decay is achieved by varying the geometry of the accelerator cells in a careful controlled manner [2]. We have investigated Gaussian and Sech functional behavior in the fall-off of the long-range wakefield. Eventually the modes would re-cohere and, in order to damp these modes [3] down to acceptable levels we couple out a significant fraction of the remaining wakefield to 4 attached manifolds.

These detuned and moderately damped accelerating structures have been verified to behave as expected from simulations in several ASSET (Accelerator Structure Setup) experiments [4] conducted in the SLC. However, modes can readily become trapped in the regions of the fundamental mode RF couplers. We refer to these modes being trapped in the sense that they are localized in the waveguide coupler [5] and the next cell. They are weakly coupled to the regular cells and output waveguides. We make the distinction between these modes and the structure modes with some fields in the coupler region [3]. The trapped modes can cause transverse instabilities which may significantly dilute the beam emittance. It is the purpose of this paper to carefully analyze these modes and ascertain their influence on the beam dynamics.

The following section provides an analysis of these modes based on experimental measurements of the scattering matrix properties of the coupler and on *HFSS* [6] modeling of the eigenmodes of the structure. The impact of the trapped modes on the beam dynamics is presented in the final main section.

MEASUREMENT AND SIMULATION OF TRAPPED EIGENMODES

Reflection and transmission were measured using one port of the fundamental coupler and an antenna inserted into the beam pipe. To measure the frequency and Q of the trapped mode it was necessary to insert the probe in the field of the trapped mode. The inserted probe, obviously perturbs the frequency and Q of the mode. The perturbation is minimized by withdrawing the probe to the extent that the resonance in S_{11} is just discernable. We observed two highest Q modes in this accelerator structure: each are located in the regions of the input and output coupler. The Qs of these modes are determined entirely by the copper losses.

The eigenmodes together with their Q values were calculated with its eigenmode module of *HFSS*. The complete set of modes simulated for a waveguide coupler, a matching iris and the first iris of the structure, are shown in Fig. 1. Further modes were observed during the experimental measurements but only those we believe to be modes trapped in the region of the coupler are shown in Fig. 1. The highest Q modes are illustrated in Fig. 1A and Fig. 1B. All of the modes displayed are dipole-like in character, except the mode in Fig. 1F. This mode is monopole-like with a finite quadrupole field. This mode has some focusing in one plane and defocusing in the other. Properties are of such modes are discussed in [7]. A summary of the experimentally determined frequencies and those computed with *HFSS* is given in Table 1. Additionally we have made limited *Omega3P* [8] simulations of the high Q input and output modes. These *Omega3P* calculations indicate that the input fundamental coupler has a mode frequency of 10.658 GHz and the output fundamental mode coupler is 11.534 GHz. These values are in better agreement with the experimentally determined frequencies. This may be due to the *Omega3P*

† Supported by the DOE, grant number DE-AC03-76SF00515

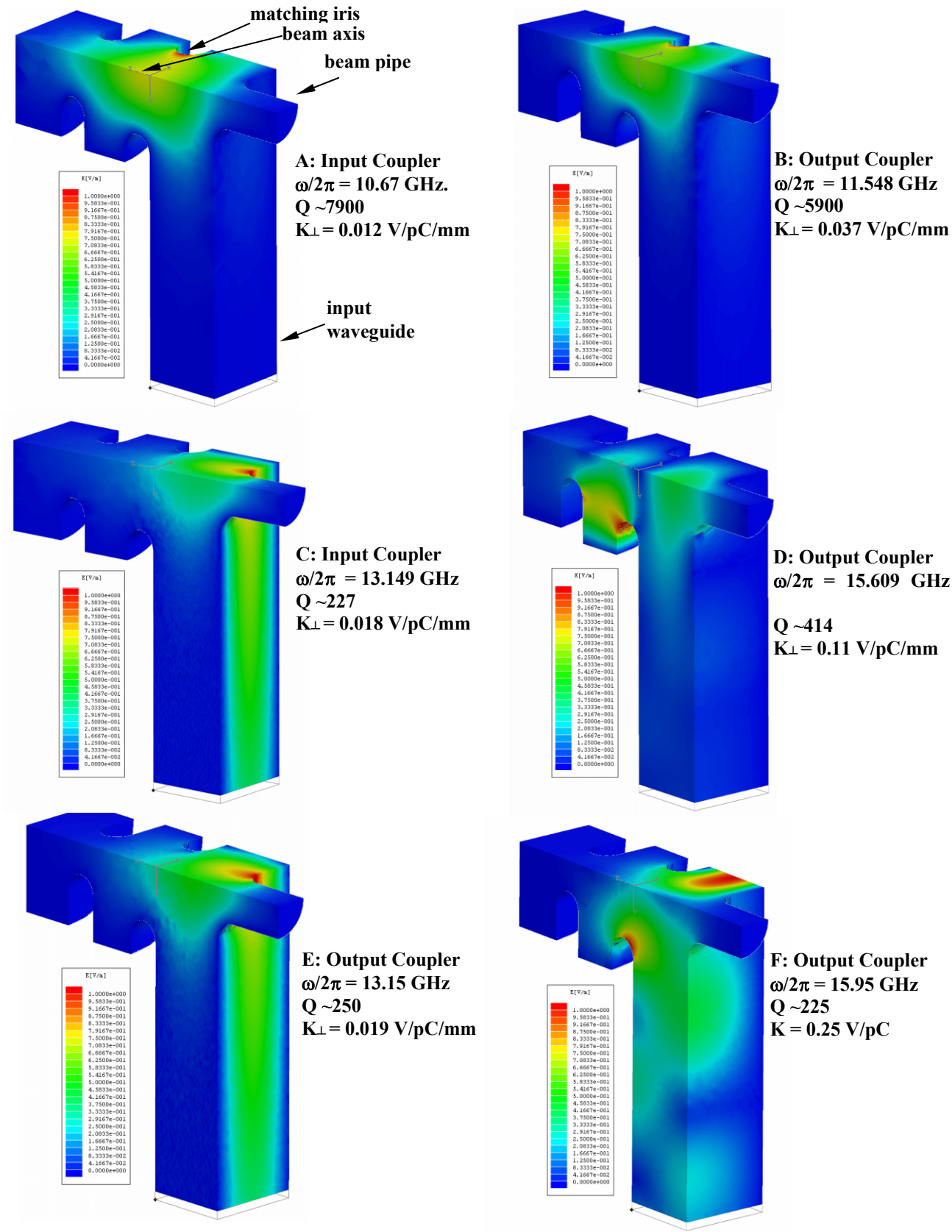

Figure 1: Surface electric fields of the trapped modes in the input and output fundamental couplers of the accelerator structure known as H60VG4S17-III-SN2. The resonant frequency (ω/2π), Q value and the dipole mode kick factor (**K⊥**), are indicated except for the monopole-like mode in F, where the monopole loss factor (**K**) is indicated. One quarter of the geometry was simulated with appropriate boundary conditions.

code allowing a more natural representation of the structure geometry, although it is not altogether clear that this is the case. It is also notable that frequencies in the *HFSS* simulations in the neighborhood of 16 GHz are also in remarkably good agreement with the experimental measurement. In the next section the affect of these modes on the beam dynamics is investigated.

Table 1: Experimentally measured and *HFSS* calculations of mode frequencies (GHz) for both the input and output mode coupler

Measured Freq., Output Coupler	11.530	13.101	15.600	15.954
Calculated Freq., Output Coupler	11.548	13.151	15.609	15.950
Calculated Q, Output Coupler	5900	250	414	225
Measured Freq., Input Coupler	10.651	13.114		
Calculated Freq., Input Coupler	10.672	13.149		
Calculated Q, Input Coupler	7900	414		

BEAM DYNAMICS

The degree which the modes disrupt the beam is represented by the beam kick factor [9] and this is indicated next to each field pattern in Fig. 1. These results are shown collated in Fig. 2, where, for the purpose of comparison, the kick factor of the center cell is also shown. The largest trapped-mode kick is at 15.6 GHz and it is notable that it has a rather low Q value (~414) as it radiates out through the waveguide coupler. The other kick factors are all almost an order of magnitude smaller than the centre cell's kick factor and

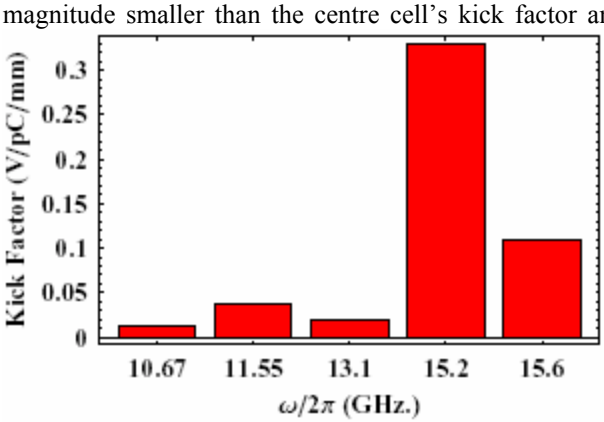

Figure 2: Comparison of trapped mode kick factors with cell 28, the middle cell of the accelerating structure. The middle cell has a mode frequency of approximately 15.2 GHz.

all have relatively low Qs. The effect on the beam is further elucidated by considering the sum of the wakes of all bunches preceding a particular bunch (computed at the locations of each preceding bunch) and this is defined as the sum wakefield. The RMS of the sum wakefield for the GLC/NLC baseline design [10] with the kick factor given in Fig. 1A added to it, is shown in Fig. 3. The nominal bunch spacing is varied in order to ascertain the sensitivity to systematic frequency errors (since varying the bunch spacing by a small fraction is equivalent to changing all cell frequencies by a fixed amount). The mode frequency ($\omega/2\pi$) is varied from that of Fig. 1A (~10.67 GHz) in order to reveal the location of any neighboring peaks in the S_{RMS}. Earlier work [11] has indicated that large a S_{RMS} gives to a BBU instability and thus the peak values must be avoided. There are indeed large trough regions in S_{RMS} and the present trapped modes are rather fortuitously confined to these regions.

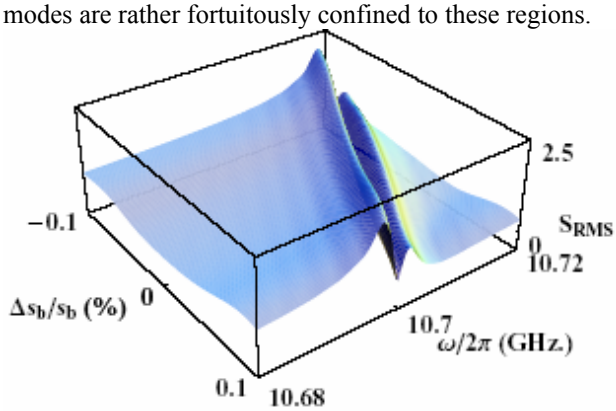

Figure 3: Surface of S_{RMS} (V/pC/mm/m), the RMS of the sum wakefield in the vicinity of the peak value. The trapped mode frequency is given by $\omega/2\pi$ and, $\Delta s_b/s_b$ is the fractional change in the bunch spacing from 1.4 ns. The large peaks occur close to harmonics of the bunch frequency (714 MHz at the nominal bunch spacing).

Beam tracking simulations were undertaken with the computer code LIAR [12] in which all trapped modes were included in the wakefield. The resulting emittance is diluted by less than 0.1%. Thus, provided the mode frequencies of the trapped modes with high Qs do not lie in the vicinity of harmonics of the beam frequency (*i.e.* multiples of 714 MHz.) little emittance dilution is expected to occur over the length of the complete linac.

Additional simulations indicate that the effect of well-damped modes ($Q \leq 500$) on the beam dynamics is rather benign as S_{RMS} is below unity for the full frequency range considered (10.5 GHz to 16 GHz).

REFERENCES

[1] S. Döbert, these proceedings, 2004.
[2] R.M. Jones *et al.*, NLC-Note-24, 1997.
[3] X. Zhan, Ph.D. thesis, Stanford University, 1997.
[4] R.M. Jones *et al.*, LINAC96, SLAC-PUB7287, 1996.
[5] C. Nantista *et al.*, Phys. Rev. STAB, Vol.7, 2004.
[6] www.ansoft.com.
[7] S. Heifets, A. Wagner, B. Zotter, SLAC-A110, 1998.
[8] Y. Sun, *et al.*, Proc. of 18th Annual Review of Progress in Appl. Computational Electromagnetics, ACES-02, Monterey, CA, 2002.
[9] P.B. Wilson, SLAC-PUB 4547, 1989.
[10] R.M. Jones *et al*, PAC03, SLAC-PUB 9868, 2003.
[11] R.M. Jones *et al.*, LINAC02, SLAC-PUB-9407,2002.
[12] R. Assman *et al.*, LIAR, SLAC-PUB-AP-103, 1997.

EMITTANCE-IMPOSED ALIGNMENT AND FREQUENCY TOLERANCES FOR THE TESLA LINEAR COLLIDER

N. Baboi, DESY, Hamburg, Germany and R.M. Jones†, SLAC, Stanford, CA 94309, USA

Abstract

One option in building a future 500 GeV c.m. linear collider is to use superconducting 1.3 GHz 9-cell cavities. However, wakefields excited by the bunch train in the TESLA (TeV-Energy Super Conducting Linear Accelerator) collider can resonantly drive the beam into unstable operation such that a BBU (Beam Break Up) mode results or at the very least significant emittance dilution occurs. The largest kick factors (proportional to the transverse fields which kick the beam off axis) are found in the first three dipole bands and hence multi-bunch emittance growth is mainly determined from these bands. These higher order dipole modes are damped by carefully orientating special couplers placed at both ends of the cavities. We investigate the dilution in the emittance of a beam with a random misalignment of cavities down the complete main linac. The beneficial effects of frequency errors on ameliorating the beam dilution are discussed.

INTRODUCTION

The fundamental consideration in a linear collider is the luminosity of the colliding beams at the interaction point. The luminosity of flat beams is proportional to $L \propto P_b / \sqrt{\varepsilon_{y,n}}$, where $P_b \propto f_{rep} n_b q$ is the beam power and $\varepsilon_{y,n}$ the normalized vertical emittance at the interaction point. For TESLA a high P_b is achieved by compensating the low pulse repetition frequency, f_{rep}, with a high bunch charge q, and a large number of bunches n_b. In order to maximize the luminosity it is however also important to minimize the vertical emittance.

As the highly charged bunches traverse the linac any misalignment in the structure, focusing magnets, or initial offset in the leading bunch, gives rise to wakes [1] which dilute the emittance and the beam may break up down the linac. This BBU [2] can result from short range wakes over the bunch itself, in which the head drives the tail, or from a long range wake, in which trailing bunches are driven by leading ones and BBU occurs due to the coupled motion of the bunches.

Table 1: Fundamental L-band TESLA RF parameters

Quantity	Symbol	L
Accelerating freq. (GHz.)	f_{acc}	1.300
Loaded gradient (MV/m)	G_{acc}	23.4
Bunch train length (T_{fill})	T_b	2.3
Bunch spacing (T_{RF})	T_{bb}	438
Charge per bunch (10^{10})	N_e	2
Structure Iris radius (λ_{RF})	A	0.15
Bunch length (μm)	σ_z	300
Pulse rate	f_{rep}	5

We investigate the emittance dilution due to the long-range wakefield left behind accelerated bunches in the main linacs of the TESLA collider [3,4]. RF parameters for the linacs of this L-band collider are given in Table 1. For the TESLA design, as the cavities are superconducting, the losses are minimal and the fill time and the length of the train of particle bunches can be very long. For this reason 2820 bunches are in the charged particle train, which is 950 μs long. Each cavity consists of 9 cells, operating in the standing wave mode and with a π phase advance per cell. A typical 9-cell cavity structure is illustrated in Fig. 1. There will be close to 21,000 of these cavities in the collider.

Figure 1: Fabricated nine-cell niobium TESLA cavity.

In this paper, due to space considerations, we concern ourselves entirely with how the emittance of the beam is diluted due to misaligned accelerator cavities. However, we refer the interested reader to [5] for an analysis of the impact on emittance dilution of a beam injected offset from the axis of the accelerator.

This paper is organized in two main sections. The following section describes the transverse wakefields calculated from numerically evaluated kick factors, and measured Qs and synchronous frequencies. The second section investigates the alignment tolerances that are allowable for a specified emittance dilution.

TRANSVERSE WAKEFIELDS

For the TESLA cavities, there are no more than a few modes that interact strongly with the beam in the first three pass-bands. Using HOM couplers attached to the beam pipe at either side of each cavity, the Q of these modes is reduced from the order of 10^9 to below 10^5. Measurements made in the majority of cavities built to date indicate this damping level is achieved. Fig. 2 shows the Qs and kick factors [6] of the dipole modes. It is clear that only a few modes have appreciable kick factors. The frequencies and quality factors given here are results from

† Supported by the U.S. Department of Energy grant number DE-AC03-76SF00515

measurements of 36 cavities made in the single-cavity test setup [7].

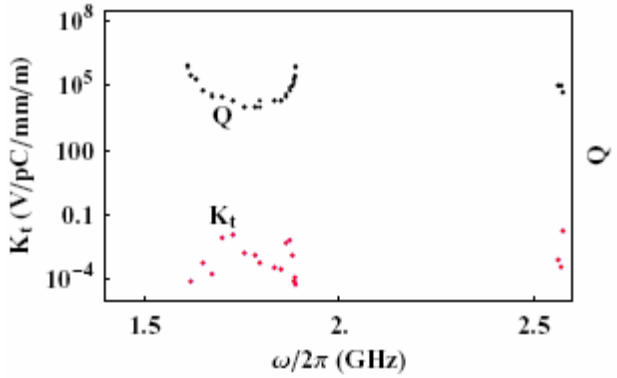

Figure 2: Calculated transverse kick factors and measured Q values for TESLA accelerating cavities.

The envelope of the long-range transverse wakefield, a distance s behind the first bunch, is calculated from the absolute value of the modal sum:

$$\hat{W}(s) = 2\left|\sum_{n=1}^{N} K_n e^{i\omega_n s/c} e^{-\omega_n s/2Q_n c}\right|, \qquad (1)$$

where N is the number of modes, the n^{th} mode has a quality factor of Q_n, a kick factor K_n and a synchronous frequency $\omega_n/2\pi$. The envelope of the wakefield obtained from applying Eq. (1) is illustrated in Fig. 3. The characteristic 'e-folding' length ($=2cQ_n/\omega_n$) for a mode with Q ~ 10^5 is ~ 6.4 km and at this distance

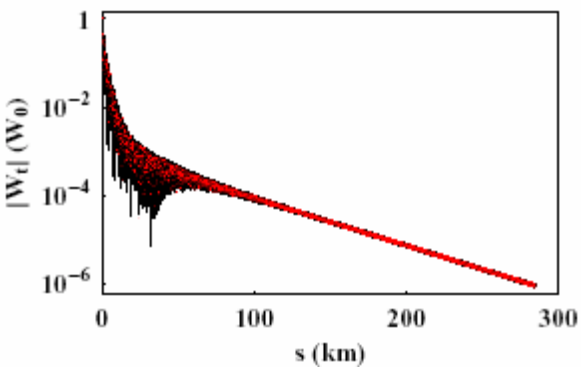

Figure 3: Envelope of the TESLA transverse wakefield. The abscissa runs over the distance of the complete bunch train. The ordinate has been normalized with respect to W_0, (0.11V/pC/mm/m). The red dots indicate the location of the individual bunches.

the mode has decayed by 63 %. However, up until 6.4 km there are ~ 65 bunches and thus we would expect significant emittance dilution to occur if no action is taken to prevent the resonant build-up of the wake.

We investigate the impact of this wakefield on the emittance dilution of a beam traversing a linac composed of randomly misaligned accelerator structures in the next section.

MISALIGNMENT TOLERANCES

Introduction

In the process of fabricating the collider, accelerating cavities of length approximately 1 meter must be aligned with respect to each other in order to prevent significant emittance dilution occurring over the 14 km of the entire L-band linac. In order to assess the impact of the long-range transverse wakefield on the emittance of the beam we track the progress of the beam down the linac using MAFIA-L [8] allowing random transverse cavity misalignments with an RMS value of 500 μm.

The results of such a tracking simulation with no frequency errors included in the simulation are illustrated in Fig 4. The abscissa used in Fig. 4 is the percentage change in the bunch spacing and this corresponds to a systematic error in the frequencies of all accelerating cavities. At the nominal bunch spacing of 337 ns ($\Delta s_b/s_b = 0$) the emittance dilution is appreciable as it is of the order of 10^3 %. There is a peak value of $9.7\cdot10^5$ % in

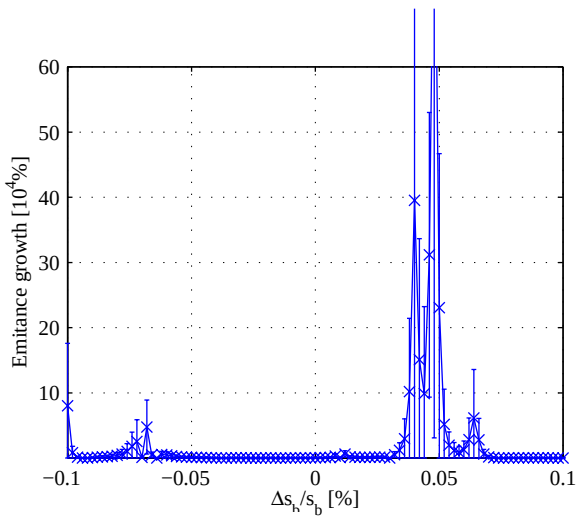

Figure 4: Percentage emittance dilution down the linac for randomly misaligned cavities with an RMS value of 500 μm. versus $\Delta s_b/s_b$, the percentage change in the bunch spacing.

the emittance dilution at $\Delta s_b/s_b \approx 0.05$ % (corresponding to a systematic shift in the frequencies of all cavities of the order of 800 kHz).

Clearly these emittance dilutions are disturbingly large. However, in the fabrication of the collider small errors in the dimensions of the cavities lead to small errors in the dipole frequencies of the cavities. These frequency errors will be randomly distributed throughout the entire linac and they will randomize the overall kick that the beam receives. It is anticipated that these errors will reduce the emittance dilution significantly.

The effectiveness of such frequency errors in reducing the emittance dilution to acceptable values is investigated in the following section.

Fabrication Errors

In the process of fabricating several thousand accelerating cavities, frequency errors will be an unavoidable part of the manufacturing process. The effect of these errors on the emittance growth for misalignments of 100 μm, 500 μm and 1 mm is illustrated in Fig. 5. For

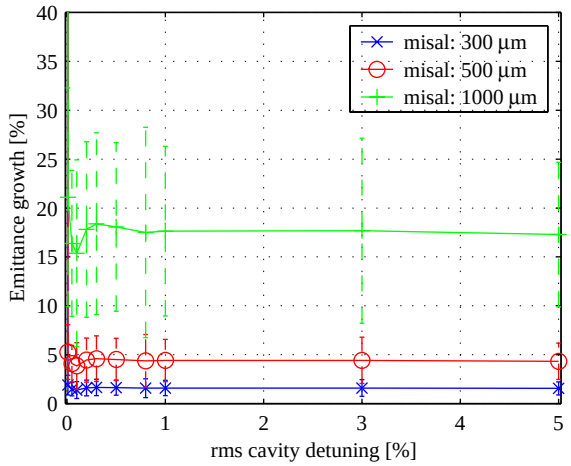

Figure 5: Percentage emittance growth versus the RMS value of the random frequency detuning (expressed as a percentage of the unperturbed dipole frequencies). Three random misalignment cases are illustrated.

the design specification of 500 μm RMS misalignment one sees that even a small frequency error of 0.01% (~200 kHz) has a remarkably beneficial effect, reducing the beam emittance from 10^3 % to about 5 %, and the high peak in Fig. 4 ($\Delta s_b/s_b \approx 0.05$ %) to about 12 % (not shown in Fig. 5).

It is also important to point out that the emittance dilution is rather independent of the degree of random

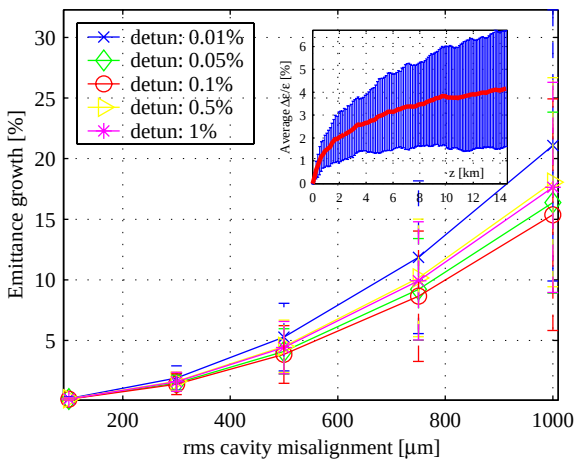

Figure 6: Percentage emittance growth versus the RMS value of the random cavity misalignment for a wide range of frequency detuning errors. Shown inset is the percentage emittance dilution down the linac for RMS random misalignment tolerance of 500 μm and a 1 % frequency detuning error. The red curve in the inset represents the mean emittance dilution along the main linac taken over 80 samples.

detuning of the HOM frequencies. Indeed, for the middle curve in Fig. 5 the dilution stays between 4.2 % and 5.1 % for detuning between 0.01 % and 5 %. This shows that the RMS values of the frequency spread measured in TTF cavities, between 0.05% and 0.45%, depending on the mode, will reduce the emittance dilution markedly.

Thus, only a small frequency detuning error is required to make a dramatic improvement in the emittance dilution. This is further testified to in Fig. 6, where the emittance dilution is illustrated versus the RMS value of the random cavity misalignment. For the example given, a RMS random offset of 700 μm the dilution in the emittance of the beam is kept below 10 % for an RMS frequency detuning error as small as 0.01 % (~ 200 kHz). The inset to Fig. 6 shows the emittance dilution down the linac for the TESLA baseline design case in which the cavities are allowed an RMS misalignment offset of 500 μm and an RMS frequency detuning error of 0.1 %. The mean emittance dilution taken over 80 machines reaches a maximum of 4 % at the end of the linac.

In conclusion, a large dilution in the emittance of the beam in the TESLA linac will occur for cavities constructed with no random frequency errors. However, in reality random frequency errors will occur as a natural consequence of the fabrication process and thus rather loose transverse misalignment tolerance are allowable. In particular, a misalignment tolerance of 0.5 mm with a 0.1 % RMS detuning of cavity frequencies restricts the emittance dilution to less than 6 %. For convenience the crucial alignment tolerances are collected in Table 2.

Table 2: Percentage emittance dilution for various misalignment tolerances. The standard error of the sampled mean is also given.

RMS Frequency Detuning (%)	RMS Misalignment (μm)		
	100	500	1000
0	47.2±53.6	1180±1339	4721±5357
0.01	0.20±0.11	5.12±2.77	20.47±11.08
0.05	0.17±0.08	4.20±2.07	16.80±8.29
0.1	0.17±0.10	4.18±2.53	16.71±10.12
0.2	0.18±0.08	4.38±2.02	17.51±8.08
0.3	0.18±0.09	4.55±2.30	18.19±9.21
0.5	0.19±0.10	4.68±2.44	18.71±9.74
0.8	0.18±0.10	4.58±2.41	18.31±9.66
1.0	0.17±0.08	4.20±2.00	16.79±8.01
3.0	0.18±0.09	4.42±2.32	17.66±9.29
5.0	0.19±0.08	4.67±2.11	18.66±8.44

REFERENCES

[1] P.B. Wilson, SLAC-PUB-4547, 1989
[2] K. Yokoya, DESY Report 86-084, 1986
[3] ILC-TRC 2nd Report, SLAC-R-606, 2003
[4] R. Brinkmann *et al.* (editors), TESLA Report 2001-23
[5] R.M. Jones *et al.*, EPAC04, SLAC-PUB-10556, 2004
[6] R.M. Jones *et al.*, LINAC02, SLAC-PUB-9467, 2002
[7] G. Kreps, private communication
[8] The MAFIA Collaboration, MAFIA-L, CST GmbH, Darmstadt, 1994

LINAC ALIGNMENT AND FREQUENCY TOLERANCES FROM THE PERSPECTIVE OF CONTAINED EMITTANCES FOR THE G/NLC

R.M. Jones†, SLAC, Stanford, CA 94309, USA

Abstract

The next generation of linear colliders will consist of several tens of thousands of accelerating structures and this will entail inevitable errors in the dimensions and alignments of cells and groups thereof. These errors result in a dilution of the beam emittance and consequently a loss in overall luminosity of the collider. For this reason it is important to understand the alignment tolerances and frequency tolerances that are imposed for a specified emittance budget. Here we specify an emittance dilution of no more than 10% of the injected nominal value of 20 nm.rads and we track the progress of the beam down the linac whilst accelerating structures (and sub-sections thereof) are misaligned in a random manner. Random frequencies are also incorporated in the misalignment analyses. Tolerances are specified for both frequency errors and misalignment errors.

INTRODUCTION

The main X-band linacs of the G/NLC (Global/Next Linear Collider) [1] are required to sustain an unloaded gradient of 65 MV/m (with a loaded gradient of 55 MV/m) and be able to accelerate 192 bunches of charged particles for almost 14 km. In order to prevent breakdown occurring in the accelerating structures, surface cleanliness, surface electromagnetic fields and several other parameters have been carefully studied and the breakdown events have been reduced to manageable rates [2].

It is also important to minimize the wakefield left behind each accelerated bunch in the train as cumulative BBU [3] or severe emittance dilution [4] will occur. The wakefield is reduced by almost 2 order of magnitude at the first trailing bunch by detuning the cell frequencies such that the characteristic modal frequencies add destructively [5]. However, soon thereafter the wakefield re-coheres and further down the train succeeding bunches would experience a wake large enough to drive a BBU instability. This is prevented by coupling out the wake from each cell to four waveguide-like manifolds [6] that lie co-linear with the axis of the accelerating structure. This method of wakefield damping has been successful in reducing the wakefield for earlier structures [7].

However, the latest structures, motivated by electrical breakdown considerations [2], are a factor of 3 shorter than the original DDS series [5]. Reducing the accelerating structure's length increases the dipole wakefield mode spacing and hence reduces the effectiveness of the overlapping of neighbouring modes. For this reason we interleave the modes of neighbouring structures and effectively fill-in the space between modes in a single structure. The focus herein is on the G/NLC baseline design structure H60VG3S17. This accelerating structure is 60 cm in length and consists of 55 cells with an initial fundamental group velocity of 0.03c. The average iris to free space wavelength is 0.17.

† Supported by the Department of Energy, grant number DE-AC03-76SF00515

The final emittance of the beam can be diluted by a beam injected off axis (injection offset) and by misalignment of cells. Space considerations prevent the former being presented. However, we refer the interested reader to [8] for some details on the remarkably loose frequency tolerances for a beam subjected to an injection offset.

Here we investigate the emittance growth due to long-range transverse wakefields for misaligned cells in the accelerator structure. We study the case of a beam injected on-axis but with misaligned cells (and groups thereof). In particular, we include frequency errors and calculate their impact on misalignment tolerances.

The paper is organized such that the next section discusses the wakefield of the G/NLC baseline design and the second main section analyzes misalignment tolerances.

TRANSVERSE WAKEFIELDS

The G/NLC baseline design uses four-fold interleaving of the dipole frequencies of accelerator structures [9]. The dominant first dipole band wake [10] that results from this process is illustrated in Fig. 1. For the sake of comparison, the decay in the envelope of the wakefield that occurs due to purely Ohmic damping together with that which occurs due to detuning the cell frequencies is also shown. Detuning the cell frequencies gives rise to destructive interference of the modes and results in the

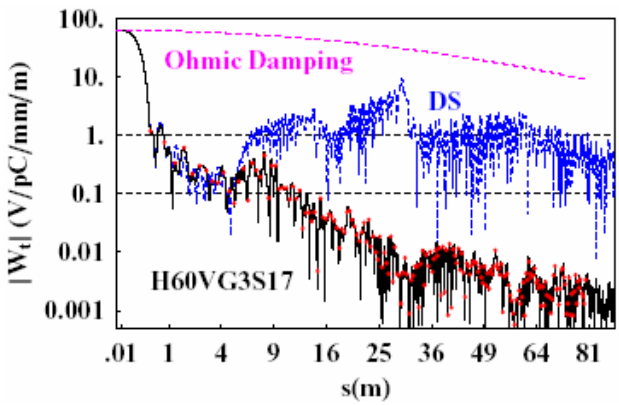

Figure 1: Envelope of the four-fold interleaved long-range transverse wakefield $|W_t|$ for H60VG3S17. The red dots indicate the location of each bunch. Also shown, in blue, is the wake that results from detuning only (DS), and in magenta, the decay of the wake that results from copper losses in the cells (Ohmic damping).

Gaussian functional fall-off in the envelope of the wakefield for the first few meters, illustrated in Fig. 1. However, eventually the modes recohere. The recoherence position is set by the minimum mode spacing. For this particular accelerator structure the dashed blue curve in Fig.1 gives a recoherence position of ~ 6.4 m. In H60VG3S17 a portion of the remaining wakefield is coupled out through a slot cut into each cell to four attached collinear waveguide-like manifolds and this reduces the wakefield to below 1 V/pC/mm/m (refer to the black line in Fig. 1).

MISALIGNMENT TOLERANCES

Introduction

Misalignments from cell-to-cell and groups thereof (structure-to-structure in particular) cause a dilution in the emittance of the beam. In addition to cell misalignment errors there are frequency errors that are caused by fabrication errors and by errors in the original design. We constrain the emittance dilution to be no more than 10 % of the injected emittance and we consider the misalignments that are allowable both with and without random frequency errors. To begin, we consider the case excluding frequency errors and we make an analytical estimate for the misalignments. The analytical estimate is compared with tracking simulations performed with LIAR [11].

Analytical Estimation of Emittance Dilution

In order to estimate the growth of the projected emittance $\Delta\varepsilon$ of a train of bunches caused by misaligned accelerator structure cells the following formula for the expectation value of [12] is used:

$$\langle \Delta\varepsilon \rangle = r_e^2 N^2 \bar{\beta}_0 L_s^2 \langle \Delta S_k^2 \rangle \frac{1-(\gamma_0/\gamma_f)^{1/2}}{\gamma_0^{1/2}\gamma_f^{3/2}} \qquad (1)$$

where r_e is the classical electron radius, N is the number of is the number of particles in the bunch, $\bar{\beta}_0$ is the average value of the beta function at the beginning of the linac, N_s is the number of structures in the linac, L_s is the length of the structure, γ_0 and γ_f are the initial and final relativistic factors of the beam. The sum wakefield of the k^{th} bunch is defined in terms of the wakefield at the location of bunch w_k as: $S_k = \sum_{i=1}^{k} w_k$ and the RMS value by: $S_{RMS} = \langle \Delta S_k^2 \rangle^{1/2}$ where ΔS_k is the difference between S_k and the average value $\langle S \rangle = N_b^{-1} \sum_{k=1}^{N_b} S_k$. Here, N_b is the number of bunches.

Eq. (1) is derived excluding frequency errors and assuming a lattice with the beta function smoothly increasing along the linac as $\bar{\beta} \propto E^{1/2}$.

For small misalignments, w_i is a linear function of cell offsets, $W_i = \sum_{s=1}^{N_c} w_{is} y_s$ (N_c = Number of cells). The matrix W for the G/NLC structure H60VG3S17 with 55 cells is based on the method in [13]. It has a dimension of N_b x N_c. In our calculation we used N_b = 192 for a bunch spacing of 1.4 ns and N_c = 55

Eq. (1) is utilized to obtain the RMS alignment tolerances on cells and this is compared with tracking simulations in the next section.

Tracking Simulations

The beam is tracked down the complete linac under the influence of misaligned groups of cells and the emittance dilution is recorded. The results of such simulations are illustrated in Fig. 2 where the emittance growth due to cell-to-cell and structure-to-structure misalignments are shown. For each point we make 50 tracking simulations and take the mean emittance dilution. There is a clear quadratic dependence on RMS misalignment. We perform similar simulations for groups of cells and extract the RMS offset that allows no more than 10 % dilution in

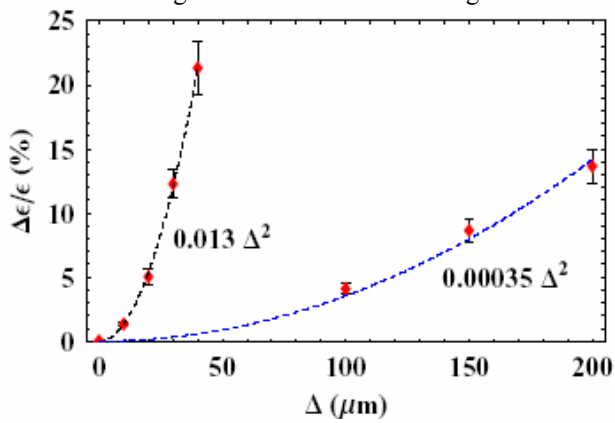

Figure 2: Percentage emittance growth $\Delta\varepsilon/\varepsilon$ versus RMS offset Δ for both single-cell and single-structure misalignments (illustrated by the black line and the blue line, respectively). The quadratic fit is also shown for each misalignment type. Error bars are for the standard error of the sampled mean.

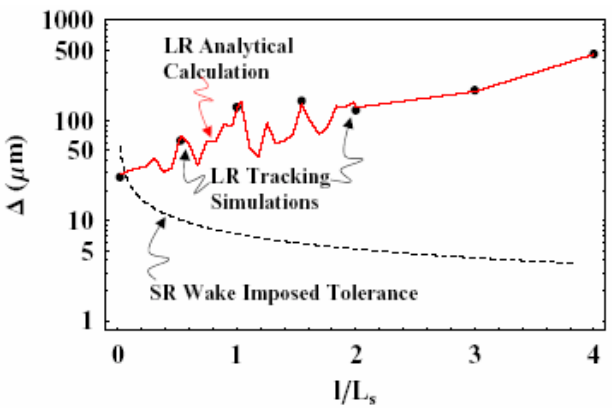

Figure 3: Tolerance Δ for random-random errors versus misalignment length l in units of the structure length L_s (0.60m). The solid red curve shows the result of an analytic calculation for the long-range (LR) wakefield tolerance based on Eq. (1) and the dots are calculated by tracking the beam down complete linac. The dashed line shows the short range (SR) wakefield tolerance.

the beam emittance. The large number of wakefiles are processed with a *Python* [14] code, prior to tracking the beam down the linac. These results are displayed in Fig. 3 together with those obtained from Eq. 1. The agreement is excellent. Also shown is the alignment tolerance that results from the short-range wakefield. This is of the order of 7 μm from one structure-to-the-next and it will be achieved by beam-based alignment (from the dipole signal radiated to the manifolds).

Similar simulations are performed for structure bows and tilts. This results in a random misalignment tolerance of 83 μm for the saggitta of a bowed structure and 0.4 mm.rads for the angular tilt of a structure.

Including Random-Systematic Frequency Errors

Frequency errors that are random within a given structure but are repeated from structure-to-structure are referred to herein as random-systematic errors. These errors are unlikely to occur in the fabrication process as it is more likely that errors from structure-to-structure will also be random. Nonetheless, we investigate the tolerances that are imposed for a 10 % emittance dilution for random-systematic errors and these results are presented in Fig. 4. In this simulation frequency errors with an RMS value of 5 MHz have been used. Each of the dashed lines corresponds to a machine made with a given error repeated from structure-to-structure throughout the linac. This type of error can give rise to tight alignment tolerances, since the lowermost line, for example in Fig. 5 specifies a structure-to-structure alignment of ~ 50 μm. Thus, in designing and fabricating the structures care must be taken to avoid such systematic errors.

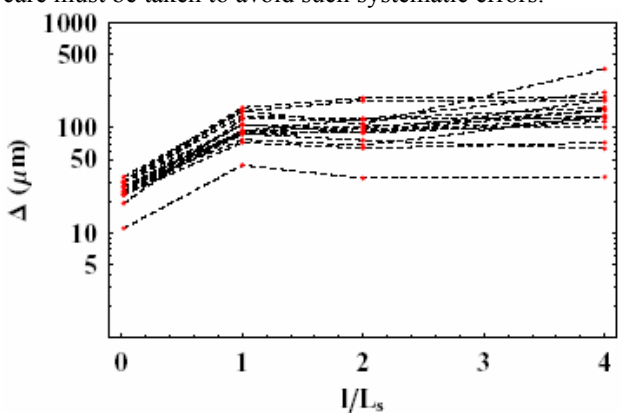

Figure 4: Tolerance Δ for random-systematic errors versus misalignment length l in units of the structure length L_s (0.60 m). The dots indicate the results of the tracking simulation. The tolerance is for long-range wakefields.

Including Random-Random Frequency Errors

Errors that are random within a given structure and are randomly distributed throughout the entire linac are considered here. This is representative of tool wear in machining several tens of thousands of structures, for example.

In particular, frequency errors with an RMS value of 3 MHz and 5 MHz are used in the alignment tracking simulations. The results of these simulations are presented in Fig. 5 where they are compared with the case where frequency errors are excluded. It is clear that the introduction of frequency errors makes the alignment tolerances tighter. For the G/NLC baseline design there

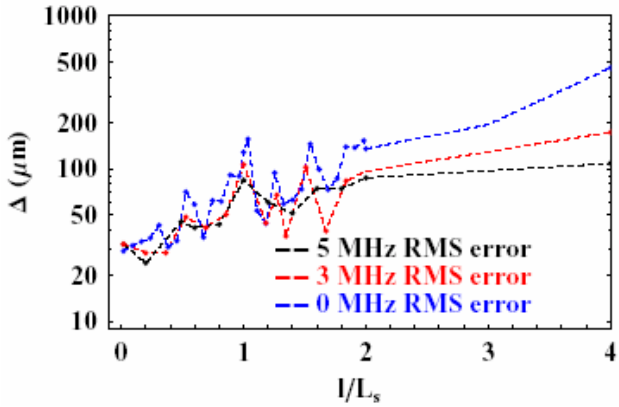

Figure 5: Tolerance Δ for random-random errors versus misalignment length l in units of the structure length L_s (0.60 m). The blue curve and dots are the results of a tracking simulation with no frequency errors included.

are 4 structures per girder so that, with reference to Fig. 5, the girder-to-girder alignment is ~ 200 μm for and ~100 μm for frequency errors with an RMS value of 3 MHz and 5 MHz, respectively.

CONCLUSIONS

To operate the collider with reasonable alignment and frequency tolerances we adopt a random-random dipole frequency tolerance of 3 MHz (which is comparable with that on the fundamental mode which is ~1 MHz) [15]. The cell and structure alignment tolerances are then approximately 28 μm and 100 μm, respectively.

ACKNOWLEDGEMENTS

This work has benefited greatly from stimulating discussions in the parameters meetings at SLAC organized by Tor Raubenheimer. I am grateful to Peter Tenenbaum for modifying the code LIAR.

REFERENCES

[1] ILC/TRC 2nd Report, SLAC-R-606, 2003
[2] S. Döbert, WE101, these proceedings, 2004.
[3] K. Yokoya, DESY Report 86-04, 1986
[4] R.M. Jones *et al.,* PAC99, SLAC-PUB-8101, 1999
[5] R.M. Jones *et al.*, PAC97, SLAC-PUB-7537, 1997
[6] M. Seidel *et al.*, Linac96, SLAC-PUB-7289, 1996
[7] R.M. Jones *et al.*, Advanced Accelerator Concepts, Lake Tahoe, CA, SLAC PUB-7387, 1996
[8] R.M. Jones *et al.*, EPAC04, SLAC-PUB-10556, 2004
[9] R.M. Jones *el al.*, PAC03, SLAC-PUB-9868, 2003
[10] R.M. Jones, MOP28, these proceedings, 2004
[11] R. Assman *et al.*, LIAR, SLAC-PUB AP-103, 1997
[12] K.L.F. Bane *et al.,* EPAC94, SLAC-PUB-6581, 1994
[13] R.M. Jones *et al.,* Linac96, SLAC-PUB-7287, 1996
[14] www.python.com
[15] J.W. Wang *et al.*, Linac00, SLAC-PUB-8583, 2000

THE IMPACT OF LONGITUDINAL DRIVE BEAM JITTER ON THE CLIC LUMINOSITY

D. Schulte, E. J. N. Wilson, F. Zimmermann, CERN

Abstract

In the Compact Linear Collider (CLIC) now under study at CERN, the RF power which accelerates the main beam is provided by decelerating a high current drive beam. Errors in the timing and intensity of the drive beam can turn into RF phase and amplitude errors that are coherent along the whole main linac and the resulting error of the final beam energy, in combination with the limited bandwidth of the beam delivery system, can lead to a significant loss of luminosity. We discuss the stability tolerances that must be met by the drive beam to avoid this loss. We also examine one of the most important sources of this jitter, which stems from the combination of RF jitter in the drive beam accelerator and subsequent bunch compression. Finally we give details of a potential feedback system that can reduce the drive beam jitter.

MAIN LINAC RF JITTER TOLERANCE

The RF can jitter in phase and amplitude; both result in a change of the effective gradient. The RF jitter tolerance is given by two main constraints. First, the luminosity loss should be limited to less than 2%. Second, the energy jitter should not lead to a significant widening of the luminosity spectrum at collision. Since the mean RF phase in the linac is about 15°, a coherent error of the RF phase all along the main linac of 0.225° corresponds to an effective gradient error of about $\Delta G/G \approx 10^{-3}$. The final energy error and the luminosity loss will be quite similar in the two cases.

In CLIC the single bunch RMS energy spread is about $\sigma_E/E \approx 3.5 \times 10^{-3}$. Consequently a beam energy jitter of $\sigma_{jitt}/E \approx 1 \times 10^{-3}$ leads to a negligible broadening of this spread, while $\sigma_{jitt}/E = 2 \times 10^{-3}$ results in probably acceptable but noticeable change of the total spread to $\sigma_E/E \approx 4 \times 10^{-3}$. We prefer to aim for $\sigma_{jitt}/E \leq 10^{-3}$.

To estimate the luminosity loss resulting from the RF jitter integrated simulations of the main linac, beam delivery system and beam-beam interaction have been performed, using PLACET [1] and GUINEA-PIG [2]. It has been found that the jitter tolerance arising from the luminosity loss due to multi-pulse emittance growth in the main linac is more relaxed than that from the above energy stability [3]. However, the limited bandwidth of the current beam delivery system results in a tighter energy error tolerance of $\sigma_{jitt}/E = 0.7 \times 10^{-3}$ for 2% luminosity reduction [5], see Fig. 1. This limitation is to a large extent due to the collimation system. Removing it from the simulation yields a tolerance of $\sigma_{jitt}/E = 1.2 \times 10^{-3}$.

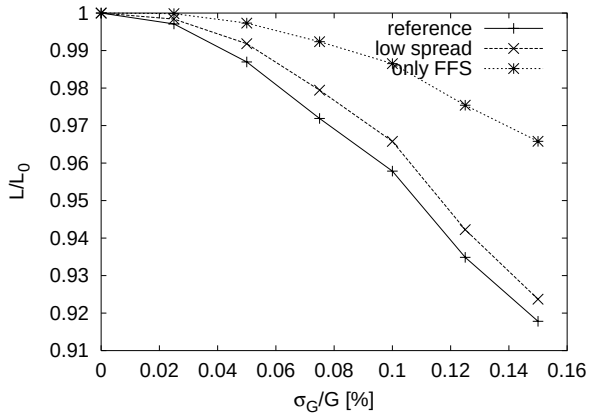

Figure 1: The relative luminosity as a function of a coherent gradient error in the main linac.

Table 1: Some important drive beam parameters.

parameter	symbol	unit	value
particles per bunch	N	$[10^{10}]$	6
energy before DBA	E_0	[MeV]	50
energy after BDA	E_f	[MeV]	2000
bunch length before DBA	$\sigma_{z,0}$	[mm]	4
bunch length after DBA	$\sigma_{z,f}$	[mm]	0.4

DRIVE BEAM TOLERANCES

The RF phase and amplitude in the main linac depends directly on the drive beam; the drive beam intensity and phase tolerances are hence $\delta I/I \leq 10^{-3}$ and $\delta\Phi \leq 0.225^\circ$ (equivalent to $\delta z \leq 6\mu\mathrm{m}$), respectively. After a short overview of the drive beam generation system one of the main jitter generation mechanisms will be discussed, focusing on coherent errors of the whole drive beam.

The drive beam is generated in a complex that is located centrally between the two linacs, for parameters see table 1. Each $92\mu\mathrm{s}$ long drive beam pulse is produced in the drive beam injector complex and then accelerated in the drive beam accelerator (DBA), with an RF frequency of $30.0/32\mathrm{GHz} = 937\mathrm{MHz}$. In a delay loop the pulse is then split into $130\mathrm{ns}$ long sub-pulses. At the end of the delay loop these pulses are pairwise merged forming new pulses of $130\mathrm{ns}$ length but with twice the previous bunch frequency. In two following combiner rings 16 of these new pulses are again merged, increasing the beam intensity as well as the bunch frequency by another factor of 16. Each of the generated 22 pulses is then sent through a transport line to the start of one drive beam decelerator, where it will arrive in time to produce the RF power needed for the main beam.

Table 2: The parameters of the two drive beam bunch compression stages. The tolerances for a coherent error causing an energy error in the main linac of $\delta E_f/E_f = 0.001$ are also given. Full beam loading was assumed.

variable	unit	first	second
L_1	[m]	2	16
G_1	[MV/m]	13	13
ϕ_1	[°]	60	-60
$R_{56}^{(1)}$	[m/MV]	0.0022	-0.00025
$\delta N/N$	$[10^{-3}]$	0.3	
δz	[μm]	70	
$\delta E_0/E_0$	$[10^{-3}]$	6	
$\delta G/G$	$[10^{-4}]$	200	2.8
$\delta\phi$	[°]	0.8	0.01

Short bunches of $\sigma_z \approx 0.4\mathrm{mm}$ are required in the decelerators for efficiency, while the drive beam bunches are likely to be as long as $\sigma_{z,0} \approx 4\mathrm{mm}$ [6] at injection into the DBA. The required bunch compression can turn energy errors into longitudinal bunch position and hence RF phase errors. If all the compression were performed after the DBA without further RF one would require a total compression $R_{56} = 0.4\mathrm{m}$ for the maximum allowed correlated beam energy spread of $\sigma_E/E = 0.01$. The drive beam mean energy error tolerance would then be $\delta E/E \approx 1.6 \times 10^{-5}$, putting strong limits on the DBA RF phase and gradient tolerance; also the beam current needs to be stable to this level, since the DBA is fully loaded.

To develop a first order concept of the bunch compression system a simple program has been developed to simulate longitudinal drive beam effects. It takes the single and multi-bunch beam loading into account and assumes compression chicanes and bends which couple only the longitundinal particle positions and energies linearly with a given R_{56}. With the bunch compressor detailed in table 2, a number of tolerances can be largely relaxed. The compressor uses opposite RF phases in the two stages, and is optimised to be independent of the initial energy error of the bunches. The charge stability tolerance is somewhat tighter than that required from the amplitude stability (10^{-3}). It can be relaxed if structures with less than 100% beam loading are used; reducing the loading to 75% (in power) would increase the tolerance to $\delta N/N = 6 \times 10^{-4}$ and require only $\approx 30\%$ more compressor power.

The remaining tight tolerance is the RF phase stability; this is unavoidable because the RF phase defines the final timing of the bunches. It could only be avoided if no bunch compression were required, e.g. by using an RF injector that could produce bunches with $\sigma_z \leq 0.4\mathrm{mm}$. However, it is not obvious that such an injector can be constructed. Also the longitudinal jitter tolerance for the bunches of this injector would be very tight, namely $\delta z \leq 6\mu\mathrm{m}$.

The tolerance of the main beam to a longitudinal shift of the whole drive beam pulse can be largely improved by using the drive beam to generate the power for the main beam bunch compressors. If the bunch compressor beam loading effects are small, the main beam bunches will always be set to the same drive beam phase. If one drive beam generator is used for both main linacs, even the relative timing between the electron and positron beam will be correct.

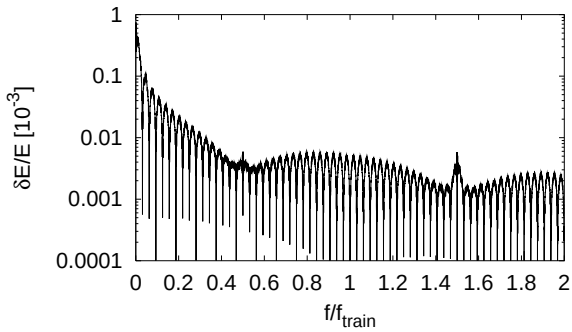

Figure 2: The maximum main beam final energy error due to the drive beam phase jitter resulting from an RF phase error of $0.01°$ in the second drive beam bunch compressor stage as a function of the frequency of the RF error. The results for an RF amplitude error in the same stage of 2.8×10^{-4} are comparable.

If an error is not coherent along the whole drive beam pulse, the effect on the main beam is more complicated since the effect of the merging of drive beam sub-pulses needs to be included. In this case, the effect of most frequencies averages out, except for those close to harmonics of the sub-pulse frequency $f_{train} = 1.0/130\mathrm{ns}$. The main linac energy variation is shown in Fig. 2 for the important example of a $0.01°$ klystron RF phase jitter of the second bunch compressor stage. The bunch compressor structures were modelled as constant impedance structures with no losses. A fill time of twice the sub-pulse length ($260\mathrm{ns}$) was used. This efficiently suppresses the dangerous harmonics of the sub-pulse frequency. As can be seen, the effect is strongly reduced for high frequencies. But the tightest low frequency tolerance is $0.013°$ and is barely visible in the figure. However, these low frequency errors can be controlled using a feedback on the klystron level [7].

PHASE COMPENSATION FEEDBACK

Another improvement of the tolerances can be expected from beam-based feedback. First, the phase of the RF needs to be measured. This can be achieved by fully compressing the beam and measuring its phase. The bunches will then need to be uncompressed again and recompressed before the decelerator. This would be a convenient choice if the beam is fully compressed in the DBA. Another option would be to measure the phase and the beam energy error in a dispersive point, so that one can predict the phase after compression. One can also measure the phase at two points which are separated by some R_{56}. Several possibilities exist to correct the measured phase error, e.g. one can modulate the beam energy by use of an accelerating struc-

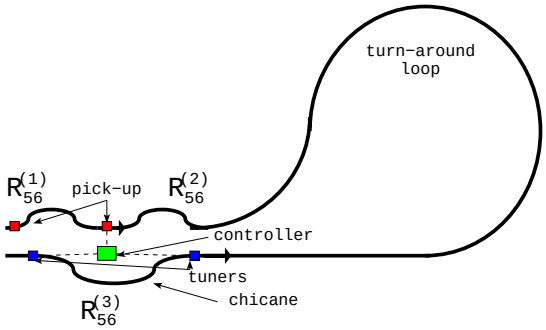

Figure 3: An example layout of a phase feedback.

ture before the final bunch compression. Or one can use transverse deflectors to introduce a half-sine-wave perturbation in the central orbit in a dispersive and anisochronous section of beam line. To first order the path length between the deflectors will be proportional to the amplitude of the deflection. The amplified measured phase signal must arrive at the deflectors before the beam. Such a feedback can be placed in many locations, e.g. before or after the combiner rings or at each turn-around that bends a drive beam pulse into a decelerator; the optimum will have to be determined. Here we present the example of the feedback in the final turn around, with the detector before and the deflectors in a chicane of four bending magnets as shown in Figure 3.

This chicane would contain bends to convert transverse deflection to path length. It would have to be achromatic and isochronous in its overall properties to avoid compression or further phase errors. However, it would contain a non isochronous section between the deflectors that need to be spaced in betatron phase by exactly π. It would be convenient if the total bending angle would be zero to preserve the line of the turned around beam.

To introduce significant path length, the bending angles, θ, in the chicane must be large since they contribute a term proportional to $\theta \sin\theta$ to the ratio between path length and deflection. The focusing lattice into which the magnets are embedded is not trivial and must be chosen to have two points exactly π apart for the deflectors.

A much simpler alternative is to place the deflectors in the final quadrant of the turn-around lattice thus saving the need for an additional chicane. In order to demonstrate the feasibility we chose the final quadrant of the combiner ring lattice, which is achromatic and isochronous from end to end. It is rather easy to find two places for the deflectors which are exactly π apart, (D1 and D2) in Fig. 3.

For the matrix element that relates horizontal deflection to path length, we find $R_{52} = \Delta s/\Delta x' = -0.756\mathrm{m}$, using MAD8 to compute this value from D1 to D2. This would provide a range of path length adjustment of $\pm 100\mu\mathrm{m}$ with deflectors of $\pm 0.13\mathrm{mrad}$.

The transverse deflectors we consider are based upon an S-band structure designed for use as part of an RF separator

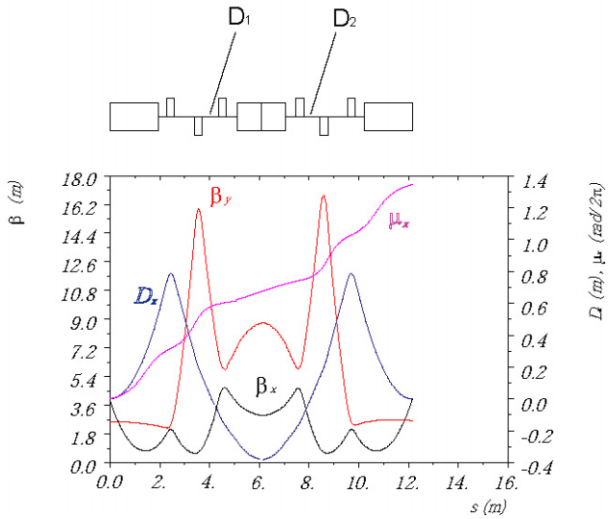

Figure 4: The lattice of the feedback.

project [8]. The use of wall mounted stripline deflectors or fast pulsed magnets could be feasible, such as those used in the TESLA damping ring. A 15GHz scaled down version of the S-band deflecting cavities has been calculated[9]. It has an aperture of $9.4\mathrm{mm}$ and a length of $0.65\mathrm{m}$; with an input power of $1.82\mathrm{kW}$ it could deflect the $2\mathrm{GeV}$ beam by $0.13\mathrm{mrad}$.

CONCLUSION

The longitudinal jitter of the CLIC drive beam has to be strictly limited in order to avoid significant luminosity loss. One of the main sources for such jitter is the combined effect of energy errors during drive beam acceleration and the bunch compressor. Some examples of means to cope with the problem have been shown.

REFERENCES

[1] D. Schulte, E. T. D'Amico, G. Guignard and N. Leros, "Simulation package based on PLACET," (2001) CERN-PS-2001-028-AE and PAC 2001.

[2] D. Schulte, "Beam-beam simulations with GUINEA-PIG," eConf **C980914** (1998) 127 and CLIC Note-387.

[3] D. Schulte, "Effect of RF-Phase Jitter on the Main Beam Emittance in CLIC". (2000) CLIC-Note 432.

[4] D. Schulte, "The Drive Beam Accelerator of CLIC". (1998) CERN/PS 98-042 (LP)

[5] D. Schulte and F. Zimmermann, "RF Phase and Amplitude Tolerance in the CLIC Main Linac". (2003) CLIC-Note 588.

[6] G. Guignard (ed.). (2000) CERN 2000-08.

[7] E. Jensen and I. Syratchev. Private communication.

[8] Ph. Bernard, H. Lengeler, V. Vaghin, "New disk-loaded waveguides for the CERN rf separator".(1970)CERN 70-26

[9] L. Thorndahl. Private communication.

ELECTRON-CLOUD EFFECTS IN THE POSITRON LINACS OF FUTURE LINEAR COLLIDERS

A. Grudiev, D. Schulte, F. Zimmermann, CERN; K. Oide, KEK

Abstract

Inside the rf structures of positron (or electron) linacs for future linear colliders, electron multipacting may occur under the combined influence of the beam field and the electro-magnetic rf wave. The multipacting can lead to an electron-cloud build up along the bunch train. Electrons are also created by collisional and field ionization of the residual gas. We present simulation results of the electron build up for various proposed designs, and discuss possible consequences.

INTRODUCTION

Table 1 lists beam and rf parameters for the linacs of 3 different linear-collider projects. In the following, we discuss the primary-electron generation, electron accumulation and multipacting under the influence of beam and rf fields, as well as mechanisms of emittance degradation.

Table 1: Beam and RF cell parameters

design	TESLA	N(G)LC	CLIC
particles/bunch N_b [10^9]	20	7.5	4
bunch spacing $L_{\rm sep}$ [ns]	337	1.4	0.67
rms bunch length σ_z [μm]	300	110	35
initial energy E_b [GeV]	5	8	9
rms hor. size σ_x [μm]	260	57	14
rms vert. size σ_y [μm]	11	6	2
norm. h. emit. $\epsilon_{N;x}$ [μm]	8	3.6	0.55
norm. v. emit. $\epsilon_{N;y}$ [nm]	20	40	5
beta function $\beta_{x,y}$ [m]	80	14	5
pressure [ntorr]	10	10	10
frequency $f_{\rm rf}$ [GHz]	1.3	11.42	30
radius R [mm]	107	10.4	4
cell length L [mm]	115	7.5	3.3
rf wave length $\lambda_{\rm rf}$ [mm]	230	26	10
field E_0 [MV/m]	23.4	45.1	150

IONIZATION RATES

Primary electrons are created by ionization of the residual gas. The collisional ionization cross section $\sigma_{\rm ion}$ is abut 2 Mbarn for nitrogen or carbon monoxide molecules at utrarelativistic beam energies, yielding 6×10^{-8} electrons per meter and per positron for a pressure of 10 ntorr. Another ionization process that can become important in linear colliders is field ionization [1]. In the quasistatic limit, its ionization rate is [2, 3]

$$w = 4\omega_0 \left(\frac{E_i}{E_h}\right)^{5/2} \frac{E_a}{E} \exp\left[-\frac{2}{3}\left(\frac{E_i}{E_h}\right)^{3/2}\frac{E_a}{E}\right] , \quad (1)$$

where $\omega_0 = \alpha^2 m_e c^2/\hbar$ is the atomic frequency unit, E_h and E_i are the ionization potentials of hydrogen (13.6 eV) and the gas atom or molecule in question (11.26 eV for carbon monoxide, 14.5 eV for nitrogen), and $E_a = m_e c^2\alpha^4/(r_e e)$ is the atomic unit of the electric field. A different formula whose numerical evaluation yields similar results was given in [1]. The ionization probability is further enhanced at high frequencies [4], i.e., for short bunch lengths σ_z and large ionization energies E_i [3], namely at $E_i > e^2E_0^2\sigma_z^2/(4m_ec^2)$; the right-hand side is 24.1 eV for TESLA, 12.0 eV for NLC/GLC and 13.5 eV for CLIC. Field ionization may also occur for electron beams and could there enhance fast beam-ion instabilities. The probability of field ionization rises steeply from 0 to 1 at a field of about 20 GV/m. Such beam fields are expected at higher beam energies in CLIC and possibly in NLC/GLC. Assuming that, at 500 GeV/c, the beam is ionized within a few rms beam sizes, the ionization rate amounts to the production of several 10^7 electrons per meter and per passing bunch, which is some orders of magnitude more than from collisional ionization. The progress of field ionization over successive bunches depends on the thermal motion of molecules. At room temperature, the rms vertical distance travelled by a gas molecule between two successive bunches is about 0.3–1 σ_y for CLIC, and larger for the other designs.

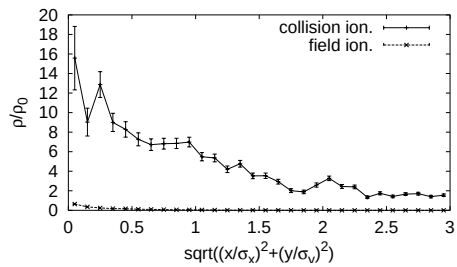

Figure 1: Electron density in units of local gas density as a function of the radial position in units of 0.1σ during a bunch passage at the end of the CLIC linac for collisional and field ionization.

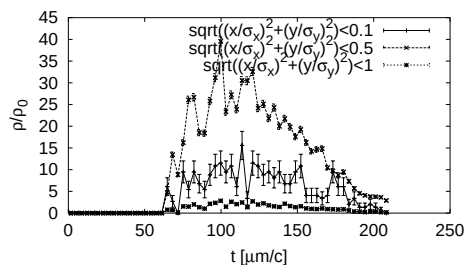

Figure 2: Average electron density, inside the 3 ellipses defined by $((x/\sigma_x)^2+(y/\sigma_y)^2)^{1/2}$ equal to 0.1, 0.5 and 1, in units of the local gas density as a function of time during the passage of a CLIC bunch with field ionization.

Figure 1 shows the radial distribution of electrons during a bunch passage at the end of the CLIC linac. The com-

bined effect of electron creation by ionization and pinch near the bunch center is evident. Electrons inside the bunch perform 1–2 oscillations in the beam potential at the start of the linac and about 3 times more at its end, for all 3 projects. In the case of collisional ionization the peak electron density in Fig. 1 is about 70% of the local gas density, which, at 10 ntorr, is 3×10^{14} m^{-3}. With field ionization, the electron density is about 15 times higher than the gas density. Figure 2 illustrates the time evolution along the bunch of the central electron density with field ionization.

ELECTRON BUILD UP

The electrons are subjected to the field of the beam and to the electric and magnetic fields of the rf. The peak electric field of the rf becomes comparable to the peak field of the beam at a transverse distance $r_{\rm crit} \approx 2N_b r_e m_e c^2/\left(\sqrt{2\pi}\sigma_z(eE_0)\right)$, which is about 1/2–1/3 of the iris radius for GLC/NLC and CLIC, and $1/10$ of the iris radius for TESLA. Therefore, the beam field appears important during the creation of the electrons and the initial acceleration close to the beam, but not for the electron motion at larger amplitudes. An electron starting from rest, during half an rf cycle passes a longitudinal distance

$$\Delta z \approx \int_0^{T_{\rm rf}/2} \sqrt{\frac{\frac{e^2E_0^2}{\omega_{\rm rf}^2}(1-\cos\omega_{\rm rf}t)^2}{m_e^2+\frac{e^2E_0^2}{\omega_{\rm rf}^2c^2}(1-\cos\omega_{\rm rf}t)^2}}\,dt\,, \qquad (2)$$

which amounts to 0.08 m, 4 mm, and 2 mm for TESLA, GLC/JLC and CLIC, respectively. These distances are a significant fraction of the cell lengths in Table 1. The maximum energy gain in half an rf cycle is

$$\Delta E \approx \sqrt{\left(\frac{eE_0c}{\pi f_{\rm rf}}\right)^2 + m_e^2c^4} - m_ec^2\,, \qquad (3)$$

or 1.3 MeV, 120 keV, and 190 keV for TESLA, NLC/GLC and CLIC, respectively.

The primary ionization electrons are either trapped near the centre of the chamber by the beam field and rf fields, possibly accelerated in the longitudinal direction, or they escape radially towards the wall, where they can induce multipacting. The electron cloud build up is modeled by a modified version of the code ECLOUD. It is important to use a sufficient number of time steps (typically several 1000 between bunches) in order to avoid spurious multipacting: a position error of 1 μm, with an rf field of 200 MV/m yields an electron energy of 200 eV, close to the maximum of the secondary emission yield.

To obtain a realistic description of the rf forces acting on the electrons, a 'snapshot' of the complex amplitudes for the longitudinal and radial electric field and the azimuthal magnetic field of the rf inside a CLIC cell as function of the radial and longitudinal coordinates were computed by HFSS. These fields are read into the ECLOUD code. Depending on the longitudinal position at the moment of its creation during a bunch passage, a complex phase factor is determined for each individual electron, such that the local rf phase is correctly synchronized with the bunch arrival. If an electron moves longitudinally the time relation between the rf wave and the beam forces of later bunches will dephase from the exact value. This is difficult to avoid in the present version of ECLOUD, where the bunch arrives 'everywhere in z' at the same time. The present aproximation is valid, if the beam field is important primarily after the electron creation inside or near the bunch, while at later times, when the electrons reside at larger ampitudes, the rf fields dominate. The phases of the rf field are kept synchronized with the electron motion throughout the simulation. The rf force on an electron is obtained by linear interpolation between the field values on the grid points computed by HFSS. The beam force is computed as for free space. A boundary with iris was introduced at either end of the cell, such that electrons are lost and produce secondaries when they impact on this boundary. At the opening of the iris quasi-periodic boundaries are applied with an appropriate shift in rf phase of 120 degrees per cell length, so that, e.g., electrons leaving the cell at large z are re-injected at $z = 0$ with a proper shift in their complex phase factor. For the other projects we scaled all dimensions of the CLIC cell with the inverse of the rf frequency and adjusted the gradient to the target value. This does not represent the exact fields in the TESLA or GLC/NLC rf structures, but may reveal the dependence on frequency and gradient.

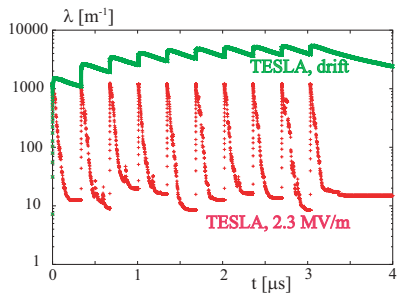

Figure 3: Evolution of electron line density during the passage of 10 bunches for TESLA without rf and with an rf field 10 times smaller than nominal.

Figures 3 and 4 display preliminary simulation results for a maximum secondary emission yield of $\delta_{\rm max} = 1.7$. Figure 3 shows that a weak rf field suppresses the electron build up which is present without rf. In Fig. 4 a higher rf field causes a linear increase in electron number along the bunch train. Figure 5 presents the energy of the electrons hitting the wall for the same two rf fields as in Fig. 4. Electrons acquire energies of several keV or 10s of keV. Most of the electrons hit the wall close to the horizontal plane, which is a reflection of the pinch inside the bunch field and the large vertical disruption. The electron distribution in the horizontal-longitudinal plane at the end of the last bunch passage is shown in Fig. 6 for GLC/NLC with the nominal rf gradient. The figure reveals that electrons are concentrated inside the beam and at the wall. An accumulation of electrons is visible also near the left iris. Interestingly, at 10 times higher gradient (not shown), electrons impact primarily on the right iris, presumably due to the higher efficiency of acceleration towards the right, i.e., in beam direction. An electron trajectory for this case

is shown in Fig. 7. Initially the electron is accelerated in the direction opposite to the positron beam motion, but at a later time it slows down and starts moving towards the right. The longitudinal turning point coincides with a moment of fast acceleration in the transverse direction.

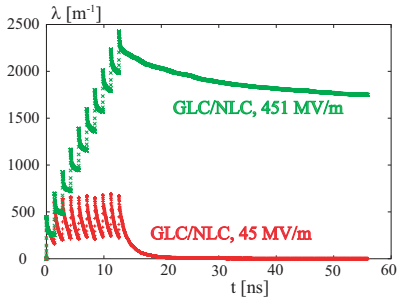

Figure 4: Evolution of electron line density during the passage of 10 bunches followed by a gap for GLC/NLC with nominal and 10 times higher rf gradient.

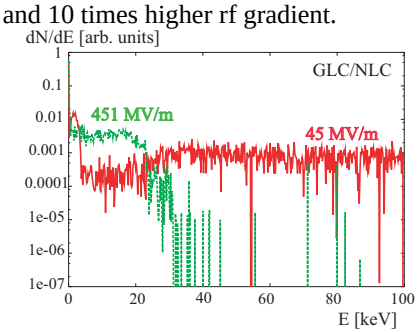

Figure 5: Energy distribution of electrons hitting the cell wall in GLC/NLC for two rf gradients.

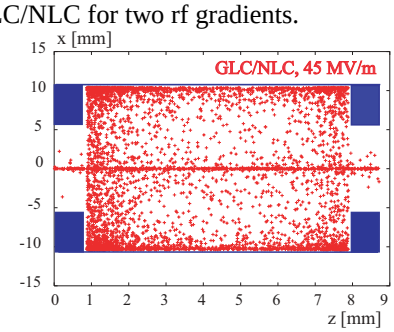

Figure 6: Snapshot of electron $z - x$ distribution after the last bunch passage for GLC/NLC at nominal rf gradient.

CONSEQUENCES

If electrons are present near the beam, they can drive beam instabilities, change the single-particle optics, and cause particle losses by scattering.

We can estimate the beam break-up instability driven by ionization electrons from a two-particle model with acceleration. Taking the electron wake field acting on the trailing particle from [5], assuming that the beta function along the linac grows as $\sqrt{\gamma}$, and modifying the treatment of [6] to account for the increase of the wake (beam-size decrease) along the linac, we estimate the beam break up parameter $\Upsilon_{\rm BBU} \approx 2\pi\rho_{e,i} r_e L\beta_i/\gamma_i^{3/2}$, where the subindex i refers to quantities at the start of the linac, and $\rho_{e,i}$ is the electron volume density generated by the leading half of the bunch, which amounts to 7×10^{10} m^{-3}, 2×10^{11} m^{-3}, and 1.4×10^{12} m^{-3}, for TESLA, NLC/GLC and CLIC, respectively. The parameter Υ, describing the enhancement

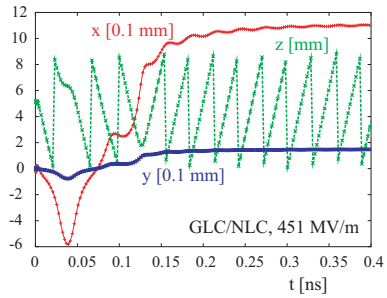

Figure 7: Sample trajectory, showing the horizontal, vertical, and longitudinal motion of an electron for GLC/NLC at an rf gradient equal to 10 times the nominal.

of an oscillation at the bunch tail, is of the order 10^{-3}, if the only electrons present are those due to collisional ionization. Hence, the beam break up is weak in this case.

The focusing effect of a uniform electron cloud inside the bunch is described by $\Delta\phi(L) = 2\pi r_e \rho_e \beta L/\gamma$. Since $\rho_e \propto \gamma/\beta$, if the electron creation is solely due to collisional ionization, the right-hand side does not depend on the beam energy, and, in this case, we have $\Delta\phi(L)^{\rm ion} \approx r_e N_b \sigma_{\rm ion}/(\sqrt{\epsilon_x \epsilon_y})(p/(k_B T))L$, which amounts to 5°, 2°, and 6° phase shift for a length of 10 km in the TESLA, GLC/NLC and CLIC linacs, respectively. With field ionization also present, the phase shift could exceed 360^o.

The probability for scattering of beam positrons off individual electrons was estimated to be negligible.

CONCLUSIONS

At elevated vacuum pressure, collisional ionization can lead to electron densities which degrade the beam quality. For high beam energies, also field ionization becomes important, supplying a larger number of electrons. Rf fields have a profound influence on the electron dynamics: moderate fields can suppress the build up; higher rf gradients trap or accelerate the primary electrons, which may acquire energies up to 10s or 100s of keV. The simulation of the electron dynamics in strong high-frequency fields requires special care in the choice of integration steps. Our simulation model is only approximate and should be reviewed in future work. Without multipacting, the possibility of beam-break up due to ionization electrons appears remote, thanks to rapid acceleration. Also, though focusing errors between several and 360 degrees may occcur along the length of the linac, and be different from bunch to bunch, the resulting emittance growth is small, roughly equivalent to that caused by a momentum error of a few permille. Incoherent scattering off electrons is negligible. In electron linacs, the fast beam-ion instability [7] may be a limitation.

REFERENCES

[1] T. Raubenheimer and P. Chen, Linac'92, Ottawa (1992).
[2] P.B. Corkum, Phys. Rev. Letters 62, 11 (1989).
[3] A. Murokh, PAC 2003 Portland (2003).
[4] S.D. Ganichev et al., Phys. Rev. Lett. 80, 11, p. 2409 (1998).
[5] K. Ohmi, F. Zimmermann, PRL 85, 3821 (2000).
[6] F. Zimmermann, JAS'2000, CERN-SL-2000-069 (AP).
[7] T. Raubenheimer, F. Zimmermann, PRE 52, 5499 (1995).

A POTENTIAL SIGNAL FOR LUMINOSITY OPTIMISATION IN CLIC

D. Schulte, CERN, Geneva, Switzerland

Abstract

Luminosity optimisation will be challenging in the compact linear collider (CLIC) studied at CERN. In particular, the signals which can be used for luminosity optimisation need to be identified. The strong beam-beam interaction in CLIC will give rise to the emission of a few megawatts of beamstrahlung; this is a potential candidate for such a signal. In this paper luminosity optimisation using the beamstrahlung is attempted for realistically shaped bunches.

INTRODUCTION

In the Compact Linear Collider (CLIC) [1], very small emittance beams are focused to a vertical spot size of about $0.7\mathrm{nm}$ in the interaction point, see table 1. The collision parameters, such as collision offset and angle, need to be carefully tuned in order to maximise luminosity. In order to optimise these parameters a fast luminosity signal is needed. Three candidate processes that could provide such a signal have been investigated in [3], beamstrahlung, bremsstrahlung and incoherent pair creation. In CLIC also a fourth process, the coherent pair creation is significant enough to be used as a signal.

Beam-Beam Interaction and Beamstrahlung

Due to the high beam density at collision each beam produces strong electro-magnetic fields, which focus the oncoming beam. The resulting acceleration of the particles towards the beam axis leads to a reduction of the effective beam size during collision, which results in increased luminosity. However, this acceleration also leads to the emission of beamstrahlung, a process comparable to the emission of synchrotron radiation in a magnetic field. Due to this effect, each particle emits on average about 1.5 photons, which carry away about 20% of the particle energy. The total energy of the photons depends on the dimensions and charges of the beams but also on other parameters, e.g. their relative offsets.

Bremsstrahlung

The bremsstrahlung or radiative Bhabha scattering has frequently been used for luminosity measurements. If two charged particles collide the exchange of a virtual photon can induce the emission of a real photon by one of the beam particles and hence a significant energy loss. The emitting particles receive little transverse kick and needs to be seperated from the beam by use of dispersion. In CLIC, these particles cannot be distinguished from beam particles which lost most of their energy by emission of beamstrahlung.

Incoherent Pair Creation

Two colliding beamstrahlung photons can produce a secondary electron-positron pair. Equivalently a pair can be produced by the collision of a photon and an electron or positron, in which case the original electron or positron is preserved. Finally a colliding electron-positron pair can create an additional pair. The total number of these particles is of the order of 10^5 per bunch crossing and most of them have small transverse momenta at production but are deflected by the beam fields. The electron of the pair can either fly into the direction of the electron or the positron beam. If it follows the electron beam it will be focused by the positron beam. If it flies in the other direction it will be deflected away from the axis by the electron beam. The pair particles can therefore reach quite large angles. This makes it possible to detect them at some distance from the beam. While the total number of pairs depends on many variables it is strongly dependent on the luminosity. By measuring the integrated energy of the pairs above a certain angle with respect to the beam axis it is thus possible to obtain a signal for luminosity optimisation [2][3]. The procedure consists of modifying one beam parameter at the time (e.g. the longitudinal position of the waist) and aiming to maximise the pair signal. In the case of CLIC the low energy tail of the particles from coherent pair creation may mask the incoherent pairs.

Coherent Pair Creation

In a very intense field the beamstrahlung photons can directly turn into an electron-positron pair. This is called coherent pair production because the photon interacts with the coherent field of the oncoming particles. The number of these pairs depends strongly on the field strength; in the case of CLIC it is only one order of magnitude smaller than the number of original beam particles.

The coherent pairs are deflected by the beam fields in the same way as the incoherent ones. The coherent pairs add a significant positron component to the spent electron beam and vice versa, which can easiliy be seperated from the rest of the spent beam using a dipole field. The power of the coherent pairs will in many cases depend in a similar fashion on the beam properties as the beamstrahlung, so it can also be used as a tuning signal. The relative changes

Table 1: Important main beam parameters of CLIC.

parameter	symbol	unit	value
centre-of-mass energy	E_{cm}	TeV	3
particles per bunch	N	10^9	4
hor. beam size at collision	σ_x	nm	≈ 60
vert. beam size at collision	σ_y	nm	≈ 0.7
hor. emittance end of linac	ϵ_x	nm	680
vert. emittance before linac	ϵ_y	nm	5
vert. emittance end of linac	ϵ_y	nm	10

of the pair power, e.g. with offset, can be even more pronounced than the change in the beamstrahlung, since the field strength during collision enters twice, in the generation of the beamstrahlung photons and in the transformation of these photons into coherent pairs.

SIMULATION PROCEDURE

In order to use realistic bunch shapes at the interaction point the beam transport through the main linac and the beam delivery system is fully simulated using the code PLACET [4]. The elements of the main linac are offset according to the anticipated alignment errors. Full beam-based alignment of the linac is then simulated. It is assumed that the beam delivery system is aligned perfectly but the non-linear and synchrotron radiation effects in this system are taken into account. The beams obtained in this way are collided pair-wise using the beam-beam simulation code GUINEA-PIG [5].

A number of random processes occur in the simulation procedure. The initial misalignments of the elements in the main linac is random. This corresponds to the real situation where each element has a fixed, if unknown, position error. One can thus only predict the mean luminosity with an uncertainty due to the fact that the actual misalignments are unknown. The luminosity for a fixed machine can be simulated only with limited precision. To chose the initial particle distribution in PLACET a random number generator is needed. Also the emission of sychrotron radiation in the beam delivery system is a stochastic process. In the beam-beam simulation the generation of beamstrahlung as well as the generation of coherent pairs from beamstrahlung photons require random number generators. Since the number of macro-particles used in the simulation is much smaller than the number of beam particles in the real machine (5×10^4 as compared to 4×10^9), the simulations tend to fluctuate noticeably. In order to reduce the fluctuation each machine is simulated five times and the average luminosity and luminosity signal is used.

RESULTS

Optimisation of Collision Offset and Angle

The tuning is performed in two steps. First the vertical offset between the beams is varied in order to find the position that minimises the production of coherent pairs. Then the crossing angle is varied in the same way again minimising the total energy in the coherent pairs. A total number of 50 machines has been simulated. In the first step, using the machines optimised with the pairs an average of about 99.6% of the optimum performance was obtained. The optimisation of the crossing angle yields again 99.7% of the achievable optimum luminosity.

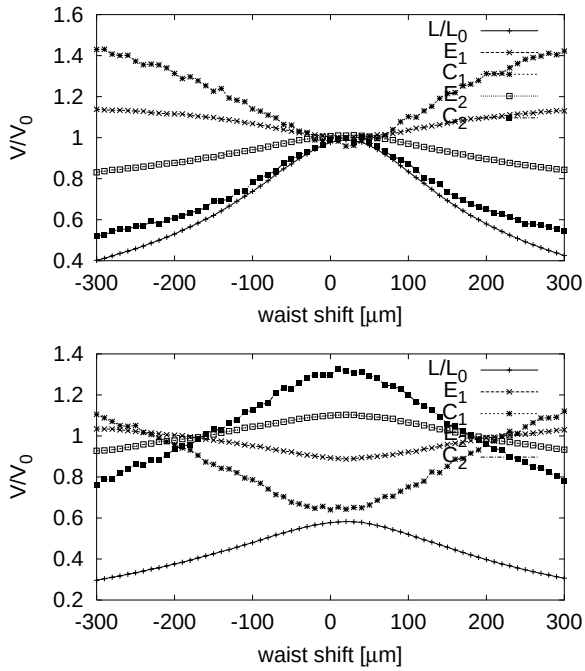

Figure 1: Examples of the waist optimisation. In the upper plot, the waist of beam 2 is in optimum position and beam 1 is scanned. The variables E_i and C_i are the beamstrahlung and coherent pair power of beam 1 and beam 2, respectively. The coherent pair power gives a more pronounced signal. In the lower plot, beam 2 has a waist shift of 200μm.

Optimisation of the Waist Position

The longitudinal position of the beam waists will need to be frequently optimised. Here we base the algorithm on the observation from reference [2]. If the vertical size of the first beam is larger than that of the second, the first beam will emit more beamstrahlung and the second less. In principle, the size of one beam can thus be minimised by minimising the beamstrahlung it emits. It should be noted that the beamstrahlung is almost independent of the absolute vertical beam size but only depends on the relative size of the two beams.

Figure 1 shows two examples of a beam size scan using simplified Gaussian beams at the interaction point. The size of beam 1 is changed by moving it's vertical waist; in one case the waist of the unmoved beam 2 is in optimum position, in the other it is shifted by 200μm. The optimum

waist position of beam 1 is recovered in both cases.

To evaluate the procedure with realistic bunches the same simulation procedure as for the offsets was used to generate the bunches. Then the waist of one beam was scanned and the position with the minimum power of coherent pairs used. The average luminosity achieved was 98.8% of the actual optimum. A slightly better result can be obtained by using the minimum of $P_{coh,1} - P_{coh,2}$, namely 99.1%. Using the beamstrahlung yields similar results.

The coherent pairs or beamstrahlung thus provide a signal that can be used for waist optimisation. In contrast, reference [3] concluded that this is not the case. The difference arises from the fact that the angular acceptance of the beamstrahlung monitor in that reference was limited, while here the full power is measured.

Optimisation of a Tuning Bump

The results above indicate that an increase in the vertical beam size may be tuned out using the coherent pair signal. However, in some cases the vertical beam size increase is not coherent along the bunch. Transverse wakefield effects for example introduce a correlation of the vertical offset of the beam particles with their longitudinal position in the bunch. The projected beam size is in this case increased but for short slices of the bunch it is not.

In order to stay below the tolerable emittance growth in the main linac, emittance tuning bumps will be used in the main linac. These bumps consist of accelerating structures that can be moved transversely. This allows to compensate the integral of the transverse wakefield kicks due to the misalignment of the accelerating structures in the linac. The strength of the kick the structure applies to the beam particles depends on their longitudinal position. After some initial optimisation in order to minimise the emittance, these bumps can also be used to directly optimise the luminosity.

Here, only a single bump is simulated for each of the 50 realistic machines. The same procedure as for the waist shift was applied, only that the position of the structures in the tuning bump was varied rather than the waist position, see Fig. 2. This procedure was able to recover 99.2% of the possible luminosity. It remains to be investigated if the coherent pair monitor performs equally well if a number of tuning bumps is optimised one after the other.

A potential disadvantage of using the coherent pair signal or some other luminosity related signal to optimise the bumps is that in this case the electron and positron linac cannot be treated independently as is the case if the emittance of the two linacs is optimised. However, there are potential advantages. First, one wants to optimise the luminosity and use a signal as closely related to luminosity as possible should give best performance. Secondly, the emittance measurement is a lengthy procedure. The beam profile has to be scanned using a laser wire, so a number of pulses are required for each measurement. The pair signal is available parasitically for each pulse. The best strategy for the bump optimisation will need to be determined taking into account the advantages and disadvantages of both methods.

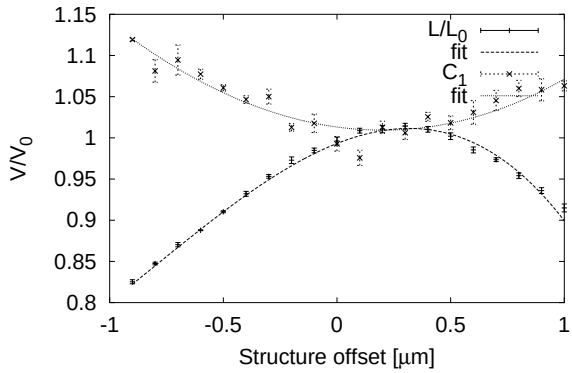

Figure 2: Example of the optimisation of a main linac bump for beam 1. The luminosity (normalised to the mean of the 50 different machines) and the coherent pair power of beam one are shown (also nomralised to the mean of 50 machines). The error bars were derived running the smae case five times using different seeds for the random number generators.

CONCLUSION

Fast signals are needed that can aid to speed up the luminosity optimisation in CLIC. Several signals can be used for this purpose, e.g. the incoherent pair creation, the beamstrahlung and the coherent pair creation. While the latter two are not proportional to the luminosity they can be used to optimise single collision parameters. The vertical offset between the beams can be optimised by performing an offset scan in order to minimise the total beamstrahlung or coherent pair power. In the same fashion one can optimise the collision angle.

A more complex tuning of the collision is also possible. The longitudinal position of the waist can be optimised. Also the main linac tuning bumps can employ the beamstrahlung and coherent pairs as a tuning signal.

Further studies should derive a more complete tuning strategy and include dynamic effects, such as the jitter of beamline elements or of the accelerating RF.

REFERENCES

[1] G. Guignard (ed.). CERN 2000-08.

[2] D. Schulte, “Study of Electromagnetic and Hadronic Background in the Interaction Region of the TESLA Linear Collider”. (thesis). TESLA 1997-08.

[3] O. Napoly and D. Schulte, “Luminosity Monitor Options for TESLA” (1998) Linac 98.

[4] D. Schulte, E. T. D’Amico, G. Guignard and N. Leros, “Simulation package based on PLACET,” CERN-PS-2001-028-AE and PAC2001 (2001).

[5] D. Schulte, “Beam-beam simulations with GUINEA-PIG,” eConf **C980914** (1998) 127 and CLIC Note-387.

EXPERIMENTAL INVESTIGATION OF THE LONGITUDINAL BEAM DYNAMICS IN A PHOTOINJECTOR USING A TWO-MACROPARTICLE BUNCH

R. Tikhoplav, A.C. Melissinos, University of Rochester, Rochester, NY 14627, USA
P. Piot, Fermi National Accelerator Laboratory, Batavia IL 60510, USA
N. Barov, D. Mihalcea, Northern Illinois University, DeKalb, IL 60115, USA

Abstract

We have developed a two-macroparticle bunch to explore the longitudinal beam dynamics through various component of the Fermilab/NICADD photoinjector laboratory. Such a two-macroparticle bunch is generated by splitting the photocathode drive laser impinging the photocathode. The presented method allows the exploration of rf-induced compression in the 1+1/2 cell rf-gun and in the 9-cell TESLA cavity. It also allows a direct measurement of the magnetic chicane bunch compressor parameters such as its momentum compaction.

INTRODUCTION

Linear accelerators designed to drive FEL-based light sources or advanced accelerator physics R&D experiments (e.g. plasma wakefield accelerators) need to provide small emittance high peak current electron bunches. In order to achieve such high-brightness beams, the bunch, after generation, is generally manipulated both in the transverse (e.g. emittance compensation in photo-injector) and longitudinal (e.g. bunch compression) phase spaces. The beam dynamics associated with such beams is intricate since both external and space charge forces play an important role in the dynamics. It is, therefore, difficult to set-up or optimize the beam manipulation process by simply measuring the bunch properties. Instead, it is first necessary to make sure the lattice is set in a proper way, e.g. as devised by numerical simulations. Directly measuring the lattice properties is generally an easy task in the transverse phase space. However, it is not such an easy matter as far as the longitudinal phase space is concerned. In the present paper we propose a simple method based on generating a bunch that consists of two macroparticles. There are two main advantages of the two-macroparticle method. Firstly, measuring the change of the separation between two macroparticles is much easier than measuring the change of the bunch size. On the other hand the space charge force is negligible for the two-macroparticle case and the evolution of their relative separation is truly a measurement of the longitudinal focussing properties.

EXPERIMENTAL SET-UP

The experimental tests of the two-macroparticle method were performed at the Fermilab/NICADD photoinjector laboratory (FNPL). The bunch length measurement can be performed by a streak camera that streaks optical transition radiation (OTR) pulses emitted as the bunch strikes an Al-coated mirror. An alternative frequency-domain bunch length diagnostics based on Martin-Puplett interferometry of coherent transition radiation is also available. For measurements reported hereafter, only the total power of the CTR emission was detected using a pyroelectric detector. The CTR signal only provide a way to monitor and minimize the bunch length (by maximizing the CTR emission). Downstream of the beamline, the electron beam can be horizontally bent in a dispersive section, to measure the beam energy distribution using a fluorescent screen located downstream at a (horizontal) dispersion of $|\eta_x| = 31.7\,\mathrm{mm}$.

The double-beam optical set-up used to create a two-macroparticle bunch was initially developed for the witness probe/plasma wake-field experiment. The photoinjector laser beam is split into two and then recombined in such a way that a time-delay is introduced between the two pulses. The delay can be remotely varied from ∼7 to ∼35 ps. A calibrated potentiometer provide a read-out for the delay between the two pulses. When such double-pulse impinges the photocathode it creates two electron bunches with a time separation much smaller than the rf period (769 ps). Hence both macroparticles fall into the same rf bucket and can be treated as a single bunch. This bunch is henceforth

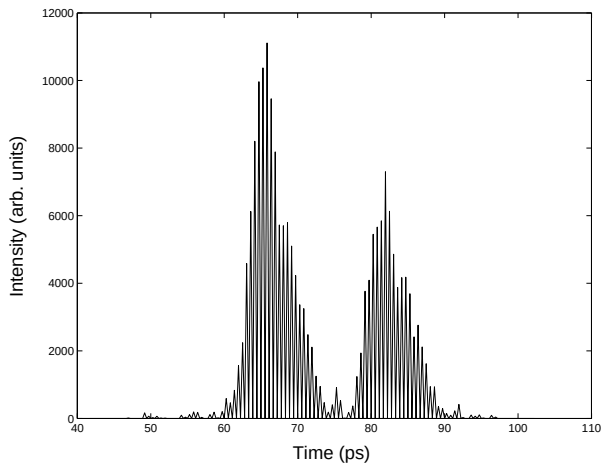

Figure 1: Example of two optical pulse streak camera measurement. The two pulses do not have exactly the same intensity in this measurement.

refer to as two-macroparticle bunch. The macroparticle which is delayed is refered to as a witness pulse (or witness macroparticle) in the following. The witness macroparticle can be "turned off" by the means of a mechanical shutter located in the delayed path. An example of two-pulse profile obtained via streak camera measurement is presented in Fig. 1.

STUDY OF VELOCITY BUNCHING

Theoretical Background

We briefly elaborate how bunching in an rf-structure occurs. A more detailed discussion is given in Reference [2, 3, 4]. An electron in an rf standing wave accelerating structure experiences the longitudinal electric field: $E_z(z,t) = E_o \cos(kz)\sin(\omega t - \psi_o)$, where E_o is the peak field, $k = \omega/c$ and the rf wavenumber and ψ_o the injection phase of the electron with respect to the rf wave. Let $\psi(z,t) = \omega t - kz + \psi_o$ be the relative phase of the electron w.r.t the wave. The evolution of $\psi(t,z)$ can be expressed as a function of z solely:

$$\frac{d\psi}{dz} = \omega\frac{dt}{dz} - k = \frac{\omega}{\beta c} - k = k\left(\frac{\gamma}{\sqrt{\gamma^2-1}} - 1\right). \quad (1)$$

Introducing the parameter $\alpha \doteq \frac{eE_o}{kmc^2}$, we write for the energy gradient [2]:

$$\frac{d\gamma}{dz} = \alpha k\left(\sin(\psi) + \sin(\psi + 2kz)\right). \quad (2)$$

The system of coupled differential equations (1) and (2) with the initial conditions $\gamma(z=0) = \gamma_0$ and $\psi(z=0) = \psi_0$ describes the longitudinal motion of an electron in the rf structure. In structure, where an incoming low-energy beam (e.g. in a rf-gun $\gamma_0 = 1$) is injected, the there is a relative longitudinal motion of the particle within the bunch: this can lead to bunch compression/decompression.

Experiment

The nominal rf-gun phase is set to 45° w.r.t. to the zero-crossing. The booster cavity phase was adjusted to obtained the maximum energy gain. The double-pulse set-up was set to have a 20 ps optical path difference between the two laser pulses and the charge was approximately 1.5 nC per macroparticle. In a first experiment the rf-gun phase was varied while keeping the booster cavity phase "on-crest". For each rf-gun phase the separation between the two macroparticles within the electron bunch was measured and then computed a compression ratio by normalizing the measured time separation on the electron beam by the laser time separation: $\Delta\tau_f/\Delta\tau_{cath}$. The results are compared with numerical simulations performed with the program ASTRA [6] in Fig.2. In a second set of experiment, the booster cavity phase was varied while keeping the rf-gun phase at its nominal value of 45°. Streak camera measurements of the macroparticle time separation versus the phase. The results are shown in Fig.3. The compression ratio is calculated by normalizing the macroparticle time separation to the time separation when the cavity is operated on crest. Similarly to the previous measurement, numerical simulations performed with ASTRA agree with the experimental measurement within the error bars. Unfortunately during this experiment we were limited to phases $\phi \in [-40^\circ, +40^\circ]$ off-crest, trying to go further off-crest resulted in large transverse envelope (due to rf-induced defocussing and chromatic aberrations) difficult to transport up to the streak camera, we could not measure the on-set the simulation predict at $\sim \pm 70^\circ$.

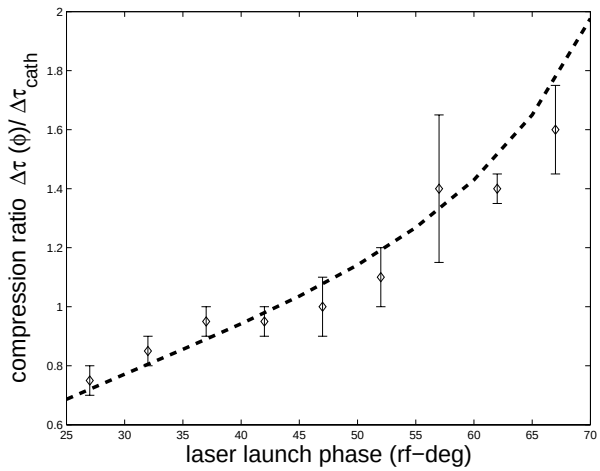

Figure 2: Velocity bunching in the rf-gun cavity. Diamonds are experimental measurements and dashed line corresponds to numerical simulations.

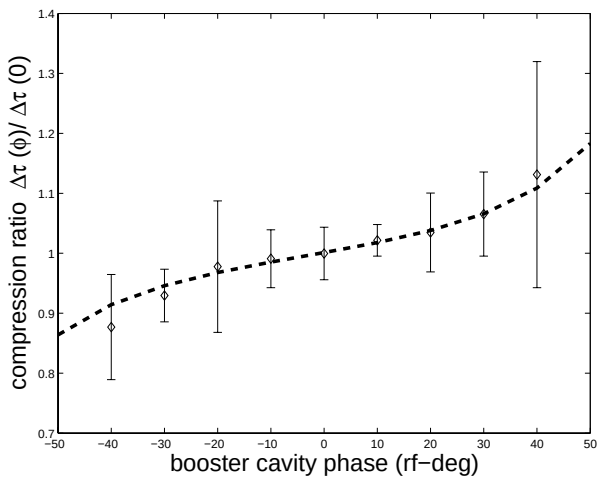

Figure 3: Velocity bunching in the booster cavity. Diamonds are experimental measurements and dashed line correspond to numerical simulations.

MAGNETIC BUNCH COMPRESSION

Theoretical Background

In magnetic-based bunch compressor an energy-dependent path length is introduced via a series of dipole forming a chicane. The incoming, to be compressed, bunch is first passed through an accelerating section operated off-crest so to introduced a time-energy correlation along the bunch (a chirp). The correlation is so that the bunch head has a lower energy than the tail. When such a bunch propagate though the magnetic chicane it gets compressed. Under a single-particle approach and using the TRANSPORT formalism, an electron with coordinate (t_i, δ_i) in the longitudinal phase space within the bunch is mapped downstream of the bunch compressor following:

$$ct_f = ct_i + R_{56}\delta_i - \frac{3}{2}R_{56}\delta_i^2, \text{ and,} \quad (3)$$

$$\delta_f = \delta_i. \quad (4)$$

R_{56} is the so-called first order momentum compaction for the bunch compressor, c is the velocity of light [1]. The coordinate of the electron in the longitudinal phase space is time t_i and fraction energy spread $\delta_i \doteq (\mathcal{E}_i - \langle\mathcal{E}\rangle)/\langle\mathcal{E}\rangle$. Note that minimum bunch length is achieved (i.e. $t_f = 0$ under single-particle linear dynamics) provided the incoming chirp, $d\delta_i/dt_i$ and momentum verify:

$$\frac{d\delta_i}{dt_i} = \frac{c}{R_{56}}, \quad (5)$$

Finally we note that in the case of two macropaticles, the evolution of the macropaticle separation downstream of the bunch compressor is given by:

$$\Delta\tau_f = \Delta\tau_i + \frac{R_{56}}{c}\frac{\Delta\mathcal{E}}{\mathcal{E}}\left[1 - \frac{3}{2}\frac{\Delta\mathcal{E}}{\mathcal{E}}\right], \quad (6)$$

where $\Delta\mathcal{E}$ is the macroparticle energy difference and $\tau_{i,f}$ their initial and final time separations. Thus a measurement of the separation and energy difference between the two macroparticle provide a way to infer the momentum compaction of the chicane.

Experiment

The booster cavity phase was operated "on-crest", i.e. to the phase corresponding to the maximum energy gain (henceforth refer to $\phi = 0^\circ$); the corresponding beam energy was 16.06 MeV. The charge was set to $\sim$ 2 nC per macroparticle and the double-beam tuned to obtained a 16 ps time separation between the two pulses. The dipoles of magnetic chicane were excited to their nominal value (corresponding to a bending angle of 22.5 deg). The CTR signal was used to find the phase corresponding to the best compression for each macroparticle; the results are: -42° and -34° for the reference and witness beam (macroparticle) respectively; the corresponding phase difference is $\Delta\phi = 8^\circ$. The next step was to go back to the uncompressed scenario (i.e. magnetic chicane dipoles unexcited and degaussed) and take the energy and time measurements. The energy was measured to be 13.07 MeV and the macroparticle fraction energy spread was $\Delta\mathcal{E}/\mathcal{E} = 9\%$. The time separation between the two macroparticles was measured with the streak camera: $\Delta t_i = 16.3$ ps. From Eq.6 this yields the value $R_{56} = 6.3$ cm. We can cross-check our direct results with corresponding phase measurements. The time between the macroparticles of 16.3 ps correlates well with their phase difference of 8° which corresponds to 17.1 ps. The energy drop from the "on-crest" position (16.06 MeV) to the "best-compression" position (13.07 MeV) corresponds to the 41.4° off-crest (4 MeV rf-gun energy was assumed). The measured phase values for each particle (-42° and -34°) yield 8.6% energy difference. The momentum compaction experimentally measured is 30% lower than what we expect from numerical simulation ($R_{56}^{simu} = 8.3$ cm), this discrepancy is not yet understood.

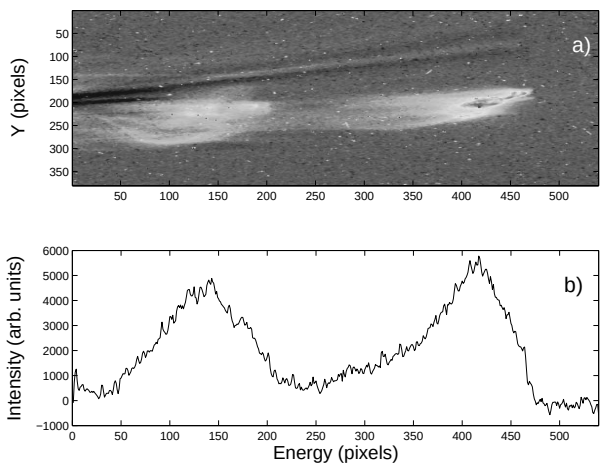

Figure 4: Example of data set for measurement of energy separation between the two macroparticles. **a)**: beam density on dispersive viewer, **b)**: corresponding projection.

REFERENCES

[1] http://nicadd.niu.edu/fnpl/

[2] K.-J. Kim, *Nucl. Instr. Meth.*, **A275**, 201-218 (1989)

[3] B. Carlsten *et al.*, *Part Accel.*, **56**, 127-145 (1997)

[4] L. Serafini, M. Ferrario, "Velocity bunching in photo-injectors", in *Physics of, and science with, the X-ray free-electron laser* edited by S. Chattopadyay et al., AIP conference proceedings **581**, 87-106 (2001)

[5] T.O. Raubenheimer, *et al.*, *proc PAC 1997*, 635-637 (1993)

[6] K. Flöttman, *Astra user manual* DESY

[1] we have expanded the t coordinate to second order and noted that $T_{566} = -3/2R_{56}$ for a magnetic chicane [5]

LIMITING EFFECTS IN THE ROUND-TO-FLAT BEAM TRANSFORMATION

Y.-E Sun*, K.-J. Kim†, University of Chicago, Chicago, IL 60637, USA
P. Piot, FNAL, Batavia, IL 60510, USA

Abstract

In the present paper we study the chromatic effects on transverse beam emittances in the transformation of an angular-momentum-dominated round beam into a flat beam. Analytical results are compared with numerical simulations and found in good agreement. We also attempt to study the effects caused by the asymmetries in the four dimensional transverse phase space distribution.

INTRODUCTION

The theory of generating a beam with high transverse emittance ratio, i.e., a flat beam, from an incoming angular-momentum-dominated beam is treated in several papers [1, 2, 3]. In this paper, we follow the theoretical treatment based on four dimensional beam matrix presented in [4], in which the round-to-flat beam (RTFB) transformation analysis was performed assuming that the beam and the transport channel upstream of the flat beam transformer are cylindrically symmetric and that the particle dynamics is symplectic. The experimental demonstration of such a round-to-flat transformation at Fermilab/NICADD Photoinjector Lab (FNPL) by using a RTFB transformer consists of three skew quadrupole channel is reported in [5].

CHROMATIC EFFECTS

The strength of a quadrupole is related to the particle's momentum. Consider an electron with a small fractional momentum deviation $\delta = \frac{p-p_0}{p_0}$ around the average beam momentum p_0. In practical units, the quadrupole strength q for an electron with momentum p is given by:

$$q[1/\mathrm{m}] = \frac{300g[\mathrm{T/m}]l_{eff}[\mathrm{m}]}{pc[\mathrm{MeV}]} = q_0(1-\delta+\delta^2+\mathcal{O}(\delta^3)),$$

where g the transverse magnetostatic field gradient, l_{eff} is the effective length of the quadrupole and c the speed of light, $q_0[1/\mathrm{m}] \doteq \frac{300g[\mathrm{T/m}]l_{eff}[\mathrm{m}]}{p_0c[\mathrm{MeV}]}$. Correspondingly, in thin lens approximation, the 2×2 transfer matrix M_Q of a normal quadrupole may be written as:

$$M_Q(q,\delta) \approx \begin{bmatrix} 1 & 0 \\ q_0 & 1 \end{bmatrix} + \delta \begin{bmatrix} 0 & 0 \\ -q_0 & 0 \end{bmatrix} + \delta^2 \begin{bmatrix} 0 & 0 \\ q_0 & 0 \end{bmatrix}.$$

Consider a RTFB transformer composed of three skew quadrupoles of strengths q_1, q_2, q_3 and separated dy drift space of lengths d_2 and d_3. The 4×4 transfer matrix of such a transformer takes the form of:

$$M(q_1,q_2,q_3,d_2,d_3) \approx M_0 + \delta\Delta_1 + \delta^2\Delta_2, \qquad (1)$$

where M_0 is the transfer matrix for reference particle with momentum p_0, Δ_1 and Δ_2 are the corrections to the transfer matrix to the first and second order of δ.

The general form of a cylindrically symmetric beam matrix [4] at the entrance of the RTFB transformer is:

$$\Sigma_0 = \begin{bmatrix} \sigma^2 & 0 & 0 & \kappa\sigma^2 \\ 0 & \kappa^2\sigma^2+\sigma'^2 & -\kappa\sigma^2 & 0 \\ 0 & -\kappa\sigma^2 & \sigma^2 & 0 \\ \kappa\sigma^2 & 0 & 0 & \kappa^2\sigma^2+\sigma'^2 \end{bmatrix}, \qquad (2)$$

where $\sigma^2 = \langle x^2\rangle = \langle y^2\rangle, \sigma'^2 = \langle x'^2\rangle = \langle y'^2\rangle, \kappa = \frac{eB_z}{2p}$, B_z is the longitudinal magnetic field on the photocathode and e the electron charge. The beam matrix at the exit of the RTFB transformer is:

$$\Sigma = M\Sigma_0\widetilde{M}, \qquad (3)$$

where $\widetilde{M}$ stands for the transpose of M. Since $\langle\delta\rangle$ vanishes, keeping only the first order modification to the beam matrix, from Eq. 1 and Eq. 3, we have:

$$\Sigma \approx M_0\Sigma_0\widetilde{M_0} + \langle\delta^2\rangle(M_0\Sigma_0\widetilde{\Delta_2} + \Delta_1\Sigma_0\widetilde{\Delta_1} + \Delta_2\Sigma_0\widetilde{M_0}). \qquad (4)$$

Given proper transfer matrix M, the first term of Eq. 4 can be block diagonalized and the two transverse emittances are given by (see, for example, Ref. [4]):

$$\varepsilon^0_{x,y} = \varepsilon_{eff} \mp \mathcal{L}, \qquad (5)$$

where $\varepsilon_{eff} = \sigma\sqrt{\sigma'^2+\kappa^2\sigma^2}$, $\mathcal{L} = \kappa\sigma^2$.

When there is a relative momentum spread in the beam, the beam matrix varies as a function of it. The two transverse emittances can be calculated as the square roots of the determinants of the top left and bottom right 2×2 sub-matrices of the beam matrix expressed in Eq. 4. Let's rewrite the second term of Eq.4 as:

$$\langle\delta^2\rangle \begin{bmatrix} \Delta_{11} & \Delta_{12} \\ \Delta_{21} & \Delta_{22} \end{bmatrix} \doteq \langle\delta^2\rangle(M_0\Sigma_0\widetilde{\Delta_2} + \Delta_1\Sigma_0\widetilde{\Delta_1} + \Delta_2\Sigma_0\widetilde{M_0}). \qquad (6)$$

By using the convenient relation for the determinant of the sum of two 2×2 matrices P and Q,

$$|P+Q| = |P| + |Q| + Tr(P^\dagger Q), \qquad (7)$$

* yinesun@uchicago.edu
† Also APS, ANL, Argonne, IL 60439, USA

where "| |" stands for the determinant, "Tr" for the trace of a matrix, and $P^\dagger$ is the symplectic conjugate of P, $P^\dagger = J^{-1}\widetilde{P}J$, where J is the 2×2 unit symplectic matrix:

$$J = \begin{bmatrix} 0 & 1 \\ -1 & 0 \end{bmatrix},$$

we can write an expression for the transverse emittances in the presence of the aforementioned chromatic effect:

$$\begin{aligned} \varepsilon_x &= \sqrt{(\varepsilon_x^0)^2 + \langle\delta^2\rangle^2[|\Delta_{11}| + (\varepsilon_x^0)^2 \mathrm{Tr}(T\Delta_{11}^\dagger)]}, \\ \varepsilon_y &= \sqrt{(\varepsilon_y^0)^2 + \langle\delta^2\rangle^2[|\Delta_{22}| + (\varepsilon_y^0)^2 \mathrm{Tr}(T\Delta_{22}^\dagger)]}. \end{aligned} \quad (8)$$

As a numerical application we consider parameters (see Table 1) close to those achieved for the FNPL flat beam experiment. Note the normalized beam emittance upstream of the RTFB transformer is taken to be equal to the thermal emittance at the photocathode ($\gamma\sigma\sigma' = 1$ mm mrad, γ is the Lorenz factor). This underestimation of the emittance leads to higher transverse emittance ratio. In turn this means the calculations presented hereafter are more sensitive to chromatic effects.

Table 1: Parameters used as a numerical example for chromatic effects in flat beam generation

parameter	value	units
γ	30	
σ	1.00	mm
κ	0.78	m^{-1}
σ'	0.033	mrad
d_2	0.35	m
d_3	0.85	m

Using the thin lens approximation, and including the thermal emittance, the skew quadrupole strengths are calculated from Ref.[6] to be:

$$q_1 = 1.729 \text{ m}^{-1}, \quad q_2 = -1.339 \text{ m}^{-1}, \quad q_1 = 0.628 \text{ m}^{-1}.$$

The normalized flat beam emittances (from Eq. 5) are:

$$\varepsilon_x^n = 0.021 \text{ mm mrad}, \quad \varepsilon_y^n = 46.82 \text{ mm mrad}.$$

The analytical calculations of the two transverse emittances and their ratio, as a function of relative momentum spread, are first compared with simulation results from ASTRA[7], ELEGANT[8] and SYNERGIA[9]. These results agree well in general, see Fig. 1.

On the other hand, we can see that the agreement between the analytical results and simulations is better for lower relative momentum spread values. To further explore the difference, each particle used in the simulation is tracked through the transfer matrix for both the cases when the quadrupole are thick and thin lenses, using the transfer matrix as shown in Eq. 1. We found that in the thick lens case, the tracking results almost overlap with the simulation

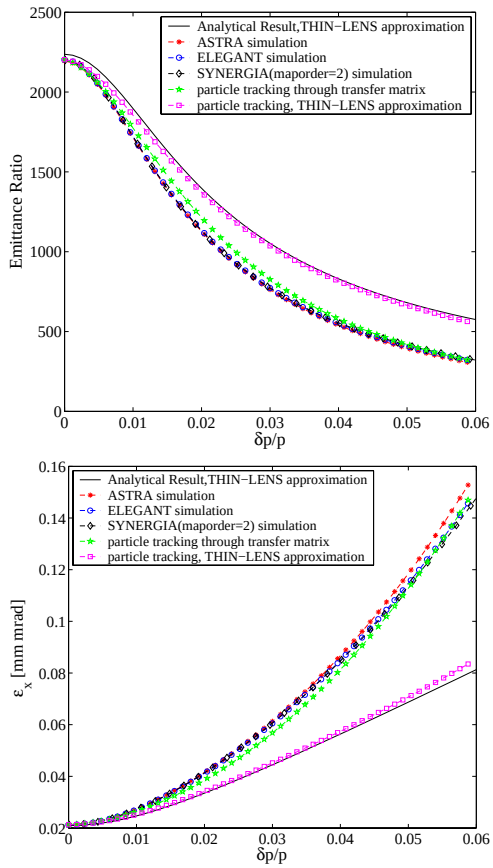

Figure 1: Chromatic effects on emittance ratio (top) and horizontal emittance (bottom). Solid line is obtained from Eq.8. Dashed lines with markers are computed using numerical methods.

results, while the thin lens approximation tracking results agree quite well with the analytical predictions. Hence the difference between analytical and numerical results can be attributed to the fact that the thin lens approximation used in analytical model does not hold as the energy spread is introduced.

ASYMMETRIES

Some elements in the beam line, such as the RF gun coupler, could cause asymmetry in the beam before it enters the RTFB transformer. In this case, the emittances of the flat beam is effected and the flat beam ratio is lowered comparing to the cylindrically symmetric beam case.

Suppose the y, y' deviate from the symmetric beam by the amount of ξ and η, respectively:

$$\begin{aligned} y &\to y + \xi, \\ y' &\to y' + \eta, \end{aligned}$$

where η and ξ could be functions of y. The beam matrix at the entrance of the RTFB transformer is:

$$\Sigma = \Sigma_0^* + \Delta, \quad (9)$$

where Σ_0^* is of the form of Eq. 2 with $\mathcal{L}$ replaced by $\mathcal{L}^* \doteq \kappa(\sigma^2 + \mu)$ and it can be block diagonalized; Δ is given by:

$$\Delta = \begin{bmatrix} 0 & 0 & 0 & -\kappa\mu \\ 0 & 0 & -\kappa\mu & 2\kappa\nu \\ 0 & -\kappa\mu & 4\mu + \langle\xi^2\rangle & 2(\mu+\nu) \\ -\kappa\mu & 2\kappa\nu & 2(\mu+\nu) & \langle\eta^2\rangle \end{bmatrix},$$

with $\mu \doteq \frac{1}{2}\langle y\xi\rangle$, $\nu \doteq \frac{1}{2}\langle y\eta\rangle$.

Δ generates x-y phase space coupling terms in the beam matrix at the exit of the RTFB transformer. It also modifies the two transverse emittances of the flat beam. As an example, we use the same initial beam matrix as used in previous section, plus Δ induced by the RF gun coupler kick [10]:

$$\Delta = \begin{bmatrix} 0 & 0 & 0 & 0 \\ 0 & 0 & 0 & 0 \\ 0 & 0 & 0 & a_1\sigma_-^2 \\ 0 & 0 & a_1\sigma_-^2 & a_1^2\sigma_-^2 + (ka_2\sigma_y\sigma_z)^2 \end{bmatrix},$$

where $\sigma_-^2 = \sigma_y^2 - h^2$, σ_y is the vertical rms bunch size, h the difference in vertical direction between the geometry and the electro-magnetic axes due to the RF coupler kick, k the rf wave number, σ_z the rms bunch length, $a_1 \doteq \alpha k \sin(kl)\sin(2kz_m)$, $a_2 \doteq \alpha k \sin(kl)\cos(2kz_m)$, where $l = z_f - z_i$, $z_m = \frac{l=z_f+z_i}{2}$, z_i and z_f be the start and end of the coupler region, $\alpha \doteq \frac{eE_0}{2mc^2k}$ [11], where E_0 is the gun peak accelerating field, m the electron mass. Take the following typical values at FNPL:

$f = 1.3$ GHz $\rightarrow$ k $= 27$ m^{-1},
$E_0 = 35$ MV/m $\rightarrow \alpha = 1.27$,
$\sigma_z = \sigma_y = 1$ mm,
$h = 1$ mm [12],
$z_i = 0.11$ m, $z_f = 0.19$ m $\rightarrow z_m = 0.15$ m, $l = 0.08$ m,
$\varepsilon_y^0 = 1$ mm mrad.

All the elements of Δ matrix vanish apart from $\Delta_{44} = 7.65 \times 10^{-10}$. For a beam without energy spread, this increases the smaller one of the two transverse emittances of the flat beam by 30%. The emittance ratio drops from 2237 to 1715, see Fig. 2 for the emittance ratio and horizontal emittance as a function of fractional momentum spread.

SUMMARY

We have shown that both the chromatic and asymmetric effects induce some residual x-y coupling downstream of the RTFB transformer, comparing to the symmetric beam without energy spread case. However the transverse emittances calculated when these two latter effects are considered remain constant in the downstream transport line, as long as no element in the beam line introduces x-y coupling.

As far as chromatic effects are concerned, we find our simple analytical treatment provide some insight regarding the dependencies of the transverse emittances on chromatic effect. Our predictions are in decent agreement with simulations taking into account that our model assumes the quadrupoles to be thin lenses. Regarding the impact of RF asymmetries, we have estimated the effects on the flat beam emittances but not yet compared with simulations.

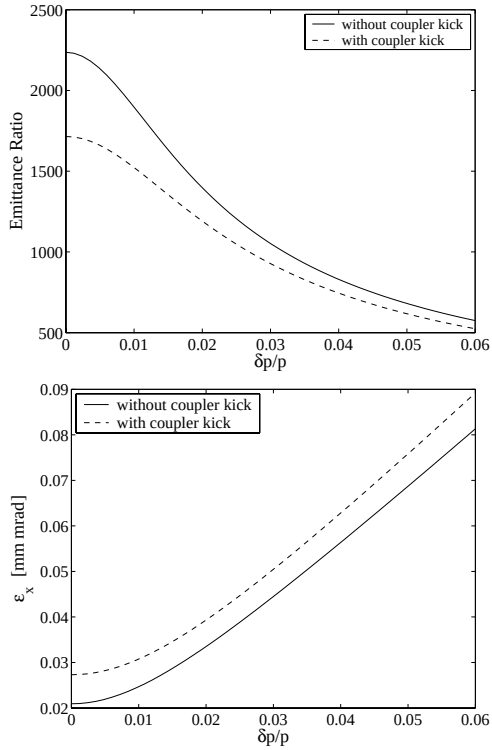

Figure 2: Asymmetry in the initial beam matrix caused by gun RF coupler kick effects emittance ratio (top) and horizontal emittance (bottom).

The next step will be trying to find a possible cure for the aforementioned limiting effects on the round-to-flat beam transformation.

REFERENCES

[1] Ya. Derbenev, UM-HE-98-04 (1998).
[2] A. Burov *et al.*, *Phys. Rev. ST A&B* **3**, 094002 (2000).
[3] R. Brinkmann *et al.*, *Phys. Rev. ST A&B* **4**, 053501 (2001).
[4] K.-J. Kim *et al.*, *Phys. Rev. ST A&B* **6**, 104002 (2003).
[5] D. Edwards *et al.*, proc. LINAC 2000, 122-124 (2000).
[6] E. Thrane *et al.*, proc. LINAC 2002, 308-310 (2002).
[7] K. Flöttman, *Astra user manual* DESY.
[8] M. Borland, Advanced Photon Source LS-287 (Sept. 2000).
[9] J. Amundson *et al.*, proc. PAC 2003, 3195-3197 (2003).
[10] Y.-E Sun, P. Piot, unpublished (June 2004).
[11] K.-J. Kim, NIM A275 201-218 (1989).
[12] M. Krassilnikov, *et al.*, in Proc. EPAC 2002, 1640 - 1642 (2002).

GAMMA - RAYS AND X-RAYS PRODUCTION FOR EXPERIMENTS AT ELSA FACILITY

J.-L. Lemaire

CEA/DAM, Bruyères-le-Châtel, France

Abstract

The ELSA facility is a high brightness 18 MeV electron source dedicated to electron irradiation, γ-rays and picosecond hard and soft X-rays. It consists of a 144 MHz RF photo-injector producing short bunches which are further accelerated to an energy varying from 2 to the maximum energy of 18 MeV thanks to three 433 MHz cavities. Former beam compression design used a half turn magnet compressor system. It was recently replaced by a double alpha magnet compressor. Electron beams are now delivered to a new experimental room. We present the new panel of interests offered by this facility in terms of short pulses X-ray production.

INTRODUCTION

The ELSA facility was designed in the late 80's, as a test bench for physics and technology of high efficiency FELs [1]. It consists of a RF photo-injector followed by a linear accelerating structure, a compressor magnet and adapted undulators. After the demonstration of free electron laser operation in the IR range was completed, improvements of the accelerator were needed. Main concerns were on the cavity of the photo-injector and on the stability of the laser system. A renewed cavity was built to fit with ultra high vacuum for photo-cathode life time requirements (10^{-10} mbar is the typical vacuum pressure at present time). The pulse-to-pulse fluctuations of the drive laser which can operate at either 532 nm or 236 nm, depending upon the choice of cathode type, were also solved. In response to new needs, the facility is now mainly used as a high-brightness electron source or as a picosecond hard X-ray source via bremsstrahlung on high Z materials. Due to lack of room to set the experimental devices in the former facility, a contiguous experimental area has been added. In order to achieve short pulses a magnetic compressor was re-design. It is now made of two alpha-magnets type (with field index of 1) [2]. The beam is also tightly radialally focused on production targets. In this ELSA2 facility, new dedicated beam lines built in this experimental area, are now commissioned. This allows to users a panel of versatile experimental conditions with short pulses of electrons, X-rays or γ-rays.

ELSA FACILITY

The ELSA overview facility is presented on figure 1. It is made of a 144 MHz photo-injector delivering for nominal operating conditions, trains of electron bunches at 2.5 MeV. The temporal structure consists of macropulses of 20 to 150μs duration. Maximum repetition rate is 10 Hz. A macropulse is made of 20 ps long micropulses (individual bunch) at a repetition rate of 14.4 MHz (see figure 2). The acceleration is completed by three 433 MHz accelerating cavities. These cavities operate at room temperature. The photo-injector cavity is powered by a tetrode tube supplying 1.5 MW of peak power. This gives an accelerating gradient of 30 MV/m.

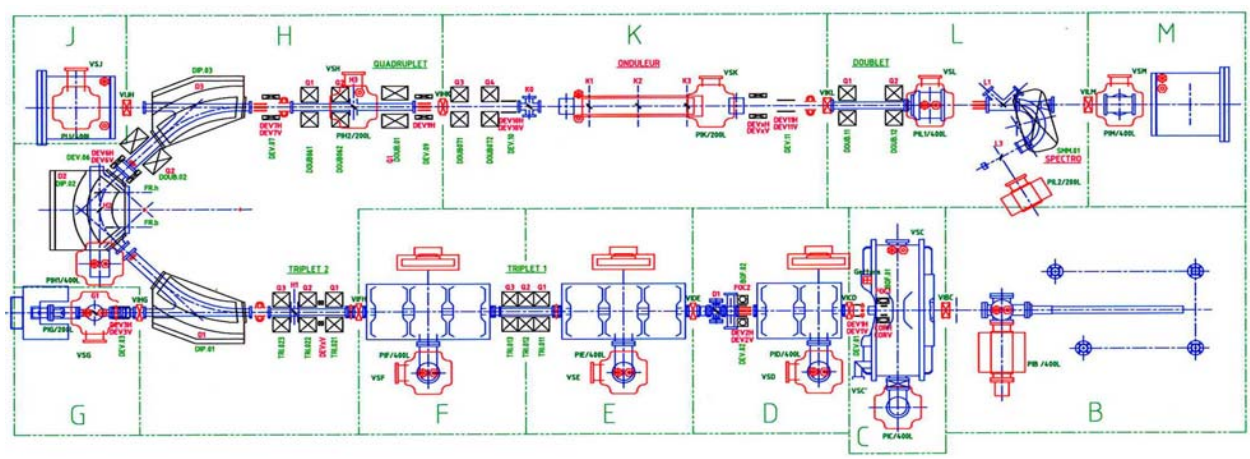

Figure 1: Former overview of the ELSA facility: room size is 12 m x 5 m and beam is bent to 180 ° through a half turn compressor magnet system made of three dipole magnets.

The 433 MHz accelerating RF cavities are powered by a unique klystron (TH2118) for which peak power of 6MW is split between the cavities. Focusing elements (solenoids at the extraction, quadrupole triplets further downstream) and a set of steering coils provide the proper beam transport tuning through the overall structure. For the benefit of experimenters, any beam energy value is easily obtained starting at 2 MeV at the expenses of some beam quality for low energies. Routinely, 20-30 ps duration laser pulses (FWHM) shining a 6 mm diameter photo-cathode permit to extract a charge of 5 nC per bunch. Two types of cathodes K_2CsSb and Cs_2Te depending upon the laser wavelength operating choice can be used. The bunch absolute charge is measured at 4 different locations along the beam propagation. As instance, G1(see figure 1) stands for the Faraday cup measurement location.

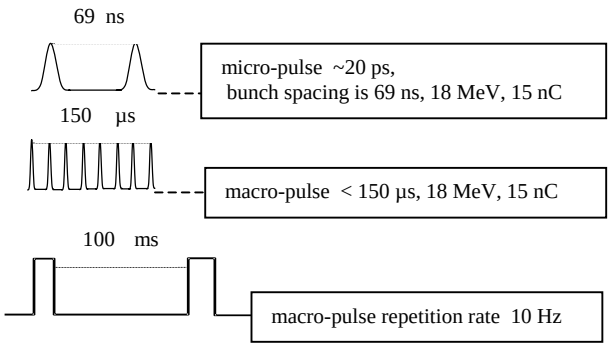

Figure 2: Typical train of bunches.

For some studies the charge contained into a single bunch can be raised as high as 50 nC. Bunch pulse is longer in this case (200 ps) [3], but 15 nC is a more usual extracted charge value corresponding to 60 ps bunch durations.

TRANSVERSE AND LONGITUDINAL PHASE SPACES QUALITIES

Measurements of the beam phase space showed that, at low charge (1nC, 60 ps), the transverse normalized rms emittance is as low as 1 µm, very close to the theoretical thermal emittance value of RF guns emittance [4]. The ability to accelerate such high bunch densities while maintaining small emittance values , is a direct benefit of the low frequency operation of the RF accelerating cavities.

This transverse emittance is measured at G1 location by means of the quadrupole scanning technique (beam transverse profiles are measured by OTR screens while acquisition is made with an intensified CCD camera [5]. Normalized measured rms emittance for a bunch carrying 10 nC is 2.5 µm.

The electron bunch and drive laser temporal pulse lengths and shapes can be simultaneously measured ahead and after the bend thanks to a synchroscan streak camera. Whilst at 5 nC the bunch length is still close to the 60 ps time duration of the driving laser pulse value, due to space charge effects it lengthens to 65 ps for 10 nC and to 90 ps for 15 nC [5].

ELSA LAYOUT

Figure 3 shows the ELSA2 experimental area layout.

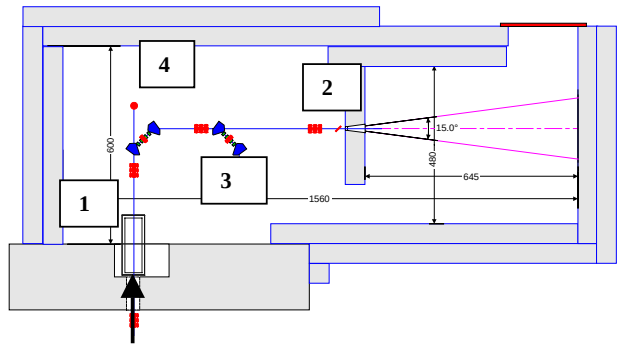

Figure 3: New experimental area (~80 m^2). On this figure the electron beam comes from the bottom (shown by the arrow).

The aim of the entire project was also to upgrade the beam energy after the beam has been compressed down to a small value of ~10 ps [6]. A post acceleration given by a 1300 MHz RF accelerating structure is intended to boost the energy up to 40 MeV. Only the first part of the ELSA 2 project has been commissioned but this latter phase has been postponed. At the end of the linac, the electron beam crosses a thick wall which separates the main accelerator room from the experimental area. It is then compressed (the compressor which deviates the beam vertical is not visible on figure 3).

After compression, the beam can be distributed to 4 different locations (schematically shown on figure 3 . The beam lines have specific features.

Beam line 1 for which the beam goes straight can handled high intensity beams dedicated to high bunch intensity measurements (spot size measurements, dose, X-ray imaging, direct irradiation by electrons)

Beam line 2 is mainly used for γ-ray production from bremsstrahlung interaction on a thick target (labelled T on figure). The photon beam is collimated whereas electrons are damped. Large room behind the production target is provided to house X-ray imaging experiments.

Beam line 3 will be dedicated to low back ground or high average intensity experiments

Beam line 4 belongs to the phase 2 of the project where a Thomson source is to be built.

IRRADIATION AREA

The electron beam from beam line 1 can be used either for beam dynamics studies or direct irradiation by electrons. Beam dynamics involves the handling and behavior of high charged bunch beams and final radial focusing to tight spot size. These studies are related to

a project called RX2 where a RF linac coupled to a photo-injector is proposed as a new versatile radiographic machine. Irradiations by electrons in the 800 keV - 2.5 MeV range are also of great interest for precise calibration of displacement energy measurements in irradiated materials. Studies on the evolution of the electrical resistivity of material samples under irradiation have been also carried out.

γ-RAY PRODUCTION

As mentioned previously, beam line 2 delivers bunched electron beam to a bremsstrhalung production target. A large room, well hardened against parasitic radiations, is used for X-ray imaging experiments. Calibration of impulse response of CdTe detectors as X-ray diagnostics for the future carries on. Also, it is a test facility for fission chambers developments dedicated to measurement of cross sections in photo-fission reactions. Yield point against high electron fluxes for mechanical strength is still an issue for such developments in view of measuring the temporal distribution of delayed neutrons in photo-fission reactions.

SOFT X-RAY PRODUCTION

The possibility to use an electron linac as a driver for an X-ray transition radiation source (XTR) has been considered both on theoretical and experimental aspects for several years. At the ELSA facility soft X ray pulses as short as 10 to 20 ps, in the energy range 0.5 to 2 KeV, can be produced by means of this process [7]. In many experiments as plasma physics, fluorescence measurements, exploration of atomic processes involved in plasma physics, temporal investigation of physical property of matter, the continuous aspect of a X-ray source issued from synchrotron radiation is useless despite the high photon flux since only single-pulse mode operation is of interest for those special applications. As far as photon brightness is concerned, even if it cannot compete with synchrotron radiation sources, a photo-injector driven linac X-ray source makes sense for these specific fields. The production target design stays a key issue in order to achieved enough signal. Proper designs include the foil stack and the multi-layer arrangement. A demonstration experiment has been carried out to consider the possibility of installing such a soft X-ray source on the ELSA facility. Very encouraging results were obtained, but too much of background noise due to the environment imposed a re-design of the production set up. Beam line 3 is intended to reactivate this X-ray production source thanks to its low back ground design .

THE THOMSON SOURCE PROJECT

Several groups have demonstrated proof-of-principle generation of soft X-rays in the keV range through interaction of picosecond or femtosecond laser with MeV electron beam in collinear or orthogonal geometry [8]. Taking advantage of the ELSA low emittance electron beam and of the synchronous drive laser for which the energy would be amplified to 100 mJ for this use, an experimental demonstration could be carried out as a first step at 20 MeV. In a second step, energy upgrade to 40 MeV is expected to enhance the performances of such a source (brigthness should be one order of magnitude higher, energy range for X-rays would be extended from 10 keV to 50 keV).

CONCLUSION

A new panel of interests offered by the upgrade ELSA 2 facility is now proposed to users in terms, electron irradiation, γ-ray and x-ray productions. Short pulse beams (10ps, 14 MHz, 150 μs), high repetition rate (10Hz), high charged bunch (15 nC) delivered in 4 different experimental spots are the main features of this 18 Mev electron beam facility which can accommodate a wide range of user requirements.

ACKNWOLEDGMENTS

The author wishes to thank the ELSA team for helpful assistance and accomplishment in commissioning the ELSA 2 facility.

REFERENCES

[1] R.Dei-Cas and al. “Status report on the low frequency photo-injector and on the infrared FEL experiment (ELSA)” Nucl. Instr. and Meth. A296 (1990) 209.

[2] H.A. Enge, ”Achromatic magnetic mirror for ion beams”, Rev.Sci. Instr. 34 (1964) 385.

[3] N. Pichoff, “Extraction of high charged electron bunch from the ELSA RF injectot: comparison between simulation and experiment” this conference

[4] W.S Graves and al. “Measurement of thermal emittance for a copper photocathode”, Proceedings of the PAC 2001 Conf, Chicago, USA.

[5] J-G Marmouget, A.Binet, P.Guimbal, J-L.Coacolo, “Present performance of the low-emittance, high-bunch charge ELSA photo-injected linac”, Proceedings of the EPAC 2002 Conf, Paris, France.

[6] Ph.Guimbal, P.Balleyguier, A.Binet, A.Bloquet, D.Deslandes, J-L.Flament, V.LeFlanchec, A.Godefroy, H.Leboutet, J-G.Marmouget, “Status of the ELSA-2 project”, Proceedings of the EPAC 2002 Conf, Paris, France.

[7] G.Haouat, C. Couillaud, S.Striby, “Soft X-ray production by means of an electron beam”, Proceedings of the EPAC 1996 Conf, Stiges, Spain.

[8] R.P.Fisher and al;, “Generation of tunable, monochromatic X-rays in the laser synchrotron source experiment”, Proceedings of the EPAC 2002 Conf, Paris, France.

STATUS AND OPERATING EXPERIENCE OF THE TTF COUPLER

D. Kostin, W.–D. Möller, for the TESLA Collaboration, DESY, D-22607 Hamburg, Notkestr. 85

Abstract

Five accelerating modules are installed in the VUV-FEL [1] linac so far. This includes 40 high power couplers connected to the superconducting cavities, eight in a module. All of them are processed and operated up to the cavity performance limits. The coupler processing procedure is described. The performance in relation to the test results on the coupler test stands and the operating experience are discussed.

INTRODUCTION

In the frame of the TESLA Collaboration [2] RF power couplers for superconducting cavities are developed. Three different types [3], [4] of the couplers are fabricated, tested and installed at the 5 modules in the Tesla Test Facility (TTF). The basic design parameters for the TTF couplers are:

- Frequency: 1.3 GHz
- Pulse length: 500 µs rise time, 800 µs flat top with beam
- Repetition rate: 10 Hz
- Coupling: adjustable, Q_{ext}= 10^6-10^7
- Safety: two ceramic windows, protection of the cavity during assembly and against window failures

During the last year the TTF is converted to a Vacuum-Ultra-Violet Free-Electron-Laser (VUV FEL) user facility. The cavities in the 5 modules are processed and operated successfully as described in [5].

Two high gradient tests with electro polished (EP) cavities and TTF3 couplers in the horizontal cryostat (CHECHIA) have been carried out. In these tests the cavity is fully equipped and corresponds to a 1/8th of a module [6].

One of the high gradient EP cavities is installed in the module ACC1 and was tested with beam.

RF COUPLER PROCESSING ON THE TEST STAND AND IN THE HORIZONTAL CRYOSTAT

Prior to the assembly on a cavity all couplers are tested and preconditioned on a test stand at room temperature. On the test stand the couplers are backed at 150 – 200 C and 24 hours. The processing is done with travelling waves. The power is cycled from low to high values, starting with short pulses (20 µs, 2 Hz). After reaching 1 MW the pulse length is doubled and the power rise starts again at low power. This procedure is repeated up to the operating pulse length of 1.3 µs. The rate of the power increase is limited by the different thresholds, set for the coupler vacuum, light and charged particles (e-) in the coupler vacuum. A hardware interlock can switch off the power at high readings of vacuum, light, electrons or ceramic temperature.

The average processing time for such a pair of couplers is 70 to 125 hours (see Fig. 1).

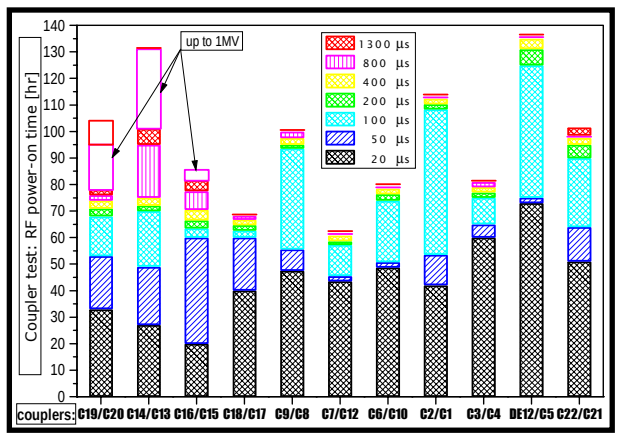

Figure 1: RF Processing times for pairs of couplers on the coupler test stand. The colours distinguish between the different pulse lengths.

After disassembly from the test stand the coupler parts are stored under dry Nitrogen atmosphere.

Due to the limited time schedule, only some of the couplers are tested together with the fully equipped cavities in the horizontal cryostat CHECHIA. Baking of the coupler is done in situ at 150 C and 24 h. The RF processing procedure before cooldown of the cavity is nearly the same that at the test stand.

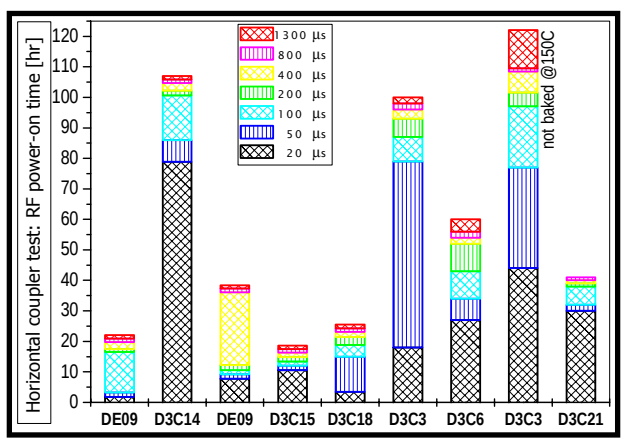

Figure 2: RF processing times for some couplers assembled to the cavities in the horizontal cryostat. The colours distinguish between the different pulse lengths. Without backing the coupler in situ the longest time is needed. Notice the big difference of needed time.

But with the cavity off resonance we have full reflection of power. The cool down is usually started during the RF processing procedure. The needed RF processing times in average is shorter (see Fig. 2). Without coupler baking in situ the longest time was needed. But also with baking the RF processing time for the couplers is very different. We believe this is due to the difference in the cleanliness during handling at assembly from test stand and to the cavity. The procedures for handling and storage have to be improved.

RF COUPLERS IN THE VUV-FEL

In Table 1 is shown were the different coupler types on the modules are installed. Due to a reassembly of the modules ACC 1, 2 and 3, we have a mix of different couplers in these modules. Module ACC 4 is completely equipped with TTF 2 couplers and the module ACC 5 with the latest coupler design TTF 3 (see Fig. 3 & 4).

Table 1: Coupler types in the different modules of the VUV FEL

Coupler type	FNAL	TTF 2	TTF 3
cold window	conical	cylindrical	cylindrical
warm window	flat wave guide	flat wave guide	cylindrical
bias	no	yes	yes
fabricated totally	16	20	62
tested	16	20	24
used in TTF modules	12	19	11
assembled in modules	ACC 1, 2	ACC 2, 3, 4	ACC 1, 5
operated	1997-2004	1998-2004	2001-2004

The assembly of the modules was done long time before the installation in the linac tunnel: ACC in 4 July 2001, ACC 5 in March 2002 and ACC 3 in February 2003.

There are two different module designs for TTF: In the older one the coupler has to follow during cool down and warm up the axial movement of the cavities of 15 mm in the extreme positions. In the newer design (ACC 4 & 5) the cavities are kept in there positions by an Invar rod. The lateral movement of the couplers at different temperatures is here only 1.5 mm.

A common pumping line for every module is connected to the coupler vacuum of 8 couplers which are pumped by one titan sublimation pump.

The 8 couplers of module ACC 3 are connected to a 5 MW klystron while the 16 couplers of modules ACC 4 & 5 are driven by a 10 MW multi beam klystron [4]. The wave guide distribution system consists of a directional coupler, a circulator and a remote controlled wave guide tuner (phase control) for every coupler / cavity.

All couplers are protected by a technical interlock system. It consists out of e- pick ups, light detectors, vacuum readouts and temperature sensors on both windows.

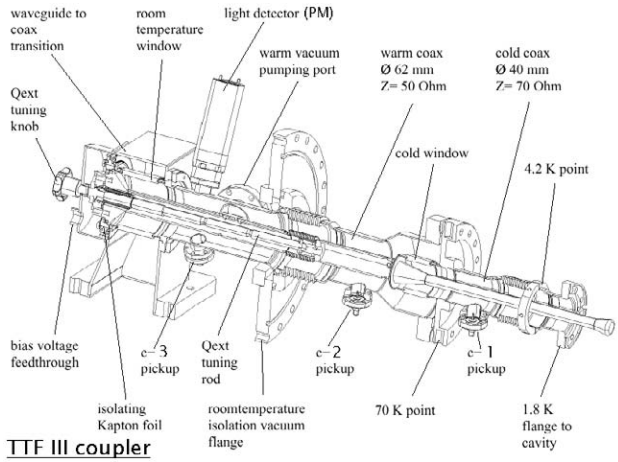

Figure 3: Latest coupler design TTF 3 with two cylindrical windows.

Figure 4: Module ACC 5 equipped with the TTF 3 couplers. Above the couplers the common pumping line for all 8 couplers is seen. Below the couplers the wave guide distribution system with the remote controlled three stub wave guide tuners, directional couplers and circulators is assembled.

RF COUPLER PROCESSING IN THE MODULES

During the period of June to September 2003 the couplers in modules ACC 3, 4 and 5 have been processed.

The RF processing procedure is comparable to the one in the horizontal cryostat. But the big difference is the parallel processing of 8 respectively 16 couplers at a time. The consequence is that always the slowest coupler sets the time needed for the whole module. The couplers are not backed in situ after the assembly to the modules. This leads to a higher starting pressure in the coupler vacuum during processing compared to the previous tests in the

horizontal cryostat. In addition the maximum power in the individual coupler was limited to 310 kW for ACC 3 and 350 kW for ACC4&5 by the klystron. In Tab. 2 the processing time for the module ACC 3, 4&5 is shown. Much longer time was needed for the processing up to the full operating pulse length of 1.3 ms compared to the processing on test stand and Chechia.

Two reasons could be responsible for the long processing time: first the parallel processing and second the poor vacuum in the couplers.

For the modules ACC4&5 we always observed the limitation in processing progress by the TTF 2 couplers. The latest design (TTF3) never showed an interlock event during processing on the modules.

Table 2: The needed RF processing time for modules ACC3, ACC4 & 5. The total power on time is only 67 % respectively 54% of the available time

ACC 3	
Total time	1858 hr
P_{for} > 2kW (RF on)	1238 hr (67%)
P_{for} > 100kW	745 hr
P_{for} > 200kW	216 hr
ACC4 & 5	
Total time	1858 hr
P_{for} > 2kW (RF on)	997 hr (54%)
P_{for} > 100kW	627
P_{for} > 200kW	193

For the klystrons 4 and 5 and their modulators together with the low level RF it was the first operating time. The remote control of the klystron modulator interlock for both klystrons was not completed. This caused an only 67% respectively 54% RF on time.

HIGH GRADIENT CAVITY TESTS

After applying the electrolytic polishing (EP) as an alternative surface preparation of 9 cell cavities, gradients >35 MV/m could be shown in the low power continuous wave test. Three of these cavities were equipped with helium tanks, high power couplers (TTF3), HOM coupler antennas and tuners for high power tests in the horizontal cryostat. The results of the cavity measurements are described in [6].

The cavity AC73 and the TTF3 coupler has been operated for more than 1100 hours at a gradient of 35 MV/m. The forward power was just above 600 kW (due to the not compensated Lorentz Force detuning). During setup of the low level RF system breakdowns in the coupler and quenches in the cavity were caused. Neither the cavity nor the coupler was showing any sign of degradation in their performance.

In module ACC 1 the high gradient EP cavity AC 72 was installed equipped with a TTF3 coupler. The coupler was processed at a short time and the cavity was operated with beam successfully.

INDUSTRIALIZATION

The last generation of the TTF3 couplers were ordered and produced completely by industry. Except the TiN coating of the ceramic windows, all fabrication steps have been performed by the companies. In the frame of a collaboration between the Institut National de Physique Nucleaire et de Physique des Particules – IN2P3 France and DESY, Germany the production was conducted. A new coupler preparation and test area including a clean room, ultra pure water system, vacuum oven for coupler baking and a klystron and test stand was installed. Now the first couplers from the industrial production are tested. It is foreseen to develop faster processing procedures and a reduced interlock system for the future use in a big linear accelerator.

Next steps are industrial studies on the coupler fabrication. The goal is to reduce the costs of the mass production of high power couplers.

CONCLUSION

All couplers in the VUV FEL linac could be processed to the power level needed. The parallel processing of 8 respectively 16 couplers at the modules is slower than at the test stands or in the horizontal cryostat.

TTF3 couplers are tested together with cavities at gradients of 35 MV/m (600 kW) without degradation of cavity or coupler.

Next steps in coupler development are industrial studies on the mass production of couplers with the goal of price reduction.

ACKNOWLEDGEMENT

I am thanking all the many colleagues from the TESLA collaboration who made it possible to develop, fabricate prepare assemble test and operate the described couplers.

REFERENCES

[1] A VUV Free Electron Laser at the TESLA Test Facility – CDR, DESY TESLA-FEL-95-03, 1995.

[2] J. Andruszkow et al., TESLA Technical Design Report, DESY 2001-011, ECFA 2001-209, TESLA Report 2001-23, TESLA-FEL-05

[3] W.-D. Moeller for the TESLA Collaboration, High Power Coupler for the TESLA Test Facility, 9th Workshop on RF Superconductivity, 1999, Los Alamos National Lab, USA

[4] B. Dwersteg at al., TESLA RF Power Coupler Development at DESY, 10th Workshop on RF Superconductivity, 2001, Tsukuba, Japan

[5] D. Kostin, New Accelerating Modules RF Test at TTF, this conference

[6] L. Lilje for the Tesla collaboration, Achievement of 35 MV/m in the Tesla superconducting Cavities using Electropolishing as a Surface Treatment, EPAC 2004, Lucerne, Switzerland

ENERGY SPREAD IN BTW ACCELERATING STRUCTURES AT ELETTRA

P. Craievich, R. J. Bakker, G. D'Auria, S. Di Mitri, Sincrotrone Trieste, Trieste, Italy

Abstract

The FEL project FERMI@ELETTRA will use the existing 1.0 GeV Linac, based on Backward Travelling Wave (BTW) structures, to produce VUV radiation between 100-10 nm. The project will be articulated in two different phases (100-40nm/40-10nm) and will require high quality beam with short bunches (500/160 fsec). Hence, wakefield effects have to be considered with respect to the electron beam quality. The single bunch energy spread induced by the short-range longitudinal wakefield is analyzed and results of start-to-end simulations are reported.

INTRODUCTION

The Fermi@Elettra project aims to construct a single-pass FEL user-facility in the spectral range 100-10 nm using the existing normal conducting 1.0 GeV linac. Fig.1 shows the proposed machine layout for the two phases of the project: FEL-I (100-40 nm) and FEL-II (40-10 nm) [1]. At present the linac is operated less than two hours a day as injector of the storage ring Elettra and, at least for the next two years, until the new injection system will be fully commissioned, this function has to be preserved. This implies that all the activities related to FERMI have to be scheduled without interfering with the normal operation of the machine.

More details on the machine upgrading and layout modifications can be found in [2].

The new scheme for the machine foresees an RF photo-cathode gun [3], providing a high quality electron beam, whose parameters are directly related to the ones required at the entrance of the undulator lines (table 1). Then, a 100 MeV pre-injector, composed by two 3 m accelerating sections with focusing solenoids, get the beam out of the space-charge energy domain and creates an energy-position correlation for bunch compression.

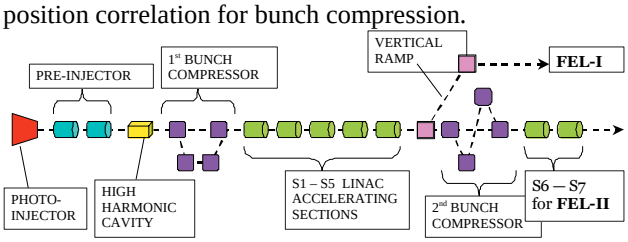

Figure 1: Schematic layout of the configuration for the FEL-I and FEL-II stages.

After the first magnetic chicane, five accelerating structures of the existing linac, equipped with an RF pulse compression system (SLED), allow the beam to reach the target energy required by FEL-I, 700 MeV. In total the present linac includes seven 6 m accelerating sections, 3/4π backward travelling wave (BTW), composed by 164 nose-cone cavities magnetically coupled. The remaining two accelerating sections will be located after the second bunch compression and will be used for the second phase of the project FEL-II up to 1.0 GeV. Quadrupole triplets between the sections provide the necessary transverse focusing. As reported in table 1, FEL operations require a high quality beam with ultra short bunches, hence the wakefield effects have to be considered carefully. That is, the short-range longitudinal wakefields increase the single bunch energy spread, while short-range transverse wakefields may increase the emittance of the bunch.

In this paper the single bunch energy spread induced by short-range longitudinal wakefields and accelerating voltage is analyzed for the FEL-I. The minimum single bunch energy spread at the exit of the linac has been calculated by varying the energy gain and RF phase of the BTW sections. Finally the results have been compared with those obtained from start-to-end simulations with ELEGANT [4] in presence of longitudinal wakefields.

Table 1: Electron beam parameters at the end of the linac for FEL-I and FEL-II

	FEL-I	FEL-II	
Wavelength target	100 40	40 10	nm
Beam energy	0.70	0.55 1.00	GeV
Bunch charge	1.0	1.0	nC
Peak current	0.8	2.5	kA
Bunch duration (σ_t)	500	160	fs
Energy spread (σ_δ)	0.7	1.0	MeV
Emittance	1.5	1.5	μm
Repetition rate	50	50	Hz

LONGITUDINAL DYNAMICS IN FEL-1

The FEL-I wavelengths foresees the acceleration to 700 MeV of a bunch with σ_z=120μm and total charge Q= 1nC at in five BTW sections. Note that with a negligible beam loading each section of the present linac can provide an energy gain up to 170 MeV. The beam energy spread is determined by the accelerating field produced by the external generator and the wakefields excited by the beam in the accelerating structures. For our BTW structures the wake potentials have been numerically evaluated and the wake function obtained by a fitting based on analytical estimations [5]. Figure 2 shows the numerical results obtained for the longitudinal wake potentials of Gaussian bunches with lengths ranging from 1000 μm up to 50 μm (solid lines); the black dashed line represents an analytic approximation of the longitudinal wake function.

As already shown in [6], for a Gaussian bunch the RMS energy spread can be easily evaluated by knowing four integral parameters of the wake fields: the loss factor $K_{\|}$, the average wake energy spread ΔW and the Fourier

sine/cosine part $I_{sin,}/I_{cos}$. Table 2 summarizes the computed integral parameters in our case.

To minimize the single bunch energy spread at the end of the linac we have used a routine that allows the compensation of the longitudinal wakefields through the tuning of the RF phase and amplitude of the accelerating sections. We have individually set each accelerating module, fixing their maximum energy gain and RF phase, in order to reach the minimum energy spread with the constraint of a final energy of 700 MeV. Note that in practice, on the present plant, we can do that with an extreme flexibility since we have one RF plant for each accelerating section.

The optimization has been made under the assumption that the initial energy spread, at the exit of the first bunch compressor, is negligible with respect to the total energy gain for section. Furthermore we have considered an initial energy of 68.3 MeV [7] and a maximum energy gain for section of 170 MeV with a gradient of 28 MV/m. The results show that the optimization foresees identical parameters for the five BTW sections, in terms of maximum energy gain U_0 and optimum RF phase ϕ_{opt}, table 3 summarizes the obtained values. The minimum relative energy spread at ϕ_{opt}=-40.8° RF phase is roughly 2.5 times smaller than the corresponding at ϕ_{opt}=0°, on crest acceleration and energy spread due to the wakefields only, but we have to accept an accelerating efficiency reduction of 24%.

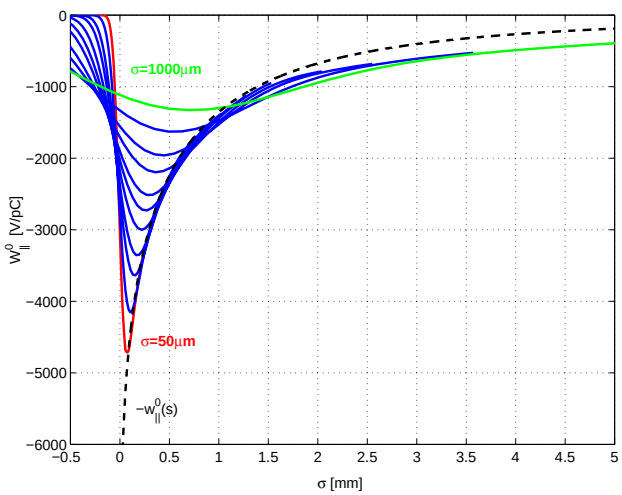

Figure 2: Longitudinal wake potentials (solid lines) and longitudinal wake function (black dashed line) of the BTW structure.

Table 2: Integral parameters of the wake potentials in the BTW structure

σ_z [μm]	$K_{\|}$ [V/pC]	I_{cos} [V/pC]	I_{sin} [V/pC]	ΔW [V/pC]
120	-2298.3	-0.009598	-7.860948	1118.4

Figure 3 shows the energy gain as a function of the distance s to the bunch center for different input phases ϕ_{opt}. The effect of the compensation of the wakefields can be seen as a decreasing of the difference between the relative maximum and minimum of the energy gain in the range considered $-3\sigma_z/3\sigma_z$.

Table 3: Minimum single bunch energy spread vs. the maximum energy gain in the BTW structure

U_0 [MeV]	ϕ_{opt}	$\Delta U/\langle U\rangle$ %
128.6	0.0°	0.80
129.0	-4.3°	0.75
130.0	-8.3°	0.70
140.0	-23.2°	0.53
150.0	-31.0°	0.44
160.0	-36.5°	0.37
170.0	-40.8°	0.32

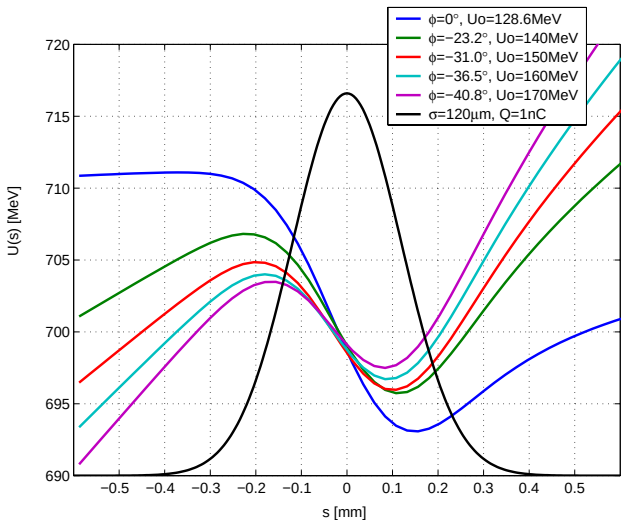

Figure 3: Energy gain of an electron inside the bunch as a function of the distance to the bunch center at the end of the linac.

RESULTS FROM START-TO-END SIMULATION

The results carried out with the previous analytical method have been compared with those obtained with the tracking code ELEGANT [6] in presence of longitudinal wakefields. As input we have used a relativistic Gaussian bunch distribution with negligible energy spread, compared with the total energy gain along the five BTW sections, 120μm bunch length, 1 nC charge. The optimization has been made using the same parameters for the BTW sections of the previous case and maximum energy gain per section of 150 MeV (keeping a safe margin of more than 10%).

Figure 4 shows the obtained results. With the same RF phase, ϕ_{opt}=-31°, the two energy gain distributions, analytical method (red curve) and ELEGANT tracking (green points), show an excellent coincidence with a final correlated energy spread obtained with ELEGANT of 0.45%.

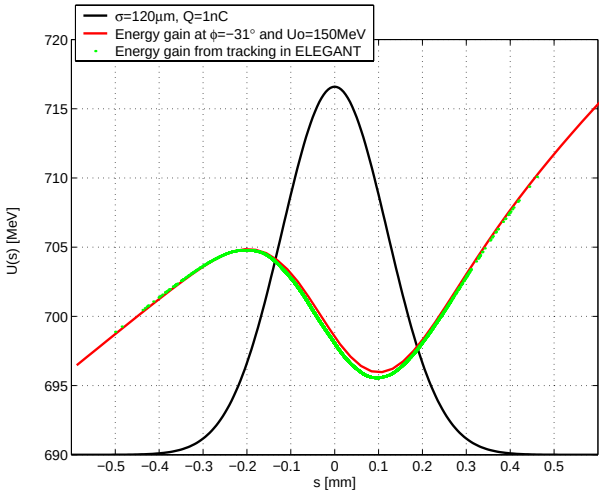

Figure 4: Energy gain comparison between analytical method (red line) and ELEGANT (green line).

More realistic conditions describing the initial energy and charge distributions (i.e. taking into account a non-negligible energy spread) produce results in good agreement with those discussed.

As an example, assuming 4 % or 2.7 MeV input energy spread after the pre-injector (see Fig. 1), we can obtain an electron bunch with an RMS length of σ_z = 128 μm and a correlated energy spread of σ_δ = 0.2 % at a central energy of 699.5 MeV, see Fig. 5. This value is slightly higher than the one quoted in Tab. 1. However, the FEL performance is determined by the uncorrelated slice-energy spread at the maximum current, i.e., the total energy spread over a cooperation length of the FEL [8]. In our case the typical cooperation length (L_c) is less than 2 μm [7]. From Fig. 5 and Fig. 6 it follows that at the peak of the bunch-current the correlated energy spread is linear. Hence, the total energy spread within a cooperation length can thus easily be estimated by $L_c \cdot \sigma_\delta / 2\sigma_z = 1.6 \cdot 10^{-5}$, well below the limit stated in Tab. 1. We also note that the estimated peak current of ~ 1 kA for FEL-1 fully satisfies the condition quoted in the table.

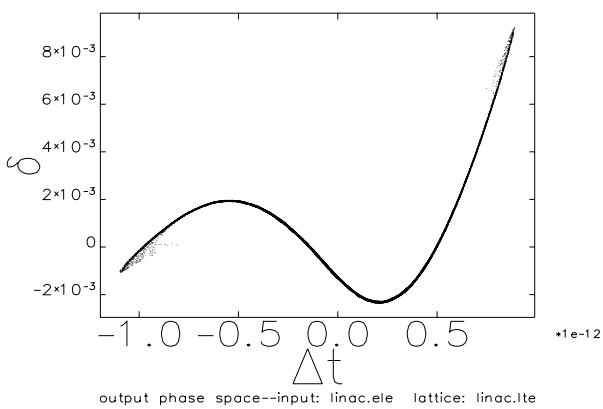

Figure 5: Longitudinal phase space (relative energy spread vs. time) at the exit of the FEL-I linac after the wakefield compensation.

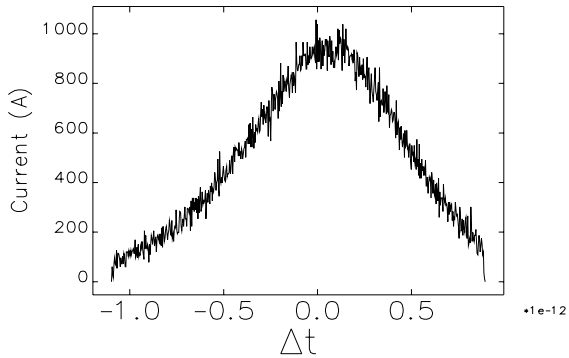

Figure 6: Current distribution along the bunch at the exit of the optimised FEL-I linac.

CONCLUSION

The single bunch energy spread induced by longitudinal wakefields and accelerating voltage of the BTW sections of the FERMI project has been analyzed for the first phase of the project FEL-I. We have carried out a very simple optimization to compensate the effect of the longitudinal wakefields foreseeing identical RF parameters for the five BTW sections utilized for FEL-I. Start-to-end simulations have also been performed, both to confirm the previous results, and to support the consistency of the ELEGANT tracking. Excellent agreements between two methods have been found.

The results obtained in more realistic case analyzed with start-to-end simulations have shown that the longitudinal wakefields in the BTW sections are not critical for the FEL-I stage. Actually, the correlated energy spread has been minimized down to the 0.2% RMS. It provides slice features concerning the longitudinal dynamics in full agreement with the specifications.

REFERENCES

[1] FERMI@ELETTRA machine project update, Sincrotrone Trieste, 2003.
[2] G. D'Auria et al, "Linac Upgrades for FERMI@ELETTRA", this Conference.
[3] V.A. Verzilov et al., "Photo-injector study for the ELETTRA linac FEL", FEL-2003 (September 2003, Tsukuba, Japan).
[4] M. Borland, http://www.aps.anl.gov/asd/oag/
[5] P. Craievich, T. Weiland and I. Zagorodnov, "The short-range wakefields in the BTW accelerating structure of the ELETTRA Linac", presented at ICAP2004, Saint Petersburg, 2004.
[6] A. Novokhatski, M. Timm and T. Weiland, "Single Bunch Energy Spread in the TESLA Cryomodule", TESLA Report 99-16, 1999.
[7] S. Di Mitri et al., "Start-to-end simulation for the FERMI project at ELETTRA", presented at FEL conference 2004, Trieste, Italy.
[8] P. Emma, "Accelerator Physics challenges of X-RAY FEL SASE sources", Proc. Of the EPAC2002, Paris, France, p. 49 (2002).

NUMERICAL CALCULATION OF COUPLING IMPEDANCES IN KICKER MODULES FOR NON-RELATIVISTIC PARTICLE BEAMS

B. Doliwa, T. Weiland, TEMF, Technische Universität Darmstadt, Germany

Abstract

In the context of heavy-ion synchrotrons, coupling impedances in ferrite-loaded structures (e.g. fast kicker modules) are known to have a significant influence on beam stability. While bench measurements are feasible today, it is desirable to have the coupling impedances in hands already during the design process of the respective components. To achieve this goal, as a first step, we have carried out numerical analyses of simple ferrite-containing test systems within the framework of the Finite Integration Technique. This amounts to solving the full set of Maxwell's equations in frequency domain, the particle beam being represented by an appropriate excitation current. With the resulting electromagnetic fields, one may then readily compute the corresponding coupling impedances. Despite the complicated material properties of ferrites, our results show that their numerical treatment is possible, thus opening up a way to determine a crucial parameter of kicker devices before construction.

INTRODUCTION

Within the design work of the planned heavy-ion synchrotron at the GSI accelerator facility, detailed impedance studies are required. Due to the target vacuum quality of 10^{-12} mbar and particle currents of up to 1 A, beam instabilities would have tremendous effects on the operability of the synchrotron. One unknown is the beam response to the ferrite-loaded kickers. Vice versa, heating of the kicker components may be a problem.

Caspers has addressed the measurement of coupling impedances via the so-called coaxial-wire technique [1], which is most accurate for ultra-relativistic particle beams. The obvious drawback of this approach is that a prototype component has to be at hand. During the design process of new components, therefore, simulations may be helpful.

In this paper we consider the numerical determination of the longitudinal coupling impedance [2]

$$Z_{||}(\omega) = \frac{1}{q^2} \int \mathrm{d}x\mathrm{d}y \rho(x,y) \int \mathrm{d}z E_z(x,y,z;\omega) e^{i\omega z/\beta c} \tag{1}$$

where $\rho(x,y)$ is the transverse charge distribution of the particle beam and $q = \int \mathrm{d}x\mathrm{d}y\rho(x,y)$. The electric field in the above expression is generated by the current density

$$\boldsymbol{J}_{\text{ext}}(x,y,z;t) = \beta c \hat{z} \rho(x,y) \delta(z - \beta c t), \tag{2}$$

which corresponds to an infinitesimally short bunch of particles travelling with velocity βc along the positive z direction. The equivalent expression in frequency domain is

$$\boldsymbol{J}_{\text{ext}}(x,y,z;\omega) = \hat{z} \rho(x,y) e^{-\mathrm{i}\omega z/\beta c}. \tag{3}$$

In the case of kicker impedances, we will restrict ourselves to frequencies below 100 MHz, which are of primary interest for the planned heavy-ion synchrotron.

COMPUTATIONAL APPROACH

In order to determine $Z_{||}$ for a given geometry and excitation current we need to calculate the electric field. Our starting point is

$$\boldsymbol{\partial} \times \nu \boldsymbol{\partial} \times \boldsymbol{E} - \omega^2 \epsilon \boldsymbol{E} = -\mathrm{i}\omega \boldsymbol{J}_{\text{ext}},$$

a descendant of Maxwell's equations in frequency domain. Here $\nu \equiv 1/\mu$, with possibly complex permeability μ and ϵ denoting permittivity.

Within the Finite Integration Technique[3], we carry out an appropriate discretization, which leads to a matrix counterpart of the former equation,

$$\left(\tilde{\boldsymbol{C}} M_\nu \boldsymbol{C} - \omega^2 M_\epsilon \right) \boldsymbol{e} = -\mathrm{i}\omega \boldsymbol{j}_{\text{ext}}. \tag{4}$$

In the presence of ferrites, this system of linear equations may become highly ill-conditioned due to the large jumps in permeability. We therefore do not attempt to solve the matrix equation as a whole but proceed as follows: Firstly, an electrostatic problem is solved yielding a divergence-free source term $\boldsymbol{j}'_{\text{ext}}$ and the 'static' part of the electric field solution. We then note that, at low enough frequencies, the term $\omega^2 M_\epsilon \equiv b$ is small compared with $\tilde{\boldsymbol{C}} M_\nu \boldsymbol{C} \equiv B$ (in the sense of some matrix norm). One may then expand the solution in terms of bB^{-1} (symbolically). It has turned out in our simulations that keeping up to six terms of this series expansion is sufficient (below 100 MHz). The inversion of the matrix B in each expansion term formally corresponds to solving a standard magnetostatic problem, which will therefore not be discussed here.

We finally remark that simulations are carried out using the software tools CST MICROWAVE STUDIO® [4] and MATLAB [5].

BOUNDARY CONDITIONS

One problem in modelling an elementary particle beam traversing an accelerator component is the question of appropriately chosen boundary conditions. This is crucial since the fourier transform of a short bunch, Eq. 3, extends from $z = -\infty$ to $+\infty$. Since our computational domain is finite we have to take one of the following options:

- open boundary conditions, e.g. by using perfectly-matched layers[6]
- periodic boundary conditions

- no special prerequisite despite long enough pieces of beam pipe leading to the accelerator component

For reasons of simplicity we have chosen the last option. This is possible since the frequency range of interest (< 100 MHz) is well below the cutoff frequency of the beam pipe (radius 10 cm). We will now shed some light on whether this approach is practical in numerical simulations.

To this end let us consider the z dependent imaginary part of the integrand of Eq. 1 on the beam axis, i.e.

$$\mathrm{Im}\left(E_z(0,0,z;\omega)e^{\mathrm{i}\omega z/\beta c}\right), \qquad (5)$$

which will help us to display the boundary effects. Consider the test system consisting of two pieces of a perfectly conducting beam pipe (20 cm $\times$ 20 cm quadratic cross section, variable length) connected to a cubic cavity (60 cm edge length, again perfectly conducting), as sketched in Fig. 1, top. Figure 1, bottom, shows a comparison of

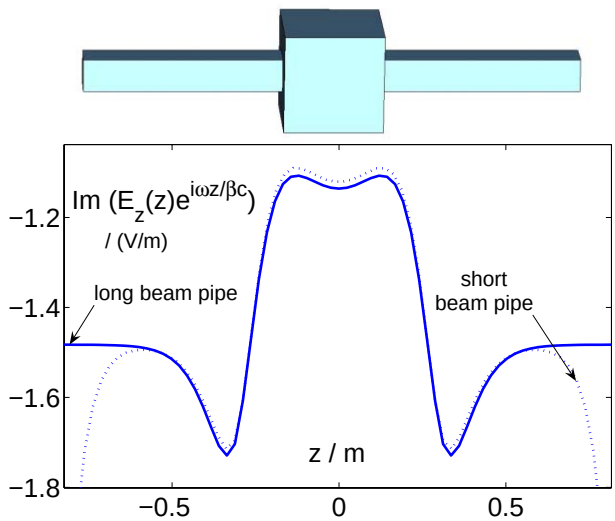

Figure 1: Top: sketch of the test system (length 300 cm). Bottom: integrand, as given by Eq. 5, for short beam pipes (length 120 cm each, dashed line) and long beam pipes (length 270 cm each, solid line), at $\omega/2\pi = 1$ MHz and $\beta = 0.85$.

the integrand, Eq. 5, at $\omega/2\pi = 1$ MHz, between two versions of the test system, one having overall length 300 cm, the other 600 cm. For $|z| > 50$ cm, the solid curve is a constant reflecting the space-charge impedance per length within the beam pipe (see next section). In the case of short beam pipes (dashed curve), boundary effects lead to a deviation from this expected behavior. For $|z| < 50$ cm, both curves are nearly identical. Thus, the impedance contribution of the cavity is correctly reflected by both simulations.

We have observed that boundary effects generally become larger towards lower frequencies (not shown here), which implies the need for longer beam pipe pieces in the simulation. At high frequencies, in contrast, boundary effects pose a less serious problem.

In summary, simulations with no other prerequisite than long enough adjacent beam pipes are sufficient for the calculation of coupling impedances. However, a further quantification of the reported effects would be useful. Moreover, one may imagine that more sophisticated kinds of boundary conditions (see above) would lead to more economic simulations. This will be one of the subjects of our further research.

SPACE-CHARGE EFFECTS

For $\beta \to 1$ the electric field of a point charge assumes a nearly 'plate-like' shape, meaning that its Coulomb interaction with preceding or following particles is negligible. For $\beta < 1$, however, these interactions (called space-charge effects) have a negative contribution to the imaginary part of the longitudinal coupling impedance.

As a test of our simulations, we have quantified this contribution for the case of an infinitely long beam pipe of either cylindrical or quadratic cross section. The walls are assumed to be perfectly conducting.

Due to the simple geometries of these examples, analytical expressions for the coupling impedances are available which we compare to the ones obtained from simulation.

Cylindrical beam pipe

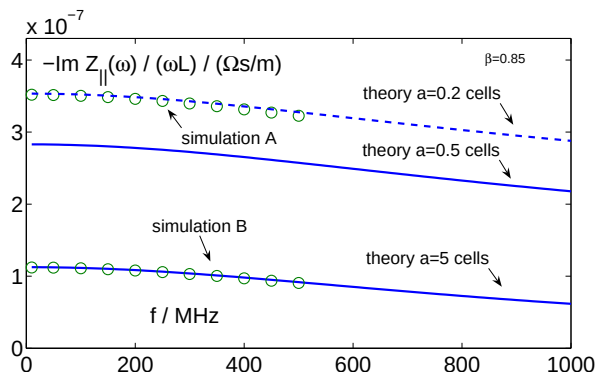

Figure 2: Negative imaginary part of the coupling impedance per unit length and frequency of a cylindrical beam pipe (radius 20cm, length 3m). Simulation A uses a current based on a single grid line along the z axis, whereas simulation B mimics a cylindrical current using grid lines within distance five from the origin of the transverse plane.

The expression for the longitudinal impedance for this case can be found in [7] and is not repeated here. We only remark that the impedance sensitively depends on the radius, a, of the particle beam. In Fig. 2, we see the comparison between theory and simulation in the case where the beam current has been imprinted on the central grid line along the z axis. Expressed differently, in each transverse plane, one 'dual' grid cell has been used to model the current. One may ask what radius should be assigned to this

current. Firstly, Fig. 2 clearly shows that a radius of half the grid spacing is in contradiction to theory. Secondly, matching analytical results to simulation (dashed line), we find $a \approx 0.2$ times the grid spacing (only equidistant grids are used in this section). This finding agrees with the results of Waldschmidt and Taflove [8] who investigated the effective extension of current filaments. Thirdly, when modelling the beam current using several cells per transverse plane (i.e. a bundle of grid lines along the z axis) simulation data and theory coincide, as expected. This is also shown in Fig. 2 for the case of a bundle of grid lines with transverse diameter of 10 cells.

Rectangular beam pipe

The impedance for this case can be calculated exactly via textbook methods. A comparison with simulations then leads to a plot similar to Fig. 2, which we omit here due to the limited space. Again, assuming an effective radius of ca. 0.2 cell sizes for a single-line current leads to the agreement of theory and simulation.

FERRITE-LOADED COMPONENTS

We finally come to the main objective of our work, i.e. impedance calculations for kicker modules. Figure 3 shows the model under investigation here. It is similar to the SIS injection/extraction kicker operated at GSI, with respect to the key features, i.e. the design of ferrite modules (held by 20 mm-thick steel plates) and the dimensions of vacuum cavity and adjacent beam pipes. Simplifications have been introduced by assuming perfectly-conducting walls and by omitting finer geometric details. The material specifications (permittivity, complex frequency dependent permeability) for the used ferrite 8C11 have been obtained from the supplier's data sheet (*www.ferroxcube.com*).

The motivation behind treating an existing accelerator component is to be able to compare our numerical results with measurements.

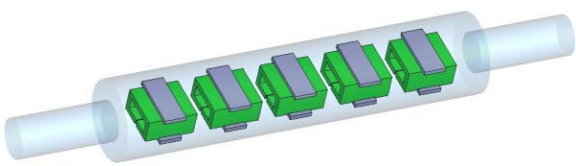

Figure 3: Model similar to GSI's existing SIS kicker, total length is 290 cm, cavity radius 20 cm, beam-pipe radius 10 cm. We put five ferrite modules here.

Figure 4 shows the coupling impedance below 100 MHz stemming from numerical simulation as described above. The z integration (see Eq. 1) extends over the whole cavity, the beam pipe parts being omitted.

Since the ferrite permeability possesses a considerable temperature dependence, we have to fix the simulation temperature (here to room temperature).

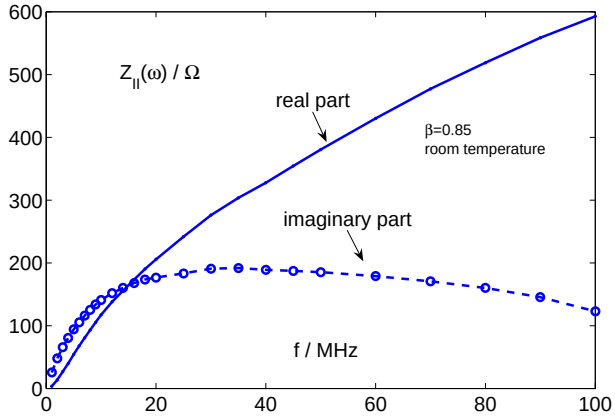

Figure 4: Longitudinal coupling impedance of the model shown in Fig. 3.

OUTLOOK

Further steps in our work will cover two main subjects: Firstly, we will further improve our numerical approach (use of different boundary conditions, multi-grid solvers). Secondly, comparison with measurements is needed. To this end, it would be desirable to measure the coupling impedance of the existing SIS kicker either within accelerator operation or on-bench, e.g. by the coaxial wire method.

ACKNOWLEDGEMENTS

We thank U. Blell and O. Boine-Frankenheim for helpful discussions and for the supply of the SIS-kicker geometry data, and W. Müller for proofreading the manuscript. B. Doliwa's work has been funded by the GSI and the 'Graduiertenkolleg Physik und Technik von Beschleunigern' at the Technische Universität Darmstadt.

REFERENCES

[1] Caspers F. *Handbook of Accelerator Physics (A.W. Chao, M.Tigner, Eds.)*, Chapter 7.5.1, 1999.

[2] U. van Rienen and T. Weiland. *IEEE Trans. Magn.*, 26(2):743, 1990.

[3] T. Weiland. *AEU-Int. J. Electron. Commun.*, 31(3):116, 1977.

[4] CST GmbH. *Bad Nauheimer Str. 19, 64289 Darmstadt, www.cst.com*.

[5] The Mathworks GmbH. *Adalperostr. 45, D-85737 Ismaning, Germany*.

[6] J. P. Berenger. *J. Comput. Phys.*, 114(2):185, 1994.

[7] A. M. Al-Khateeb, O. Boine-Frankenheim, I. Hofmann, and G. Rumolo. *Phys. Rev. E*, 6302(2):026503, 2001.

[8] G. Waldschmidt and A. Taflove. *IEEE Microw. Guided Wave Lett.*, 10(6):217, 2000.

WIRE MEASUREMENT OF IMPEDANCE OF AN X-BAND ACCELERATING STRUCTURE†

N. Baboi, DESY, Hamburg; R.M. Jones, J.R. Lewandowski, G.B. Bowden,
S.G. Tantawi, V.A. Dolgashev, J.W. Wang, SLAC, Stanford, USA

Abstract

Several tens of thousands of accelerator structures will be needed for the next generation of normal conducting linear colliders known as the GLC/NLC (Global Linear Collider/Next Linear Collider). To prevent the beam being driven into a disruptive BBU (Beam Break-Up) mode or at the very least, the emittance being significantly diluted, it is important to damp down the wakefield left by driving bunches to a manageable level. Manufacturing errors and errors in design need to be measured and compared with prediction. In this paper a bench-top method of measuring transverse impedances in X-band accelerating structures is described. Utilizing an off-axis wire the S parameters are measured and converted to impedance. Measurements in a damped and detuned structure built for GLC/NLC are presented and the results are discussed.

INTRODUCTION

One option in building a next generation of linear collider is to use normal conducting X-band accelerating structures. These structures have been carefully designed and studied for over a decade for the GLC/NLC [1]. One main concern in their design is the minimization of wakefield effects. Wakefields are excited by charged particles in the accelerating structures and influence the motion of subsequent particles or bunches. In particular, transverse fields are of concern, as they cause large increase in the emittance or, in the worst case, BBU [2].

To prevent this, the frequencies of the modes which comprise the wakefield are forced to add de-constructively by detuning the frequencies of the cells. Initially the wake decays with a Gaussian functional form. However, as there are a finite number of cells, eventually the modes must add coherently. This causes the wakefield to rise to unacceptably large values. To prevent this from occurring, a fraction of the wake is coupled out to four manifolds, which run collinear with the axis of the accelerator. Several such damped and detuned structures have been built and studied. The most advanced in this series is the RDDS1 (rounded damped detuned structure) [3]. It has a length of 1.8 m with a $2\pi/3$ phase advance per cell. A 60 cm accelerator structure with a $5\pi/6$ phase advance per cell is currently being fabricated [4].

Even though electromagnetic field simulation codes as well as circuit models have proven to give accurate results, the increasing complexity of the structures requires wakefield measurements to be performed in order to be sure that the fabricated structures behave as expected. Previously, the main setup for such measurements in GLC/NLC structures has been the ASSET facility [5], where transverse fields are excited and sampled by a beam. Although this method is quite precise, it has the drawback of requiring expensive beam time at an accelerator facility.

An alternative and somewhat complementary method is the wire method [6,7]. Here a metallic wire takes the place of the beam and a high frequency measurement is conducted in the laboratory. The fundamental idea behind the wire method is to simulate the beam-structure interaction by propagating a short current down a wire inserted in an accelerating structure.

Alternatively, one can measure the transmission curve in the frequency domain in order to study the transverse impedance, which is related to the wakefield $W_\perp$ by:

$$Z_\perp(\omega) = \frac{-i}{c}\int_{-\infty}^{\infty} W_\perp(\zeta)\exp\left(-i\omega\frac{\zeta}{c}\right)d\zeta\,, \qquad (1)$$

where ω is the angular frequency and c the light velocity. In the frequency domain one can distinguish the individual resonances of the structure, the higher order modes (HOM), constituting the wakefield:

$$W_\perp(\zeta) = \sum_n 2k_{\perp,n}\sin\left(\omega_n\frac{\zeta}{c}\right)\exp\left(-\frac{\omega_n}{2Q_n}\frac{\zeta}{c}\right). \qquad (2)$$

Here ω_n, Q_n and $k_{\perp,n}$ are the angular frequency, quality factor and kick factor of mode n.

In our measurements we chose to measure in the frequency domain. For transverse wakefields, two wires placed symmetrically around the axis have been used previously. This kind of measurement has the advantage of decoupling the odd and even modes. On the other hand, aligning the two wires may be rather difficult, particularly for X-band structures. For this reason we chose to use a single off-axis wire for our measurements.

In the next section we present the setup, built at SLAC, to measure transverse wakefields. The measurements made in RDDS1 are described in the final main section.

METHOD

Setup

Fig. 1 shows the setup of the wire measurement. A wire of diameter 300 μm is placed at an offset in the device

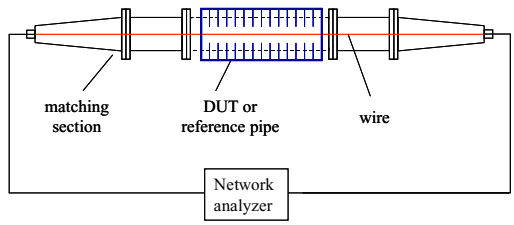

Figure 1: Sketch of the wire measurement setup.

† Supported by the U.S. DOE grant number DE-AC03-76SF00515

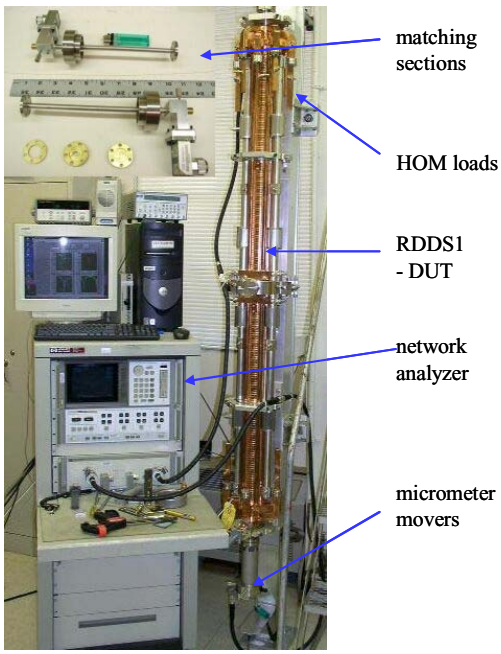

Figure 2: Wire measurement setup.

under study (DUT). Two adapters are utilized to match the impedance of the wired structure to a 50 Ω high frequency cable. A network analyzer is utilized to measure the scattering (S) parameters. In Fig. 2 one can see a picture of the setup. The 1.8 m long RDDS1 structure is mounted vertically, in order to avoid an appreciable saggitta in the wire. The supports to the lower matching section can be seen. The upper inset shows the matching sections together with the purposely built calibration elements. The wire can be moved transversely by slightly bending the tubes of the adaptors.

The network analyzer has been calibrated at the ports constituted by the flanges of the structure. The setup has a broad bandwidth, which ranges from 11 GHz to 18 GHz. The elements which limit the bandwidth are the waveguide-to-coax adaptors. This setup is sufficiently broadband to measure the entire first dipole pass-band in RDDS1.

Principle

Alignment of the wire is based on the amplitude of the transmission parameter S_{21} of modes at the low and high frequency end of the first dipole band. These two extremes correspond to alignment in cells in the first and last part of the detuned structure.

S_{21} is measured for various positions of the wire, for the DUT (S_{21}^{DUT}) and, for a reference tube (S_{21}^{REF}) having the same length as the structure. The impedance can be calculated based on various models. We use the so-called log formula, as it is best suited for long structures [8]:

$$Z_{\parallel} = -2Z_0 \ln\frac{S_{21}^{DUT}}{S_{21}^{REF}}\left(1 - \frac{1}{2\gamma_0 d}\ln\frac{S_{21}^{DUT}}{S_{21}^{REF}}\right), \qquad (3)$$

where Z_0 and γ_0 are the characteristic impedance and the propagation constant of the coaxial line and d is the length of the structure.

MEASUREMENTS

Transmission Parameter S_{21}

S_{21} measured for a relative position of the wire, with respect to an arbitrary reference, of x = 0.24 mm (the plane containing the input coupler) and y = -0.48 mm is shown in Fig. 3. The wire is about centered in the y plane and at an offset in x. The dipole band is present between about 14 and 16.5 GHz. In the presence of the wire, the mode frequencies are shifted with respect to the unperturbed case [9]. In Fig. 3 one can distinguish some of the individual dipole resonances, particularly between about 14.5 and 15.5 GHz. Although they are rather difficult to distinguish, detailed spectra indicate that there are also HOMs present at higher and lower frequencies.

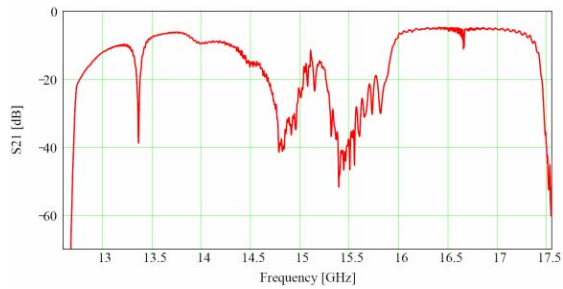

Figure 3: S_{21} as a function of frequency for x = 0.24 mm and y = - 0.48 mm.

In principle, one expects to see an overall Gaussian-like S_{21} curve [10]. However a fabrication error in the central region of this structure, has led to a deformation of the frequency spectrum in the neighborhood of 15 GHz. The larger peak at about 15.8 GHz is due to the decoupling from the manifold of the last few cells of the structure. The high peak at about 13.4 GHz is not a structure mode and has been observed in previous measurements.

The red continuous curve in Fig. 4 is a detail of the spectrum in Fig. 3. About five individual HOM peaks can be distinguished in frequencies between approximately 14 GHz and 14.2 GHz. The same plot shows other curves for several x positions. One observes how while the wire moves in one direction, both the frequency and the amplitude of the modes change. One can decouple the individual peaks and extract information about individual modes from this curve, in particular about the modal loss

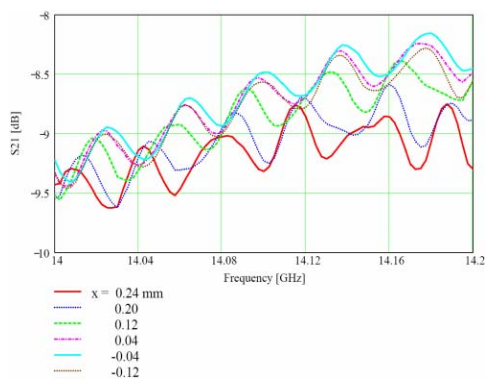

Figure 4: S_{21} as a function of frequency for several wire positions (y = -0.48 mm).

factor. This will be the subject of a future paper.

From S_{21} the frequencies of the modes can be estimated for each wire position. This is shown in Fig. 5 for the same frequency window. One can clearly follow the quadratic variation of the frequency of each mode with the wire position. This shows that the wire measurement is also suitable for measuring cell misalignments in detuned structures, where each mode couples strongest to the beam (or wire in our case) in a certain cell.

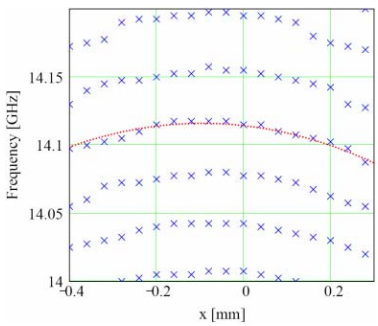

Figure 5: Peak frequencies as a function of the x wire position (y = -0.48 mm).

Transverse Impedance

From the S_{21} measurement one can calculate with eq. (3) the impedance of the dipole pass-band as a function of frequency. In order to obtain the transverse impedance (in principle independent of the transverse position of the wire) the longitudinal impedance is normalized with respect to $(c/\omega)/(x^2 d)$. Fig. 6a displays the impedance obtained from the transmission parameter shown in Fig. 3 and an application of eq. (3). For the sake of comparison, the spectral function of RDDS1 as predicted by a circuit model [11] (where the frequency errors that occurred during fabrication are included) is illustrated in Fig. 6b. It is interesting to observe in both curves frequency errors in the neighbourhood of 15 GHz. One can distinguish in the measurement recorded in Fig. 6a a rise in the impedance above 14.5 GHz. The modes below this frequency have a low kick factor and therefore they couple weaker to the wire and give a lower signal. The same reasoning applies at high frequencies.

Apart from the difficulties inherent in the method (e.g. applicability of the model used and sufficiently good electrical contacts), complications arise from the errors in the fabrication of this structure. This impedes quantitative comparisons with spectral function predictions. Also, wire movements in both planes were coupled, making the normalization of the transverse impedance to the offset from the structure axis rather difficult.

In conclusion, the setup has been improved and the two transverse planes are now adequately decoupled. Furthermore, the reason for the frequency errors occurring in the center of the structure is well understood and will be avoided in future structures. Thus, it is anticipated that there will be minimal frequency errors in the forthcoming damped and detuned structures planned

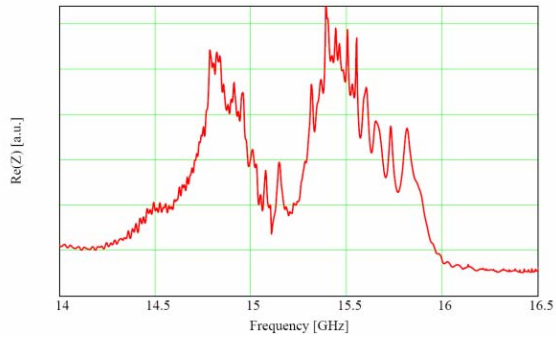

Figure 6a: Impedance obtained from the S_{21} in Fig. 3.

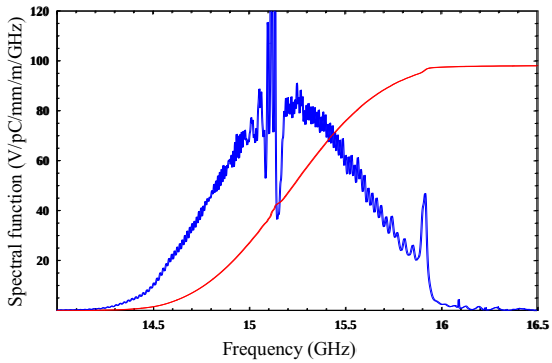

Figure 6b: Spectral function [10] as obtained from a circuit model [11]. The frequency errors in the middle of the spectrum, due to the deformation of the middle cells, are taken into account.

for measurement later this year. Also, we intend to explore the possibility of extending the measurement technique to investigate the modes in L-band TESLA [12] accelerating cavities in the context of the ILC (International Linear Collider) [13]. Finally, we note that integration of the beam impedance will allow an estimation of the individual kick factors of the dipole pass-band.

Acknowledgements We would like to thank the colleagues from the RF Structures group, High Power RF group and NLC group, for their illuminating discussions.

REFERENCES

[1] International Study Group, SLAC-R-559, 2000
[2] K. Yokoya, DESY Report 86-084, 1986
[3] R.M. Jones *et al.*, PAC97, SLAC-PUB-7537, 1997
[4] J.W. Wang *et al.*, THP33, this conference.
[5] C. Adolphsen *et al.*, SLAC-PUB-7519, 1997
[6] M. Sands and J.R. Rees, PEP-0095, 1974
[7] A. Faltens *et al.*, Proc. 8th Int. Conf. on Accel., Geneva, p. 338, 1971
[8] E. Jensen, PS/RF Note 2000-001, 2000
[9] R.M. Jones *et al.*, EPAC02, SLAC-PUB-9245, 2002
[10] R.M. Jones *et al.*, Linac96, SLAC-PUB-7287, 1996
[11] R.M. Jones *et al.*, EPAC96, SLAC-PUB-7187, 1996
[12] R. Brinkman *et al.* (editors), TESLA Report 2001-23
[13] www.interactions.org/linearcollider

SIMPLE THEORY OF THERMAL FATIGUE CAUSED BY RF PULSE HEATING

S.V. Kuzikov, Institute of Applied Physics, Russian Academy of Sciences, Nizhny Novgorod, Russia

Abstract

The electron-positron linear colliders projects imply that accelerating structures and other RF components will undergo action of extremely high RF fields. Except for electrical the breakdown threat there is an effect of the copper surface damage due to multi-pulse mechanical stress caused by Ohmic losses in the skin layer [1].

A new theory of the thermal fatigue is presented. The theory is based on the consideration of the quasi-elastic interaction between neighborhood grains in the metal due to the thermal expansion of the skin-layer. With a proposed method one can estimate a total number of the RF pulses needed for surface to fracture depending on temperature rise, pulse duration, and average temperature. The parameters necessary for the final equation were found, using experimental data points obtained at 11.4 GHz for the copper [2]. Experimental studies of the pulsed heating fatigue of the copper surface at 30 GHz are also under way [3].

FATIGUE MODEL

The copper crystal has a cubic structure. Ideally, each atom has 6 links with neighbors (Fig. 1). Probability to break any link is given by next equation:

$$p_j = \exp\left(-\frac{U_c}{k_B T_c}\right), \qquad (1)$$

which shows that the higher the temperature the higher the probability. Here U_c – energy of the coupling of the atoms, T_c is a stationary temperature, and k_B is a Boltzman's constant. If T_c>0, the probability is not zero and there are some broken links. Should mention that because of (2), the value of p_j is rather small for the temperatures less than metal melting point.

$$\frac{U_c}{k_B T_c} >> 1, \qquad (2)$$

.

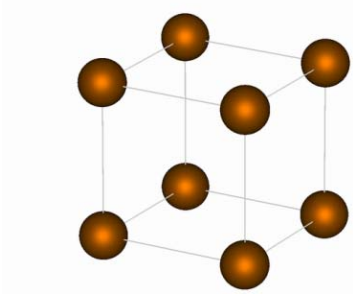

Figure 1: Structure of copper's crystal.

However, real copper has many defects. In particular, any bulk copper consists of grains (Fig. 2). Energy of coupling between grains is weak compared to the ideal crystal, and there is certain expansion of the grains if surface is hot.

During RF pulse, the Ohmic skin layer δ_{ohm} represents a thermal source. A thin layer of copper δ_T, which is exposed to the temperature increase, is a thermal skin layer. Next we suggest that the thermal skin layer is significantly smaller than the typical size of the individual copper grain. In this case the expansion in the thermal skin layer brings to situation when grains start to push each other (Fig. 3). As a result, additional elastic forces come to scene, thus increasing the probability to break links between atoms.

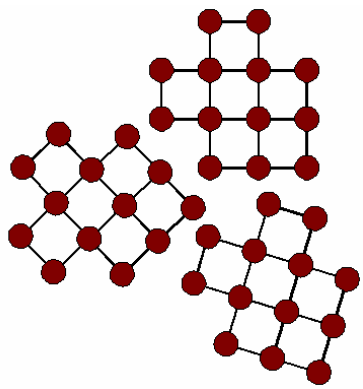

Figure 2: Schematic view of copper's grain structure.

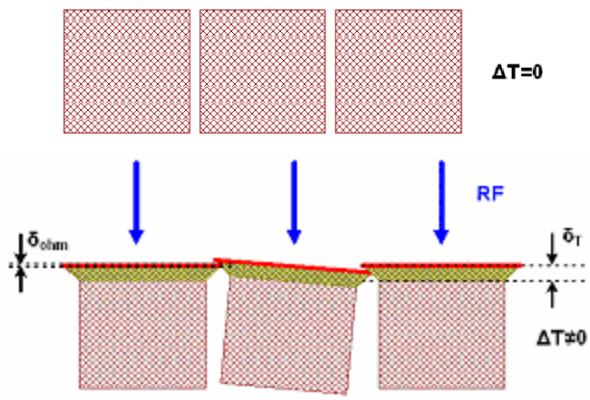

Figure 3: Interaction of grains under pulse RF heating.

High Temperature Region Approach

In the presence of the elastic forces the equation (1) has to be modified:

$$p_j = \exp\left(-\frac{U_c - \overline{U}}{k_B T_c}\right), \qquad (3)$$

where $\overline{U}$ is an energy of the external forces breaking the given link. In assumption that individual grain has n_s links with the other grains, the probability to break all these links can be expressed as:

$$p = \prod_{j=1}^{j=n_s} p_j . \quad (4)$$

The probability to break all n_s links after N thermal cycles is:

$$P = 1 - (1 - p)^N , \quad (5)$$

Taking into account (2), the above equation (5) can be rewritten in a simple way:

$$P = N \cdot p. \quad (6)$$

Obviously, large enough critical value of P exists, when the copper surface start to fracture. See [2] for example. Using (3), (4), (6) one can express the total number of pulses needed to develop the cracks on a surface as:

$$N_f = P_c \cdot \exp\left(\frac{U_c n_s}{k_B T}\right) \cdot \exp\left(-\frac{\overline{U} \cdot n_s}{k_B T}\right), \quad (7)$$

where P_c is the critical value.

Next we will look at how the elastic forces energy depends on the temperature rise ΔT and pulse duration τ. Taking into account that these forces have elastic nature, for the given grain with n_s links we can write now:

$$\overline{U} = \frac{kx^2}{2} \cdot \frac{1}{n_s}, \quad (8)$$

Following equation (9) expresses the linear thermal expansion of the individual grain with typical size l_0:

$$x = \alpha \cdot l_0 \cdot \Delta T, \quad (9)$$

where α is a coefficient of thermal expansion. Defining k, as $k = E \cdot S / l_0$, where $S = \delta_T \cdot l_0$ and E is Yung's module we finally get:

$$\overline{U} = \frac{E \cdot \alpha^2 \cdot \delta_T \cdot l_0^2 \cdot \Delta T^2}{2 \cdot n_s}, \quad (10)$$

Taking into account the δ_T dependence on the pulse duration:

$$\delta_T = \beta \cdot \sqrt{\tau}, \quad (11)$$

where β is a constant, we end up with a general equation for the number of pulses necessary to fracture the copper surface:

$$N_f = P_c \cdot \exp\left(\frac{U_c n_s}{k_B T}\right) \cdot \exp\left(-\frac{E \cdot \beta \cdot \alpha^2 \cdot l_0^2 \cdot \sqrt{\tau} \cdot \Delta T^2}{2 k_B T}\right), \quad (12)$$

As an important consequence one can see that the bigger the size of the copper grains, the less number of the pulses are needed to fracture the surface. Another conclusion is that this number is a strong function of the bulk steady temperature.

In equation (12) there are several coefficients, which could not be defined exactly. That is why we rewrite this equation in the most general form, which contains two principal unknown coefficients only:

$$N_f = B \cdot \exp\left(-\zeta \cdot \sqrt{\tau} \cdot \Delta T^2\right) \quad (13)$$

As a guess, these coefficients (B and ξ) we suggest to extract from the experimental data taken from [2] for example.

In Fig. 4 the experimental data points in coordinate system N_f - ΔT are represented by boxes. They correspond to τ equal to 1000 ns. Following equation (13), the number of pulses to failure as a function of the temperature rise of the copper surface is shown in Fig. 4 (blue line).

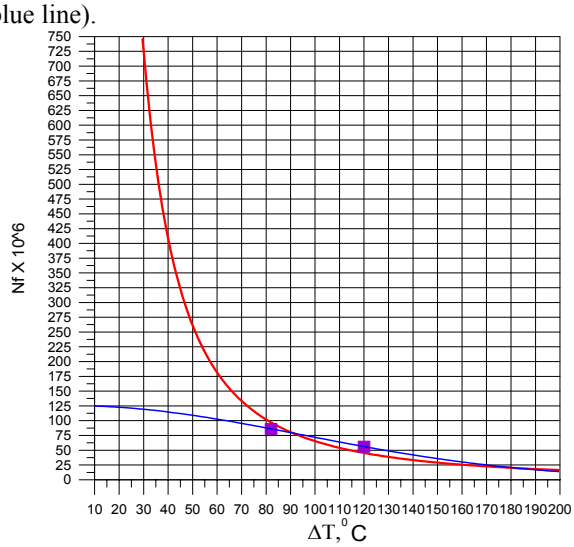

Figure 4: Total number of pulses needed for degradation (τ=1000 ns): lilac boxes taken from [2], blue curve – high temperature rise approach, red curve – the modified theory.

Extrapolation of the High Temperature Approach to the Low Temperature Region

As it follows from Fig. 4 the equation (13) predicts finite number of pulses even under condition when ΔT=0, which certainly does not respect the reality. This means that the proposed model is rather simple and is valid only for the high temperature region. That is why, next we studied the processes in more details, see Fig. 5.

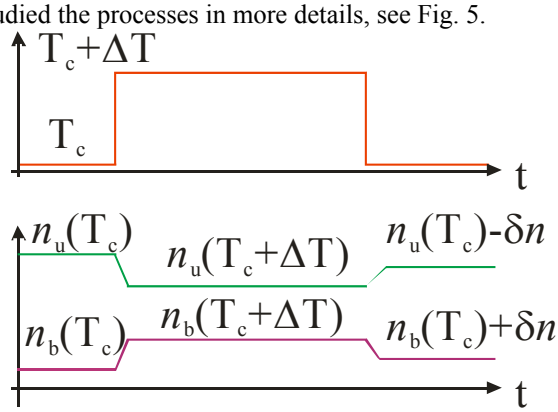

Figure 5: Scheme of the balance between concentrations of broken (n_b) and unbroken (n_u) links.

In general, the heating increases the probability of the atomic links breaks. Nevertheless, after the end of the thermal cycle, this probability recovers its initial value and most of the broken links are recovered too. However, there is certain number of the links which are not recovered because of the irreversible nature of the crystal defects.

It will be naturally to suggest that the probability to create the irreversibly broken link is proportional to the difference of probabilities during temperature rise and before (or after) RF pulse. This make it possible to modify equation (13) in a following way:

$$N_f = \frac{C}{\exp\left(\zeta \cdot \sqrt{\tau} \cdot \Delta T^2\right) - 1}. \qquad (14)$$

The constants C and ξ are defined now using the same experimental data points as before. The results are shown in Figs 6-7, where the plots of N_f versus ΔT and τ are presented.

Now one can see that following the modified equation, the number of pulses to failure goes to infinity, when ΔT goes to zero. If ΔT is high enough, the formula (14) and formula (13) do agree well.

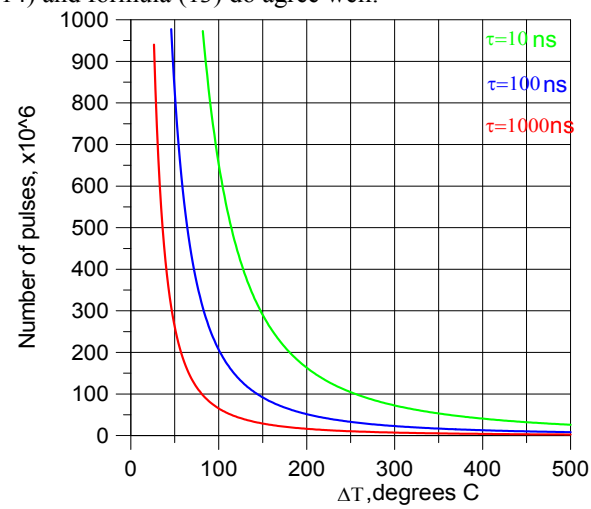

Figure 6: Total number of pulses needed for degradation Vs temperature rise for different pulse durations.

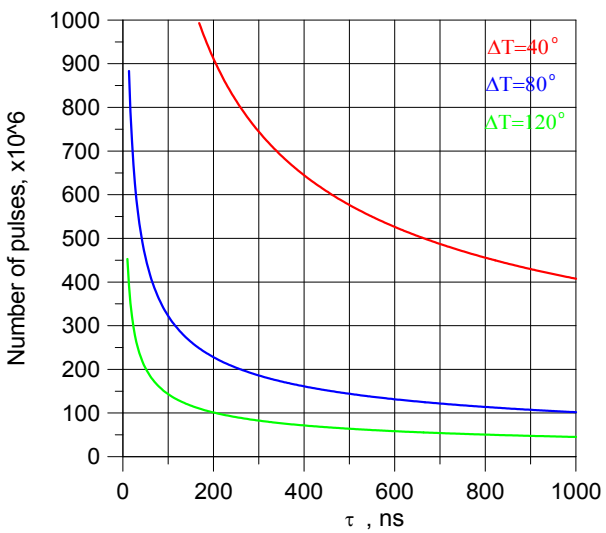

Figure 7: Total number of pulses needed for degradation Vs pulse durations for different temperature rise values.

CONCLUSION

The proposed method make it possible to find a simple way to estimate the number of the thermal cycles to fracture the metal surface using few (two at least) experimental data points.

ACKNOWLEDGMENT

The author would like to express his acknowledgment to I.Syratchev for the inspiration of these studies and many useful discussions.

REFERENCES

[1] V F.. Kovalenko. Introduction to microwave electronics. Sov. Radio, M, 1971. (in Russian).

[2] D.P. Pritzkau et al. Experimental Study of RF Pulsed Heating on Oxygen Free Electronic Copper, Physical Review Special Topics – Accelerators and Beams, Vol. 5, 2002, pp. 112002-1 - 112002-21.

[3] S.V.Kuzikov et al. Experiment to Study Effects of Multi-Pulse Heating in a 30 GHz Resonant Cavity, Proc. of the Strong Microwaves in Plasmas Conf., Vol. 1, 2003, pp. 195-198.

CALCULATION OF RF PROPERTIES OF THE THIRD HARMONIC CAVITY

K. Rothemund†, D. Hecht, U. van Rienen, Universität Rostock, Institut für Allgemeine Elektrotechnik, D – 18051 Rostock, Germany

Abstract

Recently a third harmonic structure has been proposed for the injector of the TTF-FEL to avoid nonlinear distortions in the longitudinal phase space. This structure consists of four nine cell TESLA-like cavities. For the use of this structure in combination with the TTF-FEL it might be interesting to investigate higher order modes (HOM) in the structure and their effect on the beam dynamics. In the 5th dipole passband one mode with a frequency around 9.05 Ghz was found to be almost trapped in the cavity with very small fields in the end cells and the beam pipes. CST MicrowaveStudio® (MWS) and Coupled S-Parameter Calculation (CSC) have been applied to investigate this frequency range. The CSC method [1] is based on the scattering parameter description of the rf components found with field solving codes or analytically for components of special symmetry. This paper presents the results of the calculation of frequencies and field distributions of dipole modes in the frequency range around 9.05 GHz.

INTRODUCTION

A 3.9 GHz 3rd harmonic superconducting section for the photoinjector of the TTF 2 has been proposed [2] and designed [3] recently. This section consists of four nine cell cavities. Its purpose is to correct for nonlinearities of the longitudinal phase space to produce highly charged bunches. The basic rf parameters for many monopole, dipole and quadrupole modes for one nine cell cavity of the 3rd harmonic section have been calculated [4] using MAFIA eigenmode solver [5]. As a result of these calculations a dipole mode in the frequency range around 9.05 GHz was found which has almost no electric field in the beam pipes and even in the cavity end cells. Therefor this mode might be difficult to be damped by the HOM-couplers.

This paper presents the first results of CSC calculations of frequencies and field distributions for dipole modes in this frequency range and compares the results with the results of calculations done with CST Microwave-Studio® [5] for the same frequency range.

CSC THEORY

The reflection and transmission of waves between the ports of any rf system can be described by scattering-parameters (S-parameters). In general, each S-parameter is a complex function of the frequency containing information about amplitude and phase. S-parameters can be represented by the scattering matrix **S**:

$$\mathbf{b_k} = \mathbf{S_k}\,\mathbf{a_k} \tag{1}$$

with the vectors $\mathbf{a_k}$ and $\mathbf{b_k}$ describing all input- and output-signals of the k-th object, respectively.

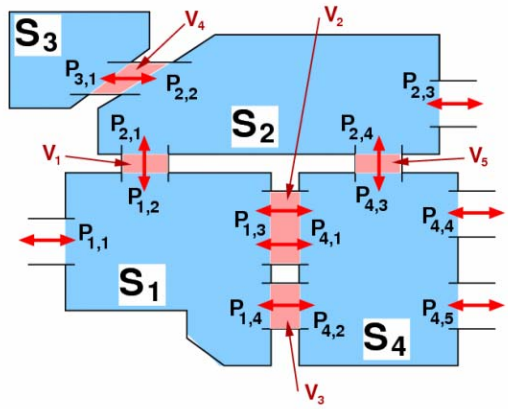

Figure 1: Complex rf-structure consisting of four substructures S_1, S_2, S_3, S_4, connected to each other by the connections V_1, V_2, V_3, V_4, with external ports $P_{1,1}$, $P_{2,3}$, $P_{4,4}$, $P_{4,5}$ and internal ports $P_{1,2}$, $P_{1,3}$, $P_{1,4}$, $P_{2,1}$, $P_{2,2}$, $P_{2,4}$, $P_{3,1}$, $P_{4,1}$, $P_{4,2}$, $P_{4,3}$.

For a complex structure consisting of several subsections the S-parameters of all subsections are arranged in a block diagonal matrix **S**:

$$\mathbf{b} = \mathbf{S}\,\mathbf{a} = \begin{pmatrix} \mathbf{S_1} & \cdots & \mathbf{0} \\ \vdots & \ddots & \vdots \\ \mathbf{0} & \cdots & \mathbf{S_N} \end{pmatrix} \begin{pmatrix} \mathbf{a}_1 \\ \vdots \\ \mathbf{a_N} \end{pmatrix} = \begin{pmatrix} \mathbf{b}_1 \\ \vdots \\ \mathbf{b_N} \end{pmatrix} \tag{2}$$

Next all incident signals are collected in a vector $\mathbf{a_{inc}}$ and all signals travelling from one subsection into a neighbouring subsection are grouped together in a coupling vector $\mathbf{a_{cop}}$. These rearrangements are performed by two permutation matrices **P** and **F**:

$$\mathbf{a} = \mathbf{P}\begin{pmatrix} \mathbf{a}_{\mathrm{cop}} \\ \mathbf{a}_{\mathrm{inc}} \end{pmatrix} \quad ; \quad \begin{pmatrix} \mathbf{a}_{\mathrm{cop}} \\ \mathbf{a}_{\mathrm{sct}} \end{pmatrix} = \mathbf{P}^{-1}\,\mathbf{F}\,\mathbf{b} \tag{3}$$

$\mathbf{a_{sct}}$ is the vector of all signals leaving the structure at the external ports. These signals are kept untouched. The combination of the above equations yields:

$$\begin{pmatrix} \mathbf{a}_{\mathrm{cop}} \\ \mathbf{a}_{\mathrm{sct}} \end{pmatrix} = \underbrace{\mathbf{P}^{-1}\,\mathbf{F}\,\mathbf{S}\,\mathbf{P}}_{\mathbf{G}} \begin{pmatrix} \mathbf{a}_{\mathrm{cop}} \\ \mathbf{a}_{\mathrm{inc}} \end{pmatrix} \tag{4}$$

where the matrix $\mathbf{G} = \mathbf{P^{-1}FSP}$ describes the structure of the whole system. According to the dimensions of vectors $\mathbf{a_{cop}}$, $\mathbf{a_{sct}}$ and $\mathbf{a_{inc}}$ this system matrix **G** can be split into submatrices:

† karsten.rothemund@etechnik.uni-rostock.de

$$\mathbf{G} = \begin{pmatrix} \mathbf{G}_{11} & \mathbf{G}_{12} \\ \mathbf{G}_{21} & \mathbf{G}_{22} \end{pmatrix} \quad (5)$$

which allows to solve eq. (4) for $\mathbf{a}_{sct}$:

$$\mathbf{a}_{sct} = \left(\mathbf{G}_{21} \left(\mathbf{I} - \mathbf{G}_{11} \right)^{-1} \mathbf{G}_{12} + \mathbf{G}_{22} \right) \mathbf{a}_{inc} . \quad (6)$$

From eq. (6) the overall scattering matrix of the whole structure, denoted as $\mathbf{S}^{(T)}$ can thus be written as $\mathbf{S}^{(T)} = \mathbf{G}_{21} (\mathbf{I} - \mathbf{G}_{11})^{-1} \mathbf{G}_{12} + \mathbf{G}_{22}$. It describes scattering at all open ports including all possibly existing multi mode scattering.

A resonator has no open (external) ports and dim ($\mathbf{a}_{inc}$) = dim ($\mathbf{a}_{sct}$) = 0 holds, only the coupling between the internal ports remains. For this case the block matrices **G12**, **G21** and **G22** vanish and eq. (6) reduces to:

$$\left(\mathbf{I} - \mathbf{G}_{11} (\omega_0) \right) \mathbf{a}_{cop} = 0 \quad (7)$$

Eq. (7) is fullfilled for discrete frequencies only, the resonant frequencies aimed for. In order to find these frequencies ω_0 the eigenvalues of $(\mathbf{I} - \mathbf{G}_{11}(\omega))$ have to be calculated. A resonant frequency is found, if at least one eigenvalue equals zero. In that case the vector $\mathbf{a}_{cop}$ holds the amplitudes of the waveguide modes at the positions of the internal ports.

APPLICATION

The CSC method was applied to the investigation of higher order modes in the third harmonic section which is planned to be installed in the TTF-FEL. Especially in the 5th dipole passband one mode with a frequency in the range of about 9.05 GHz was found to be almost trapped in the cavity. This mode was found to have very small fields in the end cells and in the beam pipes.

For all calculations the geometry of the Fermilab 3rd harmonic 3.9 GHz cavity was used, see figure 2.

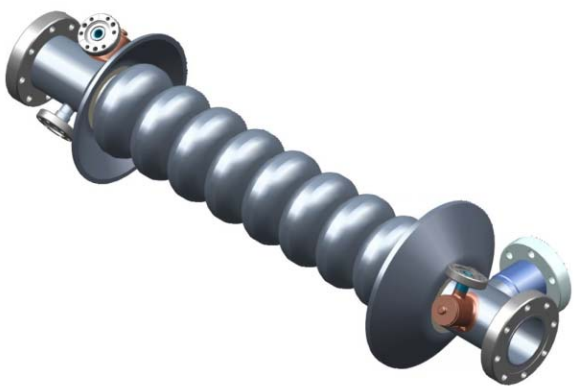

Figure 2: Design of 3rd harmonic 3.9 GHz niobium cavity (geometry provided by N. Solyak, Fermilab).

RESULTS OF CALCULATIONS

For the investigation of the dipole modes in the 5th dipole passband the field distribution of some modes in the frequency range around 9.05 GHz was computed using CST MicrowaveStudio®. Utilising the symmetry of the 9 cell cavity, field distributions were only calculated for the structure shown in figure 3.

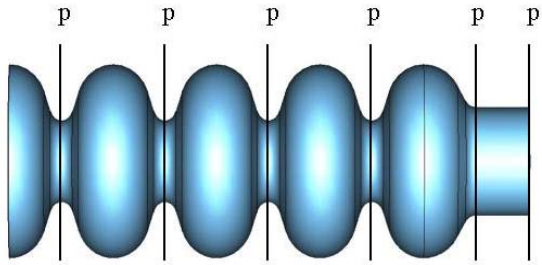

Figure 3: Geometry used for CST MicrowaveStudio® calculations, p indicates the positions of the ports used for CSC calculations of single cells.

The boundary conditions at the left and right boundary of the structure were choosen to electric – electric, electric – magnetic, magnetic – magnetic and magnetic – electric. The dipole modes in the 5th dipole passband in the frequency range around 9.05 GHz have nearly no field in the beam pipe, therefor no significant change occurred in the calculated field distributions with the same boundary conditions at the right boundary (at the beam pipe). The results of the MWS calculations are presented in figures 4 and 6.

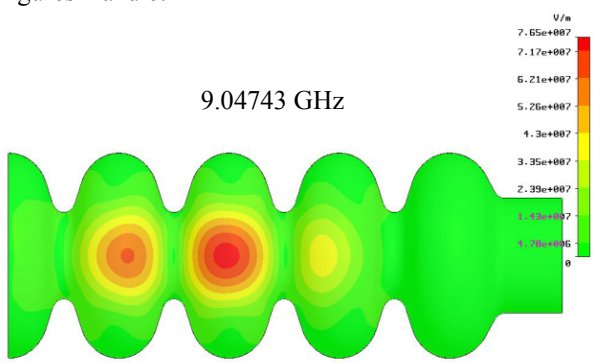

Figure 4: Contour plot of the absolute value of the electrical field of a dipole mode, calculated with MWS.

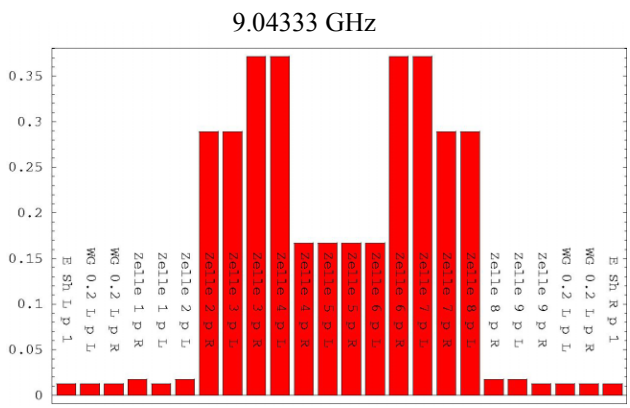

Figure 5: Absolute value of wave amplitudes of electrical field of a dipole mode at the ports of the single cells, calculated with CSC (L, R … left, right; E Sh … electrical short; WG 0.2 … waveguide with 0.2 m length).

CSC calculations were performed for a 9 cell cavity with the beam pipes shorted. The results, presented in the figures 5 and 7, were composed of the calculation of each single cell taking into account the identical geometry of the inner cells. Within a first step of these calculations the frequencies and the absolute value of the wave amplitudes of the electric field of dipole modes in the 5th dipole passband at the ports of the single cells were calculated. For the coupling between the ports of the single cells only TE 11 mode was taken into account. This was sufficient to reproduce the frequencies calculated with MWS. S-parameters of the beam pipe and of the shorts were calculated analytically.

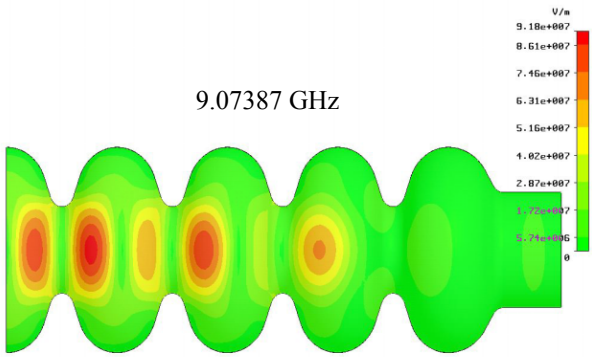

Figure 6: Contour plot of the absolute value of the electrical field of a dipole mode, calculated with MWS.

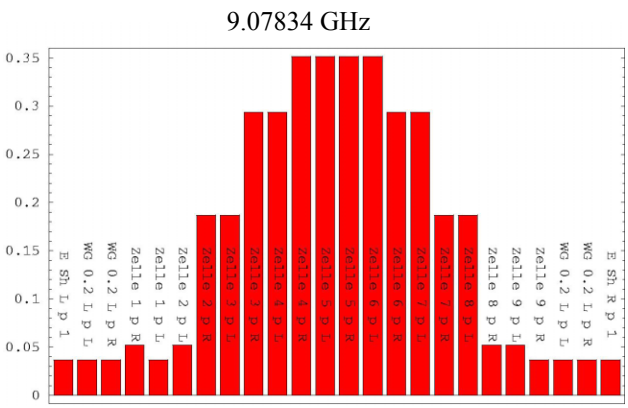

Figure 7: Absolute value of wave amplitudes of electrical field of a dipole mode at the ports of the single cells, calculated with CSC (L, R … left, right; E Sh … electrical short; WG 0.2 … waveguide with 0.2 m length).

For the evaluation of the results, obtained with CSC, these results have to be compared with the results, obtained with MWS (figure 5 – figure 4; figure 7 – figure 6). The difference of the frequencies is lower than 5 MHz. The field distributions, calculated with MWS, have to be compared with the field distributions, calculated with CSC at the location of the ports of the correspondding cells of the cavity. This comparison also shows, that the results of the CSC calculations fit well to the results of MWS calculations.

CONCLUSIONS

CST MicrowaveStudio® and CSC calculations were performed for the investigation of dipole modes in the 3rd harmonic 3.9 GHz cavity. Results of the calculations with both methods yield evidence for the existence of trapped dipole modes in the frequency range around 9.05 GHz. Frequencies and field distributions, calculated with CSC fit well to the results of MWS calculations and may be used for further calculations of beam relevant parameters of modes in the structure, completely equipped with HOM- and input-couplers.

REFERENCES

[1] H.-W. Glock, K. Rothemund, U. van Rienen, CSC - A Procedure for Coupled S-Parameter Calculations, IEEE Trans. Magnetics, vol. 38, pp. 1173 - 1176, March 2002
H.-W. Glock, K. Rothemund, U. van Rienen, CSC – A System for Coupled S-Parameter Calculations, TESLA-Report 2001-25, DESY, Hamburg 2001

[2] K. Flöttmann, T. Limberg, Ph. Piot, Generation of ultrashort electron bunches by cancellation of nonlinear distortions in the longitudinal phase space, TESLA-FEL 2001-06, DESY, Hamburg 2001.

[3] J. Sekutowicz, R. Wanzenberg, W. F. O. Müller, T. Weiland, A Design of a 3rd Harmonic Cavity for the TTF 2 Photoinjector, TESLA-FEL 2002-05, DESY, Hamburg 2002

[4] T. Khabibouline, N. Solyak, R. Wanzenberg, Higher Order Modes of a 3rd Harmonic Cavity with an Increased End-cup Iris, TESLA-FEL 2003-01, DESY, Hamburg 2003.

[5] MAFIA, CST MicrowaveStudio®, CST GmbH, Bad Nauheimer Str. 19, D-64289 Darmstadt, Germany

TESLA RF POWER COUPLER THERMAL CALCULATIONS

Dohlus M., Kostin D., Möller W.-D., DESY, D-22607 Hamburg, Germany

Abstract

The main RF power coupler is one of the key elements of the accelerating module for the superconducting linac. It provides RF power to the cavity and interconnects different temperature layers in the module. Therefore statistical and dynamical thermal losses have to be optimised. Different operating modes as well as geometries were investigated. Coupler design optimisation studies are carried out for TESLA and for the XFEL case. Especially long pulse operation for the XFEL is being investigated.

THEORETICAL BACKGROUND

Heat Conduction Equations

The general heat conduction equation (see Eq. 1) for the steady state in one dimension becomes the Eq. 2, *P* is internal heating power source, λ - thermal conductivity, ν - material index.

$$\rho C_p \frac{\partial T}{\partial T} = \nabla(\lambda \nabla T) + \frac{dP}{dV} \tag{1}$$

$$\frac{dT}{dz} = R'(z,T(z)) \cdot p(z),\ R'(z,T) = \left(\sum_{\nu} A_{\nu}(z) \lambda_{\nu}(T) \right)^{-1} \tag{2}$$

The thermal resistance *R(z,T)* describes the thermal properties of the material, it can be calculated as:

$$R_i(T_a,T_b) = (T_b - T_a) \frac{l}{A} \Big/ \int_{T_a}^{T_b} \lambda(T) dT \text{ , } l \text{ - length} \tag{3}$$

The radiational thermal resistance is (k_{em} is the emissivity and σ - Boltzmann constant 5.67×10^{-8}):

$$R_{rad}(T_1,T_2,A_{rad}) = \frac{T_1 - T_2}{A_{rad}(T_1^4 - T_2^4) k_{em} \sigma} \tag{4}$$

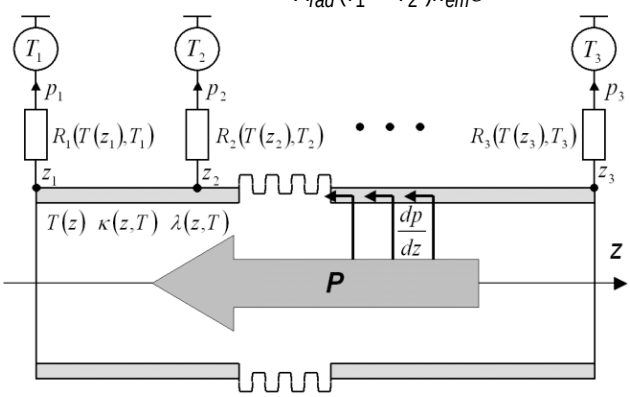

Figure 1: The Boundary Problem.

The problem to solve is a boundary problem with internal power sources introduced by RF power losses and fixed temperature points as boundary conditions (see Fig. 1). RF power losses was calculated using MAFIA and recalculated using Eq. 5, where κ is the electrical conductivity. The coupler bellows are simulated by geometry coefficient *gb(z)>1* (ratio of the material length along the bellow surface to the bellow length, see Eq. 6).

$$\frac{dp}{dz} = \underbrace{\left(\frac{dp}{dz}\right)}_{\substack{\kappa=\kappa_0,\\ P=P_0\\ \text{MAFIA}}} \cdot \frac{P}{P_0} \cdot \sqrt{\frac{\kappa_0}{\kappa(z,T)}} \tag{5}$$

$$\frac{dT}{dz} = R'(z,T(z)) \cdot p(z) \cdot gb(z),\quad gb(z) = \frac{d\tilde{z}}{dz} \tag{6}$$

Numerical Solution

The coupler was simulated by set of discrete elements (see Fig. 2) similar to the electrical circuits, in this case the resistive elements are the thermal resistances, currents are power flows and voltages are the temperature differences (see Eq. 7), for element ***n*** one can write Eq. 8. and for the whole system the matrix equation with tridiagonal matrix **G(t)** (see Eq. 9), solved using method of iterations in MathCAD (See Eq. 10).

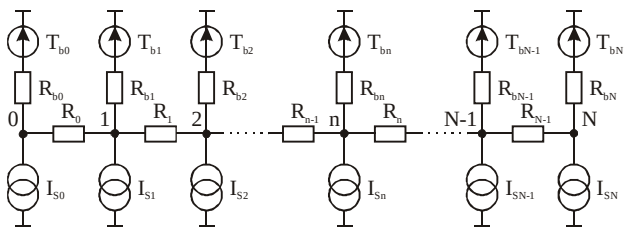

Figure 2: Equivalent Circuit Diagram.

$$G = 1/R, \mathbf{t} = (T_n), \mathbf{i} = (I_n) = \mathbf{i}(\mathbf{t}), I_n = \frac{dp}{dz} \delta z \tag{7}$$

$$(-1/R_{n-1}) T_{n-1} + (1/R_{n-1} + 1/R_n + 1/R_{bn}) T_n + + (-1/R_n) T_{n+1} = (I_{sn} + T_{bn}/R_{bn}) \tag{8}$$

$$\mathbf{i}(\mathbf{t}) = \mathbf{G}(\mathbf{t})\mathbf{t} + \mathbf{G}_b(\mathbf{t},\mathbf{T}_b)\mathbf{T}_b \tag{9}$$

$$\mathbf{i}(\mathbf{t}_n) = \mathbf{G}(\mathbf{t}_n)\mathbf{t}_{n+1} + \mathbf{G}_b(\mathbf{t}_n,\mathbf{T}_b)\mathbf{T}_b$$
$$\mathbf{t}_0 \rightarrow \text{linear between } T_1 \text{ and } T_N \tag{10}$$

TESLA RF POWER COUPLER

The RF power input coupler specifications are presented in the Table 1. The coupler is shown in Figure 3, it has 4 fixed temperature points: outside connection to 300 K, 70 K shield connection, 4 K shield connection and the cavity flange at 2K. Coupler inner and outer conductors are made from stainless steel coated by copper, coupler antenna is a whole copper made. Coupler has 2 ceramic windows (warm and cold) and 3 bellows.

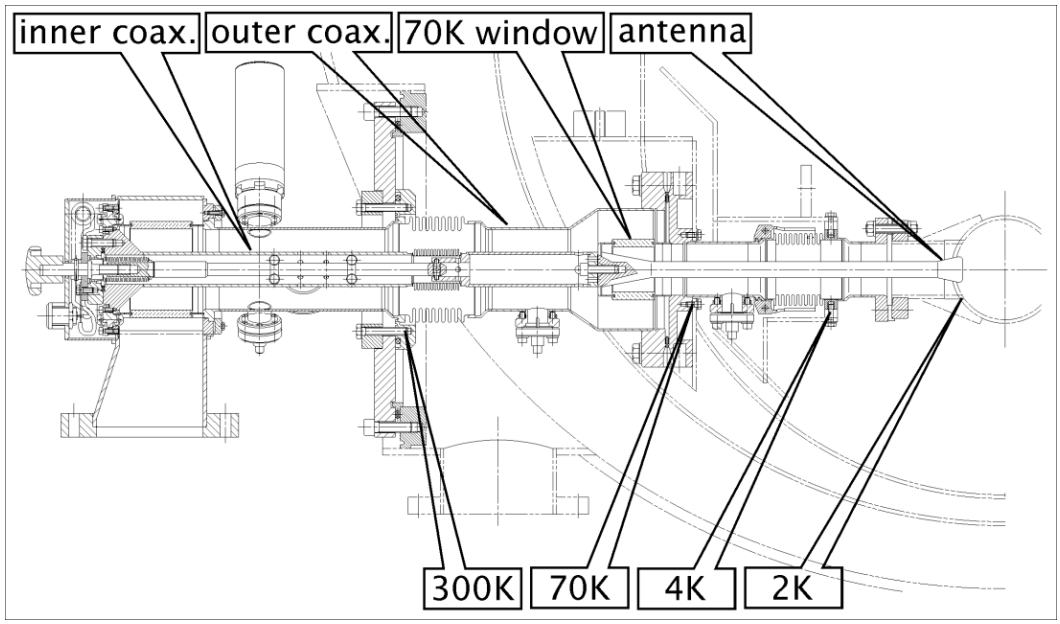

Figure 3: TTF III Coupler Design.

Table 1: RF Power Coupler Specifications

	TTF	TESLA	XFEL
frequency [GHz]	1.3		
operation	pulsed: 500 μs rise time, 800 μs flat top with beam		
2 K heat load [W]	0.06		
4 K heat load [W]	0.5		
70 K heat load [W]	6		
peak power [kW]	250	250 – 500	150
rep. rate [Hz]	10	5	10
average power [kW]	3.2	3.2 – 6.4	1.9

CALCULATIONS RESULTS

RF Power Losses

Calculated RF power losses using MAFIA 4.0 are shown in Fig. 4. Travelling wave regime calculations done for the copper, $\kappa_0=5.8\times10^7$ 1/(Ω×m) (300K), power losses in the 70K ceramic window (ε=9, tgδ=10^{-4}): $P_{loss.win}/P_{in} = 1.94\times10^{-4}$.

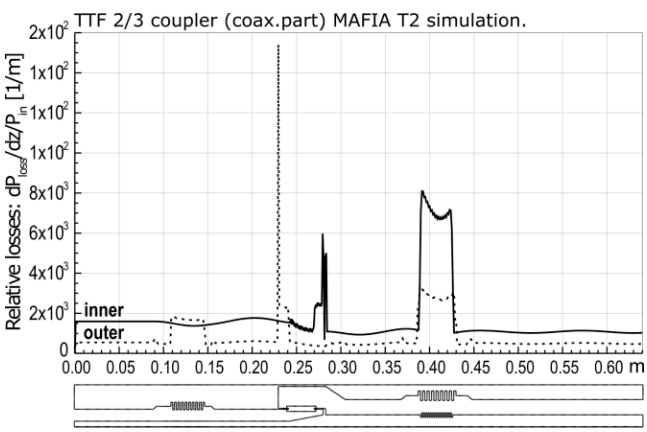

Figure 4: RF Power Losses.

Material Properties

The material properties of the materials used in the simulations are shown in Figures 5a and 5b. Calculations done for the copper with RRR 10 and 100.

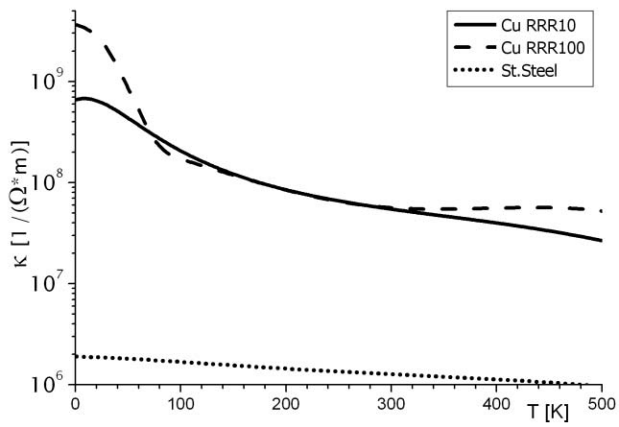

Figure 5a: Electrical Conductivities with Temperature.

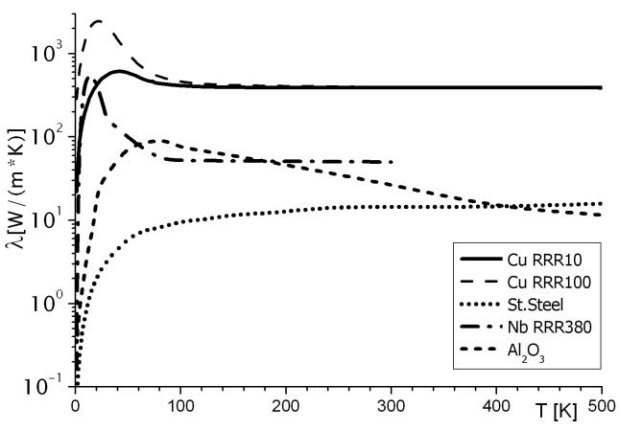

Figure 5b: Thermal Conductivities with Temperature.

Calculated Data

Temperature distributions along the TTF III coupler as well as the cryogenic power losses (statical and dynamical) were calculated for different sets of parameters. The copper coating thickness and RRR as well as average input power were varied. The obtained data are presented in the Table 2 and in the Figures 6a, 6b, 7 and 8.

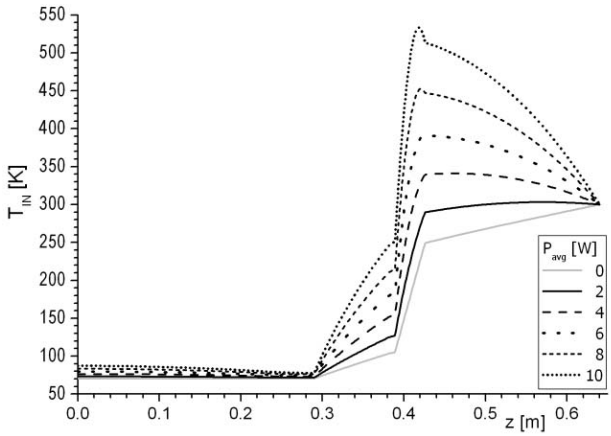

Figure 6a: Inner conductor temperature distribution.

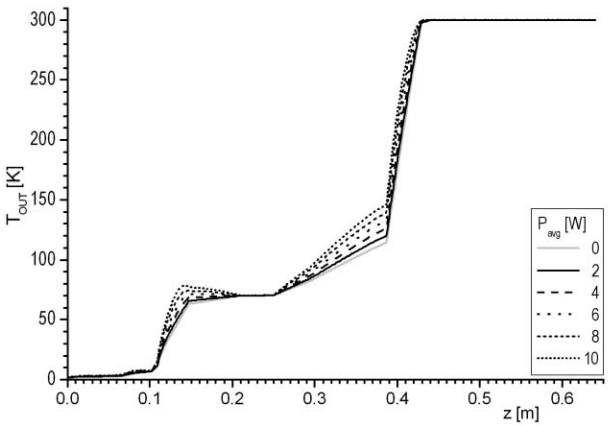

Figure 6b: Outer conductor temperature distribution.

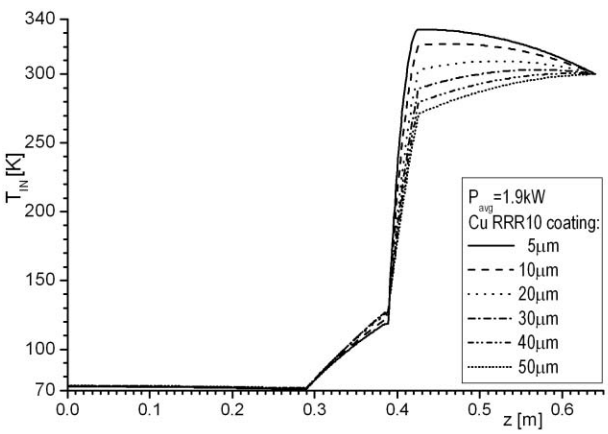

Figure 7: Cu coating of inner conductor.

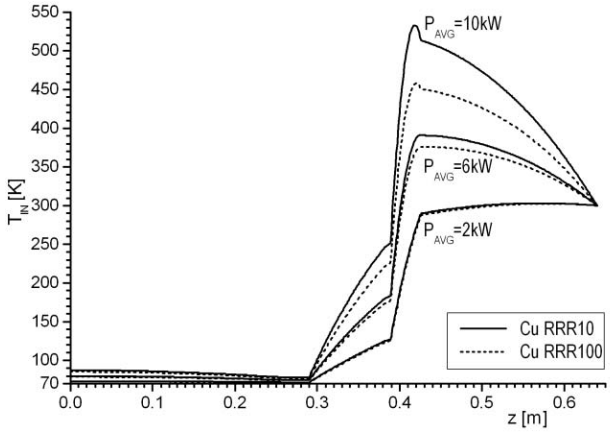

Figure 8: RRR of Cu coating of inner conductor.

Table 2: Cryogenic Power Losses

Cu coating		P_{avg}	P Σ	P Σ	P in	P out	P win	P Σ
in	out		2K	4K	70K			
μm		kW	W					
Cu RRR = 10								
10	30	0.0	0.02	0.2	0.8	1.1	0.0	1.9
		1.9	0.04	0.3	2.3	1.5	0.4	4.1
		4.0	0.05	0.4	4.0	2.0	0.8	6.8
		6.0	0.07	0.5	5.8	2.5	1.2	9.6
		8.0	0.09	0.6	7.8	3.1	1.6	12.4
		10.0	0.11	0.7	10	3.6	1.9	15.6
10	5	1.9	0.04	0.3	1.7	1.5	0.4	3.6
	10				1.8			3.7
	20				2.1			3.9
	30				2.3			4.1
	40				2.5			4.3
	50				2.6			4.5
5	30	1.9	0.03	0.2	2.3	1.3	0.4	3.9
10			0.04	0.3		1.5		4.1
20			0.05	0.5		1.9		4.6
30			0.06	0.6		2.3		5.0
40			0.08	0.8		2.8		5.4
50			0.09	0.9		3.2		5.8
Cu RRR = 100								
10	30	1.9	0.10	0.5	2.3	1.2	0.4	3.8
		6.0	0.11	0.6	5.9	2.1	1.2	9.2
		10.0	0.13	0.7	9.7	3.1	1.9	14.8

CONCLUSIONS

TTF III coupler fulfils the cryogenic losses requirements for TESLA and XFEL. At higher average power levels the inner conductor bellow becomes overheated. Average power level limit is about 6 kW (without cooling of the inner conductor). The copper coating of the inner (30±10 μm) and outer (10±5 μm) is optimal. The RRR value for the copper (10..100) is not critical up to 6 kW of average power.

RIBBON ION BEAM DYNAMICS IN UNDULATOR LINEAR ACCELERATOR*

E.S. Masunov, S.M. Polozov,
MEPhI, Moscow, 115409, Russia

Abstract

The possibility of non-synchronous radio frequency field harmonics using for ribbon ion beam focusing and acceleration in linac is discussed. In periodical resonant structure the accelerating force is produced by the combination of two spatial harmonics of RF field (two RF undulators). The examples illustrating the efficiency of the proposed method of acceleration are given for longitudinal and transverse undulators.

INTRODUCTION

The space-charge influence is the main factor limiting the beam intensity in low energy RF linac. The ion ribbon beam can be used in order to increase current in linac. The stable motion of ribbon ion beam can be provided by using an external focusing devices or a special configuration of RF fields (RF focusing). The latter approach seems to be more promising for low energy ions. In a conventional RF linac ion beams are accelerated by a synchronous wave. Non-synchronous wave will be used for focusing a charged particles only.

The values of synchronous and nonsynchronous harmonic amplitudes must be chosen to provide both longitudinal and transverse stability. For two wave approach (synchronous and one nonsynchronous harmonics) RF focusing conditions were founded for axisymmetric (ARF) and ribbon (RRF) beams in Ref. [1-2].

Another method to accelerate ions in the RF periodical structure without synchronous wave was suggested in Ref. [3-4]. In this case the acceleration force is to be driven by a combination of two non-synchronous waves (two undulators) and transverse focusing is realized by means of each RF undulator. The peculiarity of a ribbon ion beam focusing and acceleration in RF undulator linear accelerator (UNDULAC-RF) is discussed in this paper.

RF FIELD IN PERIODICAL RESONATOR

The UNDULAC-RF can be realized using an interdigital H-type resonator. The especial form of electrodes must be used in order to provide the transverse focusing along the ribbon width (see Fig.1, [4]). The field excited in a periodical resonator can be found as a periodic solution of the Maxwell equations. Under the assumption that the cross-section size of the accelerator channel is much smaller than the wavelength of the RF field, the Fourier series coefficients for field can be calculated with quasi-electrostatic approximation. The potential of RF field in periodic resonator can be represented as the sum of the spatial harmonics:

$$U = \sum_{n=0}^{\infty} U_n(x,y)\cdot\sin(\int h_n dz + \alpha)\cos(\omega t) \quad (1)$$

where $h_n = \mu / D + 2\pi n / D$ is a longitudinal wave number of field harmonic, μ is a phase advance of the field per period of RF structure, n is the harmonic number. The n-th harmonic amplitude U_n can be found from the equation

$$\Delta_\perp U_n = h_n^2 U_n \quad (2)$$

Two solutions of this equation are existent: $U_n(x,y) \sim \cosh(h_{n,x}x)\cosh(h_{n,y}y)$ and $\alpha = 0$ for longitudinal radio frequency undulator and $U_n(x,y) \sim \cosh(h_{n,x}x)\sinh(h_{n,y}y)$, $\alpha = \pi/2$ for transverse one. Here $h_{n,x}$ and $h_{n,y}$ are transverse wave number, $h_{n,x}^2 + h_{n,y}^2 = h_n^2$. The ratio $h_{n,x}/h_{n,y}$ is defined by the electrodes form and it's value is small for ribbon beams with large aspect ratio.

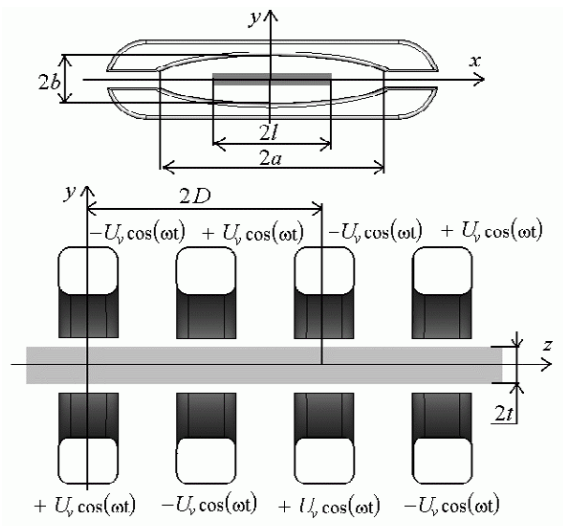

Figure 1: The structure of transverse UNDULAC-RF.

EQUATION OF MOTION

Let us consider the equation of motion for a non-relativistic ion beam in RF field (1) assuming that the particle velocity v differs from the phase velocity of all harmonics: $v_{ph,n} = \omega / h_n$, n=0,1,2… . In general, the interaction of the particles with the non-synchronous harmonic of the RF field does not change the average

*The work was supported by RFBR. Grant 04-02-16667

energy of the beam but causes the fast oscillations in the longitudinal and transverse directions. The synchronism between the beam particles and the spatial harmonics of the RF field is absent in UNDULAC-RF. The effective beam-field interaction takes place if the beam velocity is close to the combined wave phase velocity $v_c = \omega / h_c$ in this case [3]. The value $h_c = (h_n + h_p)/2$ defines the wave number of the combined wave resulting when fields of the *n*-th and *p*-th harmonics are added. Introducing a slowly varying coordinate $\bar{r}$ and phase $\varphi = \int h_c \mathrm{d}\bar{z} - \omega t$ and averaging over the fast oscillations as it is done in Ref. [3-4], one can obtain the equation in the Hamilton's form:

$$\frac{\mathrm{d}^2 \bar{\boldsymbol{r}}}{\mathrm{d}t^2} = -\frac{\mathrm{d}}{\mathrm{d}\bar{\boldsymbol{r}}} U_{eff}\,, \qquad (3)$$

where the function U_{eff} depends on the amplitudes of the RF field harmonics $\boldsymbol{E}_{n,p}$. The transverse and the longitudinal electric RF field components in periodical resonant structure can be found from (1): $\boldsymbol{E}_{\perp,n} = -\nabla_\perp U_n(x,y)$; $E_{z,n} = h_n U_n(x,y)$, if $h_n \neq 0$, and $E_{z,0} = \mathrm{const}$, if $h_0 = 0$. The function U_{eff} can be considered as the effective potential function that specifies the Hamiltonian of the beam-wave system. The study the 3D beam dynamics in the smooth approximation can be provided by means of this function. The existence of the absolute minimum of U_{eff} is necessary condition for effective beam focusing and acceleration, as it follows from Eq. (3).

It can be introduced the reference particle for analysis of the beam stability in polyharmonic RF system. The reference particle velocity is equal to the combined wave velocity, v_{c}, and it's phase in this wave, φ_c, remains constant. The longitudinal bunching and acceleration of the beam are possible if v_{c} and φ_c are slow varying with the longitudinal coordinate. From the equation

$$\frac{\mathrm{d}v_c}{\mathrm{d}t} = -\frac{\mathrm{d}}{\mathrm{d}z} U_{eff}\Big|_{x=0,y=0} \qquad (4)$$

one can find the law of v_{c} variation, the structure period *D* and the range for the reference particle phase, φ_c, when the bunching of the ion beam is the most efficient.

The beam acceleration and focusing in UNDULAC can be realized using longitudinal or transverse undulator, where RF field is generated at $\mu = \pi$ and $\mu = 0$ modes. Let us consider the plane UNDULAC-RF structure with two fundamental harmonics *n*=0, *p*=1. Introducing the dimensionless values of the field harmonic amplitude $e_{\perp,z} = e\lambda E_{\perp,z} / 2\pi mc^2$, the particle velocity β, and the slowly varying coordinates $\boldsymbol{R} = [\rho,\eta,\varphi]$, $\rho = 2\pi\bar{x}/\lambda$, $\eta = 2\pi\bar{y}/\lambda$, $\xi = 2\pi\bar{z}/\lambda$, where λ is a wavelength; $\tau = \omega t$, one can write the dimensionless equation of motion in the form

$$\frac{\mathrm{d}^2 \boldsymbol{R}}{\mathrm{d}\tau^2} = -\frac{\mathrm{d}}{\mathrm{d}\boldsymbol{R}} \bar{U}_{eff} \qquad (3a)$$

The dimensionless function $\bar{U}_{\mathrm{eff}}$ is equal

$$U_{eff} = \frac{v}{4}\left[k_0 e_0^2 + k_1 e_1^2 + 2\left(\boldsymbol{e}_{0,z}\cdot\boldsymbol{e}_{1,z} - \boldsymbol{e}_{0,\perp}\cdot\boldsymbol{e}_{1,\perp}\right)\cos\left(2\varphi + 2\alpha\right)\right] \qquad (5)$$

Here amplitudes $\boldsymbol{e_0}(x,y)$ and $\boldsymbol{e_1}(x,y)$ are the functions of transverse coordinates. The coefficients are equal k_0=10/9, k_1=26/25, $\nu = 1$ for $\mu = \pi$ mode, and k_0=1, k_1=5/9, $\nu = 1/2$ for $\mu = 0$ mode.

The equation (4) for the reference particle velocity can be written using the effective potential function (5):

$$\frac{\mathrm{d}\beta_c}{\mathrm{d}\tau} = e_{eff} \sin 2\varphi_c\,, \qquad (4a)$$

where $e_{eff} = \nu \cdot e_0 \cdot e_1 / \beta_c$ is the effective amplitude of combined wave. The longitudinal beam stability is possible if the reference particle phase in the combined wave lies in the intervals of [π/4, π/2] and [5π/4, 3π/2] and the particle velocity *v* is close to the reference particle velocity v_{c}. In this case two bunches per one RF field period will be configured.

BEAM DYNAMICS IN LONGITUDINAL UNDULATOR

We will consider the beam dynamics in UNDULAC-RF linac for deuterium ions. This accelerator consists of two sub-section: the gentle buncher section of length L_b and acceleration sub-section of length *L*. In the buncher the field harmonic amplitude smoothly increase as $E(z) = E_m \cdot \sin(\pi z / 2L_b)$ and the reference particle phase in combined wave φ_c linearly decreases from π/2 to 3π/8 or from 3π/2 to 11π/8. The harmonic amplitude, E_{m}, and the reference particle phase, φ_c, remains unchanged at the acceleration sub-section. In the simplest case one can account the ratio of RF field harmonics amplitudes $\chi = E_1 / E_0$ is constant.

It is interesting to compare the beam focusing and acceleration conditions in longitudinal UNDULATOR where the field is generated at the modes π and 0. Let us suppose that the particle velocity differs significantly from the phase velocities of zero, β_{s0}, and first, β_{s1}, RF field harmonics. In our case $\beta_{s0} = 2\beta_c$, $\beta_{s1} = 2\beta_c / 3$, $\beta_c = D/\lambda$ for $\mu = \pi$ mode and $\beta_{s0} = \infty$, $\beta_{s1} = \beta_c / 2$, $\beta_c = 2D/\lambda$ for $\mu = 0$ mode. The vertical size of the separatrix for the combined wave is shown in Fig. 2, curve 1. This figure is plotted for the next parameters: E_0=150 kV/cm, χ=0.9, the buncher length L_b=1.2 m, accelerator length *L*=1.3 m, λ=1.5 m, the initial energy of the deuterium ions W_{in}=100 keV. The variation of longitudinal velocity of the reference particle (with initial phase φ(0)=π/2 in bunch) is shown for the smooth

approximation (curve 2) and for polyharmonic field (curve 3).

The separatix sizes for the zero (curve 4) and the first RF field harmonics (curve 5) are shown in the same figure also in assumption that the beam velocity is close to β_{s0} or to β_{s1} accordingly. One can show that for small value of RF field amplitudes ratio ($\chi = 0.1$-0.3) the combined wave separatix does not overlap first harmonic separatix, but of the longitudinal beam velocity in polyharmonic field can be outside of separatix for combined wave. For large χ ($\chi \geq 0.5$) the oscillation amplitude is small, but these separatrixes are overlapping. In both cases, the particle velocity value can attain the first harmonic separatrix and the ions can be recatched by first RF field harmonic or loused. The analysis of a equation solution for π mode shows that the choice of the parameter χ influences on the beam dynamics and optimal χ value must be found for realization of large current transmission coefficient K_t. In our case the optimal value χ is equal 0.3-0.4. In the smooth approximation coefficient K_t for UNDULAC-RF with $\mu = \pi$ mode is equal 90-95 %.

In the UNDULAC-RF for $\mu = 0$ mode the distance between the separatrixes of combined wave and first RF field harmonic is larger and the influence of χ is smaller comparatively $\mu = \pi$ mode. The current transmission coefficient K_t is equal 85-90 % for $\mu = 0$ mode in the smooth approximation.

The transverse beam dynamics can be analyzed by means of the effective potential function too. In the longitudinal undulator the amplitude of a rapid transverse oscillations is small, and the beam envelop in smooth approximation is closely to real size. One can be shown that the transverse focusing condition is satisfied for the all χ value in UNDULAC-RF when $\mu = \pi$ mode of the RF field is used. In the UNDULAC-RF for $\mu = 0$ mode the transverse focusing is realized when the parameter χ>1 only for paraxial particles. Detailed study of the transverse beam focusing for $\mu = 0$ mode is shown that it is no effective because this focusing is provided by means of the first RF field harmonic only.

BEAM DYNAMICS IN TRANSVERSE UNDULATOR

The focusing and acceleration of particles is possible both in the longitudinal and the transverse RF field. In the last case the beam acceleration can be realized when electric field has only transverse components on the axis. In this case the amplitude of the rapid transverse oscillation is the largest then longitudinal one. The averaged equation of motion can be derived by means of the effective potential function (4) and all above results are valid for transverse undulator. The Hamiltonian of the beam-wave system determines the connection between the longitudinal and transverse dynamics. For analysis of the longitudinal motion it is sufficiently the smooth approximation. In the longitudinal phase space there is only one separatix and the current transmission coefficient K_t is equal 95 % in this case.

The rapid transverse oscillations influence on the effective transverse emittans. The value of emittans increases in size and the particles can be lost due to the bounded aperture of the channel. As in the longitudinal undulator, the transverse beam focusing for $\mu = 0$ mode is less effective than for $\mu = \pi$ mode. The current transmission coefficient is equal 30 % for this case. It is clear that this type of undulator linac is not interesting.

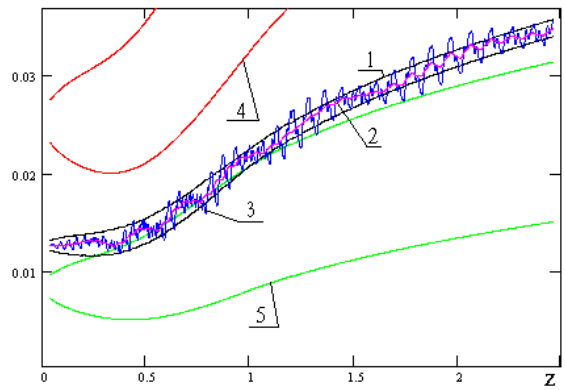

Figure 2: The separatrixes of combined wave and RF field harmonics.

CONCLUSION

The results of analytical investigation of the ribbon beam dynamics in UNDULAC-RF accelerator are discussed. It was shown that the undulator with the longitudinal RF field for $\mu = \pi$ mode is more preferable system for ion ribbon beam acceleration. The RF periodical structure for UNDULAC-RF is simpler for realization, than RRF accelerator where parameter $\chi = 10$ [2]. The zero RF field harmonic amplitude is smaller than in RRF linac for the same acceleration gradient. In the consider range of the energy, the UNDULAC-RF can be used for acceleration of high current ion beam.

REFERENCES

[1] E.S. Masunov, N.E. Vinogradov, Phys. Rev. ST Accel. Beams, 2001, No 7, 070101.
[2] E.S. Masunov, S.M. Polozov, N.E. Vinogradov. Problems of Atomic Science and Technology, № 5, 2001, issue 39, p. 71-73.
[3] E.S. Masunov. Sov. Phys. – Tech. Phys., vol. 35, № 8, pp. 962-965. 1990.
[4] E.S. Masunov. Technical Physics, Vol. 46, No. 11, 2001, pp. 1433-1436.

RF CONTROL MODELLING ISSUES FOR FUTURE SUPERCONDUCTING ACCELERATORS

A.S. Hofler, J.R. Delayen, TJNAF, Newport News, Virginia, USA
V. Ayvazyan, A. Brandt, S.N. Simrock, DESY, Hamburg, Germany
T. Czarski, WUT, Warsaw, Poland; T. Matsumoto, KEK, Ibaraki, Japan

Abstract

The development of superconducting accelerators has reached a high level of maturity following the successes of ATLAS at Argonne, CEBAF at Jefferson Lab, the TESLA Test Facility at DESY and many other operational accelerators. As a result many new accelerators under development (e.g. SNS) or proposed (e.g. RIA) will utilize this technology. Covering all aspects from cw to pulsed rf and/or beam, non-relativistic to relativistic particles, medium and high gradients, light to heavy beam loading, linacs, rings, and ERLs, the demands on the rf control system can be quite different for the various accelerators. For the rf control designer it is therefore essential to understand these issues and be able to predict rf system performance based on realistic rf control models. This paper will describe the features that should be included in such models and present an approach which will drive the development of a generic rf system model.

INTRODUCTION

Nowadays the designer of an rf control system for superconducting accelerators can make use of powerful digital processing hardware including digital signal processors (DSPs) and field programmable gate arrays (FPGAs) allowing processing times reaching from a few hundred nanoseconds for basic field control algorithms to several microseconds or more for complex algorithms. In cases where lowest possible latency is critical (to achieve higher feedback gain and immediate feedback response) the designer may want to choose an analog feedback solution, possibly a hybrid system with fast analog feedback and digital control of operating parameters, built-in diagnostics, and exception handling. In all cases it is desirable to develop a model for the rf control system to be able to predict the expected performance while assuming realistic noise source and performance limitation of the llrf subsystems. The model will allow for comparisons between different controls concept and aid the designer in the synthesis of the optimal controller design [1,2].

RF CONTROL REQUIREMENTS

The rf control requirements for amplitude and phase stability are usually derived from the desired beam parameters. The beam parameters include emittance, energy spread, bunch length and arrival time of the bunch which is critical for seeded XFEL applications. Since the bunch-to-bunch energy spread ranges from around 1% to better than 0.01%, the typical categories for field control are of the order:

Table 1: Typical requirements for field stability rf control

Category	1[a]	2[b]	3[c]
σ_A/A	1e-2	1e-3	1e-4
σ_φ [deg.]	1	0.1	0.01

a. SNS, RIA main linac
b. CEBAF, TESLA, XFEL main linac
c. XFEL critical sections (bunch compressor)

The requirements in Table 1 are considered uncorrelated errors for category 1 and 2 (the correlated error budget is certainly tighter) and correlated errors for class 3 (only few cavities before bunch compressor). The requirements for the phase stability become also more severe for off-crest operation. In the case of the control of the vector-sum of several cavities driven by one klystron, the requirement for the phase calibration of the vector-sum components may become critical depending on the magnitude of microphonics.

Besides field stabilization the RF control system must provide diagnostics for the calibration of gradient and beam phase, measurement of the loop phase, cavity detuning, and control of the cavity frequency tuners. Exception handling capability must be implemented to avoid unnecessary beam loss. Features such as automated fault recovery will help to maximize accelerator up-time. A thorough understanding of the RF system will allow for operation close to the performance envelope while maximizing accelerator availability. Often the RF control must be fully functional over a wide range of operating parameters such as gradients and beam current. For efficiency reasons the RF system should provide sufficient control close to klystron saturation. The cavities are limited in their maximum operable gradients by quench, field emission or coupler sparks. Maximum operable gradient can be achieved with proper exception handling.

SOURCES OF PERTUBATIONS

An essential feature of the rf model will be the appropriate accounting for noise. Evaluating control schemes requires a clear understanding of sources of pertubations and its implementation.

A first classification distinguishes between a modulation of parameters of the model and noise that is added at certain points of the model. The resonance frequency of superconducting cavities is a parameter that undergoes modulations due to mechanical and electromagnetic

effects (in the case of normal conducting resonators even due to thermal effects).
Therefore, the system response of the cavity model is likely to become non-linear to a non-negligible degree.
Further, in the case of pulsed mode simulation, the model should incorporate the possibility for repetitive noise in addition to statistical noise. Many components of the cavity drive system turn out to have repeating imperfections, such as the high-voltage characteristics of a klystron.

Modulation of the Cavity Resonance Frequency

The center frequency of accelerating structures is exposed to changes mainly due to excitation of low-frequency mechanical resonances (microphonics) and mechanical distortions based on strong electromagnetic fields (Lorentz force detuning). Mechanical distortions are always present and are caused by vacuum, cryogenic devices and ground motion. The typical variation of the resonance frequency is of the order of 5-10 Hz with frequencies ranging from 0.1Hz up to a few hundred Hz, reflecting the convolution of mechanical resonances with the spectral components of the sources of pertubations. The steady state resonance frequency changes due to Lorentz force detuning is at the order of 1Hz/(MV/m)^2. In the case of changing gradients, especially in pulsed mode operation, the mechanical resonances of the cavities will be excited resulting in a time varying detuning even during the flat top portion of an rf pulse.

Cavity Drive Signal

A number of effects affecting the high power drive signal of the cavities need to be considered. The HV-Pulse of microwave amplifiers usually shows modulation in the order of a few percent. Additionally, in pulsed operation, there are fluctuations from pulse to pulse. HV instabilities cause errors on the high power drive signal in amplitude and phase. It can be exposed to a ripple caused by the power supply. Additionally, phase noise from the master oscillator, jitter on the timing signal and mismatch in the power distribution as well as non-linearities in the (high power) amplifiers influence the quality of the field and need to be included adequately.

Beam Loading

Fluctuations in the beam current and the impact of pulsed beam transient can be modelled as well as the effects of wake fields. The beam can excite higher order modes and other passband modes, which may increase the demands on the cavity model to include several modes each with its own coupling to the beam.

Other

It can be necessary to model other effects, such as multipacting and field emission in the cavity, thermal drifts of various components of the control system, the response of the feedback system and recovery of interlock trips.

The designer of the noise model needs to carefully decide the level of detail of each source of noise suggested here. He may come to the conclusion that some sources are negligible compared to others. The required accuracy of each noise source implementation strongly depends on the queries made towards the model.

ACCELERATOR TYPE SPECIFIC ISSUES

The design of the acceleration system (cavity + frequency tuner, fundamental coupler, HOM coupler, rf power source, rf power distribution) is based on

- type of beam (relativistic (electron) or non-relativistic (proton or heavy ion))
- beam current (high or low)
- pulsed or cw operation (rf and/or beam)
- control of individual cavities vs. vector-sum control

which in turn determine cavity type and affects operating parameters such as

- cavity single and multi-cell, beta=1 or beta<1, elliptical, HWR, QWR, spoke, RFQ etc.
- loaded Q high (>1e7) or low (<1e6)
- on-crest or off-crest operation

The rf model must be able to support the accelerator specific requirements for the differents types of accelerators. For non relativistic beam it is desirable to model sections with several cavities including simple longitudinal beam dynamics to study the effects of beam loading variations caused by cavity field fluctuations. For high currents linacs it will be important to include beam based feedforward in the rf control system for beam loading compensation. In the case of lightly beam accelerators such as ERLs where the cavity loaded Q is high it will be important to implement a self-excited loop scheme in the controller and to provide resonance control with VCX or fast ferrite phase shifters.

RF SUBSYSTEMS

The RF system consists of various subsystems which are illustrated in Figure 1.

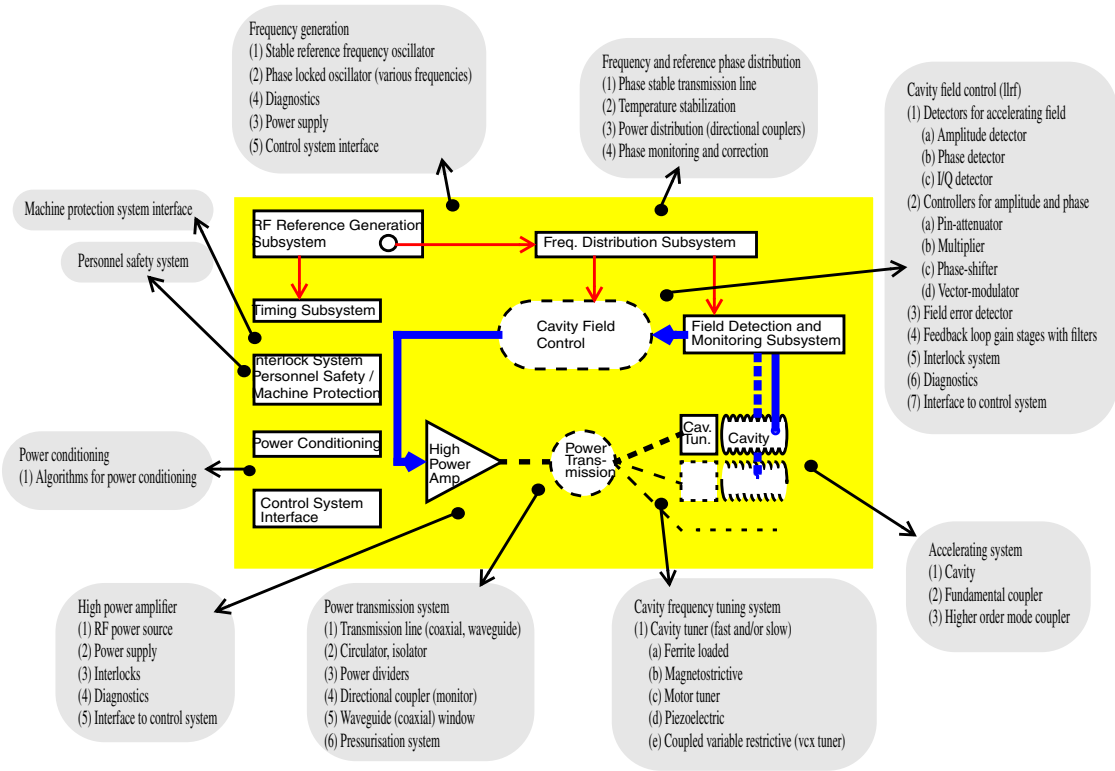

Figure 1: Typical rf system configurations.

RF MODEL IMPLEMENTATION

The design process should be accompanied by a certain set of rules that guarantee the reusability of the model and maximize its output.

• Modularity

On the implementation level, one should follow modern programming guidelines in order to minimize dependencies among program units. This eases the cooperation of different programmers as well as a fast modification of single program parts without affecting the rest. Many programming languages offer the use of libraries (either precompiled or interpreted), such as Matlab or C++.

• Flexibility

The modularity should be continued on the front end side of the model. It is desirable to split the components of the rf model into separate units that can be connected, repeated and exchanged without big effort. Ideally, every type of subsystem of different laboratories has an rf model implementation that can easily be exchanged. Matlab Simulink for example offers blocks of active elements with well-defined in- and output channels that can be replaced very quickly.

• Scalability

The model should be designed in a way, that the number of (repeated) subsystems as well as the degree of precision can be adjusted. Experience has shown that during the operation of the model questions and expectations towards it change. Scalability therefore can mean the freedom to reduce or increase the number of accelerating structures that are controlled by a single feedback loop. It can also mean to trade off the precision of a simulation against its execution time.

• Portability

In a world where many incompatible platforms compete against each other, it is desirable to not depend on a single one of them.

CONCLUSION

For the design of future superconducting accelerators extensive rf control modelling will be required. While the main goal of the model will be to predict the expected amplitude and phase stability of a given design, also other aspects of the rf system will be studied. The model must be flexible enough to accommodate accelerator type specific issues. A generic rf model following a modular architecture should be able to cover wide spread needs.

REFERENCES

[1] T. Schilcher, S.N. Simrock, L. Merminga, D.X. Wang, “A Design and Performance Analysis Tool for Superconducting RF Systems”, PAC’97, Vancouver, Canada, 1997

[2] A. Vardanyan, V. Ayvazyan, S.N. Simrock, “An Analysis Tool for RF Control for Superconducting Cavities”, EPAC’02, Paris, France, 2002

A PASS BAND PERFORMANCE SIMULATION CODE OF COUPLED CAVITIES

Tao Xiaokui, Tong Dechun
Tsinghua University, Beijing 100084, P. R. China

Abstract

A simulation code of coupled cavities named PPSC is developed by the solutions of the microwave equivalent circuit equation. It can give the pass band performance of periodic or non-periodic coupled cavity chain, such as the dispersion frequencies and the reflection factor of the cavity, the field distribution of each mode and so on. The natural parameters of the cavity chain, such as the number of the cavities, the resonant frequencies and Q-factors of each cavity, the coupling factor between two cavities and the locations of the couplers, can be changed easily to see the different results of the simulation. The code is written based on MS Visual Basic under MS windows and a user-friendly interface is made. Some simple examples were simulated and gave reliable results.

INTRODUCTION

The tuning of the pass band performance of the coupled cavities is an essential part of the development of a RF linear accelerator. Usually, we need know the pass band performance even on the physical design stage. In general, there are two way to study the coupled cavities. One is to solve the Maxwell equations under certain boundary conditions. The other is based on equivalent circuit model of coupled cavity chain.

For the first way, many codes are developed in recent years, such as URMLT, Superfish, MAFIA, HFSS, ANSYS, etc. These codes can simulate the pass band performance of a RF structure accurately. But for long multi-cell, non-uniform or very complex cavities, the calculating procedure becomes very complicated and time consuming. Sometimes it is almost impossible on a normal PC.

On the contrary, the equivalent circuit method is very simple relatively. It can give the pass band performance of periodic or non-periodic coupled cavity chain, such as the dispersion frequencies and the reflection factor of the cavity, the field flatness, and so on. The natural parameters of the cavity chain that the calculation need are all obtainable by experiments.

During our development of low energy medical linacs and non-destructive inspection linacs, a simulation code (PPSC) based on the equivalent circuit method is written. While designing and tuning a real coupled structure, the information provided by PPSC can be used as a predictive tool to adjust the normal modes and field flatness.

PPSC is a standard Microsoft Windows code. It is written by Microsoft Visual Basic, which allow programmers write large programs easily with user-friendly interfaces by the Object-oriented technology. The idea of this technology is similar to a person's thinking process, so the program is much easier to read.

FUNDAMENTAL PRINCIPLE

The fundamental principle of PPSC is based on the equivalent circuit model of a coupled cavity chain [1] (shown in Figure1).

f_i and Q_i are the resonant frequency and quality factor of the *i*-th cell *(i=1,2,...,N);* k_{0i}*(i=1,2,...,N-1)* and k_{1i} *(i=1,2,...,N-2)* are the nearest and next nearest neighbour couplings between cells. β_1/β_2 is the coupling factor between the waveguide with the input/output coupler respectively.

The equivalent circuit model gives the following matrix:

$$\begin{bmatrix} a_1 & \frac{k_{01}}{2} & \frac{k_{11}}{2} & & & & 0 \\ \frac{k_{01}}{2} & a_2 & \frac{k_{02}}{2} & & & & \\ \frac{k_{01}}{2} & \frac{k_{02}}{2} & a_3 & & & & \vdots \\ \vdots & & & \ddots & & & 0 \\ & & & & & & \frac{k_{1N-2}}{2} \\ & & & & \cdots & a_{N-1} & \frac{k_{0N-1}}{2} \\ 0 & & & 0 & \frac{k_{1N-2}}{2} & \frac{k_{0N-1}}{2} & a_N \end{bmatrix} \bullet \begin{bmatrix} X_1 \\ X_2 \\ X_3 \\ \vdots \\ \vdots \\ \vdots \\ X_N \end{bmatrix} = \begin{bmatrix} I_1 \\ I_2 \\ I_3 \\ \vdots \\ \vdots \\ \vdots \\ I_N \end{bmatrix} \quad (1)$$

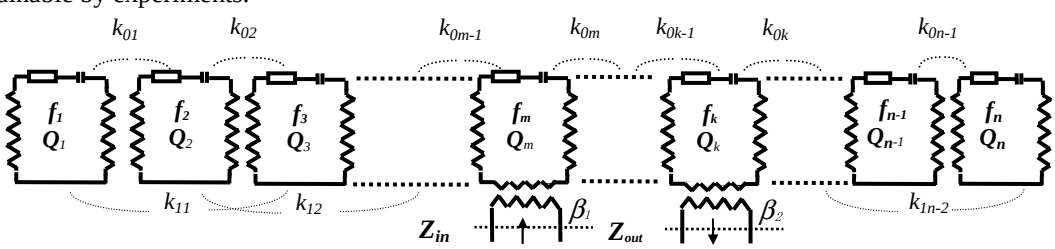

Figure 1: Equivalent circuit model of a coupled cavity chain.

In (1) $I_m = \dfrac{E_m}{jF\sqrt{2L_m}}$ is the source, $X_i = \sqrt{2L_i}\,i_i$

$$a_m = 1 - \frac{f_m^2}{F^2} - j\frac{f_m(1+\beta_1)}{fQ_m}$$

$$a_k = 1 - \frac{f_k^2}{F^2} - j\frac{f_k(1+\beta_2)}{fQ_k}$$

$$a_i = 1 - \frac{f_i^2}{F^2} - j\frac{f_i}{fQ_i} \quad i \neq m,\ k$$

Here, F is the working frequency.

For a standing wave cavity chain, if the position number of input coupler is *p*, then, from (1) we can get the input impedance

$$Z_{in} = -1 + j\frac{FQ_p}{f_p\beta_1 X_p} \tag{2}$$

and the reflection coefficient:

$$\Gamma(F) = \frac{Z-1}{Z+1} = 1 + j\frac{2f_p\beta_1 X_p}{FQ_p} \tag{3}$$

So $|\Gamma|(F)$ can be calculated by solving (1) if f_i, Q_i, k_{0i}, k_{1i}, $\beta_1(\beta_2)$ and the positions of couplers are known, A typical pass-band performance curve $|\Gamma|(F)$ is shown in Fig.2.

IMPLEMENTATION AND USER INTERFACE

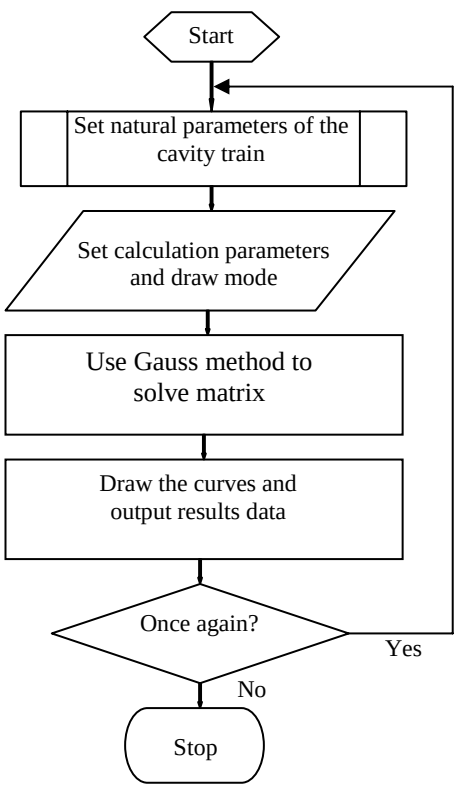

Figure 2: Flow process chart of PPSC.

A step-by-step procedure for the PPSC code with the Gauss method to solve matrix (1) can be described by the flow chart shown in Fig. 2. [2]

First, PPSC initialize a blank window to wait the users' choice: open a new work or a exist work. When open a new one, a dialog interface is shown like Figure 3 to 5. In this interface users can set the natural parameters of the cavity chain, the calculation parameters, the drawing mode, etc.

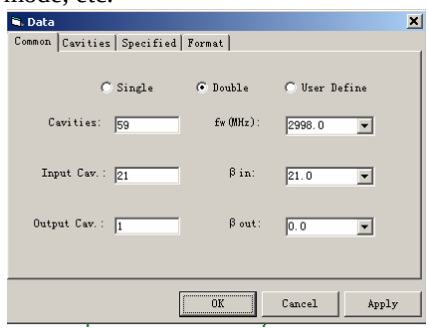

Figure 3: Cavity chain parameters.

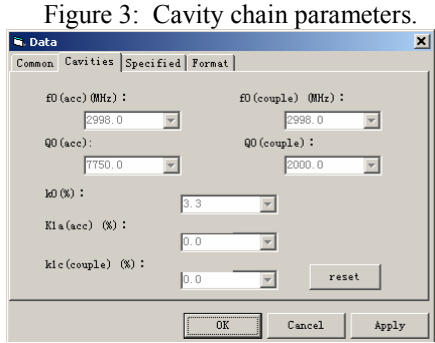

Figure 4: Cell parameters.

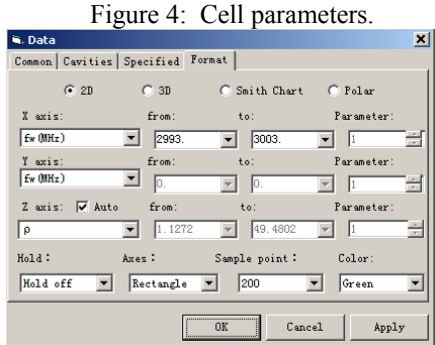

Figure 5: Drawing mode.

After setting the parameters, the main interface shown like figure 6.

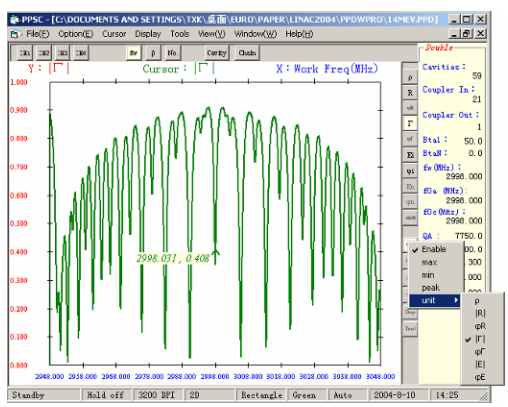

Figure 6: Main interface.

The interface looks just like a front panel of a vector network analyzer. By this interface, the pass band performance curves can be calculated and plotted and the parameters of the calculation and the curves can be change dynamically. A cursor can be displayed on the curve to show the numerical value. The peak and valley points can be found out easily by the cursor. The type, colour, precision and scale of the curve can be changed conveniently, too.

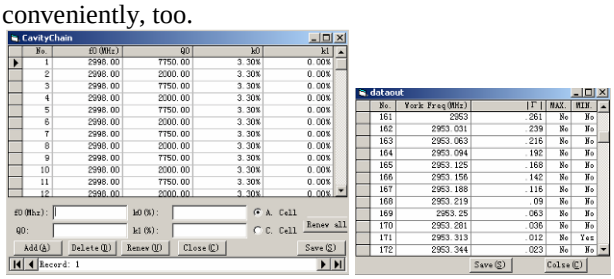

Figure 7: Cavity chain and Output data interface.

Users can also change the parameters of the cavity chain conveniently in a separate window and the calculated result curves can be saved as graphic files or transfer into data files (figure 7).

EXAMPLES

Figure 8 shows a Γ-f curve of a certain SW linac. PPSC can help to adjust the normal modes by finding the best location of the coupler and the tolerance of the detune of each cavity.

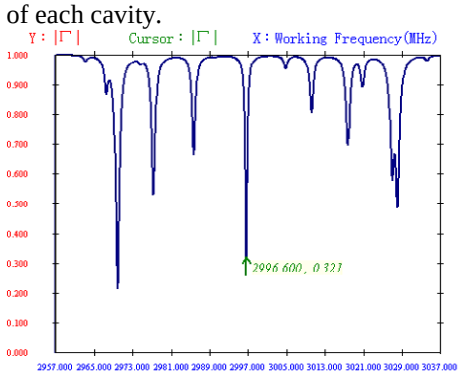

Figure 8: Γ-f curve.

Figure 9 shows the $\pi/2$ mode ρ - β curves of a cavity chain with 3, 11, 19, 29 cavities. By this simulation, the best coupling factor of the 29-cavity chain can be gotten with only 3 cavities. This is very helpful for the linac guide tuning.

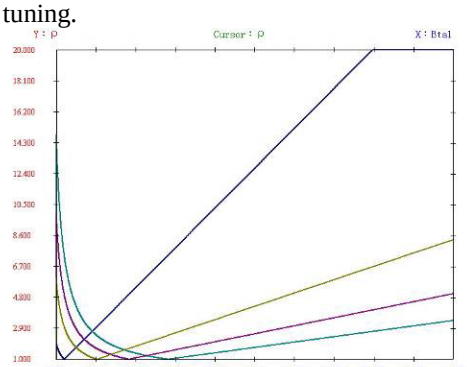

Figure 9: ρ - β curve.

The PPSC code can also help to adjust the field flatness of a cavity chain. Figure 10 gives a simulation result of the test guide of our on-axis coupled standing-wave accelerator energy switch. [3]

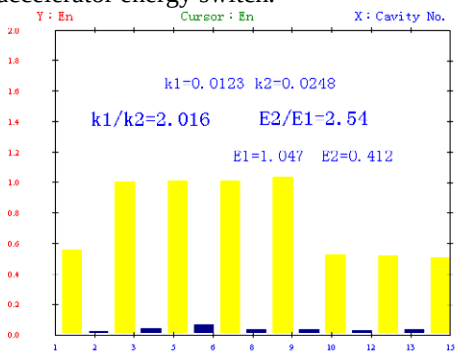

Figure 10: Field flatness.

Smith chart is also a curve type of PPSC simulation result. During the R&D of our S-band 9MeV TW linac for the fixed type container inspection system, PPSC was used as a predictive tool for the tuning of input and output couplers (Figure 11).

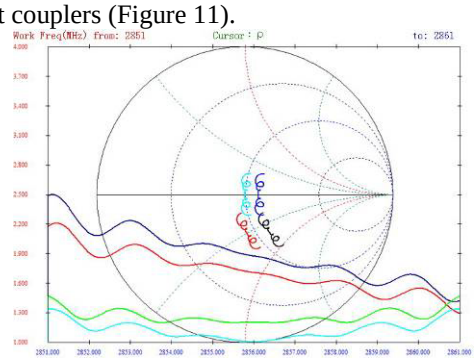

Figure 11: Smith chart.

CONCLUSION

As a powerful predictive tool of the design and tuning of coupled cavity, PPSC has an user friendly interface and is very easy to use. Further improvement of such a simulation code PPSC will be done. A MATLAB version considering the beam loading effect will be completed soon. [4]

REFERENCES

[1] D. E. Nagle, E. A. Knapp and B. C. Knapp, "Coupled Resonator Model for Standing Wave Accelerator Tanks," The Review of Scientific Instruments, Vol. 38, No.11, p1583, Nov, 1967.

[2] Huang Hai, "Study of the microwave performance of a coupled cavity chain," Beijing, 1991.

[3] Tao Xiaokui, "Study on the Energy Switch in an On-Axis Coupled Standing-Wave Accelerator," Beijing, March 1999.

[4] Zheng Shuxin, "Study on a backward travelling wave accelerating structure," Beijing, 2000.

ADVANCED BEAM-DYNAMICS SIMULATION TOOLS FOR RIA*

T. P. Wangler, R. W. Garnett, LANL, Los Alamos, NM, USA
K. R. Crandall, Tech Source, Santa Fe, NM, USA
J. Qiang, R. Ryne, LBNL, Berkeley, CA, USA
N. Aseev, P. Ostroumov, ANL, Argonne, IL, USA
D. Gorelov, R. York, Michigan State University, East Lansing, MI, USA

Abstract

Understanding beam losses is important for the high-intensity RIA driver linac. Small fractional beam losses can produce radioactivation of the beamline components that can prevent or hinder hands-on maintenance, reducing facility availability. Operational and alignment errors in the RIA driver linac can lead to beam losses caused by irreversible beam-emittance growth and halo formation. We are developing multiparticle beam-dynamics simulation codes for RIA driver-linac simulations extending from the low-energy beam transport (LEBT) line to the end of the linac. These codes run on the NERSC parallel supercomputing platforms at LBNL, which allow us to run simulations with large numbers of macroparticles for the beam-loss calculations. The codes have the physics capabilities needed for RIA, including transport and acceleration of multiple-charge-state beams, and beam-line elements such as high-voltage platforms within the linac, interdigital accelerating structures, charge-stripper foils, and capabilities for handling the effects of machine errors and other off-normal conditions. In this paper we present the status of the work, including examples showing some initial beam-dynamics simulations..*

INTRODUCTION

The present concept for the Rare Isotope Accelerator (RIA) project [1] includes a 1.4-GV CW superconducting driver linac. The driver linac is designed for multicharge-state acceleration [2] of all stable species, including protons to 900 MeV and uranium to 400 MeV/u. In conventional heavy-ion linacs, a single charge-state beam of suitably high intensity is extracted from an electron-cyclotron resonance (ECR) ion source and injected into the linac. The linac typically contains one or more strippers at higher energies to further increase the beam charge state and improve acceleration efficiency. However, the limitation to a single charge state from the ion source and from each stripper significantly reduces the beam intensity. This disadvantage is addressed in the RIA driver-linac design concept by the innovative approach of simultaneous acceleration of multiple charge states of a given ion species, which results in high-power beams of several hundred kilowatts for all beams ranging from protons to uranium. Initial beam-dynamics studies [2], supported by experimental confirmation at the Argonne ATLAS facility [3], have demonstrated the feasibility of this new approach.

However, the high-power beam associated with the multiple charge-state acceleration introduces a new design constraint to control beam losses that cause radioactivation of the driver linac [4]. Radioactivation of the linac-beamline components will hinder routine maintenance and result in reduced availability of the facility. Therefore, it will be important for the RIA project to produce a robust beam-dynamics design of the driver linac that minimizes the threat of beam losses. As an important consequence of this design requirement, it will be necessary to develop a computer-simulation code with the capability of accurately modeling the beam dynamics throughout the linac and computing the beam losses, especially at high energies where beam loss translates into greater activation.

The driver linac is made up of three sections. The first is the pre-stripper accelerator section consisting of an ECR ion source, and a low-energy beam transport (LEBT) line, which includes a mass and charge-state-selection system, and a buncher/radiofrequency quadrupole (RFQ) injection system. This is followed by the initial linac stage consisting of a room-temperature RFQ linac, a medium-energy beam transport (MEBT) line, and the low-velocity (low-β) superconducting accelerating structures. The pre-stripper section, accelerates the beam, consisting of two charge states for uranium, to an energy of about 10 MeV/u, where the beam passes through the first stripper and new charge states are produced.

The second section of the linac uses medium-β superconducting structures to accelerate the multicharge-state beam from the first to the second stripper at an energy of about 85 MeV/u. This medium-β section accelerates about five charge states for uranium. This is followed by the third and final section of the linac, which uses high-β superconducting structures to accelerate typically four charge-states for uranium to a final energy of 400 MeV/u.

The overall performance of the driver linac is crucially dependent on the performance of the LEBT and RFQ. The LEBT is designed to focus, bunch, and inject two charge states for uranium into alternate longitudinal buckets of the RFQ. The LEBT RF buncher system consists of two main components. The first RF buncher cavity system (multiharmonic buncher) uses four harmonics and is designed to capture 80% of each charge state within the longitudinal acceptance of the RFQ. A

* This work is supported by the U. S. Department of Energy Contract W-7405-ENG-36

second RF buncher cavity matches the velocity of each charge state to the design velocity of the RFQ.

To avoid problems from beam-induced radioactivation, beam losses must be limited to less than about 1 watt per meter [5],[6], particularly in the high-energy part of the accelerator. This low beam-loss requirement imposes a challenge for controlling the emittance growth throughout the driver-linac, especially because of the complication of multiple charge-state beams. In addition to increasing the intensity, acceleration of multiple charge-state beams produces a larger total longitudinal emittance, increasing the threat of beam losses. For any proposed design it is imperative to compute the high-energy beam losses with sufficient accuracy to ensure that the beam-loss requirements are satisfied. Such a computation normally requires the use of simulation codes that accurately track the beam particles through the whole accelerator using a physics model that includes all effects that can lead to emittance growth and possible beam losses.

A significant amount of accelerator design work has already been done at two institutions, Argonne National Laboratory (ANL) [5] and Michigan State University (MSU) [7]. The LANA code [7,8] is presently used at MSU for superconducting linac simulations. The code TRACK [9] is used at ANL. The LANA code was used extensively during the design and commissioning of the radioactive beam linac ISAC-1 at TRIUMF [10]. It was benchmarked as a result of the commissioning measurements, and is also being used for the design of ISAC-II, a superconducting linac for production of ion beams with energies above the Coulomb barrier.

Although much code development has already taken place for RIA, more work to develop faster end-to-end simulation tools will be important for accurate computation of beam losses. The development of such a simulation tool is the primary objective of our work. Additionally, the importance of demonstrating an understanding of the beam-losses justifies the development of more than one such code to provide necessary cross checks of the simulations.

CODE DEVELOPMENT APPROACH

Our starting point for the development of these codes for RIA has been to modify the well-established, and benchmarked, multiparticle-beam-dynamics codes PARMTEQM [11] and IMPACT [12]. The IMPACT code was originally developed to run on parallel-processor machines and models the high-energy superconducting accelerator of the driver linac. However, to provide the necessary speed and statistical accuracy for the low-energy sections, a new parallel-processor version of PARMTEQM, now called RIAPMTQ, has been developed to model the LEBT, RFQ, and MEBT of the RIA driver linac.

RIAPMTQ

The Fortran 90 version of PARMTEQ distributed through the Los Alamos Accelerator Code Group was the basis for RIAPMTQ. For convenience in debugging the code, a PC version of RIAPMTQ was developed simulatneoulsy with the parallel version. This allowed direct comparison of results between the two codes when the NERSC version was run in the single-processor mode. Comparison with results from the PC version was crucial in identifying some programming errors related to the MPI implementation at NERSC.

The code was "parallelized" by incorporating the necessary Message Passing Interface (MPI) commands to allow the code to run in the parallel-multi-processor environment at NERSC. Optimization of the code using "domain decomposition" was not thought to be necessary, therefore, the simpler, more straightforward approach of "particle decomposition" was used. All calls to Windows-based graphics were removed, as were all machine-environment dependent I/O statements. To preserve similarity with the PC-based code, which was our starting point, identical input file formats were retained. The most significant code modifications were required in the parallelization of the space-charge calculations which consume the majority of the computing time in multi-particle simulations. The following RIA-specific modifications were made to RIAPMTQ: transport and acceleration of multiple-charge-state beams (2 at present), beam-line elements including high-voltage platforms within the linac, interdigital accelerating structures, charge-stripper foils, and capabilities for simulations of the effects of machine errors including misalignments, and other off-normal operating conditions.

IMPACT

The IMPACT code is a parallel particle-in-cell (PIC) beam dynamics code. It has a large collection of beamline elements, calculates the acceleration numerically using RF cavity fields obtained from electromagnetic field-solver codes, and calculates 3D space charge with several boundary conditions. Because of already being "parallelized," the IMPACT code has required only minimal modifications for RIA. These include adding the multiple-charge-state capability, modelling of bending magnets, and the stripping models. The multiple-charge-state capability has already been tested. Some benchmarking against the ANL TRACK code, including comparison of energy gain and rms beam properties has been completed. Initial studies of beam loss have also been completed.

SIMULATION RESULTS

Several RIAPMTQ simulations were run as part of the debugging and benchmarking process. A sample input file containing a representative RIA LEBT and RFQ was used. Simulations were run at NERSC using two charge states (28 and 29) of uranium 238. Simulation results at the exit of the RFQ were compared for a single processor on a single node up to 256 processors (16 processors on 16 nodes). Variations in output transverse and longitudinal emittances of up to 11% and 22%,

respectively, were observed as the number of processors used or the number of macro-particles was varied. However, average variations in beam transmission were less than 1%. Some numerical noise is expected and a saturation effect should be observed as the number of macro-particles is increased, whereby significant variations in the rms beam properties as a function of the number of particles should diminish.

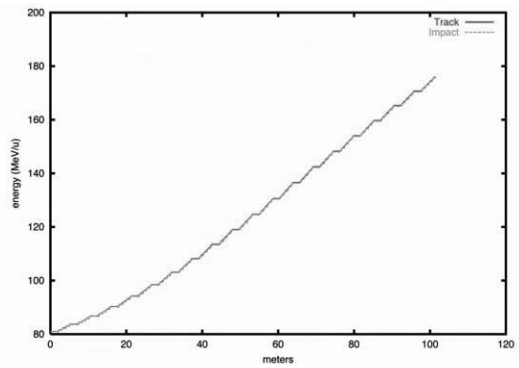

Figure 1: Comparison of IMPACT and TRACK simulations through a portion of the high-beta linac (81 to 177 MeV), showing plots of rms kinetic energy versus distance along the beam line in the superconducting linac.

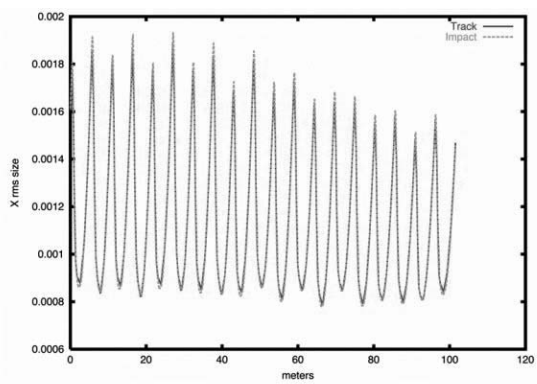

Figure 2: Comparison of IMPACT and TRACK simulations showing plots of horizontal rms beam size versus distance along the beam line in the superconducting linac.

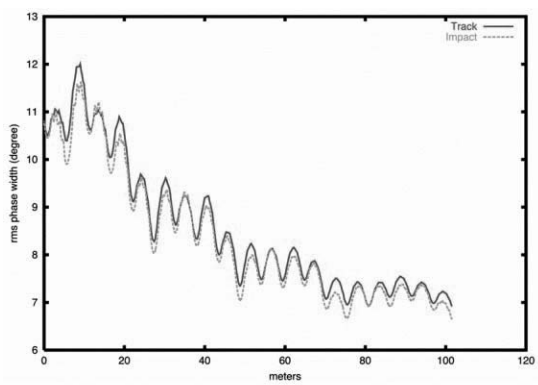

Figure 3: Comparison of IMPACT and TRACK simulations showing plots of longitudinal rms beam size versus distance along the beam line in the superconducting linac.

Figures 1-3 show comparisons of IMPACT simulation results with TRACK through a portion of the RIA high-β linac (81 to 177 MeV). Figure 1 shows a plot of the rms beam energy versus distance in the superconducting linac. Figures 2 and 3 show the horizontal and longitudinal rms beam sizes, respectively, versus distance. Excellent agreement is observed between the two codes (IMPACT and TRACK results overlap). Our next major effort will be to run an end-to-end simulation of a representative RIA driver linac and to do some additional benchmarking against the TRACK and LANA codes.

REFERENCES

[1] C.W.Leemann,"The Rare-Isotope Accelerator (RIA) Facility Project," Proc. XX International Linac Conference, Monterey, CA, August 21-25, 2000, p. 331.

[2] P.N.Ostroumov and K.W.Shepard, "Multiple-Charge Beam Dynamics in an Ion Linac," Phys. Rev. ST Accel. Beams 3, 030101 (2000).

[3] P.N.Ostroumov, R.C,Pardo, G.P.Zinkann, K.W.Shepard, and J.A.Nolen, "Multiple Charge State Beam Acceleration at Atlas," Phys. Rev. Lett. 86, 2798-2801 (2001).

[4] P. N. Ostroumov, "Heavy-Ion Beam Dynamics in the Rare Isotope Accelerator Facility", presented at 2003 Particle Accelerator Conf., Portland, OR, May 12-16, 2003.

[5] P. N. Ostroumov, "Development of a Medium-Energy Superconducting Heavy-Ion Linac", Phys. Rev. ST Accel. Beams 5, 030101 (2002).

[6] P. N. Ostroumov, "Sources of Beam Halo Formation in Heavy-Ion Superconducting Linac and Development of Halo Cleaning Methods", presented at the HALO-03 ICFA Advanced Beam Dynamics Workshop, Montauk, NY, May 19-23, 2003.

[7] D. Gorelov, T.L.Grimm, W. Hartung, F. Marti, X. Wu, R.C.York, H. Podlech, "Beam Dynamics Studies at NSCL of the RIA Superconducting Driver Linac," Proc. European Particle Accelerator Conf., Paris, France, 2002, p. 900.

[8] D.V.Gorelov, and P.N.Ostroumov, "Application of LANA Code for Design of Ion Linac," Proc. of European Particle Accelerator Conf. 1996, Barcelona, Spain, Vol.2, 1996, p. 1271.

[9] P. N. Ostroumov and K. W. Shepard, "Correction of Beam-Steering Effects in Low-Velocity Superconducting Quarter-Wave Cavities", Phys. Rev. ST Accel. Beams 4, 110101 (2001).

[10] D.V.Gorelov, P.N.Ostroumov, and R.E.Laxdal, "Use of the LANA Code for the Design of a Heavy Ion Linac," Proc. of 1997 Particle Accelerator Conf. Vancouver Canada, 1998, p. 2621.

[11] K. R. Crandall and T. P. Wangler, "PARMTEQ - Beam Dynamics Code for the RFQ Linear Accelerator", AIP Conf. Proc. 177, Linear Accelerator and Beam Optics Codes, C. Eminhizer, ed., 1988, pp. 22-28.

[12] J. Qiang, R. D. Ryne, S. Habib, and V. Decyk, J. Comput. Phys. **163**, 434 (2000).

RF BREAKDOWN IN ACCELERATOR STRUCTURES: FROM PLASMA SPOTS TO SURFACE MELTING*

Perry B. Wilson, SLAC, Stanford CA 94309, USA

Abstract

Plasma spots are known to form at field emission sites in regions of high dc or rf electric field. Several mechanisms for the formation of plasma spots in an rf field have been proposed, and one such mechanism which fits experimental data is presented in this paper. However, a plasma spot by itself does not produce breakdown. A single plasma spot, with a lifetime on the order of 30 ns, extracts only a negligible amount of energy from the rf field. The evidence for its existence is a small crater, on the order of 10 μm in diameter, left behind on the surface. In this paper we present a model in which plasma spots act as a trigger to produce surface melting on a macroscopic scale (~ 0.1 mm^2). Once surface melting occurs, a plasma that is capable of emitting several kiloamperes of electrons can form over the molten region. A key observation that must be explained by any theory of breakdown is that the probability of breakdown is independent of time within the rf pulse—breakdown is just as likely to occur at the beginning of the pulse as toward the end. In the model presented here, the conditions for breakdown develop over many pulses until a critical threshold for breakdown is reached.

INTRODUCTION

The theory presented here assumes that, for a gradient-limiting breakdown event to develop in an accelerator structure, a fairly large area near an iris tip (0.01mm^2 or more) must be brought to the melting point in a fairly short time at the beginning of each of many rf pulses. Such an event will produce serious surface damage, and a few hundred of them will produce a measurable change in the iris geometry. The sequence of events leading to such a breakdown starts with the formation of a plasma spot at a field emission site (for a description of the physics of plasma spots see [1]). A proposed mechanism for the formation of plasma spots is given in the next section. Following that, we construct a field emission based model for the breakdown rate after a structure has undergone initial processing, but at gradient levels below the surface damage threshold. Next, we examine the conditions necessary to produce rapid, large-scale surface melting, including the dependence on the physical properties of the surface metal. The predictions of the theory are then compared with experiment. Finally, we give a theory for the development of geometric surface forms over many rf pulses that lead to a gradient-limiting breakdown event.

*Work supported by Department of Energy Contract DE-AC03-76SF00515

LIQUID DROPLET MODEL FOR THE FORMATION OF PLASMA SPOTS

Once initial field emission sites have been processed off, only emitters depending on the topography of the base material remain. A plasma spot formation mechanism must kick in which depends only on the geometry of these emitters. We propose a model that is closely related to the "mechanical breakup" model of Norem *et al.* [2]. In this model the force due to the intense surface field at the emitter tip exceeds the tensile strength of copper, causing a fragment of the tip to break loose. Once this micro-particle has separated from the emitter tip, it is subjected to bombardment and vaporization by the field emission beam from the remaining tip. The rate of vaporization, and the resulting vapor density, is proportional to the field emission current for a given surface field. The rate of ionization in the metallic vapor cloud is proportional to both the vapor density and the current. *Thus the ionization rate should vary roughly as the square of the field emission current.*

A variation in this scenario assumes that tip of the emitter begins to melt due to resistive heating rather than to mechanically break off. The radius of curvature of the molten tip is set by a balance between the force per unit area, F_A, due to the E^2 force pulling on the surface and the surface tension α of the liquid metal (1.3 Nt/m for copper). It is given by [3]

$$r_0 = 2\alpha/F_A = 8\alpha/\varepsilon_0 E_S^2. \quad (1)$$

As the E-field increases the radius of curvature of the molten tip decreases until an unstable point is reached. The tip begins to neck down (possibly due to a pinch effect from the increasing magnetic field associated with the FE current??) and a droplet or a train of droplets are pinched off and pulled away. Many experimental measurements on field emitters have shown that the maximum surface field at the tip of the emitter cannot exceed about 7–10 GV/m before the emitter is destroyed. Also, it is observed that emitters in superconducting cavities cannot be processed (implying creation of a plasma) unless the emitter area is greater than about 10^{-15} m^2 [4]. Using α = 1.9 Nt/m for niobium and E_S = 7 GV/m, Eq. (1) gives an effective emitter area ($\approx 2r^2$) of 2.4×10^{-15} m^2.

A FIELD EMISSION MODEL FOR TRIGGERING BREAKDOWN EVENTS

In the initial stages of processing, we expect that the field emission features with the highest beta values will be burned off first, leaving single isolated craters. When a

crater is formed, it leaves behind its own beta distribution due to the topography of the crater rim and the presence of ejected material. At this point, new plasma spots will tend to form on or near the rims of existing craters, beginning the process of crater clustering. This second spot will wipe out 1/3 of the rim of the first crater, so that the total rim circumference is 1-2/3, or 2^X where x = 0.74. A third spot is most likely to occur where two crater rims intersect. The geometry of the situation (see Fig. A-7 in [5]) gives x = 0.70. For a large number of overlapping craters, x approaches 2/3. A reasonable assumption is that the probability for the formation of an additional plasma spot in a crater cluster is proportional to the total rim circumference $dN/dt \sim N^{2/3}$. An integration shows that the total rim circumference varies as t^2. Next, assume that the probability per unit time of having a critical number of plasma spots alive at the same time in the crater field, so as to produce surface melting and a breakdown event, is proportional to the total rim circumference, t^2, at a given value of the collective field emission current from the crater cluster. We assume that, as a function of FE current, the breakdown probability is proportional to the ionization rate, or to the square of the FE current. The net breakdown probability per pulse is

$$p = AT^3\exp(-C/\beta_{BD}E_S \qquad (2)$$

Here $\beta_{BD} = \beta/2$, where β is the usual field enhancement factor and $C = 7x10^4$ for copper. The factor of two in the betas is verified by measurements at SLAC on NLC accelerator structures. From dark current measurements on several structures the betas ranged from 30 to 47, while the β_{BD}'s ranged from 18 to 25 [6]. Now define normalized variables $g = \beta_{BD}E_S/C$ and $\tau = T(A/p)^{1/3}$. Then $g = [3\ \ln(\tau)]^{-1}$. Suppose the variation in gradient over a range in pulse length is modeled by the power law expression $g \sim T^{-n}$. By equating the values and slopes of the two preceding expressions at the center of the range, the exponent n is related to g by n = 3g. From measurements on a typical structure, values of $\beta_{BD} = 22$ and g = 0.051 at 70 MV/m were obtained [6] giving n = 0.153. This is quite close to the measured value of 1/6.

SURFACE MELTING PRODUCED BY MULTIPLE PLASMA SPOTS IN A CRATER CLUSTER

A typical plasma spot emits about 10 A of electron current in an rf field. In a wide rf gap, half of this current is emitted into the rf field and the other half returns to back to hit the emitting surface (see [7] for a discussion of electron motion in an rf gap). A back-bombarding electron has a typical energy of 50 keV and power per spot of about 250 keV dissipated in the surface layer of the metal. A complicating factor in calculating the temperature rise produced at a metal surface by the impacting electrons is the fact that these electrons can penetrate a substantial distance into the metal for typical impact energies. The penetration depth is given by [8] X_P (μm) = .0276 $(A/\rho Z^{0.89})[V(kV)]^{1.67}$, where A is the atomic mass, Z is the atomic number and ρ is the density in g/cm^3. As a first approximation, we can assume that the energy is deposited uniformly to depth X_P and is zero beyond this. As energy is being deposited in the region up to X_P, heat is also flowing out of this region following the equation for heat diffusion. The equation can be solved analytically for the temperature as a function of X and t, but the limit in which power is absorbed in a relatively thin region close to the surface provides a reasonable approximation for estimating the surface temperature rise. The diffusion depth as a function of time for this case is $X_D(\mu m) = 1\times 10^4\ (Dt)^{1/2}$ where $D = K/\rho C_S$ is the diffusivity in cm^2/sec, K is the thermal conductivity in W/cm-°C and C_S is the specific heat in J/gm-°C. The surface temperature rise is given by $\Delta T = (2P_A/\pi^{1/2}K)(Dt)^{1/2}$, where $P_A(W/cm^2)$ is the incident power per unit area. We will find later that, for a gradient-limiting breakdown to occur, surface melting must take place in a time that is relatively short compared to the pulse length. In general, the diffusion depth, x_D, for such short times will be considerably smaller than the penetration depth, x_P, of a typical back-bombarding electron. Crudely, the surface power per unit area driving diffusive heating is the total incident power density, P_A, multiplied by the ratio x_D/x_P. The temperature rise due to diffusive heating is then given by $\Delta T \sim P_A(x_D/x_P)(x_D/K)$. A figure of merit can now be formed as $\Delta T/T_m \sim x_D^2/(x_P K T_m)$, where T_m is the melting point. Values for this figure of merit for various metals of interest are given in the table below. Tables giving values for the melting point, density, specific heat, thermal conductivity, resistivity, diffusivity, diffusion depth at 30 ns and penetration depth for a 50 keV electron are given in [8].

Figure of Merit for Surface Melting
$FM = x_D^2/(x_P K T_m)\times 10^4$

Metal	Cu	Au	Mo	SS*	W	Nb	Be	Cr
FM	1.24	2.96	0.73	0.75	0.84	0.72	0.32	0.55

*304 Stainless Steel

The relative breakdown levels for copper, gold, and stainless steel surfaces have been measured by Tantawi and Dolgashev [9]. The measured ratios of breakdown field levels, and the ratios predicted from the table are

	Measured	Theory
Au/Cu	0.71	0.65
SS/Cu	1.36	1.28

The agreement between theoretical and experimental values is seen to be quite good.

FROM SURFACE MELTING TO BREAKDOWN

Figure 1 shows the geometric features formed by exposing a thin layer of molten metal to a dc electric field. We propose that similar features also form when an rf field acts on the liquid surface layer produced by back-bombardment heating in a cluster of plasma spots. These

features follow a somewhat regular pattern. Many of them have a roughly conical base with a vertical column or jet emerging from the apex. The sides of the cones make a

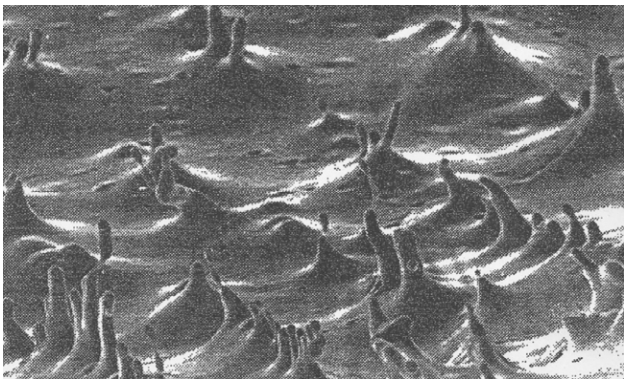

Figure 1: Surface features after action of an electric field on a thin layer of molten metal on a planar electrode [10].

roughly 45° angle with respect to the base. In the following, we develop a model based on this shape.

The model first assumes that the back-bombarding electrons produce sufficient heating to melt a thin layer of the surface in 30 ns or so at the beginning of each rf pulse, cooling and solidifying between pulses. Since the molten material cannot move very far in one rf pulse, geometric features with a scale of tens of microns must develop over hundreds or even thousands of pulses. Next assume that there are random height perturbations on the liquid surface, and that these can be modeled as portions of a spherical surface with radius r_0, as given by Eq. (1), where the surface field E_S is approximately equal to the unperturbed electric field, E_0, at the surface. The field will actually be slightly enhanced at the surface of the perturbation causing it to grow higher, which enhances the field still more etc. Following the shape of the surface projections suggested by Fig. 2, we model the growing perturbation as a conical pyramid with sides making angle ϕ with respect to the base. We assume that the cone is capped by a segment of a sphere with radius r, as show in Fig. 2. We assume that the analytic part of the growth process, where the cap radius is set by the condition for hydrostatic equilibrium (Eq. (1), starts with a spherical segment of radius r_1 as shown in Fig. 3. As the height of the cone increases the radius of the cap decreases and the surface field E_S and enhancement factor $\beta = E_S/E_0$ also increases. Simulations show that beta can be modeled as $\beta \sim r^{-n}$, where n is a function of ϕ. For the molten cap to be in hydrostatic equilibrium, the radius must vary as $r/r_1 = E_1^2/E_S^2$, giving $\beta = \beta_1 (r/r_1)^{-1/2}$, where β_1 is the value of beta at $r = r_1$. Simulations show that for n to be exactly 1/2 the base angle ϕ must be 40.0 degrees with $\beta_1 = 1.90$.

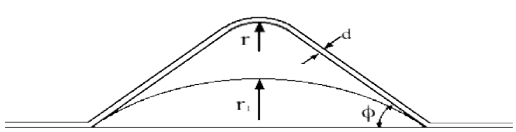

Figure 2: Geometry modeling growth of features in Fig. 1.

We next develop a model for the growth of the cone height with time. The liquid metal in the molten cap is under negative pressure from the E^2 force per unit area, F_A, pulling on the surface. This force also acts at the junction between the cap and the side of the cone, serving to pull the viscous molten metal up the side. The average flow velocity of the material follows the expression $v = \varepsilon_0 E_S^2 d/8\eta$, where η is the viscosity. This can be converted to a growth rate in height and hence in β. With a little algebra, we obtain

$$\beta = 1.9[1 - BE_0^4 T]^{-1/6}, \qquad (3)$$

where $B \approx 6d^2\varepsilon_0^2/\alpha\eta r_1$ and T is the integrated time (repetition rate times the pulse length, with some initial melting time ~ 30ns subtracted from the pulse length). Note that $E_0^4 T$ is a constant at the singularity, in agreement with experiment [9].

The scale of these geometric forms is set by Eq. (1). Small initial perturbations on the liquid surface would have small heights and large radii of curvature. The enhanced field at the crest of the perturbation sets up a pressure gradient along the surface that pulls liquid material toward the crest, building up the height. This pressure gradient, proportional to the gradient of E_S^2, is also responsible for pulling molten metal up the side of the cone shown in Fig. 3. It is essentially a ponderomotive force acting in the direction of increasing E_S.

ACKNOWLEDGEMENTS

I would like to thank Chris Nantista for producing Figure 2, and Valentin Ivanov for calculating the field enhancement factor for the geometry shown in the figure.

REFERENCES

[1] P.B. Wilson, "A Plasma Model for RF Breakdown in Accelerator Structures", Linac 2000 (Also SLAC–PUB–8653),

[2] J. Norem et al., *PRST–AB* **6,** 072001(2003).

[3] See, for example, O. G. Tietjens, *Fundamentals of Hydro – and Aeromechanics (Dover Publications, New York, 1934) p.61*.

[4] Jens Knobloch, "Advanced Thermometry Studies of Radio Frequency Superconducting Cavities", Ph.D. Thesis (Cornell University, August, 1997) Fig. 5.38.

[5] Perry Wilson, "Status of a Theory of High-Gradient Breakdown in Accelerator Structures", presented at ISG-11, KEK, Japan, December 2003 (http://lcdev.kek.jp/ISG/ISG-11).

[6] S. Doebert and C. Adolphsen, private communication.

[7] Perry B. Wilson, "Gradient Limitation in Accelerator Structures Imposed by Surface Melting", PAC03 (Also SLAC–PUB–9953).

[8] Electron Microprobe Notes: Electron Interaction with Matter, p.4 (http://jan.ucc.edu/~wittke/interaction.html.

[9] V. A. Dolgashev and S. G. Tantawi "RF Breakdown in X-band Waveguides", EPAC 2002 (Also SLAC–PUB–10355).

[10] G. A. Mesyats, *Explosive Electron Emission* (URO–Press, Ekaterinburg, 1998) p.29.

DEVELOPMENT OF A PERMANENT MAGNET ECR SOURCE TO PRODUCE A 5 mA DEUTERON BEAM AT CEA/SACLAY

R. Gobin*, P-Y Beauvais, G. Charruau, O. Delferrière, D. De Menezes, R. Ferdinand, Y. Gauthier, F. Harrault, Commissariat à l'Energie Atomique, CEA-Saclay, DSM/DAPNIA, 91191 Gif sur Yvette Cedex, France
N. Comte, Commissariat à l'Energie Atomique, CEA-Saclay, DEN/SAC/DSP/SPR, 91191 Gif sur Yvette Cedex, France
P. Leherissier, J-Y. Paquet, GANIL, Bd Henri Becquerel, 14076 Caen Cedex 5. France

Abstract

The high intensity light ion source (SILHI) is an ECR ion source operating at 2.45 GHz which produces high intensity (over 100 mA) proton or deuteron beams at 95 keV. This encouraged us to propose a permanent magnet source based on the SILHI design to fit in with the injector of the Spiral 2 project, requesting 5 mA of D^+ beam with an energy of 40 keV and a normalized rms emittance lower than 0.2 π mm.mrad. The new source has been recently assembled and the first beam (proton) extracted. The source design improvements and the preliminary results are reported.

INTRODUCTION

In France, CEA and CNRS have been working on high beam power accelerators for several years. In a first step, the SILHI source has been built to produce high intensity proton beams. Experiments were also devoted to the production of deuterons for irradiation tools. Deuterons are now also needed by the future SPIRAL 2 facility [1] and a "low" intensity (5 mA) deuteron source is presently under study at CEA Saclay.

The goal of SPIRAL 2 at GANIL, consists in extending the possible radioactive beam types. SPIRAL 2 is based on the fission of a Uranium carbide target induced by neutrons. The neutron flow will be produced by interaction of deuteron beam with a Carbon target. SPIRAL 2 requires a maximum of 5 mA - 40 keV CW D^+ beam (at the RFQ entrance) with rms normalized emittances lower than 0.2 π mm.mrad. To answer these requirements, an ECR source has been proposed, extending the SILHI design with permanent magnets.

SOURCE DESIGN

Magnetic Structure

The SILHI ECR ion source, operating at 2.45 GHz, is producing more than 100 mA proton beams [2] with a high reliability. Taking into account the deuteron experiments already successfully performed with SILHI (130 mA at 100 keV in pulsed mode) [3], the design of such a source fulfilling the SPIRAL 2 requirements has been undertaken. The reproducible performance led us to propose a permanent magnet 2.45 GHz ECR source: the magnetic field is provided by 3 ring shaped permanent magnets instead of 2 solenoidal coils on SILHI. Electromagnetic simulations have been carried out to reproduce at best the SILHI magnetic field profile on the axis [4]. The plasma chamber and the RF power chaine keep the SILHI design. In order to increase the plasma density, 2 Boron Nitride discs are also located at both ends of the plasma chamber.

No problem occurred when assembling the source but a 6 % deviation has been observed between the magnetic measurements and the simulations. Even if the ECR resonances have been easily placed, we discovered experimentally a major problem. It came from the particular permanent magnet configuration built with no shielding. Consequently, in the extraction region, the magnetic field was 40 times higher than in the SILHI case with coils and magnetic shielding, reaching a value of about 0.2 T. This high magnetic field contributed to initiate a discharge between the electrodes when the high voltage increases. The extraction system is designed for electric fields as high as 60 kV/cm and only few kV/cm between electrodes led to important currents in glow discharge and to a vacuum increase.

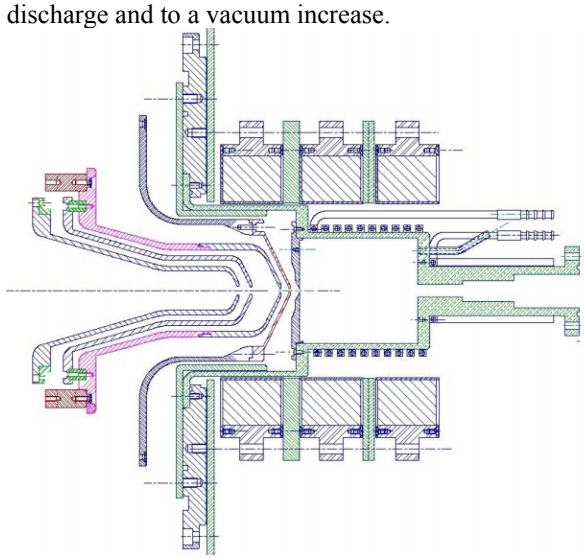

Figure 1: Permanent magnet ECR source with magnetic shielding and discs.

So, new magnetic configurations have been tested to lower the magnetic field between electrodes. But magnetic shielding leads to a decrease of the magnetic field in the plasma chamber. A compromise has finally

been found by inserting two iron discs of 13.5 mm and 5 mm width between the permanent magnet rings (Fig. 1) in addition with two 5 mm thick shielding plates in front of the first electrode (Fig. 2). The first one is located under vacuum in the accelerator column and the second one is positioned outside the vacuum between the first ring and the flange. The field is now comparable even lower than for SILHI in the extraction system.

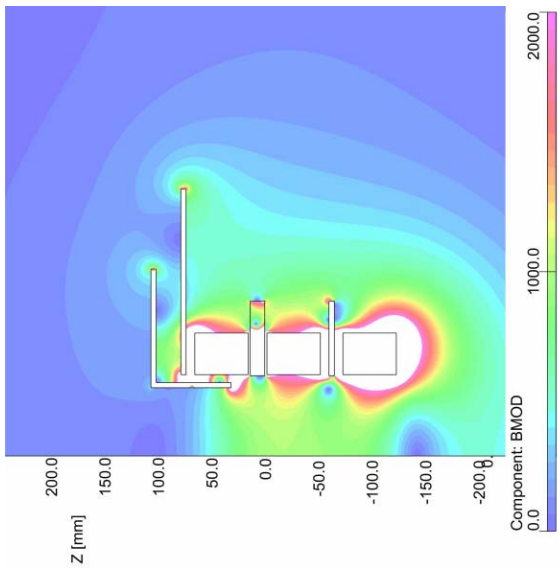

Figure 2: Magnetic simulations with shielding and discs.

Extraction System

The extraction system has been designed to be tuneable continuously at 40 keV, between 0.1 to 5 mA D^+ beam, by using 2 intermediate electrodes to adjust the accelerating gap [4]. The first simulations for a 6.4 mA total beam current have been done using AXCEL, without space charge compensation. The beam divergence and emittance optimisation has led to the first electrode configuration with a 2.5 mm diameter and 64° angle plasma electrode. The two intermediate electrodes have 3 mm and 3.5 mm diameter respectively. The 4th electrode is the – 2 kV electron repeller. The divergence was going from 10 mrad for 0.1 mA to 60 mrad for 5 mA. The rms normalized emittance given by AXCEL was very low, between 6 10^{-3} and 1.2 10^{-2} π.mm.mrad.

The extraction hole had to be enlarged to ensure a better pumping of the plasma chamber (see section III). Further simulations with AXCEL have been performed with 3 mm and 4.8 mm (Fig. 3) plasma electrode diameter. Other calculations have been done with PBGUNS in order to compare both codes. The 4.8 mm diameter plasma electrode is designed with an angle of 60°. The other electrodes have been modified with larger diameters and adjustment of their relative distances. The electrode potentials are respectively 40, 30, 10, - 4 and 0 kV from the plasma electrode to the ground. The calculated rms normalized emittance, at 7.6 mm from the hole, is about 2.3 10^{-2} π.mm.mrad with ion temperature set at 0.2 eV. The divergence is kept under 40 mrad (Fig.4). PBGUNS simulations indicate bigger tails on the emittance plot, compared to AXCEL.

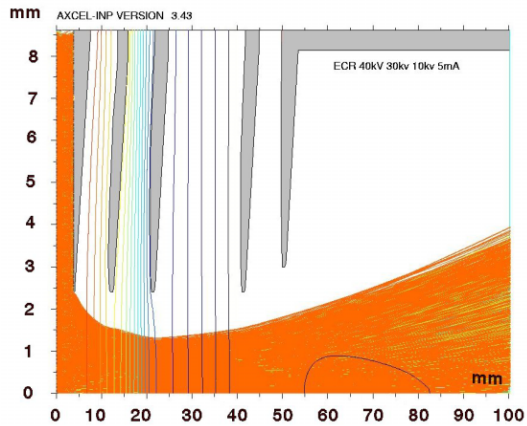

Figure 3: 4.8 mm diameter hole extraction system.

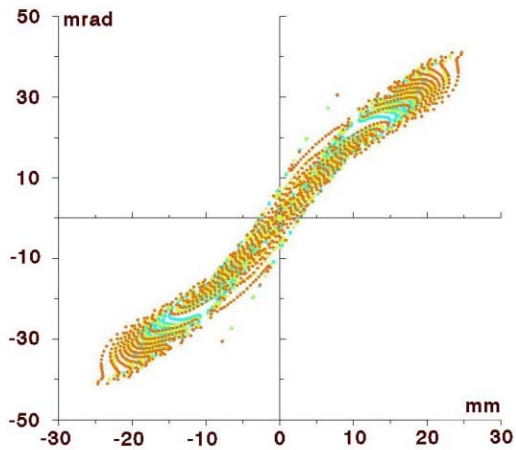

Figure 4: Emittance at 7.6 mm from extraction hole.

PRELIMINARY RESULTS

Even at low energy, deuteron beam leads to 2.45 MeV neutron emission due to the d,D reaction when the D^+ ions hit the deuterium molecules at the surface of the target. So, the new source originally started by producing H^+ beams. To keep a good plasma density, the preliminary simulations led to a 2.5 mm diameter aperture instead of 9 mm for SILHI. As the plasma chamber is only pumped through this hole, the small conductance led to tuning difficulties and finally, no efficient running mode was obtained in this configuration.

Therefore, the extraction aperture diameter has been enlarged to 3 mm and a specific turbomolecular group has been installed to directly pump the plasma chamber. By tuning the magnetic field (ring position and addition of iron plates, see section II), more than 7 mA total beams, with 1 kW RF power, have been extracted with less than 10 % of impurities and 77 % of protons. Emittance measurements have given a normalised rms value of 0.15 π mm.mrad.

Recently, deuterium gas replaced the hydrogen gas, and the total extracted beam reached 6.5 mA with 65 % of deuterons, for 1.1 kW RF power. In these conditions, the first measured D^+ beam emittance indicated a normalised rms value of 0.11 π mm.mrad (Fig. 5), largely higher than the estimated AXCEL's value

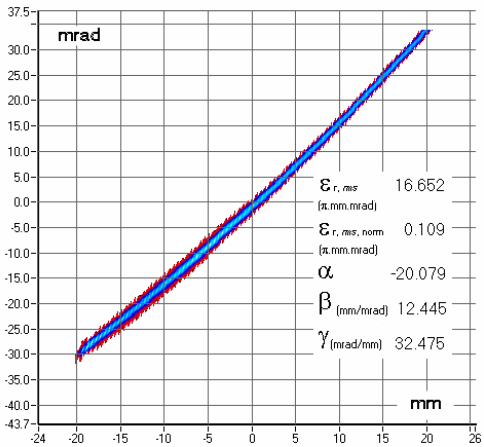

Figure 5: First beam emittance measurement (D^+ current = 4.2 mA).

NEUTRON PRODUCTION

Preliminary neutron production measurements were done [5] while the SILHI source was equipped with a small diameter (4.8 mm) extraction system to reduce the intensity. A 5 mA – 40 keV CW deuteron beam was produced. The neutrons were measured online with a LB 6411 probe under permanent control of the security staff. This experiment allowed acquiring data on 2.45 MeV neutron emission from d,D reaction.

After a short period in pulsed mode, the beam was rapidly produced in CW mode. Finally the source produced a deuteron beam for 4 days (6 hours per day). The beam was collected on a water cooled copper plate installed downstream the first solenoid, at about two meters from the extraction aperture. The neutron probe was located 0.40 m from the beam stop, outside the beam line, behind a 25 mm thick flange. A maximum neutron production saturated dose of 420 µSv was observed. The neutron emission appears isotropic around the copper target and follows the $1/r^2$ decay rule. As the beam starts, the neutron emission rise time is rather short and reaches a saturated level which linearly depends on the beam intensity. The neutron emission rise time is about 1 hour with a 5 mA-40 keV deuteron beam on a cleaned target and shorter after a beam restart on a deuterium polluted target. The neutron emission goes immediately down to 0 when the beam stops.

Moreover, the neutron emission decreases rapidly by changing the extracted particles. Just after switching from D^+ beam to H^+ beam, the neutron emission fall time goes down from 415 to 25 µSv/h after 6 min and to 0.5 µSv/h after 30 min. This residual emission is due to gas mixing in the pipes for few minutes.

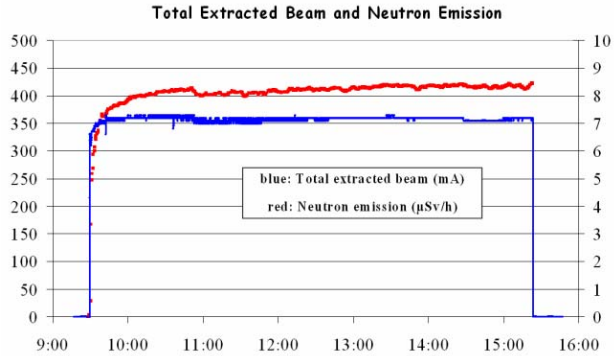

Figure 6: Neutron Emission and Extracted Current vs time.

On Figure 6, the red curve presents the neutron emission (plotted each 30 sec.) acquired by the LB 6411 probe with total extracted beam between 7 and 7.3 mA (blue curve). These measurements have been performed over a 6 hour long run with no beam off. New measurements are needed to confirm these results with systematic data record and specific shielding.

CONCLUSION

The permanent magnet technology can not simply replace a coil magnetic configuration. New magnetic simulations were needed to face the important problems leading to glow discharge. The source is now producing its first deuteron beams and the complete beam characterization is expected for the end of September.

ACKNOWLEDGMENTS

The authors would like to thank all the IPHI group members who participate to the SILHI program. In addition, people from the SPIRAL 2 group are also thanked especially M.H. Moscatello and J.M. De Conto. We do not forget L. Ando and L. Celona from INFN Catania who participated in fruitful discussions. The Saclay security staff is also gratefully acknowledged, especially F. Fardeau and H. Guillo who ensured the control for neutron measurements.

REFERENCES

[1] M-H. Moscatello, "SPIRAL2 at GANIL", This conference
[2] R. Gobin et al, "Status of the light ion source developments at CEA/Saclay", 2003 ICIS Conference, Dubna, Russia, to be published in RSI (2004)
[3] R. Ferdinand et al.; Proceedings of EPAC conference, Paris, France, June 2002, (p. 894-896)
[4] O. Delferrière and D. De Menezes, "Extraction design and LEBT optimization of space charged dominated multispecies ion beam sources", 2003 ICIS Conference, Dubna, Russia, to be published in RSI (2004)
[5] N. Comte et al, "Compte rendu d'expérience de mesures neutroniques avec un faisceau intense de deutons (5 mA – 40 keV) sur SILHI", internal report.

RECENT RESULTS OF THE 2.45 GHz ECR SOURCE PRODUCING H- IONS AT CEA/SACLAY

R. Gobin*, K. Benmeziane, O. Delferrière, R. Ferdinand, F. Harrault, Commissariat à l'Energie Atomique, DSM/DAPNIA/SACM, 91 Gif/Yvette, France
A. Girard, Commissariat à l'Energie Atomique, DSM/DRFMC/SBT, 38 Grenoble, France

Abstract

Low frequency ECR plasma sources have demonstrated their efficiency, reproducibility and long life time for the production of positive light ions. In 2003, the new 2.45 GHz ECR test stand based on a pure volume H^- ion production, developed at CEA/Saclay, showed a spectucar increase of the extracted H^- ion beam intensity. In fact, a stainless steel grid now divides the plasma chamber in two different parts: the plasma generator zone and the negative ion production zone. By optimizing the grid position and its potential with respect to the plasma chamber, the negative ion current reached nearly 1 mA. Ceramic plates covering the plasma chamber walls help electron density and lead to an optimisation of the ion production. A 1.32 mA H^- extracted current has been measured. New Langmuir probe measurements have also been done on both sides of the grid. The last results are reported and discussed. This work is supported by the European Union under contract HPRI-CT-2001-50021.

INTRODUCTION

Future high intensity proton accelerators like SNS, ESS or neutrino factories ask for reliable and efficient H^- ion production to inject in compressor rings. These facilities have been planned to work in pulsed mode (roughly 1 to 2.5 ms pulse length at a frequency ranging from 15 to 50 Hz). Many existing machines such as HERA, ISIS, LANCSE and others are also interested in source developments. Taking into account these demands, CEA has undertaken an important R&D program on high intensity light ion sources.

Since the SILHI source [1] showed a good efficiency for high intensity proton beam production with a very long source life time, parallel programs are in progress. A permanent magnet deuteron source is now delivering its first deuteron beams [2] for the SPIRAL 2 project. In parallel, the development of the 2.45 GHz ECR negative ion source is still in progress and the H^- ion production slightly increases.

One year ago, measurements performed with a plasma chamber separated into 2 zones showed an important improvement [3]. These results are shortly reported in the next section. The third section will insist on the last results obtained by testing different materials. Then recent Langmuir probe measurements are presented.

* e-mail : rjgobin@cea.fr

ELECTRIC FILTER

To produce negative hydrogen ions, the sources are generally based on the same principle. In the plasma creation zone, energetic electrons of about 20 to 40 eV interact with the gas to excite the molecules and then in a second zone, slow electrons (about 1 eV) react with these excited molecules to give an H atom and an H^- ion. This process is called the dissociative attachment. Generally, both zones are separated by a magnetic filter to limit the high energy electron flux entering into the negative ion production zone.

At Saclay, the preliminary design of the source based on plasma generated by electron cyclotron resonance, followed this principle. And only few µA of H^- ions have been observed [4].

So the small H^- ion production may be attributed to negative ion destruction close to the plasma electrode. It is possible that microwave power not completely absorbed by the plasma contributes to H^- loss. Simulations show that a simple metallic grid with a large transparency can stop the microwave penetration. As a result, an important improvement has been observed when the plasma chamber has been effectively separated in 2 zones by a stainless steel grid. This grid is polarised at the same potential than the plasma electrode.

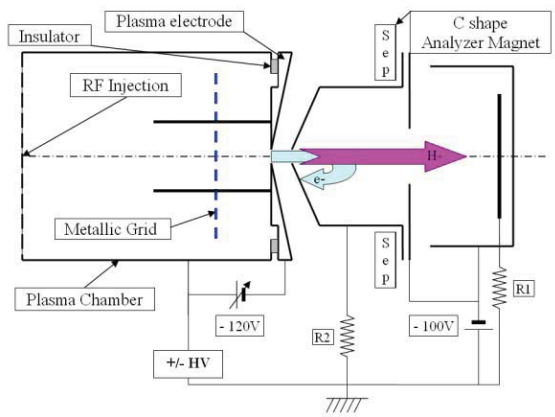

Figure 1: Scheme of the H^- ECR source.

After optimisation of the grid position, the maximum H^- current occurred while the grid was located at 30 mm from the plasma electrode. By tuning the potential of the grid and plasma electrode from 0 to – 120 V compared to

the plasma chamber, the 10 kV H^- extracted current rose from the precedent maximum value (84 µA) to 950 µA.

MATERIAL DEPENDENCE

The above-mentioned results were obtained with a stainless steel grid and a molybdenum plasma electrode. The rectangular plasma chamber is made of water-cooled copper and a 2 mm thick boron nitride disc is inserted between the RF ridged transition and the plasma chamber. The source was typically working in pulsed mode (1 ms – 10 Hz) 5 days a week for several months. And no degradation has been observed. The first stainless steel grid, installed in June 2003, has never been changed excepted during the Tantalum grid test reported hereinafter.

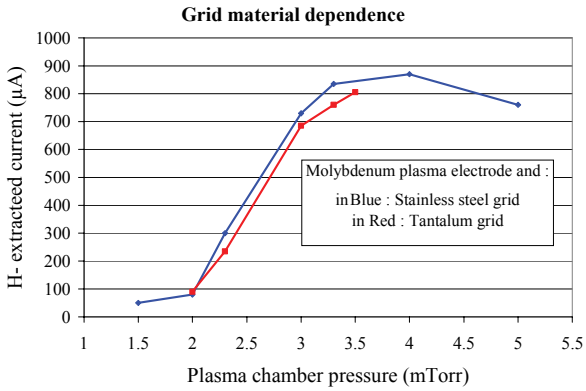

Figure 2: Extracted H^- current vs pressure with Tantalum grid (black) and Stainless steel grid (red).

Several authors already reported hydrogen negative ion production improvements while using Tantalum material inside the plasma chamber [5, 6]. So a Tantalum grid has been tested while the Saclay source operated at 10 kV and the performances did not change dramatically (Fig. 2). But if both the grid and the plasma electrode are made of Tantalum, the extracted H^- current decreases by about 25 % (Fig. 3).

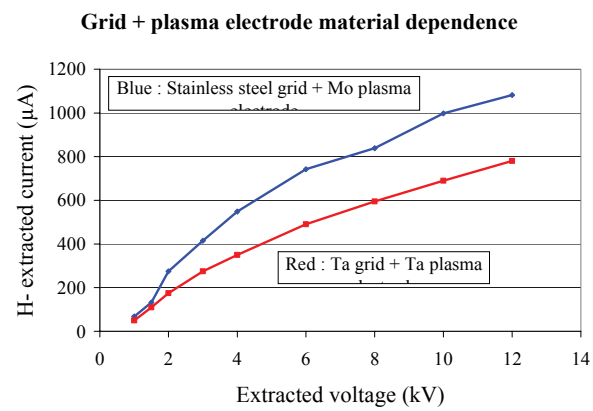

Figure 3: Extracted H^- current vs extraction voltage with:
- Ta grid and plasma electrode (red)
- Stainless steel grid and Mo plasma electrode (black).

Measurements indicated [3] that the extracted current continuously increases from 140 to 850 µA while the RF power rises from 380 to 950 W. The continuous increase of the RF power can be associated to an increase of the electron production in the plasma generator zone. And simulations [7] predict the increase of the H- ion production as a function of the electron density.

Ceramic materials like quartz, alumina or boron nitride produce an important amount of secondary electrons under plasma particle bombardment. So to confirm the dependence of the H- ion production with respect to the primary electron density, 4 boron nitride plates have been installed in the plasma creation zone. And the H^- extracted current increased from 950 µA to 1.32 mA with the same source running conditions.

LANGMUIR PROBE ANALYSIS

To better understand the plasma behavior in both parts of the source, Langmuir probe measurements have been done. A 2 mm diameter molybdenum probe has been placed perpendicularly to the source axis. In the plasma creation zone, it was located at 58 mm from the plasma electrode (28 mm from the grid). At this location, the solenoïdal magnetic field reaches nearly 500 Gauss. Hence the Langmuir probe characteristics are not easy to interpret. Figure 4 seems to indicate that, in these conditions, the electron temperature increases in this region when the grid potential varies from – 0 to – 90 V. This may be explained since the negative polarization of the grid accelerates backward all electrons with low energy.

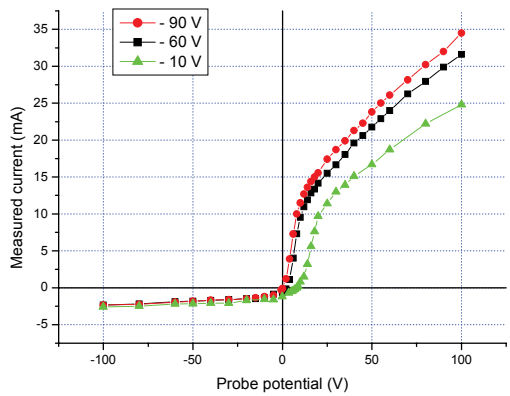

Figure 4: Probe characteristic at 2.4 mTorr pressure in the electron production chamber.

In the second part of the plasma chamber, i.e. in the negative ion production zone, the same probe has been installed, downstream the grid, at 6 mm from the plasma electrode. Here the axial magnetic field is much lower (around 200 Gauss). Figure 5 compares the probe characteristics in both zones for the same grid polarization. We can observe that the grid has an important effect on reducing the electron temperature in the H^- production zone. This electron energy reduction

allows an important improvement of the H^- ion extraction current.

The red curve shows a negative floating potential equal to – 8 V which points out the presence of very high energy electrons in the source. This curve confirms the assumption on the electron energy obtained in the ECR ion source. With no use of polarized grid the negative ion production is much lower since high energy electrons are the cause of H^- ion losses.

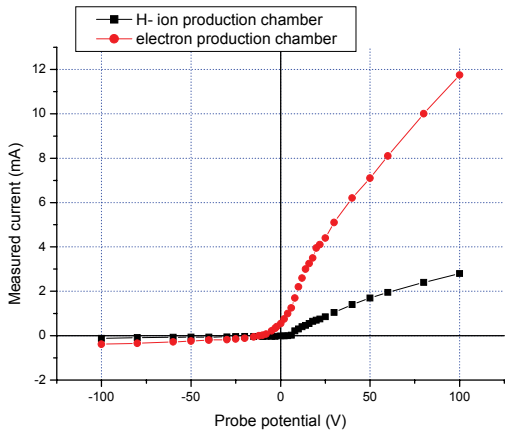

Figure 5: Comparison of probe characteristics in both parts of the plasma chamber.

By analyzing the extracted current while the probe is located close to the extraction aperture (6 mm), the maximum H^- current is obtained for – 30 V grid polarization instead of – 120 V. This confirms the plasma perturbation due to the probe. New extraction analysis will be performed when the probe is installed a little bit further from the axis to minimize the harmful effect.

10 GHz SOURCE

Moreover in the last 2 years, a new source based on 10 GHz ECR plasma generator has been studied at CEA/Grenoble. The design is now completed, the magnetic field will be provided by an octopolar permanent magnet structure. This research program will be transferred to Saclay in the near future. The construction of the source is expected at the beginning of next year. The aim of this new test stand is to verify the well-know frequency scaling law applied in the heavy ion source community: the increase of the frequency allows a better gas ionisation. As a result a larger amount of hydrogen excited molecules and an H^- ion production improvement are expected.

ACKNOWLEDGMENTS

The support of the European Community (Contract HPRI-CT-2001-50021) is gratefully acknowledged. This work could not be carried out without the technical assistance of G. Charruau and Y. Gauthier, and finally, many thanks to the IPHI team members for their contributions, especially M. Desmons and A. France. The help of J. Sherman from Los Alamos was also greatly appreciated for this development. The authors would also like to thank T. Steiner from CERN and K. Stervinou (a training student) who participated in probe measurements. Moreover, the participation of G. Gousset from the Orsay University in theoretical studies is also acknowledged.

REFERENCES

[1] R. Gobin et al., “Status of the light ion source developments at CEA/Saclay”, 2003 ICIS Conference, Dubna, Russia, to be published in RSI (2004)

[2] R. Gobin et al., “Development of a permanent magnet ECR source to produce a 5 mA deuteron beam at CEA/Saclay”, this conference

[3] R. Gobin et al., “Development of an H^- ion source based on ECR plasma generator at CEA/Saclay”, 2003 ICIS Conference, Dubna, Russia, to be published in RSI (2004)

[4] R. Gobin et al., "The CEA/Saclay 2.45 GHz microwave ion source for H^- ion production", Proceedings of the 9th Intern. Symposium on Negative Ion Sources and Beams, Saclay, France, May 2002, AIP Conference Proceedings, 639, pg: 177.

[5] J. Peters, RSI, Vol 71, N° 2, Feb. 2000.

[6] D. Spence et al, Proceedings of LINAC Conference August 1996.

[7] K. Benmeziane et al, “Study and preliminary results for a new type of ECR H^- ions source”, 2003 ICIS Conference, Dubna, Russia, to be published in RSI (2004)

H⁻ DISTRIBUTION IN THE HERA RF-VOLUME SOURCE

J. Peters DESY, Hamburg, Germany

Abstract

The HERA RF-Volume Source is the only source that delivers routinely a H⁻ current of 40 mA without Cs. The production mechanism for H⁻ ions in this type of source is still under discussion. Laser photodetachment measurements have been started at DESY in order to measure the H⁻ distribution in the source. The measurements were done also under extraction conditions at high voltage. Measurements with and without extraction are contributions for the H⁻ sheath theory. Knowing how the H⁻ are distributed and where they are produced makes further source improvements possible.

INTRODUCTION

Photodetachment measurements in order to measure the density of negative ions have been done as early as 1969 [1]. First density measurements of H^- are reported in 1979 [2]. In the HERA source a modification of a technique with a cylindrical metal probe (langmuir probe) aligned parallel to a laser axis [3] was used. The HERA volume H^- source is a RF source with an antenna outside of the plasma chamber. The antenna is shielded by a ceramic. For HERA a current pulse of 40 mA, 120 µsec long is extracted at 35 kV. The details of the source are given in several papers [4],[5],[6].

MEASUREMENT SET UP

The power applied at the RF coil of the HERA H⁻ source is pulsed. With a positive bias (U_{LP}) of 5V close to saturation one draws an electron current to the tip of the probe. This current (I_{LP}) is measured with a toroid (see Fig.1). The current signal is shown in Fig.2a. The affinity of the electron attached to the hydrogen atom is with 0.75eV very low [1]. By photodetachment $H^- + h\nu = H + e^-$ an increase in electron density is produced.

To clearly interpret the signals it has to be made sure that no other photon processes like photoionisation take place. Fig. 2b shows the increase in electrons detected when a 9 nsec, 1064 nm puls of a Nd: YAG laser travels on the axis of the source. The maximum pulse energy of our laser was 650 mJ per pulse. The 8 mm ∅ laser beam was compressed to 3mm ∅ with an optical system.

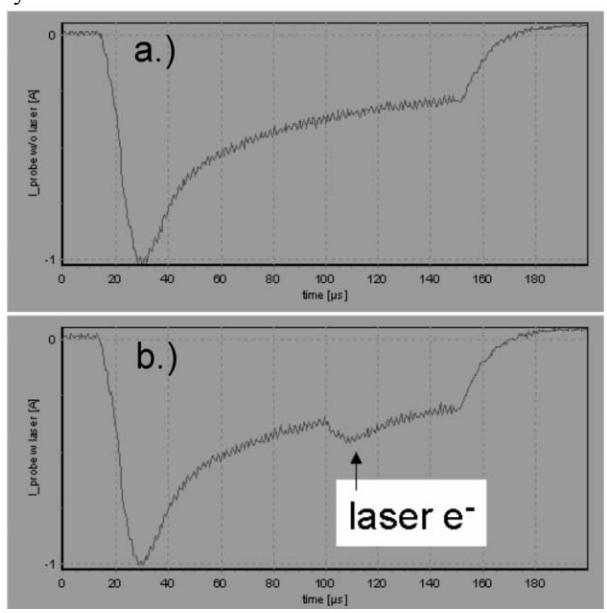

Figure 2: Current pulse of the Langmuir probe (I_{LP}) without laser beam (a) and with photo detached electrons (b).

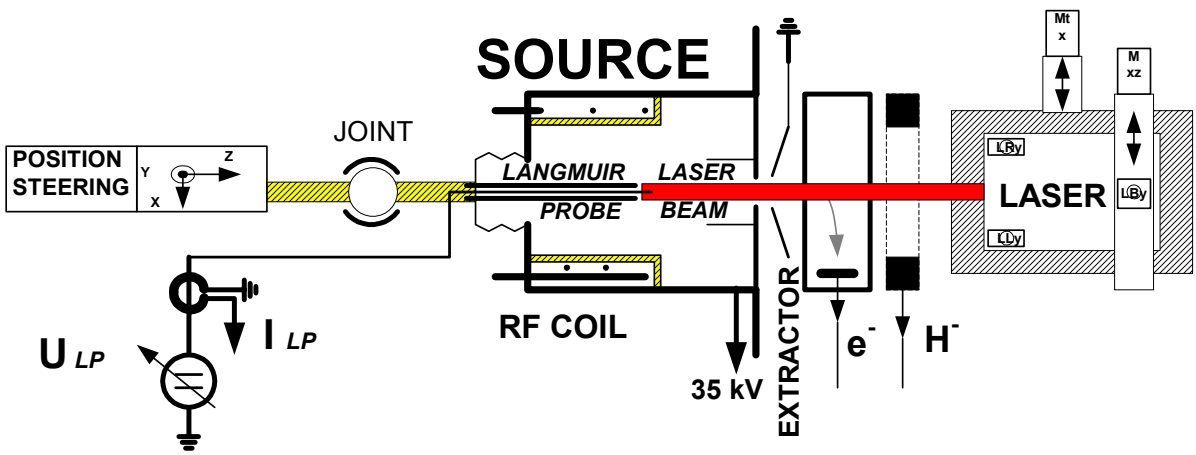

Figure 1: HERA RF source with mounted langmuir probe on the back side and a laser beam shooting through the extractor hole.

The beam was dumped on the probe or on a ceramic dump surrounding the end of the probe. A set up where the laser beam is dumped outside of the source is given in [7]. The probe tip and inner conductor are a molybdenum wire of 0.4 mm ∅. The center wire is shielded by a metal tube which is completely isolated from the plasma with sealed ceramic tubes (see Fig. 3).

Due to the environment there is noise on the signals in Fig.2. By averaging over many pulses it was possible to get very stable values.

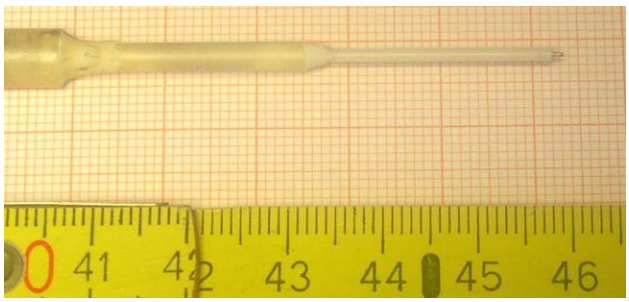

Figure 3: Ceramic shielded probe with tip

We tried different ways [8] to detect the increase in the number of electrons due to the laser beam. First the signal without laser beam was subtracted from the signal with laser beam. It turned out that detecting in the same pulse the difference between maximum and the minimum before the laser starts delivers the same results.

The laser beam was fixed on axis of the source. The probe tip was moved step by step in rectangular planes perpendicular to the beam axis (see Fig. 1). The x and y movement is done by turning the probe in a joint the z motion by pulling the probe in and out. The movements in x, y and z are done with a three table system. A long bellow is used for transforming the movements into the vacuum.

The size of the planes over which measurements were done varied from 4mm x 4mm in the collar area to 10mm x 10mm in the RF coil range and had in the final part of the source a size of 6mm x 6mm. All measurements were done with a 0.5 mm step size. The z planes were measured in 5mm steps.

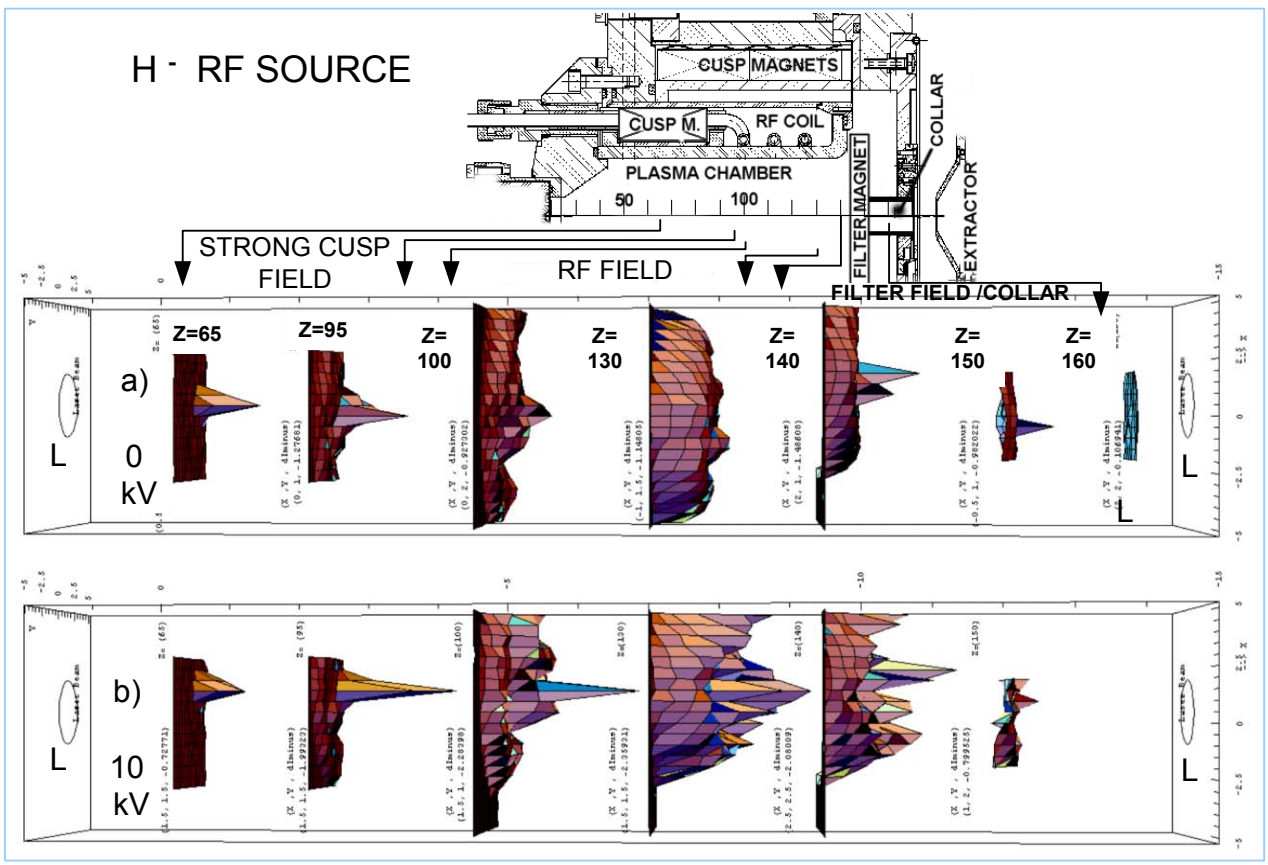

Figure 4: H ⁻ intensities along the source axis without extractor gap voltage (a.) and with 10 kV applied (b.). L marks the laser beam diameter.

RESULTS

Fig. 4 gives a 3D sample presentation of typical H^- intensities measured on selected rectangular areas along the source. It was possible to associate measurement patterns to different zones of the source. The H^- intensity (Nh^-) is proportional to the additional electron current delivered due to the laser pulse . The Nh^- measurements were taken along the central axis of the source in arbitrary units. Measurements were taken at 0 V and at 10 kV extractor gap voltage.

Strong Cusp Magnet Field Area

In the range between z=65mm and 95mm a strong multicusp field is present in the source. Only a small maximum was detected in an area of about 1.5mm times 1.5mm which is a factor 2 smaller than the laser beam diameter. Significant peaks with a Nh^- value around 1 were measured.

RF Field Area

Between z=100 mm and 130-140 mm a strong RF field is applied to the plasma. The cusp field is reduced and the dipole filter field starts only at the end of the range. One finds now laser produced electrons in a circle with 10mm diameter. A plateau is formed and in addition there are spikes. The spikes become more numerous when the acceleration voltage is applied. Apparently the freed electrons are accelerated by the RF field and this movement is modulated by the acceleration voltage. In this range a maximum Nh^- value of 2.28 was found.

Filter Field Area (in front of the collar)

A dipole field is applied which has a maximum of about 20 mT at z= 157 mm and goes to zero in the middle of the acceleration gap. The plateau becomes lower which could be due to a reduced RF field. Just in front of the collar the size of the measurement plane was reduced in order to avoid damage. Here the H^- densities were less than half the maximum values.

Collar Area

In this region only one measurement was done without acceleration voltage due to sparking which occurred under high voltage. With the 6.5 mm plasma aperture the plasma density is here reduced. The H^- density (Nh^-) is only about 5% of the maximum values detected. In case of an applied acceleration field there would be a competition between the field from the probe tip and the accelerating field.

Acceleration Voltage (On/Off)

Contrary to expectations a large intensity change was found when an extraction voltage of 10 kV was applied. This difference is most obvious in the RF field area. The voltage was applied in the usual operation mode with extractor at ground and the source at high voltage. The mechanic for the probe was grounded and isolated from the probe and source bucket.

Alignment

In the strong cusp magnet field area the position of the maximum intensity varies only 0.5 mm, the step size. In the RF field area the variation is bigger and with HV applied many peaks occur. In case of the filter field range without HV the adjustment was lost due to a power failure.

CONCLUSIONS

Photodetachment measurements of the H^- ions show that the extraction voltage has an unexpected effect on the H^- distribution in the plasma. The photodetached electrons are strongly influenced by the different magnetic fields and the RF which is coupled into the source plasma. It will be interesting to change these fields and study the change in the H^- distribution not only on axis but in the whole source. The magnetic and RF fields together with the laser light should be carefully measured. Varying the filter field and observing the change in the plasma transition (sheath) will be of special interest.

ACKNOWLEDGEMENTS

The author is grateful for the contribution of the following colleagues at DESY: I.Hansen, H.Sahling and R.Subke. The thesis (Diplomarbeit) of C. Sehnke [8] was an important basis for our studies. The author also wishes to thank H. Weise and the technical groups at DESY for their support and M.Lomperski of DESY for helpful suggestions to the wording of the article. The support of EEC (Contract HPRI-CT-2001-50021) is gratefully acknowledged.

REFERENCES

[1] J. Taillet, C. R. Acad. Sci., Ser. B 269, 52 (1969)
[2] M. Bacal and G. W. Hamilton, Phys. Rev. Lett. **42**, 1538 (1979).
[3] M.Bacal, Rev. Sci. Instrum., Vol. 71, No. 11, November 2000
[4] J.Peters, Rev. Sci. Instrum., Vol. 75, No. 5, May 2004.
[5] J.Peters, Proceedings of the XXI International LINAC Conference, Gyeongju, Korea, August 19-23, 2002.
[6] J.Peters, Ph.D. thesis, Universität Frankfurt,2001.
[7] Y.Matsumoto et al, Rev. Sci. Instrum., Vol. 73, No. 2, February 2002.
[8] C. Sehnke, Entwurf u. Implementierung eines modularen Sofwaresystems zur Plasmadiagnostik mittels Langmuir-Kurven u. Photodetachment, Diplomarbeit, FH Wedel, Februar 2004

ULTRA-HIGH-VACUUM PROBLEM FOR 200 KEV POLARIZED ELECTRON GUN WITH NEA-GaAs PHOTOCATHODE

T. Nakanishi[a], M. Yamamoto[a], N. Yamamoto[a], S. Okumi[a], F. Furuta[a], M. Kuwahara[a], K. Naniwa[a], K. Yasui[a], H. Kobayakawa[b], Y. Takashima[b], H. Matsumoto[c], M. Kuriki[c], and M.Yoshioka[c]
[a]Dept. of Physics, Nagoya University, Nagoya 464-8602, Japan
[b]Faculty of Engineering, Nagoya University, Nagoya 464-8602, Japan
[c]KEK High Energy Accelerator Research Organization, 1-1 Oho, Tsukuba 305-0801,Japan

Abstract

A high gradient electron gun with an NEA-GaAs-type photocathode is indispensable to produce the high intensity (polarized) electron beam for a future e^+-e^- linear collider (LC) and the low emittance CW beam for energy recovery linac (ERL) projects. Motivated by these needs, a 200keV (polarized) electron gun has been constructed at Nagoya Univ. The source emittance measurement system is also constructed and preliminary results are obtained. However, the lifetime of the NEA surface is not yet sufficiently long, and this problem is discussed with the efforts for improvement.

INTRODUCTION

A proto-type of 200keV polarized electron gun has been constructed for applications to the LC and ERL projects. As well known, the warm-technology-based LC requires high-intensity (>5A peak current), multi-bunch structure (~500ps bunch width, 1.4ns separation) beam with low emittance (<10π·mm·mrad) at gun exit[1]. The ERL requires large average current (~100mA) beam with the lowest emittance (<0.5π·mm·mrad)[2].

In such applications, the NEA (Negative Electron Affinity) surface makes an indispensable role to extract electrons in conduction band minimum into vacuum. It assures high polarization (P≅90%), high quantum efficiency (QE≥0.5%) [3] and lowest initial emittance (ε≅0.1 π·mm·mrad) [4] of the extracted beam.

On the contrary, there is a serious NEA lifetime problem. The NEA surface is realized by a mono-layer of electric-dipole-moment of Ga(-)–Cs(+) formed by the Cs deposition to the GaAs surface. Thus this surface state is extremely delicate against environment. In fact, the NEA surface is easily degraded by (a) desorption of residual gas molecules, (b) desorption of additional gas molecules created by the dark currents from high voltage electrode, and (c) NEA surface back-bombardment of the positive ions produced by the beam itself. In order to reduce these effects, high quality ultra-high-vacuum (UHV) is required in the vicinity of NEA surface.

The dark current induced by field emission from the cathode electrode surface is enhanced by secondary electron and ion productions. It must be also suppressed below 10nA level to maintain the UHV condition.

For keeping the lowest initial source emittance, on the other side, the higher gradient field at the NEA surface is required to prevent the beam divergence due to the space charge effect. It means that the NEA lifetime problem becomes more and more serious, if we require the higher field gradient to realize the lower source emittance.

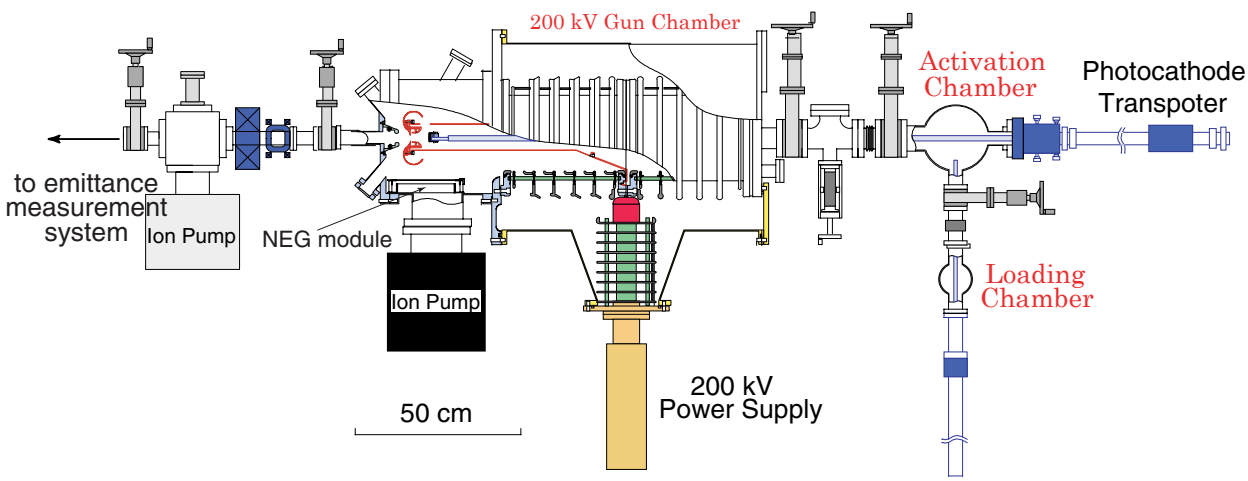

Figure 1: A schematic view of the 200keV polarized electron source.

DESIGN OF 200 KEV GUN

The mechanical structure of the 200keV gun is shown in Fig. 1. The gun consists of three sections which are isolated by gate valves. The photocathode is transferred between these chambers by two magnetic manipulators. The preparation chamber introduces the photocathode from atmosphere to UHV, and makes the surface cleaning by atomic hydrogen gas. After the photocathode is further cleaned by the RF heating, the NEA activation is made by deposition of Cs and O_2 or NF_3 in the activation chamber.

The load-lock system worked well and the gun could already produce the highly polarized electrons from a thin layer of GaAs-GaAsP strained superlattice structure [3]. The high QE (7.0%@633nm and 1.2%@780nm) was also achieved using the 15minutes atomic-hydrogen cleaning at <400ºC and the 2 hours heat cleaning at ~450ºC).

High voltage of 200kV is applied to a centre of double ceramic insulators, to which the cathode supporting tube is also fixed. In order to suppress the leakage currents along the ceramic surface and the corona discharge to the ground, the dry nitrogen is fulfilled into the insulation gas tank with pressure above 3.6atm.

ULTRA-HIGH-VACUUM

Pumping System

The high quality UHV is indispensable for the long lifetime of NEA surface. The original pumping system of the gun chamber was designed to have a 360l/s ion pump and an 850l/s non-evaporable getter (NEG) pump. The total pressure and partial pressures of residual gas were monitored by an extractor gage (IE514; Leybolt) and a residual gas analyser (TH200; Leybold), respectively. After bake-out of the gun chamber at 200ºC for 100hours, the vacuum pressure fell down to 3.2×10^{-9} Pa and the partial pressure of H_2O became to 1.1×10^{-10} Pa. However, the QE lifetime for a photocathode was rather short of ~40hours, in either case of a 200keV CW beam operation with ~100nA, or an intermittent QE measurement by a 5keV beam. The latter is so called as dark lifetime measurement.

These data suggested that the QE lifetime is limited by degradation of the NEA surface by adsorption effect of harmful residual gases. In order to achieve the extra-high-vacuum $<10^{-10}$ Pa by relaxing this effect, the following improvement were introduced.

- All valves used in the gun chamber were replaced from viton-seal to metal-seal for proof against the bake-out at higher temperature (≤200ºC).
- The additional NEG pumping modules were installed to reinforce the pumping speed under UHV.

The total pumping speed was reinforced up to 4650l/s using eight NEG pump modules (WP950×8; Saes Getters) that were installed around a photocathode. They are fixed to a rigid frame as shown in Fig. 2. The designed activation temperature was ~450ºC with 35A supplied current for each module. The mesh of stainless-steel is used to cover inner-side of the frame for masking the NEG modules from the high voltage electrode. The NEG module system was insulated from the ground so that the emitted current from the electrode to the mesh could be monitored.

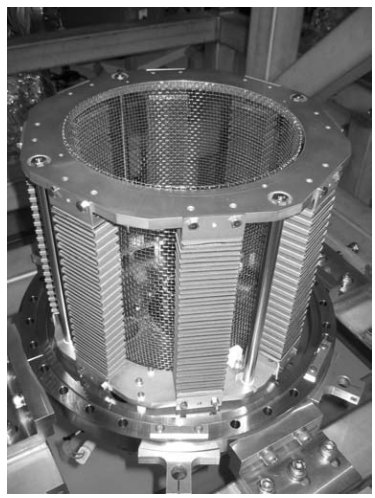

Figure 2: The NEG modules fixed to the rigid frame.

Preliminary Results of UHV

The results of preliminary UHV-test are as follows. The baking of the gun chamber with various parts was done at 200ºC for 100 hours. The heating temperature of NEG modules was as same as the baking temperature of 200ºC, due to a trivial accident of current supply circuit. It means the pumping speed of NEG modules was expected to be lower than the designed speeds.

The total pressure, wall temperature and partial pressures of H_2, CH_4, H_2O, CO/N_2, CO_2 were monitored with time as shown in Fig.3. It shows the H_2 and CH_4 were dominant components before the NEG pumps activation, and then the CH_4 component decreased while H_2 still remained.

The total pressure was improved from 3.2×10^{-9} Pa to 5.7×10^{-10} Pa, in spite of the incomplete activation of the NEG modules. The partial pressures of harmful gasses were also reduced to 2.6×10^{-11} Pa for H_2O and 5.1×10^{-11} Pa for CO_2, respectively. They are summarized in Table 1.

Table 1: Improvement of total and partial pressures of residual H_2O and CO_2 in the gun chamber

	Pressure	H_2O	CO_2
Before	3.2×10^{-9}Pa	1.1×10^{-10}Pa	2.3×10^{-10}Pa
After	5.7×10^{-10}Pa	2.6×10^{-11}Pa	5.1×10^{-11}Pa

Preliminary Results of Lifetime

A preliminary dark-lifetime measurement is done using a He-Ne laser (λ=633nm) at a bias-voltage of -5kV

under the above UHV condition. The QE decrease with time is shown in Fig. 3, together with previous data.

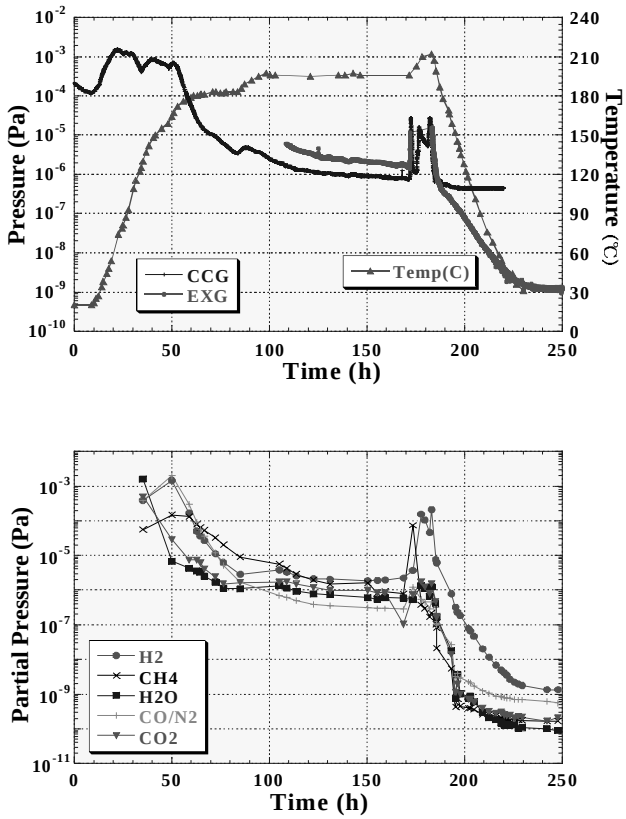

Figure 3: The total pressure, the wall temperature and the partial pressures of H_2, CH_4, H_2O, CO/N_2, CO_2 were monitored during the baking of the gun chamber.

The dark-lifetime is improved from 40 to 150 hours, and it is reconfirmed that the reduction of harmful residual gasses (in particular, H_2O and CO_2) is so important to preserve the NEA surface state.

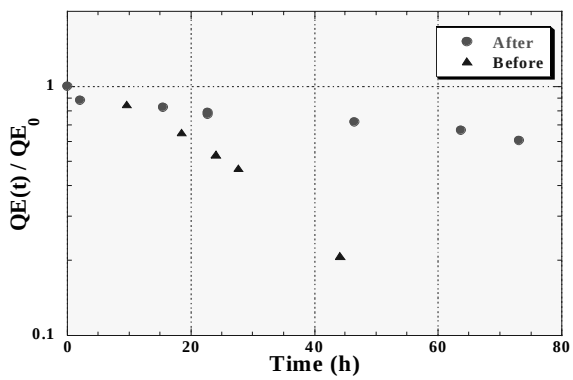

Figure 4: Preliminary result of dark-lifetime measurement.

EMITTANCE MEASUREMENT

An emittance measurement system employing a high-precision pepper pot technique has been introduced to our gun system. It was developed at KEK for the emittance measurement of a thermionic cathode gun [5] and now is modified for the NEA-GaAs cathode gun.

As shown in Fig. 4, the beam shot from the gun is masked by pepper pot placed at a distance ~1m from the photocathode, and the beamlets that pass by the mask drift about 56mm and hit a screen of scintillator film. The signal light (λ=375nm) passes through an IR-cut-filter to eliminate the background due to laser light (λ=780nm for Ti:Sapphire, λ=633nm for He-Ne). Small luminous spots on the screen are magnified by a telescope, amplified by an image-intensifier and finally converted into the electrical images by a CCD camera. The source emittance less than 0.7π·mm·mrad can be measured by this system.

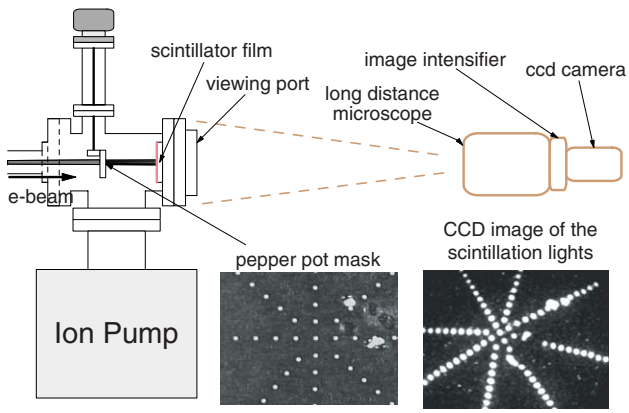

Figure 5: Pepper pot type emittance measurement system.

Preliminary results of the emittance measurement are obtained using a test beam from the 200keV gun.

SUMMARY

We have tried to improve the lifetime of NEA-GaAs photocathode by reinforcing the pumping power and also making the high temperature baking for the gun chamber. The dark-lifetime of preliminary test shows 150hours and the better lifetime will be obtained by increasing the NEG activation temperature from 200ºC to 450ºC. The precise measurement of source emittance becomes also possible.

Studies to improve the dark-lifetime and increase the field gradient by new electrode with Mo-cathode and Ti-anode are in progress [6]. Other experiments using this gun system are also scheduled to produce the nanosecond multi-bunch polarized beam for the LC project and the low emittance CW beam for the ERL project.

REFERENCES

[1] T. Nakanishi et al., KEK-Report 97-1 (1997) 36-49
[2] CHESS Technical Memo 01-003 (2001)
[3] T. Nakanishi et al., This proceedings [THP24]
[4] S. Pastuszka et al., J. Appl. Phys. 88 (2000) 6788
[5] Y. Yamazaki et al., N.I.M. A322(1992) 139-145
[6] T. Nakanishi et al., This proceedings [THP23]
F. Furuta et al., submitted to N.I.M.

DESGIGN PARAMETERS OF THE NORMAL CONDUCTING BOOSTER CAVITY FOR THE PITZ-2 TEST STAND

V.V. Paramonov, N.I. Brusova, A.I. Kvasha, A.A. Menshov, O.D. Pronin,
A.K. Skasyrskaya, A.A. Stepanov, INR, 117312 Moscow, Russia
A. Donat, M. Krasilnikov, A. Oppelt, F. Stephan, DESY, Zeuthen, Germany
K. Floettmann, DESY, Hamburg, Germany

Abstract

The normal conducting booster cavity is intended to increase the electron bunch energy in the Photo Injector Test (DESY, Zeuthen) stage 2 experiments [1]. The normal conducting cavity is selected due to infrastructure particularities in DESy Zeuthen. The L-band cavity is designed to provide the accelerating gradient up to 14 MV/m with the total input rf power up to 8.6 MW, rf pulse length up to 900 mks and repetition rate 5 Hz. The multi-cell cavity is based on the CDS compensated accelerating structure with the improved coupling coefficient value. The main design ideas and decisions are described briefly together with cavity parameters - rf properties, cooling and pumping circuits.

GENERAL PARAMETERS

Table 1: Cavity parameters

Parameter	Unit	Value
Operating frequency	MHz	1300
Particle velocity	relative	1.0
Nominal gradient E_0T	$\frac{MV}{m}$	12.5
Maximal gradient E_0T	$\frac{MV}{m}$	14.0
Nominal energy gain	MeV	20.18
Maximal surface field	$\frac{MV}{m}$	40.0
Maximal rf pulse power	MW	8.6
Maximal rf pulse length	μks	900
Nominal repetition rate	Hz	5
Aperture diameter	mm	30.0
Number of periods		14
Coupling coefficient	$\%$	7.2
Calculated Q-factor		23700
Required Q-factor	at $20C^o$	20100
Cavity length	m	≈ 1.8
Operating temperature	C^o	≈ 44
Cooling water consumpt.	$\frac{m^3}{h}$	4.5
Residual gas pressure	$Torr$	$\leq 10^{-7}$

The booster cavity is the component of the test stand for investigations of high brightness electron beam formation. The cavity should combine different, some time contradictory, properties as operating parameters flexibility, reliability, minimal own emittance perturbations. Additionally the cavity realize (in maximal parameters) the full scale high power prototype of the high gradient cavities in the TESLA Positron Pre-Accelerator [2].
The cavity general parameters are summarized in Table 1.

Accelerating structure and beam dynamics

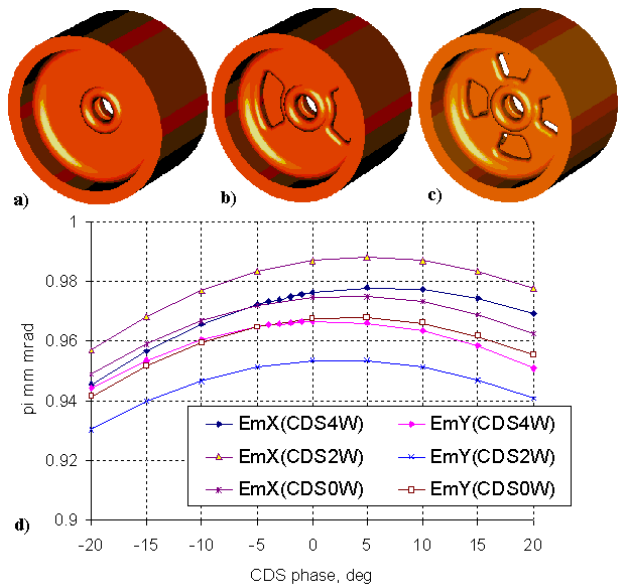

Figure 1: Top - the structure options for BD investigations, a) - axial symmetrical (CDS0W), b) - with two (CDS2W) and c) with four coupling windows. Bottom - d) the transverse rms beam emittance for different CDS options.

The cavity should provide the maximal energy gain for the maximal gradient $E_0T = 14\frac{MV}{m}$ with input rf power $P_i = 8.6MW$ and the structure effective shunt impedance Z_e should be reasonably optimized. The CDS structure [3], which combines improved coupling coefficient k_c, high Z_e value and small dimensions, is chosen. The options with two (CDS2W), Fig. 1b, and four (CDS4W), Fig. 1c, were considered. The axially symmetric option (CDS0W), Fig. 1a, is used as a reference. The moderate, not maximal possible, k_c values, $k_c^{2W} = 9.55\%$ and $k_c^{4W} = 7.2\%$, are chosen to obtain higher Z_e values, which are $Z_e^{2W} = 0.995Z_e^{0W}$ and $Z_e^{4W} = 1.03Z_e^{0W}$ (calculated values). To have higher Z_e value, the coupling windows edges - the place of maximal rf current density - are rounded. It leads to higher sensitivity of k_c value on win-

dows dimensions (and rounding radius) deviations, but we consider the achieved Z_e rise $\approx 5\%$ as more important.
The emittance perturbation by the cavity should be minimal. The beam dynamics simulations, taking into account space charge and real 3D fields maps, have performed by using ASTRA code [4]. The plots of transverse rms emittance as the functions of the phase difference between rf gun and CDS booster are shown in Fig. 1d. The visible quadruple addition in the magnetic field distribution near axis was founded for CDS2W option. Nevertheless, for small nominal relativistic ($\gamma > 10$) beams the difference in rms emittance between different CDS option is very small and beam dynamics requirements is not a point for the structure option definition.
The CDS2W option is more simple for construction, but due to:
- higher shunt impedance value;
- higher vacuum conductivity;
- more uniform field distribution in the aperture;
- more effective cooling circuit,
the CDS4W option has been adopted for the booster cavity.

CAVITY DESIGN

The cavity general view is shown in Fig. 2. The cavity has 11 regular CDS4W cells, rf coupler cell and two end cells. Each regular cell has 8 bind holes for frequency tuning after cavity final brazing by wall deformation.
Two rf probes (Fig. 2 - 4) are intended for direct rf phase

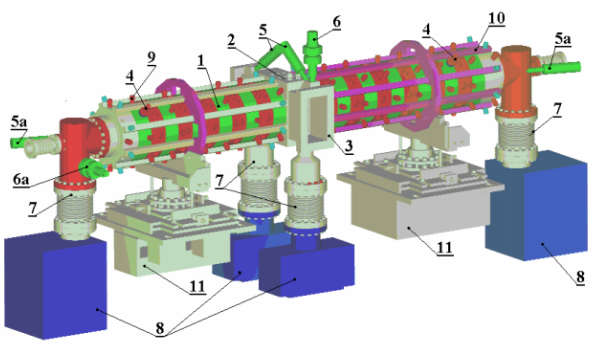

Figure 2: Booster cavity. 1 - regular cells, 2 - rf coupler cell, 3 - rf connecting flanges, 5 - photo multipliers, 5a - reserve photo multipliers, 6 - vacuum gauge, 6a- reserve vacuum gauge, 7 - pumping tubes with bellows, 8 - ion pumps, 9 - internal cooling circuit outlets, 10 - outer cooling circuit, 11 - support and adjuctment.

measurements in the cavity. As shows the rf gun experience, the Photo-Multiplier (PM) is the mostly fast and sensitive sensor to detect sparking and electric breakdowns in the rf gun cavity. Two PMs, one for each ceramic window, are foreseen in the rf coupler cell, Fig. 2 - 5. The CDS structure is not so transparent optically, as rf gun cavity. Two additional PMs are foreseen, for safety, at the cavity ends (Fig. 2 - 5a) - may be a problems, related to X-rays flux along the cavity axis.

RF coupler

RF coupler cell (Fig. 2 -2)is the most complicated part of the cavity and comprises a lot of contradictory requirements. The cavity will be driven with standard TESLA $10MW$ klystron, which is designed with two output windows. Due to a lot of reasons, the symmetrical rf coupler, Fig. 3, is adopted for CDS booster. Such coupler provides minimized oqtupole field perturbations. One half of the total rf power ($\approx 4.3MW$) will be transmitted through each coupler shoulder, allowing the applications of well tested $5MW$ ceramic rf windows. To minimize the electric field value at matching slots, the inductive type slots (Fig. 3 - 2) are chosen. The slots rounding, together with slots cooling, is foreseen to reduce the maximal rf current density and keep the surface temperature within limits $T_{max} < 45C^o$. The preliminary estimations for matching slots dimension were done following [5].
To meet requirements of matching and frequency tuning,

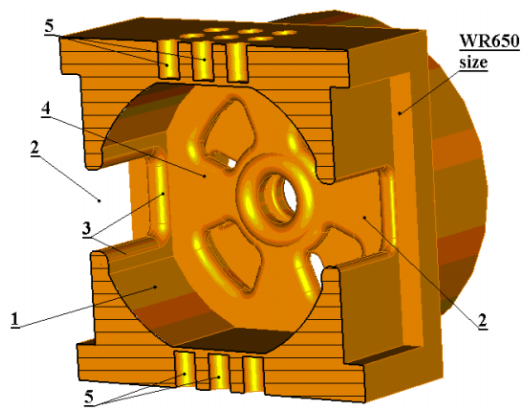

Figure 3: Symmetrical rf coupler. 1 - rf coupler cell, 2 - matching slots, 3 - rounding, 4 - diaphragm, 5 - blind holes.

reasonable construction, the rf coupler cell has a simplified shape (Fig. 3 - 1) with Z_e value $\approx 10\%$ lower as compared to regular CDS4W cells. Straight plates are foreseen for matching slots placing, Fig. 3 - 2, to simplify matching condition tuning, and for operating frequency tuning. Preliminary frequency tuning, before the cell brazing, is foreseen by material removal from straight parts. For fine narrow range frequency tuning after cavity brazing, 18 blind holes (Fig. 3 - 5) are used for reversible ($\pm\delta f_a$) tuners, developed and tested at the PITZ rf gun.

Pumping and cooling circuits

The own vacuum conductivity of the CDS4W structure is estimated as $\approx 300\frac{l}{sec}$ with main contribution due to coupling windows configuration. Four pumping ports are foreseen in the cavity (Fig 2 - 7, 8) - at the each cavity end (with Varian Vacion 150 pumps) and two in the middle of

the cavity - through rf grids in the waveguide shoulders of rf coupler - with Vacion 75 pumps. To improve the vacuum conductivity of the end cells, four narrow radial slots are in the end wall, simultaneously compensating partially the oqtupole field perturbation from the coupling windows at opposite wall of the end cells.
Assuming the out-gassing rate $q_g \approx 7 \cdot 10^{-11} \frac{Torr \cdot l}{sec}$ after cavity rf conditioning, the maximal residual gas pressure is expected as $\approx 8 \cdot 10^{-9} Torr$. This pumping scheme has a good reliability and the maximal pressure $\approx 1 \cdot 10^{-7} Torr$ is expected even for simultaneous failure of two pumps.
The residual pressure value can be estimated by measuring the pumps currents. Additionally one vacuum gauge is foreseen in rf coupler shoulder (Fig. 2 - 6) for direct pressure measurement. Additional gauge, Fig. 2 - 6a, is recommended at the cavity end, closer to rf gun (vacuum requirements for rf gun are more severe).
The maximal average rf power, dissipated in the cavity, is $38.7kW$, or $\approx 2.8kW$ per structure period. To keep the surface temperature reasonably low, both drift tube region, and outer wall cooling are required. The cooling scheme (Fig. 4a) has two circuits - for for regular cells webs internal cooling, Fig. 4a - 1, and for outer one, Fig. 4a -2. Inside each circuit several channels are connected in series in groups and groups are connected in parallel. The flow velocities in circuits are chosen (and are in safe limits - $\approx 1.8 \frac{m}{sec}$ and $\approx 2.1 \frac{m}{sec}$) to have the same temperature rise ($\approx 7C^o$), providing the most efficient conditions for cavity cooling. The thermal-stress analysis has been performed following [6]. The expected temperature distribution at the cell surface for maximal power, assuming the input water temperature $30C^o$, is shown in Fig. 4b, corresponding to frequencies shifts $\approx -270kHz$ for the operating mode and $\approx -105kHz$ for the coupling one, taking into account the cooling water temperature rise. The equivalent cavity temperature increasing, with respect input water temperature, is $\approx 13C^o$.

For the adopted cooling scheme the maximal internal

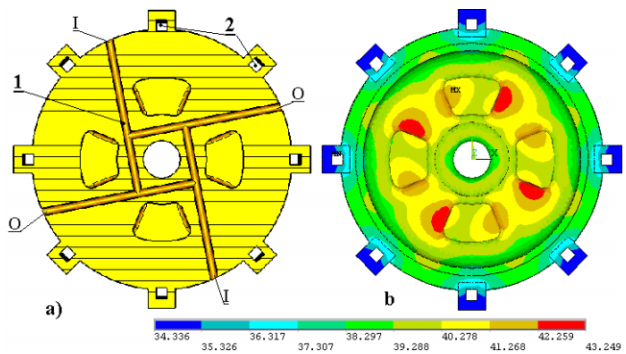

Figure 4: The cooling scheme (a) and temperature distributon (b) for regular cells. 1 - internal channels, 2 - external circuit.

stress, due to non uniform cells rf heating, are well inside safe limit - three times less than yield stress for OFC copper.

CAVITY TECHNOLOGY

For higher operational reliability the cavity is designed as the totally brazed device. RF contacts with vacuum sealing are used just at the flange (Fig. 2 - 3) for connection with $5MW$ rf ceramic input windows. This case we use the same flange design as tested at rf gun cavity.
The standard solution - one structure period consists from two half-cells - is adopted for regular cells. The cavity material is the OFC copper Class 1. For higher vacuum reliability the cooling circuits design has been performed to avoid all 'water - vacuum' brazed joints. it is the reason for non symmetric internal cooling channels scheme, Fig. 4a.
The surface roughness is specified as $R_a \sim 0.1 \mu km$ at the drift tube noses, to decrease the possible dark current field emission. For lathe treated parts of the cell surface the requirements $R_a \sim 0.2 \mu km$ and for milling reated parts (coupling windows) - $R_a \leq 0.4 \mu km$. With such requirements to the surface roughness for the totally brazed cavity after rf tuning we expect the cavity quality factor 85% from the calculated one.
The tolerances for cell dimensions were fixed following to the procedure [7] to have the relative rms field deviation $\sigma_E \leq 1\%$. The booster cavity is not too long and coupling coefficient deviations define mainly σ_E value. Both the requested tolerances $\pm(20 \div 50) \mu km$ and the surface roughness are not a problem for present technology.
The cavity will be constructed by DESY Hamburg in cooperation with industry. The construction begins now with the plan to have the conditioned cavity in the 2005 end.

ACKNOWLEGMENTS

The authors thank a lot of people both in INR and in DESY, both in Zeuthen and Hamburg, for valuable discussions, comments, proposals and support of this development.

REFERENCES

[1] A. Oppelt et al., Future plans at the Photo Injector Test Facility at DESY Zeuthen. Proc. of the 2003 FEL Conference, 18-23 September, Tsukuba, Japan, 2003

[2] K. Flottmann, V. Paramonov (ed.) Conceptual design of a positron injector for the TESLA linear collider. TESLA report 2000-12, Hamburg, DESY, 2000.

[3] V.V. Paramonov, The Cut Disk Structure for High Energy Linacs, Pros. 1997 PAC, v.3, p. 2962. 1998.

[4] K. Floettmann. ASTRA user guide, `www.desy.de/~mpflo/ASTRA_documentation`

[5] S. Kurennoy, L. Young. RF coupler for high-power CW FEL photoinjector. Proc. of the 2003 PAC, p. 3515, 2003

[6] S.C. Joshi, V.Paramonov et. al., The complete 3D coupled RF-Thermal-Structural-RF analysis procedure for a normal conduction accelerating structure for high intensity hadron linac. Proc. of the 2002 Linac Conference, p. 218, 2003

[7] V. Paramonov, A. Skasyrskaya. The technique for the numerical tolerances estimations. THP90, this Conference.

DEVELOPMENT OF ADAPTIVE FEEDBACK CONTROL SYSTEM OF BOTH SPATIAL AND TEMPORAL BEAM SHAPING FOR UV-LASER LIGHT SOURCE FOR RF GUN

H. Tomizawa[1], H. Dewa[1], T. Taniuchi[1], A. Mizuno[1], T. Asaka[1], K. Yanagida[1], S. Suzuki[1], T. Kobayashi[1], H. Hanaki[1], and F. Matsui[2],
Accelerator Division, Japan Synchrotron Radiation Research Institute (SPring-8),
1-1-1 Kouto, Mikazuki-cho, Sayo-gun, Hyogo 679-5198, Japan[1]
Creative & Advanced Research Department, Industrial Technology Centre of Fukui Prefecture,
61 Kawaiwashiduka-cho, Fukui City 910-0102, Japan[2]

Abstract

We have been developing a stable and highly qualified UV-laser pulse as a light source for the rf gun, which is a potential injector for future light sources. Our gun cavity is a single-cell pillbox, and the copper inner wall is used as a photo cathode. At present, the short pulse energy stability of laser has been improved, with a reduction to 1.3~1.5% (rms) for third harmonic generation.

In this improvement we only passively stabilized the system. We considered environmental controls in the clean room to reduce optical damage accidents and constructed a new humidity-controlled clean room in 2003. We then re-installed the entire laser system in this room in 2004. The relative humidity of this new clean room at room temperature is in the region of 50~60%, with a stability less than 2% (peak-to-peak). On the other hand, the ideal spatial and temporal profiles of a shot-by-shot single-laser pulse are essential in order to suppress the emittance growth of the electron beam from an rf gun.

This laser-shaping project has proceeded in two steps since its inception in 2002. In the first successful test run in 2002, with a microlens array as a simple spatial shaper, we obtained a minimum emittance value of 2π mm•mrad with a beam energy of 3.1 MeV, holding its charge to 0.1 nC/bunch. In the next test run in 2004, we prepared a deformable mirror for spatial shaping and a spatial light modulator based on fused-silica plates for temporal shaping. We are applying both types of adaptive optics to automatically shape both the spatial and temporal UV-laser profiles simultaneously with a feedback routine. We report here the principle and developing process of our laser beam quality control system.

INTRODUCTION

We have been developing a photo-cathode rf gun [1] as a highly qualified electron beam source to achieve future X-ray light sources (FEL (free electron laser), Compton back scattering, etc.) since 1996 in a test facility at the SPring-8 site. Future X-ray light sources will require an electron beam source with a low emittance of ~1 π mm•mrad. Our development of this type of gun is oriented toward a long-lived stable system for user experiments. It is necessary for the copper cathode of the rf gun to have a UV-laser pulse with a pulse width of ~10 ps and a photon energy of ~4 eV.

Since we started to develop the test facility, two issues regarding the laser light source have appeared. One is the energy stability of the UV-laser light source. The other concerns the spatial and temporal laser profiles. The quality of the laser beam is essential to stabilization and generation of a low-emittance electron beam.

We passively stabilized the system. Environmental controls were considered in the clean room to reduce optical damage accidents, and a new humidity-controlled clean room was constructed (relative humidity at room temperature: 50~60%). The pumping source of the laser system was stabilized with a temperature-controlled base plate. As a result of the passive stabilization, the pulse energy stability of the laser has been improved with a reduction to 1.3~1.5% (rms; 10 pps; 10000 shots) for third harmonic generation (THG).

On the other hand, optimal spatial and temporal profiles of a shot-by-shot single laser pulse are essential in order to suppress the emittance growth of the electron beam from a photo-cathode rf gun. This laser-shaping project has proceeded in two steps since its start in 2002. Specifically, higher stability of the pulse energy is required and homogeneous Silk-hat (cylindrical flattop) spatial and rectangular temporal profiles of the UV-laser light source must be generated.

In the first spatial shaping test run, we shaped the laser spatial profiles with a microlens array. Consequently, the horizontal emittance was significantly improved from 6 to 2 π mm•mrad at a beam charge of 0.1 nC/bunch. This experimental data represents a new record for the minimum emittance of an electron beam from a single-cell-cavity rf gun [2].

In the next test run, we applied both types of adaptive optics to automatically shape both the spatial and temporal UV-laser profiles with a feedback routine simultaneously. We prepared a deformable mirror for spatial shaping and a spatial light modulator based on fused-silica plates for temporal shaping. Both adaptive optics were installed in the UV-laser optical transport. The development process of our beam quality control systems are reviewed in the remainder of this paper.

EXPERIMENTAL SET-UP

Configuration of CPA - Ti: Sa Laser System

The UV-laser light source for the rf gun consists of a mirror-dispersion-controlled Ti: Sapphire laser oscillator (Femtolasers Produktions GmbH) operated at a repetition rate of 89.25 MHz, a chirped pulse amplification system (Thales Lasers Co., Ltd.) operated at a repetition rate of 10 Hz, and a third harmonic generator system. The fundamental laser oscillates at a central wavelength of 790 nm with a spectral bandwidth (FWHM (full-width at half maximum)) of 50 nm. The pulse energy of the fundamental laser is 30 to 60 mJ/pulse after the multi-pass amplifier. After the third harmonic generation (central wavelength: 263 nm), the laser pulse energy is 200 to 400 μJ/pulse with a repetition rate of 10 Hz. The best pulse energy stability of the original laser system was 2% for generation of the fundamental harmonic and 3% for the third harmonic. This original system cannot keep the laser spatial profile homogeneous for long periods of operation due to damage and misalignments.

Environmental Control System for the Laser

In principle, we planned only passive stabilization of the system. We considered environmental controls in the clean room to reduce optical damage accidents and then constructed a new humidity-controlled clean room in 2003. The relative humidity of the new clean room at room temperature is in the region of 50~60% with a stability of less than 2% (p-p). The temperature was kept constant at 21 ℃ (±0.3 ℃) on the laser table. Also, the laser pumping sources are stabilised with a water-cooled base plate. As a result, the short pulse energy stability of laser has been improved, with a reduction to 1.3~1.5% (rms; 10 pps; 10000 shots) at the THG (263 nm).

At the present state of development, long-term stability depends only on the stability of mode locking at the oscillator laser. If the oscillator is stable without out-of-mode locking, the overall laser system can be stable for long-term operation with short pulse energy stability as mentioned above.

Figure 1: New humidity-controlled laser clean room.

Tested Optics for Laser-Profile Shaping

Microlens array as a spatial homogenizer - This laser system produces an inhomogeneous spatial profile. Therefore, we used several microlens arrays as a homogenizer for the first test run [2]. This microlens array is a collection of small hexagonal convex lenses with a pitch of 250 μm. The transmission of this optical array is about 80% in the ultraviolet region. This makes it possible to shape any laser spatial profile as a Silk-hat (cylindrical flattop) by combining with a convex lens. The main difficulty in utilizing this optical system is the manner in which the homogenized laser profile transports toward the cathode surface while focusing. Even if the entire wave front of the laser does not reach the cathode at the same time, the laser spot on the surface should be within the depth of focus.

Deformable mirror and SLM - Consequently, we used a deformable mirror (left upper in Figure 2) as a spatial shaper for the second test run. This deformable mirror consists of an aluminium-coated, multilayer silicon nitride membrane and 59 small hexagonal mirror-actuators behind the reflective membrane with a center-to-center distance between the actuators of 1.75 mm. The outermost layer of the reflective membrane is protected with an MgF_2 coating to keep reflectivity at about 70% in the ultraviolet region. Adjusting the voltages between the control electrodes on the boundary actuators performs fine adjustment of each mirror-actuator. The adjustable region of the control voltages is between 0 and 255 V with a step of 1 V. This makes it possible to shape any laser spatial profile with a total forming possibility of $256^{59}(\sim 10^{110})$. However, such a high adjustability makes manual as well as simple algorithm adjustment impossible. Thus, this spatial shaping method needs a sophisticated algorithm. One concept for a sophisticated program based on this genetic algorithm for a deformable mirror has been developed through a joint project [3].

Figure 2: Adaptive-optics complex for shaping both spatial and temporal laser profiles.

To control the temporal parameters of the laser pulses, we are preparing a programmable pulse shaping system in the fundamental wavelength region using a spatial light modulator (SLM) based on fused-silica plates (Cyber Laser Inc.: right in Figure 2). The temporal profile is measured with a streak camera.

We installed a deformable mirror and an SLM in the UV-laser transport while developing a sophisticated program to examine the spatial and temporal shaping ability of inhomogeneous original UV-laser profiles.

EXPERIMENTAL RESULTS FOR SPATIAL SHAPING

Results and Effects of Spatial Shaping with Microlens Array (In First Test Run)

The laser spatial profile without homogenization is shown on the left-hand side in Figure 3. The profile was spatially shaped by a microlens array as a quasi-Silk-hat profile (see the right-hand side of Figure 3). These profiles were measured with a laser beam profiler (Spiricon Inc., LBA300-PC). By spatially homogenizing, the emittance improved from 3.3 to 2.3 π mm•mrad at a beam charge of 0.1 nC/bunch. While it was not perfectly Silk-hat-shaped, laser profile was greatly improved.

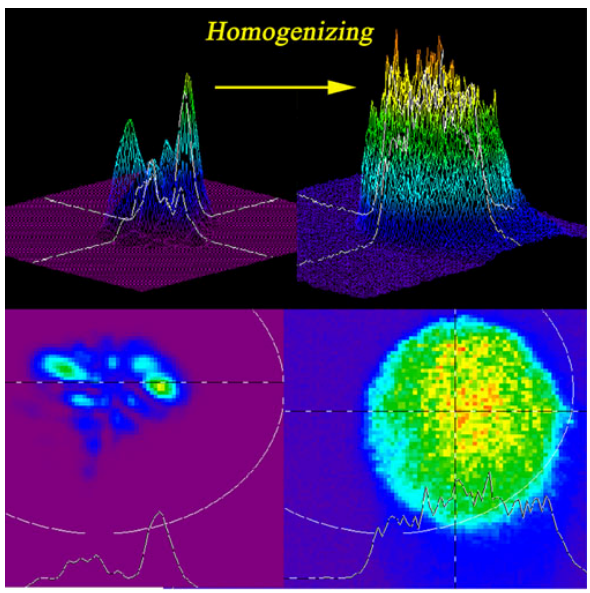

Figure 3: Homogenization results with microlens array.

Result of Spatial Shaping with Deformable Mirror (In Second Test Run)

The laser spatial profile was shaped manually for test purposes with the deformable mirror. The profile was spatially shaped by a deformable mirror as a quasi-Gaussian profile (Figure 4). This profile was also measured with the laser beam profiler. While the laser spatial profile was improved by this shaping technique, it was far from Silk-hat-shaped in this test. For perfectly Silk-hat-shaping, the amount of deformation possible with this mirror is not large enough.

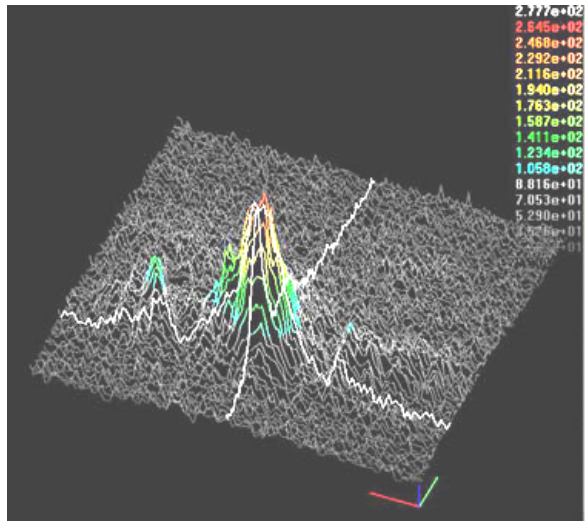

Figure 4: Spatial shaping result with a deformable mirror.

FUTURE PLANS AND DISCUSSION

Comparing the results of the spatial profiles between the two different test runs shown in Figures 3 and 4, we can see that both spatial shaping methods were successful. Especially in the shaping with the microlens array, the horizontal emittance significantly improved from 6 to 2 π mm•mrad at a beam charge of 0.1 nC/bunch. However, the amount of deformation with this type of deformable mirror (electrostatic actuator) is not large enough. For perfect Silk-hat-shaping, it is necessary to combine the method with aspheric lenses. A sophisticated program to control the spatial and temporal shaping is under development. However, the shot-by-shot optimization of each laser pulse profile can be difficult. Thus, the laser system should first be passively stabilized by environmental controls. At present, the short pulse energy stability of the laser has been improved to 1.3~1.5% at the THG (263 nm). This stability is sufficient for shot-by-shot automatic optimization with adaptive optics. The long-term stability depends only on the stability of mode locking of the oscillator laser.

In the future, we intend to shape both profiles of each electron beam bunch generated by each UV-laser pulse. An OTR monitor will be used to measure the electron beam profiles. The profile data will be used for the feedback routine to automatically optimize the electron beam pulse profiles. With this procedure, ideal electron beam profiles can be generated with compensation for some of the optical distortions and the inhomogeneous distribution of the quantum efficiency of a cathode.

REFERENCES

[1] T. Taniuchi et al., Proc. of 18th. Int. Free Electron Laser Conf., Vol. 2, 137, Rome, 1996.
[2] H. Tomizawa et al., Proceedings of the 2002 European Particle Accelerator Conference, 1819, Paris, July 2002.
[3] T. Itatani, AIST Today, p. 18, April 2003.

ANALYSIS OF THE QUALIFICATION-TESTS PERFORMANCE OF THE SUPERCONDUCTING CAVITIES FOR THE SNS LINAC*

J. R. Delayen#, J. Mammosser, J. Ozelis, Thomas Jefferson National Accelerator Facility,
12000 Jefferson Avenue, Newport News, VA 23606, USA

Abstract

Thomas Jefferson National Accelerating Facility (Jefferson Lab) is producing superconducting radio frequency (SRF) cryomodules for the Spallation Neutron Source (SNS) cold linac. This consists of 11 medium-beta (0.61) cryomodules of 3 cavities each, and 12 high-beta (0.81) cryomodules of 4 cavities each. Before assembly into cavity strings the cavities undergo individual qualification tests in a vertical cryostat (VTA). In this paper we analyze the performance of the cavities during these qualification tests, and attempt to correlate this performance with cleaning, assembly, and testing procedures. We also compare VTA performance with performance in completed cryomodules.

CAVITY AND CRYOMODULE PERFORMANCE ANALYSIS TOOLS

Jefferson Lab has developed a web-based system that integrates commercial database, data analysis, document archiving and retrieval, and user interface software into a coherent knowledge management product called *Pansophy*. *Pansophy* provides key tools for the successful pursuit of major projects such as accelerator system development and construction by offering elements of process and procedure control, data capture and review, and data mining and analysis. *Pansophy* is being used in Jefferson Lab's SNS superconducting linac construction effort as a means for structuring and implementing the QA program, for process control and tracking, and for cavity and cryomodule test data capture and analysis.

Using *Pansophy*, critical process and performance parameters for individual cavities and cryomodules can be entered in the underlying database, in a systematic fashion, by using a set of "travelers" that provide process control and data input. Typical examples of these data include cavity dimensional data, cavity rinse time, rinse water particulate count, BCP etch rate, cavity performance (gradient, Q_o, radiation onset), and cryomodule performance (gradient, Q_o, radiation onset, tuner performance, thermal behavior, probe couplings, etc.).

* Work supported by the U.S. Department of Energy under contracts DE-AC05-84-ER40150 and DE-AC05-00-OR22725.
#delayen@jlab.org

These data can be analyzed and mined using various standard and user-defined queries. These query tools allow for straightforward investigation of correlations and dependencies between cavity performance parameters and cavity processing variables. For example, the onset of field emission during vertical cavity tests can be investigated with respect to High Pressure Rinse (HPR) water particulate level, with the hope that any observed correlations can be utilized as predictors of cavity performance or water system integrity. Likewise, comparisons between cavity performance in vertical tests and in completed cryomodules can be compared and assessed. The results of such queries can be downloaded to a spreadsheet, or saved as a text file to be used with other analysis programs.

Cavity and Cryomodule *Performance Overview* pages have been added to *Pansophy*. They provide "Single-click" performance summary of cavities tested in the VTA (along with downloadable data and plots), and cryomodules tested in CMTF. An example for such a page for a cavity is shown in Fig.1.

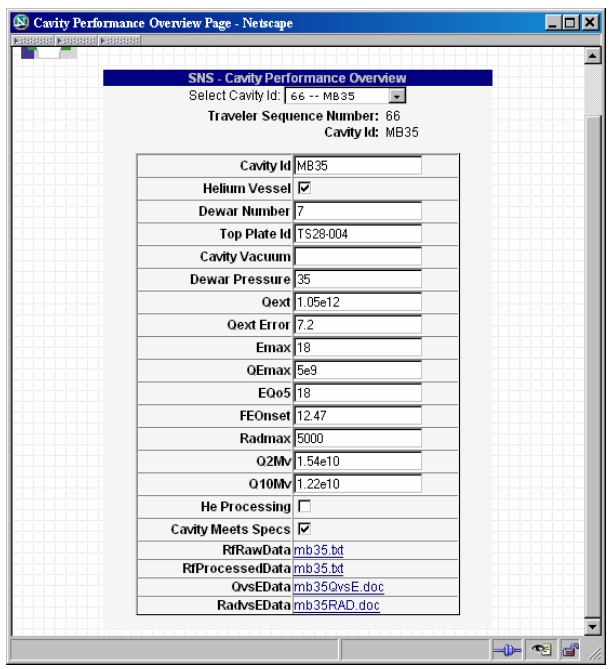

Figure 1: *Performance Overview* page provided by *Pansophy* summarizing processing, testing, and performance data on a cavity.

ANALYSIS OF TEST RESULTS

The following figures show a summary of the experimental results obtained to-date during the qualification tests of the medium-β and high-β cavities for SNS.

Figure 2 shows, chronologically, the accelerating gradient at the specification Q of 5 x 10^9. The red triangles are for the medium-β and the blue squares are for the high-β cavities. The red and blue dashed lines are the specification gradients corresponding to peak surface fields of 27.5 MV/m for the medium-β and 35 MV/m for the high-β. Figure 3 shows the Q_0 at the design gradients of 10.1 MV/m for the medium-β and 15.6 MV/m for the high-β. The dashed line is the specification of 5 10^9.

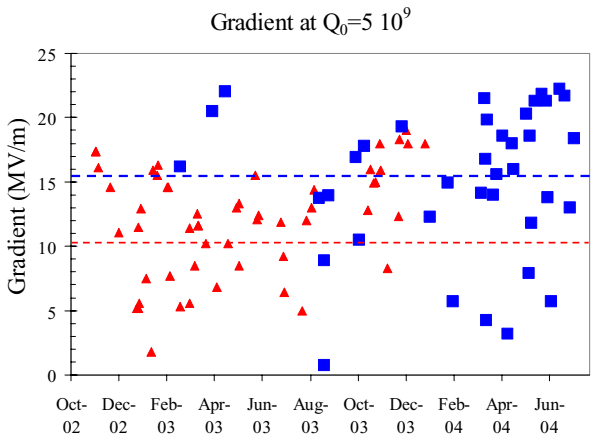

Figure 2: Gradient of SNS medium (triangles) and high (squares) β cavities measured at the Q_o specification of 5 x 10^9 during all vertical cavity tests at 2.1 K. The lower (upper) curve represents the gradient specifications for the medium (high) β cavities, respectively.

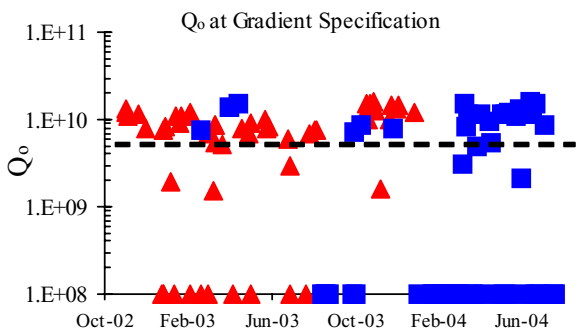

Figure 3: Cavity Q_o measured at the respective gradient specification for SNS medium- (triangles) and high- (squares) β cavities. Cavities that did not meet the required gradient specification are shown with a Q_o of 1 x 10^8.

Figure 4 and 5 show for the medium-β and high-β, respectively, the number of tests in the vertical dewar required to qualify a particular cavity, ordered chronologically by date of the first test. The effect of process improvements initiated during the medium β cavity production cycle can be seen in Figure 4, by the decline in number of tests required. These process improvements were maintained for the high β cavity production cycle.

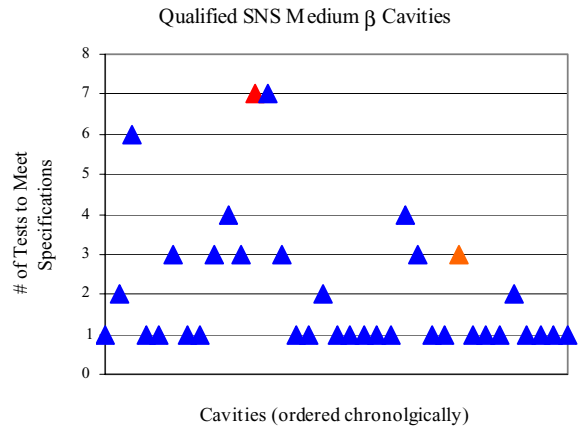

Figure 4: Number of vertical dewar tests required to reach acceptable cavity performance levels for each SNS medium-β cavity, ordered chronologically by date of 1st test.

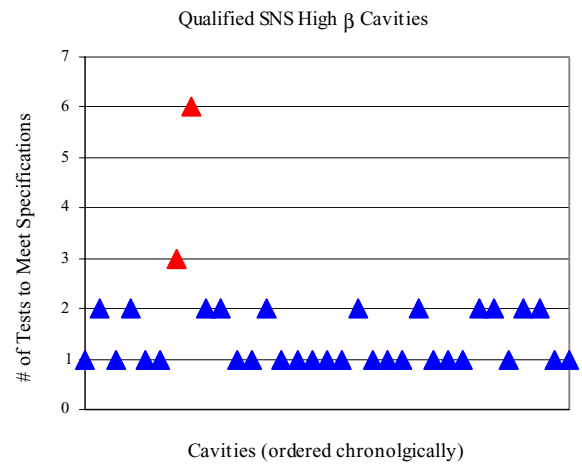

Figure 5: Number of vertical dewar tests required to reach acceptable cavity performance levels for each SNS high-β cavity, ordered chronologically by date of 1st test. The cavities denoted in red were used for additional procedure tests.

Figure 6 compares the performance of the medium-β cavities in the VTA and in the cryomodules. No performance degradation was observed between the former and the latter.

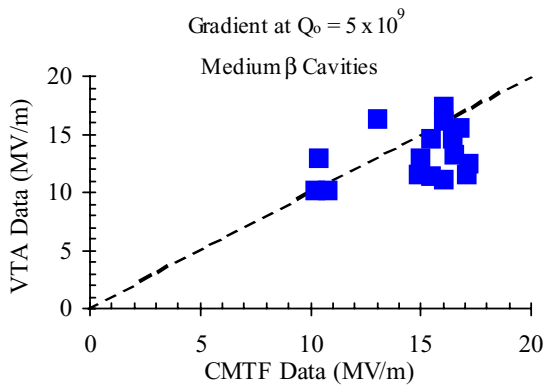

Figure 6: Comparison of measured cavity gradient at the Q_o specification of 5 x 10^9 for the SNS medium-β cavities, as measured in CW mode during vertical dewar tests and in pulsed mode in the completed cryomodule.

Figure 7 shows an attempt at finding a correlation between the performance of a cavity and the number of particulate in the water used during the high-pressure rinsing. While performance still varies significantly between tests, to-date no obvious correlation has been found between performance and any of the measured processing parameters.

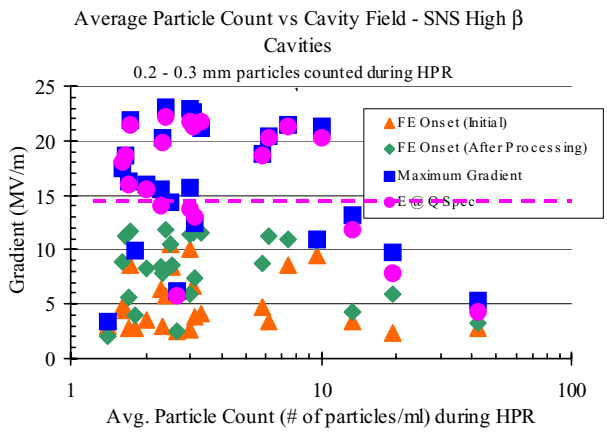

Figure 7: Effect of particulate density in the water during high-pressure rinsing on various cavity fields for the SNS high-β cavities.

MULTIPACTING IN HIGH-β CAVITIES

To date, thirty four of the production high beta cavities were RF tested at 2.1 K. Analysis of the RF test data for these cavities shows that thirty one of them exhibited multipacting (MP) during testing and only four of these showed that the barrier was completely processed away during the test. Two cavities did not show any multipacting while one cavity failed to reach the gradient typical for MP onset. One of the two cavities that did not show multipacting was electropolished.

There originally was a concern that lower-frequency, intermediate-velocity elliptical structures might be more prone to multipacting than the higher-frequency, high-velocity ones. For this reason, simulations were performed and prototypes were tested. No obvious MP behavior was observed in the prototype cavities and in the production medium-β cavities.

Simulations were performed on various cavity shapes including the SNS high-β by W. Hartung [3] which showed that MP in these cavity structures could occur at gradients of 10 to 13.7 MV/m with electron impact energies up to 31 eV. The analysis of vertical test data on high-β cavities shows that the onset occurred from 9.5 to 18.6 MV/m with a mean of 11.7 MV/m, and a standard deviation of 1.8 MV/m. Onset of multipacting was defined as the gradient at which a sudden drop in Q-value was first observed. Typical results are shown in Fig. 8.

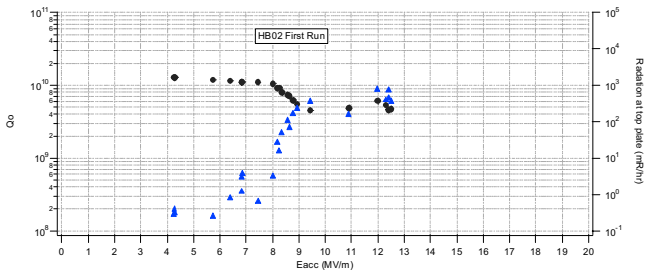

Figure 8: Experimental results on a high-β cavity showing typical multipacting behavior. Black circles show the Q and the blue triangles shown the radiation level measured outside the dewar.

One possible mechanism contributing to the spread in the onset of the MP could be the condition of the niobium surface after processing and evacuation. It is known that cleanliness and level of absorbates present during testing can influence secondary electron yield of the surface.

Simulations of the medium beta cavity shape also showed the potential for multipacting between 10 and 13.7 MV/m with impact energies up to 28 eV. Multipacting was not observed during any of the medium-β production RF tests. The fact that the impact energy in the high-β structures was higher than in the medium-β structures could explain why MP was frequently observed in the former but never in the latter.

REFERENCES

[1] C. Reece, V. Bookwalter, and B. Madre, "A System for Managing Critical Knowledge for Accelerator Subsystems: Pansophy," *Proc. 2001 Part. Acc. Conf.*, Chicago, June 2001.

[2] V. Bookwalter, B. Madre, J. P. Ozelis, C. Reece, "Utilization of Integrated Process Control, Data Capture, and Data Analysis in Construction of Accelerator Systems," *Proc. 2003 Part. Acc. Conf.*, Portland, OR (USA) May 2003.

[3] W. Hartung *et al.*, Studies of Multipacting in Medium Axisymmetric Cavities for Medium-Velocity Beams", *Proc. 2001 SRF Workshop*, Tsukuba, Japan, September 2001

SRF CAVITY AND MATERIALS R&D AT FERMILAB *

P. Bauer, L. Bellantoni#, T. Berenc, C. Boffo, R. Carcagno, C. Chapman, H. Edwards, L. Elementi, M. Foley, E. Hahn, D. Hicks, T. Khabiboulline, D. Mitchell, A. Rowe, N. Solyak, Y. Terechkine, FNAL, Batavia, IL 60510, USA
M. Jewell, D. Larbalestier, P. Lee, A. Gurevich, A. Polyanskii, A. Squitieri, Applied Superconductivity Center, University of Wisconsin-Madison, WI 53706, USA

Abstract

Fermilab has been steadily developing its SRF cavity expertise, infrastructure and technology base. We particularly emphasize here recent developments in understanding basic material properties and developing a new chemistry treatment facility.

INTRODUCTION

Two types of 3.9 GHz superconducting RF cavities are under development at FNAL for use in the upgraded A0 photo-injector facility. A TM_{110} mode cavity will provide streak capability for bunch slice diagnostics, and a TM_{010} mode cavity will provide linearization of the accelerating gradient before compression for better emittance. Fig. 1 shows the upgraded A0 facility beam line layout including the 3.9 GHz transverse deflecting and 3rd harmonic modules. The performance of recent prototype cavities is given in [1]. The use of a TM_{010} cavity for TESLA bunch compression is discussed in [2].

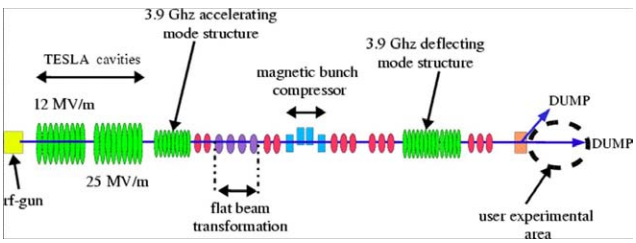

Figure 1: Upgraded A0 facility beam line layout.

CAVITY FABRICATION

We purchase RRR 300 Nb sheet from industry, cut disks via wire EDM, and stamp, coin, and machine them into cells. Prior to forming, the disks are inspected for imperfections and inclusions with an eddy current scanner. The eddy current scanning, which was formerly performed at DESY, is now done at FNAL with a scanner on loan from SNS. RRR measurements on select samples are performed to check if the material meets the specifications. The latest batch of material received from Wah Chang achieves a high RRR~450. Electron beam welding is performed near FNAL at Sciaky Inc. Our vacuum bake facility (1200°C) is used for annealing and hydrogen removal. 1:1:2 BCP acid etching can be done in-house for cavity parts. The fully assembled cavities, however, have been kindly etched for us by Jlab. We are in the process of commissioning a small manual acid etch facility operated jointly with K. Shephard, M. Kelly and M. Kedzie at Argonne National Lab. Additionally, a new, larger, remotely controlled, semi-automatic chemistry facility for FNAL cavities is under development. After commissioning at FNAL, the facility will be transferred to ANL to become a part of the ANL-FNAL Surface Treatment Facility, located at ANL. Recent developments regarding this new chemistry facility are going to be discussed in further detail below. A high pressure rinse with 18 MΩ H_20 in a class 10 clean room can be done on-site. RF field flatness tunings are all performed on-site, as is mechanical 3-dimensional high resolution profilometry. We have contracted with Advanced Energy Systems in Medford, NY to fabricate two cavities, the first of which is currently in the welding stage.

*Supported by the U.S. Department of Energy.
#bellanto@fnal.gov

CHEMISTRY FACILITY

Chemical treatment with BCP is a well-established procedure that allows the removal of a mechanically damaged and chemically contaminated layer of Nb from the cavity surface. It is used several times during the cavity fabrication with varying thicknesses of Nb removed at each step.

Fig. 2 shows the full-scale mockup of the BCP facility at FNAL, where it is being tested with water. The facility will be installed in a ventilated leak-proof process compartment in order to provide acid containment in case of a spill. This facility is designed not only for 3.9 GHz cavities but also for treatment of the larger 9-cell, 1.3 GHz TESLA-type cavities, which require up to 250 liters of acid. Up to one TESLA-sized cavity a day can be processed. To maintain a precise control over the processing time, the cavity fill-time is required to be 1 minute or less. This requirement is met by elevating the gravity feed tank for acid and by using a large (50 mm) diameter filling pipe. The system operates in the pump-through mode with a minimum acid flow speed through the cavity of 1.1 liters/min. When a TESLA-type cavity is processed at a typical etching rate of 1 μm/min, the power required to keep the solution temperature constant (including heat loss) is about 1 kW. A 2 kW heat exchanger keeps the temperature of the acid at 15°C. For a 1 m^2 Nb surface area, about 15 liters of NO_2 are released each minute. Besides NO_2, there is also emission of NO, HNO_3 and HF – fumes that are considered dangerous pollutants. The facility is designed for air exchange and subsequent scrubbing at a rate of 700 m^3/h (200 l/sec).

The acid will be brought into the chemical isolation room in double-walled barrels (HDPE outside, Teflon

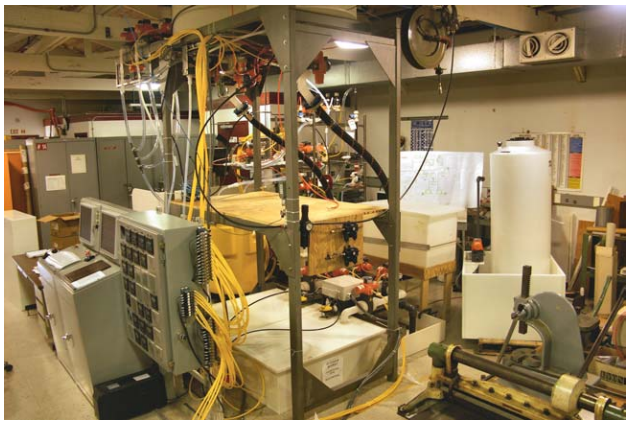

Figure 2: BCP chemistry facility assembly at FNAL.

inside) placed in DOT-approved over-packs (HDPE) and connected to the cooling and filling circuits. All the acid circulation circuits are confined to the interior of the chemical confinement room.

The acid mix in the barrel is cooled, and then transferred into the process tank where the BCP process starts. The inner and outer surfaces of the cavity are processed separately, by using different "protection jackets". Acid used for etching is collected and can be reused if the Nb concentration in the acid does not exceed 10 g/l. Rinse water is quite acidic and will be neutralized in an automated system. After acidity rinsing, the cavity is moved to an adjacent clean room for rinsing without the jacket, until a high resistivity is achieved in the outflow rinse water.

A semi-automated operating mode is used to control the different etch process steps. An interlock system prevents accidental or unauthorized access to the manual mode. Sensors provide all the relevant information about the status of the system at each stage of the process to a control system [3]. Temperature gauges measure both acid and coolant temperature, and a differential pressure gauge is used to measure the status of the acid filter. Resistivity meters are used as acid indicators to warn of spills due to equipment failure.

The process compartment is lined from the inside with PVC sheets and equipped with sealed doors to form a watertight container. Most of the critical components are provided with double containment vessels. Pieces of piping with joints and valves where acid is circulating for a long time are equipped with gutters to confine acid spills. In the case of a spill, acid is collected in a sump area with 250 liters capacity. It can be sensed by an appropriate gauge and pumped out before the room is rinsed with water and treated to neutralize remains of the spill.

MATERIAL STUDIES

Material studies are an important part of FNAL's SRF effort. The purpose of these studies is both to check the cavity manufacturing process and to understand the observed surface resistance and field-emission effects in the first prototypes of the transverse deflecting and 3rd harmonic cavities. In-house measurement capabilities now available include scanning electron microscopy, energy dispersion X-ray analysis, RRR measurements and eddy-current scanning. In addition, FNAL has a collaboration with the Applied Superconductivity Center at the University of Wisconsin-Madison, which has access to a wide variety of electron microscopes and surface analysis systems and where there is an extensive facility for testing superconducting materials. These are, just to mention the most important, SQUID magneto-meters, magneto-optics, and high precision transport measurements.

Microscopy and Grain Size

Microscopy studies are conducted on small samples subjected to the various steps of cavity fabrication. Fig. 3 shows high resolution images obtained on a sample prepared with our baseline processing. The major preparation steps consisted of a 100 µm BCP followed by an 800°C, 5 hour heating (in vacuum) and a final 20 µm etch. The surface appearance obtained is more or less consistent with that obtained with BCP in other labs [4]. Grain size measurements were performed on samples before and after heat-treatment. The (linear) grain size is typically 50 µm, changing only by a few percent during the heat treatment. Grains are much larger, on the scale of 1 mm, in the electron-beam welds at the iris and equator, with one micron deep V-grooves at the grain-boundaries (measured from SEM stereo pairs). It is well known that

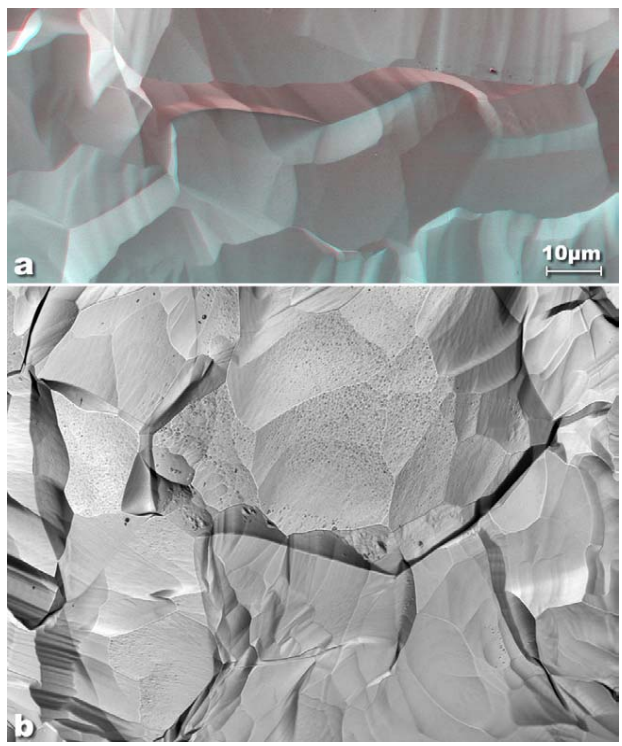

Figure 3: a) 3D red-blue anaglyph FESEM image and b) Laser Confocal Microscope (Olympus LEXT courtesy Erich Zeiss of Leeds Precision Instruments). Images at similar magnification of BCP etched surface representative of the FNAL cavities.

even smoother surfaces can be obtained with electro-polishing. FNAL is currently undertaking first steps in exploring the electro-polishing technology.

RRR Measurements

RRR studies are done to measure the impact of the cavity fabrication steps on the niobium purity. RRR measurement equipment has been developed over the last few years at FNAL [5]. Fig. 4 shows that the RRR of the Wah-Chang material used for the latest FNAL cavity prototypes is ~450 and remains unchanged throughout the etchings and heat treatments applied in the cavity production stages. The "after treatment" samples were etched ~100 µm with BCP, heat treated in vacuum (800°C, 5 hrs) and then lightly etched with BCP (~20 µm). The RRR is defined as the ratio of the sample resistance at room temperature to that at ~10 K (just above the transition point). There is a particular interest in the thermal properties of Nb in weld seams, because the magnetic field in TM_{110} mode cavities is sharply concentrated in the weld region. The RRR in welds was measured and, to within the 5% measurement accuracy, no particular change of RRR was found to occur.

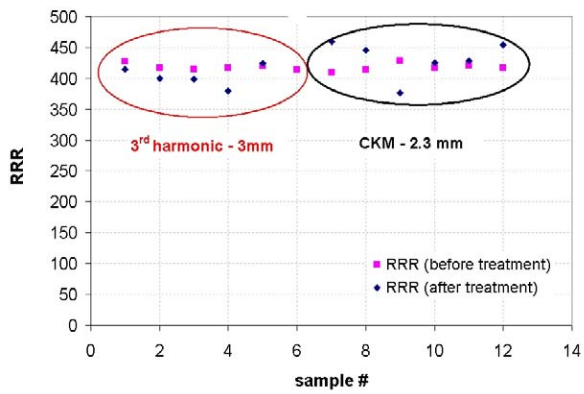

Figure 4: RRR for material used in the fabrication of prototype3rd harmonic and transverse deflecting cavities.

Magnetization Measurements

The measurement of DC magnetization provides, information about the annealing state of the material used for the cavities. Both FNAL and the University of Wisconsin have performed such measurements. Fig. 5 shows the magnetization measured at FNAL on a sample (made from a sheet bent into a cylinder), before and after an 800°C, 5 hrs heat treatment and BCP etching. The plot clearly shows a narrowing of the magnetization hysteresis, which is interpreted as the result of the removal of flux pinning sites due to the annealing. Note that in order to obtain the samples for the magnetization measurements the sheet was heavily cold-worked. Of course, the deep-drawing process used to form the 1/2 cell shapes for cavity manufacture is also a work-hardening process. Comparison to magnetization measurements

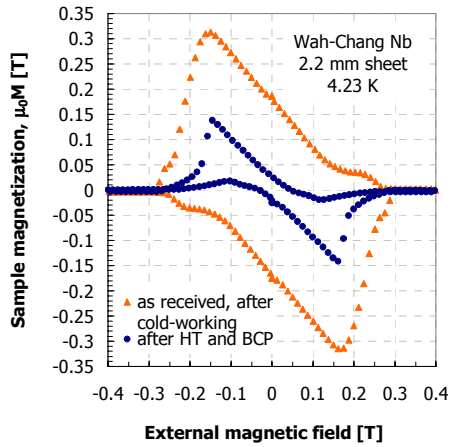

Figure 5: Magnetization of an "open" niobium cylinder with height 40 mm and diameter 16 mm at 4.2 K.

performed on similar material and following comparable treatments at the University of Hamburg show reasonable agreement [6]. The University of Wisconsin's magnetization measurements at 1.8 K revealed flux jumps.

Grain Boundary Experiments

FNAL in collaboration with the Applied Superconductivity Center at the University of Wisconsin is also involved in basic research on superconducting RF materials. We are investigating the effect of grain boundaries on the RF surface resistance, using a combination of magneto-optics and transport measurements [7]. Preliminary magneto-optical measurements on mm-size grain samples indicated preferential flux penetration through the grain-boundaries. This is an indication of depressed superconductivity in the grain boundaries. New experiments are on the way to measure the inter-grain critical current.

REFERENCES

[1] THP85, this conference.
[2] WE104, this conference; P. Piot and W. Decking, "A Modified Post-Damping Ring Bunch Compressor Beamline for the TESLA Linear Collider", FNAL TM-2235.
[3] C. Boffo, D. Connolly, L. Elementi, Y. Terechkine, "Control System for BCP Processing Facility at FNAL", SRF-03, DESY, Germany, Sept. 2003.
[4] X. Singer, "High Purity Niobium for Tesla Test Facility," Proc. Xth UHPM, Materiaux et Techniques 7-8-9 2003.
[5] P. Bauer, "RRR Measurements on Niobium for Superconducting RF Cavities at FNAL", SRF-03, DESY, Germany, Sept. 2003.
[6] S. Casalbuoni et al., "Surface Superconductivity in Niobium for Superconducting RF Cavities", TESLA report 2004-06.
[7] http://www.asc.wisc.edu/SCRF/

FIRST CRYOGENIC TESTS WITH JLAB'S NEW UPGRADE CAVITIES*

P. Kneisel, G. Ciovati, G.R. Myneni, G. Wu, Jefferson Lab, Newport News, VA 23606, USA
J. Sekutowicz, DESY, Notkestrasse 85, 22607 Hamburg, Germany
J. Halbritter, Forschungszentrum Karlsruhe, Karlsruhe, Germany

Abstract

Two types of 7-cell cavities have been developed for the upgrade of CEBAF to 12 GeV. The High Gradient type (HG) has been optimized with respect to the ratio of E_{peak}/E_{acc}. The Low Loss (LL) type has optimized shunt impedance and improved geometric factor. Each cavity type features four DESY–type coaxial Higher Order Mode (HOM) couplers and a waveguide input coupler. Design goals for these cavities have been set to E_{acc} = 20 MV/m with an intrinsic Q_o of $8\cdot10^9$ at 2.05 K. A niobium prototype of each cavity has been fabricated at JLab and both cavities have been evaluated at cryogenic temperatures after appropriate surface treatment. In addition, pressure sensitivity as well as Lorentz force detuning were evaluated. The damping of approximately 20 HOMs has been measured to verify the room temperature data. Several single cell cavities were tested in addition to multi cell cavities. We present in this contribution a summary of tests performed on the prototypes of the proposed cavities.

INTRODUCTION

The rationale for developing two different types of cavities for the upgrade of CEBAF to 12 GeV has been discussed in a previous paper [1] and will be repeated only briefly here. Typically, superconducting niobium cavities are limited in their high field performance by field emission. By optimizing the geometry, the ratio of the surface electric field E_{peak} to the accelerating field E_{acc} can be reduced for a given onset of field emission. The HG cavity has this ratio of E_{peak}/E_{acc}=1.89 making it less sensitive to the field emission phenomenon. A reduction in the cryogenic losses of a cavity can be achieved by maximizing the shunt impedance R/Q and the geometry factor G. These optimised parameters result in lower stored energy and wall losses at a given accelerating gradient compared to non-optimized cavity shapes. Given a fixed cryogenic capacity of the LHe plant higher end energies can be achieved in the CEBAF accelerator with such cavities (LL).

In Figure 1 the shapes of inner cells of both "upgrade" cavities developed at JLab are compared with the original cavities used at present in the accelerator. Table 1 lists their rf parameters.

CAVITY FABRICATION AND SURFACE TREATMENT

Several single cell cavities and one 7-cell cavity of each type were fabricated from high purity niobium with a RRR value of ~250 by the standard method of deep drawing of subcomponents and electron beam welding.

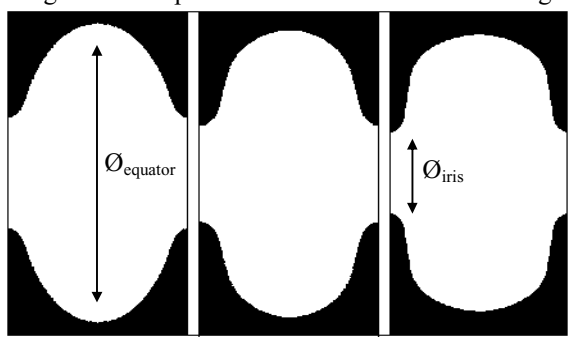

Figure 1: Geometry of the inner cells of the "original CEBAF" (OC) shape and the HG and LL shapes.

Table 1: Parameters of inner cells

Parameter		OC	HG	LL
$Ø_{equator}$	[mm]	187.0	180.5	174.0
$Ø_{iris}$	[mm]	70.0	61.4	53.0
k_{cc}*	[%]	3.29	1.72	1.49
E_{peak}/E_{acc}	[-]	2.56	1.89	2.17
B_{peak}/E_{acc}	[mT/(MV/m)	4.56	4.26	3.74
R/Q	[Ω]	96.5	111.9	128.8
G	[Ω]	273.8	265.5	280.3
R/Q·G	[Ω·Ω]	26422	29709	36103

*cell-to-cell coupling

The single cell cavities were used to develop surface treatment procedures and to verify the absence of multipacting as predicted by simulation [2]. The 7-cell cavities (Fig. 2) feature stiffening rings to resist the Lorentz force. At each end of a multi-cell cavity is a Nb55Ti helium vessel end-dish for an integrated helium vessel and two HOM couplers of the DESY type [3]. The coupling of the rf to the cavity is accomplished by a waveguide coupler situated at one beam pipe 80 mm away from the end cell iris. It provides a Q_{ext}~ $2\cdot10^7$.

All flanges are made from Nb55Ti and Al_3Mg gaskets are used [4] for sealing.

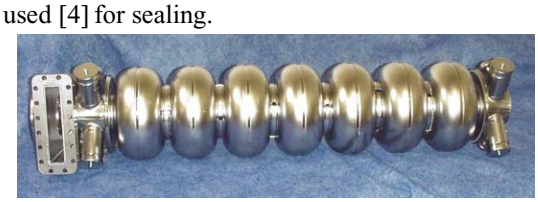

Figure 2: LL seven cell cavity.

* Supported in part by DOE contract DE-AC05-84ER40150
!kneisel@jlab.org

As fabricated, the cavities had a field flatness of roughly 70%. They have been tuned to > 97 % prior to buffered chemical polishing (BCP). The surface treatment provided a non-uniform material removal (40% less removal at equators) and a non-ideal surface finish with many radial flow marks on the upper half cells, especially on the LL prototype (Fig. 3).

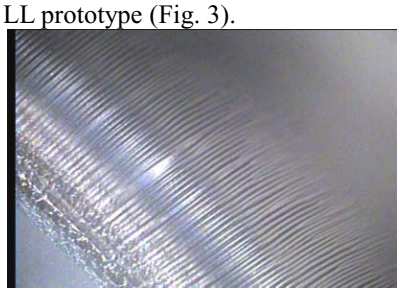

Figure 3: Surface of LL cavity end cells, showing severe flow marks.

The single cell cavities went through several BCP treatments as well as heat treatments and "in- situ" baking cycles. The final treatment, after assembling a cavity in a class 10/100 clean room for a cryogenic test, was always a high pressure rinse with ultra-pure water at a nominal (at the pump) pressure of ~ 80 bar.

EXPERIMENTAL RESULTS

Two LL single-cell cavities with the end-cell and the middle-cell shapes and one HG cavity with end-cell shape have been manufactured. The LL cavities were tested several times as described below.

Tests of LL Cavities #1 and #2

The main purpose of these tests was to find out about potential problems with multipacting and surface cleaning because of the small iris diameter and the relatively flat side wall angle.

Cavity #1 (end-cell geometry): after a nominal material removal of ~ 200 µm, a surface field of E_{peak} ~ 58 MV/m was measured at 2K and no limitations by multipacting were observed. In a subsequent treatment, the cavity was post purified with Ti at 1250 C for 3 hrs; app. 100 micron were removed from the surface and after 1 hr of HPR and horizontal drying in the class 10 clean room for 12 hrs the cavity was re-tested. The performance of the cavity had improved to a surface field of E_{peak} = 63 MV/m, but showed a strong "Q-drop" starting at E_{peak} ~ 45 MV/m. Further improvements were achieved after an "in situ" baking at ~ 100 C for 48 hrs – the "Q – drop" was shifted to a "quench" field of E_{peak} ~ 87 MV/m and was much reduced.

In Figure 4 the cavity performance before baking and after baking is shown; measurements were done at 3 different temperatures. After baking, the Qo vs. E_{peak} curves show the typical three ranges of dependences: a low field Q–slope, an intermediate slope and a high field Q-drop.

In LL#2 (inner cell shape) an E_{peak} of 60 MV/m was measured after ~ 150 µm of material removal by BCP, however, field emission loading started at ~ 40 MV/m. No signs of multipacting were detected.

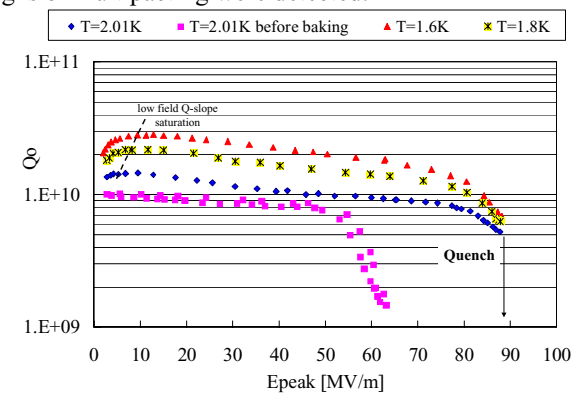

Figure 4: Performance of LL single cell cavity #1 after post- purification heat treatment and "in-situ" baking.

HG Cavity (Inner Cell Shape)

The half cells of the HG cavity were electropolished (EP) using the Siemens method [5] prior to welding-on beam pipes and completing the equator weld. Hydrogen degassing at 600 C for 10 hrs followed. We chose this manufacturing method in order to find out whether it is possible to achieve reasonably good cavity performance even if some manufacturing steps remain to be performed and very little final surface treatment can be applied. This might be a valuable method for closed cavities such as e.g. a sc gun cavity. It turned out that the initial cavity performance was rather poor (quenches, low Q), but with subsequent BCP steps continuous improvement in fields was achieved and the cavity eventually improved to E_{peak} ~ 42 MV/m; as indicated in Figure 5. Despite the BCP, the cavity surface remained as shiny as after the initial EP. We conclude at this point that the manufacturing method chosen for this cavity has no advantages over the standard method and that EP should be applied to the full cavity rather than to its parts.

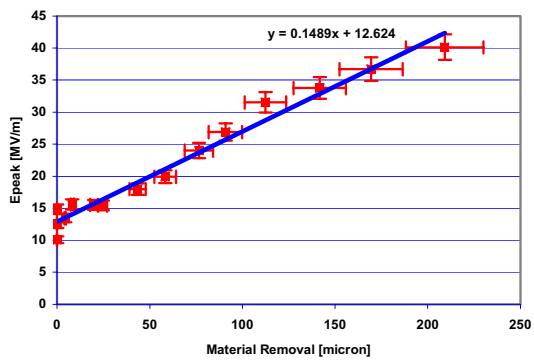

Figure 5: Improvement in quench field with material removal for HG single cell cavity.

Seven Cell Prototypes

HG Prototype

After initial removal of 200 µm of material a heat treatment at 600 C for 10 hrs followed to remove

hydrogen from the preceding chemical treatment. After an additional 50 µm of BCP the cavity reached a gradient of E_{acc} = 21.5 MV/m, limited by field emission, which started at ~ 18 MV/m. In this test the Lorentz force detuning coefficient was measured to be -2.5 Hz/(MV/m)^2. In a subsequent test, rf feedthroughs with copper probe tips were mounted onto the four HOM coupler ports; the test showed unacceptable heating of the probes already at fields as low as 3 MV/m and the Q-value dropped into the 10^8 range at ~4.5 MV/m. After switching off the rf, it took ~ 2 hrs until the low field Q-value was restored as shown in Fig. 6. As a subsequent analysis indicated, several Watts of heat were dissipated in the copper tip and the very poor thermal design of the rf feedthroughs prevented a rapid heat transfer to the helium bath. Efforts are underway to create a thermally superior feedthrough [6] needed for the CEBAF upgrade; it will be used with niobium instead of copper probes.

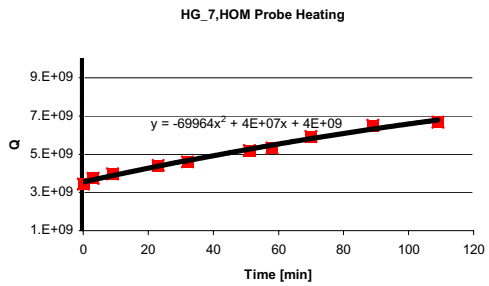

Figure 6: Recovery of the Q-value after probe heating.

LL Prototype

As mentioned already above (see Fig. 3) the surfaces of the LL cavity showed severe flow– and etch– patterns, especially in the end cells. The rf performance of the cavity was disappointing in the fundamental mode and in all modes with high field in the end-cells; strong Q-degradation at fields around 10 MV/m was observed. The end groups were cut off from the cavity to get access to the end cell for mechanical grinding. After this operation and extension of the beam tubes, the cavity reached E_{acc} = 20 MV/m without any signs of multipacting limited by available power because of a strong intermediate Q-slope. We believe that the slope is caused by insufficient material removal after the severe grinding. Additional BCP should improve the situation and is in progress. The Lorentz-force detuning coefficient was measured to be –3.1 Hz/(MV/m)^2.

HOM damping

The external Q -values of 20 dangerous HOMs were measured at 4.2 K (Fig. 7). For both prototypes the room temperature damping was confirmed.

SUMMARY

Both cavity types for the CEBAF upgrade have been prototyped and – after some unexpected problems with surface treatment, which have been solved on subsequent cavities by flipping – reached the gradient design goal of E_{acc} = 20 MV/m. Improvements in contamination control are necessary to avoid field emission and related Q-degradation. The absence of multipacting in both cavities confirmed the calculations [2]. A severe problem was encountered in the heating of the HOM pick-up probes and a better thermally designed feedthrough is under development. In addition, the analysis of the data from the HG prototype tests indicates that a superconducting probe tip is essential.

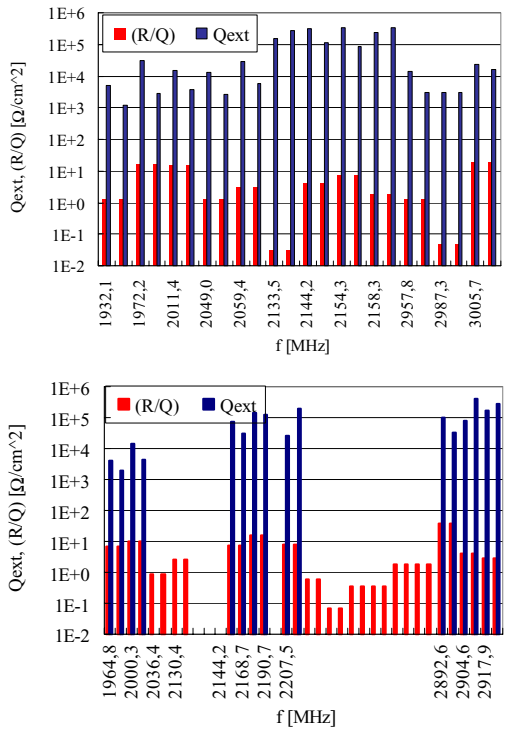

Figure 7: HOM damping at LHe: HG upper diagram, LL lower diagram.

ACKNOWLEDGEMENT

We would like to thank all our colleagues, who supported this work. Special thanks go to L. Turlington, B. Manus, G. Slack, S. Manning, R. Afanador, B. Golden, I. Daniels, J. Mammosser , P. Kushnick and S. Thomas.

REFERENCES

[1] J. Sekutowicz et al.; "Cavities for JLab's 12 GeV Upgrade", PAC 2003, paper TPAB085, http://accelconf.web.cern.ch/accelconf/p03/INDEX.HTM
[2] W. Hartung; private communication
[3] J. Sekutowicz; "HOM Couplers at DESY", Report ANL-Phys-88-1,Vol. II, p.597, Argonne, Ill (1988)
[4] K. Zapfe-Dueren et al.; "A New Flange design for the SC Cavities for TESLA", Report LNL-INFN (Rep) 133/98, p.457, Abano Terme,Italy (1997)
[5] H. Diepers et al.; "A New Method of Electropolishing Niobium", Phys.Lett. 37A, 139, (1971)
[6] C. Reece, private communication

INFLUENCE OF TA CONTENT IN HIGH PURITY NIOBIUM ON CAVITY* PERFORMANCE: PRELIMINARY RESULTS

P. Kneisel *!, G.R. Myneni *, D. Proch +, W. Singer+, X. Singer+, T. Carneiro++, C. Klinkenberg#, M. Imagumbai##,
* Jefferson Lab, Newport News, VA; USA; + DESY, Hamburg, Germany; ++ Reference Metals Co., Inc., Bridgeville, PA, USA; # Niobium Products Co., GmbH, DÜsseldorf, Germany; ## CBMM Asia , Tokyo, Japan

Abstract

In a previous paper [1] a program for reducing the costs of high purity niobium was outlined. This program was based on the fact that niobium prices could be reduced, if a higher content of Ta, which does not significantly affect the RRR–value, could be tolerated for high performance cavities. This contribution reports on the execution of this program and its present status.

Four ingots with different Ta contents have been melted and transformed into sheets. In each manufacturing step material quality has been monitored, using chemical analysis, thermal conductivity measurements and evaluation of mechanical properties. The niobium sheets have been scanned for defects by an eddy current device.

Two single cell cavities (CEBAF geometry) have been fabricated from each of three ingots, with Ta concentrations of 150, 600 and 1300 wtppm. A series of tests have been performed on each cavity with increasing amount of material removal.

This contribution reports on the test results and gives an analysis of the data.

INTRODUCTION

High purity niobium with RRR–values > 250 is exclusively used for the fabrication of high performance cavities for SRF accelerator projects such as SNS, TESLA, RIA or CEBAF Upgrade. Material cost is a significant fraction of total cavity cost, and one reason for the high costs is related to the specifications for tantalum content, which is in some cases required to be < 500 wtppm. Naturally occurring niobium–containing deposits such as columbite/tantalite or pyrochlore typically have high Ta content. Low Ta content in high purity niobium can only be obtained from niobium oxide, which appears as a byproduct of Ta production. Limited supply may be a big barrier to price stability and reliability for large projects such as TESLA.

The RRR–value (and therefore the thermal conductivity) of high purity niobium is mainly determined by interstitial impurities such as nitrogen, oxygen, hydrogen and carbon [2]. The contribution of Ta to the residual resistivity is significantly lower. It seems therefore quite reasonable to investigate the influence of Ta content in high purity niobium. However, one has also to make sure that the Ta is uniformly dispersed throughout the material, avoiding Ta clusters, which have in some cases been identified as causes of premature quenches in cavities. This is done by careful eddy current scanning of the sheets used for cavity fabrication [3].

In 2001 a project was launched to pursue this study with the following major objectives:

- Manufacturing of four niobium ingots with different Ta contents (< 150 wtppm,~ 600 wtppm, ~ 1200 wtppm and ~ 1300 wtppm)
- In these ingots only the Ta content was to be varied, content of other interstitial impurities was kept the same and verified by chemical analysis
- QA steps such as thermal conductivity measurements of ingots and rolled sheets and evaluation of mechanical properties of the rolled sheets accompanied production
- From the niobium sheets two single cell cavities each of the CEBAF variety were fabricated for Ta contents of < 150 ppm, ~ 600 ppm and 1300 ppm
- The rf performance of these cavities was measured at several stages during material removal from the surfaces

In the following the execution of this plan and the results from a total of 21 cavity tests are reported.

NIOBIUM SHEET MANUFACTURE

Ingot Production

The starting material for ingot production was pyrochlore as found at CBMM's deposit in Araxa, Brazil. Standard processing procedures [4] converted the ore to niobium ingots after triple electron beam melting of aluminothermically reduced niobium oxide. Addition of different amounts of Ta produced the four different ingots as mentioned above.

Material samples were taken from each ingot and the RRR-values were measured; the results are listed in Table 1.

Sheet Production

The ingots were converted into 2.8 mm thick sheets at the Tokyo Denkai facility in Japan in accordance with their standard processing procedures [5]. The RRR-values

* Supported in part by DOE contract DE-AC05-84ER40150
!kneisel@jlab.org

of sheets with different Ta content were measured on samples before and after a post-purification vacuum heat treatment at 1400 C for 3 hrs (Table 1).

Table 1: Residual Resistivity Ratios for different Ta contents for ingot and sheet

Ta content Sheet #	RRR Ingot	RRR sheet	RRR sheet heated
150 ppm 1161	180	178	323
~600 ppm 1162	170	231	345
~1200 ppm 1163	150	177	266
1300 ppm 1164	150	168	240

As expected, the post – purification heat treatment increased RRR, however, because of the relatively low interstitial impurity content, the improvement remained modest.

Mechanical Properties

Stress-strain curves for the different materials are shown in Figure 1. The strain rate was chosen as 2.2×10^{-5} /sec, which gives good resolution in the "Hooke's Law" region.

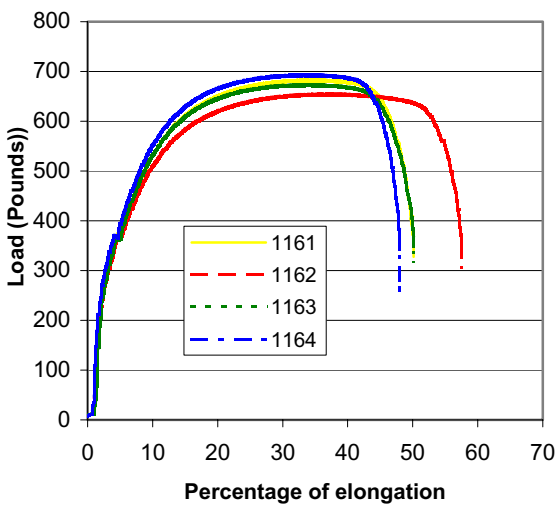

Figure 1: Stress-strain curves for the different materials.

Impurities

As mentioned above, impurity levels during ingot production were carefully controlled and kept at the same level for the materials with different Ta contents. Analyses were performed by 5 different laboratories with the average values for interstitial impurities as follows (in wtppm): oxygen: 7; hydrogen: 5; nitrogen: 4; carbon: 3.

CAVITY FABRICATION AND TESTING

Cavity Fabrication

Standard fabrication techniques were applied: half cells were deep drawn, machined to dimension with a self centering welding recess and a beam pipe/flange assembly was electron beam welded (EBW) to the half cells. After mechanical polishing to remove any surface imperfections and a removal of app. 30 µm from the surface by Buffered Chemical Polishing, (BCP) the two half cells were joined at the equator by EBW.

Surface Treatment

All six cavities were subjected to the following – equal – surface treatments:

- Degreasing in a soap/water solution with ultrasonic agitation for 30 min.
- (BCP), followed by thorough rinsing with ultra pure water and 30 min of high pressure rinsing (HPR) with a fan generating spray nozzle. Removal of 100 µm, 200 µm and 300 µm with rf measurements in-between.
- After HPR each cavity was dried in a class 10 clean room for 2 hrs prior to assembly of the rf input – and output coupling probes and evacuation on the test stand.
- After 12 hrs on the test stand the cavity vacuum had improved to the low 10^{-8} mbar range, and the cavity was cooled down to liquid helium temperature.

RF Tests

The subsequent rf tests consisted of measuring the surface resistance between 4.2K and 2K and the dependence of the Q-value on accelerating gradient (Q vs. E_{acc}) at 2K. The following observations were made:

- All cavities "quenched" at the field levels indicated in Table 2; no field emission was observed. No improvement in performance with additional material removal was observed.
- All cavities showed a strong Q-drop at gradients $E_{acc} > \sim 20$ MV/m as shown in Figure 2
- Residual resistances ranged between 12 nΩ and 3 nΩ; no systematic trend with material removal was observed
- Energy gap values $\Delta / k\ T_c$ ranged between 1.72 and 1.82; no systematic trend with material removal was observed.

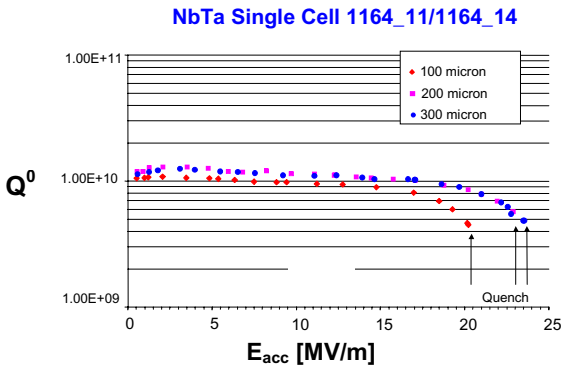

Figure 2: Typical cavity performance after removal of 100, 200 and 300 micron of material from the surface.

A summary of the tests is shown in Table 2

Heat Treatment

As a first step in assessing different heat treatments, one cavity of each Ta content was subsequently heat treated in vacuum at 800 C for 6 hrs in a Ti box. No improvement in quench fields was observed after removal of an additional 100 µm of material. Post–purification heat treatment to improve the thermal conductivity will be the next step.

SUMMARY

A systematic investigation of the effect of Ta contents in high purity Nb on cavity performance was conducted: no significant differences in performances for 150 wtppm < Ta < 1300 wtppm was found. Additional heat treatment at 800 C did not improve cavity performance. No improvement of quench fields was observed with increased material removal as has been seen in previous investigations [6]. This might suggest that no "defect gradient" exists in this material. The presence of a Q-drop in each of the tests around 20 MV/m (~ 100 mT) is not too surprising since it has been observed in cavities made from low Ta content niobium with RRR – values up to 300.

The achieved accelerating gradients of ~23 MV/m are not yet acceptable for an accelerator such as TESLA; however less demanding requirements for e.g. RIA, SNS, CEBAF Upgrade or the X-ray FEL can be accommodated. Further post purification heat treatments are needed to determine the limiting capability of the materials. It is also planned to fabricate a multi-cell cavity from the high Ta content material for further qualification.

ACKNOWLEDGEMENT

We would like to thank our colleagues from Jefferson Lab – Larry Turlington, Gianluigi Ciovati, Robert Manus, Gary Slack, and Peter Kushnick and Sherry Thomas – for their support of this work.

REFERENCES

[1] T. Carneiro et al; http://conference.kek.jp/SRF2001/
[2] K.K. Schulze, "Preparation and Characterization of Ultra-High-Purity Niobium", Journal of metals, Vol. 33 (5), May 1981, p. 33-41
[3] W. Singer et al.; "Quality requirements and Control of High Purity Niobium for SC RF cavities", Physica C386 (2003), 379-384
[4] H.R. Salles Moura, "Melting and Purification of Niobium", Proc. Intern. Symposium Niobium 2001, Dec. 2-5, 2001, Orlando, FL, p. 147
[5] H. Umezawa, "Impurity Analysis of High Purity Niobium in Industrial Production", Matereaux & Techniques, Vol. 7-9, p.33 (2003)
[6] E. Mahner et al.; "Effect of Chemical Polishing on the Electron Field Emission of Nb Samples and Cavities", Proc. 6th Workshop on RF Superconductivity, Newport News (1993),1085

Table 2: Summary of cavity tests

Material # Sheet #	Ta content [wtppm]	Test #1 100 micron E_{acc}[MV/m]	Test #2 200 micron E_{acc}[MV/m]	Test #3 300 micron E_{acc}[MV/m]	Average E_{acc}[MV/m] H_p [mT]
1164_12_12	1300	**18.1**	**15.7**	**20.6**	**18.1 / 83**
1164_11_14	1300	**20.2**	**22.9**	**23.6**	**22.2 / 102**
1161_31_34	~150	**22.3**	**22.2**	**21.2**	**21.9 / 100**
1161_32_33	~150	**23.6**	**22.5**	**23.7**	**23.2/ 106**
1162_33_34	~600	**23.3**	**22.6**	**23.5**	**23.1 / 106**
1162_32_35	~600	**20.4**	**23.4**	**22.8**	**22.2 /102**

COLD TEST RESULTS OF THE ISAC-II MEDIUM BETA HIGH GRADIENT CRYOMODULE

R.E. Laxdal, I. Bylinskii, G.S. Clark, K. Fong, A.K. Mitra, R.L. Poirier, B. Rawnsley,
T.R. Ries, I. Sekachev, G. Stanford, V. Zvyagintsev,
TRIUMF, 4004 Wesbrook Mall, Vancouver, BC, Canada, V6T2A3

Abstract

Many proposals (RIA, Eurisol, ISAC-II) are emerging for a new generation of high gradient heavy ion accelerators. The ISAC-II medium beta cryomodule represents the first realized application that encorporates many new techniques to improve the performance over machines presently being used for beam delivery. Developments include upgraded tuner and coupling loop designs, electronic alignment monitoring systems and a high density lattice using superconducting solenoids. The new developments are described and the results of the first cold tests are presented.

INTRODUCTION

TRIUMF is now preparing a new heavy ion superconducting linac as an extension to the ISAC facility [1], to permit acceleration of radioactive ion beams up to energies of at least 6.5 MeV/u. The superconducting linac is composed of two-gap, bulk niobium, quarter wave rf cavities, for acceleration, and superconducting solenoids, for periodic transverse focussing, housed in several cryomodules. The linac is grouped into low, medium and high beta sections. An initial installation of 18 MV of medium beta cavities ($\beta = 5.8\%$, 7.1%) is due for commissioning in 2005. The first major milestone, reported here and achieved in June 2004, is the first rf cold test of the completed cryomodule.

The ISAC-II medium beta cavity design goal is to operate up to 6 MV/m across an 18 cm effective length with $P_{cav} \leq 7$ W. The gradient corresponds to an acceleration voltage of 1.1 MV, a challenging peak surface field of $E_p = 30$ MV/m and a a stored energy of $U_o = 3.2$ J and is a significant increase over other operating heavy ion facilities. This goal not only demands clean rf surfaces but an rf system capable of achieving stable performance. To achieve stable phase and amplitude control the cavity natural bandwidth of $\pm$0.1 Hz is broadened by overcoupling to accomodate detuning by microphonic noise and helium pressure fluctuation. The chosen tuning bandwidth of $\pm$20 Hz demands a cw forward power of $\sim$200 W and peak power capability of $\sim$400 W to be delivered to the coupling loop.

The large accelerating gradients produce a large rf defocussing. A linac lattice consisting of modules of four cavities with a single high field (9 T) superconducting solenoid in the center is adopted. Beam diagnostics are positioned between modules at a waist in the beam envelope. The lattice is compatible with acceleration of multi-charge beams of $\Delta Q/Q \leq 7\%$.

MEDIUM BETA CRYOMODULE

The engineering description and cryogenic tests are reported in a separate article.[6] The vacuum tank consists of a stainless steel rectangular box and lid. All services and feedthroughs are located on the lid. A serial LN2 piping circuit cools both the copper panels formed into a thermal shielding box and the rf coupling loops. Magnetic shielding in the form of high μ sheet is suspended between the warm wall and the cold shield. Cavities and solenoids are suspended from a common support frame itself suspended from the tank lid (Fig. 1). Each cryomodule has a single vacuum system for thermo-isolation and beam acceleration. This demands extreme cleanliness of internal components and precludes the use of volatile lubricants and flux, as well as particulate generators, to avoid superconducting surface contamination. Assembly is done in the new ISAC-II clean room.

Figure 1: Cryomodule top assembly in the assembly frame prior to the cold test.

Alignment

The cavities must be aligned to within 0.4 mm and the solenoid to 0.2 mm. A wire position monitor (WPM)[7] system has been developed to monitor the position of the cold mass during thermal cycling. The monitors each consisting of four striplines are attached to the cavities and solenoid by off-center 'L' brackets. A wire running parallel to the beam axis and through the monitors carries an rf signal that is measured by the striplines and is converted to an x-y position. In addition optical targets are placed in

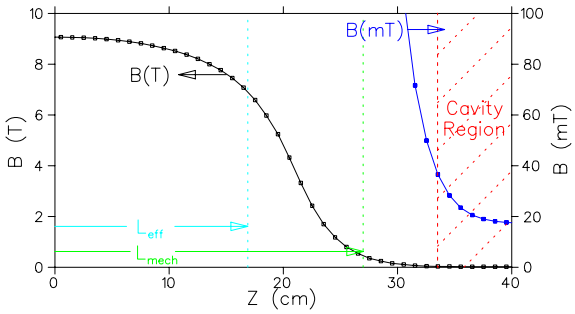

Figure 2: ISAC-II solenoid axial field map showing fringe field in the cavity region.

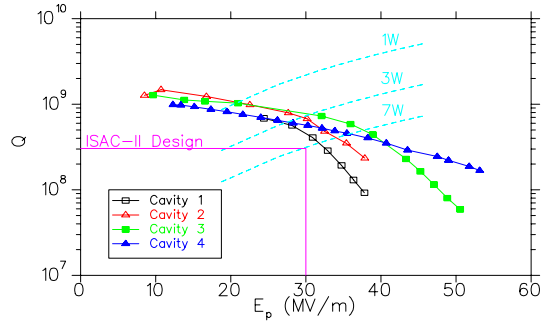

Figure 3: Characterization curves for the four cavities of the test cryomodule as measured in the single cavity cryostat.

each cavity and in the entrance and exit bore tube of the solenoid.

Solenoid

The 9 T solenoids, fabricated by Accel, have a bore of 26 mm, an effective length of 340 mm and a mechanical length of 540 mm. The magnets are mounted in a liquid Helium vessel fed from the common Helium header. The power leads are vapor cooled. Due to the close packing of the lattice the solenoids are equiped with bucking coils to actively limit the fringe field in the adjacent cavity to less than 100 mT to prevent reduction in cavity performance. The axial field map of the Accel solenoid is shown in Fig. 2 with the fringe field strength highlighted. The map indicates that the fringe field in the cavity region is less than 40 mT.

Cavities

The cavities, originally developed at INFN-LNL[2], are two-gap bulk niobium quarter wave cavities of design velocity $\beta_o \sim 7\%$. The cavities are equiped with a mechanical damper which limits microphonics to less than a few Hz rms. A demountable flange on the high field end supports the tuning plate. Rf coupling is done through a side port. After fabrication the cavities are chemically polished and rinsed with high pressure water before rf characterization in the single cavity cryostat. Results of these tests are presented in Fig. 3. All cavities reach the ISAC-II specified performance although Q degradation at high fields due to field emission is apparent.

RF Systems

RF Controls: The RF Control system [3] is a hybrid analogue/digital system. Each system consists of a self-excited feedback loop with phase-locked loops for phase and frequency stabilization. Amplitude and phase regulations, as well as tuning control, are performed using digital signal processors.

LN2 Cooled Coupling Loop: Initial cavity studies at TRIUMF were done with an adjustable coupling loop designed at INFN-Legnaro suitable for operation with lower gradients and lower forward power. A new coupler has been developed[4] that reduces the helium load to less than 0.5 W at the design gradient of 6 MV/m and $P_f = 200$ W. The coupler has a stainless steel body for thermal isolation and a copper outer conductor cooled with LN2. Cooling of the inner conductor is achieved by adopting a thermally conducting Aluminum Nitride dielectric localized in the coupling loop. The rf drive cable is uncooled but thermal radiation to 4K surfaces are intercepted by an LN2 cooled copper tube surrounding each cable.

Mechanical Tuner: A new high resolution mechanical tuner[5] has been developed. The tuning plate is actuated by a vertically mounted permanent magnet linear servo motor, at the top of the cryostat, using a 'zero backlash' lever and push rod configuration through a bellows feedthrough. The system resolution at the tuner plate center is $\sim 0.055\mu$m (0.3 Hz). The tuning plate is radially slotted and formed with an 'oil can' undulation to increase the flexibility. The demonstrated dynamic and coarse range of the tuner are ± 4 kHz and 33 kHz respectively. The demonstrated mechanical response bandwidth is 30 Hz. The tuner on-line performance is measured by altering the cavity frequency by forced variations of the helium pressure that induces an eigenfrequency change of 2 Hz/Torr. Fig. 4 shows the pressure change, the associated position signal from the tuner and the corresponding control loop error parameters while operating in ISAC-II conditions; $E_a = 6$ MV/m and $P_{for} = 200$ W. The cavity remains locked throughout but the amplitude regulation goes out of range when the rate of eigenfrequency change exceeds 60 Hz/sec.

CRYOMODULE TESTING

The cryomodule assembly and commissioning tests are conducted in the clean laboratory area in the new ISAC-II building. Thus far two cold tests have been completed. An initial cold test in April 2004, without rf ancillaries installed, characterized cryogenic performance and determined the warm off-set required to achieve cold alignment[6]. Briefly, the static helium load without rf ancillaries is 11 W and the required LN2 flow is 5ℓ/hr in line with predictions.

Preparation

Following the initial test the four rf sub-systems consisting of tuner, coupling loop and rf pick-ups are installed.

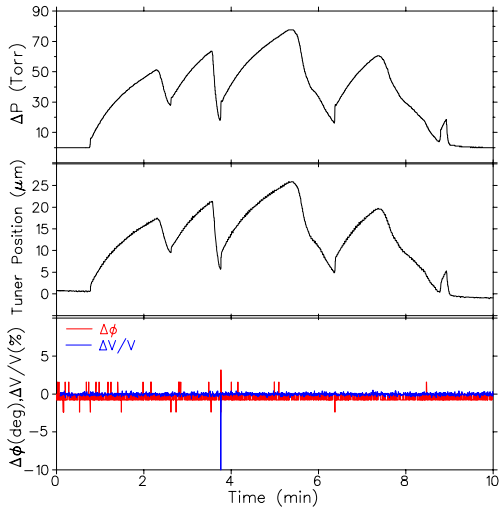

Figure 4: Tuner position response for forced pressure fluctuations in the helium space. The cavity maintained phase lock during the test. The bottom plot shows the phase and amplitude error. The cavity gradient is 6 MV/m with a bandwidth of ±20 Hz.

Cables for the rf and tuners systems are run from a multi-cavity controller cabinet and rf amplifier unit located outside the clean room. A single cavity cold test confirmed the integrity of each of the controller and cabling systems. Information collected during the first cold test is used to establish the warm alignment positions of the cavities and solenoid. Optical targets are installed in each element to check the alignment during the second cold test.

Exhaust gases from the cryomodule are passed through vaporizers and the flow is monitored by gas meters. A local computer records WPM information. Control and data acquisition are done with an EPICS control system.

Test Results

Cavities The cavities are first baked at ∼80°C for 24 hours. The cold mass is pre-cooled with LN2 to about 200°K before helium transfer. The quality factor of each cavity is determined by measuring the time constant of the field decay in pulsed mode at critical coupling. The Q values, presented in Table 1 are similar to those measured in the single cavity cryostat (Fig. 3) indicating that the μ-metal reduces the remnant magnetic field to a sufficient level. Also shown are the field values reached for a cavity power of 7 W. Cavity 2 high field results are not available due to a problem with the coupling loop. The results are below the design specification. The cavities were not rinsed prior to the test since system integrity and not high gradient are the immediate goal. As well there was insufficient helium to adequately condition the cavities.

Solenoid: The solenoid tests were done to determine the effect, if any, on cavity performance due to the high operating field or induced remnant fields. The solenoid was ramped up to 9 T with cavity 2 and 3 on. The cavities remained on and the measured Q values did not change. The solenoid and cavities were then allowed to warm above transition. After subsequent cooldown the cavity Q values were again measured. There was no change in the values showing that fields induced by the solenoid in the region of the cavities are tolerably small.

Table 1: Cavity performance during cold test

Cavity	Q_o	E_a@7 W (MV/m)	E_p@7 W (MV/m)
1	1.5×10^9	4.3	22
2	1.4×10^9	-	-
3	1.5×10^9	5.4	27
4	1.3×10^9	5.4	27

RF Control and Tuning One of the cavity control boards was shown to have a hardware fault so not all cavities could be locked simultaneously. However cavities 1,3,4 and cavities 2,3,4 were simultaneously locked to a common external frequency. In a final system test cavities 1,3,4 were each set to ISAC-II control conditions, $P_{cav} =\sim 4$ W and $P_{for} = 200$ W, and the solenoid was turned on to 9 T. The cavities remained locked to an external frequency while undergoing forced helium pressure fluctuations of 60 Torr.

CONCLUSIONS

Given the complexity of the undertaking the test was very successful. Cryogenically the cryomodule performed well with helium and LN2 consumption near expected values. Simultaneous locking of multiple cavities to an external frequency was demonstrated. The operation of the high field solenoid did not negatively impact the cavity performance. Future tests will involve a high pressure rinse and final clean assembly to reach for the design gradients.

REFERENCES

[1] P. Schmor, et al, “Development and Future Plans at ISAC”, this conference.

[2] A. Facco, et al, “The Superconducting Medium β Prototype for Radioactive Beam Acceleration at TRIUMF”, PAC2001, Chicago, June 2001.

[3] K. Fong, et al, “Status of RF Control System for ISAC-II Superconducting Cavities”, this conference.

[4] R. Poirier, et al, “Rf Coupler Design for the TRIUMF ISAC-II Superconducting Quarter Wave Resonators”, this conference.

[5] T. Ries, et al, “A Mechanical Tuner for the ISAC-II Quarter Wave Superconducting Cavities”, PAC2003, Portland, May 2003.

[6] G. Stanford, et al, “Engineering and Cryogenic Testing of the ISAC-II Medium beta Cryomodule”, this conference.

[7] W. Rawnsley, et al, “A Wire Position Monitor System for the ISAC-II Cryomodule Components Alignment”, this conference.

CONCEPTUAL LAYOUT OF THE EUROPEAN X-FEL LINEAR ACCELERATOR CRYOGENIC SUPPLY

H.Lierl, B.Petersen, A.Zolotov, DESY, Hamburg, Germany

Abstract

As a source for the European X-ray Free Electron Laser (European X-FEL project) at DESY a superconducting linear accelerator will deliver a pulsed electron beam of about 20-GeV. A conceptual layout for the cryogenic supply of the linac is presented. The linac will consist of about 1000 superconducting niobium 1.3-GHz 9-cell cavities, which will be cooled in a liquid-helium bath at a temperature of 2-K. In addition to the main linac of about 1.6-km length, two injector sections have to be supplied separately by means of helium refrigerators and the related helium distribution system.

THE EUROPEAN X-FEL PROJECT

In order to reach the X-ray region (0.1 nm) by means of a Free Electron Laser the European X-FEL-Project is presently under development at DESY [1].

A new superconducting linear accelerator will supply a pulsed electron beam of 20-GeV for the operation of the FEL. The TESLA technology will be applied for the linear accelerator:

The X-FEL linear accelerator will consist of about 1000 superconducting niobium 1.3-GHz 9-cell cavities, which will be cooled in a liquid-helium bath at a temperature of 2-K. Eight cavities and one superconducting magnet package will be assembled in cryomodules of 12.2-m length. The 2-K cryostat will be protected against heat radiation by means of two thermal shields cooled to temperatures of 5-K to 8-K and 40-K to 80-K respectively. A cross-section of a cryomodule is shown in Fig. 1.

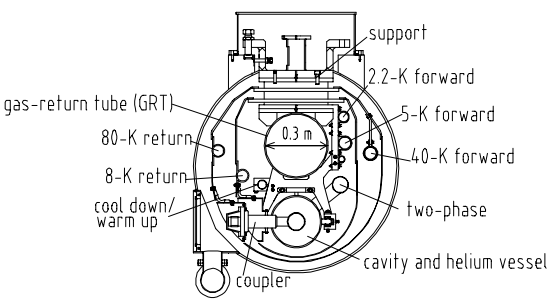

Figure 1: A cross-section of a XFEL-cryomodule.

CRYOGENICS

The XFEL-linac consists of two parallel injector cryomodules, a booster section, a bunch compressor section and the main linac cryomodules. The cryogenic supply of the two parallel injector cyromodules is separated from the supply of the booster and the cryomodules in the main tunnel. From the cryogenic point of view the four booster cryomodules including 3rd harmonic cavities and the main linac cryomodules are treated as one unit of about 1.6-km length. The 2-K cryogenic supplies of the main linac unit will be separated in 10 parallel cryogenic sections each of 12 cryomodules. These sections are called 'strings.' Including the booster cryomodules, 108 cryomodules of the main linac unit will be normally used for beam acceleration. Twelve spare cryomodules are kept in stand-by.

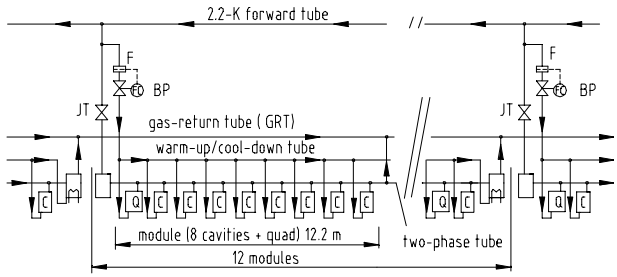

Figure 2 : A simplified scheme of the equipment and instrumentation of a XFEL-linac cryogenic string, which consists of 12 cryomodules, is shown. 'Q' corresponds to a superconducting magnet package.

The strings are separated by string connection boxes. Each box contains a Joule-Thomson valve (JT) for the steady-state operation and a bypass valve (BP) for the cool-down/warm-up. The JT-valves are supplied with helium at a temperature of 2.2-K and a pressure of 0.12 MPa by means of the 2.2-K forward tube (see Fig.1 and Fig.2). Here the helium is expanded to 0.0031-MPa into the two-phase tube and the individual helium vessels of the cavities are filled with liquid helium at 2-K. The helium vapour is directed back to the refrigerator by means of the gas return tube (GRT, see Fig.1). The string connection boxes are equipped with a vacuum barrier, which separates the insulation vacuum of the strings. The GRT as well as the supply and return tubes of the thermal shields will not be separated in string sections. At the end of each cryomodule the two-phase tube is connected to the GRT. The first string of the main linac unit is sub-divided by a bunch compressor section of 120 m length. This warm section separates the first four booster cryomodules from the main linac cyromodules. The bunch compressor section is bridged by a bypass transfer line (BCBTL), which contains all cryogenic process tubes. Inside the BCBTL the process tube diameters can not be reduced to smaller sizes, if unacceptable large

helium flow pressure drops shall be avoided. The large GRT diameter and the corresponding large diameter of the vacuum tube of the BCBTL will occupy a significant amount of space in the tunnel and at the connections to the adjacent cryomodules in particular.

Cryogenic Loads

Table 1 shows the static and dynamic losses of one cryomodule. In addition to the initial design operation of the linac at 20-GeV beam energy, the cryogenic supply has to be prepared for a wide range of operation parameters, which might exceed the loads given in table 1. The cryogenic capacities of one TESLA-Model-Refrigerator (TMR) [2] are assumed here as a reasonable limit for the design of the X-FEL-linac facilities (see table 2). The overall loads for the 20 GeV design as well as the loads for a fictive set of parameters, which correspond to the 2-K cooling capacities of a TMR are also summarized in table 2. In order to compare the different requirements and capacities at different temperature levels, the corresponding 4.5-K cooling capacity equivalents have been added to table 2. Also estimates for the primary power consumption are shown.

Table 1: The cryogenic loads of one XFEL-cryomodule containing 8 cavities and one quadrupole package at 2-K. The dynamic loads are calculated for an accelerating field of E_{acc} = 23.5 MV/m, a macro pulse of 1.35 ms and a pulse repetition rate of 10 Hz at an unloaded RF-quality factor of $Q_0 = 1*10^{10}$ corresponding to a beam energy of 20 GeV for the linac

cooling circuit	static load [W]	dynamic load [W]	sum of loads [W]
2 K	1.44	8.75	10.19
5-8 K	8.64	5.70	14.34
40-80 K	70	117	187

Overall Structure of the Cryogenic Supply

The overall structure of the cryogenic supply is shown in fig. 3. The refrigeration is separated in two sections: one (or more) helium refrigerators supply the cooling capacities from room temperature to 40-K and 5-K respectively. The 2-K helium circuit is supplied by a separate set of cold compressors and low temperature heat exchangers, which are connected to a distribution box. The distribution box branches the different helium circuits coming from one (or more) refrigerators to the injectors and the main linac. For the independent supply of the injectors an additional valve box is required, which splits the helium flows to the individual feed-boxes of the injectors. The different cryogenic components are connected by multiple tubes helium transfer lines. The cryogenic equipment of the main linac consists of a feed-cap, an end-cap, the string connection boxes and BCBTL. The BCBTL is connected to the adjacent cryomodules by means of feed-caps. One of these feed-caps acts also as an additional string connection box.

Table 2 : The overall cryogenic loads for the XFEL linear accelerator. The loads include a design factor of 1.5 . The loads in the 27 GeV column correspond to a fictive set of parameters for the linac, which come close to the 2 K capacities of the TMR (Eacc= 31.2 MV/m, 10Hz, $Q_0 = 0.5*10^{10}$). The cryogenic loads of the cryogenic distribution system are also included. A conversion factor of 3.5 is applied to the 2 K loads in order to estimate the 4.5 K equivalent capacities with reference to the TMR coefficients of performance (COP) [2]

cooling circuit	static loads linac	20 GeV linac	27 GeV linac	TMR	one HERA refrig.
2 K load [W]	500	1893	4253	4253	
2 K mass flow [kg/s]	0.025	0.089	0.199	0.199	
5-8 K load [W]	2042	2964	3320	7465	
5-8 K mass flow [kg/s]	0.073	0.105	0.118	0.250	
40-80 K load [W]	17637	36534	55230	80788	20420
40-80 K mass flow [kg/s]	0.084	0.173	0.262	0.383	
4.5 K equivalent [W]	3800	9590	18206	22350	8400
electrical power [MW]	0.94	2.23	4.00	5.13	2.68

Refrigerator Options

With reference to the experience with other large superconducting accelerator facilities like HERA or the VUV-FEL-linac at the TESLA test facility, it is expected that the cryogenic supply of the XFEL-linac has to be maintained across a period in the order of several years without any major shut-down of the cryogenic plant. The availability should exceed 99.7 % (utilities excluded). A new designed and constructed 'state-of-the-art' cryogenic plant could deliver the cooling capacities at the different temperature levels for the XFEL-linac (see table 2) in a most effective and straightforward way, following the concepts of the TMR [2]. A new cryogenic refrigerator will consist of a cold box, a multi-stage screw compressor system and the utilities. Compared to the HERA refrigerators about 17 – 41 % of primary power could be saved by means of a 'state-of-the-art' facility with reference to the LHC-refrigerators at CERN or the TESLA concepts [2] respectively. According to an internal study [3] two modificated HERA refrigerators

could also deliver the requested final cooling capacities for the X-FEL linac, which are shown in Table 2. The HERA cryogenic plant consists of three independent refrigerators. The capacities on one HERA refrigerator are given in table 2. Two of these refrigerators will supply the HERA accelerator until the end of the operation in the year 2007. One of the refrigerators will be used for the supply of the VUV-FEL linac at the TESLA test facility and the X-FEL-accelerator module test facility beyond the year 2007. Already for the initial supply of the 20 GeV linac significant up-grades would be required for the HERA-refrigerators: one cold box could supply the main part of the 40/80-K cooling capacity, the complete 5-K shield cooling circuit and the cool down of the 2-K helium mass flow from 16-K to 5-K. The second cold box could cool down the 2-K helium flow from 300-K to 16-K and support the 40/80-K circuit.

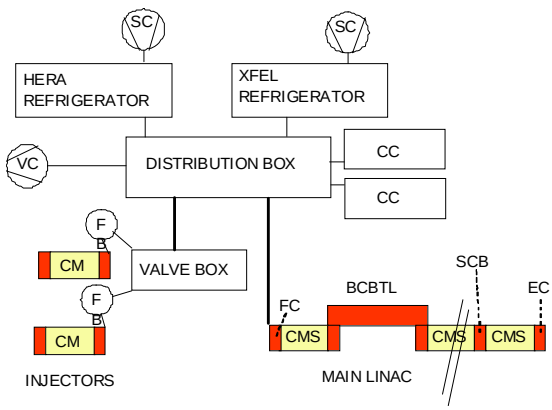

Figure 3: Block diagram of the XFEL-cryogenic supply. SC = screw compressors, VC = vacuum compressors, CC = cold compressors, F = feed box, FC = feed cap, SCB = string connection box, EC = end cap, BCBTL = bunch compressor bypass transfer line, CM = cryomodule, CMS = cryomodules.

This operation of the HERA cold boxes would require modifications of the internal tubing of the cold boxes and the installation of an additional turbine in each of the cold boxes. Other turbines have to be replaced by machines of more capacities. If the analysis is restricted only to the modifications in the cold boxes, a significant amount of investment cost could be saved compared to the procurement of a new refrigerator. On the other hand, the core of the HERA plant will have an age of about 26 years when the operation of the XFEL-linac will be started in 2012 and the highest possible availability will be requested for at least another 15 years of operation. Therefore several components will have to be replaced in addition to the cold box modifications. Some of these components are listed in table 3. As a consequence, the use of the HERA cryogenic plant will imply the risks of 'hidden' investments in addition to the obvious modifications, including the risks of a critical supply of spare parts for expired equipment. The overall efficiency will be lower than for a new 'state-of-the-art' plant.

Table 3: A comparison of advantages and disadvantages in the use of the HERA cryogenic facilities for the XFEL-linac

pro	contra
lower initial investment costs	risk of 'hidden' investment costs
technical possible	critical supply of spare parts
	replacement of screw compressor oil cooling systems
	replacement of control I/O
	replacement of valve actuators
	modifications of warm gas distribution systems
	complicated operation of 2 parallel cold boxes, mixing of helium across the CBs
	lower efficiency
	risk of lower availability
	interferences with the operation of the VUV-FEL linac and the accelerator module test facility

CONCLUSIONS

For the time being, a new 'state-of-the-art' refrigerator is considered for the cryogenic supply of the XFEL-linac, according to the concepts of the TMR. In a first step, only about half of the compressor capacity of the TMR will be installed in order to serve the requests for the 20-GeV X-FEL-linac (see table 2). All the other cryogenic equipment will be sized for the final maximum cryogenic capacities and helium mass flows of a TMR.

The HERA cryogenic plant can be used as a back-up system and can be linked to the X-FEL- distribution box as shown in Fig. 3 with only minor modifications. As soon as the tests of the XFEL-cryomodules in the accelerator module test faclity will be finished, warm vacuum compressors from the test facility could also be connected to the distribution box. By means of one HERA refrigerator and the vacuum compressors parts the XFEL-linac and the injectors can be commissioned independently from the commissioning of the new XFEL-refrigerator. In addition, one HERA refrigerator could supply the cooling capacities for the static cryogenic loads of the XFEL-linac during shut-down periods of the new XFEL-refrigerator.

REFERENCES

[1] TESLA XFEL Technical Design Report Supplement, edited by R. Brinkmann et al., Deutsches Elektronen-Synchrotron, Hamburg, 2002.

[2] H.Quack, C.Haberstroh, M.Kauschke, H.Lierl, B.Petersen, S.Wolff, "The TESLA Cryo-Plants, "TESLA Report, TESLA 2001-38, December 2001.

[3] H.Quack and A.Kutzschbach, "Über die Möglichkeit des Umbaus der HERA-Kälteanlage für TESLA", Internal Report, July 2002.

RF COUPLER DESIGN FOR THE TRIUMF ISAC-II SUPERCONDUCTING QUARTER WAVE RESONATOR

R. Poirier, K. Fong, P. Harmer, R. Laxdal, A. Mitra, I. Sekatchev, B. Waraich, V. Zvyagintsev,
TRIUMF*, Vancouver, 4004 Wesbrook Mall, Vancouver, Canada, V6T2A3

Abstract

An rf Coupler for the ISAC-II medium beta (β=0.064 and 0.074) superconducting quarter wave resonators was designed and tested at TRIUMF. The main goal of this development was to achieve stable operation of superconducting cavities at high acceleration gradients and low thermal load to the helium refrigeration system. The cavities will operate at a 6 MV/m acceleration gradient in overcoupled mode at a forward power of 200 watts at 106 MHz. The overcoupling provides ± 20 Hz cavity bandwidth, which improves the stability of the rf control system for fast helium pressure fluctuations, microphonics and environmental noise. Choice of materials, cooling with liquid nitrogen, aluminum nitride rf window and thermal shields insures a small thermal load on the helium refrigeration system by the Coupler. An rf finger contact, which caused micro dust in the coupler housing, was eliminated without any degradation of the coupler performance. Rf and thermal calculations, design and test results on the coupler are presented in this paper.

INTRODUCTION

The ISAC II [1] medium beta cavities have a design gradient of 6 MV/m. This corresponds to a peak surface fields of ~ 30 MV/m and ~60mT, and a stored energy of U=3.2 J. This is a significant increase over other operating heavy ion facilities. To achieve stable phase and amplitude control the natural bandwidth of +/- 0.1 Hz is broadened by overcoupling to accommodate detuning by microphonic noise and helium pressure fluctuations (~1-2 Hz/Torr). The ISAC II medium beta cavities are outfitted with a passive mechanical damper [2] and the microphonics are not expected to be more than a few hertz RMS. The chosen tuning bandwidth of +/- 20 Hz demands a cw forward power of 200 watts and a peak power capability of 400 watts to be delivered to the coupling loop at the cavity.

The various prototypes of the coupler design are reported in [3]. We started with a copy of an INFN-Legnaro design for gradients of 3-4 MV/m and forward power of 50 W, which we identified as Mark I. In the Mark II design we changed the loop assembly materials and added LN2 cooling. We initially tried to cool the outer conductor of the cable with an LN2 cooling loop as well but opted to add a thermal shield inside the cryostat along the rf drive cable which performed a more efficient job in reducing the added thermal load on the helium system. The thermal shield is connected to the LN2 shield of the cryostat and restricts heat radiation flux from the coupler rf cable to the helium system. In the Mark III version we added a 1-inch long split ring piece of Aluminum Nitride (AIN) dielectric to thermally connect the inner and outer conductors of the loop near the heat exchange block to reduce inner conductor heating. In the Mark IV prototype shown in Fig.1, the outer conductor and heat exchange block are formed from a solid piece of copper and a cooling channel running through the block allows direct cooling with LN2. All of these modifications allowed us to reach our design goal of 200 watts forward power at the coupling loop with less than 1 watt of power being added to the helium load. The Mark V (Fig.2 and Fig.6) is the final design for the cryomodule and differs from the Mark IV only by the heat exchange block design, which is adapted for the cryomodule assembly. The thermal shield and heat exchange block are cooled with the same LN2 flux.

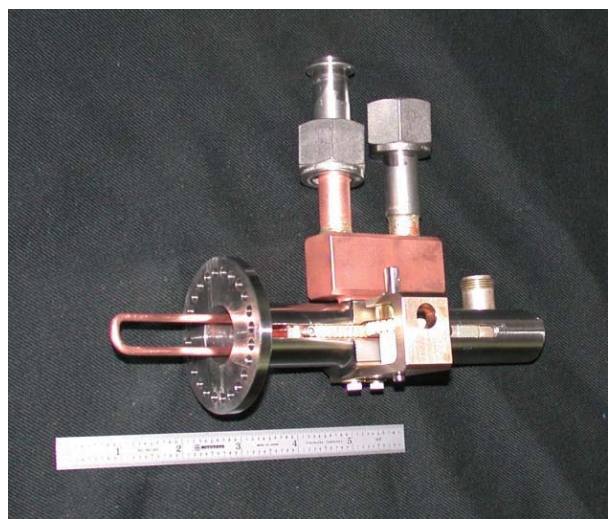

Figure 1: Mark IV Coupling Loop Assembly ready for installation into the cavity.

RF COUPLER

Coupling Loop Assembly

The housing of the coupling loop is made from thin stainless steel for thermal isolation from the cavity. The inner and outer conductors of the coupling loop assembly are made of copper. The outer conductor, which includes an integrated heat exchange block, is driven in and out through a rotating shaft attached to a stepping motor on the cryostat lid via a rack and pinion mechanism on the loop housing. The position of the AIN dielectric and the

* TRIUMF receives funding via a contribution agreement through the National Research Council of Canada

LN2 cooling circuit is shown in a cut-away rendering of the Mark V coupling loop assembly in Fig. 2.

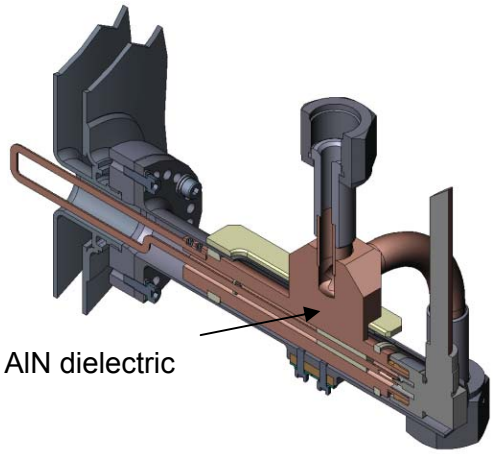

Figure 2: A cut-away rendering of the Mark V coupling loop assembly showing the position of the AlN dielectric and the LN2 cooling block.

Internal Coaxial Cable

In the initial rf tests we used Flexco FC445 coaxial cable which did the job but was very expensive. We are now using an Andrews ETS50 coaxial cable, which is less expensive and has better thermal conduction from the inner conductor to the outer conductor of the cable, even though the attenuation is bit more and the maximum power rating is less. The comparison is shown in Table 1.

Table 1: Comparison of coaxial cables for use inside the cryostat at 106 MHz

	FC445	ETS50	Comparison*
Maximum Power, W	9.6	6.0	37% less
Attenuation, dB/m	0.037	0.041	10% more
Velocity of propagation, %	84	83	
Transverse thermal conductivity of dielectric, W/(m*K)	0.27	0.50	84% more
Price, $/m	250	120	53% less

*Parameters of Andrew ETS50 cable in comparison with Flexco FC445.

In the test cryostat the length of coaxial cable required from the coupling loop assembly to the top feed through flange is 1.65 meters. This turns out to be an unfortunate length for a cable at this frequency with a VSWR, which positions a current maximum at the flange connection. However for the cryomodule the length of the cable is reduced to 1.25 meters, which greatly reduces the current density and the consequent heating problem at the flange (see Fig.3). The peak current at the flange for the cryomodule is 1.9 amps compared to 5.4 amps for the test cryostat.

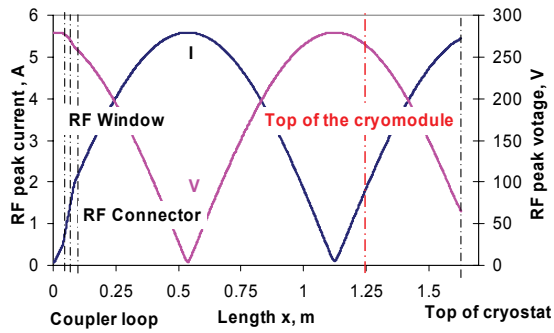

Figure 3: The voltage and current distribution along the coupler line inside of the test cryostat at nominal operating parameters (Ea=6 MV/m, Pf=200 W).

Thermal Measurements

Thermal measurements are done by first measuring the static heat loss based on the helium boil-off rate after full thermalization. The cavity is then powered until thermal equilibrium is reached and the new static heat load is measured. Several sensors during power on and power off cycles monitor the temperatures of the loop assembly. The position of the sensors on Mark IV design are shown schematically in Fig.4 and table 2 is the temperature of the sensors with rf off after full thermalization of the He cooling system and with rf on after thermal equilibrium is reached. TS8 is mounted on the heat shield and although it is showing a high temperature in the table, it was found that this was mostly due to a poor thermal contact of the thermal shield with the LN2 shield.

The measurements were taken with a forward power at the loop of 250 watts and a gradient (Ea) in the cavity of 6 MV/m. Under these conditions the loop heating caused approximately an extra 0.5 watts to the helium static load.

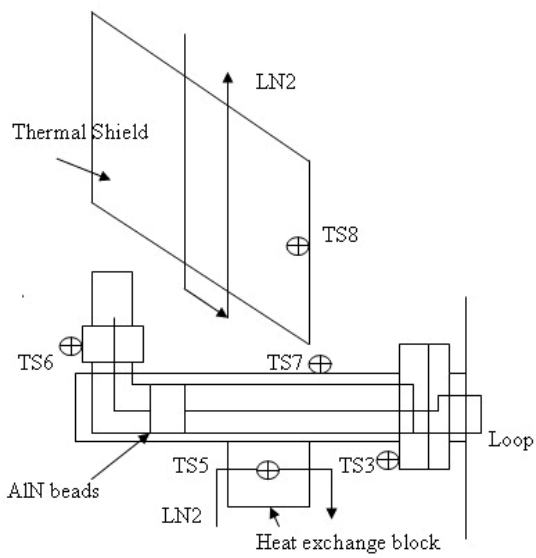

Figure 4: Schematic presentation of the temperature sensors on the coupling loop assembly.

Table 2: Temperature readings of the sensors on the coupling loop assembly shown in Fig. 4

	TS3,^{0}K	TS5,^{0}K	TS6,^{0}K	TS7,^{0}K	TS8,^{0}K
RF off	7.7	77	84	16.8	87.5
RF on	12.8	96.5	169.8	28.5	130.4

Fingerstock

RF fingerstock was initially installed in the coupling loop assembly to connect the outer conductor of the coupling loop assembly to the outer stainless steel housing. This provided an rf path to ground for any rf leakage from the cavity through the coupling loop penetration. However this also caused micro dust in the coupling loop housing and the possibility of eliminating it was investigated.

Figure 5 presents a segment of the HFSS model of the coupler for the fingerstock simulation. The total HFSS model consists of a lossless quarter wave resonator and a 50 Ohm loaded coupler set close to nominal coupling. The fingerstock plane boundary condition changes from a perfect conductor (with fingerstock) up to a minimum capacitance, of the coupler body to ground, of 20 pfd. The results from the Eigensolver calculations for resonant frequency and external quality factor with and without fingerstock was the same (f_o=105.941 MHz, Q_{ext}=3.5*10^6). The fingerstock could indeed be eliminated without any degradation to the coupler performance.

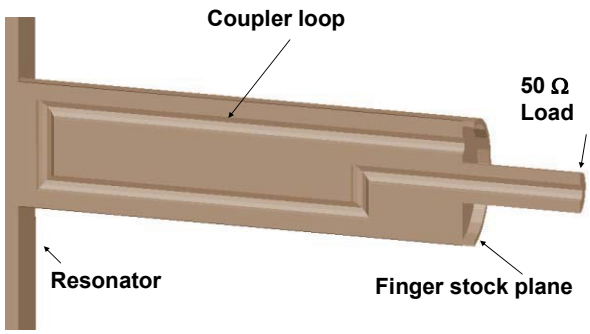

Figure 5: HFSS model for fingerstock simulation.

The only noticeable difference was an increase in the rf leakage as noted by an offset in some of the temperature sensor readings.

Mark V Coupler Assembly

The cryomodule, with four medium cavities equipped with Mark V coupler assemblies, were successfully tested up to 700 watts of rf forward power. Fig.6 shows two of the cavities with their coupler installed and their associated heat shields. One can also see the arrangement of the LN2 cooling lines.

CONCLUSIONS

When we started out with Mark I we could not go to higher powers without significantly heating both the cable and the loop assembly and several watts of power were added to the helium load even at low power levels. In the Mark II design the temperature of the inner conductor of the coupling loop assembly was high enough to increase the length of the coupling loop and caused an increase in the coupling beta. This increase in beta was sufficient to cause the power at the coupling loop to increase from 140 watts to 200 watts for the same field gradient in the cavity. The added heat load to the helium system for this arrangement was 4.5 watts. The addition of the heat shield around the cable and loop assembly further reduced the additional helium heat load to 2.5 watts but the temperature of the inner conductor was still high enough to increase the length of the coupling loop. In the Mark III design, the addition of the AIN dielectric reduced the temperature of the inner conductor sufficiently to prevent the length of the coupling from increasing for a more stable operation. In addition the improvement in the thermal path reduced the thermal equilibrium time from 6 hours to 2 hours. The added power to the helium load under these conditions was 1.5 watts. The Mark IV design has now allowed us to take the last step in achieving our design goal of less than 1 watt added to the helium load for 250 watts forward power at the coupling loop.

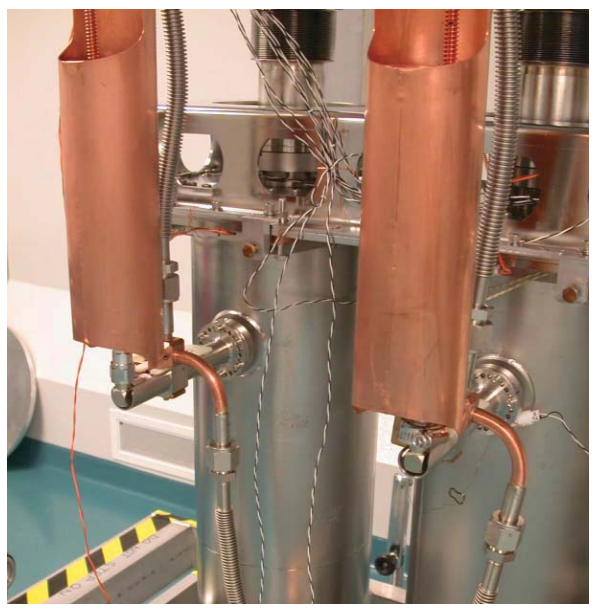

Figure 6: Mark V Coupler Loop Assembly installed on the cavity in the Cryomodule.

REFERENCES

[1] R.E. Laxdal, et al, The ISAC-II Upgrade at TRIUMF: Progress and Developments, PAC2003

[2] A. Facco, et al, Mechanical Mode Damping in Superconducting Low-beta resonators, Proc. of the Eight RF Superconductivity Workshop, Abano, 1997.

[3] R.E. Laxdal, et al, A Mechanical Tuner and rf Drive Line System for the ISAC II Quarter Wave Superconducting Cavities, SRF2003

A WIRE POSITION MONITOR SYSTEM FOR THE ISAC-II CRYOMODULE COMPONENTS ALIGNMENT

W. Rawnsley, Y. Bylinski, G. Dutto, K. Fong, R. Laxdal, T. Ries, TRIUMF, Vancouver, Canada
D. Giove, INFN, Milan, Italy

Abstract

TRIUMF is developing ISAC-II, a superconducting (SC) linac. It will comprise 9 cryomodules with a total of 48 niobium cavities and 12 SC solenoids. They must remain aligned at liquid He temperatures: cavities to ±400 µm and solenoids to ±200 µm after a vertical contraction of ~4 mm. A wire position monitor (WPM) system based on a TESLA design has been developed, built, and tested with a prototype cryomodule. The system is based on the measurement of signals induced in pickups by a 215 MHz signal carried by a wire through the WPMs. The wire is stretched between the warm tank walls parallel to the beam axis providing a position reference. The sensors, one per cavity and two per solenoid, are attached to the cold elements to monitor their motion during pre-alignment, pumping and cool down. A WPM consists of four 50 Ω striplines spaced 90° apart. A GaAs multiplexer scans the WPMs and a Bergoz card converts the rf signals to dc X and Y voltages. National Instruments I/O cards read the dc signals. The data acquisition is based on a PC running LabVIEW. System accuracy is ~7 µm. The paper describes system design, WPM calibration and test results.

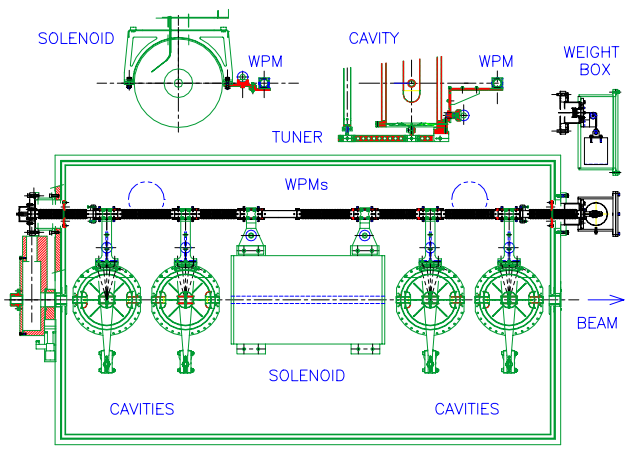

Figure 1: A plan view of a medium beta cryomodule and cross-sections of the wire weight box and WPM mounting brackets.

INTRODUCTION

TRIUMF is now constructing an extension to the ISAC facility, ISAC-II, to permit acceleration of radioactive ion beams up to energies of at least 6.5 MeV/u for masses up to 150. The proposed acceleration scheme will use the existing ISAC RFQ (E = 150 keV/u) with the addition of an ECR charge state booster to achieve the required mass to charge ratio ($A/q \leq 30$) for masses up to 150. A new room temperature IH-DTL will accelerate the beam from the RFQ to 400 keV/u followed by a post-stripper heavy ion SC linac designed to accelerate ions of $A/q \leq 7$ to the final energy. The SC linac will be composed of two-gap, bulk niobium quarter wave rf cavities for acceleration and SC solenoids for periodic transverse focussing, housed in several cryomodules. A total of 48 cavities and 12 solenoids will be used. The center line of each cavity must be aligned to within ±400 µm of the true beamline centre while those of the solenoids must be within ±200 µm.

We will discuss the system that has been designed to monitor changes in the alignment of the cavities and solenoids during pump out and cool down. The system has been tested in the first of five medium beta cryomodules, each containing four cavities and a single solenoid, figure 1 [1,2,3].

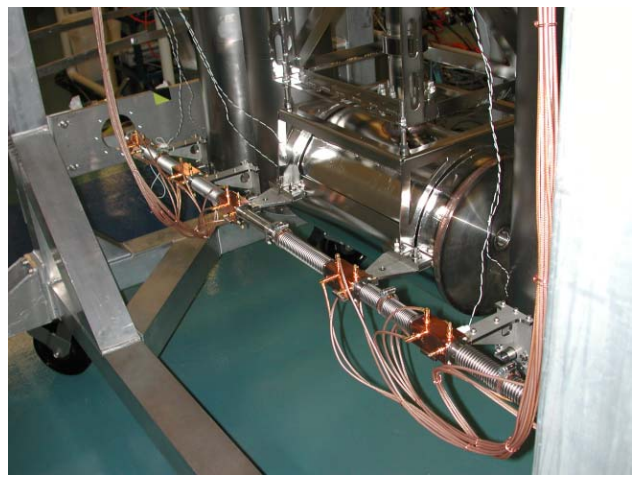

Figure 2: The WPMs and bellows form a coaxial structure. The stripline signals are brought out by 24 rf cables.

MEASUREMENT SYSTEM

WPMs

A stretched wire alignment system based on a TESLA Test Facility system has been developed at TRIUMF [4,5]. Six WPMs, one per cavity and two on the solenoid, are positioned along a wire displaced 30.48 mm horizontally from the beam axis to measure lateral displacements. The wire, stretched between the tank walls, provides a position reference and carries a 215 MHz rf signal. The WPMs are supported from the cold masses by stainless steel brackets, figure 2.

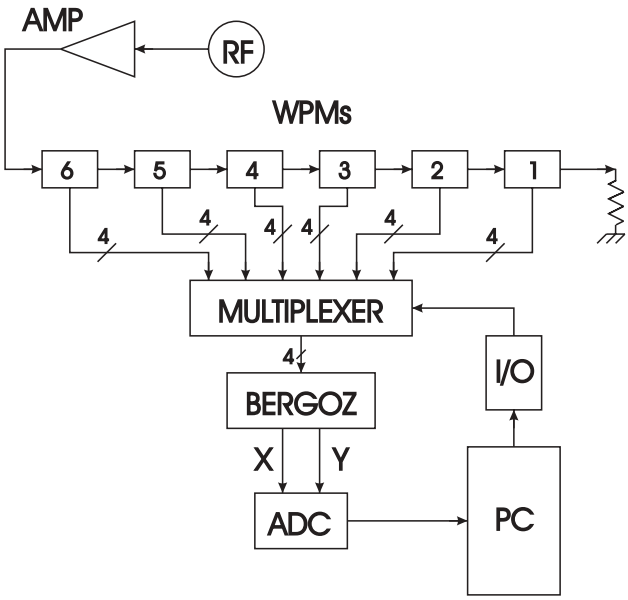

Figure 3: A block diagram of the data acquisition electronics.

Each WPM is similar to a beam position monitor. It contains four Cu plated Al antennas supported by SMA jacks. The downstream ports are connected to the readout electronics which measure the signal amplitudes while the upstream ports are terminated by 50 Ω loads. The striplines are 0.254 mm wide and 61 mm long in a housing with a 28 mm bore. Their heights are set to give 50 Ω impedance using a network analyzer in time domain reflectometry (TDR) mode. Bench tests were performed on a single WPM using rf applied to a rod rigidly supported 3 mm off centre by end caps. The apparatus was cooled using LN_2 in a small cryostat in air and an average change in readings of 16 µm was measured. Some of the change may have been due to condensation or temperature differentials, however.

Position Reference Wire

The 0.5 mm diameter bronze-Cu wire has a sag of 0.162 mm over a length of 2 m with a tensioning load of 4.55 kg provided by a pulley and a weight in the vacuum. The wire passes through pin holes in dielectric disks at each end to define its path. It runs inside thin walled stainless steel bellows between monitors in order to form a flexible coaxial transmission line. The corrugations of the bellows create a slow wave structure. The ends of each bellows are welded to square plates which are screwed to the monitors.

A TDR measurement indicated a wire impedance of 251 Ω. The sum of the signal strengths from each WPM varies by about ±7% along the wire indicating little loss. The rf signal source is not matched to the wire impedance. Instead the rf passes through 10 dB of attenuators and a vacuum feedthrough on the weight box and is connected to the wire by a jumper. The far end of the wire passes through a vacuum feedthrough and is terminated by a 220 Ω resistor. This provides a directivity of 7 dB at the end WPM which is a measure of the quality of the termination. We wish to minimize the reflection as it provides a contribution to the stripline signal strengths which varies with their load resistances.

Cables

The signals are carried to the tank lid SMA feedthroughs by 2.28 m long RG-303 cables. They have FEP and Teflon insulation but are not ideal as their centre conductors are silver plated copper clad steel. 18.3 m long RG-223 double shielded cables carry the signals to the electronics. The total cable loss is 4 dB.

Electronics

The TRIUMF built rf multiplexer uses M/A-Com SW-221 GaAs switches yielding greater than 60 dB isolation and 1.2 dB insertion loss, figure 3. Each of the four channels (l,r,d,u) is housed in a single width NIM module which selects one of the WPMs. The unselected inputs are switched to 50 Ω loads. The Bergoz Instrumentation BPM-mux card is based on a four channel rf multiplexer, a down converter, a single AGC IF amplifier and a homodyne amplitude detector [6]. The card takes care of the rf to dc conversion and is insensitive to rf phase. With our bore and a bandwidth of 10 Hz the Bergoz card contributes a noise to the position measurement of only 0.8 µm rms. A National Instruments PCI bus 16 bit ADC card reads the dc signals and a digital I/O card controls the multiplexer. The PC uses Windows XP and runs a LabVIEW program written by the SIDeA Corporation of Milan. We record the positions only once every 20 s and allow a long settling time of 1 s after selecting WPMs. A Channel Access server is being implemented in the PC to provide an interface to the EPICS control system data archiver.

Calibration

The WPMs are non-linear and must be individually calibrated along with their rf cable sets. A pair of Oriel

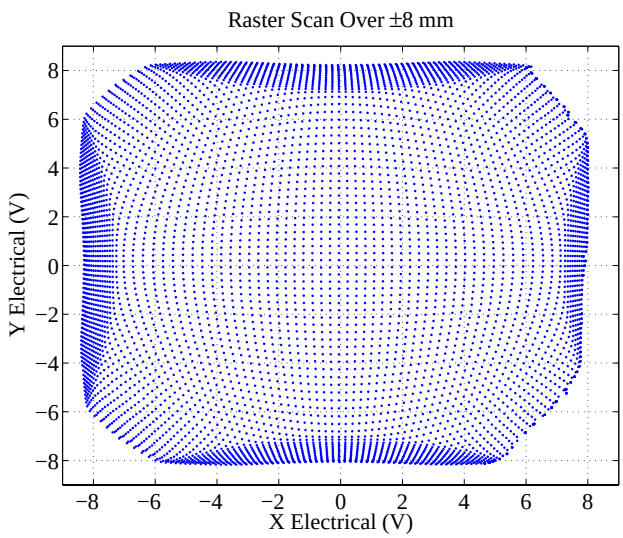

Figure 4: The X and Y voltages from the Bergoz unit are plotted for a calibration raster scan.

translator stages mounted at right angles are used to move a WPM about a stretched wire. The servo motor units contain optical encoders with a resolution of 0.1 µm. The weight box and flanges from the cryomodule are used and the scan is computer controlled. A raster scan with 0.2 mm steps over a range of ±8 mm is shown in figure 4. A 2D, third order polynomial curve fit is used to reduce the data to a set of 20 polynomial coefficients. Beyond ±4.8 mm the electronics sharply compresses the response and though still useable, these points were not included in the curve fits. A fitting error of better than 20 µm was achieved over most of the ±4.8 mm range, exceeding it only near the ends of the range. The overall WPM system accuracy is limited by the precision of the translators, the Bergoz card and the ADC. We estimate it to be 7 µm or less.

RESULTS

Comparison with Optical Measurement

The cryomodule tank was fitted with a pair of optical windows to allow sighting along the beam axis with a telescope. A pair of optical targets was installed in the upstream and downstream cavities. Optical measurements were taken periodically to check for unexpected differences between the WPM position and the position of the cold mass, figure 5. They also provided a calibration of the thermal contraction of the WPM brackets.

Vibration Studies

The WPM system was used to measure mechanical vibrations. The X and Y signals from the Bergoz card were taken to an HP 35665A analyzer. The Bergoz unit completes a sampling of its four inputs at a 2 kHz rate. For small input level changes that do not cause large AGC swings, the bandwidth is the Nyquist limit of 1 kHz. The tuners were used to shake the cavities with a step function, figure 6. The predominant resonance near 6 Hz

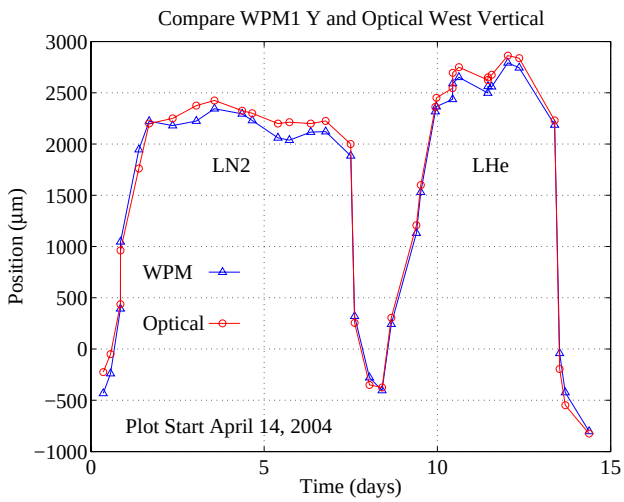

Figure 5: A comparison of the WPM measurements with optical measurements during two cool downs.

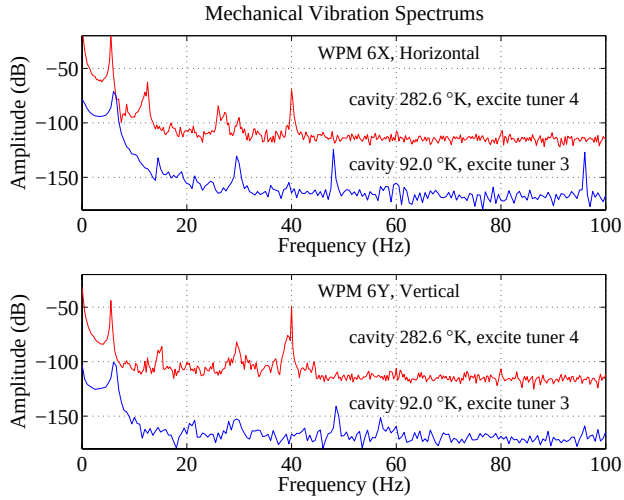

Figure 6: The mechanical vibration spectrum of the cryomodule assembly. The warm spectrums were moved up 60 dB w.r.t. the cool spectrums for clarity.

corresponds to a mainly horizontal movement of the structure with the largest movement being at the downstream end where there is a single support from the tank lid rather than two as at the upstream end. The resonance frequencies increase as the cavity temperatures decrease. The background vibration noise measured during a cool down was less than 7 µm rms.

CONCLUSIONS

The WPM system has advantages over the optical method as it records continuously and does not require personnel to take the readings. It has a high bandwidth and resolution which allow measurement of vibrations.

REFERENCES

[1] G. Stanford et al, "Engineering and Cryogenic Testing of the ISAC-II Medium Beta Cryomodule", this conference

[2] W.R. Rawnsley et al, "Alignment of the ISAC-II Medium Beta Cryomodule with a Wire Monitoring System", 20th International Cryogenic Engineering Conference, Beijing, China, (2004)

[3] W.R. Rawnsley, D. Giove, "ISAC-II Cryomodule Alignment Monitor", TRIUMF Design Note (2003), TRI-DN-03-02

[4] D. Giove, A. Bosotti, C. Pagani, and G. Varisco, "A Wire Position Monitor (WPM) System to Control the Cold Mass Movements Inside the TTF Cryomodule", PAC (1997)

[5] A. Bosotti et al, "On Line Monitoring of the TTF Cryostats Cold Mass with Wire Position Monitors", INFN/TC–00/02, Mar 17, 2000, CERN Library

[6] K.B. Unser, "New Generation Electronics Applied to Beam Position Monitors", Beam Instrumentation Workshop (1996)

SIMULATION OF THE RF COUPLER FOR TRIUMF ISAC-II SUPERCONDUCTING QUARTER WAVE RESONATORS

V. Zvyagintsev, TRIUMF*, 4004 Wesbrook Mall, Vancouver, Canada, V6T2A3

Abstract

The inductive RF coupler for the TRIUMF ISAC-II 106 MHz superconducting accelerating quarter wave resonators [1, 2] was used as a basis for the simulation model of stationary transmission processes of RF power and thermal fluxes. Electromagnetic simulation of the coupler was done with ANSOFT HFSS code. Transmission line theory [3] was used for electromagnetic wave calculations along the drive line to the Coupler. An analogy between electric and thermal processes allows the thermal calculations to be expressed in terms of electrical circuits [4]. The data obtained from the simulation are compared to measured values on the RF coupler.

INTRODUCTION

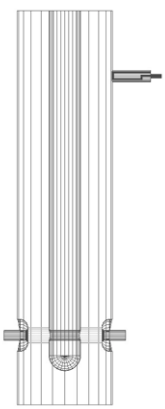

fo	MHz	106
E_a	MV/m	6
P	W	4
Q_o		5.5E+08
U	J	3.3
B_p	mT	60
Δf	Hz	40
β		200
P_f	W	200

$$1/Q_L = 1/Q_o + 1/Q_e \qquad \beta = Q_o/Q_e$$

$$P_f = P\frac{(\beta+1)^2}{4\beta} \qquad \Delta f_L = f_o/Q_L$$

Figure 1: HFSS model of SC TRIUMF ISAC-II medium-β QWR with inductive coupler.

The inductive coupler for the TRIUMF ISAC-II 106 MHz superconducting accelerating quarter wave resonators was designed and successfully tested. The main goal of the design is achieved: the coupler provides more than 200 W forward power which is needed to get an accelerating field E_a=6 MV/m with a bandwidth 40 Hz to maintain a stable cavity operation disturbed by noise and helium pressure fluctuations and thermal load for helium system from the coupler is less than 1 W. Coupler R&D was done with test cryostat and the first TRIUMF ISAC-II cryomodule with 4 medium-β cavities was equipped with new couplers and succesefully tested [1].

* TRIUMF receives funding via a contribution agreement through the National Research Council of Canada

This paper is some attempt to collect the calculation experience from this R&D which can be used for coupler design for next TRIUMF ISAC-II cryomodules which will be equipped with high-β resonators.

HFSS COUPLER SIMULATION

Coupling and Loop Power Dissipation

Due to very high Q of the cavity it is not possible to use the driven mode solution so the eigenmode solution was used instead. For simulation purposes it was assumed that the cavity and coupler were perfect conductors. The coupler port is loaded with an equivalent impedance of 50 Ω. The mesh is refined in the beam and coupler region. The power dissipation on the loop was calculated in the Postprocessor by using normalization for acceleration

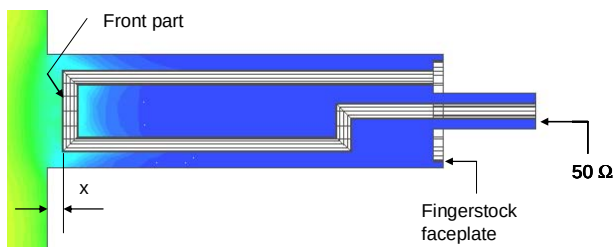

Figure 2: Magnetic field and port bondary condition for HFSS coupling loop model.

field E_a=6 MV/m and conductivity of copper. P_{loop} is the total power dissipated on the loop and P_{front} is the power dissipated on the front part of the loop which is used for analytical check. Data obtained in HFSS calculations at different loop positions are shown in Table 1. Power dissipated on the loop is due to field penetration from the cavity and rf current to the 50 Ω load. In the driven mode which is the real condition for overcoupled operation, the rf current will be very small because a current node appears at the loop as shown in Fig.7. Power dissipation in the load is inversely proportional to the quality factor. By using the external quality factor Q from table 1, and power dissipation P and quality factor Q_o from Fig.1, then power dissipation in the load and power dissipation on the loop due to the rf current through the load P_{loop}* can be calculated (to make a coorection for driven mode). Power dissipation on the loop P_{loop}** for strong overcoupled driven mode is a difference between power dissipation for eigen mode P_{loop} and P_{loop}*. The external quality factor can be defined from the following expression:

$$1/Q_e = 1/Q + 1/Q_{loop} \qquad (1)$$

Loop quality factor defined from loop power dissipation

$$Q_{loop} = 2\pi f_o \frac{U}{P_{loop}} \quad (2)$$

Coupling, bandwidth and forward power (Table 2) are defined according to the well known expressions which are shown in Fig. 1.
Fig.3 is a graph which was created from Table 2 and may be used to define the operating parameters of the

Table 1: HFSS eigensolver calculations of coupling and loop power dissipation for E_a=6 MV/m, f_o=105.940 MHz

x	Q	P_{loop}	P_{front}	P_{loop}*
mm		W	W	W
0	1.37E+06	15.7	10.6	1.495
3	3.49E+06	7.64	4.82	0.585
6	9.35E+06	2.69	1.72	0.219
9	2.50E+07	1.06	0.67	0.082
12	6.75E+07	0.38	0.25	0.030
15	1.85E+08	0.15	0.10	0.011
18	5.12E+08	0.06	0.04	0.004
21	1.48E+09	0.02	0.01	0.001

Table 2: Interpretation of eigensolver HFSS calculations for coupling parameters of the QWR at E_a=6 MV/m

x	Q_L	β	Δf	P_f
mm			Hz	W
0	1.35E+06	410	78.5	412
3	3.43E+06	161	30.9	163
6	9.10E+06	60.0	11.7	62.1
9	2.36E+07	22.5	4.49	24.5
12	5.96E+07	8.31	1.78	10.4
15	1.38E+08	3.04	0.77	5.37
18	2.65E+08	1.10	0.40	4.01
21	4.02E+08	0.38	0.26	5.00

cavity for the ISAC II operation at Ea=6 MV/m. For example, for a bandwidth of 40 Hz the loop position is 2.5 mm, the forward power is 200 watts and the power on the loop is is ~8 watts. After correction by Ploop* value which is ~1 W, power dissipation on the loop becomes ~7 W.

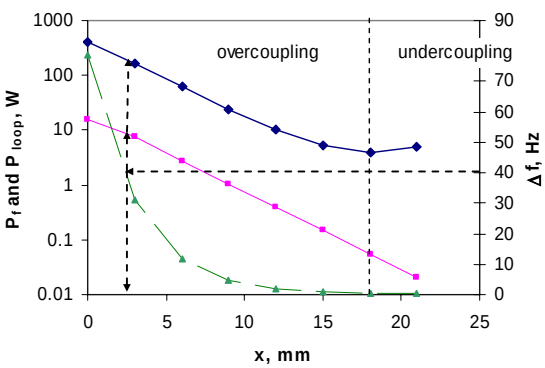

Figure 3: Operating rf parameters of the coupled QWR.

This value should be considered in the thermal design as a potential thermal load for the helium system. During the TRIUMF coupler test we observed effects of loop heating producing a change in the coupling.

Analytical Check

Power dissipation on the front part of the loop (P_{front}) was checked analytically by considering the penetration of the field from the cavity to the coupler housing for the lowest H_{11} mode. The critical wavelength [4] for the coupler housing cylinder with a radius 11 mm is 38 mm and the constant of penetration is γ=167. The field attenuation for loop position of 21 mm is

$$A_{dB} = 20\lg(e^{-\gamma x}) \approx 30dB \quad (3)$$

which is consistent with the P_{front} variation for x values from 0 to 21 mm in Table 1.
Considering the QWR as a lossless transmission line with longitudinal cosine field distribution and using Ampere's law, the magnetic field on the front part of the loop at x=0 is given by:

$$H_{loop} = H_p \frac{r}{R}\cos\left(\frac{2\pi}{\lambda} l_c\right) \quad (4)$$

where r and R are inner and outer radius of the QWR, lc is the distance from the shorted flange of the QWR to the coupler loop. Power dissipation on the front part of the loop is given by:

$$P^*_{front} = \frac{R_s}{2}\int_S |j|^2 ds \approx \frac{R_s}{2}\cdot S \cdot H_{loop}{}^2 \approx 15W \quad (5)$$

By using formula (3) for field attenuation and 15 W for P_{front} at x=0 we can calculate this power for different loop positions. Fig. 4 shows the comparison of numerical and analytical results for power dissipation on the front part of the loop Pfront. Numerical and analytical results are consistent.

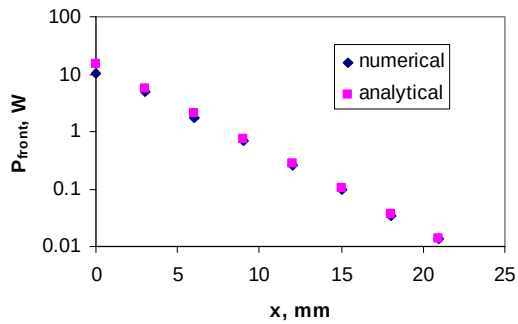

Figure 4: Numerical and analytical Pfront comparison at E_a=6 MV/m.

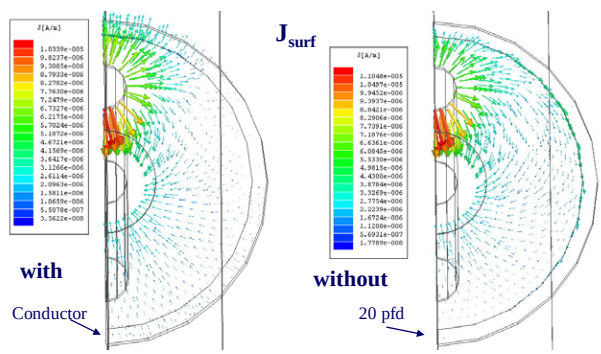

Figure 5: Rf current density distribution on the faceplate of the coupler with and without fingerstock

Fingerstock Problem

Rf fingerstock was initially installed in the coupling loop assembly to provided an rf path to ground for any rf leakage from the cavity through the coupling loop penetration. However this also caused micro dust in the coupling loop housing. To simulate the coupler without fingerstock the boundary condition on the figerstock faceplate (Fig. 2) was changed from a perfect conductor to a capacitive impedance which is eqiuvalent to minimum capacitance of 20 pfd between the coupler body and the coupler housing. This calculation was done for x=3 mm which is close to the operation condition of the cavity. Without fingerstock the same values of resonant frequency and quality factor were obtained. This means that removing the fingerstock does not cause coupling degradation. A coupler test without the fingerstock showed the same coupler performance but more rf leakadge was observed indicated by increased noise on some temperature sensors.

Without the fingerstock the current is no longer perpendicular to the faceplate edge which implies more rf radiation as can be seen in Fig. 5.

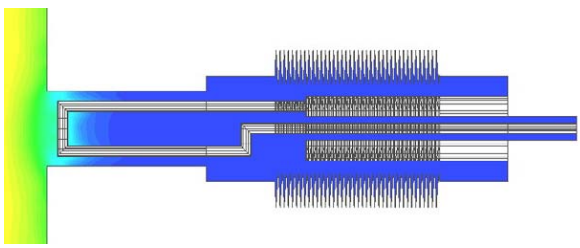

Figure 6: Magnetic field in the HFSS model of coupler with bellows.

Another option to avoid rf leakage is a coupler with bellows which could be used for a separate vacuum design. A HFSS model simulation (Fig. 6) showed a good performance and very low rf losses on the bellows.

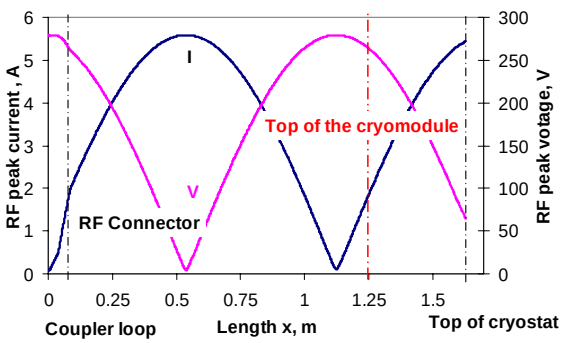

Figure 7: The voltage and current distribution along the coupling line inside of the test cryostat at nominal operating parameters (E_a=6 MV/m, P_f=200 W).

Coupler Drive Line

The most critical part of the coupler drive line is inside of the cryostat. The voltage and current distribution along the line (Fig. 7) are calculated by using well known transmission line theory [3] and considering the line as a chain of elements from the coupling loop (which is a load) to the rf feedthrough on the top of the cryostat (which is the input). Power dissipation on the line at such frequency arises mainly from Joule heating and it is very important to keep rf connectors away from maximum current regions. One can see from Fig. 7 that the length of the coupler line inside of the cryostat is unfortunate and puts the rf feedthrough at a current maximum which caused heating problems. However for the cryomodule the connector is closer to the current minimum and caused no trouble during the test [1].

Thermal Calculations

Thermal calculations were conducted by using an analogy of electrical and thermal processes [4]. Fig.8 shows an example of cell element schematic for thermal analysis which presents power dissipation as current sources and resistors represent properties of the elements for longitudinal and transverse thermal conductivity and heat radiation. The temperature of heat sinks is presented as potentials. The model can be

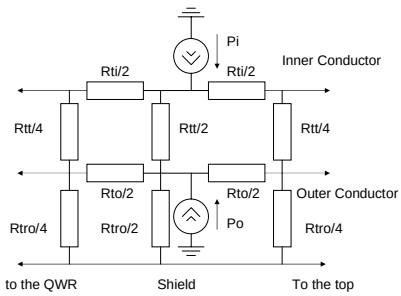

Figure 8: Example of electro-thermical equivalent cell.

solved with standard schematic solvers like PSpice. This technique can be used just for comparison of design options because it is very difficult to predict real cryogenics thermal parameters of contacts.

CONCLUSIONS

The goal for the coupler design is to provide a good rf performance at minimum heat load for helium cryogenics system. HFSS simulation of coupler and coupler line calculations provide some values of thermal loads which should be considered in thermal considerations and calculations to estimate ways to maintain good cryogenic performance of the coupler system.

REFERENCES

[1] R. Poirier, et al, RF coupler design for the TRIUMF ISAC-II superconducting quarter wave resonator, LINAC 2004, MOP88.

[2] A. Facco, et al, Superconducting medium beta prototype for radioactive beam acceleration at TRIUMF, PAC 2001, MPPH134.

[3] J. Dunlop, D. G. Smith. Telecommunications Engineering, 3rd edition 1994.

[4] DOE Fundamentals Handbook. Thermodynamics, heat transfer and fluid flow. Volume 2 of 3.

ENGINEERING AND BUILDING RF STRUCTURES – THE WORKS*

Dale L. Schrage†
Los Alamos National Laboratory, Los Alamos, NM, USA, 87545

Abstract

The translation of the physics designs of linear accelerators into engineering and manufacturing requirements is discussed. The stages of conceptual design, prototyping, final design, construction, and installation are described for both superconducting (LANL $\beta = 0.175$ Spoke Cavity) and normal-conducting (APT/LEDA 6.7 MeV RFQ) accelerators. An overview of codes that have linked accelerator cavity and thermal/structural analysis modules is provided.

INTRODUCTION

Over the past few decades, the field of design of linear accelerators has progressed as the programmatic needs have evolved to requirements for better performance in terms of higher duty factor, higher beam current, and higher accelerating gradient. The requirements for normal-conducting proton accelerators have advanced from such low-power applications as the Beam Experiment Aboard a Rocket (BEAR) of 30 mAmps 1 MeV of H^- at 0.025% duty factor, average beam power of 8 watts [1], to the Low Energy Demonstration Accelerator (LEDA) of 100 mAmps 6.7 MeV of H^+ at CW duty factor, average beam power of 670 Kwatts [2]. These high beam power applications become thermal management challenges. The lower duty factor applications can become similarly difficult if the accelerating gradient becomes sufficiently high that the RF thermal load is high.

For superconducting accelerators, the requirements have advanced from the Continuous Electron Beam Accelerator Facility (CEBAF) at 0.1 mAmps of e^- at CW duty factor with a gradient of 5 Mvolts/meter [3] to pulsed applications of non-relativistic beams such as the Spallation Neutron Source (SNS) [4], 30 mAmps of H^- at $\beta = 0.65$ and pulsed at 60 Hz and to the TESLA accelerator with $\beta = 1$ cavities operated at a gradient of 35 Mvolts/meter [5]. The medium-β ($0.5 \leq \beta < 1.0$) pulsed accelerators, which utilize elliptical cavities, present significant structural challenges in dealing with the Lorentz force detuning and the effects of vibration. Both phenomena cause deformation of the cavity structure and interact with the cavity fields and frequency.

Low velocity applications have advanced from the heavy ion cavities (split-ring resonators @$\beta = 0.06$) for the ATLAS Project [6] to the higher-β spoke cavities for waste transmutation, 30 mAmps of H^+ [7]; both are at CW duty factor. Recent developments on the RIA Project [8] have led to consideration of use of spoke cavities at up to $\beta = 0.6$ [9]. These low-β accelerators utilize much stiffer geometries such as 1/4-λ and spoke resonators. For these, the Lorentz force coefficients are much lower and the structural dynamics considerations are less severe. However, with the low beam current and resulting high loaded Q, there are microphonics concerns that must be addressed. And, there are still static loading issues (e.g., vacuum) and the matter of tuning forces. For spoke cavities with more than two gaps, the development of frequency tuning schemes involves interaction of the RF and structural analyses.

During the past decade, commercial codes have been developed that link the RF cavity, thermal, fluid dynamics, and structural analyses to a single CAD model. The first finite element codes in the US were developed in the 1950's for the structural design of military aircraft. Linked thermal analyses modules were added to these in the 1980's. Three-dimensional RF cavity codes and computational fluid dynamics (CFD) codes were developed independently during the 1980's. In the mid-1990's, the code vendors began linking the CFD module to the thermal module and created RF cavity modules that were then linked.

NORMAL-CONDUCTING CAVITIES

The analysis of normal-conducting cavities falls into two categories: cavities that are basically 2-dimensional and those that have significant 3-dimensional features. Except for the end regions, RFQs are basically two-dimensional structures. The cavity can be analyzed using SUPERFISH [10] for the determination of resonant frequency, quality factor, peak electric and magnetic fields, RF thermal loads, and tuning sensitivity. It is possible to create FORTRAN or C^{++} code to parse the input and output files of SUPERFISH to extract the cavity geometry, RF thermal loads, and tuning sensitivity information and to produce files that can be input to commercial thermal and structural finite element analysis (FEA) codes. The thermal module of the FEA code is run to determine the temperature distribution and that is then input to the structural module to determine the displacements and stresses. The displacement output file of the FEA code is then convolved with the tuning sensitivity data from SUPERFISH to predict the frequency shift. These programs can be run in batch mode and iteratively to solve for the coolant temperature necessary to maintain the cavity on resonance.

This procedure worked very well for the LEDA RFQ [2]. This 8-meter long cavity (Figure 1) had longitudinally variable electric field and vane skirt width. Thus, multiple

* Work Supported by the US Department of Energy
† dls@lanl.gov

SUPERFISH and FEA runs were required. The key requirement here was to maintain the longitudinal temperature increase in each of the coolant passages to be equal so that the thermal expansion of the cavity would be uniform and dipole modes would not be created. In order to accomplish this, the cross-sections and locations of the coolant passages were iterated until that condition was met. This required multiple iterations of SUPERFISH and the FEA code. Success was achieved as determined by the actual coolant temperatures required to maintain resonance being within 1.0 °C of the values predicted by the analysis.

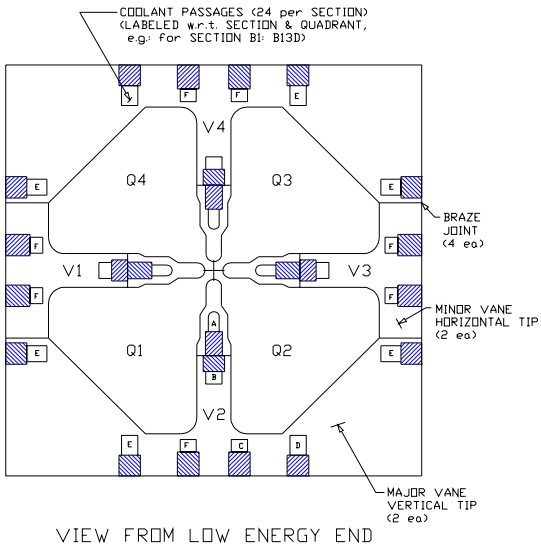

Figure 1: APT/LEDA RFQ CAVITY.

Accelerators do not always end up operating at the levels that were planned for. There are two significant examples. The RFQ for the Superconducting SuperCollider Laboratory (SSC) [11] was specified at a very low duty factor, 0.05%. This RFQ was operated successfully until the demise of the SSC. Following that, the linac was obtained as surplus equipment by a manufacturer of medical isotopes. With no modifications, the SSC RFQ is operated at 3% duty factor for the production of radioisotopes [12]. Fortunately, the 0.05% duty factor was above the level at which natural convection cooling would have been suitable so water-cooling passages were incorporated into the cavity.

A more recent case was the LEDA RFQ (Figure 2). It was not possible to achieve the specified transmission (95%) at the design electrical field level. It was necessary to increase the RF field level by 10%, corresponding to a 21% increase in RF power and thermal load on the cavity [13]. Fortunately, this was well within the design margins. A comparison of the design and operating levels of the SSC and LEDA RFQs is given on Table 1.

The incorporation of a CFD module linked to the thermal FEA module allows analysis of complex 3-dimensional cavity geometries with spatially variant high (~100 watts/cm^2) RF thermal loads. The APT/LEDA CCDTL [14] is an example of such a cavity that was analyzed using such a code. Figure 3 shows a half-cell of a 3-gap CCDTL cavity along with its coolant passage arrangement.

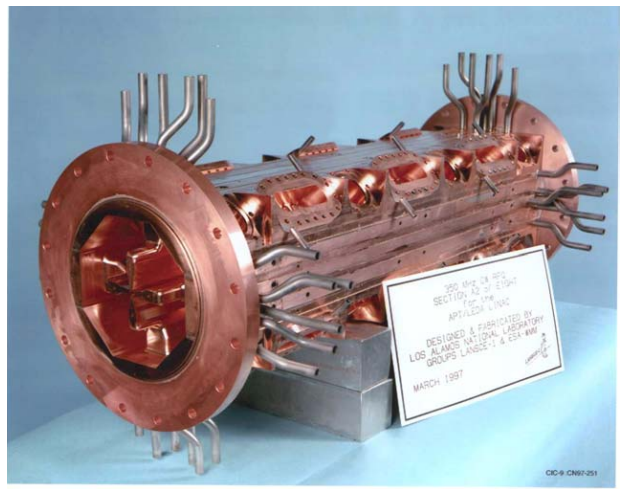

Figure 2: LEDA RFQ Section.

Table 1: RFQ Power Levels

	SSC 1992		LEDA 1995	
	Design	**Oper.**	**Design**	**Oper.**
Duty Factor	0.05%	3%	CW	CW
Energy MeV	2.5	2.5	6.7	6.7
Peak Current mAmp	27.	27.	100.	100.
Average Current mAmp	0.014	0.81	100.	100.
Beam Power kWatts	0.034	2	670.	670.
Cavity Power Kwatts/m	0.06	3.7	150.	182.
Average Heat Flux watt/cm^2	0.01	0.63	13.	16.
Peak Heat Flux watt/cm^2	0.05	3.2	65.	79.

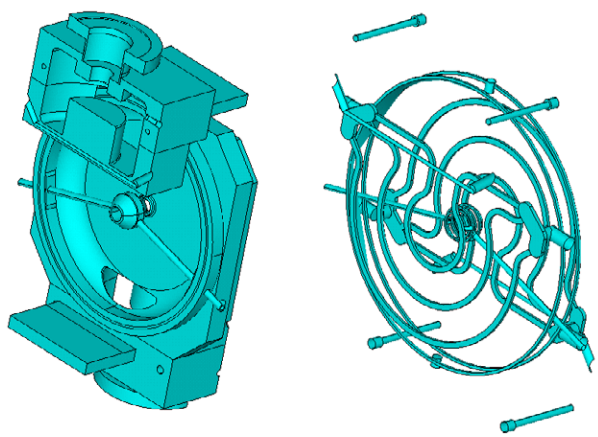

Figure 3: APT/LEDA CCDTL CAVITY & COOLANT PASSAGES [16].

Linked RF/CFD/thermal/structural analysis of the APT/LEDA CCDTL cavity was carried out using ANSYS

[15]. The predictions [16] closely matched the values of temperature and frequency shift measured on the full-power engineering model of the cavity. Similar analysis of a very high power RF photoinjector cavity [17] has been done.

The CFD modules may be used in two fashions: full CFD calculation resulting in the prediction of heat transfer coefficients or input of heat transfer coefficients obtained from empirical relations. Use of the full CFD calculation requires solution of the Navier-Stokes equations and requires considerable computing time. This is seldom justified given the good performance of the empirical predictions of the heat transfer coefficients.

The fabrication of normal-conducting accelerator cavities usually involves furnace brazing of OFE copper (ASTM F-68-99 Class 2 or better) structures. Cavities for very low duty factor applications [1] have also been fabricated from copper-plated aluminum. LANL's 30+ years of experience has been almost exclusively with "atmospheric" brazing. Brazing in an atmosphere of H_2 has the advantages of convection heating and de-oxidizing ("fluxing") of the parts. The convection heating allows better spatial control of the temperature within the furnace and assures that all parts, large and small, reflective and non-reflective, are heated nearly uniformly. Other institutions have successfully utilized vacuum furnace brazing in the manufacture of linac cavities. The advantage of vacuum brazing is that hydrogen absorption is not a concern. There are brazing job shops that provide excellent services for both atmospheric and vacuum furnace brazing.

SUPERCONDUCTING CAVITIES

The main issues in the engineering design of superconducting cavities are structural. For elliptical cavities, the RF/structural issues are generally axi-symmetric loads (Lorentz pressure or vacuum) on axi-symmetric cavities. So, the use of SUPERFISH in conjunction with a commercial structural code will suffice in most cases. For issues of structural dynamics, the non-axi-symmetric features such as the end regions (power coupler & HOM ports) and the attachment to the cryomodule are significant and thus full 3-dimensional structural analysis is required.

Pulsed Applications of Elliptical Cavities

The main concern in pulsed operation of elliptical cavities is the Lorentz force de-tuning. This can be predicted via SUPERFISH and commercial structural FEA codes. LANL uses COSMOS/M [18] for this application. The use of axi-symmetric plane elements allows the effects of weld preparations (thinned regions) to be accurately modeled. The link to SUPERFISH is as described in Section 2.

Personnel at the National Institute of Nuclear Physics (INFN) at Milan have developed a very powerful user-friendly tool for analysis of elliptical superconducting cavities [19]. This code links SUPERFISH to ANSYS and facilitates analysis of single- and multi-cell axi-symmetric cavities. The code provides prediction of Lorentz force de-tuning, vacuum frequency shift, and tuning sensitivity as well as calculation of stresses for stiffened and un-stiffened cavities. The code is linked to a database manager that keeps track of all analysis cases run. Thus it is quite easy to study the effects of variations of the cavity geometry. The INFN code was used for the design of the superconducting elliptical cavities for the Spallation Neutron Source [20].

Low-β Applications

The low-β cavities are very much 3-dimensional in terms of both their RF and structural properties. A typical spoke resonator cavity, the LANL/AAA β = 0.175, 2-Gap, 350 MHz Cavity [21], is shown on Figures 4 and 5. This is a very complex cavity and very little can be learned about such a cavity through the use of axi-symmetric or 2-dimensional analysis codes.

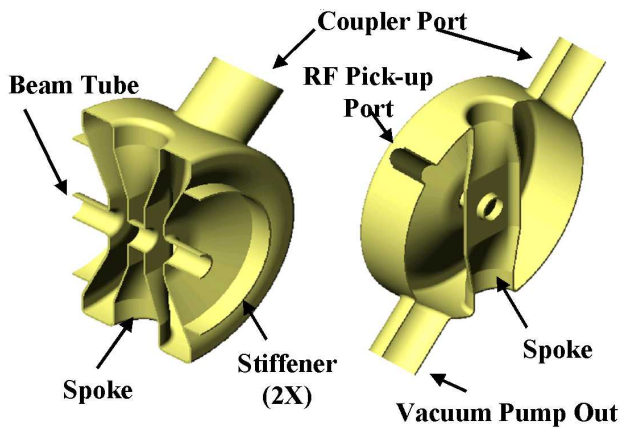

Figure 4: Cross-Section of LANL/AAA β = 0.175, 2-Gap, 350 MHz Cavity.

Figure 5: LANL/AAA β = 0.175, 2-Gap, 350 MHz Cavity.

The RF design of this cavity was performed using Microwave Studio [22]. The solid model of the cavity volume was created using the UNIGRAPHICS CAD system [23] and exported via "Standard ACIS Text" (SAT) file.

Linked RF/structural analysis was performed using MICAV [24] linked to COSMOS/M [18]. For this analysis, the cavity volume is "shelled out" to form the sheet metal niobium structure. The RF cavity module meshes the cavity volume while the structural module meshes the structural shell. The nodes on the cavity surface are merged to the nodes on the interior surface of the structural model. The resonant frequency was predicted to within 0.3% and was possible to predict the tuning sensitivity and vacuum frequency shift to an accuracy of about 20% [25]. That is reasonable agreement considering the uncertainties in precisely modeling the weld joints of the cavity stiffeners.

A similar analysis and measurements was carried out on an ANL β=0.34, 2-gap cavity [26] with results having similar accuracy. The prediction of the RF resonant frequency was again better than 0.3 %.

Most elliptical and low-β superconducting cavities are constructed of high purity (high RRR) niobium. The manufacturing technology was developed at Cornell University and at ANL more than 20 years ago. There are vendors in Europe, Japan, and the US that will produce very fine cavities on a firm, fixed-price basis. None of the vendors presently has the capability of high-temperature processing.

Larger (lower frequency) elliptical cavities are often constructed of copper with a very thin layer of niobium sputtered onto the RF surfaces. These cavities are also built in industry.

CODE VERIFICATION

The RF cavity codes that we had access to were run to determine the accuracy of the calculation of the normal-conducting resonant frequency of the ANL β = 0.34, 2-Gap, 340 MHz Cavity. A model consisting of one-quarter of the cavity was created using SOLIDWORKS [27]. A "Standard ACIS Text" (SAT) file was created from the solid model and this served as the input geometry file for all of five codes that were tested. The geometry is shown on Figure 6. The facets shown in the figure are for visual clarification; they do not represent the elements for the analysis.

The results are given in Table 2. The comparison among the codes is excellent. None of the analysis cases were optimized with respect to node and element density in order to maximize the accuracy. The characteristic of this (and many other) superconducting cavity shapes is that the cavity frequency is established prior to making the final closure weld so precision of greater than 0.3% (1 MHz for this cavity) is not required.

These commercial codes were not written specifically for the analysis and design of accelerator cavities. So, there are parameters that are not calculated directly. Depending upon the code, these may include stored energy, transit time factor, shunt impedance, and other parameters. In most cases, it is possible to extract data from the results file and to process that data to calculate the desired parameters.

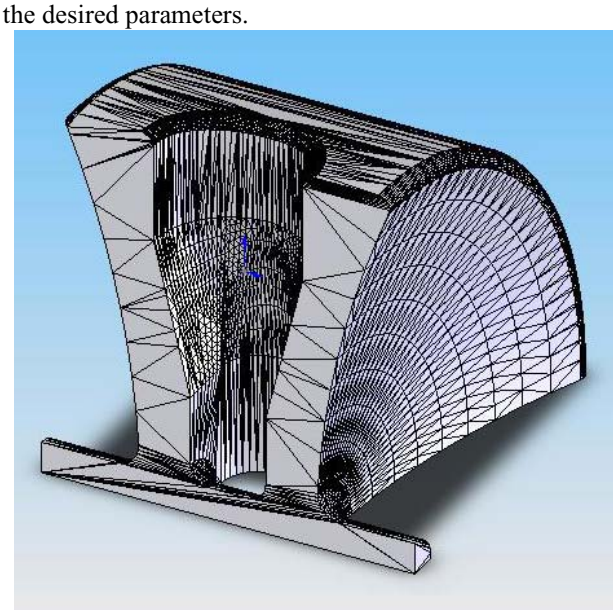

Figure 6: 1/4 Model of ANL β = 0.34, 2-Gap, 340 MHz Cavity for RF & Structural Analysis.

Table 2: Comparison of Frequency Results

CODE	REF	FREQ	Q_o	TTF
MAFIA	22,28	340.01	4621	0.905
ANALYST	28,29	340.50	4694	0.906
MICAV	24,28	340.33	4799	0.900
MWS	22,28	340.56	4554	0.905
ANSYS	15,30	340.77	4463	0.886
MEAS.	26	339.70	4815	N/A

CONCLUSIONS

The linked RF/thermal/CFD/structural codes do work. Workers at laboratories throughout the world have been successful in predicting the thermal and structural performance of accelerator cavities using these codes. Use of these codes allows accurate prediction of resonant frequencies, Lorentz force de-tuning, tuning sensitivities and mechanical resonant frequencies. Most important, these codes allow cost-effective optimization of the cavity geometry and, for superconducting cavities, the location and shape of external stiffeners.

RECOMMENDATIONS

It is clear that we now have some very powerful tools for the simulation and analysis of the RF, thermal, and structural behavior of accelerator cavities, both normal-conducting and superconducting. So, the obvious question is "can we abandon the use of low-power facsimile cavities, engineering models, and 'hot' models?"

The answer is very definitely "NO!" Simulation is no substitute for experiment. The only thing that can come out of a simulation is what was put into it. Unknown and/or forgotten phenomena will not appear in simulation results. So, some experimentation will continue to be required. However, the availability of these powerful linked codes does serve to mitigate the amount of experimentation required.

A good example of where simulation could not have substituted for experiment was in the development of the segmented resonantly coupled RFQ [31]. None of the codes that we have available today incorporate the features that made this development possible.

Secondly, while these codes work reasonably well for the prediction of the resonant frequencies and tuning sensitivities of accelerator cavities, account must be taken of manufacturing tolerances. These codes can be used to study the effects of manufacturing tolerances to bound the range of frequencies. They are most valuable in determining the tuning sensitivities of the cavities.

So, the general recommendation is that these linked codes be utilized to design the cavity geometry, specify the arrangement of cooling passages, specify the arrangement of stiffeners, predict the effect of vacuum loading,

ACKNOWLEDGEMENTS

Individuals who contributed advice to this paper include Frank Krawczyk (LANL), Richard LaFave (Varian Medical Systems), Tom Schultheiss (Advanced Energy Systems), Lloyd Young (TechSource) and Rick Wood (LANL).

REFERENCES

[1] D. Schrage, et al, "A Flight Qualified RFQ for the BEAR Project," Proc. of the 1988 LINAC Conference, Williamsburg, VA
[2] D. Schrage, et al, "CW RFQ Fabrication and Engineering," 1998 Linear Accelerator Conference, Chicago, IL, August, 1998
[3] C. Reece, et al, "Performance Experience with the CEBAF SRF Cavities," Proc. of the 1995 Particle Accelerator Conference, Dallas TX
[4] J. Wei, "The Spallation Neutron Source Project – Physical Challenges," Proc. of the 2002 European Particle Accelerator Conference, Paris, FR
[5] L. Lilje, et al, "Achievement of 35 MV/m in the Superconducting Nine-Cell Cavities for TESLA," TESLA Report 2004-05
[6] L. Bollinger, "The Argonne Tandem-Linac Accelerator System," Proc. of the 1983 Particle Accelerator Conference, Santa FE, NM
[7] G. Lawrence, "High-Power Accelerator Technology for ATW," International ATW Workshop, Washington, DC, 1999
[8] J. Nolen, "The U.S. Rare Isotope Accelerator Project, "Proc. of the 2002 Linear Accelerator Conference, Gyeongju, South Korea
[9] K. Shepard, P. Ostroumov, & J. Delayen, "High-Energy Ion Linacs Based on Superconducting Spoke Cavities," Physics Review of Science & Technology - Accelerator Beams, Vol. 6, 2003
[10] J. H. Billen and L. M. Young, "Poisson SUPERFISH," Los Alamos National Laboratory Report LA-UR-96-1834 (revision July 15, 2002).
[11] D. Schrage, et al, "Radio Frequency Quadrupole Linac for the Superconducting Super Collider," Proc. of the 12th International Conference on the Application of Linear Accelerators in Research & Industry, Nuclear Instrumentation & Methods, 1992
[12] www.traceradiochemical.com
[13] L. Young, et al, "Low-Energy Demonstration Accelerator (LEDA) Radio-Frequency Quadrupole (RFQ) Results," Proc. of the High Brightness Beams Workshop, November 1999
[14] R. Wood, et al, "Thermal/Structural Design And Fabrication Development Of High Power CCDTL & CCL Structures," Proc. of 1996 Linac Conference, Geneva, Switzerland, Aug. 1996
[15] www.ansys.com
[16] T. Schultheiss, "Analysis to Determine Steady State Temperature and Stress Distributions of the APT LEDA Hot Model Cavity Assembly Operating at Full Field Levels," AES-R-00-016, Feb. 2000
[17] S. Kurennoy, et al, "RF Couplers for Normal-Conducting Photoinjector of High-Power CW FEL," submitted to the Annual Meeting of the American Physical Society, Denver, CO, April 2004
[18] www.cosmosm.com/
[19] P. Pierini, et al, "Cavity Design Tools and Applications to the TRASCO Project," Proc. of the 9th Workshop on RF Superconductivity, Santa Fe, NM, 1999
[20]G. Ciovati, et al, "Superconducting Prototype Cavities for the Spallation Neutron Source (SNS) Project," Proc. of the 10th Workshop on RF Superconductivity, Tsukuba, Japan, September 2001
[21] T. Tajima, et al, "Test Results of two LANL β = 0.175, 350-MHz, 2-Gap Spoke Cavities," Proc. of the 2003 IEEE Particle Accelerator Conference, Portland, OR
[22] www.cst.de/
[23] www.ugs.com/products/nx/
[24] www.electromagneticworks.com/main.html
[25] R. LaFave, "MICAV Validation," Memo, LANL, LANSCE-1:01-005, January 2001
[26] T. Tajima, et al, "Evaluation and Testing of a Low-β Spoke Resonator," Proc. of the PAC 2001 Conference, Chicago, IL
[27] www.solidworks.com/
[28] F. Krawczyk, LANL, personal communication
[29] www.staarinc.com/
[30] T. Schultheiss, AES, personal communication
[31] L. Young, "Segmented Resonantly Coupled Radio-Frequency Quadrupole (RFQ)," Proc. of the 1993 IEEE Particle Accelerator Conference, Washington, DC. 1993.

SURVEY OF ADVANCED ACCELERATION TECHNIQUES

C. Joshi, UCLA, Los Angeles, CA 90095 USA

Abstract

In this paper I will survey some of the notable progress that has been made on advanced techniques for particle acceleration. Rather than trying to cover every technique superficially I will restrict myself to talking about three schemes that are showing promise: the inverse free electron laser (IFEL), the laser-wakefield acceleration (LWFA), and the beam-driven plasma-wakefield acceleration (PWFA). The progress made in all these schemes was recently presented at the AAC2004 Workshop at Stonybrook in June and in many instances the results presented by the authors are as yet unpublished.

INVERSE FREE ELECTRON LASER RESEARCH (IFEL)

In an IFEL, one uses a periodic magnet array (a.k.a., a wiggler or an undulator) to cause electron trajectory to oscillate as the electron beam traverses the array (Fig. 1). A laser beam is co-propagated with the electron beam. Now net energy exchange is possible from the laser beam to the electron if the resonance condition

$$\gamma^2 = \frac{\lambda_w}{2\lambda_L}\left(1+\frac{K^2}{2}\right) \qquad (1)$$

is satisfied. Here γ is the relativistic Lorentz factor, λ_w and λ_L are the wavelengths of the wiggler and the laser respectively, and $K = eB_o\lambda_w/2\pi mc$ is the wiggler strength parameter. Clearly, as the beam energy (γ) increases one has to either increase λ_w by tapering the wiggler or increase K or both.

The IFEL principle can be used to bunch the electron beam on the laser wavelength scale. Here the idea is to velocity modulate the electron beam by sending it through a short section of an undulator. The velocity modulated beam then bunches as it goes through a magnetic chicane.

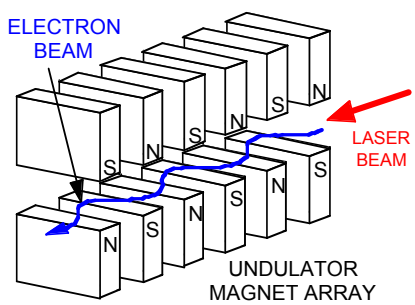

Figure 1: Schematic of the Inverse-Free Electron Laser.

Recent Experiments on the IFEL Scheme

There have been two notable recent experiments on the IFEL scheme. In the first experiment, knows as STELLA[1] for Staged Electron Laser Acceleration, a beam of nominally 45 MeV electrons from the Advanced Test Facility (ATF) at BNL was first sent through an IFEL pre-buncher magnet. This magnet was followed by a chicane compressor and then a second tapered undulator. A CO_2 laser was sent collinearly with the electron beam. The laser was focused at the center of the tapered wiggler to give a peak intensity of $\sim 2 \times 10^{12}$ W/cm^2. This meant that the laser intensity in the pre-buncher section was much lower. Nevertheless, it was sufficient to achieve a ±0.5% momentum modulation. The chicane delivered a bunched beam at the entrance of the tapered undulator. Since the same CO_2 laser beam is used to microbunch the beam and accelerate the pre-bunched beam, phasing between the two is preserved. A spectrometer which analyses the beam exiting the tapered undulator shows acceleration of the pre-bunched beam with an average gradient of 27 MeV/m. The capture efficiency of the pre-bunched beam under optimum condition was over 80% and the accelerated beam has $\lesssim$1% energy spread.[2]

This experiment is extremely significant because it showed many firsts: staged laser acceleration, acceleration of monoenergetic beam and extremely good capture efficiency.

The STELLA collaboration is now planning to do a much higher gradient two-staged laser acceleration experiment. In this method an IFEL prebuncher is used as before to micro-bunch the electron beam on the laser wavelength scale. However, this is followed by a plasma wave excited by the same intense laser in a plasma. Since gradients on the order 1 GeV/m are readily observed in plasmas, it is hoped that mono-energetic acceleration at high gradients can be demonstrated using this two-stage approach that combines IFEL and plasma wakefield technologies.[3]

In a second recent experiment at UCLA's Neptune laboratory, a more powerful, 300 GW, CO_2 laser was used in conjunction with a strongly tapered undulator. Consequently, the nominally 14 MeV electron beam was accelerated out to more than 30 MeV with a peak gradient of > 50 MeV/m.[4] These gradients are beginning to get interesting to be of use in practical devices.

LASER WAKEFIELD ACCELERATOR (LWFA)

Now I will describe recent breakthroughs in the laser-plasma accelerator field. In particular I will confine my remarks to the so-called LWFA scheme (see Fig. 2) where

a short but intense pulse of photons, approximately half a plasma wavelength long excites a relativistic, $v_\phi \sim c$, wake behind the laser pulse[5]. Simple estimates using Gauss' law show that the longitudinal electric field associated with such wakes scales as $\sqrt{n_e}$. This scaling has been shown to be valid over a range of densities from 10^{16}cm^{-3}–10^{20}cm^{-3} and maximum gradients of up to 200 GeV/m have been obtained over a mm.[6] Thus typical energy gains have been in the range from tens to 200 MeV with monotonically decaying electron energy distribution up to some maximum energy. The electrons have been mostly self-trapped by a process known as wavebreaking.[7] The charge emitted from the plasma has been in the few nanocoulomb range and the angular divergence of the emitted electrons has been narrow (few degrees). Clearly, the next challenges facing the laser-plasma accelerator researchers are: a) increasing the energy gain up to the so-called dephasing limit by increasing the interaction length , b) demonstrating that a "monoenergetic" beam can be produced from such accelerators and that this beam is short compared to the wavelength of the accelerating structure and c) staging.

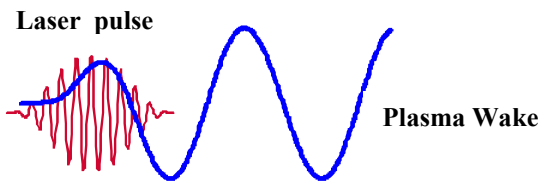

Figure 2: Schematic of the laser wakefield accelerator.

Recent Experiments on Increasing the Plasma Length

The length of the region over which a plasma wake can be excited is limited by the diffraction of the laser beam to roughly $L_{diff} = \pi\lambda_R = \pi^2 w_o^2/\lambda$. To overcome this limit the laser beam must be guided in a waveguide formed in the plasma. Fortunately a plasma with a parabolic transverse density profile with a minimum on its axis acts as a guiding structure for photons. (see Fig. 3)

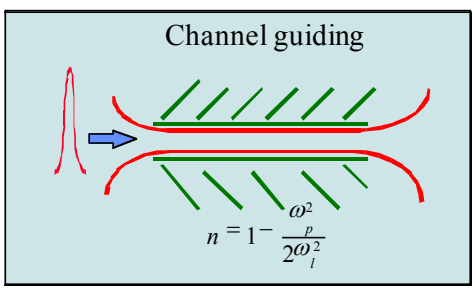

Figure 3: Schematic of a plasma channel for guiding a laser beam.

Researchers are pursuing different schemes for generating plasma channels for guiding high power laser beams. These basically fall into four categories: a) plasma heating followed by hydrodynamic expansion of the heated column[8], b) ablation of wall material in a capillary discharge[9], c) z-pinch discharges[10], and d) gas filled capillary discharges[11]. Of these hydrodynamically formed plasma channels have been shown to guide the highest intensity (~2×10^{18} W/cm^2) laser pulses. On the other hand hydrogen filled capillary discharges promise much longer length plasma waveguides approaching the dephasing length limit of $L_{dph} \sim (\lambda_p/2)/(1-v_g/c)$.

Recent Experiments "Monoenergeitc Beam" Generation

In a rf driven particle accelerator, the energy spread of the beam is small because, the bunch length is much smaller than the rf wavelength. In LWFA experiments the plasma wavelength is on the order 10 μm (30 fs) and the challenge of externally injecting a pre-bunched beam is made far more challenging than in the IFEL case by the extremely large radial fields ($E_r \sim E_z \sim 100$ GeV/m). So the ultrashort bunches must somehow be generated in situ. Various methods for locally triggering the trapping of electrons from the plasma itself using a second laser pulse have been proposed but to-date none has been shown to produce the desired effect. However, recently, three groups LBNL (USA), L.O.A. (France) and RAL (U.K.)[12] have independently and serendipitously shown quasi-monoenergetic acceleration of ~ hundred pico-coulomb charge of electrons to ~ 100 MeV. In all three schemes an extremely short laser pulse blows out the plasma electrons mainly radially which snap back behind the laser pulse forming an accelerating bucket (both in real space and in phase space). Some of the electrons are self-trapped from the walls of this bucket and begin to be accelerated. The beam loading due to these self-trapped electrons in so severe that the trapping soon terminates. At the same time laser pulse evolves both in the frequency domain and in the time domain such that the group velocity of the modified pulse slows down. Now the dephasing length is reduced and some of the accelerating electrons overtake the accelerating portion of the longitudinal field and begin to slow down while electrons trapped later are still gaining energy. The fortuitous confluence of this extremely nonlinear laser and wake evolution leads to a relatively monoenergetic beam of electrons in phase space.[13]

Using more powerful 100 TW class lasers that are coming online it should be possible to obtain relatively monoenergetic bunches of electrons containing 0.5 nC of charge with energies around 500 MeV in the near future.

Staging

Recently, the NRL (USA) group[14] has attempted to do a two-stage plasma acceleration experiment. Here field ionization of a nitrogen gas with an intense laser produces forward going, mildly relativistic electrons that

were subsequently further accelerated by a wakefield produced in a helium plasma. Only when electrons from nitrogen field-ionization were injected with the appropriate delay was there an enhanced emission of electrons with energies greater than 20 MeV indicating a causal relationship. Further results from this group are awaited with interest.

BEAM-DRIVEN PLASMA WAKEFIELD ACCELERATION

Plasma Wakefield Acceleration (PWFA) is one of the most vigorously pursued advanced acceleration scheme at this time. In this scheme the high-gradient wakefield is driven by an intense, high-energy charged particle beam as it passes through the plasma. In the case of an electron beam the space-charge of the bunch blows out the plasma electrons which rush back in and overshoot setting up a plasma oscillation (See Fig. 4). A second, appropriately phased accelerating beam, containing fewer particles than the drive beam, can now be accelerated by the wake. Both electron and positron beams can be used to drive plasma wakes. In the case of a positron beam the plasma electrons are "pulled in" instead of being expelled as in the case of an electron beam driver. The PWFA scheme is very attractive because of its potential to double the beam energy of a high energy accelerator beam in a single stage of acceleration that is only tens of meters long using existing state-of-the-art driver beams.

Recently there have been breakthrough developments

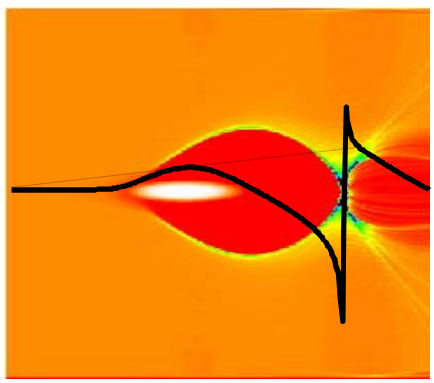

Figure 4: Schematic of the PWFA scheme.

on this scheme by the E164X collaboration[15] of scientists from UCLA, USC and SLAC using the 28.5 GeV electron beam from the Stanford Linear Accelerator. In earlier experiments this collaboration demonstrated acceleration of both electrons and positrons using typically 4 ps long bunches that contained a peak current of about 1 kA. When such e^+/e^- bunches were propagated through a 1.4 m long, ~ $5 \times 10^{14} cm^{-3}$ density lithium plasma gradients on the order 50 MeV/m for e^+ and 200 MeV/m for e^- were observed. The gradient scales as inverse square of the bunch length for a fixed number of particles. This scaling has been confirmed in computer simulations and useful gradients on the order 50 GeV/m

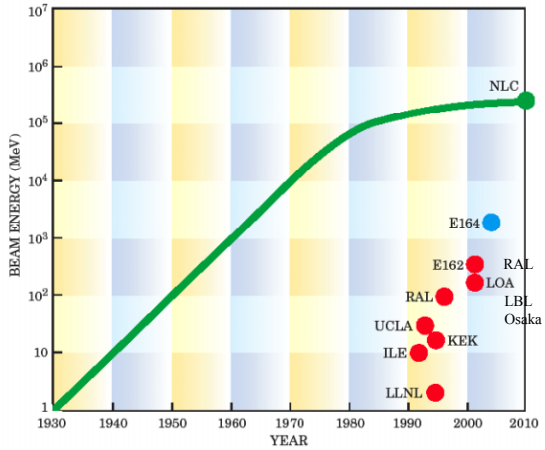

Figure 5: Maximum electron energies achieved in plasma acceleration experiments in different laboratories around the world.

have been observed using 35 μm long bunches with a peak current of ~10kA. Fortunately the Sub-Picosecond Pulse Source (SPPS) at SLAC has been able to deliver bunches as short as 20 μm. The self-fields of such short, intense bunches is large enough to field-ionize Lithium to produce long homogeneous plasmas with densities in the $10^{17} cm^{-3}$ range. Using such short beams the E164X experiment has conclusively demonstrated acceleration of electrons by up to 4 GeV in just 10 cm long plasma. Furthermore, the energy gain is limited by the energy acceptance of the Final Focus Test Beam (FFTB) beamline. If this were not the case energy gains of 10 GeV and perhaps even greater may be possible by simply extending the plasma length.

CONCLUSIONS

As one can see the Advanced Acceleration field is thriving with creativity and ingenuity. The beam-driven PWFA scheme is showing energy gain that are of interest to the HEP community and laser-plasma accelerator development is getting closer to delivering a GeV class accelerator on a "desktop."

I thank all the coworkers in the field of Advanced Acceleration technique whose work is mentioned in this paper. This work is supported by a DOE grant DE-FG03-92ER40727 at UCLA.

REFERENCES

[1] W. D. Kimura et al, Phys. Rev. Lett. 86, 4041-4043 (2001).
[2] W. D. Kimura et al., Phys. Rev. Lett. 92, 54801 (2004.
[3] W. K. Kimura, private communication.

[4] P. Musumeci et al., Proceedings of the AAC 2004 Workshop, Long Island, June 2004.
[5] T. Tajima and J. Dawson, Phys. Rev. Lett. 43, 267 (1979).
[6] C. Clayton et al., Phys. Rev. Lett. 54, 2343 (1985).
M. Everett et al., Nature, 368, 527 (1994).
V. Malka et al., Science 298, 1596 (2002).
[7] D. Gordon et al., Phys. Rev. Lett. 80, 2133 (1995).
A. Modena et al., Nature 337, 606 (1995).
[8] C. G. Durfee and H. Milchberg, Phys. Rev. Lett. 71, (1993).
[9] Y. Ehrlich et al, Phys. Rev. Lett. 77, 4186 (1990).
[10] T. Hosokai et al., Opt. Lett. 25, (2000).
[11] D. Spence and S. M. Hooker, JOSA B (2000).
[12] C. Geddes et al, submitted for publication.
J. Faure et al., submitted for publication.
K. Krushelnick et al., submitted for publication.
[13] F. Tsung et al., submitted for publication/
[14] T. Ting et al., private communication.
[15] M. Hogan and P. Muggli et al., private communication.

DEVELOPMENT OF THE UNILAC TOWARDS A MEGAWATT BEAM INJECTOR

W. Barth, L. Dahl, J. Glatz, L. Groening, S. Richter, S. Yaramishev*
Gesellschaft für Schwerionenforschung, D-64291 Darmstadt, Germany

Abstract

For the future Facility for Antiproton and Ion Research (FAIR) at Darmstadt the present GSI-accelerator complex, consisting of the linear accelerator UNILAC and the heavy ion synchrotron SIS 18, is foreseen to serve as U^{28+}-injector for up to 10^{12} particles/s. After a new High Current Injector (HSI) was installed, many different ion species were accelerated in the UNILAC for physics experiments. In 2001 a high energy physics experiment used up to $2\cdot10^9$ uranium ions per SIS18-spill (U^{73+}) while a MEVVA ion source was in routine operation for the first time. In the past two years, different hardware measures and careful fine tuning in all sections of the UNILAC resulted in an increase of the beam intensity to $9.5\cdot10^{10}$ U^{27+}-ions per 100 µs or $1.5\cdot10^{10}$ U^{73+}-ions per 100 µs. The contribution reports results of beam measurements during the high current operation with uranium beams (pulse beam power up to 0.5 MW). One of the major tasks was to optimize the beam matching to the Alvarez-DTL. In addition further upgrades, including improved beam diagnostics, are described, which allow to fill the SIS 18 up to the space charge limit (SCL) of $2.7\cdot10^{11}$ U^{28+}-ions per cycle. We acknowledge the support of the European Community-Research Infrastructure Activity under the FP6 "Structuring the European Research Area" programme (CARE, contract number RII3-CT-2003-506395) and INTAS (project 03-54-3543).

INTRODUCTION

The conceptual design of the international Facility for Antiprotons and Ion Research (FAIR) at GSI in Darmstadt (Fig. 1) has evolved from the science requirements: higher intensities will be achieved, compared to the present GSI accelerator facility, through faster cycling and, for heavy ions, lower charge state which enters quadratically into the SCL. The desired energy of up to 1.5 GeV/u for radioactive beam production is delivered by the synchrotron SIS 100, which also generates intense beams of energetic protons up to 30 GeV for pbar-production. The energy of 30 GeV/u for heavy ions is generated by using higher charge states in combination with the slower cycling synchrotron SIS 300. The SIS 300 can also be used as a stretcher for radioactive beams, which can be injected, cooled and stored in a system of rings with internal targets and in-ring experimentation. The various rings may be shared for the use with different beams.

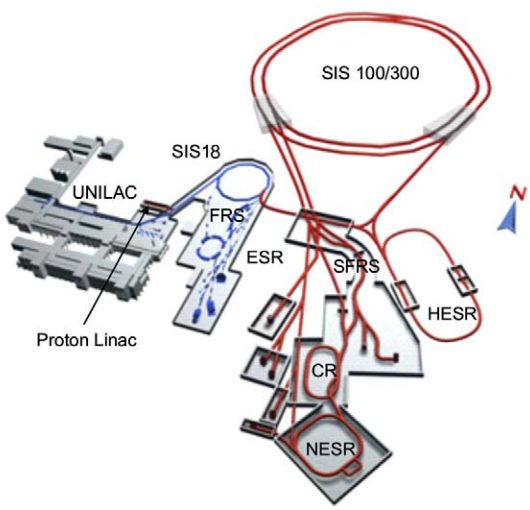

Figure 1: The proposed Accelerator facility FAIR at GSI in Darmstadt [1].

Table 1: Design uranium beam parameters at UNILAC and SIS 18 injection [2]

	HSI entrance	HSI exit	Alvarez entrance	SIS 18 injection	**Required for FAIR**
Ion species	$^{238}U^{4+}$	$^{238}U^{4+}$	$^{238}U^{28+}$	$^{238}U^{73+}$	**$^{238}U^{28+}$**
El. Current [mA]	16.5	15	12.5	4.6	**15.0**
Part. per 100µs pulse	$2.6\cdot10^{12}$	$2.3\cdot10^{12}$	$2.8\cdot10^{11}$	$4.2\cdot10^{10}$	**$3.3\cdot10^{11}$**
Energy [MeV/u]	0.0022	1.4	1.4	11.4	**11.4**
ΔW/W	-	$4\cdot10^{-3}$	$\pm1\cdot10^{-2}$	$\pm2\cdot10^{-3}$	**$\pm2\cdot10^{-3}$**
$\varepsilon_{n,x}$ [mm mrad]	0.3	0.5	0.75	0.8	**0.8**
$\varepsilon_{n,y}$ [mm mrad]	0.3	0.5	0.75	2.5	**2.5**

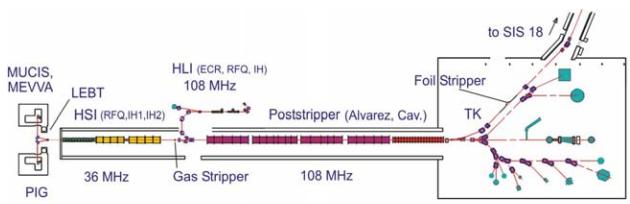

Figure. 2: Schematic overview of the GSI UNILAC [3].

The present GSI accelerator complex will serve as an injector for high intensity heavy ions to fill the SIS 100 to its space charge limit. In the last three years GSI put some effort in increasing the delivered uranium intensities to the SIS 18. An additional upgrade program for the UNILAC is foreseen to reach the required beam brilliance. For uranium (reference ion) the UNILAC has to deliver $3.3\cdot10^{11}$ U^{28+}-particles per 100 µs (see Table 1) to the present synchrotron SIS 18. Currently for a 15 emA $^{238}U^{4+}$ beam from the HSI [4] up to $4\cdot10^{10}$ U^{73+} particles should be delivered to the SIS 18 (during 100 µs), while the SIS 18-SCL is reached by a 20 turn injection into the horizontal phase space. The HSI-front end consists of ion sources of MEVVA-, MUCIS- or Penning-type and a low

* on leave from ITEP, Moscow, Russia.

energy beam transport system (LEBT). The 36 MHz IH-RFQ accelerates the ion beam from 2.2 keV/u to 120 keV/u. In the following short 11 cell adapter RFQ (Super Lens) the beam is matched to the IH-DTL, consisting of two separate tanks accelerating the beam up to the final HSI-energy of 1.4 MeV/u. The HSI-beam is stripped and one charge state is selected (e.g. 28+ for uranium beams). In the Alvarez DTL the high intensity HSI beam is accelerated without significant particle loss. The transfer line (TK) to the SIS 18 provides for a foil stripper and another charge state separator system.

The existing UNILAC had been designed for heavy ion operation. It could provide proton beams at 18 MeV with currents of max. 0.25 mA and an emittance of 1 µm. However, the resulting brilliance is at least one order of magnitude below the FAIR-requirements. For the proposed time sharing scenario beam intensities of 70 mA and an energy of 70 MeV are required. Accordingly, a dedicated proton injector linac being designed within FAIR will be operated independently from the existing UNILAC [5].

Additionally, medium heavy ion beam with a high duty factor have to be developed to increase the target luminosity for the super heavy element production during the next five years. Plans are to investigate and to build a sc 28 GHz-ECR ion source [6], which should increase the primary beam intensities. The beam coming from the new ECR source will be delivered to the GSI-High Charge State Injector by a second LEBT-system. An upgrade program for the rf-amplifiers and the rf-structures is foreseen to increase the duty factor from 30 % to 50 % [7].

The decelerator for HITRAP (Heavy Ion TRAP) [8] is another (linac-) project described in a technical design report. The HITRAP-facility should provide for ions of selected charge states up to U^{92+} at cryogenic temperatures. It is intended to be ready for operation within 30 months after the start of the project. An IH-cavity and a 4-rod RFQ are the main decelerator structures. One of the HITRAP features will be the ability to decelerate heavy highly-charged ions from 4 MeV/u down to rest after ejection from the Experimental Storage Ring (ESR). After successful operation at the ESR the HITRAP set-up will be an integral part of FAIR behind the NESR (New Experimental Storage Ring).

HSI-UPGRADE

Especially for the requested operation with intense uranium beams the performance of the UNILAC was significantly improved [9]: the MEVVA-ion source was renewed. The use of stabilized internal grids resulted in a long operation life (typically 7 days) and in high ion source beam availability. The pulse to pulse stability was enhanced. With the additional application of a strong pulsed magnetic field an U^{4+} fraction of up to 67 % was reached. Enhancements of the extraction system resulted in a higher extraction voltage and, accordingly, in a higher total current density. Due to the high rf surface field in the RFQ and in the Super Lens, rf-conditioning has to be taken into account if low charged heavy ions must be accelerated in the HSI. Permanent rf-conditioning with a low duty factor (approx. 0.3 %) in a time sharing mode with the regular beam time allows for the required rf-amplitudes. In 2002 the Super Lens was completely dismounted. In an upgrade scheme the rf-performance was significantly improved: the maximum surface field strength was slightly decreased, the surface quality was improved and a new plunger design was applied [10].

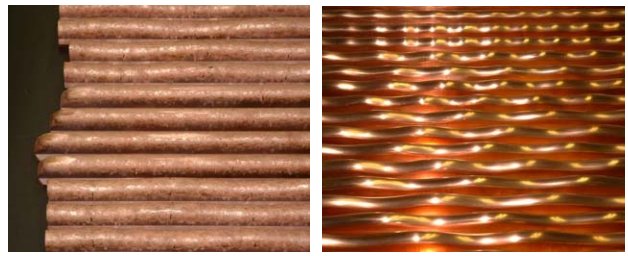

Figure 3: Upgrade of the HSI-RFQ; RFQ-electrodes after five years of operation (left), new electrodes before assembly (right).

Since the end of May 2004 a comparable upgrade measure for the RFQ has been in progress. In Fig. 3 (left) some of the dismantled RFQ-electrodes are shown. After five years of operation the electrode surface was damaged along the whole structure, requiring significantly higher input rf-power during operation at the design limit. The electrodes were reproduced; additional copper plating should lead to a reduction of "dark current" contributions during high power operation.

The RFQ input radial matcher (IRM) was redesigned to improve the matching to the RFQ with the DYNAMION-code. The new matching leads to a smaller beam diameter in the quadrupole channel, resulting in improved particle transmission. While the RFQ was de-installed for the proposed upgrade measures, the matching was investigated using beam transformers and emittance measurement devices before and after the quadrupole quartet in the LEBT-section. As predicted by simulations, based on high current uranium emittance measurements, the measured gain in particle number is close to 15 % (see Fig. 4). During recomissioning of the RFQ a high intensity Ar^{1+} beam was used. In Fig. 5 the measured beam transmission as a function of the rf-voltage is presented together with the data before the upgrade. At the working point the expected gain in RFQ-transmission is verified. The achieved maximum Ar-intensity (after RFQ) is 10.6 emA, being above the design limit (10 emA).

After a breakdown inside the IH1-structure of the HSI at the beginning of 2003 an inner triplet lens was substituted. The new advanced design provides for an improved electromagnetic performance and the outer walls of the big drift tube are now directly water-cooled. As shown in Fig. 6 the geometry of the subsequent small drift tube was slightly changed, leading to a different field distribution (E_z) and lower “dark current” contributions during operating at the highest rf-power level [11].

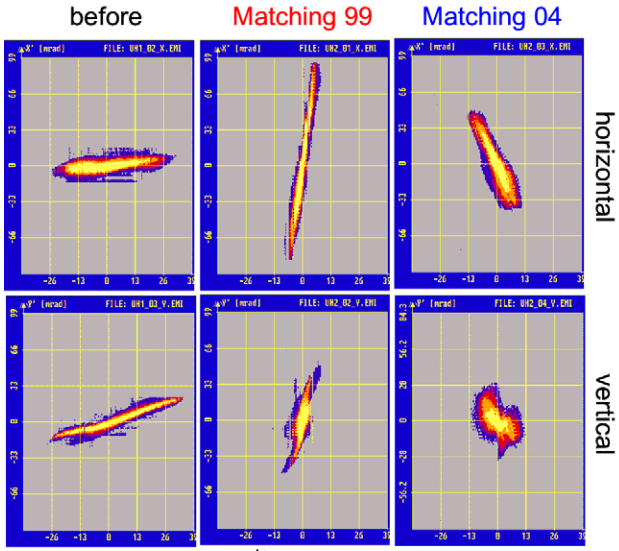

Figure 4: Measured U^{4+} emittance before and after the quadrupole quartet (left) for the two matching cases. The transmission for the new matching (2004) is 15 % higher.

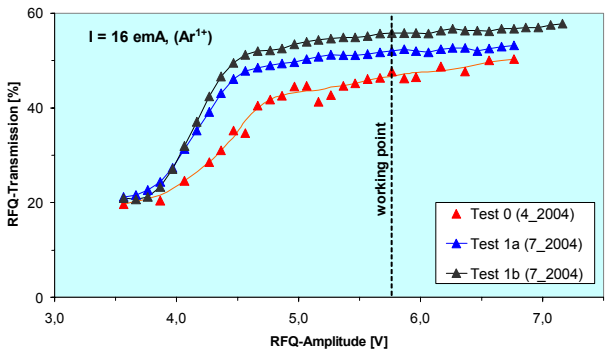

Figure 5: Measured transmission for a high current argon beam before and after the upgrade of the RFQ-electrodes.

A bottleneck behind the Alvarez section was eliminated by the reduction of the number of the single gap resonators from 15 to 10 – allowing beam transport with smaller beta-function modulation and better transmission. Adjustments along all sections of the UNILAC were performed additionally with high accuracy.

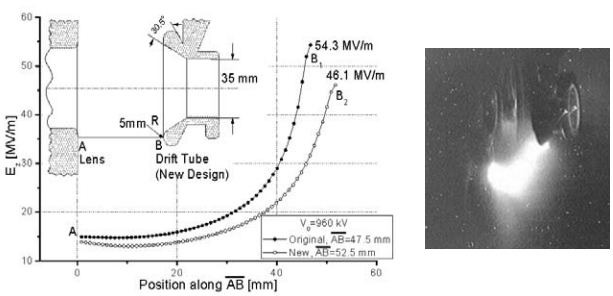

Figure 6: Maximum electric field between the first big drift tube (housing a triplet lense) and the subsequent small drift tube (left); before the improved drift tube geometry was applied (right).

GASSTRIPPER PERFORMANCE

With the reduction of the available apertures in the stripper box, it was possible to increase the stripper gas density by 50 %. For medium intense uranium beams (6.5 emA, U^{4+}) this leads to the expected gain for the desired charge state 28+ (up to 12.8 %). The desired equilibrium charge state distribution is reached for a 70 % higher gas density. Currently the power of the vacuum pumps is not sufficient to compensate this gas ballast. For a temporary 70%-increase of the gas density the measured total uranium current (all species) was increased to 41 emA. The defocusing effect of the space charge forces leads to particle loss in the transport section after the stripping area. This can be compensated by increasing the transverse beam spot in the space charge dominated beam transport. The high stripper gas density for the necessary enlarged apertures has to be provided by an enhanced vacuum pumping speed. For the proposed higher uranium intensities the present stripper section is not sufficient to meet the FAIR-requirements and has to be redesigned.

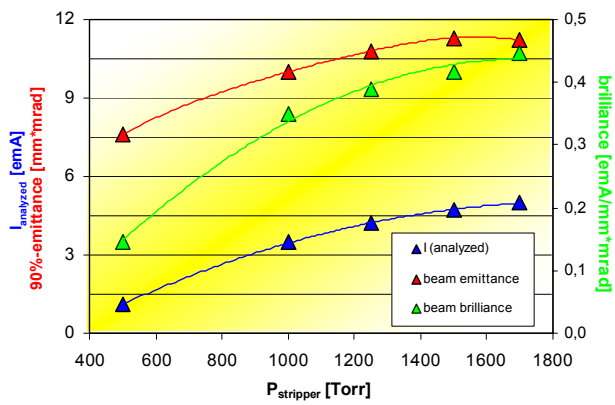

Figure 7: Measured U^{28+}-current, -emittance and -brilliance after charge state separation as a function of the stripper gas density; the input U^{28+}-current is 6 emA.

BEAM MATCHING TO THE ALVAREZ

Usually empirical matching can be done by variation of the quadrupole settings preceding the DTL until a sufficient transmission through the Alvarez section of more than 90% is achieved. In order to increase the transmission close to 100 %, a systematic matching procedure was proposed and realized during machine experiments. In general the beam is mismatched with an enlarged beta function oscillation along the Alvarez accelerator, which may cause transmission losses and emittance growth. Using the quadrupole settings in the first cells of the DTL the periodic solution for the Alvarez tank is calculated. To match the periodic DTL solution, a fitting routine involving the five matching quadrupoles is applied. For the highest available uranium intensity the losses along the Alvarez section are reduced from 8 % to less than 1 % [12].

The postaccelerator performance can also be improved by the optimization of the quadrupole settings in the

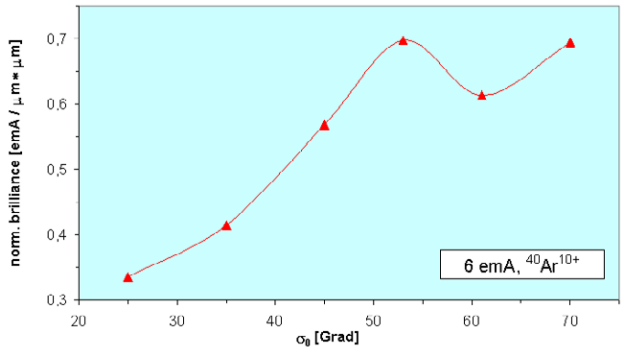

Figure 8: Normalized beam brilliance for a high current argon beam after the 4th Alvarez-tank as a function of σ_0.

Alvarez DTL, being most important in the 1st Alvarez tank. Due to the high mass over charge ratio (m/ζ) of $^{238}U^{28+}$ ions, the maximum zero current phase advance σ_0 in the Alvarez DTL is limited to 45° mainly by limitations of the quadrupole power supplies. For a $^{40}Ar^{10+}$ beam the m/ζ is lower; so that the phase advance influence on the transmission in the Alvarez DTL can be investigated in the interesting range of σ_0-values. As shown in Fig. 8, a phase advance $\sigma_0 > 50°$ is required for an improved beam brilliance for the SIS-injection.

IMPROVED TRANSFER TO THE SIS 18

The optimized matching of space charged dominated ion beams is essential for a loss free injection into the SIS 18. Transverse beam emittance measurements at different positions along the TK were done. In particular, different foil stripping modes were investigated. For the high current heavy ion beam operation e.g. a sweeping mode is routinely applied to minimize the thermal stress of the carbon stripper foil. A longitudinal emittance measurement set-up was commissioned at the entrance to the TK. It is used extensively to tune the rebuncher cavities in the UNILAC. In addition, a test bench is in use for measurements of longitudinal bunch profiles, which enables the investigation of the final debunching to SIS 18. Multi particle simulations by means of the PARMILA-code were performed allowing for a detailed analysis of experimental results for different ion currents [13].

^{238}U-BEAM INTENSITIES FOR THE SIS 18

Table 2: uranium beam intensities

	ζ	Dec 01	Dec-03
LEBT	4+	7,5	11,7
HSI	4+	3,75	6,4
gas stripper	4+	2,5	5,3
Alvarez	28+	1,8	4,8
Single Gap Resonators	28+	1,17	4,8
Foil Stripper	28+	0,94	4,5
SIS 18-Injection	73+	0,3	2.0

In Fig. 9 the achieved uranium intensities in the UNILAC and TK are summarized (2001-2003), reached by the measures mentioned above and by an extended experimental program dedicated to improve the overall UNILAC performance for heavy ion high current operation. In December 2003 an U^{73+} intensity of 2.0 emA (27.5 pµA) was reached for the first time at the injection to SIS 18, which corresponds to $1.7 \cdot 10^{10}$ particles per 100 µs. Before foil stripping 4.5 emA (160 pµA) of U^{28+} beam intensity was achieved ($1.0 \cdot 10^{11}$ particles per 100 µs). The optimized total particle transmission through HSI, stripper section, Alvarez DTL, Single gap resonator chain, and TK is 50 %, if the particle losses during charge separation after the two strippers are taken into account. Compared to the design transmission (90 %) the lack is mainly caused by a bottle neck in the front end area of the HSI-linac.

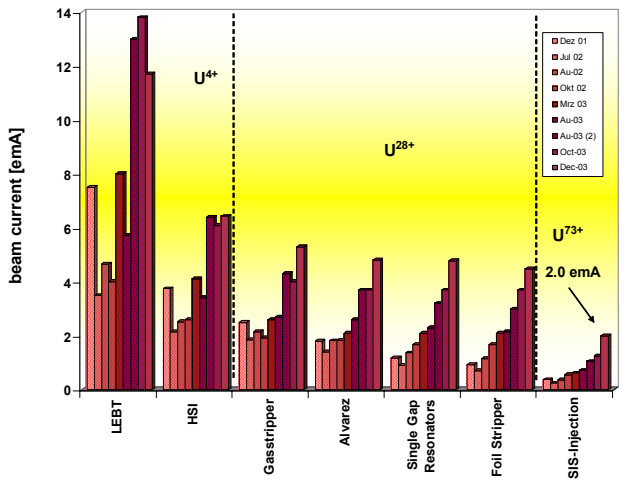

Figure 9: Improvement of the UNILAC-uranium beam intensities during the last three years.

A NEW GSI-PROTON LINAC

The antiproton physics program of FAIR is based on a rate of $7 \cdot 10^{10}$ cooled antiprotons per hour. To provide the primary proton intensities a proton linac is planned. The

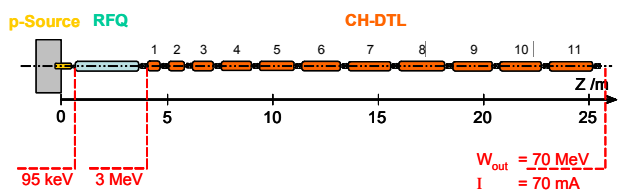

Source	H^+, ECR, 95 keV, 110 mA
LEBT	2-solenoid focusing 95 keV, 100 mA, 0.3 µm*
RFQ (4-rod or 4-windows)	3 MeV, 90 mA, 0.4 µm* *(norm.,rms)
DTL – Section rel. momentum spread rf pulse length beam pulse length max. repetition rate	352.21 MHz, rt, 11 CH-structures 70 MeV, 70 mA, 2.8 µm** ± $5 \cdot 10^{-4}$ 250 µs 100 µs 5 Hz **(norm., tot)

Figure 10: The proposed high current proton linac for the injection into the SIS 18 [5].

proposed linac (see Fig. 10) comprises a proton source, an RFQ, and a DTL, both with an operation frequency of 352 MHz allowing for acceleration up to 70 MeV. For the first time normal conducting Crossed-bar H-cavities (CH) [14] promising high shunt impedances in the required energy range are used. The beam pulses with a length of 25 µs, a current of 70 mA, and total transverse emittances of 7 µm will allow filling the existing synchrotron SIS 18 within a multi-turn-injection up to its SCL of $7 \cdot 10^{12}$ protons. The maximum SIS 18 ramping rate limits the applied proton linac repetition rate to 4 Hz.

A DECELERATOR FOR HIGHLY CHARGED HEAVY IONS FROM THE ESR

The GSI accelerator facility delivers highly-charged ions up to U^{92+} by stripping the ions at 400 MeV/u in the transfer line from the SIS 18 to the ESR. The ESR itself provides high quality beams by means of stochastic@electron cooling. Deceleration down to 4 MeV/u has already been successfully demonstrated. After suitable rebunching, further deceleration down to 6 keV/u is done by a combination of an IH-DTL and an RFQ-structure. All cavities are operated at 108 MHz. Recently the HITRAP-project was described in a Technical Design Report. The layout of the decelerator is shown in Fig. 11.

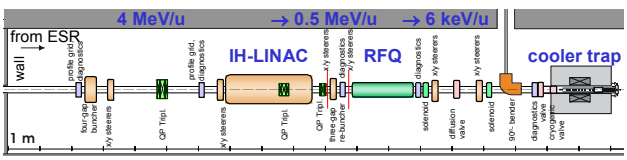

Figure 11: Outline of HITRAP in the re-injection channel between ESR and SIS 18 [8].

CONCLUSION AND OUTLOOK

An extended upgrade program in the UNILAC and TK in combination with machine investigations resulted in a seven times higher uranium beam intensity offered for the injection into the synchrotron SIS 18. Mainly the improved ion source performance, an upgrade of the HSI-structures, the increased stripper gas density, the optimization of the Alvarez-matching, the reduction in the Single Gap Resonator section, the applied sweeper mode for foil stripper operation, and the use of various newly developed beam diagnostics devices were responsible for the successful development program. The UNILAC-upgrade already started will be continued with the investigation of a new front end for U^{4+} [15], stronger power supplies for the Alvarez quadrupoles, a charge state separator system [16] in the foil stripper section and versatile (partly non-destructive) beam diagnostics devices [17], sufficient for the operation with megawatt heavy ion beams. Additionally, the offered primary proton beam intensities will be increased by a new ambitious proton linac, which should be commissioned in 2007. The decelerator for the HITRAP is another GSI-linac project, ready for operation in 2008. Last but not least, the advanced experimental program for the production of super heavy elements requires efforts to improve the average target luminosity for medium heavy ions in the MeV/u-range – for this a five year linac development program is proposed.

REFERENCES

[1] W. Henning, An International Accelerator Facility for Research with Ions and Antiprotons, EPAC2004, Luzern, Switzerland, to be published

[2] W. Barth, et. al., Achievements of the High Current Beam Performance of the GSI UNILAC, EPAC2004, Luzern, Switzerland, to be published

[3] W. Barth, Commissioning of the 1.4 MeV/u High Current Heavy Ion Linac at GSI, LINAC2000, Monterey, U.S.A., p. 1033 (2000)

[4] U. Ratzinger, The New GSI Prestripper Linac for High Current Heavy Ion Beams, LINAC96, Geneva, Switzerland, p. 288 (1996)

[5] L. Groening, et. al., A Dedicated Proton Linac for the Antiproton Physics Program of FAIR at Darmstadt, these proceedings

[6] ISIBHI, A Joint Research Project in the EURONS, CEA, GANIL, ISN (France), INFN (Italy), GSI, HMI (Germany), CERN (Suisse), JYFL (Finland), KVI (Netherlands), TSL (Sweden)

[7] Research Programme: Physics of Hadrons and Nuclei (2005-2009) p. 42 (2004)

[8] L. Dahl, et. al., The HITRAP-Decelerator for Heavy Highly-Charged Ions, these proceedings

[9] R. Hollinger, et. al., Beam Emittance Measurements at the HSI at GSI, Proc. of the 9th ICIS-conference, Oakland, U.S.A., p. 1024 (2001)

[10] W. Barth, Experience during Operation with High Current U^{4+} Beams in the new HSI, LINAC2002, Gyeongju, Korea, p. 347 (2002)

[11] W. Barth, et. al., GSI-an. rep. p. 207 (2003)

[12] S. Yaramishev, et. al., Investigation of the Beam Matching to the GSI-Alvarez DTL under Space Charge Conditions, these proceedings

[13] S.Richter, High current Beam Transport to SIS 18, these proceedings

[14] R. Tiede, et. al., KONUS Beam Dynamics Design of a 70 mA Proton CH DTL for GSI-SIS 12, these proceedings

[15] L. Dahl, et. al., Transport and Injection of heavy ion Beams with High Brilliance for the GSI-HSI, LINAC2002, Gyeongju, Korea, p. 350 (2002)

[16] J. Glatz. B. Langenbeck, The High Current Charge Stripper, Charge Separator, and their Magnets for the Beam Transfer line to the Heavy Ion Synchrotron SIS, Conf. on Magnet Technology, IEEE Transactions on Magnetics (2000)

[17] W. Barth, et. al, Application of Beam Diagnostics for Intense Heavy Ion Beams at the GSI UNILAC, DIPAC 2003, Mainz, Germany, p. 161 (2003)

DEVELOPMENTS AND FUTURE PLANS AT ISAC/TRIUMF

P. W. Schmor, TRIUMF, Vancouver, Canada

Abstract

The ISAC (Isotope Separator and Accelerator) at TRIUMF uses the ISOL (On Line Isotope Separator) technique with up to 100 microamperes of 500 MeV protons from the TRIUMF cyclotron driver available to create exotic isotopes in a thick target. An ion beam formed from these exotic isotopes is transported at 2 keV/u, mass separated, injected into a room temperature RFQ Linac and then into a five-tank drift tube linac that provides variable-energy accelerated exotic-beams from 0.15 to 1.8 MeV/u for nuclear astrophysics experiments. Super conducting rf cavities are presently being added to the linac chain to permit a further increase in the maximum energy of the exotic beams to 6.5 MeV/u. An ECR-based charge state booster is also being added in front of the RFQ to increase the available mass range of the accelerated isotopes from 30 to about 150. A second proton beam line and new target station for target and ion source development have been proposed for ISAC. In the future this new target station could be used as an independent simultaneous source of exotic beams for the experimental program.

INTRODUCTION

The availability of short-lived exotic beams has become an important goal in the search for solutions to a number of important questions in science. The science includes nuclear astrophysics, nuclear structure, atomic physics & condensed matter physics. There are two main techniques for creating these exotic beams, namely, the fragmentation method and the ISOL method. At TRIUMF the ISOL approach is used.

ISOL type facilities typically use a light-ion driver-accelerator to produce a variety of isotopes in a target. These isotopes are transferred by effusion and diffusion processes to an adjacent ion source where the isotopes are ionized, extracted and formed into an ion beam. A particular isotope is then selected by slits at the focal plane of a mass separator and transported to experimental stations either prior to or following further acceleration. The required beam quality, the beam intensity, the beam energy and the momentum spread of the accelerated exotics depend on the particular experiment. For ISAC the user input led to a continuously variable energy from 0.15 to 1.5 MeV/u for isotopes having an $a/q \leq 30$.

At TRIUMF the driver is an H-, 500 MeV, cyclotron that has been shown to have the capability of accelerating over 400 μA to 500 MeV. The TRIUMF cyclotron can simultaneously extract multiple independent proton beams into different locations. A transport beamline from the cyclotron to the target in ISAC is designed for a maximum of 100 μA of 500 MeV protons. The isotope production target material is located in a tube (2 cm diameter and up to 20 cm long) and the material composition varies depending on the particular isotopes that are being optimized. The target and ion source can be biased up to a voltage of 60 keV. The extracted beam is transported through a beamline with electrostatic focusing and steering elements. This focusing approach allows isotopes with adequate intensities to be used for tuning purposes and then, to adjust only the mass selecting system to the low flux isotopes. These fluxes cannot be, in general, observed on the normal beam diagnostic elements. However, with the electrostatic focusing elements, the beamline tune is not sensitive to the mass, only to the beam energy and that is kept constant. Therefore the low intensity isotope can be transported through the line without needing to readjust the beam optics elements and a minimum of low intensity diagnostics for optimizing the transport efficiency to the experimental target. An off line ion source (OLIS) is used to provide stable beams for commissioning beamlines, accelerators, setting up tunes and experimental calibrations. Figure 1 shows the layout of the TRIUMF facility indicating by color coding the existing and planned modifications.

ISAC I

Although the ISAC I accelerators were initially designed for a maximum energy of 1.5 Mev/u for beams having a $m/q \leq 30$ ratio, isotopes have been accelerated from the injection energy of 2 keV/u up to a maximum energy of 1.8 MeV/u. The accelerating system consists of a multi-harmonic pre-buncher, a cw RFQ, a medium energy beam transport (MEBT) section, an electron stripper, a re-buncher, a cw drift tube linac. The pre-buncher provides a pseudo saw tooth velocity profile at a fundamental frequency of 11.8 MHz, thereby providing approximately 86 nS between beam buckets. Bunched beam from the pre-buncher fills every third bucket of the 35 MHz, cw, 8 m long, split-ring, RFQ. The singly-charged beam out of the RFQ, at energy 0.15 Mev/u, is focused (transversely and longitudinally) and stripped to a higher charge state in the medium energy beam transport line (MEBT). The MEBT has an 106 MHz bunch rotator to provide a time focused beam at the stripper and a double frequency rf chopper to select cleanly separated rf bunches separated by either 85 or 107 ns. The stripped beam is magnetically bent through 90 by two 45 dipoles where silts are used to select only those isotopes having a chosen m/q ($3 \leq m/q \leq 6$) and re-bunched prior to injection into the first tank of the DTL. The DTL provides a beam that can be continuously varied in energy from 0.15 to 1.8 MeV/u. The DTL is a separated-function structure with five DTL tanks, each operating at 0° synchronous phase, with magnetic

triplets located between each tank and three split-ring, three gap, bunchers located between tanks 2,3, and 4. As the DTL system operates cw at 106 MHz, only 1 in 9 rf buckets are nominally filled (beam bursts are at the pre-buncher fundamental frequency). Two additional bunchers are located in the high-energy beam transport (HEBT) beam line prior to the experimental stations to optimize the longitudinal timing at the experiments. For bunching the lower beta beams an 11.8 MHz triple gap structure is used and a 35.4 MHz spiral buncher is used for bunching the higher beta beams. A more detailed description can be found in the proceedings of the previous conference [1]. This accelerator has provided a wide range of isotopes over the full energy range to the experimental stations for the past four years. The request for beams of stable isotopes has been greater than initially anticipated. Two ion sources are being presently used to provide the stable beams from the off line ion source (OLIS). There is a need to add a more universal ion source to meet these needs. Proposals have suggested that OLIS might even be useful for longer lived isotopes that were produced by one of the other four cyclotron on site and delivered to the OLIS ion source in gas bottles after chemical separation.

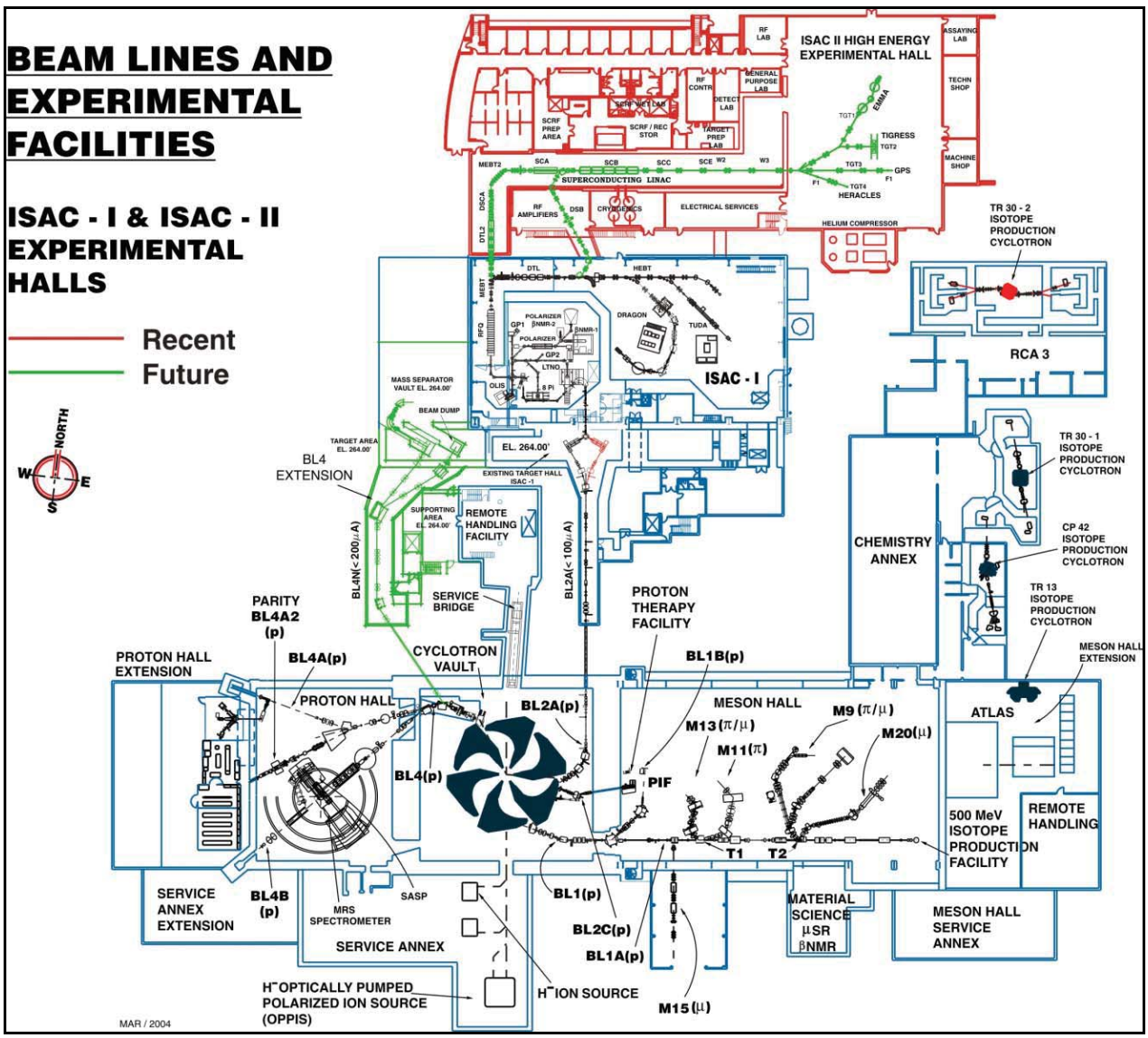

Figure 1: A schematic layout of the TRIUMF facility. The red lines indicate the building envelop for the recently completed ISAC II civil construction. The green lines labeled as BL4 extension, indicate the proposed building envelop for the proposed new high power target test facility. The ISAC II high beta cryomodules have been omitted in the schematic. Instead the HEBT beamline to the experimental hall is shown after completion of medium beta cryomodule installation in 2005 when the first ISAC IIexperiments are planned.

ISAC II

As mentioned above, the ISAC I facility is currently accelerating radioactive ions (with q = ±1 and m ≤ 30) up to 1.8 MeV/u. Although heavier masses are being produced in the targets and extracted from the ion sources, the high-pressure conditions near the ion sources permit only singly ionized ions to be extracted at reasonable intensities. These heavier masses could be accelerated if their charge state was increased to within the required m/q. In order for experimenters to reach the Coulomb barrier (roughly 6.5 MeV/u) with masses up to 150, it is necessary to increase both the length of the ISAC accelerating system and the maximum mass that can be accelerated. In order to increase the maximum mass of ions accelerated by the RFQ, a 1+ to n+ charge state booster (CSB) is required. Electron-cyclotron-resonance (ECRIS) ion sources have been shown to reach the required q/A ≥ 1/30 for many elements. The installation of a charge-state-booster in ISAC would allow the acceleration of all masses to 0.15 MeV/u. However, the beam intensities for masses beyond A ≈ 70 would most likely be too low to be useful if the ions require further stripping at 0.15 MeV/u before injection into the DTL. The stripper, in ISAC I, is located at 0.15 MeV/u and reasonable beam intensities with a q/A of 1/6 cannot be achieved for masses beyond about 70 for beams that require stripping at this low velocity. The optimum stripping energy for 30 ≤ A ≤ 150 with q/A ≥ 1/7 is about 0.4 MeV/u. To accelerate the ion beam from 0.15 to 0.4 MeV/u, requires a new linac (DTL2).

A plan to achieve the ISAC II requirements in a phased approach is being followed that allows experiments to begin prior to completion of the full accelerator capability. The plan is to optimize and install an electron cyclotron resonance ion source (ECRIS), operating in a 1+ to n+ charge state booster (CSB) mode, after the mass separator. Beams from the ECRIS CSB will be transported through the low energy beam transport (LEBT), accelerated to 1.5 MeV/u and then diverted into a new accelerator hall. In the first phase, at the end of 2005, the accelerator would contain only 20 medium-beta superconducting cavities and bring the beam to 4.3 MeV/u for m/q = 6 and, of course, somewhat higher for isotopes that can be charge boosted to a lower m/q. At least one experimental station will be prepared to use the ISAC II beams at this time. By the end of 2007, on completion of the second phase, 20 more cavities will be added to bring the final energy up to 6.5 MeV/u. By the end of 2009, on completion of the third phase, the ISAC I MEBT would be extended from the RFQ to a DTL in ISAC II, that would allow acceleration of the beams from the RFQ to 0.4 keV/u. This would provide an alternative for accelerating elements that are not efficiently charge boosted and require additional stripping for acceleration in the superconducting ISAC II linac. A short superconducting low beta section would be added to bring the energy up to the 1.5 MeV/u required for injection into the medium beta superconducting linac. The accelerator layout with respect to each of these three phases is shown in figure 2.

Civil Construction

The ISAC facility has been expanded with the addition of a new building to the north of the existing ISAC I structure. This new building includes floor space for the superconducting linac, the helium cryogenic plant, the experimental stations, a clean room for accelerator assembly and offices. The building was initially occupied in the spring of 2003. The clean room and cryomodule assembly space became operational during the fall of 2003. The first half of the cryogenic system will be installed and commissioned in the fall of 2004. The first medium beta (actually number three in the chain) will be installed in the fall of 2004. Planning has started on evaluating additional ion sources on OLIS in order that the heavier, stable-masses can be accelerated at intensities and charge states suitable for ISAC II needs.

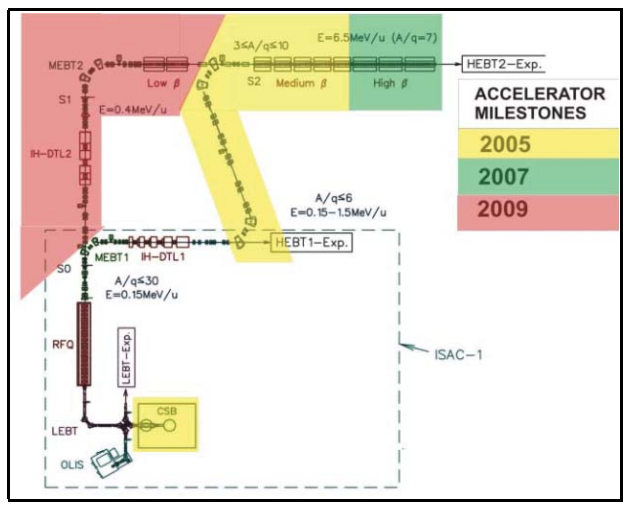

Figure 2: ISAC II accelerator layout with the projected completion dates for the three phases color-coded.

CSB (Charge State Booster)

The CSB is a Phoenix based ECRIS. TRIUMF is collaborating with ISN, Grenoble on its further development. The ECRIS has been assembled on an extension of the existing ion source test stand where its performance will be measured and optimized during the next year. An initial charge state boosted beam has just been observed, using a separate ECR as the 1+ injector. The CSB booster will be installed in the mass separator pit at the target level, downstream of the mass separator, in the January 2006 shutdown. The initial LEBT structure will be installed during the previous year (2005).

LINAC

The ISAC II LINAC has been described at the previous conference[1]. Briefly the completed system will include a cw DTL to increase the energy of the beam from the RFQ to 400 keV/u before stripping to a higher charge state. A superconducting linac with cavities designed for

β_o = 4.2% (8 low beta cavities at 70.7 MHz), 5.7% (8 medium beta cavities at 106 MHz), 7.1% (12 medium beta cavities at 106MHz) and 10.4% (20 high beta cavities at either 141 or 106 MHz)[2]. The design fields for these cavities are specified to achieve the ISAC II design energy (6.5 MeV/u) for m/q = 6. Solenoids are located between groups of cavities for transverse focusing and to enhance multi-charge acceleration when strippers are used. The HEBT from the existing 1.5 MeV/u linac to the medium beta cryomodules is currently being installed. The first cryomodule (#3) has been completed and cold tested[3,4]. The tests have successfully shown that the heat load is within expectations, that solenoid field does not impact the cavity performance, that cavity alignment tolerances are achievable and the rf tuners allow the cavity frequency to be locked[5,6,7,8]. The cryogenic plant has been purchased from Linde and should be commissioned before the end of 2004. The cold distribution system is scheduled to be completed in the fall of 2005, along with all five medium beta cryomodules. By the end of 2005, a 1.5 MeV beam from the ISAC I DTL will be transported to and accelerated by the medium beta section to 4.4 MeV/u. The high beta section will be built and installed with full operation to 6.5 MeV/u to begin at the end of 2007. Finally, the low beta cryomodule, DTL2 and connection to the RFQ will be completed by the end of 2009.

HEBT

Many of the elements required for the HEBT, both from the existing DTL to the medium beta cryomodules and the HEBT from the cryomodules to the ISAC II experimental stations have already been acquired. The section joining ISAC I to ISAC II is being installed and will be completed by the end of 2004.

FUTURE PLANS

TRIUMF has for the past 10 years been funded in 5 year cycles with schedules and resource requirements determined from a 5 year plan developed by TRIUMF and based on submissions to TRIUMF from the Canadian subatomic Physics community. The next 5 year plan (2005-2010) is currently being reviewed by the Canadian federal government. In this plan, the ISAC accelerators would be completed, the cyclotron would be upgraded to both improve reliability and increase the proton current and a new proton beam line would be built from the cyclotron to a new target development facility in an extended ISAC building.

High power target development and the experimental program compete for the same beam time from ISAC. Target development scheduling requires a substantial overhead and is inconsistent with the beam reliability demanded by the user community. Experience has shown that high power target development must be done on line with proton beam. Therefore to maintain a viable experimental program, TRIUMF has decided that it is necessary to build a dedicated target development facility. A rarely used (recently) extraction port will be upgraded for high current operation and a beam line constructed to a new target hall in ISAC, capable of operating at the nominal 50 kW. The facility will include the ISAC style target station modules, a mass separator and yield station. The facility will make use of the existing remote-handling capability, the existing nuclear exhaust system and the existing hot cells. It will operate independently of the other cyclotron beam lines and therefore target development can be carried out simultaneously with the ISAC experimental program. The expansion is being done in such a manner that in the future when the target development facility is not being used for target development a second RIB beam could be transported to any of the ISAC experimental stations. This would permit the facility to operate multiple RIB experiments simultaneously.

GENERAL CONSIDERATIONS

There are several international proposals to build new multi-purpose, high-intensity radioactive ion beam facilities. ISAC experience has shown that successful operation of a RIB facility introduces several unique accelerator constraints that need to be preplanned in order to make efficient and cost effective use of the rare exotic beams.

The interesting exotic beams are rare and require diagnostics that cannot conveniently be packaged into the space constraints of normal beam diagnostics. The costs and complexity for these low-intensity beam-monitors (using nuclear counting techniques) imply that the accelerators must be initially tuned with a stable higher-intensity beam that is an analog of the beam of interest and then switched to the exotic beam with a minimum of tuning.

The facility should include an ion source for stable beams in order to commission the accelerator, provide analog beams for experimental set up and for experimental calibrations. ISAC initially installed a compact microwave ion source for commissioning the accelerators with ions from a range of gases, modified the microwave ion source to also obtain some metallic ions, then added a thermal surface ion source to accommodate experimental requests and is now evaluating how to modify the off-line ion source (OLIS) in order to better satisfy the user community.

For a high-intensity ISOL facility, it is essential that the driver linac operate in a cw or near cw mode with a beam stability of a few percent. The intensity of an extracted exotic beam is not solely determined by the production cross section. The temperature of the target is largely determined by the deposited power from the driver beam. The intensity of the exotic beams depends on the diffusion and effusion times from production to ionization. These times are temperature dependent. Consequently for a short-lived isotope the variation of its intensity can be amplified compared to the variation of the intensity of the driver beam.

Target development cannot be reliably simulated for high power operation. On line target development has a

large time overhead that takes beam time away from the scientific program. However, on line target development is essential. Therefore, it is essential to have a dedicated development facility that can operate simultaneously with the production target used for the scientific program. Moreover, the driver must be capable of varying the power independently two these two areas. The TRIUMF cyclotron, was designed to provide multiple, simultaneously independent beams. The addition of an on line target development facility is a high priority project within the next TRIUMF five-year plan. Figure 2 shows the planned proton beam line and target development facility. The plan also includes a 100 kW beam dump for tuning the cyclotron for reliable high current operation. This project should be complete by 2009.

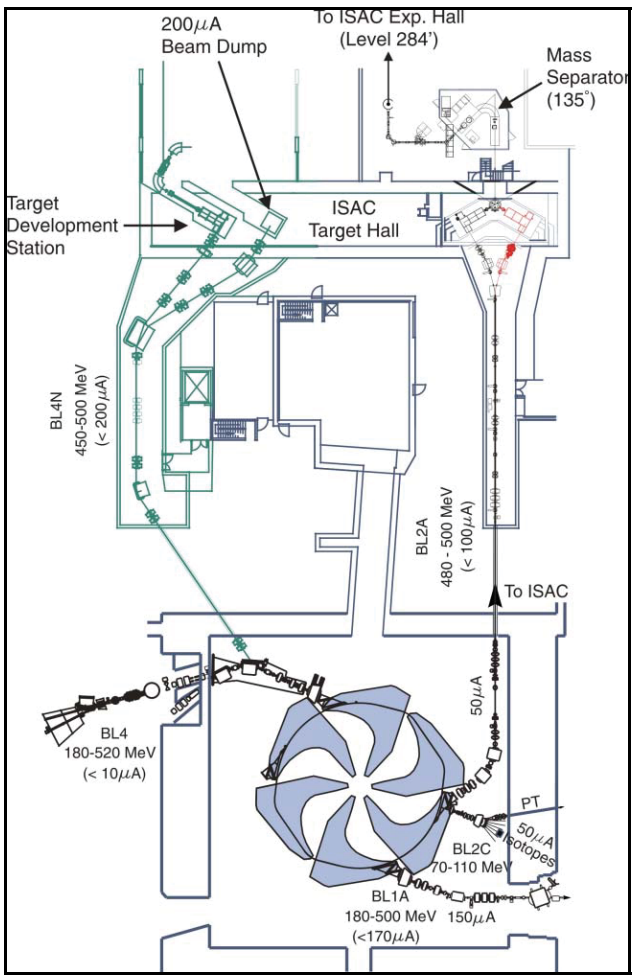

Figure 3: The BL4 cyclotron extraction port will be used to provide beams for high target development in an underground expansion of the ISAC target hall (shown in green).

SUMMARY

The accomplishments described in this paper were realized by a team effort. Without presenting the many names individually, I must nevertheless acknowledge them for these achievements.

The success of a facility is ultimately measured by its science output. The nuclear astrophysics experimental facility has attracted experimental groups internationally because of its unique capabilities. Experimental groups are already acquiring and setting up the apparatus needed for the ISAC II science program. The three major facilities will include TIGRESS (a high efficiency gamma array), TUDA (a silicon strip detector array), HERACLES, and EMMA (a recoil mass spectrometer).

REFERENCES

[1] R.E. Laxdal, "ISAC-I and ISAC-II at TRIUMF: Achieved Performance and New Construction", Proceedings of LINAC 2002, Gyeongju, Korea, p. 296.

[2] R.E. Laxdal et al, "High Beta Cavity Optimization for ISAC-II", these proceedings

[3] G. Stanford et al, "Engineering and Cryogenic Testing of the ISAC-II Medium Beta Cryomodule" these proceedings.

[4] R.E. Laxdal et al, "Cold Test Results of the ISAC-II Medium Beta High Gradient Cryomodule" these proceedings

[5] V. Zvyagintsev, "Simulation of the RF Coupler for Triumf ISAC-II Superconducting Quarter Wave Resonators", these proceedings

[6] R. Poirier et al, "RF Coupler Design for the TRIUMF ISAC-II Superconducting Quarter Wave Resonators", these proceedings

[7] W. Rawnsley et al, "A Wire Position Monitor System for the ISAC-II Cryomodule Components", these proceedings

[8] K. Fong et al, "Status of RF Control System for ISAC II Superconducting Cavities" these proceedings

THE KEK C-BAND RF SYSTEM FOR A LINEAR COLLIDER

H. Matsumoto#, Shigeru Takeda, S. S. Win, M. Yoshida, KEK, Tsukuba Japan
H. Baba, T. Shintake, SCSS Group, RIKEN, Harima Japan
J. S. Oh, PAL/POSTECH, Pohang, Republic of Korea
Y. Takasu, University of Tokyo, Tokyo Japan
F. Furuta, University of Nagoya, Nagoya Japan

Abstract

C-band (5712-MHz) RF-system hardware R&D for an e^+e^- linear collider started in 1996 at KEK. We have already developed three conventional 50-MW class klystrons, a smart modulator, and a novel HOM-free accelerator structure (Choke-mode type, full-scale high power model) [1], [2], [3], [4]. A very stable ceramic high voltage monitor was successfully tested up to 367-kV with 4.5-µsec pulses. Very good agreement in the expected division ratio and signal waveform fidelity was observed in high power tests. A new C-band SiC type high power rf-load, extending the power handling capability up to 50-MW is now being designed. It should have excellent mass production characteristics as it uses circularly symmetric TM_{011} chained cavities [5]. For the first ever, a high power prototype rf compressor (SLED III) cavity made of a low thermal expansion material (Super Invar) was designed to provide stable operation even with a very high Q of 200-k, it was operated up to a 135-MW peak output power in 0.5-µsec rf pulses compressing input 45-MW 2.5-µsec pulses [6]. The C-band linac rf-system will be used for production work in the SASE-FEL (Spring8 Compact SASE Source, SCSS) project at SPring-8 [7]; SCSS will also serve to not only verify the design concepts and components, but will also provide realistic experience and lessons which can eventually be deployed in the main linac rf system for a future large scale linear collider.

INTRODUCTION

The C-band main linac design and development has been motivated by the increasingly urgent need for a linear collider capable of undertaking the next essential physics programs. Choosing a C-band technology entails a minimum of R&D thus facilitating early deployment and reliable operation. The goal is to enable an early start to the physics program, so as to be as concurrent as possible with the LHC operation. Once a new particle threshold is opened with LHC, all angles of the new physics regime can be thoroughly studied in the more straightforward clean experimental environment of e^+e^- collisions.

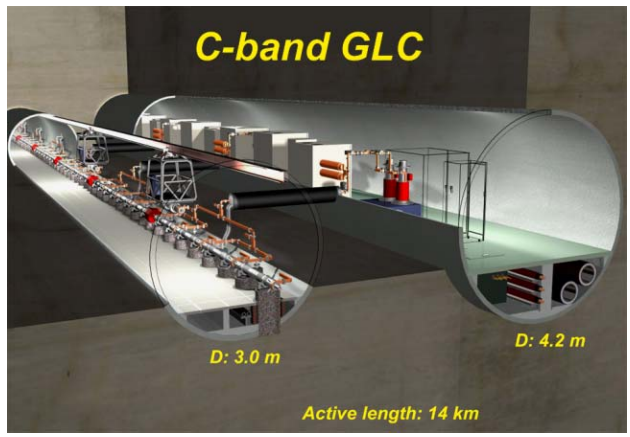

Figure 2: C-band main linac tunnels. The klystron gallery is 4.5-m in diameter and the linac tunnel is 3.0-m in diameter.

The main linac system is the heart of the linear collider. It is a huge system, composed of thousands of repetitions of common RF-units. Therefore, in order to realize a successful physics program, these RF-units have to meet strict requirements for: (1) High reliability, (2) Simplicity, (3) Easy operation, (4) Reasonable power efficiency, and (5) Low cost.

These desiderata provide boundary conditions for our design work. Especially the first three items are crucial for such a large scale system to be operated at all; only after clearing them are the detailed discussions about energy efficiency or upgradeability meaningful. As the C-band frequency is only two times higher than the S-band, the size of the accelerator structure is reduced by half. But more importantly, currently available technology for fabricating the components can easily meet the accuracy required for the C-band, thus removing the risk of a non-manufacturable design. This single choice thus directly results in possibilities for high reliability, simplicity, and hence low cost.

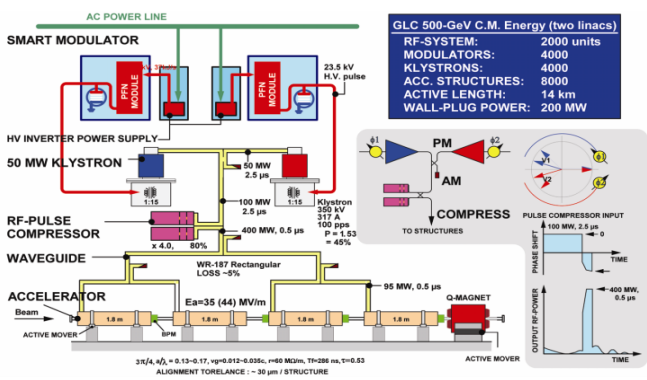

Figure 1: One unit of the C-band main linac.

#hiroshi.matsumoto@kek.jp

The total C-band main linac rf-system for a 500-GeV C.M. energy includes about 2000 rf-units as shown in Figure 1. In total about 8000 accelerating structures and about 4000 klystrons with modulators are needed for the two main linacs. The numbers of each component are large, but still not enough to bring about the drastic cost reduction allowed by full mass-production. Therefore, from the start of the design of each component, maximum efforts toward cost reduction for mid-scale production are absolutely necessary. Accordingly the C-band group has been inventing novel ideas and carrying out special cost reduction R&D.

We propose that the C-band frequency allows the best set of trade-offs for meeting the demands. And the SCSS project will give an opportunity for a realistic application of the C-band rf technology.

SYSTEM DESCRIPTION

Each unit in the main linac rf-system is composed of two 50-MW klystrons, their pulse modulators, one rf-pulse compressor, four 1.8-m-long choke-mode accelerating structures and an associated wave-guide-system as shown in Fig. 1. The accelerating gradient is 35-MV/m under full beam loading. This was chosen as a practicable accelerating gradient after studying results from the S-band frequency high gradient tests done between 1987 and 1994 at KEK.

The system will be installed in two concentric tunnels with circular cross section diameters of 3-m and 4.5-m for the accelerator and klystron galleries, respectively. For structural stability, the tunnels as shown in Figure 2 have to be constructed in a very stable stratum such as granite.

HARDWARE R&D RESULTS

We started hardware R&D in April 1996, and with the exception of the high-power rf pulse compressor, by June 2003 we had developed most of the hardware components and tested their performances.

Waveguide Components

We chose a conventional rectangular EIA-WR187 (47.55-mm x 22.15-mm) waveguide to make the system simple. The rf transmission loss in the waveguide is –0.032 dB/m, which allows keeping the waveguide rf power loss budget to less than 5%. We have developed various new waveguide components: among which there is a low cost yet highly reliable unisex type rectangular vacuum coupling flange (so-called MO type) [8]. It is now commonly used in various facilities not only for C-band applications.

Klystron R&D

We have successfully developed a 50-MW class solenoid focus type klystron (the TOSHIBA E3746 series), which meets the requirements for a 500-GeV linear collider.

We have a clear design goal of ensuring high reliability over long-term operation. Accordingly we decided conservatively on a ceiling value of 300-400 Jules/pulse for the beam power in the klystron, while keeping the maximum cathode emission loading to less than 10 A/cm^2, and with the maximum surface electrical gradient of the electrodes to less than 22-kV/mm [4]. The experimental test results of the three klystrons are summarized in Table 1. The first tube (E3746-#1) employed a conventional design such as having only a single-gap output structure. Its main propose was to fix the mechanical dimensions of the electron gun, beam dump (collector), and the output rf windows; and also to characterize the C-band performance. The 2nd and 3rd klystrons were developed (in 1997 and 1998) to increase rf power efficiency, this was accomplished by the newly introduced 3-cell traveling wave output design. Power efficiency improved to 44% for the 2nd and to 45% for the 3rd klystron. Agreement to within 1% over the operating range was found between simulation (FCI code) and a precision calorimetric power measurement system. Figure 4 shows a typical experimental result for the traveling-wave 3-gap klystron.

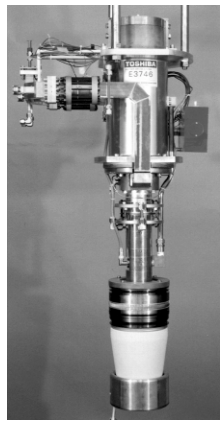

Figure 3: TOSHIBA-E3746.

Table 1: The experimental result for C-band klystrons

E3746	No. 1	No. 2	No. 3
Output power [MW]	50 (48)	54	55
Pulse width [μsec]	1 (2.5)	2.5	2.5
Repetition rate [pps]	50 (20)	50	50
Power efficiency [%]	42	44	45
Output gap	1	3[1)]	3[1)]

1) travelling-wave 3-gap output cavity.

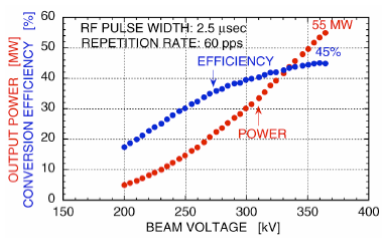

Figure 4: Typical efficiency and RF output power characteristics at saturation output rf power as a function of beam voltage.

Modulator Power Supply

We focused our modulator R&D work on reducing the fabrication cost and improving the reliability. As a first step, we developed a prototype modulator, with features: (1) Direct HV charging from an inverter power supply, (2) No de'Q-ing circuit, (3) Much smaller in size than the usual modulator, (4) Using existing low-risk reliable circuit components, such as the thyratron tube for the PFN switching.

To reduce modulator size and permit removing the de'Q-ing circuit from the PFN, we employed an inverter type DC-HV power supply (the EMI-303L, U.S.A). A first model was built in a compact metal cabinet with di-

mensions 1.6-m (W) x 2-m (H) x 1.2-m (D). The fluctuation in the measured output voltage was measured to be less than ±0.17% (at 3σ), which meets the energy stability requirement for the linear collider. The timing jitter and drift of the pulse output is around 2-nsec (at 3σ) over a 4-hour run at 50-pps [9]. In 2003, this modulator concept was accepted in China for the Shanghai light source. They fabricated it there themselves, and it was tested in May 2004.

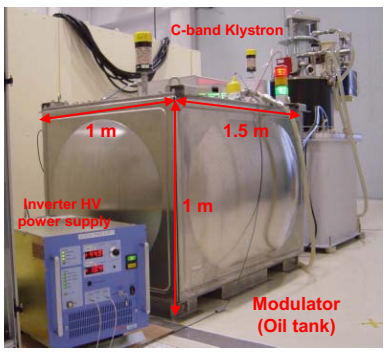

Figure 5: A new developed oil-filed modulator.

The next step in the modulator development was to install everything except for the inverting H.V. power supply in an insulating oil-filled metal tank or cabinet of very compact size as shown in Figure 5 [10]. This is also very compact, being only 1.5-m (W), 1-m (H) and 1-m (D). The prototype was developed by the NICHIKON Co in Japan. Testing was begun in March 2003 at SPring-8. We obtained the expected results as to pulse wave shape, voltage and flatness, and were able to verify the operational repeatability of the unit and also its markedly reduced EMI and noise generation. The main parameters for the modulator and new inverter power supply are listed in Table 2.

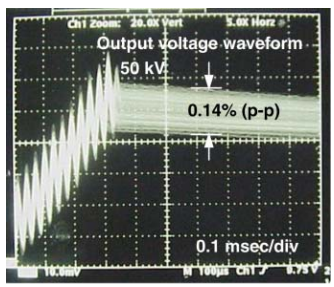

Figure 6: Measured output voltage stability at 50 kV and 60 pps repetition rate.

A new inverter H.V. power supply was developed by the TOSHIBA Co. in Japan and it was tested along with the rest of the modulator beginning in March 2003 at SPring-8. It generates a maximum output voltage of 50-kV and provides an average power of 30-kW (or a peak of 37.5-kJ/sec); this supply can drive a 50-MW klystron at up to a 60-pps repetition rate delivering a 350-kV beam voltage. As shown in Figure 6, we obtained an output voltage regulation of within ±0.1% with this first prototype model.

Table 2: Main parameters of oil filed new modulator

Modulator peak output power:	111	MW
Average output power	46.7	kW
PFN charging voltage Nominal:	44	kV
Maximum:	50	kV
Peak switching current:	5.4	kA
HV pulse width:	3.5	µsec
Pulse repetition rate (max):	60	pps
Output voltage reputability:	±<0.5	%
Thyratron timing jitter:	<5	nsec
PFN impedance:	4.3	Ω
PFN cell number:	18	Sections
Transformer step-up ratio:	1:16	
Cabinet size (W) x (H) x (D):	1.5 x 1 x 1	m
Inverter output voltage:	0 ~ 50	kV
Output current (peak):	30 (37.5)	kJ/sec
Output voltage regulation:	±<0.07	%
Power factor at full load:	>85	%
Power efficiency at full load:	>85	%
Cabinet size (W) x (H) x (D):	48 x 45 x 63	cm

RF Pulse Compressor

At the present, initial testing of a high power rf pulse compressor was begun at KEK at the end of 2003. The prototype rf cavity uses a copper plated Invar metal, this permits simplifying the temperature control system for the rf compressor and thus contributes to reducing the cost of the total system [6]. Figure 7 show a very preliminary experimental result of a 135-MW peak output power, 0.5-µsec pulse width at a 50-pps repetition rate with a total multiplication factor of 3.0. From in this figure, we see the need to improve the flatness of the top of the output waveform, and also need to increase the power gain factor from 3 to 3.3 for a realistic application.

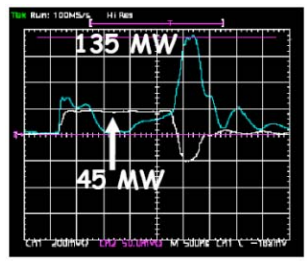

Figure 7: Typical pulse compressor cavity rf power waveforms.

The thermal stability of these rf compressor cavities provides an order of magnitude better performance than that of copper alone. No unusual vacuum out-gassing was found even while in high power operation.

Unfortunately, after a high power test in March 2004, a large water leak developed in one of the compressor cavities, which was flooded. This caused corrosion to start at the junction between the bare Invar and copper metal.

RF Structure

The C-band Choke-Mode type damped rf structure was developed in 1998, and its performance has been confirmed with the ASSET facility at SLAC [3]. A cut-away view of the cavity is shown in Fig. 8. The dark square shapes (top and bottom) in Fig. 8 show where the ring shaped SiC HOM absorbers go in the assembly.

One particular advantage is that since all of the parts are completely axially symmetric, they can be machined on a turning lathe, this easier machined type of cavity is very advantageous in

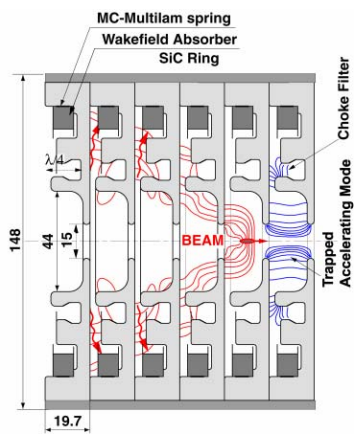

Figure 8: A cut away view of the C-band choke-mode rf structure.

mass production. The first high power prototype model is being fabricated by the MITSUBISHI HEAVY IINDUSTRY Co. in Japan. The main parameters of the rf structure are listed in Table 3.

Table 3: Main parameters of Choke-mode rf structure

Frequency:		5712	MHz
Phase-shift per cell:		3π/4	
Field distribution on the axis:		Quasi-C.G	
Quality factor (average):		10300	
Attenuation parameter:		0.53	
Filling time:		290	nsec
Shunt impedance (average):		58.5	MΩ/m
Electric filed ratio of Es/Ea:		2.2	(max)
Iris aperture	up-stream:	17.330	mm
	down-stream:	13.587	mm
Disk thickness:		4	mm
Number of cells:		91	
Number of coupler: (field symmetry & double irises)		2	
Structure active length:		1.8	m

We decided to use a quasi-constant-gradient for the electric field distribution along the axis of the structure; this minimizes the surface electrical gradients, which contribute strongly to breakdown problems in high gradient operation. Doing this, we have successfully kept Es/Ea to a maximum of only 2.2. Higher trapped modes (HOM) of small amplitude appeared at 20-, and 23-GHz in first prototype rf structure. To eliminate them, the absorber disk thickness will be changed from 3- to 4-mm. Fig. 9 shows a MAFIA simulation of the single bunch wake field. As can been seen, the wake field amplitudes are damped enough before the arrival of the 2nd bunch, and also there are no higher trapped modes found in the new rf structure.

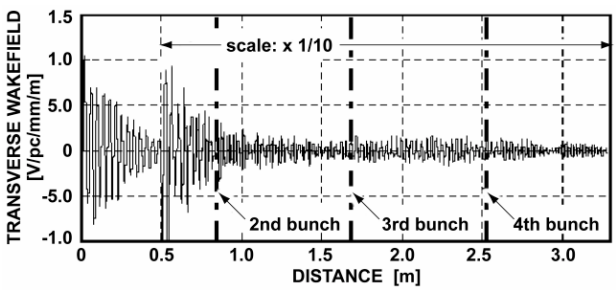

Figure 9: A single wake field simulation of the C-band Choke-mode rf structure.

High Gradient

A series of dark current measurements have been made on two kinds of electrodes made of Molybdenum (Mo) and Titanium (Ti). A new analysis method has been conceived of to separate the primary field emission current from the observed dark current. The analysis shows that the primary field emission current from cathode surface is quite small for a Mo surface, and the enhancement effect is small for a Ti surface. From this analysis, it is strongly suggested that Mo is most suitable material for the cathode and Ti for the anode. This was verified by experiment using Mo cathode and Ti anode electrodes; a field gradient of 130-MV/m was achieved with a total dark current below 1-nA when the separation gap was 0.5-mm as shown in Figure 10.

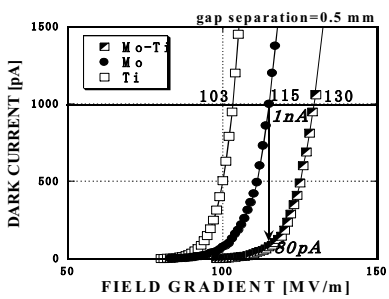

Figure 10: Dark currents for Mo-Ti, Mo-Mo, and Ti-Ti electrodes as a function of field gradient at the cathode surface with a gap separation of 0.5-mm.

Roller Cam Precise Active Mover

The new roller cams mover unit is comprised of two roller cams, their stepping motors drivers, two linear sliders and support frames as shown in Fig. 11. We used 72-mm diameter roller cams to provide ±1.4-mm of positioning area in the horizontal and vertical respectively. We do not use V-blocks and flat plates fixed to the structure (such as is used in the magnet positioning roller cams system in the SLAC FFTB).

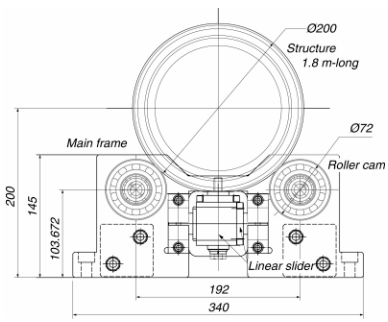

Figure 11: A cutaway drawing of the roller cams mover unit. 72-mm diameter roller cams give an adjustable range ±1.4-mm.

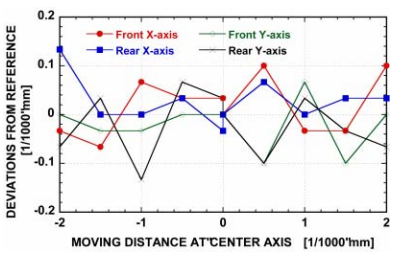

Figure 12: Deviations of roller cams mover from reference.

The expected maximum adjustable range of ±1.4-mm was measured, and then the position repeatability was tested and found to be less than ±0.1-μm anywhere within the positioning range while loaded with a 50-kg dummy weight, shown in Figure 12.

Pulsed High-Voltage Monitor

We have developed a very stable and accurate high-voltage monitor, to be used for observing the klystron pulse voltage [11]. Since it uses a ceramic material in a capacitive type voltage divider (CVD), the capacitance division ratio can be kept quite stable even under temperature changes, or changes in set-up configuration, or changes in the mechanical stresses applied to the monitor port through the input lead. We successfully operated the monitor up to 367-kV, and 4.5-μsec pulses. The maximum voltage for the CVD test was limited by the available modulator output voltage.

A New C-band 50-MW SiC Type RF Load

There are no commercially available 50-MW class vacuum rf loads for C-band frequencies. Therefore we have constructed a new type rf load using SiC ceramic indirectly cooled by water flowing through the structure; this upgraded the power handling density of the SiC material from 100-W per cc to 300-W per cc, allowing a much more compact overall size. The design uses a chain of circular mode TM_{011} absorbers [5]. One particular advantage is that since the main parts are completely axially symmetric, they can be machined on a turning lathe; thus this type of cavity has a big advantage in mass production because of its easier machining.

REALISTIC APPLICATION

SCSS will provide one realistic application of one or a few rf-units in its linac. SCSS will be a soft X-ray SASE-FEL machine aiming at demonstrating FEL operation below 10-nm wavelength with 1-GeV electron beam in 2006~2007 [7]. The combination of a short period in-vacuum type undulator and the high gradient C-band main accelerator makes the machine compact, enabling it to fit within a 100-m long tunnel.

The first project goal will be to generate 60-nm FEL from a 250-MeV energy beam by November 2005.

Machine Configuration

In the SCSS project, the following three key technologies contribute to the compactness of the machine. (1) High gradient C-band accelerator. The accelerating gradient can be as high as 40-MV/m, thus an accelerator only 30-m long is enough to reach 1-GeV. (2) In-vacuum undulator, which enables creating a shorter period undulator thus the required beam energy is lower, again reducing the accelerator size. It also contributes to shortening the FEL gain length. (3) Low emittance beam injector. The short undulator period does require a low emittance electron beam.

We chose a HV (500-kV) pulse DC gun using a single crystal CeB_6 thermionic cathode, which has the potential to generate a very small emittance beam while providing for a long lifetime.

To saturate the FEL lasing in the 22.5-m long undulator line, a low emittance beam current with as much as 2-kA peaks is required. The high peak current is generated by first compressing the bunch length in the injector and then further in a magnetic-chicane bunch compressor. We will use four units of the 40-MV/m accelerating gradient C-band accelerator, which should produce a beam energy reaching 1-GeV with only a 30-m long accelerator; and the shortest radiation wavelength should be 3.6-nm as shown in Figure 13.

REFERENCES

[1] T. Shintake et al., "C-band Main Linac RF System for Linear Collider ", KEK preprint 96-122, September. 1996.

[2] H. Matsumoto et al, "Fabrication of the C-band (5712 MHz) Choke-Mode Type Damped Accelerator Structure", KEK preprint 98-143, September 1998.

[3] T. Shintake et al., "The first Wakefield Test on the C-band Choke-Mode Accelerating Structure", KEK preprint 99-11, May 1999.

[4] H. Matsumoto et al., "DEVELOPMENT OF THE C-BAND (5712 MHz) 50 MW CLASS PPM Klystron (II)", 26th Linear Accelerator Meeting in Japan, Aug.01~03,2001, Tsukuba, Japan

[5] S. S. Win et. al., "A new C-Band 50 MW Class SiC RF load. II", Proc. of 14th Symposium on Accelerator Science and Technology, November 11-13, 2003, Tsukuba Japan.

[6] M. Yoshida et al., "RF Pulse Compressor System", 27th Linac meeting August 7-9, 2002, Kyoto.

[7] T. Shintake et al., "Status of SCSS Project", proc. of PAC2004, March 22-25, 2004, Gyeongju, KOREA.

[8] H. Matsumoto et al, "Development of C-band (5712 MHz) High Power Waveguide Components", KEK preprint 97-50, May 1997.

[9] J-S. Oh et al, "Efficiency Analysis of the First 111-MW C-band Klystron–Modulator System for Linear Collider", KEK Preprint 98-32, March 1998.

[10] H. Matsumoto et al., "Closed type Compact Modulator for 50 MW C-band Klystron", Power Modulator Conference & High Voltage Workshop, June 30 – July 3, 2002, Hollywood, CA.

[11] Y. Takasu et al., "Pulsed High Voltage Monitor Using Ceramic", 27th Linac meeting August 7-9, 2002, Kyoto.

[12] http://www-xfel.spring8.or.jp

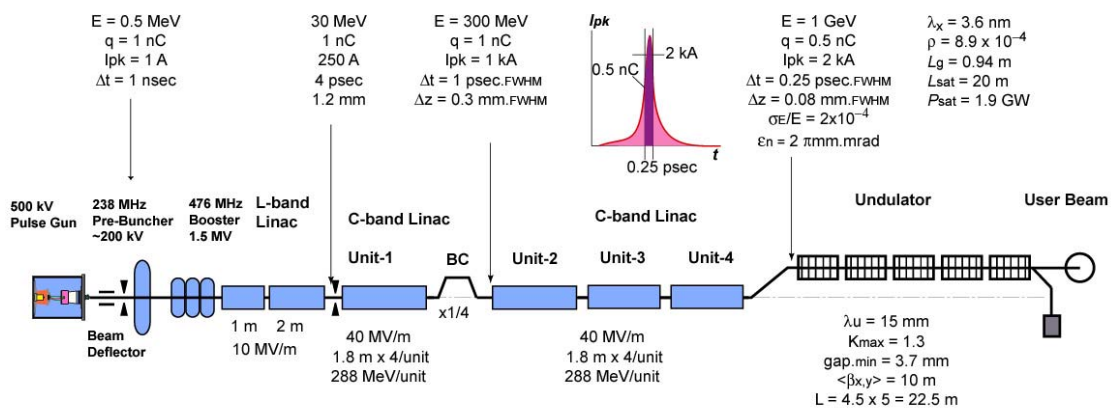

Figure 13: Beam line layout in SCSS of 1-GeV case.

LOW EMITTANCE 500 KV THERMIONIC ELECTRON GUN

K. Togawa*, T. Shintake, H. Baba, T. Inagaki, K. Onoe, T. Tanaka, SPring-8 / RIKEN Harima Institute, Hyogo 679-5148, Japan
H. Matsumoto, High Energy Accelerator Research Organization (KEK), Ibaraki 305-5148, Japan

Abstract

A low emittance 500 kV thermionic gun has been developed for the injector system of the X-ray FEL project at SPring-8. A single-crystal CeB_6 cathode is chosen as a thermionic emitter, because of its excellent emission properties, i.e., high resistance against contamination, uniform emission density, and smooth surface. A gun voltage of -500 kV was chosen as a compromise between the need for suppressing emittance growth and reducing the risks of high voltage arcing. We have succeeded in producing a 500 keV beam with 1 A peak current and 3 μsec width. A normalized rms emittance of 1.1π mm.mrad has been measured by means of double-slit method. In this paper, we describe the design of the CeB_6 gun and report on the result of the emittance measurement.

INTRODUCTION

In X-ray FEL theory, it is well known that the fine structure of the beam dominates the FEL gain. To achieve the SASE-FEL in Angstrom wavelength region, the sliced emittance of the beam should be very low and the peak current should be of the order of kA. Moreover from the application point of view, the FEL machine should be stable for long periods of operation.

In the SASE-FEL, the electron beam generated by the gun is accelerated in the main linac, then it is directly injected into the long undulator and generates the X-ray beam there. Therefore, any electron bunch fluctuation in transverse position, timing, size, charge, etc., will directly affect the X-ray lasing. This is markedly different from the storage ring type machine situation. As a result, the stability of the electron gun is essential for producing stable X-ray FEL light.

We decided to use a thermionic cathode followed by a buncher system [1]. Basically, this is a traditional injector system used in many types of electron accelerators. High stability and long lifetimes have been routinely achieved in the present day injectors, however, for these conventional applications, the typical emittance is ~30π mm.mrad or larger. In order to reduce the emittance, we have added the following modifications and upgrades:

1) Small size cathode. The initial emittance of the gun is dominated by its cathode size. We use a single crystal CeB_6 cathode with a 3 mm diameter. The theoretical thermal emittance is 0.4π mm.mrad at ~1400°C. A high beam current of 3 A can be produced from the CeB_6 crystal at this temperature without jeopardising long lifetime.

2) Elimination of the cathode control grid. The emittance of the traditional thermionic cathode gun is degraded by the electric field distortion caused by the grid mesh.

3) Applying 500 kV to the cathode. In order to minimize emittance growth due to space charge effects, a higher gun voltage is desirable. We use a 500 kV pulse just a few μsec in width.

4) Fast beam deflector. To form a nsec single bunch from the long pulse generated by the gun, we use a fast pulsed beam deflector after the gun.

5) Adiabatic bunching and acceleration. In order to minimize emittance growth due to the rf-field, a lower rf frequency is desirable. We use a 238 MHz sub-harmonic buncher, followed by a 1.6 m drift section, and then a 476 MHz booster cavity which raises the beam energy up to 1 MeV. A following S-band pre-linac is used to accelerate the bunch to 20 MeV before injection into the C-band main linac.

THE CEB6 GUN

We have designed and constructed a 500 kV electron gun with a CeB_6 cathode [2]. A side view of the CeB_6 gun with an emittance monitor bench is shown in Fig. 1, and the beam design parameters at the gun exit are summarized in Table 1.

Table1 : The beam design parameters at the gun exit.

Beam energy	500 keV
Peak current	3 A
Pulse width (FWHM)	1.6 μsec
Repetition rate	60 Hz
Normalized emittance (rms)	0.4π mm.mrad

CeB_6 Cathode

The normalized rms thermal emittance of electrons emitted from a hot cathode is described by

$$\varepsilon_{n,rms} = \frac{r_c}{2}\sqrt{\frac{k_B T}{m_e c^2}},$$

where r_c is the cathode radius, k_B is Boltzman's constant, and T is the cathode temperature. From the above relation, in order to obtain the small emittance less than 1π mm.mrad required for the X-ray FEL, the diameter of the cathode must be in the range of a few mm at the temperature of 1000-1500°C. On the other hand, very high emission density (~50 A/cm^2) is required to produce a several ampere peak current from the small surface. Only the rare-earth hexaborides, such as LaB_6 or CeB_6 can emit such an intense current over long lifetimes. A single crystal is preferable for obtaining low emittance because of its extremely flat surface (roughness ≤1 μm)

* togawa@spring8.or.jp

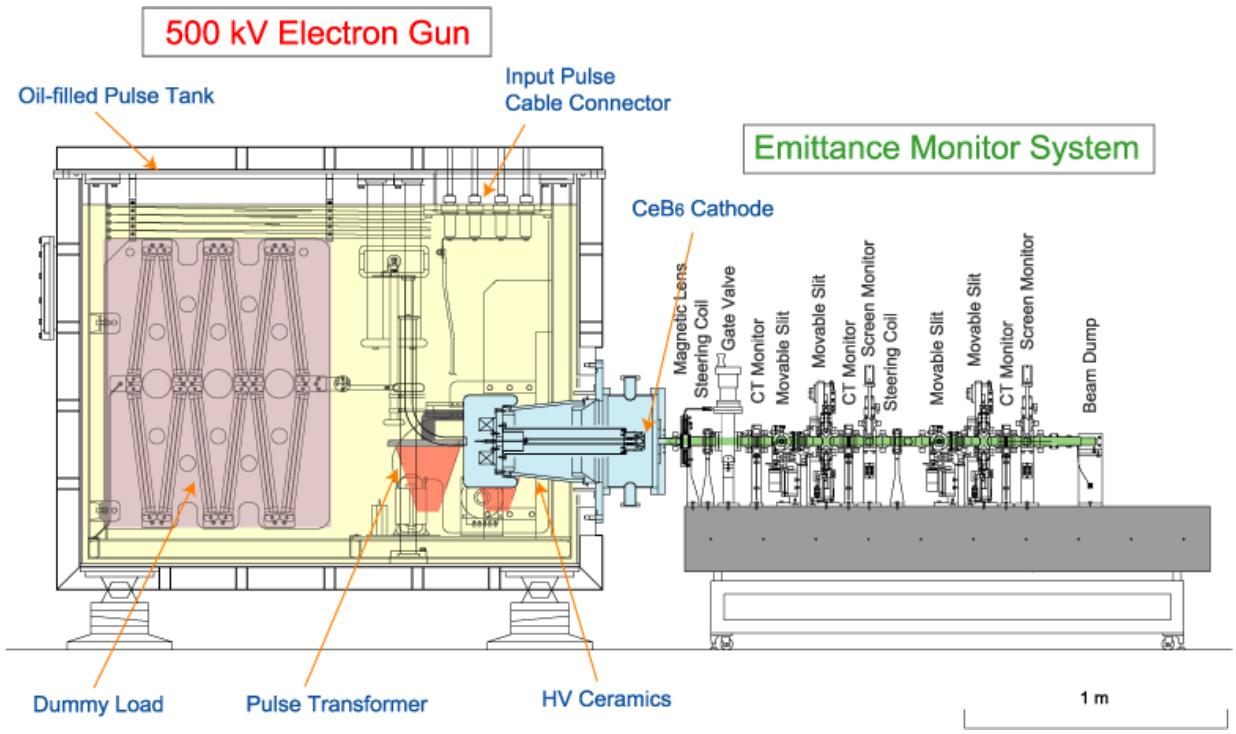

Figure 1: A side view of the CeB_6 electron gun with an emittance monitor bench.

with low porosity after surface material evaporation [3]. The emission density is more uniform because the crystal orientation is the same over the whole surface. In recent years, single crystal CeB_6 cathodes are widely used for electron microscope and superior stability has been demonstrated [4]. It is reported that CeB_6 is very resistant to carbon contamination as compared with LaB_6. Also the operational temperature of CeB_6 can be lower than that of LaB_6 because of its lower work function (~2.4 eV).

For the above reasons, we decided to use a single-crystal CeB_6 cathode with a [100] crystal face. The diameter of our CeB_6 cathode is 3 mm. 3 A peak current will be produced when heated to ~1400°C. The theoretical thermal emittance is 0.4π mm mrad.

Fig. 2 shows the CeB_6 crystal, the cathode assembly and the cathode being heated in the test chamber. The CeB_6 crystal is mounted in a graphite sleeve. This produces a uniform electric field over the entire cathode surface. This is quite important for elimination of any beam emission halo coming from the cathode edge, which could cause damage to the undulator magnets.

We use a graphite heater rather than the conventional metallic filament made of tungsten or the like. Graphite is mechanically and chemically stable even at very high temperatures and does not evaporate like other metals. Since its electrical resistance does not change much as a function of temperature, it is easy to control the heater power. The heater resistance is 0.18 Ω.

A tantalum cylinder covers the graphite heater to shield the thermal radiation from its surface. A base plate for the cathode assembly is made of silicone nitride, which is mechanically strong even when thermal stresses are applied.

The cathode was heated up to ~1400°C in the test chamber by applying 210 W of heater power (see the

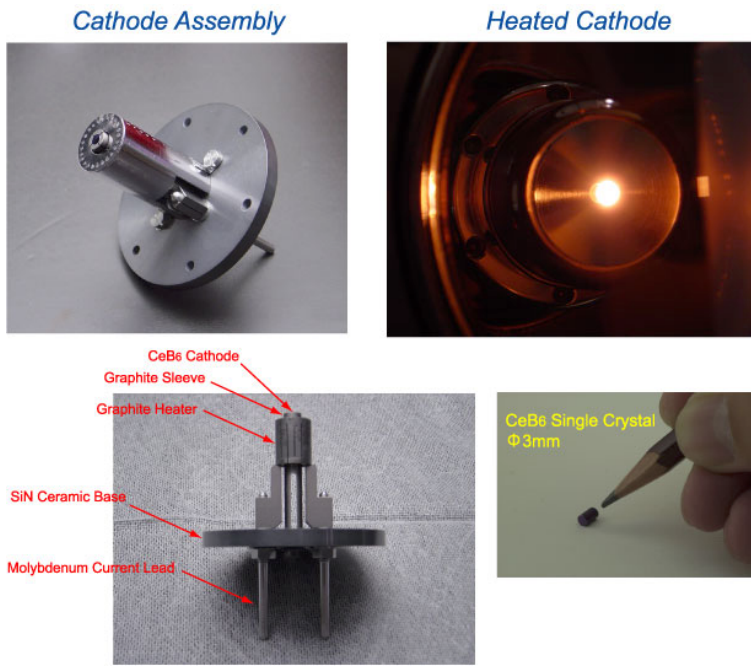

Figure 2: CeB_6 cathode assembly.

upper right side of Fig. 2). A reference temperature was measured from the graphite sleeve surrounding the cathode by means of a radiation monitor. We still need more study in order to determine the cathode temperature distribution precisely. Up to now, the cathode has been operated for 4000 hours without failure.

Accelerating Electrode

The accelerating electrode was carefully designed and manufactured because it controls the initial condition of the emerging low energy beam. We chose a flat Wehnelt rather than the common Pierce-type electrode. The reasons for this are as follows: (1) The Pierce electrode was originally designed to produce a parallel beam whose space charge field is balanced by a focusing electric field. However, if the cathode is not exactly centred due to misalignment of cathode mount or shifts in cathode position due to heating, an asymmetric focusing field acts on the beam. This may cause emittance growth. The flat Wehnelt does not have such an effect. (2) We planned to vary the beam current over a wide range in order to tune the accelerator system. The gun would be operated in a temperature limited region. The Pierce electrode is not suitable for such an operational mode, because at a low current, the beam is over-focused. The flat Wehnelt does not over-focus the beam.

Space charge limited current is described by

$$I_{scl} = \frac{4}{9}\varepsilon_0\sqrt{\frac{2e}{m_e}}\frac{S}{d^2}V^{3/2}\cdot F\,,$$

where V is the gap voltage, d is the electrode gap distance and S is the cathode area. In the case where the cathode radius is much smaller than d, the space charge limited current becomes higher than that of an infinite parallel electrode case of the equation's derivation. In order to take this effect into account, we introduce an enhancement factor, F into Child's law. By performing both an analytical evaluation and computer simulation using the EGUN code, it was found that the enhancement factor is a function of r_c/d. We set the gap distance d to be 50 mm. In this case, F becomes 4.5 and the space charge limited current is 10.5 A. Since this is much higher than the required current, the cathode will be operating in the temperature limited region. In that case, the electric field near the cathode surface is higher than it would be in the space charge limited region. Since the beam near the cathode is immediately accelerated, it is expected that emittance degradation due to space charge effects would be minimized.

We performed a computer simulation for 500 keV, 3A beam operation using the EGUN code. As shown in Fig. 3, the beam trajectory does not diverge much by the electrode gap. When the calculation mesh size is set very fine, the phase space plot becomes a straight line, and the emittance without initial thermal motion converges to less than 0.1π mm.mrad for mesh sizes below 0.05 mm.

The maximum field on the Wehnelt edge is calculated to be 26 MV/m at 500 kV using the POISSON code. The electrode is carefully manufactured to avoid breakdown discharge problems at this high field. Ultra-clean stainless steel is used for the electrode material. The surface was chemically etched and rinsed with ultra-pure water to remove any hydrocarbon contamination which promotes discharges.

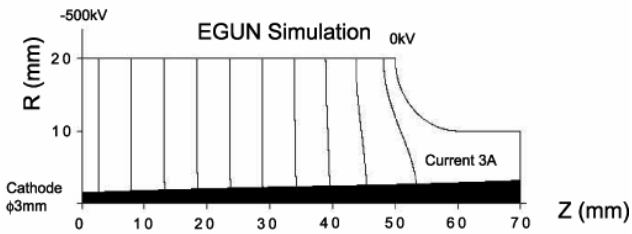

Figure 3: Beam trajectory near the gun electrode.

High-voltage Tank

The circuit diagram for the high-voltage tank is shown in Fig. 4. Basically, it follows the design conventional for a klystron tank. Nowadays, it is technically feasible to produce 500 kV pulses in high power devices, such as X-band klystrons. Therefore, we are able to use the same model C-band klystron modulator [5] to also feed a -24 kV pulsed voltage to the gun high-voltage tank. The

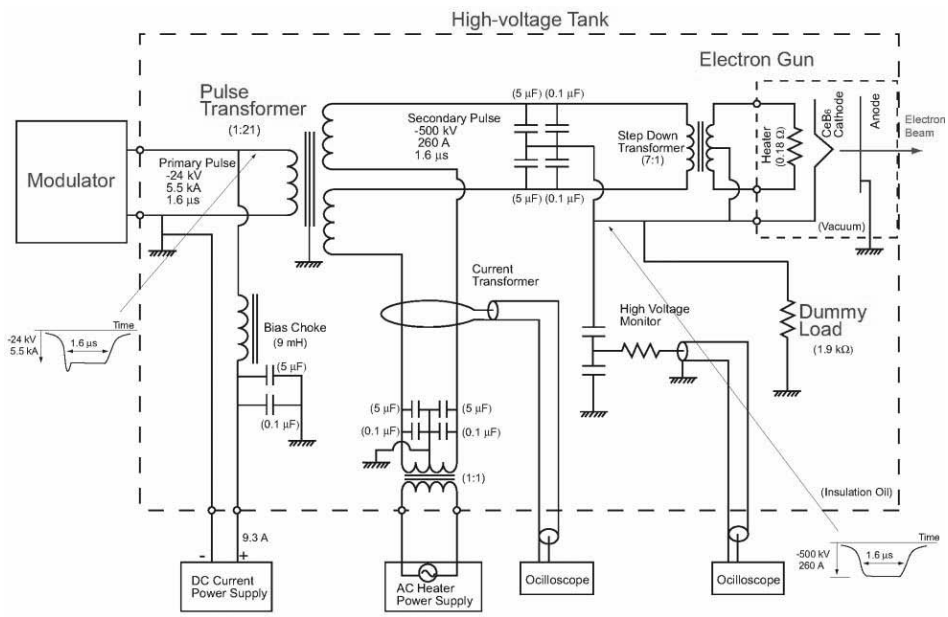

Figure 4: Circuit diagram of the gun high-voltage tank.

primary pulse is stepped-up to a -500 kV by a pulse transformer, with a turn's ratio of 1:21. In order to match the impedance of the gun to the modulator PFN output circuit, a 1.9 kΩ dummy load is connected in parallel with the cathode. AC power for the cathode heater is fed through the secondary winding of the pulse transformer. Since the heater current is very high (>30 A), a step-down transformer, whose turn's ratio is 7:1, is used to reduce the IR power loss in the transmission line from the power supply to the cathode.

Since we need to apply a -500 kV pulse voltage to the cathode, all the high-voltage components, namely, the ceramic insulator, pulse transformer, dummy load, etc., are immersed in insulating oil to eliminate discharge problems. Before operation, the high-voltage tank is pumped out to eliminate gases remaining in the oil and the high-voltage components.

Fig. 5 shows the waveform of the gun voltage and beam current. The beam current was measured by a current transformer (CT) located in the beam line right after the gun. The beam energy is 500 keV, and the peak current is 1 A. The flat-top portion of the pulse is about 0.8 μsec, which is sufficient to generate a nsec bunch.

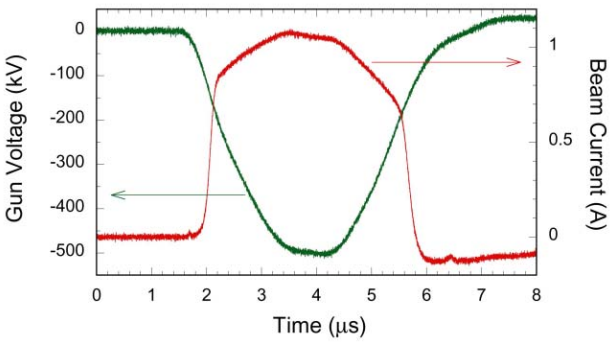

Figure 5: Waveform of the gun voltage and beam current.

EMITTANCE MEASUREMENT

We measured the beam emittance by the so-called double-slits method (Fig. 6). The upstream slit cut out a sheet shaped beamlet from the round beam, which spreads after passing through the drift space due to transverse thermal motion and space charge. The downstream slit measures the beamlet profile. By scanning the both slits throughout the whole beam area, the intensity profile in the phase space can be obtained.

We prepared four slits, two for horizontal (x-direction) scan and two for vertical (y-direction) scan. The upstream x-slit are located at 50 cm downstream from the cathode, followed by a 60 cm drift space and the downstream slit. The opening width must be narrow enough to ignore the beamlet broadening due to space charge. Fig. 7 shows the beamlet intensity profiles for several upstream slit width (25, 50, 100, 200 μm). The original beam energy and current was 400 keV and 0.9 A, respectively. The downstream slit width was set to 25 μm. Accuracy of the width and position is better than 10 μm. The profile became Gaussian for the narrow width less than 100 μm, as expected from the thermal spread. The beamlet broadening due to space charge is ~15% of the thermal spread at 50 μm width in the experimental condition.

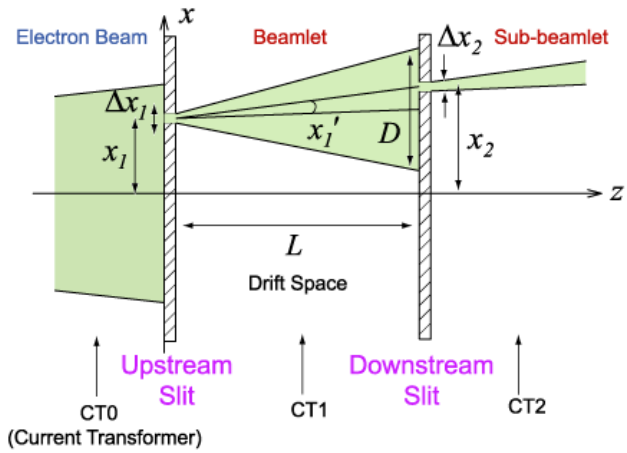

Figure 6: Principle of emittance measurement.

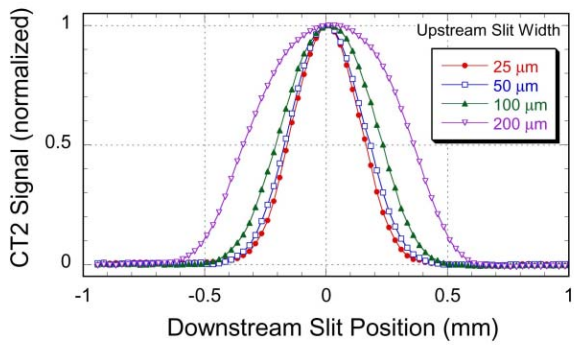

Figure 7: Beamlet profiles for different upstream slit width.

We found that the combination of a slit and a CT monitor with a digital scope is a very powerful tool to analyse the beam dynamics in time domain. The sub-beamlet current waveform provides the information about the time evolution of the phase space intensity at a certain point. From about 1500 waveforms stored by the slit scan, the time evolution of the phase space profile can be reconstructed. Fig. 8 shows an example of the animation screens of the phase space profile evolution.

Using a pair of vertical and horizontal slits, a time-resolved beam profile can be also measured by the same method.

We have measured the current density profile for the 500 keV beam with 1.0 A peak current. Fig. 9 shows the

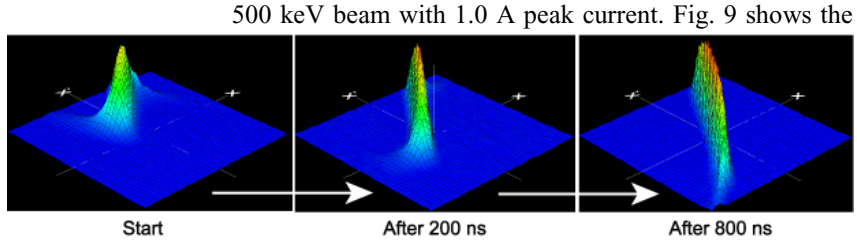

Figure 8: Time evolution of the phase space profile.

3-demensional plot of the current density profile. The width for both the x- and y-slits was set to 0.5 mm × 0.5 mm and the scan step was 0.5 mm. It shows fairly flattop shape as we expected from the cathode geometry.

Fig. 10 shows the 2-demensional plot of the phase space profile (x-direction) measured for the same beam parameters. The width for both the upstream and downstream slits was set to 50 μm and the scan step was 0.25 mm for the upstream slit and 0.1 mm for the downstream slit. From the phase space profile, we analysed the normalized rms emittance, defined as

$$\varepsilon_{n,rms} = \beta\gamma\sqrt{< x^2 >< x'^2 > - < xx' >^2} ,$$

where $<x^2>$, $<x'^2>$ and $<xx'^2>$ denote mean square values weighted by current. The result was 1.1π mm mrad. The demonstrated beam parameter at gun exit are summarized in Table 2.

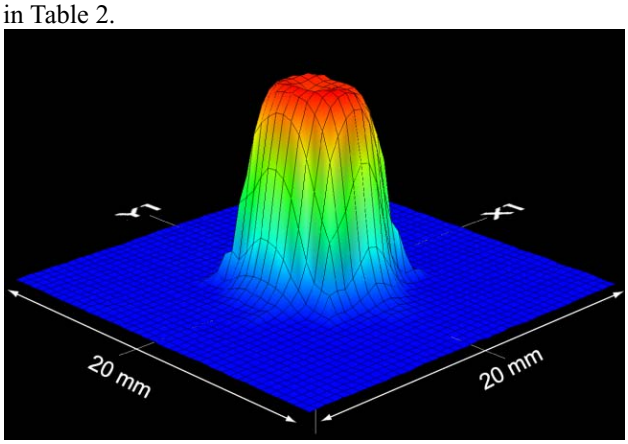

Figure 9: Current density profile of the 500 keV, 1.0 A beam.

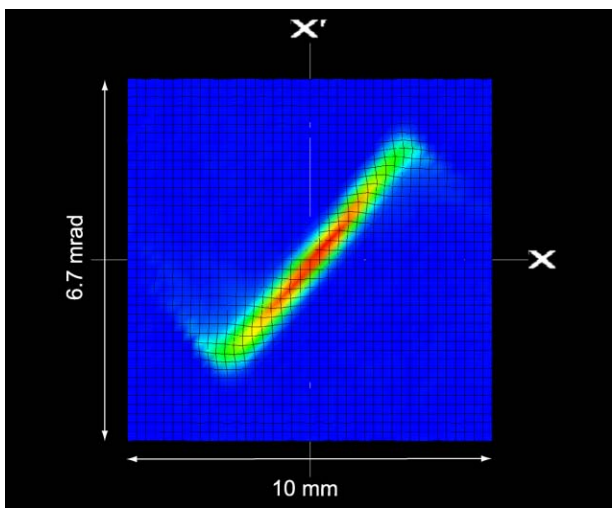

Figure 10: Phase space profile of the 500 keV, 1.0 A beam.

Table 2: Demonstrated beam parameters at gun exit.

Beam energy	500 keV
Peak current	1 A
Pulse width (FWHM)	3 μsec
Repetition rate	10 Hz
Normalized emittance (rms)	1.1π mm.mrad

IMPROVEMENTS FOR X-RAY FEL

Based on the experimental results, the following improvements will be done for the real injector system:

1) Beam current: We need to increase the beam current by a factor of 3 for operation. The current cathode emission may not be activated well as possible. The increase in cathode temperature to obtain a 3 A peak current is estimated to be ~120°C.

2) Pulse width: The high-voltage pulse width turned out to be two times longer than the design value. The fairly big stray capacitance of the dummy load resistors no doubt causes the pulse to be stretched out to this long duration. As a result, the heat load that must be removed from the high-voltage tank was higher than the design expectation. The large size of the high-voltage tank is also determined by the resistors. In order to shorten the pulse width and to make the tank more compact, we are now developing an electron tube dummy load, which will replace the load resistors.

3) Emittance: We successfully achieved a very small emittance, but even so, it was somewhat larger than the theoretical predicted value. A small tail at the profile edge, which may be generated by the space charge effect, is a source of the emittance increase. The emittance without this tail can be roughly estimated by making the product of the rms diverging angle at the beam centre ($\sigma_{x'}$) and the rms beam radius ($\sim r/2$). The 0.6π mm.mrad value obtained is near the theoretical thermal emittance. Since the nonlinear tail comes from the edge region of the round beam, it could be removed by using a beam collimator. We expect that doing that we should realize the required small emittance of less than 1π mm.mrad.

REFERENCES

[1] T. Shintake et al., "SPring-8 Compact SASE Source, SPIE2001, San Diego, USA, June 2001

[2] K. Togawa et al., "CeB_6 Electron Gun for the Soft X-ray FEL Project at SPring-8", FEL2003, Tsukuba, Japan, Sept. 2003, Nucl. Instr. Meth. A 528 (2004) 312

[3] H. Kobayashi et al., Emittance Measurement for High-Brightness Electron Guns, 1992 Linear Accelerator Conference, Ottawa, Canada, August 1992

[4] http://www.feibeamtech.com/

[5] H. Matsumoto et al., "A Closed Compact Modulator for 50 MW C-band (5712 MHz) Klystron" 25th International Power Modulator Symposium and 2002 High Voltage Workshop, Hollywood, USA, 2002, ISBN 0-7803-7540-8

[6] K. Togawa et al., "Emittance Measurement on the CeB_6 Electron Gun for the SPring-8 Compact SASE Source FEL Project", APAC2004, Gyeongju, Korea, March 2004

HIGH PRESSURE, HIGH GRADIENT RF CAVITIES FOR MUON BEAM COOLING*

R. P. Johnson#, M. M. Alsharo'a, R. E. Hartline, M. Kuchnir, T. J. Roberts, Muons, Inc., Batavia, IL
C. M. Ankenbrandt, A. Moretti, M. Popovic, Fermi National Accelerator Laboratory, Batavia, IL
D. M. Kaplan, K. Yonehara, Illinois Institute of Technology, Chicago, IL
K. Beard, A. Bogacz, Y. Derbenev, T. Jefferson National Accelerator Facility, Newport News, VA

Abstract

High intensity, low emittance muon beams are needed for new applications such as muon colliders and neutrino factories based on muon storage rings. Ionization cooling, where muon energy is lost in a low-Z absorber and only the longitudinal component is regenerated using RF cavities, is presently the only known cooling technique that is fast enough to be effective in the short muon lifetime. RF cavities filled with high-pressure hydrogen gas bring two advantages to the ionization cooling technique. First, the energy absorption and energy regeneration happen simultaneously rather than sequentially, and second, higher RF gradients and better cavity breakdown behavior are possible due to the Paschen effect. A first step in a program to develop ionization cooling using pressurized cavities is the measurement of RF breakdown of hydrogen at high density. In the study reported here, the linear dependence of breakdown on pressure was verified in an 800 MHz hydrogen-filled test cavity up to 80 MV/m, which was the surface gradient limit of the molybdenum electrodes of the cavity. We note that the conditioning of the electrodes was unusually fast in the gas and needed only a few hundred thousand pulses. Planned research includes experimental measurements of pressurized RF cavity behavior in strong magnetic and ionizing radiation fields. Analytical and simulation calculations are also being made to examine how these cavities might be used in a practical cooling channel, effectively a rather complex Linac.

INTRODUCTION

Accelerators and colliding beam storage rings for High Energy Physics research have used protons and/or electrons and their antiparticles. Muons, despite their short lifetime, have several advantages to make them attractive candidate particles for the next generation of energy frontier colliders. Muons are point like, rather than composite, so that all of their collision energy can be used to create new states of matter. Thus a muon collider can have an energy and footprint one tenth that of the equivalent proton collider. Muons are more massive than electrons so that problems with synchrotron radiation are greatly diminished. Thus a muon collider can be a multi-turn ring of high-field magnets and each beam will not be disrupted by the electromagnetic field of the other at interaction regions. Because of the reduced disruption, a muon collider can be built with center of mass energy much greater than the 1.5 TeV that linear electron-positron colliders are likely to be limited to.

The muon advantage that is the subject of the studies reported here, however, has to do with passage through matter. Unlike protons, muons do not interact through the strong interaction and rarely suffer large scattering angles. Unlike electrons, muons create few electro-magnetic showers since they are more massive. Thus, muons have one other important virtue compared to protons and electrons in that they can pass through material with losses and scattering small enough to still be useful in accelerators, storage rings, and colliders.

This paper describes efforts to use this muon virtue of acceptable scattering through matter to rapidly cool a muon beam and quickly accelerate it to high energy. The new idea that is being exploited is that RF cavities used for muons can be filled with high-pressure gas to suppress high voltage breakdown. The gas, if it is low-Z, can also be the energy absorber for ionization cooling.

Ionization Cooling

Neutrino Factories or Muon Colliders, which require intense beams of muons, are dependent on a scheme to quickly reduce or cool the emittance of a muon beam before it can be injected into a practical accelerator[1]. Ionization cooling of a muon beam involves passing a magnetically focused beam through an energy absorber, where the muon transverse and longitudinal momentum components are reduced, and through RF cavities, where only the longitudinal component is regenerated. After some distance, the transverse components shrink to the point where they come into equilibrium with the heating caused by multiple coulomb scattering.

The equation describing the rate of cooling is a balance between these cooling (first term) and heating (second term) effects[2]:

$$\frac{d\varepsilon_n}{ds} = -\frac{1}{\beta^2}\frac{dE_\mu}{ds}\frac{\varepsilon_n}{E_\mu} + \frac{1}{\beta^3}\frac{\beta_\perp (0.014)^2}{2E_\mu m_\mu X_0}.$$

Here ε_n is the normalized emittance, E_μ is the muon energy in GeV, dE_μ/ds and X_0 are the energy loss and radiation length of the absorber medium, $\beta_\perp$ is the transverse beta-function of the magnetic channel, and β is the particle velocity.

Setting the heating and cooling terms equal defines the equilibrium emittance, the very smallest possible with the given parameters:

* This work is supported in part by US DOE STTR grant DE-AC02-ER86145 and SBIR grant DE-FG02-03ER83722
# Rol@muonsinc.com

$$\varepsilon_n^{(equ.)} = \frac{\beta_\perp (0.014)^2}{2\beta m_\mu \frac{dE_\mu}{ds} X_0}.$$

A cooling factor ($F_{cool} = X_0 dE_\mu/ds$) can be uniquely defined for each material, and since cooling takes place in each transverse plane, the figure of merit is F_{cool}^2[3]. The inverse of F_{cool}^2 corresponds to the best equilibrium emittance that can be achieved. Super-conducting solenoidal focusing is used to give a value of $\beta_\perp$ as low as 10 cm. Figure 1 shows F_{cool}^2 for many materials of interest, where gaseous hydrogen is twice as effective as helium, the next best material from the standpoint of the final equilibrium emittance. Also, since the exponential cooling rate depends on the difference between the initial and final emittances, it provides the very best cooling rate.

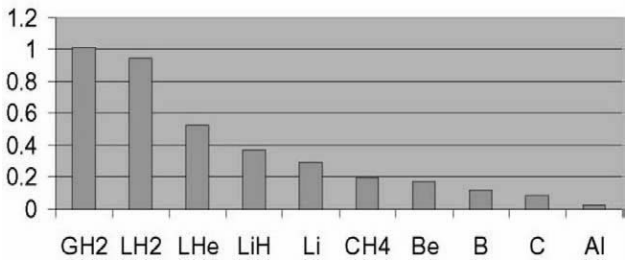

Figure 1: A comparison of F_{cool}^2 for light materials relative to gaseous hydrogen. The equilibrium beam emittance in each transverse plane is inversely proportional to the product of the energy loss and the radiation length. F_{cool}^2 for a material is independent of density, since $dE_\mu/ds \sim \rho$ and $X_0 \sim 1/\rho$.

Up to now, liquid hydrogen has been the energy-absorbing medium of choice, with $dE_\mu/ds = 30$ MeV/m and $X_0 = 8.7$ m. Most liquid hydrogen cooling channel designs use an energy absorber with a total length that corresponds to twice the energy of the initial beam. Thus a 200 MeV beam would require 400 MeV of energy loss, or about 13 meters of liquid hydrogen separated into about 40 flasks, each 33 cm long in the beam direction and a similar useful diameter. In between each flask, 3 or 4 RF cavities operating in vacuum occupy about 2.2 meters, giving an effective average energy loss of about 4 MeV/m. The gaseous hydrogen channel advocated here would have a higher average energy loss, perhaps as much as 15 MeV/m and be correspondingly shorter and cheaper.

Paschen's Law

Most RF cavities associated with particle accelerators operate in as good a vacuum as possible to avoid electrical breakdown. This is done so that ions that are accelerated by the high voltages in the RF cavity rarely encounter atoms of the low-pressure residual gas, and so the avalanche process of breakdown is inhibited. Other RF systems that do not require the ultrahigh vacuum of an accelerator typically suppress RF breakdown by using dense insulating materials between electrodes. Ions passing through these materials, which include high-pressure and/or high-density gases, have such a short mean free path between collisions that they do not accelerate to energies high enough to create an avalanche.

The relationship in the high-pressure regime between the electrical breakdown voltage and the pressure times gap width is known as Paschen's Law[4]. Here we use gradient and pressure to express the same relationship. The goal of the study below is to examine this relationship for hydrogen gas to a pressure of 110 atmospheres at 77K, where the gas density is about half that of liquid hydrogen. Extrapolated from the measurements below, hydrogen at that density will support almost 700 MV/m. Also seen below, hydrogen suppresses breakdown about six times better than helium at the same pressure.

HIGH-PRESSURE TEST CELL

Earlier measurements with the "Mark I" prototype test cell and copper electrodes have been reported[5]. Figure 2 shows a schematic of the "Mark II" RF test cell used for the measurements reported here, which were carried out in Fermilab's Laboratory G using molybdenum electrodes. The construction uses copper-plated, 5 cm thick, stainless steel disks that are bolted onto a cylinder of the same material with 0.4 mm aluminum gaskets.

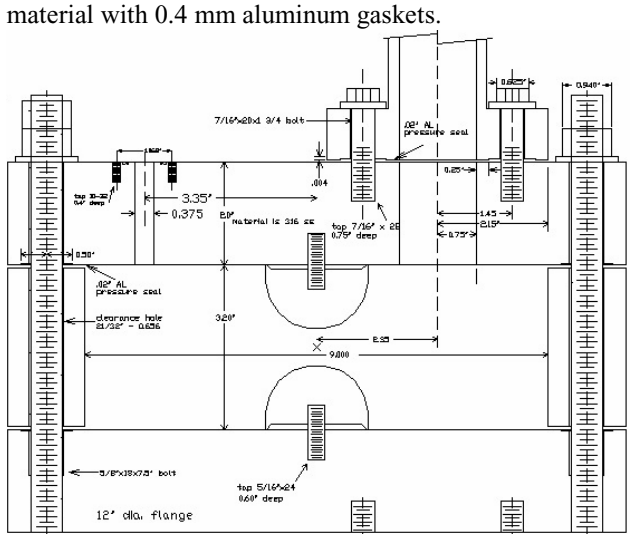

Figure 2: A schematic of the Mark II 805 MHz test cell (TC) used at Fermilab Lab G to measure the electrical breakdown properties of gases under extreme conditions. The top and bottom disks and the cylinder are copper-plated stainless steel. The TC is easily opened to allow inspections and to change the doorknob electrodes for cavity tuning or studies of RF breakdown. The central conductors of the coax feed line and of the pick-up are not shown.

Power from the Lab G klystron was fed through a stainless steel coaxial line that has a segment with an epoxied central conductor that acts as a room-temperature pressure barrier located well above the liquid nitrogen

bath that surrounds the test cell. A smaller coaxial pick-up is used to monitor the voltage in the test cell. Both the feed and the calibrated pick-up are capacitively coupled to the test cell. Two removable hemispherical doorknob electrodes inside the test cell define the resonant frequency and the breakdown location. Figure 3 is a picture of the stainless steel disks and cylinder before copper plating. Details of the construction and operation of the test cell can be found in a MuCool Note[6].

Figure 3: Picture of the Test Cell Stainless Steel Disks and Cylinder before copper plating.

Figure 4 shows the 800 MHz RF envelope as measured by the calibrated pick-up. Conditioning and measurements were with 20 microsecond pulses at 5 Hz. Measurements started at high pressure then gas was released for subsequent measurements so that it was not necessary to wait for the gas to come to thermal equilibrium with the test cell and liquid nitrogen bath.

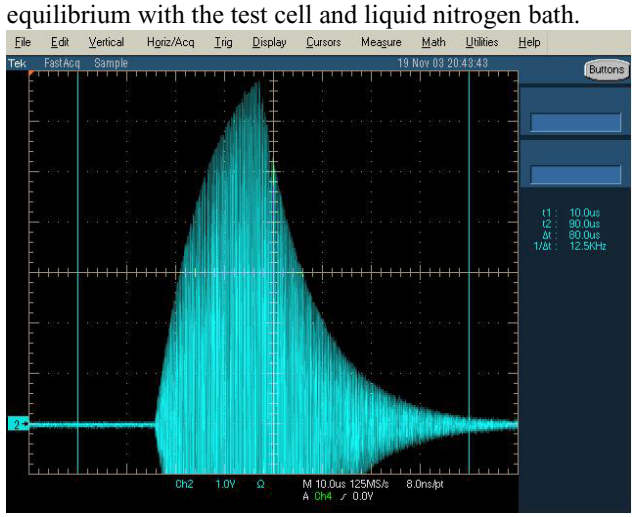

Figure 4: The probe signal taken during the last hours of operation at 250PSI and 77K. The pulse time of 20 μs corresponds to the rising part of the 800MHz envelope.

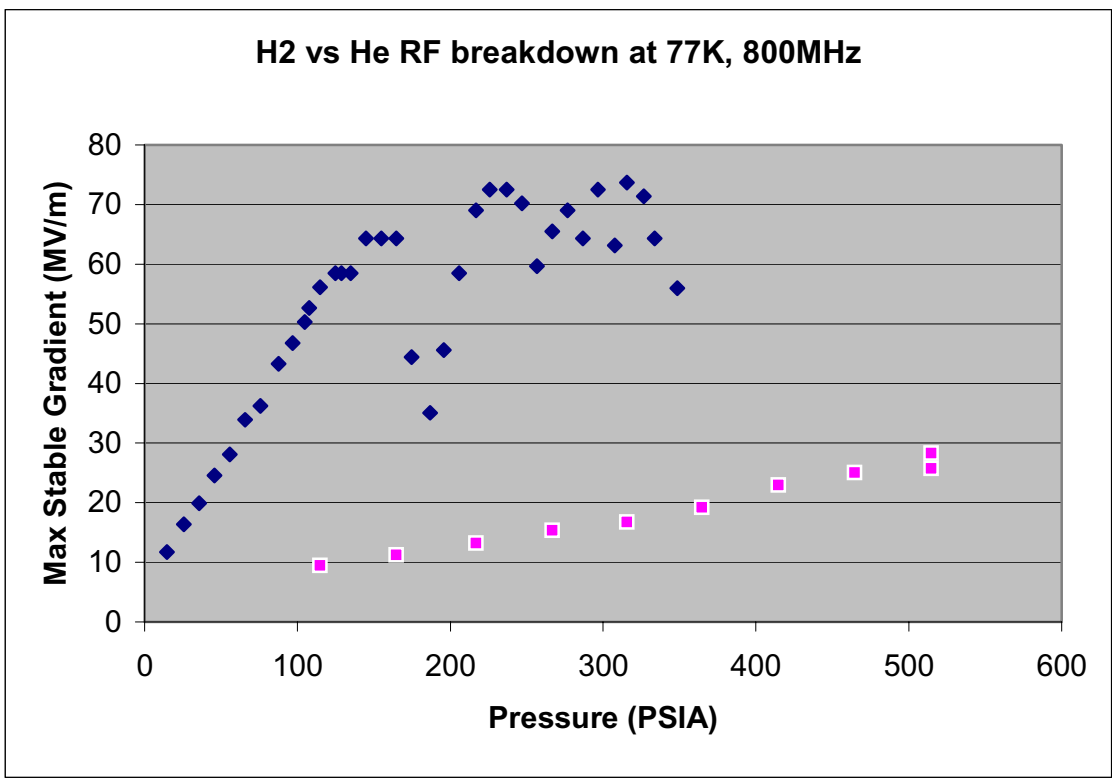

Figure 5: Paschen curve measurements for hydrogen (black diamonds) and helium (red squares) at liquid nitrogen temperature. Each datum was determined by first setting the klystron frequency at reduced voltage, raising the voltage until breakdown occurred regularly, then reducing the voltage until breakdown did not occur.

LAB G MEASUREMENTS

Figure 5 shows the measurements of the Paschen curves for hydrogen and helium at 77K. The linear Paschen region can be seen in the plot for helium over the entire range and for hydrogen below 150 PSIA. The dip around 190 PSIA in the hydrogen data corresponds to a breakdown in the transmission line from the klystron. The hydrogen data at higher pressure are dominated by breakdown at the surface of the molybdenum electrodes. The gold star represents the result of the last 3 hours of conditioning with hydrogen at 265 PSIA, where a maximum stable gradient of 79.9MV/m was attained

The next steps are to demonstrate that such cavities will work in the high magnetic and radiation fields expected in an actual cooling channel. Soon we will operate the test cell in a 5T solenoid to compare to the breakdown behavior we have measured without a field and to the behavior of the evacuated cavities that have been already tested in the solenoidal field.

The extrapolated breakdown gradient of almost 700 MV/m for hydrogen gas in our expected operating conditions gives confidence that the cavities will handle ionizing radiation well. Nevertheless, the demonstration of this prediction is the ultimate goal of this project. Our top priority is to make sure that Fermilab will have beam for us as soon as possible. We are hopeful and enthusiastic that a beam line design can be implemented so that we can do the required tests in 2005.

In order to push the technology for RF cavities, both evacuated and pressurized, we have begun to study construction materials and their breakdown behavior. The molybdenum results reported here are encouraging, and we look forward to our next tests with chromium and beryllium.

COOLING CHANNEL DESIGNS WITH GASEOUS HYDROGEN

In addition to the development of the high-pressure RF cavities themselves, there is considerable effort to develop cooling channels that could use them. One such effort involves the possibility that a continuous gaseous energy absorber in a magnetic channel with dispersion can be used to cool the momentum spread of a muon beam by exploiting the fact that higher-momentum particles have longer path length and therefore larger energy loss. This approach to emittance exchange and six-dimensional cooling has been described analytically[7] and is now the subject of simulation efforts. As an example, figures 6 and 7 show the side and end view of a segment of a six-dimensional cooling simulation that incorporates a continuous solenoid with helical dipole and quadrupole magnets to achieve a channel with good dispersion and acceptance. The simulation code G4Beamline is based on the Geant4 program and is under development by our collaboration[8].

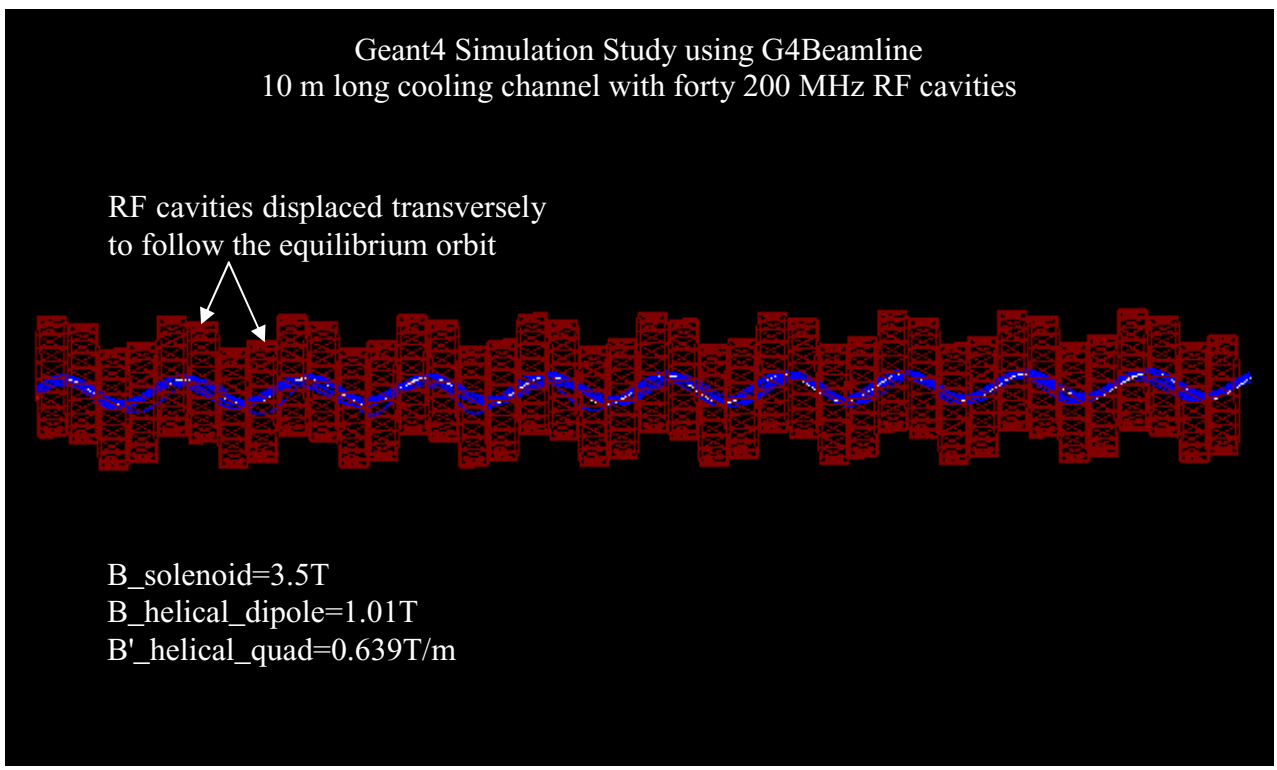

Figure 6: G4Beamline display of the helical cooling channel that is being simulated. In this simulation, superimposed magnetic fields with solenoidal and helical components provide focusing and dispersion as the muons pass through the hydrogen-filled RF cavities. Muon trajectories are shown in blue as they oscillate about the equilibrium orbit shown in white.

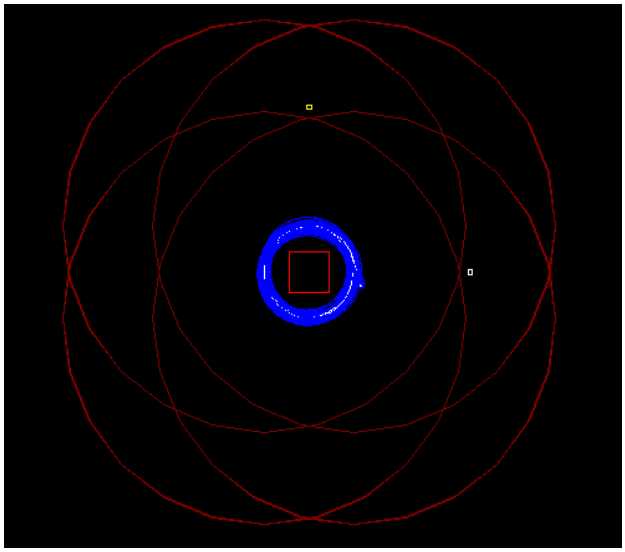

Figure 7: The same as conditions as figure 6, but viewed looking down the cooling channel. The beam here is at 200 MeV/c with a helix radius of 11 cm. The outlines of the radially displaced RF cavities are shown in red. The red box shown for orientation in the center is 10 cm on a side.

CONCLUSIONS

Some new ideas to cool muon beams are being explored. The use of a gaseous hydrogen energy absorber for ionization cooling seems particularly promising in that the gas can fill the RF cavities of a cooling channel to good advantage. First measurements indicate that such cavities will operate at higher gradients, have shorter conditioning times, and have reduced dark currents. Tests in high magnetic fields and in intense ionizing radiation are needed to verify that pressurized RF cavities will work satisfactorily in muon cooling applications. New ideas in cooling channel designs that will incorporate these cavities are starting to be developed as well. If an effective six-dimensional muon beam cooling channel can be developed, the chances for an affordable neutrino factory and a realistic muon collider will be greatly increased.

REFERENCES

[1] M. M. Alsharo'a et al., *Recent progress in neutrino factory and muon collider research within the Muon Collaboration.* Phys. Rev. ST Accel. Beams 6, 081001 (2003)

[2] Daniel M. Kaplan**,** *Introduction to Muon Cooling,* http://www.slac.stanford.edu/econf/C010630/papers/M102.PDF

[3] R. P. Johnson, et al. *Gaseous Hydrogen and Muon Accelerators.* International Workshop on Hydrogen in Materials and Vacuum Systems, Newport News, Virginia, 11-13 Nov 2002. Published in **AIP Conf.Proc.671:328-336,2003.**

[4] Sanborn C. Brown, **Basic Data of Plasma Physics, The Fundamental Data on Electrical Discharges in Gases**, American Vacuum Society Classics, AIP Press, 1993. http://home.earthlink.net/~jimlux/hv/paschen.htm

[5] R. P.Johnson et al., *Gaseous Hydrogen For Muon Beam Cooling*, PAC2003 Portland, OR. http://warrior.lbl.gov:7778/pacfiles/papers/TUESDAY/PM_POSTER/TPPB087/TPPB087.PDF

[6] R. E. Hartline, R. P. Johnson, M. Kuchnir, C. M. Ankenbrandt, A. Moretti, M. Popovic D. M. Kaplan, K. Yonehara, *Mark II High-Pressure RF Test Cell Measurements with Molybdenum Electrodes at Lab G.* http://www-mucool.fnal.gov/mcnotes/public/pdf/muc0285/muc0285.pdf

[7] Yaroslav Derbenev and Rolland P. Johnson*, Six-dimensional muon beam cooling using a homogeneous absorber*, http://www-mucool.fnal.gov/mcnotes/public/pdf/muc0284/muc0284.pdf

[8] http://www.muonsinc.com

EFFECT OF HIGH SOLENOIDAL MAGNETIC FIELDS ON BREAKDOWN VOLTAGES OF HIGH VACUUM 805 MHz CAVITIES

A. Moretti, A. Bross, S. Geer, Z. Qian, (FNAL) , J. Norem, (ANL), D. Li, M. Zisman, (LBNL), Y. Torun, (IIT), R. Rimmer, (TJNAL), D. Errede, (UIUC)

Abstract

There is an on going international collaboration studying the feasibility and cost of building a muon collider or neutrino factory [1,2]. An important aspect of this study is the full understanding of ionization cooling of muons by many orders of magnitude for the collider case. An important muon ionization cooling experiment, MICE [3], has been proposed to demonstrate and validate the technology that could be used for cooling. Ionization cooling is accomplished by passing a high-emittance muon beam alternately through regions of low Z material, such as liquid hydrogen, and very high accelerating RF Cavities within a multi-Tesla solenoidal field. To determine the effect of very large solenoidal magnetic fields on the generation of dark current, x-rays and on the breakdown voltage gradients of vacuum RF cavities, a test facility has been established at Fermilab in Lab G. This facility consists of a 12 MW 805 MHz RF station and a large warm bore 5 T solenoidal superconducting magnet containing a pill box type cavity with thin removable window apertures. This system allowes dark current and breakdown studies of different window configurations and materials. The results of this study will be presented. The study has shown that the peak achievable accelerating gradient is reduced by a factor greater than 2 when solenoidal field of greater than 2 T are applied to the cavity.

INTRODUCTION

The concept of a Muon Collider has been under study internationally for a number of years. High intensity muons are produced from a high-energy high-intensity proton beam hitting a high Z material. Pions are captured and subsequently decay into muons. The capture section consists of a high Z target surrounded by a very high solenoidal capture field of several T. This produces a muon beam of very large 6-D phase space. In order to produce muon beams of high enough quality to be used for a collider, this large phase space must be cooled several orders of magnitude and done quickly, because of the short life time of the muon. Ionization cooling can accomplish the task of cooling the muon beam many orders of magnitude. Ionization cooling consists of passing a high-emittance muon beam alternately through regions of low Z material, such as liquid hydrogen, and very high accelerating RF Cavities within a multi-Tesla solenoidal focusing channel. As the particles pass through the low Z material, they lose momentum in 3-D phase space. The longitudinal component (accelerating frame) is then restored by the RF cavities. This is repeated many times to produce a beam of the quality required for a collider. Although not necessarily required, muon ionization cooling can be used to improve the performance of a neutrino factory.

A key element of the feasibility study is the demonstration of ionization cooling. The Muon Ionization Cooling Experiment, MICE [3], has been proposed and is being planned to demonstrate 10 % cooling which will be enough to validate the technology. This experiment is an international collaborative effort with the US, Europe and Japan as the principle partners. This experiment is planned to take place at Rutherford Appelton Laboratory in England.

Important to any demonstration of muon ionization cooling is the accelerating cavity technology. For the past three years, studies of the limitations of very high electric field gradients in linac type vacuum RF cavities have been taking place in a test facility in Lab G at Fermilab. The purpose of the facility is to determine the effect of very large solenoidal magnetic fields on the generation of dark current and x-rays and its effect on the breakdown voltage gradients of vacuum RF cavities. This facility allows us to test methods and materials to increase the breakdown limit and reduce dark current emissions. Increasing the achievable accelerating gradient would reduce one of the major cost drivers of a future collider or neutrino factory.

THE LAB G TEST FACILITY

The Lab G facility consists of a Fermilab upgrade Linac modulator and controls, a 12 MW pulsed klystron and its waveguide system, a 5 T superconducting magnet with a large warm bore for cavity insertion, cooling water and high vacuum systems for the test cavity and a radiation shielded interlocked test cave. Figure 1 shows a picture of the 5 T superconducting solenoid with the first test cavity (an open cell cavity) being tested in the facility [4]. At its ends are shown thin 125 μm Ti vacuum windows for dark current and x-ray measurements. The facility permits research and development on methods and materials to increase the breakdown limit and reduce dark current emissions. It also allows us to test RF components and qualify RF technology for a future muon collider, neutrino factory or MICE .

The arrangement for the second set of measurements on the LBL Pill box cavity is shown in Figure 2. The single cell LBL cavity is shown in the center of figure 2, [5,6]. It has been designed with removable vacuum end pieces. This arrangement was chosen so that a variety of window configurations and materials could be tested rapidly for

This work supported by the US Department of Energy
Under Contract Number DE-AC02-76H0300.

their breakdown limit and dark current emission. There is a thin 125 μm Ti thick window at the downstream end of the cavity for dark current measurements. [Note: the solenoid has two separate coils. They can be powered to add field (solenoid mode), in opposition (gradient mode), or one coil alone (single coil mode).]

EXPERIMENTAL RESULTS ON THE LBL SINGLE CELL CAVITY

The chart, Figure 3, presents the breakdown limit versus magnetic field results from about a 2 year period of study. The graph shows the limit above which surface damaging sparks occur during a relatively short RF commissioning period of time. Spending long periods, hours, above this limit results in a very large permanent increase in dark current and x-ray emissions. The graph shows the safe gradient operating limit in a magnetic field. Operating near this or at this limit results in little increase in dark current and x-ray emissions over time. The data were taken with the three magnetic field configurations as parameters and are plotted as a function of the field level at the window. This shows that the breakdown limit is strongly correlated with the value of the magnetic field at the site of the window. It also shows a reduction in the breakdown limit of greater than a factor of two above 2 T.

Examination of the damage by SEM and optical microscope showed molten copper disks 100 to 125 μm in diameter scattered over the Be window surface, Figure 4. There was no spark damage observed in the Be or in the TiN coating of the window. Spark damage was only observed in the copper parts of the cavity. The SEM analysis of the molten copper spots indicate they were mainly composed of copper with just a small trace of other elements. Other studies with copper windows inserts were observed to behave in a similar manner. This demonstrates that copper is the weak link in reaching high gradient in large magnetic fields and that Be has a greater intrinsic breakdown limit. It would be impractical and extremely expensive to build the accelerating cavity entirely out of Be. A major portion of the cavity still needs to be made of copper. A research effort is being planned to find a coating that can protect and therefore greatly enhance the breakdown limit of copper.

Figure 5, shows typical x-ray level measurements as a function of gradient without magnetic field over a period of one month. Time starts with the top curve and ends 30 days later at the bottom curve. This demonstrates an observation of a curing effect. As the RF commissioning time goes on, the x-ray levels go down as long as the breakdown limit is not exceeded. However, as soon as a damaging spark occurs, the x-ray emission greatly increases and never recovers to the previous low background level even with continuing RF commissioning. It should be observed that the curves end just below the breakdown limit. This seems to demonstrate that breakdown is determined by the dark current emission near or at breakdown and no matter at what level it starts out ii reaches the same limit point.

Figure 1: Picture of the open cell test cavity in the Solenoid.

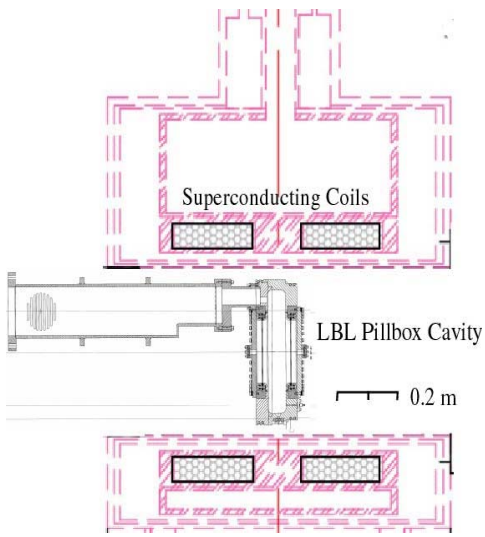

Figure 2: The single cell cavity in the superconducting 5 T solenoid.

Figure 6, shows typical x-ray level measurements as a function of gradient with the magnetic field as a parameter for three field levels. The magnetic field levels increase from bottom to top. This demonstrates a large increase in x-ray levels with increasing magnetic field at lower gradient levels. The x-ray background levels are also higher than without magnetic field because of the focusing effect of the magnet. As the RF commissioning time goes on, the x-ray levels go down as long as the

breakdown limit is not exceeded. However, as soon as a damaging spark occurs, the x-ray emission greatly increases and never recovers to the previous low, even after long RF commissioning runs.

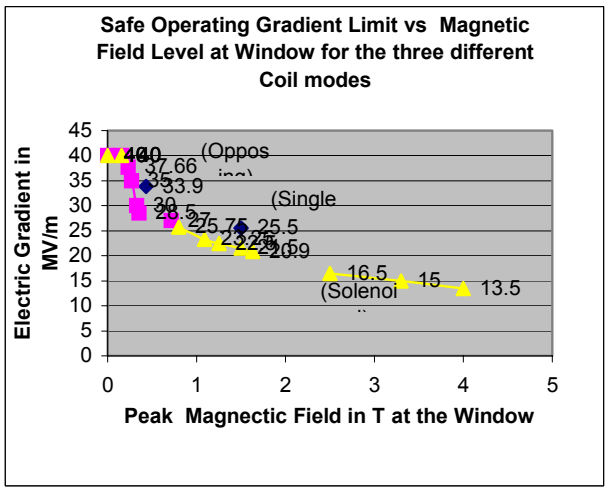

Figure 3: Safe operating electric gradient for the three different coils excitations. Operating above these limits produced damaging sparks that produce large increases in x-ray levels which never fully recover.

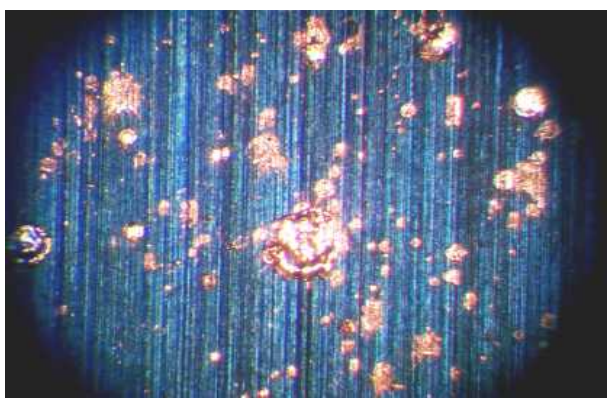

Figure 4: Copper Splatter on Be Window

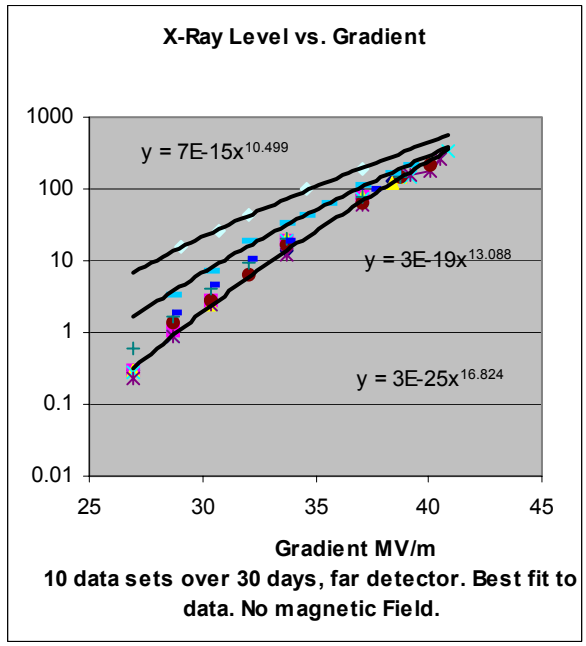

Figure 5: X-ray level in far detector 3 m away from the cavity [vertical scale mrem/hr].

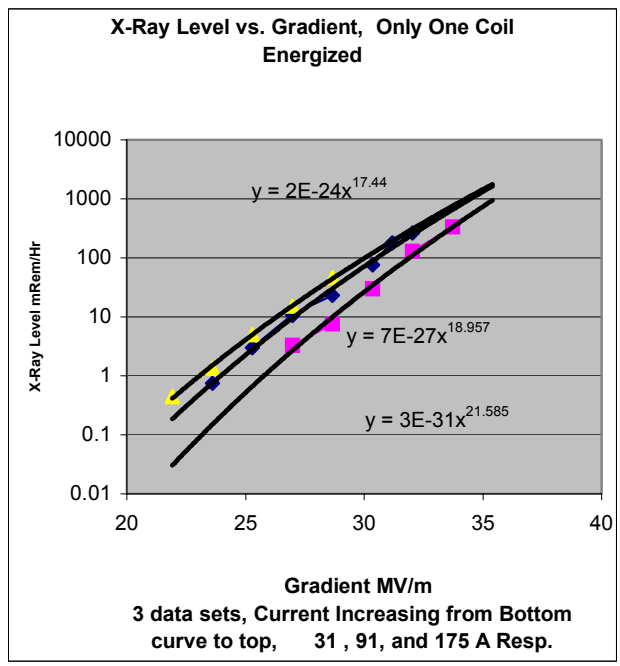

Figure 6: X-ray level in far detector 3 m away from the cavity with magnetic field levels of 0.3 T, 0.91 T and 1.7 T respectively.

SUMMARY AND FUTURE PLANS

A two year study of the breakdown limit of the LBL single cell cavity with large applied solenoidal fields has been completed. The early studies were conducted with copper window inserts and the later studies were done with thin Be windows coated with TiN to suppress multipactoring. In general the breakdown limit is much lower when a solenoidal magnetic field is applied. In addition the dark current and x-ray emissions are much larger after the occurrence of sparking at very high electric and magnetic field levels (above the safe limit curve shown in Figure 3). Even after long RF commissioning runs, the cavity does not return to the previous recorded low background level. The Lab G facility has been recently shut down and the equipment is being moved to the new Fermilab MuCool Test Area (MTA) Figure 7, [7]. Figure 8 shows the high power 805 MHz and 201 MHz transmission lines at top of linac shielding being installed to the MTA.

A modification of the cavity which will allow for the insertion of small button size sample pieces has been designed and is under construction. This will allow for more rapid testing of various materials and coating processes. Materials under consideration for study are chromium, tungsten, and molybdenum [8].

Figure 7: Picture of the MTA at the south end of the Fermilab linac.

Figure 8: Picture of the high power 805 MHz and 201 MHz transmission lines at top of linac shielding being installed to the MTA.

REFERENCES

[1] D.Finley, N.Holtkamp,' Feasibility Study on Neutrino Based Storage Ring' http://www.fnal.gov/projects/ muon_collider/reports.html
[2] E. Ozaki, et al, 'Feasibility Study II of a Muon Based Source', http://www.cap.bnl.gov/mions/studyii/FS2-report.html
[3] http://mice/iit/edu
[4] J. Norem, Wu, Moretti, Popovic, Qian, Ducas, Torun and Salomey Phys. Rev. STAB, 6, 072001, (2003)
[5] J. Norem, et al, Proc of 2003 PAC p1183
[6] D. Li, et al, Proc. of 2003 PAC, p1246
[7] M. Popovic, 'Muon Test Area at Fermilab", EPAC04, Lucerne Switzerland.
[8] J. Norem, This Conference.

HIGH POWER CW SUPERCONDUCTING LINACS FOR EURISOL AND XADS

J-L. Biarrotte#, CNRS / IN2P3/ IPNO, Orsay, France

Abstract

A multi-MW superconducting proton linac is proposed as the baseline solution for the EURISOL and the XADS driver accelerators. In the EURISOL project, which studies the design of the next-generation European ISOL facility, it is used to produce both neutron-deficient and neutron-rich exotic nuclei far from the valley of stability. In the PDS-XADS project, which aims to the demonstration of the feasibility of an ADS system for nuclear waste transmutation, it is used to produce the neutron flux required by the associated sub-critical reactor. In this paper, we report the main results and conclusions reached within these preliminary design studies. A special emphasis is given on the on-going and future R&D to be done to accomplish the demonstration of the full technology. Both of these works have been supported and funded by the EC 5th Framework Program, under contracts n° FIKW-CT-2001-00179 (PDS-XADS) and n° HPRI-1999-CT-50001 (EURISOL).

INTRODUCTION

During the period 2000-2004, the European Commission, within its 5th Framework Program, has been supporting in the field of nuclear physics two distinct projects having between them a high level of synergy due to their rather similar driver accelerators.

The EURISOL Project

The first one is the EURISOL project [1], which looks at the feasibility study of a new European isotope-separation-on-line (ISOL) radioactive ion beam facility, aiming at providing exotic beams which are orders of magnitude higher in intensity than presently available. In the light of this general objective and the inherent limits imposed by practical target considerations, a high power proton driver accelerator has been proposed as the base-line solution for producing both neutron-deficient and neutron-rich exotic nuclei far from the valley of stability.

The EURISOL proton beam main specifications are summarized in Table 1. The beam final energy is 1 GeV, with a 2 GeV upgrade capability, and two main intensity regimes are required: at intensities around a few hundred μA, the driver would be operated as a classical ISOL facility, while the full beam power (5 mA mean current) would be used to generate neutrons from a spallation target, which in turn would be used for producing fission products (converter method). Moreover, because of current interest in some cross section properties of heavy-ion induced reactions, the EURISOL proton accelerator should exhibit a strong heavy-ion capability for low-mass species, with ion beam powers of hundreds of kW.

biarrott@ipno.in2p3.fr

The PDS-XADS Project

The second project is the PDS-XADS one, which looks at the feasibility study of an experimental Accelerator Driven System (ADS) for nuclear waste transmutation. Consecutive to the work of the European Technical Working Group on ADS [2], this preliminary design study was launched in 2001 within a large European collaboration [3]. Five work packages (WP) cover the relevant issues, and the WP3 is dedicated to the design of the high power proton accelerator providing the neutron flux to the sub-critical reactor via a spallation target.

The XADS accelerator's main specifications are also quite usual for such a machine (see Table 1): 600 MeV final energy, 6 mA maximum mean beam current on target (10 mA for the demonstration of concept), 2 % beam power stability, 10 % beam size stability on target. On the other hand, less than a few (in the order of 5 per year) beam stops longer than one second are allowed for the successful demonstration of the ADS coupling. Given the state-of-the-art in the field of accelerator reliability, this requirement appears to be highly challenging, and could reveal itself as being a "show-stopper" for ADS technology. From this extremely hard requirement, it is clear that suitable design strategies had to be followed early in the conception stage of the XADS accelerator.

Table 1: EURISOL & XADS beams specifications

	EURISOL	**XADS**
Final proton beam energy	1 GeV	600 MeV
Proton beam mean current	• 5 mA (2-step production mode) • 0.2 to 0.5 mA (direct production mode)	• 6 mA max. on target • 10 mA rated
Main additional specifications	Heavy-ion capability for ions with A/q = 2 & 3	Less than 5 beam trips (>1sec) per year
	The machine must be up-gradable to a 2 GeV machine	The concept must stay valid for a 1 GeV, 20 mA industrial machine

Beam Time Structure

In principle, to avoid thermal stresses on the ADS beam window, target and sub-critical assembly, or in the radioactivity-releasing ISOL target, the maximum smoothing-out of the beam structure is favoured: a continuous wave (CW) beam would thus be the best solution. However, a pulsed operation of the beam could also be feasible, under the condition that the time scales of thermal inertia of the different components of the target and the reactor are much longer than that of the beam

period. The use of a "pulsed beam mode" of the accelerator is anyway needed in both projects. In the EURISOL case, sharp beam interruptions for quite variable periods of time are required for measurements of target release properties. In the XADS case, short and well-defined beam interruptions are mandatory to enable the in-line measurement, during normal operation, of the sub-criticality level through dynamic measurements. The possibility to produce short (a few tens of μs) proton pulses is also needed during operation starting phases.

From the accelerator point of view, it is an important design issue to decide between a CW RF machine and a pulsed RF machine, no matter what the beam time structure is. Operation in a CW RF mode is generally preferred to a pulsed one in this kind of high power machine. As a matter of fact, a quantitative analysis has been made for the EURISOL driver machine [4], leading to the conclusion that a CW RF machine solution is recommended: reliability is maximum (lower peak RF power), the Lorentz forces problem vanishes in the superconducting accelerating cavities, the R&D effort is significantly lower, and the machine is simpler and more flexible. With such a solution, the RF remains continuously applied on the RF structures, but the beam intensity can still be arbitrary shaped when needed within a very broad range.

Finally, an accelerator operating in a CW RF mode and accelerating a beam with a CW-based time structure appears to be a natural and simpler choice both for the EURISOL and the XADS projects. Figure 1 shows for example the agreed specifications concerning the XADS nominal beam time structure: additional short and well-defined (sharp edge) beam interruptions of 200 μs are implemented in the CW beam, with a repetition frequency in the order of 1 Hz; these beam holes, shutting down the neutron power source from time to time, should enable continuous and very accurate on-line measurements and monitoring of the reactor sub-criticality.

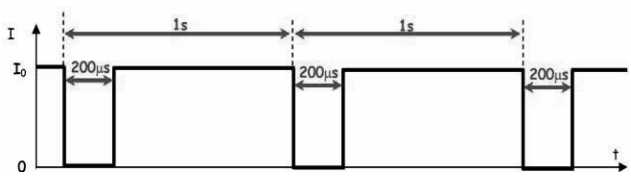

Figure 1: XADS beam time structure (normal operation).

BASIC ACCELERATOR CONCEPT

With the present state-of-the-art in accelerator technology, only two basic concepts of accelerators have shown to be able to deliver proton beams with mean intensities in the mA range. These namely are sector-focused cyclotrons and linear accelerators (linacs). Typical examples, running since a quarter century, are the 590 MeV separated-sector cyclotron of the Paul Scherrer Institute (PSI) at Villigen, Switzerland, and the 800 MeV linear accelerator of the Los Alamos Neutron Science Center (LANSCE) in New Mexico, USA. The PSI cyclotron is a CW-type machine of which the maximum average intensity has been continuously improved: starting initially with 100 μA, steady improvements allow at present to extract up to 2 mA from the machine [5]. The LANSCE's linac [6], designed for (100 Hz) pulsed-beam operation, delivers an average intensity of 1 mA. That means that the instantaneous intensity in the 625 ms lasting beam pulses amounts to 16.5 mA. The high-current capability of linear accelerators, due to the intrinsic strong focusing, is also demonstrated by the 50 MeV CERN injector LINAC-2, which reaches 170 mA during its 150 ms pulses [7]. In principle, strong focusing is also present in a FFAG-synchrotron, and some R&D is presently underway at Kyoto University in Japan [8]. However, this type of accelerator is not sufficiently advanced for assessing the very large extrapolation to the required XADS and EURISOL machines parameters.

Concerning cyclotrons, a final energy of 600 MeV is well established, with the experience of the PSI machine, and it is felt in the cyclotron community that a value of 5 mA should be considered as safely reachable [9]. However, extrapolating up to 10 mA is more questionable, and might require a complex of at least two cyclotrons with the two beams being funneled together. Moreover, for energies reaching the 1 GeV range, the intrinsic limits of the very principle of cyclotrons are reached because the proton is becoming too relativistic. None of all these limitations are present in a linac where intensities can reach more than 100 mA without any intrinsic energy limit. In addition, a cyclotron is basically a CW machine, and the requirement to provide sharp pulses is a major difficulty for a cyclotron of such power.

The minimisation of the number of beam trips, in order to match the XADS specifications, is a very specific and challenging requirement. It was clearly established by the XADS WP3 group that reliability can be implemented into an accelerator by adopting, in a very dedicated manner, the triple concept of over-design, redundancy and fault tolerance [10]. This strategy requires a highly modular system where the individual components are operated substantially below their performance limit. In contrast to circular machines like cyclotrons (and FFAG), a superconducting linac, with its many repetitive accelerating sections, conceptually meets this reliability strategy. It further allows keeping the activation of the structures rather low, which is important for radioprotection and maintenance issues, whereas the extraction channel of high power circular accelerators is in this respect a considerable concern.

For all these reasons, it was concluded that the reference solution should be a superconducting linac both for the EURISOL and the XADS projects. This assessment is corroborated by the one of OECD/NEA on ADS accelerators [11]: "Cyclotrons of the PSI type should be considered as the natural and cost-effective choice for preliminary low power experiments, where availability and reliability requirements are less stringent. CW linear accelerators must be chosen for demonstrators and full-scale plants, because of their potentiality, once properly designed, in term of availability, reliability and power upgrading capability".

THE EURISOL DRIVER ACCELERATOR

The general layout of the EURISOL proton driver (see Figure 2) is classicaly composed of three main parts: the "low-energy section" (up to 5 MeV), the "intermediate section" (up to around 100 MeV) and the superconducting "high-energy section" (up to 1 GeV).

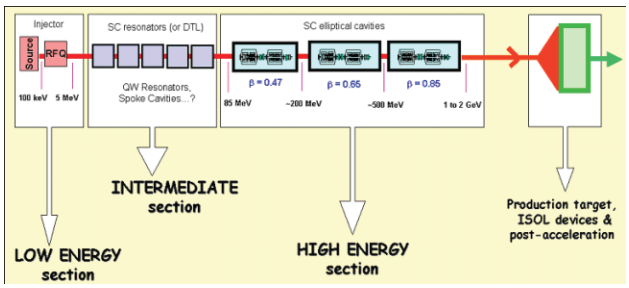

Figure 2: Layout of the EURISOL proton linac.

The Low-Energy Section (Injector)

The injector section is quite straightforward because of the relatively low proton beam current. The source is an Electron Cyclotron Resonance (ECR) ion source, based on the experience accumulated in many laboratories around the world [12,13,14]. It is followed by a room-temperature copper RFQ that has two main functions: it prepares the particles in bunches separated by the RF period and it accelerates the beam to an energy of 5 MeV while maintaining a strong confinement. It operates at a frequency of 352.2 MHz, which is a good compromise between lower sensibility to space charge effects & relaxed fabrication tolerances at lower frequencies, and higher shunt impedance & smaller dimensions at higher frequency. This frequency choice also relies on the existing RF technology at this rather common frequency, traditionally used e.g. at CERN.

The Los Alamos National Laboratory was the first to operate such a 350 MHz injector, LEDA, at intensities of the level of 100 mA CW [15]. In Europe, INFN is building a 30 mA injector in Italy within the TRASCO programme [16], while in France, the IPHI project is composed of an ECR source (SILHI) routinely delivering a 95 keV 100 mA proton beam, followed by a 3 MeV RFQ presently under construction at Saclay [17]. In the three cases, very good performances have been achieved, that fully demonstrates the feasibility of a 5 MeV 5 mA CW proton injector for EURISOL.

The High-Energy Section

There is also a general agreement that the high-energy section should be made of superconducting (SC) multi-cell elliptical cavities. These have been demonstrated to be extremely efficient and cost-effective, and a lot of experience and knowledge has been accumulated. Moreover, large size machines using SC RF Cavities have been constructed (like the TTF injector in DESY, Germany) or are currently under construction (like the SNS at Oak Ridge, USA), giving confidence in the achievable performance for the EURISOL accelerator.

The proposed SC linac for the high-energy section of the EURISOL driver operates at 2K and 704.4 MHz, and has been settled using all the optimisation criteria developed by the French-Italian collaboration [18,19] for the cavities' design, and the beam dynamics studies. Due to the varying velocity of the moderately relativistic protons, the 85 MeV - 1 GeV high-energy section of the EURISOL linac is divided in three parts, each covering an energy range with a single type of structure. The geometrical β values of these structures are 0.47, 0.65 and 0.85 respectively. The transition energies are set to approximately 200 and 500 MeV, and the last family of cavities, bringing the beam up to 1 GeV, could operate to 2 GeV without great losses of efficiency. The transverse focusing is provided by a periodic array of quadrupole doublets between which the SC cavity "cryomodules" are placed. Comfortable margins on critical values have been chosen in the study to ensure a design as robust as possible. These margins leads especially in limiting, in a reasonable way, the minimum beam apertures, the field in the cavities, the phase advances along the linac, the sensibility to beam mismatch, or the possibility of halo creation, leading to very smooth and safe beam behaviors through the linac. In particular, peak surface magnetic and electric fields of respectively 50 mT and 30 MV/m have been used as upper limits for SC cavity operation.

The Intermediate Section

For this range of energy (5–85 MeV), two solutions with the same frequency (352 MHz) have been discussed: a room-temperature solution, based on a DTL structure, and a cold solution, using superconducting resonators. Comparing the two options, it appears that the investment cost and the overall length for both solutions seem to be of the same order. On the other hand, the AC power difference between the two options is very large (about 7 MW) and makes a huge difference in the operating cost, in the order of 2 M€/year [4]. Moreover, the superconducting option gives higher safety (larger beam tubes), and has great potential in terms of reliability and flexibility thanks to its independently phased structures.

As a consequence, the EURISOL intermediate section will use, a priori, superconducting cavities. Two different preliminary designs have been proposed by INFN Legnaro [20] and IPN Orsay [21], the first using half-wave and 4-gap ladder resonators, the second using 2-gap spoke cavities. The "warm" DTL-like solution, while less attractive from the point of view of efficiency, cost and flexibility, still exists as a back-up solution.

Heavy-Ion Capability

The development of a superconducting version for the intermediate section of the EURISOL driver is crucial if one wants to fullfill the heavy-ion capability requirement. As a matter of fact, in order to be able to accelerate both protons and heavy-ions in the linac, the number of gaps per accelerating structure has to be kept small, and the phase in the successive accelerating structures has to be independently controlled so as to provide a large velocity

acceptance. Different heavy ion capability scenarios have been identified within the EURISOL study [4]. The conclusion is that, owing to the principle of independent phasing and some margin in the maximum surface fields, acceleration of A/q=2 ions is potentially feasible up to 500 MeV/u, under the condition that a second dedicated 5 MeV injector is constructed. Acceleration of A/q=3 ions can also be envisaged, but it would need significant modifications in the linac architecture.

THE XADS DRIVER ACCELERATOR

The layout of the XADS driver accelerator is of course very similar to the EURISOL one, with the only difference that reliability is here a major issue. In particular, the design should look at the ability to either maintain the beam under safe conditions, or to recover the beam through, in less than one second, to avoid any core shutdown. This is a new feature, not required for any other accelerator application, which is quite specific to ADS linacs. Thus, the philosophy prevailing on current machines to cope with component failures should be reconsidered, taking into account this requirement. The main guidelines that have been highlighted to drive the study are a strong design (which makes extensive use of component derating and redundancy) and a high degree of fault tolerance (i.e. the capability to maintain beam operation within nominal conditions under a wide variety of accelerator component faults). A reference solution based on a linear superconducting accelerator with its associated doubly achromatic final beam line has been worked out up to some detail by the XADS WP3 group [22], including studies on radioprotection and maintenance aspects. It is shown on Figure 3.

The XADS Reference Accelerator

The XADS reference design is optimized for reliability, and all selected components have the capability to accelerate higher beam currents (~ 40 mA) without major changes. It uses a “classical”proton injector (ECR source + normal conducting RFQ), followed by additional warm IH-DTL, developed by IBA (Belgium), or/and superconducting CH-DTL structures, developed by Frankfurt University [23], up to a transition energy still to be defined between 5 and 50 MeV. At this point, a fully modular independently-phased superconducting linac accelerates the beam up to the final energy.

Up to the transition energy (linac front end), fault-tolerance is guaranteed by means of a "hot stand-by" spare, keeping the possibility to switch the second injector on if the first one fails or have any long beam trip. Above this energy, spoke and, from 90 MeV on, elliptical cavities are used. An individual cavity failure in this part can be handled at all stages without loss of the beam. This characteristic relies on the use of highly “de-rated” and independently powered accelerating components, associated to a fast digital feedback system and adequate diagnostics. Note that these SC cavities (spoke and elliptical) are subject of important R&D programmes presently underway, e.g. at CEA Saclay, IPN Orsay and INFN Milano. The performance of the prototypes has been measured to exceed the operational characteristics by a very comfortable safety margin [24,25,26], that ensures the overdesign criteria imposed by the reliability strategy.

Besides this fault-tolerance, another remarkable feature of the concept is its validity for a very different output energy range: 350 MeV for the smaller-scale XADS require for example nine β=0.65 elliptical cavities cryomodules; in order to obtain 600 MeV, simply ten more cryomodules have to be added (7 with β=0.65 and 3 with β=0.85) and 12 additional (β=0.85) boost the energy to 1 GeV. Therefore, already the small-scale XADS accelerator is fully demonstrative not only of the 600 MeV XADS, but even for an industrial machine.

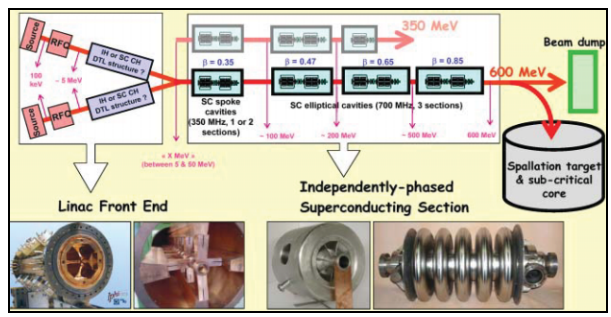

Figure 3: XADS reference accelerator layout (Photos, from left to right: RFQ, CH-DTL, spoke and 5-cell elliptical cavity).

Fault-Tolerance Capability

The fault-tolerance concept is a crucial point in the design of the overall XADS accelerator. The state of the art in RF system technology is indeed not reliable enough to envisage an operation of the XADS accelerator during several months without any beam trip. We can actually foresee at least a few tens of failures per year, only due to these RF systems, based on parts count reliability estimates. Therefore, even if a great effort can be directed at improving the MTBF of RF systems, it seems difficult to reach the reliability requirement without implementing any fault-tolerance philosophy for the linac design.

The fault-tolerance principle of the independently-phased superconducting section has been thoroughly analysed by means of beam dynamics multiparticle simulations. The calculations have been performed on the basis of a 5 MeV - 600 MeV superconducting linac (see Table 2) using the “local compensation” method (see Figure 4): if a cavity (or quadrupole) fails, the nominal beam is recovered by retuning as fast as possible a few accelerating cavities and/or quadrupoles neighbouring the failing element.

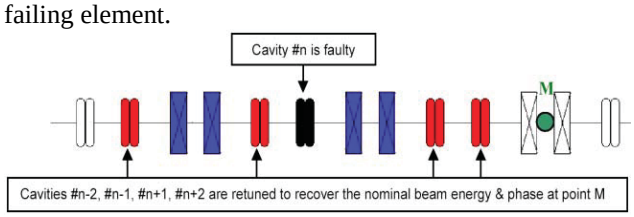

Figure 4: The “local compensation” method.

Table 2: Layout of the SC linac used for the fault-tolerance simulations; focusing is ensured by warm quadrupole doublets

SC linac sections	Energy range	Nb of cavities
Spoke 2-gap, 352.2 MHz, β=0.15 (~30 metres)	5 - 17 MeV	36 (2 per lattice)
Spoke 2-gap 352.2 MHz, β=0.35 (~50 meters)	17 - 91 MeV	63 (3 per lattice)
Elliptical 5-gap, 704.4 MHz, β=0.47 (~60 meters)	91 - 192 MeV	28 (2 per lattice)
Elliptical 5-gap, 704.4 MHz, β=0.65 (~100 meters)	192 - 498 MeV	51 (3 per lattice)
Elliptical 6-gap, 704.4 MHz, β=0.85 (~25 meters)	498 - 615 MeV	12 (4 per lattice)

A systematic study of the XADS linac fault-tolerance capability has been performed, optimizing the retuned values to be applied for local compensation in the case of the failure of most of the linac cavities and quadrupoles. The conclusion of the study [27] is that in every case, with an appropriate retuning, the beam can be transported up to the high energy end without any beam loss (100 % transmission, reasonable emittance growth), and within the nominal target parameters. It is also recommended to switch off the whole quadrupole doublet if one quadrupole fails.

PERSPECTIVES

The 6th European Framework Program is now running. The EURISOL and XADS preliminary design studies will be pursued within, respectively, the EURISOL Design Study, and the EUROTRANS Integrated Project. The final goal is to be ready to launch an eventual construction of these machines at the end of 2008. In the meanwhile (2004-2008), a huge R&D program will be undertaken, focusing on two main items.

The first one concerns basic R&D and prototyping for the intermediate energy section (5 MeV – 100 MeV) of such linacs. The construction and test of HWR and ladder resonators at Legnaro [28], of spoke cavities at Orsay, of a SC CH-DTL at Frankfurt, of a normal conducting IH-DTL by IBA, and of their associated equipments (coupler, tuner, cryostat, LLRF system...) should allow to choose the best technical option in this energy range. This R&D should also enable to qualify the reliability of these different components. The second item concerns indeed the accelerator reliability, which is a crucial issue in the XADS case. The reliability of the injector section will be experimentally determined by means of a long test run of the 3 MeV, 100 mA accelerator IPHI, presently in construction by CEA Saclay and IPN Orsay. Concerning the high-energy section, a complete elliptical cryomodule with all subsystems running at rated power and nominal temperature will be built, tested and qualified by INFN Milano and IPN Orsay. Finally, studies on fault-tolerance will be pursued with the development of more adapted beam dynamics simulation code, and the development by CEA Saclay of an adequate LLRF system, able to handle beam trips as quickly as possible using the local compensation method.

This R&D program should finally lead to a frozen design of the XADS and EURISOL linacs, with assessed reliability and costing.

ACKNOWLEDGEMENTS

The author would like to thank all the colleagues from Ansaldo, CEA Saclay, CERN, ENEA, ESRF, Framatome ANP, Framatome GmbH, FZ Jülich, GANIL, IAP Frankfurt, IBA, INFN Legnaro, INFN Milano, IPN Orsay, ITN Lisboa, having actively participated to these preliminary design studies.

REFERENCES

[1] "The EURISOL Report", Published by GANIL, December 2003.
[2] "A European Roadmap for Developing ADS for Nuclear Waste Incineration", ISBN 88-8286-008-6, Rome, Italy, 2001.
[3] See, e.g., B. Carluec, "The European project PDS-XADS", Int. Wor. for P&T and ADS, Mol, Belgium, 2003.
[4] "The driver accelerator for EURISOL", Report of the EURISOL Driver Accelerator Task Group, December 2003.
[5] Th. Stammbach et al., "The PSI 2mA beam and future applications", 16th Int. Conf. on Cyclotrons and Their Applications, East Lansing, USA, 2001.
[6] F. Merrill & L. Rybarcyk, "Beam dynamics simulations of the LANSCE linac", XIX Int. Linac Conf., Chicago, USA, 1998.
[7] C.E. Hill et al., "Tests of the CERN proton linac performance for LHC-type beams", XX Int. Linac Conf., Monterey, USA, 2000.
[8] M. Tanigaki et al., "Construction of FFAG Accelerator Complex for ADS Research in KURRI", 4th Int. Workshop on Utilisation and Reliability of HPPA, Daejeon, Korea, 2004.
[9] Th. Stammbach et al., "The Feasibility of High Power Cyclotrons", *Nucl. Inst. & Meth.*, B113-1, 1995.
[10] P. Pierini, "ADS reliability activities in Europe", 4th Int. Workshop on Utilisation and Reliability of HPPA, Daejeon, Korea, 2004.
[11] See proc. of the Int. Workshops on Utilisation and Reliability of High Power Proton Accelerators, organized by the OECD NEA.
[12] J. Sherman & al., "A 75 keV, 140 mA proton injector", Rev. Sci. Instrum., Vol. 73, n°2 , p. 917, 2002.
[13] R. Gobin & al., "High Intensity ECR ion source developments at CEA/Saclay", Rev. Sci. Instrum., Vol. 73, n°2 , p. 922, 2002.
[14] G. Ciavola & al, "The TRASCO high current proton source and its LEBT", XXI Int. Linac Conf., Gyeongju, Korea, 2002.
[15] H.V. Smith & al., "Status report on the low energy demonstration accelerator LEDA", XX Int. Linac Conf., Monterey, USA, 2000.
[16] A. Pisent et al., "TRASCO RFQ", XX Int. Linac Conf., Monterey, USA, 2000.
[17] P-Y. Beauvais, "Status report on the construction of the French high intensity proton injector (IPHI)", EPAC 2002, Paris, France.
[18] H. Safa, "Superconducting proton linac for waste transmutation", 9th SRF Workshop, Santa Fe, USA, 1999.
[19] P. Pierini & al, "Status of the high current proton accelerator for the TRASCO Program", EPAC 2002, Paris, France.
[20] A. Pisent & al, "Study of a superconducting 100 MeV linear accelerator for exotic beam", EPAC 2002, Paris, France.
[21] J-L. Biarrotte & al, "High-intensity proton SC linacs using spoke cavities", EPAC 2002, Paris, France.
[22] A. C. Mueller, "The PDS-XADS reference accelerator", Int. Wor. for P&T and ADS, Mol, Belgium, 2003.
[23] H. Podlech et al., "Status of the SC 352MHz CH Prototype Cavity", 11th SRF Workshop, Travemünde, Germany, 2003.
[24] B. Visentin et al., "Performances improvement for the French multicell SC cavity prototype dedicated to proton LINAC projects", this conference.
[25] A. Bosotti et al., "RF tests of the β=0.5 5-cell TRASCO cavity", EPAC 2004, Lucerne, Switzerland.
[26] G. Olry et al., "Recent developments on SC β0.35 and β015 spoke cavities at IPN for low and medium energy sections of proton linear accelerators", EPAC 2004, Lucerne, Switzerland.
[27] J-L. Biarrotte & al., "Beam dynamics studies for the fault tolerance assessment of the PDS-XADS linac design", EPAC 2004, Lucerne, Switzerland, and 4th Int. Workshop on Utilisation and Reliability of HPPA, Daejeon, Korea, 2004.
[28] A. Pisent, "Recent results in the field of high intensity CW linac development for RIB production", this conference.

FUTURE DEVELOPMENTS IN ELECTRON LINAC DIAGNOSTICS*

Marc C. Ross, SLAC, Stanford, CA 94025, USA

Abstract

The next generation of electron linacs will fill two different roles:

1. ultra-low emittance, very high power accelerators for linear colliders and

2. ultra-short bunch, high stability accelerators for SASE X-ray production.

In either case, precision control based on non-invasive, reliable, beam instrumentation will be required. For the linear collider, low emittance transport is an important concern for both warm and superconducting linacs. Instrumentation will be used for control and diagnostics will be used to validate emittance preserving strategies, such as beam based alignment and dispersion - free steering. Tests at the KEK ATF and the SLAC FFTB have demonstrated the required performance of beam position and beam size monitors. Linacs intended for FEL's will require precision bunch length diagnostics because of expected non-linear micro-bunching processes. A wide variety of devices are now in development at FEL prototypes, including TTF2 at DESY and SPPS at SLAC. We present a review of the new diagnostic systems.

INTRODUCTION

The last ten years have seen unprecedented growth in electron linac technology development, driven by two main forces: 1) development of ultra-short pulse single pass free electron lasers (FEL) [1] and 2) development of high energy linear colliders (LC) [2]. The underlying physics for these machines has been well understood for 10 – 20 years and the intervening time has been devoted to demonstrations of key subsystems, such as accelerating structures, high-brightness beam generation and related instrumentation. In this paper we review 3 types of beam instruments that play a significant role in this work: 1) sub-micron resolution cavity beam position monitors (BPM's), 2) laser-based profile monitors (laserwires), and 3) bunch length monitors based on deflecting structures.

Demonstration of new beam instrumentation requires substantial accelerator test facilities to provide beams with smaller dimensions, higher brightness and greater stability. Indeed, the development of the instrumentation and the performance of the test facilities are strongly linked. Each is needed to validate and support the operation of the other and this is what has happened at the SLAC Final Focus Test Beam (FFTB) [3], the KEK Accelerator Test Facility (ATF) [4] and the DESY TESLA Test Facility (TTF) [5]. Since starting operation in the mid-1990's, these machines have been used to demonstrate 1) demagnification beyond that needed for the LC (FFTB), 2) generation of ultra-low emittance beams (ATF) and 3) generation of ultra-short pulse saturated ~100nm FEL radiation (TTF). Each of these tests has boosted and allowed aggressive development of related FEL/LC projects.

ULTRA-HIGH RESOLUTION BEAM POSITION MONITORS

The development of high resolution beam pickups for bunched electron beams lags substantially behind proton machine pickups, typically used for un-bunched (or weakly bunched) beams. Those devices, developed roughly 30 years ago for use with broad-band stochastic cooling, typically operate near the thermal, black-body radiation limit and are often cryogenically cooled in order to extend that limit as far as possible. In contrast to the needs of Schottky - signal based devices; most electron machine BPM requirements have been well served by devices that operate well away from the thermal noise limit. This is no longer true.

Third generation light sources require sub-micron resolution and stability, which is achieved using multi-turn digitization schemes that average over many hundreds of thousands of turns [6]. The Stanford Linear Collider (SLC) linac BPM system had 10 micron single reading resolution and an absolute precision of about 5 times larger [7]. This level of performance was well matched to the requirements of the machine. A good, practical way to interpret resolution requirements (r) in an LC or FEL is the view them in units of the beam size. Of course, the size of the vacuum chamber is also critical, so that the two key parameters are: 1) $j=r$/beam size and 2) $p=r$/vacuum chamber diameter. In operational terms, j allows the determination of sources of beam instability (such as poorly performing magnet power supplies or collective effects) with precision that is good compared to the beam's own emittance. In the SLC, with typical beam sizes of 50 μm and a one inch diameter beam tube, 10 μm resolution worked well for the identification most instability sources [8]. At the LC, with expected beam sizes almost 50 times smaller, and a larger beam tube, resolution performance must be substantially improved. Typical beam tube sizes in the FEL will be smaller. Table 1 summarizes these parameters, illustrating the challenge of the next generation linacs.

*Work supported by DOE-AC03-76SF00515.
#mcrec@slac.stanford.edu

Beyond the beam size and beam vacuum chamber size, there are several more critical performance parameters: 1) the loss factor of the pickup, 2) the monopole suppression factor, 3) the system bandwidth and 4) the dynamic range. The loss factor must be optimized between collective effects, such as transverse impedance wakes, and needed signal strength. The thermal noise power P_n depends on the system bandwidth in a simple way $P_n=ktb$ (where k is the Boltzmann constant, t is the temperature in degrees K and b is the system bandwidth). The cryogenic linac, with large beam inter-bunch spacing, is well adapted for a narrow band position monitor system, using cavity BPM's with a ~100ns decay time.

For the cavity BPM engineer, the most important component of P_n is the electronic noise figure.

A system with roughly appropriate parameters, but with a rather large loss factor, has been tested several places [9] and we present here results from tests now underway at the ATF, using the damped, extracted ATF beam. The system uses C-band TM110 dipole mode cavities, designed and constructed at the Budker Institute, coupled to a simple two stage heterodyne down-mixer. The final IF mixer output is repeatedly sampled by a 100 MHz 14 bit commercial digitizer. Table 2 lists the parameters of the test cavity BPM system.

Table 1: BPM performance parameters, achieved and suggested, based on the practical rule (j ~ 0.2). The first four rows in the table describe the BPMs typical of the machine. The last row lists the performance parameters of the system presently in test at ATF. The sensitivity scaled to the vacuum chamber size, p, is excellent at the test system at ATF, but the loss factor of the BINP cavity BPMs is too large for use in an LC linac.

Machine	typical beam size (μm)	Beam tube diameter (mm)	bunch spacing (ns)	suggested/achieved resolution (μm)	j (= r/σ)	p (= r/d)
SLC	50	25	60	10	0.2	5e-4
ATF	5	25	2.8/330	1	0.2	4e-5
LC	1	75	330	.2	0.2	3e-6
FEL (LCLS)	1	10	-	.2	0.2	1e-4
ATF test (see below)	5	20	-	0.02	0.004	1e-6

Table 2: Parameter table for the BINP cavity BPM system

Parameter	
Cavity dipole mode frequency	6426 MHz
1/angular frequency	7.4 mm
Intermediate IF	476 MHz
Final IF	23 MHz
Cavity gap length	10 mm
Coupling β	1 (not known exactly)
System gain	48 dB
Electronic bandwidth	20MHz
Noise figure	3 dB
Loss factor	3.9e10 Joules/C^2/mm^2
mV/nm at 1e10	1
electronic noise (rms)	1mV
Electronic dynamic range	20 μm
Estimated resolution (preliminary)	15 nm

An RF cavity BPM with operating angular frequency close to one over the bunch length and with a gap near this same characteristic length is subject to additional complications associated with the so-called 'transit time effect' and the bunch's own tilt or y-z correlation [10]. This signal appears in phase quadrature with the basic radial offset signal and must be properly accounted for in any high performance cavity BPM system. Table 2 shows the magnitude of these effects at ATF, where they are large and can be studied in some detail. Figure 1 shows typical signals from the system, showing a nominal IF signal along side a more peculiar one. The top part of the figure shows a nominal decaying exponential, typical of most beam pulses. A reference cavity is used to determine the phase (sign) and normalize the pulse amplitude, here about 1e10 particles / bunch. The scale is approximately 350 ADC counts (peak amplitude) per micron. In this example case the beam is about 300 nm from the electrical center of the cavity (if the offset is purely axial). The bottom half of the figure shows a beam pulse with a smaller offset – perhaps less than 100 nm – but with a very large offset in the other plane (x) showing coupling between the TM modes. This figure also clearly shows the monopole transient.

In order to study BPM performance in the presence of 1) expected performance beyond our ability to hold a set of BPMs still with respect to each other, 2) transit time effects and 3) limited dynamic range beyond our ability to perform ab-initio alignment, we constructed an extremely stiff flexure-based mover system with full 6 degrees of freedom that can support a set of three BPMs. This device

is used for precision displacement calibration. Three BPMs is the minimum number required to determine system resolution using a zero-constraint linear regression fit. Figure 2 shows typical performance of the system at ATF. The figure shows the residual (actual-predicted) vertical beam position measurement over a sequence of beam pulses during which the BPM mover is adjusted in one micron steps. The width of the distribution of data points roughly indicates the resolution, in this case around 16 nm. Effects related to stray field fluctuation, thermal stability, beam energy pulse to pulse jitter and wake fields are under analysis as of December 2004.

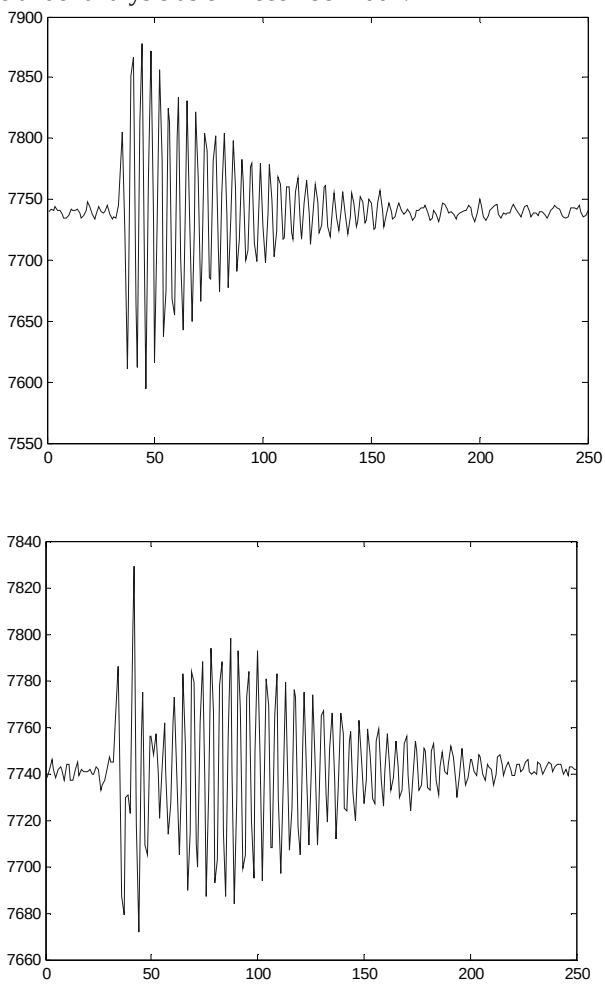

Figure 1: Sample IF waveforms from the ATF/BINP/SLAC cavity BPMs. The vertical scale is ADC counts and the horizontal scale is sample number of the 100 MHz sampling ADC.

An important use of precision beam position monitors is in the energy spectrometer device planned for the LC beam delivery section [11]. Such a device must have good resolution and stable long-term electrical and mechanical offsets. While the detailed spectrometer performance parameters have not yet been set, we expect the ATF system to be capable of proving cavity BPMs for this purpose.

LASER-BASED PROFILE MONITORS

Both the FEL and LC performance depend strongly on the beam phase space, and the ability to transport cleanly generated beams long distances through precisely matched lattices. The job of matching and compensating collective effects in a single pass system is quite different in practice from the similar task in a third generation light source storage ring. While precise, high resolution BPMs are, in both cases, the most important beam instrument for this purpose, in a single pass machine a second system is needed to verify that the job has been adequately done and to serve a tool for finishing the job. This was demonstrated at SLC [12], where sophisticated BPM-based optics tuning procedures were backed up by groups of wire scanners, typically four each, to allow full transverse phase space determination between major subsystems (damping ring, linac, arcs and beam delivery) [13]. At the peak SLC performance, however, three effects showed the inadequacy of filamentary wire scanners: 1) the wire was too fragile and cumbersome to replace when broken [14] and 2) the presence of the wire in the beam, however transient, generated too many secondaries and degraded particles to allow continued high power operation and finally (perhaps most importantly) 3) the wires could not be made small enough for accurate measurements of the low emittance beam. The latter was especially important as the machine performance moved to another regime where new effects made more precise measurements critical.

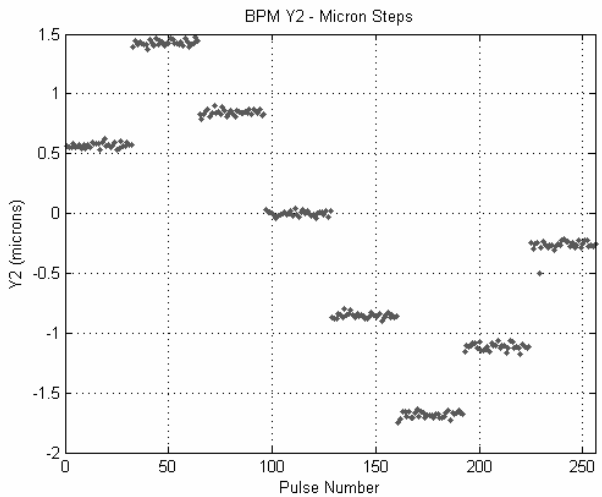

Figure 2: Preliminary cavity BPM data from a sequence of pulses at ATF, showing the difference between the predicted (using adjacent BPM's) and actual reading as the support struts were moved one micron steps. Some mover mechanical backlash (~150nm) is clearly visible.

These effects forced the development of a more complex, but much more powerful beam size monitor, one based on Compton scattering of the particle beam with a finely focused laser beam. The laser beam is not material so it cannot be trivially broken, its power can be adjusted remotely, allowing the number of degraded particles to be reduced if circumstances require and it can be focused to

well below the typical 1 μm beam size. Key technical issues are 1) the degraded particle (or neutral beam) detector, 2) the stability and calibration of the laser beam itself and 3) the large number of mechanical and operational issues associated with the laser, its controls, transport line and optical focus system.

It is important to consider two 'resolution'-like performance parameters: 1) the dynamic range of the system, i.e. the range of beam sizes can be effectively measured, and 2) the real resolution of the system, i.e. the reproducibility of the instrument given identical particle beam conditions. Table 3 lists these for some beam profile monitors. It is important to understand system requirements, especially for 2), because tuning procedures will depend critically on this and it may be very advantageous to develop devices with good resolution.

Table 3: Performance parameters for selected wire scanners and laserwires

Laserwire	σ_l	σ_e	P_l/wire mat'l	Resolution
SLC wires	NA	50	W/C/SiC	10%
SLD	.35	.8	100 MW	20%
ATF	5	5	1000 W	1%
PETRA	50	80	10 MW	

Several such systems have been built and tested and it seems that laserwires will become an effective tool [15]. The challenge of stabilizing the laser, perhaps at the expense of optical beam power, has been met by the ATF group who built the most heavily used laserwire system to date. This device has been the subject of several written thesis reports and remains subject to active development while at the same time proving critical for understanding ATF performance. Figure 3 shows a typical scan, illustrating the extreme stability of the system. Recent developments include a 'pulse-stacking' system that allows a substantial increase in peak power with fixed average power.

BUNCH LENGTH MONITORS

The performance of an FEL depends very strongly on the peak bunch current. As beam bunches are made shorter (10 μm σ_z) this is fresh territory for machine operation in several ways, a substantial world-wide RD effort is underway to prove practical ways making 1) accurate, 2) relative (high resolution) or 3) simple ways of bunch length estimation. This topic, along with a related topic of understanding bunch timing, has been central to a series of recent ACFA workshops which provide a comprehensive picture of the state of the art. Here we describe only one such system; that based on high power transverse deflecting structures.

What transverse deflecting structures lack in simplicity, they make up in precision. The principle of operation is simple, namely that a strong correlation between y (or x) and z, of well known amplitude is generated and then a y (or x) image is viewed using a conventional video – based profile monitor. The technique was first used almost 40 years ago, but has recently been revived as the need to make bunches shorter than 1 mm arose. Two such structures have been recently installed [16] and are either in use or in commissioning. At the DESY TTF, a 4 m long S-band structure, capable of monitoring 10 μm σ_z was installed in late 2003 and is now being commissioned. Table 4 shows the performance parameters of the system. First results are expected in early 2005.

Table 4: Performance Parameters of the TTF transverse deflecting structure 'LOLA IV'

Power	18 MW
Length	3.7 m
Peak deflecting Voltage	25 MV
Wavelength	105 mm
Incoming vertical beam size	300 μm
Differential kick /μm	40 μm
Required phase stability	0.1 ps

REFERENCES

[1] J. Andruszkow et al., First Observation of Selfamplified Spontaneous Emission in a Free Electron Laser at 109-nm Wavelength. Phys.Rev.Lett.85:3825-3829,2000.

[2] International Linear Collider Technical Review Committee. Second Report. 2003. SLAC-R-606.

[3] V.A. Alexandrov et al., 'Results of Final Focus Test Beam'. IEEE PAC 1995:2742-2746.

[4] Y. Honda et al., Achievement of Ultralow Emittance Beam in the ATF Damping Ring. Phys.Rev.Lett.92:054802,2004

[5] Pedro Castro, Performance of the TESLA Test Facility LINAC. EPAC 02 876-878

[6] M. Boge, J. Chrin, P. Pollet, T. Schilcher, V. Schlott, 'Orbit Control at the SLS Storage Ring'. Paris 2002, EPAC 02* 2067-2069.

[7] M.C. Ross, Beam Diagnostics and Control for SLC. Washington PAC 1987:0508

[8] J.T. Seeman, R.L. Holtzapple, M.C. Ross, 'Induced Beam Oscillations from Quadrupole Vibrations in the SLC LINAC'. IEEE PAC 1993:3564-3566 (QCD183:P3:1993)

[9] V. Balakin et al., Experimental Results from a Microwave Cavity Beam Position Monitor'. New York 1999, Particle accelerator, vol. 1* 461-464

[10] P. Tenenbaum, J. Frisch, D. McCormick, M. Ross, S. Smith, 'Beam Tilt Signals as Emittance Diagnostic in the Next Linear Collider Main LINAC'. Paris 2002, EPAC 02, 512-514.

[11] See presentation material from the 2002 ICFA 'NanoBeam' Workshop. http://icfa-nanobeam.web.cern.ch/

[12] L. Hendrickson, P. Raimondi, Automated Tuning and Feedback Systems at the SLC. CERN-OPEN-2000-224 (Dec 1998)
[13] M.C. Ross, Wire Scanner Systems for Beam Size and Emittance Measurements at SLC. Batavia 1990, Proceedings, Accelerator Instrumentation Workshop, 88-106
[14] C. Field, D. McCormick, P. Raimondi, M. Ross, Wire Breakage in SLC Wire Profile Monitors. In *Stanford 1998, Beam instrumentation 440-445.
[15] G.A. Blair et al., R & D Towards a Laser Based Beam Size Monitor for the Future Linear Collider. Paris 2002, EPAC 02* 1912-1914.
[16] R. Akre, L. Bentson, P. Emma, P. Krejcik, 'Bunch Length Measurements Using a Transverse RF Deflecting Structure in the SLAC LINAC'. In Paris 2002, EPAC 02* 1882-1884.

RFQ DRIFT-TUBE PROTON LINACS IN IHEP

Yu.A. Budanov#, O.K. Belyaev, S.V. Ivanov, A.P. Maltsev, I.G. Maltsev,
V.B. Stepanov, S.A. Strekalovskyh, V.A. Teplyakov, V.A. Zenin
IHEP, Protvino, Moscow Reg., 142281, Russia

Abstract

The major RFQ Drift-Tube proton Linacs (RFQ-DTL) of IHEP-Protvino are described. The unique feature inherent in these accelerators is use of spatially periodic quadrupole RF focusing. Prospects are outlined for a further progress in R&D of this brand of linacs in IHEP.

PREAMBLE

Stability of a particle motion in a linear accelerator can be attained via choosing a dedicated geometry for accelerating gaps such as to force transverse components of accelerating field to exert the RF quadrupole focusing effect. Primary feasibility studies for this kind of focusing were, mostly, theoretical and foresaw either a weak focusing effect, or an unacceptably low accelerating rate.

A proposal by V.A. Teplyakov [1] to supplement an accelerating gap with a spacer electrode (or, generally, with a few of them), charged under an intermediate potential, has allowed for a noticeable upgrade in performance of the focusing mechanism at issue. Careful tailoring the period geometry allows to attain nearly the same minimal transverse frequency for all phases along bunch which improves beam quality [2].

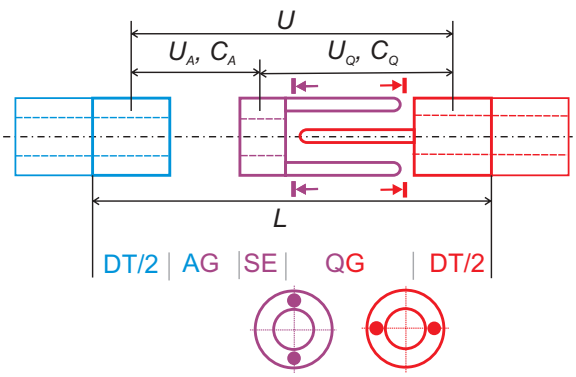

Figure 1: Schematic layout of accelerating cell.

Fig. 1 sketches such an accelerating cell with one spacer electrode SE (AG and QG are accelerating and quadrupole gaps, U_A and U_Q are voltages across them, total $U = U_A + U_Q$, and DT/2 is half of a drift tube, $L = \beta\lambda/2$). It is this structure that is employed in the first sections of URAL-30 and URAL-30M linacs of IHEP (URAL is a Russian acronym for **a**ccelerator **r**esonant **a**uto-focusing and **l**inear — a local code name for the machines).

Since then, a comprehensive R&D program has been pursued in IHEP to manufacture and run RFQ-DT linacs in which accelerating & focusing structure is driven at π-mode by a standing-wave cavity oscillating at a longitudinal-magnetic-field fundamental mode (an *H*-cavity).

In what follows, a 20-year long experience of IHEP-Protvino in R&D of RFQ-DTLs is reviewed.

RFQ-DTL FACILITIES

URAL-30

In 1968, the first experimental model of a linac based on the RFQ principle was assembled [3]. This event has encouraged feasibility studies for implementing RF focusing at lower energies. In 1969, I.M. Kapchinsky (ITEP-Moscow) and V.A. Teplyakov (IHEP-Protvino) put forward the concept of spatially uniform (smooth) quadrupole RF focusing (RFQ). By 1972, initial testing was accomplished, and the first accelerated beam was obtained [3].

The URAL-30 proton linac was commissioned in 1977. It applies a through front-to-end RFQ-focusing up to the top energy of 30 MeV. For a few years to follow diverse and instructive experimental studies of the machine were performed, and a sound practical experience acquired.

Since 1985 till now, this facility routinely operates as an injector to booster proton synchrotron, thus feeding the entire accelerator complex of IHEP (see Fig. 2).

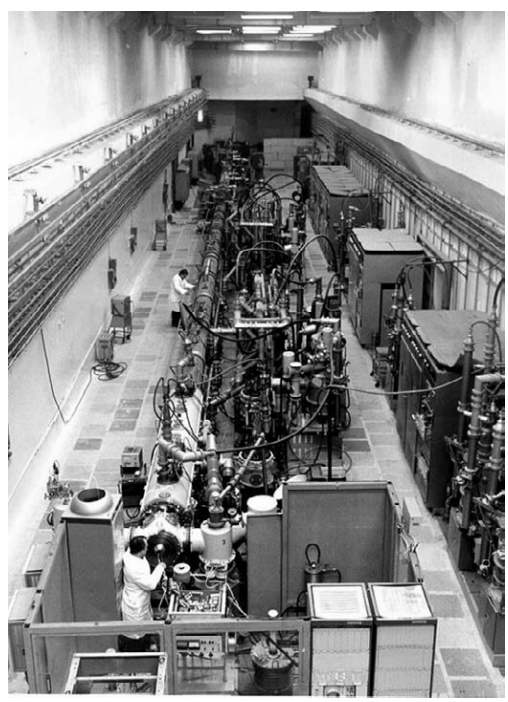

Figure 2: URAL-30 linac in the machine hall. Direction downstream of beam — away from the viewpoint.

#budanov51@mail.ru

Table 1 specifies major parameters of URAL-30. Its RFQ-DTL part comprises two segments, either being divided into two sections, four in total.

Table 1: Parameter list of URAL-30

Parameter	RFQ	RFQ-DTL	
	S # 0	S # 1,2	S # 3,4
Beam energy, in, MeV	0.1	1.98	16
Beam energy, out, MeV	1.98	16	29.99
Max. current, mA	100	100	100
Voltage, kV	150	304	352
Max. E-field on surface, kV/cm	225	380	370
Momentum spread, %	±1.5	±0.47	±0.42
Bunch width, deg	45	20	12
Stable phase angle, deg	–(90-30)	–30	–30
Gap efficiency	0.002–0.3	0.63–0.87	
Number of cells	136	65	57
Phase advance, μ	0.96	1.5–1.38	
Acceptance, πcm·mrad	1.12	0.85	
Emittance @ 90% and 100 mA, π cm·mrad	0.18	0.26	0.32

Beam pulse length is 10 μs. Pulse repetition rate is 25 Hz inside a packet, packet-to-packet recurring frequency being 0.2 Hz. Operating radio frequency is 148.5 MHz. Length of accelerator is 25.3 m. Tank shell is manufactured of steel, copper-coated from inside. Electrodes are wholly tooled of OFC-grade copper.

The operational experience gained by now tells that, given careful manufacturing and accurate tuning, the RFQ-DTL is well commeasurable to a conventional Alvarez DTL in reliability and physical parameters yielded.

On putting URAL-30 into operation, a few more advanced models of RFQ and RFQ-DTL accelerators are being developed and assembled in IHEP.

URAL-30M

By now, many parts and subsystems of URAL-30 no longer comply with up-to-date requirements and thus call for replacement. A-few-year-long scientific research efforts and computer simulations ([5], [6], [7] etc) allowed to launch design of a novel, upgraded machine intended to yield far a better functionality than URAL-30.

This accelerator, URAL-30M (**m**odernized), is currently being manufactured in IHEP. For the time being, a conventional (smooth) RFQ and two of four RFQ-DTL sections (up to 15 MeV) are assembled and subjected to pre-commissioning tests. Others are being fabricated.

In this machine, measures are foreseen to facilitate a better section-to-section matching of beam. The particular attention is paid to interface between RFQ and RFQ-DTL. To this end, accelerating rate at exit from RFQ approaches that at entry to RFQ-DTL. Longitudinal emittance of beam is minimized. A more regular transverse focusing pattern is foreseen — FD periodicity is applied in both, RFQ and RFQ-DTL sections. On the contrary, the RFQ-DTL section of URAL-30 relied on the FFDD layout.

To ensure the improved stability of operation, maximum E-field on the surface tips of electrodes is lowered down to ≤ 350 kV/cm. Voltage jumps in between sections are reduced noticeably. Vane-to-vane voltage U is now ramped along the cavity length, downstream of beam motion. This allows to compensate for a descent in accelerating rate $\propto 1/\beta$ inherent in an invariable-voltage option (e.g., that of URAL-30).

The accelerating structure itself diverges essentially from that of URAL-30. Both, cavity and tanks are manufactured of a copper-plated aluminum alloy; which eliminates corrosion problems and lowers outgassing rate. Electrodes are tooled of bulk OFC copper. An old-fashioned *H*-cavity (refer to Fig. 3) is used only in the first section of URAL-30M. Other sections employ the so-called sector *H*-cavity (an *SH*-cavity). These exhibit a higher shunt impedance and enable much an easier assembly of the electrodes. The latter procedure is not a trivial task since it should yield the prescribed partition of overall voltage U in between accelerating (U_A) and focusing (U_Q) gaps. To this end, support stems of intermediate (spacer) electrodes must be installed at a well-controlled angle with respect to the vertical plane of the cavity symmetry. The design goal is to provide constant voltage U_Q across quadrupole gaps, while keeping the voltage across accelerating gaps ramped along beam path, $U_A \propto \beta$. Contrary to URAL-30, URAL-30M has lengths of accelerating gaps varying along the cavity section.

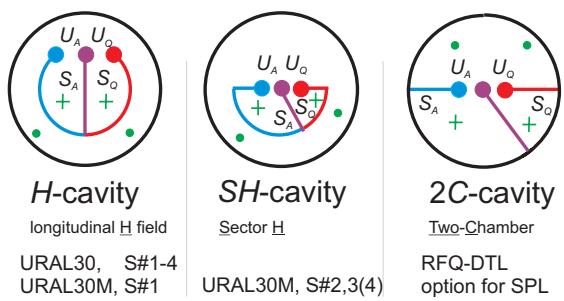

Figure 3: Three *H*-cavity options for the RFQ-DTLs.

Preliminary testing of the first two RFQ-DT sections of URAL-30M indicates that emittance growth is now significantly lower, as compared to its predecessor. All the more, URAL-30M has a shorter length of 23.4 m.

Tuning the accelerator

This procedure is of crucial importance for the facility in question. It must provide: (i) the prescribed partitioning of the net cell voltage $U = U_A + U_Q$ through a distributed series capacitive divider,

$$U_A/U_Q = C_Q/C_A ,$$

(ii) a proper ramp of U longitudinally along beam axis, and (iii) ensure ultimate tuning the entire loaded cavity to the preset operating radio frequency.

In URAL-30M, the capacitive tuners for $C_{A,Q}$ are placed onto the cavity vanes. Since, generally, $U_A \neq U_Q$, one has to install support stem of an intermediate (spacer) electrode so as to cancel out electrical current from the stem to the cavity body. This demand is met by obeying the ratio

$$\int_{S_A} H_A dS \Big/ \int_{S_Q} H_Q dS = C_Q / C_A \ ,$$

which dictates inclination angle of stem with respect to vertical. Here, S_A and S_Q are cross-areas in between respective vanes and the spacer electrode (see Fig. 3). First, this angle is calculated theoretically. Then, its value is subjected to bench verification. If required, proper stem position is adjusted iteratively, Fig. 4.

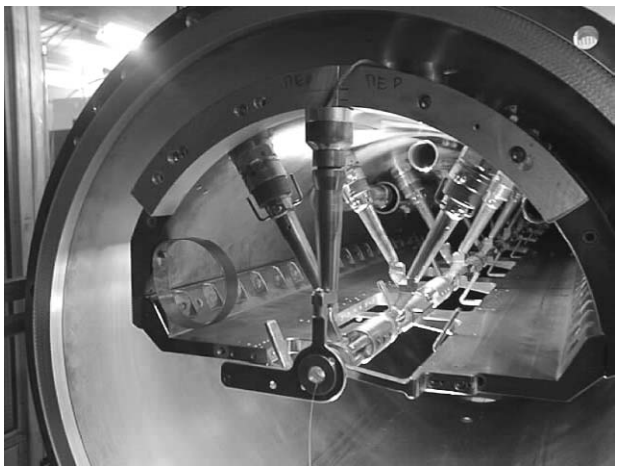

Figure 4: Open *SH*-cavity in a tuning process.

A smaller-scale *H*-cavity has a rather low stored energy, about an order of magnitude less as compared to its Alvarez counterpart. Therefore, on the one hand, tolerances on the field stability under beam in RFQ-DTLs get tougher. To handle this problem, two quite novel automatic control systems were developed and implemented in IHEP [8]. On the other hand, lower stored energy alleviates aftermaths of electrical breakdowns, which is crucial for a heavy-duty-factor regime.

Dedicated long-life-time (of 4 years ca) ion sources for URAL-30 and URAL-30M were custom-made in situ [9].

Other activities with RFQ-DTLs

During the recent years, there was an apparent trend observed word-wide towards R&D of new ion linacs to be operated at higher radio frequencies, under heavier duty-factors, and having decreased geometrical dimensions.

At the moment, IHEP is getting involved into R&D and manufacture of a prototype first section for 40 MeV RFQ-DTL at 352.2 MHz — the intended RFQ-DTL option for the warm front-end part of the CERN SPL project. It is a tri-lateral endeavor of CERN-Geneva, IHEP-Protvino and RFNC-VNIIEF-Sarov, supported by the Moscow-based International Science and Technology Center (ISTC) [10].

A tentative parameter list of the prototype to be manufactured is specified in Table 2. The cavity option proposed is the so-called 2*C*-cavity (refer to Fig. 3).

Table 2: Parameter list of 352.2 MHz RFQ-DTL

Beam energy, MeV	3.0–11.27
Beam current, mA	40
Length of accelerating channel, mm	3243.6
Voltage across cell, kV	170–219.7
Voltage across accelerating gap, kV	80–129.7
Voltage across quadrupole gap, kV	90
Max. E-field on surface, kV/cm	325
Acceptance, π mm·mrad	5.5
Focusing pattern	FFDD
Phase advance, μ	0.6
Min. transverse frequency, minν	0.46
Stable phase angle, deg	–30
Gap efficiency	0.68–0.85
Normalized transverse r.m.s. emittance @ 40 mA, π mm·mrad	0.33–0.34
Normalized longitudinal r.m.s. emittance @ 40 mA, π deg·MeV	0.25–0.26
Aperture radius, mm	4.5
Number of cells	65

CONCLUSION

The concept itself of accelerating protons to 30-40 MeV with RFQ-DTL has not yet exhausted itself. Further activity in that direction is well promising and can result in new effective facilities.

REFERENCES

[1] V.A. Teplyakov. Pribory & Tekhnika. Experimenta, 1964, v.6, p.24.
[2] A.P. Maltsev, S.M. Ermakov, V.A. Teplyakov. Atomic Energy, 1967, v.23, p.195.
[3] A.P. Maltsev, V.B. Stepanov, V.A. Teplyakov. Preprint IHEP 69–2, Serpukhov, 1969.
[4] N.I. Golosay et al. Atomic Energy, 1975, v.39, p.123.
[5] Yu.A. Budanov et al. Vestnik Atomnoy.Nauki & Tekhniki, 1985, v.3, p.48.
[6] Yu.A. Budanov. Sov. Physics JTP, 1991, v.61, p.162.
[7] I.G. Maltsev et al. Preprint IHEP 85–158, 1985.
[8] I.G. Maltsev, V.A. Teplyakov. Preprint IHEP 76-137, Serpukhov, 1976.
[9] V.V. Nizhegorodtsev et al. Proc. of 5-th All-Union Charged Particle Accelerator Conference., Moscow, 1977, v.1, p.368.
[10] ISTC Project # 2889 (the AD stage), http://tech-db.istc.ru/istc/db/projects.nsf/all-projects/2889.

DEVELOPMENT OF A 352 MHZ CELL-COUPLED DRIFT TUBE LINAC PROTOTYPE

Y. Cuvet, J. Genest, C. Völlinger, M. Vretenar, CERN, Geneva, Switzerland
F. Gerigk, RAL, Chilton, UK

Abstract

At linac energies above 40 MeV, alternative structures to the conventional Drift Tube Linac can be used to increase efficiency and to simplify construction and alignment. In the frame of the R&D activities for the CERN SPL and Linac4, a prototype of Cell-Coupled Drift Tube Linac (CCDTL) at 352 MHz has been designed and built. This particular CCDTL concept is intended to cover the energy range from 40 to 90 MeV and consists of modules of ~5 m length made of 3-gap DTL tanks linked by coupling cells. The focusing quadrupoles are placed between tanks, and are aligned independently from the RF structure.

The CCDTL prototype consists of two half tanks connected by a coupling cell and requires an RF power of 120 kW to achieve the design gradient. RF tests will be made at low and high power, the latter up to a 20% duty cycle. This paper introduces the main features of this CCDTL design and describes the RF and mechanical design of the prototype.

THE CERN CCDTL

The new Linac4 presently under study at CERN will accelerate an H^- beam to a kinetic energy of 160 MeV, making use of 352 MHz RF equipment (klystrons, waveguides and circulators) recuperated from the LEP machine [1]. This frequency is almost ideal for an H^- linear accelerator, offering a good compromise between size, maximum gradient, efficiency and focalization in the RFQ.

After the RFQ and a 3 MeV chopper line, the present Linac4 layout foresees an Alvarez-type Drift Tube Linac (DTL). The first DTL tank will be equipped with Permanent Magnet Quadrupoles, while the other tanks will have conventional electromagnets. The DTL structure is expensive to build because of its large dimensions and because of the accurate alignment required for the drift tubes. Moreover, the difficult access to the drift tubes is of concern if repairs are needed. However, for a high-intensity linac where beam optics has to be smooth, the choice of the conventional Alvarez DTL is unavoidable at low energy because of its short focusing periods. When the beam energy exceeds a few tens of MeV, the focusing period can become longer, and alternative structures can be considered.

Different alternatives to the DTL have been developed, all relying on the principle of separating the focusing from the RF structure, alternating quadrupoles with short accelerating tanks. Some solutions are based on TE modes, which provide a high shunt impedance, but require relatively long tanks and unconventional beam optics solutions, difficult to apply for high intensity operation due to the longer focusing periods. Other solutions retain the TM010 mode of the DTL, using shorter DTL tanks containing drift tubes of smaller diameter, without quadrupoles which are then placed between tanks. These structures have a lower capacitance between drift tubes than the standard DTL, but have increased losses due to a higher number of end walls, thus arriving at similar shunt impedance values to a conventional DTL. They go under the name of Separated DTL (SDTL) when the accelerating tanks are decoupled one from the other and fed by their own RF coupler, and of Cell-Coupled DTL (CCDTL) when the tanks are coupled together via coupling cells, forming a single resonator. The CCDTL was originally developed at Los Alamos at a frequency of 805 MHz [2].

The solution retained at CERN, shown in Fig. 1, is a CCDTL at the same RF frequency as the DTL, 352 MHz, and composed of 3-gap DTL-like accelerating tanks, connected by standard coupling cells [3]. Single quadrupoles are placed between tanks, giving a focusing period of 7 $\beta\lambda$. A string of 4 tanks forms a module, operating in the $\pi/2$ mode between tanks and coupling cells, which is directly fed by a 1 MW klystron.

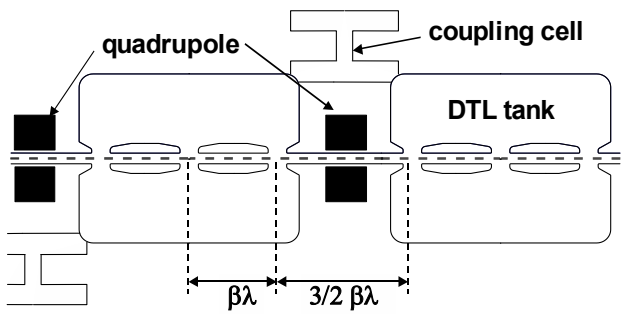

Figure 1: Outline of the CERN Cell-Coupled DTL.

The quadrupoles outside of the tanks can be easily accessed, aligned and cooled. Machining and plating of the relatively small CCDTL tanks requires a smaller and less expensive infrastructure than needed for a DTL. The alignment of the drift tubes is much less critical than in the DTL, the tolerances required for the alignment of an RF gap at this energy being between 5 and 10 times less stringent than for the alignment of the quadrupole. The module is directly fed by a klystron, clearly defining the tank phases and amplitudes. Finally, a CCDTL allows for a continuous focusing lattice, without the DTL intertank spacings, thus reducing the risk of beam mismatch.

Fig. 2 compares the computed shunt impedance of this CCDTL design with a CCDTL design with 2-gap tanks and with two standard DTL designs. In the energy range

between 40 and 80 MeV the 3-gap CCDTL presents a shunt impedance slightly higher than the DTL.

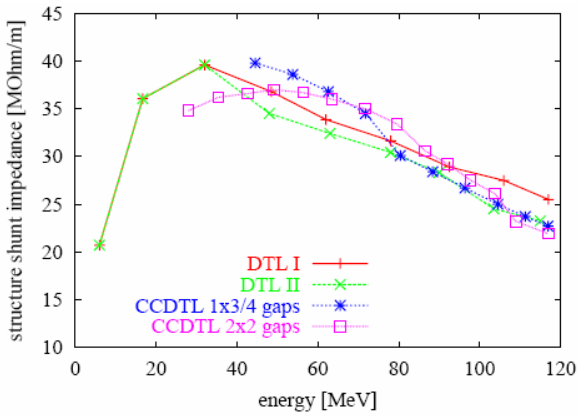

Figure 2: Comparison of shunt impedances for two CCDTL and two DTL designs.

The present CCDTL layout for Linac4 covers the energy range between 40 MeV and 90 MeV with 7 modules of four 3-gap cavities each, for a total length of 30 m. The RF input is from a coupler placed in one of the central tanks. The main design parameters are presented in Table 1 and a view of a CCDTL module in Fig.3.

Table 1: Parameters of the CCDTL design for Linac4

Input Energy	40	MeV
Output Energy	90	MeV
RF Frequency	352.2	MHz
Number of tanks	28	
Gradient E_0	3	MV/m
Lattice	FD	
Max. surface field	1.3	Kilp.
Aperture radius	14 - 16	mm
Synchronous phase	-25	deg
Length	30.1	m
Peak beam current	30	mA
Max. duty cycle	14	%

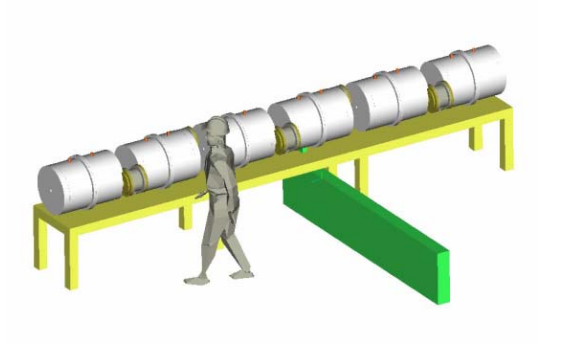

Figure 3: View of a CCDTL module.

RF DESIGN OF THE PROTOTYPE

In order to define the mechanical engineering of this CCDTL structure and to test the cooling and the high power behavior, a CCDTL prototype has been designed and is presently in construction at the CERN workshop. It has the minimum size necessary to obtain the desired field and loss distribution, i.e. two half tanks connected by a coupling cell, with dimensions corresponding to 40 MeV beam energy. Its basic geometry is shown in Fig. 4. The coupling between tanks and coupling cells is via a slot of 102 mm x 48 mm, providing a coupling factor of 1 %, as calculated by 3D simulation codes, sufficient for the short CCDTL modules. The estimated RF power dissipation to reach the nominal field in the prototype is 120 kW peak.

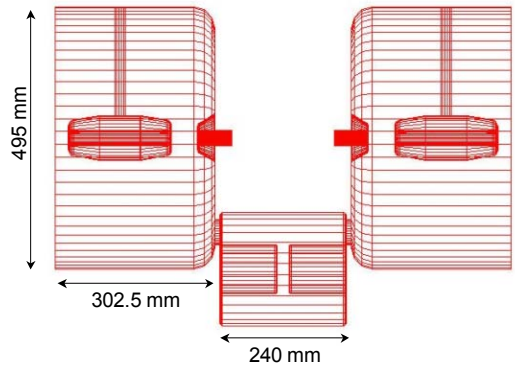

Figure 4: Geometry of the CCDTL prototype.

The CCDTL will have a single waveguide coupler for 1 MW peak power, and a maximum average power of 140 kW. A commercial waveguide window will be used, and the RF power will be coupled via an iris in one of the tanks. The dimensions of the iris have been defined using 3D RF simulations (Fig. 5), computing first of all the Q_0 of the tank-waveguide assembly and then its Q_{ext} by closing the waveguide with a perfectly matched layer. The ratio of the two Q-values gives the value of the coupling β. The waveguide is tangential to the tank, and closed with a short-circuit at λ/4 distance from the centre of the coupling iris. This arrangement allows precise matching of the line to the resonator, compensating for the final Q-value of the cavity and for the inaccuracies of the simulations, by changing the position of the short-circuiting plane before its brazing in the final position.

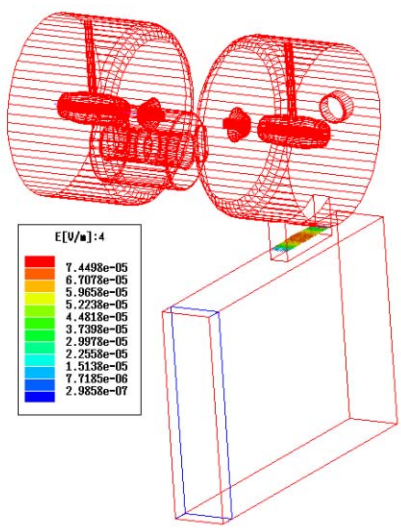

Figure 5: 3D simulation of the waveguide coupler showing the electric field on the coupling iris.

MECHANICAL DESIGN

A preliminary analysis of the cooling requirements for 14% duty cycle indicated that the tank can be made out of copper-plated stainless steel, with cooling channels directly machined in the external part of the tank cylinder. The drift tube has to be made in copper, and cooled via the supporting stem. To ease assembly and to minimise the number of joints, half tanks are connected via a helicoflex joint in the tank middle plane, while the end walls are electron beam welded to the tank cylinder. The basic tank structure is shown in Figs. 6 and 7.

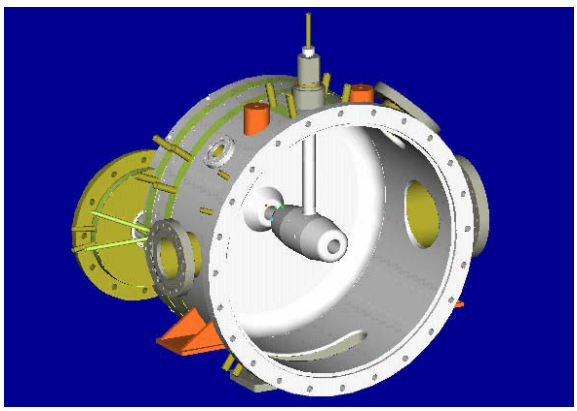

Figure 6: CCDTL prototype half tank.

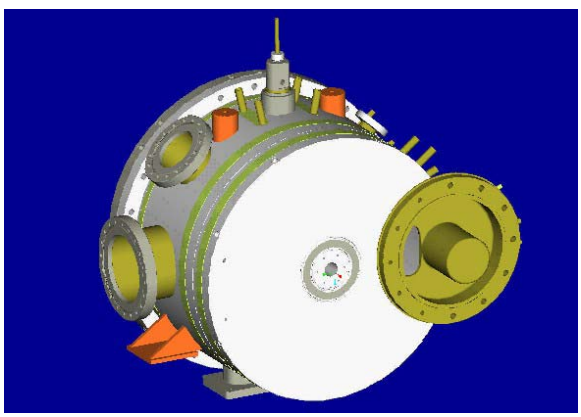

Figure 7: Rear view of the CCDTL half tank.

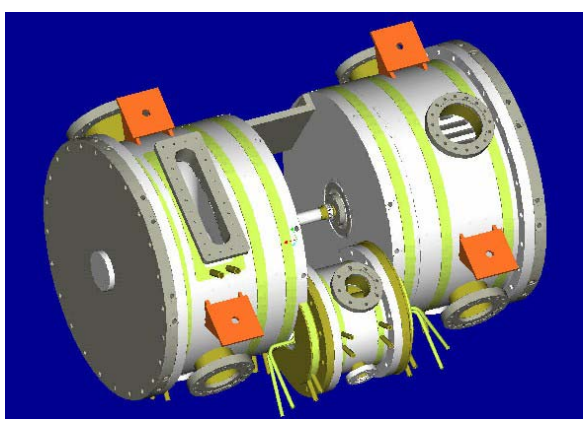

Figure 8: Assembled CCDTL prototype.

The end wall of the coupling cell is connected to the tank by electron beam welding around the coupling slot, visible in Fig. 7. The prototype, Figure 8, is finally assembled using helicoflex joints. The large iris for RF coupling is clearly visible.

The thermal calculations performed on the prototype (Fig. 9) show a maximum temperature of about 100º on the pumping port grid, while 85º are reached on the cavity body. A critical spot is the coupling slot, which can go to 120º when the coupling cell is not cooled. By adding some cooling, the temperature is reduced to 52º. The temperature of the copper drift tube is limited to 30º. The calculated frequency shift due to heating is 200 kHz.

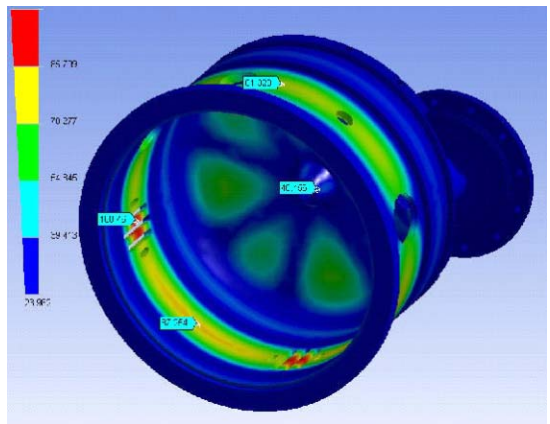

Figure 9: Thermal calculation for the CCDTL prototype.

PRESENT STATUS AND PERSPECTIVES

Machining and welding of the prototype have been finished and the components are presently waiting for copper plating. High-power RF testing is scheduled to begin at the SM18 test stand at CERN in March 2005.

The construction of a larger size CCDTL prototype is planned in the frame of an ISTC project involving the Russian laboratories BINP (Novosibirsk) and VNIITF (Snezinsk) and CERN. The engineering of the CCDTL will be adapted to the construction technologies available in Russia, and a prototype made of two full tanks will be built and tested with RF power at CERN in 2006.

ACKNOWLEDGEMENTS

We acknowledge the support of the European Community-Research Infrastructure Activity under the FP6 “Structuring the European Research Area” programme (CARE, contract number RII3-CT-2003-506395).

REFERENCES

[1] R. Garoby, F. Gerigk, K. Hanke, A. Lombardi, C. Rossi, M. Vretenar, “Design of Linac4, a new Injector for the CERN Booster”, this conference.

[2] J. Billen, F. Krawczyk, R.Wood, L.Young., “A New RF Structure for Intermediate-Velocity Particles”, Linac 94, Tsukuba.

[3] F. Gerigk, M. Vretenar, Design Choices for the SPL normal-conducting Front-end, PS/RF Note 2002-038.

DESIGN OF LINAC4, A NEW INJECTOR FOR THE CERN BOOSTER

R. Garoby, K. Hanke, A. Lombardi, C. Rossi, M. Vretenar, CERN, Geneva, Switzerland
F. Gerigk, RAL, Chilton, UK

Abstract

A new H^- linac (Linac4) is presently under study at CERN. This accelerator, based on normal conducting structures at 352 and 704 MHz, will provide a 30 mA 160 MeV H^- beam to the CERN PS Booster (PSB), thus overcoming the present space-charge bottleneck at injection with a 50 MeV proton beam. Linac4 is conceived as the first stage of a future 2.2 GeV superconducting linac (SPL) and it is therefore designed for a higher duty cycle than necessary for the PSB.

This paper discusses the design choices, presents the layout of the facility and illustrates the advantages for the LHC and other CERN users. The R&D and construction strategy, which mainly relies upon international collaborations, is also presented.

INTRODUCTION

A 2.2 GeV, 4 MW Superconducting Proton Linac (SPL) [1] represents a very interesting option for the long-term future of CERN (beyond 2010). This linac would serve as high power driver for neutrino production and/or radioactive ion physics. At the same time, as a high-brightness injector, it would modernise and improve the LHC injection chain, paving the way for an LHC upgrade. The low energy part of the SPL, up to 160 MeV, is normal conducting. It could be built first and used to inject H^- in the PSB, advantageously replacing the present 50 MeV proton Linac2. This new linac injector being the 4th hadron linac to be built at CERN would be named Linac4. Re-using part of the 352.2 MHz RF equipment from the decommissioned LEP accelerator and profiting from the available space and infrastructure in the Proton Synchrotron (PS) South Hall, the construction of Linac4 can be particularly cost-effective.

The main expected benefit of Linac4 is the doubling of the intensity and brightness of the beam from the PSB because of the charge-exchange H^- injection and because of the reduction in the space charge induced tune shift at low energy. That will result in an increased proton flux to the CERN users and an increased bunch population for the LHC. The energy of the new linac is set by the requirement for the PSB to deliver to the PS the LHC beam intensity in a single batch as compared to the present double batch, which corresponds to doubling the intensity per bunch in the PSB. Assuming that the maximum intensity at injection is inversely proportional to the tune shift, which in turn scales like $1/\beta\gamma^2$ (at constant normalized emittances), one can estimate that an energy increase from 50 to 160 MeV, corresponding to a factor 2 in $\beta\gamma^2$, will approximately double the maximum injection intensity. Recent simulations have confirmed this expectation. [2].

A recent study has compared different intensity upgrade scenarios for the CERN accelerators, recommending the construction of Linac4 in the medium term [3]. The estimated performance of the CERN complex with Linac4 together with the decrease of the PSB repetition period from 1.2 to 0.9 s and with upgrades to PS and SPS for higher intensity is shown in Table 1 and compared to present performance. The improvement for neutrino experiments is a factor 1.7, while for radioactive ions a factor of 3.5 is expected. The higher beam brightness would allow the bunch population at PS exit to reach 2×10^{11} protons in a 72 bunch train, corresponding to the LHC ultimate luminosity.

Table 1: Possible improvement to the CERN p beams

	Normal	Improved	
Flux to CNGS (ν beam)	4.5	7.5	$\times10^{19}$ pot/yr
Avg. current to ISOLDE	1.9	6.4	μA
LHC bunch population at PS exit	1.5	2.0	$\times10^{11}$ ppb

PARAMETERS AND LAYOUT

Linac4 will operate in two modes, initially as PSB injector at a maximum repetition frequency of 2 Hz and, at a later stage, at 50 Hz as front-end of the SPL. For injection in the PSB, the beam current is 30 mA, allowing the required number of protons per pulse to be reached in 500 μs, for a duty cycle of 0.1%. For the nominal SPL mode, the available RF power in the SC section limits the beam current to 13 mA, while the pulse length is 2.8 ms, for a duty cycle of 14%. Taking into account the chopping at low energy and the collimation in the front-end, the current required from the source is 50 mA and 30 mA respectively for the two operating modes. The linac structures are designed for the high duty cycle, but they will be operated in a first stage only at low duty cycle. Table 2 summarises the main design parameters.

Table 2: Linac4 parameters

	Phase 1 (PSB)	Phase 2 (SPL)	
Beam Energy	160		MeV
Maximum repetition rate	2	50	Hz
Source current	50	30	mA
RFQ current	40	21	mA
Chopper beam-on factor	75	62	%
Current after chopper	30	13	mA
Pulse length (max.)	0.5	2.8	ms
Average current	15	1820	μA
Max. beam duty cycle	0.1	14	%
Transv. norm. emitt. (rms)	0.33	0.33	π mm mrad
Long. emittance (rms)	0.24	0.24	π deg MeV

The basic Linac4 building blocks are sketched in Fig. 1 and the main layout parameters reported in Table 3 [4]. A chopper line section generates the beam time structure required for longitudinal injection into the PSB. The transition energy of 3 MeV between RFQ and DTL is considered as the highest value still giving negligible irradiation in case of beam loss, the cross-section for nuclear reactions in Cu still being very small at 3 MeV.

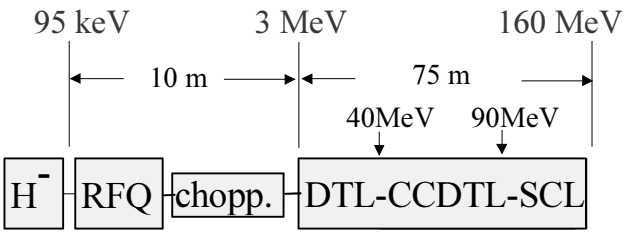

Figure 1: Schematic Linac4 layout.

Table 3: Linac4 layout

Section	Output energy (MeV)	No. of cavities (tanks)	RF Freq. (MHz)	Peak RF power (MW)	No. of klystr.	Length (m)
LEBT	0.095	-	-	-	-	2
RFQ	3	1	352.2	0.9	1	6
Chopper	3	3	352.2	0.1	-	3.7
DTL	40	3	352.2	4.8	5	16.7
CCDTL	90	27	352.2	5.6	6	30.1
SCL	160	20	704.4	13.8	5	27.8
Totals		54	-	25.2	17	86.3

THE FRONT-END

The Linac4 front-end, up to the energy of 3 MeV, is already in construction, and will be extensively tested in a dedicated test area at CERN [5]. It will use the RFQ of the IPHI project, designed and built by CEA and IN2P3 in France, which at the end of a series of tests at Saclay in 2007 will be transferred to CERN to be used in the new injector. This RFQ is designed to operate in CW mode, while at CERN it will be used at a reduced duty cycle.

An H^- source of the ECR type, preferred for its high reliability, is being developed at CERN in connection with the European network on Negative Ion Sources.

The chopper line is being designed and built at CERN, partly using existing quadrupoles and power supplies, to be extensively tested with the RFQ beam in 2007-08. The 3.6 m long line is based on a FODO focusing structure and contains two 500 mm long chopper structures placed inside quadrupoles, a chopper dump, three bunching cavities as well as diagnostics and focusing elements.

ACCELERATING STRUCTURES

An Alvarez DTL structure follows the RFQ, up to an energy of 40 MeV. The DTL is made of 3 tanks, the first one fed by one klystron, and the others by two klystrons each. Tank 1 is equipped with Permanent Magnet Quadrupoles (PMQ), while the other tanks have conventional electromagnetic quadrupoles (EMQ). Simulations indicate that the quadrupoles in the chopper line allow matching to the fixed gradient focusing channel of Tank 1 for a wide range of beam currents. FFDD focusing has been preferred for all the DTL [4].

With the support of the International Science and Technology Centre (ISTC), the ITEP (Moscow) and VNIIEF (Sarov) laboratories in Russia are presently building a prototype of DTL Tank 1 in collaboration with CERN. Additional contributions to the Alvarez DTL development come from CEA and IN2P3 (France), under the EU-funded HIPPI (High Intensity Pulsed Proton Injector) Joint Research Activity (JRA). High-power RF tests of the prototype are scheduled to take place at CERN in 2006.

Above 40 MeV the focusing periods can be longer than $\beta\lambda$, and alternative structures can be adopted, with quadrupoles outside of the drift tubes,. For Linac4, a particular Cell-Coupled Drift Tube Linac (CCDTL) design at 352 MHz has been selected [4, 6]. This structure is made of short 3-gap tanks connected by bridge couplers. The quadrupoles placed between tanks are mechanically independent of the RF structures, and can be easily aligned. Each klystron feeds a module made of 5 or 4 tanks via a single input coupler. A high-power prototype of 2 half CCDTL tanks is being made at CERN, while another ISTC project with BINP (Novosibirsk) and VNIITF (Snezinsk) will build a high-power prototype made of two complete tanks, again to be tested at CERN in 2006. The CCDTL development is also integrated in the HIPPI JRA.

Above approximately 90 MeV, the shunt impedance of 0-mode DTL-like structures starts to decrease drastically, and a Side-Coupled Linac (SCL) design at 704 MHz has been adopted to cover the energy range to 160 MeV. The SCL is made of 20 tanks with 11 accelerating cells each, connected into 5 modules of 4 tanks, each fed by a 4 MW klystron. Cell-to-cell coupling is 3%, and tanks are connected by 3-cell bridge couplers. The development of the SCL is also part of the HIPPI JRA, IN2P3 and CEA being the main contributors, while ISTC funds the construction of a 2-cell full-copper technological model at BINP Novosibirsk.

Alternative solutions for the low and high-energy part of the linac are under investigation. As a possible alternative to the Alvarez DTL, an ISTC project involving IHEP (Protvino) and VNIIEF (Sarov) will build a prototype of RFQ-DTL tank, from 3 MeV energy. This TE-mode structure offers a high shunt impedance, but is technologically challenging at this relatively high frequency and is based on non-conventional RFQ-type focusing. At high energy, another option is represented by superconducting cavities, a reasonable choice for the high duty cycle of the SPL, but already attractive at the low duty PSB operation. Two superconducting alternatives to the SCL (90-160 MeV) are presently under study in the HIPPI JRA, to be adopted in case they could outperform the SCL. The first is based on 704 MHz elliptical cavities at β=0.5, while the other consists of 4-gap spoke cavities at 352 MHz.

RADIO-FREQUENCY SYSTEMS

The 352 MHz RF system uses 12 klystrons plus circulators and waveguides from the LEP RF inventory presently stored at CERN. Tests have shown that the 1 MW LEP klystrons can be effectively operated in pulsed mode, by pulsing the modulating anode which was originally foreseen for conditioning and testing. When equipped with a storage capacitor bank, the LEP klystron power supplies have been shown to be usable in pulsed mode and potentially able to drive 6 klystrons simultaneously. However, their needs in terms of infrastructure are rather costly and not really justified for the low duty cycle of PSB operation. For this reason, a simpler pulsed power supply design will be used, presently under development at GSI. It will already be employed for the klystrons of the 3 MeV test stand.

The five 704 MHz klystrons will operate at 4 MW, considered as the limit for safe operation of the windows. The necessary power supplies will be developed at CERN when the construction of Linac4 will be authorised.

BEAM DYNAMICS

Linac4, as a first stage of the SPL, is designed to operate at high beam power, and particular care has been given to the beam dynamics, to avoid activation due to losses at high duty cycle operation. To this end, the transverse and longitudinal phase advances at each stage of acceleration have been carefully chosen to avoid resonances and emittance exchange for the nominal beam [4]. In general, abrupt changes in phase advance both transversely and longitudinally have been avoided wherever possible. The only region where, due to hardware constraints, this precaution could not be taken is in the 3 MeV line between the RFQ and the DTL. The chopper itself is about 1 m long and imposes a break in the continuity of a FODO structure which, at this energy and frequency, amounts to about 10 cm in length. Therefore, movable scrapers and a rudimentary collimation system are implemented to remove halo particles coming from the source and/or the RFQ and/or the line itself before acceleration to higher energies where neutron production cross sections are non-negligible.

The ratio between aperture and rms beam size is maintained all along the linac to a value between 7 and 8. This conservative value is chosen with the aim of absorbing a variety of distributions from the source. End-to-end simulations under ideal and slightly-perturbed conditions have validated the overall design [7].

LAYOUT ON SITE AND SCHEDULE

Linac4 will be installed in the South Hall of the PS, in the direct continuation of the test stand beam line. A 100 m long concrete bunker will be built, with a wall thickness between 80 and 200 cm. The klystrons, accessible during operation, are placed on the floor next to the machine bunker, the shielded waveguide access ducts being on the other side, close to the PS ring shielding wall. A switched magnet at the linac end sends the beam into a 200 m long transfer line, parallel to an existing ion transfer line, towards the PSB. After an upgrade for the higher energy, the existing beam measurement lines at the PSB entrance will be used for the Linac4 beam.

The decision on the construction of Linac4 is foreseen at the end of 2006, when the 3 MeV test stand will be ready to operate, the ISTC projects will be concluded and the HIPPI JRA will be more than half way to conclusion. If construction effectively starts at the beginning of 2007, a first beam could be available by the end of 2010. A possible schedule, including the test stand and a tentative schedule for the SPL, is shown in Figure 2.

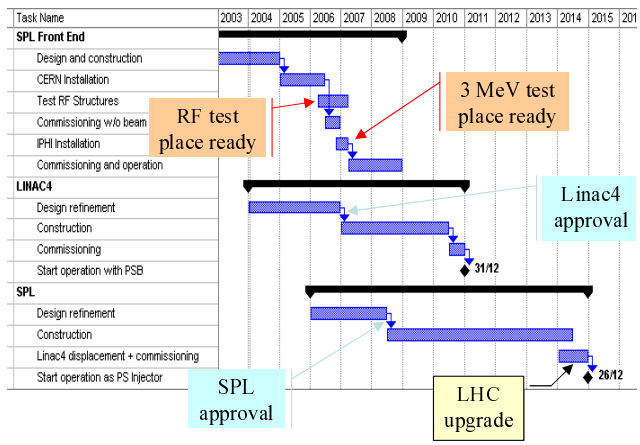

Figure 2: Possible schedule (Front-End, Linac4 and SPL).

ACKNOWLEDGEMENTS

We acknowledge the support of EU through the CARE I3, contract number RII3-CT-2003-506395 and the continuous and fruitful help of many CERN Groups.

REFERENCES

[1] M. Vretenar (ed.), "Conceptual Design of the SPL", CERN 2000-012.

[2] M. Martini, C. Prior, "High-Intensity and High-Density Charge-Exchange Injection Studies into the CERN PS Booster at Intermediate Energies", EPAC04, Luzern, July 2004.

[3] M. Benedikt, K. Cornelis, R. Garoby, E. Métral, F. Ruggiero, M. Vretenar, "Report of the High Intensity Protons Working Group", CERN-AB-2004-022.

[4] F. Gerigk, M. Vretenar, "Design of a 120 MeV H^- Linac for CERN High-Intensity Applications", Linac 2002, Gwangju, August 2002.

[5] C. Rossi et al., "The SPL Front-End: a 3 MeV H^- Test Stand at CERN", this conference.

[6] M. Vretenar, Y. Cuvet, J. Genest, C. Vollinger, F. Gerigk, "Development of a 352 MHz Cell-Coupled Drift Tube Linac Prototype", this conference.

[7] F. Gerigk, E. Benedico, A. Lombardi, E. Sargsyan, M. Vretenar, "Beam Dynamics for a New 160 MeV H^- Linac at CERN (Linac4)", this conference.

THE SPL FRONT END: A 3 MeV H⁻ TEST STAND AT CERN

C. Rossi, L. Bruno, F. Caspers, R. Garoby, J. Genest, K. Hanke, M. Hori, D. Kuchler, A. Lombardi, M. Magistris, A. Millich, M. Paoluzzi, E. Sargsyan, M. Silari, T. Steiner, M. Vretenar, CERN, Geneva, Switzerland
P.-Y. Beauvais, CEA, Saclay, France, P. Ausset, CNRS, Orsay, France

Abstract

In the frame of the SPL (Superconducting Proton Linac) study at CERN, a new 160 MeV proton injector for the CERN PS Booster is presently under development. This linear accelerator (Linac4) would not only be a first step towards a future, multi-MW superconducting linac, but would also improve in the medium term both the beam availability and beam quality for CERN's proton users. Within the framework of the Linac4 study and with the support of the EU funded Joint Research Activity HIPPI (High Intensity Pulsed Proton Injectors), a 3 MeV test stand is under construction at CERN. This test stand will explore some of the most critical issues of the linac, such as the beam dynamics at low energy, with special emphasis on the chopper line that has been designed to generate the required time structure of the beam, to clean the beam halo, and to match it to the subsequent RF structures. In this context, a new Beam Shape and Halo Monitor is under construction. The beam acceleration will be performed by an RFQ that is being developed in France within the IPHI collaboration between CEA and CNRS. Moreover, the test stand will be equipped with an additional 1 MW RF klystron to test different 352 MHz RF structures that are being developed for the Linac4.

INTRODUCTION

During the setting up of the LHC injector chain (Linac2-PSB-PS-SPS) it has been demonstrated that the intensity in the PS ring for the 25 ns LHC beam is limited to 1.5×10^{11} ppb, slightly more than nominal, mainly because of space charge effects at 50 MeV injection into the PS Booster (PSB). This is why the proposal has been made to build the low energy part (160 MeV) of the SPL and use it as an upgraded PSB injector, calling it Linac4 [1], [2]. The charge exchange injection that will be used in the PSB, combined with the higher injection energy, will substantially increase the intensity and brightness of the PSB beam. As a result, the intensity per bunch within the nominal transverse emittances is expected to reach 2.0×10^{11} ppb at the PS exit.

The technology and the beam dynamics issues at low energy, up to 3 MeV, are critical for the performance of Linac4, especially in its potential role as an SPL front-end. The halo formation mechanism has to be accurately studied and the techniques for chopping the beam with the appropriate time structure have to be validated. For these reasons a 3 MeV beam test stand is being built and installed in the position where it will later operate as the Linac4 front-end.

3 MEV TEST STAND LAYOUT

The 3 MeV test stand is designed to become the low energy part of Linac4. As a test stand, its main goal will be to validate the chopper line and to characterize the beam parameters and halo at low energy.

The preliminary layout is shown in Fig.1, integrated in the building where it will be assembled, the PS South Hall Extension.

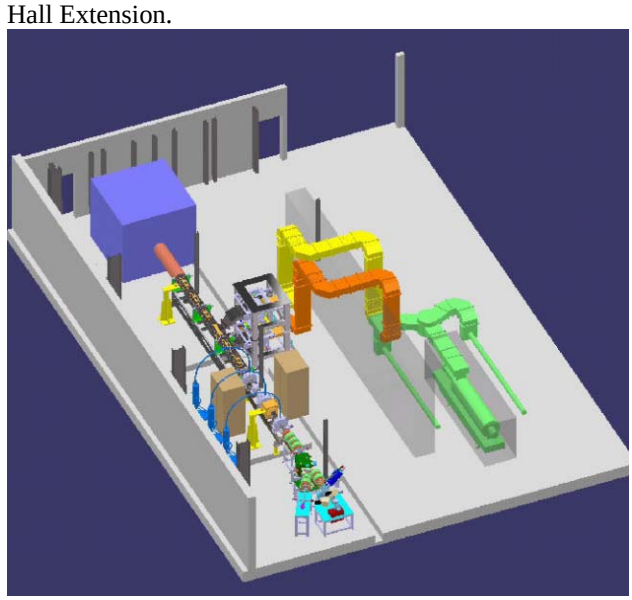

Figure 1: Layout of the 3 MeV test stand.

The test stand is composed of four areas, described below.

Ion Source and LEBT

A high intensity, high performance, micro-wave driven source is presently under development at CERN. It is designed for the requirements of the SPL, that can be considered as a long term development of the less demanding Linac4 H⁻ source.

In Table 1 the parameters for the two cases are listed.

Table 1: Main H⁻ source parameters

Parameter	Linac4	SPL
Instantaneous current	50 mA	>40 mA
Pulse length	0.5 ms	> 2.0 ms
Repetition rate	2 Hz	50 Hz
Extraction voltage	95 kV	95 kV
Duty cycle	1 ‰	15 %

The decision to develop a micro-wave driven source is based on the very satisfying operational experience with

ECR ion sources for heavy ions, especially in terms of reliability and life-time. Different magnetic structures for the source will be tested to maximize the H^- output. At present a multi-cusp structure is under investigation. Although the extracted current is very small (~300 μA), the influence of different source parameters (gas flow, RF power, RF tuning, bias of the plasma electrode, wall materials and additional gases) are being tested to get a better understanding of the H^- production. One of the next steps will be to redo the present tests with a solenoidal field structure. Based on the experience gained from these measurements a new source design will be made before the end of 2004. A test stand will be prepared for a prototype low energy beam transport (LEBT) equipped with a duoplasmatron proton source. The LEBT is based on a two solenoid structure and will contain some beam diagnostics, beam steering and possibly a pre-chopper.

Accelerator System

The core of the test stand is represented by a 6 m long RFQ that is being built within the framework of the IPHI collaboration between CEA and CNRS [3]. The RFQ has been designed to provide a continuous proton beam current of 100 mA for high intensity beam studies. After a one year test period at Saclay, this device will be made available for CERN to use for its new projects. In the 3 MeV test place and in Linac4, the RFQ will be operated at a 1/1000 duty cycle with 0.5 ms pulse length and 2 Hz repetition rate. In the SPL the duty factor will reach 15%.

The RF power source for feeding the RFQ will be a overhauled LEP klystron (352.21 MHz, 1 MW CW) that will be operated in pulsed mode. After some preliminary tests with the original LEP power supplies [4], it has been decided to develop a dedicated pulsed power supply. This will be done in collaboration between CERN and GSI, which also needs such converters to power the LEP klystrons of their future 70 MeV proton linac. According to the present terms of the agreement under negotiation, GSI will provide two HV pulsed power supplies, each capable of driving a 1 MW LEP klystron at full power with 0.7 ms pulse length and 2 Hz repetition rate. The first power supply will be delivered by the end of 2005 and the second by the end of 2006.

Chopper Line

The 3 MeV chopper line is meant to produce the beam time structure required by the different users and perform the delicate matching (transverse and longitudinal) between the RFQ and the DTL. In a high intensity machine, these two operations are crucial to maximize the beam transport and keep the beam losses along the accelerator at the lowest possible level. The line has been kept as compact as possible (3.7 m) and the chopper deflection structures are located inside quadrupoles. The two 500 mm long structures are made of a double meander stripline built on an alumina substrate [5]. With a drive voltage of ±500V between the two parallel meander lines, the chopped beam is deviated by 7 mrad. This results in a 2.0 cm separation between the beam centres at the beam dump, 1 m downstream from the last chopping cavity. The chopper driver must be very flexible and able to provide the required voltage excitation at a maximum repetition rate of 45 MHz, with a pulse length varying from 8 ns to 2 μs while keeping a 2 ns rise/fall time.

The transverse focusing is designed as a five-cell FODO structure and simulations show that a rather wide range of currents (from 20 mA to 60 mA) can be matched from the RFQ to the DTL.

The longitudinal matching of the beam from the RFQ output to the DTL input is assured by three buncher cavities, equally spaced, operating at 352 MHz. Two types of nose-cone equipped pillbox cavities, B30 and B40, have been designed, differing in beam aperture (30 mm for the B30 and 40 mm for the B40). Two B30 are placed at the beginning and at the end of the line, while the B40 is situated in the chopping region (and for this reason needs a larger aperture). A gap voltage of 140 kV is required for the B30s and 100 kV for the B40. Multi-particle simulations indicate transmission of the main beam as high as 98% and the chopped beam is eliminated to better than 0.02%. Under nominal conditions the computed longitudinal emittance growth is limited to 4% and the transverse emittance growth to 8%. Again, the simulations show that this chopper line is rather insensitive to misalignment of its component and that a positioning accuracy of 0.2 mm and 1 mrad is sufficient to achieve the required performance.

Diagnostics

In order to monitor the correct functioning of the chopper and to precisely measure the beam distribution in all three planes, a dedicated “Beam Shape and Halo Monitor” (BSHM) is being developed. This monitor has to fulfil two tasks: 1.) to measure the time structure of the beam and detect the remaining beam in chopped bunches down to 10^3 particles in the vicinity of a bunch populated with 10^8 particles; 2.) to provide a transverse image of the beam, allowing observation and study of the beam halo (diameter 4 cm, 10^3 particles/cm^2), and the beam core (diameter 1 cm, 10^9 particles/cm^2). The monitor is based on a thin carbon foil, which is inserted into the beam to generate secondary electrons. These electrons are accelerated towards a multi-channel plate (MCP), where they are transformed into light, which is transported via a fibre optics bundle to a CCD camera. Fast gating and a high-quality CCD camera provide the required dynamic range of 10^5-10^6. Further diagnostics will come from the IPHI installation and includes beam current transformers upstream and downstream of the chopper, as well as a set of devices following the chopper line, including a wire scanner, beam position monitors, pick-ups for beam energy measurement by means of the time of flight technique and a spectrometer magnet.

MEASUREMENT PROGRAMME

The purpose of the 3 MeV test stand is threefold. The primary goal is to validate the whole 3 MeV injector,

including the chopper system, the second one is to study the beam dynamics in the line and verify the simulation codes, and the third one is to measure the real beam parameters at 3 MeV so that the design of the downstream accelerator can be optimised. After a series of "routine" measurements (transmission, energy and energy spread) during setting up, we will concentrate on characterising the chopper and the matching to a DTL.

Validation of the Chopper

The chopper system is composed of three elements: the chopper itself, which provides the kick to the beam; the quadrupole after the chopper structure, which magnifies the kick; and the dump which collects the deviated beam. Each component will be tested individually. The effective kick received by the beam will be measured on a screen downstream, with a pencil beam and the quadrupole switched off. Two spots will be observed, corresponding to the main and the chopped beams. In the absence of quadrupole, the distance between them is proportional to the effective chopper voltage. The current in the quadrupole will then be progressively increased until the second spot on the screen disappears; in this condition we will be sure that the centre of the chopped beam is on the dump and that the main beam goes through the line. The rise and fall times of the chopper will then be estimated with the BSHM, both for the pencil beam and for the full beam. At the end of that series of measurements, the chopper line itself as well as all its components will be fully characterised.

Beam Matching and Halo Studies

The transverse emittance will be estimated from a series of profile measurements at varying quadrupole strength and the longitudinal emittance will be derived from energy spread measurements at varying buncher voltages. This method should be applied carefully in presence of space charge. In our case [6], we can achieve accuracy of the order of 10%. This method will also provide a good estimate of the flexibility of the line to meet different requirements for matching at the entrance of the next accelerator. After having assessed the envelope properties of the beam we will make use of the 2D readout system of the BHSM to study the halo. The halo will be measured (shape and intensity) for various settings of the source, the RFQ and the line and the results will be compared to simulations. Finally these parameters will be used to optimise the performance of the collimation system.

PLANNING

The start of such a rich scientific program is foreseen in 2007, when the IPHI RFQ and diagnostic line will have completed their testing phase at Saclay under continuous beam conditions. To avoid interference with the work of LHC installation, the preparation of the test place has started early, in 2003, and the design phase will be completed in the first half of 2005. The fabrication of all the major components is advancing and should be finished by the end of 2005. In the meantime, during the second half of 2005, the technical infrastructure will be fully prepared and a first RF system will be installed in order to make tests of prototype RF structures in 2006. The integration of the 3 MeV test stand (SPL Front End) project into the Linac4 realization and the possible SPL construction is shown in Fig.2.

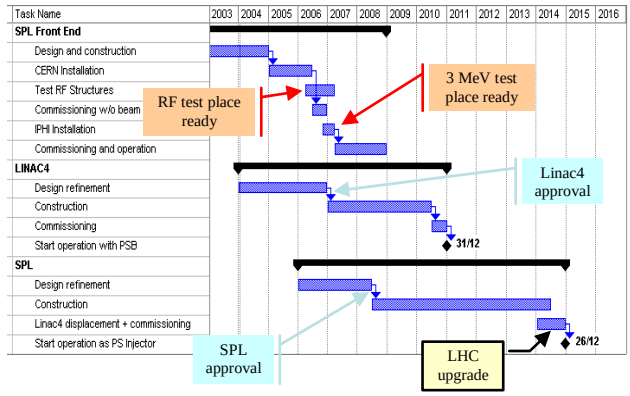

Figure 2: Integrated planning of the 3 MeV test stand (SPL Front End), of the Linac4 and of the SPL.

ACKNOWLEDGMENTS

The progress reported is the result of the commitment and enthusiasm of numerous scientific and technical contributors from many different teams at CERN, who managed to support this realization while fulfilling at the same time their responsibilities towards the LHC project. The active assistance and collaborative spirit of the members of the CEA-CNRS is also gratefully recognized. We acknowledge the support of the European Community-Research Infrastructure Activity under the FP6 "Structuring the European Research Area" programme (CARE, contract number RII3-CT-2003-506395).

REFERENCES

[1] F. Gerick et al., "Beam Dynamics for a new 160 MeV H^- Linac at CERN (LINAC4)", this conference.
[2] M. Vretenar et al., "Design of the LINAC4, a New Injector for the CERN Booster", this conference.
[3] P.-Y. Beauvais, "Recent Evolutions in the Design of the French High Intensity Proton Injector (IPHI)", EPAC04, Lucerne, July 2004, Switzerland.
[4] H.Frischolz, D.Valuch, "Operation of the LEP CW Klystrons in Pulsed Mode", PAC03, Portland May 2003, Oregon USA.
[5] F. Caspers, "Review of fast beam chopping", this conference.
[6] E. Sargsyan, K. Hanke, A. Lombardi, "Simulations of the beam diagnostics line for the SPL 3MeV chopper line,", AB-Note-2004-053 (SPL).

BEAM DYNAMICS FOR A NEW 160 MeV H $^-$ LINAC AT CERN (LINAC4)

F. Gerigk, RAL, Chilton, UK
E. Benedico Mora, A. M. Lombardi, E. Sargsyan, M. Vretenar, CERN, Geneva, Switzerland

Abstract

Linac4 is a normal conducting H^- linac proposed at CERN to provide a higher proton flux to the CERN accelerator chain. It should replace the existing Linac2 as injector for the PS booster (PSB). The same machine can also operate in the future as the front end of the SPL, a 2.2 GeV superconducting linac with 1.8 mA average current. At present Linac4 consists of a Radio Frequency Quadrupole (RFQ), a chopper line, a Drift Tube Linac (DTL), and Cell Coupled DTL (CCDTL) all operating at 352.2 MHz and finally a Side Coupled Linac (SCL) at 704.4 MHz. This paper discusses the overall beam dynamics concept, presents the optics for the different sections of the machine and compares end-to-end simulations realised with two tracking codes (PATH and IMPACT). The influence of phase/energy errors is discussed and the challenging features in the current design are highlighted.

CONCEPT

The guidelines for the design of Linac4 are high beam quality, low losses, low activation and, where possible, reuse of existing equipment. In the initial stage Linac4 will be used as a new injector for the PS Booster, providing 30 mA of H^- at 160 MeV in 0.5 ms long pulses at a 2 Hz repetition rate. At the same time it is conceived and designed as the normal conducting "front-end" of a 2.2 GeV superconducting proton linac with an average power of 4 MW, delivering a 13 mA beam with 2.8 ms pulse length and a repetition rate of 50 Hz [1]. With such high beam power involved, beam quality and halo formation must be carefully controlled in order to avoid activation and to ensure hands-on-maintenance. For this purpose the lattice is designed to provide a smooth evolution of the phase advance per metre across all transitions. This could be achieved for the whole of Linac4 (Fig. 1) with the exception of the LEBT and chopper line where mechanical constraints prevent this approach. Furthermore an effort was made to avoid resonant emittance exchange by adapting the transverse phase advance to the longitudinal one, yielding, in our case, a full current phase advance ratio of $0.5 < k_l/k_t < 0.8$ throughout the machine which successfully prevents any exchange of emittances between the planes (compare Fig. 3).

The fundamental frequency of 352.2 MHz was chosen in order to re-use the LEP klystrons, and the source extraction energy of 95 keV was determined by the availability of the IPHI RFQ [2].

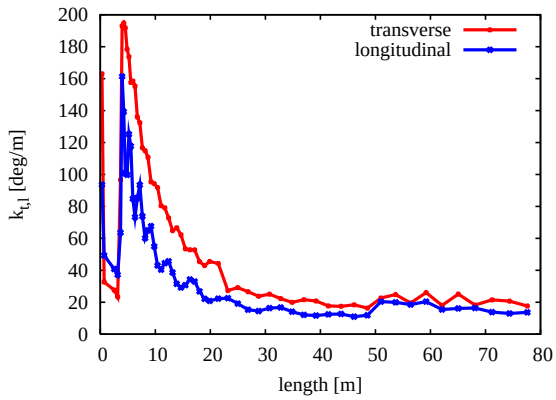

Figure 1: Phase adv. per metre from RFQ (out) to 160 MeV.

BEAM DYNAMICS

LEBT and RFQ

The Linac4 source beam will be matched into the RFQ by means of 2 solenoids and provision is made to house a pre-chopper between the two of them. Space charge effects are not severe as the beam is continuous and they can be compensated for by the solenoids. They account for less than 1% of the simulated emittance increase. The energy spread, expected to be around 4%, has instead a very strong effect, not only generating transverse emittance increase up to 30%, but also significantly spoiling the beam distribution because of the strong chromatic distortion when focused into the RFQ acceptance. The RFQ has been designed and optimised for 100 mA CW operation. It shows excellent transmission and good beam qualities also at 40 mA. The emittance increase, however, which occurs mostly in the first coupling gap, is more pronounced in the presence of the source energy spread.

Chopper Line

The chopper line dynamics is dominated by the chopper structure itself [3], [4]. The requirements for fast rise time (2 ns) and the timing structure of the CERN NuFact accumulator [1]) limit the maximum effective voltage to 800 Volts. In order to separate the beam by more than 1% we are forced to use a 1 m long chopper. The chopper line consists of 5 FODO cells with 2 periods on each side to match from the fast phase advance in the accelerating structures to a slow phase advance in the chopper (see Fig. 2). The chopping takes place in the (20 $\beta\lambda$ long) central FODO cell. The chopper itself is housed inside the first focussing quadrupoles (F5 and F6) and provides a 7 mrad kick to the beam. The separation in phase space is then ampli-

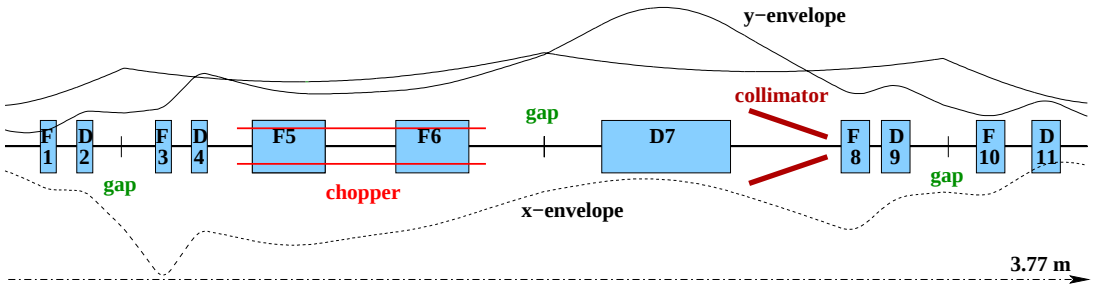

Figure 2: Chopper line and beam envelopes from TRACE3D.

fied and transformed by the second defocussing quadrupole (D7) into a physical separation at a cone shaped collimator which acts as a beam dump for the chopped bunches. In order for the chopping to work properly the centre of the beam must experience 90 deg phase advance between the (centre of) the chopper and the dump. The transverse matching to the DTL is guaranteed by the last two FODO periods. The matching was optimised, starting from the conventional envelope matching, by a genetic algorithms routine which has been implemented in the tracking code PATH [5] and which optimises the lattice elements for maximum transmission and minimum emittance growth. The longitudinal matching is done with 3 bunchers, equally spaced in the line.

DTL, CCDTL, SCL

The DTL section uses a FOFODODO structure which is able to provide strong transverse focussing, even with the relatively short quadrupoles, at 3 MeV and 352.2 MHz. A field and phase ramp in the first DTL tank ensures that the longitudinal zero-current phase advance per period stays below ≈ 65 deg. Thus the maximum transverse phase advance can be pushed to values close to 90 deg in order to prevent resonant emittance exchange between the planes as well as unstable envelope oscillations at or above 90 deg phase advance. At 40 MeV longer focussing periods become possible and the beam is matched into a CCDTL (FODO) structure using short 3-gap DTL tanks, coupled with single cell cavities in the $\pi/2$ mode. From 90 MeV onwards a Side Coupled Linac (SCL) structure (FODO) at 704.4 MHz is used to accelerate the beam to its final energy of 160 MeV. Before and after each transition (between DTL tanks, DTL/CCDTL, and especially around the frequency jump CCDTL/SCL) the synchronous phase is ramped either to compensate for the "missing gaps" between the structures or to squeeze the beam into the shorter bucket of the SCL.

OVERALL PERFORMANCE & CODE COMPARISON

For these first end-to-end simulations we use an input beam of 95 keV with 4% energy spread as it is expected from the H^- source. The linac has been simulated with PATH using cross-checks with IMPACT [6] and TRACE_WIN [7]. Using this "nominal" beam we observe a total rms emittance growth of 73% in the transverse plane and 18% in the longitudinal plane. The seemingly large transverse emittance growth occurs mainly in the front-end and breaks down into: 33% within the LEBT, 14% in the RFQ, 5% in the chopper line and the remaining 8% in the DTL, CCDTL, and SCL (see Table 1).

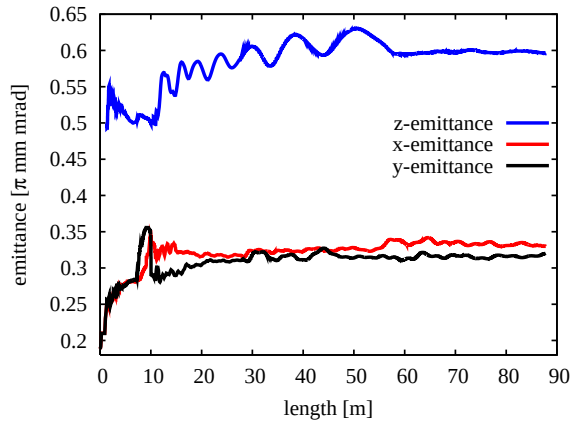

Figure 3: End-to-end (LEBT to 160 MeV) rms emittance evolution (from PATH).

The initial 4% energy spread was identified to double the "intrinsic" transverse emittance growth in the linac (Fig. 4) and it was found that source distributions with less than 2% energy spread can dramatically reduce these values.

In Fig. 5 we show a comparison of rms emittance evolution between PATH and IMPACT. The differences in the transverse plane can be explained by slightly different amounts of lost particles in the chopper line, which are due to differences in the geometric modelling of the two codes. Longitudinally, however, the simulations show up to 20% difference, which still has to be understood. Using IMPACT with nonlinear Lorentz Force integration instead of the standard linear transfer maps further enhances the differences in the results. At this point it is also not clear why the longitudinal emittance growth starts to differ ≈ 0.5 m after entering the DTL.

Despite the frequency jump at 90 MeV, energy & phase jitter remain very limited. 90% of all bunch centres are within values of ± 0.2 MeV and ± 3.4 deg as depicted in

Table 1: Emittance growth, transmission, and energy per section from PATH (50000 particles).

section	freq. [MHz]	length [m]	W_{out} [MeV]	$\varepsilon_{rms,t}$* [πmm mrad]	$\varepsilon_{rms,l}$ [πmm mrad]	$\Delta\varepsilon_{rms,t}$* [%]	$\Delta\epsilon_{rms,l}$ [%]	transm. [%]
LEBT		1.27	0.095	0.188	-	33	-	100
RFQ	352.2	5.96	3	0.25	-	14.4	-	98.9
CHOPPER	352.2	3.77	3	0.286	0.5	4.9	0.6	91
DTL	352.2	16.71	40	0.3	0.5	5.0	16.3	99.9
CCDTL	352.2	30.54	90	0.315	0.58	3.8	1.2	100
SCL	704.4	27.78	160	0.327	0.59	-0.6	0.2	100
TOTAL		86.03	160	0.325	0.59	73	18	89.9

* average

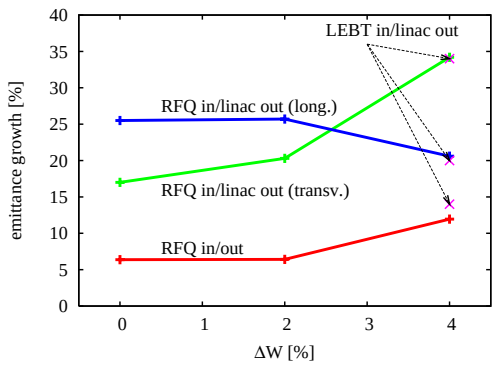

Figure 4: Influence of source energy spread on rms emittance growth.

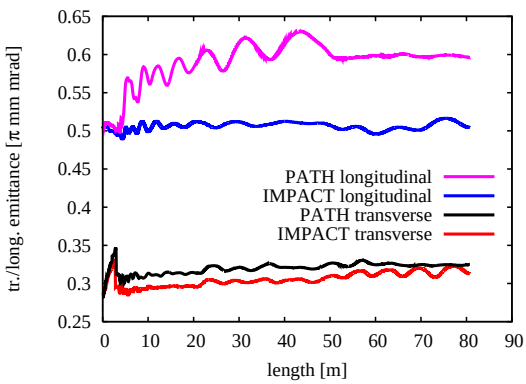

Figure 5: Rms emittance evolution simulated with PATH and IMPACT.

Fig. 6 and are thus close to earlier estimates which formed the basis of the transfer line design to the PS booster. [8].

SUMMARY

The first end-to-end simulations for Linac4 predict a substantial transverse emittance growth of ≈ 73%, which can be reduced considerably by assuming less than 2% source energy spread instead of the estimated 4%. Nevertheless, the overall design seems to be feasible and neither the chopper line dynamics nor the frequency jump seem to

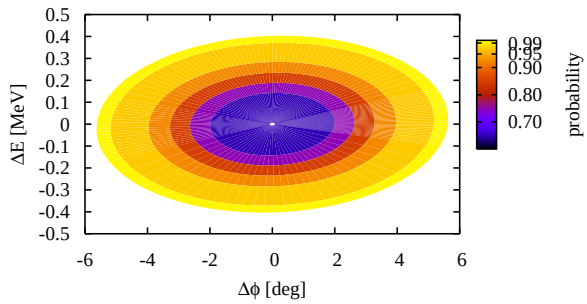

Figure 6: Energy & phase jitter at the linac output, assuming $\pm 0.5\%$ and ± 0.5 deg variation (rms with Gaussian distribution and cut-off at 2·rms) in all RF systems.

pose any unsurmountable difficulties. Comparative simulations with PATH and IMPACT show differences in emittance growth that remain to be understood but which do not endanger the performance of the design.

ACKNOWLEDGEMENTS

We acknowledge the support of the European Community-Research Infrastructure Activity under the FP6 “Structuring the European Research Area” program (CARE, Contract No. RII3-CT-2003-506395). We would also like to thank Beatrice Hadorn for helping to set up the PATH run file.

REFERENCES

[1] M. Vretenar, editor, CERN 2000-012

[2] P.-Y. Beauvais, Recent Evolutions in the Design of the French High Intensity Proton Injector (IPHI), EPAC 2004

[3] F. Caspers, Review of Fast Beam Chopping., this conference

[4] R. Garoby et al, The SPL Front End: A 3 MeV H^- Test Stand at CERN., this conference

[5] A. Perrin, J.F. Amand, Travel v4.06, user manual, 2003

[6] J. Qiang, R.D. Ryne, S. Habib, and V. Decyk, J. Comput. Phys., **163**, 434, 2000.

[7] N. Pichoff, D. Uriot, TRACE_WIN, *DSM/DAPNIA/CEA 2000/45*

[8] F. Gerigk, CERN-NUFACT-NOTE 133, 2003

RESULTS OF THE HIGH-POWER CONDITIONING AND THE FIRST BEAM ACCELERATION OF THE DTL-1 FOR J-PARC

F. Naito*, S. Anami, J. Chiba, Y. Fukui, K. Furukawa, Z. Igarashi, K. Ikegami, M. Ikegami
E. Kadokura, N. Kamikubota, T. Kato, M. Kawamura, H. Kobayashi, C. Kubota, E. Takasaki
H.Tanaka, S. Yamaguchi, K. Yoshino, KEK, Tsukuba, JAPAN
K. Hasegawa, T. Itou, T. Kobayashi, Y. Kondo, A. Ueno, Y. Yamazaki, JAERI, Tokai, JAPAN

Abstract

The first tank of the DTL for Japan Proton Accelerator Research Complex (J-PARC) was installed in the test facility at KEK. The DTL tank is 9.9 m in length and consists of 76 cells. The resonant frequency of the tank is 324 MHz. After the installation of the tank, the high-power conditioning was carried out deliberately. Consequently a peak rf power of 1.2 MW (pulse repetition of 50Hz, pulse length of 600 μsec) was put into the tank stably. (The required power is about 1.1 MW for the designed accelerating field of 2.5 MV/m.) Following the conditioning, An H^- ion beam, accelerated by the RFQ linac up to 3 MeV, was injected into the DTL and accelerated up to its design value of 19.7 MeV. The peak current of 30 mA was achieved with almost 100 % transmission in November of 2003.

INTRODUCTION

The construction of a high-intensity proton accelerator facility for J-PARC has been started at Tokai campus of JAERI. The accelerator consists of a 181-MeV linac (which will be extended to 400MeV in near future), a 3-GeV rapid cycle synchrotron and a 50-GeV synchrotron[1]. The 181-MeV injection linac is comprised of the an H^- ion source, an radio frequency quadrupole (RFQ) linac, a drift-tube linac (DTL), a separated DTL (SDTL)[2], and several beam transport lines. The resonant frequency of the RFQ, the DTL and the SDTL is 324 MHz.

The Alvarez-type DTL accelerates the H^- ion beam from 3 to 50 MeV. It consists of the three independent tanks of which the length is about 9 m. Furthermore each tank is comprised of three short unit tanks of which length is approximately 3 m. The inside diameter of the tank is 560 mm. Each drift tube (140 mm in diameter) accommodates the electro-quadrupole magnet. The DTL-1 has 77 magnets. The DTL-2 and -3 have 44 and 28 magnets, respectively.

HIGH-POWER CONDITIONING

The DTL-1 was assembled very precisely and the accelerating field was stabilized by the post-couplers [3]. After the tuning of the field, The DTL-1 was installed in the tunnel of the test facility at KEK for the beam acceleration experiment.

* fujio.naito@kek.jp

Installed DTL-1 into the beam line is shown in figure 1. Left side component in the figure is the MEBT placed precisely in the area between the RFQ and the DTL. The properties of the beam ejected from the DTL are measured by the beam test line which has the current transformer (CT) , the beam position monitors (BPM), the transverse emittance monitor (EM) and the Faraday cup (FC) which works as a beam dump. The emittance monitor and the Faraday cup are installed in the area covered by concrete blocks for radiation shield. The blocks are seen at right side of the figure. The schematic view of the beam test line are shown in figure 2.

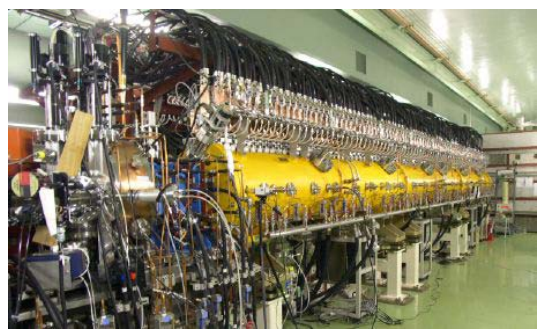

Figure 1: DTL-1 in the beam line.

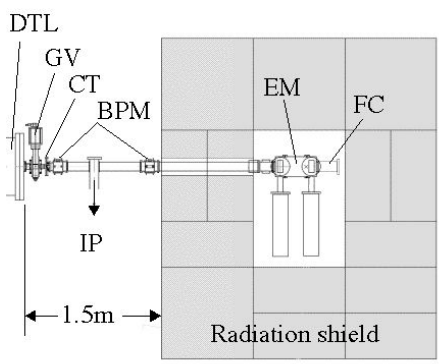

Figure 2: Beam test line.

A lot of black lines on the DTL shown in the figure 1 are the power lines for the quadrupole magnets. Each magnet is supplied the electric power independently. The power sources can supply both DC (600A in maximum) and pulse (1000A in maximum) currents to the magnet.

Adjustment of the input couplers

The rf power from the klystron is transferred in the WR2300 rectangular waveguide. The waveguide is converted to the WX203D coaxial one in the tunnel. The coaxial waveguide is connected to the input coupler.

The rf-power is fed into tank by two input couplers so that the load of each coupler is reduced by half. Furthermore the excitation of the TM_{011} and TM_{012} modes is suppressed since each coupler is located at one fourth of the total length from the end plate. The coupling constant of the coupler is tunable since the loop of the coupler is movable. The schematic view of the coupler is shown in figure 3.

Figure 4 shows the the relation between the coupler position and the value of the coupling constant. It also shows the loaded- (Q_L)and unloaded-Q (Q_0) values measured by changing the coupling constant (β_1 and β_2). Because the observed unloaded-Q value is 48700 and the calculated Q-value by the superfish without the effect of the post-couplers is 52900, the observed Q_0 is approximately more than 92 % of the theoretical value. Finally the coupling of the each coupler was adjusted to 0.5 so that the total coupling of the couplers is critical one. The reason why the critical coupling was chosen is described in the next section.

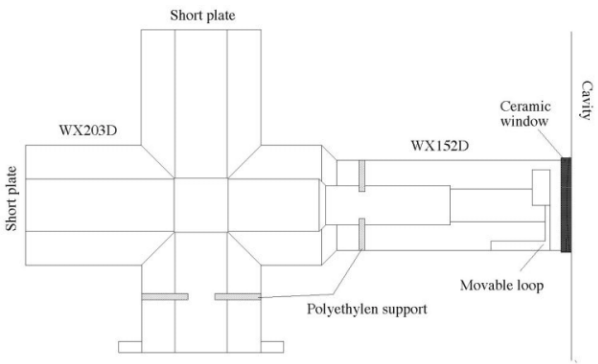

Figure 3: Design of the input coupler.

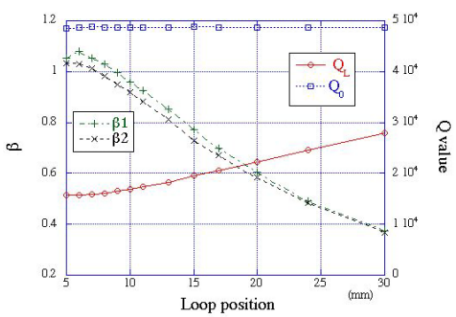

Figure 4: Measured Q-values and the coupling constants of the coupler.
Abscissa shows the gap length between the loop and the window.

High-power conditioning

High-power conditioning has been done for the DTL-1 very carefully. The conditioning history is shown in figure 5. The coupling constant of each coupler was adjusted to 0.6 at the beginning of the conditioning. It means that the total coupling constant was 1.2 (over coupling) at first. The following items are the history of the conditining.

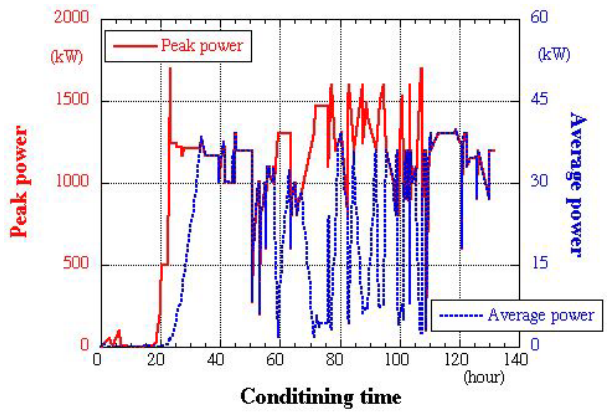

Figure 5: Conditioning history for DTL-1.

(1) 0 to 18 hours: In the beginning of the conditioning, almost input rf power was reflected from the coupler window. The rf pulse width was extended to 780 μsec with 50 Hz repetition in this period. Peak power was less than 6 kW. The conditioning in this period is considered as aging of the coupler window.

(2) 18 to 23 hours: When the rf power entered the tank through the window, real tank conditioning starts. During this period, the rf conditioning was done with the rf pusle of the low duty factor, (puse length of 100 μsec, repetition rate of $\leq$ 10 Hz). It is the same procedure as the conditioning of the SDTL [4]. The input peak power was increased gradually up to 1.7 MW in maximum, which is approximately 1.5 times the desired value (the rf power of 1.1MW is required for the designed acceleration field of 2.5 MV/m) for the tank.

(3) 23 to 33 hours: After the achievement of the maximum value of rf power, the rf duty factor then has been extended gradually to the maximum value of 3% (600 μsec in the pulse length, 50 Hz in the repetition rate) with the peak power of 1.2 MW. The maximum duty was achieved soon. However the tank condition was not stable yet. Discharges happened frequently around the ceramic window. The rate of the discharge was approximately once per 5 minutes.

(4) 33 to 108 hours: The conditioning was being continued by changing the duty factor and/or the rf peak power. However the tank was still unstable.

(5) 108 to 120 hours: Finally we decreased the coupling constant of the coupler from 1.2 (figure 6 (a).) to 1.0 (critical coupling shown in figure 6 (b)) by removing the coupler loop from the window since the luminescence pattern on the window had the similar shape of the loop of the

coupler. As a result the tank became stable. (See figure 6 (b).)

(6) 120 to 130 hours: Because the tank achieved the stable condition, the tuning of the rf feed-back system was started for the beam acceleration.

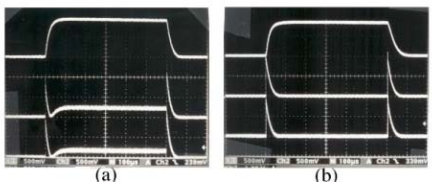

Figure 6: RF pulse shapes. (a) β = 1.2 (b) β = 1.0
Top: Tank rf level. Other lines:Reflection from the DTL.

FIRST BEAM ACCELERATION

The H^- ion beam was already accelerated by the RFQ linac up to 3 MeV [5]. Furthermore the MEBT line between the RFQ and DTL-1 was studied also by the beam from the RFQ [6]. The beam tuned by using the results of previous experiments was injected into the DTL-1 and accelerated up to its design value of 19.7 MeV. The energy was measured by the time of flight method with two beam position monitors, which works as a fast current transformer. The initial goal of the peak current of 30 mA was achieved after the tuning of the components in the MEBT. The observed current pattern is shown in the figure 7. Top of the figure is the beam current injected to the DTL-1 and bottom one is the beam from DTL-1. The beam pulse width is 20 μsec and the repetition rate of the beam is 12.5 Hz.

Quadrupole magnets in the DT were operated with DC current. The value of the current are shown in figure 8. The value of the current was fixed by using the previously observed transverse emittance of the RFQ. One of the main subject of the beam experiment is to find the reasonable operating condition of the quadrupole magnet in the DTL-1.

In the first beam acceleration, only the beam energy and the current were measured. The beam experiment is being carried out in order to study the beam properties (which are the emittance measurement, the bunch shape, the beam position, etc.). [7].

CONCLUSION

The high-power rf conditioning of the DTL-1 for J-PARC, which is installed in the test facility at KEK, was carried out deliberately. Consequently the peak rf power of 1.2 MW (pulse repetition rate of 50Hz, pulse length of 600 μsec) was put into the tank almost stably. (Recently the tank accepts stably the rf-power of 1.4 MW with the full duty factor.) Then H^- ion beam of 3 MeV energy was injected to the DTL. The beam which has 30 mA peak current was accelerated up to its design value of 19.7 MeV

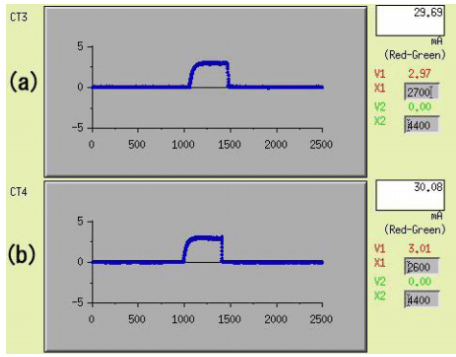

Figure 7: Output of the current monitor.
(a) Beam current at the end of the MEBT.
(b) Beam current ejected from the DTL-1

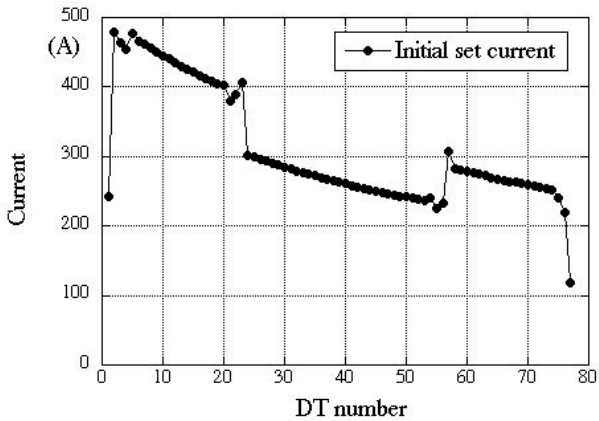

Figure 8: The set DC current for DTQs.

with almost 100 % transmission. The beam experiment will be continued till the autumn of 2004.

REFERENCES

[1] F. Naito, "The JAERI/KEK Joint Project and its Performance" Proc. of LAC 2002, Gyeongju, KOREA, 566 (2002)

[2] T. Kato, "Proposal of a Separated-type Proton Drift Tube Linac for a Medium-Energy Structure", KEK Report 92-10 (1992)

[3] F. Naito, et al, "Tuning of the RF Field of the DTL for the J-PARC", Proc. of PAC 2003, Portland, OREGON, 2835 (2003)

[4] F. Naito, et al, "High-power Test of the SDTL for the JAERI/KEK Joint Project", Proc. of LAC 2002, Gyeongju, KOREA, 427 (2002)

[5] A. Ueno, et al, "Beam Test of a Front-end System for the JAERI-KEK Joint (JKJ) Project ", Proc. of LAC 2002, Gyeongju, KOREA, 358 (2002)

[6] M. Ikegami, et al, "Beam Commissioning of the J-PARC Linac Medium Energy Beam Transport at KEK", Proc. of PAC 2003, Portland, OREGON, 1509 (2003)

[7] Y. Kondo, et al., "Beam Commissioning of the J-PARC linac DTL-1 at KEK", Proc. of 29th linac Meeting in Japan (in Japanese), Funabashi, JAPAN, 156 (2004)

A LINAC-TO-BOOSTER INJECTION LINE FOR TRANSVERSE MATCHING AND CORRELATED INJECTION PAINTING*

R. W. Garnett, L. J. Rybarcyk, LANL, Los Alamos, USA

Abstract

In this paper we discuss a compact linac-to-booster ring transfer line originally proposed for the Los Alamos Advanced Hydrotest Facility design to vertically inject a 157-MeV H^- beam from the linac into a 4-GeV booster. TRACE 3-D and PARMILA simulations were used to demonstrate the performance of the transfer line to deliver the required transverse beam to the foil while also allowing correlated longitudinal injection painting. Schemes for both transverse and longitudinal matching are important for high-intensity ring applications where low beam loss operation is desirable. The main features of the beam line layout, a proposed longitudinal painting scheme, and the simulation results will be discussed. This work is supported by the U. S. Department of Energy Contract W-7405-ENG-36.

INTRODUCTION

The most recent design of the Advanced Hydrotest Facility (AHF) assumes an injector linac that is a duplication of the SNS linac up to 157 MeV [1]. The linac is followed by an injection line that allows both transverse matching and correlated longitudinal injection painting [2,3] into a 4-GeV booster ring, followed finally by a 50-GeV main ring and associated beam lines for radiography. Here we propose a layout of an injection line that includes the required horizontal and vertical bends necessary to deliver the desired beam to the booster injection foil. Preliminary beam parameters required at the foil, which constrain the proposed transfer line design, and information regarding the booster lattice geometry were provided by the booster designers [4]. TRACE 3-D, PARMILA, and ESME2K simulations were used to demonstrate the performance of the transfer line to deliver the required transverse beam to the foil while also allowing longitudinal injection painting.

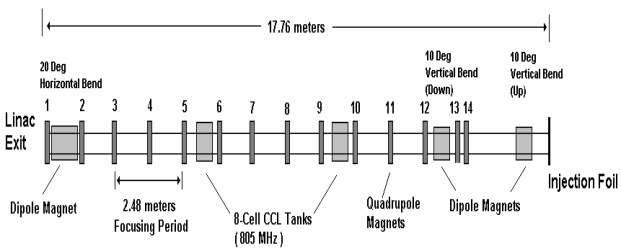

Figure 1: Unfolded layout of the booster transfer line.

TRANSFER LINE LAYOUT

Figure 1 shows the unfolded layout of the transfer line, including its various components. The layout of the transfer line relative to the booster ring is not shown, however, its length constrains the horizontal bend required with respect to the linac beam axis. The horizontal bend angle was chosen to allow sufficient separation between a separate linac tune-up line and the booster transfer line. A 20°-bend angle gives a sufficient separation to allow space for the required shielding so that linac tune-up activities can be in progress while maintenance activities, etc. are performed in the adjacent booster tunnel.

The transfer line focusing lattice is an extension of that used in linac. It was found that doing so maintains the beam size required to clear the relatively small radial apertures (r=1.5cm) of the 805-MHz 8-cell coupled-cavity linac (CCL) tanks of the transfer line that are used to do the correlated painting.

These cavities are identical to those of the last tank of the SNS CCL in order to save construction costs. The first tank will be operated in the bunching mode (ϕ= -90°). The second tank will be varied in phase about -90° and over a range sufficient to give the desired energy variation required to do the painting (typically $-120° \leq \phi \leq -60°$). The amplitude settings of the tanks are not identical, but are well within the expected operating range for SNS.

The quads in the transfer line are all set to identical gradient values with the exception of the final 4 quads (11-14 as shown in Fig. 1) that are used to obtain the transverse beam parameters required at the injection foil. From simulation results it was found that the dispersion at the foil could be reduced significantly by operating the last part of the linac and the transfer line at nearly 90° transverse zero-current phase advance. This results in somewhat higher quadrupole gradients as previously specified for SNS, but well within their operational limits.

Table 1 gives some of the transfer line mechanical and operational parameters. The total unfolded length of the transfer line from the linac exit to the foil is 17.8m. The magnetic field for all three bending dipoles is limited to 0.75 Tesla to avoid magnetic stripping of the H^- beam [5].

BOOSTER INJECTION REQUIREMENTS

Figure 2 shows the vertical injection region into the booster. It has been assumed that all magnets in this region will be operating in DC-mode. The long straight section in the booster is approximately 8.4m long. The injection region is assumed to occupy approximately 7m of the straight section as is shown in the figure. The combination of dipoles in the injection region will bend the beam upward by 10° and then back to horizontal at a new elevation. This displaces the beam approximately 0.53m off the booster axis during injection. This

particular geometry requires the linac beam centerline to be approximately 1.3m above the ring axis with a gradual change in elevation to the ring axis after the downward 10°-bend in the transfer line. A vertical clearance of approximately 0.9m between the booster magnets and the elements in the transfer line where the two lines tangentially and vertically merge.

Table 1. Transfer line parameters.

Transverse Focusing Lattice	Quadrupole Singlet
Transverse Focusing Period	2.48 m
Zero-Current Transverse Phase Advance / Period	≈ 90 degrees
Quadrupole Effective Length	8 cm
Focusing Quads	26.67 T/m
Matching Quads Q11, Q12, Q13, Q14	-37.97 T/m, 17.40 T/m, -41.28 T/m, -41.28 T/m
8-Cell CCL Tank Length	76.62 cm
Tank 1 Accel Gradient (EoT)	1.80 MV/m
Tank 2 Accel Gradient (EoT)	2.30 MV/m
CCL Bore Radius	1.5 cm
Dipole Magnetic Field, B	0.75 Tesla
Dipole Radius of Curvature, ρ	2.52 m

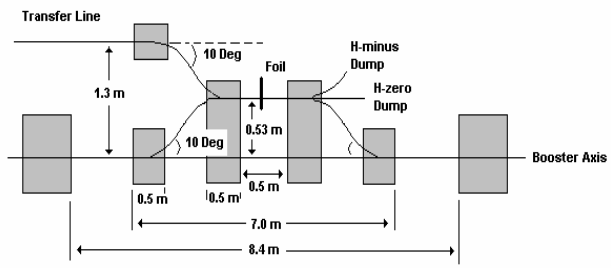

Figure 2: Booster injection region geometry. The final four transfer line quads were adjusted to meet the beam requirements at the foil.

TRANSFER LINE SIMULATIONS RESULTS

The TRACE 3-D beam envelope code was used initially to determine the transfer line layout. The location of the first CCL tank was selected by observing how rapidly the beam de-bunches as it exits the linac. The first tank was placed at a location where the total phase width of the beam is less than approximately 20°. This was specifically done to reduce the nonlinear effects on the beam distribution by the tank RF fields. The position of the second tank is chosen to minimize both the phase width and energy width at the foil. This solution leads to minimum variations in the longitudinal phase space of the beam as the second tank phase is varied to shift the beam energy centroid. Based on these simulation results, the expected x- and y-dispersion values are -0.348 m/frac and -0.035 m/frac, respectively; well within the requirements.

Multi-particle simulations using the PARMILA code were used to verify the beam envelope calculations. Design input files describing the SNS linac were obtained from the SNS project along with input beam distributions that are believed to be representative of the experimentally measured RFQ output. Simulations were completed using this input beam distribution to obtain the input distribution at the entrance to the transfer line. Table 2 gives the linac output beam parameters at the injection foil as calculated by PARMILA as a function of the CCL tank 2 phase settings. We have met the requirements specified above with our layout and choice of operational parameters. Figure 3 shows simulation results for the three nominal CCL-tank-2 phase settings of -60°, -90°, and -120°. The longitudinal phase space plots are shown.

CORRELATED PHASE-ENERGY PAINTING

The chopper in the low-energy beam transport of the linac. Along with the two CCL tanks of the transfer line, will be used to structure the train of micropulses in time. As described earlier, the second CCL tank will be used to change the central energy of the beam micropulses over the duration of a macropulse. By synchronizing the chopper and the energy-slewing cavity, a correlated longitudinal distribution can be produced. A simplified diagram of this system is shown in Figure 4**.** In this scheme, a gate signal will be simultaneously sent to the chopper and to a ramp generator which feeds a phase shifter on the low-level RF (LLRF) drive for the generator powering the CCL tank. The gate signal will enable a pre-programmed chopper pattern to begin. The LLRF drive signal will be modulated with a linear phase ramp which shifts the phase of the RF, as seen by the beam, by 100° over the macropulse. This will result in an almost linear variation of the beam energy across the macropulse. A negligible 10.5-kHz detuning of the 805-MHz tank is expected during the required phase variation of the cavity for a 25-turn injection (26.4 μs) into the booster. The field amplitude in the tank will operate at approximately 62% of the nominal design value (2.1 MV/m vs. 3.37 MV/m).

The goal of employing this scheme is to inject a matched beam into the booster RF bucket to minimize losses. The separatrix of a stationary RF bucket made up of RF harmonic h=1 has the shape of $\pm\Delta W \cdot \mathrm{Cos}(\phi/2)$ where $-180° \le \phi \le 180°$ and ΔW is the maximum energy extent of the bucket relative to the nominal injection energy of the booster. The energy of the injected beam will be swept in a monotonic fashion from $-\Delta W$ to $+\Delta W$ over the duration of the macropulse. During each "turn" of injected beam in the booster, the phase duration of that train of micropulses will be truncated by the beam chopper to match it to the phase width of the RF bucket

Table 2: Output beam parameters at the foil as calculated from the PARMILA simulations.

Tank 2 Phase	α_x	α_y	β_x (mm/mrad)	β_y (mm/mrad)	ε_x (π-cm-mrad, norm)	ε_y (π-cm-mrad, norm)	Beam Energy
-60°	-0.006	-0.058	9.98	9.61	0.0329	0.0519	157.91
-90°	0.023	-0.062	10.02	9.57	0.0331	0.0524	157.04
-120°	0.089	-0.047	9.68	9.37	0.0331	0.0520	156.19

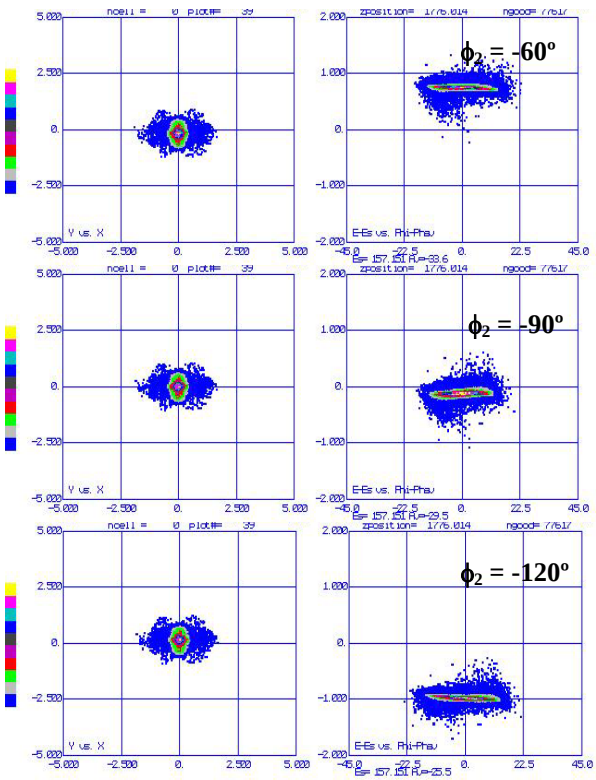

Figure 3: PARMILA simulation results: xy-beam spot at the foil and the longitudinal phase space distribution for the three CCL tank 2 phase settings.

for that energy offset. Figure 5 shows the longitudinal phase space distribution in the booster at the end of the 25-turn injection for a beam created in this fashion and simulated using ESME2K**.** To create this matched beam, three output distributions from PARMILA simulations described earlier were used, i.e. for tank 2 phase = -90° and ±50° from the nominal (-40° and -140°). These distributions were analyzed to determine the average energy and energy width of each distribution. This information was used along with a simple representation of the second CCL tank RF field, i.e. V·Sin ϕ, to produce the energy variation versus turn needed to paint into the RF bucket. The number of particles injected during each turn was adjusted by the amount of chopping done to the beam. A constant peak current from the linac was assumed. The beam was chopped to a maximum phase extent of ±170° to better match the pseudo-stationary RF bucket. To achieve the required 5×10^{12} protons injected into the booster (156m circumference) over the 25 turns (in 26.4 μs), at a nominal injection energy of 140 MeV, an average current of ~30.3 mA over the macropulse will be required. This is equivalent to a 50.3-mA-peak-beam current during the macropulse..

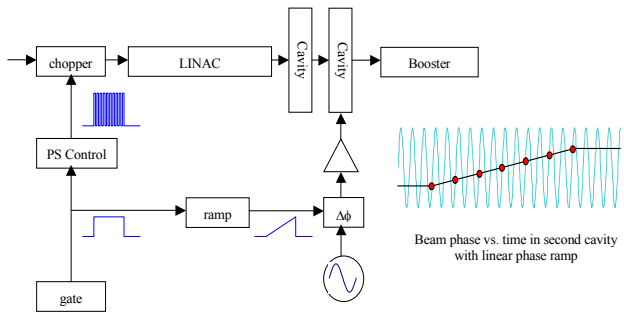

Figure 4: Schematic of the correlated longitudinal painting system. The drive signal to the sweeping cavity is phase modulated with a linearly-increasing phase to sweep the beam across the desired range of phase over the macropulse. The modulation is synchronized with the chopping pattern and the booster RF.

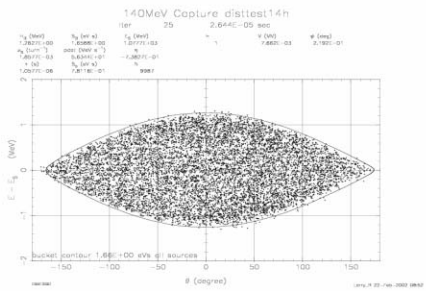

Figure 5: ESME2K simulation results showing the matched beam distribution injected into the booster over 25 turns. The second CCL tank provided ~1.15 MeV of energy variation over a range of 50° of phase as seen by the linac beam.

REFERENCES

[1] AHF Quarterly Report, April 25, 2002.
[2] R. Garnett and L. Rybarcyk, "AHF Linac Simulations Including Correlated Painting," Los Alamos National Laboratory Technical Memorandum, LANSCE-1:02-015, February 26, 2002
[3] L. Rybarcyk, "ESME Simulation Results for Matched Beam Injection into AHF Booster with Resonant Magnet Power Supplies", Los Alamos National Laboratory Technical Memorandum, LANSCE-1:02-012TN, February 26, 2002.
[4] F. Neri, private communication.
[5] A. Jason, D. Hudgings, and O. van Dyck, "Neutralization of H- Beams by Magnetic Stripping," IEEE Transactions on Nuclear Science, Vol. NS-28, No. 3, June 1981.

CARBON ION INJECTOR LINAC FOR A HEAVY ION MEDICAL SYNCHROTRON*

D.A. Swenson, Linac Systems, Albuquerque, NM 87109, USA

Abstract

The design of a Carbon Ion Injector Linac for a heavy ion medical synchrotron will be presented. The linac is designed to accelerate quadruply-ionized carbon ions ($^{12}C^{+4}$) with a charge/mass ratio (q/A) of 0.333, and all other ions with the same or higher charge/mass ratios, such as H^{+1}, H_2^{+1}, D^{+1}, T^{+1}, $^3He^{+1}$, $^4He^{+2}$, $^6Li^{+2}$, $^{10}B^{+4}$, and $^{16}O^{+6}$ to an output energy of 7 MeV/u. The 200-MHz linac consists of a Radio Frequency Quadrupole (RFQ) linac to accelerate the ions from an input energy of 0.008 MeV/u to an intermediate energy of 0.800 MeV/u, and an Rf-Focused Interdigital (RFI) linac to accelerate these ions to the output energy. The combined linac structures have a total length of 7.8 meters and a total peak rf power requirement of about 600 kW. The RFQ linac employs a radial-strut, four-bar design that is about twice as efficient as the conventional four-bar RFQ design. The RFI linac, which is basically an interdigital drift tube structure with rf quadrupole focusing incorporated into each drift tube, is about 5 times more efficient than the conventional Drift Tube Linac (DTL) structure. Details of the linac structures and their calculated performance will be presented.

CARBON LINAC (7 MEV/U)

Linac Systems has designed a 7-MeV/u, Carbon+4 Linac to serve as an injector linac for a heavy-ion synchrotron for medical applications. The linac is designed to operate at 200 MHz and consists of a Radio Frequency Quadrupole (RFQ) linac section, an Rf-Focused Interdigital (RFI) linac[1,2] section, an rf power system, a stripper foil assembly, a debuncher cavity, and associated vacuum, temperature control, and linac control systems. The two linac structures, shown in Fig. 1, have a total length of 7.8 meters and a total peak rf power requirement of about 600 kW.

The low rf power requirement is a tribute to the rf efficiencies of the RFQ and RFI linac structures. The RFQ linac structure employs a radial-strut, four-bar design that is about twice as efficient as conventional four-bar designs. The RFI linac structure[1,2], which is basically an interdigital linac structure with rf quadrupole focusing incorporated into each drift tube, is about 5 times more efficient than the conventional Drift Tube Linac (DTL) structure. Two features of the RFI linac structure contribute to its higher efficiency; namely, the interdigital configuration and the rf electric focusing. The efficiency of the interdigital configuration follows from the fact that the rf electric fields are concentrated in the vicinity of the drift tubes, resulting in very low amounts of electric and magnetic stored energies. The rf electric focusing results in smaller diameter beams, which allows smaller diameter drift tubes, which in turn further reduces the capacitive loading of the structure and associated rf power losses.

The linac system is designed to accelerate quadruply-ionized carbon ions ($^{12}C^{+4}$) with their charge/mass ratio (q/A) of 0.333, and all other ions with higher charge/mass ratios. As all of the accelerating and focusing forces are electric, driven by rf power, the only change required to accommodate the different ion species is a change in the rf drive power. By reducing the rf electric fields by a factor of 3, the accelerating and focusing forces in the linac are appropriate for the acceleration of protons at currents as high as 8 mA.

The rf pulse duty factor requirement for this application is very low. The required beam pulse length is less than 50 μs and the required repetition rate is less that 1 per second. However, for operational and rf conditioning reasons, we have designed for an rf pulse length of 100 μs and a repetition rate of 10 Hz, resulting in a duty factor of 0.1%. The average rf power in the RFQ and RFI linac combination is about 600 W.

The resonant frequency of the resonant units will be maintained by a temperature-controlled, recirculating coolant system mannaged by dedicated temperature control units. The rf frequency of the rf power system will be locked to the resonant frequency of the ensemble of resonant units. The setpoints of the temperature control units will be controlled by the linac control system.

The vacuum system is based on turbomolecular vacuum pumps. Two turbo pumps will be mounted on each of the three resonant units to maintain the vacuum level down to about $5x10^{-7}$ Torr. Several "dry scroll pump" are used to rough down the linac sections and back-up the turbo pumps. The vacuum system will be controlled and monitored by the linac control system.

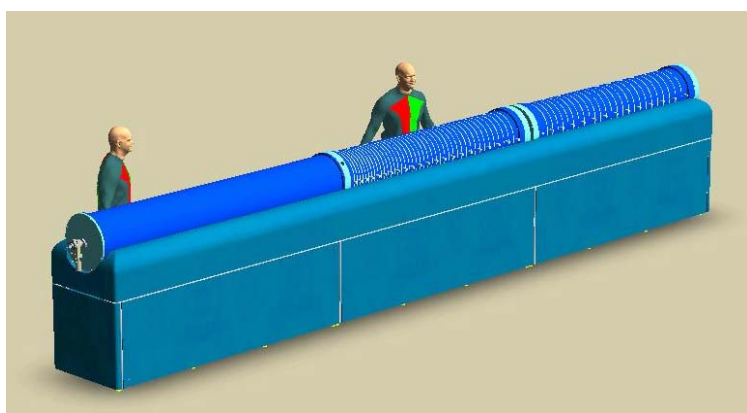

Figure 1: 7-MeV/u, Carbon+4 Injector Linac.

A distributed, Ethernet-based linac control system with fiber-optic links to the main synchrotron control system is proposed. There is little, however, to control. The acceleration and focusing actions of the linac structures depend solely on the distribution of the rf electric fields within the three resonant units, namely the RFQ linac section and the two RFI linac tanks. The distribution of the fields within each resonant unit is determined by the geometry of the unit. The three resonant units are resonantly coupled together, which locks their relative amplitudes and phases.

A variety of data will be monitored by the linac control system for diagnostic and maintenance purposes. The beam current into and out of the linac will be monitored. The forward and reflected powers from the rf power system will be monitored. The amplitude of the rf fields will be monitored in at least two locations in each resonant unit. The outlet temperature of the coolant from the many parallel coolant circuits will be monitored. As there are no steering magnets or focusing magnets, there are no magnet power supplies to be controlled or monitored. Diagnostic procedures will be in place to test the "health" of the rf power, vacuum, and temperature control systems.

Preparation for "Operation" requires simply that the vacuum pumps and temperature control systems are on and working properly. The rf power system is then brought up to "stand-by" condition. The next step is to excite the linac structures with rf power to the desired level, depending on the ion species to be accelerated. After checking that the rf field levels at the monitor loops are at their expected values, and opening a couple of beamline vacuum valves, the linac is ready to go. All of these operations will be automated through the control system.

RFQ LINAC

The RFQ linac for this system will be of the four-bar type. It will capture the 8 keV/u ion beams from the low energy beam transport system, and accelerate them to a suitable energy for acceptance by the RFI linac. Because of the exceptional low-energy capabilities of the RFI linac structure, the RFQ will only need to accelerate the ion beams to an energy of 0.80 MeV/u.

The bore radius is 3.6 mm and the length is 2.73 m. The rf cavity inner diameter of 288 mm and a strut spacing of 228 mm results in a resonant frequency of 200 MHz. The rf dipole mode for this configuration is several MHz above the quadrupole mode and does not present a problem with rf field stability. The peak rf power requirement is 105 kW, which for the 0.1% duty factor, results in an average rf power of only 105 W.

The main structural element of the RFQ is the heavy-wall aluminum rf cavity. The bars are extruded aluminum, with a longitudinal hole for cooling purposes. Each bar is supported by ten struts. The four-bar/strut assemblies are cooled by four separate cooling circuits. A counterflow arrangement will be employed so that the average temperature at all locations along the structure will be the same. The RFQ linac structure will be mounted inside a vacuum tank that provides the high-vacuum conditions required by the beam, the rf power, and the linac structure. The RFQ vacuum tank will be pumped by two 400 l/s turbomolecular vacuum pump and will typically operate in the $5x10^{-7}$ Torr range.

RFI LINAC

The RFI linac structure represents an effective combination of the Wideröe (or interdigital) linac structure, used for many low frequency, heavy ion applications, and the rf electric quadrupole focusing used in the RFQ linac structure and the Rf-Focused Drift tube (RFD) linac structure. The rf focusing is introduced into the RFI linac structure by configuring the drift tubes as two independent pieces operating at different electrical potentials as determined by the rf fields of the linac structure. Each piece (or electrode) of the RFI drift tube supports two fingers pointed inwards towards the opposite end of the drift tube forming a four-finger geometry that produces an rf quadrupole field along the axis of the linac for focusing the beam.

We have adopted what we call the "Stacked Cell" approach, where the basic unit of the structure is a single cell, complete with a two-piece drift tube, supported by major and minor stems in a short section of the outer wall. The linac structure is assembled by stacking up a sequence of these cells, each with the proper dimensions. The stack is held together by tie-bolts running along the structure or by welding the cells together into a single unit.

The RFI linac section will be configured as two tanks. The first tank accelerates the beam from 0.8 MEV/u to 3.88 MeV/u. The second tank accelerates the beam to the final energy of 7.0 MeV/u. The bore radius for both tanks is 6 mm and the total length of the two tanks is 4.47 m. The peak rf power requirement for the two tanks is 500 kW, which for the 0.1% duty factor, results in an average rf power of only 500 W.

RF POWER SYSTEM

The rf power system[3] consists of a low level rf system, a solid state amplifier, two one-tube intermediate power amplifiers, a final power amplifier (FPA), and an output directional coupler. It is designed to provide 800 kW of 200-MHz power at 0.1% duty factor. The rf power amplifier utilizes six GB-35B planar triodes in parallel in an axial array around the output coax. Each tube is capable of 140 kW of peak power output up to 1 GHz. Each tube has its own cathode bias and heater power circuit. The cathode bias circuit adjusts the bias on each tube to maintain a programmed level of cathode current. In order to make a compact amplifier, the anodes will be liquid cooled.

The directional coupler provides rf samples proportional to the forward and reflected wave amplitudes in the output coax. The forward amplitude signal is used

in the frequency control circuit to lock the rf system to the accelerator resonant frequency. A pickup loop in the cavity provides a signal that is used in the frequency control loop and in the amplitude control feedback circuit. The reflected amplitude signal is used for fault protection due to high VSWR.

RFI BEAM DYNAMICS

The beam dynamics of the RFI linac structure was investigated with the aid of TRACE-3D, a well-known, linear beam dynamics computer program, and PARMIR, a PARMILA-like beam dynamics code that simulates multi-particle beam dynamics in drift tube and interdigital linacs that employ rf focusing inside the drift tubes. TRACE-3D calculations for the Carbon+4 linac, configured in the + + - - focusing sequence, were made for cell lengths of 30, 45, 60, 75, and 90 cm, corresponding to the carbon ion energies of 0.75, 1.68, 3.00, 4.70, and 6.78 MeV/u. The phase advance of the transverse oscillation ranges from 36 degrees for the shortest cell to 47 degrees for the longest cell. The Twiss beta parameter varies from 0.26 cm/mrad for the shortest cell to 0.62 cm/mrad for the longest cell. The beam radius is 2 mm or less throughout the linac.

Due to the similarity in the transverse focusing forces in the RFQ and RFI linac structures (rf electric quadrupole focusing in both cases), very little is required to match the beam from the RFQ structure into the RFI structure. There is very little space between the two structures – the RFQ rods end only millimeters from the first half cell of the RFI structure. The RFQ structure ends in a "transition cell", which reduces the angular content of the output beam from the RFQ in both transverse planes. The RFI structure begins at a point of symmetry in the + + - - focusing sequence, which reduces the angular content of the input beam for the RFI in both transverse planes. Only minor changes to the lens strengths in the first four cells of the RFI structure are required to match the beam from the RFQ into the RFI. Figure 2 shows the TRACE-3D simulation of the matched beam in the last 10 cells of the RFQ, through the very short drift between the two structures, through the slightly modified first four cells of the RFI, and then through the rest of the RFI structure. This simulation also demonstrates that a constant-aperture, constant-voltage RFI lens, with a length that is a constant fraction of the cell length (1/3), results in a constant diameter beam.

The RFI linac structure offers a "one knob" accommodation for ions of other charges and masses. As all of the acceleration and focusing forces are electric and proportional to the rf field strength, a change in the magnitude of the rf field strength is all that is needed to accommodate other ion species. For example, to change from Carbon+4 to proton acceleration, the only change required is to reduce the rf electric field strength by a factor of 3. In the beam dynamics simulations, changing the charge/nucleon from 0.3333 (for Carbon+4) to unity (for protons) and reducing the acceleration and focusing field strengths by a factor of 3, the resulting beam profiles and phase spaces are indistinguishable from the carbon results.

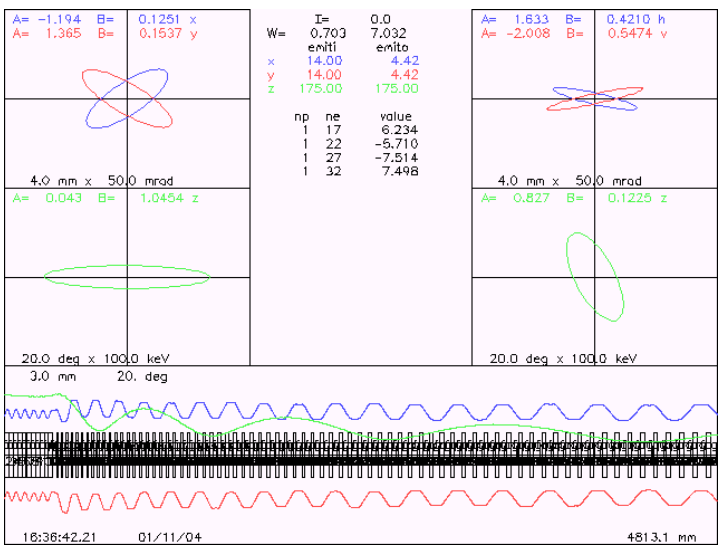

Figure 2: Trace Display showing beam in last ten cells of the RFQ and all of the RFI for Carbon +4.

ACKNOWLEDGEMENTS

The author acknowledges the contributions of his associates: Joel Starling, Frank Guy, Ken Crandall, and Jim Potter.

REFERENCES

[1] D.A. Swenson, "An Rf-Focused Interdigital Linac Structure", 2002 Intern. Linac Conf., Korea, 2002.

[2] D. A. Swenson, "An Rf Focused Interdigital Ion Accelerating Structure". CAARI Conf., Denton, TX, 2002.

[3] JP Accelerator Works, www.jpaw.com

THE HEIDELBERG HIGH CURRENT INJECTOR: A VERSATILE INJECTOR FOR STORAGE RING EXPERIMENTS

R. von Hahn[1], M. Grieser, R. Repnow, D. Schwalm, C.P. Welsch,
MPI-K Heidelberg, Germany

Abstract

The High Current Injector (HCI) was designed and built as a dedicated single turn injector for the Test Storage Ring in Heidelberg to deliver mainly very high intensities of singly charged Li- and Be-ions for laser cooling experiments. After start of routine operation in 1999 the HCI delivered high quality beams for about 25% of the experiments with very high reliability.
Due to the experimental requirements the HCI mutated from a specialized injector to a versatile multipurpose instrument, able to deliver a large variety of atomic and molecular light ions with either positive or negative charge. In addition provisions are far advanced to implement a custom built 18 GHz high power ECR-source for the injection of highly charged heavy ions suitable for further acceleration.
This paper gives an overview of the experience gained so far and presents the status of the upgrade of the HCI.

INTRODUCTION

The High Current Injector (HCI) consists of an ion source, a 6 m long RFQ section [1] and eight drift tube structures with seven accelerating gaps [2]. Most of the components have been designed and built in house. After final construction the first phase of the accelerator was commissioned successfully in 1999 and since then the machine is routinely operated for experiments [3]. The output energy can be flexibly varied from 0.5 MeV/u (RFQ only) to 2 MeV/u (with all 7 gap resonators) and can be boosted up to 5 MeV/u using the room temperature post accelerator of the MP Tandem.
Until now the HCI performed about 10 to 15 one week beam times per year with a large variety of molecules as well as positively or negatively charged ions at the low RFQ-energy or up to the design energy of 1.7 MeV/u with the 7-gap-Linac. Although the second rebuncher is not yet available, the coupling with the post accelerator was successfully used in a few beam times.
The accelerating structures are preferably used at design velocity. After determination of the correct amplitudes and phases in several test runs with $^4He^+$-ions only linear scaling for amplitudes and magnet settings is necessary to achieve beams with good transmission for all ion species in the design range A/q Ò9.
After successful commissioning of the custom built ECR-source at its present test location, various modifications were necessary preparing the second phase of the HCI -project. The platform of the CHORDIS source power supplies was raised up to a height of 3 m to create enough space for the ECR-injection.
The charge-state separator between the HCI and the post accelerator was designed and installed. Moreover, in collaboration with the Moscow University we started to investigate the lifetimes of thin foils for additional stripping behind the HCI [4]. However the time schedule for the installation of the ECR at the HCI or at a new application is presently under discussion as changes in the future orientation of physics research at MPI-K are envisaged.

[1] robert.von.hahn@mpi-hd.mpg.de

THE RFQ

The transmission of the 6 m long RFQ consisting of two directly coupled RFQs was measured as a function of the beam intensity. Up to mass to charge ratio 4:1 the available rf power is sufficient to operate the LINAC in CW mode which is more convenient for rf- and beam diagnostics than pulsed mode operation. With higher masses up to the maximum mass to charge ratio of 9:1 the pulsed mode operation with 20 ms long pulses and a duty cycle of 25% is required. The majority of required beam times were done in CW mode.

The following figures 1 and 2 demonstrate a significant dependence on the beam intensity starting at about 500 µA in CW-mode. At low intensities a bad transmission can be attributed to larger emittances of different ion sources rather than of the RFQ.

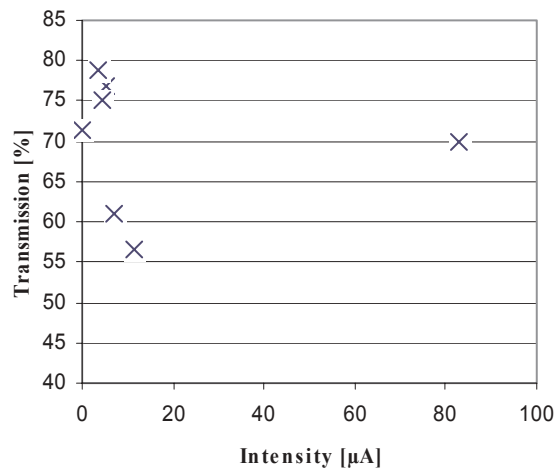

Figure 1: Transmission as a function of the beam intensity in pulsed beam operation.

A reason for losses at intensities close to 1 mA might be the fact that the early codes did not work well enough for the space charge effects. The adaptation to the RFQ possibly can be improved with a solenoid instead of the quadrupole presently used.

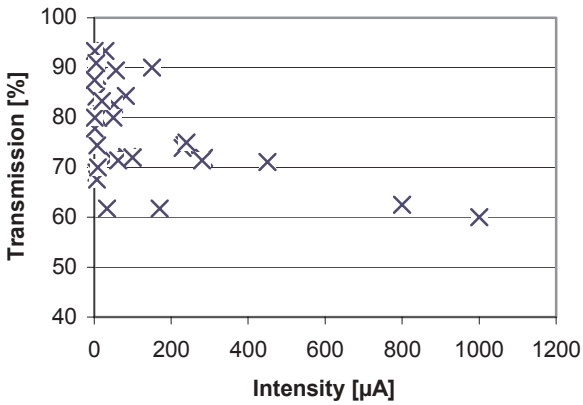

Figure 2: Transmission as a function of the beam intensity in CW operation.

OPERATION AND DEVELOPMENTS AT THE HCI

During the last years the High Current Injector (HCI) delivered a large variety of different molecular and atomic ions for experiments at the Test Storage Ring and for test purposes, Table 1. For difficult beams with very weak intensities from the ion source more prolific pilot beams were used for preparation and tuning of the required beams. The beam intensities reported in Table 1 were limited in most cases by the experiment. The reduction was achieved by a chopper in front of the RFQs or the TSR chopper.

In 2001 we started to deliver beams from a negative sputter ion source (MISS) instead of the standard CHORDIS in order to fulfil the demands for negatively charged ions. After a modification of the extraction system of the MISS to adapt it to the High Current Injector, the combination of MISS and HCI was very effective. Only two lenses have now to be switched to opposite polarity to accelerate also negative ions. In addition, newly developed sources like e.g. an ultra-cold liquid nitrogen cooled source for the preparation of rotational and vibrational cold molecules of H_3 were successfully installed.

For a D^--beam time only half of the RFQ-energy was required. This was achieved by operating the first RFQ in the standard mode and shifting the phase of the second RFQ by 180 degrees as compared to the standard phase. Thus a 1µA D^- beam of 0.5 MeV could be produced.

A variety of beam diagnostics are in use, in which beam profiles at higher intensities are determined using wire grids. The maximum power dissipation on the grid wires limits the applicable beam current to a few µA depending on the ion species and energy. To be able to observe the beam profiles also at higher currents, a beam profile monitor using residual gas ionization was developed. This device consists of two plates with an electrical field in between at a pressure of a few 10^{-7} torr. Residual gas atoms are ionized by the beam and accelerated to the segmented imaging electrode, where an arrangement of 32 collecting strips made of copper is used to detect the ions. The read out system was designed in such a way that the electronics used for the profile grids can be used with small modifications also for the residual gas monitors.

First measurements with 360 µA $^4He^+$ at an energy of 1.9 MeV demonstrated the functionality of this new system. To compare the measured beam profile of the residual gas monitor with the profile grid measurements a pulsed current of 78 µA with 1.5 ms pulse length was used. The profiles measured at the same position agreed within 0.1 mm to the measured FWHM value of the beam.

Table 1: Beams delivered by the HCI

Beam	Energy [MeV]	Intensity [µA]
$^1H^-$	0.5	0.6
$^4He^+$	7.67	30
$^2D_2^+$	6.56	3
$^1H_2^+$	3.1	30
$^2D_3^+$	1.4	0.25
$^9Be^+$	4.5	0.3
$^2D^-$	1	1
LiH_2^-	4.5	0.1
$^7Li^-$	5.6	0.2
$^1H_3^+$	1.46	10
LiH_2^-	4.3	0.08
HD^+	1.5	5
D_2H^+	2.4	5
D_2H^+	5.3	5
$^4He_2^+$	4	0.0003

THE ECR

In preparation of phase II of the High Current Injector, a state of the art 18 GHz-ECR-Source, Fig. 3, for the production of highly charged ions was bought and installed on a test bench. The test bench consists of the source itself, a solenoid and a double focusing magnet to resolve the ion source spectra.

During the acceptance tests at the manufacturer we achieved stable operating conditions at the maximum voltage of 36 kV and reproduced the ion intensities from the specifications (Table 2).

Table 2: Design specifications of the ECR

Ion	Mass	Charge	Intensity [eμA]
Ar	40	11^+	80
Xe	129	25^+	10
Pb	208	33^+	3

In 2002, all infrastructure work of the test bench was finished and we could start to operate the source in order to reproduce the design parameters and gain experience for routine operation. As a first step we run the source in the gas mode operating with H, He, N, O and Ar. A versatile new scan and analysis routine was very convenient to evaluate the complex ion spectra delivered from the ECR.

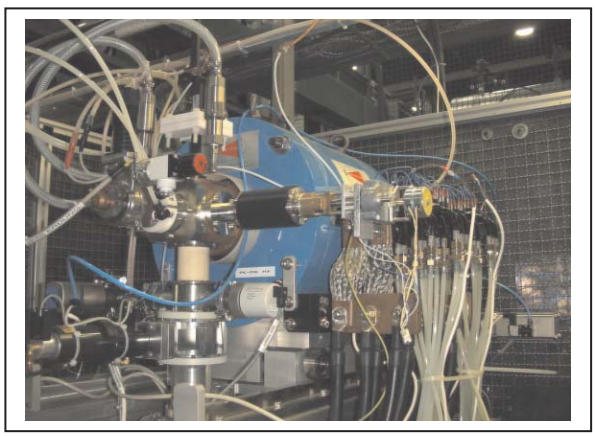

Figure 3: Photograph of the ECR ion source.

A typical spectrum of Argon is shown in Fig. 4. The source was optimized for Ar^{8+} resulting in a current of 400 μA in this charge state. The maximum charge state of Ar was Ar^{11+} up to now.

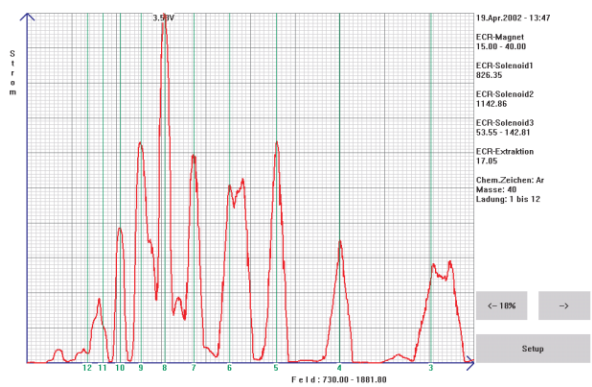

Figure 4: Spectrum of an Argon beam with 17 kV extraction voltage.

Though basically operational the ECR still has to be adapted to the spatial restrictions and the optical requirements of the HCI injection system. The design consists of the ECR, a singlet, an 180° bender and a triplet to focus the beam into the RFQ-section.
A stripper will be required in phase II to increase the ionic charge before further acceleration in the post accelerator. To separate the charge states, a separator system consisting of 4 identical 45 degree bending magnets has been designed and built. Allowing for edge angles of 22.5 degree these magnets are rectangular magnets and fulfill the requirement that the dispersion after the separator is zero. The magnets are already adjusted in the beam line and are routinely in use to determine the beam energy.

CONCLUSION

The principle of two directly coupled RFQs was successfully proven for the first time. Since 1999 the HCI is a very stable and reliably running machine in spite of permanent changes of ion species or required energy.

REFERENCES

[1] M. Madert, R. Cee, M. Grieser, R. von Hahn, C.-M. Kleffner, S. Papureanu, H. Podlech, R. Repnow, D. Schwalm, The RFQ accelerator for the Heidelberg High Current Injector, Nucl. Instr. and Meth. B139 (1998) 437-440

[2] R. von Hahn et al. , Development of 7-gap resonators for the Heidelberg High Current Injector, Nucl. Instr. and Meth. A328 (1993) 270-274

[3] R. von Hahn et al., First year of operation of the Heidelberg High Current Injector, EPAC 2000, Vienna, 596-598

[4] V. Kh. Liechtenstein et al., Recent developments and applications of thin diamond-like carbon (DLC) foils, Nucl. Instr. and Meth. A 521 (2004) 197-202

DESIGN OF A DEUTERON RFQ FOR NEUTRON GENERATION

Z.Y. Guo[1,#], C. Zhang[1,2], A. Schempp[2], J.E. Chen[1], J.X. Fang[1],
Y.R. Lu[1,2], S.X. Peng[1], Z.Z. Song[1], J.X. Yu[1], K. Zhu[1]
[1] Institute of Heavy Ion Physics, Peking University, Beijing 100871, P.R.China
[2] Institute for Applied Physics, Johann Wolfgang Goethe University, Frankfurt am Main, Germany

Abstract

A 201.5 MHz 2.0 MeV deuteron RFQ accelerator for neutron generation has been designed. The general considerations, particle dynamics and RF structure design of the RFQ cavity are discussed. The progress of the studies on ion source, LEBT and RF transmitter are presented.

INTRODUCTION

Neutron has been widely used in various fields. In addition to nuclear reactors, accelerators played an important role in neutron sources. The energy of accelerated proton or deuteron beams ranged from around 100 keV to about 1 GeV depending on the application demand. Low energy accelerators, like DC high voltage accelerator, cyclotron and RFQ, have been used for neutron radiography, boron neutron capture therapy, neutron activation analysis, etc [1].

The neutron sources based on RFQ or RFQ+DTL have been developed in LLNL[2], South Africa[3] and Indiana[4]. In this paper the design of a deuteron RFQ for neutron generation is described.

BASIC DESIGN CONSIDERATIONS

The main design objectives are to get the higher neutron yield with lower RF power. The fast neutron yield depends on the particle species, target element, particle energy and the average beam current. The reaction Be(d, n) was chosen because the Be target is easier to be handled than Li and the beam energy could be lower with deuteron than proton for the same neutron yield (Fig. 1).

The designed parameters of RFQ accelerator largely depend on the available RF output power of transmitter. We decided not to use klystron due to its big dimension and higher cost. The Thales TH781 was chosen as the final RF output tube, which can deliver 400 kW peak power with more than 10% duty factor at around 200 MHz. Considering the available RF power the deuteron energy at exit of RFQ was set to 2.0 MeV, and the peak current of deuteron beam was designed as 50 mA. So the peak beam power is 100 kW and the peak power consumed in RFQ cavity should be limited below 260 – 280 kW. The frequency of RFQ was chosen as 201.5 MHz. From Fig. 1 the expected 4π fast neutron yield is 4×10^{12} n/s.

At the frequency around 200 MHz, both four-vane and four-rod type structure can be used for RFQ cavity. The four-rod structure was chosen due to its smaller diameter and lower machining precision.

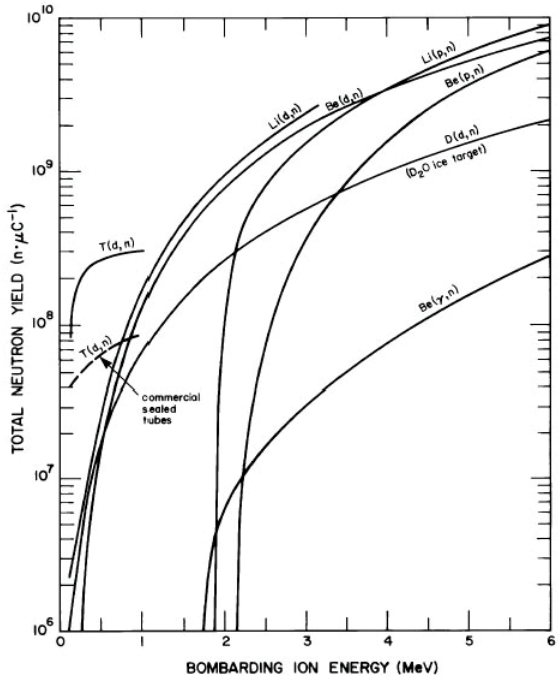

Figure 1: Neutron yields for low energy particle beam reactions[5].

The whole accelerator consists of ion source, LEBT, RFQ cavity and HEBT (Fig. 2), which will be described in the following sections.

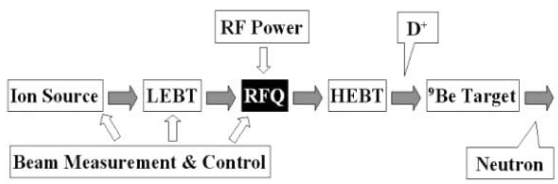

Figure 2: Scheme of the accelerator subsystem.

RFQ CAVITY DESIGN

The RFQ beam dynamics design has been performed with PARMTEQM using the LANL Four Section Procedure[6], but the beam loss is more than the expectation. In order to improve the beam transmission efficiency, two optimization concepts were combined in the new design: (1) the variation of the focusing parameter was adjusted along the RFQ to keep a certain ratio between the focusing force and the space-charge force; (2) main beam dynamics parameters' variation

#zhyguo@pku.edu.cn

were adequately smoothed, especially at the critical point between the sections of gentle buncher and accelerator. Those optimization not only reduced the beam loss greatly (Fig. 3) but also shortened the structure length. After the optimization, the transmission rose from 91.0% to 98.5%, and the electrode length reduced from 2.91m to 2.71m[7].

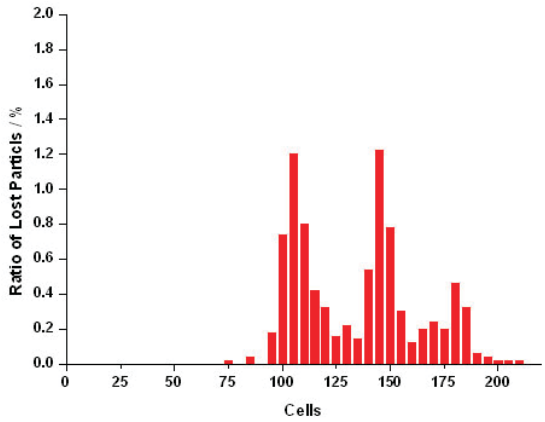

(a) Particle lost when the four section procedure was used

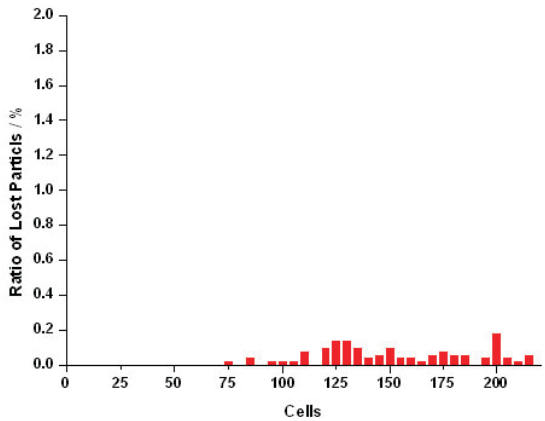

(b) Particle lost after the optimization

Figure 3: Transmission improvement by optimization.

The 4-rod RFQ structure with mini-vanes was designed with Microwave Studio (MWS). To get desired frequency, higher electrode voltage and less power loss, higher and thicker stems were adopted. The frequency and shunt impedance are sensitive to the distance between stems, so it should be optimized, too. Every stem is designed with a suitable balancing slope namely a shortcut to decrease the dipole effect. Most sharp angles inside every stem are chamfered to avoid sparking and decrease power consumption. Fig. 4 shows the designed 4-rod RFQ structure.

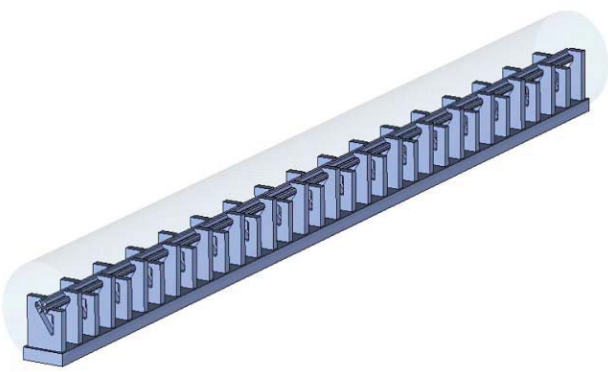

Figure 4: Four-rod RFQ structure designed with MWS.

RF TRANSMITTER

The scheme of RF transmitter is shown in Fig. 5. The 201.5 MHz RF signal is modulated by a PIN modulator, then input to a broad band solid state amplifier, which can give 1 kW RF output. The front stage power amplifier uses a FU-113 tube, which can deliver 20 kW peak RF power. The final power amplifier uses TH-781 tetrode, and its peak RF output power can reach 400 kW. Both front and final power amplifiers are modulated by a pulsed modulator. The PIN modulator and pulsed modulator are controlled by a timer, which generates 0.3 – 1 ms tunable square wave pulse signal with the frequency of 100 – 160 Hz. The 400 kW circulator has an insert loss less than 0.5 dB.

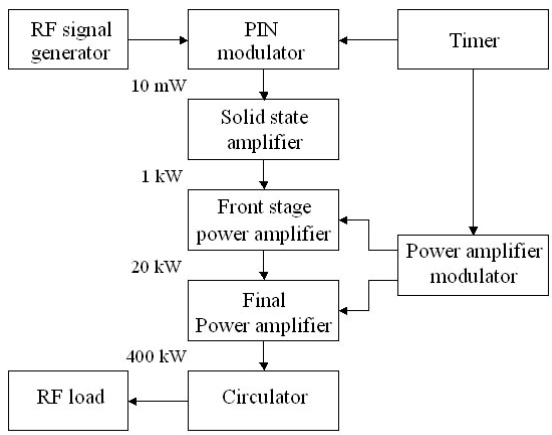

Figure 5: Scheme of the RF transmitter.

ION SOURCE AND LEBT

The deuteron ions are generated by a 2.45 GHz ECR ion source, but the axial magnetic field in the source is a bit higher than the ECR value. A prototype of the ion source with NdFeB permanent magnet rings has been developed. The outer diameter of the source body is 100 mm, and the length is 100 mm, too. The diameter of the discharge chamber is 50 mm, and the total weight is less than 5 kg (Fig. 6). The ion source can be run in either DC or pulsed mode. With pulsed mode more than 100 mA peak current of proton beam can be extracted, the proton ratio is about 80%, and the normalized rms emittance is less than 0.2 π mm.mrad.

A test bench is being set up to investigate the magnetic solenoid performance, space charge compensation and the entrance match of RFQ. A high current ion beam emittance measurement unit has been constructed, too.

Figure: 6 ECR ion source on the test bench.

CONCLUSIONS

A 201.5 MHz 2 MeV deuteron RFQ accelerator has been designed to fit the 400 kW peak RF power. Its transmission was greatly improved by optimization, and its 4-rod mini-vane RF structure was carefully designed. The studies on ion source, LEBT and RF transmitter are in progress. The whole accelerator is expected to give high current deuteron beam for neutron generation in the near future.

REFERENCES

[1] Gillespie GH, McMichael GE, Applications of MeV proton and deuteron linear accelerators. Proc. PAC95, p107.

[2] J. Hall et al., Development of high-energy neutron imaging in support of NDE applications, 3rd Working Group 1 Meeting of COST-Action 524, Munich, Germany, Sept. 13, 2001.

[3] R.W. Hamm et al., Characterization of a variable energy deutron RFQ system for neutron production, Proc. Linac98, p1010.

[4] D.V. Baxter et al., LENS, a university-based pulsed cold neutron source for research and education, 16th Meeting of the International Collaboration on Advanced Neutron Sources, Duesseldorf-Neuss, Germany, May 12-15, 2003.

[5] M.R. Hawkesworth, Neutron radiography: Equipment and Methods, Atomic Energy Review 15: 169-220, 1977.

[6] C. Zhang et al., Design of a high current RFQ for neutron production, Nucl. Instru. and Meth., A 521: 326-331, 2004.

[7] C. Zhang et al., Investigation on Beam Dynamics Design of High-Intensity RFQs, Linac2004.

HIGH CURRENT RFQ USING LASER ION SOURCE

M. Okamura, R. A. Jameson, J. Takano, K. Yamamoto, RIKEN, Saitama, Japan

H. Kashiwagi, JAERI, Gunma, Japan, T. Hattori, N. Hayashizaki, TIT, Tokyo, Japan

A. Schempp, R. Becker, IAP, Goethe-Universität, Frankfurt, Germany

Y. Iwata, NIRS, Chiba, Japan, T. Fujimoto, S. Shibuya, AEC, Chiba, Japan

Abstract

A new RFQ was built for demonstrating a capability of the "Direct Plasma Injection Scheme". After a few months commissioning period, we could obtain 50 *mA* of Carbon beam from the RFQ. This new heavy ion production scheme could be applied to Cancer therapy facilities and high energy nuclear physics accelerator complexes.

INTRODUCTION

Recently, high current and highly charged state heavy ion sources have been studied intensively in the world. Electron Beam Ion Source (EBIS), Laser Ion Source (LIS) and Metal Vapour Vacuum Arc ion source (MEVVA) are typical sources in this category. Among them, we focused on high brightness of induced plasma in LIS and have studied how to utilize the high density of plasma ablated from solid material.

The plasma is produced by a laser shot on the target and is expanded adiabatically normal to the target surface, with energy of a few hundred *eV*. In the established type of LIS, the plasma drifts with about 100 % momentum spread until obtaining the desired pulse period and then reaches an extraction electrode followed by Low Energy Beam Transport line, LEBT. In order to get about 10 μs of the pulse length, the plasma has to be drifted about 2 *m*. As a result, a solid angle captured by the extraction electrode is very small relative to an emitted angle of the ablation plasma. In addition, we had difficulty overcoming the space charge effect in the LEBT due to highly charged state, voltage limitation in the extractor and relatively higher current compared to standard ion sources, like Electron Cyclotron Resonance (ECR) ion sources.

To prevent the beam loss in the LEBT and take the advantage of the density of the laser plasma, Direct Plasma Injection Scheme (DPIS) has been developed. In general recipe, the beam being injected to an RFQ has to be focused. This scheme is not only for acceptance matching but also having a large beam size in the LEBT to prevent the beam loss caused by the space charge effect. In case of DPIS, we do not need to obey this strategy, because enough injected beam intensity into the RFQ can be achieved even if using diverging injection beam. The diverging beam has a large emittance, but enough beam is accepted by the RFQ. The space charge effect can be neglected during transportation from the source to the RFQ entrance, because the plasma is induced in the box directly attached to the RFQ and the ions fly from the target to the entrance of the RFQ with neutralized plasma state. Moreover the ion source part can be made extremely compact. There are no magnetic or micro wave devices and all the power for ionization is fed by laser light.

Since 2001, we have had experiments to verify the DPIS using an existing RFQ in TITech, Tokyo. Obtained maximum current of Carbon beam was 9.2 *mA* and this value agreed well with our simulation[1]. Upon this experience, we decided to construct a new RFQ to achieve higher current using the DPIS. We believe this new technique will impact the heavy ion accelerator field.

THE NEW RFQ FOR HIGH CURRENT HEAVY ION BEAM

In order to demonstrate the intrinsic performance of the DPIS, the new RFQ was constructed at Institute for Applied Physics, Goethe University, Frankfurt. This RFQ was designed to accelerate Carbon 4+ and 6+. A goal current was set to 100 *mA* with C^{4+}. Operation frequency was chosen as 100 *MHz* by availability of an RF amplifier system. The resonant structure is the 4 rod type, which is well established in IAP and suited for this frequency region and low duty factor operation. It has a reasonably small diameter, and the field distribution is easy to tune. Also it is not difficult to replace vanes in future modification. Total vane length was decided as 2 *m* considering future modification however output beam energy is 100 keV/u limited by a radiation safety regulation. The beam is accelerated up to 100 keV/u within first 1.42 *m* section and then transported through un-modulated vanes to the end of the RFQ. In the un-modulated section, the accelerated beam is completely de-bunched and this will help to reduce space charge effect in an analyzing section, which will be constructed in the near future. The input energy of the beam is a very important value, because in DPIS a high voltage biased slit is located at the entrance of the RFQ and might cause discharge. Part of the very high intensity plasma is guided through the several mm diameter hole in the biased slit and enter the RFQ. To minimize the beam size emitted from the hole, the slit needs to be close to the vanes. At

the same time, we have to avoid sparking and an effect on the resonant cavity. We adopted 60 *KV* as total input beam energy based on our experience. In case of C^{4+}, the value corresponds to 20 *keV/u* as the injection energy. The position of the slit can be adjusted. A picture and summarized design parameters of the RFQ are shown in Fig. 1 and Table 1 respectively. The vane parameters of the RFQ were designed to maximize beam acceptance. These parameters are indicated in Fig. 2. To confirm the particle dynamics in the RFQ, PteqHI was used. This code was developed by one of authors and can simulate multiple charge states simultaneously.

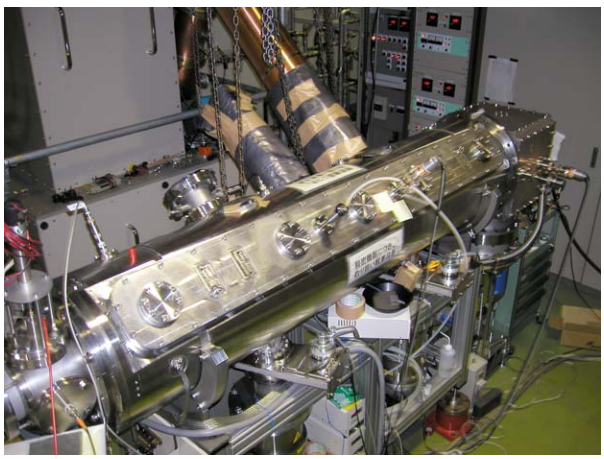

Figure 1: 100 MHz RFQ.

A cube box behind the RFQ is the ion source.

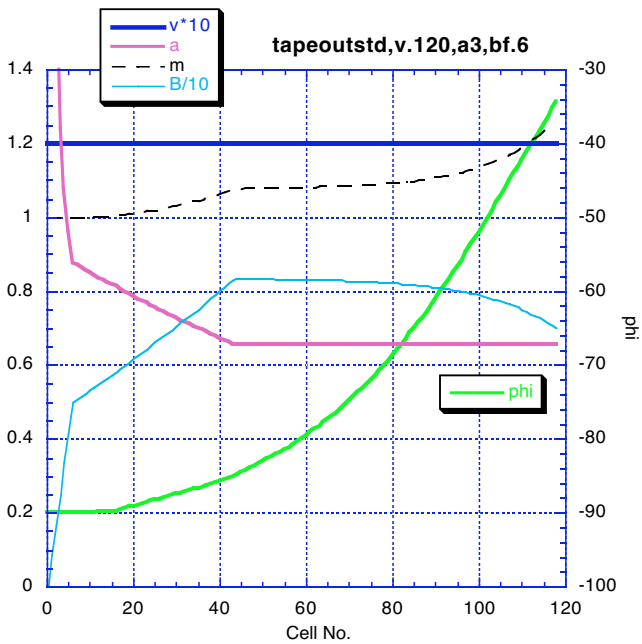

Figure 2: Vane parameters of the RFQ.

Table 1 : Basic design parameters of the RFQ

Frequency	100 MHz
Total length	2.0 m
Modulated vane length	1.42m
Limit of intervane voltage	120 kV
I_{out} at 100 mA C^{4+} in	76 mA
Saturated I_{out}, C^{4+} only	155 mA
I_{in} for saturated I_{out}	~300 mA
Acceptance	0.14 cm.rad
Aperture	0.655 cm (βλ/3)

LASER SYSTEM FOR PLASMA PRODUCTION

We have been investigating two types of laser system for plasma production. Currently a CO_2 laser is used for our experiment. The maximum output energy of the CO_2 laser is 8 J, however emitted energy to the carbon target was measured as 1.2 J with 85 ns (FWMS) of pulse width. Our plasma measurement experiment shows that this condition of the laser system produce mainly C4+ (50 %) and rest of the ions comprised with C5+ (35 %) and C3+ (15%). We can assume that these three charged states ions are injected to the RFQ. We also measured the property of the plasma induced by a Nd-YAG laser system. This laser has output energy of 300 mJ and can produce mainly C6+ (50 %). This laser system is now planed to be used in next DPIS experiment. The measured result also shows that the Nd-YAG laser plasma also can provide enough beam current to the RFQ.

PLASMA TARGET CHAMBER

Ion source parts, including the plasma production solid target and the space which will be filled by the ablated plasma, have to be isolated electrically and kept at high voltage which corresponds to the beam injection energy of the RFQ. 60 kV is applied to the ion source part and this voltage is too high to insulate in the air condition. Therefore, high voltage parts are located in a vacuum box as shown in Fig. 3. The high voltage connector is at the bottom of the TEFLON sleeve that is 30 cm long, and a cable from the high voltage power supply is inserted to the sleeve. The high voltage parts are not shown from outside of the vacuum box. As we mentioned all the fed energy to the plasma is provided by laser shot. This means that both a large terminal stage and safety fence are not needed and the ion source part can be made extremely compact and simple. Behind the vacuum box, laser beam is injected through double NaCl windows and guided to the high voltage region. A concave mirror reflects and focuses the laser beam on to the Carbon target. Then plasma is induced and expanded towards the RFQ. Finally the expanding plasma which can be

accommodated by the high voltage slit is injected to the RFQ.

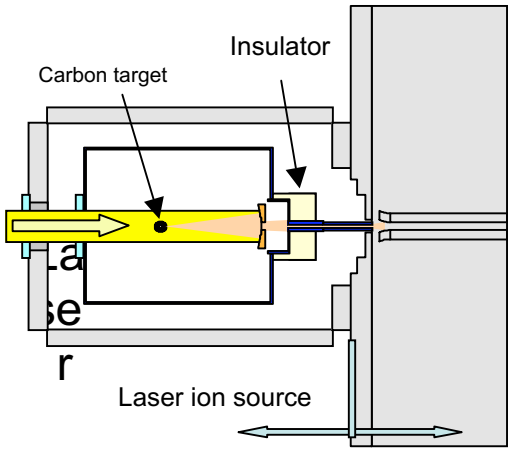

Figure 3: Target Chamber.

ACCELERATION TEST WITH CARBON TARGET

We got the first beam in June 2004 after overcoming sparking problem. The measured peak current reached 30 mA with a slit having 4 mm diameter hole. We optimized various parameters for C^{4+} beam and obtained a maximum peak current of more than 50 mA. In this condition, the inner diameter of the slit is 6 mm. A typical beam shape is shown in Fig. 4. This signal was from a Faraday cup just after the RFQ.

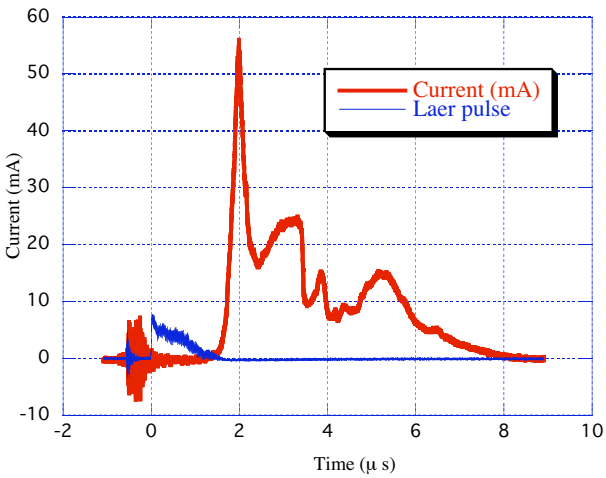

Figure 4: Accelerated beam out of the RFQ.
Red: Current measured by a Faraday Cup after the RFQ.
Blue: Laser pulse shape.

The input current and emittance have not been measured. At the C^{4+} peak, estimates indicate that with a 4 mm extraction slit, ~100 mA with emittance ~0.45 cm.rad enters the RFQ. The RFQ simulation then shows that ~40% is transmitted. With the 6 mm extraction slit, ~200 mA with emittance ~0.6 cm.rad enters the RFQ and ~25% is transmitted. The input estimates are in accord with our analysis of the effect of the dc field in the entrance region of the RFQ. Also, in this regime, output current saturation is expected.

APPLICATION OF THE DPIS

The DPIS can provide intense heavy ion beam efficiently and easily. We expect there will be various applications. Here we emphasize typical applications.

Cancer Therapy

Carbon beam is used in a cancer therapy facility like NIRS. We propose to use the intense carbon beam from DPIS in such a facility. The very high current beam can eliminate the necessity for multi turn injection in a synchrotron. Also enough heavy ions can be obtained after collimation to reduce the beam size. These will make magnets smaller. A laser source can easily produce fully stripped Carbon beam. A contamination of the carbon beam, which is frequently pointed out as an issue, strongly depends on the purity of the solid target in LIS. We expect that DPIS has an advantage in the contamination, because residual gas is not involved in plasma production process, not like ECR or EBIS. The fully stripped carbon beam can eliminate a stripper foil which is usually placed just before the main ring and enables a lower injection energy of the synchrotron to be adopted. Also it can shorten the length of injector linacs. In our next step the Nd-YAG laser is planned to be used to produce C^{6+} beam.

High Energy Physics Accelerator

The DPIS is also applicable to produce heavier species like lead and gold. These kind of heavy species have not been tested yet, however we believe highly charged high current beam can be obtained easily using an adequate laser system. Especially for injecting to a large size synchrotron, a longer beam pulse might be desired. In the case of a solid laser device, several shots with intervals of a few μs can be emitted sequentially and a long beam pulse can be achieved.

REFERENCES

[1] Scheme for Direct Plasma Injection into an RFQ Linac, M. Okamura et al, LASER AND PARTICLE BEAMS, (2002), 20, 451-454

[2] Nd-YAG laser ion source for direct injection scheme, H. Kashiwagi, et al, Review of Scientific Instruments, 75-5 (2004) 1569-1571

TEST AND FIRST EXPERIMENTS WITH THE NEW REX-ISOLDE 200 MHZ IH STRUCTURE*

T. Sieber#, CERN, Geneva, Switzerland
D. Habs, O. Kester, LMU, Garching, Ludwig Maximillian Universität, Physics Department

Abstract

For the REX-ISOLDE accelerator, a new accelerating structure is at the moment installed and tested. It will raise the final energy from the present 2.3 MeV/u to 3 MeV/u. The aim is to increase the mass range of the nuclei available for nuclear spectroscopy from mass 40 to mass 80. The new accelerator component is a 0.5 m IH-structure, working at the double REX frequency of 202.56 MHz. It was originally developed as a 7-Gap resonator for the MAFF [1] project and later adapted to the requirements at REX by changing from a 7-Gap to a 9-Gap resonator to match the lower injection energy. We present the design of the resonator and the results of the rf-tests, commissioning and first operation during the 2004 running period.

INTRODUCTION

In order to make a wider range of isotopes from ISOLDE/CERN available for nuclear physics experiments at REX-ISOLDE [2], an energy upgrade of the REX accelerator has been proposed. It was decided to do the upgrade in two separate steps (see fig. 1). The first step – increasing the energy from the previous 2.3 MeV/u to 3 MeV/u – was recently achieved by installing an additional IH 9-gap cavity in the REX beam line. The second step includes major changes in the setup of the machine By replacing two of the existing 7-gap resonators with a 1.5 m IH structure, the energy will be raised from 3 MeV/u to ~4.2 MeV/u. Since this energy is beyond the limits of several currently installed beam optics elements, a redesign of the high energy beam transport is required at the same time.

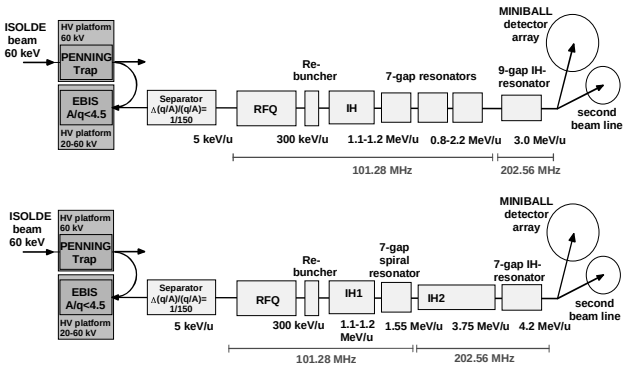

Figure1: Upgrade of the REX-ISOLDE Linac.

For the MAFF project a design has been worked out for two identical short 7-gap IH structures, providing the desired energy variation for the MAFF-Linac. The main advantage of this accelerator type compared to the split-ring resonators of REX-ISOLDE lies in the higher shunt impedance, allowing a variation of the final energy over a comparatively wide range (3.7 – 5.9 MeV/u) with only two short cavities. Since acceleration and deceleration must be possible to cover this energy range, the particle dynamics design at MAFF was very similar to the 7-gap resonators of REX-ISOLDE, which means constant gap lengths and a synchronous phase defined by the phase the particles experience in the middle gap.
In the first design for the REX 3MeV/u upgrade, it was foreseen to change the MAFF resonator from a 7-gap to a 9-gap resonator – keeping a constant cell length, corresponding to 2.5 MeV/u synchronous particle energy. Nine gaps were necessary to match the lower injection energy of 2.2 MeV/u instead of 3.7 MeV/u. However, measurements at the Tandem accelerator of the Maier-Leibnitz Laboratory in Garching showed that this gap geometry leads to a rather low transit time factor [3]. Thus the drift tube geometry was changed to a $\beta\lambda/2$ profile for fixed input and output energies. Table 1 shows the geometry and rf-parameters of the resonator.

Table 1: Resonator parameters of the 9-gap IH-cavity

	IH 9gap
Frequency [MHz]	202.56
outer tank length [mm]	676
inner tank length [mm]	520
half shell radius [mm]	145
cell length [mm]	38.5 – 58.5
gap length [mm]	19 - 27
drift tube length [mm]	32
drift tube diameter in./out. [mm]	16 / 22
maximum rf-power [kW]	100
duty cycle [%]	10
Kilpatrick	1.5
shunt impedance (pert.) [MΩ/m]	218
Q_0	10100

The above 9-gap design includes a smaller diameter of the drift tubes compared to the original 7-gap structure to keep the resonant frequency at 202.56 MHz. The gap voltage distribution used for the LORASR simulations

*work supported by the BMBF and the DFG, # Thomas.Sieber@cern.ch

was calculated with MAFIA and verified first on a 1:1 copper model and later on the power resonator.
Figure 2 shows the resonator after installation in the REX beam line, before the lead shielding was installed.

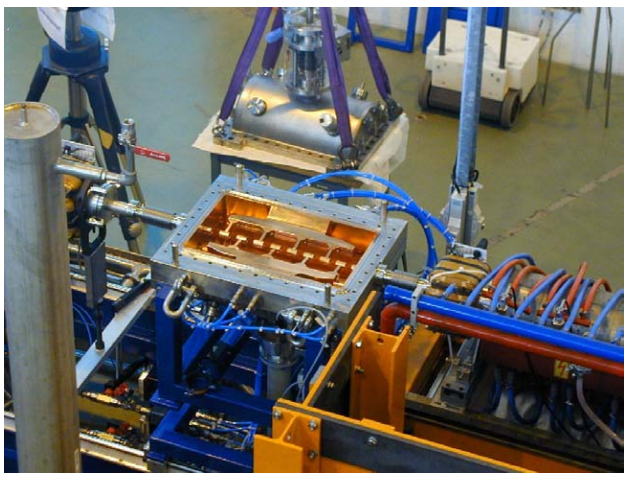

Figure 2: Open tank of the IH 9-gap accelerator, installed in the REX beam line.

BEAM DYNAMICS CALCULATIONS

The input for the LORASR simulations is delivered by the original LINAC design calculations for the 7-gap resonators, which were verified in detail during the commissioning phase of REX-ISOLDE [4]. The main goal of the calculations (after having once fixed the drift tube geometry) was to find out to what extend the structure is still energy variable, even if it has a design for a fixed input and output energy. Due to the short length and the small number of gaps as well as the relatively high injection energy, one can expect that the beam quality and transmission after the 9-gap resonator are much less sensitive to changes in the accelerating voltage than it is found in long IH structures at lower energies.

The design injection energy produced by the 7-gap resonators is 2.25 MeV/u at a phase spread of ± 15° (after 1.3m drift) and at an energy spread of ± 0.45 %. Transversely, the beam is injected with an emittance of $\varepsilon_{n,x,y}$ = 1.4 π mm mrad in both planes convergent, whereby only slightly converging beams led to the best transmission.

To test the energy variation, the resonator voltage was changed in steps according to the measurements at different rf-power levels. This downscaling of the gap voltages was done – starting from the design voltage at 3 MeV/u - using the pickup values measured at the power levels shown in the diagrams. The spectra in figure 3 show that the transmission as well as the energy spread stay in a reasonable range down to an output energy of 2.55 MeV/u. With this result (which could be verified during the measurements shown below) the REX accelerator becomes continuously energy variable over a range from 0.8 MeV/u to 3 MeV/u.

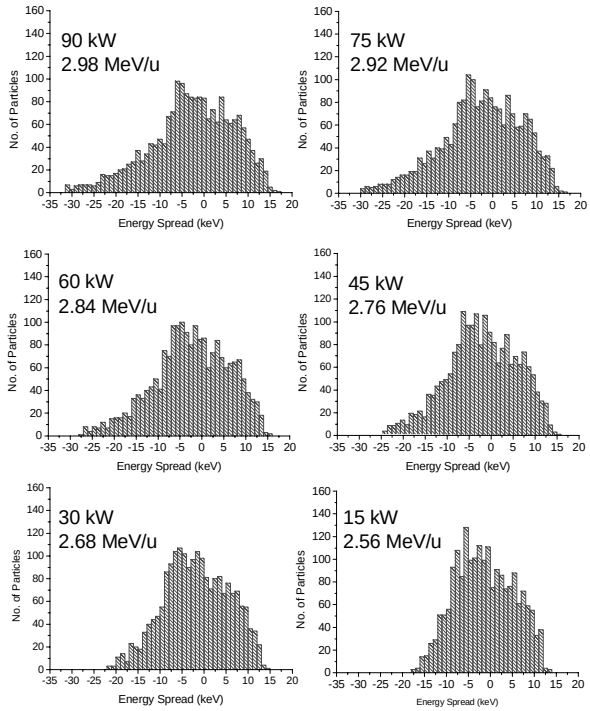

Figure 3: Energy spectra at different acceleration voltages.

The calcuated transit time factors in the fifth gap – which is taken here as a reference - always stay between 0.855 and 0.865. The good flexibility in output energy of the accelerator allows a wider range of mass to charge ratios to be available at energies around 3.0 MeV/u, than limited by the currently maximum available rf-power. With an rf-power level limited to 90 kW, the maximum A/q at 3.0 MeV/u is at the moment A/q = 3.5. Thus, during the first runs with radioactive ions, compromises could be found, like e.g. accelerating $^{76}Zn^{20+}$ ions (A/q = 3.8) at 90kW to ~2.9 MeV/u. Table 2 shows the calculated parameters of the 9-gap resonator for regular operation at 3 MeV/u and for the variable energy.

Table 2: Design parameters of the 9-gap IH-cavity

	IH 9gap
input energy [MeV/u]	2.2
output energy [MeV/u]	2.55 - 3.0
energy spread [%]	1.0 – 1.6
phase spread [°]	25
transmission [%]	100
TTF on axis in gap No. 5 (2.55 – 3.0 MeV/u)	0.855 – 0.866
maximum A/q (90kW)	3.5
radial acceptance $\alpha_{x,y,norm}$ [π mm mrad]	1.4

BEAM TESTS

From the low level measurements and LORASR calculations we expected for the IH structure an effective shunt impedance of 163 MΩ/m. An energy gain of 0.75 MeV/u requires for ions with A/q = 3.5 an effective acceleration voltage of 2.63 MV, which corresponds at the given shunt impedance and structure length to an rf-power of 85 kW. We therefore performed the tests with a N^{4+} residual gas beam from the REXEBIS. The injected current was in the range of 50 pA in the beginning and went down to ~10 pA because of the slits in front of the energy spectrometer, which were used to reduce the emittance influence on the energy spectra. Figure 4 shows the measured spectra.

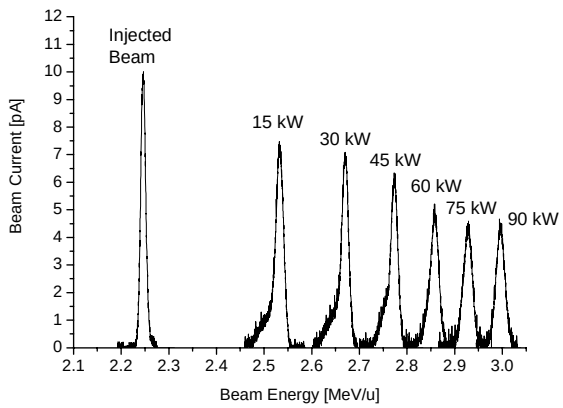

Figure 4: Energy spectra measured with a A/q = 3.5 beam.

The measured final energies are in good agreement with the calculations. The decrease of the beam current at higher energies occurs because the beam transport was optimized for a parallel 2.25 MeV/u beam through the spectrometer instead of a convergent injection into the 9-gap. With an optimized injection and a beam transport scaled to the different energies, the transmission was close to 100 %.

The energy peaks at lower power levels show a tail towards the low energy side, which might be the result of a slightly wrong injection phase. However, the FWHM of the peaks correspond remarkably well to the design calculations.

Calculating the effective shunt impedance for an effective acceleration voltage of 2.63 MV at 90kW gives a value of η_{eff} = 154 MΩ/m. With an average transit time factor of 0.865 we derive a shunt impedance of η = 205 MΩ/m. If the decrease of the shunt impedance at higher power levels due to the heating of the resonator is taken into account, this value fits nicely to the η = 218 MΩ/m from perturbation measurements.

CONCLUSION

With the successful test and first operation during nuclear physics experiments, the first stage of the REX-ISOLDE energy upgrade has become reality. At the same time it could be shown that the REX-LINAC is still fully energy variable from 0.8 MeV/u up to the final energy of now 3.0 MeV/u. To increase the maximum A/q of the ions at 3 MeV/u, work is under progress to reach the nominal rf-power of 100 kW. In parallel we will investigate the possibility of increasing the injection energy.

REFERENCES

[1] H. Bongers et al., The IH-7-Gap Resonators of the Munich Accelerator for Fission Fragments (MAFF) Linac, proceedings of the PAC2001, Chicago, June 2001, p.3945

[2] O. Kester et al., Status of REX-ISOLDE, this conference

[3] O. Kester et al., An Energy Upgrade of the REX-ISOLDE Linac, PAC'2003, Portland, Oregon, USA, May 2003, p.2869

[4] S. Emhofer et al., Commissioning results of the REX-ISOLDE LINAC, PAC'2003, Portland, Oregon, USA, May 2003, p.2872

STATUS OF THE RFI LINAC PROTOTYPE*

D.A. Swenson and W.J. Starling, Linac Systems, Albuquerque, NM 87109, USA

Abstract

A prototype of the Rf Focused Interdigital (RFI) linac structure is currently under construction at Linac Systems. The RFI linac structure is basically an interdigital (or Wideröe) linac structure with rf quadrupole focusing incorporated into each drift tube. The 200-MHz RFI Prototype, consisting of a short RFQ linac followed by a short RFI linac, will accelerate a 20-mA beam of protons from an injection energy of 25 keV to an output energy of 2.50 MeV in a total linac structure length of 1.44 meters. The linac structures are designed for continuous (cw) operation, and will be tested initially at a 33% duty factor. The peak structure power of 66 kW and peak beam power of 50 kW will be supplied by a 144-kW, 33% duty rf power system. A microwave ion source will supply the proton beam and an articulated Einzel lens will steer and focus the beam into the RFQ aperture. The mechanical design of the linac structures will be presented, the calculated performance will be described, the status of the components will be reported. The prototype is scheduled to come into operation in the fall of this year.

THE RFI PROTOTYPE

The Rf Focused Interdigital (RFI) linac structure[1,2] represents an effective combination of the Wideröe (or interdigital) linac structure, used for many low frequency, heavy ion applications, and the rf electric quadrupole focusing used in the Radio Frequency Quadrupole (RFQ) and Rf-Focused Drift tube (RFD) linac structures[3,4]. As in the RFD linac structure, rf focusing is introduced into the RFI linac structure by configuring the drift tubes as two independent pieces operating at different electrical potentials as determined by the rf fields of the linac structure. Each piece (or electrode) of the RFI drift tube supports two fingers pointed inwards towards the opposite end of the drift tube forming a four-finger geometry that produces an rf quadrupole field along the axis of the linac for focusing the beam.

The RFI linac structure is two-to-six times more efficient and three times smaller in diameter than the conventional Drift Tube Linac (DTL) structure in the energy range from 0.75 to 12 MeV. It is ten times more efficient than the RFQ linac structure in the 0.75 to 6 MeV range. This high efficiency reduces the rf power dissipation in the rf structures and the problems associated with cooling them, thereby promoting the prospect for cw operation, which in turn, allows large increases in the average beam currents. This linac structure promises to have significant size, efficiency, performance, and cost advantages over existing linac structures for the acceleration of low energy ion beams of all masses (light to heavy).

An operating prototype of the RFI linac structure, shown in Fig. 1, is under construction at Linac Systems. The RFI Prototype will be designed for an output energy of 2.5 MeV and an output current of 20 mA. It is designed for both pulsed and cw operation. This prototype will serve to verify the performance of the RFI linac structure and demonstrate its capabilities.

The RFI Prototype consists of a microwave ECR ion source, a low energy beam transport (LEBT) system, an RFQ linac section, an RFI linac section, a short beam diagnostics section, an rf power system, a vacuum system, a cooling system, and a computer control system.

ION SOURCE

A 2.45-GHz Microwave Ion Source, similar to the IUCF Ion Source[5], a lower current derivative of the LEDA Ion Source[6], is under construction[7] for the RFI Prototype. The source is designed for a peak proton current of 30 mA at 25 keV, and can be operated in either a continuous (cw) mode or a pulsed mode, with pulse lengths adjustable from 10 to 100 μs and repetition rates adjustable from 10 to 3000 Hz. The magnetic field is supplied by two water-cooled 15,000 A-turn solenoid magnets. The microwave power is adjustable up to 800 W and is capable of cw or pulsed operation.

The performance of the source was analyzed and optimized to the desired parameters with the PBGUNS

Figure 1: The 2.5 MeV, 20 mA RFI Prototype.

* Supported by the U.S. Dept. of Energy.

code. The extraction geometry consists of four elements, namely a plasma electrode, a puller electrode, an electron suppressor electrode, and a final ground electrode. The extraction aperture is 7 mm in diameter and all four electrodes are conical with a cone angle of 56 degrees from the axis. A steel flange is mounted close to the source exit to limit the extent of the magnetic field along the beam path.

LEBT

The LEBT is based on a single articulated Einzel lens. The total distance from the ion source extraction aperture to the RFQ entrance aperture is 24.2 cm. The length and aperture of the Einzel lens electrode are 6.3 cm and 6.6 cm respectively. This electrode is centered about two thirds of the way from the ion source aperture to the RFQ aperture and mounted on a 3-axis stage controllable manually through the side of the LEBT vacuum tank. The range of motion is ±5 mm in the two transverse directions and ±20 mm in the longitudinal direction. The transverse motions will be used to steer the beam into the RFQ aperture. The lens voltage and longitudinal motion will be used to optimize the capture of the beam by the RFQ linac.

The 3D beam dynamics code, SCALA[8], and the 2D beam dynamics code, AXCEL, were used to analyze and optimize the performance of the LEBT. Both codes gave similar results, where the beam reaches a diameter of about 5 cm inside the Einzel lens. This arrangement suggests the capture and transmission of about 84% of the 30-mA beam from the ion source through the RFQ linac.

RFQ LINAC

The RFQ linac for the RFI Prototype is of the four-bar type. It will capture and bunch the ion beams from the ion source and accelerate them to a suitable energy for acceptance by the RFI linac. Because of the exceptional low-energy capabilities of the RFI linac structure, the RFQ linac section need only accelerate the beam to an energy of 0.75 MeV.

We have chosen to employ a radial strut design, where the individual bars are supported by radial struts emanating from the walls of the cavity with four-pole symmetry. The RFQ linac structure is mounted inside a vacuum tank that provides the high-vacuum conditions required by the beam, the rf power, and the linac structure. The RFQ vacuum tank is pumped by a 400 l/s turbomolecular vacuum pump and typically operates in the 5×10^{-7} Torr range.

The bore radius is 3.6 mm. The rf cavity inner diameter is 256 mm and a strut spacing of 160 mm results in a resonant frequency of 200 MHz. The rf dipole mode for this configuration is several MHz above the quadrupole mode and does not present a problem with rf field stability.

The rf efficiency of the RFQ is expressed in terms of a transverse shunt impedance, Z_{TR} (MΩ-m), defined as V^2/P_L, where V is the bar-to-bar voltage and P_L is the rf power per unit length in the structure. The shunt impedance of the radial strut design is 0.12 MΩ/m, about twice the value of conventional four-bar RFQs.

RFI LINAC

The RFI linac section is designed to operate at 200 MHz and accelerate the beam from 0.75 MeV to 2.5 MeV. It is 0.54 m long and involves 13 unit cells, ranging in length from 3.1 to 5.4 cm in length. In general, the inner radii of the cells must increase with energy to maintain resonance. However, the tank termination scheme requires the radii of the first two and last two cells of a tank to be increased to achieve a flat field distribution in the vicinity of the tank terminations.

The two-part drift tubes of the RFI structure comprise a minor piece (upstream) supported on a minor stem and a major piece (downstream) supported on a major stem, each with two fingers that form a four-finger geometry, which when excited with rf energy produces an rf quadrupole field along the axis for focusing the beam. In order to excite the four-finger geometries, it is necessary to couple to some of the longitudinal rf magnetic fields in the structure. This requires the minor stems be offset to one or both sides of the major stems. For symmetry and mechanical rigidity, we choose a minor stem geometry that extends symmetrically on both sides of the major stem.

We have adopted a radial stem approach, where the minor stems are essentially radial members extending from the tank wall, and offer unlimited coupling (from 0% to nearly 100% of the cell voltage) to the magnetic fields of the structure. We have adopted what we call the "Stacked Cell" approach, shown in Fig. 2, where the basic unit of the structure is a single cell, complete with a two-piece drift tube, supported by major and minor stems in a short section of the outer wall. The linac structure is assembled by stacking up a sequence of these cells, each with the proper dimensions. The stack is held together by tie-bolts running along the structure or by welding the cells together into a single unit as shown also in Fig. 2. The 13 unit cells for the RFI Prototype are nearing completion.

RF POWER SYSTEM

The peak rf power requirement for the 2.5-MeV, 20-mA RFI Prototype is 122 kW. The rf power system, currently under construction[7], will be capable of producing a pulsed output of 192 kW at 25% duty, a pulsed output of 144 kW at 33% duty, or a cw output of 48 kW. This will allow testing of both the RFQ and RFI linac sections, independently, at full power and duty without beam, and running the combination, complete with 50 kW of beam, at a 33% duty cycle.

The final power amplifier (FPA) for this system is based on the same parallel planar triode concept used in the rf power system for our previous prototype of the RFD linac structure at 600 MHz. This time we will use GB-35B planar triodes, which are rated for operation as high as 1000 MHz and have an anode power rating of 2.5 kW in water-cooled operation. The basic configuration involves a total of 24 tubes, in two 12-tube arrays, in a push-pull configuration, driving a double-ended output cavity. The tubes in each array are attached to separate heat sinks in each end of the double-ended output cavity.

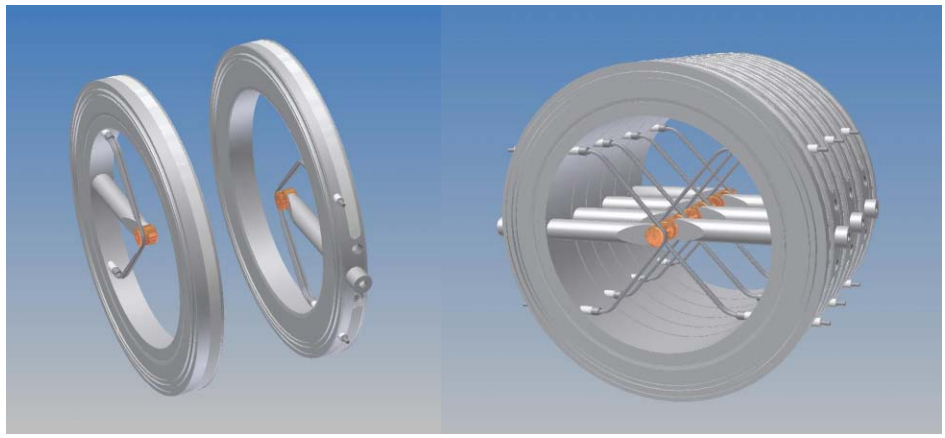

Figure 2: The "Stacked Cell" Approach to RFI Linac Fabrication.

The intermediate power amplifiers (IPAs) will use the same GB-35B tubes. The first unit (IPA1) uses a single tube. Its output will be split two ways to drive two additional intermediate power amplifiers (IPA2). Each two-tube IPA2 amplifier will drive one ring of 12 tubes in the FPA. A phase shifter in one of the IPA2 inputs will provide the 180° phase shift required for push/pull operation.

The IPA2 and FPA tubes will operate at 4 kV for cw operation and at 8 kV for pulsed operation. The dc power supply will be configured as a multiplicity of 1 kV units, each with an insulated gate bipolar transistor (IGBT) series switch. The 1-kV units will be series connected as two 4-kV supplies for 48 kW cw or pulsed operation, or series connected as one 8-kV supply for 144 kW pulsed operation. The IGBT switches will eliminate the need for crowbar switches to protect the equipment. In the event of a load fault, current sensing circuitry in the IGBT control logic will turn off the IGBT switches so rapidly that the peak rating of the devices are not exceeded.

COOLED FOR CW OPERATION

The RFQ and RFI linac structures are designed for CW operation. In this mode, the total rf power dissipation in the RFQ is 40 kW and the total rf power dissipation in the RFI is 26 kW. Both structures are cooled by a large number of parallel cooling circuits. The total coolant flow through each structure is independently controlled by a throttle valve.

The RFQ consists of a cylindrical rf cavity and four bar assemblies, each supported on five struts. Thirty percent of the power (12 kW) is dissipated on the cylindrical body of the structure, while the remaining power is dissipated on the four bar/strut assemblies (7 kW per bar/strut assembly). There are 8 cooling channels bored through the length of the cylindrical body. The average power associated with each of these cooling channels is 1.5 kW. There are 5 cooling circuits in each bar/strut assembly. The average power associated with each of these cooling circuits is 1.4 kW.

The RFI consists of 13 unit cells, each with three separate cooling circuits, namely the cell wall, the major stem/drift tube assembly, and the minor stem/drift tube assembly. Fifty-four percent of the power is dissipated on the cell walls for an average of 1.2 kW per unit cell wall, forty-two percent of the power is dissipated on the major stem/drift tube assembly for an average of 0.9 kW per major stem assembly, and four percent of the power is dissipated on the minor stem/drift tube assembly for an average of 0.1 kW per minor stem assembly.

A pressure of 4.4 psi across the RFQ cooling manifold will push 44 GPM of water through the 28 parallel cooling circuits of the RFQ for a temperature rise of about 2.5 C. A pressure of 1.6 psi across the RFI cooling manifold will push 53 GPM of water through the 39 parallel cooling circuits of the RFI for a temperature rise of about 2.0 C.

REFERENCES

[1] D.A. Swenson, "An Rf-Focused Interdigital Linac Structure", 2002 Intern. Linac Conf., Korea, 2002.
[2] D. A. Swenson, "An Rf Focused Interdigital Ion Accelerating Structure". CAARI Conf., Denton, TX, 2002.
[3] I.M. Kapchinskiy and V.A. Tepliakov, Prib. Tekh. Eksp. 2, 19-22 (1970) & 4, 17-19 (1970).
[4] D.A. Swenson, "RF-Focused Drift Tube Linac Structure", 1994 Linac Conf., Tsukuba, Japan, 1994.
[5] V.P. Derenchuk, "A Continuous Wave Microwave Proton Ion Source and Low Energy Beam Transport for the IUCF Cyclotrons", RSI Vol. 75(5) pp.1851, May 2004.
[6] L.D. Hansborough, et. al., Proc. 1997 Particle Accelerator Conf., IEEE 97CH37167, 2740(1998).
[7] JP Accelerator Works, http://www.jpaw.com
[8] VectorFields, Inc., http://www.vectorfields.com[1]

SPACE CHARGE COMPENSATION IN LOW ENERGY PROTON BEAMS

A. BenIsmaïl#, R. Duperrier, D. Uriot, CEA Saclay, DSM /DAPNIA, 91191 Gif sur Yvette,
N. Pichoff, CEA Bruyères-le-Châtel, DIF /DPTA, BP12, 91680 Bruyères-le-Châtel, France

Abstract

High-power accelerators are being studied for several projects including accelerator driven neutron or neutrino sources. The low energy part of these facilities has to be carefully optimized to match the beam requirements of the higher energy parts.
In this low energy part, the space charge self force, induced by a high intensity beam, has to be carefully controlled. This nonlinear force can generate a large and irreversible emittance growth of the beam.
To reduce the space charge (SC), neutralization of the beam charge can be done by capturing some particles of the ionised residual gas in the vacuum chamber. This space charge compensation (SCC) regime complicates the beam dynamics study. Modelling the beam behavior in such a regime would be a significant contribution to the development of high intensity accelerators.

INTRODUCTION

In the low energy part of an accelerator, a high intensity beam is space charge dominated. Such a beam can be transported in a neutralization regime using the charge of the ionized residual gas. This regime occurs naturally when the beam propagates through a residual gas. Gas ionization takes place inside the beam and produces electrons and positive ions. For positive beams, electrons are trapped as long as the SC is not fully compensated.

As many experiments show [1], the beam charge is not always fully neutralized. Inside a Low Energy Beam Transport line (LEBT), the time dependent SCC is not necessarily homogeneous in space. These conditions contribute to emittance growth induced by non-linear forces and may lead to particle losses.
The knowledge of such regime is important to predict the optical qualities of the transported beam.

In this paper, we first describe a code CARTAGO for SCC modelization. This PIC code simulates the SCC mechanism during the transient and steady state regimes. We then present a numerical investigation of the SCC behavior for a continuous (DC) and a bunched (AC) proton beam through a drift section.

This work is a part of the theoretical and experimental work for the IPHI project [2].

CARTAGO ALGORITHM

Cartago is a beam dynamics simulation code including the effect of the non linear SCC. The scheme used to simulate the beam and plasma dynamics is composed of four basic parts (Fig.1):

Part1 At each time step, new particles produced by gas ionization are added according to the angular end energy differential cross section [3]. The beam is defined by a particle cloud carrying the main current.

Parts2&3 The charge distribution, is obtained in a 1D mesh (r) with a PIC scheme. The Poisson equation is solved with the grid by integration of the Gauss law. Forces extracted from the resulting potential, are applied to particles via the step by step "leap frog" scheme [4]. This scheme allows to integrate the equation of motion including the SC calculation.

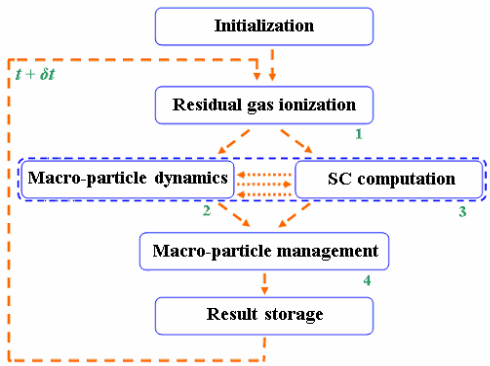

Figure 1: Cartago algorithm.

Part4 The residual gas plasma evolves taking into account the ionization intensity and the extend of the particle losses. This macro-particle system is simulated by using a "chained lists" method [5]. Every particle species is classified on separated lists. The size of each list increases when adding ionized particles, and decreases if some particles are lost on the vacuum chamber walls. Having roughly an idea of the plasma time scale stabilisation [6], and estimating the size for these lists for this moment, we deduce the number of macro-particles generated at every time step. Using this method, we simplify the Read Access Memory management during the computation.

Typical outputs of Cartago are electrostatic field, potential and radial distributions of the studied species. For further information, particle clouds may also be investigated at each time step. The SCC degree at a given azimuth of the beam direction is defined by:

$$\tau(t) = 100 \cdot \left(1 - \frac{\int_0^{r_{beam}} r \cdot \left\| \vec{F}_{SC\_C}(r) \right\| \cdot \rho(r) \cdot dr}{\int_0^{r_{beam}} r \cdot \left\| \vec{F}_{SC}(r) \right\| \cdot \rho(r) \cdot dr} \right), \qquad (1)$$

where $\vec{F}_{SC}$, $\vec{F}_{SC\_C}$ and ρ are respectively SC forces of the initial beam, forces in presence of the SCC and the beam distribution. This SCC degree gives the average reduction of the force acting on the beam. It is 0 if no compensation and 100 if the SC is fully compensated.

#bismail@cea.fr

SCC OF A DC RIGID BEAM

In this section, the study is restricted to a drift region with a 3 cm constant beam radius. The proton beam (95 keV, 100 mA) is uniform, cylindrical and rigid.

The residual gas consists of H_2 molecules at 3.8 10^{-4} hPa and 300 K. We assume that the only source of secondary charges is the gas ionization. The drift radius is 0.1 m.

We studied the SCC of this particular beam during 20 µs. The SCC degree reaches 99% and still increasing very slowly (Fig.2.a). This result gives a good agreement with our expectation. With these beam and gas parameters, ionization dominates all beam-plasma interactions which favours continuously the SCC.

First studies of some other Coulomb collisions show that the SCC degree at the steady state is lower than 100% if we include only the beam-electron Coulomb scattering.

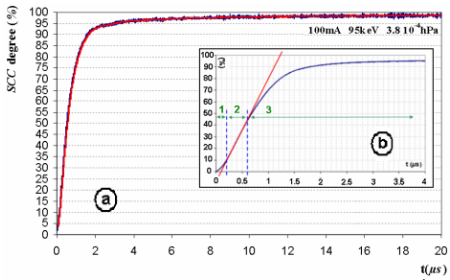

Figure 2: SCC of a rigid beam at 3.8 10^{-4}hPa.

Before reaching the steady state regime, we can divide the SCC transient phase (up to 4 µs) into 3 stages (Fig.2.b).

The stage 1 is characterized by a slow SCC evolution. The ions are not immediately repelled (heavy particles created without initial energy) (Fig.3.a). This point will have an important effect on the bunched beam neutralization.

In the stage 2, the ions are lost at a constant rate. This condition makes the SCC evolution similar to the classical description proposed in [5]. By measuring the second stage slope (Fig.2.b), we find the same value of the SCC time scale (T_{SCC} = 1 µs) as given by:

$$T_{SCC} = (\sigma_i \cdot n_g \cdot v_f)^{-1}, \qquad (2)$$

where v_f (m/s), n_g (m^{-3}), σ_i (m^2) are respectively the beam velocity, the gas density and the ionization cross section.

During the stage 3, the negative charge compensates gradually the positive charge beginning by the beam centre. This particular evolution implies a non linear SC field (Fig.3.c). The emittance growth of a transported beam will depend on the amplitude of this non-linearity.

The hollow electron density (Ne) is due to the fact that each electron gets some orbital kinetic moment at the creation. This gives to the radial electron oscillation an elliptical trajectory and reduces the total electron density near the beam centre [7].

SCC OF A TRANSPORTED DC BEAM

We study in this section the beam transport in a drift section of 0.25 m without longitudinal SC effects. We consider, at the drift entrance, a uniform proton beam (95 keV, 100 mA) with ε_{rms}=0.2 π.mm.mrad the rms normalized emittance. The Twiss parameters are α=-2 and β=1.74 mm/π.mrad (Fig4.a). Gas pressure is 3.8 10^{-4} hPa.

This beam is then transported through the drift section in a time dependent SCC regime.

At the beginning of the simulation, the radial SC force of the uniform beam is linear. The head of the beam propagates then through the drift without emittance growth (Fig.4.b).

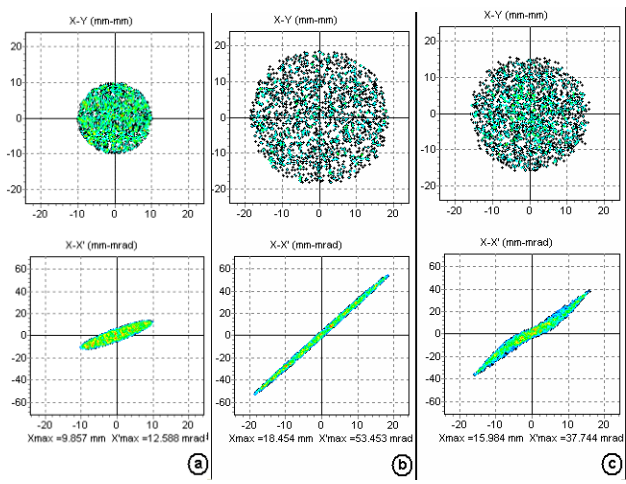

Figure 4: Beam profile and emittance, (a) at the drift entrance, at the drift exit (b) at 58 ns, (c) at 600 ns.

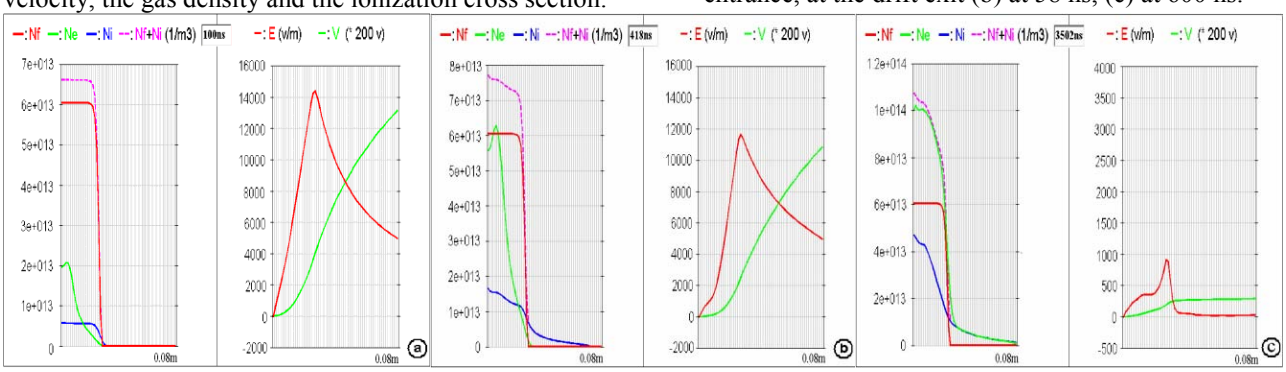

Figure 3: Radial distributions Nf (beam), Ne (electrons), Ni (ions), electrostatic field E and potential V, (a) at 0.1 µs, (b) at 0.4 µs, (c) at 3.5 µs.

When the residual gas is being ionized, the resulting SC force becomes non-linear. This non-linearity is verified, for example at 600 ns (Fig.4.c), when the normalized beam emittance reaches 0.3 π.mm.mrad.

With the same evolution showed in Fig.2.a, SC is nearly compensated at about 10 µs inside the whole drift.

Figure 5 gives the relative emittance growth at the drift exit as a function of the SCC degree.

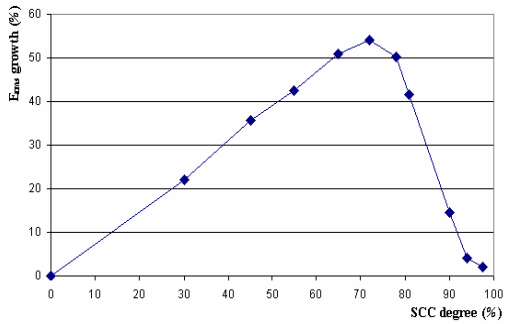

Figure 5: The emittance growth at the drift exit vs. the SCC degree.

When the SC is entirely compensated, the beam transport conditions become similar to the case of linear transport with 0 mA. The emittance of the uniform beam is then conserved inside the whole drift.

SCC OF A BUNCHED BEAM: THE CASE OF THE IPHI MEBT

We study in this section the SCC of a bunched beam using the same parameters of the studied DC rigid beam but at 3 MeV. The bunch length and frequency are respectively 60° and 352 Mhz [2].

At a given azimuth, the electrons see successively the focusing forces induced by the proton bunch, followed by a drift time between bunches. The forces induced by the passage of a bunch have been studied by several authors [8]. Assuming that SC force results only from the beam charge, a criterion for electron stability and accumulation has been established:

$$f_{RF} > (f_{RF})_c = \frac{r_e \cdot u \cdot c}{2 \cdot e} \cdot \frac{I_f}{b^2} \quad , \qquad (3)$$

where u and r_p are respectively the atomic unit mass and the classical electron radius; I_f, b, f_{RF} are respectively the beam current, radius and frequency.

Using only the beam SC, we verified that results obtained by the Cartago code correspond to the stability criterion (Eq.3). The electrons are being accumulated and SC is compensated for frequencies greater than 17.17 MHz.

In the second part of the bunched beam study, we include ions and electrons in the SC computation. The SCC evolution of the bunched beam is showed in figure 6.

The SCC final degree is about 13%. The result is nearly the same at 3.8 10^{-5} hPa, but the rise time is 10 times longer.

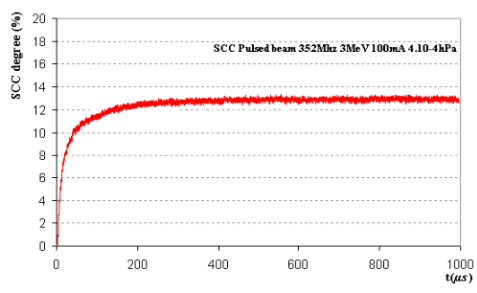

Figure 6: SCC of the bunched beam at 3.8 10^{-4} hPa.

In the particular case studied, the SCC and consequently the beam dynamic become stables after ~0.2 ms. This rise time is important for the commissioning where pulsed beams will be used to tune the machine for the CW regime. It may also be a problem for pulsed machines.

CONCLUSION AND PERSPECTIVES

Numerical investigations of SCC evolution in a drift section have been realized. The study, in the case of a rigid beam, verifies that space charge can be fully neutralized when the ionization is the only effective process. The transient regime study is in good agreement with theoretical expectations [3,6,7].

The emittance growth during the transient regime is computed from the transport of a continuous beam.

Theoretical study of a bunched beam, with some specifics hypotheses [8], successfully compare with numerical results. When including the full SC (beam, e^- and ions), the numerical study shows that the bunched beam SC is partially neutralized after a relatively long rise time.

Special effort is presently made to understand and to introduce other collision processes. To take into account the longitudinal effects, the Poisson solver is being modified. Specific SCC measurements in the IPHI LEBT line are planed this year. They will be compared with Cartago predictions.

REFERENCES

[1] R. Ferdinand, J. Sherman, RR Stevens Jr., and T. Zaugg, "Space-charge neutralization measurement of a 75kev, 130mA H+ beam", PAC97, Canada.

[2] P.Y. Beauvais, "Status report on the construction of the French High Intensity Proton Injector (IPHI)", EPAC 2002, Paris.

[3] X. Fleury, "Modelization and simulation of proton beam space charge compensation", PhD thesis, Polytechnic School – France, June 2000.

[4] W.H. Press et al, "Numerical Recipes", second edition, Cambridge University Press, p.833, 1992.

[5] N. Pichoff, Private communication.

[6] Y. Baconnier, A. Poncet, P.F.Tavares, "Neutralisation of accelerator beam by ionisation of the residual gas", Jyväskylä 1992, CERN 94-10, p. 525.

[7] A. Ben Ismail, "Space charge compensation of high intensity beam", SFP Accelerators Days, Porquerolles, October 2003.

[8] Y. Baconnier and G.Brianti, "The stability of ions in bunched beam machines", CERN-SPS 80-2, 1980.

INVESTIGATION ON BEAM DYNAMICS DESIGN OF HIGH-INTENSITY RFQS

C. Zhang*,#,1,2, Z.Y. Guo[1], A. Schempp[2], J.E. Chen[1], J.X. Fang[1]
[1] Key Laboratory of Heavy Ion Physics at Peking University, Ministry of Education, Beijing, China
[2] Institute for Applied Physics, Johann Wolfgang Goethe University, Frankfurt am Main, Germany

Abstract

Recently various potential uses of high-intensity beams bring new opportunities as well as challenges to RFQ accelerator research because of the new problems arising from the strong space-charge effects. Unconventional concepts of beam dynamics design, which surround the choice of basic parameters and the optimization of main dynamics parameters' variation along the machine, are illustrated by the designing Peking University (PKU) Deuteron RFQ. An efficient tool of LANL RFQ Design Codes for beam dynamics simulation and analysis, RFQBAT, is introduced. Some quality criterions are also presented for evaluating design results.

INTRODUCTION

Started by Kapchinsky and Teplyakov in 1970, the Radio Frequency Quadrupole (RFQ) accelerator has been developed as a kind of standard linear accelerator structure for low energy particles. No matter as injectors of large accelerators or independent facilities, a general tendency in the RFQ research field is to work for high-intensity beams.

Because neutrons have widely important applications e.g. clean nuclear power production, non-destructive detection and cancer treatment, the interest of using high-intensity proton or deuteron accelerators to produce neutrons as secondary particles is increasing in the world. As an essential component of such accelerator-based neutron source projects e.g. SNS, China ADS and IFMIF, the RFQ is expected to greatly improve its performance to satisfy some new severe requirements. For example, very low beam loss is a basic demand to limit the possible induced radioactivity to an acceptable level.

A 50 mA, 2.0 MeV RFQ is proposed for neutron radiography at PKU. In the case of high-intensity beams, two obvious negative influences from strong space-charge effects are defocusing and emittance growth. Therefore, some special considerations and optimization methods are required in the design work.

RFQ beam dynamics design is actually a process of choice and optimization for a multi-parameter system. All parameters could be roughly divided into two groups: (a) basic ones giving the boundary conditions of the design, e.g. frequency; (b) three relatively independent functions namely $a(z)$, $m(z)$ and $\varphi_s(z)$.

CHOICE OF BASIC PARAMETERS

Basic parameters are mainly decided by four kinds of factors: (a) motivations of projects, (b) available resources like funding, equipments and applicable technologies, (c) analysis from the physical standpoint, (d) practical feasibility. In practice, a basic parameter could not be determined independently. A general case is that basic parameters are chosen as the tradeoffs of several or all kinds of factors.

Usually frequency is the first parameter to be chosen. Singly from the beam dynamics, high-intensity RFQs should use lower frequency for stronger focusing strength, which benefits to capture and accelerate higher current beams (Formula (1)).

$$B = \left(\frac{q \cdot V}{m_0 \cdot f^2 \cdot a^2} \right) \cdot \left(\frac{I_0(ka) + I_0(mka)}{m^2 \cdot I_0(ka) + I_0(mka)} \right) \quad (1)$$

where a=aperture, f= RF frequency, I_0=first order Bessel function, k=wave number, m=electrode modulation, m_0=rest mass, q=charge, V=inter-electrode voltage.

However, lower frequency will significantly increase the cavity dimensions consequently the costs, and higher one could lower the charge per bunch, which is advantageous to avoid undesired resonances and emittance growth in high-intensity RFQs.

For enough neutron production, the ^{9}Be(d, n) reaction using a 50 mA, 2.0 MeV deuteron beam is chosen for the PKU RFQ. Numerical studies show that ~200MHz frequency is suitable for high current deuteron RFQs with adequate focusing strength and aperture size. The available RF power source at ~200 MHz, the THALES tetrode TH781 [1], is adopted for the PKU D^+ RFQ. Consequently, the frequency, the duty factor and the total peak power are fixed at 201.5 MHz, 10% and 400 kW respectively.

Inter-electrode voltage mainly governs the transverse focusing strength (Formula (1)), the current limits and the acceleration efficiency. An integrated consideration of favorable transmission and structure length, ease of machining, low power consumption and the Kilpatrick Law is done for the PKU RFQ. The 80 kV of voltage i.e. $1.8E_k$, which is a reasonable max. surface field proved by the practice of the LEDA RFQ, is finally adopted.

The 50 keV of input energy W_i is a compromising choice of emittance concerns. Lower W_i goes against the

* Supported by Gottlieb Daimler-Karl Benz Stiftung & GSI, Germany
# zhang@iap.uni-frankfurt.de or zhangc@pku.org.cn

transverse emittance at the entrance to RFQ where space-charge effects are remarkable. Furthermore, as there are few acceleration in the shaper and gentle buncher sections which need be long enough for preparing a beam well in transverse and longitudinal directions, lower W_i normally leads to a shorter structure due to cell length=βλ/2.

Basic parameters of the PKU RFQ are listed as below.

Table 1: Basic parameters of the PKU RFQ

Frequency [MHz]	201.5
Input/Output energy [MeV]	0.05 - 2.00
Peak beam current [mA]	50
Inter-electrode voltage [kV]	80
Duty Factor [%]	10

BEAM DYNAMICS OPTIMIZATION

The LANL Four-Section Procedure, which conceptually divides an RFQ into Radial Matching section (RM), Shaper (SH), Gentle Buncher (GB) and Acceleration section (ACC), has been the standard solution for RFQ beam dynamics designs.

Regarding the transition point between the GB section and the ACC section as a borderline, these four sections could be simply distinguished into two phases: preparing period and accelerating period. The RM section serves to get high transverse capture at the entrance to the RFQ, the SH and GB sections aim to longitudinally change the beam from continuous to well bunched. The real acceleration is achieved by the ACC section.

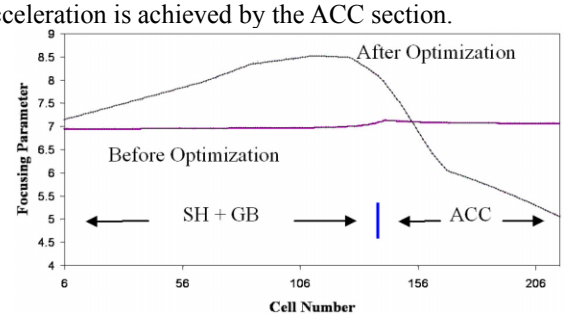

Figure 1: Variation of *B* before and after optimization.

Obviously, before the ACC section, the space-charge forces of intense beams are increasing with decreasing beam bunch size at low velocities and behave most significantly at the end of the GB section. Then they will be reduced because of the maximum acceleration rate.

For a typical four-section design, the focusing parameter *B* is held constant after the RM section in order to adapt the beam to a time-independent transverse focusing system. But from the above analysis, *B* is not necessary to and should not be fixed due to the changing space-charge forces along the RFQ. Therefore, the method of adjusting the variation of the focusing parameter to keep a certain ratio between the focusing force and the space-charge force is employed in the optimization design of the PKU RFQ. Fig.1 shows that *B* has a nearly linear growth to the maximum value until the end of GB section and then decreases gradually to the exit of the RFQ. The average focusing parameters are similar before and after optimization. This method also has the merit of getting a bigger aperture at the high energy end.

In addition, numerical simulation studies show that the peaks of beam losses usually appear at the transition points between neighboring sections, where beam parameters vary steeply. Naturally, another opmization concept of smoothing parameters' variation especially at the critical point between the GB section and the ACC section is combined into the PKU RFQ design. Fig.2 shows that the two sections are smoothly merged into together, which means particles get more acceleration in the GB section and more focusing in the ACC section. It is also helpful to short the total length of the electrodes.

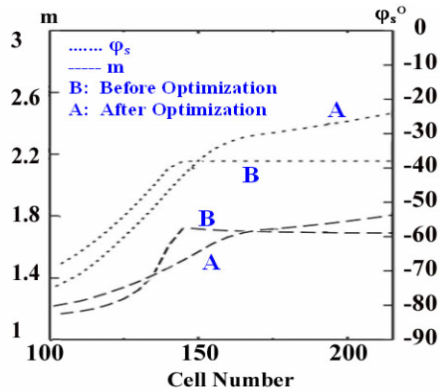

Figure 2: Smoothing optimization φs & m along the RFQ.

Table 2: Main parameters of the PKU RFQ

Parameters	Before Optimization	After Optimization
Synchronous phase [°]	-90 – -38	-90 – -25
Electrode modulation	1 – 1.73	1 – 1.79
Minimum aperture [cm]	0.26	0.28
Electrode length [m]	2.91	2.71
Cell numbers	216	216
Beam transmission [%]	91.0	98.5

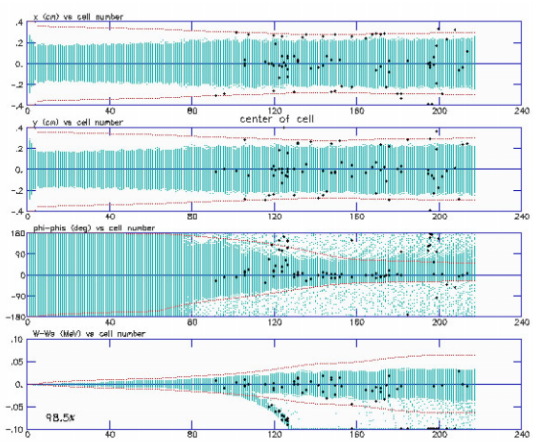

Figure 3: Beam transport simulation along the PKU RFQ.

The results based on the above two optimization methods are favourable. The beam transmission effiency increases from 91.0% to 98.5% for 5000 macroparticles. Also the RFQ is shorted to 2.71 m from 2.91 m. Fig. 3 is the beam transport plot of the optimized design.

The comparisons of main parameters and the beam losses before and after optimization are presented in the Table 2 and the reference [3] respectively.

RFQBAT COMPUTER CODE

The LANL RFQ Design Codes are the most popular beam dynamics simulation software for RFQ accelerators. A complete process of design includes the following four stages, namely calculating the current limit for a given RFQ design by CURLI, exploring the parameter space of interest and developing reference designs by RFQUICK, calculating the electrode modulation by PARI and generating the detailed RFQ design and integrating multi-particle bunches through the machine by ParmteqM [4].

To get a design scheme with very high performance, normally the optimization of beam dynamics parameters takes a lot of times, e.g. the design process of the India ADS RFQ [5]. The main disadvantages of the DOS-based LANL codes are low efficiency and poor management of input and output data. Therefore, a Windows code, RFQ Beam Analysis Tools (RFQBAT), has been developed for accelerating and extending the LANL codes since 2002.

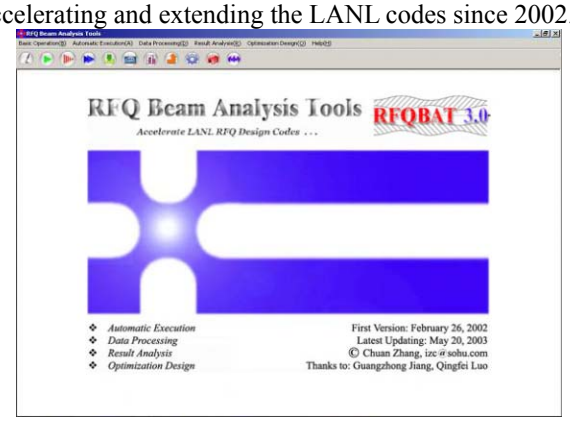

Figure 4: Start Window of the RFQBAT Code.

Though the source code of the LANL codes is not available, RFQBAT still successfully controls its running from outside with the script files saving all input data and commands. The main features of this efficient software are automatic execution, batch run, data processing, result analysis and optimization design.

It lets the running of the LANL codes need not to manually input parameters one by one any more. One automatic execution based on script files could save about 2/3 of the regular running time. After setting a certain variable and the step length, the function of batch run makes the study on the influence of an interesting parameter possible without any human workload. The RFQBAT database could not only save the input data and record all important values located in different output files for one calculation but also give the opportunity to compare and analysis relative calculations.

DESIGN QUALITY CRITERIONS

The RFQBAT Code brings the investigation on various design schemes to an easy case. Then how to evaluate the quality of a design scheme should be a critical point.

To some degree, designing RFQ accelerators is an engineering problem rather than a physical one, so the design quality criterions depend on a lot of practical factors, like the purpose of the machine, the construction costs and the ease of maintenance, etc. Here several general design quality criterions especially for high current RFQs are described.

Firstly, high beam transmission efficiency is a very important standard. Being used to produce neutrons, for example, most high current proton and deuteron RFQs require as high as possible transmission efficiency for radioactivity protection.

Secondly, a reasonable energy distribution of lost particles is very important. When some particles could not stay in the bucket of stabile oscillations around the synchronous phase at a certain moment, normally they will not be lost at once. Some of them could fly forward a distance by means of inertia without or with a little energy gain, then they hit the cavity wall and appear to be lost. Therefore, it does make sense to investigate the energy of lost particles.

Thirdly, the sensitivity of design schemes should be checked. Ion sources and input matching are not perfect, so the non-ideal beams will affect the beam transmission. A stable design scheme is important for practice [6].

In addition, the cavity size, emittance growth and aperture size should be also taken into account as functions of demands.

ACKNOWLEDGEMENTS

The author C. Zhang appreciates the support of Gottlieb Daimler-Karl Benz Stiftung and GSI, Germany, and the initiatives of Prof. H. Klein. This work has benefited a lot from the personal discussions with Dr. R. A. Jameson. Special thanks go to Mr. G. Z. Jiang and Mr. Q. F. Luo for helps on developing of the RFQBAT Code.

REFERENCES

[1] THALES Electron Devices Company
[2] A. Schempp, “New Development in High Duty Cycle, High Current RFQs”, Proceedings of LINAC2002, Gyeongju, Korea (CERN, 1996), pp539-543
[3] Z. Y. Guo et al., “Design of a Deuteron RFQ for Neutron Generation”, this conference (LINAC 2004)
[4] Manual of RFQ Design Codes, LANL
[5] S. A. Pande et al., “Preliminary Design Studies of a 100MeV H^-/H^+ Linac as injector for SNS Synchrotron/ADS Linac”, Pramana-Journal of Physics, Vol. 59, No.5, Nov. 2002, pp. 859-869
[6] C. Zhang et al., “Design of a high current RFQ for neutron production”, Nuclear Instruments and Methods in Physics Research, A, Vol 521/2-3 pp 326

BEAM DYNAMICS ISSUES OF SPES-1 LINAC

E. Fagotti, Universita' degli studi di Milano, Milano, Italy - INFN/LNL, Legnaro, Padova, Italy
M. Comunian, A. Palmieri, A. Pisent, INFN/LNL, Legnaro, Padova, Italy

Abstract

An Independent Superconducting Cavity Linac able to accelerate 10 mA CW proton beams up to 20 MeV has been studied for the SPES-1 project. This paper presents the results of beam dynamics studies through SPES linac including mapped fields effects on cavities.

INTRODUCTION

The first time step of SPES [1] realization is the creation of a two-way facility able, on one hand, to accelerate a 10 mA protons beam up to 20 MeV for nuclear studies and, on the other hand, to accelerate a 30 mA protons beam up to 5 MeV for cancer therapy and preliminary ADS studies. TRASCO RFQ [2] is used to accelerate beam up to 5 MeV in both cases. Utilization of an accelerator optimized for high current, for relatively low current requires some care [3]. Even if transversal dynamics may be readjusted through beam re-matching at RFQ input, this is not the case for longitudinal one. Separatrix width results larger than necessary and betatron oscillations are too small in number to let good thermalization of longitudinal distribution.

Linac structure has been optimized for this particular distribution in order to guarantee the lowest possible transversal and longitudinal emittance increase, minimum halo formation and complete transmission.

LINAC DESIGN

Linac is structured in two large cryostats (see Fig. 1) with a warm doublet in between that facilitates transversal matching. The linac lattice is based on a doublets structure. The focusing elements are short quadrupoles mounted inside cryostats; the number of cavities between quadrupoles increases with β. The required quadrupole gradient can be reached both by normal conducting and superconducting magnets. Superferric quadrupoles [4], combining a very compact size with a low power dissipation in the cryostat, have been found to be an excellent solution for this linac. A potential drawback is the residual magnetic field of the iron core, which must be shielded below 1 μT during cavity cooldown to prevent performance degradation of the nearby superconducting cavities. To ensure full transmission, cylindrically symmetric (thus dipole free) reentrant cavities [5] are chosen as accelerating elements. Table 1 summarizes beam characteristics at linac input, while Table 2 presents linac configuration used in matching and tracking calculations.

Table 1: Beam characteristics at Linac input

Current	10 mA	
Energy	5 MeV	
Emit. norm. rms	x	0.208 mm-mrad
	y	0.204 mm-mrad
	z	0.240 deg-MeV

Table 2: Main linac parameters

Period Type	**Type 1**	**Type 2**	**Type 3**
No. Periods	6	3	4
No. Cavity / Period	2	3	4
Energy Range (MeV)	5.0→9.5	9.5→13.2	13.2→20.1
Lattice Type	Doublet		
Lattice Period (m)	0.69	0.87→1.13	1.05
Energy Gain / Period (MeV)	0.6→0.8	1.0→1.4	1.1→2.0
RF Phase	-30°		

BEAM DYNAMICS SIMULATIONS

Trace 3D [6], PARMILA [7] and PARMELA [8] codes are used for beam dynamics simulations, while SUPERFISH [9] is used for cavity real fields generation. Few fundamental rules are followed for beam dynamics calculation:

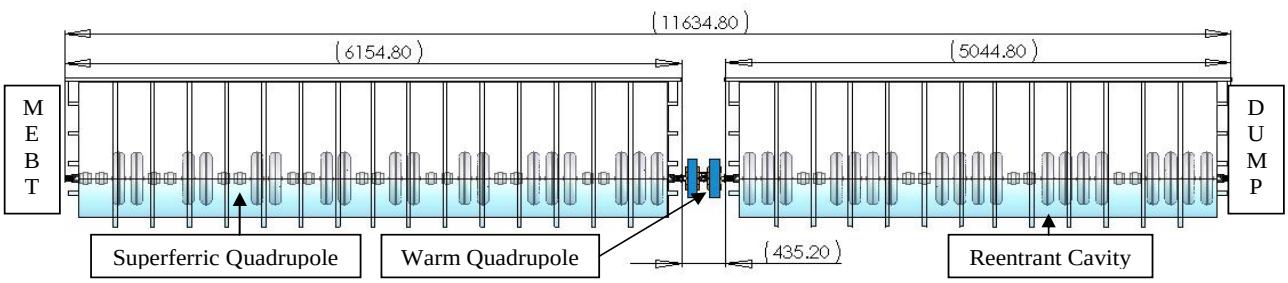

Figure 1: Linac layout. It consists of two large cryostats with a warm section in between.

- Zero current phase advances is less than 90 degrees per period in the entire structure in order to avoid instabilities for every current regime.
- Transversal phase advance is everywhere greater than longitudinal ones except in the matching section where match has precedence.
- Structure is as compact as possible to increase real estate gradient.
- The bore to rms ratio is the greatest as possible to guarantee full transmission.

These constraints, together with cavity choice, fix the number of cavities per period. Beam matching is carried out using the code TRACE 3D. The TRACE 3D code transports a beam ellipse in 6D phase space linearly through a user-defined lattice. Space charge forces are treated linearly using a uniform density model. The initial step in the matching is the calculation of periodic solutions in the first period for each type. Solutions are then matched adjusting quadrupole field gradients and RF amplitudes in few periods before type transition. Match is optimized to maintain continuous phase advances per unit length for both transverse and longitudinal motion across the transitions. Fig. 2 shows phase advances per unit length compared with quadrupoles strength and effective gap voltage (VT) in cavities.

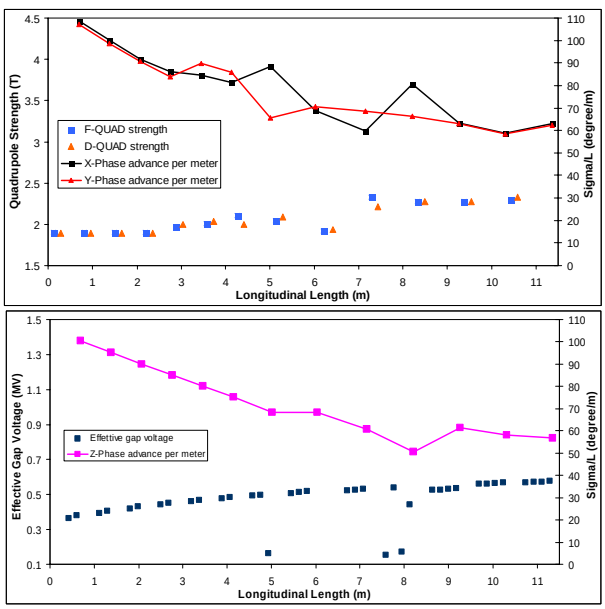

Figure 2: Comparison between phase advance per unit length and quadrupoles (up) and cavities (down) strength.

In order to verify the overall architecture and matching, a more detailed beam dynamics calculation is carried out using PARMILA code with the 3D Picnic space charge routine. Simulations proceed step by step with a feedback procedure that compares rms beam parameters obtained, with rms parameters found with TRACE 3D. At the beginning a uniform distribution of 300000 macroparticle is used as linac input. If results are well-matched uniform distribution is substituted by a 6D waterbag and simulation is repeated. If results are compatible again, input distribution is replaced with the result of beam transport through RFQ and MEBT [10] starting with a 4D waterbag distribution at RFQ input. This simulation is analyzed in more detail not only comparing rms results but also studying emittance, bore to rms ratio and envelope instabilities in relation to phase advances. If results are not satisfactory the procedure is repeated restarting from TRACE 3D and readjusting phase advance. This method guarantees convergence towards good parameters optimization. Final test is simulation of this structure with PARMELA code implementing real cavity fields.

SIMULATIONS WITHOUT ERRORS

Simulations results (see Fig. 3) show that both transverse and longitudinal rms emittance increase remains lower than 10 percent in the whole linac. Oscillation of longitudinal emittance is due to beam redistribution in longitudinal phase space. Phase-energy distribution generated by RFQ at low currents presents a two picked shape with a halo structure. Existence of this structure affects little transversal plane but has serious consequences on longitudinal plane that have to be studied in more detail. A particular of the structure is presented in Fig. 4, while beam distributions at the beginning and at the end of linac are presented in Fig. 5 and Fig. 6.

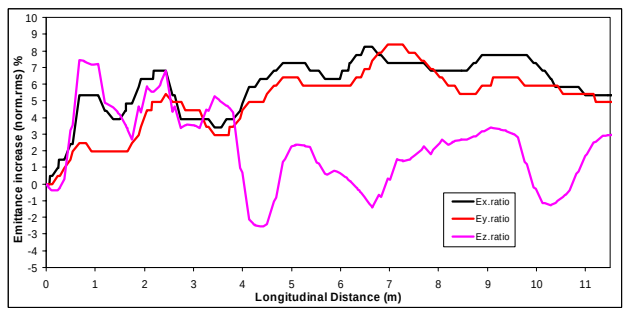

Figure 3: PARMELA calculation of the RMS beam emittances through the matched SC linac.

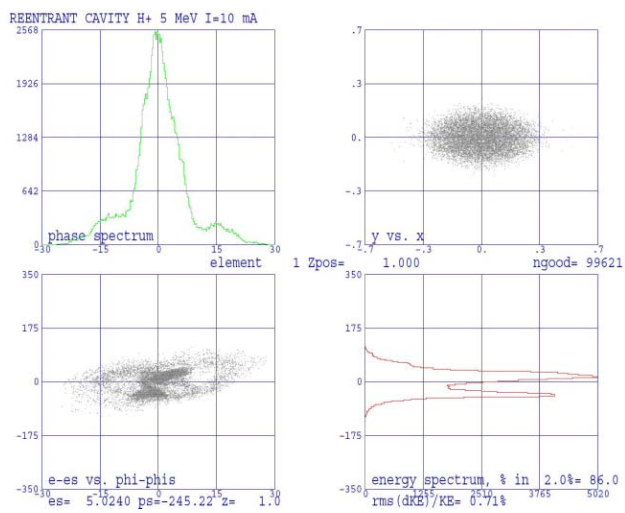

Figure 4: Longitudinal beam distribution at MEBT exit. Beam appears to be double picked in energy spread plane.

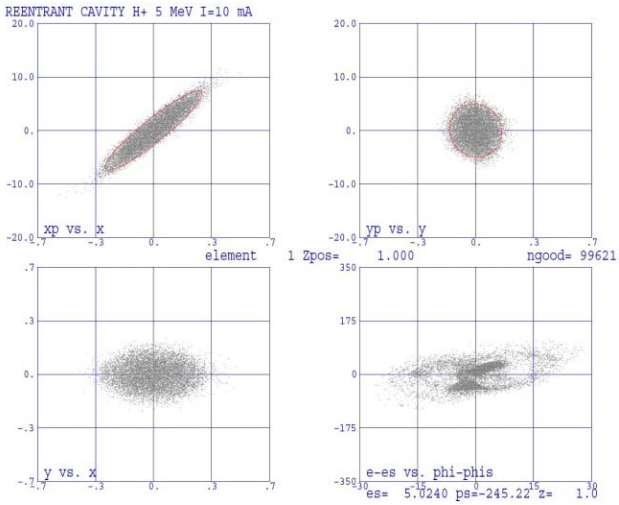

Figure 5: Beam distributions at the beginning of the SC linac at the design energy of 5 MeV.

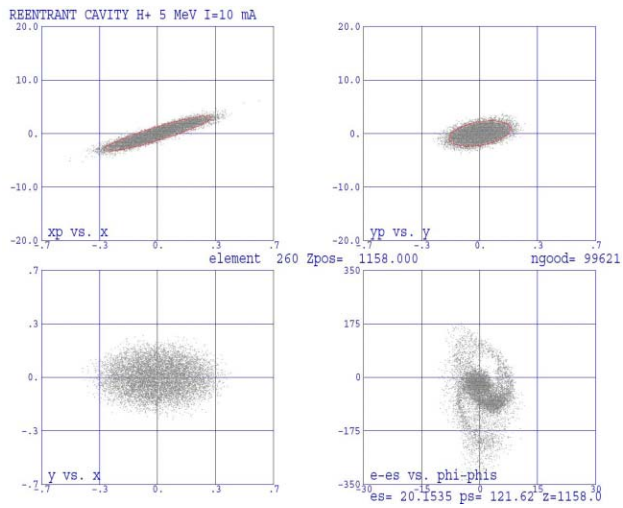

Figure 6: Final beam distributions at the end of the SC linac.

SIMULATIONS WITH ERRORS

A preliminary study on the tolerances of possible errors in the superconducting linac is carried out. Errors in positioning of focusing elements have been considered and are presented in Table 3. Fig. 7 shows the maximum values of beam transverse extent for 200 calculations. Each calculation uses different random number seeds, thus simulating 200 independent linacs with errors. The number of macroparticles used in the simulations is 100000. Full transmission is achieved and the maximum transverse extent of the beam radius is well below bore limits.

Table 3: Values of the error limits of the linac

Quadrupole transverse displacements	0.2 mm
Quadrupole tilt	3.5 mrad
Quadrupole roll	3.5 mrad

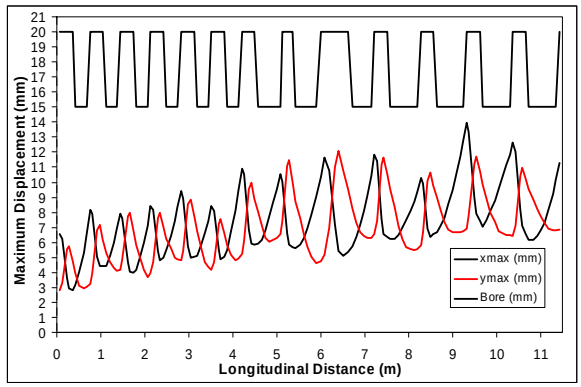

Fig. 7: Maximum transverse extent of the macroparticles in the beam versus longitudinal length for 200 independent runs with about 100000 macroparticles. Each run has been done with different random number seeds for simulating errors.

CONCLUSIONS

The structure presented fulfils the requirements of SPES-1 project. Other studies are being performed to further investigate this architecture: sensitivity to focusing errors and cavities failure. Up to now loss level is below 2 Watt in the whole linac.

REFERENCES

[1] A. Bracco, A. Pisent, “SPES-Technical Design for an Advanced Exotic Ion Beam Facility at LNL”, LNL-INFN, (REP) 181/02, June 2002.

[2] A. Pisent, et al., “TRASCO RFQ” Proc. of the XX Int. Linac Conf., Monterey, California, August 21-25, 2000.

[3] E. Fagotti, et al, “Characterization of beam parameter and halo for a high intensity RFQ output under different current regimes”, this conference.

[4] A. F. Zeller, et al, “Magnetic elements for the A1900 Fragment Separator”, Advances in Cryogenic Engineering, vol. 43B, pp. 245-252, 1998.

[5] A. Facco, V. Zviagintsev, B.M. Pasini, “A superconductive, low beta single gap cavity for a high intensity proton linac”, in Proceedings of the Linac 2000 Conference, Monterey, USA, 2000.

[6] K. R. Crandall, D. P. Rusthoi, “TRACE 3-D,” Los Alamos National Laboratory report LA-UR-97-886 (revision January 29, 2004).

[7] H. Takeda, J. H. Billen, “PARMILA” Los Alamos National Laboratory report LA-UR-98-4478 (revision January 10, 2004).

[8] L. M. Young, J. H. Billen, “PARMELA Version 3” Los Alamos National Laboratory report LA-UR-96-1835 (revision June 8, 2004).

[9] J. H. Billen, L. M. Young, “POISSON SUPERFISH” Los Alamos National Laboratory report LA-UR-96-1834 (revision January 29, 2004).

[10] M. Comunian, et al, ” TRASCO-RFQ as injector for the SPES-1 project”, this conference.

CHARACTERIZATION OF BEAM PARAMETER AND HALO FOR A HIGH INTENSITY RFQ OUTPUT UNDER DIFFERENT CURRENT REGIMES

E. Fagotti, Universita' degli studi di Milano, Milano, Italy - INFN/LNL, Legnaro, Padova, Italy
M. Comunian, A. Pisent, A. Palmieri, INFN/LNL, Legnaro, Padova, Italy

Abstract

The characterization of the beam distribution at the exit of a high intensity RFQ is a crucial point in view of a correct simulation of beam behaviour in the following linac structure. At this scope we need to know the beam halo quantification as a function of the input beam and RFQ parameters. In this paper, the description of beam halo based upon moments of the particle distribution at the exit of the TRASCO-RFQ [1] is given.

INTRODUCTION

The first time step of SPES [2] realization is the creation of a two-way facility able, on one hand, to accelerate a 10 mA protons beam up to 20 MeV for nuclear studies and, on the other hand, to accelerate a 30 mA protons beam up to 5 MeV for cancer therapy and preliminary ADS studies. This two-way facility, forces the TRASCO RFQ (Fig. 1), which is used to accelerate beam up to 5 MeV in both cases, to work with two very different current regimes. Considering that RFQ design has been optimized for a 50 mA protons beam, it is evident that a very deep RFQ parameters optimization is needed.

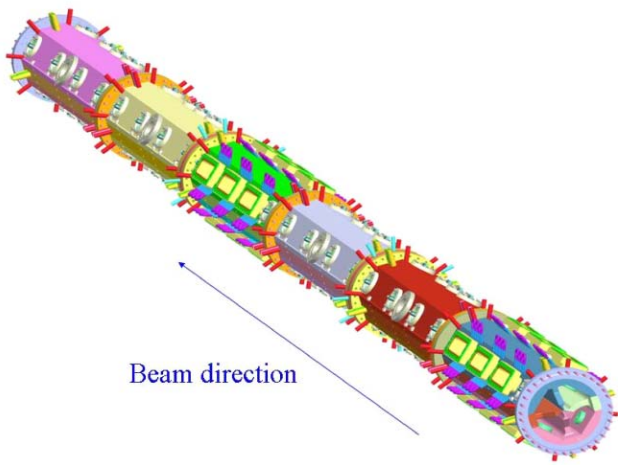

Figure 1: TRASCO-SPES RFQ design.

RFQ BEAM DYNAMICS

Beam dynamics has been simulated with PARMTEQM [3] code. All the simulations are executed starting with a 4-D Waterbag distribution of 100000 macroparticles at RFQ in. All results are obtained analyzing the full distribution output file. Therefore, it has been possible to evaluate parameters that simulation program normally do not calculate. In Tab. 1 and Tab. 2 summarize the main RFQ nominal parameters [4] and Twiss parameters at RFQ in/out for the two current regimes.

Table 1: RFQ characteristics (1)

Particle	Proton
Energy	0.08 – 5 MeV
Frequency	352.2 MHz
Duty Factor	100 %
Length	713 cm
Maximum surface field	<33 MV/m (1.8 Kilpatrick)
RF Power consumption	<800 kW

Table 2: RFQ characteristics (2)

Current (mA)		**10 mA**		**30 mA**	
Transmission		99.6 %		98.0 %	
		in	*out*	*in*	*out*
E.n.rms. *(mm-mrad) (deg-MeV)*	*x*	0.2	0.205	0.2	0.216
	y	0.2	0.2	0.2	0.212
	z	-	0.253	-	0.191
Alpha	*x*	1.37	-1.13	1.57	-1.27
	y	1.37	0.15	1.57	0.29
	z	-	0.288	-	0.05
Beta *(mm/mrad) (deg/MeV)*	*x*	0.049	0.27	0.054	0.32
	y	0.049	0.10	0.054	0.11
	z	-	439.9	-	435.4
H (halo parameter)	*x*	0.25	0.39	0.25	0.68
	y	0.25	0.35	0.25	0.60
	z	0	1.06	0	2.09

Fig. 2 shows simulation results for the two current values. Each plot is divided into four sub-plots showing beam projections in phase space. In particular, x-x', y-y', x-y and $\Delta\varphi$-ΔW plane are plotted from top left to bottom right. As regard the low current case, it can be noticed that phase-energy distribution presents a two picks structure. This has two main reasons: non linear effects due to space charge are too small to remix distribution, separatrix width results larger than necessary allowing beam to expand in longitudinal phase space. Associated with current increase there is a halo formation. In other

words, a small fraction of particles acquires enough transverse energy from the repulsive space-charge forces within the beam to form halo. A measure of halo is important because halo particles can be lost on the walls of the beam line structures, where they will induce unwanted radioactivity. A halo parameterization is important in order to compare real beam halo with that calculated for different known distributions. Uniform distribution must be the starting point for comparisons. Transport matrix codes use in general this distribution to make dynamics simulations and space charge routines implemented in multiparticle codes such as PARMTEQM, are based on an elliptical uniform symmetry of the beam. Other significant distributions for comparison are Parabolic, Gaussian and Hollow. Therefore, it is necessary to evaluate beam halo parameter and compare it with that obtained for the mentioned distributions.

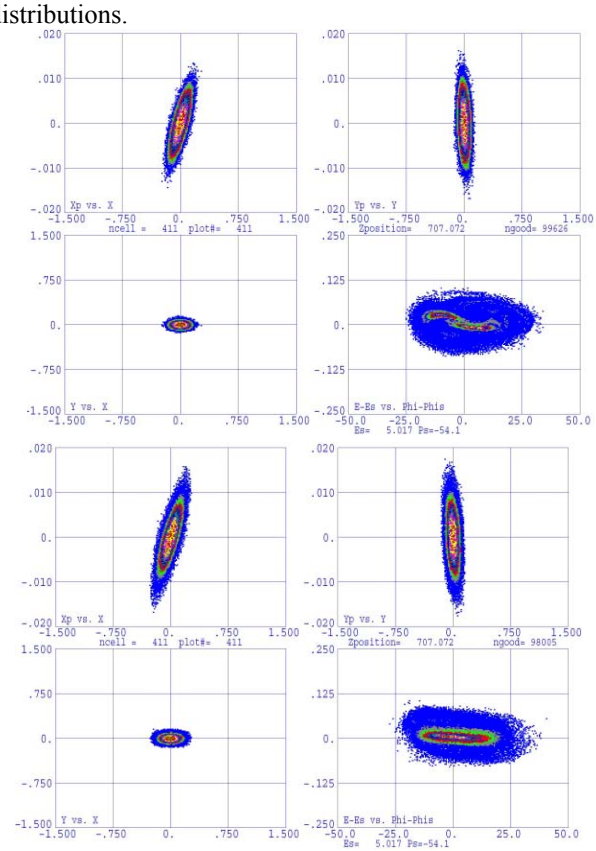

Figure 2: RFQ out for 10 mA (up) and 30 mA (down).

Wangler and Crandall [5] introduced the beam *halo parameter (H)* that gives a very good halo description:

$$H = \frac{\sqrt{3I_4}}{2I_2} - 2$$

$$I_2 = \langle q^2 \rangle \langle p^2 \rangle - \langle qp \rangle^2$$

$$I_4 = \langle q^4 \rangle \langle p^4 \rangle + 3\langle q^2 p^2 \rangle^2 - 4\langle qp^3 \rangle \langle q^3 p \rangle$$

In situation of elliptical symmetry in phase space, H has a value *0* for KV distribution, a value *0.25* for 4-D Waterbag distribution and unitary value for Gaussian distribution. Multiparticle simulations show that significant halo in the 2D phase-space projection corresponds to H > 1.

RFQ PARAMETRIZATION

With the help of *halo parameter*, RFQ dynamics is presented in the next pictures. The effect of current increase on transmission and on rms emittance is shown in Fig. 3. Transmission as a function of input emittance is not shown because it remains almost constant. In Fig. 4, the parameter halo (H) is plotted for different input currents. While halo formation is controlled on transversal plane, it can be seen a halo increase in longitudinal plane even for low current values (> 5 mA).

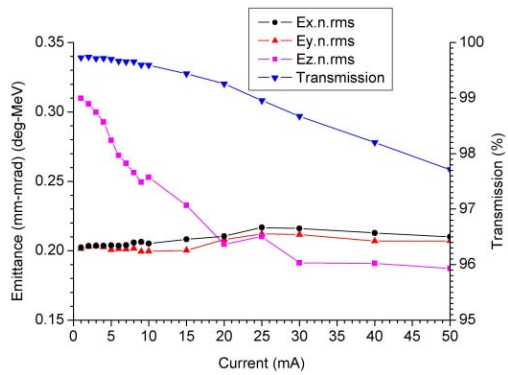

Figure 3: Transmission and rms emittance as a function of input current.

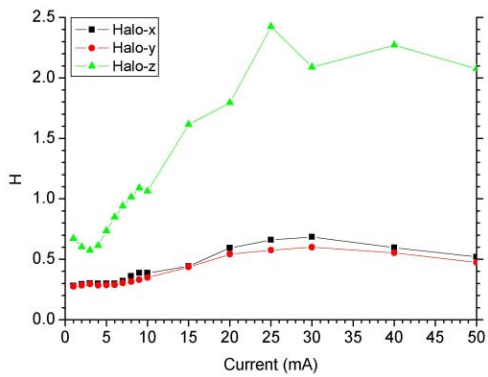

Figure 4: Parameter halo as a function of input current.

Transversal phase-space may be considered halo free in low current region (1-10 mA) where parameter halo is similar to that of the parabolic distribution *(H=0.25)*. For high currents there is an acceptable halo increase causing short tails formation. This effect is not phase-plane dependent (it's almost the same for x-x' and y-y'). Longitudinal phase-space presents a halo structure that increase with current as for transversal plane, but in this case halo is more evident. Halo structure assumes

Gaussian* behaviour up to 10 mA, while it overcomes Gaussian limit for higher currents.

RESULTS AND IMPROVEMENTS

In order to improve RFQ performances at low current, electrode voltage and input emittance may be varied. A wide emittance region (0.06-0.25 mm-mrad) has been investigated and for each emittance value electrode voltage has been varied to +-5 percent. Results show that the effect of voltage variation on beam halo is very small (Fig. 5).

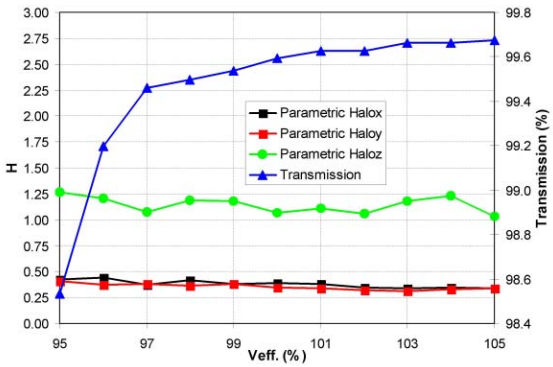

Figure 5: Beam halo and transmission as a function of electrodes voltage.

As regard emittance, decreasing beam current from 30 mA to 10 mA means to decrease beam perveance of the same amount. Considering envelope equation, it is simple to see that to restore previous balance between space charge term and emittance term, it is sufficient to decrease rms emittance by a factor $\sqrt{3}$ that is at 0.12 mm-mrad. This partially solves the problems of limited space charge and has some effects in longitudinal plane allowing the two picks approach themselves but it is not a painless operation. Low current separatrix is larger than high current one. This means that beam has much more space to evolve in longitudinal dimension. This effect combined with the apparent space charge created by low input emittance allows beam halo to increase. Results presented in Fig. 6 show that parameter halo increases with emittance decrease. Fig. 7 shows simulation results for low current and low input emittance.

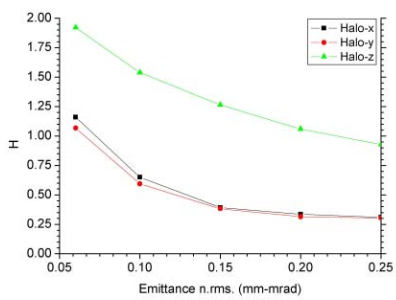

*It is referred only to tails distribution and not to the beam core that might be very different from a Gaussian. This is implicit in the halo parameter definition that is very little sensitive to beam core.

Figure 6: Beam halo as a function of rms emittance.

With very low emittance values, the multi-picks problem is completely solved, but apparent space charge effects cause degradation of transversal beam quality. On the other hand, high input emittance values guarantee low transverse and longitudinal halo, but sharp multi-picks structure.

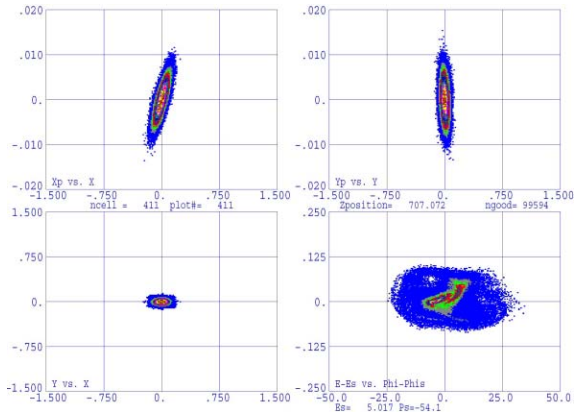

Figure 7: RFQ out for 10 mA and low emittance.

CONCLUSIONS

RFQ analysis shows that good quality beam transmission requires some care. Other studies are in progress to upgrade simulations, substituting 4-D Waterbag distribution at RFQ input, with distribution simulated by source extraction and LEBT transport [6]. An important result in understanding RFQ future behaviour will be the possibility to implement the measured LEBT distribution as input distribution. All the results will be valued taking into account the effects on halo development in the following Linac.

REFERENCES

[1] A. Pisent, A. Comunian, A. Palmieri, E. Fagotti, G. V. Lamanna, S. Mathot "The TRASCO-SPES RFQ", this conference.

[2] A. Bracco, A. Pisent, "SPES-Technical Design for an Advanced Exotic Ion Beam Facility at LNL", LNL-INFN, (REP) 181/02, June 2002.

[3] K. R. Crandall, T. P. Wangler, et al. "RFQ Design Codes" Los Alamos National Laboratory report LA-UR-96-1836 (revision July 15, 2004).

[4] M. Comunian, G.V. Lamanna, A. Pisent, "TRASCO RFQ design", LNL-INFN, TRASCO note, 01/00.

[5] C.K. Allen, T.P. Wangler, "Beam Halo definitions based upon moments of the particle distribution", Phys. Rev. Spec. Top. A. B., Vol.5, 124202 (2002).

[6] E. Fagotti, M. Comunian, A. Pisent, "Design of SPES-1 LEBT", this conference.

SOME RELEVANT ASPECTS IN THE DESIGN AND CONSTRUCTION OF A 30-62 MEV LINAC BOOSTER FOR PROTON THERAPY

D. Davino, University of Sannio, Italy, A. D'Elia, INFN and University of Naples, Italy,
S. Falco, University of Naples, Italy, M.R. Masullo, INFN, Italy,
V. G. Vaccaro*, INFN and University of Naples, Italy

Abstract

Recent results in accelerator physics showed the feasibility of a coupling scheme between a cyclotron and a linac for proton acceleration. Cyclotrons with energies up to 30MeV, mainly devoted to radioisotopes production, are available in a large number of medical centres. This suggested to design a linac booster able to increase the proton energy up to 62MeV as required for treating tumours like the ocular ones. In this paper we will discuss the basic design of a compact 3GHz SCL (Side Coupled Linac). Among the many challenges of such a project one of the most interesting is the tuning of the cavities. Because the tuning can be done only after assembling the system, it is difficult to detect which cavities are responsible for the detuning: indeed the resonant behaviour of single cavity is lost since the resonances merge into the resonant modes of the whole system. It is shown how, from the measured mode frequencies of the system, it is possible to derive the unknown resonances of each cavity and then refine the tuning. The proposed procedure is quite general and is not restricted to the SCL. This procedure is quite attractive because its use may relax the fabrication tolerances and avoids any bead pull procedure. In addition to this one may foresee even an on line computer driven tuning. Examples were given for 13 cavities fed at $\pi/2$ mode.

INTRODUCTION

The effectiveness of proton therapy of deep-seated solid tumours is now well established for the great numbers of the accumulated clinical data since when Bob Wilson proposed this therapy in 1947 in his visionary paper [1].

The potential of proton cancer therapy is now widely accepted. It has already been identified by an EU working group as deserving of priority support [2]. More than 36.000 patients [3] have already been treated world wide with proton beams of energy ranging between 60MeV to 220MeV, according to the tumour depth. The therapeutic activity, which was beforehand mainly concentrated around nuclear physics laboratories, is now moving to ad hoc conceived hospital units. Only in 1991, with the completion of the LOMA LINDA facility, proton therapy became available in a hospital site. Since then several hospital based centres have been developed [3,4,5].

The idea of designing a linac booster able to increase the proton energy up to values adequate for protontherapy was born at the beginning of 90s. A detailed description of the development of this idea and of its outcome can be found in ref. [6,7]. The PALME project concerns the design of a 3GHz linac able to accelerate up to 62MeV proton beams delivered by existing cyclotrons of 30MeV. Many of these cyclotrons are already in use for isotope production in nuclear medicine. The goal is to achieve a mean energy gradient of 11MeV/m, so that the total linac length should not exceed 3m. With 30MeV injection energy booster connected to their cyclotrons these centres could extend their activities to cancer therapy with investments lower than those required for separate installations with the same functions.

THE ACCELERATOR

The SCL is formed by a chain of large number of accelerating cavities (AC) connected via irises to off-set coupling cavities (CC). The principle which governs the frequency behavior of such a device is the resonant coupling [8]: when coupled, the all equal resonances of the cavities split into the resonant modes of the whole system. Each mode is characterized by the phase advance between adjacent cavities. This implies that when excited, all the cavities resonate on this mode with their own phase advances. Therefore, the peculiar aspect of this configuration is the possibility of having only one RF feeder for a very large number of cavities (almost fifty elements AC+CC). For SCL compact accelerators the RF power frequency is matched to the so called $\pi/2$ mode: this means that each second cavity is empty of energy and it has the role of coupling adjacent cavities.

In general the SCL basic bricks are tiles, on the opposite sides of which a half-CC and a half-AC are machined. The fabrication tolerances play a crucial role in the performances of these devices because of the extreme high frequency of the feeder. In fact, the fabrication errors produce deviations from the design nominal values of the most relevant parameters.

Even if we are dealing with devices working in the GigaHertz range, lumped circuit representation very well suits the SCL behaviour [8]. In the next section we resort to the transmission matrix representation of the two-port device for the tiles and we investigate on the overall behaviour of the SCL. In the case of N identical two-port device chain, the whole system exhibits N+1 resonant frequencies, each characterised by its own mode (phase advance). These frequencies are given by simple analytical formulas [9]. The actual situation is quite intricate: after machining the tiles are unequal and the lumped parameter values of the device exhibit slight

*vaccaro@na.infn.it

differences from tile to tile; furthermore these parameters, after assembling and brazing the tiles, exhibit additional random errors. At this stage it is impossible to make direct measurements of the single two port device, the only measurement allowed being on the whole system.

THE LUMPED CIRCUIT MODEL

The electromagnetic behaviour of a single tile can be represented by a two-port device made of two lumped resonant series circuits coupled by a coupling coefficient. The overall SCL behaviour is so described by a two-port device chain. The transmission matrix of this chain is studied. Our goal is to study the overall behaviour of a SCL structure in order to find out tools useful for the design, the analysis, the diagnostics and the correction of the single cavities. We consider two-port devices which are similar but exhibit slight differences, essentially due to fabrication errors which produce deviations of the cavity parameter nominal values. We allow for the transmission matrix representation [10], denoting each cavity by the index p. The quantity T_p is therefore defined as:

$$\begin{pmatrix} V_p \\ I_p \end{pmatrix} = \begin{pmatrix} t_{11}^p & t_{12}^p \\ t_{21}^p & t_{22}^p \end{pmatrix} \begin{pmatrix} V_{p+1} \\ I_{p+1} \end{pmatrix} = \mathbf{T}_p \begin{pmatrix} V_{p+1} \\ I_{p+1} \end{pmatrix} \tag{1}$$

We suppose that each two-port device is composed by two lossy resonant series circuits [10] as shown in Fig. 1.

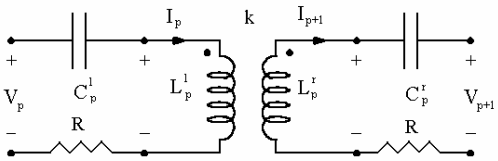

Figure 1: The generic two-port device representing two resonant circuit coupled by a coupling coefficient k.

In this device the parameters differ for different values of p. Furthermore we assume that the r.h.s parameters differ from the l.h.s. ones, as shown in Fig. 1, where the indices *r* and *l* stand for right and left. We may assume that the resistance does not depend on index p.

We may define for each tile two resonant frequencies (the end tiles only one) as:

$$f_p^l = 1/2\pi\left(L_p^l C_p^l\right)^{1/2} \quad \text{and} \quad f_p^r = 1/2\pi\left(L_p^r C_p^r\right)^{1/2} \tag{2},$$

for the l.h.s and r.h.s. of the p-th two-port device, where p=1,.. N+1 for the index l and p=-1,.. N for the index r. Resorting to formulas, which can be found in the literature [8, 9] we get, for lossless all equal devices, the resonant mode frequencies, F_s:

$$F_s = \frac{f_0}{\sqrt{1 + k\cos[s\pi/(N+2)]}} \qquad 1 \le s \le N+1 \tag{3},$$

where f_o is the resonant frequency of the unperturbed two port device of Fig 1. The quantity sπ/(N+2) is the phase advance of the field along the chain and it is a characteristics of each mode. We are particularly interested in the π/2 mode (s=1+N/2), since of its stability with respect to the errors.

THE PERTURBATIVE MODEL

Consider now a chain of N different two-port devices, where N is an even number. The chain transmission matrix has been studied by means of a perturbation analysis. We look for the resonant frequencies without any restriction to the mode.

The overall transfer matrix is:

$$\mathbf{T}_{tot} = \prod_{p=1}^{N} \mathbf{T}_p \tag{4}.$$

. The equation to be solved is [10]:

$$Z_c^l \left(\prod_{p=1}^{N} \mathbf{T}_p \right)_{21} + Y_c^r \left(\prod_{p=1}^{N} \mathbf{T}_p \right)_{12} = 0 \tag{5},$$

where Z_c^l and Y_c^r are the left hand and right hand loads of the chain.

We define the deviation of the resonant frequencies for each cavity as:

$$\Delta f_p = \Delta f_{p-1}^r + \Delta f_p^l \tag{6}.$$

From eqs. (5), resorting to perturbative techniques, after some algebra, we get [10] an expression for the perturbed frequency of the modes ΔF_s as a linear combination of the perturbed resonant frequencies Δf_p of the cavities:

$$\frac{\Delta F_s}{F_s} = \frac{2}{(N+2)} \sum_{p=1}^{N+1} \frac{\Delta f_p}{f_0} \sin^2 \frac{ps\pi}{N+2} \tag{7}.$$

In the system (7) the equations of indices s and N+2-s, are identical. As consequence, the number of the independent equations is the first integer equal to 1+N/2. This property implies that the system (7) cannot be solved respect to Δf_p. However, defining the new unknown

$$\Delta \bar{f}_p = \Delta f_p + \Delta f_{N+2-p} \tag{8},$$

in the system of equations (7) the number of unknowns ($\Delta \bar{f}_p$) is equal to the measurable quantities (ΔF_s); the determinant of the system is finite; so that eq. (7) can be inverted as:

$$\frac{\Delta \bar{f}_p}{f_0} = \sum_{p=1}^{E\left(\frac{N}{2}\right)+1} A_{ps} \frac{\Delta F_s}{F_s} \tag{9},$$

where $E(x)$ means the minimum integer larger than x.

THE TUNING

It is customary, after a preliminary tuning by means of ad hoc machining, to refine the tuning in order to better equalise and maximise the field. This is done by introducing small pistons in the accelerating cavities (all the cavities) for π/2 mode (π-mode). All pistons are inserted inside the cavity of the same amount. Monitoring is made by means of the bead pull. We will call this method as Uniform Piston Advancement (UPA) tuning.

The proposed tuning, named System Mode Sounding (SMS), consists in: 1) the detection of the mode frequencies, the sounding the system in the frequency band $f_o(1\pm k)$; 2) the calculation of the correction by means of eq. (9); 3) the introduction (extraction) of tuners producing the desired tuning refinement. The procedure can be iterated. Because of eq. (8) the iteration stops

when the sum of the frequency deviations of symmetrical resonators is zero. The tuning converges very fast: in general two iterations are sufficient. The detection of the mode frequencies is made by feeding a variable frequency signal in the first cell and by picking up the response in the last one. The application of SMS gives an equalization and maximisation of the field in the cavities.

We made a virtual measurement by means a program with Matlab code for 13 cavities (N=12) fed via the central one at π/2 mode (f_o=3GHz and k=4%). Eq. (5) is numerically solved with respect to the mode frequencies. We allow the cavities to be detuned by random errors with an uniform distribution in the interval (0, f). We "measure" the mode frequency shifts and the voltage at the gaps and then we adopt SMS and UPA procedures .

The results are shown in the following Fig.2 and 3.

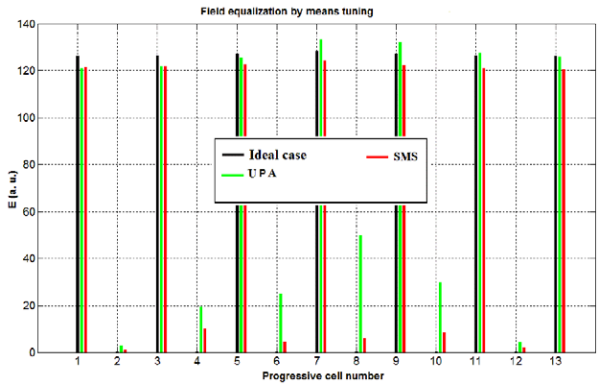

Figure 2. Comparing UPA and SMS, f= 10MHz.

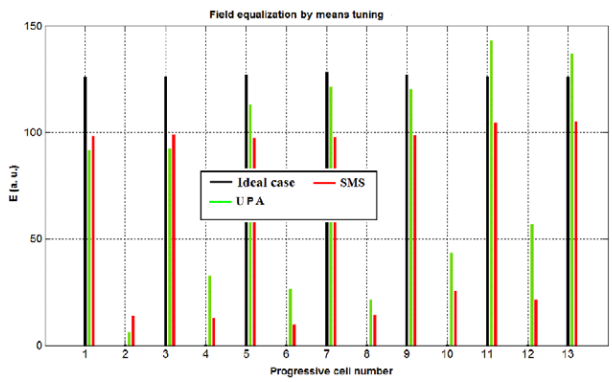

Figure 3. Comparing UPA and SMS, f= 20MHz.

From the comparison of the two techniques one has to look at the field uniformity and the power losses in CC's. From Fig. 2 and 3 we see that SMS gives a good field uniformity in any condition, better than UPA. Furthermore SMS tuning shows lower losses than UPA. The results are summarised in Tab. 1.

Table 1: Field non uniformity and power efficiency

	Field non-uniformity		Power efficiency	
	SMS	UPA	SMS	UPA
f= 10MHz	1.0%	3.4%	99.8%	96.2%
f= 20MHz	3.0%	15.9%	97.5%	92.9%

We made also a test by combining the two tuning methods. The results confirm that SMS tuning is a very good tuning method and it is the faster one: indeed the combination of SMS + UPA gives only a higher mean value of the field with the same field uniformity.

CONCLUSIONS

In this paper we showed a new tuning method. By using a circuit model it is possible to find out useful formula's to connect the mode frequency response of a coupled structure to the frequency shift of the resonators. The formula's are quite general and they show that, in order to tune the mode, the symmetrical sum of the single resonator errors must be zero. The UPA tuning technique was adopted for LIBO [7]. We have tested our method with a system of 13 cavities fed at π/2 mode. We have seen that for the cavity detuning characterised by a large spread (0.33%) a quite good field equalization and maximisation can be reached by our SMS tuning. Our method is better then UPA and it is even more, if one takes into account the losses in the coupling cavities. For even larger spreads (0.67%) a quite good field equalisation is obtained by means of SMS tuning as shown in Fig.3, while UPA produces field values with a larger spread and a significant amount of losses in the CC's. The power losses play a role in favour of SMS.

REFERENCES

[1] R. R. Wilson "Radiological Use of Fast Protons", Radiology, 47, pp 487-491, July 1946

[2] "European Strategy for Cancer Research" Commission of European Communities DG XII-Medical Division (1991): XII/F-6-AV/nv/91001P

[3] Particles NewsLetter (PTCOG) n. 31, January 2004, pag 10 - Edt: Janet Sisterson Ph.D., NPTC

[4] E. Pedroni, "Status of Proton Therapy : Results and Future Trends" Proceedings of the Fourth European Particle Accelerator Conference, London 1994

[5] R. Orecchia et al.,"Particle Beam Therapy (Hadrontherapy): Basis for Interest and Clinical Experience", Eur.J. of Cancer, vol. 34 no.4, 1998.

[6] V.G. Vaccaro et al., "Study of a Linac post-accelerator for Proton Therapy in the 30-62 MeV Energy range", accepted and to be printed on Proceedings of EPAC 2004, Luezern, Switzerland (July 2004)

[7] U. Amaldi et al., "LIBO – A LInac-BOoster for Protontherapy: Construction and Test of a Prototype", NIM A, 521 (2004), 512.

[8] D.E. Nagle, E.A. Knapp, B.C. Knapp, "Coupled resonator model for standing wave accelerator tanks" The Review of Scientific Instruments, vol.38 n.11, pp 1583-1587,1967.

[9] T. Wangler, "Principles of RF Linear Accelerator Technology", ed. Wiley Series in Beam Physics and Accelerator Technology, (Aprile 1998).

[10] V.G.Vaccaro et alii "Perturbative techniques applied to a lumped circuit model of an SCL" in preparation.

BEAM DYNAMICS DESIGN OF J-PARC LINAC HIGH ENERGY SECTION

Masanori Ikegami, Takao Kato, Shuichi Noguchi, KEK, Tsukuba, Ibaraki 305-0801, Japan
Hiroyuki Ao, Tomohiro Ohkawa, Akira Ueno, Kazuo Hasegawa,
Yoshishige Yamazaki, JAERI, Tokai, Ibaraki 319-1195, Japan
Noriyosu Hayashizaki, TIT, Meguro, Tokyo 152-8550, Japan
Valentin V. Paramonov, INR RAS, Moscow 117312, Russia

Abstract

Recently, the beam dynamics design of the high-energy part of J-PARC linac has been revised to reduce construction cost. The modifications are described in this paper together with 3D particle simulations results for the revised design.

INTRODUCTION

ACS (Annular-Coupled Structure linac) is the high-energy part of the J-PARC linac, which accelerates 190-MeV negative hydrogen beams up to 400 MeV [1, 2]. Recently, the beam dynamics design of the ACS part has been improved to reduce construction cost. The beam matching section between preceding SDTL (Separate-type Drift Tube Linac) and ACS is also revised correspondingly. The modifications of the design are described in this paper together with 3D particle simulation results for the revised design.

As presented in the reference [1], we start beam commissioning with lower linac energy of 181 MeV, in which the ACS part is replaced with a beam transport line compatible with swift energy upgrade to 400 MeV. Simulation results for the lower energy operation is also presented.

REVISED ACS

Figure 1 shows the layout of a revised ACS module, which consists of two ACS tanks connected with a bridge coupler, and quadrupole doublets placed at inter-tank spacings. Two neighboring ACS tanks are driven by a 2.5-MW klystron. The inter-tank spacing is $4.5\beta\lambda$ with β and λ being the beam velocity scaled by the speed of light and the RF wave length, respectively.

In the original design [3], ACS part consisted of 46 ACS tanks, and each ACS tank had 15 accelerating cells. The total length including inter-tank spacing was 108.3 m.

In the revised design, the number of ACS tanks is reduced from 46 to 42. To maintain the total energy gain, the number of accelerating cells in an ACS tank is increased from 15 to 17. With this design change, the number of klystrons is reduced by two, curtailing the margin for RF power by around 5 %. The averaged field strength E_0 is reduced from 4.26 MV/m to 4.12 MV/m to keep the increase of RF power load in the sustainable range. The total length of the ACS section is slightly reduced to 107.1 m. Cell geometries of an accelerating cell and a coupling cell are not modified. Bridge couplers are placed below the quadruople doublets in the inter-tank spacing, while we originally plan to place them above the beam line. This layout is selected to enable easy handling of beam instrumentation installed in the inter-tank spacing. Table 1 summarizes the main specifications of the revised ACS.

Table 1: Main specifications of the revised ACS

Input beam energy	190.8 MeV
Output beam energy	400.0 MeV
Operation frequency	972 MHz
Beam particle	Negative hydrogen ion
Peak beam current	50 mA
Beam pulse width	0.5 msec
Repetition	50 Hz (25 Hz initially)
Num. of cells per tank	17
Num. of tanks per module	2
Num. of modules	21
Num. of klystrons	21
Inter-tank spacing	$4.5\beta\lambda$
Bore radius	20 mm
Average accelerating field E_0	4.12 MV/m
Synchronous phase	-30 deg
Max. surface field	0.82 Kilpatrick
Peak RF power	42.5 MW
Peak wall loss	32.0 MW
Peak beam loading	10.5 MW
Total length	107.1 m

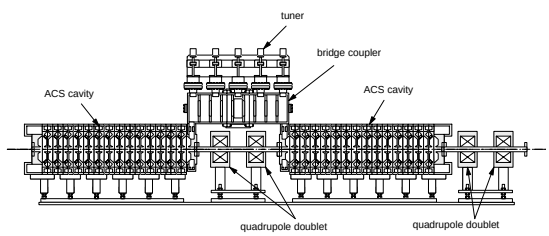

Figure 1: Layout of a revised ACS module. Although the bridge coupler is shown above the beam line in this figure, we plan to place it below.

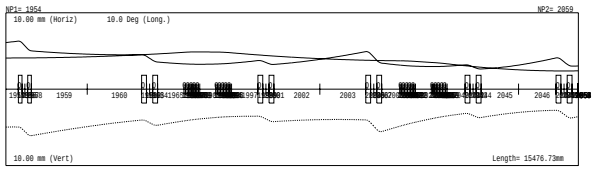

Figure 2: Trace3D output for the revised MEBT2.

Table 2: Normalized rms emittances (400-MeV operation)

	ϵ_x πmm·mrad	ϵ_y πmm·mrad	ϵ_z πMeV·deg
RMS			
RFQ exit	0.205	0.206	0.115
SDTL exit	0.298	0.300	0.149
ACS entrance	0.289	0.288	0.168
ACS exit	0.309	0.312	0.157
RCS injection	0.319	0.294	0.368
99.5 %			
RFQ exit	2.155	2.158	1.556
SDTL exit	4.327	4.558	2.406
ACS entrance	4.407	4.156	2.517
ACS exit	4.827	5.065	2.416
RCS injection	5.173	4.720	5.207

REVISED MEBT2

We have a beam matching section between SDTL and ACS to which we refer as MEBT2 (Medium Energy Beam Transport 2). The main purpose of this beam transport line is to realize smooth matching absorbing the effects of three-fold frequency jump from SDTL (324 MHz) to ACS (972 MHz).

For the longitudinal matching, we have two 972-MHz buncher cavities of ACS-type. A buncher module consists of two 5-cell ACS tanks connected with a short bridge coupler [2, 3, 4]. For the transverse matching, we have six quadrupole doublets. While both SDTL and ACS have doublet-focusing lattices, their period lengths are different. To absorb the difference smoothly, we adopt a "quasi-doublet focusing lattice" for MEBT2, in which the period length is gradually reduced. As the period length in the ACS has been changed from $12\beta\lambda$ to $13\beta\lambda$, the layout (spacing between quadrupole doublets) has been changed accordingly. With this modification, the total length of MEBT2 is reduced from 15.9 m to 15.4 m.

Figure 2 shows a typical beam profile along MEBT2 calculated with Trace3D [5], where middle four quadrupole doublets are mainly used for the transverse matching.

PARTICLE SIMULATION

In this paper, particle simulations are performed with PARMILA [6] from the exit of RFQ to RCS injection. In the simulations, we assume the peak current of 50 mA,

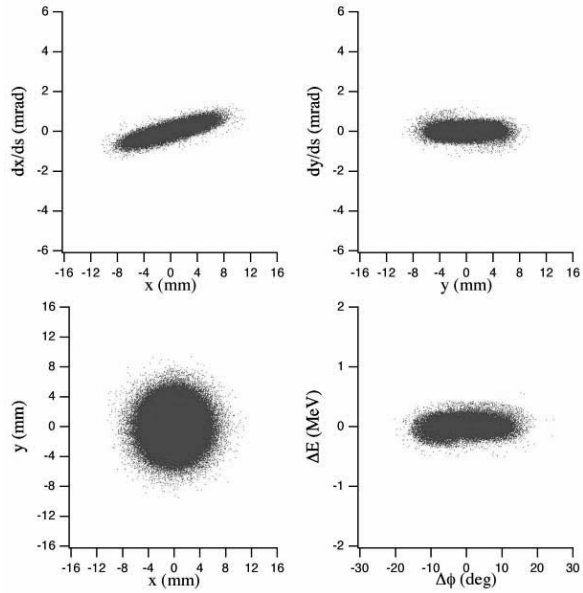

Figure 3: Phase-space distributions at SDTL exit (400-MeV operation).

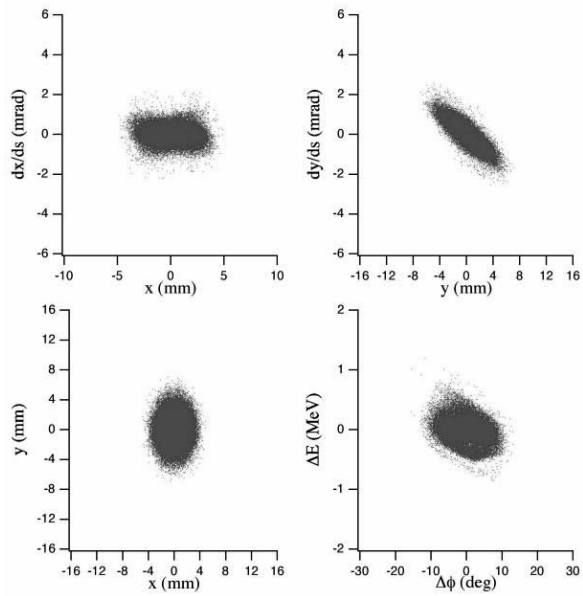

Figure 4: Phase-space distributions at ACS injection (400-MeV operation).

which is the design value for our linac. The initial distribution at the exit of RFQ is obtained with PARMTEQM with the similar procedure described in the reference [7]. The number of simulation particles is 94,720 and the number of meshes is set to 20x20x40. We use the 3D space-charge option. Equipartitioned setting has been assumed for the quadruple magnets in DTL, SDTL, and ACS sections, and no error has been applied.

Table 2 summarizes the evolution of the emittance along the linac, in which phase deviation is measured for 324

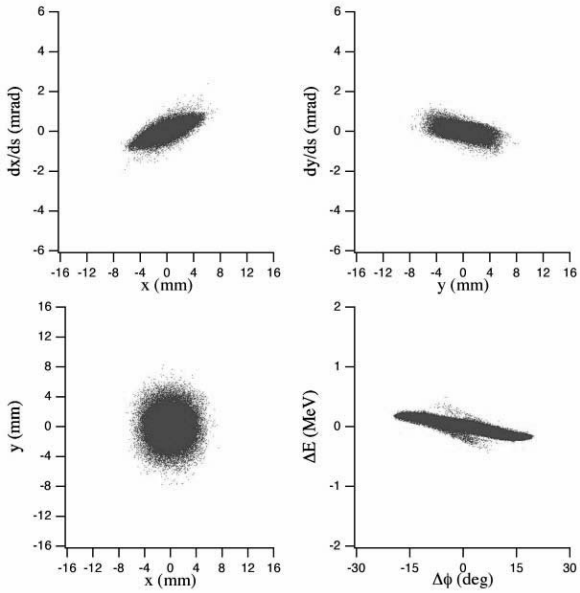

Figure 5: Phase-space distributions at RCS injection (400-MeV operation). The horizontal axis for the right-bottom figure is the phase deviation for 324 MHz.

MHz. As shown in Figs. 3 and 4, slight distortion of the longitudinal distribution occurs in MEBT2. However, the final distribution satisfies the requirement for the momentum spread at RCS injection, ± 0.1 %, as seen in Fig. 5. In the beam transport line from the linac to RCS, the bunch has been rotated in the longitudinal phase-plane to minimize the momentum spread with two 972-MHz debunchers located before and after the 90-degree arc section.

PARTICLE SIMULATION FOR LOWER ENERGY OPERATION

As we start beam commissioning with the beam energy of 181-MeV [1], the lattice design of the high-energy part should be compatible with the lower energy operation. To see its compatibility, PARMILA simulation has also been performed for the 181-MeV operation, where ACS is replaced with a beam transport line. The design consideration of the ACS has been deeply related to the design of the substituting beam transport line, because the capability of swift installation of ACS modules is required to minimize the accompanying beam shut-down period. For the detailed design of the beam transport line, refer to the reference [1].

The simulation conditions are the same with those for 400-MeV operation except that the beam current is assumed to be 30 mA (design value for 181-MeV operation) and the number of particles is slightly increased to 95,322.

Table 3 summarizes the evolution of the emittance along the linac. Figure 6 shows the obtained phase-space distributions at the injection point to RCS. From these results, we have concluded that the revised ACS and MEBT2 satisfy the requirement for the lower energy operation.

Table 3: Normalized emittances (181-MeV operation)

	ϵ_x πmm·mrad	ϵ_y πmm·mrad	ϵ_z πMeV·deg
RMS			
RFQ exit	0.212	0.212	0.0913
SDTL exit	0.262	0.260	0.0958
RCS injection	0.275	0.254	0.262
99.5 %			
RFQ exit	2.075	2.048	1.323
SDTL exit	4.015	3.838	1.370
RCS injection	4.322	3.754	4.078

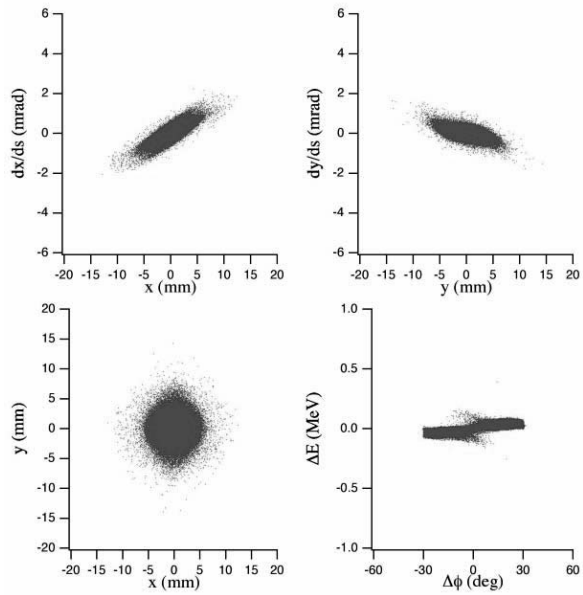

Figure 6: Phase-space distributions at RCS injection (181-MeV operation). The horizontal axis for the right-bottom figure is the phase deviation for 324 MHz.

REFERENCES

[1] Y. Yamazaki, "Status of the J-PARC Linac, Initial Results and Upgrade Plan", in these proceedings.

[2] Y Yamazaki ed., "Accelerator Technical Design Report for J-PARC", KEK Report 2002-13; JAERI-Tech 2003-044.

[3] M. Ikegami et. al., "Beam Dynamics Design of the Annular-Coupled-Structure Lianc and Its Beam Matching Section for the KEK/JAERI Joint Project", in Procs. of LINAC2002, p. 631 (2002).

[4] H. Ao et.al., "Cold-model Tests and Fabrication Status for J-PARC ACS", in these proceedings.

[5] K. R. Crandall, "TRACE: An Interactive Beam Dynamics Code", in AIP Conference Procs. **177**, p. 29 (1988).

[6] H. Takeda, "PARMILA", Los Alamos National Laboratory Report, LA-UR-98-4487 (1998).

[7] Y. Kondo et.al., "Particle Distribution at the Exit of the J-PARC RFQ", in these proceedings.

A SIMULATION STUDY ON CHOPPER TRANSIENT EFFECTS IN J-PARC LINAC

Masanori Ikegami, KEK, Tsukuba, Ibaraki 305-0801, Japan
Tomohiro Ohkawa, Yasuhiro Kondo, Akira Ueno, JAERI, Tokai, Ibaraki 319-1195, Japan

Abstract

J-PARC linac has a chopper system to reduce uncontrolled beam loss in the succeeding ring. The chopper system is located in MEBT (Medium Energy Beam Transport line) between a 3-MeV RFQ and a 50-MeV DTL, and consists of two RFD (Radio-Frequency Deflection) cavities and a beam collector. During the rising- and falling-times of the RFD cavities, the beams are half-kicked and cause excess beam loss downstream. In this paper, the behavior of these half-kicked beams is examined with 3D PARMILA simulations, and resulting beam loss and beam quality deterioration are estimated.

INTRODUCTION

J-PARC linac [1, 2] has a chopper system to reduce uncontrolled beam loss in the succeeding RCS (Rapid Cycling Synchrotron). While we are preparing two-stage chopping system utilizing both LEBT and MEBT choppers [2], we are considering to start beam commissioning only with MEBT chopper, taking account of the following circumstances, namely; we decided to start beam commissioning with lower peak current of 30 mA [1], which eases the heat load problem of the chopper target (collector), and we have experimentally confirmed that surviving ratio in the chopper-on period is less than 10^{-4} only with MEBT chopper [3]. While the experimental data is for the case with 5 mA, it encourages us to seek the possibility of "one-stage chopping" in which the combined transient effects of LEBT and MEBT choppers are avoided. In this paper, we focus on the transient effects in one-stage chopping where only MEBT chopper is used.

The chopper system is located in MEBT between a 3-MeV RFQ and a 50-MeV DTL, and consists of two 324-MHz RFD (Radio-Frequency Deflection) cavities and a beam collector [2, 4]. With this RF chopper system, an intermediate-pulse (or pulse-train) structure is generated as schematically shown in Fig. 1. In the intermediate-pulse structure, the beam-on period continues for $\sim$ 500 nsec followed by the beam-off (chopper-on) period of $\sim$ 500 nsec. The repetition of the intermediate-pulse structure is synchronized with the frequency of the RCS RF system. The intermediate-pulse width will be optimized to have the maximum beam power within the tolerable beam loss limit in RCS. In the beam-off period, beams are horizontally deflected by the RFD cavities and collected by the collector. During the rising- and falling-times of the RFD cavities, the beams are half-kicked and can cause excess beam loss downstream.

Survived half-kicked beams can also cause a beam loss problem in RCS, exceeding the transverse dynamic aperture limit. We have a requirement for the transverse emittance at the injection to RCS to enable effective painting, namely; the normalized transverse emittance should be less than 4πmm·mrad. To achieve the requirement for the transverse emittance, we have transverse halo collimators in the beam transport line between linac and RCS [2]. The collimator edge position is supposed to be set to satisfy the requirement for the transverse emittance, and it is practically important to estimate the collimator load, i.e., the fraction of a beam that must be eliminated with the halo collimators. One of our aims in this simulation study is to estimate the increase of the collimator load during chopper transient.

In this paper, the behavior of these half-kicked beams is examined with 3D PARMILA[5] simulations, and resulting excess beam loss and halo-collimator load are estimated.

SIMULATION CONDITIONS

As discussed in a separate paper [1], we plan to start beam operation with the lower linac energy of 181-MeV. In this paper, simulations are performed with PARMILA from the exit of RFQ to the injection point to RCS for the 181-MeV case. In the simulations, we assume the peak current of 30 mA, which is the design value for 181-MeV operation. The initial distribution at the exit of RFQ is obtained with PARMTEQM [6]. The number of simulation particles is 95,322 and the number of meshes is set to 20x20x40.

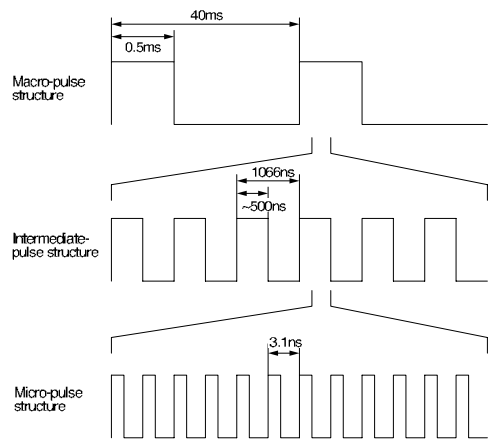

Figure 1: Pulse structure for J-PARC linac (181-MeV injection).

The quadruple magnets in DTL and SDTL sections are set to satisfy the equipartition condition. No halo collimation has been assumed.

In this paper, the RFD cavities are modeled as thin elements which provide transverse kick, and the collector as a rectangular aperture. The collector edge position is set to 12 mm from the beam axis.

In this paper, we consider the following four cases:

- Case-I: No error is assumed.
- Case-II: Run#18 of the reference [7].
- Case-III: Run#9 of the reference [7].
- Case-IV: Run#17 of the reference [7].

In the reference [7],we tried 20 cases with realistic errors. Case-II is a typical case in those 20 cases. Case-III corresponds to the case with the largest horizontal emittance growth. Case-IV corresponds to the case with the largest beam loss in DTL. In Case-IV, a simple beam orbit collection is assumed at the exit of MEBT to minimize beam loss, but it still has the beam loss of about 2 % mostly localized in DTL1.

SIMULATION RESULTS

Figure 2 shows the dependence of the transmission ratio through the linac on the deflection angle provided with the RFD cavities. In Fig. 2, the horizontal axis is the sum of deflection angles given by the two RFD cavities. Figure 2 shows that the required deflection angle in the beam-off period is around 18 mrad.

Figure 3 shows the dependence of the downstream beam loss on the deflection angle. The downstream beam loss is defined as the ratio of the number of particles lost after the collector to that at the entrance of MEBT. Figure 3 shows that the downstream beam loss maximizes at the midst of the rising- or falling-times. The loss is mostly localized in the low energy part of DTL as illustrated in Fig. 4. Beam loss increase is not observed after DTL1 except for Case-III, where the excess loss of 0.5-0.7 % has been observed in the midst of rising- and falling-times at the DTL-SDTL transition.

Figure 5 shows the dependence of the collimator load on the deflection angle. The collimator load is the fraction of the particles which must be eliminated to satisfy the requirement for the transverse emittance. The halo collimator edge position is supposed to be set to satisfy the requirement in the beam-on period (where the RFD cavities provide no deflection). Here, we define the collimator load for deflected beams as the fraction of the particles located outside the 4πmm·mrad ellipse of the un-deflected beam. The situation is illustrated in Fig. 6 where the phase-space distributions at the injection to RCS are shown for Case-I. In Fig. 6, only the transverse phase-plane is shown. The blue ellipses in Fig. 6 show the 4πmm·mrad ellipse for the un-deflected beam. The halo collimator edge is supposed to be

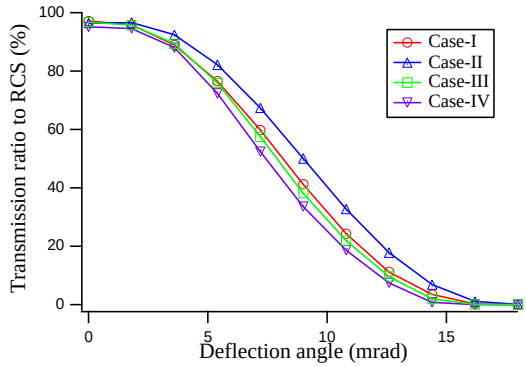

Figure 2: Transmission ratio vs deflection angle.

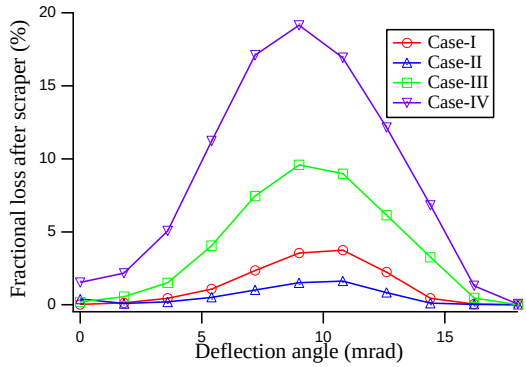

Figure 3: Downstream beam loss vs deflection angle.

set to eliminate the particles outside this boundary. Then, we label the particle outside this boundary as the particle supposed to hit the halo-collimator. The collimator load is found as the ratio of the number of the labeled particles to that at the entrance of MEBT.

DISCUSSIONS

With the beam test of the RF chopper system, we have confirmed that the rising- and falling- times of the chopper system is around 10 nsec [4], which means six micro-bunches are half-kicked in one intermediate-pulse cycle (three in the rising time and three in the falling time). Supposing that these six micro-bunches, respectively, have 20 %, 20 %, 50 %, 50 %, 80 % and 80 % of the design deflection angle (18 mrad in this case), total charge lost downstream becomes 8.9 % of a micro-bunch in Case-I. As an intermediate-pulse typically consists of 150 micro-bunches, the averaged excess beam loss due to beam chopping is estimated to be 0.059 %. Similarly, the excess beam losses are estimated to be 0.024 %, 0.19 %, and 0.41 % for Case-II, III, and IV, respectively. The excess halo-collimator load can also be estimated in a similar way, in which we find they are 0.18 %, 0.30 %, 0.18 %, and 0.11 % for Case-I, II, III, and IV, respectively.

These estimates depend on the initial supposition on the

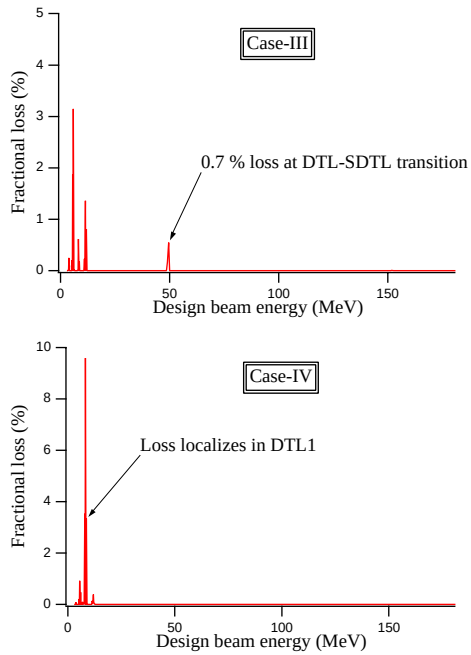

Figure 4: Loss profiles along the linac with the deflection angle of 9.0 mrad for Case-III (top) and Case-IV (bottom).

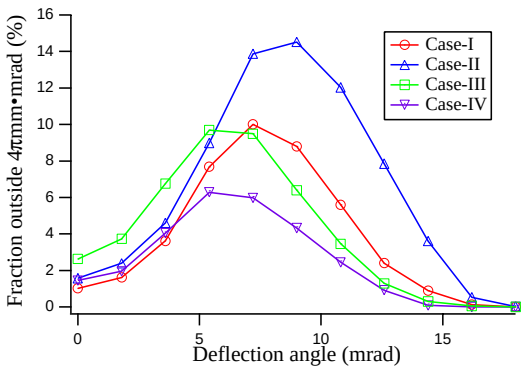

Figure 5: Halo-collimator load vs deflection angle.

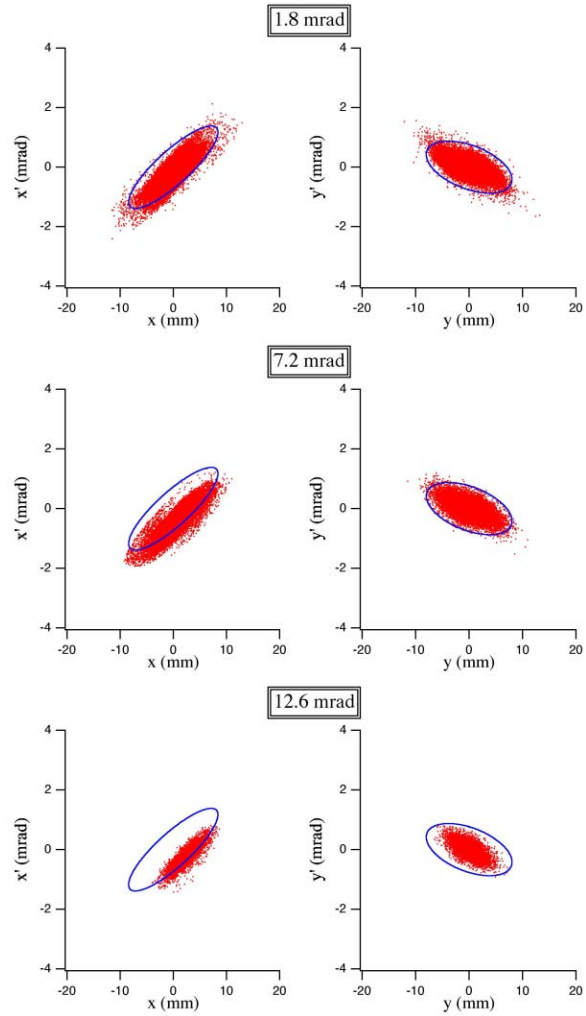

Figure 6: Phase-space distributions at the injection to RCS (Case-I). Phase-space distributions for three different deflection angles at the RFD cavities, i.e., 1.8 mrad (top), 7.2 mrad (middle), and 12.6 mrad (bottom), are shown. Blue ellipses show the 4πmm·mrad ellipses for the case without deflection.

fractional kicks for six half-kicked bunches. For example, supposing 10 %, 10 %, 40 %, 40 %, 70 % and 70 % of the design deflection angle, the excess-loss estimates decreases by 0.063 %, and the excess-collimator-load estimates increases by 0.19 % for Case-I.

To be noted here is that the excess beam loss is mostly localized in DTL1. While some excess beam loss after DTL1 is also anticipated, it is expected to be localized at the DTL-SDTL transition region and its amount is around 0.01 % level in average, which corresponds to around 2 W in 181-MeV operation.

REFERENCES

[1] Y. Yamazaki, "Status of the J-PARC Linac, Initial Results and Upgrade Plan", in these proceedings.

[2] Y. Yamazaki ed., "Accelerator Technical Design Report for J-PARC", KEK Report 2002-13; JAERI-Tech 2003-044.

[3] Y. Kondo, private communication.

[4] T. Kato et.al., "Beam Study with RF Choppers in the MEBT of the J-PARC Proton Linac", in Procs. of PAC2003, p. 1455 (2003).

[5] H. Takeda, "PARMILA", Los Alamos National Laboratory Report, LA-UR-98-4487 (1998).

[6] Y. Kondo et. al., "Particle Distribution at the Exit of the J-PARC RFQ", in these proceedings.

[7] M. Ikegami et.al., "A Simulation Study on Error Effects in J-PARC Linac", in these proceedings.

A SIMULATION STUDY ON ERROR EFFECTS IN J-PARC LINAC

Masanori Ikegami, KEK, Tsukuba, Ibaraki 305-0801, Japan
Tomohiro Ohkawa, Yasuhiro Kondo, Akira Ueno, JAERI, Tokai, Ibaraki 319-1195, Japan

Abstract

In this paper, effects of realistic errors on beam loss and beam-quality deterioration in J-PARC linac are examined with systematic simulations with PARMILA. Necessity of transverse collimation is also discussed.

INTRODUCTION

Requirements on the momentum spread and transverse emittance are severe for J-PARC linac [1, 2] to realize effective injection to the succeeding RCS (Rapid Cycling Synchrotron). The requirement for the momentum spread at the RCS injection is less than $\pm 0.1\%$ including beam centroid momentum jitter, and that for the normalized transverse emittance is less than 4πmm·mrad. To achieve the requirement for the transverse emittance, we have transverse halo collimators in the beam transport line between linac and RCS [2]. To meet the requirement for the momentum spread, we have two debuncher cavities in the beam transport line to the RCS, with which the bunch is rotated to minimize momentum spread [2, 3].

As losses and beam-quality deterioration are mainly caused by various errors, such as misalignment, RF setpoint errors, etc, it is essentially important to perform particle simulations for J-PARC linac with as realistic errors as possible to estimate their effects. In this paper, effects of realistic errors on beam loss and beam-quality deterioration in J-PARC linac are examined with systematic 2D and 3D simulations with PARMILA [4].

SIMULATION CONDITIONS

As discussed in a separate paper [1], we plan to start beam operation with the lower linac energy of 181-MeV. In this paper, simulations are performed with PARMILA from the exit of RFQ to the injection point to RCS for the 181-MeV case. In the simulations, we assume the peak current of 30 mA, which is the design value for 181-MeV operation. The initial distribution at the exit of RFQ is obtained with PARMTEQM [5]. The number of simulation particles is 95,322 and the number of meshes is set to 20x20x40 for 3D cases and 20x40 for 2D cases.

The quadrupole magnets in DTL and SDTL sections are set to satisfy the equipartition condition. No halo collimation has been assumed in the simulation.

EFFECTS OF STATIC ERRORS

In error analyses, dynamic errors and static errors should be treated separately. For example, beam orbit distortion is mainly caused by the alignment errors of quadrupole magnets, which are static by nature. Another obvious example is the beam centroid momentum jitter, which is solely determined by the dynamic component of the RF errors. We here refer drift or sway of RF phase and amplitude as "dynamic" regardless of their time-scale, and tuning errors of RF setpoints as "static".

Table 1: Assumed static errors

Errors	Range
Quad alignment error (transverse displacement)	± 0.1 mm
Quad alignment error (roll error)	± 5 mrad
Quad gradient error	$\pm 0.25\%$
RF amplitude error	$\pm 1\%$
RF phase error	± 1 deg

At first, we consider the static errors listed in Table 1. The errors are uniform-randomly distributed in the range. 20 cases with different random seeds have been considered. Simplified beam-orbit correction has been assumed only in the cases where the beam loss is significant, while we have an elaborated beam steering system in the actual linac. At the end of MEBT (in Run #8, 11, 14, and 17), we give a tilt to the beam to minimize the beam loss in DTL1. At the entrance of SDTL (in Run #8), we simply shift the beam center to the origin to avoid the loss in SDTL. Similarly, we shift the beam center to the origin at the exit of SDTL (in Run #5, 9, 11, 16, and 19) to avoid the loss in the beam transport line to RCS.

Figure 1 shows the obtained normalized emittance at the injection to RCS. The result for the case without errors is also shown. As seen in Fig. 1, the emittance exceeds 4πmm·mrad in most cases, and the particles outside 4π ellipse should be eliminated with halo collimators. Then, we estimate the collimator load by counting the number of particles locating outside the 4π boundary. We find that the collimator load ranges from 1 to 3 % and it is typically around 1.5 %, which is tolerable with the current radiation shielding of the halo collimator.

In the 20 cases, we have the beam loss of up to 2 % (typically less than 0.2 %), but they are mostly localized in the first DTL tank as shown in Fig. 2. While small amount of loss (up to 0.2 %) is observed at the DTL-SDTL transition, we have confirmed that it can be reduced to less than 0.01 % (2 W) level with beam steering at MEBT.

Figure 3 shows the energy spread and the longitudinal emittance at RCS injection. While substantial momentum spread increase have be observed, we have confirmed that dynamic RF errors plays a more dominant role in determining the final momentum spread as discussed later. As seen

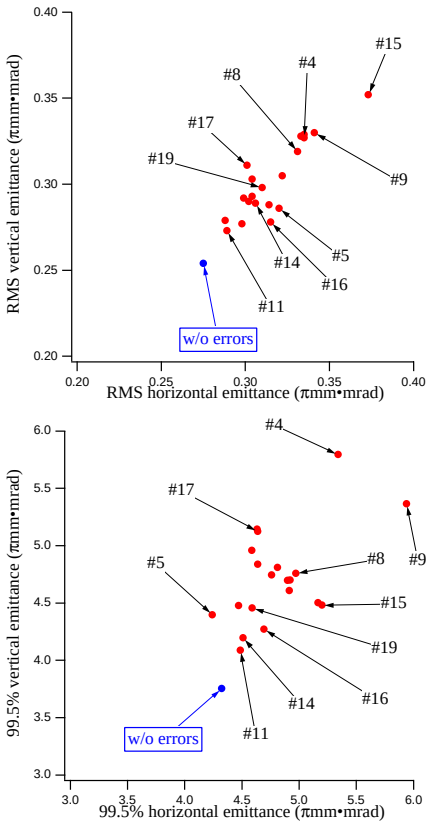

Figure 1: The normalized rms (top) and 99.5% (bottom) transverse emittances. Run numbers are labeled for the cases with characteristic results and those with beam orbit corrections.

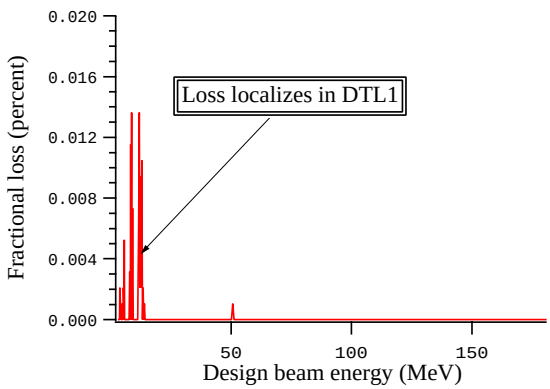

Figure 2: Typical beam loss profile (Run #1).

in Fig. 4, the phase-space distribution looks similar to the the case without errors [6].

EFFECTS OF DYNAMIC ERRORS

We have confirmed that the longitudinal filamentation in the debunching process is the primary source of the momentum spread at ring injection, and the dynamic RF errors play a dominant role in the filamentation [3]. In this section, we concentrate on the effect of dynamic RF errors, because satisfying the requirement for the momentum spread is one of toughest challenges in the J-PARC lianc commissioning.

The mechanism with which the filamentation occurs is simple. If the output beam energy from SDTL deviates, the energy deviation is translated into large phase deviation at debuncher location because of the long drift length between them. For example, energy deviation of 0.4 MeV at the

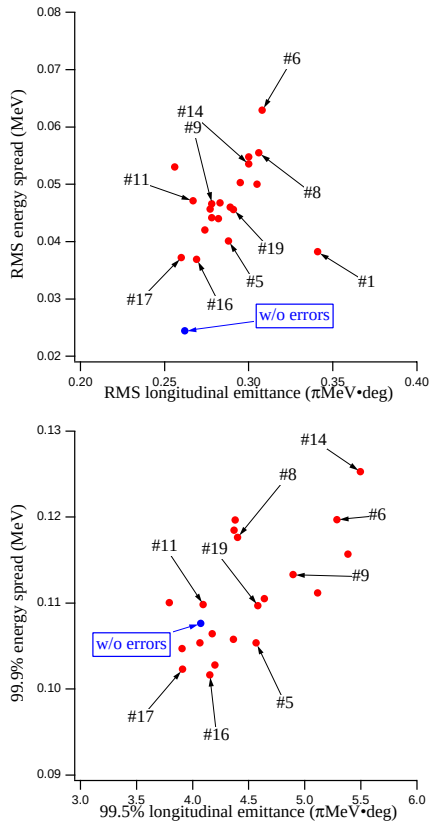

Figure 3: The rms energy spread vs the longitudinal rms emittance (top), and the 99.9% energy spread vs the 99.5% longitudinal emittance (bottom).

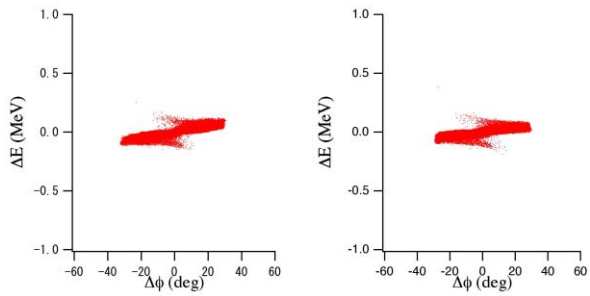

Figure 4: Longitudinal phase-space distribution for the cases with the largest energy spread (static RF errors). Run #6 (left) and Run #14 (right).

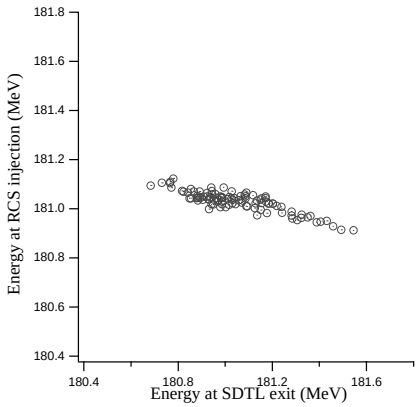

Figure 5: Beam centroid energy at RCS injection vs beam centroid energy at SDTL exit.

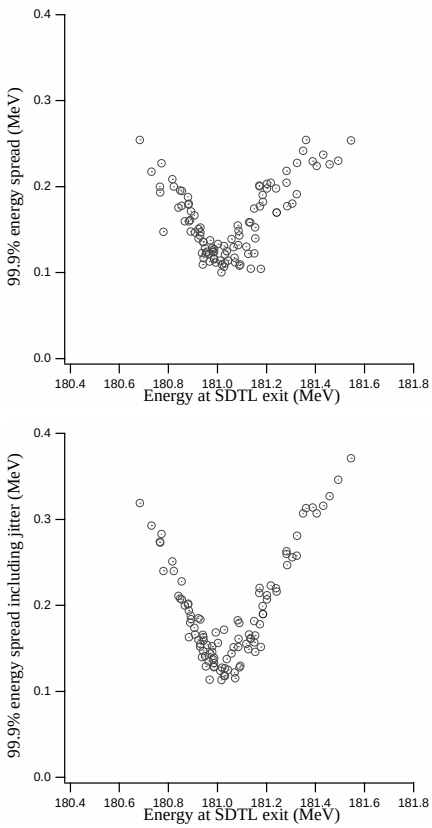

Figure 6: Energy spread at RCS injection. 99.9% energy spread (top) and that including beam centroid energy jitter (bottom).

exit of SDTL causes phase deviation of 32 deg at the first debuncher. To be noted here is that we don't have the large phase deviation for static RF errors, because the debuncher phase is adjusted to the shifted beam phase in a beam-based tuning procedure in that case.

To evaluate the effect of dynamic RF errors of debunchers, we have performed 100 2D runs with the dynamic RF errors of 1 deg and 1 % (Our goal for the dynamic RF error is 0.5 deg and 0.5 %). Figure 5 shows the beam energy jitter at RCS injection, which is reduced to around ± 0.1 MeV by debunchers. In Fig. 6, it is clearly seen that the beam with larger energy deviation at SDTL exit has larger energy spread at RCS injection. In spite of the severe filamentation as shown in Fig. 7, the energy spread meets the requirement (less than ± 0.333 MeV for 181-MeV operation) for RCS injection mostly, which is consistent with 3D simulation study [3] .

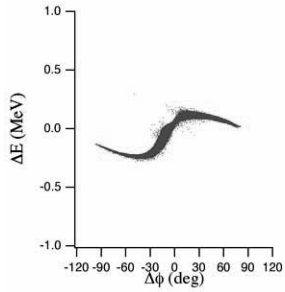

Figure 7: Longitudinal phase-space distribution for the case with the largest energy spread (dynamic RF errors).

SUMMARY

The effect of realistic errors are examined with 3D PARMILA for J-PARC linac. Transverse collimation is necessary to meet the requirement for the normalized transverse emittance at RCS injection. The fraction of 1.5 % should be eliminated at halo collimators in typical cases. While visible beam loss is observed in some cases, it is reasonably localized in the low-energy section of DTL. The energy spread meets the requirement for RCS injection mostly, although substantial increase of energy spread is anticipated due to dynamic RF errors. Because it is obvious that the linac output energy deviation is the primary source of the energy spread increase, feedback of the linac energy to the phase or amplitude of the last klystron is foreseen to eliminate the effects of slow drift of RF properties.

REFERENCES

[1] Y. Yamazaki, "Status of the J-PARC Linac, Initial Results and Upgrade Plan", in these proceedings.

[2] Y. Yamazaki ed., "Accelerator Technical Design Report for J-PARC", KEK Report 2002-13; JAERI-Tech 2003-044.

[3] T. Ohkawa et.al., "Design of the Beam Transportation Line from the Linac to the 3-GeV RCS for J-PARC", submitted to EPAC2004.

[4] H. Takeda, "PARMILA", Los Alamos National Laboratory Report, LA-UR-98-4487 (1998).

[5] Y. Kondo et.al., "Particle Distribution at the Exit of the J-PARC RFQ", in these proceedings.

[6] M. Ikegami et.al.,"Beam Dynamics Design of J-PARC Linac High Energy Section", in these proceedings.

ALTERNATING PHASE FOCUSING IN LOW-VELOCITY HEAVY-ION SUPERCONDUCTING LINAC*

P.N. Ostroumov#, A.A. Kolomiets†, K.W. Shepard, Physics Division, ANL, 9700 S. Cass Avenue,
E.S. Masunov, MEPhI, Moscow, Russia.

Abstract

The low-charge-state injector linac of the RIA post-accelerator (RIB) is based on ~ 60 independently phased SC resonators providing a total of ~70 MV accelerating potential. The low charge-state beams, however, require stronger transverse focusing, particularly at low velocities, than is used in existing SC ion linacs. For the charge-to-mass ratios considered here (q/A = 1/66) the proper focusing can be reached by using strong SC solenoid lenses with a field of up to 15 T. Both the number of the solenoids and field can be reduced applying Alternating Phase Focusing (APF). A method to set the rf field phases has been developed and studied both analytically [1] and with the help of the three-dimensional ray tracing code TRACK [2]. The paper discusses the results of these studies.

INTRODUCTION

The design goal for the RIB linac is to accelerate heavy ions up to 10 MeV/u and higher in the mass range from 6 to 240, starting with ions at charge state 1+ [3]. The initial section of the RIB linac is a low- charge-to-mass-ratio superconducting rf linac (SRF) which will accelerate any ion with q/A≥1/66 to at least ~1 MeV/u. The low-energy RIB linac will be based on 4-gap quarter wave SC cavities, which can provide typically ~1 MV of accelerating potential per cavity in the velocity range 0.011c<v<0.06c. The initial section of the linac consists of four classes of those cavities designed for different geometrical beta as listed in Table 1. The input beam is formed by upstream RFQs operating at room temperature. The initial normalized transverse emittance is ε_T =0.1 π · mm·mrad and the longitudinal emittance is ε_L =0.3 π · keV/u·nsec. The RIB linac described in this paper is designed using the 4-gap resonators designed for the RIA driver linac. These resonators, modified slightly to match the ATLAS operating frequency [3] are completely applicable for the RIB lianc.

REFERENCE DESIGN

As a reference design of the RIB linac we consider the focusing by high-field SC solenoids alternating with SC resonators. The main parameter which defines specifications to the focusing system is the defocusing factor which is significant due to the high accelerating field in the SC resonators and low velocity of ions.

The phase advance per focusing period of the betatron oscillations μ is defined as

$$\mu^2 = \mu_0^2 + \alpha \sin\varphi , \qquad (1)$$

where $\alpha = \dfrac{\pi eqUL}{2Am_e c^2 \lambda \beta^3 \gamma^3}$, μ_0 is the phase advance without any acceleration, α is the defocusing factor, φ is the particle phase with respect to the accelerating field crest in the resonator, eq and A are the charge and mass number of ion, L is the length of the focusing period, m_e is the atomic unit mass, c is the speed of light, λ is the wavelength of the rf field, β is the ion velocity in units of c. The formula (1) is valid for any particle phase with respect to the crest of the rf electric field in the cavity. There is a large phase slippage of the bunch in a SC resonator therefore it is convenient to introduce an effective phase φ_e which is measured with respect to the maximum energy gain phase angle in the resonator.

The transverse phase advance and average accelerating rate are inversely proportional to the length of the focusing period L. However the lowest possible value of L is limited by practically achievable focusing fields. Figure 1 shows transverse phase advance as a function of the solenoid field. The calculations have been performed for realistic field distributions both in the resonators and solenoids. The effective length of the solenoid is 280 mm,

Table 1: Resonators developed for the RIA driver linac.

Design beta of cavity	Frequency (MHz)	Maximum field (MV/m)	Voltage (MV)
0.017	57.5	20	0.82
0.024	57.5	20	1.07
0.031	57.5	20	1.25
0.061	57.5	20	1.35

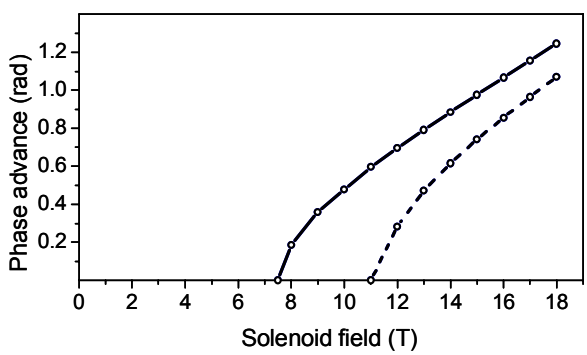

Figure 1: Transverse phase advance as a function of the solenoid field. The solid line corresponds to the bunch center and the dashed line - to the outermost particle phase.

*Work supported by the U.S. Department of Energy, Office of Nuclear Physics, under Contract No. W-31-109-ENG-38.
#ostroumov@phy.anl.gov
† On leave from ITEP, Moscow, Russia

L=700 mm and effective phase angle is φ_e=-20°. The solid line corresponds to the reference particle and the dashed line corresponds to the outermost particle in the longitudinal phase space with respect to the reference particle for the first period of the reference design. As is seen, a focusing field higher than 10 Tesla is required to provide stable motion of all particles in the bunch.

For the acceleration of heavy ions with q/A=1/66 from 75 keV/u to 1.0 MeV/u with effective phase angle -20°, the RIB linac requires a total of 63 resonators of four different types shown in Table 1. The constant average beam radius along the linac can be provided with average focusing field 14.7 T. The field varies along linac within ± 3% due to slightly different energy gain in the cavities. The full beam size does not exceed half of the aperture.

The cavities and solenoids will be distributed in seven cryostats with ~7 m length. The design of the cryostats is similar to those described in ref. [4]. There is a drift space between the cryostats [4] which the inter-cryostat distance 50 cm. Appropriate beam matching in both transverse and longitudinal phase space can be provided without any additional accelerating or focusing elements. However, careful tuning of the solenoids and resonator phases at each cryostat interface is required.

Beam dynamics simulations in the reference design of the RIB linac performed with the code TRACK [2] have shown that there is minor emittance growth along the structure as is seen from Fig. 2.

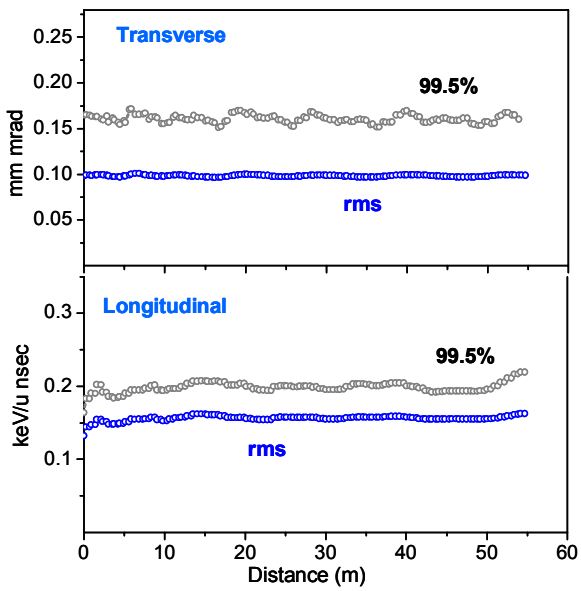

Figure 2: Emittance evolution along the baseline structure simulated by the TRACK code.

COMBINED FOCUSING STRUCTURE

The reference design completely meets the specifications for the RIB linac. However, it is achieved with a significant number of solenoids and the linac is long. As a result the real-estate accelerating gradient is ~30% of the gradient provided by the SC cavities. Also, very high-field SC solenoids are required. As was mentioned, above the required solenoid parameters are mostly defined by the high value of the defocusing factor α in the SC resonators. The strong defocusing can be converted to focusing by applying an alternating phase focusing (APF) [1]. As a result, the real-estate accelerating gradient can be increased. To create the APF, the effective phase must be alternated between positive and negative values. The analytical estimate has shown [1], that simultaneous stability of the transverse and longitudinal motion can be achieved despite significant phase slippage of up to 100^0 in an individual cavity. However to create a sufficient stability area, large values of the effective phases $|\varphi_e|$ in the cavities are required. The area of stability can be extended even for lower values of $|\varphi_e|$ by adding a focusing solenoid into the focusing period which will also allow separate control of transverse and longitudinal beam dynamics. The combined focusing structure (CFS) includes both SC solenoid and APF in every focusing period. Figure 3 shows phase advances in the CFS for two phase settings: 1) (φ_{e1}=-20^0, φ_{e2}=0^0) and 2) (φ_{e1}=-30^0, φ_{e2}=10^0). As is seen the phase advance in the CFS can be similar to those in the reference design. Unlike in the reference design, the focusing fields in solenoids are appreciably lower. The frequency of small longitudinal oscillations is similar to the reference design case but the real-estate accelerating gradient is higher because the focusing period consists of two or more resonators.

Figure 4 presents transverse beam envelopes along the first two cryomodules of the CFS simulated by the TRACK code. In the second cryomodule, the number of resonators per focusing period is increased up to three and four which is necessary to provide sufficient focusing while the parameter α drops as the ion energy increases. In the CFS shown in Figure 5, the average absolute value of the effective phase is equal to 20° as in the reference design while the required number of SC solenoids is significantly lower. In addition, the solenoid field is lower. The beam matching between the cryomodules is provided by appropriate adjustment of the effective phases in the outermost resonators and solenoid fields. As

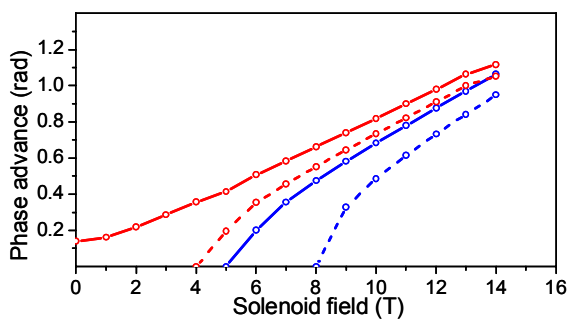

Figure 3: Transverse phase advance as a function of the solenoid field in the CFS. The blue lines correspond to the case (φ_1=-20^0, φ_2=0); the red lines are for the case (φ_1=-30^0, φ_2=-10^0). The solid line corresponds to the bunch center and the dashed line - to the outermost particle phase.

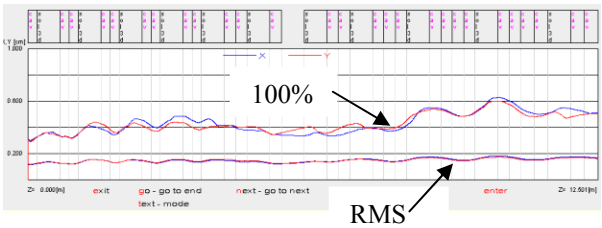

Figure 4: Transverse beam envelopes in first two cryomodules of the CFS.

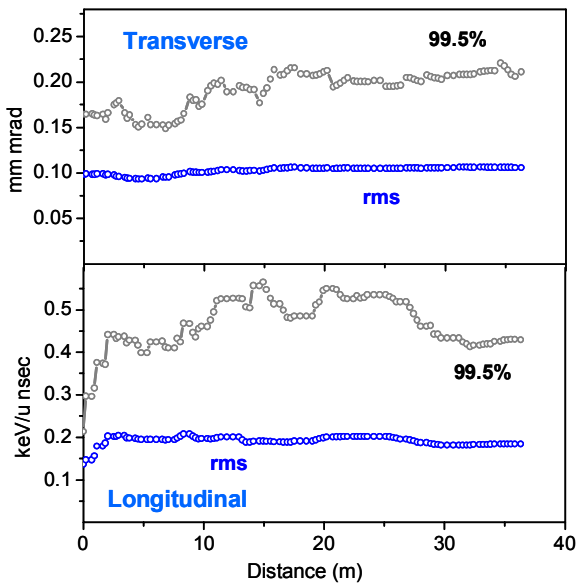

Figure 5: Emittances along the baseline structure simulated by TRACK code. Blue lines – rms, gray – for 99.5% simulated particles.

is seen from Fig. 3 the inter-cryostat transition does not disturb the beam envelope.

The disadvantage of the CFS is in strong coupling of the transverse and longitudinal degrees of ion motion. Figure 5 shows an evolution of transverse and longitudinal emittances in the CFS. As in the reference design there is no transverse emittance growth while the longitudinal rms emittance growth is 35% and emittance containing 99.5% of particles increases even more. The longitudinal emittance growth is a consequence of the electric field dependence from the radial coordinate in the low-velocity accelerating structures. This effect takes place in the first several resonators and can be minimized by lowering accelerating gradient or re-arranging the focusing period. Some additional studies are required to minimize the longitudinal emittance growth in the CFS.

COMPARISON OF TWO OPTIONS

The main parameters of two different lattices of the RIB linac, one based solely on high-field solenoid focusing and the other based on combined focusing by solenoids and APF are shown in Table 2. As is seen, the CFS allows reduction of the number of solenoids more than 50% and reduces the real-estate length of the linac. In addition the required solenoid fields are lower. A significant saving in the total cost of the accelerator is expected.

Table 2: Comparison of the main parameters of the reference and combined focusing structure.

Parameter	Reference design	Combined focusing
Average phase, deg	-20	-20
Number of resonators	63	73
Number of solenoids	69	27
Number of cryomodules	7	6
Average length of the cryomodule, m	7	5.5
Total length, m	54.7	36
Average real-estate accelerating gradient, MV/m	1.06	1.67
Solenoid field, T	15.0 – 13.5	14.0 – 12.0
Transverse phase advance	0.866 – 0.323	1.083 – 0.357
Longitudinal phase advance	1.00 – 0.245	0.549 – 0.256
Transverse rms emittance growth	< 1%	8%
Longitudinal rms emittance growth	22%	35%

CONCLUSION

Two options of the RIB linac section for acceleration of heavy ions with charge-to-mass ratio 1/66 have been studied: the reference design with periodic solenoid focusing and a combined focusing structure (CFS) with solenoids and APF. The CFS has obvious advantages compared to the reference design and can significantly reduce the cost of the RIB linac. However, additional studies to minimize longitudinal emittance growth in the CFS are necessary.

REFERENCE

[1] E.S. Masunov, et al. Proc. of the EPAC'04, Lucerne, Switzerland, paper TUPLT111.
[2] P.N. Ostroumov, V.N. Aseev, and B. Mustapha. Beam loss studies in high-intensity heavy-ion linacs, Accepted for publication in Phys. Rev. ST Accel. Beams, August 3, 2004.
[3] P.N. Ostroumov, et al. NIM, Section B, **204**, 2003, p. 433.
[4] J.D. Fuerst, K.W. Shepard. A cryomodule for RIA driver linac, 19th Intl. Cryogenic Engineering Conf., Grenoble, France, July 22-26, 2002.

ACCELERATION OF SEVERAL CHARGE STATES OF LEAD ION IN CERN LINAC3

V. Coco, J. Chamings, A. M. Lombardi, E. Sargsyan and R. Scrivens, CERN, Geneva, Switzerland

Abstract

CERN's LINAC3 is designed to accelerate a 100 μAe lead 25+ ion beam from 2.5 keV/u to 4.2 MeV/u. The beam is then stripped using a carbon foil and the resulting 25 μAe 54+ beam is accumulated and cooled in the Low Energy Ion Ring (LEIR) before transfer to the Proton Synchrotron (PS) and ultimately to the Large Hadron Collider (LHC). The lead 25+ ions are selected with a spectrometer from a mixture of ten charge states produced by an Electron Cyclotron Resonance (ECR) source.

In view of the fact that the stripping efficiency to lead 54+ is mostly dependent on energy and not on initial charge state, the feasibility of simultaneously accelerating to 4.2 MeV/u several charge states has been investigated. In this paper we report two possible technical solutions, their advantage in terms of intensity for the downstream machines and the experimental results supporting these conclusions.

MOTIVATION

LINAC3[1], the CERN lead ion injector has been operational since 1993 and providing an intensity of 25 μA of lead 54+ at 4.2 MeV/u to the Proton Synchrotron Booster (PSB). The beam is obtained by selecting a 2.5 keV/u 27+ lead ion beam from an ECR source and further accelerating it to 4.2MeV/u onto a 100 μg/cm^2 carbon foil. The acceleration is done in two stages: a 100MHz RFQ increases the beam energy to 250 keV/u and subsequently a system of three IH tanks (first one at 100MHz, the others at 200MHz) increases the beam energy to 4.2 MeV/u. The theoretical and experimental acceleration efficiency is around 85%, the stripping efficiency around 15% [2]. After stripping one charge state is selected and debunched to prepare for injection into the PSB. From 2006 the LINAC3 beam will be accumulated and cooled in a Low Energy Ion Ring (LEIR) before acceleration to LHC injection energy. The present set-up of LINAC3 is sufficient to meet the LHC needs [3]. Nevertheless, studies for exploring LINAC3 bottlenecks and possible improvements to its output current were pursued in the framework of the Ions for LHC (I-LHC) program. In view of the very good transmission of LINAC3 significant improvements can come either from a new source or from a new approach to producing lead 54+ at 4.2 MeV. In this paper we deal only with the second option. The efficiency of ionisation from lead 27 to lead 54 is quite low, because of the statistical nature of the interaction between charged particles and matter. This means that a good fraction of the intensity is lost due to the fact that more than 80% of the incoming ions are ionised to the "wrong" charge state. For this very same reason, a high charge state can be the result of the ionisation of a slightly different incoming charge state, i.e. lead 54+ can be obtained by stripping 25+ or 26+ or 27+ with the same foil thickness. Therefore, if we had more than one charge state simultaneously on the stripper within the nominal transverse emittance and energy spread, we could increase the overall useful current delivered by LINAC3. In the following we will report some theoretical and experimental observation on how to bring several charge states onto the LINAC3 stripper with minimum modification to the present set-up.

MULTICHARGE OPERATION

The ECR source of LINAC3 delivers, in the afterglow mode, 800 μA of lead shared between about 10 charge states. The source is optimised for delivering a maximum current made of 27+ lead ion and about 400μA of the total current is made of 24+,25+,26+, 27+ and 28+[4].

Low Energy Beam Transport (LEBT)

The LEBT is designed to select a pure single charge state lead ion beam. The 135 degrees spectrometer placed after the source is composed of two 67.5 degrees bending spaced by 700 mm. After the selection, a system of three quadrupoles and a solenoid matches the beam to the RFQ. We have analysed two solutions to bring several charge states at the RFQ entrance. The first one involves eliminating the spectrometer and putting the source in line with the RFQ: the new LEBT line, 2.4 m in length and equipped with three solenoids would allow all the charge states (5 of which also well matched) to the RFQ entrance. This solution, conceptually the easiest, involves major modifications to the present set-up and acquiring a new solenoid. It will be referred to as the "straight injection" solution and its beam dynamics can be seen in Fig. 1.

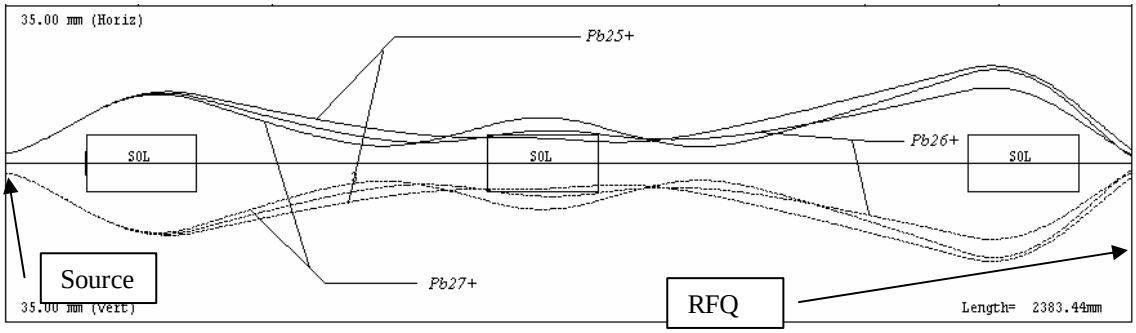

Figure 1: Beam dynamics in the LEBT for the straight injection solution.

An alternative solution aiming at nullifying the dispersion and its derivative without uprooting the present set-up involves adding a third magnet to the spectrometre with opposite bending field. In particular the following constraints were taken into account: that the total bending angle should be the same as the initial one, that the space available between the two nominal bending magnets is limited to about 200mm, and that the overall emittance of all the recombined charge states should be matched to the RFQ acceptance of 200 pi mm mrad. A magnet with an effective length of 80 mm and average field of 0.5 T placed between the two main spectrometre magnets would allow three charge states to be matched to the RFQ with an efficiency of 75% (9 % losses on the vacuum chamber 16% outside the RFQ acceptance). This solution, referred to as the "reverse bending", can cohabitate with nominal operation. The dynamics in the reverse bending and in the matching to the RFQ is shown in Fig 2 and 3.

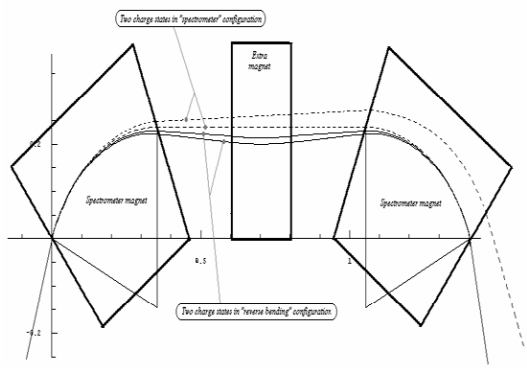

Figure 2: Principle of the reverse bending.

The proof of principle of the reverse bending solution was experimentally tried with a magnet which could give only 10% of the required field: a decrease of the dispersion was observed but stronger magnet is required for a fully conclusive experiment.

Radio Frequency Quadrupole (RFQ)

The LINAC3 RFQ is designed for a 25+ lead ion beam with excellent transmission and beam quality. We want to evaluate its efficiency when several charge states are injected simultaneously. The beam dynamics issues are the following: the different charge states have a different input longitudinal velocity and they receive a different acceleration per cell in the RFQ. Those two factors which are equivalent to a bigger overall input energy spread and a voltage jitter inside the RFQ have an impact on the overall output longitudinal emittance. The source extraction voltage and the RFQ vane voltage are the two parameters that can be used for the optimisation. Theoretical studies have shown that the minimum output longitudinal emittance for a population of three charge states is reached when the voltage in the RFQ is set correctly for the charge state with the biggest offset in input energy. The theoretical prediction was verified experimentally, by passing one charge state population at the time without changing the setting of the optics line matching to the RFQ. With these measurements we could verify the transmission of the nominal and adjacent charge state in presence of transverse mismatch and verify the prediction on the voltage settings. One should note that this procedure is valid if there are no collective effects, which is what we observe in simulations.

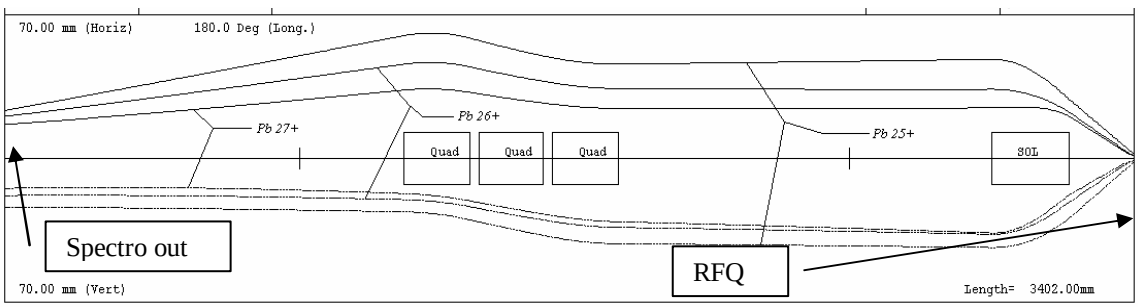

Figure 3: Beam dynamics in the LEBT for the reverse bending solution.

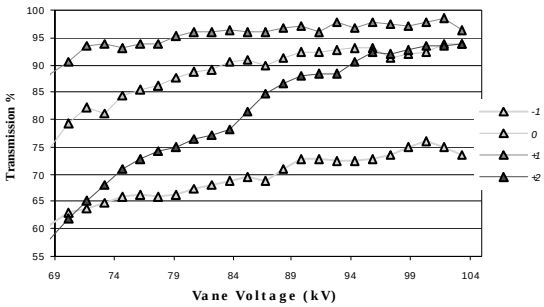

Figure: 4: Measured transmission vs. RFQ vane voltage for four adjacent charge states (0 is the charge state for which the matching to the RFQ has been optimised).

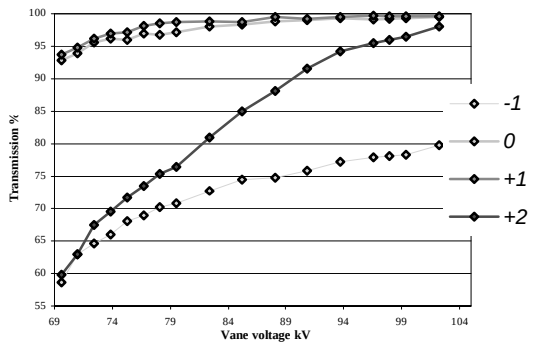

Figure 5: Calculated transmission vs. RFQ vane voltage for different charge states. Each charge state was individually matched to evaluate the effects of mismatch by comparison with the data on Fig4.

From Fig 4 and 5 we can learn that four charge states can be accelerated in the RFQ simultaneously, that the effect of mismatch for the adjacent charge state is noticeable only for one charge state and that it can be compensated by increasing the RFQ vane voltage.

Interdigital H-Structucture (IH)

The IH structure is very sensitive to any longitudinal mismatch and its acceptance is very tight hence particular care has been used to optimise the longitudinally matching of the three charge states from the RFQ. Designed for Pb25+, the IH Linac cannot accelerate lower charge states, while acceleration for two higher charge states is rather good. As lower charge states receive an energy gain less than the design one, they stay in an unstable area, and are lost already in the first tank. With these preliminary considerations we look at the possibility of accelerating simultaneously Pb25+, 26+ and 27+. The overall transmission for three charge states has been optimised both transversally and longitudinally [6]. In particular, quadrupoles are optimised for maximum possible total transmission and, RF phase and voltage in tanks are used mostly to ensure beam quality. Tank 1 and Tank 2 voltages are suitable for tuning the beam transmission and longitudinal parameters while the voltage in Tank 3 acts mainly on the output energy of the beam. Experimental results are reported in Fig. 6.

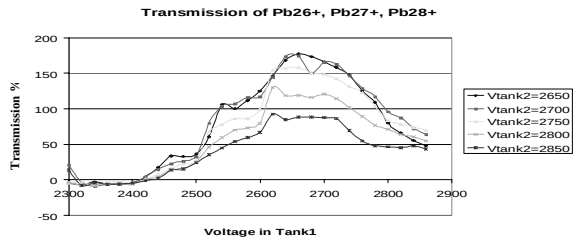

Figure 6: Transmission of three charge states through the LINAC3 IH. For reference the single charge state transmission is 85%.

Comparison of the Proposed Solutions

In order to estimate the advantages of the multicharge solution over the present single charge acceleration scheme, we have performed an end-to-end simulation of the different set-ups starting from the source up to the end of the line which selects the lead 54+ for injection into LEIR. We have used the same beam at the source and transported it through the optimised configuration for each case. The figure of merit is the intensity of lead 54+ inside the typical transverse emittances and momentum spread expected by LEIR (2.1 mm mrad rms and 0.1 % dp/p-5sigma) [7]. This figure of merit accounts for the losses in the accelerator as well as for any transverse and longitudinal emittance increase, resulting in the effective gain as seen from the downstream accumulator. The results are that both solutions give abut twice as much particles: 80% if the reverse bending solution is chosen or up to 150% more if the straight injection solution is chosen.

CONCLUSIONS

It is possible to accelerate simultaneously 3 charge states of lead ion through the RFQ and the IH of LINAC3. This possibility allows us to increase the intensity delivered to LEIR, the low energy ion ring for the LHC ion program, by a 80% or 150% depending on the technical solution chosen for the LEBT.

REFERENCES

[1] D. Warner editor, “CERN Heavy Ion Facility Design Report”, CERN 93-01, Apr. 1993.
[2] J. Chamings, V. Coco, A.M. Lombardi, R. Scrivens, “Measurements of Emittance and Twiss Parameters in LINAC3”, AB-Note-2004-002-ABP
[3] K. Schindl,”Ion Injector Issues”, LHC Project Workshop, CHAMONIX XIII,19-23 January 2004 .
[4] J. Chamings, “Charge state distribution scans on LEBT of LINAC3”, AB-Note-2004-056-ABP
[5] V. Coco, A.M. Lombardi, E. Sargsyan, R. Scrivens, “Restudy Of Linac 3 For Acceleration Of Several Charge States Of Lead”, AB-Note-2004-033-ABP
[6] E. Sargsyan, V. Coco, A.M. Lombardi, “Interdigital H-Type Linac Simulations And Measurements In The Framework Of Cern Linac 3 Restudy”, AB-Note-2003-083-ABP
[7] C. Carli private communication

PROTON BEAM DYNAMICS OF THE SARAF LINAC

A. Shor, D. Berkovits, G. Feinberg and S. Halfon, Soreq NRC Yavne 81800 Israel
K. Dunkel, ACCEL Instruments GmbH, Bergisch-Gladbach, Germany

Abstract

We have performed proton beam dynamics simulations for the SARAF (Soreq Applied Research Accelerator Facility), 40 MeV and 4 mA, linac. The simulations are performed using the GPT code and includes effects of space charge. They demonstrate that for an initial 6D ellipsoid Waterbag distribution beam, a tune can be obtained with a longitudinal rms emittance growth of 5% and a transverse normalized rms emittance growth of 20%. Beam loss is estimated by fitting a radial Gaussian to the particle distribution along the linac. A 1 nA beam envelope is obtained by extrapolating the tail of the radial-Gaussian function. The 1nA beam envelope for an initial Waterbag distribution is well within the beam bore radius. However, benchmark simulations with an initial 6D ellipsoid Gaussian distribution, with the same rms quantities, exhibit a more extended tail that may result in higher beam loss.

INTRODUCTION

Beam dynamics simulations for the SARAF [1] linac (fig. 1) are presently being performed at Soreq. We present results of the simulations performed with the General Particle Tracer (GPT) simulation code [2] and the LANA [3] code. Both codes enable precise calculations of particle tracking, taking into account realistic 3D fields of accelerating and focusing elements and also effects of space charge. GPT contains provisions for generating random particles, and for incorporating user supplied codes.

The SARAF accelerator consists of an ECR ion source (20 keV/u), a low energy beam transport (LEBT), a 176 MHz 4-rod RFQ for bunching and pre-accelerating to 1.5 MeV/u, a medium energy beam transport (MEBT), and a linac. The linac is based on independently phased superconducting (SC) 176 MHz half-wave resonator cavities (HWR) and SC solenoids. The accelerator is based on the ACCEL design [4], consists of two types of HWRs, one optimized for η_0=0.09 and a second for η_0=0.15 [5]. The linac consists of six self-contained SC modules. The first module, referred to as the PSM (Prototype SC Module), consists of three solenoids, each followed by two η_0=0.09 HWRs. The remaining five modules consist of 4 solenoids, each followed by two η_0=0.15 HWRs. Figure 1 shows a schematic of the SARAF linac.

Typically, particles simulations generate the initial particle distribution according to a 6D ellipsoid, with either a Waterbag (WB) or Gaussian (Gauss) distribution. The 6D ellipsoid establishes the particle distribution and correlations in x-x', y-y', and z-z', or π-÷E spaces. The WB option establishes a uniform distribution within the 6D ellipsoid, while the Gauss option establishes a density profile with a Gaussian falloff. ACCEL has performed extensive beam dynamics simulations of the linac assuming an initial 6D ellipsoid with a WB distribution. We use the ACCEL linac lattice and tune and repeat their simulation with the codes GPT and LANA.

INITIAL DISTRIBUTION GENERATOR

GPT version 2.52 has no provisions for a 6D ellipsoid, but it does contain option for linking a user routine to the GPT code. We embarked on developing algorithms for creating a 6D ellipsoid, with a WB or Gauss distribution, and incorporating a reliable code into the GPT particle generator. This code was tested and checked for consistency and reliability.

In the algorithm for generating events within a 6D ellipse we first generate random numbers for x, x', y, y', z and z' uniformly distributed within the given boundaries, according to:

$$4\sqrt{\kappa_x\eta_x}\ \Omega x\ \Omega\sqrt{\kappa_x\eta_x} \text{ and } 4\sqrt{\kappa_x\nu_x}\ \Omega x'\ \Omega\sqrt{\kappa_x\nu_x} \qquad (1)$$

and similarly in the y and z plans, where κ is the emittance and η and ν are the Twiss parameters.

If the event is inside the ellipse, i.e. if the inequality in eq.(2) is satisfied then we accept, otherwise, reject the event. This procedure populates a 6D ellipsoid with a uniform particle distribution (except for statistical fluctuations) - a Waterbag distribution.

We base our algorithm for a 6-D Gauss distribution on the acceptance-rejection method of von Neumann [6]. First, we generate an event according to the prescription described above for the 6D WB. The left side of eq.(2),

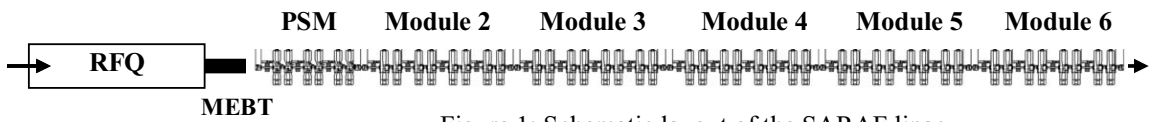

Figure 1: Schematic layout of the SARAF linac.

defined as $\wedge$, represents the fraction of the total for the ellipsoid encompassing the chosen point. $\sqrt{\wedge}$ represents the fraction of maximum extent within the ellipse at the selected orientation. We then generate a random number $0<U<1$. If the inequality, $\exp(4/\sqrt{\wedge}N_\omega^2/2)\{U$, where N_ω is the number of standard deviations desired, is satisfied, then we accept the event. This populates a 6D Gauss up to N_ω standard deviations.

$$\left\{\begin{array}{l}\frac{1}{\kappa_x}\left(\nu_x x^2+2\zeta_x xx'+\eta_x x'^2\right)\\ \frac{1}{\kappa_y}\left(\nu_y y^2+2\zeta_y yy'+\eta_y y'^2\right)\\ \frac{1}{\kappa_z}\left(\nu_z z^2+2\zeta_z zz'+\eta_z z'^2\right)\end{array}\right\}\le\Omega^2 \qquad (2)$$

LINAC TUNE

We performed proton beam dynamics simulations of the MEBT+linac using the GPT code and benchmarked the PSM simulation using LANA. The simulations contained the real 3D field maps for the HWRs as calculated by ACCEL using MWS, and included the Scheff prescription for space charge. We generate 5000 macro-particles at 4 mA. The initial particle distribution in GPT was taken as a 6D ellipsoid with a WB or Gauss distribution. The longitudinal rms emittance was 74 ϕ keV deg with Twiss parameters ζ_z=0 and η_z=0.771 deg/keV. The transverse rms normalized emittance was 0.2 ϕ mm mrad, with ζ_x=-1.38 and η_x=0.46 mm/mrad and ζ_y=0.96 and η_y=0.61 mm/mrad. At this stage, misalignment, fabrication and operation errors are not included in the GPT simulation.

A good tune was obtained with small longitudinal and transverse emittance growth, and with a small rms transverse envelope (fig.2) by using exactly the same HWR's amplitude and phase and solenoids field as in ACCEL's PARMELA beam dynamics simulation [7].

We have performed a benchmark simulation of protons in the PSM using LANA. We find a good agreement in the longitudinal phase space in term of bunch width, ion energy and rms emittance. In the transversal phase space there is a good agreement in the rms emittance and a difference in the r_{rms} envelope (fig.3). This difference is caused by the solenoid field approximation. While LANA uses the hard-edge approximation GPT is using a field parameterization that predicts a much closer approximation to the field of the solenoid simulated by ACCEL using OPERA.

We have also performed beam dynamics calculations for 5000 protons with an initial 6D ellipsoid Gaussian distribution. Using the same tune as for the WB distribution we obtained a 33% normalized transversal rms emittance growth along the linac. The r_{rms}

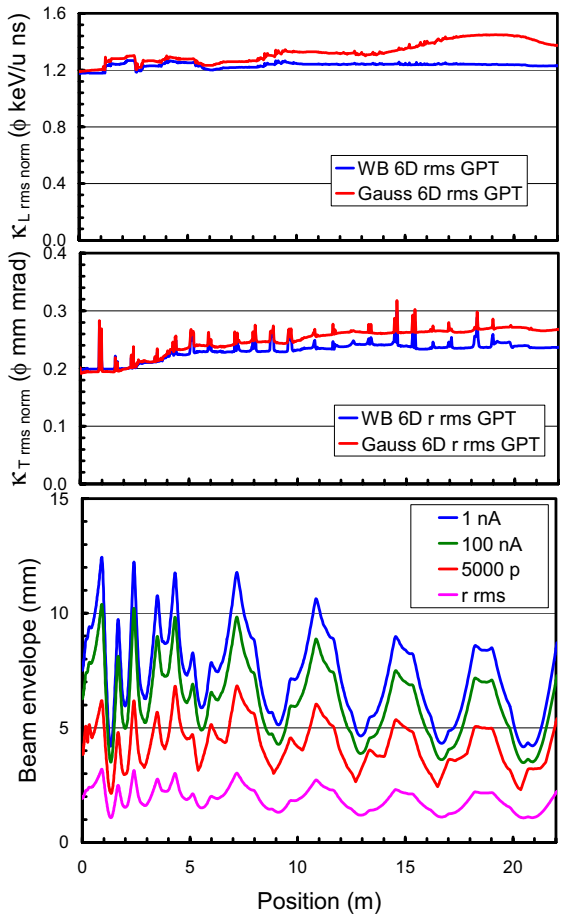

Figure 2: Longitudinal (top) and Transversal (middle) normalized rms emittance along the 22 m of the linac for initial WB and Gauss proton distributions. Bottom: the rms and 5000proton 6D WB simulated envelopes and the prediction of the 1 and 100 nA envelopes along the linac based on eq.(4). The jumps in κ_T are due to the tangent velocity at the solenoids entrance and exit.

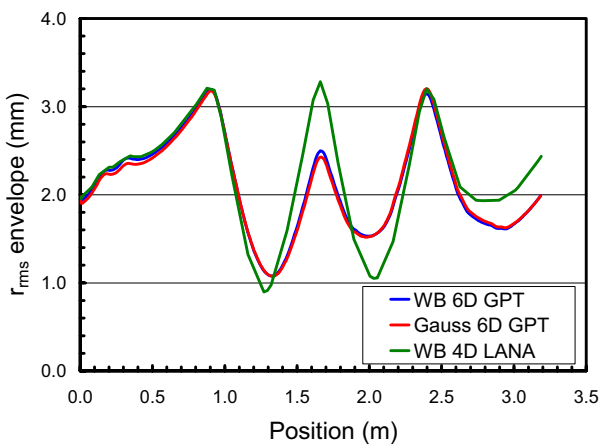

Figure 3: Benchmark simulations of the PSM for different initial proton distributions using GPT and LANA.

($r = \sqrt{x^2 + y^2}$) envelope along the linac for an initial 6D Gauss is very similar to that of the 6D WB (fig.2).

BEAM LOSS PREDICTION

Beam dynamics calculations that contain real 3D fields for the RF cavities and include space charge effects for intense beams are very time consuming. To determine the Hands-On maintenance criterion of 1 nA beam loss out of a 4 mA beam would require a simulation containing at least $4\Delta 10^6$ macro-particles. Instead, extrapolations relying on simulations with a modest number of macro-particles will provide a rough estimate on the expected beam loss.

At various locations along the linac, histograms are made of the transverse deflections of the simulated particles. Each histogram is fit with a radial Gaussian function. Using this function, an extrapolation is made to the beam bore radius to determine the fraction of events that hit the beam pipe. Alternately, an extrapolation for a 1 nA beam profile can be made.

For our calculations, we assume that the transverse beam has a cylindrical symmetry. This is justified since the MEBT delivers a beam symmetric in x and y to the linac. Although the HWRs introduce a relatively small quadropole effect, the solenoid magnets rotate the beam transversely and help maintain a beam symmetric in x and y. We parameterize the transverse spread as a "modified radial Gaussian" function in r, as follows:

$$\div I = k \left[\frac{r}{\omega^2}\right] \left[e^{(4^{(r4\eta)^2}/2\omega^2)}\right] \div r \qquad (3)$$

where r_1 is a free parameter, I is the beam current and K is a normalization factor.

Figure 4 shows probability function histograms of the transverse distribution of the 5000 macro-particles at the location of the 3rd and 8th solenoids, where the largest transverse size occurs. Also superimposed on the histogram is a best fit of the "modified radial-Gaussian" probability function of eq.(3). The events in the tail of the histogram lies below the curve of this modified radial-Gaussian fit for the initial 6D WB distribution, however, the initial 6D Gaussian simulation show events that deviate significantly from the "modified radial-Gaussian" fit.

For a beam pipe bore radius $R>>r_1$ (and approximating $r_1=0$) the beam loss is given by:

$$\frac{I_{loss}}{I_0} = \exp\left(-\frac{R^2}{2\omega^2}\right) \quad \text{and} \quad \omega = \frac{r_{rms}}{\sqrt{2}} \qquad (4)$$

$$\frac{1\,nA}{4\,mA} = 2.5 \times 10^{-7} \quad \Rightarrow \quad R = 5.5\omega$$

The method for determining the 1 nA transverse beam profile is straightforward. We take the profile for r_{rms} and multiply by a factor of 5.5/· 2, as shown in eq.(4). The result is the 1 nA profile as shown in fig.2. This 1 nA envelope is well within a beam bore radius of 15 mm.

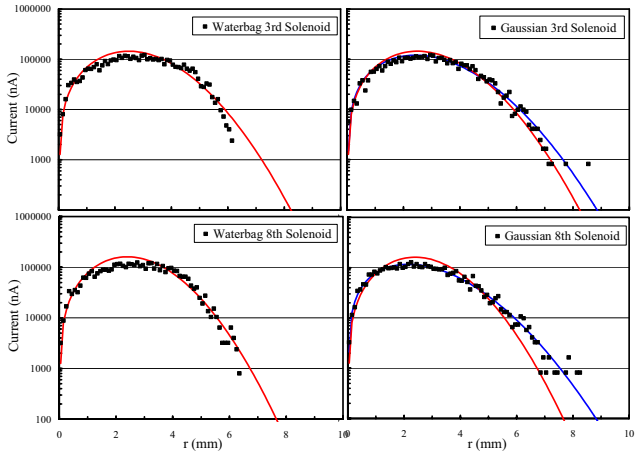

Figure 4: Proton transverse distribution probability function at the location of the 3rd solenoid (top) and the 8th solenoid (bottom) for initial WB and Gauss 6D distributions and best fits to the data using eq.(3). The fitting curve of the WB distribution (in red) is presented on top of the Gauss histograms (right) in order to guide the eye.

CONCLUSIONS

The SARAF proton beam dynamics simulation demonstrate that for an initial 6D WB distribution a tune with rms emittance growth less than 5% longitudinally and 20% transversally and envelope well within the beam pipe is obtained. The 1 nA radial-Gaussian extrapolation appears to be justified for an initial 6D WB distribution. However the 6D Gauss distribution exhibits a more extended tail than the prediction of the "modified radial-Gaussian" curve.

REFERENCES

[1] H. Watzman, Nature 410(2001)399.
[2] General Particle Tracer (GPT), release 2.52, Pulsar Physics Ltd., The Netherlands.
[3] D. Gorelov, MSU, LANA code version 9.4.8 (1996-2002).
[4] K. Dunkel, M. Pekeler, C. Piel, H. Vogel, P. vom Stein, Proc. of EPAC 2004, Lucerne, 5 to 9 July (2004).
[5] M. Pekeler, K. Dunkel, C. Piel, H. Vogel, P. vom Stein, Proc. of EPAC 2002, Paris, (2002) 936.
[6] R. Rubinstein, "Simulation and the Monte Carlo Method", Wiley & Sons, 1981.
[7] N. Pupeter and C. Piel, ACCEL Instruments GmbH, internal report no. 1290-BP-1552-0, October 31 (2003).

MULTI-BUNCH BEAM DYNAMICS STUDIES FOR THE EUROPEAN XFEL

N. Baboi*, DESY, Hamburg, Germany

Abstract

In the X-ray free electron laser (XFEL) planned to be built at DESY the acceleration of the electron bunches will be made by 9-cell superconducting cavities. These cavities have been initially developed within the TESLA (TeV Energy Superconducting Linear Accelerator) linear collider study. The impact of the higher order modes (HOM) has been shown to be within the acceptable beam dynamics limits for the collider. For the XFEL the dynamics is relaxed from the point of view of multi-bunch effects (e.g. lower bunch charge, higher bunch emittance). However the lower energy and different time structure of the beam make the study of the HOM effects in the XFEL linac desirable. Multi-bunch beam dynamics simulations have been made. The results of the HOM measurements at the TESLA Test Facility are used. Several options for the beam structure and energy are studied.

INTRODUCTION

In the European XFEL [1, 2, 3] a beam of up to 400 electron bunches with 10 to 20 GeV energy will generate ultrashort, high-intensity, coherent X-rays in long undulators. The design is based on the superconducting technology developed for the TESLA linear collider study [1, 4]. For the SASE FEL process, a good alignment, low emittance and small energy spread of the beam are essential. The main cause of degradation of the multi-bunch beam dynamics is the long-range wakefields generated by each bunch in the accelerating cavities. These may lead to accumulating deflections of the subsequent bunches, so that the multi-bunch emittance increases. The study of the wakefield effects is therefore important.

No dedicated multi-bunch beam dynamics simulations have been made so far for the XFEL. However many estimations could already be made based on the extensive studies made for TESLA [1, 5]. In the linear collider two beams, one of electrons and one of positrons, would be accelerated against each other to an energy of 500 GeV c.m. in an initial stage, and later up to 800 GeV c.m. The emittance preservation in the XFEL is less critical than in the case of TESLA due to the lower bunch charge and length and the higher design emittance (see Table 1). Therefore smaller wakefield effects are expected. However one should take into account some major differences, such as the lower energy, where the wakefield kicks are stronger and the different pulse structure. Therefore a series of simulations have been made of the multi-bunch emittance dilution along the XFEL linac. The results are discussed hereafter.

* nicoleta.baboi@desy.de

Table 1: Comparative parameters for XFEL and TESLA

	XFEL	TESLA
bunch length (fs)	80	1000
bunch spacing (ns)	min. 200	337
bunch train length (μs)	max. 800	950
bunch charge (nC)	1	3.2
beam energy (GeV)	max. 20	250
normalized emittance (m·rad)	$1.4{\cdot}10^{-6}$	$3{\cdot}10^{-8}$

MULTI-BUNCH DYNAMICS SIMULATIONS

Linac layout For the multi-bunch tracking, we have considered the linac design previously used in simulations of single-bunch effects [6]. The layout has been recently slightly changed, to two bunch compression stages in order to increase jitter tolerances [3, 7]. These changes should not affect the multi-bunch effects. A photo-injector produces electrons bunches of 1 nC which are immediately accelerated by four cryo-modules. Each cryo-module contains eight 1 m long 1.3 GHz accelerating cavities (TESLA cavities). Fig. 1 shows the beta function along the linac starting with the last cavity of the first module, where our simulations begin. The linac elements are also schematically shown.

After the first TESLA modules, the bunches pass through a cryo-module with eight cavities working at 3.9 GHz, used to compensate for non-linear distortions of the longitudinal phase space. Two subsequent bunch com-

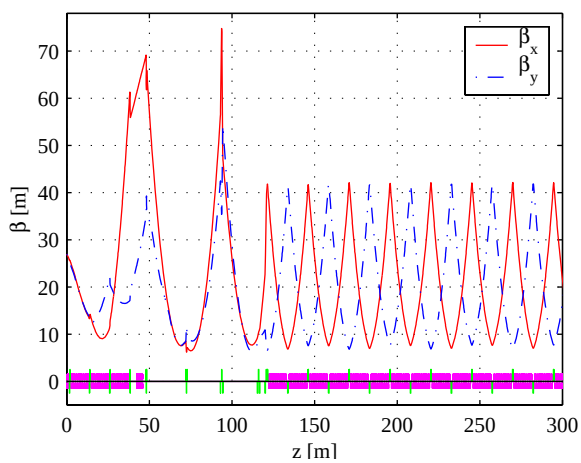

Figure 1: Beta function along the linac. The cryo-modules and quadrupoles are also sketched. The 3.9 GHz module is situated at z ≈ 45 m. Two bunch compressors are placed between about 50 and 120 m.

pressors reduce the bunch length to 80 μs. Then 57 FODO cells containing each 2 cryo-modules and 2 quadrupoles bring the electrons to a maximum energy of 20 GeV. The figure shows only the first few FODO cells, which repeat themselves up to a total length of about 1.5 km. From here the bunch train is directed into the undulators where the FEL beam is produced.

HOMs in the TESLA cavities The long-range wakefield, excited by each bunch at the passage through an accelerating cavity, are given by the sum of many individual resonances, the higher order modes (HOM). The main effect on the beam is given by dipole modes.

The frequencies and quality factors of the modes from the first 2 dipole bands have been measured in a single cavity test setup in most cavities built for the TESLA Test Facility (TTF) [8]. It has been found that in most cavities all modes are well damped by the special couplers mounted at each side of the cavities. For the simulations the average frequencies resulted from these measurements are considered. For the quality factors (Q) higher quantities than the most likely values are assumed. For the simulations we take into account all modes from the first 2 bands and 3 modes with highest loss factor in the 3rd band. However there are only few modes with a large loss factor, i.e. with a strong interaction between the mode and the beam [9].

Simulation assumptions For the simulations we have used the MAFIA-L code [10]. The beam is injected on-axis with an energy of 117 MeV into the last cavity of the first cryo-module, where the simulation is started. In the first four cryo-modules and the 3.9 GHz cavities the acceleration is made off crest, for bunch compression. The electrons are accelerated here up to about 730 MeV. The phase in the cavities of the FODO cells is adjusted for maximum acceleration. The gradient is 20.65 MV/m. The beam reaches a final energy of approximately 20 GeV. All the modes from the first 2 dipole passbands as well as 3 modes from the 3rd passband are considered, although only about 5 dipole modes will effectively contribute to emittance dilution. The wakefields in the 3.9 GHz cavities has been neglected. The cavities have a misalignment of 500 μm rms. The HOM frequencies have a spread among the cavities of 0.1% rms. The bunch spacing is 200 ns, and the maximum number of bunches is 4000. Other bunch distances, train lengths and final energies have been considered as well. 100 random machines have been calculated in each case.

Results

Reference bunch train We consider first the case of 200 ns bunch spacing and 800 μs pulse length (4000 bunches). Fig. 2(a) shows typical offsets of the bunches at the end of the linac, while in Fig. 2(b) the bunch train is displayed in the phase space. The rms of the bunch positions is in this case 0.7 μm (5.7%). While the maximum oscillation of the bunch offsets of 20 μm may be a problem

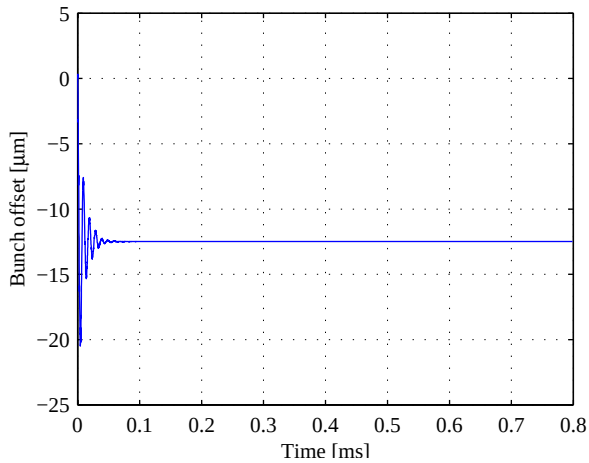

(a) bunch offsets

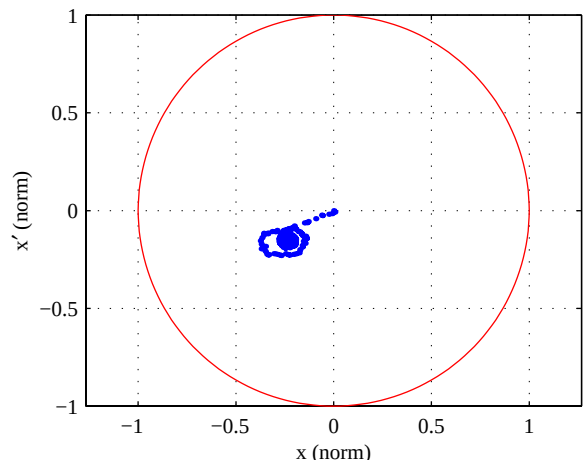

(b) phase space

Figure 2: Typical bunch train at the linac end for 4000 bunches spaced by 200 ns. The energy is 20 GeV.

for the FEL process, it is important to note that the variations are concentrated in the first less than 50 μs. This part could be deflected towards a dump and only the high quality tail of the beam be used in many experiments. On the other hand, the deflections in subsequent beam pulses are almost identical, as it was shown for TESLA [11]. Therefore the unwanted offset (and angle) variations along the trains can be corrected with a feedback system.

Fig. 3 shows the emittance dilution along the linac. The average over all machines has been made. The emittance growth relative to the design slice emittance $\Delta\varepsilon/\varepsilon$ is $0.02 \pm 0.02\%$, which is negligible.

Various pulse length and bunch spacings If the pulse length is shortened as compared to the reference case above, the steady state is not reached (see first part of the beam in Fig. 2(a)). The emittance increases significantly. In particular for a train length of 20 μs a multi-bunch emittance growth of $0.62 \pm 0.69\%$ is reached. In many situations one can accelerate a pulse longer than the desired

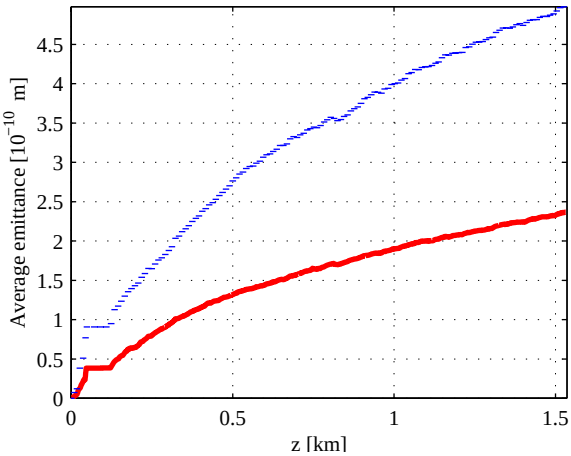

Figure 3: The emittance growth along the linac for 4000 bunches spaced by 200 ns. The energy is 20 GeV. The emittance is averaged over 100 random machines. The upper lines represent the limit of standard deviation bars.

length and then retain only the steady state part. However the question remains about the unconventional pulse structures needed by various experiments, e.g. with mini-train within each bunch train. In this case the steady state is not reached. This will be the object of future studies.

For larger bunch spacings, multiple of 200 ns the situation can only improve. This is shown in Table 2 in terms of emittance growth, in comparison to the reference case. The double of the smallest spacing is considered. Although not planned to be used, the results for a distance of 337 ns, which is the design spacing for TESLA, are also displayed. It is remarkable that the latest case gives much smaller values than for 400 ns. This is due to a concurrent relationship between the bunch spacing and the mode frequencies.

Table 2: Emittance growth $\Delta\varepsilon/\varepsilon$ (in %) for various beams. Each number is the average over 100 linacs. The standard deviation is of the same order of magnitude.

Spacing [ns]	**Bunch train length** [μs]		
	800	120	20
200	0.017	0.11	0.62
400	0.003	0.022	0.11
337	0.0005	0.003	0.016

Lower beam energy The results mentioned above are for the maximum energy needed in the linac. For lower bunch energies the HOM kicks on the beam are stronger and therefore the beam quality is deteriorating. Indeed, simulations show an emittance growth of $0.86 \pm 0.95\%$ for a beam of 20 ns, with 200 ns spacing, and a final energy of 15 GeV (gradient in the FODO cells of 15.34 MV/m). For the 10 GeV case (gradient 10.05 MV/m), the same beam has an emittance growth of $1.5 \pm 1.6\%$. As mentioned above, the relative bunch offsets can be compensated with the feedback system.

Energy spread The three strongest longitudinal monopole HOMs, which are situated in the second monopole band of the TESLA cavities, have also been included in the calculations. The rms energy spread is 5.15 MeV for a pulse length of 20 ns. For a full bunch train (800 μs) the rms spread is 0.88 MeV. A final peak-to-peak energy spread of 17 MeV has been obtained. For a 20 GeV beam this represents 0.085%, while for 10 GeV it is 0.17%.

As for the bunch offsets, the energy variation occurs in the first part of the bunch train. For short pulses this should be compensated by the RF system.

SUMMARY

The simulations we present in this paper show a somewhat large effect of the wakefields on the bunch offsets within the train for short bunch trains and low beam energies. However, on one hand the negative effects are concentrated in the first part of the beam, which gives us the option to dump this part of the beam and send to the undulator only the high quality tail. On the other, the multibunch excitation is quasi-static, which makes easy the compensation of the bunch offsets by a feedback system. The energy spread may require compensation by the RF system for short trains. Unconventional pulse configurations remains to be studied.

Last but not least, we would like to mention that the possibility to align the beam in the cryo-modules based on the HOM signals is under study at TTF2 [12]. This is important particularly at low energy and would further contribute to the improvement of the beam quality.

Acknowledgments The author is thankful for the comments and discussions with its colleagues, in particular with W. Decking and R. Brinkmann.

REFERENCES

[1] R. Brinkmann et al. (eds.), TESLA Report 2001-23
[2] R. Brinkmann et al. (eds.), TESLA-FEL 2002-09
[3] R. Brinkmann, MO102, these Proceedings
[4] ILC/TRC, 2nd Report, SLAC-R-606, 2003
[5] N. Baboi, DESY-THESIS-2001-052
[6] Y. Kim, EPAC2004, Lucerne, July 5-9, 2004
[7] Y. Kim et al., TUP58, these Proceedings
[8] G. Kreps, private communication
[9] R.M. Jones et al., EPAC2004, Lucerne, July 5-9, 2004
[10] The MAFIA Collaboration, MAFIA: L - The Linear Accelerator Tracking Code, CST GmbH, Darmstadt, 1994
[11] N. Baboi and R. Brinkmann, TESLA 2000-28
[12] N. Baboi et al., MOP36, these Proceedings

BEAM OPTICS STUDIES FOR THE TESLA TEST FACILITY LINAC

V. Balandin, P. Castro and N. Golubeva, DESY, Hamburg, Germany

Abstract

The aim of the TESLA Test Facility Phase 2 (TTF2) Linac is to create electron bunches of small transverse emittance and high current with energies up to 1 GeV for the VUV-FEL at DESY. A study of the (linear) beam optics of the linac is presented for the case of beam commissioning for FEL. The requirements of each part of the linac upon the optics are discussed in detail and an appropriate solution for each case is shown, as well as the matching solution to the rest of the accelerator. The chromatic properties of the linac have been studied also.

ACCELERATOR OVERVIEW

Details on components and parts of the TTF2 linac are documented in many technical reports and publications (see, for example, [1, 2, 3, 4] and references therein). The machine layout for the start of operations is shown in Fig. 1.

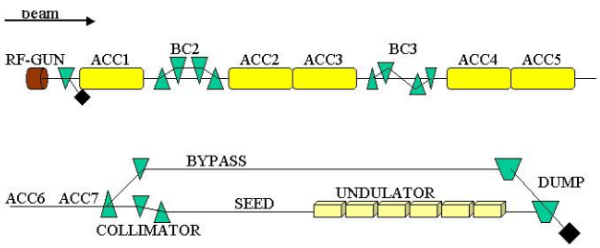

Figure 1: Schematic of TESLA Test Facility Linac.

Electron bunches are produced in an RF gun and accelerated by five cryomodules (ACC1 - ACC5) each containing eight nine-cell superconducting niobium cavities and a doublet of superconducting quadrupoles. To achieve high peak current in the undulator, the bunch is longitudinally compressed in two magnetic chicanes. Downstream the first bunch compressor BC2 (a four bend chicane) there is a diagnostic section arranged in a FODO lattice for the measurement of beam parameters. A second compression stage takes place after the passage through ACC2 and ACC3 and is performed using a S-type chicane (BC3). The last accelerating section, presently containing only two cryomodules (ACC4 and ACC5), accelerates the beam to the chosen final energy. Longitudinal beam profile diagnostics are located in the temporary beam line reserved for two more cryomodules (ACC6 and ACC7). Then, the electron beam is either guided to a bypass beam line (BYPASS) or brought through a collimator section (COLLIMATOR) to the FEL undulator. The collimator section has a dogleg shape and contains transverse and energy collimators for undulator protection purposes. Besides that, the collimator section incorporates a fast orbit feedback system and has to ensure the matching into the downstream beam line. Before the bunch enters the undulator, it passes an FEL seeding section (SEED), which at present is substituted by a temporary beam line with FODO type of focusing. Finally, the electron beams from the undulator and bypass are dumped in the same absorber (DUMP).

OPTICS SEARCH STRATEGY

The transverse optics discussed in this paper starts from the quadrupole doublet of the ACC1 cryomodule and uses as initial values (which eventually have to be corrected after measurement of actual beam parameters) the same Twiss functions which are used in [5]. We consider neither the beam dynamics in the gun area nor the choice of bunch compression schemes. A detailed description of these questions can be found, for example, in [1, 2].

Lattice Constraints

There are several requirements on the local behaviour of the optical functions, which we consider as constraints to the optics design.

- The TTF2 undulator section is a periodic structure consisting of six identical cells. Each cell is built up of an undulator segment (made of permanent magnets) followed by a doublet of electromagnetic quadrupoles to accomplish strong focusing [3, 6]. The quadrupole strength has to be optimized to provide good FEL performance.
- A special choice of Twiss parameters at the entrances of bunch compressors BC2 and BC3 reduces emittance growth due to coherent synchrotron radiation (CSR). That results in an asymmetric behaviour of betatron functions through bunch compression sections with a maximum at the entrance and a minimum between last two dipoles [7, 8, 9].
- The selection of optical functions in the dogleg of the collimator section are completely determined by the need to suppress the linear and second order dispersions and to shape a beam envelop suitable for collimation purposes [10].
- Beam emittance measurements in sections BC2 and SEED are obtained from the beam sizes measured at four separated locations inside a FODO structure. This emittance measurement technique provides its best accuracy for periodic Twiss functions and a 45° phase advance per cell [11].
- Beam spot size at the exit window location should be not smaller than the safety limit defined by the window (and dump) material properties and design. Al-

though dispersion helps to enlarge the beam spot area, it is better to keep it about zero to ensure independence of beam position at the dump on beam energy variation [12].

Energy Dependence

Transverse optics of the TTF2 linac can not be designed in such a way that it will stay invariable after linear scaling of magnet settings with change of the beam energy. One has to take into account focusing properties of RF cavities and undulator permanent magnets.

RF Radial Focusing. To obtain a better understanding of the RF focusing effects in the TTF2 linac we did not rely on any approximate analytical formulas because they have a certain (limited) range of applicability. The transport matrices corresponding to the passage through an RF cavity were obtained using the FMN2 code [13], which is capable to accurately calculate them using the knowledge of on-axis accelerating field profile and beam injection phase and energy. Another option of this code, which was used, is that these matrices can be printed in the format directly insertable into input file of the MAD program [14].

Natural Undulator Focusing. The electrons, when moving in the planar magnetic field of an undulator segment, undergo horizontal oscillations and experience vertical (natural) focusing. Effect of this additional focusing was analyzed with the help of the FMN2 program using measured field data not only for undulator segments, but also for undulator quadrupoles [15]. An example of this analysis is shown in Fig. 2.

Note that the focusing effect of extended fringing fields of dipole magnets, which is somewhat similar to the natural undulator focusing, was also taken into account during optics design.

Operational Regimes

Several possible scenarios of the linac operation during commissioning are foreseen to help to establish the primary goal, the SASE FEL operation. One can guide the beam either through the undulator or through the bypass. For both regimes the operations with bunch compressors on or off (one or both of them) are proposed, which may require the re-matching of the optics to compensate the differences in the path length and in the focusing properties (focusing of dipoles). The number of operational regimes is further doubled by the proposal to use the dipole magnets, which bend the beam down into the dump, as a spectrometer. Besides that, the bypass accommodates a material test facility, however the special requirements for its operation are not discussed in this paper.

Special Feature of Bypass Operation. For space reasons the bypass beam line starts with a section which is tilted with respect to the principal linac planes. The first part of this section is a dogleg with suppressed first and second order dispersions. Three additional tilted quadrupoles, placed downstream, make the total transport matrix of this section rotationally invariant that avoids the generation of the phase space coupling at the exit of this section [16]. In order not to destroy dispersion and coupling compensation, we assume that the setting of magnets of the tilted section (once established) will be frozen for all operational regimes.

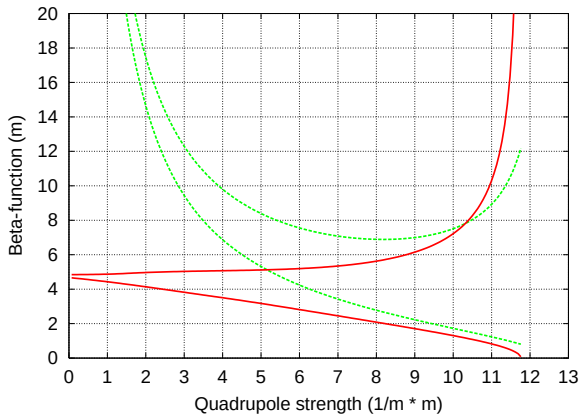

Figure 2: Minimal and maximal values of horizontal (green) and vertical (red) periodic $\beta-$functions achivable within the TTF2 undulator cell as a function of the quadrupole strength k (with doublet setting $k_1 = -k_2 = k$). The natural undulator focusing for a beam energy of 445 MeV is included here.

Usage of Dump Dipoles as Spectrometer. To get a good energy resolution, a small beam size at the OTR screen located downstream of spectrometer dipole is required [12]. Besides the necessity to have a special optical solution for these measurements, the beam intensity should be reduced in order not to damage the exit window and the OTR screen itself.

Optics Design Procedure

At the first step we concentrated on the design of the beam optics which could be used for the SASE FEL operation. After satisfying chosen requirements on the local behaviour of the optical functions, the remaining freedom was used for the matching between different linac parts and for improvement of the chromatic lattice properties. Considering the other operational regimes, we tried to satisfy their particular requirements with a minimum number of changes in order to keep the same optics in the other sections.

COMMISSIONING OPTICS

The commissioning of the TTF2 linac starts with the beam energy corresponding to a photon wavelength of 30 nm, which is 445 MeV. All necessary details about the proposed acceleration regime, which defines the focusing

properties of an RF cavities, and beam compression strategy can be found in [17]. We only note, that, according to [17], the ACC5 module is not used in calculations presented in this paper and the ACC4 module operates at relatively low accelerating gradient of about 7.8 MeV/m (accelerating on-crest).

Fig. 3 and 4 presents two beam optics solutions (shown from the entrance of the ACC1 quadrupole doublet up to the dump dipole) [18], which can be used for the start of the commissioning of the SASE FEL operation. As a working point for the undulator quadrupoles we use the values $k_1 = 10.92\ \mathrm{m}^{-1}$ and $k_2 = -10.57\ \mathrm{m}^{-1}$. These settings, under the assumption that the beam is uncoupled and perfectly matched to the undulator entrance, minimize the beam spot size averaged over the length of an undulator segment.

Note that this optics is set to the transport of beam envelop parameters. The influence of transverse space charge effects on the propagation of the high peak current part of the bunch and the necessary changes in optics will be described in separate paper.

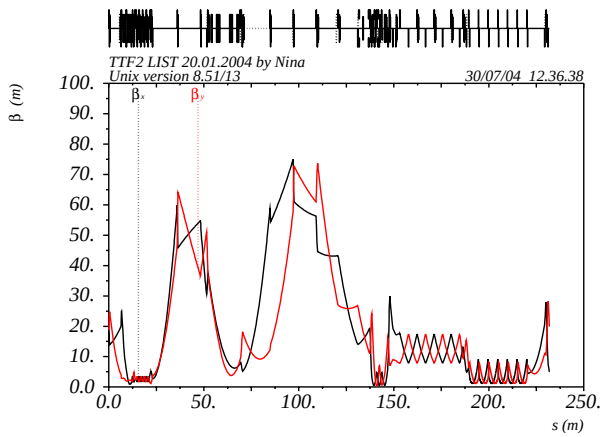

Figure 3: Commissioning 445-MeV optics of the TTF2 linac which satisfies all lattice constraints considered.

ACKNOWLEDGEMENTS

We would like to thank R. Brinkmann and K. Flöttmann for their careful reading of the manuscript and many useful comments. We are specially grateful to J. Roßbach for many valuable discussions and his support to our work.

REFERENCES

[1] The TTF FEL team, “SASE FEL at the TESLA FACILITY, Phase 2”, TESLA-FEL 2002-01, June 2002.

[2] K. Flöttmann, Ph. Piot, “An Upgraded Injector for the TTF FEL-user Facility”, EPAC 2002, Paris, France, 1798 (2002).

[3] J. Pflüger, U. Hanh, B, Faatz, and M. Tischer, “Undulator system for the VUV FEL at the TESLA test facility phase-2”, Nucl. Instr. and Meth. A 507 (2003) 228-233.

[4] M. Körfer, “The TTF-FEL status and its future as a soft X-ray user facility”, FEL’01, Darmstadt, Germany, 2001.

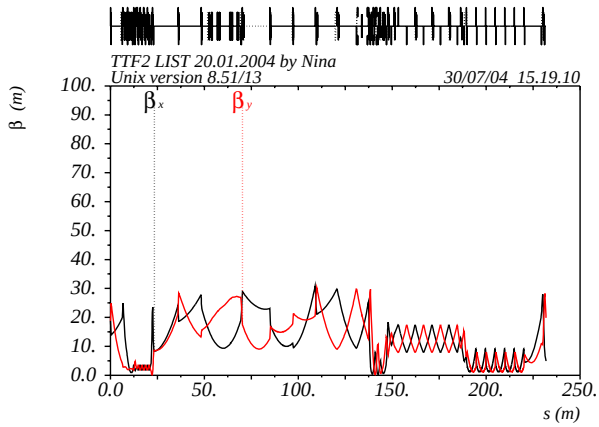

Figure 4: Commissioning 445-MeV optics of the TTF2 linac which makes the maximal beta functions smaller in comparison with the optics presented in Fig. 3, but does not provide the special behaviour of beta functions in the bunch compressor BC3 and moderately changes the beta functions through the collimator section.

[5] V. Balandin, K. Flöttmann, N. Golubeva, “Beam Power Limitations during the TTF2 Injector Commissioning”, TESLA 2004-07, April 2004.

[6] B. Faatz, J. Pflüger, “Different focusing solutions for the TTF-FEL undulator”, Nucl. Instr. and Meth. A 475 (2001) 603-607.

[7] P. Emma, R. Brinkmann, “Emittance Dilution Through Coherent Energy Spread Generation in Bending Systems”, SLAC-PUB-7554, May 1997.

[8] M. Dohlus, A. Kabel, T. Limberg, “Optimal Beam Optics in the TTF-FEL Bunch Compression Sections: Minimizing the Emittance Growth”, PAC’99, New York, 1999.

[9] F. Stulle, “TTF2 BC3 LIST 11.07.02 by Frank Stulle”, private communication.

[10] V. Balandin, K. Flöttmann, N. Golubeva, M. Körfer, “Studies of the Collimation System for the TTF Phase 2”, TESLA 2003-17, May 2003.

[11] P. Castro, “ Monte Carlo Simulations of Emittance Measurements at TTF2”, Technical Note 2003-03, DESY.

[12] M. Schmitz, “How to operate Spectrometer and Dump Safely?”, TTF2 Review Meeting in Salzau, January 2003.

[13] V. Balandin, “The FMN2 Program. User’s Reference Manual”, unpublished.

[14] F. Christoph Iselin, “The MAD Program. User’s reference Manual”, CERN/SL/90-13 (AP).

[15] V. Balandin et. al., “Betatron Motion in the TTF2 Undulator: Effect of Natural Undulator Focusing on Periodic Beam Transport”, in preparation.

[16] G. Hoffstätter, “Requirements for the Tilted TTF Bypass Line”, TESLA 2001-31, June 2001.

[17] P. Castro, B. Faatz, “TTF2 commissioning for first lasing: beam energy”, http://www.desy.de/pcastro/TTF2/documents/meeting_11dec02.ps.

[18] N. Golubeva, ”Studies of Optical Functions for TTF Phase 2”, http://www-mpy.desy.de/AccPhySemDESY/y2003/index.html.

THE SUPERCONDUCTING CW DRIVER LINAC FOR THE BESSY-FEL USER FACILITY*

J. Knobloch for the BESSY-FEL Design Group
BESSY GmbH, Albert-Einstein-Str. 15, 12489 Berlin, Germany

Abstract

A CW FEL User Facility for the VUV to soft X-ray spectral range using a cascaded HGHG-FEL scheme is planned at the BESSY site. Beam acceleration to 2.3 GeV is provided by a 144-cavity superconducting driver linac based on TESLA technology modified for CW operation. Initially, a high-rep-rate normal-conducting photoinjector will be used but a fully CW superconducting version is being investigated for a future upgrade. The required 2 kA peak current is achieved with two bunch compressors. An overview of the linac layout is provided here. Also discussed are the impact of CW operation, modifications to the TESLA technology that are necessary, as well as the expected linac performance.

INTRODUCTION

Numerous CW FELs are now being proposed to meet the demand of the synchrotron-light community for high-brilliance, fully coherent and short-pulse (fs) light in the VUV to x-ray range. These include the BESSY FEL in Berlin, whose Technical Design Report was published recently[1], and the 4GLS at Daresbury[2].

Such CW machines, which must use superconducting cavities, are very attractive because their intrinsic high average flux and brightness enable multi-beamline operation at a level not possible with pulsed linacs. Furthermore, CW operation provides additional flexibility to tailor the bunch structure to the users' needs. Due to the success of the TESLA Test Facility (TTF) at demonstrating the reliable operation of TESLA technology[3] for FEL applications, these new proposals are also based on this technology.

The BESSY-FEL facility, shown schematically in Fig. 1, comprises a CW linac driving three cascaded High-Gain-Harmonic-Generation (HGHG) FELs. These cover a continuous photon-energy range from 24 eV to 1000 eV.

For efficient lasing, the linac must provide a beam energy of 2.3 GeV at a peak current of 2 kA (2.5 nC per bunch) with a slice emittance of order 1.5 π mm mrad. Bunch compression is achieved in a two-stage system. An arc is included in the layout to reduce the physical length of the machine, leaving space for future upgrades and expansions. Fast kickers[4] at 1020 MeV and 2300 MeV then distribute the electron beam among the three FELs. A collimator section[5] prior to each FEL protects the undulators.

Although much of the pulsed TESLA technology will be transferred directly to the BESSY FEL several issues unique to CW operation have been investigated and necessitate some design and layout changes. These include cryogenic aspects, RF control and the RF distribution which are addressed later.

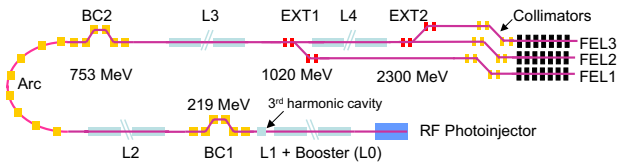

Figure 1: Layout of the driver linac for the BESSY FEL.

INJECTOR

Initially the injector will use a high-rep-rate normal-conducting (NC) RF photogun, but a future upgrade to a fully CW superconducting system is planned.[6] The NC gun is based on the operational PITZ design, which has achieved a *projected* emittance of 1.7 π mm mrad at a peak cavity field of 40 MV/m. Simulations of a layout optimized for 2.5-nC operation have demonstrated that, given a 38 ps flat-top temporal laser profile with short rise and fall times (4 ps), a slice emittance of less than 1.5 π mm mrad can be achieved at the exit of the booster section (L0) (2.1 π mm mrad projected emittance).[6]

Three bunches are accelerated in a 6 μs pulse at a repetition rate of 1 kHz. They are distributed among the three FELs using high-speed kickers[4], so that each FEL is also operated at 1 kHz. But the relatively large duty factor (ca. 2.5% when rise and fall times are included) produces a 75 kW heat load in the RF gun, nearly three times that of PITZ, so that the cooling had to be improved.

The NC, pulsed injector represents a conservative system that will be used to commission the BESSY FEL. However, to fully exploit the CW capability of the main linac, a CW injector will eventually be required. Such systems are currently being investigated[7, 8]. A split superconducting cavity/compensation solenoid layout is also being studied at BESSY. Preliminary simulations of such a layout suggest that the required slice emittance can be achieved at an accelerating field of 34.5 MV/m.

The L0 section, consisting of eight TESLA cavities, follows directly after the RF gun. The average field is 15.7 MV/m, chosen to minimize and preserve the emittance out of the gun. Acceleration is off crest, as in the L1 and L2 linac, to provide an energy chirp which later is used for bunch compression. A third harmonic cavity compensates for the curvature of the RF field as well as the T_{566} of the dispersive sections downstream.

* Work funded by the BMBF and the Land Berlin.

MAIN LINAC

Modules and cryogenics

The main linac consists of a further 17 TTF-style modules housing eight 9-cell cavities each (Fig. 2(a)). Details of the original TTF design and its philosophy are given in numerous references.[9, 10, 11] As in TTF, several modules are grouped together into cold sections.[12]

For a linac energy of 2.3 GeV, the average field is a conservative 15–16 MV/m. This was chosen for a number of reasons:

- Simpler cavity preparation. Cavities operating at 20 MV/m are now produced and assembled routinely.
- Improved reliability of the linac. Underperforming cavities can be compensated for by increasing the field of others, while remaining below 20 MV/m.
- High Q values can be achieved.
- Manageable cryogenic load per cavity.

Assuming a (measured) 2.0-K Q factor of 1.3×10^{10}[13] the average dynamic heat load is of order 20 W/cavity, for a total of 2.8 kW. However, the linac is designed for 1.8-K operation, and an improvement to $Q\approx2\times10^{10}$ is expected, therefor reducing the cryogenic cost significantly.

Compared to TTF, the heat load per cavity still is 10 to 20 times greater. To exhaust this heat, the helium-tank design was modified slightly. In particular the diameter of the two-phase supply line spanning the modules and the chimney supplying helium II to each tank were enlarged to 100 mm and 90 mm (ID), respectively, as shown in Fig. 2(a).

For the helium distribution, the scheme in Fig. 2(b) was chosen. This creates two independent legs of nearly equal length. The main advantages lie in the ability to operate/commission the two sections independently and a reduced pressure drop in the gas return pipe (GRP) that returns the helium to the refrigeration plant.

Simulations of the cryogenic distribution system with a 4.5-kW heat load (roughly a 100% safety margin) have been performed to better understand the He flow and pressure drop given the large heat load. These simulations demonstrated that stable stratified two-phase flow is maintained in the entire linac (see Fig. 2(c)), provided always eight cavities are supplied with He-II by a JT valve, as in Fig. 2(a) (18 supply valves in total). This is in contrast to the layout for the XFEL, where only one JT valve for every 10 modules is required.

RF system

Beam loading will be, at most, 1.5 kW/cavity, so that each cavity is equipped with its own RF transmitter. This provides a large degree of operational flexibility and reliability and improves the RF control.

However, the cavity bandwidth is small (order 10–50 Hz) and microphonic detuning increases the *peak* power demand to about 15 kW while the average power is less

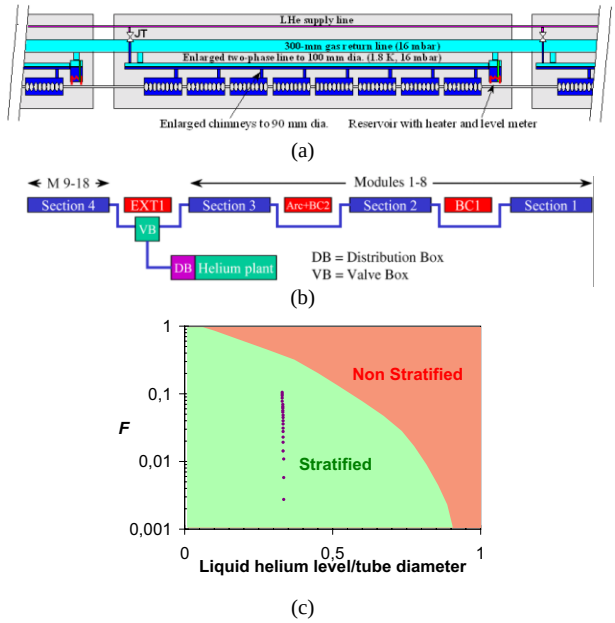

Figure 2: (a) Schematic of the CW module, (b) Helium distribution in the BESSY FEL. (c) Simulated flow pattern for 1.8 K He II in the two-phase supply line of the most critical module. The dimensionless parameter F, as defined in [14], determines whether flow is stratified or not.

than 5 kW.[1] For such operation, IOTs have a higher efficiency than klystrons. Two systems have been developed for 1.3 GHz so far (E2V & CPI VKL7811) and they will be evaluated in the HoBiCaT facility[15, 16] to test their suitability for the BESSY FEL.

TTF type-III couplers[17] in conjunction with waveguide tuning stubs provide the coupling to the cavities. This combination yields a coupling range of nearly two decades which not only offers the flexibility to adapt cavities to changing beam-loading conditions and performance, but also enables high-power processing of cavities.

To compensate the beam loading and microphonics of order 5 Hz rms, about 4–5 kW CW RF power is needed per cavity for 20 MV/m operation. The coupler has been tested to 4 kW CW at Rossendorf, this being limited by the heating of the inner-conductor bellows. However, this coupler was tested warm and a further increase under normal (cold) operating conditions is expected. Cold tests will be carried out in the HoBiCaT facility soon. Also, design changes required to significantly boost the power capability (50 kW) have already been identified, should the need arise.[18]

RF control will be implemented using a digital FPGA-based system. This is currently being developed for testing in HoBiCaT.[19] For efficient light generation, the HGHG scheme requires a bunch-to-bunch energy stability of 10^{-3} and a timing jitter of less than 50 fs at the linac exit.

Simulations were made to better understand the achievable performance of the linac. For these, the cavity voltage was evolved in time in the presence of beam loading, microphonics, Lorentz-force detuning, and other noise terms. The beam was tracked through all 144 cavities, as well as

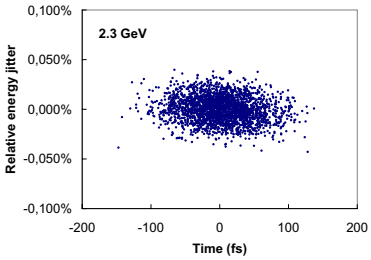

Figure 3: Simulated bunch-to-bunch energy distribution.

the bunch compressors and 3rd-harmonic cavities.

Although a number of the assumed initial conditions still need to be verified experimentally, these simulations have demonstrated that the requirements for energy and time jitter can indeed be met. Fig. 3 depicts one result of the jitter at 2.3 GeV. The dominant noise source are the microphonics, an rms value of 5 Hz being assumed, and the energy/phase jitter of the injector. Passive and active means of reducing the microphonics will be investigated in HOBICAT. In particular, piezo compensation potentially can improve the cavity performance significantly and will likely be implemented in the BESSY FEL.

Bunch compression

In principle, the bunch compression could be done in one step. Non-linearities arising from wakefields, coherent synchrotron radiation (CSR) and space-charge effects, however, limit this and a two-stage scheme was adopted for additional flexibility. This was optimized in view of the emittance, peak current and energy spread at the linac exit.

By accelerating off crest at $-13.3°$ in the L0 and L1 section, and at $-5°$ in the L2 section the longitudinal energy profile is chirped. This is then translated into a bunch shortening in the dispersive bunch compressors.

The first bunch compressor (BC1) was placed at the lowest possible energy (219 MeV) to minimize the summation of non-linearities imposed by the RF potential on the relatively long bunches. An energy limit is set by space charge effects. A six magnet chicane, rather than four, was chosen to reduce the magnet strengths, thereby avoiding emittance dilution due to CSR effects.

The arc must be placed before the second bunch compressor (BC2) to avoid strong CSR effects due to short bunches. BC2 then follows immediately so that adiabatic damping does not diminish the energy chirp unnecessarily. The arc/BC2 combination is placed at the highest possible energy to save space and to increase the beam's rigidity, thereby reducing its sensitivity to disturbances. This energy is limited by the CSR effects in BC2 to about 750 MeV.

Eight dipoles are used in BC2, again to reduce their strength and hence CSR effects. Two additional quadrupoles provide extra control of the beta functions. The arc, which "naturally" would have a positive momentum compaction, has been tuned to be isochronous to prevent bunch lengthening that otherwise would have to be compensated for in BC2 by an increased field strength.

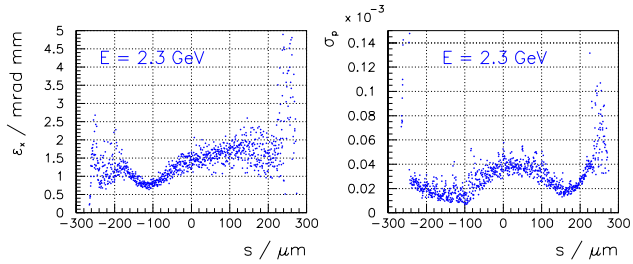

Figure 4: Slice analysis of the beam simulations at the collimator exit.[1] (a) Emittance, (b) relative momentum.

START-TO-END SIMULATIONS

Several programs were used to simulate the full BESSY FEL.[1] Calculations from the gun to the first bunch compressor (where space-charge-effects cease to be important) were performed with ASTRA using 100,000 particles. The 6-D phase-space output was then converted and passed on to ELEGANT for calculations up to the linac end. Finally, calculations of the HGHG scheme were performed in ELEGANT. The slice emittance of 1.5 π mm mrad, as shown in Fig. 4(a), is preserved throughout the linac. Also the slice momentum spread (Fig. 4(b)) is less than 5×10^{-5}. Both values are well suited for the HGHG cascade.

REFERENCES

[1] D. Krämer et al., editors, The BESSY Soft X-ray Free Electron Laser (BESSY (Berlin), 2004), ISBN 3-9809534-0-8.

[2] M. Poole et al., Proc. 2003 PAC, pp. 189–191, 2003.

[3] R. Brinkmann et al., editors, TESLA Technical Design Report—Part II, DESY report 2001-011.

[4] J. Feikes et al., Proc. 9th EPAC, Luzern, 2004.

[5] T. Kamps et al., Proc. FEL 2004 (to be published).

[6] F. Marhauser, Proc. 9th EPAC, Luzern, 2004.

[7] J. Sekutowicz et al., Physical Review Special Topics AB (submitted for publication).

[8] J. Teichert et al., Proc. 9th EPAC, Luzern, 2004.

[9] J.G. Weisend et al., Adv. Cryog. Eng. 45A (2000) 825.

[10] C. Pagani et al., Adv. Cryog. Eng. 45A (2000) 939.

[11] C. Pagani et al., (2001), TESLA report 2001-36.

[12] S. Wolff et al., DESY report TESLA 2001-37.

[13] W.D. Möller et al., Proc. 10th Workshop on RF Superconductivity, S. Noguchi, editor, p. 212, Tsukuba, Japan, 2001.

[14] N. Cheremisinoff, editor, Encyclopedia of Fluid Mechanicsvolume 3 (Gulf Publishing, 1986) pp. 403–474.

[15] J. Knobloch et al., Proc. 11th Workshop on RF Superconductivity, (2003).

[16] J. Knobloch et al., Proc. 9th EPAC, Luzern, 2004.

[17] W.D. Möller et al., Proc. 9th Workshop on RF Superconductivity, edited by B. Rusnak, Santa Fe, New Mexico, 1999.

[18] V. Veschcherevich et al., Proc. PAC 2003, pp. 1201–1203, Portland, Oregon, 2003.

[19] A. Neumann and J. Knobloch, Proc. 9th EPAC, Luzern, 2004.

LINAC UPGRADES FOR FERMI@ELETTRA

G. D'Auria, R.J. Bakker, C.J. Bocchetta, P. Craievich, M. Danailov, G. De Ninno, S. Di Mitri, B. Diviacco, M. Ferianis, G. Pangon, L. Rumiz, L. Tosi, V. Verzilov*, D. Zangrando,
Sincrotrone Trieste, SS 14 - km 163,5 in AREA Science Park, 34012 Basovizza, Trieste ITALY

Abstract

To fulfill the stringent requirements expected from the FERMI@ELETTRA project, the existing linac needs some modifications in the layout and an upgrading of the present plants. Moreover, for the next two years, until the new injection system, now under construction, is fully commissioned, the linac has to be kept in operation as injector for the ELETTRA Storage Ring. Therefore most of the planned activities have to be carried out without interfering with the normal operation of the machine. Details on the new linac layout and related activities are discussed.

INTRODUCTION

The FERMI@ELETTRA project [1] is an initiative among Sincrotrone Trieste, INFM and other Italian Institutes, to construct a single-pass FEL user facility located next to the third generation Synchrotron Light Source ELETTRA, utilizing the existing 1.0 GeV linac. The spectral range of the laser will go from 100 nm to 10 nm with two undulator beamlines implemented on the machine in two different phases:

- Phase 1 (FEL-1) will aim to cover 100-40 nm.
- Phase 2 (FEL-2) will extend the FEL wavelength up to 10 nm.

The first proposal of the FERMI project [2] was submitted to Italian Ministry of Education, University and Scientific Research in February 2002, in response to the Italian Government's call for proposals for a multipurpose pulsed laser X-ray source. In July 2004 the project was funded.

Ongoing activities are now evolving from a conceptual design phase to an early stage of a detailed technical design. Table 1 summarizes the main beam parameters for the two phases of the project.

Table 1: Electron beam parameters for phase 1 and 2

	FEL-1		FEL-2		
Wavelength	100	40	40	10	nm
Beam energy	0.7		0.55	1.0	GeV
Bunch charge	1.0		1.0		nC
Peak current	0.8		2.5		kA
Bunch duration	500		160		fs
Energy spread	0.7		1.0		MeV
Emittance	1.5		1.5		10^{-6} m
Repetition rate	50		50		Hz

To produce a beam with the required beam characteristics the existing linac needs some layout modifications, an upgrading of the RF plants, the implementation of a new synchronization system as well as a review of the whole beam optics, including the installation of two bunch compressors.

Figure 1 shows the present layout of the machine (a), the proposed FEL schemes with the two beamlines and the main modifications to be implemented on the existing machine (b) [2], and the new layout to guarantee the injection in the storage ring (c). At present the linac is operated less than 2 hours a day as the ELETTRA injector, the time remaining is completely available for all the activities connected to the FEL development. Therefore, with careful planning, most of the foreseen upgradings could be already activated.

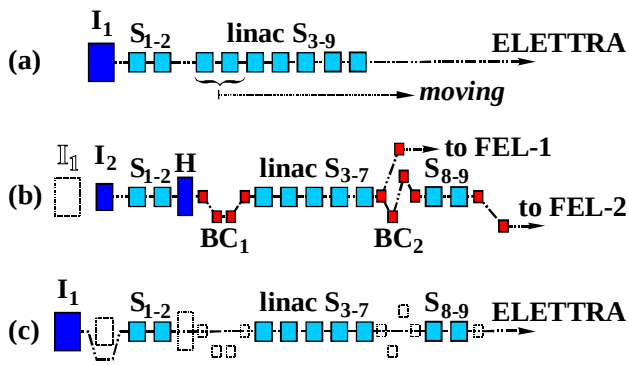

Figure 1: Linac layouts.

Labels meaning:

- I_1: present injector, thermionic gun and bunching sections, beam energy at exit 4.5 MeV.
- I_2: high brightness photoinjector.
- $S_{1\text{-}2}$: 3.2 m long accelerating sections, 2/3π forward TW, iris diameter 16-22 mm, without sled.
- H: 3rd harmonic cavity.
- BC_1 and BC_2: magnetic bunch compressors.
- $S_{3\text{-}9}$: 6.1 m long accelerating sections, 4/5π backward TW, each equipped with its own sled system.

LINAC MODIFICATIONS

Figure 2 gives a schematic overview of the linac building complex with the layout modifications and the expected installations.

Concerning the civil engineering, the present tunnel of the machine is adequate in length to house all the required modifications: roughly 40 m of free space are available at the end of the present accelerator for the relocation of two 6.1 m accelerating sections and the installation of the second bunch compressor as indicated in the FEL layout. The 3rd harmonic cavity, the first bunch compressor and the new diagnostics will be taken up in the space left free from the two moved sections. Additional space, roughly 15 m, is needed for the klystron gallery to relocate two RF plants.

* Now at TRIUMF, Vancouver, B.C., Canada

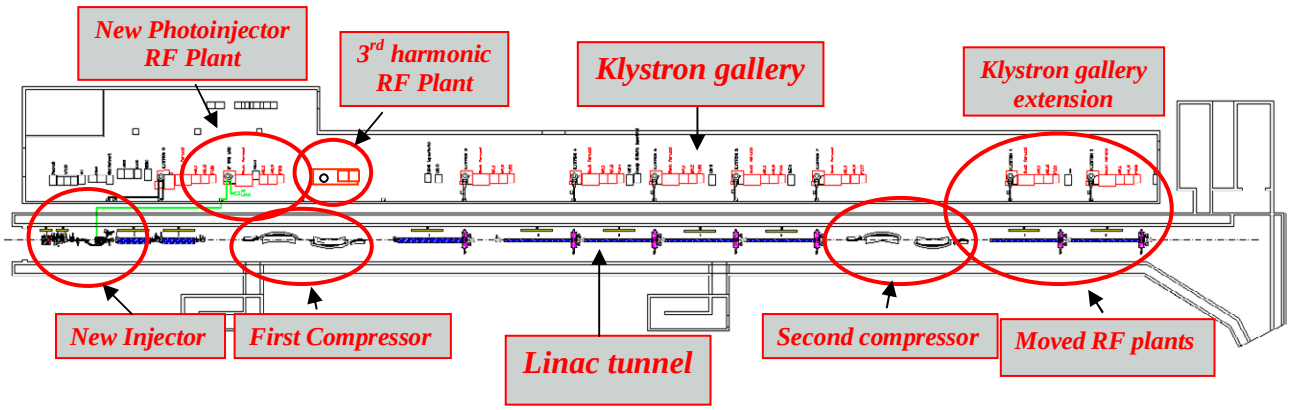

Figure 2: Overview of the linac building complex with the new installation.

Photocathode and New Injection Scheme

At present the linac does not match the beam requirement especially in terms of normalized brightness ($B_n=I_{pk}/4\pi\varepsilon_n^2$). To overcome this problem the actual thermionic electron source will be replaced with a high brightness photocathode. At the same time, at least for the next two years, the original gun must remain operational, to guarantee injection into the storage ring. To fulfil both requirements a new injection layout has been proposed with the new electron source in place of the old thermionic one, which will be relocated 3 m upstream. The scheme shown in figure 3 fits the space available in the present tunnel and all the modifications will be implemented in order to achieve a fast switching between the two modes of operation.

For the RF Gun three different options have been considered: a 1.6-cell developed by BNL/SLAC/UCLA for LCLS [3], scaled to 2998 MHz, a 2.6-cell gun developed at the TUE [4], and a 1-cell higher order mode (HOM) gun developed by Lewellen at the APS [5].

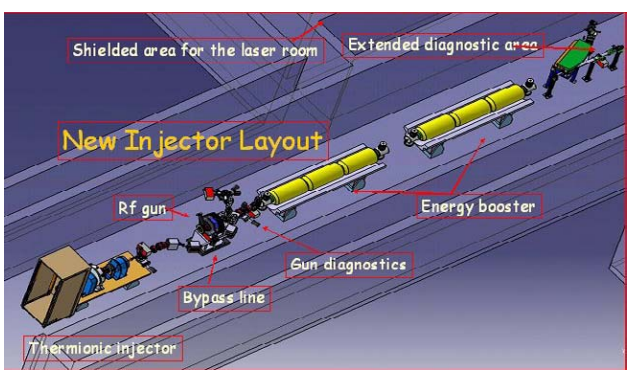

Figure 3: New injection layout.

Preliminary beam dynamics simulations have been performed with ASTRA [6] only for the first two options. We have considered the whole system photoinjector-booster linac up to 120 MeV utilizing the first two SLAC type accelerating sections of the present machine, $S_{1\text{-}2}$, both fed by the same klystron and embedded in their own solenoid with a maximum field up to 0.25 T, which is of great importance to control the beam envelope and the emittance oscillations. For the LCLS gun we have considered two values of the peak electric field at the cathode 120 MV/m and 140 MV/m. Table 2 summarizes the obtained results that are in a good agreement with the required parameters.

Table 2: Output beam characteristics and gun parameters

	LCLS	LCLS	TUE	
Gun field	140	120	100	MV/m
Beam energy	119	111	123	MeV
Norm. emit. (rms)	0.57	0.63	0.57	μm
Energy spread (rms)	0.21	0.27	0.36	%
Bunch length (rms)	0.90	0.93	1.0	mm
Peak current	104	102	93	A
RF peak power	11.1	8.2	8.2	MW
Heat flux @4μs, 10Hz	1.56	1.14	0.77	W/cm^2
Solenoid field	3.02	2.64	4.01	KG
S_1 average gradient	16.5	14.3	18	MV/m
S_1 focusing field	0.6	0.6	0.7	KG
S_2 average gradient	22	22	22	MV/m

In particular the TUE gun seems to be very interesting for the lower gradient of operation and a better performance in terms of heat production/dissipation. The same gun seems to be very promising also for its ideal rotational symmetry due to the axial coupling with the the RF generator. Nevertheless, at present the 1.6 cell LCLS choice seems the most appropriate for reasons of reliability and for the great experience matured on it in many laboratories during the last ten years.

Once the present injector will be relocated 3 m upstream and the transfer line for the storage ring injection commissioned (activities to be scheduled during a long shutdown period), it will be possible to install and test the new photoinjector as a stand-alone set-up before the definitive connection to the main linac.

The diagnostic section in the drift between the gun and the booster linac will provide the control over the main beam parameters and the space available will fit that

required for the emittance compensation. More details on the new injection system can be found in [7,8].

Laser System

The laser system will be placed in an existing shielded area located on one side of the linac tunnel, only few meters away from the gun. We plan to assemble a system based on a commercially available Ti:Sapphire laser and amplifier modules upgraded with additional units and control loops. The main requirements of the laser system for a copper cathode based photoinjector are well established and limit the choice to a 10-20 mJ range Ti:Sapphire system based on consecutive regenerative multi-pass amplifier stages. Although the application of a purely diode pumped systems would be preferable for reducing the pulse-to-pulse energy fluctuations (and amplifier induced timing jitter), at the present status of these systems the use of one lamp-pumped multi-pass amplifier end stage seems unavoidable. Temporal pulse shaping for obtaining the necessary 10 ps range 'flat-top' low energy infrared pulses can be done by different methods, however the obtaining of high energy UV pulses with such shape is a serious challenge. We are now examining different possible solutions, including also shaping in the UV region, which would avoid problems with pulse deformations during amplification and frequency conversion.

RF Plant Modifications

At present the RF plants are operated with a repetition rate of 10 Hz. To increase the beam average power we are considering to extend the pulse repetition rate up to 50 Hz, compatible with the klystron TH2132A and some of the components already mounted on our plants, i.e. accelerating sections, sled cavities, thyratrons, etc. On the other hand, to deal with the 50 Hz average power increasing, many other components installed on the pulsed modulators need to be modified or completely substituted, i.e. the HV power supply, the PFN (Pulse Forming Network), etc.

Moreover, since FEL operation calls for an overall improvement of the stability of the machine, many other sub-assemblies have to be checked, modified or completely replaced. In particular:

- it will be necessary to improve the pulse to pulse stability of the HV modulators as well the ripple of the klystron anodic pulses to avoid unwanted phase rotation in the emitted RF;
- all the wave guides and the power distribution systems from klystrons to accelerating sections need to be modified and temperature stabilized;
- the RF low level system, the klystron drivers, etc. have to be replaced with high stability equipments with control loops and feedbacks supplied;
- the accuracy and stability of the water cooling system of the accelerating sections have to be improved to limit the phase errors between adjacent cells.

Concerning the layout modifications it will be necessary to relocate the first two 6 m accelerating sections S_3 and S_4 with their RF plants at the end of the tunnel leaving the space for the installation of the first bunch compressor and the 3rd harmonic cavity. Two more RF plants have to be installed in the klystron gallery: one for the 3rd harmonic cavity, the other for the photoinjector and eventually an RF deflecting structure for bunch length measurements. Most of the activities above described can be gradually implemented on the plants during normal shutdown periods, without interfering with ELETTRA operation. The modularity of the RF plants and in particular the layout of the present accelerating systems (one HV modulator with its own klystron feeds only one accelerating section) guarantees minimal disruption to machine operation since plants can be selected and upgraded one at a time.

Timing System

Timing and synchronization between different sub-systems will be a fundamental issue. The present timing system will be completely revised in terms of global stability and a frequency reference will be properly distributed around the machine allowing the implementation of local phase control loops. Several options are now under investigation for the reference distribution (coax, optical fiber, etc). We have also started a sub-ps jitter analysis and a study on phase measurement that will be crucial subjects for achieving the beam parameters required by the laser.

CONCLUSIONS

A brief overview of the main modifications and upgradings required from the Trieste linac to fulfil the expected performances required for FERMI has been given. Moreover, for each of the above mentioned activities, it will be necessary to carry out a detailed technical design and an accurate time schedule for its implementation according to operational needs of ELETTRA.

REFERENCES

[1] FERMI@ELETTRA, Preliminary Conceptual Design Report, Sincrotrone Trieste, February 2002.
[2] R.J. Bakker et al., "FERMI@ELETTRA: 100 nm - 10 nm Single Pass FEL User Facility" EPAC 2004, Zurigo CH.
[3] LCLS CDR, SLAC-R-593, 2002.
[4] M.J.deLoos et al., "A high brightness pre-accelerated RF-Photo Injector", EPAC 2002, Paris, France.
[5] J.W. Lewellen, "Higher-order mode RF guns, "Phys. Rev. ST Accel. Beams 4, April 2001.
[6] K. Flottmann, ASTRA User Manual.
[7] V.A. Verzilov et al., "Photo-injector study for the ELETTRA linac FEL", to be published in Nucl. Instr. Meth. In Physics Research A (NIM-A).
[8] S. Di Mitri et al., Optics for a transfer line from the present thermionic gun to the main linac', ST/M-04/03.

EXTENDED PARAMETRIC EVALUATION FOR 1Å FEL – EMITTANCE AND CURRENT REQUIREMENTS

M. Pedrozzi, G. Ingold, PSI, Villigen, Switzerland

Abstract

In the synchrotron radiation community there is a strong request for high-brightness, coherent X-ray light pulses, especially in the 1 to 0.1 nm wavelength range. A Free Electron Laser (FEL), driven by a linear single-pass accelerator, is today the most promising mechanism able to produce such radiation. Since the electron beam brightness plays a major role in the laser saturation process and in the final energy of the driving linac, many laboratories are presently working on a new generation of low emittance sources. The present analysis will give an indication about the FEL behaviour versus the undulator parameters and the slice beam quality (emittance, current, energy spread).

INTRODUCTION

At short wavelength the transversal coherence of the FEL radiation and therefore the gain length can strongly be compromized due to the transversal emittance of the electron beam. As shown by L-H Yu and S. Krinsky [1], with an external focusing the normalized emittance will have a negligible effect on the FEL interaction if :

$$\varepsilon_n << \varepsilon_{nc} = \frac{\beta}{L_g}\frac{\gamma\lambda_s}{2\pi} \qquad (1)$$

where β is the betatron function, γ the Lorenz factor, λ_s the radiation wave length and L_g the gain length.

According to equation (1) the beam energy can be reduced and therefore the facility costs only if the emittance is "sufficiently" small.

The present state of the art electron sources intended for the next generation of light source facilities (LCLS [2] and TESLA-FEL [3]) can provide 1 nC beams with normalized slice emittances close to 1 mm mrad [4]. Recently, the importance of developing high brightness beam sources with emittances at least one order of magnitude smaller than the present status has been emphasized [5], and new gun designs proposed [6,7,8]. A systematic parametric analysis of the FEL interaction with an ultra-bright beam is therefore necessary to achieve a consistent set of specifications for the gun, the LINAC and the undulator.

Model

In this analysis we are using the analytical theory developed by L-H Yu et al. [9] which simultaneously includes the effects of the energy spread, emittance, and focusing of the electron beam, as well as the diffraction and the optical guiding of the radiation field. A Gaussian beam energy distribution, a uniform longitudinal density and a uniform water-bag distribution U(R,R') in the 4-dimensional transverse phase space R=(x,y) and R'=(x',y') are assumed:

$$U(\vec{R},\vec{R}') = \frac{\beta^2 n_0}{\pi R_0^2}\ \Theta\left(\frac{R_0^2}{\beta^2} - \frac{R^2}{\beta^2} - R'^2\right) \qquad (2)$$

where Θ(v)=1 for v>0 and Θ(v)=0 for v<0. The transverse electron density profile is then parabolic:

$$g(\vec{R}) = n_0\left(1 - \frac{R^2}{R_0^2}\right) \quad \text{for } R < R_0 \qquad (3)$$

The gain length is calculated by numerically solving the dispersion relation resulting from the linearized Maxwell-Vlasov equations (see [9] for details).

PARAMETRIC ANALYSIS

Reference Case

As a reference we assume a normalized emittance close to the state of the art ε_n=1.2 10^{-6} mrad, and an energy spread σ_E near 10^{-4}, which is comparable to the energy spread induced by the quantum fluctuation along the undulator [10] for energies near 20 GeV. All our evaluations are made for planar undulators.

Table 1: Reference case parameters

ε_n	1.2 10^{-6}
σ_E	10^{-4} and 2 10^{-4}
Peak	5000 [A]
Beta func. β	31 [m]
Radiation λ	1 Å

The gain lengths at optimum detuning versus the undulator period are shown in Fig. 1, and the corresponding beam energies in Fig. 2.

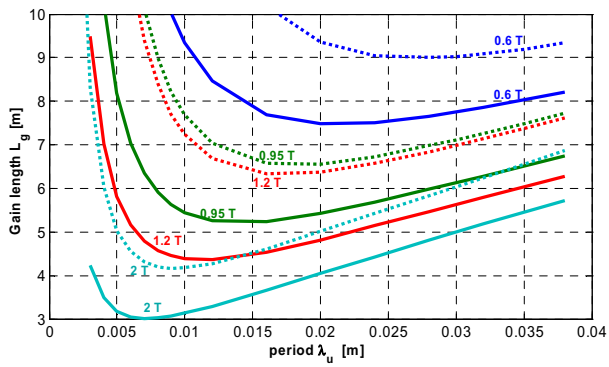

Figure 1: Reference case, gain length vs. undulator period for four peak magnetic fields. Continuous line σ_E =10^{-4}, dotted line σ_E =2 10^{-4}.

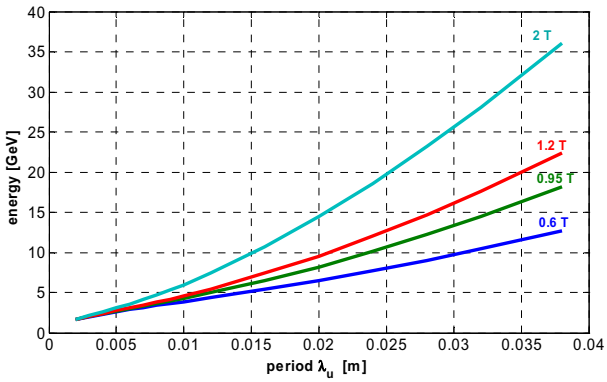

Figure 2: Electron beam energy vs. undulator period (resonant condition).

In this case a high magnetic field is clearly preferable in term of saturation length and final linac energy but undulators above 1 T with periods below 15 mm would require a challenging narrow physical aperture, typically g≈3 mm for λ_u=10 mm. This has to be compared with present designs such the TESLA XFEL[3], with an undulator of 38 mm period, 10 mm gap and 1.06 T. Wake field effects on short pulses with high peak current may limit the minimal undulator aperture.

Emittance and Peak Magnetic Field

A smaller emittance has a strong impact on the FEL gain length and allows operation at lower peak current. The possibility to reduce the charge could considerably help to preserve the emittance at low energy at the source where space-charge effects are dominant. The optimum β function decreases with the emittance:

$$\beta_{opt}\sim 16\ \text{m} \quad \text{for } \varepsilon_n = 5\ 10^{-7}\ [\text{mrad}]$$
$$\beta_{opt}< 1\ \text{m} \quad \text{for } \varepsilon_n < 1\ 10^{-7}\ [\text{mrad}]$$

Operation at β optimum for emittances smaller than 10^{-7} is difficult to realize. However the gain length (~1.5m) only increases smoothly with the β function. For the two lowest emittances a β of 4.77 m has been chosen, in those cases the gain length can degrades of ~35%.if increasing β to 15.9 m

Table 2: Parameters at low emittance

ε_n [mrad]	σ_E	β [m]	I [A]
$5\ 10^{-7}$	10^{-4}	15.9	500
1.10^{-7}	10^{-4}	4.77	500
$5\ 10^{-8}$	10^{-4}	4.77	500

Comparing Fig. 3a with the reference case we note that increasing the current by a factor 10 largely compensates the emittance degradation from ε_n=5 10^{-7} to ε_n=1.2 10^{-6}. This is roughly in agreement with the analytical scaling of the gain length L_g given by Saldin et al. [11], which at low energy spread is:

$$L_g \propto \varepsilon_n^{5/6} \Big/ \sqrt{I} \qquad (4)$$

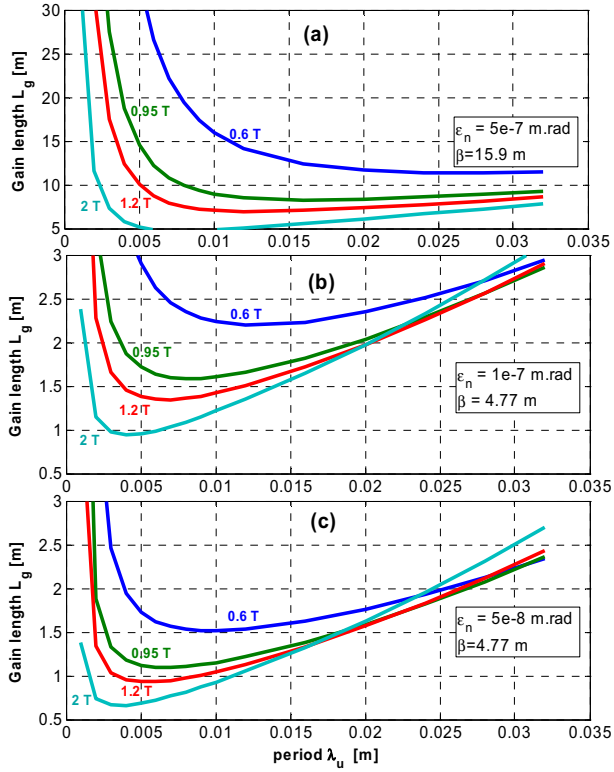

Figure 3: Gain length vs. undulator period for different peak magnetic field and emittances: (a) ε_n=5 10^{-7} mrad, (b) ε_n=10^{-7} mrad, (c) ε_n=5 10^{-8} mrad.

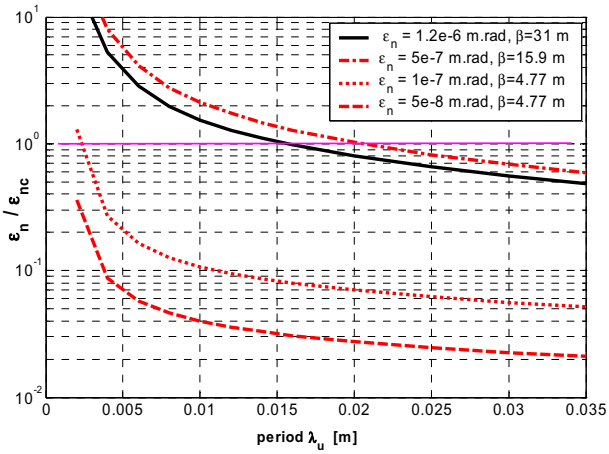

Figure 4: Ratio between normalized emittance ε and critical emittance ε_{nc} as given in Eq (1) for 0.95 T peak magnetic field.

Analyzing in Fig. 4 the criteria given by Eq. (1) for the case with 0.95 T peak field, we observe that the regimes covered by the reference case and the ε_n=5 10^{-7} [m rad] scenario are still emittance dominated, while for the two lowest emittances the criteria is fulfilled down to approximately 5mm undulator period. In Fig. 3 the gain length scales approximately linearly with the emittance according to Eq. (4), although we are slightly outside the parameter range considered by Saldin.

From figure 3b and 3c we conclude that for small emittances there is no advantage to use a high field undulator for periods λ_u>15 mm, where an undulator K factor of 1.4 should be sufficient.

Current

In order to reach a reasonable gain length currents up to 5kA are foreseen in the present 1Å FEL proposals. At low emittance the peak charge can be reduced according to (4), and many problems related to wake field, compression chicanes and beam collimation someway relaxed.

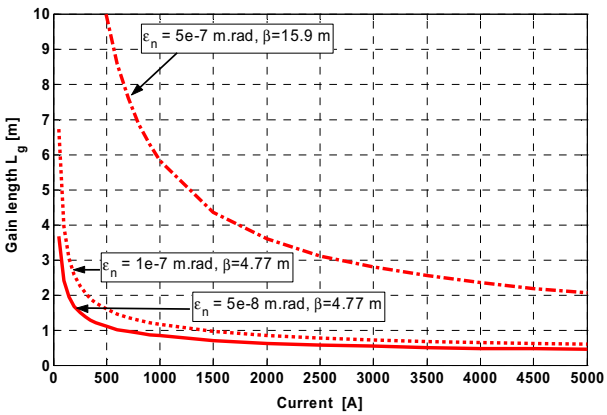

Figure 5: Gain length versus peak current for an undulator period of 8 mm and 0.95 T peak field. Continuous line ε_n=5 10^{-8}, dotted line ε_n=1 10^{-7}, dash dotted line ε_n=5 10^{-7}.

Fig. 5 shows the gain length behavior versus current for an undulator period of 8mm and a peak field of 0.95 T. For the parameters considered in Fig. 5 the Gain length shows a slightly different scaling with current for the different emittances: Table 3 summarize the scaling factors obtained from a fit on the numerical results and clearly indicates that the gain length scaling vs. current is more favorable at higher emittances.

Table 3: Scaling versus current

ε_n [m rad]	L_g scaling
5. 10^{-7}	$L_g \propto I^{-0.69}$
1. 10^{-7}	$L_g \propto I^{-0.49}$
5. 10^{-8}	$L_g \propto I^{-0.43}$

According to the present analysis a current of 500 A seems a good compromise for emittances 1 10^{-7} [m rad].

CONCLUSIONS

The parametric analysis for 1Å FEL versus an improved electron beam emittance shows that an undulator period between 10 and 15 mm operating at a gap between 3 and 5 mm can be used. The resulting linac energy could then be adjusted around 5GeV, which is quite positive concerning the accelerator size and cost.

At emittances below 1 10^{-7} mrad the current needed to reach a reasonable gain length relaxes considerably. The charge produced by the electron gun could be decreased from the usual 1 nC to 0.1 nC reducing the space-charge contribution to the emittance growth at low energy.

Beside the difficulties inherent the low emittance electron sources a major R&D effort as to be made as well concerning the undulator technology. Beside Super Conducting undulators, the recent works on cryogenic permanent magnet undulators presented by T. Hara et al [12] shows that a short period undulator (table 4) with peak magnetic fields matching the scenarios presented in this paper may be feasible.

Table 4: Possible cryo undulator

period [mm]	Gap [mm]	Peak field [T]
8	3	0.94
10	3	1.28
10	5	0.64
15	5	1.07

REFERENCES

[1] L-H Yu, S. Krinsky, “Betatron Oscillation in a FEL”, N.I.M in Physics Research A272 (1988), 436-441.
[2] M. Cornacchia et al, “LCLS design study report”,SLAC-R-521,1998.
[3] .R. Brinkmann, et al, “Tesla XFEL Technical design report supplement”, Desy 2002 167, October 2002.
[4] A. Oppelt et al,”Future plans at the Photo Injector Test Facility at DESY Zeuthen”, FEL2003
[5] K.-J.Kim et al ,”Towards Advanced Electron Beam Brightness Enhancement and Conditioning”, ANL/APS/LS-305, (2004) http://www.aps.anl.gov/techpub/lsnotes/ls305.pdf
[6] R. Ganter et al, ”Ultra-Low emittance electron gun project for FEl application”, THP27 proceedings this conference.
[7] M.J. de Loos et al, ”A High brightness pre-accelerated RF-Photo injector”, EPAC 2002, Paris, France
[8] Togawa, et. al., “Emittance Measurement on the CeB_6 Electron Gun for the SPring-8 Compact SASE Source FEL project,” APAC 2004 (MOP-20006).
[9] L.H. Yu, et al, “Calculation of Universal Scaling Function for Free-Electron-Laser Gain”, Phsy.Rev. Letters, vol 64, no 25 (1990).
[10] E.L. Saldin, et al, “Calculation of energy diffusion in an electron beam due to quantum fluctuations of undulator radiation”, N.I.M. in physical research, A381 (1996), 545-547.
[11] E.L. Saldin, et al, “Design formulas for short-wavelength FELs”, DESY 04-012, January 2004.
[12] T. Hara, et al, “Cryogenic permanent magnet undulators”, Physical review special topics – Accelerators and beams, vol. 7, 050702 (2004)

A NEW CONTROL SYSTEM FOR THE S-DALINAC[‡]

M. Platz[§], A. Araz, U. Bonnes, M. Brunken, H.-D. Gräf, M. Hertling,
A. Karnaukhov, O. Patalakha, A. Richter, O. Titze, B. Truckses,
Institut für Kernphysik, Technische Universität Darmstadt,
Schlossgartenstrasse 9, 64289 Darmstadt, Germany
W. Ackermann, W. F. O. Müller, B. Steiner, T. Weiland,
Institut Theorie Elektromagnetischer Felder, Technische Universität Darmstadt,
Schlossgartenstrasse 8, 64289 Darmstadt, Germany

Abstract

Recent results with respect to the development of a new control system for the superconducting cw electron accelerator S–DALINAC are presented. The system is based on common industrial standards. Due to the exceptionally large number of devices necessary to control the beam at the S–DALINAC, a simple and inexpensive communication interface is required to replace the current proprietary bus topology. The existing devices will be extended by a microcontroller based CAN-Bus interface as a communication path to one or more control servers. These servers utilize a TCP/IP connection to give application programs (clients) access to the device parameters. The protocol for this communication is composed of a special binary protocol and a text protocol based on XML.

INTRODUCTION

The superconducting recirculating electron accelerator S–DALINAC [1] is designed to deliver a continuous wave (cw) electron beam for nuclear and radiation physics experiments and has commenced operations in 1991. It provides an electron beam with an average current of up to 60 μA at energies of up to 130 MeV. A variety of nuclear physics experiments require the development of a new photoinjector electron gun as well as the increase of energy and intensity of the electron beam. For all experiments a reliable operation of the accelerator based on a modern control system is needed.

The accelerator and its beam transport system shown in fig. 1 consists of about 200 magnets, 80 targets and cameras and several special setups [2], e.g. Faraday cups for beam current measurements, beam position monitors or Compton diodes, to be controlled. The possibility and the demand of controlling additional devices, e.g. new diagnostic elements or parameters of the Helium liquifier, require the development of a new control system which will be realized in three steps.

The human device interface (HDI) used to control the S–DALINAC is a so-called knob board. A knob board is a thumb device emulating an analog tuning of the accelerator. A counter adds up the increments of a rotary encoder and sends the result to a knob server. Button switches are used for digital inputs, e.g. for switching power on/off or toggling between the dial mode for selecting a device from a list, which is defined for a special mode of operation, and the set mode for changing the set value of the selected device. Depending on the mode of operation the server recalculates an internal value, changes the device parameters and displays the result in the LCD elements.

The control system currently used [3] consists of a remote part based on VMS and PSOS including a knob server with an MC68020 processor, giving the possibility of selecting and turning devices, and a VAX 3800 acting as client. As control computers MC68020 microcomputers running under PSOS as operating system (OS) and two AXPvme boards using VxWorks as OS are used. While the MC68020 systems accessing the devices through a local VMEbus, e.g. the HF Control System, the gross of the devices were connected to the AXPvme via a proprietary bus topology. For the communication between the clients and servers, the Linac Control Protocol (LCP) based on Ethernet/DECnet was developed.

Although a reliable operation of the accelerator is possible, this solution has several drawbacks:

- Due to the proprietary bus, an implementation of new types of devices is rather difficult.
- The support for the AXPvme Single Board Computer (SBC) is discontinued.
- The AXPvme board architecture is no longer supported by new versions of VxWorks.
- Therefore, no hardware manufacturer supports the combination of SBC and OS.
- The clients are using VMS as OS.

THE NEW CONTROL SYSTEM

The aim of the new control system is to use a standard transport protocol like TCP/IP instead of the unique LCP used before, which will allow the definition of an application layer protocol independent of operating systems.

[‡] Supported by the Sonderforschungsbereich 634 "Nuclear Structure, Nuclear Astrophysics and Fundamental Experiments at low Momentum Transfer at the Superconducting Darmstadt Electron Accelerator (S–DALINAC)" and by the Graduiertenkolleg 410 "Physics and Technology of Accelerators"

[§] platz@ikp.tu-darmstadt.de

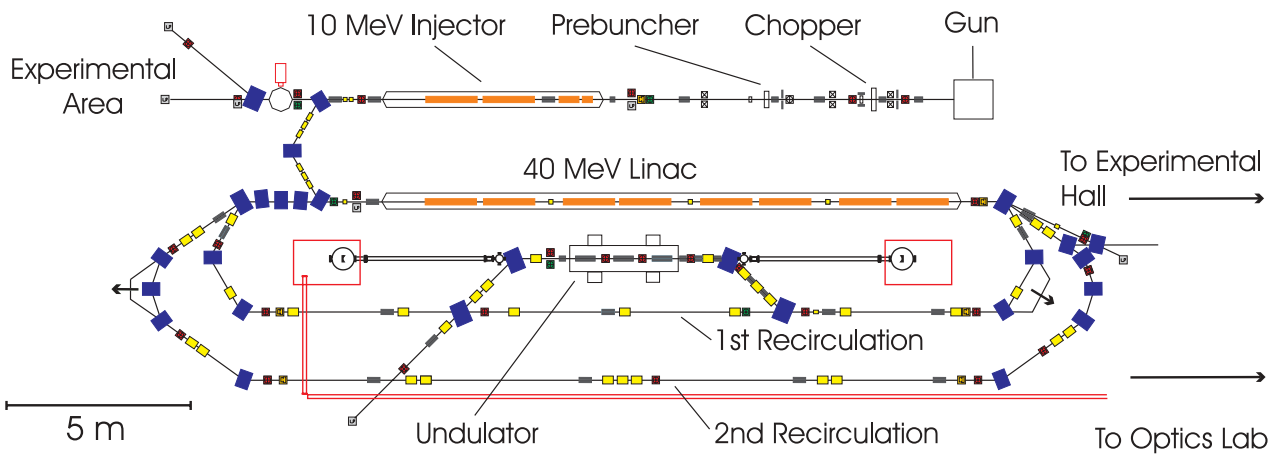

Figure 1: Layout of the S–DALINAC.

Requirements

From the experience gained in the last years several requirements for the new system could be defined:

- Low cost and reliable.
- Knob boards are to be retained.
- The system should allow easy maintenance.
- Simple integration of new elements in soft- and hardware.
- No real time beam alignment necessary.

Since the machine and personal interlock is completely hardwired, the control program should be able to retrieve and record the status. Furthermore, only this control program is going to be used for adjusting the machine parameters whereas an automatical beam alignment will not be implemented in the first step. Since the manual adjustment of the beam alignment is considered to be a rather slow process, neither a fast interaction between devices nor a common timescale (trigger) is required. Since the devices are distributed over the entire area around the accelerator, the rewiring and positioning of the control computers have to be considered carefully.

Layout

A schematic layout of the new control system is shown in fig. 2. As mentioned above, the first aim is to control all devices by a control computer, there will be no need for an implementation of a direct interaction of two devices. If a fast control operation is required, e.g for the HF control, this can be realized by a special hardware bypassing the control program. In case of major beam losses the machine and personal interlock system will stop the beam. By implementing dynamically selectable devices used for beam diagnostics into the control system, slow drifts of the beam might be compensated automatically. This will be developed in the future.

The control system is based on several control servers. The server functionality is implemented in the core of the application running on the control computer, allowing clients to request a TCP/IP connection. The functionality necessary to handle the particular devices is loaded to the application program by initialization in form of plugins. The information about the plugins needed and the devices to be controlled is inquired by the server from a global database. This database is also used by clients to find the addresses of the servers handling the devices to control.

Clients and servers exchange new device settings as follows. The client application sends a packet over a TCP/IP connection to the control server. The first byte is a protocol ID defining the structure of the following data, e.g. the ASCII value of ”<” in the special case of an XML based protocol. Usually a packet is dedicated to a specific device and is thus handled by a specific driver, i.e. only this driver is able to understand the request. Therefore a dispatcher task receives the packet from the TCP/IP socket, extracts the command for the specified driver and calls the driver entry point with the command as argument. After the driver has executed the requested operation (synchronous or asynchronous) it notifies the dispatcher task in order to

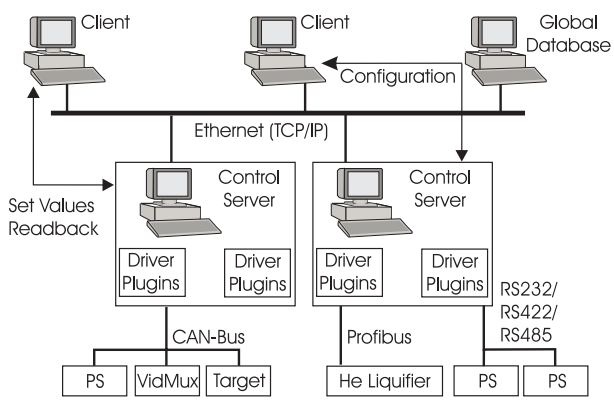

Figure 2: Layout of the control system, where PS denote a power supply for the magnets and VidMux denotes the Video Multiplexer.

initiate the reply to the client application. It turns out that this leads to software interfaces between drivers and server applications which are device independent, but they depend on the protocol. Therefore these interfaces have to be defined carefully to allow further extensions of the system.

All noncommercial devices will have the same bus interface. The device specific part of the hardware is controlled by the microcontroller attached to the bus controller, leading to a distributed system of ”intelligent” devices. While the software for the bus communication is planned to be the same for each device, the software controlling the device specific part has to be developed in conjunction with the new hardware.

As common bus interface the CAN-Bus was chosen, because it is a simple, inexpensive and reliable multimaster field bus, defined by an ISO standard for the automotive industry. Compared to other commonly used buses, like Ethernet, the speed is low, the packet size is small and it therefore suits the demands of the devices equipped with a low cost microcontroller, namely a small memory and a low computing speed. The ISO standard defines the bus on the OSI Layer 2 (datalink layer) as an object oriented bus, i.e. an object ID is defining the type of the packet. Each destination programmed to recognize this object ID will then receive the packet. The priority of the packet is determined by the object ID; the higher the object ID, the lower the priority This is to overcome conflicts in case of different controllers trying to get access to the bus simultaneously. Because of the necessity to address special devices instead of a common set of devices, the datalink layer has to be extended. This is done by redefining the object ID of a packet in that way that it contains the address and the type of service definition of the device. Thus it is possible to create reliable connections between two peers, allowing the transmission of packets as well as setting up streams.

Client Applications

Among the set of different client applications the tuning of the accelerator by using the knob boards is one of the most important. In this scope a Window based application for driving targets and selecting video multiplexer channels, giving information about the beam position and shape, is essential. By omitting the proprietary LCP, clients may be allowed to easily access the control servers automatically. In the simplest approach this could be used for beam simulation calculations, e.g. based on the V-Code [4], or will in a more complex way lead to the possibility of automatic beam emittance measurements, which is not possible presently. Finally, specific clients may be used to control slow drifts, depending on operator defined machine premises.

Current Status

The implementation of a new control system into a running accelerator is a rather difficult and complex task. So far, prototypes for the required hardware, e.g. improved knob boards and the CAN-Bus interfaces, have been designed and built. Currently this hardware is tested. The second major issue is the development of new software. As far as the application clients are concerned, a preliminary application has been accomplished and tests are currently been carried out. The global database for the storage of the data for devices and the monitored parameters have been successfully tested. The computer program for the microcontrollers is almost finished and will be tested accurately thereafter.

SUMMARY AND OUTLOOK

While designing the new control system special attention was payed to the flexibility, reliability and simplicity. Regarding the hardware the extension of the control system is achieved by a simple field bus system sufficient for slow control operation of the S–DALINAC. By using the same interface for all uncommercial devices a well-defined set of functions merged in a library could also be used to implement new types of devices.

By using TCP/IP as transport layer the development of clients is possible employing all well established operating systems. The lynchpin is the application layer protocol used to exchange the information between clients and servers. Utilizing XML as an object oriented markup language a set of common device requests could be defined. From that new device request classes can easily be derived.

By extending the server application with plugins, new drivers could be easily added after off line development and testing. The software interface between server application and driver plugin is an entry point receiving the device request that is defined by the application layer protocol. After the first device driver able to execute the common request has been developed, the others could be derived from it. The realization of the control system described in this paper will give the possibility of a flexible and extremely convenient operation of of S–DALINAC.

REFERENCES

[1] A. Richter, Proc. EPAC96, ed. by S. Myers et al., IOP Publishing, Bristol, Barcelona (1996) 110.

[2] H.-D. Gräf, J. Herrmann, M. Hüning, U. Laier, P. Mohr, M. Platz, A. Richter, B. Schweizer, S. Watzlawik, H. Weise, NIM A **512** 3 (2003) 453.

[3] H. Genz, H.-D. Gräf, J. Horn, V. Huck, K.D. Hummel, M. Knirsch, C. Lüttge, A. Richter, T. Rietdorf, K. Rühl, P. Schardt, E. Spamer, A. Stiller, F. Thomas, O. Titze, J. Töpper, H. Weise, Proc. EPAC92, ed. by H. Henke, M. Homeyer and Ch. Petit-Jean-Gomez, Edition-Frontières, Gif-sur-Yevette Cedex (1992) 53.

[4] W. Beinhauer, R. Cee, W. Koch, M. Krassilnikov, A. Novokhatski, S. Ratschow, T. Weiland, P. Castro, S. Schreiber, Proc. PAC2001, Chicago, Illinois, USA, 06/18-06/22/2001.

THE PHOTO INJECTOR TEST FACILITY AT DESY ZEUTHEN: RESULTS OF THE FIRST PHASE

A.Oppelt*, K.Abrahamyan, J.Bähr, I.Bohnet, U.Gensch, H.-J.Grabosch,
J.H.Han, M.Krasilnikov, D.Lipka, V.Miltchev, B.Petrosyan, L.Staykov,
F.Stephan, DESY, D-15738 Zeuthen, Germany
M.v.Hartrott, E.Jaeschke, D.Krämer, D.Richter, BESSY, 12487 Berlin, Germany
J.P.Carneiro, K.Flöttmann, S.Schreiber, DESY, D-22603 Hamburg, Germany
P.Michelato, C.Pagani, D.Sertore, INFN Milano, 20090 Segrate, Italy
I.Tsakov, INRNE Sofia, 1784 Sofia, Bulgaria
W.Sandner, I.Will, Max-Born-Institute, D-12489 Berlin, Germany
W.Ackermann, W.F.O.Müller, S.Setzer, T.Weiland, TU Darmstadt, D-64289 Darmstadt, Germany
J.Roßbach, Inst. f. Experimentalphysik, Univ. Hamburg, D-22761 Hamburg, Germany

Abstract

The photo injector test facility at DESY Zeuthen successfully concluded it's first phase of operation in November 2003 (PITZ1). After a complete characterization of the injector, the gun has been transfered to Hamburg and has already been taken into operation on the VUV-FEL.

The measurement program for the year 2003 included RF commissioning, emittance studies, momentum and bunch length measurements, and studies of the influence of the drive laser parameters. We provide an overview on the latest achievements in all of these topics and an outlook on the future plans at PITZ.

INTRODUCTION

The Photo Injector Test Facility at DESY Zeuthen (PITZ) has been built in order to test and optimize electron sources for Free Electron Lasers (FELs) and future linear colliders. The goal of PITZ is to produce intense electron beams with small transverse emittance and short bunch length as required for FEL operation.

The photo injector consists of a 1.5 cell L-band RF gun with a Cs_2Te photo cathode, a solenoid system for space charge compensation, a photo cathode laser system which generates long pulse trains with variable temporal and spatial pulse shape, and an extended diagnostics section. A schematics of the PITZ1 setup is shown in figure 1.

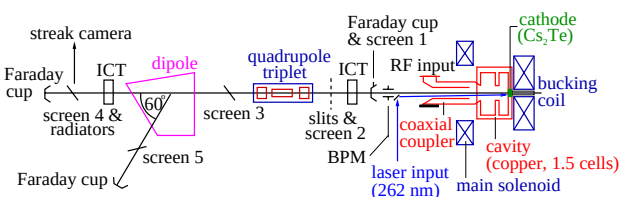

Figure 1: Scheme of the PITZ1 setup.

PITZ has been taken into operation in January 2002. The first stage of the project (PITZ1) has been successfully completed with the transfer of a completely characterized RF gun to the VUV-FEL at DESY Hamburg in November 2003. The results obtained with this gun are briefly summarized in the following section. Meanwhile, a new gun has been installed and conditioned at PITZ. Recent improvements and first measurement results as well as plans for the future of PITZ are reported below.

* corresponding author: anne.oppelt@desy.de

RESULTS OF PITZ1

The measurement program of PITZ1 in the year 2003 included RF commissioning, emittance studies, momentum and bunch length measurements, and studies of the influence of the drive laser parameters.

RF conditioning. The smooth commissioning of the gun allowed an operation with up to 900 μs long RF pulses at 10 Hz repetition rate and about 3.3 MW peak power in the gun. This corresponds to an accelerating gradient at the cathode of about 42 MV/m, and an average power of 27 kW in the gun with 0.9% duty cycle [1]. Such a long RF pulse operation fulfills the TTF2 VUV-FEL requirements.

Photo cathode laser. The optimization of the photo cathode laser parameters included longitudinal and transverse profile. In order to minimize the space charge influence on the transverse beam emittance, a longitudinal flat top profile of 20 ps duration (FWHM) and rise/fall times of 2 ps should be realized. The transverse laser profile is needed to be radially homogeneous, and of adjustable rms size. In reality, these ideal parameters could not yet be reached. Typically, a longitudinal profile of 23 ps FWHM with 6 ps rise/fall time has been used, and a relatively homogeneous transverse profile of size $\sigma_{rms} = 0.5 \ldots 0.6$ mm.

Bunch charge. Detailed studies of the produced electron bunch charge as function of the RF phase and the solenoid settings were performed [1], and comparisons with simulations allowed to improve the understanding of the photo injector. The nominal bunch charge is 1 nC and can be adjusted by tuning the photo cathode laser power.

Momentum and momentum spread. Extensive measurements have been undertaken in order to study longitudinal

momentum and momentum spread of the electron beam. A maximum mean momentum of 4.72 MeV/c has been measured. The minimum momentum spread was found to be 33 keV/c. For more details see [2].

Bunch length. The bunch length has been measured for different conditions [2]. A minimum length (FWHM) has been measured to be (21.04±0.45stat±4.14syst) ps.

Normalized emittance. For measurements of the normalized projected beam emittance, the slit mask scan technique is used [1]. The optimization of the photo cathode laser properties together with RF field and solenoid parameters yielded an average emittance of $\sqrt{\varepsilon_x \varepsilon_y} = 1.7\ \pi$ mm·mrad [3], see figure 2. Thus, the start-up conditions of the TTF2 VUV-FEL on normalized projected beam emittance [4] have been fulfilled.

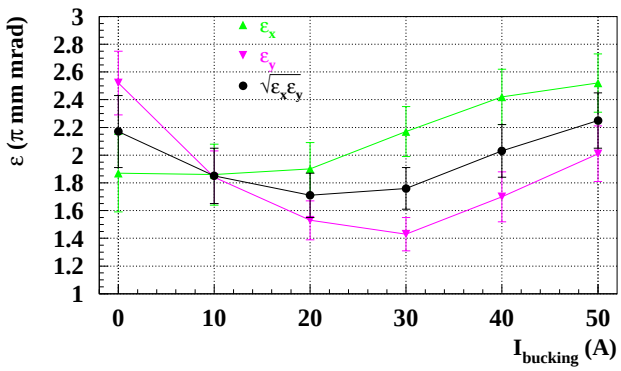

Figure 2: Measured transverse normalized emittance as function of the current in the bucking solenoid (responsible for compensating the magnetic field of the main solenoid at the cathode plane) for the optimized RF phase and main solenoid current [3]. The measurements in both planes, x and y, are shown as well as the geometric average $\sqrt{\varepsilon_x \varepsilon_y}$.

RECENT IMPROVEMENTS

After the fully characterized gun has been transfered to DESY Hamburg and taken into operation at the TTF2 VUV-FEL, a new gun cavity has been installed at PITZ. This gun has extensively been conditioned, and measurements of the electron beam properties are ongoing. The most recent measurement results comprise (see also [5]):

RF commissioning. The limited input peak power of the 5 MW klystron allows for a maximum power in the gun of about 4 MW. In order to reach a high average power, the pulse length has been increased up to 1300 μs. An average power of about 33 kW has been reached in July 2004 [5].

Dark current studies. The behaviour of the dark current emitted from the gun has been studied. Due to the high rf gradient and the limited surface quality of this gun, a high amount of dark current has been measured and was found to be the reason for destruction of vacuum components (e.g. view screens) and photo cathode surfaces [6].

Laser optical beamline. In parallel to these activities, the optical beamline of the photo cathode laser has been modified, resulting in a significant improvement of the homogeneity of the transverse laser profile at the photo cathode. Figure 3 shows an example of the laser spot at the cathode plane.

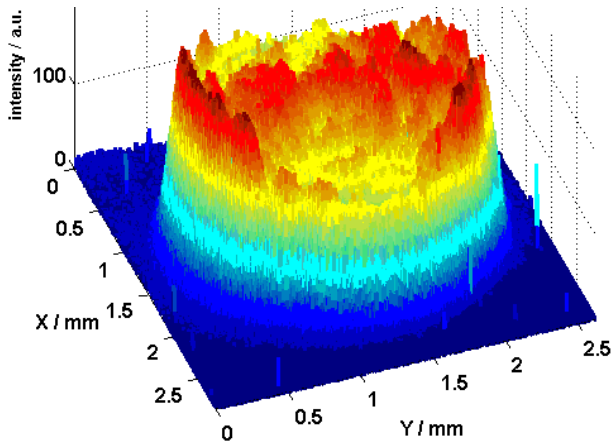

Figure 3: 3D image of the transverse laser profile at the position of the photo cathode.

Emittance measurements. Thermal emittance measurements at low charge (few pC) were performed in June 2004. An average kinetic energy of the photo electrons after emission has been found to be about 0.8 eV [3]. The normalized projected beam emittance measurements and the parameter space optimization for high gradients are ongoing. As a preliminary result, the minimum measured emittance was about 2.5 π mm·mrad at the nominal charge of 1 nC [3].

Longitudinal phase space. Momentum measurements in August 2004 resulted in a maximum momentum of 5.2 MeV/c. First measurements of the momentum spread indicated, that the minimum momentum spread could be as low as 22 keV/c, which would be considerably smaller than the PITZ1 measurements. Bunch length measurements still have to be performed.

PITZ2

The second stage of PITZ, called PITZ2, will be a large extension of the experimental setup and its measurement program [7]. The main intention is a further improvement of the electron beam quality with the goal to approach the requirements of the European XFEL. This needs an optimization of the photoinjector and all subsystems, including laser, photo cathodes, and guns, as well as simulation tools.

Booster cavity. In order to conserve the small beam emittance produced at the gun, a booster cavity will be installed. Using a preliminary booster, the beam energy will be increased from about 5 MeV to $\sim$ 16 MeV. This booster has been tuned and is presently under vacuum preparations. It will be conditioned before its installation at the beamline, which is foreseen to happen in early spring 2005. Later, the beam energy will be further increased to about 30 MeV, using a final booster specially designed for

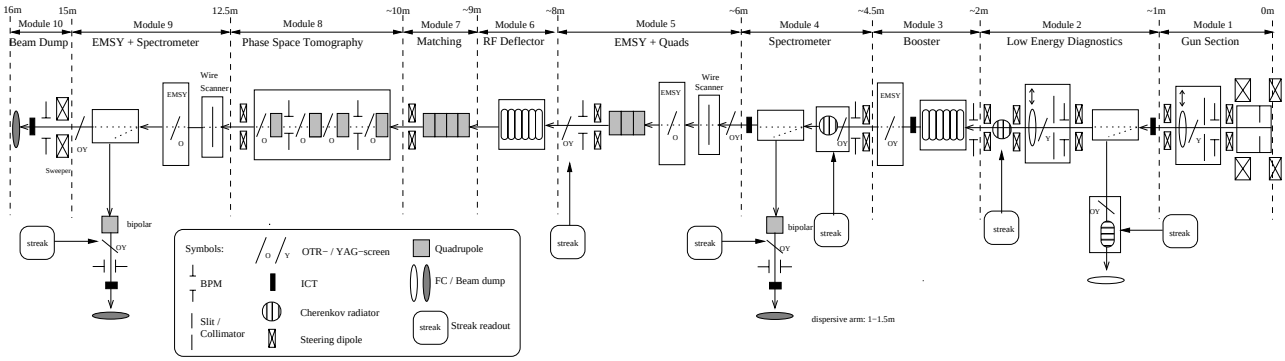

Figure 4: Preliminary layout of PITZ2.

PITZ.

RF system. In order to operate the booster cavity, a second rf system has been installed and is being taken into operation. Since reaching a higher gradient in gun and booster is essential for producing low emittance beams, the existing 5 MW klystrons will be replaced by 10 MW klystrons in the year 2005.

Beam diagnostics. The increased beam energy requires new, adapted diagnostics tools. For this reason, a completely new diagnostics beamline will be installed at PITZ, suitable for the higher beam energy. Beside standard beam diagnostics devices like e.g. OTR view screens, possibilities for slice emittance measurements and phase space tomography are foreseen to be implemented. In order to test the emittance conservation principle, the emittance development along the beam axis has to be monitored. For that purpose, three emittance measurement stations and several quadrupoles are distributed along the beamline. A preliminary layout of the complete PITZ2 beamline is shown in figure 4.

As a first step towards the PITZ2 beamline, a simplified setup with only a limited number of diagnostics devices will be realized. The design of this minimum version of the PITZ2 setup has been finished, and the beamline elements are currently under construction. Before the booster cavity can be taken into operation, a beam dump needs to be commissioned. This is a critical point, since long bunch trains and small spot sizes require special design considerations.

Laser system. The transverse and longitudinal laser profile have been found to be crucial for the production of low emittance beams. The goal is to reach the parameters determined by simulations: a longitudinal flat top distribution of 20 ps length (FWHM) with rise/fall times of 2 ps, and a very homogeneous, circular transverse laser profile. These requirements can only be realized by a special development of the laser system (a two-channel mixing system, mixing high power gaussian and low power rectangular laser pulses) and a further improvement of the optical beamline.

Further optimization. In order to reach optimum electron beam parameters and improve the theoretical understanding of the photo injector, the optimization of all subsystems is needed. For that purpose, extensive beam dynamics simulations have to be done and compared to measurements. This includes improvements on the simulation tools.

Furthermore, it is planned to improve the existing gun design and develop a gun for the European XFEL with improved geometry and cooling. This is a precondition for the exploration of the European XFEL parameter space and high duty cycle operation. For that, studies of the photo cathode materials are also necessary and foreseen.

SUMMARY

The first phase of PITZ has successfully concluded in November 2003 with the full characterization of the photo injector. The main results have been summarized. A large extension of the existing setup and the measurement program is planned. Preparations for the PITZ2 project are ongoing, and results of the first improvements have been presented.

REFERENCES

[1] M. Krasilnikov et al., Characterization of the Electron Source at the Photo Injector test facility at DESY Zeuthen", FEL 2003, Tsukuba, Sept. 2003.

[2] D.Lipka, Investigations about the logitudinal phase space at a photo injector for minimized emittance, PhD thesis, Humboldt University Berlin, May 2004.

[3] V.Miltchev et al., Transverse emittance measurements at the Photo Injector Test Facility at DESY Zeuthen, FEL 2004, Trieste, Sept. 2004.

[4] "SASE FEL at the TESLA Facility, Phase2", DESY Report TESLA-FEL 2002-01, June 2002.

[5] F.Stephan et al., Recent Results and Perspectives of the Low Emittance Photo Injector at PITZ, FEL 2004, Trieste, Sept. 2004.

[6] J.H.Han et al., Conditioning and high power tests of the rf guns at PITZ, EPAC 2004, Lucerne, June 2004.

[7] A.Oppelt et al., Future plans at the Photo Injector Test Facility at DESY Zeuthen, FEL 2003, Tsukuba, Sept. 2003.

PROGRESS REPORT ON THE FLAT BEAM EXPERIMENT AT THE FERMILAB/NICADD PHOTOINJECTOR LABORATORY

Y.-E Sun*, K.-J. Kim, University of Chicago, Chicago, IL 60637, USA
P. Piot†, K. Desler, H. Edwards, M. Hüning,
J. Santucci, J. Wennerberg, FNAL, Batavia, IL 60510, USA
N. Barov, Northern Illinois University, DeKalb, IL 60115, USA
R. Tikhoplav, University of Rochester, Rochester, NY 14627, USA
S. Lidia, LBNL, Berkeley, CA 94720, USA

Abstract

We report on our present progress toward the investigation on the generation of flat beam from an incoming angular momentum-dominated beam. In the present paper we compare our latest experimental results with numerical simulations.

INTRODUCTION

The generation of flat beam from an incoming angular momentum-dominated (magnetized) beam proposed in Reference [1] in the linear collider context has found, since then, other applications, e.g. in the linac-based light source [2]. A proof-of-principle experiment was performed at the Fermilab/NICADD photoinjector laboratory (FNPL) [3] and reported in various papers [4, 5]. In the present paper, we discuss the first results of a second series of experiment dedicated to better understand the production of magnetized beams and the subsequent removal of the longitudinal angular momentum with the round-to-flat beam (RTFB) transformer. The RTFB transformer (see

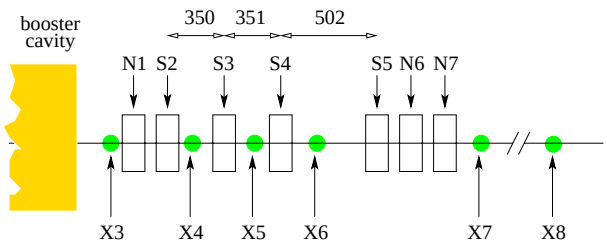

Figure 1: Overview of the RFTB section. The letters N, S and X represents normal and skew quadrupoles, and diagnostic stations. Dimension are in mm.

Fig. 1) consists of four skew quadrupoles located downstream of the booster cavity, at an energy $E \simeq 16$ MeV. Several optical transition radiation (OTR) or scintillating (YaG-based) screens allow the measurement of beam transverse density evolution through the RFTB transformer. The beam transverse emittances can be measured based on the multi-slit, or the quadrupole scan techniques. These emittance diagnostics are available both upstream and downstream of the RFTB section. Compared to the first series

* yinesun@uchicago.edu
† piot@fnal.gov

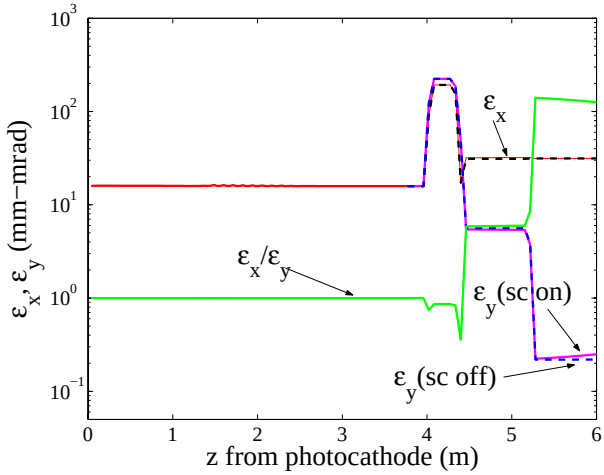

Figure 2: Simulated evolution of transverse emittances along the FNPL beamline for standard nominal settings.

Table 1: Typical settings for the rf-gun, accelerating section, and the photo-cathode drive-laser

parameter	value	units
laser injection phase	25 ± 5	rf-deg
laser radius on cathode	0.6-1.6 ($\pm$ 0.05)	mm
laser pulse duration	4 ($\pm$ 0.5)	ps
bunch charge	0.2-1.6	nC
E_z on cathode	34-35 $\pm$ 0.2	MV/m
B_z on cathode	200-1100	Gauss
booster cavity acc. gradient	~ 12	MV/m

of experiment, our main motivation for reorganizing the RFTB section was to locate all the RFTB section components upstream of the magnetic chicane. Such a relocation was motivated by the potential production of compressed flat beams at a later phase of the flat beam experiment. The typical operating parameters of the photo-injector subsystems during data taking for the flat beam experiment are gathered in Table 1. A series of simulations were performed to study the performance of the RFTB section in term of what transverse emittance ratio could be achieved. An example of evolution of the transverse emittance along the beamline is presented in Fig. 2 for the a magneto-

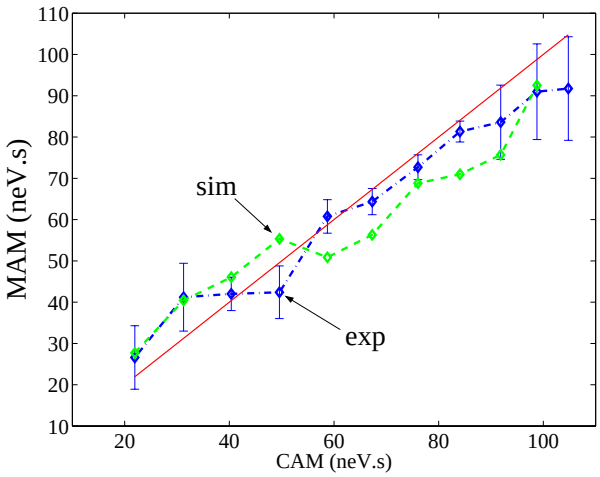

Figure 3: Mechanical angular momentum (MAM) compared to the canonical angular momentum (CAM) calculated from the longitudinal magnetostatic field at the photocathode. The labels "exp." and "sim." correspond respectively to experimentally measured data points and simulated value after modeling of the measurement technique.

static field $B_z = 829$ G on the photocathode surface (at $z = 0$ m). As one can see, this set of daily achievable beam parameters has the potential to generate a flat beam with transverse emittance ratio $\tilde{\varepsilon}_y/\tilde{\varepsilon}_x \simeq 31.39/0.23 \simeq 136$. We also note in Fig. 2 that space charge effects within the RFTB section are insignificant. But an increase of the smaller of the flat emittances is observed as the beam propagates downstream of the transformer – this is a critical issue that need to be taken into account when measuring the flat beam transverse emittances.

STUDY OF ANGULAR MOMENTUM-DOMINATED BEAMS

Given the B-field at the photocathode and the uncorrelated transverse emittance in the Larmor frame, ϵ_u, the flat beam transverse emittances, $\epsilon_\pm$, are respectively given by [6]:

$$\epsilon_\pm = \sqrt{\epsilon_u^2 + \mathcal{L}^2} \pm \mathcal{L}, \text{ with } \mathcal{L} = \kappa\sigma_c^2, \qquad (1)$$

wherein σ_c is the rms drive-laser spot size on the photocathode and $\kappa \doteq eB_z/(2p)$, e is the electron charge, B_z the longitudinal magnetic field on photocathode and p the particle momentum. For a cylindrically symmetric beam, $\mathcal{L}$ is related to the canonical angular momentum through [7]:

$$\langle L \rangle = 2p\mathcal{L}. \qquad (2)$$

We use the technique to measure the mechanical angular momentum from a measurement of beam rms spot sizes, σ_1 and σ_2, at two longitudinal locations z_1 and $z_2 (> z_1)$ and the measurement of rotation angle, θ, of beamlets pattern at z_2 produced by inserting a multi-slit mask at location z_1: the averaged mechanical angular momentum is obtained from $\langle L \rangle = p\sigma_1\sigma_2 \sin\theta/(z_2 - z_1)$.

A set of measurement of the evolution of mechanical angular momentum evolution versus B-field on the photocathode was reported in Ref. [7]. Here such an experiment was performed varying the B_z-field over a wider range ($B_z \in [200, 1100]$ Gauss) – see details in Ref. [8]. The measurement technique aforementioned was also numerically tested for each experimental data point. In Figure 3 we compare the measured mechanical angular momentum with the canonical angular momentum calculated, given the B-field on the photocathode, from Eq.2. The measured val-

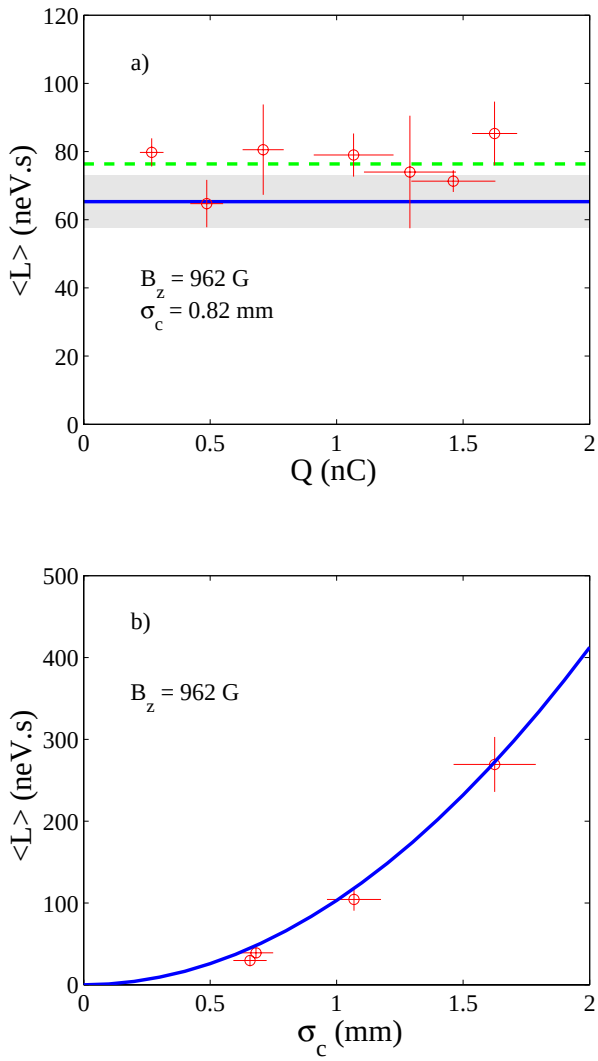

Figure 4: Angular momentum versus charge **a)** and photocathode drive-laser spot size **b)**. The experimental data (circles) are compared with theoretical value of the canonical angular momentum calculated from the longitudinal magnetostatic field. In **a)**, the dashed line represent the average value of all the data points, and the shaded area corresponds to the uncertainty on the canonical angular momentum.

ues include both experimental data and simulated values, i.e. values that have been retrieved after a numerical simulation of the measurement.

The dependence of angular momentum on the charge was also explored, in this experiment the laser spot size was set to $\sigma_c = 0.98$ mm, and laser intensity was varied by the mean of a wave plate attenuator located in the ultraviolet path of the laser. The results, shown in Fig. 4(a), indicate the angular momentum is charge-independent, confirming our assumption that the beam dynamics is angular momentum-dominated.

Finally the dependence of angular momentum versus σ_c was investigated, in this experiment σ_c was varied using a remotely controllable iris. The laser intensity was held constant and the B-field on the photocathode was identical to the previous experiment ($B_z = 962$ G). The measurements (see Fig. 4(b)) support the expected quadratic dependence of the angular momentum on σ_c.

REMOVAL OF ANGULAR MOMENTUM

The incoming angular momentum-dominated beam is converted into a flat beam using only three quadrupoles (S2, S3, S5 in Fig. 1) for the series of measurement presented hereafter. Given the photoinjector parameters, numerical simulations of the upstream beamline are performed using the tracking program ASTRA[9]. From the transverse phase space obtained at the transformer entrance, the correlation matrix defined as $\mathcal{C} \doteq \langle Y\widetilde{X}\rangle\langle X\widetilde{X}\rangle^{-1}$ is calculated, wherein $\widetilde{X} = (x, x')$, $\widetilde{Y} = (y, y')$ and $\widetilde{\ }$ stands for the transpose operator. The required skew quadrupole strengths are then computed such that the quantity $\chi^2 \doteq \sum_i \sum_j |\mathcal{C}_{i,j}|^2$ evaluated downstream of the RFTB transformer is minimized. The starting values for the minimization algorithm are the one derived under the thin lens approximation in Reference [5].

Experimentally further optimization around the predicted values is generally needed to insure the angular momentum is totally suppressed (as inferred by observation of the x-y coupling at several location downstream of the RFTB section). Presently we observed an agreement between the predicted values and those experimentally optimized of about 10 to 20%. The evolution of beam transverse density throughout the RFTB section is in very good agreement with the expectations from simulation, as depicted in Figure 5.

SUMMARY AND FUTURE PLANS

The dependence of mechanical angular momentum on B-field, charge and laser spot size on the cathode have been measured. A new configuration for the round-to-flat beam transformer has been commissioned, and good qualitative agreement is observed between numerical simulations and experiment. To date we have not yet attempted to precisely measure the achieved emittance: further work on the emittance measurement is first needed.

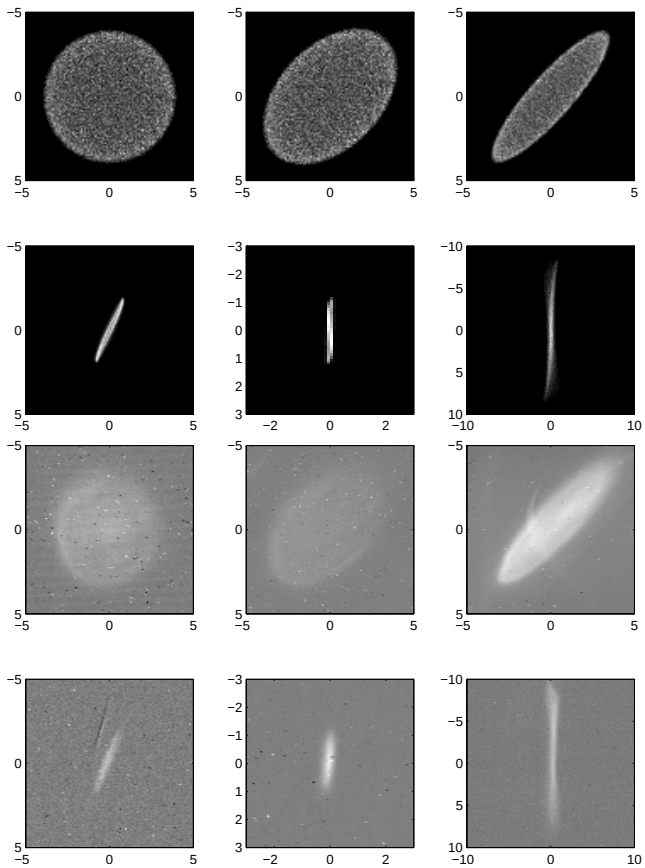

Figure 5: Simulated (top six plots) and measured (bottom six plots) beam transverse density evolution in the RFTB section. The consecutive plots corresponds to location X3, X4, X5, X6, X7 and X8. Dimensions are in mm.

ACKNOWLEDGEMENTS

The authors wish to thank W. Muranyi, M. Heinz, M. Rauchmiller, P. Padilla and P. Prieto for their excellent technical support.

REFERENCES

[1] R. Brinkman *et al.*, *Phys. Rev. ST A&B* **4**, 053501 (2001)

[2] J. Corlett *et. al*, proc. EPAC 2002, 668-670 (2002)

[3] K. Desler et. al, this conference

[4] D. Edwards *et al.*, proc. LINAC 2000, 122-124 (2000)

[5] E. Thrane *et al.*, proc. LINAC 2002, 308-310 (2002)

[6] K.-J. Kim *et al.*, *Phys. Rev. ST A&B* **6**, 104002 (2003)

[7] Y.-E Sun *et al.*, proc. PAC 2003, 2682-2684 (2003)

[8] Y.-E Sun and P. Piot, Beams Document 1254-v1 July 2004 (unpublished) available at http://beamdocs.fnal.gov/cgi-bin/public/DocDB/DocumentDatabase

[9] K. Flöttman, *Astra user manual* DESY

SIMULATIONS OF THE ION-HOSE INSTABILITY FOR DARHT-II LONG-PULSE EXPERIMENTS

K. C. Dominic Chan, Carl A. Ekdahl Jr., LANL, Los Alamos, NM 87545, USA
Thomas C. Genoni, Thomas P. Hughes, ATK-MRC, NM 87110, USA

Abstract

Computer simulations of the ion-hose effect typically use Particle-In-Cell (PIC) computer codes or codes using the spread-mass model. PIC simulations, though offering more reliable results, require extensive running time on large computers. In order to support commissioning experiments in the DARHT-II induction linac at Los Alamos National Laboratory, we have improved a spread-mass code so that we can survey quickly the parameter space for the experiment. In this paper, we describe the code modifications and the benchmarking against a PIC code, and present results of our simulations for the DARHT-II commissioning experiment.

INTRODUCTION

During Phase-II commissioning of the DARHT (Dual-Axis Radiographic Hydrodynamics Test) Facility [1], beam physics tests (also known as Long-Pulse Experiments, LPE) will focus on the stability of the 2-μs beam pulse against beam-breakup and ion-hose effects. The goal is to demonstrate that beam-breakup and ion-hose instabilities will not cause the DARHT-II beam to become unacceptable for radiographic uses.

The ion-hose instability was studied previously for the DARHT-II induction linac using computer simulations including Particle-In-Cell (PIC) and Spread-Mass (SM) methods [2, 3]. PIC simulations, though offering more reliable results, require extensive running time in large computers. Our goal is to improve a SM simulation code, which has a typical running time of a few minutes, so that it can be used to give fast and reasonably reliable guidance during commissioning.

In this paper, we will describe modifications to the SM code. Numerical results obtained using the improved SM model are compared to PIC simulations to assess the accuracy of the SM simulations. Then we will describe SM simulation results for LPE of Phase-II commissioning.

IMPROVED SPREAD-MASS SIMULATION CODE

Previously, SM simulations for DARHT assumed beam and accelerator parameters that were uniform along the length of the accelerator. These parameters include the solenoidal magnetic field, beam energy, and beam radius. To improve the SM simulations, we modified the SM code to include these parameters as a function of longitudinal distance along the accelerator (z). We also included the effect of the radial magnetic field due to the varying longitudinal magnetic field. This latter effect will introduce a rotation of the beam centroid around the accelerator axis.

Our SM code was based on the SM code written by Genoni with uniform accelerator parameters. Our development and solution of the equations follows closely that by Genoni in Ref. [2], which in turn was a generalization of the original ion-hose SM formulation by Buchanan in Ref [4]. Since details of Genoni's work can be found in Ref. [2], we will highlight here only the new modifications.

Equation (1) in Ref. [2], which considers only the linear ion-hose force, was modified by adding the effect of the radial magnetic field by including a third term on the left-hand side of the equation, i.e.

$$\frac{\partial^2 b}{\partial z^2} = -k_{\beta e}^2 (b-d) + ik_{ce}\frac{\partial b}{\partial z} - ik_{ce}\left(\frac{B_r}{rB_z}\right)b \qquad (1)$$

where b and d, respectively, are the beam and ion-channel centroid-displacements from the axis. In the third term, B_r and B_z are the radial and longitudinal components of the solenoidal magnetic fields and r is the radial position of the beam. Equation (2) in Ref. [2] remains unchanged, i.e.

$$\frac{\partial^2 d}{\partial \tau^2} = -\omega_{\beta i}^2 (d-b) - i\omega_{ci}\frac{\partial d}{\partial \tau} \qquad (2)$$

In equations (1) and (2), $k_{\beta e}^2$ and $\omega_{\beta i}^2$ are given as:

$$k_{\beta e}^2 = \frac{f\nu}{\gamma R^2} \quad and \quad \omega_{\beta i}^2 = \frac{m_e \nu c^2}{m_i R^2}$$

where m_e and m_i are the electron and ion masses, γ is the electron relativistic factor, $\nu = {eI_b}/{m_e c^3}$, $\tau = t - {z}/{c}$, I_b is the beam current and f is the fractional neutralization. k_{ce} and ω_{ci} are defined as:

$$k_{ce} = \frac{eB_z}{\gamma m_e c^2} \quad and \quad \omega_{ci} = \frac{eB_z}{m_i c}$$

Equations (1) and (2) were further transformed by adding the SM formulation and nonlinearity as in Ref. [2], arriving at equations similar to equations (27) and (28) in Ref. [2]. These equations were then solved numerically with the solenoidal magnetic field, beam energy, and beam radius as functions of z.

BENCHMARKING OF SM SIMULATIONS

We benchmarked our SM code against results obtained using LSP, a 3-D PIC code from ATK-MRC [5]. Four

cases were compared: a) H_2O gas excited with a 12-MHz input beam displacement oscillation; b) H_2O gas excited by a broadband beam displacement oscillation; c) Ar gas excited with an 8.4-MHz input beam displacement oscillation; and d) Ar gas excited by a broadband beam displacement oscillation. The frequencies of 12 and 8.4 MHz were chosen because they were the estimated ion-hose resonance frequencies. The broadband oscillation spectrum is represented by a sum of 100 sinusoidal oscillations with discrete frequencies distributed uniformly over a frequency range from 0 to 60 MHz. Both SM and PIC simulations used same initial displacements and accelerator parameters for Phase I Commissioning as listed in the 'Benchmark' column in Table 1.

Table 1: Accelerator parameters used for the benchmark and LPE simulations

Parameters	Benchmark	LPE
Accelerator length (cm)	2250	2750
Initial Beam Energy (MV)	4.2	3.1
Final beam Energy (MeV)	11.34	8.1
Average rms beam radius (mm)	7.2	5.5
Average Bz (Gauss)	700	625
Gas pressure (torr)	$1x10^{-6}$	0.1-1 x 10^{-6}

Typical PIC and SM results are shown in Figures 1a and 1b, respectively, for cases (a) and (c). The beam displacements are plotted as a function of time (τ) measured back from the head of the pulse. Some general conclusions can be drawn. PIC and SM results show good qualitative agreement. The SM results have more pronounced oscillations. Agreement is better for single-frequency excitation, probably due to differences in random excitations used for the broadband cases. With the results of the four benchmark cases, we conclude that the SM simulations can predict the ion-hose excitations to better than a factor of two and are lower than the PIC results.

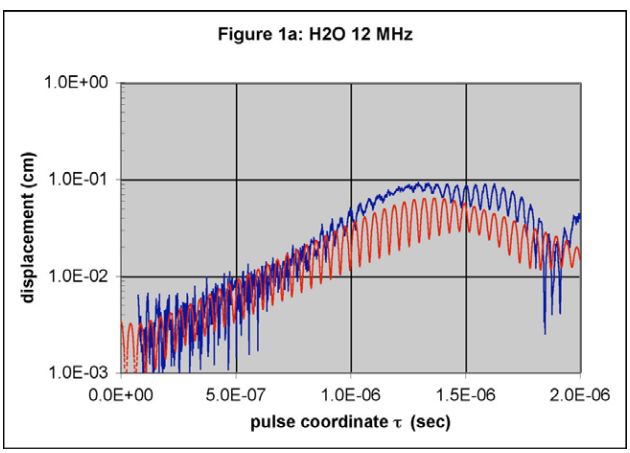

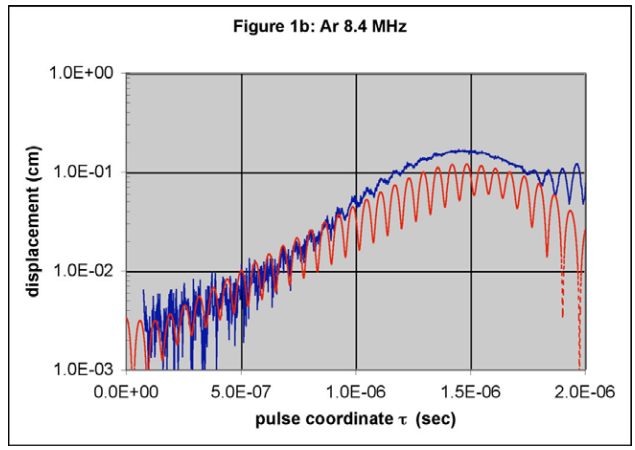

Figure 1: Comparison of LSP (blue) and SM (red) results for benchmark cases (a) and (c) are shown, respectively, in Figure 1a and 1b.

SPREAD-MASS RESULTS FOR PHASE-II COMMISSIONING

The plan for LPE is to observe ion-hose effects using some of the following gases: H_2O, Ar, Kr, Xe, or N_2 in a pressure range of 1 x 10^{-7} to 1 x 10^{-6} torr. The relevant accelerator parameters are summarized in Table 1.

Using the improved SM code, we obtained results for the LPE assuming a broadband excitation. The broadband excitation was represented by a sum of sinusoidal oscillations at 100 discrete frequencies equally spaced between 0 and 50 MHz. The initial amplitudes of these oscillations were 0.001 cm.

Typical results are shown in Fig. 2 for gases (a) Ar and (b) Xe, respectively. The beam displacements along the pulse were plotted for four different pressure levels in the beam pipe. To summarize the results of beam displacement as a function of pressure, we have plotted in Fig. 3 the average beam displacements of the last quarter of the beam pulse (between 1.5 and 2.0 μs) as a function of pressure for different gases. Results show the instability growth with increasing pressure levels and towards the back of the pulse.

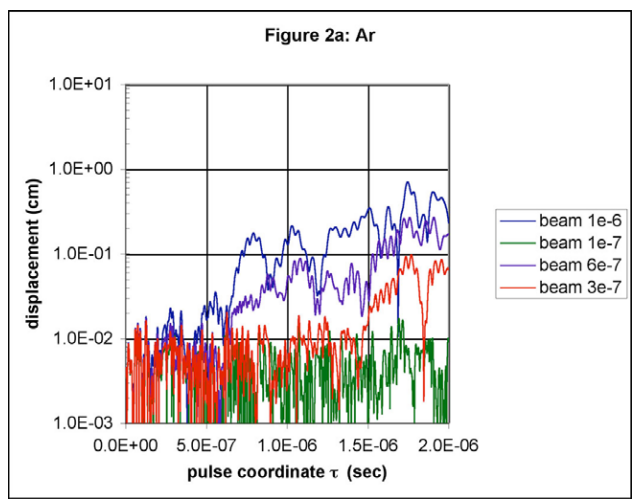

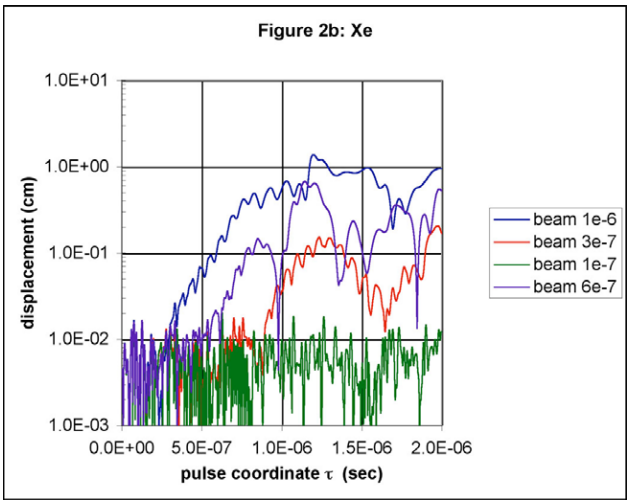

Figure 2: Typical results for (a) Ar and (b) Xe, showing the beam displacements along the beam pulse for different pressures.

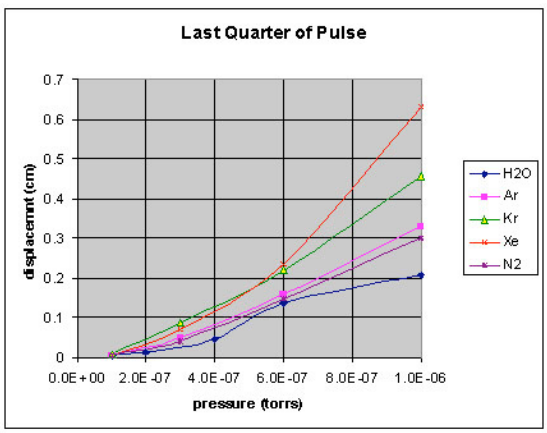

Figure 3: Average beam displacements for the last quarter of the beam pulse as a function of pressure for different gases.

The runtime for each run using the SM code was less than 15 minutes. We found that good results could be obtained when the time and z resolutions used in integrating equations (1) and (2) were, respectively, 2 cm and 1 ns, or better. The SM code is presently configured to read the z-dependent parameters from a file, which, in our runs, is produced with a beam envelope code (XTR) routinely used at DARHT. Other needed inputs are entered interactively while the code is running so that cases with different parameter values can be tried.

SUMMARY

Simulation results of ion-hose effects were obtained for different gases in support of Phase II commissioning of DARHT II induction linac. The results were obtained with a computer code using the spread-mass model. This code was designed to give quick results to support commissioning. It differs from other spread-mass codes in that it includes the z dependence of accelerator parameters. Results from this code compare well with the more reliable results obtained using time-consuming 3-D Particle-In-Cell simulations.

ACKNOWLEDGEMENT

This work was supported by the US National Nuclear Security Agency and the US Department of Energy under contract W-7405-ENG-36.

REFERENCES

[1] Ekdahl et al., First Beam at DARHT-II, Proceedings of Particle Accelerator Conference 2003, Portland, Oregon, May 12-16, 2003, p. 558.
[2] Genoni and Hughes, Ion-hose instability in a long-pulse linear induction accelerator, Phys. Rev. Special Topics-Accel. And Beams, Vol. 6, 030401, 2003
[3] Caporaso and McCarrick, Ion-Hose Instability in Long Pulse Induction Accelerators, Proceedings of the 2000 International Linac Conference, Monterey, CA, August 21-25, 2000, p.500.
[4] H.L. Buchanan, *Phys. Fluids*, 30:221, 1987.
[5] LSP is a software product of ATK Mission Research (http;//www.mrcabq.com).

CUMULATIVE BEAM BREAKUP WITH TIME-DEPENDENT PARAMETERS*

J. R. Delayen#, Thomas Jefferson National Accelerator Facility, Newport News, VA 23606, USA

Abstract

A general analytical formalism developed recently for cumulative beam breakup (BBU) in linear accelerators with arbitrary beam current profile and misalignments [1, 2] is extended to include time-dependent parameters, such as energy chirp or rf focusing, in order to reduce BBU-induced instabilities and emittance growth. Analytical results are presented and applied to practical accelerator configurations.

FORMULATION AND SOLUTION

In a continuum approximation, the transverse motion of a relativistic beam under the influence of focusing and BBU can be modeled by [1]

$$\left[\frac{1}{\gamma}\frac{\partial}{\partial\sigma}\left(\gamma\frac{\partial}{\partial\sigma}\right)+\kappa^2\right]x(\sigma,\zeta) = \varepsilon\int_0^\zeta d\zeta_1\, w(\zeta-\zeta_1)F(\zeta_1)x(\sigma,\zeta_1) \tag{1}$$

where γ is the usual energy parameter; $\sigma = s/\mathbf{L}$, is the distance from the front of the accelerator normalized to the accelerator length; κ is the normalized focusing wave number; $\zeta = \omega\left(t-\int ds/\beta c\right)$, is the time made dimensionless by the frequency ω and measured after the arrival of the head of the beam at location σ; $F(\zeta) = I(\zeta)/\bar{I}$, the current form factor, is the instantaneous current divided by the average current; $w(\zeta)$ is the wake function, which, in the case of a single dipole mode, is assumed to be $w(\zeta) = u(\zeta)\,\sin\zeta\, e^{-\zeta/2Q}$; ε is the coupling strength between the beam and the dipole mode, and includes properties of the beam and the deflecting mode of the accelerating structure.

While Eq. (1) assumes a perfectly aligned accelerator, misalignment of the cavities and focusing elements can also be included in the following analysis in a straightforward fashion.

Without loss of generality, we will assume a coasting beam. As shown in [1], the analytical results can be extended to an accelerated beam by suitable coordinate and variable transformations. Under these assumptions, the equation of motion becomes

$$\frac{\partial^2}{\partial\sigma^2}x(\sigma,\zeta)+\kappa^2x(\sigma,\zeta) = \varepsilon\int_0^\zeta d\zeta_1\, w(\zeta-\zeta_1)\,F(\zeta_1)x(\sigma,\zeta_1). \tag{2}$$

* Work supported by the U.S. Department of Energy under contracts No. DE-AC05-84-ER40150 and DE-AC05-00-OR22725

#delayen@jlab.org

In the following we will make the additional assumption that the injection offsets (lateral displacement and angular divergence) are time-independent. Again, time-dependent injection parameters can be included in the following formalism.

Time-independent Parameters

In [1], Equation (2) was solved under the assumption of constant, time-independent BBU coupling and focusing strengths (ε and κ). Applying to Eq. (2) the Laplace transform with respect to σ: $\mathcal{L}\left[x(\sigma,\zeta)\right] = x^\dagger(p,\zeta)$, we obtain

$$x^\dagger(p,\zeta) = \sum_{n=0}^{\infty}\frac{\varepsilon^n}{\left(p^2+\kappa^2\right)^{n+1}}\left[\,x_0\,p+x_0'\,\right]f_n(\zeta), \tag{3}$$

with

$$f_{n+1}(\zeta) = \int_0^\zeta f_n(\zeta_1)\,w(\zeta-\zeta_1)\,F(\zeta_1)\,d\zeta_1, \qquad f_0(\zeta) = 1. \tag{4}$$

Applying the inverse Laplace transform gives

$$x(\sigma,\zeta) = \sum_{n=0}^{\infty}\varepsilon^n\left[x_0 j_n(\kappa,\sigma)+x_0' i_n(\kappa,\sigma)\right]f_n(\zeta) \quad , \tag{5}$$

where

$$i_n(\kappa,\sigma) = \frac{1}{n!}\left(\frac{\sigma}{2\kappa}\right)^n\frac{1}{\kappa}\sqrt{\frac{\pi\kappa\sigma}{2}}J_{n+\frac{1}{2}}(\kappa\sigma)\ ,$$
$$j_n(\kappa,\sigma) = \frac{1}{n!}\left(\frac{\sigma}{2\kappa}\right)^n\sqrt{\frac{\pi\kappa\sigma}{2}}J_{n-\frac{1}{2}}(\kappa\sigma)\ . \tag{6}$$

Time-dependent Parameters

When the BBU coupling and focusing strengths are time-dependent [$\varepsilon(\zeta)$ and $\kappa(\zeta)$] the beam displacement $x(\sigma,\zeta)$ is not given by Eqs. (3)-(6) anymore and the procedure for solving Eq. (2) needs to be modified. This can be done simply by splitting the focusing strength $\kappa(\zeta)$ in two parts, one constant and the other time-dependent, such that:

$$\kappa^2(\zeta) = \kappa_0^2\left[1+\Delta\kappa(\zeta)\right] \tag{7}$$

The displacement $x(\sigma,\zeta)$ and its Laplace transform $x^\dagger(p,\zeta)$ are then given by

$$x^\dagger(p,\zeta) = \sum_{n=0}^{\infty}\frac{\left[\,x_0\,p+x_0'\,\right]}{\left(p^2+\kappa_0^2\right)^{n+1}}f_n^*(\zeta) \quad , \tag{8}$$

$$x(\sigma,\zeta) = \sum_{n=0}^{\infty}\left[x_0 j_n(\kappa_0,\sigma)+x_0' i_n(\kappa_0,\sigma)\right]f_n^*(\zeta), \tag{9}$$

$$f^*_{n+1}(\zeta) = \varepsilon(\zeta)\int_0^\zeta f^*_n(\zeta_1) w(\zeta-\zeta_1)\, F(\zeta_1)\, d\zeta_1 - \kappa_0^2\, \Delta\kappa(\zeta)\, f^*_n(\zeta), \quad (10)$$

$$f^*_0(\zeta) = 1,$$

$$i_n(\kappa_0,\sigma) = \frac{1}{n!}\left(\frac{\sigma}{2\kappa_0}\right)^n \frac{1}{\kappa_0}\sqrt{\frac{\pi\kappa_0\sigma}{2}}\, J_{n+\frac{1}{2}}(\kappa_0\sigma)\ ,$$
$$j_n(\kappa_0,\sigma) = \frac{1}{n!}\left(\frac{\sigma}{2\kappa_0}\right)^n \sqrt{\frac{\pi\kappa_0\sigma}{2}}\, J_{n-\frac{1}{2}}(\kappa_0\sigma)\ . \quad (11)$$

There is some arbitrariness in the way the focusing strength $\kappa(\zeta)$ is split in two parts according to Eq. (7). For example, it could be assumed that $\kappa(\zeta)$ has no constant term ($\kappa_0 = 0$) and only a time-dependent part. In this case $x(\sigma,\zeta)$ would be given by

$$x(\sigma,\zeta) = \sum_{n=0}^{\infty}\left[x_0\, j_n(0,\sigma) + x_0'\, i_n(0,\sigma)\right] f^\circ_n(\zeta), \quad (12)$$

with

$$f^\circ_{n+1}(\zeta) = \varepsilon(\zeta)\int_0^\zeta f^\circ_n(\zeta_1) w(\zeta-\zeta_1)\, F(\zeta_1)\, d\zeta_1 - \kappa^2(\zeta)\, f^\circ_n(\zeta), \quad (13)$$

$$f^\circ_0(\zeta) = 1,$$

$$i_n(0,\sigma) = \frac{\sigma^{2n+1}}{(2n+1)!}, \qquad j_n(0,\sigma) = \frac{\sigma^{2n}}{(2n)!}. \quad (14)$$

While expressions (9)-(11) and (12)-(14) for $x(\sigma,\zeta)$ look quite different they are mathematically equivalent and represent the same solution of Eq. (2). They differ however in the speed of convergence with (12)-(14) converging very slowly. For expressions (9)-(11) to be of practical use the separation of $\kappa(\zeta)$ in two parts, as given by Eq. (7), needs to be done in such a way that the time-dependent part $\Delta\kappa(\zeta)$ is kept as small as possible.

Form Eq. (10) we see that

$$f^*_1(\zeta) = \varepsilon(\zeta)\int_0^\zeta w(\zeta-\zeta_1)\, F(\zeta_1)\, d\zeta_1 - \kappa_0^2\, \Delta\kappa(\zeta), \quad (15)$$

and choosing a time-dependent focusing such that

$$\kappa_0^2\, \Delta\kappa(\zeta) = \varepsilon(\zeta)\int_0^\zeta w(\zeta-\zeta_1)\, F(\zeta_1)\, d\zeta_1 \quad (16)$$

will yield $f^*_{n>0}(\zeta) = 0$ and

$$x(\sigma,\zeta) = x_0\cos\kappa_0\sigma + x_0'\frac{\sin\kappa_0\sigma}{\kappa_0}\ . \quad (17)$$

Equation (16) is the general condition for eliminating cumulative BBU by BNS damping [3].

SINGLE SHORT BUNCH

In the case of a single very short bunch, the wakefield can be assumed to be linear $[w(\zeta)=\zeta]$. If one assumes further that the bunch charge density is constant $[F(\zeta)=1]$, that the BBU coupling strength ε is constant and that the time-dependent focusing is of the form

$$\kappa^2(\zeta) = \kappa_0^2\left[1+\eta\,\zeta^2\right], \quad (18)$$

then the functions $f^*_n(\zeta)$ can be easily calculated:

$$f^*_n(\zeta) = \frac{\zeta^{2n}}{(2n)!}\prod_{k=1}^{n}\left[\varepsilon-(2k-1)(2k)\kappa_0^2\,\eta\right] \quad (19)$$

This, together with Eqs. (9) and (11), defines completely the displacement $x(\sigma,\zeta)$. If η is chosen such that $\eta = \varepsilon/(2\kappa_0^2)$, then $f^*_{n>0}(\zeta) = 0$ and the coupling between the beam and the dipole mode is suppressed.

In the case of a linear time dependence of the focusing

$$\kappa^2(\zeta) = \kappa_0^2\left[1+\eta\zeta\right], \quad (20)$$

the functions $f^*_n(\zeta)$ can be obtained through the recurrence relations

$$f^*_n(\zeta) = \sum_{k=n}^{2n} a_{n,k}\zeta^k\ ,$$
$$a_{0,0} = 1\ , \quad (21)$$
$$a_{n,k} = \frac{\varepsilon a_{n-1,k-2}}{k(k-1)} - \kappa_0^2\,\eta\, a_{n-1,k-1}\ .$$

FINITE TRAIN OF POINT-LIKE BUNCHES

The results of the previous sections will be applied here to a finite train of N identical point-like bunches separated, in the laboratory frame, by τ, so that bunch M is defined by $\zeta = M\omega\tau$. The displacement of bunch M is then given by

$$x_M(\sigma) = \sum_{n=0}^{\infty} f^*_n(M\omega\tau)\left[x_0\, j_n(\kappa_0,\sigma) + x_0'\, i_n(\kappa_0,\sigma)\right] \quad (22)$$

$$f^*_{n+1}(M\omega\tau) = \omega\tau\,\varepsilon(M\omega\tau)\sum_{k=0}^{M} f^*_n(k\omega\tau)\, w[(M-k)\omega\tau] - \kappa_0^2\,\Delta\kappa(M\omega\tau)\, f^*_n(M\omega\tau) \quad (23)$$

Table 1: Nominal top-level linear-collider design parameters [1,4,5]

Parameters	Value
Total initial energy	10 GeV
Total final energy	1 TeV
Linac length **L**	10 km
Number of betatron periods	100
Bunch charge	1 nC
Number of bunches N	90
Bunch spacing τ	2.8 ns
Deflecting-wake frequency $\omega/2\pi$	14.95 GHz
Deflecting-wake quality factor Q	∞
Deflecting-wake amplitude w_0	10^{15} VC^{-1}m^{-2}

As an example, the analytical results expressed by Eqs. (22) and (23) will be applied to a beam representative of a

linear collider. For comparison, we will use the same parameters as those used in [1, 4, 5], and which are listed in Table 1. The time-dependent focusing is assumed to be of the form

$$\kappa^2(M\omega\tau) = \kappa_0^2\left[1+\eta\frac{M}{N-1}\right] \qquad (24)$$

where η represents the relative variation of the focusing strength during the bunch train.

Results of the application of Eqs. (22) and (23) to the beam described in Table 1 are shown in Fig. 1 for $\eta = 0$, 0.01, 0.02, and 0.03. Since this is an accelerated beam, the variable and coordinate transformations described in Appendix A of [1] were applied to Eq. (22); in particular Fig. 1 shows the effect of adiabatic damping. The lower plot of Fig. 1 $(\eta = .03)$, which was obtained by direct calculation using the analytical results given by Eqs. (22) and (23), is identical to Fig. 4 of [5] which was obtained numerically by tracking successive bunches as they progress along the accelerator.

The incorporation of a finite Q for the deflecting mode or the use of a different time-dependence of the focusing is straightforward.

SUMMARY

This paper presents a formalism to address analytically cumulative beam breakup in linear accelerators with time-dependent parameters, such as energy chirp or rf focusing. It allows, in principle, direct calculation, at any time and location, of the transverse displacement of beams of arbitrary current distribution. When applied to a collider-like accelerator, the analytical results reproduce exactly the results of numerical simulations that were done previously.

While we assumed here constant injection offsets and a perfectly aligned accelerator, time-dependent offsets and misalignment of the cavities and focusing elements, as well as acceleration, can be included in this formalism and will be presented in another publication.

REFERENCES

[1] J. R. Delayen, Phys. Rev. ST Accel. Beams **6**, 084402 (2003)

[2] J. R. Delayen, Phys. Rev. ST Accel. Beams **7**, 074402 (2004)

[3] V. Balakin, A. Novokhatsky, and V. Smirnov, *Proc. 12th Conf. High Energy Accel*, Fermilab, 1983, p. 119

[4] C. L. Bohn and K.-Y. Ng, Phys. Rev. Lett. **85**, 984 (2000)

[5] C. L. Bohn and K.-Y. Ng, *Proc. XX International Linac Conference*, Monterey, CA, p. 31 (2000)

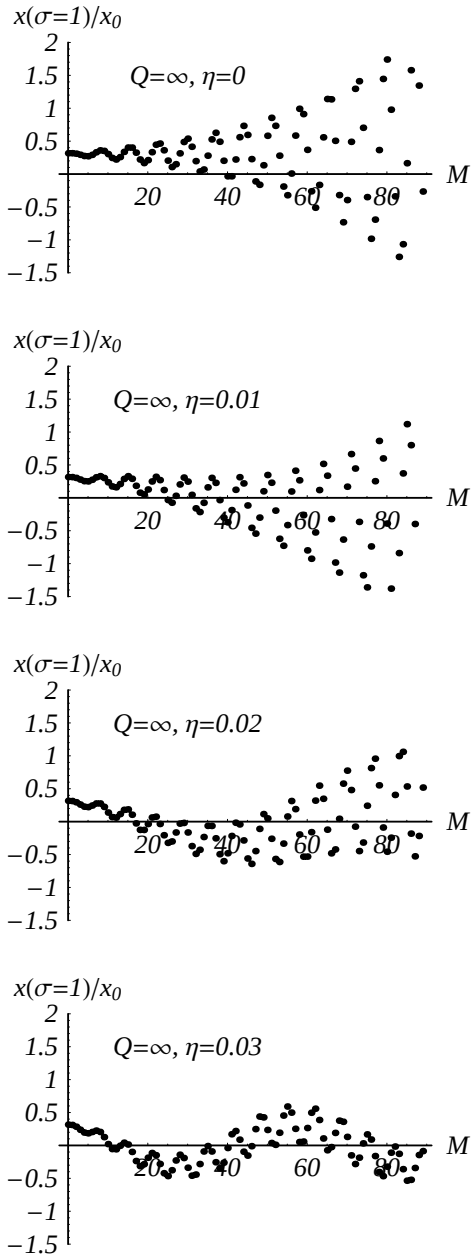

Figure 1: Normalized lateral displacement of a finite train of point-like bunches at the exit of a nominal linear collider. See Table 1 for the choice of parameters and Eq. (24) for the definition of η.

METHODS FOR MEASURING AND CONTROLLING BEAM BREAKUP IN HIGH CURRENT ERLS*

C. Tennant#, K. Jordan, E. Pozdeyev, R. Rimmer, H. Wang, TJNAF, Newport News, VA, 23606
S. Simrock, DESY, Hamburg, Germany

Abstract

It is well known that high current Energy Recovery Linacs (ERL) utilizing superconducting cavities are susceptible to a regenerative type of beam breakup (BBU). The BBU instability is caused by the high impedance transverse deflecting higher-order modes (HOMs) of the cavities. This multipass, multibunch instability has been observed at Jefferson Laboratory's FEL Upgrade driver. Some preliminary measurements are presented. To combat the harmful effects of a particularly dangerous mode, two methods of directly damping HOMs through the cavity HOM couplers were demonstrated. In an effort to suppress the BBU in the presence of multiple, dangerous HOMs, a conceptual design for an injector beam-based transverse feedback system has been developed. By implementing beam-based feedback, the threshold for instability can be increased substantially.

INTRODUCTION

The BBU measurement and suppression techniques described in this paper have application to any ERL based machine. However, for simplicity we will restrict ourselves to Jefferson Lab's Free-Electron Laser (FEL) Upgrade. The driver is an energy-recovery based linear accelerator used to condition an electron beam for high power lasing [1]. Electrons are injected at 10 MeV and are accelerated to 145 MeV through three cryomodules (each containing 8 superconducting niobium cavities). The beam is transported to a wiggler where up to 10 kW of laser power is generated. The spent electron beam is recirculated and phased in such a way that the beam is decelerated through the linac region on the second pass. Upon exiting the linac, the 10 MeV beam is extracted to a dump.

MULTIPASS, MULTIBUNCH BBU

At sufficiently high average beam current, ERLs are susceptible to a regenerative type of beam breakup (BBU). The BBU instability is caused by the high impedance transverse deflecting higher-order modes (HOMs) of the cavities. The underlying mechanism is that with insufficient damping of cavity HOMs, a positive feedback loop will be created between the cavity and the recirculated beam. This feedback can create an energy exchange between the cavity fields and beam which can lead to exponential growth of the beam offset. For a single cavity, containing one HOM oriented at an angle α with respect to the horizontal axis and with a single recirculation, the expression for the threshold current of the instability is given by

$$I_{th} = -\frac{2V_b}{k(R/Q)Q\,M_{12}^{*}\sin(\omega T_r)}$$

$$M_{12}^{*} \equiv M_{12}\cos^2\alpha + (M_{14}+M_{32})\sin\alpha\cos\alpha + M_{34}\sin^2\alpha$$

where V_b is the beam voltage at the cavity, k is the wavenumber of the mode, $(R/Q)Q$ is the shunt impedance of the HOM, T_r is the recirculation time and the M_{ij} are the elements of the recirculation transport matrix (which can describe coupled transverse motion) [2]. The purpose of this paper is to present methods of increasing the threshold current by using feedback methods to effectively modify the shunt impedance of the HOM or the M_{12}^{*} term. Other means of suppressing the onset of BBU by a judicious choice of beam optics are given elsewhere [3] [4].

BBU MEASUREMENTS

On May 27, 2004 the multipass, multibunch beam breakup instability was observed at 3 mA of average beam current at the FEL for the first time. Using Schottky diodes on each of the two HOM ports per cavity (8 cavities x 2 ports = 16 diodes total) we were able to monitor the total HOM power levels from each cavity in the second cryomodule – which, for these operating conditions, exhibits insufficient HOM damping. At the onset of the instability we saw the HOM power levels in cavity 4 grow exponentially until the beam losses tripped off the machine (see Figure 1).

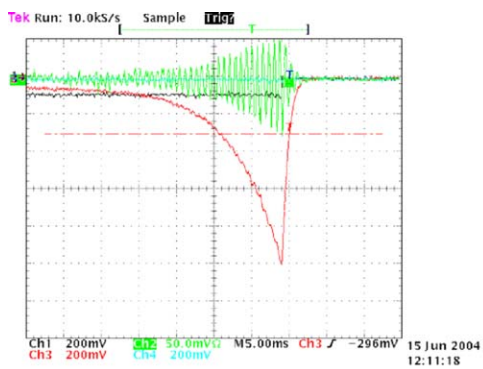

Figure 1: An oscilloscope trace from a BBU induced machine trip. The green trace is the cavity HOM voltage and the red trace is the total HOM power as measured from the Schottky diode. The time scale is 5 msec/div.

Repeated BBU-induced trips continued to be caused by cavity 4, leaving no doubt that the mode causing the instability was located in this cavity. Having successfully located the offending HOM, the next step was to extract

*supported by US DOE Contract No. DE-AC05-84ER40150
#tennant@jlab.org

the frequency of the mode causing the breakup. To do this, we measured the HOM voltage from cavity 4 during a BBU induced machine trip. A Fast-Fourier Transform (FFT) of the signal yielded an HOM frequency of 2114.156 MHz, in agreement with simulation results [5] and previous RF measurements of the frequencies and quality factors of the dipole modes. With the knowledge that beam breakup is a real limitation to machine operation, the focus turns to finding means of suppressing the instability.

HOM DAMPING SCHEMES

In an effort to provide a relatively quick method for raising the threshold current in the FEL, two HOM damping schemes have been developed. These methods are intended to be short-term solutions. The primary disadvantage of these damping methods is that they are effective for damping only a single HOM per cavity.

Active Damping

The first scheme uses a self-excited feedback loop to damp a dangerous HOM. The idea is as follows: couple power from one of the HOM ports, shift the signal 180 degrees in phase, amplify the signal and feed it back through the same HOM port. A measurement to prove the validity of such a scheme was performed on a cold cavity (without beam). For a specifically chosen HOM (1936 MHz) the loaded Q was lowered by a factor of ~ 4 (see Figure 2). Because the threshold current is inversely proportional to the Q of the offending mode, the ability to provide a factor of 4 reduction in the loaded Q corresponds to an increase in the threshold current by the same amount. In optimizing the setup, one must ensure that the gain of the feedback loop is less than unity otherwise the loop becomes unstable. Ideally, one would use a bandpass filter to allow only the frequency of the HOM of interest through to the feedback loop. Without a filter, the quality factors of other HOMs can be damped - or even enhanced - depending on the phase advance of the feedback loop.

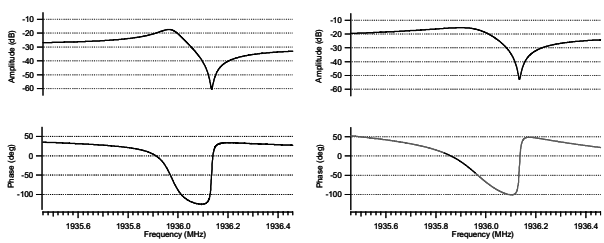

Figure 2: Demonstration of active damping of an HOM. The effect of the damping (right picture) is to decrease the loaded Q by a factor of ~ 4.

Passive Damping

We adopted a concept similar to that of the active damping scheme by connecting a 3-stub tuner between the HOM coupler and the damping load. Three stubs ($\lambda/4$ apart) can act as a reactive tuner to match any load at any location. In other words, this passive device can simply reflect the HOM wave back to the HOM coupler input. With this circuit setup without a beam present, we measured a factor of 2 reduction in the loaded Q on a chosen HOM (2106.007 MHz). A quantitative analysis of reactive coupling by a network method has been successfully applied in the operation of CEBAF. The 3-stub tuners there are used to increase or decrease the external Q of RF input couplers [6].

BEAM-BASED FEEDBACK SYSTEMS

Although the aforementioned HOM damping schemes are promising, they require a very accurate knowledge of the frequency of the HOM causing beam breakup and the cavity in which it is located. Furthermore, the method is only effective for a single mode per cavity. To suppress BBU due to many HOMs (whose identity may not be known), the more conventional method of beam-based feedback systems can be utilized. We describe two systems in particular, both of which are well suited for ERL-based accelerators.

Bunch-by-Bunch Feedback System

Initially the feasibility of a bunch-by-bunch feedback system [7] was investigated for use in the FEL Upgrade driver. The essential algorithm requires two position measurements from Beam Position Monitors (BPM) separated by 90 degrees of betatron phase. With sufficient knowledge of the recirculator optics, the two positions can be used to generate a correction signal used to drive downstream kickers [8]. Unlike a bunch-by-bunch feedback system in a storage ring where the transverse oscillations can be slowly damped over many turns, in an ERL electrons are dumped after two passes through the linac (in a 2-pass machine) after which, new electrons are injected. Thus the kickers need to provide enough power to completely damp the oscillation within the same turn on which the oscillations are detected. This type of feedback system may be suitable for larger ERL based machines; however, upon further inspection it became clear that such a system is not optimally suited for a machine like the FEL Upgrade driver. The issues prohibiting the implementation of this type of feedback are:

- *Relative size and geometry of the machine*. The FEL is a relatively small accelerator, with a recirculation time of 433 ns and consequently, there is not sufficient time to allow for the required signal processing.
- *Relative phase advances between the pairs of pickups and kickers*. For the feedback to be most efficient, the two pickups should be separated by 90 degrees of betatron phase and likewise for the two kickers. Due to the limited space available on either side of the linac, this requirement becomes difficult to achieve.

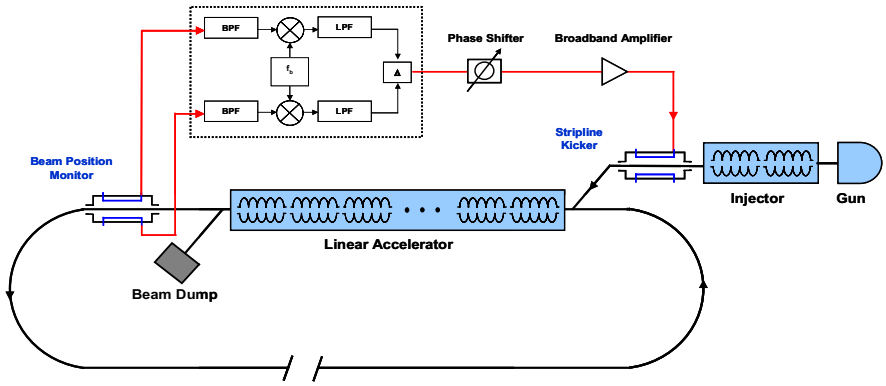

Figure 3: Schematic for an injector beam-based feedback system. A heterodyne receiver mixes down a BPM signal which is shifted in phase, amplified and used to drive a kicker in the injection region.

- *Small betatron functions at the locations of the pickups and kickers*. The feedback system operates most efficiently when the pickups and kickers are in regions of large betatron functions. However, for the nominal FEL optics configuration, the smallest betatron functions are found precisely in the locations where the pickups and kickers would need to be placed (on either side of the linac).

Injector-Based Feedback

To alleviate the stringent requirements of a bunch-by-bunch feedback system, we propose the injector beam-based feedback system as shown in Figure 3. The basic idea is that the signal from a BPM located downstream of the linac is amplified, shifted in phase by 180 degrees and then used to drive a kicker in the injection line. The primary advantage of this system is that the strict time requirements are eliminated since it is not a bunch-by-bunch feedback. In addition the requirements on the kicker power needed to produce a suitable correction signal are greatly relaxed since the kicks will be imparted in the low energy (injector) region. This is especially important for future ERL machines which will have injection energies on the order of 10 MeV and final energies of several GeV. Thus, rather than investing in specially designed kickers and powerful amplifiers to correct a GeV beam, this scheme which uses a stripline kicker and relatively low power amplifier to correct a low energy beam in the injector, may be sufficient.

CONCLUSIONS

The best defense against the beam breakup instability is to fabricate cavities which provide adequate HOM damping. However, in the event that beam breakup does pose a threat below nominal operating beam currents, then the suppression techniques described in this paper may be required. The encouraging results of our preliminary evaluations suggest that these schemes should be pursued.

The following activities are expected to take place in the near future:

- After the successful commissioning process, a thorough and systematic study of beam breakup in the FEL Upgrade driver will take place.
- Experimentally determine the effectiveness of increasing the beam breakup threshold current by means of the HOM damping schemes described in this paper
- Incorporate the injector beam-based feedback scheme into our BBU simulation code and assess the effectiveness of such a system.

REFERENCES

[1] Behre, C., et. al., "The JLab THz/IR/UV Light Source Facility", Proceedings of the 10th FEL Users Workshop (2003).

[2] Pozdeyev, E., Tennant C., "Equation for the Multipass Beam Breakup Threshold Current for a Single Mode and a 4x4 Recirculation Matrix", JLAB-TN-04-019 (2004).

[3] Rand R., Smith T., *Beam Optical Control of Beam Breakup in a Recirculating Electron Accelerator*, Particle Accelerators 1980, Vol. II, pp. 1-13.

[4] Tennant, C., et. al., "Suppression of Multipass, Multibunch Beam Breakup in Two Pass Recirculating Accelerators", To be presented at the 2004 International FEL Conference (2004).

[5] Tennant, C., et. al., "Estimated Beam Breakup Threshold Currents in the 10 kW FEL due to HOMs in the 7-Cell Cryomodule", JLAB-TN-04-008 (2004).

[6] Wang H., Tienfenback M., "Waveguide Stub Tuner Analysis for CEBAF Machine Application", These Proceedings.

[7] Yunn, B., "A Method to Control Multipass Beam Breakup in Recirculating Linacs", Proceedings of the 2003 Particle Accelerator Conference (2003).

[8] Tennant, C., "Modeling a Transverse Feedback System for an Energy Recovering Linac", JLAB-TN-03-045 (2003).

TEMPORAL PROFILE OF THE LCLS PHOTOCATHODE ULTRAVIOLET DRIVE LASER TOLERATED BY THE MICROBUNCHING INSTABILITY*

Juhao Wu†, P. Emma, Z. Huang, C. Limborg, SLAC, Menlo Park, CA 94025, USA
M. Borland, APS, ANL, Argonne, IL 60439, USA

Abstract

The LCLS electron beam generated in the photoinjector is subject to various instabilities in the downstream acceleration and compression. The instability can be initiated by e-beam density modulation at birth. In this paper, we prescribe the tolerance on the initial e-beam density modulation possibly introduced by the ultraviolet (uv) laser at the cathode. Our study shows that the initial rms density modulation of the e-beam at the photocathode shall be less than 5 % to ensure the FEL lasing and saturation.

Introduction

The success of FEL calls for a high quality e-beam, which is, however, subject to various impedance in the downstream acceleration and compression after being generated from a photocathode. Specifically, the impedance (space charge, wakefield, and CSR) and momentum compaction factor act as an amplifier for initial density and energy modulations. Since the slice emittance and energy spread are extremely small, Landau damping is not effective in suppressing instabilities, which can increase the slice energy spread and emittance, and therefore degrade FEL lasing. FEL operation calls for best achievable beam quality; yet, unnecessarily high quality renders it more susceptible to instabilities described above. To address this quandary, a laser-heater [1] is introduced into the LCLS beamline. The laser-heater is designed to be an adjustable control, which will impose a limited increase on the slice energy spread to the level where FEL lasing is still guaranteed. This 'procured' increase is designed to enhance Landau damping such that downstream instabilities can be suppressed. Density and energy modulations can be initiated by shot noise in the e-beam born at the photocathode. Also, temporal modulation on the ultraviolet (uv) laser pulse itself can be transferred to the e-beam at birth. These initial e-beam density or energy modulations can be amplified to affect the FEL lasing. Hence, we study the tolerance of the e-beam density modulations at birth.

Simulation details and results

In our study, we take the nominal LCLS accelerator system setup including the laser-heater, with parameters in Table 1. The laser-heater is to be installed where the e-beam $E = 135$ MeV. Parameters for the laser-heater are in Table 2. We use a total temporal compression factor of 30. Hence, if we require the rms slice relative energy spread $\sigma_\delta \approx 1 \times 10^{-4}$ at $E = 14.1$ GeV, then the laser-heater should give a maximum rms slice energy spread $\sigma_E \approx 47$ keV, assuming the conservation of the longitudinal phase space area. This slice σ_E then determines the Landau damping strength to suppress instabilities. The laser-heater introduces energy modulation at wavelength of 800 nm; however, the chicane provides an R_{52} large enough, so that the laser-heater induced energy modulation is washed out by the second half of the chicane. Hence, the laser-heater induced energy modulation becomes purely slice energy spread; and will not be converted into density modulation.

In our study, we take two approaches. In the first one, we introduce a density modulation at the injector end ($E = 135$ MeV). In the second one, we introduce a density modulation in the e-beam at birth. Details are the follows.

Approach I: we take a PARMELA output distribution at

Table 1: Main parameters for the LCLS FEL.

Parameter	Symbol	Value
electron energy	γmc^2	14.1 GeV
bunch charge	Q	1 nC
bunch current	I_f	3.4 kA
transverse norm. emittance	$\varepsilon^n_{x,y}$	1 μm
average beta function	$\beta_{x,y}$	25 m
undulator period	λ_u	0.03 m
undulator field	B	1.3 T
undulator parameter	K	3.64
undulator length	L_u	130 m
FEL wavelength	λ_r	1.5 Å
FEL parameter	ρ	4.8×10^{-4}

Table 2: Main parameters for the LCLS laser-heater.

Parameter	Symbol	Value
electron energy	$\gamma_0 mc^2$	135 MeV
average beta function	$\beta_{x,y}$	10 m
transverse rms beam size	$\sigma_{x,y}$	190 μm
undulator period	λ_u	0.05 m
undulator field	B	0.33 T
undulator parameter	K	1.56
undulator length	L_u	0.5 m
laser wavelength	λ_L	800 nm
laser rms spot size	σ_r	175 μm
laser peak power	P_L	1.2 MW
Rayleigh range	Z_R	0.6 m
maximum energy modulation	$\Delta\gamma_L(0)mc^2$	80 keV
rms local energy spread	$\sigma_{\gamma_L}mc^2$	40 keV

* Work supported by the U.S. Department of Energy under Contract No. DE-AC03-76SF00515, and No. W-31-109-ENG-38.

† jhwu@SLAC.Stanford.EDU

Table 3: Summary of the parameters and results for the microbunching and final slice relative energy spread.

		Approach I							Approach II		
Energy modulation amplitude at cathode	keV	0							0		
Density modulation amplitude at cathode	%	0							8		
Energy modulation amplitude at injector end	keV	0							0.3	3.1	1.2
Density modulation amplitude at injector end	%	1						4	0.7	1.0	1.3
Density modulation wavelength	μm	15	30	60	100	150	200	150	50	150	300
Final slice rms relative energy spread at 14 GeV	10^{-4}	0.9	0.9	0.9	0.8	0.9	0.8	1.0	1.1	1.0	1.0

the injector end at 135 MeV with $200,000$ macroparticles with no density or energy modulation. We then find out the longitudinal momentum correlation, the local slice energy spread correlation, the transverse emittance and its correlations. Preserving all these information, we then use Halton-sequence 'quiet-start' in 6-D to generate 2 million macroparticles and superimpose an initial $\pm 1\%$ density modulation with 6 different wavelengths. We also did one simulation with an initial $\pm 4\%$ density modulation to check linearity. Here, the laser-heater introduces a slice $\sigma_E \approx 40$ keV with results in Table 3. The slice σ_δ is the average of the central 20 μm portion of the e-beam. Each slice is 0.5 μm to match the FEL slippage distance.

Approach II: here, 1 million macroparticles with an initial $\pm 8\%$ density modulation for 3 different wavelengths are generated at the cathode. They are tracked through the photoinjector via ASTRA code [2], and the rest of accelerator system via Elegant code [3]. Here, the laser-heater introduces the maximum allowable slice $\sigma_E = 47$ keV, with results in Table 3. In contrast to the e-beam in approach I, there exists energy modulation at injector end.

To further reduce the noise effect, a high pass filter is introduced in the Elegant simulation [1]. In our study, we simulate a single frequency modulation. When the gain is high enough, the instability can run into the nonlinear regime, where harmonics will show up. To account for this, we set the high pass filter slightly higher than the second harmonic. In doing so, modulation with frequencies higher than the second harmonic is filtered out, however, modulations with frequencies between the second harmonic (included) and the original frequency are preserved.

To illustrate how the beam instability degrades the longitudinal phase space, and how effectively the laser-heater can Landau damp the instability, here we show a typical comparison between a matched laser-heater and no laser-heater. (A matched laser-heater is a device where the transverse laser beam size is approximately equal to that of the e-beam.) Figure 1 shows the longitudinal phase space at the undulator entrance without laser-heater, and Fig. 2 with a matched laser-heater. These figures are the approach II simulation at wavelength $\lambda = 150$ μm. In Fig. 1, we find a very large final energy modulation at period about 150 μm$/30 = 5$ μm. This indicates that the initial 150 μm density modulation leads to a large energy modulation after the 30 times compression. Besides this initial 150

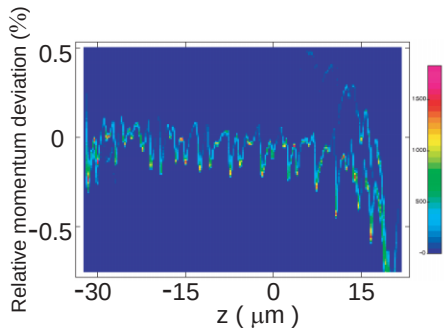

Figure 1: (Color) Longitudinal phase space at the undulator entrance. An initial $\pm$ 8% density modulation at 150 μm in Approach II simulation without laser-heater.

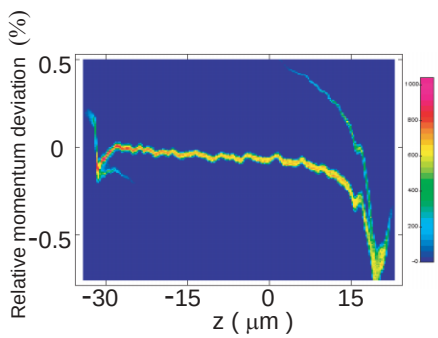

Figure 2: (Color) Longitudinal phase space at the undulator entrance. An initial $\pm$ 8% density modulation at 150 μm in Approach II simulation with a matched laser-heater.

μm modulation, the second harmonic is also clearly shown. This indicates that the system has evolved into the nonlinear regime. With a matched laser-heater, the results differ significantly as in Fig. 2. The effectiveness of the matched laser-heater is seen in the greatly reduced amplitude of energy modulation at the 5 μm period. The quantity which will affect the FEL lasing is the slice energy spread within the slippage length. We then plot, in Fig. 3, the slice σ_δ along the e-beam. The matched laser-heater clearly limits $\sigma_\delta < 1.0 \times 10^{-4}$ at the central portion of the e-beam. In

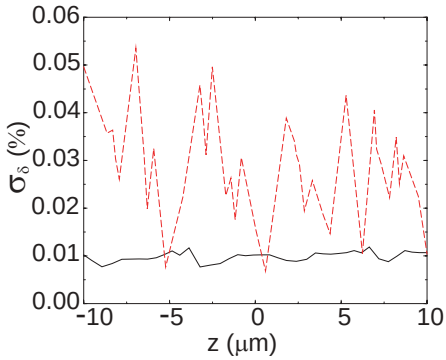

Figure 3: (Color) Slice σ_δ at the undulator entrance. An initial $\pm$ 8% density modulation at 150 μm in Approach II simulation. Solid curve: a matched laser-heater; and dashed curve: no laser-heater.

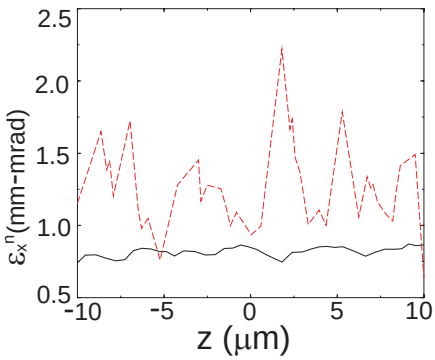

Figure 4: (Color) Slice ϵ_x^n at the undulator entrance. An initial $\pm$ 8% density modulation at 150 μm in Approach II simulation. Solid curve: a matched laser-heater; and dashed curve: no laser-heater.

contrast, without laser-heater, σ_δ is much too high. Similarly, for the slice normalized x emittance ϵ_x^n, Figure 4 shows that $\epsilon_x^n < 1$ mm-mrad along this central portion of the e-beam with a matched laser-heater. Without laser-heater, the ϵ_x^n is much larger. For the other wavelength, the conclusion is the same.

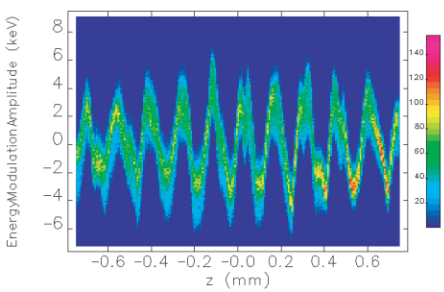

Figure 5: (Color) Energy modulation along the bunch at the injector end, but prior to the laser-heater. An initial $\pm$ 8% density modulation at 150 μm in Approach II simulation.

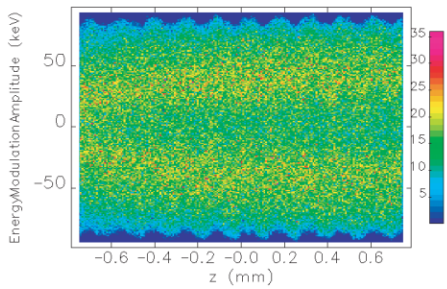

Figure 6: (Color) Energy modulation along the bunch at the end of a matched laser-heater. An initial $\pm$ 8% density modulation at 150 μm in Approach II simulation.

Discussion and conclusion

It is important to clarify the distinction between approach I and II. Table 3 shows that the initial $\pm$8% density modulation is reduced after the injector. However the known space-charge oscillation results in an accumulated energy modulation. This residual energy modulation can be reconverted back into a density modulation without the laser-heater. A matched laser-heater induces a slice $\sigma_E \approx 40$ keV to enhance Landau damping and smear out the residual energy modulation. To demonstrate this, in Figs. 5 and 6, we chose the 150 μm wavelength example in approach II. It is seen in Table 3 that the density modulation is reduced to the $\pm$1% level and the accumulated energy modulation has increased from zero to $\pm$3 keV. Relative to the 3 keV slice σ_E, this is a 100% modulation as in Fig. 5. By contrast, Fig. 6 shows that with a matched laser-heater, this accumulated energy modulation is only about 7% of the slice σ_E. Landau damping suppresses the reconversion of this residual energy modulation back to a density modulation in BC1, and suppresses the instability effectively.

In our study, all the simulations are done for density modulation at a specified frequency. The results show that without the laser-heater, the gain of the microbunching is too high to make FEL lasing possible. Use of a matched laser-heater indicates that the FEL requirement of slice $\sigma_\delta < 10^{-4}$ and slice $\epsilon_x^n < 1$ mm-mrad can be met with a peak-to-peak e-beam density modulation as much as $\pm$8% at the photocathode. This we interpret as the maximum density modulation tolerance at birth. From the $\pm$8% modulation for all wavelengths and a relative insensitivity to wavelength in 50 μm to 300 μm interval, we determine this maximum tolerance to be a 5% rms value. Because the e-beam density modulation is driven by the uv laser pulse. This is therefore the upper limit to the rms noise on the temporal profile of the uv laser pulse.

References

[1] Z. Huang *et al.*, PRST AB, **7**, 074401 (2004).
[2] C. Limborg *et al.*, *EPAC'04*, 2004.
[3] M. Borland, ANL/APS Report No. LS-287, 2000.

RESISTIVE-WALL WAKE EFFECT IN THE BEAM DELIVERY SYSTEM*

J.R. Delayen, Thomas Jefferson National Accelerator Facility, Newport News, VA 23606, USA
Juhao Wu†, T.O. Raubenheimer, SLAC, Menlo Park, CA 94025, USA
Jiunn-Ming Wang, NSLS, BNL, Upton, NY 11973, USA

Abstract

General formulae for resistive-wall induced beam dilution are presented and then applied to the final beam delivery system of linear colliders. Criteria for the design of final beam delivery systems are discussed.

Equation and Solution

Recently, the beam breakup (BBU) problem due to the resistive-wall impedance was studied for uniform single bunch and also point-like bunch train [1, 2]. However for linear collider, the beam at the interaction point normally has some microstructure. This is evidenced by start-to-end simulation. Hence, in this paper, we study the resistive wall BBU problem for the case of arbitrary beam current profile.

We denote the location along the beamline by the variable s. The beam travels in the positive s direction, and the entrance to the beamline is located at $s = 0$. We assume in this paper that the accelerator is uniform and that there is no acceleration. This is not unduly restrictive [3]. In a continuum approximation, the transverse motion $y(\tau, s)$ of a beam in a misaligned beamline under the combined influence of focusing and wake field can be modelled by [4]

$$\frac{\partial^2 y(\sigma,\zeta)}{\partial\sigma^2} + \kappa^2\left[y(\sigma,\zeta) - d_f(\sigma)\right] = \varepsilon\int_0^\zeta w(\zeta-\zeta_1)F(\zeta_1)\left[y(\sigma,\zeta_1) - d_c(\sigma)\right]d\zeta_1\,, \quad (1)$$

where $\sigma = s/\mathcal{L}$, with $\mathcal{L}$ being the length of the element where wakefield is generated; $\zeta = \omega_0\,\tau$, with ω_0 being a reference angular frequency, and $\tau = t - s/v$ describes the relative longitudinal position of the particle inside the bunch, v is the particle velocity; $\kappa = k_y\,\mathcal{L}$, is the betatron phase advance with k_y being the betatron focusing strength; $F(\zeta) = I(\zeta)/\bar{I}$, the current form factor, is the instantaneous current $I(\zeta)$ divided by the average current $\bar{I}$; $d_f(\sigma)$ and $d_c(\sigma)$ are the lateral displacement of the focusing elements and element where the wakefield is generated. The right hand side of Eq. (1) represents the effects due to the wakefield $\mathcal{W}(\tau)$, which is introduced via

$$(\mathcal{L}^2/\omega_0)\,\mathcal{W}(\tau) = \varepsilon\,w(\zeta)\,. \quad (2)$$

The exact meaning of ε and ω_0 will be made clear in the following. The general solution of Eq. (1) is [3]

$$y(\sigma,\zeta) = \sum_{n=0}^{\infty}\varepsilon^n[y_0\,h_n(\zeta)\,j_n(\kappa,\sigma) + y_0'\,g_n(\zeta)\;i_n(\kappa,\sigma)\,] - \sum_{n=0}^{\infty}\varepsilon^{n+1}f_{n+1}(\zeta)\,i_n(\kappa,\sigma) * d_c(\sigma) + \kappa^2\sum_{n=0}^{\infty}\varepsilon^n f_n(\zeta)\,i_n(\kappa,\sigma) * d_f(\sigma) \quad (3)$$

where $i_n(\kappa,\sigma) * d(\sigma) = \int_0^\sigma du\, i_n(\kappa,u)\,d(\sigma-u)$. Via inverse Laplace transform, $i_n(\kappa,\sigma)$ and $j_n(\kappa,\sigma)$ are

$$\begin{aligned} i_n(\kappa,\sigma) &= \mathbf{L}_\sigma^{-1}\left[\frac{1}{(p^2+\kappa^2)^{n+1}}\right] \\ &= \frac{1}{n!}\left(\frac{\sigma}{2\kappa}\right)^n\frac{1}{\kappa}\sqrt{\frac{\pi\kappa\sigma}{2}}J_{n+(1/2)}(\kappa\sigma)\,, \quad (4)\\ j_n(\kappa,\sigma) &= \mathbf{L}_\sigma^{-1}\left[\frac{p}{(p^2+\kappa^2)^{n+1}}\right] \\ &= \frac{d}{d\sigma}i_n(\kappa,\sigma) = \frac{\sigma}{2n}i_{n-1}(\kappa,\sigma) \\ &= \frac{1}{n!}\left(\frac{\sigma}{2\kappa}\right)^n\sqrt{\frac{\pi\kappa\sigma}{2}}J_{n-(1/2)}(\kappa\sigma)\,. \quad (5)\end{aligned}$$

In the absence of focusing $i_n(\kappa,\sigma)$ and $j_n(\kappa,\sigma)$ reduce to $i_n(0,\sigma) = \sigma^{2n+1}/(2n+1)!$, and $j_n(0,\sigma) = \sigma^{2n}/(2n)!$.

The functions $f_n(\zeta)$, $g_n(\zeta)$, and $h_n(\zeta)$ are defined as

$$\begin{Bmatrix} f_{n+1}(\zeta)\\ g_{n+1}(\zeta)\\ h_{n+1}(\zeta)\end{Bmatrix} = \int_{-\infty}^{\zeta}\begin{Bmatrix} f_n(\zeta_1)\\ g_n(\zeta_1)\\ h_n(\zeta_1)\end{Bmatrix} w(\zeta-\zeta_1)\,F(\zeta_1)\,d\zeta_1\,, \quad (6)$$

where

$$f_0(\zeta) = 1\,, \quad (7)$$

$$y_0'\,g_0(\zeta) = y_0'(\zeta) = \frac{\partial}{\partial\sigma}y(\sigma,\zeta)\Big|_{\sigma=0}\,, \quad (8)$$

$$y_0\,h_0(\zeta) = y_0(\zeta) = y(\sigma=0,\zeta)\,. \quad (9)$$

Resistive-Wall Wake

If the wakefield source is the resistive-wall of a circularly cylindrical pipe, then the long-range wakefield is [5]

$$\mathcal{W}(\tau) = \frac{A}{\sqrt{\tau}} \quad \text{for} \quad \tau > 0\,, \quad (10)$$

where

$$A = (4c^2\bar{I})/(v\gamma b^3 I_{\text{Alfvèn}})\sqrt{\epsilon_0/\pi\sigma_c}\,. \quad (11)$$

In the above expression, c is the speed of light in vacuum, γ is the Lorentz factor, b is the radius of the pipe, $I_{\text{Alfvèn}} = 4\pi\epsilon_0 mc^3/e \approx 17,045$ Amp is the Alfvèn current, $\epsilon_0 =$

* Work supported by US Department of Energy under contract No. DE-AC05-84-ER40150 (JRD), No. DE-AC05-00-OR22725 (JRD), No. DE-AC03-76SF00515 (JW&TOR), and No. DE-AC02-98CH10886(JMW).

† jhwu@SLAC.Stanford.EDU

8.8542×10^{-12} C^2/(N m^2) is the vacuum permittivity, and σ_c is the pipe conductivity. According to Eq. (2), we have

$$\varepsilon = (\mathcal{L}^2 A)/\sqrt{\omega_0}, \tag{12}$$

so that

$$w(\zeta) = 1/\sqrt{\zeta}. \tag{13}$$

Hence, the series solution in Eq. (3) would converge quickly if $\varepsilon \ll 1$.

Note that Eq. (10) is only an approximation [6, 7] for

$$\tau_s \equiv \left(\frac{b^2}{Z_0\sigma_c c^3}\right)^{1/3} \ll \tau \ll \min\left[\frac{Z_0\sigma_c b^2}{c}, \frac{Z_0\sigma_c \Delta r^2}{c}\right] \equiv \tau_l, \tag{14}$$

with $Z_0 \approx 376.7\ \Omega$ being the vacuum impedance; and Δr the thickness of the wall. In particular $\mathcal{W}(0) = 0$, and

$$\mathcal{W}(\tau \to \infty) \approx B \equiv 2\bar{I}v/(I_{\mathrm{Alfvèn}} c b^2) \tag{15}$$

in the thin wall approximation [8].

Single Bunch

For a bunch of uniform current distribution — $F(\zeta) = 1$— we get from Eq. (6)

$$f_n(\zeta) = \frac{\left[\Gamma\left(\frac{1}{2}\right)\right]^n}{\Gamma\left(\frac{n}{2}+1\right)} \zeta^{\frac{n}{2}}. \tag{16}$$

We further assume that $y_0(\zeta) = y_0$ and $y_0'(\zeta) = y_0'\mathcal{L}$, so that $g_n(\zeta) = h_n(\zeta)\mathcal{L} = f_n(\zeta)\mathcal{L}$. For arbitrary current profile $F(\zeta)$, Eqs. (3-9) and (13) set up the calculation frame.

Periodic Bunch Train

For a steady-state periodic bunch train, the current form factor $F(\zeta)$ is given by

$$F(\zeta) = \sum_{k=-\infty}^{\infty} F_k e^{i(2\pi/\omega_0\tau_b)k\zeta}, \tag{17}$$

where τ_b is the laboratory-frame period of the longitudinal beam modulation, or the bunch separation in a bunch train. The meaning of previously introduced ω_0 is clear now. We could set it to be $\omega_0 = 2\pi/\tau_b$, even though not have to. The corresponding general solution is

$$\begin{aligned} y(\sigma,\zeta) &= \sum_{n=0}^{\infty} \frac{1}{n!}\left(\frac{\varepsilon\sigma}{2\kappa}\right)^n \sqrt{\frac{\pi\kappa\sigma}{2}} \left[y_0 J_{n-(1/2)}(\kappa\sigma)\right. \\ &+ \left.\frac{y_0'\mathcal{L}}{\kappa} J_{n+(1/2)}(\kappa\sigma)\right] f_n(\zeta), \end{aligned} \tag{18}$$

where

$$f_n(\zeta) = \sum_k \exp\left[i\frac{2\pi}{\omega_0\tau_b}k\zeta\right] f_{n,k}, \tag{19}$$

with the following recursion relation $f_{0,k} = \delta_{0,k}$, and $f_{n+1,k} = \tilde{w}_k \sum_{k_1} F_{k_1} f_{n,k-k_1}$; where, $\tilde{w}_k = \tilde{w}[(2\pi/\omega_0\tau_b)k]$, and $\tilde{w}(Z) = \int_{-\infty}^{\infty} d\zeta w(\zeta) e^{-iZ\zeta}$ is the Fourier transform of the wake $w(\zeta)$, i.e., the impedance.

Now, suppose a beam is composed of bunches of constant current density, separated by $\omega_0\tau_b$, of length $\alpha\omega_0\tau_b$. The parameter α allows a continuous transition from a dc beam ($\alpha = 1$) to a beam composed of $\delta-$function bunches separated by $\omega_0\tau_b(\alpha = 0)$. Choosing $\zeta = 0$ as being in the middle of a bunch, the Fourier coefficients of the current form factor are $F_k = [\sin(k\alpha\pi)/(k\alpha\pi)]$.

For the resistive-wall wake, the impedance is

$$\tilde{w}(Z) = \sqrt{\frac{\pi}{Z}} e^{-i\pi/4}. \tag{20}$$

Since $Z > 0$, the Fourier integral contour is chosen at the lower-right quarter in the complex $\zeta-$plane. Hence,

$$\tilde{w}_k = \tilde{w}\left[\frac{2\pi}{\omega\tau}k\right] = \sqrt{\frac{\omega\tau}{2k}} e^{-i\pi/4}. \tag{21}$$

Notice that there is a singularity at $k = 0$ or $Z = 0$. This is artificial, since the wakefield in Eq. (10) is an oversimplified form. Detailed calculation shows [8]

$$\tilde{w}_0 = \frac{B\sqrt{\omega_0}}{A}, \tag{22}$$

where A and B are defined in Eqs. (11) and (15).

dc beam: For a dc beam, the general solution is

$$y(\sigma,\zeta) = y_0 \cos\left[\sigma\sqrt{\kappa^2 - \varepsilon\tilde{w}_0}\right] + y_0'\mathcal{L}\frac{\sin\left[\sigma\sqrt{\kappa^2 - \varepsilon\tilde{w}_0}\right]}{\sqrt{\kappa^2 - \varepsilon\tilde{w}_0}}. \tag{23}$$

For the resistive-wall wake, $\tilde{w}_0$ is given in Eq. (22).

$\delta-$**function beam**: In the case of a bunch train comprised of $\delta-$function bunches, for $\zeta = M\omega_0\tau_b$, i.e., for bunch M, the displacement becomes

$$y(\sigma, M\omega_0\tau_b) = y_0 \cos\left[\sigma\sqrt{\kappa^2 - \varepsilon\tilde{W}_0}\right] + y_0'\mathcal{L}\frac{\sin\left[\sigma\sqrt{\kappa^2 - \varepsilon\tilde{W}_0}\right]}{\sqrt{\kappa^2 - \varepsilon\tilde{W}_0}}. \tag{24}$$

For the resistive-wall wake, we have $\tilde{W}_0 = \sqrt{\omega_0\tau_b}\mathrm{Zeta}(1/2) + B\sqrt{\omega_0}/A$.

Transient Periodic Beam

Let us analyze a periodic bunch train that was turned on at $\zeta = 0$. For the case of $y_0(\zeta) = y_0$ and $y_0'(\zeta) = 0$, the general solution is [3]

$$y(\sigma,\zeta) = y_0 \sum_{n=0}^{\infty} \frac{1}{n!}\left(\frac{\varepsilon\sigma}{2\kappa}\right)^n \sqrt{\frac{\pi\kappa\sigma}{2}} J_{n-(1/2)}(\kappa\sigma) h_n(\zeta), \tag{25}$$

where $h_0(\zeta) = H(\zeta)$, with $H(\zeta)$ being the Heaviside function. The recursion relation is $h_{n+1}(\zeta) = \int_0^{\zeta} h_n(\zeta_1) F(\zeta_1) w(\zeta - \zeta_1) d\zeta_1$.

dc beam: For a dc beam, in the case of resistive-wall wake, we have for $n = 0, 1, 2, \cdots$

$$h_n(\zeta) = \frac{\left[\Gamma\left(\frac{1}{2}\right)\right]^n}{\Gamma\left(\frac{n}{2}+1\right)} \zeta^{\frac{n}{2}}. \tag{26}$$

This together with Eq. (25) defines completely the transverse displacement at an arbitrary location σ and time ζ.

$\delta-$**function beam**: For a bunch train comprised of point-like bunches turned on at $\zeta = 0$, the displacement of bunch M at location σ is given by [3]

$$y_M(\sigma) = y_0 \sum_{n=0}^{M} \frac{1}{n!}\left(\frac{\varepsilon\sigma}{2\kappa}\right)^n \sqrt{\frac{\pi\kappa\sigma}{2}} h_n(M\omega_0\tau_b) J_{n-(1/2)}(\kappa\sigma).$$

Here $h_n(M\omega_0\tau_b)$ is defined as $h_n(M\omega_0\tau_b) = \frac{1}{2\pi i}\oint z^{M-1}\check{h}_n(z)dz$, where $\check{h}_n(z) = \frac{z}{z-1}[\omega_0\tau_b\check{w}(z)]^n$, and $\check{w}(z) = \sum_{k=0}^{\infty} z^{-k} w(k\omega_0\tau_b)$. In the case of the resistive-wall wake, $w(\zeta) = 1/\sqrt{\zeta}$, so that $\check{w}(z) = \mathrm{PolyLog}\left(1/2, z^{-1}\right)$. Notice that, this is only an approximation for $\check{w}(z)$, since $w(\zeta) = 1/\sqrt{\zeta}$ is not valid for $\zeta \to \infty$, though we have used the fact that $w(0) = 0$.

Finite train of finite bunches: For a bunch train of finite but identical bunches turned on at $\zeta = 0$, the current form factor is $F(\zeta) = H(\zeta)\sum_{k=-\infty}^{\infty} F_k \exp\left(i\frac{2\pi}{\omega_0\tau_b}k\zeta\right)$. The first-order term is [3]

$$h_1(\zeta) = \int_{-\infty}^{\zeta} H(\zeta_1)F(\zeta_1)w(\zeta-\zeta_1)d\zeta_1 = \int_0^{\zeta} F(\zeta-\zeta_1)w(\zeta_1)d\zeta_1$$
$$= \sum_k F_k \tilde{w}_k e^{i\frac{2\pi k\zeta}{\omega_0\tau_b}} - \sum_k F_k e^{i\frac{2\pi k\zeta}{\omega_0\tau_b}} \int_{\zeta}^{\infty} e^{-i\frac{2\pi k\zeta_1}{\omega_0\tau_b}} w(\zeta_1)d\zeta_1. \quad (27)$$

Notice that the first term is the steady state obtained previously, while the second term is the transient that decays when $\zeta \to +\infty$. For the resistive-wall wake, we obtain

$$h_1(\zeta) = \sqrt{\omega_0\tau_b}\sum_k \frac{F_k}{\sqrt{k}} e^{i\frac{2\pi k\zeta}{\omega_0\tau_b}} \left\{ \mathrm{FresnelC}\left(2\sqrt{\frac{k\zeta}{\omega_0\tau_b}}\right) + i\left[-1 + \mathrm{FresnelS}\left(2\sqrt{\frac{k\zeta}{\omega_0\tau_b}}\right)\right]\right\}. \quad (28)$$

Application and Discussion

Now let us study the USWarm and USCold linear collider design [9]. According to the design, there will be about 300 meter long transformer with large $\beta-$function in the final beam delivery system. There is essentially no focusing, hence the resistive-wall effect need be studied. Typical parameters are given in Table 1. Notice that $\kappa\sigma \approx 0$, according to Eqs. (3-5), and (16), in the case of $d_c = 0$ and $d_f = 0$, we have

$$y(\sigma,\zeta) = \sum_{n=0}^{\infty} \varepsilon^n \frac{\left[\Gamma\left(\frac{1}{2}\right)\right]^n}{\Gamma\left(\frac{n}{2}+1\right)} \zeta^{n/2} \frac{1}{n!}\left(\frac{\sigma}{2}\right)^{2n} \frac{\sqrt{\pi}}{\Gamma\left(n+\frac{1}{2}\right)} \times \left\{ y_0 + y_0'\mathcal{L}\frac{\sigma}{2}\frac{1}{n+\frac{1}{2}}\right\}; \quad (29)$$

and $y'(\sigma,\zeta)$ similarly. It is interesting to observe that $\varepsilon \propto 1/\sqrt{\omega_0}$, while $\zeta \propto \omega_0$, hence in the above $y(\sigma,\zeta)$ and $y'(\sigma,\zeta)$, the arbitrary parameter ω_0 is gone.

	USWarm	USCold
Bunch charge (nC)	1.2	3.2
Single bunch rms length (μm)	110	300
Bunch separation τ_b (ns)	1.4	337
Bunch number	192	2820
Pipe radius b (cm)	2	2
Pipe length $\mathcal{L}$ (m)	300	300
Conductivity σ_c ($10^7\Omega^{-1}\mathrm{m}^{-1}$)	3.47	3.47
k_y (m^{-1})	1/50000	1/12500
Beam energy (GeV)	250	250
$\Delta\sigma_y/\sigma_y$ (Single) (%)	0.6	2.5
$\Delta\sigma_{y'}/\sigma_{y'}$ (Single) (%)	19.3	7.8
$\Delta\sigma_y/\sigma_y$ (Multi) (%)	1.3	4.9
$\Delta\sigma_{y'}/\sigma_{y'}$ (Multi) (%)	26.1	9.0

Table 1: Parameters for the USWarm and USCold design.

Given the parameters in Table 1, we compute the bunch spot size increase $\Delta\sigma_y/\sigma_y$, and the angular divergence increase $\Delta\sigma_{y'}/\sigma_{y'}$. The calculation indicates that to maintain a relatively small increase, we need to use Aluminum and keep the pipe radius to be larger than 2 cm. Given these, the increase at a single bunch tail due to the wakefield of a single bunch, and that at the bunch train tail due to the wakefield of the entire bunch train are given in Table 1. We find that the majority contribution of $\Delta\sigma_{y'}/\sigma_{y'}$ comes from the single bunch effect; while for $\Delta\sigma_y/\sigma_y$, contribution of single bunch and multi bunch effect are almost equal.

Investigation in this paper indicates that the resistive-wall effect in the final beam delivery system needs to be considered in design. As we pointed out in Eq. (14), the wake given in Eq. (10) is only an approximation. Suppose that the wall thickness is $\Delta r = 3$ mm, we have $\tau_l \approx 0.39$ ms, since $b >> \Delta r$. Therefore, the wake given in Eq. (10) fails at the bunch train tail in the USCold. The long-range wake decays even faster [8] than that in Eq. (10). However, since the single bunch effect dominates, especially for the angular divergence, the long-range wake will only introduce a small correction. For the other limit, with $b = 2$ cm, and Aluminum pipe, $\tau_s \approx 100$ fs, hence a more accurate calculation utilizing the short-range wake [7] should be considered, whenever it is needed.

REFERENCES

[1] J.-M. Wang, S.R. Mane, and N. Towne, *EPAC'00*, p. 1179.

[2] J.-M. Wang and J. Wu, PRST AB **7**, 034402 (2004).

[3] J.R. Delayen, PRST AB **6**, 084402 (2003).

[4] A.W. Chao *et al.*, Nucl. Instrum. Methods **178**, 1(1980).

[5] P.L. Morton *et al.*, J. Appl. Phys. **37**, 3875 (1966).

[6] A.W. Chao, *Physics of Collective Beam Instabilities in High Energy Accelerators*, (Wiley-Interscience Publication, 1993).

[7] K.L.F. Bane and M. Sands, SLAC-PUB-7074, 1995.

[8] A. Burov and V. Lebedev, *EPAC'02*, p. 1452.

[9] http://www.slac.stanford.edu/xorg/accelops/.

SIMULATION OF RF BREAKDOWN EFFECTS ON NLC BEAM *

V.A. Dolgashev, T. Raubenheimer,
SLAC, Menlo Park, CA, 94025, USA

Abstract

The linacs of the Next Linear Collider (NLC) / Global Linear Collider (GLC) will contain several thousand traveling wave X-band accelerator structures operating at aninput power of about 60 MW. At this input power, prototypes of NLC/GLC structures have breakdown rates lower than one breakdown in ten hours. RF breakdowns disrupt flow of energy inside the structure and create arcs with electron and ion currents. Electromagnetic fields of these currents interact with the NLC beam. We simulated the deflection of the NLC beam caused by breakdown currents using the particle-in-cell code MAGIC. In this paper we present modeling considerations and simulation results.

INTRODUCTION

In the NLC/GLC, electron and positron multibunch beams traverse thousands of traveling wave accelerating structures. Each beam consists of 190 bunches spaced at 1.4 ns. Each 60 cm X-band accelerating structure is driven by about 60 MW of rf power and produces a 65 MV/m unloaded gradient. To fill the structure and accelerate the beam the effective rf pulse length is set to about 400 ns.

RF breakdown in a structure disrupts its operation. Because of that, the NLC has a stringent limit on the breakdown rate: it should be less than one breakdown per few million pulses. With this breakdown rate one breakdown will occur in the linac every few seconds. The structures operate below threshold for breakdown damage, so the rf power does not have to be switched off after the breakdown. Therefore only the beam that is in the linac during the breakdown get distorted. In this report we will discuss the effect of breakdown currents on the NLC beams.

RF Breakdown

RF breakdown is a phenomenon that abruptly and significantly changes transmission and reflection of rf power directed to the structure. Breakdown is accompanied by a burst of x-rays and by a bright flash of visible light. There is copious experimental data on rf breakdowns in the NLC/GLC structures obtained at the Next Linear Collider Test Accelerator (NLCTA) [1, 2]. Listed here are some properties of the rf breakdown phenomenon in the structures [3]:

1. During breakdown the transmitted power drops to unmeasurable levels in 20–200 ns. During the rf pulse the transmission never recovers.
2. Up to 80% of the incident rf power is absorbed by the arc.
3. At the NLCTA the beam current is measured using low-Q cavities located a few centimeters away from the output end of the structure. These current monitors detect a short (order of 10 ns) burst of current concurrent with the first signs of breakdown in rf signals. Typically the sinal from the monitors corresponds to amps of current averaged over an rf pulse.

Breakdown Currents

Knowing that the instantaneous rf power absorbed by the arc reaches 80%, and assuming that this power is absorbed by the electrons, we can estimate the amplitude of the current. The average electron energy for current emitted from a spot on the cell iris tip is about 100 keV (as calculated by a particle tracking code), and the incident rf power is about 100 MW. To absorb this power, the amplitude of the electron current should be about 1 kA. This kA current will interact with the primary electron (or positron) bunches being accelerated in the structure, kick the bunch centroid (assuming that currents are not axially symmetric) and perhaps dilute the beam emittance.

Below, we report results of simulation of the breakdown kick on the centroid of the primary bunch in NLC/GLC structures. We used the commercially available Particle-In-Cell (PIC) code MAGIC3D [4] for the calculations.

PARTICLE-IN-CELL SIMULATIONS

To obtain the beam kick from rf breakdown we have built a 3D PIC model of a 3 cell travelling wave structure. It is a disk loaded waveguide with 120° phase advance per cell, cavity radius of 10.875 mm, period of 8.75 mm, iris radius 4.45 mm, and iris thickness 1.66 mm (the iris tip is rounded). This model was developed for 3D self-consistent simulations of breakdown currents [3]. The geometry is built in cylindrical coordinates with z = constant being the (x, y) plane. The model consists of one cell and two coupler cells that match the impedance of a coaxial waveguide to the impedance of the structure at a frequency of 11.424 GHz (with VSWR better than 1.2). Snapshots of the MAGIC3D screen with the geometry are shown in Fig.1.

To simulate the breakdown, the tip of an iris was divided into upstream and downstream parts. Then one half-tip sector was assigned to emit copper ions using EMISSION BEAM model with current 20 A. The same area is also assigned as a source of space-charge limited electron current. For that we used EMISSION EXPLOSIVE model. EMISSION BEAM and EMISSION EXPLOSIVE are keywords

* This work was supported by the U.S. Department of Energy contract DE-AC02-76SF00515.

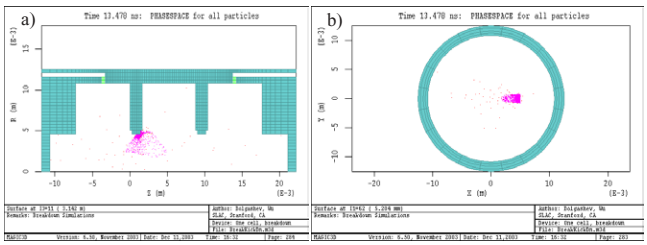

Figure 1: Snapshots of MAGIC3D screen with geometry of the travelling wave structure: electrons (red), and copper ions (magenta). a) (r, z) plane, b) (x, y) plane. Beam and rf energy move left to right in a); emission spot is at right in b), with $y = 0$. Emission spot is on downstream half of first iris.

in MAGIC3D. The amplitude of the ion current is set by requirements on drop-off of the transmitted power, since this drop-off is a feature observed in every breakdown. With ion currents equal to or higher than 20 A, the transmitted power drops from 70 MW to a fraction of a MW in about 25 ns after the start of emission. During this time, emitted electron current reaches 8 kA. Most of the electron current returns to the emission spot, and about 1 kA fills the cell and intensively interacts with the driving rf fields. For the breakdown kick simulations we set emission spot area to 2 mm^2. We note that the electron current, and reflected and transmitted rf power depend mostly on the amplitude of the ion current and weakly on the size of the emission spot.

The calculation of the breakdown kick was divided into two steps. First, we set up initial conditions: a model of a structure (without emission) is filled with 70 MW of rf power, and after one fill time (15 ns) all fields are dumped into a file. Then the simulation is restarted with one of the iris half-tips emitting copper ions and electrons. We stop the simulation after about 20 ns, when the transmitted power was significantly reduced. During the run with emission, all components of electric and magnetic fields along the trajectory of a primary beam are saved (with a 2.3 ps time step).

Then the transverse kick caused by the radial component of electric field and the azimuthal component of the magnetic field is integrated, assuming the bunch moves with the speed of light. Since the PIC code does not separate the rf and ion-electron fields, we verified that in absence of currents the transverse kick is zero, as it should be for a cylindrically symmetric structure.

RESULTS

The on-axis transverse kick for a cell breakdown (emission spot is located on the downstream tip of the first iris) is shown in Fig. 2, Fig. 3, and Fig. 4. The kick for coupler breakdown (emission from upstream tip of the first iris) is shown in Fig. 5, Fig. 6, and Fig. 7. Qualitatively, the results of the simulation are similar to results of a calculation of the transverse kick from dark currents [5]. The time dependence of the kick is almost periodic, with a period of one rf cycle. Within a period, the kick strongly depends on the rf phase, and this dependance slowly (in tens of nanosecond) changes with time.

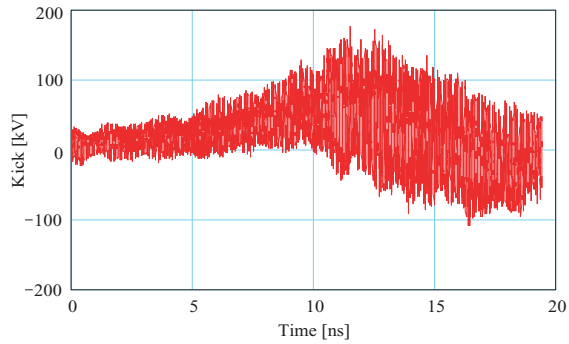

Figure 2: Transverse kick induced by arc current in a cell.

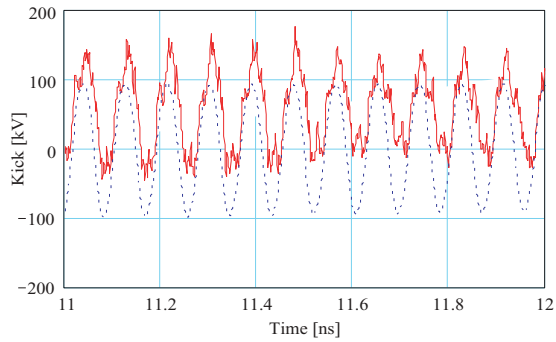

Figure 3: Transverse kick (solid) induced by arc current in a structure cell, after 11 ns. The dashed curve is one tenth of acceleration.

We find that the kick is largest when the primary beam "collides" with the emitted electrons near the emission site.

In the NLC/GLC linacs the bunch is accelerated at different rf phases to maintain BNS energy spread. At low energies, it is at +10°. Then it is almost on crest. At the end of the linac, the phase is close to -30°. Because of its dependence on the rf phase, the bunch kick will vary with

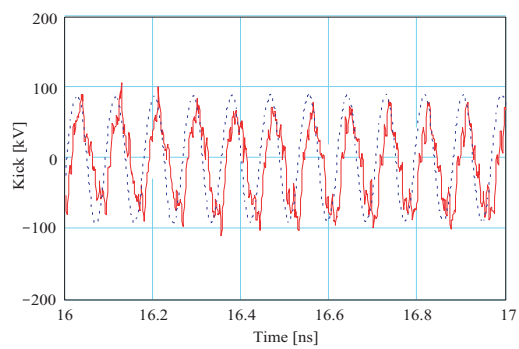

Figure 4: Transverse kick (solid) induced by arc current in a structure cell, after 16 ns. The dashed curve is one tenth of acceleration.

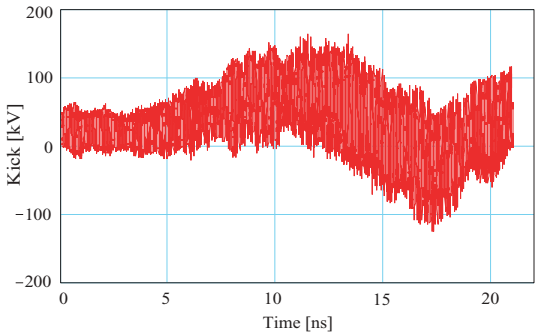

Figure 5: Transverse kick induced by arc current in a structure coupler.

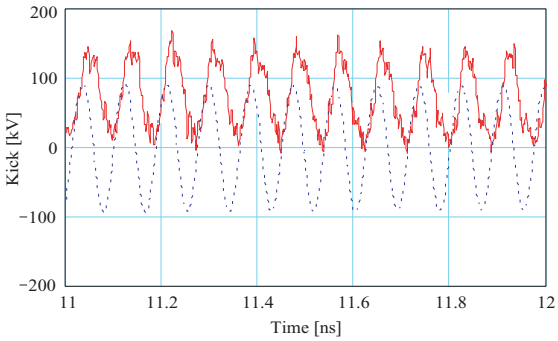

Figure 6: Transverse kick (solid) induced by arc current in a structure coupler after 11 ns. The dashed curve is one tenth of acceleration.

the beam position in the linac (assuming all breakdown parameters are the same). To show how the kick is distributed in reference to the rf phase, in figures 3, 4, 6, and 7 we plot the acceleration. The negative part of the sinusoidal acceleration curve corresponds to acceleration of electrons; the positive part to positrons. We note that, without a breakdown, maximum acceleration is 1.7 MV.

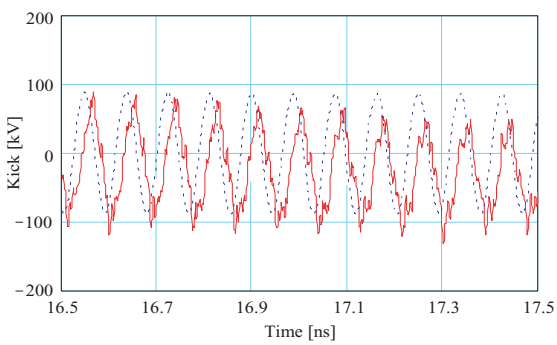

Figure 7: Transverse kick (solid) induced by arc current in a structure coupler, after 16.5 ns. The dashed curve is one tenth of acceleration.

SUMMARY AND DISCUSSION

We have calculated transverse kicks induced on the primary beam by a breakdown in an X-band travelling wave accelerating structure. The maximum on-axis kick is about 150 keV/c for positrons and about 100 keV/c for electrons, assuming a 20 A copper ion current. To hit the NLC collimators, the kick mast be larger then 300 keV/c if the breakdown occurs in the beginning of the linac where its effect is strongest. During the first 20 ns of the breakdown, the kick reaches maximum at a negative acceleration rf phase. In the NLC this corresponds to the last part of the linac, where the effect of the kick on the beam is less significant.

We note that even though the PIC model explains the breakdown rf signals, it does not predict the behavior of the currents detected by the monitors in the beam pipes. The model shows that on he order of a 100 A current is launched into the beam pipes continually during the breakdown. In experiments, the monitors register a short burst of amps of current. The physics of this contradiction is not understood.

Recent measurements of the breakdown kick at NLCTA have shown that most of the kicks are within 30 keV/c [2, 6]. This number is well below the critical 300 keV/c needed to deflect the beam into the collimator, but since the measurements were done for a limited set of parameters (on-crest electrons), more experimental data is needed to verify the kick properties and to check the validity of the simulation results.

Other effects of breakdown current on the primary bunch, such as wakefields due to the breakdown plasma, *etc.*, are likely to be less critical for the NLC operation then the bunch centroid kick, but reqire further investigation.

REFERENCES

[1] C. Adolphsen, ROPC006, Proceedings of the PAC03, 2003, pp. 668 - 672.

[2] S. Döbert this conference.

[3] V.A. Dolgashev *et al.*, SLAC-PUB-8866, Proceedings of the PAC01, 2001, pp. 3807 - 3809.

[4] http://www.mrcwdc.com/Magic/

[5] V.A. Dolgashev *at al.*, "Effect of Dark Currents on the Acclerated beam in an X-band Linac," WEPLT155, EPAC 2004, Lucerne, Switzerland, 2004.

[6] C. Adolphsen and S. Döbert of SLAC, private communication.

ALTERNATIVE LINAC LAYOUT FOR EUROPEAN XFEL PROJECT

Yujong Kim*, K. Flöttmann, and T. Limberg, DESY, D-22603 Hamburg, Germany
Dongchul Son and Y. Kim, The Center for High Energy Physics, Daegu 702-701, Korea

Abstract

To control the microbunching instability at the European XFEL linac, we had optimized one linac layout with a double chicane. However, to relax jitter tolerance further, and to clean ignorable space charge force effects at the second bunch compressor, we have newly designed an alternative linac layout with two bunch compressor stages for the European XFEL project. In this paper, we describe design concepts, Start-to-End (S2E) simulations, and operational flexibility of our alternative linac layout for the European XFEL project.

INTRODUCTION

To supply coherent, ultra-fast, and ultra-bright SASE sources in hard X-ray region, DESY has a plan to construct the largest SASE FEL facility in the world, European XFEL [1]. Its main required parameters are summarized in Table 1. Recently, to control the microbunching instability at bunch compressors for the European XFEL project, we had optimized one linac layout (13JAN04 version) as shown in Fig. 1(top). Here only one bunch compressor (BC) stage with a double chicane is used to obtain a large slice energy spread before the second bunch compressor (BC2) [2], [3]. However it was reported that the jitter tolerance of an FEL driving linac with one BC stage is tighter than that of the other case with two BC stages [4]. Therefore we had investigated the impact of jitters on FEL performances for our current linac layout (13JAN04 version) [3]. According to our recent S2E simulations, rms bunch length, bunch arriving time, and saturation power of SASE source have somewhat large variations under jitters [3]. Since our current linac layout does not have any accelerating module between BCs, space charge force may be increased if bunch length is highly compressed at BC2. Therefore, to avoid any beam quality dilution due to space charge force, we put the double chicane at a somewhat higher beam energy of 510 MeV. According to our CSRtrack simulation considering CSR and space charge force in BCs, the beam quality dilution due to space charge force is ignorable at 510 MeV [3]. By the help of well-damped CSR effects and microbunching instability, all projected and slice beam parameters of our current linac layout are much better than our requirements for the European XFEL project [3]. However, to relax jitter tolerance further, and to clean ignorable space charge force effects at the BC2, we have newly optimized an alternative linac layout (10AUG04 version) with two BC stages for the European XFEL project. In this paper, we describe design concepts, S2E simulations, and operational flexibility of our alternative linac layout for the European XFEL project.

* E-Mail : Yujong.Kim@DESY.de, URL : http://TESLA.DESY.de

Table 1: Main parameters for XFEL project

Parameter	Unit	Value
beam energy E	GeV	20
single bunch charge Q	nC	1
slice normalized rms emittance ϵ_{ns}	μm	1.4
slice rms relative energy spread $\sigma_{\delta s}$	10^{-4}	1.25
peak current I_{pk}	A	5
maximum bunch train length	μs	650
bunch train repetition rate	Hz	10
minimum bunch spacing in a train	μs	0.2
wavelength of SASE source	nm	0.08-6.4
saturation length of SASE source	m	95-170
total undulator length	m	140.3-250.1

ALTERNATIVE LINAC LAYOUT

Generally, the minimum slice emittance is limited by thermal emittance, which is proportional to beamsize on the cathode [4], [5]. After considering two facts that decelerating electric field at the cathode due to space charge force is inversely proportional to the square of rms beamsize at the cathode, and the available maximum gradient of the L-band RF gun is around 60 MV/m at the cathode, we have reduced the rms beamsize on the cathode from 0.75 mm to 0.70 mm to reduce thermal emittance. Recently, by the help of a flat-top laser profile with about 21 ps (FWHM) length and about 7 ps rising and falling time, TTF2 gun (originally PITZ1 gun) had generated high quality electron beams with a projected normalized rms emittance of about 1.7 μm without any booster linac [6]. Therefore we expect that our XFEL injector can supply much higher quality electron beams by increasing the maximum gradient of gun, by improving uniformity of gun driving laser, by reducing rising and falling time of gun driving laser, and by accelerating beams quickly with a booster linac. According to our new ASTRA optimizations, XFEL injector can supply higher quality electron beams with a projected normalized rms emittance of around 0.88 μm by upgrading TTF2 gun. Detail injector re-optimizations for the European XFEL project are described in reference [7], and its optimized results are summarized in Table 2.

Basic bunch compressor design concepts are well described in reference [8], which is related with the SCSS bunch compressor, and detail bunch compressor design concepts of our current linac layout are described in ref-

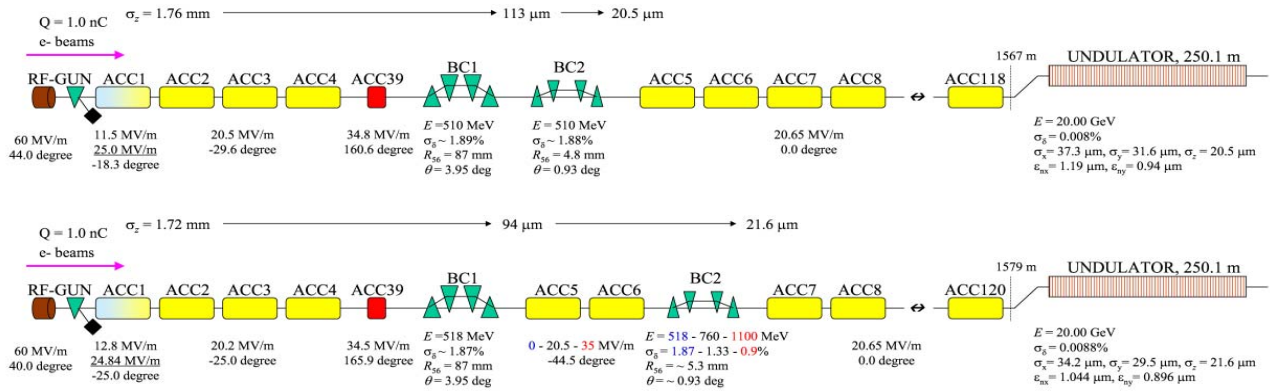

Figure 1: Current (top) and alternative (bottom) linac layout for XFEL project. Here all parameters are projected ones.

erence [3]. The same design concepts in references [3] and [8] are used in designing bunch compressors in our alternative linac layout.

To relax jitter tolerance, to clean ignorable space charge force effects at BC2, and to get operational flexibility, we have adopted followings in our alternative linac layout as shown in Fig. 1(bottom): First, after considering two facts that there is 30 m long drift space between the first bunch compressor (BC1) and BC2 in our current linac layout, and energy spread at BC2 should be high enough to control microbunching instability and CSR, we have added two TESLA modules with a high gradient of 35 MV/m between BCs. During the nominal operation, those modules will be operated with a middle accelerating gradient of 20.5 MV/m. In this case, beam energy at BC2 is about 760 MeV, which is good enough to clean ignorable space charge force effects at BC2. By operating those modules with the highest accelerating gradient of 35 MV/m, beam energy at BC2 can be increased up to 1.1 GeV. Note that our alternative linac layout can be returned to our current linac layout with a double chicane only by turning off those two modules and by rematching optics. In this case, microbunching instability will be effectively damped [3]. Second, generally, tight jitter tolerance can be improved by operating accelerating module with more klystrons. Therefore two klystrons will be dedicated to each module between BCs to relax the jitter tolerance further.

To avoid slice parameter dilution due to the microbunching instability in BCs, we have adopted followings in our alternative linac layout as shown in Fig. 1(bottom): First, to reduce overall CSR strength, we choose only two bunch compressors with the normal chicane instead of S-type chicane. Second, to keep the slice rms relative energy spread at the entrance of BC2 large, we put BC2 at a low beam energy of around 760 MeV. In this case, BC2 has still a large projected rms relative energy spread of around 1.33%. Third, during compression in BCs, slice energy spread generally becomes larger to conserve the normalized longitudinal emittance. Therefore slice rms relative energy spread before BC2 can be further increased up to 3.8×10^{-5} by compressing bunch length at BC1 strongly. Since the compression factor at BC1 is high, we put BC1 at 518 MeV to avoid any beam dilution due to space charge force.

Table 2: S2E simulation results for XFEL project

Parameter	Unit	Value
RF frequency of gun and TESLA module	GHz	1.3
gun cell number	cell	1.5
laser spotsize at cathode σ_r	mm	0.70
laser pulse length (FWHM)	ps	20
laser pulse rising and falling time	ps	1.5
normalized thermal emittance	μm	0.60
maximum longitudinal solenoid field	T	0.198
maximum gradient at the cathode	MV/m	60
gun phase from zero crossing	deg	40
low / high accelerating gradient in ACC1	MV/m	12.8 / 24.8
ACC1 phase from on crest	deg	-25
projected emittance before BC1 / BC2	μm	0.88 / 1.00
slice emittance before BC1 / BC2	μm	0.75 / 0.75
bunch length before BC1 / BC2	mm	1.72 / 0.09
beam energy before BC1 / BC2	MeV	518 / 760
projected energy spread before BC1 / BC2	%	1.87 / 1.33
slice energy spread before BC1 / BC2	10^{-5}	0.86 / 3.8
projected emittance after BC2 / LINAC	μm	1.17 / 1.04
slice emittance after BC2 / LINAC	μm	0.75 / 0.75
bunch length after BC2 / LINAC	μm	21.6 / 21.6
beam energy after BC2 / LINAC	GeV	0.76 / 20.0
projected energy spread after BC2 / LINAC	%	1.3 / 0.009
slice energy spread after BC2 / LINAC	10^{-4}	1.17 / 0.05

To avoid projected emittance dilution due to CSR in BCs, we have adopted followings in our alternative linac layout as shown in Figs. 1(bottom) and 2: First, to reduce CSR, we should choose a smaller momentum compaction factor R_{56} of chicane. This is possible by choosing a somewhat larger projected rms relative energy spread σ_δ [8]. Af-

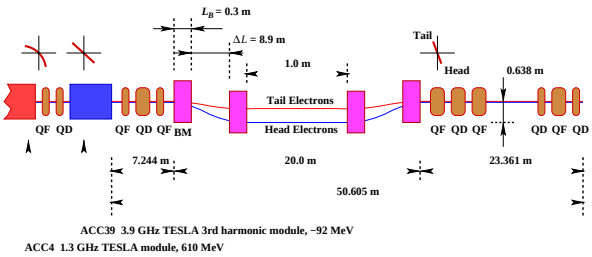

Figure 2: BC1 layout for XFEL project. BC2 chicane has the same layout except $\Delta L = 9.9$ m.

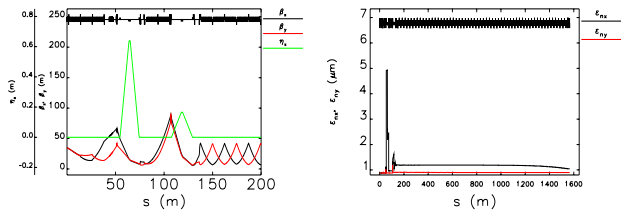

Figure 3: Twiss parameters around BCs (left) and projected emittances along XFEL linac (right).

ter considering the emittance growth due to chromatic effect, we choose $\sigma_\delta \simeq 1.87\%$ at BC1. Second, we choose short quadrupoles around BCs to reduce emittance growth due to chromatic effect. Third, for a required R_{56}, we can reduce dipole bending angle (hence, CSR) further by using a longer drift space ΔL between the first dipole and the second one as shown in Fig. 2 [8]. In case of BC2 which is located at a smaller σ_δ, we increase ΔL by 1.0 m to choose a smaller bending angle of 0.93 degree. Fourth, generally, CSR is weaker at BC1, and CSR becomes stronger at BC2 as bunch length is compressed. Hence, we choose a higher compression factor at BC1 and a lower compression factor at BC2 to reduce overall CSR effects in our two BCs. Fifth, we reduce CSR further by installing a 3rd harmonic module (ACC39) before BC1 to compensate nonlinearities in the longitudinal phase space as shown in Fig. 2 [8]. After considering about 92 MeV beam deceleration by ACC39 and difficulty in compensating of accumulated higher-order nonlinearities in longitudinal phase space due to geometric wakefields and RF curvature along TESLA superconducting modules (ACC1 to ACC4), ACC39 is moved from the downstream of ACC1 to the downstream of ACC4 in our alternative layout. Sixth, the projected emittance dilution due to CSR can be reduced further by forcing the beam waist close to the last dipole where α-functions are zero, and β-functions are their minimum as shown in Fig. 3 [8]. Since chromatic effects becomes smaller at BC2 due to smaller σ_δ, we choose much higher β-functions at the upstream of BC2 to give strong focusing in BC2 as shown in Fig. 3(left) [8]. In this case, the projected emittance growth due to CSR can be effectively reduced at BC2.

To check performance of our alternative linac layout, we have performed S2E simulations with ASTRA and ELE-

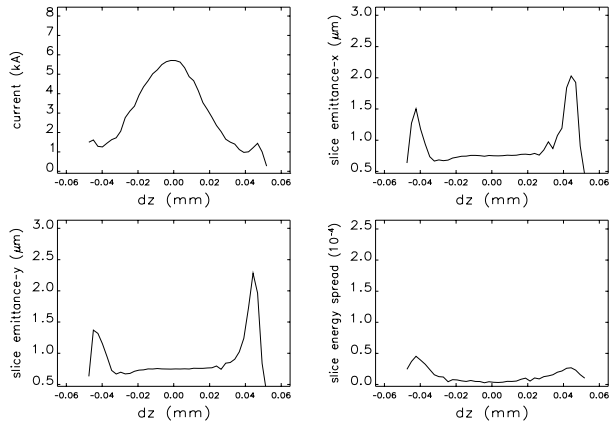

Figure 4: Slice parameters at the end of XFEL linac.

GANT codes as shown in Figs. 1(bottom) and 3(right), and as summarized in Table 2. Here emittance, energy spread, and bunch length are estimated in *normalized rms*, *rms relative*, and *rms*, respectively, and slice parameters before BC2 (after BC2) are estimated at ± 0.1 mm (± 0.02 mm) core region. In these simulations, we have included all important impedances such as space charge force in gun and ACC1, CSR and incoherent synchrotron radiation (ISR) in BCs, and short-range wakefields in all modules. According to our S2E simulations, all obtained slice parameters at the end of the XFEL linac are much better than our requirements as summarized in Table 2 and shown in Fig. 4.

SUMMARY

Although two accelerating modules are added between BCs of our alternative linac layout, slice energy spread before BC2 is around 3.8×10^{-5}, which is about three times higher than that of TTF2. Since slice energy spread and beam energy at BC2 can be widely changeable by adjusting gradient of two modules between BCs, we expect that our alternative linac layout is safe from ignorable space charge force effects at BC2 and the strongest microbunching instability with 2.0 ps modulation period [2], [3]. We expect that jitter tolerance becomes looser by adding two modules between BCs and by dedicating total four klystrons to those two modules. Now, we are under investigating jitter tolerance in our alternative linac layout.

REFERENCES

[1] http://XFEL.DESY.de
[2] Yujong Kim *et al.*, Nucl. Instr. and Meth. A 528 (2004) 427.
[3] Yujong Kim *et al.*, in *Proc. EPAC2004*, 2004.
[4] LCLS CDR, SLAC-R-593, 2002.
[5] C. Travier, Nucl. Instr. and Meth. A 340 (1994) 26.
[6] M. Krasilnikov *et al.*, in *Proc. EPAC2004*, 2004.
[7] Yujong Kim *et al.*, in these proceedings.
[8] Yujong Kim *et al.*, Nucl. Instr. and Meth. A 528 (2004) 421.

EXTRACTION OF HIGH CHARGE ELECTRON BUNCH FROM THE ELSA RF INJECTOR – COMPARISON BETWEEN SIMULATION AND EXPERIMENT

N. Pichoff, P. Balleyguier, A. Binet, R. Bailly-Salins, J.-M. Lagniel, V. Le Flanchec, J-L Lemaire, M. Millerioux, C. Quine
CEA/DAM, Bruyères-le-Châtel, France

Abstract

A new scheme based on a photo-injector and an RF linear accelerator operating at 352 MHz has been recently proposed as a versatile radiographic facility. Beam pulses of 60 ns duration containing 20 successive electron bunches that are extracted at 2.5 MeV from a photo-injector are accelerated through the next structure to the final energy of 51 MeV. Bunches carrying 100 nC are required for this purpose. As a first demonstrating step, mora than 50 nC electron bunches have been produced and accelerated to 2.5 MeV with the 144 MHz ELSA photo-injector at Bruyères le Châtel. For this experiment, we compare the results and the numerical simulations made with PARMELA, MAGIC and MAFIA codes.

INTRODUCTION

A proposal for the project named RX2 has been made in view of producing high-flux of short X-ray pulses from a very intense 50 MeV electron beam impinging a high Z material production target. The facility consists of a photo-injector followed by a linear accelerating structure. The beam is finally tightly focused to the target. The 60-ns electron pulse is made of 20 bunches repeated at 352 MHz. Each bunch of 100 ps duration is issued from the photo-injector and carries a 100 nC charge. Several simulation codes have been used to design the photo-injector: PARMELA [1], MAGIC [2], MAFIA [3] and M2V [4].

The space-charge limit is the maximum amount of charge that can be extracted from a gun (at fixed beam size and time duration). This limitation happens when the field induced by the extracted charges (space-charge field) cancels out the gun acceleration field on the cathode. In a stationary 1D model, this is known as the Child-Langmuir current density limit. In the RX2 gun, this limit calculated with the codes [1], [2], [3], [4] is about 600 nC within 20% dispersion from code to code (figure 1). According to these simulations, the RX2 gun 100 nC working point is much lower than the space-charge limit.

To ensure that one can rely on the space-charge limit predicted by the codes, we decided to validate these codes against experimental measurements. In this paper, we present the space charge-limit measured on the ELSA RF photo-injector [5] and we compare it to the code results.

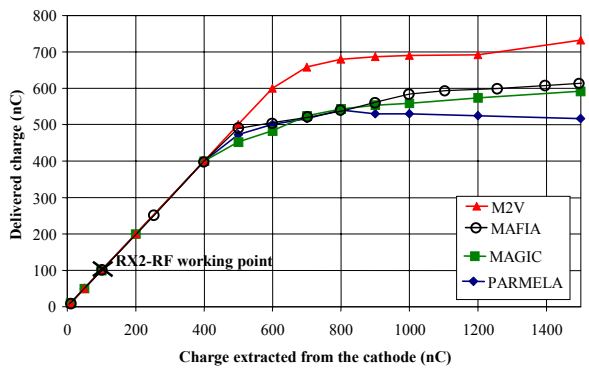

Figure 1: Prediction by four codes for the delivered charge as a function of the expected charge produced from the photo-electric effect. RX2 working point is well below the space charge limit.

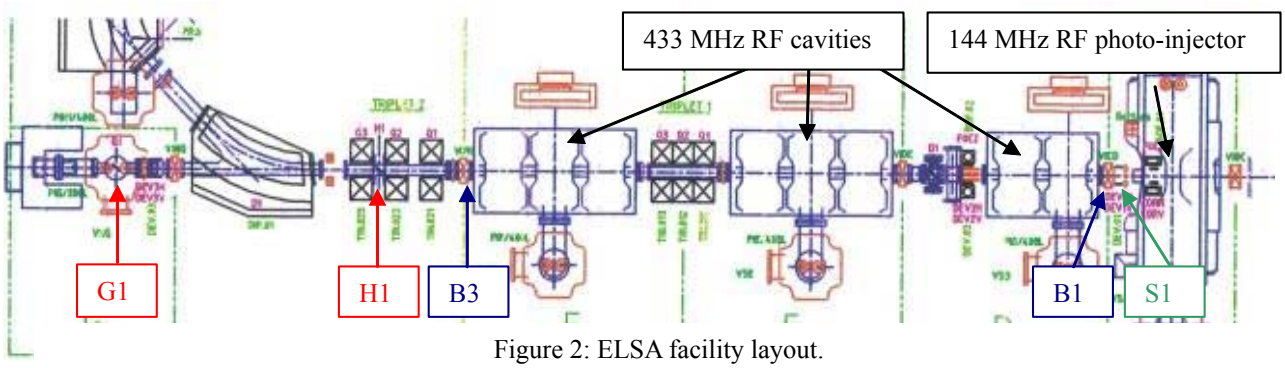

Figure 2: ELSA facility layout.

ELSA LAYOUT

The ELSA layout is presented on figure 2. It is made of a 144 MHz photo-injector delivering 2.5 MeV bunches, followed by three 433 MHz accelerating cavities (not powered in this experiment), focusing elements (triplets, solenoids) and a set of steering coils. The beam reaches currently a final energy of 18 MeV. S1 stands for the extraction solenoid coil. The bunch absolute charge is measured at H1 with a current transformer and at G1 on a Faraday cup. Distance between the photo-cathode and G1 is ~7 m. B1 and B3 are beam position monitors (BPM). By summing the four antenna signals BPM's deliver a signal proportional to the bunch charge. Then, after calibration, they have been used to measure the absolute charge.

CALIBRATION OF BPM's FOR CHARGE MEASUREMENTS

The signals obtained on each of the four BPM antennas are summed. The sum signal is amplified in a logarithmic amplifier before being transported along a 30 m coaxial line to an oscilloscope where the signal is measured through a 50 Ω load (figure 3).

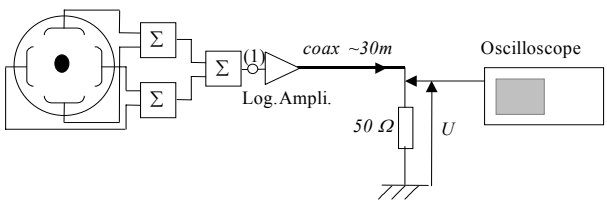

Figure 3: Signal measured on a BPM.

The voltage U delivered by the log-amp depends on the charge Q. More precisely, Q should be proportional to: $10^{\alpha U/20}$, where α is the slope of the log-amp in dB/V. Actually, this slope shows some variation in the range of the log-amp, and it is worth to replace the term αU by a third degree polynomial (figure 4) resulting from a preliminary characterization of the log-amp with a 1-ns square signal at its input (noted °1 on figure 3).

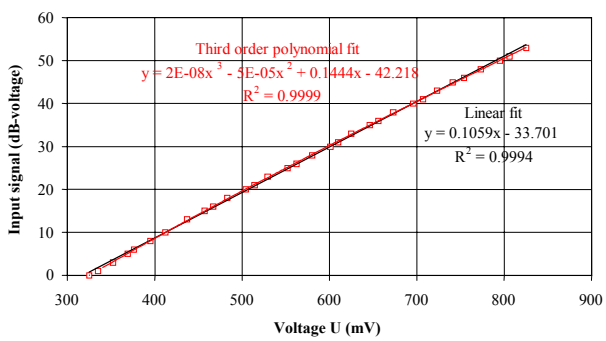

Figure 4: Polynomial fit of the log-amp response signal. Actually, our range of interest stands between 450 and 600 mV.

Thus, the relation between the charge and the measured voltage becomes :

$$Q = Q_0 \cdot 10^{\frac{1}{20}\sum_{i=0}^{3} a_i U^i} .$$

The second factor of the right hand term gives the relative evolution of the beam charge with respect to the measured voltage. The Q_0 coefficient tells the absolute charge.

To determine Q_0, we made some correlated beam charge measurement on B1, B3, H1 and G1 at low charge transport assuming no beam loss (figure 5).

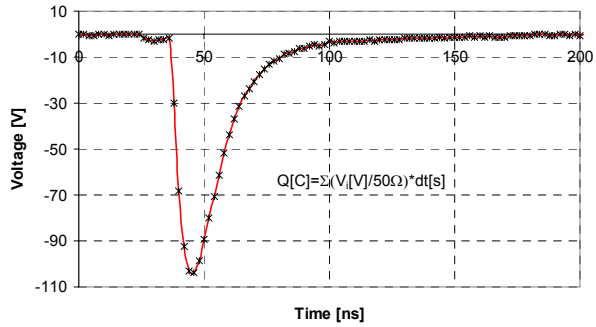

Figure 5: Signal recording for charge measurements: calibration is 1 nC/ 2 10^7 V.s.

At low laser power delivering 0.5 nC per bunch, we measured the signal at the four positions versus the extraction solenoid current. A beam transport with no loss should show in G1 or even H1 some plateau of maximum charge versus the solenoid current. This was experimentally observed as shown in figure 6

Doing the same procedure for four different laser powerings, four Q_0 values are obtained. These four coefficient values, which are in agreement within +/- 5%, are averaged to give the final coefficient.

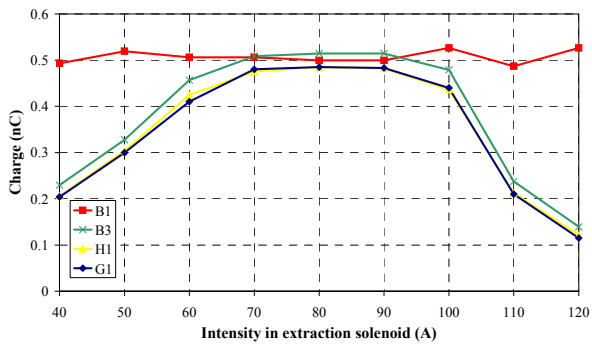

Figure 6: Calibration of the charge at low current: the signals are measured at B1, B3, H1 and G1.

SPACE-CHARGE SATURATION

The laser spot size on the cathode is 8 mm diameter. The "average" transverse beam profile has been modelled by a 2.75 mm sigma gaussian truncated to +/- 4 mm. Its duration is 200 ps FWHM and it has been modelled by a 85 ps sigma gaussian truncated to +/- 170 ps.

In a photo-injector, the number of electrons pulled out of the cathode is proportional to the laser power through the quantum efficiency. When this power is low, all the

pulled out electrons are extracted from the gun i.e the total charge extracted is proportional to the laser power. Above a threshold of laser power, the field on the cathode cancels out and reverses due to the remaining pulled out electrons. Only a fraction of these electrons is extracted from the gun.

We have experimentally measured the effective charge extracted from the ELSA photo-injector (B1 viewing station) as a function of the laser power. Typical signal recording is shown on figure 6 Assuming the pulled out charge is proportional to the laser power and that this charge is totally extracted (as long as this charge is low), the extracted charge can be plotted as a function of the pulled out charge.

In figure 7 the experimental results are compared to the simulations obtained with the 3 codes PARMELA, MAGIC and MAFIA. Note that the MAFIA limit (about 50 nC here) is much lower than the 500 nC value obtained in a previous simulation [6] where the emission radius were much larger (15 mm).

The experimental error bars have been deduced from calibration of the charge measurement at B1. It does not take into account the beam parameters stability. The 15% errors bars on MAGIC and PARMELA simulation results come from simulations assuming 10% uncertainties on laser parameters (radial and longitudinal profiles).

MAGIC is in good agreement with the experimental results. MAFIA, even if using the same model as MAGIC, gives a space-charge saturation about 40% lower. This difference have not been explained so far.

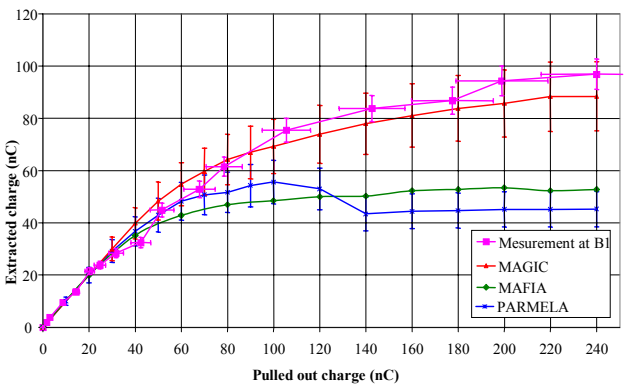

Figure 7: Evolution of the extracted charge from the gun as a function of the charge pulled out of the cathode. Experimental and simulation results are compared.

PARMELA shows some particle losses on the extraction cavity nose as indicated in figure 8 These losses are not observed with MAGIC or MAFIA simulations. During the experiments, we had unfortunately no way to measure the beam losses in the extraction cavity if any.

At full pulled out charge, about 20 nC are lost in the cavity (about 70 nC are extracted from the cathode, as only 50 nC are extracted from the gun). The calculation of the transverse force is clearly different in PARMELA and in MAGIC. This difference could come from a more basic phenomena related to the space-charge model used in PARMELA (indeed the SCHEFF routine assumes no retarded potential and calculated electrostatic field in the beam frame).

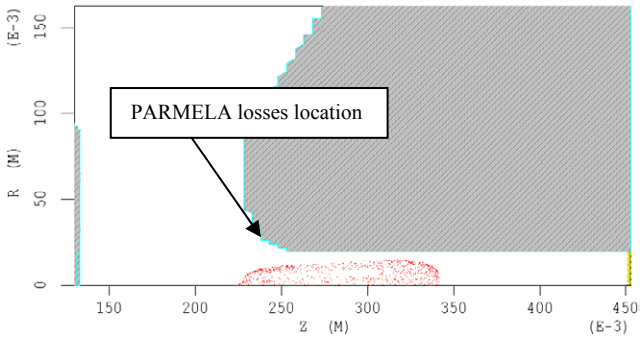

Figure 8: Extracted charge propagation from PARMELA simulations.

We are probably reaching here the limits of PARMELA. At any rate it is still the fastest and the easiest used code at present time. It remains also in good agreement with other codes when used far from the space-charge limit.

CONCLUSION

Different codes (PARMELA, MAGIC, MAFIA and M2V) have been used to design the RF-RX2 accelerator project. These codes predict that the RX2 gun charge retained for operation is much lower than the space-charge limit. To make sure of this, we have measured the space-charge limit on ELSA RF photo-injector and compared it with simulations. MAGIC simulations are in good agreement with experimental results. However MAFIA and PARMELA seem to under-estimate the total charge that can be extracted from the gun.

Moreover, PARMELA predicts beam losses not shown by the other codes. Nevertheless, this discrepancy between code results is much lower than the difference between the space-charge limit prediction for RX2 and does not affect the chosen working point. We are then confident that the RX2 gun can extract the required 100 nC per bunch at 2.5 MeV.

REFERENCES

[1] L. M. Young, J. H. Billen, "Parmela documentation", LA-UR-96-1835, revised July 17, 2003.
[2] http://www.mrcwdc.com/Magic/index.html
[3] http://www.cst.de/Content/Products/MAFIA/Overview.aspx
[4] J. Segré “utilisation du code DEGAS2D”, internal report
[5] S.Joly, S.Striby “The ELSA Linear Accelerator”, revue Chocs n° 18, CEA, DRIF, march 1998.
[6] P.Balleyguier, Ph.Guimbal, " Simulation of high charge extraction from the ELSA RF Photo-injector", Particle Accelerator Conference, Portland, Mai 2003.

BEAM ANALYSIS USING THE IPNS LINAC ESEM*

J.C. Dooling, F.R. Brumwell, LI. Donley, G.E. McMichael, and V.F. Stipp
Argonne National Laboratory, Argonne, IL 60439, USA

Abstract

The Energy Spread and Energy Monitor (ESEM) is an on-line, non-intrusive diagnostic used to characterize the output beam from the 200-MHz, 50-MeV linac. The energy spread is determined from a 3-size, longitudinal emittance measurement and energy is derived from TOF analysis. Presently, a single particle distribution is used to yield energy and energy-spread results. Effort is on-going to allow for more realistic distributions to be included. Signals are detected on terminated 50-ohm, stripline BPMs. Each BPM is constructed with four striplines: top, bottom, left and right. Until recently, the ESEM signals were taken solely from bottom striplines in four separate BPM locations in the transport line between the linac and synchrotron. We have begun to use the top stripline data to examine, in more detail, beam position and attempt to measure beam size.

INTRODUCTION

Stripline beam position monitors (BPMs) are an important on-line diagnostic tool[1]. The IPNS BPMs are constructed with four 50-Ω striplines aligned with the horizontal and vertical axes of the accelerator. Each stripline is terminated on the downstream end in its characteristic impedance (50-Ω). A BPM module is shown in Figure 1. There are seven BPM modules in the 50 MeV transport line between the linac and synchrotron; the first four are also used for ESEM measurements.

Figure 1: IPNS 50 MeV line stripline BPMs.

* This work is supported by the US DOE under contract no. W-31-109-ENG-38

The ESEM diagnostic makes use of a three-size technique to determine the beam's longitudinal momentum and energy spread[2]. A drift-length parameter is used to adjust the four three-size permutations until satisfactory agreement is achieved between them. The four BPM permutations are 123, 124, 134, and 234. Figure 2 shows the section of beamline relevant to the ESEM diagnostic.

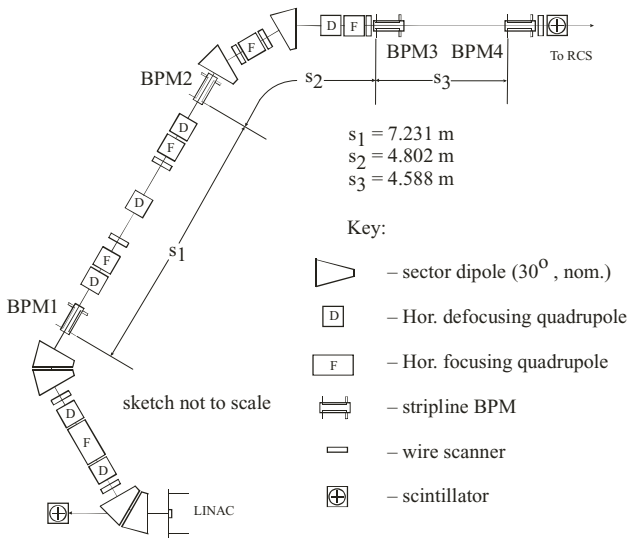

Figure 2: 50-MeV transport line with location of the ESEM stripline BPMs.

BEAM SIZE ANALYSIS

A heuristic approach is used to determine the transverse beam size using stripline BPMs. Two-point models have been used elsewhere[3] to describe beam motion and stability; here, a rigid, two-point model is used to study the beam size.

Two Beamlet Approach

The measurement assumes the beam bunch of charge Q can be represented by two equal point charges of Q/2 separated in one transverse plane by 2a. The center of the two point charges is offset from the axis of the BPM by x_0. The two-beamlet approach is shown schematically in Figure 3. A fraction of the total charge from each beamlet appears on the stripline within a polar angle of $\pi/2\gamma$, centered about $\theta=\pi/2$, where γ is the relativistic ratio of total to rest-mass energy. The charge density on each strip can be expressed as,

$$q_j = \sum_i (Q/2)\cdot(2\pi r_{ij}\, s_{ij})^{-1}\phi_{ij} \qquad (1)$$

where s_{ij} represents the image length on stripline j from charge i; also, ϕ_{ij} is the azimuthal angle defined as $2\tan^{-1}(w/2r_{ij})$ where w is the width of the stripline. For stripline 1, the charge density can be written as,

$$q_1 = \frac{Q}{4\pi}\left(\frac{\phi_{11}}{r_{11}s_{11}} + \frac{\phi_{21}}{r_{21}s_{21}}\right) \quad (2)$$

where $r_{11}=b-a-x_0$, $r_{21}=b+a-x_0$, $s_{11}=2r_{11}\tan(\pi/4\gamma)$, $s_{21}=2r_{21}\tan(\pi/4\gamma)$, b is the stripline radius (3.85 cm), x_0 is the beam offset, and a is the beam half-width. The sign of x_0 can be either positive or negative. Likewise on stripline 2, the charge density is given as,

$$q_2 = \frac{Q}{4\pi}\left(\frac{\phi_{12}}{r_{12}s_{12}} + \frac{\phi_{22}}{r_{22}s_{22}}\right) \quad (3)$$

where the other length parameters may be inferred from Fig. 3. The stripline current can be obtained by integrating the product of charge density and bunch velocity over the azimuthal widths. It is important to note that the axial charge distribution on the stripline is not uniform but will vary with the distance from the beamlet within each polar angle. Averaging the density over the longitudinal extent of the image charge, the average current within the polar angles of both beamlets for stripline 1 is approximately,

$$I_1 = \frac{Q}{4\pi}\left(\frac{1}{r_{11}s_{11}} + \frac{1}{r_{21}s_{21}}\right)w\beta c \quad (4).$$

where βc is the average bunch velocity.

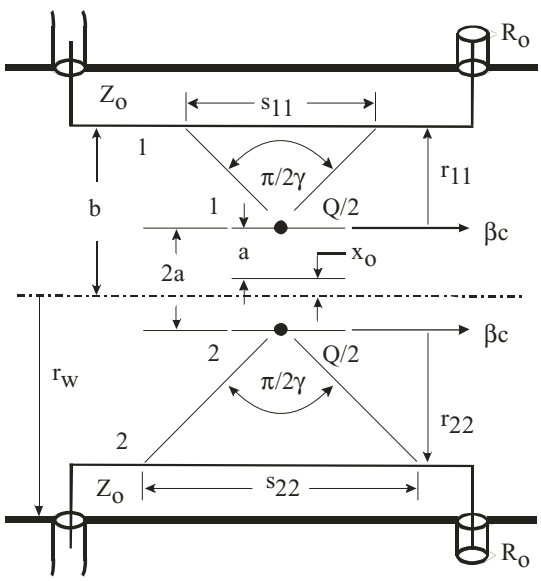

Figure 3: Cross-section of a BPM module showing the parameters used in the two-beamlet approach for measuring beam size.

Outside of the inner polar angle, the current drops to,

$$I_1 = \frac{Q}{4\pi}\frac{w\beta c}{r_{21}s_{21}} \quad (5)$$

From this simple model, it can be seen that the temporal shape of the image current will depend on the separation between the beamlets; therefore the shape of the image current provides information on the size of the beam.

Beam Size Calculation

BPM 4 is located near a waist in the horizontal and vertical dimensions of the 50 MeV beam. This location has periodically been used as a target site for nuclear physics experiments and several beam size diagnostics have been placed here, including wire scanner (WS), scintillator, and segmented Faraday cup (SFC). The BPM beam size measurement begins with the collection of H- macropulse data from both horizontal striplines using a fast, deep memory oscilloscope (Tektronix TDS7254-3M). All BPM signals are recorded as 8-bit data at a rate of 5 samples per ns. Data acquisition continues for 100 μs to completely encompass the length of the <80 μs macropulse. A 500 kilosample (kS) data set is generated for each sampled stripline. Deterministic noise is removed from the data sets, where feasible, up through the fifth harmonic of the linac[4]. An FFT of a 400-ns window of data (2 kS) is used to examine the average microbunch structure. Working in the frequency domain, the spectra are corrected for cable attenuation. The time-domain signal is reconstructed using the amplitudes of the principal harmonics and rectangular pulse-train phasing to provide the minimum pulsewidth. The time-domain signal is then modelled with a double Gaussian function as shown in Figure 4. The two functions represent the profiles from the left and right beamlets. From Fig. 3, the axial length of the charge distribution may be written as,

$$\tan\left(\frac{\pi}{4\gamma}\right) = \frac{s_{22}}{2r_{22}} = \frac{s_{12}}{2r_{12}} \quad (6)$$

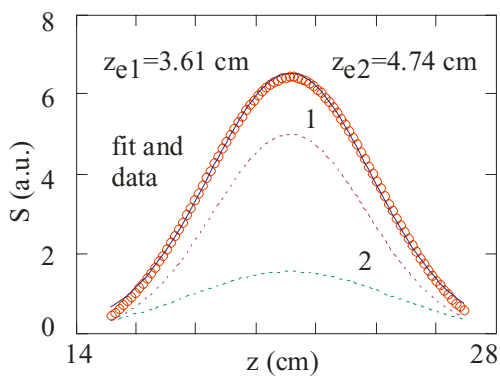

Figure 4: Reconstructed time domain signal, BPM 4R; composite 1/e-width = 3.88 cm.

representing one equation and two unknowns, a and x_0. The offset is determined by the ratio of the left and right amplitudes and is expressed approximately as,

$$x_o = \left(\frac{R-L}{R+L}\right)\frac{b}{2} \qquad (7)$$

Using s_{22} and converting the e-width to FWHM values ($s_{22}=2(\ln 2)^{1/2}z_{e1}$), the beam size expression becomes,

$$a = b - x_o - \frac{s_{22}}{\tan\left(\frac{\pi}{4\gamma}\right)} \qquad (8)$$

Performing the measurement on four separate linac macropulses near the midpoint (40 μs) of each pulse, the following result is obtained,

$a = 0.61 \pm 0.09$ cm,

for a FWHM value of 1.22 ±.17 cm. The BPM size result is compared with fits to WS, scintillator, and SFC data in Table 1.

Table 1: Horizontal beam size measurements near BPM 4

DIAGNOSTIC	FWHM (cm)
BPM	1.22
WS8	1.32
Scintillator	1.87
SFC	1.26

Measurement Challenges and Discussion

The BPM striplines are raised up above the inner radius of the BPM chamber by approximately 0.8 cm. Magnetic field generated by the beam can penetrate the loop formed by the stripline and its support structure. On the downstream end, the structure is tied immediately to a 50-ohm terminator. The voltage induced by the time-varying magnetic field can be equal to or greater than that generated by the image charge of the beam, especially at the upstream end of the 50 MeV line where the microbunch pulsewidths are shortest. We are presently considering building a new BPM where the striplines are approximately flush to the inner surface to negate the effects of the linked magnetic field.

Solutions to the double Gaussian fitting procedure are not unique. The opening angle of the charge on the stripline is only estimated here, but should be calculated more precisely. Also, the microbunch is not a point source but is extended in the direction of motion.

An advantage of this approach, is that it does not preclude the use of round beams as is the case when employing radial magnetic fields to monitor beam size[5,6]. As shown by the scintillator image in Figure 5, the beam at the BPM 4 location is roughly circular.

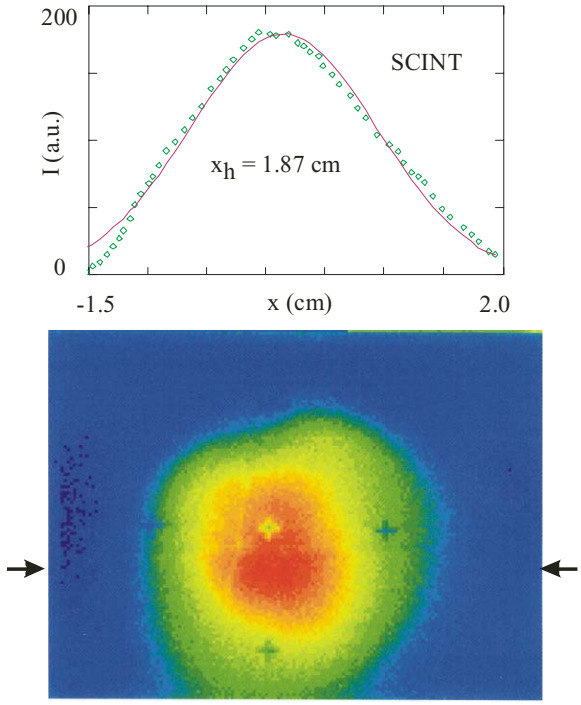

Figure 5: False-color scintillator image, digitized horizontal data (arrows), and fit.

ACKNOWLEGDEMENT

This work is made possible by the effort and dedication of the IPNS Operations Group

REFERENCES

[1] R. E. Shafer, Proc. 1989 Accel. Instrum. Workshop, BNL, AIP Conf. Proc. **212**, 26(1990), and R. E. Shafer, Proc. 1993 Beam. Instrum. Workshop, Santa Fe, AIP Conf. Proc. **319**, 303(1994).

[2] C. Dooling, et al., Proc. 20th LINAC Conference, SLAC-R-561, Monterey, CA, August 2000, p 193.

[3] A. W. Chao, *Physics of Collective Beam Instabilities in High Energy Accelerators*, Wiley, New York, 1993, p. 3. .

[4] J. C. Dooling, submitted to the Proc. BIW, May 3-6, 2004, Knoxville, TN.

[5] R. H. Miller, et al., Proc. 12th International Conf. on High-Energy Accelerators, Fermilab, 1983.

[6] A. Jansson, Phys. Rev. STAB, **5**, 072303(2002).

THE FIRST RESULTS OF BUNCH SHAPE MEASUREMENTS IN THE SNS LINAC

A. Feschenko*, V. Gaidash, Yu. Kisselev, L. Kravchuk, A. Liyu, A. Menshov, A. Mirzojan,
Institute for Nuclear Research, Moscow 117312, Russia
S. Assadi, W. Blokland, S. Henderson, D.-O. Jeon, E. Tanke, ORNL/SNS, Oak Ridge, Tennessee

Abstract

Three Bunch Shape Monitors with transverse scanning of low-energy secondary electrons have been developed and fabricated for the SNS Linac. A novel feature of the detectors is the use of energy separation of the electrons. The separation allows minimizing the influence of detached electrons originated from dissociation of H-minus ions in the detector wire target. The first detector was used at the exit of the first DTL tank during its commissioning. The results of Bunch Shape measurements are presented and discussed. These results were used to verify beam quality, to set parameters of the accelerating field, to estimate longitudinal beam halo and to estimate the longitudinal beam emittance.

INTRODUCTION

Bunch Shape Monitors (BSMs) are used to measure longitudinal microstructure of the accelerated beam in a number of accelerators. A review report [1] includes details of the principle of operation and description of BSM parameters as well as thorough list of references. Briefly, the principle of operation is based on the coherent transformation of a longitudinal distribution of charge of the analyzed beam into a spatial distribution of low energy secondary electrons through transverse RF modulation. The main parameter of the monitor is its phase resolution. Typically the value of resolution is about 1° at the frequencies of hundreds of MHz.

In the case of an H-minus beam the results of measurements are distorted by the electrons detached from the ions in the wire target of a BSM [2]. The influence of the detached electrons essentially depends on the analyzed beam energy. In the majority of cases this influence is not essential for bunch core measurements but is of extreme importance for measurements of a longitudinal halo. Information on halo intensity is vital for the new generation of high intensity linear accelerators. That is why a special measure for diminishing the influence of the detached electrons has been foreseen in BSMs developed for the SNS linac. Due to the difference in energy of the low energy secondary electrons used for bunch shape measurements and the detached electrons, an effective way of diminishing the influence of the latter ones is energy separation of the two electron fractions [3]. The standard configuration of the BSM (fig. 1) was modernised by adding bending magnet 5 along with slit 6 between output collimator 4 and electron collector 7. Bending magnetic field is selected to provide separation of electrons with the energy corresponding to target potential U_{targ} (typically 10 kV) Separated energy range must be sufficient to provide loss-less propagation of the low energy secondary electrons. With the radius of 47 mm, the slit size of 3 mm and the image size of 1 mm the energy range equals about 20%.

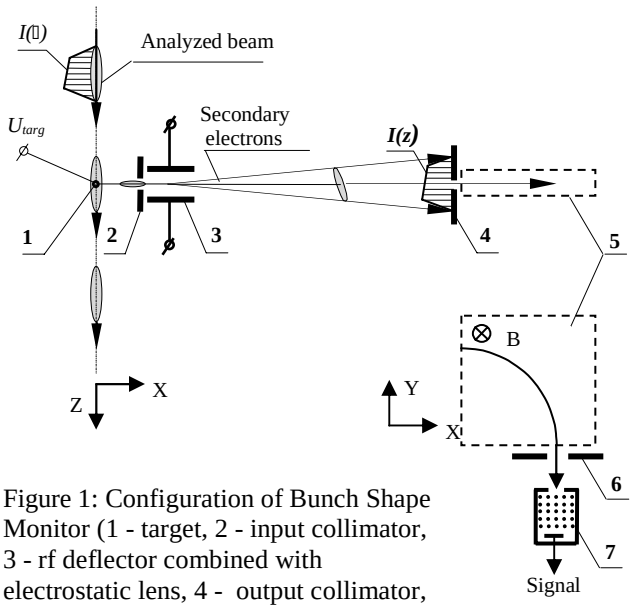

Figure 1: Configuration of Bunch Shape Monitor (1 - target, 2 - input collimator, 3 - rf deflector combined with electrostatic lens, 4 - output collimator, 5 – bending magnet, 6 – collimator, 7 – Secondary Electron Multiplier).

Energy separation also improves halo measurements due to decreasing the influence of electrons inelastically scattered on the plates of input collimator 2.

Three Bunch Shape Monitors have been built for the SNS linac. Now they are installed in intersegments 7, 9 and 11 of CCL Module #1. The first one, shown in fig. 2, was used during the commissioning of the DTL Tank 1 in autumn 2003.

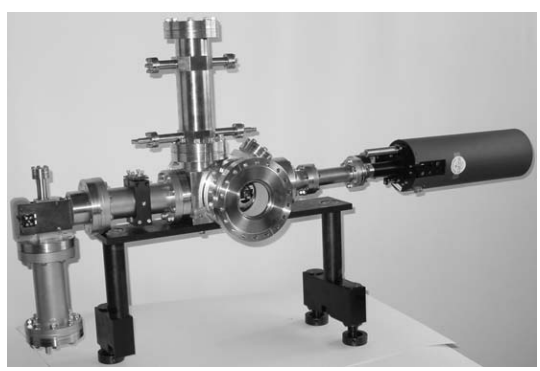

Figure 2: General view of BSM.

*feschenk@inr.troitsk.ru

EXPERIMENTAL RESULTS

The first BSM was installed in D-plate 1.27 m downstream of Tank 1 exit. Tank 1 is a 4.152 m drift tube cavity operating at 402.5 MHz and accelerating the beam from 2.5 MeV to 7.5 MeV. To avoid thermal destruction of a BSM wire target the beam pulse repetition rate and the beam pulse duration were limited to 2 Hz and 50 μs correspondingly. The pulse current was about 12-18 mA.

During the bunch shape measurement the phase of the deflecting field is adjusted between beam pulses: that is, different points of the longitudinal distribution are measured for different beam pulses. This feature implies a repeatability of beam parameters from pulse to pulse. A signal from the electron collector is digitized along the beam pulse. The result of the measurement is a two-dimensional array of data representing the evolution of the bunch shape within the beam pulse. A typical experimental distribution for nominal accelerator parameter settings is given in fig. 3.

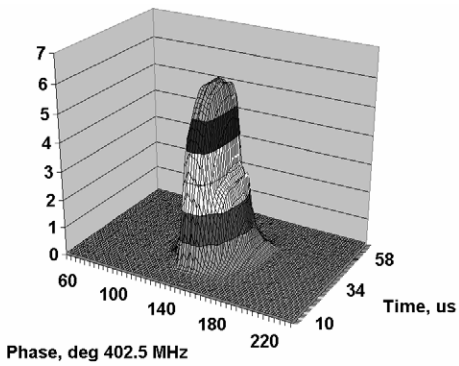

Figure 3: Typical evolution of bunch shape along the beam pulse.

Longitudinal Halo Measurements

To detect the electron intensity a Hamamatsu R596 Electron Multiplier 7 (fig. 1) is used. Changing of the multiplier supply voltage enables to adjust its gain over 5 orders of magnitude resulting in the possibility of more precise measurements of bunch tails. The results of bunch shape measurements done for relative gains 1, 5, 30 and 150 are shown in fig. 4. After removing the points with signal saturation at higher gains one can reconstruct the bunch and present it in a wide intensity range (fig. 5). A background level is also presented in fig. 5. The latter was measured with a decreased current of bending magnet 5 (fig. 1) to 75% of the nominal value. It was observed that variation of the bending magnet current below 90% of the nominal value does not change the background level.

After subtracting the background level a percentage of beam particles within a given phase range can be found (fig. 6). One should note that phase range of measurements of BSM is equal to half a period of the deflecting field: the signal from electron collector represents a superposition of two points in longitudinal distribution shifted by 180°. With this the result in fig. 6 is valid assuming that the amount of particles in a phase range shifted by 180° with respect to the bunch is negligible.

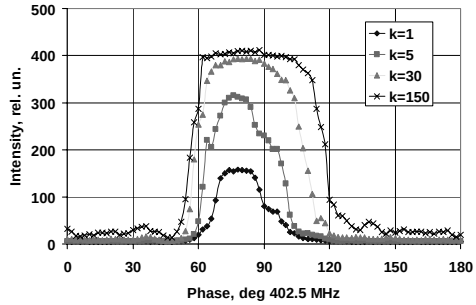

Figure 4: Result of Bunch Shape Measurement for different electron multiplier gains.

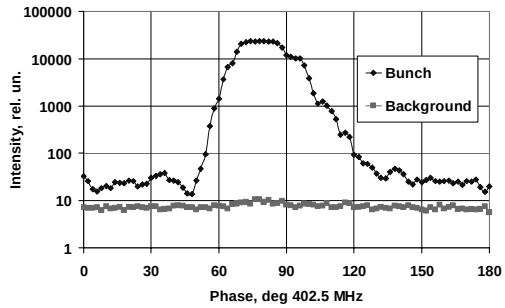

Figure 5: Presentation of bunch shape in a wide intensity range.

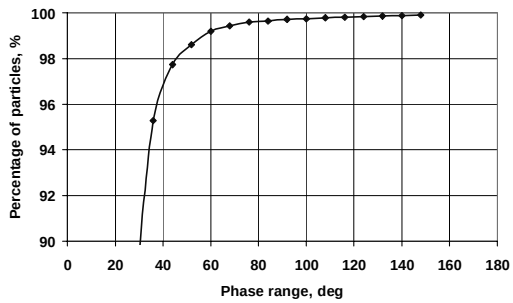

Figure 6: Particle portion as function of phase range.

Longitudinal Emittance Measurements

The method of longitudinal emittance measurement [4] is similar to the one widely used for transverse phase space. The emittance is found as an equivalent phase ellipse in the phase - energy plane using the results of several bunch length measurements downstream of the element(s) providing known linear transformation of the ellipse. To restore the ellipse at the entrance of Tank 1, bunch shape measurements were executed for different amplitudes of accelerating field with appropriate adjustment of tank phase to stay in the vicinity of the synchronous phase. The transformation matrix from Tank 1 entrance to the BSM position for different amplitudes was calculated numerically.

The calibration of amplitude was done by comparing the measured dependence of the variation of bunch center

phase position Φ on Tank 1 phase shift φ with a calculated function. Indeed the derivatives $d\Phi/d\varphi$ of experimental and calculated functions were used for comparison. Fig. 7 shows bunch shapes measured for different tank phases and the behavior of bunch center. Comparing the tilt of experimental function $d\Phi/d\varphi$=1.45 at the inflection point with the theoretical curve (fig. 8), one can find the current accelerating field amplitude to be 1.02 of the nominal value. One should note that the tank phase corresponding to inflection point (φ =-124°) agrees well with the tank synchronous phase found preliminary using a phase scan method.

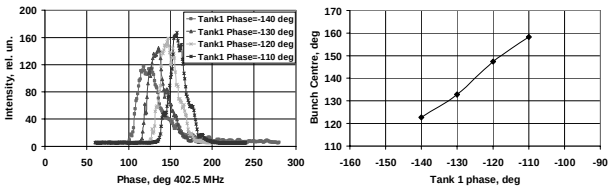

Figure 7: Bunch phase position for different Tank 1 phases.

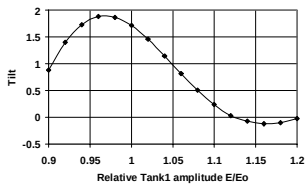

Figure 8: Theoretical dependence of $d\Phi/d\varphi$ on field amplitude.

Bunch shapes have been measured for eight Tank 1 amplitudes within the range of (0.96÷1.17) with respect to nominal value. The rms bunch length has been found for four cut off levels with respect to maximum: 0.025, 0.05, 0.1 and 0.2. The results of the measurements are summarized in Table 1.

Table 1: Results of bunch phase length measurements

Tank 1 Amplitude	Rms bunch phase length for different cut-off levels, deg			
	0.025	0.05	0.1	0.2
$1.17E_0$	21.0	18.6	16.2	13.6
$1.14E_0$	19.3	17.1	14.2	10.5
$1.11E_0$	16.0	14.0	10.9	7.6
$1.08E_0$	13.6	11.8	8.7	6.5
$1.05E_0$	9.8	8.8	7.6	6.6
$1.02E_0$	10.1	9.6	9.0	8.0
$0.99E_0$	15.5	14.1	12.5	9.8
$0.96E_0$	16.7	14.8	12.3	10.5

The values of rms bunch phase lengths were used to plot boundary lines of phase ellipse. These lines transformed to the entrance of Tank 1 for one cut off level are shown in fig. 9. The optimum ellipses inscribed inside the polygons produced by the lines are presented as well. The values of emittance for different cut off levels are given in table 2.

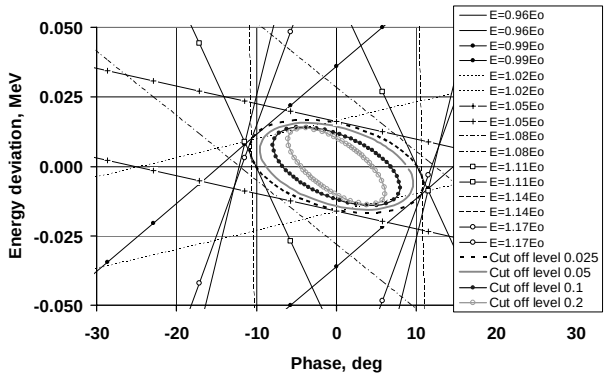

Figure 9: Phase ellipses at the entrance of Tank 1 for different cut off levels (The tangents are shown for 0.025 cut off level).

Table 2: Longitudinal emittance value

Cut off level	0.025	0.05	0.1	0.2
Emittance, MeV·deg	0.171	0.138	0.095	0.062

Figure 10 shows the ellipses for a cut off level of 0.05 transformed to the exit of Tank 1 and to the BSM position for nominal amplitude.

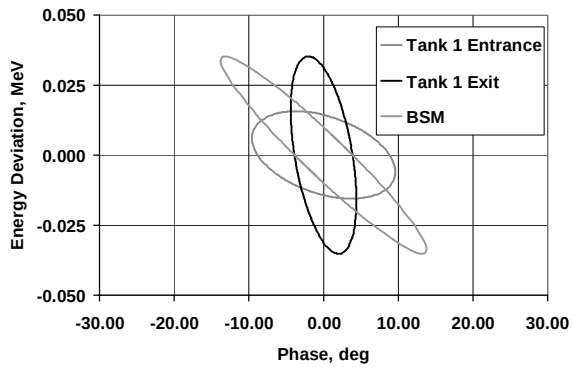

Figure 10: Phase ellipses at the entrance of Tank, the exit of Tank 1 and at the BSM position.

ACKNOWLEDGEMENTS

The authors express their gratitude to Dr. N. Holtkamp for the support of this work.

REFERENCES

[1] A.Feschenko. PAC2001, Chicago, June 2001, V. 1, p. 517.

[2] A. Mirzojan et al. Voprosy Atomnoi Nauki i Tekhniki. V. 4,5 (31,32), Kharkov, 1997, p. 92 (in Russian)

[3] A.V.Feschenko et al. Proc. of the 1992 Linear Acc. Conf., August 1992, Ottawa, V. 2, p. 662.

[4] Yu.V.Bylinsky et al. Proc.of the 1991 Particle Acc. Conf., San-Francisco, May 1991,. p.3062.

BUNCH LENGTH MEASUREMENTS AT LEBRA

K.Yokoyama [#,*,A)], I.Sato [A)], K.Hayakawa [A)] , T.Tanaka [A)] , Y.Hayakawa [A)], K.Nakao[B)]
A) Laboratory for Electron Beam Research and Application, Institute of Quantum Science, Nihon University 7-24-1 Narashinodai, Funabashi, 274-8501
B) College of Science and Technology, Nihon University 7-24-1 Narashinodai, Funabashi, 274 -8501 Japan

Abstract

The high-gain FEL amplification in near IR and SASE have been observed at LEBRA (Laboratory for Electron Beam Research and Application). A very short bunch of the electron beams have been achieved by the achromatic bending system, as the bunch compression system due to apt on the accelerating phase in the last accelerating section. The bunch length was estimated from the phase ellipse parameters which is deduced from the dependence of the beam spread on the accelerating phase. The bunch length of FWHM was estimated approximately 0.33 mm from the results of the experiments. Besides, the pulse length of the FEL lights around the wavelength of 1.5 micrometer was measured by means of the autocorrelation. The pulse length was less than 0.06 mm according to the number of interference waves. The pulse length of the FEL lights corresponds to around 20% of the electron bunch length.

INTRODUCTION

The high-gain FEL amplification has been obtained and the result of the simulation extracted from the FEL gain indicates that the bunch length could be around 1 ps or less [1]. SASE has also been observed using the electron beam with a low macropulse beam current and a very short bunch with considerable bunch compression in the achromatic bending system [2]. In order to investigate the bunch length which yields the high gain FEL amplification, the electron bunch length was measured by means of the simple theory about the phase ellipse instead of using a streak camera, which provides a direct and convenient way to measure bunch lengths but a high-accuracy one is very expensive. The pulse length of the FEL lights around the wavelength of 1.5 μm was also measured by means of the autocorrelation to compare the results of the bunch length.

The part of the main accelerating at LEBRA consists of three 4-m accelerating sections [3, 4]. The accelerating RF is provided by two 20-MW klystrons, which are operated at 2856 MHz with a pulse length 20 μs. The Phase flatness of the pulse error within 0.3° was achieved [5]. Klystron #1 is used for the injector and the first accelerating section and klystron #2 is used for the two accelerating sections. The electron beam accelerated in the linac is transported to the FEL system through the 90° achromatic bending and analyzer magnet system. The energy spread of the beam is restricted to about 1% by a slit of the momentum analyzer. The FEL system consists of an undulator of 50 periods of a Halbach-type permanent magnet array and an optical cavity and the cavity length is about 7 m.

[#]kazue.yokoyama@kek.jp
* Present affiliation: High Energy Accelerator Research Organization, KEK, 1-1 Oho, Tsukuba, 305-0801 Japan

EXPERIMENTAL METHOD [6]

The input RF phase of klystron #2 and the accelerating phase in accelerating section #3 can be changed by two phase shifters independently as shown in Fig. 1. The energy spectrum can be obtained by utilizing the first 45° bending magnet of the momentum analyzer as a spectrometer. The bunch length was estimated from the energy spread by using the method as below.

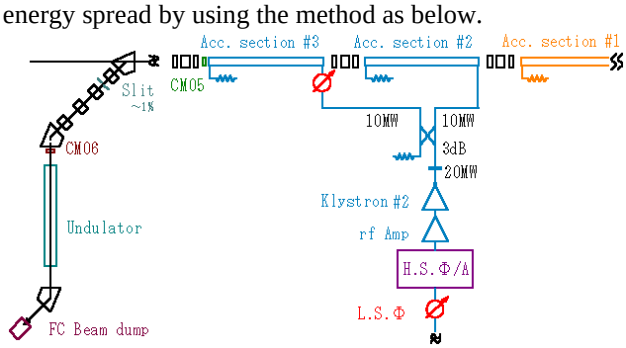

Figure 1: Layout of the FEL LINAC at LEBRA.

Maximum Energy Gain

The maximum electric field of the accelerating RF, E_P, is obtained from the maximum energy of the energy spectrum depending on the accelerating RF phase. E_0 is the total accelerating energy which beams obtain until acc-section #2 and the beam loading in acc-section #3, E_i is the beam energy after acc-section #3 and ϕ_i is the accelerating phase in acc-section #3. This correlation can be written

$$E_i = E_0 + E_P \cos\phi_i \qquad (1),$$

where the original point of ϕ_i is based on the phase with the maximum energy. E_0 and E_P can be obtained by the least-square method from the experimental data of E_i and ϕ_i.

Ellipse Parameters

To describe a beam in phase space, assuming that the distribution of the beam at any other place along the transport line is to be an ellipse space, it can be expressed

$$\gamma_0 \Delta l^2 - 2\alpha_0 \Delta l \Delta E + \beta_0 \Delta E^2 = \varepsilon \qquad (2)\ [7],$$

where α_0, β_0, γ_0 and ε are ellipse parameters and $\sqrt{\varepsilon\beta_0}$ represents the bunch length and $\sqrt{\varepsilon\gamma_0}$ represents the energy spared of the electron beam.

The vector in the longitudinal phase space at the entrance of acc-section #2 can be represented as (Δl_0, ΔE_0) and it can be transferred to (Δl, ΔE) at the linac exit, the electron beam passing through acc-section #2 and #3. Δl_0 and ΔE_0 represent position and energy relative to the electron along the central orbit, respectively. The matrix formulation can be expressed by

$$\begin{pmatrix}\Delta l\\ \Delta E\end{pmatrix}=\begin{pmatrix}1 & 0\\ g(\theta,\Delta\theta) & 1\end{pmatrix}\begin{pmatrix}\Delta l_0\\ \Delta E_0\end{pmatrix} \quad (3).$$

By using the same transfer matrix, the ellipse parameters are transformed as

$$\begin{pmatrix}\beta & \alpha\\ \alpha & \gamma\end{pmatrix}=\begin{pmatrix}1 & 0\\ g & 1\end{pmatrix}\begin{pmatrix}\beta_0 & \alpha_0\\ \alpha_0 & \gamma_0\end{pmatrix}\begin{pmatrix}1 & g\\ 0 & 1\end{pmatrix} \quad (4).$$

Three equations below can be obtained from Eq.(4);

$$\alpha(g)=\beta_0 g(\theta,\Delta\theta)+\alpha_0 \quad (5)$$

$$\beta(g)=\beta_0 \quad (6)$$

$$\gamma(g)=\beta_0 g(\theta,\Delta\theta)^2+2\alpha_0 g(\theta,\Delta\theta)+\gamma_0 \quad (7),$$

where the accelerating phase in acc-section #3 is expressed as $\theta+\Delta\theta$ when θ represents the accelerating phase in acc-section #2 and V_2 represents the maximum energy gain of acc-section #2 and #3. Approximating by the first order, $g(\theta,\Delta\theta)$ can be defined as;

$$g(\theta,\Delta\theta)=-2V_2\cos\frac{\Delta\theta}{2}\sin\left(\theta+\frac{\Delta\theta}{2}\right)\frac{2\pi}{\lambda} \quad (8).$$

At this time, Eq.(7) becomes Eq.(9) by multiplying both sides by ε because the energy spread is $\delta E=\sqrt{\varepsilon\gamma_0}$.

$$\delta E^2=\varepsilon\beta_0 g(\theta,\Delta\theta)^2+\varepsilon 2\alpha_0 g(\theta,\Delta\theta)+\varepsilon\gamma_0 \quad (9)$$

Hence, the whole electron beam can be described by knowing the ellipse parameters of Eq.(9) which are obtained from the energy spread as a function, $g(\theta,\Delta\theta)$, of θ and $\Delta\theta$ and the bunch length can be also calculated from Eq. (6).

Bunch Length Through the Analyzer System

The ellipse parameters are also transferred to Eq. (10) after the achromatic bending system;

$$\begin{pmatrix}\beta' & \alpha'\\ \alpha' & \gamma'\end{pmatrix}=\begin{pmatrix}1 & h\\ 0 & 1\end{pmatrix}\begin{pmatrix}\beta(g) & \alpha(g)\\ \alpha(g) & \gamma(g)\end{pmatrix}\begin{pmatrix}1 & 0\\ h & 1\end{pmatrix} \quad (10)$$

$$h\equiv\frac{2\rho(\vartheta-\sin\vartheta)}{E_M}=0.00125 \quad (11)$$

where ρ is the orbital radius (550 mm) and ϑ is the bending angle (45°) and E_M is the central energy depending on the purpose of experiment, respectively. The matrix formulation Eq. (10) becomes;

$$\alpha'=\alpha(g)+h\cdot\gamma(g) \quad (12)$$

$$\beta'=\beta(g)+2h\cdot\alpha(g)+h^2\gamma(g) \quad (13)$$

$$\gamma'=\gamma(g) \quad (14)$$

These equations can be calculated from the ellipse parameters in Eq. (9) and Eq. (5), (6), (7). The bunch length through the achromatic bending system can be also calculated from Eq. (13).

To investigate the bunch length of the electron beam at FEL oscillation, the energy spectra with the same central energy, which means E_M is constant, depending on the combination of θ and $\Delta\theta$ are measured.

Autocorrelation Method

The pulse length of the FEL lights around the wavelength of 1.5 μm was measured by using the interferometer based on the autocorrelation [8]. The interferometer is a Michelson-Moley type, which consists of two beamsplitters, a movable mirror and a fixed mirror as shown in Fig. 2. The interferogram is derived from the deference in path length between the light pulses split into two by a beamsplitter1 which works as a half mirror around 1.5 μm. Detector1 measures a fundamental light of the FEL and Detector2 is used for a reference. The movable mirror can move in steps of 0.1 μm. The optical pulse length is roughly estimated from multiplying the number of the interference wave by the half of the FEL wavelength.

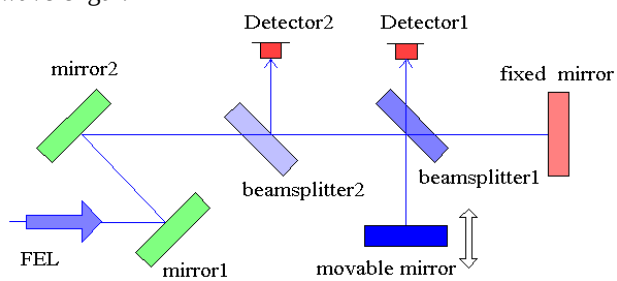

Figure 2: Layout of the interferometer.

RESULTS AND DISCUSSION

Electron Bunch Length

The result of the peak energy extracted from the energy spectrum as a function of the accelerating phase on acc-section #3 is shown in Fig. 3. Applying the least-square method, Eq. (1) was obtained as;

$$E_i=62.02+40.35\cos(\phi_i'-70) \quad (15)$$

where E_p = 40.35 comes from the result. The value of E_p corresponds to V_2 in the Eq. (8).

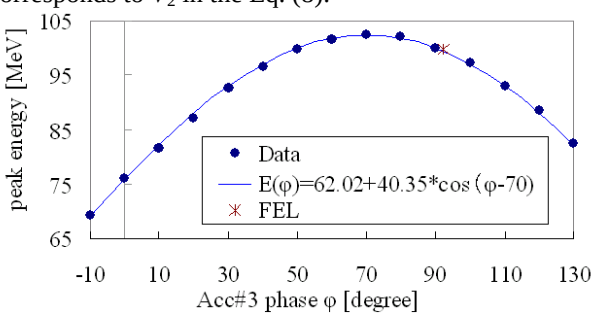

Figure 3: The electron peak energy depends on the accelerating phase. (* means the point of the observation of the maximum FEL power).

The energy spread extracted from energy spectrum which measured was by changing the accelerating phase are shown in Fig. 4. From fitting experimental data,

$$\delta E^2 = 1.94\times10^{-7} g(\phi)^2 + 2.75\times10^{-4} g(\phi) + 0.397 \quad (16)$$

was obtained. The bunch length (FWHM) at the linac exit is 0.88 mm (2.9 ps) from $2\sqrt{\varepsilon\beta_0}$ given by Eq. (6).

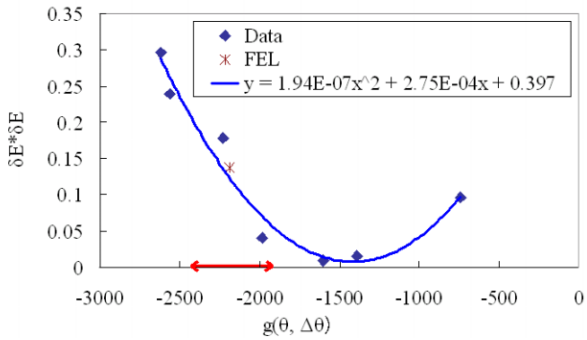

Figure 4: $g(\theta, \Delta\theta)$ and δE^2 as a function of accelerating phase and the ellipse parameters. (* means the point of the observation of the maximum FEL power. ↔ means the region of the FEL observed.).

Figure 5 shows the bunch length and the energy spread of the electron beam which supplied to FEL system. The central energy E_M is around 100 MeV and the macropulse current is about 80 mA. The point of (*) means the experimental data of which the highest power of the FEL was observed. The FEL gain was around 9% and the power was approximately 8 mJ/macropulse. The energy spread is 0.74% and the bunch length is 0.33 mm (1.1 ps) at this time. The peak current is expected to be 20 A or more.

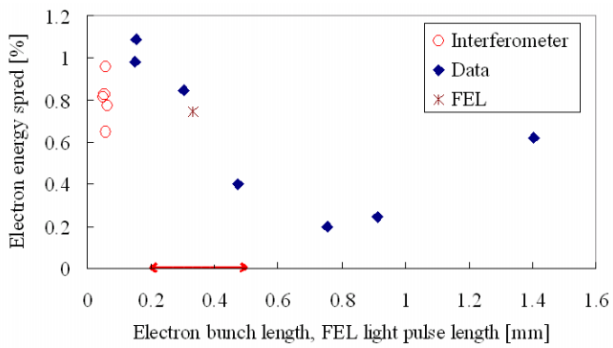

Figure 5: Electron bunch length and pulse length of the FEL light depending on the electron beam energy spread (FWHM). (* and ↔ mean the same as Fig. 4.).

Optical Pulse Length

The typical interferogram of the autocorrelation is shown in Fig. 6. The experimental beam parameter is the same as the bunch length measurements and the FEL wavelength is around 1.5 μm (3rd: 512 mm). The pulse length of the FEL light depending on the accelerating phase was measured when the FEL power is strong enough to get the interference wave from 5 to 8 mJ /macropulse. The results were shown in Fig. 5. The pulse length of the FEL light is around 0.06 mm (0.2 ps). The optical pulse length is 20% or less of the electron bunch length from the experimental results. The distribution of the electron beam which is high-density and attributable to the FEL oscillation could be narrow as interacting with the optical pulse emitted from the electrons in the undulator.

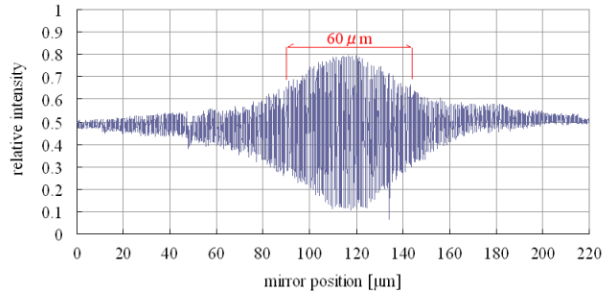

Figure 6: The typical interferogram of the autocorrelation.

CONCLUSION

It was confirmed experimentally that the bunch length at the FEL oscillation was 0.6-1.7 ps, by measuring the energy spread vs accelerating phase. The bunch length of the electron beam at the high-gain FEL amplification was around 1ps. This experimental result is consistent with the simulation [1].

The pulse length of the FEL light was extremely narrow to compare with the electron bunch length. The simulation about the correlation between the bunch length of the electron beam and the pulse length of the FEL light has proceeded at LEBRA.

REFERENCES

[1] Y.Hayakawa et al., "Characteristics of the Fundamental and 3rd Harmonic FEL at LEBRA", Nucl. Instr. and Meth. A507 (2003) 404.

[2] T.Tanaka et al., "Observation of SASE in LEBRA FEL system", To be published in Nucl. Instr. and Meth. A, Proc. of the 25th International Free Electron Laser Conference and 10th FEL Users Workshop (Tsukuba, Ibaraki, Japan, Sep.8-12, 2003).

[3] K.Hayakawa et al., "Performance of the FEL Linac at Nihon University", Proc. of this Conf.

[4] T.Tanaka et al., Proc. of the 1st Asian Particle Accelerator Conference (1998) 722.

[5] K.Yokoyama et al., "Improvement of the PFN Control system for the Klystron Pulse Modulator at LEBRA", To be published in Nucl. Instr. and Meth. A, Proc. of the 25th International Free Electron Laser Conference and 10th FEL Users Workshop (Tsukuba, Ibaraki, Japan, Sep.8-12, 2003).

[6] D.H.Dowell et al., "Longitudinal emittance measurements at the SLAC gun test facility", Nucl. Instr. and Meth. A507 (2003) 331.

[7] H.Wiedemann, Particle Accelerator Physics 1, Springer (1993) 152.

[8] C.Settakorn et al., "Impact of Experimental Conditions on Autocorrelation Bunchlength measurements", Proc. of the 2nd APAC, Beijing, China, 2001, p.728.

RF TUNING SCHEMES FOR J-PARC DTL AND SDTL

Masanori Ikegami, KEK, Tsukuba, Ibaraki 305-0031, Japan
Yasuhiro Kondo, Akira Ueno, JAERI, Tokai, Ibaraki 319-1195, Japan

Abstract

In the beam commissioning of J-PARC linac, RF phase and amplitude of RF cavities will be tuned based on the beam-phase or beam-energy measurement. In this paper, planned beam-based tuning schemes for the DTL and SDTL are presented together with the beam diagnostic layout for the tuning.

INTRODUCTION

In high-current proton linacs, precise tuning of RF amplitude and phase is indispensable to reduce uncontrolled beam loss and beam-quality deterioration. Especially, accurate RF tuning is essential for J-PARC linac [1, 2], because requirement for the momentum spread is severe ($\pm 0.1\%$ at the ring injection including jitter) to realize effective injection to the succeeding RCS (Rapid Cycling Synchrotron). To meet the requirement, tuning goals for the RF phase and amplitude are, respectively, set to ± 1 degree and $\pm 1\%$. In the beam commissioning of the linac, RF phase and amplitude are tuned based on the beam-phase or beam-energy measurement.

In this paper, planned tuning schemes for the DTL and SDTL (Separate-type DTL) are presented together with the beam diagnostic layout for the tuning. We have three DTL tanks and 32 SDTL tanks, which constitute middle energy portion of J-PARC linac. Each DTL tank is driven by a 3-MW klystron, and two neighboring SDTL tanks are driven by a 3-MW klystron. Only the klystron phase and amplitude is tuned based on the beam measurement. The relative phase and amplitude between the SDTL pair are tuned with low- and high-level RF measurements, and its procedure is out of scope of this paper.

TUNING SCHEMES

In the tuning of RF phase and amplitude of an RF cavity, a phase-scan method has widely been adopted [3]. There are a variety of phase-scan methods with different monitor setup and different approach. In the tuning of J-PARC DTL and SDTL, we are considering the following three schemes;

- Scheme I: Tank phase and amplitude are scanned with measuring the beam phase just after the tank under tuning. The output beam phase is measured with an FCT (Fast Current Transformer). Only the relative variation of output beam phase is used to find adequate RF phase and amplitude.
- Scheme II: Tank phase and amplitude are scanned with measuring the beam energy after the tank under tuning. The output beam energy is measured with two FCT's based on the TOF (Time Of Flight) method. While the beam energy is measured, only the relative variation of the beam energy is used to find adequate RF phase and amplitude.
- Scheme III: The setting is essentially the same with Scheme II, but the knowledge of the absolute output energy is used to find adequate RF phase and amplitude.

The setups for these tuning schemes are schematically shown in Fig. 1. It should be noted that the two FCT's in Scheme II and III have more than one DTL or SDTL tank in-between in our linac layout, and these tanks are detuned to avoid interference to the TOF measurement. In Scheme I and II, the required scanning ranges are modest, namely, the phase and amplitude are scanned about ± 10 deg and $\pm 5\%$, respectively. Contrary, we need a wider phase-scan (360 deg is desirable) for Scheme III. It is obvious that Scheme I is the most preferable considering its simplicity and the absence of the possible influence of idle detuned cavities, and that Scheme III is the least preferable where absolute beam energy measurements are involved. However, the applicability of these schemes is deeply dependent on the cavity characteristics. Then, we have determined the tuning schemes for each tank evaluating the applicability with PARMILA[4] simulations.

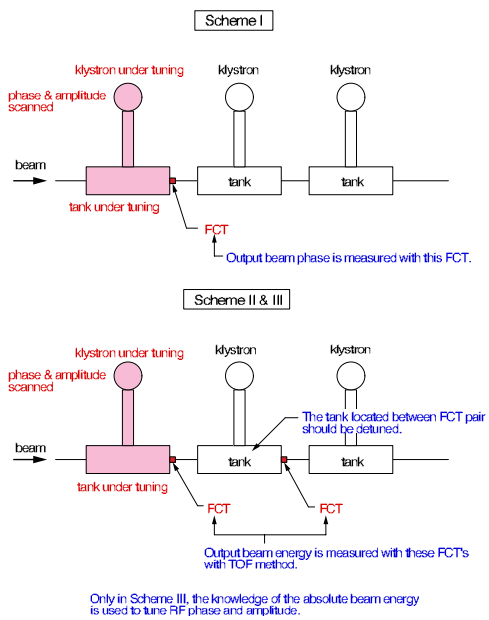

Figure 1: A schematic for RF tuning schemes.

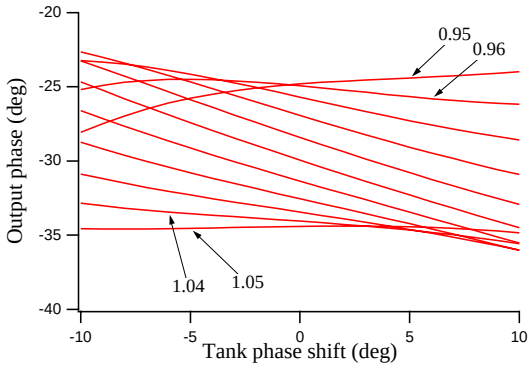

Figure 2: Simulated phase-scan curves for DTL1 (Scheme I). 11 phase-scan curves are shown for 11 different tank levels. For example, the phase-scan curve with 95 % of the design tank level is labeled as “0.95”.

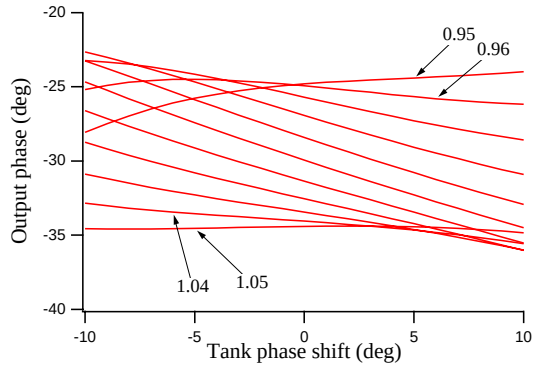

Figure 3: Simulated phase-scan curves for DTL1 (Scheme II).

DTL TUNING

DTL1 Tuning

We plan to adopt Scheme I for RF tuning of DTL1 (the 1st DTL tank). Figure 2 shows the phase-scan curves for DTL1 obtained with a PARMILA simulation. In Fig. 2, Scheme I is assumed, and 11 phase-scan curves are shown for 11 different tank-levels. The curve labeled with 0.95 shows the phase-scan curve with 95 % of the design tank level. In Fig. 2, it is readily seen that the phase-scan curve becomes flat (insensitive to the tank phase) in the right-hand side of the figure with the tank-level of 0.955, and in the left-hand side with the tank level of 1.045. Using these characteristic curves, the tank level will be calibrated. After the tank level is calibrated, the tank phase will be found using the crossing point of two phase-scan curves with different tank levels. In the RF phase calibration, two tank levels, with which phase-scan curves cross with a large crossing angle, should be selected to realize accurate phase calibration. To enable this tuning, the resolution of the phase measurement should be better than 1 deg.

DTL1 can also be tuned with Scheme II. Figure 3 shows the phase-scan curves for DTL1 with Scheme II. It is seen in this figure that the curve becomes flat with the design tank-level. We plan to adopt Scheme II as a back-up method, which needs the energy resolution of around 10 keV.

DTL2 and DTL3 Tuning

We plan to adopt Scheme II for RF tuning of DTL2 (the 2nd DTL tank) and DTL3 (the 3rd DTL tank). Figure 4 and 5, respectively, show the phase-scan curves for DTL2 and DTL3 obtained with PARMILA simulations. In these figures, Scheme II is assumed, and 11 phase-scan curves are shown for 11 different tank-levels. It is readily seen that the phase-scan curve becomes flat for DTL2 with the tank-level of 1.005. It becomes flat for DTL3 with the tank

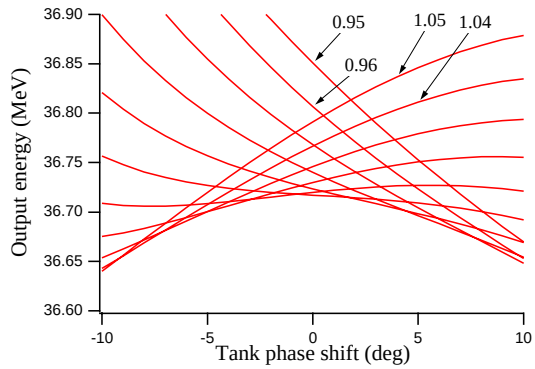

Figure 4: Simulated phase-scan curves for DTL2 (Scheme II).

level of 0.97. Using these characteristic curves, the tank level will be calibrated. After the tank level is calibrated, the tank phase will be found using the crossing point of two phase-scan curves with different tank levels. To enable these tuning, the energy resolution of around 10-20 keV is required.

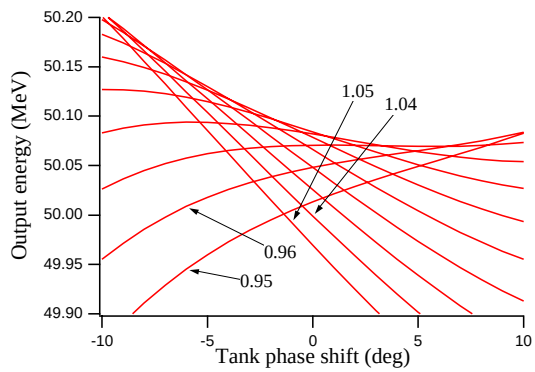

Figure 5: Simulated phase-scan curves for DTL3 (Scheme II).

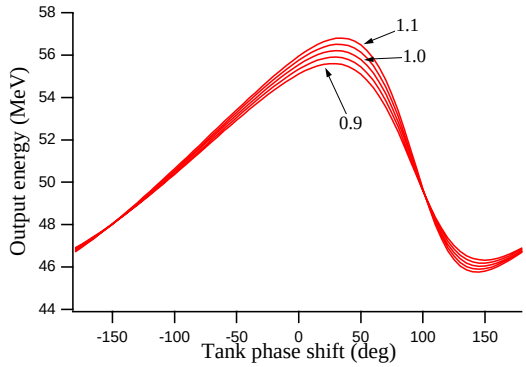

Figure 6: Simulated phase-scan curves for SDTL1-2 (Scheme III).

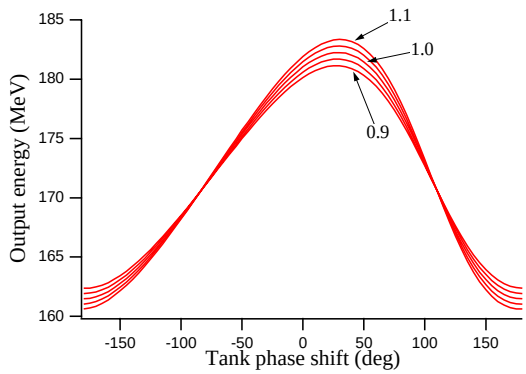

Figure 7: Simulated phase-scan curves for SDTL29-30 (Scheme III).

SDTL TUNING

As seen in the previous section, a flat part and a crossing point of phase-scan curves are required to be in the vicinity of the operation point to utilize Scheme I or II. However, the phase-scan curves for SDTL tanks are more-like a sinusoid, and they do not have a flat part and a crossing point with large crossing angle. Then, we have decided to adopt Scheme III for RF tuning of SDTL tanks. Figure 6 and 7, respectively, show the phase-scan curves for SDTL1-2 (the 1st SDTL module) and SDTL29-30 (the last SDTL module in 181-MeV operation [1]) obtained with a PARMILA simulation. In Scheme III, the phase is scanned in wider range (360 deg), and the RF amplitude will be obtained by measuring the maximum and minimum energy gain. After the RF amplitude is adjusted, the RF phase is set to give the design energy gain. To enable these tuning, the accuracy of the beam energy measurement should be better than $\pm 0.1\%$.

FCT LAYOUT

To enable RF tuning described in the previous two sections, we plan to install 45 FCT's in DTL and SDTL sections. The layout of FCT's is schematically shown in Fig. 8. In SDTL section, the TOF measurement will be performed with three idle SDTL tanks in-between to achieve required accuracy. To attain the accuracy of the TOF measurements, we plan to measure the distance between FCT's with a laser tracker with the accuracy of 0.2 mm. FCT pairs with shorter drift length are also prepared for rough TOF measurement. Utilization of these FCT pairs is discussed in a separate paper [5].

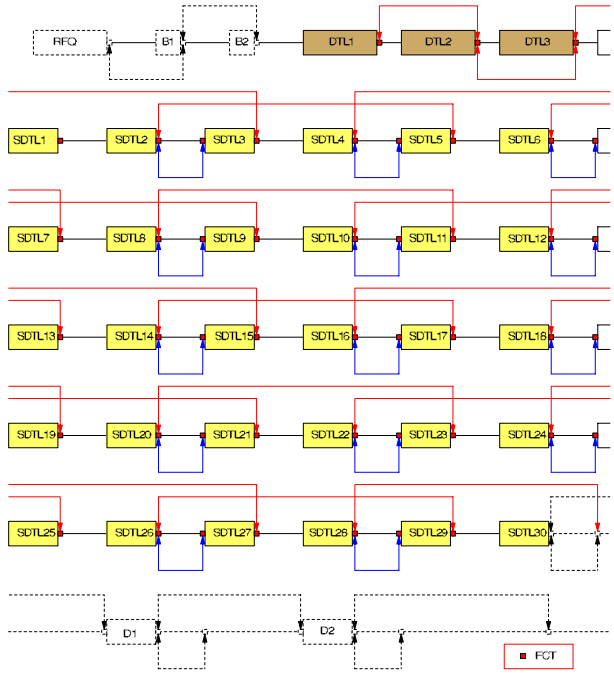

Figure 8: FCT layout in DTL and SDTL sections. Small red rectangles show FCT locations. Red arrows indicate FCT pairs for precise TOF measurement, and blue ones for rough TOF measurement.

SUMMARY

The beam-based RF tuning schemes for J-PARC DTL and SDTL are determined with PARMILA simulation. Basically, we adopt phase-scan schemes, but we use three different approaches to fit tank characteristics. FCT layout is determined to realize the tuning.

REFERENCES

[1] Y. Yamazaki, "Status of the J-PARC Linac, Initial Results and Upgrade Plan", in these proceedings.

[2] Y. Yamazaki ed., "Accelerator Technical Design Report for J-PARC", KEK Report 2002-13; JAERI-Tech 2003-044.

[3] D. Jeon et.al., "Longitudinal Tune-up of SNS Normal Conducting Linac",in Procs. of LINAC2002, p. 370 (2002).

[4] H. Takeda, "PARMILA", Los Alamos National Laboratory Report, LA-UR-98-4487 (1998).

[5] M. Ikegami et.al.,"An Alternative Scheme for J-PARC SDTL Tuning",in these proceedings.

AN ALTERNATIVE SCHEME FOR J-PARC SDTL TUNING

Masanori Ikegami , KEK, Tsukuba, Ibaraki 305-0801, Japan
Yasuhiro Kondo, Akira Ueno, JAERI, Tokai, Ibaraki 319-1195, Japan

Abstract

In the beam commissioning of J-PARC linac, we plan to perform phase-scan with precise TOF (Time Of Flight) beam-energy measurement to tune RF phase and amplitude of SDTL tanks. As a back-up method, we are considering to prepare a simpler RF tuning scheme with rough TOF measurement for SDTL which does not involve TOF measurements with idle SDTL tanks in-between. In this paper, the principle of this scheme is presented, and its advantages and disadvantages are discussed based on a systematic particle simulation.

INTRODUCTION

In the beam commissioning of J-PARC linac [1, 2], RF phase and amplitude are tuned based on the beam phase or beam energy measurement. As presented in a separate paper [3], we plan to perform phase-scan with precise TOF (Time Of Flight) beam-energy measurements in RF tuning of SDTL (Separate-type DTL) tanks. However, that scheme is presupposing an accurate TOF measurement of absolute beam energy having idle detuned cavities between beam phase monitors, which may involve technical difficulty. Then, we are considering to prepare an RF tuning scheme with rough TOF measurement as a back-up method for SDTL tuning. In this paper, the principle of this scheme is presented, and its advantages and disadvantages are discussed based on a systematic particle simulation.

ALTERNATIVE TUNING SCHEME

We have 30 SDTL tanks in SDTL section in 181-MeV operation [1], and the neighboring two SDTL tanks are driven by a 3-MW klystron. The beam energy measurement in SDTL section is performed based on the TOF (Time Of Flight) method utilizing two FCT's (Fast Current Transformers). Figure 1 schematically shows the FCT layout in SDTL section. Precise beam energy measurement is performed with a FCT pair which has three idle detuned SDTL tanks in-between. Although the accuracy of precise measurement is expected to reach 0.05 %, the measurement cannot be performed while nominal beam operation. For the beam energy measurement while nominal beam operation, additional FCT pairs with shorter drift length are prepared, to which we refer as "rough TOF pairs".

With these FCT pairs, we are able to perform rough TOF measurement of the beam energy without interfering with beam operation. The drift length in a rough TOF pair is around $2\beta\lambda$ with β and λ being the beam velocity scaled by the speed of light and the RF wave length, respectively. The accuracy of the beam energy measurement is limited to be around 0.5 % because of its short drift length. While the measurement accuracy is limited, it is advantageous that the measurement can be performed while nominal beam operation without possible influence of idle detuned cavities. We are considering two roles for the rough TOF pairs. One is the continuous watching of RF tuning to detect long-term drift or sway of RF properties. The other is the utilization for initial RF tuning of SDTL modules. The sensitivity of the former utilization is closely related to the achieved tuning accuracy of the latter. In this paper, we seek the possibility of using these pairs for initial RF tuning of SDTL tanks. It will also provide us information on the sensitivity for the watching of the long-term RF stability.

The accuracy of beam energy measurement is insufficient for precisely determining the RF phase and amplitude of an individual RF module. Our strategy for the RF tuning is to avoid undesirable build-up of the effect of errors, tolerating large phase and amplitude errors for individual RF modules. The rough TOF pairs are located after every SDTL module, and, hence, the output energy of every SDTL module can be monitored. In this tuning scheme, we first perform rough preset of the RF phase and amplitude of SDTL modules with, for example, low- and high-power RF

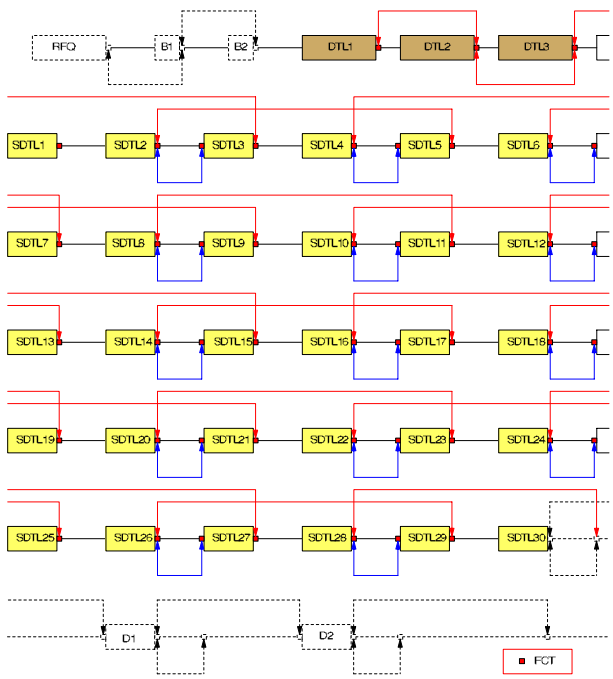

Figure 1: Schematic layout of FCT's in SDTL section (181-MeV operation). A red arrow indicates a FCT pair for presice TOF measurement, and a blue arrow rough TOF measurement.

measurements, and then we fine-tune the RF phase and amplitude to make the beam-energy deviation from its design value lower than the detectable limit at all the 15 measurement points. The RF phase and amplitude of individual SDTL module are assumed to be preset with the accuracy of around 5 deg and 5 %, respectively. In this paper, we examine the feasibility of this approach with a systematic PARMILA[4] simulation.

SIMULATION CONDITIONS

In this paper, simulations are performed with PARMILA from the exit of RFQ to the injection point to RCS for the 181-MeV case [1]. In the simulations, we assume the peak current of 30 mA, which is the design value for 181-MeV operation. The initial distribution at the exit of RFQ is obtained with PARMTEQM[5]. The number of simulation particles is 95,322 and the number of meshes is set to 20x20x40 (XxYxZ) for 3D cases and 20x40 (RxZ) for 2D cases. The quadrupole magnets in DTL and SDTL sections are set to satisfy the equipartition condition. No error has been assumed except for the RF phase and amplitude of DTL and SDTL. We assume the RF phase and amplitude of DTL tanks are set with the accuracy of 1 deg and 1%. We also assume the RF phase and amplitude of SDTL modules are preset with the accuracy of 5 deg and 5 %. The RF phase and amplitude errors are assumed to be uniform-randomly distributed in the above-mentioned range.

SIMULATION RESULTS

At first, we tried 400 cases with different random seeds with 2D space-charge option. Figure 2 shows the longitudinal rms emittance at the SDTL exit obtained in the simulation. The horizontal axis is the maximum of the output energy deviations observed at the 15 measurement points, to which we refer as “the maximum enery deviation”. It is seen in Fig. 2 that there is clear dependence of the longitudinal emittance on the maximum energy deviation, which suggests that the excess longitudinal emittance growth can be avoided by eliminating large energy deviation.

Here, we assume that we can avoid the case if the enegy deviation at the measurement points exceeds 0.5 %. The energy deviation after each SDTL module is checked for each case, and we find 42 cases in the above 400 cases which pass the test. For the selected 42 cases, we perform 3D PARMILA simulations to see the beam quality at the RCS injection in more detail. Figure 3 shows 99.9 % energy spread at the RCS injection. The requirement for the momentum spread at RCS injection is $\pm 0.1\%$ including jitter, which corresponds to ± 0.333 MeV in energy spread. The energy spread is increased by around 50 % compared to the cases with the reference tuning scheme in which each klystron is tuned with the accuracy of 1 deg and 1 % [3, 6]. However, we have confirmed that the contribution of RF setpoint errors on the final energy spread is rather small compared to that of RF dynamic errors [6]. Then, there

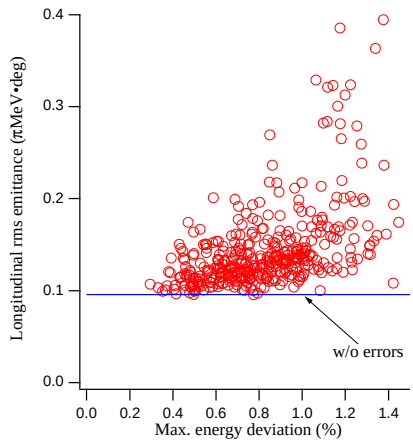

Figure 2: Longitudinal rms emittance at SDTL exit vs maximum energy deviation at 15 measurement points (2D case).

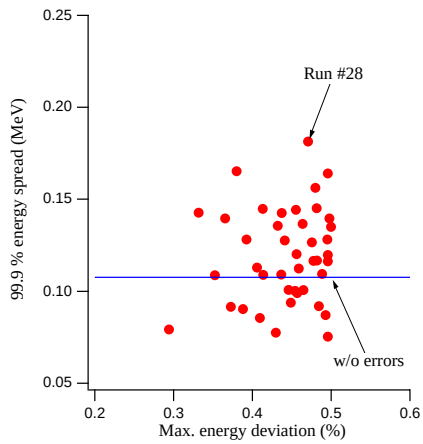

Figure 3: 99.9 % energy spread (half width) at RCS injection vs maximum energy deviation (3D case).

is a reasonable possibility to meet the requirement for the energy spread with the rough TOF-based tuning.

Figure 4 shows the 99.5 % transverse emittance at the RCS injection, in which considerable emittance growth is observed. We also have a requirement for the transvese emittance at the RCS injection (4πmm·mrad in normalized), and we have a halo collimator section in the beam transport line to meet the requirement. An excess emittance growth results in an increase of the collimator load, i.e., the fraction of a beam which must be removed at the halo collimator. Figure 5 shows the collimator load in these cases. While the collimator load nearly reaches 5 % in some cases, it is still tolerable in the 181-MeV operation. However, to be compatible with 400-MeV operation, the collimator load should be reduced to less than $\sim$ 1.5 % level, which means we need to improve the accuracy of rough TOF measurements to 0.3-0.35 %.

Figures 6 and 7 show the phase-space distributions obtained for the cases with the largest energy spread and

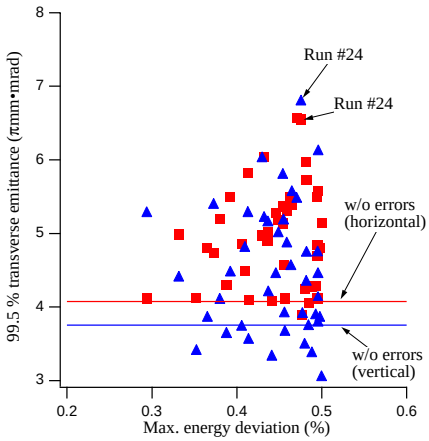

Figure 4: 99.5 % transverse emittance at RCS injection vs maximum energy deviation (3D case). Red squares show the horizontal emittance, and blue triangles the vertical.

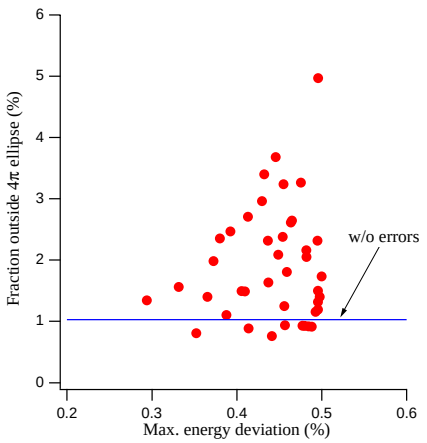

Figure 5: Halo collimator load vs maximum energy deviation (3D case).

largest vertical emittance, respectively. Figure 6 shows complicated filamentation due to combined effects of RF errors and the debunching effects, and clear halo development is seen in Fig. 7.

DISCUSSIONS

An alternative scheme for the SDTL RF tuning is proposed in this paper. Our basic strategy is to avoid undesirable build-up of the effect of errors, by eliminating the combinations of errors whose energy deviation can be detected with an array of rough TOF pairs. The proposed scheme is based on a statistical approach. Therefore, it is difficult to completely eliminate the possiblity that the undesirable effects of RF errors, which are undetectable with the rough TOF pairs, cause intolerable beam-quality deterioration. However, the simulation results suggest that these possiblities can be reduced by improving the accuracy of TOF measurements, and there is a reasonable possibility

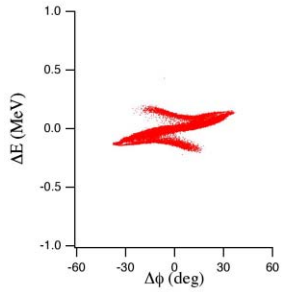

Figure 6: The longitudinal phase-space distribution at RCS injection for the case with the largest energy spread (Run #28).

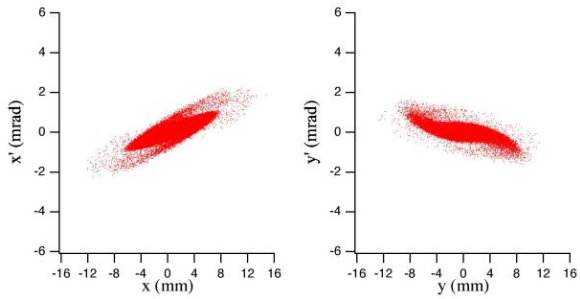

Figure 7: The transverse phase-space distribution at RCS injection for the case with the largest vertical emittance (Run #24).

that our requirement for 181-MeV operation can be met with the accuracy of 0.5 %. Based on these findings, we have concluded that it is worth while preparing the rough TOF pairs, while we need to continue the effort to improve the accuracy of rough TOF measurement. We plan to use the rough TOF pairs as both a long-term monitor of RF tuning and a back-up scheme for the initial RF tuning. We expect that it also enables swift RF retuning of SDTL modules with minimum interference with beam operation.

REFERENCES

[1] Y. Yamazaki, “Status of the J-PARC Linac, Initial Results and Upgrade Plan”, in these proceedings.

[2] Y. Yamazaki ed., “Accelerator Technical Design Report for J-PARC”, KEK Report 2002-13; JAERI-Tech 2003-044.

[3] M. Ikegami et.al., “RF Tuning Schemes for J-PARC DTL and SDTL”, in these proceedings.

[4] H. Takeda, “PARMILA”, Los Alamos National Laboratory Report, LA-UR-98-4487 (1998).

[5] Y. Kondo et.al., “Particle Distributions at the Exit of the J-PARC RFQ”, in these proceedings.

[6] M. Ikegami et.al., “A Simulation Study on Error Effects in J-PARC Linac”, in these proceedings.

BEAM-BASED ALIGNMENT MEASUREMENTS OF THE LANSCE LINAC*

R. C. McCrady#, L. J. Rybarcyk, LANL, Los Alamos, NM 87545, USA

Abstract

We have made measurements of the alignment of the Los Alamos Neutron Science Center (LANSCE) Drift Tube linac (DTL) and Side Coupled linac (SCL) using beam position measurements and analyzing them with linear models. In the DTL, we varied the injection steering and focusing lattice strengths, measured the beam position after each DTL tank, and analyzed the data with a linear model using R-matrices that were either computed by the Trace-3D computer program or extracted from analysis of the data. The analysis model allowed for tank-to-tank misalignments. The measurements were made similarly in the SCL, where the analysis model allowed for misalignments of each quadrupole doublet lens. We present here the analysis techniques and the resulting beam-based alignment measurements.

INTRODUCTION

The LANSCE linac accelerates protons and H^- ions from 750keV to 100MeV in a DTL and to 800MeV in an SCL. During beam operations, the presence of misalignments became apparent. During short (<1 day) accelerator development periods we used the particle beams to make measurements of the relative misalignment of the focusing elements in both the DTL and the SCL. These data were intended to supplement data from optical instruments that require more time, preparation and access to the beam tunnels.

Measurements of beam positions were made with profile monitors, as no beam position monitors are available in the areas of interest. To facilitate these measurements, a smaller emittance, 1mA peak beam was used.

DTL ALIGNMENT MEASUREMENTS

The DTL consists of four tanks. The drift tubes contain quadrupole magnets for transverse focusing of the beam. We can measure the beam position and angle at the entrance and exit of the DTL and the beam position between each pair of tanks. Two types of measurements were made: 1) We varied the position and angle of the injected beam and measured the effect on the beam position and angle downstream; 2) We varied the strength of the quadrupole magnets in the drift tubes and measured the effect on the beam position and angle downstream. The assumptions of the analysis models are: 1) The focusing lattice within each of the tanks is straight, 2) No x-y coupling is present, 3) A linear beam optics model is valid.

*Work conducted at Los Alamos National Laboratory, which is operated by the University of California for the United States Department of Energy under contract W-7405-ENG-36.
#mccrady@lanl.gov

Suppose the beam is injected into the DTL with measured injection position and angle (x_0, θ_0) and that there is a misalignment $(\delta_{0,1}, \phi_{0,1})$ between the injection measurement system and tank 1. The position of the beam as it exits tank 1 of the DTL will be:

$$x_1 = R_{11}\left(x_0 + \delta_{0,1}\right) + R_{12}\left(\theta_0 + \phi_{0,1}\right) + \delta_1 \qquad (1)$$

where δ_1 is an offset in the measurement and R_{mn} is the $(m,n)^{th}$ element of the transport matrix[1] from the injection point through DTL tank 1 to the beam position measurement device. This equation can be applied to both the vertical and horizontal planes. A set of such equations can be formed by making N measurements of x_1 with different injection parameters or with different focusing lattice strengths (which varies the R-matrix elements.) To determine the misalignment parameters and measurement offset, the set of equations can be written in the form $A \cdot x = b$ where A is an $N \times 3$ matrix, b is a vector of the N measurements and x is the vector of the three quantities to be estimated. This over-determined matrix equation can be solved by a variety of techniques; we employed the method of singular value decomposition. (See, for example, reference [2].)

When the injection parameters are varied, the matrix equation is:

$$\begin{bmatrix} R_{11} & R_{12} & 1 \\ R_{11} & R_{12} & 1 \\ \vdots & \vdots & \vdots \end{bmatrix} \begin{bmatrix} \delta_{0,1} \\ \phi_{0,1} \\ \delta_1 \end{bmatrix} = \begin{bmatrix} x_1(1) - R_{11}x_0(1) - R_{12}\theta_0(1) \\ \vdots \\ x_1(N) - R_{11}x_0(N) - R_{12}\theta_0(N) \end{bmatrix}$$

When the focusing lattice strength is varied, the matrix is equation is:

$$\begin{bmatrix} R_{11}(1) & R_{12}(1) & 1 \\ \vdots & \vdots & \vdots \\ R_{11}(N) & R_{12}(N) & 1 \end{bmatrix} \begin{bmatrix} \delta_{0,1} \\ \phi_{0,1} \\ \delta_1 \end{bmatrix} = \begin{bmatrix} x_1(1) - R_{11}(1)x_0 - R_{12}(1)\theta_0 \\ \vdots \\ x_1(N) - R_{11}(N)x_0 - R_{12}(N)\theta_0 \end{bmatrix}$$

(The indices in parentheses indicate the measurement number.) The R-matrix elements can computed using a model of the DTL and the Trace-3D computer program[3], however for tank 1 we were able to extract the values of the R-matrix elements from the data.

One cannot distinguish the three fit parameters by varying the injection alone since each produces a constant offset in the measurements. These measurements can be useful when combined with those taken when the focusing lattice strength is varied.

For measurements of the beam position made downstream of DTL tanks 2, 3 and 4 additional terms for tank-to-tank misalignments must be included in Equation 1. The beam position measured downstream of tank j will be:

$$x_j = R_{11}^{0\to j} x_0 + R_{12}^{0\to j}\theta_0 + \sum_{i=0}^{j-1}\left(R_{11}^{i\to j}\delta_{i,i+1} + R_{12}^{i\to j}\phi_{i,i+1}\right) + \delta_j$$

where $R_{mn}^{i\to j}$ is the $(m,n)^{th}$ component of the transport matrix from the beam position measurement device downstream of tank i to that downstream of tank j (with i=0 indicating the injection area,) ($\delta_{i,i+1}$,$\phi_{i,i+1}$) are the misalignment offset and angle between tanks i and $i+1$, and δ_j is the offset in the measurement device downstream of tank j.

Measurement of R-matrix Elements

The analysis model for the misalignment measurements relies on our ability to calculate the transport matrix elements through the DTL tanks; we were especially concerned about our ability to accurately calculate the transport matrices in tank 1 since the focusing by the accelerating field is strongest in this tank due to the low kinetic energy (<5MeV) of the beam. Because we measure the position and angle of the beam at the injection into tank 1 and the position at the exit, we can measure $R_{11}^{0\to1}$ and $R_{12}^{0\to1}$, the R-matrix elements from the injection through tank 1, by making measurements with N settings of the injection parameters and solving a matrix equation of the following form:

$$\begin{bmatrix} x_0(1) & \theta_0(1) & 1 \\ \vdots & \vdots & \vdots \\ x_0(N) & \theta_0(N) & 1 \end{bmatrix}\begin{bmatrix} R_{11} \\ R_{12} \\ c \end{bmatrix} = \begin{bmatrix} x_1(1) \\ \vdots \\ x_1(N) \end{bmatrix}$$

where the constant c is the constant offset produced by the misalignment and the measurement offset.

Table 1: Comparison of measured and calculated transport matrix elements for H^- beam through DTL tank 1

	Measured	Calculated
R_{11}	+0.9 ±0.2	+0.7 ±0.2
R_{12} (mm/mrad)	+0.00 ±0.06	+0.15 ±0.05
R_{33}	+0.9 ±0.2	+1.1 ±0.2
R_{34} (mm/mrad)	+0.10 ±0.01	+0.07 ±0.05

The uncertainties shown for the calculated values reflect the effect of small changes to the accelerating fields in the model.

Because of additional uncertainties in the calculated values of the transport matrix elements, we used these measured values in the analysis of the misalignment data.

Measurements of Tank-to-Tank Misalignments

The results of the beam-based tank-to-tank misalignment measurements are shown in Table 2. We did not get a good measurement of the misalignment between tanks 1 and 2 because of the uncertainty in computing the transport matrix elements through tank 1. (We couldn't measure all that were required for the analysis, namely R_{21} and R_{43}, because there is no way to measure the beam angle between these two tanks.)

Ultimately we will compare these beam-based measurements with optical survey data. We have recently acquired a laser tracker and associated tooling for this purpose, and measurements are in progress.

Table 2: Beam-based misalignment measurements of the DTL

Parameter	Beam-Based Measurement
Horizontal $\delta_{0,1}$	−0.8 ±0.5 mm
Horizontal $\phi_{0,1}$	+6.4 ±1.5 mrad
Vertical $\delta_{0,1}$	+1.7 ±0.2 mm
Vertical $\phi_{0,1}$	+0.6 ±1.5 mrad
Horizontal $\delta_{2,3}$	+0.9 ±0.1 mm
Horizontal $\phi_{2,3}$	−1.3 ±0.2 mrad
Vertical $\delta_{2,3}$	+0.4 ±0.1 mm
Vertical $\phi_{2,3}$	−0.5 ±0.1 mrad
Horizontal $\delta_{3,4}$	−3.6 ±0.2 mm
Horizontal $\phi_{3,4}$	+0.6 ±0.1mrad
Vertical $\delta_{3,4}$	+0.7 ±0.1mm
Vertical $\phi_{3,4}$	+0.9 ±0.1 mrad

Sources of Errors and Improving the Measurements

The uncertainty in the actual distribution of the accelerating fields in the DTL complicate the calculation of the transport matrices, especially where the beam energy is low. Making the measurements with the accelerating fields turned off could make these calculations more reliable, however the focusing lattice strength would need to be changed drastically from the operational condition since the un-accelerated beam is not stable in the normal lattice.

One assumption in the model for these measurements is that each tank of the DTL is straight, i.e. that the magnetic centers of all of the quadrupole magnets lie on a line. Tanks 2, 3 and 4 are each 15 to 20m long and mechanically supported at locations between the two ends. Bending moments produced by these supports or by thermal gradients in the structures could distort the magnetic axis and render this assumption invalid. Additionally, random or other systematic misalignments of the drift tubes within a tank could render this assumption invalid. One could determine a lower limit on the straightness by attempting to find a beam trajectory upon which no beam deflection occurs as the quadrupole strengths are varied; we have not yet made this measurement.

SCL ALIGNMENT MEASUREMENTS

The SCL at LANSCE accelerates beams from 100MeV to 800MeV. The focusing lattice consists of quadrupole doublets between each pair of accelerating tanks. We wished to measure the misalignment offsets of the

quadrupole doublets, i.e. misalignment angles were not considered.

When a beam that is traveling at a position and angle specified by (x_{in}, θ_{in}) relative to the reference trajectory traverses a quadrupole doublet whose center is displaced by a distance δ from the reference trajectory, the beam exiting the doublet will travel as specified by:

$$x_{out} = \left(R_{11}{}^{Q} x_{in} + R_{12}{}^{Q} \theta_{in}\right) + \delta(1 - R_{11}{}^{Q})$$

$$\theta_{out} = \left(R_{21}{}^{Q} x_{in} + R_{22}{}^{Q} \theta_{in}\right) - \delta R_{12}{}^{Q}$$

where the R-matrix elements $R_{mn}{}^{Q}$ are those from the entrance to the exit of the quadrupole doublet. The measured position of the beam at location j after passing through M such doublets will be:

$$x_j = x_0 R_{11}{}^{0\to j} + \theta_0 R_{12}{}^{0\to j} + \sum_{i=1}^{M} \delta_{Q(i)} \left[R_{11}{}^{Q(i)\to j} (1 - R_{11}{}^{Q(i)}) - R_{11}{}^{Q(i)\to j} R_{11}{}^{Q(i)} \right] + \delta_j$$

The sum is over all quadrupole doublets upstream of the measurement location. As before, δ_j is the offset in the measurement device and (x_0, θ_0) are the injection parameters. The transport matrix elements $R_{mn}{}^{Q(i)}$ and $R_{mn}{}^{Q(i)\to j}$ are those from the entrance to the exit of the doublet, and from the exit of the doublet to the beam position measurement location respectively. $R_{mn}{}^{0\to j}$ is the transport matrix element from the injection point to the j^{th} beam position measurement device. The accelerating fields were turned off during these measurements in order to enable more reliable calculation of the transport matrices.

One can make measurements of beam positions in the linac with several sets of injection parameters, create an over-determined set of linear equations and solve the equations for the quantities of interest, namely the $\delta_{Q(i)}$'s and δ_j's. However a system of equations where only the injection parameters are varied does not allow one to distinguish misalignments from measurement offsets; one must vary the quadrupole strengths.

A data set, where the beam injection alone was varied, is in hand. In future beam development periods we will collect data with variations in the focusing lattice strength.

SUMMARY

One can make measurements of DTL tank-to-tank misalignments and of the misalignments of the individual quadrupole doublets in an SCL using particle beams. Because these measurements are made with the beam itself, they are an essential complement to optical measurements.

In order to distinguish between component misalignments and offsets in the measurements one needs to make measurements with various settings of the focusing lattice strength. Varying the beam injection steering reduces the uncertainties in the measurements and allows direct measurement of the transport matrix elements that are required in the analysis of the data.

The ability to accurately calculate transport matrices through the DTL was a limiting factor in the analysis presented here. Making the measurements with the accelerating fields turned off, as was done in the SCL, would reduce the uncertainty in the calculation, but this requires extensive manipulation of the focusing lattice strength, and thus a great deal more time. Additionally it may change the effective centerline of the tank since the defocusing of the accelerating fields would be removed.

REFERENCES

[1] K. L. Brown, F. Rothacker, D. C. Carey, Ch. Iselin, "TRANSPORT A Computer Program for Designing Charged Particle Beam Transport Systems," CERN 80-04, 1980.

[2] W. H. Press, B. P. Flannery, S. A Teukolsky, W. T. Vetterling, "Numerical Recipes," Cambridge University Press, 1986.

[3] K. R. Crandall and D. P. Rusthoi, "Trace-3D Documentation," LA-UR-97-886, 1997.

THE LANSCE LOW MOMENTUM BEAM MONITOR*

Rob Merl#, Floyd Gallegos, Chandra Pillai, Stuart Schaller, Fred Shelley, Andy Steck, Los Alamos National Laboratory, Los Alamos, NM 87545, USA
Benjamin J. Sanchez, ORNL, Oak Ridge, TN 37831, USA

Abstract

A diagnostic has been developed at the Los Alamos Neutron Science Center (LANSCE) for the purpose of identifying low momentum beam tails in the linear accelerator. These tails must be eliminated in order to maintain the transverse and longitudinal beam size. Instead of the currently used phosphor camera system, this instrument consists of a Multi Wire Proportional Chamber (MWPC) detector coupled to an EPICS compliant VME-based electronics package. Low momentum tails are detected with a resolution of 5 mm in the MWPC at a high dispersion point near a bending magnet. While phosphor is typically not sensitive in the nano amp range, the MWPC is sensitive down to about a pico amp. The electronics package processes the signals from each of the MWPC wires to generate an array of beam currents at each of the lower energies. The electronics has an analog front end with a high-speed analog to digital converter for each wire. Data from multiple wires are processed with an embedded digital signal processor and results placed in a set of VME registers. An EPICS application assembles the data from these VME registers into a display of beam current vs. beam energy (momentum) in the LANSCE control room.

ARCHITECTURE

The diagnostic is composed of a MWPC detector wired to a VME crate containing eight custom data acquisition and processing boards as shown in figure 1.

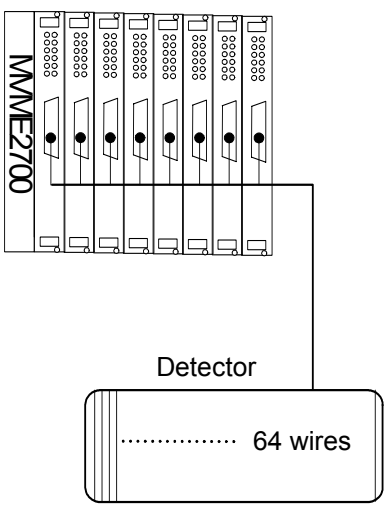

Figure 1: The 64 detector wires are supported by a remote VME crate with eight custom processing boards and a Motorola MVME2700 processor.

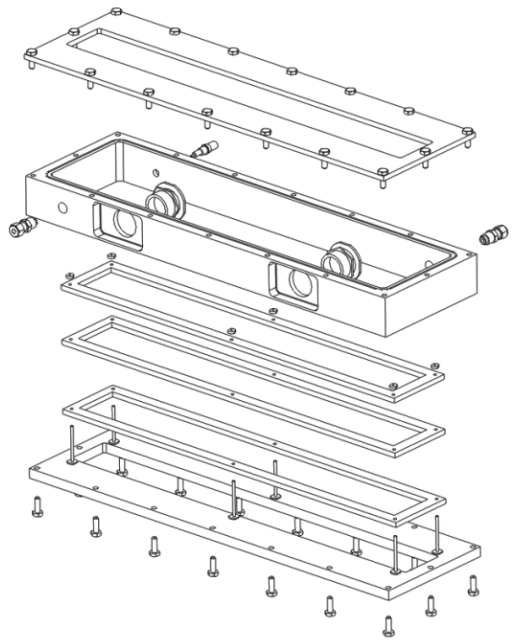

Figure 2: Solid Model drawing of detector assembly.

The detector is gas filled and contains 64 wires. The electronics supports them with 64 individual parallel processing channels in the VME crate.

There are cables containing 64 individual twisted pairs running from the detector to the VME crate. Each custom VME board handles eight of the 64 detector wires. The detector is located in the LANSCE beam tunnel just down stream and inboard from the XDBM04 bending magnet.

800 MeV beam entering this magnet is bent toward the experimental areas. Beam components at lower energies, however, are bent in a tighter radius and hit an inboard beam stop. These are the low energy components that should be eliminated. The detector is placed between this bending magnet and the beam stop so it can measure the magnitude spectrum of beam currents over a range of unwanted low energies [1].

MULTIWIRE CHAMBER

The chamber contains 64 gold plated tungsten wires that are stretched across a fiberglass frame. The wires are 5 mm apart and sit between two high voltage plates. The high voltage plates are made of 25 μm aluminum foil also supported by fiberglass frames. The area inside the frames is 50 cm x 6 cm or 300 square cm. The wires and high

*Work supported by the U.S. Department of Energy.
#merl@lanl.gov

voltage plates are housed in an aluminum enclosure with hermetic gas, high voltage, and signal connectors. The enclosure is filled with a 10% methane – 90% argon gas mixture. A 100 μm thick aluminum foil window allows beam to enter the enclosure [2].

When a particle traverses the detector, it produces electrons by ionization, which are then multiplied by the strong electric field around the wire. The gain of the detector increases with the amount voltage on the foil plates. The current multiplication factor, M, for this multiwire chamber is given by equation (1) below [3].

$$M = \exp\left[2\sqrt{\frac{akNCVo}{2\pi\varepsilon_o}}\left(\sqrt{\frac{Vo}{Vt}}-1\right)\right] \quad (1)$$

Where k = 1.81×10^{-17}cm^2/V, which the Townsend constant, N is the number of molecules per unit volume, C is the capacitance between the wire and the plate, ε_0 is

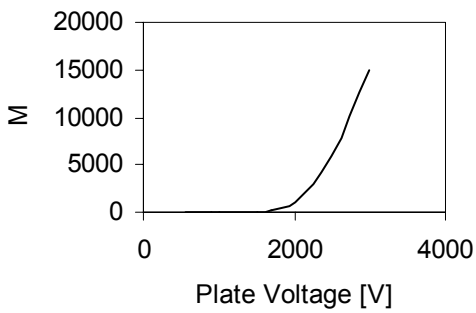

Figure 3: The multiplication factor, M, plotted as a function of plate voltage.

8.85pF/m, and a is the radius of the wire. Vo is the voltage on the foil and V_t is the threshold voltage, which is 1500 volts in this case.

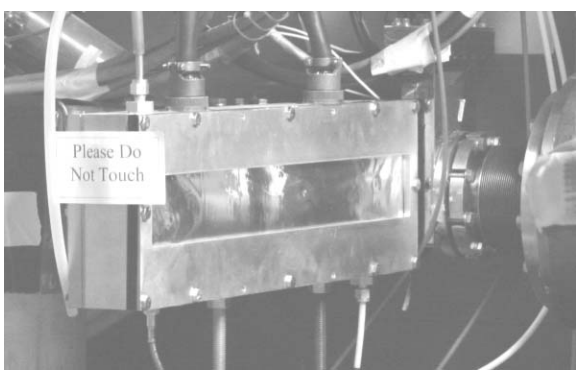

Figure 4: The detector in place in the LANSCE switchyard beam tunnel.

The multiplication factor is plotted vs. plate voltage in figure 3. At 3kV, the multiplication factor is 1.5×10^4.

SIGNAL

When a particle traverses the detector wire a fast current pulse is produced. The simplest processing method is to count these pulses and the electronics have been designed to do this in addition to a more sophisticated integration technique. Integration of the pulses is preferred because the bandwidth of the cable plant is slow compared to the raw pulses, which causes pile-up. Once that happens, individual pulses can no longer be separately counted.

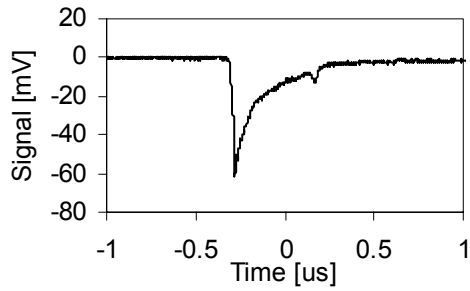

Figure 5: Raw pulse from detector wire showing pile-up problem.

A typical pulse from a detector wire is shown above in figure 5. The pile-up problem can be observed with a -20 mV pulse partially absorbed into the –60 mV pulse that preceded it. Integrating, on the other hand, allows us to calculate the rate at which charge is collected on each detector wire.

DIGITAL SIGNAL PROCESSING

Each detector wire has its own signal conditioning electronics, analog to digital converter (ADC), and field programmable gate array (FPGA) for digital signal processing [4]. Furthermore, there is a dedicated digital signal processor for every eight wires used to perform floating-point math. Frequency analysis of the input signal has shown that there are no significant components above 1.5 MHz [1]. The signal is then bandwidth limited to 5 MHz by an analog signal conditioner and digitized at 10 MHz. The FPGA processes the digitized data at the full 10 MHz.

The gate for this integration is generated internally by the FPGA based on a trigger pulse from the LANSCE master timer [5]. Gates at LANSCE are not longer than 1 ms and the hardware supports programmable gates up to 6.5 ms. Integrals have to be calculated at the LANSCE beam repetition rate, which is 120 Hz.

The integral, equation (2), is formed partially in the FPGA and then completed in the DSP as shown by the signal processing block diagram in figure 6. In equation (2), and in figure 6, n is the sample number within the integration gate, x_n is the digitized sample, T is the sample time, 1 / 10 MHz, and y_n is the integrated output.

The FPGA uses an accumulator-based technique to form a partial integral using fixed-point math. It can do this in real time at the full rate of the ADC.

$$y_n = T\left[\frac{1}{2}[x_0 + x_n] + \sum_{i=0}^{n-1} x_i\right] \qquad (2)$$

The FPGA collects the first sample, x_0, the last sample, x_n, and accumulates all the samples in between. It then hands this information off to the DSP at 120 Hz to form the complete integral using floating-point math. The result is further processed by the DSP with a six pole low pass filter before being delivered to the EPICS control system for display in the LANSCE central control room [6].

A block diagram of the process is shown in figure 6. A 14-bit digital signal flows into the left side of the block diagram and is processed by the FPGA. Inside the FPGA, the timing hardware selects the first and last sample inside the integration gate and stores them in the registers marked x_0, and x_n, respectively. It accumulates the samples in between, x_1 and x_{n-1}. The analog and digital

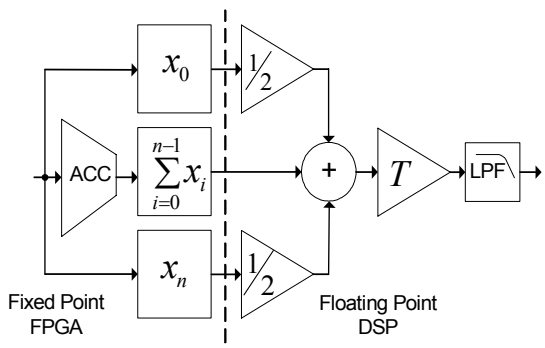

Figure 6: Signal processing block diagram.

electronics are bipolar and the accumulator can accommodate both negative and positive values in real time using two's complement math. The FPGA operates at 10 MHz while the integration gate is open, then stops and holds its values when the gate closes. The floating point DSP on each VME board then reads the x_0, x_n, and $\Sigma(x_n)$ values for further processing. This method allows for complete processing of the signal inside the VME crate. Only low bandwidth results need to be sent over the network. The resulting spectrum may be displayed directly on an EPICS screen.

MEASUREMENT

A first order measurement with this detector has been performed using a cobalt-60 source. With the source placed about 2 cm from the detector an end-to-end measurement was made. The spectrum measured with the source in front of wire #16 is shown in figure 7. For this measurement, only the first 40 of the full set of 64 wires were used.

The graph shows that the detector, electronics, and cable plant can process low energy beam components down to less than 20 pA or around 10,000 particles per wire.

FUTURE

Now that the detector is installed and the electronics have been tested, we are looking forward to tuning the LANSCE linear accelerator with the aid of this new diagnostic.

In practice, all 64 wires will be used and the x-axis will be relabeled for the beam energy each wire corresponds to 350 MeV to 750 MeV.

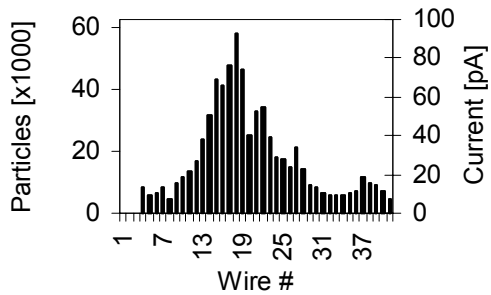

Figure 7: Measured spectrum using a Cobalt-60 source.

REFERENCES

[1] Rob Merl, Charles Burns, Floyd Gallegos, Chandra Pillai, Fred Shelley, Andy Steck "A Multiwire Proportional Chamber System For Monitoring Low Momentum Beam In Accelerators," PAC 2003, Portland OR, May 2003.

[2] Jim Witt, Los Alamos National Laboratory, private communication.

[3] "Experimental Techniques in High Energy Physics", Allan Wylde, 1987, Addison-Wesley, p 130.

[4] R. Merl, F. Gallegos, C. Pillai, F. Shelley, "High Speed Epics Data Acquisition And Processing On One VME Board", PAC 2003, Portland OR, May 2003.

[5] Michael Oothoudt, Stuart Schaller, Eric Bjorklund, Mary Burns, Gary Carr, John Faucett, David Hayden, Mathew Lusk, Robert Merl, Jerry Potter, Jerome Reynolds, Dolores Romero, and Fred Shelley, Jr, "The LANSCE Rice Control System Upgrade PAC 2003, Portland OR, May 2003.

[6] L. R. Dalesio, et al., "The Experimental Physics and Industrial Control System Architecture: Past, Present and Future," Proceedings of the International Conference on Accelerator and Large Experimental Physics Control Systems, 1993, pp. 179-184.

PRECISION ALIGNMENTS OF STRIPLINE BPM'S WITH QUADRUPOLE MAGNETS FOR TTF2

D. Noelle, G. Priebe, M.Wendt and M. Werner,
Deutsches Elektronen Synchrotron DESY, Notkestr. 85, D-22603 Hamburg

Abstract

Due to the absence of synchrotron radiation in a linac like the TESLA Test Facility (TTF2), it is possible to install the beam position monitors (BPMs) inside the quadrupoles, defining the optical axis of the accelerator. This paper reports on an alignment setup and the procedure, using the stretched wire technique to calibrate the BPMs with respect to the magnetic axis of the quadrupole magnet.

INTRODUCTION

The control of the beam orbit is essential for the operation of linear accelerators for future linear colliders (LC), as well as for free electron laser (FEL) drive linacs. The transport of the beam, by preserving its low emittance, requires a precise measurement of the beam orbit with respect to the magnetic axis of the quadrupoles. As a beam based alignment procedure is not always applicable (common quadrupole power supplies), or sometimes may not give satisfactory results (shot-to shot beam jitter), a stretched wire alignment measurement for quadrupole and BPM pickup can be used as an alternative or add-on.

MEASUREMENT PRINCIPLE

The optical axis of an accelerator is defined by the magnetic axis of the focussing elements, i.e. the quadupoles. Only if the beam is following this axis as close as possible, the machine will achieve optimum performance. Therefore, it is essential to have the BPMs as close and as well aligned to the quadrupoles as possible. Since there is almost no synchrotron radiation in a linac, it is possible to install the BPM inside the quadrupoles without the danger that movements of the vacuum chamber due to heat load will move the quadrupole or the BPM with respect to the quadrupole.

Due to the rigid connection between the two units, it is also possible to determine the offset of the BPM and quadrupole, caused by manufacturing tolerances, before installation on a test bench.

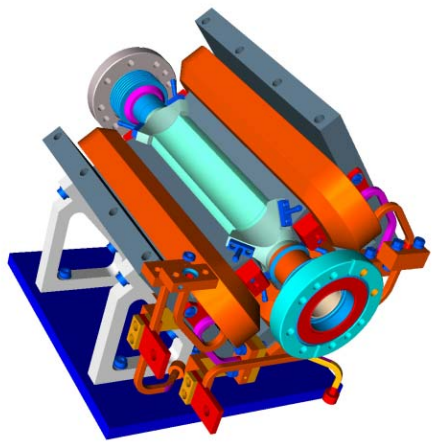

Figure 1: Drawing of a TTF2 stripline installed inside a quadrupole magnet.

The test bench uses a stretched wire, to determine

a) the magnetic axis of the magnets, by measuring an minimizing movements of the wire introduced by current pulses: If a current pulse is passing the wire, while the magnetic field of the quadrupole is present, Lorence force will induce movements of the wire, except if the wire is passing on the magnetic axis.
b) To determine the electrical axis of the BPM within the same reference frame, by using the wire as an antenna for incoupling of an RF signal. This signal is read by two opposite pickups of the BPM. If the wire is exactly on the electrical axis, the difference of the two signals will cancel.

Since we are dealing with no perfect mechanical systems, one has to find the minimum signal for wire movement and antenna signal. The difference of the transverse positions, where the minimum signals are found, is then the BPM offset, to be used as calibration data for the orbit measurement system.

THE STRECHED WIRE TEST BENCH

This idea [1] was already adapted for a few stripline BPM-quadrupole units, used at the S-Band Test Facility linac [2], and is now applied under cleanroom conditions for larger quantities for TTF2.

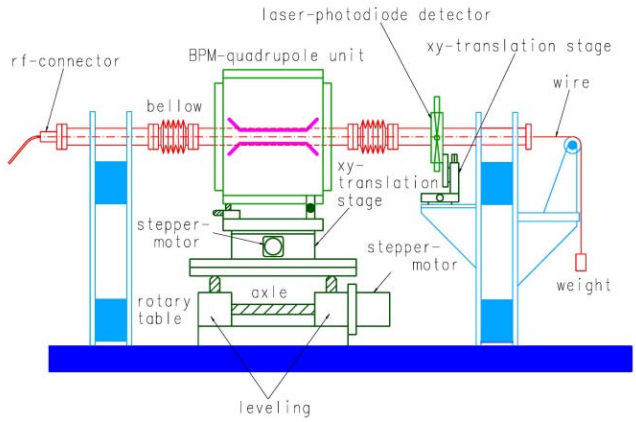

Figure 2: Schematic view of the stretched wire alignment setup.

Fig. 2 shows a schematic view of the stretched wire test bench with it's basic elements. An aluminium plate carries the BPM-quadrupole unit on a stepper-motor movable xy-translation stage. Two rigid pillars fix the beam-pipe sections, which adapts to the movable BPM pipe in the center via bellows. A 130 µm diameter, copper-beryllium wire is stretched in the center of the beam pipe and forms a coaxial transmission line. The current pulses to measure the magnetic axis, and the rf-signals to find the electrical axis of the BPM are feed from an upstream N-connector. A laser-photodiode detection system, located on the downstream pillar, is used to detect movements of the wire, in order to find the magnetic center of the quadrupole. The distance between this detector and the end of the wire has to be longer than the half of the magnet length, in order to separate signal and reflections. Other parts of the test bench are a defined mass to stretch the wire and some mechanical elements to compensate a tilt between BPM-quadrupole and wire. The laser-photodiode detector can also be moved by a manual xy-translation stage.

The calibration procedure is done in two steps:

CALIBRATION OF THE MAGNETIC CENTER OF THE QUADRUPOLE

A method to measure the effect of a magnetic field on a stretched wire, excited with a strong, but short pulse of charge Q is described in [3], [4]. The *Lorenz* force accelerates the part of the wire, on which the magnetic field B acts, in transverse direction. This displacement of the wire

$$x(z_0,t)=\frac{Q}{2\mu c}\int_{z_0}^{z_0-ct}B(\bar{z})d\bar{z} \qquad (1)$$

moves with the wave velocity $c=\sqrt{T/\mu}$ towards upstream and downstream fixpoints of the wire and can be detected at a location z_0 behind the magnet with the laser-photodiode detector (μ is the weight per unit length of the wire, T is the tensile force to which the wire is stretched).

Before starting the calibration procedure the magnet was cycled using a bipolar power supply. Then the magnet was powered with 25 % of it's nominal current (≈100A). A pulse of 400V, 20A and 10µs lengths was feed into the stretched wire. The magnet was then moved in a way that the signal from the photodiodes gets minimum value. This reading corresponds to the magnetic axis of the quadrupole, and defines the *reference position*.

The movement of the BPM-quadrupole unit was done by computer controlled stepper motors with a resolution of 5µm (hor.) resp. 0.6µm (vert.) Being close to the magnetic center also the tilt between wire and magnetic axis was minimized.

From this reference position –micrometer gauges and step counter are set to zero – we started the second step of the procedure:

CALIBRATION OF THE ELECTRICAL CENTER OF THE STRIPLINE BPM

In this step the wire is used as an antenna to produce RF-signals on the electrodes of the BPM. A difference signal of two opposite electrodes of the stripline BPM was produced by wiring well calibrated, phase-stable semi-rigid coaxial cables and a *M/A-COM H-9* 180° broadband hybrid. With a network analyzer a frequency-domain $|S21(f)|$ measurement was set up between stretched wire and the Δ-signal output. Reflections in the non terminated stretched wire pipe are not important, as the measurement was performed for a single frequency (zero-span mode). By moving the BPM-quadrupole unit with the stepper motors and appropriate settings of the network-analyzer (*f*center = 180MHz, *f*RBW= 100Hz, *t*sweep= 5s) it was easily possible to minimize $|S21|$ down to the -100dBm noise level. The signal minimum could be identified clearly within a single step in the horizontal (step size: 5µm) and 2..3 steps in the vertical plane (step size: 0.6µm).

When both planes show a minimum of the Δ-signal transfer, the wire was in the electrical center of the stripline BPM. The *xy-offset* between magnetic center of the quadrupole and electrical center of the stripline BPM was evaluated by counting the driven steps, and cross-checked with the micrometer gauge readings.

RESULTS

23 BPM-quadrupole units were calibrated with the stretched wire alignment setup. Each measurement was performed twice, the setup was de-adjusted and partially demounted between individual measurements. The results are shown in Fig. 3. As expected 200...300 µm offsets typical for mechanical construction tolerances show up. While the resolution to identify the BPM center is in the range 1...2 µm, the identification of the magnetic center is

limited to 10...20 µm, dominating the resolution of the complete setup. This is due to several facts, like stray fields, wire diameter, laser focussing, mechanical vibrations, etc. and, in the horizontal plane, the rather large step size of the motor system.

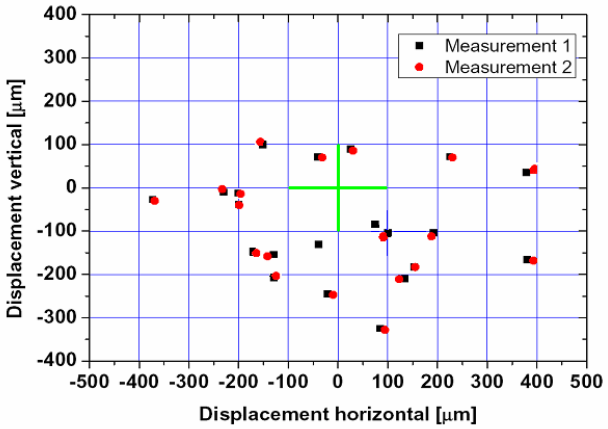

Figure 3: Results of the stretched wire alignment procedure.

The offset data taken by this measurement will be included as calibration data in the BPM readout system.

REFERENCES

[1] G. E. Fischer, et. al., “Finding the Magnetic Center of a Quadrupole to High Resolution”, SLAC-TN-89-01, 1989, U.S.A.

[2] F. Brinker, et. al., “Precision Alignment of BPM’s with Quadrupole Magnets”, Proc. of the 18rd Int. Linac Conf. LINAC 96, Geneva (1996), Switzerland, pp.502-504

[3] R. W. Warren, “Limitations on the Use of the Pulsed-Wire Field Measuring Technique”, NIM A272 (1988), pp.257-263

[4] A. Geisler, et. al., “The Pulsed-Wire Method”, DELTA Int. Rep. 94-4 (1994), University of Dortmund, Germany

SYSTEMATIC CALIBRATION OF BEAM POSITION MONITOR IN THE HIGH INTENSITY PROTON ACCELERATOR (J-PARC) LINAC

S. Sato*#, Z. Igarashi†, S. Lee†, T. Tomisawa*, F. Hiroki*, J. Kishiro*,
M. Ikegami†, Y. Kondo*, K. Hasegawa*, A. Ueno*, T. Toyama†,
N. Kamikubota†, K. Nigorikawa†, M. Tanaka‡, H. Yoshikawa*
* JAERI: Japan Atomic Energy Research Institute, Tokai, Ibaraki, 319-1195 JAPAN
† KEK: High Energy Accelerator Research Organization, Tsukuba, Ibaraki, 305-0801 JAPAN
‡ Mitsubishi Electric System & Service, Tsukuba, Ibaraki, 305-0045 JAPAN

Abstract

As a joint project of KEK and JAERI, a MW class of high intensity proton accelerator (J-PARC), consisting of Linac, 3 GeV-RCS, 50 GeV-MR, is under construction. For this accelerator, it is required to minimize the beam loss (typically, lower than 0.1~1 W/m at the linac). To achieve the requirement, beam trajectory needs to be controlled with accuracy of some 100 μm. The first stage of the acceleration (up to 181 MeV during the first stage of construction) is done by linac. The beam position monitor (BPM) in the linac utilizes 4 stripline pickups (50 Ω) on the beam transportation chamber. In this paper, systematic calibration of the BPM is described.

DESIGN OF PICKUP LINE IN BPM

First stage of acceleration (181 MeV in the 1st phase of construction) in J-PARC is done by linac. For the beam position monitoring in the linac, stripline type of pickup electrodes (50 Ω) are placed inside beam transporting chambers. In order to minimize the space and to get the accuracy of the positioning of BPM, each BPM module is supported by pole faces of a quadrupole magnet. For the pickup electrodes it is important to maintain impedance matching, in order to avoid the reflection and to keep the signal balances between the electrodes. In the linac, there are 5 sizes of the beam transporting chamber, namely (from up stream) 37.7, 40, 70, 85, 120 mm in diameters. For BPMs in the 2 smaller types of diameter, flat-shape (in cross section) pickup plates are chosen because the mechanical structure is relatively simpler [1].

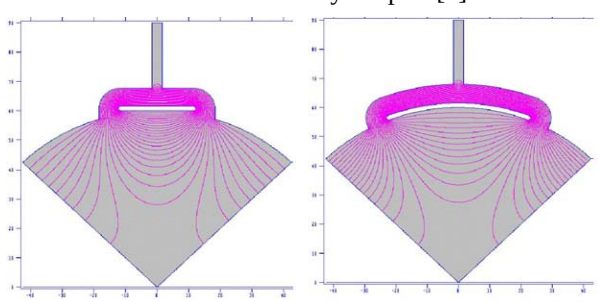

Figure 1: Cross section of the pickup electrode plates in BPM. Left; flat type. Right; round-shape type. (Due to the symmetry in the shape of BPM, only a quarter of BPM is shown.

#susumu.sato@j-parc.jp

For the BPMs in the 3 larger types of diameter, it is designed to use round-shape pickup plate along with the chamber circumference, in order to tale larger width of the electrode to achieve better sensitivity (S/N ratio). Figure 1 shows the two types of cross section of the pickup electrode plate with electric field shape in the BPM. The field shapes are calculated by POISSON [2] code which is used for the impedance optimization. As there are symmetries of the shape in each of 4 (up, down, right, left) electrodes, only a quarter of cross section is shown in the figure. The flat type and the round-shape type of pickups are shown in the left side and the right side, respectively.

CALIBRATION OF BPM

Calibrations of the BPM take two steps. The first step is taken before installation, and with the dedicated calibration bench which has a stainless wire (100μm) carrying 324 MHz (acceleration frequency) as dummy signal simulating the beam. In this step, an electrical zero point of pickup electrode is calibrated with respect to the mechanical center. The second step is taken after the installation with beam in low intensity, and is called beam based calibration (BBC). Displacement between the electrical center of BPM and the practical field center of the quadrupole magnet is calibrated.

Calibration before Installation (Calibration Bench Based)

Before installation, electrical zero point of pickup electrode for each BPM is calibrated by a calibration bench with a wire which carries 324 MHz simulating beam. Figure 2 shows a schematic (upper) and a photograph (lower) of the calibration bench, looking from the side. The BPM is sustained in the center of the calibration bench. The wire is placed inside the BPM and is straightened from both sides by hinges soldered on core pins of N-type connectors. The wire can be moved inside the BPM in order to simulate possible beam positions. On both edges of the BPM, dummy pipes are attached to simulate beam pipes, and are connected to the outer-line of the N-type connector. One side of the N-type connector is conducted to the 324 MHz generator and the other side is conducted to a terminator. Mechanical test of wire scanning has been already done.

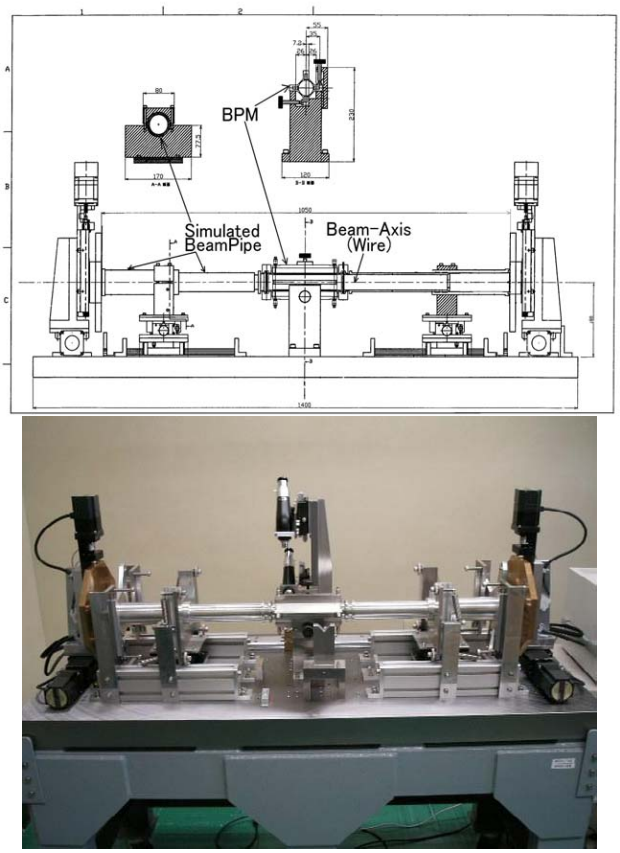

Figure 2: A schematic and photograph of BPM calibrator.

Calibration after Installation (Beam Based Calibration; BBC)

After installation in the quadrupole magnets, when low intensity beam is available, displacement between electrical center of the BPMs and magnetic center of the quadrupole magnet can be calibrated by using the actual beam. To calibrate a BPM mounted in a corresponding quadrupole magnet (called the "*housing quadrupole*" with an "*examined BPM*" here), diagnostic devices are needed both in the upstream side and in the downstream side as follows.

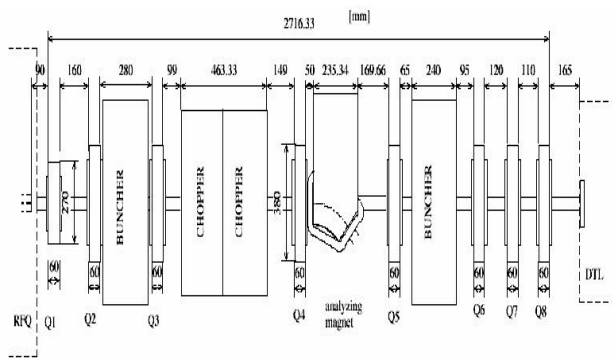

Figure 3: Alignment of 8 quadrupole magnets (Q1 ~ Q8) in the MEBT. In each quadrupole, a BPM is installed (BPM1 ~ BPM8, respectively). Steering coils are installed in Q1, Q2, Q4, Q6, and Q8.

- In the upstream, a magnet to steer the beam is needed (called as a "*steerer*" here). Some of quadrupole magnets in the MEBT have steering coils, which are controllable independently of quadrupole coils.
- In the downstream, another BPM as a probe (called as a "*probing BPM*" here) is needed.

The calibration and analysis is done in the following 6 procedures with real beam, and one additional procedure to confirm readout electronics

- Procedure 1: Steer the beam by a *steerer* (step by step, of the order of millimeter).
- Procedure 2: For each step of steering beam in the procedure 1, change quadrupole field of the *housing quadrupole* (step by step, of the order of percent off nominal value).
- Procedure 3: For each step of quadrupole field in the procedure 2, read positions measured by a *probing BPM*.
- Procedure 4: Plot the positions measured by the *probing BPM* as a function of field strength of the *housing quadrupole*. And extract the slope of this correlation, assuming a linear correlation.
- Procedure 5: For each step of steering beam in the procedure 1, plot the gradient of the slope in the procedure 4, as a function of the position measured by the *examined BPM*.
- Procedure 6: Interpolate (or extrapolate) linearly the beam position given by the *examined BPM*, by requiring zero slope in the correlation studied in procedure 5. Because the zero slope corresponds to the situation where the beam running at the center of the *housing quadrupole*, the interpolated (or extrapolated) beam position is displacement of the electrical center of the *examined BPM* from the quadrupole's center.
- Additional procedure: Independently of procedures from 1 to 6, measure the output value of readout electronics (a logarithmic ratio amplifier and an ADC), when exchanging the inputs of readout electronics (between up and down, or between right and left). This additional procedure provides an internal offset of the readout electronics.

These procedures are tested at the MEBT (beam transporting line between RFQ and DTL) which is currently being commissioned at KEK. Figure 3 shows the alignments of 8 quadrupole magnets (Q1 ~ Q8) in MEBT [3]. In each quadrupole, a BPM is mounted (BPM1 ~ 8). The steering coils are installed in Q1, Q2, Q4, Q6, and Q8.

The calibration and analysis is done based on the SAD [4] scripts, which is developed for design and commissioning of accelerators. The SAD is chosen for the reason of continuity to the latter stages of accelerators in J-PARC, namely 3-GeV RCS, and 50 GeV-MR synchrotrons, for which the SAD has varieties of tools.

It became possible to measure in some 15 minutes per one BPM by optimizing scanning configuration, for example, concentrating the scanning region and absolute

value of the *steerer* strength and the *housing quadrupole* strength during the calibration. These automatic measurements can be viewed also by the existing display tool developed by J-PARC control subgroup [5]. Figure 4 shows one of the examples of the beam based calibration. In this example, a *steerer* is in Q4, an *examined BPM* is BPM6 mounted in its *housing quadruple* Q6, and a *probing BPM* is BPM8. Left side of figure 4 shows the procedures 1 to 4, where horizontal axis is the field strength (unit: percent off nominal value) of the *housing quadrupole*, and vertical axis is measured position (unit: millimeter) by the *probing BPM*. The right side of figure 4 shows the procedure 5 and 6, where horizontal axis is measured position (unit: millimeter) by the examined BPM, and vertical axis is the slope of the left figure (unit: millimeter per percent).

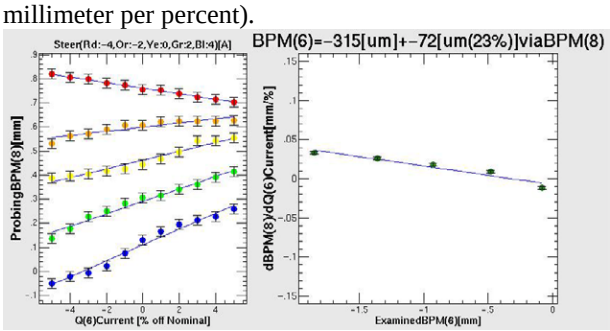

Figure 4: An example of the beam based calibration. (detail in the text). In the left figure, the *steerer* current is set to -4, -2, 0, 2, 4 (Ampere) from the top.

The early stage of experiment of the beam based calibration is done, and the results there are summarized in table 1. It is seen that evaluation with error of the order of some 10 μm is achievable for the displacement between centers of the BPM and the quadrupole, by optimizing the configuration of the BBC.

APPLICATION OF CALIBRATION RESULTS

As an application of the beam based calibration results, comparison is performed between measured data by BPM and simulation for MEBT. TRACE3D [6] is used for simulation of beam size (upper figure) and beam centroid (lower figure) as shown in figure 5. For the vertical centroid position, data points measured by the BPM to which the calibration results (BBC only) are applied, are plotted in the lower figure. In the simulation, field strength of quadrupole magnet is based on the measured current to the magnet. Three types of parameters are applied to the simulation, (a) initial beam position, (b) initial beam tilting angle, and (c(1~8)) kick angle for each quadrupole magnet due to e.g. position misalignment of magnet. Development of better optimization procedure is kept going for best parameter set {a, b, c}, as there are some parts which have discrepancies of the order more than some tens μm still (in distance between simulation and data, or in misalignment distance corresponding to kick angle parameter).

Table 1: Results of early stage of experiments of beam based calibrations

Calibrated BPM (Vertical, Horizontal)		Steering Magnet(L), Probing BPM (R)		Center [μm]	error [μm]
BPM2	V	1	5	29	93
	H	1	5	-265	109
BPM3	V	2	4	36	32
	H	2	4	-313	222
BPM4	V	2	6	379	76
	H	2	6	-442	292
BPM5	V	4	8	-371	126
	H	4	6	-185	-
BPM6	V	4	8	-315	72
	H	4	7	-46	-
BPM7	V	4	8	100	88
	H	6	8	17	-

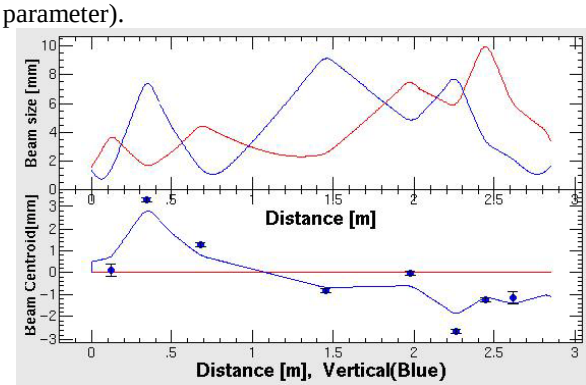

Figure 5: Comparison between measured data (points) and simulation (TRACE3D). Upper is beam size (simulation only), and the lower is beam centroid (vertical only).

SUMMARY

Beam position monitors (BPMs) for J-PARC LINAC with the stripline type pickup electrode, are calibrated with real beam. It has been understood that evaluation between electrical center and quadrupole center was achievable of the order of some tens μm. Some comparisons between the data applied calibration results and the simulation were done. Calibration with bench setup is under going, and developments to optimize parameters in simulation are kept going.

REFERENCES

[1] T. Tomisawa, et al., Design of 4-Stripline Beam Position Monitors of the J-PARC LINAC SDTL., Proceeding of 1st Annual Meeting of Particle Accelerator Society of Japan. Aug. 8. 2004.

[2] Poisson Manual, J.Billen, L.Young, LANL, LA-UR-96-1834.

[3] J-Parc Design Report (JAERI-Tech 2003-044, KEK Report 2002-13) from Fig. 3.1.2.3.10

[4] SAD Manual and SAD home page http://acc-physics.kek.jp/SAD/SADTkinter.pdf and sad.html

[5] M. Takagi, et al., Beam-monitor Software at the KEK 60-MeV Proton Linac, (Fig4 during BBC) Proceeding of 1st Annual Meeting of Particle Accelerator Society of Japan.

[6] Trace3D Manual (3rd ed.) K.Crandall, D.Rusthoi, LANL, LA-UR-97-886.

HIGHLY SENSITIVE MEASUREMENTS OF THE DARK CURRENT OF SUPERCONDUCTING CAVITIES FOR TESLA USING A SQUID BASED CRYOGENIC CURRENT COMPARATOR

W. Vodel, S. Nietzsche, R. Neubert, Friedrich Schiller University Jena, Germany
A. Peters, GSI Darmstadt, Germany
K. Knaack, M. Wendt, K. Wittenburg, DESY Hamburg, Germany

Abstract

A newly high performance SQUID based measurement system for detecting dark currents, generated by superconducting cavities for the upcoming TESLA project (X-FEL) at DESY Hamburg, is proposed. It makes use of the Cryogenic Current Comparator principle and senses dark currents in the pA range with a measurement bandwidth of up to 70 kHz.

INTRODUCTION

The 2×250 GeV/c TESLA linear collider project, currently under study at DESY [1], is based on the technology of superconducting L-band (1.3 GHz) cavities. The two 10 km long main LINACs (linear accelerator) are equipped with a total of nearly 20,000 cavities. A gradient of 23.4 MV/m is required for a so-called superstructure arrangement of couples of 9-cell cavities. To meet the 2×400 GeV/c energy upgrade specifications, higher gradients of 35 MV/m are mandatory.

The dark current, due to emission of electrons in these high gradient fields, is an unwanted particle source. Two issues are of main concern:

- Thermal load: An emitted electron from the cavity surface follows a path along the electric field lines and will most probable hit somewhere else onto the cavity wall. This leads to an additional thermal load in the cryostat, which has to be covered by the liquid helium refrigerator.
- Propagating dark current: If the energy gain is sufficient, the electrons will generate secondary particles when hitting the cavity wall which then also may generate secondaries. In the following avalanche process some electrons may pass through the iris of the cavity cell and will be further accelerated. In this case the dark current along the LINAC would grow exponentially if on average more than one electron passes the complete FODO (focus/defocus lattice) cell.

Recent studies [2] show that the second case seems to be the more critical one. It limits the acceptable dark current on the beam pipe "exit" of a TESLA 9-cell cavity to approximately 50 nA. Therefore the mass-production of high-gradient cavities with minimum field emission requires a precise, reliable measurement of the dark current in absolute values. The presented apparatus senses dark currents in the nA range. It is based on the cryogenic current comparator (CCC) principle, which includes a highly sensitive LTS SQUID as magnetic field sensor. Further on the setup contains a faraday cup and will be housed in the cryostat of the CHECHIA cavity test stand.

REQUIREMENTS FOR DARK CURRENT MEASUREMENT APPARATUS

Electrons can leave the niobium cavity material if the force of an applied external electric field is higher than the bounding forces inside the crystal structure. The highest field gradients occur at corners, spikes or other discontinuities, due to imperfections of the cavity shape. Another potential field emitter is due to any kind of imperfection on the crystal matter, like grain boundaries, inclusion of "foreign" contaminants (microparticles of e.g. In, Fe, Cr, Si, Cu) and material inhomogeneity. At these imperfections the bounding forces are reduced and electrons are emitted under the applied high electromagnetic fields [3]. With a series of special treatments the inner surface of the TESLA cavities are processed to minimize these effects. A reliable, absolute measurement of the dark current allows the comparison of different processing methods and a quality control in the future mass-production.

TESLA will be operated in a pulse mode with 5 Hz repetition rate. The 1.3 GHz r.f. pulse duration is 950 µs. During this time the dark current is present and has to be measured. Therefore a bandwidth of 10 kHz of the dark current instrument is sufficient. As field emission is a statistical process, the electrons leave the cavity on both ends of the beam pipe. Thus, half of the dark current exits at each side, and has to be measured on one side only. With the 1.3 GHz r.f. applied, we expect that the dark current has a strong amplitude modulation at this frequency. This frequency has to be carefully rejected from the instrument electronics to insure its proper operation and to avoid a malfunction of the SQUID. This were done by the help of careful r.f. shielding, appropriate filtering of all leads feeding to the SQUID input coil, and the low pass characteristic of the transformer used.

The use of a cryogenic current comparator as dark current sensor has some important advantages:

- measurement of the absolute value of the dark current,
- independence of the electron trajectories,
- accurate absolute calibration with an additional wire loop, and
- extremely high resolution.

The required working temperature of 4.2 K (boiling temperature of LHe) for the apparatus is unproblematic to provide because the CHECHIA test stand includes the

whole cryogenic infrastructure for cooling the niobium cavities. In order to enable the CCC to measure the magnetic field of the dark current only, an effective shielding against external magnetic fields has to be realized.

THE CRYOGENIC CURRENT COMPARATOR (CCC)

In principle, the CCC is composed of three main components (see Fig. 1):

- the superconducting pickup coil,
- the highly effective superconducting shield, and
- the high performance LTS-SQUID system.

The CCC, first developed by Harvey in 1972 [4], is a non-destructive method to compare two currents I_1, I_2 (see fig. 1) with high precision using a meander shaped flux transducer. Only the azimuthally magnetic field component, which is proportional to the current in the wires, will then be sensed by the pick-up coil. All other field components are strongly suppressed. The very small magnetic flux coupled into the coil is mostly detected by a SQUID.

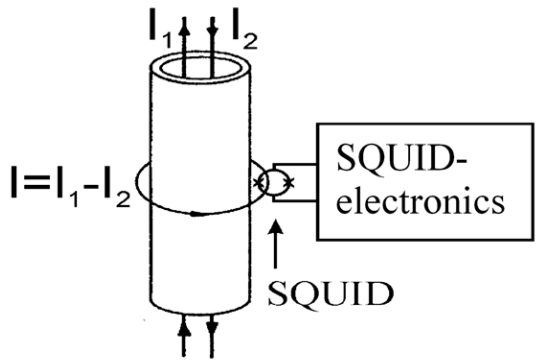

Figure 1: Simplified scheme of a LTS SQUID-based cryogenic current comparator.

The design of the CCC for measuring of dark currents is realized as co-operation of DESY Hamburg, Jena University and GSI Darmstadt. The apparatus will be placed in the CHECHIA cavity test stand and operates at 4.2 K.

Pickup Coil

A single turn pickup coil is formed as superconducting niobium toroid with a slot around the circumference. It contains a Vitrovac 6025-F core (Vacuumschmelze GmbH, Hanau, Germany) providing a high permeability of about 30,000 at liquid helium temperatures [5]. According to our experience 6025-F cores give the lowest noise level in comparison to other materials tested. The material inhomogeneity of the core is averaged by complete encapsulation of a toroidal niobium coil.

Superconductive Shields

The resolution of the CCC is reduced if the toroidal pickup coil operates in presence of external disturbing magnetic fields. As external fields are in practice unavoidable, an extremely effective shielding has to be applied. A circular meander ("ring cavities") shielding structure (see Fig. 2) allows to pass only the azimuthal magnetic field component of the dark current, while the non-azimuthal field components are strongly attenuated. The attenuation characteristics of CCC shieldings were analytically analyzed in great detail [6-8]. Applied to the shielding of the TESLA CCC an attenuation factor of approximately 120 dB for transverse, non-azimuthally magnetic field components is estimated. This result is based on the superposition of the analytic results for the different shielding substructures, here: coaxial cylinders and "ring cavities" (as shown in [9]).

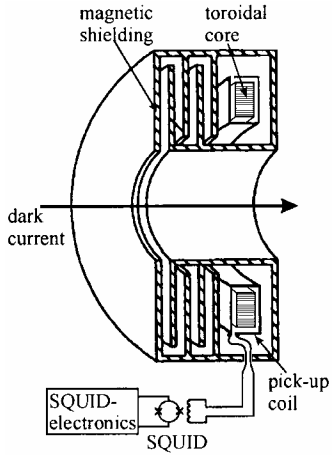

Figure 2: Simplified schematic view of the magnetic shielding, the toroidal pick-up coil, and the SQUID.

SQUID Measurement System

The key component of the CCC is a high performance DC SQUID system developed and manufactured at Jena University. The system makes use of the sensor UJ 111 [10], which is designed in a gradiometric configuration and based on Nb-NbO_x-Pb/In/Au window-type Josephson tunnel junctions with dimensions of 3 µm×3 µm. To couple a signal into the gradiometer-type SQUID an input coil system is integrated on the chip consisting of two coils of 18 turns each, connected in a gradiometric configuration. The input inductance of the SQUID is about 0.8 µH. In most applications the SQUID works in a feedback regime at constant flux. The feedback is realized by a one turn flux modulation coil inductively coupled only to one half of the SQUID loop system.

The SQUID electronics consists of the low noise preamplifier and the SQUID control and detector unit. The low source impedance of the SQUID (about 1 Ω) is stepped up to the optimal impedance of the preamplifier by means of a resonant transformer. The d.c. bias and flux modulation current (modulation frequency 307 kHz) are fed into the SQUID via voltage-controlled current sources situated in the preamplifier and the controller, respectively. The amplification and detection of the SQUID signal is achieved by the state-of-the-art design, i.e. the preamplifier is followed by an AC amplifier and a phase sensitive detector (lock-in) with a PI-type integrator. The output signal returns via a resistor to the modulation coil to close the feedback loop.

For an optimal choice of bias and flux modulation point, a white flux spectral density of 2×10^{-6} $\Phi_0/\sqrt{\text{Hz}}$ for

the SQUID system was found. This flux noise corresponds to an equivalent current noise through the input coil of 0.9 pA/√Hz, an effective energy factor of 543×h, and an energy resolution of 3.6×10^{-31} J/Hz. Using optimum electric and magnetic screening of the sensor the 1/f noise knee was found below 0.1 Hz even in a normal laboratory environment [10].

In a DC coupled feedback loop, the field of the dark current to be measured is compensated at the SQUID by an external magnetic field generated from the attached electronics. Due to the superconductivity of all leads in the input circuitry (pick-up coil, transformer, SQUID input coil) the CCC is able to detect even DC currents. For an optimum coupling between the 1-turn toroidal pick-up coil (40 µH) and the SQUID a matching transformer is necessary. The overall current sensitivity of the CCC was calculated to 175 nA/Φ_0.

Using a modulation frequency of 307 kHz the measurement system provides a over-all bandwidth of 20 kHz (signal level 1 Φ_0) or 70 kHz (signal level 0.1 Φ_0), respectively. Thus, it will be possible to characterize the pulse shape of the dark current beam (300 µs rise time, 950 µs flattop, 300 µs fall time, 10 Hz repetition rate) which is dominated by the r.f. structure applied to the cavities.

Faraday Cup

Because of the fact that the energy of dark current electrons is relatively small at CHECHIA, the design includes a faraday cup to have a second measurement system for comparison. We installed the faraday cup at the end of the cavity vacuum chamber. The readout electronics will measure the current to ground. Also it will be needed for stopping the electrons of the dark current in the test facility. This requires a high voltage-screen to absorb the secondaries from the stopper electrode. The simplified scheme of the main components of the CHECHIA's CCC is shown in fig. 3.

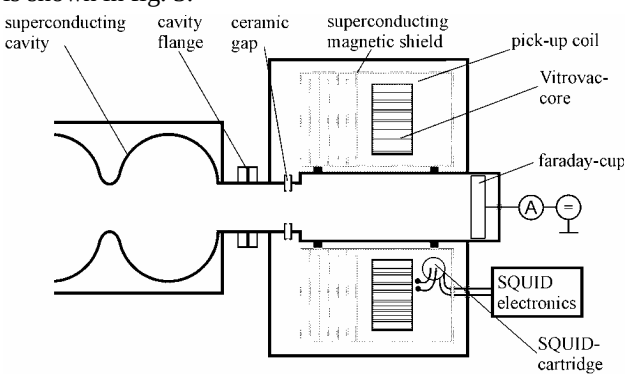

Figure 3: Schematic design of the CHECHIA's CCC.

RESULTS AND OUTLOOK

Test measurements with all special cabling and feed throughs were successfully done at the cryogenic laboratory of Jena university and a special pick-up coil to emulate the real pick-up coil under fabrication (see Fig. 4) was applied. As signal source a current generator was used to simulate the expected dark electron beam pulses.

In this test configuration a system current sensitivity of 167 nA/Φ_0 was reached using a calibration wire fed through the pick-up coil to emulate the beam. The flux noise of the system in the white noise region was measured to be as low as 8×10^{-5} Φ_0√Hz. These values correspond to a noise limited current resolution of the CCC of 13 pA/√Hz which is much better than required. According to our experience, in the final system the current resolution will be decreased by at least one order of magnitude because of the additional noise contribution due to the core material of the pick-up coil and external disturbing magnetic fields.

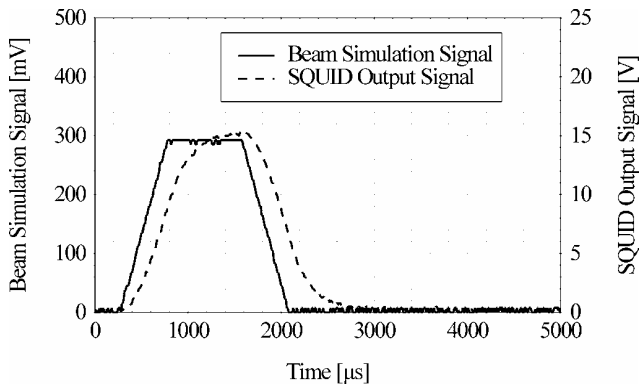

Figure 4: Test signal and SQUID output signal.

The mechanical construction of the CHECHIA CCC is completed. Tests of the manufacturing of critical components, i.e. the niobium shielding, are under way. The SQUID electronics including special cabling and feed throughs are ready for installation at DESY. The final installation is planned at the end of 2004.

REFERENCES

[1] R. Brinkmann; TESLA Technical Design Report.
[2] R. Brinkmann; Dark Current Issues; TESLA Collab. Meeting - CEA Saclay 4/2002.
[3] G. R. Werner, et al.; Proc. of the Part. Acc. Conf. PAC 01, pp. 1071-73.
[4] I. K. Harvey, "A precise low temperature dc ratio transformer", Rev. Sci. Instrum., vol. 43, p. 1626, 1972
[5] Datasheet "Toroidal strip-wound cores of VITROVAC 6025 F" and private communication from Vacuumschmelze Hanau, Germany.
[6] K. Grohmann, et. al.; CRYOGENICS, July 1976, pp. 423-429.
[7] K. Grohmann, et. al.; CRYOGENICS, October 1976, pp. 601-605.
[8] K. Grohmann and D. Hechtfischer; CRYOGENICS, October 1977, pp. 579-581.
[9] P. Gutmann and H. Bachmair; in V. Kose, Superconducting Quantum Electronics, 1989, pp. 255-259.
[10] W. Vodel, K. Mäkiniemi, "An ultra low noise SQUID system for biomagnetic research", Meas. Science and Technology Vol 3, No 2, pp. 1155-1160, Dec. 1992

TTF2 BEAM MONITORS FOR BEAM POSITION, BUNCH CHARGE AND PHASE MEASUREMENTS

D. Nölle, M. Wendt
Deutsches Elektronen Synchrotron (DESY),
Notkestr. 85, D-22607 Hamburg, Germany

Abstract

An overview of the basic beam instrumentation with regard to electromagnetic beam monitors for the TESLA Test Facility phase 2 (TTF2) is given. Emphasis is put on beam position monitor (BPM) and toriod transformer systems for beam orbit and bunch charge observations. Furthermore broadband monitors, i.e. wall current and bunch phase monitors, are briefly presented.

INTRODUCTION

During the past 10 years, the TESLA Collaboration has established the TESLA Test Facility (TTF) on the DESY site in order to develop the technology for a superconducting linear electron-positron collider and a X-ray free electron laser facility. The first phase of this project, TTF1, was successfully completed in 2002 with an extended operation period for first scientific applications of the saturated FEL beam below 100 nm wavelength [1].

Convinced of the unique possibilities provided by this new kind of radiation source, DESY is now upgrading the TTF accelerator and implementing the VUV-FEL user facility [2]. As in case of TTF1 the task in operating TTF2 will be twofold:

- Test accelerator for further development of superconducting L-Band (1.3 GHz) acceleration structures in the frame of a HEP linear collider, as well as for DESY's upcoming XFEL project.
- Drive linac for the 4th generation synchrotron radiation user facility based on a SASE FEL-undulator with a wavelength regime down to 6 nm.

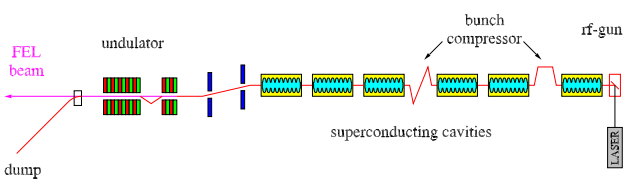

Figure 1: Schematic overview of TTF2.

Fig. 1 sketches the major components of TTF2, a new photoinjector (already tested with beam), five superconducting accelerator modules (a sixth module, for a 1 GeV upgrade, is under construction) of the TESLA type each containing eight L-band 9-cell cavities, two bunch-compressors, a collimation section and finally a 30 m long SASE FEL-undulator (divided in six 5 m long sections).

Based on the experience with TTF1 and other accelerators on the DESY side, a set of monitors for the basic beam instrumentation have been developed for TTF2. Emphasis was put on homogenous systems with high reliability, good maintenance and operational properties, rather than on "high-end instrumentation".

Table 1: Parameters of the TTF2 electron beam

max. beam energy	=	800 MeV (1 GeV)
max. rep. rate f_{rep}	=	10 Hz
macro pulse length t_{pulse}	=	800 μs
bunch spacing $\Delta\, t_b$	=	*110 ns or 1 μs*
N_e per bunch	=	*0.1...4 nC*
bunch length σ_z	$<$	50 μm
norm. emmittance ϵ_{norm}	=	2 mm mrad

Table 1 presents the beam parameters of TTF2, relevant for beam instrumentation. All monitors have to resolve single bunch information, thus the measurement (integration) time has to be $<$ 110 ns. Due to the use of high gradient superconducting cavities, special care has to be taken to avoid dust or other particles in the vacuum system, even though most of the diagnostics is installed outside of the cryostats.

BEAM POSITION MONITORS

About 60 *beam position monitors* (BPM) are installed in the warm sections of TTF2, half of them are stripline and half of them button BPMs, mainly installed in sections with limited space, e.g. in the undulator. Resonant cavity and re-entrant cavity type BPM's, with special read-out electronics, as they are used in the cold accelerating modules are not covered here.

Stripline BPM's

Based on a design for the S-Band LC test facility, the TTF2 *stripline-BPM's* are manufactured in two slightly different versions for the two standard vacuum chambers diameters of of 34 mm resp. 44 mm diameter. Since the outer shape of the BPMs maps to the contour of the poles inside the quadrupoles, it was possible to install the BPMs *inside* the quads, i.e. where the optical axis of the machine is defined. A stretched-wire calibration procedure was applied to these BPM-quadrupole units to measure the difference between electrical axis of the monitor and magnetic axis of the quad.

Fig. 2 shows the orthogonal arrangement of the four 20 cm long, longitudinal slotted coaxial electrodes, fixed with ceramic spacers, in the BPM body.

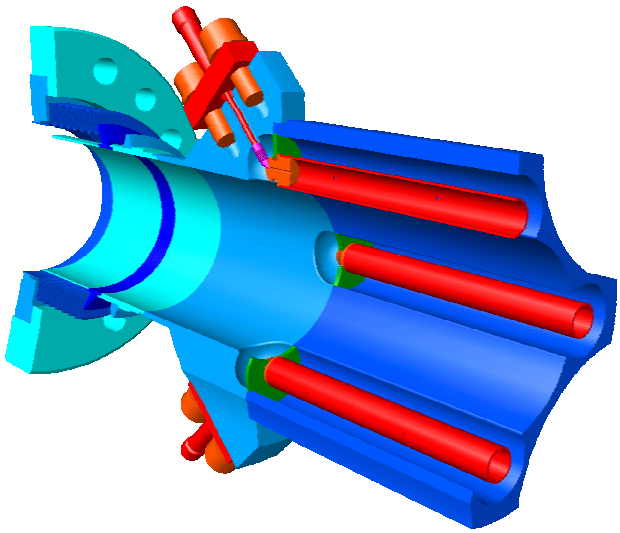

Figure 2: Sectional view of a TTF2 stripline-BPM.

Key characteristics of the TTF2 stripline BPM's are:

- Installation inside and collinear to the quadrupole axis. Calibration of BPM and quad axis with respect to each other with a resolution of 10...20 μm, using a stretched-wire technique [3].
- Strong signal levels, already at these moderate frequencies, allows a sufficient long integration period in the read-out electronics and results in a high S/N-ratio, even at bunch spacings of 110 ns.
- The resistive 50 Ω source impedance minimizes reflection effects between BPM pickup and read-out electronics, and therefore improves the single bunch measurement capability.
- The normalized position sensitivity (signal ratio) close to the center is ≈ 2 dB/mm.
- The coupling coefficient for a centered beam is $k \approx 6.5$ %.
- Two BPM versions for 34 (resp. 44) mm diameter aperture with 6 (8) mm diameter "semi"-coaxial stainless steel tube electrodes ($Z_0 = 50\,\Omega$) of 20 cm length ($f_{\text{center}} = 375$ MHz).
- Cleanroom class 100 approved construction, copper-plated stainless steel monitor body with brazed end-pieces.

Electrostatic "Button" BPM's

In regions of limited space, i.e. the injector, the bunch-compressors and of course in the undulator section *electrostatic "button"-type BPM's* are installed. Depending on the space requirements and beam pipe diameter two types of flange mounted pickup electrodes are used:

"Trumped" styled button (custom made by *Metaceram*) of 8 mm diameter, are flange-mounted in an 90^0 orthogonal arrangement in the 34 mm vacuum chamber of the injector. They are also used in an "array"-like arrangement in the flat, rectangular vacuum chamber of the bunch-compressors.

Tiny, pin-style electrostatic BPM electrodes are used in the 10 mm diameter vacuum chamber of the FEL undulator [4]. The space limitations inside the FEL undulator dictates a non-orthogonal arrangement of these flange mount, commercial feedthrough electrodes (custom made by *Meggitt, ex. Kaman*). With the change of the beam optics in TTF2 the need of BPM's *inside* the FEL undulator sections is relaxed. Two BPM pairs installed inside, plus one BPM between undulator sections allows a beam orbit monitoring every 30^0 phase advance.

Read-out Electronics

The *read-out electronics* has to interface the electrode signals of BPM pickup's to the analogue input of the existing VME-based data acquisition system. Therefore the successful operated undulator BPM read-out electronics of TTF1 [5] was re-designed, upgraded and modified to accomplish all the TTF2 needs:

- Monopulse and ringing band-pass versions of the *AM/PM normalization* based electronics to read-out both, button-, as well as stripline-BPM's.
- Remote controlled settings for offsets, timing, etc. to allow in tunnel operation.

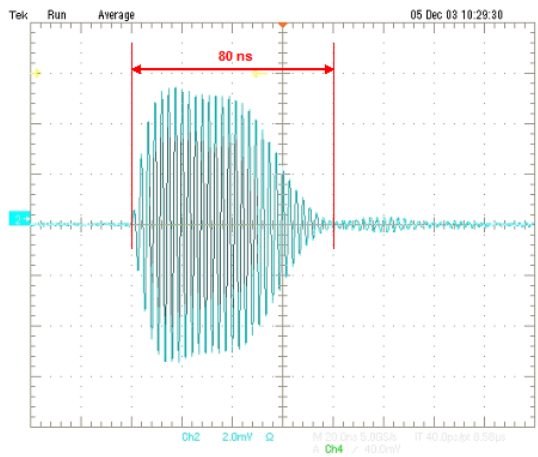

Figure 3: Measured TD impulse response of the band-pass input filter – stripline version of the read-out electronics.

For the stripline version of the read-out electronics, a new ringing band-pass input filter was developed. It is based on a rectangular impulse response low-pass prototype. Fig. 3 shows it's time domain response, which gives ≈ 20 oscillations of 375 MHz, well damped within 110 ns to insure the single bunch detection capability.

The electronics hardware is realized as VXI C-size mainboard, holding 9 rf submodules which keep the critical analogue functions. This rf building block concept simplifies future changes, features easy adaption to new monitors and supports maintenance and improvement aspects.

BUNCH CHARGE MONITORS

The bunch charge (beam intensity) measurements in TTF2 are based on *inductive, broadband toroidal transformers* (toroids). Fig. 4 sketches the tunnel-installed hardware, consisting out of the actual toroid, a set of signal combiners (only one shown), a low-pass pulse-forming network and broadband amplifiers. For compatibility and maintenance reasons the in-house developed toroid was preferred to a commercial version, since it is cut in two half rings. Therefore it can be (dis)mounted without breaking the vacuum. Due to the unavoidable air-gaps the lower cut-off frequency is limited, the usable bandwidth ranges $\approx$ 10 kHz...$>$ 100 MHz.

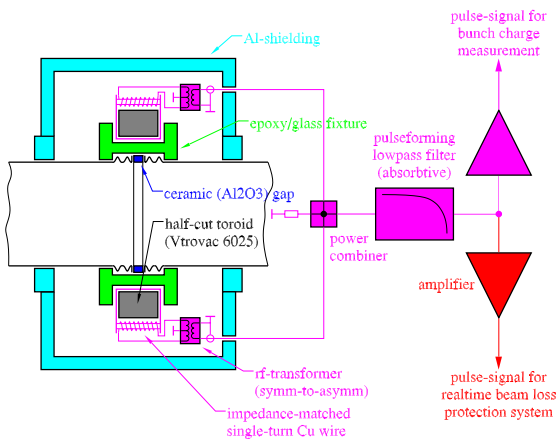

Figure 4: Toroidal transformer with front-end electronics for beam intensity measurements.

11 toroid units matched to the 3 different vacuum pipe diameters are installed along the TTF2 linac to keep track of the accelerated charge and therefore the transmission through the accelerator. Selected pairs of toroids are also used for beam loss monitoring; as source for the fast protection system [6]. In order to provide a sufficient beam loss resolution we have to matched the transfer responses of these toroid couples to $< 10^{-3}$.

OTHER BROADBAND MONITORS

Bunch Phase Monitors

The operation of a SASE FEL, like TTF2, is very sensitive to the compression of the beam in order to reach the required high peak currents. This process depends critically on the phase of the rf-voltages, used to produce the energy chirp within the bunch. Therefore, the a precise tuning of the rf-phase with respect to the beam to the 0.1^0 level or even better is essential. Furthermore, beam related trigger signals, to determine arrival time or to evaluate jitter properties on the some 100 fs level are required. Therefore a *bunch phase monitor* is used to pickup a beam position independent, broadband bunch signal. It consists out of a simple *ring electrode* of 100 Ω characteristic impedance, fixed by two adjacent 50 Ω rf-feedthroughs. This arrangement was simply integrated into a thick flange.

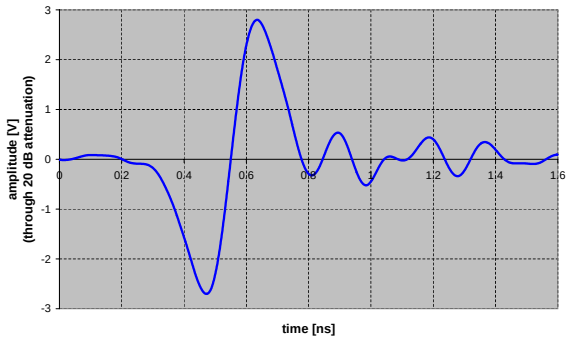

Figure 5: Time domain signal from a bunch phase monitor.

The monitor delivers a well differentiated output signal, as first preliminary measurements indicates (here limited by the 4 GHz bandwidth of the observation instrument, Fig. 5). The theoretical band-limitation is expected in the 8...10 GHz region, due to the ring diameter and reflection effects at the feedthroughs. In TTF2 phase monitors are installed after each section including dipole magnets plus one injector before the compression stages. Thus it is possible to locate phase jumps, introduced by rf-systems, through a time-of-fight measurement. Further monitors are installed to extract timing signals.

Wall Current Monitors

A set of very simple *wall current monitors*, based on the ceramic gap of the toroids, is installed in TTF2. The time-constant is build from the gap capacitance of $C_{\text{gap}} \approx 55$ pF and eight gap resistors $R_{\text{gap}} = 25/8\,\Omega$ in parallel with eight passive summed load-lines $R_{\text{load}} = 50/8\,\Omega$, and leads to an upper frequency limit of $f \approx 1.4$ GHz.

This broadband bunch current monitor is only required for unusual operating modes, i.e. a bunch spacing $\ll$ 110 ns, as used during the TTF1 HOM measurement experiments, etc.

REFERENCES

[1] M. Körfer, et. al., Proc. of the 23rd FEL Conf., Darmstadt (2001), Germany, pp. 34.

[2] B. Faatz, et. al., Proc. of the 24rd FEL Conf., Argonne (2002),Illinois, U.S.A., pp. II-55-56.

[3] G. Priebe, et. al., this proceedings.

[4] R. Lorenz. et. al., Proc. of the DIPAC 1997, Frascati (1997), Italy, pp.73-75.

[5] M. Wendt, Proc. of the DIPAC 2001, Grenoble (2001), France, pp.63-65.

[6] D. Nölle, et al., Proc. of the DIPAC 2003, Mainz (2003), Germany, pp.62-64.

BEAM INSTRUMENTATION USING BPM SYSTEM OF THE SPring-8 LINAC

K. Yanagida*, T. Asaka, H. Dewa, H. Hanaki, T. Kobayashi,
A. Mizuno, S. Suzuki, T. Taniuchi, and H. Tomizawa
Japan Synchrotron Radiation Research Institute, Mikazuki, Hyogo, 679-5198, Japan

Abstract

Beam position monitors were installed in a SPring-8 linac's dispersive sections, and the entire beam trajectory could be measured along the linac. A fast and synchronized accumulating database system started, that accumulated beam position data from all forty-seven BPMs simultaneously at 10-pps operation of the linac. Feedback control of steering magnets and an energy compression system for beam position stabilization were also successfully examined.

INTRODUCTION

In a SPring-8 linac a beam position monitor (BPM) system has been developed and installed for several years. BPMs for the non-dispersive section were installed in August 2000. The non-dispersive section BPM is an electrostatic stripline monitor whose aperture is a circule of ϕ32 mm [1]. Its stripline length is 27 mm, and the detection frequency is 2856 MHz. Signal processors were installed in March 2001 whose basic processes are filtering by a band pass filter, detection by a logarithmic detector (AD8313), and analog-to-digital conversion [2]. At this time a simple data acquisition system from signal processors to an operator console was started to measure the trajectory of the non-dispersive section.

In August 2003 BPMs were installed in the dispersive section, and an entire beam trajectory could be measured along the linac. Finally, in November 2003 a fast and synchronized accumulating database system was started. After completion of the BPM system, the next task is to prepare beam instrumentation using the BPM system. The final goal is automatic tuning or operation of the linac. First beam position and energy feedback programs were developed, examined, and designed for long term stabilization in a top-up operation of the SPring-8 and the NewSUBARU storage rings [3] [4]. An examination of the programs was successfully carried out in July 2004, and they will be implemented from September 2004.

INSTALLATION OF DISPERSIVE SECTION BPM

The structure of the dispersive section BPM is the same as the non-dispersive section BPM, except that the cross-sectional aperture is larger. Its aperture is 62 $\times$ 30 mm ellipse as shown in Fig. 1 that was carefully designed to block RF noises around the detection frequency (2856 MHz), generated outside of BPM. Almost all BPMs were installed into quadrupole magnets. Figure 2 shows the location where the dispersive section BPMs were installed.

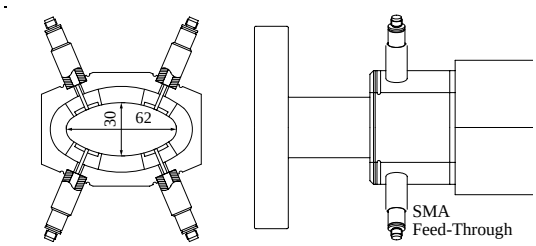

Figure 1: Schematic drawing of dispersive section BPM.

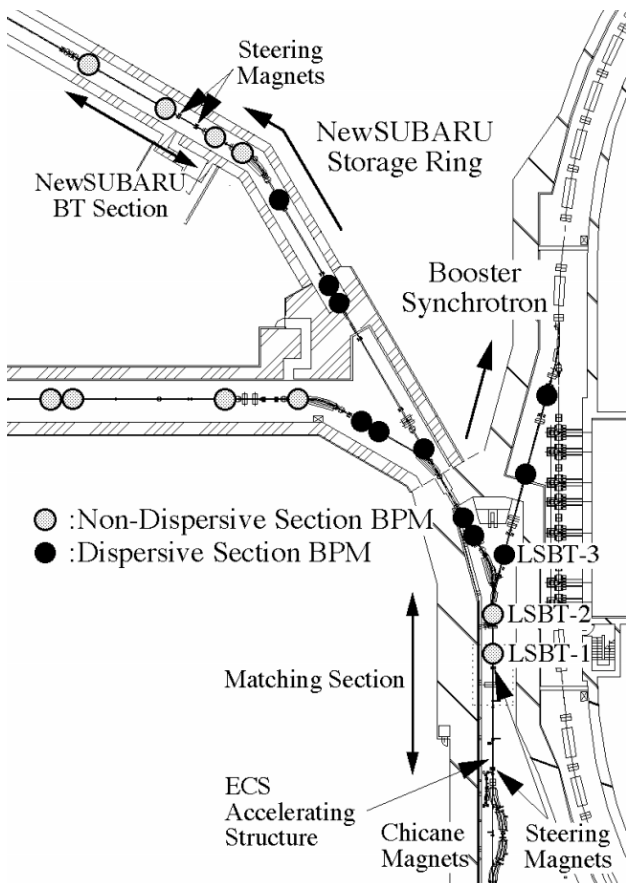

Figure 2: Location of installed dispersive section BPMs.

* ken@spring8.or.jp

DATA ACCUMULATION DATABASE

The database system is designed to collect all beam position data from forty-seven BPMs that synchronize every beam shot. The collected data are accumulated automatically into the database. The accumulated data can be always extracted from the database for beam diagnosis.

The maximum beam repetition of the linac is originally 60 pps. Therefore a database system was required to process data acquisition even at 60 pps operation of the linac. Software framework with a shared memory network has been developed to satisfy this requirement [5]. The most important thing is that all accumulated data must be completely synchronized, even if an acquisition error occurs.

At present the data acquisition rate into the database is not fast enough to collect all the data at 60 pps operation of the linac, but it is sufficiently fast at 10 pps operation. The beam repetition of the linac has now been reduced to less than 10 pps to prolong life of linac's components, e.g. thylatrons and klystrons, and to reduce electrical power consumption. Thus a serious acquisition error has not occurred during usual operations.

Figure 3 shows processed data and variations of horizontal beam trajectories along the linac. Trajectory variation was induced by a kicking perturbation imposed at the injector section, which is located upstream of the linac where beam energy is $\sim$60 MeV. Trajectories are expressed as the differences from the reference trajectory at 14:00:48.32. They clearly exhibit betatron oscillations along the linac.

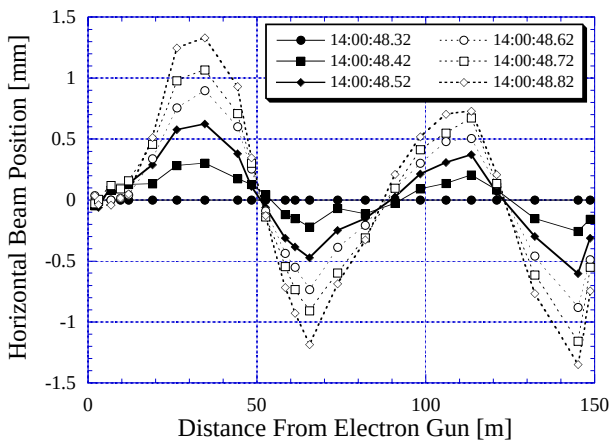

Figure 3: Horizontal beam trajectories along the linac. Trajectories are expressed as differences from reference trajectory at 14:00:48.32.

BEAM POSITION FEEDBACK

A beam trajectory of the linac sometimes varies based on a room temperature. Trajectory variation affects beam injection to the booster synchrotron or the NewSUBARU storage ring. Therefore, beam trajectory must be as stable as possible. A beam position feedback control program was developed in order to stabilize the beam positions at the following three sections.

In the linac there is at least one steering magnet for one BPM so that the steering magnets can correct beam position at each BPM. However, beam angle cannot be simultaneously corrected because one steering magnet can either correct beam position or beam angle. There are only three sections where both the position and angle can be corrected. Each of them was designed with double steering magnets in their drift space upstream of the two BPMs. The three sections are the injector section, a matching section and a NewSUBARU beam transport (BT) section.

The matching section is located upstream of the switching magnet for the booster synchrotron or NewSUBARU storage ring as shown in Fig. 2. The NewSUBARU BT section is located downstream of the second bending magnet toward the New SUBARU storage ring (see Fig. 2).

The position feedback control scheme is quite simple. The program consists of three feedback loops corresponding to the injector, matching, and NewSUBARU BT sections. The program calculates the excitation current of the steering magnets by using of measured beam positions. The program adjusts the excitation current of the steering magnets to keep the beam position within a tolerance. Each feedback loop works locally and independently in each section. Therefore a trajectory change due to an upstream feedback loop may interfere with the correction of the downstream feedback loop. Weight factors are introduced for each feedback loop to avoid serious interference expressed as correction ratios for one feedback loop. The weight of the upstream feedback loop is small, and the weight of the downstream feedback loop is large. The weight of the injector, matching, and NewSUBARU BT sections are 12.5%, 25% and 50%, respectively.

Figure 4 is an example of the horizontal position feedback examination. The tolerance of the position feedback control was $\pm$30 μm. All the sections - injector, matching, and NewSUBARU BT - work together. A kicking perturbation was created by a steering magnet located upstream of the injector section. A variation of the magnet excitation current gave the beam positions large initial displacement; they finally converged within the tolerance. The feedback interference resulted in a slight overshooting of the beam positions observed in the matching and NewSUBARU BT sections.

BEAM ENERGY FEEDBACK

The linac has a beam energy compression system (ECS) that compensates for or stabilizes beam energy [6]. However, small beam energy drift at the downstream of the ECS was observed when the room temperature changed. This unwanted energy drift slightly affected the injection efficiency of the booster synchrotron and the NewSUBARU storage ring. For additional stabilization of the beam energy or injection efficiency, beam energy feedback control was developed and examined.

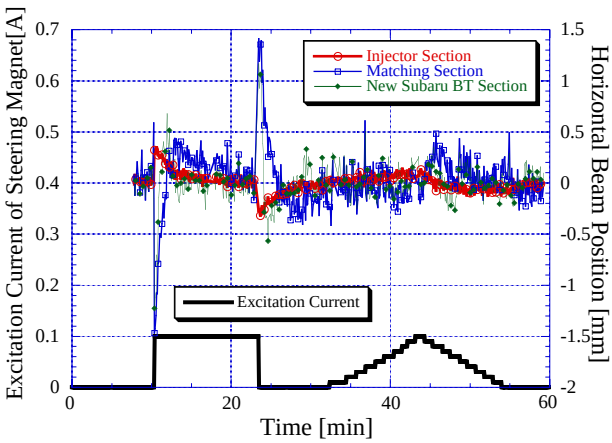

Figure 4: Example of horizontal position feedback control.

The energy feedback scheme is also quite simple. The horizontal beam positions in the matching section are corrected within double tolerance of the position feedback control, and an energy feedback program adjusts the ECS phase shifter to keep the beam position within the tolerance of the energy feedback control in the downstream dispersive section.

The energy feedback program was examined in July 2004. The tolerances of the position and energy feedback control were ± 30 μm and ± 0.5 mm ($\sim \pm 0.05\%$ of beam energy), respectively. A perturbation was created by varying RF power and phase of ECS klystron that feeds RF power to the ECS accelerating structure: The actual varied parameter was the pulse forming network (PFN) voltage of the modulator for the ECS klystron. A 1 kV variation of the PFN voltage corresponds to a phase compensation of more than 10° for ECS.

Figure 5 shows the variation of PFN voltage as a perturbation and the phase set values given by the program. Figure 6 is the behavior of the horizontal beam position. First, beam positions of LSBT-1 and LSBT-2 (see Fig. 2) were corrected by the position feedback program. Next, the beam position at LSBT-3 was automatically corrected within the tolerance.

CONCLUSION

A BPM system of the SPring-8 linac was completed. The database system is regularly collecting and accumulating beam position data. These accumulated data are always available or can be extracted from the database system. The application programs of beam position and energy feedback control were successfully examined. The beam positions displaced by a kicking perturbation eventually converged. These programs will be implemented from September 2004.

Remaining tasks includes tuning the database system faster, tuning the feedback program more reliably, and developing other application programs such as automatic tuning or operation of the linac.

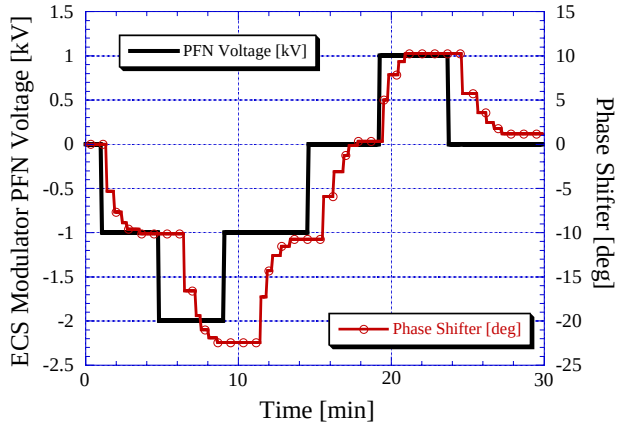

Figure 5: ECS PFN voltage and phase of ECS phase shifter on beam energy feedback examination.

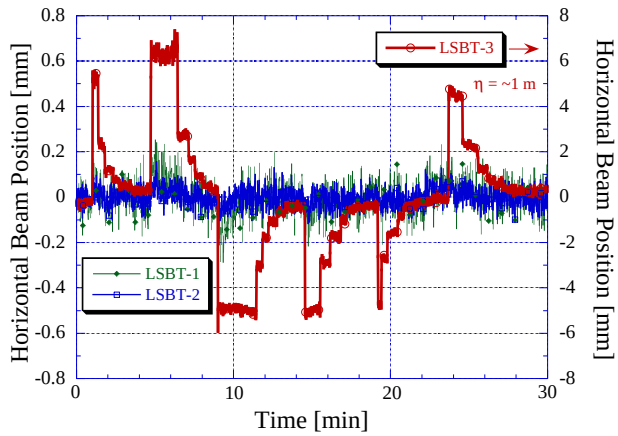

Figure 6: Horizontal beam positions in non-dispersive section (LSBT-1 and LSBT-2) and in dispersive section (LSBT-3) on beam energy feedback examination.

REFERENCES

[1] K. Yanagida, et al., "A BPM System for the SPring-8 Linac," Proc. of the 20th Int. Linac Conf., Monterey USA, Aug. 2000, pp. 190-192.

[2] K. Yanagida, et al., "Signal Processor for SPring-8 Linac BPM," Proc. of the 5th European Workshop on Diagnostics and Beam Instr., Grenoble France, May 2001, pp. 162-164.

[3] H. Tanaka et al., "Top-up Operation at SPring-8 Towards Maximizing the Potential of a 3rd Generation Light Source," Proc. of the EPAC 2004, Lucerne Switzerland, July. 2004. To be published.

[4] Y. Shoji et al., "NewSUBARU Storage Ring Operational Progress in These Three Years," Proc. of the APAC 2004, Kyonju, Korea, March. 2004. To be published.

[5] T. Masuda et al., "Data Acquisition System with Shared Memory Network", Proc. of ICALEPCS'01, San Jose, USA, 2001, pp. 567-569.

[6] T. Asaka et al., Nucl. Instr. and Meth. A, 516 (2004) 249-269.

THE BEAM DIAGNOSTICS SYSTEM IN THE J-PARC LINAC

S.Lee[A)], Z. Igarashi[A)], M.Tanaka[B)], S. Sato[B)], H. Akikawa[B)], F. Hiroki[B)], T.Tomisawa[B)], H.Yoshikawa[B)], J. Kishiro[B)] and T. Toyama[A)]

[A)] KEK, Tsukuba, Ibaraki, 305-0801, Japan

[B)] JAERI, Tokai, Naka, Ibaraki, 319-1195, Japan

Abstract

The beam diagnostics system has been developed to tune and investigate the high intensity proton beam in the J-PARC linac. Beam monitors are required to measure wide dynamic range of beam intensities and energies in linac. In this paper, construction and application of beam monitor system are described. Preliminary results of demonstration of beam position monitor (BPM), fast/slow current transformer (FCT/SCT), wire scanner (WS) and beam loss monitor (BLM) in the KEK-DTL1 (20MeV) are also discussed.

INTRODUCTION

The J-PARC (Japan Proton Accelerator Research Complex) linac aims to provide high intensity beams of peak current 50mA, kinetic energy 181/400MeV, pulse width 0.5mA and repetition rate 25Hz [1]. The goal of 133 kW beam power and hand-on maintenance will place significant demands on the performance and operational reliability of accelerator diagnostics systems. Beam diagnostics system is required to verify proper transverse focusing and matching of the magnetic focusing lattice of the linac. Large number of beam monitors will be installed in MEBT, DTL, SDTL, ACS and L3BT (Fig. 1). Progress and R&D results of beam monitors are evaluated in detail.

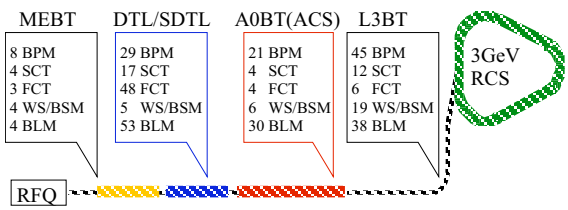

Figure 1: Designed beam monitor system in the J-PARC linac.

BEAM MONITORS IN THE J-PARC LINAC

Beam Position Monitor

Beam position monitors (BPM) have about 40mm-130mm bore and 4-stripline electrodes with one end shorted by 50 Ω terminations (Fig. 2) [2]. Electrostatic computations are used to adjust the BPM cross-section parameters to obtaine 50 Ω transmission lines. BPMs are sustained by pole edge of quadrupole magnet, and designed to reduce the offset between quadrupole magnet and BPM electrical centers of less than 0.1mm. A procedure of beam based calibration/alignment (BBC/BBA) method to evaluate the displacement of linac BPMs are examined [3]. The BPM electronics uses both amplitude-modulation-to-phase-modulation (AM-PM) method and conventional log-ratio method [4]. Prototype of BPM system with log-ration electronics have been constructed and examined in KEK MEBT1 and DTL1.

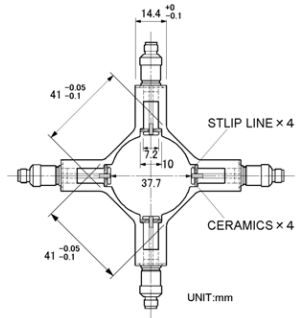

Figure 2: Schematic of beam position monitor in MEBT1.

Slow/Fast Current Transformer

Two types of current transformers have been developed to measure beam intensity and bunch phase (Fig. 3). The slow current transformer (SCT) have dynamic renge of 0.1-80 mA, a droop of 3% for a pulse width of 500 μs and time response of <50ns. The SCT has been chosen with 50 turns and additional winding to provide a calibration/test input capability. The fast current transformer (FCT) have response of relative bunch phase <1%. To measure the beam energy at every accelerator tank and injection point of 3GeV RCS, phase differences of two FCTs are used (time-of-flight: TOF), and 10^{-4} order energy resolutions can be expected. The SCT will also contribute to personal-protection-system (PPS). Integrated current signal will be evaluated to guarantee the normal operation of beam dumps.

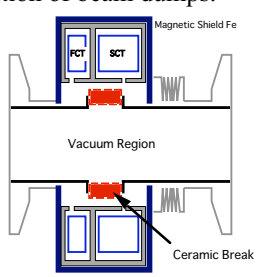

Figure 3: Cross sectional view of slow/fast combined type current transformer. FINEMET core is placed at outside the vaccum chamber to avoide the out gas. Outer wall is composed of iron to reduce the noise level.

Beam Loss Monitor

To prevent the activation and heat load by intense beam loss, fast time response of loss signals is required. The beam loss monitor (BLM) system is composed of scintillator (S-BLM) and Ar+CO_2 gas filled proportional

counter (P-BLM, Fig. 4), which detect γ-ray, neutron and charged particles induced by lost particle [5-7]. It is necessary to measure wide dynamic range of loss intensity for various beam energies.

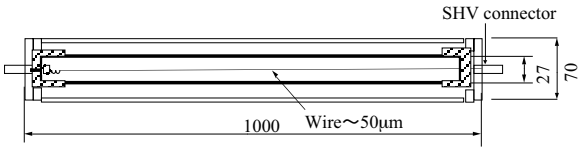

Figure 4: Schematic of proportional counter type beam loss monitor. Dual tube structure was designed to reduce the noise level and measure the residual activation level.

Beam Profile/Size Monitor

Profile measurements are used to determine the beam emittance of a matched beam in a periodic focusing lattice. The thin sensing wire (WS: carbon, diameter 7~100 μm) is scanned to obtain a current density distribution of the beam. Beam size and halo profiles will also be evaluated by movable beam scraper (BSM). The heat flux of single wire and scraper frame have been evaluated to avoid heat damage or thermionic emission.

EXPERIMENTAL RESULTS IN THE KEK MEBT1 AND DTL1

Figure 5 shows the distribution of beam monitor system and an example of BPM out put signal in MEBT1.

BPMs are sustained by pole edges of quadrupole magnets (Q-mag), and the absolute accuracy of beam position monitors were confirmed by beam based calibration method. It has been evaluated that the displacements between magnetic center of Q-mag and electrical center of BPMs are less than 0.2mm [3,8].

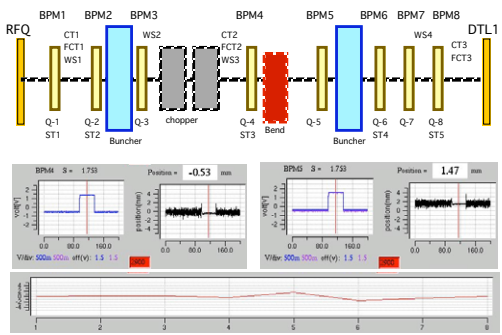

Figure 5: Installed beam monitors in MEBT1 and typical out put signal of BPM by using the Experimental Physics and Industrial Control System (EPICS) software [9].

The P-BLM and S-BLM (GSO: radiation hardness type scintillator) are installed on KEK DTL1. Figure 6 shows an example of SCT, S-BLM and P-BLM signals. Sufficient sensitivity and fast time response of S-BLM <1μsec are confirmed for low energy region of linac (20MeV). P-BLM also shows the rise time of several μsec for input impedance of 10 kΩ [1,10]. Gas amplifier ratio was evaluated for various beam current of 5mA~24mA. Output signal is proportional to bias voltage and agree with Diethorn plot except the saturation at high voltage operation [11,12]. The lineality between the P-BLM signal and the relative beam loss at transport line from DTL1 to faraday cup (beam dump) have been confirmed. It was assumed that the difference of current transformer (SCT4) and faraday cup (F. C.) signals represent the relative beam loss at transport line. A large amount of beam loss is intentionally induced to evaluate the BLM sensitivity. The dynamic range of 10^3 order was obtained with only gas amplifier. The relation of the loss signal and the scraped beam current have to be surveyed in lower beam loss operation.

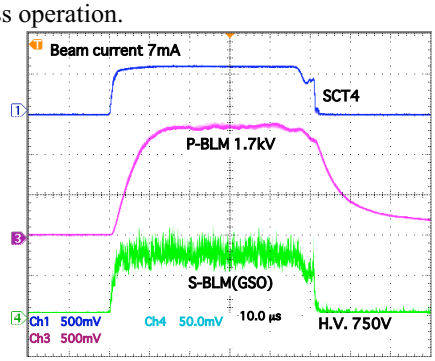

Figure 6: Beam current and loss signals of SCT, S-BLM and P-BLM at transport line from DTL1 to beam dump. Fast time response of S-BLM is confirmed. Bias voltage were -1.7 kV and -0.75 kV for P-BLM and S-BLM photomultiplier tube (PMT).

The degradation in gain of Ar+CH_4 gas filled P-BLM due to the deposit of polymerized material on wire was reported [6]. So that the sensitivity degradation of P-BLM includes other stopping gas (Ar+CO_2) should be surveyed with Co-60 γ-ray source. The sensitivity reduction of Ar+CO_2 P-BLM was not observed up to the charge accumulation of 0.0035 C/mm, which correspondes to more than several years operation in J-PARC. The constant sensitivity of radiation hardness scintillators and quartz window PMT (GSO, SCSN-81 and H3695-10: Hamamatsu Phot. K.K.) was also examined up to the irradiation of 7 kGy [13].

Vertical and horizontal beam profiles are measured by 4 wire scanners in MEBT1 [14]. Time averaged (30 μsec) beam pulse signals were processed for each sample positions. Typical out put signal of WS is shown in Fig. 7(a). The measured rms widths of WS4, between Q-mag 7 and Q-mag 8, are 1.45 and 1.04 mm for the horizontal and vertical distributions respectively. The observed results agree with calculated rms widths within 20% differences. The out put signal of WS has been supposed to depend mainly on beam energy, wire diameter and materials. The bias potential should also be determined by measuring the wire signals as a function of bias potential. The resulting data (Fig. 7(b)) shows that the out put signal is saturated in bias potential of higher than 100V. An expected mechanism of interaction between thin wire and H^- beam is that, as the wire is biased positively, the current

component due to the intercepted H^- ion are clarified because of a reduction in secondary electron emission.

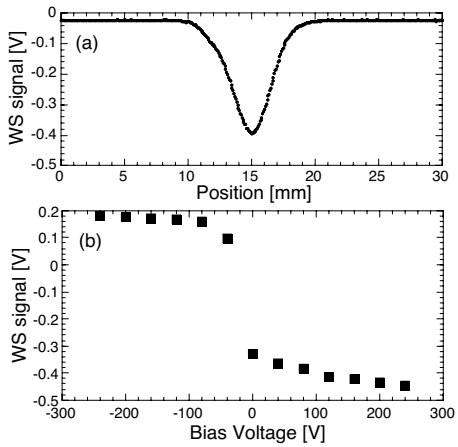

Figure 7: An example of transverse beam profile in MEBT1(a), and net signal during the beam pulse as a function of applied bias potential(b).

Stripline pickups can also be used as a beam width monitors to measure the beam size (quadrupole moment), from which the momentum spread is inferred [15,16].

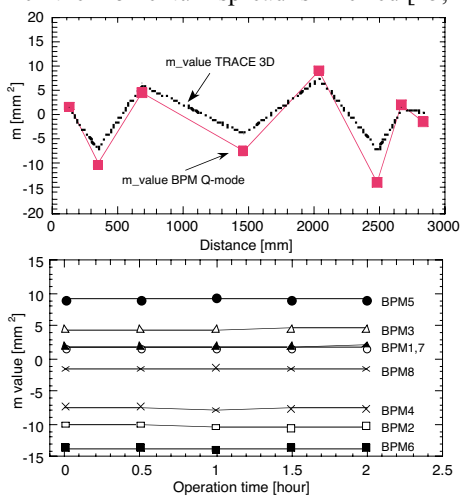

Figure 8: Experimental and calculated results of beam size term (a). Sufficient reliability of beam size measurement during the practical long time period was also confirmed (b).

A non-destructive beam momentum spread measurement using a BPM has been examined in order to investigate and control the momentum spread of J-PARC linac beams. The momentum spread of less than 0.1% is required for 3GeV rapid cycling synchrotron (RCS) injection to avoid uncontrolled beam losses. The 4-stripline monitor has to be mounted on a L3BT beam line of large dispersion to compare the difference of horizontal and vertical beam size. The momentum spread is obtained from following equation as:

$$\frac{\Delta P}{P} = \frac{1}{\eta}\sqrt{m - (\varepsilon_x\beta_x - \varepsilon_y\beta_y)} \qquad (1)$$

$$m = \sigma_x^2 - \sigma_y^2 \qquad (2)$$

The absolute measurement of the beam size term m is also represented as:

$$Q = \frac{(V_1 + V_3) - (V_2 + V_4)}{V_1 + V_2 + V_3 + V_4} = \frac{C}{R^2}(\sigma_x^2 - \sigma_y^2 + x_0^2 - y_0^2) \qquad (3)$$

Figure 8(a) shows a plot of the observed and calculated (TRACE 3D) results of beam size term, good agreements were confirmed in MEBT1. The sufficient accuracy and stability, m<0.5 mm^2 for 2hours, have also be evaluated (Fig. 8(b)) experimentally [17].

SUMMARY

Prototype of beam monitors for J-PARC linac have been performed in KEK MEBT1 and DTL1. BPM pickups and electronics provide a sufficient accuracy and stability (<0.2 mm). A non-destructive beam momentum spread measurement using a 4-stripline pickups was examined. Beam loss signals could also be observed with fast rise time (<1μsec) and very high sensitivities. The wire scanners practically contribute to the beam commissioning in MEBT1 and DTL1. However the interaction mechanism between thin wire and H^- ions for various beam energies have to be investigated in future.

REFERENCES

[1] Y. Yamazaki, eds. *Accelerator Technical Design Report for J-PARC,* KEK Report 2002-13.
[2] T.Tomisawa *et al.,* Proc. of the 1st annual meeting of particle Accelerator Society of Japan, 6C07.
[3] S. Sato *et al.,* "Systematic Beam Position Monitoring in the High Intensity Proton Accelerator (J-PARC) LINAC" These proceedings.
[4] R. E. Shafer, American Institute of Physics, **212**(1989).
[5] S. Lee *et al.,* Proc. of EPAC2004, THPLT074.
[6] S. Lee *et al.,* Proc. of 14th Symp. Accel. Sci. and Tech., (2003)482, S-188.
[7] T. Nakamura, *Radiation Physics and Accelerator Safety Engineering*, 2nd Edition (2001).
[8] S. Sato *et al.,* Proc. of the 1st annual meeting of particle Accelerator Society of Japan, 6C08.
[9] M. Takagi *et al.,* Proc. of the 1st annual meeting of particle Accelerator Society of Japan, 5P38.
[10] W. Bambynek, Nucl. Instr. and Meth. **112**(1973)103.
[11] G. F. Knoll, *Radiation Detection and Measurement*, 3rd Edition (John Wiley & Sons, inc, 2000).
[12] M. Tanaka *et. al.,* Proc. of the 1st annual meeting of Particle Accelerator Society of Japan, 5P27.
[13] M. Tanaka *et. al.,* Proc. of the 1st annual meeting of Particle Accelerator Society of Japan, 5P26.
[14] H. Akikawa *et. al.,* Proc. of the 1st annual meeting of Particle Accelerator Society of Japan, 6C06.
[15] R. H.Miller *et al., HEAC'83*, Fermilab,1983,pp.602
[16] R. Assmann *et al.,* Proc. EPAC2000.p1693.
[17] S. LEE *et al.,* Proc. of the 1st annual meeting of Particle Accelerator Society of Japan, 5P46.

THE HIGH ACCURACY RF PHASE DETECTOR RESEARCH FOR 200 MEV LINAC

Dong Sai, Zhou Yingui, Li Ge, Huang Guirong, Jia Dachun,
National Synchrotron Radiation Laboratory,
University of Science and Technology of China,
Hefei, Anhui 230029, P.R.China

Abstract

The basic configuration of one experimental RF Phase detector and its application in Hefei 200MeV RF Linear accelerator are introduced. The 200MeV linac, which is the injector of Hefei Light Source (HLS), is cascaded by 5 accelerator tubes. The beam energy could be stabilized and controlled accurately by implementing RF Phase detectors of the 5 cascaded accelerator tubes into a phase locked system. The tabletop experiments are given and the RF Phase detector is tuned in the off-line status. The microwave in 2856MHZ under CW mode is differentiated accurately by the developed RF phase detector. The measured results are better than prediction. The accuracy of the basic configuration of the RF Phase detector is verified, which establishes foundations for further experiments.

INTRODUCTION

200 MeV electron linac is an injector of HLS (Hefei Synchrotron Radiation Light Source), as shown in Figure 1. The Linac has been running for 17 years. Its typical operation parameters are energy of 200 MeV, Current of 50 mA and energy spread of 0.8%[1]. Its energy shift during the injection period suggest its cure by implementing RF Phase detectors of the 5 cascaded accelerator tubes into a phase locked system.

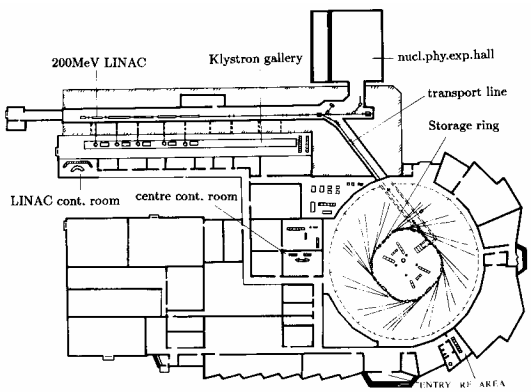

Figure 1: Layout of Hefei SLS.

In Phase-II Project of the National Synchrotron Radiation Laboratory, the old RF drive system of 200MeV Linac[2] is transformed into a high peak power RF solid-state amplifier as illustrated in Fig. 2. The main parameters of the RF power solid-state amplifier are operating frequency of 2856 MHz, peak power of 300W, pulse width (flat top) of 2.0μs, RF repetition rate of 300 pps. The new RF drive system consists of a medial power klystron amplifier and a medial power modulator. The RF solid-state amplifier drives the first high peak power klystron to amplify the 300Watt of the solid-state amplifier to a level of 8.5 MW. This power will be fed to the first accelerating tube, buncher and prebuncher. Simultaneously, a level of 15 kW from the first klystron is divided into 5 branches to drive other 5 high power klystrons along the new main drive line.

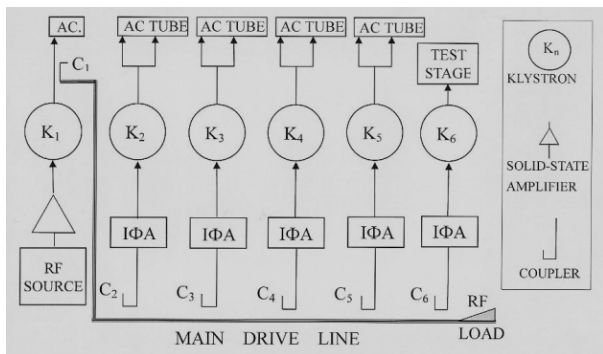

Figure 2: The New RF drive system of 200 MeV LINAC.

Free Electron Laser (FEL) is the only light source with over 20 eV photo energy and GW peak power [3-7], which covers the spectrum from mm wave to x-ray. Linac based FEL requires state-of-the-art performance from the all linear subsystems, especially RF power (within 0.1% shot-to-shot) and phase (less than 1^o rms jitter shot-to-shot and 5^o rms long-term drift). To satisfy such tight criteria, both low-level and high-power RF systems are under evaluation together with development of a precision on-line phase detector system for FEL [8-12].

The high accuracy RF Phase detector is not only necessary for reliable and stable operation of Linac as injector for storage ring [10-13], but also plays one important role in developing future Free Electron Laser system driven by the 200MeV Linac.

In 2003, National Synchrotron Radiation Laboratory, Univ. of Science and Technology of China was awarded

two grants (Innovative Research fund from Chinese Science Academy and No. 10375061 of Natural Science Foundation of China) to develop high accuracy RF phase detector and to assess its applications for RF Linear accelerator and Free Electron Laser system. These efforts are focused on RF phase detector in 2856MHZ, its application to the present 200MeV RF Linear accelerator, and potential system configuration of Free Electron Laser driven by the 200MeV RF Linear accelerator. Until now, the tested resolution of the designed RF phase detector in 2856MHZ is better than 0.3 degree. This paper describes the configuration of the high accuracy RF Phase detector as well as the architecture, trade-offs, and progress in the development of these RF phase detectors for RF accelerators and Free Electron Laser.

SYSTEM DESCRIPTION

In the multi-section RF accelerators employed in high energy RF Linac, the beam is tuned to sit on the top of RF traveling wave to get the best acceleration with RF phase shifter and energy spectrum target. Due to lots of objective reasons such as temperature, pressure and voltage fluctuations, the beam is shifted with RF phase. The process can not be automatically tuned and drawn back by personal computer (PC) to the required phase for absence of "eye"-the phase detector to monitor the RF phase deviation to the beam.

The HLS 800MeV electron storage ring is injected by 200MeV electron Linac and ramping up to 800MeV for synchrotron radiation use. The RF system to drive the 200MeV Linac has no phase detector and feedback system presently, which needs upgrading for more stable and reliable injection to the storage ring as well as FEL investigation based on Linac.

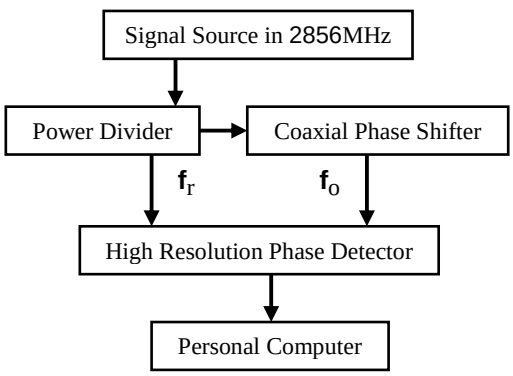

Figure 3: Configuration of Precise Phase Detector.

The configuration of the RF phase detector is illustrated in Fig. 3 The precise coaxial phase shifter is used to simulate all RF phase distortion due to temperature, pressure and voltage fluctuations. The multi-section RF accelerator could then be stabilized by implementing the developed high resolution RF phase detector in 2856MHz with the feedback loop.

The RF upgrade of Hefei 200MeV Linac with the developed RF phase detector is shown in Fig. 4 Successful implementation this RF system in HLS will benefit not only the storage ring with more stable injection, but also FEL research based on Linac.

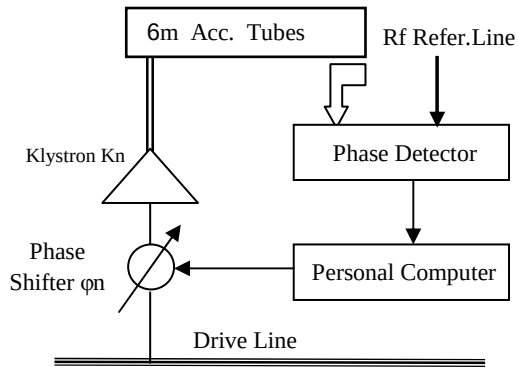

Figure 4: RF upgrade for Hefei 200MeV Linac.

PRIMARY IN-SITU EXPERIMENTS

The precise RF phase detector illustrated in Fig. 3 is tested in Hefei 200MeV RF Linac, as illustrated in Fig. 5 The signals in the downstream of klystron 5 and main drive line are coupled out for measuring. The results are listed in table 1, which states that the resolution of the precise phase detector is better than 0.3 degree.

.

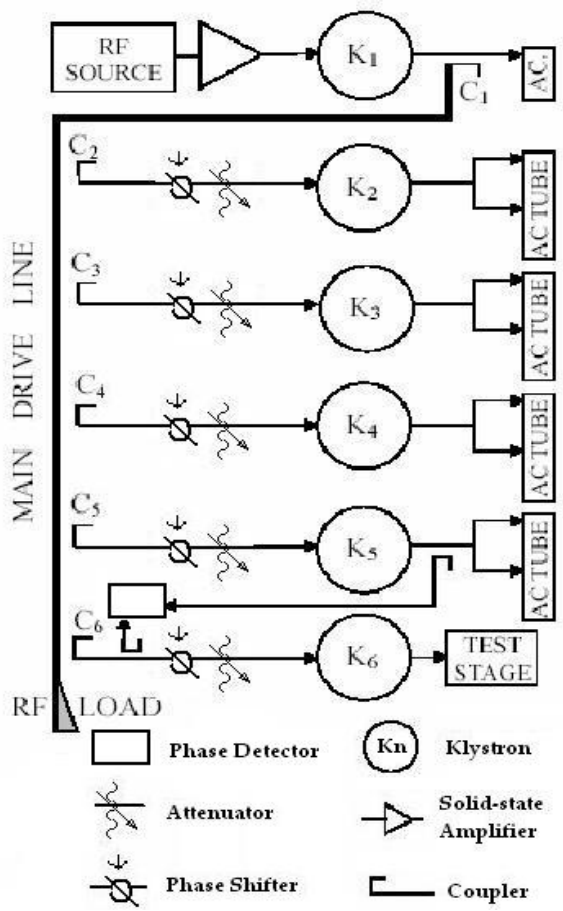

Figure 5: In-situ Experiments of Precise Phase Detector.

Table 1: The in-situ Measured Phases dated on 27-4-2004

Phase Shifter Position	The Measured Phase/degree	Time
189	-82.0	11:23
170	-56.0	11:27
170	-56.2	11:31
180	-67.7	11:34
180	-65.1	11:35
189	-81.4	11:40
189	-82.6	11:41

SUMMARY

The high accuracy RF Phase detector in 2856MHz is designed, built and tested, which underpins solid foundations for more stable injection for HLS as well as the development of linac based FEL in HLS. It's connected to the PC by Fiber optical cable. The measured phase resolution in 2856MHz is better than 0.3 degree, which could be further enhanced to 0.1 degree in the near future. Primary desktop and in-situ experiments with klystron give us confidence about its application in the phase control system of RF accelerators, where the beam energy and the energy chirp can be accurately controlled. Particularly in photo cathode RF gun, the cavity is excited by combined fundamental and third harmonic RF sources matched with suitable amplitudes and phases of them, the beam emittances are reduced from 0.6 to 0.3 microns or less over the main body of the bunch [18-20]. Therefore, the saturation length of the FEL system can be significant decreased, especially in the process of developing the short wavelength FEL [12-13, 16-17].

REFERENCES

[1] Y.J.Pei, D.F.Wang, D.H.He, Proc. of the 3rd International Conference on Synchrotron Radiation Instrumentation, Review of Scientific Instruments, Vol. 60, No. 7, 1701 (1989)

[2] Zhiang Yuan, "Design and Performance of RF Drive system for 200 MeV LINAC", Proc. of the International Conference on Synchrotron Radiation Application, May 9-12, 1989

[3] C. Limborg, "Design considerations for the LCLS," Nuclear Instruments and Methods in Physics Research A 507 (2003) 378–381

[4] J. Rossbach, "Demonstration of gain saturation and controlled variation of pulse length at the TESLA test facility FEL," Nuclear Instruments and Methods in Physics Research A 507 (2003) 362–367

[5] Dinh C. Nguyen and Henry P. Freund, "Possibility of a high-power, high-gain FEL amplifier," Nuclear Instruments and Methods in Physics Research A 507 (2003) 120–124

[6] Vladimir N. Litvinenko, "New results and prospects for harmonic generation in storage ring FELs," Nuclear Instruments and Methods in Physics Research A 507 (2003) 265–273

[7] Kui, ZHAO, "FEL Investigation Based on Superconductor Accelerator," in Chinese 973 Programme 2002-2007. Available: http://www.973.gov.cn in Chinese, Beijing, Ministry of Chinese Science and Technology.

[8] T.L. Smith et al, "RF SYSTEM UPGRADES TO THE ADVANCED PHOTON SOURCE LINEAR ACCELERATOR IN SUPPORT OF THE FEL OPERATION," in Proc. of XX Linac 2000 □ Monterey□California□August 21-25□2000.

[9] A. E. Grelick et al, "Phase control & intra-pulse phase compensation of the APS linear accelerator," in Proc. IEEE PAC'95, Dallas, May 1995, pp. 1082-1084, 1996.

[10] A. E. Grelick et al, "The High-Power S-band Feed Subsystem for the APS Injector Test Stand," in Proc. IEEE PAC'2001, Chicago, May 2001, pp. 1393-1395.

[11] S. V. Milton, E. Gluskin and N. D. Arnold et al. Exponential Gain and Saturation of a Self-Amplified Spontaneous Emission FEL[J], Science, Vol. 292, 15 JUNE 2001, PP2037-2041.

[12] S.V. Milton et al, "Observation of Self-Amplified Spontaneous Emission and Exponential Growth at 530 nm," PRL 85(5), pp. 988-991, July 2000.

[13] C. Pellegrini, "High power femtosecond pulses from an X-ray SASE-FEL," Nuclear Instruments and Methods in Physics Research A 445 (2000) 124-127

[14] J. Y. Liu, C. Z. Diao and D. H. He et al, "COHERENT HARMONIC GENERATION EXPERIMENT ON HEFEI SYNCHROTRON RADIATION SOURCE," in Proc. IEEE PAC'2003, May 2003, pp. 968-970.

[15] Dong Sai, Huang Guirong, Jia Dachun, Pei Yuanji, et al, "RF Drive System with High Power Solid-State Amplifier for 200MeV LINAC," in Proc. of Linac 2002 □ Gyeongiu □ Korea □ August 19-23 □ 2002.

[16] L.-H. Yu, M. Babzien, I.Ben-Zvi et al. "High Gain Harmonic Generation FEL", Science, Vol. 289, Aug. 11, 2000, PP932-934.

[17] Patrick G. O'Shea and Henry P. Freund, "Free-Electron Laser: Status and Application", Science, Vol. 292, 8 JUNE 2001, PP1853-1858.

[18] D.H. Dowell, M. Ferrario, T. Kimura, J. Lewellen, C. Limborg, P. Raimondi, J.F. Schmerge, L. Serafini, T. Smith and L. Young, "A Two-Frequency RF Photocathode Gun," Tsukuba, Japan, (2003)

[19] L. Serafini et al, NIM A318 (1992)301-307, T.I. Smith, Proc. Linear Acc. Conf., SLAC PUB-303.

[20] Robert M. Phillips and Daryl W. Sprehm, "High-Power Klystrons for the Next Linear Collider," Proc. of the IEEE Vol. 87(5), pp. 738-751, May 1999.

ADAPTIVE FEEDFORWARD CANCELLATION OF SINUSOIDAL DISTURBANCES IN SUPERCONDUCTING RF CAVITIES *

T. Kandil, T.L. Grimm, W. Hartung, H.K. Khalil, J. Popielarski, J. Vincent, R.C. York†
Michigan State University, East Lansing, MI 48824, USA

Abstract: A control method, known as adaptive feedforward cancellation (AFC) is applied to damp sinusoidal disturbances due to microphonics in superconducting RF (SRF) cavities. AFC provides a method for damping internal, and external sinusoidal disturbances with known frequencies. It is preferred over other schemes because it uses rudimentary information about the frequency response at the disturbance frequencies, without the necessity of knowing an analytic model (transfer function) of the system. It estimates the magnitude and phase of the sinusoidal disturbance inputs and generates a control signal to cancel their effect. AFC, along with a frequency estimation process, is shown to be very successful in the cancellation of sinusoidal signals from different sources. The results of this research may significantly reduce the power requirements and increase the stability for lightly loaded continuous-wave SRF systems.

INTRODUCTION

The control of the resonance frequency of SRF cavities is highly desirable in view of the narrow bandwidth of operation. Detuning of SRF cavities is caused mainly by the Lorentz force (radiation pressure induced by high RF field) and microphonics (mechanical vibrations). In continuous-wave (cw) accelerators, microphonics is the major concern. It is natural to think of using fast mechanical actuators to compensate for, i.e., attenuate, the effect of mechanical vibrations on detuning. This concept was applied successfully by Simrock et al [1] to a simple quarter wave resonator (QWR) with a fast piezoelectric tuner. However, the high-gain feedback approach used in [1] is too complex to apply to multi-cell elliptical cavities, which is the subject of this work. In fact, in a previous work by Simrock [2] for elliptical cavities it is stated that "the large phase shift over this frequency range makes it clear that feedback for microphonics control using the RF signal will not be possible with the piezo actuator." To date, there has been no demonstration of microphonics control on multi-cell SRF cavities, and the current paper presents the first such demonstration.

We start by formulating the microphonics control problem from a control theory viewpoint and exploring various standard control approaches. We conclude that AFC is the most appropriate for the task because it handles sinusoidal disturbances, which are the main source of microphonics, it is developed for stable systems, as in the current case, and it does not require an analytic model of the system to design a feedback controller. Then, we review the main elements of the theory of AFC, and present our experimental demonstration of its successful use in microphonics control of elliptical cavities.

*This work was supported in part by the Michigan State University Foundation IRGP grant # 3699 and US Department of Energy under grant number DOE DE-FG02-00ER41144.

†T. Kandil and H.K. Khalil are with the Department of Electrical and Computer Engineering, and T.L. Grimm, W. Hartung, J. Popielarski, J. Vincent, and R.C. York are with the National Superconducting Cyclotron Laboratory.

PROBLEM FORMULATION AND PRELIMINARY WORK

The starting point is to develop a mathematical model that describes how the mechanical vibrations and the control actuator determine the cavity detuning. It is shown in [3, Section 3.2] that the relationship between the cavity detuning $\Delta\omega = \omega_0 - \omega$ and the phase angle ψ (between the driving current and cavity voltage) can be approximated by a parallel RLC circuit; consequently,

$$\tan\psi = 2Q_L\left(\frac{\Delta\omega}{\omega}\right) \tag{1}$$

where ω is the RF generator frequency, ω_0 is the cavity eigenfrequency, and Q_L is the loaded Q factor, defined by

$$Q_L = 2\pi\cdot\frac{\text{Stored energy}}{\text{Total power dissipation/cycle}}$$

From (1), we see that detuning can be reduced by reducing the phase angle ψ. Towards that end, we develop a model for ψ. Two basic assumptions in developing this model are:

- Mechanical vibrations, which affect the cavity in a distributed way, can be modelled by an equivalent lumped disturbance that affects the system at the same point where the control actuator is applied. In other words, the input to the system can be represented as the sum $u-d$, where d is the disturbance input and u is the control input.
- The system with input $u-d$ and output ψ is linear and time-invariant. Hence, it can be represented by a transfer function $G(s)$ from $u-d$ to ψ.

From a control theory viewpoint, the problem reduces to designing the control u to reject or attenuate the effect of the disturbance d on the output ψ. We started our investigation by examining six different control techniques for disturbance rejection: (1) Proportional (P), (2) Proportional-Integral (PI), (3) Proportional-Integral-Derivative (PID), (4) High-gain band-limited, (5) Servocompensator design, and (6) Adaptive Feedforward Cancellation (AFC). The six techniques were investigated in the internal report [4] using simulation of an experimentally-determined model of a

single-cell copper RF cavity at room temperature. The simulation studies showed that the traditional P, PI, and PID controllers would not achieve the desired level of disturbance attenuation because the controller gains are limited by stability requirements. In the high-gain band-limited control design, a controller is designed to have a high loop gain over the frequency band of interest, while rolling off the controller's frequency response rapidly at high frequency to ensure the stability of the closed-loop system. The drawback of this design is the relatively high-order of the controller. It is worthwhile to note that this technique is used by Simrock et al. [1] in microphonics control of a quarter wave resonator with a fast piezoelectric tuner. However, our investigation indicates that the complexity of the controller and the demand on the control effort in such design will be prohibitive for multi-cell cavities because the order of the controller will be very high. Even in the simple experiment of [1], the controller's order is 20, i.e., the degree of the denominator polynomial of the controller's transfer function is 20.

Microphonics is known to be caused, primarily, by mechanical vibrations that are almost periodic; in particular, the disturbance signal can be represented as the sum of a finite number of sinusoidal signals. For this type of disturbance, the techniques of servocompensators, e.g. [5], and AFC, e.g. [6], are more appropriate because they are designed to work with this particular class of signals. Both approaches performed satisfactorily in the simulation study [4], but the AFC has the advantage that the only information about the transfer function $G(s)$ that is needed is its magnitude and phase at the input frequencies, which can be easily obtained from the experimentally-determined Bode plots. Mathematical analysis of the system illustrated that we can tolerate up to 90 deg phase error, while magnitude error will only affect the speed of convergence of the adaptive algorithm and will not alter its stability. For the servocompensator approach, we have to obtain an analytic model of the system in the form of a rational transfer function to use in designing the compensator. Because of the simplicity of the AFC method, we have adopted it in the experimental part of our work.

ADAPTIVE FEEDFORWARD CANCELLATION

Consider a linear stable system represented by the transfer function $G(s)$. Let y be the output of the system and suppose the input is the sum of two signals $u-d$, where u is the control input and d is an unknown disturbance that can be modelled as the sum of sinusoidal signals of known frequencies, but unknown amplitudes and phases, that is,

$$d=\sum_{i=1}^{n}A_i\sin(\omega_i t+\theta_i)\stackrel{\text{def}}{=}\sum_{i=1}^{n}[a_i\sin(\omega_i t)+b_i\cos(\omega_i t)] \quad (2)$$

where ω_i, for $i=1,\cdots,n$, are known but a_i and b_i are unknown. The goal is to design the control input u, so as to attenuate the output y in the presence of the disturbance d.

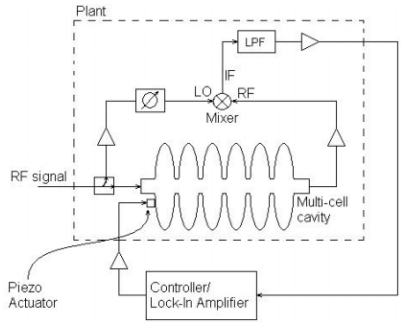

Figure 1: Physical setup of the cavities with the control unit or lock-in amplifier.

Had we known the amplitudes and phases of the sinusoidal signals, we could have cancelled the disturbance by

$$u=\sum_{i=1}^{n}[a_i\sin(\omega_i t)+b_i\cos(\omega_i t)]$$

To cope with the uncertainty in the parameters a_i and b_i, we use the control

$$u=\sum_{i=1}^{n}[\hat{a}_i\sin(\omega_i t)+\hat{b}_i\cos(\omega_i t)] \quad (3)$$

where $\hat{a}_i$ and $\hat{b}_i$ are estimates of a_i and b_i, respectively, obtained by the adaptive algorithm

$$\dot{\hat{a}}_i(t) = -\gamma_i y(t)\sin(\omega_i t+\theta_i) \quad (4)$$

$$\dot{\hat{b}}_i(t) = -\gamma_i y(t)\cos(\omega_i t+\theta_i) \quad (5)$$

where $\gamma_i>0$ are positive adaptation gains. Since $G(s)$ is stable, by choosing the adaptation gains γ_i small enough so it follows from [7, Theorem 4.4.3] that, in the absence of measurement noise, the adaptive algorithm ensures convergence of the parameter estimates $\hat{a}_i$ and $\hat{b}_i$ to the true parameters a_i and b_i, respectively, and convergence of the output $y(t)$ to zero. In the presence of bounded measurement noise, we can invoke standard perturbation analysis to show that, after finite time, the output will be of the order of the measurement noise.

EXPERIMENTAL DEMONSTRATION

The setup is shown in Figure 1, where the estimated noise signal is added to the system by directly shaking an SRF 6-cell elliptical cavity, cooled to 2 K, using a piezoelectric actuator (PI, model P-842.60). The controller can also be replaced by a lock-in amplifier to generate the Bode plot of the system. The block diagram of the AFC algorithm is shown in Figure 2 for the case of a single-frequency disturbance. It is an implementation of Equations (4) and (5). In Figure 2, ω is the angular frequency of the disturbance signal that is calculated from an FFT of the RF error signal, θ is a phase advance introduced to ensure maximum stability of the system, and γ is the adaptation gain. Both θ and γ are determined from a numerically saved Bode plot, where θ is the phase at the frequency to be cancelled and γ is calculated from the magnitude information such that its value is large at small magnitudes and relatively small at large magnitudes.

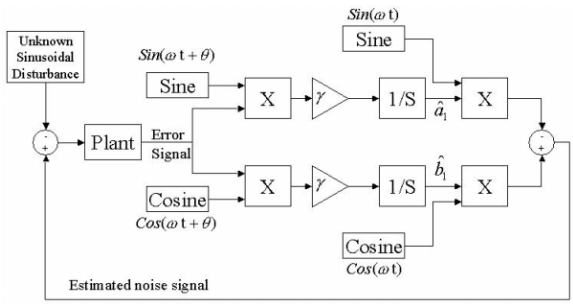

Figure 2: Implementation of the AFC on Simulink.

Experimental setup

A prototype 805 MHz cryomodule has been tested to demonstrate the required performance for the Rare Isotope Accelerator [8, 9]. An external PC is used for modelling the controller in Simulink, which is then built in dSPACE CONTROLDESK developer version that communicates with an external hardware (dSPACE RTI1104 board), with 16 I/O ports. The user's interface is through dSPACE CONTROLDESK developer version for parameters adjustments to achieve optimum control.

The Bode plot is obtained using an SRS digital lock-in amplifier model SR850, as shown in Figure 1. The lock-in amplifier sends out a sinusoidal signal to the piezo-electric actuator that is swept through the desired frequency range, step size, and sampling rate, then the output of the plant is fed back into the lock-in amplifier compared to the output signal of the lock-in amplifier to produce a Bode plot, which is saved in the form of a look-up table. The FFT of the RF error signal is generated from a LeCroy Waverunner LT342 digital oscilloscope, from which the largest frequency components are picked for damping.

Experimental Results

We observed two types of microphonics vibrations: internal (helium oscillations) and external (motors, pumps, etc.). The results of applying AFC to both types are shown in Figures 3 and 4. Figure 3 shows cavity detuning due to internal helium oscillation at 6.5 Hz. It shows an FFT of the detuning for the undamped and damped responses. After applying a cancellation signal at 6.5 Hz, the internal energy shifted to 13 Hz, where another cancellation signal was applied. The first peak at 6.5 Hz was reduced by a factor of 6 from 59 Hz to 10 Hz, while the second peak at 13 Hz was reduced from 13 Hz to 4 Hz.

Figure 4 shows the undamped and damped responses due to external vibrations from a motor that was turned on purposely for demonstration. The noise appeared at 57.5 Hz, and it was successfully damped by a factor of 7.4 from 31 Hz to 4.2 Hz.

CONCLUSIONS

We have demonstrated the successful use of piezoelectric actuators and adaptive feedforward cancellation control to damp sinusoidal disturbances due to microphonics in SRF cavities. The next step in our research is to equip the AFC algorithm with a mechanism to identify the frequencies of the disturbance inputs, and to implement it using field programmable gate arrays (FPGA).

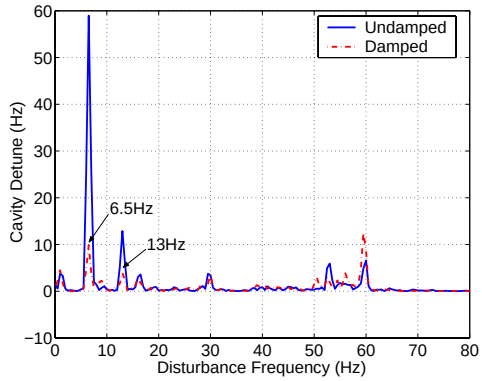

Figure 3: Active damping of helium oscillations at 2K.

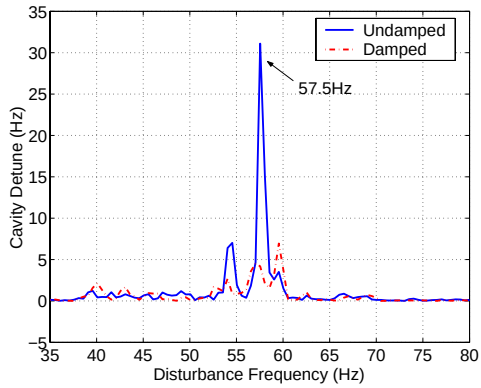

Figure 4: Active damping of external vibration at 2K.

REFERENCES

[1] S. Simrock et al. First demonstration of microphonic control of a superconducting cavity with a fast piezoelectric tuner. In 2003 Particle Accelerator Conference, pages 470-472, Portland, OR, 2003.

[2] L. Lije, S. Simrock, D. Kostin, and M. Fouaidy. Characteristics of a fast piezo-tuning mechanism for superconducting cavities. In 2002 European Particle Accelerator Conference, pages 2256-2258, Paris, 2002.

[3] T. Schilcher. Vector sum control of pulsed accelerating fileds in Lorentz force detuned superconducting cavities. PhD thesis, University of Hamburg, Germany, 1998.

[4] S. Seshagiri. Active control of microphonics detuning. Technical report, Michigan State University, East Lansing, 2003.

[5] A. Isidori, L. Marconi, and A. Serrani. Robust Autonomous Guidance: An Internal Model Approach. Springer, London, 2003.

[6] M. Bodson, A. Sacks, and P. Khosla. Harmonic generation in adaptive feedforward cancellation schemes. IEEE Trans. Automat. Contr., 39:1939-1944, 1994.

[7] S. Sastry and M. Bodson. Adaptive Control. Prentice-Hall, Englewood Cliffs, New Jersey, 1989.

[8] T.L. Grimm et al. Experimental Study of an 805 MHz Cryomodule for the Rare Isotope Accelerator. In LINAC 2004, Lubeck, Germany, 2004.

[9] T.L. Grimm et al. Measurement and Control of Microphonics in High Loaded-Q Superconducting RF Cavities. In LINAC 2004, Lubeck, Germany, 2004.

STATUS OF RF CONTROL SYSTEM FOR ISAC II SUPERCONDUCTING CAVITIES

K. Fong, M. Laverty, S. Fang, TRIUMF, Vancouver

Abstract

The rf control system for the ISAC II superconducting cavities is a hybrid analogue/digital system using a self-excited feedback loop. It has undergone more than a year of testing. Improvements have been made to every aspect of the system including phase detection, loop regulation, data acquisition, as well as communication with EPICS. With a loaded Q of 100,000, amplitude regulation bandwidth of 400 Hz and phase regulation bandwidth of 100 Hz have been achieved. Simultaneous operation of 3 cavities under typical ISAC 2 operating conditions has also been demonstrated.

INTRODUCTION

The design of the RF system has been described in several previous papers[1][2]. Based on the experience gained in tests under superconducting conditions, the present system has eliminated some shortcomings in the original design and has incorporated several important improvements. Crosstalk between different feedback paths has been eliminated. This resulted in much improved regulation bandwidth in the phase/frequency loop. A higher dynamic range phase detector is used which enables self-excited operation at both high and low power levels. However, the most important improvements are in the supervisory software, particularly in the area of EPICS communication and multi-thread synchronization.

RF CONTROL SYSTEM

System Model

The transfer function representation of the self-excited system with quadrature control with perfect alignment in static loop phase is given by[3]:

$$\begin{bmatrix}\delta V\\ \delta\Omega\end{bmatrix}=\begin{bmatrix}G_{aa} & G_{ta}\\ G_{a\omega} & G_{t\omega}\end{bmatrix}\begin{bmatrix}\delta v_i\\ \delta v_q\end{bmatrix} \qquad (1)$$

where

$$G_{aa}=\frac{\gamma}{1+\tau s},\qquad G_{ta}=0,$$

$$G_{a\omega}=-\frac{1}{v_i}\frac{\Omega}{(1+\tau s)},\qquad G_{t\omega}=\frac{1}{v_i\tau}\equiv\eta, \qquad (2)$$

$\tau=\dfrac{2Q}{\omega_c}$ is the time constant of the cavity,

$\Omega=\omega-\omega_c$ is the detuning of the cavity, with γ is

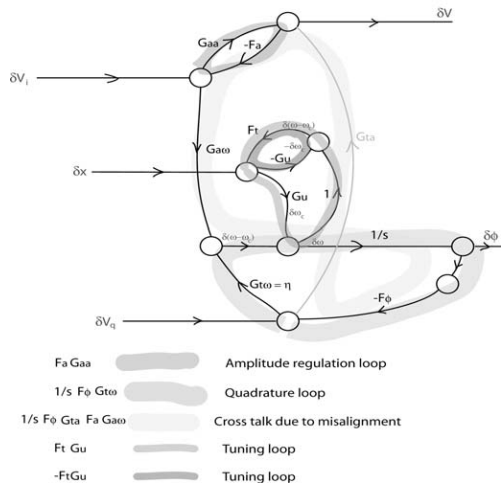

Figure 1: Signal Flow Graph of the Amplitude, Phase and Tuning Loops.

the voltage transformation ratio, ω_c the natural resonance frequency of the cavity and Q the loaded cavity quality factor. Eq. 1 is used to form the signal flow graph of the complete RF control system in Fig. 1, where F_a, F_ϕ and F_t/s are the amplitude, quadrature and tuner feedback coefficients, respectively. The $1/s$ factor from the tuner feedback coefficient arises due to that fact we have implemented velocity feedback in the tuner control. The sensitivity of frequency to tuner movement is given by

$$G_u=\frac{\partial\omega_c}{\partial x} \qquad (3)$$

and depends only on the geometries of the cavity and the tuning mechanism. From the signal flow graph we get the various open loop gains of the feedback system: Amplitude loop gain is given by:

$$G_a=F_aG_{aa}=\frac{\gamma F_a}{1+s\tau} \qquad (4)$$

and phase loop gain is given by:

$$G_\phi = \frac{F_\phi G_{t\omega}}{s} = \frac{F_\phi \eta}{s} \quad (5)$$

Furthermore, closed loop gains of the feedback system are:

$$\frac{\delta V}{\delta v_i} = \frac{G_{aa}}{1+F_a G_{aa}} \approx \frac{1}{s\tau + 1 + F_a}, \quad (6)$$

$$\frac{\delta \phi}{\delta v_q} = \frac{\eta(s+F_t G_u)}{s^2 + F_\phi \eta(s+F_t G_u)}, \quad (7)$$

$$\frac{\delta \phi}{\delta x} = \frac{sG_u}{s^2 + F_\phi \eta(s+F_t G_u)}, \quad (8)$$

$$\frac{\delta v_q}{\delta x} = \frac{sF_\phi G_u}{s^2 + F_\phi \eta(s+F_t G_u)} \quad (9)$$

From Eq. 6, 7, and 9 we see that if one requires zero steady-state errors for both amplitude and phase errors, then one requires at least a pole at the origin in both F_a and F_ϕ. To minimize rf power, one also requires the steady-state error for quadrature drive be zero. This can be achieved when F_t is a constant. Thus Proportional-Integral-Differential controllers are used in the amplitude and phase loops, and a proportional controller is used in the tuner loop.

System Hardware

Each cavity controller consists of two VXI modules: the rf module, colored pink in Figure 2, and the DSP modules, colored green in Figure 2. A total of four controllers are housed inside a VXI mainframe. Another VXI module generates the different phase references for the 4 controllers. An Agilent FireWire VXI slot 0 controller controls all of these modules. The feedback controller consists of three main regulation loops - the amplitude loop, the quadrature phase/frequency loop, and the tuning loop. As seen in Figure 2, part of the feedback signal is amplitude limited.

This amplitude limited signal is used for both amplitude and phase detection. Synchronous demodulation is used in the amplitude detector because it has good amplitude linearity and large dynamic range. The detected signal is filtered, sampled and digitized at 66 k samples/sec and fed into a Motorola DSP56002 Digital Signal Processor. The DSP is configured as a Proportional-Integral controller, providing amplitude regulation. The limiter output is also compared with an external master frequency source using a phase/frequency discriminator. The difference in phase is filtered by the same DSP running a parallel PID controller task, whose output is used to control the quadrature part of the amplifier output. The same amplitude limited signal is mixed with an amplitude limited signal from the input side of the cavity using an edge-triggered JK flip-flop, and the mixing product is filtered, digitized

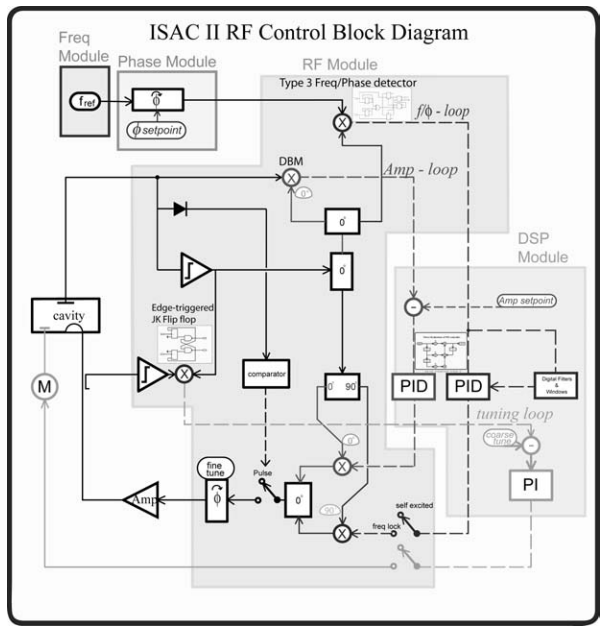

Figure 2: Block Diagram of Superconducting RF cavity control system.

and processed by a separate DSP to form the velocity signal for the tuning servo motor, which is described in a separate paper in this conference[4].

System Software

There are three levels of software in a module controller. The first level controls each individual DSP in each feedback loop. It resides in the program memory of the DSPs and performs open loop output, closed loop regulation, as well as output limiting. It is written in assembler and is loaded into the DSP program memory at power up and executed automatically. It can also be dynamically changed via the VXI interface.

The second level software is the supervisory process for individual cavity control. It sends instructions to the first level software to set feedback loop parameters and power up sequencing. It also performs data acquisitions and most of the cavity controls. These are done via separate threads and access to the DSPs and the ADCs are coordinated with lightweight intra-process thread synchronization, in critical sections. These are 4 such multi-thread processes running per cryomodule, each controlling a single cavity. The software is written in C++ and resides in a rack-mounted PC and communicates with the VXI modules via a FireWire (IEEE 1394) interface. The third level manages VXI modules that are common to all the cavities, other resources, safety interlocks, and communication with the central control system. Communication between the first level of the VXI modules is also done via the same FireWire interface. Data exchange between the second level and the third level is done via a shared memory Dynamic Linking Library. This software also has an embedded EPICS virtual IOC for site-wide communication. Figure 3

shows the deployment diagram of the system software at the second and the third level.

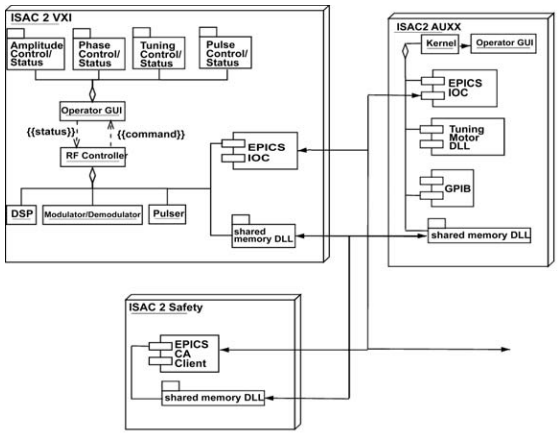

Figure 3: Deployment Diagram of ISAC 2 Control System.

System Performance

Figures 4 and 5 show the achieved open loop gains in the amplitude and phase loops, respectively, under typical operating condition. With PID controllers, the open loop gains of Eq. 4 and 5 can be rewritten as

$$G_a = \gamma K_{a_i} \frac{(1+s\tau_a)}{s(1+s\tau)},\ G_\phi = \eta K_{\phi_i} \frac{(1+s\tau_\phi)}{s^2}$$

Since the resonator pole τ and the zero of the amplitude PID controller τ_a are only slightly different in frequency, their effects are almost cancelled. The overall response is similar to that of a simple pole at zero frequency. The unity gain bandwidth for the amplitude loop is 400 Hz, with 90° phase margin and gain margin well in excess of 20dB.

In the phase loop, the system starts with a double pole at very low frequencies. The phase detector and the phase PID controller each contribute a simple pole. The zero of the PID controller τ_ϕ restores the system to that of a single pole response above 100 Hz. The unity gain bandwidth is 120 Hz, with similar gain and phase margin to that of the amplitude loop. The system is thus unconditionally stable in both the amplitude and phase loops, with the accuracy of regulation limited only by the available rf power. The performance of the tuner loop depends primarily on the processor speed and the servo motor controller speed. With a 350 MHz Intel Pentium processor, an update rate of 200 Hz is achieved with four controllers running simultaneously.

CONCLUSION

The rf control system has been tested in every aspect of the system and has performed satisfactory, including phase detection, loop regulation, data acquisition as well as communication with EPICS. With a loaded Q of 100,000, amplitude regulation bandwidth of 400 Hz, phase regulation bandwidth of 100 Hz has been

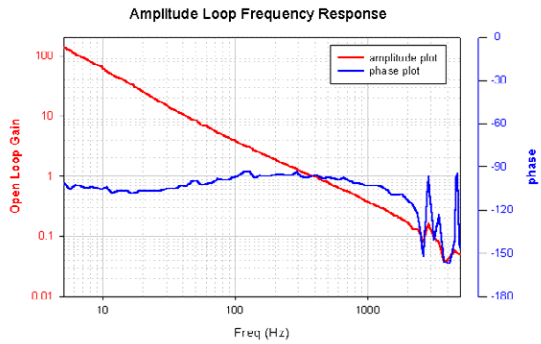

Figure 4: Amplitude Loop Bode Plot.

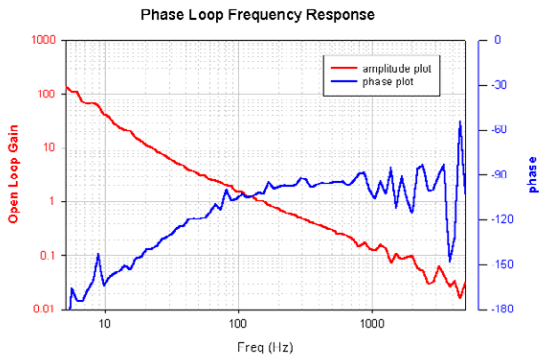

Figure 5: Phase Loop Bode Plot.

achieved. Simultaneously operation of 3 cavities under typical ISAC 2 operating conditions has also been demonstrated.

REFERENCES

[1] K. Fong, M. Laverty, S. Fang, “RF Control System for ISAC II Superconducting Cavity Test Stand”, Proceedings of the LINAC 2002, Gyeongju, Korea, August 2002.

[2] K. Fong, S. Fang, M. Laverty, “RF Control System for ISAC II Superconducting Cavities”, Proceedings of the 2003 Particle Accelerator Conference, Portland, USA, May 2003.

[3] J.R. Delayen, "Phase and Amplitude Stabilization of Beam-Loaded Superconducting Resonators", Proc. Linac 92, p. 371.

[4] R.E. Laxdal et al, “Cold Test Results of the ISAC-II Medium Beta High Gradient Cryomodule”, This proceeding.

DIAGNOSTICS FOR THE LOW LEVEL RF CONTROL FOR THE EUROPEAN XFEL

T.Jezynski*, P.Pucyk*, S.Simrock#
*Warsaw University of Technology, Inst. Electronic Systems, Poland, # DESY, Germany

Abstract

One of the most important goal of the diagnostic system is to provide the high reliability. This article describes the concept and the proposal for a diagnostics for the Low Level Radio Frequency system for EU-XFEL. It enables immediate location of faults and understanding of their causes, tests the functionality of LLRF system, tests each of the electronic boards and connections. The diagnostic system checks different LLRF subsystem components. Hardware, software and database aspect of diagnostic system is presented. The main part of this paper is devoted to the hardware and software specification of the diagnostic.

INTRODUCTION

The X -ray free-electron laser EU-XFEL, that is begin planed at the DESY research center will produce high-intensity ultra short X-ray flashes with the properties of laser light. The commissioning of the facility could start in 2012. The total length of the tunnel will be about 2.1 km. The access to the whole electronics placed inside the tunnel will be possible only during the maintenance day (once a month or even more seldom). One of the requirements for the electronic subsystems is the long lifetime and continues work. The LLRF devices will be installed inside the tunnel and exposed on some small level of the radiation. This radiation can cause Single Event Upset (SEU) an active electronic components. Therefore an additional systems redundancy is needed as well as the radiation hardness hardware to ensure the continues work. It is impossible to predict all ways it can fail. Therefore a diagnostic system is needed in order to monitor the hardware and in case of failure switch the system off or run the redundant one. It should also be able to perform offline tests of the device and diagnose the reason of the failure. Because of the scale of the accelerator it is also important to give the information about the placement of the broken part. Due to the complexity of the LLRF system and dependencies between its parts the diagnostic system should monitor as much devices as it is possible. All devices should also provide some hardware and software interfaces through which tests can be preformed. Diagnostic system itself should provide an user interface for experts and operators.

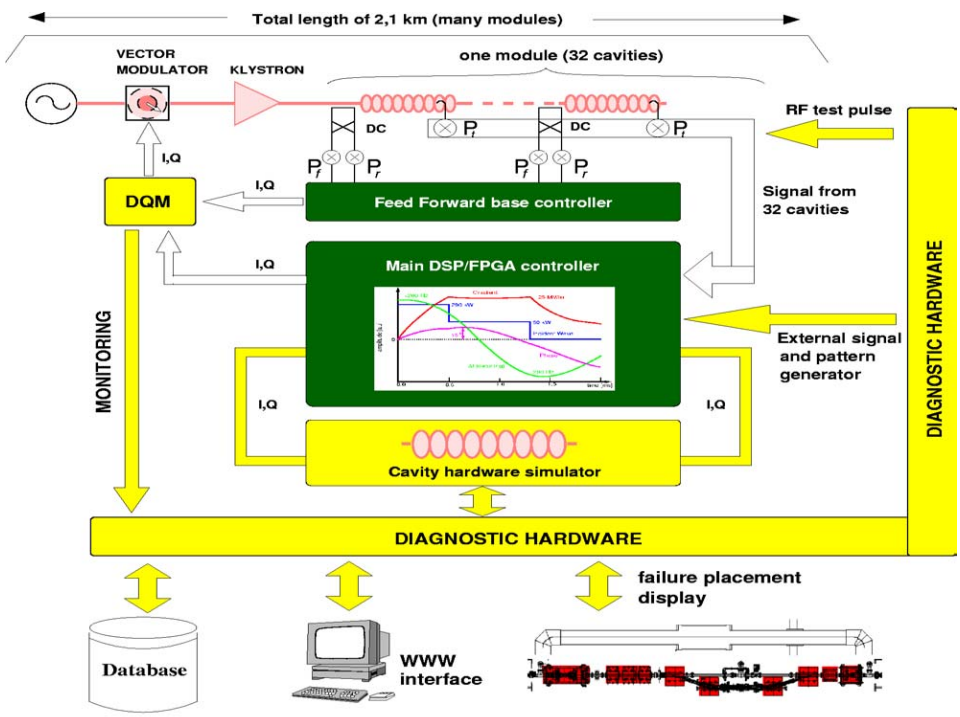

Figure 1: The structure of LLRF and the diagnostic system.

CONCEPT OF THE DIGNOSTIC SYSTEM

Electronics in LLRF

To design a good diagnostic system means to possess the appropriate knowledge about the LLRF implementation. its structure. The LLRF system will control the electromagnetic field inside the cavity. It consists of probe which measures the field in the cavity, downconverter which decreases frequency from 1.3GHz to 250kHz, in new version to 81 MHz, controller boards with ADCs, DACs, DSP and FPGA [1] chips, timing and trigger distribution system, vector modulator and other components. The system was described in [2]. One module consists of 32 cavities, one vector modulator (VM) and DSP/FPGA controller. The downconverted probe signal is digitized by the ADCs and sent to DSP/FPGA controller. The controller has implemented feed-forward and feedback algorithm. It produces signal I and Q which drive VM. For the output signal calculation the algorithm uses the vector sum electromagnetic field form 32 cavities

The Diagnostic System

The main tasks of the diagnostic software are:

- Monitoring power, temperature, etc.
- Failure detection.
- Perform the complex test of the all electronic boards.
- Examination of the connection between boards.
- Checking logic and algorithm.
- Checking the timing.
- Analysis of the correlation between failures.
- Storing result in database.
- Presentation result of test.

The general concept of the diagnostic system is given in Figure 1. The diagnostic system consists of the hardware and software layer. The signal from the cavity is connected to downconverter and then to DSP/FPGA controller. A simple version of the controller, which allows to use feed-forward tables is running parallel with DSP/FPG controller. The diagnostic system is distributed among different hardware devices. These simple block measures forward and reflected power and can estimate field inside the cavity. The outputs from both controllers are connected to voting system, which can choose the better driving signal. In case any errors, an error signal is sent to the main diagnostic software. At the moment only one controller can drive the VM. In case of error in main controller, another controller will drive VM. The stability driven by the feed-forward controller is slightly degraded but sufficient for operation. It is possible to switch controllers during RF pulse. When main controller is disabled, it is possible to start diagnostic process with the cavity simulator. More sophisticated tests are possible with dummy data. When a problem is diagnosed, it is possible to use modified algorithm and continue the operation. For example if the one ADCs is broken, it is possible continue the operation with the algorithm that estimates the missing data from other sources.

Database is one of the most important elements of the diagnostic system. It stores information about the expected performance, interfaces between boards, placement whole electronics in the tunnel, configuration data, setup files, test results, calibration and system documentation including description of used electronic boards, known problems. Access to database is possible through WWW as well as with dedicated stand-alone applications.

Hardware

The hardware of the diagnostic system consists of:

- dedicated diagnostic and monitoring modules, integrated with the electronic board. This module allows to access any register, memory and chips on the board.
- sources of test signals
- cavity simulator.

The control board for the LLRF is shown in the Figure 2. This board is equipped with the diagnostic module. It includes the FPGA, with implemented DSP blocks, memory, ADCs, DACs, digital inputs and outputs. The PC manages the data transfer from the internal bus to the VME bus. There is also possible to read and write data from the internal bus through Ethernet. This is additional feature, which allows to test the board independently from VME. On the board there is a temperature sensor and a power monitor. The diagnostic module is connected to the internal and VME bus, that allows to access all components on the board. The diagnostic module is equipped with modules, which allows to calculate histogram the given values or count events.

Tests of the particular subsystems may require an additional input signals, which are defined by the user and specific for the particular device. Such a signal, connected to the input of the system (e.g. probe from the cavity) can test the whole chain of devices – from down-converter up to VM.

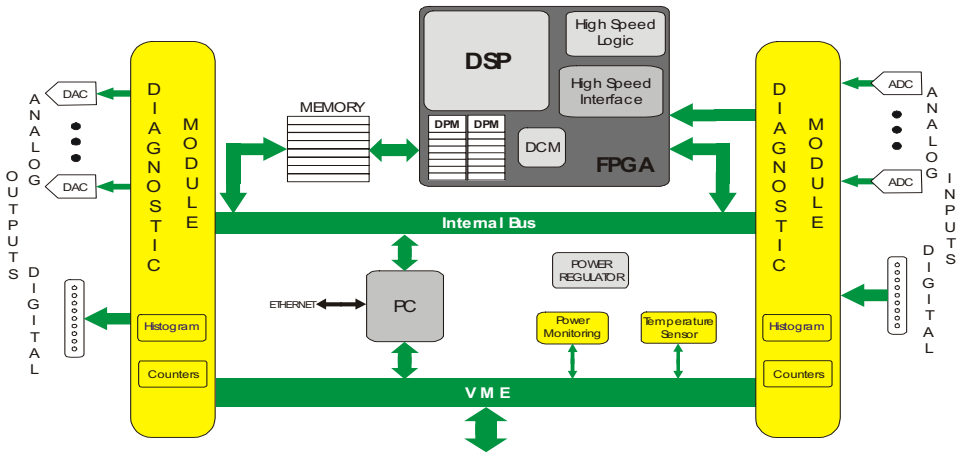

Figure 2: The examples board, control board equipped with diagnostic module.

There are two kinds of test signals:

- *RF test pulse*, allows to examine functionality, logic and connection. The test signal is being put on the input of the system. For the given test signal, diagnostic system knows the proper output signal. This known output signal is being compared with the real output from the tested system. If these signals are not equal this means system failure.
- *signal and pattern generators* allows to examine ADC channels, logical inputs. It can be a part of the bigger chain. Result of tests of the diagnostic system can read immediately from the diagnostic module and compare with predicted values.

The last diagnostic hardware is the cavity simulator, described in [3] and [4]. This device allows to test very precisely the logic, algorithm of the feedback and errors in real time. The cavity simulator can work in a step mode operation. It is very useful option that allows to debug algorithm and the boot file for FPGA step by step. All hardware diagnostic modules allow to test the system on-line, between pulses. This ensures that the possible error can be detected before the next pulse and appropriate procedures can be triggered (switching into redundant system, reconfiguring, etc.) in order to keep the system working.

Software and Database

- The complete analysis of data from the diagnostic modules is done by the software. The diagnostic software controls all the diagnostic hardware through VME bus. Access to VME bus is possible via VME controller – SUN SPARC – or in reasonable cases via Ethernet.

Information about connections, placement of hardware, base addresses of the boards are stored in database. The diagnostic system can be run only from control room, but it is possible to observer diagnose process through web browser (WWW). The configuration data, result of the calibration, and other diagnostic results are also stored in database for further analysis.

System Integrity Monitoring

The important goals of the on-line diagnostic system is to monitor: power and temperature on boards, collect information about events and collecting them in the database. The off-line analyze can correlate an event with data from database. The diagnostic system takes data from input and output of DSP/FPGA controllers, calculated output and compare predicted output witch output from the controller.

CONCLUSION

An initial of the overall feedback system with a cavity simulator has been demonstrated successful. The diagnostic system allows to maintain LLRF components. Collected diagnostic data can be used by designers, experts to improve the construction and algorithms. Presented solution does not severely increase the cost of the design and manufacturing of the electronic devices, but ensures the longer operation time of the whole system and can safe money and effort used for the maintenance .

REFERENCES

[1] A.Burghard; FPGA Based RF Control; TESLA Notes no. 2003-16

[2] S.Simrock; The RF Control System for the DESY X-FEL; Proceedings of SPIE, Bellingham, WA, USA, Vol. 5125, 2003.

[3] S.Simrock at el. Cavity Control System, Models Simulations for TESLA Linear Accelerator; TESLA Notes no. 2003-09

[4] .Czarski at el. Cavity digital control testing system by Simulink step operation method for TESLA linear accelerator and free electron laser; Proceedings of SPIE, Bellingham, WA, USA, Vol. 5125, 2003.

A NEW RF SYSTEM FOR THE CEBAF NORMAL CONDUCTING CAVITIES*

C. Hovater#, H. Dong, A. Hofler, G. Lahti, J. Musson and T. Plawski,
Jefferson Lab, Newport News, VA, USA

Abstract

The CEBAF Accelerator at Jefferson Lab is a 6 GeV five pass electron accelerator consisting of two superconducting linacs joined by independent magnetic transport arcs. CEBAF also has numerous normal conducting cavities for beam conditioning in the injector and for RF extraction to the experimental halls. The RF systems that presently control these cavities are becoming expensive to maintain, therefore a replacement RF control system is now being developed. For the new RF system, cavity field control is maintained digitally using an FPGA which contains the feedback algorithm. The system incorporates digital down conversion, using quadrature under-sampling at an IF frequency of 70 MHz. The VXI bus-crate was chosen as the operating platform because of its excellent RFI/EMI properties and its compatibility with the EPICS control system. The normal conducting cavities operate at both the 1497 MHz accelerating frequency and the sub-harmonic frequency of 499 MHz. To accommodate this, the new design will use different receiver-transmitter daughter cards for each frequency. This paper discuses the development of the new RF system and reports on initial results.

RF SYSTEM

The chopper and separator cavities are both beam deflecting cavities. In the case of the chopping cavities two orthogonal modes (Q_L 11,000) are excited in a single copper structure, with mode isolation being greater than 40 dB. The electron beam is chopped and then "de-chopped" after the beam has been modified. The separator cavities use a TEM dipole mode (Q_L 2500) that can deflect multiple beams [1]. The field control requirement for these cavities is relatively undemanding at 1% and 1 ps rms amplitude and phase control. In the case of the chopping cavities, the amplitude is rarely changed, but in the case of the separator, amplitude is adjusted to reflect the deflection needed for different beam energies. In both cases phase is adjusted upon initial start up of the accelerator and then tweaked as needed. Therefore the RF system can be rather simple.

Figure 1 shows a block diagram of the low level RF control system (LLRF). This architecture has become the common model for single cavity control LLRF systems, with 4 RF inputs and 2 RF outputs utilizing a modern large field programmable gate array (FPGA). We have chosen the VXI platform for both convenience and its RFI/EMI properties. The system utilizes a mother - daughter board with the FPGA on the motherboard and the daughterboard hosting the RF hardware and analog to digital converters (ADC) and digital to analog converters (DAC) for both the receiver and transmitter. The motherboard will also be used in other applications at CEBAF such as a cavity BPM [2].

The RF system down converts the cavity frequencies (499 MHz and 1497 MHz) to an IF of 70 MHz. This allows us to use the local oscillator (LO) and IF signals that are already distributed around CEBAF. The receiver IF signals are then quadrature demodulated using harmonic under sampling (56 MHz clock). The transmitter output is a single IF output at 70 MHz where the quadrature components are digitally recombined inside the FPGA [3]. The signal is then filtered and up converted to the cavity frequency. Both forward and reflected powers are also monitored. The control system is a digital generator driven resonator (GDR), using a basic proportional and integral (PI) algorithm for field control [4]. All adjustable parameters such as gain, phase and gradient are embedded in the FPGA.

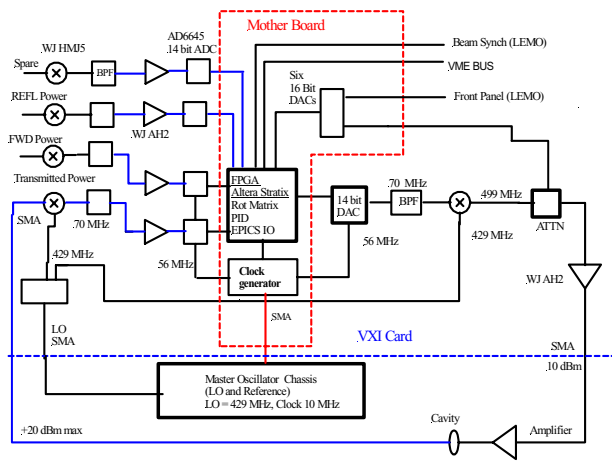

Figure 1: RF system block diagram.

Receiver/Transmitter

The receiver/transmitter mates as a daughterboard to a VXI motherboard. FET mixers (WJ HMJ5) were chosen because of their linearity (IP3 ~ 40 dBm) and high dynamic range. To minimize amplitude drifts a product called Thermopads is being considered (an attenuator product with selectable tempcos). This will allow us to offset any temperature induced amplitude drifts in the RF signal path. A commercial IF filter was chosen for its low group delay ~ 80 ns. In addition, a gentle lumped-element band pass filter designed to remove most of the out-of-band noise precedes the ADC. By including this we reclaim 1-2 bits of dynamic range in the ADC. The fast ADCs (AD6645) and a dual DAC (AD 9767) are included on this card. Because isolation between channels is also a

*This work was supported by DOE contract No. DE-AC05-84ER40150.
#hovater@jlab.org

concern, we have specified this to be 60 dB for the cavity transmitted power and 50 dB for all other channels. We intend to use diode ring mixer for the transmitter since the IP3 requirements are not as stringent.

The receiver has been modeled and tested in a variety of ways. First a simple spreadsheet was used to look statically at the systems gains, IP3 and SNR. If system properties such as saturations and/or any other non-linearity's appear normal, we then model the system with SystemView (a commercial software for receiver and RF design). This allows for dynamic modeling of the chosen components. Following this, bench testing commenced (IMD, dynamic range, tangential sensitivity etc.) on selected parts and any unknown data is fed back into the receiver model. In addition critical parts have been tested in an environmental chamber to measure temperature induced phase drifts. This design process has produced an extremely linear receiver. A complete receiver (2-channel) is presently being assembled for testing and evaluation.

VXI Motherboard

The VXI motherboard contains the digital electronics necessary to process digital signals to and from the daughterboard, interface to the VXI bus, and 10/100 Ethernet. As shown in Figure 2, the board features one Altera Stratix FPGA, 64Kx16 DPRAM, 1Mx32 RAM, 1Mx32 FLASH, Phase Lock Loop (PLL), six 16-bits 500K-sample DACs, 10/100 Ethernet, general purpose digital IO, and infrared input and output. The motherboard uses two 100-pin and two 20-pin stackable connectors to support daughter board(s). Each 100 pin connector has 70 digital I/O, PLL clock output, FPGA clock input, and digital powers. Each 20 pin connector provides VXI analog powers (+/-12V, +/-24V).

We chose an Altera Stratix FPGA with 18,000 to 25,000 logic elements (LE are the basic electronics building blocks), 80 eight-bit multiplier/ accumulators, and can support both hard coding and a soft microprocessor core (NIOS) simultaneously. Various operating systems including Linux can be loaded, and with its Ethernet support, the board can communicate with EPICS directly, thus bypassing the traditional EPICS IOC. We plan to use the NIOS processor as an EPICS IOC for future designs, migrating out of the VXI environment.

Care was taken in the design of the clock PLL to achieve a jitter of less than one ps. The PLL takes in an analog (or digital) signal from a front panel SMA connector and generates a square wave that is phase locked to the input. The clock signal is double buffered and distributed to the FPGA and to both 100-pin connectors. The signal from the SMA connector is buffered and distributed to both 20-pin connectors.

As shown in Figure 3, the connectors (100 and 20 pin) are situated on the board to support either one or two separate daughterboards. The 100-pin connectors provide the digital interface and the 20-pin connectors provide clean analog power. In addition, 16 digital IO (TTL) points are available on an internal connector. Two digital inputs are available via the front LEMO connectors. These inputs are clamped to 4.7V and buffered with JFET. Infrared input and output are Agilent HFBR-241X and HFBR-141X respectively. Six analog outputs are available at the front panel LEMO connectors. Their magnitude and polarity are configurable from –14V to +14V.

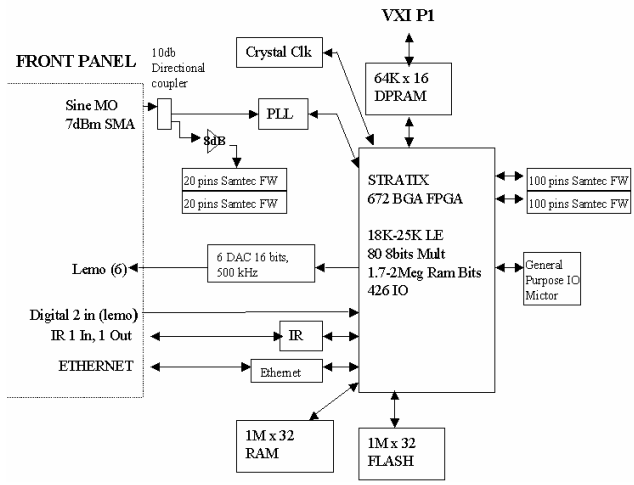

Figure 2: Motherboard Components.

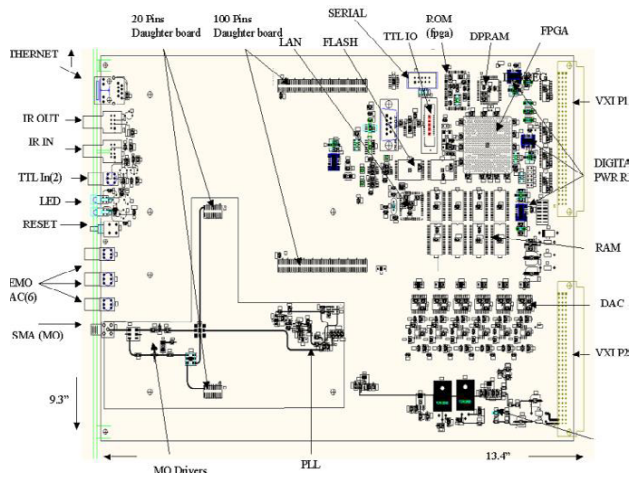

Figure 3: VXI Motherboard.

MODEL & SYSTEM CONTROL

System control was modeled and tested for a variety of cavity scenarios. The separator cavities and chopper cavities have much different Q_L's (2500 vs. 10000). This ultimately affects the loop bandwidth and hence the gain parameters of the LLRF system. In the case of the chopping cavities the loop bandwidth is set by the cavity at ~25 kHz. This gives us adequate margin for Proportional (P) gain. Not so for the case of the separator cavity since it has a bandwidth of ~ 100 kHz. For the separator P gains < 3 are expected (limited by system delay). System delays have been measured in the evaluation system and we have settled on ~ 1.0 μsec total

delay (the latency from ADC to DAC was measured to be ~ 0.5 μsec).

We did investigate lowering the loop pole digitally with an IIR filter, but because of high clock frequencies, 56 MHz, and low loop filters needed ~ 1 kHz, realization of these filters was not easily implemented [5]. The filter poles land very close to the stability circle on the z plane, and when programmed into the evaluation system, the loop tended to oscillate. It may have been possible to decimate down and implement the IIR filters at a lower frequency but we did not investigate this.

Model Results

Jefferson Lab uses Matlab and Simulink to model the response of its low level RF control systems [6]. The models for the warm RF cavities contain the basic elements of the two systems: a controller, a cavity, and cable and digital processor delays. While integral to the systems as a whole, the RF power amplifier and its effects are neglected in this initial set of models and will be included in subsequent versions. The controller consists of a 28 MHz sampling mechanism and PI controller. The cavity is modeled by its fundamental mode using the resonant cavity equivalent circuit equations, and the cable and digital processor delays are lumped together into one delay that feeds into the controller. Figure 4 along with Table 1 show the model and relevant modeling parameters.

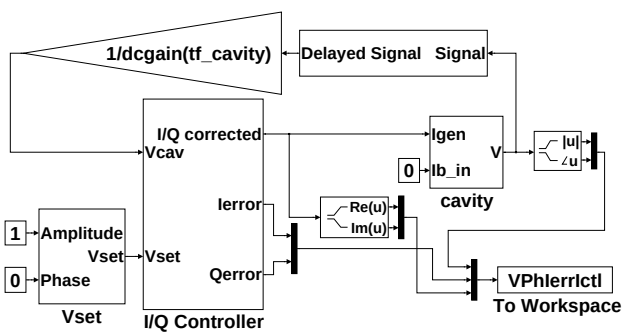

Figure 4: Simulink Model for 499 MHz cavity simulations.

Table 1: Cavity Characteristics used in Cavity Model

	Chopper	Separator
f_0	499 MHz	499 MHz
r/Q	14.4 Ω	$44.7\,\mathrm{k\Omega/m}\times 0.3\,\mathrm{m} = 13410\,\Omega$
Q_L	10000	2500
Bandwidth	24.95 kHz	99.8 kHz
Transfer Function	$\frac{2.257\times10^{10}}{s+1.568\times10^{5}}$	$\frac{2.102\times10^{13}}{s+6.271\times10^{5}}$

The cavity models were used to explore the P and I gain space to find a suitable integral gain and corresponding range of proportional gains that allowed the system to run without a loop filter. Simulations indicate that with an integral gain of 10000, the proportional gain can vary between 1 and 9 for the chopper system and between 1 and 2.5 for the separator system. Figure 5 shows two cases for each system. The baseline case for each system has the integral gain set to zero and the proportional gain set to one which results in a negative feedback system with unity gain. The other case represents the maximum proportional gain for the integral gain that gives the least overshoot with the quickest settling time.

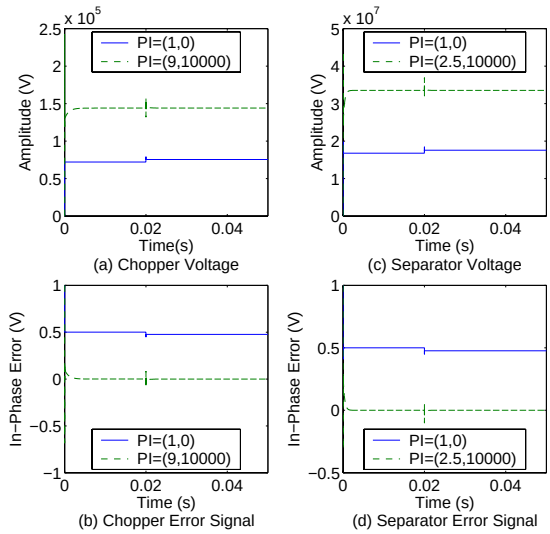

Figure 5: Simulation results for the chopper and separator cavities. Plots (a) and (c) show the amplitude of the cavity voltage for the baseline and maximum gain cases. Plots (b) and (d) show the in-phase component of the cavity voltage error signal for the baseline and maximum gain cases.

SUMMARY

Many of the major parts of the system have been tested on an evaluation platform (ADC, FPGA, DAC, control system firmware) using a simple cavity simulator. The motherboard has been designed and is undergoing tests. The receiver/transmitter card should follow shortly. The next step is to verify the model vs. the final hardware. We intend to install the new system in the spring and summer of 2005.

REFERENCES

[1] C. Leemann and G. Yao, "A Highly Effective Deflecting Structure", 1990 LINAC conference proceedings, Albuquerque, New Mexico
[2] HAPPEX experiment BPM
[3] L. Doolittle, LBNL, private communication. http://recycle.lbl.gov/%7Eldoolitt/plan50MHz/
[4] S. Simrock, DESY, private communication
[5] J. Hereford, Murray State University, private communication
[6] A. Hofler et al., "RF System Modeling for the 12 GeV Upgrade and RIA", 2003 SRF Workshop Proceedings, Lubeck, Germany

A LONG-PULSE MODULATOR FOR THE TESLA TEST FACILITY (TTF)

W. Kaesler, Puls-Plasmatechnik GmbH, Feldstr.56, D-44141 Dortmund, Germany

Abstract

TESLA will be a TeV-Energy Superconducting Linear Accelerator where superconducting (sc) 9-cell Niob-cavities with field gradients of more than 25MV/m will be the key elements. For the TESLA Test Facility (TTF) "long-pulse"-klystron modulators must generate 1.6 ms output pulses with an output power up to 20 MW which is flat to within 1% during 1.5 ms. The main goal of the development at PPT is to optimize the existing modulator design towards a reliable and cost-effective design to allow for a industrial series production of pulse modulators for sc-accelerator operation.

Based on the first design of Fermilab [1] the main features of the redesigned new pulse modulator sub-assemblies are: 1) a compact 300-kW/12-kV switched mode power supply; 2) a volume optimized 1.4-mF storage capacitor bank using high energy capacitors with self-healing segmented PP-foil technology; 3) a rugged , compact solid-state switch stack with seven 4.5-kV IGCT`s, integrated gate units and a current turn-off capability up to 4 kA; 4) a solid-state crowbar switch assembly based on light-triggered high current thyristors replacing the ignitron tubes.

INTRODUCTION

The TESLA cavities will be used in the linac cryo-modules of the TTF2-Free Electron Laser (FEL) project, further for the 35-GeV-linac, driving the European X-ray FEL at DESY and the planned electron-positron linear collider TESLA. One important characteristic number of sc-cavities is the 'quality factor' Q. Q_{sc}-values > 10^{10} exceed the Q-values of conventional normal conducting cavities by more than 10^5. This high Q_{sc}-values increase the filling time of cavities; the TESLA-cavities with an operating frequency of 1.3 GHz need a filling time of more than 0.5 ms. With a required rf-flattop of up to 1.0ms the TESLA rf-source must generate ms-pulse lengths.

In the TTF-project different accelerator subsystems are under test. For the rf-generation different types of 1.3-GHz-klystron tubes are in operation: A 5-MW conventional single beam klystron TH2104, a special developed 10-MW multibeam klystron TH1801 from THALES and at the end of 2004 alternative multibeam klystrons from CPI and Toshiba.

Tab. 1 shows some features of the THALES-klystron.

Table 1: Technical data of "Long-pulse" klystrons

Klystron		TH2104	TH1801
		max	max
Klystronperveance	$AV^{-1,5}$	2,0E-06	3,4E-06
Number of beams		1	**7**
Cathode Voltage	kV	130	120
Anode Current	A	92	140
Impedance	kOhm	1,41	0,86
Input Power	MW	11,96	16,80
Efficiency (min)	**%**	42	60
Output Power	MW	5,0	10,1

TTF MODULATOR

HV-Power Supply

To operate the TTF-klystron modulators the HVPS´s must be able to deliver an electrical peak power up to17 MW with a dc-output voltage up to 12 kV. The load is a 1.4-mF capacitor bank with a storage energy up to 100 kJ - which must deliver periodically current pulses up to 1700 A and pulse lengths up to 1.6 ms. The maximum droop of the the capacitor voltage is about 16 % which must be recharged by the HVPS. The pulse repetition rate may vary in steps from 0.1 to 10 Hz. This operation modus requires a rms-power of about 300 kW. To run large numbers of modulators this units mustbe operated in "constant-power-mode" in order to minimize the generation of low-frequency disturbances on the mains. An essential HVPS-part to achieve this constant power mode is a fast intelligent regulating system which has been developed at DESY.

Pulse Generator

The pulse generator is a solid-state-switched capacitor discharge which will be droop-compensated by an appropriate L-C-ringing circuit (bouncer) [1]. The main components of the pulse generator are: The storage capacitor bank, the crowbar switch, the solid-state high power switch, the droop-compensating bouncer circuit, the undershoot circuit and the backup switch.

PPT tries to reduce the construction efforts and to minimize costs focussing on components widely used in industrial applications.

The main redesigned sub-assemblies of the new, improved pulse generator are:

A volume optimized storage capacitor bank using self-healing Polypropylen capacitors; a rugged, compact12-kV IGCT-switch stack with a 4-kA current turn-off capability and a 100-kA solid-state crowbar switch with light-triggered thyristors.

Storage Capacitor Bank

The original storage capacitor bank designed by Fermilab was based on fifty-six 12-kV-capacitors of 25µF. These dc-filter capacitors are built in aluminum foil technology with paper dielectrics. This technology needs special protection against catastrophic discharge of capacitor bank members into one subunit in case of a capacitor failure. The controlled self-healing technology with segmented, metallized polypropylen films has been evolved for the use in high voltage/high energy capacitors and further improved by the use of internal "fuse gates". No catastrophic failure with an internal high energy discharge will occur even without any external protection circuit. The new technology combines two benefits: First, a controlled self-healing behaviour and second, a superior energy density due to impregnation. The result is a very compact capacitor with stored energies of about 100kJ within a volume of less than $0.75m^3$.

Table 2: Comparison of different capacitor banks

Company			GE	AVX
Type			TTF1/3	TTF
Capacitance	C	uF	25	488
Cap bank no			56	3
Rated dc voltage	Vdc	kV	12	12
Storage energy	Wc	kJ	1,8	33,6
Total cap-bank				
Capacitance	CF	uF	1400	1464
Storage energy	Wc	kJ	100,8	100,8
Fault current	If	kA	120	150
Lifetime (min)		h	90.000	139.000
Weight (total)		kg	2.184	585

Solid State On-/Off- Switch

A characteristic feature of the "long-pulse", high power klystron modulator is the use of a solid state on-/off-switch. This switch assembly must be able to sustain dc-voltages up to 12 kV and to switch off currents up to 1700 A during normal operation and at least 3000 A under fault conditions. The first three generators built at Fermilab used a series combination of six GTO's and later twelve 1600V high-current IGBT-modules.

In the new TTF-generators built at PPT a new IGCT-switch assembly in a rugged, compact stack arrangement is used. An Integrated Gate Commutated Thyristor (IGCT)-switch is a solid state switch derived from former GTO-switch topology. The IGCT-wafer is packed in a new, extreme low-inductive ceramic housing with a ring electrode as gate terminal.

This gate geometry allows for direct coupling of the power switch to the gate driver board.

Due to the low inductance of the integrated gate circuit the IGCT shows a nearly instantaneous turn-off behaviour. There is no dv/dt-limitation. To give the main switch a high immunity and safety against fast powerful pulse-spikes a compact R-C-D-snubber network and a high power varistor stack are parallel to the IGCT-stack. Integrated low-inductive gate driving units and a common trigger distribution box using optical fibre technique are further parts of the compact main switch. The trigger box includes a trigger signal logic which inhibits different malfunctions.

Table 3: High voltage, high current ON/OFF switches

		TTF1	TTF2/3	TTF4/6
Single Switch type		GTO	IGBT*	IGCT
VDRM / VCES*	kV	4,5	1,6*	4,5
ITSM	kA	16	8	25
ITCM	kA	3	2,4 @ 1ms	4
tgq @ dIGQ/dt	us	20	<1,5	< 4
Manufacturer		GEC	EUPEC	ABB
Main switch members		6	12	7
Forw. Blocking voltage	kV	36	24	31,5
Losses per switch	W	< 80	< 200	< 90
Switch volume		moderate	great	moderate
Switch construction		simple	complexe	simple

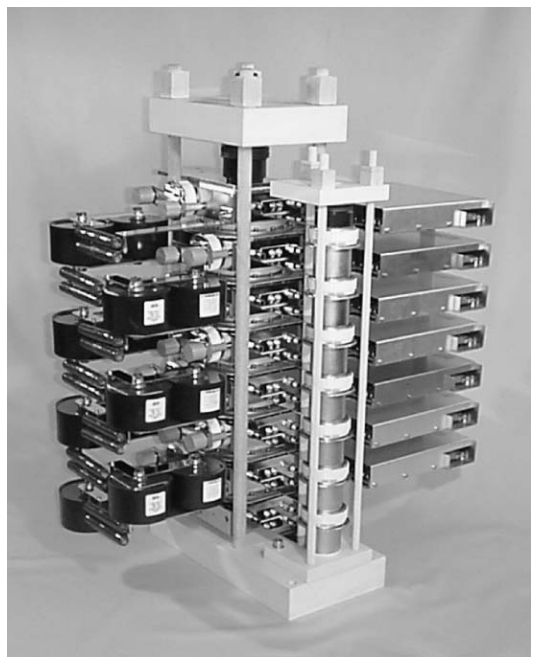

Figure 1: 12-kV IGCT-stack with integrated gate units, R-C-D snubber and MOV-stack.

Solid State Crowbar Switch

In case of a malfunction of the main IGCT-switch the klystron must be protected by discharging the 100-kJ capacitor bank by a fast, 100-kA crowbar switch. The first modulators used two redundant ignitron switches. In order to avoid the use of mercury filled tubes PPT

replaced these conventional crowbar units by light-triggered, high current thyristor stacks.

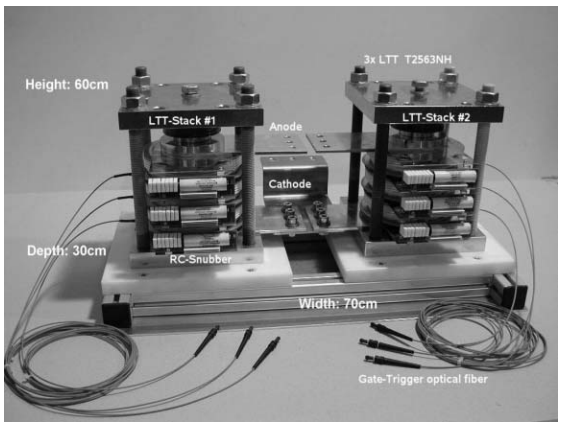

Figure 2: 100kA-crowbar switch unit with light-triggered, high current thyristors.

SUMMARY

The main improvements made in the redesign of the modulator refer to the integration of modern power components like new capacitors, IGCT-switches and LTT crowbar switches. These features are marked in the following schematic (Fig.3).

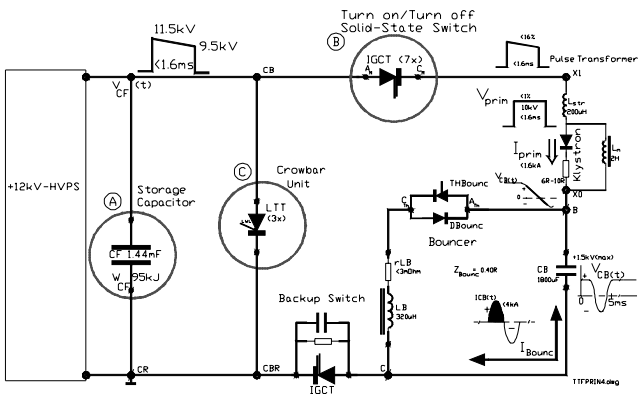

Figure 3: Schematic of the improved TTF modulator.

In the meantime eight TTF-modulators have been built by PPT. Five modulators are running in the laboratories at DESY/Hamburg, DESY/Zeuthen and LAL/Orsay. Typical pulse shapes are shown in Fig. 4.

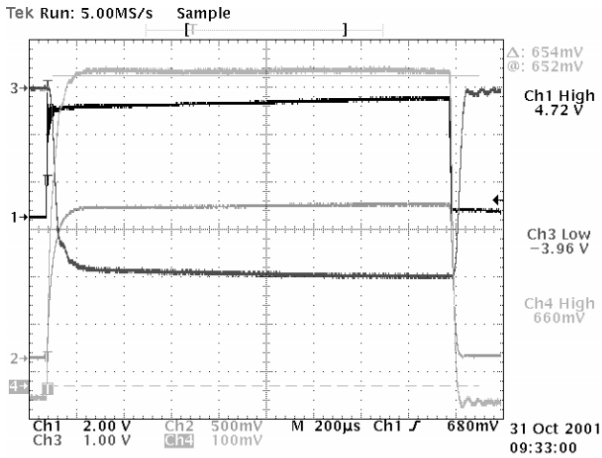

5MW Klystron TH2104C V_{CF}: 10kV / t_p: 1,7ms

CH1	V_prim	(2kV / 1V)	black
CH2	I_prim	(500A / 1V)	green
CH3	V_Klystron	(27.5kV / 1V)	red
CH4	I_Klystron	(100A / 1V)	blue

Figure 4: Voltage and current pulse shapes of the improved TTF modulator.

The new design has led to a compact arrangement of all modulator parts. Fig.5 shows all main modulator cabinets except the control unit cabinet.
The klystron and the pulse transformer tank assembly are located at the rear side.

Figure 5: HVPS- / Pulser cabinets of the new modulator.

REFERENCES

[1] H.Pfeffer,L.Bartelson, K.Bourkland, D.Wolf, C.Jensen, Q.Kerns, P.Pietro, G.Saewert "A Long Pulse Modulator For Reduzed Size and Cost" 24th IEEE PMS Costa Mesa p48-51,1994

SUPERSTRONG ADJUSTABLE PERMANENT MAGNET FOR A LINEAR COLLIDER FINAL FOCUS

T. Mihara, Y. Iwashita, Kyoto University, Kyoto, Japan
M. Kumada, NIRS, Chiba, Japan
C. M. Spencer, SLAC, CA, USA
E. Sugiyama, NEOMAX, Osaka, Japan

Abstract

A superstrong permanent magnet quadrupole (PMQ) is one of the candidates for the final focus lens for the linear collider because of its compactness and low power consumption. The first fabricated prototype of our PMQ achieved a 300T/m superstrong field gradient with ϕ100mm overall magnet radius and ϕ7mm bore radius, but a drawback is its fixed strength. Therefore, a second prototype of PMQ, whose strength is adjustable, was fabricated. Its strength adjustability is based on the "double ring structure", rotating subdivided magnet slices separately.

This second prototype is being tested. Some of the early results are presented.

INTRODUCTION

A 4.45T high magnetic field has been demonstrated with just permanent magnets. It is based on the modified Halbach's configuration, which introduces some saturated iron to enhance the field strength [1,2]. This technique has been applied to a quadrupole to generate a high gradient (see Fig. 1). The first prototype was fabricated and tested [3]. This PMQ, which is compact and strong, is good to use as the final focus lens in a linear collider because the outgoing beam from the interaction point passes very close to the final focus lens (separated by only 7cm).

The remanent field strength of a permanent magnet changes with temperature. NdFeB, which is used for the PMQ has a relatively large temperature coefficient. A special temperature compensation alloy, MS-1, was added to the core to cure this problem. Then the temperature coefficient decreased from -7×10^{-4} to -3×10^{-5} [4,5].

DOUBLE RING STRUCTURE

The final focus lens for the linear collider needs a strength-adjustable quadrupole with 1% adjustment steps. A method for varying the strength is to divide the magnet into sections along the beam axis and rotate the sections separately [3, 4, 5]. Any section is rotated only by 90° so as not to introduce any skew multipoles.

Because mechanical errors in rotation may introduce unwanted skew components and a shift in the magnetic field axis (i.e. the magnetic center where the field is zero), we extended this technique into a "double ring structure" (Fig. 2). The inner region of a PMQ has a larger influence on its field quality in the bore than its outer region. If we split a PMQ into two nested concentric rings and rotate only the outer ring or parts of it, to change the total strength, while the inner ring is fixed, then, we supposed, the skew component would be reduced, and also any shift of the quad's magnetic axis. We confirmed this by calculations and computer modeling [4].

We fabricated a second prototype of a PMQ with a double ring structure. This prototype also has the temperature compensation material. We will make long term measurements to confirm these features.

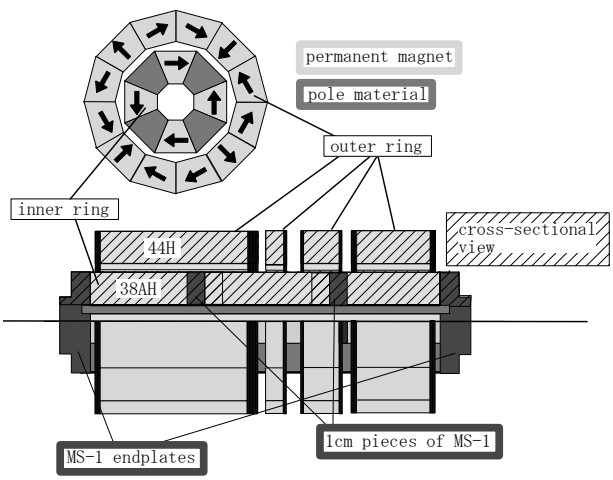

Figure 2: The double ring structure.

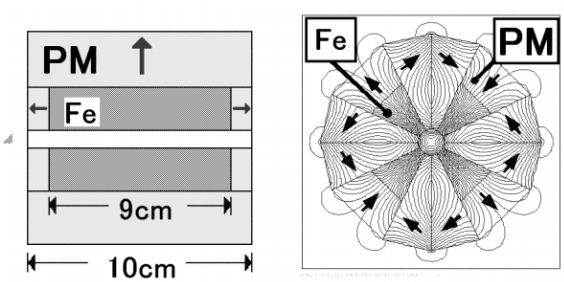

Figure 1: The first prototype of the PMQ.

SECOND PROTOTYPE OF THE PMQ

Figure 3 shows the second prototype of a PMQ, with the "double ring structure" and hence adjustable. The outer rings are rotated by worm gears powered by DC motors [6]. The design parameters are shown in Table 1. The pole material is Permendur. Four poles are welded onto two endplates made of MS-1, which compensates for the NEOMAX strength variation with temperature [4]. Considering that the maximum length of a permanent magnet piece that can be fabricated is about 5cm, three

5cm permanent magnets are installed in each quadrant (see Fig.2). Two 2cm spaces between the 5cm permanent magnets are available for either permanent magnet or MS-1 material. We filled each space with 1cm magnet and 1cm MS-1 material as the initial configuration. Although this configuration has a smaller maximum integrated strength (25.2T) than that filled by all magnets (28T), it can reduce the risk of demagnetization. It also enables us to investigate the overcompensated case.

The second prototype of our PMQ has four outer rings that can be separately rotated from their strong position ("on") to weak position ("off"). Therefore it can generate 16 levels of integrated gradients (see Table 2). It takes less than 1 minute to rotate an outer ring from "on" to "off" and vice versa and these rotations are controlled remotely.

MEASUREMENT

The measurement of the field strength of the adjustable PMQ has been performed with a rotating coil system at SLAC. The measurement set up is shown in Figure 4. The room temperature was kept to 21.7±0.2°C.
We measured its integrated strength at different ring positions.

Integrated Gradient

The adjustable PMQ can generate 16 levels of integrated gradients. When all of the outer rings are switched "on" ("off") the integrated gradient has its maximum (minimum) value. The integrated strength will be measured at 16 combinations of positions (see Table 2) Combination No.1 corresponds to the strongest case and No.16 corresponds to the weakest case. The integrated gradient is designed to change by 1.4T with each step from No.1 to No.16. In a preliminary measurement these 6 positions were measured in the following sequence: 16,1,8,12,14 and 15.

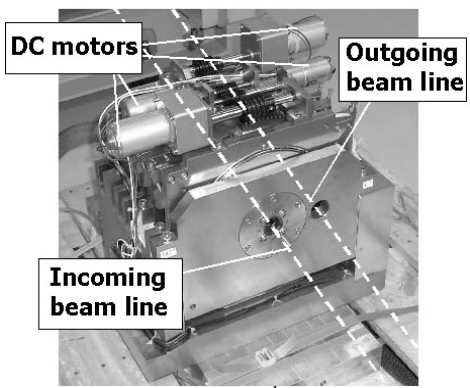

Figure 3: Fabricated 2nd prototype PMQ.

Table 1: Design Parameters

Bore radius	1cm
Inner ring radii	In 1cm out 3cm
Outer ring radii	In 3.3cm out 5cm
Outer ring section length	1cm, 2cm, 4cm, 8cm
Physical length	23cm
Pole material	Permendur
Magnet material(inner ring)	NEOMAX38AH
Magnet material(inner ring)	NEOMAX44H
Integrated gradient(strongest)	25.2T
Integrated gradient(weakest)	4.8T
Int. gradient step size	1.4T

Table 2: 16 cases of positions of the outer rings

No.	8cm	4cm	2cm	1cm	No.	8cm	4cm	2cm	1cm
1	on	on	on	on	9	off	on	on	on
2	on	on	on	off	10	off	on	on	off
3	on	on	off	on	11	off	on	off	on
4	on	on	off	off	12	off	on	off	off
5	on	off	on	on	13	off	off	on	on
6	on	off	on	off	14	off	off	on	off
7	on	off	off	on	15	off	off	off	on
8	on	off	off	off	16	off	off	off	off

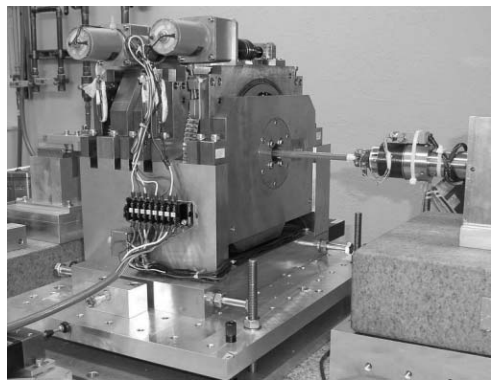
Figure 4: The measurement of PMQ.

PRELIMINARY RESULTS

Some preliminary data is available. Figures 5 and 6 show repeated measurements of integrated strength over several hours in the strongest case and weakest case respectively. Each strength measurement takes about 3 minutes. The strongest and weakest integrated strengths are 24.2T and 3.48T, respectively. The discrepancy between the design value and the measured value is about 5% in the strongest case. The discrepancy of the weakest case is also about 5 % of the strength in the strongest case. We consider that they are not far from the design values.

Figures 5 and 6 also show that the integrated strength of the PMQ changes very slightly with time. These variations are well correlated with the temperature of the magnet. The strength of the strongest case changes by about 10^{-4} T in four hours. That of the weakest case fluctuates about 10^{-3} T over 80 hours of repeated measurements. The effective temperature coefficients of the strongest and weakest case are -4×10^{-4}/°C and 2×10^{-3}/°C. The designed values of the temperature coefficient in the strongest and weakest cases are -1×10^{-4}/°C and 2×10^{-3}/°C, respectively. The effect of the temperature compensation is a little less than the design value. This difference can be explained as following.

The Curie Temperature of MS-1 fluctuates from batch to batch by as much as 20% variation in its saturated magnetic flux density. Whereas the design calculation was performed with the catalogue values of MS-1 parameters.

The "switched-on" length is defined as the summation of the lengths of the outer rings in the strong position. Figure 7 shows the measured strength of six cases at various "switched-on" lengths. The strength is proportional to the cumulative "switched-on" length as expected.

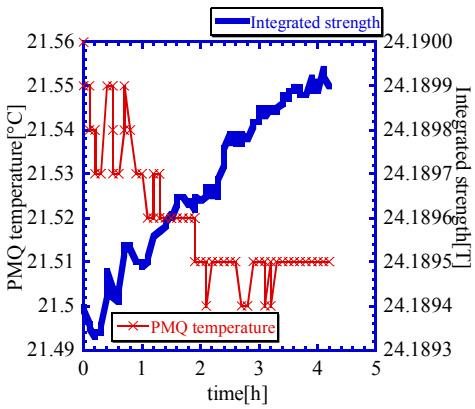

Figure 5: The strongest integrated strength vs time.

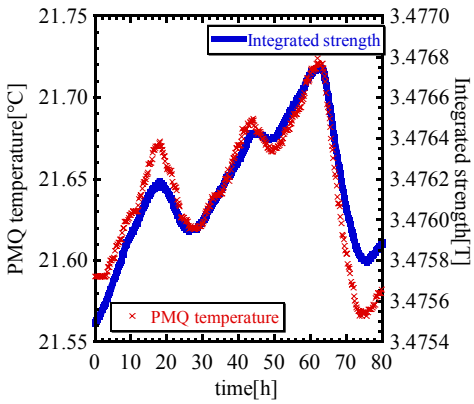

Figure 6: The weakest integrated strength vs time.

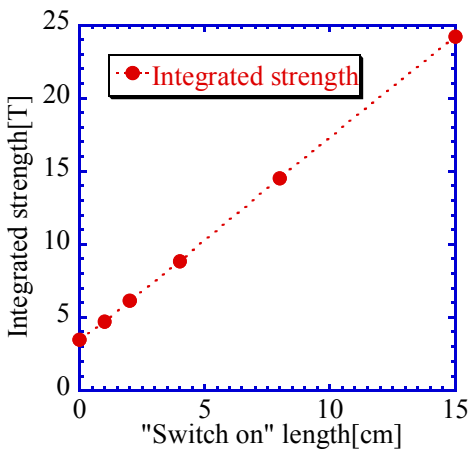

Figure 7: The variation of integrated strength.

CONCLUSIONS

The Integrated Strength

The integrated strength of the strongest case and weakest case of PMQ were 24.2T and 3.48T, respectively. They agree with the calculated values within 5%.

The integrated strength will be increased to its final value by replacing the inner ring with one that is filled with permanent magnet pieces.

Temperature Coefficient

The effective temperature coefficients of strongest and weakest cases were $-4\text{x}10^{-4}$/°C and $2\text{x}10^{-3}$/°C, respectively. The difference of the temperature coefficient between the strongest case and weakest case comes from the overcompensation of the inner ring.

Strength Adjustability

Figure 7 shows that the integrated strength can be varied in proportion to the "switched on" length. The step size is 1.4T/cm. It agrees with the calculated value well. We will have more measurements to confirm that the PMQ can generate 16 levels of the integrated strength with a 1.4T step between them.

Possible Improvement

The strength of the PMQ can be made further stronger by replacing inner and/or outer ring permanent magnet pieces with stronger ones. The strength can be 5% more when the inner magnet (NEOMAX 38AH) and the outer magnet material (NEOMAX 44H) are replaced by NEOMAX44AH and NEOMAX50BH, respectively.

REFERENCES

[1] K.Halbach, IEEE, Trans., NS26 (1979), 3882, NIM169 (1989)1, NIM 187(1981)109, NIM 198(1982)213

[2] M.Kumada et al., patent pending. CERN Courier, **41**, 7, Sep. 2001, p.9.

[3] Y.Iwashita, T.Mihara, E.Antokin, M.Kumada, M.Aoki "Permanent Magnet Quadrupole for Final Focus for Linear Collider", PAC03, May 12-16, 2003, Portland

[4] T. Mihara, Y.Iwashita, M. Kumada. C.M. Spencer, E. Antokhin "Super Strong Permanent Magnet Quadrupole for a Linear Collider" IEEE trans. Appl. Supercond. Vol 14, no.2, pp.469-472, June 2004.

[5] T.Mihara, Y. Iwashita, M. Kumada, E. Antokhin,E. Sugiyama, C.M.Spencer, "A Super Strong Permanent Magnet for the Final Focus Quadrupole in a Linear Collider", APAC04, May 22-26,2004, South Korea.

[6] T. Mihara, Y. Iwashita, M. Kumada, C.M.Spencer, E. Sugiyama "A Superstrong Permanent Magnet for the Linear Collider Final Focus." EPAC04, Jul. 5-9, 2004, Lucerne.

LOW ENERGY BEAM TRANSPORT USING SPACE CHARGE LENSES

O. Meusel, A. Bechtold, J. Pozimski, U. Ratzinger, A. Schempp, H. Klein,
Institut für Angewandte Physik der Johann Wolfgang Goethe Universität,
Robert-Mayer-Str. 2-4, D-60054 Frankfurt am Main, Germany

Abstract

At the frontend of an accelerator the transversal focusing suffers from high space charge forces. Space charge lenses (SCL) provide strong cylinder symmetric electrostatic focusing by a confined nonneutral plasma. The density distribution of the enclosed space charge is defined by the enclosure conditions in transverse and longitudinal direction. For a homogeneous charge density distribution the resulting electrostatic field and therefrom the focusing forces inside the space charge cloud are linear. Additionally, in case of a positive ion beam, the space charge of the confined electrons causes compensation of the ion beam space charge forces.
To study the capabilities of a Gabor double lens system to match an ion beam into an RFQ a testinjector was installed at the IAP and put into operation successfully. Beam profiles and emittance measurements as well as measurements of the beam energy and energy spread have already been performed and show satisfactory results and no significant deviation from the theoretical predictions. To investigate the beam focusing of bunched beams using this lens type at beam energies up to 500 keV a new high field Gabor lens was built and installed behind of the RFQ.

THEORY

The focal strength of a SCL is determined by the spatial space charge density distribution. The space charge density distribution is a function of the transversal and longitudinal enclosure conditions [1,2]. Gabor showed [3] for a radial confinement by a magnetic field, that in absence of external electric fields, the transversal enclosure condition is given by the Brillouin flow [4] and therefrom the maximum electron density can be calculated by:

$$n_{e,rad} = \frac{\varepsilon_0}{2m_e} B_z^2 \qquad (1)$$

The upper limit for the longitudinal enclosure can be calculated by the space charge potential of a homogeneous cloud of radius r_A, which has to be smaller then the anode potential V_A, resulting in:

$$n_{e,l} = \frac{4\varepsilon_0 V_A}{e r_A} \qquad (2)$$

Both of these relations solely overestimate the space charge density significantly. Additionally the longitudinal enclosure condition is drastically influenced by thermalization of the enclosed particles and therefrom due to losses of fast particles in the Maxwellian tail. By measurement of the focal length the average electron density can be determined. Applying the thin lens approximation for a homogeneously space charge filled cylinder the average electron density is given by:

$$\frac{1}{f} = \frac{r'}{r_0} = k^2 \cdot l = \frac{\bar{n}_e \cdot e}{4\varepsilon_0 \cdot W_B} \cdot l \qquad (3)$$

(refraction power k, divergence angel r´, beam radius r_0 and energy W_B, the length of the space charge cloud l, focal length f). The length of the cloud can be estimated by the distance between the two grounded electrodes (see fig. 5). Introducing the radial and longitudinal filling factors [5] $\kappa_{r,l}$ [$0 \leq \kappa_{r,l} \leq 1$] and using Eq. (1),(2) and (3) the trapping efficiency can be expressed by:

$$\kappa_r = \frac{\bar{n}_e}{n_{e,r}} \quad ; \quad \kappa_l = \frac{\bar{n}_e}{n_{e,l}} \qquad (4)$$

THE HE$^+$ - TEST INJECTOR

A test injector to study the matching of a space charge dominated ion beam into an RFQ has been constructed and installed at IAP. The schematic layout of the experiment is shown in figure 1.

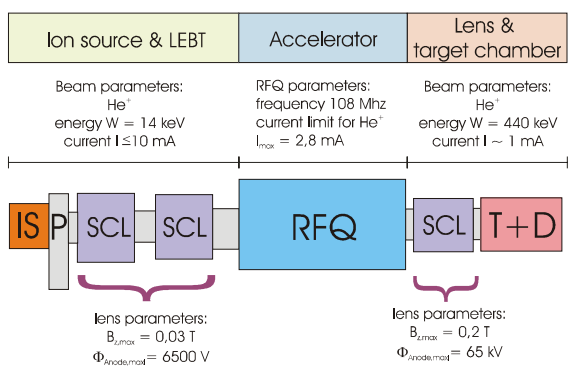

Figure 1: Schematic drawing of the experimental set up.

In a first step the low energy beam transport (LEBT) and the injection of a space charge dominated ion beam into an RFQ using Gabor lenses was studied. After beam acceleration by the four rod RFQ, the beam passes a high field Gabor lens. This allows to investigate beam focusing after an increase of the beam energy by a factor of 30 and including a more or less pronounced micro bunch structure, depending on the drift length RFQ – Gabor lens.

LOW ENERGY BEAM TRANSPORT

The front end of the injector consists of a volume type ion source, a differential pumping stage, the Gabor lens LEBT system and several beam diagnostic devices.

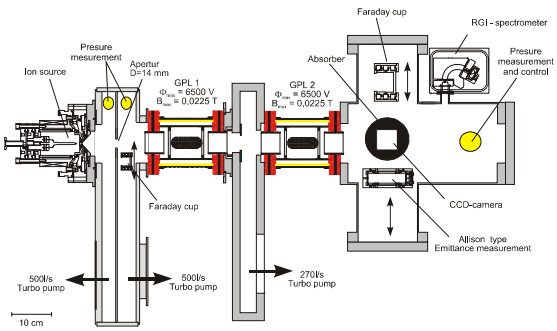

Figure 2: Schematic drawing of the front end of the injector.

The ion source delivers a maximum beam current of 10 mA He^+ at 14 keV. After commissioning of the ion source the emittance of the beam behind of the differential pumping stage was measured (see fig. 3 left, He^+, 14 keV, 4.5mA, $\varepsilon_{n,rms,100\%}$ = 0.0225 πmmmrad).

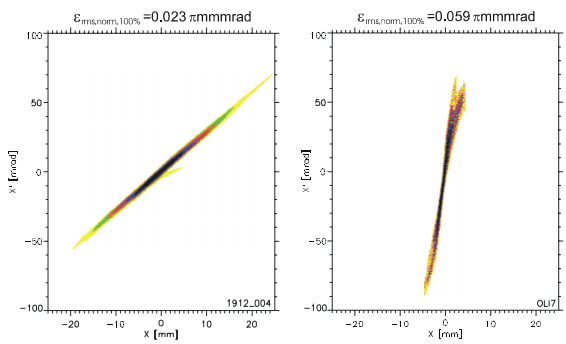

Figure 3: Measured beam emittance behind the differential pumping stage (left) and behind the LEBT – system (right) at I=8.4mA.

After installation of the two Gabor lenses the emittance at the RFQ injection point was measured using improved ion current (see fig. 3 right, He^+, 14 keV, 8.4 mA, $\varepsilon_{n,rms,100\%}$ = 0.0598 πmmmrad). In figure 3 (right) the phase space distribution just behind the focus of the beam is shown. The following lens parameters were used: first lens V_A = 1.8 kV and $B_{z,max} = 5.76 \cdot 10^{-3}$ T, second lens V_A = 2.1 kV and $B_{z,max} = 6.24 \cdot 10^{-3}$ T for the presented results. For these measurements the calculated focal lengths were f = 0.366 m for the first and f = 0.22 m for the second lens. Therefore the filling factors are κ_r = 38 % and κ_l = 49 % respectively. Our hitherto experience shows a good reproducibility of the gained results.

THE RFQ

After finalization of the LEBT measurements the RFQ was installed behind of the second Gabor lens. The design beam energies at the RFQ entrance and exit are 3.5 AkeV and 110 AkeV respectively. The maximum beam current is limited by space charge forces to 0.7 mA·A/q, the design ion being N^+. The beam energy spectrum proofs that the necessary design power for the acceleration of He^+ is 8 kW as predicted by simulations [6]. For a power level of 8 kW the measured energy spread is below 5 % and the accelerated beam current already reached 50 % of the RFQ space charge limit. Beam profile and emittance measurements have already be performed. In figure 4 the measured phase space distribution behind the RFQ is shown (left, x-plane, $\varepsilon_{n,rms,100\%}$ = 0.175 πmmmrad, right, y-plane, $\varepsilon_{n,rms,100\%}$ = 0.192 πmmmrad).

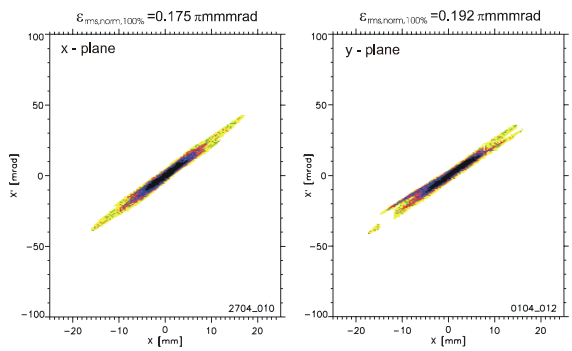

Figure 4: Measured beam emittance behind the RFQ in x-plane (left) and in y-plane (right), beam current I = 1,15 mA.

The intense centre of the beam is predicted by beam transport simulations, while the low intensity wings in the phase space distribution are due to unaccelerated halo particles (see chapter 5.).

THE HIGH FIELD GABOR LENS

Finally the test injector was extended by the high field Gabor lens. Figure 4 shows a cross sectional view and a picture of this lens.

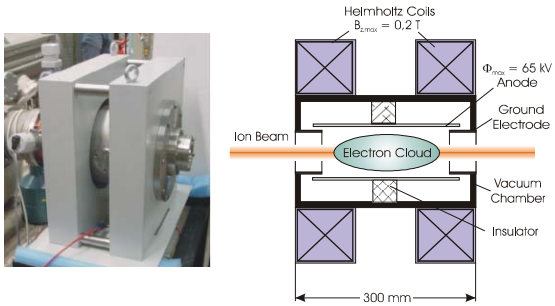

Figure 5: Picture and cross sectional view of the high field Gabor lens.

For the radial confinement the magnetic field of Helmholtz coils (up to 0.2 T on axis) is used while the longitudinal confinement is provided by an anode with radius r_A = 0.032 m and $U_{A,max}$ = 65 kV. In figure 6 the very first measured emittances behind the lens are shown. For the presented results the lens settings of V_A = 25 kV and $B_{z,max}$ = 46 mT was used. The phase space distribution in the x-plane (left, $\varepsilon_{n,rms,100\%}$ = 0.066 πmmmrad) and in y-plane (right, $\varepsilon_{n,rms,100\%}$ = 0.094 πmmmrad) are presented in figure 6.

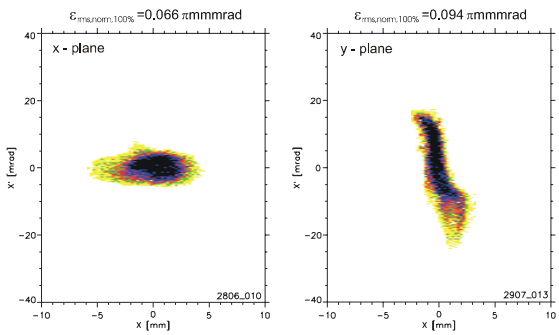

Figure 6: measured beam emittance behind the high field Gabor lens x-plane (left) and y-plane (right) using following lens settings: V_A = 25 kV and $B_{z,max}$ = 46 mT.

It is shown that the divergence angel of the core of the phase space distribution was decreased from 20mrad to 0mrad in x-plane and from 20mrad to –20mrad in y-plane. Furthermore the unaccelerated halo particles are lost due to over focusing. The beam radii at the lens centre in the x and y plane are 5mm and 10mm, respectively. For the presented emittances the focal length is approximately 0.25m and the filling factors can be calculated to be κ_r = 24 % for radial confinement and κ_l = 61 % for longitudinal confinement. The beam radius in the y-plane is a little bit larger than the radius of the space charge cloud. This causes the observed emittnace growth [7].

CONCLUSIONS

The injection of a space charge dominated ion beam into an RFQ by space charge lenses was performed successfully. The experiments show for the LEBT-system a low emittance growth, high transmission and reasonable filling factors in the Gabor lens. The injected beam was accelerated successfully by the RFQ at the design input power and the extracted beam has already reached 50% of the space charge limit for He^+. Experiments using the high field Gabor lens have started. The first beam measurements of the emittance show a good performance for beam radii smaller than the radius of the space charge cloud (see fig. 6, x-plane).

REFERENCES

[1] J.Pozimski, P.Groß, R.Dölling and T.Weis: “First experimental studies of a Gabor plasma-lens in Frankfurt”, Proc. 3rd EPAC Conf. 1992 Berlin

[2] O. Meusel, J. Pozimski, A. Jakob, A. Lakatos ”Low energy beam transport for HIDIF” HIDIF 2000 Meeting San Diego, USA, NIM A 464 (2001) p. 512-517

[3] D.Gabor: “A Space charge lens for the focusing of ion beams”, Nature 160 (1947)

[4] L. Brillouin, “A theorem of Lamor and its importance for electrons in magnetic fields”, Phys, Rev. 67, 260 (1945)

[5] Reiser, “Comparison of Gabor lens, gas focussing and electrostatic quadrupol focusing for low energy beams”, Proc. PAC Conf. 1989, Chicago, USA

[6] A.Bechtold, “Construction of an heavy ion RFQ accelerator with high duty cycle” Diploma thesis 1997

[7] J.Pozimski: “Untersuchungen zum Transport raumladungskompensierter niederenergetischer und intensiver Ionenstrahlen mit einer Gabor Plasma-Linse“, Dissertation Inst. f. Angew. Phys.,J.W.Goethe-Univ., Frankfurt am Main (1997)

RESULTS OF THE MAGNETIC FIELD MEASUREMENTS OF THE DTL QUADRUPOLE MAGNETS FOR THE J-PARC

E. Takasaki#, F. Naito, H. Tanaka, K. Yoshino, KEK, Tsukuba, Japan
T. Ito, JAERI, Tokai, Japan
H. Ino, Z. Kabeya, S. Kakizaki, T. Kawasumi, MHI, Nagoya, Japan

Abstract

A quadrupole electromagnet is installed in the drift tube, which has an outer diameter of 140 mm and its minimum length of 53 mm. Hence, a coil of this magnet was made by the advanced periodic reverse copper electroforming method (PR-method) instead of the conventional hollow conductor. 149 quadrupole electromagnets were completed and then installed in the drift tube within a high accuracy. The magnetic field measurements have been carried out by a rotating coil at each stage of the manufacturing process of the drift tube. The discrepancies between the magnetic field center and the mechanical center are within about ± 25 μm after installation of the quadrupole magnet inside the drift tube. Recently, drift tubes have been aligned into 9 unit-tanks. This paper describes results of the magnetic field measurements and summarizes results of the drift tube alignments in the unit tanks.

INTRODUCTION

The Alvarez-type drift tube linac (DTL) accelerates the H^- ion beams from 3 MeV to 50 MeV. It consists of the three tanks (DTL-1, DTL-2 and DTL-3), of which the length is about 9 m. Each tank is composed of three short unit tanks. The inner diameter of the tank is 560 mm.

The 149 drift tubes, in which an electromagnetic quadrupole magnet (Q-magnet) is installed, are aligned into DTL precisely within the required accuracy. The specifications of all the Q-magnets in the DTL are given in Table 1 with the size of the drift tube.

Now all the magnets have been completed and installed into the drift tubes (DT). All the drift tubes have been aligned into the 9 unit tanks within the high accuracy of ± 50 μm, which was determined from requirement of the beam dynamics. The first tank (DTL-1) accelerates the H^- ion beam from 3 MeV to 19.7 MeV, successfully.

CONSTRUCTION OF QUADRUPOLE

Since the resonance frequency of the DTL is 324 MHz, the size of the DT becomes smaller. The pulsed Q-magnet is selected to suppress deformation of the DT by the released heat of the coil. Hence, as a coil, the electroformed hollow coil [1-3] has been developed at KEK. Furthermore, beam dynamics requires that the deviation of the quadrupole center from the mechanical center should be within ± 50 μm. Hence, we decided on ± 25 μm as a tolerable deviation of the magnetic field center from the mechanical center of the Q-magnet and the DT. Figure 1 shows some components for the Q-magnet.

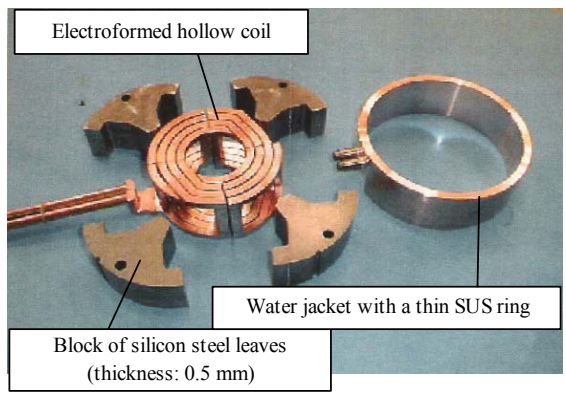

Figure 1: Components for the Q-magnet

Especially, the water jacket with a thin SUS ring has been used to fasten four long blocks together with thermal shrinkage of a water jacket.

The magnetic field of the Q-magnet has been measured by a rotating coil to investigate if the deviation of the magnetic field center from the bore center would be within the required accuracy. The measured results are shown in Figure 2. As seen in the Fig. 2, the discrepancies of all the magnets are within ± 25 μm.

Table 1: Specifications of all quadrupoles in the DTL

DTL tank	DTL-1					DTL-2		DTL-3
DT Nos.	1 to 6	7 to 23	24 to 56	57	58 to 77	78	79 to 121	122 to 149
Type of Q-mag.	A type	B type	C type		D type		E type	F type
Outside diameter of Q-mag./ DT (mm)	115/140	115/140	115/140	115/140	115/140	115/140	115/140	115/140
Core length (mm)	33	35	50	76	80	80	90	125
Bore diameter (mm)	15.6	16	16	21	21	25	25	29
Number of magnets	6	17	33	1	20	1	44	28
Inside diameter of beam pipe (mm)	13	13	13	13|18	18	22	22	26

#eiichi.takasaki@kek.jp

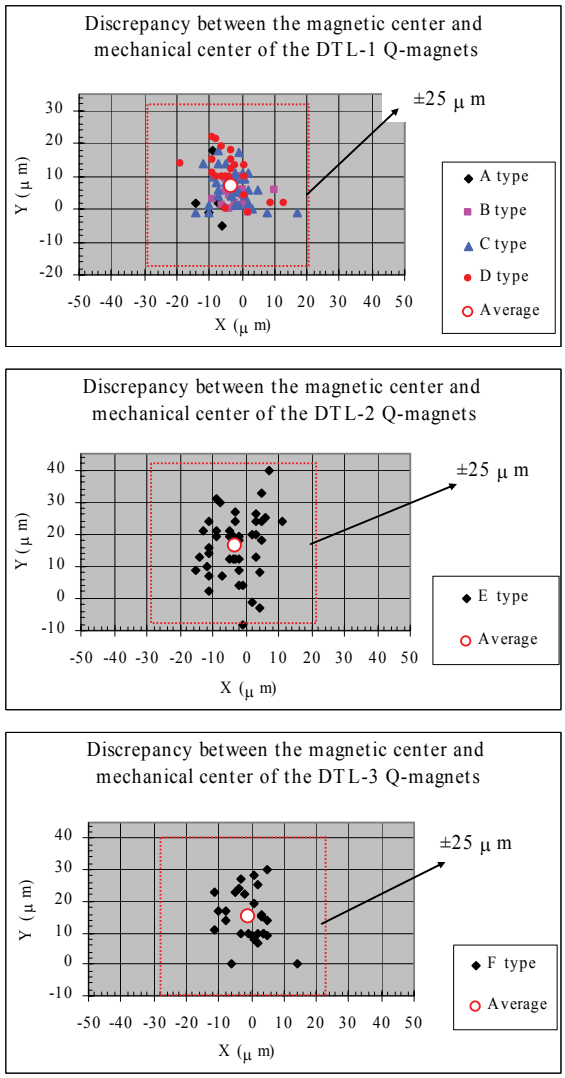

Figure 2: Measured discrepancies between the magnetic field center and the mechanical center of the Q-magnet.

DT FABRICATION

The drift tube was assembled with a Q-magnet, a stem (34 mm in diameter) and some components, which were two drift tube shells, a beam pipe and a stem base made of stainless steel. The size of the drift tubes is given in Table 1.

The manufacturing process of the drift tube is described as follows. At first, a Q-magnet is installed in the standard drift tube shell with a high accuracy in order to transfer the mechanical center from the bore of the Q-magnet to the inside of a beam pipe of the DT. Secondly, another shell and a stem base are assembled and then are welded by an electron beam welding (EBW). A stem is also welded by TIG-welding. After this process, the magnetic field measurement is carried out for checking the position shift of the magnetic field center by the thermal stress due to the EBW and the TIG-welding. In practice, we have observed the position shift after the EBW of the stem base. Hence, the beam pipe has reclaimed for correcting the measured discrepancy. Thirdly, the copper having thickness of over 1 mm is electroformed all over the surface of the drift tube except the inner surface of the beam pipe by the PR-method. And then the surface is precisely machined to obtain the proper size. Fourthly, the drift tube is impregnated with the epoxy resign by the vacuum impregnation method and finally the surface of the drift tube is electro polished (EP) in order to remove abrasive particles and denatured layers. At this stage, the DT is completed. After completion of the DT fabrication, we have measured the discrepancy between the magnetic field center and the mechanical center, which means the center of the inside of the beam pipe. The measured discrepancies are shown in Figure 3. Figure 4 shows the magnetic field measurement system.

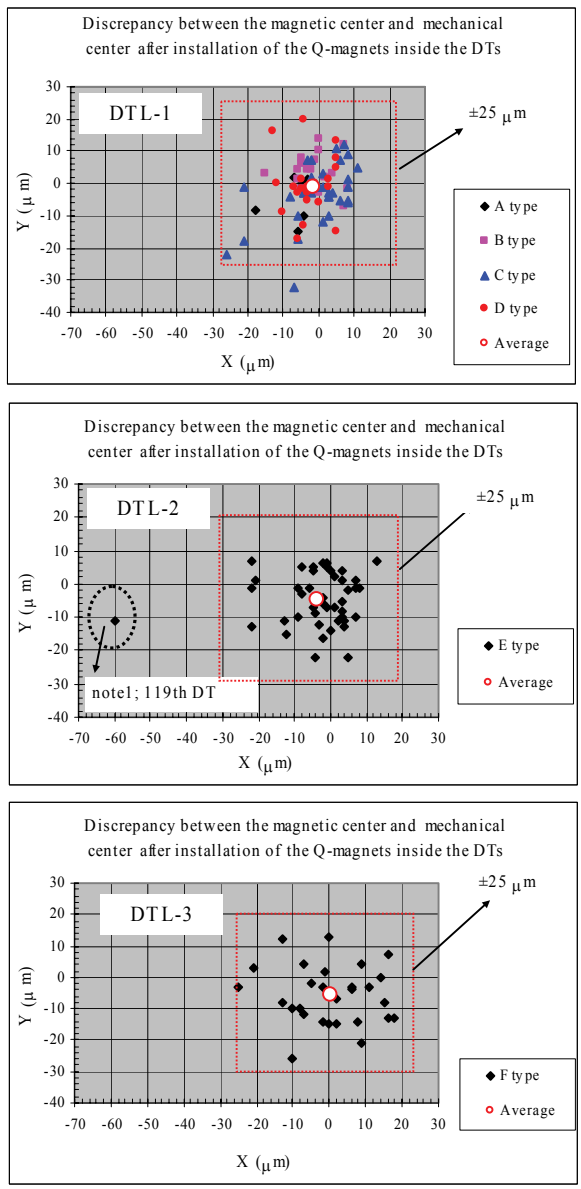

Figure 3: Measured discrepancies between the magnetic field center and the mechanical center of DTs.

Unfortunately, we observed the bad discrepancy for the 119th DT. This bad discrepancy (-60 μm for the 119th DT) would be caused by an impact during the transportation process. This accident happened before the magnet was finally fixed inside the drift tube and the coil was completely insulated by the vacuum impregnation of the epoxy resin. Hence, the discrepancy of 119th drift tube will be corrected when the drift tube will be aligned in the tank (DTL-2).

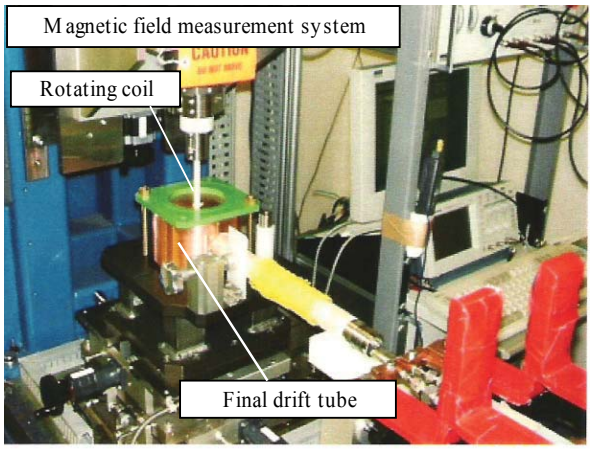

Figure 4: Magnetic field measurement after the final fabrication process.

DT ALIGNMENT

It is most important to align the drift tubes in the tanks with a high accuracy. The required tolerance of the alignment errors is ± 50 μ m in the vertical plane (X-Y plane) to the beam axis and ± 100 μ m along the beam axis (Z-axis). At first we have set up the optical telescope for fixing an optical axis, which is the center of the unit tank, by installing the templates at the extremities of the tank. The optical target has been installed inside the beam pipe and the DT has been aligned by using the optical telescope. The center position has also been measured by the optical telescope. The position of the DT along the beam axis has been measured by the laser interferometer and the special instrument for the z-measure. The systematic error in this alignment system has been estimated to be within about ± 10 μ m. Hence, we have estimated that total systematic error in the procedure aligning the magnetic field center would be within about ± 18 μ m, considering the errors in the magnetic field measurement system.

The aligned results are shown in figure 5. Figure 5 shows that all the drift tubes are sufficiently aligned with the required accuracy of ± 50 μ m within the estimated errors.

Now, the DTL-1 accelerates the negative hydrogen beams from 3 MeV to 19.7 MeV with a beam intensity of about 30 mA, successfully [4]. As for the DTL-2 and the DTL-3, adjustment of tuners is carried out in order to obtain the uniform accelerating field on the beam axis. Furthermore, the post-couplers also are adjusted to stabilize the accelerating field distribution [5].

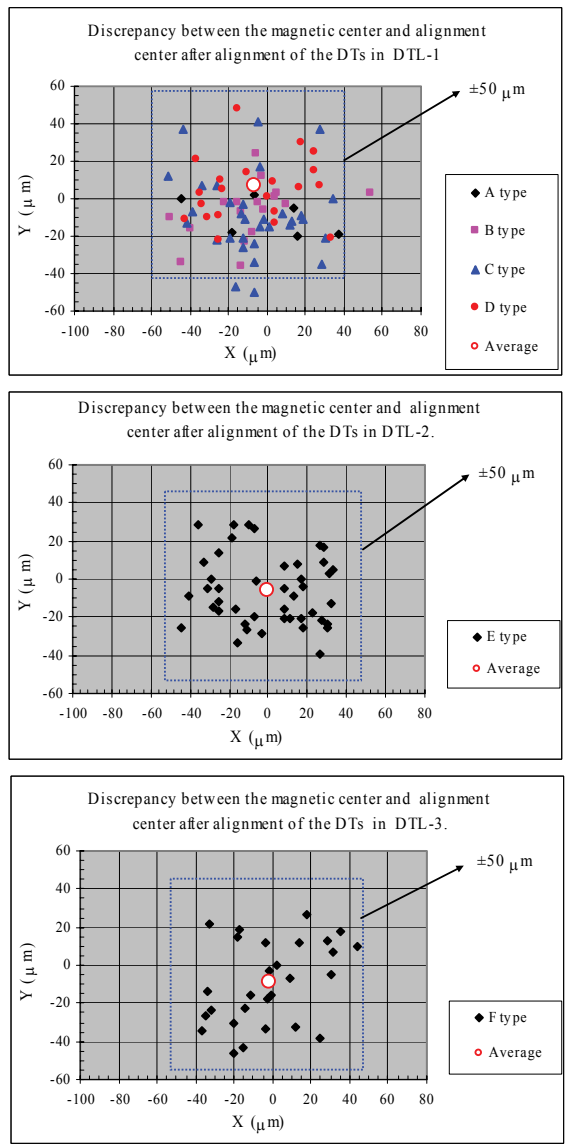

Figure 5: Discrepancies after all the drift tubes are aligned in the tank.

REFERENCES

[1] H. Ino, et al., "Advanced copper lining for accelerator components", Proc. of LAC 2000, California, USA, 1015 (2000).

[2] K. Yoshino, et al., "Development of a DTL quadrupole magnet with a new electroformed hollow coil for the JAERI/KEK joint project", Proc. of LAC 2000, California, USA, 569 (2000).

[3] F. Naito, et al., "Mechanical and RF properties of the DTL for the JAERI/KEK joint project", Proc. of LINAC 2002, Gyeongju, Korea, 361 (2002).

[4] F. Naito, et al., "Results of the High-Power Conditioning and the First Beam Acceleration of the DTL-1 for J-Parc", TUP06, this conference.

[5] H. Tanaka, et al., "Measured RF Properties of the DTL for J-Parc", THP89, this conference.

SPECTROGRAPHIC APPROACH TO STUDY OF RF CONDITIONING PROCESS IN ACCELERATING RF STRUCTURES

H. Tomizawa[1], T. Taniuchi[1], H. Hanaki[1], Y. Igarashi[2], S. Yamaguchi[2], A. Enomoto[2]
Accelerator Division, Japan Synchrotron Radiation Research Institute (SPring-8)
1-1-1 Kouto, Mikazuki-cho, Sayo-gun, Hyogo 679-5198, Japan[1]
High-Energy Accelerator Research Organization (KEK)
1-1 Oho, Tsukuba, Ibaraki 305-0801, Japan[2]

Abstract

The acceleration gradient of a linac (linear accelerator) is limited by rf breakdown in its accelerating structure. We applied an imaging spectrograph system to study the mechanism of rf breakdown phenomena in accelerating rf structures. Excited outgases emit light during rf breakdown, and the type of outgases depend on surface treatments and rinsing methods for their materials. To study rf breakdown, we used 2-m-long accelerating structures and investigated the effects when high-pressure ultrapure water rinsing (HPR) treatment was applied.

We performed experiments to study the outgases under rf conditioning with quadruple mass spectroscopy and imaging spectrography. As a result, we were able to observe instantly increasing signals at mass numbers of 2 (H_2), 28 (CO), and 44 (CO_2) but not 18 (H_2O) just after the rf breakdown. We also conducted spectral imaging for the light emissions from atoms in a vacuum that are excited by rf breakdown. Without HPR, we observed atomic lines at 515 nm (Cu I), 622 nm (Cu II), and 711 nm (C I). With HPR, 395 nm (O I), 459 nm (O II), 511 nm (Cu I), 538 nm (C I), 570 nm (Cu I), 578 nm (Cu I), 656 nm (H I), and 740 nm (Cu II) were observed.

INTRODUCTION

Recently, rf structures have become necessary for higher-gradient acceleration. A range of contaminants and micron-sized particles may remain on the surface following different treatments. Those contaminants are field emitters, and outgassed due to the rf breakdown in rf structures. The lower the outgassing rates and the fewer the contaminating particles, the lower the breakdown rate.

It has been reported that the high-pressure ultrapure water rinsing (HPR) technique is very effective in improving the field gradients for normal conducting and superconducting rf structures [1]. This is because HPR treatment eliminates particle contamination on the surface, which is thought to be one of the causes of field emission.

To study rf breakdown, we applied this technique to the S-band 2-m-long disk-loaded accelerating structure. Microsecond-pulsed rf power (average accelerating field of 45 MV/m at maximum) was fed into these rf structures.

We performed experiments using quadrupole mass spectroscopy and imaging spectrography of atomic lines to study outgassing from the surface of rf structures. This imaging spectrograph system is useful for observing irreproducible phenomena such as rf breakdown, even for non-ultra-high vacuum conditions. Condensed gas and electrons play important roles in triggering the formation of aggressive plasma that acts against the copper surface. In our work, excited neutral and ionized gases in this plasma were observed as atomic lines in the real accelerating structures. Additionally, to reduce outgas rate, we applied chemical etching for rf pill-box-type single cavity (rf gun). With this treatment, we could achieve 206 MV/m of the maximal surface field.

EXPERIMENTAL SETUP

Tested accelerating structure

We performed experiments using the high-power test stand at KEK. We chose two S-band 2-m-accelerating structures which were prepared with the following fabrication processes:

A. A high-precision turning lathe with a diamond byte machined the disks and cylinders.
B. The electroplating fabrication method was applied to fix the disks and cylinders together.
C. HPR was applied to the assembled accelerating structure.

Note that these accelerating structures have a crescent-shaped cut opposite the waveguide iris (see Figure 1) to correct the asymmetry of the electromagnetic field.

For comparison, we prepared two different treated accelerating structures with and without HPR treatment (process C). One of the accelerating structures, while moving vertically (60 mm/min) and rotating (6.5 rpm), was rinsed by a nozzle-equipped pipe that jets high-pressure ultrapure water under optimal conditions.

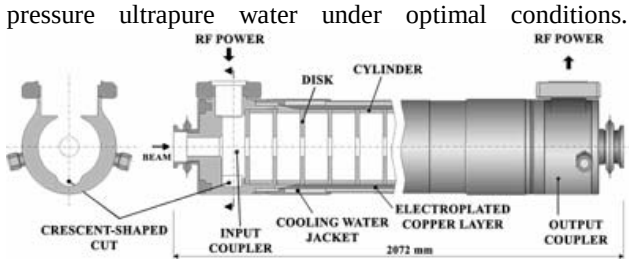

Figure 1: Schematic drawing of the accelerating structure

Following the HPR process, a scroll pump immediately dried the rf structure, and valves were attached in a clean room. After that, the structure was evacuated and then inserted into a high-power test stand without exposure to the atmosphere after assembly in the clean room.

Imaging spectrograph system

The imaging spectrograph monitor consists of three parts: a spectrometer (SPECIM; ImSpector), an image intensifier (SWAROVSKI; MK500) and a CCD-camera.

The spectrometer was used as an imaging spectrograph that captures a line image and disperses it into a spectrum in a direction orthogonal to the line image. These optics are based on the Prism-Grating-Prism (PGP) technique, yielding a direct-sight imaging spectrogram in which light passes through a straight optical axis. After an image is converted to a spectral line image, the image intensifier (I.I.) amplifies the light by a factor of more than 10^4, making it possible to take a spectrogram of a light emitter with low brightness. The CCD camera then changes the intensified spectral line images into video frames.

All image data were recorded on digital videotapes since rf breakdown is unpredictable. Each frame contains the line pixels in one dimension (spatial axis) and the spectral pixels in the other dimension (spectral axis), providing full spectral information for each line pixel. It was possible to obtain spectral information over the entire visible region (380 - 780 nm). For this spectrograph system, we calibrated the absolute wavelength with an He-Ne laser (633 nm) and a mercury lamp (shortest spectral line: 404 nm). We obtained a resolution and geometrical resolution of 8.9 nm and 2.4 nm/dot, respectively. Note that, if two spectral lines are separated by more than 8.9 nm, the spectral peaks' wavelength accuracy is 2.4 nm.

The data analysis system was specially developed for this imaging spectrograph. It automatically searched video frames for rf breakdown phenomena. The selected frames had an integrated pixel brightness along the spectral axis that was greater than the threshold level. In this experiment, most of the frames were full of radiation noise during rf breakdown. This method is very effective for avoiding background noise on the video images.

Experimental setup in high-power test stand

We constructed a test stand for high-power tests on the accelerating structures. A klystron with a maximum peak rf power of 45 MW and a SLED-type pulse compressor, used to generate a high-power rf pulse, were installed on the stand. The pulse width and repetition rate of the rf pulse were 4.0 μsec and 50 Hz, respectively, and the klystron output power level was gradually increased. The reflection of the rf power from the accelerating structure, or waveguides, and the vacuum pressure of the ion pumps were used as an interlock to stop the rf power. The vacuum pressure of the accelerating structure was maintained at around $1{\cdot}10^{-6}$ Pa during rf conditioning.

We installed a quadrupole mass spectrometer and an imaging spectrograph system to study the gases released from the surface of accelerating structures during rf conditioning. In order to improve sensitivity, an ABB Extrel quadrupole mass spectrometer with 19-mm diameter rods was employed. We installed the imaging spectrograph camera to directly view the crescent-shaped cuts in the coupler cavities. These were some of the most likely locations for rf breakdown, because the surface current densities at these locations are 10 times higher than those at other sections [2]. Indeed, we often observed blackened areas damaged by rf breakdown in these cuts.

EXPERIMENTAL RESULTS

Spectrography of rf breakdown in the accelerating structure without HPR

The initial test was carried out in the accelerating structure but without HPR treatment. After the rf conditioning, an average accelerating field of 40 MV/m was obtained after $1.0{\cdot}10^8$ shots (542 hours). Also, the high-power test was terminated due to a time limit. The system experienced 4559 trips due to interlocks with VSWR, which measures rf reflection due to rf breakdown in the accelerating structures. An imaging spectrogram and the light spectrum of light emission as a result of rf breakdown after rf conditioning (elapsed time: 631 hours) are shown in the upper and lower parts of the right side of Figure 2, respectively. The light spectrum clearly shows the atomic lines of outgases at 515 nm (Cu I) 622 nm (Cu II), and, as the most dominant line, at 711 nm (C I).

Spectrometer and I.I.-camera for the imaging spectrograph

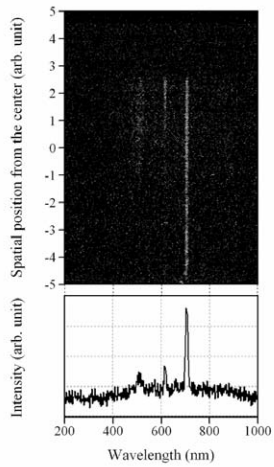

Figure 2: Spectrogram (upper) and light spectrum (lower) of light emission as a result of rf breakdown in the rf-conditioned accelerating structure without HPR treatment (elapsed time: 631 hours; average accelerating field: 30 MV/m)

Spectrography of rf breakdown in the accelerating structure with HPR

The next test was carried out using the accelerating structure with HPR treatment (average water pressure: 5.0 MPa). After the rf conditioning, an average accelerating field of 45 MV/m was obtained after $6.4{\cdot}10^7$ shots (356

hours); however, this gradient was limited by the klystron output power. The system experienced 1894 trips due to interlocks with VSWR. The left and right sides of Figure 3 show two imaging spectrograms with the light spectra at elapsed times of 307 (during rf conditioning) and 677 (after rf conditioning) hours, respectively. The left spectrogram and light spectrum in Figure 3 shows the atomic lines at 395 nm (O I), 515 nm (Cu I), 570 nm (Cu I), 578 nm (Cu I), and, as the most dominant lines, 459 nm (O II) and 656 nm (H: Balmer alpha). In the right spectrogram and light spectrum of Figure 3 only 538 nm (C I), 656 nm (H: Balmer alpha), and 740 nm (Cu II) were observed. After rf conditioning (elapsed time: 677 hours), we observed only these three lines.

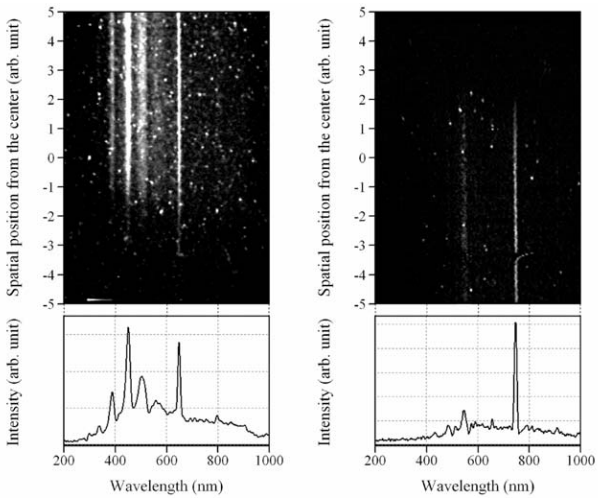

Figure 3: Spectrograms (upper) and light spectra (lower) of light emission as a result of rf breakdown in the accelerating structure with HPR treatment

The spectrograms (upper) and light spectra (lower) during rf conditioning (elapsed time: 307 hours; average accelerating field: 42 MV/m) and after rf conditioning (677 hours; 45 MV/m) are shown at left and right, respectively.

Results of gas and surface analysis

As a result of the gas analysis, we were able to observe instantly increasing signals at mass numbers 2 (H_2), 28 (CO), and 44 (CO_2) but not 18 (H_2O) just after rf breakdown in the accelerating structures. The mass spectrum without rf power is not significantly different from the spectrum before rf breakdown.

In addition, an XPS (X-ray photoelectron spectroscopy) surface analysis was performed on blackened areas of the crescent-shaped cuts in the coupler cavities (without HPR treatment). It was found that with the exception of copper, carbon (graphite) was the most dominant element on the blackened surface of rf-conditioned surfaces.

SUMMARY

We performed experiments to study the gas release from the surface of rf structures by employing quadrupole mass spectroscopy and imaging spectrography of atomic lines. This spectrographic method proved to be particularly useful for observing instantaneous irreproducible phenomena such as rf breakdown. Generally, in both of the accelerating structures, we were able to observe increasing quantities of H_2, CO, and CO_2 molecules immediately after the rf breakdown. These molecules may be either a result of being released from the surface or else generated in the recombination plasma induced by rf breakdown. According to the spectrograms of this recombination plasma, we mainly observed atomic lines of evaporated copper. Using an accelerating structure without HPR treatment, we observed that the atomic carbon line was the most intense, but no oxygen was detected. However, with HPR treatment, we observed only the atomic oxygen and hydrogen lines as the most dominant lines in the early stages of rf conditioning.

According to our experimental results, the HPR treatment can remove dust particles, although it causes different contaminant layers on the copper surface of the accelerating structure. One of these layers could be a thin oxidized layer, because an oxygen line glows in the early stages of rf conditioning but not after rf conditioning. This indicates that, by the end of rf conditioning, the copper surface of the accelerating structure became almost oxygen-free. This is noteworthy, as an oxidized layer is an insulator and allows rf breakdowns to become concentrated on the oxidized layer. Consequently, after rf conditioning, oxygen lines were not observed.

As a result, we found that the structure treated by the HPR process reached 45 MV/m with an rf-conditioning period 1.5-times shorter, a lower rf breakdown rate, and a lower dark current than the untreated one [2].

According to XPS, the most dominant element on the blackened surface, with the exception of copper, was carbon (graphite). We concluded that carbon ions in the plasma recombine with electrons on the copper surface due to the much higher electron density and low electron temperature in the material as compared with the vacuum.

In an additional high power test of rf gun with a chemical etching treatment, we could not measure any spectrum in visible region, because any significant rf breakdown has not occurred. For the next step, we are preparing a new system for imaging spectrography in the UV-region (200 – 400 nm). To study spectra at this shorter wavelength, rf breakdown phenomena will be easier to observe (even for not significant rf breakdown) due to the plasma chemical reactions described in this paper.

REFERENCES

[1] K. Saito, et.al. Proceedings of the 6th Workshop on Superconductivity, 4-8 October, 1993, CEBAF, Newport News, USA, pp. 1151-1159.

[2] Y. Igarashi, S. Yamaguchi, A. Enomoto, T. Oogoe, K. Kakihara, S. Ohsawa, H. Tomizawa, T. Taniuchi, and H. Hanaki, Proceedings of the 2003 Particle Accelerator Conference, 12-16 May, 2003, Portland, Oregon, in printing.

J-PARC LINAC ALIGNMENT

Masanori Ikegami, Fujio Naito, Hirokazu Tanaka, Kazuo Yoshino, Chikashi Kubota, Eiichi Takasaki
KEK, Tsukuba, Ibaraki 305-0801, Japan
Takatoshi Morishita, Hiroyuki Ao, Takashi Ito, Naoki Nakamura, Akira Ueno, Kazuo Hasegawa
JAERI, Tokai, Ibaraki 319-1195, Japan

Abstract

J-PARC lianc has the total length of more than 400 m including the beam transport line to the succeeding synchrotron. In this paper, planned schemes for the linac alignment is presented together with instrumentation for the long-term ground-motion watching.

INTRODUCTION

J-PARC linac has the total length of more than 400 m including the beam transport line to the succeeding RCS (Rapid Cycling Synchrotron) [1, 2]. In high-current proton accelerators, precise alignment of accelerator components is indispensable to reduce uncontrolled beam loss and beam-quality deterioration. It is of essential importance to achieve precise alignment and to maintain its long-term accuracy for realization of the high-power proton beams.

Although we originally planned to develop a laser-based alignment system for J-PARC linac [3], we totally revised the alignment scheme to reduce construction cost and R&D burden. Main difficulty in the original system was the avoidance of the effect of air-turbulence on the measurement. It was also anticipated to be difficult to use the system for continuous observation of the alignment, because its silicon-photo-diode sensors are supposed to be vulnerable to radiation damage. In the revised system, the emphasis is put on the continuous watching of the ground motion as well as the accuracy of the initial alignment. In this paper, the revised alignment scheme for J-PARC linac is described.

ALIGNMENT GOALS

Tolerances for the transverse displacement from the design axis, Δx and Δy, the longitudinal displacement from the adjacent elements Δz, and the roll error, θz, are listed in Table 1. These tolerances are not margins for the alignment procedure, but include various errors in the machining and assembling procedures of a component. The requirement for the transverse displacement of quadrupole magnets, including DTQ (Drift Tube Quadrupole), is especially severe to avoid orbit distortion and resulting emittance growth. However, it has been confirmed that a gradual deflection of the alignment axis is tolerable, and the tolerance for the monotonous deflection is around 0.05 mm/10 m.

INITIAL ALIGNMENT

Link to the Global Survey

Before the commencement of the accelerator alignment, we need to know the relative position of the linac building with the other J-PARC buildings. To this end, we set up a metrological network on the ground which covers the whole J-PARC facility. It also has a few GPS (Global Positioning System) measurement points to link with a global coordinate system. Because the metrological network is set up on the ground level, we need to have access holes to the linac accelerator tunnel (that is located at 13.5 m underground) to introduce the coordinate. We have three access-holes to the linac accelerator tunnel from the ground level (klystron gallery). Just below the access-holes, we have three "primary reference points" for the linac tunnel, which will be the starting points of the linac tunnel survey. Through the access-holes, the height reference of the whole J-PARC facilities is also introduced into the linac tunnel.

Alignment Reference on the Components

The horizontal and longitudinal alignment are planned to be performed with a laser-tracker. Although a laser-tracker can be used for the vertical measurement, we plan to use a digital level (Leica DNA03) for the vertical alignment to improve the accuracy [4, 5]. As a back-up scheme for the horizontal alignment of straight sections, we are preparing a stretched-wire method with capacitive wire-position sensors (Fogale nanotech WPS2D). In addition, we will use an alignment-telescope (Taylor-Hobson 112/2582) in prealignment of the accelerator elements. The rotation about the beam axis will be avoided with a digital inclinometer (Wyler Minilevel NT). To enable these alignments, each accelerator element has "alignment reference bases" which are standardized for J-PARC accelerators. The alignment base is a stainless steel plate which has a standardized reference hole at the center of its top surface. The position of the reference hole is adjusted to a certain position with respect to the beam axis before the installation of the component. Various targets, including a CCR (Corner Cube Reflector) for a laser-tracker, an optical target for an alignment telescope, a leveling staff for a digital level, and a capacitive wire-position sensor, can be mounted on the reference base via dedicated attachments with precise position reproducibility. Figure 1 shows an example of these attachments, in which a drawing of a wire-position-sensor holder for DTL and SDTL tanks is shown. To attain the precise position reproducibility, we use a preside attach/detach sys-

Table 1: Tolerances for alignment

	Δx, Δy	Δz	θ_z
DTQ, quadrupole magnets	± 0.1 mm	± 0.1 mm	± 5 mrad
SDTL tanks, other RF cavities	± 0.3 mm	± 0.1 mm	

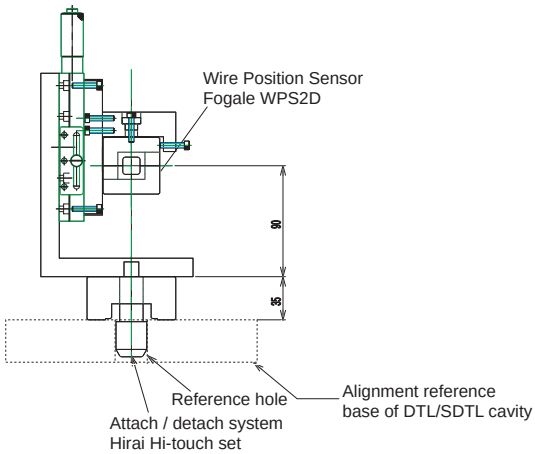

Figure 1: A wire-position-sensor holder for DTL and SDTL tanks.

tem (Hirai High-touch set) for these attachments.

Horizontal and Longitudinal Alignment

The concept of alignment with a laser-tracker is shown in Fig. 2. The procedure is conventional, in which a laser-tracker is placed at a position (red circle in Fig. 2), and measure the positions of reference bases and wall monuments, and then it is moved to the next position (blue circle). Some of the measurement points for the new tracker-position are overlapped with the previous ones in order to find out the movement of the laser-tracker itself. Repeating this procedure, the whole linac and the beam transport line will be covered. Each element, i.e., RF cavities, quadrupole doublets, has two or more reference bases for a CCR.

The main concern in using a laser-tracker for linac alignment is the possible gradual deflection of the alignment axis, which might be resulted from the insufficient accuracy of angular measurement [4]. The narrow tunnel width is also an obstacle to setup a secure metrological network sustainable for the measurement errors. Our strategy is to setup a fine metrological network which minimizes the statistical errors of the coordinate measurements with geometrical considerations [6]. If we find an unacceptably large deflection of the alignment axis (which is supposed to be detected with an alignment-telescope), we plan to use a WPS (Wire Positioning System) for the horizontal alignment of the straight section (in which case, the longitudinal alignment can be performed with a tubular inside-micrometer). Figure 3 shows a conceptual view of alignment with WPS. A stretched wire is located above the reference bases for DTL and SDTL tanks. A WPS sensor is placed on the reference base with a removable attachment. The attachments for the quadrupole magnets have a long arm, because the reference bases for quadrupole magnets are located above the beam axis which is 460 mm horizontally from the wire axis. We prepare several sets of WPS attachments, and we measure the horizontal position of each element utilizing them. The maximum length of a stretched wire is 120 m, and DTL (27m) and SDTL section (90 m) can be covered with one wire. A stretched wire can cover the ACS section (107 m) also. To avoid the tilt between these two wires, we plan to set up an additional wire which overlaps with these two wires [4]. We also plan to use WPS for the halo scraper section after the first arc of the beam transport line.

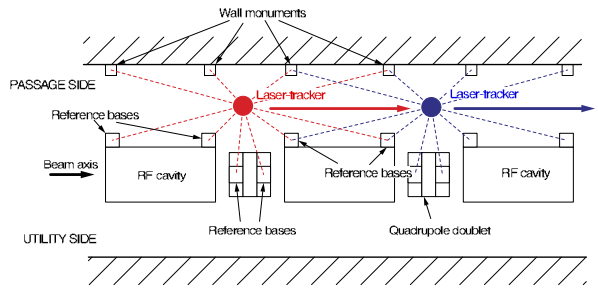

Figure 2: Conceptual view of alignment with a laser-tracker.

Vertical Alignment

In the vertical alignment, we plan to use an HLS (Hydrostatic Leveling System) as the reference in order to avoid accumulating errors of the height measurements. We plan to install 13 HLS sensors (Fogale nanotech HLS) along the linac and the beam transport line between the linac and the succeeding RCS. Figure 4 shows the schematic layout of the HLS sensors. Spacing between HLS sensors is about 50 m, except for the vicinity of expansion joints and a partition wall where sensors are densely populated. The HLS sensors are fixed on steel base plates on which accelerator components are placed, and the base plates are fixed to a structural concrete slab of the tunnel floor. Based on the communicating vessel principle, the height difference among sensor positions can be obtained by measuring the difference of the water levels. The HLS sensor has a high-precision capacitive water-level sensor and a reference sphere nest for connection to the metrological measurement.

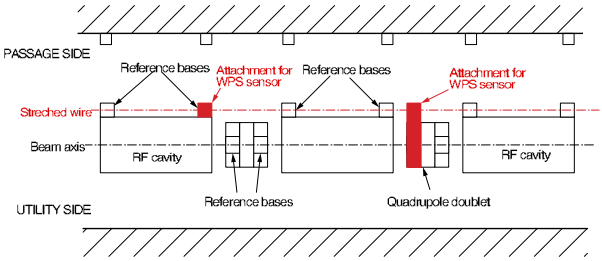

Figure 3: Conceptual view of alignment with WPS.

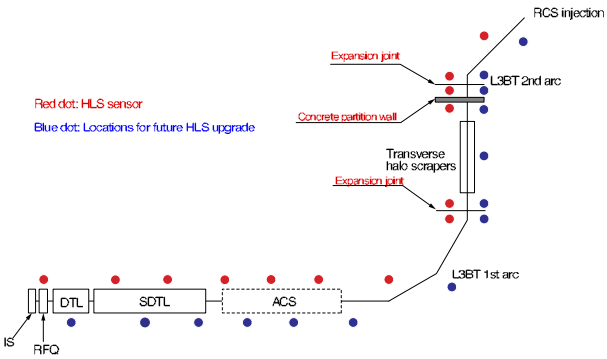

Figure 4: Schematic layout of HLS sensors.

CONTINUOUS WATCHING

We plan to use HLS sensors and WPS sensors for continuous watching of the ground motion. The HLS sensors installed as the reference for vertical alignment will be used for this purpose. The HLS sensors are densely populated in the vicinity of the expansion joints to closely watch the movement bordering the joints. We also plan to place some WPS sensors, which has been prepared as a back-up for horizontal alignment, for the continuous monitoring. Figure 5 shows a schematic layout of the WPS sensors for the continuous watching. Because we don't have enough sensors, we plan to focus on DTL section at the beginning, and then increase the number of sensors and extend the coverage to downstream sections.

The sensor electronics of both HLS and WPS are separated and placed in the sub-tunnel to avoid radiation damage. The cable between a sensor and sensor electronics is extended to 20 m to enable these layout. While the cable extension increases the noise level, the resulting deterioration ofthe sensor resolution is expected to be around $\pm 4\mu$m, which is negligible for our purpose.

To watch more large-scale movement, i.e., relative movement between the linac building and the RCS building, we utilizes the access-holes mentioned above. Using these access-holes we can measure the relative position between the linac tunnel and other J-PARC buildings. Performing metrological measurement using these access-holes occasionally, the large-scale movement of J-PARC facilities can be measured.

The data obtained with the long-term monitoring will be used for realignment scheduling and, possibly, a slow feedback of the beam orbit correction.

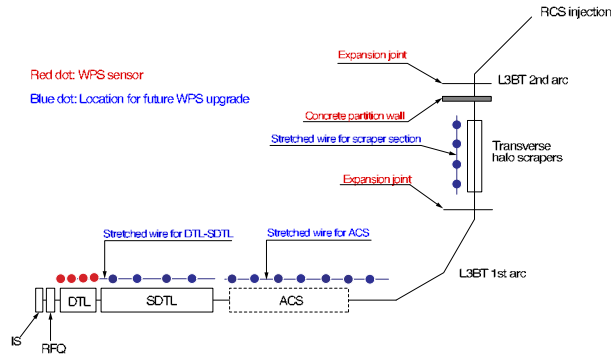

Figure 5: Schematic layout of WPS sensors.

SCHEDULE

Metrological measurement of the accelerator tunnel and marking for component installation will be performed in March 2005. The installation of main components will be started in May 2005. The fine alignment will be performed in May-June 2006. Fundamental testing of HLS sensors and WPS sensors has been started.

SUMMARY

We plan to perform J-PARC linac alingment with a laser-tracker (horizontal and longitudinal) and a digital level (vertical), basically. As a reference for the vertical alignment, we prepare HLS sensors along the linac. We prepare WPS sensors as a back-up method for the horizontal alignment. We plan to use the HLS sensors and WPS sensors also for the long-term monitoring of the floor motion.

ACKNOWLEDGMENT

Authors would like to thank Prof. R. Sugahara of KEK and Dr. K. Mishima of PASCO Corp. for valuable discussions and suggestions.

REFERENCES

[1] Y. Yamazaki,"Status of the J-PARC Linac, Initial Results and Upgrade Plan", in these proceedings.

[2] Y. Yamazaki ed., "Accelerator Technical Design Report for J-PARC", KEK Report 2002-13; JAERI-Tech 2003-044.

[3] M. Ikegami et.al, "Laser-based Alignment System for J-PARC Linac", in Procs. of PAC2003, p. 2393 (2003).

[4] R. Sugahara, private communication.

[5] K. Mishima, private communication.

[6] K. Mishima, "Study on the Precise Alignment of Accelerator (in Japanese)", Doctoral thesis, 2002.

COUPLER DEVELOPMENT AND GAP FIELD ANALYSIS FOR THE 352 MHz SUPERCONDUCTING CH-CAVITY*

H. Liebermann, H. Podlech, U. Ratzinger, A. Sauer,
Institut für Angewandte Physik, Frankfurt, Germany

Abstract

The cross-bar H-type (CH) cavity is a multi-gap drift tube structure based on the H-210 mode currently under development at IAP Frankfurt and in collaboration with GSI. Numerical simulations and rf model measurements showed that the CH-type cavity is an excellent candidate to realize s.c. multi-cell structures ranging from the RFQ exit energy up to the injection energy into elliptical multi-cell cavities. A 19-cell, beta=0.1, 352 MHz, bulk niobium prototype cavity is under fabrication at the ACCEL-Company, Bergisch-Gladbach. This paper will present detailed MicroWave Studio [1] simulations and rf model measurements for the coupler development of the 352 MHz superconducting CH-cavity. It describes possibilities for coupling into the superconducting CH-cavity. First results of the measurements of different coupler concepts, e.g. capacitive and inductive coupling at different positions of the CH-cavity are reported.
Additionally the rf quadrupole content in CH-type gaps was investigated quantitatively.

INTRODUCTION

Present H-mode structures are all operated at room temperature. Many future accelerator projects require cw operation. But the achievable gradients of room temperature cw operated H-mode cavities are limited due to power losses and cooling problems. The superconducting CH-cavity can be realized in the frequency range from 150 to 800 MHz, the beam energy can be chosen between 5 AMeV and 150 AMeV which corresponds to a β-range from 0.1 to 0.5. The CH-structure can be used for proton as well as for heavy ion beams. The superconducting version seems to be quite attractive for high current proton linacs like XADS [2] or deuteron linacs like IFMIF [3].

SUPERCONDUCTING (SC) STRUCTURES

In sc cavities there is no cooling problem as in cw operated rt (room temperatur) linacs. In general, sc linacs can be operated at higher gradients above a certain duty factor. On the other hand, at low duty factors and high beam currents rt structures are very favourable because they are less expensive and can tolerate dark current contributions. To demonstrate the capabilites of the CH-DTL, it is foreseen to test a sc CH cavity prototype. A design and engineering study has been performed in close cooperation with industry[1]. This study shows the feasibility of the production of superconducting CH cavities. The cavity production started in 2003 and the delivery is expected in October 2004 [4]. The CH protoype with 19 gaps will be made of

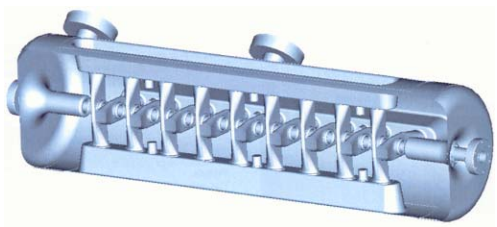

Figure 1: The sc 352 MHZ CH prototype with matched end cell geometry.

bulk niobium, the diameter is 28 cm, the length is 105 cm. At an operation frequency of 352 MHz, this corresponds to a particle β of 0.1. One important issue during the design phase was the minimization of the electric and magnetic peak fields to reduce the risk of field emission and of thermal break down. An accelerating gradient of 4 MV/m results in an electric peak field of 26.4 MV/m and in a magnetic peak field of 30 mT which is a moderate value.

Table 1: Main design parameter of the s.c. prototype CH-cavity

β	0.1
Frequency [MHz]	352
Diameter [m]	0.28
Tank length [m]	1.05
$R_a/Q[\Omega]$	3220
E_p/E_a	6.59
B_p/E_a [mT/(MV/m)]	7.29
$Q_0(R_s = 150n\Omega)$	$3.7 \cdot 10^8$

METHODE FOR THE EXTERNAL Q VALUE

For calculation of the external Q value, we use the method described by Balleyguier [5]. If a lossless cavity is weakly coupled to an infinite line, this line drives out a certain RF power P and the energy stored in the cavity gradually decreases. The external Q then is:

$$Q_{ext} = \omega W/P.$$

If we assume, that the line mode is a TEM and the dielectric is vacuum: $\eta^2 = \mu/\epsilon$. Then, the external Q can be

* Supported by GSI Darmstadt, EU and by BMBF, contr. no. 06F134I
[1] ACCEL Company, Bergisch Gladbach, Germany

expressed as:

$$Q_{ext} = \frac{\omega \iiint_{cavity} |F|^2 dV}{c \iint_A |F|^2 dA}. \quad (1)$$

F being either the electric (E) or magnetic (H) field. According to the superposition theorem, we can add these two solutions (fig. 2). So it is possible to solve these problem by two MicroWave Studio runs.

At the first run, the line can be terminated at the refer-

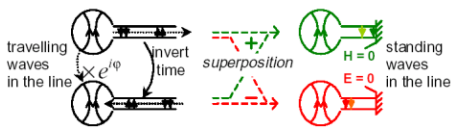

Figure 2: Transforming a travelling-wave problem into a standing-wave one [5].

ence plane with the appropriate boundary condition (perfect magnetic wall). Using the same formal expression as in equation (1), we can define the quantity Q as:

$$Q_1 = \frac{\omega \iiint_{cavity} |E_1|^2 dV}{c \iint_{ref.plane} |E_1|^2 dA} = \frac{|1+e^{i\phi}|^2}{4} Q_{ext}.$$

At the second run, the line can be terminated with other boundary condition (perfect electric wall). So we can define the quantity Q_2 as:

$$Q_2 = \frac{\omega \iiint_{cavity} |H_2|^2 dV}{c \iint_{ref.plane} |H_2|^2 dA} = \frac{|1-e^{i\phi}|^2}{4} Q_{ext}.$$

As for any value of ϕ, $|1+e^{i\phi}|^2 + |1-e^{i\phi}|^2 = 4$, we have then: $Q_{ext} = Q_1 + Q_2$.

CH CAVITY COUPLING

For coupling into superconducting structures the external Q-value must be between 10^6 and 10^9. If you want to reach these different kinds of couplers were examined with MicroWave Studio and measured at a copper model. First a capacitive coupling through the girder of the CH-structure (fig.3) was examined. The inner conductor of the coaxial line is facing a drift tube with opposite polarity.

It turned out that by this method external Q-values from 10^4 to 10^{11} can be achieved (fig.4). In order to verify the calculations with MicroWave Studio, measurements of the copper model were accomplished. These show a good agreement with the calculations.

After getting confidence in the simulations from the comparison with model measurements,calculations for the superconducting prototype of the CH structure were performed. The results of the calculations are represented in figure 5.

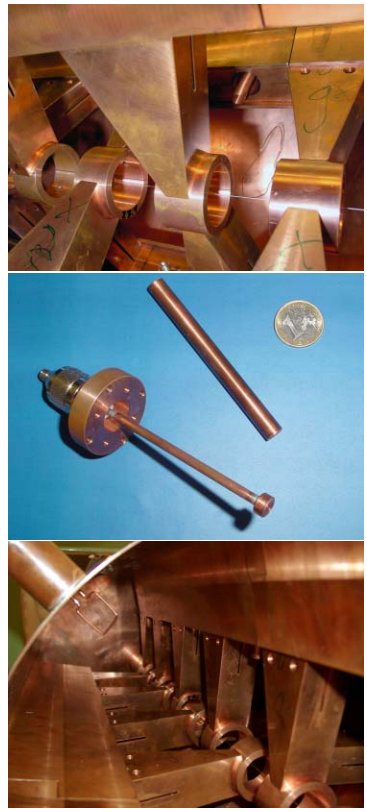

Figure 3: Capacitive coupling through one girder between two stems in the same plane (upper), Capacitive Couplers for the measurements at the copper-model (middle) and Inductive coupler at the CH-Copper-model (lower).

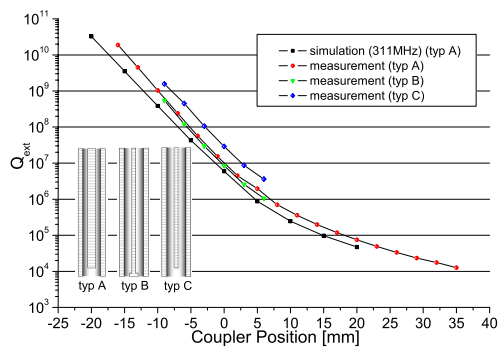

Figure 4: Calculations and Measurements for capacitive couplers for the Copper-model of the CH-Cavity. 0mm corresponds to the girder surface plane.

It showed that with a coupler position between -10 and +10 mm external Q-values between 10^5 and 10^9 can be achieved (fig.5). Additionally, magnetic coupling by a loop was investigated.Two positions were examined: In the midplane of the structure and at the cavity end. Both positions were located transversly between the girders under 45 degrees. In fig.6 the results of the calculations are showed.

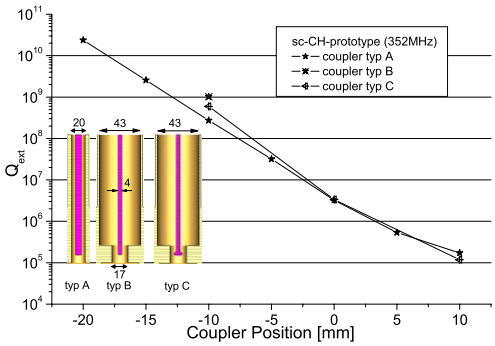

Figure 5: Calculations for capacitive couplers for the s.c. prototype of the CH-Cavity.

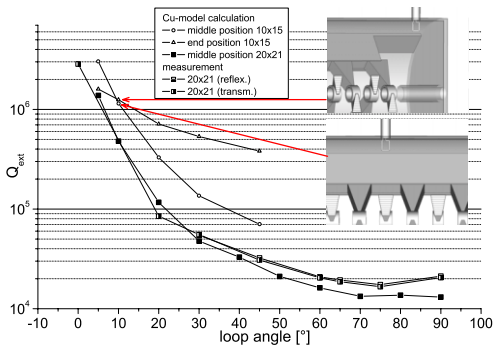

Figure 6: Calculations and Measurements for inductive couplers for the Copper-model of the CH-Cavity.

RF QUADRUPOLE CONTENT IN CH-GAPS

In the CH-DTL structure, the tubes are supported alternately in the X and Y planes, which generates quadrupole fields, as fig.7 shows. It means that two kinds of transverse

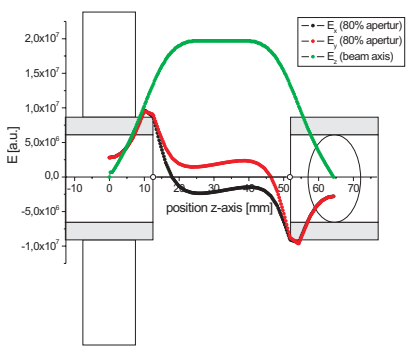

Figure 7: Schematic view of the CH-DTL.

fields exist inside the CH-gaps, which were generated by stems and tubes, respectively. The transverse total E-field consists of the cylinder-symmetrical and of the quadrupole field components.

$$E_{x,tot.}(z) = E_r(z) + E'(z)\cdot x + \ldots$$
$$E_{y,tot.}(z) = E_r(z) - E'(z)\cdot x + \ldots$$

$$\rightarrow E_{x,tot.}(z) - E_{y,tot.}(z) \simeq 2\cdot E'(z)\cdot x$$

The stem orientation of the input drift tube defines the focusing quadrupole direction of each gap for accelerating rf phases between -90 and +90. In case of the CH-structure the quadrupole orientation is changed in every gap (FODO). The Quadrupole strength of one CH-gap can be written as:

$$\int_{CH} E'dz = \int_{CH} \frac{E_{x,tot.}-E_{y,tot.}}{2\cdot x}dz$$

The quadrupole strength is compared to an idealized drift tube structure with quadrupole fingers, where the quadrupole is generated by the gap voltage amplitude $\pm$ V/2 at the aperture radius a along the gap length g. This result in a reference quadrupole strength $E'\cdot g = \frac{V}{a^2}\cdot g$ and in a related strength factor for the CH-gap with $\eta_Q = \frac{\int_{CH}|E'|dz}{\int_{CH}E_z dz}\cdot\frac{a^2}{g}$.

In Fig.8 η_Q is plotted against varying gap lengths.

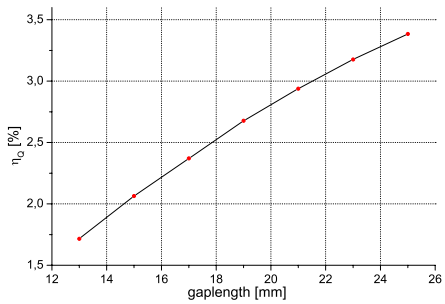

Figure 8: quadrupole strength factor η_Q at different CH gap lengths and constant period length $\beta\lambda/2 = 42.857mm$, stemm geometry like in Fig.1.

OUTLOOK

The calculations have shown that the best way to couple into the CH-structure is to couple with an antenna to the electric field, because we can reach external Q-value between 10^5 and 10^9 and it is the easiest method.

For the first cold tests it is planned to couple with an capacitive coupler of type B. The quadrupole content in the gap-fields of CH-structures were studied quantitytively and will be included in future beam dynamics calculations with LORASR.

REFERENCES

[1] http://www.cst.com

[2] Requirements for the XADS Accelerator and Technical Anwers, DAPNIA-02-302, September 2002, France

[3] A. Sauer, H. Deitinghoff, H. Klein, H. Liebermann, H. Podlech, U. Ratzinger, R. Tiede, End-To-End Simulations of a Superconducting Deuteron CH-DTL for IFMIF, Proceedings of the PAC 2003, Portland, OR, USA

[4] H. Podlech, Development of Superconducting and Room Temperature CH-Structures, these proceedings

[5] P. Balleyguier, External Q Studies for APT SC-Cavity Couplers, Proceedings of the LINAC 1998, Chicago, IL, USA

TECHNOLOGIES OF THE PERIPHERAL EQUIPMENTS OF THE J-PARC DTL1 FOR THE BEAM TEST

K. Yoshino#, C. Kubota, E. Takasaki, E. Kadokura, F. Naito, H. Tanaka, T. Kato, Y. Fukui, KEK, Tsukuba, Japan
T. Ito, JAERI, Tokai, Japan

Abstract

First beam test of the DTL1 was performed in November of 2003 at KEK site. A 30-mA H^- beam was successfully accelerated from 3 to 19.7 MeV. In order to accomplish the successful beam test, various peripheral equipments were developed: the electrode plates for connecting the hollow-conductor coil and the power cable were developed since quadrupole electromagnets are built in all DTs (77 sets) of the DTL1 [1], the water-cooled multiconductor copper tubes (Control Copper Tube) were used as the power cable from the electrode plates to power supplies, and the interlock system assembled by PLCs (Programmable Logic Controller) was also prepared for the surveillance of many cooling channel.

INTRODUCTION

High Energy Accelerator Research Organization (KEK) and Japan Atomic Energy Research Institute (JAERI) are together constructing the high intensity proton accelerator at Tokai site, which is called Japan Proton Accelerator Research Complex (J-PARC) Project. We are conducting the beam test of the first tank of DTL (DTL1) at the Proton linac test facility at KEK site. A negative hydrogen beam was accelerated to its design value of 19.7 MeV. A peak current of 30 mA was achieved with almost 100 % transmission at a 12.5 Hz repetition rate in a 20-microsecond pulse width [2].

It is required for the beam test that the wiring from the power supply to the quadrupole magnet (Q-magnet) copes with the following technical subjects:

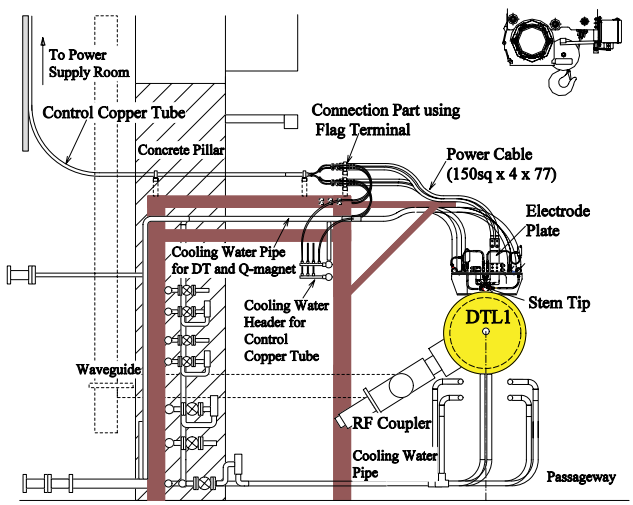

Figure 1: Schematic drawing of the wiring in the tunnel.

1) Suppressing cable vibration with the pulse excitation of the Q-magnet.
2) Design of the electrode which connects the power cable and the Q-magnet in small installation space.
3) Assembling procedure of the electrode in order to minimize the effects on the position of the stem. (Because the electrode can push the stem, it may shift the position of the drift tube.)
4) The performance test of the busduct which is intended to use mainly as the power cable in Tokai site.
5) Construction of a local interlock system for errors in the magnet power supplies, the cooling water system and the vacuum pump controllers.

Investigated results for these subjects are described in the following sections.

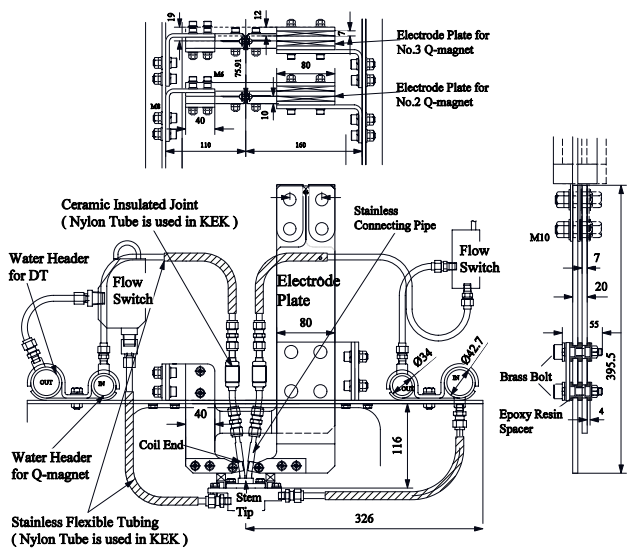

Figure 2: Schematic drawing of the connection part between the power cable and the electrode at the top of the stem.

WIRING COMPONENTS

Schematic drawing of the wiring in the tunnel at kek is shown in Fig. 1. All magnets were wired by the cables which satisfy the pulse excitation specification (Max. 1000 A, 50 Hz). Therefore wiring was done after the confirmation test that the effects of the pulse vibration of those cables were negligible for the DT alignment.

#kazuo.yoshino@kek.jp

Connection Between the Power Cable and the Electromagnet

The end of the hollow conductor coil was extended by only about 3 cm from the stem tip, since the extension length was limited by the assembling procedure of the DT in the tank [3]. It was observed in the preliminary assembling test that the position of DT deviated from the initial position when the connection of the power cable to the end of the coil was done without careful attention to the load of the stem. Then, we decided to connect the coil-end and the power cable by using electrode plate (see Fig.2) which is finally fixed on the DTL so that the direct effects on the stem due to the load of the power cable can be prevented. The gap of both positive and negative electrodes were made as small as possible in order to reduce the amplitude of the vibration by pulse excitation of the Q-magnet. Moreover, the position of the electrode plate was fine-tuned by using the larger screw hole when the electrode is connected to the coil. In addition, the thermostat was attached in all electrode plates in order to observe temperature rise of the power line.

Control Copper Tube

The copper pipes (Control Copper Tube) were used for the main wiring from the power supplies to the Q-magnets for the beam test at KEK; CCPP-EE 7x8x6 (No. of Pipe x Outside Diameter x Inside Diameter) made by Hitachi Cable, LTD (see Photo 1) [4]. They were applied for 73 lines among 77 lines. The reasons for using Control Copper Tube are as follows:

1) It can be expected that pulse vibration reduces compared with the power cable, since the Control Copper Tube has twist structure of the multi-core.
2) The thermal influence on waveguide near a wiring can be reduced, since the heat from the power line is suppressed by cooling water.
3) The material cost of Control Copper Tube is lower than the power cable.
4) It is comparatively easy to do wiring work, since it is lightweight and flexible. Moreover, a required installation area is small since the cross-section per line is much smaller than that of the busduct and/or other air-cooled cables.

After relocation to Tokai site the busduct and the thick power cable will be used instead of Control Copper Tube, since the water-cooled power line for the Q-magnets are not permitted to be used as the power cable in JAERI.

Connection between Control Copper Tube and the Power Cable

Since the tube fittings for cooling-water is attached to the terminal of Control Copper Tube, it is impossible to connect the magnet power supply or the magnet coil to the Control Copper tube directly. Then, the short power cable was used to connect them.

After testing various types of clamps, it was found that the flag terminal (J.S.T. Mfg. Co., Ltd : SF38-12) was the best way and it costs lower [5].

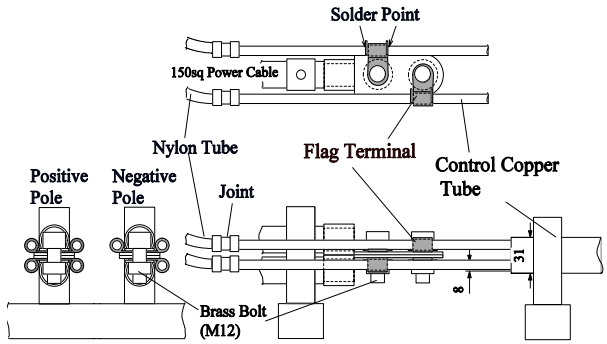

Figure 3: Schematic drawing of the connection part between Control Copper Tube and the power cable.

The outline of the connection part using the flag terminal is shown in Fig.3. Fixing of the terminal has been done by soldering both ends after cramping to the Control Copper Tube moderately.

Busduct

We used the busduct for the main wiring of 4 lines among 77 lines instead of the Control Copper Tube. The E-BD type made by KYODO KY-TEC CORP was chosen as the busduct [6]. Since the structure of the bus duct is a 4-wire x 2-stage, it is connectable with four magnets by one set (see Fig.4). The conductor is made of aluminum with the insulator of a polyester sheet.

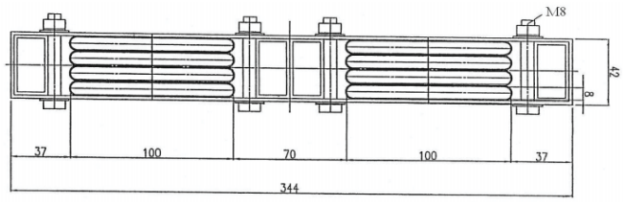

Figure 4: Cross-sectional drawing of the busduct.

PLC

We are using PLC (Yokogawa Electric Corp. : FA-M3) as a cooling-water interlock system for DTL. For the beam examination, signals from flow switches of DT's and Q-magnets (electrodes) has been connected to the magnet power supplies via PLC. However, signals from flow switches of DT's and Q-magnets will be connected to the magnet power supplies directly at Tokai site. The number of input and output signals to PLC of DTL1 is shown in table 1. This system links "Beam operating and safety system" [7] and stops a beam at the alarm.

PRELIMINARY TEST RESULTS

The preliminary test of each equipment was done before the actual run.

Preliminary Test of the Electrode Plate

The prototype model of the electrode plate was made and installed on the DTL test cavity for the preliminary examination (see Photo 2). The bolting procedure has

been investigated in order to decrease the deviation of the drift tube within an allowable limit.

Next, the electrode and the magnet power supply were connected by using the Control Copper Tube and the flag terminal, and then, a pulse excitation examination was done. In the beginning, the maximum difference of temperature the electrode-surface and the tank-wall was approximately 20 degrees centigrade. So, the following countermeasures were taken. (1) The material of the bolt was changed from SUS to brass. (2) Each cable terminal was fixed to the plate of the electrode one by one since the large thermal gradient was observed when the terminal was fixed to a pair of plates simultaneously. As a result, a temperature difference decreased below 15 degrees centigrade.

There were few vibrations of the Control Copper Tube and the electrode plate in comparison with the power cable. It will be necessary to consider how to reduce the vibration more about wiring of the power cable in Tokai site. The connection part of the flag terminal was satisfactory.

Table 1: The number of input and output signals to PLC of DTL1

	INPUT	OUTPUT
Flow Switch	214	
Resistance Temperature Detector	58	
Thermostat	77	
Power Supply Status	77	
To Power Supply		77
Beam, RF, etc		3
TOTAL	426	80

Preliminary Test of the Busduct

Because each line in the busduct is close in the structure, it is expected that the influence of the electromagnetic induction by pulse excitation is sufficiently small. So, on the condition that one line was connected to the test Q-magnet, and other 3 lines were short-circuited, an influence on each line in the busduct was measured. In this case the neighboring line had the reverse polarity. As a result, the measured voltage induced by the mutual coupling was 0.3 % in maximum shown in Figure 5. Therefore, it can be concluded that the stability within 1 A can be achieved if voltage polarity is reverse and pulse shape is the same.

PLC Response Examination

The delay, from when the alarm happens to the time when the power supply is cut off, is about 18 msec. Therefore, there was no problem because the measured delay time was less than the repetition rate of the pulse operated magnet power supply.

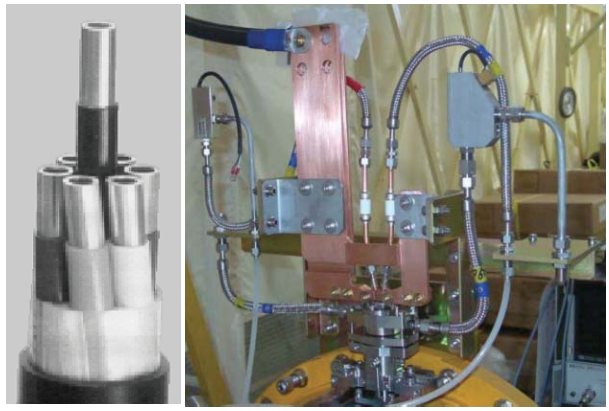

Photo 1 (Left): Control Copper Tube.

Photo 2 (Right): Preliminary test of the electrode plate.

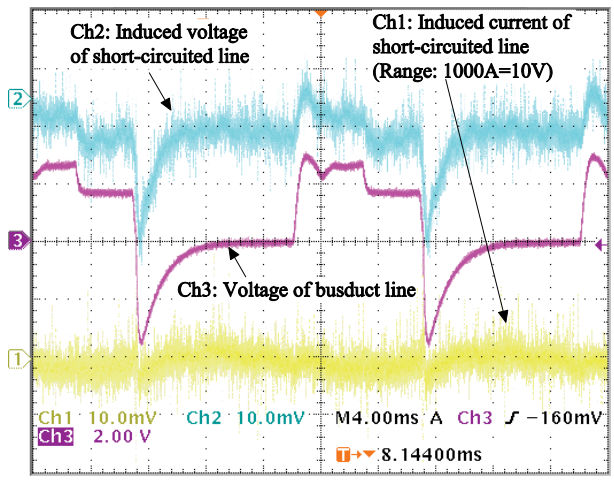

Figure 5: Induced voltage of the short-circuited line.

REFERENCES

[1] K. Yoshino et al., "Development of a DTL quadrupole magnet with a new electroformed hollow coil for the JAERI/KEK joint project", LINAC'00, California, August 2000, p. 569.

[2] F. Naito et al., "RESULTS OF THE HIGH-POWER CONDITIONING AND THE FIRST BEAM ACCELERATION OF THE DTL-1 FOR J-PARC", in this conference.

[3] F. Naito et al., "MECHANICAL AND RF PROPERTIES OF THE DTL FOR THE JAERI/KEK JOINT PROJECT", LINAC'02, Gyeongju, August 2002, p. 359.

[4] http://www.hitachi-cable.co.jp/catalog/h-001/pdf/cable.pdf, p. 150

[5] http://www.jst-mfg.com/ProductGuideJ/pdf_j/A-G4.pdf.

[6] http://www.ky-tec.co.jp/enter_04.html.

[7] E. Kadokura, S. Noguchi, "BEAM OPERATION AND SAFETY SYSTEM FOR THE PROTON LINAC OF THE JAERI/KEK JOINT PROJECT" APAC'01, Beijing, September 2001, p. 884.

CLIC MAGNET STABILIZATION STUDIES

S. Redaelli*, R. Aßmann, W. Coosemans, G. Guignard,
D. Schulte, I. Wilson, F. Zimmermann. CERN, Geneva, Switzerland.

Abstract

One of the main challenges for future linear colliders is producing and colliding high energy e^+e^- beams with a transverse spot size at the collision point in the nanometre range ("nanobeams"). The Compact LInear Collider (CLIC), presently under investigation at CERN, aims at colliding e^+e^- beams with a vertical spot size of 0.7 nm, at a centre-of-mass energy of 3 TeV. This requires a vertical stability to the 1.3 nm level for the 2600 linac quadrupoles and to the 0.2 nm level for the two final doublets at either side of the interaction point. In the framework of the CLIC Stability Study, it has been demonstrated for the first time that CLIC prototype quadrupoles can be stabilized to the 0.5 nm level in a normal working area on the CERN site.

INTRODUCTION

The Compact LInear Collider (CLIC) study [1] at CERN is investigating the feasibility of building an e^+e^- linear collider with centre-of-mass energies up to 5 TeV, at a luminosity of 10^{35} cm^{-2}s^{-1}. High luminosities will be achieved by colliding opposing e^+e^- beams with transverse spot sizes of $\approx 60 \times 0.7$ nm^2 (horizontal$\times$vertical), which imposes tight tolerances on the stability of the focusing quadrupoles. The CLIC tolerances for a 2 % luminosity reduction for uncorrelated RMS displacements above 4 Hz are summarized in Table 1 for the 2×1300 linac quadrupoles and for the 2×2 final focus quadrupoles [2]. The SLC experience has shown that beam-based feedback systems can efficiently compensate *slow* motions up to $\approx 1/25$ of the pulse repetition frequency [3] (100 Hz for CLIC). *Fast* vibration above ≈ 4 Hz must then be mechanically stabilized to ensure the required luminosity performance. To achieve the ambitious CLIC stability goal, it is not possible to rely only on the stability of a given site because the natural ground stability is strongly increased by the accelerator environment (pumps, ventilation, cooling water, ...). This was demonstrated by vibration measurements at LEP [4], where the motion was increased from 0.2 nm to more than 20 nm. Dedicated stabilization technologies must therefore be developed to meet the requirements of future linear colliders.

In the last years, the magnet stabilization problem has attracted the interest of various high-energy physics laboratories and universities worldwide. At CERN, a CLIC stability study was started in 2001 [5] to investigate the feasibility of colliding nanometre-size beams in CLIC in a realistic accelerator environment. Following the encouraging results obtained in stabilizing low-energy nanobeams for electron transmission microscopy [6] and in various other domains, the CLIC study pursued the approach of using state-of-the-art stabilization devices to find out what level of magnet stability could be achieved by using the presently available technology from industry (see Fig. 1). This report summarizes the experimental achievements obtained from January 2001 to December 2003.

Table 1: Tolerance on the uncorrelated RMS motion above $f_{\min}$ of the CLIC quadrupoles for a 2 % luminosity loss

Magnet type	N_{magnet}	$f_{\min}$	I_x	I_y
Linac	2600	4 Hz	14.0 nm	1.3 nm
Final focus	2	4 Hz	7.8 nm	0.2 nm

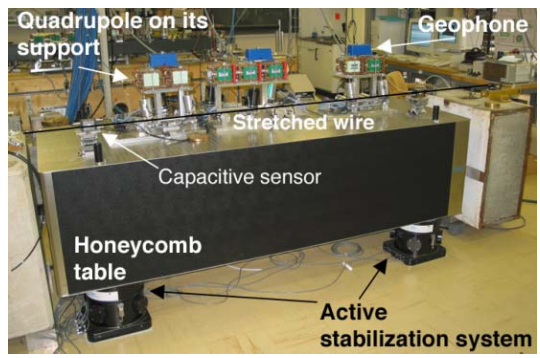

Figure 1: Photograph of the CLIC stability study test stand, with the detail of a geophone installed on a quadrupole.

THE CLIC TEST STAND

Basic notation

Vibration measurements are performed with high-resolution *geophones*, which measure vibration velocities versus time. The employed sensors have a sub-nanometre resolution in the 4 Hz to 315 Hz range (e.g., 0.28 nm resolution on the RMS motion above 4 Hz). Detailed comparisons with several other vibration devices [7], indicate an error of 10 % on the geophone calibration provided by the manufacturer. Here, the basic notation for data analysis is briefly reviewed. The vibration velocity, $v(t_n)$, is measured at the discrete times $t_n = n\Delta t$, with $n = 1, 2, ...N$ ($\Delta t = 0.001$ s). The power spectral density of the displacement, $P(f_k)$, is defined for the discrete frequencies $f_k = \frac{k}{N\Delta t}$ as:

$$P(f_k) = \frac{N\Delta t^3}{2\pi^2 k^2} \left| \sum_{n=1}^{N} v(n) e^{-2\pi i \frac{kn}{N}} \right|^2 . \qquad (1)$$

The integrated RMS displacement induced by vibrations

* Work done in the framework of a PhD program at the University of Lausanne, CH, High Energy Physics Institute (UNIL-IPHE).

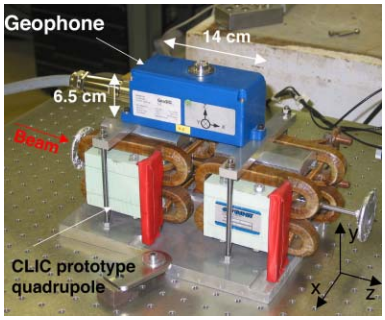

Figure 2: A CLIC prototype quadrupole with a geophone to measure vibrations

above $f_{\min} = k_{\min}/(N\Delta t)$ is given by:

$$I(f_{\min}) = \sqrt{\frac{1}{N\Delta t}\sum_{k'=k_{\min}}^{k_{\max}} P(f_{k'})}. \qquad (2)$$

Here, $k_{\max}$ is the maximum measurable frequency and is equivalent to infinity for our purposes. The spectra $P(f)$ are calculated as the average of several consecutive data sets before integration. The reference frame (x, y, z) is shown in Fig. 2: x and y are the horizontal and vertical directions with respect to the beam trajectory, z.

Experimental setup

The CLIC experimental test stand was located on purpose in a normal working area of the CERN site, close to various sources of noise (streets, workshops, offices, running accelerators, ...). The vibration level of the chosen site was measured to be up to 12-15 nm, i.e. up to 70 times larger than the tightest CLIC tolerance (Table 1) and hence suitable for testing the efficiency of stabilization techniques. A photograph of the overall CLIC test stand for the vibration studies and magnet stabilization is shown in Fig. 1 (see [2, 7] for more details). The available equipment includes, amongst others: (1) Four high-resolution geophones for measuring sub-nanometre vibrations from 4 Hz to 315 Hz; (2) One low-frequency, high-resolution geophone for vibrations from 0.03 Hz to 50 Hz; (3) Two distinct devices for passive and active vibration damping: (a) a *stiff* system (STACIS2000 from TMC) consisting of four independent actively stabilized feet and (b) a *soft* system (PEPS-VX from TMC) based on four air-pressure pistons; (4) A honeycomb support structure (table, dimensions 2.4 m×0.8 m×0.8 m), used to support the magnets, with minimal structural resonances above 230 Hz; (5) Prototypes of CLIC quadrupoles (Fig. 2), with the possibility to connect them to an adjustable flow of cooling water; (6) A stretched wire system for measuring the magnet alignment with respect to the surrounding ground in a wide range of times (seconds to weeks). It is noted that by combining the measurements of the two available types of geophones, vibrations over four orders of magnitude, from 0.033 Hz to 300 Hz, can be measured. An example of ground vibrations is given in Fig. 3.

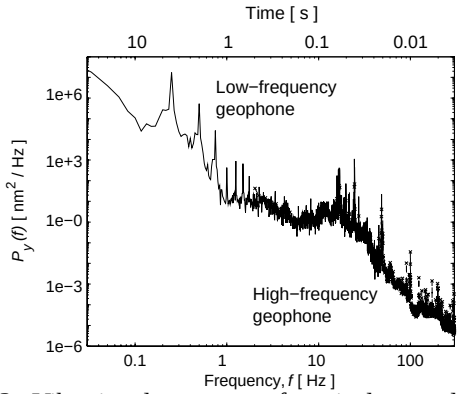

Figure 3: Vibrational spectrum of vertical ground motion versus frequency as measured in the CLIC test stand.

ACHIEVED QUADRUPOLE STABILITY

The best damping of quadrupole fast vibrations ($f \gtrsim 1$ Hz) is obtained by directly fixing the magnets on the table, as in Fig. 2, and by using the stiff piezo-based isolators (the performance achieved with the soft system was reported in [2, 7]). The measured vertical and horizontal quadrupole motion is shown in Fig. 4. The motion of the supporting ground is also given as a reference. In Table 2 the total RMS motion above some lower frequency limits is summarized for all directions. These results were achieved in the CLIC test stand during working hours (02/2003).

Above 4 Hz, a CLIC quadrupole doublet was vertically stabilized to (0.43 ± 0.04) nm with a ground motion of (6.19 ± 0.62) nm. This is the first time that an accelerator magnet is stabilized to the sub-nanometre level. The quadrupole vertical (y) vibration is within the CLIC linac tolerance (1.3 nm) and only a factor 2 larger than the final focus tolerance (0.2 nm). The horizontal (x) RMS motion above 4 Hz was (0.79 ± 0.08) nm compared to (3.04 ± 0.30) nm on the ground, i.e. factors 10 and 18 smaller than the linac and final focus tolerances (14.0 nm and 7.8 nm). The longitudinal (z) RMS motion above 4 Hz was (4.29 ± 0.43) nm compared to (4.32 ± 0.43) nm on the ground.

Table 2: RMS motion above different minimal frequencies (f) as measured on the ground and on a quadrupole prototype stabilized with the stiff isolation system.

	Ground	Quadrupole
Vertical RMS motion [nm]		
$f \geq 4$ Hz	6.19 ± 0.62	0.43 ± 0.04
$f \geq 20$ Hz	2.67 ± 0.27	0.36 ± 0.04
$f \geq 60$ Hz	1.01 ± 0.10	0.14 ± 0.01
Horizontal RMS motion [nm]		
$f \geq 4$ Hz	3.04 ± 0.30	0.79 ± 0.08
$f \geq 20$ Hz	0.50 ± 0.05	0.49 ± 0.05
$f \geq 60$ Hz	0.20 ± 0.02	0.12 ± 0.01
Longitudinal RMS motion [nm]		
$f \geq 4$ Hz	4.29 ± 0.43	4.32 ± 0.43
$f \geq 20$ Hz	0.63 ± 0.06	0.63 ± 0.06
$f \geq 60$ Hz	0.28 ± 0.03	0.14 ± 0.01

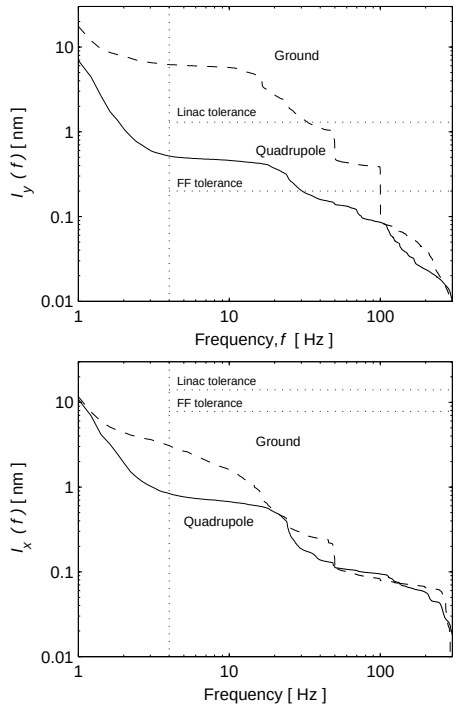

Figure 4: Vertical ($I_y(f)$, top) and horizontal ($I_x(f)$, bottom) integrated RMS motions versus frequency, f, as measured on the ground (dashed line) and on a stabilized CLIC quadrupole (solid).

The performance of the stiff stabilization device was continuously monitored over several consecutive days. The achieved vertical RMS motion above $4\,\mathrm{Hz}$ is displayed versus time in Fig. 5. The quadrupole was steadily kept below a maximum value of $(1.00 \pm 0.10)\,\mathrm{nm}$, with an average value of $(0.77 \pm 0.10)\,\mathrm{nm}$ and $(0.67 \pm 0.06)\,\mathrm{nm}$ during days and nights, respectively. The horizontal (x) and longitudinal motions were always below $(1.47 \pm 0.15)\,\mathrm{nm}$ and $(9.07 \pm 0.91)\,\mathrm{nm}$, respectively.

The long-term alignment stability of the stabilized table was monitored with the stretched-wire system, which measures table drifts with respect to the ground. An example of measured vertical and horizontal table positions versus time is given in Fig. 6 (top graphs), together with the ambient temperature (bottom graph). The table position depends on the temperature due to the volume variations of the rubber used as a passive damper. A maximum vertical variation of $\approx 40\,\mu\mathrm{m}$ was measured. Horizontally, the variations are three to four times smaller. The slow temperature variations (e.g., $\approx 20\,\mu\mathrm{m}$ in 5 hours due to a variation of $\approx 1.5\,^{\circ}\mathrm{C}$, corresponding to $\approx 1\,\mathrm{nm/s}$) will be efficiently compensated by beam-based feedbacks.

CONCLUSIONS

In the framework of the CLIC stability study, the principle feasibility of stabilizing accelerator magnets to the levels required by future linear colliders has been demonstrated by stabilizing a quadrupole vertically to $(0.43 \pm 0.04)\,\mathrm{nm}$ in a normal working environment, with the supporting ground moving ≈ 15 times more. Simultaneously, horizontal and vertical quadrupole motions of $(0.79 \pm 0.08)\,\mathrm{nm}$ and $(4.29 \pm 0.43)\,\mathrm{nm}$ were recorded. It has been verified that the device used is in principle suitable for an accelerator environment because it reliably stabilized a magnet below the 1 nm level for a period of several consecutive days. Detailed studies of vibrations from cooling water or structural resonances suggest that these effects can be kept under control with a proper magnet design. Some critical aspects, however, such as the effects of electromagnetic noise and radiation resistance, need further study. Future studies will be focused on implementing the stabilization technology in an experimental region, with more realistic magnet designs.

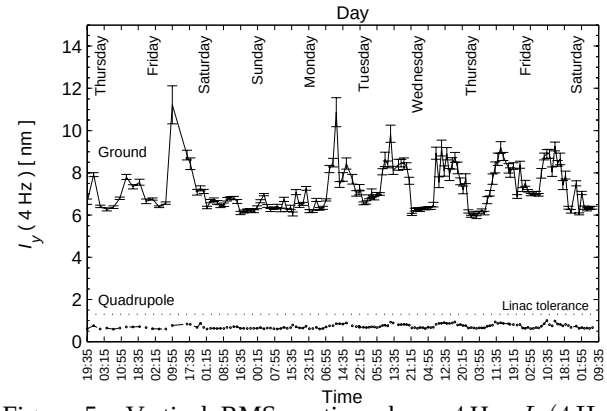

Figure 5: Vertical RMS motion above $4\,\mathrm{Hz}$, $I_y(4\,\mathrm{Hz})$, versus time as measured on the ground and on a CLIC quadrupole. The first Thursday is a Geneva bank holiday.

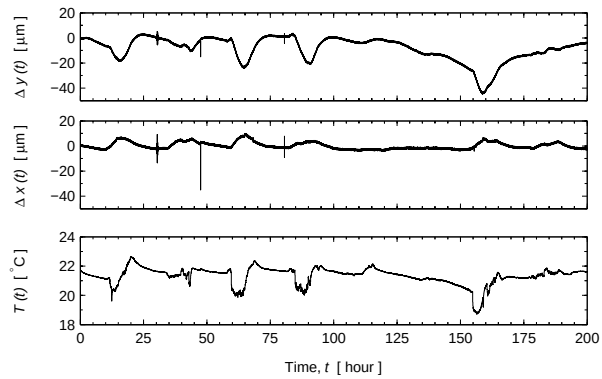

Figure 6: Vertical ($\Delta y(t)$, top graph) and horizontal ($\Delta x(t)$, middle) table positions and ambient temperature ($T(t)$, bottom) versus time, t.

REFERENCES

[1] The CLIC Study Team, **CERN-2000-008**.

[2] R. Aßmann *et al.*, "The CLIC Stability Study on the Feasibility of Colliding High Energy Nanobeams," Proc. *Nanobeam2002*, Lausanne, CH (2002).

[3] A. Seryi, **SLAC-PUB-8893** (2001).

[4] V. M. Juravlev, *et al.*, **CERN-SL-93-53** (1993).

[5] M. Aleksa, *et al.* , **CERN-SL-2001-045-AP** (2001).

[6] P.E. Batson, *et al.*, Nature **418** (2002).

[7] S. Redaelli, PhD thesis (2003), also as **CERN-AB-2004-026**.

STATIC ABSOLUTE FORCE MEASUREMENT FOR PRELOADED PIEZOELEMENTS USED FOR ACTIVE LORENTZ FORCE DETUNING SYSTEM

P. Sekalski, A. Napieralski, DMCS, Technical University of Lodz, Poland
S. Simrock, L.Lilje, DESY, Hamburg, Germany
A. Bosotti, R. Paparella, F. Puricelli, INFN, Milan, Italy
M. Fouaidy, IN2P3, Orsay, France

Abstract

To reach high gradients in pulsed operation of superconducting (SC) cavities an active Lorentz force detuning compensation system is needed. For this system a piezoelement can be used as an actuator (other option is a magnetostrictive device). To guarantee the demanded lifetime of the active element, the proper preload force adjustment is necessary. To determine this parameter an absolute force sensor is needed which will be able to operate at cryogenic temperatures. Currently, there is no calibrated commercial available sensor, which will be able to measure the static force in such an environment. The authors propose to use a discovered phenomenon to estimate the preload force applied to the piezoelement. The principle of the proposed solution based on a shape of impedance curve, which changes with the value of applied force. Especially, the position of resonances are monitored. No need of specialized force sensor and measurement in-situ are additional advantages of proposed method.

INTRODUCTION

For the X-Ray Free Electron Laser (XFEL) and for the TeV Superconducting Linear Collider (TESLA) a tuning system is developed. Its main goal is to keep the internal resonance frequency of the cavity constant. Perturbations in cavity shape have two main sources. One of them is a microphonics and another is a Lorentz force [1÷3].

One tuning system was designed to compensate both effects. Moreover, it is integrated with the existing step motor system, used for cavity pretuning [1]. The tuning system consists of the frame in which two piezo elements (PEs) are assembled. One of them works as a dynamic force sensor, while the second one as an actuator. PE devices are identical, hence there is possible to use them as a sensor or an actuator or use both as actuators.

The PEs must work during each pulse, thus the proper lifetime must be guaranteed. For ten years working period without any breakdown with repetition rate up to 20Hz more than 10^{10} cycles is foreseen. The PEs might reach such a lifetime, only if they are properly preloaded. From literature and manufacturers datasheets of piezostacks, one might conclude that the best preload is around a half of the blocking force. For our case the blocking force is 3kN, hence the preload should be set between 1,0kN and 1,5kN. Unfortunately, an access to PE is only possible during module assembly but mentioned preload ought to be reached at the cryogenic temperature (CT) - below 2K and low pressure (several mBars). The precise preload force adjustment becomes difficult task due to the complexity of system and the different thermal coefficient of expansion (TCE) of used materials. Also during changing the pressure additional forces appears. As a consequence it is very hard to calculate or estimate the preload force change during cooling down and pumping. Even if a proper approximation will be done, there is need to verify the result. Therefore an absolute force measurement is needed. Currently, a commercial-use absolute force sensor for temperature below 10K does not exist.

The authors propose to use one of two observed effect caused by applied force: either a capacitance change of PE or a impedance resonances shift of the PE. The detailed information about performed experiment is presented in following chapters.

Currently, five types of PEs are investigated in three institutes (DESY, INFN, IN2P3). The devices come from five different manufacturers: EPCOS (PZT/Nd34), PI Ceramics (PICMA), PiezoMechanik (PSt150/10/60), NOLIAC (Pz27 and Pz29) and Piezo JENA (#9222). The EPCOS PE has been tested for 2 years; the others are quite new ones. As a consequence this publication will focus mainly on the EPCOS PE.

Four types of experiment were done. Firstly, the resonances were measured at room temperature (RT); secondly the characteristic of the PEs was investigated at CT. Then, the calibration was used to determine the preload force in real system in CHECHIA cryostat. At the end, the capacitance change due to the applied force at RT is presented.

ROOM TEMPERATURE EXPERIMENTS

The electrical impedance was first measured at RT, during PE classification. The impedance resonances were the parameters, which were investigated.

Each PE was characterized individually. It was assembled in series with a piezoresistive force sensor - model 8415-6002 from BURSTER Company. At the top of the fixture there was a screw to adjust the force applied to devices. The stiffness of the frame was more than 10 times higher than stiffness of PE.

The impedance was measured using a dynamic Signal Analyzer (SR785) for frequency range from 50Hz up to 100kHz.

According to the theory of piezoelectricity, a single resonance and anti-resonance pair should be observed. For multilayer piezoelectric (i.e. for NOLIAC) devices several such a pair was observed. Usually, there was two main resonances pairs which were investigated.

The frequency of resonances depends on boundary condition. When the PE is stressed the resonance is shifted to higher frequency values. A resonance frequency shift versus an applied force for EPCOS PE is shown in figure 1.

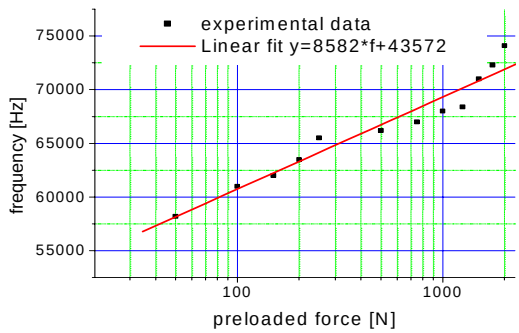

Figure 1: Resonance position frequency shift caused by applied force at RT.

The correlation between measurement points and the exponential approximation is over 0.97. Numerous run was performed to verify stability in time. The resulting spread is less than 2%. The impedance measurement was also performed for several PE from the same manufacturer line. The obtained statistics shows that PEs behaves in similar way (the value of resonance frequencies might vary from actuator to actuator by around 5%).

Encouraged by the preliminary tests at RT, the decision to perform similar experiment at CT has been made.

LOW TEMPERATURE EXPERIMENT

To perform impedance measurement at 4K for different PE preload, a dedicated cryostat was developed. A possibility to apply a known force to PE has been implemented. A proper device was built in INFN, Milan.

An insert for a vertical cryostat has been designed to support measurements in the liquid helium (LHe) environment. This insert allows to mount the PE in a box under isolation vacuum.

The design of the experimental setup is presented in figure 2. The insert grants the possibility to exert a known force on the DUT, keeping it under cryogenic conditions. This is achieved via an external device, placed at the top of the insert, in which spring-washers are coupled to a screwed ring to generate the test force (up to 2.5 kN). This force is transferred by a long steel (G10) rod to the PE. A calibrated load cell, working at RT, is in series and measures the generated force.

The box is immersed in LHe in order to cool the PE down to 4.18 K. This temperature can be considered as a good approximation of the real operating temperature of

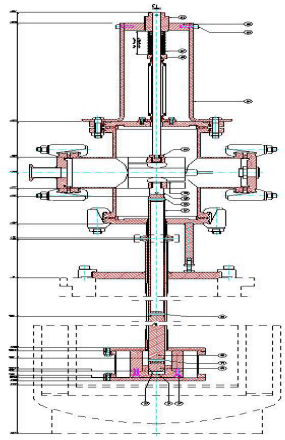

Figure 2: Vertical cryostat setup.

the PE, with respect to the electro-mechanical properties of the PE itself. Unfortunately, as the tests show the PE temperature was unstable and varies from 4K up to 10K. The temperature inside the box was even unstable, when the box was completely surrounded by liquid helium for some hours. Also compressing the actuator leads to a temperature increase proportional to the increasing load. Moreover, to reduce self-heating effect during tests the PE was supplied by only 100mV voltage.

Up to now, two PEs from EPCOS (type LN 01/8002) were characterized. As previously the impedance curve shows two resonances: the series resonance around 30 kHz and parallel resonance (so-called anti-resonance) above 53 kHz – both values for an unloaded piezo.

Data points were spread on different temperature values due to temperature stabilization failure. The 3D interpolating function was developed considering the temperature as a parameter. The results are plotted in figure 3.

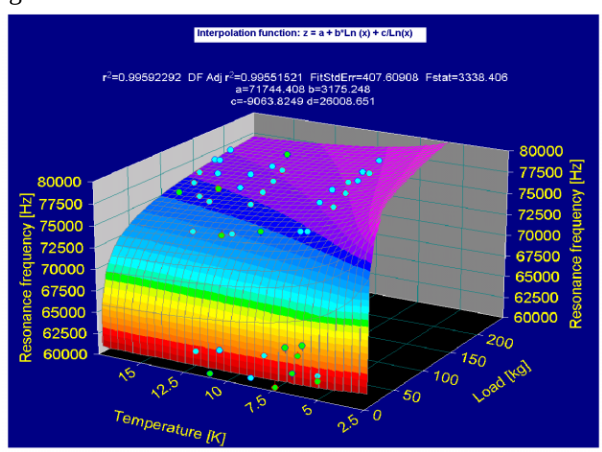

Figure 3: 3D interpolation of position of resonance versus applied force and temperature for EPCOS piezo.

CHECHIA TEST

At the end, an impedance measurement for PE assembled in a CHECHIA cryostat was performed. CHECHIA is a horizontal cryostat, in which a single high gradient cavity with full equipment i.e. couplers,

a pretuning system with a step motor and active detuning compensation system with PE, is installed.

Because those two mentioned structure interact to each other, so it is possible to change the force applied to piezo by moving the step motor. The step motor can move up to 1 million steps what corresponds to 3µm. of length change of piezo fixture. The resonance frequency versus position of step motor is presented in figure 4.

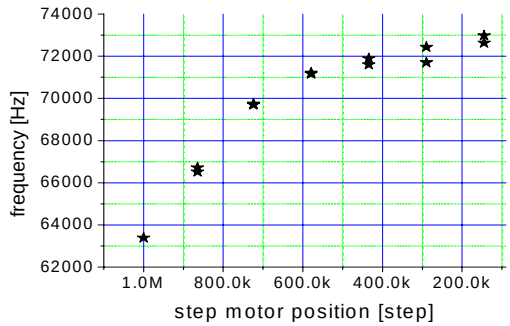

Figure 4: Resonance frequency of EPCOS piezo versus position of step motor.

By comparing the data presented in figure 3 and in figure 4, it is possible to estimate the force applied to PE in CHECHIA cryostat. The force on PE changes from 0,7kN for 0 step motor position to 70N for one million steps movement. The last result indicates that the piezo was almost completely loose and could fall out of the fixture. As a consequence, to maximize lifetime, the PEs should be stronger preloaded at RT, during its assembly (the preload force should be in range between 1,0kN to 1,5kN).

CAPACITANCE CHANGE

Recently, a measurement of capacitance change versus applied force was performed in IN2P3 [4]. As it was expected, the preliminary results done with Piezo JENA (#9222) stack shows that, the capacitance is also changing versus the piezo preload (see figure 5).

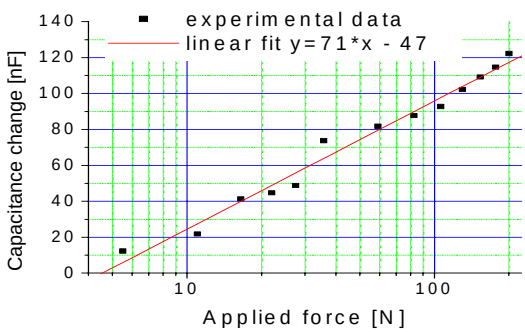

Figure 5: The change of capacitance of Piezo JENA (9222) versus applied force at RT.

The behavior of change is also exponential, as it was with resonance shift. It seems, that capacitance change is better method to determine the preload. However, to fully understand what happened with stressed PE, there is a need to perform more experiments. It also helps to develop a model, based on physical properties of piezostack.

CONCLUSION

Performed experiments are only the preliminary, but they prooved that it is possible to estimate the PE preload inside cryostat without any additional force sensor. To calculate an applied force it is necessary to measure impedance of piezoelement and compare with the calibration curve made before at desired crygenic temperature. However, the proposed method has some small disadvantages (i.e. many new resonances arise and significantly modulate the shape of amplitude and phase of the PE impedance with load, so it is hard to identify the resonance shift).

In principle, the series-resonance position (minimum of the impedance value) might be also characterized as a function of applied load.

Different types of piezoelectric actuators will be tested soon at CT and RT. In particular the PE from NOLIAC and PI should grant higher performances, due to their higher mass and greater dimensions. It means, that they should have lower resonance and anti-resonance frequencies and they should imply a sufficient sensitivity at the requested preload force.

Moreover, the capacitance change seems to be a good parameter for comparison. Nevertheless, there is need to perform more test especially at cryogenic temperatures. The capacitance change due to a PE breakdown (i.e. stack shortcut) need to be investigated carefully.

At the end, to be sure that our estimation is correct, the strain gauge sensor based on piezoresistive effect will be build and tested in Milan cryostat.

ACKNOWLEDGEMENT

We acknowledge the support of the European Community-Research Infrastructure Activity under the FP6 “Structuring the European Research Area” program (CARE, contract number RII3-CT-2003-506395)

REFERENCES

[1] T. Schilcher, “Vector Sum Control of Pulsed Accelerating Field in Lorentz Force Detuned Superconducting Cavities“, PhD thesis

[2] P. Sekalski, S. Simrock, L. Lilje, C. Albrecht, “Lorentz Force Detuning Compensation System For Accelerating Field Gradients Up To 35 Mv/M For Superconducting Xfel And Tesla Nine-Cell Cavities”, MIXDES 2004, Poland

[3] S.N. Simrock, “Lorentz Force Compensation of Pulsed SRF Cavities”, Proceedings of LINAC 2002, Gyeongju, Korea

[4] M. Fouaidy, N. Hammoudi, ”Characterization of Piezoelectric Actuators Used for SRF Cavities Active Tuning at Low Temperature”, SRF 2003.

IMPROVEMENTS OF RF CHARACTERISTICS IN THE SDTL OF THE J-PARC PROTON LINAC

S. Wang*, IHEP, P.O.Box 918, 100039, Beijing, China
T. Kato, KEK, Oho, Tsukuba-shi, Ibaraki-ken, 305-0801, Japan
V.V.Paramonov, RAS/INR, Moscow, Russian Academy of Sciences Institute for Nuclear Research

Abstract

A separated drift tube linac (SDTL) was adopted as an accelerating structure of Japan Proton Accelerator Complex (J-PARC), which follows the DTL. The SDTL of J-PARC consists of 32 five-cell short tanks, ranging from 1.5 to 2.5 m in length. A design of frequency tuners of the SDTL was performed by taking account of 3-D field distribution calculated with MAFIA. The effects of stems on the resonant frequency and field distribution were also analyzed. An easy and effective compensation method for perturbation by stems of both end cells was proposed and applied to the SDTL tanks.

INTRODUCTION

An Alvarez drift-tube linac (DTL) is widely used for accelerating low-energy proton beams. It is a complicated and sophisticated structure since drift-tubes contain focusing magnets. A separated-type drift-tube linac (SDTL) was proposed [1] as an accelerating structure for the medium-energy region because of both high shunt impedance and ease of construction. Higher shunt impedance can be realized by eliminating focusing devices from drift tubes. Instead, the focusing elements are placed between two adjacent SDTL tanks. Since one of the merits of the SDTL structure is simplicity of both rf properties and mechanical issues in construction, any kinds of stabilizing devices (post couplers or multi-stems) are not usually installed. Thus, the number of cells in a tank is also important from the viewpoint of rf stabilization.

The SDTL was adopted as the accelerating structure of J-PARC linac [2], which connects the DTL and the ACS. The SDTL of J-PARC consists of 32 short five-cell tanks. A normal unit cell in the tank consists of an accelerating gap, two tubes of half-size and two half stems. Table 1 shows the parameters of the SDTL tank.

Table 1. Parameters of SDTL tank for J-PARC

Frequency	324 MHz
Tank diameter	520 mm
Drift tube diameter	92 mm
Stem diameter	36 mm
Cell length	0.29– 0.51m
Tank length	1.47 – 2.56m
Energy	50 – 190 MeV

As the first constructed SDTL linac in the world, the tuner of the SDTL was designed based on the detailed calculation by using MAFIA. The special attention should be taken for both end cells, where there is no half stem on the end plate usually. An easy and effective compensation method for the perturbation of the stem to the accelerating field was studied by the simulations.

*Email: wangs@ihep.ac.cn

THE DESIGN OF THE TUNER

The Positions for Installing Tuners

As shown in Table 1 for J-PARC, the maximum length of SDTL tanks is 2.56 m, and the number of the tuner is expected within three. Fig.1 shows the sketch of a five-cell SDTL tank and the candidate positions for tuners in the longitudinal direction.

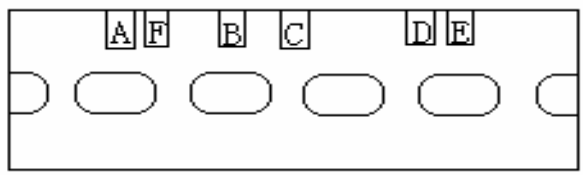

Figure 1: The sketch of a five-cell SDTL tank and the candidate positions (A~F) for tuner in the longitudinal direction.

In case of adopting 3 tuners, there are two choices for the distribution of tuners in the longitudinal direction. One choice is installing in the positions of F, C and D, in which C is in the center of the tank, and F and D are at L/4 from the both end plates respectively, with L the length of the tank. In this case, the distribution of the tuner is uniform in longitudinal direction, but all the tuners are not located in the center of the tube, where is the most effective tuning position. The other choice is installing in the positions of A, B and E, with A, B and E the center of the drift tube, but in this case three tuners are not regularly distributed in the longitudinal directions. To decide the distribution of the tuner, the simulations were made by MAFIA, for investigating the difference of the tuning efficiency among different positions. For all SDTL tanks, the diameter of the tuner was chosen as 90 mm.

Fig. 2 shows the simulated frequency shift of one tuner with different insertion length for different positions in the 97-MeV tank. For the insertion length more than 5 cm, the tuner positioned at A is much more effective than tuners positioned at the other two places. The power losses on the tuner surface at different positions were almost equal.

According to the simulation results, the tuners should be positioned at the position of the center of the drift tube in longitudinal direction. In case of installing three tuners,

the positions should be A, B and E. Another reason for selecting mid point of the drift tube for tuner position is that the positions of F, C and D are located at the gap-center or near the gap-center, and in this case, the total frequency shift decreases rapidly as the tank length increases. Therefore, for the 2.5 m (190-MeV) tank, a three-tuner system of gap-center tuner position does not work well.

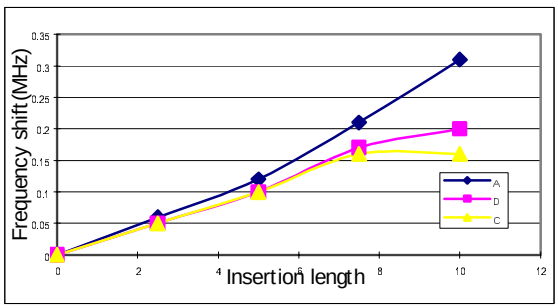

Figure 2: Frequency shift vs. different insertion length for different longitudinal positions.

Tuning Effects for Different Number of Tuners

Figure 3 shows the simulated tuning effects vs. different number of tuners at 97-MeV tank. One tuner is positioned at A, two tuners are positioned at A and its symmetric position E, while three tuners are positioned at A , E and B. The total tuning effect is proportional to the number of tuners. The final number of tuners installed in each tank should be determined by the requirement of the tuning ability (a range of frequency shift and the deviation of the field distribution).

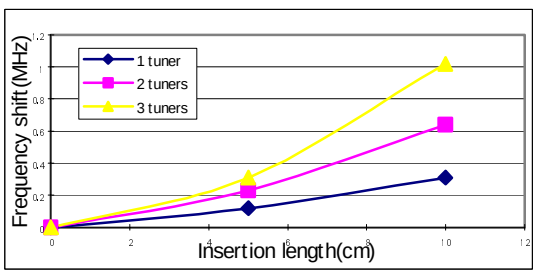

Figure 3: Frequency shifts vs. different insertion length for the different number of tuners.

Tuning Effects for Different Tank

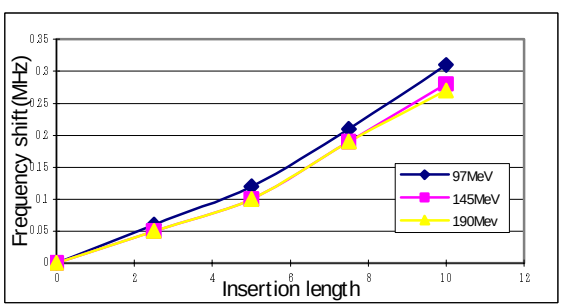

Figure 4: Frequency shift vs. different insertion length for different tank.

To compare the tuner effect for different tanks with the same tuner diameter, simulation was done with one tuner. One tuner was positioned at position A. Fig. 4 shows the tuning effects for different tanks. With the same diameter of tuner, the tuning ability was decreased with the increase in the length of the tank, but the decrease in the tuning ability was within 10%. Therefore, the tuner of the same size can be adopted for all SDTL tanks.

Tuning Effects for Different Angle From Stem

The simulations were done for comparing tuning effects with 45° and 60° angles between the tuner and the stem. The small angle means the tuner is much close to the stem. The insertion length is fixed to 7.5cm, and only one tuner at position A is used. Table 2 indicates that for the 45° and 60° angles between the tuner and the stem, the tuning effects are equal, and the power losses on the surface of the tuner are also nearly equal. In table 2, the values of power loss and E were the relative values to that of the 60°. To save the space in the tunnel, 45° angle between tuner and stem was chosen.

Table 2. Some results for different angles

	45°	60°
Tuning effect	0.21MHz	0.20MHz
Power loss on the surface	0.99	1
Ez at top surface of the tuner	0.99	1
Er at top surface of the tuner	0.56	1

The simulation shows that when the insertion length was more than 10cm, the increased tuning effect for frequency was very small, and the additional mode would be induced. The maximum insertion length of tuner should be 10 cm.

COMPENSATION FOR THE FIELD PERTRUBATION INDUCED BY STEMS

There are two special end cells in the SDTL tank, where there is no half stem on the end plate usually. The design field distribution is uniform in a SDTL tank, but the uniform distribution would be deformed because of the lack of the half stem at the end cell. Fig. 5 shows the simulated field distribution of the first SDTL tank without end cell compensation, in which the deviation of the field distribution was 1.7%. Taking the advantage of the near symmetry of the geometry in the longitudinal direction, simulation was made for the half SDTL tank.

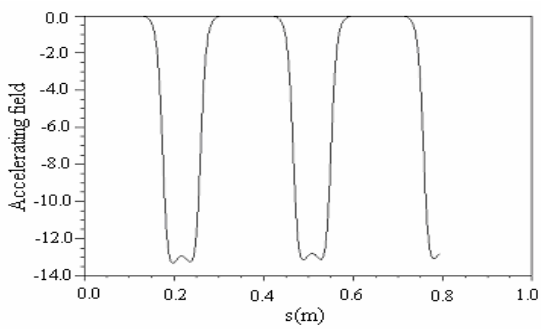

Figure 5: The simulated field distribution of the first SDTL tank without end cell compensation, made by MAFIA.

To compensate the stem effect, a direct method is using a half stem at each end plate, but this simple method becomes complicated in fabrication. An easy and effective compensation method for the perturbation of the stem to accelerating field was proposed [3]. A thin circular disk was added on the end plate instead of a half stem: a thickness and a radius of the disk was chosen so that a frequency shift due to the increase in the volume of the end plate may be equal to that of the virtual half-stem on the end plate. In order to keep the cell length and the gap length, the outer radius of the disk was less than the radius of the tank. The inner radius of the disk was selected to be the same as the radius of the drift tube because of ease of fabrication.

For studying the effect of the compensation, some simulations were made for the first SDTL tank by using MAFIA. The simulated accelerating field distribution without end-cell compensation is shown in Fig. 5, and the corresponding simulation results with compensation by adding a thin circular disk on the end plate is shown in Fig. 6, in which the thickness of the disk was 1.5 mm and the radius of the disk was 250 mm. It shows that, the field deviation was perfectly compensated, and field distribution became uniform in the simulation. The effect of the compensation with a disk of 1.5 mm in thickness was equal to that by adding a half stem on the end plate, as shown in Fig.6. When a disk of 1.0mm in thickness was used in the simulation, the deviation of the field distribution was 0.58%, as shown in Fig.7, which was still within the tolerance (±1%).

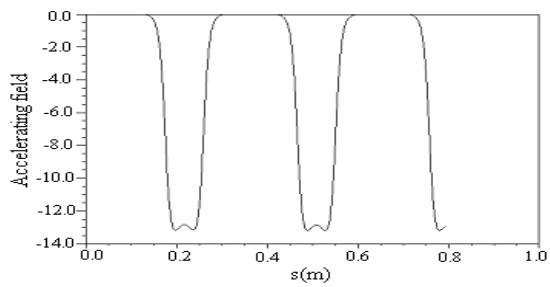

Figure 6: Simulated field distribution in the first SDTL tank with compensation by adding a thin circular disk at the end plate. The thickness of the disk was 1.5 mm and the radius of the disk was 250 mm

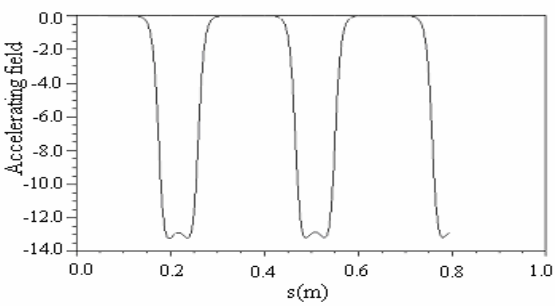

Figure 7: Simulated field distribution in the first SDTL tank with compensation by adding a thin circular disk at the end plate. The thickness of the disk was 1.0 mm and the radius of the disk was 250 mm

PERTURBATION OF THE TUNER TO THE FIELD DISTRIBUTION

The perturbations of the tuner to the field distribution were studied by simulation for the 50-MeV tank. Fig. 8 shows the MAFIA model used in the simulation, in which there are two circular disks at the end plates. The thickness of the disk was 1.5 mm and the radius of the disk was 250 mm, and the insertion length of the three tuners were all 7.5 cm. As shown in Fig.6, the field distribution was uniform without tuner. With the perturbation of the tuners, the field distribution is shown in Fig. 9, the deviation of the field distribution was ±0.8%.

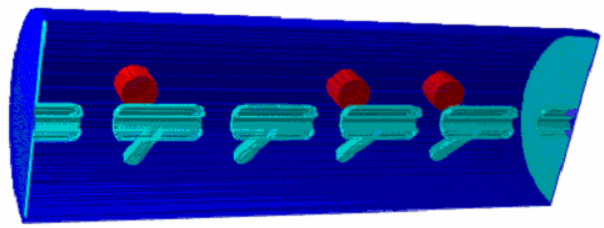

Figure 8: MAFIA model with tuners and circular disks

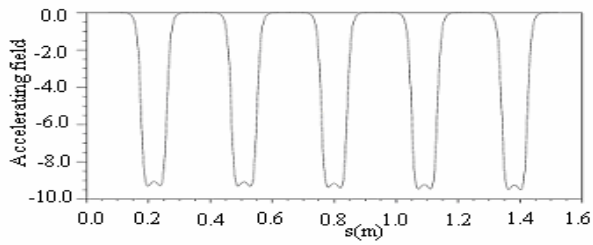

Figure 9: The field distribution of the 50-MeV SDTL tank with tuners and circular disks

CONCLUSION

The tuner of the SDTL tank of J-PARC was designed based on the detailed calculation by using MAFIA. The tuner should be positioned in the center of the tube at longitudinal direction, instead of symmetric assembly; with 45° angle from stem; the maximum insertion length of the tuner should be not larger than 10cm; for all SDTL tanks, the tuner of the same diameter could be used. An easy and effective compensation method for the perturbation of the stem to accelerating field was studied by the simulations. It shows that with a disk of 1.5 mm in thickness and 250 mm in radius adding to the end plate, the field distributions were correctly adjusted.

REFERENCES

[1] T. Kato, Proposal of a Separated-type Proton Drift Tube Linac for a Medium-Energy Structure. KEK Report 92-10 (1992).

[2] JHF Project Office, "JHF Accelerator Design Study Report", KEK Report 97-16 Chapter 4 (JHF-97-10), 1998, Accelerator Technical Design Report for J-PARC, KEK Report 2002-13 (2003).

[3] T. Kato et al., Compensation for the Stem Effects of the End Cells for the J-PARC SDTL Structure, to be published in KEK Report.

COMPACT ELECTRON-LINAC DESIGN CONCEPT FOR A GAMMA RAY SOURCE

K. C. Dominic Chan, Bruce E. Carlsten, Gregory E. Dale, Robert W. Garnett, Hugh C. Kirbie, Frank L. Krawczyk, Steven J. Russell, Thomas P. Wangler, LANL, Los Alamos, NM87545, USA
Edward Wright, CPI, Palo Alto, CA 94303, USA

Abstract

Gamma-ray sources, particularly sources that are easily transportable, are in high demand for different applications. We have carried out a review of commercially available electron-linac-based sources, and have investigated alternative compact electron-linac systems that use updated technologies compared with sources that are available commercially. As a result, we propose to develop a new source using an electron linac operating at 17-GHz. It uses a klystron, instead of a magnetron, and an IGBT-switched HV power supply. The source design takes advantages of the advances in X-band linac technology and solid-state HV technology. The higher frequency and upgraded technologies offer smaller size, lighter weight, better efficiency, easier operation, and higher reliability, compared with commercially available linacs. In this paper, we will describe the source design and our choice of technologies.

REQUIREMENTS OF AN ELECTRON-LINAC-BASED GAMMA-RAY SOURCE

For most applications, an electron-linac-based gamma-ray source is required to produce a dose rate up to 1500 cGy/min on axis one meter away from the source. The electron beam energy is typically between 6-10 MeV. The exact dose rate and energy will depend on the specific application and material to be penetrated. A pulsed linac is usually needed to allow for beam-off time for data acquisition. The typical pulse format is a repetition rate of 50 Hz, a 10-μs pulse length, and a nominal peak current of 70 mA. For some applications, a compact system is also required. A compact system provides transportability, ease of radiation shielding, and low cost. Ease of use and reliability will also be important.

STATUS OF TECHNOLOGY

We have carried out a study of electron-linac-based sources and associated technologies. The results are summarized in a report [1] and this paper is a summary of that report.

Presently, commercially available electron-linac-based gamma-ray sources are derived from medical linac technology. Such sources usually consist of a Linac Subsystem, a RF Subsystem, an HV Subsystem, and a Support Subsystem for cooling, vacuum, and control. The general features of presently available gamma-ray sources include:

- A S-band (3 GHz) linac
- Powered by magnetrons
- High-voltage modulated by a pulse-forming network (PFN) and a HV transformer
- Limited flexibility in energy and pulse format
- Dimensions of each component about a few feet on each side
- Weight of each component about 500-1000 pounds; with total weight about 1800 pounds.

AN GAMMA-RAY SOURCE WITH IMPROVED TECHNOLOGY

In our study, we concluded that using an electron linac at 17 GHz, a klystron as the RF source, and a solid-state Marx generator as modulator can make an improved electron-linac-based gamma-ray source. By updating the technology in these three aspects, the system will improve in efficiency, reliability, flexibility, size, weight, and cost. In this section, we will describe the subsystems using these updated technologies.

Linac Subsystem

The nominal parameters of the Linac Subsystem are given in Table 1. The linac will operate at an optimum frequency of 17 GHz. A higher-frequency linac operating at 17 GHz offers many advantages over the currently available S-band linacs because linac performance improves with linac frequency. The copper loss is reduced by a factor of 2.3. The linac is less prone to RF field breakdown with the breakdown limit higher by the same factor. The structure radius decreases linearly with frequency, resulting in a structure weight reduction by a factor of 25.

Table 1: Nominal Parameters of a Linac Subsystem

Linac frequency (GHz)	17
Beam energy (MeV)	8
Beam current (mA)	68.2
Beam Power (kW)	545
Structure power (kW)	1170
Total power required (kW)	1715
Length of structure (cm)	25
Acceleration gradient (MeV/m)	32
Diameter of structure (cm)	2.7
Number of cells	55
Ratio of mode spacing to mode width	3.2
Shunt impedance (MΩ/m)	219
Unloaded quality factor	5725
Cell to cell coupling coefficient	0.048

Our investigation shows that 17 GHz is nearly the optimum linac frequency for this application. Frequencies higher than 17 GHz, even better in linac efficiency, may lead us to linac operation with multiple RF-structure modes [2], and consequently unstable

operation. A higher-frequency linac structure may also have such tight mechanical tolerances that fabrication of the structure may require more novel techniques than conventional machining. In the last ten years, Stanford Linear Accelerator Center (SLAC) has been developing electron linacs for the Next Linear Collider (NLC) at 11.5 GHz, close to our proposed 17 GHz. Results of their development in mechanical fabrication techniques and RF sources can readily be adapted for our application.

Our proposed linac structure, as shown in Fig. 1, will operate in the standing-wave mode for efficiency. The structure is a biperiodic structure operating in the $\pi/2$-coupled mode for best stability and efficiency. The buncher and main linac will be uncoupled to allow more flexibility in varying beam energy. Focusing will be provided by a periodic permanent-magnet (PPM) channel for compactness and high efficiency.

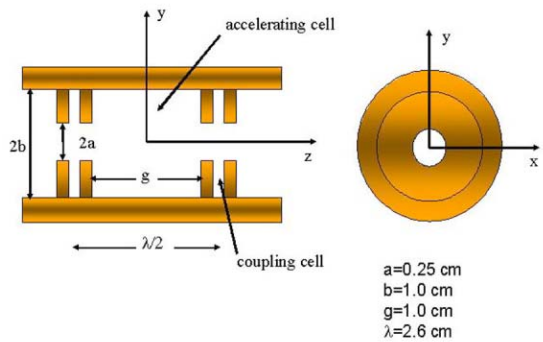

Figure 1: Cross sections of a 17-GHz linac structure.

Klystron Subsystem

A klystron will be used to power the linac for excellent controllability and reliability. Nominal 17-GHz klystron parameters are given in Table 2. Klystrons, being amplifiers, amplify well-defined low-level input signals with high fidelity. By formatting the low-level input signals, a variety of pulsing schemes can be reliably provided. This is an improvement compared to magnetrons, which are oscillators starting by amplifying noise. Magnetrons also are not chosen because it is difficult to push magnetron technology to our required higher frequency of 17 GHz at high power.

Table 2: Nominal parameters of a X-Band klystron

Frequency	17.136 GHz
Peak RF Output Power	2000 kW
Pulse length	20 μs
Pulse repetition rate	50 Hz
Average Power	2000 W
High-voltage subsystem requirements Voltage Current	 115 kV 29.3 A
Diameter	16.3 cm
Height	53.4 cm
Weight	60 lb

Klystrons with peak power of 75 MW have been developed by industry for the NLC. Designs of such klystrons can easily be adapted for our need of 2 MW. A diagram of a proposed commercial 17-GHz klystron is shown in Fig. 2. It uses a PPM array for beam focusing and an air-cooled collector/beam dump to improve compactness and efficiency [3]. Similar design was also proposed by SLAC. Success of higher power X-band klystron at SLAC klystron indicates that the development of a 17-GHz klystron for our application will be of relatively low risk.

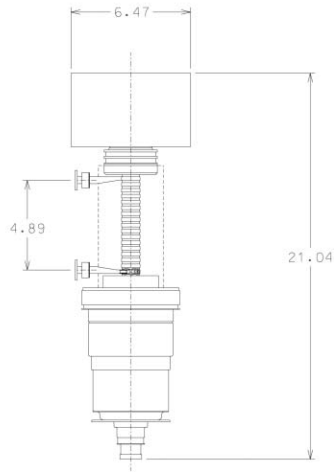

Figure 2: Schematic of a 2-MW 17-GHz klystron. Dimensions are in inches.

High-Voltage Subsystem

A solid-state Marx generator [4] will be used to provide the high-voltage to the klystron. The requirements of the HV subsystem are given in Table 3.

Table 3: Nominal parameters of a HV-Subsystem

Pulse width	10–40 μs
Pulse Voltage	130 kV
Peak Load Current	30 A
Peak Output Power	3.5 MW
Pulse Repetition Frequency	25–100 Hz
Pulse Droop	1–2 %
Energy per Pulse	70 J
Duty Factor	0.1%
Average Output Power	3.5 kW
Available Utility Power	3.3 kW (110 V, 30 A)

The advantages of a solid-state Marx generator are improved reliability, flexibility in pulse format, and compact size. As shown in Fig. 3, the solid-state Marx generator charges a collection of energy-storage capacitors in a parallel configuration at low voltage and uses solid-state switches to reconnect the capacitors into a series configuration to provide the required high-voltage. The switches are high-power IGBTs (Insulated Gate Bipolar Transistors), available only in the last five years. They will be operated by optical links that provide the high-voltage insulation. Although this is a relatively new technology, three designs at 50 to 500 kV have been

proposed and one prototype is being built in Los Alamos [5] and at SLAC. A 2-μs, 11-kV device is presently in use driving a traveling-wave tube at SLAC.

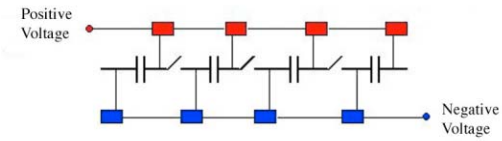

Figure 3: Schematic of a basic Marx-generator module.

The solid-state Marx generator offers many advantages compared to conventional modulator technology using a pulse-forming network and a high-voltage transformer. Its pulse format is flexible, tailored simply by sending on/off signals to quick-recovering IGBT switches. It is built by stacking identical Marx circuit boards that contain a few low-voltage capacitors (Fig. 4). Such a modular design allows the basic module to be well tested and the full unit easily reconfigured to different output voltages. With all solid-state components, the unit will share the long service life and high reliability typical for solid-state devices. Additionally, a solid-state Marx generator has small size (a fraction of a cubic foot) and is lightweight (about 50 pounds), compared to conventional units.

Figure 4: Photograph of a single Marx circuit board showing 4 IGBTs, 4 optical receivers, and 8 charging diodes.

Overall System

The proposed gamma-ray source design is very compact. Table 4 shows a comparison between our proposed system and a commercially available unit. Instead of the truck size of a commercial unit, our proposed design is approximately the size of a filing cabinet. The system can be designed to operate using electrical power supplied by readily accessible 110-220-volt household circuits. Portable power and a self-contained cooling system can also be considered.

Development Plan

The proposed design, although not based on off-the-shelf technology, is based on reasonable extensions of known technologies. We have proposed a 3-year development plan that will result in a demonstration of this new technology and would only require a minimal R&D effort. Our development plan would have three phases:

- Phase I: Review and optimize design parameters (six months)
- Phase II: Design, build, and test prototype subsystems (twenty two months)
- Phase III: Test prototype of full-unit (six months)

Industry should be brought in at the beginning of the technology development process. They can play a major role, particularly in Phase III, contributing to the integrated design of the full system. The system packaging is important for achieving a minimum overall size; an area where industry has significant experience and expertise.

Table 4: Comparison of sizes and weights of major subsystem of the proposed gamma-ray source design to a typical commercially available unit.

Subsystem	Commercial Unit	Proposed Design (Estimated)
HV Modulator	35 ft^3, 700 lbs	1.5 ft^3, 50 lbs
RF Source	8 ft^3, 350 lbs	2.5 ft^3, 60 lbs
Linac	21 ft^3, 1600 lbs	2.5 ft^3, 60 lbs

ACKNOWLEDGEMENT

This work was supported by the US National Nuclear Security Agency and the US Department of Energy under contract W-7405-ENG-36.

REFERENCES

[1] K. C. D. Chan (edited), An Accelerator-Based Gamma-Ray Source For the Detection of Highly Enriched Uranium, Los Alamos National Laboratory Report LA-UR-04-3194 (2004).
[2] T. P. Wangler, et al, Importance Of Mode Spacing In The Design Of Very High Frequency Linacs, presented at 2004 Meeting of the American Physical Society Denver, CO, May 1-4, 2004.
[3] Edward Wright, CPI, private communication, 2004.
[4] Jeffery A. Casey, et al., Solid-State Marx Bank Modulator for the Next Linear Collider, Proceedings of the 14th IEEE International Pulsed Power Conference, Dallas, TX, June 15-18, 2003, p.641
[5] G.E. Dale, H. C. Kirbie, J. D. Doss, and M. A. Serrano, Solid-State Marx Modulator Development, Conference Record of the Twenty-Sixth International Power Modulator Symposium and 2004 High Voltage Workshop, San Francisco, CA, May 23-26, 2004 (to be published)

RESULTS OF A 3D-EM-CODE COMPARISON ON THE TRISPAL-CAVITY BENCHMARK

P.Balleyguier CEA/DPTA Bruyères-le-Châtel, France

Abstract

Several 3D electromagnetic codes (MAFIA, CST MicroWave-Studio, Vector-Fields Soprano, Ansoft HFSS, SLAC Omega3P) have been tested on a 2-cell cavity benchmark. Computed frequencies and Q-factors were compared to experimental values measured on a mock-up, putting the emphasis on the effect of coupling slots. It comes out that MAFIA limitations due to the staircase approximation is overcome by all other codes, but some differences still remain for losses calculations in re-entrant corners.

INTRODUCTION

Up to recent times, we mainly used the MAFIA code to design cavities for particle accelerators applications in Bruyeres-le-Chatel. Despite of its proper quality, the meshing method used by this software introduces a "staircase" approximation causing some artifacts on calculated results. In many cases, a proper choice of the mesh grid and a proper post-processing permit to get rid of these artifacts (see for example [1]).

To correct the artifacts, the first step is to start from an accurate 2D simulation, and in a second step, to take into account every 3D aspect of the structure: coupling holes, tuning plungers, RFQ vane ends, pumping grids... Their effect can be estimated individually with a fair accuracy by the comparison of two simulations using an identical mesh, with and without each considered 3D aspect. This method gives good results for global structure parameters (frequency resonance, Q-value, R/Q, external Q), but can be difficult to apply for local parameters such as local losses or peak fields. And, of course, it can only be applied on "2D-like" structures.

Because of these limitations, and to take advantage of computer and software evolutions, we considered to change our tool, and compared on the same benchmark MAFIA and four other 3D EM codes (fig. 1):

- Microwave Studio 4.3 (CST)
- Soprano (Vector Fields)
- High Frequency Structure Simulator 9.0 (Ansoft)
- Ω3p (eigen mode solver developed at SLAC)

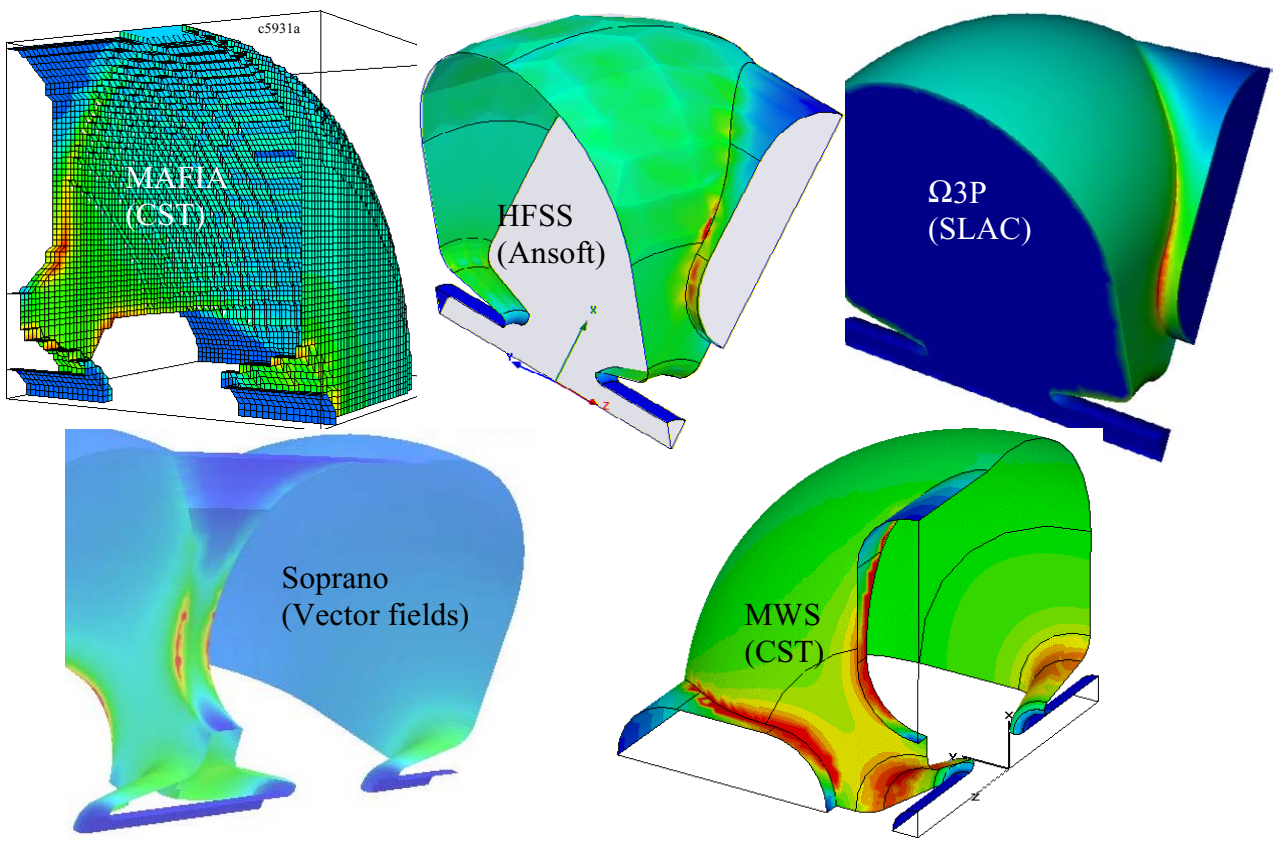

Figure 1: Losses in Trispal benchmark for tested 3D-codes (pi-mode).

BENCHMARK

The benchmark is the cavity mock-up build at the time of the Trispal project (fig. 2). This modular structure can be mounted in a single-cell (and purely axi-symmetrical) configuration. It can also be mounted in a 2-cell configuration in which the cells are coupled through coupling holes or slots (fig. 3). This cavity was accurately measured in term of resonance frequency and Q-value in 1997 [2].

A major issue is to get a reliable Q value in spite of successive assembling and dismantling. The electrical seal is made of a 0.8-mm soft solder wire squeezed to 0.4 mm with a mechanical limitation that makes the contact quality independent of the tightening strength. To estimate the quality factor reliability, we made a series of measurements alternating both configurations (single or double-cell) and changing the seal each time. After a few first tries to train the operator, the statistical r.m.s deviation for Q between nine successive measurements is about 0.4 %.

Measured data exhibit a Q-drop caused by coupling holes. This is due to the high increase of surface current density in the edge of the holes. Simulating such a case is a good way to test how a code deals with local losses in re-entrant corners, and it was used to validate the new MAFIA algorithm for computation of RF losses [3].

The high increase of magnetic field in re-entrant corner had already been measured on the IPHI RFQ mock-up, and compared to MAFIA and Soprano simulations [4]. But the conclusions at that time were not clear quantitatively, because losses were deduced from magnetic field measurements based on the bead-pull technique which brings some artifacts.

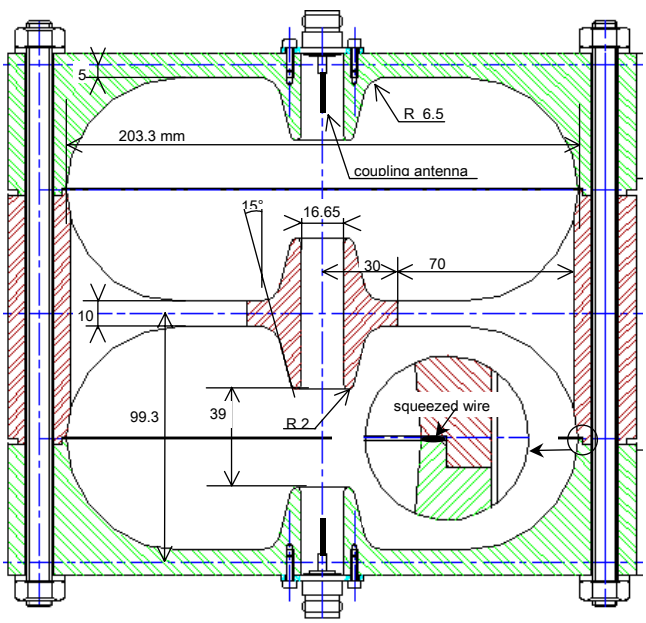

Figure 2: Transverse section of the Trispal cavity mock-up (2-cell configuration).

Single Cell Results

Measured and computed values are displayed in table 1. The 51 nΩ.m estimated resistivity of the material (a 96% Al and 4% Cu alloy) is taken into account in displayed Q values.

MAFIA gives a frequency resonance +0.75% above experimental value, which is not so bad considering the staircase approximation. All of the other codes (including Superfish) gave a resonance frequency of the single-cell cavity very close to the experimental value (1080.8 MHz). We observe that Soprano, HFSS, Ω3p and Superfish are all gathered around +0.10% from measurement, while MWS is -0.03%. But the mechanical machining is not precise enough to tell which code is the best.

From a Q-factor point of view, all the codes (except MAFIA) are between +3% and +5.5% above measurement. Such a positive difference of a few percent is expected because of surface imperfection and seal losses in the real cavity. Again, the unrealistic MAFIA result (-16 % vs. measurement) is an artifact due to the staircase approximation.

Dual-Cell Results

In the 2-cell cavity, the fundamental TM010 mode splits into two modes (0 an π) depending on the field condition in the symmetry plane between the cells. Dual-cell results are appreciated from a relative point of view by comparing the two modes either to each other or to the single-cell mode. This compensates most of mesh induced bias and puts the emphasis on coupling holes.

We define the following parameters, where indices π, 0 and 1 indicate pi-mode, 0-mode and single-cell mode, respectively:

- frequency shift due to hole volumes : $\alpha = 2(f_1-f_0)/f_0$
- coupling coefficient : $\gamma = 2(f_0-f_\pi)/f_0$,
- pi-mode Q-drop : $\delta Q_\pi = Q_\pi^2/Q_1^2-1 \approx 2(Q_\pi-Q_1)/Q_1$
- 0-mode Q-drop : $\delta Q_0 = Q_0^2/Q_1^2-1 \approx 2(Q_0-Q_1)/Q_1$.

The folding factor 2 is to be compatible with an infinitely long structure with coupling holes on both side of each cell.

Compared to experimental values, the frequency shift α and the coupling coefficient γ are both slightly underestimated by all the codes. The discrepancies, referred to absolute frequency, are always (including MAFIA) less than 0.2% for α and 0.1 % for γ. Though these discrepancies seem low, they are non negligible compared to typical α and γ values (about 1.4%) and cannot be attributed to errors in coupling slots dimensions. Ω3p values are the closest from experimental values, probably because of the smaller mesh grid used in this simulation.

On the other hand, extra losses due high current density on the edge of coupling slots in π-mode (specially along the re-entrant corner) are diversely computed. Simulated losses are displayed for different software on figure 1. As MAFIA, MWS HFSS and Ω3p predictions

for δQ_π are between -19.4% and -24.9 % (-22.5% measured), Soprano underestimates this phenomenon (-5.6%). The same thing happens if the zero-mode is considered: while MAFIA, MWS HFSS and Ω3p values for δQ_0 are between -1% and +3% (+1% measured), Soprano gives +11%. We observe that MAFIA and MWS used with the old algorithm for Q-calculation [3] give about the same discrepancies than Soprano.

CONCLUSION

Though they use different techniques and mesh types, the four newly tested codes give all very good results in frequencies. About losses, they also give satisfactory values, except that Soprano still underestimates losses in re-entrant corners. All of them overtake the limitation suffered by MAFIA users due to staircase approximation.

The author thanks Jerôme Mollet from CST for MWS test lending, David Presto from Ansoft for HFSS test lending, Kwok Ko from SLAC for Ω3p simulations and Olivier Delferriere from CEA-Saclay for Soprano Simulations.

REFERENCES

[1] P. Balleyguier, "3D design of the IPHI RFQ cavity", 20th Linear Accelerator Conference, Monterey, 2000.
[2] P. Balleyguier, "Coupling slots measurements against simulation for Trispal accelerating cavities", 19th Linear Accelerator Conference, Chicago, 1998.
[3] P. Balleyguier, R. Schuhmann, "Improvement in 3D computation of RF-losses in resonant cavities", 20th Linear Accelerator Conference, Monterey, 2000.
[4] P.Balleyguier, F.Simoens, "Simulations vs. Measurements on the IPHI RFQ Cold Model", 8th European Particle Accelerator Conference, Paris, 2002 .

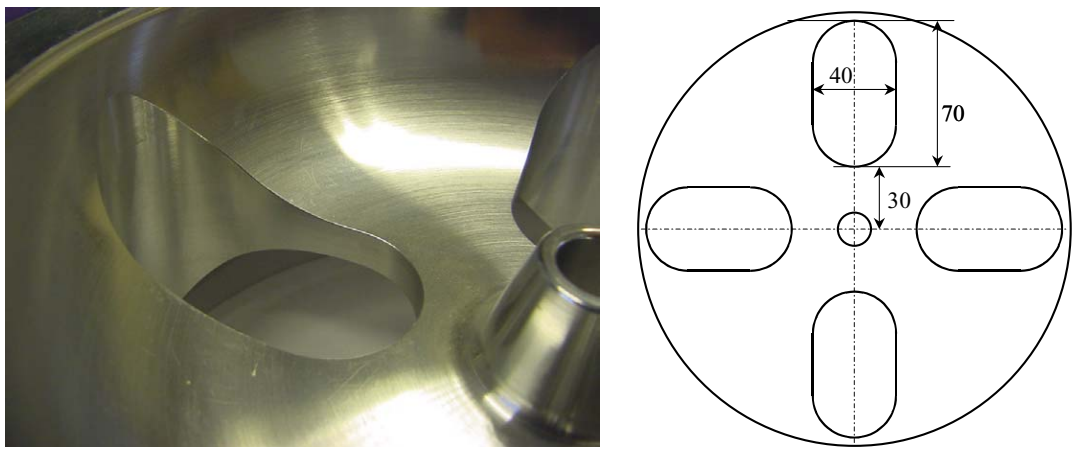

Figure 3: Coupling slots.

Table 1: Frequency and Q-factors for single-cell and 2-cell modes

		measurment	Superfish	Mafia	MWS	Soprano	HFSS	Ω3p
H wall	fq	1064.415		1073.912	1064.796	1066.673	1066.800	1066.090
(π mode)	Q	11340		9724	11665	12901	11789	12111
E wall	fq	1072.412		1081.556	1072.605	1074.267	1074.700	1074.100
(0 mode)	Q	12938		11023	13481	13982	13536	13738
single-cell	fq	1080.841	1081.770	1088.948	1080.451	1081.828	1082.200	1082.250
	Q	12880	13584	11032	13285	13275	13601	13509
coupling γ		1.49 %		1.41 %	1.46 %	1.41 %	1.47 %	1.49 %
fq.shift α		1.57 %		1.37 %	1.47 %	1.41 %	1.40 %	1.52 %
δQ(π)		**-22.5 %**		**-22.3 %**	**-22.8 %**	**-5.6 %**	**-24.9 %**	**-19.6 %**
δQ(0)		**+0.9 %**		**-0.2 %**	**+3.1%**	**+10.9 %**	**-1.0 %**	**+ 3.4 %**

PARALLEL PARTICLE IN CELL COMPUTATION OF AN ELECTRON GUN WITH GdfidL

W. Bruns, WBFB, Berlin, Germany *

Abstract

The paper describes an efficient algorithm to integrate the equations of a fast moving charge cloud of small size in a large electron gun. Particle in cell computation of a realistic electron gun is challenging due to the large discrepancy between the size of the cavity and the size of the cloud. A fine grid must be used to resolve the small volume of the charge, with a grid spacing in the order of 0.1 mm. The cavity has extensions of about 100 mm. Therefore one has to deal with about 1000 million gridcells. Such a large grid is handled best with parallel systems. Each node of the parallel system computes the electromagnetic field in its subvolume. As the extension of the charge keeps being small during the flight, at each timestep the charged particles will be located in only a few subvolumes of the nodes of the parallel system. This would lead to a strong load imbalance, if the particle related computations for each particle would be performed by the node where the particle is in. GdfidL instead spreads the data of most particles over all processors, which then perform the particle related computations, and send back the results to the processors where the particles are in.

THE PHOTO GUN

The resonator has a diameter of 10cm, and the height of the most interesting part of the gun is about 10cm. At the bottom of the gun, a charge with a diameter of 3mm is emitted via a laser-pulse. The duration of the pulse is so short, that the emitted charged cloud has a length of 5 mm. Because the gradient in the gun is about 100 MV/m, the emitted charge is accelerated very rapidly to relativistic velocities. The size of the charge cloud therefore stays small.

The geometry itself is rotational symmetric, and the charge ideally would be rotational symmetric. To investigate what effect an offset of the laser pulse from the axis would have, one needs to perform a three dimensional computation, without any planes of symmetry.

Because the charge has an extension in the order of 3 mm, one needs a gridspacing of 0.1 mm or less. Because we want to resolve small effects due to a small deviation from a rotational symmetric case, we want to compute with a homogeneous grid, minimising dispersion errors and reflections due to an inhomogeneous grid. This leads to a total number of gridcells in the order of 1000 millions. A naive implementation of the FDTD-algorithm would then require about 50 GBytes of RAM. Such large grids are best handled by clusters of PCs.

* bruns@gdfidl.de

DOMAIN SUBDIVISION

The computational volume is partitioned in many more subvolumes than the number of available processors. Each subvolume is inspected, whether it is filled only with electric conducting material. The fully electric conducting subvolumes are discarded and the remaining ones are spread evenly over the processors. This way, each processor has about the same number of interesting gridcells to compute the fields in, leading to a good load balancing for the field computation.

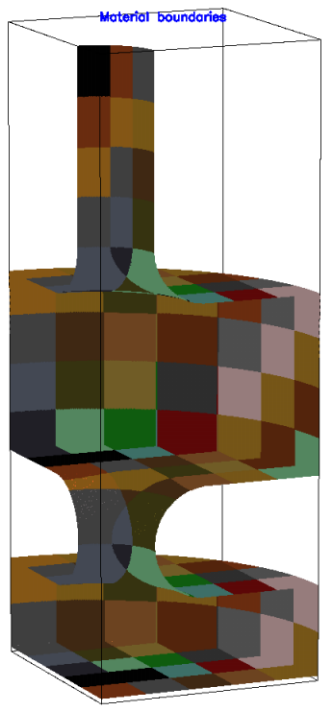

Figure 1: A model of the gun. The grid spacing is 0.1 mm. The total number of gridcells in this quarter of the total volume is 212 millions. Less than 40% of the computational volume is filled with vacuum cells. The different colours indicate the used subvolumes. The shown volume is partitioned in 325 subvolumes, of which 167 are discarded, since they do not have a single vacuum cell. A naive implementation of FDTD in this quarter of the volume would require 10 GBytes of RAM. GdfidL uses 4.3 GBytes, spread evenly over the available processors.

Local Field Computation

Each processor computes the electromagnetic fields in its local subvolumes. The tangential electric and magnetic fields of the neighbour volumes are boundary conditions

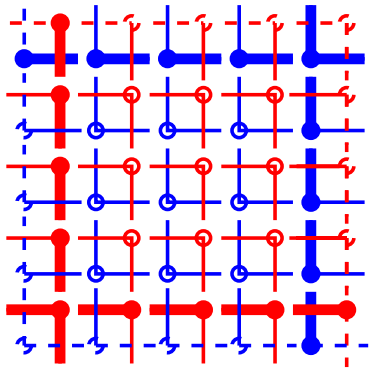

Figure 2: The blue lines and circles represent the electric field components in a local volume. The red ones represent the magnetic field components. The tangential E field components at the upper boundaries of the local volume (thick blue) and the tangential H field components at the lower boundaries (thick red) can be computed from the local information. These components are sent to the neighbour volumes. The tangential E field at the lower boundaries (dashed blue) and the tangential H field at the upper boundaries (dashed red) cannot be computed from the local information. These components are received from the neighbours.

for the local field computation, and are communicated between the processors at each timestep.

SIMULATING FREE MOVING CHARGES

Moving charges change the electric field in their immediate vicinity, and they are accelerated by the electric field and rotated by the magnetic field at their actual positions.

The computation of the acceleration and rotation is performed by an algorithm invented by Boris [Boris 1970]. The optimised implementation of Buneman, as can be found in the TRISTAN code, is used.

Moving charges show up in MAXWELLS equations as a current density. The change of electric flux through a face must equal the total amount of charge which enters a grid-cell through that face. The computation of the charge is done with an algorithm similiar to the one described by Villasenor [Villasenor 1992], extended for a grid with uneven spacings and charged particles of arbitrary size.

Since the computation of the acceleration requires knowledge about the electromagnetic field at the positions of the particles, and since the electric field near the particles are changed due to their convection current, it is natural to perform all the charge related computations on the processor who is responsible for computing the electromagnetic field within the volume where also the charge is in. While the charges are drifting through the computational volume, they eventually leave the domain of one processor and enter the domain of another processor. At each timestep, the data of the leaving charges must be sent to the processor who is responsible for the volume they are entering.

When simulating a photo-gun on a parallel system, this approach leads to a strong load-imbalance, as the charged cloud in a photo-gun has small extension during the flight through the gun. For most timesteps, almost all macroparticles are within the subvolume of a single processor. When that single processor has to perform all charge related computations, the other processors will have to wait for completion of the computations.

Instead, a small rectangular volume is selected, where almost all macroparticles are in, see figure 3. The data of the contained macroparticles are spread evenly over the processors. Each processor performs the charge related computations for its part of macroparticles within the box.

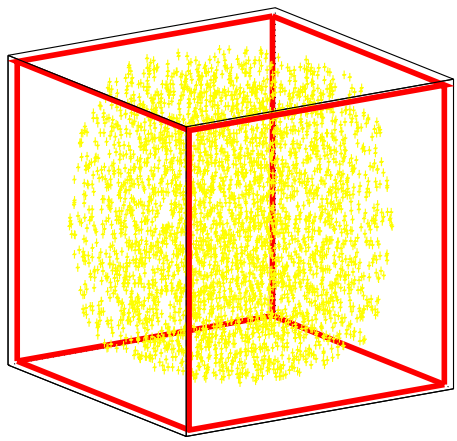

Figure 3: A cloud of macroparticles in a box which encloses 99% of the particles. The macroparticles within the box are spreaded evenly over the available processors. The electromagnetic field within this box must be sent to all processors, and the parts of the convection current due to the macroparticles is computed by each processor and sent to selected processors. The time required for these communications is proportional to the volume of the box. The time dependend borderplanes of the volume are found via adapting their positions at each timestep.

The macroparticles are accelerated by the electric field and rotated by the magnetic field. For computing this acceleration and rotation, the processors must know the electromagnetic field near the center of mass of the macroparticles. For this, the electromagnetic field within this box is gathered from the processors which know that field, and scattered to all processors.

In MAXWELLS equation, the moving charges show up as a convection current, and therefore change the electric field in their vicinity. The total convection current due to the macro-particles in the small box is computed by each processor for its macroparticles. The sum of all the convection currents is sent to the processors which are responsible for computing the electromagnetic field within the box.

The computations for the macroparticles outside of the small box are performed by the processors who are responsible for the subvolume they are in.

Additional Communication

The quoted times and numbers in this section refer to a quarter of the gun. For the photo gun, the size of the box can be so small that the box contains less than 150.000 gridcells, see figure 4. The average is 100.000 cells. This is less than 0.04 % of the total number of gridcells. In each timestep, the electromagnetic field of these 100.000 gridcells must be gathered and scattered. With a logarithmic communication scheme, this requires $2\times(\log_2(N_{CPUs})-1)$ communication steps, each transferring 100.000 x 6 x 4 Bytes. The gathering and scattering of the convection current also requires $2\times(\log_2(N_{CPUs})-1)$ communication steps, each transferring 100.000 x 3 x 4 Bytes. Using up to 16 CPUs connected via 100mbit ethernet, the communication requires about $2\times(\log_2(16)-1)\times 100.000\times(6+3)\times 4\ \ \mathrm{Byte}/(10\ \mathrm{MByte}/s) = 2.2$ seconds. Using a cluster of 12 AMD-Athlon processors, the wall clock time per timestep is 11 seconds, see figure 5. The communication due to the gathering and scattering of the box-data therefore requires 20 % of the total time.

The total wall clock time to simulate the acceleration of 2 million macroparticles in a mesh of 220 million gridcells is 25.000 seconds = 7 hours on a cluster of 12 AMD-Athlons.

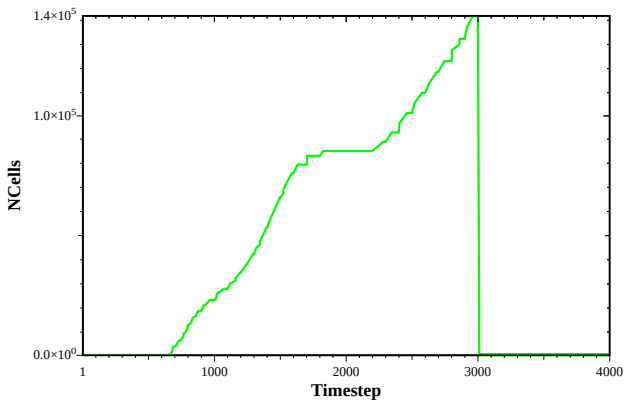

Figure 4: The number of gridcells in the charged box as a function of time. The charge is emitted near the 600.th timestep, and it exits the computational volume near the timestep 3000.

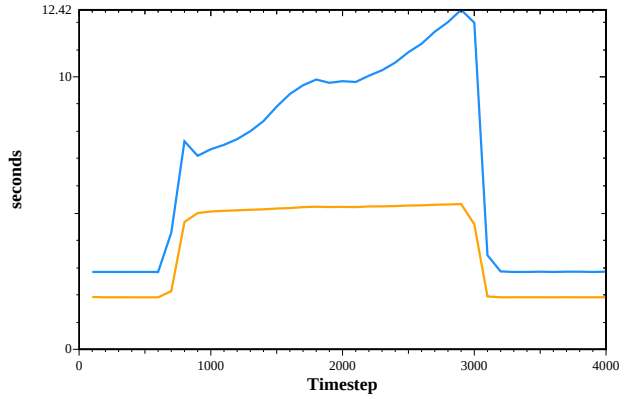

Figure 5: Upper curve: The wall clock time to compute a timestep as a function of time. Lower curve: The CPU time per processor. The wall clock time rises because the required communication rises strongly due to the growing box. The needed CPU time rises slightly because the gathering and scattering of the box-data in the growing box also consume CPU time. The charge is emitted near the 600.th timestep, and it exits the computational volume near the timestep 3000.

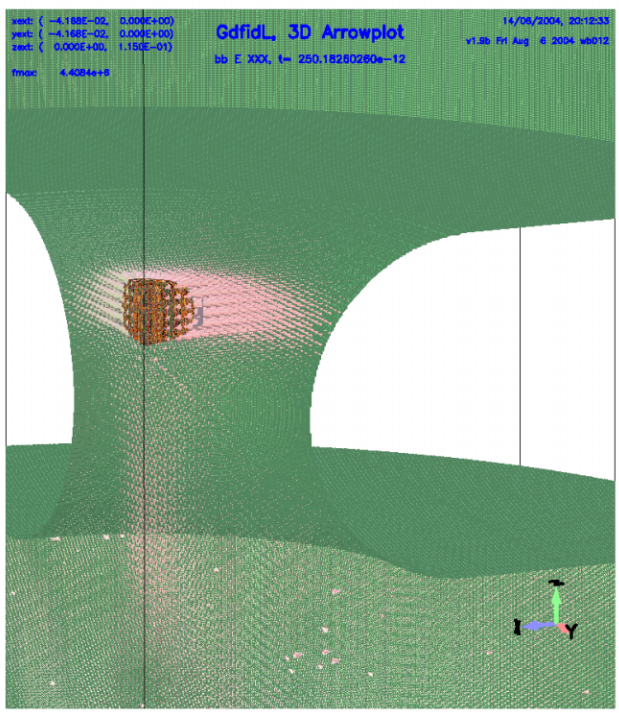

Figure 6: The bunch and the wakefield of the bunch when they just enter the second cell of the cavity. There are 2 million macroparticles in the bunch. Only the wakefield is shown. The fieldstrength of the wakefield is 5 MV/m, while the gradient of the accelerating field is 100 MV/m. The particles are already accelerated to a velocity of $\beta = 0.98$. The volume which contains 99% of the macroparticles consists of less than 60.000 gridcells.

REFERENCES

[1] Boris, J. P., "Relativistic plasma simulation-optimization of a hybrid code", in *Proceedings of the Fourth Conference on the Numerical Simulation of Plasmas* Naval Res. Lab., Wash. D.C., 1970.

[2] J. Villasenor, O. Bunemann, "Rigorous charge conservation for local electromagnetic field solvers", Computer Physics Communications 69 (1992) 306

[3] http://webserv.gsfc.nasa.gov/ESS/exchange/contrib/macneice/pic-tristan.html

EVALUATION OF MAGNETIC FIELD ENHANCEMENT ALONG A BOUNDARY

Y. Iwashita, ICR, Kyoto Univ., Kyoto, JAPAN
T. Higo, KEK, Tsukuba, JAPAN

Abstract

Only the high electric field gradient on boundaries has been thought to cause sparking in a cavity, and designers have been taking much attention on avoiding sharp edges in such an area to reduce peak electric field gradient. Recently, not only the electric field but also magnetic field on an edge can cause the spark problem through heating up of the very local surface material by concentration of the magnetic field density. The effects were numerically evaluated through a simplified model.

INTRODUCTION

There are three requirements for the accelerator structure of the main linac of the linear collider GLC/NLC[1]:

1) high gradient (50MV/m),
2) suppression of wake field and
3) low cost in mass production.

The first two items are of concern in the present paper. The second requirement was proved to be met by the DDS (Damped Detuned Structure) that can suppress the long wake field [2]. In order to meet the first requirement, the design parameters have been evolved for a few years to date to adopt low group velocity and high phase advance features [3]. The resultant recent shape of the relevant constituent disk is shown in Fig. 1.

It was known that the magnetic field that crosses a ridge-like geometry was enhanced at the ridge. The enhanced field results in a huge temperature rise within a pulse (see Fig. 2). Typical example was described in [4] where copper surface with low electric field but high magnetic field was cracked and/or eroded identified after numerous number of breakdowns near the ridge. Considering these, we designed and fabricated the HDDS disks, which does not have any area where severe magnetic field enhancement did not appear. In the present paper are described the enhancement characteristics relevant to this HDDS disks. Understanding the sensitivities on relevant parameters and proper tolerance setting is very important to pursue the structure mass production stably in an inexpensive manner.

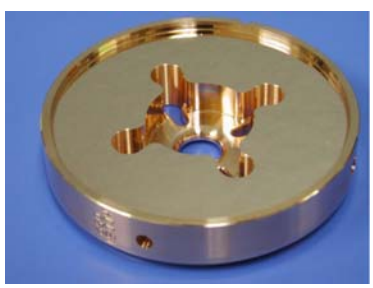

Figure 1: The HDDS cell.

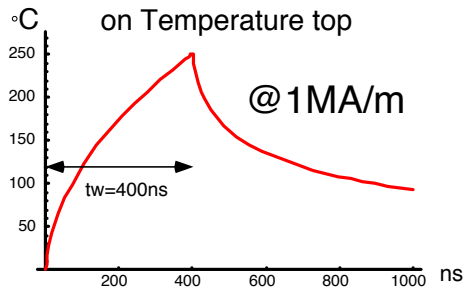

Figure 2: Pulse temperature rise on a flat copper surface where the pulse surface current is 1MA/m and the duration is 400ns. The temperature value should be scaled with the square of the surface current. A reference value of a surface current for a 2D cell without a local enhancement is 0.2MA/m, which reaches 1MA/m when the enhancement factor at a convex corner is 5. This temperature rise becomes more at a convex corner, where a heat capacity is less.

SURFACE CONFIGURATION

As seen in Fig. 3, there are two areas, shown in red, where magnetic field is naturally large. The first is the opening from accelerator cell to HOM manifold. The second is located at each slot, which is needed to extract HOM dipole filed to manifold. From these features, the enhancement at these two areas is inevitable. We evaluated on these geometries.

The assumed geometry is a parallel cut into the outer diameter of a pillbox. The width of the opening and the edge angle are the important parameters. The very edge of the opening is assumed to be rounded by 5 microns reflecting to the fact that these disks are chemically etched by about 3 microns in the fabrication stage so that the similar amount of rounding, 5-micron radius, is assumed at the very edge.

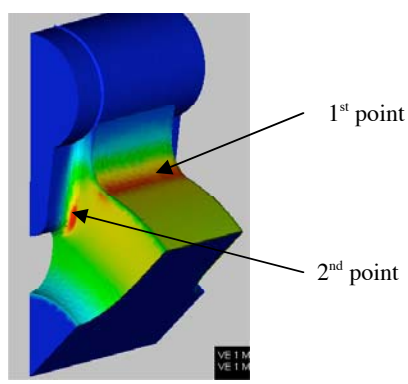

Figure 3: Magnetic field distribution on the surface.

SIMULATION

Although the objects to be evaluated have 3D boundaries, we need a simple model to extract the characteristics. A cylindrical cavity with two waveguide ports is considered in 2D and the problem region is reduced to one quarter because of the symmetries in horizontal and vertical directions (see Fig. 4). Axisymmetric modes TM_{010} in the cylindrical cavities are analyzed as Eigenvalue problems with Finite Element Method. The convex edge with the crossing angle X between the two-machined surfaces (lathed surface with radius R11 and milled surface with radius r) is assumed to be rounded to with 5-μm radius by an etching rinse. Consequently, there are only round corners and concave edges on the boundary. In order for us to ignore the presence of the bottom (a short plane) for any cases, the waveguide depth is set to twice of its width, which is well below the cut off wavelength.

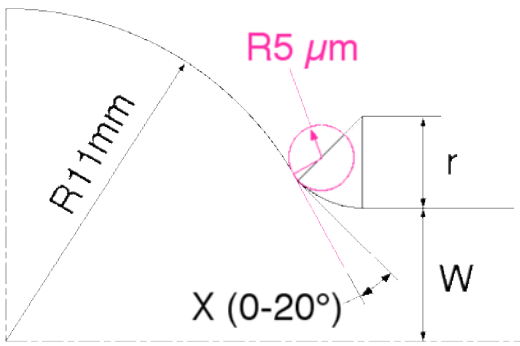

Figure 4: Simplified model for the field enhancement factor.

The problem is analyzed by PISCES-II [5], which uses second order isoparametric finite elements. Because a very fine mesh that can express 5μm radius boundary in 11mm radius area, has more than thousand times ratio in mesh size, a new mesh generator that uses Delauny triangulation [6] is prepared. It generates smooth mesh

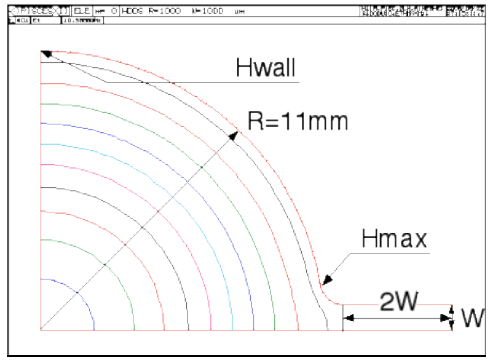

Figure 6: Contour plot of Ez represents magnetic field lines. The enhancement factor is defined by Hmax/Hwall.

where the ratios of the elements sizes between the adjacent elements are less than two (see Fig. 5). The input file format has the same format as that of POISSON/SUPERFISH rel.4.12 for the compatibility.

The magnetic field enhancement factor is defined as the ratio of the fields between two locations Hmax/Hwall: the maximum magnetic field (usually appears at the sharpest curve boundary) Hmax and the magnetic field Hwall at the farthest point from the waveguide (the top of the region). Fig. 6 shows the locations. The Eigenfrequency varies with the parameters while the cavity cell radius is fixed as 11mm. This effect is ignored because it is not serious to the evaluation of the enhancement factor.

PISCES-II can evaluate all Eigenmodes in an axisymmetric boundary including dipole mode (SUPERFISH can obtain only TM0 modes). In order to evaluate the problems described above, capability to analyze in the Cartesian coordinates is added before the series of calculations.

The boundary considered here does not have a convex corner that causes an electromagnetic singular point; the boundary lines and arcs are smoothly connected. The isoparametric second order elements (used in PISCES-II) can express such curved boundaries appropriately and the evaluation becomes accurate.

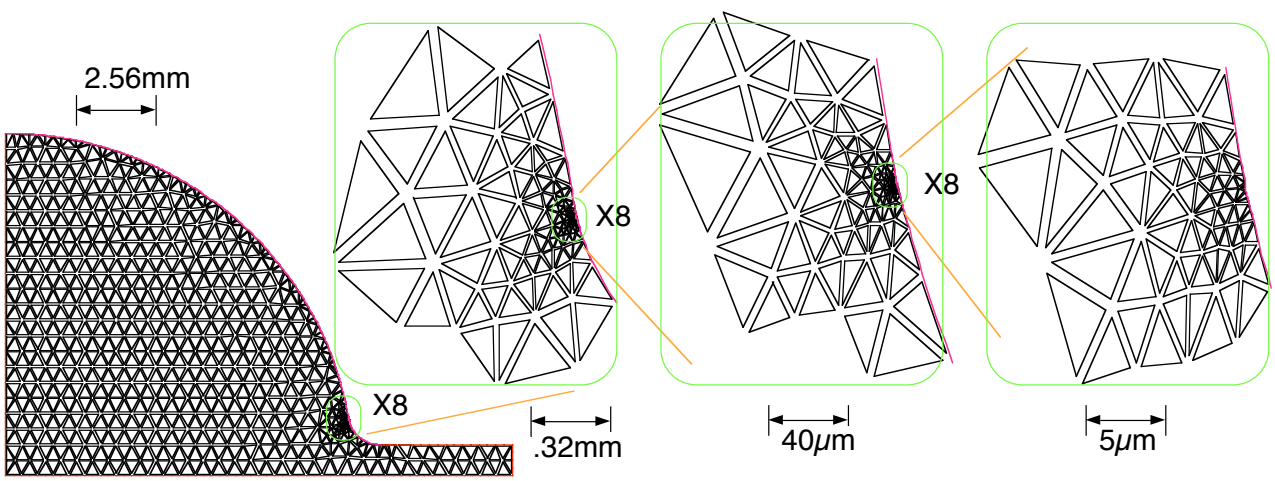

Figure 5: Example of generated mesh with large ratio in mesh size.

RESULTS AND DISCUSSION

The effects on three parameters (W, r and X in Fig. 4) are investigated, where the ranges of the parameters are listed in Table I. The first and the second points in Fig. 3 correspond to (W=3mm, X<5°, r=2mm) and (W=1mm, X~8°, r=0.5mm), respectively. A typical curve for the enhancement factor along the boundary is shown in Fig. 7. The boundary consists of smoothly connected three arcs and straight lines: a concave arc with radius 11mm, a convex 5μm arc and a convex arc with radius r.

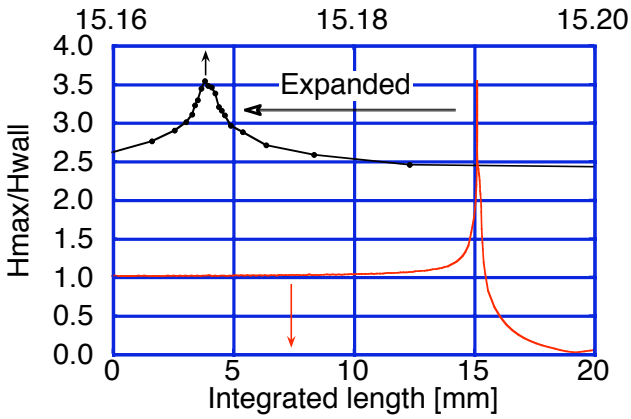

Figure 7: Field enhancement factor along the boundary corresponding to (W=2mm, X=20°, r=200μm). The abscissa shows the integrated distance from the top point where H_{wall} is referred.

Table 1: Input parameters

Half port width	W mm	1, 2, 3, 5
Crossing angle	X degree	0, 5, 12, 20
Radius of opening port	R mm	0.2, 0.5, 1

The enhancement factors for X=0° as functions of r are shown in Fig. 8, where they show $r^{-1/3} \sim r^{-1/4}$ dependences. In order to keep the reproducible connection between the two major arcs in fabrication, a finite crossing angle is needed [7]. The enhancement factors at W=5mm are shown in Fig. 9. This shows the dependencies of power function and the effect of finite crossing angle is prominent when the curvature is small. Fig. 10 shows the dependencies on the crossing angle and the slot width. Three tendencies are shown from the results: 1. the larger the slot width, the higher the enhancement factor, 2. large r reduces the enhancement, 3. large crossing angle decreases the above reduction effect.

In the current cell geometries, the enhancement factors that correspond to the first and second points in Fig. 3, are about 1.5 when the crossing angle is 0°. Although the enhancement factors increase with the finite crossing angles, they can be kept below 2 for the first point if X=5° with W=3 and for the second point if X=8° with W=1 case. From these results, we conclude that practical design is possible for the real cavity cells.

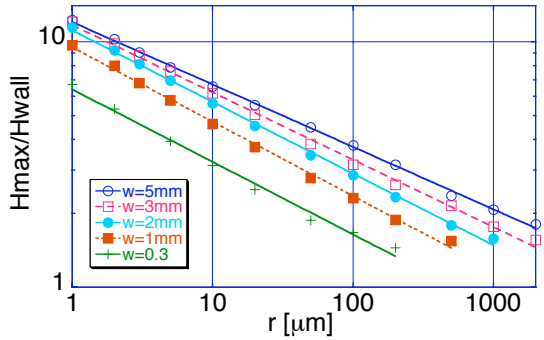

Figure 8: Enhancement factors as functions of r: X=0.

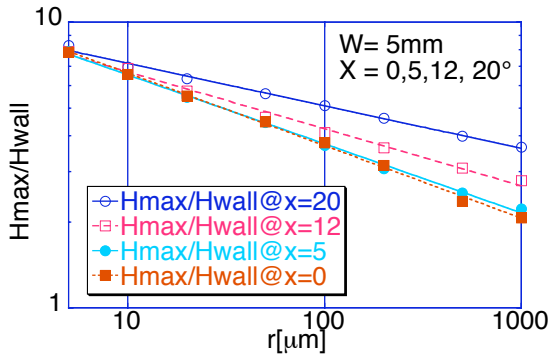

Figure 9: Enhancement factors at finite crossing angles.

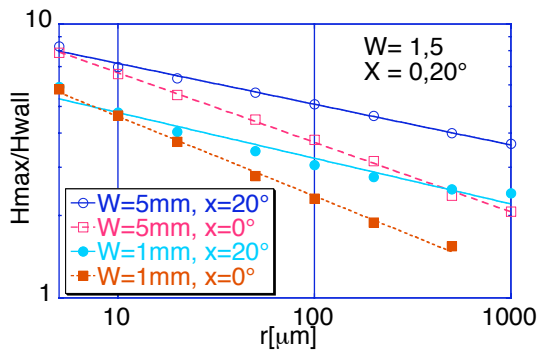

Figure 10: Enhancement factors at finite crossing angles.

REFERENCES

[1] GLC: KEK Report 2003-7, 2003 and http://lcdev.kek.jp/ProjReport/, 2003 and NLC: SLAC Report 474, 1996.
[2] KEK Report 2000-7, SLAC-R-559, April 2000.
[3] J.W. Wang et al.: "Recent progress in R&D of Advanced Room Temperature Accelerator Structures", TH464, Proc. of LINAC2002, Gyeongju, Korea, 2002.
[4] V. Dolgashev, KEK-SLAC ISG9 Meeting, Dec. 2002 at KEK, http://lcdev.kek.jp/ISG/ISG9.html
[5] Y. Iwashita: "PISCESII: 2.5D RF Cavity Code with High Accuracy", Beam Science and Technology, ICR Kyoto Univ., **7**, 14-18 ISSN 1342-033X (2002)
[6] T. Taniguchi: Morikita Shuppan Co. Ltd., ISBN: 627914008, 1992 in Japanese.
[7] T. Higo et al.: "Improved HDDS cell fabrication", GLCX-006, http://lcdev.kek.jp/TechNotes/, 2003

MECHANICAL STABILITY SIMULATIONS ON A QUARTER WAVE RESONATOR FOR THE SPIRAL II PROJECT

H. Saugnac, G. Olry, S. Blivet, J.L. Biarrotte, S. Bousson, T. Junquera, M. Fouaidy, IPN Orsay, CNRS/IN2P3, France

Abstract

In the framework of the SPIRAL II project, IPN Orsay is studying a 88 MHz beta 0.12 super conducting quarter wave resonator prototype. Due to its low RF bandwidth (around 60 Hz) the resonator must have a very high mechanical stability and have small sensitivity to dynamic mechanical loads. To simulate the effects of geometrical deformations on the fundamental RF frequency a three dimensional analysis is required. The simulations were made by coupling mechanical FEM analysis performed in COSMOS/GEOSTAR© with the RF electromagnetic FEM code MICAV© integrated in the COSMOS/GEOSTAR© interface.

Static mechanical loads were first studied to reduce the effects of external pressure on the RF frequency shift and evaluate the tuning sensitivity of the cavity. Then, simulations of the dynamic response of the resonator, using the modal superposition analysis method, with random external pressure variations and harmonic excitation of the cavity were performed.

This paper presents the results of the simulations and mechanical solutions chosen to increase the cavity RF frequency stability.

NUMERICAL CODES AND METHODS

Numerical simulations where performed with the finite element codes COSMOS/GEOSTAR© for the mechanical study and MICAV/EMW© for the RF frequency simulations. MICAV© being integrated in COSMOS© it is possible, after some data treatments on the input and output files, to create a shell mechanical model and a solid RF model with corresponding meshing patterns. RF frequency perturbations are then computed without numerical interpolation [2].

Dynamic simulations are performed using the modal superposition analysis method [3] where the overall response of the structure is the sum of a set of modal responses for specific loading and boundary conditions.

Each mode *i*, considered as a single freedom degree element, has the harmonic stationary relative response :

$$u_i(t) = \frac{1}{2\xi_i\sqrt{1-\xi_i^2}} \cdot X \cdot \sin(\omega_i t + \pi/2)$$

Assuming, for small displacements, proportionality between RF frequency shift, and cavity wall deformation:

$$\Delta f_i \approx \left(\frac{\Delta f}{u}\right)_i \cdot u_i = K_i \cdot u_i$$

K_i is computed with COSMOS/GEOSTAR© and MICAV©.

For a combination of harmonic excitations having the same phase, and amplitude X_j and pulsation Ω_j once have the overall response :

$$\Delta f\ (t) \approx \frac{1}{N}\sum_j\sum_i H(h_{i,j}) \cdot X_{i,j} \cdot K_i \cdot \sin(\Omega_j t + \varphi_{i,j})$$

$$H(h_{i,j}) = \sqrt{\frac{1}{(1-h_{i,j}{}^2)^2 + 4\cdot\xi_i{}^2\cdot h_{i,j}^2}} \quad \& \quad \varphi_{i,j} = \arctan(2\xi_i \cdot \frac{h_{i,j}}{1-h_{i,j}^2})$$

$$\xi_i = \frac{1}{2Q_i} \qquad \& \qquad h_{i,j} = \frac{\Omega_j}{\omega_{0i}}$$

Q_i being the modal mechanical quality factor.

$X_{i,j}$ is the harmonic excitation amplitude.

For harmonic acceleration of amplitude γ_j or harmonic displacement of amplitude Z_{mj} once have:

$$X_{i,j} = \frac{\gamma_j}{\omega_i^2} \qquad \text{or} \qquad X_{i,j} = h_{i,j}^2 \cdot Z_{mj}$$

STATIC ANALYSIS

Simulations on static changes of cavity geometry were performed to stand cavity and cold tuning system design parameters. The tuning sensitivity was calculated at various positions on the external cavity body in order to optimise the ratio between the tuning sensitivity and the mechanical stiffness.

Static pressure variation effects as well as cool down and chemical etching induced frequency shift are presented in table 1 for two studied models (figure 1).

Table 1: Static frequency shifts numbers

	Model I	Model II
Tuning. Sens.	~ 15 kHz/mm	~ 15 kHz/mm
Tuning stiffness	~ 15 kN/mm	~ 15 kN/mm
Pressure. Sens.	-5.5 kHz/bar	-4.5 kHz/bar
Chemical etching sens.	~ -5kHz/0.1mm	~ -5kHz/0.1 mm
Therm. sens. @4K	~150 kHz	~150 kHz

These data will give a first evaluation of the design frequency target and the overall tuning range taking into account the manufacturing incertainities that will be measured on a first prototype planed for October 2004.

DYNAMIC ANALYSIS

Mechanical coupling between the helium tank and the cavity is mainly at the helium tank jointing ring (compensating bellows have high compliance).

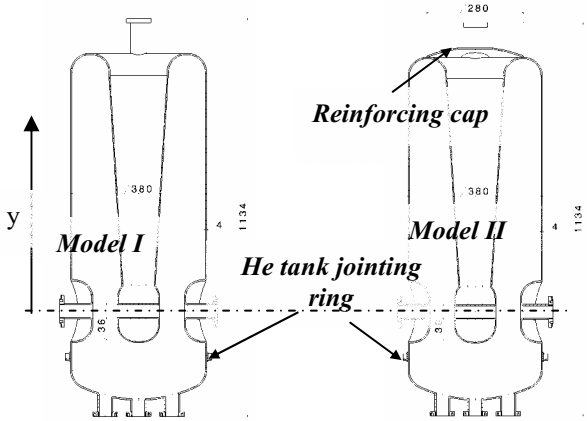

Figure 1: QWR Models.

The displacement boundary conditions (fixing and harmonic base excitation) are then applied only on the helium tank jointing ring.

A number of 60 modes giving a modal mass participation factor of ~80 % in all directions, from 50 Hz to 1100 Hz, where computed to describe the dynamic mechanical response of the cavity. For the base excitation study 10 modes (Model II) were chosen to form the frequency shift modal basis (figure 2). A random dynamic pressure excitation simulation with a white noise PSD shows that only one mode can be used to describe the RF frequency shift due to dynamic pressure loads with a good accuracy. Quality factors values, from 10 to 200, were chosen according to different measured values on bulk niobium super conducting cavities [4].

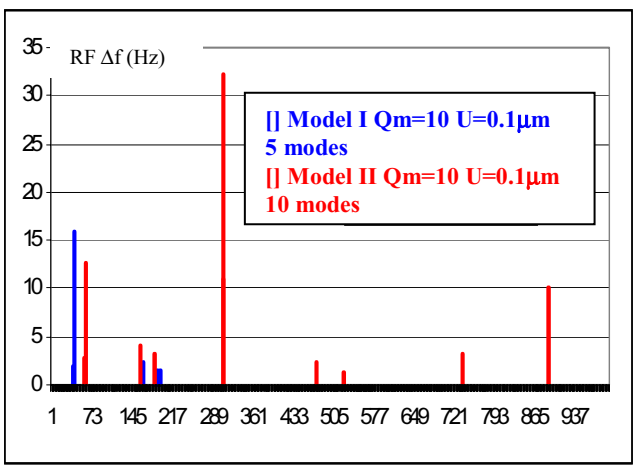

Figure 2: Modal harmonic response for base excitation Model I & Model II.

Base Excitation Analysis

These simulations describe the effects of environmental vibrations transmitted to the cavity from the soil or the cryogenic tubing submitted to rotating machines vibrations (helium compressor, vacuum pumps …).

A comparison for low frequency excitations between the two models is shown figure 3.

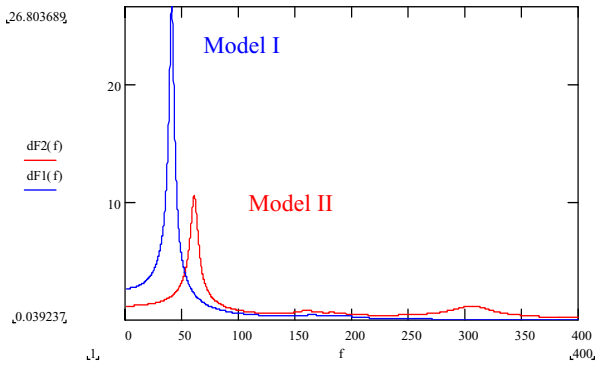

Figure 3: RF frequency Shift (Hz) for 0.01 m/s^2 constant acceleration amplitude.

The reinforcing cap on the model II, increases the first mode frequency from 40 Hz to 60 Hz, and lead to a better RF frequency stability for low frequency mechanical excitations.

Pressure Excitation Analysis

Spiral II resonators are to be cooled with liquid He I at 4.2 K. Bubbles, created during pool boiling, have random characteristics (diameters, formation frequency, distribution on the surface…) which depend on various parameters: surface history, roughness … The pressure forces can be roughly (predictions are not well established) evaluated from mathematical correlation [5]. Assuming a number of nucleation sites of $10^6/m^2$, a maximum 150 µm bubble diameter, a homogenous distribution on the surface and a formation frequency at the most sensitive QWR resonant mode, we can make a conservative evaluation (Table 2) that shows that this effect should be small compare to other mechanical perturbations.

Table 2: Nucleate boiling induced frequency shift

	Model I (197 Hz)	Model II (277 Hz)
ΔP = 10-3 mbar Qm=200	1.53 Hz	0.68 Hz

CRYOMODULE DESIGN CRITERIA

Dynamic simulations on the cavity support rods (figure 4) has been done with a constant acceleration amplitude harmonic excitation roughly established from measured values on an accelerator environment [6]. These simulations show that risks to have RF frequency shifts greater than our QWR bandwidth are possible for excited mechanical eigen modes with high quality factors.

For small quality factors the frequency shift remains low even when resonant modes are excited. Lowering the mechanical quality factors of the QWR [7], the cavity support and the cryostat/soil interface[8] is then an issue for the cryomodule design.

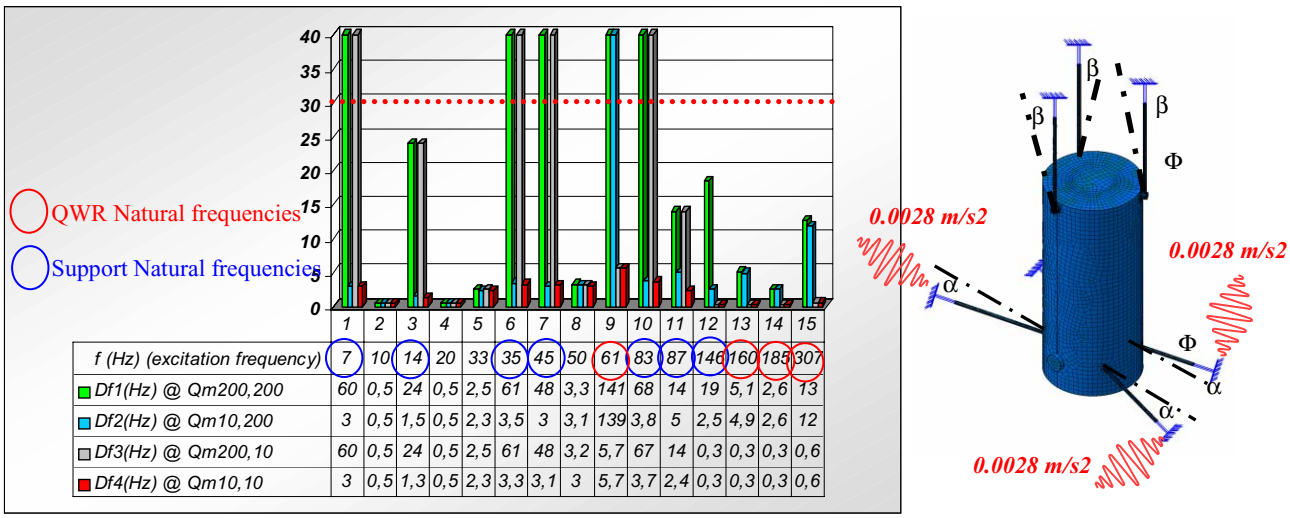

Frequency shift response for a harm. acceleration excitation amplitude 0.0028 m/s2. Qm i,j : mechanical quality factor of the support rods (i) and the QWR (j). *For* ***QWR Model II & Tank Model α=0, β=0, Φ= 10***

Figure 4: Frequency shift for cavity support / QWR integrated model.

An other direction, aiming to avoid excitation of the natural frequencies of the cavity support rods, is to allow an adjustment of the rods geometrical parameters α, β or Φ (figure 4) which have a sufficient effect on the eigen frequencies values. Qualitative solutions to decrease the influence of the vacuum pumps, cryogenic tubing and cold tuning system stepping motor lead to reduce the vibration transmission to the QWR (bellows, distance, working conditions…). First design numbers and qualitative goals are presented table 3.

Table 3: Design numbers

Soil vibration intensity	U < 20 nm f >5 Hz
Cryostat / soil transmission	T < 0.5
1 st QWR mode Quality factor	Qmj < 20
Cavity support Quality factors	Qmi < 20
First cavity support Mode	f > 15 Hz
No excitation of the natural modes by the tuning system stepping motor → effect on the working speed	
No common resonant frequency between : Cryostat, Cavity support, QWR	
Vac. Pumps, cryo. tubing, tuner.	To be evaluated
He bath pressure stability	+/- 1 mbar
QWR RF frequency Fab. Incertainities	Δf < +/-10 kHz

CONCLUSION

Despite the incertainities on the boundary conditions values (acceleration and displacement intensities, mechanical Q factors…), these simulations give a basis for the construction choices and the design concepts of the beta 0.12 SPIRAL II cryomodule. From vibration tests on a first QWR prototype, planed for 2005, the numerical model validity will be checked and the QWR mechanical modal quality factors will be evaluated.

The next step is to manufacture a prototype cryomodule and measure the dynamic response of the whole mechanical structure.

REFERENCES

[1] T. Junquera & al., "High Intensity Linac Driver for the SPIRAL-2 Project : Design of Superconducting 88 MHz Quarter Wave Resonators (beta 0.12), power couplers and cryomodules", EPAC'04, Luzern, July 2004.

[2] F. Krawczyk & al., " An integrated design for a beta=0.175 spoke resonator and associated power coupler", EPAC'02, Paris, June 2002.

[3] N. Ouchi & al., "Pulsed SC proton LINAC"," LINAC 2000, Monterey, August 2000.

[4] L. Lilje & al., "Characteristics of a fast piezo-tuning mechanism for superconducting cavities" EPAC'02, Paris, June 2002.

[5] W.B. Bald "Cryogenic heat transfer research at Oxford", CRYOGENICS, August 1973, p 457.

[6] J. Welch, "Ground vibration and siting of the Cryogenics Facility for Cornell ERL Prototype", ERL reports 2002.

[7] A. Facco & al. "On-line performance of the LNL mechanically damped superconducting low beta resonator", EPAC'00, Stockholm, June 2000.

[8] R. Assmann & al. "The CLIC stability study - Stabilizing Accelerator Magnets to the Sub-nm Level", ELAN Workshop Frascati, Italy, May 2004.

SOME ESTIMATIONS FOR CORRELATION BETWEEN THE RF CAVITY SURFACE TEMPERATURE AND ELECTRICAL BREAKDOWN POSSIBILITY

V.V. Paramonov, INR, 117312 Moscow, Russia

Abstract

The electrical breakdown in accelerating cavities is the complicated phenomenon and depends on many parameters. Some reasons for breakdown can be avoided by appropriate vacuum system design and the cavity surface cleaning. This case for normal conducting accelerating cavities free electrons - the dark currents due to Fowler-Nordheim emission can be considered as the main reason of possible electrical breakdowns. It is known from the practice the combination of the high electric field at the cavity surface with high surface temperature is the subject for risk in the cavity operation. In this paper the dependence of the dark current density on the surface temperature is considered and effective electric field enhancement is discussed.

INTRODUCTION

As it is well understood now, the electron current, emitted from the rf cavity surface, is one reason for electrical breakdown. When the electron current reach some threshold value, the sparking and further breakdown take place.
The investigation of electron emission is a special branch of technical physics and a lot of researchers worked in this field. Extensive special bibliography exists related to the investigation of emitting surface parameters on the emitting current. The systematic review one can find in [2] with related references.
The purpose of this report is not to find new relationships - just, referring to the well known in the emission study effects, estimate the influence of the surface temperature in normal conducting cavities on the dark current emission.

ELECTRON EMISSION

The electron emission from metals is quantum tunneling effect through potential barrier. The probability of the electron tunneling depends on both the barrier parameters - width, height - and the electrons energy state. Several physical processes can change the electron energy state - the external electric field, the temperature of material, the external photons. The quantitative description of electron emission, taking unto account all processes, is very complicated and just under simplifications we can obtain some analytical conclusions.
The electron field emission has been explained in [1] for the limiting case $T_c = 0^o K$,

$$j_0(E_s) = \frac{A(\beta E_s)^2}{\phi} exp(-\frac{B\phi^{3/2}}{\beta E_s}), \qquad (1)$$

where E_s is the surface electric field, in $\frac{MV}{m}$, ϕ is the work function of the material, in eV ($\phi = 4.47eV$ for copper), $A = 1.54 \cdot 10^6 \frac{eVA}{(MV)^2}$, $B = 6830 \frac{MV}{m(eV)^{3/2}}$, β is the ratio of local field at the emitter to the average surface field E_s. For the case of very high electric fields it can be corrected [3] as:

$$j_0(E_s) = \frac{A(\beta E_s)^2}{\phi} exp(-\frac{B\phi^{3/2}}{\beta E_s})(1 - \frac{5\beta E_s}{18B\phi^{(3/2)}}). \quad (2)$$

Anyhow, both (1) and (2) are obtained in the assumption of absolute zero material temperature. The estimations of the material temperature influence were done in [4] and extended in [5]. The parameter with temperature dimension is the inversion temperature T_i, K^o, related with the external field strength E_s as:

$$T_i = \frac{0.567 E_s}{\sqrt{\phi}}. \qquad (3)$$

Emitting electrons can either absorb the heat from thee emitter ($T_i > T_c$), or generate it, if ($T_i < T_c$) - Nottingham effect. The inversion temperature T_i is the linear function of the external electric field E_s and, to estimate values, $T_i = 134K^o$ for $E_s = 500 \frac{MV}{m}$.
Analytical results in [4], [5] are obtained for the case of 'low temperature' and 'high electric field', when temperature addition can be considered as small. According [4], the current density j_{T_c}, emitted from the surface with the temperature T_c is:

$$j_{T_c} = j_0 \frac{\frac{\pi T_c}{2T_i}}{sin(\frac{\pi T_c}{2T_i})}, \qquad (4)$$

for the temperature range $0 < T_c < 1.2T_i$. Extended temperature region $1.2T_i < T_c < 2.2T_i$ is considered in [5] and

$$j_{T_c} = j_0 \cdot 1.16 \cdot exp(0.31 \frac{T_c^3}{T_i^3}). \qquad (5)$$

The plot of the current ratio densities $\frac{j_{T_c}}{j_0}$ for temperature range $0 < T_c < 2.2T_i$ is shown in Fig. 1. The plot in Fig. 1 exhibits fast rise of the current density for $T_c > 1.5T_i$. Unfortunately, we can not extend the plot for higher ratio values $T_c > 2.2T_i$ - it is out of physical assumptions, done in the obtaining these analytical estimations.
The extension to higher temperatures requires numerical simulations. Such results are known, see, for example [6], and shows significant current density rise with the surface temperature increasing (up to order) for relatively low electric fields. For higher temperatures T_c the current density

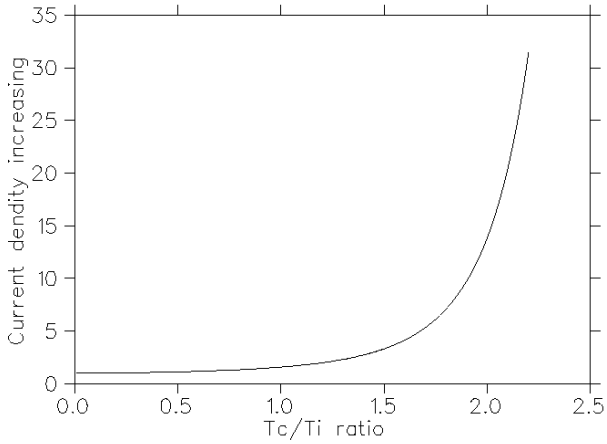

Figure 1: The current density increasing with the surface temperature rise.

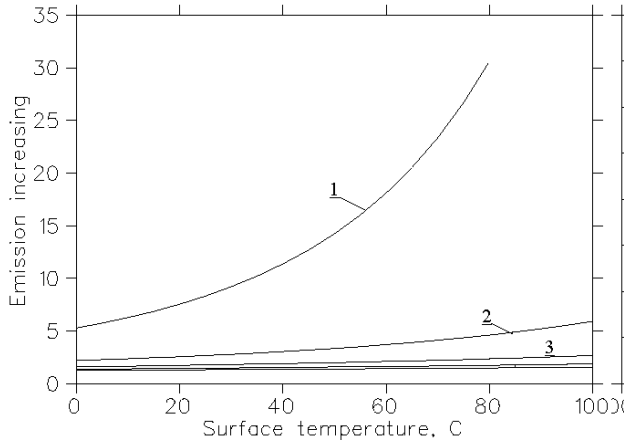

Figure 2: The current density increasing with the surface temperature rise for different E_s values. 1 - $E_s = 600\frac{MV}{m}$, 2 - $E_s = 800\frac{MV}{m}$, 3 - $E_s = 1000\frac{MV}{m}$.

increasing is not so large, as one can expect from continuation of the plot in Fig. 1, some saturation take place. Using in this paper the known analytical estimations, we can consider the results obtained for the emitted current increasing as the low estimations.

For normal conducting cavities we are interesting in the surface temperature $T_c \sim (293 \div 373)K^o$. We do not assume the higher temperatures, which can lead to high internal stresses and surface destruction.

According (1), the current density j_0 rises very fast with E_s and parts of surfaces with high electric field $E_s \geq 10^3 \frac{MV}{m}$ provide the main contribution in the emitted current. But, such electric field leads (3) to high $T_i \geq 300K^o$ value and the effect of emitting current increasing for moderate cavity temperature $T_c \sim 300K^o$ is not important, according (4) for such parts.

The low inversion temperature $T_i \leq 100K^o$ corresponds to the surface field value $E_s \leq 380\frac{MV}{m}$. For such E_s values one can expect the large current increasing with surface temperature, but original current density j_0, according (1), is negligibly small.

In Fig. 2 the plots of the current density j_{T_c} increasing with the surface temperature T_c rise for different E_s values are shown. Significant increasing of the total emitted current we can expect at the part of the cavity surface with 'moderate' electric field $E_s \sim (500 \div 800)\frac{MV}{m}$. Normally, at the well treated cavity surface the electric field is much lower and only special surface imperfectness generate very high E_s value and serve as effective emitters.

EMITTERS MODEL

As it is known from practice, see, for example, [7] and related references, the field emission takes place at the average surface field values, much lower, than predicted by (1). It is explained now, and can be explained only by the existence at the regular cavity surface of point-like emitters with very high local electric field.

Regular Surface

To have the high quality value Q, close to the design one, the cavity surface should be treated with the surface roughness $R_a \leq 0.2\delta$, where δ is the skin depth at the operating frequency f_0. For $f_0 \sim 1000MHz, \delta \approx 2\mu km$ and should be surface roughness $R_a \leq 0.4\mu km$. It defines the average height of lugs and the deepness of growth at the cavity surface after mechanical treatment. Instead the lugs can be sharp with the high local field at the ends, there is the limitation [8] to the field emission possibility, which provide the relation between the minimal height of the lug h_{min} and the

$$E_{s_{min}} > \frac{4\phi}{eh_m}, \tag{6}$$

where e is the electron charge. For a field emission the high field is necessary both on the emitter surface, and in the nearest finite vicinity. The small sharp emitters can result in high β value and high local field at the end, but the field decreases very fast with the distance from the emitter end and finally can not extract electron from the metal. For $h_{min} = R_a = 0.4\mu km, E_{s_{min}} > 50\frac{MV}{m}$. It is approximately two times higher as Kilpatrick limit at L-band frequency and normally exceed the maximal surface field in operating regime. The contribution of the well treated regular surface in the emitted field current should be small.

Single Emitters

At the cavity surface exist, see, for example [7], a lot of small (micron scale size) objects - hairlike strands, cone shaped bumps, shiny spheres, sphere on sphere - which can provide the field enhancement and serve as effective emitters. The real emitter shape is less important as compared to the produced β value. Let consider a single emitter as a half of ellipse with axis dimensions $a > b = c$ and axis a is directed perpendicular to the cavity surface. For such model the field distribution is known and the maximal elec-

tric field E_{sm} at the ellipse end is [8]:

$$E_{sm} = E_s \frac{x^3}{(\frac{1}{2}ln(\frac{1+x}{1-x}) - x)(1-x^2)}, \quad (7)$$

where $x = \sqrt{\frac{a^2-b^2}{a^2}}$. The plot of field enhancement $\beta = \frac{E_{sm}}{E_s}$ is shown in Fig. 3. Along the ellipse envelope the field decreases as $E_{sm}cos(\Theta)$, where Θ is the angle between the normal vector to the ellipse surface and a-axis.

For such emitter model we can calculate the emitted current values for different $E_s, \frac{b}{a}, T_c$.

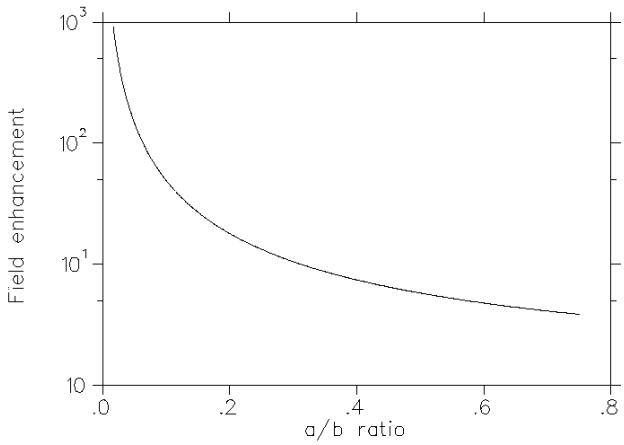

Figure 3: The field enhancement of the elliptical emitter as the function of $\frac{b}{a}$ ratio.

The primary effect on the field emission has the local electric field value, which can achieve $E_{sm} \sim 10\frac{GV}{m}$ at $E_s \approx 40\frac{MV}{m}$, corresponding to $\beta \approx 200$ [7]. The field emission is a strongly nonlinear process and the rapid rise of current with local field heavily weights result toward the effective emitters with highest fields, which provide the main part of the emitted current.

During cavity rf conditioning, the initial dark current value decreases at least in two orders. It can be explained either by the reduction of effective emitters number, or, by reduction of emitters efficiency due to emitters shape smoothing and local filed decreasing. To decrease the dark current intensity in two orders, it is required to remove emitters with $\beta > 150$.

Let consider a set of elliptical emitters with $10 \leq \beta \leq 150$ and calculate the ratio of the total emitted current I_0 assuming zero-temperature approximation (1) and I_t - assuming the temperature correction (4), (5). We neglect the emitter heating due to Joule losses - it is essential for effective emitters, which should be destroyed during rf conditioning. The plot of $\frac{I_t}{I_0}$ is shown in Fig. 4 for $E_s = (10 \div 60)\frac{MV}{m}$ and $T_c = (0 \div 100)C^o$.

As one can see from Fig. 4, significant value of the ratio is at low E_s values. As a rule, maximal electric field is at the restricted part of the cavity surface, at drift tubes, at the iris ends. The main part of the surface has a lowered (as compared to maximal) E_s value. Due to strong nonlinearity of the field emission, the unit area in such part provides a small contribution to the total dark current value, but total effect can be significant.

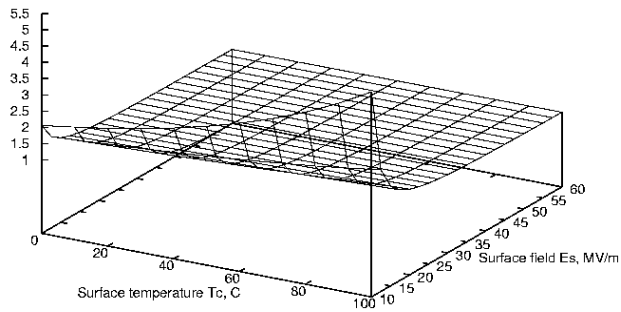

Figure 4: The ratio of total currents I_0 and I_t, emitted by the set of elliptical emitters for $E_s = (10 \div 60)\frac{MV}{m}, T_c = (0 \div 100)C^o$.

CONCLUSION

In this paper some estimations related to the cavity surface temperature influence on the field emitted (dark) current. For room temperature range the cavity surface temperature is not a primary effect in the dark current emission. The main effect is from enhanced electric field at the effective emitters. But increasing of surface temperature leads to the emission increasing from noneffective emitters, which can be widely distributed at the surface. Also it involves in the field emission the parts of the cavity surface with lowered, as compared to maximal value, surface field. As the result, the total dark current value increases, increasing the breakdowns possibility.

REFERENCES

[1] R.H. Fowler, L. Nordheim, Proc. Roy. Soc., v. 119, n. A781, p. 173, 1928

[2] G.A. Mesjaz et al., Autoemission and explousure emission processes in vacuum discharges. Uspechi Phizicheskih nauk, Moascow, Nauka, v. 139, n.2, p. 265, 1983 (in Russian)

[3] A.M. Brodsky, Yu.A. Gurevich. Theory of electron emission from metals. Nauka, 1973 (in Russian)

[4] E.L. Murphy, R.H. Good. Thermionic emission, field emission and the transition region. Phys. Rev., v. 102, n. 6, p. 1464, 1956

[5] S.G. Christov. General theory of electron emission from metals. Phys. Stat. Sol., v. 17, n. 1, p. 11, 1966

[6] M. Elinson et al, About the theory of field and thermionic emission from metals and semiconductors. Radiotechnika i electronika, v. 6, n. 8, p. 1342, 1961 (in Russian)

[7] J. Norem et al., Dark current, breakdown, and magnetic field effects in multicell, 805 MHz cavity. PRST-AB, v. 6, 072001, (2003)

[8] I.N. Slivkov. Processes under high voltage in vacuum. Moscow, Energoatomizdat, 1986 (in Russian)

THE FINITE STATE MACHINE FOR KLYSTRON OPERATION FOR VUV-FEL AND EUROPEAN X-FEL LINEAR ACCELERATOR

W. Cichalewski, B. Kosęda, A. Napieralski, Technical University of Lodz, POLAND
F.R. Kaiser, S.N. Simrock, Deutsches Elektronen-Synchrotron Hamburg, GERMANY

Abstract

In order to provide a pulsed RF power signal that fulfills all designers and users demands the development on power supplies, pulse transformers, wave-guides, and klystrons has to be well coordinated. Because operators and not experts engineers will operate the user facility therefore software has to be implemented in order to automate the enormous quantity of hardware operation accompanying regular operation of *linear accelerator*. A finite state machine provides an adequate formal description of reactive systems that has become starting point for designing our control software. To present the complexity of the task that establishing a FSM for klystron and modulator system would be, one has to become acquainted with the complexity of the system itself. Therefore this article describes the construction and principles of the klystron and modulator as well as ideas concerning the implementation of a FSM for such a system.

INTRODUCTION

In present time all this equipment, which work for VUV-FEL and X-FEL together with hardware control systems, has to be monitored and operated through a computer system. At DESY DOOCS has been developed (Distributed Object Oriented Control System DOOCS [3]) that is a computer system of multi layer servers working together for optimal operation of the whole system. Beside the typical hardware servers like ADC or DAC servers, there are also servers designed especially for Finite State Machine purposes. Such FSM allows minimizing user intervention during system operation to "one button" action. One of the part of the whole system that requires such a structure is a system responsible for supplying cavities with energy necessary for particle acceleration.

Superconducting cavities are supplied with RF power needed for electron acceleration from multibeam 10MW klystrons working in pulse mode.

KLYSTRON SYSTEM DESCRIPTION

In order to provide a pulsed power signal that fulfils all designers and users demands the work on power supplies, pulse transformers waveguides and klystrons has to be well coordinated. As in the phase of commissioning the device (like VUV-FEL) such a system can be operated manually that in a final solution operator has to be replaced by robust FSM software working in the DOOCS environment

In the whole klystron and modulator system one can distinguish several subsystems that form main sections. Each of this section has to be carefully managed to achieve best system performance.

Modulator - High Voltage Power Supply (HV-PS)

HV-PS is a section responsible for high voltage (HV) pulse for klystron. There is possibility to regulate HV pulse parameters as duration or voltage level and repetition rate in order to achieve requested portion of the energy for the klystron.

Electrical power is delivered to the system as AC 440V 50Hz signal in 3 phases. After conversion (in a transformer) the signal is filtered and the energy is stored in 1,4mF capacitor (*Cap Bank*). Next to the capacitor *the crowbar* system is installed. If there is an arcing effect in the klystron tube this system makes a short circuit for the Capbank and sends the energy from the capacitor to the ground. This system is not used during normal operation.

The switch is present for releasing the energy from capacitor bank. This *main switch* is based on seven Integrated Gate-Commutated Thyristors devices.

This power is send to *the pulse transformer.*

Because of the slope that occurs on a high voltage envelope there is compensation needed. In order to achieve a flattop the bouncer system is used. A bouncer is a resonance circuit that stores energy and when triggering signal appears this energy is released in order to compensate the slope on the main circuit signal. Bouncers counterbalance signal minimizes the fluctuations of the high voltage signal to the level of +-0,5 %.

Pulse Transformer

The *pulse transformer* (PT) is a subsystem that converts signal achieved from HVPS to the HV signal that supplies the klystron tube [4]. For the efficient use of magnetic core, there is also biasing introduced through one of the section of the secondary windings.

In order to decrease thermal power losses, the whole pulse transformer body is cooled by mineral oil. The level, temperature and also humidity of the oil are monitored at all times.

Klystron Section

The HV pulse is delivered to the klystron, where *collector* is grounded and high voltage is applied to the *cathode*.

To achieve sufficient electron emission from the cathode, this part of the klystron must be heated to the particular temperature. *The filament* subsystem is responsible for this process. A heater subsystem contains special controller hardware for slow increasing the temperature that is necessary for efficient and longtime filament and cathode use.

According to the data achieved from cathode examination the pearvance of the klystron is measured. Afterwards some correction of the filament preparation

process can be performed (like increasing heating time or increasing current step level).

When filament heating is finished and all security systems are ready HV can be applied into the klystron.

In order to achieve focused beam current *external solenoids* are installed. Information about the voltage and current of the PS powering the solenoid are given.

For XFEL purposes the klystron will work up to 10Hz pulses with 1.7ms time of power release.

The Drive RF Signal Delivering

The small RF drive signal is introduced to the klystron tube with an antenna placed before first bunching cavity of the klystron. The signal from this antenna causes beam modulation with 1,3 GHz and shape bunches in such a way to achieve signal responding required RF envelope shape. Then in the following cavities – resonators the bunching process is continued and finally with another coupler (in the last klystron cavity) power is coupled out and distributed in wave-guide system through the two arms of the klystron. The gain of the power is determined by DC power from HVPS subsystem and signal efficiency by bunching process.

Klystron cavities as well as a wave-guide system and the output coupler from the klystron are designed and made in such a way that the signal of the output of the klystron is a 1,3 GHz signal.

Klystron Machine Protection and Safety Subsys.

In the klystron section there are a couple of security interlocks systems that examine the online klystron environment and provide necessary information about overcoming fault thresholds or even activate the interlock.

- Vacuum pump system

In order to keep high vacuum in the klystron tube there are three pumps installed. In case of not clean environment the pump starts to evacuate the tube. If the device overcome specified current level appropriate action in interlock take place.

- Solenoid status check

For convenient beam focusing voltage and current of solenoid have to be checked. Monitored signals have to be compared with the technical specification.

- Cooling system check:

Because of low efficiency of the klystron and the magnets (about 50-60%) this parts are heated during operating time and have to be equipped with a cooling system. All the parts are cooled by water flow.

- RF Leakage subsystem:

Because of the waveguide power distribution system complexity it is not possible to keep the system completely shielded for RF signal. That is why dedicated subsystems monitor the RF leakage level. Subsystem gives information to the interlock channel if safe leakage level has been overcome. This signal can be read as well from DOOCS interlock server. If RF leakage will be detected at the excessive leakage interlock protection will switch off all the other subsystems.

RF Signal Distribution – Klystron Driver

After achieving modulated and corrected RF signal from the Low Level RF control system *klystron driver* section amplifies this signal in an RF amplifier.

There is also a RF switch present that allows switching off the RF signal during some stages of klystron operation, for example during changing the HV level or if interlock action occurs.

OPERATION AUTOMATION

In order to achieve system automation a *Distributed Object Oriented Control System (DOOCS)* has been designed and developed. A finite state machine [2] is the adequate formal description of reactive systems. Therefore two very helpful tools - *FSM server* and *FSM C++ server code generator* have been included in *DOOCS* environment. As the *FSM DOOCS server* one understand a computer program that is compatible with DOOCS and its algorithm is based on FSM formalism. The standard graphical editor DOOCS Data Display (DDD)[1] developed to display and control the TTF equipment has been extended to allow the creation of FSM designs. The FSM code generator can generate a template for the FSM server straight from *state charts (Fig.1)*. Foregoing scenario is a usual way of creating applications that drive subsystems of *linear collider*. The following part of the article presents some new ideas, which will be realized during the development of the FSM for *klystron subsystem.*

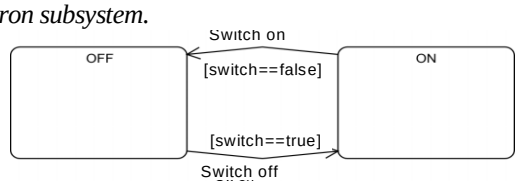

Figure 1: State chart - representation of FSM formalism.

Requirements Analysis

One has carried out the requirement analysis, which revealed that the main difficulties in case of *klystron FSM* creation could be the changes in the hardware and software during FSM development and maintenance.

Because this software will work for at least 10 years challenges related to long-term maintenance would be present. Next problem concerns documentation management. It would be very helpful if FSM were "self-describtive". For the time being FSMs are mainly made as monolithic programs. A new approach considers creation of small (and common for all klystrons) generic FSM's and set of binaries that will work as drivers for particular subsystems. These components will be implemented as independent processes but connected with each other with communication channels. This solution aims to create a machine that will consist of a many well programmed and tested binaries (*subsystem drivers*) that will work under the command of one generic state machine. To make FSM more flexible and easy configurable one consider whether is not better to move all configuration which is related to DOOCS environment to plain XML files, definitions of DOOCS members as well as definitions of the simple algorithms.

Modularization and Interface Generalization

Proposed approach aims to create a reliable set of well-tested small applications. Additional advantage is that several people can work on one FSM independently. It also means that each *subsystem driver* can be written and maintained by person who understands relevant subsystem. In order to simplify the development process one has to design common and simple interface between the FSM and the generic *subsystem driver*. It will make it possible to easily extend number of subsystems that will be driven by the FSM without recompiling it. Only changes in the FSMs configuration file will be necessary. The crucial task in the achievement of such solution is to apply inter-process communication protocol that will be able to handle inter-object communication with sufficient efficiency and reliability.

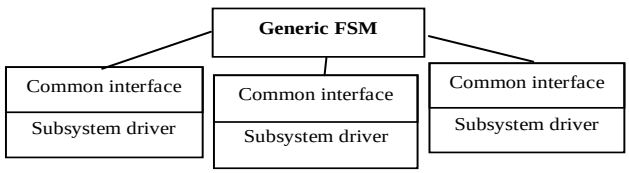

Figure 2: Modular architecture of FSM.

Hierarchy and Dependency

From observations that has been taken (one has observed how engineers work with klystrons) follows that *the klystron system* should be divided into several dependent subsystems i.e. cooling, vacuum, plenty of power suppliers, personal and hardware interlocks etc. Dividing software into modules supports this aspect of structure, but additional effort in designing object-oriented structure, which can handle such dependencies, has to be made. If we can represent such dependencies as tree-like structure it will help in system error handling, since errors affect "parent" systems in case of affecting "child" ones.

Configuration Instead of Recompilation

One considers design structure of XML document that will be the configuration file for *subsystem driver*. Maybe not all issues can be solved this way. Still remains difficulty with using the algorithms which are performed by special software i.e. Matlab. But it can help in case of change *DOOCS* property name or meaning or even in change in some algorithm (which can be represented as series of reads and writes to certain properties). By the way well formed XML files can very precise describe functionality of its binaries. Therefore one considers creating fully automated solution that will generate documentation from those configuration files and store this data in the easy readable form.

Taking Advantages of Existing Solutions

Because the FSM will be incorporated in the DOOCS environment one cannot omit solutions developed so far. To communicate between the state machines ClientLib will be used. Also FSM will need to be controlled somehow even if it has only a few control buttons. Therefore main FSM will be implemented as regular DOOCS FSM server. One consider to include DOOCS server interface in every *subsystem driver* in order to use existing watchdog to improve reliability of the system.

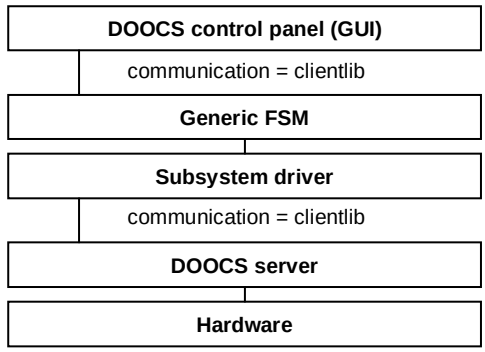

Figure 3: Communication between DOOCS and new FSM.

CONCLUSIONS

The requirement analysis revealed several problems like for example a need for ease software modifications during accelerator operation and development without compromising machine work or well-defined and efficient way for a new part of the system description. In order to solve them one has to design new architecture for the FSM for klystrons. First idea is to split the FSM for one generic FSM for all klystrons and set of programs will act as drivers for relevant klystron subsystems. To handle dependencies between subsystems a hierarchical tree-like structure class structure has to be designed and implemented.

Because the klystron equipment will work in radiation environment for at least 10 years one cannot omit challenges related to long-term maintenance. Therefore software which is designed have to be flexible, easy reconfigurable and well documented.

ACKNOWLEDGEMENTS

We acknowledge the support of the European Community-Research Infrastructure Activity under the FP6 "Structuring the European Research Area" program (CARE, contract number RII3-CT-2003-506395).

REFERENCES

[1] K.Rehlich, "An Object Oriented Data Display for the TESLA Test Facility", ICALEPCS 97 , Beijing.

[2] Harel, David, "Statecharts: A Visual Formalizm for Complex Systems." Science of Computer Programming 8, 1987, pages 231-274.

[3] O.Hensler, K.Rehlich, et al " DOOCS : A Distributed Object-Oriented Control System on PC]s and Workstations ", PCaPAC conference, 1996

[4] P.A. Bak et. all, "A Pulse Transformer for a 10MW Klystron Power Supply".

[5] A. Aghababyan, V. Kocharyan, K.Rehlich, "An Integrated Finite State Machine to Automate TTF Operation ", DESY, Hamburg, 2000.

GRADIENT LIMITATIONS FOR HIGH-FREQUENCY ACCELERATORS*

S. Döbert, SLAC, Menlo Park, CA 94025, USA

Abstract

The main gradient limitation for high frequency accelerators is rf breakdown. While the physics of this gradient limitation still lacks a full theoretical understanding, a fairly complete empirical picture has emerged from the experimental work done in the past few years to characterize this phenomenon. Experimental results obtained mostly in the framework of the NLC/GLC project at 11 GHz and from the CLIC study at 30 GHz will be used to illustrate the important trends. The dependence of achievable gradient on pulse length, operating frequency and fabrication materials will be described. Also, the performance results most relevant to linear colliders will be presented in some detail. Specifically, these related to the requirements that the structures sustain a certain gradient without incurring damage, and that more importantly, they run reliably at this gradient, with breakdown rates less than one in a million pulses. In this context, long term operation results will be discussed as well as the result of controlled venting experiments. Finally, a very brief idea of the theories related to rf breakdown will be presented.

INTRODUCTION

Choosing a high rf operating frequency offers the advantage of a more compact accelerator design and less rf energy per pulse for efficient acceleration. Drawbacks include the difficulty of generating high peak powers at higher frequency and the tighter alignment tolerances required to cope with the higher transverse wakefields. However, these impediments can be overcome, and high rf frequencies were chosen by normal-conducting linear collider projects, specifically, NLC and GLC [1] and by CLIC [2], which aims for multi-TeV energies. The NLC/GLC collaboration has developed accelerating structures at 11.4 GHz with an unloaded design gradient of 65 MV/m with 400 ns long pulses. The CLIC group studies structures at 30 GHz aiming for an unloaded gradient of 170 MV/m at a pulse length of 130 ns (recent optimization studies suggest a much shorter pulse length of about 60 ns). These gradient choices were motivated in part by early measurements that showed achievable gradient increases monotonically with frequency. Recent results suggest that this assumption is probably not valid anymore at frequencies above X-band [3]. Beyond just achieving these gradients, the structures must operate reliability for decades in a linear collider, which makes it imperative that rf breakdown limitations be well understood. Although a dynamical model of rf breakdown has yet to be fully developed, the phenomenon can be sketched from an empirical view as follows: rf breakdown is a fast and local dissipation of stored energy. Several Joules of rf energy can be absorbed in a single cell, and in the process, surface melting and evaporation occurs in an area of a few 100 μm^2. Strong electron emission, acoustic waves, gas desorption, X-rays and visible light is observed during a breakdown event. The majority of breakdowns are concentrated in areas of high surface electric fields. However a strong exponential correlation between surface field distribution and breakdown location is not always observed, as would be expected from a purely field emission driven process. In areas with high surface currents but not necessarily high electric fields, surface defects like particles, voids and contaminants have been found to be sources of breakdown. The stress imposed on the copper surface by pulsed heating resulting from high surface currents alone is also believed to lead to breakdown. Structure designs with a pulsed temperature rises < 50 K appear to be safe in this respect.

HIGH GRADIENT PROCESSING

High frequency accelerators have to be conditioned to their high operational gradients. The process of rf conditioning is not well understood but it is believed to be a combination of physically smoothening, degassing and cleanup of the surface as a result of the energy dissipated during breakdown. Clean fabrication and assembly procedure seem to speed up rf conditioning but never eliminate it. Typically, the conditioning starts with a pulse width much shorter than the design value. The structure is processed to a field 10-25% above the design gradient and then this process is repeated with progressively longer pulses. As an example, Figure 1 shows the processing

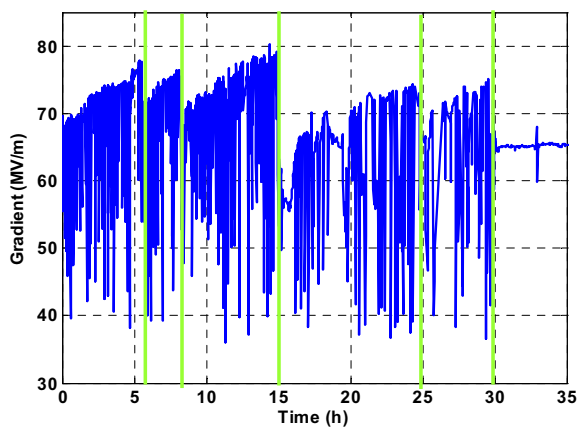

Figure 1: Processing history of a pair of 60 cm structures. The green vertical lines indicate changes in the rf pulse length (50, 100, 170, 240,400 ns).

* Work supported by the US Department of Energy, under contract DE-AC03-76SFF00515

history for a pair of NLC/GLC structures tested in the Next Linear Collider Test Accelerator (NLCTA). After about 30 hours of processing in this case, the structures where operated at the design gradient (65 MV/m) and pulse length (400 ns).

The conditioning times and final performance of the structures do not seem to depend on the differences in the fabrication methods used. Most of the NLC/GLC structures have been built by two groups using somewhat different procedures. The FNAL group starts with cells fabricated by poly-crystal diamond turning, assembles them using conventional brazing in low a pressure argon atmosphere and then vacuum bakes them at 500 °C for 72 hours [4]. The KEK/SLAC group starts with cells fabricated by single-crystal diamond turning, diffusion bonds them in a hydrogen furnace and then vacuum bakes them for 15 days at 650 °C. In each case, the structures are back-filled with nitrogen after assembly. A 250 °C in-situ bake had been performed after the structures were installed in NLCTA for testing, but it was eliminated after faster conditioning times were achieved without it.

A series of venting experiments were recently conducted to determine the influence of gas exposure to the conditioning process. Venting and purging a pair of previously processed structures with filtered, boiled-off nitrogen resulted in almost no degradation of structure performance. Both structures came up to the design gradient with only a few breakdowns and the subsequent breakdown rate was unchanged for one structure and a factor of 2 higher for the other during the first 24 hours. The structures were then exposed to filtered laboratory air. In this case, they came up to the design gradient after a few dozen breakdowns and continued to breakdown at a rate (~ 0.5/hr) that is 10 times higher than the pre-test levels. However, after 50-100 hours, the rates came down to the earlier values. It appears that the addition of water vapor and the thin oxide layer that results enhances breakdown activity, but only temporarily as these sites are quickly processed. More importantly, a rf conditioned surface doesn't loose this quality after a exposure to filtered nitrogen or air.

RELIABILITY

Due to the large number of components in a linear collider, the reliably requirements are very demanding. The NLC/GLC linacs contain about 18,000 X-band structures, so the trip rate from rf breakdown needs to be very small to not impact accelerator availability and emerged therefore to a figure of merit for their performance. Also, the transverse fields generated during breakdown will deflect the beam so there concern as to the magnitude of the kicks (e.g., do they cause beam loss).

As for availability, the NLC/GLC design assumes that after breakdown in any structure in an rf unit (which contains 8 structures), the unit would be shut off for 10 seconds. During this time, another unit from a 2% pool of spares (overhead) would be turned on so there would be a reduction in beam energy for a single rf pulse only.

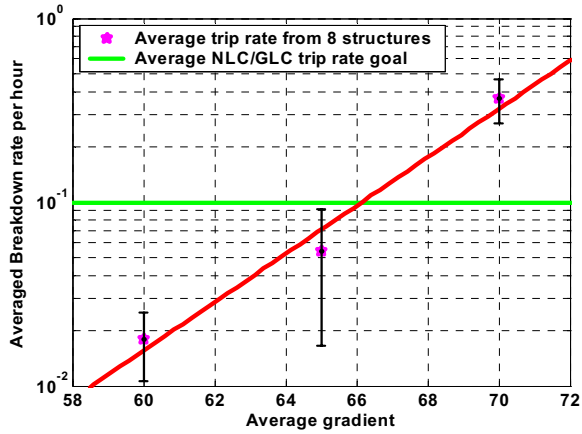

Figure 2: Average breakdown rate for 8 NLC structures as a function of average gradient.

Measurements of the beam kicks show them to be large enough to cause some luminosity loss from off-center beam collisions, but not large enough to cause the beams to hit the collimators. These considerations have lead to the adoption of a breakdown rate limit of 1 in 10 hours per structure at the 60 Hz rate used for testing (the collider rate is 120 Hz). For NLC/GLC operation, this would ensure that the pool of spares would rarely be depleted (once a year) and the luminosity loss from beam deflections would be well below 1%.

To achieve this very low trip rate at the design gradient of 65 MV/m required several years of structure development by the NLC/GLC groups. The breakdown rates obtained this year in an ensemble of 8 structures tested together in NLCTA is shown in figure 2. The breakdown rate is an exponential function of the average gradient. The slope of the fitted curve is one decade in breakdown rate for 7 MV/m of average gradient independent of pulse length. The breakdown probability also grows exponentially with pulse length at a fixed gradient [5]. The observed spread in performance is most likely reflecting the variability in the current structure production. More rigorous quality control and monitoring should improve the reproducibility.

Tests done in NLCTA indicate that most of the breakdowns are single events and the field recovers for the following pulse. Therefore it may be not necessary to shut off the rf unit in case of a single breakdown. The ensemble of 8 structures has been operated for about 1600 hours at the design gradient of 65 MV/m. A very encouraging observation during this period was that the breakdown rates steadily decreased (see figure 3). The reduction is compatible with a 1/sqrt(t) behavior. This is similar to the outgassing rate dependence in a diffusion limited vacuum system, which makes one wonder if the two phenomena are related (although other time dependencies fit the statistics-limited rate data just as well). Similar trends in the breakdown rate dependence on operation time have been observed in the proton linac at FNAL [6].

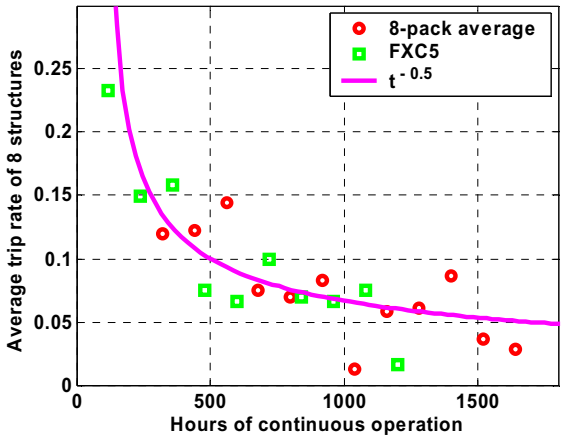

Figure 3: Long term operation of multiple NLC accelerating structures at 65 MV/m and 400 ns. The reduction of the breakdown rate with time is shown.

PULSE LENGTH DEPENDENCE

The dependence of the maximum gradient in a high frequency accelerator on the rf pulse duration is shown in figure 4 for NLC X-band structures. The presented data follows a $G \sim t_p^{-1/6}$ dependence. The upper data points represent the onset of saturation in the processing curve and correspond to a breakdown rate of a few tens per hour while the two lower data points have a breakdown rate of 0.1/h. It is interesting to note that a 30 GHz copper cavity at CERN measured at 16 ns matches the trend in terms of surface field (see figure 6) [7]. The observed dependence on pulse length is predicted by a plasma spot multiplication model [8] and has been observed experimentally for vacuum surface flashovers involving a dielectric insulator [9]. Pulse length dependences following a $G \sim t_p^{-1/4}$ law have been reported by other experiments and suggest that pulsed heating may determine this dependence [10]. The breakdowns in the X-band structures occur fairly uniformly during the pulse, which is true even immediately after the pulse length is increased. The dependence of the achievable gradient as a function of pulse length might well be the most restricting limitation for high frequency accelerators.

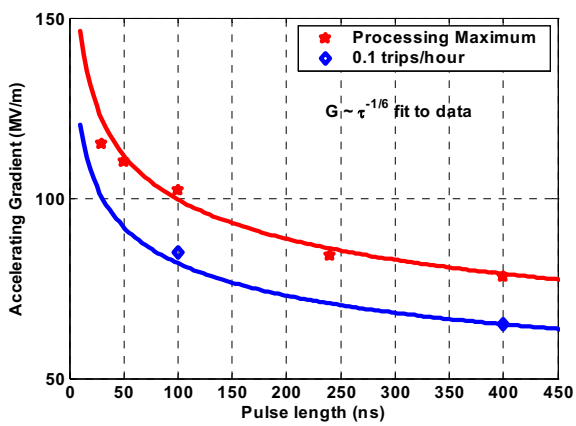

Figure 4: Pulse length dependence of the achievable gradient in X-band structures.

FREQUENCY DEPENDENCE

At frequencies below S-band one finds the empirically well established square-root frequency dependence of the attainable surface field. This dependence first established by Kilpatrick could be explained by rest gas ions being accelerated and bombarding the cavity wall, although the field limits predicted have been largely exceeded [11]. Until about five years ago, it was believed that this trend continued at higher frequencies where there were few measurements for comparison. Newer experiments however suggest that the increase in gradient with frequency is much weaker in this regime. A frequency scaling experiment conducted at CERN using single cells between 20 and 40 GHz did not see an increase of the attainable surface field in this frequency range [3]. The same limiting surface fields were found for copper cavities at 30 GHz by the CLIC study and by the NLC group at 11 GHz.

Currently there is no model of the limiting mechanism describing the available. Figure 5 shows data from copper cavities in a frequency range between 3 and 40 GHz obtained by various groups (KEK [12], SLAC [5, 10], MIT [13], and CERN [3, 7]). Two eye-guiding curves have been added to suggest certain trends in an otherwise confusing data landscape. The straight line at 350 MV/m is meant to indicate the ultimate limit in copper that is determined by breakdown-related damage. Surface fields this high can be obtained over the entire frequency range using low power cavities and brut-force processing. Subsequent autopsies of these cavities however revealed serious erosion and melting on the high field surfaces. Practical structures on the other hand group around the second curve ($G \sim f^{1/4}$), which follows from the observed pulse length dependence on gradient ($G \sim t_p^{-1/6}$) for a fixed breakdown rate, and structure fill time dependence on frequency ($t_p \sim f^{-3/2}$) assuming the 'natural' pulse length scales with the fill time. Thus the data appear to be bounded by material limits and pulse length dependent effects.

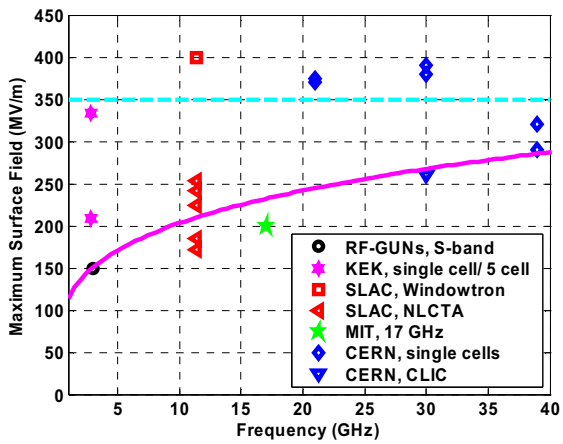

Figure 5: Maximum surface field as a function of frequency. The data points are measured at different pulse lengths (see further explanation in text).

CHOICE OF MATERIALS

Copper is the most common material choice for high voltage applications due to its superior conductivity. However many applications suffer from erosion due to local melting during breakdown events. This shortcoming has prompted the high voltage switch industry, for example, to look at alternative materials to enhance switch lifetime. Materials combining both a higher melting point and reasonable conductivity such as tungsten, molybdenum and their alloys with copper have been investigated and successfully implemented. The CLIC group likewise tried to use these materials to achieve higher gradients, and have had spectacular success [7]. As part of this program, three electrically identical 30 GHz constant impedance accelerating structures were built using copper, tungsten and molybdenum and tested in the CLIC Test Facility at the maximum available rf pulse length of 16 ns. The copper structure was built the traditional way, while for the other two structures, the irises were made out of the refractory metals and then clamped between copper disks to form the cells (hence the highest fields are only on the new materials). These structures were then mounted in a vacuum container for high power testing. The copper structure reached a surface field of 260 MV/m on the first iris while the tungsten and the molybdenum structure went up to 340 MV/m and 430 MV/m respectively. Post-mortem inspections of the irises revealed local melting and micro cracking therefore, indicating that these fields are close to the damage limits for these materials.

High power tests using X-band waveguides made out of copper, gold and stainless steel have been conducted at SLAC [14]. The results favor stainless steel over copper and gold with respect to the achievable surface fields. The measured surface fields ranging between 50 and 100 MV/m are not comparable with those obtained in X-band accelerating structures.

Inspired by the success of the 30 GHz experiments, the CLIC group built an X-band structure with molybdenum irises for testing at NLCTA, where longer pulse lengths are possible. The structure is a scaled version of the 30 GHz constant impedance structure discussed above. It was processed for more than 700 h and conditioned very slowly compared to NLC/GLC copper structures. Furthermore the structure did not exceed field values obtained for X-band copper structures. When the test ended due to time and program constraints, the gradient was still slowly increasing, which may mean higher gradients are still possible. More details about the experiment and the post analysis could be found in [15, 16]. The maximum surface fields achieved with different materials at various frequencies are plotted in figure 6 as a function of pulse length. It is remarkable that the copper results connect at short pulse length despite the different structure designs at different frequencies.

The molybdenum X-band structure shows the same pulse length dependence as the copper structures, but lower field levels. This contrasts with the 30 GHz results and DC spark experiments, which show molybdenum to be superior to copper in the field levels that can be achieved [17]. At pulse lengths of 30 ns and smaller, it should be noted that the molybdenum results were power limited. With only one test, it would be premature to drawn a definite conclusion as to the performance of molybdenum at X-band.

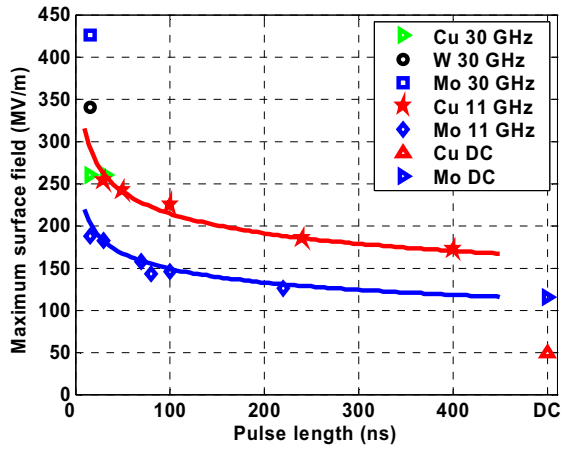

Figure 6: Pulse length dependence of the maximum surface field for different materials.

Material properties such as the melting point, yield strength, vapor pressure and vaporization energy seem to be important in determining gradient limits. Which parameter or combination of parameters is the most relevant is not yet understood and clearly more work has to be done to be able to use the full potential of alternative materials.

REMARKS ABOUT THEORY

Currently there is no consistent theoretical description of rf breakdown. The theory of explosive electron emission which was developed for DC breakdown is certainly also relevant for the rf case too, but it cannot describe all the aspects of the rf breakdown [18]. Field emission is most likely the starting point of rf breakdown. A long standing mystery in this regard is the field enhancement factors (β) in the Fowler-Nordheim theory of field emission. Without this enhancement the local surface fields are not high enough to generate the observed emission currents. The measured β-values should probably be considered as fudge-factors that account for multiple surface properties such as roughness, oxide layers, grain boundaries etc. During breakdown, local plasma has to be created and maintained to account for the amount of charge observed and the erosion. This plasma can consist out of copper ions from melting or vaporization processes and out of gas ions desorpted by particle bombardment or local heating. A plasma spot model has been developed which can predict pulse length, gradient and material dependencies [9]. An alternative to field emission as the trigger of breakdown is surface fracturing directly from the high surface field forces [19].

The surface magnetic field seems to play a role in the breakdown dynamics as well. Large surface currents can provide additional local heating that enhances field emission and subsequent melting. Also, the application of an external magnetic field may enhance damage by confining the breakdown induced plasma.

The potential damage to the surface from a breakdown should be related to the available energy therefore a limit for breakdown proportional to power and square-root of pulse length ($G \sim P\, t_p^{1/2}$) was suggested [20].

One of the most puzzling aspects of rf breakdown is its stochastic nature. That is, why is there breakdown in a particular pulse after millions of non-breakdown pulses? This must involve a yet unknown, low probability dynamical process.

CONCLUSIONS

The NLC/GLC collaboration has demonstrated that normal-conducting high-frequency accelerator technology is suitable for a large scale linear collider. An ensemble of eight accelerating structures has been operated reliable at the design gradient of 65 MV/m at 400 ns for more than 1500 hours with a breakdown rate below 0.1/h. In addition, experience from venting experiments and long term operation shows the structures to be rather robust and easy to maintain. These results are a major milestone in the quest for a next generation linear collider.

The results from various high gradient studies show there is little margin to increase the operating gradient in practical structures made of copper. Nevertheless, the choice of higher frequencies for the linear collider application still appears to be the right one due to the cost benefits of a more compact machine and the lower rf energy requirements.

Rf breakdown still lacks a complete understanding and therefore there might be still some room for optimizations and performance improvements. On the other hand the experimental data presented encircles a large fraction of the available parameter space for copper structures. One can almost predict the expected performance as a function of gradient, frequency and pulse length. Among those the pulse length dependence is probably the most limiting and the most interesting to understand better in the future.

The only hard physical limit seems to be the melting point of copper. Therefore the exploitation of alternative materials is very appealing but challenging at the same time. New fabrication methods have to be developed and material quality standards have to be defined. Yet it is not clear which material parameters are most relevant for better breakdown resistance. The first results obtained are very promising and might be therefore the right way towards gradients above 100 MV/m necessary for multi-TeV energies.

ACKNOWLEDGMENT

The data presented in this paper was obtained by the CLIC-study at CERN and by the NLC/GLC collaboration using the test and manufacturing facilities at KEK, FNAL and SLAC. Many thanks to all the colleagues which worked on these projects for their excellent work.

REFERENCES

[1] International Linear Collider, Technical Review Committee, Second Report 2003, SLAC-R-606.

[2] The CLIC Study-Team, 'A 3 TeV e+e- Linear Collider based on CLIC Technology', edited by G. Guignard, CERN Report No. 2000-008, 2000.

[3] H.H. Braun, S. Döbert, I. Wilson, W. Wuensch, Phys. Rev. Letters, 90, 224801 (2003)

[4] T. Arkan et al.,'Fabrication of X-band Accelerating Structures at FERMILAB', Proc. 9th EPAC, Lucerne, Switzerland, (2004)

[5] C. Adolphsen, 'Normal-Conducting rf Structure Test Facilities and Results', Proc. Particle Accelerator Conference 2003, Portland; Oregon, USA (2003), 668

[6] E. McCory, T. Kroc, A. Moretti, M. Popovic, 'Continued Monitoring of the Conditioning of the Fermilab Linac 805 MHz cavities', Proc. XX International Linac Conference, Monterrey, USA, (2000)

[7] W. Wuensch, C. Achard, H.H. Braun, S. Döbert, I. Syratchev, M. Taborelli, I. Wilson, 'A Demonstration of High-Gradient Acceleration', Proc. Particle Accelerator Conference 2003, Portland; Oregon, USA (2003), 495

[8] P.B. Wilson, 'RF Breakdown in Accelerator Structures: From Plasma Spots to Surface Melting', this proceeding

[9] W.A. Stygar, 'Flashover of a vacuum-insulator interface: A statistical model', Phys. Rev. ST-Accelerators and Beams, Vol.7, 070401 (2004)

[10] L. Laurent, 'High Gradient rf Breakdown Studies', Ph.D. Dissertation, UC Davis, 2002

[11] W.D. Kilpatrick, Rev. Sci. Instr. 28, 824 (1957)

[12] H. Matsumoto, 'Dark Currents', Proc. XVIII LINAC, Geneva (1996) 626

[13] W.J. Brown et al, 'Low emittance electron beam formation with a 17 GHz rf gun', Phys. Rev. ST-Accelerators and Beams, Vol.4, 083501 (2001)

[14] V. Dolgashev, S. Tantawi, 'RF Breakdown in X-band waveguides', Proc. 8th EPAC, Paris, France, (2002)

[15] W. Wuensch et al. 'A high-power test of an X-band molybdenum-iris structure', this proceeding .

[16] S. Döbert et al.,'High gradient test of a molybdenum iris clamped X-band accelerating structure at NLCTA', SLAC-PUB-10551

[17] T. Nakanishi,'A Molybdenum-Titanium Paired Electrode Used for a High Gradient DC Gun to Minimize Field Emission Dark Currents', this proceeding

[18] G.A. Mesyats, 'Explosive Electron Emission', URO-Press, Ekaterinburg, 1998

[19] J. Norem, Z. Insepov, 'Triggers for rf breakdown', Proc. 9th EPAC, Lucerne, Switzerland, (2004)

[20] V. Dolgashev, private communication

STATE OF THE ART SRF CAVITY PERFORMANCE

Lutz Lilje#, DESY, Hamburg. Germany

Abstract

The paper will review superconducting RF cavity performance for β=1 cavities used in both linear and circular accelerators. These superconducting cavities are used in two kinds of applications: High current storage rings and efficient high duty cycle linacs. In recent years the performance of those cavities has been improving steadily. High accelerating gradients have been achieved using advanced surface preparation techniques like electropolishing and surface cleaning methods like high pressure water rinsing. High intensity beams can be handled with advanced higher-order-mode damping schemes.

INTRODUCTION

Superconducting radiofrequency (SRF) cavities are used for several applications. All species of particles are accelerated using SRF for several reasons:

- Surface resistance at microwave frequencies is a few nOhm (10^6 times smaller than for normal conductors)
- High efficiency for transforming wall-plug to beam power
- Continuous-wave operation
- Low frequencies
  - Large aperture
  - Large acceptance
  - Smaller wakefields
- Potential for energy recovery operation
- High accelerating gradients

This paper will describe the state-of-the-art for cavities used for electron acceleration (β=v/c=1). Electron accelerators are used for elementary particle physics (storage rings, linear collider) or light sources (storage rings, linacs).

SUPERCONDUCTING CAVITY TECHNOLOGY

For superconducting cavities at very high electrical and magnetical surface field great care has to be taken during manufacturing and preparation for beam acceleration. Normalconducting inclusions in the material and contaminations on the surface need to be avoided. For example, the preparation and assembly in in clean rooms and ultrapure water supplies for rinsing the surfaces are a must. In this paper the focus will be on the surface preparation with electrochemical methods before the final high pressure rinsing.

Material Quality

The niobium bulk material used for cavity fabrication needs to have good thermal conductivity as the heat produced on the inner side of the cavity needs to be conducted to the coolant (liquid helium) on the outside. The thermal conductivity is usually not quoted as the figure of merit but the RRR (residual-resistivity ratio) value. Typical RRR values in the cavities described in this paper is around 200-300 and 500-600 for cavities subjected to a postpurification using a furnace treatment at 1300°C with a titanium getter layer.

As an example of quality control for the niobium sheet material an eddy-current scanning system which currently is used for SNS (build by company based on a design by Bundesanstalt für Materialforschung and DESY) is shown in figure 1. A similar system is in use for the TESLA cavities [1,2]. The eddy-current system also allows to certain degree to determine the type of inclusion. Any niobium sheet showing defects is rejected from the cavity manufacturing process. The rejection rate is about 5 %. Most of the rejected sheets will be recoverable by applying some chemical etching. The iron inclusions were caused by mechanical wear of the rolls used for sheet rolling. In the meantime new rolls have been installed. The eddy-current check has turned out to be an important quality control not only for the cavity manufacturer but also for the supplier of the niobium sheets.

Figure 1: Setup for quality control of niobium sheet material for SNS.

Surface Treatment

The niobium sheets are deep drawn and electron beam welded to fabricate a cavity. A damage layer of about 100 μm thickness is removed from the inner surface to obtain optimum performance in the superconducting state. Often cavities have been chemically etched [2,3]. Niobium metal has a natural Nb_2O_5 layer with a thickness of about 5 nm which is chemically rather inert and can be dissolved only with hydrofluoric acid (HF). Chemical etching of niobium consists of two alternating processes: dissolution of the Nb_2O_5 layer by HF and re-oxidation of the niobium by a strongly oxidizing acid such as nitric acid (HNO_3) [4,5]. To reduce the etching speed a buffer substance is added, for example phosphoric acid H_3PO_4 (concentration of 85%) [6], and the mixture is cooled

#lutz.lilje@desy.de

below 15°C. The standard procedure with a removal rate of about 1 µm per minute is called buffered chemical polishing (BCP) with an acid mixture containing 1 part HF, 1 part HNO_3 and 2 parts H_3PO_4 in volume.

An alternative surface preparation method to etching is electrolytic polishing (EP). The material is removed in an acid mixture under the flow of an electric current. Sharp edges or tips are smoothed out and a very glossy surface can be obtained. This is an essential difference to the BCP process which tends to enhance the steps at grain boundaries (see micrographs in Fig. 2). Using electrolytic polishing, scientists at the KEK laboratory in Tsukuba (Japan) achieved gradients of up to 40 MV/m in single-cell cavities [7].

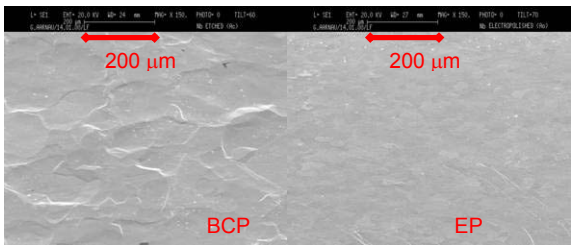

Figure 2: SEM surface picture of etched (BCP=Buffered Chemical Polish) and electropolished surface.

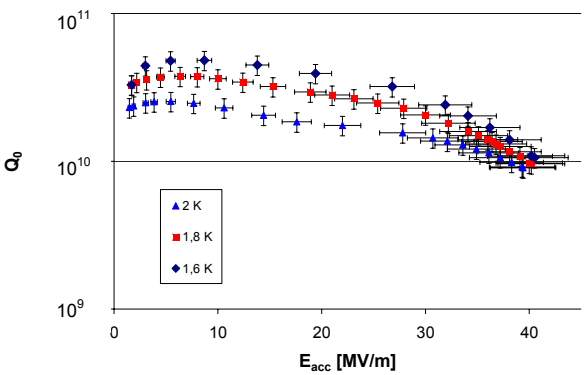

Figure 3: Performance of a TESLA cavity after EP at DESY. A gradient of 40 MV/m was achieved in the low power continuous wave measurement.

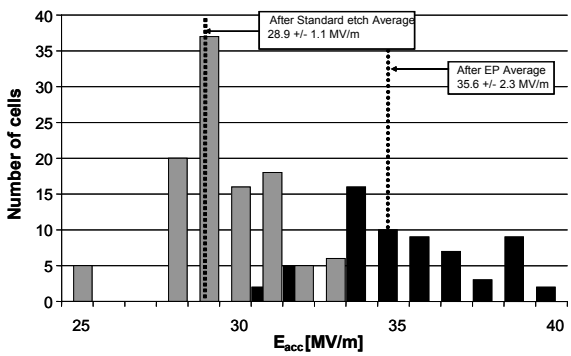

Figure 4: Comparison of the achieved gradients in the individual cells of several nine-cell cavities after standard etching (grey) and after electropolishing (black).

The EP technique has been successfully transferred to nine-cell cavities within a joint KEK-DESY R&D program [8]. Cavities were sent to KEK/Nomura Plating after furnace treatment at DESY (5 cavities treated 800°C, 4 cavities at 1400°C) where electropolishing and first high pressure rinsing were carried out. Final assembly, final high pressure rinsing and bakeout at 120°C were carried out at DESY.

For an energy upgrade of TESLA to center-of-mass energy of 800 GeV (TESLA-800) a gradient of 35 MV/m at a Q_0 of 5×10^9 is needed. Out of the 9 cavities from the last production series of TTF cavities four cavities achieved this specification and six cavities more than 30 MV/m. Two cavities were strongly loaded with field emission. One of these cavities has been electropolished for the second time in the EP facility at DESY. The test results of this cavity at helium temperatures between 1.6 and 2.0 K are shown in figure 3. Accelerating fields of up to 40 MV/m have been reached which is a record for multi-cell niobium cavities.

The clear advantage of electropolishing can be seen in figure 4. The single cell statistics derived from the coupled mode measurements are compared for chemically etched and electropolished nine-cell cavities. The average maximum gradient is 28.9 MV/m for BCP-treated cavities and 35.6 MV/m for EP-treated cavities.

Additionally high power tests have been performed on electropolished cavities: Several measurements at nominal pulse length (500 µs, filling time, 800µs flat-top) at a repetition rate of 1-10 Hz confirmed the very good performance of the cavities in the vertical test (figure 5). The quality factor of larger than 7×10^9 at a gradient of 35MV/m is larger than required for TESLA-800 in all cases. One cavity achieved a gradient of 37 MV/m at a Q_0 of 1×10^{10}. Warm-ups of the cavity to 300 K and 150 K respectively did not change the cavity behaviour in any case.

In a long term test of more than 1100 hours at 35 MV/m there was no sign of performance degradation. Thermal breakdowns (quenches) of the cavity induced during the setup of the LLRF (Low-level RF system) were not influencing the quality factor. This is a well-known behaviour for superconducting cavities. Breakdowns in the coupler also caused during setup of the Low Level RF system were not detrimental to the coupler performance.

Another cavity was installed into an accelerator module for TTF. The final preparation and assembly (e.g. cavity-to-cavity connection) for the module did not change the performance of the cavity. At a gradient of 35 MV/m the cavity has been measured with a quality factor of 9×10^9 which is far above the specification for TESLA-800. The RF gradient calibration was crosschecked using an energy gain measurement of the electron beam.

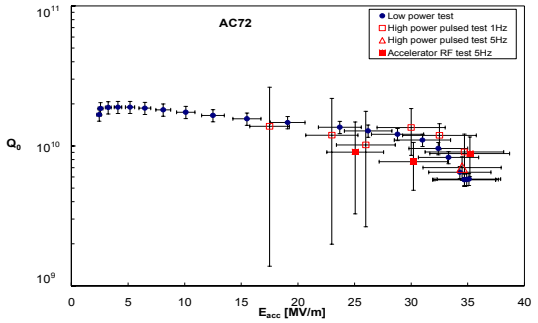

Figure 5: High power test of an electropolished TESLA nine-cell in the TTF linac. 35 MV/m were achieved with a quality factor of 9×10^9.

Pulsed Operation of Cryomodules

The performance of full TESLA accelerator modules in use today demonstrates that the gradient achieved in the low-power acceptance tests can be used in the accelerator. (figure 6)[9]. This is a sign that the final assembly steps are well enough defined for reproducible results. The most recent module assembled with has an accelerating gradient of more than 25 MV/m limited by the last cavity. Some cavities show gradients of 30 MV/m which seems near the maximum which is achievable using post-purified (RRR~500), etched cavities. The results of the acceptance test are also shown in figure 6.

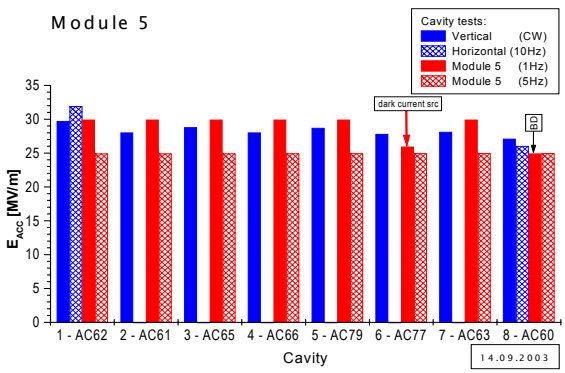

Figure 6: Performance of a TESLA accelerating module assembled with etched cavities. The maximum gradient achieved in the module is compared to the gradient achieved in the acceptance test[9].

CW Operation of Cryomodules

CW operation is typically limited to gradients around 15 MV/m for economical reasons. JLab has build a module for the infrared FEL which can deliver more than 15 MV/m in seven out of eight cavities [10]. The module is also build from etched cavities. The cavities have not been subjected to a post-purification treatment like the TESLA cavities in TTF. The single cavity test yields a higher gradient than the operational gradient as the beam energy requested by the FEL users was lower. At the lower energy no trip of the system was observed for several weeks.

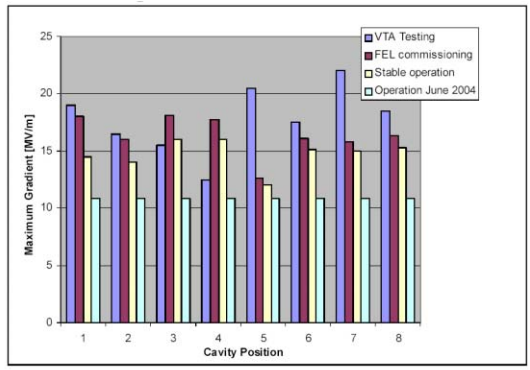

Figure 7: Performance of the IR-FEL module build at JLab[10].

CAVITY DESIGN

With the accelerating gradient approaching the theoretical limit and fabrication technology in hand the new challenges for SRF cavities are increasing the beam current further thus introducing many new ideas about cavity shapes and HOM damping. This will be illustrated using three examples: The superstructure concept, the CEBAF upgrade cavity shapes and the HOM damping concepts for the Cornell ERL prototype.

Superstructure Concept

In striving for highest collider energies not only the gradient in the cavities but also the active acceleration length have to be maximized. There are, however, two effects which limit the number of cells N_c per resonator. With increasing N_c it becomes more and more difficult to tune the resonator for equal field amplitude in every cell: the sensitivity of the field homogeneity to small perturbations grows with N_c^2. Secondly, in a very long multicell cavity 'trapped modes' may be excited by the short particle bunches. These are coupled oscillations at high frequency which are confined to the inner cells and have such a low amplitude in the beam pipe sections that they cannot be extracted by the higher-order mode (HOM) couplers mounted the beam pipe. Trapped modes may have a detrimental influence on the beam emittance and must be avoided. The number $N_c = 9$ chosen for TESLA appears a reasonable upper limit.

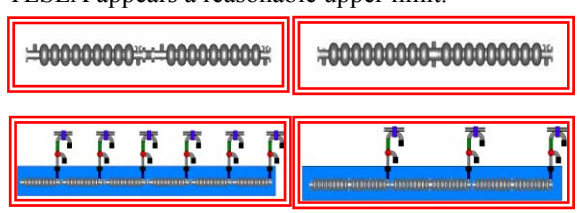

Figure 8: Comparison of the standard TESLA layout (left) with the superstructure layout (right).

The limitation in the number of cells can be overcome by the *superstructure* concept proposed by J. Sekutowicz [11]. Several multicell cavities are joined by beam tubes of length $\lambda/2$ ($\lambda = 230$ mm is the wavelength of the accelerating mode). Within each cavity there is an rf

phase advance of π from cell to cell, while the phase advance between adjacent multicell units is zero. This ensures that the particles experience the same accelerating field in all cells of the superstructure. The superstructure is supplied with rf power by a single input coupler at one end. The interconnecting pipes have a sufficiently large diameter to permit the flow of rf power from one cavity to the next.

For the TESLA electron and positron linacs a superstructure consisting of two 9-cell cavities is envisaged [1], see figure 8. Compared to the layout with separated 9-cell cavities, this superstructure improves the filling factor by 6 % and saves a factor of two in input couplers and waveguide components.

The coupling between two adjacent cavities in a superstructure is about two orders of magnitude smaller than the cell-to-cell coupling within each subunit. To demonstrate that this small coupling is compatible with the requirement of a low beam energy spread a proof-of-principle experiment of two 2x7-cell superstructures was carried out at the TTF linac [12]. The rf power flow through the interconnecting pipe was found to be sufficient to replenish the stored energy in each cell between successive electron bunches. The measured bunch-to-bunch energy fluctuation was within the TESLA specification of $\Delta E/E$ (rms) $\leq 5 \cdot 10^{-4}$ (see figure 9). Besides this, it was confirmed that a field homogeneity of better than 90% could be achieved in the superstructure. The excitation of beam-induced higher-order-modes was thoroughly studied and sufficient damping was verified.

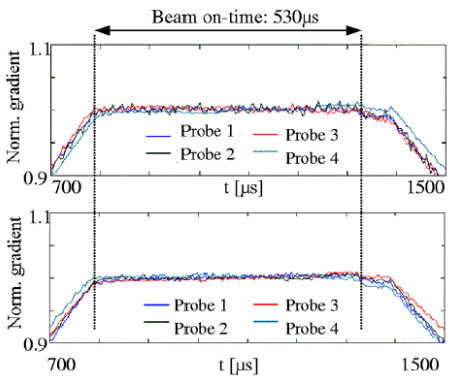

Figure 9: Measured: $\Delta E/E$ (rms) $\leq 2 \cdot 10^{-4}$ in the prototype superstructure .The TESLA-Specification is $\Delta E/E$ (rms) $\leq 5 \cdot 10^{-4}$.

Besides this, it was confirmed that a field homogeneity of better than 90% could be achieved in the superstructure. The excitation of beam-induced higher-order-modes was thoroughly studied and sufficient damping was verified (figure 10).

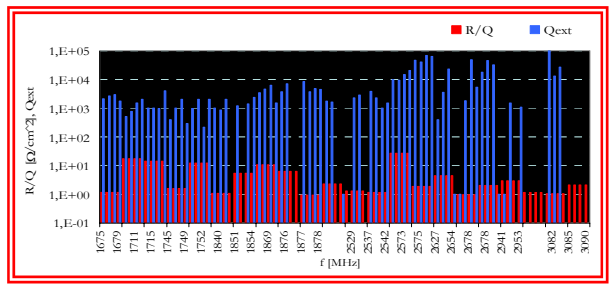

Figure 10: The damping of dipoles with (R/Q) ≥ 1 Ω/cm2 which are relevant for the TESLA beam was by factor 5 to 100 better then the specification.

CEBAF Upgrade Cavity Shape

For the CEBAF upgrade two new cavity shapes have been proposed (figure 11) [13]. One is optimized for high-gradient operation (HG) which features a lower E_{surf} to reduce field emission. The second shape is called low-loss (LL) and maximizes the shunt impedance and geometric factor to achieve the maximum gradient with a given cryo power (see table 1).

Tests on single cell cavities demonstrated that the shapes are multipacting-free. One cavity of the low-loss variety achieved an electric peak surface field of 87 MV/m (figure 12). Seven-cells have achieved 20 MV/m in first tests.

The HOM damping of niobium prototypes confirms calculations and copper model measurements. For the final application improved feedthroughs with better thermal design are under fabrication.

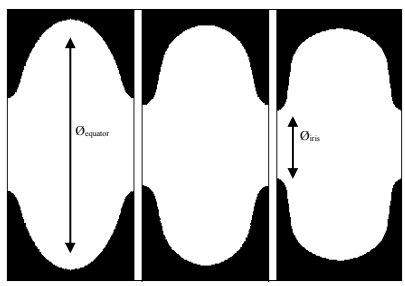

Figure 11: Geometrical shapes for the CEBAF upgrade cavities[13].

Table 1: Parameters for the cavity shapes for the CEBAF upgrade cavities

Parameter		OC	HG	LL
$Ø_{equator}$	[mm]	187.0	180.5	174.0
$Ø_{iris}$	[mm]	70.0	61.4	53.0
k_{cc}*	[%]	3.29	1.72	1.49
E_{peak}/E_{acc}	[-]	2.56	1.89	2.17
B_{peak}/E_{acc}	[mT/(MV/m)]	4.56	4.26	3.74
R/Q	[Ω]	96.5	111.9	128.8
G	[Ω]	273.8	265.5	280.3
R/Q·G	[Ω·Ω]	26422	29709	36103

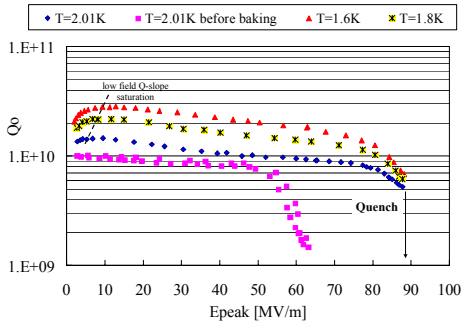

Figure 12: Test of a single cell of the low-loss shape. Very high electric surface field could be reached.

HOM Damping of the Cornell ERL Prototype Injector Cavities

Cornell University, in collaboration with JLab is exploring a 100 MeV CW prototype ERL with a beam current of 100 mA to study the energy recovery concept with high current, low emittance beams [14]. A key element of this machine is a high brightness injector with every bunch filled.

The injector system needs to deliver 150 kW per cavity to the beam through the input couplers. More than a hundred watts per cavity of beam induced power must be removed through HOM couplers. Power delivery and extraction must be accomplished without introducing an asymmetry that can lead to emittance dilution. This is done using two input couplers and HOM broadband absorbers in a region with enlarged beam tube which allows propagating of all HOMs. Figure 13 illustrates the injector cavities.

.

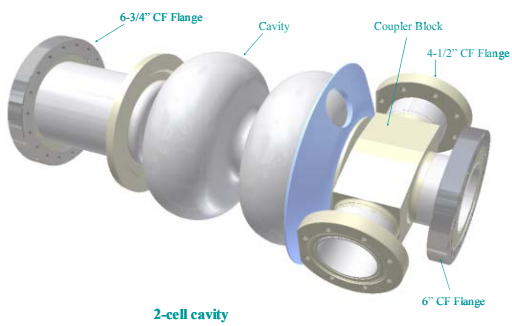

Figure 13: Two-cell injector cavity for the Cornell ERL prototype.

CONCLUSION

SRF cavities approach the physical limit in terms of maximum magnetic peak field. For electropolished cavities of the TESLA-type accelerating gradients of more than 35 MV/m have been achieved in multi-cell cavities in low and high power test. A test in the TTF accelerator shows that the means of assembling such high gradient cavities are at hand principally. Continuous wave operation of full cryomodules near the economically reasonable gradient of about 15 MV/m has been achieved at JLab. New cavity concepts like superstructures and heavily HOM damped structures are being explored thus opening up a new regime of increased beam currents suitable for a variety of accelerator projects.

ACKNOWLEDGEMENT

The author would like to thank the colleagues from the TESLA collaboration for providing data and support. The material provided by P. Kneisel, J. Sekutowicz, G. Hoffstätter, M Kelly, H. Padamsee is gratefully acknowledged.

REFERENCES

[1] R. Brinkmann, et al. (editors), *TESLA - Technical Design Report*, volume II. DESY, March 2001. ECFA 2001-209, TESLA Report 2001-23.

[2] B. Aune et al. The Superconducting TESLA Cavities. *Phys. Rev. ST-AB*, 3(9), September 2000. 092001.

[3] H. Padamsee and J. Knobloch and T. Hays, RF Superconductivity for Accelerators, John Wiley & Sons, 1998

[4] B. Hillenbrand, N. Krause, K. Schmitzke, and Y. Uzel. Abschlussbericht - Supraleitende Resonatoren. Technical Report NT 2024 7, Siemens AG, Dezember 1982. BMBF Forschungsbericht.

[5] Gmelin, *Handbuch der anorganischen Chemie*, volume 49 (Nb). Springer Verlag Berlin, 1970.

[6] J. Guerin, *Etude du bain de polissage chimique de niobium*, Technical Report TE/LC/157/89, CERN, October 1989.

[7] K. Saito et al. Superiority of Electropolishing over Chemical Polishing on High Gradients. In V. Palmieri, editor, *Proceedings of the 8th Workshop on RF Superconductivity*, volume I+II, pages 759 - 813, Abano terme, October 1997. INFN.

[8] L. Lilje, Peter Schmüser et al., Achievement of 35 MV/m in the Superconducting Nine-Cell Cavities for TESLA. Nucl. Inst. Meth. A 524 (1-3); 2004; pp. 1-12.

[9] D. Kostin, THP32, This conference.

[10] A.M. Valente, EPAC04

[11] J. Sekutowicz, M. Ferrario and Ch. Tang, Phys. Rev. ST Accel. Beams, vol. 2, No. 6 (1999)

[12] J. Sekutowicz et al., Phys.Rev. ST-AB, Vol. 7, 012002 (2004)

[13] P. Kneisel et. Al, MOP84, This conference.

[14] I. Bazarov, et al., "Phase I Energy Recovery Linac at Cornell University", Proceedings of the 8th European Particle Accelerator Conference, Paris, France, June 2002, pp. 644-646.

STATE OF THE ART IN RF CONTROL

S.N. Simrock, DESY

Abstract

Nowadays the designer of a new rf control system has access to a wealth of powerful digital, analog, and rf circuitry. The requirements for the rf control system have changed from only controlling the amplitude and phase of the accelerating field to the required degree to stability. Additional tasks include exception handling and extensive build-in diagnostics while pursuing issues related to reliability, operability, and maintainability. Also operation close to the performance limit must be supported while maximizing the availability of the accelerator. With many accelerator projects in planning or under construction several state-of-the art rf control designs have evolved. This paper will present an overview of this new technology and discuss its performance.

INTRODUCTION

The architecture of a typical RF control system is shown in Figure 2. A power amplifier provides the rf power necessary for establishing the accelerating fields in the cavities. The cavity field is measured and the compared to a setpoint. The resulting error signal is amplified and filtered and drives a controller for the incident wave to the cavity. A frequency and phase reference system provides the necessary rf signals. The requirements for the stability of the accelerating fields range from 1% in amplitude and 1 degree in phase for high power H^- accelerators to 0.01% in amplitude and 0.01 degree in phase for the critical sections such as compressors in XFELs. Since many of the present and near future accelerator based facilities are employing superconducting cavity technology this review will focus on rf control systems for sc-cavities. Accelerator projects making use of the present state of the art technology include SNS, J-PARC, CEBAF upgrade, RIA, the European X-FEL, the BESSY soft X-Ray Laser, the Cornell ERL, and many others. Descriptions of the design of the llrf system that have been developed recently for the various accelerator projects can be found in [1-21].

RF CONTROL SUBSYSTEMS

The subsystems shown in the architecture of the rf system in Figure 2 are shown in more detail in Figure 5. Most recent advances in technology have been achieved in the area of the digital controllers including high speed analog I/O and powerful signal processing, the area of field detection, frequency conversion and actuators for field control, fast piezoelectric and magnetostrictive cavity frequency tuners, low noise reference frequency oscillators and highly stable frequency distribution systems.

CAVITY FIELD DETECTION

The cavity field detection can be accomplished with traditional amplitude and phase detectors or with IQ detectors which operated directly at the rf operation frequency or at an intermediate IF frequency which contains the amplitude and phase information. Another possibility if the a scheme employing digital IQ detection where the IF (or the RF signal) is sampled directly by an ADC which usually samples alternating the real and imaginary components of the cavity. This of course requires correct timing of the data acquisition.

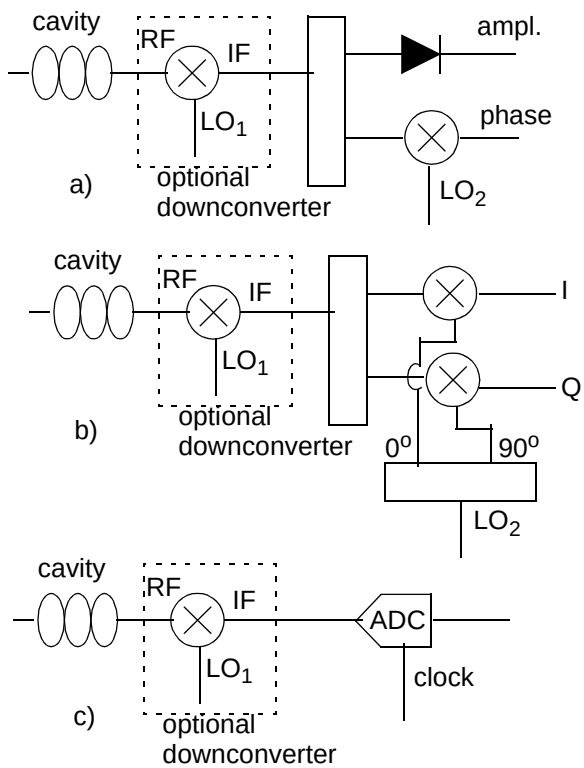

Figure 1: Field detection schemes. a) amplitude and phase detection, b) IQ detection, c) digital IQ detection.

With the rapid development of the telecommunication market industry had developed a variety of single chip solutions for amplitude detection, phase detection, and IQ detection based on analog multipliers. Examples are:

- AD8343 analog multiplier
- RF2411 analog multiplier
- AD8361 linear video detector (temperature stabilized)
- AD8302 logarithmic video detector and phase detector
- HMC 439 digital phase detector

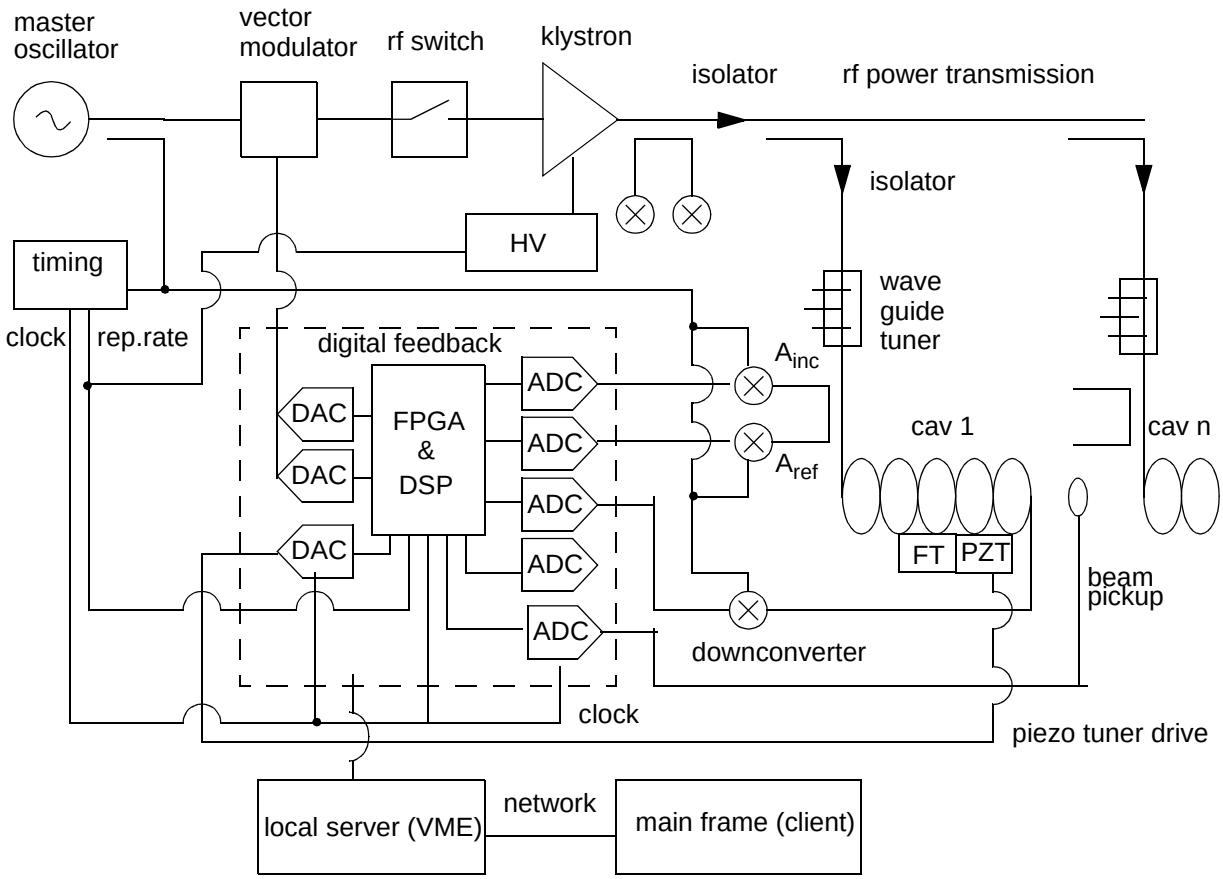

Figure 2: Typical configuration of an RF control system using digital feedback control.

• AD8347 IQ detector

The same circuits are also used to detect the incident wave and reflected wave vectors usually described as forward and reflected power. Examples of the excellent performance of these detectors are shown in Figure 3. The

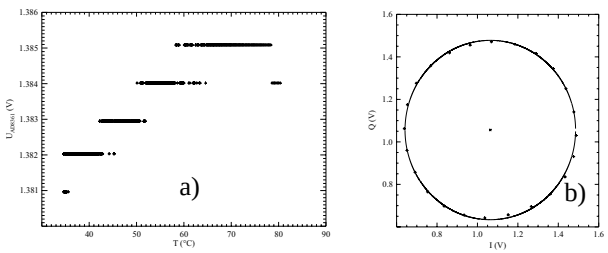

Figure 3: a) Temperature stability of the amplitude detector AD861 and b) linearity of IQ detector AD8347.

ACTUATORS FOR FIELD CONTROL

Similar circuits as used for field detection are also used for the control of the incident wave. Since analog multipliers can be also used for control of the amplitude of an rf wave they can be used in upconverters and for amplitude control. The digital downconversion scheme can also be used in an upconversion mode where the frequency f_1 (discrete samples) written to the DAC which is clocked at f_2 generates a sideband (among many others) of f_1+f_2 which contains the control vector and is filtered and upconverted to the operating frequency of the cavity. Examples for vector modulators are:

• RF 2480

• AD8346

• HMC 495 and 497

The linearity of a vector modulator is shown in Figure 4.

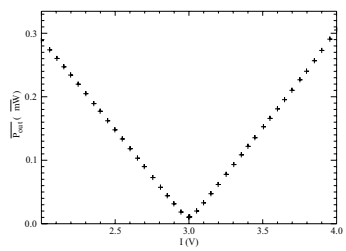

Figure 4: Linearity of the vector modulator RF 2480.

DIGITAL RF CONTROL

The key elements of a digital feedback system are the ADCs for the measurement of the detector signals for the cavity field and forward and reflected power, the DACs

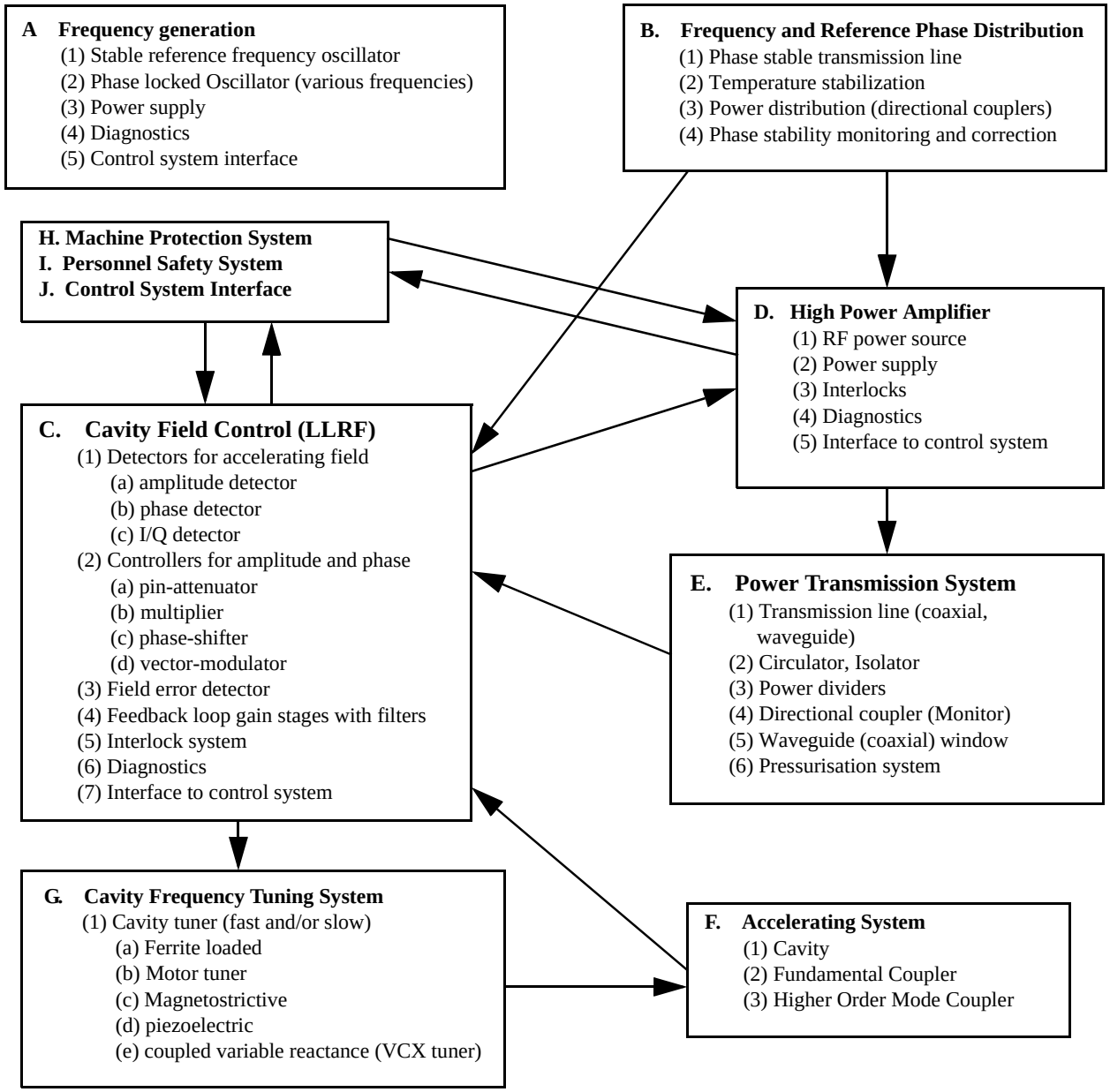

Figure 5: Breakdown of RF Control Subsystems and some choices for implementation.

which drive the actuators for field control, and the signal processing unit(s). The signal processing is performed by powerful FPGAs and DSPs allow low latencies from ADCs clock to DAC output ranging from a few 100ns to several μs depending on the chosen processor and the complexity of the algorithms. Gigabit Links the high data rates between a large number of analog IO channels and the digital processor as well as for communication between various signal processing units. Typical parameters for the ADCs and DACs are a sample rate of 65-125 MHz at 14 bit resolution (example AD6644). For the signal processing one has the choice of FPGAs with several million gates, including many fast multipliers cores and even with power PCs on the same chip such as Virtex2Pro from Xilinx or the Stratix GX from Altera. More complex algorithm are implemented on slower floating point DSPs such as the C6701 from Texas Instruments or the Sharc from Analog Devices. Typical configurations of the digital feedback hardware can are documented in [1-21].

ALGORITHMS AND PROCEDURES

The algorithms and procedures implemented in the digital feedback system should support automated operation with minimal operator intervention. A list of possible algorithms is shown figure 6. The feedback algorithms should be optimized for best field stability (i.e. lowest possible rms amplitude and phase errors) while being robust against parameter variations, allow for fast trip recovery, and support exceptional handling routines. Beam based

A. FIELD CONTROL ALGORITHMS
- (1) Feedback
  - (a) PID filter
  - (b) Kalman filter
  - (c) adaptive filters
  - (c) Smith predictor
  - (d) optimal controller
- (2) Feedforward
  - (a) beam loading compensation
  - (b) beam energy feedback
  - (c) bunch length feedback
- (3) Klystron linearization
- (4) Exception handling
  - (a) quench detection and handling

B. LLRF System Measurement Algorithms
- (1) Loop phase rotation matrix
- (2) Field calibration rotation matrix
  - (based on rf, beam based transients, and spectrometer)
  - (a) gradient calibration
  - (b) phase calibration
- (3) Vector-sum calculation
- (4) Measurement of incident phase (vector-sum !)
- (5) Beam phase measurement
- (6) forward/reflected power calibratio
  - (a) correct for directivity of couplers
- (7) Cavity detuning
  - (a) average during pulse
  - (b) detuning curve during pulse
- (8) Loaded Q

C. Cavity Resonance Control
- (1) Slow tuner
  - (a) maintain average resonance frequency
  - (b) maximize tuner lifetime
- (2) Fast tuner (ex. piezoelectric tuner)
  - (a) dynamic Lorentz force compensation
  - (b) microphonics control
  - (c) minimize rf power required for control

D. High level procedures
- (1) Adaptive feedforward
  - (a) response matrix based
  - (b) transferfunction based
  - (c) robust
  - (d) different beam modes
- (1) System identification
  - (a) beam phase and current
  - (b) loaded Q
  - (c) incident phase
- (3) Waveguide tuner control
- (4) Momentum management system
- (5) Field control parameters optimization
- (6) Operation at different gradients
- (7) Operation at the performance limit
  - (a) maximize availability
  - (b) maximize field stability
- (8) Hardware diagnostics
- (9) On-line rf system modelling

E. Miscellaneous
- (1) RF System Database
  - (a) calibration coefficients
  - (b) subsystem characteristics
- (2) Alarm and warning generation
- (3) Automated fault recovery
- (4) Finite state machine

Figure 6: Algorithms and procedures required for an automated digital feedback system.

feedforward will further enhance the field stability. Also important is the automated control of the resonance frequency of the cavities with slow motor controlled tuners and fast piezo actuator based tuners for Lorentz force compensation in pulsed rf systems.

REFERENCE FREQUENCY SYSTEM

With the increasing demands on the emittance and bunch length of the electron bunches for linear colliders and X-FELs the requirements for amplitude and phase stability of the accelerating fields have also become more stringent. Frequency distribution systems for linear colliders must provide a phase stability of better than 1 ps while X-FELs may require as much as 10 fs stability. This seems feasible with a combination of fiber laser oscillator and actively stabilized fiber optic distribution systems. This level of stability has been demonstrated successfully in the lab environment and is expected to be available in accelerator within the next 2 years.

SUMMARY

The rapid advances in digital technology allows the designer of an rf control system to employ real time digital feedback control with latencies in the range of a few hundred ns to a few μs at sampling frequencies of up to 100 MHz at 14-bit resolution which is sufficient for regulation to the 1e-4 level for amplitude and better than 0.1 deg. for phase. The powerful signal processing capability of FPGAs and DSPs support the implementation of complex algorithms which support a high degree of automation of operation. Recently a large number of detectors and actuators for amplitude, phase and in-phase and quadrature-phase (IQ) components, and up- and downconverters have been developed which simplify the design of the field

detectors drastically while guaranteeing low noise performance. These detectors are usually based on analog multiplies using Gilbert cell technology. In the area of low noise oscillators and highly phase stable rf reference frequency distribution system the application of laser oscillators and actively stabilized fiber distribution system it is expected that short and long term stabilities of the order of some 10 fs will be achieved in the next years.

REFERENCES

[1] S.N. Simrock, "Achieving Phase and Amplitude Stability in Pulsed Superconducting Cavities", Proceedings of the 2001 Particle Accelerator Conference, Chicago

[2] M. Liepe, S. Belomestnykh, J. Dobbins, R. Kaplan, C. Strohman, LEPP, Cornell, "A New Digital Control System for CESR-c and the Cornell ERL", Proceedings of the 2003 Particle Accelerator Conference, Portland

[3] A. Regan et al., "The SNS Linac RF Control System", Proceedings of the 2002 Linac Conference, Gyeongju, Korea

[4] M. Champion et al , "The Spallation Neutron Source Accelerator Low Level RF Control System", Proceedings of the 2003 Particle Accelerator Conference, Portland

[5] A. Regan et al., "Newly Designed Field Control Module for the SNS", Proceedings of the 2003 Particle Accelerator Conference, Portland

[6] L. Doolittle et al., "Operational Performance of the SNS LLRF Interim System", Proceedings of the 2003 Particle Accelerator Conference, Portland

[7] K. Fong et al., "RF Control System for ISAC II Superconducting Cavities", Proceedings of the 2003 Particle Accelerator Conference, Portland

[8] T. Plawski , T. Allison, J. Delayen, C. Hovater, T. Powers, , "Low Level RF System for Jefferson Lab Cryomodule Test Facility", Proceedings of the 2003 Particle Accelerator Conference, Portland

[9] S. Michizono et al., "Digital RF Control System for 400-MeV Proton Linac of JAERI/KEK Joint Project", Proceedings of the 2002 Linac Conference, Gyeongju, Korea

[10] A. Büchner, F. Gabriel, H. Langenhagen, "Noise Measurements at the RF System of the ELBE Superconducting Accelerator", Proceedings of the 2002 EPAC Conference, Paris, France

[11] T. Naito, K. Ebihara, M. Suetake, E. Ezura, "RF Reference Distribution Using Fibre-Optic Links for KEKB Accelerator", Proceedings of the 2001 Particle Accelerator Conference, Chicago

[12] C. Hovater et al., "RF System Development for The CEBAF Energy Upgrade", Proceedings of LINAC 2002, Gyeongju, Korea

[13] I. H. Yu et al., "The Low Level RF System for 100MV Proton Linac of KOMAC", Proceedings of the 2003 Particle Accelerator Conference, Portland

[14] R. Wilcox, L. Doolittle, J.W. Staples, "A Fiber Optic Synchronization System for LUX", Proceedings of the 2004 EPAC Conference, Lucerne, Switzerland

[15] A. Rohlev, J. Broere, R. Garoby, I. Kozsar, J. Serrano, "All Digital IQ Servo-system for CERN Linacs", Proceedings of the 2004 EPAC Conference, Lucerne, Switzerland

[16] M. Huening, P. Bauer, G.W. Foster, "Simulation of RF Control of a Superconducting Linac for Relativistic Particles", Proceedings of the 2004 EPAC Conference, Lucerne, Switzerland

[17] M. Laverty, S. Fang, K. Fong, "TRIUMF ISAC II RF Control System Design and Testing", Proceedings of the 2004 EPAC Conference, Lucerne, Switzerland

[18] D. Valuch, H. Frischholz, J. Tuckmantel, C. Weil, "First Results with a Fast Phase and Amplitude Modulator for High Power RF Application", Proceedings of the 2004 EPAC Conference, Lucerne, Switzerland

[19] J. Knobloch, A. Neumann, "RF Control of the Superconducting Linac for the BESSY FEL", Proceedings of the 2004 EPAC Conference, Lucerne, Switzerland

[20] S. Michizono et al., "Control of Low Level RF System for J-Parc Linac", Proceedings of the 2004 Linac Conference, Luebeck Germany

[21] J. Mourier et al., "Low Level RF Including a Sophisticated Phase Control System for CTF3", Proceedings of the 2004 Linac Conference, Luebeck Germany

STATE-OF-THE-ART ELECTRON BUNCH COMPRESSION

P. Piot *
Fermi National Accelerator Laboratory, Batavia, IL 60510, USA

Abstract

Many accelerator applications such as advanced accelerator R&D, free-electron laser drivers and linear colliders, require high peak current electron bunches. The bunch is generally shortened via magnetic compression. In the present paper we review various bunch compression schemes and discuss their limitations.

INTRODUCTION

There is a growing demand for generating and transporting very bright electron bunches. Applications range from linac-based light sources (both free-electron laser (FEL) and spontaneous emission-based), future linear colliders, to novel electron beam-driven acceleration schemes (e.g. plasma wake-field acceleration). The generation of bright electron bunches directly out of an electron sources is generally not an easy task. Instead it is preferred to create relatively low peak current bunches at the source. Beam manipulations are subsequently implemented in the downstream transport in order to obtain short electron bunches. Several proposed projects [1, 2] call for peak current in the multi-kiloamps regime resulting in bunch length of as low as $\sim$20μm (corresponding to a duration of $\sim$ 70 fs). The process of manipulating an electron beam so to enhance its peak current is called bunch compression. Many other schemes aimed to produce short bunches have been proposed, either with special design of electron source [4] or by selecting only one part of the bunch, e.g. via dispersive collimation or spoiling. These latter "selective" techniques are not addressed in the present paper and a review in the context of light source short radiation pulse production is given in Reference [3]).

MAGNETIC COMPRESSION SCHEMES

Principle

A magnetic bunch compressor, in its simplest form, consists of two elements: an energy "modulator" and a non-isochronous achromatic sections. The energy modulator provides a time-energy correlation (or chirp) along the bunch length, the non-isochronous section introduces an energy-dependent path length. Thus a proper tuning of the modulator parameters to impart the needed chirp along the bunch results in compression as the bunch propagates in the non- isochronous section.

* piot@fnal.gov

Let's first discuss the magnetic compression scheme by considering a single particle linear model. Consider an electron with longitudinal phase space coordinate (z_0, δ_0) w.r.t. the bunch center upstream of the energy modulator (δ denotes the fractional energy offset of the electron with respect to the bunch center). Downstream of the modulator, the longitudinal phase space coordinate, (z_m, δ_m), are

$$\begin{aligned} z_m &= z_0, \text{ (assuming } \gamma \gg 1) \\ \delta_m &= \frac{eV_{rf}}{\mathcal{E}_m}\left(\cos(kz_0+\varphi)-\cos\varphi\right) \doteq \kappa z_0 + \mathcal{O}(z^2) \end{aligned} \quad (1)$$

wherein e is the electron charge, V_{rf} and φ are the accelerating voltage and operating phase of the energy modulator section, k is the rf wavenumber ($k = 2\pi/\lambda_{rf}$, λ_{rf} being the rf-wavelength), and $\mathcal{E}_m \doteq \mathcal{E}_0 + eV_{rf}\cos(\varphi)$ ($\mathcal{E}_0$ being the initial electron energy). After passing through a non-isochronous section characterized by its first order momentum compaction, R_{56}, the electron coordinates are mapped, to first order, to the following:

$$z_c = z_0 + R_{56}\delta_m, \text{ and } \delta_c = \delta_m. \quad (2)$$

Thus the final electron position with the bunch, z_c, is related to the initial position, z_0, via $z_c = (1+\kappa R_{56})z_0$ which gives the longitudinal matching condition $\kappa = -1/R_{56}$ for minimizing the bunch length in a single stage magnetic compressor. The constant κ is the bunch chirp and can be tuned via V_{rf} and/or φ variable. If one consider rms quantities, the final rms bunch length downstream of the compressor is:

$$\sigma_{z,c} = \left((1+\kappa R_{56})^2\sigma_{z,0}^2 + (R_{56}\sigma_{\delta,0}\mathcal{E}_0/\mathcal{E}_m)^2\right)^{1/2}. \quad (3)$$

When the longitudinal matching condition is satisfied, we have $\sigma_{z,c} = R_{56}\sigma_{\delta,0}\mathcal{E}_0/\mathcal{E}_m$. Therefore compression at higher energy ($\mathcal{E}_m \to \infty$) would results in shorter minimum bunch length. The above linear theory holds under the condition (i.e. $k\sigma_z \ll 1$). In a real accelerator such a condition is not a fortiori satisfied: e.g. in a photo-injector it is common [5] to generate a long bunch length so to properly compensate transverse emittance growth. The bunch compression is then performed once this bunch has been accelerated to high enough energy to sufficiently damp space charge forces. As the bunch is accelerated in the structure, the longitudinal phase space accumulates some curvature due to the cos-like time dependence of the rf-field and the fractional energy spread downstream of the accelerating structure is expanded as $\delta_m = \kappa z_0 + \mu z_0^2 + \mathcal{O}(z_0^3)$ instead of Eq. 1. In turn the bunch compressor needs to be

treated to second order in energy (we consider the bunch as a line charge and ignore transverse effects for the sake of simplicity), and the electron longitudinal coordinate downstream of a bunch compressor now writes:

$$z_c = z_i + R_{56}\delta_m + T_{566}\delta_m^2, \quad (4)$$

wherein the constant T_{566} is the second order momentum compaction of the bunch compressor. Expression of momentum compactions (R_{56}, and T_{566}) for various bunch compressors can be found in Reference [6]. Similar to the linear case we can calculate the rms bunch length downstream of the compressor:

$$\begin{aligned}\sigma_{z,c}^2 &= (1+\kappa R_{56})^2\sigma_{z,0}^2 + \langle z^4\rangle(\mu R_{56}+\kappa^2 T_{566})^2 \\ &\quad +2\langle z^3\rangle(1+\kappa R_{56})(\mu R_{56}+\kappa^2 T_{566}) + \\ &\quad R_{56}\sigma_\delta^2 + T_{566}\langle\delta^4\rangle, \quad (5)\end{aligned}$$

wherein $\langle A^n\rangle$ is the n-th order centered moment of A. The minimum bunch length is no more achieved for the aforementioned "linear" matching condition. A way to correct for the second order aberration in Eq. 5 is either to (1) design a bunch compressor with the proper ratio R_{56}/T_{566} or (2) to include higher frequency accelerating section(s) in order to render the accelerating potential constant over the bunch length [7, 8]. The use of an higher harmonic rf-field provides an independent control of μ and κ parameters and it has been preferred in recent designs (e.g. [10]) because it does not introduce coupling between longitudinal and transverse phase spaces contrary to a bunch compressor designed to have the proper R_{56}/T_{566} ratio. This higher harmonic compensation scheme is integrated in the LCLS and TESLA X-ray FEL designs [9, 10]. The results of linearizing the longitudinal phase space along with its impact downstream of the compressor are illustrated in Fig. 1. Theoretically, it is conceivable to synthesize an arbitrary pulse shape by introducing an arbitrary number of rf harmonics.

In the spirit of trying to tailor the bunch distribution, it is planned at Neptune Lab (UCLA) to use a dogleg type non-isochronous system to compress and shape the beam current distribution as a linear ramp [11]. Such a ramped current profile has applications in plasma-wakefield acceleration to maximize the so-called transformer ratio, i.e. the accelerating over decelerating longitudinal field excited as the beam passes through the plasma. The dog-leg, which has a positive R_{56} in our convention, incorporates sextupoles to tune the values of T_{566} given the R_{56}.

We have, up to now, considered the modulator wavelength to be much longer than the incoming bunch length ($\lambda_{rf} \gg \sigma_z$) so that the modulator effectively introduces a chirp along the bunch. Recently the use of an inverse free-electron laser (IFEL) as a modulator was studied, and simulations showed the possibility to reach bunch durations in the sub-femtosecond regime [13]. In such a proposal, a laser with wavelength $\lambda = 0.8$ μm interacts via an undulator with a 100 MeV electron bunch. The thereby imparted energy modulation along the bunch allows to compress the bunch in a subsequent magnetic compressor; the bunch then consists of a train of microbunches with width of $\sim$ 200 attoseconds.

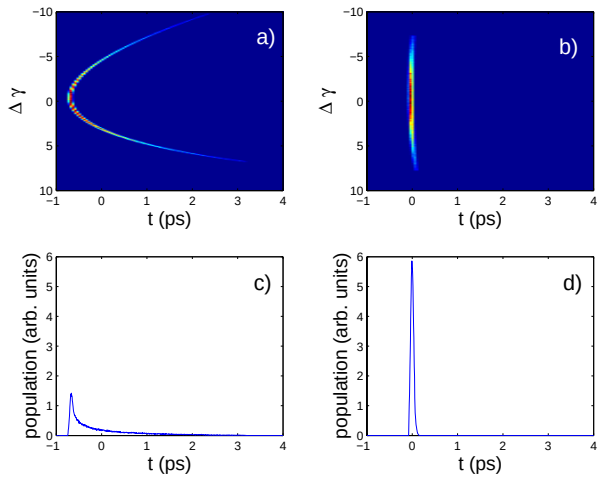

Figure 1: longitudinal phase spaces downstream of a bunch compressor (top plots) and corresponding time-distribution (bottom plots) with (right plots) and without (left plots) an harmonic rf-section to linearize the phase space upstream of the compressor.

Finally, the energy chirp along the bunch can also be introduced by the beam self-field, for instance by resistive or geometric wakefields. The use of these latter effects to chirp the bunch prior to a compressor was proposed as a last (optional) stage bunch compression for the TESLA X-ray FEL [14] and has recently been realized at the SPPS facility at SLAC (see below).

Limiting Effects

The main limitation associated to magnetic bunch compression comes from synchrotron radiation: as an electron travels on a curved trajectory, e.g. in bending magnets, it emits radiation due to centrifugal acceleration. This emission process causes the electron to loose energy as $\propto \gamma^4 I_2$, and the corresponding fractional energy spread dilution and bend-plane emittance growth for a bunch of electrons are respectively proportional to $\propto \gamma^6 I_5$ and $\propto \gamma^5 I_3$ wherein the I_n's stand for the n-th synchrotron integrals [15]. Radiation emitted by a collection of electrons have two regimes: coherent and incoherent as illustrated in Fig. 2(a). The coherent radiation results in a significant self-interaction: at a retarded time the radiation can overtake the bunch on a straight line and interact with electrons ahead in the bunch. This bunch self-interaction is relevant when the path length in the bend is comparable to the so-called overtaking length, $(24\sigma_z\rho^2)^{1/3}$, where ρ the curvature radius. This is the regime of coherent synchrotron radiation (CSR) – the power radiated [16] is $\propto N^2$ (N being the number of electrons in the bunch). This effect is favored in magnetic bunch compressors employed in FEL's and linear colliders, where short (ps-level) and highly charged ($Q \simeq 1$ nC) bunches travel through magnets with small bending radii

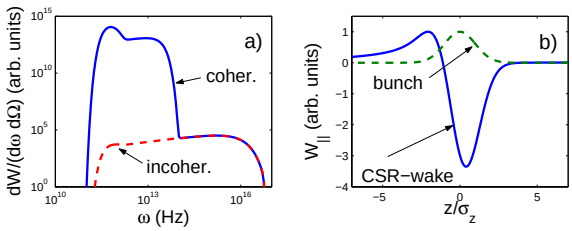

Figure 2: Synchrotron radiation spectrum associated to a Gaussian bunch **a)**, and corresponding coherent synchrotron radiation overtake function as the bunch orbit on a curved trajectory with radius of 1.6 m **b)**. The bunch energy is 140 MeV, its charge 1 nC and rms length $\sigma_z = 250$ μm.

($\rho \sim 1$ m). The magnitude of CSR longitudinal wake function scales as [17]:

$$\widehat{W_{||}} = \frac{Q}{\epsilon_0 (2\pi)^{3/2} 3^{1/3} \sigma_z^{4/3} \rho^{2/3}}, \qquad (6)$$

ϵ_0 being the electric permittivity for vacuum. Eq. 6 assumes the bunch has a Gaussian charge density. The CSR overtake function is presented in Fig. 2. Although CSR-induced beam degradation is a major limitation, scheme to neutralize the deleterious impact on bend-plane emittance dilution have been proposed: possible solutions include split chicane or periodic F0D0 arcs with proper betatron phase advance [18, 19].

CSR studies via simulation unveiled a micro-bunching instability [20] that was analyzed in References [21, 22, 23]. Such an instability is deleterious for FEL performances, since it affects the beam parameters on time scale comparable to the so-called cooperation length. It was later realized that any energy or density modulations in the longitudinal phase space can be amplified in a magnetic bunch compressor system [24, 25]. In Fig. 3 we present an example of gain calculation for the CSR microbunching instability [23]. Although the gain can be substantial, it can be significantly reduced via Landau damping, e.g. by introducing energy spread via the IFEL process [24, 26].

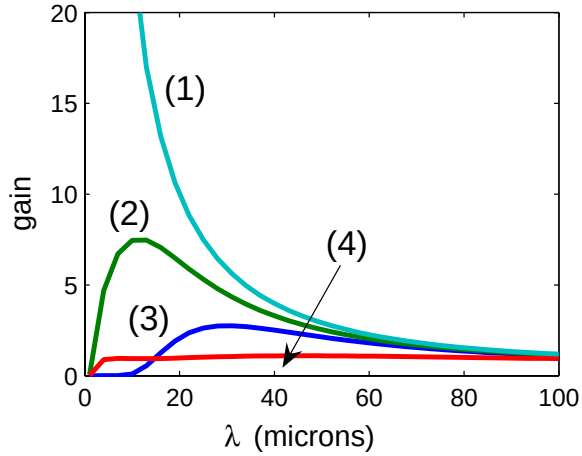

Figure 3: Microbunching gain calculation for a bunch compressor located at 5 GeV, with a $R_{56} = 25$ mm. The bunch is not compressed and its peak current is kept to 6 kA. The four cases presented are: (1) $\tilde{\varepsilon} = 1 \times 10^{-3}$ mm-mrad, $\sigma_\delta = 2 \times 10^{-6}$, (2) $\tilde{\varepsilon} = 1$ mm-mrad, $\sigma_\delta = 2 \times 10^{-6}$, (3) $\tilde{\varepsilon} = 1$ mm-mrad, $\sigma_\delta = 2 \times 10^{-5}$, and (4) $\tilde{\varepsilon} = 20$ mm-mrad, $\sigma_\delta = 2 \times 10^{-6}$.

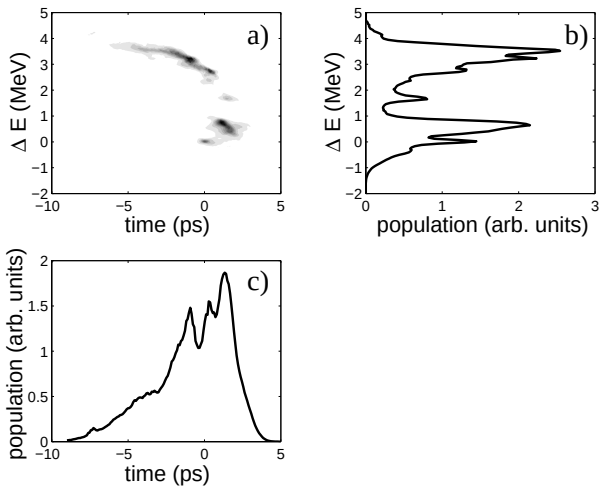

Figure 4: Measured longitudinal phase space at the TTF-1 accelerator **a)** with corresponding energy **b)** and density **c)** profiles. Note positive time corresponds to bunch head.

Example of Experimental Results

The Tesla Test Facility - phase 1 (TTF1), at DESY, has driven a FEL in the saturation regime in the vacuum ultraviolet (VUV) spectrum. A key parameter for achieving such a results was the peak current. During commissioning, the longitudinal phase space was measured [27] and the expected banana shape of the phase space (see Fig. 1) was observed as depicted in Fig. 4. However due to resolution limit of the measurement, it was not possible to obtain a precise value for the peak current. From the achieved FEL performances (gain length, number of mode, etc...) a posteriori simulations were used to reconstruct the bunch profile, and the peak current was estimated to be $\simeq$2.5-3 kA [28].

The sub-picosecond photon pulse source (SPPS) [29], at SLAC, currently holds the record in achieved peak current. The compression occurs in three stages and the final current reaches up to $\sim$30 kA. First the bunch out of the damping ring is compressed by a factor 6, down to 1.2 mm in the ring-to-linac transfer line. The bunch is then accelerated off-crest to 9 GeV and compressed through a four-bend chicane [30] down to $\sigma_z \simeq 50$ μm. Finally the bunch is accelerated to 28.5 GeV and the geometric wakefield of the S-band linac provides a chirp than allows further compression down to $\sim$12 μm in the FFTB dog-leg.

VELOCITY AND BALLISTIC COMPRESSION SCHEMES

Principle

In this section we elaborate a simple model that describes how the velocity bunching works. A more detailed discussion is given in Reference [31]. An electron in an rf traveling wave accelerating structure experiences the longitudinal electric field:$E_z(z,t) = E_o \sin(\omega t - kz + \psi_o)$, where E_o is the peak field, k the rf wavenumber and ψ_o the injection phase of the electron with respect to the rf wave. Let $\psi(z,t) = \omega t - kz + \psi_o$ be the relative phase of the electron w.r.t the wave. The evolution of $\psi(t,z)$ can be expressed as a function of z solely:

$$\frac{d\psi}{dz} = \omega\frac{dt}{dz} - k = \frac{\omega}{\beta c} - k = k\left(\frac{\gamma}{\sqrt{\gamma^2-1}} - 1\right). \quad (7)$$

Introducing the parameter $\alpha \doteq \frac{eE_o}{kmc^2}$, we write for the energy gradient [32]:

$$\frac{d\gamma}{dz} = \alpha k \sin(\psi). \quad (8)$$

The system of coupled differential equations (7) and (8) with the initial conditions $\gamma(z=0) = \gamma_o$ and $\psi(z=0) = \psi_o$ describes the longitudinal motion of an electron in the rf structure. Such a system is solved using the variable separation technique to yield:

$$\alpha\cos\psi + \gamma - \sqrt{\gamma^2-1} = \mathcal{C}. \quad (9)$$

Here the constant of integration is set by the initial conditions of the problem: $\mathcal{C} = \alpha\cos\psi_o + \gamma_o - \sqrt{\gamma_o^2-1}$. The latter equation gives insights on the underlying mechanism that provides compression. In order to get a simpler model, we consider the limit: $\psi_\infty \doteq \lim_{\gamma\to\infty}\psi(\gamma) = \arccos\left(\cos(\psi_o) + \frac{1}{2\alpha\gamma_o}\right)$; we have assumed $\gamma_o \gg 1$. After differentiation of Eq. 9, given an initial phase $d\psi_o$ and energy $d\gamma_o$ extents we have for the final phase extent:

$$d\psi_\infty = \frac{\sin(\psi_o)}{\sin(\psi_\infty)}d\psi_o + \frac{1}{2\alpha\gamma_o^2\sin(\psi_\infty)}d\gamma_o. \quad (10)$$

Hence depending upon the incoming energy and phase extents, the phase of injection in the rf structure ψ_o can be tuned to minimize the phase extent after extraction, i.e. to ideally (under single-particle dynamics) make $d\psi_\infty \to 0$. We note that there are two contributions to $d\psi_\infty$: the first term $\partial\psi_\infty/\partial\psi_o$ comes from the phase slippage (the injection and extraction phases are generally different). The second term $\partial\psi_\infty/\partial\gamma_o$ is the contribution coming from the initial energy spread. To illustrate the compression mechanism we consider a two macro-particles model. In Figure 5 we present results obtained by numerically integrating the equation of motion for two non-interacting macro-particles injected into a 3 m long traveling wave structure. Given the incoming phase $\Delta\psi_o$ and energy $\Delta\gamma_o$ spreads between the two macro-particles, and the accelerating gradient of the structure (taken to be 20 MV/m), we can optimize the injection phase to minimize the bunch length at the structure exit.

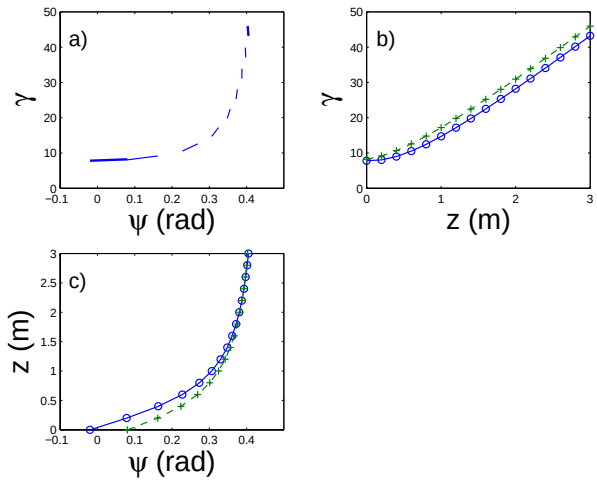

Figure 5: Simple two-macropaticle illustration of the velocity bunching scheme. Snapshots of the longitudinal phase space **a)**, and energy **b)** and phase **c)** spread evolutions as the two macroparticle are transported in a 3 m long traveling wave structure operated with an accelerating gradient of 20 MV/m. The initial energy of ∼4.5 MeV corresponds to the beam energy upon exit from an rf-gun.

Similarly to velocity bunching, ballistic bunching occurs for non-ultra-relativistic electron bunches. In such a scheme, an energy chirp is imparted along the bunch and the compression occurs in the downstream drift (the momentum compaction of a drift of length L is $R_{56} = -L/\gamma^2$). Ballistic bunching is of common use in conjunction with DC-gun electron sources e.g. as planned for the production of polarized electron beam for linear colliders [33], or for CW high power FELs [34].

Limiting Effects

Velocity and ballistic bunching have to occur at low energy, downstream of the electron source. In the case of rf-gun, the accelerating structure, located immediately downstream of the gun, plays also an important role in the so-called transverse emittance compensation process [35]: it needs to be operated to provide acceleration as prescribed by the so-called invariant envelope matching condition [36]. Such a requirement is, at first, incompatible with operating this first structure far off-crest. This limitation was taken into account for the design of SPARC-FEL [37] and a magnetic field superimposed on the first accelerating structure was proposed to prevent significant transverse emittance growth [38]. This technique is however not applicable for a superconducting linacs.

Recent Experimental Results

To date a series of experimental results have been obtained at several facilities.

At the deep ultraviolet FEL (DUVFEL) in Brookhaven [39], a 3 m long S-band (f=2.856 GHz) linac located immediately downstream of an rf-gun was used to bunch the beam [40]. The bunch was injected at various phases, and the bunch length was measured, after being accelerated to ∼70 MeV, via the zero-crossing method [41, 42]. An example of measurement of bunch length compared to the expectation is presented in Fig. 6 – sub-picosecond bunch length were achieved with a bunch charge of ∼ 0.5 nC.

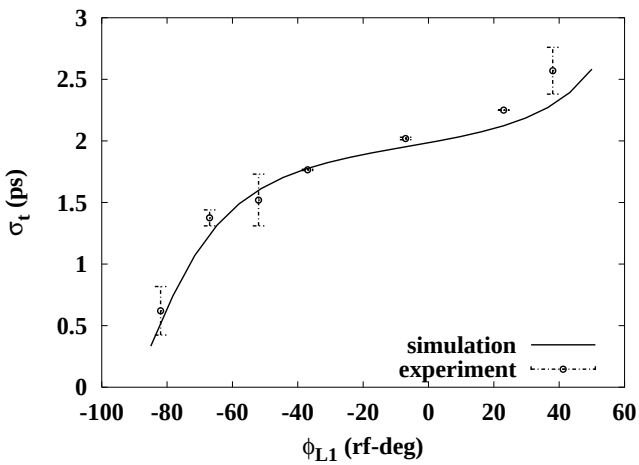

Figure 6: Measured bunch length variation as the phase of the linac located downstream of the rf-gun is varied. The measurements were performed at the DUVFEL in BNL.

At the Neptune Lab [43] of UCLA, a similar experiment was performed and the transverse emittance growth as the rf-section far operated far off-crest was also measured [44].

CONCLUSION

We reviewed two types of compression either employed in currently operating linear accelerators or included in the design of foreseen accelerators. We have not however addressed the integration of such compression schemes in an accelerator complex. In present designs [1, 2, 12], it is common to compress the bunch in a staged fashion. Such a staged compression is needed to (i) avoid driving the beam back into the space-charge dominated regime, (ii) to be less sensitive to time/energy jitter, (iii) to mitigate coherent synchrotron radiation effects. Among the two compression schemes we discussed, magnetic bunch compression, despite its limitations, seems well mastered and most of the current state-of-art accelerators (either operating or under design study) rely on this type of compression.

REFERENCES

[1] *LCLS Conceptual Design Report*, SLAC-R-593 (2002)
[2] *TESLA Technical Design report*, TESLA-FEL-01-05 (2001)
[3] P. Emma, *Proc. EPAC'04*; preprint SLAC-PUB-10535 (2004)
[4] F. B. Kiewiet, et al., *Proc. EPAC'00*, p. 1660 (2000)
[5] K. Flöttmann, et al., *Proc. EPAC'02*, p. 1798 (2002)
[6] T. O. Raubenheimer, et al, *Proc. PAC'93*, p. 635 (1993)
[7] T. Smith, et al., *Proc. LINAC'84*, SLAC-303, p. 421 (1986)
[8] D. Dowell, et al., *Nucl. Instr. Meth.* **A398**,p. 273 (1997)
[9] P. Emma, et al., LCLS TN-01-1 (2001)
[10] K. Flöttmann, et al., report TESLA-FEL-2001-06 (2001)
[11] R. Englang, et al,. *Proc AAC'02*, AIP **CP647**, p. 884 (2002)
[12] T. Limberg, et al., *Proc. EPAC'02* Paris (2002)
[13] A. Zholents, et al., *Proc. PAC'01*, p. 723 (2001)
[14] H. Schlarb, et al., *Proc. PAC'97*
[15] M. Sands, report SLAC 121 (1970)
[16] J.S. Nodvick, et al., *Phys. Rev.* **96**, p. 180 (1954)
[17] Ya. Derbenev, et al., report TESLA-FEL-1995-05 (1995)
[18] P. Emma, et al., *Proc. PAC'97* , p. 1679 (1997)
[19] D. R. Douglas, report JLAB-TN-98-012 (1998)
[20] M. Borland, ICFA CSR workshop 2002, Zeuthen Germany
[21] E. Saldin, et al., report TESLA-FEL-2002-02 (2002)
[22] S. Heifets, et al., *Phys. Rev. ST*, **A&B 5**, 064401 (2002)
[23] Z. Huang, et al., *Phys. Rev. ST*, **A&B 5**, 074401 (2002)
[24] E. Saldin, et al., report TESLA-FEL-2003-02 (2003)
[25] Z. Huang, et al., *Proc. PAC'03*, p. 3138 (2003)
[26] Z. Huang, et al., *Phys. Rev. ST*, **A&B 7**, 074401, (2004)
[27] M. Hüning, et al., *Nucl. Instr. Meth.* **A475**, p. 348 (2001)
[28] M. Dohlus, et al., *Phys.Part.Nucl.Lett* **1**, p. 114 (2004)
[29] M Cornacchia, et al., SLAC-PUB-8950 (2001)
[30] L. Bentson, et al., *Proc. EPAC'02*, p. 683 (2002)
[31] L. Serafini, et al., *in AIP conf. proc* **581**, p. 87 (2001)
[32] K.J. Kim., *Nucl. Instr. Meth.* **A275**, p. 201 (1989)
[33] A. Curtoni, et al., report TESLA-2001-22 (2001)
[34] P. Piot, et al., *Proc. EPAC'98*, p. 1447 (1998)
[35] B. Carlsten, *Nucl. Instr. Meth.* **A285**, p. 313 (1989)
[36] L. Serafini, et al., *Phys. Rev.* **E55**, p. 7565 (1997)
[37] L. Serafini, et al., *Nucl. Instr. Meth.* **A528**, p. 586 (2004)
[38] L. Serafini, et al., *Proc. PAC'01*, p .2242 (2001)
[39] L.-H. Yu, et al., *Proc. PAC'01*, p. 2830 (2001)
[40] P. Piot, et al., *Phys. Rev. ST*, **A&B 6**, 033503 (2003)
[41] D.X. Wang, et al., *Phys. Rev.*, **E 57**(2), p. 2283 (1998)
[42] W. Graves, et al., *Proc. PAC'01*, p. 2224 (2001)
[43] S. Anderson, et al., *Proc. PAC'99*, p. 2006 (1999)
[44] P. Musumeci, et al., *Proc. PAC'01*, p.2117 (2001)

RESULTS FROM THE INITIAL OPERATIONS OF THE SNS FRONT END AND DRIFT TUBE LINAC*

A. Aleksandrov for SNS collaboration, ORNL, Oak Ridge, TN 37830 USA

Abstract

The Spallation Neutron Source accelerator systems will deliver a 1 GeV, 1.44 MW proton beam to a liquid mercury target for neutron scattering research. The accelerator complex consists of an H^- injector, capable of producing one-ms-long pulses at 60 Hz repetition rate with 38 mA peak current, a 1 GeV linear accelerator, an accumulator ring, and associated transport lines. The 2.5 MeV beam from the Front End is accelerated to 86 MeV in a Drift Tube Linac, then to 185 MeV in a Coupled-Cavity Linac and then to 1 GeV in a Superconducting Linac. The staged beam commissioning of the accelerator complex is proceeding as component installation progresses. The Front End and Drift Tube Linac tanks 1-3 have been commissioned at ORNL. The primary design goals of peak current, transverse emittance and beam energy have been achieved. Beam with 38 mA peak beam current, 1 msec beam pulse length and 1 mA average beam current have been accelerated through the DTL tank 1. Results and status of the beam commissioning program will be presented.

INTRODUCTION

The Spallation Neutron Source accelerator complex will provide a 1 GeV, 1.44 MW proton beam to a liquid mercury target for neutron production. The accelerator complex consists of an H^- injector, capable of producing one-ms-long pulses at 60 Hz repetition rate with 38 mA peak current, a 1 GeV linear accelerator, an accumulator ring, and associated transport lines. The SNS accelerator systems are comprehensively discussed elsewhere [1]. The baseline linac beam has a 1 msec pulse length, 38 mA peak current, is chopped with a 68% beam-on duty factor and repetition rate of 60 Hz to produce 1.6 mA average current. The staged beam commissioning of the accelerator complex is proceeding as component installation progresses. At this point, the H^- injector (Front End) and Drift Tube Linac tanks 1, 2 and 3 (of 6) have been commissioned at ORNL. A summary of baseline design parameters and beam commissioning results is shown in Table 1.

FRONT-END PERFORMANCE AND COMMISSIONING RESULTS

The front-end for the SNS accelerator systems is a 2.5 MeV injector consisting of the following major subsystems: the rf-driven H^- source, the electrostatic low energy beam transport line (LEBT), a 402.5 MHz RFQ, the medium energy beam transport line (MEBT), a beam chopper system and a suite of diagnostic devices. The front-end is required to produce a 38 mA beam of 2.5 MeV energy at 6% duty factor. The 1 ms long H^- macro-pulses are chopped at the revolution frequency of the accumulator ring (~1 MHz) into mini-pulses of 645 ns duration with 300 ns gaps. After construction and initial commissioning at LBNL the Front End was shipped to Oak Ridge in the summer of 2002, installed at the SNS site and re-commissioned using a dedicated beam stop. The Front End has been providing beam for commissioning the rest of the linac since then and more than 2000 hours of operation time have been accumulated so far.

Table 1. SNS design vs. achieved beam parameters

	Baseline Design or Goal	Achieved
MEBT peak current [mA]	38	52
DTL1 peak current [mA]	38	40
DTL1-3 peak current [mA]	38	38
DTL1 beam pulse length [msec]	1.0	1.0
DTL1 average current [mA]	1.6	1.05
MEBT horiz. emittance [π mm mrad (rms,norm)]	.27	< .3
MEBT vertical emittance [π mm mrad (rms,norm)]	.27	< .3
DTL1 horiz emittance [π mm mrad (rms,norm)]	0.3	0.30 (fit), 0.40
DTL1 vertical emittance [π mm mrad (rms,norm)]	0.3 (RMS)	0.21 (fit), 0.31 (RMS)
DTL1 beam duty factor	6.0%	3.9%
MEBT Beam Energy [MeV]	2.5	2.45 ± 0.010
DTL2 output energy [MeV]	22.89	22.94 ± 0.11

Ion Source and LEBT Performance

Details of the ion source and LEBT design can be found in [2]. General performance of the ion source during commissioning is summarized in Fig.1, where operational current is shown for each day of the last commissioning run. Since there are no beam diagnostics in the ion source or LEBT, the beam current is measured in the MEBT after the RFQ. A maximum current of 51 mA was achieved, significantly exceeding the base line requirement of 38 mA. An R&D program on the ion-source hot spare stand [3] yielded a significant increase of the ion source

* SNS is managed by UT-Battelle, LLC, under contract DE-AC05-00OR22725 for the U.S. Department of Energy. SNS is a partnership of six national laboratories: Argonne, Brookhaven, Jefferson, Lawrence Berkeley, Los Alamos and Oak Ridge.

availability: starting at 85.6%, it increased to 92.4% in the second, and finally to 97.8% in the most recent DTL1-3 run.

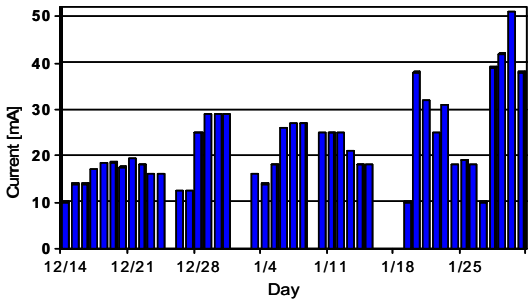

Figure 1: Peak beam current (average over 24 hours) at the MEBT exit for each commissioning day.

RFQ Performance

The design of the 3.72 m long 4-vane RFQ with p-mode stabilizers is described in detail elsewhere [4]. It operates at 402.5 MHz and accelerates H^- beam from 65 kV to 2.5 MeV. Since the only tunable parameter for RFQ is the RF power, we used measurements of the RFQ transmission vs. RF power in order to establish the nominal set point. Since we couldn't measure the beam current injected into the RFQ from the LEBT, the absolute value of the RFQ transmission couldn't be calculated. Instead, we compared measured data with PARMTEQ simulations and derived the set point and expected transmission from the model, see Fig. 2.

The RFQ output energy was measured by a time-of-flight technique in the MEBT and found to be 2.45±0.01 MeV, compared with 2.50 MeV nominal design energy.

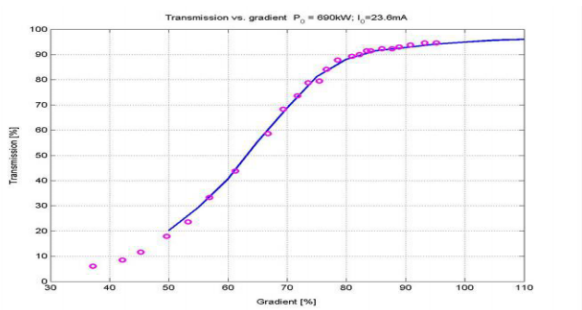

Figure 2: RFQ transmission vs. RF power. Measurements (red) and model fit (blue) .

MEBT Performance

The MEBT is a complex beam transport line [5]. It matches the beam from the RFQ through the MEBT chopper system and into the drift-tube linac. Fourteen quadrupole magnets and four bunching cavities provide transverse and longitudinal focusing. The MEBT is equipped with a suite of beam diagnostics [6] including two beam current monitors (BCM), six beam position and phase monitors (BPM) installed within quadrupole magnets, and five dual- plane wire scanners (WS). A temporary slit/collector type emittance device was installed at the MEBT exit for transverse emittance measurements during initial commissioning. It allowed measurements in one plane (vertical or horizontal). In order to switch to another plane vacuum had to be broken and the device physically rotated, therefore no simultaneous measurements in both directions were obtained. Typical emittance scan plots are shown in Fig.3.

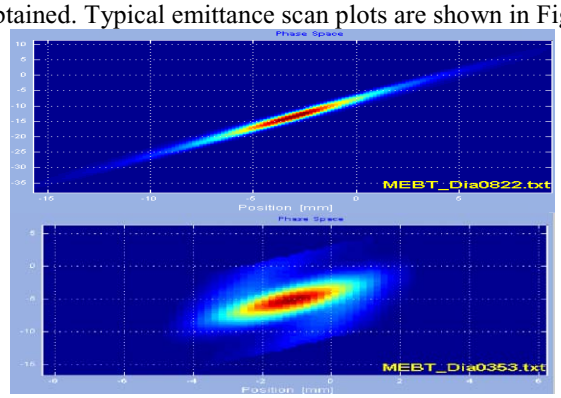

Figure 3: Typical beam vertical (upper) and horizontal (lower) transverse phase space measured at the MEBT exit.

The horizontal emittance scan in Fig. 3 clearly shows an S-shaped distortion caused by non-linear space charge forces. Even in the presence of the emittance growth due to non-linearity, the rms emittance values satisfy the requirements in a wide range of beam currents as illustrated in Fig. 4, where the output r.m.s. emittance is plotted vs. beam current.

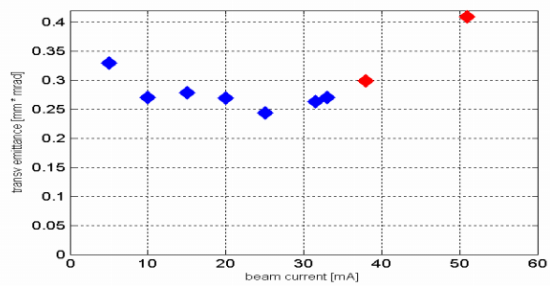

Figure 4: Transverse normilized rms emittance at the MEBT exit vs. beam current.

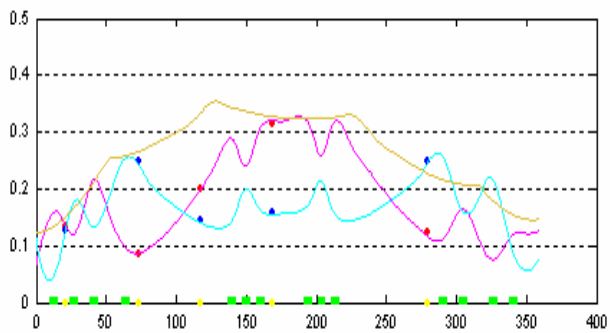

Figure 5: Beam profile (cm) vs. distance in the MEBT (cm). The points show measured horizontal and vertical beam profiles and the curves show the predicted horizontal profile (red), vertical profile (blue) and longitudinal profile (brown).

After proper tuning beam losses in the MEBT are below the measurement accuracy of the BCMs as illustrated by Fig. 7. In this picture the beam current pulse at the MEBT exit is shown on top of the beam pulse at the MEBT entrance.

Good understanding of the MEBT transverse optics was demonstrated. Figure 5 shows excellent agreement between measured horizontal and vertical beam profiles and those predicted from a model-based fit to the input Twiss parameters.

Chopping

The 1 ms long H^- macro-pulses have to be chopped at the revolution frequency of the accumulator ring into mini-pulses of 645 ns duration with 300 ns gaps. Beam chopping is performed by two separate chopper systems located in the LEBT and MEBT. The LEBT chopper removes most of the beam charge during the mini-pulse gaps, and the MEBT chopper further cleans the gap and reduces rise and fall time of the mini-pulse to 10 ns. The last lens in the LEBT is split into four quadrants to allow for electrostatic chopping using the RFQ entrance flange as a chopper target. The LEBT chopper system is complemented by a traveling-wave chopper in the MEBT that provides faster rise and fall times to 10 ns and further attenuates the beam in the gap to a level of 10^{-4} [7]. Transient times of the gap produced by LEBT and MEBT choppers in the beam were measured using a BPM and fast oscilloscope - see Fig. 6 upper and lower signals respectively. The oscilloscope resolution did not allow an extinction ratio measurement to the design level of 10^{-4}. Nevertheless, a laser based system capable of measuring rise/fall time with 5 ns resolution and beam extinction ratio with 10^{-4} resolution was installed and tested but not with nominal chopped beam. Details can be found in [8].

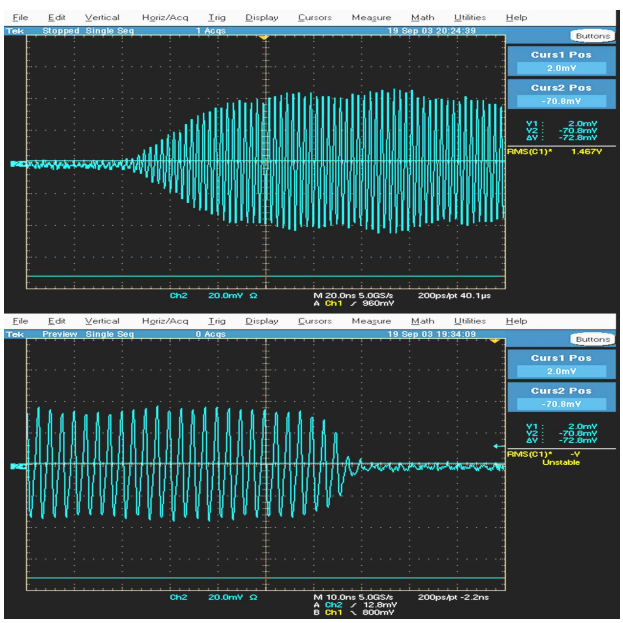

Figure 6: LEBT chopper rise time (upper trace) and MEBT chopper fall time (lower trace) measured at the MEBT exit.

DRIFT TUBE LINAC PERFORMANCE AND COMMISSIONING RESULTS

The Drift Tube Linac consists of six accelerating tanks operating at 402.5 MHz with final output energy of 87 MeV. The transverse focusing is arranged in a FFODDO lattice utilizing permanent-magnet quadrupoles. Some empty drift tubes contain beam position monitors and dipole correctors. The intertank sections contain BCMs, wire scanners and energy degrader/faraday cups (ED/FC).

The first three of six DTL tanks have been commissioned with beam in two separate runs. The goals of the commissioning runs [9] have been to demonstrate full system functionality, demonstrate beam acceleration with design beam parameters to the limits of the available beamstop, test and validate beam commissioning algorithms, and commission the installed diagnostic devices.

DTL Tank 1

In the first run, DTL tank 1 (with output energy 7.5 MeV) was commissioned into a dedicated Diagnostics System [10] (the "D-plate") equipped with energy degrader/faraday cups, wire scanners, beam position monitors, a slit/harp emittance system, and a Bunch-Shape Monitor (BSM) [11], to enable detailed characterization of the output beam parameters, as well as a full-power beamstop for a test of high-power operation. DTL Tank 1 commissioning results are summarized in Table 1. The design peak current of 38 mA was readily achieved. A 1 msec long beam pulse was generated at 20 mA average current during the pulse (at low duty factor). Finally, a 1 mA average current beam was accelerated in DTL1 with 100% beam transmission. For this demonstration, a beam pulse of 26 mA peak current, 650 microsecond pulse length at 60 Hz (7.6 kW beam power) was achieved. Figure 7 shows an overlay of Beam Current Monitor signals in the MEBT and DTL1 during this high-power demonstration run. This was an important milestone, in that it shows the injector is capable of 1 MW-class SNS operation.

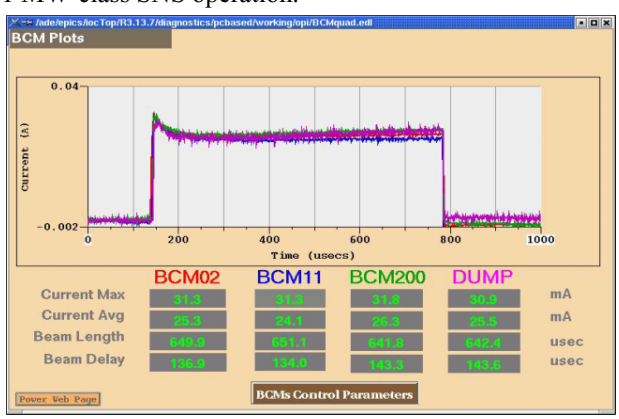

Figure 7: Beam current monitor traces during the DTL1 high-power run. The traces show the beam current after the RFQ (red), after the MEBT (blue), after DTL1 (green) and at the beamstop (purple).

The basic procedure for setting the RF phase and amplitude of the DTL tanks relies on the acceptance scan method utilizing the ED/FC located after each tank. The degrader thickness is chosen to absorb beam particles with energy just below the nominal acceptance. The phase and amplitude are determined by comparing the phase profile of the transmitted current with beam dynamics simulations. An example measurement is shown in Figure 8.

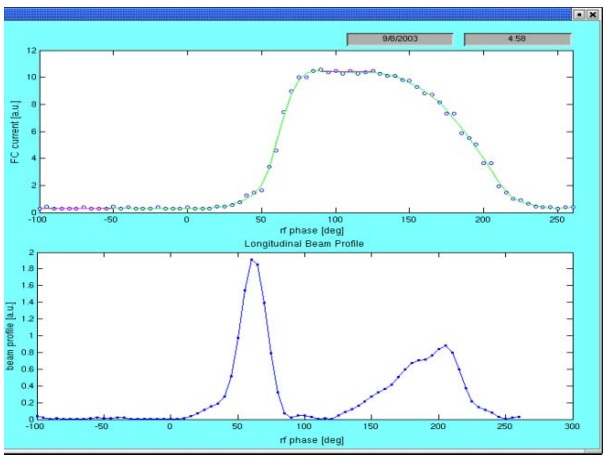

Figure 8: DTL tank 1 acceptance scan. The top curve shows the transmitted current through the degrader measured on the Faraday cup as a function of DTL1 phase. The lower curve is the derivative of the upper curve.

Extensive DTL1 output beam emittance measurements were performed with a slit-collector system. Figure 9 shows a horizontal emittance measurement at 38 mA peak current.

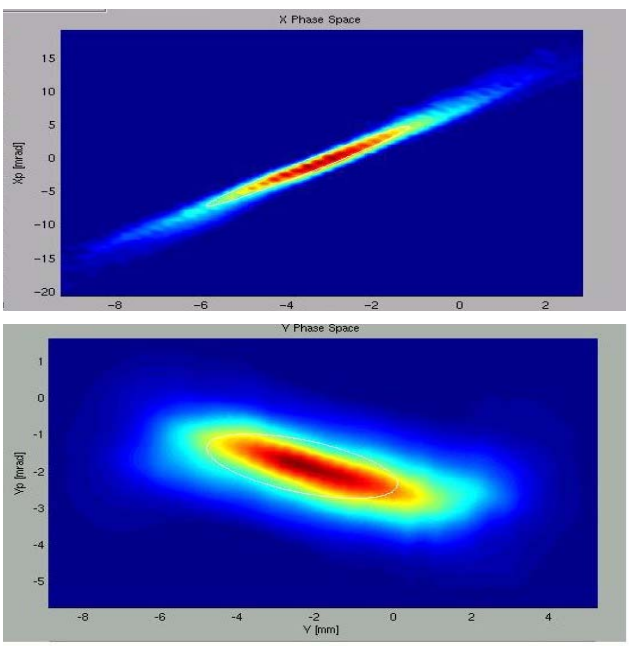

Figure 9: Horizontal (upper) and vertical (lower) output emittance from DTL tank 1 at 38 mA peak current. Angle (mrad) is plotted vs. position (mm).

The data are analysed in two ways. First, a Gaussian fit is performed to the two-dimensional beam distribution in position-angle space to obtain an emittance that can be considered representative of the beam core. Values obtained in this way are 0.21 π mm mrad (rms, normalized) in the vertical plane and 0.30 π mm mrad in the horizontal plane at 38 mA peak current, both of which achieve the emittance goal. In a second analysis, the RMS of the beam distribution is calculated with a 1% threshold (relative to the peak beam intensity) to remove spurious noise. Values obtained in this way are somewhat larger than the core emittances: 0.31 π mm mrad, and 0.40 π mm mrad in the vertical and horizontal respectively. A number of systematic effects in the emittance data are being investigated. For example, we see evidence of a large slit-scattering component that produces an opposite-sign signal (since the H^- ion is stripped to protons) which reduces the beam signal. Analysis and modelling of slit-scattering and its correction is underway. We also observed a discrepancy between emittance device and wire scanner measurements in the horizontal plane, which is under investigation.

A number of measurements pertaining to the longitudinal dynamics were obtained from BSM measurements and will be discussed in a separate publication [11].

DTL Tanks 2 and 3

In a third commissioning run, DTL Tanks 1-3, with output energy of 40 MeV, were commissioned into a low-power beam stop. Again, a peak current of 38 mA was readily transported through all three tanks with 100% transmission (within the 2-4% BCM measurement uncertainty). The beamstop limited pulse lengths to less than 50 microseconds, and repetition rates to 1 Hz. It is notable that the trajectory errors with all dipole correctors turned off remains within ±1.5 mm in the MEBT/DTL1-3 system. Correction of the trajectory makes no measurable improvement in beam transmission.

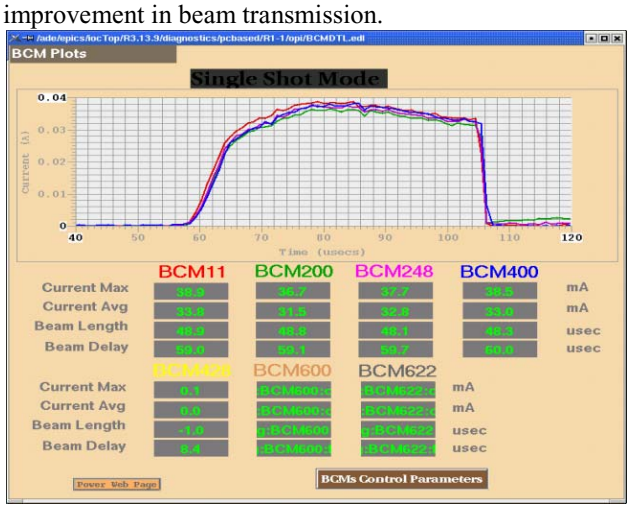

Figure10: Beam current monitor traces during the DTL1-3 run. The traces show the beam current after the MEBT (red), after DTL1 (green), after DTL2 (purple) and after DTL3 (blue).

A second technique for determining DTL tank phase and amplitude setpoints, as well as determining the input energy, was explored. In this method, based on the "phase-scan signature matching" approach [12], the beam phase from a single BPM, or the phase difference between two BPMs downstream of a DTL tank, are measured as a function of the tank phase and amplitude.

Figure 10 shows an example for DTL1, in which three sets of measured phase differences were recorded from BPMs located after DTL tank 1. The data are limited only to those points where more than 7 mA of beam current was transported in order to ensure a reliable beam phase measurement. One scan was taken at nominal RF amplitude, one at 5% above nominal, and the other at 5% below nominal. As is evident in the figure, the signatures are quite sensitive to the RF amplitude. A model-based fit was then performed to these three phase-scan "signatures" to obtain the RF amplitude, relative phase of beam and RF, and the input energy. Interestingly, the input energy of 2.45 MeV, measured in this way, agrees with that measured by TOF in the MEBT. This is a powerful method that promises to offer more accurate determination of DTL setpoints than the acceptance scan method utilizing an ED/FC.

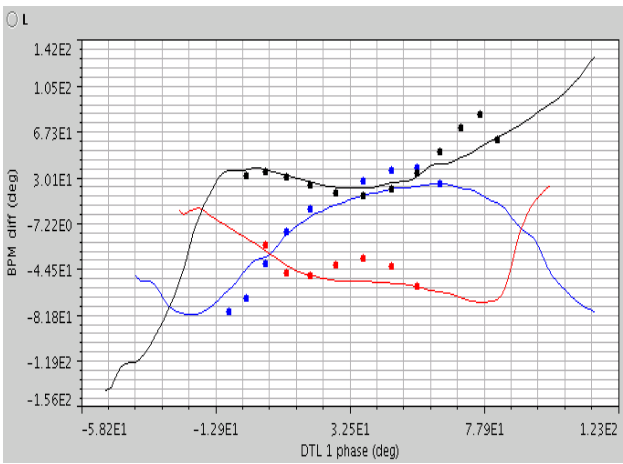

Figure 11: Curves show the measured phase difference (degrees) between two BPMs downstream of DTL1 as functions of DTL1 RF phase for nominal RF amplitude (blue), 5% below nominal (red) and 5% above nominal (black). The points show the result of a model-based fit to the data.

Time-of-flight measurements were also performed. Using BPMs located in DTL3 with the tank unpowered, a DTL2 output energy of 22.94±0.11 MeV was measured, which agrees with the design value within measurement uncertainty. The energy jitter and long-term drift were also measured. Averaging all data taken during a 30-minute period results in 0.08% rms output energy stability, which corresponds to 0.6 degree phase stability measured on a single BPM.

OPERATIONAL STATISTICS

One of the important results of the commissioning activity is the improvement of the hardware reliability. A summary of operational statistics for all three commissioning runs is shown in Table 2. Beam availability has been steadily improving despite an increase in the number of hardware systems under commissioning in each run, and reached 75% during the DTL1-3 commissioning run.

Table 2. Operational statistics

	Run 3 (DTL1-3)	Run2 (DTL1)	Run1 (FE)
Total time [hours]	288	1136	800
Beam available [%]	75	62	53
Planned shutdown [%]	6	2	2
Equipment breakdown[%]	19	36	45
Breakdown statistics by equipment group [%]			
RF	15	28	34
Power supplies	0	22	4
Ion Source	6	21	32
Diagnostics	0	6	7
Controls	4	17	12
Water, vacuum, etc.	75	6	11

CONCLUSIONS

Commissioning of the SNS linac has been progressing well. Acceleration to 40 MeV of beam pulses with the peak design current of 38 mA has been readily achieved. The Front End and DTL1 were operated at 1 mA average current. Beam availability increases steadily with each commissioning run.

The remaining DTL tanks 4-6 and CCL have been installed in the tunnel and RF processed to the nominal power. They will be commissioned in the next commissioning period in fall 2004.

REFERENCES

[1] N. Holtkamp, Proc. PAC 2003, p. 11.
[2] R. Keller et al., in "9th Int. Symp. on the Production and Neutralization of Negative Ions and Beams", edited by M. Stockli, AIP Conf. Proc. No. 639, p. 47.
[3] R. Welton et al, Proc. PAC 2004.
[4] A. Ratti et al., Proc. EPAC 2000, p. 495.
[5] J. Staples et al., Proc. LINAC 2000, p. 250.
[6] S. Assadi , Proc. PAC 2003, p. 498.
[7] R. Hardekopf et al., PAC 2004.
[8] A. Aleksandrov et al., PAC 2003, p. 1524.
[9] E. Tanke et al., Proc. LINAC 2002, p. 353.
[10] M. Plum et al., Proc. PAC 2001, p. 2374.
[11] A. Feshenko et al., these proceedings.
[12] T. Owens et al., Part. Acc. **48** (1994) p. 169.

RECENT RESULTS IN THE FIELD OF HIGH INTENSITY CW LINAC DEVELOPMENT FOR RIB PRODUCTION

A. Pisent, INFN/LNL, Legnaro, Padova, Italy

Abstract

High Intensity CW Linacs have been proposed as driver accelerators for RIB production in various projects, since they can drive in steady conditions a MW power range target for the production of spallation neutrons that induce fission in a natural uranium target. The necessity to develop a superconducting intermediate energy part with good power conversion efficiency is particularly important for this application, with a relatively low beam current. The second specific requirement of RIB facility drivers, which is also fulfilled by a superconducting intermediate energy linac, is the necessity to keep some flexibility in the species that can be accelerated (deuterons or light ions). In EURISOL RTD project, a 1 GeV 5 mA proton linac has been proposed for this application. In the SPES project, recently approved for its initial phase at LNL, a lower energy proton beam will be used on a solid target. The results of the specific R&D programs in the field of CW RFQ and superconducting low energy linacs will be illustrated. In particular for LNL the status of the RFQ construction and the superconducting cavities prototype tests will be given.

HIGH INTENSITY FOR RIB PRODUCTION

In the last years the availability of new intense radioactive ion beams (RIB) has been recognized as a fundamental tool for future research in Nuclear Physics, and new major facilities have been proposed worldwide (Table 1). By means of RIBs it is possible to study the properties of nuclei that, due to their short life-time, cannot be used as a target. Therefore RIBs allow to extend the knowledge of nuclear structure to exotic compounds and to study conditions that are relevant for the understanding of the early stage of the Universe and for the nucleo-synthesis.

Of the two complementary methods for RIB production, the In Flight (IF) and the ISOL (Isotope Separation On Line), the second one takes directly advantage of the development of cw high intensity linacs.

The basic scheme of an ISOL facility [1] is the following: the primary accelerator beam induces a nuclear reaction in a thick target, producing unstable nuclei. During their short life-time the isotopes evaporate from the target (kept at high temperature), are pumped into an ion source, ionized, extracted, selected by a magnetic spectrometer, accelerated and sent into the experimental apparatus. The RIB intensity actually delivered to the experiments is mainly the product of the primary beam intensity, the cross section of the specific production and the various efficiencies. These efficiencies take into account the particle losses occurred during the effusion from the hot target and the diffusion in the ion source, the nuclei that decay before reaching the experiment and the transmission of the spectrometer and of the reaccelearator. Even if the improvement of the efficiencies and of the ion selectivity of the spectrometer are under many aspect the key points for the success of an ISOL facility, a large flux of primary particles is the initial point.

In Europe the future for the IF method is assured by the GSI project FAIR[2], while for the ISOL method a large group of research institutions, including the major Nuclear Physics laboratories, have joined the EURISOL project, funded by EU, for the determination of the most competitive new generation ISOL facility for Europe. The resulting EURISOL report[3] has been published last year, and more recently the EU has positively evaluated a second stage design work (EURISOL-DS), now in negotiation stage, that includes the funding of prototypes of some critical issues.

Thanks to the complementarity with FAIR, EURISOL is mainly concentrated on the use of a 1 GeV high power proton linac, while the American project RIA, including IF method, considers a lower intensity linac able to accelerate ions up to uranium. For this reason this paper will be centred on European development, even if at present the most performing cw proton beam for RIB production is produced by a cyclotron in America (ISAC at TRIUMF[4]).

In particular in EURISOL design the direct use of a p beam of "moderate" intensity (tenths of mA) on a solid target will allow in most cases to operate at the limit of the target possibility (in terms of power dissipation density) with RIBs intensity much larger than the one available today.

Neutron reach isotopes are instead most efficiently produced by fission reaction with the two targets method: a very high fission rate (exceeding $10^{15}s^{-1}$) can be induced in a depleted uranium carbide target by fast neutrons; the fast neutrons are produced by spallation in a MW class (liquid metal) target.

Therefore, the EURISOL reference facility foresees three 100 kW target stations and one 5 MW target. Correspondently, the linac will have two modes of operation, at 100 μA and at 5 mA. Moreover, the possibility to accelerate light ions with the same driver has been explored; in particular the upgrading of the injectors needed to accelerate ions with A/q=2 up to 500 A MeV and A/q=3 up to 100 A MeV have been considered.

To assure the continuity in RIB research development some new ISOL facilities are proposed in Europe for the next decade (Tab. 2). In EURISOL-DS proposal and in NuPECC Long Range Plan a "EURISOL road map"

Table 1: Main new RIB facilities under discussion worldwide

Location	Driver	Post-accelerator	Fragment separator	Type of facility
Europe: GSI (Germany)	synchrotron, heavy ions: 1.5 A GeV	-	'Super-FRS'	In-Flight
Europe: EURISOL	protons, 1 GeV, 1-5 MW	CW Linac, up to 100 *A* MeV	-	ISOL
USA: RIA Rare Isotope Accelerator	900 MeV protons heavy ions: 400 *A* MeV, 100 kW	Linac up to 8–15 A MeV	4-dipole separator	ISOL, In-Flight
JAPAN: RIKEN RIB Factory	Ring-cyclotrons up to 400 *A* MeV (light ions); up to 150 *A* MeV (heavy ions)	-	3 fragment separators storage & cooler rings	In-Flight

Table 2: New ISOL facilities in EUROPE

Location	RIB Starting Date	Driver	Post-accelerator
SPIRAL-II: GANIL Caen, France	2008	SC linear accelerator LINAG deuterons up to 40 MeV heavy ions up to 15 *A* MeV	cyclotron CIME $K = 265$, 2–25 *A* MeV
MAFF Munich, Germany	2008	reactor 10^{14} *n/cm².sec*	linac up to 7 *A* MeV
SPES Legnaro, Italy	2008 (Initial phase)	SC proton linac 100 *MeV* Initial phase 20 *MeV*	ALPI linac 15-20 *A MeV*
ISOLDE upgrade CERN	2008	PS booster p, 1.4 GeV, 10 µA	linac up to 5 *A* MeV

with the realization of these new facilities on National Laboratory scale is described.

In particular SPIRAL2 [5] at GANIL, using a low frequency (88 MHz) superconducting linac, will explore the production of RIBs with deuteron primary beam, and the double target method, with a fission rate of $10^{13}s^{-1}$or more. The facility SPES[6] at LNL will develop a superconducting proton linac (100 MeV, operating at 352.2 MHz) with the same characteristics of the intermediate energy section of EURISOL driver; this proton beam (with a solid converter in Be or ^{13}C and a UC_X target) will also allow to exceed 10^{13} fissions s^{-1}. Both SPIRAL2 and SPES linacs are open to the implementation of a second injector for heavier ions.

PROTON DRIVER

In Fig. 1 the schematic layout of the EURISOL proton linac is shown. Since the main choices are determined by the high energy section, the layout will be described backwards.

Main Linac

The high energy part of the linac will be superconducting as well as established with SNS experience; 704 MHz elliptical cavities with high gradient (above 10 MV/m) can be used. In EURISOL TDR 5-cell cavities are used, with β=0.47, β=0.65 and β=0.85 up to 1 GeV, for a total number of 134 cavities and a linac length of 270 m [3,7]. An intense prototype program for these cavities is under

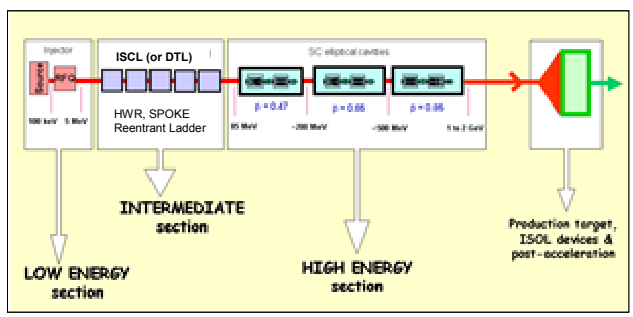

Figure 1: Schematic lay-out of EURISOL proton driver.

way at CEA-CNRS France and at INFN Italy for RIBs and ADS applications. In Fig 2 a prototype of a β=0.65, 5-cell cavity recently fabricated in France and successfully tested is shown[8]; the β=0.47, 5-cell cavity built in Italy has also exceeded the nominal performances[9].

The superconducting main linac guarantees high gradient, low power consumption and therefore convenient real estate length and power conversion efficiency for this linac which has to work in a wide range of beam currents.

For RIB users the time structure of the primary beam is not a requirement since they see the continuous beam after the effusion from the hot target. It is therefore convenient to build a CW linac since, besides avoiding thermal shocks in the target, the linac operation is simplified due to the absence of Lorenz force detuning in

the transient. Moreover, with CW operation the RF power per cavity is minimized (below 50 kW), the couplers can

Figure 2: Prototype of a β=0.65, 5-cell cavity fabricated in France.

be easily developed and low power RF units can be installed for each cavity, with an important simplification of phase control.

On the other hand, the analysis done by EURISOL target working group shows that a pulsed linac, with repetition rate higher than 50 Hz, is acceptable for the high power target. As a consequence, if EURISOL shared the driver with other applications (as for example at CERN using SPL), the driver could be pulsed. This also implies that it is preferable that all the superconducting cavities developed for RIB production have the capability to work in pulsed mode.

The Low Energy Linac

The low energy driver linac is based on independently phased superconducting cavities (ISCL) with a capability of 5 mA. The beam current choice is convenient for this linac, since a power level below 15 kW per amplifier can be achieved with solid state technology.

The RFQ Injectors. The front end of the linac delivers a cw beam of 5 mA at 5 MeV. RF ion sources like SILHI and TRIPS are perfectly capable to produce this beam with good emittance and reliability.

The RFQ structure has to operate at 352 MHz, since a lower sub-multiple of 704 MHz would generate a larger longitudinal emittance difficult to be managed in the superconducting linac with a high power beam.

It exists a well established development of cw RFQ for protons at this frequency, with the successful operation of LEDA [5] (100 mA, 6.7 MeV) at LANL and the two European projects IPHI (100 mA, 5 MeV) at CEA-CNRS [10] and TRASCO (30 mA, 5 MeV) at INFN-LNL [11]. These two accelerators, conceived for ADS development, will both be used for fundamental physics (and partly for RIB production).

IPHI RFQ will be built up to 3 MeV (one of the modules has already been brazed) and, after being tested cw at CEA Saclay, it will operate at CERN in pulsed mode as front-end of Linac4[12]. TRASCO RFQ will be used as injector of SPES (two modules have already been brazed) and will be used at full current for interdisciplinary applications.

The beam loading in RIB case is rather small (25 kW), in comparison with the power dissipated in the copper

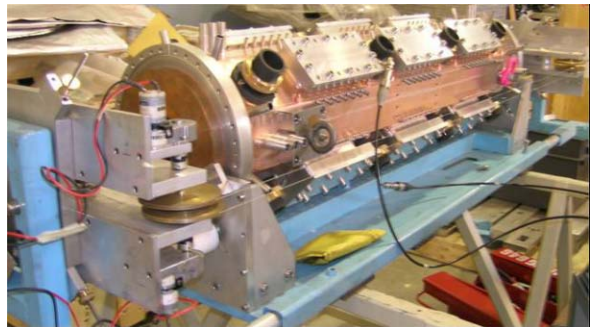

Figure 3: First module of TRASCO RFQ during final RF measurements.

(700 kW in TRASCO and more than 1 MW in IPHI) and this makes the RFQ rather inefficient from an energy consumption point of view. Thus a lower intervane voltage structure like TRASCO RFQ suits better since in this case for 30 mA beam current the problems of an RFQ with a beam loading almost negligible with respect to the copper power (150 kW vs 700 kW) has already been faced. In this respect this RFQ is optimized also for 5 mA.

In particular the power dissipation is minimized, a single LEP klystron is used, and the construction procedure is simplified to reduce the costs, at the expenses of a worst control of the non linear components of the focusing field. This last simplification is possible since both for 5 mA and 30 mA the non linear space is not predominant.

From the beam dynamics point of view a 30 mA RFQ can accelerate a 5 mA beam, with virtually full transmission, good emittance and low beam halo parameter [13]. The MEBT has of course to be flexible enough to match the different Twiss parameters. Moreover, in TRASCO RFQ simulations (PARMTEQM) the appearance at low current of a structure with two peaks in the longitudinal phase plane distribution has been observed, due to the very incomplete mixing of the subsequent longitudinal oscillations. This structure survives in the intermediate energy linac (without any dangerous consequences), but its effects in the main linac have still to be investigated.

The possibility to use a superconducting RFQ for this cw low beam loading application has also been taken into consideration. Indeed for these parameters 1% beam losses can correspond to 250 W dissipated in the cryostat at 4.2^0K, a too large number to be managed by the cryogenic system. It is very difficult to envisage beam losses lower than 1% in a RFQ, especially with the mechanical tolerance achievable in a Nb construction, so that unfortunately it will not be possible to use the LNL successful development in SRFQ for this application. On the contrary an SRFQ is very well suited as first element for the reacceleration of RIBs.

Intermediate Energy Superconducting Linac. For the intermediate part of the linac, between 5 and 85 MeV, covered by normal conducting DTL in present linacs, we considered the use of an ISCL; this implies the use of

many superconducting cavities evolution of those developed for heavy ion linacs. Proton low beta cavities are under development in many laboratories, starting from the early works more than one decade ago (see for example [14]). In Fig.4 the realized prototypes of some of the cavities considered in EURISOL-TDR are shown (re-entrant[15], half wave coaxial [16]and spoke[17]).

In EURISOL-TDR the normal conducting and superconducting options were compared, showing a similar capital cost but, for the specific application (5 mA cw), a running cost much higher for the normal conducting DTL (about 2M€/year difference).

A key (and not uniquely solved) problem for this kind of structure is the choice of the focusing structure, to allow the efficient use of high performance cavities and the achievement of a high real estate gradient. Typical values for the energy gain per cavity (at ϕ_s=0) ΔW go from the 0.6 MeV of re-entrant cavities, to 1-1.5 MeV for multi gap structures.

The beam dynamics has to cope with space charge effect and possible single particle and envelope resonances, so that starting with a realistic distribution out of the RFQ the beam quality in the main linac is maintained and beam losses are negligible. A well designed ISCL has to generate a beam quality comparable with a DTL, that has the advantage of a shorter focusing period.

In particular the parametric resonance, occurring when the longitudinal phase advance is about twice the transverse phase advance, must be avoided to preserve beam quality. A more conservative criterion, that takes into account also other low resonances, is $\sigma_{0L} \le \sigma_{0T}$. Moreover the transverse phase advance per period σ_{0T} is limited to $\pi/2$ due to the envelope instability. As a consequence $\sigma_{0L} \le \sigma_{0T} \le \pi/2$ limits the period length L and ΔW, since:

$$\sigma_{0L} = L\sqrt{\frac{eE}{mc^2}\frac{2\pi\sin(-\phi_s)}{\beta^3\gamma^3\lambda}} \approx \sqrt{\frac{n\Delta WL}{\lambda}}\sqrt{\frac{2\pi\sin(-\phi_s)}{mc^2\beta^3\gamma^3}}$$

with E real estate average accelerating field, n number of cavities per period, β and γ relativistic parameters and λ RF wavelength. In other words, the use of a low number of high performance cavities (high ΔW), that is economically advantageous, requires the compactness of the period and of the cavities themselves. These problems are much worst at low energy.

The first consequence is that the use superconducting quadrupoles to be installed inside the cryomodule is almost necessary at low energy (even if the solution with many short cryostats has been considered[17]); secondly the doublet lattice is preferable respect to the FODO lattice, allowing a larger space for cavities during each period (even if 4-gap ladder cavities and FODO lattice can be assembled in a very efficient linac [18]). Finally, very compact cavities in longitudinal direction are needed, even when this has to be compromised with smaller beam bore aperture.

For example in the nominal layout studied for SPES linac between 5 and 10 MeV, 37 re-entrant cavities and 12 superconducting quadrupole doublets are assembled in two long cryostats with a short focusing period (0.7 m in the first cells), and an overall real estate gradient of about 1.3 MV/m [19]. Above 20 MeV HWRs, housed in cylindrical cryostats (similar to ALPI modules) and external normal conducting doublets can be used. The total length of this linac (5-100 MeV) is about 50 m, with full transmission under fair construction error conditions and an rms emittance increase below 10%.

Moreover, a linac of this kind is an open structure, since ions with A/q up to 3 and higher can be accelerated substantially to the same energy per charge unit. The flexibility of this kind of linac allows also to cope with the possible failure of some of the hardware, as studied in details for ADS applications.

Figure 4: Reentrant cavity and HWR (β=0.31) prototypes, developed at LNL, and Spoke cavity (β=0.35) prototypes developed at CNRS Orsay.

PERSPECTIVES

The long range ISOL facility will be on European scale (EURISOL), based on a high intensity linac as driver and a superconducting linac for the reacceleration. The technology of the driver (and of the converter) is common to other applications like spallations sources for Material Science and Nuclear Waste Transmutation, or new High Energy Physics applications, so that synergies are possible and necessary.

There is an intermediate phase with an essential role for National Laboratories, like SPES project at LNL and SPIRAL2 at GANIL.

The first step in Italy will be the construction of the first phase of SPES, SPES-1 in the next five years. This project will be a first significant step in the direction of SPES and EURISOL, a very good test for the high intensity community (ADS), and will be able to serve a community of interdisciplinary physics and medical users.

The specific investment, approved by INFN in Autumn '03, includes (Fig. 5):

1. the completion and installation of the 5 MeV 30 mA proton injector (TRASCO source and RFQ),
2. the development and construction of the thermal neutron facility ($\geq 10^9$ s^{-1} cm^{-2} thermal neutrons, low gamma and fast neutron contamination) for BNCT

(Boron Neutron Capture Therapy) experimental studies[20,21], based on the 150 kW RFQ beam impinging into a Be target.

3. the development and realization of the superconducting p linac up to 20 MeV, 10mA current, cw.
4. the continuation of the R&D program on RIB production targets, and in particular the rotating converter done in ^{13}C and natural graphite, and the development of UCx fission targets.

It should be noted that with respect to the EURISOL requirements the current accelerated by the superconducting linac has been increased from 5 mA to 10 mA. This allows a better use of the intensity available from the RFQ, and makes the linac development relevant for the other high intensity applications (ADS).

Finally for RIB experiments this opens an additional possibility: a 10 mA 40 MeV proton beam hitting a thick ^{13}C graphite or Be target would produce a neutron flux and a fission rate interesting for experiments. Another possibility under study is the direct use of the proton beam (1 mA 40 MeV) in a thin fission target (some mm), such as leaving the Bragg peak outside. If the R&D on these concepts will be successful, LNL will be able to propose a compact and cost effective RIB source to be coupled to ALPI reaccelerator.

There is therefore an integrated plan for the development of ISOL facilities in Europe, and good perspectives for the implementation of the relative Physics programs.

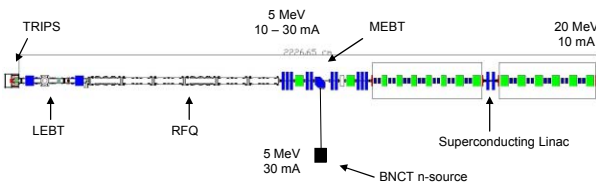

Figure 5: The SPES-1 project layout at LNL-INFN.

AKNOWLEDGMENTS

The author wishes to thank A. Mueller, coordinator of the Driver Accelerator task of EURISOL, G. Fortuna, spoke person of EURISOL-DS and M.H. Moscatello for very informative discussions.

REFERENCES

[1] see for example M. Lindroos "Review of ISOL-Type Radioactive Beam Facility" EPAC 04, Lucerne, in publication.
[2] W. Henning "FAIR-An International Accelerator Facility for Research With Ions and Antiprotons" ibid.
[3] EURISOL report (coordinator J. Vervier) available on line http://www.ganil.fr/eurisol/
[4] P. Schmor "Developments and Future Plans at ISAC/ TRIUMF" This conf. p. 306.
[5] M.H. Moscatello this conference and http://www.ganil.fr/research/developments/spiral2/ index.html
[6] SPES Technical design report (A. Bracco and A. Pisent editors) LNL-INFN(REP) 181/2002 and http://www.lnl.infn.it/~spes/
[7] J-L. Biarrotte et al. "High Intensity Driver Accelerators For EURISOL" Proc. of EPAC 02, p. 1007
[8] B. Visentin et al "Experimental results on 700 MHz multicell superconducting cavity for proton linac" Proceedings of 2003 PAC, p.1303
[9] A. Bosotti et al. "Rf Tests Of The Beta=0.5 Five Cell TRASCO Cavities" EPAC 04, in publication.
[10] P-Y Beauvais "Recent evolutions in the design of the French High Intensity Proton Injector (IPHI)" EPAC 04, in publication.
[11] A. Pisent, M. Comunian, A. Palmieri, E. Fagotti, G.V. La manna, S. Mathot "The TRASCO-SPES RFQ" this conference.
[12] M. Vretenar et al "Design of The LINAC4, A New Injector for The CERN Booster" these proc. p. 353.
[13] E. Fagotti et al "Characterization of beam parameters and Halo for a High intensity RFQ output under different current regimes" this conference.
[14] J. R. Delayen et al., Nucl. Instr. Meth. B56/57, 1025 (1991).
[15] A. Facco et al "RF testing of the TRASCO Superconducting Reentrant Cavità for High Intensity Proton Beams" proc of EPAC 2002, Paris, 2002.
[16] A. Facco et al. "Construction and testing of the β=0.31, 352 MHz Superconducting Half Wave Resonator for the SPES project" Proceedings of EPAC04, to be published, 2004.
[17] G. Olry et al "Recent Developments on Super-conducting β035 and β015 Spoke Cavities at IPN for low and Medium Energy Sections of Proton Linear Accelerators" Proceedings of EPAC04, to be published, 2004.
[18] V. Andreev et al. "Ladder resonator: A novel superconducting structure for the very low beta part of high current linacs" Phys. Rev. ST Accel. Beams 6, 040101 (2003)
[19] E. Fagotti et al." Beam Dynamics Issues of SPES-1 Linac" this proc. p. 395
[20] Agosteo S., et al. "Advances in the INFN-Legnaro BNCT Project for Skin Melanoma". Proc. of Int. Physical and Clinical Workshop on BNCT. Candiolo (Torino), February 7, 2001
[21] A. Pisent and J. Esposito "An Accelerator Based BNCT Facility: The Project SPES at INFN Legnaro" Proc of the International Workshop on Neutron Capture Therapy, November 28th, 2003 S. Cataldo, Pisa .

Challenges of Linac Driven Light Sources

C. Bocchetta, ELETTRA, Basovizza, Trieste

Abstract

The use of linacs allows novel light sources to be conceived by not being limited by equilibrium dynamics or IBS effects. These new sources can be single pass or recirculated (with or without energy recovery) or linac augmented storage rings. They allow tuneable polarised radiation of unprecedented brilliance, short pulse lengths that may reach the atto-second scale and full coherence. Both SC and NC machines are being proposed, designed and constructed. Photon output characteristics range from incoherent synchrotron radiation to SASE to seeded HGHG. The proposed beams can be low to high average current and pulse time structures range from CW to highly variable with mutual exclusion amongst different forms of operation. The multiple challenges of these machines reside not only in the requirement of beams of extremely high quality (energy, emittance, energy-spread and temporal stability) for the brightest, shortest wavelength sources but also in the demanding technologies and control of beam-machine interactions for the high current energy recovery ones. The paper gives an overview of these broad challenges and of the directions taken to reach the objectives of a user facility.

NO SUBMISSION RECEIVED

PAL LINAC UPGRADE FOR A 1-3 Å XFEL

J. S. Oh, W. Namkung, Pohang Accelerator Laboratory, POSTECH, Pohang 790-784, Korea
Y. Kim, Deutsches Elektronen-Synchrotron DESY, D-22603 Hamburg, Germany

Abstract

With the successful SASE FEL saturation at 80-nm wavelength at TTF1, TTF2 will begin re-commissioning in the fall of 2004 as an FEL user facility to 6 nm with 1-GeV beams. The high gain harmonic generation is also confirmed by the DUV-FEL experiments at 266 nm with seeding wavelength at 800 nm. In order to realize a hard X-ray SASE FEL (SASE XFEL) with a lower energy beams, we need a long in-vacuum mini-gap undulator and a GeV-scale FEL driving linac that can supply an extremely low slice emittance, a high peak current, and an extremely low slice energy spread. PAL is operating a 2.5-GeV electron linac as a full-energy injector to the PLS storage ring. By adding an RF photo-cathode gun, two bunch compressors, and a 0.5-GeV S-band injector linac to the existing PLS linac, and by installing a 60-m long in-vacuum undulator, the PLS linac can be converted to a SASE XFEL facility (PAL XFEL) which supplies coherent X-ray down to 0.3-nm wavelength. The third harmonic enhancement technique can supply coherent hard X-ray beams to 0.1 nm. The technical parameters related to these goals are examined, and preliminary design details are reviewed for the PAL linac upgrade idea for a 1-3 Å PAL XFEL.

INTRODUCTION

The requirements of X-ray from scientific users are radiation wavelength of 0.1nm, pulse length of 20 fs (FWHM). PAL operates a 2.5-GeV electron linac, the 3rd largest in the world, as a full-energy injector to the PLS storage ring [1]. The PAL 2.5-GeV linac can be converted to an X-ray free electron laser (XFEL) facility driven by a self-amplified spontaneous emission (SASE) mode, which supplies coherent X-rays down to 0.3-nm wavelength. The third harmonic enhancement technique on the electron beam or advanced X-ray laser optics will be applied to obtain radiation wavelengths of 0.1 nm. The design goal is for the undulator to be less than 60 m in total length. The linac should supply highly bright 3-GeV beams to a 60-m long in-vacuum undulator with a 3-mm gap and a 12.5-mm period, of which emittance of 1.5 mm-mrad, a peak current of 4 kA, and a low energy spread of 0.02% [2].

Table 1 shows the comparison of single bunch specifications between the PLS linac and PAL XFEL. Normalized emittance should be 100 times improved, which requires a low emittance gun and high gradient acceleration at low energy region to preserve the emittance. The suitable bunch compression is one of key technique to realize the high peak current, also.

Questions are how to utilize the existing 2.5-GeV linac and how to keep the operation mode as a full energy injector for PLS 2.5-GeV storage ring.

Therefore we have to minimize the modification of existing linac layout. We have to find matching conditions to provide flexible beam operation for both applications. Also the site is already fixed and limits the maximum size of a new machine scale. The performance and stability of the 2.5-GeV linac is also challenging to meet the strict SASE requirements.

Table 1: Bunch specifications of PLS linac and XFEL

Parameter	PLS Linac	XFEL
Beam energy	2.5 GeV	3.0 GeV
Normalized emittance	150 μm-rad	1.5 μm-rad
FWHM bunch length	13 ps	0.23 ps
RMS energy spread	0.26%	0.02%
Bunch charge	0.43 nC*	1.0 nC
Peak current	33 A*	4 kA
Repetition rate	10 Hz	60 Hz

* 2-A gun current and 62% transmission

PAL XFEL PROGRAM

The fundamental radiation wavelength λ_x of an undulator is given by

$$\lambda_x = \frac{\lambda_u}{2\gamma^2}(1 + K^2/2), \quad \gamma = E_o / 0.511, \quad K = 0.934 B_u \lambda_u ,$$

where E_o is the beam energy in MeV, B_u is the peak magnetic field of the undulator in Tesla, and λ_u is the undulator period in cm. The peak magnetic field B_u of a 45°-magnetized undulator with $H = \lambda_u/2$ is given by

$$B_u = \frac{4\sqrt{2}B_r}{\pi} \sum_{n=1,5,9}^{\infty} \frac{1}{n}(1 - e^{-2n\pi H/\lambda_u}) e^{-n\pi g/\lambda_u} ,$$

where B_r is assumed 1.19 Tesla with $Nd_2Fe_{14}B$ magnets, H is the block height, and g is full-gap length [3]. Fig. 1 shows the undulator geometry with 45°-magnetization.

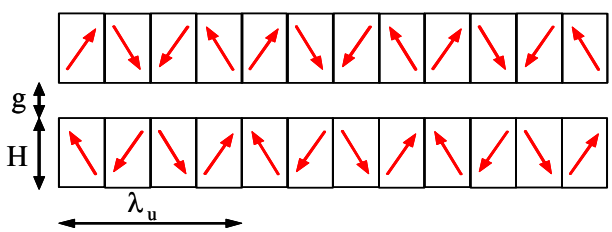

Figure 1: Undulator geometry with 45°-magnetization.

Either a short-period undulator or a high-energy beam can provide short-wave radiation. A short-period undulator will give a compact FEL machine for a short-wave radiation. It is important to keep reasonably large undulator parameter K to obtain a short saturation length. An in-vacuum mini-gap undulator can meet this idea that was introduced by the SCSS project at SPring-8 [4]. Fig. 2 shows the 0.3-nm XFEL curves with saturation lengths of 40, 50, 60 m and beam energy of 2.5, 3.0, 3.5 GeV, respectively. The one of possible solution that is reasonably economic, to meet the saturation length less than 60 m with margin is to use 3-GeV beam with a 3-mm gap and a 12.5-mm period for a undulator.

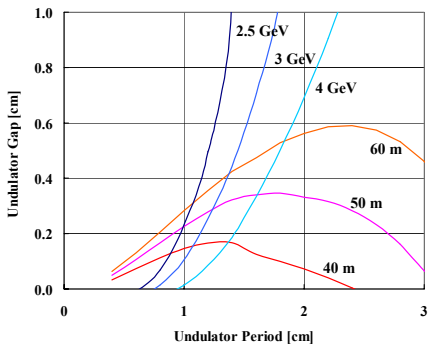

Figure 2: Undulator period and gap length for 0.3-nm SASE for saturation lengths (40, 50, 60 m) and beam energy (2.5, 3, 4 GeV).

Table 2 summarizes the FEL parameters for a 0.3-nm PAL-XFEL. The undulator beta value is adjusted to obtain as short a saturation length as possible. Undulator saturation length is approximately 20 times 3D gain length L_g.

Table 2: FEL parameters for 0.3-nm PAL XFEL

Undulator period [mm]	12.5
Undulator gap [mm]	3.0
Peak magnetic field [T]	0.97
Undulator parameter, K	1.14
Beta [m]	15
Saturation length [m]	52
FEL parameter	4.3e-4
1D gain length [m], L_{1d}	1.35
3D gain length correction, η*	0.97
Gain length [m], L_g	2.67
Peak power [GW]	2.1
Peak brightness [x 10^{32}]**	1.4

* $L_g = (1+\eta)\, L_{1d}$

** photons/sec-mm^2-mrad^2-0.1%BW

The 3D gain length correction and 3D gain length according to normalized emittance are calculated according to M. Xie [5] and shown in Fig. 3. In general, the electron beam emittance is required to be equal or less than the natural emittance of the FEL radiation. The gain correction factor of PAL XFEL is a bit larger than the LCLS and TESLA XFEL due to rather large normalized emittance relative to the natural radiation emittance. However, due to the small periodic length of an undulator, the gain length becomes small. Therefore, it is possible to realized compact X-ray FEL by an in-vacuum undulator with small period and rather a low energy linear accelerator.

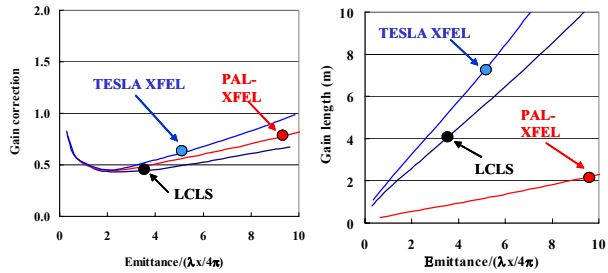

Figure 3: 3D Gain length and 3D gain correction factor.

The solid line 'PAL XFEL' in Fig. 4 shows the expected peak brilliance of the fundamental radiation of PAL-XFEL. The three circles on the line correspond to beam energies of 2.0, 2.5, and 3.0 GeV. The peak brilliance of PAL-XFEL is 10^{12} time higher than the U7 undulator radiation from the PLS 3rd generation storage ring. The spontaneous radiation from the undulator of PAL XFEL is also a hard X-ray and 10^{10} times brighter than the synchrotron radiation from the PLS bending magnet.

The 'PAL VUV FEL' assumes to use a conventional undulator with a period of 3 cm and a gap length of 1.2 cm to generate 1-4 nm VUV radiation by changing the beam energy from 1.5-3.0 GeV. The 'PAL 0.1-nm XFEL' denotes the possible 0.1-nm PAL-XFEL with the third harmonic enhancement technique employing an additional undulator with a shorter periodic length.

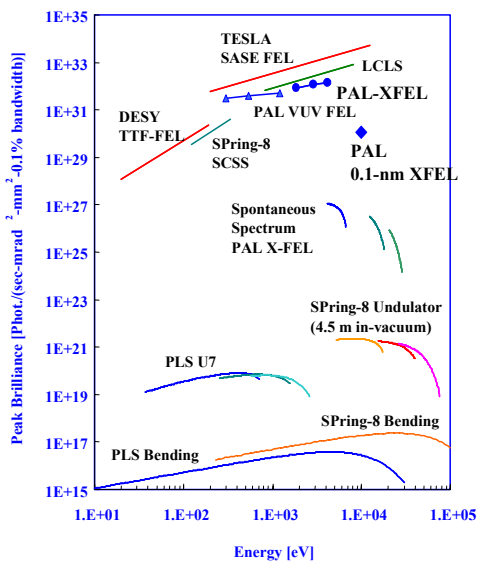

Figure 4: Peak brilliance for PAL XFEL.

PLS LINAC UPGRADE

The existing 2.5-GeV S-band PLS linac can be converted to X-ray FEL driver with a new S-band photo-injector, and a new S-band FEL injector linac, two bunch compressors. Fig. 5 shows one of possible upgrade layout of the PAL linac including a new undulator system (U1 to U13). The injector consists of a low-emittance laser-driven photo-cathode gun, three S-band accelerating modules (X1, X2, X3), and two bunch compressors (BC1, BC2).

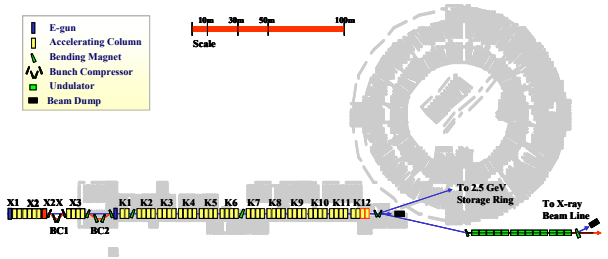

Figure 5: PLS linac upgrade scheme for PAL XFEL.

The previous design concept of an injector system presented in FEL2003 is somewhat improved in this work [2]. First of all, the dog-leg scheme in the new injector is modified to align the center line of the new injector to the one of existing linac to suppress emittance degradation due to CSR as possible as. Also two bunch compressors are located in the new injector system to minimize the modification of existing layout of PLS 2.5-GeV linac.

The S-band photo-injector is consisted of a Cu cathode and 1.6-cell S-band RF cavity. Table 3 shows beam parameters at the cathode. The photoelectron beam is generated by 10-ps, 500-μJ, and 260-nm UV laser. It is accelerated to 7 MeV by a high gradient of 120 MV/m within 16.8-cm length. The high gradient acceleration is essential to preserve the beam emittance under high space charge force at the low energy.

Table 3: Beam parameters at the cathode

Bunch length	10 ps (FWHM), 2.9 ps (rms)
Rise time (10-90%)	0.7 ps
Spot size	0.6 mm (rms)
Thermal emittance	0.6 μm
Peak gradient	120 MV/m
Peak solenoid field	2.71 kG at 19.1 cm

The lattice design is shown in Fig. 6 from the new injector to the end of main linac. The existing quadrupole magnets along the main linac are optimised as it is. Twiss parameters in the existing linac are possible to be re-optimised. Lattice optimisation is to find solution to minimize the second term in the following equation for the relative emittance growth [6]. The optimum condition is given when the alpha value is about 0 and beta function is about 3.

$$\frac{\varepsilon}{\varepsilon_o}=\sqrt{1+\frac{(0.22)^2}{36}\frac{\gamma_e^2 N^2}{\gamma\varepsilon_N\beta}\left(\frac{|\theta|^5 L_B}{\sigma_z^4}\right)^{\frac{2}{3}}[L_B^2(1+\alpha^2)+9\beta^2+6\alpha\beta L_B]}$$

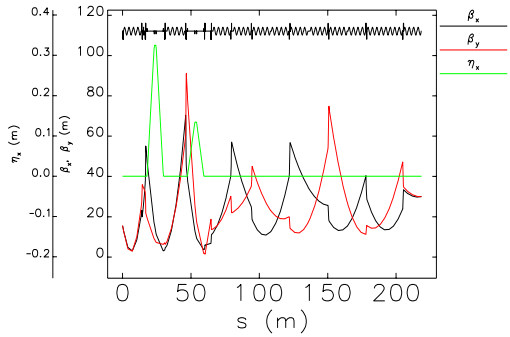

Figure 6: Lattice profile along the linac.

Against projected parameter dilution due to CSR and chromatic effect, adopted lattice design concepts are as follows: long drift space to reduce bending angle for a required momentum compaction R56, small bending angle at a large energy spread, large compression factor at BC1 and small compression factor at BC2. Strong focusing lattice around BC to reduce CSR induced emittance growth, small quadrupole length around BCs to reduce the chromatic effects, smaller maximum beta-function of ~ 60 m at BC1 entrance, larger maximum beta-function at BC2 entrance after reducing energy spread at BC2 are also effective. Against slice parameter dilution due to the micro-bunching instability, following design concepts are adopted: normal 4-bend chicane instead of S-type chicane, large uncorrelated energy spread at BC2 by putting the BC2 at low energy region. We do not consider laser beam heater or super conducting wiggler. Against the tight jitter tolerance, followings are considered: two stage BC, RF gun driven by its own klystron, each S-band accelerating column before BC2 driven by each own klystron, X-band correction cavity possibly driven by two X-band klystrons. Fig. 7 shows the detail layout of a new FEL injector linac including two bunch compressors and new accelerators. X2 is a modulator to make suitable energy spread for bunch compression. X2X is a linearizer of non-linear energy spread caused in the modulator.

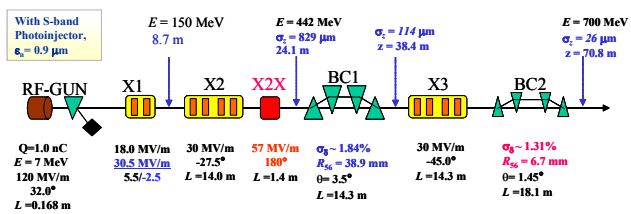

Figure 7: BCs and a new accelerator layout.

Detail layout of BC1 is shown in Fig. 8. The net chicane length is 12.2 m. Maximum beam offset from the centerline is 33 cm. The total chicane length becomes 17 m including focusing quadruples.

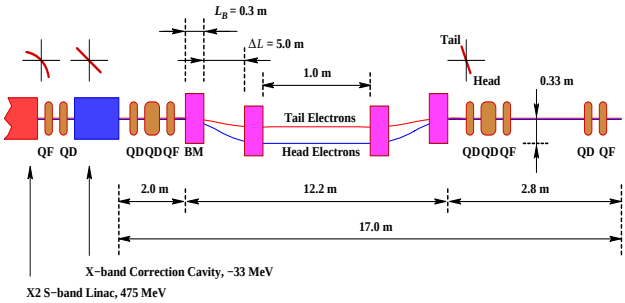

Figure 8: Detail layout of BC1.

Table 4 shows the design parameters of bunch compressor BC1 and BC2. BC2 layout is almost same as BC1. All uncorrelated energy spread is estimated at ± 0.1 mm core region. Initial uncorrelated energy spread at BC2 is increased after compression by BC1. The uncorrelated energy deviation at BC2 is larger than $1x10^{-5}$ that is required to suppress the micro-bunching instability.

Table 4: Design parameters of bunch compressors

Parameter	BC1	BC2
BC type	Two stage	Two stage
Beam energy	442 MeV	700 MeV
Relative energy spread	1.84%	1.31%
Uncorrelated energy spread	$9.2x10^{-6}$	$4.3x10^{-5}$
Bending angle	3.50 deg	1.45 deg
Momentum compaction R56	38.9 mm	6.70 mm
Total chicane length	12.2 m	12.2 m
Dipole length	0.3 m	0.3 m
Drift length ΔL	5.0 m	5.0 m
Initial rms bunch length	820 μm	114 μm
Final rms bunch length	114 μm	26 μm
Compression factor	7.2	4.38
Initial projected emittance	0.90 μm	1.01 μm
Final projected emittance	1.01 μm	1.12 μm

S2E SIMULATION

We examined beam parameters by the ASTRA simulation considering the space charge force at low energy. Lattice is designed by using ELEGANT code from X2 accelerating unit to the end of existing linac, which includes CSR effect in the bunch compressor and geometric wake field effect in the accelerating columns. The number of simulated particles is 200,000 in this study.

The energy spread along the bunch length is linearized by X-band linac as shown in Fig. 9. At the entrance of BC1, beam energy is 441.5 MeV, energy spread is 1.835%, beam size is 230 μm (σ_x), and 147 μm (σ_y), bunch length is 829 μm, emittance is 0.953 μm (ε_{nx}) and 0.945 μm (ε_{ny}).

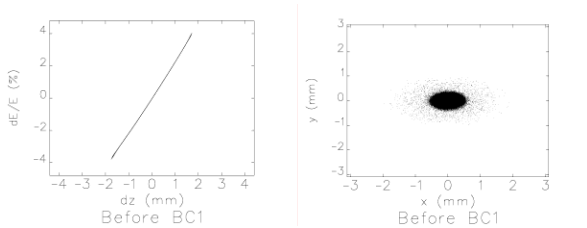

Figure 9: Phase spaces before BC1.

At the end of linac, beam energy is 3.389 GeV, energy spread is 0.033%, beam size is 68.1 μm (σ_x), and 61.9 μm (σ_y), bunch length is 26 μm, normalized emittance is 1.116 μm (ε_{nx}) and 1.004 μm (ε_{ny}) in this simulation. Longitudinal short-range wake-field damps the energy spread at the tail region so that the energy profile along the bunch becomes more flat and uniform as shown in Fig. 10.

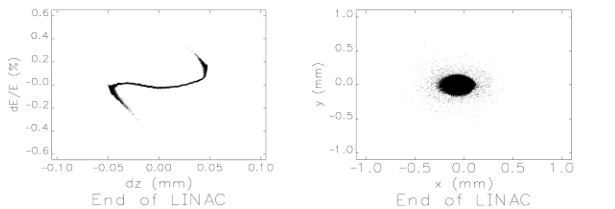

Figure 10: Phase spaces at the end of linac.

Fig. 11 shows the variation of the energy spread and the bunch length along the linac. The relative energy spread is continuously increased to 1.84% until the entrance of BC1 to fit the necessary compression factor. The variation of energy spread in the BC2 is kept low by small CSR effect. Increasing the beam energy, the energy spread is continuously decreased to 0.03% at the end of linac. The large compression at BC1 and small compression at BC2 are clearly shown in the figure.

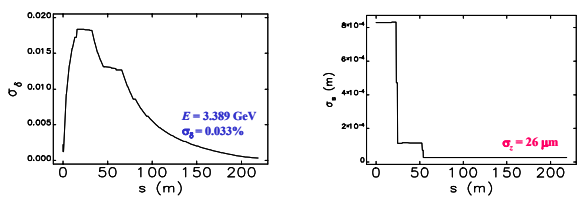

Figure 11: Energy spread and bunch length along linac.

Fig. 12 shows the beam quality at the end of linac. The required beam parameters for FEL lasing at the undulator entrance correspond to dotted lines for the peak current of 4 kA, normalized emittance of 1.5 μm, and energy spread of 0.02%. The normalized emittance, that is most sensitive FEL parameter, is well below the requirement along the whole bunch, which gives reasonable margin for safe saturation within 60-m long undulator. The lowest peak current along the bunch is about 20% less than 4 kA. The slice emittance is also 20% lower than the nominal value of 1.5 μm. Because the saturation length is

more sensitive to the emittance, it is safe to make saturation along the whole bunch.

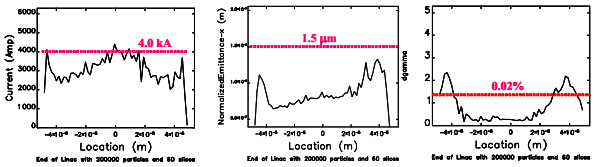

Figure 12: Beam quality at the end of linac.

DISCUSSION

Fig. 13 shows the sensitivity of saturation length on the system performance for beam emittance, energy spread, bunch length, and undulator beta value. The system parameters are normalized by the nominal values. The most sensitive parameter is the emittance of the electron beam. Therefore a low emittance gun is essential for PAL XFEL.

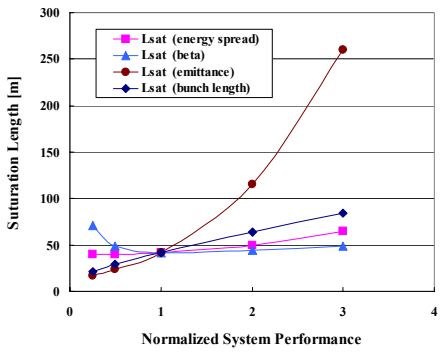

Figure 13: Saturation length vs. system performance.

Fig. 14 shows the distribution of uncorrelated energy spread along the bunch length. At the entrance of BC1, uncorrelated energy deviation at ± 1.0 mm core is 4 keV at the beam energy of 442 MeV. It is increase to 30 keV by high compression factor at the BC1. If we consider space charge force, this will be increased further at BC2. The increased uncorrelated energy spread at the BC2 suppresses micro-bunching instabilities.

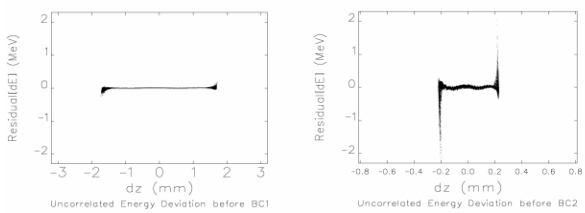

Figure 14: Uncorrelated energy spread at the entrance of BC1 and BC2.

The bunch length can be made shorter by the slit placed in the middle of bunch compressor [7]. The bunch length at the center of BC2 is 70 μm and the transverse beam size is 1.74 mm as shown in Fig. 15. The shaded area represents a 300-μm slit at this location. By adding the slit, the head and tail parts of the bunch can be removed. Then the bunch length can be further reduced down to 20 fs.

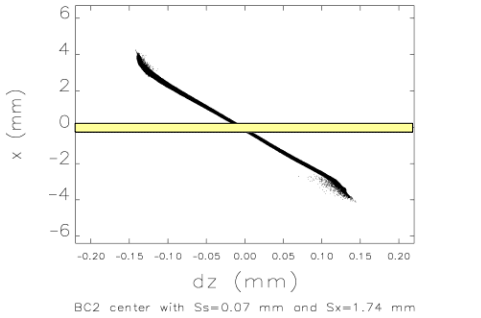

Figure 15: Beam size at the center of BC2.

The wake field effect on the electron beams in the undulator and the beam quality degradation due to the magnet field error are sensitive to FEL process. The jitter and sensitivity analysis on the combined parameter space is to be intensively followed. It is necessary to analyse hardware upgrade scheme and stability requirements with related technical parameters.

ACKNOWLEDGMENTS

This work is supported by POSCO and the Ministry of Science and Technology (MOST) of Korea.

REFERENCES

[1] http://pal.postech.ac.kr/
[2] J. S. Oh et al., “0.3-nm SASE FEL at PAL,” Nucl. Instr. Meth. A528, 582 (2004)
[3] Maréchal X., Chavanne J., Elleaume P., On 2D periodic magnetic field, ESRF-SR/ID 90-38 (1990)
[4] T. Shintake et al., “SPring-8 Compact SASE Source (SCSS),” in Proc. the SPIE2001, San Diego, USA, 2001; http://www-xfel.spring8.or.jp
[5] M. Xie, “Design Optimization for an X-ray Free Electron Laser Driven by SLAC Linac,” LBL Preprint No-36038, 1995
[6] T. Limberg, “Emittance Growth in the LCLS due to Coherent Synchrotron Radiation,” SLAC internal note, Oct. 1997
[7] P. Emma et al. SLAC-PUB-10002

KEKB INJECTOR LINAC AND UPGRADE FOR SUPERKEKB

S. Michizono#, for the KEK electron/positron Injector Linac and the Linac Commissioning Group, KEK, Tsukuba, Japan

Abstract

The KEB injector linac delivers electrons and positrons to four rings (KEKB LER, KEK HER, PF and PF-AR). The operational status of the KEKB injector linac is summarized. The R&D work concerning diagnostics of the klystrons and the beam-quality are also described. An upgrade plan of the injector linac using a C-band rf system is under consideration for SuperKEKB. A C-band acceleration structure was installed in the KEKB linac after rf conditioning at more than 40 MW. An energy gain of more than 40 MV/m was confirmed by the beam acceleration. The C-band acceleration unit has been operated continuously for a stability test.

INTRODUCTION

The KEKB Injector linac has provided 8 GeV electrons to KEKB HER and 3.5 GeV positrons to KEKB LER [1]. KEKB has recorded the highest luminosity to which the linac contributes with an advanced operational stability for about 7,000 hours per year. Double bunch injection and continuous injection (CI) schemes have been adopted.

The SuperKEKB project [2], aiming for a ten-times higher luminosity, is under consideration as an upgrade of KEKB. In this upgrade, the injector linac has to increase the positron acceleration energy from 3.5 GeV to 8 GeV [3]. One of the plans for this upgrade is to double the acceleration field (from 20 to 40 MV/m) with a C-band (5712 MHz) rf system. The newly developed components are summarized.

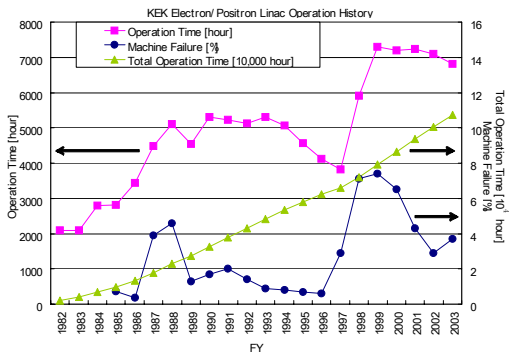

Figure 1: Operation history of the KEKB linac.

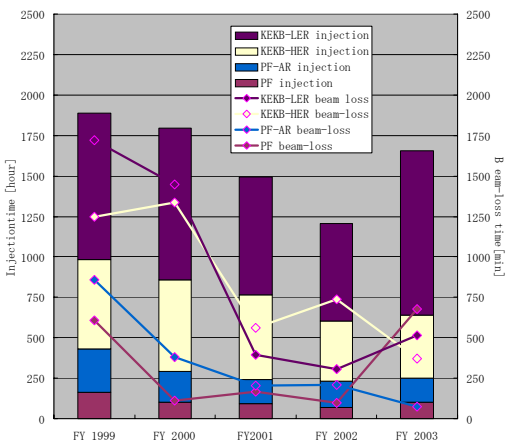

Figure 2: Injection time and beam-loss time to PF, PF-AR, KEKB LER and KEKB HER.

#shinichiro.michizono@kek.jp

OPERATION STAUS OF KEKB LINAC

Operation History and Statistics

Construction of the linac started in 1978, and operation started in 1982. Electron/positron beams were injected to Tristan from 1986 to 1994. The KEKB rings started their operations from 1998. The operation time is presently about 7,000 hours per year. The history of the operation time is shown in Figure 1. The accumulating operation time reached 100,000 hours on Mar. 3, 2003. The failure ratio has been about 5%. Figure 2 shows the injection time delivered to 4 kinds of rings. The KEKB injection time is more than 80% of the total injection time. The beam-loss time is shorter than the value obtained from the machine failure in Figure 1 because many of failed modules can be replaced by one of the stand-by modules before beam operation. The larger beam-loss time at PF in FY 2003 was caused by a problem of old modules in the trigger system. It was replaced last spring.

Continuous Injection (CI) Scheme

From January, 2004, the CI scheme to KEKB started for higher luminosity operation. CI operation enables us to increase the accumulation luminosity by about 20-

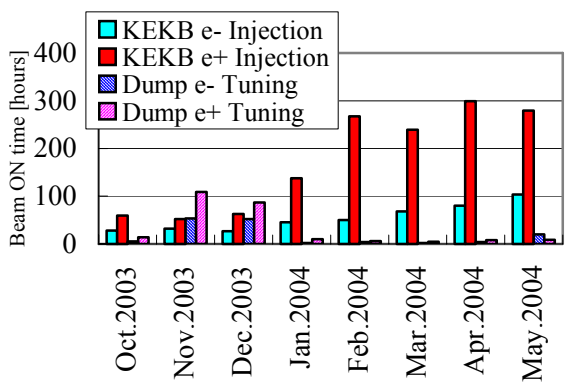

Figure 3: Status of the beam on time. The CI scheme started from Jan, 2004, the beam on time for LER (e+) increased and the tuning time (Dump) decreased.

30%, and it reaches about 1/fb/day. The positron and electron beams are switched about every 10 minutes. The injection rates at CI are 1.0 mA/s for electrons at 10 Hz and 0.5 mA/s for positrons at 10 Hz, respectively. Figure 3 shows the beam-injection time this year. Since the accumulated current is larger and the lifetime of the positrons in LER is shorter than that of HER, the beam on time is longer compared with that of electrons (HER). After CI started, it became difficult to have time for "tuning", including beam-optics correction and/or rf phase optimization. This tuning is now carried out on demand.

Dip Test of the Klystrons

Figure 4 shows the operation time of the klystron-assemblies. Many assemblies have been used for more than 40,000 hours. These were installed during the KEKB construction and failures caused by the emission decrease can become a serious problem in the near future.

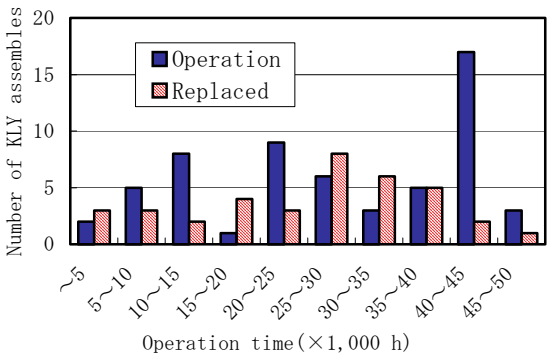

Figure 4: Operation and replaced time of the klystron assemblies. The assemblies installed at the beginning of the KEKB were used for more than 40,000 hours.

In order to catch a slight indication of the emission decrease with a limited diagnostic time (less than 10 minutes), dip tests [4] have been applied to all of the klystrons periodically [5]. Figure 5 shows an example of a dip test. The heater of the klystron is cut for 60 seconds and the emission decrease is monitored. A gradual increase in the dips with operation time is observed, which corresponds to the emission decrease. Such a klystron is replaced during the shutdown time or maintenance time.

Strip Line-Type BPM with Eight Electrodes

Non-destructive procedures are required to diagnose of the beam quality, especially at the CI scheme. The important parameters of the beam quality are the beam energy, beam position, energy spread and emittance. Feedback systems for the beam energy and the beam position are successfully operated at the KEK linac [6]. As for the beam emittance, wire-scanner measurements have been made during injection [7]. The energy spread had been measured using a screen monitor during the beam dump time for linac tuning.

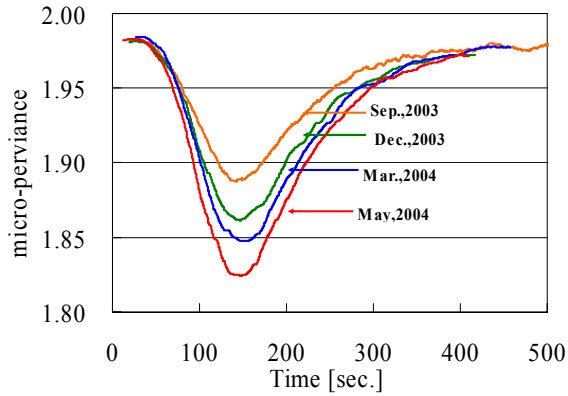

Figure 5: Result of the dip test. This example shows the decrease in emission with time. Such a klystron is replaced prior to a serious emission decrease.

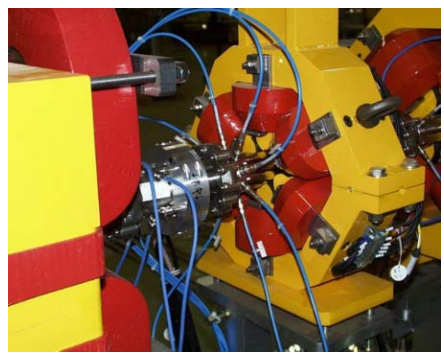

Figure 6: Photograph of the eight-electrodes BPM.

In order to measure the energy spread during injection, a stripline-type BPM with eight electrodes (Figure 6) is utilized [8,9]. This BPM has also been tested as the energy spread feedback for the electron beam and will be tested for the positron beam in this year.

UPGRADE FOR SUPER-KEKB

Upgrade Plan

Figure 7 shows one of the upgrade plans of the KEKB injector for SuperKEKB. Positrons with 8 GeV energy and electron with 3.5 GeV energy are required in this plan. The positron energy is boosted by the C-band accelerator modules. Electron/positron injections are switched by the kicker before the target, and both beams go through independent beam lines. The emittance of the positron beam is reduced with a damping ring. Both of the 2 bunches are used for positron and electron beams.

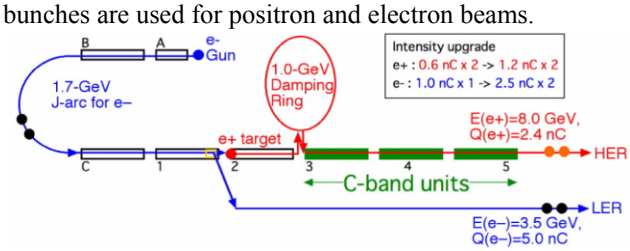

Figure 7: Layout of the linac upgrade for SuperKEKB.

In this plan, twice the number of modulators should be installed in the C-band units. Compact modulators with inverter power supplies are adopted. Figure 8 shows a schematic layout of the rf modules.

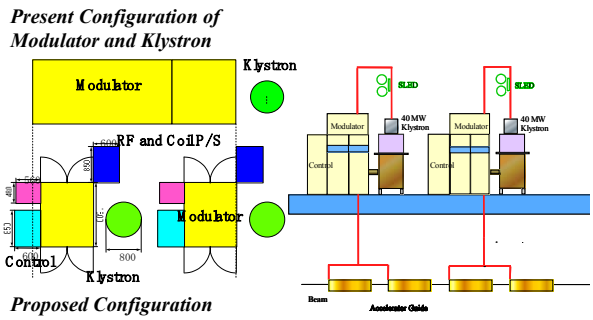

Figure 8: Schematic of the configuration of modulators and klystrons.

A C-band unit will consist of a compact modulator, a klystron, a waveguide window, a pulse compressor (SKIP) and two acceleration structures. In order to develop this upgrade, the C-band components are being examined. The layout of the rf system is shown in Figure 9.

RF Source

A driver klystron (100 kW) will drive eight high-power klystrons. The existing C-band 200 kW klystron for a weather observation station (Mitsubishi Electric Company) is being examined by retuning. The driver klystron (SB) can deliver more than 100 kW (at the applied voltage of 35 kV). The same modulator and high-voltage supply as that to the existing S-band system is used.

A high-power klystron (Toshiba E3726, 50 MW, 50 pps [10]) is used to examine the rf components and to test the beam acceleration. The existing pulse transformer (1:15) and oil tank are reused in this experiment. The operation conditions of a high-power klystron are compared with the existing S-band unit in Table 1.

Table 1: Operation parameters of the C-band klystron

	S-band	C-band
RF output	41 MW	40 MW
Typical charging voltage	42 kV	41 kV
Typical applied voltage	290 kV	325 kV
Pulse duration	4 μs	2μs

Inverter Power Supply

An inverter power supply is a key device for a compact modulator. A photograph of the inverter power supply is shown in Figure 10. The maximum output voltage is 50 kV with a voltage regulation of ±0.1%. Several problems, such as IGBT breakdowns, were found during operation. Improvements of the IGBT circuits and adoption of the durable IGBT have been applied and it runs in the klystron gallery.

Figure 10: Photograph of the inverter power supply. The size is 449mm(H)x 480mm(W)x 630mm(D).

Pulse Compressor (SKIP)

A C-band pulse compressor (SKIP: SuperKEKB Injector Pulse Compressor) was designed and tested this summer. The specifications of the pulse compressor are summarized in Table 2. Since the Q value decrease at high frequency, the TE_{038} mode (same mode to LIPS in CERN [11]) was chosen instead of the present TE_{015} mode at the C-band pulse compressor. The dimensions of

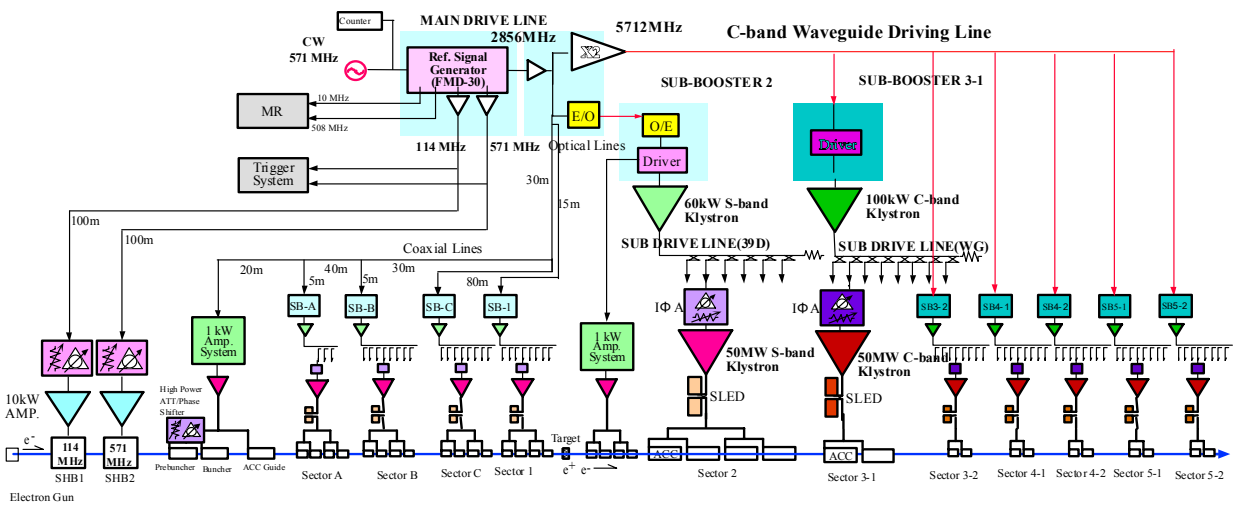

Figure 9: Rf system planned for the linac upgrade.

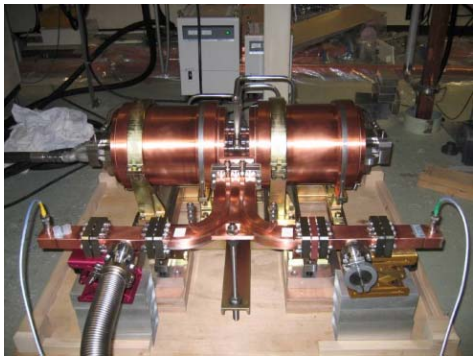

Figure 11: Photograph of SKIP.

the cavity become almost the same as that of the present KEKB-SLED.

Figure 11 shows a photograph of the SKIP. The maximum output power of 200 MW is obtained and the power magnification factor is 4.7 [12]. It will be installed in the klystron gallery for long-time operation with beam acceleration.

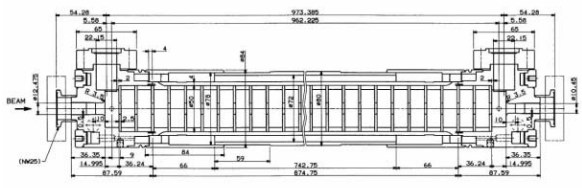

Figure 12: C-band acceleration structure.

Acceleration Structure

The acceleration structure is designed based on the present S-band acceleration structure (Figure12). High-power tests were carried out up to more than 43 MW at the test stand [13]. During the high-power test, an analysis of the breakdown location was carried out by rf signals and acoustic sensors. It revealed that the input coupler was one of the sources of the breakdown, probably due to the thin and sharp-edged coupler iris [13]. At the second model, the coupler structure has been re-designed. A high-power test of the second model is scheduled for this September.

RF Window

An rf window is utilized in a waveguide system in order to isolate the vacuum and pass rf power. A mix-mode window [14] has been designed [15]. The calculated electric fields at the center and the edge of the ceramics are 20% and 50% less, respectively, compared with the present S-band window. The window has a sufficient band-width of more than 200 MHz (<VSWR 1.2). Figure 13 shows a photograph of the window.

In order to examine the rf window, a resonant ring has also been designed. The resonance condition of the ring is controlled by the operation frequency after adjusting the total length roughly by spacers. The window has been tested up to 300 MW [15]. The window after operation

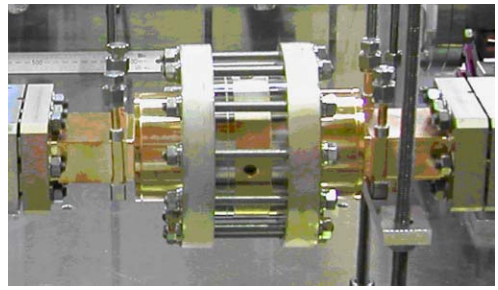

Figure 13: Photograph of the mix-mode window.

showed no damage, and it was installed in the klystron test stand.

Dummy Load

A dummy load is designed based on the present dummy load at the S-band linac. A photograph of the dummy load is shown in Figure 14 The load is used at the C-band acceleration structure, and as a load of the pulse compressor. It has been tested up to a 100 MW peak (at the test of SKIP) and a 2 kW average.

Table 2: Comparison between KEKB-SLED and C-band SKIP

	KEKB-SLED	C-band SKIP
Frequency	2856 MHz	5712 MHz
Resonance mode	TE_{015}	TE_{038}
Length	33.59 cm	30.72 cm
Cavity diameter	20.51 cm	23.28 cm
Qvalue (Q_0)	90,000	130,000
Coupling	6.4	6.6

Figure 14: Photograph of the dummy load.

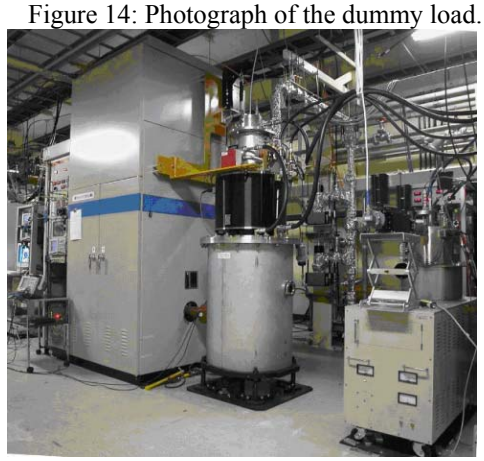

Figure 15: Photograph of the C-band unit installed in the klystron gallery.

Figure 16: Photograph of the C-band acceleration unit installed in the beam-line.

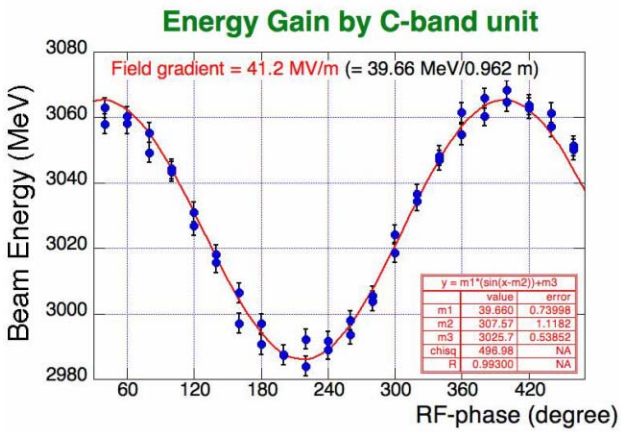

Figure 17: Result of beam-acceleration.

Operation Status at Klystron Gallery

A C-band unit (a driver klystron, a high-power klystron with a compact modulator, an rf window and an acceleration structure) was installed in the klystron gallery and beam line of the linac in Aug., 2003. The first model was installed into the beam line of the KEKB linac (Figures 15 and 16) in August, 2003. An acceleration gradient of more than 40 MV/m has been achieved as shown in Figure 17. The acceleration structure has been operated in the beam line, and it has also been confirmed that the smaller aperture of the C-band structure does not induce any beam characteristics. The unit has been operated for about 6,000 hours, and breakdown statistics of the acceleration structure and a long-time test of the components have been carried out [16]. SKIP was installed in the klystron gallery this summer, and beam acceleration tests with SKIP and a acceleration structure will be examined this Autumn.

SUMMARY

The KEKB linac delivers electron/positron-beams to 4 kinds of rings. The stability of the linac, where the failure rate is less than 5%, supports an efficient operation of the rings. The continuous-injection mode of the KEKB rings requires high-quality managements of the components. Dip tests of the klystrons are helpful to diagnose the klystrons. The eight-electrodes BPM has been tested concerning the feedback of the beam energy spread.

An upgrade for the Super KEKB is under consideration, and the C-band components have been tested. The acceleration structure, a pulse compressor (SKIP), has showed the good performance at a high-power test. Other components, such as the inverter power supply, rf window and dummy load have also been examined, and satisfy our specifications. Beam acceleration tests using SKIP, and high-power tests of the second acceleration structure are scheduled for this Autumn.

REFERENCES

[1] S.Kurokawa and E.Kikutani, Nucl. Instrum. Methods Phys. Res. A 499 (2003) 1.
[2] SuperKEKB Letter of Intent (LoI), KEK Report 04-4 ,August,2004, http://belle.kek.jp/superb/loi/
[3] T.Kamitani, EPAC 2002, Paris, p.1088.
[4] A.S.Gilmour jr., Ch.5 of "Principles of Traveling Wave Tube", Arthch House INC.,1994.
[5] K.Nakao et al., Proc. of the 29th Linear Acclerator Meeting in Japan, Aug. 2004. (in Japanese)
[6] K.Furukawa, "THE PRESENT PERFORMANCE AND FUTURE UPGRADE OF THE KEKB ELECTRON LINAC", Linac2002, Gyeongju,p.380.
[7] I.Abe et al., Nucl. Instrum. Methods Phys. Res. A 499 (2003) 167.
[8] T.Suwada, M.Satoh, and K.Furukawa, Phys. Rev. ST Accel. Beams 6 (2003) 032801.
[9] M.Satoh, et al.,"Fast Data-Acquisition System for the Beam-Energy-Spread-Monitor", Proc. of the IX Int. Conf. on Accelerator and Large Experimental Physics Control System 2003, Gyeongju, p.2000.
[10] Y.Ohkubo et al.," THE C-BAND 50MW KLYSTRON USING TRAVELING-WAVE OUTPUT STRUCTURE", Linac98, Chicago, p.932.
[11] A.Fiebig et al.," Design Consideration, Construction and Performance of a SLED Type Radiofrequency Pulse Compressor using very high Q Cylindrical Cavities" , PAC1987, Washington D.C., p.1931.
[12] T.Sugimura et al., "SKIP - a pulse compressor for SuperKEKB Injector ", this conference.
[13] T.Kamitani et al., "Development of C-band accelerating section for SuperKEKB", this conference.
[14] S.Yu.Kazakov, "A New Traveling-Wave Mixed-Mode RF Window With a Low Electric Field in Ceramic-Metal Brazing Area", KEK preprint 98-140, Aug. 1998.
[15] S.Michizono et al., "Development of C-band high-power mix-mode rf window", this conference.
[16] S.Ohsawa et al.,"Development of C-band Accelerator Unit for Super KEKB", this conference.

STATUS OF THE J-PARC LINAC, INITIAL RESULTS AND UPGRADE PLAN

Y. Yamazaki for the J-PARC Accelerator Group,
JAERI, Shirakata-Shirane 2-4, Tokai-mura, Naka-gun, Ibaraki-ken, Japan, and KEK, Oho 1-1, Tsukuba-shi, Ibaraki-ken, Japan

Abstract

The J-PARC linac comprises the voulume-production type negative hydrogen ion source, the 50-keV low-energy beam transport, the 3-MeV RFQ linac with π-mode stabilizing loop, the 50-MeV, 324-MHz Dift-Tube Linac (DTL) with electro quadrupole magnets therein, and 180-MeV separate-type DTL. The construction is on schedule for starting the beam commissioning in September, 2006. The first cavity of DTL already accelerated the beams up to 20 MeV in November, 2003. The beam study results are reported with the measured values of the emittances. The chopper installed to the medium-energy beam transport was already beam-tested with designed rise and falling times. Since the expected beam power of the 3-GeV rapid-cycling synchrotron is only 0.6 MW with an injection energy of 180 MeV, the construction budget for the linac energy recovery to 400 MeV will be immediately submitted to the funding agency after the completion of the present phase of the project. The further upgrade plans to several-MW neutron source and neutrino factory are also presented.

INTRODUCTION

The High-Intensity Proton Accelerator Facility in Japan [1-9], which is a joint project between JAERI (Japan Atomic Energy Research Institute) and KEK (High Energy Accelerator Research Orgainzation), has been referred to as J-PARC, which is the acronym of Japan Proton Accelerator Research Complex. The J-PARC project as agreed by JAERI and KEK comprises the 600-MeV linac, the 3-GeV rapid-cycling synchrotron (RCS), and the 50-GeV proton synchrotron (Main Ring, MR). The 400-MeV beams from the linac are injected to the RCS with a repetition rate of 25 Hz, while the beams are further accelerated up to 600 MeV by the superconducting (SC) linac to be used for the basic study of the Accelerator-Driven Nuclear Waste Transmutation System (ADS). The maximum average current is 333 μA for each of RCS and ADS. The 1-MW beams from the RCS are mostly extracted to the Materials and Life Science Experimental Facility (MLF), where the muon-production and neutron-production targets are located in a series. The 10 % of the beams are used for the muon production. Every 3.3 second, the beams are transported and injected to the MR four times. The ramping time is 1.9 s, while the deceleration takes 0.9 s. The accelerated beams are slowly extracted to the Nuclear and Fundamental Particle Physics Experimental Facility (NPF), and are fast extracted to produce the neutrino beams, which are sent to the SUPERKAMIOKANDE detector located 300-km west. The MR beam power is 0.75 MW at 50 GeV (15 μA). This is a full scope of the J-PARC project as agreed between JAERI and KEK.

When the project was funded to start in Japanese Fiscal Year (JFY) 2001 as a six-year project, the following facilities were shifted to the Phase II (the funded project is referred to as Phase I).

1) The Neutrino Facility
2) The ADS Facility
3) The SC linac from 400 MeV to 600 MeV
4) Half of the NPF Experimental Hall
5) The fly-wheel electric power generator for the MR, which means that the MR can be operated only up to 40 GeV with the above ramping time (if the ramping time is longer, the acceleration up to 50 GeV will be possible).

In the next section the project status and the overall schedule will be reported. Then, the linac scheme is summarized together with its reasoning. After the construction status is reported, the initial results of the beam commissioning up to the 20-MeV Drift-Tube Linac (DTL) are presented in detail. Finally, the upgrade plans proposed so far are described.

PROJECT STATUS

The following three major changes came into the project. First, the Neutrino Facility was approved for the construction starting from April 2004 to complete in March 2009, implying that the Neutrino Facility was moved up from Phase II to Phase I.

Second, the linac energy was decreased from 400 MeV to 180 MeV in order to compensate the budget overflow in the linac and RCS. Here, we will construct all the accelerating structures up to 190 MeV, but the two cavities, to accelerate the beams from 180 MeV to 190 Mev in future, will be used as debunchers rather than accelerators for the time being. Although the RCS beam power is reduced from 1 MW to 0.6 MW by this, the MR the same beam power may be kept as original by increasing the time duration of the injection from the RCS to the MR. The present building can accommodate the 400-MeV linac, and the energy recovery to 400 MeV will be submitted to the funding agency immediately after the completion of Phase I. Since it needs several-year beam operational experience to achieve the full performance of 0.6 MW, the 1-MW full power operation will not be delayed by recovering the linac energy to 400 MeV within a few years.

Third, the funding to the linac and the RCS was delayed by one year. The scheudule for the MR building had been delayed by more than one year for the archaeological investigation of the ancient salt pans. However, the delay in the beam commissioning schedule was managed to decrease to half a year. The updated construction schedule is shown in Fig. 1.

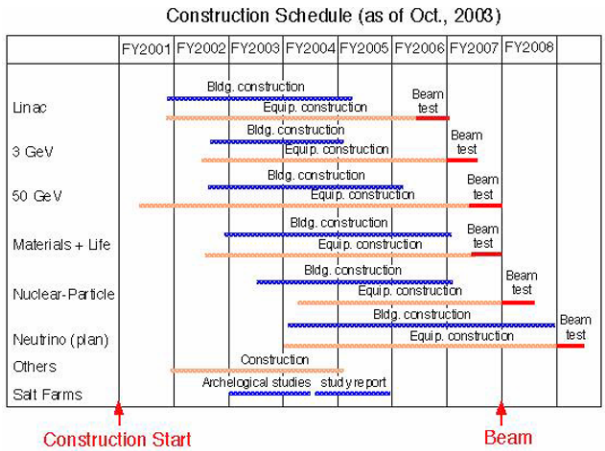

Figure 1: Construction Schedule Updated.

LINAC SHEME

The J-PARC linac scheme is summarized in Fig. 2. The volume-production type of the negative hydrogen ion source is followed by the 50-keV Low-Energy Beam Transport (LEBT), which uses the solenoid focusing. The Radio-Frequency Quadrupole (RFQ) linac accelerates the beams to 3 MeV, being equipped with the π-mode Stabilizing Loop (PISL) [10-12]. The 3-MeV Medium-Energy Beam Transport (MEBT) [13] comprises eight quadrupole magnets to transversely match the RFQ beams to the following DTL and two bunchers for longitudinal matching. In addition, the RF chopper [14] is installed in the MEBT. The 50-MeV DTL [15-21] comprises three cavities, being followed by the Separate type of DTL (SDTL) [22], which has no quadrupole magnets (QMís) inside. The shape of the Drift Tubes (DTís) can thus be adjusted for optimizing their shunt impedances. Since the QMís are installed outside the five-cell SDTLís, the transverse transition is located between DTL and SDTL systems. The 32 SDTL cavities accelerate the beams to 190 MeV, where the high-energy structure starts with an accelerating frequency three times as high as that of RFQ and DTL. Thus, the longitudinal transition is located there. The Annular-ring Coupled Structure (ACS) [23-32] was chosen for the high-energy structure. The ACS is also used for the bunchers located in the beam transport from the SDTL system to the ACS system, and for the debunchers in the beam transport (L3BT) [33] to the RCS.

The key issue of the parameter choices [34] is the RF accelerating frequency of the DTL. The higher frequency is preferable for increasing the beam current, since the larger number of the bunches can be accelerated per unit time. This choice is also advantageous, regarding the smaller sizes of the RF components. In particular, the feasibility to use the klystrons contributes to the stability and reliability of the RF system. On the other hand, the smaller size of the DTís do not accommodate the electro quadrupole magnets with hollow conductors. For this reason, the 432-MHz DTL was developed with the permanent QMís (PQMís) [35] for the Japan Hadron Project (JHP) [36]. Although the PQMís are very advantageous regarding their maintenance-free character, one has to lose the flexible knob for the focusing parameters. In particular, the matching between the beam emittance and the lattice parameters are important in order to reduce the emittance growth and the halo formation. The matching condition may be different from the designed one, depending upon the beam current or the ion source condition. Also, one has to avoid the unknown resonances, if they exist. For this reason, we decided to develop the water-cooled electromagnets with the minimum size. The water channels of the coils were formed by the electroforming technique, while the coils were machined out by means of wire-cutting technology [15]. In this way, the 324-MHz DTL starting from 3 MeV was realized, being powered by the klystron.

The DTL can start from 3 MeV rather than 2 or 2.5 MeV, since the long RFQ linac is made possible by the invention of the PISL [10]. The beams should be chopped at the MEBT in order to avoid the beam loss inherent to the adiabatic capture process for the ring injection. The beams with the energy much higher than 3 MeV are difficult to chop. This is the reason for the choice of the MEBT energy.

The RF chopper [14] is another invention for the J-PARC. The prechopper installed at the LEBT chops the beams with rather slow rise and falling times. The prechopper, based upon the FINEMET induction linac, decreases the injection energy to the RFQ linac, which was designed to work as a sharp energy filter. The RF chopper then chops the remaining beams with fast rise and falling times of 10 ns by the deflecting RF electric fields of TE111-like mode.

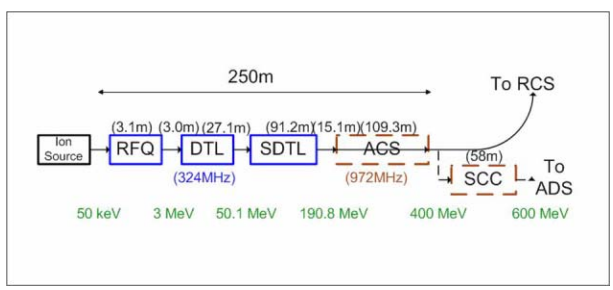

Figure 2: Scheme of J-PARC Linac.

ACCELERATOR STATUS

Ion Source

Three negative hydrogen ion sources are produced for the linac. All are of the volume production type. The first one is of the pure volume production type without cesium designed by KEK. Its filament is made of LaB_6. This is

used for the beam test at present. The shortcoming of this ion source is a long rise time. The longest flat top so far obtained is 360 μs with a repetition of 25 Hz [37]. The second one was designed and tested by JAERI in order to study the parameter dependence of the ion source performance. With cesium, the peak current of 72 mA was obtained with a full duty factor [38]. Its filament is made of tugsten, the life time of which could be elongated to 258 hours by optimising the filament shape. Since this is specialized for the study of the ion production mechanisms and for the parameter search with adjustable cusp fields, the ion source cannot be used for injecting the beams to an RFQ linac. The third one was produced for the use in the real machine with improved design for the stability of the beam current. This is now under test without cesium. The peak current of 28 mA has been already obtained and is increasing (a pulse length of 600 μs and a repetition of 10 Hz, at present). The use of the RF fields are planned for the arc excitation rather than the filament in collaboration with the SNS ion source group.

LEBT, RFQ, MEBT, Choppers and DTL1

These components are already under beam-commisioning to be detailed in the next section.

DTL2, DTL3 and SDTL

The low-power tuning of the DTL2 has been finished with field uniformity better than 1 %, while that of the DTL3 is under way. The components of all the SDTL cavities will be completed by the end of this year. The seven cavities have been assembled, while the three were power-tested.

RF Power Sources

Among twenty klystrons for RFQ, DTL and SDTLís the sixteen have been assembled, while the seven were power-tested. All the twenty anode-modulators and the five cathode power supplies were ready.

BT to RCS

Most of the Beam Transport (BT) components from the linac to the RCS will be completed by March, 2005, while some will be finished one year later.

Building, Installation and Alignment

The linac building will be completed by October, when the electricity and the air conditioning system start to be installed. Everything will become ready by May, 2005, for the installation of accelerator, although some installation will begin much earlier. Most of the linac components are tested and stored in the KEK site. Thus, their shipping to Tokai is an issue, in particular, for the DTL cavities with long DT stems delicately aligned. The laser tracker will be fully used for the alignment [39] rather than the laser-beam alignment first planned.

INITIAL RESULTS

The beam test of the RFQ linac and the MEBT has been conducted in the KEK site from 2002 to March, 2003. The results of the emittance measurements and the beam chopper tests were reported in Refs. [13,14]. The DTL1 was then installed to the tunnel and the RF power was fed in the DTL1 cavity. The detail of the DTL is reported in Refs. [15-21]. The photograph of the DTL1 being used for the beam study is shown in Fig. 3.

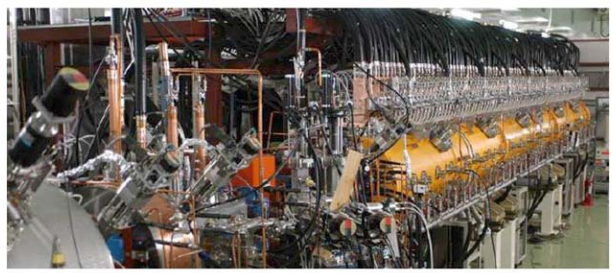

Figure 3: The DTL1 and MEBT ready for the beam study.

The beam commissioning of the DTL1 started on October 30th, 2003, when the peak current of 5 mA was accelerated. On the second day (November 6th) of the beam commissioning, the peak current of 30 mA was obtained with a transmission of 100 % (the accuracy of the used current transformer is typically a few per cent). The beam pulse length is 20 μs with a repetition rate of 12.5 Hz. The duty factor is limited by the radiation shielding capacity of the beam dump (in the case of the 3-MeV MEBT the pulse length of 250 μs with a repetition rate of 25 Hz was tested).

Just after this beam test, the turbo-molecular vacuum pump installed to the downstream of the DTL1 was broken, resulting in the serious damage on the nearby vacuum chamber. After the repair of the damaged components the beam study restarted in February 2004. Until May, the beam has been mainly used for the basic test and study of the beam monitors installed to the MEBT. In June, the improved emittance monitor was installed at the downstream of the DTL1. The emittance measurement then started.

At the 2782-mm down stream from the end plate of the DTL1 the first slit for the emittance measurement was located. The distance between the two slits is 340 mm. The slits are 0.1-mm wide and 5-mm thick. The beam current was measured by both the slow current transformer (SCT) just after the DTL1 and the Faraday Cup (FC) just after the second slit. The beam energy was measured by the time-of-flight method between the Fast Current Transformer (FCT) and the Beam Position Monitor (BPM2) 1.1-m apart.

The preliminary results of the emittance measurements [40] are shown in Table 1 together with the simulation result by PARMILA for comparison. It is seen that the measured emittances are 1.5-times as high as the calculated ones. In order to eliminate the space-charge effect, the emittance measurements were also performed at the peak current of 5 mA. The horizontal emittance became close to the simulated one, while the vertical one was still larger.

Table 1: Measured and Calculated Emittances (normalized rms in π mm mrad)

	Horizontal	Vertical
After MEBT[a)] (Measured at 29 mA)	0.25	0.21
After DTL1 (Measured at 30 mA)	0.39	0.49
After DTL1 (calculated)	0.25	0.27
After DTL1 (Measured at 5 mA)	0.26	0.37

a) Ref. [13]. This is in reasonable agreement with the simulation result by IMPACT [41].

Since the phase and amplitude tuning of the DTL1 is essential for the results, the phase scan method was tested to obtain the best tuning. The tuning thus obtained was close to that which was used to minimize the emittances. The further investigation is ongoing to find the reason of the observed emittance growth.

LINAC ENERGY RECOVERY PLAN AND HIGH-ENERGY STRUCTURE

It is agreed among the two institutes, the user community and the ministry that the linac energy recovery to 400 MeV should be done at first as mentioned in the previous section. The two ACS cavities are already under construction to be used from 190 MeV to 400 MeV. The two ACS bunchers are also under production for the beam transport from the 190-MeV SDTL to the ACS. The three klystrons have been ordered, while the two is under power test.

The ACS first appeared in Ref. [23] had been long useless for its Q degradation, although its advantage regarding the axial symmetry has been realized [34]. The 1300-MHz ACS was developed for JHP [36] in KEK, with deep insight to the RF characteristics of the structure [24]. The prototype of the ACS with two five-cell cavities bridged by a five-cell bridge coupler was first power-tested up to more than designed field with a pulse length of 600 μs and a repetition of 50 Hz [25-27]. Afterwards a few ACS cavities were fabricated and power-tested with different β values and different coupling slots [28].

After the J-PARC project started, the new 972-MHz ACS cavity [29-32] was developed in order to keep the same size as that of 1300-MHz ACS in close collaboration with Institute for Nuclear Research (INR), Moscow, and Tokyo Institute of Technology. One disadvantage of the ACS cavity is its big size, since the ACS can be formed by rotating the side-coupled structure around the beam axis, geometrically speaking. This disadvantage is partly compensated by this new structure. The present version of the ACS is the one thus developed.

FUTURE UPGRADE PLAN

The future upgrade plan may be divided into two categories. The first one is the Phase II of the J-PARC project, which has been already agreed between the two institutes. The second one comprises facilities proposed by the J-PARC users as extensions of the present J-PARC facilities.

Phase II of J-PARC Project

As mentioned in the introduction, several facilities originally included in the J-PARC project were moved to the Phase II except for the neutrino facility. For the future extension to the 600-MeV linac, the present linac beam dump and the shielding there were built removable. In particular, the removable shielding concrete blocks surround the beam dump, since the activated soil cannot be removed later.

The development of the SC linac is in progress by the budget for the ADS development outside the J-PARC budget. One cryomodule comprising two nine-cell cavities for $\beta = 0.725$ was fabricated and low-power tested at 2°K in June [42, 43]. The high-power test is planned in this fall.

On the other hand, a branch tunnel was built from the present linac tunnel in order to extract the 400-MeV beams to the ADS facility. In this way, the ADS experiment can use the 400-MeV beams before the construction of the 600-MeV SC linac.

Upgrade Plan in Letter of Intent

Among thirty Letters of Intent (LoIís) [44] collected for the use of NPF, six letters proposed additional rings which accelerate or store the secondary beams produced by the MR beams, including the neutrino factory. The fast extraction system was made bi-polar in order to extract the beams either inside or outside the ring. The former is for the long base-line neutrino experiment, while the latter is for the future upgrade (for the abort at present). The present beam abort dump and the shielding can be removed by the same means as described in the above subsection.

Neutron Source Upgrade Plan

The scientific community for the pulsed spallation neutron source has been requesting the more powerful source beyond 1 MW. Until the J-PARC project was agreed between the two institutes, JAERI had been promoting the Neutron Science Project (NSP) including GeV-class linac. The present 180-MeV linac can be extended to the 1-GeV linac outside the MR area. Since the 1-GeV beam line is straightly extended through the shielding concrete wall of the MR tunnel, the wall was built so as to have the beam transport tunnel in order to keep the future upgradability. Inside the MR area the additional RCS or the compressor ring can be built together with an experimental facility building. The high-power RCS technology will be fully developed by realizing the present RCS. The 1-GeV injection to the

RCS will make possible a several-MW pulsed neutron source.

One of the serious problems for the future upgrade plan is that some plans in the LoIís do not seem geologically compatible with the several-MW neutron source. Some new methods such as extremely deep tunnels are necessary for solving this problem.

CONCLUSION

The J-PARC linac is under construction for the beam commissioning starting in September, 2006, at Tokai site. In general, the construction is on schedule. The beam study for the front end up to 20 MeV is in progress at KEK site.

The other topics, including the control and beam diagnostics, cannot be mentioned in this report for the limited space. These are detailed in Refs. [45-52].

REFERENCES

[1] "The Joint Project for High-Intensity Proton Accelerators", KEK Report 99-4, JHF-99-3 and JAERI-Tech 99-056 (1999).
[2] Y. Yamazaki et al., PAC'99, THDL1 (1999).
[3] Y. Yamazaki et al., EPAC'00, THOAF201(2000).
[4] Y. Yamazaki et al., LINAC'00, TUD07 (2000).
[5] Y. Yamazaki, PAC'01, WOAA007 (2001).
[6] Y. Yamazaki, EPAC'02, TUZGB003, pp. 163 (2002).
[7] "Accelerator Technical Design Report for High-Intensity Proton Accelerator Project, J-PARC," KEK Report 2002-13 and JAERI-Tech 2003-44.
[8] Y. Yamazaki, PAC'03, ROPA002 (2003).
[9] Y. Yamazaki, EPAC'04, TUPLT085 (2004).
[10] A. Ueno and Y. Yamazaki, Nucl. Instr. Meth. **A300**, 15 (1990).
[11] A. Ueno et al., LINAC'96, 293 (1996).
[12] A. Ueno et al., LINAC'02, TU423 (2002).
[13] M. Ikegami et al., PAC'03, TPAG035 (2003).
[14] T. Kato et al., PAC'03, TPAG014 (2003).
[15] F. Yoshino et al., LINAC'00, TUD10 (2000).
[16] F. Naito et al., LINAC'02, TH102 (2002).
[17] F. Naito et al., PAC'03, RPAB049 (2003).
[18] F. Naito et al., "Results of the High-Power Conditioning and the First Beam Acceleration of the DTL-1 for J-PARC", LINAC'04, TUP06 (2004).
[19] E. Takasaki et al."Results of the Magnetic Field Measurements of the DTL Quadrupole Magnets for J-PARC", LINAC'04, TUP83 (2004).
[20] K. Yoshino et al., "Technologies of the Peripheral Equipments of the J-PARC DTL1 for the Beam Test", LINAC'04, TUP87 (2004).
[21] H. Tanaka et al., "Measured RF Properties of the DTL for J-PARC", LINAC'04, THP89 (2004).
[22] T. Kato, "Proposal of a Separated-Type Proton Drift Tube Linac for Medium-Energy Structure", KEK Report 92-10 (1992).
[23] V. G. Andreev et al., Proc. 1972 Proton Linac Conference, 114 (1972).
[24] T. Kageyama, Y. Yamazaki, and K. Yoshino, Part. Accel. **32**, 33 (1990).
[25] T. Kageyama et al., LINAC'90, 150 (1990).
[26] Y. Morozumi et al., LINAC'90, 153 (1990).
[27] K. Yamasu et al., LINAC'90, 126 (1990).
[28] T. Kageyama et al., LINAC'94, 248 (1994).
[29] V. V. Paramanov, "The Annular Coupled Structure Optimization for JAERI/KEK Joint Project", KEK Report 2001-14 (2001).
[30] S. C. Joshi, "RF-Thermal-Structural Coupled Analysis of Annular Coupled Cavity Structure for the Joint Project of KEK/JAERI", KEK Internal 2001-6 (2001).
[31] H. Ao et al., PAC'03, RPAB046 (2003).
[32] H. Ao et al., "Cold-Model Tests and Fabrication Status for J-PARC ACS", LINAC'04, MOP18 (2004).
[33] M. Ikegami et al., "Beam Dynamics Design of J-PARC Linac High Energy Section", LINAC'04, TUP21 (2004).
[34] Y. Yamazaki, LINAC'96, 592 (1996).
[35] F. Naito et al., LINAC'96, 137 (1994).
[36] Y. Yamazaki and M. Kihara, LINAC'90, 543 (1990).
[37] A. Ueno et al., Rev. Sci. Instrum. **75**, 1714 (2004).
[38] H. Oguri et al., Rev. Sci. Instrum., **73**, 1021 (2002).
[39] M. Ikegami et al., "J-PARC linac alignment", LINAC'04, TUP85 (2004).
[40] Y. Kondo et al., Proc. 1st Annual Meeting of Part. Accel. Soc. Japan and 29th Linear Accel. Meeting in Japan, 156 (2004) (in Japanese).
[41] J. Qiang et al., J. Comput. Phys., **153**, 434 (2000).
[42] N. Ohuchi et al., EPACí04, TUPKF033 (2004).
[43] E. Kako et al., EPACí04, TUPKF036 (2004).
[44] "Letters of Intent for Nuclear and Particle Physics at the J-PARC, " J-PARC 03-6 (2003).
[45] Y. Kondo et al., "Particle Distributions at the Exit of the J-PARC RFQ", LINAC'04, MOP19.
[46] M. Ikegami et al., "A Simulation Study on Chopper Transient Effects in J-PARC Linac", LINAC'04, TUP22.
[47] S. Sato et al., "Systematic Calibration of Beam Position Monitor in the High Intensity Proton Accelerator (J-PARC) LINAC", LINAC'04, TUP70.
[48] S.Lee et al., "The Beam Diagnostics System in the J-PARC Linac", LINAC'04, TUP74.
[49] T. Kobayashi et al., "RF Reference Distribution System for J-PARC Linac, " LINAC'04, THP52.
[50] S. Michizono et al., "Control of the Low Level RF System for the J-PARC Linac," LINAC'04, THP56.
[51] S. Michizono et al, "Digital Feedback System for J-PARC Linac RF Source, " LINAC'04, THP57.
[52] F. Naito, "Longitudinal Bunch Shape Monitor Using the Beam Chopper Of J-Parc," LINAC'04, THP88.

OVERVIEW OF HIGH INTENSITY LINAC PROGRAMS IN EUROPE

M. Vretenar, R. Garoby, CERN, Geneva, Switzerland

Abstract

Recent years have seen a boost in the support by the European Union (EU) of accelerator research in Europe. Provided they coordinate their efforts and define common goals and strategies, laboratories and institutions from the member states can receive a financial support reaching 50% of the total project cost. In the field of High Intensity Linacs, the EU has already supported the EURISOL initiative for nuclear physics, which this year is applying for funding of a Design Study, and the development of linacs for Waste Transmutation. More recently, an initiative for high-energy physics has been approved, which includes a programme for the development of pulsed linac technologies. The coordination and synergy imposed by the EU rules increase the benefit of the allocated resources. Combined with the ongoing internal projects in the partner laboratories, these European initiatives represent a strong effort focussed towards the development of linac technologies.

This paper summarises the requests from the various European communities and gives an overview of linac R&D activities sponsored by the EU, together with some information on parallel national/local projects. The parameter choices as well as the main technical features of the different projects are presented and compared.

INTRODUCTION

Recent years have seen an increasing worldwide interest in high-intensity linear accelerators for protons and H^- primarily aimed at the production of intense beams of secondary particles. Secondary beams of scientific interest include:

- Intense neutrino beams for particle physics, produced by the decay of pions, muons or radioactive beta emitters.
- Radioactive ions for nuclear physics, astrophysics and natural science.
- Spallation neutrons as a probe for condensed matter studies or feeding sub-critical reactors for energy production and waste transmutation.

In these applications as "proton drivers", linacs are attractive with respect to circular accelerators for their capability to operate at high repetition rates, up to CW, with limited current per bunch. For pulsed applications at low duty cycle and high energy (1 GeV and above), they are in competition with Rapid Cycling Synchrotrons, while for CW applications at low energy, they compete with cyclotrons. In the past, linacs have always been considered expensive in comparison to circular accelerators. However, thanks to the recent advances in superconducting RF technology and to the increasing optimisation of linac designs, their energy reach, size and cost are improving, so that more projects rely on high-energy high-intensity linear accelerators. Moreover, the strict limits on acceptable beam loss required to minimise radiation and allow hands-on maintenance are more easily met in linear machines, less disturbed by harmful beam resonances than circular machines.

EUROPE AND ACCELERATOR R&D

Any one of these future high energy and high power linacs has such important needs in terms of space and overall infrastructure that it can only be hosted in a large laboratory. With the exception of CERN, the landscape of European accelerator research is rather made-up of a large number of small national laboratories and Universities, with very competent teams, but none having the critical mass required either for a large scale project or for its associated R&D. The basic mission of CERN is for large projects in high energy physics, however its present resources are focused on the construction of the LHC with a very limited support for future options beyond its start-up. Therefore R&D for new European accelerator projects can only be pursued through the collaboration of many different laboratories.

This situation in accelerator research is common to many branches of European science, a fact that is pushing the European Union (EU) commission towards taking a more active role in creating a real European Research Area. In the frame of the 6th EU Framework Programme (FP), covering the period 2004-2009, European research institutions are invited to propose Integrated Projects (IP), i.e. a coordinated research programme for a particular topic involving a certain number of EU scientific centres, which establish a common schedule and share their resources and the results of their work. The approved projects can be financially funded up to a maximum of 50% of the total cost (material and personnel). The evaluation is made not only on the scientific case, but also on the level of integration involved in the proposal.

For high intensity proton linacs, the EU has expanded the support already given to pioneering projects in the FP5, by approving the CARE (Coordinated Accelerator Research in Europe) Initiative. The EURISOL and EUROTRANS Design Studies have also been positively evaluated and are expecting approval. In parallel, support for the ADS (Accelerator Driven Systems) activities is continuing through the EURATOM agency of the EU.

It must be stressed that, due to the fierce competition, projects are never funded at the maximum allowed level, the priorities being defined by the EU committees. For example, inside the CARE initiative, the Joint Research Activity (JRA) dedicated to R&D for high-intensity low-energy linacs, has been very positively evaluated but has obtained EU funding for only about 25% of the total

project cost, a value to be compared to the important amount of overhead in handling the meetings and paperwork (periodic reports) required by Brussels. However, the added value of the integrated EU projects comes more from the synergies among the participating laboratories than from the simple financial contribution.

PARTICLE PHYSICS APPLICATIONS

Particle physics is one of the leading communities pushing for a high-intensity proton facility in Europe, for the production of intense neutrino beams. The recent discovery of neutrino masses has opened new horizons for physics and cosmology, and the new physics of neutrino oscillations is proving extremely rewarding and demands long term experimentation with accelerator neutrinos. Long baseline experiments are in preparation, based on intense beams of neutrinos sent from an accelerator complex to a large underground detector, at distances of hundreds of kilometers.

For the production of neutrino beams orders of magnitude more intense than provided at present facilities, three techniques are presently considered:

a. from conventional pion decay (called "Superbeam").
b. from the decay of muons, previously accelerated and stored in a decay ring ("Neutrino Factory")
c. from the beta decay of radioactive ions, produced in a nuclear physics facility and then accelerated and stored in an accelerator complex ("Beta-beams").

In all three cases, a high power proton driver is needed, with a beam power that has been normalised in the European studies to 4 MW, considered as a (challenging) limit for target technology.

For pion (and muon) production, the intensity of the pion beam is roughly proportional to beam power above a threshold that simulations situate at some 2 GeV, an energy still economically reachable by a linear accelerator. The choice of the proton energy will be strongly influenced by the results of the HARP experiment recently performed at CERN, once its data has been fully exploited [1]. For the Superbeam and Neutrino Factory scenarios, an accumulator and eventually a compressor ring are needed after the high-energy linac. The amount of usable pions being proportional to beam power, alternative scenarios for neutrino production make use of a higher energy proton beam (15-30 GeV) delivered by a cascade of Rapid Cycling Synchrotrons (RCS). Preliminary estimations indicate comparable costs for the Linac/Accumulator and the RCS scenarios. While an RCS is ideally suited to concentrate the beam in a small number of short bunches, a high-energy linac provides more flexibility, offering several possible operation modes and upgrade scenarios.

Table 1 compares three European scenarios for particle physics proton drivers with three corresponding US designs and with the highest beam power facilities in operation or close to commissioning.

Table 1: Proton driver parameters

	Linac (MeV)	Ring(s)	Beam Power (MW)	Rep. freq. (Hz)
ISIS	70	800 MeV RCS	≤ 0.24	50
SNS	1000	accumulator	1.24	60
JPARC (n)	400	3 GeV RCS	1	25
JPARC (ν)	400	50 GeV RCS	0.75	
CERN SPL	2200	accumulator	4	50
CERN RCS	180	2.2 GeV RCS 30 GeV RCS	4	8
RAL	180	2×1.2 GeV RCS 2×5 GeV RCS	4	2×25
FNAL 1	600	8 GeV RCS (+ Main Ring)	1.9	15-0.65
FNAL 2	8000	(+ Main Ring)	2	10
BNL	1200	(+AGS 28 GeV)	1	2.5

The Superconducting Proton Linac at CERN

The Superconducting Proton Linac (SPL) study was started at CERN in 1997, aiming at the construction of a 2.2 GeV linear accelerator using the large inventory of 352 MHz RF (klystrons, waveguides and cavities) recuperated from the LEP machine [2]. The energy of this linac has been chosen in order to fit the needs of a neutrino factory and at the same time to be an improved injector for the CERN Proton Synchrotron (PS), increasing the brightness of its beam by a factor 3. For a neutrino factory, the SPL would feed particles to a 1 km circumference accumulator ring followed by a compressor of the same size, and the 4 MW of beam power would finally be sent onto a target in the form of a 3 μs train of 1 ns rms long bunches. For the generation of a neutrino super-beam, the compressor would not be needed. In parallel to the high power operation, the facility could provide via the PS-SPS a beam of very high brightness to the LHC, an essential ingredient of most of the proposed upgrade options for the LHC.

A second Conceptual Design Report of the SPL is in preparation, to be ready by mid-2005. The low energy part will still delivered beam bunched at 352 MHz, but the transition from normal to superconducting cavities will be changed from 120 MeV to 180 MeV. In the superconducting part, state-of-the-art bulk niobium superconducting cavities operating at 704 MHz will be used instead of the aging low-gradient LEP cavities considered in the initial design so that, for the same output energy, the linac will be shorter, or, for a similar length, the energy will be higher. Also being considered is another frequency jump, to a high-energy linac section at 1408 MHz, where even higher gradients could eventually be achieved, with possible synergies with the TESLA developments. The main SPL beam parameters are reported in Table 2 and Fig. 1. In the present CERN plans, the decision of construction is envisaged in 2008. However, the normal-conducting part of the SPL, called Linac4, could already be built between 2007 and 2010, as a replacement to the present injector of the PS Booster.

This would benefit the present users by increasing the intensity and the brightness of the beam provided by the PSB, and the PS could then deliver the "ultimate" beam required by the LHC [3].

Table 2: SPL Parameters (CDR 2)

Ion species	H-	
Kinetic energy	2.2	GeV
Mean current during the pulse	30	mA
Beam duty cycle	6	%
Mean beam power	4	MW
Pulse repetition rate	50	Hz
Beam pulse duration	1.2	ms
Bunch frequency	352.2	MHz
Duty cycle during the pulse	62	%
Normalized rms transv. emittances	0.4	πmm mrad
Longitudinal rms emittance	0.3	π deg MeV

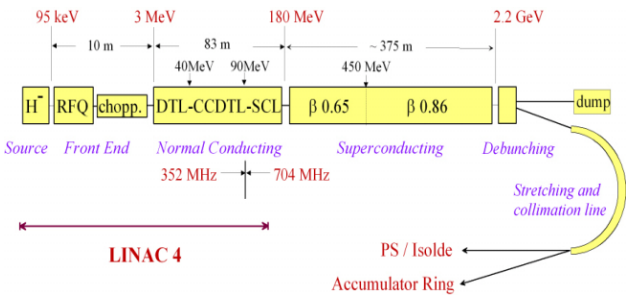

Figure 1: Layout of the SPL (CDR 2).

NUCLEAR PHYSICS APPLICATIONS

Owing to the increasing interest for the scientific applications of Radioactive Ion Beams (RIB), going well beyond the traditional field of Nuclear Physics, a strong community is advocating the construction in Europe of an RIB facility with an intensity three orders of magnitude higher than the present ones. Such a laboratory could meet the demands of a wide science programme covering solid state physics, biophysics, nuclear astrophysics, studies of fundamental symmetries and interactions, and a full programme on structure and reaction studies of atomic nuclei very far from the valley of beta stability. Two parallel and complementary RIB programs are foreseen in Europe, one based on the in-flight projectile fragmentation around 1 GeV/u, to be pursued at GSI, as part of the FAIR project, and another one based on the Ion Separation on Line (ISOL) method, in another location. The ideal ISOL driver is a high-intensity 1 to 2 GeV proton accelerator, operated in two power levels: around a few hundred kW as a classical ISOL facility or at a few MW when generating radio-active ions by bombardment with spallation neutrons from the target. Instantaneous power deposition in the target is a major concern, and for this reason the beam has to be CW or pulsed at a high repetition rate, 50 Hz being considered as the lowest acceptable value.

The EURISOL Design Study

The European scientific community working on RIB was present already in the 5th FP of EU, and has now submitted the EURISOL Design Study in the frame of the 6th FP, aiming at the preparation of a detailed design for an ISOL facility [4]. The baseline EURISOL CW driver (Figure 2) is composed of a 5 MeV front-end based on a proton source and an RFQ, followed by a 352 MHz superconducting section at intermediate energy using Quarter-Wave or Spoke type resonators, and finally by a 704 MHz high energy superconducting section made of elliptical cavities. An additional feature of this design is the capability to accelerate low-mass ions, as required by some experiments.

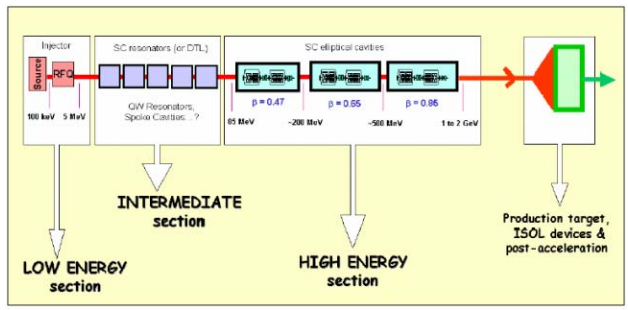

Figure 2: EURISOL layout.

EURISOL at CERN and the Beta-beams

An interesting option has been recently proposed which shows a remarkable synergy between a neutrino and an RIB facility [5]. Using a single proton driver like the SPL, it is based on an ISOL type facility, providing the radio-active ions needed for nuclear physics and simultaneously producing intense beams of beta emitting ions (^{6}He and ^{18}Ne). These beta emitters are accelerated in a dedicated post-accelerator and then in the existing CERN accelerator complex (PS and SPS). After acceleration in the SPS, they are injected in a storage ring, where their decay produces intense streams of neutrinos at the end of two long straight sections (Figure 3). The analysis of the technological issues of the beta-beam option is one of the work packages in the EURISOL Design Study.

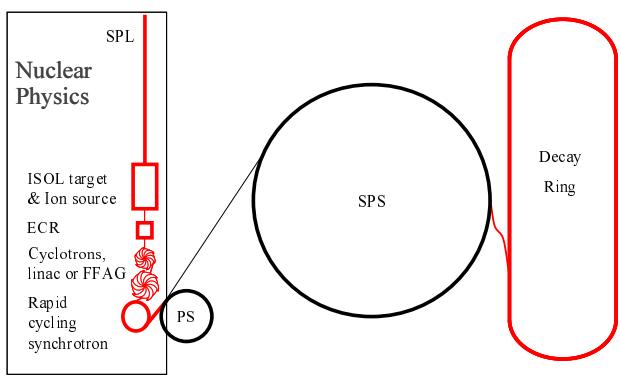

Figure 3: Concept of the beta-beam facility.

The SPES Programme at INFN-LNL

The SPES machine under construction at INFN Legnaro is a high-intensity proton linac at low energy (20 MeV in the initial stage, 100 MeV final energy), intended to feed an ISOL facility. A 352 MHz CW RFQ for 30 mA current is followed by a superconducting linac made of re-entrant cavities. The machine is designed to be operated at a later stage with deuterons (with a different RFQ), to obtain a larger neutron yield at low energy [6].

NEUTRON APPLICATIONS

An intense proton beam can be converted into streams of neutrons in a spallation target. The use of neutrons ranges from basic science and condensed matter studies, to feeding sub-critical reactors. European activities are on-going on both fronts, for the ESS and the ADS studies.

The European Spallation Source (ESS)

An accelerator based Neutron Spallation Source for Europe was the subject of the ESS Study. After the preparation of a detailed proposal, at the beginning of 2003, the partner governments have delayed the decision of construction by 4-5 years and requested the refinement of the technological layout. The new ESS SC reference design (Fig. 4) includes a 1120 MHz superconducting section, starting at 400 MeV energy. The low-energy part is based on two 280 MHz H^- linacs funnelled at 20 MeV followed by normal-conducting structures at 560 MHz. It includes an innovative fast chopper/collector system, for the double operating mode (short and long pulse, at 5 MW each) that is a unique feature of the ESS [7].

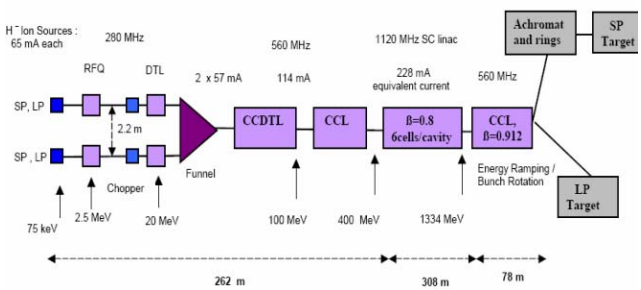

Figure 4: ESS SC reference linac layout.

Accelerator Driven Systems (ADS)

The preliminary ADS design study funded by EU has recently compared linac and cyclotron layouts for a 600 MeV, 6 mA current CW driver for transmutation, taking into account the high reliability required by ADS systems, with less than 5 beam trips (>1 s) allowed per year. The outcome of the study is that CW superconducting linacs should be chosen for demonstrator and full scale plants, because of their potentiality in terms of availability, reliability and power upgrading capability. Cyclotrons are considered attractive in cost, but at the limit of feasibility for the required parameters, not upgradeable and far less reliable. The PDS-XADS reference layout (Fig. 5) is based on a double front-end for higher availability, made of a 352 MHz normal-conducting RFQ followed by superconducting structures from the lowest possible energy. Spoke and CH-cavities are considered for the low-beta part of the linac, while the high-energy sections are made of 704 MHz elliptical cavities. The EUROTRANS Integrated project is presently being submitted to the EU, focused mainly on reliability issues and on demonstration experiments.

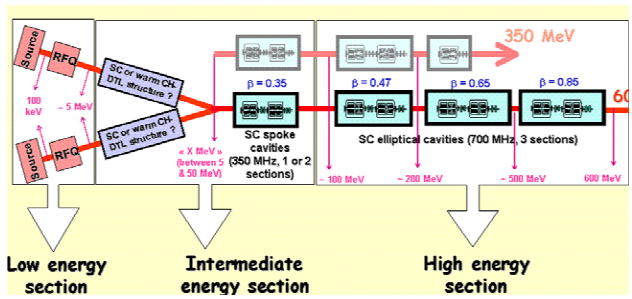

Figure 5: The PDS-XADS reference accelerator layout.

TECHNOLOGICAL ISSUES

Front-end

The technological and beam dynamics issues of the front-end (source, RFQ and MEBT) are crucial for a high-intensity linac, and need to be addressed as early as possible, well before the construction of the rest of the linac. The particle distribution is generated in the front-end, and source extraction fields, RFQ multipoles, changes of beam size and focusing period in the MEBT can create harmful halos, which will finally produce losses in the following linac sections. Moreover, the front-end presents many technological challenges, like performance and reliability of the source, power dissipation, field adjustment and coupler design in the RFQ, chopping and collimation in the MEBT. To address these questions two teams in Europe are presently building high-power RFQ's: CEA-CNRS in France and INFN/LNL in Italy. Both RFQ's were originally designed as ADS-type demonstrators, but will be finally used as front-ends for linacs devoted to physics research.

The CEA-CNRS IPHI RFQ is a 100 mA CW RFQ, whose design has been recently revised and the energy, originally 5 MeV, reduced to 3 MeV for this RFQ to be used as injector for the CERN Linac4 and SPL. After a first series of CW tests at Saclay planned in 2006, mainly to assess reliability of an ADS front-end, the RFQ will be sent to CERN in 2007, where it will be installed in a test stand equipped with an H^- source and a complete MEBT, for extensive beam tests [8]. The LNL RFQ, also conceived for the TRASCO transmutation study, will be now the preliminary injector of the SPES linac at Legnaro. It goes up to 5 MeV with 30 mA of beam current. It is based on a simpler mechanical design than the IPHI RFQ, and should be finished in about the same time [9]. Testing will take place at Legnaro.

Superconducting Linac

Presently, all European high-intensity linac projects include a superconducting high-energy section. The transition energy between normal and superconducting depends on the operation mode and ranges from the 5 MeV of EURISOL (CW, proton and deuteron operation mode requiring individually phased cavities) to the 180 MeV of the SPL and the 400 MeV of the ESS. The frequencies are also standardised for most of the projects to 352 MHz and multiple harmonics, the main reason for this "European" frequency choice being the availability of RF equipment and expertise at this frequency from the old LEP RF system.

The development of 704 MHz low-beta elliptical cavities, as well as of different alternative designs at 352 MHz (spoke, QWR, HWR, re-entrant, etc.) is progressing at several European laboratories. Moreover, some projects are envisaging to push even higher the SC RF frequency (1.4 GHz for the SPL, 1.1 GHz for the ESS) to reduce the size of cavities and cryostats while reaching higher gradients, profiting in this way from the developments made for TESLA.

The instabilities induced by cavity vibrations due to the pulsed mode of operation are being studied, stiffening techniques have been proposed and compensation schemes are under investigation in many laboratories. CERN is testing a prototype high power phase and amplitude modulator intended to facilitate the stabilisation of a string of superconducting cavities fed by a single klystron [10].

Beam Dynamics and Halo

A considerable effort is devoted to beam dynamics calculations and to the study of halo generation and removal. In particular, there is a clear interest in understanding the mechanism of halo formation in the front-end. Realistic distributions from the source are included in the simulations. Modern simulation codes allow calculations with a large number of particles, but in order to have a realistic view of the beam behaviour long end-to-end simulations are needed, either including statistical error distributions for the entire machine, or introducing artificially in the beam an equivalent mismatch to that generated by the error distribution [11].

THE HIPPI JOINT RESEARCH ACTIVITY

In order to address the issues involved in the low-energy part of pulsed high-intensity linacs, the CARE Initiative recently approved by the EU includes the HIPPI (High Intensity Pulsed Proton Injectors) Joint Research Activity, covering the period 2004-2008. The goal of HIPPI is the common development of the technological basis for three proposed new linac injectors, the CERN Linac4, the new 180 MeV linac at RAL and the new GSI proton injector, analyzing jointly the different options and problems for linacs in the energy range between 3 and 200 MeV. HIPPI partners are 9 laboratories from 5 countries: RAL, CEA-Saclay, CERN, FZ-Jülich, GSI, IAP-Frankfurt, INFN-Milan, IPN-Orsay and LPSC-Grenoble. Inside HIPPI, different technologies are developed in parallel, some in collaboration between laboratories, and some by individual HIPPI members. The results of the development will be jointly analyzed, to come to a common assessment on the technologies and on their applicability to the different linac upgrades.

HIPPI is divided in four technical work packages. The first one will compare four Normal Conducting structures, DTL, H-mode linac, SCL and CCDTL, by building prototypes and scaled models. In this activity three collaborations between CERN and Russian laboratories, that will build prototypes of 352 MHz linac structures to be tested at CERN in 2006, have also been integrated.

The second work package is devoted to the study of superconducting cavities as an alternative to normal-conducting at energies between 90 and 200 MeV. Two different elliptical cavities at β=0.5 will be built and tested in a new 704 MHz test stand for 1 MW RF power under preparation at Saclay, aiming for gradients >10 MV/m. In parallel, prototypes of spoke cavity and CH-cavity at 352 MHz will be built and tested.

The third work package will compare two alternative chopper designs and integrates the chopper study into the development and beam testing of the critical MEBT line.

Finally, the fourth work package groups the beam dynamics activities, and aims for a common comparison and assessment of different beam dynamic codes, through extensive simulations and comparison with beam measurements, together with a common development of beam diagnostics.

REFERENCES

[1] http://harp.web.cern.ch/harp/
[2] M. Vretenar (ed.), "Conceptual Design of the SPL", CERN 2000-012.
[3] R. Garoby, F. Gerigk, K. Hanke, A. Lombardi, C. Rossi, M. Vretenar, "Design of the Linac4, a new Injector for the CERN Booster", this conference.
[4] The Driver Accelerator for EURISOL, Dec. 2003, http://www.ganil.fr/eurisol/Final_Report/APPENDIX-B.pdf .
[5] P. Zucchelli, "A novel concept for a neutrino factory: the beta-beam", Phys. Let. B, 532 (2002) 166-172 .
[6] L. Tecchio, "The Radioactive Ion Beam Facility Project for the Legnaro Laboratories", PAC 99, NY.
[7] A. Letchford, K. Bongardt, ESS Update Report, 2003 http://neutron.neutron-eu.net/n_ess/n_ess_documentation.
[8] R. Garoby et al., The SPL Front-End: a 3 MeV Test Stand at CERN, this conference.
[9] A. Pisent et al., "The TRASCO-SPES RFQ", this conference.
[10] D. Valuch, H. Frischholz, J. Tückmantel, "First Results with a Fast Phase and Amplitude Modulator for High Power RF Application", EPAC04, Luzern.
[11] F. Gerigk, "Beam Halo in High-Intensity Hadron Accelerators caused by Statistical Gradient Errors", PRSTAB, vol. 7, 064202 (2004).

SUMMARY OF THE ARGONNE WORKSHOP ON HIGH GRADIENT RF

J. Norem*, Argonne National Laboratory, Argonne, IL 60439, USA

Abstract

The Workshop on High Gradient rf was held at Argonne, Oct. 7-9, 2003. This workshop reviewed the progress in a number of accelerator technologies approaching high gradient limits. In addition to progress reports, one aim of the workshop was to involve materials scientists and look at trigger mechanisms and surface interactions. Talks were presented on superconducting rf, progress with high and low frequency copper cavities, and dielectrics. The focus was on both experimental and theoretical aspects of the problem. The overall picture presented at the workshop will be summarized.

INTRODUCTION

This paper will attempt to review the highlights presented at the workshop, summarize in a little more detail ongoing work not otherwise mentioned at this conference, and discuss some of the open questions in the field of high gradient rf. Since many of the participants in this workshop are also presenting more recent results at LINAC 2004, and it is desirable to avoid repetition and discussion of older data, the emphasis will be on topics not covered in this conference, and on general conclusions that could be extracted from the workshop.

Effort on the Workshop was begun as an attempt by members of the Muon Collaboration to explore how much overlap there was between the problems of building muon cooling linacs, with very low frequencies (200 MHz) but comparatively high gradients, and the better understood problems of high frequency electron linacs. There was also a strong feeling that the material dependence of rf breakdown was an important and not well understood aspect of this problem, and it might be possible to productively involve materials scientists in a study of this problem. There was an organizational meeting at PAC03, in Portland Oregon and the workshop was held at Argonne, Oct. 7-9, 2003. A short summary of the workshop was published in the CERN Courier [1].

The website, with copies of all talks given at the workshop, is located at http://www.hep.anl.gov/rf/ [2]. In order to simplify this paper, contributions will be identified by name and not referenced individually.

LINAC DEVELOPMENTS

The majority of the effort on high gradient rf has been done as part of the NLC, CLIC and TESLA effort to produce TeV scale electron linacs for the next generation of particle accelerators. This work has been done by an international group centered at SLAC, FNAL, KEK, DESY and CERN, with important contributions from many other laboratories and individuals.

* norem@anl.gov

Linear Collider Work

Although the emphasis of the workshop was on normal conducting rf, two talks were given on superconducting rf technology. A. Matheisen described SRF surface preparation techniques, and K. Saito discussed recent results with high field SC cavities. The techniques used in this technology involve enormous effort to insure that the metals and surfaces are as free of defects and contamination as possible, the manufacturing process are clean, and assembly and testing do not further contaminate the structures. In many cases this has been done to the point where there is no field emission even at the highest fields. While these methods are widely respected, there is some doubt if they are applicable to high frequency cavities, which are somewhat harder to clean and seem prone to produce damage sites when first exposed to high powers.

The majority of the effort devoted to the linear collider has been adequately summarized elsewhere in this conference. At the workshop C. Adolphsen gave an overview the NLC structure tests done by KEK, SLAC and others, showing that the specifications of the NLC design were being met by prototypes. This was followed by S. Tantawi, who talked about breakdown experiments in waveguides of different dimensions (local B/E ratios) and single cell traveling wave structures. V. Dolgashev described the effects of magnetic fields and input power levels on test cells in the NLCTA and simulations of breakdown. S Doebert looked at gradient limitations on high frequency accelerators showing how breakdown depended on a number of variables (pulse length, power, electric field etc.), but ultimately seemed to occur when the product $\beta E_s \sim 7$ GV/m. S. Harvey presented results of autopsies on structures following high power processing, which showed cracks, craters, and a variety of inclusions and sparking sites, extending the description of surface defects from that published recently by Pritzkau and Siemann [3]. T Higo, showed some preliminary data on the effects of high pressure rinsing of cavities and other treatments. Some of these resulets are shown in Figs. 1-4.

The CLIC effort was summarized by W. Wuensch, who described the work done at the CLIC test facility, which produces high power rf from structures exposed to high energy bunched beams, and uses this power to drive accelerating structures. Results were presented which showed that the breakdown rates seemed to be essentially independent of frequency and initial temperature.

Other Structures

High gradient structures are under construction at other facilities. S. Yamaguchi described a very thorough construction, cleaning and conditioning program for a high gradient test of a new S band structure at KEK.

Among other things, the data showed that during conditioning, the enhancement factor, β, decreased as the surface field, E, increased with almost the same exponential time constant, During this time the product remained constant, and equal to 6 - 7 GV/m, see Fig 5. This value is significant since it is roughly equal to the surface field at breakdown measured in a number of rf and DC experiments over the years, and is close the field where *tensile stress = tensile strength* for copper. They found that high pressure rinsing of the structure cut the conditioning time of the structure by about half and also cut the flux of dark current electrons to one third of the untreated case.

S. Fukuda described a high gradient test of a C band structure built for the SuperKEKB built to increase the positron beam energy to 8 GeV, and showed how the cavity conditioned to the 42 MV/m design field in less than two months.

H. Haseroth described the history of the ion source at CERN, showing the importance of eliminating contamination, particularly pump oils, from the vacuum system.

M. Shapiro showed results from a new photoelectric gun that operates at peak surface fields of 200 MV/m at 17 GHz.

Muon Cooling

The Muon Collaboration effort has been aimed at developing 200 MHz cavities that can operate at gradients of 10 – 20 MV/m, the initial goal for this program is to build cavities for the Muon Ionization Cooling Experiment (MICE), and eventually neutrino sources or muon colliders. The development of the 201 MHz test cavity was described by D. Li, and the Muon Test Area (MTA) built near the linac at Fermilab, which has high power available at 201 and 805 MHz, was described by M. Popovic. Some results of 805 MHz cavity tests, done in Lab G, were described by J. Norem, Fig 6, and A. Moretti, who reported new data on the magnetic field dependence of the maximum useful electric field and new results using Be windows.

HIGH GRADIENT DEVELOPMENT

While much of the work presented directly described linac developments, there were other topics that were covered which were relevant to high gradient rf.

High Pressure Cavities

An effort by Muons Inc. looking into the breakdown properties of cavities with high-pressure hydrogen, which would satisfy both the acceleration and absorber requirements of a muon cooling system, was reported by R. Johnson.

Dielectric Accelerators

The status of high gradient dielectric cavities was covered in three talks. Y. Y. Lau described the theory of multipactor in dielectrics. A. Neuber discussed an experimental program designed to understand the limits of high power rf windows Fig. 7. J. Power described efforts to develop high gradient dielectric accelerators, which are presently limited by multipactor effects.

DC Studies

Although the subject of the workshop was high gradient rf, one of the basic questions of the field is how rf phenomena compare with DC processes and systems. G. Werner, described DC studies motivated by the high gradient rf program, and described similarities between the starbursts seen in DC and SCRF systems.

Gas Cluster Ion Beams (GCIB)

Z Insepov described how Gas Cluster Ion Beams (GCIB) which consist of charged clusters of argon atoms accelerated to a few kV/atom can be used to alter the surface of a metal Fig 8. This technique is now used in the semiconductor industry to achieve the highest level of local smoothing, down to 1.7 Angstroms rms. The technique has a possible application to smooth and clean rf cavity surfaces such as the NLC cavity sections or TESLA structures. This technology was developed by Epion Corp [4], and is in wide use in the semiconductor industry.

MODELING AND ANALYSIS

Although the problems of high gradients in vacuum have been studied for 100 years, there seems to be no agreement on the cause of breakdown, and no unambiguous recipe for minimizing the frequency or damage it produces. The situation was summed up by S. Tantawi:

- Breakdown seems to be a mysterious process, with no clear theory that enables understanding of the phenomenon.
- Most of the experimental work is done with complicated structures that make interpretation of the data very hard.

In spite of this, there are a number of modeling efforts underway, with a variety of goals and approaches. Historically there have been two efforts at SLAC and Cornell.

Modeling

At Cornell simulations of breakdown is continuing from an effort begun with Padamsee and Knobloch [5]. Particle in cell models showing the development of electron and ion clouds around a potential breakdown site implied that the breakdown events began in a few rf cycles with back-bombardment of the wall, Fig 9. G. Werner described how the process would work once some trigger produced an initial concentration of electrons and ions.

A somewhat similar model was presented by V Dolgashev, at SLAC, who looked at the development of breakdown in a rectangular waveguide. Modeling the

development of an event from an initial low concentration of ions to complete absorption of all stored energy in the cavity in a few cycles, he showed how the model agreed with measurements of transmitted and reflected power on recent NLC prototype cavities.

An effort at Argonne, aimed at understanding the trigger mechanisms has also involved some theoretical and experimental work. J. Norem summarized a model in which breakdown seems to be triggered at the local fields where tensile stresses in the field are comparable to the tensile strength of the material. Z. Insepov showed simulations of a molecular dynamics code displaying individual atoms being torn off an asperity by electric fields, Fig 10. I. Konkashbaev showed calculations of field evaporation and field emission and discussed their consequences. Data was presented that showed that high current densities can produce high electric fields at grain boundaries and defects of the sort seen by Pritzkau and Siemann [3] and Harvey.

Calculations of field emitted electrons were presented by V. Ivanov, who showed the trajectories these electrons would follow and the secondary electrons they would produce when they hit the walls.

Y. Iwashita showed how the surface current density could be calculated with high precision with variable mesh sizes.

Open Questions

There are a number of questions that may be worth wider discussion. There was no agreement on the nature of the enhancement factor β, this quantity is used to relate the field at an emitter to the average surface field, but there is some doubt if these geometrical enhancements actually exist. It seems that all cavities see field emitted electrons, which the Fowler-Nordheim formalism says are only produced above 5 GV/m, and this may imply the enhancements are real.

The "Fowler-Nordheim Plot" seems to be the most common way of plotting field emitted currents as a function of surface field. Unfortunately, this method seems to be unnecessarily complex, somewhat unintuitive and difficult to associate with experimental or fitting errors. Simply plotting the current as a function of the field may have a number of advantages. The primary variables are the emitter area and enhancement factor, and this method clearly expresses these quantities in perhaps more intuitive way. The effects of experimental uncertainties such as saturation and noise can also be understood more directly.

CONCLUSIONS

Although the meeting itself did not have time for long discussion periods, a number of conclusions that seem to present themselves.

Although the linear collider effort has been pursuing high gradients more aggressively than is done at lower frequencies, the problems they are finding seem similar to those seen at lower frequencies and even DC systems. The local fields of 6 - 10 GV./m are almost always associated with breakdown events or unstable operation, and lowering the fields by a small amount reduces the sparking rates considerably.

It seems possible to find engineering solutions without a good physical understanding. Experiments are difficult, and comparisons between the results are even more difficult, primarily because the hardware is complex. The NLC/GLC effort has found and cured the primary source of breakdown in their structures with very minor modifications.

A wide, and increasing, range of instrumentation is being used to attack the problems of breakdown.

Breakdown fields are a function of a number of variables and there were no clear understanding the majority of problems faced at high gradients. There may be more than one mechanism responsible for breakdown and these have not been well documented. There could be more effort on the physics of high gradients.

ACKNOWLEDGEMENTS

While many people helped set up the conference, special thanks go to P. Malhotra, who took care of all the administrative details and registration problems, and Y. Torun, who handled the talks, and communications. This work was supported by the USDOE, Department of High Energy Physics and Argonne National Laboratory.

REFERENCES

[1] J. Norem, CERN Courier, Jan/Feb 2004, p21.
[2] http://www.hep.anl.gov/rf/.
[3] D. Pritzkau and R. H. Siemann, Phys. Rev. STAB, 5, 112002, (2002).
[4] Epion Corp. Billerica, Ma.
[5] J. Knobloch, PhD Thesis, Cornell University, (1997)

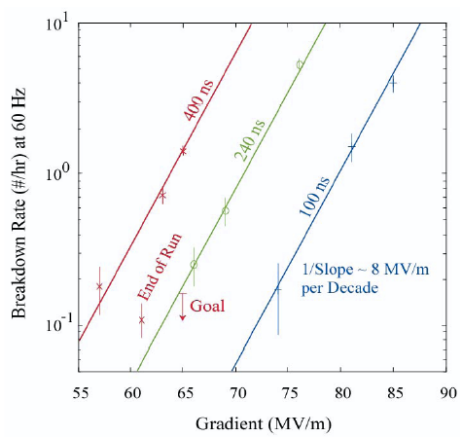

Figure 1: Breakdown rate vs. Gradient for NLC prototype structures (Adolphsen).

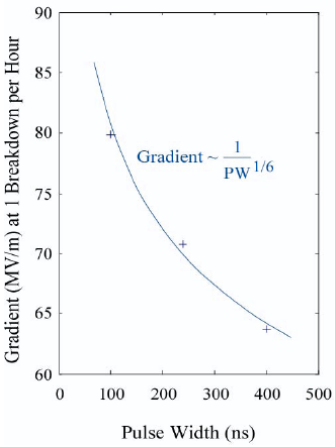

Figure 2: Maximum gradient vs. pulse length for NLC/GLC structures (Adolphsen).

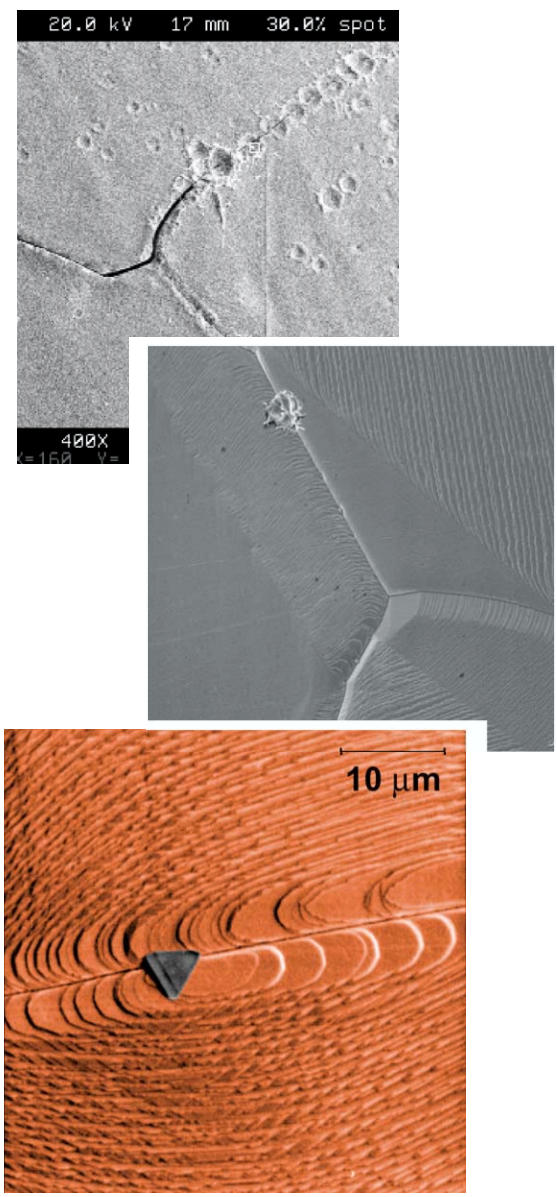

Figure 3: Various SEM pictures from autopsies, with false color (Harvey).

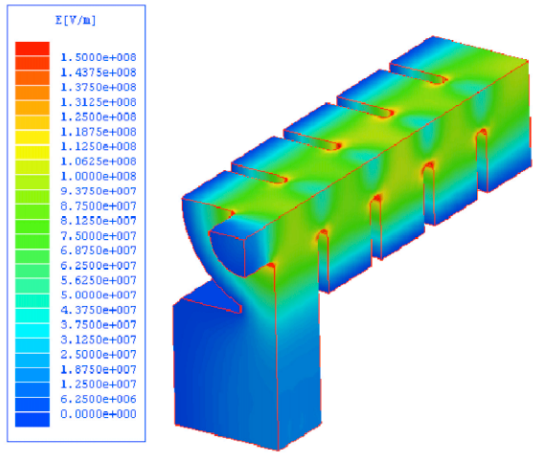

Figure 4: Electric fields in a NLC/GLC structure (Dolgashev).

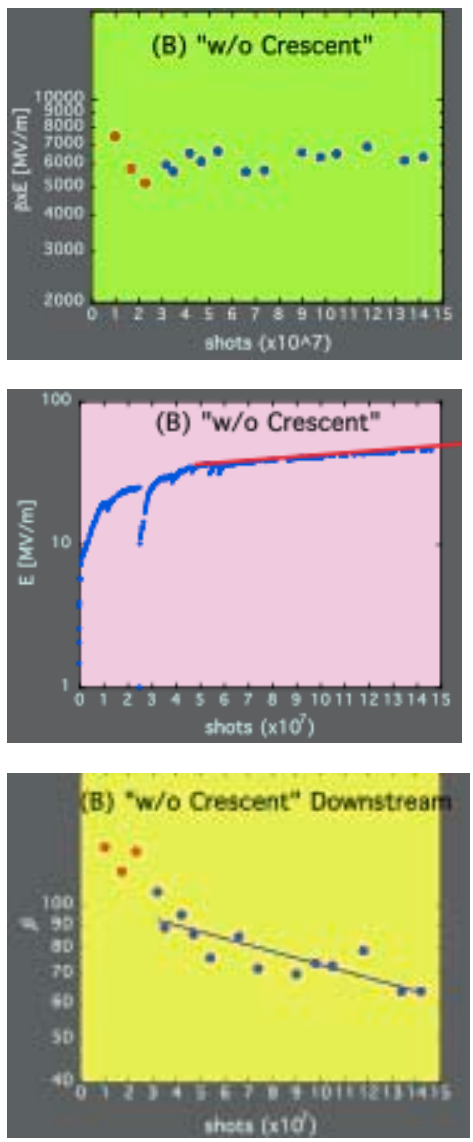

Figure 5: Enhancement factor, surface field and the local surface field during condidtioning of structures. (Yamaguchi).

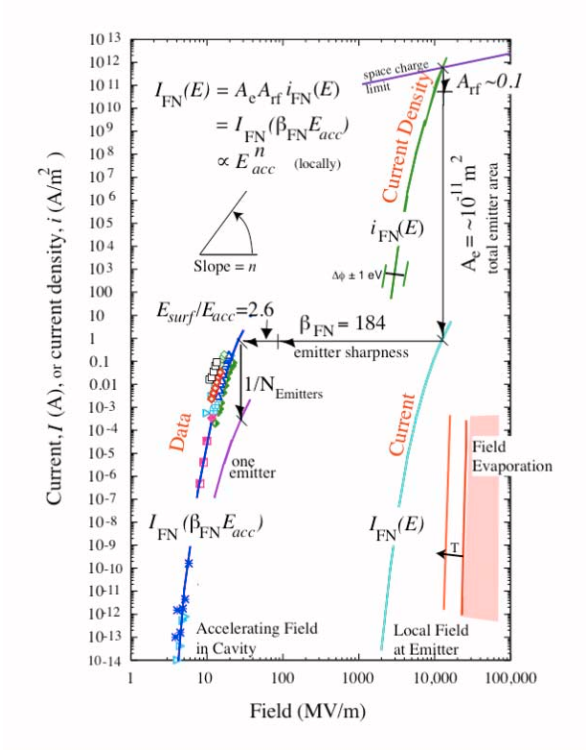

Figure 6: 805 MHz data with FN model and other processes (Norem).

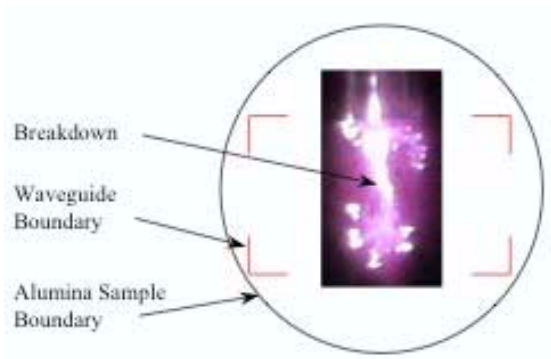

Figure 7: Breakdown in a dielectric window (Neuber).

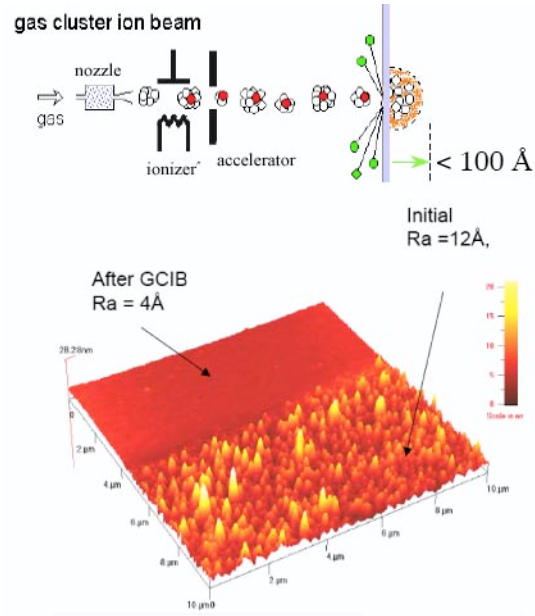

Figure 8: Gas Cluster Ion Beams (Insepov).

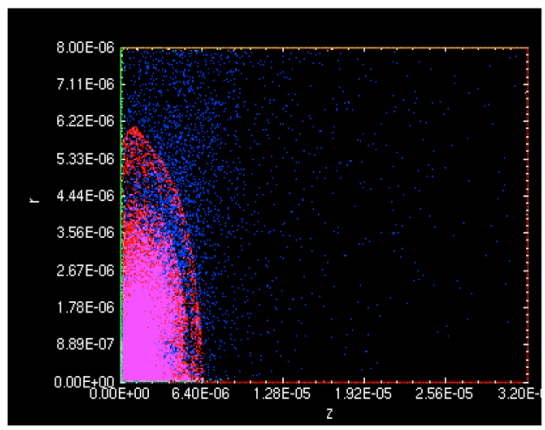

Figure 9: Simuations of the first few cycles of rf breakdown (Werner).

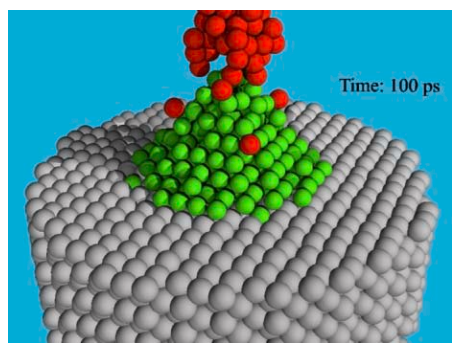

Figure 10: Modeling of cluster emission (Insepov).

INDUSTRIAL RF LINAC EXPERIENCES AND LABORATORY INTERACTIONS *

M. Peiniger, ACCEL Instruments GmbH, Bergisch Gladbach

Abstract

For more than two decades ACCEL Instruments GmbH at Bergisch Gladbach (formerly Siemens/ Interatom) has supplied accelerator labs worldwide with key components like rf cavities and power couplers, s.c. magnets, insertion devices, vacuum chambers and x-ray beamline equipment. Starting with the design and production of turn key SRF accelerating modules in the late 80th, meanwhile ACCEL is now engineering, manufacturing, on site commissioning and servicing complete accelerators with guaranteed beam performance. Today, with a staff of more than 100 physicists and engineers and about the same number of manufacturing specialists in our dedicated production facilities, ACCEL's know how and sales volume in this field has accumulated to more than 2000 man years and several hundred Mio €, respectively. Basis of our steady development is a cooperative partnership with the world's leading research labs in the respective fields. To give an example, we established a very fruitful partnership with DESY for the supply of a turn key 100 MeV injector linac for the Swiss Light Source, and meanwhile also for the Diamond Light Source as well as for the Australian Synchrotron Project.

INTRODUCTION

In the last years there have been different talks by people from industry [1], [2] or labs [3] on international accelerator conferences concerning the relation between the labs and the supplying industry for this worldwide research market. The scope of industrial supplies and services ranges from job shop and build to print work over standard and special equipment to turn-key systems. The lab's choice of type of relation is generally depending on their individual capabilities and strategies. While there exist a broad range of companies for performing work on a job shop/build to print level or supplying standard and special equipment there exist only very few companies worldwide with the know-how and capabilities for supplying complete accelerator systems or subsystems with guaranteed beam performance.

ACCEL Instruments GmbH is supplying advanced technology special equipment as well as turn-key linear and circular accelerators for research, industry and medical purposes worldwide. In the following I will try to give a picture on ACCEL's experiences and interactions with the international accelerator labs in the field of rf linac components and complete systems within the last years.

SRF CAVITIES AND MODULES

Within the last two decades ACCEL has manufactured more than 600 superconducting rf cavities out of bulk niobium, by Nb sputter coating of copper cavities or by Nb/Cu explosion bonding techniques. As examples we built all the 360 niobium cavities for CEBAF, the 109 medium and high ß cavities for SNS/ORNL (fig. 1) [4] and in the meantime more than 50 TESLA type cavities (fig. 1) for DESY, Stanford University, FZ Rossendorf and BESSY [5]. Our production know-how for these key components is based on a very intense, long term co-operation especially with DESY, CERN, JLAB, Cornell and Wuppertal University.

Figure 1: SNS (upper) und TESLA (lower) Cavity.

While in the past the cavity production was performed more or less on best effort basis, today customers are asking more and more on a performance guarantee especially for the accelerating field (E) and the cavity Q of the naked cavity, sometimes including the LHe vessel.

For BESSY we have been contracted for manufacturing, chemically treating (BCP) and high pressure rinsing (HPR, fig. 2) two TESLA type cavities [5]. The 800 °C heat treatment (fig. 2) and the vertical cold test have been performed at DESY with the help of DESY personnel. In fig. 3, the resulting Q versus E curves are shown in comparison with results of TESLA cavities manufactured by us but finally treated by and at DESY. We think these first results of accelerating fields above 20 MV/m at a Q of 1 E10 are very promising.

For future projects upon customer's request we plan to perform all preparation steps on TESLA type cavities under full responsibility of ACCEL, using DESY Nb material inspection, furnace and test infrastructure under service contract.

Figure 2: TESLA Cavities for BESSY during HPR at ACCEL (left) and vertical testing at DESY (right).

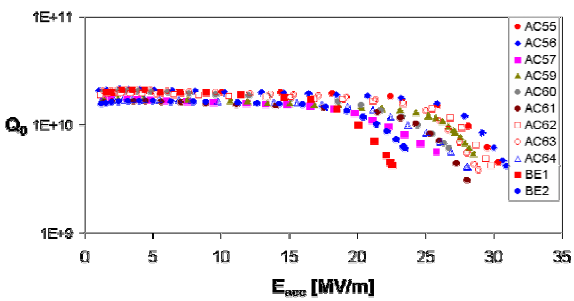

Figure 3: Q versus E curves of the two TESLA type cavities for BESSY (BE1, BE2) in comparison with those finally prepared by DESY (ref. TESLA TDR, DESY 2001). Most of the AC cavities have been titanium heat treated at 1400 °C, while the BE cavities did undergo only the standard 800 °C annealing process.

For an increasing number of labs, like CERN (LEP200), JAERI (FEL), LANL (pion momentum compaction), FZJ (ESS prototyping), BESSY, Cornell University (CESR), NSRRC, CLS, DLS (all synchrotron light sources) and Daresbury lab (4GLS prototype) we have delivered or are supplying complete SRF modules with guaranteed performance.

In figure 4 a complete LEP 200 module with four 352 MHz 4 cell Nb sputter coated copper cavities is shown together with 3 more cavity/LHe tank/tuner assemblies in front of our class 10 clean room. After a very intense technology transfer from CERN, which took about half a year, we were able to accomplish the manufacture, sputter coating and final preparation of the huge 352 MHz cavities. Before module assembly on our site all of the 88 cavities had been cold tested at CERN. This quality assurance step basically allowed us to issue guarantee for the performance of the modules.

Figure 4: LEP 200 module and 3 single cavity/LHe tank assemblies in our assembly hall. In the back is a 15 m long clean room, the quality of which has since been improved from class 100/10 to class 10/1.

The design of the four 500 MHz SRF modules for the JAERI free electron laser (FEL) and for FZ Jülich (for ESS prototyping [6]) was based on a DESY layout and then completely engineered by ACCEL. For the worldwide supply of the CESR type 500 MHz single cell modules, including valve-box, instrumentation and system control [7] (see figure 5), we concluded a technology transfer agreement with Cornell University which also regulates the use of university infrastructure for testing cavities and higher order mode absorbers as well as conditioning the high power rf windows.

Figure 5: Cornell type module with electronics and valve-box delivered to NSRRC and CLS.

Meanwhile this design has also been further engineered especially to stay in line with the European pressure vessel regulations. The status of the projects with Cornell, NSRRC/Taiwan, CLS/Canada and DLS/UK is given elsewhere [8].

The 1.5 GHz third harmonic Landau module for BESSY [9](fig. 6) is completely based on our own design. The required very short flange to flange distance made a rather complex cryostat design and cryogenic loss simulation necessary.

Figure 6: Turnkey 1.5 GHz SRF Landau module for BESSY.

Generally transportation to the final destination takes place in specially designed shock absorbing frames by trucks (in Europe) and/or by plane (intercontinental). Up to now the overall cavity and module transportation distance has exceeded 200.000 km and in all cases of proper transportation, no deterioration in cavity Q and maximum acceleration field has been observed. This documents that SRF cavity and module transportation should not be a technical issue especially when considering possible world spanning projects like an international linear collider (ILC).

In the beginning of 2004 we settled a license agreement with FZ Rossendorf for the production and worldwide sale of the twin TESLA cavity modules (fig. 7). The design is based on the technology developed by the world spanning TESLA collaboration and optimised by FZR in cooperation with Stanford University for cw operation for the FEL project ELBE. Meanwhile we have been contracted by Daresbury lab for supplying two such modules on a turn-key basis with guaranteed performance for the 4GLS prototype project in UK.

Our future goal is to also build and sale turn-key TESLA/XFEL type modules with guaranteed performance for worldwide FEL and energy recovery linac (ERL) applications.

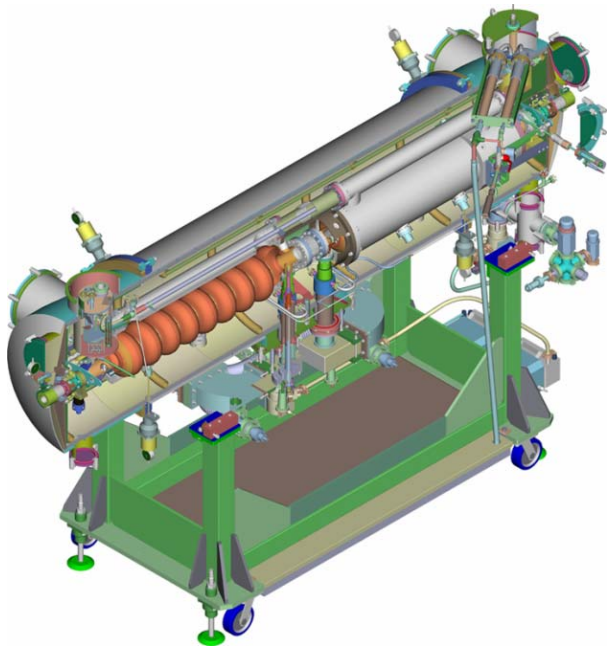

Figure 7: Twin cavity accelerator module, designed by FZR for cw operation in the ELBE FEL on the basis of TESLA module technology.

CU CAVITIES AND MODULES

In parallel to our SRF activities more than 200 normal conducting rf structures, couplers and modules in the frequency range between 52 MHz and 4.9 GHz have been manufactured for accelerator labs like CERN (LEP, CLIC), ESRF, ANL, LBL, BNL, DESY, SLAC, ORNL/SNS, SLS, CLS, DLS, ASP and Mainz University.

To give an actual example, for the SNS project we manufactured, assembled, aligned and rf tuned all the 4 CCL modules (fig. 8). Here we had a very intense technology and know-how exchange with LANL e.g. on the brazing technique and on the rf tuning procedures.

Figure 8: Completely aligned CCL module for SNS during rf test at ACCEL.

LINACS WITH GUARANTEED BEAM PERFORMANCE

Some years ago, a further step into systems technology was accomplished by developing, constructing, on site assembling and commissioning a complete 100 MeV S-Band electron injector linac for the Swiss Light Source at PSI (fig. 9) [10]. The settlement of a license agreement with DESY on the S-Band accelerating structures and electron gun, developed for linear collider applications at that time, together with a very fruitful co-operation with DESY and Dortmund university, made it possible to put the complete linac into operation with guaranteed beam performance on schedule. As of today three more such types of linacs are in production for DLS, ASP, and PTB, respectively [11].

Figure 9: Turn-key S-Band injector linac for SLS at PSI.

Two years ago, after a very thorough assessment study, we have been contracted to design, build and install a turn-key proton/deuteron linac injector for SARAF/Israel (fig. 10) for cw operation with a beam current of up to 2-4 mA [12]. Key subsystem of the accelerator is a prototype SRF module with 6 half wave resonators (HWR, fig.11) with a frequency of 176 MHz. The assessment study included beam dynamic simulations as well as error analysis. Since then the first prototype HWR (fig. 12) has been fabricated and first cold tests are expected soon. After a successful run of this injector the energy is foreseen to be upgraded to 40 MeV by means of an adequate number of additional superconducting modules. ACCEL is chosen to supply the complete accelerator including all the rf supply.

In order to satisfy these requirements we have defined - as we do for all contracted projects - a project team, consisting of project managers and engineers, several rf, srf and beam dynamics experts as well as manufacturing and assembly specialists. An intense inhouse R&D effort has been combined with a very strong cooperation with the world's leading accelerator labs in this field like INFN LNL, Frankfurt University, FZ Jülich, ANL, MSU; LANL, ORNL; PSI and AECL.

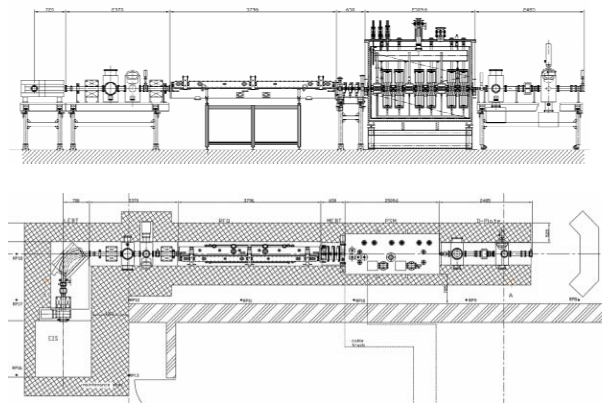

Figure 10: Scheme of the proton/deuteron injector linac for SARAF/Israel.

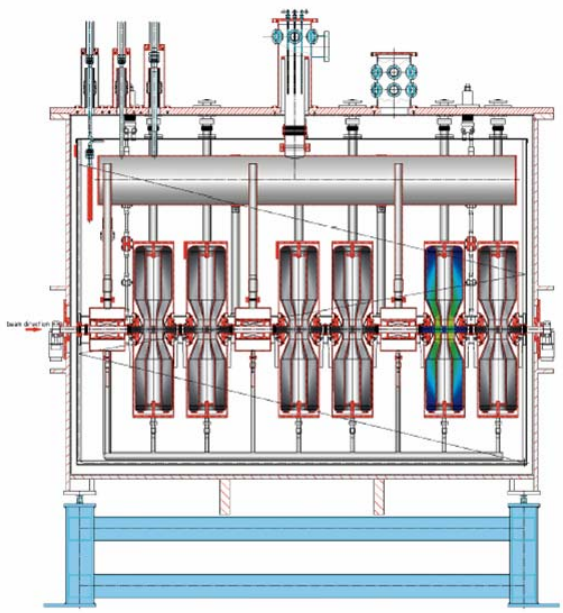

Figure 11: Scheme of the prototype SRF module for SARAF with 6 bulk niobium HWR and 3 superconducting solenoids. The beam vacuum is separated from the cryostat vacuum.

CONCLUSIONS

ACCEL's mission is to serve as an industrial partner for the worldwide labs on supplying advanced technology equipment and turn-key systems with guaranteed performance as well as co-operating with the labs on rf accelerators and its respective technologies. Therefore ACCEL is investing substantially in specialised production capabilities and in human resources.

Figure 12: Bulk niobium 176 MHz half wave resonator for the prototype superconducting module for SARAF.

We are observing that an increasing number of young and motivated lab physicists and engineers are deciding to join ACCEL for working as accelerator specialists or project managers, thus combining their individual know-how with the company's experience and capabilities.

Baseline of our technological development is an intense co-operation with the world's leading labs in the respective fields. This allows us to evaluate and compare the different experiences of those labs for gaining best solutions on running and future projects.

It is our impression that an increasing number of labs and people accept the role of the specialised industry and take advantage of a partnership under flexible but well defined conditions. This gives us – the industry – the necessary basis to stabilize and continuously expand our activities.

Our long term experience with the research organisations of the different countries shows us in view of both technical/operational and legal/administrative aspects, that all the different contractual systems give enough room for a flexible handling of the project, but it is up to the individual people on both sides to use and take advantage of it.

Successful partnership can only be accomplished by human beings on both sides with mutual respect and understanding. A growing acceptance of a dependence on each other and a common understanding of the benefits from the synergies within the partnership can even create more in the future.

REFERENCES

[1] B. Nielsen, Relations between accelerator institutes and industry, EPAC, Paris, 2002

[2] H. U. Klein, An Example of Cooperation in the Field of High Technology, EPAC, Wien, 2000

[3] D. Krämer, Experience with industry during the construction of a large accelerator, EPAC, Paris, 2002

[4] M. Pekeler et al., Fabrication of superconducting cavities for SNS, this conference, 2004

[5] S. Bauer et al., Test results of superconducting cavities produced and prepared completely in industry, EPAC, Lucerne, 2004

[6] W. Diete et al., A superconducting accelerating test module for the European spallation source, PAC, New York, 1999

[7] e.g. S. Bauer et al., Industrial production of turn key superconducting accelerator modules for high current storage rings, PAC, Chicago, 2001

[8] e.g. S. Bauer et al., Fabrication, test and first operation of superconducting accelerator modules for storage rings, PAC, 2003

[9] P. vom Stein et al., A superconducting Landau accelerator module for BESSY 2, PAC, Chicago, 2001

[10] C. Piel et al., design and construction of a turn-key 100 MeV Linac for the swiss light source , EPAC, Vienna, 2000

[11] K. Dunkel et al., Custom design of medium energy linear accelerator systems, EPAC, Lucern, 2004

[12] M. Pekeler et al., Design of a 40 MeV linear accelerator for protons and deuterons using superconducting half wave resonators, EPAC, Paris, 2002

IOT RF POWER SOURCES FOR PULSED AND CW LINACS

H. Bohlen, Y. Li, R. Tornoe,
CPI Eimac Division, San Carlos, CA, USA

Abstract

For many years, klystrons have been the preferred RF power amplifiers for both pulsed and CW linacs at UHF and higher frequencies. Their properties have earned them that position. But in recent years, in UHF terrestrial television transmitters, the earlier predominant klystron has been replaced by the Inductive Output Tube (IOT) because the IOT provides higher efficiency and , due to its excellent linearity, can handle the simultaneous amplification of both the vision and the sound signal. Its robustness and life expectancy equals that of a klystron, and it more than compensates its lower gain by a lower price and a smaller size. Pulsed operation of an IOT can be achieved without the help a high-voltage modulator. Since the beam current is grid-controlled it is sufficient to pulse the drive power. For linac operation, derivates of UHF TV IOTs, capable of up to 80 kW CW output power, are already available and operating. In L-Band, they are presently joined by recently developed 15 to 30 kW CW IOTs. HOM-IOTs are expected to extend the CW range in UHF to 1 MW and beyond.

LINAC RF SOURCE REQUIREMENTS AND BASIC IOT PROPERTIES

Every linac has certain requirements regarding its RF power source. The most common ones are (not necessarily in this order): high efficiency, reliability and ruggedness, long-term stability, low pushing factors (AM/AM and AM/PM), long life, and all that at a price that does not jeopardize the project. For many years, klystrons have provided most of these properties, and they still do so. So, why and when use IOTs instead?

In now almost two decades of TV operation the IOT has developed into a device that equals the klystron in terms of reliability and ruggedness, long-term stability and life. That by itself is remarkable, but it would not serve as a prudent reason for a change. However, there are areas where the IOT shows significant superiority compared to the klystron.

Efficiency and Linearity

The IOT, also known as a klystrode*, is by its nature a special tetrode. The bunches in its electron beam are generated by means of a control grid and not by velocity modulation, as in a klystron. This results in several advantages. The first one is basic efficiency. Like a tetrode the IOT can be operated in class C mode, providing efficiency figures in the order of 73 % and higher. The second advantage is that the IOT's high basic efficiency can actually be fully exploited.

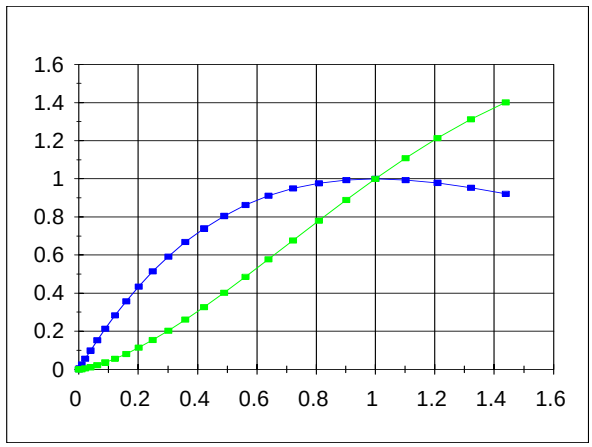

Figure 1: Normalized characteristics of output power (vertical axis) vs. drive power (horizontal axis) for klystrons (blue, saturating) and IOTs (green, not saturating).

Figure 1 highlights this very important feature for accelerator operation. In order to apply fast feedback control when using a klystron, a back-off in the order of 10 % of output power from the point of maximum efficiency (1/1 in the figure) is necessary, due to the change of slope in the characteristic at that point. An IOT, on the other hand, does not require a back-off; full use of its already higher basic efficiency can be made since its characteristic does not saturate at its nominal output power level.

A third advantage is superior linearity, resulting in low pushing factors. The characteristic in Figure 1 already reveals the lower AM/AM conversion in the vicinity of the operation point, compared to that of a klystron. AM/PM conversion is likewise much more benign in an IOT.

Costs

IOTs are simple devices. Basically, they contain only one RF circuit (the so-called input circuit is merely an impedance-matching device between the input line and the low-impedance cathode-grid structure). The whole tube is considerably shorter than a comparable klystron, resulting in a significantly lower price for both the IOT proper and the assembly hardware, including the focusing magnet.

A drawback is the lower gain of the IOT (in the order of 23 dB) which requires a more powerful driver, but this is usually more than compensated by reduced costs for power supplies and cooling devices, due to the higher efficiency. And, naturally, there are considerable savings in the power bill, especially in CW operation.

In pulsed operation, the power bill savings may not be that attractive. But in this case, another IOT feature that is

* Klystrode® is a trademark of CPI

based on grid control can save a considerable amount of capital costs: no expensive high-voltage modulator is required; a simple PIN modulator placed at a low level in the driver will serve the purpose.

EXAMPLES OF UHF IOTS

Already in Use in Accelerator Operation

Aided by intensified cooling (water-cooled anode and output cavity, improved air-cooling of the output window), TV-IOT derivates like the CPI/Eimac K2H80W shown in Figure 2 are able to provide CW output power up to 80 kW at efficiencies between 70 and 76 %.

Figure 2: K2H80W, an 80 kW CW UHF IOT with complete hardware assembly.

The double-tuned output circuit provides an additional feature: The almost flat top of the frequency-response curve permits an offset between operating and central frequency, which leads to a further increase in efficiency.

Maintaining High Efficiency when Modulating

Adding two or more collector stages that are operated at potentials lower than the IOT's body potential (with respect to the cathode) permits to slow down considerable portions of the spent beam before it hits a collector surface. This saves energy. The IOT depicted in Figure 3 (CPI/Eimac K3130WC) features 3 collector stages, those at high voltage potential being oil-cooled.

The improvement in efficiency due to Multi-Stage Collector Depression (MSDC) is especially high at power levels lower than the nominal power, as shown by the graph in Figure 4 (efficiency levels presented are relatively low because they represent a TV transmitter application). Collector depression therefore becomes useful in applications with varying power levels, while the additional effort may be wasted for the small efficiency gain in CW operation close to nominal output power.

Figure 3: 3-Stage Depressed Collector IOT K3130WC.

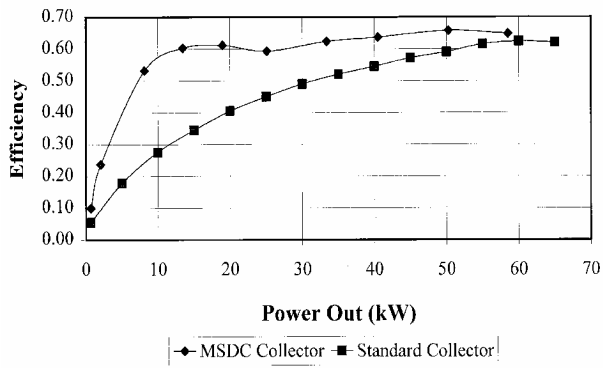

Figure 4: Characteristics of efficiency vs. output power. Top: 3-stage MSDC. Bottom: standard collector.

High-Power and Super-Power Options

For output power levels exceeding 80 kW, and for higher frequencies than UHF, internal cavities replace the external ones. Shown in Figure 5 is the CPI/Eimac (Varian/Eimac) 2KDW250PA, the so called "Chalk River Tube", which provides 250 kW CW output power at 267 MHz with 73 % efficiency.

But there is an IOT option for even higher power levels. The Higher-Order Mode IOT (HOM-IOT) uses multiple beams (or large electron beams with quasi-

annular cross-section) that interact with the outer voltage maxima in TM_{0n0} mode cavities. The advantage: low beam voltages, low emission densities, low energy densities on surfaces and in cavities.

Figure 5: 250 kW CW "Chalk River" IOT.

Table 1 compares the capabilities of an HOM-IOT and a klystron, both for 1 MW CW output power in UHF.

Table 1: Comparison of HOM-IOT and klystron properties at 1 MW CW output power in UHF

Property	HOM-IOT	Klystron
Effective efficiency	**73 %**	**60 %**
Rel. power consumption	**82 %**	**100 %**
Assembly volume (approx.)	**30 cbf**	**200 cbf**
Assembly weight (approx.)	**1,000 lbs**	**5,000 lbs**
DC voltage	**45 kV**	**90 kV**

Figure 6 shows the first (and so far only) HOM-IOT in test. It has been developed by CPI for Los Alamos National Laboratories for their abandoned APT (Accelerator Production of Tritium) project and has been moth-balled together with it. Its target specification: 1 MW CW at 700 MHz.

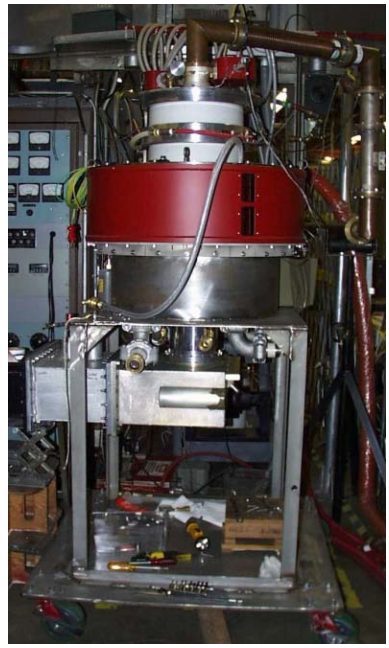

Figure 6: 1 MW / 700 MHz HOM-IOT in test.

IOTS IN L-BAND

Basic Considerations

The cathode-grid configuration of modern IOTs is well proven. There have been scarcely any grid failures reported. Thus there are good reasons to maintain this configuration when designing an IOT for higher frequencies. That these well established assemblies are well-suited for L-Band operation is documented by the simulation of the fundamental-frequency currents versus operation frequency of an existing IOT electron gun in class B operation at in this case 22 kV, as shown in Figure 7.

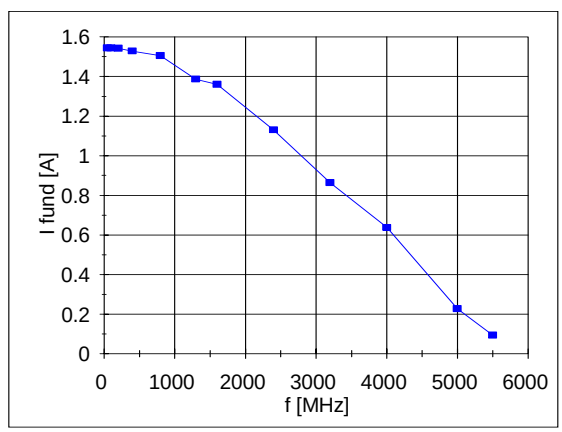

Figure 7: Simulated fundamental frequency current of existing IOT gun vs. frequency at 22 kV (Class B).

The characteristic proves that reasonable operation results can be expected using such a gun up to 2 or even 3 GHz.

Birth of a New IOT Generation

A 1.3 GHz IOT has been developed at CPI / Eimac, based on considerations like those explained above. Figure 8 depicts the tube.

Figure 8: 30 kW CW L-Band IOT by CPI / Eimac.

The following table 2 lists the test results of the third prototype tube at 1.3 GHz.

Table 2: L-Band IOT test results

Voltage(kV)	Current(A)	Drive(W)	Output(kW)	Gain(dB)	Eff(%)
24	0.79	208	10.0	17	52.7
25	1.10	203	15.1	19	54.9
26	1.46	183	20.6	21	54.3
32	1.35	192	25.7	21	59.5
34	1.39	253	30.2	21	63.8

The test results confirm the computer simulations: the almost 64 % efficiency, achieved at 30 kW CW output power, are in good agreement with the about 10 % of predicted loss in fundamental current at 1.3 GHz, compared to UHF. This power range is well positioned to satisfy the requirements of fourth-generation light sources.

Figure 9 shows the L-Band IOT in its hardware set, in this case equipped with a coax-waveguide transition at the output.

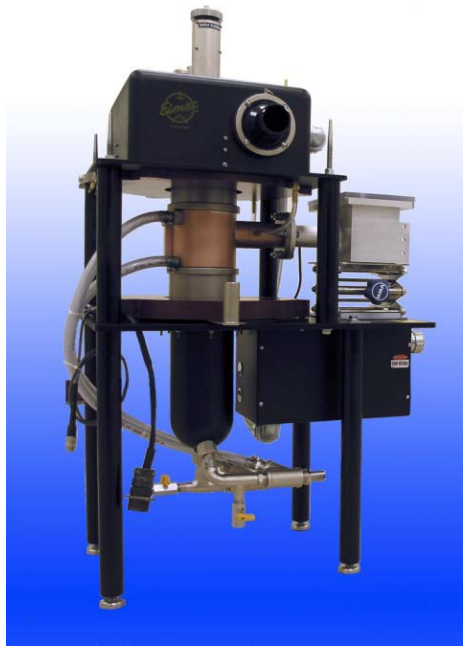

Figure 9: 30 kW L-Band IOT in hardware set.

CONCLUSION AND OUTLOOK

Less than twenty years after the design of the first modern IOT the device has established itself as a reliable and very efficient amplifier for medium power levels in UHF, and it is on the verge of expanding its area of use into the UHF super-power range and into medium- and high-power L-band applications, especially in fourth generation light sources.

ACKNOWLEDGEMENTS

The authors wish to thank all members of the CPI / Eimac IOT team for their inventiveness and their dedication to the task, and many of the present and future IOT users for lots of suggestions.

REVIEW OF FAST BEAM CHOPPING

F. Caspers, CERN, Geneva, Switzerland

Abstract

Several types of fast beam chopping systems in use or under construction are presented. Emphasis is given to their specific technologies and in particular their various fields of application. Important parameters are duty cycle, rise- and fall-time, ringing and overall bandwidth. Certain systems have very specific driver concepts, since the generation of multi-kW peak power with nanosecond transients, high repetition rate and very good pulse shape fidelity is not a trivial issue. The design of driver amplifier and actual chopper structure are not always mutually independent and thus some of the limiting aspects will be discussed.

INTRODUCTION

Over the recent years different chopper structures and chopper systems (e. g. RAL-ESS, LANL-SNS, JAERI CERN-SPL) have been designed and tested. Some of them are already in operation, others still under construction and / or in development. Many of these chopper structures contain slow wave deflectors, since the beam to be chopped has a fairly low momentum, usually with $\beta = v/c$ values between 5 and 10 %. The specifications for the chopper systems differ largely in terms of duty cycle, rise-and fall-time as well as required deflection angle. Thus there is no unique solution for all existing machines and the structures and hardware presently available has been optimised for each individual application.

DISCUSSION OF CHOPPER CONCEPTS

In the following sections the properties and design concepts of the four chopper systems mentioned above will be shown and subsequently discussed. Obviously this selection cannot be complete and priority is deliberately given to the most recent projects.

THE RAL-ESS CHOPPING SCHEME#

This is an example of a chopping scheme for a next generation spallation neutron source [1]. Chopping is restricted to the 2.5 MeV medium energy beam transfer (MEBT) line, where a low level of emittance growth is predicted [2,5]. The proposed 'fast-slow' chopping technique addresses the requirements for a ~ 2 ns transition time, a 200 ns to 0.1 ms chopping duration, and a programmable duty cycle [2]. Components of the European Spallation Source (ESS) front-end are shown in schematic form in Fig. 1. ESS front-end specifications call for significant technical development and the design may be considered to be very relevant for next generation spallation sources and neutrino factories [3].

#Supported by EC Research Infrastructure Activity FP6 "Structuring the European Research Area" program, CARE –RII3-CT-3003-506395

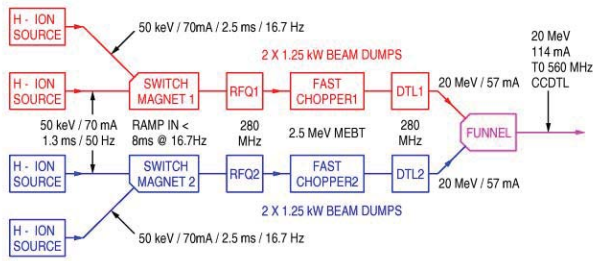

Figure 1: ESS front-end schematic [2].

A schematic drawing of the 2.5 MeV ESS MEBT line is shown in Fig. 2. and a corresponding table of key parameters can be found in [2].

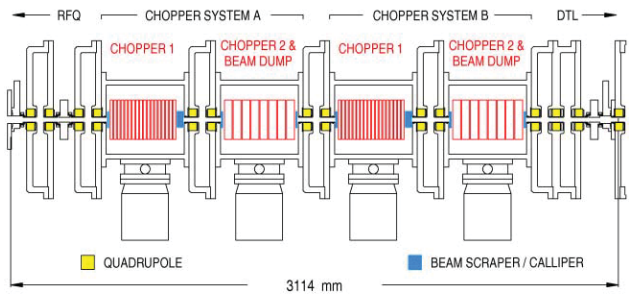

Figure 2: ESS MEBT line with 'Tandem' chopper [2].

The configuration has evolved from a previously reported design [4], and utilises two slow-wave E-field chopper systems operating in 'Tandem'. The design reduces beam dump power dissipation, and high voltage pulse generator repetition frequency by a factor of two, without incurring excessive emittance growth.

Simulated r.m.s beam radii and emittances from a revised optical design [5] return beam radii around 2 mm in both planes [2]. Input matching from the RFQ, use of regular lattice functions with the same beam aspect ratios in the channel cells, and a final six parameter output matching section, result in an acceptably low level of emittance growth and halo development. Optical amplification of beam deflection has not been attempted, and chopping fields are therefore higher than in other designs [6]. Key parameters and a timing schematic for one sub-system of the 'Tandem' chopper configuration are shown in Table 1, and Fig. 3, respectively.

'Tandem' sub-systems are identical in operation and operate alternately at a repetition frequency of 25 Hz. Each sub-system consists of an upstream fast chopper with a meander type slow-wave electrode structure [7]

and a downstream (slower) main chopper (Fig. 3 top) with water-cooled lumped element electrodes, which also serve as a beam dump.

Table 1: Key parameters for the ESS chopper system [2]

	Prechopper	Chopper
Beam energy	2.5 MeV	
Chopping factor	30 % (ring stacking regime)	
Electrode voltage	± 2.2 kV	± 6.0 kV
Electrode length	340 mm	360 mm
Electrode gap	14 mm	11 mm
Deflection angle	16 mrad	66 mrad
Pulse transit. (10-90%)	~ 2 ns	~12 ns
Pulse duration	12 ns	240 ns-0.1 ms
Pulse repetition freq.	2.4 MHz	1.2 MHz
Burst duration	1.5 ms	
Load impedance	50 Ω	35 pF / 60 nH
Repetition rate	50 Hz (two systems @ 25 Hz)	
Beam power on dump	2.5 kW (2 systems @1.25 kW)	

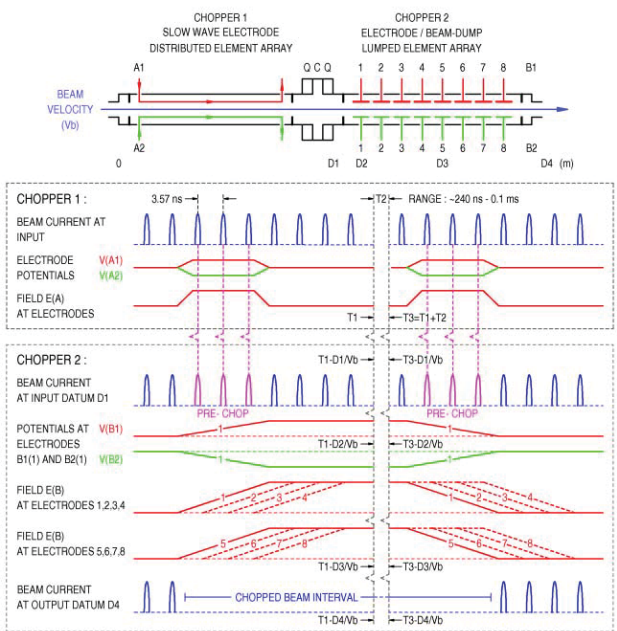

Figure 3: Two stage (fast-slow) chopping scheme [2].

Slow-wave chopper 1 produces a uni-polar pulsed field that deflects just three adjacent bunches through ~ 16 mrad. into scraper S2, S3 and chopper 2 beam dump electrodes, creating two ~ 14 ns duration gaps in the bunch train at the beginning and end of each chopped beam interval. These gaps ensure that no partially chopped bunches result from the slower field transition time of chopper 2.

Fig 4, and 5 shows 'General Particle Tracer' (GPT) [8] simulations of particle tracking with space charge for the cases of fast (pre-post) chopping, and main chopping, respectively. Eight pairs of adjustable scrapers control beam halo, beam displacement during fast chopping and function as diagnostic beam "callipers".

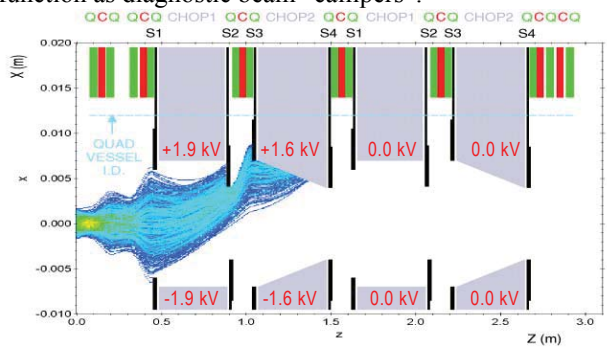

Figure 4: Fast chopping / Bunch 1-3 and 63-66 chopped.

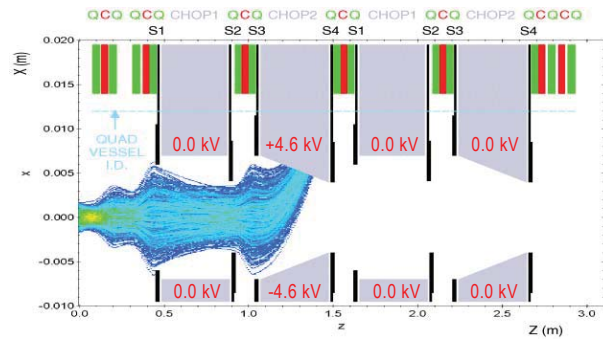

Figure 5: Slow chopping / Bunch 4-62 chopped.

THE LANL-SNS CHOPPING SCHEME

Structure (SNS-MEBT)

The MEBT chopper matches the deflecting electric wave velocity along the beam axis to the beam particle velocity, thus providing a rise and fall time determined mainly by the rise and fall times of the electric pulse. The parameters of this chopper are given in Table 2.

Table 2: SNS MEBT chopper parameters

Parameter	Value	Comments
Beam energy	2.5 MeV	β=0.073
Structure length	35 cm	
Meander width	96 mm	
Gap	18 mm	Adjustable
Pulser voltage	±2350 V	Max. ±2500V
Deflection angle	18 mrad	
Chopping period	945 ns	
Duty factor	32 %	Beam on:68 %
Structure rise/fall time	1.5 ns	
Pulser rise / fall time	10 ns	2-98 %

The current structure is based on the meander-folded notched strip-line with separators [9, 10, 11], see Fig. 6. The notched meander line provides the proper wave phase velocity along the beam path while keeping the characteristic impedance of the line equal to 50 Ω. The separators (metallic ridges situated between adjacent meander elements) reduce the strip-to-strip coupling and thus minimize the dispersion due to this mutual coupling.

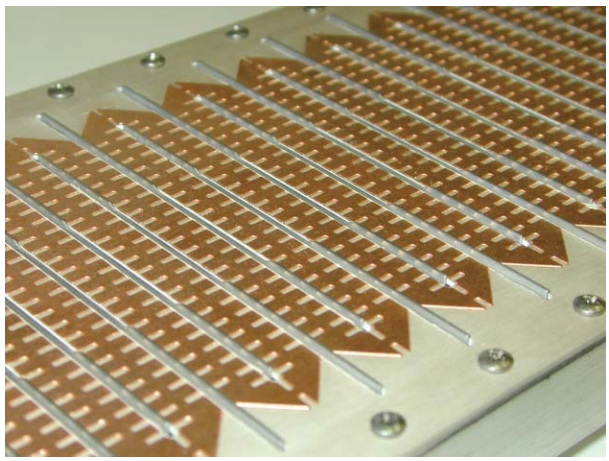

Figure 6: Close-up view of the notched-meander current structure [9].

Technology (SNS MEBT)

The notched meander line is supported by a T-shaped dielectric support that goes all along the strip-line length. The support is carved from a continuous dielectric plate of Rogers' duroid RT/6002 and afterwards the notched meander pattern is chemically etched on the copper coating of the dielectric plate. The copper thickness in the transmission line is 0.25 mm, and the dielectric is 2.5 mm thick. The metal width in the line is 8 mm, and the meander period is 1 cm; it leaves 2-mm gaps between the straight strips. The grounded metal separators protrude into these gaps through the narrow cuts in the dielectric. The notches on the line serve to slow down the TEM wave along the line straight sections to 0.68*c*. The notches are 3 mm deep and 1 mm wide, and their period is 4 mm. The whole structure is clamped by bolts near its sides to the metal ground plate, and the dielectric supports are glued to the ground plate with a special epoxy. The ground plates are fabricated of 6061-T6 aluminum alloy.

Pulser (SNS MEBT)

The chopper pulser has a peak voltage of 2.35 kV, higher by a factor 2.6 compared to its original specification of 900 V, so that the peak current through the meander line is about 47 A. It results in a power dissipation along the chopper structures of between 10-20 W. Active water cooling will be used. The original rise time requirement for the chopper system was set at below 2.5 ns, which led to the development of the fast current structure. Later beam dynamics simulations have shown that partially chopped bunches would not lead to extra beam loss in the SNS linac or the ring transfer line. The requirement for the pulser voltage was changed to 2.35 kV with a slower rise and fall time, below 10 ns, thus allowing up to 3 partially-chopped bunches in the beginning and at the end of each chopper pulse, which lasts around 300 ns. The pulser was developed by Directed Energy Inc. (Fort Collins, CO); it uses 4 FETs in series for each voltage source, positive and negative.

The SNS MEBT chopper system was tested with beam at ORNL in 2003. All the results satisfy the chopper system requirements [13].

LANSCE CHOPPER

The SNS travelling-wave chopper is based on the same principle as the strip-coax helical structure [12] successfully used at LANL for many years. The present chopper system at Los Alamos Neutron Science Center (LANSCE) was constructed for the Proton Storage Ring (PSR) in the early 80s. It works at beam energy of 750 keV and provides a rise time of approximately 7 ns with a larger contribution from the pulse modulator. The current structure itself is capable of providing a pulse front slightly longer than 2 ns, with an overshoot on the 10% level ringing for a few nanoseconds. This coax-plate structure is 1 m long and consists of two parallel plates each interfaced with many small strips. These are connected with coaxial cables on the reverse side of each plate to form a circuit that is continuous along the structure.

The LANSCE pulse modulator was developed in the early 80s as a fast vacuum-tube-driven device. In the 90s it has been revised to a solid-state model, which is easier to maintain at peak performance, but with a slower rise time. Both LANSCE pulsers give 500 V. The old pulser used 8 vacuum tubes in parallel; it was very fast (about 2.5 ns rise / fall "on a good day", typically 50% slower), but its tuning was fairly difficult. Its reliability was a serious issue, so it has been replaced later with a slower, but more reliable solid-state pulser.

THE J-PARC CHOPPER SYSTEM

The J-PARC linac has a two-stage chopping system with an LEBT pre-chopper and an MEBT chopper [14]. A. parameter list is given in Table 3. The LEBT pre-chopper is an energy modulation induction cavity, with which one can drive bunches beyond the longitudinal acceptance of the RFQ. The MEBT chopper is an RFD (RF deflection cavity) with short time-constant or low Q – value (around 10) driven by fast RF bursts from a high power RF amplifier. Bunches are kicked horizontally with the RFD and removed with a collector downstream. With the cavity modulating the LEBT beam energy, the downstream RFQ operates as an "energy filter" by letting the off-momentum beam arrive outside the momentum

acceptance of the RFQ. The MEBT chopper has been tested, and, as shown in Fig. 7, the design rise/fall time of 10 ns has been achieved [15]. It has also been confirmed that the residual current during "chopper-on" periods is less than 10^{-4} of the nominal current (5 mA). Further testing of the chopper performance is now in progress during beam commissioning of the J-PARC linac front-end at KEK [16].

Table 3: Parameter list for the J-PARC chopper

Beam energy	3 MeV
Type	RFD
Operation frequency	324 MHz
Operation mode	TE11
Number of cavities	2
Number of gaps per cavity	1
Cavity length	172 mm
Bore radius	5 mm
Gap length	20 mm
Full rise / fall time	15 ns
Deflection field voltage	1.6 MV/m
Beam-on duty factor	56 %
RF power source type	Solid state amp.
Number of cavities per RF source	2
Peak RF power per cavity	30 kW

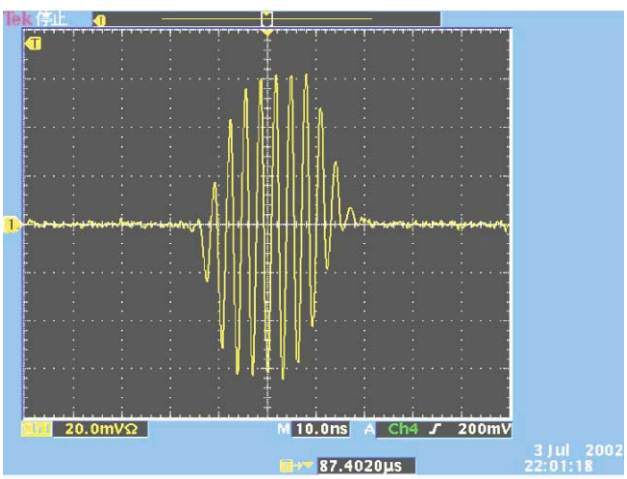

Figure 7: Waveform of a chopped beam obtained with a beam position monitor in MEBT. The horizontal scaling is 10ns/div. The pulse duration is shortened to demonstrate the chopper performance [16].

THE CERN-SPL CHOPPER*

The fast chopper for the CERN SPL (Super conducting Proton Linac) consists of a double meander structure with $\beta = v/c$ of 0.08 printed on an alumina substrate for the deflecting plates. For the parameters see Table 4. Each chopper unit is 50 cm long and housed in a quadrupole magnet surrounding the vacuum chamber.

The deflecting plates are driven simultaneously in a dual mode of operation. For frequencies above about 10 MHz the travelling wave is used mode and below the quasi-electrostatic deflection. These structures are water-cooled to handle heating from beam losses as well as from the deflecting signal.

For the actual chopping structure a printed circuit design has been selected using a double meander type micro-strip line on a 3 mm thick alumina substrate (c.f. figure 8.). Details of the production process for this printed circuit are given in [16]. We used a MoMn layer (fired at 1500º C in an H_2/N_2 atmosphere) which has several layers of other metals added. It is given its final shape by a chemical etching process. Results of extensive numerical simulations as well as measurements on the rise- and fall-times and the deflecting efficiency have been presented in [18]. The main motivation for this kind of approach was to keep the actual chopper structure as short as possible and to obtain moderate requirements for the deflection voltage by taking advantage of beam-optics related deflection enhancements.

Table 4: Selected Parameter list for the SPL Chopper

Beam energy	3 MeV
Overall length	3.7 m
Number of chopper structures	2 inside quads
Number of quadrupoles	11
Chopper plate length	400+400 mm
Chopper plate distance	20 mm
Separation chopped/ un-chopped beam	15 mm
Chopper structure rise-and fall time	<2ns (10-90%)
Chopper voltage pulse (per plate)	500 V
Effective chopper voltage pulse	400 V
Max. chopper frequency	44 MHz
Pulse length	8-1700 ns
Max chopping factor (duty cycle)	40%
Repetition rate	1-50 Hz
Output transverse emittance (rms, norm)	0.27 π mm mrad with collimator
Chopper deflection angle	6.8 mrad

The dual mode operation for the deflecting plate has been selected in order to obtain an optimum combination of bandwidth, pulsing parameter variation range and power to be provided from the pulser. Note that nearly all the power delivered from the pulse generator has to be dissipated later in a load.

*Supported by EC:(HIPPI inside CARE), contract number RII3-CT-2003-506395

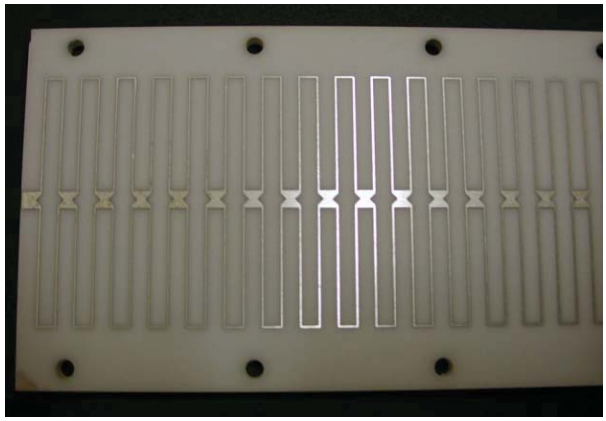

Figure 8: The alumina ceramic plates with printed meander structure (MoMn + 30 micron Ag); mounting holes for M2.5 screws are at the sides [17].

Thus the 50 Ohm termination travelling wave mode, essentially required for fast transients is only used above roughly 10 MHz and below the high impedance electrostatic deflection is used Details of these dual mode pulse amplifiers, which are presently under construction are given in [17].

Finally a 3D view of the complete chopper with its vacuum tank, water cooling system (beam loss related heating!) and triaxial feedthroughs is shown in Fig. 9.

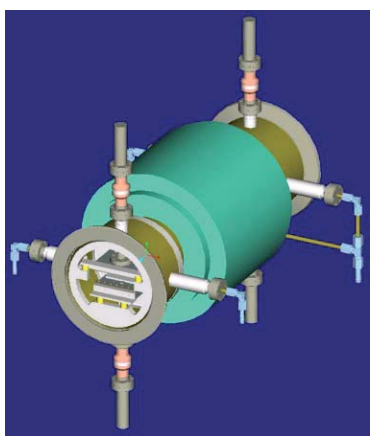

Figure 9: Complete chopper with vacuum tank mounted in a quadrupole [17].

CONCLUSIONS

Different concepts and ways of implementation for fast chopping structures have been shown and discussed. The main technological challenges for present developments are the pulse driver or power amplifier as well as the management of beam losses in the MEBT lines. Practical experience in the coming years will show which of the systems discussed above has the best performance and advances in solid state switching technology may lead to modifications in the deflector hardware.

ACKNOWLEDGEMENTS

This paper would not have been written without the extensive discussion and contributions in particular from M. Clarke-Gaither, S. Kurennoy as well as R. Garoby, M. Vretenar, M. Paoluzzi, A. Lombardi.and M. Ikegami. The author would also like to thank R. Garoby and T. Linnecar for support and for reading the manuscript.

REFERENCES

[1] "The ESS Project, Volume III Update: Technical Report – Status 2003", ISBN 3-89336-345-9.
[2] M. A. Clarke-Gayther, "A fast beam chopper for next generation high power proton drivers", Proc. of EPAC 2004, Lucerne.
[3] W. Chou, "Spallation neutron source and other high intensity proton sources", FNAL Report No. FERMILAB-Conf-03/012.
[4] M. A. Clarke-Gayther, "Modulator Systems for the ESS 2.5 MeV Fast Chopper", Proc. of PAC 2001, Chicago, USA, p. 4062-4065.
[5] F. Gerigk, "Revised ESS front-end 2.5 – 20MeV", 2003, ESS Report No. ESS 03-138-A.
[6] F. Caspers, K. Hanke, A. Lombardi, A. Millich, A. Mostacci, et al "Design of a chopper line for the CERN-SPL", Proc. of the 21st Linac Conf., Gyeongju, Korea, 19-23 August, 2002, p. 76-78.
[7] M. A. Clarke-Gayther, "Slow-wave electrode structures for the ESS 2.5 MeV fast chopper", Proc. of PAC 2003 , Portland, Oregon, USA, p. 1473-1475.
[8] "General Particle Tracer", www.pulsar.nl.
[9] S.S. Kurennoy, J.F. Power, D.L. Schrage, "Meander-line Current Structure for SNS Fast Beam Chopper", Proc. of PAC'99, New York, 1999, p.1399.
[10] S.S. Kurennoy and J.F. Power. "Development of Meander-Line Current Structure for SNS Fast 2.5-MeV Beam Chopper," Proc of EPAC00, Vienna, 2000, p.336.
[11] S.S. Kurennoy et al., "Progress with SNS Fast Beam Chopper", Proc. of PAC01, Chicago, IL, p.1435.
[12] J. Lunsford and R. Hardekopf, "Pulsed Beam Chopper for the PSR at LAMPF", Proc. of PAC83, Santa Fe, NM, IEEE Trans. NS-30 (1983) 2830.
[13] R.A. Hardekopf, S.S. Kurennoy, et al. "Design, Construction and Initital Operation of the SNS MEBT Chopper system" Proc of EPAC2004, Luzern.
[14] Y. Yamazaki ed., "Accelerator Technical Design Report for J-PARC", KEK Report 2002-13; JAERI-Tech 2003-044.
[15] T. Kato et al., "Beam Study with RF Choppers in the MEBT of the J-PARC Proton Linac", Proc. of PAC2003, p.1455 (2003).
[16] Y. Yamazaki, "Status of the J-PARC Linac, Initial Results and Upgrade Plan", in these proceedings.
[17] F. Caspers, J. Genest, M. Haase M. Paoluzzi, A. Teixeira, "The CERN-SPL Chopper Concept and Final Layout", Proc of EPAC 04, Luzern.

High Power Targets

H. Kirk, BNL, Upton, Long Island, New York

Abstract

The accelerator physics community is responding to developing theoretical arguments for the search of new physics beyond the Standard Model by conceiving and proposing new high-intensity proton machines in the multi-megawatt class. These new machines will allow for the production of a variety of useful secondary beams but only if the proper target configurations are first developed and then implemented. In this paper, important target issues will be discussed and world-wide approaches and prospects for new targets will be reviewed.

NO SUBMISSION RECEIVED

END-TO-END BEAM DYNAMICS SIMULATIONS FOR THE ANL RIA DRIVER LINAC*

P.N. Ostroumov#, Physics Division, ANL, 9700 S. Cass Avenue, Argonne, IL, 60439

Abstract

The proposed Rare Isotope Accelerator (RIA) Facility consists of a superconducting (SC) 1.4 GV driver linac capable of producing 400 kW beams of any ion from hydrogen to uranium. The driver is configured as an array of ~390 SC cavities, each with independently controllable rf phase. For the end-to-end beam dynamics design and simulation we use a dedicated code, TRACK [1]. The code integrates ion motion through the three-dimensional fields of all elements of the driver linac beginning from the exit of the electron cyclotron resonance (ECR) ion source to the production targets. TRACK has been parallelized and is able to track large numbers of particles in randomly seeded accelerators with misalignments and a comprehensive set of errors.

INTRODUCTION

A detailed configuration of the 1.4-GV RIA driver linac was described in ref. [2]. The linac consists of a front-end and three sections of SC linac: low-, medium- and high-β sections. The front-end includes an ECR ion source, a Low Energy Beam Transport (LEBT) system, a Multi-Harmonic Buncher (MHB), a Radio Frequency Quadrupole (RFQ) and a Medium Energy Beam Transport (MEBT) system. The three sections of the linac are each separated by two stripper areas with a stripper foil or film and a post-stripper Magnetic Transport System (MTS). Beam dynamics in the driver linac are the most challenging for the multiple-charge-state uranium beam [2]. The baseline design of the driver linac has been optimized for simultaneous acceleration of two charge states (28^+ and 29^+) in the front-end and the first section of the linac up to the first stripper and optimized for five charge states between the two strippers (average charge state is 74^+) and five charge states in the high-β section (average charge state is 88^+). The acceleration of multi-q beams not only increases the total intensity but also reduces significantly the power to dump at the strippers. For example, the five charge states after the second stripper represent 98% of the total intensity. The linac lattice is optimized for multiple-charge-state uranium beams and includes 220 SC drift tube based resonators between the front end and the second stripper. The stripping energies for uranium beam, 12 MeV/u and 89.86 MeV/u, are optimized to minimize the longitudinal effective emittance of multi-q beams at the location of the strippers. The baseline design includes 172 SC cavities of elliptical type beyond the second stripper. The most recent parameters of the RIA driver baseline design were reported in the RIA R&D workshop [3].

With cw operation of the driver linac, the space charge effects are negligible in all accelerator sections except the ECR source, the ECR extraction optics and the LEBT. The required beam intensity in the LEBT is 500 μA for protons and 250 μA for uranium to produce 400 kW accelerated cw beams. After separation and selection of ion species the beam optics become emittance dominated and the space charge effects produce small perturbations with respect to the "zero-current" beam optics. Downstream of the LEBT the space charge effects are negligible.

FRONT END

ECR-LEBT

Detailed design, optimization and simulation of the front-end is extremely important to produce a realistic beam distribution in the six-dimensional phase space at the entrance of the SC linac. Several publications have been devoted to this problem [4-6].

Beam parameters at the entrance of the LEBT have been obtained from simulations of multi-component ion beams through extraction and acceleration system of the ECR, including the extraction electrodes, solenoid lens and accelerating tube (Fig. 1). The total accelerating voltage is 100 kV. The calculations performed by the code TRACK, including static electric and magnetic field distributions and beam space charge, are consistent with the recent experimental data [7]. The achromatic section of the LEBT has been optimized to select two charge state heavy-ion beams and obtain a ~6 mm diameter beam at the location of the MHB. Figure 2 shows transverse phase space plots of dual charge state ion beam at the location of mass-analyzing slits and at the entrance of the MHB. The total extracted beam current is 3.9 mA with each charge state of U^{28+} and U^{29+} carrying 125 eμA. The simulations show that the system separates charge states reliably over full range of total input beam currents and provides at the MHB similar Twiss parameters for transverse emittances for both charge states.

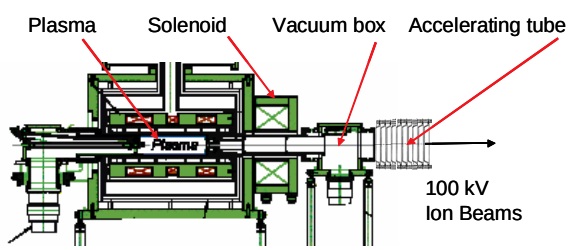

Figure 1: Beam extraction from the ECR.

Work supported by the U.S. Department of Energy, Office of Nuclear Physics, under Contract No. W-31-109-ENG-38.
#ostroumov@phy.anl.gov

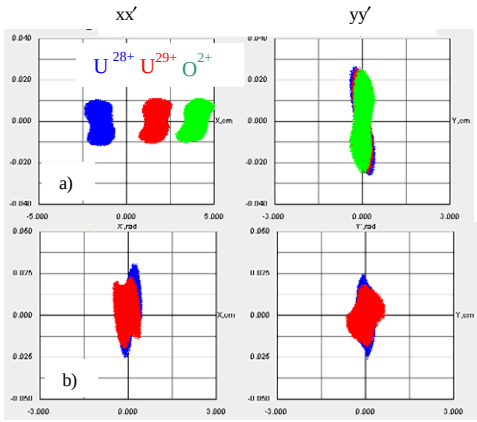

Figure 2: Beam phase space plots of a dual charge-state uranium beam at the location of the selection slits (a) and at the entrance of the MHB (b).

MHB-RFQ-MEBT

The front-end includes different types of ion-optics devices including the MHB, RFQ and MEBT. The MEBT matches two-charge state beams to the 6D acceptance of the SRF linac. The MEBT consist of focusing elements, rebunchers, beam diagnostics tools, steering magnets and one or more choppers.

Several options for the MEBT have been studied: e.g. focusing by doublets, triplets and solenoids. It was shown that the focusing by SC solenoids is the best system for the transport of two-charge state beams. The solenoidal channel is less sensitive to the particular charge state and does not introduce additional mismatch for two-charge state beams. The beam exiting the RFQ is matched to the axial- symmetric channel by three strong electromagnet quadrupoles. The MEBT has been designed using the code TRACE3D [8] and verified by the code TRACK [1].

After the final optimization of the front-end system, the simulations including space charge of multi-component ion beams have been carried out with different numbers of particles from $2 \cdot 10^3$ to 10^6. Figure 3 shows the rms envelopes of a dual charge state uranium beam along the MHB-RFQ-MEBT section obtained from the simulation of 10^6 particles. Fig. 4 shows the fraction of particles $1\text{-}N/N_0$ outside of a given longitudinal emittance. The simulation of larger numbers of particles reveals an increased beam halo. The MHB forms an extremely low longitudinal emittance of 1.6 π keV/u nsec containing 99% of particles. However, as is seen from Fig. 4, the total emittance for 100% of all accelerated particles which is $8.23 \cdot 10^5$ can reach ~12 π keV/u nsec.

The beam dynamics including space charge effects in the LEBT and RFQ has been simulated [1] and shows a 100% transmission through the RFQ including a 17.7% fraction of non-accelerated particles. The latter can be intercepted by collimators between the quadrupole lenses.

TWO OPTIONS FOR THE LINAC

Massive parallel-computer end-to-end simulations

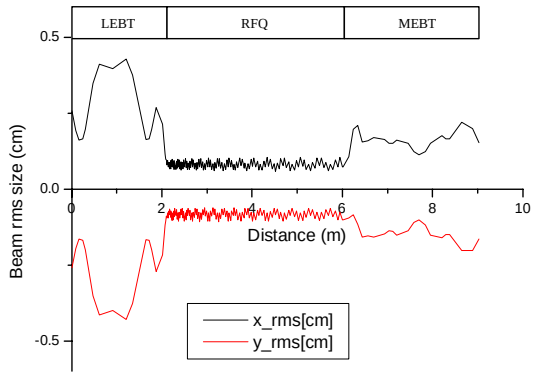

Figure 3: Two charge-state uranium rms beam size along MHB, LEBT, RFQ and MEBT. The vertical size is shown with negative sign.

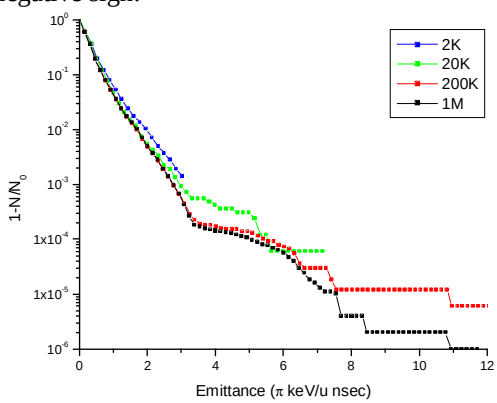

Figure 4: Fraction of particles outside of the given emittance as a function of the emittance.

have been performed for two options of the SC driver linac in order to investigate possible beam losses and determine the exact location of these eventual losses. The first option is the baseline design of the driver linac the latest update of which was described in refs. [1,3].

The second option of the driver linac is based on triple-spoke resonators (TSR) in the high-β section of the linac [9]. In what follows we refer to the first option as the elliptical-cell linac (ECL) and the second option as the triple-spoke linac (TSL). As was mentioned in ref. [9] the obvious advantage of the TSL option is a significantly larger longitudinal acceptance compared to the ECL option. Significant cost saving in the TSL are possible primarily by reducing number of required resonators by 40 as compared to the ECL and through 4K rather thane 2K operation.

Both MTSs following the strippers are provided by the set of collimators [10]. The main collimator is located in a highly dispersive area used to dump all unwanted charge states. Five other collimators are designed to clean the beam halo in the transverse phase planes. Both the ECL and TSL are designed to accept 5 charge states of uranium beam in the high-β section, therefore only 2% of the initial intensity (about 2 kW) has to be dumped after the second stripper. The transverse acceptance of the MTS with collimators is about 10 times smaller than the acceptance of the subsequent high-β section of the linac.

In the linac sections there are no uncontrollable mechanisms for beam halo formation, the main source of halo being the strippers. Therefore, appropriate beam collimation in the post-stripper MTS is the key solution to avoid or minimize beam losses associated with the beam dynamics.

END-TO-END SIMULATIONS

The particle distribution exiting the front-end has been used as an initial distribution for the simulation of the SC linac. Important considerations of the accelerator "tune" include: a) beam matching between the different focusing periods; b) providing minimal beam size at the stripper location; c) transformation of the multi-q beams in the six-dimensional phase space by the MTS after the stripper; d) setting of the reference phases of the resonators to provide minimal effective emittance of the multi-q beam at the location of the strippers; e) adjustments of the collimator openings in the MTS.

Figures 5 shows the evolution of beam envelopes and emittances along the baseline linac (ECL) obtained from the simulation of 82.3% of the million particles injected into the front-end system. In these calculations, the stripper thickness fluctuation was set at 5% FWHM. After the first and second strippers 0.3% and 0.2% of particles with the accepted charge states are intercepted, respectively, by the collimators in the MTS. The sharp peaks in the beam maximum envelopes seen on Fig. 5a occur just upstream of the collimators. The controlled beam losses are mainly related to the large scattering angle and energy loss of individual particles after the stripper. The simulation without errors does not show any uncontrolled losses along the linac. Furthermore, the total transverse emittances of the beam after the MTS are defined by the set of collimators. The horizontal emittance is very similar to the vertical emittance shown in Fig. 5b. The TSL option of the linac has similar behavior for beam envelopes and emittances.

Simulations with errors

We may classify the possible sources of error into three groups: a) Misalignment errors affecting all the elements of the accelerator system: accelerating cavities, quadrupoles, solenoids,... b) Rotation errors affecting mainly quadrupoles, multipoles and bending magnets. c) RF field errors affecting the field level as well as the phase of an accelerating cavity. For heavy ions requiring stripping another important source of error is the fluctuation in the thickness of the stripper foil or film [10]. The errors are of two types: static and dynamic. Misalignments of accelerator elements are considered as static errors. A jitter of RF and focusing fields is an example of a dynamic error. The phase and amplitude setting of the accelerating cavities when first tuning the accelerator or when restoring a tune is also a source of static errors.

Table 1 lists the errors considered as well as their typical amplitudes. We have studied the effects of individual type of errors on beam dynamics by varying individual amplitudes through wider range than is shown in Table 1. In practice, we expect alignment within ±200 μm, as was demonstrated at TRIUMF [11]. The errors in the beam dynamics simulations are generated randomly based on appropriate distributions [1].

Beam-based correction

The most critical errors affecting transverse beam motion of multi-q ion beams are the misalignments of transverse position of focusing elements and low-beta SC resonators. As was discussed in ref. [12] multi-q beams require corrective steering in order to avoid emittance growth. A minimization algorithm has been developed that can correct both position and angle in the four-dimensional transverse phase space. The algorithm has been fully integrated into the code TRACK. The details of the method can be found in ref. [13]. As a beam-based

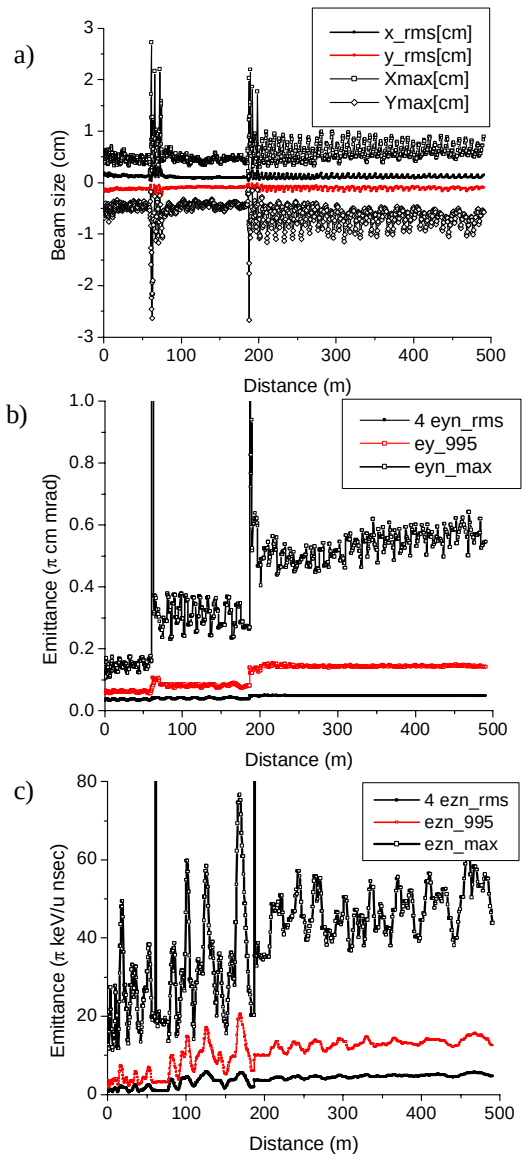

Figure 5: Beam envelope (a), transverse emittance (b) and longitudinal emittance (c) evolution along the linac.

Table 1: Sources of static errors and their typical values. For solenoid displacements, the error depends on the solenoid length.

	Description	Value
1	Cavity end displacement	0.05 cm
2	Solenoid end displacement	0.015-0.05 cm
3	Quadrupole end displacement	0.01 cm
4	Multipole rotation	2 mrad

method, one of the essential features is that it can be implemented experimentally. The beam-based steering algorithm is applied to every randomly generated accelerator seed to determine the steering correctors setting along the whole linac for the given set of the element misalignments. The final tracking of large number of particles occurs in the misaligned accelerator with corrective steering applied. To achieve effective steering for the whole linac, the latter is divided into 10-15 short sections to which the steering algorithm is applied. Figure 6 shows the beam centroid evolution along the linac. The misalignment amplitudes are taken from Table 1. Note, without corrective steering a major fraction of the beam would be lost.

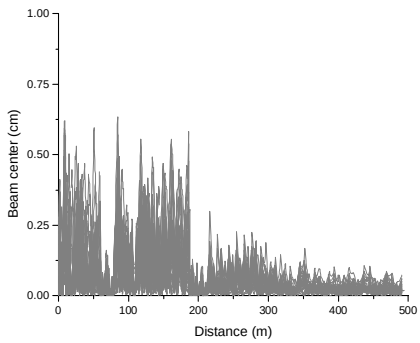

Figure 6: Multi-q beam center $\sqrt{X_c^2 + Y_c^2}$ as a function. of the distance. The figure shows trajectories of multi-q beam center along the linac for all 50 accelerator seeds.

BEAM LOSS ANALYSI S

In this section we apply all of the errors simultaneously and study the beam dynamics and the eventual beam losses. Different combinations of amplitudes for RF errors and stripper thickness fluctuations are used as shown in Table 2. Additional errors have the same values as shown in Table I and are kept unchanged in each calculation. Both the baseline and triple-spoke designs of the accelerator were simulated using 200 sets of errors for each combination. For each set $2 \cdot 10^5$ particles are tracked for a total of 40 million particles. Figure 7 shows particle coordinates at the exit of the accelerator for the different error combinations accumulated for all seeds. From these plots we notice that while the transverse beam size is unchanged for the triple-spoke design it is increasing for the baseline (ECL) design as is the longitudinal emittance. This may be due to a coupling of the transverse and longitudinal motion for particles near the separatrix in

Table 2: Combinations of RF field amplitude, phase errors and foil thickness fluctuations. Uncontrolled beam losses are given for the ECL and TSL options of the driver linac.

Comb.	Rms RF errors	Thick. fluct.	ECL	TSL
1	0.3%, 0.3°	5%	3.0×10^{-8}	0.
2	0.3%, 0.3°	10%	8.2×10^{-7}	0.
3	0.5%, 0.5°	5%	5.5×10^{-5}	0.
4	0.5%, 0.5°	10%	2.7×10^{-4}	0.
5	0.7%, 0.7°	5%	1.4×10^{-3}	0.
6	0.7%, 0.7°	10%	2.6×10^{-3}	0.

the longitudinal phase space. Some of these particles may lose stability and eventually be lost. Table 2 shows the fraction of beam lost in the high-β sections of the linac for the different error combinations and both accelerator designs. The values in Table 2 are the average of 200 sets for each combination of errors defined in columns 2 and 3. The baseline and triple-spoke designs have very similar low and medium energy sections therefore the ~0.3% loss (in addition to the losses of unwanted charge states) in the stripper areas are similar for both designs and independent of the combination of errors. Beam losses are observed in the high-β section for the baseline design whereas no losses are observed for the triple-spoke design. The losses seem to increase with both the RF errors and the fluctuation in the stripper thickness. The recommended values of errors for the baseline design of the driver linac should therefore be less than or equal to those listed in row 3 in Table 2. 'Combination 4' already produces power losses on accelerator structures higher than 1 W/m [1]. In the simulations we have not included radioactive products generated on the second stripper. However, the uncontrolled losses of radioactive ions should not exceed several units of 10^{-6} according to analytical estimations.

This study clearly indicates that the current baseline design imposes more stringent error tolerances, whereas, the triple-spoke design is more tolerant of errors.

ACKNOWLEDGEMENT

The author is grateful to the colleagues Drs. V.N. Aseev, A.A. Kolomiets, E.S. Lessner, B. Mustapha, J.A. Nolen, R.C. Pardo, K.W. Shepard, T. Wangler who made possible the extensive beam dynamics studies in the driver linac by their significant contributions and stimulating discussions.

REFERENCES

[1] P.N. Ostroumov, V.N. Aseev, and B. Mustapha. Beam loss studies in high-intensity heavy-ion linacs, Accepted for publication in PRST-AB, June 9, 2004.

[2] P.N. Ostroumov. Phys. Rev. ST Accel. Beams 5 (2002) 030101.
[3] K. Shepard, RIA R&D Workshop, Washington, D.C., August 26-28, 2003, paper 2.2.3.
[4] P.N. Ostroumov, et al., Proc. of the LINAC'2000, Monterey, CA, p. 202.
[5] P.N. Ostroumov, et al., Phys. Rev. ST Accel. Beams 5 (2002) 060101.
[6] A.A. Kolomiets et al., Proc. of the PAC-2003, Portland, OR, p. 2875.
[7] D. Leitner, ECR Ion sources for RIA, RIA Facility Workshop, March 9-13, 2004, http://meetings.nscl.msu.edu/ria2004/talks_dl.php.
[8] K.R. Crandall, TRACE 3-D Documentation, Report LA-11054-MS, Los Alamos, 1987.
[9] K.W. Shepard, P. N. Ostroumov, and J. R. Delayen, Phys. Rev. ST Accel. Beams 6 (2003) 080101.
[10] P.N. Ostroumov, in Proceedings of the 29th ICFA Advanced Beam Dynamic Workshop, Montauk, New York, 2003, AIP Conf. Proceedings, 693, p. 53.
[11] B. Rawnsley, et al. A Wire Position Monitor System for the ISAC-II Cryomodule Components Alignment. Paper MOP89 in this proceedings.
[12] P.N. Ostroumov and K. W. Shepard, Phys. Rev. ST Accel. Beams 3, 030101 (2000).
[13] E.S. Lessner and P.N. Ostroumov, Proc. of the EPAC'04, Lucerne, Switzerland, paper TUPLT147.

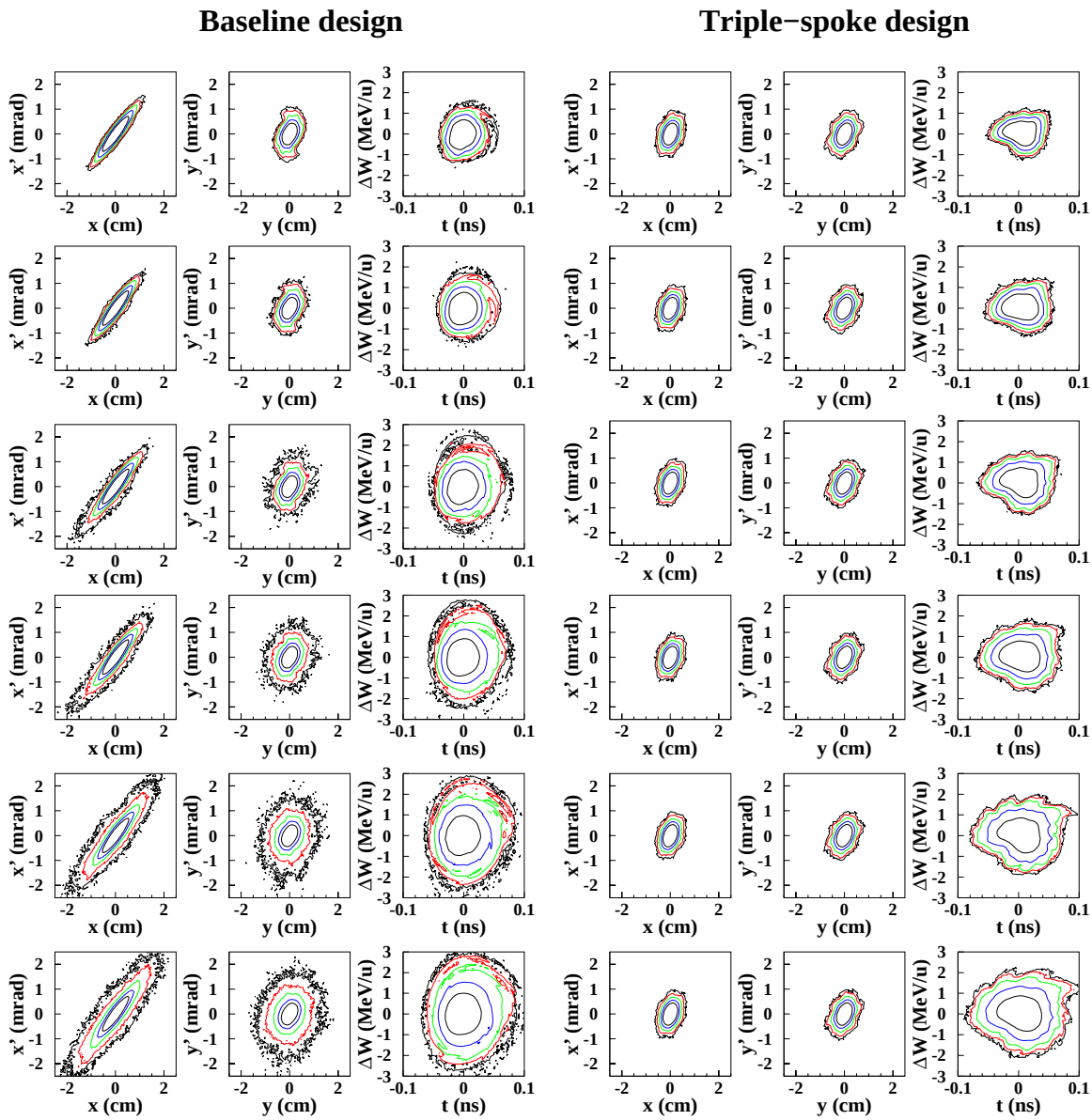

Figure 7: Phase space plots for the both accelerator designs and error combinations of table II. The six rows here correspond to the six rows in Table 2. The logarithmic density isolines are represented by different color.

INTERMEDIATE-VELOCITY SUPERCONDUCTING ACCELERATING STRUCTURES*

J. R. Delayen#, Thomas Jefferson National Accelerator Facility, Newport News, VA 23606, USA

Abstract

In the last decade, one of the most active areas in the applications of the superconducting rf (SRF) technology has been for the acceleration of ions to medium energy (~1 GeV/amu). One such accelerator is under construction in the US while others are being proposed in the US, Japan, and Europe. These new facilities require SRF accelerating structures operating in a velocity region that has until recently been unexplored, and new types of structures optimized for the velocity range from ~0.2 to ~0.8 c have been developed. We will review the properties of these intermediate-velocity structures, the status of their development, as well as present an over view of the medium-energy superconducting ion accelerator designs being developed world-wide.

OVERVIEW OF MEDIUM-ENERGY ION ACCELERATORS

Medium-energy superconducting ion accelerators can be grouped into three broad categories: high-current cw, high-current pulsed, and low-to medium current cw.

High-current cw accelerators

The main application of cw high-current ion accelerators is for accelerator driven systems, either for energy production, waste transmutation or (some time ago) tritium production [1-3].

The main technical issues and challenges are:

- Beam losses (< 1 W/m in order to allow hands-on maintenance)
- Activation
- High cw rf power
- Higher order modes
- Cryogenics losses

The implications for SRF technology are:

- Cavities with high acceptance
- Development of high cw power couplers
- Extraction of HOM power
- Cavities with high shunt impedance

High-current pulsed accelerators

Accelerators in this category are mostly H^- or proton accelerators for neutron production; the best example of these machines is the Spallation Neutron Source (SNS) under construction at ORNL as collaboration between several laboratories [4], or the proposed European Spallation Source. A different application, although with similar beam parameters, is the 8 GeV injector linac at Fermilab [5].

The main technical issues and challenges are:

- Beam losses (~ 1 W/m)
- Activation
- Higher order modes
- High peak rf power
- Dynamic Lorentz detuning

The implications for SRF technology are:

- Cavities with high acceptance
- Development of high peak power couplers
- Extraction of HOM power
- Development of active compensation of dynamic Lorentz detuning

Low-to-medium current cw accelerators

The best example of low-to-medium current cw accelerator is the Rare Isotope Accelerator (RIA) under consideration in the US [6]. The RIA driver would be capable of initially producing a 100 kW, 400 MeV/u uranium beam and also a ~ 1 GeV proton beam.

The main technical issues and challenges are:

- Microphonics, frequency control
- Cryogenic losses
- Wide charge to mass ratio
- Multicharged-state acceleration
- Activation

The implications for SRF technology are:

- Cavities with low sensitivity to vibration
- Development of microphonics compensation
- Cavities with high shunt impedance
- Cavities with large velocity acceptance (few cells)
- Cavities with large beam acceptance (low frequency, small frequency transitions)

ACCELERATING STRUCTURES

The majority of the superconducting structures that are being developed for medium-energy accelerators fall into two categories: those based on $\lambda/2$ resonant transmission line modes (TEM-like) and those based on a transverse magnetic (TM) mode [7-9]. The former can be of either the coaxial half-wave or spoke geometry, the latter are compressed versions of the familiar "elliptical" geometry used in high-energy accelerators.

* Work supported by the U.S. Department of Energy under contracts DE-AC05-84-ER40150 and DE-AC05-00-OR22725.
#delayen@jlab.org

TEM-class cavities

The λ/2 structures that have been developed and are under consideration for proposed applications are of two types: the coaxial half-wave (mostly in the low-velocity region) [10, 11], and the spoke geometry (mostly in the medium-velocity region) [10, 12]; the latter having the advantage of being able to be used as a building block for longer multi-gap structures [13-16]. When the number of loading elements is large and they are rotated by 90° from one to the next, these cavities are sometime referred to as H-type cavities [15]. A number of laboratories worldwide are now involved in the development of spoke cavities [14-26].

Fig 1: Examples of single-, double-, and triple-spoke cavities [11, 16, 26].

TM-class cavities

All the superconducting cavities in operation today for velocity-of-light particles are of the same design with only subtle differences. They are of the so-called elliptical geometry, *i.e.* rounded pill-box cavities operating in the TM_{010} mode with transverse dimension close to λ. This geometry can straightforwardly be extended to lower β by reducing the length of the cells while maintaining a constant frequency.

A number of TM mode cavities have been designed and tested for β's as low as 0.47 [27-35].

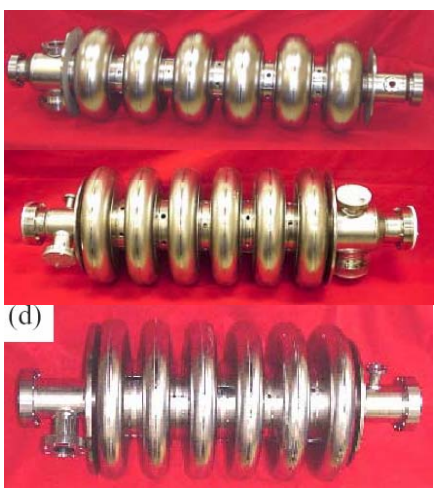

Figure 2: Examples of β=0.81, 0.61, and 0.47 elliptical cavities [27, 35]

DESIGN CONSIDERATIONS

General considerations

Intermediate-velocity ion accelerators usually are not designed to operate at very high gradients and, unlike high-energy electron accelerators, will not push the SRF technology in that direction. Operational gradients are in the 8-15 MV/m region and are limited by practical considerations. In cw applications, operating fields are limited by the load to the cryogenic system. In high current applications, the fields are limited by the capability of the fundamental power couplers. In the low-current applications, the fields are limited by the rf power required for field control. For cw applications, a high shunt impedance is often a more important objective than high gradient.

To various degrees, beam losses and activation are fundamental issues for medium-energy accelerators and important considerations in the design of the accelerating structures and the accelerators.

Superconducting ion accelerators in the medium-energy range are mostly used for the productions of secondary species: either neutrons in spallation sources, or exotic ions in the radioactive beam facilities. This is accomplish by having a medium-power (~ 100s kW) or high-power (~MWs) primary beam impinging and depositing its energy on a target. Thermal properties and the thermal dynamics of the target are important considerations in the design of the facility and the operation of the accelerator, and put strict constraints on the rate, duration, and recovery from beam interruption. Beam interruptions of a few ms may be without consequences, but could affect the lifetime of a target when they last several seconds. The implications on the cavity and accelerator designs are that the cavities should not be operated "close to the edge" and be provided with an ample frequency control window

- Low cryogenics losses
  - High $QR_s * R_{sh}/Q$
  - Low frequency
- High gradient
  - Low E_p/E_{acc}
  - Low B_p/E_{acc}
- Large velocity acceptance
  - Small number of cells
  - Low frequency
- Frequency control
  - Low sensitivity to microphonics
  - Low energy content
- Large beam acceptance
  - Large aperture (transverse acceptance)
  - Low frequency (longitudinal acceptance)

Peak surface fields

As mentioned earlier, medium-energy accelerators usually do not require, or cannot afford, operation of the cavities at very high gradients. Nevertheless, it is always good practice to limit the peak surface fields both electric and magnetic. We do not have, at present, extensive experience in this velocity and frequency range, especially in continuous operation, however peak surface fields around 27.5 MV/m and peak surface magnetic

fields around 80 mT seem reasonable. It may turn out that these values are conservative but they still need to be demonstrated in large scale, routine operation.

Figure 3 shows the peak surface to accelerating fields that have been achieved in intermediate-velocity cavities. In the intermediate velocity region TEM- and TM-class cavities show similar peak surface to accelerating field values.

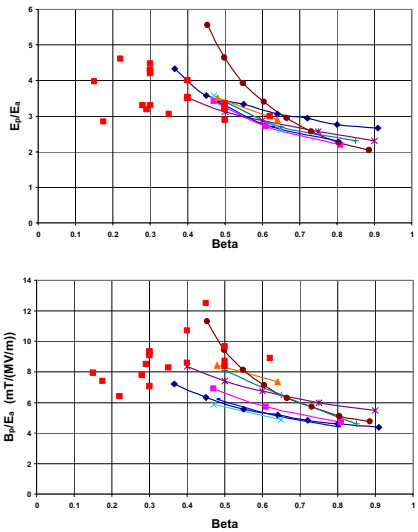

Figure 3: Peak surface electric field (upper) and magnetic field (lower) normalized to accelerating field. Data points joined by lines are for TM-class structures, isolated points (red squares) are for TEM-class structures.

Power dissipation

In cw operation the load imposed on the cryogenic system is a major consideration and is often the main limitation on the operating gradient. The power dissipation in an accelerating cavity at a given field is obtained from two parameters, one that his purely geometrical, and one that depends on the material properties of the cavity (the effective surface resistance R_s).

$$P = \frac{E^2 l^2}{R_s \, R_{sh}} R_s \qquad (1)$$

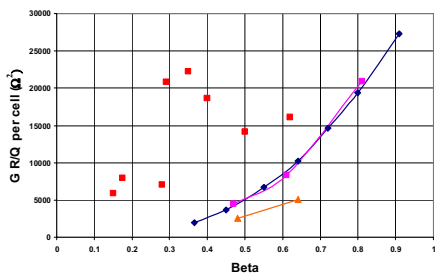

Figure 4: Product of shunt impedance and surface resistance (R_{sh} R_s) per cell or loading element.

The geometrical parameter [denominator in Eq. (1)], is the product (in Ω^2) of the shunt impedance R_{sh} of the structure and the surface resistance R_s and depends only of the shape of the structure. Since it is proportional to the number of cells, it is shown per cell in Fig. 4 for the structures for which that data is available. Everything else being constant, TEM structures require less power dissipation than TM structures to provide energy gain.

Energy Content

The effect of the energy content is already included in the above parameters but is important in itself for the low current applications (such as RIA). When the beam loading is negligible, the amount of rf power involved in phase stabilizing a structure at a given gradient with a given amount of detuning (microphonics) is given by the product of the energy content and the detuning. When stabilization is obtained by negative phase feedback the rf power that needs to be available from the rf source is $P = U \, \Delta\omega$. When stabilization is obtained *via* an externally controlled reactance the amount of reactive rf power that must be switched or controlled is given by $P = 4 \, U \, \Delta\omega$.

Not only is the energy content proportional to the number of cells or loading elements but it also depends on the gradient and frequency as $U \propto E^2 \, \omega^{-3}$. The numbers quoted will be per cell or loading element, at 1 MV/m, and for a geometry scaled to 500 MHz. At the same gradient and frequency TEM-class cavities have much lower energy content than TM-class cavities.

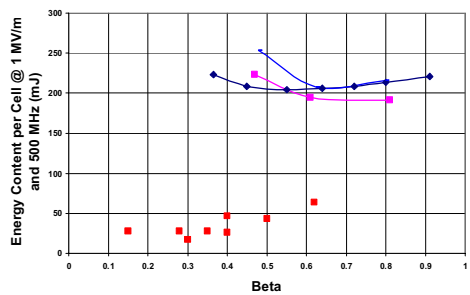

Figure 5: Energy content per cell or loading element at 1 MV/m for 500 MHz structures.

Lorentz Detuning and Microphonics

The Lorentz detuning coefficient (both static and dynamic) and the sensitivity to microphonics depend on the geometry of the cavity but are also strongly dependent on the details of the mechanical design (material thickness, stiffening, boundary conditions, *etc,*) and the environment. This is particularly true of the dynamic Lorentz coefficient where a small shift in the frequency of a mechanical mode can make it to correspond to a harmonic of the rf repetition rate and drastically increase the frequency excursion in pulsed mode. Measurement of the dynamic Lorentz coefficient on the SNS cryomodules showed large differences between supposedly identical cavities. However, use of piezo tuners has been very effective in reducing the frequency excursions during pulsed operation to acceptable levels [36].

Maintaining the level of vibration-induced frequency excursions (microphonics) to a low level is an important consideration in low-current applications since they determine the amount of rf power that will be needed to power the cavity and stabilize the fields. In most cases microphonics can be modeled by a number of parallel harmonic oscillators (the mechanical modes of the cavity) excited by white noise and the probability density of the microphonics would be gaussian (Fig. 6 left). In some cases there is a dominant single-frequency driving term and the probability density would have the characteristic double maximum (Fig. 6 center). If the probability density is measured over a long time it sometimes can be represented by the sum of 2 gaussians (Fig.6 right); this is indicative of an enhanced driving term of short duration. It is important to remember that, for large facilities comprised of a large number of cavities where the probability of any cavity being out-of-lock must be small, it is those rare occurrences of large levels of microphonics that must be accommodated by the rf control window. If the probability density is assumed to be gaussian then the probability of any cavity being out-of-lock of $<10^{-5}$ requires the control window to be at least 12 times the rms value of the microphonics [37].

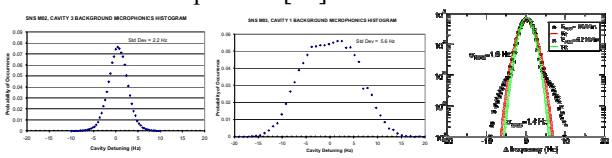

Figure 6: Probability density of microphonics. Left: Gaussian; modes driven by noise [36]. Center: bimodal; modes driven by single-frequency term [36]. Right: dual Gaussian; non-stationary driving term [38].

In the intermediate-velocity region, both TEM-class and TM-class cavities that have been developed so far have demonstrated levels of microphonics that are similar in magnitude although it is difficult to generalize since they are dependent on the environment and the cryostat design and have shown large variations between supposedly similar cavities [39]. The frequency spectra of the microphonics are, however, very different between the two types of cavities. TM-class cavities show a rich spectrum where many mechanical modes are excited form a few 10s to several 100s Hz [39]. For the TEM-class cavities, the microphonics are dominated by low-frequency modulations caused by fluctuations in the cryogenics system with a few high-frequency mechanical modes being excited and contributing little to the microphonics [40]. The low-frequency excursion ought to be easily removed with a piezo-tuner-based feedback system. A piezo-based feedforward system has also been demonstrated to reduce single-frequency-driven microphonics in elliptical cavities [41].

The same can be said of the Lorentz transfer functions (response of the cavity frequency to a sinusoidal modulation of the field). TM-class cavities show a very rich spectrum [39], while TEM-class cavities show a response at only a few high-frequency modes [38].

EXPERIMENTAL RESULTS

It would be impossible to present all the experimental results obtained to date. The best representative sample for the TM-class cavities is that of the 805 MHz cavities for SNS shown in Fig. 7 (upper). For the TEM-class cavities Fig. 7 shows results for a 345 MHz, β=0.4, double-spoke from ANL (lower left) [16]; and 352 MHz, β=0.35 single-spoke from Orsay (lower right) [25].

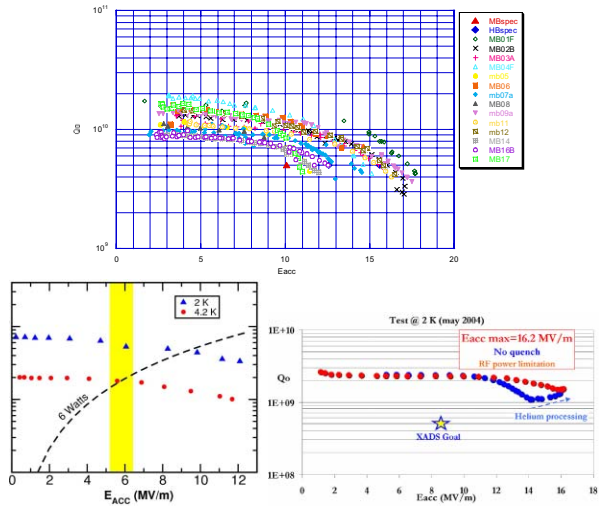

Figure 7: Experimental results for TM-class elliptical cavities (upper) and TEM-class spoke cavities (lower).

REFERENCES

[1] A. Facco, "High Intensity Proton Sources," *Proc. 11th SRF Workshop*, Travemunde (Germany), Sept. 2003.

[2] A. Mosnier, "Survey of High-Power Proton Linacs," *Proc. XXI Linear Acc. Conf.*, Gyeongju (Korea) 2002.

[3] R. L. Sheffield, "Superconducting Technologies for the Advanced Accelerator Application Program," *Proc. 10th SRF Workshop,* Tsukuba (Japan) 2001.

[4] N. Holtkamp, "Status of the SNS Project," *Proc. 2003 Part. Acc. Conf.*, Portland, OR (USA) May 2003.

[5] G. W. Foster and J. A. MacLachlan, "a Multi-Mission 8 GeV Injector Linac as a Fermilab Booster Replacement," *Proc. XXI Linear Acc. Conf.*, Gyeongju (Korea) 2002.

[6] J. A. Nolen, "The U.S. Rare Isotope Accelerator Project", *Proc. XXI Linear Acc. Conf.*, Gyeongju (Korea) 2002.

[7] J. R. Delayen, "Medium-β Superconducting Accelerating Structures," *Proc. 10th SRF Workshop,* Tsukuba (Japan) 2001.

[8] Sang-ho Kim, "Challenges and the Future of the Reduced-beta SRF Cavity Design," *Proc. XXI Linear Acc. Conf.*, Gyeongju (Korea) 2002.

[9] K. W. Shepard, "Status of Low and Intermediate Velocity Superconducting Accelerating Structures," *Proc. 2003 Part. Acc. Conf.*, Portland, OR (USA) May 2003.

[10] J. R. Delayen, "Superconducting Accelerating Structures for High-Current Ion Beams," *Proc. 1988 LINAC Conf.*, Newport News, VA (USA) Oct. 1988.
[11] J. R. Delayen, C. L. Bohn, and C. T. Roche, "Experimental Results in Superconducting Niobium Resonators for High-brightness Ion Beam Acceleration," *Proc. 1990 LINAC Conf.*, Albuquerque, NM (USA) Sept. 1990.
[12] J. R. Delayen, W. L. Kennedy, and C. T. Roche, Design and Test of a Superconducting Structure for High-Velocity Ions," *Proc. 1992 LINAC Conf.*, Ottawa (Canada) 1992.
[13] J. R. Delayen, C. L. Bohn, and C. T. Roche, "Application of rf Superconductivity to High-brightness Ion Beam Acceleration," *Proc. 1990 LINAC Conf.*, Albuquerque, NM (USA) Sept. 1990.
[14] F. Krawczyk, "Report from the LANL Spoke Cavity Workshop in Octover 2002," *Proc. 11th SRF Workshop*, Travemunde (Germany) Sept. 2003. http://laacgl.lanl.gov/spokewk/
[15] E. N. Zaplatin, "Low-β SC RF Cavity Investigations," *Proc. 10th SRF Workshop,* Tsukuba (Japan) 2001.
[16] M. P. Kelly, J. D. Fuerst, M. Kedzie, and K. W. Shepard, "Cold tests of the RIA Two-cell Spoke Cavity," *Proc. 11th SRF Workshop*, Travemunde (Germany) Sept. 2003.
[17] K. W. Shepard, M. Kedzie, J. R. Delayen, J. Mammosser, C. Piller, "Prototype 350 MHz, Niobium Spoke-Loaded Cavities," *Proc. 1999 Part. Acc. Conf.,* New York, March 1999
[18] F. L. Krawczyk *et al.,* "Design of a Low-β 2-Gap Resonator for the AAA Project," *Proc. 2001 Part. Acc. Conf.*, Chicago, June 2001.
[19] E. Zaplatin, W. Braeutigam, and S. Martin "Design Study for SC Proton Linac Accelerating Cavities," *Proc. 1999 Part. Acc. Conf.*, New York, March 1999.
[20] K. W. Shepard, M. Kedzie, M. P. Kelly, and T. Schultheiss, "Superconducting Intermediate-Velocity Drift-Tube Cavities for the RIA Driver Linac," *Proc. 2001 Part. Acc. Conf.*, Chicago, June 2001.
[21] T. Tajima *et al.*, "Evaluation and Testing of a Low-β Spoke Resonator", *Proc. 2001 Part. Acc. Conf.*, Chicago, June 2001.
[22] E. Zaplatin, "Design of Superconducting RF Accelerating Structures for High Power Proton Linac," ESS 104-00-A, July 2000.
[23] T. Tajima *et al.*, "Status of the LANL Activities in the Field of rf Superconductivity," *Proc. 11th SRF Workshop*, Travemunde (Germany) Sept. 2003.
[24] G. Olry *et al.*, "Development of SRF Spoke Cavities for Low and Intermediate Energy Ion Linacs," *Proc. 11th SRF Workshop*, Travemunde (Germany), Sept. 2003.
[25] G. Olry *et al.,* "Recent Developments on Superconducting β035 and β015 Spoke Cavities at IPN for Low and Medium Energy Sections of Proton Linear Accelerators," *Proc. EPAC 2004*, Lucerne (Switzerland) 2004.
[26] K. W. Shepard, "Development of Superconducting Intermediate-velocity Cavities for the U. S. RIA Project," *Proc. 11th SRF Workshop*, Travemunde (Germany) Sept. 2003.
[27] G. Ciovati *et al.*, "Superconducting Prototype Cavities for the Spallation Neutron Source (SNS) Project," *Proc. 2001 Part. Acc. Conf.*, Chicago, 2001.
[28] T. Tajima *et al.,* "Developments, of 700 MHz 5-Cell Superconducting Cavities for APT," *Proc. 2001 Part. Acc. Conf.*, Chicago, June 2001.
[29] C. Pagani *et al.*, "Status of the High-Energy SC Linac for the TRASCO Program," *Proc. 2001 Part. Acc. Conf.*, Chicago, June 2001.
[30] A. Facco, V. Zviagintsev, and B. M. Pasini, "A Superconductive Low Beta Single Gap Cavity for a High Intensity Proton Linac," *Proc. 2000 LINAC Conf.*, Monterey, August 2001.
[31] D. Barni *et al.*, "SC Beta Graded Design for a Proposed 350 MHz Linac for Waste Transmutation and Energy Production," *Proc. EPAC'98*, Stockholm (Sweden) June 1998.
[32] T. L. Grimm *et al.*, "Superconducting rf Activities for the Rare Isotope Accelerator at Michigan State University," *Proc. 11th SRF Workshop*, Travemunde (Germany) Sept. 2003.
[33] T. Junquera, "Superconducting rf Activities at the IPN Orsay Laboratory," *Proc. 11th SRF Workshop*, Travemunde (Germany), Sept. 2003.
[34] S. Noguchi *et al.*, "Prototype Cryomodule for the ADS Linac," *Proc. 11th SRF Workshop*, Travemunde (Germany) Sept. 2003.
[35] W. Hartung *et al.,* "Status Report on Multi-cell Superconducting Cavity Development for Medium-velocity Beams," *Proc. 2003 Part. Acc. Conf.*, Portland, OR (USA) May 2003.
[36] J. R. Delayen, G. K. Davis, "Piezoelectric Tuner Compensation of Lorentz Detuning in Superconducting Cavities," *Proc. 11th SRF Workshop*, Travemunde (Germany) Sept. 2003.
[37] J. R. Delayen, L. H. Harwood, "Determination of Low Level RF Control Requirements for Superconducting Cavities from Microphonics Measurements," *Proc. 2003 Part. Acc. Conf.*, Portland, OR (USA) May 2003.
[38] M. Kelly, private communication.
[39] J. R. Delayen, G. K. Davis, "Microphonics and Lorentz Transfer Function Measurements on the SNS Cryomodules," *Proc. 11th SRF Workshop*, Travemunde (Germany) Sept. 2003.
[40] M. P. Kelly *et al.*, Microphonics Measurements in SRF Cavities for RIA," *Proc. 2003 Part. Acc. Conf.*, Portland, OR (USA) May 2003.
[41] T. Kandil *et al.*, "Adaptive Feedforward Cancellation of Sinusoidal Disturbances in Superconducting Cavities," these proceedings.

END-TO-END BEAM SIMULATIONS FOR THE MSU RIA DRIVER LINAC*

X. Wu†, M. Doleans, D. Gorelov, Q. Zhao, T. L. Grimm, F. Marti and R. C. York,
National Superconducting Cyclotron Laboratory, Michigan State University, E. Lansing,
MI 48824, USA

Abstract

The Rare Isotope Accelerator (RIA) [1] driver linac proposed by Michigan State University (MSU) will use a 10th sub-harmonic based, superconducting, cw linac to accelerate light and heavy ions to final energies of ≥ 400 MeV/u with beam powers of 100 to 400 kW. The driver linac uses for acceleration superconducting quarter-wave, half-wave, and six-cell elliptical cavities with frequencies ranging from 80.5 MHz to 805 MHz, and for transverse focusing superconducting solenoids and room temperature quadrupoles. For the heavier ions, two stages of charge-stripping and multiple-charge-state acceleration will be used to meet the beam power requirements and to minimize the requisite accelerating voltage. End-to-end, three-dimensional (3D), beam dynamics simulations from the Front End to the output of the driver linac have been performed. These studies include a 3D analysis of multi-charge-state beam acceleration, evaluation of transverse misalignment and rf errors on the machine performance, and modeling of the charge-stripping foils and stripping-chicane performance. The results of these beam dynamics studies will be presented, and further planned beam dynamics studies will be discussed.

INTRODUCTION

RIA beam dynamics studies [2,3] have been performed at Michigan State University since 1999 as part of an overall effort to establish a comprehensive design for RIA and in support of the on-going Superconducting Radio Frequency (SRF) R&D program. To meet the beam power (≤400 kW) specification, multi-charge state beam acceleration for heavy ions is required. To meet beam loss criteria ($\leq 10^{-4}$) for hand-on maintenance, adequate acceptances and limited emittance growths must be achieved. The MSU RIA driver lattice design [4] was predominantly motivated by the minimization of technical risk and maximization of simplicity, leading to higher probability of achieving performance and increased operational efficiencies. The 10th sub-harmonic or 80.5 MHz was chosen, compared to 14th sub-harmonic or 57.5 MHz proposed by ANL [5], as the lowest linac frequency to significantly reduce microphonics in the first segment of the Superconducting Linac (SCL), allowing a simple solution utilizing a mechanical damper and modest rf while avoiding the VCX tuner reliability concerns. The design requires only three rf frequencies and six SRF cavity types for the driver linac.

*Work supported by MSU and DOE.

†xwu@nscl.msu.edu

Figure 1 shows the Rare Isotope Accelerator (RIA) driver linac layout that is being evaluated at MSU. A folded MSU RIA driver linac option also exists by bending the beam 180° in the 2nd charge-stripping chicane. It consists of a room temperature Front End, and three segments of superconducting rf linac, separated by two charge-stripping sections that provide a cost-effective method of achieving the final beam energy for a wide range of ions from proton to uranium. A beam switchyard will deliver up to 400 MeV/u ion beams to the Isotope Separation On Line (ISOL) and Particle Fragmentation (PF) target area. The RIA driver linac will be operated in a continuous-wave (cw) mode, effectively providing a 100% duty factor.

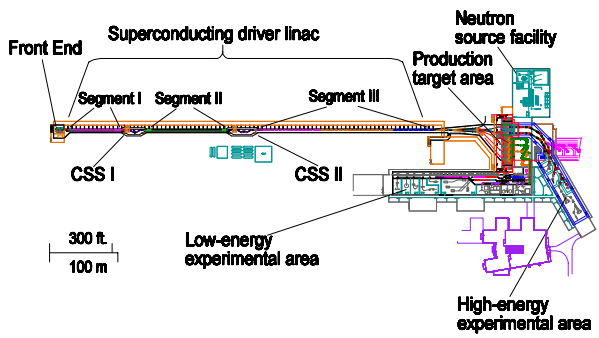

Figure 1: Layout of the MSU RIA driver linac.

End-to-end beam simulations were performed to quantify the driver linac performance and evaluate the full effects of alignment and rf errors through all three segments of the driver linac, given a realistic initial input beam from the ECR ion source. A model of the charge stripping foil including the effects of multiple scattering, energy loss and straggling, and variation in foil thickness was also included in the simulations. Since the multi-charge state beam acceleration for heavy ions [6] is the most challenging, our end-to-end simulations assumed an initial beam consisting of a two-charge state ^{238}U beam from the ECR going through two charge-stripping targets during acceleration in RIA driver linac. Charge states of 28+ and 29+, 71+ to 75+, and 87+ to 89+ will be accelerated in Segments I, II and III, respectively.

Various computer codes were used for beam dynamics studies. The simulations for the Front End were done primarily using PARMELA and PARMTEQ to include space-charge effects. LANA [7] was used for the longitudinal beam dynamics studies, 6-D phase space particle tracking, and rf error analysis in the SCL segments. DIMAD [8] and COSY INFINITY were used to study the transverse focusing structure, beam matching,

and transverse misalignment and high-order aberration correction schemes. The charge-stripping foil model was based on simulation results from TRIM. Collaborations between MSU, Lawrence Berkeley National Laboratory (LBNL) and Los Alamos National Laboratory (LANL) have been initiated to provide an additional simulation tool based upon PARMTEQm and IMPACT.

END-TO-END BEAM SIMULATIONS FOR THE RIA DRIVER LINAC

Initial Beam and RIA Front End Simulations

The MSU RIA driver linac Front End is comprised of several ECR ion sources, achromatic charge-selection sections, a Low Energy Beam Transport (LEBT), a Radio Frequency Quadrupole (RFQ), and a Medium Energy Beam Transport (MEBT) system. The objective is to accelerate a wide range of selected single- or multi-charge state beams from the ECR to about 300 keV/u and provide the required longitudinal bunching and transverse matching into the following SRF linac segments. The LEBT uses a Multi-Harmonic Buncher (MHB) and a Velocity Equalizer (VE) to efficiently prebunch the selected dc beam for injection into the 80.5 MHz RFQ. Magnetic and electrostatic quadrupole magnets and solenoid magnets are used for transverse focusing and matching.

As part of RIA collaborations, the VENUS ECR ion source has been developed at LBNL as a possible ion source. Recently, a 3 pμA $^{27+}$Bi from VENUS [9] has been measured with a normalized rms emittance of ~ 0.08π mm-mrad, which is comparable with the input beam required for RIA. The initial phase spaces of a two-charge state ^{238}U beam at the entrance, shown in Figure 2, are based on the VENUS emittance measurement results and used in our end-to-end beam simulations. The assumed total two-charge state beam intensity was 8 pμA to achieve a beam power of 400 kW.

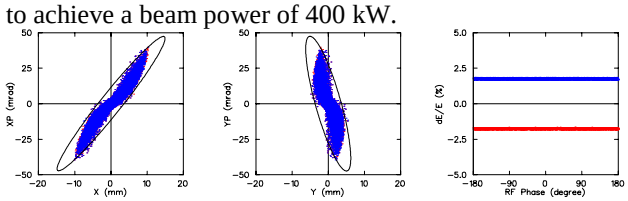

Figure 2: Horizontal (left), vertical (middle), and longitudinal (right) phase spaces of a two charge-state uranium beam at the entrance of the RIA Front End.

The two-charge-state uranium beam was simulated using PARMELA and PARMTEQ through the LEBT, RFQ and MEBT [10], and the phase spaces at the exit of the RIA Front End are shown in Figure 3. The longitudinal and transverse normalized emittances (99.5%) for a two charge-state uranium beam entering SCL Segment I will be 1.2π keV/u-ns and 0.9π mm-mrad, with rms values of 0.1π keV/u-ns and 0.09π mm-mrad. Our previous simulations [2] used a matched 4D water bag for the beam distribution. For the experimentally-based beam distribution used here, only the 99.5% transverse emittances are relatively larger. No significant space-charge effects were observed with the assumed beam intensity in our simulation. The small transverse emittance growth in the Front End is primarily due to the offset of the two charge states in transverse phase spaces.

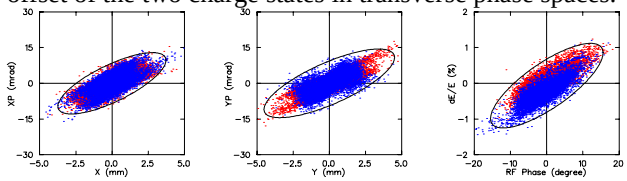

Figure 3: Horizontal (left), vertical (middle), and longitudinal (right) phase spaces of a two charge-state uranium beam at the exit of the RIA Front End.

Misalignment and RF Errors

The misalignment of SRF cavities and focusing elements lead to distortion of the beam centroid orbit, envelope growth, and transverse and longitudinal emittance growth, due mainly to the non-linear field distribution in the SRF cavities. These effects are especially strong in Segment I where the beam energy is low. Orbit correction is necessary to prevent significant emittance growth and possible beam loss. Since the transverse de-focusing due to the SRF cavities is much weaker than the focusing provided by the solenoids and quadrupoles, the impact on the beam transverse motion from the rf field errors is limited, and the SRF cavities are much less sensitive to the alignment errors. However, the rf field errors have a significant effect on the longitudinal emittance growth. Previous beam dynamics studies [11] of SCL segments have established the alignment and rf error tolerances listed in Tables 1 and 2, which were used in the end-to-end simulations. The misalignment includes all SRF cavities and focusing elements assuming a Gaussian distribution (±2σ), while a uniform distribution was used for rf errors. The correction of the beam centroid orbit was done using beam position monitors between cryomodules, dipole windings in the solenoids of Segments I and II, and dipole corrector magnets at quadrupoles in Segment III.

Table 1: Alignment Tolerances

RIA driver linac Segment	Misalignment $\sigma_{x,y}$ (mm)	
	SRF Cavity	Focusing element
I	1.0	0.5
II	1.0	0.5
III	1.0	1.0

Table 2: RF Error Tolerances

RIA Driver Linac Segment	SRF Cavity RF Errors	
	Phase	Amplitude
I	±0.25°	±0.25%
II	±0.50°	±0.50%
III	±0.50°	±0.50%

Charge-Stripping Foil Modeling

To achieve the required beam energy, heavy ions like uranium will pass through two charge-stripping foils to increase the acceleration efficiency. The model used for stripping foils is based on simulation results from the code TRIM that include elastic and inelastic scattering, and energy loss for ionization. A small transverse beam spot (~3 mm) and short bunch length (~8°) on both charge-stripping targets were obtained to minimize the beam transverse and longitudinal emittance increase due to multiple scattering and energy straggling in the stripping material.

Carbon foils were used in our end-to-end simulations. In addition to multiple scattering and energy straggling, foil thickness variation also contributed to the beam emittance growth; ±5% was assumed for the foil thickness variation. Due to the high beam energy at the end of Segment II, a much thicker foil was required for the 2nd charge-stripper. Table 3 gives the carbon foil parameters for the RIA driver linac. The estimated emittance growth will not significantly degrade the overall performance. Experimental work has been performed at NSCL using the beam from the K1200 Superconducting Cyclotron to explore the feasibility of carbon and other foils, and tests using diamond foils and lithium jets as charge-strippers for RIA are in progress in Argonne National Laboratory (ANL) and other institutes.

Table 3: Charge-Stripping Foils Parameters

Stripping location	Stripping Energy (MeV/u)	Ave. Foil Thickness (μm)	Emittance Growth	
			Trans.	Longi.
1st	11.9	1.8	~ 20%	~ 65%
2nd	89.2	64.4	~ 45%	~103%

SCL Segment I – Low β Section

Segment I of the RIA diver linac will be used to accelerate two-charge state Uranium beams to ~12 MeV/nucleon. It uses two types of Quarter Wave Resonators (QWR) with β_{opt} of 0.041 and 0.085 operating at 80.5 MHz with peak surface electric field (E_p) of 16.5 MV/m and 20 MV/m, respectively. The focusing lattice will consist of 76 solenoids, each having independent dipole windings to provide horizontal and vertical orbit corrections. The beam position monitors are located in the warm regions between cryomodules.

Figure 4 shows the transverse and longitudinal phase spaces at the end of Segment I using LANA with an initial phase space shown in Figure 3 without alignment or rf errors. Figure 5 shows the evolution of the normalized (rms) emittance. The total longitudinal emittance displays an oscillatory behavior along Segment I because the two charge states of uranium perform coherent oscillations in longitudinal phase space due to their different charge-to-mass ratios. The transverse and longitudinal emittance (rms) growth factors for the perfect lattice of Segment I were ~1.0, and ~1.35, respectively. The calculated longitudinal acceptance to emittance ratio at the entrance of Segment I was 2.9:1.

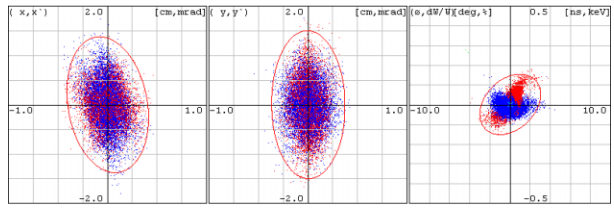

Figure 4: Horizontal (left), vertical (middle), and longitudinal (right) phase spaces of a two charge-state uranium beam at the end of Segment I.

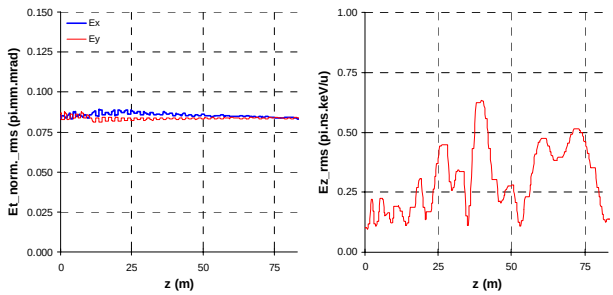

Figure 5: Transverse (left), and longitudinal (right) beam emittance (rms) for a two charge-state uranium beam in Segment I without errors.

Beam simulations using LANA were performed to investigate the influence of the transverse misalignment and rf phase and amplitude errors on beam quality. With the alignment and rf error tolerances listed in Tables 1 and 2, and alignment correction applied with 100 random seeds, no beam loss was observed in Segment I. Confidence plots for the transverse and longitudinal emittances (rms) at the end of Segment I are shown in Figure 6. With 90% confidence, the transverse and longitudinal emittance (rms) growth factor due to combined transverse misalignment and rf errors in Segment I are ~ 1.8 and 4.3, respectively. The maximum beam envelope in Segment I is ~10.4 mm from all 100 random seed runs. With an SRF cavity radial aperture of 15 mm, the ratio of aperture to beam envelope is ~1.4:1 with errors, indicating that Segment I has adequate transverse acceptance. Further improvement could be achieved via transverse collimation of the beam tails in the MEBT.

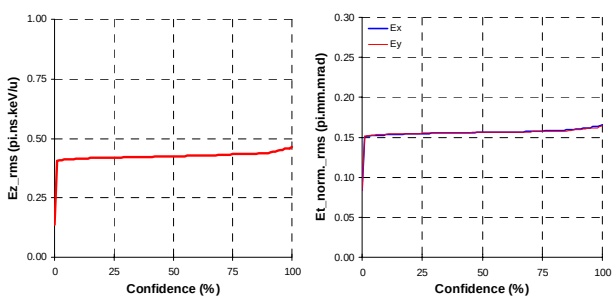

Figure 6: Transverse (left) and longitudinal (right) rms emittances at the end of Segment I for multi-charge uranium beam with errors vs. statistical confidence.

SCL Segment II – Medium β Section

Segment II of the RIA driver linac will accelerate the multi-charge uranium beam (71+~75+) from ~12 MeV/u to about 90 MeV/u. It uses a total of 208 superconducting Half-Wave cavities in 26 cryomodules, operating at a frequency of 322 MHz with a design peak surface electric field of 25 MV/m. The transverse focusing will use 2 superconducting solenoids per cryomodule for a total of 52 focusing elements. Each solenoid will also have independent dipole windings to provide horizontal and vertical orbit corrections. The beam position monitors used for corrections are located in the warm region between cryomodules as for Segment I.

Figure 7 shows the transverse and longitudinal phase spaces without alignment or rf errors at the end of Segment II for the five charge-state uranium ion beam continued from Segment I. Figure 8 shows the evolution of the normalized transverse and longitudinal (rms) emittance in Segment II. Due to the higher beam energy in Segment II, the beam's longitudinal motion is more adiabatic and matching between cavities and cryomodules is easier. No transverse and only a small longitudinal emittance growth were observed. The transverse and longitudinal emittance (rms) growth factors for the perfect lattice of Segment II are ~1.0, and ~1.3, respectively.

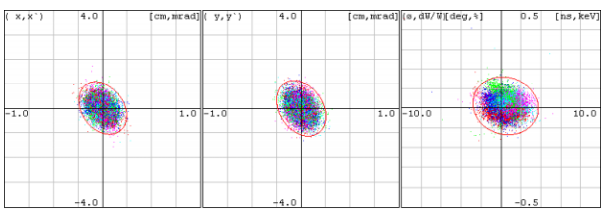

Figure 7: Horizontal (left), vertical (middle), and longitudinal (right) phase spaces of a five charge-state uranium beam at the end of Segment II.

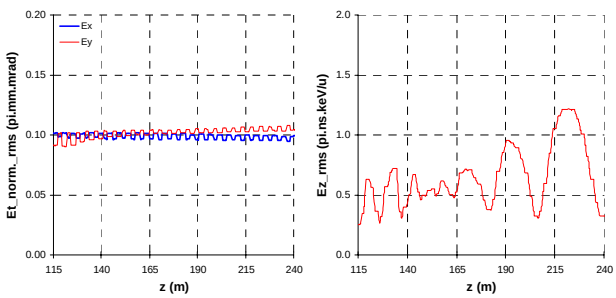

Figure 8: Transverse (left), and longitudinal (right), beam emittance (rms) for a multi-charge state uranium beam in Segment II without errors.

The transverse misalignment and rf errors in Segment II were then included to continue beam simulations from Segment I using LANA for 100 random seeds. As in Segment I, no beam loss was observed in Segment II. Confidence plots for the transverse and longitudinal emittance (rms) at the end of Segment II are shown in Figure 9. With 90% confidence, the transverse and longitudinal emittance (rms) growth factors in Segment II with transverse misalignment and rf errors were increased to ~ 1.1 and 1.8, respectively. The sensitivities to misalignment and rf errors are significantly less than those in Segment I. The maximum beam envelope in Segment II is ~9.6 mm from all 100 random seed runs. With an SRF cavity radial aperture of 15 mm, the ratio of aperture to beam envelope will be about 1.6:1 with errors and after orbit correction, indicating that Segment II also has adequate transverse acceptance. Since the longitudinal acceptance at the entrance of Segment II is ~ 20 π keV/u-ns, the beam longitudinal emittance (99.5%) of ~ 6.2π keV/u-ns at the entrance of Segment II from our simulations leads to an adequate longitudinal acceptance to emittance ratio of 3.2:1.

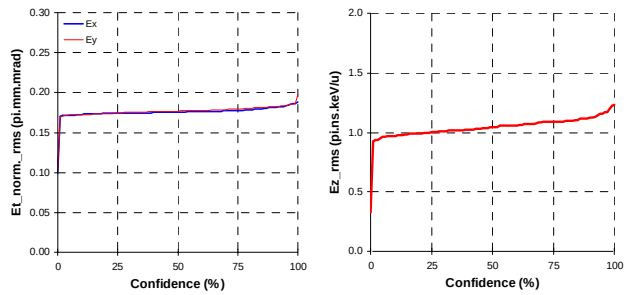

Figure 9: Transverse (left) and longitudinal (right) rms emittances at the end of Segment II for multi-charge uranium beam with errors vs. statistical confidence.

SCL Segment III – High β Section

Segment III will accelerate the multi-charge uranium beam (87+~89+) to the final energy of 400 MeV/u. It uses a total of 164 6-cell SRF elliptical cavities in 41 cryomodules, operating at a frequency of 805 MHz with a design peak surface electric field of 32.5 MV/m. The focusing lattice will use in each inter-cryostat warm region a room temperature quadrupole doublet with a pair of corrector magnets to provide horizontal and vertical orbit corrections.

Figure 10 shows the transverse and longitudinal phase space without alignment or rf errors at the end of Segment III for the multi-charge state uranium beam continued from Segment II. Figure 11 shows the evolution of the normalized (rms) emittance evolutions in Segment III. The transverse and longitudinal emittance (rms) growth factors for the perfect lattice of Segment III are ~1.0, and ~1.27, respectively.

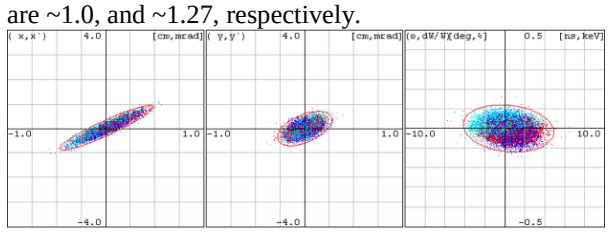

Figure 10: Horizontal (left), vertical (middle), and longitudinal (right) phase spaces of a multi-charge uranium beam at the end of Segment III without alignment or rf errors.

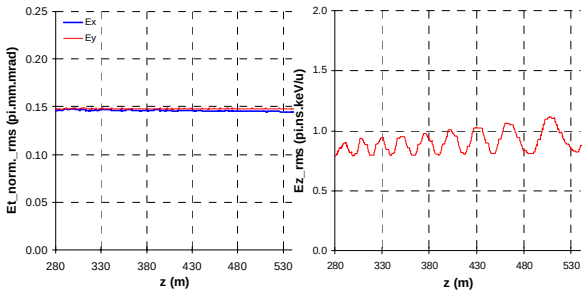

Figure 11: Transverse (left) and longitudinal (right) beam emittance (rms) for a multi-charge state uranium beam in Segment III without errors.

Beam simulations from Segment II were continued using LANA with alignment and rf errors in Segment III. Since the orbit correctors were paired with the relatively weak focusing quadrupoles with a beam position monitor in each focusing cell, the orbit correction was much more effective than that for Segments I and II. No beam loss was observed in Segment III. The confidence plots for the transverse and longitudinal emittances (rms) at the end of Segment III are shown in Figure 12. The alignment and rf errors have no significant impact on lattice performance in Segment III. With 90% confidence, the transverse and longitudinal emittance (rms) growth factors have only been increased to ~ 1.05 and 1.3, respectively, due to transverse misalignment and rf errors. The maximum beam envelope in Segment III is ~ 12 mm from all 100 random seed runs. Since the elliptical cavities used in Segment III have a much larger radial aperture (38.5mm), the ratio of aperture to beam size was about 3.2:1 with errors. Assuming a focusing quadrupole radial aperture of 25mm, the ratio of aperture to beam size with errors is about 2.1:1, indicating that Segment III also has adequate transverse acceptance. Compared to 345 MHz Triple-spoke cavities, the 805 MHz elliptical cavities used in Segment III have a smaller longitudinal acceptance of ~ 115 π keV/u-ns mainly due to the higher frequency. The longitudinal emittance (99.5%) of ~ 20.2π keV/u-ns at the entrance of Segment III was obtained from our end-to-end beam simulations with errors, leading to an adequate longitudinal acceptance to emittance ratio of 5.7:1.

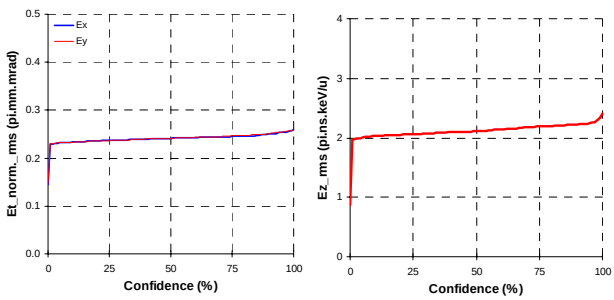

Figure 12: Transverse (left) and longitudinal (right) rms emittances at the end of Segment III for a multi-charge uranium beam with errors vs. statistical confidence.

SUMMARY AND CONCLUSIONS

End-to-end beam simulation results with experimentally-based input beams including alignment and rf errors and charge-stripping foils, indicate that the MSU 10th sub-harmonic RIA driver linac option has adequate transverse and longitudinal acceptances to achieve the beam power and beam loss requirements for RIA even for the most challenging multi-charge state heavy ion beams. The alignment and rf error tolerances are reasonable and have been shown to be achievable from past experience. Further beam dynamics studies will include developing an automated SRF cavity tuning procedure for multi-charge beam acceleration, performing lattice element failure analysis, and establishing failure tolerances to meet the high availability desired for RIA. Advantage will be taken of the parallel computing capabilities of PARTEQm and IMPACT currently being developed at LBNL and LANL for beam simulations.

REFERENCES

[1] C. W. Leemann, "The Rare-Isotope Accelerator (RIA) Facility Project", proceedings of the XXth Int. Linac Conference, Monterey, California, 2000.

[2] D. Gorelov, T. Grimm, W. Hartung, F. Marti, H. Podlech, X. Wu and R. C. York, "Beam Dynamics Studies at NSCL of the RIA Superconducting Driver Linac", proceedings of EPAC 2002, Paris, France, 2002.

[3] X. Wu, "Beam Dynamics Studies for RIA at Michigan State University", RIA R&D Workshop, Bethesda, Maryland, August 2003.

[4] "The Rare Isotope Accelerator (RIA) at Michigan State University", RIA R&D Workshop, Bethesda, Maryland, August 2003.

[5] P. N. Ostroumov, "Design Features of high-intensity medium-energy superconducting heavy-ion linac", proceedings of the XXI Linac Conference, Gyeongju, Korea, August 2002.

[6] P. N. Ostroumov et al., "Multiple-charge Beam Dynamics in an Ion Linac", proceedings of the XX Linac Conference, Monterey, CA, August 2000.

[7] D. Gorelov, and P. N. Ostroumov, "Application of LANA Code for Design of Ion Linac", EPAC'96, Sitges, June 1996

[8] R. Servranckx, K. Brown, L. Schachinger, and D. Douglas, "User's Guide to the Program Dimad", SLAC Report 285, UC-28, May 1985.

[9] D. Leitner, RIA Facility Workshop, East Lansing, MI, March 2004.

[10] Q. Zhao, et al., "Design Improvement of the RIA 80.5 MHz RFQ ", these proceedings.

[11] X. Wu, D. Gorelov, T. Grimm, W. Hartung, F. Marti, and R.C. York, "The Beam Dynamics Studies of Combined Misalignment and RF Errors for RIA", proc. of PAC 2003, Portland, Oregon, 2003.

DESIGN IMPROVEMENT OF THE RIA 80.5 MHZ RFQ

Q. Zhao*, V. Andreev, M. Doleans, D. Gorelov, T. Grimm, W. Hartung, F. Marti, S.O. Schriber, X. Wu, R.C. York, NSCL, Michigan State University, East Lansing, MI 48824, USA

Abstract

An 80.5 MHz, continuous-wave, normal-conducting, radio-frequency quadrupole (RFQ) was designed for the front end of the Rare Isotope Accelerator (RIA) driver linac. It will accelerate various ion beams (hydrogen up to uranium) from 12 keV/u to about 300 keV/u. The 4-meter-long RFQ accepts the pre-bunched beams from the low energy beam transport (LEBT) and captures more than 80% of the beams with a current of ~0.3 mA. Beam dynamics simulations show that the longitudinal output emittance is small for both single- and two-charge-state ion beams with an external multi-harmonic buncher. A 4-vane resonator with magnetic coupling windows was employed in the cavity design to provide large mode separation, high shunt impedance, and a small transverse dimension. The results of beam dynamics as well as the electromagnetic simulations are presented.

INTRODUCTION

To minimize beam losses in the RIA driver linac, the superconducting (SC) linac requires the front end to provide a longitudinal beam emittance of about 1.2 π·keV/u·ns (99.5% particles) with minimum transverse emittance growth. Since the beam current is not very high in the RIA driver linac, the dc beam selected from the ion source can be efficiently pre-bunched by an external multi-harmonic buncher before injection into the RFQ. This scheme can produce a smaller longitudinal output emittance [1], and enhance the RFQ's acceleration efficiency. In previous designs of the front end RFQ [2,3], the longitudinal output emittance was larger than the requirement when using a more realistic input beam from LEBT that includes unbunched particles. Therefore, we optimized the initial longitudinal acceptance and its evolution to remove the tails while still maintaining the transverse emittance. Beam dynamics simulations showed about 83% of the injected beam was accelerated with required output emittances. In addition, an improved 4-vane RFQ structure with coupling windows was adopted to achieve improved mode separation and smaller power dissipation.

The driver linac will provide ion beams from protons up to uranium. To meet the final beam power requirement for heavier ions, two charge-state beams will be injected and accelerated in alternate longitudinal buckets of the RFQ [4]. Since the heaviest ion beams are the most challenging, the baseline design has been primarily focused on the uranium beam with charge states of 28+ and 29+. Therefore, the RFQ must be able to operate with a wide range of power levels to accommodate the different ion species. To minimize the range of voltages, we proposed to use triatomic hydrogen molecule ions (e.g. H_3^+ instead of H^+ for proton) from the ion source through the RFQ and first segment of SC linac until stripped into monatomic ions at first stripper, which also reduces the beam current by a factor of 3 at the low energy side.

* zhao@nscl.msu.edu

DESIGN PHILOSOPHY

The 100% duty factor, normal conducting RFQ will accelerate ion beams from 12 keV/u to about 300 keV/u. The input energy is determined by the high voltage platform of ion source, while the output energy is set to obtain a transit time factor of 0.5 for the first SC cavity in the driver linac and is a tradeoff between the acceptance of the SC linac and the size of RFQ. The 80.5 MHz frequency is chosen to be the same as the successive quarter-wave superconducting structures.

The design goals are the minimization of the longitudinal and transverse emittance, RF power requirements and structure size. For the RIA beam currents, an external harmonic buncher with a quasi-linear bunching field can generate a small longitudinal emittance beam for RFQ. To obtain a low output emittance, the RFQ should only accept the well-bunched core particles for further acceleration avoiding capture of the small fraction particles in the tails of the distribution. Since the beam is already bunched at the entrance of RFQ, an initial synchronous phase of -30^o and a modulation factor of 1.03 are chosen so that the longitudinal acceptance is truncated, as shown in Fig. 1. These values represent an optimization between the removal of tail particles and providing a linear field for the bunched particles. The modulation factor as well as the synchronous phase is then smoothly increased to accelerate just the core particles.

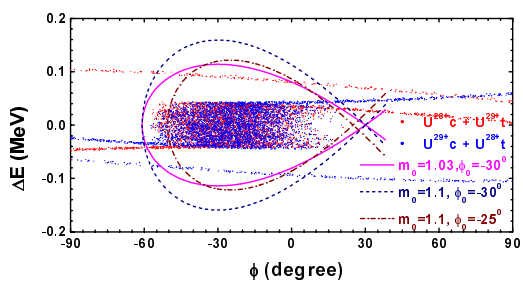

Figure 1: Initially reduced separatrices with bunched beams.

Even though the beam is pre-bunched, a four-cell radial matcher was found to be of benefit especially for a two-charge-state beam. A reduced adiabatic bunching design before the acceleration section is necessary to achieve stable bunches and control the blowup of emittances. Particles with large transverse amplitudes may result in

large longitudinal amplitudes due to the coupling between the two motions. Hence, proper transverse focusing must be provided to maintain a small beam envelope. The transverse phase advance is larger than the longitudinal one to avoid a coupling resonance.

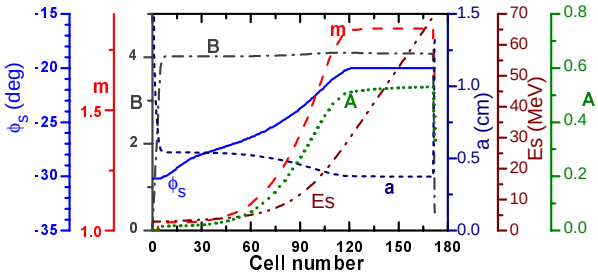

Figure 2: Evolution of the synchronous phase (ϕ_s), modulation factor (m), transverse focusing strength (B), minimum radius aperture (a), synchronous beam energy (E_s), and acceleration efficiency (A) along the RFQ.

Fig. 2 shows the main RFQ parameters as a function of cell number. The focusing strength was held constant (B=4.1) along the structure leading to a constant average aperture radius of 5.5 mm, keeping the capacitance independent of longitudinal position to facilitate cavity tuning. In this scheme, the minimum vane radius decreases with the increase of modulation factor along the RFQ and determines the normalized transverse acceptance of about 1.4 π·mm·mrad. A nominal inter-vane voltage of 70 kV was adopted in the design resulting in a moderate peak surface electric field of $1.58 \cdot E_{kilpatric}$. The transverse phase advance per focusing period is around 25° and is almost constant along the RFQ, while the phase motion of the longitudinal oscillation is approximately 15°. The transverse geometry of the vane-tip is circular with the same transverse radius of curvature throughout the RFQ making fabrication easier. The ratio between the vane tip radius and the average radial aperture was chosen to be 0.82 as a compromise between the peak voltage and the effect of multi-poles. A radial matcher at the exit of the RFQ [5] was used to obtain an output beam with similar Twiss parameters in both horizontal and vertical planes to match to the downstream solenoidal focusing.

BEAM DYNAMICS

The beam dynamics simulations of the RFQ were performed with the PARMTEQ code [6]. The baseline design was for $^{238}U^{28+}$ and $^{238}U^{29+}$ with charge-to-mass of 0.12. PARMELA output from the LEBT was used as the input beam distribution for PARMTEQ. The phase spaces of the two-charge state beam at the RFQ entrance and exit are plotted in Fig. 3, where $^{238}U^{28+}$ and $^{238}U^{29+}$ were plotted in the same spaces, although they were separated by an rf period [4]. The longitudinal input phase space was determined by the harmonic buncher in the LEBT. Fig. 4 illustrates the evolution of the rms beam emittance and transmission along the RFQ for the two-charge-state beam. About 83% of the beam was captured and accelerated by the RFQ. There was no transverse emittance increase of the two-charge-state beam throughout the RFQ. The rms and 99.5% of longitudinal output emittances are 0.1 and 1.2 π·keV/u·ns, respectively, which is slightly larger than that of the single-charge-state beam. This increase is mainly due to the phase-shift between the beams and may be minimized.

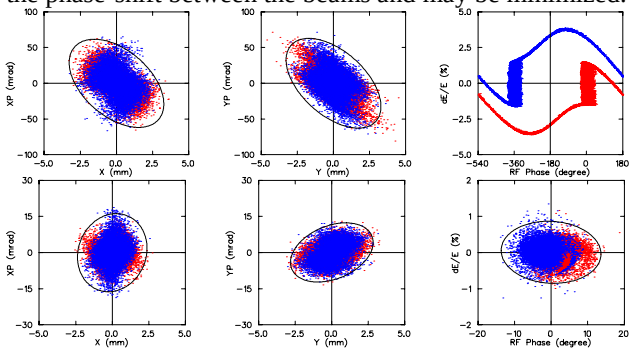

Figure 3: Phase space distributions of two-charge-state uranium beam at the entrance (above) and the exit (below) of RFQ ($^{238}U^{28+}$ in red, $^{238}U^{29+}$ in blue).

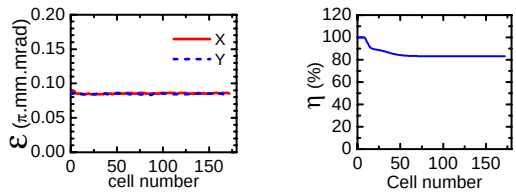

Figure 4: Variations of normalized transverse rms emittance and beam transmission along RFQ for $^{238}U^{28+}$ and $^{238}U^{29+}$.

The beam dynamics of other ions are similar after scaling the inter-vane voltage according to the corresponding charge-to-mass ratios. Triatomic hydrogen molecule H_3^+ instead of H^+ will be accelerated in the RFQ to increase the operation voltage. Fig. 5 shows the phase space of a H_3^+ ion beam at the entrance and exit of RFQ, which are analogous to those of two-charge-state beam.

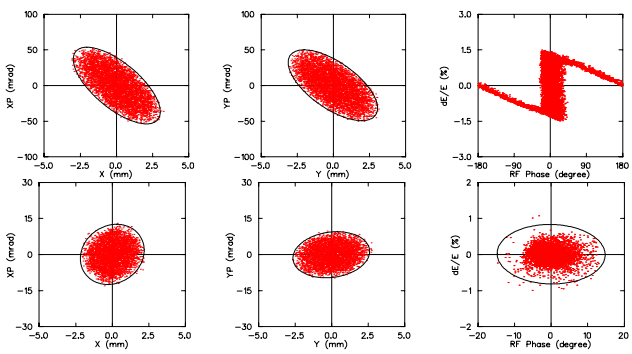

Figure 5: Phase space distributions of H_3^+ beam at the entrance (above) and the exit (below) of RFQ.

RESONANT STRUCTURE

The design of the RFQ cavity is based on the improved 4-vane resonator with magnetic coupling windows [7], as shown in Fig. 6. The windows improve the azimuthal and longitudinal stabilization of the operating mode (a

combination of TE_{211} and coaxial one) by increasing the separation from parasitic modes, and significantly reduce the transverse dimensions of the resonator. Test results of such structures confirmed the high RF efficiency as well as the simplicity of alignment and tuning [8].

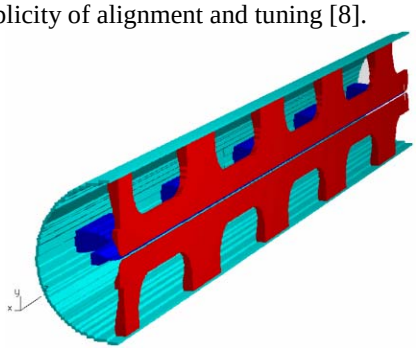

Figure 6: Layout of the ½ resonator without end flanges.

The resonator was designed using MAFIA version 4.1. Table 1 lists the main parameters of the structure. Increasing resonant cell length and window area improve mode separation, but also reduces shunt impedance of the resonator. A separation of 13.3 MHz from the nearest dipole mode was obtained, which would be sufficient to avoid problems of alignment and tuning from experience [8]. The shape of the windows has been optimized to reduce the extra magnetic flux density and rf losses. The magnetic field in y-z plane and electric field in x-y plane are shown in Fig. 7, respectively. Sufficient water-cooling is provided to maintain a good thermal stability during cw operation.

Table 1: Main parameters of the RFQ resonator

Name (unit)	Value
Resonator length (m)	4
Tank inner diameter (m)	0.54
Resonant cell number	9
Window width (m)	0.56
Window height (m)	0.17
Average aperture radius (cm)	0.55
Vane tip radius (cm)	0.45
Operating mode frequency (MHz)	80.5
Nearest quadrupole mode (MHz)	88.6
Nearest dipole mode (MHz)	93.8
Specific shunt impedance (kΩ·m)	389
Quality factor	13000
Inter-vane voltage (kV)	70
Peak electric field (MV/m)	14
Peak magnetic field (mT)	11
Total power dissipation (kW)	51

A flat inter-electrode voltage along the vanes has been achieved, as plotted in Fig.8, by properly tuning the end cells of the cavity with a 3-cm undercut on the vanes at both ends of the structure. The ripple of the inter-vane voltage, an inherent feature for all longitudinally non-uniform RFQs, is ±0.35%. In addition, 9 tuners with diameter of 8 cm will be used in each quadrant to provide misalignment compensation and frequency tuning.

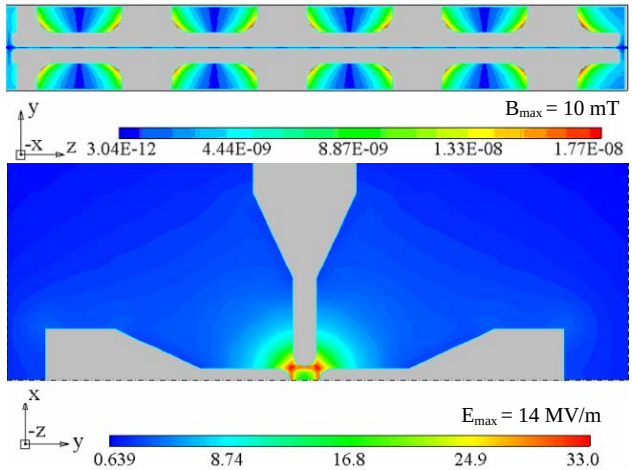

Figure 7: Magnetic flux density in y-z cross section (vertical vanes) on the top, and electric field in x-y cross section (half of the resonator) on the bottom.

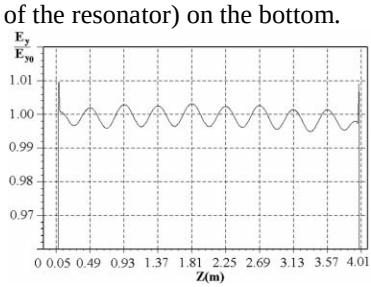

Figure 8: Distribution of the normalized inter-vane voltage.

SUMMARY

Beam dynamics simulations show the RFQ can produce required output emittance for both two and single charge-state beams with the input from the LEBT. The resonator has good mode separation, low power dissipation, and small inter-vane voltage variation.

ACKNOWLEDGEMENTS

We are grateful to Drs. T. Wangler at LANL, H. Podlech at IAP and R. Duperrier at CEA for the helpful discussions, and wish to thank Drs. L. Young, J. Billen and R. Garnett at LANL to provide the simulation codes. This work has been supported by Michigan State.

REFERENCES

[1] J.W. Staples, Proc. Linac'94, Tsukuba, Japan, p755.
[2] H. Podlech, et al., Proc. EPAC'02, Paris, France, p.945.
[3] R. Duperrier, NSCL internal report, 2002
[4] P.N. Ostroumov, et al., Proc. Linac'00, Monterey, USA, p202.
[5] K. Crandall, Proc. Linac'94, Tsukuba, Japan, p.227.
[6] K. Crandall, et al., LANL Report 96-1836, 2004.
[7] V.A. Andreev and G. Parisi, Proc. PAC'93, Washington DC, USA, p3124; V.A. Andreev and G Parisi, Proc. EPAC'94, London, UK, p1300.
[8] V.A. Andreev, et al., Proc. PAC'97, Vancouver, Canada, p1090; G. Bisoffi, et al., Proc. EPAC'00, Vienna, Austria, p324.

FABRICATION OF SUPERCONDUCTING CAVITIES FOR SNS

M. Pekeler, S. Bauer, J. Schwellenbach, M. Tradt, H. Vogel, P. vom Stein,
ACCEL Instruments GmbH, Friedrich-Ebert-Str. 1, 51429 Bergisch Gladbach, Germany

Abstract

During the last three years ACCEL fabricated almost all 109 superconducting cavities for the Spallation Neutron Source (SNS) in Oak Ridge, Tennessee. Two series of 35 medium beta (beta=0.61) and 74 high beta (beta=0.81) cavities will be delivered until October 2004. Besides cavity manufacturing ACCEL also performed RF tuning and chemical surface preparation. We give an outline on the current manufacturing experience and comment on future developments for industrial cavity production.

INTRODUCTION

In August 2001 the contract for the production of in total 109 elliptical 6-cell 805 MHz superconducting niobium cavities was awarded to ACCEL by JLAB. Two families of cavities had to be produced, 35 cavities of the medium beta type optimised for β=0.61 particle velocity and 74 cavities of the high beta type optimised for β=0.81 particle velocity needed to be produced within a 3 years period.

In addition to the manufacturing, the contract also included the surface removal of 30 µm from the outside and 100 µm from the inside by buffered chemical polishing.

The last step before delivery is field flatness tuning of the π-mode to accuracy better than 5% in amplitude and adjustment of the external Q of the fundamental mode of the HOM couplers to values above 10^{12}.

CAVITY MANUFACTURING

At the time of the contract award prototype cavities of both families were already produced at Jefferson Laboratory. After contract award major milestones for the successful run of the project were:

- Engineering review of manufacturing procedures of the prototype cavities.
- Develop production drawings to reflect different manufacturing methods used at ACCEL compared to the JLAB used procedures for the prototype cavities.
- Establish QA plan for the cavity production and detailed workshop travellers.
- Design and manufacturing of all tooling for metal forming, turning, milling, electron beam welding, leak check, tuning, inner and outer BCP needed for the series production.
- Determine optimum electron beam welding parameters for all weld geometries.

The engineering review of the cavity manufacturing methods lead to the decision to change production details compared to the prototype cavities. The main changes were:

- Deepdrawing of half cells using a stamp and a cushion instead of inner and outer die. This technique requires fewer production steps and results in better accuracy of cell geometry.
- Production of raw end groups (see figure 1) out of one sheet of reactor grade niobium by deep drawing and nipple pulling.
- Production of the HOM coupler bodies out of reactor grade niobium cans (ordered from Heraeus GmbH).

The finished cavities can be seen in Figure 2 (medium beta cavity) and Figure 3 (high beta cavity) ready for shipment to JLAB.

Figure 1: Raw end groups produced for SNS cavities by deep drawing and nipple pulling from one reactor grade niobium sheet.

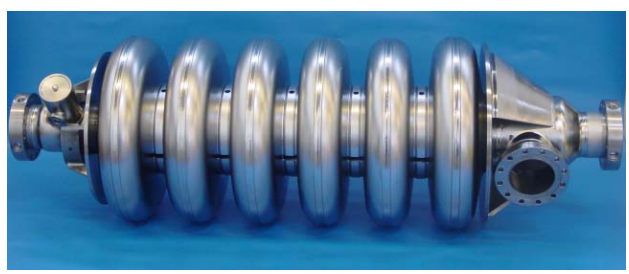

Figure 2: Medium beta 6 cell 805 MHz cavity produced for the Spallation Neutron Source Linac. The production of the medium beta cavities is finished.

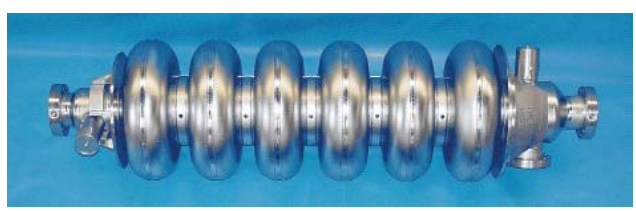

Figure 3: High beta 6 cell 805 MHz cavity for SNS. The series production of the 74 high beta cavities is scheduled to be completed in October 2004.

The surface removal after final welding of 30 µm from the outside and 100 µm from the inside is done in our closed loop chemistry cabinet using buffered chemical polishing (BCP 1:1:2). The acid temperature control during the etching process to values below 15 °C ensures that no hydrogen contamination of the niobium can take place. Thus no Q-disease has been observed in any of the cavities treated at ACCEL so far.

Before shipment an integral leak check to demonstrate leak tightness with a leak-rate below $2 \cdot 10^{-10}$ mbar·l/s followed by a careful dimensional control of the cavity is performed. It should be noted, that all cavities delivered to JLAB meet the required dimensions especially the length of all cavities is in the tolerance of +/- 3mm after tuning to the correct frequency. To achieve the correct length safely, the frequencies of all produced dumbbells were measured during the production and depending on the individual frequency measurement result the length of the dumbbells before final welding was adjusted. Beside achieving the right frequency this also helps to achieve a field flatness of already < +/- 25 % (deviation from mean value in amplitude) in the cavities directly after final welding and thus the tuning effort is greatly reduced. Normally a field flatness of +/- 1 % in amplitude is easily achieved after final tuning.

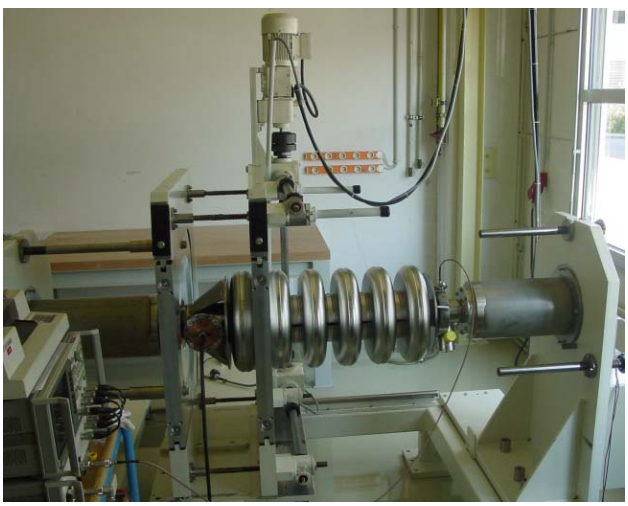

Figure 4: Tuning apparatus for SNS medium beta and high beta cavities. A field flatness of +/- 1% in amplitude is easily achieved.

TIME SCHEDULE

The time schedule for the project included a first article cavity production of medium and high beta cavity each. The first article medium beta cavity production included the tooling development and took one year, thus in August 2002 the first cavity was shipped to JLAB for vertical test and to demonstrate, that the specified cavity performance of 11.2 MV/m accelerating gradient with Q_0 values above $5 \cdot 10^9$could be achieved. This result was needed to launch the electron beam welding of the medium beta series production. Some single parts for the medium beta cavity series were already produced in parallel to the first article.

The remaining manufacturing work, chemical treatment and tuning of the additional 34 medium beta cavities was then finished within another 8 months. (Last medium beta cavity delivered in beginning of April 2003).

Some time during the production of the medium beta and later also of the high beta cavities was lost due to the finding from JLAB, that for all end groups originally requested to be produced out of reactor grade (RRR 40) material, a RRR value in the order of RRR 100 was needed for safe and stable operation in the SNS linac at the design fields and design currents. For this purpose all endgroups were shipped after deepdrawing and nipple pulling to JLAB for additional post purification in a vacuum furnace. At 1000 °C, the endgroups were annealed wrapped in titanium foil to increase the RRR. Some samples were taken from annealed endgroups to demonstrate the required increase in RRR and also to show that the mechanical properties of the niobium were not reduced due to that heat treatment.

In parallel to the work on the medium beta series cavity production, the first article high beta cavity was produced and delivered to JLAB for qualification vertical RF test 17 months after contract award (February 2003). The series production of single parts for the high beta cavities was started in June 2002. The first series high beta cavity was finished in June 2003. Since then, we are shipping cavities to JLAB with a rate of approximately 6 cavities every 6 weeks. The last lot of cavities is scheduled to be delivered to JLAB in October 2004. A comparison of planned and achieved time schedule for the main tasks of the project is shown in Figure 5. Only for the first article cavities, some delay was observed, caused by the additional work for annealing the raw endgroups and by the prototype character of this work.

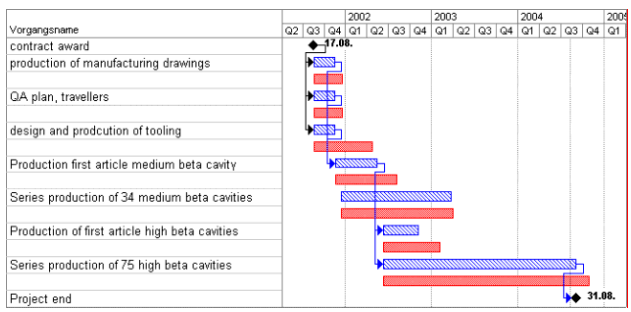

Figure 5: Comparison of planed (blue) and achieved (red) time and delivery schedule of SNS cavities. In summary the originally time schedule could be fulfilled.

CAVITY TEST RESULTS

No delivered SNS cavity has been reported to not exceed the specified and guaranteed design parameters of

$$Q_0 = 5 \cdot 10^9 \text{ at } E_{acc} = 11.2 \text{ MV/m}$$

for the medium beta cavities and of

$$Q0 = 5 \cdot 10^9 \text{ at } E_{acc} = 15.1 \text{ MV/m}$$

for the high beta cavities during the vertical cold RF test at a bath temperature of 2.1 K. Sometimes a cavity needed to be tested more than once in order to reach the

desired performance, the limiting effect being field emission loading by most probably insufficient high pressure water rinsing [1].

In figure 6 typical cold RF test results of a medium and high beta cavity are shown in comparison to the design specifications.

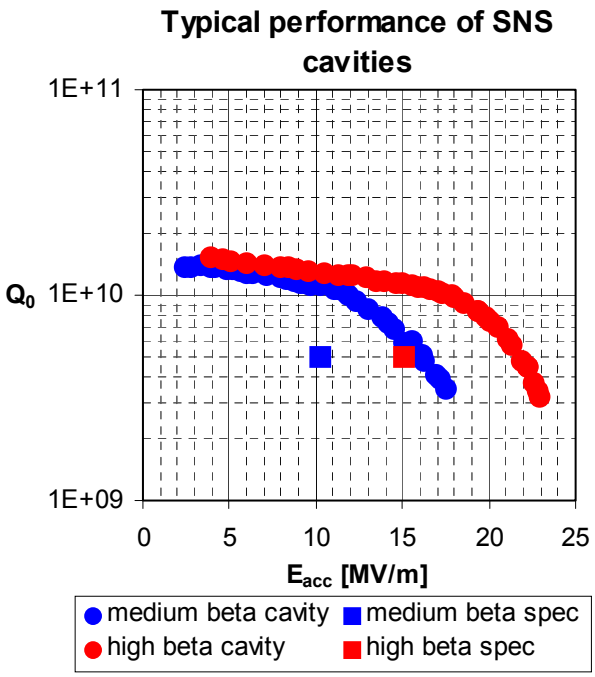

Figure 6: Typical cold test result of medium and high beta cavities for SNS. Accelerating gradients of up to 23 MV/m were achieved in the high beta cavities.

REQUIRED PERSONNEL

In average the contract was finished with approximately 10-15 people working on the project.

Figure 7 shows the relative distribution of engineers and skilled technicians involved in the project.

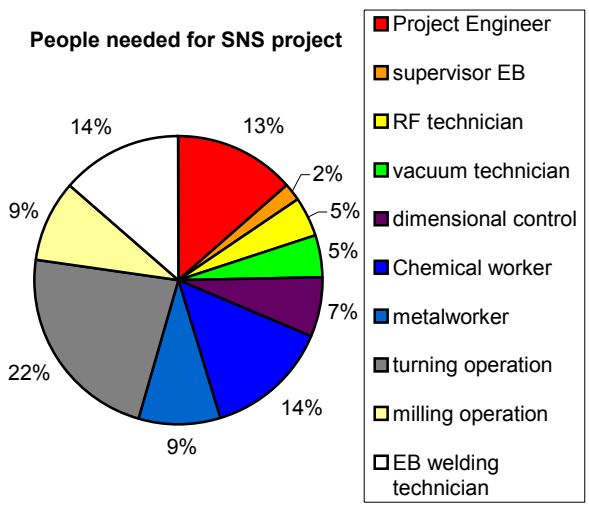

Figure 7: Relative distribution of engineers and skilled technicians involved in the SNS project.

Besides specific tasks like dimensional control and leak checks performed by vacuum technicians, QA work is included in the engineering, supervision of EB and RF technician work.

As can be seen, the heaviest work load is for turning operation followed by chemical workers (chemical treatment before welding and final chemistry), project engineering and EB welding. For the SNS project our two electron beam welding machines were loaded in a one shift operation to approximately 75 %.

With a view to future possible industrial cavity manufacturing projects with an even higher number of cavities produced per time, we would like to comment this additionally as follows:

- The two required cavity types for SNS reduced the number of similar cavities to maximum 73 during series production. This number is still too low to implement highly efficient mass production tools. Less engineering per cavity will be required for higher cavity numbers.
- The two first article cavities and design of all tooling also required a relative high percentage of engineers involved in the production.
- The tools for electron beam welding and the electron beam welding machines itself have still potential for further optimization when producing higher cavity numbers. There is still some room to reduce the needed electron welding machine time for one cavity and increasing the number of completed cavities per time.
- All involved machines and services were not exclusively dedicated to this project during the whole contract period. Storage of parts and internal transport can be reduced when machines and locations are dedicated to only one big mass production project.
- Milling and turning capacity can be easily enlarged for high cavity numbers by establishing a two or three shift operation. For the SNS project, turning and milling machines were operated in a one shift operation only.

ACKNOWLEDGEMENT

We thank Peter Kneisel and Tim Cannella from Jefferson Laboratory for the fruitful collaboration during this work.

We thank Joe Ozelis from Jefferson Laboratory for providing SNS cavity cold test results.

REFERENCES

[1] Peter Kneisel, private communication

SUPERCONDUCTING β=0.15 QUARTER-WAVE CAVITY FOR RIA

M.P. Kelly, Z.A. Conway, J.D. Fuerst, M. Kedzie, K.W. Shepard
Argonne Physics Division, Argonne National Laboratory, Argonne, IL 60439, USA

Abstract

A 109 MHz niobium quarter-wave cavity, fully configured with an integral stainless steel helium jacket, has been built and tested as part of the R&D for the Rare Isotope Accelerator (RIA) driver linac. The two-gap cavity is designed to accelerate ions over the velocity range 0.14<β<0.24. Final processing of the cavity RF surfaces, including high-pressure rinsing and assembly of the cavity with a high-power, variable rf coupler, were all performed under clean-room conditions. Cold test results including high-field cw operation, microphonics, and helium pressure sensitivity are discussed..

INTRODUCTION

A superconducting (SC) linac for the Rare Isotope Accelerator (RIA) ion driver requires several hundred SC cavities of several different types spanning the velocity range 0.02<β<0.8 [1]. We report here on the first cold tests of a prototype for one of these types, a β=0.15 niobium quarter-wave resonator (QWR). Although the QWR cavity discussed here will initially be used in an energy upgrade of the existing ATLAS accelerator, it has been developed specifically for the RIA driver linac as one of a set of three SC cavities spanning the intermediate velocity range 0.12<β<0.5. The other two cavities are a half-wave cavity, reported elsewhere at this conference [2], and a two-cell spoke-loaded cavity which has been reported previously [3]. The cold-test results for the QWR cavity discussed below represent the completion of development of the entire set of three cavities, in all of which the performance substantially exceeds the requirements of RIA.

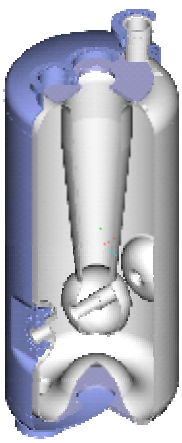

Figure 1: A partially cut away view of the RIA quarter-wave cavity generated in Pro/Engineer. The active length along the beam axis is 25 cm.

DESIGN AND CONSTRUCTION

The design of the β=0.15 QWR is shown in Figure 1. The inner niobium shell is shown in gray while the stainless-steel helium vessel is shown in blue. Electromagnetic parameters are listed in Table I. The cavity design was developed using numerical finite-element models in full 3D, using Pro/Engineer for the mechanical properties and CST Microwave Studio for the electromagnetic properties..

The useful accelerating range spans the velocity region 0.10<β<0.30, a velocity somewhat higher than for most existing quarter-wave structures. A correction for beam steering, inherent in quarter-wave structures due to the rf magnetic field in the beam region, has been incorporated by tilting the drift-tube faces by approximately 9° [4] The top and bottom of the QWR cavity are terminated in a large-radius toroid to avoid sharp corners and facilitate both chemical processing and rinsing, and also high-pressure water rinsing.

Frequency	109.13	MHz
Geometric Beta	0.144	v/c
Active Length	25	cm
QRs	40	ohm
R/Q	548	
below for Eacc = 1 MV/m		
Epeak	3.2	MV/m
Bpeak	58.3	Gauss
RF Energy	0.17	Joule

Table I: Electromagnetic properties of the QWR cavity

The cavity was formed of high-purity, RRR > 250, 3mm niobium sheet. The center conductor, toroids, and drift-tube faces were hydroformed, while the outer housing was rolled from flat niobium sheet. The niobium cavity-shell is enclosed in an integral stainless-steel helium vessel, as is the case for all of the ANL-developed RIA cavities. The stainless jacket is joined to the niobium at the cavity ports by a vacuum braze with pure copper. All nb-nb joints are electron-beam welded..

SURFACE PROCESSING

Chemical processing

It is well established that electropolishing of a niobium surface gives a substantially smoother and brighter rf surface than a heavy buffered chemical polish (BCP) and experimental data indicate that rf losses are reduced

Figure 2: The electropolished rf surface of the QWR just prior to the final closure weld.

particularly at real operational surface fields of >20 MV/m [5].

The following technique has been used at Argonne for electropolishing drift-tube cavities with small aperture ports, where electropolishing of the closed cavity is impractical. As applied to the QWR cavity, prior to completion of the closed cavity, each of four major niobium sub-assemblies was given a heavy electropolish (100~150 microns), as can be seen in Figure 2. The sub-assemblies were then electron-beam welded together, following which a very light BCP (8μm) was used to remove any residual oxide, etc. resulting from the weld.

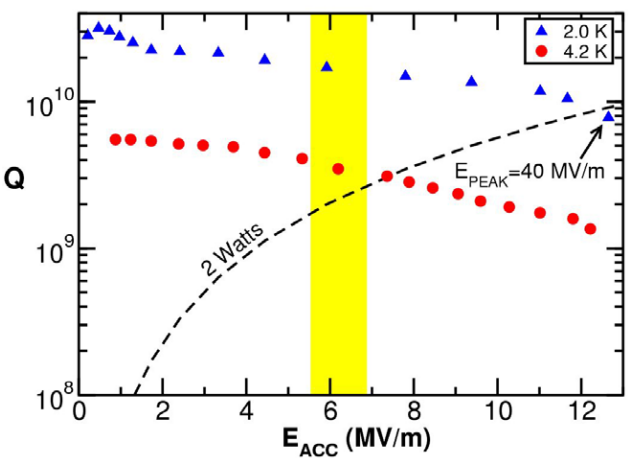

Figure 3: Initial test results for the RIA quarter-wave resonator. The value of Q at 4.2 K exceeds 10^9 even at peak surface fields as high as 40 MV/m.

High-pressure rinse and assembly

After BCP, the cavity was cleaned with a high-pressure water rinse (HPR) for 90 minutes and dried in the clean-room. It was then transported to a clean assembly area where a variable coupler and the cavity vacuum system, also cleaned by HPR, were connected, completing the cavity vacuum system. The sealed system was then removed from the clean area and installed in the test cryostat.

COLD TESTS

The oil-free cavity vacuum system was allowed to pump to a few 10-7 torr for 24 hours prior to cooldown. The cavity was cooled to 4.2 K with particular care to limit the time between 80 and 150K to about 30 minutes in order to avoid hydride formation.

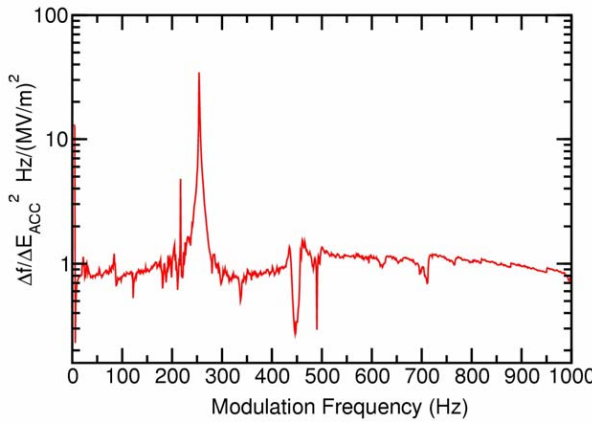

Figure 4. The amplitude of the Lorentz force transfer function. There are no low lying modes below 200 Hz.

Supeconducting performance

The cavity was cooled to 4.2 K, cooling rapidly (~1/2 hour) from 150 K to 80K to avoid hydride formation. Following a brief period of conditioning with up to 200 watts of power, primarily to 'burn through' low-level MP barriers, the performance detailed in Figure 3 was observed.

No significant electron-loading was observed. We note that the nominal residual resistivity is 3 nΩ at 4.2 K and less than 2 nΩ at 2 K. Very little 'Q-slope' is observed at either 2 K or 4.2 K, and the Q remains high even at the highest gradients. The gradients were finally limited by a thermal-magnetic quench at an accelerating field above 12 MV/m, corresponding to a peak surface electric field of more than 40 MV/m.

The cavity performs sufficiently well at 4 K that no refrigeration advantage would be gained by operation at 2 K.

Microphonics

Microphonics is an important issue for all RIA cavities, since beam loading will be relatively small and any additional RF bandwidth required for microphonics could impact the cost of RF power.

The relevant acoustic properties of the QWR cavity are characterized by the Lorentz-force transfer function,. which identifies mechanical modes which couple to the rf

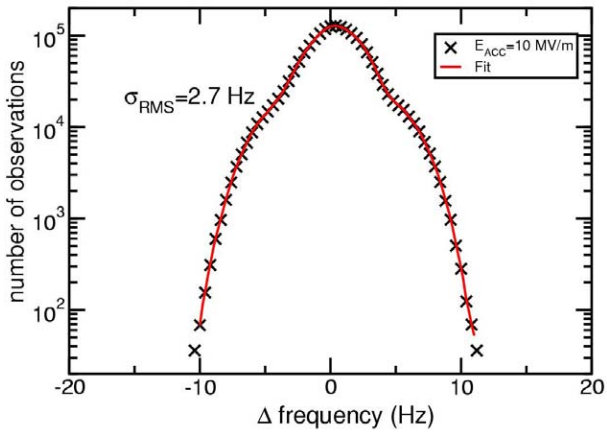

Figure 5: Probability density for quarter-wave eigenfrequency deviations for cw operation at E_{ACC}=10 MV/m.

eigenfrequency. The transfer function, shown in Fig 4, was measured by modulating the rf drive power and observing the resulting cavity rf frequency response. No significant acoustic modes were observed below a frequency of 200 Hz.

The measured probability density of rf eigenfrequency shifts in stable cw operation is shown in Figure 5. for operation at T=4.2 K and E_{ACC}=10 MV/m. Data was collected for a total of 300 seconds in three separate measurements and then summed. Measurements were performed using a very low noise reference (HP 8665B) and a cavity resonance monitor (CRM) device. The

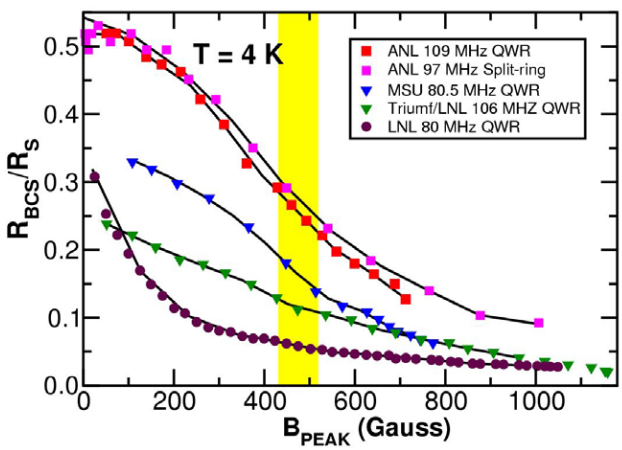

Figure 6: A comparison of recent experimental results to the BCS limit for surface resistance. ANL cavities received a heavy electropolishing.

spectral shape is well described as a pair of Gaussians. The rms frequency jitter is only 2.7 Hz even though we have not yet incorporated a planned mechanical damper.

DISCUSSION AND CONCLUSIONS

A measure of the cavity surface quality for the RIA QWR along with five other quarter-wave cavities at similar frequencies is shown in Figure 6. The curves comes from published electromagnetic parameters and Q-curve data, shown here in the form of the reciprocal of the effective surface resistance $1/R_S$, as a function of the (peak) surface rf magnetic field. This quantity is normalized to the calculated BCS surface resistance [6] for each cavity, a value of $1/R_S$ equal to one represents the theoretical maximum.

Results in figure 6. are all for cavities tested recently and assembled with some manner of clean handling. We note the cavity surfaces were prepared by BCP, except for the those cavities processed at ANL, where we use electropolishing and generally observe smoother surfaces than for BCP. All of the cavities shown operated at rf magnetic fields as high as 1000 Gauss or more. The two electropolished cavities, however, show substantially higher values of Q_0 (R_{RES}~3-4 nΩ) and, more importantly for actual use, reduced Q-slope and lower surface resistance (R_{TOTAL}~15 nΩ) at operationally useful field levels.

We have designed a QWR cavity suitable for production and tested the prototype in a realistic accelerator environment. The results substantially exceed the RIA design goals in all respects, and demonstrate that it is possible to produce drift-tube cavities capable of operating at 4.3K at peak surface electric fields well above 20 MV/m while maintaining a high-field Q well above 10^9.

ACKNOWLEDGMENTS

The authors wish to acknowledge the contributions of John Rathke and Ed Peterson of Advanced Energy Systems and of Ted Hejna of Sciaky, Inc. in the tooling, forming, and eb-welding of the prototype cavity.

This work was supported by the U.S. Department of Energy Office of Nuclear Physics under contract number W-31-109-ENG-38.

REFERENCES

[1] J. A. Nolen, in Proc. 2002 Linear Accelerator Conference, Gyeongju, South Korea, August 2002

[2] M.P. Kelly, Z.A. Conway, J.D. Fuerst, M. Kedzie, K.W. Shepard, paper THP06 in these proceedings.

[3] M.P. Kelly, K.W. Shepard, J.D. Fuerst, M. Kedzie, in Proc. 11th Workshop on RF Superconductivity, September 8-12, 2003, Lubeck, Germany

[4] P.N. Ostroumov† and K.W. Shepard, , in Proc. 21st Linac Conference, Gyeongju, Korea, August 19-23, 2002.

[5] J. Knoblach, R.L. Geng, M. Liepe, H. Padamsee, in Proc. 9th Workshop on RF Superconductivity, Santa Fe, New Mexico, USA, November 1-5, 1999.

.[6] H. Padamsee et al., "RF Superconductivity for Accelerators", p. 88.

COLD TESTS OF A SUPERCONDUCTING CO-AXIAL HALF-WAVE CAVITY FOR RIA

M.P. Kelly, J.D. Fuerst, M. Kedzie, K.W. Shepard
Argonne Physics Division, Argonne National Laboratory, Argonne, IL 60439, USA

Abstract

This paper reports cold tests of a superconducting niobium half-wave cavity with integral helium vessel, the design of which is suitable for production for the Rare Isotope Accelerator (RIA) driver linac. The cavity operates at 172 MHz and can provide more than 2 MV of accelerating voltage per cavity for ions with $0.24<\beta<0.37$. Cavity rf surfaces were prepared using electropolishing, high-pressure rinsing and clean assembly. Measurements of Q_0 show a residual rf surface resistance R_S = 5 nΩs in both 2 K and 4 K operations. The cavity can be operated at 4.5 K with E_{Acc} >10 MV/m (E_{Peak} >30 MV/m). Performance exceeds RIA specifications of an input power of 12 Watts at 4.5 K and E_{Acc} = 6.9 MV/m. RMS frequency jitter is only 1.6 Hz at E_{Acc} = 8 MV/m and T = 4.5 K as determined from microphonics measurements in a realistic accelerator environment connected to the ATLAS refrigerator.

INTRODUCTION

The Rare Isotope Accelerator (RIA) superconducting (SC) multi-ion driver requires ~390 SC cavities of several different types spanning the velocity range $0.02<\beta<0.8$ [1]. We report here on the cold tests of a prototype for one of these types, a β=0.26 niobium half-wave resonator (HWR). The HWR cavity discussed here will initially be used in an energy upgrade of the existing ATLAS accelerator, however, it has been developed specifically for the RIA driver linac as one of a set of three SC cavities spanning the intermediate velocity range $0.12<\beta<0.5$. The other two cavities are a quarter-wave cavity, reported elsewhere at this conference [2], and a two-cell spoke-loaded cavity which has been reported previously [3]. The complete set of three cavities all substantially exceed the performance requirements of RIA.

Figure 1: A partially cut away view of the RIA half-wave cavity generated in Pro/Engineer. The active length along the beam axis is 30 cm.

FABRICATION

The design of the β=0.25 half-wave resonator (HWR) is shown in Figure 1. with electromagnetic parameters in Table I. The inner niobium shell is shown in gray while the stainless-steel helium vessel is shown in blue. The cavity design was developed using numerical finite-element models in full 3D, using Pro/Engineer for the mechanical properties and CST Microwave Studio for the electromagnetic properties.

Table 1: Electromagnetic properties of the HWR cavity

Frequency	170	MHz
Geometric Beta	0.26	v/c
Active Length	30	cm
QRs	57	ohm
R/Q	241	
below for Eacc = 1 MV/m		
Epeak	2.9	MV/m
Bpeak	78	Gauss
RF Energy	0.338	Joule

The useful accelerating range spans the velocity region $0.24<\beta<0.40$. The top and bottom of the HWR cavity are terminated in a large-radius toroid to avoid sharp corners and facilitate both chemical processing and rinsing, and also high-pressure water rinsing.

The cavity was formed of high-purity, RRR > 250, 3 mm niobium sheet. The center conductor, toroids, and drift-tube faces were hydroformed, while the outer housing was rolled from flat niobium sheet. The niobium cavity-shell is enclosed in an integral stainless-steel helium vessel, as is the case for all of the ANL-developed RIA cavities. The stainless jacket is joined to the niobium at the cavity ports by a vacuum braze with pure copper. All nb-nb joints are electron-beam welded.

PROCESSING AND ASSEMBLY

Electropolishing

Electropolished surfaces like those shown in Figure 4. are known to be substantially smoother than those achieved using standard buffered chemical polish (BCP). Electropolishing has been used here to remove between 100 and 150 microns of niobium from all of the critical rf surfaces. Results shown here together with other recent results for ANL cavities indicate that electropolishing

Figure 2: Electropolished niobium components of the RIA half-wave cavity.

reduces Q-slope in drift-tube cavities operating at 4 K as had been previously observed for elliptical cell cavities running at 2 K.

The following technique has been used at Argonne for electropolishing drift-tube cavities with small aperture ports, where electropolishing of the closed cavity is impractical. As applied to the HWR cavity, prior to completion of the closed cavity, each of four major niobium sub-assemblies was given a heavy electropolish (100~150 microns), as can be seen in Figure 2. The sub-assemblies were then electron-beam welded together, following which a very light BCP (8μm) was used to remove any residual oxide, etc. resulting from the weld.

Clean room assembly

Clean processing and assembly techniques have been systematically applied for the first time to drift-tube cavities at ANL and our results show that clean techniques may be used to repeatably achieve high gradients in drift-tube cavities.

Techniques and facilities currently in place at Argonne and used with the half-wave cavity include:

- A versatile electropolish apparatus which can accomodate various drift-tube parts
- An ultra-pure water high-pressure rinsing apparatus which can be tilted for different cavity geometries
- A large curtained cleanroom area for the assembly of cavities and couplers (See Figure 3)
- A pair of test cryostats, one vertical and one horizontal which for a separate and clean cavity vacuum system

Figure 3: Clean room assembly of the HWR together with a variable coupler and pumping system.

COLD TESTS

After installation into the vertical test cryostat the oil-free cavity vacuum system was allowed to pump to the low 10-7 Torr range for 24 hours prior to cooldown. The cavity was cooled to 4.2 K while limiting the time between 80 and 150K to about 30 minutes in order to avoid hydride formation.

Performance

The cavity was conditioned through multipacting in a couple of hours using up to 200 Watts of available rf power. No significant electron-loading was observed. 'Q-slope' is minimal for both 2 K or 4.2 K operations, and the Q remains high even at the highest gradients. The gradients were finally limited by a thermal-magnetic

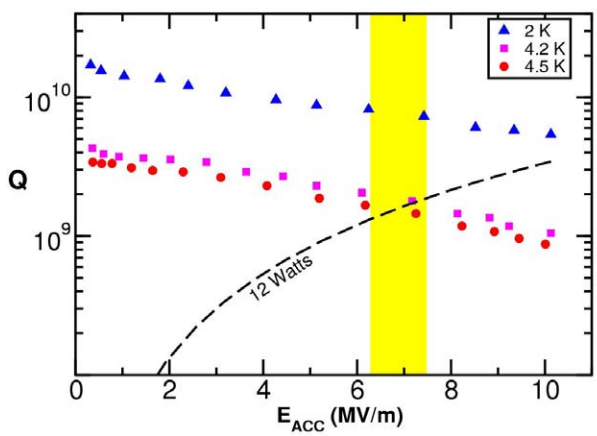

Figure 4: RIA half-wave resonator test results. The band indicates the RIA performance goal. The electropolished rf surface shows little Q-slope even in 4 K operation.

quench at an accelerating field above 10 MV/m, corresponding to a peak surface electric field of more than 30 MV/m. Cavity performance at 4.2 K is such that no refrigeration advantage would be gained by operation at 2 K.

MICROPHONICS

Microphonics levels in the RIA cavities will be key to determining both the cost of rf power for the driver linac and the fast tuning requirements. Microphonics measurements on the half-wave cavity have been performed here using an ultra-low noise rf signal generator and cavity resonance monitor (CRM) electronics capable of resolving eigenfrequency shifts as small as 0.1 Hz.

Measured eigenfrequency shifts for the half-wave cavity operating at both low and high fields are shown in Figure 5. The sample rate for each data set was 10 kHz with a sample time of 60 seconds each.

Observed frequency jitter is only 1.6 Hz rms, nearly independent of the rf power dissipated in the cavity. This observation is consistent with the very low helium pressure sensitivity measured to be –5 Hz/Torr and a measured Lorentz detuning coefficient of only -0.68 Hz/(MV/m)^2.

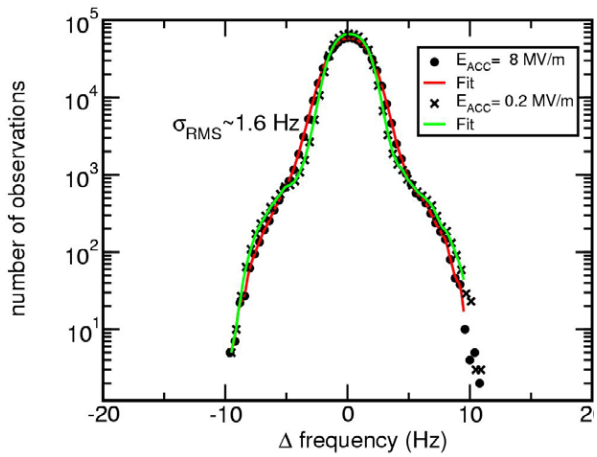

Figure 5: Microphonics measurements in the RIA half-wave cavity at low field level (crosses) and at E_{ACC}=8 MV/m (circles).

With the good mechanical stability of this half-wave geometry, the microphonics lie well within the expected beam loaded bandwith for RIA. An estimate of the beam loaded cavity bandwidth based on a voltage gain per half-wave cavity of 2 MV, a stored energy of 0.34 mJ and beam current of 0.5 mA for protons gives a value of 10 Hz or 6x the measured rms microphonics even with no additional fast tuner. However, additional fast tuning, such as with a VCX, piezoelectric device or overcoupling, will almost certainly be used to ensure phase stability.

CONCLUSION

We have designed and built a HWR cavity suitable for production and tested the prototype in a realistic accelerator environment. The results substantially exceed the RIA design goals in all respects, and demonstrate that it is possible to produce drift-tube cavities capable of operating at 4.2 K at peak surface electric fields well above 20 MV/m while maintaining a high-field Q above 10^9.

ACKNOWLEDGMENTS

The authors wish to acknowledge the contributions of John Rathke and Ed Peterson of Advanced Energy Systems and of Ted Hejna of Sciaky, Inc. in the tooling, forming, and eb-welding of the prototype cavity.

This work was supported by the U.S. Department of Energy Office of Nuclear Physics under contract number W-31-109-ENG-38.

REFERENCES

[1] J. A. Nolen, in Proc. 2002 Linear Accelerator Conference, Gyeongju, South Korea, August 2002.

[2] M.P. Kelly, Z.A. Conway, J.D. Fuerst, M. Kedzie, K.W. Shepard, paper THP05 in these proceedings.

[3] M.P. Kelly, K.W. Shepard, J.D. Fuerst, M. Kedzie, in Proc. 11th Workshop on RF Superconductivity, September 8-12, 2003, Lubeck, Germany.

PERFORMANCE IMPROVEMENT OF THE MULTICELL CAVITY PROTOTYPE FOR PROTON LINAC PROJECTS

B. Visentin[#], J.P.Charrier, G. Devanz, Y. Gasser, J.P. Poupeau, D. Braud, P. Sahuquet, B. Coadou,
CEA-Saclay, DSM/DAPNIA/SACM - 91191 Gif / Yvette Cedex - France
H. Saugnac, H. Gassot, S. Bousson, Ph. Szott
IPN-Orsay, Accelerator Division - 91406 Orsay Cedex - France

Abstract

The CEA-Saclay / IPN-Orsay collaboration allowed to manufacture a multicell superconducting RF cavity prototype for proton linac. Since the first experimental results [1], obtained in a vertical cryostat and the horizontal cryostat CryHoLab, the accelerating field E_{acc} has been recently increased up to 19 MV/m with a quality factor $Q_0 = 9.10^9$ and a limitation by quench.

However some improvements are still needed, in particular to suppress the field emission above 16 MV/m.

INTRODUCTION

The French R&D program on superconducting RF cavities dedicated to fit the high energy section (>100 MeV) of high intensity proton linear accelerators (see Fig.1) is mainly supported by two European projects:

- XADS, Preliminary Design Study of an eXperimental Accelerator Driven System. In this concept, neutrons are produced from spallation processes induced by the proton beam interaction with a heavy material target (Pb). These neutrons make up the external neutron source for a subcritical nuclear reactor to sustain transmutation of nuclear wastes,
- EURISOL, Research and Technical Development for the EURopean Isotope Separator On-Line, a radioactive beam facility in Europe. Rare isotopes are produced after the proton beam interaction with the target.

In this context, the CEA-Saclay and IPN-Orsay Laboratories started few years ago a collaboration to design, build and test a multicell cavity prototype for medium beta (β=0.65). At the same time an international collaboration was also established with INFN-Milan for the low beta superconducting cavities (β=0.47) for the Italian TRASCO program [2]. This R&D on multicell superconducting cavities should be continuing within the 6th European framework program with the Integrated Project EUROTRANS (XADS continuation), the EURISOL Design Study and the CARE-HIPPI (High Intensity Pulsed Proton Injector) program linked to the SPL (Superconducting Proton Linac) project at CERN.

CAVITY FEATURES

The five-cell A5-01 cavity (700 MHz, β=0.65), manufactured by CERCA from Wah Chang Niobium sheets (thickness 4 mm - RRR>250), is characterized by ratios of E_{peak}/E_{acc} and B_{peak}/E_{acc} surface peak to accelerating fields, respectively about 2.32 and 4.48 mT/(MV/m). Conflat® flanges, and liquid helium vessel, made from 316 L stainless steel, are copper-brazed on niobium. The mechanical stiffness of the cavity is ensured by the stainless steel frame (20 mm thick) and bracing rods, without stiffening rings between cells. Moreover, the cavity has been annealed under vacuum in furnace (650°C, ~ 1.10^{-7} mbar) to prevent the Q-disease during the RF test in the horizontal cryostat.

EXPERIMENTAL RESULTS

Preliminary Results

The first RF results achieved on this cavity have been discussed in previous papers [1,3]. During these tests, some problems occurred:

- a vacuum leak due to the acid attack of the brazing metal. This leak was temporarily sealed with a Stycast® epoxy compound,

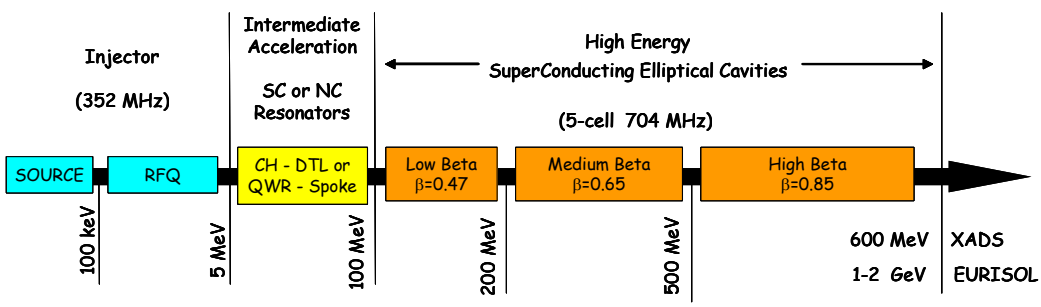

Figure 1: Schematic layout of a high intensity proton linear accelerator.

[#] bvisentin@cea.fr

• the limitation by strong resistive losses of the accelerating field around 16 MV/m for the test in vertical cryostat and only 10 MV/m in CryHoLab.

New Tests in Vertical and Horizontal Cryostats

To solve the leak problem a new flange has been successfully designed with sealing by indium gasket instead of Helicoflex® rings.

To improve the cavity performances additional chemistries have been applied on its inner surface. Niobium thickness of 35 µm has been removed since the preliminary tests. The chemical treatment procedure is to fill and empty several times the cavity with 55 liters of acid. After a first water rinsing, the cavity is rinsed at high pressure (85 bars) with ultra-pure water (18 MΩ.cm) in clean room of class 100.

After cavity cooldown to the liquid He temperature the surface resistance versus temperature has been measured between 4.2 and 1.7 K (Fig.2). The data fit with the BCS theory by using the Nb parameters (λ_L = 31 nm, ξ_0 = 62 nm, T_C = 9.22 K) allowed to obtain the values of the electron mean free path (190 nm) and the very low residual resistance (2.2 nΩ).

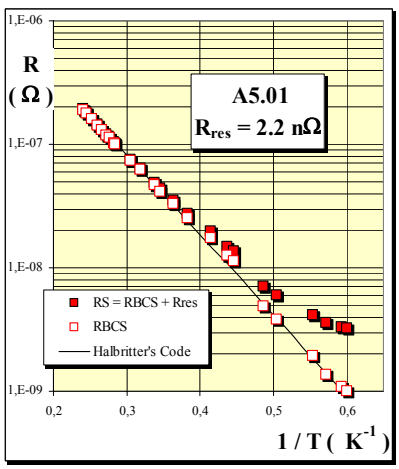

Figure 2: Surface resistance measurement between 4.2 and 1.7 K fitted by the BCS theory.

The quality factor versus accelerating field (E_{acc}) is shown in Fig.3. The accelerating gradient reaches 19 MV/m with a quality factor of 9.10^9 for the RF test in vertical cryostat. Consistent results (18 MV/m - 6.10^9) have been achieved with test in the horizontal cryostat CryHoLab. These values of E_{acc} correspond to electric and magnetic peak fields on cavity surface of about 43 MV/m and 83 mT.

No problems were encountered to easily go through the multipacting barriers. Field emission appeared above 16 MV/m. The cavity performances were limited by thermal quench located in the cell n°1 or n°5. This localisation of the quench became possible by means of the TM_{010} - 4π/5 mode, because in this case, the energy is mainly stored in the end cells of the cavity.

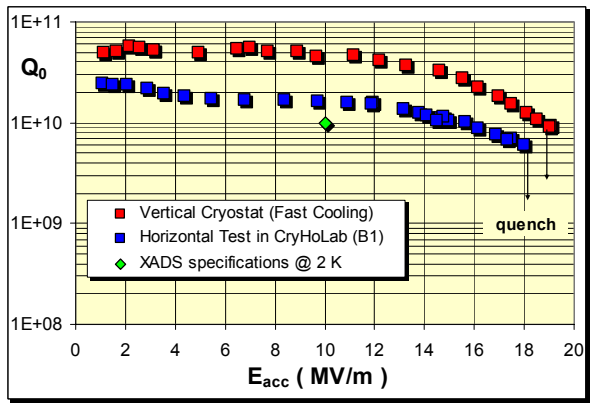

Figure 3: Q_0 vs. E_{acc} in vertical and horizontal cryostats.

Comments

• The improvement of the cavity performances by comparison with the previous results [1] is probably due to a better surface quality achieved after additional chemistries. In particular the non understood phenomenon (local defect) that limited the accelerating field last year did not appear this time.

• We can see in Fig.3 a difference of the quality factor value between the vertical and horizontal RF tests, for low and middle accelerating fields. The cause is probably a less efficient magnetic shielding of the horizontal cryostat CryHoLab: change of intensity in the magnetic coils (dynamic shielding) modifies the Q_0 values (white and blue squares in Fig.4).

• On other hand no change is observed in vertical test when the cavity is cooled down quickly (red data in fig. 4) or slowly with a stage of several hours around 100 K (white and red squares). Therefore, since the cavity heat treatment at 650°C the hydrogen did not pollute the niobium during the seven successive chemistries (total thickness removed 85 µm).

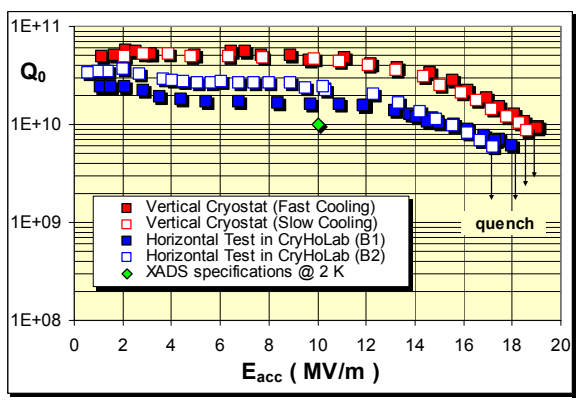

Figure 4: Q_0 vs. E_{acc} for A5-01 at 1.7 K showing the influence of magnetic shielding and slow cooling down.

LORENTZ FORCE DETUNING

A deformation of the cavity shape appears at high accelerating fields because of the radiation pressure. The result is a resonance frequency shift, characterized by the Lorentz force coefficient K_L:

$$\Delta f = K_L \, E_{acc}^2$$

This coefficient has been calculated [4] with the finite element code CAST3M in different boundary conditions for the cavity stiffness (see Table 1).

Table 1: K_L theoretical values computed with CAST3M code

	Fixed End	Helium Vessel & Tuner	Free
K_L Hz / $(MV/m)^2$	- 2.27	- 4	- 30

During the RF tests we have measured the frequency variation of the cavity Δf versus E_{acc}, but the experimental boundary condition was different from the three conditions above. The cavity was equipped with its helium vessel but without tuner and the stiffness element was the "stainless steel frame – bracing rods" system shown in Fig.5.

Figure 5: Stainless steel frame and bracing rods as cavity stiffness.

The experimental determination of K_L during several tests in vertical cryostat was around -7 Hz / $(MV/m)^2$, this value is in the range of the computed values and shows the relative efficiency of the stiffness system.

But in the horizontal cryostat this value was strongly deteriorated (-13 Hz / $(MV/m)^2$ in Fig.6). The reason seems to be due to the combination of the lack of stiffening rings between cavity cells and the heat treatment at 650°C causing a diminution of the mechanical stiffness of the whole system. In horizontal position the bare cavity showed indeed sag of few millimetres in the middle of the cavity length. Simulations are started to see if it is the only cause of this K_L degradation.

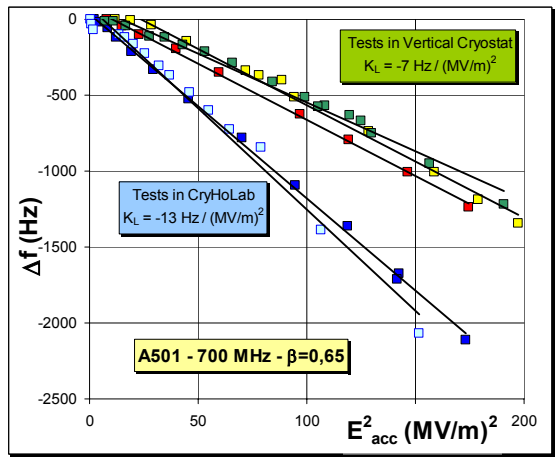

Figure 6: K_L experimental measurements in vertical cryostat and CryHoLab.

CONCLUSION

By comparison with the preliminary RF tests [1] carried out on the 5-cell cavity A5-01, we have found with these new series of tests a more usual behaviour of the cavity with an accelerating field limited by thermal quench around 19 MV/m.

Nevertheless some technical modifications should be undertaken in the future:

- the nozzle design of the high pressure rinsing to suppress the electron field emission which appears systematically for this cavity shape, whereas we do not observe such electron emission on TTF cavities.
- the magnetic screening of CryHoLab to decrease the residual resistance and increase Q_0 at low accelerating fields. A passive shielding with mu-metal sheets around the helium vessel could be considered.
- the cavity stiffness, especially if we want to use this cavity design for pulsed proton accelerator projects.

REFERENCES

[1] B. Visentin et al., "Experimental Results on 700 MHz Multicell Superconducting Cavity for Proton Linac", 20th PAC, p. 1303, Portland USA (2003) – PAC 2003: TPAB047

[2] A. Bosotti et al., "RF Tests of the β=0.5 Five-Cell TRASCO Cavities", 9th EPAC, Lucerne SWITZERLAND (2004) – EPAC 2004: TUPKF026.

[3] H. Saugnac et al., "CryHoLab, Horizontal Cavity Test Facility", 11th SRF Workshop, Travemunde GERMANY (2003) - SRF2003: MoP46

[4] H. Gassot, "Etude de la Stabilité Mécanique des Cavités Supraconductrices…", Thesis - Paris XI University (2001)

THE FRANKFURT FUNNELING EXPERIMENT*

J. Thibus†, U. Bartz, N. Müller, A. Schempp, H. Zimmermann, IAP,
J.W. Goethe-University, Frankfurt a.M., Germany

Abstract

Funneling is a procedure to multiply beam currents of rf-accelerators at low energies. In the ideal case the beam current can be multiplied in several stages without emittance growth. The Frankfurt Funneling Experiment consists of two ion sources, a Two-Beam RFQ accelerator, two different funneling deflectors and a beam diagnostic equipment system. The whole set-up is scaled for He^+ instead of Bi^+ for the first funneling stage of a HIIF driver. The progress of our experiment and the results of the simulations will be presented.

INTRODUCTION

The maximum beam current of a linac is limited by the beam transport capability at the low energy end of the accelerator. For a given ion source current and emittance the linac current limit is proportional to $\beta = v/c$ for electric and to β^3 for magnetic focusing channels and ideal emittance conservation. The funneling scheme is making use of the higher current limits at higher beam energies by doubling the beam current combining two bunched beams preaccelerated at a frequency f_0 with an rf-deflector to a common axis and injecting into another rf-accelerator at frequency $2 \cdot f_0$ as shown in figure 1. Ideally the beam emittance could be staying as low as for one single beam. Extracting twice the beam from a single ion source would result in at least twice the emittance for the following accelerators.

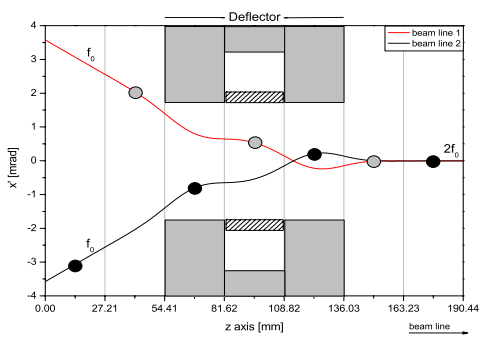

Figure 1: Principle of funneling demonstrated at a 3 cell deflector. To reduce the bending voltage drift tubes can be placed in the wider electrode apertures (shaded rectangle).

* Work supported by BMBF
† thibus@iap.uni-frankfurt.de

A tree of ion linacs is planned to increase the heavy ion beam current from 25 mA Bi^+ at the first linac to 400 mA at 10 MeV/u for the main linac.

The first linac is an RFQ with two beam channels in one resonator. By the use of the Two-Beam RFQ the distance of the two beams are very small while they are still radially and longitudinally focused. Additional discrete elements like quadrupole-doublets and -triplets, debunchers and bending magnets, as they have been proposed in first funneling studies, might not be necessary [1, 2, 3]. A short rf-funneling deflector is placed at the beam crossing position behind the RFQ [4].

EXPERIMENTAL SETUP

The Two-Beam RFQ accelerator is designed for He^+-ions instead of Bi^+ to reduce experimental expenses, facilitate operation and beam diagnostics (fig. 2,3). Two small multicusp ion sources [5, 6] and electrostatic LEBT lenses are used. The LEBTs are directly mounted at the front of the RFQ. The angle of both beam axes is 75 mrad.

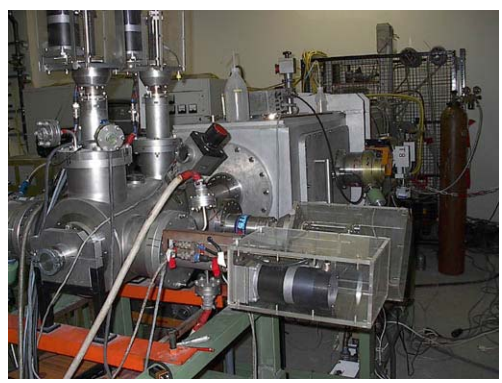

Figure 2: Picture of the experiment.

The Two-Beam RFQ consists of two sets of quadrupole electrodes, where the beams are bunched and accelerated driven by one resonant structure. The RFQ electrodes are divided in two sections. The first section, which is about two thirds of the total length of 2 meters, bunches and accelerates the beam to a final energy of 160 keV. At first the second part has been used as a transport section with unmodulated RFQ electrodes. For first beam tests only one RFQ-channel has been replaced by a section that matches the beam to the funneling deflector to optimize beam radius and phase width. This allowed us to compare both RFQ channels directly.

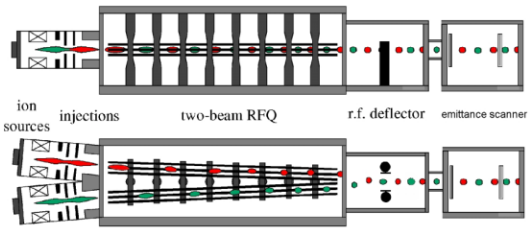

Figure 3: Scheme of the experimental set-up.

THE NEW RFQ ELECTRODES

The old transport section had unmodulated electrodes with constant aperture. In the new design the aperture increases and the last 8 of the total 12 cells have a modulation up to $m = 1.4$ to bunch the beam with the time focus at the funneling deflector. At the same time the focusing is made stronger to avoid a diverging beam and get more beam into the aperture of the deflector. Thus the RFQ provides a longitudinal and radial focus at the deflector.

Figure 4 shows the comparison of beam dynamics simulations for the old and the new RFQ electrode end matching section. The new electrode design reduces the beam radius from $r = 1.7$ cm to $r = 0.9$ cm and phase spread from $\Delta\varphi = 100°$ to $\Delta\varphi = 25°$ at the position of the funneling deflector, which is 54 cm behind the RFQ.

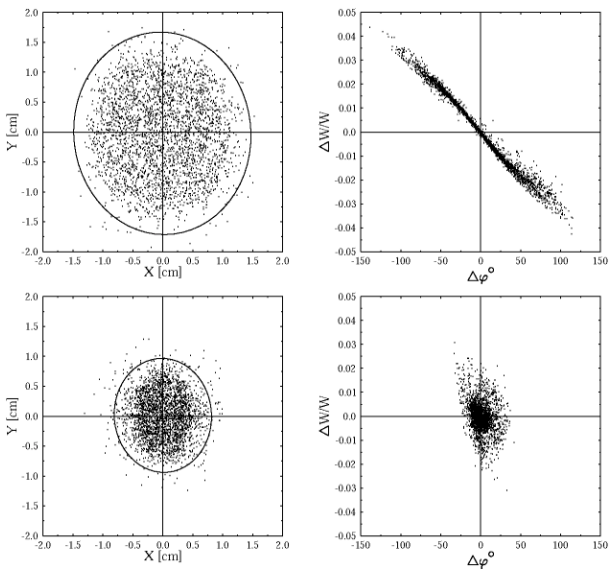

Figure 4: RFQSIM results with old (top) and new (bottom) RFQ electrode matching section.

BEAM TESTS

We have done a number of beam experiments to test the new matching out section. Figure 5 shows the beam pulses of the RFQ at the point of the beam crossing. The matching section in the new beam line reduces the pulse length. The Faraday cup used has only a restricted bandwidth and cannot resolve the pulses with high resolution. But the results clearly show the improvement of the pulse width for the new matching.

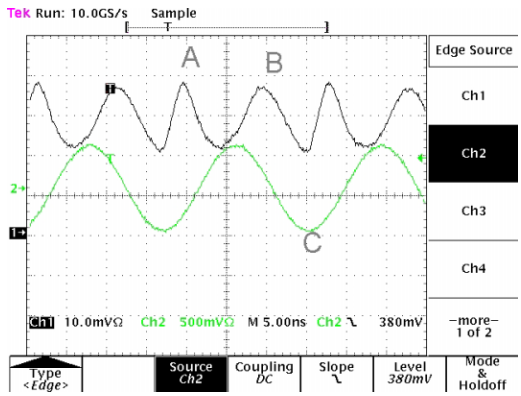

Figure 5: Bunch measurements with both beams.
A: New matching electrode end section
B: Unmodulated electrode end section
C: 54 MHz RF-trigger-signal

Figure 6 illustrates an emittance measurement with both beams at the point of beam crossing. The emittance from the beamline with the matching section reduces the beam radius. The measurements are in good agreement with our simulations shown in figure 7.

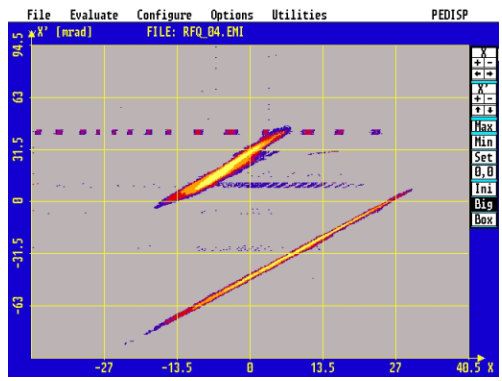

Figure 6: Measured emittances of old (bottom) and new (top) RFQ channels.

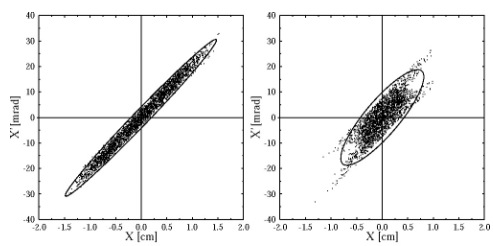

Figure 7: Simulated emittances of old (left) and new (right) RFQ channels.

THE SIM CODES

All simulations were done with *RFQSIM* and *DEFTRA*. *RFQSIM* is a beam dynamic transport program for RFQ accelerators. It transports macro particle bunches in the 6-dimensional phase space segmentally through the RFQ and more than 15 transport modules such as bunchers, quadrupole, lenses and drift tubes. These modules can be placed before and behind the accelerator.

DEFTRA is used to simulate two beam lines through a funneling deflector. It needs a particle distribution file from *RFQSIM*. Furthermore the 3D structure and the potential matrices $\Theta(x, y, z)$ and $\Phi(x, y, z)$ of the funneling deflector with fringe ranges computed by *DEFGEN* are required [8]. The bunch of each beam line is transported segmentally through the structure and the fringe ranges.

DEFLECTOR SIMULATION

To reduce beam losses, beam divergency and phase spreading of our 17 cell funneling deflector several shorter versions are investigated. The existing single deflector has the disadvantage that the large bending voltage of about 21 kV for He^+ corresponds to MV for Bi^+ (HIDIF). Figure 8 illustrates the potential distribution of a funneling deflector with 9 cells at a bending voltage of approximately 6.4 kV. The electrode aperture in the short gaps start from 30 mm to 20 mm, the drift tubes in the large gaps vary from 15 mm to 12 mm.

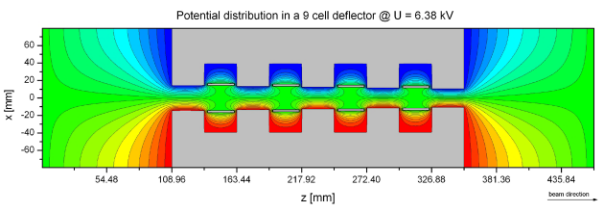

Figure 8: Intersection at the beam axis of the 9 cell deflector in top view of the potential distribution matrix.

The (x, x') and $(\Delta W/W, \Delta\phi)$ emittances behind the 17 and the 9 cell deflector for one beam line are shown in figure 9. Due to different deflector lengths a drift of 11 cm has been placed behind the 9 cell deflector for true comparison. The phase width is reduced from $\Delta\varphi = 150°$ to $\Delta\varphi = 55°$.

Further investigations have to be done.

CONCLUSIONS

Our first experiments with the two beam RFQ accelerator have shown that funneling can be done, but the beams were not matched to the funneling deflector [9].

By adding the new 3D matching section to one RFQ channel we were able to improve the matching.

The second RFQ channel is now modified with the new matching electrodes too [10]. Next step will be new funneling experiments with the two matched beams.

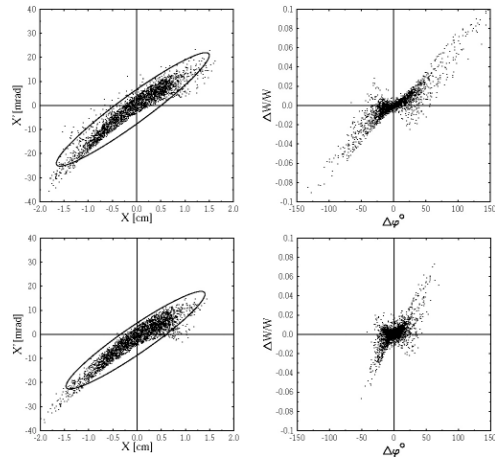

Figure 9: Emittances of the existing 17 cell deflector (top) and a newer 9 cell deflector (bottom). For better comparison only one beam line is shown.

REFERENCES

[1] K. Bongardt and D. Sanitz, “Funneling of Heavy Ion Beams”, Primary Report, Kernforschungszentrum Karlsruhe, 11 04 02P14C (September 1982)

[2] J.F. Stovall, F.W. Guy, R.H. Stokes and T.P. Wangler, “Beam Funneling Studies at Los Alamos”, Nucl. Instr. and Meth. A278 (1989), p.143

[3] K.F. Johnson, O.R. Sander, G.O. Bolmer, J.D. Gilpatrick, F.W. Guy, J.H. Marquardt, K. Saadatmand, D. Dandoval and V. Yuan, “A Beam Funnel Demonstration: Experiment and Simulation”, Particle Accelerators, Vols. 37-38 (1992), p. 261

[4] A. Schempp, “Design of Compact RFQs”, Proc. LINAC 96, CERN 96-07, p. 53

[5] K.N. Leung, “Multicusp Ion Sources”, Rev. Sci. Instrum. 65(4) (1994) p. 1165

[6] R. Keller in: The Physics and Technology of Ion Sources, Edited by I. G. Brown, Wiley-New York

[7] A. Schempp, “Funneling Experiments”, NIM A464 (2001), p.395

[8] J. Thibus, A. Schempp, “Numerical simulations for the Frankfurt Funneling Experiment”, Proceedings EPAC 2004, Lucerne, Switzerland

[9] H. Zimmermann, A. Bechtold, A. Schempp, J. Thibus, “Funneling with the Two-Beam-RFQ”, XX Int’l Linac Conference 2000, Monterey, California, p. 791-793

[10] H. Zimmermann, U. Bartz, N. Müller, A. Schempp, J. Thibus, “The Frankfurt Funneling Experiment”, Proceedings EPAC 2004, Lucerne, Switzerland

TUNER DESIGN FOR HIGH POWER 4-ROD-RFQs*

A. Schempp#, L. Brendel, B. Hofmann, H. Liebermann
Institut für Angewandte Physik
Johann Wolfgang Goethe-Universität, 60054 Frankfurt am.Main, Germany

Abstract

The performance of high power RFQ linacs, as used in spallations sources and proposed for projects like ADxy, IFMIF or high duty factor drivers for RIB application are limited by beam dynamic properties as well as technical limits like sparking, power density, cooling and thermal stresses. A "one piece structure" even possible in theory has to have means for tuning the real fields like exchangable or moving tuners. Tuner design features will be discussed and results will be presented.

INTRODUCTION

The low energy section of a modern ion linac consist of an RFQ-DTL combination in which the beam from the ion source is shaped to match the experiment or the following accelerator, an high energy linear or circular accelerator.

The beam dynamics and rf-structure designs for moderate beam currents and pulsed structures are proven and there is a lot of experience and tools to match and shape for different special requirements.

For high average beam power and e.g. cw-operation of linacs the freedom of parameter is limited and the interference of beam dynamics with rf-design and mechanical engineering is much stronger.

There are high duty factor heavy ion machines and some experience with cw high current RFQ prototypes but new projects like the IFMIF / XADS [1] type of projects require new parameter ranges which cannot be achieved by just extrapolating low power structures.

The succesful tests of the LEDA RFQ with 100mA cw proton beam illustrates the magnitude of problems to be solved [2].

One important point is the tuning of a long structure. Starting from designs for an ideal cavity the frequency of the resulting structure can be determined in the order of some percents precision. The more homogenous the structure the more precise the simulation can be. But, e.g. with the modulation of the RFQ electrodes structure and by this varying capacity along the RFQ the simulation are less precise and in addition some design ask for a tilted field distribution, while in the normal designs the field amplitude is just a constant factor.

Tilted field designs are even more difficult to simulate and mechanical tolerances bring unavoidable field and frequency errors.

One point which brought some reduction in length sensitivity was the development of resonantly coupled sections and distributed rf-feeds and vacuum pumping ports. Still the LEDA-RFQ has 132 tuners to compensate for discontinuities and field balance.

The 4-rod-RFQ-structure is less sensitive to mechanical asymmetries, a typical number is 10 tuners for a 4 m long RFQ at 200 MHz. There are two kind of tuners: static ones to tune the frequency and dynamic ones to compensate for temperature changes. For lower average rf-powers this is no real problem. 30A/cm scale down to average currents of less than 1A/cm and rather low power losses on the contacts between tuner blocks and the tank base, which can be simple spring fingers, special developed finger stock like for tunable cyclotrons or metal vacuum seals.

We have made an attempt to investigate these problems, because for possible application of the 4-Rod as cw structure the straightforward finger stock material used so far is at its limits.

RFQ TUNER

The 4-Rod-RFQ consists of a chain of interlaced λ/2 resonators operating in π0-mode, generating the homogenous quarupole voltage distribution along the RFQ electrodes. Basicly the capacitively loaded stem structure is a loaded chain of strongly coupled resonators. The frequency of theses resonators should be identical, then the fields will be constant along the RFQ. Mechanical inhomogeneities, ports etc. and the varying electrode shape detune the chain.

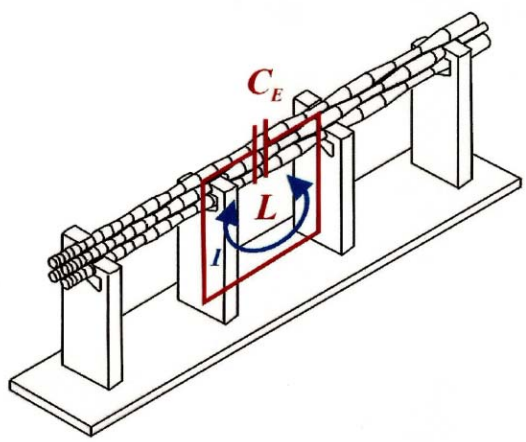

Figure 1: Basic 4-Rod-RFQ cell.

*supported by the BMBF
#a.schempp@em.uni-frankfurt.de

Small changes can be achieved by bringing in copper cups, which perturb the magnetic field, raising the frequency of the pertubated cell and by coupling also of the chain of cells and such compensating thermal changes in operation, where these tuners serve in a feedback loop. Typically for a 4-Rod structure of 2 m length one tuner is sufficient.

A contact to the cavity is not necassary, unlike tuners like for a spiral cavity which act capacitively and add capacity to the tank outside. There is a net current flow over the tuner stem to the tank, requiring a good sliding contact at the base.

Tuners in e.g. reentrant cavities and Alvarez structures tune the magnetic fields (change of the net volume of the tank) and they change the current path. They need a contact between tank and tuner if their change of the field distribution should be small. Simple and mostly used solution is a deep slot, which brings the net current flow on the contact down to a very small rest.

As indicated in the scheme of the basic cell of a 4-rod RFQ in fig.1 the cross section of the current loop is prop.. to the inductivity and making this loop smaller, e.g. by introducing some (copper) material on the base plate, will raise the frequency. Fig. 2 show the structure used in the following examples (stem distance 77 mm, stem height 95mm) together with calculated currents in the middle of the base plate and E-fields resp. voltages between the electrodes in the middle between the stems.

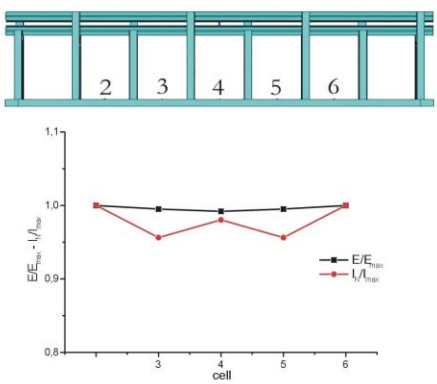

Figure 2: Voltages and currents in the cell centers between the stems along a short 8-stem 4-Rod RFQ.

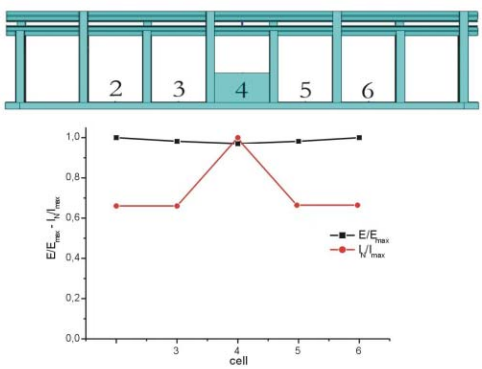

Figure 3: Voltages and currents along a short 8-stem 4-Rod RFQ with a central tuning block (Δf=2%).

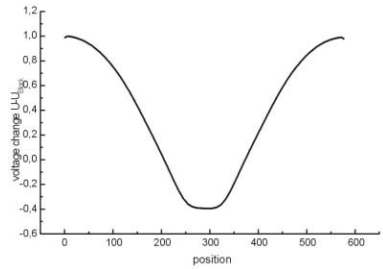

Figure 4: Electrode field changes induced by the central tuning block.

Introducing a tuning block (height 40mm) in the central cell will raise the frequency by 2%, lower the field in the middle cell and increase the current in the middle cell as shown in Fig. 3. Such an current increase of about 50% [3] can lead to overload of these contacts between stems and tuning block.

The variation of the E-field along the electrodes is localised around the tuned cell as shown in fig. 4.

The current distribution with a tuning block is investigated in more detail in figs. 5-8, where the current across the RFQ cell is plotted for different paths, showing that the full current is in the slot.

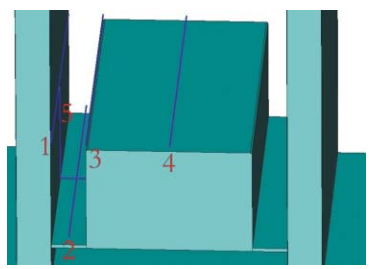

Figure 5: RFQ tuning block between stems with slots.

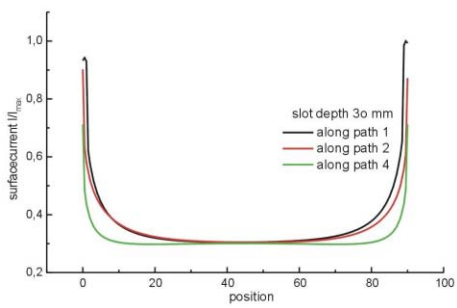

Figure 6: current distribution across the RFQ-cell at different points.

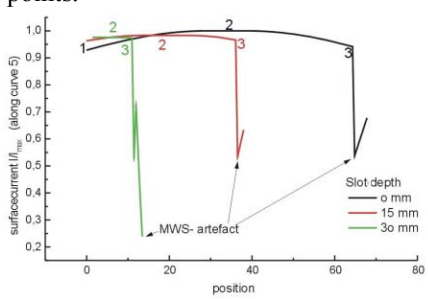

Figure 7: Current distribution along the cell center at different points (parameter: slot depth).

Figs. 9-12 show the same for a partial slot of only 30 mm length. There the current in the slot is strongly reduced. MWS has limited precision at sharp corners, resp. we must use higher resolution for more details. But the present results show clearly the current paths and magnitudes in the different cases, where contacts have to be placed.

Fig.11 and 12 show ALGOR calculations of the temperature distribution in a 4-Rod cell. In this example a constant power load per area and only cooling of the base plate and the electrodes are assumed.

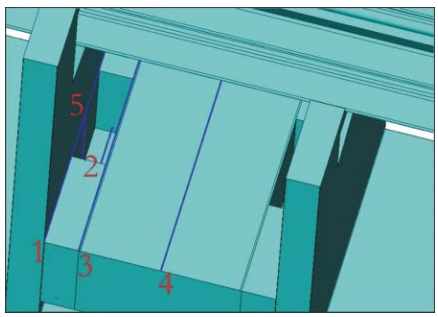

Figure 8: RFQ tuning block between stems with a short central slot (30mm).

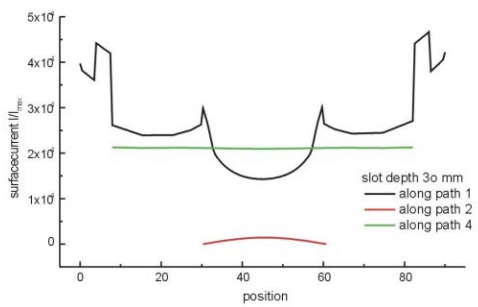

Figure 9: Current distribution across the RFQ-cell at different paths.

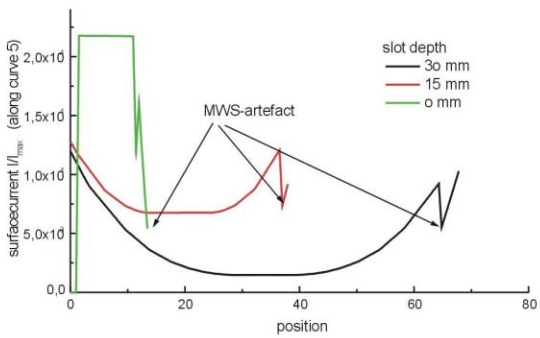

Figure 10: Current distribution along the cell center, (parameter: slot depth).

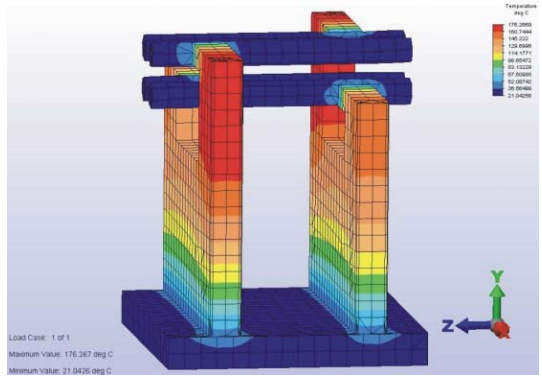

Figure 11: Simulation of temperature distribution of one RFQ cell with constant power/area. Base plate and electrodes cooled.

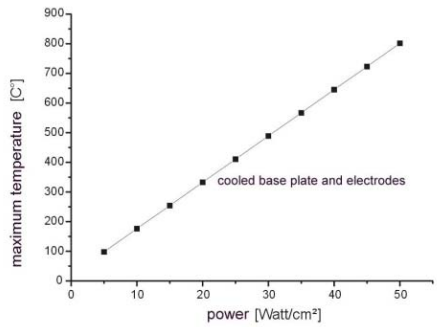

Figure 12: Maximum temperature in a RFQ cell with constant power/area. Base plate and electrodes are cooled.

REFERENCES

[1] M. Sugimotoa,, R. A. Jameson, V. Teplyakov, D. Berwald, B. Blind, D. Bruhwiler, H. Deitinghoff, R. Ferdinand, M. Kinsho, H. Klein, J. -M. Lagniel, A. Miyahara, M. Olivier, M. Peakock, E. Piechowiak, J. Pozimski, J. Rathke, Y. Tanabe and K. Volk, "Accelerator conceptual design of the international fusion materials irradiation facility", Journal of Nuclear Materials, Vol. 258, (1998), p. 367.

[2] D. Schrage, L. Young, P. Roybal, A. Naranjo, D.Baca, W. Clark, F. Martinez, H. Haagenstad, J. Mitchell, D. Montoya, A. Rendon, F.," CW RFQ Fabrication and Engineering", Linac98, p. 680

[3] H. Liebermann, Int. Note 03

DESIGN OF A 352 MHZ-PROTON-RFQ FOR GSI *

B. Hofmann, L. Brendel, A. Schempp#,
Institut für Angewandte Physik,
Johann Wolfgang Goethe-Universität, 60054 Frankfurt am.Main, Germany

Abstract

Part of the future project of GSI is a new p-linac for the production of Antiprotons. The 4-Rod-RFQ operating at 352 MHz has to accelerate up to 100mA protons from an ECR source. Design studies have been made using the RFQsim- and Microwave Studio codes to optimize beam dynamics properties and the field distribution of the RFQ. Results of the design studies will be presented.

INTRODUCTION

The plan for the future GSI accelerator system is based on the existing UNILAC and SIS18 as injectors to a complex Synchrotron storage ring system, which should be able to deliver unique beams for the study of the structure of matter [1]. A key feature of the facility is the generation of intense, high-quality secondary beams of rare isotopes as well as antiprotons. To serve as an injector, the UNILAC intensity has to be upgraded by a factor of appr. 100. Refering to the experience of CERN the primary proton beam pulse intensity for the production of antiprotons has to be in the order of 50mA, while the maximum proton beam currents from the UNILAC, which is optimized for Uranium beams, are only I_p < 1mA. Therefore plans to built a new dedicated P-linac have a high priority.

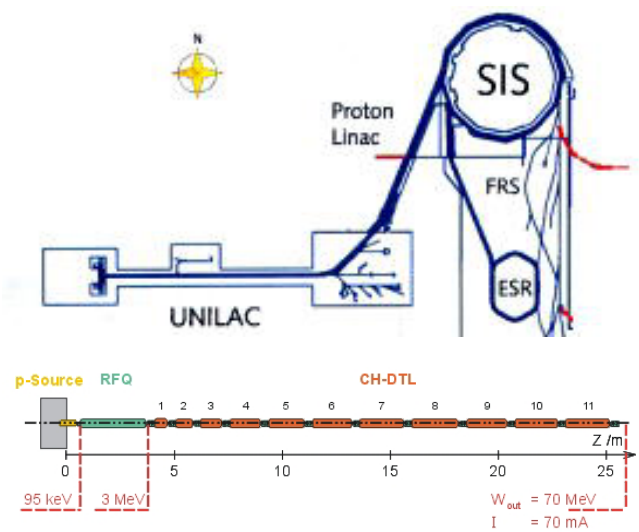

Figure 1: Scheme of the future GSI-p-linac with ECR-source, RFQ and CH-DTL linac.

*supported by the BMBF
#a.schempp@em.uni-frankfurt.de

Table 1: Basic P-Linac Parameters

Frequency	352 MHz
pulse rate,length	5 Hz, 0.1msec
Output energy	70 MeV
Beam current	70 mA
transv, emittance rms norm.	1.5 π mm mrad
energy spread	± 1%

This new 70 MeV proton linac will directly inject into the SIS18 and should deliver high quality 70 mA beams. It is planned to built a very compact linac, making use of the recent progress in accelerator technology by building an ECR-RFQ-CH linac with a total length of ca. 26 m. The choice of the operating frequency of 352 MHz is set by the availability of LEP-type Klystrons which shall drive the linac [2,3].

RFQ-BEAM DYNAMICS

Preliminary design studies fixed the injection energy of the RFQ to 95 keV and the final energy to 3 MeV. The beam current should be 70 mA, but a current upgrade up to 90mA should be possible without big changes.

Table 2: Basic RFQ Parameters

Frequency	352 MHz
Input energy	95 keV
Output energy	3.0 MeV
Beam current	70/90 mA
output emittance rms norm.	0.4 π mm mrad
energy spread rms	150 deg.keV
Electrode voltage	90 kV
RFQ length	3.22 m
cell number	272
min - max aperture	2.35-3.6 mm

The beam dynamics design is based on the results for the proton RFQs for DESY, RAL and Debtec with adiabatic variation of electrode parameters, it aims at a short structure at low electrode voltage to save rf-power and facilitate rf-tolerances and peak power problems preserve emittance and high transmission.

The beam dynamics design,based on the parameters of Table 1, led to a RFQ with electrode voltage of 90 kV and a length of 3.2 m as summarized in table 2.

The design procedure allows for a transmission of more than 95% even at the high input current of 100 mA, with a very small emittance growth.

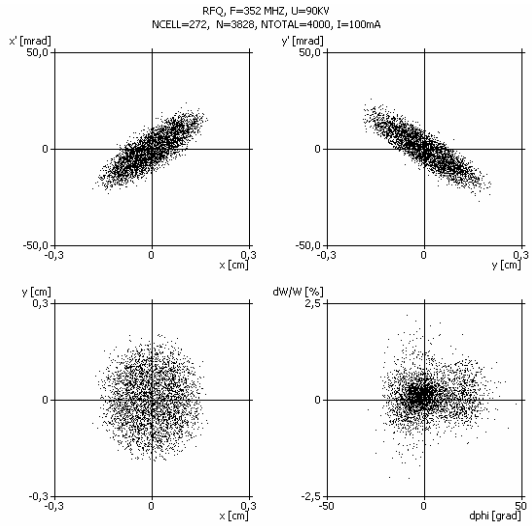

Figure 2: RFQ output distribution. Input beam current 100 mA, output current 95.7 mA, input emittance 0.3 π mm mrad rms n, output emittance 0.27 π mm mrad rms n.

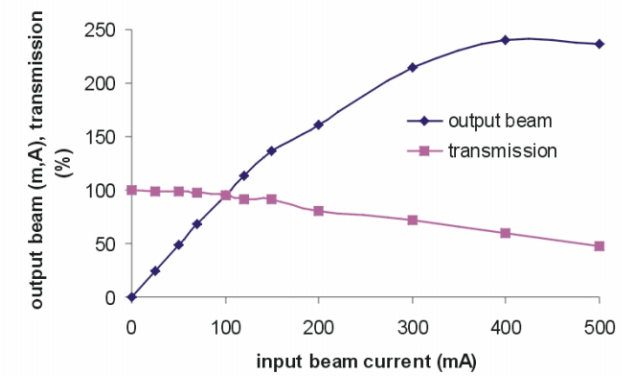

Figure 3: RFQ output proton current as a function of the input proton beam current.
Transmission as function of the input beam current.

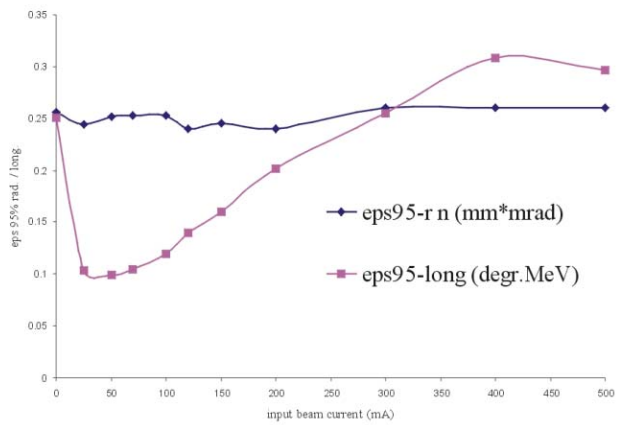

Figure 4: RFQ output emittance (95%) as a function of the input proton beam current.

Fig. 2 shows the output distribution for an input emittance of $\varepsilon_{in} = 0.3\ \pi$ mm mrad rms normalized.

An even higher transmission is possible on cost of structure length. More important seems the behaviour as function of the input current, where one could see in fig. 3 and fig. 4 that the real limit is far above the design value. The radial emittance stays nearly constant even for input currents as high as 500 mA. The output current saturates at appr. 250 mA, the current limit of that design.

RFQ STRUCTURE

A 4-Rod-RFQ structure will drive the RFQ electrodes. The basic cell is a interlaced capacitively loaded λ/2 transmission lines in π0-mode.

Up to now 4-Rod RFQs have been built in the frequency region between 2.5 MHz and 216 MHz for protons, H- and mostly heavy ions up to mass to charge ratios of A/q = 1000.

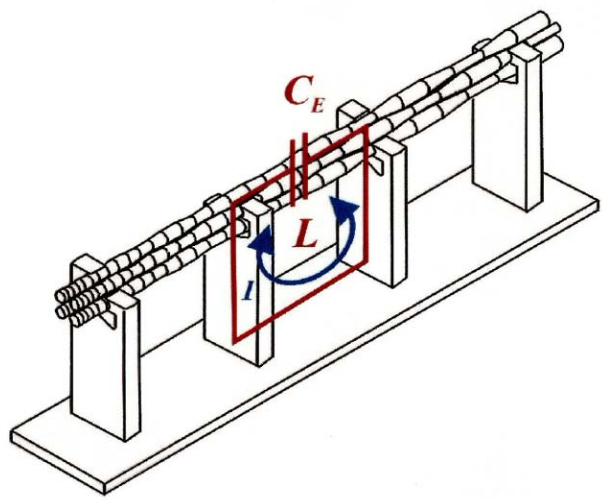

Figure 5: Basic 4-Rod-RFQ Cell.

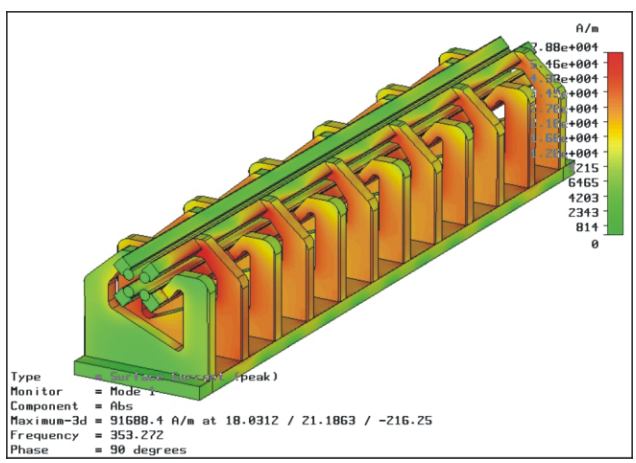

Figure 6: MWS simulation of current densities in the 350 MHz 4-Rod-RFQ structure.

We have developed a design for 352 MHz, which is mainly by reducing the distance between the stems and the shape of the stem [4]. The electrodes have to stay more or less the same as for 200 MHz. Fig. 6 shows current- and power-distribution. Fig 7 and fig. 8 the E-fields in basic mode and the first higher longitudinal mode at 410 MHz.

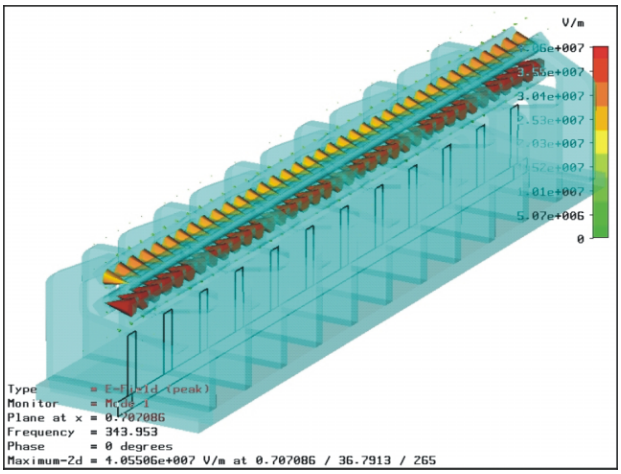

Figure 7: Electric field distribution in the π0-Mode.

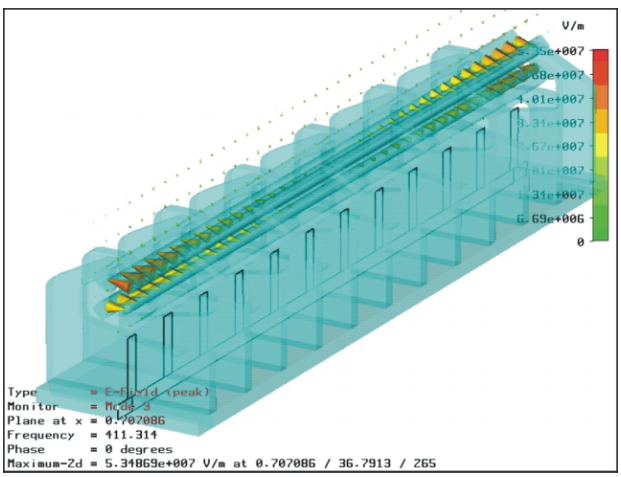

Figure 8: Electric field distribution in the π1-Mode.

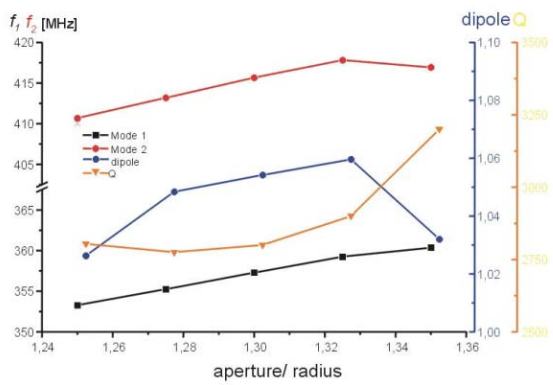

Figure 9: Mode frequencies, Dipoles and Q as function of the aperture radius.

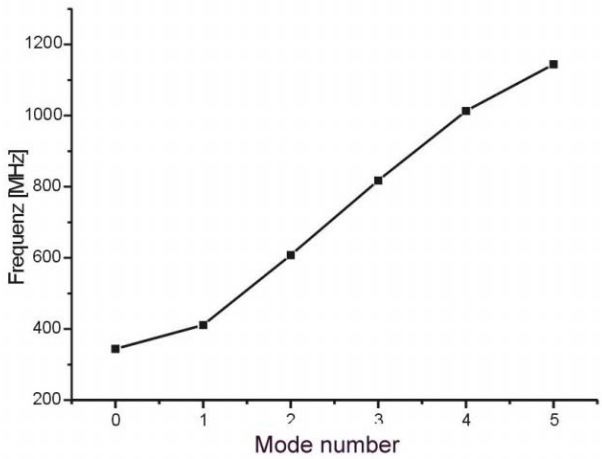

Figure 10: Brillouin diagram for the first 6 modes.

The variation of the aperture to electrode radius does vary the frequency of all modes and in addition influences the dipole mode across the stems and the Q-value of the resonator as shown in fig.9. Fig 10 shows the frequency of the first 6 modes of this 12-stem structure with its big longitudinal coupling.

REFERENCES

[1] W.F. Henning, "FAIR – an international accelerator facility for research with protons and antiprotons", EPAC04, Luzern, CH, July 2004.

[2] L. Groening, W. Barth, L. Dahl, R. Hollinger, P.S. Spädtke, S. Yaramishev, B.H. Hofmann, Z. Li, U. Ratzinger, A. Schempp, R. Tiede, "A Dedicated 70 MeV Proton Linac for the Antiproton Physics Program of the Future Facility for Ion and Antiproton Research at Darmstadt", LINAC04, Lübeck, August 04

[3] H. Podlech,,"Development of Superconducting and Room Temperature CH-Structures", LINAC04, Lübeck, August 04

[4] B. Hofmann, diploma thesis, Univ. Frankfurt, 2004

SUPERCONDUCTING RFQS IN THE PIAVE INJECTOR*

G. Bisoffi, G. Bassato, G. Bezzon, A. Calore, S. Canella, F. Chiurlotto, A. Lombardi, P. Modanese, A.M. Porcellato, S. Stark, INFN LaboratoriNazionali di Legnaro, I 35020 Legnaro (Italy)

Abstract

Two superconducting (sc) RFQ's (SRFQ1 and SRFQ2, resonating at 80 MHz, 0.8 m in diameter and 1.34 m and 0.74 m long), were mounted in their common cryostat and connected to the TCF50 refrigerator in the linac building. The SRFQs follow an ECR source on a 350 kV platform and external bunching, and precede 8 sc quarter wave resonators. They are the very low velocity accelerating structures of the new heavy ion injector PIAVE [1], which will soon expand the mass range of accelerated projectiles at INFN-Legnaro up to the heaviest ones. After thorough "off-line" resonator testing was completed and dealt with on previous publications ($E_{sp,n}$> 25.5 MV/m – the design value, Q-values between 5 and 8 x10^8, stability issues in He-to-recovery mode), this paper describes the very first on-line results.

THE BUMBY ROAD TOWARDS BEAM COMMISSIONING

After assemblying both RFQs in their common final cryostat more than a year ago, a number of inconveniences had to be overcome and tests to be made, before the resonators could undergo on-line tests in June this year, prior to their use for beam acceleration.

First of all, their delicate alignment with respect to the beam line (~0.2 mm precision) was complicated by manufacturing errors of the cryostat, which were brought up both at room T and at 77 K (April-September 2003). Then a few months were intensely invested in searching for a cold leak, which was eventually found on one innermost indium sealing (September 2003 – January 2004). At that stage, we had already realized that both mechanical tuners of SRFQ1 were not working at cold temperatures. Aware that an additional disassembly was hence unavoidable later, after fixing the problem, we opted for proceeding anyway with the overall assembly of the cryostat in the linac vault, with a view of addressing then all possibly arising problems in once. Automatic refrigeration with Linde Kr. TCF50 was hence successfully performed on the SRFQ cryostat between February and March 2004. Immediately afterwards, the first on-line testing started, till the beginning of April. Two months were then spent to perfect a significant refurbishing of the slow tuners mechanics (new articulated joints, ball and roller bearings wherever appropriate), to perform their warm and cold off-line tests and to assemble the cryostat once more (see fig.1). June 2004 was then dedicated to prepare the resonators, check the linear response of the slow tuners and eventually investigate the best possible locking conditions, while stepwise approaching with the cryogenic system the conditions of best pressure stability in operation.

Figure 1: Assembly of SRFQ1 and SRFQ2 on the final cryostat.

PREPARATION FOR THE LOCKING TESTS

Following cryostat evacuation, both SRFQs underwent bakeout at 340÷350 K for about 30 h. With the intermediate shields at 77 K, resonant field emission (RFE) was processed at room temperature. After cool-down to 4 K, residual RFE low level processing (up to peak surface fields $E_{s,p}$ = 3.2 MV/m for SRFQ1 and up to $E_{s,p}$ = 6.2 MV/m for SRFQ2) took 8 h and 2.5 h respectively. Both cavities have always shown a very last RFE level at ~ 9 MV/m: to overcome this and to He-process non resonant field emission (FE) took further 2 h and 9 h respectively.

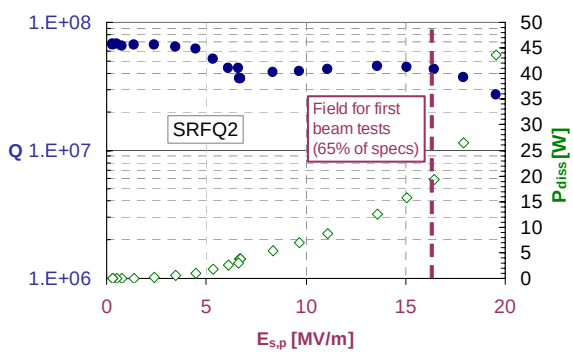

Figure 2: On-line Q-curve of SRFQ2 (Q and P_{diss} are loaded by the VCX, cooled at 77 K)

The on-line Q-curves of the resonators (fig.2 shows the curve of SRFQ2) deserve two comments. First of all, the Q-values are appreciably loaded by the presence of the fast tuner (VCX) loops (refrigerated separately at 77 K). Versus a Q_L~ $7x10^7$, we measured from He gas evaporation a critical Q_0 ~ $5x10^8$, i.e. unaltered with respect to off-line tests. The same holds for SRFQ1. Secondly, since the very first beam test requires only 65% of the design field ($E_{sp,n}$), this was taken in general as a reference value for both FE conditioning and locking tests (this limit was then pushed up to 100% when locking SRFQ1 with the fast tuners, as shown later in this paper).

The four refurbished mechanical tuners were cautiously limited in range by a factor 3 (i.e. the end plates were allowed to be pushed/pulled within ±1 mm with respect to their zero): this allowed windows of ± 10 kHz per tuner. At the beginning of operations tuner A (the first on the beam line) was completely pulled out (+10 kHz), while tuner B was completely pushed in (-10 kHz); as described elsewhere [2], the software slow feedback control system makes tuner A to counteract slow frequency drops and tuner B to counteract slow frequency growths. Since all slow frequency changes are linked to the pressure variations of the liquid He bath outside the resonators, the long term net P change is close to zero: as a consequence the two tuners, which have a similar response, tend to reach the opposite extremes of their setup range more or less simultaneously. When the first of the two reaches its end, the motion of both tuners is inverted. Within the conservative ±1 mm range fixed in the June tests, the inversion of motion, which shall also be handled by the control system shortly, occurred every 5÷12 hours, the time varying in relationship to the pressure history of the relevant period.

For this slow tuning feedback to work, it is essential that the mechanical tuner behaviour is monotonic in the whole range of operation, while some variation in the response slope can be tolerated. This was checked quite carefully on all tuners, by sampling portions of the tuning range (separated by 1000 steps) with a 4 step (~ 0.8 Hz) sensitivity.

LOCKING OF SRFQ1 AND SRFQ2 ON THE BEAM LINE

In order to guarantee a stable beam operation, the natural (unlocked) resonant frequency should not differ by more than a few tens of Hz from the master oscillator reference. To achieve this basic condition, both slow liquid He pressure drifts (seconds) and quick mechanical or electro-mechanical vibrations (a few ms or less) have to be controlled.

Off-line tests had shown [2] that the mechanical tuners were capable to control frequency changes up to ~ 2 Hz/s, corresponding to 2.5÷3 mbar/min pressure change speed in the He tank, consistently with the specifications set for the TCF50 refrigerator. The resonators had also been excited through a powerful frequency swept shaker and a heavy hammer and it was preliminarily concluded that they seemed rather stiff with respect the mechanical vibrations. However, the last word on cavity locking could only be said when both resonators would be mounted on their final common cryostat, in the linac hall and connected to the actual refrigeration system, what eventually happened this time.

In June 2004 the 4 refurbished tuners of SRFQ1 and SRFQ2, which would compensate He pressure changes, were all working reliably. Both resonator controllers housed a vector modulator (CPM) [3], capable to control ±10 Hz by strong overcoupling with a 700 W amplifier, and a VCX fast tuner [4]. The window of the VCX was measured to be 80 [Hz] (SRFQ1) and 210 [Hz] (SRFQ2). It was soon noted, however, that the overcoupling of SRFQ1 was insufficient for reliable locking and hence SRFQ1 was then operated with the VCX only.

On the other hand, during preliminary tests a short was induced on a Pin Diode Switch of the SRFQ2 fast tuner. Despite the procedures to solve this inconvenience in real time had been made promptly available by ANL, manufacturer of the VCXs [5] we opted for cautiously postponing this operation and decided to try locking SRFQ2 with the CPM only.

A software tool combining the slow frequency control through the mechanical tuners (two per cavity, as mentioned above) with fast frequency control (either the CPM or the VCX) was implemented with success.
A total period of about 36 h was devoted to check independent or simultaneous locking of SRFQ1 with the VCX and SRFQ2 with the CPM.

The SRFQ2 resonator could be locked reliably (via slow tuner and CPM) up to 50% of $E_{sp,n}$. At 65% of $E_{sp,n}$ (target value in June), the situation was less stable.

Concerning SRFQ1, locking was fairly stable at 65% of $E_{sp,n}$ (12 h long test). Locking tests at 80% and 100% were also made, for a few hours each. Fig. 3 shows a small fraction of the locking test at 80% $E_{sp,n}$. While the picture samples a period of larger instability with respect to average, it was chosen since it represents an interesting collection of the variety of out-of-lock events observed.

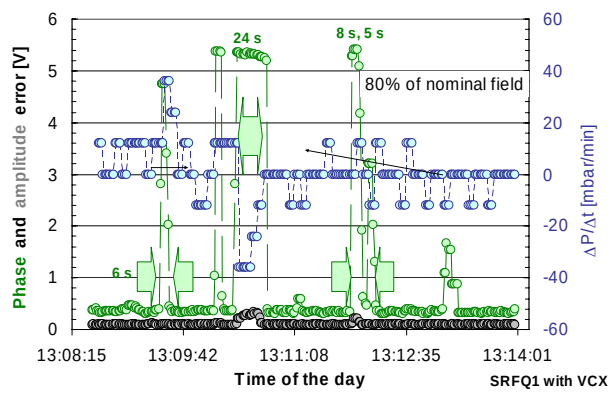

Figure 3: Samples of locking and out-of-lock periods of SRFQ1, with the VCX fast tuner and 80% of the nominal field. Every second, the maximum of $|\Delta\phi|$ and $|\Delta A|$ detected in the last 400 ms is shown on the graph.

As can be seen in fig.3, most out-of-lock events are clearly related to changes of the liquid He bath pressure which are larger than specified, while few are not. Moreover, the 24 s long out-of-lock event in the middle of the graph corresponds to the on/off switching of the TCF50 internal purifier: this is by far the largest kind of pressure change observed during the tests and shall be eliminated in the near future by the cryogenics experts. In all cases, locking can get lost for periods of 5÷10 s at most, every one or more minutes. It remains to be assessed whether this can be an acceptable operating condition for initial beam tests.

As far as slow He pressure variations in general are concerned, the following comments can be made. After good systematic work of the cryogenics engineers, conditions were found where the pressure change could be kept within ±5 mbar/min for periods of hours. The threshold on the rate of pressure fluctuations that can be safely compensated by the mechanical tuner seems to be ~ 5 mbar/min. The large frequency window given to SRFQ1 by the VCX offers an additional margin (the threshold moves from ~5 to ~10 mbar/min) for those cases in which a slow variation of such rate does not last longer than a few seconds. This is another reason, why we find it compulsory to use the VCX fast tuner with SRFQ2 too, in the near future.

Additional systematic work is required on the cryogenic system to further improve conditions, which are already reasonably satisfactory.

ELECTRO-MECHANICAL VIBRATIONS

Noting that some out-of-lock events were "not" related to sharp He pressure fluctuations, preliminary mechanical spectra were taken. Accelerometers were placed outside the cryostat on the bars which directly hold the SRFQs through their liquid He tanks. They were hence rather sensitive to cavity vibrations, despite being rather far and at room T. Accelerometers placed on the pumping system of the cryostat excluded, incidentally, any influence of the latter on the cavity vibration spectrum.

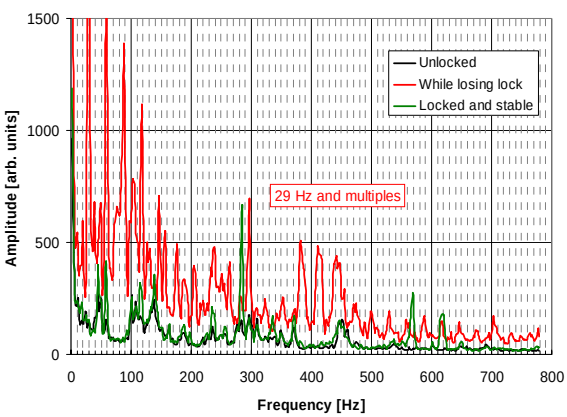

Figure 4: Spectra were taken on the suspension bar of SRFQ2 in three conditions: out-of-lock cavity (black line); stable locked cavity (green line); transition period during which the cavity is losing lock (red line).

Fig. 4 compares the spectra of unlocked and locked resonators with the spectrum measured in the time span while the cavity is losing lock and the feedback control system is trying to compensate for the significant phase and amplitude errors which are increasingly high. The out-of-lock resonator is the most stable. On the contrary, the transition from the lock to out-of-lock conditions triggers a well reproducible spectrum of a 29 [Hz] fundamental frequency and all its multiples, which tends to hinder the previous spectrum. The green curve (fairly stably locked resonator) is an interesting combination of the modes of the other two graphs, particularly below 250 Hz where the vibration energy is higher.

A possible explanation of fig.4 is that the action of locking (or losing lock) triggers an electro-mechanical vibration of the resonator itself, which is strong enough to be clearly detected outside the cryostat.

This might also explain why, on a relevant fraction of cases during the June tests (around 30%), the action of locking SRFQ2 drove the previously VCX-locked SRFQ1 out of lock (mechanical shaking transmitted through the cryostat).

These experimental investigations deserve to be conducted more systematically in the near future.

CONCLUSION

The experience of the latest tests (VCX working only on SRFQ1), described in this paper, has shown that the SRFQs are already in the condition to accelerate beam at more than 50% of the nominal peak surface field $E_{sp,n}$ (which is 25.5 MV/m).

Operation of the VCX on SRFQ2 and possible broadening of the SRFQ1 VCX window (from 80 to the design 200 [Hz]) should soon make it possible to work reliably at 65% $E_{sp,n}$, reducing number and length of out-of-lock events.

Further work on the TCF50 refrigerator parameters is expected to reduce to a minimum those out-of-lock events which are related to fluctuations of the liquid He pressure. We shall continue to work, so as to reach reliable locking at 100% $E_{sp,n}$.

ACKNOWLEDGMENT

The skilful contribution of E. Bissiato, D. Conventi, S. Marigo and F. Stivanello was essential in the mechanical upgrades of the resonators and the on-line cryostat.

REFERENCES

[1] A. Lombardi et al., Proc. of the 1999 PAC, New York, USA, 1324

[2] G. Bisoffi et al., "Results on INFN-LNL Niobium RFQ Resonators", 11th Workshop on RF Superconductivity,Travemünde (D),Sept. 2003,in print

[3] G. Bassato et al., NI&M A238 (1993) 195-198

[4] V. Andreev et al., Proc. of EPAC2000, Vienna, Austria, June 2000, 2013

[5] G. Zinkann (Argonne Nat. Laboratory), p.c.

Construction of a 161 MHz, β=0.16 Superconducting Quarter Wave Resonator with Steering Correction for RIA

A. Facco, INFN/LNL, Legnaro, Padova
C. Compton, T.L. Grimm, W. Hartung, F. Marti, R.C. York, NSCL, East Lansing, Michigan
V. Zvyagintsev, TRIUMF, Vancouver

Abstract

We have built a 161 MHz, β=0.16 superconducting Quarter Wave Resonator with steering correction for the low beta section of RIA. This bulk niobium, double wall cavity, compatible with both separate vacuum between beam line and cryostats or unified one, was designed in collaboration between MSU-NSCL and LNL. The design is suitable for extension to other frequencies, e.g. to obtain the 80 MHz, β=0.085 cavity required in RIA. The shaped drift tube allows correction of the residual QWR steering that can cause emittance growth especially in light ions; this could make this resonator a good alternative to Half-Wave resonators in high intensity proton-deuteron linacs, like the SPES injector project at LNL. First test results will be presented.

NO SUBMISSION RECEIVED

HIGH BETA CAVITY OPTIMIZATION FOR ISAC-II

R.E. Laxdal and V. Zvyagintsev, TRIUMF, Vancouver, Canada
Z.H. Peng, CIAE, China Institute of Atomic Energy, Beijing, China

Abstract

The linac for ISAC-II comprises twenty cavities of medium β quarter wave cavities now in the production phase. A second stage will see the installation of ~ 20 MV of high β quarter wave cavities. The cavity structure choice depends on the efficiency of operation, cost, stability, beam dynamics and schedule. Two main cavity types are considered; a low frequency 106 MHz option and a high frequency 141 MHz cavity. We compare and contrast the cavity choices.

INTRODUCTION

TRIUMF is now constructing an extension to the ISAC facility, ISAC-II, [1], to permit acceleration of radioactive ion beams up to energies of at least 6.5 MeV/u for masses up to 150. Central to the upgrade is the installation of a heavy ion superconducting linac designed to accelerate ions of $A/q \leq 7$ to the final energy. The superconducting linac is composed of two-gap, bulk niobium, quarter wave rf cavities, for acceleration, and superconducting solenoids, for periodic transverse focussing, housed in several cryomodules. The cryomodules are grouped into low, medium and high beta sections corresponding to cavities with optimum velocities of $\beta_o = 4.2\%$, $\beta_o = 5.8, 7.1\%$ and $\beta_o = 10.4\%$ respectively.

Due to experimental pressure and budget limitations the installation of the linac has been grouped into three stages highlighted in Fig. 1. The initial Stage 0 to be completed in 2005 includes the installation of a transfer line from the ISAC DTL ($E = 1.5$ MeV/u) and the medium beta section to produce 18 MV of accelerating voltage for initial experiments. Stage 1 to be completed two years later includes the installation of the three high beta modules for a further 18 MV. The ISAC-II accelerator final Stage 2 is foreseen for 2010. The twenty medium beta cavities are installed four per cryomodule in a total of five modules now in production. The design effort on the high beta section is now intensifying.

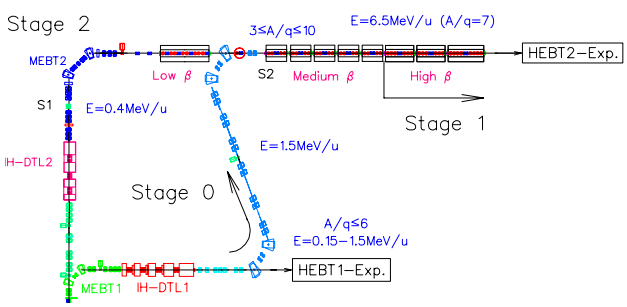

Figure 1: Stages 0, 1 and 2 for the ISAC-II upgrade.

CAVITY VARIANTS

Three cavity variants are considered and shown in Fig. 2. The benchmark cavity, (a) *round141*, has identical transverse dimensions to the medium beta cavity[2] but is designed as a 141 MHz cavity by shortening the overall length and adjusting the gap. In a second variant, (c) *round106*, the cavity frequency is kept at 106 MHz but the cavity transverse dimensions are scaled to increase the beta from 7.1% to 10.4%. The quadrupole asymmetry in the accelerating fields [3] is somewhat larger in the high frequency case by virtue of the smaller inner conductor. A third variant, (b)*flat141*, is also considered where the 141 MHz cavity inner conductor is flattened near the beam ports to produce a smaller quadrupole asymmetry. This variant has a lower optimum beta, 9%, suitable for use in the beginning of the high beta section.

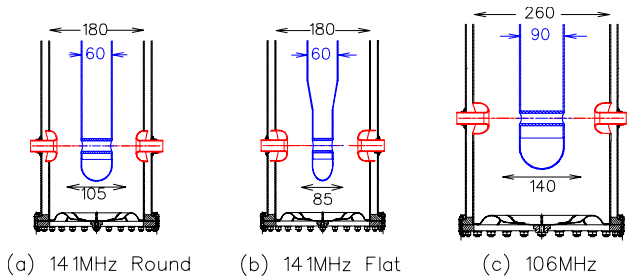

Figure 2: Three cavity variants considered in the study.

BEAM DYNAMICS

The field asymmetries from the three models are summarized in Fig. 3 over the operating velocity range required of the cavity for an accelerating gradient of 6 MV/m, an ion of $A/q = 3$, and a phase of $\phi_s = -30°$. Shown are the corrected vertical steering components and the vertical and horizontal defocussing perturbations for a 1 mm displacement from the electrical axis. The dipole steering components can be reduced to less than 0.1 mrad over the whole velocity range, for even the lightest beams, by shifting the cavities down by 1.3,1.0 and 2 mm respectively for the *round141*, *flat141* and *round106* cases with respect to the beam and solenoid axis. In particular the beam port position with respect to the inner conductor tip is varied to reduce the required shift and minimize the steering effect.

Linac Variants

The beam dynamics of the three cavity types are studied in three linac variants. The benchmark variant consists of twenty 141 MHz high beta cavities divided into two modules of six cavities and one module of eight cavities with one solenoid in each module. In a second vari-

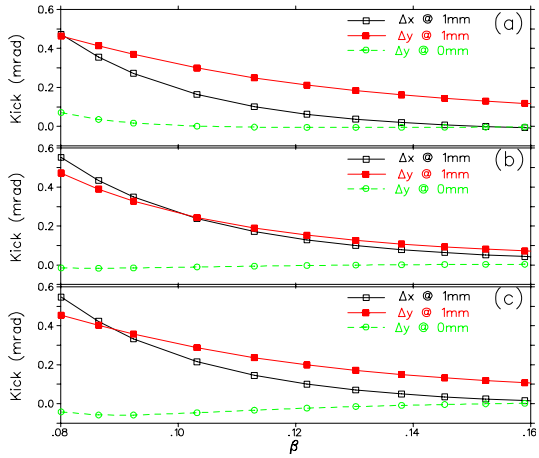

Figure 3: Focussing and steering perturbations for the three cavity geometries (a) *round141* (b) *flat141* (c) *round106* as calculated in LANA based on HFSS fields. Shown are the corrected vertical steering components (dashed lines) and the vertical and horizontal defocussing perturbations for a 1 mm displacement from the electrical axis.

ant the six cavities in the first high beta module are replaced with the flat 141 MHz cavities to reduce the impact of the quadrupole asymmetry. In the last variant fourteen 106 MHz cavities are used divided into two modules of four cavities and one module of six cavities. A plot of accelerator efficiency as a function of particle A/q values is given in Fig. 4. All variants give an overall efficiency of 80% for light ions and 90% for heavy ions as compared to the optimum efficiency (accelerating always at β_o).

A summary of the beam dynamics calculations for the Stage 1 linac using the three linac variants is given in Fig. 5 and Fig. 6. Given are the transverse beam envelopes and the beam centroids. In each case a single charge state beam with intial emittance of 1.8πmm-mr and 12πkeV/u-ns (ten times the expected emittances) is simulated. The large beam is used to characterise differences in the effective dynamic aperture of the three variants. Also shown

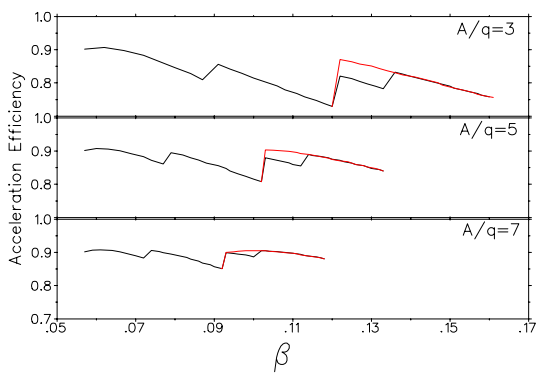

Figure 4: The acceleration efficiency for various A/q values for the Stage 1 linac for the benchmark case and for the first six high beta cavities replaced by the *flat141* cavity.

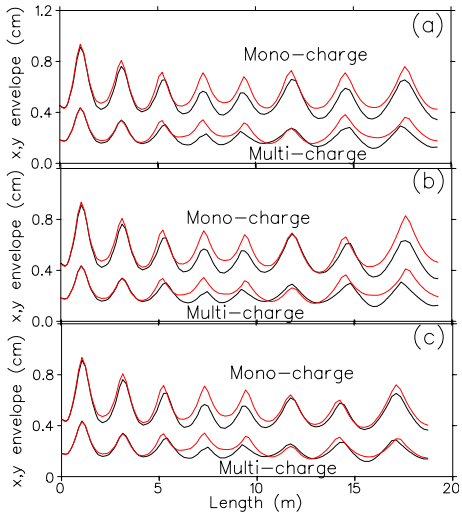

Figure 5: The transverse beam envelopes as a function of longitudinal position along the medium and high beta sections for (a) *round141* (b) *flat141*/*round141* variant (c) *round106* variant. In each case a single charge state beam with initial emittance of 1.8πmm-mr and 12πkeV/u-ns (ten times the expected emittances) is simulated. Also shown is a multi-charge beam ($\Delta Q/Q = \pm 5\%$) with initial emittances of 0.3πmm-mr and 2.πkeV/u-ns.

are results for a multi-charge beam with initial emittances of 0.3πmm-mr and 2.πkeV/u-ns. The reduced quadrupole asymmetry in the *round106* cavity results in less asymmetry in the transverse envelope compared to the other two 141 MHz variants. However the transverse and longitudinal emittance growth for the three cases are virtually identical. The beam centroid shifts are tolerably small in all cases.

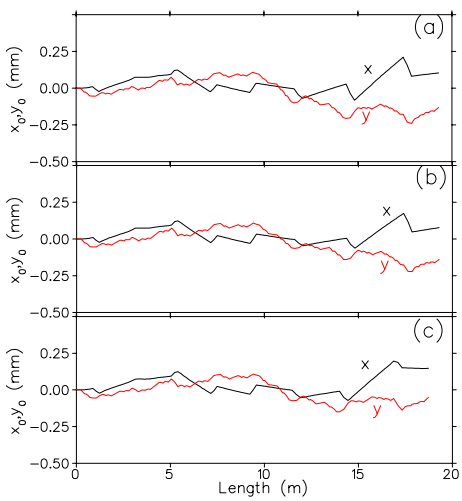

Figure 6: The transverse beam centroids as a function of longitudinal position along the medium and high beta sections for (a) *round141* (b) *flat141*/*round141* variant (c) *round106* variant.

RF CHARACTERISTICS

The rf paramters of the three cavity variants are given in Table 1. The cavity rf properties are simulated in HFSS.

Table 1: Parameters of cavity variants

Parameter	*round141*	*flat141*	*round106*
f (MHz)	141.4	141.4	106.1
β_o	0.104	0.09	0.103
TTF_o	0.089	0.086	0.093
bore (mm)	20	20	20
gap (mm)	45	45	50
drift tube (mm)	60	40	90
L_{eff} (mm)	180	180	260
Height (mm)	577	577	737
Δy (mm)	1.3	1.0	2.0
f_{mech} (Hz)	150	150	134
E_a (MV/m)	6	6	6
V (MV)@6MV/m	1.08	1.08	1.56
E_p/E_a	4.7	5.6	4.6
B_p/E_a(mT/MV/m)	10.3	10.5	9.9
U/E_a^2(J/(MV/m)^2)	0.073	0.078	0.194
$R_sQ_0(\Omega)$	24.8	24.9	26.8
$R_{sh}/Q(\Omega$	499	470	521

We compare all cavities at a gradient of 6 MV/m calculated over the cavity length defined as the inside diameter of the outer rf surface. There is little difference between the two 141 MHz variants except for the higher peak surface field in the *flat141* variant. Instead we concentrate here on the comparison of the *round141* and the *round106* variants. Due to the increased voltage the main practical difference is that fewer sub-systems (14 as compared to 20) would be required for the lower frequency. However due to the higher stored energy and somewhat higher Q_0 (see below) more power is required to provide a sufficient tuning bandwidth.

Let us examine the role of rf frequency in cavity scaling. The surface resistance is given by

$$R_s = R_{BCS} + R_{mag} + R_0$$

where

$$R_{BCS} = 2 \times 10^{-4} \frac{1}{T} (\frac{f}{1.5})^2 e^{-17.7/T}$$

and

$$R_{mag} = 0.3 n\Omega \cdot H_{ext}(mOe)\sqrt{f(GHz)}$$

Results of these expressions are shown in Table 2 assuming a magnetic field attenuation factor of five from the earth's field. The TRIUMF medium beta cavity has a typical Q of 1.5×10^9 at low field that droops to 5×10^8 at a gradient of 6 MV/m. Since $R_sQ = 19\Omega$ for this cavity this corresponds to surface resistance values of 12.7 and 38.2 nΩ. Assuming R_0 is independent of frequency we can estimate that the high-field surface resistance for the 141 MHz cavity is enhanced due to the increased values of R_{BCS} and R_{mag} to be 42.5 nΩ an increase of 11%. Using these values of R_s and the tablulated values of R_sQ_o gives expected Q_0 values of 5.8×10^8 and 7×10^8 respectively for the *round141* and *round106* cavity respectively. The cavity power dissipation, $P_{cav} = \omega_o U/Q_0$, is listed in Table2.

Table 2: Frequency dependence of surface resistance and cavity power

f (MHz)	106	141
R_{BCS}(nΩ)	3.5	6.3
R_{mag}(nΩ)	9.8	11.3
R_0(nΩ)	25	25
R_s(nΩ)	38.2	42.5
Q_0@6MV/m	7×10^8	5.8×10^8
P_{cav}(W)@6MV/m	6.7	4.2
β	280	230
P_{amp}(W)@6MV/m	1200	620

The increased quality factor of the 106 MHz cavity increases the amount of overcoupling required to achieve a specified rf bandwidth (in our case $\Delta f/f = 4 \times 10^{-7}$). The forward power can be calculated from the coupling factor, β, and the cavity power using $P_f = P_{cav} * (\beta + 1)^2/(4\beta)$. To provide for the bandwidth the peak amplifier power must be sufficent to deliver twice the required forward power after considering the line losses. These deliberations lead us to estimating that the required amplifier would be almost a factor of two larger in the 106 MHz case.

CONCLUSION

There is no strong beam dynamics argument to choose one variant over another. The total dissipated cavity power is 17% less in the high frequency cavity and the total amplifier power is 29% less. The high frequency cavity is also somewhat more mechanically stable. These advantages are not sufficient to force a cavity choice. The two most compelling arguments are that the design time for the 141 MHz cavity and ancillaries will be significantly less. This is balanced somewhat by the attractiveness of reducing the number of sub-systems by adopting the lower frequency. The final choice will be based on a review of the schedule and cash flow.

ACKNOWLEDGEMENT

The authors would like to thank R. Eichhorn for useful discussions and D. Gorelov for help with LANA.

REFERENCES

[1] P. Schmor, et al, "Development and Future Plans at ISAC", this conference.

[2] A. Facco, et al, "The Superconducting Medium β Prototype for Radioactive Beam Acceleration at TRIUMF", PAC2001, Chicago, June 2001.

[3] M. Pasini, *et al, Beam Dynamics Studies on the ISAC-II Post Accelerator at TRIUMF*, EPAC2002, Paris.

ENGINEERING AND CRYOGENIC TESTING OF THE ISAC-II MEDIUM BETA CRYOMODULE

G. Stanford, Y. Bylinsky, R.E. Laxdal, W. Rawnsley, T. Ries and I. Sekachev,
TRIUMF, 4004 Wesbrook Mall, Vancouver, BC, Canada, V6T 2A3

Abstract

The medium beta section of the ISAC-II Heavy Ion Accelerator consists of five cryomodules each containing four quarter wave bulk niobium resonators and one superconducting solenoid. A prototype cryomodule has been designed and assembled at TRIUMF. This paper describes the system engineering, alignment procedures and test results.

INTRODUCTION

The ISAC-II[1], superconducting linac is composed of two-gap, bulk niobium, quarter wave RF cavities, for acceleration, and superconducting solenoids (9 T), for periodic transverse focusing, housed in several cryomodules and grouped into low, medium and high-beta sections. Each cryomodule has a single vacuum system for thermo-isolation and beam. This demands extreme cleanliness of internal components and precludes the use of volatile lubricants or flux as well as particulate generators to avoid superconducting surface contamination. An initial stage to be completed in 2005 includes the installation of the medium-beta section consisting of five cryomodules. An initial cryomodule[2] has been designed and assembled at TRIUMF.

CRYOMODULE ENGINEERING

The stainless steel vacuum tank has dimensions $\sim 2 \times 2 \times 1$m. The superconducting elements are supported on a beam that is suspended from the lid by struts (Fig. 1). The struts are slung from three support points, two upstream and one downstream, that are laterally and vertically adjustable. There is an independently mounted liquid helium reservoir (120ℓ inventory) suspended from the lid attached to the superconducting elements by soft bellows. Except for the niobium cavities the cold mass is predominantly made from 316L stainless steel. The efficiency of cooldown is improved by a manifold and distribution system 'spider', connected to the LHe transfer line, that delivers cold gas and liquid to the bottom of each element through 5 mm Cu tubing. Once the liquid begins to collect in the reservoir a pre-cool valve on the distribution manifold is opened and LHe flows directly into the reservoir.

The entire cold mass is surrounded by a forced flow, liquid nitrogen cooled, thermal shield. The shield consists of several Cu panels riveted together to form a box with 10 mm ID Cu tubing soldered to the panels to form a serial LN2 circuit. After soldering the panels are nickel plated to improve emissivity. A μ-metal magnetic shield, consisting of 1 mm Conetic panels is attached to the inside of the vacuum tank outside the LN2 shield. A single LN2 panel

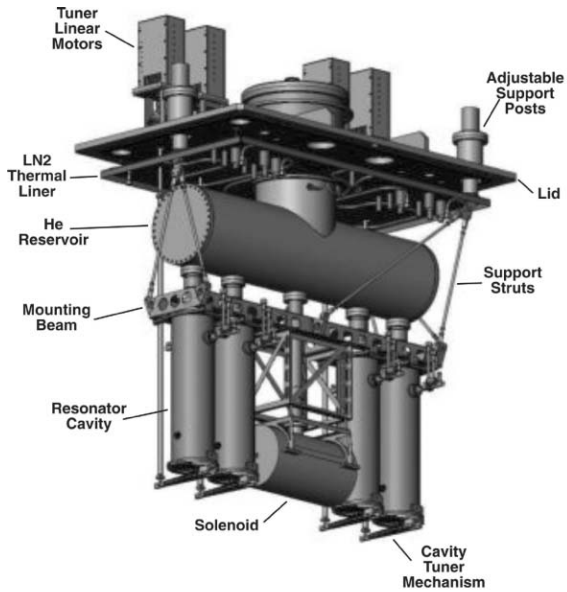

Figure 1: Cryomodule top plate assembly.

and μ-metal shield suspended from the lid make up the top thermal and magnetic enclosure respectively.

Alignment During Assembly and Installation

An assembly stand (Fig.2) is used to assemble the tank internals to the lid. The stand mimics the vacuum tank and uses the same lid location dowel arrangement. The line of sight (LOS) location of the beam and wire position monitor (WPM) ports on the tank are transferred to the adjustable end plates on the assembly stand via a transfer fixture and optical telescope. The tank internals are aligned with respect to the LOS using optical targets in the beam ports. The WPM alignment monitors are aligned with respect to the line of wire (LOW) also with optical targets.

The WPM system[3] provides an off-axis measure of the cavity and solenoid positions during cooldown. The monitors, each consisting of four striplines, are attached to the cavities and solenoid by brackets that position them 0.31 m horizontally from the beam axis. A wire running parallel to the beam axis and through the monitors carries an rf signal that is measured by the striplines and is converted to an x-y position. The cryomodule tank is also outfitted with a pair of optical windows and alignment targets to set up and monitor an external optical reference line with a telescope. Optical targets are installed in each cavity and in the upstream and downstream ends of the solenoid. Optical measurements, taken periodically, serve to check for

Figure 2: Top plate assembly in assembly stand.

unexpected differences between the WPM position and the position of the cold mass. During cooldown they provide a calibration of the thermal contraction of the WPM brackets.

The solenoid is required to be centered on the beam axis while the cavities are aligned on the horizontal axis but 750μm below the vertical beam axis. The required alignment tolerance is $\pm$400μm and $\pm$200μm for the cavities and solenoid respectively. Once the internal alignment is complete the cryomodule is installed in the accelerator vault and the beam ports are aligned to the theoretical beam centerline. Three target posts on the lid can be characterized in space relative to building benchmarks such that, in future, when the accelerator is operational, a cryomodule can be removed and reinstalled to the same position.

CRYOMODULE COMMISSIONING

The cryomodule assembly and commissioning tests are conducted in the clean laboratory area in the new ISAC-II building. LN2 for shield cooling is fed from a transfer line coming from an external tank. Helium is presently fed from local dewars (plans are underway to add a transfer line from the soon to be installed LHe refrigerator). Exhaust gases from the cryomodule are passed through vaporizers and the flow is monitored by gas meters. A local computer records WPM information. Control and data acquisition are done with an EPICS control system.

Warm measurements

To accurately predict final cold mass position it is necessary to measure the effect or repeatability of initial lid positioning, vacuum pumpdown, helium space pressure and thermal contraction. Lid positioning studies involve loosening the top bolts, lifting the lid off the o-ring, repositioning the lid and torquing the lid bolts. For five cycles the vertical measurements repeat within $\pm$20μm. The horizontal position skewed after the first cycle but repeated within $\pm$75μm thereafter hence the location of the lid to the tank via the dowel pair is adequate. It is assumed that built in stresses were relieved during the first cycle. During repeated vacuum pumpdowns the position of the WPM's in both horizontal and vertical planes was repeatable to within $\pm$20μm.

Cold Measurements

The cryomodule has undergone two cold tests. The first established the cryogenic and alignment performance and the second characterized the rf and solenoid performance as well as checking the accuracy of alignment shimming. The initial test includes three temperature cycles from room temperature to LN2 temperature and one cooldown to helium temperature. The second test includes one helium and one LN2 cycle.

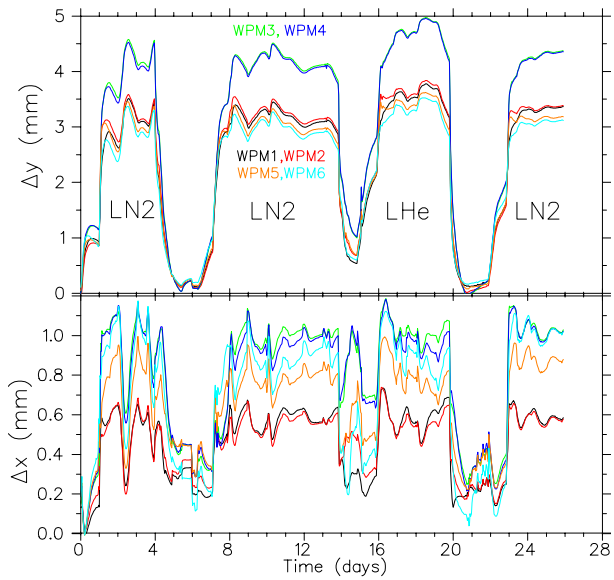

Figure 3: Vertical and horizontal wpm positions for three LN2 cycles and one LHe cycle.

Alignment: The main goal is to determine the repeatability of the cooldown process and to establish offset values for each cavity and the solenoid to enable warm positioning compatible with alignment at cold temperatures. Vertical and horizontal wpm positions are given in Fig. 3 for the four thermal cycles during the first cold test. Due to the different materials involved the solenoid experiences more vertical contraction, with $\sim$4.4 mm at LN2 and $\sim$5 mm at LHe temperatures while the cavities contracted $\sim$3.3 mm at LN2 and $\sim$3.8 mm at LHe temperatures. In the horizontal direction there is a 0.45 mm difference between the movement of WPM1 and WPM6, evidence that the cavity support beam is yawing laterally during cooldown. A change of pressure in the helium space inflates the bellows resulting in a net force on the cavity support frame yielding a measured deflection of 30μm/100Torr pressure variation. The same pressure variation also causes a side load on the support frame skewing the frame by 10μm/100Torr.

The position of the cold mass is analyzed at three cold LN2 temperatures. The differences in position between cycle 2 and cycle 1 and 3 are summarized in Fig. 4. The positions are repeatable to within $\pm 50\mu$m vertically and $\pm 100\mu$m horizontally. The horizontal position of the downstream end is found to be less stable than the upstream end since the two main struts at the downstream end are slung from the same support tower while in the upstream end the two main struts are slung from separate towers.

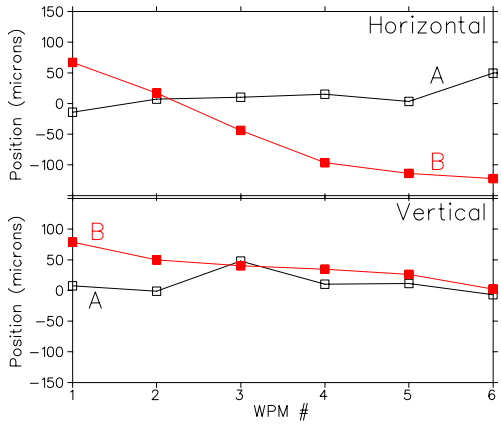

Figure 4: Relative WPM positions for three LN2 cooldown cycles.

The cryomodule is warmed, opened and the elements adjusted to the warm offset position established during the initial cold test. Alignment correction is achieved horizontally via threaded adjusters and vertically by the machining of support shims. The tank is then reassembled, recooled and the alignment checked with both WPM and optical targets. The solenoid is warm aligned on the LOS and during cooldown the adjusters on the three external support posts are used to position the cold solenoid back on the LOS. The warm off-set position and final cold position with respect to the specified positions of the six optical targets are given in Fig. 5. The final position in the vertical plane is within $\pm 150\mu$m. However, a temperature dependent skew in the horizontal position of the solenoid was noted during the cooldown. The surprising result is that the skew is not apparent in the WPM data leading us to believe that the solenoid bore tube is somehow warping during cooldown. This result was also observed during a second LN2 thermal cycle. Further investigations are required.

Cryogenic tests: During the commissioning tests the cold mass is pre-cooled with LN2. The helium space is pumped and purged prior to helium transfer. During helium transfer the distribution 'spider' effectively distributes the helium to the bottom of all cold masses. Due to the difference in mass and geometry the cavities cool at a rate of 70°K/hr while the solenoid cools at 20°K/hr for a transfer rate of $\sim 80\ell$/hr. We are presently designing a new three position manifold valve that can force cold gas preferentially to the solenoid.

In the first test the final static load on the helium, after

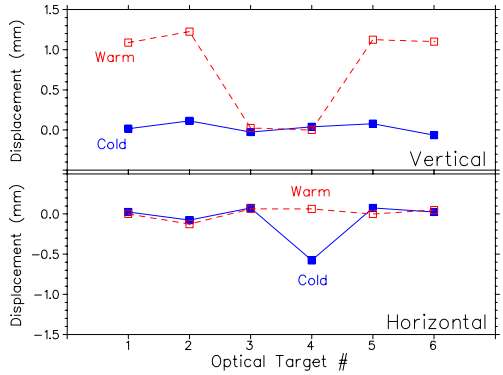

Figure 5: Measured positions of the six optical targets relative to their specified positions for warm and cold conditions.

thermalization, as measured from the gas boil-off is 11 W. In the second test after adding rf cables, tuner actuators and solenoid leads the static load rose to 16 W. This can be compared to the design estimate of 13 W. Removal of the wpm cabling will reduce the static load. However we are presently reviewing the equipment added during the second test with the aim to further reduce the final load. The LN2 flow required to keep the side shield less than 100°K is measured to be $\sim 5\ell$/hr matching design estimates.

Mechanical studies:The characterization of the mechanical modes is useful to diagnose the source of spectral noise in the rf error signal during rf cold tests. The mechanical modes of the cryomodule assembly are measured in two ways. In the first an accelerometer is attached to a cavity to measure transvere motion. Various parts of the assembly are struck with an impulse and the induced signal is passed to a spectrum analyzer. In the second the raw wpm signal is passed to the spectrum analyzer and the assembly is excited by stepping a mechanical tuner[4] attached to the bottom of one of the cavities through a long actuator rod. The studies give similar results except that the wpm signal also contains the wire resonant frequency of 43 Hz. Simulations predict the lowest frequency mechanical mode of the cryomodule assembly to be 14.3 Hz. Measurements do confirm the mode at 14 Hz but also clearly show a mode at 6 Hz. It is thought that the lower mode is due to a small backlash in the support strut spherical joint couplings that 'loosen' the mechanical system.

REFERENCES

[1] P. Schmor, "Development and Future Plans at ISAC/TRIUMF", this conference.

[2] G. Stanford, et al, "Design of the Medium Beta Cryomodule for the ISAC-II Superconducting Heavy Ion Linac", Proceedings of the CEC-ICMC2003, Sept. 2003, Anchorage.

[3] W. Rawnsley, et al, "A Wire Position Monitor System for the ISAC-II Cryomodule Components Alignment", this conference.

[4] R.E. Laxdal, et al, "Cold Test Results of the ISAC-II Medium Beta High Gradient Cryomodule", this conference.

PROGRESS IN THE DEVELOPMENT OF THE TOP LINAC

L. Picardi, C. Ronsivalle, ENEA, Frascati (Rome), Italy, S. Frullani, ISS, Rome, Italy

Abstract

The TOP Linac (Oncological Therapy with Protons), under development by ENEA and ISS is a sequence of three pulsed (5 μsec, 300 Hz) linear accelerators: a 7 MeV, 425 MHz RFQ+DTL (AccSys Model PL-7), a 7-65 MeV, 2998 MHz Side Coupled Drift Tube Linac (SCDTL) and a 65-200 MeV, variable energy 2998 MHz Side Coupled Linac (SCL). The first SCDTL module is composed by 11 DTL tanks coupled by 10 side cavities. The tanks has modified to overcome vacuum leakage that occurred during brazing, and now the module has been completed, and is about to be ready to be tested with protons. The 7 MeV injector will be installed in September at the ENEA Frascati laboratories for preliminary test, before being transferred to a large oncologycal hospital in Rome (Istituto Regina Elena or Ospedale S. Andrea).

INTRODUCTION

Protontherapy is nowadays a reality in the oncologycal radiotherapy and several accelerators are being developed worldwide for this application, but they are mainly cyclotrons and synchrotrons while the accelerator described in this paper is the only linac. The reasons why walking this unusual road are: the modularity of the construction, as the linac can be expanded in at least 3 steps, each of them able to be operated for a specific task, the compactness, as the linac extends in the area used by beam transport lines in other types of machine, and the flexibility, as a fully 3D scanning irradiation with energy, current and position variable on a pulse-to pulse basis is possible.

Moreover, the use of 3 GHz accelerating structures in a large part of the machine makes the use of the facility closer to the electron conventional radiotherapy accelerators as to time structure, maintenance and dosimetry.

The TOP (Terapia Oncologica con Protoni) Linac [1] is a proton medical linac designed to produce at least the following beams (fig. 1):

- a 7 MeV, 700 W beam for F-18 radioisotope production;
- a 65 MeV, 10nA (average) beam for proton eye therapy;
- a 100-200 MeV, 10 nA (average) beam for deep seated tumours proton therapy.

The linac is composed of a 7 MeV 425 MHz injector, a 7-65 MeV 3 GHz linac booster, named SCDTL (Side Copled Drift Tube Linac) from the accelerating structure name, a second 65-200 MeV 3 GHz linac booster named SCL, and the various beam lines to the application rooms. The time structure is pulsed with typical hundreds of Hz rep rate and a few μs pulses. The fully 3-D scanning irradiation of deep seated tumours requires a beam whose position, energy and pulse charge can be varied on a pulse-to pulse basis, that is energy between 130 and 200 MeV, pulse current between 0.1 and 10 μA (a factor 100) and pulse duration between 1 and 5 μs pulses at 100-250 Hz repetition frequency.

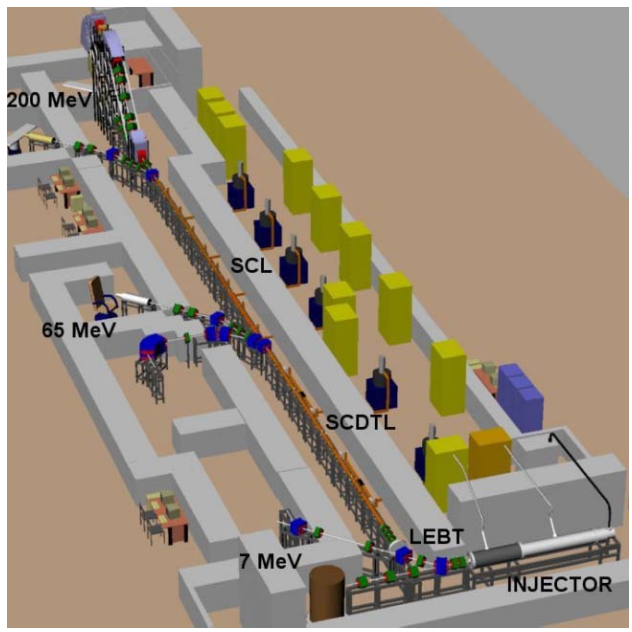

Figure 1: TOP Linac design layout.

The design [2] was developed by ENEA in collaboration with CERN, INFN and TERA and it was approved by ISS (National Institute of Health) and funded in 1997 but only with about 4.5 M€ against the 22 M€ estimated for the high technology devices of the facility. Despite this, construction started within a cooperation agreement between ENEA and ISS and installation was agreed to be done in Rome at a large Oncologycal Hospital. Up to now unfortunately no additional funding has been available so that work is carried on at ENEA Frascati laboratories, where a proper temporary site was set up for the first machine tests, up to 20 MeV. Interest for the installation has been evidenced by S. Andrea Hospital in Rome.

THE 7 MEV LINAC INJECTOR

The injector linac was bought from AccSys Inc., USA. It is a PL-7 model modified to meet the TOP requirements [3]. It is actually installed in a test bunker at Frascati and scheduled to be put in operation in September. It will be used for three main purposes: Fluorine-18 production (F-Mode, high current), Protontherapy beam injection and radiobiology experiments (P-mode, low current). In the high-current mode the pulse current will be 8 mA for 60 μs and 60-100 Hz rep. rate. In the low-current mode the pulse current

will be variable between 1 and 30 μA for 7 μs and up to 250 Hz rep. rate.

The injector linac is composed of a pulsed 30 keV duoplasmatron proton source a 3 MeV RFQ and a 4 MeV DTL. The total length is 4.6 m. The source is followed by a single einzel lens and a water-cooled current limiting aperture that can be inserted by remote control to reduce the linac current by a factor of 100 for operation in the proton therapy mode. The two main 425 MHz RF amplifiers, one for RFQ and the other for DTL are based on a parallel arrangement of twelve EIMAC YU176 tubes. The injector was successfully tested at factory [4]. In protontherapy mode up to 300 Hz (maximum flat top pulse length of 2 μs), and steadily at 250 Hz with flat top of 7 μs. It is possible to vary the pulse current by a factor more than 100 acting on the ion source arc voltage, gas pressure and magnet current, on the Einzel lens voltage combined with the limiting aperture. Another factor of 4-5 can be obtained by an appropriate phasing of injection line cavities.

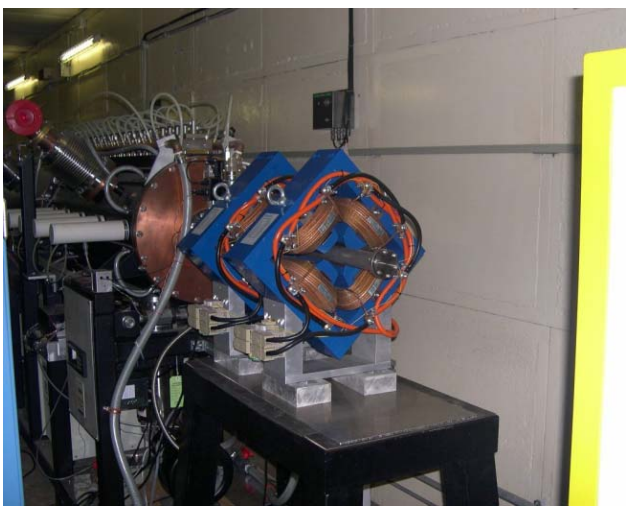

Figure 2: PL-7 Injector linac at CR Frascati.

As to the F-mode, numerous radioisotope production tests at 7 MeV confirmed the possibility of F-18 production rate of about 1 Ci for 2 h irradiation time. In the test arrangement at CR Frascati (fig.2) in a 1-m wall thickness bunker, a couple of quadrupoles has been installed to size the beam on F-18 target, which will be placed inside a polyethylene-lead beam dump.

7 MEV LEBT

In the reference layout of the TOP linac (fig. 1), after the 7 MeV injector 2 quadrupoles are placed, and then the high current beam can go straight to the radioisotope production (shaped by using other quadrupoles and eventually octupoles to flatten the beam distribution on target) while the low current beam is transferred, through the LEBT to the following accelerating sections. The LEBT is composed by a 90° achromatic bend system to preserve the horizontal emittance, and a sequence of two RF cavities and four quadrupoles to adapt the total beam phase space to the SCDTL acceptance. The longitudinal matching is obtained by allowing the bunch to lengthen to much more than one 2998 MHz RF period, under the velocity spread, and then by using two RF cavities, the first (425 MHz, 65 KV) reducing the beam energy spread and the second (2998 MHz, 16 KV) for re-bunching at 2998 MHz to increase the beam capture in the SCDTL. An aluminium model of the 425 MHz cavity, has been built. The 3 GHz prebuncher has been realized (fig. 3).

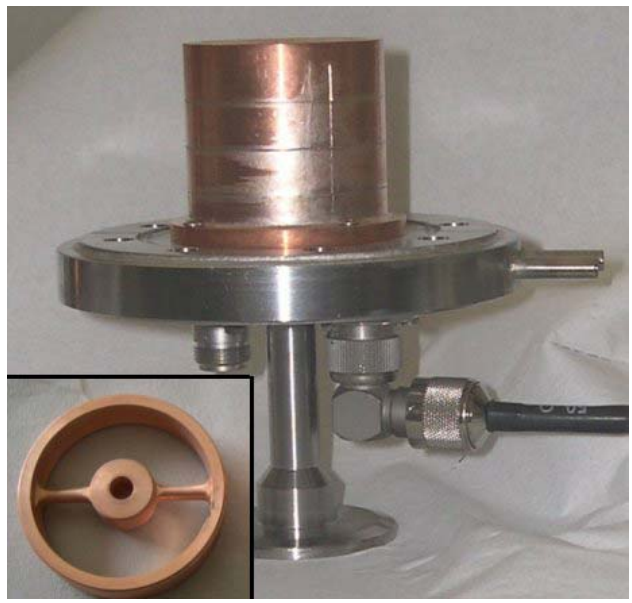

Figure 3: 3GHz prebunching cavity. In the frame the drift tube-stem. Cooling is achieved by contact with CF flange.

It is a three-gap cavity with slanted noses drift tubes each supported by a couple of 4 mm diameter stems. It is bolted to a cooled CF flange where also the connectors to RF input and pick-up loops are placed. The geometry is a compromise between efficiency due to transit time factor (larger gaps) and multipactoring suppression (shorter gaps) at the given voltage. In fig. 4 the measured field on axis is shown. The Superfish Qo value increased, as usual by 25% is 5500. First measurements indicate a similar value. In this condition, 20 kV require 750 W of RF power.

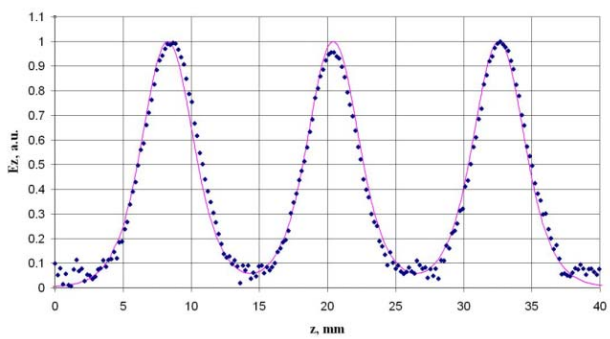

Figure 4: 3GHz prebunching cavity field on the axis: dots are measurements, continuous line is Superfish output.

SCDTL 7-65 MEV

The Intermediate energy (7-65 MeV) part of the TOP Linac is a 3 GHz linac booster bases on the SCDTL (Side Coupled Drift Tube Linac) accelerating structure, that was developed to satisfy the requirement of a high shunt impedance in the low-beta part of the TOP Linac. According to the original design the SCDTL tanks are grouped in seven modules of similar length (around 1.4 m each): the first three boost the energy to 30 MeV and the other four to 65 MeV. A total RF power of 7.5 MW is required, that should be given by two klystrons. An alternative scheme switching at 30 MeV to the easier structure SCL (Side Coupled Linac), tolerating the RF power increase (about 10 MW) due to the lower shunt impedance of SCL at these energies.

The SCDTL structure has been described in several papers [1, 3]. It consists of short DTL tanks coupled together by side cavities. The DTLs are short tanks, each having 5 to 7 cells of $\beta\lambda$ length, and the side cavity extends in a space left free on the axis for the accommodation of a very short (3 cm long, 2 cm o.d., 6 mm i.d.) PMQ (Permanent Magnet Quadrupole) for transverse focusing.

All tanks and coupling cavities of the first module (7-13.4 MeV, 1.32 m long, 11 DTL tanks, 5 cells per tank) were built. All the intermediate brazing steps were performed but for the final braze. The whole structure was bolted and measured on RF bench [1]. With the structure correctly tuned at the proper frequency the electric field was adjusted with tuning screws in the coupling cells to obtain the axial distribution uniform within ±2% among the 11 average tank fields and ±5% among the 55 cells fields. Unfortunately, vacuum leakage occurred during the intermediate brazing steps in about 40% of the tanks. The reason was that cooling channels were obtained by a complicated manufacture of the stem/drift tube assembly as described in a previous paper [5], and some brazing alloys re-melted and opened a leak just on the drift tube. As this was not recoverable, major modifications were introduced in the stem/drift tube manufacture of all the tanks. The final shape is shown in fig. 5 on the right.

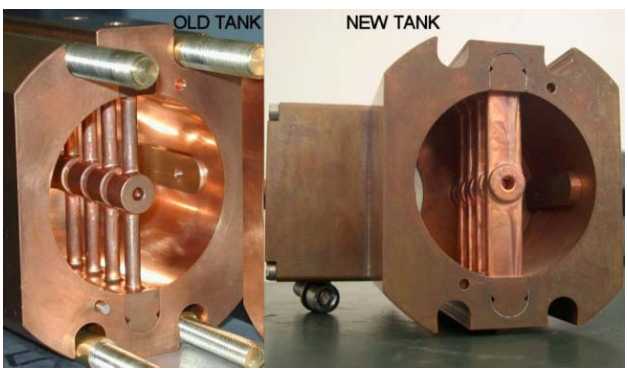

Figure 5: SCDTL tank: old stem (Left), new stem (right).

The stem and drift tube are machined from a solid piece and two parallel 1.5 mm diameter holes are drilled trough the 60 mm long rectangular stem with smoothed edges, for the coolant flow. Each stem is then TIG welded to the tank outer surface to provide for vacuum/coolant tightness, while thin channels are drilled at the inner surface of the tank body and filled with brazing alloy that will melt during final braze and will provide the correct electric contact between surfaces. Due to some manufacture delay, not all tanks are ready; the ones already manufactured have been measured and are within the frequency specifications. The structure is expected to be completed within this year.

Passing from the old to the new structure one of the prices to pay is that shunt impedance lowers by 12%. Due to the however high shunt impedance, this increment does not seem harmful, and the structure is much safer and we are confident that this task will be carried out without other problems.

SCL 65-200 MEV

The development of the final part of the TOP Linac has been left to a second priority. It will be based on conventional SCL structure at 3 GHz, suitably graded to follow the particle velocity. A prototype of a similar structure was built in 2002 by the TERA group [6]. Also in this case the cavities are grouped in tanks and connected by bridge couplers. Several klystrons are foreseen to manage the peak Required RF peak power is in the range of 30 MW and the total length is about 12 m.

CONCLUSIONS

The temporary site (a 20 m long bunker) in ENEA Frascati Laboratory is now available, and the injector has been installed and will be put in operation in September. Almost all the components of the 7 MeV LEBT are ready. Within a few months the first module of the SCDTL structure will be completed, and if the cold test are passed, a beam line will be arranged to test it with the 7 MeV protons from injector. Any future development is subjected to the definitive funding of the total project.

REFERENCES

[1] L. Picardi et al. “Advances in TOP Linac construction”, Proc. EPAC2002, Paris, Fr., p.248

[2] L. Picardi, C. Ronsivalle, A. Vignati “Progetto del TOP Linac”, in Italian, ENEA Technical Report RT/INN/97/17, 1997

[3] L. Picardi, C. Ronsivalle, R. Hamm “Beam injection study of the TOP linac using an AccSys Model PL-7 linac”, EPAC2000 Proc., p. 1675.

[4] L. Picardi et al. “The TOP Project status”, Proc. PAC2001, Chicago, USA, p.2491

[5] L. Picardi, C. Ronsivalle, B. Spataro “New structural design of SCDTL structures for the TOP Linac”, EPAC1998 Proc., p. 2333.

[6] C. De Martinis et al. “Beam tests for a proton linac booster for hadrontherapy”, Proc. EPAC2002, Paris, p.2727

THE ACCELERATION TEST OF THE APF-IH LINAC

K.Yamamoto[a) b)], M. Okamura[a)], T. Hattori[b)],S. Yamada[c)]
[a)] The Institute of Physical and Chemical Research (RIKEN), Japan
[b)] Tokyo Institute of Technology (TITech), Japan
[c)] National Institute of Radiological Sciences (NIRS), Japan

Abstract

An IH linac with Alternating Phase Focusing scheme has been fabricated to study a high efficiency cavity for a medical accelerator injector. This linac was designed to accelerate C4+ ions from 39 keV/u up to 1.9MeV/u. In order to test this linac, a test stand was just assembled which consists of a P.I.G. ion source, bending magnets and focus lenses. The total length of the test stand is less than 5 m including 1.5 m of linac tank length. The operation frequency of the cavity is 97.6MHz. We will report linac design, fabrication and the test bench.

INTRODUCTION

Now tumor therapy is being one of major applications of hadron accelerators. Typically a chain of linacs occupies large area in tumor therapy facilities. For instance, an injector of HIMAC (Heavy Ion Medical Accelerator in Chiba; Japan), consists of RFQ linac and Alvarez linac, accelerates C4+ ions up to 6MeV/u and the length is over 30 m[1)]. In particularly such a medical accelerator complex, not only machine performance but also construction cost and operation cost are very important. Therefore compact and reliable linac design is needed. For this purpose, we designed an Interdigital-H mode linac with alternating phase focusing (APF) as a new high efficiency cavity for the injector. The IH structure has an advantage of high shunt impedance in low energy region. The technique of APF has been proposed for the design of short low beta structures, because its inherent focusing capability could eliminate the need of external transverse focusing by drift tube quadrupoles[2)-5)].

DESIGN

Initial parameters were determined for C4+ acceleration. An injection energy, output energy and operation frequency are 2 MeV/u, 40 keV/u, and 100 MHz respectively. Electric field strength in gaps is limited by twice of Kirpatric's limit and an acceleration ratio is 5MeV/m. Based on this condition, a length of the linac is 1.5m long. A number of cell was determined as 22 which was given by the linac length divided by an average cell length (about 70mm).

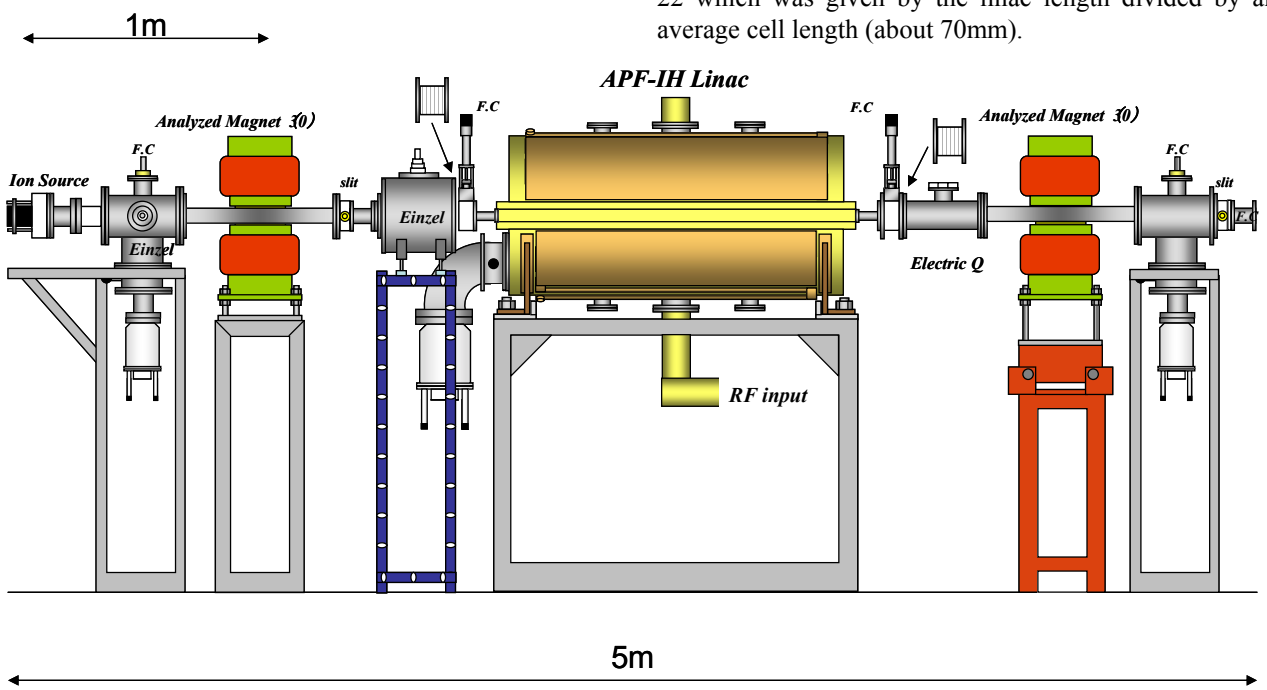

Figure 1: Acceleration test bench.

A total acceleration voltage was divided into cells keeping constant electric field distribution. Then, we optimized to find a best phase pattern working APF effectively by means of a matrix code using thin lens approximation. The results are shown in Figureure1. Next, we calculated 3D electric fields by a 3D-calculater (High Frequency Structure Simulator: H.F.S.S.) to find an end ridge tuner length to get required voltage distribution. The length of cut area was expected as 120mm. We made a half-scale cold model to check the distribution by perturbation method; a small Aluminium ball are put into the gap by a stepping motor controlled by LabVIEW and measured the electric fields by a variation of the frequency. The result is shown in Figureure2 and the final main parameters are shown in table1. Based on these parameters, a beam dynamics was calculated again.

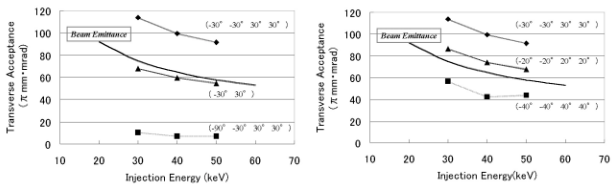

Figure 2: The comparisons of several phase pattern.

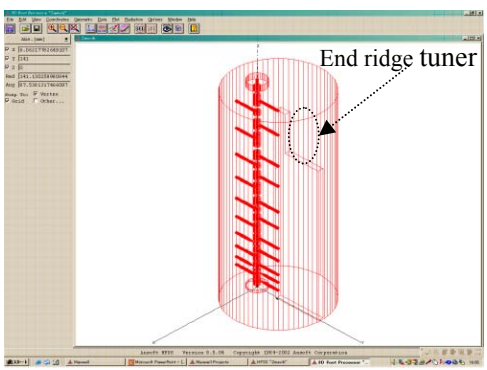

Figure 3: End Ridge tuner length=120mm by H.F.S.S.

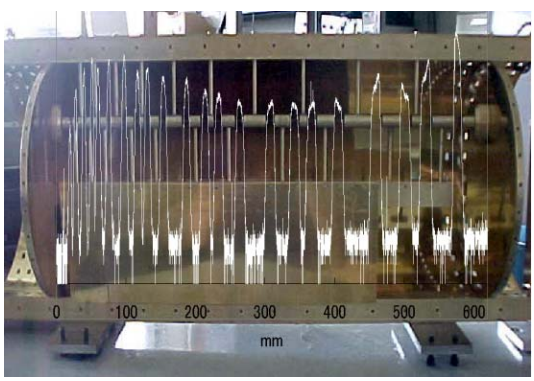

Figure 4: The electric field distribution by model test.

Table 1: Main parameters of the linac

Acceleration Particle	q/A ≥ 1/3
Input Energy	39 keV/u
Output Energy	1.9 MeV/u
Operation Frequency	97.5 MHz
Synchronous Phase	-30 , -30 ,+30 ,+30
Number of Cell	22
Cavity Length	1280 mm
Diameter of Cavity	ϕ560 mm
Focusing Sequence	-30 , -30 ,+30 ,+30
Dia. of drift tube	ϕ38, ϕ14

MANUFACTURE

The cavity was separated into 3 parts for easy fabrication and easy modification of the drift tubes. The middle plate was manufactured from single stainless plate by NC machining centre within ±0.1mm error. After plating Cu, the drift tubes were aligned and the length of each gap was lined as under ±1%. The top and bottom vessels were also manufactured and checked vacuum before assembling. After gathering each part, the frequency and the Q-value were indicated as 97.60MHz and about 10000 respectively by a Network Analyzer.

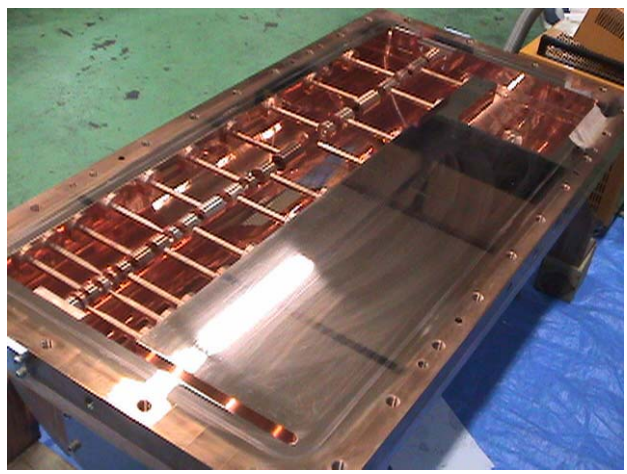

Figure 5: Photograph of the linac.

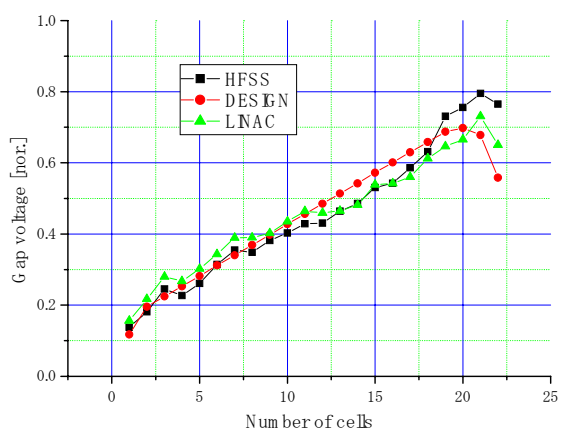

Figure 6: Comparison of the gap voltage distribution.

ACCELERATION TEST BENCH

A shunt impedance of the linac is expected as 215MΩ/m and a required RF power is 134 kW to accelerate C4+ ions. At current facility, only 30 kW power supply is available, so we will use protons for acceleration test; it will need about 14kW of RF power. The whole length of an acceleration test bench using proton is less than 5m including the 1.5m linac (Figure.1). We use P.I.G. ion source to supply protons. An extraction voltage is 15kV and an acceleration tube accelerates the beams up to injection energy. This ion source was newly manufactured and then the emittance was measured using a pepper pot and a micro channel plate. The obtained emittance was 0.04 mmmrad(nor.). For low energy beam transport, there are bending magnet to select only proton, and focusing lenses before and after the magnet. Extraction energy is analyzed by another bending magnet after focusing by an electric quadrupole. There are slits after the each magnet to improve the resolution.

The resonance frequency of the cavity is 97.6MHz, however the power supply can provide within 100±2MHz. So, we change the frequency to output 97.6MHz efficiently modifying the tuning plate. Figureure 8 shows the power at this frequency. The power is almost half compared to the capacity but enough to accelerate protons. We succeed to input the power into the linac about 14kW without sparking. Figureure9 shows the analyzed beam when the power is input. Unfortunately the analyzing magnet need to be modified to measure fully accelerated beams due to heavy saturation. In this measurement, the RF power was swept with 1 kHz repetition. A small peak appeared at 1.3 MeV seems partially accelerated protons with a particular condition which was given by lower RF fed power. Similar phenomena had been observed in our experience.

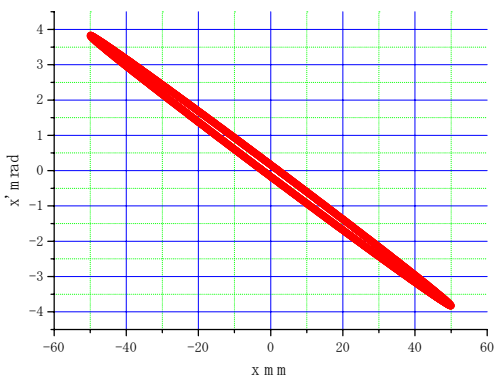

Figure 7: Emittance from the ion source.

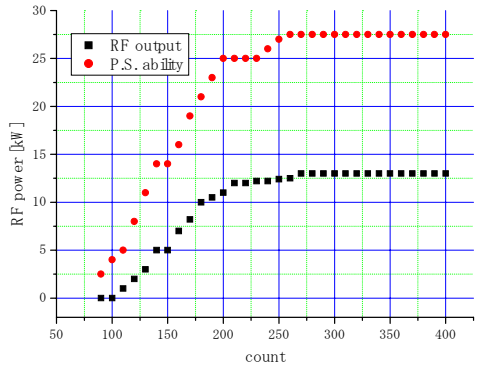

Figure 8: Ability of the RF power suply.

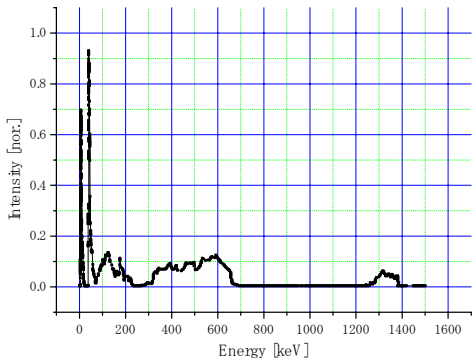

Figure 9: Analyzed beam when the RF power input.

SUMMARY

We designed and manufactured the new high efficiency cavity for the cancer therapy injector. The beam dynamics were calculated by a thin lens approximation matrix code. The RF structure of the linac was designed by a 3D-calculator (H.F.S.S.) and confirmed by the scale model. The cavity was machined by a NC machining centre and after Cu plating, drift tubes were aligned under ±1% error. In order to test the new IH linac, all devices for proton acceleration test were aligned under ±0.5mm error. After tuning of RF feed line, required RF power was successfully input without sparking. We are almost ready to commission the linac.

REFERENCES

[1] S.Yamada et al.,"HIMAC and Medical Accelerater Projects in Japan",APAC'98,pp885-889

[2] T.Hattori et al., "Compact IH-APF type linac for PIXE and RBS analysis " , Nucl . Instr. & Meth. , Sect. B, vol.161-163, pp1174, 2000

[3] N.Hayashizaki et. al.,"Compact injector with alternating phase focusing-interdigital H-mode linac…",Rev.of Scient. Instr.,vol.71,no.2.p.990,2000

[4] V.V.Kushin et.al.,"ITEP Heavy Ion Alternating Phase Focusing Linac" 1993 in proceedings of the Particle Accelerators,pp1798-1800

[5] D.A.Swenson,"Alternating Phase Focused LINACS",1976 in Proceedings of the Particle Accelerators,Vol.7,pp61-67

CALCULATION OF ELECTRON BEAM DYNAMICS OF THE LUE−200 ACCELERATOR

A.P. Sumbaev#, V.S. Aleksandrov, N.Yu. Kazarinov, V.F. Shevtsov,
JINR, Moscow region, 141980, Dubna, Russia

Abstract

The results of calculations of the focusing and transportation systems of the electron beam of LUE-200 accelerator – the driver of a pulse source of resonant neutrons IREN [1], JINR (Dubna), are presented. Simulations of the beam dynamics in the traweling wave accelerator were carried out by means of PARMELA code [2]. The calculations have been fulfilled for various parameters of the focusing magnetic field in the accelerator and the channel, various currents of the beam and various initial distributions of electrons.

INTRODUCTION

The intense resonant neutron pulse source IREN is a traditional JINR combination of a driver (an electron LINAC) and a converter - target with a booster multiplier. The LINAC is designed at the Budker INP of the Siberian Branch of the Russian Academy of Sciences. The design prototype is the preinjector of the VEPP-5 accelerator complex [3]. For ensuring the design parameters of the IREN, the average power of the electron beam must be about 10 kW that defines the electron energy to be 200 MeV if the pulse duration is 250 ns, the electron current is 1.5 A, and the repetition frequency is 150 Hz. The mean rate of the energy gain in the accelerating structures should not be less than 35 MeV/m because the restrictions related to the placement of the accelerator in the available building.

LUE-200 ACCELERATOR

The accelerator (Figure 1) consists of an electron gun (C−A), an accelerating system, and an electron beam transport channel up to the target (T).

The accelerating system consists of a buncher (B) and two accelerating sections (AS1, AS2).

The *buncher* [4] is four coupled resonators (3 cells and a converter of wave type) with an operational frequency 2855.6 MHz and 4π/3 operating mode. Figure 2 shows the distribution of the longitudinal electric field along the axis of the buncher.

The accelerating sections are round disk-loaded waveguides of constant impedance. The major parameters of the section are given in [3]. Each section is fed by RF power from independent klystron amplifiers based on the 5045 SLAC klystron operating at the frequency 2856 MHz.

The *focusing system* consists of a solenoid focusing channel and a quadrupole focusing channel.

The *solenoid focusing channel* is used at the bunching step and at initial acceleration from the energy 200 keV to 100 MeV. It consists of magnetic lenses AS, ML1 and ML2 of the electron source, and of a solenoids system of the buncher (BC) and the first accelerating section (S1). During the design, the configuration of the solenoid focusing channel was evolved. In the first version of the design [3], focusing of the beam in the first accelerating section was performed by two solenoids S1 (length ~0.75 m, field strength ~1.5 kG) and S2 (length ~2.1 m, field strength ~4.0 kG) with opposite directions of the field. After optimization of the fields, the system of two solenoids was replaced by a single sectioned solenoid S1 (16 coils).

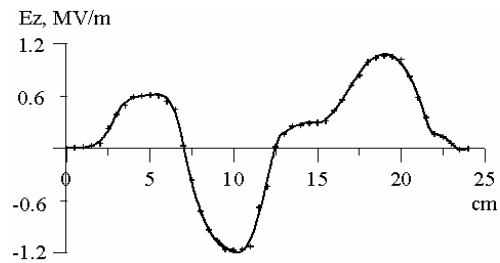

Figure 2: Distribution of the longitudinal electric field strength along the axis of the buncher.

The *quadrupole focusing channel* is used after the exit of the first accelerating section. The channel consists of nine quadrupole lenses Q1–Q9. The correcting lens Q1 is combined with the beam displacement corrector. Two doublets Q2–Q3 and Q4–Q5 are mounted on the second accelerating section and aimed at guiding the beam through the small-aperture channel inside the section.

Two more doublets Q6–Q7 and Q8–Q9 aimed at guiding and focusing the beam to the target (T).

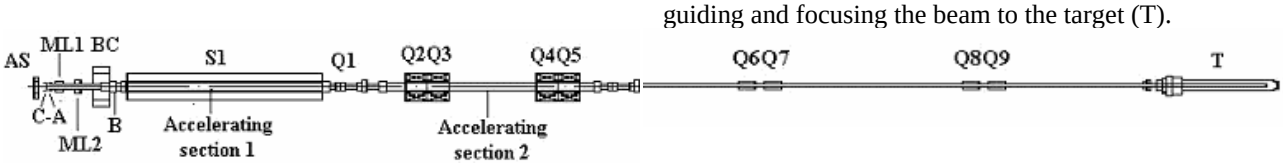

Figure 1: Layout of LUE-200 accelerator.

#sumbaev@nf.jinr.ru

SIMULATION OF THE BEAM DYNAMICS

Simulation was aimed at the following objectives:

- optimization of the values and distribution of the longitudinal magnetic field in the neighbourhood of the cathode unit and buncher;
- testing the possibility to decrease the magnetic field in the solenoids and to avoid reversion of the field in the neighbourhood of the first accelerating section;
- optimization of the parameters for the quadrupole focusing channel that should provide the required beam parameters.

Beam dynamics was computed with the PARMELA code. Initial beam parameters are contained in Table 1.

Table 1: Initial beam parameters

Electron energy	200 keV
Maximum beam current in a pulse	3 A
Duration of a beam current pulse	250 ns
Beam transverse size (radius)	4 mm
Beam emittance (upper bound)	$\leq 0.01\ \pi$ cm rad
Energy spread	≤ 2 keV

Required beam parameters on the target are contained in Table 2.

Table 2: Required beam parameters

Electron energy	200 MeV
Beam current in a pulse	1.5 A
Duration of the beam current pulse	250 ns
Beam radius on the target	10 mm

In the computation, the following input electron density distributions were used:

Vladimirsky–Kapchinsky distribution in the transverse phase space and uniform distribution in the initial phases (from 0 to 2π) and in the energy spread;

Gaussian distribution in the transverse cross section of the beam and uniform distribution in the initial phases at zero emittance and energy spread.

Amplitudes of the Fourier coefficients for the electric field shown in Figure 2 were used in the simulation of particle motion in the buncher by the PARMELA code. The second section was divided into five domains to take into account the quadrupole focusing. Accelerating electric fields in the domains were tuned to gain the required energy on the length of the section.

In the simulation of acceleration and transportation of various bunches of the electron beam, the electric field was decreased according to [5] to obtain the mean energy of a bunch with the beam-loading effect taken into account.

SIMULATION RESULTS

Computations with the POISSON code used the geometry (shown in Fig. 1) of the elements forming the magnetic field in the domain from the cathode to the end of the first accelerating section.

Simulation has demonstrated that the parameters required from the beam on the target can be achieved at the longitudinal magnetic field in the first accelerating section $\lesssim 2$ kG and without change of its direction.

The distribution of the magnetic field on the axis obtained at the optimal parameters of the elements is shown in Figure 3.

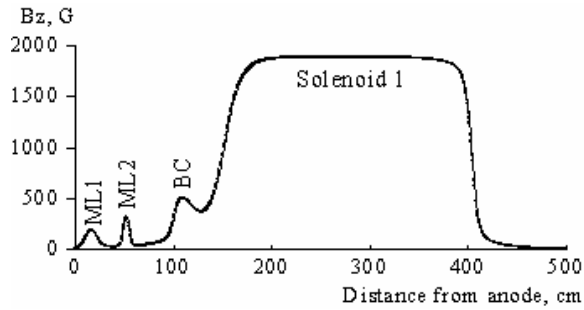

Figure 3: Distribution of magnetic field in the solenoid focusing channel.

The capture efficiency in the acceleration regime was ~80% with the magnetic field formed in the neighborhood of the cathode and the buncher. Modification of the relative positions of the quadrupoles Q6–Q9 required by the placement of the channel in the available building required optimization of the gradients of quadrupoles on the beam parameters on the target. The optimization was performed with the method and code described in [6].

The beam current transmittion along the accelerator line and in the transport channels as well as the energy gain in the acceleration process obtained in the computation, are shown in Figs. 4 and 5.

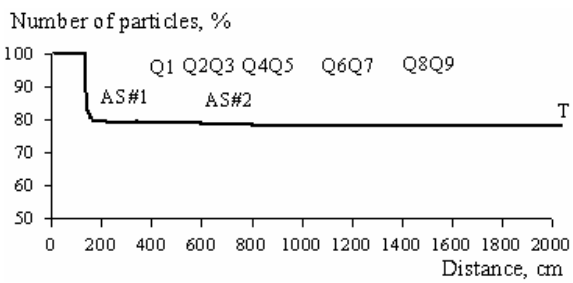

Figure 4: Beam current transmittion through the line.

The total beam losses are about 25% for the initial beam current 2 A. Most of the beam losses are taking place in the neighborhood of the buncher. For the first bunch of the current pulse, the maximal energy of electrons at the target is 204 MeV and the mean energy is 192 MeV.

The same parameters for the last (715th) bunch are 145 and 137 MeV, respectively. The standard deviation of the energy from its mean value is 23 MeV, the minimal electron energy (>65 MeV) is in the required domain, where the neutrons are produced efficiently in a phototarget (> 60 MeV [1]).

Figure 6 shows the distributions of the particles in the transverse cross section of the beam at the target for the microcanonical and Gaussian initial distributions of the

electrons. As seen, half-size of the beam at the target does not exceed 5 mm within three standard deviations for the microcanonical initial distribution and 4 mm - for the Gaussian distribution. The beam current transmittion drops till 5% with respect to the microcanonical initial distribution.

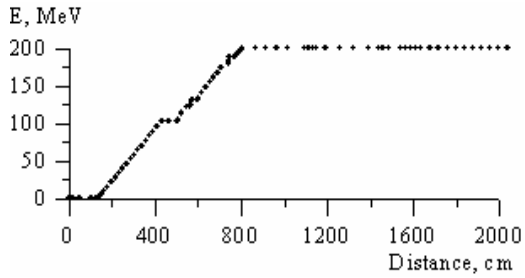

Figure 5: Energy gain along the line.

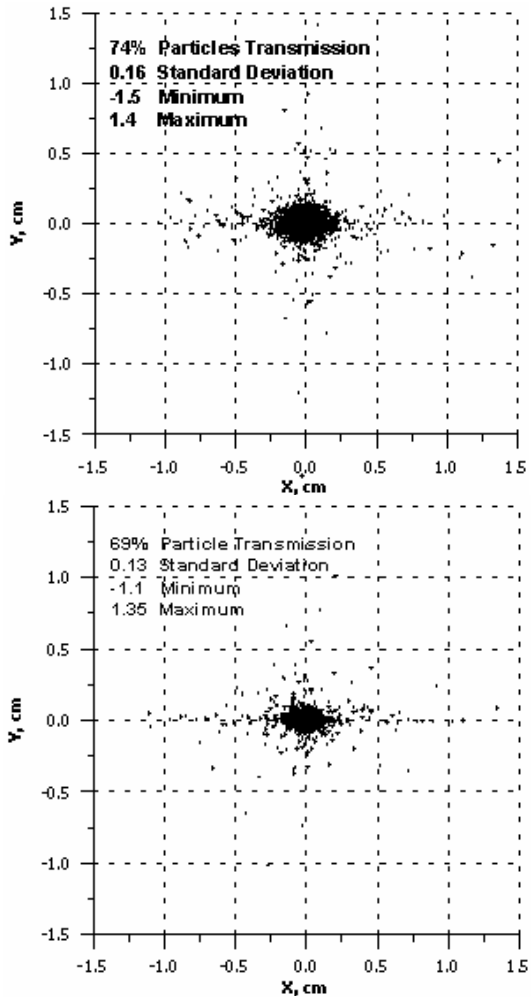

Figure 6: Beam spot at the target for the initial micro-canonical (above) and Gaussian (below) distributions.

CONCLUSIONS

1. The suggested scheme for the accelerator and transport channel is viable at the nominal parameters as well as at various configurations of the focusing magnetic field in the accelerator line, at various currents and initial distributions of electrons in the beam. The following parameters of the accelerated current were obtained: the half-size at the target is less than 10 mm, a final mean energy of 165 MeV, minimal energy >65 MeV, maximal energy of 204 MeV, and beam current transmittion is equal to 70–75% at the initial beam current 2 A. These parameters meet the requirements of the design [1–2].
2. Changing the polarity of the magnetic field in a solenoid does not influence the dynamics and the final parameters of the beam. Using an external magnetic screen for the solenoid results in a 3% increase of the magnetic field strength maximum on the axis, and does not influence the ultimate parameters of the beam.
3. Decreasing the magnetic field in the accelerating section down to 2 – 2.5 kG does not complicate production of the required beam spot on the target if the gradients of the quadrupole lenses are optimal and the beam current transmittion in the line is satisfactory.
4. For the considered range of initial currents (2–5 A) and configuration of magnetic fields of the accelerator (the maximal field of the solenoid S1 ranging from ±2 to ±5 kG) and at the given initial electron energy, placement and parameters of the transport channel lenses, and at various initial distributions, the own field of the beam (without wake field effects) does not considerably influence the dynamics of the beam. We conclude that it is possible to carry the beam while maintaining electron losses as planned (~25%) at fixed gradients of the lenses.

REFERENCES

[1] W. Furman, New Pulsed Neutron Source Of JINR – The IREN Project, In Proc. of a 3rd Int. Conference Dynamical Aspects of Nuclear Fission, Casta-Papiernichka, Slovak Republic, 1996, Ed. By J. Kliman and B. I. Pustylnik, Dubna, 1996, p. 394-414.
[2] B. Mouton, “The PARMELA Program,” LAL/SERA 93-455 (Orsay, 1993).
[3] A.V. Alexandrov et. al., "Electron-positron preinjector of VEPP-5 complex". Proceedings of the XVIII International Linear Accelerator Conference, 26-30 August 1996, Geneva, Switzerland., CERN 96-07, 15 November 1996, Vol. 2, pp. 821-823.
[4] V.M. Pavlov, Microwave Buncher of Forinjector VEPP-5 (Inst. Yad. Fiz., Sib. Otd. Ross. Akad. Nauk, Novosibirsk, 2002) [in Russian].
[5] V.S. Aleksandrov et al., “Modelling of Beam-Loading effect in the LUE-200 Accelerator,” Paper presented at V Scientific Memorial Sarantsev`s Seminar, (Dubna, 2003).
[6] V.S. Alexandrov et al., “Optimization of Transportation Channel Parameters for Beams with Large Space Charge,” in Proceedings of ISPP2002 (Mianyang, China, 2002), p. 75; N.Yu. Kazarinov and V.F. Shevtsov, Optimization of Transportation Channel Parameters for Beams with Large Space Charge, JINR Communication, P9-2002-148 (Dubna, 2002) [in Russian].

3D BEAM DYNAMICS SIMULATION IN UNDULATOR LINAC*

E.S. Masunov, S.M. Polozov, MEPhI, Moscow, 115409, Russia

Abstract

The ion beam can be bunched and accelerated in linear undulator accelerator (UNDULAC). The acceleration and focusing of beam can be realised without using a synchronous wave. In this paper the computer simulation of high intensity ion beam dynamics in UNDULAC-RF was carried out by means of the "particle-in-cell" method.

INTRODUCTION

The beam focusing and acceleration can be realized without using a synchronous wave of RF field, as it discussed in Ref. [1-2]. In this case accelerating force is to be driven by a combination of two non-synchronous waves (two undulators). Such linac was called linear undulator accelerator (UNDULAC). The ribbon ion beams can be accelerated in two types of undulator linac UNDULAC-E [1] and UNDULAC-RF [2]. In first case beam bunching, acceleration and transverse focusing are realised in combined wave field which is produced by one spatial RF field harmonic in a periodical resonator and field of electrostatic undulator. In second case the accelerator force is driven by two fundamental RF field harmonics. It should be noted that the ion beams can be accelerated in UNDULAC in low energy range using transverse or longitudinal fields [1].

The beam dynamics in UNDULAC can not be investigated by means of traditional analytical methods because it is no synchronous wave in this linac. The computer simulation and optimization of ion dynamics consist of two steps. At the first the equations of particles motion in polyharmonic fields is devised by means of smooth approximation. Hamiltonian analysis of this equation allows to find a velocity of reference particle in polyharmonic field and to formulate the conditions of effective longitudinal bunching and transverse beam focusing [3]. These conditions define the structure period and the field amplitudes distribution. At the second, using above founded characteristics, the 3D ion beam dynamics numerical simulation in an UNDULAC is provided. The space charge influence on the beam dynamics is investigated also by this simulation

The results of beam dynamics analytical study and numerical simulation for UNDULAC-E are discussed in Ref. [4-5]. The analytical investigation for UNDULAC-RF is provided in [3]. Let us consider briefly the results of this investigation. It helps to realize the numerical simulation.

*The work was supported by RFBR. Grant 04-02-16667

THE RESULTS OF BEAM DYNAMICS ANALYTICAL STUDY

The analytical investigation was provided for UNDULAC-RF using RF field with $\mu = 0$ and $\mu = \pi$ modes in Ref. [3]. The main results of ribbon ion beam dynamics analytical study in UNDULAC-RF:

1. The two sub-sections are necessary for providing of beam bunching in UNDULAC-RF. The reference particle phase must be chosen linearly decreased and fields amplitudes increased as sine function in first bunching sub-section. The synchronous phase and amplitudes are constant in second accelerating sub-section. These dependencies are providing the minimal particle loses.
2. It was shown that the optimal bunching conditions and maximal current transmission coefficient could to be driven with the optimal RF field harmonics ratio $\chi = E_1 / E_0$. The optimal value is equal χ=0.3-0.4 in UNDULAC-RF using $\mu = \pi$ mode of RF field and χ>1 for $\mu = 0$ mode.
3. In the smooth approximation the current transmission coefficient K_T is equal 90-95 % for UNDULAC-RF using $\mu = \pi$ mode of RF field (for both transverse and longitudinal fields) and 85-90 % for $\mu = 0$ mode.
4. The two bunches per one period of RF field will be configured.

BEAMDULAC CODE

The beam dynamics can not be studied completely using analytical methods only. The time-averaged motion equation and effective potential function are obtained using smooth approximation. The influence of particle phase and velocities oscillations on beam dynamics does not take into account in this approximation. The numerical simulation in polyharmonic field is also necessary. The new code BEAMDULAC has been developed specially for beam dynamics simulations in undulator linear accelerator. This code is carried out by means of Cloud-in-Cell (CIC) method for accurate treat of space charge effects that is especially important in the case of high intensity beam. The motion equation for each particle is being solved including forces due to external fields and inter-particle Coulomb field. field The Poisson equation is solving on the grid with periodic boundary conditions in order to find the potential of Coulomb. The Dirichlet boundary conditions are applied at transverse boundaries of the simulation domain. The interaction of the bunch space charge with the accelerating channel is taken into account. The Fast Fourier Transform algorithm is used to solve the Poisson equation on 3D grid with given charge density distribution. The external potential is

represented as a series of space harmonics. The BEAMDULAC code was used for ribbon ion beam dynamics study in UNDULAC-RF and UNDULAC-E. Let us discussed the results of beam dynamics in UNDULAC-RF using $\mu = 0$ and $\mu = \pi$ modes of transverse and longitudinal RF field.

LONGITUDINAL RF FIELD (π MODE)

The numerical simulation was provided for ribbon beam of deuterium ions. The basic parameters of UNDULAC and the results of beam dynamics investigation are presented in Table 1. The simulation was started with next parameters: the initial energy of deuterium ions W_{in}=100 keV; the full length of accelerator channel 2.5 m; the accelerator channel cross-section size $2a\times2b$=0.8×20 cm. The output beam energy in UDNULAC-RF using $\mu = \pi$ mode is equal 1.3-1.5 MeV with effective amplitude equal to $E_{eff} = e\lambda E_0 E_1 / 2\pi W_0 \beta = 40$ kV/cm. Here e is the charge of electron, λ is the wave length (λ=1.5 m n this case), $W_0 = mc^2$ and β is the initial beam velocity. The energy gain in accelerating part is equal 700-800 keV/m. The optimal bunching sub-section length L_b must be equal to accelerating sub-section length L approximately. It was shown that the optimal value of RF field harmonics amplitude is equal χ=0.3–0.4 (see Fig. 1). This result coincides with previously analytically founded value and this ratio can be easily realised.

The current transmission coefficient is close to 100 % in smooth approximated field as it was shown above [3]. It is appreciably reduced if the beam dynamics simulation is done in polyharmonic RF field. The current transmission coefficient is equal 75–80 % (see Fig. 1, curve 1) for paraxial injected beam (when the beam cross-section size is equal to $2l\times2t$=1×0.04 cm^2). One has obtained that K_T mightily decreased if the beam size is larger of a critical value ($2l\times2t$=5×0.3 cm^2). The size of accelerator channel can be reduced to $2a\times2b$=0.7×10 cm in this case. The particle loses are due to the fast oscillations of particle phases and longitudinal velocities for UNDULAC-RF using longitudinal RF field.

Numerical simulation of beam dynamics when a space charge field is taken into account shows that limit current in UNDULAC-RF is lower analytically predicted and its value is equal I_{max}=200–250 mA when the cross-section is equal $2l\times2t$ =5×0.3 cm^2 (see Fig. 1, curve 2). It was shown that K_T is not exceeding 60 % in this case.

The input and output beam cross-section (a), normalized transverse emittance E_y (b), phase (c) and energy (d) spectra are plotted on Fig. 2. This figure illustrates the formation of two bunches per one RF field period. The output normalized emittance E_y is twice as an initial one.

TRANSVERSE RF FIELD (π MODE)

The parameters of system for simulation are equal for UNDULAC-RF using transverse and longitudinal RF field for $\mu = \pi$ mode. The results of simulation are also close for both linac types (see Table 1). The optimal ratio of RF field harmonics amplitudes is equal χ=0.35 for UNDULAC-RF using transverse RF field. The length of bunching sub-section must be also close to the accelerator length.

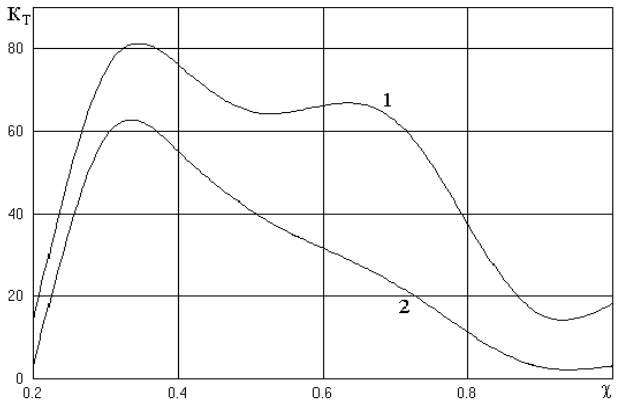

Figure 1: Current transmission coefficient versus ratio of RF field space harmonics amplitudes χ.

Table 1: The parameters of UNDULAC-RF ($\mu = \pi$ mode)

	lg.	tr.
Length of accelerator L, m	1.3	
Injection energy W_{in}, keV (β_{in})	100 (0.01)	
Amplitudes of RF field harmonics, base E_0, kV/cm	200	210
first E_1, kV/cm	80	70
Buncher length, m	1.2	
Accelerator channel size $2a\times2b$, cm	10×0.7	
Input beam size $2l\times2t$, cm^2	5×0.3	7×0.3
Input emittance E_x, mm·mrad	30π	30π
E_y, mm·mrad	0.7π	0.06π
E_φ, keV·mrad	25	40
Acceptance of accelerator channel A_x, mm·mrad	60π	60π
A_y, mm·mrad	2π	2.5π
A_φ, keV·mrad	40	40
Limit beam current I_{max}, mA	200–250	300–350
Output beam energy W_{max}, MeV (β_{max})	1.2–1.5 (0.034–0.04)	

The limit input beam size is $2l\times2t$ =7×0.3 cm^2. It is higher that for UNDULAC-RF using longitudinal field. The current transmission coefficient is equal 65 % for this input beam size. The limit current is equal 300–350 mA for this type of undulator linac. The particle loses are caused by longitudinal motion in the bunching sub-section and all loses in accelerating sub-section are caused by transverse motion and Coulomb field influence.

The transverse emittance threefold. The transverse particles velocity and beam size both. The halo is not forming. The limit initial emittance E_y is lowers that for UNDULAC-RF using longitudinal field (see Table 1).

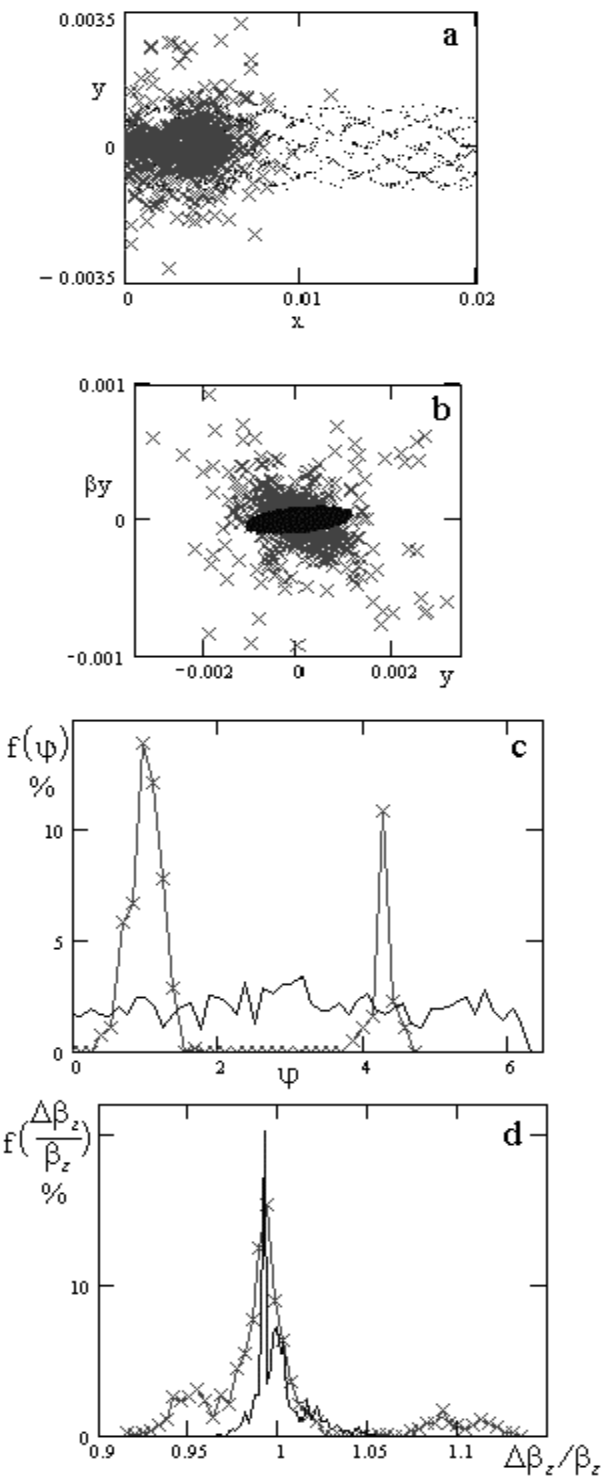

Figure 2: Input and output beam cross-section (a), normalized transverse emittance E_y (b), phase (c) and energy (d) spectra. ("points" – initial values, "×" – output).

UNDULAC-RF USING LONGITUDINAL AND TRANSVERSE RF FIELD (0 MODE)

The numerical simulation of ribbon ion beam dynamics in UNDULAC-RF for $\mu = 0$ mode of RF field shows that the current transmission coefficient is very small. The current transmission coefficient decreases to 55–60 % for paraxial injected beam if the simulation is provided in the polyharmonic field. For larger beam cross-sections current transmission coefficient reduces to 30–35 % (UDULAC-RF using longitudinal field) and to 5-10 % (using transverse field). These results are confirmed by previous analytical investigation.

The optimal value of effective amplitude of combined wave is equal E_{eff}=30 kV/cm and output energy W =0.9-1.1 MeV. The limit current was not calculated for this type of undulator linac because the current transmission coefficient is small.

CONCLUSION

The results of deuterium ion beam dynamics investigation in RF undulator linacs are presented. These results are obtained using the BEAMDULAC code. It was shown that UNDULAC-RF using $\mu = \pi$ mode RF field is more preferable for further design. The ribbon beam of deuterium ions can be bunched and accelerated up to energy W =1-1.5 MeV. The limit current is up to 350 mA and current transmission coefficient K_t=65 % in this type of undulator linac. It should be noted that the limit beam current and current transmission coefficient are lowest than in electrostatical undulator linac [5]. However the energy gain in accelerating sub-section of UNDULAC-RF is twice as larger than in UNDULAC-E. The current transmission enlarging is possible by means of numerical optimization of function of synchronous phase and RF field harmonics amplitudes variation.

It was also shown that UNDULAC-RF using $\mu = 0$ mode RF field is not perspective system for further design because the transverse beam focusing is not effective here.

REFERENCES

[1] Masunov E.S., Sov. Phys.-Tech. Phys., vol. 35, No. 8, p. 962, 1990.
[2] Masunov E.S., Tech. Phys., vol. 46, No.11, pp. 1433-1436, 2001.
[3] E.S. Masunov, S.M. Polozov. Ribbon Ion Beam Dynamics in Undulator Linear Accelerator. Proc. of LINAC'04. (see this issue)
[4] E.S. Masunov, A.S. Roshal. Proc. of PAC'1997, pp 2835 – 2837, 1997.
[5] E.S. Masunov, S. M. Polozov, A.S. Roshal. Radiation Physics and Chemistry v. 61, pp. 491-493, 2001.

AN ELECTRODE WITH MOLYBDENUM-CATHODE AND TITANIUM-ANODE TO MINIMIZE FIELD EMISSION DARK CURRENTS

T. Nakanishi[a], F. Furuta[a], S. Okumi[a], T. Gotou[a], M. Yamamoto[a], M. Kuwahara[a], N. Yamamoto[a], K. Naniwa[a], K. Yasui[a], H. Matsumoto[b], M. Yoshioka[b] and K. Togawa[c]

[a]Department of Physics, Nagoya University, Nagoya 464-8602, Japan
[b]KEK High Energy Accelerator Research Organization, 1-1 Oho, Tsukuba 305-0801, Japan
[c]SPring-8 /RIKEN, 1-1-1 Koto, Mikazuki-cho, Sayo-gun 679-5148, Japan

Abstract

A series of dark current measurements are performed for Molybdenum (Mo) and Titanium (Ti) electrodes, and the results are analyzed to separate the primary field emission current from the total observed dark current. The analysis shows that Mo exhibits very low primary field emission current as a cathode, and Ti also exhibits a lower enhancement effect of dark current due to electron and ion bombardments of cathode and anode. An electrode configuration with Mo cathode and Ti anode is thus examined, and it is confirmed that a field gradient of as high as 130 MV/m for 1 nA total dark current is possible for an electrode gap of 0.5 mm and an effective cathode area of 7 mm^2.

INTRODUCTION

The initial phase of dark current or pre-breakdown phenomenon, dominated by primary field emission is usually weak, and does not cause fatal damage in high-voltage devices. More serious breakdown phenomena that degrade device performance are triggered by the same field emissions but are enhanced by an additional positive feedback mechanism. However, for photoemission source using GaAs-type photo-cathodes with a negative electron affinity (NEA) surface to extract electrons into vacuum, even a weak pre-breakdown current significantly reduces the cathode lifetime [1]. The NEA surface realized by a surface dipole layer of Ga(−)–Cs(+) is delicate and easily destroyed by small disturbances induced by dark current. Thus, technology for reducing pre-breakdown dark current is essential for the photoemission devices using an NEA-GaAs surface. Polarized electron source (for linear collider) and low-emittance electron source (for ERL) are representatives of such devices.

The dark current properties of SUS and Cu surfaces have already been investigated using a compact test stand constructed at KEK. Based on these experiments, it has been suggested that the magnitude of dark current is dependent on both the electrode fabrication process and the purity of the crystal structure of the material [2]. Thus, using the same apparatus, our group undertook a systematic study of the dark current from Ti and Mo electrodes. This paper presents the results of these experiments, and introduces a new analysis method for separating primary field emission current from total dark current based on experimental data for the gap-separation dependence.

APPARATUS AND ELECTRODE

The test stand was built for basic study of field emission dark current under the high DC-field gradient condition (~200 MV/m) with ultra-high vacuum of $<10^{-11}$ Torr. In order to obtain a high-quality UHV, the main vacuum chamber was fabricated using re-melted stainless steel (NK-Clean-Z), which contains much less non-metallic impurities than SUS316L. The applied field gradient could be changed by controlling the gap separation of the electrodes (0–20 mm) and the bias voltage (0–100 kV), allowing the dark current under a given field gradient to be measured with respect to different gap separations. The Ti electrode was machined from JIS grade-2 pure Ti, and a mirror-like surface was obtained by buff-polishing. The Mo electrode was machined from a single-crystal Mo block (purity: 99.999%), and a mirror-like surface was prepared by diamond paste polishing. The specimens were finally treated by high-pressure rinsing (80 kg/cm^2, 5 min) with ultra-pure water in the class-100 clean room.

DARK CURRENT MEASUREMENT

To avoid trivial electrical breakdown, the dark current measurements were done very carefully using the long time current conditioning for a few days to 2 weeks. The results of dark current measurements are shown in Fig. 1, where the dark current is plotted as a function of applied field gradient at the cathode surface. The Ti and Mo electrodes exhibited no dark current up to 80 and 83 MV/m, reaching 1 nA at 103 and 115 MV/m at a gap separation of 0.5 mm, respectively. This represents much higher performance than either SUS or Cu.

The dependence of dark current on gap separation is also shown in Fig. 1. For Ti, it exhibits a dark current of ~1 pA with a 0.5 mm gap and > 100 pA with a 1.0 mm gap under the same field gradient of 80 MV/m. A stronger dependence is observed for Mo. It has a dark current of less than 1 pA for 0.5 mm gap separation, but a dark current of over 1 nA for 1.0 mm gap separation under a field gradient of 83 MV/m.

Fowler-Nordheim theory provides a fundamental viewpoint for field emission phenomena, but it is unable

to predict the dependence of dark current on gap

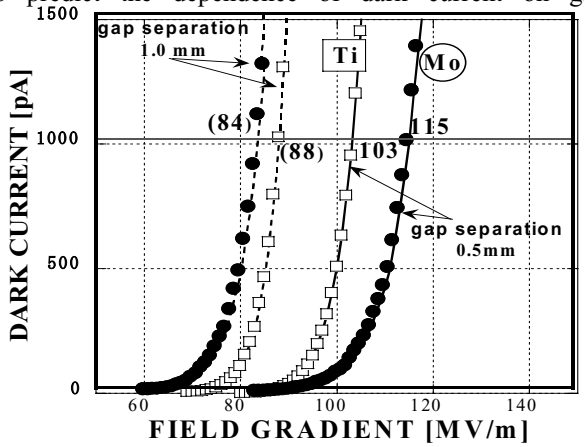

Figure 1: Dark currents from Ti (□) and Mo (●). Gap separations are 0.5 mm (—) and 1.0 mm (----).

separation [3]. The current enhancement effect due to bombardment of the anode and cathode by electrons and positive ions is expected to stimulate additional dark current. Under a given field gradient applied to the cathode surface, a wider gap results in higher kinetic energies of electrons and positive ions, and thus the enhancement effect is expected to become more significant. Table 1 lists experimental values of secondary electron yield for specific energies of incident electrons and sputtering rates under 600 eV Ar+ ion bombardment. Both rates are larger for Mo compared to Ti, and it seems quite reasonable that a larger enhancement effect and thus larger gap separation dependence is observed for the Mo electrode.

Table 1: Secondary electron yield for normal-incidence electrons and sputtering rate by 600eV Ar^+

	Ti	Mo
Secondary electron yield	0.9@280eV	1.25@375eV
Sputtering rate (atoms/ion)	0.58	0.93

SEPARATION OF PRIMARY FIELD EMISSION CURRENT FROM TOTAL DARK CURRENT

The total dark current will approach the primary field emission current with decreasing gap separation reaching coincidence at zero gap separation, as the enhancement effect must also become smaller and finally disappear. Thus, the primary field emission current under a given field gradient will be equivalent to the total dark current extrapolated to zero gap separation.

The field gradients producing a total dark current of 1 nA are plotted with respect to gap separation for the Mo and Ti electrodes in Fig. 2. The following formula was used to approximate the field gradient of *E(I,d)* [MV/m] giving the total dark current of *I* [A] at the gap separation of *d* [mm]

$$E(I,d) = \frac{E(I,0)}{1+\alpha d}. \quad (1)$$

where α is a constant representing the enhancement effect [mm^{-1}], and *E(I,0)* is the intercept of the field gradient at zero gap separation, corresponding to the magnitude of the field gradient giving the field emission current of *I*.

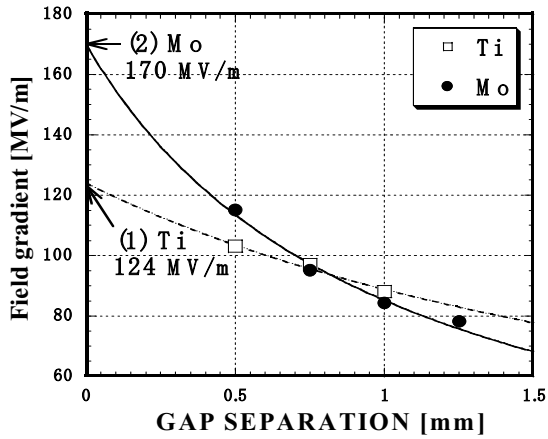

Figure 2: Fitting and extrapolation of data points for (1) Ti and (2) Mo electrodes. The field gradient corresponding to a primary field emission current of 1 nA is obtained as the intercept at zero gap separation.

Using this equation, the data points are fitted with respect to the free parameter α, yielding field gradients corresponding to 1 nA primary field emission current of 124 MV/m for Ti and 170 MV/m for Mo. A similar extrapolation was performed for dark currents between 1 pA and 1 nA. The free parameter α was adjusted in each case, but had an average value of 0.4 ± 0.02 for Ti and 1.0 ± 0.04 for Mo. This constancy of α over the entire range of dark current indicates that the gap separation dependence is well approximated by equation (1). Using the extrapolated data for *E(I,0)*, a two-dimensional plot of field emission current vs. field gradient can be

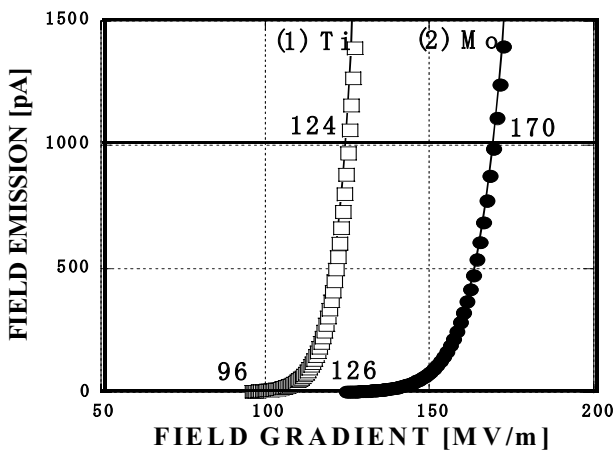

Figure 3: Estimated primary field emission current from (1) Ti and (2) Mo surfaces as a function of field gradient at the cathode surface.

constructed, as shown in Fig. 3.

Comparing the plots for Ti and Mo, it is obvious that the primary field emission from the Mo surface is much smaller than that from the Ti surface, consistent with the original expectation. As the F-N equation indicates that the field emission current is inversely proportion to the work function of the electrode material, the present analysis results seem quite reasonable, where the work functions of Mo and Ti are 4.6 and 4.3 eV, respectively.

REDUCTION OF DARK CURRENT

The above analysis showed that Mo and Ti have different advantages, that is, Mo exhibits low primary field emission, while the enhancement effect due to bombardment is weak for Ti. Thus, a Mo cathode and Ti anode may represent the best electrode combination.

Dark current measurements were made for such a Mo-Ti electrode configuration at different gap separations. The results for 0.5 mm gap separation are plotted in Fig. 4 in comparison to the results for the Mo-Mo and Ti-Ti configurations. As expected, the Mo-Ti configuration exhibits the best performance with a dark current of only 80 pA at 115 MV/m, increasing to 1 nA at 130 MV/m. The evaluated behaviour of primary field emission currents for the Mo-Ti electrode agrees quite well with that for the Mo-Mo electrode. It supports the validity of the present analysis method.

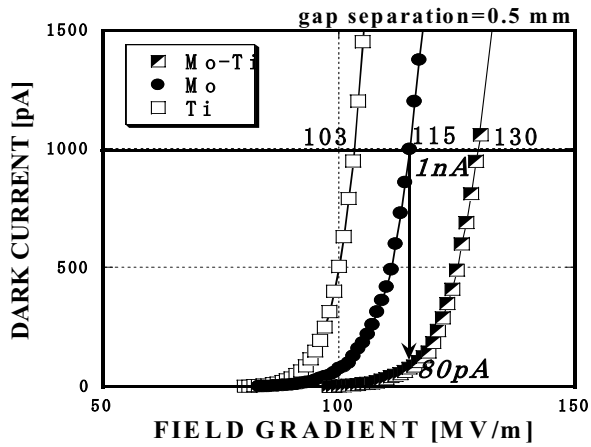

Figure 4: Dark currents for Mo-Ti, Mo-Mo, and Ti-Ti electrodes as a function of field gradient at the cathode surface for a gap separation of 0.5 mm.

FIELD ENHANCEMENT FACTOR β

Although the field enhancement factor β defined in the F-N equation is independent of gap separation [4], a clear dependence is apparent in the experimental data. Fig. 5 plots β for the Mo-Ti, Mo-Mo and Ti-Ti electrode configurations with respect to gap separation. As a gross feature, the value of β increases linearly with gap separation. It is reasonable since the dark current enhancement effect becomes more significant as the gap becomes wider and is interpreted as an increase in the local field strength in the F-N equation.

The β values for both Mo-Ti and Mo-Mo electrodes at zero gap separation must to be same (β≈23), since the same field emission current is expected for them. The straight lines fitting the gap-dependent β value for Mo-Mo and Mo-Ti electrode in Fig. 5 seem to cross the vertical axis at the same point (β≈23). This agreement in the β values by two different fitting methods demonstrates again the reliability of equation (1) for evaluating field emission dark current.

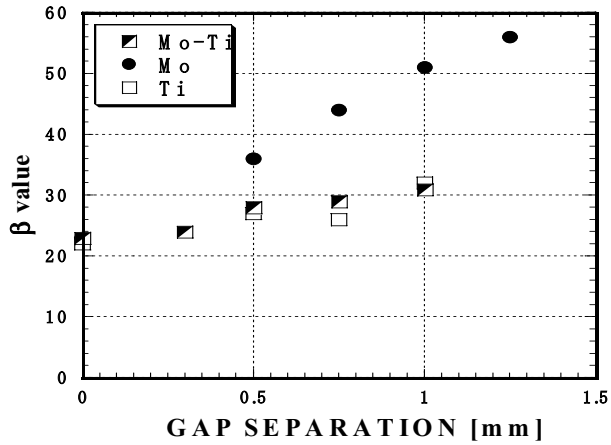

Figure 5: Dependence of enhancement factor α on gap separation for Mo-Ti, Mo-Mo, and Ti-Ti electrodes. Enhancement factors at a gap separation of zero are obtained from the F-N plot using estimated primary field emission data.

SUMMARY

Electrodes of Mo and Ti were fabricated and tested. A new analysis method was proposed to evaluate the primary field emission current component of the total dark current by using gap dependence data. Through this analysis, it was predicted that Mo is most suitable as a cathode material, while Ti is suitable for use as an anode. This is verified by experiment using the electrode configuration of a Mo cathode and Ti anode. A dark current of 1 nA was generated under an applied field of 130 MV/m at a gap separation of 0.5 mm. This result is useful for constructions of high field gradient guns to produce the low emittance electron beam in various applications. The details of this report will be published in a referred journal [5].

REFERENCES

[1] R. Alley et al., N. I. M. A 365 (1995) 1
[2] C. Suzuki et al., N. I. M. A 462 (2001) 337
[3] R. H. Fowler and L. Nordheim, Proc. Roy. Soc. A 119 (1928) 173
[4] R. V. Latham, High Voltage Vacuum Insulation, Academic Press London, 1981, Chap. 2
[5] F. Furuta et al. submitted to N. I. M.

HIGHLY POLARIZED ELECTRONS FROM GaAs-GaAsP AND InGaAs-AlGaAs STRAINED LAYER SUPERLATTICE PHOTOCATHODES

T. Nakanishi[a], T. Nishitani[a], M. Yamamoto[a], S. Okumi[a], F. Furuta[a], M.Kuwahara[a], N. Yamamoto[a], K. Naniwa[a], K. Yasui[a], O. Watanabe[b], Y. Takeda[b], H. Kobayakawa[b], Y. Takashima[b]
H. Horinaka[c], T. Matsuyama[c]
[a]Department of Physics, Nagoya University, Nagoya 464-8602, Japan
[b]Faculty of Engineering, Nagoya University, Nagoya 464-8602, Japan
[c]Faculty of Engineering, Osaka Prefecture University, 599-8531, Japan

Abstract

GaAs-GaAsP and InGaAs-AlGaAs strained-layer superlattice photocathodes are presented as emission sources for highly polarized electron beams. The GaAs-GaAsP cathode achieved a maximum polarization of 92(±6)% with a quantum efficiency of 0.5%, while the InGaAs-AlGaAs cathode provides a higher quantum efficiency (0.7%) but a lower polarization (77(±5)%). Criteria for achieving high polarization using superlattice (SL) photocathodes are discussed based on experimental spin-resolved quantum efficiency spectra.

INTRODUCTION

Polarized electron beams are conventionally produced by photoemission from GaAs-type semiconductors. The degeneracy between heavy hole (hh) and light hole (lh) bands at the valence band maximum can be resolved through the use of a strained GaAs layer, a GaAs-AlGaAs superlattice SL layer, or a strained InGaAs-GaAs SL layer, and our group has achieved experimental ESPs of 86% [1], 70% [2] and 83% [3], respectively.

In these studies it became clear that by using a modulation-doping method, the SL cathode is capable of achieving much higher quantum efficiency (QE) than the strained-layer GaAs. Thus, while heavy doping is used for surface layers to achieve large band-bending, medium doping is better for SL layers in order to avoid spin-flip depolarization.

More importantly, however, SL cathodes were found to provide a solution for the surface charge limit (SCL) problem, whereby the maximum current density that can be extracted from the NEA surface is much lower than that determined by the space charge limit. This effect is caused by a decrease in band bending at the NEA surface due to the surface photo-voltage (SPV) effect. However, a GaAs-$Al_{0.31}Ga_{0.69}As$ cathode has been demonstrated to produce a space charge-limited current of 14 A (2.3×10^{11} electrons in a 2.5 ns bunch) using a 120 keV gun with a QE of 2.0% at a laser wavelength of 752 nm [4]. This means that the use of a modulation-doped SL photocathode solves the SCL problem for this beam condition.

Encouraged by these successful results, the present authors have continued research on the development of new types of InGaAs-AlGaAs and GaAs-GaAsP strained SL structures [5]. We have also investigated the SCL problem in more detail using the SL photocathodes irradiated by a nanosecond double-bunch laser with 2.8 ns separation time [6]. In this paper, we describe experimental results demonstrating the improvements in ESP, QE and SCL effect achieved using a GaAs-GaAsP cathode. Criteria for obtaining the highest ESP are also proposed based on the spin-resolved QE spectra.

PHOTOCATHODE PREPARATION

The InGaAs-AlGaAs SL samples were fabricated by molecular beam epitaxy (MBE) at NEC, and the GaAs-GaAsP SL samples were made by metal-oxide chemical vapor deposition (MOCVD) at Nagoya University. The InGaAs-AlGaAs sample was prepared with a protective surface film of amorphous As, which was removed by heat-cleaning at 400 ºC in a vacuum. The GaAs-GaAsP sample had no protective film and was heat cleaned at 550 ºC for 2 h in a vacuum.

A number of different SL samples with various materials and crystal parameters were fabricated and tested, but in this paper, the SLSA#2 and SLSP#9 samples are selected from InGaAs-AlGaAs and GaAs-GaAsP SL families, for detailed analysis. The crystal structure and doping densities for SLSP#9 are shown in Fig. 1.

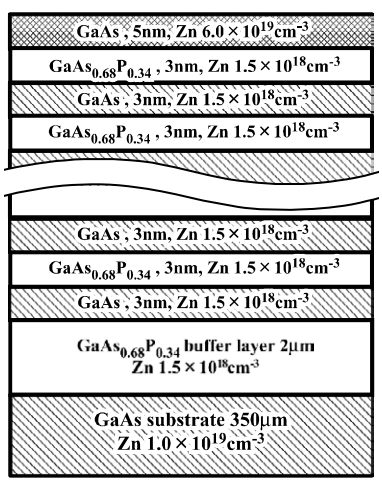

Figure 1: Crystal structure and doping density of the SLSP#9 sample.

A commercially available GaAs wafer with high Zn dopant content was used as a substrate, and a strain-

relaxed GaAsP buffer layer was formed on it to obtain large strains for the GaAs well layers. The 16 pairs of SL layers with medium Zn dopings of 1.5×10^{18}/cm^3 were terminated with a heavily doped surface layer of GaAs (Zn, 6.0×10^{19}/cm^3) to obtain a large band bending at the NEA surface. The crystal structue of SLSA#2 was already given in ref. 6 as a SL-3 sample.

The modulation doping technique was employed for whole samples. The thicknesses of the wells and barrier layers were chosen so as to obtain high large hh-lh energy splitting, and the total thickness of the samples was about 100 nm, set to minimize spin depolarization.

ESP AND QE SPECTRA

ESP and QE spectra were measured using a compact cathode test system with a 4 keV gun and a 100 keV Mott polarimeter [7]. The maximum systematic error for this ESP measurement was estimated to be ±6% (absolute value) [1].

The ESP and QE spectra for the SLSP and SLSA cathodes are shown in Fig. 2 against laser wavelength.

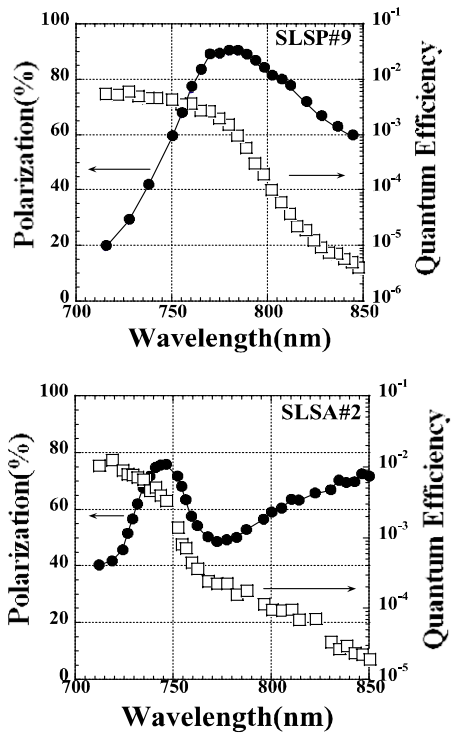

Figure 2: Observed ESP and QE spectra for SLSP#9 and SLSA#2.

Most of the SLSP cathodes achieved maximum ESPs of higher than 90%, with SLSP#9 reaching 92% with a QE of 0.5% at 778 nm. The SLSA cathodes showed lower ESPs of around 80%, but the highest QE of 0.7% was reached by SLSA#2 at 741 nm with an ESP of 77%.

Concerning the SCL effect, we demonstrated that a multi-bunch beam required by a future linear collider can be also produced using the GaAs-GaAsP photocathode in combination with a 70 keV gun and a 0.7 ns double-bunch laser. Recently, this SCL effect was also studied by an approach using core-level photo-electron spectroscopy in combination with synchrotron radiation and a laser. It was found that the SPV effect in the SL cathode is remarkably suppressed compared with that in a bulk-GaAs cathode [8].

DATA ANALYSIS

We have experimentally investigated SL photocathodes with GaAs-AlGaAs, InGaAs-AlGaAs and GaAs-GaAsP structures, and the highest ESPs obtained by these samples are 70%, 83% and 92%, respectively. The maximum ESP depends strongly on the initial polarization (P_i) of excited electrons in the conduction band, and P_i is in turn related to the coefficients of photo-absorption from the hh (A_{hh}) and lh (A_{lh}) mini-bands. The explicit relations are given by $A_{hh} = A_i(1 + P_i)/2$ and $A_{lh} = A_i(1 - P_i)/2$, where A_i is the total absorption coefficient, and the sign of P_i is defined as positive for left-handed electrons.

These photo-absorption coefficients A_{hh} and A_{lh} are proportional to the joint densities of state (JDOS) between conduction and hh or lh bands. The typical behaviors of these JDOSs in the threshold region are shown in Fig. 3, where the two dotted lines represent the JDOSs for strained layers, and the two solid lines denote those for strained SL layers. The latter exhibit a series of quantum jumps with an unit of $m/(\pi\hbar^2)$, where m is a reduced mass defined as $m_{c\text{-}hh} = (m_c\times m_{hh})/(m_c + m_{hh})$ for hh absorption, and $m_{c\text{-}lh} = (m_c\times m_{lh})/(m_c + m_{lh})$ for lh absorption. The width of the absorption edge ($W_{c\text{-}hh}$ or $W_{c\text{-}lh}$) corresponds to the sum of widths for both the conduction and the hh or lh mini-bands.

For comparison of the experimental data with the above JDOS-based A_{hh} and A_{lh} spectra it is convenient to use the spin-resolved quantum efficiencies for left-handed (Q_L) and right-handed (Q_R) electrons in an emitted beam as functions of excitation photon energy. The Q_L and Q_R spectra are related to experimental ESP and QE spectra

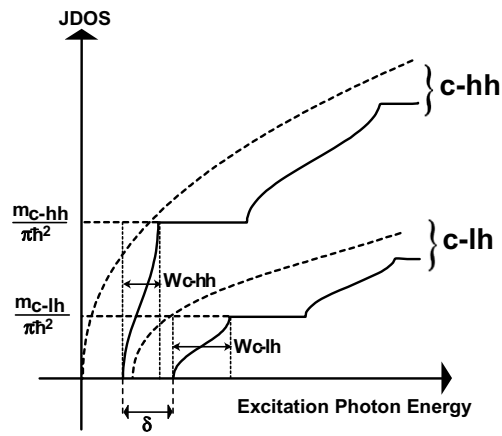

Figure 3: Schematic behaviours of JDOS's as functions of excitation photon energy for strained layer (dotted line) and strained layer (solid line) in threshold energy region.

by Q_L = QE(1 + ESP)/2 and Q_R = QE(1 – ESP)/2, where the sign of ESP is defined as positive for left-handed electrons.

The experimental Q_L and Q_R spectra are plotted in Fig. 4. As expected from the typical JDOS spectra in Fig. 3, a step-like jump in QE is clearly observed in the Q_L spectra for SLSP#9, yet is difficult to discern for SLSA#2. No such QE steps were observed in any of the Q_R spectra, probably due to the limited range of wavelengths covered by our laser system.

The parameters of the JDOS-based A_{hh} and A_{lh} spectra were determined for the SLSP and SLSA cathodes using threshold energies for hh and lh excitations calculated by the Kronig-Penny (KP) model, by approximating the shapes and widths of the hh and lh absorption edges by dispersion relation curves calculated using the KP model, and by modeling the unit of quantum absorption jump as being proportional to $m/(\pi\hbar^2)$ after the observed jump in QE.

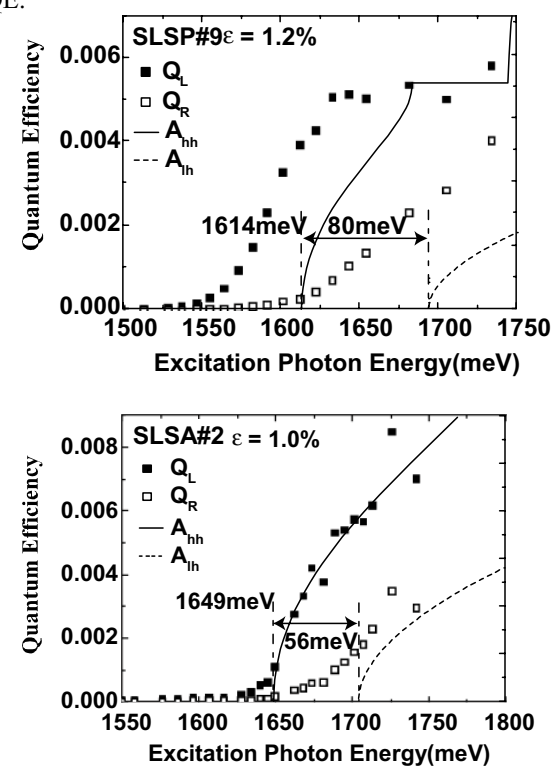

Figure 4: The Q_L and Q_R spectra (experimental) and the JDOS- based A_{hh} and A_{lh} spectra for SLSP#9 and SLSA#2.

The threshold positions for the Q_L and Q_R spectra of SLSP#9 do not coincide with those of the A_{hh} and A_{lh} spectra, instead being shifted to lower photon energies. This discrepancy can be resolved by taking the strain relaxation effect into account. The critical thickness with respect to strain relaxation can be estimated using the Matthews formula. A net strain (ε*) is defined for the SL layer as $\varepsilon^* = \varepsilon L_w/(L_w + L_b)$, where L_w and L_b are the widths of the well and barrier layers, respectively and ε is the strain induced by lattice-mismatch between the well and barrier layers. The estimated values of strain, net strain and critical thickness are 1.2%, 0.6% and 20 nm. The SLSA sample has a critical thickness about 3 times that for the SLSP cathodes and the strain relaxation seems negligible. As shown in Fig. 5, reasonable agreement is obtained for the threshold positions if the reduced strains after relaxation are assumed to be 0.66% and 0.72%.

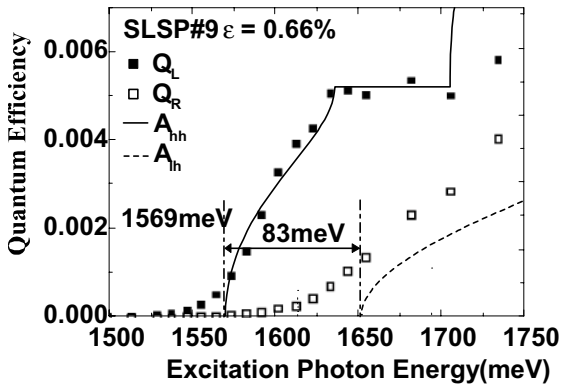

Figure 5: Q_L and Q_R spectra with shifted threshold energies calculated by using the reduced strain for SLSP#9.

Both Q_R spectra show that the threshold position is smeared by small amounts of right-handed electrons below the threshold energy level. These right-handed electrons appear to be created from left-handed electrons through spin-flip interactions, and this smearing effect looks to be an important factor determining the upper-limit of ESP.

SUMMARY

This paper reports our systematic study of strained-layer SL photocathodes with InGaAs-AlGaAs and GaAs-GaAsP structures. Our results confirm that GaAs-GaAsP SL photocathodes are capable of delivering electron beams with high ESP, high QE and high peak current. It is most promising cathode for future linear colliders.

The mechanism that determines the maximum ESP was clarified through phenomenological data analyses of spin-resolved QE spectra. It was found that the most important factors for achieving high ESP are 1) large hh-lh energy (δ) separation, 2) narrow joint widths ($W_{c\text{-}hh}$) between the conduction and hh-band, and 3) minimal depolarization inside the SL layers. Combining 1) and 2), $\delta \geqq W_{c\text{-}hh}$ was derived as the most important condition. The above criteria can explain why the GaAs-GaAsP strained SL photocathode can achieve such high ESP (92%) and QE (0.5%) simultaneously.

REFERENCES

[1] T. Nakanishi et al., Phys. Lett. 158, 345 (1991).
[2] T. Omori, et al., Phys. Rev. Lett. 67, 3294 (1994).
[3] T. Omori, et al., Jpn. J. Appl. Phys. 33, 5676 (1994).
[4] Y. Kurihara, et al., Jpn. J. Appl. Phys. 34, 355 (1995).
[5] T. Nakanishi et al., AIP. Conf. Proc. 421, 300 (1997).
[6] K. Togawa, et al., Nucl. Instr. Meth. A414, 431 (1998).
[7] T. Nakanishi, et al., Jpn. J. Appl. Phys. 25, 766 (1986)
[8] S. Tanaka et al., J. Appl. Phys. 95, 551 (2004)

DEVELOPMENT OF FIELD-EMISSION ELECTRON GUN FROM CARBON NANOTUBES

Y. Hozumi[1,A)], S.Ohsawa[B)], T. Sugimura[B)], M. Ikeda[B)]
[A)]*The graduate university for advanced studies,* [B)]*KEK, 1-1 Oho, Tsukuba, JAPAN*

Abstract

Aiming to develop a high intensity electron beam with narrow energy-spread for injector guns, we have been tested field emission cathodes of carbon nanotubes (CNTs), which have some features of easy handling and low cost. Experiments for these three years brought us important suggestions and a few rules of thumb. Now at last, anode current of 3.0 A/cm^2 was achieved with 8 kV acceleration voltage by applying short grid pulses between cathode and grid electrodes[1]. In order to proof utility, 100-kV gun system had been designed and constructed since last year. Then the value of 100 mA was obtained based on 10^{-5}~10^{-6} Pa back ground pressures. With some improvements it would be expected that anode currents of Ampere order will be obtained from the CNTs cathode gun.

INTRODUCTION

The heater-less electron guns (e-guns) are desired because of its excellent emission properties, i.e., low emittance, high brightness and low cost driving. Field emission (FE) e-guns are under investigation for injector linacs. This time, we have been fabricated and tested a new type of FE-gun using the promising material emitter called “carbon nanotubes (CNTs)”. The CNTs have strong potentials as a field emitter; actually, 1×10^9 A/cm^2 of current density has recently obtained in Japan. In the last year, it was reported that anode current of 3.0 A/cm^2 was achieved from CNT-FE e-gun by applying short grid pulses between cathode and grid electrodes [1]. The CNTs cathode which had enough current density and long life-time could be developed by some companies’ cooperation[2]. The report results were obtained with as low acceleration voltage as 8 kV, and this time, we have constructed a 100 kV practical test stand and started test of performance of the e-gun which were also designed to suited EIMAC-Y796 standard. This paper describes the basic design and the characteristics of the CNTs FE-gun.

COMPOSISIONS OF THE E-GUN SYSTEM

Measurement System and Electrical Circuits

At the gap distance between the grid and cathode (G-C) electrodes, short pulses of 50 ~ 100 ns width and 0.1 ~ -3.4 kV are applied through a BNC connector with a repetition rate of 7〜10 Hz. 50 ns is the lower limit of the pulse generator PVX-4140 produced by DIRECTED ENERGY, INC. Figure 1 shows this system outline. The 50 Ω resistance connected to the pulser in series has a role of mitigating damage of the cathode from discharge, and reflected pulses due to impedance miss match. The emitted electrons are accelerated by DC high voltage of 100 kV between the anode and grid electrodes, and then emerge from the e-gun through an anode hole. Then, electron beams are adjusted by a magnetic lens to focus on the beam catcher (BC) in solenoidal fields. The values of beam currents are measured by monitors such as a wall current monitor (WCM), a core monitor (CM) and BC, which are set along the beam line. Furthermore, a fluorescence screen is available, if necessary, by inserting in the beam line instead of BC at the same place.

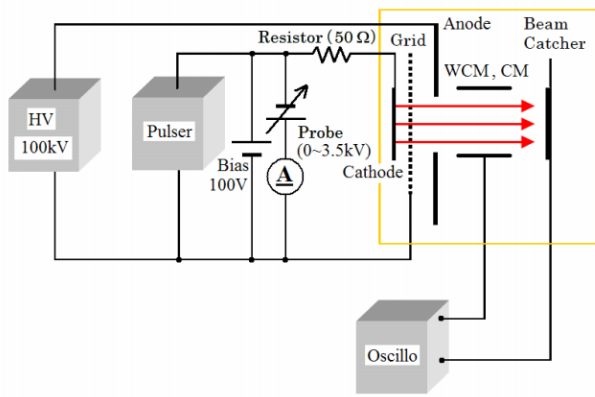

Figure 1: The main components of the e-gun system

Structures of the E-Gun

Figure 2: The e-gun view

Figure 2 shows e-gun structure viewed from the grid side. A standard vacuum flange ICF88 is adopted for the e-gun in order that it is compatible with the often used cathode EIMAC-Y796. The distance between the G-C is very important, because it determines the field gradient between the G-C with grid pulses, namely beam currents. Therefore we designed the structure of the G-C assembly

[1)] hozumiy@post.kek.jp

so that the distance is given mechanically from the components in an accuracy of 10 μm by means of compressing with a screw from BNC connector side. By changing height of a cathode base the distance will be easily changed. Furthermore it is easy to assemble the G-C mechanically it is suitable to make a test for many pieces of cathodes by changing one to another.

Figure 3 shows the Wehnelt electrode with a grid-cathode assembly at the center. The slope angle of 22.5 degrees was chosen to get a parallel beam following Pierce's theory. In the picture there is space between the Wehnelt electrode and outside of the G-C assembly. Its space is actually filled with a cover of SUS in case of measurements. Figure 4 shows an anode electrode which was made into monotonous structure, and attached the roundness of R2 to the beam hole, which was an entrance of the beam (10 mm diameter), and the anode surfaces were similarly processed like a mirror to Wehnelt electrode to avoid discharge.

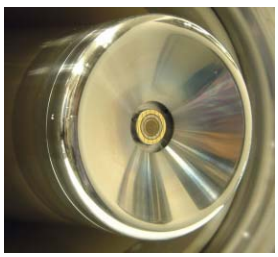

Figure 3: Wehnelt

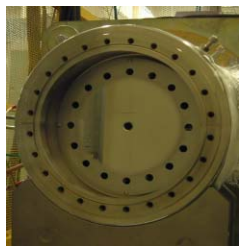

Figure 4: anode

Beam Trajectory Simulation

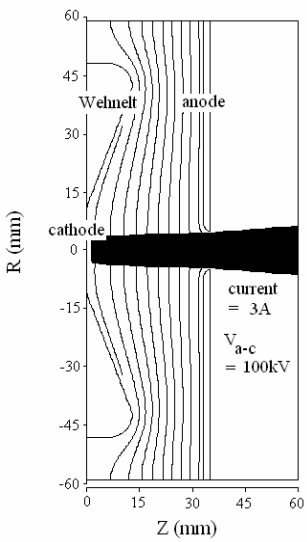

Figure 5: Simulation results image

Trajectories were simulated by the code EGUN with an assumption that electrons were uniformly emitted from the cathode surface at room temperature (defined as 300 K) with a cathode current of 3 A at an acceleration voltage of 100 kV. It was conformed that beams from a cathode of which diameter are 6 mm could be extracted satisfactorily through the anode hole.

BEAM TEST

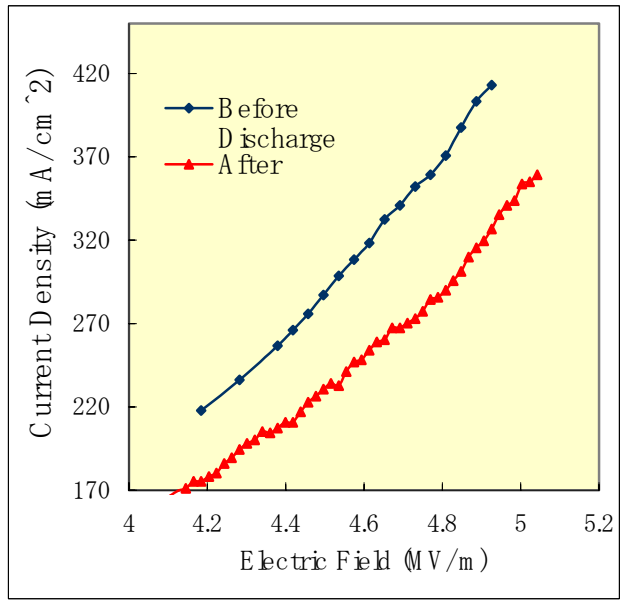

Figure 6: Reduced current density from anode current

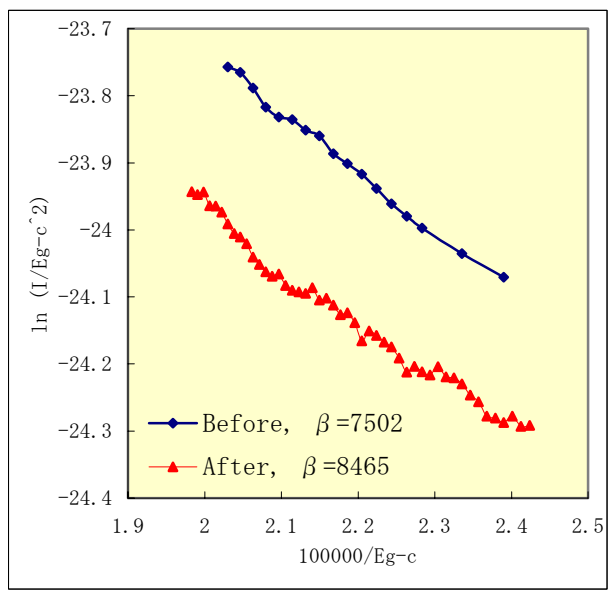

Figure 7: The Fowler-Nordheim plot of Fig.6

The beam tests were performed at the e-gun test stand, where acceleration is capable up to 120 kV. Its construction started from October last year, and completed it in February this year.

In this system, beams from the cathode are mainly controlled by pulses applied between the G-C, namely beam values such as intensity and pulse width controlled by the pulses. On the other hand, beams are accelerated by DC high voltage of 100 kV impressed between the grid and anode electrodes. Beam characteristics have been

investigated versus field strength near the cathode by changing voltage of grid pulses. Vacuum pressures achieved were in the order of 10^{-6} Pa. Figure 6 shows anode current dependence measured at BC point, versus electric fields between the G-C. Figure 7 presents Fowler-Nordheim plot of the same data, where the symbol of $E_{g\text{-}c}$ means that applied field strength between the G-C and β's are field enhancement factors. Large values of β's gotten from the plot indicate that field emission is the source of the beams as well as linearly changing dependence in the plot. The beam pulse shapes are shown in Fig. 8, which are measured by three kinds of monitors. The beam tests were performed with pulses of 65 ns width at a fixed repetition rate of 7 Hz. In Figures 6 and 7, the data measured before discharge occurred are shown with square marks, and ones with triangles are the data measured after discharge occurred three times serially. Although 400 mA/cm^2 was obtained before discharge happened, the discharge between the G-C occurred occasionally, and whenever it happened, reduction in emission current took place. Estimating from the data in Fig. 6, the rate of reduction due to a discharge was about 4 ~ 5 % in intensity.

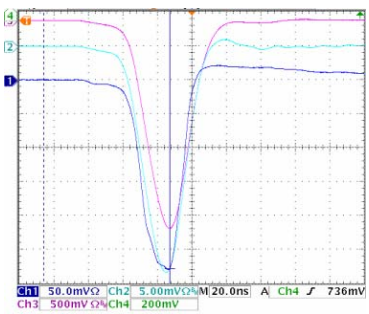

Figure 8: Monitor of beam current (CH1:WCM, CH2: CM, CH3:BC)

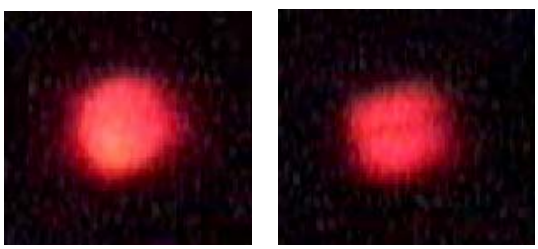

Figure 9: Beam shapes at BC before (a: left) and after discharge (b: right)

It is considered that CNTs sites emitting electrons might be broken by discharges, and number of site became fewer and fewer gradually. Then, in order to observe change in the beam shape the fluorescence screen was inserted instead of BC at the same place (see Fig. 9). The beam of Fig. 9a shows rather uniform shape which indicates uniform emission from the cathode. On the other hand, in Fig. 9b there is obviously a change in brightness: a portion of the beam disappeared due to discharges. The cathode seems to be affected by discharges. It could be said that the beam shapes observed on the fluorescence screen reflects directly the state of cathode as they are.

CNTS CATHODE SURFACE STUDY

In order to investigate directions for CNTs cathode optimization, the FE-SEM observation was performed. Figure 10 shows a FE-SEM image of a cathode sample used in this experiment, of which CNTs thin films produced on a SUS substrate. The FE-SEM observation was done in the secondary electron detection mode, at a working distance of 14.8 mm, with a probe current of 10.6 μA at 10 kV accelerating voltage. CNTs can be seen near the center of the photograph. The EDS investigation was also done to check the materials of the concavo-convex parts around CNTs substances, which revealed the materials were mainly of spherical particles of carbon-like, and partly of un-grown up CNTs. In the investigated cathode, the quite large variations were observed in CNT density and height.

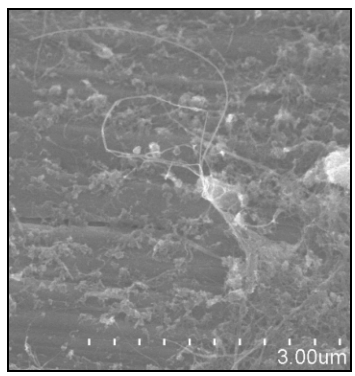

Figure 10: FE-SEM image of a CNTs cathode

SUMMARY

Anode currents were obtained as high as 100 mA from CNTs cathodes, which were equivalent to the density about 400 mA/cm^2. It became promising that Ampere order beams would come true with some improvement in vacuum pressure and CNTs cathode structure.

ACKNOLEDGEMENTS

The FE-SEM work was conducted in AIST Nano-Processing Facility, supported by Nanotechnology Support Project of the Ministry of Education, Culture, Sports, Science and Technology (MEXT), Japan.

REFERENCES

[1] S. Ohsawa et al., *Proceedings of the 28th LINAC meetings in Japan, pp. 120-122 (In Japanese).*

[2] A. Yamamoto et al., *Proceedings of the particle accelerator conference in America, pp. 3326-3328 (2003).*

COMPARISON OF 2 CATHODE GEOMETRIES FOR HIGH CURRENT (2 KA) DIODES

M. Caron, F. Bombardier, E. Merle, Ch. Noël, O. Pierret, R. Rosol, C. Vermare

CEA/DIF Polygone d'Experimentation de Moronvilliers – 51 Pontfaverger-Moronvilliers, France

N. Pichoff, DPTA/SP2A, A. Piquemal, DPTA/SPPE, CEA/DIF 91 Bruyères-le-Chatel, France

D.C. Moir, LANL-DX6 – NM Los Alamos – USA

Abstract

AIRIX (FRANCE) and DARHT axis-1 (USA) facilities are two high current accelerators especially designed for X-ray flash radiography. The produced electron beam (2 kA, 60 ns, 3.5 to 3.8 MeV at the diode output) is extracted from a velvet cold cathode. Specific calculations have demonstrated the influence of the cathode geometry on the emitted beam profiles [1]. In order to check this assumption two different experiments (DARHT march 2003 – AIRIX march 2004) have been performed. The beam characteristics with two different geometries have been compared both theoretically and experimentally. The beam simulations have been done with 3 codes: a home-made one (M2V) and 2 commercial ones (PBGUNS and MAGIC). The extracted beam current and transverse profiles, for the first experiment, have been measured and compared to simulations results. In the second one, we have mainly compared the primary current intensity that can be drawn with the two different K-designs for a given energy.

INTRODUCTION

Since the first reports on the X-ray sources like DARHT Axis 1 or AIRIX [1] [2] [3], some efforts have been devoted to improving the overall electron beam quality in order to reduce for instance the beam focal spot. One of the most relevant parameters to assess the ability for a beam to be more focused is the so-called emittance ε. ε can be seen as an intrinsic beam characteristic that can only increase all along the acceleration line. At first glance, the smaller ε onto the X-ray converter, the smaller the spot size is. Therefore, the main challenges we have to face are on the one hand to reduce the emittance as much as possible at the e-beam production stage and on the other hand to limit its growth during regular transport. This paper rather deals with the first point since reducing ε remains a key issue in the successful development of new cathode designs. We present in the first section the two different cathode geometries taken into consideration in this report as well as the numerical simulations exhibiting the expected gain in terms of beam quality. Then section 2 is dedicated to the description of the two experiments performed so far at DARHT Axis 1 and AIRIX facilities. A comparison between theoretical predictions and experimental results is done in section 3.

THEORETICAL BACKGROUND

The driving forces responsible for the major cathode developments have been quite extensively described elsewhere [1] [4] and have lead to an evolution from our regular standard K-geometry to a modified one: the so-called Pierce geometry. The main differences between them become clear from figure 1.

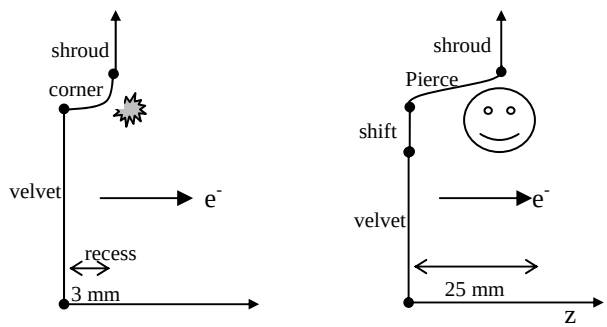

Figure 1: Cathode geometries: a: Standard; b: Pierce.

These geometrical modifications have been implemented into numerical simulation tools independently developed. The entire diode theoretical description has not only been performed by means of a home made code called M2V [5], but also with two commercial codes PBGUNS [6] and MAGIC [7] which are based on very different models. In any cases, the beam is always extracted from the cathode under space-charge limited flow. Electrons are focused out of the diode by means of a solenoid whereas another coil brings the residual magnetic field on top of the cathode down to zero. Up to now, it has been shown that the beam distribution into the (x,x') phase space simulated nearest to the anode level with M2V, PBGUNS or even MAGIC look very similar provided that stationary conditions are considered (front edges excluded) [8] [9].

According to the theoretical calculations, the main improvement expected from the use of the newest type of cathode is to get an emittance reduction of about 10 to 30 % for the same values of primary currents and energies.

EXPERIMENT

The experimental part of this work was first performed at DARHT Axis 1 on March 2003 and then at AIRIX facility on March 2004. Actually, current characterisations dealing with accelerated beams are still running on both sides but they are out of the scope of this paper. Here, we thus take a step back and concentrate on the beam analysis near the entrance of the accelerator line. Basically, such characterisation stage aims to check the validity of the theoretical predictions. In other words, for the same experimental conditions we want to compare the performances in terms of beam quality between the two cathode geometries.

DARHT Experiment

For a complete beam characterisation at the diode output the following set of data is required: the primary beam current intensity (I), the primary beam energy (E), the mean angular beam dispersion (R'), the RMS beam size (R) as well as the beam emittance (ε). The first two parameters are given in a routine way by the regular electrical captors present into the beam lines. For the last three ones, a classical beam diagnostic based on the detection of the electron induced Cerenkov radiation has been used for the present purpose. As a first step prior to a more refined analysis, we present in figure 2 and 3 the beam patterns and the related transverse profiles measured for the both types of cathodes at the same location (z=1.67 m away from K).

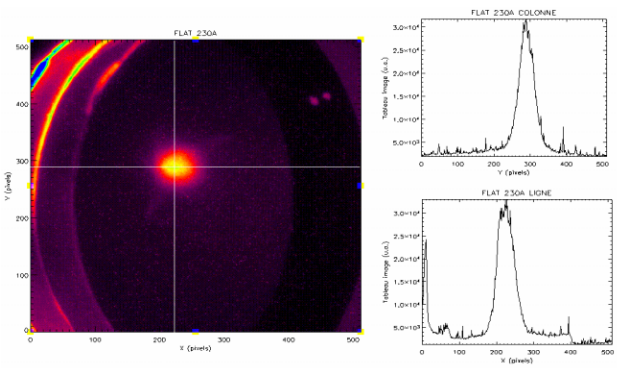

Figure 2: Beam pattern from Cerenkov light recorded for the standard cathode (I=1.84 kA, $I_{focusing\ magnet}$ = 230A)

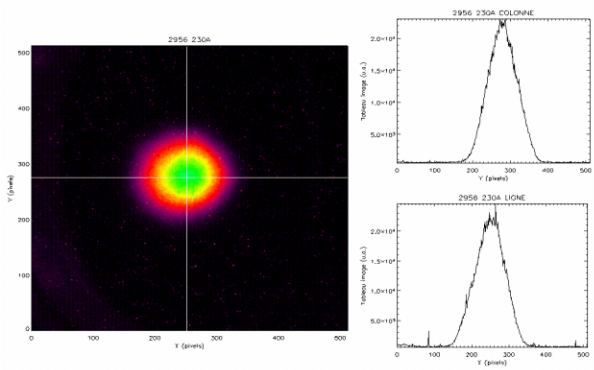

Figure 3: Beam pattern from Cerenkov light recorded for the Pierce cathode (I=1.77 kA, $I_{focusing\ magnet}$ = 230A)

First remark looking at figure 3 is that the entire set of emitted electrons falls down into a sharp contour. This remark is no longer valid for figure 2 where long wings are visible. Moreover, an additional peak to the main one rises up near the edge. A possible interpretation of such interesting findings assumes that the emitted light from the outer part is due to the superimposition of an Optical Transition Radiation to the main Cerenkov signal. The OTR contribution would be induced by electrons coming from the foot of the main distribution interacting with the metallic radiator holder. However both cathodes exhibit a clear difference with respect to their beam profiles and the main conclusion drawn is that the Pierce geometry offers the opportunity to get rid off the disturbing background signal observed while using the standard cathode. This outcome appears like the first qualitative improving point brought by the modified K-design regarding to the beam quality.

AIRIX Experiment

As already mentioned in the previous section, the same parameters E, I, R, R' and ε are required to achieve a complete beam properties investigation. From a primary beam energy spread measurement performed with a time resolved magnetic spectrometer [10] the mean beam energy value can be known while the corresponding primary current intensity is given by the magnetic loops of a Beam Positioning Monitor located in front of the spectrometer entrance. When varying the diode voltage, different (E, I) values are measured and plot together to form a kind of Voltage-Current Diode Characteristic.

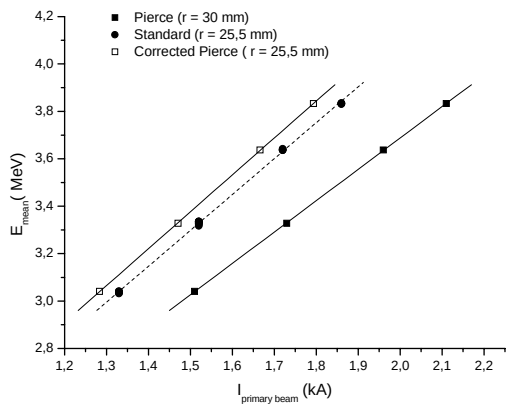

Figure 4: Energy current diode characteristics.

The full symbols correspond to the measured values. As the velvet radii are different we have tried to estimate the emitted current for a Pierce cathode with the same emitting surface (open squares). This correction has been done assuming that the emitted current intensity follows a velvet radius square law. It turns out that a small shift is observed meaning that for a given diode voltage the Pierce cathode would emit slightly less electrons.

The beam patterns from electron induced Cerenkov light have been recorded for different current intensity settings on an upstream focusing magnet and for both cathodes. The radiator is a 5 μm thick aluminium coated mylar foil, tilted with respect to the accelerator axis to the right angle in order to make light easily measurable by an intensified and a two dimensional gated camera (512 x 512 pixels^2, 8 bits, 5 ns minimum exposure time).

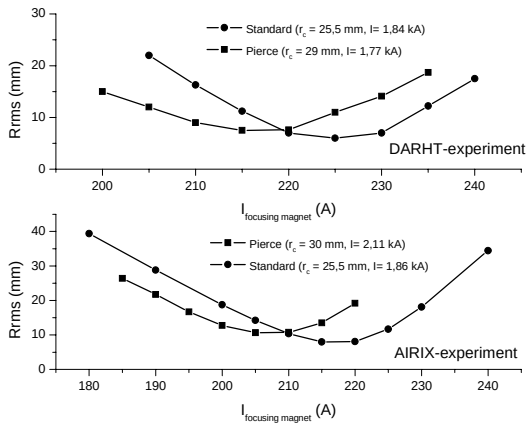

Figure 5: R_{rms} evolution as a function of the focusing magnet current intensity for both experiments (z = 2.095 m for AIRIX, z = 1.890 m for DARHT).

For the standard cathode, the RMS beam radius varies as a function of the extraction current intensity with a stronger slope than for the Pierce one near the beam-waist. This behavior might be an advantage in terms of beam stability since the beam transport from the diode to the accelerator line would be less sensitive to slight current drift into the extraction solenoid.

RESULTS AND DISCUSSION

Part of the experimental results measured either at DARHT or at AIRIX can be used now to verify and to validate the diode modelling by the different numerical simulation tools.

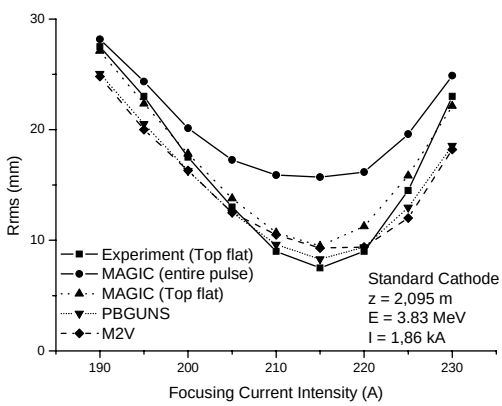

Figure 6: Envelope radius as a function of the focusing magnet current intensity.

As an example, we present above one comparison between experimental data and theoretical calculations for the standard cathode. As long as the front edges of the pulse are not taken into account in the numerical simulations the whole calculated datasets fit quite properly the measured ones. In order to make a more stringent validation of the numerical simulations we need now to measure some more refined experimental parameters like ε for instance, ideally in a more accurate way than the usual three-gradient method.

CONCLUSION AND OUTLOOK

The first results dealing with the e-beam characterisation at the diode output have shown measurable differences between the two cathodes geometries under investigation. The Pierce geometry has shown promising behaviours with respect to the beam quality like some better defined beam profiles and a smoother beam-waist at the entrance of the accelerator. This makes it very worthwhile to further investigate this cathode and see whether or not after beam acceleration the promising results obtained so far could lead to a significant reduction of the focal spot size.

AKCNOWLEDGEMENTS

We would like to thank the both accelerator operation teams from DARHT and AIRIX for their assistance before and during the experiments.

REFERENCES

[1] E. Merle et al., “Efforts to Improve Intense Linear Induction Accelerator (LIA) Sources for Flash Radiography”, Proc. of LINAC 2002.
[2] M. J. Burns et al., “DARHT Accelerators Update and Plans for Initial Operations », Proc. of PAC 1999.
[3] E. Merle et al., “Transport of the 1.92-3.1 kA AIRIX Electron Beam”, Proc. of PAC 2001.
[4] R. Bailly-Salins et al., “A New Cathode for AIRIX », internal CEA-report 1999.
[5] M2V code.
[6] J.E. BOERS, “PBGUNS: an Interactive IBM PC Computer Program for the Simulation of Electron and Ion Beams and Guns”, http://www.thunderbird simulations.com.
[7] http://www.mrcwdc.com/magic/index.html.
[8] N. Pichoff et al., “End to End Multiparticle Simulations of AIRIX”, Proc. of ENAC 2004.
[9] N. Pichoff et al., “Modélisation de la diode dans le simulateur AIRIX », internal CEA-report 2004.
[10] D. Villate et al., “AIRIX alignment and high current beam diagnostics”, Proc. of PAC1995.

ULTRA-LOW EMITTANCE ELECTRON GUN PROJECT FOR FEL APPLICATION

R. Ganter, M. Dehler, J. Gobrecht, C. Gough, G. Ingold, S.C. Leemann, M. Paraliev,
M. Pedrozzi, J.-Y. Raguin, L. Rivkin, V. Schlott, A. Streun, A. Wrulich,
Paul Scherrer Institut, Villigen, Switzerland
A. Candel, K. Li, Swiss, Federal Institute of Technology, Zürich, Switzerland

Abstract

Most of the current 1 Å Free-Electron Laser (FEL) projects are based on thermionic or photocathode guns aiming at an electron beam emittance of 0.5 to 1 mm·mrad. The design of a gun capable of producing a beam with an emittance one order of magnitude lower than the state of the art would reduce considerably the cost and size of such a FEL. Due to the recent advances in nanotechnologies and vacuum microelectronics, a field-emitter based gun is a promising alternative scheme. We present first measurements on commercial field-emitter arrays as well as 3-D numerical simulations of the electron beam dynamics for typical bunch distributions generated from field emitters in realistic gun geometries.

MOTIVATIONS

In a LINAC-driven FEL, the normalized electron beam emittance ε_n has to satisfy the condition [1]:

$$\varepsilon_n < \beta\lambda\gamma / 2\pi L_g ,$$

where λ is the radiated wavelength, β the beta function, γ the relativistic factor and L_g the gain length. For a given wavelength, a small normalized beam emittance would considerably reduce the required beam energy and thus the cost and size of the accelerator facility [2]. The required peak current to drive efficiently a FEL is also reduced when the emittance is smaller. Moreover, the emittance is limited by its initial value at the cathode which can be expressed as follows:

$$\varepsilon_n = \frac{\gamma r_c}{2}\sqrt{\frac{E_{r,kin}}{m_o c^2}} ,$$

where r_c is the cathode radius and $E_{r,kin}$ the mean transverse kinetic energy just after emission. Reducing the the size of the cathode and the mean transverse energy of the emitted electrons leads then to a lower emittance.

FIELD-EMISSION CATHODES

The standard emission mechanisms of the cathodes used in the accelerator electron guns are photoemission and thermionic emission. In both cases, the mean transverse energy of the extracted electrons is several hundreds meV due either to the difference between photon energy and cathode work function or to the cathode temperature. This already limits the minimum achievable initial transverse kinetic energy of the produced electron beam. One alternative technology is field-emitter arrays (FEA) where electrons are emitted with energies close to the Fermi level. In such cathodes, the mean transverse energy is mainly determined by the geometry of the electric field lines [3].

These FEAs consist of thousands of conductive tips in the micrometer size range separated from a conductive gate layer by a one micrometer thick dielectric layer (see Fig. 1 and 2). By applying a voltage V_{ge} between the tips and the gate layer electrons are emitted from the tip's apexes. Additional control of the electron trajectories can be achieved by integrating a focusing second grid layer.

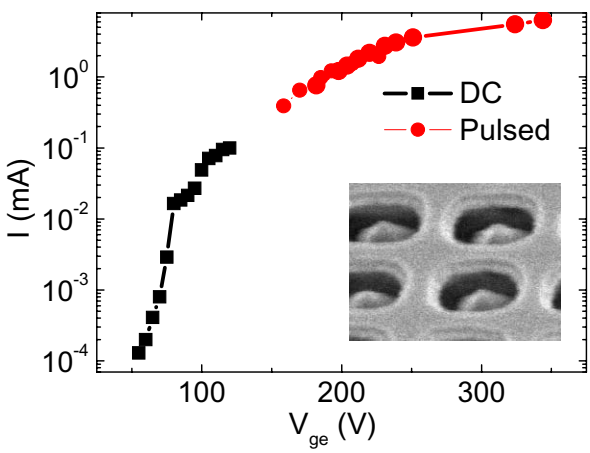

Figure 1: Current-voltage characteristic in DC and pulsed regime for a XDI Inc. FEA (170 µm diameter, 3,000 diamond tips). Insert: SEM picture of some pyramidal diamond tips.

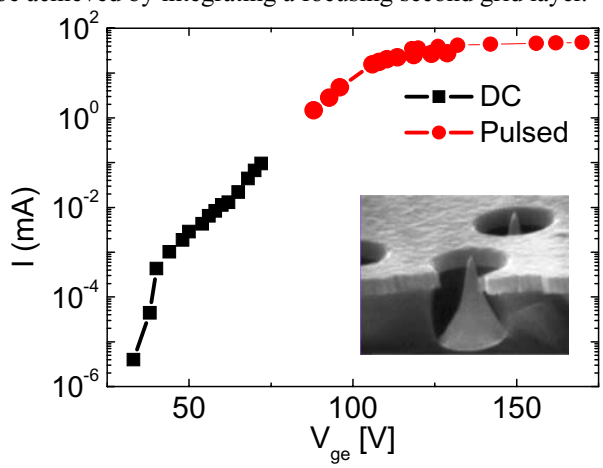

Figure 2: Current-voltage characteristic in DC and pulsed regime for a SRI Inc. FEA (1 µm diameter, 50,000 Mo tips) Insert: SEM picture of some conical Mo tips (SRI website [3]).

FIELD-EMITTED CURRENT MEASUREMENTS

The present work focuses on the maximum emitted current performances that can be obtained from FEA cathodes available on the market. The SEM pictures in Fig. 1 and 2 represent diamond tips from the company XDI Inc. [4] and molybdenum tips from SRI Inc. [5], respectively. A single tip in ZrC from APTech Inc. [6], without any gate layer, has been tested as well (Fig. 4). Field emitted currents were measured in a triode configuration where a collector was positively biased with respect to the gate layer and the tips.

In DC operation, the limiting factor for high current emission in FEAs is the thermally induced desorption of atoms and the related contamination and sputtering problems. These well-known environmental problems can lead to current emission fluctuations by changing either the work function or the tip geometry [7]. Local pressure rise can even lead to some destructive arcs. By driving the FEAs with low-frequency short voltage pulses it is possible to reduce drastically these environmental problems. Consequently, the emitted current can be increased with less risk of deterioration.

Fig. 1 shows the variation of the emitted current with the applied tip-to-gate voltage for an XDI Inc. array of about 3,000 diamond tips. The tips were distributed on a 170 micrometers diameter disc area. The measured maximum current in the continuous mode was about 800 µA but emission was subject to fluctuations, a phenomenon already pointed out in [7]. Monotonic decay with time, also mentioned in [7], was observed as well. However, in the 50-Hz pulsed regime, with 100-ns applied voltage pulses, it was possible to reach up to 6 mA peak current. In this mode of operation, emission was very stable and no decrease of the emitted current was observed after one day of operation. The maximum current performance was limited by the 25-kΩ internal resistance of the field-emitter array. This internal resistance also limits the minimum pulse length that can be applied between the gate and the tips. The current-voltage characteristic for a standard FEA from SRI Inc. (Fig. 2) shows a similar behavior. This FEA consists of about 50,000 Mo tips grown by the so-called Spindt method [7] on an area of one millimeter in diameter. Again, the sensitivity to environmental conditions was much less important in the pulsed mode than in DC. The maximum emitted current was limited by the silicon wafer resistance to values around 50 mA (see Fig. 2). Fig. 3 shows the typical 100 ns collected current pulses collected with a SRI Inc. FEA.

Fig. 4 represents some collected current pulses for a single ZrC tip. Since this tip does not have any gate layer, a copper anode was placed five millimeter away from the tip and large (several kV) voltage pulses were applied. To protect the tip from too high current values, a 10-kΩ resistor was placed in series with the tip. The effect of the resistor is the slow charging ramp on the current pulses seen in Fig. 4. Only the apex of the ZrC tip emits, the tip apex radius being less than one micrometer (specifications give values between 20 and 100 nm). Assuming an emission area of one square micrometer, the corresponding current density is as high as 100 kA/cm^2.

3-D BEAM DYNAMICS SIMULATIONS

To assess the projected emittance and the slice emittance of an electron beam generated with a pulsed DC gun equipped with a field-emission cathode, MAFIA simulations have been performed for different cathode-anode geometries. The active emitter diameter was 0.5 mm and the electron bunches were assumed to have a longitudinal Gaussian distribution such that the rms bunch length was 8.3 ps (20 ps FWHM). The applied voltage between the cathode and the anode plate was 1 MV and the cathode-anode distance was varied from 10 mm to 1 mm leading to average electric fields ranging from 100 MV/m to 1 GV/m. The iris diameter in the anode plate was accordingly varied from 4 mm to 1 mm.

The variations of the projected and slice (1 ps long) emittances with the peak current are shown in Fig. 5 and

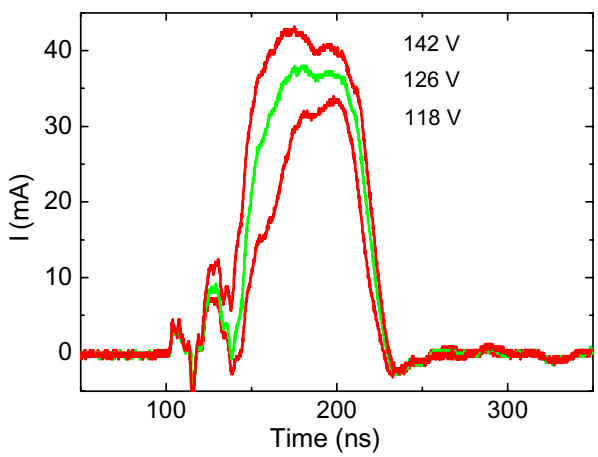

Figure 3: Collected current pulses for a SRI Inc. FEA with 50,000 Mo tips for 100 ns square applied voltage pulses of 118, 126 and 142 V.

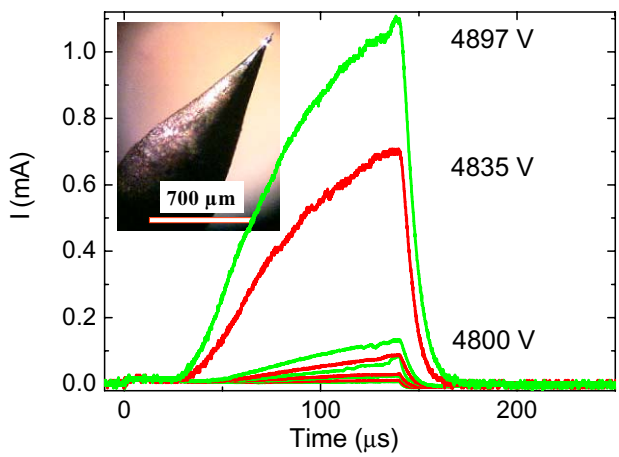

Figure 4: Collected current pulses for a single ZrC tip from APTech Inc. for different 100 µs square applied voltage pulses.

Fig. 6. For peak current below 100 mA, the projected emittances are constant for the considered four average electric fields and are less than 1.10^{-7} m·rad. In this range of peak currents the projected emittance decreases as the average electric field gradient is lowered. However, as a consequence of space-charge effects, above 5 A, there is a clear advantage to operate with large electric field gradient: the increase of the projected emittance is less pronounced as the field gradient gets higher. As for the slice emittance, similar conclusions can be drawn although the mechanism of dilution as the peak current gets higher is also due to the excitation of longitudinal wakes, a consequence of the temporal variation of the local bunch current density. In the 100 MV/m case, the slice emittance is about $0.1.10^{-7}$ m·rad for current below 100 mA and increases to reach 1.10^{-7} m·rad for a current of 10 A. In the 1 GV/M case, the slice emittance is constant and is slightly below $0.7.10^{-7}$ for peak currents less than 10 A, dilution occurring for higher currents. For currents above 25 A, the lowest slice emittance is obtained in the 1 GV/m field gradient case.

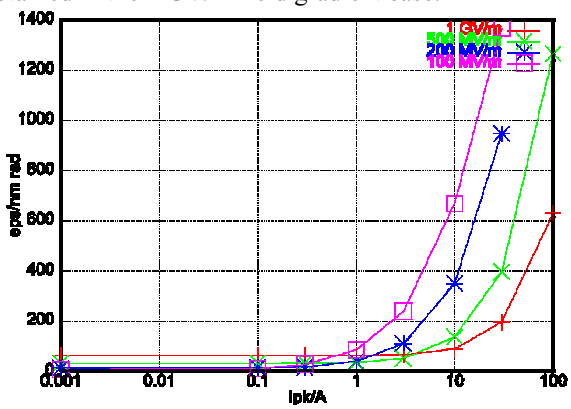

Figure 5: Projected emittance vs. peak current for a longitudinal Gaussian bunch distribution – DC gun configuration.

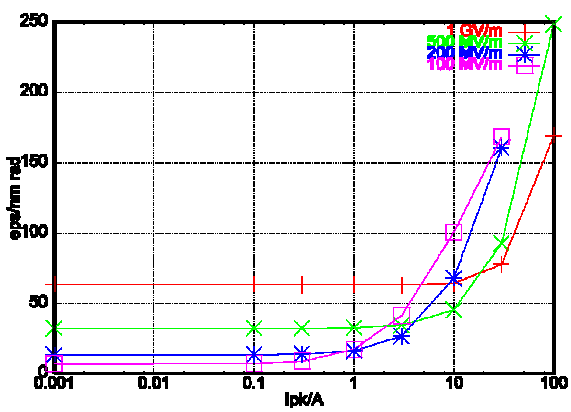

Figure 6: Slice emittance vs. peak current for a longitudinal Gaussian bunch distribution – DC gun configuration.

The above calculated emittances have been compared to the performances that could be obtained from a 3 GHz 2.5-cell RF gun configuration. MAFIA computations were performed with a modified version of a CLIC gun, the characteristics of which are described in [8]. In this RF gun, the active emitter diameter was reduced to 0.5 mm and the initial electric field gradient to 50 MV/m (peak gradient of 100 MV/m). The projected and the slice emittances along the axis of the RF structure are shown in Fig. 7 for a 3 A peak current. The projected emittance at the exit of the RF gun is about $3.6.10^{-7}$ m·rad, slightly higher than in the DC configuration. As for the slice emittance, it is about $0.25.10^{-7}$ m·rad, comparable with the value obtained in the DC gun configuration.

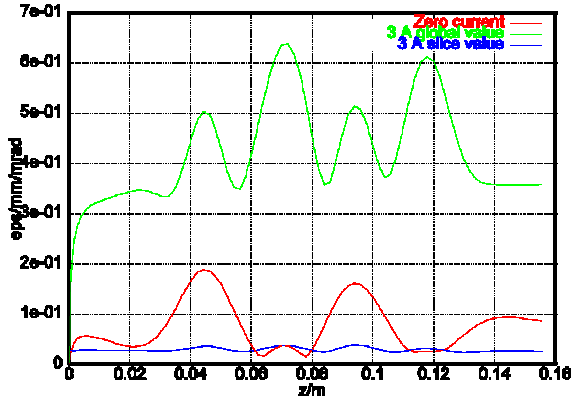

Figure 7: Emittances vs. distance – RF gun configuration.

CONCLUSIONS AND OUTLOOK

Some commercial field-emitter arrays have been tested and high and stable peak currents under pulsed operation have been obtained. For a free-electron laser application [2], the obtained peak currents are still too small. However, with shorter pulses and smaller internal FEA resistance, peak currents of at least a few amperes are expected. Beam dynamics simulations of such a cathode embedded in a DC gun configuration have shown that slice emittances smaller than $0.7.10^{-7}$ m·rad are achievable for peak currents smaller than 5 A and for an average electric field ranging from 100 MV/m to 1 GV/m. In parallel to field-emission cathode evaluations, a 100-kV gun test stand is under construction [9]. A 500-kV pulser is also under evaluation as well as studies of a combined DC/RF gun configuration.

REFERENCES

[1] L. H. Yu and S. Krinsky, NIM A, Vol. 272, pp. 436-441, 1988.
[2] M. Pedrozzi, et al., TUP45, these proceedings.
[3] Y. Liu and Y. Y. Lau, J. Vac. Sci. Technol. B, Vol. 14, pp. 2126-2129, 1996.
[4] K. D. Jamison, et al., J. Vac. Sci. Technol. B, Vol. 21, pp. 1738-1741, 2003.
[5] http://www.sri.com/psd/microsys/
[6] http://www.a-p-tech.com/
[7] P. R. Schwoebel, et al., J. Vac. Sci. Technol. B, Vol. 19, pp. 582-584, 2001.
[8] R. Bossart, et al., CLIC-Note 297, CERN, 1995.
[9] S. C. Leemann, Internal Note SLS-TME-TA-2004-0244, PSI, 2004, http://slsbd.psi.ch/pub/slsnotes/.

MULTI-MODE SLED-II PULSE COMPRESSORS

S.V. Kuzikov, Yu.Yu. Danilov, G.G. Denisov, D.Yu. Shegol'kov, A.A. Vikharev,
Institute of Applied Physics, Russian Academy of Sciences, Nizhny Novgorod, Russia
I. Syratchev, CERN, Geneva, Switzerland
V.G. Paveliev, Nizhny Novgorod State University, Russia

Abstract

Compact SLED-II pulse compressors are considered. The primary idea to use a set of the cylindrical multi-mode cavities, to be free of high-Q resonances around the 11.4 GHz, is analyzed [2]. This idea is developed, in order to provide more delaying time per miter of the line. Another idea to provide compactness is to avoid two-channel scheme with 3dB coupler usually used for SLED-II pulse compressors. A reflectionless delay line is built in this case, using coupling in a form of the non-symmetrical mode converter. SLED-II pulse compressors of higher frequency bands also are considered. It is suggested to shape these compressors on a base of the multi-mirror transmission lines. The operating mode in this case is a Gaussian wavebeam traveling between mirrors.

PULSE COMPRESSORS BASED ON A SET OF CYLINDRICAL MULTI-MODE CAVITIES

The SLED-II pulse compressor consists of two delaying lines, operated with TE_{01} modes, which are coupled by means of 3 dB coupler [1].

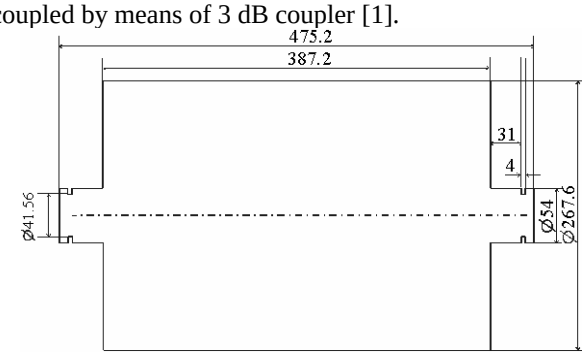

Figure 1: The 11.4 GHz elementary delaying cell.

In order to reduce the total length of delay waveguides, the idea to use a set of cavities, which are to be an equivalent of delaying line, was suggested [2]. One of cells of the mentioned type, which was calculated for 11.424 GHz, is shown in Fig. 1. Near the operating frequency the cavity does not have any high-Q resonances. The incident power in a form of TE_{01} mode passes many times inside the cavity. This provides several times larger delay time comparing to the straight waveguide of the same length as the cavity's length. Several cavities, connected in a chain, can provide delaying time up to hundreds of nanoseconds.

The necessary condition for the mentioned solution is to avoid spurious high-Q resonances in the frequency band which at least wider than spectrum width of the output compressor's pulse:

$$|f - f_0| >> \Lambda f, \qquad (1)$$

where f – is a real part of the eigen frequency of the nearest eigen mode, f_0 – is an operating frequency, and Δf – is a width of spectrum of the output pulse. The low-Q resonances are not dangerous if Q-factors are much less than:

$$Q^* = f_0 / \Lambda f. \qquad (2)$$

The conditions (1-2) are satisfied, in particular, if the cavity has spectrum of eigen modes consisted of the quasi-degenerated modes. This situation takes place in the solution presented in [2].

In order to test at low power level the idea of compact pulse compressor, the cavity with the shape, shown in Fig. 1, was chosen. The transmission and reflection characteristics of the delay line consisted of this chain are plotted in Fig. 2. Near the operating frequency the reflection is less than 1% on power. The dependence of the phase on frequency is practically linear one (Fig. 3). This means that the incident pulse has delaying only (23 ns/m) without distortions on amplitude and phase.

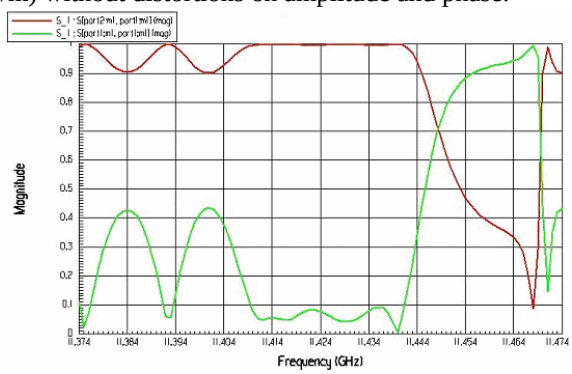

Figure 2: Reflection and transmission for the 4-cell chain (the cell shape is shown in Fig. 1).

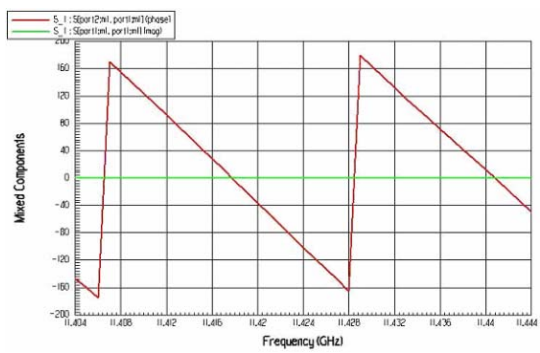

Figure 3: Phase of the reflected (red curve) wave for the 4-cell chain.

The low power tests were carried out at 34.27 GHz with the one-channel prototype (Fig. 4), where the last cell was closed by means of movable cut off reflector. This reflector was used for precise frequency tuning. The design of each cavity with scaling to 34.27 GHz

corresponded the Fig. 1. The coupling diaphragm before the first cavity was calculated separately in order to provide maximal efficiency under compression ratio 5.

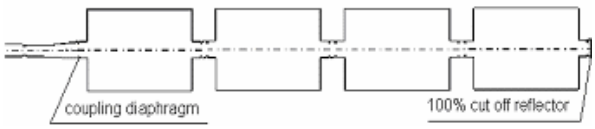

Figure 4: Scheme of the tested 4-cell pulse compressor.

The observed compression of 200 ns pulse without phase modulation (Fig. 5) as well as compression with the switched step-type phase modulation on (Fig. 6) is in good agreement with the theory. The power gain is ~2.2 without phase modulation, the power gain is about 4.5 with the π step-type phase modulation.

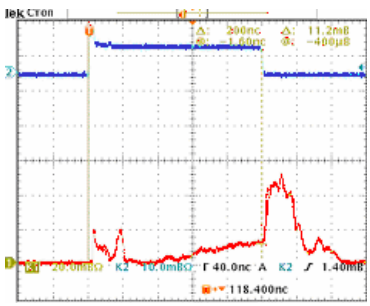

Figure 5: Experimental plot of the input (blue) and output (red) pulses formed by the compressor (no phase reverse).

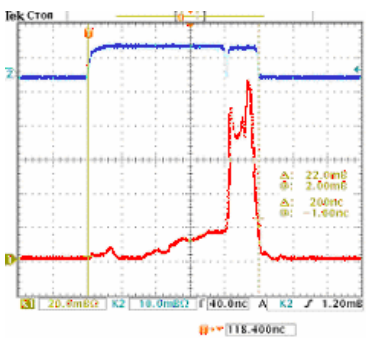

Figure 6: Experimental plot of the input (blue) and output (red) pulses formed by the compressor (with phase reverse).

In order to provide maximal compactness, it is natural to increase the diameter of delaying cavity and simultaneously to reduce the length. A compressor assembled of cavities of such design usually requires more cells, but total length is reduced dramatically. The results of such calculations are summarized at Table 1. Designations of sizes are plotted in Fig. 7.

Table 1: Parameters of the calculated cavities scaled to 34.27 GHz

Name	L1, mm	L2, mm	D1, mm	D2, mm	Delay time, ns/m	Ohmic Loss / delay time, %/ns
Kazakov cavity	14.7	129	18	89.2	22.9	0.13
"Long" cavity	5	100	14	69.3	52.8	0.16
"Short" cavity	5	25.1	11.3	171	152.3	0.21

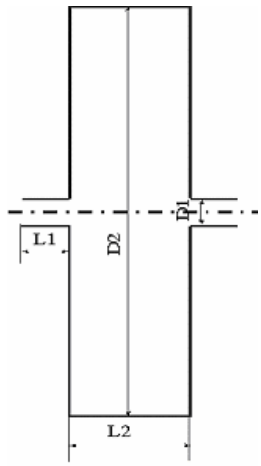

Figure 7: Sizes of the calculated cavities.

Obviously, in order to obtain most compact design, it is necessary to expand the volume of cavity. However, volume expansion means an appearance of additional eigen modes which can spoil delaying without distortion of the pulse shape. Nevertheless, the mentioned problem is solvable. There are cavities, which have the pure degenerated eigen modes only. Any frequencies between groups of these degenerated modes are free of undesirable eigen modes and could be used for compression. These are so-called two-mirror confocal cavities. In geometry-optical approach all eigen modes of them are strictly degenerated.

ONE-CHANNEL SLED-II PULSE COMPRESSOR

The principal idea of the one-channel SLED-II pulse compressor, based on a ring-like cavity, is illustrated by means of the Fig. 8. The operating mode of the axis-symmetrical cavity consists of mode *B* and mode *C*, which propagate toward each other. In particular, let us consider the compressor with *B*=TE_{01} and *C*=TE_{02}. These modes are transformed each to other in the ends of the delay line by means of special reflecting converters (Fig. 9). The feeding wave *A* is to be the TE_{11} mode, which propagates through the mentioned converters without conversion into other modes. This is reached due smooth converter's profile, which is not resonant for the TE_{11} mode.

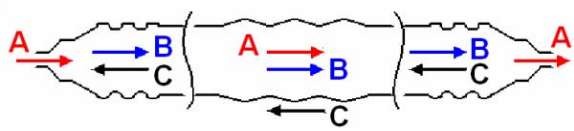

Figure 8: General scheme of one-channel SLED-II pulse compressor.

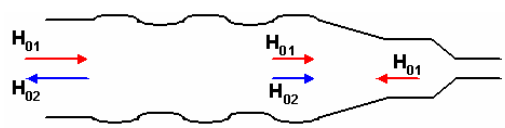

Figure 9: TE_{01}-TE_{02} mode reflector which does not perturb TE_{11} mode propagated through the compressor.

The transmitting TE_{11} mode is coupled selectively with the forward TE_{01} mode only by means of the serpent-like periodic mode converter placed in the delay line (Fig. 10). This converter should provide optimal mutual TE_{11}-TE_{01} conversion in order to obtain high compression efficiency. Note that the backward TE_{02} mode should be not perturbed by the coupling converter. The mentioned conditions are achievable due to relatively small periodic deformation of walls.

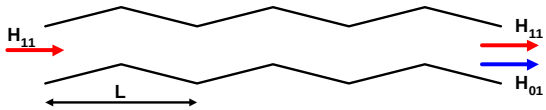

Figure 10 : TE_{11}-TE_{01} (forward modes) mode coupler.

The Figs 11-12 describe results of calculation of the 34.27 GHz pulse compressor. The first figure shows mode behavior at the TE_{01}-TE_{02} mode reflector. At the operating frequency of the compressor the mutual conversion is about 99%. The TE_{11} mode is transmitted through this reflector with efficiency 99%. For the compression ratio 4, the optimal coupling is 50% on power. That is why, in Fig. 12 mutual conversion of TE_{11} and TE_{01} modes reaches this value at the operating frequency.

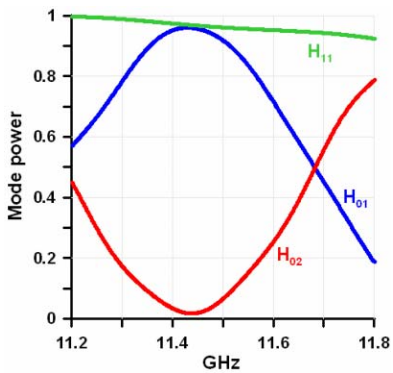

Figure 11: Calculation of modes at the TE_{01}-TE_{02} mode reflector.

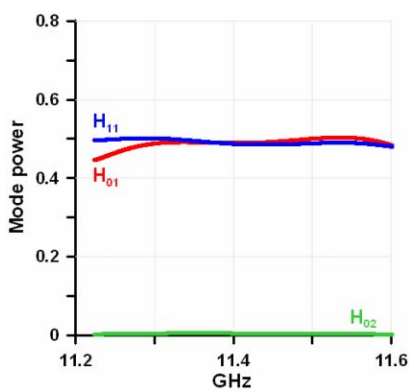

Figure 12: Calculation of the mode coupler with coupling coefficient 0.5 on power.

The mentioned modes *A*, *B*, and *C* could be arbitrary. For example, scheme with pure axisymmetrical modes (A=TE_{01}, B=TE_{02}, C=TE_{03}) seems attractive.

COMPRESSORS BASED ON MULTI-MIRROR DELAY LINES

At high frequencies the use of mirror lines becomes more natural in comparison with the closed waveguide delay lines. The mirror lines are capable to provide low-loss transmission and good compactness. The suppression of the reflected power, propagating in backward direction to the incident RF source, is achieved by means of diffraction grating (Fig. 13).

In Fig. 13 the 30 GHz pulse compressor is shown which was calculated to provide 25 ns duration of the output pulse. The total height of the compressor in vertical direction is ~1800 mm ($2a$=520 mm, b=426 mm, φ=55°). The sizes of the used mirrors are 174×143 mm^2. Each of two neighbor mirrors represents a so-called confocal pair.

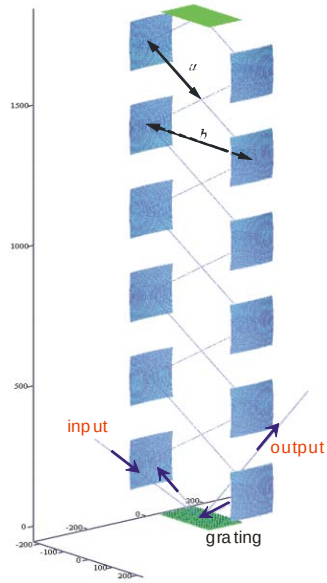

Figure 13: SLED-II pulse compressor based on multi-mirror delaying line.

CONCLUSION

The SLED-II pulse compressor, based on TE_{0n} mode cavity chains allow to reduce up to 50 times the length of delaying lines in comparison with usual delay lines.

The one-channel TE_{01}-TE_{02} SLED-II pulse compressor is suggested. It does not require the 3 dB coupler.

SLED-II pulse compressors, based on multi-mirror delaying lines, are suggested for frequencies 30-100 GHz. They allow to provide high efficiency and excellent compactness, really flat output pulse shape.

REFERENCES

[1] Farkas Z.D. et al, SLED: A Method of Doubling SLAC's Energy, Proc. 9th Conf. On High Energy Accelerator, SLAC, Stanford, CA, USA, May 2-7, 1974, p. 576, SLAC-PUB-1453.

[2] S. Kazakov, Multi-mode delay lines, ISG-XI, KEK, December 2003.

DEVELOPMENT OF C-BAND ACCELERATING SECTION FOR SUPERKEKB

T. Kamitani*, N. Delerue, M. Ikeda, K. Kakihara, S. Ohsawa, T. Oogoe, T. Sugimura,
T. Takatomi, S. Yamaguchi, K. Yokoyama, KEK, Tsukuba, Japan
Y. Hozumi, Graduate University for Advanced Studies Department
of Accelerator Science, Tsukuba, Japan

Abstract

In a future luminosity upgrade from the present KEK-B factory to the SuperKEKB, the injector linac is required to increase the positron acceleration energy from 3.5 GeV to 8.0 GeV. It could be realized by replacing some of the present S-band accelerator modules to the C-band module and doubling the acceleration field gradient (21 → 42 MV/m). Research and development of the components for the C-band module has been performed since 2002. This paper reports on the development of the first prototype of the C-band accelerating section whose design is based on a half-scale dimension of the present S-band 2-m long section. Details in the design and the fabrication are described. Results of the high-power test, beam acceleration test and ten months' operation in the KEKB injector linac are given.

INTRODUCTION

The KEK-B factory has achieved the world highest luminosity of 1.39×10^{34} cm^{-2}s^{-1} [1] but further upgrade aiming 2.5×10^{35} cm^{-2}s^{-1} has been considered [2]. In this upgrade, the stored beam energies of the electrons (8.0 GeV) and of the positrons (3.5 GeV) will be exchanged against positron beam-instability due to the electron-cloud effect. Consequently, the injector linac has to increase positron acceleration energy from 3.5 GeV to 8.0 GeV. In the present injector, the positron generation target is placed in the midway of the linac. Only the accelerator modules after the target contributes to the positron acceleration and it is sufficient for 3.5-GeV injection but not for 8.0 GeV. The 8.0-GeV positron beam is obtained if we could double the acceleration field gradient (21 → 42 MV/m). It is a general strategy to use higher rf frequency for higher field gradient as seen in the active R and D works for the linear colliders [3]. We have adopted the C-band (5712 MHz) accelerator module to replace some of the present S-band (2856 MHz) modules. The rf frequency is exactly twice of the present S-band frequency to accomodate the remaining S-band modules. Design studies of the C-band components have been performed to fit them to the specification for the KEKB injector upgrade [4]. The C-band accelerating section which cope with the rf breakdowns in the structure is one of the key components in the C-band accelerator module development.

* takuya.kamitani@kek.jp

DESIGN AND FABRICATION

The design of the first prototype of the C-band accelerating section is based on a half-scale dimension of the present 2 m long S-band section used in the KEKB linac [5]. We could take advandages of determining many design parameters just by scaling. Thus, the length of the first prototype C-band section is 1 m. It has a disk-loaded waveguide structure whose disk-iris diameter decrease linearly along the section to achieve quasi-constant field gradient. Specifications and a figure of the C-band section are shown in Table 1 and in Fig. 1.

Table 1: Specifications of the first prototype 1-m long C-band accelerating section.

operation frequency	5712.000 (MHz)
operation temperature	30.0 (degC)
no. of cells	54 regular cells + 2 couplers
section length	926.225 (mm) (55 cells)
phase advance per cell	$\frac{2\pi}{3}$-mode
cell length	17.495 (mm)
disk thickness (t)	2.500 (mm)
iris diameter (2a)	12.475 ∼ 10.450 (mm)
cavity diameter (2b)	41.494 ∼ 41.010 (mm)
shunt impedance (r_0)	74.6 ∼ 85.1 (MΩ/m)
Q factor	9703 ∼ 9676 (mm)
group velocity (v_g/c)	1.9 ∼ 1.0 (%)
filling time	234 (ns)
attenuation parameter (τ)	0.434

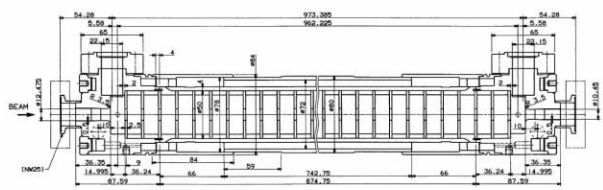

Figure 1: First prototype of C-band accelerating section.

The disks and cylindrical spacers forming regular cells of the accelerating section were made of oxygen-free copper and individually machined. The inner diameters of the spacers were adjusted by the Nodal shift measurements to achieve $2\pi/3$ phase advance per cell. After this resonant frequency adjustment of each cell, the central 50 cells out of total 54 cells were joined together by electroplating with copper. Typical radial thickness of the spacers was 4 mm

and the thickness of the electroplated copper layer outside the spacers was also 4 mm. After the electroplating process, an average resonant frequency was increased by 660 kHz, which is almost twice larger than an expectation from the S-band cases. It is supposed to come from the mismanagement of the solution concentration used in the electroplating. Besides this global frequency shift, the effect was locally smaller in the cells at both ends. It is due to the thinner electroplated layer for interface. The phase advances in these cells are 3 - 8 degrees less than the ordinary $2\pi/3$. Special care should be taken for these cells in the fabrication of the second prototype.

The couplers of the C-band section are single-feed type which magnetically couples the cavity to the waveguide through a thin small iris. While the dimensions of the regular cells could be half-scale of that of the S-band section, the coupler cells were not the case because the C-band waveguide (WR-187) connected to the coupler was not the half-scale of the S-band waveguide (WR-284). Original S-band coupler has dip structure at the opposite side from the coupling iris in order to compensate the field asymmetry. However, the high power study with the S-band structure has shown that the dip caused rf breakdowns. Thus, the dip was omitted in the first prototype C-band section and the field asymmetry was neglected. Optimum dimensions of the coupler cavity diameter and the coupling iris were approximately estimated with MAFIA-T3 simulation and precisely determined using low-power models by an iteration of the rf measurement (Kyhl method) and the machining of the cavity. Fabricated coupler cavities were jointed by the electron-beam welding (EBW) with the regular cells which were already united. Subsequently, a stainless-steel jacket for a cooling water layer was attached outside the structure by the tungsten inert gas (TIG) welding. After the EBW and TIG welding, the average resonant frequency went down by 300 kHz probably due to a deformation. Fortunately, this effect almost compensated for the excessive frequency shift by the electroplating, which resulted in the frequency deviation less than 100 kHz.

HIGH-POWER TEST

A test stand was built beside the KEKB linac for rf processing and high-power tests of the C-band components. After the high power tests of the klystron, the modulator, the sub-booster klystron, the rf window, the 3-db coupler and the dummy loads, the C-band accelerating section has installed in the test stand. rf pulse from the klystron in 500 ns duration was fed to the accelerating section at 50 Hz pulse repetition. After total 300 hours of rf processing (54 million rf pulse shots), it reaches to the level of 43.7-MW klystron output power which corresponds to the acceleration field of 41.8 MV/m assuming a theoretical shut impedance, as shown in Fig. 2.

Even at the end of the rf processing, rf breakdowns occur frequently, about ten times an hour at the highest power level. To investigate the breakdown location, rf pulse

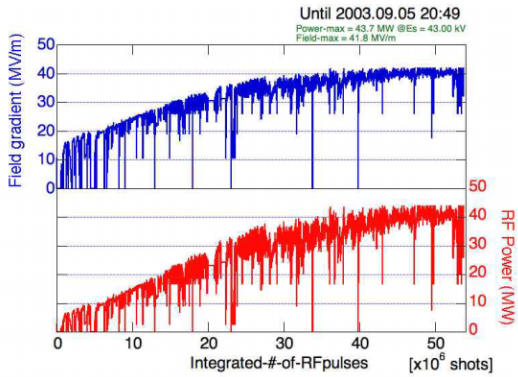

Figure 2: rf processing history.

shapes of incoming, outgoing and reflected waves of the accelerating structure were observed at each breakdown and numerically analyzed [6]. It is assumed that at the instant of rf breakdown the accelerating structure is locally short-circuited. The rf pulse propagating in the structure is divided there. Front part of the pulse propagetes forward and is observed as a terminated outgoing wave. Rear part of the pulse is reflected at the breakdown point, propagetes backward and is observed as a reflected wave. From the pulse length of the terminated outgoing wave, we can know that in what timing of the rf pulse the breakdown occurs. Figure 3(a) shows a distribution of the breakdown timing in an rf pulse. The distribution is rather flat except a peak at the beginning of the rf pulse. Likewise, information of the breakdown location can be obtained from the time difference between the end of the outgoing wave and the arrival of the reflected wave, as seen in Fig. 3(b). In this plot, the right-hand side is the input coupler and the left-hand side is the output coupler. We can see that the breakdown locations are concentrated around the input coupler.

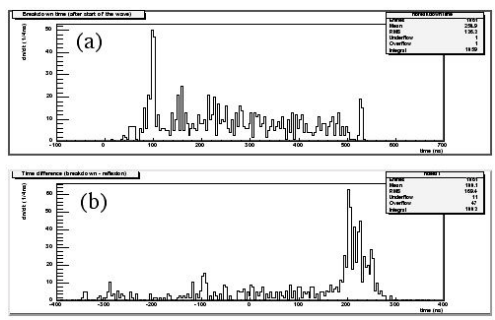

Figure 3: Breakdown location from rf pulse timing.

Acoustic sensors were also used to estimate the breakdown locations by detecting vibrations due to the breakdown [6]. Four sensors were attached on the input coupler, on the output coupler and at 1/3 and at 2/3 positions of the accelerating section in equal interval. The timing and the magnitude of the signals from the sensors were analyzed. Figure 4(a) shows a correlation between the fastest signal sensor and the largest signal sensor and figure 4(b) shows a distribution of which sensor had the fastest and the largest signal. It also suggest that most of the breakdowns occur around the input coupler.

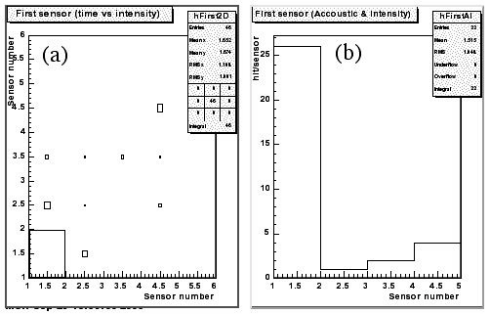

Figure 4: Breakdown location from acoustic sensor.

BEAM ACCELERATION TEST

In September of 2003, after finishing the rf processing and the high power test of the accelerating section at the test stand, a C-band accelerator module was constructed in the area of the S-band module No. 4-4 of the KEKB injector linac, which was temporary empty. A C-band klystron, the accelerating section and an rf dummy load were moved there from the test stand. A modulator and a low-power rf source including sub-booster klystron were newly installed. Unlikely to the design of a complete C-band accelerator module, only single 1-m long accelerating section was installed instead of two 2-m long sections and an rf pulse compressor was missing because it was still in a design stage. Recent status of the development of the pulse compressor will be reported by another paper in this conference [7]. In the operation of the C-band accelerator module, its energy gain has been measured at the energy analyzer in the end of the linac by changing the acceleration phase. We have used 3.0-GeV electron beams of 0.13-nC charge per pulse for injecting into the AR-SOR ring because of sufficiently good energy resolution and small beam-loading effect. Figure 5 shows that the energy gain was estimated to be 39.7 MeV which corresponds to the acceleration field of 41.2 MV/m with the klystron output power of 43.8 MW. The errors in individual data points comes from the measurement error of the beam positions. Besides these errors, the beam orbit displacement due to the field asymmetry in the couplers affects the result. This systematic error is supposed to be more than five percent, but yet to be studied.

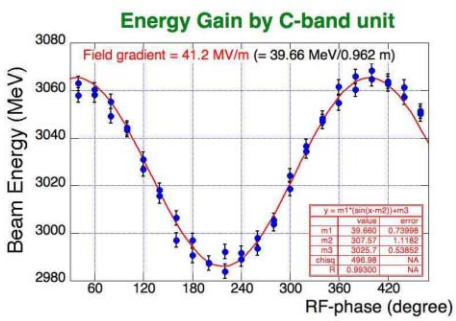

Figure 5: Measured energy gain of the C-band module.

LONG TERM OPERATION

The C-band module has been used for beam acceleration for ten months. The rf breakdown rate has become lower than the beginning, but is still five times an hour above 40 MW power level. After the ten months' operation, we have observed inside of the accelerating section using a CCD endoscope. As seen in Fig. 6(a), the iris edge in the input coupler were discolored and the surface in the suburb of the iris was turned into black. In the output coupler, these damages were not so obvious. Damage of the disk iris with plenty of small pits can be seen in Fig. 6(b). It was remarkable in the first disk connecting to the input coupler cell, but much less in the second and third disks and further less in the disks close to the output coupler. These locations of the surface damage are consistent with the distribution of the breakdown locations. In the second prototype accelerating section, we adopt thicker coupling iris, and tuning of the coupler dimension using low-power models is in progress.

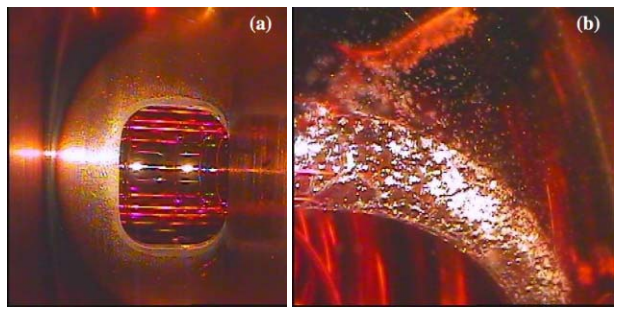

Figure 6: Surface damage in accelerating structure.

ACKNOWLEDGEMENT

The authors wish to thank Mitsubishi Heavy Industries, Ltd. and Mechanical Engineering Center of KEK for their cooperation in fabricating the accelerating section.

REFERENCES

[1] KEKB, An Asymmetric Electron-Positron Collider for B Physics, http://www-acc.kek.jp/KEKB/.

[2] SuperKEKB Letter of Intent (LoI), KEK Report 04-4, August, 2004, http://belle.kek.jp/superb/loi/.

[3] X-band R and D for GLC, http://lcdev.kek.jp/
C-band R and D for GLC and X-ray FEL,
http://c-band.kek.jp/.

[4] T. Kamitani, et. al., "R and D status of C-band accelerating unit for SuperKEKB", PAC2003 conference, Portland, OR, USA, 12-16 May 2003.

[5] I. Abe, et. al., "The KEKB injector linac", KEK Preprint 2001-157, Nucl. Instrum. Methods A, Volume 499, Issue 1, 21 February 2003, Pages 167-190.

[6] N. Delerue, "Identifying high power breakdowns in accelerating structures with acoustic sensors",
http://acfahep.kek.jp/appi/2004/TPs/Nicolas0402appi.pdf.

[7] T. Sugimura et. al., "SKIP - A pulse compressor for SuperKEKB", This proceedings.

PRODUCTION OF S-BAND ACCELERATING STRUCTURES

Kai Dunkel, Christian Piel, Hanspeter Vogel, Peter vom Stein,
ACCEL Instruments GmbH, Bergisch Gladbach, Germany

Abstract

ACCEL currently produces accelerating structures for several scientific laboratories. Multi-cell cavities at S-band frequencies are required for the projects CLIC-driver-linac, DLS and ASP pre-injector linac and the MAMI-C microtron. Based on those projects differences and similarities in design, production technologies and requirements will be addressed.

CLIC DRIVER LINAC

The production of 18 CLIC Driver Linac structures [1] is under way at ACCEL Instrument GmbH [2]. Meanwhile more than 12 structures are delivered and successfully tested at CERN. The structure consists of 35 accelerating cells including the coupling cells with symmetric rf ports. Each cell contains four Silicon Carbide absorbers, which are coupled to the accelerating cells by the slotted cavity iris for HOM suppression. The operating frequency is 2998.55 MHz in 2π/3 mode. The structure is designed for extreme high beam loading of nearly 98 %. The nominal input power is 30 MW at a pulse length of 1.5 µs resulting to an unloaded accelerating voltage of 13.5 MV.

Figure 1: Two 1.22 m long CLIC Drive Linac structures ready for delivery.

The slotted iris geometry of the accelerating cells requires extreme care during the manufacturing process. After the turning and milling operations on the accelerating cells, which is similar to other standard S-Band structures, the cell is cut from the iris up to 10 mm away from the cell equator by wire spark erosion. This makes the cells fragile and sensitive to any mechanical deformations.

To assure the correct phase and amplitude tuning of the finished structure the frequency of each cell is measured before final brazing (Figure 2). A special test setup was built up at ACCEL for the measurement of the 0-mode and π- mode frequencies of each cell. This allows to calculate the 2π/3 mode frequency of the individual cells. After the final brazing the phase advance and field distribution of each structure is checked by a bead pull measurement (Figure 3).

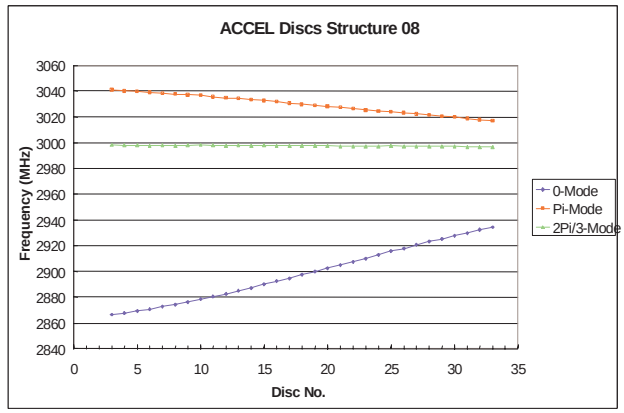

Figure 2: RF measurement of CLIC structure half cells.

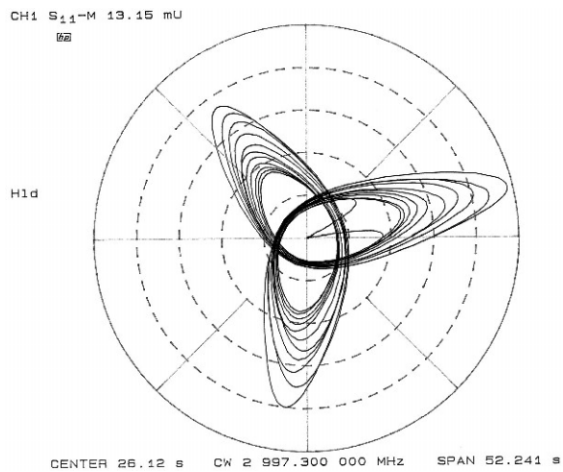

Figure 3: Bead pull measurement of a CLIC structure.

DLS AND ASP INJECTOR LINAC

ACCEL currently manufactures the 100 MeV injector linacs for the Diamond Light Source DLS [3],[4] and for the Australian Synchrotron Project ASP [5] based on 2π/3 mode travelling wave S-Band structures, operating at 2.997912 GHz.

Already four structures of this type had been delivered in the past. Two structures serve the SLS [6] injector linac at moderate accelerating fields of 11 MeV/m very reliable since April 2000. Another two structures are used at MaxLab at much higher gradients of 25 MeV/m. The manufacturing technology and design allow as well the production of 6m long structures. The design of the 5.2m long structures has been transferred from DESY to ACCEL under a technology transfer contract.

Figure 4: 5.2 m long S-Linac structure ready for delivery.

The accelerating structure incorporates the rf absorbers in the last cells, were the absorbing material is sputtered directly to the cell surface, so that only one ceramic window is required at the rf input coupler, this increase reliability of this structures and reduce required investment.

Required manufacturing technologies as precise turning, chemical cleaning, vacuum bracing of subassemblies and induction bracing of stacks, are well established technologies at ACCEL.

The quality is assured during the manufacturing process by rf measurements beside standard technologies as dimension control and vacuum leak checking. Each individual cell is measured according to its rf properties prior to stack brazing.

The final structure is tuned based on beat pull measurements and finally characterised by its field profile and cell to cell phase advance (Figure 5).

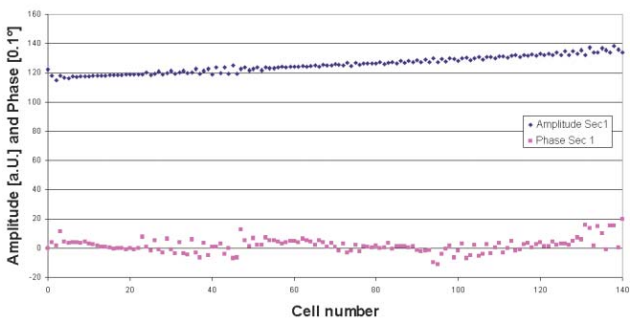

Figure 5: Bead-pull measurement after final tuning of the accelerating structure.

MAMI-C 2.45 GHZ AND 4.9 GHZ STRUCTURES

ACCEL is currently manufacturing 2.45 GHz and 4.9 GHz accelerating structures for MAMI-C at the "Institut für Kernphysik" (IKPH), University of Mainz [7],[8].

Design

The 2.45 GHz accelerating structure based on a Chalk River design and modified by IKPH is an on-axis-coupled biperiodic $\pi/2$ standing wave structure with 33 accelerating cells (AC) and 32 coupling cells (CC) and the RF input in the middle AC (Figure 7). It is vacuum brazed consisting out of 66 half cells of copper. The water cooling is realised by integrated cooling channels (Figure 6).

Figure 6: Pre-machined 4.9 GHz half cells (before coupling slot milling) and a 2.45 GHz half cell including coupling slots and tuner port.

The 4.9 GHz accelerating structure design is based on a scaled version from the 2.45 GHz structure, but has 35 AC, 34 CC and a higher coupling [9].

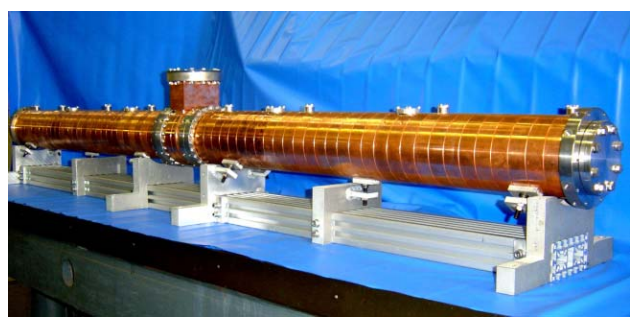

Figure 7: Complete brazed and assembled 2 m long MAMI-C 2.45 GHz structure.

Low-Level-RF Measurements

The frequency preset for machining of the half-cells is +1.5 MHz to allow a tuning step before brazing. The accuracy of machining can be determined by the frequency spread, which is σ=0.19 MHz for the manufacturing of the 2.45 GHz prototype structure. The pre-braze tuning has to be done carefully, since a post-braze tuning is not foreseen. The average difference to

target frequency of all accelerating cells of the prototype structure is df_{avg}=-0.021 MHz with σ=0.049 MHz (Figure 8).

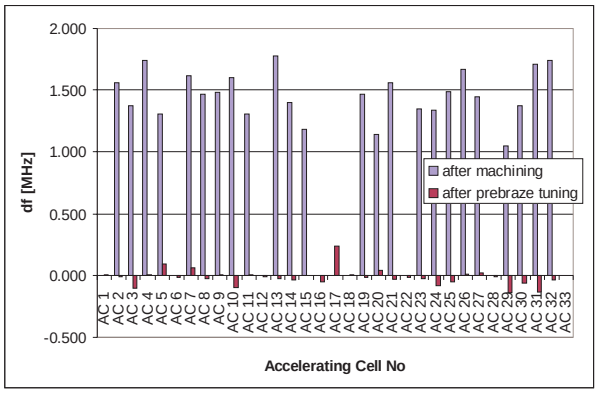

Figure 8: Frequency difference to target frequency before and after pre-braze tuning.

Bead-pull Measurements

The final proof of correct manufacturing and tuning is given by a bead-pull measurement of the complete structure after brazing and assembly. Figure 9 shows the bead-pull measurement of the 2.45 GHz prototype structure with nearly constant field in the accelerating cells. The fluctuation at the bottom line between the accelerating cells is artificial and caused by the small, but unavoidable spread of the lace diameter.

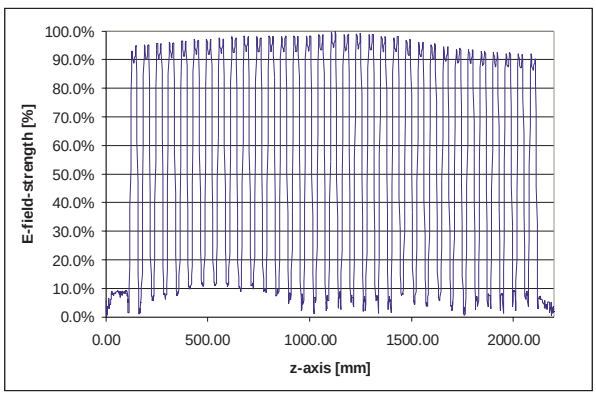

Figure 9: Bead-pull measurement after brazing at plunger norm position.

SUMMARY

Various types of S-Band type accelerating structures had been designed and/or produced at ACCEL Instruments. All projects require precise machining, brazing and close quality control by leak checks and intense rf measurements during the entire manufacturing process, generally ending in a bead pull to check amplitude distribution and cell to cell phase advance as our final quality control before delivery.

REFERENCES

[1] E. Jensen, "CTF3 Drive Beam Accelerating Structures", Proc. of LINAC 2002, Kyongju, Korea
[2] http://www.accel.de
[3] C. Christou et al., "The Pre-Injector Linac for the Diamond Light Source", these proceedings
[4] http://www.diamond.ac.uk
[5] http://www.synchrotron.vic.gov.au
[6] C. Piel, Design and Construction of a turnkey 100 MeV Linac for the Swiss Light Source, Proceedings of EPAC 2000, Wien (2000)
[7] http://www.kph.uni-mainz.de/en/
[8] A. Jankowiak et al., "Design and Status of the 1.5 GeV-Harmonic Double Sided Microtron for MAMI", Proceedings EPAC 2002, Paris
[9] A. Jankowiak et al., "Experiences in Fabrication and Testing the Prototype of the 4.90 GHz Accelerating Sections for MAMI C", these proceedings

A FOUR-CELL PERIODICALLY HOM-DAMPED RF CAVITY FOR HIGH CURRENT ACCELERATORS *

G. Wu†, R. Rimmer, H. Wang, Jefferson Lab, Newport News, VA 23606, USA
J. Sekutowicz, DESY, Notkestrasse 85, 22607 Hamburg, Germany
Sun An, Oak Ridge National Lab, Oak Ridge, TN 37830, USA

Abstract

A periodically Higher Order Mode (HOM) damped RF cavity is a weakly coupled multi-cell RF cavity with HOM couplers periodically mounted between the cells. It was studied as an alternative RF structure between single-cell and superstructure cavities in high current application requiring strong damping of HOMs. The acceleration mode in this design is the lowest frequency mode (zero mode) in the pass band, in contrast to the traditional "π" acceleration mode in multicell superconducting cavities. The acceleration mode of the four-cell cavity has been studied, along with the monopole and dipole HOMs. The frequency response through HOM ports has been simulated in HFSS™ with waveguide couplers, which shows almost constant Q_{ext} for several important HOMs, even with different number of cells. A 4x1 zero-mode cavity was studied with MAFIA time domain analysis. To understand the tuning challenge for this weakly-coupled cavity, ANSYS® and SUPERFISH codes were used to simulate the cavity frequency sensitivity and field flatness change, which will influence the design of the tuner structure. This paper presents the computer simulation of this novel accelerating structure that may be used for variety of accelerator applications.

INTRODUCTION

High current linacs require heavily HOM-damped RF cavities. In other words, the high-current accelerating structure should only confine the accelerating mode or at most the only modes within the first pass band. One such RF structure is a HOM well-damped single cell cavity, which is used in storage rings [1, 2]. To get higher voltage gain within the same machine length, one would use multi-cell cavities [3], or a superstructure cavity [4]. The multi-cell structure inevitably traps some HOMs. One would naturally think that something in between should provide a trade off between effective accelerating voltage per unit length and the good HOM damping.

One solution could be packing individually HOM damped single cell cavities in a chain to form a periodical structure, which we call the Zero Mode cavity. The other would be packing single cell cavity back to back, which is essentially a superstructure of two-cell cavities. The latter has been proposed and studied earlier [5]. This note investigates the former case, the Zero Mode cavity.

*Work performed under DOE Contract #DEAC0584ER40150
†Electronic mail: genfa@jlab.org

ZERO MODE CAVITY

An enlarged beam pipe connects individual cells. Cell-to-cell coupling is expected to be quite weak. Since the high current RF cavity would mostly run in energy recovering mode, the weak coupling is thought to be less detrimental in terms of energy re-filling. The beam test of a 2x7 superstructure indicated that the energy flow between weakly coupled subunits was not a problem at least for TESLA's beam current [6].

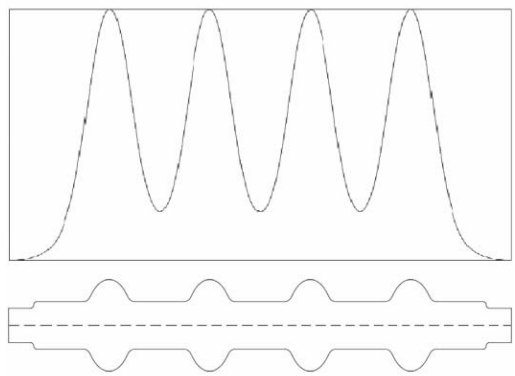

Figure 1: The four cell Zero Mode cavity and its on-axis electric field for acceleration mode.

A four-cell Zero Mode cavity is shown in Figure 1. Due to the non-zero field in the interconnecting beam pipe, lower R/Q is expected for the accelerating mode. The RF parameters are also listed in Table 1. From the E_p/E_{acc} ratio, a peak surface field 50 MV/m would be needed for a 10 MV/m accelerating gradient. The frequencies of the first pass band modes are plotted in Figure 2.

Table 1: RF parameters of Zero Mode cavity

Accelerating mode [MHz]	0	1498.703
Mode 2 [MHz]	π/4	1499.048
Mode 3 [MHz]	2π/4	1500.110
Mode 4 [MHz]	3π/4	1501.167
Cell number		1x4
Cell to cell coupling		7.91E-04
R/Q [Ohm] of accelerating mode		239
Geometric factor		277
Epk/Eacc		5.07
Bpk/Eacc [mT/(MV/m)]		8.42

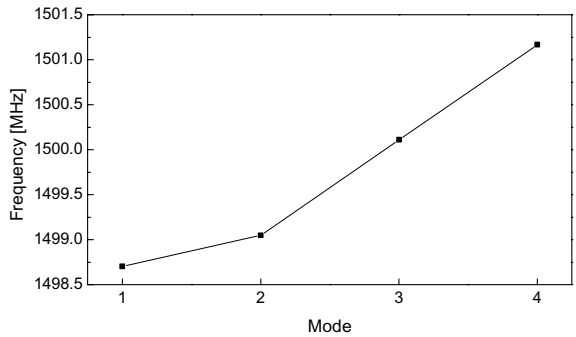

Figure 2: Frequencies of first pass band computed by Superfish.

HOM DAMPING

The interconnecting beam pipe allows the placement of HOM couplers between cells. Since this HOM damping scheme is considered very promising, shunt impedance minimization of HOMs may allow further cavity shape optimization to improve fundamental mode R/Q and Ep/Eacc ratio. For this configuration, the frequency and R/Q of the monopole and dipole modes have been calculated by MAFIA 2D as summarized in Table 3 and 4; those modes with very small R/Q values were not listed.

Table 3: Dipole modes

Mode	Frequency (MHz)	R/Q (Ω)	R/Q (Ω/cm^2)
1	1.582527	9.59	1.53
2	1.596888	1.70	0.27
6	1.868148	13.21	2.11
7	1.913363	15.63	2.50
9	2.161911	1.23	0.20
11	2.192195	29.18	4.67
12	2.193530	1.24	0.199
13	2.196425	0.80	0.13
14	2.455769	0.82	0.13
15	2.505229	3.85	0.62
16	2.575615	3.05	0.49
18	2.701776	0.91	0.15
20	2.987272	1.97	0.32
21	3.068014	1.13	0.18
22	3.129850	7.92	1.27
23	3.159913	2.65	0.42
24	3.385317	0.65	0.10
25	3.389713	11.33	1.81
26	3.403304	7.35	1.18
31	3.525925	1.77	0.28
36	3.659088	1.34	0.21
39	3.884062	1.28	0.21
40	3.886888	2.44	0.39

Table 4: Monopole modes

Mode	Frequency (MHz)	R/Q (Ω)
5	2.448852	2.56
6	2.459498	1.07
10	2.669108	1.47
11	2.709442	2.40
17	3.036354	5.24
19	3.211969	11.97
20	3.376769	2.70
21	3.378105	16.91
22	3.380678	6.10
23	3.548321	9.36
24	3.829342	24.92
25	3.844619	5.67
27	3.921957	23.34

The investigation assessed the effectiveness of rectangular waveguide couplers as HOM dampers, as a function of the number of cells in the structure. The configuration for a four-cell cavity is illustrated in Figure 3. The waveguide HOM transmission S-parameter was calculated for cavities with two, three, four cells. The result is shown in Figure 4. The S-parameter peaks for several modes are rather insensitive to the number of cells.

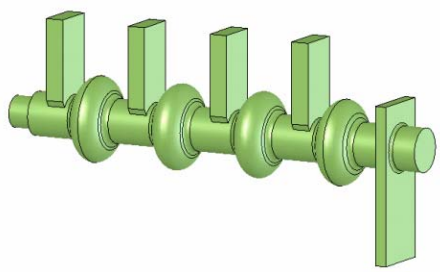

Figure 3: The model of zero mode cavity with periodic damping by waveguide HOM couplers.

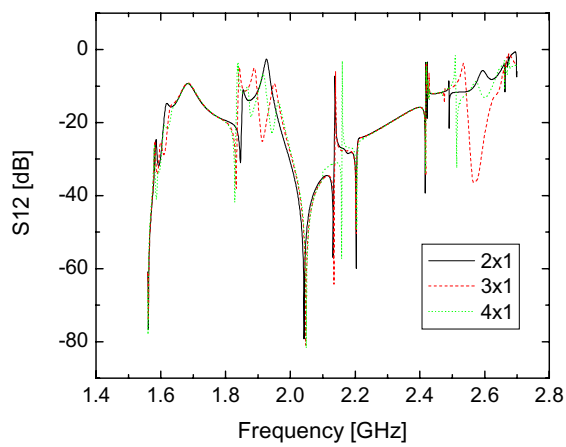

Figure 4: The transmission S-parameter computed for 2-cell, 3-cell, and 4-cell cavities.

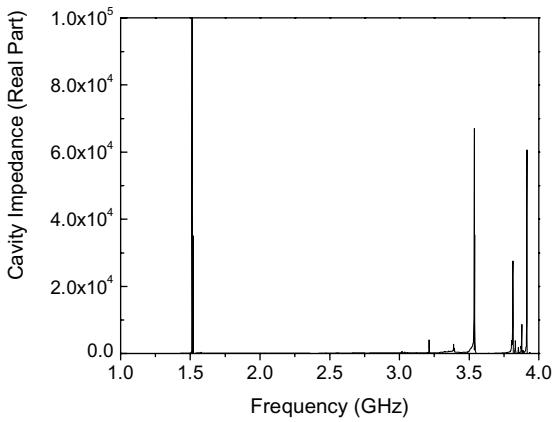

Figure 5: The cavity beam impedance showing several TM modes.

MAFIA time domain analysis [7] was used to calculate the actual Qext of monopole modes of the cavity shown in Figure 3. Since the dipole modes have quite small R/Q, effort should be focused on monopole HOMs as for superstructures [5]. Cavity impedance is plotted in Figure 5 showing several TM modes. The simulated Qext of monopoles were below 307 except two beam pipe modes in Table 4: mode 23 with 7100 and mode 27 with 2600. Beam pipes were electrically terminated in the simulation.

TUNING SENSITIVITY

Due to the weak cell-to-cell coupling, cavity field flatness may be difficult to maintain when cold. Four-cell cavity tuning sensitivity and field flatness was simulated using the same procedure that has been used for SNS type cavities [8]. When the ideal cavity geometry was assumed, the frequency change and the field flatness due to cavity stretching have remarkably similar responses to the regular π-mode multi-cell cavity [8] as shown in Figure 6. The frequency sensitivity is 700 KHz/mm. The field flatness sensitivity is 1.1%/MHz. Imperfect cavity geometry may require four individual cold tuners to help maintain field flatness, or a single cold tuner with pre-configured stress memory, which requires some development to implement.

SUMMARY

It is concluded that the damping effect is independent of the cavity cell number for this zero mode cavities. This evaluation of simple waveguide HOM couplers suggests that the structure eases the design effort for HOM damping. The cold tuner remains a costly component. Some further studies, especially cold tests, are needed to find whether a single tuner is sufficient and whether an economic solution for a cold tuner is achievable. Some optimization effort is also needed to increase the fundamental mode R/Q for the four-cell cavity.

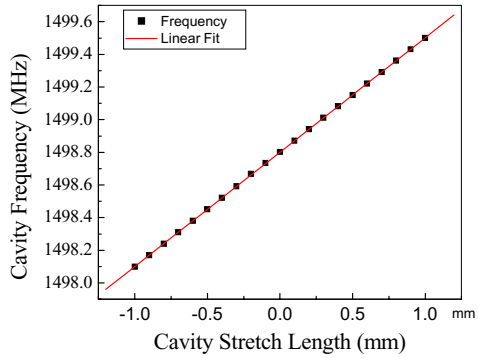

(a)

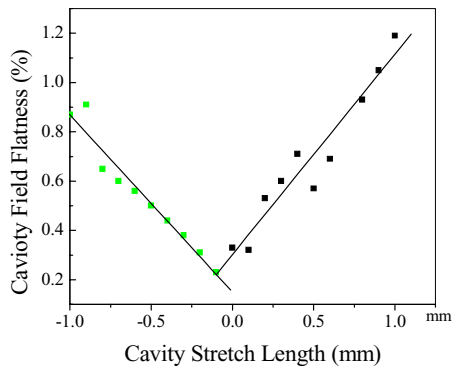

(b)

Figure 6: The tuning frequency response (a), and the field flatness degradation (b).

ACKNOWLEDGEMENT

We would like to thank G. Neil, W. Merz and W. Funk for their strong support.

REFERENCES

[1] J. Kirchgessner, Part. Accel., **46(1)**:151 (1995).
[2] T. Furuya et al., Proc. 7th Workshop on RF Superconductivity, edited by B. Bonin, Gif-sur-Yvette, France, p. 729 (1995).
[3] R. Rimmer, H. Wang, G. Wu, D. Li, Proc. PAC 2003, Portland, p. 1389.
[4] J. Sekutowicz, K. Beard, P. Kneisel, G. Wu, C. Thomas, S. Zheng, Proc. PAC 2003, Portland, p. 1575.
[5] J. Sekutowicz, P. Kneisel, G. Wu, Proposal for the development of a 1 MW FEL structure, JLAB-TN-03-020.
[6] J. Sekutowicz, et al., Proc. PAC 2003, Portland, p467.
[7] Derun Li , Robert A.Rimmer, Proc. PAC 2001, Chicago, p. 915.
[8] A. Sun, H. Wang, G. Wu, Tuner Effect on the Field Flatness of SNS Superconducting RF Cavity, this Proceeding.

NEW ACCELERATING MODULES RF TEST AT TTF

D. Kostin for the TESLA collaboration, DESY, D-22607 Hamburg, Germany

Abstract

Five new accelerating modules were installed into the TTF tunnel as a part of the VUV FEL Linac. They are tested prior to the linac operation. The RF test includes processing of the superconducting cavities, as well as maximum module performance tests. The test procedure and the achieved modules cavities performance are presented.

TTF ACCELERATING MODULES

The TESLA Test Facility (TTF) VUV FEL LINAC [1], [2], [3], [4] has now 5 accelerating modules (see Fig. 1), each module (see Fig. 2) consists of 8 9-cell niobium cavities with input RF power couplers (see Table 1) and a quadrupole in the cryomodule [5].

Figure 1: Accelerating modules ACC1 – ACC5 at TTF.

Figure 2: Accelerating module in the VUV-FEL tunnel.

Table 1: Accelerating Modules.

pos.	mod.	ready	coupler type	cold win.	warm win.
ACC 1	2*	Jan. 2004	FNAL/ TTF III	Conical /Cyl.	Planar /Cyl
ACC 2	1*	Mar. 2000	FNAL/ TTF II	Conical /Cyl.	Planar (WG)
ACC 3	3*	Feb. 2003	TTF II	Cyl.	Planar (WG)
ACC 4	4	Jul. 2001	TTF II	Cyl.	Planar, (WG)
ACC 5	5	Mar. 2002	TTF III	Cyl.	Cyl.

The cavities are operated at 2 K and have an accelerating gradient between 12 and 35 MV/m. The RF power sources for the accelerating modules are the 5 and 10 MW 1.3 GHz klystrons connected to the modules through the waveguide power distribution system (see Fig. 3). The RF power measurements are done using the waveguide directional coupler (DC) (1 coupler, forw. and refl., 1 DC pro module installed). The probe power measurement is done for the one cavity (where DC is also installed) pro accelerating module using the power meter. Power meters connected through GPIB-Ethernet network to the computers, controlling the test procedure using LabVIEW program.

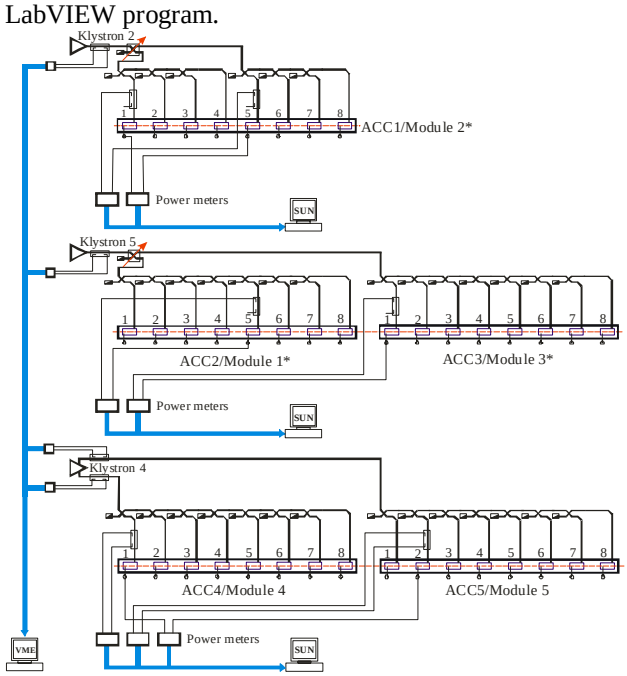

Figure 3: RF power distribution / measurement diagram.

Downconvertor/ADC channel for P_{for}, P_{ref} (from circulators) and P_{trans} (cavity probes) for each cavity is used to monitor the forward, reflected and transmitted power pulse shape. To measure power precisely enough proper power line calibration measurement must be ensured in order to get attenuation values between the power meter (PM) and measurement point. All measurement cables were calibrated before the test. To measure the accelerating gradient (E_{acc}) cavity pickup (transmitted) power value was used, calibration coefficient k_t is to be measured at lower power rectangular pulse, when pulse shape is precisely defined and E_{acc} is calculated (see Eq. 1).

$$E_{ACC} = \frac{\sqrt{4\frac{R_{sh}}{Q}Q_{load}P_{for}}}{L_{cavity}} \times \left[1 - e^{-\frac{\pi f_0 t_{fill}}{Q_{load}}}\right] = k_t \times \sqrt{P_{trans}}, [V/m] \quad (1)$$

Standard parameters values are: $R_{sh}/Q=1030\Omega$, $L_{cavity}=1.035$m, $Q_{load}=3\times10^6$, $f_0=1.3$GHz, $P_{for}\approx5$kW (for the calibration), $t_{fill}=1.3$ms (for the calibration, 500µs for flat-top pulse (FT)). In this case such a measurement was not possible for each cavity, also most of the gradient values were obtained from forward power measurement using first part of the Eq. 1, assuming the symmetrical power distribution when using only one power measurement pro module. The non-symmetry of power distribution was measured to be about ±0.2dB. Other, most important measurement error origins are cable calibration coefficients (±0.1dB), non-rectangular power pulse shape at high RF power and dependence of the DC directivity coefficients from the standing wave distribution in the waveguide. The evaluated error margins for accelerating gradients in this test are about ±10..16%.

RF TEST RESULTS

In order to get the maximum performance from the LINAC accelerating cavities and input power couplers must be conditioned. Each step in the coupler conditioning is limited by plasma density in the coupler caused by rf discharge. Standard sensors set used for coupler processing – photo multipliers, infrared temperature sensors, spark detectors and coupler pick-ups (3 pro coupler, paralleled) [6], [7]. After couplers conditioning off resonance was completed all the cavities were tuned to the resonant frequency of 1.3GHz and loaded quality factor was adjusted by changing the coupler antenna position. Cavity 4 at module 3* (ACC3) was not tested because of minor problem with the coupler, at the next LINAC run this coupler was successfully conditioned. The cavities were tested with the flat-top RF pulse with 0.5 ms rise time and 0.8 ms flat-top.

In the Fig. 4 single cavities tests results are presented, vertical test cryostat, horizontal test cryostat and accelerating module tests are compared. In the position 5 of the module 2* / ACC1 a high gradient cavity (AC72, electropolished [8]) was installed and tested successfully reaching the gradient of 35 MV/m with own quality factor $Q_0=10^{10}$. The summary of the modules tests is presented in Fig. 5, where average accelerating gradients of the modules are shown. The own quality factors Q_0 measurements done using the cryogenic losses measurement, results are summarized in Fig. 6.

Some cavities in the accelerating modules have the field emission. Module 2* / ACC1: cavity 7 is a source of a dark current, up to 10 mGy/min measured on axis. Module 5 / ACC5: cavity 6 is a source of a dark current of 1 µA (peak) at 25 MV/m. Radiation level measured at 1 m distance from module 5 dump side was about 18 µSv/min

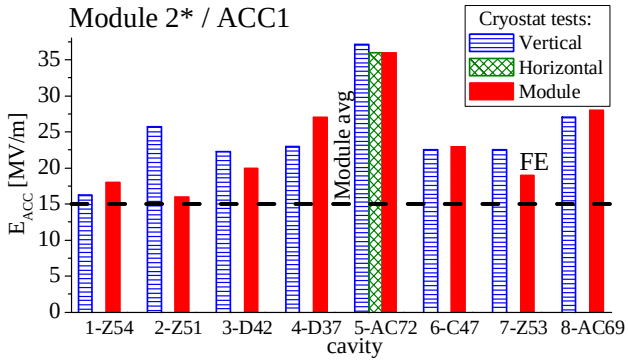

Figure 4a: Single cavities tests: ACC1.

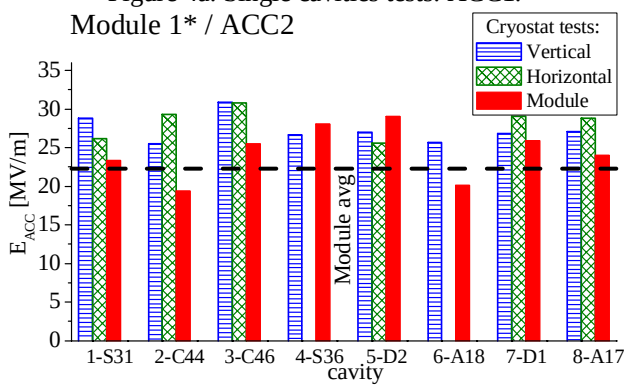

Figure 4b: Single cavities tests: ACC2.

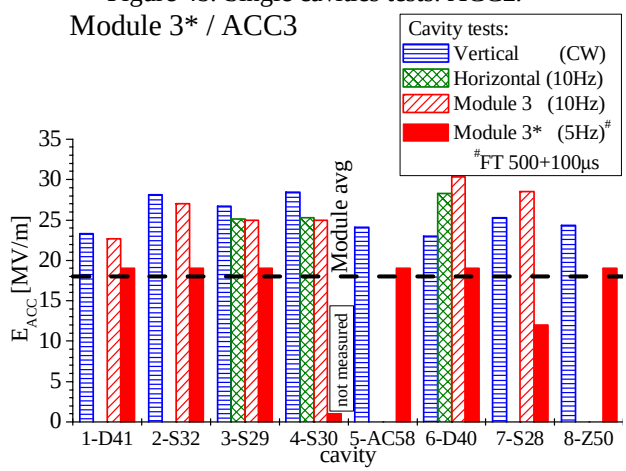

Figure 4c: Single cavities tests: ACC3.

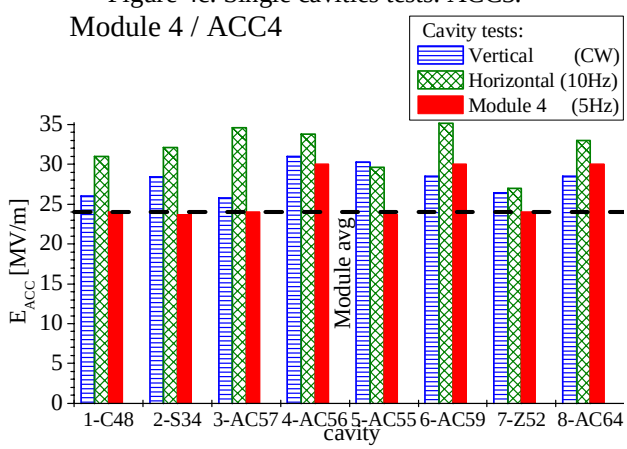

Figure 4d: Single cavities tests: ACC4.

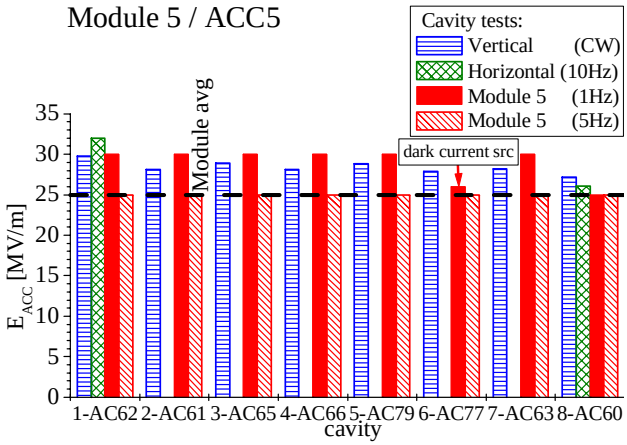

Figure 4e: Single cavities tests: ACC5.

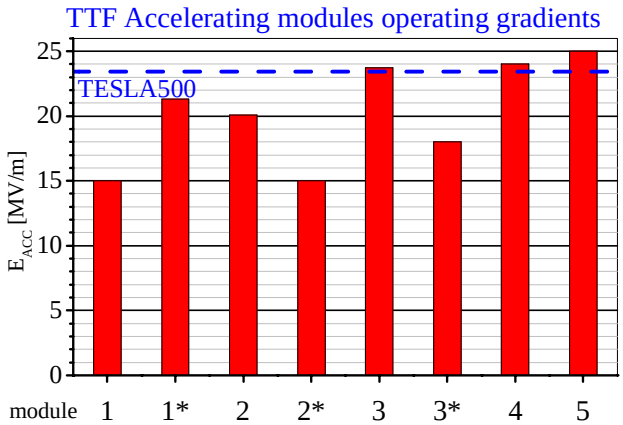

Figure 5: Modules operating (average) gradients.

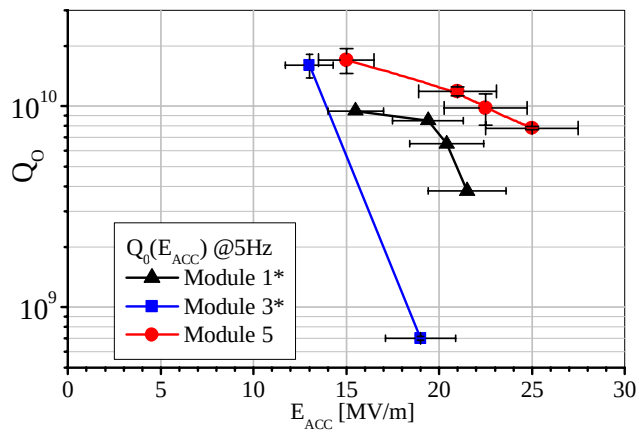

Figure 6: Q_0 vs E_{acc} measurements.

CONCLUSIONS

The last two modules, 4 and 5, fulfill the TESLA500 specifications. All modules have functioned continuously during certain periods of time, no one was taken immediately out for repair.

ACC5 / module5: tested at the repetition rate of 5 Hz was operating at the accelerating gradient of 25 MV/m, 500 + 800 μs full length flat-top pulse and quality factor of 8×10^9. Cavity 6 is a source of a dark current of 1 μA (peak) at 25 MV/m. Radiation level measured at 1 m distance from module 5 dump side: 18 μSv/min.

Module 2* / ACC1 was operated with beam for about 2 months. Cavity 5 (AC72) tested in Module 2* / ACC1 reached 35 MV/m, confirmed with beam. Cavity 7 is a source of a dark current, up to 10mGy/min measured on axis.

ACKNOWLEDGEMENT

I am thanking all the many colleagues from the TESLA collaboration who made it possible to develop, fabricate, prepare, assemble, test and operate the TTF accelerating modules.

REFERENCES

[1] D.A. Edwards, "TESLA Test Facility Linac Design Report", TESLA Report 95-01 (1995)

[2] A VUV Free Electron Laser at the TESLA Test Facility - CDR, DESY TESLA-FEL-95-03, 1995.

[3] P.Castro for the TESLA Collaboration, “Performance Of The Tesla Test Facility Linac”, Proceedings of EPAC 2002, Paris, France, pp.876-878.

[4] H.Weise, “The TESLA X-FEL Project”, Proceedings of EPAC 2004, Lucerne, Switzerland.

[5] D. Proch for the TESLA collaboration, “Activities With Superconducting Cavities At DESY”, Proceedings of the 9th Workshop on the RF Superconductivity, 1999, Santa Fe

[6] W.-D. Moeller for the TESLA Collaboration, “High Power Coupler For The TESLA Test Facility”, Proceedings of the 9th Workshop on the RF Superconductivity, 1999, Santa Fe, Vol.2, pp.577-581.

[7] W.-D. Moeller for the TESLA Collaboration, “Status And Operating Experience Of The TTF Coupler”, Proceedings of this conference.

[8] L. Lilje, et.all, “Achievement of 35 MV/m in the TESLA Superconducting Cavities Using Electropolishing as a Surface Treatment”, Proceedings of EPAC 2004, Lucerne, Switzerland.

PROGRESS TOWARD NLC/GLC PROTOTYPE ACCELERATOR STRUCTURES*

J.W. Wang#, C. Adolphsen, G. Bowden, D.L. Burke, J. Chan, J. Cornuelle, S. Doebert, V. Dolgashev, R.M. Jones, J. Lewandowski, Z. Li, R.H. Miller, C. Nantista, N. Baboi, C. Pearson, R.D. Ruth, S. Tantawi, P.B. Wilson, L. Xiao SLAC, USA
T. Higo, Y. Higashi, T. Kumi, Y. Morozumi, N. Toge, K. Ueno, KEK, Japan.
T. Arkan, C. Boffo, H. Carter, D. Finley, I. Gonin, T. Khabiboulline, S. Mishra, G. Romanov, N. Solyak, FNAL, USA

Abstract

The accelerator structure groups for NLC (Next Linear Collider) and GLC (Global Linear Colliders) have successfully collaborated on the research and development of a major series of advanced accelerator structures based on room-temperature technology at X-band frequency. The progress in design, simulation, microwave measurement and high gradient tests are summarized in this paper. The recent effort in design and fabrication of the accelerator structure prototype for the main linac is presented in detail including HOM (High Order Mode) suppression and design of HOM couplers and fundamental mode couplers, optimized accelerator cavities as well as plans for future structures.

HIGH GRADIENT TEST STRUCTURES

Since 2000, more then thirty structures with different length, aperture, phase advance and coupler design have been built and tested at the NLCTA.[1] Through the thorough comparison and analysis we have selected the following main accelerator parameters: 60 cm of length, 5π/6 phase advance /cell, low group velocity with optimal attenuation factor of 0.5-0.6 for optimal RF efficiency.

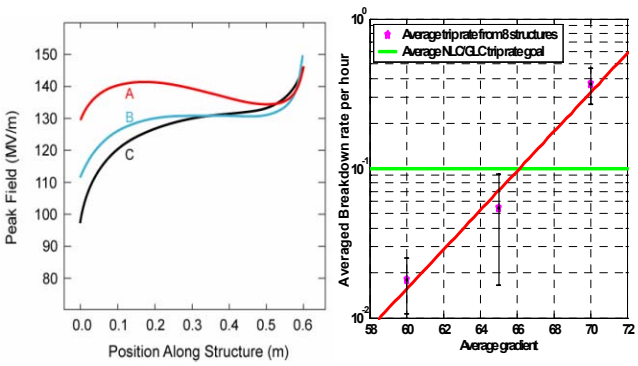

Figure 1: Maximum surface field for three types structures at unloaded gradient of 65 MV/m (left) and high power test results for eight structures (right).

The parameters of A (H60VG3S18), B (H60VG3S17) and C (H60VG4S17) are shown on Table 1. With reduced aperture a/λ=0.17, B and C have 10% higher RF efficiency than A. With asymmetric dipole mode detuning distribution, C has lowest surface field at the input end.

Table 1: Basic parameters for three typical structures

Structure Type	H60VG3S18	H60VG3S17	H60VG4S17
Other Names	FXBs (2D), KX01 (2D)	FXCs	FXDs, KX02, H60VG4SL17
Length	62 cm	62 cm	62 cm
Number of Cells	53 cells + 2 Matching Cells	53 cells + 2 Matching Cells	53 cells + 2 Matching Cells
Iris Radius	$<a/\lambda>$ =0.18	$<a/\lambda>$ = 0.17	$<a/\lambda>$ = 0.17
Phase Advance	5π/6 Per Cell	5π/6 Per Cell	5π/6 Per Cell
Group Velocity	3.27–1.24 % Speed of Light	3.56–0.78 % Speed of Light	4.50-0.82 % Speed of Light
Attenuation τ	0.533 0.508 (2D)	0.630	0.636
Filling Time	105 ns	116.5 ns	117.6 ns
Q_0 Value	~ 6640 ~ 6990 (2D)	~ 6670	~ 6660
Shunt Impedance	46.5-73.5 49.1-77.2 (2D) MΩ/m	54.7 – 68.8 MΩ/m	50.9 – 69.0 MΩ/m
Coupler Type	Mode Converter or Wave Guide Type	Waveguide Type	Wave Guide type
1st Band Dipole Mode Detuning	kdn/df Symmetric Gaussian Δf/f~10% (4.0σ)	kdn/df Symmetric Gaussian Δf/f~9.37% (3.94σ)	kdn/df Asymmetric $Sech^{1.5}$ with Δf/f~12.5% (5.1σ)
Es /Ea	2.06 - 1.90	2.04 -1.99	2.10 -1.97
Required Input Power	69 MW 63.2 MW (2D)	59 MW	58.2 MW
Unloaded Gradient	65 MV/m	65 MV/m	65 MV/m

The right plot of Fig. 1 show a summary of performance for the recent eight accelerator structures. The horizontal line is the goal line for GLC/NLC stable high power operation – less than 1 breakdown per 10 hours per 60 cm section at unloaded 65 MV/m gradient for 60 Hz RF pulses. The tilted line is a fit for average trip rates for

*Work supported by U.S. Department of Energy, contract DE-AC02-76SF00515 and part of JapanUS Collaboration Program In High Energy Physics Research.
#jywap@slac.stanford.edu

different gradients. The factor of two lower trip rate has been successfully reached. [2]

DEVELOPMENT OF H60VG4SL17

Accelerator Design

As the first generation of full featured HDDS structures, four H60VG4SL17 type of structures are in the final assembly stage of fabrication. Figure 2 shows four HOM couplers in both input and output ends. Fundamental input/output couplers are waveguide type.

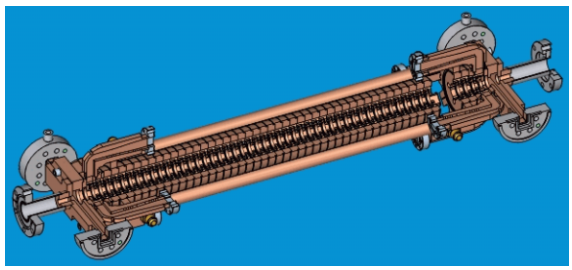

Figure 2: Cutaway view of H60VG4SL17 structure.

In order to reduce the field in the input end, the dipole mode detuned distribution becomes asymmetric. A Sech$^{1.5}$ function distribution was adopted for better dipole mode suppression. The predicted wakefield is shown in Fig. 3.

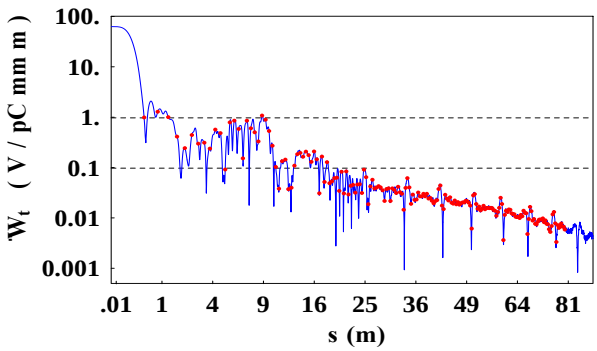

Figure 3: Envelope of simulated wakefield of two fold interleaved structures as function of the distance behind a driving bunch, dots show the location of trailing bunches.

Accelerator Cup Fabrication

Figure 1 shows one of accelerator cups for the latest structures, which are fabricated through a combination of precise milling and tuning. For KEK produced cups, final finish was done by single-diamond turning.

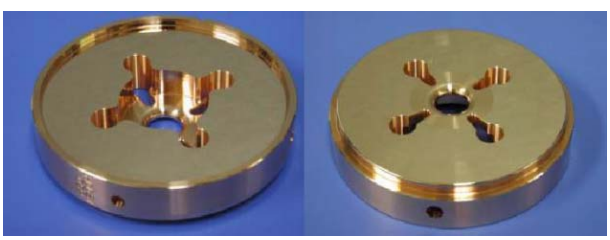

Figure 4: View from both sides of an accelerator cup.

The fundamental mode (TM01) frequencies and dipole mode (HEM) frequencies were measured by using a single cup microwave QC setup. The results for the first band of dipole mode were shown in Figure 1. The left plot shows the very smooth change for the frequencies corresponding to the cups of two interleaved structures A and B in the sequence of 3A, 3B, 4A, 4B, 5A, 5B and so on. Right plot shows the distribution of frequencies in comparison with accurately calculated theoretical values.

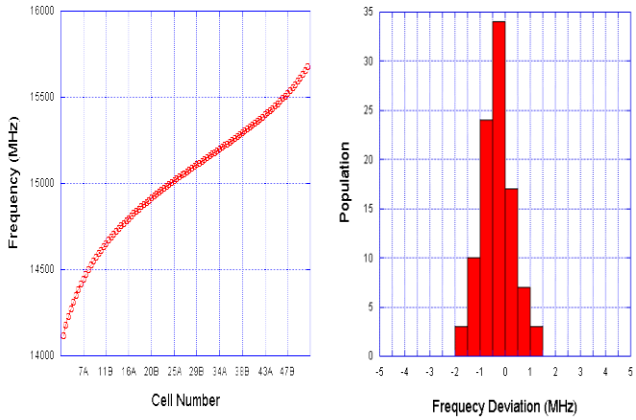

Figure 5: Measured dipole mode frequencies (left) and their tolerances.

HOM Coupler Design and Verification

HOM couplers are critical elements to connect each HOM manifold and corresponding WR62 load with good match. A scattering matrix computer code S3p was used to theoretically design the HOM couplers. Figure 6 shows a model with symmetric feeds and better than 0.1 of reflection coefficient within structure first dipole band has been reached with our design.

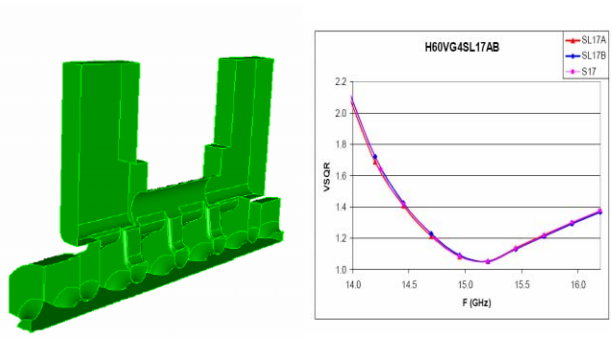

Figure 6: Simulation model for HOM coupler design (left) and match quality expressed by the VSWR in coupler pass region (right).

In order to examine the accuracy of the electrical design and mechanical fabrication for those HOM couplers, a cold test assembly of H60VG4SL17B output end HOM coupler was tested. By sequentially changing the number of cups between back-to-back HOM couplers at certain frequency, the amplitude of reflection coefficient within dipole mode pass band can be mapped out. The consistency between measurement and theory gave us the confidence to fabricate such complicated elements.

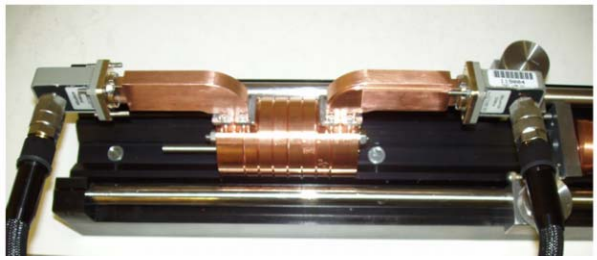

Figure 7: Microwave measurement for a HOM coupler test assembly.

NEXT PROTOTYPE STRUCTURES

Optimization of Accelerator Disks

To improve the shunt impedance of the structures by 10 to 15%, a structure incorporating rounded cells is being studied and test cups are being machined. The main technical challenge is to machine round-edged pie-shape slots along curved cavity wall. High speed ball milling is the first option. The second choice is to mill with a shaped tool in a 5-axis milling machine, then a so called "leek-head" cavity shape design is needed in order to allow the tool to cut the curved slot edges near the cavity outer wall. Fig. 8 shows accelerator cups schematically.

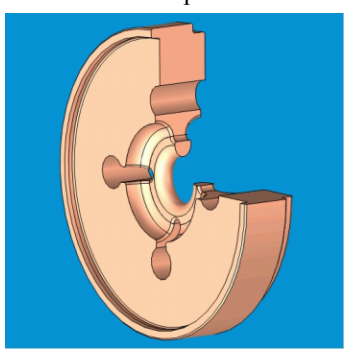

Figure 8: Cutaway view of a proposed full rounded symmetric accelerator cups.

Fundamental Coupler

We plan to adapt a compact design (shown in Figure 9), which was used in early RDDS1 structure for both input/output fundamental couplers. Trapped modes need to be studied very carefully as was done for H60VG4S17 structures. [3]

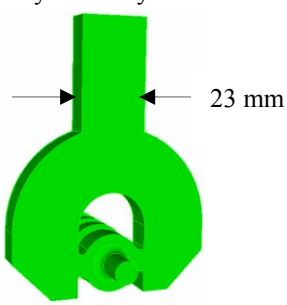

Figure 9: Compact fundamental couplers.

HOM Coupler and Load

In present design, the HOM modes are transmitted through a mitered WR62 bend to an external load and pick-up assembly. In order to reduce the complexity and fabrication cost, there are three proposed and designed configurations for HOM coupler ports as showed in Fig. 10. Design A is so called in-line load type, where microwave absorbers are located inside of manifolds. The technical challenges are good broad band HOM matching and low absorption for fundamental mode power. Design B is to braze transverse WR62 loads directly on HOM port. Design C is to use waveguide to coax adapter terminated by a coax load.

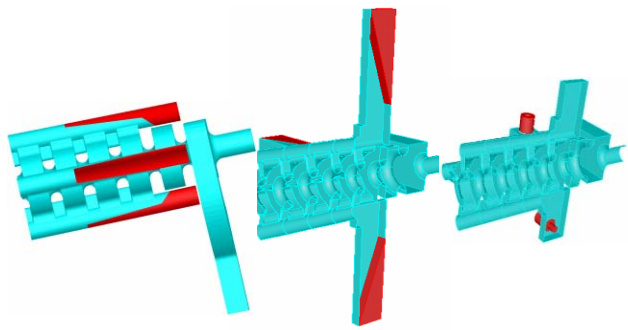

(A) (B) (C)

Figure 10: Three types of HOM coupler design.

Wire Measurement

A wire-based structure experimental method [4] is being developed to quickly and inexpensively analyze the wakefield suppression properties of accelerator structures. Using a 300-micron thick brass wire, measurements of the structure S-parameters are made to compute the impedances for the monopole band and higher dipole mode bands. The test results for a standing-wave structure, a short traveling-wave structure, and the RDDS1 structure (see Fig. 11) show a reasonable agreement with computer simulations.

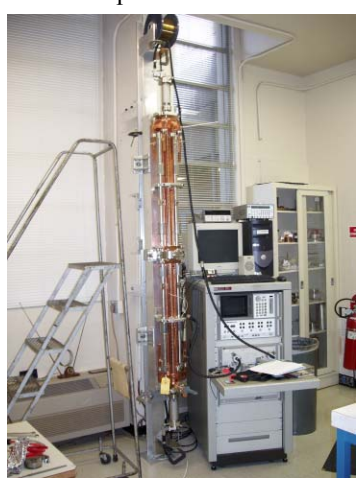

Figure 11: Wire measurement set-up with the RDDS1 structure.

REFERENCES

[1] J. Wang and T. Higo, ICFA Beam Dynamics Newsletter No. 32, SLAC-PUB-10370.
[2] S. Doebert, WE101, this conference.
[3] R. M. Jones et al., MOP40, this conference.
[4] N. Baboi, et al., MOP64, this conference.

A HIGH-POWER TEST OF AN X-BAND MOLYBDENUM-IRIS STRUCTURE

W. Wuensch, A. Grudiev, S. Heikkinen, I. Syratchev, M. Taborelli, I. Wilson, CERN, Geneva, Switzerland
S. Döbert, C. Adolphsen, SLAC, Palo Alto, California, USA

Abstract

In order to achieve accelerating gradients above 150 MV/m, alternative materials to copper are being investigated by the CLIC study. The potential of refractory metals has already been demonstrated in tests in which a tungsten-iris and a molybdenum-iris structure reached 150 and 193 MV/m respectively (30 GHz and a pulse length of 15 ns). In order to extend the investigation to the pulse lengths required for a linear collider, a molybdenum-iris structure scaled to X-band was tested at the Next Linear Collider Test Accelerator (NLCTA). The structure conditioned to only 65 MV/m (100 ns pulse length) in the available testing time and much more slowly than is typical of a copper structure. However the structure showed no sign of saturation and a microscopic inspection of the rf surfaces corroborated that the structure was still at an early stage of conditioning. The X-band and 30 GHz results are compared and what has been learned about material quality, surface preparation and conditioning strategy is discussed.

INTRODUCTION

The CLIC accelerating gradient specification is 150 MV/m, indisputably high, and a substantial development program is underway to achieve it [1]. One aspect of the program is an rf design study with the objective to design and optimize structures within experimentally determined high-power rf and simulated beam-dynamics constraints [2]. Another aspect is an experimental study which seeks to find alternative materials to copper which are able both to sustain a higher surface electric field and to resist damage during breakdown. A significant success of this experimental study has been the demonstration in CTF2 of a 193 MV/m, 15 ns peak accelerating gradient in a molybdenum iris structure [3].

The logical next step is to repeat the test at a longer pulse length since the CLIC design pulse length is 150 ns. However 30 GHz power will only become available for testing (in CTF3) at the end of 2004. In order make the test as soon as possible and to utilize the highly-developed NLCTA test area, an agreement was made to test a CERN-built molybdenum iris structure scaled to 11 GHz at the NLCTA at SLAC.

THE STRUCTURE AND INSTALLATION

The 11 GHz structure geometry was exactly scaled from the 30 GHz test in order to be able to make as direct a comparison to the previous test and also to provide frequency scaling of gradient data. The structure characteristics are summarized in table 1. The same mode-launcher coupler was used as in the 30 GHz test with only slight dimensional changes to match to WR-90 rather than WR-28 waveguide.

In addition, the irises were manufactured from the same 99.95% purity sintered and forged molybdenum bar produced by the same supplier as those of the 30 GHz test. Finally the method of assembly by clamping, a cell and iris are shown in fig.1, was maintained to keep to a minimum the number of differences between the structures.

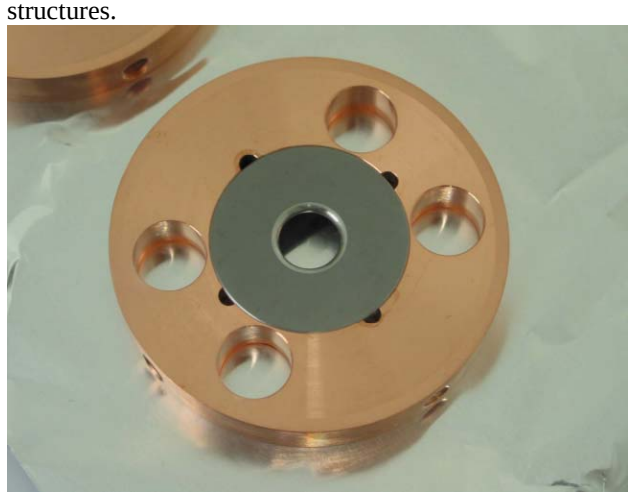

Figure 1: A molybdenum iris mounted in the copper disk which forms the cell.

Table 1: Structure Specifications

Frequency	11.424 GHz
Number of cells	30+2 matching cells
Phase advance	$2\pi/3$
Beam aperture	9.19 mm (constant)
Group velocity, v_g/c	4.6 %
Fill time	20 ns
$E_{surface}/E_{accelerating}$	2.2
Power for $E_{accelerating}$=100 MV/m	175 MW

The structure was assembled and installed in a dedicated vacuum tank at CERN and shipped to SLAC under vacuum. However the structure arrived vented and was therefore purged with hot (100°C) nitrogen for 72 hours in an attempt to reduce the water content in the rest gas. The structure vacuum level was measured by a gauge mounted directly on the tank and operated with a static pressure of the order of 10^{-8} mbar.

CONDITIONING

The high power test was performed using a single 50 MW klystron and a SLED II pulse compression system delivering a maximum of 140 MW X-band power to the structure at a pulse length of up to 240 ns. Directional couplers in the input and output waveguide were used to monitor the relevant rf power signals.

The structure was conditioned using the standard NLCTA automated processing loop. The primary pulse-to-pulse interlock on rf was a user-defined percentage of missing forward energy (integrated incident power minus transmitted power). In addition, structure vacuum and reflected power interlocks were used to protect the klystron output windows. The missing energy trip level, which is normally set to 10% for (copper) NLC structures, was set for most of this experiment to about 50%.

The conditioning was started using a pulse length of 30 ns. The conditioning curve, accelerating gradient in the first cell as a function of testing time, for the entire test is shown in fig. 2. Progress was initially limited by heavy vacuum out-gassing and the structure processed slowly to about 70 MV/m (first cell). Progress was then limited by rf breakdown. Initially most breakdowns were 'soft', missing energy below 15%, but towards the end of the processing the more typical 'hard', missing energy above 50%, breakdowns dominated.

The pulse length was changed a number of times during conditioning, which produced the abrupt changes in gradient that appear in the conditioning curve. The reasons it was changed were to investigate the behaviour near the CLIC nominal pulse length, to try to optimize conditioning speed and in order to compare directly to the 16 ns data at 30 GHz. The klystron/pulse compressor power limit of roughly 140 MW, producing 85 MV/m in the first cell, was reached for pulse lengths of 16, 25 and 30 ns.

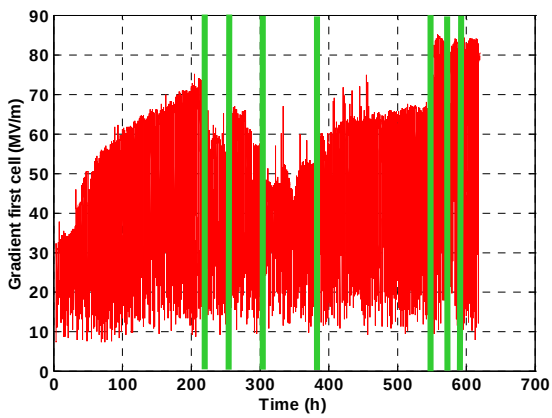

Figure 2: The conditioning curve gradient in the first cell vs processing time. A green vertical line indicates a change in pulse length and the sequence of pulse lengths was: 30, 100, 70, 240,100, 16, 25 and 30 ns.

In addition to the processing, about 100 h of testing time was used to make a number of basic high power rf measurements. More details on these measurements can be found in [4]. The dependence of breakdown rate on gradient and pulse length was similar to that observed in copper X-band structures [5]. The dependence of gradient on pulse length was $\tau^{-(1/6)}$ and thus very similar to that measured with copper structures. A Fowler-Nordheim field enhancement factor of $\beta = 30$ was measured.

The locations of breakdown in the structure were determined by timing measurements using the transmitted and reflected rf pulses. They were uniformly distributed over the length of the structure with some enhancement in the last five cells or so. The stable gradient did not change when the repetition rate was changed from 60 Hz to 10 Hz, which indicates that the cooling of the structure was sufficient – a concern in a clamped structure.

COMPARISON TO 30 GHZ AND COPPER RESULTS AND CONCLUSIONS

Although the structure ran to the available power limit for pulse lengths of 30 ns and below, it must be clearly stated that the 65 MV/m achieved for longer pulses in the nearly five week long test was a disappointment. The test has raised the questions: are the 11 GHz results consistent with the 30 GHz test, what new issues does this test highlight and do the results call into question the potential of molybdenum?

Direct comparison of the maximum achievable gradient is impossible because of the power-source limit of the 11 GHz gradient at the 16 ns 30 GHz test pulse length. In addition, the conditioning curve of the 11 GHz structure shows no sign of saturation at longer pulse lengths which indicates that it had not been taken to its ultimate gradient - more evidence follows below.

An obvious difference between the two structures is that the 11 GHz structure conditioned much more slowly with respect to testing time, even allowing for the longer pulse lengths. However since the conditioning was controlled so differently in the two tests, the 11 GHz test was interlocked and the 30 GHz test was not, comparing testing time is arguably not relevant.

One comparison which may be physically relevant is the number of breakdowns per rf surface area that the structures were subject to. This comparison is motivated by the supposition that breakdowns during conditioning improve rf surfaces by removing dirt, oxides, asperities or mechanical stresses. The surface area which individual breakdowns affect is small and not a function of rf frequency and a certain number are needed per unit area to prepare a given type of surface for a specific gradient.

A counterargument can be found by applying this logic to copper and extrapolating NLC results to 30 GHz structures. This implies conditioning within 100 breakdowns, which has not been observed [3]. Still copper and molybdenum may need a very different type of conditioning, and the numbers are considered.

In CTF2 the 30 GHz structure was driven to breakdown on approximately every fourth rf pulse (exact statistics are not available) giving nearly a 1 Hz conditioning pulse rate

and resulting in a total of about 500,000 breakdowns. In NLCTA the requirement to protect the driving klystron restricted the rate to about two per minute and resulted in a total of about 100,000 breakdowns. Normalizing by the ratio of surface areas, the 11 GH structure saw an equivalent of 15,000 breakdowns, a very early stage of conditioning from the 30 GHz data.

A microscopic analysis of the irises, shown in fig. 3, corroborates the hypothesis that the 11 GHz structure surface was subject to a much lower number of conditioning breakdowns and consequently that it was conditioned comparatively little. Taken together these two analyses imply that the two tests differed mainly in conditioning procedure – and does not indicate a specific problem with the 11 GHz structure nor a frequency dependence of breakdown.

The images also show that the surface finish of the molybdenum parts was not good and that the 11 GHz structure was the poorer of the two. Substantial progress must be made in improving both the molybdenum bulk and the surface in order to provide a more practical rf material since rf conditioning is bound to be a costly activity for a linear collider – although a more robust material may always be more difficult to condition.

Higher purity and smaller grain molybdenum than the sintered 99.95% purity used in the tests described in this report are being investigated. Both the higher purity and especially the smaller grain size should improve surface finish (and tolerances) which should speed conditioning. The higher purity may also be better with respect to breakdown.

Demonstrating these suppositions with experiments with positive results is a very high priority of the CLIC structure development program. A repeat of the 30 GHz test, but now in CTF3 with longer pulses, will be the next test of molybdenum. The test of a tungsten-iris structure will also be redone.

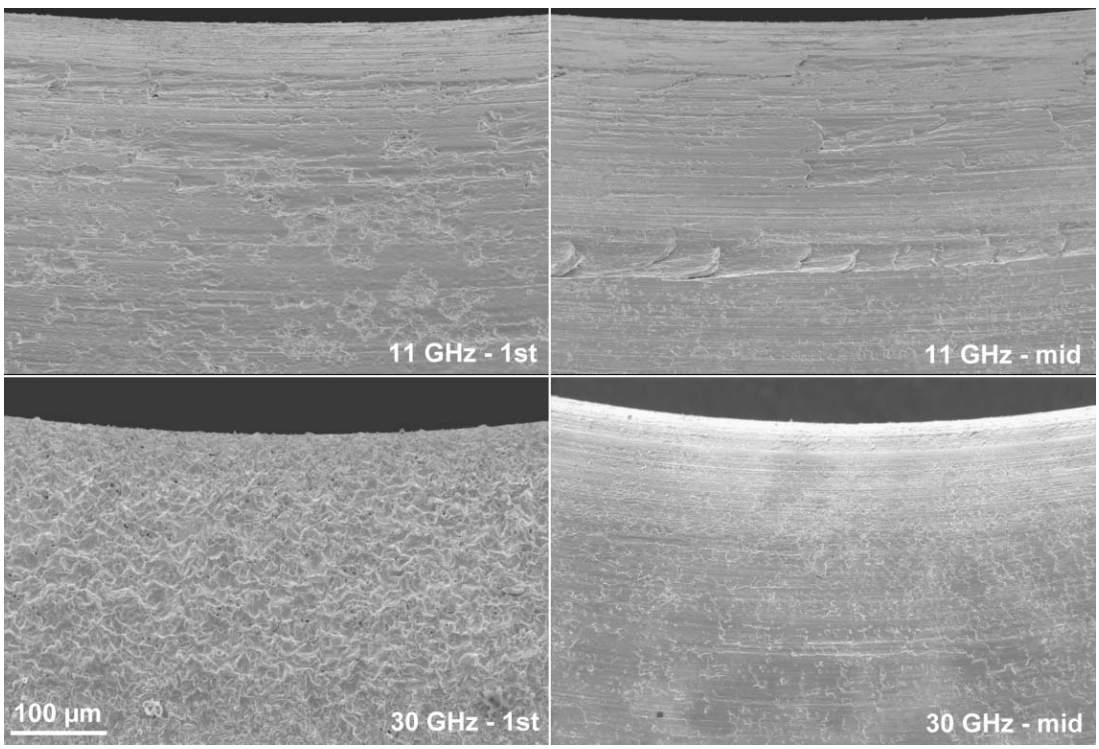

Figure 3: SEM analysis of the high electric field region of the molybdenum irises after test. The same magnification is used for all the photographs. Images of cells from the middle of the structure are shown for reference. The relative difference in conditioning is easily observed from the much higher density of melted spots on the 30 GHz iris.

REFERENCES

[1] W. Wuensch, "Major Issues for CLIC Accelerating and Transfer Structure Development", ICFA Beam Dynamics Newsletter, No.32, December 2003.

[2] A. Grudiev, W. Wuensch, “A newly designed and optimized CLIC main linac accelerating structure”, these proceedings.

[3] W. Wuensch, C. Achard, S. Döbert, H. H. Braun, I. Syratchev, M. Taborelli, I. Wilson, "A Demonstration of High Gradient Acceleration", Proc. PAC2003.

[4] C. Adolphsen S. Döbert, C. Achard, H. H. Braun, A. Grudiev, I. Syratchev, M. Taborelli, I. Wilson W. Wuensch “High Gradient Test of a molybdenum iris clamped X-band accelerating structure at NLCTA”, SLAC-PUB-10551.

[5] C. Adolphsen, “Progress on X-band Accelerator Structure Development for NLC/GLC”, EPAC 2004.

DEVELOPMENT OF A NON-MAGNETIC INERTIAL SENSOR FOR VIBRATION STABILIZATION IN A LINEAR COLLIDER*

Josef Frisch, Valentin Decker, Eric Doyle, Linda Hendrickson, Thomas Himel, Thomas Markiewicz, Andrei Seryi, SLAC, Stanford CA, USA
Allison Chang, Richard Partridge, Brown University, RI, USA

Abstract

One of the options for controlling vibration of the final focus magnets in a linear collider is to use active feedback based on accelerometers. While commercial geophysics sensors have noise performance that substantially exceeds the requirements for a linear collider, they are physically large, and cannot operate in the strong magnetic field of the detector. Conventional nonmagnetic sensors have excessive noise for this application. We report on the development of a non-magnetic inertial sensor, and on a novel commercial sensor both of which have demonstrated the required noise levels for this application.

SENSOR REQUIREMENTS

Room temperature linear colliders require relative position stability of the electron and positron beams at the Interaction point at the nanometer lever. The most sensitive beam line elements for vibration effects on the beam are the final focus doublets, which produce approximately one-to-one motion of the beam spots at the IP. With a beam rate of 120Hz, a feedback based on the beam interaction typically has unity gain around 10Hz. Gain at 1Hz is 10-1000 [1].

An accelerometer-based feedback system to mechanically stabilize the final doublets, with gain at frequencies above ~1 Hz can reduce the beam / beam motion at the IP [2]. While there is not a simple relationship between the accelerometer noise and ultimate feedback performance, it is clear that an integrated sensor noise of < 1nm for frequencies above ~1Hz is desirable, corresponding to a sensor acceleration noise of $<3x10^{-8}M/s^2/Hz^{1/2}$ at frequencies above 1Hz.

The acceleration sensors are attached to the final doublet magnets, and must operate in a detector magnetic field of the order of one Tesla. They must also be physically compact (approximately 20x20x10cm) due to volume constraints in the final focus design.

COMMERCIAL SENSORS

Good commercial piezoelectric seismometers have specified noise of $\sim 6x10^{-7}M/s^2/Hz^{1/2}$ at 1Hz [3]. Tests at SLAC measured a noise level of these sensors of $2x10^{-6}M/s^2/Hz^{1/2}$ at 1Hz with an integrated noise of 50nm above 1Hz. [4], too large for this application.

A commercial magnetic geophone of the type used in vibration stabilization experiments at SLAC [5], the GS-1 from Geospace [6] has a moving mass of 700 grams and a mechanical Q of ~0.5. The theoretical thermal noise of the sensor is $5x10^{-10}M/s^2/Hz^{1/2}$ (see below), however the actual sensor noise is not specified and may be higher.

Previous measurements of a similar sensor, a Mark Products L-4C at SLAC gave a noise of $<4x10^{-8}M/s^2/Hz^{1/2}$ (measurement limit), with an integrated noise of 0.3nm above 1Hz. This meets the noise requirements for final focus stabilization, but this type of sensor can not be used in the strong magnetic field of the detector.

Geophysics feedback seismometers such as the Streckeisen STS-2 have noise levels of $\sim 10^{-9}M/s^2/Hz^{1/2}$ with a corresponding integrated noise above 1Hz of ~.07nm [7], much better than our requirements. All commercial sensors of this type use magnetic internal components for temperature compensation and for force feedback, and cannot be used for our application. The prototype NLC vibration uses the same basic design concept, adapted for non-magnetic operation.

Micromachined accelerometers such as the "Si-flex" [8] accelerometer from Applied Mems have a specified noise of at $3x10^{-7}M/s^2/Hz^{1/2}$ at 1Hz. This does not meet our requirements, but future devices may improve on this performance.

Electrochemical Sensor

A novel commercial sensor SP-400 based on electrochemical detection of motion has recently been developed by PMD/Eentec [9]. This sensor is specified at $10^{-8}M/s^2/Hz^{1/2}$ at 1Hz, sufficient for our application. However this sensor uses magnetic coils for force feedback and cannot be used in this application without modification. The company estimates that replacing the magnetic components (which would remove the force feedback) would increase the noise by a factor of ~3, still within our requirements.

NLC SENSOR DESIGN

The lack of suitable sensors for NLC final focus stabilization led to the design of a low noise, nonmagnetic sensor. The sensor operates on the same principal as geophysics feedback seismometers, however the non-magnetic and compact size requirements lead to some design changes. The prototype sensor was designed for vertical sensing as this was considered to be the more technically challenging problem.

Sensor Noise Sources

All acceleration sensors can be modeled as a suspended mass, with a position measurement between the mass and the body of the sensor. The ultimate thermal noise of the

* Work Supported by DOE Contract DE-AC03-76SF0515

sensor is given by $A=(4K_bTw_0/mQ)^{1/2}$ [10] , with K_b Boltzman's constant, m the moving mass, Q the sensor Q, and w_0 the resonance frequency. The mass position readout can contribute to the noise of the sensor, but for most designs this noise can be made small.

At low frequencies temperature variations of the sensor typically provide the major noise source. For a vertical sensor, the suspension is acting against the $9.8M/s^2$ acceleration of gravity. Typical engineering materials will exhibit changes in length and stiffness on the order of 10^{-5}/ºC. For our requirements this corresponds to a temperature stability of 10^{-9} ºC for the suspension during a measurement time (~1 second).

Geophysics seismometers like the STS-2 use temperature compensated spring materials (eg. Nispan [11]), however these materials are magnetic and cannot be used in our application. Fortunately our requirements do not extend significantly below 1Hz, allowing thermal time constants to reduce temperature variations.

Convection currents can disturb the test mass, so most low noise sensors, including the NLC sensor are operated in vacuum. External varying magnetic fields can also produce noise in the sensor. In addition to using non-magnetic materials, with the exception of the suspension spring, the NLC sensor also uses non-conducting materials in the suspended mass in order to avoid forces from eddy currents.

Suspension Design

An ideal suspension provides a low primary resonant frequency, high Q, and low thermal sensitivity. Other modes of the suspension system should have resonant frequencies above the frequency band of interest. Since it is desirable to have a suspension frequency of ~1Hz, and higher (transverse) frequencies >~100Hz, the suspension must be very soft in one direction, stiff in the others.

The design chosen is to use a "pre-bent" leaf spring which has a 90 degree bend with no load, and is flat under gravity load. For the NLC sensor, Beryllium Copper was used as the spring material. For the first prototype sensor, an Aluminum "Y" frame was used for the cantilever, and tungsten for the mass. For the next prototype, the cantilever will be Aluminum Oxide, and for 'the mass a heavy insulator, either Hafnium Oxide, or tungsten powder loaded epoxy.

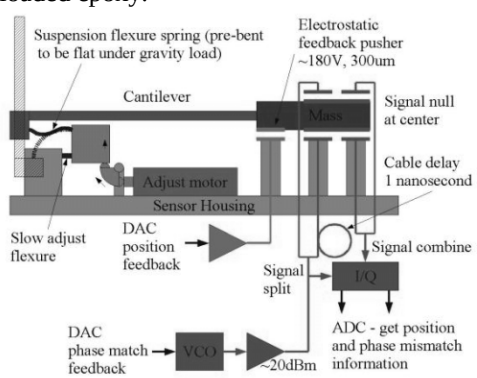

Figure 1: Sensor block diagram.

The Suspension spring creeps with time and changes with temperature. A piezoelectric motor (Picomotor [12]) is used to adjust the position of the spring support to compensate. Long term studies were conducted of the behavior of the BeCu spring under design load, and the creep was found to be acceptable for a lifetime of >10 years.

Electronics

The position of the mass relative to the sensor frame is measured using a differential RF capacitor system. RF at ~400MHz, 100mW is applied out of phase to two electrodes capacitively coupled to the mass. The summed signal on the mass is capacitively coupled to synchronous detection electronics to read the in-phase, and quadrature components. The capacitive gaps are approximately 300 microns, giving a full range of motion of 600 microns.

In-phase errors are proportional to the position error of the mass. These are corrected by moving the mass position actuator. Control is through an electrostatic pusher which applies 0-180 Volts to an electrode on the frame next to a grounded part of the test mass

Quadrature errors are proportional to errors in the 180-degree phase difference between the drive electrodes. These are corrected by changing the RF drive frequency, which in conjunction with the 180 degree RF delay results in a phase shift.

The combination of in-phase and out-of-phase loops allows nulling of the RF signal from the detector, and the use of high gain, low noise RF amplifiers.

Feedback

The in-phase and out-of-phase signals are amplified and digitized at 16 bits, 2 kHz. Feedback is performed using a TMS320C40 DSP. Presently, a PID algorithm is used for control; "optimal" control may be implemented in the future.

The force required to hold the mass position fixed (square of the applied voltage), is a measure of the acceleration of the sensor. This signal is then corrected with the residual mass position to measure motion above the feedback bandwidth.

Sensor Parameters

The sensor is enclosed in a vacuum box, 20cm long, connected to an ion pump to maintain $<10^{-4}$ Torr. The box is gold plated to reduce thermal radiation

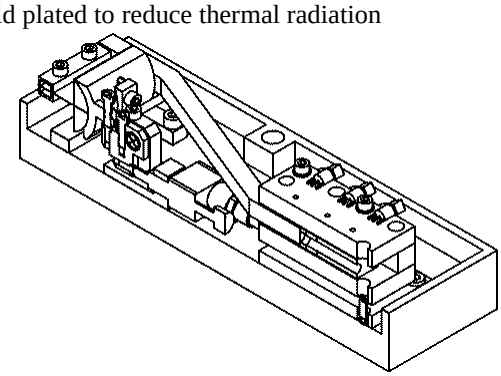

Figure 2: Sensor cut-away, leaf spring to left.

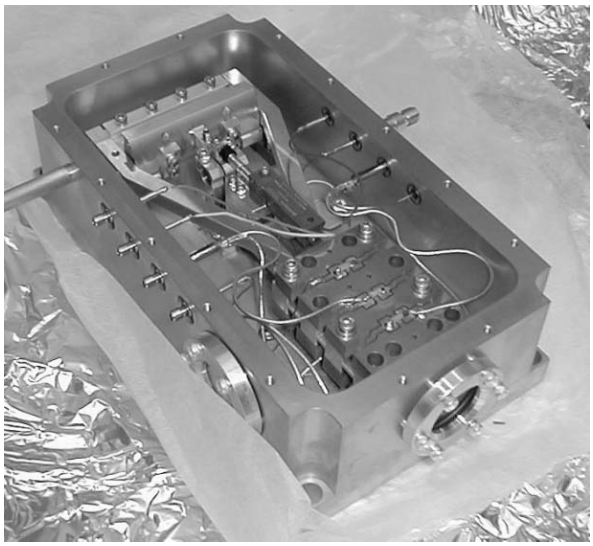

Figure 3: Photo of prototype sensor.

Table 1: Sensor Parameters

Test Mass	40 grams
Suspension Frequency	1.4Hz
Mechanical Q	>100 (but see below)
Theoretical thermal noise	$1.5 \times 10^{-10} M/s^2/Hz^{1/2}$
Capacitive sensor gap	300 microns
RF drive power	100 mW
Theoretical electrical noise	< thermal mechanical noise

SENSOR PERFORMANCE

The noise of the sensor was measured by correlating with a STS-2. Measurements were performed in a noisy environment (integrated noise ~50nm above 1Hz), and may not represent the sensor limit.

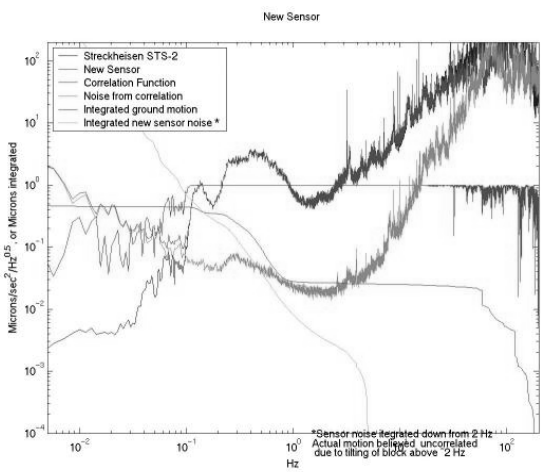

Figure 4: Sensor noise from correlation with STS-2.

The measured noise is $\sim 2 \times 10^{-8} M/s^2/Hz^{1/2}$ which meets the NLC requirement, but is substantially worse than the expected sensor noise.

A possible cause of the higher than expected noise was recently uncovered: While the mechanical Q of the sensor is >100 for large amplitude (>50 micron) motions, it is quite small for low amplitude motions see figure 5. The decay for small amplitude motion suggests hysteretic damping – possibly due to a poor connection between the leaf spring and its supports.

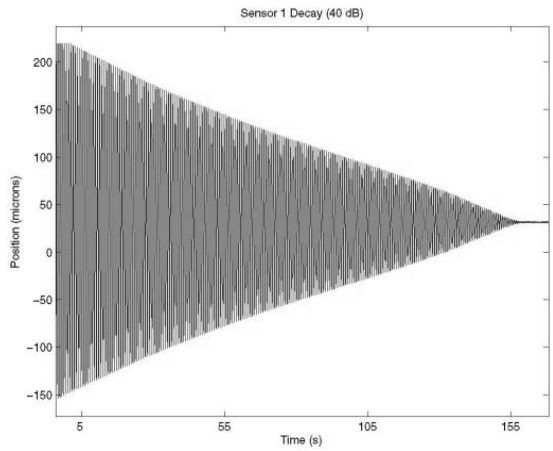

Figure 5: Evidenced of hysteretic damping in sensor. Note that apparent "beating" is an artifact of the image reproduction. Vertical scale approximate.

Work is under way to improve the spring to mount connection by either brazing, or diffusion bonding the connection.

REFERENCES

[1] L. Hendrickson, "Simulations of IP Feedback and Stabilization in the NLC" SLAC-PUB-10492, July 2004.
[2] J. Frisch, "Approaches to beam stabilization in X-band linear colliders", THP37, LINAC'04, Lubeck, August 2004. (these proceedings)
[3] PCB Piezotronics 393B31 sensor specification sheet.
[4] A. Seryi, J. Frisch, Test noise of 393B31 piezoelectric probes, 2000, unpublished.
[5] J. Frisch et al. "Vibration stabilization of a mechanical model of a X-band linear collider final focus magnet", THP37, LINAC'04, Lubeck, August 2004.
[6] Geospace Online data at http://www.geospacelp.com
[7] Zeroth-Order Design Report for the Next Linear Collider, Appendix C, SLAC-474, May 1996.
[8] www.appliedmems.cc/htmlmems/pdf/SFDigital.pdf preliminary datasheet.
[9] www.eentec.com
[10] Bernstein et al. "Low -noise MEMS vibration sensor for geophysical aplicaitons" Proc. Solid-state Sensor and Actuator Workshop 1998 p55-58.
[11] http://www.alloywire.com/nispan_alloy_c902.html
[12] http://www.newfocus.com

VIBRATION STABILIZATION OF A MECHANICAL MODEL OF A X-BAND LINEAR COLLIDER FINAL FOCUS MAGNET*

Josef Frisch, Allison Chang, Valentin Decker, Eric Doyle, Leif Eriksson, Linda Hendrickson, Thomas Himel, Thomas Markiewicz, Richard Partridge, Andrei Seryi, SLAC, Stanford CA, USA

Abstract

The small beam sizes at the interaction point of a X-band linear collider require mechanical stabilization of the final focus magnets at the nanometer level. While passive systems provide adequate performance at many potential sites, active mechanical stabilization is useful if the natural or cultural ground vibration is higher than expected. A mechanical model of a room temperature linear collider final focus magnet has been constructed and actively stabilized with an accelerometer based system.

PROTOTYPE SYSTEM

One option for the warm linear collider is to use a permanent magnet final focus. The small beam sizes at the IP of the linear collider require nanometer scale stabilization of the final doublets. Passive stabilization, interferometer based stabilization, and inertial stabilization have been considered. This paper describes a prototype of the inertial stabilization system.

The prototype system is designed to have mechanical properties similar to an actual permanent magnet final doublet and support raft, but is constructed somewhat differently, figure 1. It is referred to as the "extended object" to distinguish it from an earlier prototype consisting of a simple suspended block. [1]

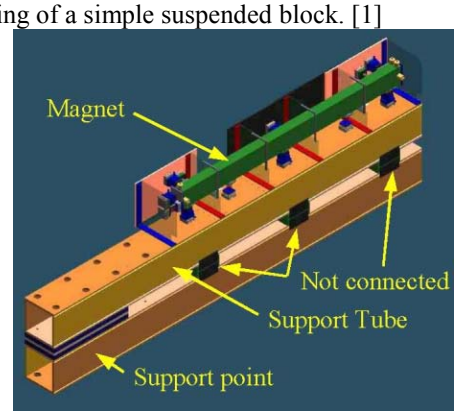

Figure 1: Vibration stabilization demonstration system.

Extended Object Mechanical Design

The extended object contains a simulated magnet support raft constructed of 4 thick-wall welded steel plates. It has the same dimensions, weight, and first two internal design mode frequencies as one of the designs for the NLC final doublet support raft.

Table 1: Simulated magnet properties

Length	3 Meters
Height	21 cm
Width	11.4 cm
Wall thickness	2.54 cm
Weight	240 Kg

The simulated magnet is supported on 6 spring mounts, designed to give the 6 rigid body degrees of freedom resonant frequencies of 2.5 to 6 Hz. This low support resonant frequency provides good attenuation of high frequency motions, which limits excitation of internal modes of the extended object and simplifies feedback.

The springs are mounted on a steel beam which has the same mass and resonant frequencies as the support tube which in an actual final focus would be cantilevered into the detector. Note that mounting the support tube rigidly to the detector risks coupling vibrations from the detector.

Table 2: Support tube properties

Length	3.35M (unsupported length)
Height / Width	40.6 cm
Wall thickness	1.6cm
Weight	1090 Kg

Figure 2: Photo of stabilization demonstration system.

Vibration Sensors

The position of the magnet mass is measured using 8 Geospace GS-1 1Hz magnetic coil seismometers [2]. These seismometer are not suitable for use in the magnetic field of a physics detector, however they have noise similar to the non-magnetic prototype seismometer being developed for the NLC [3]. These sensors are

* Work Supported by DOE Contract DE-AC03-76SF0515

specified from 1Hz to 75Hz, with an integrated noise of ~0.3 nanometers above 1Hz.

The 8 GS-1 sensors are used in a digital feedback loop to control the 6 rigid body modes, and 2 lowest bending modes of the extended object.

An Additional GS-1 sensor is mounted on the free end of the cantilevered support tube and is used in an analog feedback to damp the lowest resonance of the support tube.

Two Streckeisen STS-2, three-axis seismometers are used as an independent measurement of the motion of the extended object, and of the ground. These are very low noise sensors, with integrated noise <0.03nm above 1Hz, and <1nm integrated above 0.1Hz [4].

Feedback Actuators

The low stiffness suspension springs allow the use of low actuator forces to control the extended object position, ~0.025N for 100nm of motion.

Piezoelectric actuators are too stiff for this application, and would prevent the use of a low resonant frequency support system. Magnetic coil actuators are not suitable for use in the magnetic field of the physics detector, and so are not used in this prototype.

Electrostatic pushers - approximately 10x10cm plates, with a ~1 mm gap, and ~1KV high voltage are used for feedback. These provide sufficient force, and have very low stiffness, figure 3.

Figure 3: Close-up of sensors and electrostatic actuators.

Electronics

The eight GS-1 sensors signals are sent on differential cables to gain =100 instrumentation amplifiers (AD624 [5]), then to a set of programmable gain differential amplifiers (Frequency Devices PGA5-100 [6]), then to 500Hz, 4-pole low pass filters (Frequency devices D824), then digitized at 16 bits, at (typically) 1.5KHz (Pentek 6102 [7]). The digitized signals are read across the MIX (Pentek proprietary) bus into a TMS320C40 DSP (Pentek 4284 module). The DSP performs the feedback calculations. The output of the DSP is converted to analog at 16 bits, 1.5KHz (Pentek 6102), then amplified by 1KV, 100KHz bandwidth high voltage amplifiers to drive the pushers. Note that the DSP takes the square root of the required force to produce the drive voltage.

Feedback Algorithm-Extended *Object*

The actuators are operated over a range of frequencies (both swept sine, and random have been used), and all of the sensors are recorded. The data is fit to a model with 8 independent modes (6 rigid body, 2 lowest internal modes). From this a matrix to take sensor measurements to mode amplitudes and a matrix to take mode amplitudes to actuator strengths is created.

Orthoginalizing the problem into 8 independent mode feedbacks reduces the computational complexity. A variety of feedback algorithms for the individual modes, typical stat-space " optimal" control is used.

Note that this model of the system is only valid for relatively high frequencies. At very low frequencies (<~1Hz), the "tilt sensitivity" of the sensors becomes a problem. A horizontal sensor cannot distinguish a horizontal acceleration from a tilt (relative to gravity), thus a fixed angle tilt, appears as a fixed horizontal acceleration (2 time derivatives different). The effect is to convert the 8 independent modes now used into a fully coupled 8x8 system.

Work will begin to solve the fully coupled problem after a higher performance feedback processor (Power PC based) is installed.

Feedback Algorithm - Support Tube

In addition to the primary feedback on the cantilever, an analog feedback is used to damp the lowest order vertical resonance of the support tube. This feedback takes the signal from a GS-1 seismometer, which acts as a velocity sensor at 10Hz, and uses it to drive a second GS-1 seismometer acting as an inertial actuator.

Since force applied by the actuator is proportional to velocity, it acts as a damping term, to reduce the amplitude of the 10 Hz cantilever resonance.

In an actual NLC application (in the detector selonoid), the magnetic actuator could be replaced with a piezoelectric inertial actuator.

Performance Measurements

The GS-1 seismometers used for feedback have noise similar to the prototype NLC non-magnetic sensor. The STS-2 seismometers have very low noise, and are used as an independent measurement to quantify the performance of the system. The feedback algorithm does not use data from the STS-2s.

STABILIZATION EXPERIMENTS

The experiments were conducted in End Station B at SLAC. ESB is located near a large accelerator pumping station and cooling tower, and the site Helium liquefier, resuting in a large background vibration - approximately

40 nanometers integrated above 1Hz. This environment probably represents a worst credible case for the vibration to be expected in the experimental hall of a linear collider.

Note that the ground motion spectra in the ESB vary significantly with time, and therefore measurements taken at different times may not be consistent.

Vibration Spectra

Figure 4 shows overlaid vibration power spectra taken at different points and under different conditions.

- Ground Motion - from STS-2 seismometer
- Support tube motion from GS-1 seismometer.
- Extended object motion measured with STS-2 seismometer taken with digital feedback off
- Extended object motion with digital feedback on.

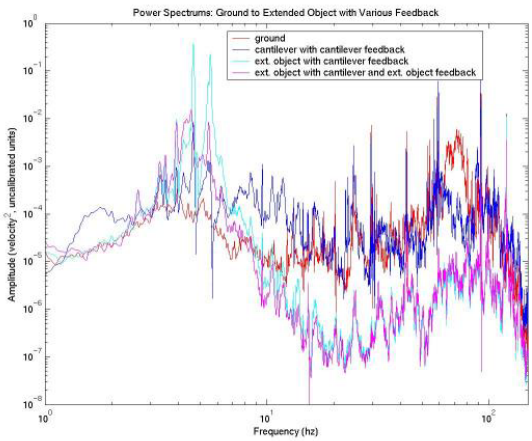

Figure 4: Vibration Spectra.

Since accelerometers cannot measure absolute position (or velocity), it is not possible to measure the "motion" of the magnet as a single number. The STS-2 sensors used provide a good indication of the motion down to approximately 0.1Hz.

Integrated Magnet and Beam Motions

Figure 5 shows the RMS integrated motion spectrum of the ground sensor, and of the magnet sensor with the feedback on and off. Note that the trace for " magnet attached to ground" is for reference. It is not practical to connect the final doublets rigidly to the ground in the accelerator due to the presence of the physics detector.

From Figures 4 and 5, it can be seen that the mechanical suspension of the magnet reduces high frequency motions (above the suspension frequency of ~5Hz), while increasing low frequency motion. The active feedback then reduces the low frequency motions introduced by the support resonance.

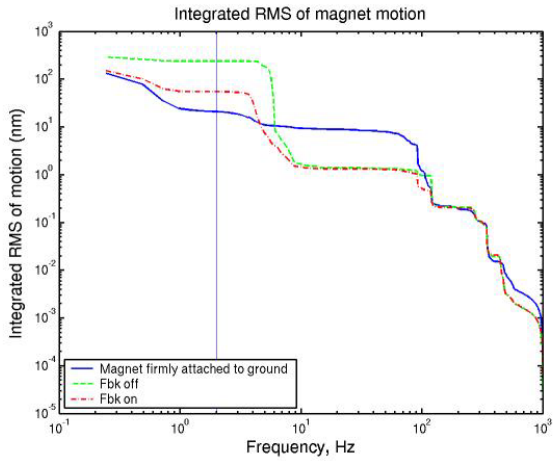

Figure 5:

The performance of the stabilization system is best evaluated by applying a simulated 120Hz beam-beam feedback to the measured magnet motion. Note that the factor of sqrt(2) is included to account for the (presumed) uncorrelated motions of the two magnets. The simulated beam-beam position from the measured magnet positions are shown in figure 6.

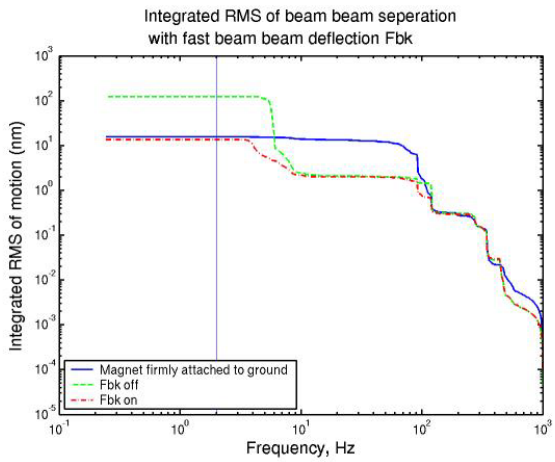

Figure 6: Beam - beam separation at IP from data.

REFERENCES

[1] Allison et al. "Active Vibration Suppression for the Next Linear Collider", SLAC-PUB-9149, August 2002

[2] http://www.geospacelp.com

[3] Frisch et al. "Development of a Non-Magnetic Inertial Sensor for Vibration Stabilization in a Linear Collider", LINAC04.

[4] "Zeroth-Order Design Report for the Next Linear Collider", Appendix C, SLAC-474, May 1996.

[5] http://www.analog.com

[6] http://www.freqdev.com

[7] http://www.pentek.com

APPROACHES TO BEAM STABILIZATION IN X-BAND LINEAR COLLIDERS*

Josef Frisch, Linda Hendrickson, Thomas Himel, Thomas Markiewicz, Tor Raubenheimer, Andrei Seryi, SLAC Stanford CA USA
Philip Burrows, Stephen Molloy, Glen White, Queen Mary University, London UK,
Colin Perry, Oxford University, Oxford UK

Abstract

In order to stabilize the beams at the interaction point, the X-band linear collider proposes to use a combination of techniques: inter-train and intra-train beam-beam feedback, passive vibration isolation, and active vibration stabilization based on either accelerometers or laser interferometers. These systems operate in a technologically redundant fashion: simulations indicate that if one technique proves unusable in the final machine, the others will still support adequate luminosity. Experiments underway for all of these technologies have already demonstrated adequate performance.

STABILIZATION OVERVIEW*

The NLC X-band linear collider is designed to operate at a 120Hz train rate with 192 bunches spaced at 1.4 nanoseconds per train. The linacs each contain approximately 600 quadrapoles containing beam position monitors, and 40 feedback corrector magnets. Beam position monitors and correctors are distributed throughout the beam delivery system. Beam stabilization simulations are described elsewhere [1], here we only quote results. Beam stabilization can be characterized with respect to its timescale, in this paper we primarily discuss feedback on relatively short timescales:

Beam Based Alignment

On approximately one month timescales, the effective centers of the Linac beam position monitors relative to the quadrapole magnetic centers are found through either quad shunting, or dispersion free steering [2].

On several hour timescales, the Linac quadrapoles are moved based on a global optimization algorithm to minimize the orbit errors in the BPMs, to minimize the corrector strengths, and to overall center the beam.

The accelerator structures contain beam position monitors (using signals from the higher order mode ports). Mechanical movers on the structures are used to minimize the transverse wakes when the quadrapoles are aligned.

Beam Based Feedback

Feedbacks distributed throughout the accelerators operate on a pulse to pulse basis at the 120Hz repetition rate of the accelerator[1]. These feedbacks are cascaded, allowing each to have information about the operation of the upstream feedbacks[3].

* Work Supported by DOE contract DE-AC03-76SF0515

The beam / beam deflection at the Interaction Point provides information on the beam separation. This deflection signal is used in a 120Hz feedback in the final focus to maintain beam collisions.

Vibration feedback

The final doublet magnets have the tightest vibration tolerances of any of the machine components [4] with an approximately 1:1 response of beam motion to magnet motion. As the 120Hz beam rate limits the effective frequency of feedbacks to frequencies below a few Hz, several options for mechanical stabilization of the final doublets have been considered, including passive, inertial based, and interferometer based feedback. To date most of the work has been directed to using accelerometers mounted on the doublets, with force feedback to control the magnet positions. The loop speed is typically 1-2 kilohertz, providing gain at frequencies from approximately 1-100 Hz. Current status of this work is described in [5], and the results are used here.

Fast Intratrain Feedback

A fast beam position monitor and kicker located near the interaction point can provide closed feedback on a timescale of tens of nanoseconds[6]. This feedback operates essentially independently from the other beam feedbacks (due to the different timescale), and can significantly improve luminosity under noisy beam conditions.

STABILIZATION STUDIES

The beam stabilization studies use a combination of real and simulated data to provide an estimated luminosity. The simulations are described in [7]. The basic procedure is:

- A series of initial machines with random errors (BPM offsets, magnet positions, etc) based on design tolerance are constructed.
- A simulated ground motion model, in this case the model "B", power spectrum shown in figure 1 is applied to the beamline components EXCEPT for the final doublet. [8].
- An additional 15nm of random jitter is applied to the linac quadrapoles to simulate, for example, water flow induced vibration . An addition 5nm of random jitter is added to the beam delivery quadrapoles.
- 120Hz linac beam feedbacks are simulated
- Final doublet positions are taken from measured data from the vibration stabilization test system [5] – a

mechanical model of a final focus doublet. Since there is only a single stabilization test system, data from two different times is taken to represent the motion of the two doublets – any motion correlations in the real system are ignored (pessimistic assumption).

- The resulting calculated beam / beam separation at the IP is used as the signal for a simulated beam feedback modeled in LIAR, whose gain is shown in figure 6.
- The resulting beam / beam separation is simulated [9] through a model of the intratrain "FONT" feedback system, based on the measured FONT system delay as tested at the NLCTA [10].
- Lumonisity from the final beam / beam separation is calculated.

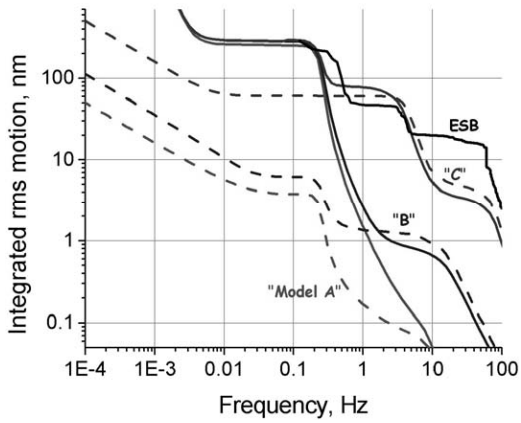

Figure 1: Ground Motion Models. Solid lines are single point motion, dashed are differential motion for 50M separation . "B used". ESB is the measured vibration at the high noise location where the vibration stabilization tests were performed.

Ground Motion Assumptions

There are large variations in ground motion between different possible accelerator sites. Model B used in the simulations roughly corresponds to ground motion in the (shallow) SLAC tunnel under quiet conditions. Figure 2.

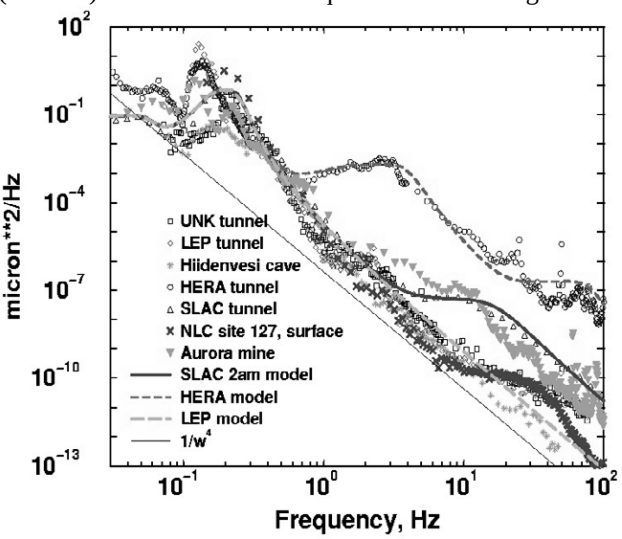

Figure 2: Ground Motion at Various Sites

Vibration Stabilization Assumptions

The final doublet stabilization experiments [5] were performed in a very noisy environment, End Station B, as shown by the line ESB in figure 1.

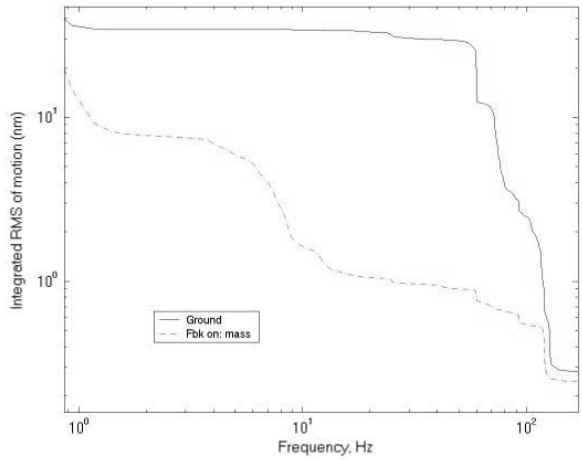

Figure 3: Ground and stabilized magnet spectra

Intratrain Feedback Assumptions

The intratrain feedback calculations assumed the system had the time delay measured in the FONT experiments conducted at the NLCTA (figures 4, 5).

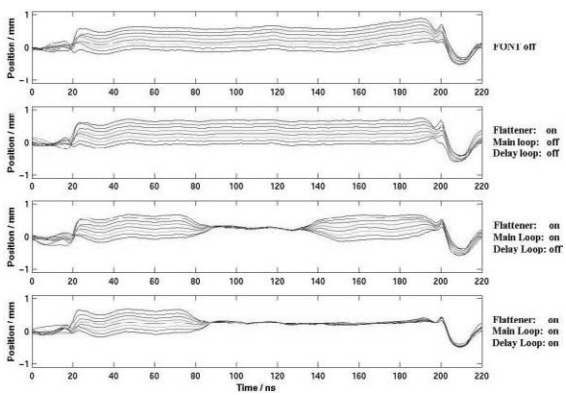

Figure 4: Intratrain feedback demonstration at NLCTA

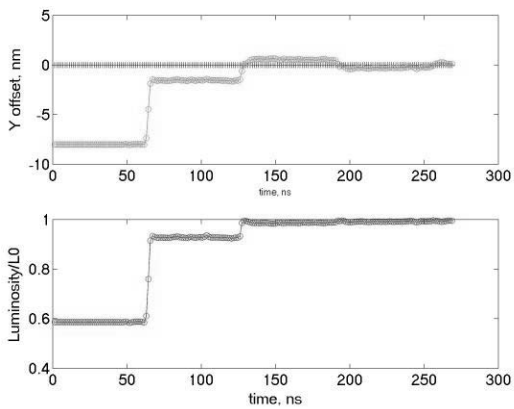

Figure 5: Calculated response of intratrain feedback to an 8 nm offset, based in measured 62ns response

Beam – Beam Feedback Assumptions

The 120Hz beam feedback at the IP is based on the beam – beam deflection which amplifies the offset to a level easily read by BPMs. A variety of algorithms are possible, the frequency response curves for two cases are shown in figure 6. The simulations were performed with a feedback similar to the design with high gain at low frequency.

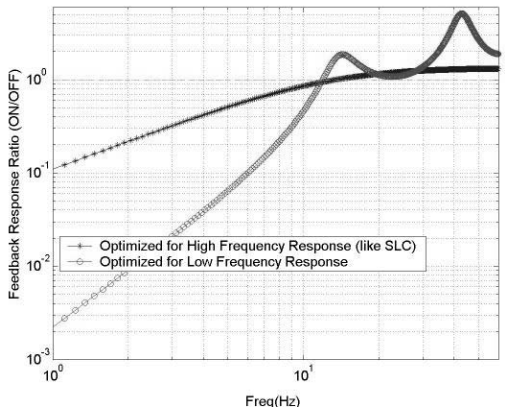

Figure 6: Design responses for 120-Hz intertrain feedback. The SLC-type design (*) is optimized for high frequency noise. An alternative design (o) is optimized for improved low frequency response.

LUMINOSITY CALCULATIONS

The luminosity of the NLC was simulated under a variety of conditions for the final focus. All simulations discussed here used the ground motion "B" model for the linac, with additional jitter applied to the quadrapoles. Statistical errors are approximately +/- 1%. In the following results.

Case 1: 30% nominal luminosity
Doublet motion taken from measurements of the motion of the triplets at the SLD: 20nm RMS.
No active vibration stabilization.
No Intratrain FONT feedback.

Case 2: 66% nominal luminosity
Doublet motion as expected from ground motion "B" model: 4nm RMS.
No active vibration stabilization
No Intratrain FONT feedback

Case 3: 71% nominal luminosity
Doublet motion measured from vibration stabilization test system: ~6nm RMS
No Intratrain FONT feedback
Note: spectrum is different from case 2.

Case 4: 93% nominal luminosity
Doublet motion measured from vibration stabilization test system: ~6nm RMS
Intratrain FONT feedback simulated with measured delay

These results indicate that reasonable luminosity can be obtained without active vibration feedback or fast intratrain feedback with nominal site ground motion levels. At a noisy site, luminosity can be recovered using the demonstrated performance of the feedback systems. In addition, the performance of both the FONT intratrain feedback, and the vibration stabilization system are expected to continue to improve.

REFERENCES

[1] L. Hendrickson et al, "Beam Based Feedback for the NLC Linac", SLAC-PUB-10493, July 2004.
[2] P. Tenenbaum, "Main Linac Single Bunch Emittance Preservation in the NLC and USColdLC Configurations", SLAC LCC-Note-0137, May 2004.
[3] T. Himel, et al., "Adaptive Cascaded Beam-Based Feedback at the SLAC", SLAC-PUB-6125 (1993).
[4] N. Phinney ed. "2001 Report on the Next Linear Collider", SLAC-R-571
[5] J. Frisch et al. "Vibration Stabilization of a Mechanical model of an X-band Linear Collider Final Focus Magnet", THP36, LINAC'04.
[6] P. Burrows, "Optimizing the Linear Collider Luminosity: Feedback on Nanosecond Timescales:, Snowmass-2001-T105, December 2001.
[7] P. Tenenbaum et al. "Use of Simulation Programs for Modeling the Next Linear Collider", PAC, New York, New York, 1999.
[8] A. Seryi, "Effects of Dynamic Misalignments and Feedback Performancd on Luminosity Stability in Linear Colliders", SLAC-PUB-9896, May 2003.
[9] G. White et al. "Simulations of a Nanosecond Timescale beam-based feedback system for the future linear collider", RPAB026, PAC2003, Portland OR, May 03. .
[10] P. Burrows et al. "Nanosecond-timescale Intra-bunch-train Feedback for the Linear Collider: Results of the FONT2 run". MOPLT107, EPAC2004, Lausanne.

HIGH PRECISION SURVEY AND ALIGNMENT OF LARGE LINEAR ACCELERATORS

J. Prenting, M. Schlösser, A. Herty[⊗], DESY, Hamburg, Germany
J. Green, G. Grzelak, A. Mitra, A. Reichold, University of Oxford, United Kingdom

Abstract

Future linear accelerators require new survey techniques to achieve the necessary alignment precision. For TESLA, the demanded accuracy for the alignment of the components is 0.5mm horizontal and 0.2mm vertical, both on each 600m section. Other proposed linear colliders require similar accuracies. These demands can not be fulfilled with common, open-air geodetic methods, mainly because of refraction in the tunnel. Therefore the RTRS (Rapid Tunnel Reference Surveyor), a 25m long measurement train performing overlapping multipoint alignment on a regular tunnel reference network is being developed. Two refraction-free realizations of this concept are being developed at the moment:

GeLiS measures the horizontal co-ordinates using multipoint alignment with stretched wires as strightness reference. In areas of the tunnel where the accelerator is following the earth curvature GeLiS measures the vertical co-ordinate using a new hydrostatic levelling system (HLS).

LiCAS is based on laser straightness monitors (LSM) combined with frequency scanning interferometry (FSI) in an evacuated system. LiCAS measures both co-ordinates with respect to its LSM-beam and thus is suitable for geometrically straight tunnel sections. Both measurement systems will be placed on a train, which could do the reference survey autonomous or semi-autonomous.

GEODETIC TASKS

A very high accuracy is demanded for the alignment of all accelerator components to run the linear collider successfully. The standard deviation of every component is postulated to be $\sigma_{l,h}$ = 0.2mm in lateral and height over the maximum betatron wavelength (e.g. 600m). Because of the influence of refraction, this requirement can not be achieved with any open-air optical survey.

CONCEPT

A basic network of reference points fixed to the wall in an equidistance of approximately 5m is installed in the tunnel. The alignment of the accelerator is split up in two major steps:

1) The reference points will be determined by an automated system (Rapid Tunnel Reference Surveyor, RTRS) in 3D space. The RTRS is described here.
2) The coordinates are transferred to the machine components with a tacheometer. This step is geodetic standard work and is not described in this paper. It is planned to integrate this second step into the RTRS.

Multipoint Alignment

With the technique of multipoint alignment the effects of refraction can be eliminated or reduced if a mechanical structure or a laser beam in vacuum is used as straightness reference. Multipoint alignment in a simplified 2D context means that the lateral distances s_{i-1}, s_i and s_{i+1} (see Fig. 1) between the straightness reference and several reference points are measured. Together with the distances $s_{i-1,i}$ and $s_{i,i+1}$ the angle β and the distances d can be calculated. This is done sequentially for every reference point in the tunnel (see Fig. 1). A traverse then is used to estimate the coordinates of the reference points. LiCAS extends this concept to a 3D-measurement

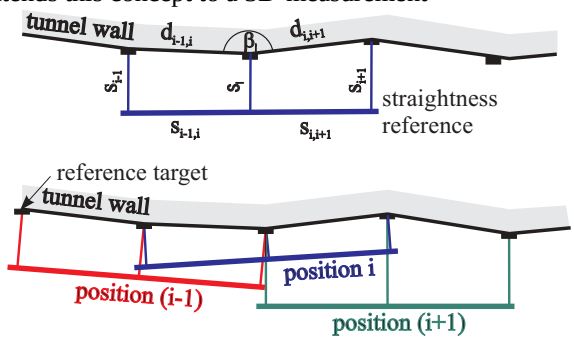

Figure 1: concept of geodetic reference survey, simplified 2D.

Rapid Tunnel Reference Surveyor, RTRS

A train with six measurement cars (blue, see Fig. 2) will overdetermine the multipoint alignment problem and provide enough redundancy to obtain the desired accuracy and reliability. For electronics and drives additional service cars (grey) are needed. This train can act autonomous and moves through the tunnel without user interaction.

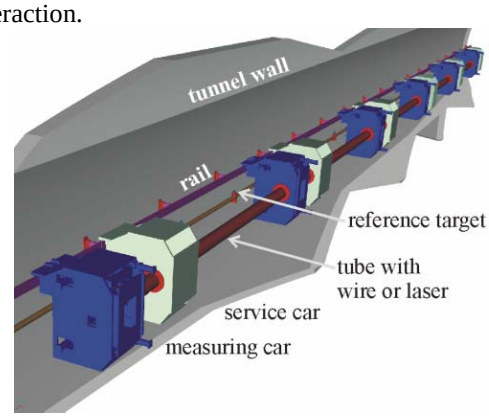

Figure 2: Measuring train on the tunnel wall.

[⊗]now CERN, Geneva, Switzerland

THE GELIS⊕ METROLOGY SYSTEM

A stretched wire is used as a straightness reference in the GeLiS-train. This wire runs through the whole train in a closed tube to prevent influences from external forces. It is fixed at the front and rear of the train only and thus provides a straight line, when projected onto the horizontal plane.

In every single car the distance between the reference target (A, see Fig. 3) and the wire (C) is measured with two optical 3D-sensors (B, D) and two incremental length gauges (E, F). The cameras (H) are used for rough positioning. (G) is the measurement vessel of the HLS. Because the measuring range of the 3D-Sensors is only a few millimetres the sensors have to be mounted on movable stages so that they can compensate for the tunnel tolerance of several centimetre. The tilt of the inner block is measured by a biaxial tilt sensor (K) and adjusted to zero with the stages. The distance between the wire (C) and the target (A) is measured with an accuracy of 3µm.

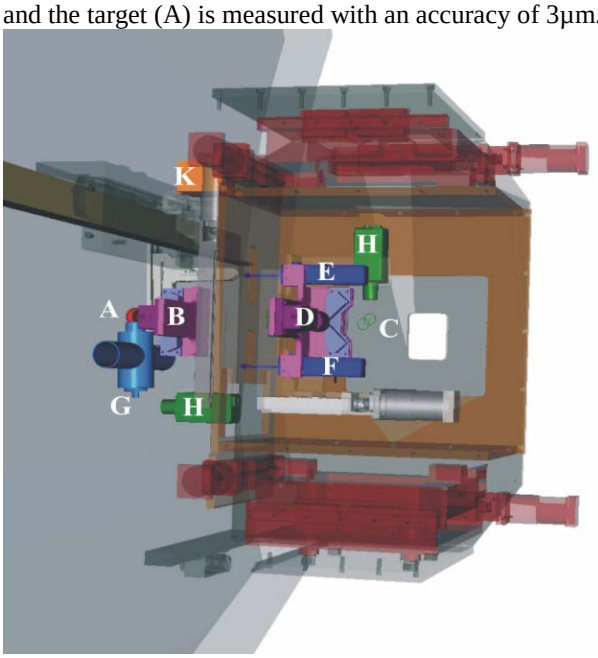

Figure 3: A GeLiS car in the tunnel.

Optical 3D-Sensor

For the contactless distance determination an optical sensor consisting of a digital camera and a split image prism is used (see Fig. 5). The distance Δy between the two image parts on the CCD gives - together with some calibration constants - the distance Δx (see Fig. 4 and 5).

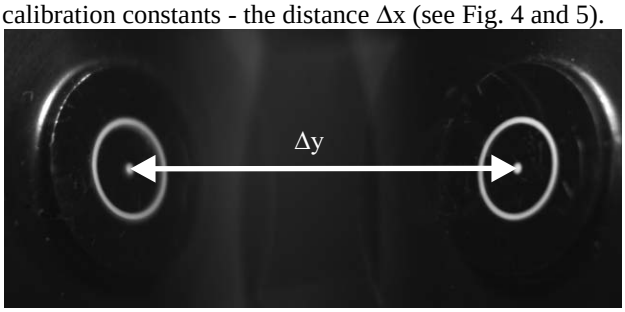

Figure 4: view from the outer 3D-sensor.

The main advantage compared to a two-camera stereo solution is that there is no special stability requirement for the relative position of the cameras. There is only the easier stability requirement of the prism.

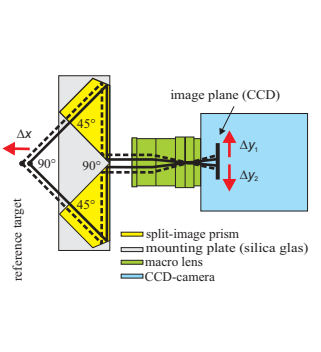

Figure 5: Optical 3D-sensor.

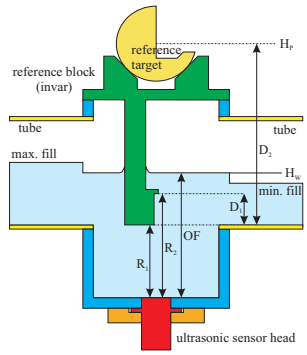

Figure 6: Ultrasonic measurement pot.

Hydrostatic Levelling System (HLS)

Since the accelerator could follow the curvature of the earth and the wire has limitations as height reference because of the sag, a drift-free HLS was developed. To eliminate the effect of temperature differences between the measurement vessels, a system with a free surface is used. No external forces provided, this surface is an equipotential expanse. The surface is then sampled using an ultrasonic system, the distances R_1, R_2 and OF (see Fig. 6) are measured simultaneously. Due to the calibrated distances D_1 and D_2 a calibrated estimation of H_P is possible.

GeLiS Prototype

To date a one car GeLiS Prototype has been constructed (see Fig. 7). Tests of functionality and repeatability are in progress. Software for the sensors and the motion stages is being improved. A mathematical model for the least squares adjustment of all measured data is also being developed.

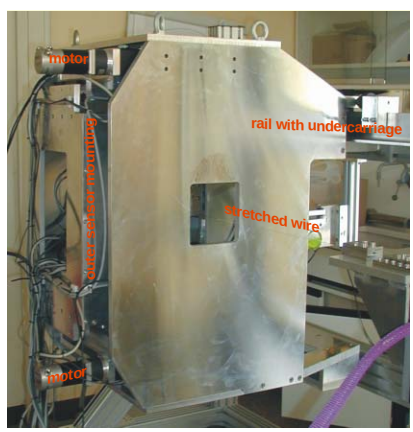

Figure 7: Protoype, view from the tunnel side.

⊕GeLiS: GEodetic measurement train for LInear accelerators and linear Synchrotron radiation sources

THE LiCAS* METROLOGY SYSTEM

The LiCAS project aims to construct a metrology system for the RTRS with the following properties:

- Capable of measuring a tunnel reference network independent of the geoid by use of a geometrical straightness and distance definition making it suitable for geometrically straight or inclined tunnels.
- Redundant and rapid measurement procedure avoiding the use of precision movers in the measurement process.
- High intrinsic sensitivity and maximum reconstruction power, enabling in-situ calibration procedures to minimise systematic errors

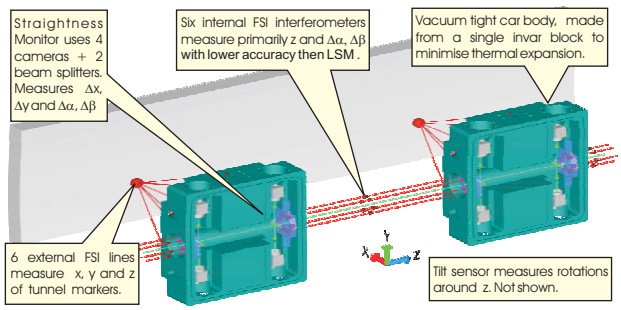

Figure 8: Two LiCAS cars without mechanical framework and vacuum system. Δα, Δβ refer to rotations around x and y.

The LiCAS cars measure their relative position and orientation using a laser straightness monitor (LSM) and an internal FSI† system. The LSM beam is launched by the first car and accurately retro-reflected by a corner cube reflector in the last car. Each car measures the LSM beam with 4 CCD cameras. This redundantly determines transverse offsets and rotations around x and y. Six internal FSI distance measurements primarily determine the relative offset in z but are also sensitive to rotations around x and y. Rotations around z are measured by a tilt sensor (not shown). All intra-car measurements are performed in vacuum to avoid refraction problems. The position of each reference marker is measured by its car with 6 external FSI lines.

Performance Simulations

To study the expected errors and correlations of reference marker position reconstruction, a geometrical simulation of the LiCAS-RTRS, using the SIMULGEO [1] software package, was performed. The long-distance operation of the train was simulated by a set of identical trains displaced by one marker separation. SIMULGEO's approach of manipulating very large matrices‡ is very time and memory consuming. Therefore a simplified analytical formula derived from a random walk model with direction correlation between steps was used to extrapolate the SIMULGEO predictions over long distances. The error on the *n*'th reference marker is then given by: $\sigma_{n,x} = \sqrt{l^2\sigma_{\alpha_x}^2 \frac{n(n+1)(2n+1)}{6} + \sigma_x^2 n}$, where l is the distance between cars, $\sigma\alpha_x$ is the angular and σx the transverse offset error between consecutive train stops.

These errors were obtained by fits to the SIMULGEO simulations. A large series of random walk trajectories was generated whose RMS-residua with respect to a straight line give the survey accuracy. **Figure 9** demonstrates that a vertical precision of O(200 μm) over 600 m is feasible.

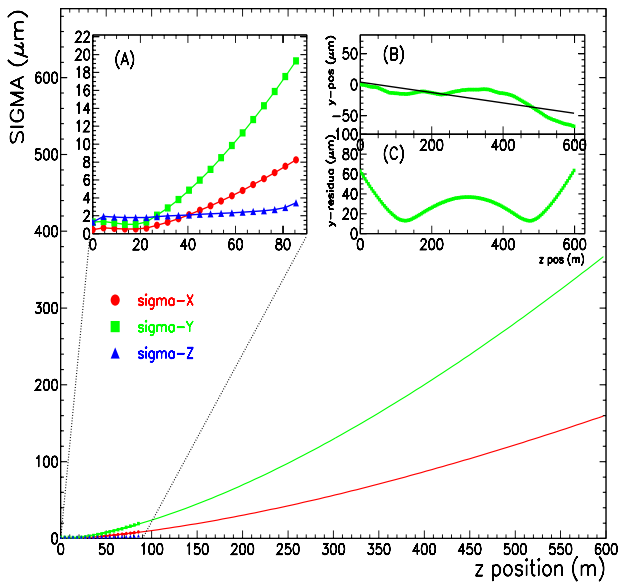

Figure 9: LiCAS train simulation: (A) Simulgeo simulation; (Main) random walk extrapolation to 600m; (B) Example of a random walk trajectory with a straight line fit. (C) RMS residua distribution of many random walk trajectories.

REFERENCES

[1] L. Brunel, "SIMULGEO: Simulation and reconstruction software for optogeometrical systems", CERN CMS Note 1998/079.

*LiCAS = Linear Collider Alignment and Survey,

† FSI = Frequency Scanning Interferometry, a method for accurate distance measurement

‡ With sizes similar to the number of measurements; eg. O(2.000) for an 80 meter tunnel segment.

Operation of a 1.3 GHz, 10 MW Multiple Beam Klystron

H.P. Bohlen, A. Balkcum, M. Cattelino, L. Cox, M. Cusick,
S. Forrest, F. Friedlander, A. Staprans, E. Wright, L. Zitelli,
CPI, Palo Alto, California
K. Eppley, SAIC, Boston

Abstract

Results will be reported for a 1.3 GHz, 10 MW multiple beam klystron that is being developed for the TESLA linear accelerator facility. The design parameters for the device are 10 MW peak RF output power with 150 kW average power, 1.5 ms pulse length, 65% efficiency, 50 dB gain, and 2.0 A/cm^2 maximum cathode loading. Initial testing of the device has validated the basic design approach. Six 120 kV electron beams of measurably identical currents of 22.9 A each have been successfully propagated through the klystron circuit with 99.5% DC beam transmission at full operating video duty and with 98.5% saturated RF transmission. A peak power of 10 MW at 1.3 GHz with 60% efficiency and 49 dB of gain has been measured.

NO SUBMISSION RECEIVED

DEVELOPMENT OF HIGH RF POWER DELIVERY SYSTEM FOR 1300 MHZ SUPERCONDUCTING CAVITIES OF CORNELL ERL INJECTOR*

S. Belomestnykh#, M. Liepe, V. Medjidzade, H. Padamsee, V. Veshcherevich,
Laboratory for Elementary-Particle Physics, Cornell University, Ithaca, NY 14853, USA
N. Sobenin, Moscow Engineering Physics Institute (State University), Moscow, Russia

Abstract

Development of a 150 kW CW RF power delivery system for 1300 MHz superconducting cavities is under way at Cornell University in collaboration with MEPhI. The system is based on a twin-coupler consisting of two identical coaxial antenna-type couplers derived from the TTF III input coupler design. Because the average power is much higher than in the TTF III coupler, the required coupling is stronger and to avoid multipacting phenomena, major changes were made to the prototype design. Presented coupler has completely redesigned cold part and significantly improved cooling of warm bellows. The results of thermal and mechanical stress calculations are reported. The magnitudes and phases of RF fields applied to each side of the twin-coupler must be very close to each other. This imposes very strict requirements upon a power dividing system. These requirements and proposed layout of a system satisfying them are discussed.

INTRODUCTION

In the Cornell Energy Recovery Linac project (ERL) [1], each of the two-cell 1300 MHz injector cavities will deliver 100 kW of CW RF power to the 100 mA beam. Individual 150 kW klystrons will drive the cavities via high-power delivery systems. Each system consists of a twin input coupler [2] and a waveguide distribution network with an adjustable hybrid and a two-stub phase tuner for precise setting of RF power split. The twin coupler consists of two identical antenna type couplers, and the magnitudes and phases of RF fields applied to each of these couplers must be very close to each other. A difference of field magnitudes on individual coupler antennae should not exceed 1-2%, and a phase difference should not exceed 1º [2]. A scheme of the power dividing system for ERL injector cavities is shown in Figure 1. This paper describes latest results in developing components of the high power delivery system that would satisfy such strict requirements.

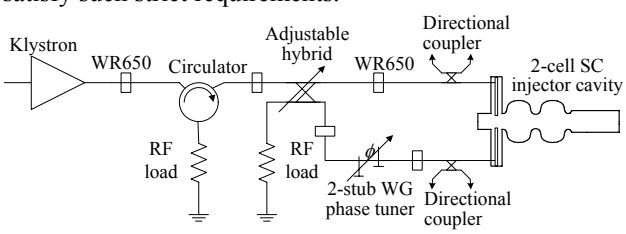

Figure 1: RF power splitting scheme for ERL injector.

*Supported by Cornell University
#sab@lepp.cornell.edu

POWER SPLIT

We proposed to use a short slot hybrid as a power divider for this precise RF power dividing system [3]. This type of hybrids seems to have better electrical properties compared with other four-port hybrid designs: low sensitivity to mismatch, a wide frequency band, and the best high power handling. For power balance, an adjustable stub in the middle point of the short slot hybrid can be used. By varying its penetration into the waveguide, one can adjust the power ratio between hybrid output arms with a very small phase error. Two versions of an adjustable short slot hybrid design were studied recently [4]. The first one uses uniform standard waveguide arms of the WR650 type and has a narrower frequency band. The second one uses narrower waveguide arms and needs additional transition pieces for connection to standard waveguides. On the other hand, it has a wider frequency band. Both types are adequate to the Cornell ERL RF system.

A two-stub device can be used as a phase tuner. Insertion of a stub into a waveguide produces capacitive admittance and an additional phase shift, these two values depending on the depth of the stub insertion. Using optimal stub separation one can reach the phase range of 20º keeping reflection below –40 dB [3].

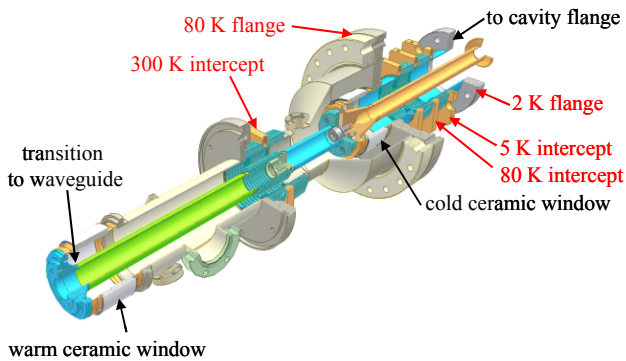

Figure 2: 3D view of the injector cavity coupler.

INPUT COUPLER

A design of the coaxial antenna type couplers is derived from the TTF III input coupler [5]. The following major modifications were made to meet our requirements. The cold part of the original coupler was completely redesigned. Instead of a 40 mm 70 Ω coaxial line, a 62 mm 60 Ω line was chosen for stronger coupling, better handling the high power and avoiding multipacting [2]. The coupler has large profiled antenna tip and the 16 mm travel range for getting the required coupling variation.

The antenna is made of a copper tube. In the cold window a bigger ceramic cylinder is used (similar to the one used in the warm window but with a reduced height). The weakest points of the TTF III coupler at high average power levels are the bellows, which are not cooled. This problem is solved in the new design by i) providing forced air cooling of inner conductor bellows of the warm coax line and ii) adding more heat intercepts to outer conductor bellows of the cold and warm coaxial lines. The general design of the coupler is shown in Figure 2. A careful thermal analysis [6] of the coupler confirmed that the design changes are adequate. Figure 3 illustrates temperature distributions along bellows. Although simulations showed that maximum temperature of the warm ceramics does not exceed 90ºC, there is significant azimuthal temperature gradient (Figure 4) so that local cooling by compressed air will be required. The coupler heat loads are approximately 0.17 W to 2 K, 2.5 W to 5 K, and 70 W to 80 K at RF power of 75 kW CW in traveling wave mode. Mechanical stress calculations did not reveal any problems in the proposed design.

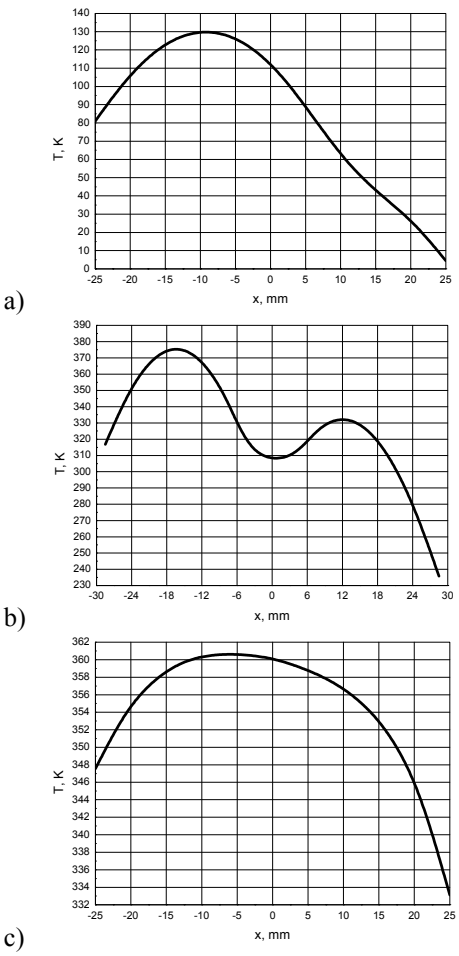

Figure 3: Temperature distribution at 75 kW CW in traveling wave along: a) cold bellows, b) warm outer conductor bellows, and c) warm inner conductor bellows.

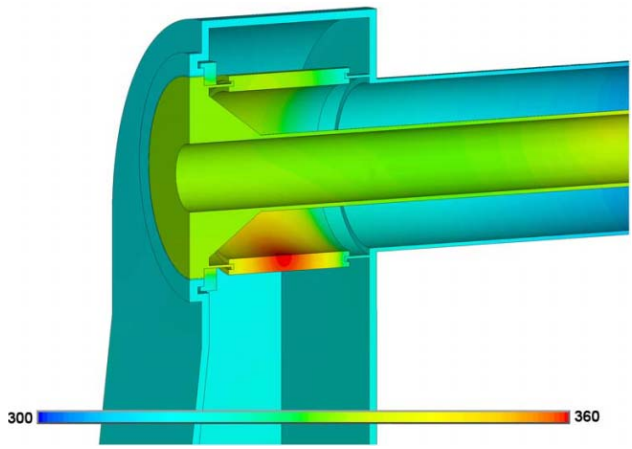

Figure 4: Temperature map of the warm window.

The cold outer conductor bellows must have a support that would provide means for alignment and would not increase significantly static heat leak to the 5 K heat intercept. The design we chose is shown in Figure 5. It allows vertical and horizontal alignment and free longitudinal movement.

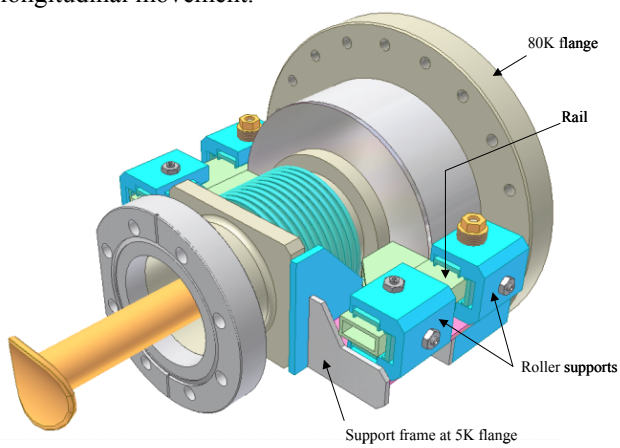

Figure 5: Alignment of the cold part of the input coupler.

TUNING THE SYSTEM

The very strict requirements to the power split come from desire to avoid field asymmetry that would transversely kick the beam traveling on axis and produce an emittance growth [2]. A procedure has to be developed to precisely tune the power delivery system. To assist in tuning, we proposed to use an equivalent diagram (Figure 6). Here RF power split with associated amplitude and phase errors are represented by two sources with corresponding amplitudes $A1$ and $A2$ and phases $\phi 1$ and $\phi 2$. Two antennae have capacitive coupling (represented by $C1$ and $C2$) to the cavity (R/Q, Q_0, f_{res}), to the ground ($C10$ and $C20$), and to each other ($C12$). Parameters of the equivalent diagram were calculated as functions of the antenna penetration depth (Figure 7) using Microwave Studio® [7]. At nominal coupling ($Q_{ext} = 9.2\times10^5$) the capacitance values are: $C10$ = 2.95 pF, $C1$ = 0.00859 pF, $C12$ = 0.116 pF. Using the

equivalent diagram allows us to make predictions easily and will help in interpreting the results of measurements.

The accuracy of final magnitude and phase balance depends not only on adjusting devices and tuning procedure, but also and mainly on measuring techniques and accuracy of measurements. We need to measure and adjust power and phase balance on output arms of the power divider. Also we need to measure phases of each coupler with the waveguide pieces attached to them. Flexible waveguide parts should not be used in waveguide assemblies between power divider and cavity couplers because they are sources of phase errors. We need to use only rigid waveguide pieces and shims. Measurements should be done using a well-calibrated network analyzer with cables being as short as possible (even the use of calibrated cables may lead to non-negligible phase errors due to their bending). The measurements of two individual cavity couplers should be made immediately one after another, using the same calibration.

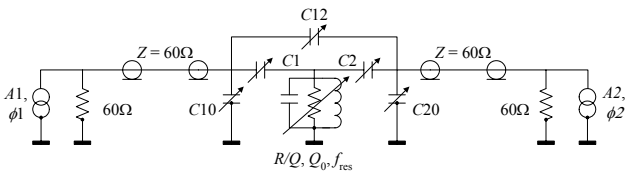

Figure 6: Equivalent diagram.

SUMMARY

The development of the 150 kW CW power delivery system for 1300 MHz superconducting cavities of the Cornell ERL Injector is in progress. The input coupler design is complete and preparations are under way to order first two prototypes from industry. The coupler will have low heat leaks and will provide adjustable coupling to the cavity. A variable power dividing scheme was proposed that would satisfy strict requirements of the ERL injector. An adjustable four-port hybrid and a two-stub waveguide phase shifter have been simulated. To assist in tuning the system, an equivalent diagram was developed and its parameters were calculated.

REFERENCES

[1] G. Hoffstaetter et al., "The Cornell ERL Prototype Project," PAC'2003, Portland, OR.

[2] V. Veshcherevich et al., "Input Coupler for ERL Injector Cavities," PAC'2003, Portland, OR.

[3] V. Veshcherevich, "On Power Splitting for Cornell ERL Injector Cavities," Cornell LEPP Report ERL 04-1, 2004.

[4] V. Veshcherevich, "An Adjustable Short Slot Hybrid for Precise RF Power Divider System for Cornell ERL Injector Cavities," Cornell LEPP Report ERL 04-3, 2004

[5] B. Dwersteg, et al., "TESLA RF Power Couplers Development at DESY," Proc. of the 10th Workshop on RF Superconductivity, Tsukuba, Japan, 2001.

[6] N. Sobenin, et al., "Thermal Calculations of Input Coupler for Cornell ERL Injector Cavities," EPAC'2004, Lucerne, Switzerland.

[7] CST GmbH, Darmstadt, Germany.

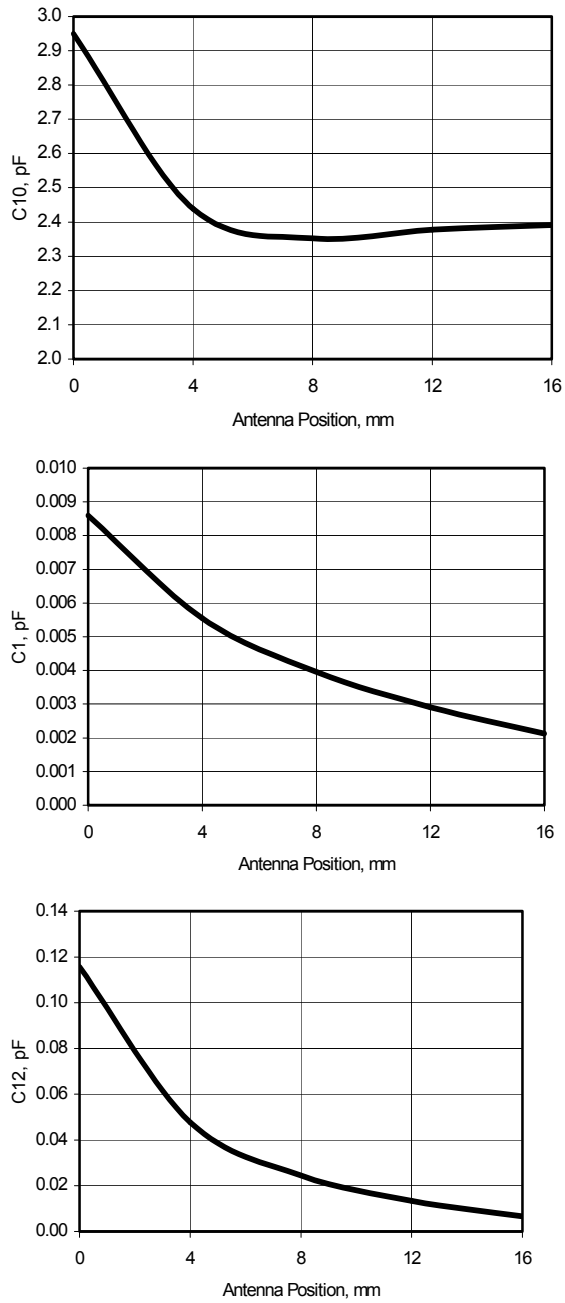

Figure 7: Parameters of the equivalent diagram as function of the antenna position.

NLC HYBRID SOLID STATE INDUCTION MODULATOR*

R.L. Cassel, J.E. deLamare, M.N. Nguyen, G.C. Pappas @SLAC,
E. Cook, J. Sullivan @ LLNL, C. Brooksby @ Bechtell Nevada

Abstract

The Next Linear Collider accelerator proposal at SLAC requires a high efficiency, highly reliable, and low cost pulsed power modulator to drive the X band klystrons. The original NLC envisions a solid-state induction modulator design to drive up to 8 klystrons to 500kV for 3µS at 120 PPS with one modulator delivering greater than 1,000-megawatt pulse, at 500kW average. A change in RF compression techniques resulted in only two klystrons needed pulsing per modulator at a reduced pulse width of 1.6µS or approximately 250 megawatts of the pulsed power and 80kW of average powers. A prototype Design for Manufacturability (DFM) 8-pack modulator was under construction at the time of the change, so a redirection of modulator design was in order. To utilities the equipment, which had already be fabricated, a hybrid modulator was designed and constructed using the DFM induction modulator parts and a conventional pulse transformer. The construction and performance of this hybrid two-klystron Induction modulator will be discussed. In addition the next generation DFM induction modulator utilizing a ten-turn secondary and fractional turn primary transformer well be presented.

PROTOTYPE MODULATOR

The prototype Solid State induction modulator for the NLC Klystron was original designed to drive eight X-band klystron in parallel requiring 500kV 2000A pulses for 3.2µS flat top at 120 PPS. [1] [2] The prototype was fabricated and tested in a water load to 500kV and into two 5045 klystron up to 420kV. The NLC program for the RF testing was modified requiring a change in the modulator to operate only four XL4 klystron at 400kV, 1300 Amps, 1.6µS flattop at 60Hz. (See figure 1)

Figure 1: "8-pack" Solid State modulator installation.

To better match the operating condition of the klystron the two parallel drivers were reduced to one driver operating at 2kV at 3600A.

The stray capacitance to ground of the XL4 klystrons, was twice that of the X-band klystron resulting in a voltage overshoot of greater than 20%. This overshoot was eliminated by delaying the turning on of 18 of the 76 driver cells. (See figure 2)

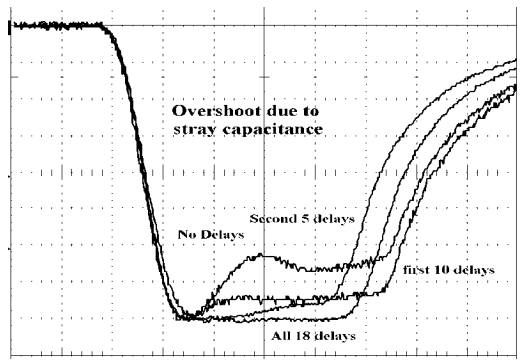

Figure 2: Overshoot correction by delaying triggers.

Delaying eliminated the overshoot without compromising the rise time and adjusted the flattop to a flatness of < 0.5%. (See figure 3)

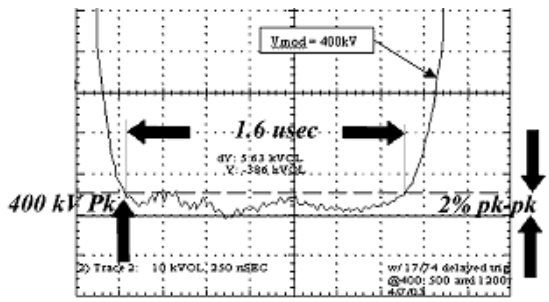

Figure 3: Pulse flattop regulation.

The prototype solid-state modulator has been operating at 60 Hz 24 hours a day for months >600hr with a minimum of intervention. Even with more than a thousand interruptions of operation for RF vacuum faults the modulator continues to operate.

Klystron Arcs

There were numerous (>15) klystrons arc at different points along the flattop pulse with no discernable effect on either klystron of modulator. (See Figure 4) The klystron and modulator resumed operation after the klystron arcs with no klystron damage. From the measurements of the klystron arcs, it is clear that the joules and coulombs under which a klystron can recover from are considerably higher than previously predicted.

* Work supported by DOE, contract DE-AC03-76SF0051

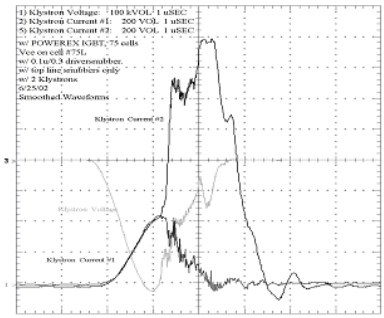

Figure 4: Klystron fault with induction modulator.

The prototype NLC solid-state induction modulator has proven itself an effective way to make a very high power pulsed modulator.

DFM1 HYBRID MODULATOR

The next stage in the Solid State induction modulator program was the development of a "Design for Manufacturability" (DFM) modulator. The ordinal design was for a modulator to drive 8 X-band PPM klystrons from one modulator to match the expected RF compression technique. The modulator had a three turn secondary with 46 cores using the available 6.5kV IGBT to deliver 500kV, 2000A, 3.2μS pulses.

DFM Cores

Each of the new DFM Metglas® cores was designed to support a 4kV pulse for 4.5μS with a one-turn primary. The cores were enclosed in a single turn stainless steel jacket, which serves as the electrical turn as well as holding the cores in place while allowing oil to flow pasted the core to prove the cooling. Two cores were used with an insulator between the cores to provide for the pulse voltage insulation. A outer cast aluminum case served to complete the grounded side of the single turn, supported the cores, and provided the oil seal. (See Figure 5) This outer casing has penetration for the electrical connection to a single turn in three locations. Two of the insulated connections are for the two IGBT driver and one for a bypass diode, used to carry the pulsed current if the IGBT drivers are delayed on turn on.

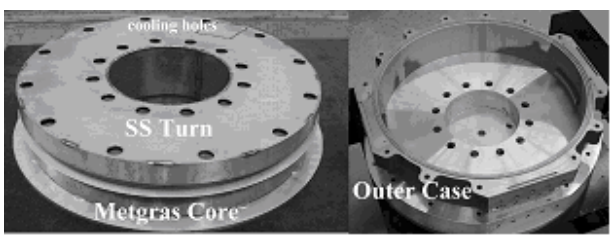

Figure 5: DFM Cores and outer Case.

DFM Drivers

The IGBT driver utilized two 37ufd 4.3kV pulsed capacitors in parallel. The capacitors are in series with a 6.5kV 600 Amp IGBT with specially design gate drive. The capacitors are change from an external source by way of a capacitor charging diode network with safety shorting relay. The driver is a plug in, strip line PC, board with the heat sink for the IGBT bolted to the outer core casing for support and cooling from the core oil cooling system. (See figure 6)

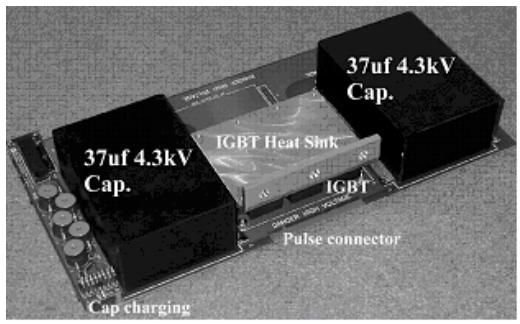

Figure 6: IGBT Driver Boards.

DFM1 Hybrid Modulator

The cores, cases and drivers were design and were in fabrication for the 8 klystron DFM modulator when the RF compression technique use to drive the accelerator structure was revised, reducing the modulator requirements to drive only 2 klystrons for 1.6μS.

A three turn secondary induction modulator is not economically the right design for driving 2 klystrons. A 10 to 12 Turn secondary winding is a better match to 2 klystron operation. With cores and cases already fabricated and not suitable for so many secondary turns the program was redirected into two parts

First, the DFM1 Hybrid modulator utilizing DFM fabricated parts with a single secondary turn driving a conventional 10 to 1 turn's ratio pulse transformer, and second the DFM2 fractional turn modulator in which the secondary has 10 turns and the primary 15 cores with single turns or a 150/1 turns ratio transformer.

The DFM1 utilized 15 of the DFM cores and 30 drivers with a single secondary turn. The core and IGBT's drivers were design to produce a 4kv 3.2μS pulse at 3kA per driver. With 15 cores and 30 drivers, the single turn primary could develop ~60kV at 6kA. With a 10 to 1 pulse transformer, the output could produce ~600kV at 600A maximum. . (See figure 7)

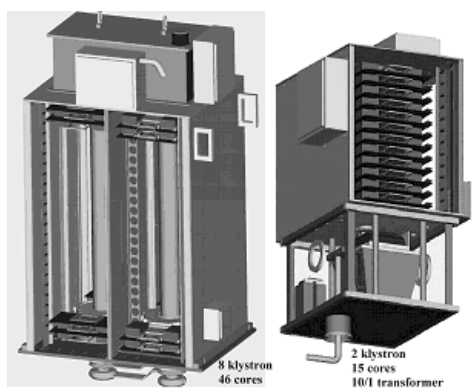

Figure 7: DFM and DFM1 Modulators.

DFM1 Installation and Testing

The DFM1 was fabricated and installed on the prototype test stand and is under test into a 1kohm water load. The current balance, thermal properties and pulse performance were measured. (See Figure 8)

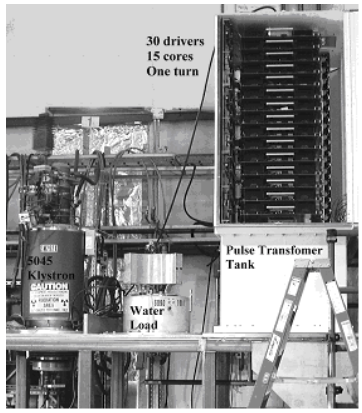

Figure 8: IGBT Driver Boards.

The use of an additional conventional designed pulse transformer, not only introduces more series inductance limiting the rise time of the voltage, but also the stray capacitance. As in the prototype modulator, the additional capacitance results in an overshoot of voltage. Delaying the turn on of 4 of the 15 cells corrects for the overshoot in voltage. The water load was driven to 500kV, 500A 1.6μS at 120Hz. (See figure 9)

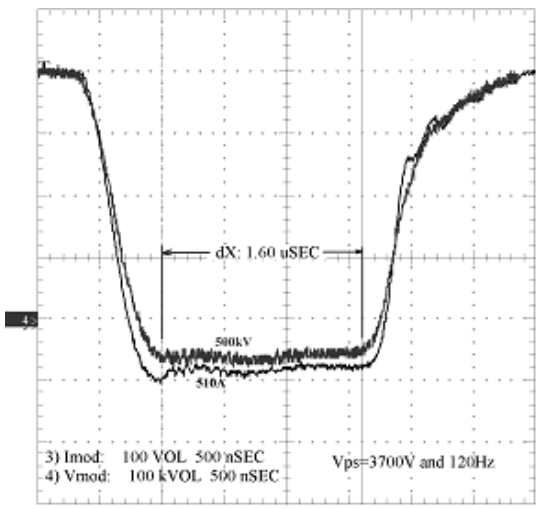

Figure 9: Waveform of DFM1 Modulators water load.

As expected the power loss and efficiency of the Hybrid modulator is not as low as would be desired ~65% It did should that the Hybrid design is a practical design.

DFM2 MODULATOR

DFM2 Conceptual Design

The hybrid modulator, although it works, is not an optimal design for driving one or two klystrons, There are two transformers in series one for the induction one turn core and the second conventional pulse transformer which increase the cost weight, and limits the rise time of the pulse. It is much preferred to combine the two transformer into one transformer. This is done be increasing the core size to accept a more conventional multi turn pulse transformer windings. (See figure 10)

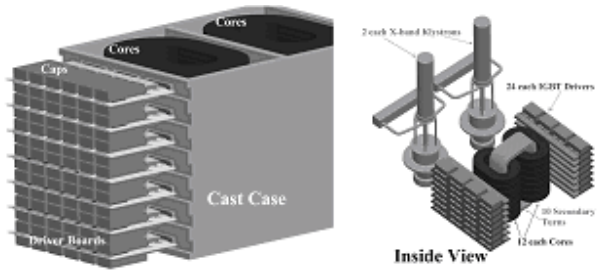

Figure 10: DFM2 conceptual design.

DFM2 IGBT Exploration

The present 6.5kV 600A IGBT modules require sophisticated gate drivers to allow for the fast turn on and protection against klystron arcs and insulation flashovers, due to the modules internal structure. As part of the DFM2 design we are exploring the used of smaller IGBT modules with integrated gate drives. A two chip IGBT package with integrated gate drives appears to work will reducing the protection problems. (See figure 11)

Figure 11: IGBT with gate drive 6.5kV.

SUMMARY

The prototype solid-state induction modulator and DFM1 have demonstrated that the solid-state fractional turn approach to modulator is workable. They have the ability to controls the wave shape, pulse width and clear faults. In order to deduce the cost and increase the performance for a two-klystron driver a fractional turn primary multiple turn secondary DFM2 appears to have a better performance and reduce cost.

REFERENCES

[1] A solid state induction modulator for SLAC NLC Cassel, R.L.; Pappas, G.C.; Nguyen, M.N.; DeLamare, J.E.;Particle Accelerator Conference, 1999. Proceedings of the 1999 ,Volume: 3 , 27 arch-2 April 1999 Pages:1494 - 1496 vol.3

[2] Three turn secondary for the prototype SLAC solid state induction modulator Cassel, R.L.; deLamare, J.E.; Nguyen, M.N.; Pappas, G.C.; Cook, E.; Sullivan, J.; Brooksby, C.;Power Modulator Symposium, 2002 and 2002 High-Voltage Workshop. Conference Record of the Twenty-Fifth International , 30 June-3 July 2002

REDUCTION OF RF POWER LOSS CAUSED BY SKIN EFFECT

Y. Iwashita, ICR, Kyoto Univ., Kyoto, JAPAN

Abstract

Skin effect on a metal foil that is thinner than a skin depth is investigated starting from general derivation of skin depth on a bulk conductor. The reduction of the power loss due to the skin effect with multi-layered conductors is reported and discussed. A simple application on a dielectric cavity is presented.

INTRODUCTION

RF current flows on a metal surface with only very thin skin depth, which decreases with RF frequency. Thus the surface resistance increases with the frequency. Because the skin depth also decreases when the metal conductivity increases, the improvement of the conductivity does not contribute much; it is only an inverse proportion to the square root of the conductivity. Recently, it is shown that such a power loss can be reduced on a dielectric cavity with thin conductor layers on the surface, where the layers are thinner than the skin depth [1]. The thin foil case is analyzed after a review of the well-known theory of the skin effect. Then an application to a dielectric cavity with TM0 mode is discussed [2].

SKIN DEPTH OF BULK MATERIAL

In materials with conductance σ ($>>i\omega\varepsilon$), Ampere's law becomes:

$$\nabla\times\mathbf{H}=(\sigma+i\omega\varepsilon)\mathbf{E}. \tag{1}$$

Suppose a system as shown in Fig. 1, Eq.1 finally becomes:

$$\partial_x^2 j = i\omega\mu\sigma j, \quad j=\sigma E_y. \tag{2}$$

Under the condition of $\sigma>>i\omega\varepsilon$, the solution of Eq.2 is:

$$j(x)=j_0 e^{-(1+i)x/\delta}, \quad \delta=\sqrt{2/\omega\mu\sigma}, \tag{3}$$

where δ is the skin depth. Considering that $\nabla\times\mathbf{E}$ has only one nonzero component of $\partial_x E_y=\partial_x j/\sigma$, the magnetic field in the conductor is derived from Faraday's law $\partial_x E_y=-i\omega\mu H_z$ as

$$H_z(x)=\frac{\partial_x E_y}{-i\omega\mu}=\frac{\partial_x j}{-i\sigma\omega\mu}=\frac{\delta^2\partial_x j}{-2i}=\frac{\delta}{2}(1-i)j(x). \tag{4}$$

Thus $j(x)$ is expressed by the magnetic field on the conductor surface $H_z(0)$:

$$j(x)=\frac{1+i}{\delta}H_z(0)e^{-(1+i)x/\delta}. \tag{5}$$

A typical value of δ in copper at the frequency of 3GHz is 1μm. Figure 2 shows the current j as a function of x/δ. By integrating j, we obtain total current in the conductor:

$$J=\int_0^\infty j\,dx=H_z(0). \tag{6}$$

The power loss in the conductor can be calculated as

$$P_{bulk}=\int_0^\infty |j|^2/\sigma\,dx=\frac{H_z(0)^2}{\sigma\delta}=\sqrt{\frac{\omega\mu}{2\sigma}}H_z(0)^2, \tag{7}$$

where $1/\sigma\delta$ is often written as surface resistance Rs.

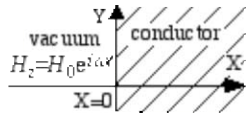

Figure 1: Half of the space is filled by conductor.

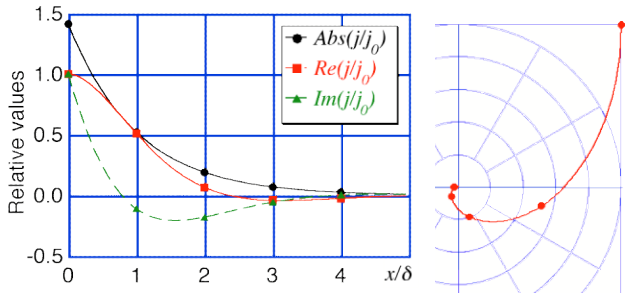

Figure 2: Left: j as a function of x/δ. Right: polar plot. Markers are put in every unit.

Although it is necessary to increase the conductance for lower RF power loss, the higher conductance leads to higher current density and thus the thinner skin depth reduces the improvement by the good conductance. It may be possible to cure this situation if we can control the current density independent of the conductance.

Typical value of σ is $5.8\text{x}10^7$ [S] for copper metal and that of $\omega\varepsilon$ is 1 in vacuum at 18 GHz. Reminding the Eq.1, if low loss dielectric material with relative permittivity of more than 10^7 at such a high frequency were available, the RF power loss could be determined by the dielectric loss other than the conductor loss. Composite material such as seen in multilayered capacitors may have such characteristics. This will be investigated in future.

SKIN EFFECT ON THIN FOIL

Let us consider a case that the thickness of the conductor is thinner than the skin depth δ (see Fig. 3) and the both sides have electromagnetic fields with different amplitudes. The solution of Eq.2 becomes:

$$j(x)=H_z(0)\left(j_f e^{-(1+i)x/\delta}+j_b e^{-(1+i)(\alpha\delta-x)/\delta}\right), \tag{8}$$

$$j_f=\frac{(1+i)e^{(1+i)\alpha}\left(e^{(1+i)\alpha}-\xi\right)}{\delta\left(e^{2(1+i)\alpha}-1\right)}, j_b=\frac{(1+i)e^{(1+i)\alpha}\left(\xi e^{(1+i)\alpha}-1\right)}{\delta\left(e^{2(1+i)\alpha}-1\right)}.$$

Figure 4 shows polar plots for $j(x)$ for the case when the magnetic fields of both sides have the same amplitude(ξ=1). They are symmetrical with respect to the origin because the currents from both sides cancel each other. The linear behaviour can be seen when the

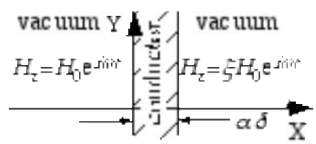

Figure 3: The thickness is thinner than the skin depth.

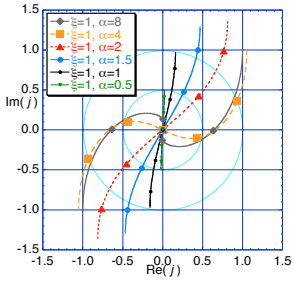

Figure 4: Polar plots of complex current densities. The markers are at centers of every 1/5 layers in depth: x=0.1δ, 0.3δ, … 0.9δ. (currents are normalized by H_0/δ).

thickness is less than the skin depth (markers are at the centers of even intervals).

Let us consider a simple example as shown in Fig. 5, where two layers of thin foils with thickness of just the skin depth δ are immersed in equally stepped RF fields (ξ=0.5). The current densities in the foils are shown in Fig. 6. The total current in each layer is just the magnetic field difference between the front and backsides: the currents of both the layers are the same. The total power loss is calculated by the similar way as Eq.7:

$$P_2 = \int_0^{\delta} \left(|j_1|^2 + |j_2|^2 \right) / \sigma \, dx \,, \qquad (9)$$

which is 70% of the bulk case. When we optimize the thickness of the first layer α and the current ratio ξ, the minimum power loss becomes 67.9% at α=0.826 and ξ=0.498. Further, when the thickness of the last layer (second layer in this case) is thick enough compared to the skin depth (α=4 in this case), the minimum power loss becomes 65.6% at α=0.785 and ξ=0.534.

When n-layers of equal thickness are immersed in n-equally-stepped RF magnetic fields, the power loss can be given by:

$$P_n = \sum_{i=1}^{n} \int_0^{d} |j_i|^2 / \sigma \, dx \,. \qquad (10)$$

Such a configuration should be more practical than a configuration with non-uniform thicknesses. Figure 7 shows the relative power losses as functions of the normalized thickness $\alpha = d/\delta$. The thicknesses that show minimum power loss decrease as the numbers of layers increase. The minimum power loss is shown in Fig. 8 as a function of the number of layers. It shows $n^{-0.5}$ dependence, which can be also derived from an expansion of the power loss formula. Therefore, the RF power loss may be reduced by this geometry, if the current on each layer is well controlled. The improvement, however, is limited by the absolute thickness of each layer: it should be enough thicker than the inter-atomic distance. On the other hand, the power loss can be more than the bulk case, which may be useful for absorber applications such as EMI shields.

Suppose a plane wave comes from the left in Fig. 3. The transmission T through the foil is shown in Fig. 9 as a function of α., where $\alpha\delta$ is the thickness of the copper

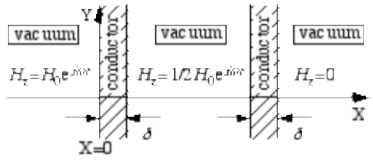

Figure 5: Two conductor layers are immersed in stepped RF fields: 100%, 50%, and 0%.

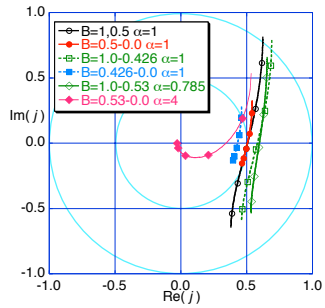

Figure 6: Polar plots of pairs of complex currents in Fig. 5.

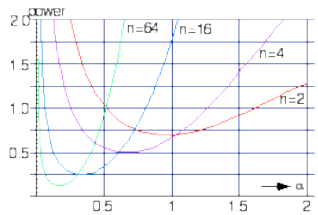

Figure 7: Relative power losses as functions of thickness, (normalized by the bulk case)

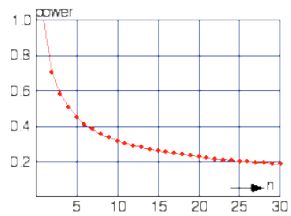

Figure 8: Minimum power loss as a function of the number of layers.

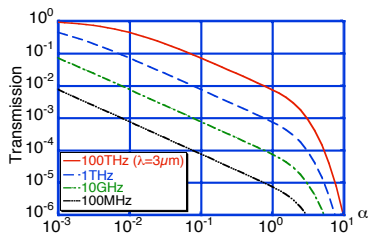

Figure 9: Transmission through a thin conductor foil with thickness of $\alpha\delta$.

foil. Because the transmission is less than 1% at 10GHz even if the thickness is one-hundredth of the skin depth, the two regions, the front side and the backside, are isolated by the foil: the left hand side field can hardly penetrate the foil and no power can be delivered to the other side. A plane wave with an angle other than normal makes a different situation from this and a solution to distribute the current to each layer is reported

in Ref[1]. This method, however, requires narrow choice in the material inserted between the conductor layers.

DIELECTRIC CAVITY WITH THIN FOIL

Let us consider a flat dielectric cylindrical cavity with TM_{010} mode as shown in Figure 10. Suppose a high dielectric constant ε_r, the boundary condition at the perimeter (r=R) is almost magnetic, where the magnetic field is normal to or zero on the boundary. The electric field E_z can be described by the Bessel function as:

$$E_z(r) = E_z(0)\,\mathrm{J}_0(kr), \quad k = x_1'/R, \tag{11}$$

where x_1' is the first root of $\mathrm{J}_0'(x)$=0. The displacement current in the dielectric material are collected on the conductor surface around the center and leaves from the conductor around the perimeter, so that the surface current density has a peak at the radius r_p (the first root of $\mathrm{J}_0(kr_p)$=0). When we put extra thin washer foils on the peak as shown in Fig. 11, part of the displace currents go into the extra thin foils and flow on them, which redistributes the current flows. The power reduction can happen when the thickness of the conductor is not much more than the skin depth: the currents on both sides of the extra electrode surface flow in the opposite directions without the cancellation and the total net current on the surface is zero and the power loss just increases, otherwise. In order to isolate the layers, the in-and-out current on the extra electrode should balance:

$$\int_{r_1}^{r_2} \dot{D}\, 2\pi r dr = 0. \tag{12}$$

Another constraint minimizing the power loss P_1 will give the radii r_1 and r_2 together with eq.15:

$$P_1 = \int_0^R \int_0^\infty \frac{|j_1|^2}{\sigma} dz\, 2\pi r dr + \int_{r_1}^{r_2} \int_0^d \frac{|j_2|^2}{\sigma} dz\, 2\pi r dr. \tag{13}$$

The minimum P_1 is 70.5% of the bulk case at r_1 =0.261R and r_2=0.921R. In order to simplify the constraint, we may use the following instead:

$$\int_0^{r_p} \dot{D}\, 2\pi r dr = 2\int_0^{r_1} \dot{D}\, 2\pi r dr \quad \left(= 2\int_{r_1}^{r_p} \dot{D}\, 2\pi r dr\right), \tag{14}$$

because the power loss density is proportional to the square of the current density and thus the peak value of the current is dominant in the power loss. The left side term is the total current at the peak (node) and is equally shared by the two conductors. The P_1 given by eq.17 is 75.4% of bulk case at r_1=0.322R and r_2=0.884R. Although this simplified constraint does not give optimum condition for minimum power loss, it is useful for multi-layered application.

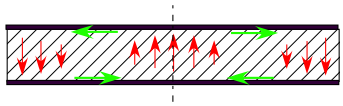

Figure 10: Flat dielectric cylindrical cavity where the dielectric constant ε_r is much larger than unity and the top and the bottom surfaces are covered by conductors.

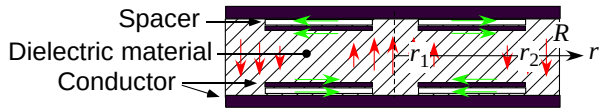

Figure 11: Dielectric cylindrical cavity with extra electrodes that have washer shape. The thicknesses are exaggerated: inside of the each conventional disc electrode, one smaller washer shape electrode is located with a small distance from the disc.

Figure 12 shows an axisymmetric simulation code result of the Q enhancement as a function of r_1/R. Although the used parameters that reduce the computing time may be unrealistic, the effectiveness can be seen from this simulation result. The used parameters are listed in the caption.

It should be noted that the space between the disc and the extra electrodes are essential; it should have lower dielectric constant than the body material. As can be seen, the width of the extra electrode is comparable to the half wavelength in the main body. Therefore the narrow space between two electrodes (not the wider one that forms the cavity itself) becomes another resonator to suck the power unless the space has enough lower dielectric constant than that of main body.

Although this example cannot be directly applicable to vacuum accelerating tubes, similar technique should be applicable to many cases. Needless to say, the number of layers can be increase to enhance the effect further.

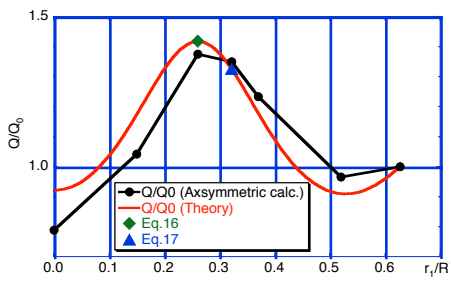

Figure 12: Q enhancement as a function of r_1/ R.

Dielectric constant of the body material:	10000
Tan δ of the dielectric material:	0
Thickness of the dielectric body:	400(200)μm
(Symmetry is used to reduce the CPU time)	
Radius of the dielectric body:	600μm
Conductance:	58MS/m
Base conductor thickness:	8μm
Thinner conductor thickness:	1μm
Space between the conductors:	1μm
Eigenfrequency:	~3HGz

REFERENCES

[1] J. Hattori, et al.: Low Profile Dielectric Band Elimination Filter using Thin Film Layered Electrode for 2GHz Band Cellular Base Station, IEEE MTT-S Digest 1999

[2] Japanese Patent Laid -Open No.2004-120516A

THE DESIGN AND PERFORMANCE OF THE SPALLATION NEUTRON SOURCE LOW-LEVEL RF CONTROL SYSTEM *,**

M. Champion, M. Crofford, K. Kasemir, H. Ma, C. Piller, Spallation Neutron Source, Oak Ridge National Laboratory, Oak Ridge, TN, USA
L. Doolittle, C. Lionberger, M. Monroy, A. Ratti, Lawrence Berkeley National Laboratory, Berkeley, CA, USA
J. Power, H. Shoee, Los Alamos National Laboratory, Los Alamos, NM, USA

Abstract

The Spallation Neutron Source (SNS) linear accelerator low-level RF control system has been developed within a collaboration of Lawrence Berkeley, Los Alamos, and Oak Ridge national laboratories. Three distinct generations of the system, previously described, have been used to support beam commissioning at Oak Ridge. The third generation system went into production in early 2004, with installation in the coupled-cavity and superconducting linacs to span the remainder of the year. The final design of this system will be presented along with results of performance measurements.

INTRODUCTION

The LLRF controller for the SNS linac has been designed with a collaborative effort among three US national laboratories, Oak Ridge, Lawrence Berkeley and Los Alamos.

The three main components of the SNS LLRF Control System are the RF field control module (FCM), the High Power Protection Module (HPM), and the reference system. The HPM and the reference systems have been described elsewhere.

The FCM is a digital feedback controller that uses a Field Programmable Gate Array (FPGA) for fast data processing. The work presented here covers the test performance and production of the field control module.

The FCM is the result of the evolution of the FPGA-based data acquisition and processing systems developed for the SNS project by Los Alamos and Berkeley[1].

The SNS project is currently under construction. The equipment described here has been used during beam commissioning of the front end and DTL systems, and is ready to support CCL commissioning. The beam commissioning for the entire linac is planned for 2005.

* This work is supported by the Director, Office of Science, Office of Basic Energy Sciences, of the U.S. Department of Energy under Contract No. DE-AC03-76SF-00098.

** The SNS project is being carried out as a collaboration of six US Laboratories: Argonne National Laboratory (ANL), Brookhaven National Laboratory (BNL), Thomas Jefferson National Accelerator Facility (TJNAF), Los Alamos National Laboratory (LANL), E. O. Lawrence Berkeley National Laboratory (LBNL), and Oak Ridge National Laboratory (ORNL). SNS is managed by UT-Battelle, LLC, under contract DE-AC05-00OR22725 for the U.S. Department of Energy.

PROTOTYPING AND TESTING

Throughout the project, we took a gradual and incremental approach towards accomplishing our goals. As a consequence of this decision, we leveraged from the experience of the first and second-generation LLRF systems, as well as that of similar components in the BPM system[2].

Shortly after deciding on the basic approach, we designed and built a prototype system, which we used for debugging and performance testing purposes[3,4]. This system was used to power up both a superconducting RF system, using the JLAB SRF cavity test stand, and a warm system at SNS.

The prototype system was an expansion over the interim system built at Berkeley and used as a benchmark and a development platform for the final system[5]. This allowed us to compare most of the performance measurements and make the necessary adjustments to enhance performance as described below before going into final production.

PRODUCTION EXPERIENCE

Once the system was successfully prototyped, we went to commercial production. In this process we combined the fabrication of the FCMs with that of the HPMs and requested that the vendor be responsible for both the manufacturing of the PC boards and the loading of its components.

In order to meet our aggressive schedule, we procured all electrical components in advance; the vendor was responsible for board procurement, nuts & bolts, loading, and flying-probe testing.

Since we need to deploy 98 systems, we planned for a full production of 100 boards, plus 25 spares. This process had no big surprises; the only problem was caused by damage to the filters in the output circuit, which were not sealed and were damaged in the cleaning process. This was discovered in a pre-production run, so for the final run we attached the filters to the board after the rest of the board was soldered and cleaned.

TEST STRATEGY

We approached testing in two phases. The first was in support of the development of the hardware and was aimed at maximizing performance and optimizing the design. The second is the ongoing acceptance testing of

the boards built in quantity. The most important performance measurements characterized channel cross-talk, digitizer noise, signal distortion and non-linear behavior.

System Testing

The input channels noise and crosstalk measurements are performed on the AFE and DFE combined, essentially using the FPGA and ADCs as a sampling scope, transmitting the raw data over the network connection, and analyzing the data at an ordinary workstation. Results are presented below.

Similarly, the DFE and RFO were used to perform linearity analyses, driving the output from the network connection through the FPGA.

The integrated system was measured for overall performance. Since the system is based on the VME/VXI form-factor, we compared the relevant measurements by testing the same hardware on the PCI platform used by the beam diagnostics group.

Acceptance Tests

Testing of the production hardware is being performed by testing the same functions and characterizing the each board either individually or as a subsystem. For example, the DFE and RFO are tested together, because there is no simpler way to feed high speed digital data into the RFO.

PERFORMANCE RESULTS AND MODIFICATIONS

One of the performance improvements we implemented in the testing phase was the adoption of a shield plane between the DFE+RFO and the VXI motherboard. Since our schedule did not allow us for further troubleshooting, this shield has effectively worked to limit the broadband noise from VXI bus transactions, which was seen in the 50 MHz output section, and then was mixed up to generate strange spurs in the RF band. The noise has recently greatly suppressed by modifying the FPGA firmware to allow for better routing of the output gates. This change might eliminate the need for the shield.

Modifications to the DFE

The differential clocks supplied to the AD6645 high speed ADC's needed careful attention, including last minute component changes, before the input ADC subsytem achieved the desired noise floor of -140 dBc/Hz. This signal comes from a low jitter differential LVPECL 80 MHz VCXO, divided by two, transformer coupled, and transmitted across approximately 12 cm of circuit board. Data-dependent noise is observed, presumably due to capacitive coupling from the ADC data lines to the clock traces. Figure 1 shows the effect, both before and after optimizing the clock trace drive circuitry, and a comparison with the interim system used as a benchmark.

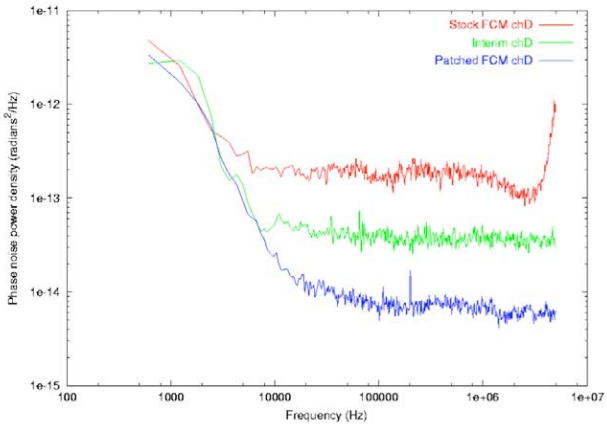

Figure 1: Clock circuit modifications on system noise.

An interesting byproduct of the noise measurements is the characterization of our signal sources. Since the noise measurements were made using various reference sources, we could extract their noise performance in our frequency range, and compare the $5 crystal with the $10,000+ signal generator or the SNS master oscillator. Needless to say, the crystal is second to none, as shown in Fig. 2.

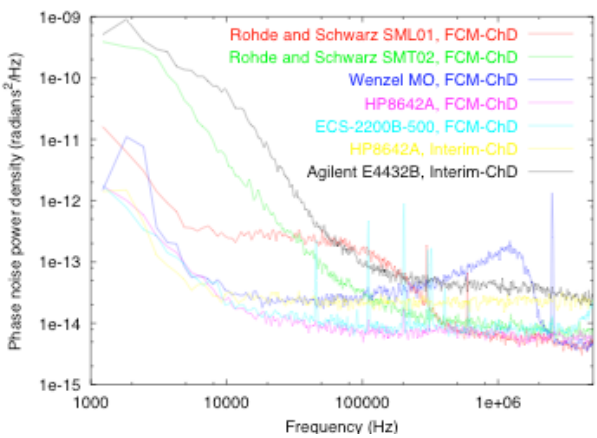

Figure 2: Phase noise comparison of several RF sources.

Results from Tests at SNS and Jab

The FCM operation was also thoroughly tested on the complete system. The results including klystron and RF cavities. The system closed loop performance already reached results well within the 1%, 1 deg. specification. While running standalone, the closed loop system demonstrated a stability of about 0.2% and 0.2 deg (Fig. 3), while during the last beam run the observed stability has been 0.5% and 0.5 deg. While these results were obtained with some effort to optimize performance, the system firmware is still under development. Improvements such as adaptive feed forward algorithms and shaping the turn-on curve are aimed at improving performance further. Such firmware will be available for operation with the SCL.

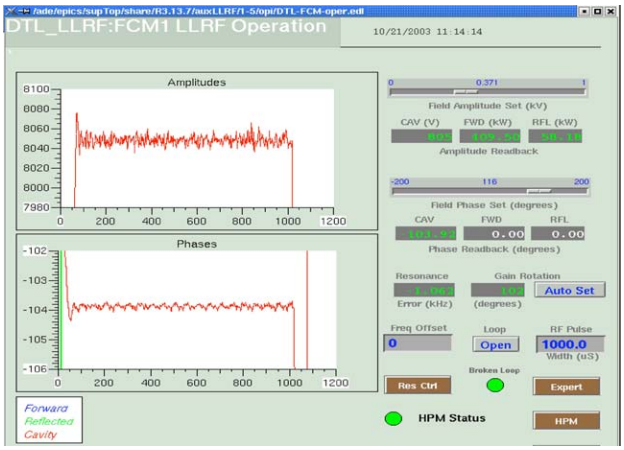

Figure 3: Test results on the DTL1 – amplitude and phase regulation to 0.2%, 0.2 deg.

Although these initial results are very encouraging, scaling these results to the large number of stations required for operation of the full linac will require adequate testing time and is certainly a challenging task.

FIRMWARE ARCHITECTURE

Since project inception, we have split tasks between firmware and controls software by assigning all actions taken within the pulse to the FPGA and those that are taken pulse-by-pulse to the software. For example, cavity tuning algorithms are implemented in software, whereas amplitude and phase feedback are a task of the firmware. The EPICS sequencer is now fully integrated in the operation of the system. The overall system architecture, which highlights the interaction between software and firmware, is shown in Fig. 4.

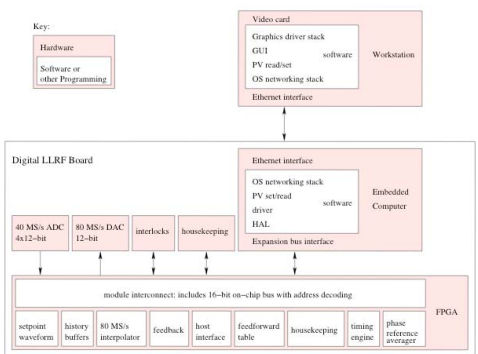

Figure 4: Software-firmware architecture.

Automated Code Generation

An important addition to the code set is that of the automated generation of a Verilog module to interconnect components: intercon.pl (241 non-blank, non-comment lines) creates a top level module to instantiate and interconnect second level modules, parse argument lists in Verilog modules, and build up the top-level Verilog program that instantiates each of them.

The intercon "framework", admittedly foreign to anyone browsing the code for the first time, is designed to minimize the amount of human-maintained overhead needed to support "real work" done in those second level modules. Along with the reduced line count should come reduced chances of introducing errors during maintenance of the code.

Each second level module defines its ports in a well defined manner, from the following categories: pins -- simply brought up as pins at the top level; interconnect -- like-named ports are interconnected to other second level modules, so the top level acts like a virtual backplane; host registers -- address ranges specified for read and/or write

PLANS FOR THE FUTURE

With the delivery of the production boards, we will be assembling and testing systems while supporting cavity installation and conditioning. A beam commissioning run is scheduled for September and it will include the linac up to the CCL system. This is the last scheduled beam run until the full linac commissioning in 2005. At this time, 35 LLRF systems have been installed in the klystron gallery.

The firmware development will continue throughout next year. While operation with superconducting cavities has been previously demonstrated, and the controller is used to condition cryomodules, a lot of development is still planned for the coming months. Lorentz force detuning and optimized turn on profiles will be studied and implemented, as well as a possible interface with a piezo-tuner controller. To further improve performance, we will also study and implement adaptive feed-forward algorithms. Auto-configuring routines will also be added to simplify settings of the linac for operator's control.

ACKNOWLEDGMENTS

The authors would like to acknowledge the precious contributions of the SNS controls group, who provided their help interfacing to their system, and the beam instrumentation group who shared assets and resources.

REFERENCES

[1] Doolittle, et al, "The SNS Front End LLRF System," Proceed. of the Linac2002 Conference, Gyeongju, Korea, August 2002.
[2] J. Power, et al, "Beam Position Monitors for the SNS Linac," Proceedings of the 2001 Particle Accelerator Conference, Chicago, IL, June 2001.
[3] M. Champion, "The Spallation Neutron Source Low Level RF Control System", Proceedings of the 2003 Particle Accelerator Conference, Portland, OR, May 2003.
[4] A. Regan, et al., "Newly designed field control module for the SNS", Proceedings of the 2003 Particle Accelerator Conference, Portland, OR, May 2003
[5] L. Doolittle, et al., "Operational Performance of the SNS LLRF interim system", Proceedings of the 2003 Particle Accelerator Conference, Portland, OR, May 2003

THE TOSHIBA E3736 MULTI-BEAM KLYSTRON

A.Yano#, S.Miyake,
TOSHIBA ELECTRON TUBES & DEVISES Co., Ltd, Otawara, Tochigi 324-8550, Japan
S. Kazakov, A. Larionov, V. Teriaev, BINP, Branch of Institute of Nuclear Physics, Russia
Y. H. Chin, KEK, High Energy Accelerator Research Organization, Tuskuba, 305-8550, Japan

Abstract

A 10-MW, L-band multi beam klystron (MBK) for TESLA linear collider and TESLA XFEL has been under development at Toshiba Electron Tubes & Devices Co., Ltd. (TETD) in collaboration with KEK. The TESLA requires pulsed klystrons capable of 10 MW output power at 1300 MHz with 1.5 ms pulse length and a repetition rate of 10 pps. The MBK with 6 low-perveance beams in parallel in the klystron enables us to operate at lower cathode voltage with higher efficiency. By choosing the coaxial cavities operated in TM_{010} mode, the cathode loading can be reduced for long life operation. This klystron is a six-cavity klystron. The 2nd harmonic cavity was employed as the 3rd cavity to satisfy the phase sensitivity requirement due to the change in the beam voltage. Tow pillbox windows with WR650 waveguide were chosen for power transmission. From the space limitation, a low-height waveguide was coupled to an output cavity. The design work and the fabrication have been accomplished and the testing is under way. We started conditioning and testing of prototype #0 from the beginning of August 2004. The preliminary testing up to a beam voltage of 100kV (specification=115kV) demonstrated the output power more than 6.2MW with an efficiency of 59%. The testing at higher voltage will start soon. The design overview and the initial test result at the factory are presented.

INTRODUCTION

Each author The TESLA project is a 33km long 500 to 800GeV electron/positron linear collider.[1] The TESLA X-FEL laboratory is a 1.5km long 20Gev electron linear accelerator for free electron laser application. [2] The superconducting cavity technology is adapted to the accelerators. The 500GeV TESLA project requires 572 klystrons operating at 10MW output power with 1.5ms pulse length. [3]

KEK has investigated a basic design X-band multi-beam klystron as power sources of Global linear collider (GLC) main linac. [4] Our design work started based on our experience of this X-band MBK design. TOSHIBA/KEK team improved the preliminary design to meet the DESY's requirements. The design parameters for the TOSHIBA E3736 klystron are shown in Table 1.

#atsunori.yano@toshiba.co.jp

Table 1: Design parameters of the E3736 MBK

Parameter	Value	Units
Frequency	1300	MHz
Output Power	10	MW
Average Output Power	150	kV
Beam Voltage	115	kV
Beam Current	132	A
Efficiency	>65	%
RF Pulse Width	1.5	ms
Repetition Rate	10	pps
Saturation Gain	47	dB
Number of Beams	6	
Cathode Loading	<2.1	A/cm^2
Structure	6	cavities
RF Window	Pill Box WR-650	
Tube Length	2270	mm
Solenoid Power	<4	KW

MULTI-BEAM KLYSTRON [5]

Fig. 1 shows the cut-away view of the multi-beam klystron E3736.

Symons reported the relationship of an RF efficiency η and the beam perveance P ($I/V^{3/2}$) can be expressed as below: [6]

$$\eta(\%) = 90 - 20 \times P(\mu perv.)$$

If a microperveance $P(\mu perv.)$ is to be chosen to be 2.0 that are typically selected for the conventional (shingle beam) klystrons operated at 10MW output power, expected RF efficiency is 50% at the maximum. A low microperveance klystron must operate at higher beam voltage. In case of long pulse klystrons, it might be cause of breakdown problem at electron gun and hence reduce the klystron reliability.

By using several low perveance electron beams in parallel in a klystron, a higher RF efficiency is expected due to the lower space charge forces that enable a tighter beam bunching.

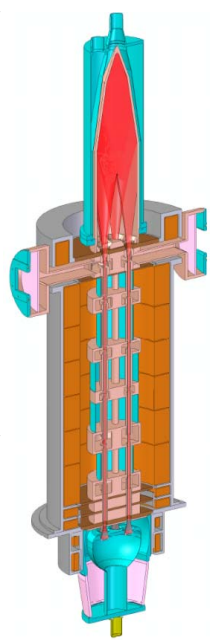

Figure 1: Cut-away view of the TOSHIBA E3736 multi-beam klystron.

For TOSHIBA MBK E3736, 6 low perveance beams of 0.56 $P(\mu perv.)$ are chosen. So achievement of efficiency of over 70% is theoretically expected.

KLYSTRON DESIGN

Design Outline

The simulation model of the input cavity is shown in Fig. 2. The cavities are ring-shaped common cavities operated in TM_{010} mode and 6 beams behave truly in a MBK way. By choosing this type of cavities, the separation of beam-lets are 120mm and the cathode diameter becomes 38mm. Therefore the cathode loading can be reduced to less than 2.1A/cm^2 for long life operation. To avoid parasitic oscillations, we investigated high order mode of each cavities.

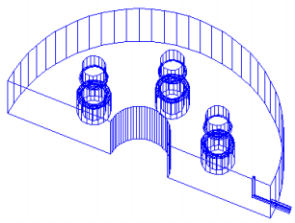

Figure 2: Cross section of an input cavity.

Electron Gun

6 low perveance beams of 0.56 $P(\mu perv.)$ are chosen. By choosing the coaxial cavities operated in TM_{010} mode, the separation of beam-lets are 120mm and the cathode diameter becomes 38mm. Therefore cathode loading can be reduced to less than 2.1A/cm^2 so that cathode life time was improved. DGUN [7] indicated that additional backing coils improve beam trajectory. The matching coils located between the gun and the input cavity can adjust the beam diameter.

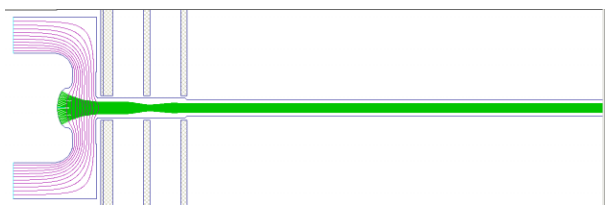

Figure 3: Electron gun design of E3736 MBK.

An "M"-type cathode [8] is adopted in order to assure the long life and the stable emission.

As mentioned in the reference, the gun surface gradients must be limited to be about 75kV/cm in DC operation. [9] Simulation results indicated that the surface gradients are less than 60kV/cm at the cathode voltage of 115kV.

One of the critical issues for gun design using off-axis electron beams is actual dimension of the gun at operating temperature. The cold dimension of electron gun was estimated by ANSYS code.

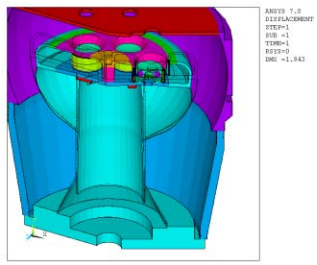

Figure 4: The thermal calculation.

Figure 5: The gun.

Interaction Cavities and Beam Simulation

The E3736 is a six-cavity klystron. The 2nd harmonic cavity was employed as the 3rd cavity to satisfy the phase sensitivity requirement due to the change in the beam voltage. The parameters of interaction cavities were optimised by FCI [10] (Field Charge Interaction 2+1/2 PIC code). The simulations show that the efficiency is close to 75% at a drive power of 150W.

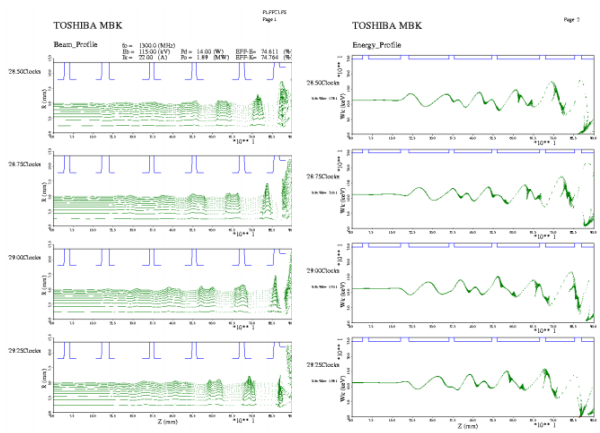

Figure 6: FCI simulation result.

Output Structure

Fig. 7 shows the simulation model of the output structure. Tow pillbox windows with WR650 waveguide were chosen for power transmission. From the space limitation, a low height waveguide was coupled to an output cavity. The matching post located the low height waveguide improves the rf transmission.

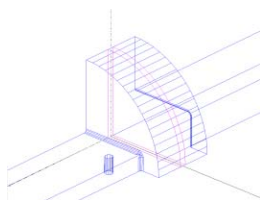

Figure 7: The simulation model of output window.

The calculated Qext of output cavity was about 44. Fig. 8 (right) indicates it as about 44.

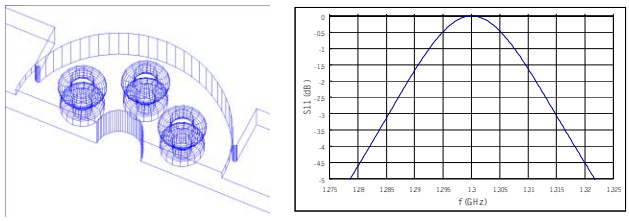

Figure 8: The simulation model and the result of the output cavity.

To suppress the multipactoring discharge, Al_2O_3 ceramic of vacuum side is coated with a TiN thin layer.

KLYSTRON PERFOMANCE

Result of Preliminary Test

Fig. 9 shows the photograph of the E3736 multi-beam klystron. Aging and testing has just started. No parasitic oscillation was found. The beam transmission rate from the gun to the collector was about 99%. At the preliminary test, the prototype #0 produced an output power of up to 6.2MW at a beam voltage of 100kV with an efficiency of 59%. After the beam test up to the beam voltage of 115kV and short pulse rf test, we will start the operation with a full rf pulse of 1.5ms.

Figure 9: The E3736 KLYSTRON.

CONCLUSION

The design and fabrication of the first prototype of E3736, 10MW, L-band multi beam klystron were completed. The E3736 MBK is designed to incorporate the coaxial cavities operated in fundamental mode. By choosing this type of cavities, the cathode loading can be reduced to less than 2.1A/cm^2 for long life operation. At initial test, no parasitic oscillation was observed. The beam transmission rate from the gun to the collector was about 99%. This result was to verify the beam transmission predicted by the electron trajectory simulation. The preliminary testing of the first prototype up to a beam voltage of 100kV (specification=115kV) demonstrated the output power more than 6.2MW with an efficiency of 59%. The testing at higher voltage will start soon. We expected that the E3736 MBK is able to generate the enough RF power required for the TESLA XFEL and the TESLA linear collider. We have been continuing the first prototype test to confirm the operation at beam voltage of 115kV with a full rf pulse of 1.5ms and reliability. We are going to modify the design for the production model based on the results of first prototype described in this paper.

ACKNOWLEDGMENTS

This development work was funded by DESY. The authors wish to thank Drs. S. Choroba, A. Gamp and D. Trines of DESY for their support and collaboration.

REFERENCES

[1] TESLA, "The superconducting Electron-Positron Collider with Integrated X-ray Laser Laboratory, Technical Design Report", DESY 2001-011, ECFA 2001-209, TESLA report 2001-23, TESLA-FEL 2001-05, March 2001

[2] TESLA XFEL, "First Stage of the X-Ray Laser Laboratory, Technical Design Report Supplement", DESY 2002-167, TESLA-FEL 2002-09, October 2002

[3] S. Choroba, "The TESLA RF System", RF2003, 2003

[4] A. Larionov et al, "Design of Multi-beam Klystron in X-Band" Proceeding of the 27th Linear Accelerator Meeting in Japan, 2002
IEDM, 1986A

[5] Some article on MBK are found in "High Energy Density Microwaves" Edited by R.M. Philips, AIP Conf. Proc. 474, 1999

[6] R.S. Symons, "Scaling laws and power limits for klystrons", IEDM, 1986

[7] A. Larionov, K. Ouglekov, " D-GUN for Simulation of Intensive Axial symmetric Electron Beam"

[8] S.Kimura et al. "Long-Life High-Reliability Ir-Coated Dispenser Cathode", IEDM, 1987.

[9] G.Caryotakis, Handbook of Accelerator Physics and Engineering, pp504-507, World Scientific, 1998.

[10] T. Shinkake, KEK Report 90-3, May 1990

CABLE INSULATION BREAKDOWNS IN THE MODULATOR WITH A SWITCH-MODE HIGH-VOLTAGE POWER SUPPLY*

A. Cours#, Argonne National Laboratory, 9700 S. Cass Ave.,
Argonne, Illinois, 60439, USA

Abstract

The Advanced Photon Source modulators are PFN-type pulsers with 40-kV switch-mode charging power supplies (PSs). The PS and the PFN are connected to each other by 18 feet of high-voltage (HV) cable. Another HV cable connects two separate parts of the PFN. The cables are standard 75-kV x-ray cables. All four cable connectors were designed by the PS manufacturer. Both cables were operating at the same voltage level (about 35 kV). The PS's output connector has never failed during five years of operation. One of the other three connectors failed approximately five times more often than the others. In order to resolve the failure problem, a transient analysis was performed for all connectors. It was found that transient voltage in the connector that failed most often was subjected to more high-frequency, high-amplitude AC components than the other three connectors. It was thought that these components caused partial discharge in the connector insulation and led to the insulation breakdown. Modification of the PFN eliminated one HV cable and significantly reduced the AC components during the pulse. A connector with higher partial discharge inception voltage was chosen as a replacement.

THE MODULATOR CIRCUITRY

The modulator power circuitry is shown in Fig. 1.

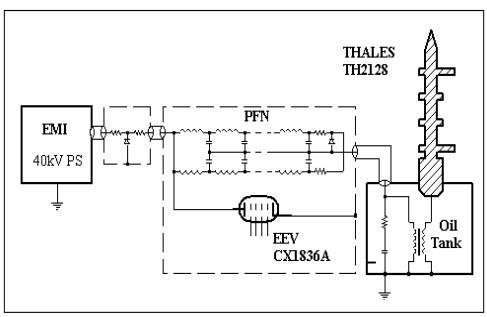

Figure 1: Modulator power circuitry.

The main elements are a 40-kV, 30-kJ/s Lambda-EMI power supply, a 2×8-cell PFN, an EEV thyratron switch, and a 15.3:1 step-up pulse transformer (PT). The charging supply charges the PFN capacitors to up to 40 kV (normal operational voltage is 34 to 36 kV), and then the thyratron switch discharges the PFN into the matched 4-Ω reflected load of the klystron cathode. The process then repeats at a 30 p.p.s. rate. The modulator has a fairly standard design and has been presented at various particle accelerator and power modulator conferences [1- 3].

HIGH-VOLTAGE CABLES

Cable Configuration

The Lambda-EMI PSs have been installed in five operational linac modulators between March 1999 and April 2000. Old PFNs have been utilized in the new modulator design. In addition to the PSs, a copper box with a PS protection circuit (PSPC) consisting of two resistors and a diode stack was placed between the PFN box and the PS (see Fig. 1).

The PS and the PSPC were connected to each other by 18 feet of high-voltage cable (Dielectric Science, model 2060). The PSPC and the PFN were connected by 10 feet of the same cable. Both cables were terminated at the ends with connectors designed by the manufacturer of the PSs (Fig. 2).

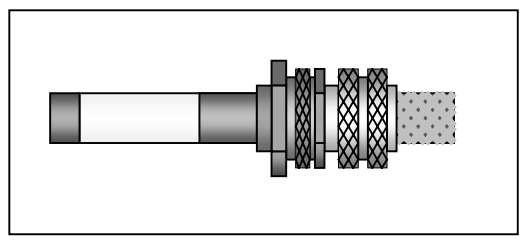

Figure 2: High-voltage cable termination.

Cable Failures

Since the first PS with the PSPC and the cables were installed in 1999, we have experienced 24 connector failures. Failure distribution over the years is presented in Fig. 3.

* Work supported by U.S. Department of Energy, Office of Basic Energy Sciences, under Contract No. W-31-109-ENG-38.

cours@aps.anl.gov

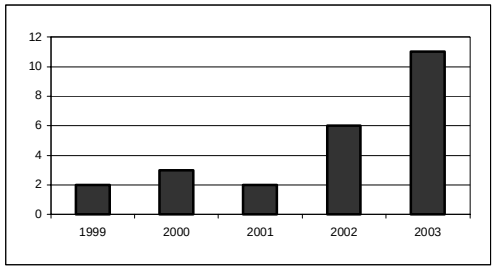

Figure 3: Cable failures per year

All failures were found to be almost identical breakdowns of the cable insulation in the area of the cable braid termination inside the connectors. We believe that increase in the number of failures is related to cable aging and rise of modulator operational voltage.

Connector Failures

The failures were distributed unevenly between four cable connectors (see Fig. 4).

In Figure 4:

- PS – Power Supply connector
- PSPC In – PSPC Input connector
- PSPC Out – PSPC Output connector
- PFN – PFN Input connector

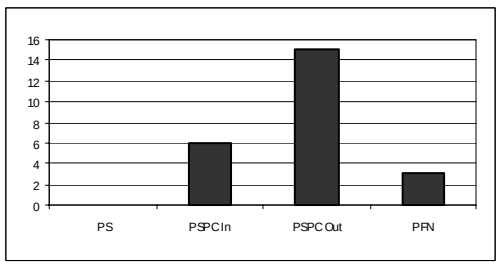

Figure 4: Failures per connector

In order to resolve the problem of such an uneven failure distribution, we performed a transient analysis for all connectors.

Transient Analysis and Direct Measurements

We found that after the thyratron switch closure, transient voltage in the connector that failed most often was subjected to more high-frequency, high-amplitude AC components than the other three connectors (see Figs. 5 though 8).

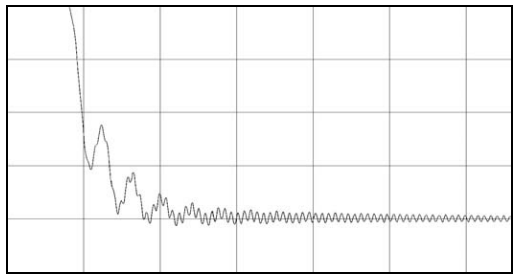

Figure 5: Transient voltage in the PS connector (simulation)

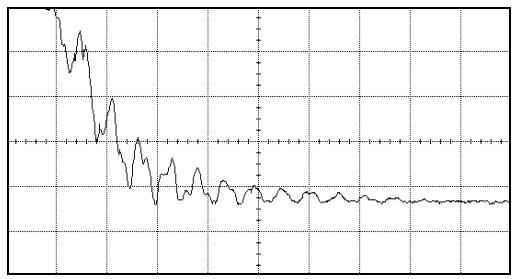

Figure 6: Transient voltage in the PSPC In connector (measured)

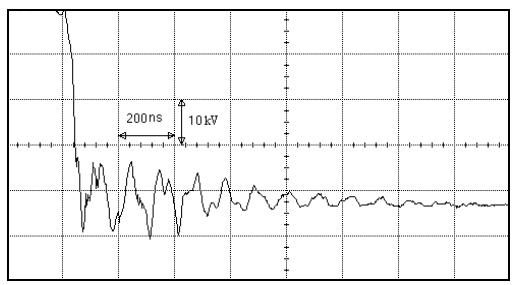

Figure 7: Transient voltage in the PSPC Out connector (measured)

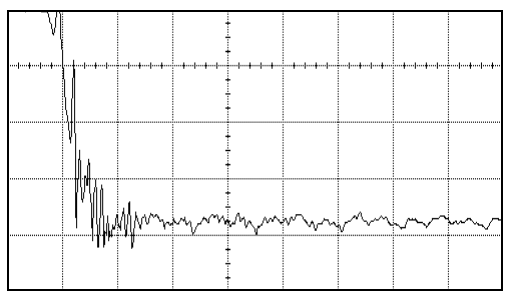

Figure 8: Transient voltage in the PFN connector (measured)

AC components in these plots have frequency of 5 to 10 MHz. It can be seen that the PSPC Output connector is the only one where voltage gets reversed a number of times during the pulse. Maximum reversed voltage in Fig. 8 is about 10 kV peak. We think that this voltage component causes partial discharge in the connector insulation and leads to the insulation breakdown.

MODULATOR MODIFICATION

We considered several different ways to modify the modulator in order to reduce or eliminate high-frequency oscillation in the connectors during the pulse and decided to perform two major modifications at the same time:

- Place the PSPC and the PFN with the thyratron switch in one copper-shielded compartment. This would eliminate one of the two HV cables and two of the four connectors (including the one that failed more often than the others) and reduce AC component amplitude during the pulse.
- Choose another HV connector with higher partial discharge inception voltage as a replacement for one of the two remaining HV connectors.

After major mechanical modulator modifications were complete, a number of different HV connectors with various cables were measured in order to find the connector-cable combination with highest partial-discharge inception voltage. It was found that the Isolation Product connector, model D-102-4, with a Dielectric Science 100-kV x-ray cable, model 2212, was the most suitable combination for this application.

The modifications that had been made to the modulators resulted in elimination of two connectors with the highest reversed voltage value and dV/dt during the pulse (Figs. 7 and 8). The AC component of the transient voltage in the PSPC Input connector has become much smaller (compare Fig. 6 and Fig. 9).

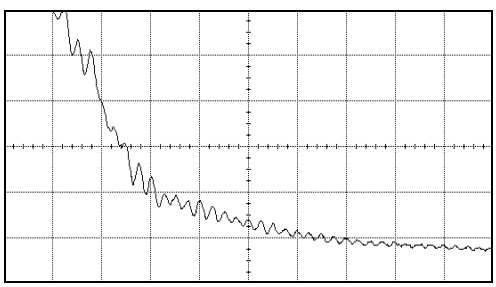

Figure 9: Transient voltage across PSPC Input connector after modulator modification (measured)

In order to make this transient voltage even smoother, a 1.2-nF capacitor was connected in parallel with the connector. Transient voltage across the connector with the capacitor is presented in Fig. 10.

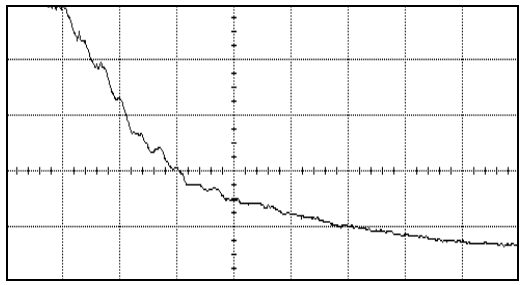

Figure 10: Transient voltage across PSPC Input connector with 1.2-nF capacitor (measured)

SUMMARY

The modulator modifications were completed for most of the APS linac modulators at the end of 2003 and the beginning of 2004. As a result, there have been no connector failures during first seven months of 2004 (see Fig. 11). Modification of other modulators will be completed in 2004.

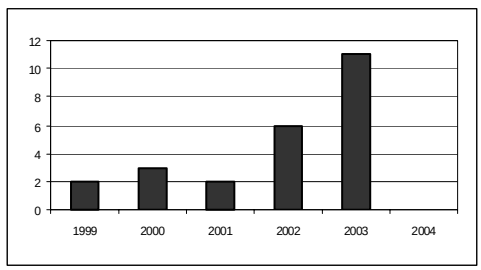

Figure 11: Cable failures per year including 2004

ACKNOWLEDGEMENTS

The authors wish to thank Howard Pfeffer, Ken Bourkland, and Chris Jensen (Fermilab) for their help with PD tests and discussions of the connector breakdown problems; and Dave Meyer, Mike Douell, and Tim Jonasson (ANL, RF Group) for their work on the modulator upgrade.

REFERENCES

[1] T. J. Russell, A. Cours, "Klystron Modulator Operation and Upgrades for the APS Linac," Proc. 1995 Particle Accelerator Conference, p. 1559, 1995.

[2] R. Fuja et al., "Constant-Current Charging Supplies for the Advanced Photon Source (APS) Linear Accelerator Modulators," Proc. 1997 Particle Accelerator Conference, p. 1269, 1998.

[3] A. Cours, T. Smith, "The Advanced Photon Source Linac Modulators. PSpice Simulation and Upgrade", Proc. Twenty-Fifth International Power Modulator Symposium and 2002 High-Voltage Workshop, p. 270, 2002.

THE RF-SYSTEM FOR A HIGH CURRENT RFQ AT IHEP

Zhang Zonghua, Qiao Jimin, Li Jian, Xu Xinan,
IHEP, Institute of High Energy Physics, Beijing100039, China

Abstract

The R&D of a high current proton RFQ is one of the most important research tasks of the Accelerator Driven Sub-critical system (ADS) basic research project. In preliminary research phase, the 352.2MHz RF system will be operated in pulse mode. CERN kindly provided IHEP with some RF equipment. Because the given RF system was used for CW operation at CERN before, to apply them to our pulse mode operation, some modifications and improvements are necessary. We have made some indispensable assemblies, and also did some tests and commissioning of every sub-system. At present, the initial high power conditioning of the klystron is carried out. A description of RF power system is given, in particularly, the performance of HV power supply, thyratron crowbar and capacitors, hard tube modulator and its control electronics, and klystron power conditioning are presented.

INTRODUCTION

The programme of building our RF power system, in brief, includes two phases--the 1st phase is to modify CERN LEP / RF equipment and to install a RF power test stand of our own for pulse mode operation. That is, klystron amplifier is directly connected to dummy load and meanwhile, R&D of long pulse hard tube modulator for klystron TH2089 is carried out. The 2nd Phase is fabrication of RF power transmission and distribution system from the klystron amplifier to the RFQ cavity; at last, we will perform RFQ power delivering and conditioning. Design features and parameters of RF system are shown in Table 1. The picture of RF power test stand can be seen in Fig. 1.

Table 1: Design features and parameters

Frequency	352.209MHz
Pulsed output RF power	1 MW max.
Waveguide system	WR2300
Klystron cathode voltage	95 kV max.
Klystron modulation anode voltage	62 kV to 0

Figure 1: Panorama picture of our RF power test stand.

HV POWER SUPPLY

General Layout

The power supply of a klystron is a 100kV, 20A power converter. It consists of four basic units: step-down transformers TR1 and TR2 (10 / 1 kV), a thyristor AC line controller and its electronics, high voltage transformers TR3 and TR4 (1 / 52 kV), diode rectifier and the filter chokes unit.

Step-down Transformers

Original HV power supply at CERN was fed from the 18 kV, 50 Hz, three-phase mains, but in China the mains feeding voltage is 10kV, therefore we specially redesigned and manufactured the step-down transformer unit in China to match CERN LEP power supply equipment. The primaries of the two step-down transformers TR1 and TR2 are fed from the 10kV, 50Hz, three-phase mains. The secondary output voltage of each transformer is 1kV line-to-line. The two transformer units are housed in one tank and are immersed in mineral oil. They are air natural / oil natural cooled. The winding configuration of the two step-down transformers is extended delta / star, so their secondaries can form phase-shift of 30 degrees between TR1 and TR2. A twelve-phase system at the HV DC output terminals is obtained. This can help to reduce the DC output ripple. The ripple of the whole power supply is no more than 1%.

Vector group of TR1 is dyn 11.5, and TR2's is dyn 0.5. That means, the phase-shift of the TR1 secondary voltage with respect to the feeding mains is +15 degrees, and the TR2's is –15 degrees. Thus, the required phase-shift of 30 degrees between TR1 and TR2 is obtained. The two transformers are designed symmetrically. It can limit the difference between the two halves of the converter and minimize sub-harmonic generation. Under the acceptance test, the phase-shift between TR1 and TR2 is 30.03 degrees. The design allowable tolerance of phase shift is 30 ± 0.1 degrees. So the result of the acceptance test is satisfying.

Thyristor AC Line Controller

The power converter can provide 0 to 100kV continuously variable output voltage. This is realized by controlling firing angle of the thyristors of the thyristor AC line controller. The different firing angle corresponds to the different current in each branch of the thyristors. The input voltage of the thyristor AC line controller is fixed at 1kV, and the output voltage can be adjusted from

0 to 1kV, then, it is fed into the diode rectifier. Input and output voltage waveforms of one module of thyristor AC line controller are given in Fig. 2.

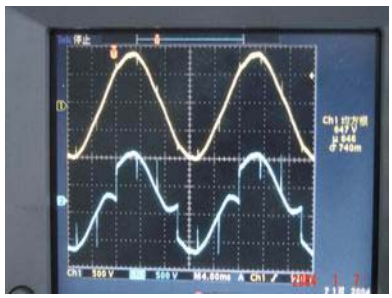

Figure 2: Input and output voltage of thyristor AC line controller.

THYRATRON CROWBAR AND CAPACITORS

In pulse mode operation, capacitor bank is necessary for energy storage. The thyratron crowbar is a klystron protection device. Since the above mentioned components are immersed in oil, they must be housed in a fireproof bunker. In the case of an arc occurring inside the klystron, the thyratron crowbar can remove the high voltage energy from the klystron within a few microseconds in order to avoid the damage of the klystron. At the same time, the thyristor AC line controller is phased back safely to bring the DC output voltage of the rectifier to zero. So the fault is cleared immediately.

The thyratron crowbar comprises the eight-gap double-ended thyratron CX2098B, made by EEV, and its electronic trigger circuit. Since the operating voltage of klystron is no more than 100 kV, the maximum voltage across each gap is thus 12.5 kV which is half specified value and, therefore, voltage breakdowns should not occur or if so very rarely [1]. We used four capacitors (2uF) for energy storage. A wideband current transformer is inserted in the low voltage line of each capacitor. The output signals of the four current transformers are connected in parallel into interlock interface electronics, then, passing on a summary fault signal to the thyristor AC line controller for turn off the HV power converter in case of internal flashover in klystron. In a simulation fault protection test, we fed a 2us-pulse trigger signal as substitute of overcurrent signal into interlock interface electronics, an output control signal can go to thyristor AC line controller within 4 us (see Fig. 3).

Figure 3: Simulated overcurrent input signal and output control signal of the interlock interface electronics.

HARD TUBE MODULATOR AND ITS CONTROL ELECTRONICS

The schematic diagram of the modulator is shown in Fig. 4. The klystron TH2089 is equipped with a modulation anode (MA). The MA voltage with respect to the cathode determines the intensity of the electron beam current departing from the cathode. By varying the MA voltage, the klystron beam current can be controlled, and hence klystron output power can be controlled while keeping RF drive level and operating voltage constant. Because ADS RFQ operates in pulse mode, emphasis of ADS RF system research is laid on the long pulse modulator, which can change duty factor and amplitude of the klystron output power. The modulator's parameters are:

- Output pulse width: up to 3ms.
- Duty factor: 1% ~ 10%, continuously adjustable.
- Output peak voltage with respect to the cathode: $\leqslant$ 62KV.

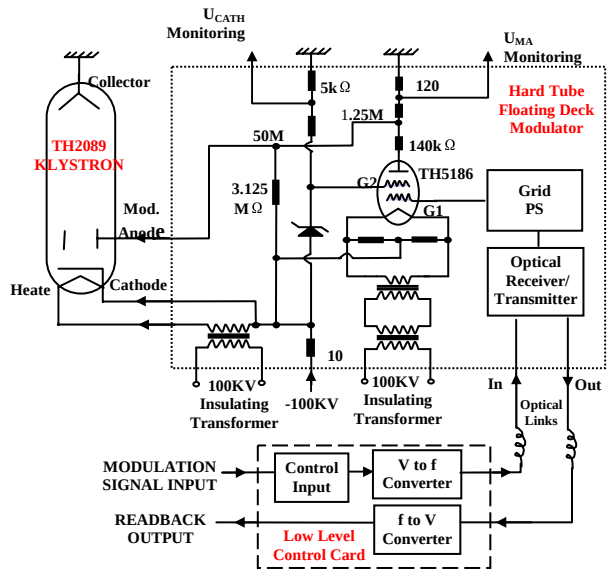

Figure 4: Schematic diagram of hard tube modulator.

The modulator is the type of the hard tube floating deck modulator. It mainly comprises the HV resistors, the HV tetrode TH5186 and its control electronics. The tetrode is suited for 100kV operation voltage, made by Thomson Company. The function of the tube is that of a variable high voltage resistor. The tube together with the HV resistors 1.25 M Ohms and 3.125 M Ohms form an adjustable resistive voltage divider, which determines the maximum and minimum MA voltage.

Because the tetrode is at cathode potential, all control signals must be insulated. For this reason, the optical fibers, the low level control card and the control electronics of the tetrode grid are employed. The low level control card is developed for converting a voltage signal to a frequency signal that passes on via optical fiber, and vice versa. A signal derived from the low level control card, the frequency of which is proportional to the voltage value of a modulation control signal, is sent via

the optical fiber to the control electronics of the tetrode grid. Through conversion by the control electronics, the tetrode grid obtains variable biasing supply (V_{G1}) (see Fig. 5). Thus, the tube represents either infinite or a very small resistance value compared to those of the HV resistors (1.25 M Ohms and 3.125 M Ohms). By means of the variable grid supply, the internal impedance of the tube can be varied between the above mentioned two extremes. The test voltage waveforms of a modulation control signal and the tetrode grid voltage (V_{G1}) are given in Fig. 6.

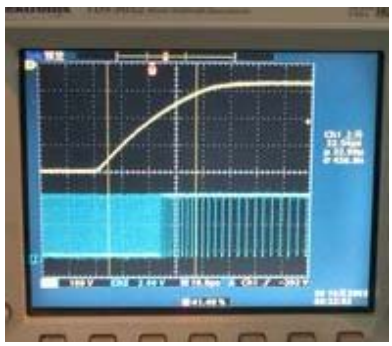

Figure 5: V_{G1} and frequency signal from the voltage to frequency converter.

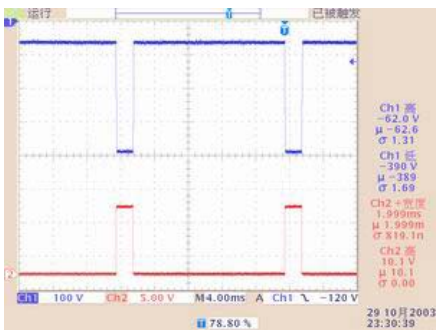

Figure 6: V_{G1} and the modulation control signal of low level control card.

Besides the HV resistors, the HV tetrode TH5186 and its control electronics, two 100kV insulating transformers and a 10-Ohms carbon-ceramic resistor are also housed in the modulator oil tank. One of the insulating transformers provides the operating voltage for the cathode heater of the klystron; the other one supplies the voltage for the heater and the grid control electronics of the tetrode. The 10-Ohms carbon-ceramic resistor is inserted in the high voltage line in series to the klystron and serves as an energy limiter in the case of an arc in the klystron.

KLYSTRON POWER CONDITIONING

Because the klystron given by CERN was a used and ever repaired tube, which stopped and stored up for four years, we must recondition it again. However, due to high storage energy of capacitor bank, only one capacitor instead of four is connected in parallel into HV power supply for the first step of power conditioning in order to protect klystron. At present, the initial high power conditioning of the klystron is carried out, and output power can reach up to 334 kW at 62 kV in CW mode and 402 kW at 66.5 kV in pulse mode. Waveforms of RF power, klystron beam current and cathode voltage are shown in Fig. 7 and Fig. 8. Next step, it will take us long time to raise conditioning power to reach nominal value. And at last, all of four capacitors will be used, and high RF power will be applied to RFQ cavity.

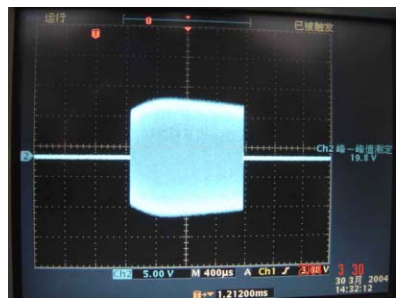

Figure 7: RF power waveform.

Figure 8: klystron beam current and cathode voltage.

ACKNOWLEDGEMENTS

The authors would like to thank Prof. Kurt Hubner and Dr. John Poole for their great support about CERN-IHEP collaboration and LEP / RF equipment that was presented to IHEP and also Dr. Tom Wegelius who was charge of LEP / RF equipment transportation from CERN side. Especially, we are also grateful to Dr. Hans Frischholz for his kind help and doing a lot of jobs for us. Thanks are also due to Prof. Fu Shinian and Prof. Guan Xialing for their great support and contribution on RF system.

REFERENCES

[1] H. Frischholz, G. Pecheur, “The High-voltage Interface for the LEP II RF Power Generation System”, 4th European Particle Accelerator Conference, London, UK, 27 Jun - 1 Jul 1994, p. 1939-1941.

A HIGH-RESOLUTION S-BAND DOWN-CONVERTING DIGITAL PHASE DETECTOR FOR SASE FEL USE

A.E. Grelick, N.D. Arnold, J. Carwardine, N.P. DiMonte, A. Nassiri, T.L. Smith,
Argonne National Laboratory, Argonne, IL 60439, USA

Abstract

Each of the rf phase detectors in the Advanced Photon Source linac [1] consists of a module that down converts from S-band to 20 MHz followed by an analog I/Q detector. Phase is calculated from one digitized sample per pulse each of I and Q. The resulting data have excellent long-term stability but are noisy enough so that a number of samples must be averaged to get a usable reading. The more recent requirement to support a self-amplified spontaneous emission (SASE) free-electron laser (FEL) has presented the need to accurately resolve the relative phase of a single pulse. We replaced analog detection with digital sampling and replaced internal intermediate frequency (IF) reference oscillators with a lower-noise external oscillator in order to control the two largest components of noise. The implementation of a central, ultra-low-noise reference oscillator and a distribution system capable of maintaining the low phase noise is described, together with the results obtained to date. The principal remaining technical issue is determining the processing power required as a function of measurement channels per processor, measured pulse repetition rate, intrapulse data bandwidth, and digital filter characteristics. The options and tradeoffs involved and the present status are discussed.

DEFINITION OF PROBLEM

Existing System and Limitations

The existing LANL-designed linac phase detectors utilize down conversion from 2856 MHz to 20 MHz (Downconverter VXI Module), followed by ovenized analog I and Q detectors that produce one 12-bit digitized sample per pulse for each of the I and Q waveforms (Vector Detector 2 slot VXI module). Software in the input/output controller (IOC) performs a rectangular-to-polar conversion on the data samples, extracting phase and suppressing amplitude. Excellent long-term stability has been achieved. However, these detectors have exhibited over one degree of noise on the measurement.

Requirements for Improved Performance

The more recent requirement to support a SASE FEL [2] has presented the need to accurately resolve the relative phase of a single pulse. The following requirements have been determined as goals for upgrade efforts.

- Compatibility with existing, VXI-based, down-converting (to 20 MHz) hardware
- Resolution of ≤ 0.1 degree rms based on single-pulse data (without averaging multiple pulses)
- Capability of supporting up to four measurements/subsystem in the operational environment
- Operational Environment:

Pulse rep. freq.	30 Hz max
Sampled pulse width	1.3 μs max
Intrapulse data bandwidth	10 MHz

DIGITAL CONCEPT AND EXPERIMENTS

An internal APS presentation [3] identified phase detection as one of a number of applications that could potentially benefit from cost-effective performance improvements associated with the use of digital signal processing (DSP).

In order to maximize the pulse envelope bandwidth, the existing design employs minimal filtering of the IF carrier. DSP easily incorporates high performance filters that could reduce carrier noise. Newly announced sampling modules using state-of-the-art flash analog-to-digital converters that could support the desired 80-MHz sampling rate were identified. DSP would allow acquisition of the phase waveform of the portion of interest of a complete pulse, which could then be averaged in different ways for different purposes. For instance, one point in a pulse could be averaged over a number of pulses to get an extremely steady phase value for screen display and long-term auto phase correction. At the same time, the entire portion of interest of a pulse could be averaged into a composite phase value, which would have low enough effective noise to be effectively compared with the equivalent value for an adjacent pulse.

A frequency quadrupler was constructed and experiments were performed comparing digital sampling to the existing analog system. A key finding from the initial experiments was that the phase noise of the 20-MHz IF reference oscillator, used by the Downconverter Module, constitutes the most critical limitation that constrains the phase measurement performance. This implementation is especially sensitive since the approximately 143X down conversion adds phase noise that is 43 dB greater than the reference oscillator phase noise to both the down-converted signal and the down-converted 2856-MHz reference. Furthermore, the digitally sampled data is degraded even more than the analog data when the noise level is as great as that of the existing system.

ULTRA-LOW-NOISE OSCILLATOR

An ultra-low-noise oscillator, from the Wenzel Associates ULN series, has been procured. This oscillator

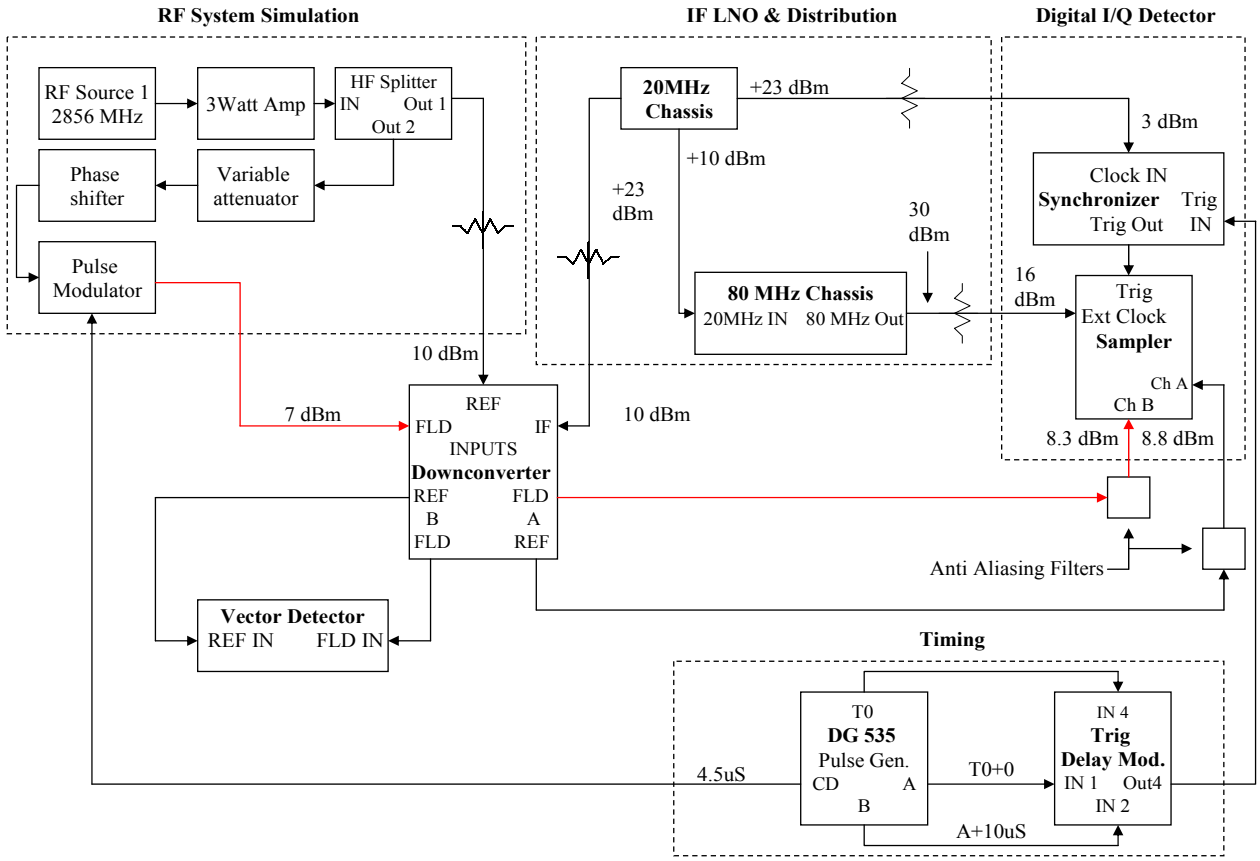

Figure 1: Phase detector comparative test configuration.

has phase noise specifications 30 dB below those of the 20-MHz IF reference oscillator that is internal to the Downconverter Module. A revised topology that replaces the internal reference oscillator with the ultra-low-noise oscillator as an external 20-MHz reference was tested. The results show that when the phase noise of the 20-MHz source is low enough, the digital phase measurement has a lower noise level than the analog. This is as expected, since carrier noise is lower. Figure 1 shows the most current version of the test configuration.

CENTRALIZED 20 MHZ AND 80 MHZ

Distribution Concept

There are seven IOCs supporting rf measurements in the Advanced Photon Source linac. The size and cost of the ultra-low-noise oscillator are both beyond comfortable limits for incorporation within a VXI module. The use of a centralized subsystem, incorporating the ultra-low-noise oscillator and the quadrupler, together with amplification and 8-way fan-out, was chosen as a cost-effective way to obtain the two required frequencies with the necessary low phase-noise characteristics.

Distribution Implementation

A key design issue was avoiding phase-noise degradation in amplifying 20 MHz. The precise noise figure of the amplifier is not critical. However, excellent effective linearity is required in order to minimize AM-to-PM conversion. The amplifier configuration selected uses an amplifier incorporating feedback with gain limited to 15 dB, followed by a phase-optimized bandpass filter having 35% band width. This identical configuration is used both before and after an 8-way splitter. Maximum power output is limited to 10 dB below typical 1-dB compression power. This configuration produces test results indistinguishable from those obtained by using the unamplified oscillator as the down-conversion reference.

The centrally distributed 20-MHz and 80-MHz subsystem has been implemented in the form of separate 20-MHz and 80-MHz chassis, which have been installed in a central location in the linac, plus Dual Distribution panels/chassis at each IOC. Each Dual Distribution panel/chassis provides eight 20-MHz jacks and four 80-MHz jacks. This subsystem has been made active as the IF reference for the Downconverter Modules. The additional 20-MHz and 80-MHz outputs that have been provided will support experimental and, later, operational digital phase detectors that will eventually supersede the Vector Detector Modules.

PROCESSOR CONSIDERATIONS

Processing requirements are minimized by the use of the 4X oversampling since the I/Q calculations require no multiplications (sin/cos of 0, 90, 180 and 270 degrees are -1, 0, +1). An MVME5100 processor is already in use at the APS and is expected to have adequate performance.

TEST RESULTS

Figure 2 shows stability test results with and without an anti-aliasing filter having a 3-dB bandwidth of 55 MHz.

OPTIONS AND TRADE OFFS

The results to date appear to meet the requirements of the application with a performance margin. Most of the data points are less than 0.07 degrees. This approach is preferred because it maintains compatibility with the existing hardware.

However, the true optimum calls for choice of a higher IF. Oscillators from the Wenzel Associates ULN series are available at higher frequencies, including 100 MHz. The lesser down conversion will result in a 14-dB decrease in noise on the down-converted signal. This is offset by a 5-dB increase in specified noise in the higher frequency oscillators, resulting in a 9-dB net improvement. The effective net improvement can be expected to be 7 dB after subtracting a 2-dB improvement from the anti-aliasing filter, which probably would not be practical for that case, meaning that most data points will be less than 0.03 degrees, i.e., a time uncertainty of 30 fs.

On the other hand, optimum performance versus total cost from scratch is likely to be produced by direct digital sampling. In this case, the aperture uncertainty of the analog-to-digital converter is the principal error. Aperture uncertainty of 100 fs is currently available

ACKNOWLEDGEMENTS

The authors wish to thank W. Yoder for his extensive help in building the new chassis and assembling and operating the test set-up. We also thank B. Epperson for graphics assistance.

This work is supported by the U.S. Department of Energy, Office of Basic Energy Sciences, under Contract No. W-31-109-ENG-38.

REFERENCES

[1] M. White et al., "Construction, Commissioning and Operational Experience of the Advanced Photon Source (APS) Linear Accelerator," Proceedings of the XVIII International Linear Accelerator Conference, Geneva, Switzerland, 26-30 August, 1996, pp. 315-319 (1996).

[2] T.L. Smith et al., "RF System Upgrades to the Advanced Photon Source Linear Accelerator in Support of the FEL Operation," Proceedings of the XX International Linac Conference, pp. 878-880 (2000).

[3] J. Carwardine, F. Lenkszus, APS internal seminar.

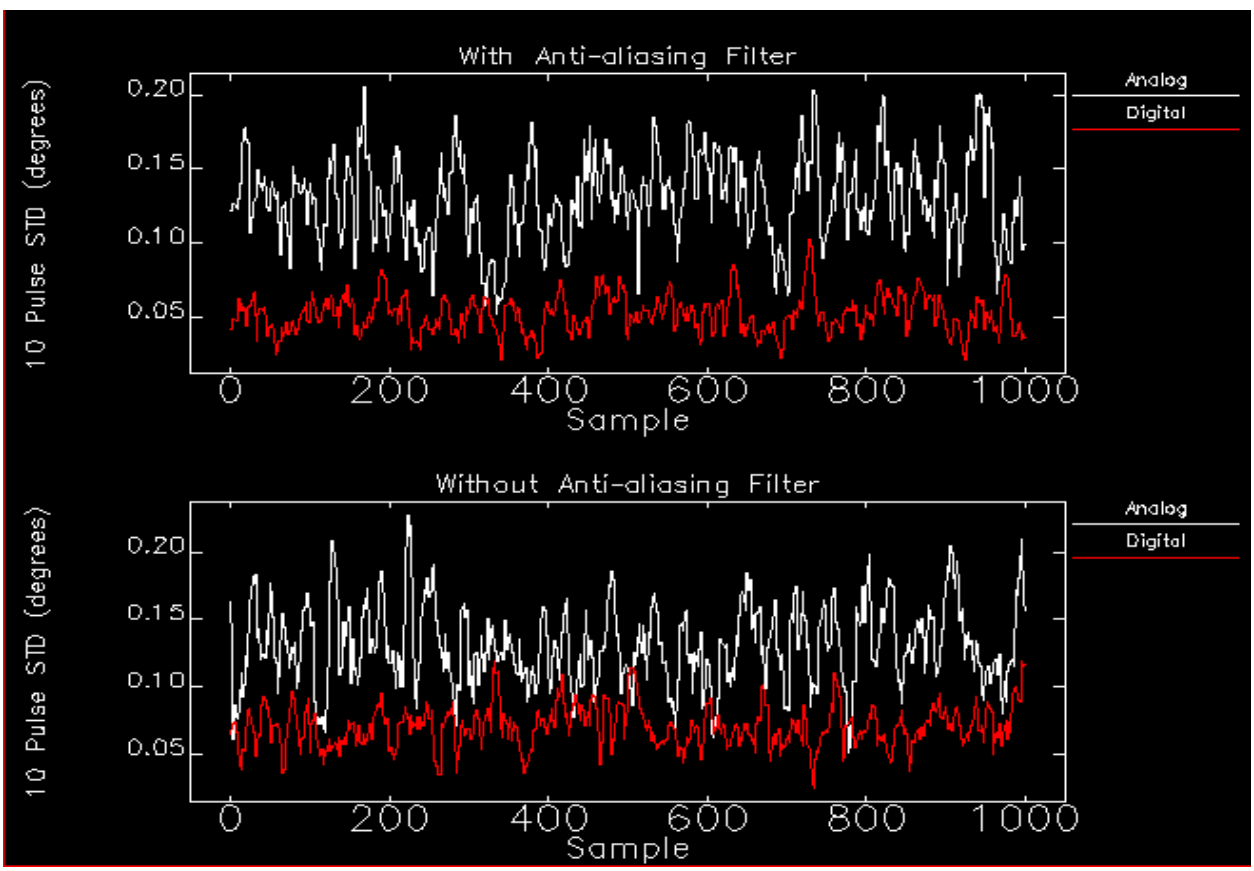

Figure 2: Comparative stability test results.

THE RF-STATION INTERLOCK FOR THE EUROPEAN X-RAY LASER

T. Grevsmühl, S. Choroba, P. Duval, O. Hensler, J. Kahl, F.-R. Kaiser, A. Kretzschmann, H. Leich, K. Rehlich, U.Schwendicke, S. Simrock, S. Weisse, R. Wenndorff, DESY, Germany

Abstract

The RF-station interlock for the European X-ray laser will be based on a 19"- 3U crate incorporating a controller with the 32-bit RISC NIOS-processor (ALTERA). The main task of the interlock system is to guarantee safety of personnel and prevent any damage from the components of the RF station and connected cavities. The interlock system must also guarantee a maximum time of operation of the RF stations which implies the implementation of self diagnostics and repair strategies on a module basis. Additional tasks are: collection and temporary storage of status information of the individual channels of the interlock system, transfer of this information to the control system, slow control functions (e.g. HV setting and monitoring) and control of inputs and outputs from and to other subsystems. In this paper we present the implementation using an ALTERA-FPGA running a 32-bit RISC NIOS-processor. Connection to the accelerator main control is provided by Ethernet using BSD-style socket routines based on ALTERA's plugs-library. The layout of the system is presented and first hardware components are shown.

INTRODUCTION

The RF system for the European XFEL consists of 35 RF stations supplying RF power at 1.3GHz for the superconducting cavities of the linear accelerator of the XFEL [1]. Each RF station generates RF pulses up to 10MW at a pulse duration up to 1.5ms and a repetition rate up to 10Hz. A station consists of a klystron, pulse transformer, pulsed high voltage power supply, a low level RF system, auxiliary power supplies and an interlock system [2]. A simplified view is shown Figure 1. The pulsed high voltage power supplies will be installed in a separate hall above ground whereas all other components will be installed in the accelerator tunnel under ground near to the cavities. Connection between the components in the hall and in the tunnel is accomplished by high voltage pulse cables and control and interlock connections. The main task of the interlock system is the protection of the different subsystems of the RF stations and of the components connected to the station. In addition it provides slow control functions for the subsystems. Since the interlock system is installed in the accelerator tunnel, where no access is allowed during beam operation, the interlock system has to provide monitoring functions, allowing the localization of failures of the RF station remotely which sets the service personnel in a position to exchange broken subunits quickly during a scheduled maintenance time. In addition all monitored signals will be transferred to the accelerator main control system, where correlations between accelerator and RF station operation can be determined. The interlock system is a modular system so that malfunctioning interlock boards can be exchanged without renewing a complete system.

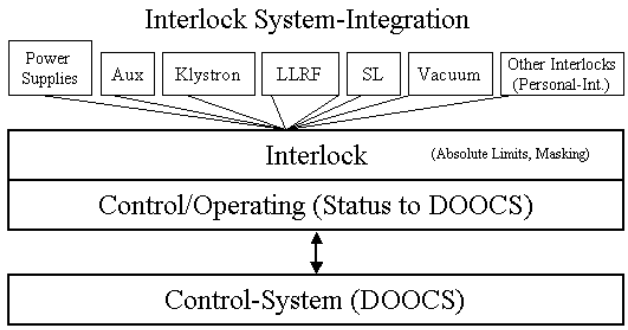

Figure 1 : RF-Station components (simplified).

REQUIREMENTS

To serve its main task the interlock system has to deal with 3 types of errors:

-hard component failures (non-reversible hardware mal-function like broken cables, damaged contacts, dead sensors, ...)
-soft errors (e.g. sparks in the klystron or wave guide system, temperature above a threshold, water-flow...)
-error conditions caused by transient noise from the RF station itself (caused by the pulsed power operation)

Errors should be treated with two types of thresholds and channel masking.

Absolute max./min. thresholds: any violation of these thresholds will force the shutdown of one ore more subsystems or of all components of the RF station.

Programmable (soft) thresholds: a violation of these boundaries will generate an alarm message to the control system. Soft thresholds are only available for analog input channels.

For any individual input channel a mask function should be implemented which allows to exclude this channel from all of the interlock functions. Masking operations via the control system are secured by password mechanism and must cause an entry into a log file [3,4].

Besides additional tasks like setting operational parameters, collecting status and diagnostic information and providing it to the main control system, a system self test at power-up has to ensure the proper operation of all interlock components. This is also true for a test during normal operation. In case of power-down status-information should be saved for diagnostics. The RF-

station interlock has to interact with other XFEL-subsystems (see Figure 2).

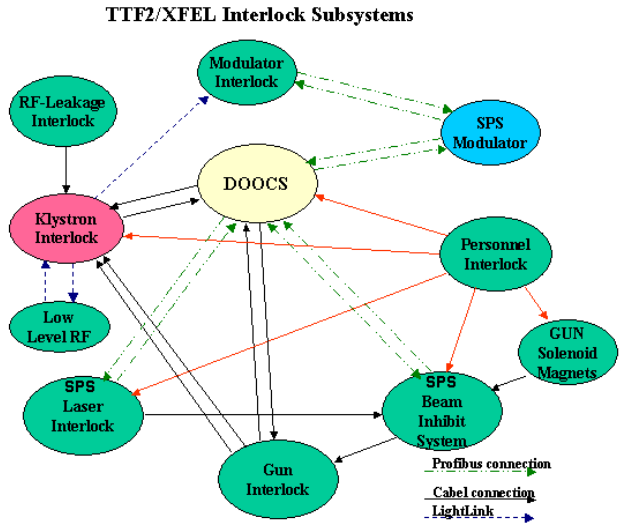

Figure 2 : Interaction of different XFEL-subsystems.

Other implementation constraints are :

- process-I/O should not use cables to/from the front side of the crate; all cabling must be done from rear site
- due to the future XFEL-tunnel layout a space saving implementation of the system is needed e.g. a combination of all interlock functions and some slow control functions into only one crate per RF-station
- perform communication between modules via a backplane (no extra cables for communication)
- connection to the main control system DOOCS via ethernet

IMPLEMENTATION

The interlock mechanics is a 19" 4U crate with dedicated backplane optimized to the application (figure 3, 4, 8).

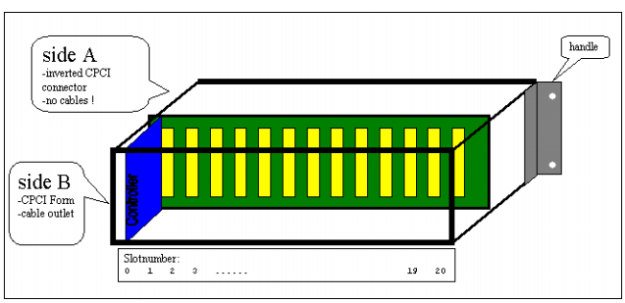

Figure 3: Interlock Crate Layout.

A 3U cPCI-like board format with two 5-row connectors is used (figure 5). 235 pins to the backplane per board give enough pin resources per slot and to the backplane to build a compact interlock/control system.

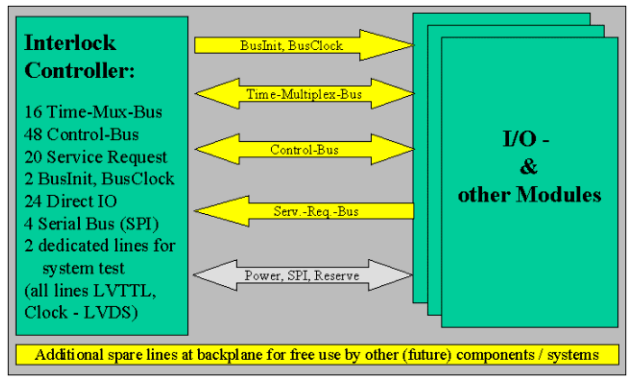

Figure 4: Dedicated Backplane Layout.

Figure 5: Interlock Controller.

Each interlock system consists of 1 controller and up to 20 I/O-modules (figure6).

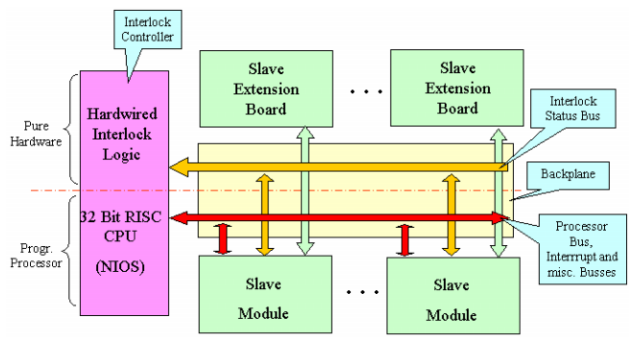

Figure 6: Interlock System Layout.

At the interlock controller board an ALTERA FPGA, a Cyclone EP1C20F400-C7 FPGA is used (figure 5, 7). Inside the FPGA the following is implemented:

- interlock function for components of one RF station based on signals pre-processed within the different IO-modules
- interface to the DOOCS control system via ethernet
- controls of the IO-modules in the crate
- master of all backplane busses
- source of the bus timing signals
- some slow control functions
- system check after power up or per command

All necessary control functions to all slave modules in the interlock crate and the interfacing to the control system are performed by a 32-bit RISC NIOS CPU inside the FPGA. It is important to recognize that the interlock functionality inside the FPGA is strictly separated from software running at the NIOS CPU. The interlock will always work independently from the state of the CPU (figure 6, 7).

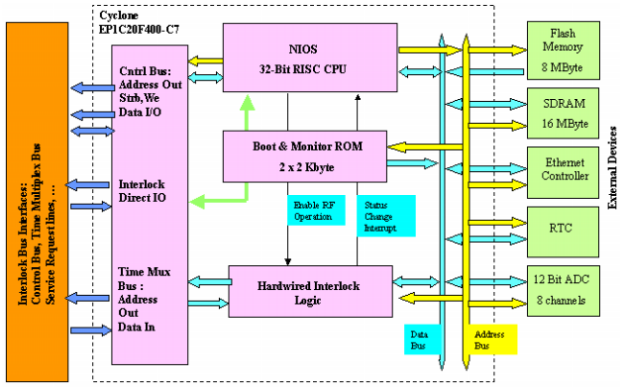

Figure 7: Interlock Controller Board Layout.

A TINE[5] server will run on the NIOS CPU and will provide the interface to DOOCS clients via Ethernet. The following is transmitted via the interface: status information, mask data, current values of analog input channels. Commands will also be available in the control system as properties, whose settings along with all other information will be made available in the DOOCS History Format.

The TINE kernel relies on BSD sockets and must somehow be interfaced to the ALTERA-FPGA plugs library. To this end, a BSD-style socket library, based on ALTERA's plugs-library, supporting UDP, TCP, and standard BSD-routines, was developed, allowing a seamless integration of the TINE kernel. This approach has decided advantages as many more NIOS-compatible ALTERA devices (irrespective of NIOS II) are supported and no additional license is needed for the upcoming NIOS II. Due to the small-footprint of the TINE NIOS kernel one can run a standard TINE FEC, as is used at the DESY accelerators, directly on an ALTERA device! Standard network protocols can be used and very compact FEC-designs are possible.

RESULTS

Several hardware components and the TINE NIOS kernel are available and tested. Parts of the design used in the actual interlock hardware at TTF2 show the stability and the reliability of the components. More IO-modules and the software for the interface to the control system are under construction. Options for the remote reconfiguration of the FPGA's are being investigated.

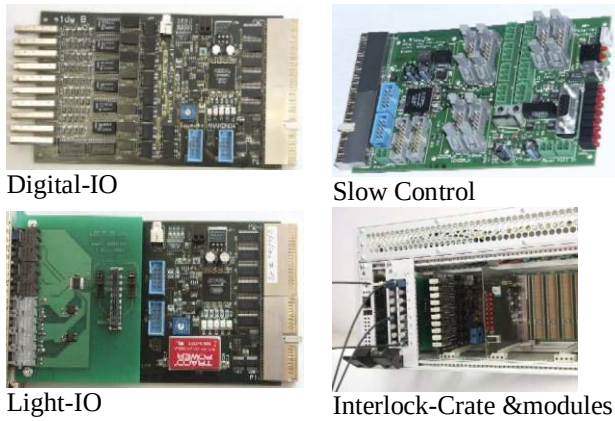

Figure 8: Hardware parts of interlock system.

CONCLUSION

A very compact, scalable interlock system for the XFEL-RF-stations has been designed and partly tested. It uses an ALTERA-FPGA running a 32-bit RISC NIOS CPU with a BSD-style socket library plus TINE kernel. The layout of the system is now almost completed. Prototypes with limited performance have been built and are in operation at the new RF stations of the DESY VUV-FEL (Tesla Test Facility). It is planned to install extended versions of these prototypes in the older VUV-FEL RF stations when the next generation of boards are available.

REFERENCES

[1] TESLA Technical Design Report, DESY TESLA-2001-011, 2001
[2] S. Choroba, The TESLA RF System, in High Energy and High Power RF, Proceedings of the 6th Workshop on High Energy Density and High Power RF, Berkeley Springs, West Virginia, 22-26 June 2003, AIP Conference Proceedings, Vol. 691, P. 1-14
[3] S. Choroba, T. Grevsmuehl, H. Leich, S. Simrock, "The TTF2 / XFEL Klystron Interlock: Requirements and Implementation" (Requirements_Draft.doc)
[4] H. Leich, Report at Spring Conference of the SEI, (SEI_290304.ppt)
[5] http://desyntwww.desy.de/tine

THE CEBAF RF SEPARATOR SYSTEM UPGRADE*

C. Hovater#, M. Augustine, A. Guerra, Rick Nelson, R. Terrel, and M. Wissmann,
Jefferson Lab, Newport News, VA, USA

Abstract

The CEBAF accelerator uses RF deflecting cavities operating at the third sub-harmonic (499 MHz) of the accelerating frequency (1497 MHz) to "kick" the electron beam to the experimental halls. The cavities operate in a TEM dipole mode incorporating mode enhancing rods to increase the cavity's transverse shunt impedance [1]. As the accelerators energy has increased from 4 GeV to 6 GeV the RF system, specifically the 1 kW solid-state amplifiers, have become problematic, operating in saturation because of the increased beam energy demands. Two years ago we began a study to look into replacement for the RF amplifiers and decided to use a commercial broadcast Inductive Output Tube (IOT) capable of 30 kW. The new RF system uses one IOT amplifier on multiple cavities as opposed to one amplifier per cavity as was originally used. In addition, the new RF system supports a proposed 12 GeV energy upgrade to CEBAF. We are currently halfway through the upgrade with three IOTs in operation and the remaining one nearly installed. This paper reports on the new RF system and the IOT performance.

INTRODUCTION

The CEBAF accelerator has been operating for 10 years steadily increasing the beam energy from 4 GeV up to 5.75 GeV. In that time the original RF amplifiers used to separate the electron beam have been pushed to their operational limit. This has resulted in increased system down time. Three years ago the RF group began an investigation to find a replacement power amplifier for the RF system. An additional requirement was to make the new amplifier compatible with the CEBAF energy upgrade. We settled on what is known as an Inductive Output Tube (IOT). The concept of the IOT was first proposed in the late 1930's – early 1940's but it was only in the last 20 years that they have become commercialized, primarily used in the broadcast industry [2, 3]. The system will ultimately incorporate four IOTs operating from a single high voltage power supply. The IOT and power supply is completely autonomous from the RF controls and self protected. The RF control system for the separator RF cavities has also changed. Where as before we had one cavity/amplifier, we now have multiple cavities/amplifier and control the field on the vector sum. To support this RF system we have incorporated inline high power coaxial phase shifters for system alignment. The existing LLRF controls have been modified to support these changes. Three of the IOTs are now operational and the system has been very reliable.

*This work was supported by DOE contract No. DE-AC05-84ER40150.
#hovater@jlab.org

RF SYSTEM

The CEBAF accelerator has the capability of extracting any one of the 5 passes and sending it to an experimental hall [4]. Each pass has a bank of RF separator cavities that can kick the beam out. The three highest energy passes all are powered by an individual IOT. While the IOT is capable of 30 kW we have limited them to 10 kW. The lowest energy passes (1 and 2) share an IOT in a slave configuration. Figure 1 shows the RF system for pass 5, the highest energy pass. A single IOT output is split 3 ways and then drives the three cavities. In two of the legs, electronically controlled high power coaxial phase shifters have been installed for phase adjustments. In addition, the RF cables from the splitter to the cavity coupler were meticulously measured and trimmed to within ~ two degrees of one another. In a similar fashion the cables for the cavities' transmitted powers have been measured and cut to a similar accuracy. Field control is maintained by summing the transmitted signals and controlling on the average. Cavity control is presently provided by the original analog CEBAF LLRF system, though this will change in the near future with the addition of a new digital controller [5].

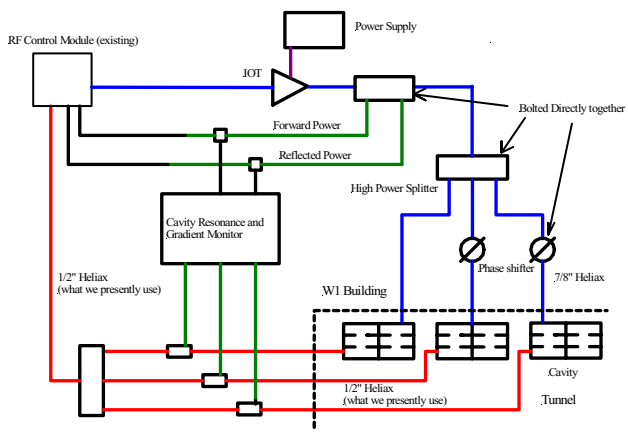

Figure 1: 5th Pass Separator RF System.

First and Second Pass

The first and second passes share a single IOT. Since required RF power goes as the square of the beam energy this can be implemented fairly easily. The energy essentially doubles between pass one and two thereby a 6 dB coupler is needed to divide the output of the IOT. For 6 Gev operations pass one needs approximately 400 watts so pass two would need 1600 watts. Figure 2 shows the First and second passes with one IOT. A coaxial jumper will allow one to choose to operate both passes or just one pass. The RF from the pass not in operation is then fed to

a high power load. A high power phase shifter is used in pass one to adjust the cavity for the proper kick. Pass two is globally adjusted with the RF control module.

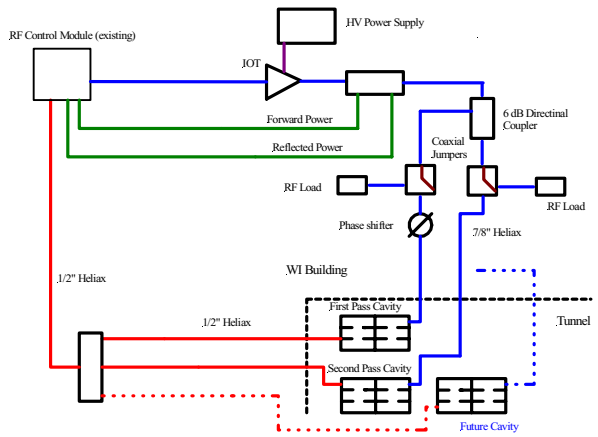

Figure 2: 1st and 2nd pass RF Separator System.

Inductive Output Tube

The inductive input output tube design has been around for many years; but only relatively recently has it been a suitable choice for the broadcast bands. Three reasons for this are its potential for high efficiency, linear operation, and ability to cover the full range of UHF TV broadcast frequencies. The frequency range for these IOTs is from 470 MHz to 860 MHz, with bandwidths of ~ 6 MHz. Output power typically is more than 30 kW. The only downside of IOTs is their relatively low gain, typically 22-23 dB.

After a competitive bid we purchased the Litton L4482**. Litton was purchased by Northrop Grumman, and later became part of L-3 Communications. We have tubes bearing all three names.** Table 1 shows the IOT specifications.

Table 1: IOT Specifications

Requirement	Value
Beam Voltage	21 kV
Beam Current	0.79 A
Quiescent Current	0.15 A
Collector Dissipation	6750 kW
Load VSWR	1.5:1 Max
Center Frequency	499 MHz
Output Power	10 kW
Bandwidth	5 MHz
Gain	23.5 dB
RF Efficiency	60.28%

Figure 3 shows the IOT assembly and trolley. It features a replaceable beam stick (tube) and is solenoid-focused (two coils). It has adjustable external cavities (single-tuned input dual-tuned output). The system requires both air (cavities) and water (body and collector) cooling. Like a klystron, the tube operates with a grounded collector, with cathode, filament, bias, and ion pump all at HV. Collector water fittings have been modified for our use. Each IOT has a corresponding floating deck unit (FDU) in the rack next to it which has the bias, filament, ion pump power supplies and instrumentation & control. System interlocks include cathode and body current, arc detectors and reflected power. There are no circulators in the system, so a reflected power interlock is set to trip at 500 watts. Due to the low gain the IOTs need a rather large driver amp that is capable of 50 watts to reach full output power. Figure 4 depicts the IOT/Trolley and rack containing the FDU and instrumentation.

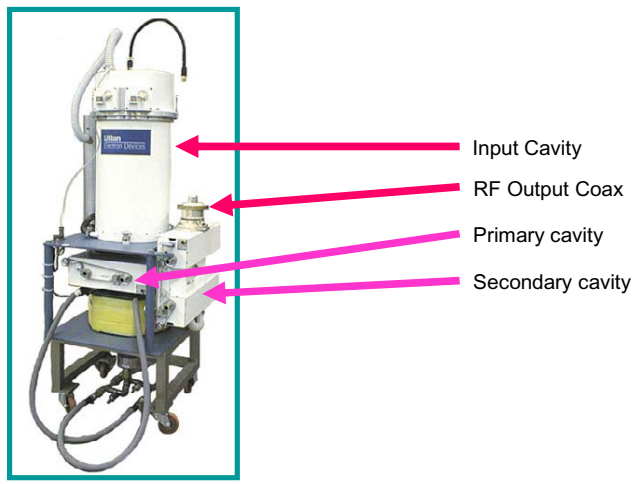

Figure 3: IOT Assembly and trolley.

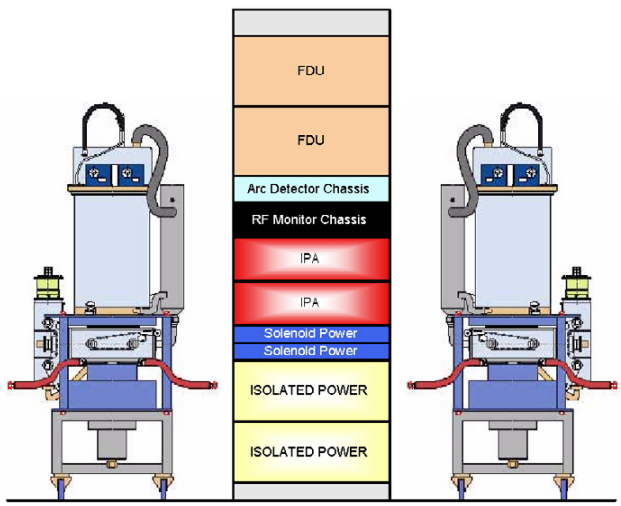

Figure 4: Shows a cartoon of the IOT and control racks.

IOT Controls

The power supply and the four IOTs are controlled using a commercial programmable logic controller (PLC, AutomationDirect 405 series). All of the digital, analog and system interlock inputs and outputs are monitored by the PLC. For the IOT controls each has an individual remote Terminator IO that floats on the high voltage deck of each IOT and is connected via fiber optic link to the main PLC. This controls the filament, bias and ion pump

parameters. In addition to the signals already mentioned above, each IOT is interlocked on water & air flow, ion pump current and cavity vacuum. A fast interlock chassis in the HV power supply monitors body and cathode current. The system is capable of both local and remote control. An Ethernet interface is used to talk directly to accelerator's EPICS control system.

Power Supply

The high voltage power supply is capable of driving four individual IOTs up to 21 kV at 4 A. The HV section is housed in a self-contained interlocked room (Figure 5). Features of the HV power supply include

- SCR front end
- Autotransformer
- 12 pulse step-up transformer
- rectifier, choke, capacitor
- Presently NOT regulated
- E2V thyratron crowbar
- LEM DC current transformers monitor cathode and body current
- Lockable HV cable disconnects for safe bypassing of unused IOTs

Figure 5: HV power supply.

Resonance Control System

The cavities are kept on resonance by a water temperature controlled resonance system. Figure 6 shows a block diagram of the water system. The resonance system uses a separate PLC (AutomationDirect 405 series). A PID algorithm inside the PLC regulates a 208 VAC, 3 kilowatt heater to maintain 120° F water at the heater's output. A mixing valve, which is controlled by a second PID loop in the PLC, then locally mixes the 120 F water with 95° F LCW (Low Conductivity Water) to maintain a constant water temperature exiting the cavity. Presently the system regulates about a fixed temperature. In the future it is intended to monitor the cavity reflected power and control the cavity frequency with the mixing valve. Similarly to the IOT/power supply PLC controls, the set points can be controlled locally by touch panel or remotely through EPICS.

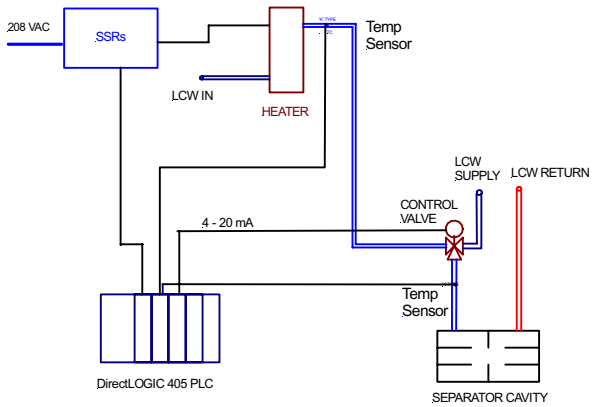

Figure 6: Cavity Resonance System.

SUMMARY

Three IOTs are presently operating on the higher energy passes. Two of them have been operating since October of 2003 and the third since April of this year. The last IOT (for pass 1 &2) is being installed. The resonance systems will be installed by the end of August 2004. The new systems have behaved flawlessly with little downtime. The only complaint so far has been too *much* kick -- a problem we are happy to fix after languishing with the old solid-state amplifiers.

REFERENCES

[1] C. Leemann and G. Yao, "A Highly Effective Deflecting Structure", 1990 LINAC conference proceedings, Albuquerque, New Mexico

[2] A.V. Haeff, "An UHV Power Amplifier of Novel Design", Electronics, February 1939, pp 30-32

[3] R. Heppinstall & G.T. Clayworth,"The inductive output tube, the latest generation of amplifier for digital television transmission", EEV Ltd, http://www.ebu.ch/trev_273-heppinstall.pdf

[4] C. Hovater et al, "The CEBAF RF Separator System", LINAC 1996 conference proceedings, Geneva, Switzerland

[5] C. Hovater , et. al , "A NEW RF SYSTEM FOR THE CEBAF NORMAL CONDUCTING CAVITIES", this conference

TUNING OF EXTERNAL Q AND PHASE FOR THE CAVITIES OF A SUPERCONDUCTING LINEAR ACCELERATOR

V.Katalev, S.Choroba, DESY, Germany

Abstract

The RF power required for a certain gradient of a superconducting cavity depends on the beam current and coupling between the cavity and waveguide. The coupling with the cavity may be changed by variation of Q_{ext}. Different devices can be used to adjust Q_{ext} or phase. In this paper three stub and E-H tuners are compared and their usability for the RF power distribution system for the superconducting accelerator of the European X-Ray Laser and the TESLA linear collider is considered. The tuners were analyzed by using the scattering matrix. Advantages and limitations of the devices are presented.

INTRODUCTION

The linear accelerators of the European XFEL and TESLA linear collider make use of the same type of superconducting cavities [1],[2]. The cavities are operated at a frequency of 1.3 GHz and an unloaded quality factor of Q_0>10^9.The accelerating gradient is 23.4 MV/m with a beam current of 9.5 mA for the TESLA linear colder and 22.9 MV/m with 5 mA of a beam current for the XFEL.

The power required by the cavity is 122 kW for the XFEL and 231 kW for TESLA with a pulse duration of 1.5 ms at a repetition rate of 10 Hz and 5 Hz respectively. To accelerate the beam with optimum consumption of RF power it is necessary to change the loaded quality factor of the cavity within several units of 10^6. With constant coupling between the cavity and the waveguide this can be achieved by changing the external losses namely by changing of Q_{ext}.

The cavities are connected to the RF power source, a klystron, by a waveguide distributing system with a circulator and a fixed dummy load in front of each cavity. In order to change the external losses of the cavity it is necessary to use an additional impedance transformer between the cavity and the circulator like a three stub tuner or an E-H tuner.

RF POWER FOR BEAM ACCELERATION

Let us consider the case of cavity operation at resonance and beam acceleration on-crest. It is possible to neglect power dissipation in the walls of the cavity in comparison with losses in the external load because Q_0>> Q_{ext}. The required RF power [3] for filling of the superconducting cavity with energy up to the required accelerating voltage V_{c0} is

$$P_{g0} = \frac{V_{c0}^2}{4\frac{R}{Q_0}Q_{ext}} \frac{1}{(1-e^{-\frac{t_{inj}}{\tau}})^2}$$

With R/Q_0 – normalized shunt impedance for a linac
τ = $Q_{ext}/\pi f$ time constant of the cavity
t_{inj} – time of beam injection

In order to accelerate the DC beam current I_b the RF power

$$P_{gb} = \frac{V_{c0}^2}{4\frac{R}{Q_0}Q_{ext}}\left(1+\frac{I_b\frac{R}{Q_0}Q_{ext}}{V_{c0}}\right)^2$$

for flattop operation is required. It is the well-known formula for the power of a generator connected to a cavity with heavy beam loading [4].

Fig. 1 shows the RF power for the XFEL and TESLA cavity P_g as a function of the external quality factor Q_{ext}. The minimum RF power for cavity filling or for beam acceleration has a minimum for different conditions. For cavity filling the condition is

$$\frac{t_{inj}\pi f}{Q_{ext}^0} = 1.256,$$

whereas for beam accelerating it is

$$Q_{ext}^b = \frac{V_{c0}}{I_b\frac{R}{Q_0}}$$

Typically Qext is chosen between these two minima.

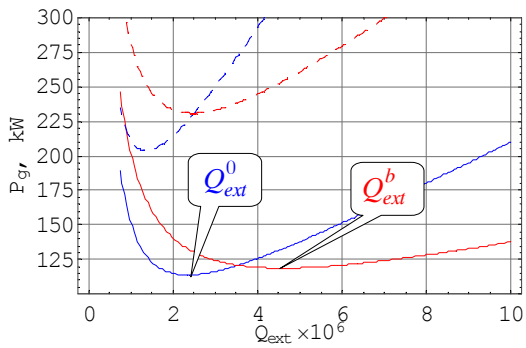

Figure 1: Cavity forward power P_{g0} (blue) and P_{gb} (red) for a XFEL cavity with gradient E=22.9 MV/m, I_b=5 mA and t_{inj}=720 μs. TESLA cavity – E=23.4 MV/m, I_b=9.5 mA t_{inj}=420 μs (dashed).

The conditions of minimum RF power for cavity filling and beam acceleration are fulfilled with $Q_{ext}^0 = 2.36\times10^6$ and $Q_{ext}^b = 4.59\times10^6$ in the XFEL case and with $Q_{ext}^0 = 1.36\times10^6$ and $Q_{ext}^b = 2.47\times10^6$ in the TESLA case, respectively. For the case of operation at a reduced cavity gradient one has to reduce the external quality factor in order to operate at minimum of RF power consumption . In the other case of a reduced beam current one might consider increasing Q_{ext} to meet the minimum condition for Q_{ext}^b. But one has to observe that by increasing Q_{ext} the RF power for cavity filling would increase dramatically (see Fig. 1). Therefore the recommended Q_{ext} value are in the range from 2.3 up to

4.6×10^6 for the XFEL and from 1.3 up to 2.5×10^6 for TESLA.

PHASE VARIATION

The phase difference caused by the accuracy of assembling the waveguide distributing system is smaller ±20°. The maximum phase shift due to thermal expansion of the waveguides is about 12°. Therefore a tuner should have the capability to adjust the phase within a range of about ±40°.

EQUIVALENT CIRQUIT

The superconducting cavity is connected to the RF power waveguide distributing system through a circulator with matched dummy load [1]. A tuner described by a scattering matrix [S] is inserted between the cavity and the circulator. The port 1 of the tuner is connected to a cavity coupler through a waveguide without losses with impedance Z_0 and fixed length l (see Fig. 2). The port 2 of the tuner is connected to the matched load Z_0 of the circulator.

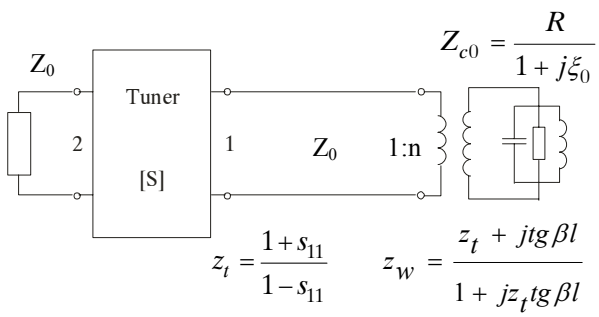

Figure 2: The equivalent circuit of a superconducting cavity with impedance Z_{c0} connected to a RF power waveguide distributing system through circulator and tuner.

A normalized tuner impedance z_t is transformed into z_w by the waveguide. This impedance is transformed by the power coupler to a cavity gap of $z_w Z_0 n^2$ in parallel to the cavity impedance. Having in mind $Q_0 >> Q_{ext}$ we get a normalized cavity impedance of

$$z_c \simeq \frac{z_w \frac{R}{Q_0} Q_{ext0}}{1 + j\xi z_w}$$

With Q_{ext0} – external quality factor without tuner
ξ – detuning of the cavity equal to $2Q_{ext0}\,\Delta f/f_0$

By changing elements of the tuner scattering matrix we can tune both the external quality factor of the cavity and the phase of the forward power. In order to phase the cavity it is necessary to fix s_{11} and vary s_{21}. For changing external losses it is necessary to keep the phase of s_{21} constant and vary the absolute value of s_{11}. The phase of s_{11} has to be fixed, otherwise the cavity resonance frequency will be changed.

THREE STUB TUNER

Three stub tuner for TESLA are made of a straight waveguide with three movable posts located 80 mm from each other. The diameter of a post is 33 mm and the maximal depth of penetration is 42 mm. The relation between the penetration depth h of the post and his normalized impedance x is determined experimentally and given by $h = 29.253 \times x^{-0.5153}$. This means that the minimum impedance of a stub can not be less than 0.5 for the maximum penetration depth of 42 mm.

By knowing the impedance of the posts and distances between them it is possible to find a scattering matrix of the three stub tuner. Calculation of the scattering matrix was carried out by Mathematica 5.0 [5]. The resulting scattering matrix has a lengthy expression. To simplify the analysis of the matrix expression the distance between the posts has been taken equal to a quarter of wave length 80.66 mm. The simplified scattering matrix is shown on fig.3.

To understand the three stub tuner when it operates as a pure phaseshifter let us assume a special case: s_{11}=0. From this condition and $x_3 = x_1$ we can get $x_2 = x_1^2/(1+2x_1)$ and correspondingly calculate the next element of the matrix $s_{21} = (-j + x_1)/(j + x_1)$. By changing the penetration depth of posts in a proper way it is possible to vary the phase by ±50° without any reflection from the tuner.

When the tuner works like an impedance transformer the phase of s_{21} must be constant. This means, that

$$x_1 = \frac{-1 + x_2 x_3 - x_3 tg\varphi_{21}}{-x_2 - x_3 + tg\varphi_{21}(1 - 2x_2 x_3)}$$

In order to keep the resonance frequency of the superconducting cavity constant the imaginary part of z_w has to be equal to 0 and therefore the following condition

$$\begin{bmatrix} \frac{j(-1 + x_1(-j + x_2 - x_3) + (j + x_2)x_3)}{j(-1 + (j + x_2)x_3) + x_1(-1 + jx_3 + x_2(j + 2x_3))} & \frac{2x_1 x_2 x_3}{j(-1 + (j + x_2)x_3) + x_1(-1 + jx_3 + x_2(j + 2x_3))} \\ \frac{2x_1 x_2 x_3}{j(-1 + (j + x_2)x_3) + x_1(-1 + jx_3 + x_2(j + 2x_3))} & \frac{j(-1 + x_1(-j + x_2 - x_3) + (j + x_2)x_3)}{j(-1 + (j + x_2)x_3) + x_1(-1 + jx_3 + x_2(j + 2x_3))} \end{bmatrix}$$

Figure 3: Scattering matrix of three stub tuner for quarter wave length between the posts and post impedances x_i.

should be satisfied

$$x_2 = 1/x_3 - ctg\varphi_{21}$$

From these two limitations and keeping in mind the minimum impedance of the stub of 0.5 we get the possible range of the external quality factor depending on the phase of the forward power without changing of cavity frequency (see fig.4).

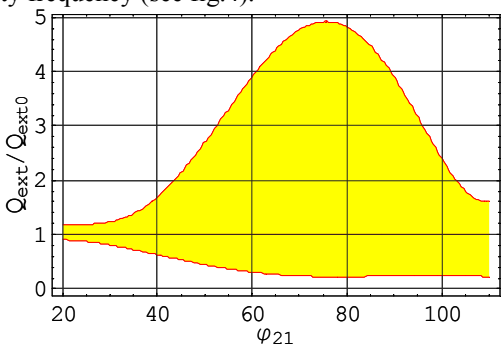

Figure 4: External quality factor Q_{ext} range relative to factor Q_{ext0} depending on phase shifts φ_{21} of forward power (yellow area).

E-H TUNER

This type of a tuner is proposed for the waveguide system for the 8 GeV Fermilab linac [6] and is considered in [7]. An E-H tuner consists of a matched magic tee and two sliding short circuits. Taking the ideal scattering matrix of the tee junction and assuming full reflection by sliding short circuits it is straight forward to get the elements of the E-H tuner scattering matrix

$$s_{11} = \frac{1}{2}\left(e^{-j\frac{4\pi l_1}{\Lambda}} + e^{-j\frac{4\pi l_2}{\Lambda}}\right)$$

$$s_{21} = \frac{1}{2}\left(e^{-j\frac{4\pi l_1}{\Lambda}} - e^{-j\frac{4\pi l_2}{\Lambda}}\right)$$

With l_1, l_2 – position of the short circuit ,

Λ – wave length in the waveguide

If l_1 and l_2 are changed in the same way in one direction the amplitudes of s_{11} and s_{21} are constant but their phases are varied. The E-H tuner works like a phaseshifter. In the other case, when l_1 and l_2 are changed in the same way in opposite directions the E-H tuner is an impedance transformer. This means that the amplitudes of s_{11} and s_{21} are varied and phases do not change.

To avoid a cavity resonance frequency change the condition $Im(z_w)=0$ must be fulfilled. It is straight forward to get the relation for the waveguide length l and the short circuit positions

$$l = \frac{1}{2}(l_1 + l_2) + n\frac{\Lambda}{2}$$

This requirement cannot be met easily if there is no additional phaseshifter between cavity and tuner. Therefore the cavity frequency will change during the adjustment of phase or external quality factor by the E-H tuner.

This dependence is shown in fig.5 for the special case when $l = n\frac{\Lambda}{2}$. This can only be avoided if either an additional phaseshifter is installed between the cavity and tuner or a frequency cavity tuner [8] is used in addition.

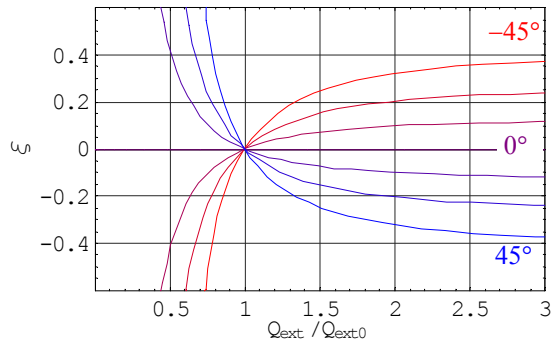

Figure 5: Detuning of cavity $\xi = 2Q_{ext0}\,\Delta f/f_0$ due to variation of Q_{ext} by an E-H tuner for different phase shifts φ_{21} of forward power.

It is also possible to use the usual quadrature coupler instead of the magic tee junction. In this case the tuner has higher power capability and has also more compact dimensions.

SUMMARY

Besides the restrictions mentioned above the power capabilities of the devices must be considered.

The measured power breakdown for three stub tuner is about 400 kW for full reflection. The power capability of E-H tuner is more than 1 MW

Three stub tuner or E-H tuner have enough dynamic range for Q_{ext} and phase settings and have acceptable power capability. Therefore they can be used for the power distributing system for the XFEL and the TESLA linac.

REFERENCES

[1] TESLA Technical Design Report, DESY TESLA-2001-011, 2001

[2] R.Brinkmann, "Accelerator Layout and Parameters", ESFRI XFEL Workshop 30./31.10.2003

[3] V.Katalev, S.Choroba, "RF power distributing waveguide systems for TESLA", RuPAC 2002

[4] F.Pedersen, "A novel RF cavity tuning feedback scheme for heavy beam loading", IEEE Trans. Nucl. Sci., NS-32, 2138

[5] Wolfram Research, Mathematica 5.0

[6] 8 GeV Injector Linac Design Study, TM-2169 Part II, FNAL, http://www-bd.fnal.gov/pdriver

[7] B.Bogdanovich,M.Ebert et., "Design of an E-H Tuner and Adjustable Directional Coupler for High-Power Waveguide Systems" EPAC 2002, Paris, France.

[8] L.Lilje, S.Simrock, D.Kostin, "Characteristics of a Fast Piezo-Tuning Mechanism for Superconducting Cavity", EPAC 2002, Paris, France

RF REFERENCE DISTRIBUTION SYSTEM FOR THE J-PARC LINAC

T. Kobayashi†, E. Chishiro, JAERI, Tokai, Naka, Ibaraki, Japan
S. Anami, S. Yamaguchi, S. Michizono, KEK, Tsukuba, Ibaraki, Japan

Abstract

The J-PARC (Japan Proton Accelerator Research Complex) linac, which is 300 m long, consists of a 324-MHz accelerating section of the upstream part and a 972-MHz section of the downstream part. In the klystron gallery, a total of about 60 RF source control stations will drive the klystrons and solid-state amplifiers.

The error of the accelerating field must be within ±1° in phase and ±1% in amplitude. Thus, high phase stability is required as an RF reference for all of the low-level RF control systems and the beam-monitor systems. The RF reference (12 MHz) is distributed to all stations optically. Low-jitter E/O and O/E with temperature stabilizers were developed. The reference is optically amplified, divided into 17 transfer lines, and delivered through PSOF (phase-stabilized optical fiber), the temperature of which is stabilized by cooling water. Each of the transmitted signals is divided more into 4 signals by an optical coupler.

Our objective concerning the phase stability of the reference aims at less than ±0.3° at a frequency of 972 MHz.

INTRODUCTION

J-PARC accelerators [1] are now under construction at the JAERI Tokai site. The linac of the J-PARC, which is about 300 m long, provides 181-MeV (400-MeV in the future) proton beam to the 3-GeV, 1-MW rapid-cycling synchrotron (RCS). For this linac, the RF source will power 20 accelerating cavity modules (an RFQ, 3 DTLs and 16 SDTL modules) operated at a frequency of 324 MHz, and 21 ACS cavities operated at a frequency of 972 MHz (Refer Fig. 1). Furthermore, solid-state amplifiers will drive the buncher, chopper and debuncher cavities. In addition to the RF systems, the beam-monitor systems, the magnet power supply, and so on, are installed in the klystron gallery. Totally, 60 arrays of 12 EIA-standard 19-inch racks will be installed as the control stations for these systems over the whole area of the klystron gallery. An RF reference signal must be distributed to all of these control stations.

Because the momentum spread (Δp/p) of the RCS injection beam is required to be within 0.1%, the RF sources must maintain the correct accelerating field within an amplitude error of ±1% and a phase error of ±1°. Therefore, the RF reference signal should be more highly stable. Our objective for the RF reference aims at within ±0.3° at a 972-MHz frequency for phase stability.

On account of pulse operation of 500-μs beam duration and 50-Hz repetition, the timing control signals must be distributed in analogy with the RF reference.

This paper presents the final design of the RF reference distribution system in detail, including the timing reference distribution.

RF REFERENCE DISTRIBUTION LINE

A block diagram of the RF reference distribution system is shown in Fig. 1. The 12-MHz RF reference is distributed to about 60 low-level RF (LLRF) control systems of klystron and solid-state amplifier stations (RFQ,

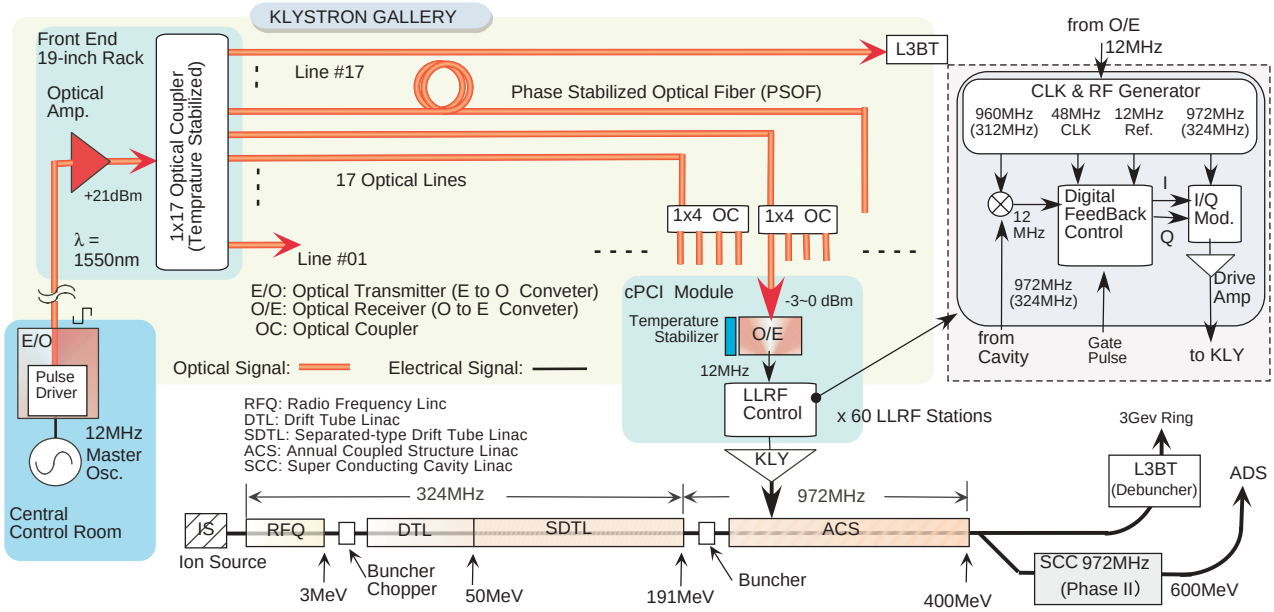

Figure 1: Block diagram of the RF reference distribution system.

†tetsuya.kobayashi@j-parc.jp

buncher, chopper, DTL, STDL, ACS and debuncher) through optical links. As shown in the figure, the electrical RF reference signal (12 MHz) generated by a master oscillator at the central control room is optically transferred to the linac klystron gallery. It is then directly amplified and divided into 17 optical transfer lines by an optical star coupler at the front end of the gallery. In order to apply an optical amplifier, a wavelength of 1.55-μm wavelength has been chosen for the optical source. One of the 17 transfer lines provides an RF reference for each of 4 klystron stations; thus, the transmitted optical signal is divided into 4 by an optical coupler. Each of them is received by an O/E and converted to an electrical signal at each station.

An accelerating RF of 324 MHz or 972 MHz is generated by a VCXO with PLL synchronizing with the distributed 12-MHz reference at each local station. Although the fast-change (over 1 kHz) phase jitter is suppressed by the VCXO-PLL, stabilizing temperature drifts of the reference becomes very important.

To stabilize the amplitude and phase of the field in the accelerating cavity, a digital feedback and feed-forward technique is used in the LLRF control system [2]. This system controls the I/Q components of the RF signal, as shown in Fig. 1. Feedback and feed-forward control is performed by a combination of FPGAs (field programmable gate array) for the fast and simple processing and DSPs (digital signal processor) for slow and complicate processing. At the present stage, a compact PCI (cPCI) bus module and a Windows OS system is used as an integrated development environment in order to make it easy for us to develop the software of FPGAs, DSPs and a CPU host.

OPTICAL CABLES

The phase stability directly depends on the characteristics of the optical components. For the optical transfer line, phase-stabilized optical fiber (PSOF) is adopted. In the 300-m signal transfer, the dispersion and power loss in PSOF are negligible when using of a Distributed Feed Back (DFB) laser diode for the E/O. The thermal coefficient of the PSOF is generally less than 1 ppm/°C, while that of normal fiber is greater than 6 ppm/°C. In order to reduce the thermal coefficient, single-mode silica fiber is coated with a liquid-crystal polymer, the thermal-expansion coefficient of which is negative [3]. However, these days, only Furukawa Electric Ind. Ltd Japan manufactures the PSOF.

The room temperature in the gallery will be controlled at 27±2 °C during operation. From our measurement result, the thermal coefficient of Furukawa's PSOF is 0.4 ppm/°C (0.2°/300m/°C for 972-MHz frequency) at a temperature range from 25 °C to 30 °C [4]. This characteristic does not satisfy the required stability. In order to keep the phase change due to the optical cable within ±0.1°, the temperature change of the PSOF should be controlled to be ±0.5 °C by a cooling water system, the temperature stability of which is ±0.1 °C. As shown in Fig. 2, optical cables and cooling water pipe will be installed in an insulated duct. The duct will be set in a cable trench under the floor. Also 1x4 optical couplers will be put in the insulated duct in consideration of the measured result of its temperature characteristic for phase stability [5].

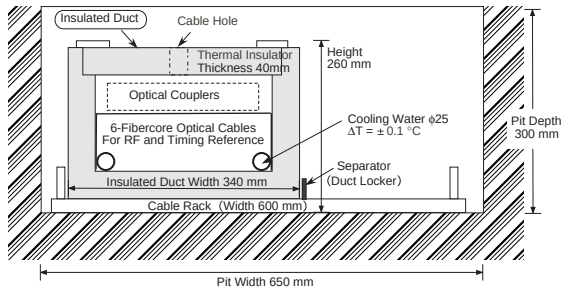

Figure 2: Cross section of the insulated duct set in the under-floor cable trench.

OPTICAL TRANSMITTER/RECEIVER

For improvements in the stability, new O/E and E/O were developed for this system. They were manufactured by Graviton Co., Ltd. Japan [6]. The O/E, which has a temperature stabilizer with a peltier device, is compact and is mounted on a cPCI board (RF & CLK generator), as shown in Fig. 3. The photo detector is pigtail type in order to finally make fusion splices for fiber connections through all optical paths in order to prevent phase instability due to connector vibration.

The E/O and O/E, the transmission bandwidths of which are wide (0.1 MHz ~ 2 GHz), have a pulse driver (limiting amp.). This makes a 12-MHz clock signal shorter rise time pulse than 200 ps to reduce the transfer jitter. Figure 4 shows the measurement result of the transfer jitter of the optical link including the optical amplifier using a Tektronix TDS8000B. It can be said that the jitter is less than 1 ps (rms), which is the design value.

The measured temperature dependence of the phase change in the E/O and O/E is shown in Fig. 5. The thermal coefficients of the E/O and O/E are 0.17 and 0.02°/°C, respectively, for a frequency of 972 MHz. The phase change due to the O/E can be lower than 0.1° for a gallery temperature change of ±2 °C. On the other hand, the E/O, which is the only one in this system, should be operated in a thermal chamber in order to keep the phase change within ±0.1°.

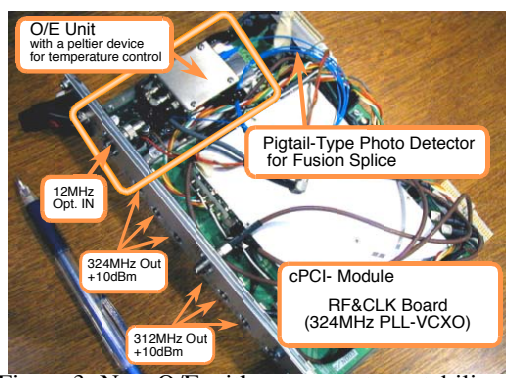

Figure 3: New O/E with a temperature stabilizer.

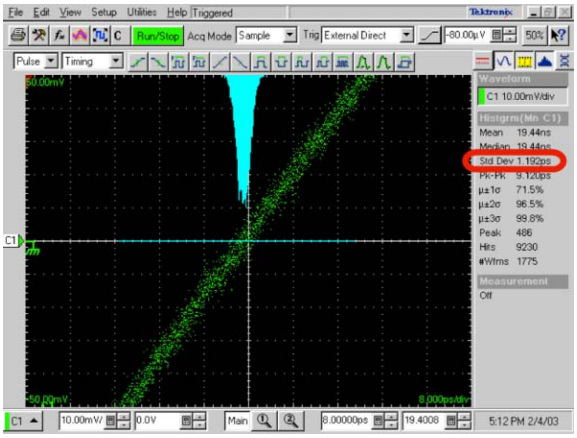

Figure 4: E/O-O/E transfer jitter measured by using a TDS8000B. Because the jitter of the measurement system is about 0.8 ps, the net jitter is Sqrt(1.2^2-0.8^2) = 0.9 ps.

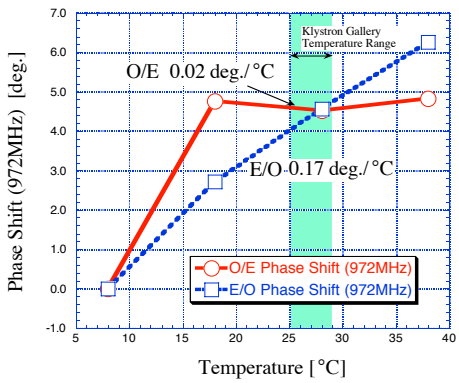

Figure 5: Temperature characteristics of the new E/O and O/E.

TIMING REFERENCE DISTURIBUTION

For 50-Hz pulse operation, a timing reference (trigger) signal is required for all control systems. The J-PARC accelerator timing system uses the following 3 signals to control the trigger timing: (1) a 50-Hz trigger clock, (2) a 12-MHz clock (master clock to count trigger delay), and (3) a control code (16-bit serial, called "Type") [7]. A set of these 3 signals is called the timing reference in this paper.

The method of distributing the timing reference in the linac follows that of the RF reference distribution as shown in Fig. 6. However, source signals are electrically divided into 17+3 signals, and will be distributed to not only the 19-inch rack control stations in the klystron gallery, but also the linac control, the ion source power supply and the DTL Q-magnet power supply rooms. A 3-channel optical transceiver and a fanout module, which can transfer the 3 signals all together, have been developed for the J-PARC timing system [7]. Normal single-mode optical cables are used for the timing reference distribution, because high phase stability is not required. However, 17 optical transfer cables are installed in the insulated duct used for the PSOF's. Then, as shown in Fig. 7, the reference signals will be provided to each control station from the optical transfer line.

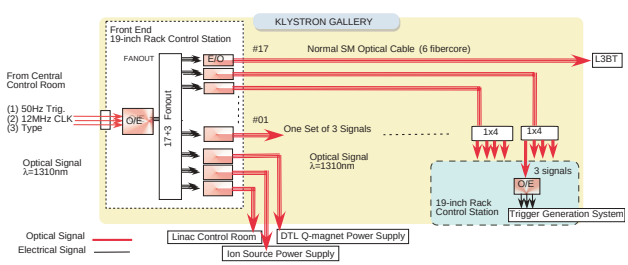

Figure 6: Layout of the timing reference signal distribution system.

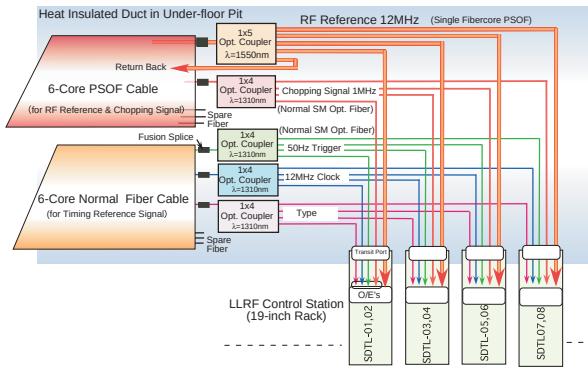

Figure 7: Providing RF and timing reference to each control station.

SUMMARY

The final design of the RF reference distribution system for the J-PARC linac is shown. The reference (12 MHz) is optically amplified and distributed to all control stations. Optical transfer cables will be installed in the insulated duct with cooling water pipes, the temperature stability of which will be ±0.1°C. A compact new O/E with a temperature stabilizer was developed. A jitter of less than 1 ps (rms) will be achieved in the optical transfer.

The timing reference (a set of the 3 timing control signals) for the whole linac will be distributed in a way similar to the RF reference distribution.

REFERENCES

[1] URL: http://www.j-parc.jp/
[2] S. Michizono, et al., "Digital Feedback System for J-PARC Linac RF Source", in this conference, 2004.
[3] T. Kakuta, S.Tanaka, "LPC coated optical fiber with zero thermal coefficient of transmission delay time", Proc. of International Wire & Cable Symp., pp. 234-240, 1987.
[4] T. Kobayashi, et al., "RF Reference Distribution System for the 400-MeV Proton Linac of the KEK/JAERI Joint Project", Proc. of the LINAC2002, MO463, 2002.
[5] T. Kobayashi, et al., "RF Reference Distribution System for J-PARC", Proc. of the Linear Accelerator Meeting in Japan, pp. 366-368, 2003
[6] URL: http://www.graviton.co.jp/
[7] F. Tamura, et al., "J-PARC Timing System", Proc. of ICALEPCS 2003, 2003

QUASI-OPTICAL COMPONENTS FOR FUTURE LINEAR COLLIDERS

S. Kuzikov, G. G. Denisov, M.Yu. Smelyov, Institute of Applied Physics, Russian Academy of Sciences, Nizhniy Novgorod, Russia
J.L. Hirshfield, Omega-P, Inc., New Haven, Connecticut, USA

Abstract

This paper presents a concept of the quasi-optical RF system for future Ka-band electron-positron linear collider. According to this concept a quasi-optical Delay Line Distribution System (DLDS) is considered. The DLDS is based on oversized waveguides. In such waveguides the so-called image multiplication phenomena are used for power launching, extracting, combining, and splitting of waves. Recent low power tests of mode launchers and other DLDS components are discussed.

INTRODUCTION

The DLDS concept is considered as one of prospect solutions for feeding of high-gradient accelerators at 11.424 GHz [1-2]. According to the projected schemes the DLDS is based on relatively oversized delay lines operated with one or several modes and mode launchers completely or partially constructed on the base of single-mode waveguides. Scaling of the mentioned projects to Ka-band seems to be not acceptable because of higher Ohmic attenuation as well as bigger RF power density, which causes a threat of breakdown. More natural way is to use pure quasi-optical solutions in the design of each DLDS component.

MODE LAUNCHERS

A key component of any DLDS project is a mode launcher, which allows feeding consequently different acceleration sections by means of proper setting the phases of RF pulses from different amplifiers. In the scheme, shown in Fig. 1, the mode launcher has four input channels and the same number of output channels providing four times power gaining. The delay lines behind the mode launcher are assumed to be oversized circular cross-section waveguides operated with axis-symmetrical TE_{01} mode.

We considered two possible versions of the mode launcher both based on image multiplication phenomena in an oversized waveguide [3-6].

Mode Launcher Based on Rectangular Cross-Section Waveguide

In this version (Fig. 2) the mode launcher is shaped of a smooth oversized (waveguide size is a) rectangular waveguide, where image multiplication occurs at one coordinate only. Four TE_{01} modes at the input of rectangular waveguide are combined into one of four output channels. The position of the resulted channel depends on the mutual phases at the input. The required length of the waveguide equals to a^2/λ.

The mode launcher was calculated using Kirhgof's approach, and results were published in paper [3]. According to these results the wider waveguide the higher efficiency of the launcher. For example, at 34 GHz, width a=120 mm, and length L=1600 mm provide 99% efficiency of the power summarizing.

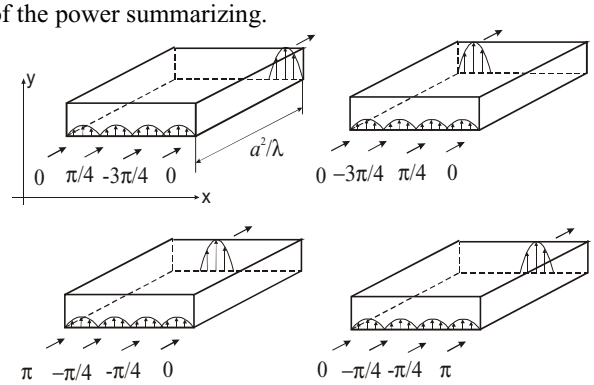

Figure 1: Mode launcher based on rectangular cross-section waveguide (principal scheme).

Figure 2: Mode launcher based on rectangular cross-section waveguide (photograph of the prototype).

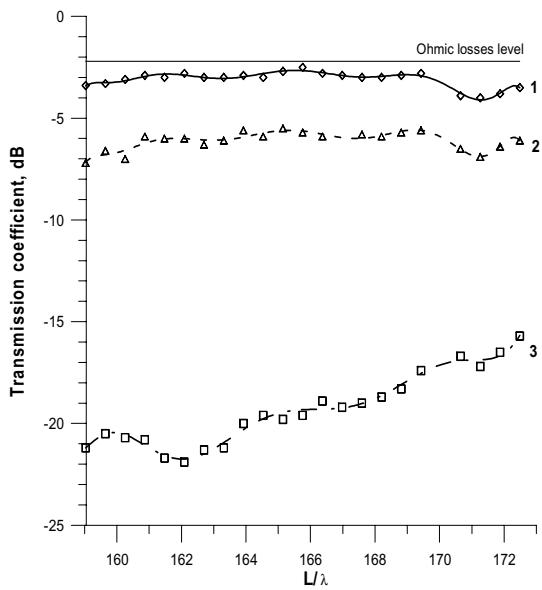

Figure 3: Measurements of mode launcher efficienc when incident wave is launched into a channel near the wall.

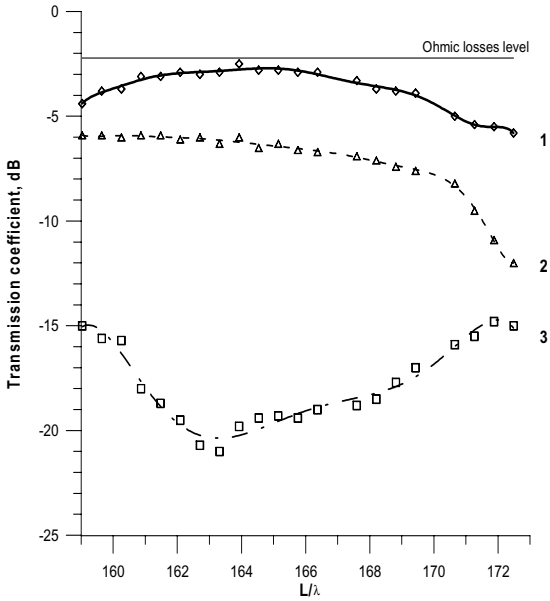

Figure 4: Measurements of mode launcher efficiency when incident wave is launched into a channel near the center of waveguide.

Preliminary tests were performed with the launcher prototype (Fig. 2) scaled to 4-times higher frequency in order to minimize launcher sizes and simplify its fabrication. This resulted in higher Ohmic losses (about two times) and more critical alignment of parts. The launcher was fed by one wave and the output field structure and reflection coefficient from specially shaped mirrors at the launcher output were measured.

The results of the measurements, carried out for two regimes, are shown in Figs. 3-4, where reflection is plotted as a function of launcher length normalized on a wavelength. The first used mirror provided phases of four reflected waves at the output end so, that the reflected waves were combined again in the input waveguide where the initial wave was radiated. The curves marked by *1* in both Fig 3 and Fig. 4 show the reflection in this case. This reflection was actually the squared efficiency of the launcher, because all other channels were opened and the scattered radiation was free to go away. The measured difference between the reflection and Ohmic losses level is rather small: 0.5 dB.

The curves marked by *2* correspond just to the flat mirror reflectors. In such a case according to image multiplication effect the reflected waves formed two identical waves at input cross-section. One of them came back into the feeding channel, but the second wave was radiated away. So, -3 dB extra losses, measured in this scheme, are agreed well with a theory.

The curves marked with *3* correspond to the case when reflected radiation was combined all power in another channel (not in the feeding channel). In this case we could measure the scattered radiation only. Its level appeared about –15-20 dB.

Mode Launcher Based on Square Cross-Section Waveguide

The second version of a mode launcher is based on image multiplication in square cross-section waveguide with the impedance corrugation of walls (Fig. 5). The infinite impedance allows combining TE_{01} modes of a circular waveguide, and thus, any mode converters, in order to match such mode launcher with TE_{01} delay lines, are not needed. The length of the launcher equals $2a^2/\lambda$.

For tests we used four-times higher frequency and selected sizes of mode launcher (Fig. 6), which provided 93% efficiency.

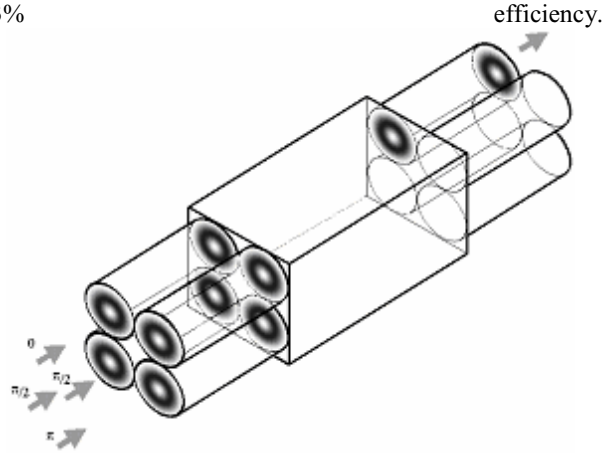

Figure 5: Mode launcher based on square cross-section waveguide (principal scheme).

The scheme of efficiency measurements coincides with the scheme chosen for the rectangular mode launcher described above. with mode purity at operating frequency estimated as 96-97%. In our tests we found out that the efficiency of such a mode launcher is very sensible to the accuracy of manufacturing. In particular, difference in sizes of the walls results in an essential drop of the efficiency in comparison with the ideal case. That was the main reason, why we measured rather high power losses (Fig. 7). Nevertheless, taking into account the actual accuracy of fabrication and purity of the incident TE_{01} mode, one concludes that the efficiency of such a component at 34 GHz is able to be high enough.

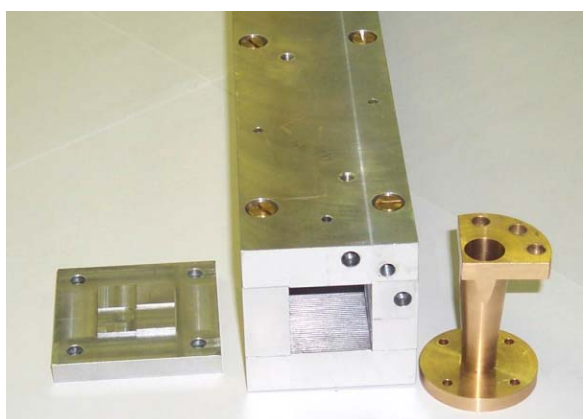

Figure 6: Mode launcher based on square cross-section waveguide (photograph of the tested prototype).

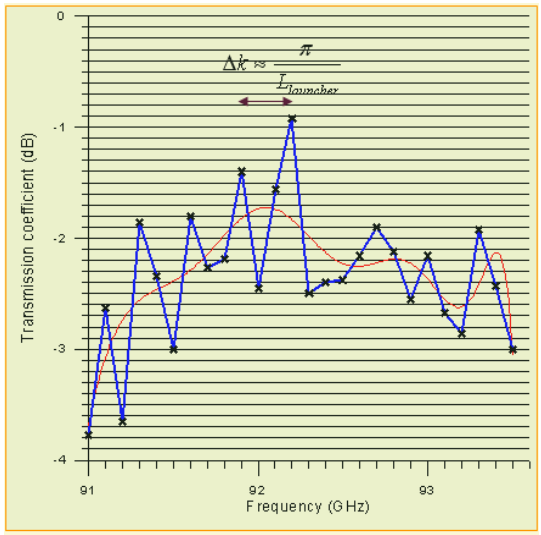

Figure 7: Measurement of efficiency of the TE_{01} mode launcher based on square cross-section waveguide.

CONCLUSION

The main components of Ka-band transmission line for future accelerator system were designed, fabricated and tested at low power experiments. The test results agree well with the design parameters. Therefore, the Ka-band DLDS seems to be feasible.

REFERENCES

[1] H. Mizuno et al. A new RF power distribution system for X band linac equivalent to an RF pulse compression scheme of factor 2^N, presented at the 17th International Linac Conference (Linac94), Tsukuba Japan, 1994.

[2] S. Tantawi. Active and Passive Multimoded Components for High Power RF Systems. 9th International Workshop on linear colliders LC2002, California, SLAC, February 4-8, 2002.

[3] S.V.Kuzikov. Wavebeam Multiplication Phenomena to RF Power Distribution Systems of High-Energy Linear Accelerators. International Journal of Infrared and Millimeter Waves, Vol. 19, No.11, 1998. pp.1523-1539.

[4] G.G.Denisov, S.V.Kuzikov. Microwave systems based on controllable interference of paraxial wavebeams in oversized waveguides, Proceedings of the Int. Workshop Strong Microwaves in Plasmas, Nizhny Novgorod, August 2-9, 1999, Vol. 2, pp. 955-960, 2000.

[5] G.G.Denisov et al. New Components for TE01 Transmission Lines, Proceedings of the Int. Workshop Strong Microwaves in Plasmas, Nizhny Novgorod, August 2-9, 1999, Vol. 2, pp. 943-948, 2000.

[6] S.V.Kuzikov et al., Proc. of the Strong Microwaves in Plasmas Conf., Vol. 1, 2003, pp. 220-226.

MOSCOW MESON FACTORY DTL RF SYSTEM UPGRADE

A.I.Kvasha•, Institute for nuclear research RAS, Moscow

Abstract

The last paper, devoted to description of the first part (DTL) RF system of Moscow Meson Factory upgrade, was published in Proceedings of PAC95 Conference in Dallas [1]. Since then some new works, directed at improvement of reliability and efficiency of the RF system, were carried out. Among them there are a new powerful pulse triode "Katran" installed in the output RF power amplifiers (PA) of three channels, modifications of the anode modulator control circuit and crow-bar system, new additional RF channel for RF supply of RFQ and some alterations in placing of the anode modulator equipment, decreasing a level of interference's at crow-bar circuits. Some new, checked at MMF RF channels, ideas concerning of PA tuning are of interest for people working in this sphere of activity.

INTRODUCTION

Developed more than 30 years ago the DTL RF system equipment of the MMF (frequency 198,2 МГц, RF pulse length - 400 μs, repetition rate - 50 Гц, pulse RF power - up to 2,5 MW, amount of RF channels - 6, including RFQ), has successfully operated for 16 years. Since the last information [1] the RF system has been in operation about 18 thousand hours. During all this time the continuous work, directed at increasing of reliability and efficiency of the RF system has been fulfilled. Some results of this activity have found the reflection in papers [2,3]. Moreover, due to improvement of the water quality in the powerful vacuum tubes cooling system, realization of preventive works and more strict maintenance of the exploitation conditions it got possible to appreciably increase powerful vacuum tubes service life. So at service life of 1000 hours, guaranteed by the manufacturer of powerful modulator (GMI-44A) and RF amplifiers (GI-51A and GI-54A) vacuum tubes, it achieves now about 5000 hours for triode GI-54A, installed in the RF output power amplifier (PA), about 6000 for tetrode GI-51A, installed in the PA driver, and about 7000 for modulator tube GMI-44A. A few vacuum tubes were in operation more than 16 thousand hours. It is necessary to have in view, that these data concern to the vacuum tubes that were manufactured 20-25 years ago.

Each RF channel consists of two main parts - the four-stage RF amplifier and two pulse modulators.

PULSE MODULATORS

There are two pulse modulators in each RF channel. The first modulator provides anode supply for the first two RF amplifiers vacuum tubes; the second one provides anode supply of the last two powerful RF amplifier vacuum tubes GI-51A and GI-54A. The first modulator also serves as a driver for the more powerful second modulator. In both anode modulators were recently used a few vacuum tubes for driving and control of output pulse voltage, because stabilization of RF amplitude voltage in the DTL tank is realized by means of the modulator pulse amplitude control (see fig.1).

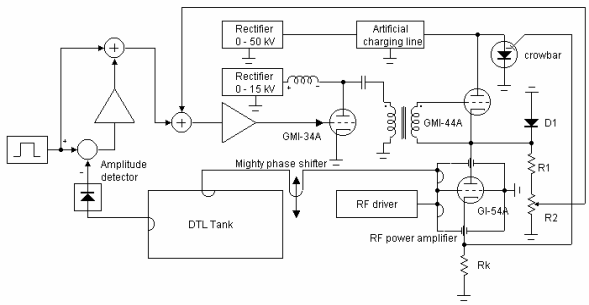

Figure 1: Common view of the DTL RF channel

During the last modernization of the pulse power supply systems were developed and established transistor pulse drivers (TPD) in all modulators. Inputting of TPD has allowed removing six vacuum tubes in each RF channel and appreciably increasing reliability of modulators operation. Besides, installation of the TPD has allowed realizing rather simply the negative feedback path around of the anode modulator (see Fig.1). The feedback increased output pulse stability and essentially improved frequency response of the modulator, which, in turn, has resulted in improvement static and dynamic characteristics of RF amplitude stabilization system in the tank. So now there are only seven vacuum tubes in every RF channel - four in RF amplifiers and three in two modulators.

Structure of the artificial charging line (ACL), as a storage device for the powerful anode modulator vacuum tube GMI-44A, was also changed so that during breakdowns in load of ACL, accompanied by crowbar operation, overcharge of ACL took place. In that way, fast (about 400μs) and reliable lock-out of crowbar thyristors is achieved. This is particularly important in a case of using the induction regulators, demanding of constant load for their operation, in alternating-current high voltage circuit. Obviously, the faster the thyristors are closed, the less load perturbations an induction regulator "fills" during crowbar operation. Besides, some useful rearrangements of high voltage equipment were performed. In particular, diode network D1 (see fig.1) was carried out from ACL chamber into the GMI-44A case. That resulted in the strong shortening of the HV

• kvasha@inr.ru

cable (from 50m to 2m) and weakening of spurious coupling between the powerful RF amplifiers and crowbar circuits, arranged in ACL chamber, that, in turn, decreases the probability of false crowbar launching emergency.

RF AMPLIFIERS

The basic modernization of the DTL RF system was connected with new powerful triode "Katran" which should be installed in the channel output RF power amplifiers instead of vacuum tube GI-54A, removed from manufacture nearly ten years ago. The first mention of the vacuum tube “Katran” took place in paper [1] when the first results of the tube tests were got. The more detailed information about development, technology of manufacture and test results of vacuum tube "Katran" are presented in paper [2]. By now, vacuum tubes "Katran" are installed in three regular RF channels. One of the tubes worked for more than 9000 hours at the level of pulse RF power near 1 MW, the second tube, mounted in 2002, has up to now worked for 4500 hours at the level of pulse RF power ~1,6 MW, and the third one, installed in 2003, has worked for 1500 hours at the level of RF power ~ 1,2 MW.

This year in connection with taking off from manufacture vacuum tube (tetrode) GI-51A, which for the last 15 years was used as the driver for the output PA, tests of vacuum tube GI-57A have begun. Vacuum tube GI-57A is the triode with output pulse RF power up to 300kW. If the expected level of pulse RF power with the triode will be achieved, tandem of vacuum tubes GI-57A and "Katran" allows finishing the full modernization of the RF amplifiers in all channels of the DTL RF system.

RFQ channel

The RFQ channel that was put in operation in 1998 [3] appreciably differs from regular ones due to excitation of RFQ by means of four cables, which have to provide identical RF field in four cavities of the RFQ structure. For realization of the RFQ drive λ/4 transformer, as a RF divider, was installed into the coaxial metal feeder 300/130 mm, attached to the PA coupling loop (see Fig.2). Wave impedance of the transformer (25 Ohm) allows matching four coaxial cables, connected in parallel, with wave impedance 50 Ohm. Wave impedance and length of the transformer are more exactly determined by taking into consideration the end capacity and inductances of the four inner conductors of cables, placed inside of the divider. Lengths of the cables were preliminarily leveled during cutting, then their lengths were corrected by measuring of every cable capacity and, final correction came out from measurement of their phase length directly after their connection to the divider. After all these procedures the dispersion of cables electric lengths did not exceed units of degrees. Position of the couple loops of RFQ was chosen so that the loaded quality factor was twice lower than own one. At that in every cable nearly traveling wave was installed in a steady state. Since the RFQ was not originally foreseen

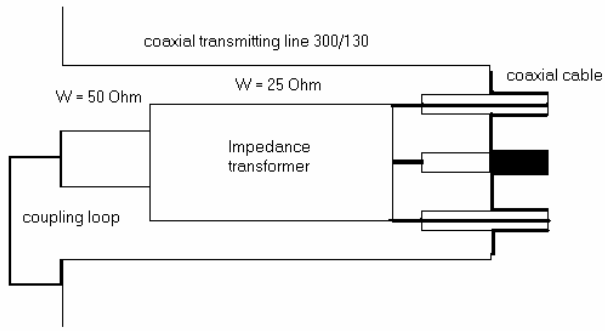

Figure 2: Construction of the RF divider

in MMF design, placement of the RF channel proved to be too far removed from the RFQ - length of cables between them achieved 24 -25 meters. At pulse RF power level in RFQ near 200 kW and specific cable attenuation value 0.05 db/m pulse RF power ~ 65 kW goes into each cable. Thus, at duty factor value 0.01 average RF power value about 300 W is dissipated in every cable. The level of RF power, dissipated inside of every cable, seems to be not so large but during a long continuous work there is an effect of accumulation of heat in them that caused the appropriate rise in temperature of cables and change of their electric lengths. It connected mainly with changing of permittivity of the coaxial cable dielectric (polyethylene) filling .As estimations show phase temperature factor of cables with entire dielectric filling is ~ 0.06deg/m*deg C at frequency 200 MHz. At long length of cables and value of warming up, which achieves 20^0C and more, a phase shift of electrical length of the cable can increase up to value of tens degrees. If synchronous changes of all four cable electrical lengths took place, RFQ accelerating field would slightly changed. However, really, at such lengths of cables it is difficult to expect absolute identity

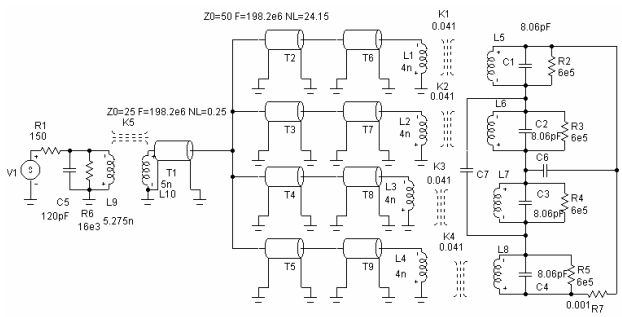

Figure 3: The RFQ RF system supply

of their behavior during heating . And indeed, during long beam sessions gradual decrease of RF amplitude in RFQ, accompanied by heating one of the cables, was observed. Attempts to restore the cavity RF amplitude resulted in further increasing of heating of the cable and breakdowns in the area of the RFQ coupling loops. For estimation of processes in cables, modeling of the RFQ

RF supply was carried out by means of program Micro Cap 7 (see fig.3). RFQ is presented as a four-vane structure, connected to the RF system by means of four ideal transmitting lines. Parameters of the cavities correspond to the real that of RFQ [3]: Q_0 = 6000, Rs = 1.5*10^{5}Ohm, f_O =198.2 MHz. Coupling of transmitting lines (TL) with the cavities is determined by coefficients K1-K4, which values are defined when all loops are connected to RF matched loads and its values are changed simultaneously so that the RFQ quality factor is twice decreased. At that, in each TL at the RFQ resonance frequency traveling wave is established. Hence amplitude of RF field in the cavity does not depend on lengths of TL, if their changes are synchronous ones. K1-K4 values, as a matter of fact, determine relations between a flow of magnetic field, run through the loop, and the whole magnetic field in the RFQ cavity. Capacities $C7=C6=C_d$ determine value of dipole frequency f_d corresponding TE_{110} mode in the RFQ: $f_d = f_q(1+C_d/C_q)^{-0.5}$, where C_q is an equivalent capacity of each of the four cavities; f_q is resonance frequency of quadrupole TE_{210} mode [4]. The external RF generator is presented as source V1 with impedance R1 and oscillatory circuit C5, L9, R6 tuned at frequency 198.2 MHz. Coupling coefficient K5 is chosen from condition of maximum RF power in the matched load. For an analysis of processes in the transmitting lines the λ/4 length line is separated in every TL. Vector values of voltage at the input $(\overline{U}_{in})$ and the output $(\overline{U}_{out})$ of the λ/4 TL allow determining the incident $(\overline{U}_{inc})$ and reflected $(\overline{U}_r)$ waves and, hence, reflection coefficient $(\overline{\Gamma})$:

$$\left|\overline{\Gamma}\right| = \frac{\left|\overline{U}_r\right|}{\left|\overline{U}_{inc}\right|} = \frac{MAG(\overline{U}_{out} + j\overline{U}_{in})}{MAG(\overline{U}_{in} + j\overline{U}_{out})} \quad (1)$$

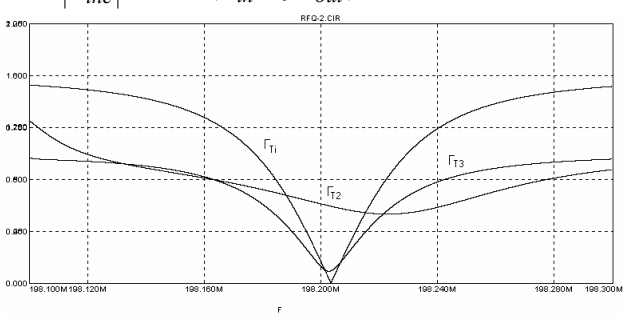

Figure 4: Reflection coefficients as a function of frequency

In figure 4 frequency responses of $\left|\overline{\Gamma}\right|$ are presented: Γ_{Ti} corresponds to a case of identical TL, equal 25λ, Γ_{T2} and Γ_{T3} - to a case when length one of TL (L_{T2}) differs from the rest of lines at small negative value (0.05λ). Fig.5 corresponds to the case when length L_{T2} differs from rest of lines at small positive value (+0.05) λ. Appearance of $\Gamma_{T2} > 1$ shows, that RF power in one cable gets off of the cavity. As follows from the dependencies, relatively small change of one of the cable length (in limits of ± 0.2% if the initial TL length is 25m) results in the strong redistribution of the RF power in the TL.

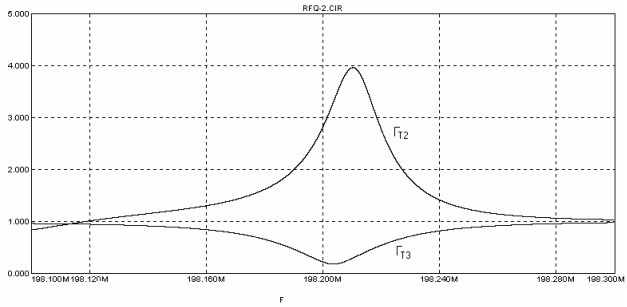

Figure 5: $L_{T2} - L_{T3} = +0.05\lambda$

At that the RF losses in the transmitting lines become different ones that, in turn, increases difference between electrical lengths of the cables due to their heating. If initial length of all TL differs from nλ/2, the distribution of RF power in the TL can be quite another one. So correct choice of the initial lengths of the long cables determines the behavior of the RF system during heating cables by RF losses. For decision of the problem at the MMF, length of metal feeder 300/130 was increased as much as possible to approach the RF divider to the RFQ and decrease the length of cables. After that length of the cables was decreased from 25m to 7m and problems, connected with long cables overheating were ceased.

It is necessary to notice that above-mentioned dependencies didn't take into account the dipole mode, though it is obvious, that if the TL lengths are different ones, exciting of dipole mode always takes place. As follows from calculations if $f_q - f_d > 0.5MHz$ the dipole mode really hasn't an influence at distribution RF power between TL and also at RF amplitude in the RFQ. When the frequencies are closer than 0.5 MHz, the influence of dipole mode becomes more appreciable. It is supposed that analysis of the above mentioned RF system in detail would be carried out in separate article.

REFERENCES

[1] E.S.Esin, L.V.Kravchuk, A.I.Kvasha "Moscow Meson Factory DTL RF System Upgrade", 1995 PAC and ICHEA Conference, May 1995, Dallas, Texis, p.1175.

[2] A.I.Kvasha et al. "A New 200 MHz Powerful Pulse Triode for the Output Power Amplifier of DTL RF System", PAC2001, June 2001, Chicago.

[3] S.K.Esin et al "Commissioning of new Injection Line at INR Proton Linac", Proceedings of the 1999 PAC, New York, 1999, p.3561.

[4] Proceedings of the CERN Accelerator School fifth advanced accelerator physics course, CERN 95-06, 22 November 1995, Volume II, p.977.

ELECTROMAGNETIC DESIGN OF NEW RF POWER COUPLERS FOR THE S-DALINAC

M. Kunze#, W.F.O. Müller, T. Weiland, TEMF, TU Darmstadt, Darmstadt, Germany
M. Brunken, H.-D. Gräf, A. Richter, IKP, TU Darmstadt, Darmstadt, Germany

Abstract

The electromagnetic design and design results of new rf waveguide-coax input power couplers for the S-DALINAC are presented. Special consideration is spent on the minimization of the transverse electromagnetic field on the beam axis which would cause an emittance growth of the electron beam.

INTRODUCTION

The superconducting Darmstadt electron linear accelerator (S-DALINAC) is a recirculating machine operating at 3 GHz [1]. Since its first operation in 1987 the S-DALINAC has continuously be improved. Presently, the third generation of components for this accelerator is under development. To allow future nuclear physics experiments with cw beam currents from 150 to 250 µA at electron energies of 14 MeV behind the injector linac rf power of up to 2 kW has to be transferred to the electron beam. The present coax-coax input power couplers at the S-DALINAC with variable coupling are limited to a maximum power of 500 W. To reach power operation up to 2 kW while keeping the emittance growth of the electron beam small waveguide power couplers [2, 3] with minimized transverse kick should be used in the accelerator upgrade.

Recently, the electromagnetic design of a single-waveguide-coax and a twin-waveguide-coax coupler, respectively, for the S-DALINAC has been published [4]. It was mentioned that the single-waveguide-coax coupler allows for a more compact design whereas the rf behavior in terms of S-parameters is similar to that of the twin-waveguide-coax coupler.

In this paper a modified design of the twin-waveguide-coax coupler and its electromagnetic design procedure is presented. It is shown that a compact design similar to that of the single-waveguide-coax coupler is possible.

COUPLER DESIGN

Fig. 1 shows the geometry of the twin-waveguide coupler and the electric field patterns of the two lowest coaxial (TEM, H_{11}) and circular waveguide modes (TM_{01}, TE_{11}), respectively. At the 3 GHz operating frequency of the S-DALINAC the TEM mode and the H_{11} mode can propagate on the coaxial line while the TM_{01} and the TE_{11} mode of the circular waveguide (beam tube in Fig.1) are still evanescent modes. At transition 2 the TE_{11} mode with its asymmetric field distribution is mainly excited by the H_{11} mode. Since the asymmetric electromagnetic field of the TE_{11} mode generates an emittance growth, the excitation of the H_{11} mode must be minimized at transition 1.

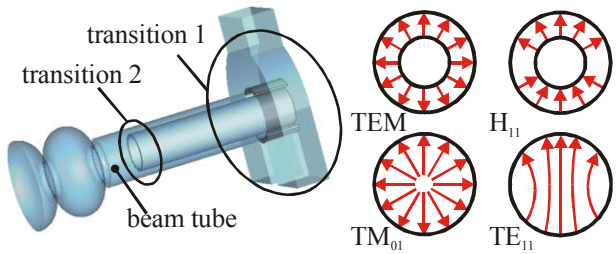

Figure 1: The twin-waveguide coupler and the electric field patterns of the two lowest coaxial modes (TEM, H_{11}) and of the circular waveguide modes (TM_{01}, TE_{11}).

In Fig. 2a the geometry of the twin-waveguide-to-coax transition (transition 1 in Fig. 1) and its parameters are given. The single-waveguide-to-coax transition presented before in [4] is again given in Fig. 2b. In both designs diaphragms are used to minimize the transverse coupler kick. The suppression of the H_{11} mode can be adjusted choosing the opening angle $\varphi_1+\varphi_2$. Once the angle $\varphi_1+\varphi_2$ is chosen the power transfer from the fundamental rectangular waveguide mode H_{10} to the TEM mode of the coaxial waveguide can be maximized by adjusting the height *h* and the stub length *s* for the single-waveguide-to-coax transition and additionally the gap width *g* and the waveguide width *w* for the twin-waveguide-to-coax transition, respectively.

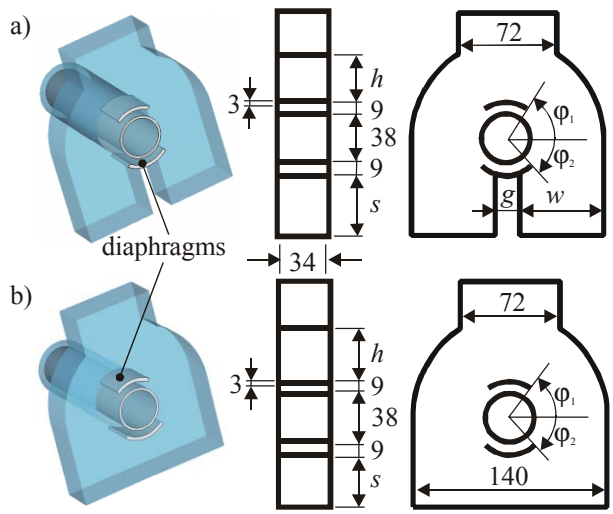

Figure 2: The twin-waveguide-to-coax (a) and the single-waveguide-to-coax (b) transition of the waveguide-to-coaxial couplers under investigation (unit of length is mm).

#kunze@temf.tu-darmstadt.de - This work is supported by the Deutsche Forschungsgemeinschaft (DFG) under contract SFB 634.

EM DESIGN PROCEDURE

The excitation of the H_{11} coaxial mode can be adjusted by choosing the opening angle $\varphi_1+\varphi_2$ of the waveguide-to-coax transitions in Fig. 2 and optimizing the remaining parameters *h*, *s*, *g*, and *w*.

In Fig. 3 the electromagnetic design procedure of the twin-waveguide-to-coax transition is illustrated. First, initial values for *h*, *s*, *g*, *w* and $\varphi_1 = \varphi_2$ are chosen. Then, the parameters *h*, *s*, *g* and *w* are varied in order to minimize the reflection of the fundamental waveguide mode H_{10}. In the next step, φ_1, and φ_2 are adjusted for a maximum suppression of the H_{11} mode at transition 1 in Fig. 1. The second and third step of the design procedure are repeated until optimized values for *h*, *s*, *g*, *w*, φ_1 and φ_2 are reached which means that the reflection $S_{H10,H10}$ and the transmission $S_{H11,H10}$ can not further be suppressed for the given opening angle $\varphi_1+\varphi_2$.

The design procedure of the single-waveguide-to-coax transition follows the same scheme except that only four parameters, namely *h*, *s*, φ_1, and φ_2 have to be adjusted.

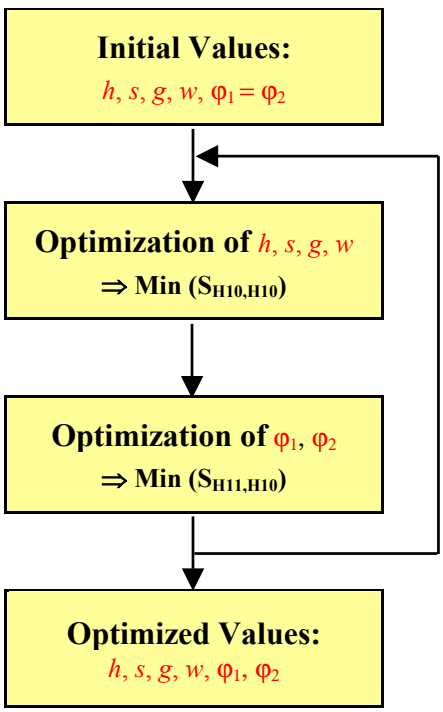

Figure 3: The electromagnetic design procedure of the twin-waveguide-to-coax transition.

WAVEGUIDE-TO-COAX TRANSITIONS

In Fig. 4 and 5 the design results of electromagnetic simulations for three twin-waveguide-to-coax transitions and three single-waveguide-to-coax transitions, respectively, with different opening angles are shown. The electromagnetic simulations were performed by means of CST MICROWAVE STUDIO ® [5] and usage of the integrated optimization tool. As can easily be seen the overall behavior of both designs is similar. Thus, the description of the twin-waveguide-to-coax transition is sufficient. An important characteristic of the modified twin-waveguide-to-coax transition (see also [4]) is that its total dimension is of the same order as that of the single-waveguide-to-coax transition.

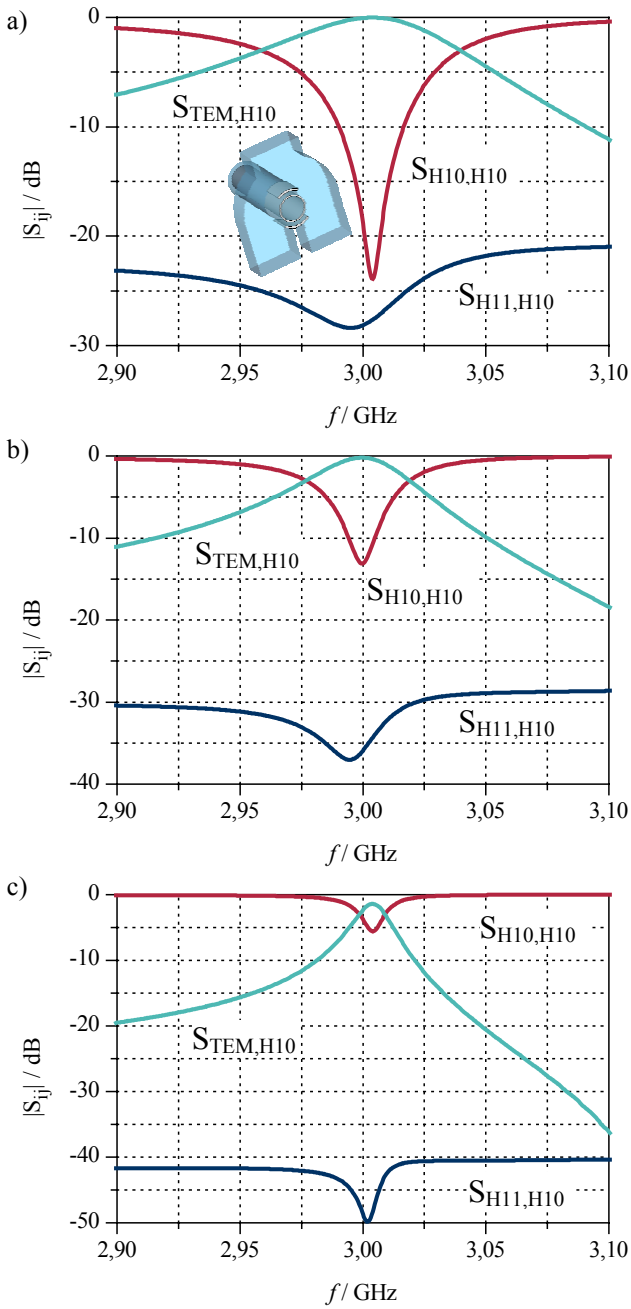

Figure 4: Reflection magnitude $|S_{H10,H10}|$ / dB and transmission magnitudes $|S_{TEM,H10}|$ / dB and $|S_{H11,H10}|$ / dB against frequency for three different twin-waveguide-to-coax transitions with different opening angles $\varphi_1+\varphi_2$:

a: $h = 34.1$, $s = 43$, $g = 18$, $w = 61$, $\varphi_1 = 56.2°$, $\varphi_2 = 49.3°$

b: $h = 36$, $s = 45$, $g = 5.6$, $w = 67.2$, $\varphi_1 = 44.6°$, $\varphi_2 = 41.6°$

c: $h = 37$, $s = 49$, $g = 2.4$, $w = 68.8$, $\varphi_1 = 32.4°$, $\varphi_2 = 28.7°$

(unit of length is mm; H_{10} is the fundamental mode of the rectangular waveguide, other modes as in Fig. 1).

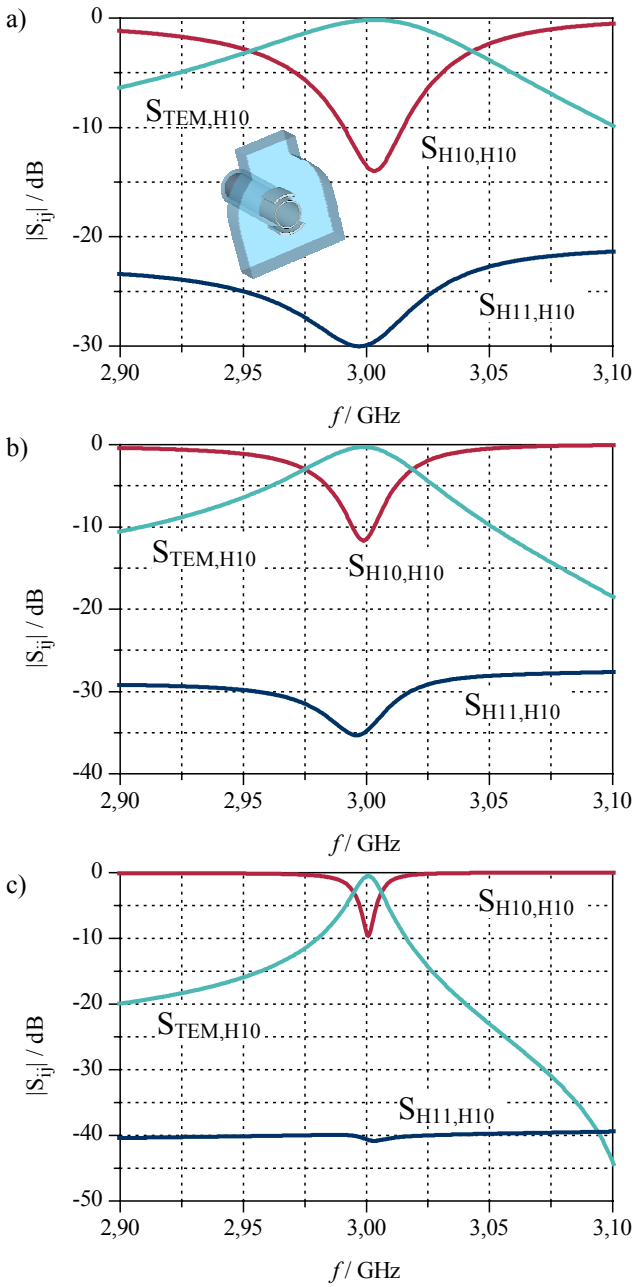

Figure 5: Reflection magnitude $|S_{H10,H10}|$ / dB and transmission magnitudes $|S_{TEM,H10}|$ / dB and $|S_{H11,H10}|$ / dB against frequency for three different single-waveguide-to-coax transitions with different opening angles $\varphi_1+\varphi_2$:

a: $h = 37.3$, $s = 36.1$, $\varphi_1 = 55°$, $\varphi_2 = 47.9°$

b: $h = 36.9$, $s = 39.5$, $\varphi_1 = 45.3°$, $\varphi_2 = 39.8°$

c: $h = 33.4$, $s = 42$, $\varphi_1 = 34.2°$, $\varphi_2 = 30.1°$

(unit of length is mm; H_{10} is the fundamental mode of the rectangular waveguide, other modes as in Fig. 1).

As can be seen from the dependence of the excitation level of the H_{11} mode from the opening angle $\varphi_1+\varphi_2$ in Fig. 4, decreasing the opening angle by about 20° reduces the excitation of the H_{11} ($|S_{H11,H10}|$) mode by some 10 dB. The excitation of the H_{11} mode is about -50 dB for an opening angle of 60°, resulting in an excitation of the TE_{11} mode in the beam tube (see. Fig. 1) by less than -50 dB. Further investigations have shown that the excitation level of the H_{11} mode can be reduced to less than -50 dB choosing an opening angle of about 40°. But this would result in a reflection of the fundamental waveguide mode H_{10} of more than -10 dB and a significant decrease of the transmission $S_{TEM,H10}$ to less than -3 dB as follows from Fig. 4. Fig. 4 provides also information on the bandwidth of the twin-waveguide-to-coax transition. Decreasing the opening angle $\varphi_1+\varphi_2$ results in a smaller bandwidth. The bandwidth is nearly 80 MHz for an opening angle of 100° (see Fig. 4a.) and approximately 10 MHz if an opening angle of 60° is chosen (see Fig. 4c.).

At this point, some general design rules for the twin-waveguide-to-coax transition and the single-waveguide-to-coax transition, respectively, can be summarized:

1. Diaphragms in the waveguide-to-coax transitions are used to minimize the transverse coupler kick. In particular the excitation of transverse electromagnetic fields in the beam tube (see Fig. 1) can be reduced to less than -40 dB.
2. The level of excitation of the H_{11} mode at transition 1 of the coupler designs (see Fig. 1) can be adjusted choosing the opening angle $\varphi_1+\varphi_2$.
3. The overall behavior for a given opening angle $\varphi_1+\varphi_2$ of the rf waveguide-coax input power couplers can be optimized varying some few coupler dimensions (see Fig. 2) .

CONCLUSIONS

A new twin-waveguide-coax coupler is proposed for the S-DALINAC upgrade. The rf behavior in terms of S-parameters and its dimensions are similar to that of a single-waveguide-coax coupler of which design data is also given in this paper. At the present state of research it seems that the main advantage of the twin-waveguide-coax power coupler over the single-waveguide-coax coupler is, that it allows for smaller transverse coupler kicks at the same opening angle $\varphi_1+\varphi_2$.

ACKNOWLEDGEMENT

The authors would like to thank M. Dohlus (DESY, Hamburg) for helpful discussions.

REFERENCES

[1] A. Richter, "Operational experience at the S-DALINAC," *in Proceedings of the 5th European Particle Accelerator Conference*, 1996, vol. 1, pp. 110 - 114.

[2] V. Shemelin, S. Belomestnykh, H. Padamsee, "Low-kick twin-coaxial and waveguide-coaxial couplers for ERL," *Cornell LEPP Report SRF 021028-08*, 2002.

[3] G. Bowden et al., "A compact rf power coupler for the NLC linac," *in Proceedings of the 18th Particle Accelerator Conference*, 1999, vol. 5, pp. 3426-3428.

[4] M. Kunze, M. Brunken, H.-D. Gräf, W.F.O. Müller, A. Richter and T. Weiland, " Electromagnetic Design of New RF Power Couplers for the S-DALINAC," *to appear in Proceedings of the 9th European Particle Accelerator Conference*, 2004.

[5] Computer Simulation Technology: www.cst.com.

CONTROL OF THE LOW LEVEL RF SYSTEM FOR THE J-PARC LINAC

S. Anami#, E. Kadokura, S. Michizono, S. Yamaguchi, KEK, 1-1 Oho, Tsukuba, Ibaraki, 305-0801,Japan; E. Chishiro, T. Kobayashi, H. Suzuki, JAERI, 2-4 Shirakata-Shirane, Tokai, Naka, Ibaraki, 319-1195, Japan

Abstract

The J-PARC 181-Mev proton linac requires twenty-four RF systems, which operate at a 620-μs pulse width, 50-Hz repetition rate, and 324-MHz frequency. The required basic functions of the low level RF (LLRF) control system for the klystron RF source are: field control, high-power protection, analog and status monitor and klystron drive. To perform these functions a programmable logic controller (PLC) is used as the main system controller. The PLC will be locally operated by a touch panel on PLC LAN and remotely by an EPICS Operator Interface (OPI) on EPICS LAN. This paper describes the LLRF hardware configurations and the system control using the PLC.

INTRODUCTION

The RF source of the J-PARC 181-MeV proton Linac is composed of four solid-state amplifiers and twenty klystron amplifiers. In each RF source, the cavity field will be stabilized within an accuracy of ± 1% in amplitude and ± 1° in phase. This field control, which is implemented by a combination of feedback (FB) and feed-forward (FF) algorithms, is the most important key function in the low level RF (LLRF) system, and requires much of our efforts [1][2]. However, seeing from the viewpoint to control the whole LLRF system, the field control is one embedded system, all of the LLRF components, such as a high power protection unit, status and analog monitors and a klystron driver, are controlled by a system controller with interfaces for local and remote operation. We adopt a programmable logic controller (PLC) as the main system controller.

OVERVIEW OF THE LLRF SYSTEM

There are twenty-four LLRF systems corresponding to each of the solid-state and klystron amplifier stations. A block diagram of the LLRF system for the klystron station, including an interface with the EPICS control system (VME/IOC and NIM/Timing), is shown in Figure 1. The required fundamental functions for the LLRF system are: 1) generation of the accelerating RF (324 MHz) and clock (12 MHz, 48 MHz and 312 MHz) signals phase-locked with a 12-MHz optical signal provided with the rf reference distribution system [3], 2) cavity field and tuning control (cPCI/Digital FB), 3) high-power protection and RF monitor (Fast Interlock, Arc Detector and VSWR Meter), and 4) klystron drive (Analog FB, 20-dB and 40-W amplifiers).

The signal generation and the cavity field and tuning control are performed by a cPCI crate system, which is composed of a host CPU module, a control input/output module (CTRL I/O), a mixer and I/Q modulator module (MIX&I/Q-M), a DSP module attached with a FPGA mezzanine card, and an RF and clock generator module (RF&CLK). All of the LLRF hardware components which are listed in Table 1 are installed in two 19”

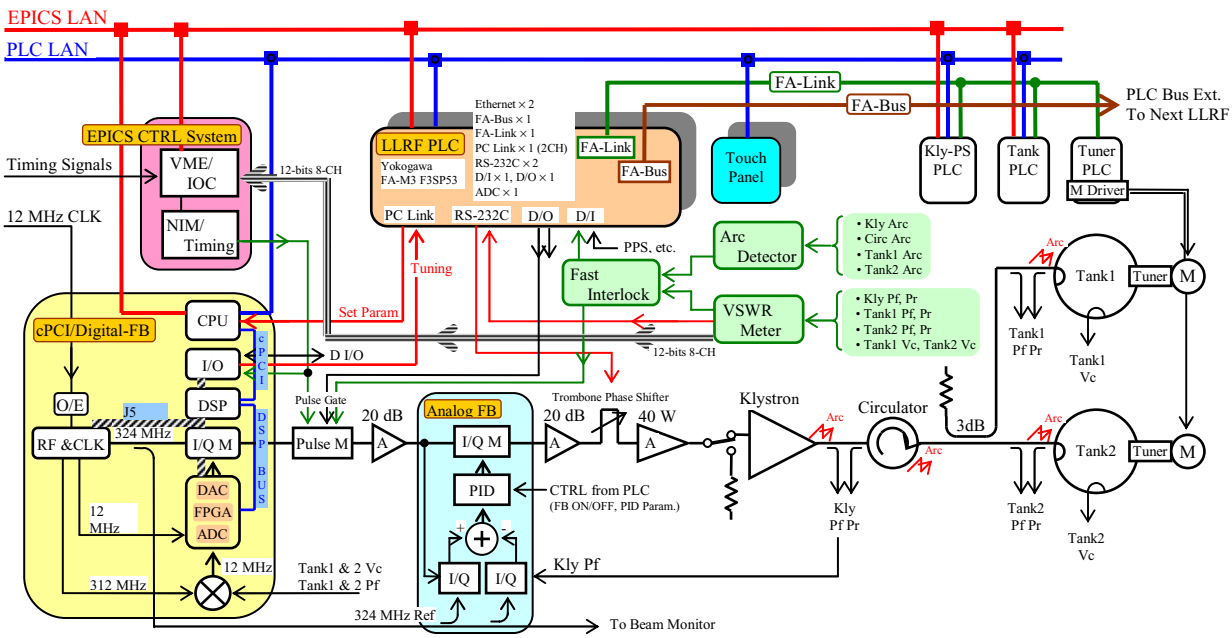

Figure 1: Block diagram of LLRF System.

#anami@post.kek.jp

standard racks (1400W × 800D × 2000H).

Table 1: LLRF hardware components and their unit size

Chassis Unit	Height (unit)	
PLC and Touch Panel	7	Touch Panel mounted on PLC chassis front panel
cPCI Crate	8	covered with noise-shield case with fans
NIM Bins	5 × 2	Pulse Mod, 3-CH 20-dB Amp, Fast INT, Arc Detect., Analog FB CTRL, Osc. Trig Delay
VSWR Meter	3	with peak power meter function
40-W Amp.	4	include dc power supply
40-W Output Unit	2	monitor couplers, circulator, coaxial SW
Tromb. Phase Shifter	side panel	motor driven (20 cm × 80 cm)
Temp. Module Panel	rear panel	4 thermocouple modules
I/O Connector Panels	3 × 2	main purpose for ground sink
1-GHz Oscilloscope	7	waveform and phase read-out
Others	10	2 fan units, MCCB

CONTROL COMPONETS OF THE LLRF SYSTEM

The components for controlling the LLRF system, as shown in Figure 1, are the PLC, Touch Panel, EPICS Control System, cPCI System, and Fast Interlock. The hardware configuration and control function for each of these components are described as follows:

PLC

Though it isn't shown in Figure 1, there are two types of PLCs: a main unit which has a CPU module in its back plane bus, and a subunit which doesn't have a CPU and is connected on the expansion bus of the main unit by an FA-Link module. The main unit is one rate in four systems, thus, one CPU works four system tasks. Figure 1 shows the case that PLC is a main unit. Differences between the subunit and the main unit are two points: the subunit has no connection to LANs and no link with other PLCs. All others are similar system configurations. The followings are explained about the system whose PLC is a main unit, as well as the paragraph mentioned above.

The modules used in the PLC are shown in Figure 1. Control functions of the PLC can be depicted in Figure 2. In order to operate the system and provide remote and local access to the PLC, there are the EPICS VME/IOC and the Touch Panel (TP). Two types of modules for serial (RS-232C) communication are used: one is a 2-channel PC-Link module which is implemented by a client program for communication with the cPCI/CPU module and the cPCI/DSP module routed through the cPCI/CTRL I/O module, and the other is Ladder Program Communication modules which are implemented by PLC ladder programs for communication with the VSWR Meter and the Trombone Phase Shifter. As a control output from the PLC, ON/OFF commands are transmitted to the cPCI/FPGA through the cPCI/CTRL I/O, Pulse Modulator, Klystron Input SW, and Analog PID. In addition parameter settings are transmitted to the Tuner PLC, cPCI/CPU, Analog PID, and Trombone Phase Sifter.

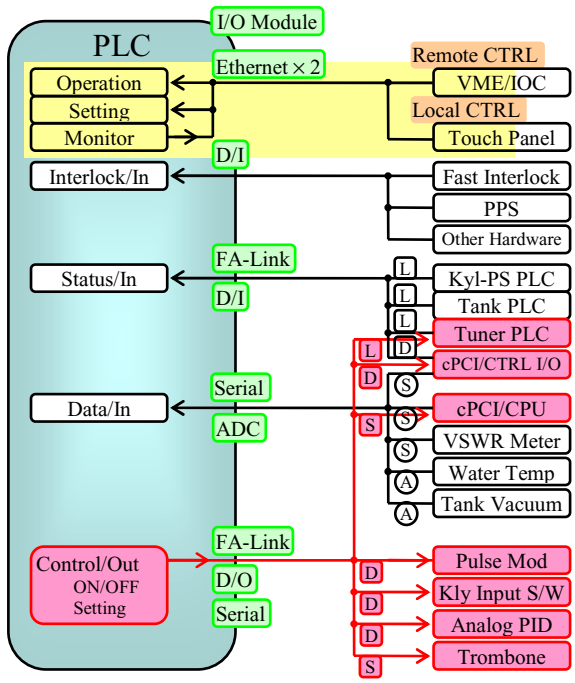

Figure 2: Control flow from/to the PLC.

Touch Panel

The Touch Panel (TP) provides a GUI for local operation and all the functions necessary to control the entire LLRF system. In addition important data such as the field amplitude and phase, the cavity tuning angle and vacuum, and the klystron output power are displayed in the trend graph.

EPICS VME/IOC

The EPICS VME/IOC is an I/O interface with EPICS which is supported by the linac control group. The PLC is remotely controlled by reading and writing from EPICS to the PLC register. The required timing signals for the LLRF system are provided by the EPICS NIM Timing system. In addition the high-refresh-rate dada from the VSWR Meter (8-CH 12-bit, 50 Hz) are saved in to the EPICS database.

cPCI System

The cPCI system composed of five modules and one mezzanine board (FPGA) is shown in Figure 3. In these modules only the CPU and DSP modules utilize the PCI system bus (J1 and J2), while the other modules utilize only the user bus (F3 and J5) and, thus, merely make use of its standard module case. The boards (CPU, DSP, FPGA and CTL I/O) relevant to control are explained as follows:

A *CPU* module used as a cPCI system host is a general purpose Pentium CPU board (ACP-128-1, AVALDATA Co., PentiumM/1.6GHz). On the front panel the PC standard communication and device I/O ports, such as Ethernet (×2), COM, keyboard, display and etc., are provided, which make it easy to locally debug and diagnose the software and system. The COM port is used for the communication of all the control data required for

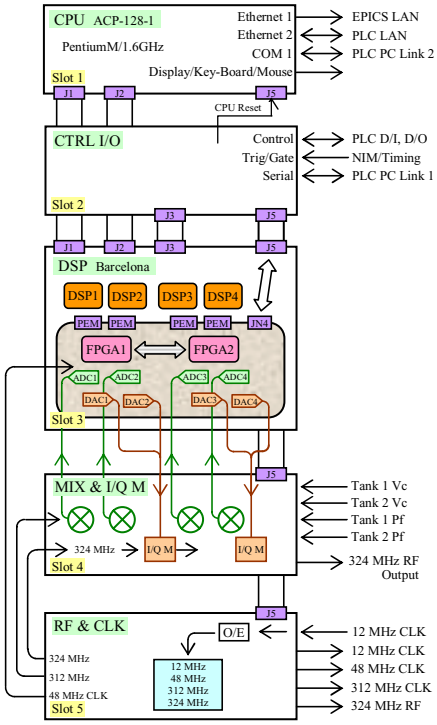

Figure 3: Block diagram of the cPCI modules.

the field control from/to the PLC. One Ethernet port is for the transmission of waveform data to the EPICS OPI as a FTP server. Another Ethernet port is connected to PLC LAN and served the network boot and the download of DSP execute and FPGA configuration files.

We adopt a Barcelona *DSP* board (Spectrum Signal Processing Inc., TMS320C6701 × 4). Each of the DSPs has an I/O port called "PEM" on the board which provides a high-speed dataflow (400 MB/s) from/to a mezzanine board inserted into the PEM connectors. The waveform data from the mezzanine (FPGA) board can be stored directly in lots of memories (512-kB SSRAM, 16-MB SDRAM) on each DSP local bus by a DMA engine, and, after processed by DPSs, transferred to the host memory on the PCI memory address space.

Besides J1 and J2 this DSP board has the J3 and J5 user bus connectors: J3 is for DSP global interrupts and serial communication, and J5 for user free I/O lines, which route a path to a 64-pin connector (JN4) on the board. We use JN4 as a signal path from the CTRL I/O to FPGA boards.

The *FPGA* board installed on the DSP board as its mezzanine board consists of two FPGAs (Xilinx Virtex-E XCV600E (FG676)), four ADCs (AD6644) and four DACs (AD9764). By equipping the FPGA board with all the PEM and JN4 ports, we obtain the expansible usability. The configuration PROMs on the board can be rewritten through the DSP serial port in the PEM ports, as well as the JTAG port, therefore we can download FPGA configuration files sent from the PC server on PLC LAN.

The Control I/O *(CTRL I/O)* board provides the signal paths from the PLC and NIM/Timing to the J3 and J5 cPCI user bus connectors. The digital I/O signals between the PLC and J5 bus are RF ON/OFF, FB ON/OFF, fault latch Reset, host CPU Reset, FPGA OK, DSP OK, etc. The timing signals are FPGA pulse control Start/Stop, RF ON Gate, Beam ON Gate, Beam Chopper Clock (~1 MHz), etc.

Fast Interlock

In order to protect the high-power components such as RF windows in case of RF discharge and over RF reflection, we must shut off the RF drive to the klystron as soon as possible. The Fast Interlock (Fast INT) module provides the high-power protection function by controlling a gate signal to the RF switch of the Pulse Mod module. The Fast INT module has many input signals, as shown in Figure 4: four arc detection signals from the Arc Detector (klystron, circulator, tank-1 input port and tank-2 input port), three set signals of an over forward power (Pf), over reflection power (Pr) and VSWR (5-μs delay for processing) from the VSWR Meter, and the RF Out Enable signal from the machine protection system (MPS).

The Fast INT module also has an output function of the "RF Acc OK" signal which informs the RF source ready for beam acceleration to the MPS.

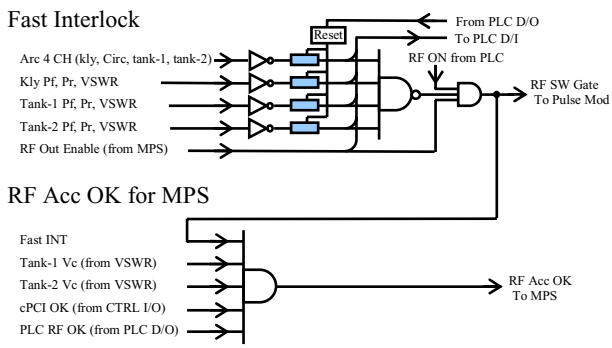

Figure 4: Block diagram of the Fast Interlock module.

CURRENT STATUS

Two prototypes of the LLRF system based on analog feedback have been operated at the DTL-1 RF station and the SDTL high-power test station in the 60-MeV test linac. All twenty-four LLRF systems will be delivered at the end of March 2005. We are developing the PLC program which includes the auto-recover process from fault down and the auto-conditioning process for cavities.

REFERENCES

[1] S. Michizono, et al, "Digital RF Control System for 400-MeV proton Linac of JAERI/KEK Joint Project," Linac 2002, Gyeongju, Korea, Aug. 2002.

[2] S. Michizono, et al, "Digital Feedback System for J-PARC Linac RF Source," this conference.

[3] T. Kobayashi, et al, "RF Reference Distribution System for J-PARC Linac," this conference.

DIGITAL FEEDBACK SYSTEM FOR J-PARC LINAC RF SOURCE

S. Michizono#, S. Anami, S. Yamaguchi, KEK, Tsukuba, Japan
T. Kobayashi, JAERI, Tokai, Japan

Abstract

At the proton linac of J-PARC (Japan Proton Accelerator Research Complex), an accelerating electric field stability of ±1% in amplitude and ±1° in phase is required for the RF system. In order to accomplish these requirements, a digital feedback system is adopted for flexibility of the feedback (FB) and feedforward (FF) algorism implementation. FPGAs are used for the real-time FB system. A DSP board is also utilized for data processing and communication between FPGAs and a crate control CPU (Host). The system was examined with the SDTL cavity, and satisfied the stability specification.

INTRODUCTION

Twenty klystrons (324 MHz, 3 MW) will be installed in the J-PARC linac. An RFQ, 3 DTLs and 16 SDTL modules are driven by klystrons [1]. The maximum pulse width and repetition rate are 620 μs, including the cavity build-up time, and 50 pps, respectively. Because the rf source should maintain the accelerating field within an amplitude stability of ±1% and phase stability of ±1°, a highly intelligent feedback system should be constructed. A digital feedback system using the FPGAs combined with DSPs has been developed for these requirements. The FPGAs are in charge of fast feedback for the cavities and the DSPs will be operated for data/program exchange and a slow feedback system, such as tuning the cavities. In this report, the hardware developments and performance of the feedback system are described.

FEEDBACK EQUIPMENT

The digital feedback system is installed in a compact PCI (cPCI crate). The backplane of the cPCI crate is specially designed so as to separate the ground line between digital and analog boards. The digital equipment, such as the CPU, DSP (Spectrum Signal Processing Inc. 'Barcelona', 4xTMS320C6701) and I/O boards, are located on left side of the cPCI crate, and analog boards, such as the RF&CLK (rf and clock generator) and Mixer&I/Q (mixers and I/Q modulators) boards, are installed on the right side. The RF&CLK board creates timing clock (f_{Tim}:12 MHz, f_{Trig}: 48MHz, f_{LO}: 312 MHz) and RF (f_{RF}: 324 MHz) signals synchronized with a distributed reference signal [2]. Since the accuracy of around 2 ps is required especially to the LO signal (312 MHz), the reference signal is planned to change from 12

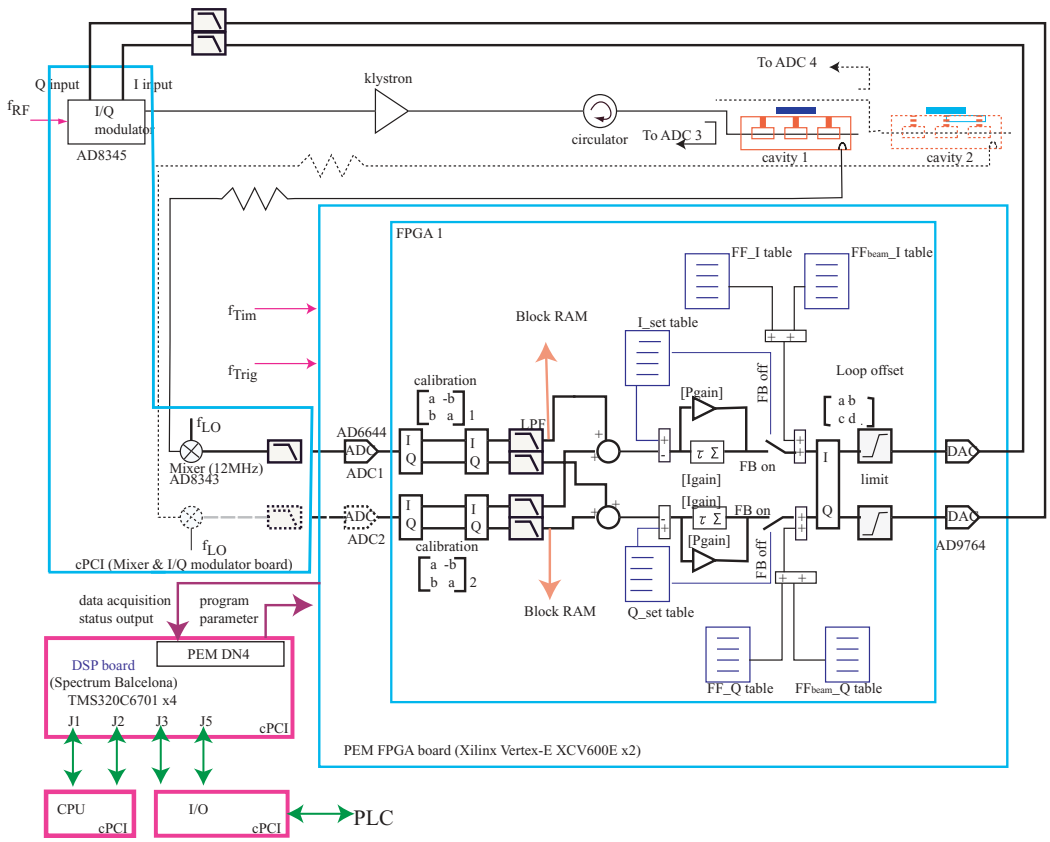

Figure 1: Schematic diagram of the digital feedback system.

#shinichiro.michizono@kek.jp

MHz to 312 MHz.

An FPGA (Vertex-E XCV600E, which will be replaced by XC2V2000 in this year) sends I and Q components to an I/Q modulator (AD8345) through 14-bit DACs (AD9764). The modified signal drives a klystron. An active mixer (AD8343) receives the rf signal from the cavity and down-converts it to an IF signal (12 MHz). The FPGA obtains I/Q components by measuring the IF signals at a 48-MHz clock through a 14-bit ADC (AD6644). One of the FPGAs works for the rf signals from cavities, and another serves as a monitor of the rf signals from cavity input ports, which is used for tuner control. Figure 1 shows a schematic diagram of the digital FB system. Simple PI control is adopted for cavity control. The FF signal is added as beam compensation. The digital FB system is controlled through a PLC [3].

FEEDBACK PERFORMANCE

The system configuration is shown in Figure 2. Prior to a high-power test using a SDTL, a low-level FB was tested using a simulation cavity [4] with a delay line. After checking the performance with the simulation cavity,

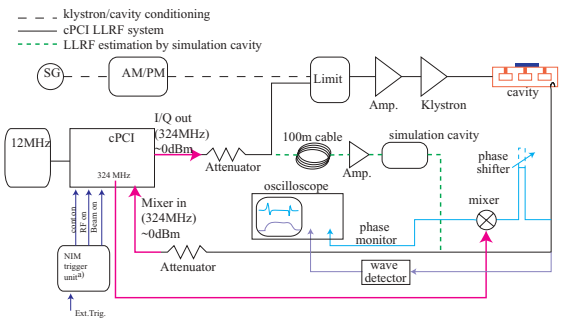

Figure 2: Schematic diagram of the LLRF system configuration.

a high-power test was carried out. Figure 3 shows the step response obtained by the digital system without FB. The measured loaded Q value from this measurement was about 22,000.

Set-values of the FB are an exponential pattern, as shown in Figure 4, for a fast build-up time with a limited

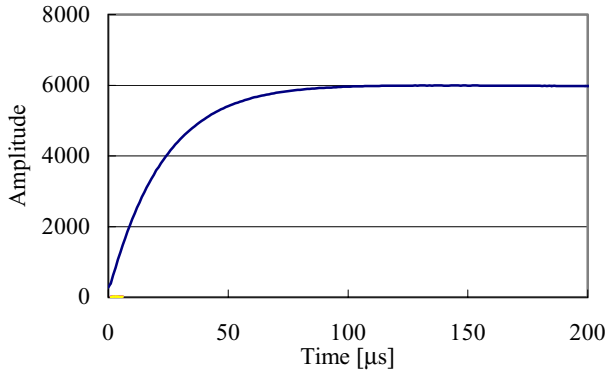

Figure 3: Step response measured by the digital system.

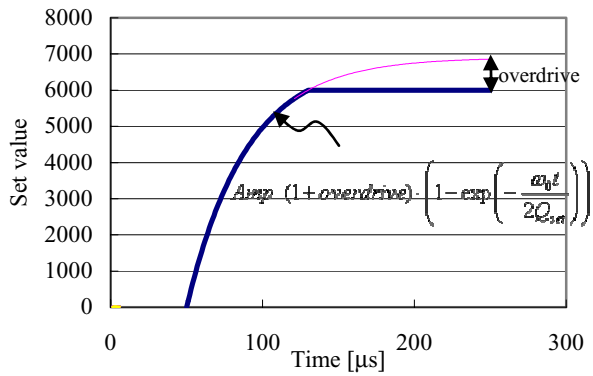

Figure 4: Set-values used for the feedback.

rf power. The parameters of the set-values are the amplitude, phase, overdrive and Q value for build-up (Q_{set}). In this test, these parameters were 6,000, 0° , 5% and 40,000, respectively. This combination of amplitude and phase corresponds to 6,000 and 0 in the I and Q components, respectively.

Figure 5 shows the I/Q components during FB (without FF). Proportional and integral gains of 10 and 15/1000 at a 48-MHz clock were adopted in this experiment. The variations of both components at flattop were less than 10. The corresponding errors of the amplitude and phase in the pulse were ±0.08% and ±0.04°, respectively. The stabilities were also evaluated using an external monitor.

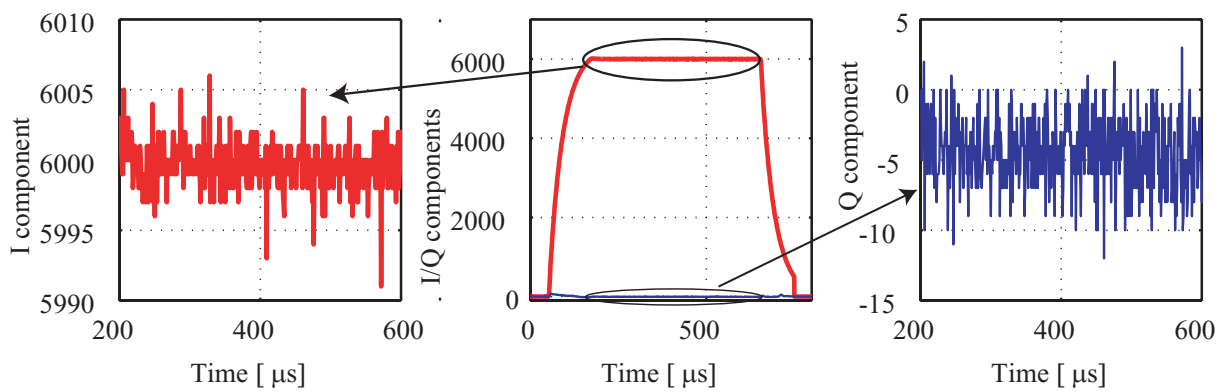

Figure 5: Measured I/Q components during rf operation. Fullscale I/Q:center, expansion I: left, expansion Q: right. No feedforward was used. The proportional and integral gains for the feedback are 10 and 15/1000 at a 48-MHz clock, respectively.

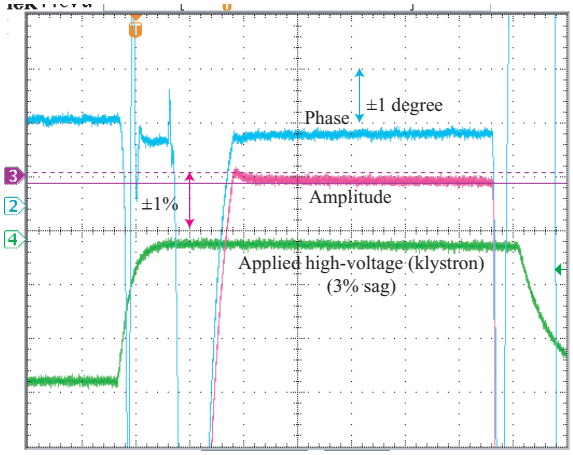

Figure 6: Waveforms of the amplitude and phase obtained by external monitors.

Figure 6 shows the amplitude and phase signals obtained with a wavedetector and a mixer, which corresponds to errors of ±0.2% in amplitude and ±0.2° in phase. The measured data with the external monitor were about 4-times larger, probably due to the ambiguity of the measurement system. Further development of the external measurement system is required for a more precise evaluation.

The measured values were compared with the calculated values based on the state equations. Theses showed good agreements, including the overshooting (Figure 7). This indicates that the system is well-modeled in the simulation, and that simulations will be helpful for developing new FB algorisms.

The stability of the system was also examined during long-time operation. The results are shown in Figure 8. Stabilities of ±0.2% in amplitude and ±0.25° in phase were achieved for more than 17 hours.

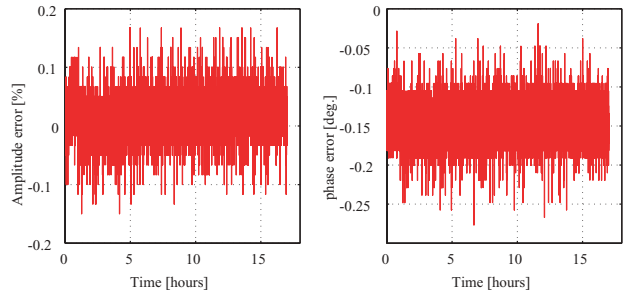

Figure 8: Trend-graphs of the amplitude and phase stabilities.

SUMMARY

A digital FB system used at the rf sources in the J-PARC linac has been developed. The requirements for the LLRF system are stabilities of ±1% in amplitude and ±1° in phase. The system was examined by a SDTL cavity, and show good stabilities of ±0.08% in amplitude and ±0.04° in phase. The stabilities remained for more than 15 hours at ±0.2% in amplitude and ±0.25° in phase.

REFERENCES

[1] S.Yamaguchi et al., "Overview of The RF System for The JAERI/KEK High-Intensity Proton Linac", LINAC2002, Gyeongju, Aug. 2002, p.452.

[2] T.Kobayashi et al., "RF Reference Distribution System for J-PARC Linac", this conference.

[3] S. Anami et al., "Control of the Low Level RF System for the J-Parc Linac", this conference.

[4] S. Michizono et al., "Digital RF Control System for 400-MeV Proton Linac of JAERI/KEK Joint Project" LINAC2002, Gyeongju,Aug. 2002, p.184.

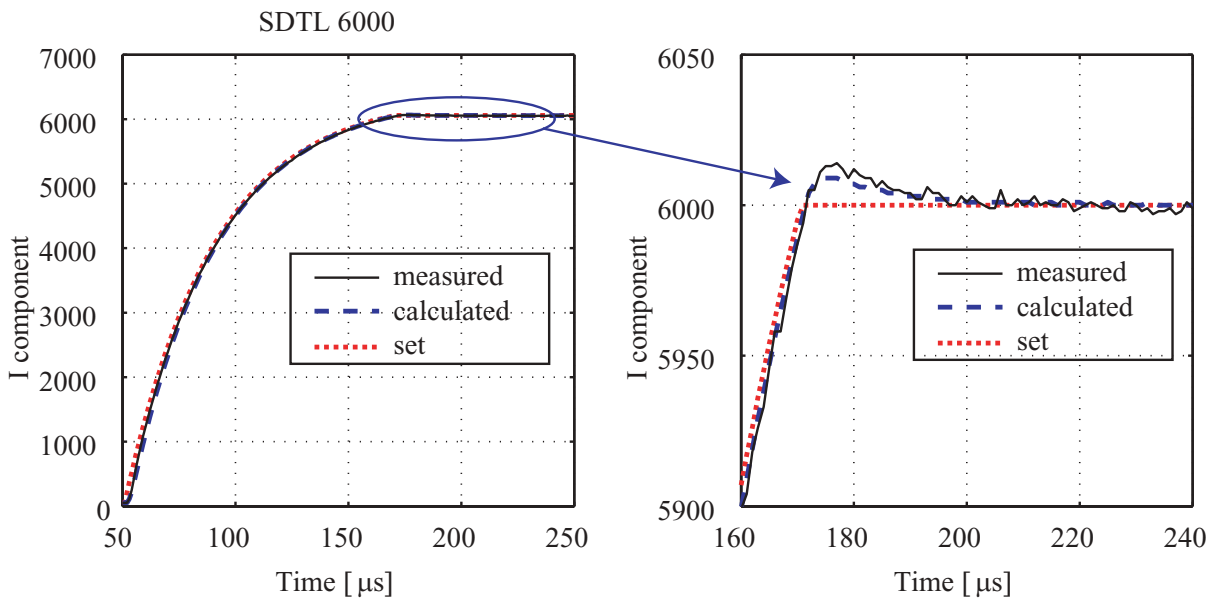

Figure 7: Comparison with the measured and calculated I-component. These show good agreements, including overshoot.

DEVELOPMENT OF C-BAND HIGH-POWER MIX-MODE RF WINDOW

S. Michizono#, T. Matsumoto, K. Nakao, T. Takenaka, S. Fukuda, KEK, Tsukuba, Japan
K. Yoshida, Mitsubishi Electric Corporation, Amagasaki, Japan

Abstract

A high-power C-band (5712 MHz) rf system (40 MW, 2 μs, 50 Hz) is under consideration for an electron-linac upgrade aimed for the super KEKB project. An rf window, which isolates the vacuum and passes rf power, is one of the most important components for the rf system. The window consists of a ceramic disk and a pill-box housing. The mix-mode rf window is designed so as to decrease the electric field on the periphery of the ceramic disk. A resonant ring has been assembled in order to examine a high-power transmission test. The window was tested up to a transmission power of 300 MW. The rf losses were also measured during rf operation.

INTRODUCTION

An upgrade of the KEKB injector linac is under consideration for the SuperKEKB project [1]. C-band rf sources (5712 MHz, 2 μs, maximum 50 MW) will be installed in the upgrade for a higher acceleration gradient of more than 40 MV/m [2]. The rf power (~40 MW) will be transmitted through an rf window and a pulse compressor, and delivered to acceleration structures. The rf window consists of an alumina ceramic disk and pill-box housing, which enables us to transmit the rf and separate the vacuum, which is one of the important components for this upgrade. A surface discharge due to electron emission at the edge of the ceramic under high rf fields results in excess surface heating, leading to punctures.

In this paper, the design of a mix-mode window [3], where the electric fields at the edge of the ceramic decrease, is described. The results of high-power tests using a resonant ring are also summarized.

DESIGN OF THE RF WINDOW

The new rf window is required to transmit rf power of 50 MW (2 μs, 50 pps). The criteria of the new C-band rf window are determined based on the electric fields of the S-band rf window. The S-band window has a long life with an MTBF of more than 100,000 hours [4] under an rf transmission of 50 MW (2856 MHz, 4 μs, 50 pps), and is reliable for long-time rf operation, even though leakage of the klystrons is one of the reasons for klystron failures. The electric field at the edge and center of the ceramic disk should be less than that of the S-band disk (84 mm in diameter and 3.2 mm in thickness). The bandwidth of the rf window should be more than 100 MHz, which is sufficiently wider than the performance of the klystron and/or the acceleration structure. The calculated values are given in Table 1. The electric fields at the edge and at the center of the ceramic are about 1.7 MV/m and 3.7 MV/m, respectively. In order to satisfy these requirements, it is necessary to enlarge the diameter of the alumina ceramic disk compared with the wavelength of the C-band, which indicates the transmission of the higher modes, such as a TM_{11} mode. By mixing the TE_{11} mode and the TM_{11} mode, lower electric fields can be accomplished, thus making a 'mix-mode window'. A high-purity alumina ceramic of HA-997 (99.7% purity, NTK Co.) having a high durability for the transmission of high power [5] has been adopted. A diameter of 78 mm and a thickness of 4 mm were chosen in order to avoid any resonant frequencies around the operation frequency (5712 MHz).

Table 1: Electric properties of the S-band rf window

Center of the ceramic	3.7 [MV/m@50MW]
Edge of the ceramic	1.7 [MV/m@50MW]
Maximum electric field on the surface of the ceramic	5.5 [MV/m@50MW]
Bandwidth (VSWR<1.2)	600 [MHz]

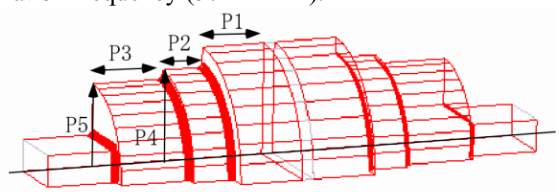

Figure 1: Schematic of the C-band window. The length of the first ring (P1), second ring (P2), third ring (P3) and inner radius of second (P4) and third ring (P5) are the parameters to be optimized.

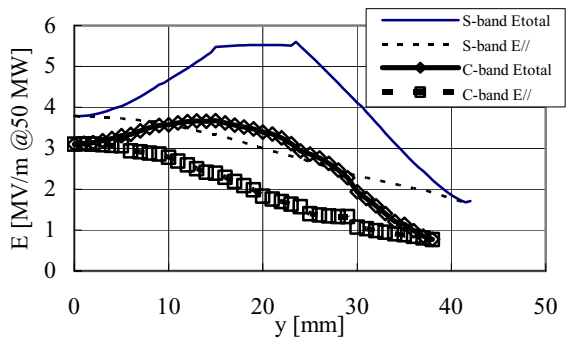

Figure 2: Electric fields on the ceramic disk calculated for C-band and present S-band rf window.

The window is constructed with a combination of three rings. Five parameters (Figure 1), which are necessary to match the two different modes in a same length, are optimized using HFSS. In order to avoid any volume resonance of TE_{012}-like and TM_{014}-like modes, the rf waves do not propagate as complete travelling waves in the ceramic disk (quasi-travelling wave). However, the

#shinichiro.michizono@kek.jp

electric fields at the center and edge of the disk are about 20% and 50% lower than the present S-band window, respectively, as shown in Figure 2. This indicates that that the electric fields at the power of 50 MW at C-band correspond to those at a power of 35 MW at the S-band, so that a longer MTBF will be expected compared with the present S-band window.

LOW LEVEL MEASUREMENTS

Several types of first and second rings having different P1 and P2 parameters were prepared for determining the final dimensions. The electric fields were measured by a perturbation method [6] using this low-level model. A cubic (3 mm) of Rutile having high permittivity is used in the measurements due to the low electric fields around the ceramic surface. The measured fields are shown in Figure 3. The electric fields were measured from the center of the rectangular waveguide (z=-100 mm) to the center of the ceramic disk (z=0). The measured and calculated data show good agreements.

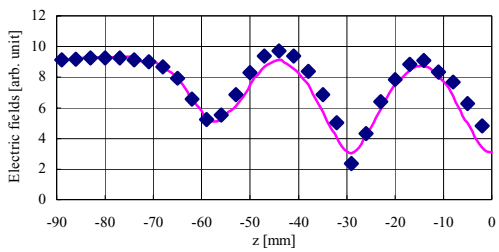

Figure 3: Measured electric fields at the center of the axis from the ceramic to the rectangular waveguide.

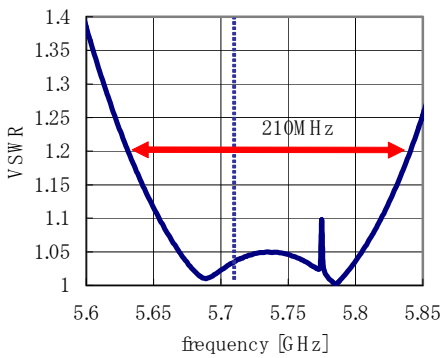

Figure 4: Bandwidth of the C-band rf window.

Table 2: Volume resonances near to the operation frequency

	Calculation	Measured
TM_{014}-like [GHz]	5.78	5.77
TE_{012}-like [GHz]	>5.85	>5.8

A window for high-power usage was coated with TiN films for multipactor suppression [7]. The measured band-width (VSWR < 1.2) is more than 200 MHz, as shown in Figure 4, which agrees well with the calculation. The volume resonances were also measured, as shown in Table 2. The TM_{014}-like mode locates at about 50 MHz higher than the operation frequency, and the resonance frequency is almost the same as the predicted one, based on a calculation using HFSS. Figure 5 shows a photograph of this C-band mix-mode window.

HIGH-POWER TEST USING A RESONANT RING

Resonant Ring

A resonant ring is designed for a high-power test of the rf window. A schematic of the ring is shown in Figure 6. The main characteristics of the ring are determined by the coupling ratio of the hybrid [8]. In this resonant ring, a coupling ratio of 14 dB is adopted, and a maximum of 18-times higher power than the klystron output is available in the ring.

The total length of the ring should be an integer of the wavelength. A rough adjustment was carried out inserting a spacer in the ring with a preciseness of 10 mm. Fine tuning was done by adjusting the operation frequency, which was 5710.2 MHz at a high-power test of the rf window. The resonant ring is evacuated by two non-evaporating getter pumps (NEGs) and two ion pumps located on both sides of the rf window. The base pressure was less than 10^{-7} Pa.

High Power Tests

High power tests were carried out with a waveguide instead of an rf window at first in order to progress the conditioning of the resonant ring. A maximum circulating power of 400 MW (2 μs) was achieved after about 10

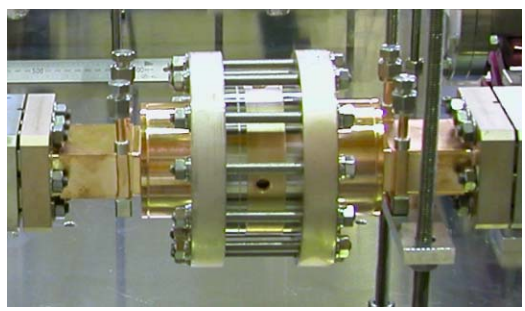

Figure 5: Photograph of the C-band rf window.

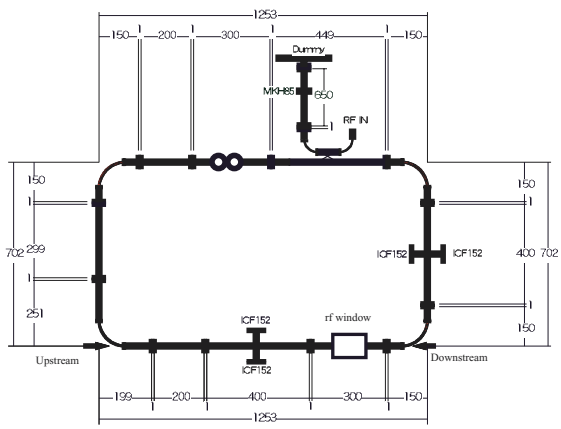

Figure 6: Schematic of the resonant ring.

days of operation. High power tests of the rf window were examined up to 300 MW (2 μs), finally. Figure 7 shows the rf power and vacuum pressure during 8 hours of operation. The rf trips took place only 3-times during operation.

The optical emission was measured during rf operation. Emission took place between about 70 MW and about

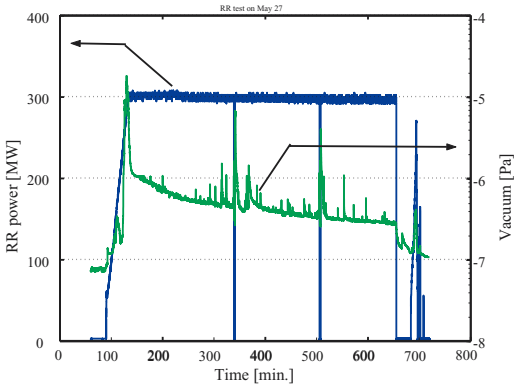

Figure 7: Rf transmission power through the rf window and vacuum pressure during 8 hours of operation.

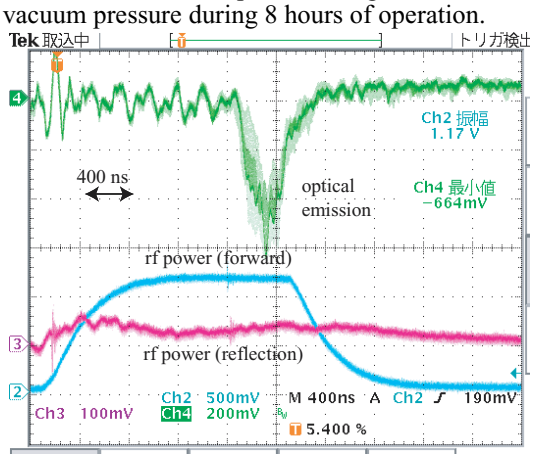

Figure 8: Rf transmission power together with the optical emission.

150 MW. The region of the optical emission depends on the past records, and it is considered that the surface charging of the ceramic disk affects the emission [9]. The spectrum of the optical emission was also measured, and it was confirmed that the emission was cathodoluminescence (luminescence induced by electron irradiation) from the alumina ceramic, caused by oxygen defects such as the F^+ center [5]. The optical emission was observed at a higher power than that of the present S-band window, probably caused by the lower electric field at the edge of the ceramic disk. The emission took place at the end of the rf pulse, as shown in Figure 8. A longer time is probably necessary to accumulate a sufficient number of electrons contributing to the optical emission.

The rf losses were measured by the increase in the temperature of the cooling water. The results are shown in Figure 9. The loss was 10 W at a transmission power of 10 kW, which is almost the same as the present S-band window. Since the ceramic thickness is 30% thicker than the S-band window, the effective rf losses per unit length

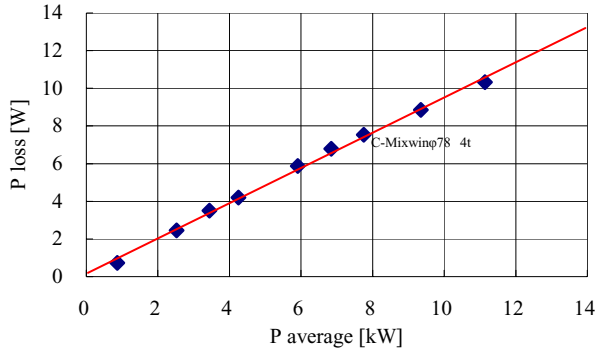

Figure 9: Rf losses at the ceramic disk measured by the temperature increase of the cooling water.

are smaller than that of the S-band window, which indicates the lower rf fields in the ceramic disk.

SUMMARY

The C-band rf window was designed based on a mix-mode structure. The electric fields at the edge of the ceramic, which are related to electric breakdown, become about half compared with that of the present S-band window. High-power tests were carried out with a resonant ring. The ring was evacuated to less than 10^{-7} Pa and was successfully operated up to 300 MW, which is about 6-times higher than the specification.

ACKNOWLEDGEMENT

The authors wish to thank Dr. Sergei Kazakov of BINP for discussions and suggestions about the calculation of the mix-mode window.

REFERENCES

[1] SuperKEKB Letter of Intent (LoI), KEK Report 04-4 ,August,2004, http://belle.kek.jp/superb/loi/

[2] S.Michizono, "KEKB INJECTOR LINAC AND UPGRADE FOR SUPERKEKB", this conference.

[3] S.Yu.Kazakov, "A New Traveling-Wave Mixed-Mode RF Window With a Low Electric Field in Ceramic-Metal Brazing Area", KEK preprint 98-140, Aug. 1998.

[4] S. Michizono et al., App. Surf. Sci., 169-170 (2001) 742.

[5] S. Michizono et al., IEEE Trans. Electr. Insul. 28 (1993) 692.

[6] C.W.Steele, IEEE Trans. on Microwave Theory and Tech. 14 (1966)70.

[7] S. Michizono et al., J. Vac. Sci. Technol. A10 (1992) 1180.

[8] L.J.Milosevic and R.Vautey, Inst.Radio Engrs. Trans., MTT-6(1958)136.

[9] S. Michizono and Y. Saito, "SURFACE CHARGING BY UV IRRADIATION AT THE ALUMINA RF WINDOW", Proc. of 20th ISDEIV, Tours, June, 2002.

LOW LEVEL RF INCLUDING A SOPHISTICATED PHASE CONTROL SYSTEM FOR CTF3

J. Mourier, R. Bossart, J.-M. Nonglaton, I. Syratchev and L.Tanner
CERN, Geneva, Switzerland

Abstract

CTF3 (CLIC Test Facility 3), currently under construction at CERN, is a test facility designed to demonstrate the key feasibility issues of the CLIC (Compact LInear Collider) two-beam scheme. When completed, this facility will consist of a 150 MeV linac followed by two rings for bunch-interleaving, and a test stand where 30 GHz power will be generated. In this paper, the work that has been carried out on the linac's low power RF system is described. This includes, in particular, a sophisticated phase control system for the RF pulse compressor to produce a flat-top rectangular pulse over 1.4 μs.

INTRODUCTION

An international collaboration is currently building CTF3 (CLIC Test Facility 3) at CERN. When completed, this facility will consist of a 150 MeV 3 GHz linac followed by two rings for bunch-interleaving and a test stand where 30 GHz power will be generated [1]. Its aim is to demonstrate the key feasibility issues of the CLIC (Compact LInear Collider) two-beam scheme [2]. At present, the linac is being constructed and commissioned in stages and well over half is completed. Six 35 MW to 45 MW 3 GHz klystrons are operational. One powers two standing-wave pre-buncher cavities and a travelling-wave buncher. The others each power two damped travelling-wave accelerating structures with a loaded gradient of 6.5 MV/m. Commissioning results in 2003 demonstrated full beam loading operation of these structures with the nominal beam current of 3.5 A [3].

CTF3 uses a large part of the infrastructure of LPI, the now decommissioned LEP pre-injector linac. This includes re-use of modulators, klystrons and LIPS pulse compressor cavities at the klystron output [4]. RF pulse compression is mandatory in order to reach the required power level of over 30 MW for the 1.5 μs pulses at each structure's input. In LPI, the phase function for compression consisted of a straightforward 180^{O} phase inversion at the klystron driver's output. However in CTF3, with much longer bunch trains of 1.4 μs, a much more sophisticated phase function was required and this was one of the principal reasons why the low level RF system needed a complete re-design. In this paper, an overview of the current status of the CTF3 low level RF system is presented, concentrating on the pulse compression phase control scheme.

AMPLITUDE AND PHASE CONTROL

The layout of the low power system for one klystron is shown in Figure 1. The 3 GHz is distributed from a master synthesizer to the low level equipment of each klystron over low-loss phase-stable 7/8-inch coaxial cable. To minimize differential phase variations with temperature, equal lengths of cable are used (100 m ±1 cm). The 360^{O} "digital" phase shifter (analogue with integrated DAC) is slow and is used for adjusting the

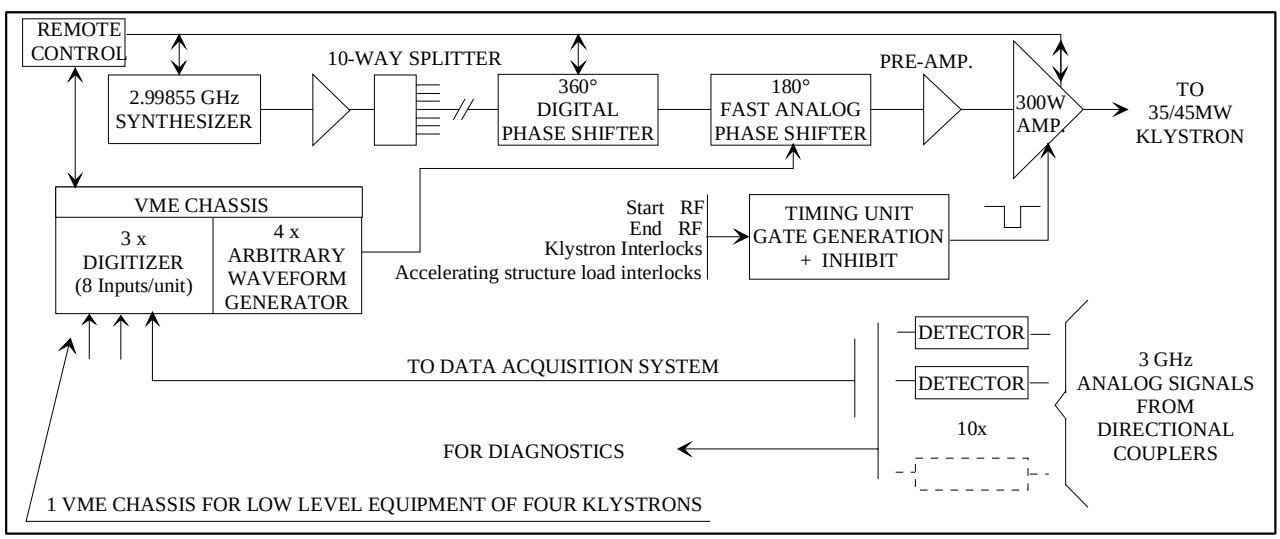

Figure 1: Simplified block diagram of low level system.

klystron phase relative to the beam. The 180^{O} analogue phase shifter has a step response of 10 ns. It is controlled by a VME-based 100 MS/s arbitrary waveform generator that produces the phase function for pulse compression. Both phase shifters have a temperature coefficient specification of less than $0.15^{O}/^{O}C$.

The continuous wave RF signal is fed to a 300 W power amplifier that incorporates an input PIN diode switch producing the pulse. Key specifications of the amplifier are the stability of amplitude and phase during the pulse of less than 0.2 dB and less than 3^{O} respectively. The first five of these amplifiers were purchased in industry. However, for reasons of economy, it was decided to fabricate the remaining amplifiers at CERN. The development work is now completed. They consist of a chain of cascaded NPN silicon class C power transistor stages on a low-loss substrate. The end of the chain is split and terminates in two 190 W stages that are combined in a hybrid. The amplifier output feeds the klystron via a circulator.

The timing unit has two functions. Firstly, it interfaces the amplifier to the machine timing system's start and end RF production events. These permit remote setting of the klystron RF pulse length. Secondly, it is part of the interlock system and, under certain conditions, will inhibit the driver output pulse. This is the case for certain modulator or klystron problems or, for example, if the power limit of the accelerating structure output loads is exceeded. This can occur with beam if the klystron phase is incorrect.

SIGNAL ACQUISITION AND DIAGNOSTICS

The low level RF system includes a data acquisition system permitting real-time display of a variety of signals such as the phase and amplitude of the klystron output, pulse compressor output and accelerating structure input and output. It consists of 3 GHz phase and amplitude detectors followed by 100 MS/s VME-based ADC cards. The system has proven indispensable during both RF conditioning and machine operation. During conditioning it facilitates the localisation of breakdowns and other anomalies. During operation the system permits real time observation of detected RF waveforms in the CTF3 control room. This is particularly important when setting

Figure 2: LIPS pulse compressor.

Figure 3: BOC pulse compressor.

up the RF pulse compression. At present there are 56 detectors, 29 of which have digitized outputs. These numbers will increase to 110 and 59 respectively when CTF3 is completed.

RF PULSE COMPRESSION SYSTEM

CTF3 requires nine RF pulse compression systems that will give a power gain of about two in klystron peak power. Since only a limited number of LIPS systems (Figure 2) was available from LPI, additional systems were built based on the Barrel Open Cavity (BOC, Figure 3). Such a system (VPM) was developed for the VLEPP linear collider [5] and an X-band version was successfully tested at KEK at an RF power level of 150 MW [6]. Unlike the LIPS system that uses two standing-wave cavities coupled via a 3 dB hybrid, BOC consists of a single cavity [7].

In order to achieve a compressed pulse with a flat top in amplitude, the RF input to the compressor follows a pre-defined phase modulation function. An example of the compressed pulses for two different klystron pulse lengths is shown in Figure 4. The typical shape of the phase modulation function and the resulting compressor output phase is shown in Figure 5. CTF3 has a stringent specification on the stability of the compressed RF pulse of ±1% in amplitude and 5^{O} in phase. To compensate the phase ramp $\Delta\phi$ introduced by the modulation, a detuning of 130 kHz is added [8]. The residual phase variation is compensated by operating alternate klystrons with an inverse phase function. To make best use of the total modulator pulse length, the RF is switched on during the rising edge of the modulator pulse.

Fine frequency tuning of both the LIPS and BOC is achieved by precise temperature control of the cavities. To keep within the required flatness of the compressed

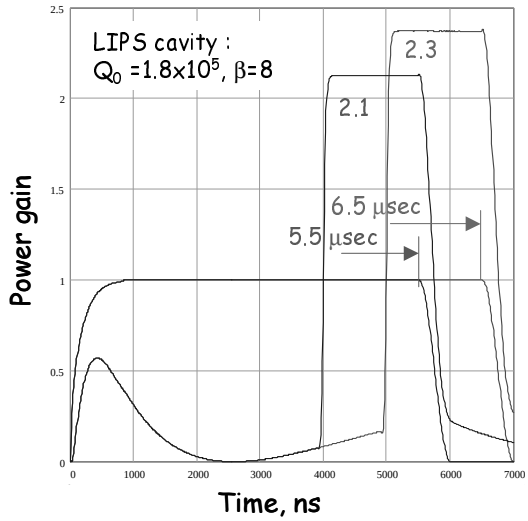

Figure 4: Compressed pulses for two different klystron pulse lengths.

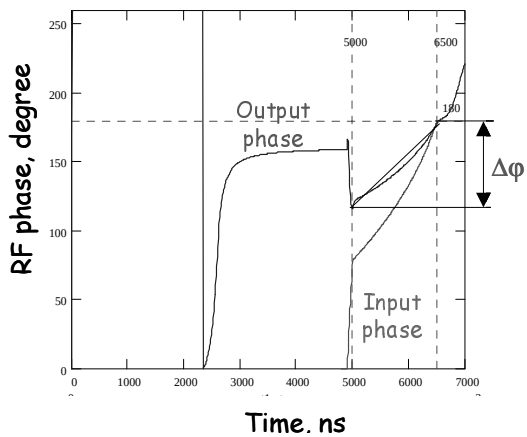

Figure 5: Input and output RF phases.

pulse, their resonant frequencies must be stabilised to ±1.5 kHz (Figure 6). This corresponds to ±0.03^{O}C of maximum permitted temperature variation. Each compressor is connected to an independent remote controlled cooling station. For the BOC cavities, this is the sole tuning method and they require a ±5^{O}C temperature range. The LIPS cavities incorporate tuners for coarse frequency control.

The phase function is generated by the VME arbitrary waveform generator modules referred to in the previous section. The 500 data points that cover the 5 μs pulse are downloaded into local memory via high-level application software. A programme has been developed that analyses the compressed RF pulse and, in an iterative process, optimises its phase and amplitude characteristics by varying the input phase function. It also compensates the parasitic phase modulation introduced by the klystron. A software check on the slew-rate of the phase function is made so as to avoid dangerous peaks of RF power at the output of the compressor cavity.

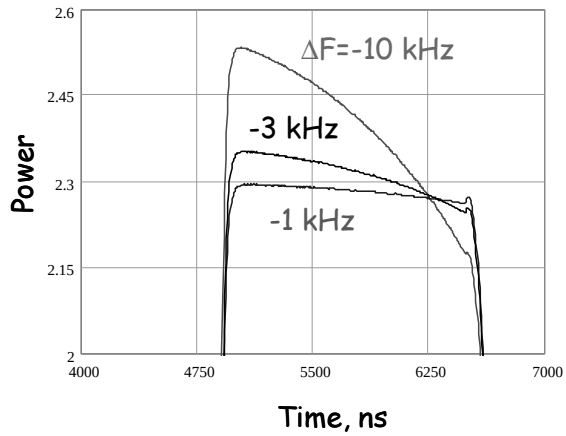

Figure 6: Sensitivity to detuning.

CONCLUSIONS

Staged commissioning of the CTF3 linac in 2003 and 2004 has already demonstrated the proper functioning of the low level RF system. The remaining 3 GHz klystrons will be equipped with the same hardware. Additional work on the CTF3 RF low level will include systems for the 1.5 GHz sub-harmonic bunchers and RF deflector. These will be required for bunch-interleaving when the two rings are constructed [1].

REFERENCES

[1] G. Geschonke and A. Ghigo (editors), "CTF3 design report", CERN/PS 2002-008 (RF).

[2] G. Guignard (editor), "A 3 TeV e^+ e^- linear collider based on CLIC technology" CERN 2000-008.

[3] R. Corsini *et al*., "First full beam loading operation with the CTF3 linac", 9th European particle accelerator conference EPAC2004, 5 to 9 July 2004, Lucerne.

[4] A. Fiebig and R. Hohbach, "Study of peak power doublers with spherical resonators", Proc. 1983 particle accelerator conference, Santa Fe, 21-23 March 1983, pp.3563-5.

[5] V. E. Balakin and I. V. Syrachev, "Status of VLEPP RF Power Multiplier", Proc. 3rd European Particle Accelerator Conference EPAC92, Berlin, 24-28 March 1992, pp.1173-5.

[6] I.V. Syrachev, V.F. Vogel, H. Mizuno, J. Odajiri, Y. Otake, S. Tokumoto. "The Results of RF High Power Tests of X-Band Open Cavity RF Pulse Compression System", Proc. int. conference Linac-94, Tsukuba, pp. 475-477, 1994.

[7] I. V. Syratchev, "RF pulse compressor systems for CTF3", Proc. 5-th MDK Workshop, Geneva, June 2001.

[8] R. Bossart, P. Brown, J. Mourier, I. V. Syratchev, L. Tanner "High-Power Microwave Pulse Compression of Klystrons by Phase-Modulation of High-Q Storage Cavities", CERN-OPEN-2004-015; CLIC Note 592.

HIGH-POWER RF DISTRIBUTION SYSTEM FOR THE 8-PACK PROJECT*

Christopher Nantista, Sami Tantawi, Jose Chan, David Schultz, SLAC, Menlo Park, CA 94025, USA, Dennis Atkinson, LLNL, Livermore, CA 94550, USA, Sergey Kazakov, KEK, Tsukuba, Japan

Abstract

The 8-Pack Project at SLAC is a prototype rf system whose goal is to demonstrate the high-power X-band technology developed in the NLC/GLC (Next/Global Linear Collider) program. In its first phase, it has reliably produced a 400 ns rf pulse of over 500 MW using a solid-state modulator, four 11.424 GHz klystrons and a dual-moded SLED-II pulse compressor [1]. In Phase 2, the output power of our system has been delivered into the bunker of the NLCTA (Next Linear Collider Test Accelerator) and divided between several accelerator structures for beam acceleration. We describe here the design, cold-test measurements, and processing of this power distribution system. Due to the high power levels and the need for efficiency, overmoded waveguide and components are used. For power transport, the TE_{01} mode is used in 7.44 cm and 4.064 cm diameter circular waveguide. Only near the structures is standard WR90 rectangular waveguide employed. Components used to manipulate the rf power include transitional tapers, mode converters, overmoded bends, fractional directional couplers, and hybrids.

INTRODUCTION

As part of the research and development for the future linear collider, SLAC has undertaken the 8-Pack Project, its goal being the realization of a working prototype rf system of the type envisioned for a machine powered by warm X-band technology, as in the NLC/GLC (Next/Global Linear Collider) designs. Employing a state-of-the-art solid-state modulator, four 50 MW klystrons, dual-moded transmission waveguides, and a novel dual-moded SLED-II pulse compression system, this project has had remarkable success in reliably generating 400 ns flat compressed pulses of 500 MW and above. This phase of the project is reported on elsewhere [1,2].

In this paper, we describe Phase 2 of the 8 Pack Project, in which the power produced in Phase 1 is used to conduct gradient tests and accelerate beam in accelerator structures. To this end, we have designed and constructed an rf distribution system to transport the high power pulses into the NLCTA (Next Linear Collider Test Accelerator) bunker and distribute them between several structures. As the use of overmoded waveguide and components is dictated by the need for high power-handling capacity and reasonable efficiency, such a system is non-trivial. Indeed, the interface between power sources and the accelerator represents an important part of an rf module, increasingly so as the design has moved toward higher peak-power pulses and shorter structures, requiring more division.

* Work supported by the U.S. Department of Energy under contract DE-AC02-76SF00515.

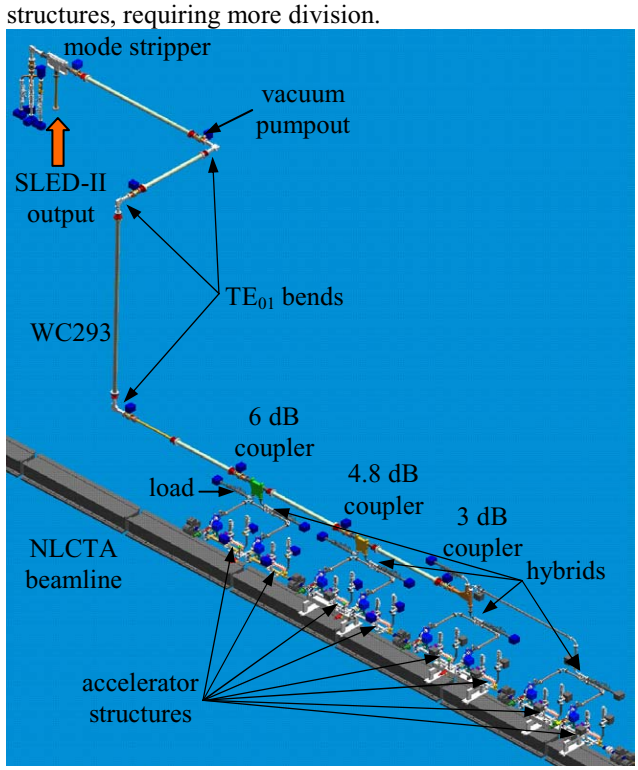

Figure 1: Physical layout of the distribution system from the 8-Pack pulse compressor to the accelerator structures.

SYSTEM LAYOUT

A scaled graphical representation of the distribution waveguide system, picking up from the output of the SLED-II system, is shown in Figure 1. The dual-moded nature of the Phase 1 system [3], along with the project title, is a vestige of the originally conceived configuration (retained for power source versatility and to test components capable of accommodating either option). The distribution system uses only the TE_{01} mode in circular waveguide. A "mode stripper" thus replaces the splitter that previously divided the output power into a series of eight loads. It directs any TE_{11} power due to source mismatch/misphasing into a smaller four-load tree while bending the desired power horizontally.

Due to the position and orientation of our pulse compression system, three more overmoded 90° bends are required to bring the power parallel and in close proximity to the NLCTA beamline. The vertical run penetrates the roof of the concrete bunker housing the

accelerator. While components are fitted with circular flanges of 1.6 inches (4.064 cm), transmission runs of significant length are made in 2.93 inch (7.442 cm) guide, for which the attenuation is reduced by a factor of nine. Short tapers connect these diameters.

Directional coupler power dividers are shown to split off first one fourth, then one third, and finally one half of the power flowing along the main transmission line. The power can thus be split equally between four pairs of structures. Directional couplers are used, rather than three-port tap-offs, so that the structures will be uncoupled in case of breakdown reflections. High-power loads are installed on the fourth ports.

A second level of power division, between each structure pair, is accomplished with hybrids of the "magic H" type [4]. Although the hybrids have double height interiors, this part of the distribution system, including bends and diagnostic directional couplers, uses standard WR90 waveguide. The power is low enough and this provides mechanical flexibility needed at the accelerator structure inputs.

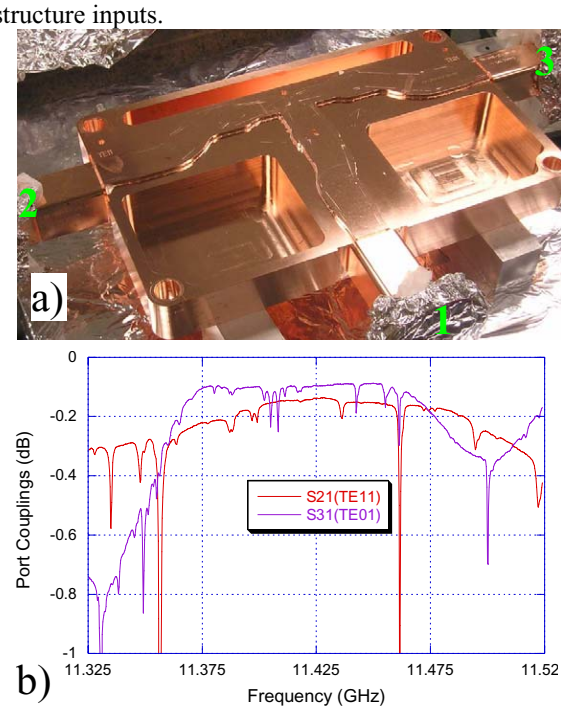

Figure 2: a) Mode stripper with brazed circular-to-rectangular tapers. TE_{11} power at the bottom input port is directed to the left port (as TE_{01}) and TE_{01} power is directed to the right port. b) network analyzer measurements of TE_{11} (red) and TE_{01} (purple) transmission. Losses and bandwidths are dominated by the mode launchers used for cold tests.

OVERMODED COMPONENTS

While circular flanges are used at all overmoded joints in the distribution system, the interiors of several components manipulate power in the TE_{10} and TE_{20} modes of over-height (1.435 inch) rectangular waveguide, as in the Phase 1 components. This facilitates the design of such components without unduly limiting their power-handling capacity. The transition from and to circular TE_{01} at the ports is accomplished with mode converting tapers described in [5].

Mode Stripper

The "mode stripper" removes TE_{11} power propagated past the pulse compressor by the Phase 1 system. In a final rf system, such power would never be launched, but rather dumped directly into a high-power load through the combining hybrid. It is in essence the same as the input of the SLED-II head which directs the modes through or past SLED-II.

After conversion of circular TE_{01} and TE_{11} into rectangular TE_{20} and TE_{10} respectively, a slight jog couples the latter two modes, creating a 50/50 mix from either. A T-junction follows, matched for both modes and precisely spaced so that the orthogonal mixes resulting from either input add in one port and cancel in the other. After a width taper and mode-converting jog, more pronounced than the mixing jog, the power sent either way enters a rectangular-to-circular converter as TE_{20} to emerge at the port as TE_{01}. Figure 2 shows the actual device and cold test measurements. TE_{11} leakage to the TE_{01} port was -39 dB.

Bends

The system uses three compact, high-power 90° TE_{01} bends. The 1.600 inch diameter ports give an effective bend radius of less than ten inches. This component is composed of two circular-to-rectangular tapers and a simple overmoded rectangular H-Plane bend. The latter is designed such that TE_{10} and TE_{20} are allowed to mix in the interior but the input mode is restored at the end. Although we use the bend here only for TE_{01}, it is actually a dual-mode bend, working equally for TE_{11}, albeit restricted to the H-plane. Figure 3 shows a drawing of the component and a field simulation of the interior.. Losses measured through these bends were on the order of one percent.

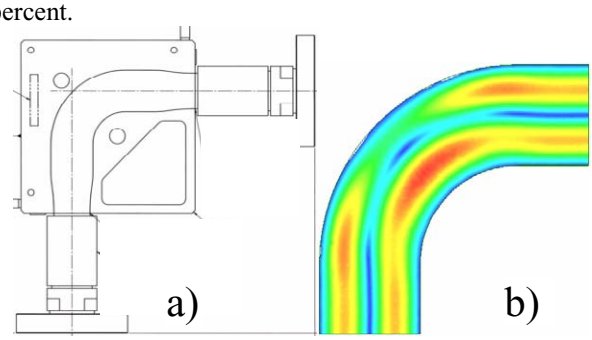

Figure 3: a) High-power TE_{01} bend with converters and b) electric field plot of interior overmoded rectangular H-plane bend.

Fractional Directional Couplers

To divide power between eight structures, one could use three levels of binary hybrid splitting. To provide more flexibility (e.g. to be able to feed six structures) we chose rather to use hybrids only for the lowest level of

splitting between pairs of structures and fractional power dividers in series in the main transfer line to extract the appropriate power for each pair – first 1/4, then 1/3 of what remains, and finally 1/2. The interior of the latter is identical, except in height, to the lower level hybrids. The former two have modified designs of the same geometry [6], for which the phase length difference of the interior waveguide for the two modes it supports is appropriately adjusted. The planar design of the 1/4, or 6 dB, directional coupler, along with an electric field plot, is shown in Figure 4a.

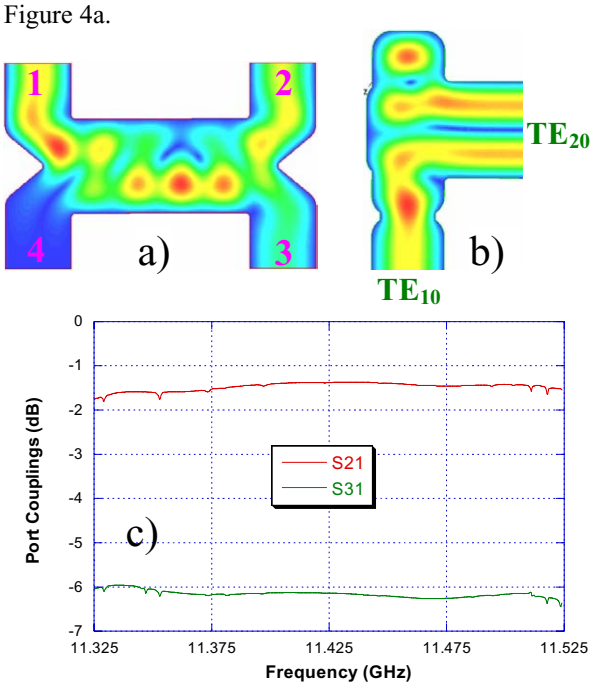

Figure 4: a) 6 dB directional coupler geometry with electric field plot, b) TE_{10}-TE_{20} mode converter attached to upper ports with field plot, and c) network analyzer measurement of power split through the device.

A new feature incorporated into two of these directional couplers is a compact right-angle TE_{10}-TE_{20} converter [5] at each port connected to the TE_{01} transfer line. It connects the 0.900 inch wide rectangular port to the rectangular-to-circular taper, replacing a mitred bend, width taper, and jog converter used in the previously fabricated 3 dB coupler. Its shape and function are shown in Figure 4b. To the lower coupler ports are brazed smooth height tapers down to WR90, through which the forward port is connected to a hybrid and the reverse port to a load.

Figure 4c is a plot of the coupling S parameters of the 6 dB coupler. The measured loss, correcting for the cold test mode launchers, is ~2%, and the split 66.3%/33.7%. For the 4.8 dB coupler, these numbers were ~0.6% and 75.1%/24.9%. For the 3 dB coupler, they were 1.3% and 49.5%/50.5%. Port matches and isolations measured from -34−-59 dB. Cold tests of the four WR90 hybrids (with double height interior) showed losses ranging from 0.8%−1.7%, largely attributable to the measurement flange adaptors, and split ratios differing from unity by 0.67% on average, 1.6% maximum.

PERFORMANCE

The rf distribution system described here has not yet been fully installed. As an intermediate step, we have powered only the last four structures with the 8-Pack by omitting the 6 dB and 4.8 dB directional couplers. The WR90 run to the final structure pair shown in the main transfer line was replaced with 1.6 inch circular waveguide to reduce losses and the risk of rf breakdown. As with any overmoded system, care had to be taken during installation to avoid resonances.

In this configuration, we have successfully performed months of high-gradient accelerator structure testing, running at the 300 MW level. Processing of the system was quick and painless, driven by the structures, although the upstream components see only about half their intended power. From the output of SLED-II to the diagnostic directional couplers at the inputs of the structures, the average efficiency of the system was measured to be ~85%, without noticeable distortion of the tailored pulse shape. An anomalously large difference (on the order of 10%) between powers measured at structures 7 and 8 may be due to a calibration error (At tens of megawatts, measurements must be made through ~95 dB of attenuation.). This will be further investigated when the structure installation schedule allows.

REFERENCES

[1] S.G. Tantawi, *et al.*, "Experimental Demonstration of an RF System for the X-Band Linear Collider," presented at the 3rd Asian Particle Accelerator Conference (APAC 04), Gyeongju, Korea, March 22-26, 2004; SLAC-PUB-10550.

[2] S. Tantawi, *et al.*, "Status of High-Power Tests of the Dual-Mode SLED-II System for an X Band Linear Collider," invited talk, these proceedings.

[3] S. Tantawi and C. Nantista, "High Power Tests of a Multimode X-Band RF Distribution System," proceedings of the 2003 Particle Accelerator Conference (PAC 03), Portland, OR, May 12-16, 2003, pp. 482-486.

[4] C.D. Nantista, *et al.*, "Planar Waveguide Hybrids for Very High Power RF," presented at the 1999 Particle Accelerator Conference, New York, NY, March 29−April 2, 1999; SLAC-PUB-8142.

[5] Christopher D. Nantista and Sami G. Tantawi, "Overmoded Rectangular Waveguide Components for a Multi-Moded RF Power Distribution System," presented at the 7th European Particle Accelerator Conference (EPAC 2000), Vienna Austria, June 26-30, 2000; SLAC-PUB-8500.

[6] Christopher D. Nantista, "Overmoded Waveguide Components for High-Power RF," proceedings of the 6th Workshop on High Energy Density and High Power RF (RF 04), Berkeley Springs, WV, USA, June 22-26, 2003, pp. 263-271; SLAC-PUB-10218.

SKIP - A PULSE COMPRESSOR FOR SUPERKEKB

T. Sugimura, T. Kamitani, K. Yokoyama, K. Kakihara, M. Ikeda and S. Ohsawa
KEK, 1-1, Oho, Tsukuba, Ibaraki, Japan

Abstract

A C-band RF pulse compressor "SKIP", which stand for SuperKEKB Injector Pulse compressor, has been developed for the SuperKEKB project aiming luminosity upgrade of the present KEK-B factory. The design of the compressor using $TE_{0,3,8}$ mode cylindrical cavity is based on the "LIPS" used in the LEP injector S-band linac. Detailed dimensions of the cavity have been optimized for C-band (5712 MHz) with low power models. In the high power test of the pulse compressor, a peak output power of 200 MW is achieved with the input RF power of 43MW in 2 μsec duration.

INTRODUCTION

KEKB attained the highest luminosity ($1.3\times10^{34}cm^{-2}s^{-1}$) in the world. SuperKEKB, an upgrade of KEKB whose target luminosity is 1-5 $\times10^{35}$ $cm^{-2}s^{-1}$ is under consideration [1]. In the SuperKEKB project, energy exchange of beams has an important role. In order to escape the influence of electron clouds, the energy of an electron beam is lowered to 3.5 GeV from 8 GeV, and the energy of a positron beam is raised from 3.5 GeV to 8 GeV. Although it is easy to lower the energy of an electronic beam, it is not easy to raise the energy of a positron beam. A positron is a secondary particle, and after generating it, the space in which a positron beam is accelerated is restricted. One of solutions is to double an acceleration field. Thus the C-band accelerator module which has double acceleration field has been developed [2]. In the summer of 2003, an accelerating structure was installed into the beam line and beam acceleration has been performed since. The acceleration gain with the accelerating structure is 40 MeV/m, feeding power from a klystron into one 1m-long structure. In the complete composition of accelerator module, one klystron feeds two 2m-long structures. Since peak power runs short with the present 50 MW class klystron in such a case, an RF pulse compressor is essential.

Modified RF pulse compressors of SLED are used in the sections of S-band [3]. The half-scale model of S-band structure was adopted in the design of an accelerating structure [4]. In the design of a pulse compressor, when the scale down model of S-band is considered, sufficient Q factor is not acquired. Then, another design plan is needed. We considered using the cavity in the $TE_{0,3,8}$ mode adopted in the LIPS cavities [5]. The Q factor of about 150,000 is expected in $TE_{0,3,8}$-mode cavity. Thereby, an energy multiplication factor of the same as SLED for S-band can be obtained.

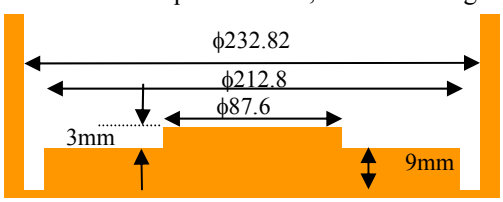

Figure 1: Sectional view of the groove

DESIGN

As already stated, the cavity in the $TE_{0,3,8}$ mode was adopted. Considering a simple cylindrical cavity, there are two adjustable parameters such as diameter and height. For the first step, a scale down model of LIPS cavity is considered. The diameter of 232.82 mm is as almost same as the present S-Band SLED type pulse compressor in KEKB injector linac. It is necessary to investigate the resonance modes of a cylindrical cavity with such form. The mode which should be most careful of is the $TM_{1,3,8}$ mode which is degenerating with the $TE_{0,3,8}$ mode. It is also necessary to take care about the $TE_{12,1,1}$ mode. In order to detune these modes, there is a groove on the base plate as shown in a Fig1. In the numerical computation by MAFIA, these modes are detuned, as shown in the Table1.

Table 1: Frequency shift by groove

Mode	F_0(MHz)	ΔF from $TE_{0,3,8}$ (MHz)
$TM_{1,3,8}$	5684.525	-12.723
$TE_{12,1,1}$	5708.321	11.073
$TE_{0,3,8}$	5697.248	0

An energy multiplication factor M is given by [6]

$$M = \gamma e^{-T_a/T_c}\left[1-(1-g)^{1+\nu}\right]\left[g(1+\nu)\right]^{-1} - (\alpha - 1),$$

where T_a is the filling time of the accelerating structure, T_c is the filling time of the cavity, $\alpha=2\beta/(1+\beta)$ and $\nu=T_a/T_c[ln(1-g)]$. The group velocity vg varies linearly with the position z according to $v_g(z)= v_{g0}(1-gz/L)$, where v_{g0} is a group velocity at position $z=0$, L is the length of the accelerating structure and g is the quantity about the gradient of a group velocity v_g variation along the structure. For the case of C-band accelerator, characteristic parameters of RF are given in Table 2. Using these values, relation between coupling factor β and energy multiplication factor is represented in Fig. 2.

Table 2: Main RF parameter

Frequency	5712 MHz
Q_0	130000
T_a	350 nsec
g	0.6
L	1.924
Full RF pulse width	2.00 μsec
Pulse width before phase inversion	1.65 μsec

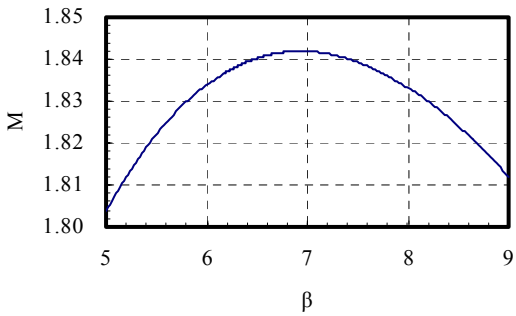

Figure 2: Energy multiplication factor as a function of coupling factor β.

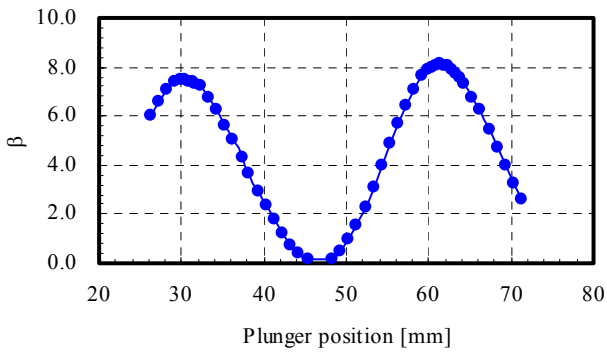

Figure 3: Measured coupling factor β as a function of position of short plane when the diameter of hole is 18.8 mm.

COLD MODEL

In order to determine the dimensions of the compressor, a cold model was manufactured and RF measurement was performed. Using the cold model, cavity length was determined so that the resonant frequency becomes 5712 MHz. +1mm of cavity length is equivalent to -8.7 MHz on frequency.

The cavity is coupled to the waveguide through two holes on the sidewall of waveguide. They are half wave length away from each other. Figure 3 shows a relation between β and position of short plane. The position of a short plane is optimized in order to maximize β and is about 3/4 wave length, which corresponds to the plunger position of 61.3 mm, off the one of coupling holes.

Figure 4 shows relations between β and Diameter of coupling hole computed by MAFIA. Three coupling plate with different thickness were prepared based on the relations, and each β and Q factor was measured with changing a diameter of the holes. Figure 5 shows a relation between the length of coupling hole and β. Although the tendency of an actual measurement result suited the calculation result, some absolute values had shifted. The diameter and length were determined by cold-model measurements to be 18.8mm and 6mm, respectively. Under these conditions, unloaded Q factor is 148000. Figure 6 shows that there are 8 resonances near 5712 MHz. By bead perturbation measurement of a field inside the cavity in the radial and longitudinal directions, it turns out that the number of nodes of the resonance "e" is consistent with the $TE_{0,3,8}$ mode as expected.

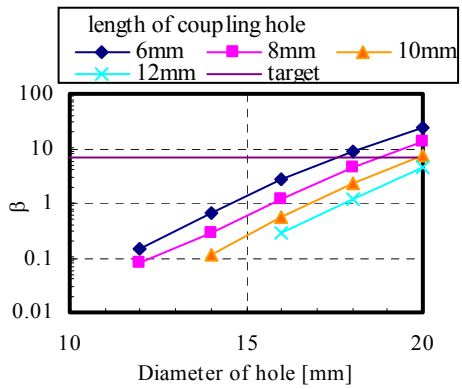

Figure 4: Calculated coupling factor β as a function of diameter of coupling hole.

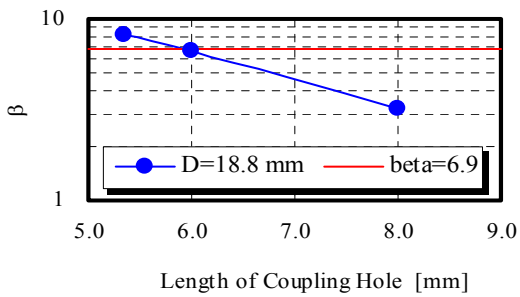

Figure 5: Measured coupling factor β as a function of length of coupling hole when the diameter of hole is 18.8 mm.

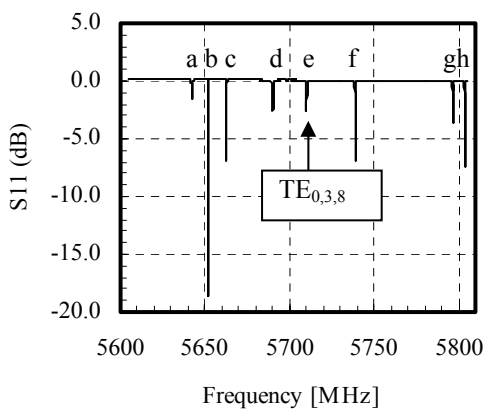

Figure 6: Reflection from the cavity (S_{11}). There are 8 resonances near 5712 MHz.

HOT VERSION

The first product is manufactured based on the dimensions determined with the cold model. However, unloaded Q value and β were smaller than those of the cold model. It is expected to come from the difference in

the processing method of a coupling plate. Although coupling plate of the cold model was processed with a lathe, the plate of the hot version was processed with a milling cutter. As a result, the roughness of the surface of a coupling plate differed, and unloaded Q value and β fell. Therefore, the length of holes was reduced to 5.35 mm from 6 mm in order to achieve sufficient β.

Results of RF measurement for hot version of cavities are listed in Table 3. A 3dB-hybrid coupler is attached to two cavities and it is completed. Figure 7 shows a whole view of the RF pulse compressor. Figure 8 shows the 3dB-hybrid coupler for the pulse compressor.

Table 3: Measured parameter of Cavities (30 centigrade, N_2 gas)

	Q_0	β
Cavity A	136000	6.71
Cavity B	137000	6.79
Cavity A,B with 3dB coupler	133000	6.59

After an RF processing of about 170 hours, the peak output power attained 200 MW at a repetition rate of 50 pps with the pulse duration of 2 μsec. Figure 9 shows some forms of RF pulses. RF power at the exit of a klystron and the exit of the pulse compressor was measured, and it turns out that the ratio of the peak output power to input power is 4.7.

This RF pulse compressor is named "SKIP" (SuperKEKB Injector Pulse compressor). SKIP is now installed into the RF system of C-band accelerator module of injector linac for KEKB, PF (Photon Factory) and PF-AR (Advanced Ring). It will be tested for a year under the real operation. The energy multiplication factor M will be measured in the beam acceleration test.

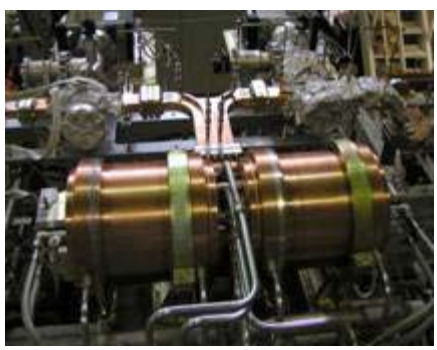

Figure 7: Whole view of the pulse compressor "SKIP" at test stand.

SUMMARY

A C-band pulse compressor SKIP with $TE_{0,3,8}$-mode cylindrical cavities is developed. It achieves a peak output power of 200 MW with the input RF power of 43 MW and the repetition rate of 50 pps.

Figure 8: Whole view of 3dB-hybrid coupler (left) and waveguide for low power RF measurement (right).

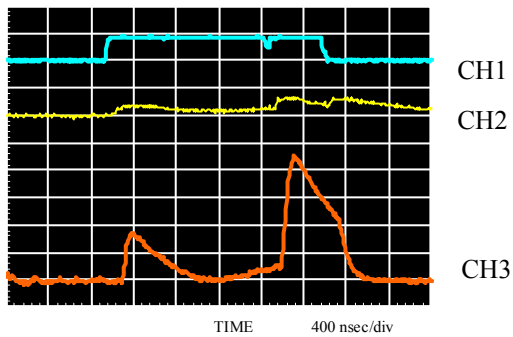

Figure 9: Form of input signal (CH1), VSWR (CH2) and output signal of SKIP (CH3). They are plotted in arbitral units in vertical axis. The peak of CH3 exceeds 200 MW.

ACKNOWLEDGEMENT

The authors would like to give their sincere thanks to Mitsubishi Heavy Industries, LTD. for their powerful cooperation.

REFERENCES

[1] J. W. Flanagan, Y. Ohnishi, et al., Letter of Intent for KEK Super B Factory, Part III: Accelerator Design, KEK Report 04-4

[2] S. Michizono, et al., "KEKB INJECTOR LINAC AND UPGRADE FOR SUPERKEKB", this conference.

[3] I. Sato, et al, "design report on PF Injector linac Upgrade for KEKB", KEK Report 95-18, in Japanese

[4] T. Kamitani, et al., "Development of C-band accelerating section for SuperKEKB", this conference.

[5] A. Fiebig, et al., "Design considerations, construction and performance of a SLED-type radiofrequency pulse compressor using very high Q cylindrical cavities", CERN/PS 87-45(RF) March, 1987

[6] Z. D. Farkas, et al., "SLED: A method of doubling SLAC's energy" SLAC-PUB-1453, June, 1974

WAVEGUIDE STUB TUNER ANALYSIS FOR CEBAF APPLICATION*

H. Wang#, M. Tiefenback, Jefferson Lab, Newport News, VA 23606, USA

Abstract

Three-stub WR650 waveguide tuners have been used on the CEBAF superconducting cavities for two changes of the external quality factors (Q_{ext}): increasing the Q_{ext} from $3.4\sim7.6\times10^6$ to 8×10^6 on 5-cell cavities to reduce klystron power at operating gradients and decreasing the Q_{ext} from $1.7\sim2.4\times10^7$ to 8×10^6 on 7-cell cavities to simplify control of Lorenz Force detuning. To understand the reactive tuning effects in the machine operations with beam current and mechanical tuning, a network analysis model was developed. The S parameters of the stub tuner were simulated by MAFIA and measured on the bench. We used this stub tuner model to study tuning range, sensitivity, and frequency pulling, as well as cold waveguide (WG) and window heating problems. Detailed experimental results are compared against this model. Pros and cons of this stub tuner application are summarized.

INTRODUCTION

Most applications of a three-stub tuner modifying a superconducting cavity input coupling are on storage rings, to match RF power to heavy beam loading and off-crest conditions. An early implementation was at DESY [1]. The analysis method used an equivalent circuit including the three-stub tuner. Recently, a similar application has been employed at CESR, Cornell. The analysis method has been improved from lumped elements to a network distributed system [2]. Reactive tuning by H or E stubs and other fast response tuning devices could also compensate Lorenz Force detuning and microphonic problems in the SRF control system [3]. In a WG iris/stub tuning design [4], reactive tuning was dominated by the fixed inductance of an iris. The stubs only change the frequency pulling. So the Q_{ext} can only be increased. Three stubs can act as both frequency tuner and reactive device to increase or decrease the Q_{ext}.

The WR650 waveguide three-stub tuners have been used at JLab on 5-cell (mean value of $Q_{ext}=5.5\pm0.8\times10^6$) cavities to reduce required klystrons' power [5]. They were also installed on the SL21 cryomodule, with new 7-cell cavities and $Q_{ext}=1.7\sim2.4\times10^7$. The heating effect on the SL21's cold WG fundamental power coupler (FPC) and warm ceramic windows have been observed [6] with little understanding. Under existing RF low level control (amplitude modulation) and high level power (5kW klystron) systems, the system Q at 8×10^6 is more tolerable. Then there is motivation to decrease the Q_{ext} to overcome the problem of Lorenz-force bump during cavity gradient ramp-up [7]. Otherwise a manual tuning of up to 3 bandwidths (225Hz) and slow increase of gradient are necessary. A network model has been developed to analyze stub tuner tuning properties, such as range, sensitivity and reactive heating effect.

NETWORK ANALYSIS MODEL

A two-port microwave network can be described by a 2×2 transmission matrix **T**:

$$\begin{pmatrix} a_1 \\ b_1 \end{pmatrix} = \begin{pmatrix} T_{11} & T_{12} \\ T_{21} & T_{22} \end{pmatrix} \begin{pmatrix} b_2 \\ a_2 \end{pmatrix} \tag{1}$$

Here a_1 and b_1 are incident and reflected waves (or voltages) on input port 1 respectively. The a_2 and b_2 are for output port 2 and reversed in raw position. So a total **T** matrix represents a cascaded wave transmission from three-stub tuner to the Field Probe (FP) of the cavity.

$$T_{tot} = T_{3st} \bullet T_{wg2} \bullet T_{tp} \bullet T_{hb} \bullet T_{wg1} \bullet T_{FPC} \bullet T_{ca} \bullet T_b \bullet T_{FP} \tag{2}$$

Here T_{wg1} and T_{wg2} are WR650 WG matrices in two section lengths l_1 and l_2 with attenuation α and propagation β constants for TE01 mode.

$$T_{wg} = \begin{pmatrix} e^{(\alpha+j\beta)l} & 0 \\ 0 & e^{(\alpha-j\beta)l} \end{pmatrix} \tag{3}$$

The T_{FPC} and T_{FP} are ideal transformer matrices for FPC (subscript 1) and FP (subscript 2), with $n_1 = \sqrt{Q_0 / Q_{1ext}}$, and $n_2 = \sqrt{Q_0 / Q_{2ext}}$ respectively:

$$T_{FPC} = \begin{pmatrix} \frac{1+n_1^2}{2n_1} & \frac{n_1^2-1}{2n_1} \\ \frac{n_1^2-1}{2n_1} & \frac{1+n_1^2}{2n_1} \end{pmatrix} \quad T_{FP} = \begin{pmatrix} \frac{1+n_2^2}{2n_2} & \frac{1-n_2^2}{2n_2} \\ \frac{1-n_2^2}{2n_2} & \frac{1+n_2^2}{2n_2} \end{pmatrix} \tag{4}$$

The T_{ca} and T_b corresponds normalized cavity and beam load shunt susceptances:

$$T_{ca} = \begin{pmatrix} 1+\frac{Y_{ca}}{2} & Y_{ca} \\ -\frac{Y_{ca}}{2} & 1-\frac{Y_{ca}}{2} \end{pmatrix} \quad T_b = \begin{pmatrix} 1+\frac{Y_b}{2} & Y_b \\ -\frac{Y_b}{2} & 1-\frac{Y_b}{2} \end{pmatrix} \tag{5}$$

The Y_{ca} is a function of cavity's intrinsic quality factor Q_0, drive frequency f (1497MHz for CEBAF) and cavity tuned resonance frequency deviation *df*.

$$Y_{ca} = 1 + iQ_0\left(\frac{f+df}{f} - \frac{f}{f+df}\right) \tag{6}$$

The Y_b is a function of beam current I_0, cavity's shunt impedance per unit length $(r/Q)Q_0$, acceleration gradient E_{acc} and the beam current to RF voltage's phase Φ_b.

$$Y_b = \frac{I_0 (r/Q) Q_0}{E_{acc}} e^{i\phi_b} \tag{7}$$

The T_{3st} is the transmission matrix for the three-stub tuner. The T_{tp}, a WG taper, transforms from WR650 to a reduced height WG (5.292″×0.986″). The T_{hb} is for a reduced height 90° H-bend. Their transmission matrices can be converted from their S-parameters.

* Work supported by the US DOE Contract No. DE-AC0584ER401050
# haipeng@jlab.org

$$\begin{pmatrix} S_{11} & S_{12} \\ S_{21} & S_{22} \end{pmatrix} = \frac{1}{T_{11}} \begin{pmatrix} T_{21} & |T| \\ 1 & -T_{12} \end{pmatrix} \text{ or } \begin{pmatrix} T_{11} & T_{12} \\ T_{21} & T_{22} \end{pmatrix} = \frac{1}{S_{21}} \begin{pmatrix} 1 & -S_{22} \\ S_{11} & -|S| \end{pmatrix} \quad (8)$$

All S-parameters can be measured on the bench with a network analyzer and TRL calibrations, or calculated by 3D simulations like MAFIA (time domain) and HFSS (frequency domain) at 1.5GHz frequency. The three-stub tuner can be divided into three individual elements. Each element has one stub plus two small sections of WG on each side. The S-parameters of each element can be characterized as a function of each individual stub height. Then three stubs can be combined like cascaded elements. Figures 1 and 2 show a good agreement between measurement and simulations. The polynomial fits can be used in the analysis.

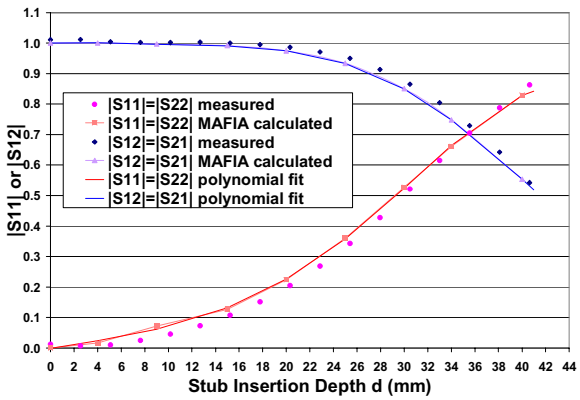

Figure 1: S amplitudes of a single stub inside of a 12" long WR650 WG.

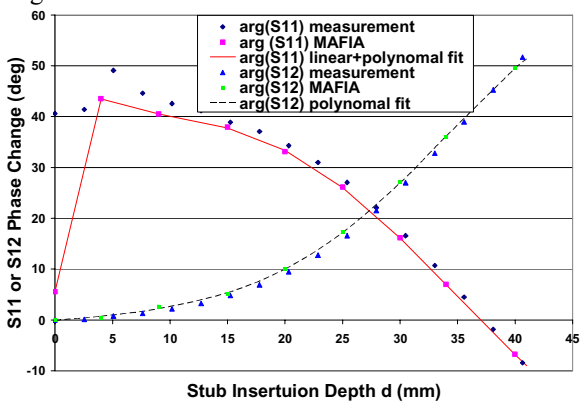

Figure 2: Phase change of S parameters of Figure 1.

After applying all parameters for a 7-cell cavity, without beam current present, we can plot */S21/* from Equation 8 for the total transmission from FPC to FP with the variables of *d1*, *d2*, *d3* (three stubs' heights) and *df* (in Figure 3). The same quantities cab be measured in a cold cavity with a network analyzer. The loaded Q of the system has been reduced (can be increased too) by different stub settings. An important observation from this graph is that even with a "flush" stub settings (d1=d2=d3=0), there is still about +4Hz frequency pulling (the peak is at *df*=4Hz) caused by the unmatched WG taper and H-bend. With the third stub in (d3=31 mm), the loaded Q dropped from 2.55×10^7 to 8.03×10^6, but frequency was pulled by -26Hz. Inserting the second stub (d2=18mm) can bring the peak back, but the Q drops further to 6.37×10^6. This behavior also has been experienced during stub tuning practice.

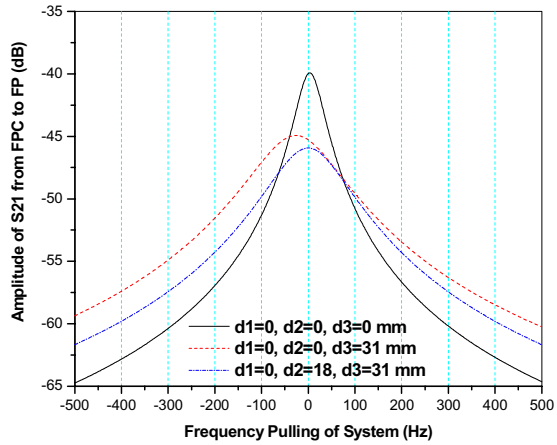

Figure 3: Three stubs with different heights change the superconducting cavity's Q_{ext}, seen by the |S21| peaks from FPC to FP.

By calculating the -3dB bandwidth on each */S21/* peak or the absolute value of the peak, we can derive and map out the equivalent external Q of the input coupling as a function of the stub settings. Figure 4 shows an example with the first stub fixed at *d1*=0, and *d2* and *d3* as variables. Q_{ext} can be tuned from its original value of 2×10^7 down to 1×10^6 or up to 2×10^8. Tuning sensitivity varies from stub to stub with travel heights. The most sensitive stub in this example is at *d3*=20 to 30 mm, being 10dB change on the Q_{ext}, or a sensitivity of is up to 10dB/cm. We can also conclude from these calculations that different stub settings can get a same Q_{ext} value but with different frequency pulls. The following analysis shows that the best stub setting is the one with minimum frequency pull from 1497MHz.

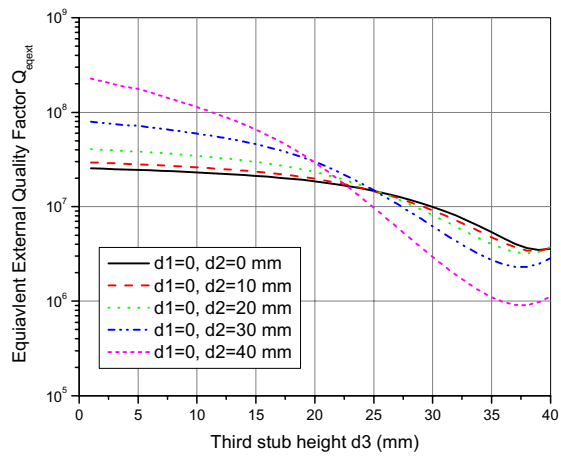

Figure 4: One case of tuning range and sensitivity of external Q with different stub settings.

Using this transmission matrices technique, we can separate the T_{wg1} into two sections in Equation (2). We shall get a WG input voltage for a known cavity voltage (or E_{acc}) first, then use the inverse of transmission matrix on the left side of the separation point in Equation (2).

We can calculate the standing wave voltage (SWV) inside of WG near the FPC as a function of the WG distance. To get an absolute SWV value, one needs to de-normalize the waves *(a, b)* by the local impedances. Figure 5 shows the result with the stub setting, frequency pull (could be due to others than the stub setting) and beam current as the variables [8].

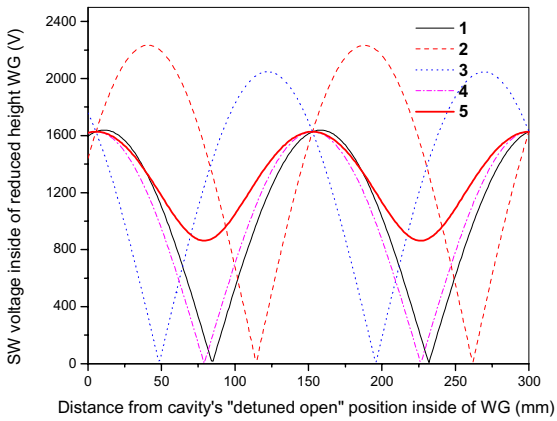

Figure 5: Standing wave voltage patterns at a constant gradient of E_{acc}=12MV/m inside of FPC's WG (either on short or long wall) with following conditions:
1. d1=0,d2=0,d3=0, peak at df=+4Hz, Q_{ext}=2.55E7.
2. d1=0,d2=0,d3=0, -3dB pt. at df=+32Hz, Q_{ext}=2.55E7.
3. d1=0,d2=0,d3=31mm, peak at df=-26Hz, Q_{ext}=8.03E6.
4. d1=0,d2=18,d3=31mm, peak at df=0Hz, Q_{ext}=6.37E6.
5. Same as curve 4, and beam I_0=0.3mA, Φ_b=0(on-crest).

One important conclusion drawn from this calculation is that when the stub tuner decreases (or increases) the external Q of the system, at a fixed gradient, a setup with a minimum frequency pulling (df) always minimizes the SWV ratio inside of the WG between the stubs and the cavity. So the heating in this section can be reduced.

EXPERIMENT RESULT

Based on this conclusion, a test plan has been carried out at SL21's #4 cavity with low temperature diodes installed on the cold section of WG. We tuned the stubs from $Q_{ext}=2\times10^7$ to 5×10^6 by every means to minimize the frequency pull with df=-20Hz only. We recorded the klystron forward power, phase angle offset in the auto-track mode of the cavity tuner. Cold WG temperature follows a parabolic shape as the klystron power's fitting shown in Figure 6. Except the drift from a phase transit, no sign of temperature increase in this stub setting. We also found the ceramic window warm temperature has no correlation with this stub setting. The cavity can ramp up to a 10MV/m gradient in 1 second.

CONCLUSION

Based on our model analysis and experimental data, we have concluded that three-stub tuner can modify (increase or decrease) the external coupling Q of a superconducting cavity over a range of 2 orders of magnitude. Stub position could be sensitive to the Q and phase change. Minimizing the frequency pulling away from the matched system is the key step to properly set up the stubs to avoid extra RF heating on the WG components. The phase drifting problem as the tunnel's temperature variation is related to the reactance change on the WG components. To relief this problem, we recommend installing the stub tuner close to the cavity inside accelerator tunnel with a stepper-motor remote control. We can use this network model study the problem further. This model can be also modified to improve the reactive tuning compensation technique [4] for other applications.

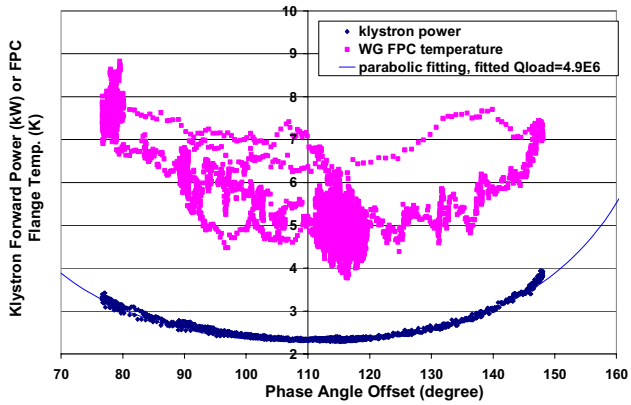

Figure 6: Cold waveguide temperature readout at SL21 cavity #4 with E_{acc}=7.8MV/m, stub tuner set as $Q_{ext}=5\times10^6$. df=-20Hz.

REFERENCES

[1] B. Dwersteg, "SC-Cavity Operation Via WG-Transformer", Proc. Of the 4th SRF Workshop, Aug 14-18, 1989, KEK, Japan, KEK report 89-21, Vol. II, p. 593.
[2] V. Veshcherevich, S. Belomestnykh, "Correction of the Coupling of CESR RF Cavities to Klystrons Using Three-Post Waveguide Transformers", Cornell LNS Report SRF 020220-02, 2002.
[3] Y. Kang, M. Tiefenback, "Reactive RF Tuning for Compensation of a Detuned Accelerating Cavity", Proc. of LINAC2002, Gyeongju, Korea, Aug. 19-23, 2002.
[4] H. Wang, "Analytical Design of a Waveguide Iris/Stub Tuning Coupler to an Overcoupled Superconducting Cavity", Proc. of PAC2003, Portland, OR, USA, May 12-16, 2003, p. 1101.
[5] C. Reece, "Optimal Loaded-Qs for CEBAF", internal AccSys Notes, Dec. 12, 2000.
[6] T. Powers, "Waveguide Heating on SL21, Cavity #3", internal report, May, 29, 2003.
[7] C. Reece, "Lorentz-force Tuning Effects in CEBAF", JLab Technote TN 98-041, Oct. 6, 1998.
[8] H. Wang, "A MathCAD Program to Calculate the RF Waves Coupled from a WR650 Three-Stub Tuner to a CEBAF Superconducting Cavity", to be published in a JLab Technote, 2004.

LOW-POWER RF TUNING OF THE SPALLATION NEUTRON SOURCE WARM LINAC STRUCTURES

C. Deibele, ORNL, Oak Ridge, TN, 38830 USA
J. Billen, LANL, Los Alamos, NM, 87545, USA
L. Young, TechSource, Santa Fe, NM, USA
A. Vasyuchenko, RAS/INR, Moscow, Russia
J. Error, P. Gibson, G. Johnson, ORNL, Oak Ridge, TN, 38830 USA
N. Bultman, J. Stovall, LANL, Los Alamos, NM, 87545, USA
J. Manolitsas, D. Trompetter, Accel Instruments, Bergisch Gladbach, Germany

Abstract

The Spallation Neutron Source (SNS) is an accelerator-based neutron source being built at Oak Ridge National Laboratory. A conventional 402.5-MHz drift-tube linac (DTL) accelerates the H^- beam from 2.5 to 86 MeV, followed by a 805-MHz coupled-cavity linac (CCL) to 186 MeV. Tuning the six DTL tanks involves adjusting post-coupler lengths and slug tuners to achieve the design resonant frequency and stabilized field distribution. A 2.5-MW klystron feeds RF power into a DTL through a ridge-loaded waveguide. The CCL consists of 4 RF modules operating in the $\pi/2$ mode. Each module contains 96 accelerating cavities in 12 segments of 8 cavities each, 11 active bridge coupler cavities, and 106 nominally unexcited coupling cavities. For each RF module, power from a 5-MW klystron splits and drives bridge couplers 3 and 9. We will discuss the procedures and special tools developed for the structure tuning.

INTRODUCTION

We describe the low-power RF tuning of the SNS warm linac designed by LANL. For each of 10 RF structures (6 DTL tanks and 4 CCL modules), the tuning goals are:

- Resonant frequency within ±20 kHz of design under normal operating conditions.
- Field distribution within ±2% of design.
- Fields stable against frequency perturbations.
- Cavity-to-waveguide coupling matched for full beam current.

We convert all frequency measurements made under ambient conditions to 20 C structure temperature under vacuum. Flowing dry nitrogen through the cavities avoids any uncertainty from inaccurate or varying humidity measurements.

DRIFT-TUBE LINAC

The six 402.5-MHz DTL cavities have between 22 and 60 1-$\beta\lambda$-long cells with half drift tubes on the end walls. A tank contains three (two for tank 1) ~2-m-long, copper-plated steel sections bolted together. Tank 1 with 60 cells and tank 2 with 48 cells have a ramped field distribution. Tanks 3-6 with 34, 28, 24, and 22 cells all have a flat field distribution. Slug tuners evenly spaced along the tank bottom (4 per section) provide each tank with 2.1 MHz of static tuning to correct for expected manufacturing dimensional tolerances. In operation, water coolant temperature controls the frequency. Water-cooled copper drift tubes (DTs) mounted on copper-plated steel stems contain focusing, steering, or diagnostic elements. The FFODDO focusing lattice uses permanent-magnet quadrupole lenses in 2/3 of the DTs. In each tank, 4 downstream DTs contain dipole steering magnets and 2 upstream DTs contain beam-position monitors. Some DTs are empty.

Post couplers (PCs) are quarter-wave resonators that provide field stabilization. Rotating the bent the PC adjusts the longitudinal field distribution. A DT-to-tank-wall spacing of ~$0.95\lambda/4$ ensures adequate coupling between the PC tip and DT. Tank 1 has 19 PCs, one at every third DT and alternating side to side. Tanks 2 and 3 have 23 and 17 PCs (one at every other DT), and tanks 4,5,and 6 have a PC at every DT location.

RF power enters the cavity through a tapered ridge-loaded waveguide that terminates in a barbell shaped iris (see Fig. 1). Because the iris is small (~2 mm wide), it has a negligible effect on the cavity frequency and field distribution.

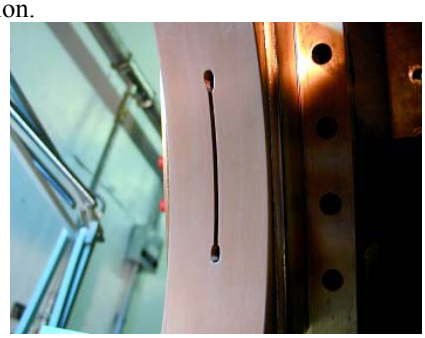

Figure 1: Iris viewed from the DTL side.

DTL Tuning

For low-power DTL tuning we adjust temporary aluminum slug tuners (STs) and PCs (see Figs. 2 and 3). Upon completed, fixed copper parts are finish machined to the measured final dimensions. For low PC excitation during operation, we adjust the STs to achieve the design field distribution before installing PCs. The PCs raise tank frequency 100 to 200 kHz when installed. From this point forward, we move all STs together to maintain the tank target frequency.

Figure 2: An adjustable aluminum slug tuner.

Figure 3: An adjustable aluminum post coupler.

Axial field measurements use the Slater bead-perturbation (BP) method [1]. A hollow aluminum sphere traverses the cavity at constant speed while a network analyzer under LabView control records the frequency at regular intervals. From frequency change data in each gap, and Superfish [2] field data for each cell, analysis code DTLplot computes each cell's average axial field E_0. Tilt Sensitivity (TS) measures field stability. TS is the cell-by-cell difference in E_0 between two BP measurements with different frequency perturbations of the end cells. We first insert a metal tube in the bore on one end to lower cavity frequency ~25 kHz. For the second measurement the tube is on the other end. DTLplot determines the end-cell frequency perturbations from stored energy ratios.

The procedure is to first stabilize the fields by tuning the PCs. We start with all PCs a bit too low in frequency (i.e., too long) and gradually pull out all PCs until the TS slope is near zero. Some individual PC adjustment results in a smooth TS curve. Once the PC lengths have been fixed, we adjust the PC orientation angle to achieve the design field distribution. Some iteration is usually needed. The left side of Fig. 4 (z = 0 to 36 m) shows E_0 and TS for the 6 DTL tanks. The TS measurements for tanks 4 and 6 show the both aluminum and copper PC data. The larger slope of the copper PC data mean that copper parts did not replicate the aluminum PC geometry as well as for other tanks. For the largest expected frequency errors of a few tens of kHz, the TS final data is still adequate.

Another measure of DTL stability is the stabilization factor $K_{st} = [\Delta S_1/\Delta f_1]/[\Delta S_2/\Delta f_2]$, where ΔS_1 and ΔS_2 are changes of the field slope in unstabilized and stabilized cavities for end-cavity frequency perturbations Δf_1 and Δf_2 [3,4]. The stabilization factor depends on the location and number of post couplers. Usually, DTLs have Kst in the range 10 to 100. The change in field slope measures the first harmonic compensation from the TM_{011} mode, which is closest in frequency to the TM_{010} mode and contributes most to the field distortion. We measured K_{st} = 15, 26, 75, 51, and 37 for tanks 1, 2, 4, 5, and 6, respectively.

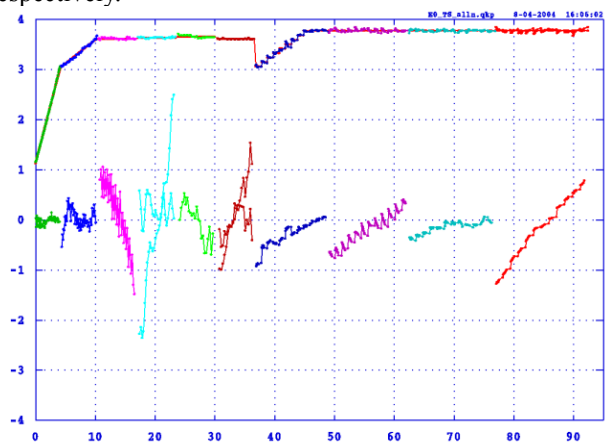

Figure 4: E_0 in MV/m (upper) and tilt sensitivity in %/MHz (lower) versus accelerating-gap longitudinal position z (m). Design E_0 is in red over the entire length. Measured E_0 for each structure (in various colors) covers up most plotted design values.

COUPLED-CAVITY LINAC

The CCL consists of 384 accelerating cavities (ACs) arranged in 48 segments of 8 identical ACs each. Segment length gradually increases to match the average particle velocity β. The length of an AC is βλ/2, and the distance between segments is 5βλ/2, where now β is the segment exit velocity. We further subdivide the 48 segments into 4 RF modules of 12 segments each. Within a module, 3-cell bridge couplers span the space between segments leaving room for quadrupole singlets and diagnostics. A module contains a total of 213 cavities: 96 ACs, 84 internal coupling cavities (CCs), 22 longer bridge CCs, and 11 powered bridge cavities (BCs).

An internal CC connects two ACs within a segment. These cavities attach above or below the ACs, alternating from top to bottom. All ACs have the same outer corner radius and septum thickness, and all the internal CCs are identical. The coupling slot between AC and CC starts as the intersection of their corner radii machined from both sides of a copper plate. We then mill the edge of the slot to specified dimensions, ensuring a consistent coupling factor within a segment. The nominal coupling factor k is 5%. Because of the increasing AC volume with β, k varies from 5.45% in segment 1 to 4.45% in segment 48.

CCL Tuning

CCL tuning is an integral part of the manufacturing process. Different AC tuning steps occur both before and after the segment braze. The first tuning of the internal CCs occurs after the segment braze. We tune the BC in a special 5-cell fixture before assembly in the module. Bridge CC tuning occurs only after module assembly.

An AC half-cell includes a raised tuning ring that we machine to make the segment's π/2 mode frequency $f_{\pi/2}$ ~200 kHz low before brazing. After brazing we first tune all internal CCs to the module's target frequency f_T, which includes a small offset that anticipates the effects of thermal gradients under power. Squeezing the CC noses together lowers frequency and prying the noses apart raises frequency. Based upon measurements $f_{\pi/2}$ and individual AC frequencies (with nearby cavities shorted in a consistent manner), we tune the 6 internal ACs by "dimpling" the outer wall. Each AC has 12 dimpling ports where the wall is only a few mm thick. Together the 12 ports provide up to 400 kHz of tuning range. The dimpling takes place while observing the frequency f_{AC} of a single AC. This mode is typically 4.5 MHz higher in frequency than $f_{\pi/2}$ because of the ~1.1% direct coupling between ACs. Metal rods inserted from the segment ends short other cavities. Each rod contains an electric antenna. We short nearby CCs with copper wedges inserted through the pumping ports.

Pushing or pulling the segment end walls tunes the end ACs. For a single segment, an end AC is tuned correctly when the adjacent CC contains no stored energy in the π/2 mode. This frequency is approximately the average of $f_{\pi/2}$ and f_{AC}. In the module, we retune only the 22 end ACs next to bridge couplers to a common frequency to change the module frequency.

The BC bolts into the center of a 5-cell tuning fixture for measurements that determine the length if its fixed slug tuner. Tuning is complete when the end cavities have the same frequency (measured individually), the 5-cell π/2-mode frequency f_T, and the two bridge CCs contain no significant RF power in the π/2 mode. After meeting these conditions using an adjustable slug tuner, we machine the water-cooled copper slug to the required length.

An important BC feature is the TE-mode tuner, which is a solid copper rod welded to the top of the cavity. The large slots (see Fig. 5) in the BC split the degeneracy between two TE_{111} modes. One mode couples strongly to the adjacent bridge CC TM_{010} field in the slot and would interfere with the proper behavior of the coupled chain of resonators. The vertical TE-mode tuner lowers the frequency of this mode to <690 MHz, well below the TM_{010} pass band. Bending the rod affects the ratio of coupling to the bridge CCs and changes the segment-to-segment field distribution.

After assembly of an entire module, we tune the 22 bridge CCs to f_T and retune the 22 end ACs to make the module's π/2-mode frequency f_T. At this point, axial BP and TS measurements begin. Analysis code CCLplot computes segment averages of E_0, TS slopes for each segment, and the step in TS between segments. We tune the bridge CCs to adjust these TS steps. Raising the frequency of the bridge CCs makes the step more positive. A slightly positive overall slope of the TS curve helps prevent a possible thermal runaway situation because the field will tend to drop in a hotter (lower frequency) segment. If the TS slopes for individual segments need adjustment, we retune the internal CCs. However, the three CCs on the segment bottom are only accessible with the segment removed from the support stand.

Because of the large slot between the BC and the bridge CCs we cannot measure reliably an isolated bridge CC frequency. If, instead, we short ACs and CCs in adjacent segments, then the π/2-mode frequency of the 3-cell system of two bridge CCs and the BC is the average frequency of the bridge CCs. The drive and pickup probes are in the bore-tube shorting rods in the gap of the adjacent end ACs. Their frequency difference comes from single-cavity measurements with a plug (see Fig. 5) in the slot, which is inserted by reaching in through the BC slug-tuner port.

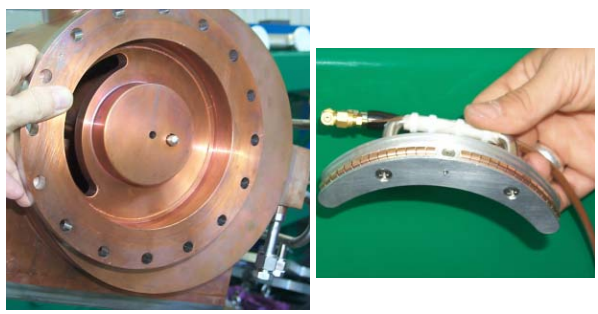

Figure 5: Left: bridge-coupler end view. Right: plug with pickup loop inserted from the BC side of the slot.

Tuning of a bridge CC occurs with the coupling-slot plug in place. A silver-plated stainless-steel screw, adjusted from the BC side, provides >5 MHz of tuning range. Power losses are negligible because the screw is in a primarily electric field region of a nominally unexcited cavity. Contacts are well inside the tapped hole. After final adjustment, another screw inserted behind the tuner locks it in place. Both screws include vacuum relief.

The right side of Fig. 4 (z = 36 to 92 m) shows E_0 and TS for the 4 CCL modules.

REFERENCES

[1] J. C. Slater, *Microwave Electronics*, D. Van Norstrand, Princeton, NJ (1950) 80-82.

[2] J. H. Billen and L. M. Young, "Poisson Superfish," Los Alamos National Laboratory report LA-UR-96-1834 (revision August 4, 2004).

[3] V.G. Kulman et al., "Studies of DTL with Post Couplers," Proc. of RTI (1973) 16 (in Russian).

[4] A. Vasyuchenko et al., "Random Errors in Measurement of the Field Stabilization for Tank 1 Cold Model", SNS-NOTE-90, http://it.sns.ornl.gov/asd/public/pdf/sns0090/sns0090.pdf

MEASUREMENT AND CONTROL OF MICROPHONICS IN HIGH LOADED-Q SUPERCONDUCTING RF CAVITIES*

T.L. Grimm, W. Hartung, T. Kandil, H. Khalil,
J. Popielarski, C. Radcliffe, J. Vincent, R.C. York,
Michigan State University, East Lansing, MI 48824

INTRODUCTION

Superconducting radio frequency (SRF) linacs with light beam loading, such as the Rare Isotope Accelerator (RIA), S-DALINAC, CEBAF upgrade, and energy recovery linacs, operate more efficiently with loaded-Q, Q_L, values greater than 10^7. The resulting narrow bandwidth puts stringent limits on acceptable levels of vibration, also called microphonics, which detune the SRF cavities and require additional rf power to maintain amplitude and phase.

RIA will use six-cell 805 MHz elliptical cavities for acceleration of uranium from 88 MeV/u to 400 MeV/u (β=v/c=0.41 to 0.72) with a final beam power of 400 kW [1]. To cover this velocity range, three geometric β, β_g, values of 0.47, 0.61 and 0.81 are used [2,3]. A multi-charge state uranium beam with three charge states centered on $^{238}U^{89+}$ and a total beam current, I_{beam}, of 0.37 mA are accelerated in the elliptical cavity section of RIA.

A prototype RIA 805 MHz β_g=0.47 cryomodule has been tested in realistic operating conditions [4]. For Q_L~10^7 operation of RIA, rf power requirements are determined, and measurement and control of microphonics have been demonstrated.

BEAM LOADING & RF REQUIREMENTS

Superconducting cavities require very little rf power to generate the accelerating gradient, and therefore, have intrinsic quality factors, Q_o, greater than 10^8. Additional rf power is required for beam acceleration and control of microphonics. If the beam current is high, beam loading is large enough so that the system bandwidth is much larger than any microphonics detuning. Under these circumstances, the rf generator power (P_g) equals the beam power (P_{beam}). But, if the cavity resonant frequency is shifted, then additional rf power is required to maintain amplitude and phase. The required P_g for a given beam loading, coupler strength ($Q_{ext} \cong Q_L$), and maximum detuning ($\pm\delta f$) is given by [5]

$$\frac{P_g}{P_{beam}} = \frac{1}{4}\frac{Q_{beam}}{Q_L}\left[\left(1+\frac{Q_L}{Q_{beam}}\right)^2+\left(\frac{\delta f}{\Delta_{beam}}\frac{Q_L}{Q_{beam}}\right)^2\right]$$

$$Q_{beam} = \frac{2\pi f U}{I_{beam}V_a\cos\phi_s} = Q_o\frac{P_o}{P_{beam}}$$

$$\Delta_{beam} = half\ \ beam\ bandwidth = \frac{f}{2Q_{beam}}$$

*Work supported by Michigan State University and DOE DE-FG02-00ER41144

Table 1: Beam loading requirements for 400 kW, 400 MeV/u uranium in RIA elliptical cavities

Type	6-cell	6-cell	6-cell
β_g	0.47	0.61	0.81
V_a(MV)	5.12	8.17	13.46
P_{beam}(W)	1660	2640	2600*
Q_{beam}	9.1×10^7	9.1×10^7	1.4×10^8
P_g(W)	3320	5280	5200
Q_L	3.0×10^7	3.0×10^7	4.7×10^7
$\Delta_{allowed}$(Hz)	25	25	16

*β_g=0.81 decreased from the maximum value due to transit time factor

For RIA, the rf generator requirements are chosen to be twice the maximum beam power. From the previous equation it can be shown that the maximum allowable detuning occurs when Q_L/Q_{beam}=0.33 for these conditions. The maximum allowable detuning for which amplitude and phase can be maintained is then $\delta f=2.8\Delta_{beam}$. Therefore, the microphonics can detune the cavity over a full bandwidth, $\Delta_{allowed}=2\delta f=5.6\Delta_{beam}$, and the amplitude and phase can still be maintained. The control bandwidth is slightly smaller than the Q_L bandwidth (f/Q_L) due to the generator requirements.

The design beam for the driver linac is 400 MeV/u uranium with a total power of 400 kW. For this case, the beam loading values are shown in Table 1 for a synchronous phase, ϕ_s, of -30°. The accelerating voltages, V_a, correspond to peak surface electric fields of 32.5 MV/m and accelerating gradients of 10-15 MV/m. Because the β_g=0.81 cavity does not accelerate uranium at the peak of its transit time curve, the maximum beam power is nearly the same as the maximum value for the β_g=0.61 cavity. The allowable detuning for RIA, assuming a generator power that is twice the beam power, is also shown in Table 1. Due to transit time effects, most of the cavities do not supply the maximum power to the beam. Therefore, most of the cavities will be able to handle significantly higher detuning than shown here. The measured microphonics with and without passive and active damping on the prototype RIA cryomodule show that the values in Table 1 are adequate for RIA.

Operation of SRF cavities with $Q_L=3\times10^7$ is done at the S-DALINAC in Darmstadt [6], and a Q_L in the low 10^7 range is proposed for the CEBAF upgrade [7]. Energy recovery linacs would benefit from Q_L in the 10^8 range. Therefore, the design bandwidth values proposed here for RIA are consistent with the goals of other projects and will be able to capitalize on the advances made for other accelerators.

Finally, Lorentz detuning which is a shift in the cavity frequency due to radiation pressure of the electromagnetic field must be compensated for during rf turn on. For RIA, a cw linac, this can be done slowly using the tuner and will not be a critical issue.

METHODS OF MITIGATION

Vibrations and pressure fluctuations cause the cavity frequency to shift (detune) only if the forces distort the cavity walls. Typical sources of vibration are rotating machinery, fluid fluctuations, and ground motion. Motors will generate discrete vibration frequencies at harmonics of their revolution rate. Fluid fluctuations such as boiling, cavitation, and turbulent flow, and ground motion will generate a broadband vibration spectrum.

There are many techniques to reduce microphonics or otherwise mitigate their effect on an SRF cavity. The mechanical frequencies of concern are usually low (less than 200 Hz). A proper cavity and cryomodule design can significantly reduce the microphonics problem. The cavity can be made more rigid with thicker material and gussets to reduce distortions, but the tuner will become more complicated and heat transfer from the rf surface to the helium bath may be degraded. Structural resonances should be eliminated or shifted to higher frequency. As an example, the lowest frequency transverse mechanical mode of the 805 MHz cavities was removed with a support at the center of the six-cell structure. Designing the cavity and helium vessel so that distortions in regions of high electric field are canceled by distortions in high magnetic field regions can reduce the frequency shift due to pressure fluctuations in the helium bath. Passive mechanical dampers can be integrated into the cavity as has become standard for quarter-wave resonators [8].

The choice of operating temperature can have a large influence on microphonics excitation. Operation at 4 K results in helium at atmospheric pressure with fluctuations from the plant and pool boiling heat transfer with its concomitant broadband vibration. Operation at 2 K has sub-atmospheric liquid helium with lower disturbances from the cryoplant, and heat transfer via conduction is enhanced due to the unique properties of superfluid.

Another system design issue is cw versus pulsed operation. Pulsed operation must deal with the transient Lorentz force detuning, which is likely to dominate all other microphonic sources.

Sources of vibration should be eliminated when possible or isolated from the cryomodule. Vibrations will be transmitted through the ground, pipes and fluids. Passive and active absorbers can reduce the amplitude before the vibrations reach the cryomodule and cavity. Examples from other disciplines are optical benches, telescopes, automobile suspension systems, and sound cancellation [9]. Vibrations that reach the cryomodule can be actively and passively damped before that motion affects the cavity.

Even with the damping and isolation techniques listed above, there will likely still be some cavity vibration. There are several methods available to compensate the microphonics. A fast mechanical tuner can distort the cavity shape and cancel the frequency shift induced by the microphonics. Another way to apply a force on the cavity is to vary the accelerating gradient by a small but acceptable amount and use the Lorentz force [10]. The cavity frequency can also be shifted using a tunable reactive element that is coupled through the input power coupler or a dedicated fast tuner coupler [11,12].

Finally, small changes in the synchronous phase can accommodate the microphonics by allowing the rf drive frequency to remain on resonance, as is done with the VCX tuner [12], with an additional correction to the voltage amplitude given the known phase error.

MEASUREMENTS

The prototype RIA 805 MHz β_g=0.47 cryomodule has two multi-cell cavities with fixed input power couplers and external tuners actuated by a room temperature piezoelectric actuator [4]. The cavities are cooled by 2 K superfluid with cryoplant temperature regulation. The coupler strength, Q_{ext}, is varied from $6x10^4$ to $6x10^9$ using an external transmission line transformer. Figure 1 shows a cross section of the cavity with tuner and coupler.

Real-time frequency detuning measurements were made for modulation rates from dc to greater than 1 kHz. Figure 2 shows the microphonics measurement technique. A stable signal generator in open loop mode is used to drive the rf cavity, and a pickup from the cavity is mixed with the input to generate an error signal that is proportional to the cavity detuning. Since Q_L is adjustable, the system bandwidth is set so the peak detuning is within the system bandwidth and generates linear error signals. This technique gives real-time error signals that can be analyzed or used for feedback/feedforward. Other methods give similar results, but require a longer acquisition time, more stable signal generator, and cannot be used for feedback [13].

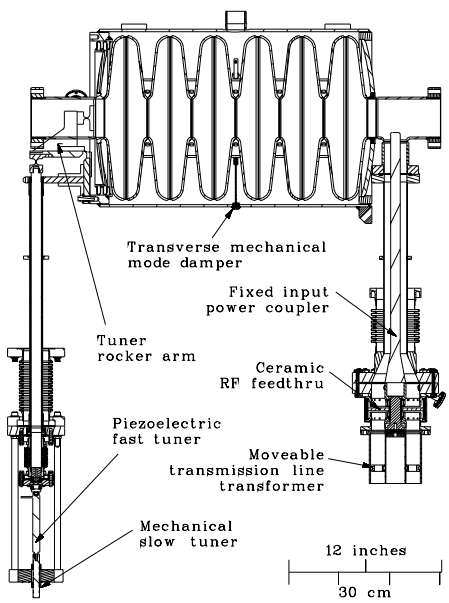

Figure 1: Side view of cavity with room temperature tuner and fixed input coupler.

At 2 K low power measurements were made with the liquid helium partially filling the distribution pipe as would be done for operation. The maximum frequency deviation using the calibrated error signal was less than 40 Hz peak-to-peak (see figure 2). The error signal was calibrated using a known frequency shift from the signal generator. The measured modulation spectrum was primarily comprised of discrete Fourier components with modulation frequencies less than 80 Hz. The main components were at 59.5 and 59.7 Hz. They could be clearly distinguished from 60 Hz electronic pickup, which was negligible in these measurements. Additional components near 54 Hz, which is the lowest frequency natural mode of the cavity, were measured and likely due to other nearby motors. Using an accelerometer, the primary sources of vibration were identified to be the two cryoplant screw compressors (rated for 1500 hp/3560 rpm and 250 hp/3550 rpm). The cryoplant was designed to cool superconducting magnets so vibration was not a consideration, and no isolation from the floor or the piping was implemented. The motors are about 20 m from the cryomodule test area. For RIA the cryoplant motors will be farther away and better isolated.

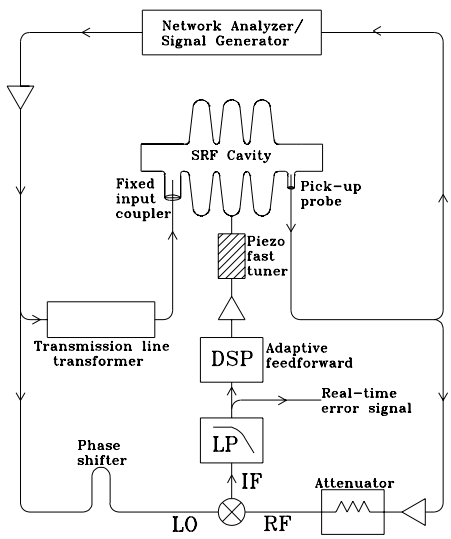

Figure 2: Microphonics measurement and control technique.

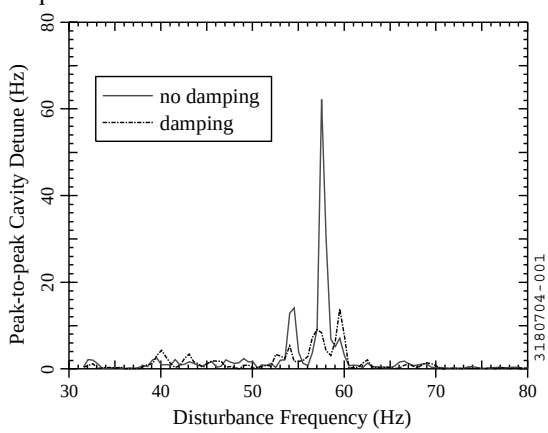

Figure 3: Fourier components of cavity detuning with and without active damping.

Since the detuning spectrum is made up primarily of discrete sinusoidal disturbances, an adaptive feedforward scheme was used to damp individual Fourier components [14]. The dominant microphonics signal was determined to consist of two closely spaced sinusoidal disturbances whose damping would be more problematic then a single peak, so for demonstration purposes a small motor with a Fourier component at about 57 Hz was placed on the cryomodule to generate a known sinusoidal disturbance. Figure 3 shows the Fourier components before and after active compensation and shows about a factor of seven damping of the 57 Hz component. The measured microphonics are near required levels for RIA without active damping, and can be brought below them using the adaptive feedforward cancellation.

REFERENCES

[1] C.W. Leemann, "The Rare-Isotope Accelerator (RIA) Facility Project," in *Proceedings of the XX International Linac Conference*, Monterey, California (2000).

[2] G. Ciovati et al., "Superconducting Prototype Cavities for the Spallation Neutron Source (SNS) Project," in *Proc. of the 2001 PAC*, Chicago (2001).

[3] W. Hartung et al.,"Status Report on Multi-Cell Superconducting Cavity Development for Medium-Velocity Beams," in *Proceedings of the 2003 Particle Accelerator Conference*, Portland, Oregon (2003).

[4] T.L. Grimm et al., "Experimental Study of an 805 MHz Cryomodule for the Rare Isotope Accelerator", these proceedings.

[5] H. Padamsee et al., "RF superconductivity for Accelerators", John Wiley & Sons, p. 391 (1998).

[6] H.-D. Gräf, "Experience with Control of Frequency, Amplitude and Phase", in *Proc. of the 5th Workshop on RF Superconductivity*, Hamburg, Germany (1992).

[7] L. Harwood, "Upgrading CEBAF to 12 GeV," in *Proc. of the 2003 PAC*, Portland, Oregon (2003).

[8] A. Facco, "Mechanical Mode Damping in Superconducting Low-β Resonators, Particle Accelerators, vol. 61, pp. 265-278 (1998).

[9] A. Hull, C. Radcliffe, S.C. Southward, "Global Active Noise Control of a One Dimensional Acoustic Duct Using a Feedback Controller", *ASME J. Dynamic Systems, Measurement and Control*, Vol. 115, pp.488-494 (1993).

[10] J.R. Delayen, "Electronic Damping of Microphonics in Superconducting Cavities", in *Proceedings of the 2001 Particle Accelerator Conference*, Chicago (2001).

[11] A.K. Mitra et al., "Coarse and fine tuners for the CERN PS 40 MHz Buncher Cavity", in *Proc. of the 1997 Particle Accelerator Conference*, Vancouver (1997).

[12] R. Pardo et al., "Long-Term Operating Experience for the ATLAS Superconducting Resonators," in *9th Workshop on RF Superconductivity*, Santa Fe, (1999).

[13] M.P. Kelly et al., "Microphonics Measurements in SRF Cavities for RIA", in *Proceedings of the 2003 Particle Accelerator Conference*, Portland (2003).

[14] T. Kandil et al., "Adaptive Feedforward Cancellation of Sinusoidal Disturbances in Superconducting RF Cavities", these proceedings.

TRAVELLING WAVE AND STANDING WAVE SINGLE CELL HIGH GRADIENT TESTS *

V.A. Dolgashev, S.G. Tantawi, C.D. Nantista, SLAC, Menlo Park, CA, 94025, USA
Y. Higashi, T. Higo, KEK, Tsukuba, Ibaraki 305, Japan

INTRODUCTION

Accelerating gradient is one of the crucial parameters affecting the design, construction and cost of next-generation linear accelerators. The present Next Linear Collider (NLC) / Global Linear Collider (GLC) designs specifies unloaded accelerating gradient of 65 MV/m at 11.4 GHz [1]. This is almost three times the present operating gradient of the S-band SLAC linac. The major obstacle to higher gradient is rf breakdown.

RF breakdown limits working power and produces irreversible surface damage in high power rf components and rf sources. For a given rf frequency, the maximum working gradient depends on the rf circuit, structure geometry and material. It is also a function of the input power, pulse width, and surface electric and magnetic fields. Here we define working gradient as a gradient with very low breakdown rate — less then one breakdown in 2×10^6 rf pulses.

The complexity of rf breakdown phenomena and the absence of a proven theory for it make it difficult to apply experimental results on breakdown limit from one rf structure to another. For example, working gradients in specialized small cavities are usually much higher than in high power waveguides and practical accelerating structures. To date, dozens of full-scale travelling wave (TW) structures [1, 2] and standing wave (SW) structures [3] have been tested at SLAC in an effort to produce accelerating structures that satisfy NLC/GLC requirements on gradient and breakdown rate. The requirements were met mainly by reducing length of a structure. To reach the same gradient while keeping average iris size, the power fed into a structure had to be reduced. Many questions about the physics of rf breakdown remain unanswered. The experiments described in this paper are designed to study the breakdown phenomena. They allow economical testing of structures with different cell geometries, materials and preparation techniques with short turn around time. The requirements were met mainly by reducing the power fed into a structure. To reach the same gradient while keeping average iris size, structure length had to be reduced. Many questions about the physics of rf breakdown remain unanswered.

MOTIVATION

The shape of the cell is one of the parameters that determines the high power performance of an accelerating structure. To study the effect of cell shape on the rf breakdown behavior of a TW structure is difficult because the geometry of the cells varies along its length and rf power decays toward the end of the structure. Here we refer to 11.424 GHz, near-constant-gradient TW structures developed for the NLC [2].

In order to study the effect of cell shape alone, we will perform an experiment with *single cell TW* structures. The idea is to build a structure that in only one cell mimics the fields near the input of a full-scale TW structure and has high electric and magnetic fields only in that cell, not in matching elements or *couplers* that transform the TE_{10} mode of rectangular waveguide into the "accelerating" circular TM_{01} mode. Another feature of the setup is the couplers, or mode launchers, which can be connected to the single cell structure with rf-compatible circular waveguide vacuum flanges. The flanges allow re-use of the same mode launchers for different structures, significantly reducing the cost of the experiments and allowing fast turn-around between tests of different structures.

We emphasize the difference between our proposed tests and earlier experiments with single cell structures [4]: the power available for breakdown and the field configuration in the single TW cell are similar to the power and fields at the beginning of the full TW accelerating structure. This was not the case in earlier experiments, which were done mostly with standing wave structures. We note that available rf power was shown in experiments [2] to have an effect on the breakdown limit in full TW structures.

Since breakdown behavior in TW structures and SW structures is different [3, 5], to study this difference and effect of SW cell shape on breakdown, we will perform *single cell SW* experiments. These will employ one of the mode launchers to feed rf power into a SW structure. Fields in the middle cell of the SW structure are similar to fields of a large-aperture SW structure already tested at high power (structure SW20a565 [3]). Fields in the other two cells are designed to be at most one half of the middle cell fields, so breakdowns will likely occur in the middle cell.

We note that shapes and field distributions in both single cell TW and single cell SW structures are identical to shapes and fields of full-length structures. We speculate that this similarity will allow us to predict the behavior of practical structures from the tests. We note another advantage of the single cell structures: small geometry allows better diagnostics of breakdown events and makes possible detailed 3D simulation of breakdown processes observed in the experiments.

SETUP

The TW single cell setup consists of two mode launchers with a TW structure in between. The SW single cell setup consists of one mode launcher and a SW structure. Mode

* This work was supported by the U.S. Department of Energy contract DE-AC03-76SF00515.

launchers and standing wave structures have have vacuum viewports to detect visible light and high frequency rf signals generated by breakdown events.

Mode Launcher

The mode launcher transforms the TE_{10} mode of WR90 rectangular waveguide into the TM_{01} mode in circular waveguide with a diameter of 0.900 inch (2.286 cm). It is designed as a single unit with rectangular and circular rf vacuum flanges and a vacuum viewport. A cutaway view of the mode launcher is shown in Fig. 1.

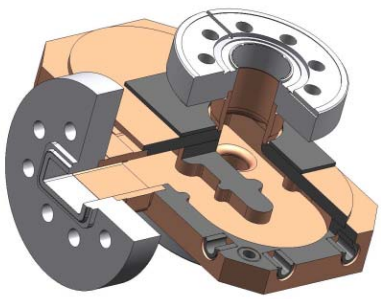

Figure 1: Cutaway view of the mode launcher.

Power in the WR90 input is split with a matched T, then symmetrically fed into the perpendicular circular waveguide. In the circular waveguide at 11.424 GHz only two modes are supported: TE_{11} and TM_{01}. With symmetric feeding, the TE_{11} mode is suppressed, and even with imperfect feeding symmetry it is poorly coupled to the rectangular TE_{10} mode (due to the field orientation). With only TM_{01} excited, a simple matching element in WR90 — a thick inductive iris — completes this launcher. Results of cold test measurement for the mode launchers are presented in [6]. Four mode launchers were built and successfully cold tested. Although the mode launcher itself was not yet tested at high power, nine couplers for travelling wave structures, based on the design, have been successfully used in the high-gradient structure program at SLAC [6].

Travelling Wave Structures

In the single cell TW setup, fields of the TM_{01} mode are first generated by the mode launcher, then transformed by a matching cell into fields of a periodic structure travelling wave (in one cell), then transformed through another matching cell back to the TM_{01} waveguide mode, to be extracted by the second mode launcher. The dimensions of the single cell are chosen to be the same as an initial cell of TW structure known as T53VG3. This is a disk-loaded waveguide with initial group velocity 3% speed of light and 120° phase advance per cell. The iris radius for the cell is 3.88 mm, the iris thickness 1.66 mm, the cell radius 10.641 mm, and the cell length 8.747 mm.

To create the travelling wave in one cell, we first match the 0.9 inch circular waveguide into a semi-infinite disk loaded waveguide using one matching cell. The matching process is described in detail in [6]. Then we make a structure with only one cell between two matching cells. Fields in this single cell structure are shown in Fig. 2. To illustrate

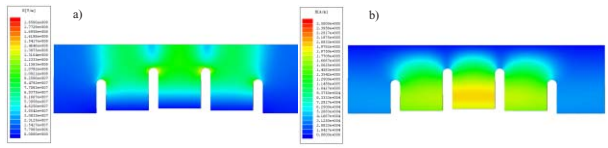

Figure 2: Amplitude of electric (a) and magnetic (b) fields in single cell TW structure for 40 MW of input power.

the properties of the structure we show calculated reflection of the TM_{01} mode from a structure made of the same matching cells and one, four, and 10 cells on Fig. 3. This

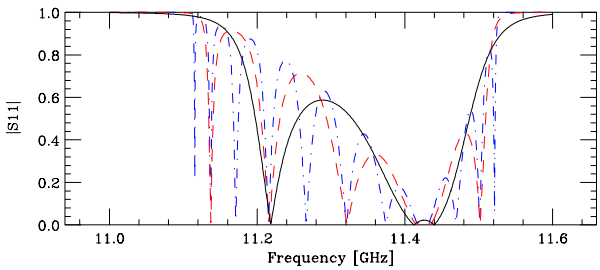

Figure 3: Reflection from a setup with different numbers of cells sandwiched between two matching cells: single cell (solid curve), 4 cells (dashed), and 10 cells (dot-dashed).

graph clearly shows that the match at working frequency, 11.424 GHz, is independent of the number of cells, *i.e.* the matching cell creates fields with space harmonic content close to that of the travelling wave in periodic disk-loaded waveguide.

A total of five TW structures were built for the test, including one structure that has iris tips made of molybdenum. All of them were successfully cold tested. In Fig. 4, we show one of the TW structures with attached mode launchers during measurement of the field profile (beadpull test).

Standing Wave Structures

For the single cell SW setup we used the dimensions of the NLC prototype SW structure SW20a565, with π phase advance per cell [3]. The SW20a565 cell dimensions are: cell radius 1.150 mm, cell length 11.312 mm, iris radius 5.65 mm, iris thickness 4.6 mm, major-axis of the elliptical iris tip 3.4 mm. In the single-cell SW structure, the cell radius was slightly modified to achieve the desired field profile.

We added two cells to the structure to create π-like fields in the test cell: a *matching cell* connected to circular waveguide and an *end cell* with a vacuum viewport. The geome-

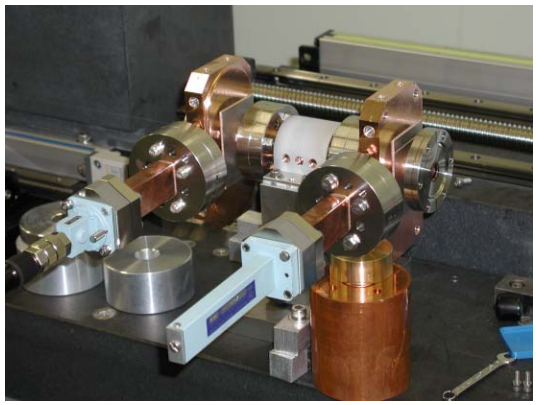

Figure 4: Single cell TW structure installed for bead-pull test.

tries of these two cells were chosen such that the structure is matched at the working frequency (critical coupling) and the maximum fields in these cells are half as large as the fields in the test cell.

The structure was designed with the 2D finite element code SLANS [7]. During the matching, four parameters were adjusted: the radii of all cells and the iris radius of the matching cell. The cell radii determine the field profile in the structure, and the iris of the matching cell determines the coupling of the structure to the circular waveguide. Afterward, the matching the solution was verified with the commercial electrodynamic code HFSS [8]. The field distribution in a copper single cell SW structure is shown in Fig. 5. We note that the same design procedure could be applied to structures with more than one cell for future study of the effect of the number of cell on breakdown behavior.

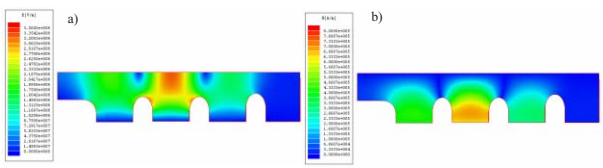

Figure 5: Amplitude of electric (a) and magnetic (b) fields in single cell copper SW structure for 10 MW of input power. The structure fed from the right, on the left, there is an opening with vacuum viewport.

We made two designs, one for testing of copper structure and another one for molybdenum. Since the resistivity of molybdenum is higher than that of copper, we changed the radii of all cells and radius of the matching iris of the molybdenum structure in order to maintain the field profile and critical coupling.

To date, a total of two copper SW structures have been built and successfully cold tested.

EXPERIMENTS

Different Materials

With copper TW and SW structures, we plan to study the effect of cell shape, circuit (SW *vs.* TW), and surface preparation methods on breakdown behavior. In addition, we have built a TW structure with iris tips made of molybdenum, and are building a TW and a SW structure made of solid molybdenum. We are going to compare breakdown limits and the conditioning behavior of these structures and the copper structures.

The structure shapes (for both SW and TW structures) and rf parameters, such as power and pulse width, for the these experiments will be close to those of practical structures. The importance of the choice of rf parameters was shown in experiments with CERN molybdenum TW structures, where short-pulse breakdown limit was higher than for copper. A similar structure operated at long-pulse length did not reach the copper breakdown limit [9].

Surface Processing

We are going to study the effect of different surface processing on breakdown behavior. We will use copper TW and SW structures for this experiment. We are going to compare standard SLAC/KEK processing of high gradient structures, high pressure water rinsing, and light etching of the assembled structure. The standard procedure includes etching of the structure cells only before bonding. All the structures will be assembled in a clean room and vacuum baked at 600° C for several days.

REFERENCES

[1] C. Adolphsen, "Normal Conducting RF Structure Test Facilities and Results," ROPC006, PAC03, Portland, Oregon, May 12-16, 2003.

[2] J. Wang and T. Higo, "Accelerator structure development for NLC / GLC," ICFA Beam Dyn. Newslett. **32**, 27 (2003).

[3] V. A. Dolgashev *et al*, "Status of X-band Standing Wave Structure Studies at SLAC," TPAB031, PAC03, Portland, Oregon, May 12-16, 2003.

[4] J.W. Wang, "RF Properties of Periodic Accelerating Structures for Linear Colliders," SLAC-Report-339, Ph.D. Dissertation, Stanford University, 1989.

[5] V.A. Dolgashev, S.G. Tantawi, "Simulations of Currents in X-band accelerator structures using 2D and 3D particle-in-cell code," FPAH057, PAC 2001, June 18-22, Chicago, Illinois. pp. 3807-3809.

[6] C. Nantista, S. Tantawi and V.A. Dolgashev, "Low-field accelerator structure couplers and design techniques," Phys. Rev. ST Accel. Beams 7, 072001 (2004), 7 pages.

[7] D. G. Myakishev *et al.* "An interactive code SLANS for evaluation of RF-cavities and accelerator structures," Proceedings of IEEE PAC01, 1991, San Francisco, Ca, pp.3002-3004.

[8] http://www.ansoft.com/products/hf/hfss/

[9] W. Wuensch *et al.*, "A High-Power Test of an X-Band Molybdenum-Iris Structure," THP34, this conference.

The Simulation Calculations And Dielectric Characteristics Investigation of a Hybrid Dielectric-Iris-Loaded Traveling Accelerating Structure

C.-F. Wu, USTC/NSRL, Hefei, Anhui

Abstract

Mafia code has been used to calculate the RF properties versus the geometric parameters and dielectric permittivity of the X-band (f=9.37 GHz) hybrid dielectric-iris-loaded travelling accelerating structure. The simulation results show that when the range of the permittivity is about 59 and the geometric parameters are optimized, the new structure may have lower ratio (about 1) of peak surface electric field at the iris to axial accelerating electric field , while r, Q, r/Q of the new structure being comparable to iris-loaded accelerating structure. The experimental investigation of the permittivity of the dielectric (ceramic)has been made by using the cavity perturbation technique. The results show that the permittivity of the ceramic is about 5.8 at the X-band and its stability is good.The above results will be applied to the design of the new accelerating structure, which may be a potential candidate of high gradient Linear accelerator.

NO SUBMISSION RECEIVED

THE TUNING STUDY OF THE COUPLED CAVITIES FOR THE RF CHOPPER SYSTEM OF J-PARC

S. Wang*, S. Fu, IHEP, P.O. Box 918, Beijing 100039, People's Republic of China
T. Kato, KEK, 1-1 Oho, Tsukuba-shi, Ibaraki-ken 305-0801, Japan

Abstract

A 3-MeV medium-energy beam transport line (MEBT) is located between the RFQ and the DTL in the linac of the Japan Proton Accelerator Research Complex (J-PARC). The MEBT accomplishes beam matching and chopping. An rf deflector (RFD) was adopted as a chopper in the J-PARC linac. A coupled RFD system was proposed in the design of chopper system for saving the cost of rf power source. The tuning of the coupled RFD system was successfully performed. The longer rise time of the second RFD and the delay of the second RFD excitation were found during the tuning of the coupled RFD system, and these phenomena were further analyzed and investigated. Both in the high power and beam tests, the chopper worked well without any discharge under 36 kW peak driving power.

INTRODUCTION

A Medium-Energy Beam-Transport line (MEBT) of Japan Proton Accelerator Research Complex (J-PARC) was installed in KEK for the beam test [1]. As a key component of MEBT, an rf deflector was proposed[2] and designed[3] as a chopper, because of its merits of high deflecting field, compact structure and easy to manufacture. An rf chopper, composed of two RFD (RFD-A and RFD-B), has been successfully developed. Because of the very low loaded-Q of the RFD, a coupled RFD system was adopted in operation for decreasing the demanded rf power by half.

Some frequency deviation was found after the construction of the RFDs. Although the bandwidth of the RFD is very large (~30 MHz), the frequency deviation of about 2 MHz still induces some negative effects: additional reflection and mismatch between two RFDs. The modifications of the RFDs were made for tuning the resonant frequency to the operation frequency of 324 MHz. In a low-level rf test, the fundamental rf properties showed good agreement with those in a design simulation. In a high-power test, the chopper worked well without any discharge under 36 kW peak driving power, and the longer rise time of the second RFD and the delay of the second RFD excitation were investigated in the coupled RFD system.

THE IMPROVEMENT OF THE RFD CAVITY DISIGN

The RFD cavity consists of two parts: the cavity body and the two end plates with large coupling loops. Fig. 1 shows the deformed waveform of the first RFD (RFD-A) when a mismatch of the resonant frequencies (~2 MHz) between RFD-A and B exists in the coupled RFD system.

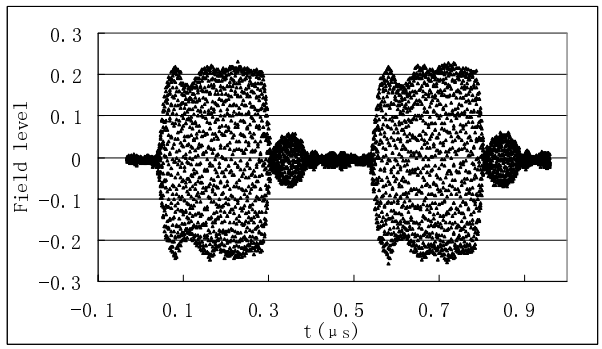

Figure1: The deformed waveform of the RFD-A of the coupled system due to mismatch (36 kW driving power).

To tune the resonant frequency back to 324 MHz, one idea is to move the large coupling loops about 3 mm towards the electrode. In practice, just about a 3mm gasket is needed between the loop and the end plate, then the resonant frequency is tuned to 324 MHz. But in this case the bandwidth of the RFD cavity is increased to 36 MHz, this means much more input power is needed than design.

To tune the resonant frequency to 324 MHz and keep the bandwidth and the other parameters unchanged, a new coupling loop was proposed, and designed by the RF simulation code HFSS.

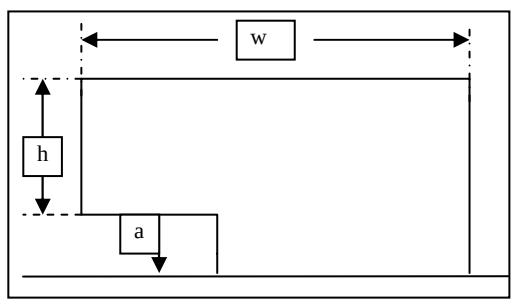

Figure 2: The shape and parameters of coupling loop.

Figure 2 shows the shape and parameters of the coupling loop. The thickness of the loop was 3mm. In design calculations by HFSS, the resonant frequencies were firstly tuned to the measured values by changing the gap distance, for RFD-A and RFD-B, respectively. In order to compensate the manufacture error of the cavities, the width *w* and height *h* of the loop of the two RFDs are

*Email: wangs@ihep.ac.cn

modified to tune the resonant frequency to operating frequency of 324MHz. Tuning the resonant frequency by modifying the coupling loop has two merits: easy for fabrication and less cost. The tuner effect with 15mm insertion is included in the calculations, and the insertion of 15 mm is set as the default value.

The above designed loops were fabricated and installed in the RFD cavities. The cold model test and high power test showed the good performance of the modification. Table 1 shows the designed and measured frequencies of RFD-A and RFD-B with new coupling loops. The measured frequencies had a good agreement with design values, and the resonant frequency was changed to 324MHz for two single RFD cavities.

Table 1: The measured and designed parameters of RFDs with new and old coupling loop

	Resonant Freq. (MHz)				Bandwidth (MHz)	
	Tuner=0mm		Tuner=15mm		RFD-A	RFD-B
	RFD-A	RFD-B	RFD-A	RFD-B		
Old loop	322.30	321.90			30	30
New loop (design)	323.75	323.75	324.00	324.00	30	30
New loop (Measured)	323.81	323.88	324.00	324.15	30	30

A high-power test of the coupled RFD was performed. The RFD worked very well up to a 36 kW peak driving power. Fig. 3 depicts the waveform from the first RFD of the coupled RFD system with improved coupling loops in the high power test. It shows that there is no mismatch between two RFD cavities in the coupled RFD system, after the resonant frequency was tuned to the operating frequency.

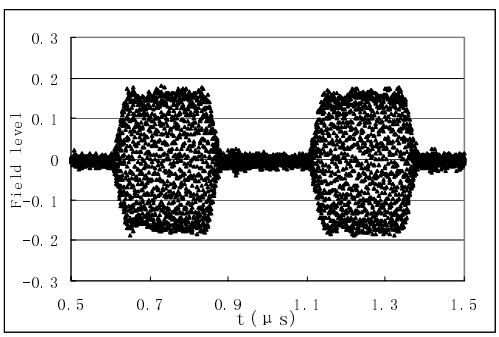

Figure 3: Waveform in the RFD-A of a coupled RFD system without mismatch (36kW driving power).

TEST OF THE COUPLED RFD SYSTEM

Setup of a Coupled RFD System

Since the loaded Q of the RFD is very low, almost all of the driving power (~99.7%) is coupled out of an RFD cavity to a matched load. If two RFD cavities are connected so that the output power from the first RFD is utilized for the second one, the total RF power demanded for the two cavities may be halved.

Two RFDs (RFD-A and RFD-B) were connected with a coaxial cable. The coupled RFD system can be regarded as a three-cavity system: two RFD cavities and a coaxial cavity. Because the distance between two gaps of the RFD cavities along the beam line is $3\beta\lambda$ (221.38 mm), the electric length between two cavities should be $n\lambda$ in order to keep the beam bunches synchronized with the rf field in the two RFD cavities. Here β is the relative velocity of a 3-MeV H^- ion, λ the free-space wavelength of RF, and n is an integer. The cable length was determined according to the results of a HFSS simulation. Taking the mechanical limitation in installation into account, the total cable length between two cavities was 942 mm. With this cable length, the measured spectrum of S_{21} in Fig. 4 shows that there are three modes, in which the second mode (324MHz) is the operating one. The measured spectrum of S_{21} gives the same feature as the simulation, in which the resonant frequency of the second mode is 323.75 MHz, with a bandwidth of 31.4 MHz and the loaded Q value of 10.4.

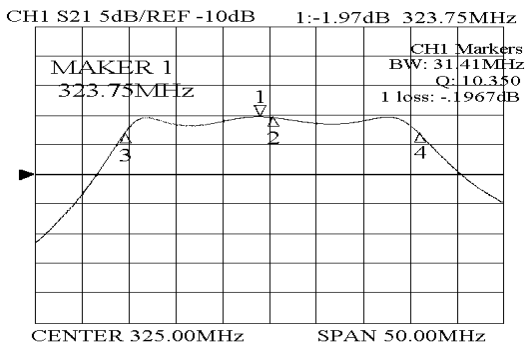

Figure 4: Measured S_{21} spectrum of the coupled RFD system.

Because the phase relations between two cavities can not be accurately checked by direct measurement, it is important to investigate the sensitivity of the deflecting effect with the phase error induced by the error of the connecting cable length. The simulation was made by using the code of TRACE3D for MEBT. The simulation showed that, within a 10° phase deviation, the influence to the deflection effect is very small.

Study on the RF Transient Behaviour

According to the measured loaded Q value (Q_L), as shown in the Fig. 4, the rise time of the cavity is $Q_L/\pi f_0$=10.6 ns, in which f_0 is the resonant frequency. The rise time of the whole RFD system is longer than that of the cavity, because of the contribution from the amplifier. The rise time of the coupled RFD system was measured by directly observing the rf response of the coupled RFD, as shown in Fig. 5, in which the dashed curve depicts the rf response from RFD-A and the solid curve the rf response from RFD-B. The rise time of the first cavity (RFD-A) is about 8 rf periods, almost the same as that of

a single cavity, but it becomes 11 rf periods for the second cavity (RFD-B).

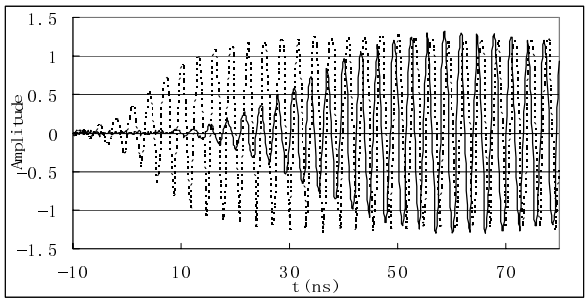

Figure 5: Measured response of the rf pulse of a coupled RFD system. The dashed curve is from the rf monitor of RFD-A, while the solid curve is from the rf monitor of RFD-B. Some delay time during transient rise time can be seen between two signals from A and B.

From Fig. 5, one can find that the delay time of the second RFD excitation was about 6 rf periods. For the $3\beta\lambda$ distance between two RFD cavities along the beam line, the 6 rf periods delay means that there were 3 micro bunches deflected by the first RFD only during the rise time; a similar case exists during the fall time.

A similar transient behaviour as that in the case of the measurement was observed in the simulation with T3 module of MAFIA, as shown in Fig. 6, in which the thin line indicates the rf signal in the gap of the RFD-A, and the dark line traces the rf signal in the gap of the RFD-B. Similar to the measurement results, the rise time of the second RFD is longer than that of the first one, and the delay time in the second RFD excitation is about 5 rf periods. The delay time obtained in the simulation is less than that in the measurement. The reason for the difference in the delay times comes from the different setups between the measurement and the simulation: in the simulation two RFDs were connected by 50 mm coaxial cable for decreasing the required computing time, while it was connected by a 942 mm cable in the measurement.

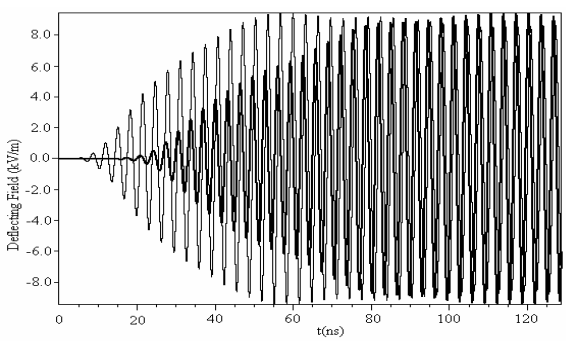

Figure 6: Simulated response of the rf pulse of the coupled RFD system made by using the T3 module of MAFIA. The thin line indicates the rf signal in the deflecting gap of the RFD-A, and the dark line traces the rf signal in the deflecting gap of the RFD-B.

It can be predicted that the two demerits, the longer rise time and the longer delay time in the second RFD will decrease the total deflection efficiency of the two RFD cavities. However, considering that the capability of the power amplifier is up to 36 kW, which is much larger than the demanded power of 22 kW in the design, these two demerits are not a problem. Fig. 7 shows the very short chopped beam signal measured by a beam position monitor in the first beam test at KEK [4]. It can be seen that both rise and fall times are about three rf periods (~10 ns), owing to the much higher deflecting field than the designed one.

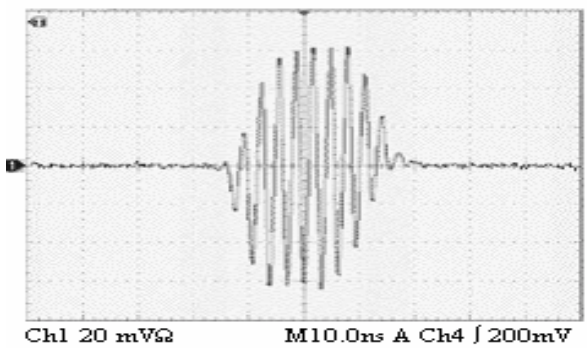

Figure 7: Signal of a chopped beam measured by the BPM. The beam current was 24 mA and driving power was 36 kW. 10 nsec/div. This is an example of a very short pulse with a fast rise/fall time after careful tuning accelerating parameters.

CONCLUSION

An rf chopper system consisting of two RFDs, has been successfully developed. A modification in the coupling loop of the chopper cavities was made for tuning the resonant frequency while keeping the bandwidth unchanged. In a high-power test, the chopper worked well without any discharge under 36 kW peak driving power. The rise time of the rf chopper system and the delay of the excitation of the second RFD in the coupled RFD system were studied by experiments and MAFIA T3 module simulations. The rise times of the chopped beam of about three rf periods (~10 ns) were obtained in the first beam test.

REFERENCES

[1] Accelerator Technical Design Report for J-PARC, KEK Report 2002-13; JAERI-Tech 2003-044.
[2] T. Kato, New Design of an RF beam Chopper, Proceedings of 7th Symp. on Accelerator Science and Technology, 228(1989).
[3] S. Fu and T. Kato, RF-chopper for JHF linac, Nucl. Instr. And Meth. A 440, 296(2000).
[4] T. Kato et al., Beam Study with RF Choppers in the MEBT of the J-PARC Proton Linac, Proceedings of PAC2003, p1455, May, 2003, Portland, USA.

EXPERIMENTAL STUDY OF AN 805 MHz CRYOMODULE FOR THE RARE ISOTOPE ACCELERATOR*

T. L. Grimm, S. Bricker, C. Compton, W. Hartung, M. Johnson, F. Marti, J. Popielarski, R. C. York
National Superconducting Cyclotron Lab, Michigan State University, East Lansing, Michigan, USA
G. Ciovati, P. Kneisel, L. Turlington
Thomas Jefferson National Accelerator Facility, Newport News, Virginia, USA

INTRODUCTION

The driver linac for the Rare Isotope Accelerator (RIA) is designed to accelerate heavy ions to 400 MeV/u ($\beta = v/c = 0.72$) with a beam power up to 400 kW [1]. To obtain these intensities, partially stripped ions are accelerated in a 1400 MV superconducting linac. The high energy section of the linac uses 805 MHz six-cell elliptical cavities with geometric $\beta \equiv \beta_g = 0.47$, 0.61, and 0.81. The first cavity was developed specifically for RIA [2]; the last two were developed for the Spallation Neutron Source (SNS) [3].

A rectangular cryomodule design that can accommodate all of the superconducting cavity and magnet types is proposed for RIA [4]. The proposed cryomodule is more compact than the SNS cryomodule, allowing for a smaller tunnel cross-section and a higher real estate gradient. The cold mass alignment is accomplished with titanium rails supported by adjustable nitronic links, similar to that used for superconducting magnet cryostats at MSU.

A prototype cryomodule for the RIA $\beta_g = 0.47$ elliptical cavities was completed in February 2004. The prototype contains 2 multi-cell cavities instead of the 4 cavities planned for production cryomodules, since the critical issues of cavity gradient, quality factor, and microphonics (which drive the linac cost via module count, cryo-plant capacity, and RF amplifier power) can still be addressed. The first cryogenic and RF tests on the prototype cryomodule were completed in May 2004. Experimental results will be presented in this paper, including alignment, cryogenic performance, RF performance, and frequency tuning. Measurements on microphonics and microphonics control for the cryomodule cavities are presented elsewhere [5, 6].

PROTOTYPE DESIGN AND CONSTRUCTION

Figure 1 shows the prototype cryomodule. The cavities were chemically treated and tested in a vertical cryostat at Jefferson Laboratory (JLab) to verify their performance before installation into the module [2]. The field unflatness between cells was less than 10%, and the π mode frequency was tuned for 805 MHz at 2 K.

The titanium helium vessel was TIG welded to Nb-Ti adapter flanges that were electron beam welded to the cavity beam tubes. Nb-Ti flanges with Al alloy gaskets were used for vacuum sealing. The cold mass was assembled in Jlab's class 10 clean room and shipped by truck to MSU. The cavities were shipped under partial vacuum due to a leaky valve, which was subsequently replaced.

Two μ-metal shields that also serve as passive thermal shields reduce stray fields to 0.5–1 μT. Liquid N_2 was used in the thermal shield, but in the RIA linac 50 K He gas will further decrease the static load to the liquid He.

The required RF power for beam loading and microphonics control is less than 10 kW [5]. The same ceramic window as SNS was used with a smaller diameter coaxial coupler [7, 8].

A room temperature external tuner with piezo-electric actuator was designed for ease of maintenance. Since RIA operates continuous wave (CW), Lorentz detuning will not require fast compensation.

A simple fixture was used to verify cavity alignment to the beam axis within ± 0.25 mm. Fiducials on the Ti rails were monitored through viewports during the cool-down.

COOL-DOWN

The cool-down to 20 K was done rapidly to avoid Q disease. Below 20 K, we proceeded slowly to economise liquid He while the cryomodule approached steady state. The cavities reached 24 K in about 2.5 hours and became superconducting after another 2.5 hours. He gas was introduced into the insulation vacuum space for about 3 hours during the cool-down to increase the heat transfer to the liquid N_2 shield. The cryomodule temperatures were nearly at their steady state values with a full He reservoir 16 hours after the cool-down started. The cavities were cooled from 4.3 K to 2 K by pumping on the He reservoir.

In the initial attempt to cool down to 4 K, the insulation vacuum was not spoiled and the He reservoir was filled rapidly—this caused problems due to the inner μ-metal shield and Ti rails still being warm. In the production cryomodules, it may be worthwhile to improve the heat sinking for these elements to simplify the cool-down.

In initial attempts to cool down to 2 K, there were 2 trapped gas volumes in the liquid He space, one in the supply bayonet and the other associated with a viewport on top of the module. These trapped gas volumes produced thermo-acoustic oscillations near the λ-point, resulting in a pressure instability. Once the liquid level was low enough so that the gas was no longer trapped, we were able to reach 2 K. This problem was eliminated by removing the supply bayonet and the viewport and plugging the holes with teflon-tipped G10 spears. (A supply bayonet was installed in the He reservoir to replace the original bayonet feeding liquid directly to the cavities.) Trapped gas volumes will

*Work supported by Michigan State and the U.S. Department of Energy under Grant DE-FG02-03ER41247.

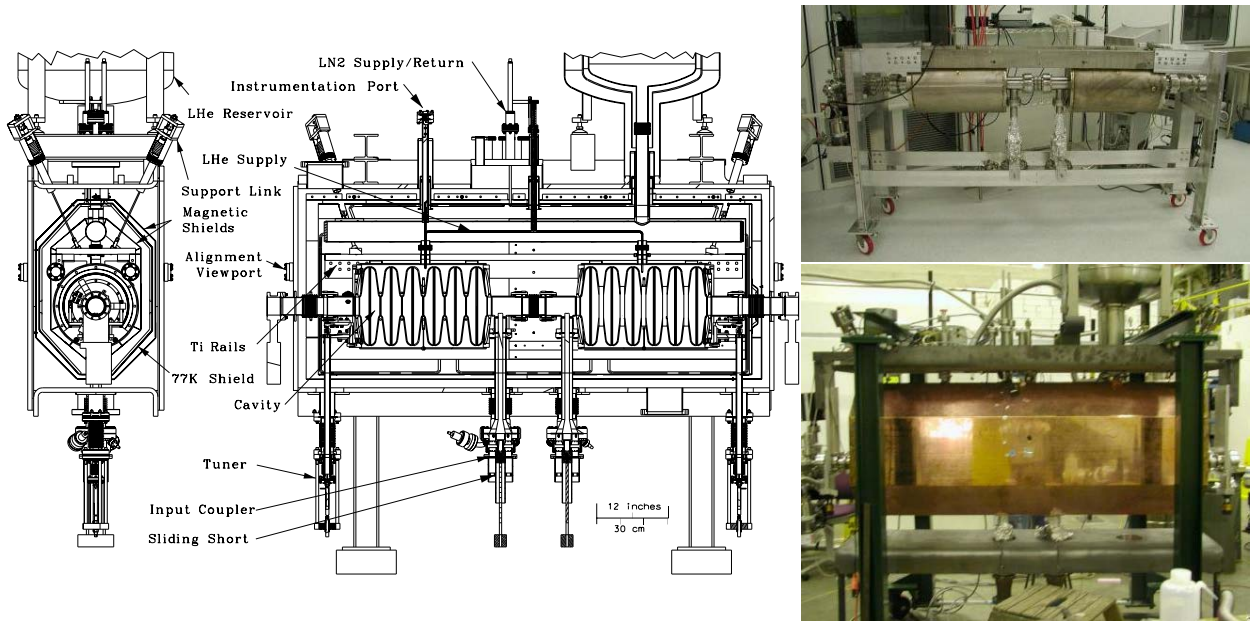

Figure 1 Left: end view and section view of the $\beta = 0.47$ prototype cryomodule. Top right: cavities inside the helium vessels after attachment of the Ti rails and input couplers. Bottom right: Cold mass after installation of the thermal shield.

be avoided in the production cryomodules.

STATIC HEAT LEAK

The static heat leak to the liquid He at 2 K was measured from the volume of He gas pumped per unit time. The pumping rate was obtained by measuring the time required to displace a known volume of water. The pumping rate was converted to heat leakage rate by calibrating it against a resistive heater in the cryomodule. In steady state conditions, the measured static heat leak to the liquid He was 10 to 11 W. The predicted heat leak was 15 W for a 4-cavity cryomodule [4], in reasonable agreement with the measurements on the 2-cavity prototype.

The static heat leak to the liquid He at 4.3 K was measured from the rate of decrease of the level in the He reservoir. As expected, the measured heat leak at 4.3 K (9 W) was similar to that at 2 K.

INPUT COUPLERS

The measured input coupling strengths were $Q_{ext} = 1.4 \cdot 10^7$ for Cavity #1 and $Q_{ext} = 1.3 \cdot 10^7$ for Cavity #2, both a bit lower than the design value ($Q_{ext} = 2 \cdot 10^7$).

Multipacting barriers were encountered at low field ($E_a \lesssim 0.1$ MV/m) with both cavities after they were cooled to 4.2 K. In both cases, we punched through the barriers after less than 1 hour of RF conditioning. Current was detected on the center conductor during the conditioning, which suggests that the multipacting was in the coupler, not in the cavity.

Since the input antennae cannot be moved, sliding shorts were installed on the coaxial lines to adjust the input coupling (see Figure 1). Loop antennae on the sliding shorts were used to couple power in and excite a standing wave in the coupler. For high field measurements, the short was moved to the detuned position to maximise the field in the cavity and minimise the field in the coupler. For low-field microphonics studies with a wide band-width, the short was moved to the tuned position. The range of measured Q_{ext} values was $6 \cdot 10^4$ to $6 \cdot 10^9$.

CAVITIES

The sliding short allowed us to set up a good match to reach high fields without high RF power, so most of the RF measurements were done with a 200 W solid state amplifier and a phase feedback loop.

The intrinsic quality factor of the cavity (Q_0) was obtained from RF measurements and checked with calorimetry. With the short present, the coaxial line has one open end and one shorted end, and hence has resonances when the length is equal to an odd integer multiple of $\lambda/4$. In the detuned position, the cavity resonance was between the frequencies of the $7\lambda/4$ and the $9\lambda/4$ resonances. We measured the Q for these adjacent resonances to estimate the power dissipation in the coupler's standing wave. We used a second loop antenna to infer the energy stored in the standing wave while we were driving the cavity. This allowed us to subtract out the estimated power dissipation in the coaxial line and calculate Q_0 directly from the RF measurements.

Field emission started at low field in the first measurements at 2 K. The field emission was especially bad in Cavity #1. Interesting images were observed with a video camera (set up to look into the cavities from a viewport on the beam tube) while driving Cavity #1. The light disappeared during RF processing of Cavity #1 and did not return. We were able to reach $E_a = 6$ MV/m in Cavity #1 and $E_a = 7.5$ MV/m in Cavity #2 after RF processing. We observed some deconditioning of Cavity #2 after conditioning of Cavity #1.

Additional pulsed processing (power ≤ 3 kW) was done

to further reduce the field emission. Figure 2 shows the cavities' performance after pulsed processing. The design gradient ($E_a = 10$ MV/m) was exceeded in both cavities, but they both still show field emission at high field: after processing, the first x-ray signals were detected at $E_a \approx 8$ MV/m, and the x-ray levels near the cryomodule reached as high as 10 rem/hour at high field. Cavity #2 does not quite meet the design goal of $Q_0 = 7 \cdot 10^9$ at the design gradient. After conditioning, both cavities exhibited some "Jekyll & Hyde" behaviour in which the field emission current (along with the RF power dissipation and x-ray flux) jumped back and forth between a lower value and a higher value. This can be seen most clearly from the double-valued Q_0 versus E_a curve for Cavity #2 at high field.

Measurements on the standing wave indicated that, at low field, the power dissipation in the coaxial line was less than or about equal to the power dissipation in the cavity; at high field, a higher proportion of the power was dissipated in the cavity. To check the RF measurements, the quality factor was obtained from a calorimetric measurement of the power dissipation. As for the static heat leak measurement, the He gas pumping rate was measured and calibrated against a heater. Measurements were done on Cavity #2 before the final round of pulsed RF processing. Useful results were obtained for $4.5 \leq E_a \leq 7$ MV/m (at low field, the RF power dissipation was small relative to the static heat leak and the uncertainty in Q_0 was excessive). The calorimetric Q_0 values were between $5 \cdot 10^9$ and $9 \cdot 10^9$, consistent with the RF measurements.

FREQUENCY ISSUES

In the first cool-down to 2 K (both tuners locked), the resonant frequencies were 805.13 MHz (Cavity #1) and 805.24 MHz (Cavity #2). The measured travel was 10 mm, with a measured tuning range of 0.95 MHz, well above the design goal of 0.5 MHz. Thus, both cavities were well within tuning range of the design frequency. A piezoelectric element was installed for fast tuning and compensation of vibrations. The range of fast tuning with up to 100 V drive signal was about 11 kHz. The piezo element was used for active damping of microphonics [5, 6].

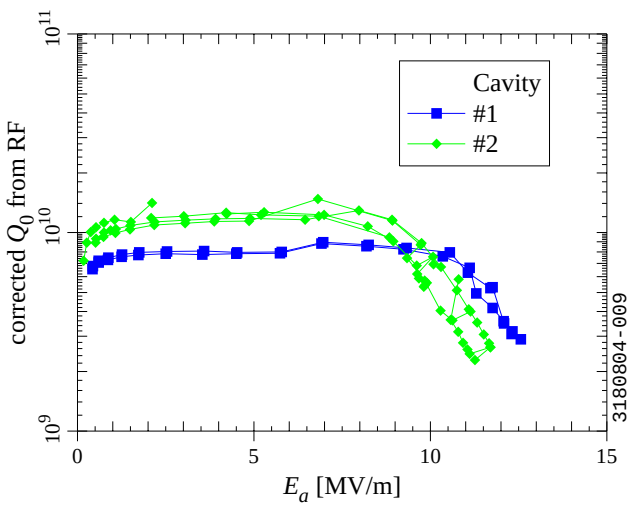

Figure 2: RF measurements on the $\beta_g = 0.47$ cavities at 2 K after RF processing.

The rate of change in the resonant frequency f as a function of the pressure P in the helium vessel was measured during the cool-down from 4.2 K to 2 K, with the result $df/dP = 0.36$ kHz/torr (Cavity #1) and $df/dP = 0.46$ kHz/torr (Cavity #2). The sign is the opposite of what was measured for single-cell cavities ($df/dP = -1.0$ kHz/torr) and vertical tests on 6-cell cavities; the pressure force on the helium vessel (present for the cryomodule cavities, absent in the vertical tests) tends to cancel the effect of the pressure force on the cavities.

The measured Lorentz detuning coefficient at 2 K was $K_L \equiv df/dE_a^2 = -16$ Hz/(MV/m)^2. This result is close to the predicted value of $K_L = -14$ Hz/(MV/m)^2 [9]. The value for the cryomodule is smaller than the measured detuning for the single-cell cavities [$K_L = -22$ Hz/(MV/m)^2], as one would expect since the single-cell cavities had no stiffening rings at the irises.

CONCLUSION

A prototype cryomodule for RIA has been constructed and tested. The cryogenic and RF performance has been demonstrated. The RF performance of one of the cavities is a bit marginal due to contamination. Note that SNS production cavities were prepared using the same facilities at about the same time (November 2003), and they showed similar problems with field emission. Corrections have since been implemented, resulting in lower field emission and better performance for SNS cavities. A valve leak might have also contributed to the contamination of the prototype module. Future goals include a demonstration of RF amplitude and phase control at full power, including microphonics control.

REFERENCES

[1] C. W. Leemann, in *Proceedings of the XX International Linac Conference* SLAC-R-561, 2000, p. 331–335.
[2] W. Hartung *et al.*, in *Proceedings of the 2003 Particle Accelerator Conference*, p. 1362–1364.
[3] G. Ciovati *et al.*, in *Proceedings of the 2001 Particle Accelerator Conference*, p. 484–486.
[4] T. L. Grimm *et al.*, in *Proceedings of the 2003 Particle Accelerator Conference*, p. 1350–1352.
[5] T. L. Grimm *et al.*, "Measurement and Control of Microphonics in High Loaded-Q Superconducting RF Cavities," these proceedings.
[6] T. Kandil *et al.*, "Adaptive Feedforward Cancellation of Sinusoidal Disturbances in Superconducting RF Cavities," *ibid.*
[7] Q.-S. Shu *et al.*, "Design and Fabrication of Input RF Coupler Windows for the U.S. Rare Isotope Project (RIA)," presented at the Eleventh Workshop on RF Superconductivity (8–12 September 2003, Travemünde, Germany).
[8] M. Stirbet *et al.*, "RF Conditioning and Testing of Fundamental Power Couplers for the RIA Project," *ibid.*
[9] D. Barni *et al.*, Tech Note JLab-TN-01-014, Jefferson Lab, Newport News, Virginia (2001).

FIRST EXPERIENCE WITH DRY-ICE CLEANING ON SRF CAVITIES

D. Reschke[#], A. Brinkmann, DESY, D-22603 Hamburg, Germany
D. Werner, Fraunhofer IPA, D-70569 Stuttgart, Germany
G. Müller, FB C, University of Wuppertal, D-42097 Wuppertal, Germany

Abstract

The surface of superconducting (s.c.) accelerator cavities must be cleaned from any kind of contamination, like particles or chemical residues. Contaminations might act as centers for field emission, thus limiting the maximum gradient. Today's final cleaning is based on high pressure rinsing with ultra pure water. Application of dry-ice cleaning might result in additional cleaning potential. Dry-ice cleaning relies on the sublimation-impulse method and removes particulate and film contaminations without residues. As first qualifying step intentionally contaminated niobium samples were treated by dry-ice cleaning. It resulted in a drastic reduction of the particle numbers and of DC field emission up to fields of 100 MV/m. The dry-ice jet caused no observable surface damage. First cleaning tests on single-cell cavities showed Q-values at low fields up to $4x10^{10}$ at 1.8K. Gradients up to 33 MV/m were achieved, but field emission still is the limiting effect. Further tests are planned to optimise the dry-ice cleaning technique.

INTRODUCTION

Despite the substantial improvement of the preparation procedures, enhanced field emission still imposes the major high gradient limitation of superconducting accelerator structures, e.g. for the 1.3 GHz nine-cell structures used in TTF at DESY [1]. In order to achieve a gradient of 23 MV/m required for the XFEL [2] or to push the performance to 35 MV/m required for TESLA [3], electric surface fields of at least 46 MV/m and 70MV/m, respectively, should be achieved reliably without field emission loading of the Q-value. Therefore, advanced final cleaning and handling procedures must be applied to avoid surface contaminations like particles, hydrocarbons, etc. and mechanical damages like scratches. The above mentioned have been shown to cause enhanced field emission (EFE) at the envisaged field levels. Though high pressure rinsing with ultrapure water has been proven to be a powerful technique to reduce the enhanced field emission of cavities [1, 4, 5], dry–ice cleaning might have additional cleaning potential. Moreover it avoids a wet cavity surface with its enhanced sensitivity against recontamination. It should be applicable to ceramics (coupler windows) without loosing the gain of an earlier conditioning. Due to these properties dry-ice cleaning is considered as very attractive for the final treatment of horizontally assembled cavities with its power coupler. According to the stimulating first results on flat Nb samples [6], the adoption of this technique to srf cavities will be reported in this paper.

[#]detlef.reschke@desy.de

DRY-ICE CLEANING

A jet of pure carbon dioxide snow loosens and removes different types of surface contaminations by its unique combination of mechanical, thermal and chemical effects. The cleaning process acts locally, mildly, dryly, without residues and requires no additional cleaning agent. The spontaneous relaxation of liquid carbon dioxide leaving the nozzle results in a snow/gas mixture with app. 45 % snow and a temperature of 194.3 K (-78.9°C). This jet is surrounded by supersonic nitrogen, which firstly gives an acceleration and focussing of the jet and secondly prevents partially the condensation of humidity at the cleaned object. The cleaning effect is based on thermo mechanical and chemo mechanical forces. The former are created by three effects: brittling the contamination as a result of rapid cooling (shock-freezing), the tough pressure and shearing forces due to the high momentum of the snow crystals hitting the surface and the powerful rinsing due to the 500 times increased volume after sublimation. Particles down to 100 nm can be removed. Chemo mechanical forces occur, when high momentum snow particles hitting the surface partially are melting at the point of impact. In its liquid phase carbon dioxide is a good solvent for non-polar chemicals, especially for hydrocarbons and silicones. The thermal effect of shock-freezing is thereby directly correlated with the snow intensity. The mechanical effect however depends on the velocity and angle of the jet and the chemical effect depends on the momentum of the crystals. An optimal cleaning impact is achieved, if the thermal gradient between contamination and substrate is high. To avoid recontamination an effective and well-defined exhaust system is necessary. In summary the advantages of the carbon dioxide dry-ice cleaning are:

- dry cleaning process,
- no cleaning agents,
- removal of particulate and film contaminations,
- no polluting residues.

NB SAMPLE EXPERIMENTS

Flat samples with a diameter of 28 mm were machined from high purity niobium (RRR = 300) and etched 80 µm with standard BCP ($HF:HNO_3:H_3PO_4$ volume ratio 1:1:2). In order to get typical EFE, each test sequence started with a new surface treatment, i.e. etching and rinsing inside a cavity [7] or intentional contamination with particles [6]. The chosen particle materials are typically ambient during the assembly of accelerating structures like latex (gloves), metal oxides, copper, iron and stainless steel. At first, these samples were inspected with

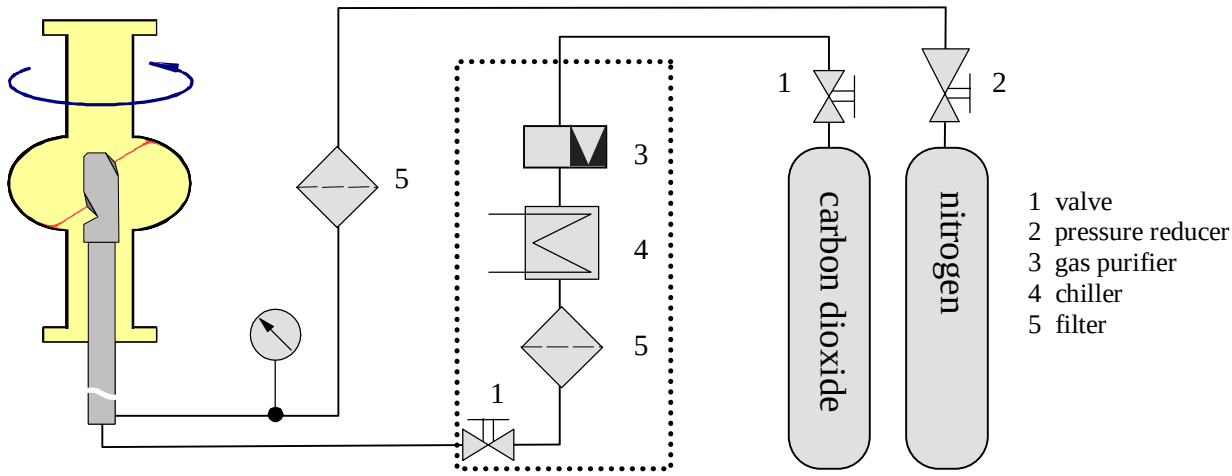

Figure 1: Schematic of the prototype set up for dry-ice cleaning of monocell cavities.

an optical microscope under cleanroom conditions (class 10000). The particle number densities of the intentionally contaminated samples varied between 400/mm^2 and 1100/mm^2. Then the EFE properties were determined with a field emission scanning microscope [8] (FESM). The dry-ice cleaning was performed in a class 10 cleanroom with a one-nozzle system perpendicular to the surface [6]. The cleaning effect was investigated with the FESM and an optical microscope (class 10) again. For the sample transfer between the laboratories, an approved clamped cap system [7] was used and opened under cleanroom or UHV conditions only.

The results achieved on 9 samples can be summarized as follows:

a) Two samples etched and ultrapure water rinsed inside a nine-cell cavity showed few emission spots before but none after dry-ice cleaning up to 100 MV/m.

b) An intentional contamination with metal particles of 5 samples created a significant number of field emission spots up to 101 at 80 MV/m before dry ice cleaning. After dry-ice cleaning, both the number of microscopically visible particles as well as the number of field emission sites decreased dramatically. On two samples no field emission was found up to 100 MV/m (typ. scanning area 6 mm x 6 mm).

c) Two samples contaminated with latex and metal-oxide particles showed nearly no dc EFE up to 100MV/m before dry-ice cleaning and were not investigated further.

d) No kind of mechanical damage was found on the dry-ice cleaned niobium samples.

CAVITY EXPERIMENTS

Dry-Ice Cleaning Apparatus and Procedures

An overview of the prototype set-up for cleaning of monocell cavities is given in figure 1. A major component is the chiller/purifier system for purifying and particle filtering of the technical-grade CO_2. The temperature of the liquid CO_2 is reduced below -5°C to increase the fraction of snow. As the cooling capacity of the available chiller was insufficient, the temperature could not be kept constant (see below). Pure nitrogen is supplied up to a pressure of 18 bar and particle filtered to < 0,05 µm. A dedicated nozzle system for cavity cleaning was developed using two opposite nozzles spraying with an angle of 30 degrees upward and downward with respect to the horizontal plane for optimised cleaning of the cavity iris area (Figs. 2 + 3). The used temporary motion unit caused severe restrictions of the experiments due to a missing gas extraction system, an insufficient heating possibility of the cavity and bearings generating particles.

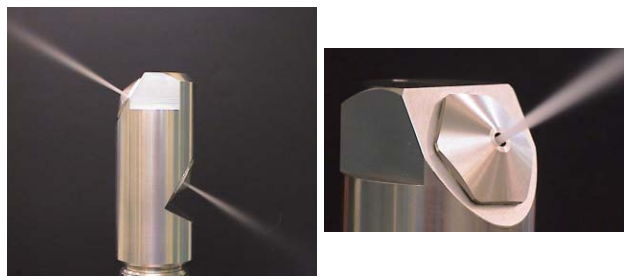

Figure 2: Nozzle system for cavity cleaning.

Each cavity was rotated and cleaned at least one time up and down. The cleaning duration was varied between 10 to 50 minutes. Due to the inadequate chiller the cleaning process had to be interrupted and restarted several times causing an enhanced danger of particle contamination. After the dry-ice process, the final assembly, evacuating and leak-checking was performed in a class 10 cleanroom.

Table 1: Dry ice cleaning parameters

CO_2-pressure	~ 50 bar
N_2-pressure	12 - 18 bar
Particle filtration	< 0,05 µm
Temperature of liquid CO_2	-5° - -40° C
Environment of cleaning	Laminar flow class 10

Figure 3: Nozzle test in a cut NbCu cavity (top) and in the beam tube of a Nb monocell (bottom).

RF Results

In total 11 niobium monocell cavities were rf tested after dry-ice cleaning. All tests show high Q-values above 10^{10} at 2 K typical for superconducting niobium cavities at 1.3 GHz. The highest Q-value of $4 \cdot 10^{10}$ at 1.8 K proves that no surface contamination is caused by dry-ice cleaning. Though gradients up to $E_{acc} = 33$ MV/m are achieved (fig. 4), still field emission is the limiting effect in most tests indicating that both, installations and cleaning process, need further optimisation.

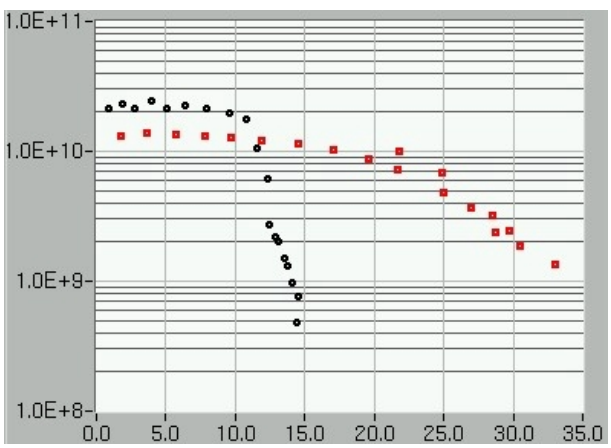

Figure 4: $Q(E_{acc})$-performance of a monocell cavity at 2 K before (black) and after (red) dry-ice cleaning.

SUMMARY AND OUTLOOK

Based on the evident experiences in semi-conductor industry and the successful cleaning of several Nb samples, dry-ice cleaning was applied for the first time to superconducting accelerator cavities. Resulting in typical high Q-values and gradients up to 33 MV/m the proof-of-principle was successful. Nevertheless significant improvements of the cleaning apparatus and optimisation of the parameters are necessary.

A more powerful chiller/purifier unit for CO_2 is ordered and an improved motion unit, capable for horizontal cleaning of one- to three-cell cavities, is under construction. An effective gas extraction system and a controlled heater system to avoid humidity condensation on the cavity are under development. During the next tests the cleaning speed as well as the dry-ice jet properties defined by nozzle diameter, N_2 pressure, CO_2 temperature will be topics of detailed investigations.

ACKNOWLEDGEMENT

We acknowledge the support of the European Community Research Infrastructure Activity under FP6 “Structuring the European Research Area” program (CARE, contract number RII3-CT-2003-506395).

The authors thank A. Guss, J. Iversen, F Kaldasch, J. Ziegler, C. Zorn for their technical support.

REFERENCES

[1] D. Reschke, Proc. 10th Workshop on RF Superconductivity, Tsukuba, Japan, p.144 (2001)

[2] Editors: R. Brinkmann et al., TESLA XFEL TDR Supplement, DESY 2002-167, TESLA-FEL 2002-09 (2002)

[3] Editors: R. Brinkmann, K. Flöttmann, J. Rossbach, P. Schmüser, N. Walker, H. Weise, TESLA TDR, DESY 2001-011, ECFA 2001-209, TESLA-FEL 2001-05 (2001)

[4] P. Kneisel, B. Lewis, Proc 7th Workshop on RF Superconductivity, Gif-sur-Yvette, France, p.311, (1995)

[5] B. Aune et al., Superconducting TESLA Cavities, Phys. Rev. ST Accel. Beam 3, 092001 (2000)

[6] D. Proch, D. Reschke, B. Günther, G. Müller, D. Werner, Proc. 10th Workshop on RF Superconductivity, Tsukuba, Japan, p. 463 (2001)

[7] G. Müller, A. Göhl, T. Habermann, A. Matheisen, D. Nau, D. Proch, D. Reschke, Proc. 6th Europ. Part. Acc. Conf., Stockholm, 1998, p. 1876

[8] E. Mahner, N. Minatti, H. Piel, N. Pupeter, Appl. Surf. Sci 67, 23 (1993)

A NEWLY DESIGNED AND OPTIMIZED CLIC MAIN LINAC ACCELERATING STRUCTURE

A. Grudiev, W. Wuensch, CERN, Geneva, Switzerland

Abstract

A new CLIC main-linac accelerating-structure design, HDS (Hybrid Damped Structure), with improved high-gradient performance, efficiency and simplicity of fabrication is presented. The gains are achieved in part through a new cell design which includes fully-profiled rf surfaces optimized to minimize surface fields and hybrid damping using both iris slots and radial waveguides. The slotted irises allow a simple structure fabrication in quadrants with no rf currents across joints. Further gains are achieved through a new structure optimization procedure, which simultaneously balances surface fields, power flow, short and long-range transverse wakefields, rf-to-beam efficiency and the ratio of luminosity to input power. The optimization of a 30 GHz structure with a loaded accelerating gradient of 150 MV/m results in a bunch spacing of seven rf cycles and 32 % rf-to-beam efficiency.

INTRODUCTION

In order to reach the CLIC design luminosity and energy (~10^{35} $cm^{-2}sec^{-1}$ and 3 TeV, respectively) in power-efficient way, multiple-bunch trains of about 0.5 nC each are accelerated on each machine cycle with an average gradient of 150 MV/m [1]. The design of an accelerating structure capable of this is constrained by a number of very demanding beam dynamics requirements and rf effects: a short-range transverse wakefields limit, long-range transverse wakefield suppression, rf breakdown and rf pulsed surface heating.

As more experimental data about rf breakdown has become available and when these constraints have been considered simultaneously, it has become clear that the existing designs of the CLIC main linac accelerating structure, the TDS (Tapered Damped Structure) [2] and later the XDS (conveX Tapered Structure) [3], are not satisfactory. In this paper, a new geometry and design approach is described giving a structure which not only finally satisfies both beam dynamics and rf constraints (at least to our present level of knowledge of them) but also brings a distinct improvement in rf-to-beam efficiency of 32% and a novel assembly technique.

The first key improvement has been to increase higher order mode damping by combining iris slots and radial waveguides – hybrid damping and hence the name HDS (Hybrid Damped Structure) - allowing the bunch spacing to be reduced from 20 to 7 rf cycles. The second key improvement is a new optimization procedure which is based on the interpolation of the structure parameters and allows millions of structures to be analysed taking into account the full and extremely complex interplay between rf and beam dynamics parameters.

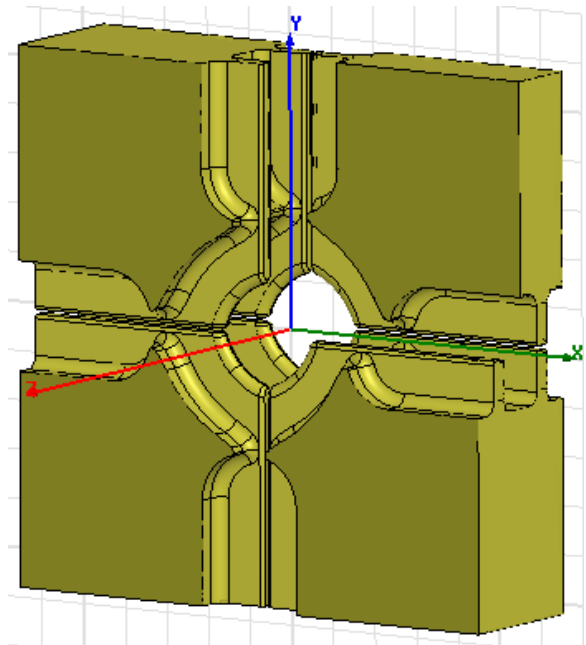

Figure 1: Geometry of the HDS cell. Two cells are shown to better demonstrate shape of the cell cavity, slotted iris and damping waveguides. For the same reason one quarter of one of the cells is removed from the picture.

HDS DESIGN

The HDS design was illuminated by the idea that iris slots could be introduced in addition to the damping waveguides in order to improve suppression of long-range transverse wakefields with little increase of the pulsed surface heating. The geometry of the HDS cell is shown in Fig. 1. In fact, the coupling in the HDS of the (dominant) lowest dipole mode to the slots becomes significantly stronger than the coupling to the damping waveguides. The waveguides are retained because there are higher-order transverse modes with the rf phase advance per cell close to 0 and longitudinal higher-order modes (TM_{0n}), which are weakly or not at all coupled to the slots. These modes are generally well damped by the waveguides.

Because the lowest dipole mode is coupled mainly to the slots rather than to the waveguides, and the weak dependence of this coupling on the damping waveguide aperture size, the surface of the cell outer wall can be increased compared to the XDS. This *reduces* pulsed surface heating, due to a lower current density, while simultaneously improving damping.

The slots however introduce a number of difficulties which have had to be addressed. One of them is that the surface electric field is enhanced in the area where the slots end in the center of the iris. This field enhancement is eliminated by composing the beam aperture out of four

circular arcs which have a radius larger than the distance from the beam axis to the iris tip *a*, which can be observed in Fig. 1. Because the ends of the slots are further from the center of the cell than the middle of the iris arcs, they are exposed to lower surface electric field. Each cell consequently consists of four quadrants which have no contact because of the slots cut both the iris and the wall between damping waveguides of adjacent cells. A structure can thus be formed from four quadrants in which the cells, irises, slots, damping waveguides and other subsystems are milled into the outside each piece as is shown in Fig.2.

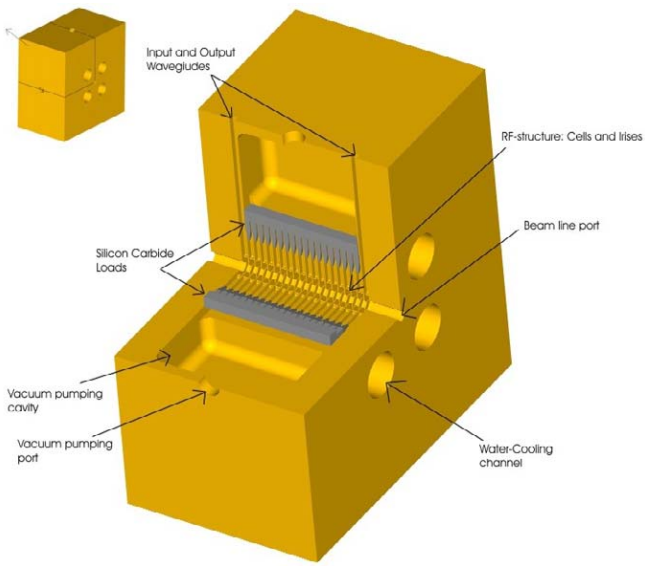

Figure 2: The HDS layout. Taking one of the quadrants out shows the inside of the structure: the chain of cells of accelerating structure, the damping waveguides, terminating loads, the vacuum pumping ports, the input and output waveguides, as well as four water-cooling channels.

This novel accelerating structure design and assembly gives a number of advantages compared to traditional structures in which individual cells are brazed together including,

- Reduction of the number of pieces per structure to four and a significantly decrease in surface area to be machined.
- Free choice of joining because of there are no rf currents between quadrants
- No water/vacuum joints nor brazed-on cooling channels.
- Excellent vacuum pumping.
- Slots can be as narrow as needed an profiled – an important feature for 30 GHz.

THE OPTIMIZATION PROCEDURE

The search for a new structure optimization procedure was motivated by the need to simultaneously vary iris diameter range, iris thickness range and phase advance while considering the effect on short-range transverse wakefield amplitude, long-range transverse wakefield suppression, rf-to-beam efficiency, surface fields and power flow. The simple approach of varying a single parameter at time was clearly impractical.

For a fixed rf phase advance, the entire procedure is repeated for different phase advances, the optimization procedure consists of three parts. In the first part, a set of nine individually optimised cell geometries are calculated for fundamental mode and lowest dipole mode characteristics of over an range of *a,* and iris thickness, *d.* This gives a two-dimensional parameter space for interpolation.

In the second part, parameters for $4 \cdot n_{d1} \cdot n_{d2} \cdot (n_{d1}-1) \cdot (n_{d2}-1)/2$ structures are calculated. Here $n_{d1}, n_{d2}, n_{d1}, n_{d2}$ mean number of variation in a_1, d_1, a_2, d_2, respectively, which are *a* and *d* in the first and last cells of a structure. For each structure the bunch charge *N* is determined from the results of beam dynamic simulations which take into account the effect of short-range wakefields on emittance growth [4]. The long-range wakefields of the lowest dipole mode is calculated based on interpolated parameters and uncoupled model. The value of the transverse wake envelope at the position of the second bunch $\|W_t\|_2$ is limited by the following condition [4]:

$$N \times \|W_t\|_2 < 4 \cdot 10^9 \times 20 \text{ V/pC/mm/m}.$$

Satisfying this condition gives the bunch separation in the number of rf cycles N_s.

In the third part of the optimization, structures are selected which satisfy the following rf constraints which are based on a structure made from CuZr alloy and Mo iris tips:

1. Surface electric field [5]: $E_{surf}^{\max} < 380$ MV/m.
2. Pulsed surface heating [6]: $\Delta T^{\max} < 56$ K.
3. Power [7]: $P_{in}\, \tau_p^{1/2} < 1225$ MW·ns$^{1/2}$.

Here $E_{surf}^{\max}$ and $\Delta T^{\max}$ refer to maximum surface electric field and maximum pulsed surface heating temperature rise in the structure, respectively. P_{in} and τ_p denote input power and pulse length. Since both $\Delta T^{\max} \sim \tau_p^{1/2}$ and $P_{in}\, \tau_p^{1/2}$ depend on pulse length conditions, 2 and 3 can always be satisfied by reducing the number of bunches in the train N_b. This reduction is however limited because the shorter the pulse the lower the rf-to-beam efficiency due to the fill time of the structure. Hence, N_b is chosen to make pulse as long as possible under pulsed surface heating and power constraints. Then, if the structure satisfies condition 1, rf-to-beam efficiency and other pulse length dependent parameters of the structure are scaled for this value of N_b.

Different optimization criteria are possible. In the case of CLIC, the main goal is to reach design luminosity and energy in the most efficient way. Hence the optimum structure must provide the highest ratio of luminosity to main linac input power. In terms of the structure parameters this corresponds to maximum of figure of merit: $L_{b\times}\eta/N$, where $L_{b\times}$ denotes luminosity per bunch crossing in 1% of energy which is obtained in the beam dynamics simulations of CLIC main linac and beam delivery system [4]. Thus, the optimum structure is that

which gives maximum of figure of merit among all structures satisfying conditions 1 through 3.

OPTIMIZATION OF THE CLIC MAIN LINAC ACCELERATING STRUCTURE

The optimization procedure section was been performed for a range of rf phase advances $\Delta\varphi$ of 50^{o} to 130^{o}. The iris radius a was varied from 1 to 2.5 mm, thickness d was varied from 0.3 to 0.75 mm for $\Delta\varphi < 90^{o}$ and from 0.5 to 1 mm for $\Delta\varphi \geq 90^{o}$. Both a and d step variation is 0.05 mm resulting in 217800 analyzed structures for each value of $\Delta\varphi$. The results show maximum figure of merit: $L_{b\times}\eta/N = 14.0$ at $\Delta\varphi = 70^{o}$. The optimisation was then performed once more at the optimum $\Delta\varphi = 70^{o}$ with smaller step (0.02 mm) of a and d variation, which results in larger number of analyzed structures: 7605000 and, consequently, in a better structure with figure of merit: $L_{b\times}\eta/N = 14.4$.

Table 1: Parameters of the best structure calculated without interpolation

Cell length: l_c [mm]	1.944
First and last iris radius: a_1, a_2 [mm]	2.14, 1.52
First and last iris thickness: d_1, d_2 [mm]	0.59, 0.37
Averaged a to wavelength ratio: $<a>/\lambda$	0.183
Number of particles in the bunch: N	2.8×10^{9}
Luminosity per bunch crossing: $L_{b\times}$ [m^{-2}]	1.22×10^{34}
Structure length: l [mm]	218
Bunch separation: N_s [rf cycles]	7
Number of bunches in the train: N_b	212
Pulse length: τ_p [ns]	58.2
Input power: P_{in} [MW]	160
Rf-to-beam efficiency: η, η_{Mo} [%]	33, 32.2

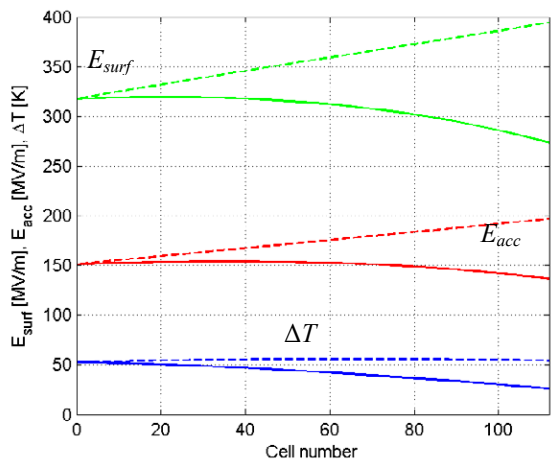

Figure 3: Pulsed surface heating temperature rise (blue), accelerating gradient (red), and maximum surface electric field (green) along the optimum structure with (solid) and without (dashed) beam loading.

A list of the optimized structure parameters, which are finally calculated without interpolation, is presented in Table 1. η_{Mo} refers to the rf-to-beam efficiency taking into account lower electrical conductivity of the Mo tips. Fundamental mode parameters as a function of cell number are shown in Fig. 3 and the transverse wake is shown in Fig. 4.

The theme obscurely stated in the parameter tables is that the overall performance of CLIC in terms of the luminosity to power ratio has been improved while simultaneously satisfying for the first time all of the beam dynamics and rf constraints described previously. Bringing the TDS or XDS designs into consistency would result in serious reductions of many previously published parameters. The main feature giving the improvement is the reduction in the bunch spacing from 20 to 7 fundamental rf cycles. This has a profound effect on the structure rf-to-beam efficiency which is increased despite the reduction of the pulse length by a factor of two and reduction in bunch charge by 30%.

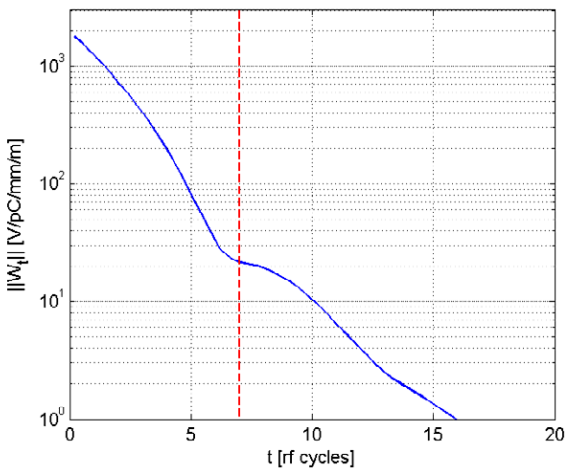

Figure 4: Envelope of the wake of the lowest dipole mode in the optimum structure.

REFERENCES

[1] The CLIC Study Team (edited by G. Guignard), "A 3 TeV e+/e- Linear Collider Based on CLIC Technology", CERN Report 2000-008.

[2] M. Dehler, I. Wilson, and W. Wuensch, "A Tapered Damped Accelerating Structure for CLIC", LINAC'98, Chicago, August 1998.

[3] J.-Y. Raguin, I. Wilson, and W. Wuensch, "Progress on the Design of a Damped and Tapered Accelerating Structure for CLIC", PAC'03, Portland, May 2003.

[4] D.Schulte, "Luminosity Limitations at the Multi TeV Linear Collider Energy Frontier", PAC'02, Paris, June 2002.

[5] W. Wuensch, H. Braun, S. Doebert, I. Syratchev, and I. Wilson, "A Demostration of High-Gradient Acceleration", PAC'03, Portland, May 2003.

[6] S. Heikkinen, http://clic-meeting.web.cern.ch/clic-meeting/, CLIC Meeting of 26 June 2003.

[7] V. Dolgashev, "Effect of Rf Magnetic Fields and Input Power on Rf Breakdown Limit", Workshop on High-Gradient RF, Argonne, October 2003.

LASER PRODUCED IONS AS AN INJECTION BEAM FOR CANCER THERAPY FACILITY*

A. Noda, M. Hashida, Y. Iwashita, S. Nakamura, S. Sakabe, S. Shimizu, T. Shirai,
T. Takeuchi, H. Tongu, ICR, Kyoto University, Uji-city, Kyoto, 611-0011, Japan
A. Fukumi, Z. Li K. Matsukado, NIRS, Inage-ku, Chiba, 263-8555, Japan
H. Daido, Kansai Research Establishment, JAERI, Umemi-dai, Kizu, Kyoto, 619-0215, Japan
T. Hosokai, H. Iijima, K. Kinoshita, K. Yoshii, T. Watanabe, M. Uesaka
Graduate School of Engineering, Univ. of Tokyo, Naka, Tokai, Ibaraki, 319-1188, Japan

Abstract

Ion production from a solid target by a high-power short-pulse laser has been proposed to replace the injector linac for the synchrotron dedicated for cancer therapy in order to reduce the size of the facility. For the reduction of the energy spread of the laser-produced ions up to ±5 %, a scheme of phase rotation is to be utilized. A quarter wave length resonator with the resonant frequency of 79.3~82.7 MHz and its power amplifier of the maximum power of 30 kW are designed and fabricated. Ion production from the solid target has also been studied and experimental results suggest the ion production from under dense plasma for the case with the presence of pre-pulse.

INTRODUCTION

High energy ion production from the solid target by a high-power laser has recently been reported [1, 2]. In such a process, target normal sheet acceleration is expected [3]. The lasers utilized for such purpose had been high power lasers mainly oriented for laser fusion and their repetition rates are, in general, very low and less than once per twenty minutes, which does not match the real application for medical use and so on. For the purpose of demonstrating the feasibility of utilization of the laser-produced ion-beam as the injection beam for cancer dedicated synchrotron, possibility of inducing target normal sheet acceleration of ion beam from the solid target with the pulse laser of much shorter pulse width and higher repetition rate as 10 Hz has been investigated. By focusing the laser to the size ~10μm in diameter, ion production up to 1 MeV has been observed even for the rather limited laser power density of ~10^{18} W/cm^2. The intensity of the laser-produced ions, however, decreases exponentially according to the increase of the ion energy. In order to remedy this situation, a scheme of phase rotation with use of the laser-synchronized RF electric field has been proposed [4], which has been developed assuming the experiments utilizing 100 TW, 20 fs, 10 Hz laser at JAERI, Kansai Research Establishment.

In the present paper, the preliminary results of experimental research on laser ion production is presented together with the design and fabrication of the quarter wave length RF cavity for phase rotation.

PRELIMINARY TEST OF LASER ION PRODUCTION

Ion production by the laser with the power ~10 TW and short pulse width (50 fs) has been performed as the preparatory work for ion production and its phase rotation with use of 100 TW, 20 fs laser, because the available time of the latter laser is rather limited.

Wth use of a 30TW, 50 fs laser at Nuclear Engineering Research Laboratory, Graduate School of Engineering, University of Tokyo, ion production from various solids targets such as polyethylene, Ti, Ta and so on, has been performed. Among these targets, Ta target, 5 μm in thickness was most preferable. In Fig. 2, comparison of energy distribution among the metal targets is shown together with the data taken using the 10 TW, 50 fs laser

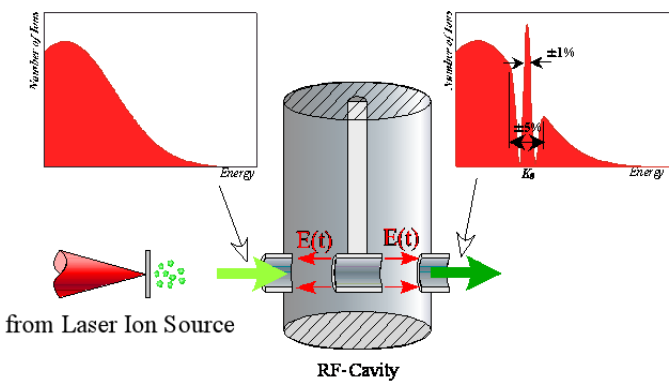

Figure 1: Schematic illustration of phase rotation of laser produced ions by a laser-synchronized laser.

*noda@kyticr.kuicr.kyoto-u.ac.jp

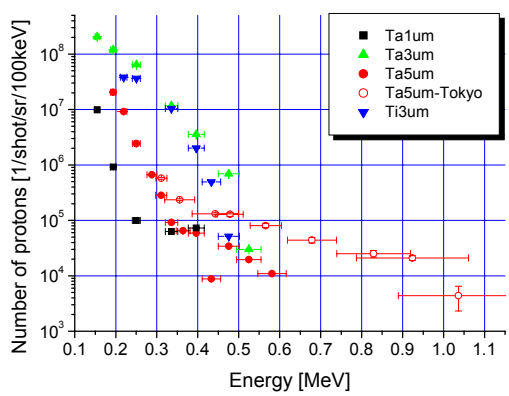

Figure 2: Comparison of energy distributions of laserproduced proton from various metal targets.

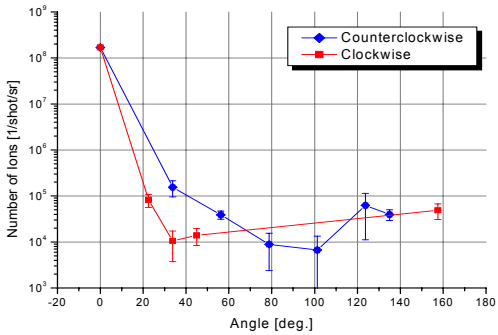

Figure 3: Angular distribution of laser produced protons.

available at JAERI, Kansai. In Fig. 3, the angular distribution of produced proton is shown, which indicates that most of laser produced protons are emitted in the direction less than 20 degree from the direction of the laser, while the solid target is set perpendicular to the laser direction.

In these experiments, there existed a rather large pre-

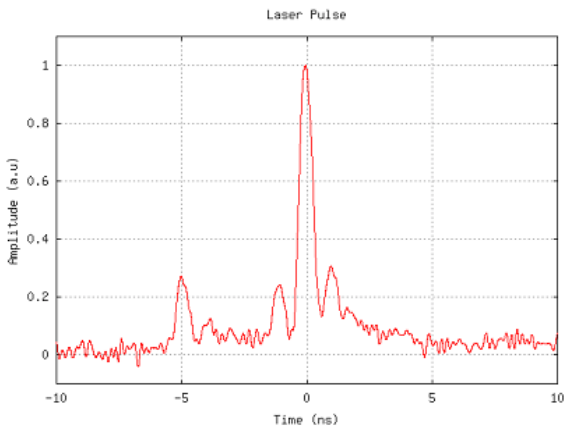

Figure 4: Temporal structure of the pulse laser.

pulse as indicated in Fig.4, which resulted in a rather promising results of producing higher energy protons as is expected by ion production from under-dense plasma compared with the case of production from over-dense

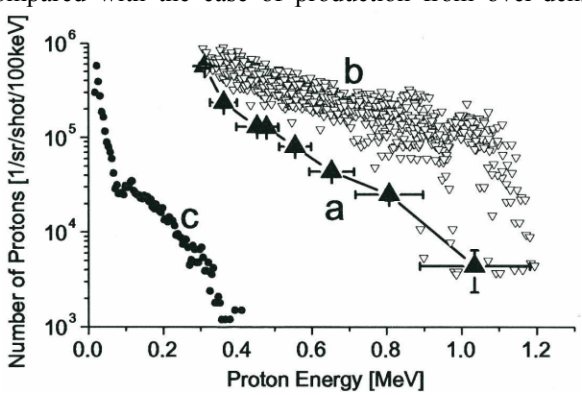

Figure 5: Energy distribution of laser produced proton in the direction of laser propagation. (a)experimental results, (b)simulation by under-dense plasma model, (c)simulation by over-dense plasma model [5].

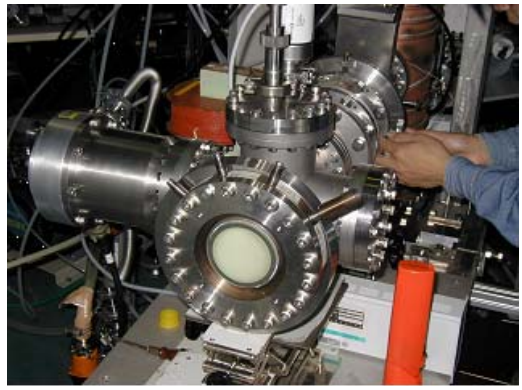

Figure 6(a): Micro-channel plate to observe the Thomson parabola of laser produced ions.

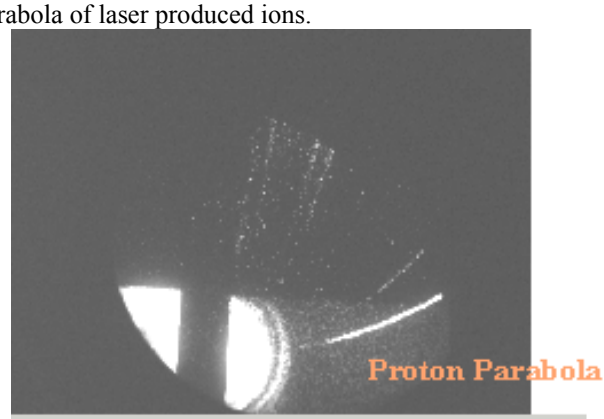

Figure 6(b): Observed Thomson parabola of produced ions by the T6 laser.

plasma as shown in Fig. 5 [5]

Ion production from a mylar target, 2.5 μm in thickness, has also been studied with use of T6 (Table-top Ten TW Ten-Hz Tunable Ti:sapphire) laser at Osaka University. With use of the michro-chanel plate as shown in Fig. 6(a), the Thomson parabola is observed for proton together with carbons of various charge states (Fig. 6(b)).

In the case of T6 laser, the suppression of the pre-pulse is considered to be very good. In such a situation, ion production to target normal direction is considered to be very sharply oriented from the experimental fact that the Thomson parabola can be observed with good reproducibility only with the target already irradiated by the laser. In the case of irradiation on the new surface of the target, usually the Thomson parabola cannot be observed. We defined the direction of ions which come into the apparatus for Thomson parabola observation with use of two collimators set at the front side. Our adjustment of the target to the collimation direction of the laser produced ion is considered not precise enough and the Thomson parabola cannot be observed for the new surface, while the target surface becomes somewhat deformed after irradiation of the laser and the "effective" target normal direction somewhat spreads. This speculation indicates the possibility that the angular distribution of the laser produced ions is much more sharp compared with Fig.3 if the pre-pulse of the irradiated pulse laser is well suppressed, which is the scope of our future experimental research.

PHASE ROTATION FOR CREATION OF ENERGY PEAK

The laser produced ions, in general, have no energy peak as shown in Fig. 2 and Fig. 5. In order to improve this situation, the phase rotation cavity has been designed and fabricated. The signal from the source laser is utilized to trigger the RF electric field on the quarter wave length resonant cavity and relative phase between the RF electric field and the pulse laser can be adjusted with use of a phase shifter.

The frequency of the source laser is 82.7 MHz and 79.3 MHz for 100 TW and 10 TW lasers, respectively and the resonant frequency of the phase rotation cavity is designed to be tuned for both frequencies with use of a fixed tuner in addition to the adjustable tuner. The phase rotation cavity, which has double gap, are designed with a quarter wave length type and fabricated as shown in Fig. 7.

A power amplifier to excite this resonator with the maximum power of 30 kW has also been completed. It is expected that the acceleration voltage up to 200 kV with the two gap can be applied. With this voltage, correction of the energy up to ±5 % of carbon ion with the kinetic energy of 2 MeV/u, which is assumed as the injection beam for the synchrotron dedicated for cancer therapy, can be realized.

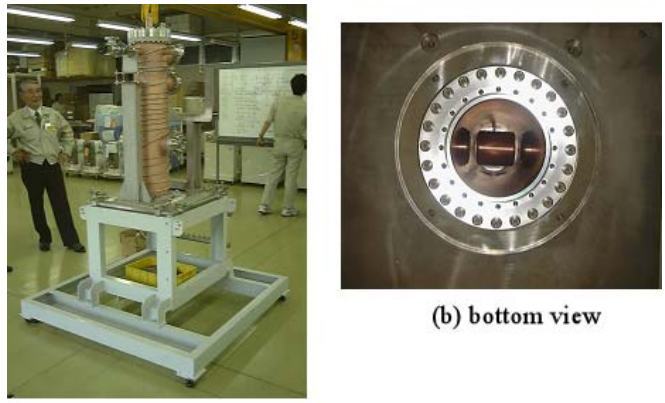

(a) overall view (b) bottom view

Figure 7: Fabricated phase rotation cavity.

PRESENT STATUS

The phase rotation experiment with use of 100 TW, 20 fs laser is scheduled in coming October. The phase rotation cavity and its power amplifier have been set at the down stream of the target chamber and fine tuning of the timing system between the pulse laser and the RF electric field has been started.

As the laser produced ion needs further reduction of energy spread after phase rotation to be utilized for cancer therapy machine [4], overall test of the phase rotation and further beam cooling of laser produced ions are planned at S-LSR, which is now under construction at ICR, Kyoto University. Utilizing the T6 laser to be moved to the laser building constructed next to the accelerator hall, the laser is guided as indicated in Fig. 8 and the phase rotation and electron beam cooling will be applied to the "real" laser produced ions.

ACKNOWLEDGEMENTS

The present work has been promoted as the research and developments for Compact Accelerator Development Project by Ministry of Education, Culture, Sports, Science and Technology of Japanese government.

REFERENCES

[1] P.Stephen et al., Physics of Plasma **7** (2000) pp2076-2082.
[2] E.L.Clark et al., Phys. Rev. Lett. **85** (2000) pp1654-1657.
[3] S.C. Wilks et al., Phys. Plasma **8** (2001)pp542-549
[4] A. Noda et al., Beam Science and Technology, **6**, 21 (2001)
[5] K. Matsukado et al., Phys. Rev. Lett. **91** (2003) 215001

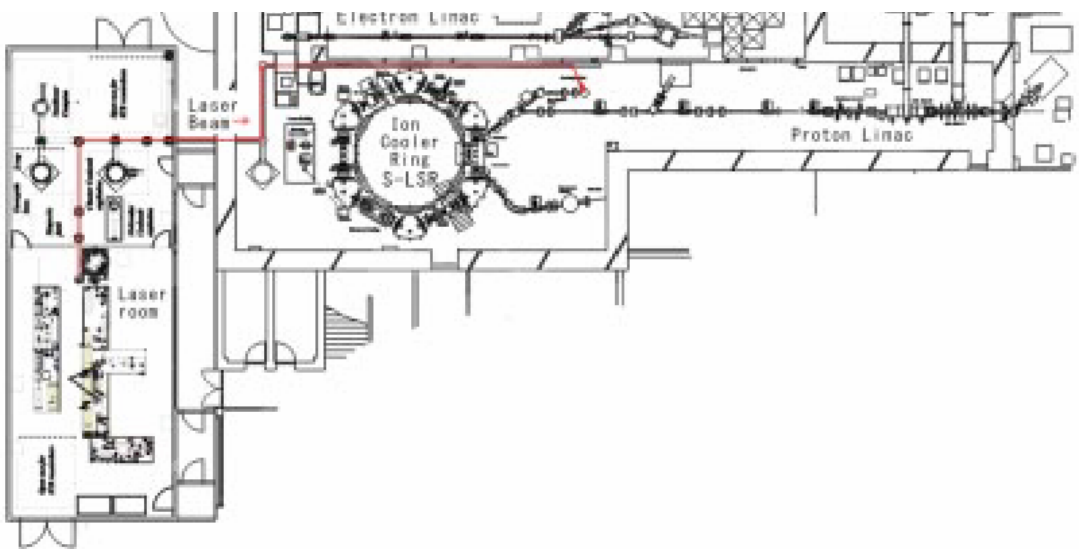

Figure 8: Layout of the combined facility of the accelerator and high power short pulse laser.

SUPERCONDUCTING ACCELERATING STRUCTURE WITH GRADIENT AS 2 TIMES HIGHER AS TESLA STRUCTURE

P. Avrakhov, V. Balakin, Physical Technical Center of P.N.Lebedev Physical Institute, Protvino, Russia

Abstract

A proposed new accelerating structure for TESLA is assumed to have an effective gradient 2 times more than existing 9-cell cavity [1]. This structure is an interlaced combination of two side-cavity-coupled standing wave substructures with $\lambda/4$ cells length. Intercell coupling provides side-coupled cavities, which are made from a special shape waveguide section. The high accelerating gradient is accomplish by 4 factors:

1) The shortened accelerating cells have transit time factor 0.9 instead of 0.64 for conventional standing wave cells with $\lambda/2$ length.

2) The side magnetic coupling has made it possible to reduce the cells beam aperture that reduce relation between the maximum surface field and the acceleration gradient.

3) Stronger intercell coupling allows extending the accelerating cavity and improving a duty factor of linac.

4) Availability of the side coupling elements enables to use them for power input and HOM-couplers. It reduces intercavity distance and enhances duty factor too.

INTRODUCTION

Under development of a superconducting linear accelerator the greatest efforts are applying to increase its effective accelerating gradient. The next significant parameter is shunt impedance. But shunt impedance of a superconducting linac is higher than 5-6 orders of magnitude for "warm" accelerators and is not so important to choice of a geometry superconducting linac. A few methods for improvement of acc. gradient are known. They are including an application of shortened cells for accelerating structure, reducing linac aperture and increasing of active length of accelerators by shortening of inter-cavity spacing. The first two methods increase acc. gradient due to reducing surface electric and magnetic fields into an accelerating cell. And third method extends effective length of accelerator. In this report a novel type of standing wave accelerating structure, which combines all these methods, is suggested.

DOUBLE-CHAIN BIPERIODIC STANDING WAVE STRUCTURE

Experience of employment of biperiodic accelerating structures with side coupled resonators (see Fig.1) showed their high efficiency in comparison with ordinary iris-loaded cavities. Due to side magnetic coupling large intercell coupling coefficient is easily obtained for any

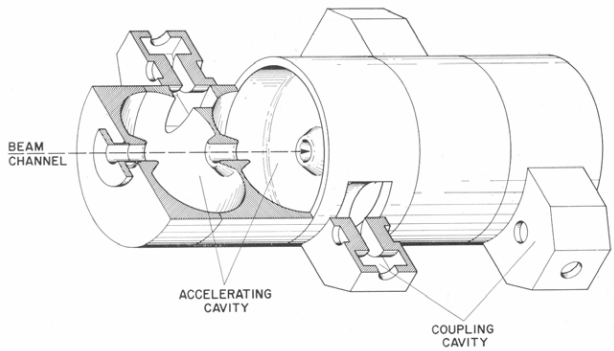

Figure 1: The side-coupled cavity chain [1].

size of beam holes. Low aperture accelerating cells have low field ratios E_{surf}/E_{acc} and H_{surf}/E_{acc}, where E_{surf}, H_{surf} means the maximal electric and magnetic fields into the cell and E_{acc} is the accelerating gradient.

In addition the high coupling allows to use long accelerating cavity because the main limitation factor of cell number for superconducting structure is field nonuniformity [4], which is proportional to $\Delta f/f \cdot N^{3/2} \cdot K_{coup}^{-1}$, where $\Delta f/f$ means average relative error of cells frequency, N is number of cells in the cavity and K_{coup} is the intercell coupling coefficient. Existence of the side resonators allows to carry out main power and HOM couplers into these resonators. Filling factor for such biperiodic structure can achieve 1.

If an accelerating cavity consists of $\lambda/4$ instead of $\lambda/2$ length cells it gives considerable gain in accelerating gradient due to rising of transit time factor. Transit time factor for single pillbox resonator can be expressed from length of pillbox as:

$$T = \frac{\sin(\theta/2)}{\theta/2} = \frac{\sin(\pi \cdot D/\lambda)}{\pi \cdot D/\lambda}$$

Where θ is transit angle and D is the resonator length. In case of $D=\lambda/2$ $T=2/\pi=0.637$ and for $D=\lambda/4$ $T=2\cdot\sqrt{2}/\pi=0.9$. Since transit time factor means ratio of effective accelerating voltage to maximum cell voltage, accelerating rate of $\lambda/4$ pillbox obtains as $\sqrt{2}=1.41$ times higher than in $\lambda/2$ length pillbox.

However the well-known biperiodic structure [2, 3] with side coupling cavity is not quite suitable for superconducting accelerator because of prohibitive gain of magnetic field in coupling slot area. It is caused by

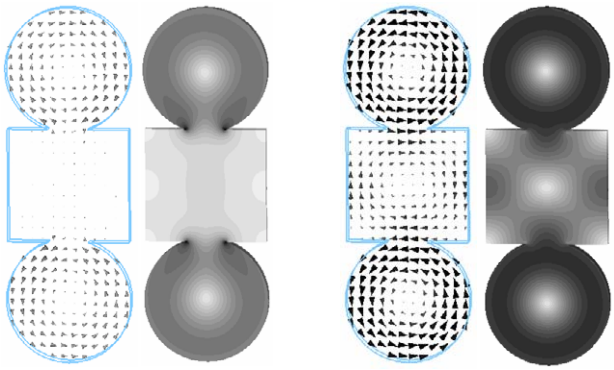

a) With high magnetic field in coupling window

b) With low magnetic field in coupling window

Figure 2: Two samples of magnetic coupling between three cavities.

penetration of strong magnetic flux from accelerating cavity to relatively empty side cavity. The penetrating magnetic field considerable gains on corners of coupling slot. Only the same magnitude and direction field in the neighboring coupling resonator can compensate and reduce parasitic transverse magnetic field in the coupling slot (see Fig. 2). In this case operation mode is π and phase shift between accelerating cells is 2π. But allowing for one hundred eighty degrees turn of every next accelerating resonator (see Fig. 3) the total phase shift for them remains π. It defines distance between accelerating cells. The minimum distance is $\lambda/2$ at the $\lambda/4$ cell length.

Figure 3: Electric field distribution for operation mode of the biperiodic structure.

From Fig. 4 it is seen that the resulting accelerating structure can be expanded an identical second one with side coupling cells oriented in transverse plane towards the first structure plane. Thus we obtain standing wave accelerator structure: a combination of two independent substructures, each operating at the π-mode, and each with an independent RF input coupler.

Proper operation of this double-chain biperiodic structure requires that both substructures are tuned to the same resonant frequency, RF power from the RF source must be divided equally between them, and a phase difference of $\pi/2$ between these two RF inputs must be provided. Therefore for beam an accelerating field of this structure will be equivalent to $\pi/2$-mode accelerating structure. But unlike conventional traveling wave accelerating structure [5] the coupling between on-line cavities through the beam aperture can be arbitrary small. It allows to choose cavity geometry with small beam hole.

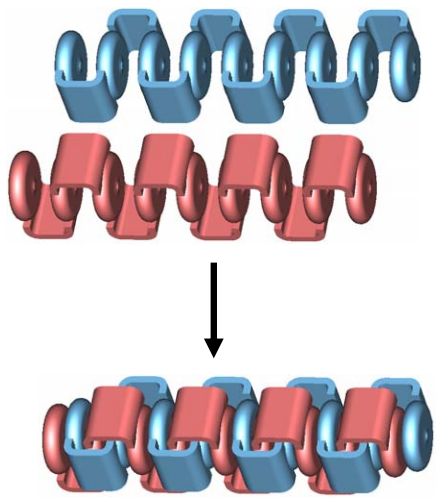

Figure 4: Union of two side-coupled cavity chains into the one SW acceleration structure.

SUPERCONDUCTING ACCELERATING STRUCTURE WITH GRADIENT AS 2 TIMES HIGHER AS TESLA STRUCTURE

As an example we will consider 18-cell double-chain biperiodic structure with 20mm aperture and resonant frequency of 1.3GHz. Geometry of two periods of the substructure is shown in Fig. 5. Since the beam aperture is no longer used to couple energy down the system, one has almost complete freedom to change the cavity parameters to optimize efficiency. At first we chose an accelerating cavity shape to minimize the maximal surface magnetic and electric fields for given gradient into the accelerating cell. After that the coupling resonator shaped to obtain proper coupling factor and tuned the cavity chain on retention low magnetic field in area of coupling slot. As coupling resonators there is a short waveguide section, which is made from WR650 with reduced height of 20mm.

The maximal surface electric and magnetic fields in the tuned-up structure achieve approximately the same value into the accelerating and the coupling resonators. If TESLA ratios of the maximal electric and magnetic field

strength on the cavity surface to the accelerating rate ($E_{surf}/E_{acc}=2$, $H_{surf}/E_{acc}=4.26mT/MV/m$) is taken as reference, then this structure has reduction of such ratios by a factor 0.62 both for magnetic and electric fields. The exact values are E_{surf}/E_{acc}=1.24 and B_{surf}/E_{acc}=2.63mT/MV/m. By choosing the cavity geometry [5] these ratios can be varied in a wide-ranging.

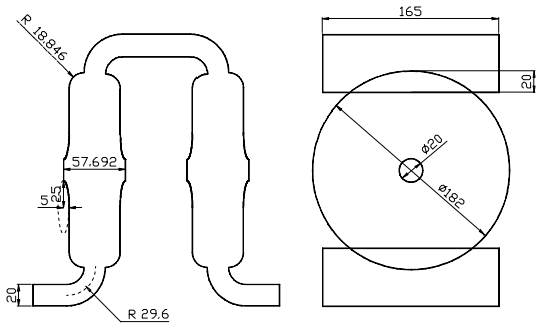

Figure 5: Two periods of the biperiodic substructure.

Dispersion curve of the substructure (see Fig.6) shows the coupling factor obtains 9.72%. It allows to have accelerating field nonuniformity like 9-cell TESLA structure for 27-cell cavity at the same cavity sizes tolerance.

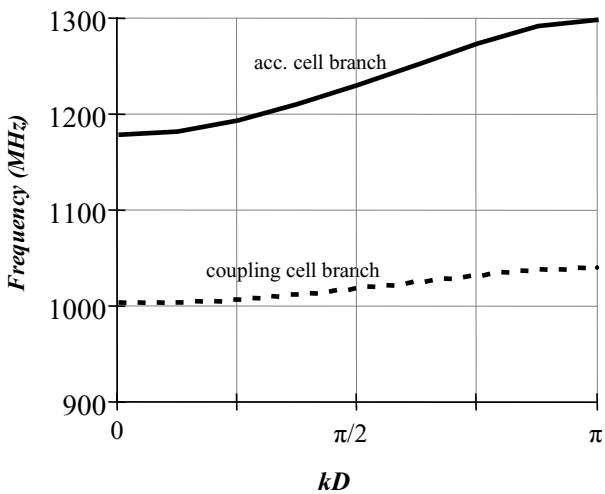

Figure 6: Dispersion curve for double-chain biperiodic structure.

In Table 1 important parameters of the double-chain biperiodic structure and two version of TESLA 9-cell structure are compared.

CONCLUSION

As a result of investigation of new type of standing wave accelerating structure showed that accelerating rate in superconducting accelerator can be significant increased for the achievable surface fields. The most gain of gradient gives small iris radius and large filling factor of the considered structure. Of course, we didn't touch many other appearing problems, which should be solved for this structure. The most evidence of them are:

- Technology of production double-chain biperiodic structure
- Beam dynamics (wake-field)
- Complication of auxiliary system and RF component

Table 1: Comparison between two layout of TESLA 9-cell cavity and double-chain biperiodic structure

Parameter	TTF-1 9-cell cavity	TESLA -500 9-cell cavity	Double-chain biperiodic structure
Active length (m)	1.038	1.038	1.038 - 1.558
Number of cells	9	9	18 - 27
Aperture diameter (mm)	70	70	20
Coupling cell to cell (%)	1.87	1.87	9.72
R/Q per cavity (Ω)	1036	1036	1293
f/ L (kHz/mm)	404	315	61
Filling factor L_{active}/L_{total}	0.747	0.786	≥ 0.94
E_{peac}/E_{acc}	2.0	2.0	1.24
B_{peac}/E_{acc} (mT/Mv/m)	4.26	4.26	2.63
Attainable effective acc.gradient (MV/m)			
at 105mT (TTF-1, 25MV/m in cavity)	18.4	19.4	37.5
at 150mT (present time, 35MV/m in cavity)	26.3	27.7	53.6
at 200mT (theoretical limit for niobium at 2°K)	35	36.9	71.5

REFERENCES

[1] B.Aune et al. "Superconducting TESLA cavities", Phys. Rev. ST – Accel. Beams 3, 092001 (2000)

[2] E.A.Knapp, B.C.Knapp, and J.M.Potter, "Standing Wave High Energy Linear Accelerator Structures", Rev. Sci. instruments, vol. 39, 7, July 1968.

[3] V.A.Vaguine, "Standing wave high gradient accelerator structure" Rev. Sci. Instrum., Vol. 48, No 12, pp. 1658 – 1660, December 1977

[4] M. Dohlus, V. Kaljuzhny, 98-26, "Relative Nonuniformity in the Amplitude of the Accelerating Field Along the M N-cell TESLA Supercavities", TESLA Reports 98-14 (1998)

[5] Balakin V.E., Solyak N.A. "Some estimation of Superconducting TW Structure with a High Accelerating Gradient", Branch of INP, Preprint 98-01 (1998)

EXPERIENCES IN FABRICATION AND TESTING THE PROTOTYPE OF THE 4.90 GHZ ACCELERATING SECTIONS FOR MAMI C[#]

A. Jankowiak, H. Euteneuer, S. Schumann, O. Tchoubarov,
Institut für Kernphysik, Johannes Gutenberg-Universität, D-55099 Mainz, Germany

Abstract

The fourth stage of the Mainz Microtron (MAMI C) is under construction as a Harmonic Double Sided Microtron [1]: by 43 recirculations through two anti-parallel linacs, one working at the MAMI-frequency of 2.45GHz, the other at 4.90GHz, the beam energy is raised from 855 to 1500MeV. The biperiodic accelerating structures used are of the on axis coupled type [2], well proven in high power cw-operation at MAMI since 1978. For 4.90GHz a further optimisation of the cavity profile was done [3]. In addition, to ensure an efficient industrial production of the ten 35AC-sections needed, a prototype section was designed, built and power tested fully in house.

We report the final cavity profile and the configuration of this 4.90GHz-section with its cooling arrangement, tuning plungers and diagnostic probes. Details of machining, fine tuning and brazing the resonator discs are given. Finally the results of the high power test up to 22kW (1.29MV/m) are presented: the conditioning behaviour and the irreversible permanent as well as the reversible dynamic changes of passband gap and resonance frequency as a function of rf input power.

RESONATOR PROFILE

A detailed discussion of our modifications of the cavity profile compared with the just 2:1 scaled 2.45GHz dimensions was given in [3]. These changes were: a larger beam hole ($\varnothing_B$=7 → 10mm) for a relaxed loss free beam transmission along the 12m long linac; a further outward positioning of the coupling slots for higher coupling (k=-4.1% → -8.7%), i.e. less stringent tuning demands, and a less sharp nose cone for easier precision machining. The total sacrifice in shunt impedance by these measures was calculated to be 18%.

With MAFIA and URMEL the sensitivities of the AC- and CC-frequencies to small changes of cavity dimensions were calculated (Table 1). Because of the high sensitivity of ν_{CC} to the CC-length l_{CC} (+163MHz/mm), bearing in mind the layer of brazing alloy with not precisely known final thickness between the endfaces, as a final modification l_{CC} was enlarged from 1.94 → 2.94mm, sacrificing 0.5mm in web thickness. The sensitivity decreased to +99MHz/mm, the coupling increased by 0.5% and the final CC- and AC-diameter is 40.23 resp. 45.39mm. In addition in Table 1 the calculated sensitivities of ν_{AC} and ν_{CC} to special cuts applied by us for fine tuning (cf. 3) are given, as well as the range of empirical values (e) gained during this tuning. For the full end cells (EC) with only one pair of coupling slots a by 50MHz higher frequency was compensated by a 0.52mm larger diameter, and the magnetic coupling slot (22.1×5.5mm through a min. 3.1mm wall) in the input coupler (IC) demanded for compensation of -47MHz by a 0.49mm smaller diameter.

SETUP OF THE 35AC-SECTION

The design of the section is shown in Fig. 1. The number of 35AC (electr./mech. length = 1.071/1.121m) was chosen for two sections being fed by one 55kW cw-klystron (THALES / TH2166): dissipated power 2×15kW, max. beam load 2×4kW, and a margin for waveguide losses and controlling the rf-amplitude to $<10^{-3}$ via the klystron input power. The coupling slot pairs in the AC were chosen to be oriented parallel: for compensation of their rf-quadrupole effect [4], a larger splitting of the TM_{110}-BBU-mode [5] and a clear fulfilling of the mirror boundary conditions when tuning finite resonator stacks. The IC is located at the symmetry point AC18, so the next excitable modes are ±19MHz away from the π/2-mode. Detailed calculations with LOOP [6] were done for this section design, concerning its tuning tolerances and the optimum position of tuning plungers and probes. It e.g.

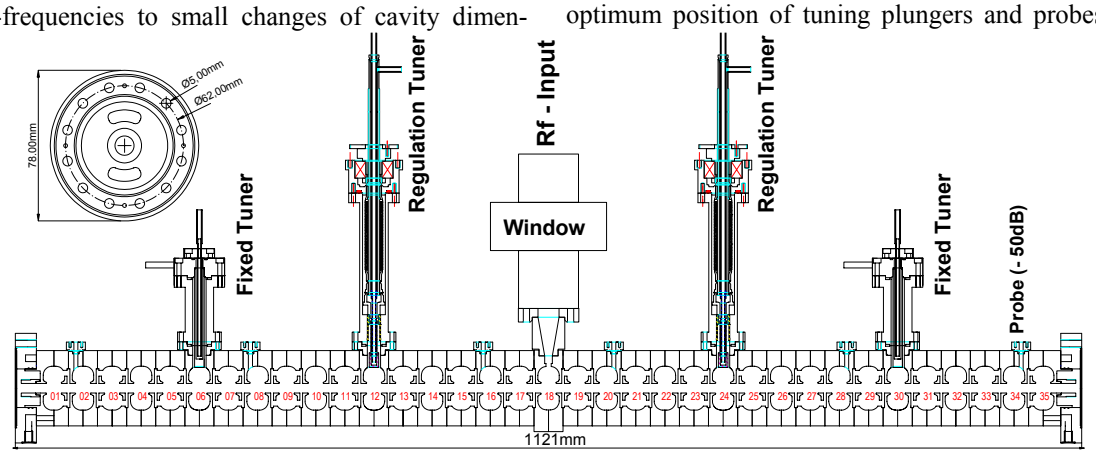

Figure 1: Scheme of the 4.90GHz section (already adapted for series production).

[#] Work supported by HBFG and DFG (SFB443)

turned out that the difference in resonance frequency of left and right half section (which are fabricated separately and then brazed to the IC) must be less then 1MHz to avoid distinct losses in quality factor by growing CC-fields; alike the tolerance for the symmetry of the pass-band gap is ca. 2MHz for an E_{AC}-unflatness <5%. For the industrial production of ten series sections the possibilities of tuning after brazing were distinctly enhanced compared to the 2.45GHz-sections fabricated in house in the 1980´s [7]. The section has four symmetrically located tuning plungers, of which two are movable to regulate the resonance frequency under power via a phase detection loop. Their design is very similar to the ones described in [7], with a tuning head of 10mm moving from -3.5 to +6.5mm in a ∅=14mm hole, for a section tuning range of 2.1MHz. The other two plungers are simple fixed cylinders, machined to the right intrusion depth to compensate for frequency deviations and asymmetries having occurred during fabrication. Moreover, the EC were constructed to be tuneable by a 3mm thin wall extending from ∅=14 to 36mm. With a hammer-tool fixed to a thread on their cutoff-pipe the end nose cones can be moved by ca. ±0.25mm, resulting in a frequency range of ±20MHz for the EC, i.e. ±1.1MHz for the whole section. It turned out that, to get a good phase and amplitude signal, the vertically mounted -50dB coaxial antenna probes should only be placed in AC with the two coupling slot pairs oriented horizontally. For cooling two sections will be connected in parallel, their 2×44 l/min water flow then going to the klystron collector. The cooling manifold consists of twelve Ø=5mm channels drilled along the circumferential wall, resulting in a flow velocity of 3.1m/s (Re=18.700) with a pressure drop of $< 1.5 \cdot 10^5$ Pa. The effective warm-up of the section under power, i.e. the necessary lab. frequency preset was calculated by the from [7] appropriately modified formula

$$\Delta\nu = -0.0823 \cdot P \cdot \left(7.17/D + 7.27/D^{0.82} + 0.447\right) \quad (1)$$

(Δν-MHz, P-kW, D-l/min). Here the first term accounts for the average warm up of the cooling water, the second for the temperature step at the copper-water boundary [8], and the third for the warm up of the rf-structure itself, including webdeformations [9]. For 15kW one gets Δν= -1.16MHz (eff. ΔT= +14.1°C).

MACHINING , TUNING , BRAZING

The materials used were OFHC-Cu (Zollern OF-Cu F20 certified) and SST304 (1.4301). This simple standard stainless steel was preferably used; because of its Ti-freeness it can be brazed to copper by Palcusil20 without Ni-plating. The machining was done in the following steps: The AC- and CC-resonator profile was machined on a CNC-lathe from copper discs with a 0.2mm skin staying all around, except on the outer diameter. As next on a CNC-milling machine the 12 cooling channels were drilled and especially very precisely (≤ 0.01mm) the holes for the two 2mm SST-centring pins between the segments. During the same step the coupling slots were milled to their final dimensions to avoid introducing any

Table 1: Sensitivity of tuning cuts at the cavity.

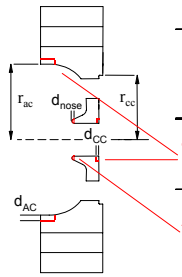

	AC	CC
Radius	$\frac{\partial \nu_{AC}}{\partial r_{AC}} = -193.1 \frac{MHz}{mm}$ (e): −185 ... −197	$\frac{\partial \nu_{CC}}{\partial r_{CC}} = -148.8 \frac{MHz}{mm}$ (e): −138 ... −186
Tuning	$\frac{\partial \nu_{AC}}{\partial d_{AC}} = -40.4 \frac{MHz}{mm}$ (e): −32 ... −38	$\frac{\partial \nu_{CC}}{\partial d_{CC}} = +150.7 \frac{MHz}{mm}$ (e): +149 ... +157
AC-Nose	flat cut d_{nose} [mm] / $\Delta\nu_{AC}$ [MHz] (e)	0.05 / 2.1 — 0.10 / 7.7 — 0.15 / 11.5 — 0.20 / 16.4

stronger stress into the webs later. These "raw" segments were thermal stress relieved at 450°C under vacuum and then finally machined. An excellent surface quality (the skin depth in Cu is 0.93µm at 4.90GHz) was obtained with the following CNC-lathe operation: cutting velocity 3.3m/s at a feed rate of 0.05mm/turn; infeed 0.1mm; cutting tool a sintered diamond circular plate with ∅=2.9mm; lubricant alcohol; special chuck with contact on the whole circumference.

At test samples without coupling slots a Q_0=11800 was measured, 99% of the reliable URMEL-value. The dimensions of the segments were for a machining preset $\Delta\nu_{AC}$= +1.5MHz and gap g= -5.2MHz; max. deviations of ±0.6MHz and ±2.1MHz respectively occurred, roughly consistent with a lathe accuracy of ±0.003mm. These presets in ν_{AC} and g were intended for easy fine tuning cuts (Table 1): an "inductive" 2mm broad ring at the outer diameter of the AC and a "capacitive" 1mm broad ring around the beam hole at the CC.

The fine tuning was done by measuring stacks of segments with a NWA in S_{11}-mode. Two ½-AC served as boundary "etalon-cells", with movable tuning stubs for e.g. compensating the detuning by the small rf-antenna. Only the accelerating mode (AM) was measured and the frequency of the coupling mode (CM) then determined by DISP-4 Par. fits [6]. It turned out, probably because of a quite strong second coupling ($k_{AC/CC}$= -8.7%, $k_{CC/CC}$= -0.7%, $k_{AC/AC} \sim 0$), that the fitted gap $g=\nu_{CM}-\nu_{AM}$ was significantly dependent on the length of a stack up to ≤ 8 segments (9 frequencies on the dispersion curve). Therefore with two segments at a time between the etalon-cells (5 frequencies) only the constancy of ν_{CM} was controlled, and then with long stacks its value for the global correction of the CC. The stacks were measured in a hydraulic press with a force of 1400kp; beyond this value the Q_0-value did not grow any more, indicating a sufficient rf-contact. However, as a bad surprise the gap changed by -5MHz for a pressing force between 300 and 1400kp. The reason for this effect was most probably the shape of the abutting faces of the segments: they had been machined with linear recess of 0.005mm from inner to outer edge of the circumferential wall, for ensuring a safe contact at the inner edge. So by the pressing the webs were slightly elastically bended, thus changing the effective length of the CC. To overcome this difficulty several test brazings on short tuned stacks were done, which with good constancy suggested a tuning preset before brazing of

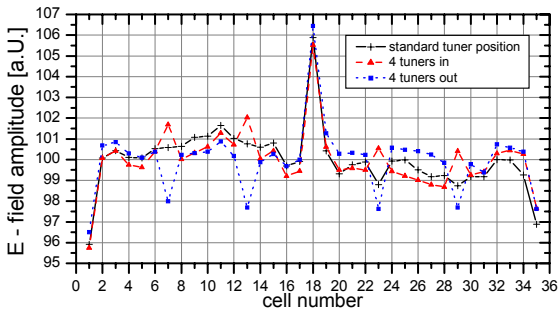

Figure 2: AC- field amplitudes for different tuner positions.

+1.3MHz and -3.6MHz for ν_{AM} and ν_{CM} respectively. For a future design, however, abutting faces with a ca. 3mm flat part and then a recess should be preferred. The full EC of the section were tuned to ν_{AM}. To do so without compensation for the symmetry breaking was decided experimentally by a bead pull measurement on a 4½-resonator stack with the EC hammer tuned in the range $\nu_{AM} \pm 20$MHz: the fields in the CC had a clear minimum for $\nu_{EC} = \nu_{AM}$, whereas the AC-fields nearly did not change, the EC being down by -3%. The tuning and match of the IC were performed by alternately measuring its frequency in the ½-cells etalon with the input waveguide pressed on it and terminated by a matched load, and by measuring the coupling factor β though the IC being pressed between the two section side parts. The adjustment of β to 1.127 (for match at 43×50μA beam loading) was done by machining in steps the length l and width w of the input slot, with roughly $\beta \sim l^5 \times w$.

The vacuum brazing was done mainly with Cusil (780°C, Cu/Cu), two 0.7mm wires in notches of the segments abutting faces at 26 and 36.5mm radius. The other alloys used were Palcusil 20 (905°C, Cu/SST304), Palcusil 10 (860°C, Cu/SST304-Ni-plated) and for the final connection of the two ready brazed and rf-measured section side parts to the input coupler Incusil 13 (720°C, Cu/Cu). The brazing presets for ν_{AM} and gap proved to be quite good, the deviations for the two 17-AC side parts were +0.57/+0.57MHz and +0.10/+0.52MHz respectively.

TESTS OF THE SECTION

The parameters measured on the ready brazed section were: shunt impedance r=81.5MΩ/m, i.e. only 14% less than the 2.45GHz scaled value; frequency ν_{AM} by 0.48MHz high; gap g= +0.31MHz and Q_0=10600. When detuning the section by ± 2.3MHz with the four tuning plungers Q_0 lowered by only 3.6%, indicating a very good field stability (CC-fields staying low) by the high coupling of k= -8.7%. This is also shown by the small changes of the AC-field amplitudes in Fig. 2. The 3-4% lower fields in the full EC were already mentioned. The 6% higher field at the IC clearly results from a design mistake: in this cell the two coupling slot pairs were oriented vertically and thus the coupling k is lowered by the big rf-input slot between them. For the series sections the orientation of the slot pairs will be changed by 90° in each

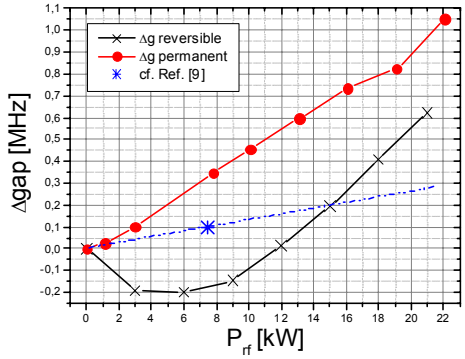

Figure 3: Permanent and reversible change of gap g.

cell and the tuner positions moved by one AC to stay with horizontal slot pairs also here.

The high power test began by heating the section without coolant flow by 1-2kW of rf-power up to 100°C and pumping it one day. Then, with the 4 tuners staying in nominal position, the power, with tightly set vacuum and reflected power interlocks, was raised up to 22kW, 47% more than the nominal dissipated power. After every advance by 2-4kW the conditioning was interrupted and the spectrum of the section measured with a NWA, to determine the permanent irreversible changes of ν_{AM} and gap. With good linearity the following values were measured: -4.7kHz/kW for the frequency and +49kHz/kW for the gap (cf. Fig. 3), indicating a permanent bending of the webs to their AC side by ca. 0.1μm/kW. An important measure was the visual observation of the sections interior under power by two glass windows at its ends: the bright glow of many microparticles gradually diminished with conditioning time, but not any blue plasma cloud, indicating a multipacting discharge, was observed. The dynamic reversible change Δg of the passband gap with input power (Fig. 3) was determined by a NWA-S_{21}-measurement of the sections spectrum through two of the diagnostic probes, with a +35dB-TWT in the 1-arm and a -70dB notch-filter in the 2-arm of the NWA. The strong nonlinearity of Δg differs significantly from the behaviour of our 2.45GHz-profile [7], and also the prediction of the thermoelastic calculation [9] done at 7.5kW input is locally not too good. Fortunately, during the design of the section this one point was used by us for a linear extrapolation to 15kW. Equation (1) was tested for coolant flows of 23, 45 and 67 l/min, the deviations to the measurement being +6%, +2.5% and 0% respectively.

REFERENCES

[1] A. Jankowiak et al., EPAC2002, Paris, p. 1085
[2] S.O. Schriber, LINAC76, Chalk River, p. 338
[3] H. Euteneuer et al., EPAC2000, Wien, p. 1954
[4] V.I. Shvedunov et al., PAC1995, Dallas, p. 3361
[5] V.I. Shvedunov et al., EPAC1998, Stockholm, p. 951
[6] S.O. Schriber, LINAC2002, Gyeongju, p. 231
[7] H. Euteneuer, H. Schöler, LINAC86, SLAC, p. 508
[8] H. Henke, I. Wilson, IEEE NS-30, No.4, 1983, p. 3590 & Handbook of Acc.Physics and Eng., p. 313 ff.
[9] V.I. Shvedunov, H. Euteneuer, Int.Note MAMI 1/99

MEASUREMENTS OF HIGH ORDER MODES IN HIGH PHASE ADVANCE DAMPED DETUNED ACCELERATING STRUCTURE FOR NLC

Gennady Romanov, Tug Arkan, Harry Carter, Timergali Khabiboulline,
FNAL, Batavia, IL 60510, USA
Gregory Linder, University of Illinois, Champaign, IL, USA

Abstract

The RF Technology Development group at Fermilab is working together with the NLC and JLC groups at SLAC and KEK on developing technology for room temperature X-band accelerating structures for a future linear collider. We have built several series of structures for high gradient tests. We have also built 150 degrees phase advance per cell, 60cm long, damped and detuned structures (HDDS or FXC series). Five of these structures have been successfully used for the 8-pack test at SLAC this summer, as part of the JLC/NLC effort to demonstrate the readiness of room temperature RF technology for a linear collider. HDSS structures are very close to the final design for the linear collider, and it was very interesting to study the properties of high order modes in the structures produced by semi-industrial methods. In this study advanced RF techniques and methods developed at Fermilab for structure low power testing and tuning have been used. The results of these measurements are presented in this paper.

INTRODUCTION

There are three basic requirements on the NLC structure design [1]: it must transfer the rf energy to the beam efficiently and demonstrate stable, long-term operation at 65-70 MV/m accelerating gradient to keep the machine cost low; it must be optimized to reduce the short-range wakefields which depend on average iris radius; and it must suppress the long-range transverse wakefield to prevent multibunch beam breakup and achieve high luminosity. During the past four years, an aggressive program has been underway by groups at SLAC, KEK and FNAL to build structures that meet the gradient requirements. Though the major emphasis has been on proving high gradient operation, an optimization of the structure for the NLC has been continuing as well, resulting in the development and adoption of a structure design (H-type Damped Detuned Structure) that basically meets performance requirements [2]. Now that significant progress in structure high gradient performance has been achieved [3], the high order modes issue must be revisited.

The NLC will require 10,000 to 20,000 accelerator structures. Each structure is comprised of about 50 accelerating cells, thus the total number of cells required is roughly one million [1]. Due to the tight tolerance requirements for these cells, quality control (QC) of RF parts is one of critical steps for this program. The full scope of QC includes many topics such as single cell and full structure QC, and RF and mechanical QC. At Fermilab, we have developed QC set-ups utilizing different microwave techniques to ensure that the machined cells are within the design tolerances, and to confirm overall RF performance of the completed structure [4]. Thus far, our routine QC procedures have not included direct control of high order modes.

The long-range dipole wakefield is suppressed in the structure design by detuning the dipole mode frequencies and damping the fields with dipole coupling channels (HOM manifolds) [2]. The dipole wakefields are the main cause of emittance increase and beam break-up in high-energy accelerators, thus understanding them is essential. Recently, we have developed methods for direct measurements of high order modes in completed structures in order to study their properties and to gain a better understanding of their relationship to single disk and full structure production.

MEASUREMENT SETUP

General

HOM measurements in a completed brazed structure requires the implementation of powerful automated bead-pull techniques. The high order modes of interest do not propagate along the axes of a tapered, detuned structure. Instead, they exist as a set of standing wave modes of different frequencies trapped in corresponding groups of cells, and it is difficult to excite and detect them in a completed brazed structure. Since the modes of interest should be coupled to the HOM manifolds and the manifolds are designed to provide good propagation for such modes, we were able to utilize the HOM manifolds for high order mode excitation and indication. For our experiments we used the FXC-001 structure (a Fermilab designation for an intermediate version of a 52 cell HDDS structure).

Simulation of Measurements

The experiments were simulated before measurements to predict what we should observe. Fig.1 shows a model of an FXC structure consisting of disks ##1,10,20,30,40,50 and 60 (there is no disk #60 in a real FXC structure, this one has extrapolated parameters). As shown in [5], a model developed with

this distribution is sufficiently accurate to describe a complete tapered structure.

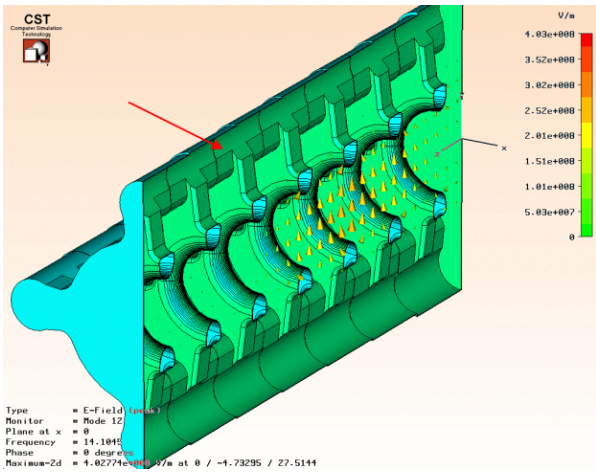

Figure 1: Distributed model of the FXC-001 structure with a simulated dipole mode trapped in the inner cells. Arrow shows HOM manifold.

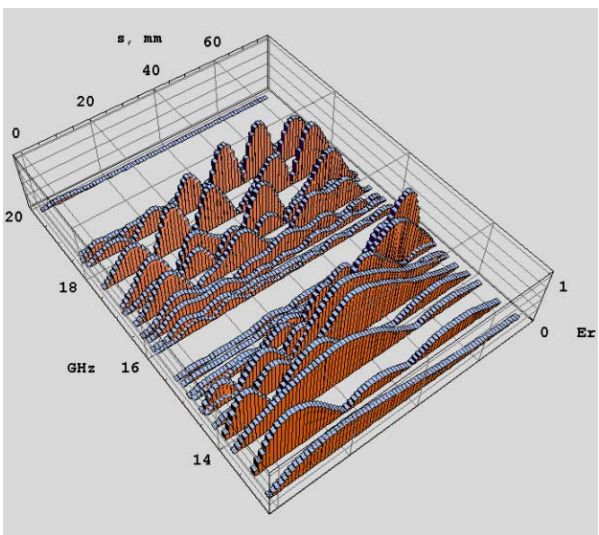

Figure 2: Distribution of E_r component of HOM field in the distributed structure model.

Fig. 2 shows the distribution of the amplitude of the radial component of the electric field along the axes for dipole modes in the 7 FXC disk stack. We referred to this data to identify numerous measured modes. Notice the clearly seen stop-band from 15.3 to 15.9 GHz, and a specific pattern of the first dipole pass-band field distribution.

FXC-001 Structure Rework

The FXC-001 structure was built for high gradient tests only, so it does not have matched HOM ports in the manifolds. Actually, the manifolds in this structure are resonant volumes rather than transmission lines. They have their own standing wave resonant modes of different field distributions. Because of this, we had to drill 12 holes in the HOM manifolds (3 holes per manifold) to position the probes (magnetic loops) so as to excite as many modes in the manifolds as possible.

Normally, HDDS structure manifolds will have matched HOM ports and stationary probes which can be used for HOM measurements, and we would be able to perform bead-pull measurements in the traveling wave regime, which is the real mode of operation.

In standing wave measurements with shorted manifolds, the HOM spectrum depends very strongly on probe locations in the manifolds. Figure 3 shows typical HOM spectra measured with probes placed in opposite manifolds at the input end, center and output end of the structure.

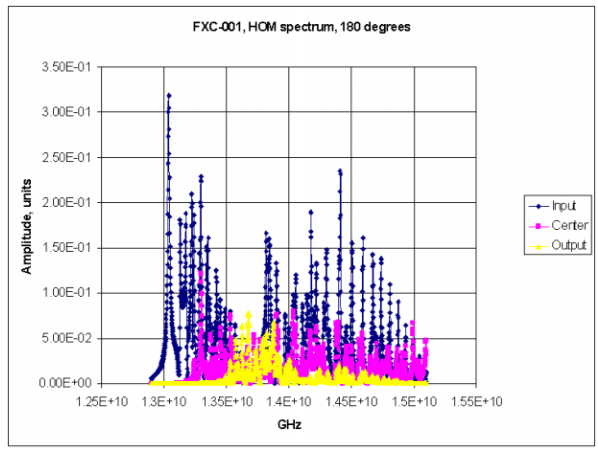

Figure 3: HOM spectra for different positions of probes.

We decided to omit measurements with the probes placed in the same manifold because we see many uninteresting modes specific to the manifold only. We also decided to omit measurements with the probes in the manifolds which are 90° apart because we observed unexpectedly strong coupling between dipole modes in orthogonal planes, and this fact requires additional consideration. Finally, we conducted measurements for different combination of loop positions in opposite manifolds.

Bead-pull Spectral Measurements

Practically, it is impossible to conduct standard bead-pull measurements of all modes seen through HOM manifolds. In order to obtain a complete picture in a reasonable period of time, we developed and applied a new method for bead-pull measurements.

In this method we first make a reference measurement of structure frequency spectra with the bead outside the structure. We then locate the bead in a structure cell, fix its position and repeat the spectra measurement. Comparison of the reference spectrum with the measured one identifies the modes that have a field in a given cell (see Fig. 4.). We then place the bead in the next cell (or next position along structure) and repeat the spectra measurements. Gradually we collect information on the HOM field distribution over a frequency interval of several GHz.

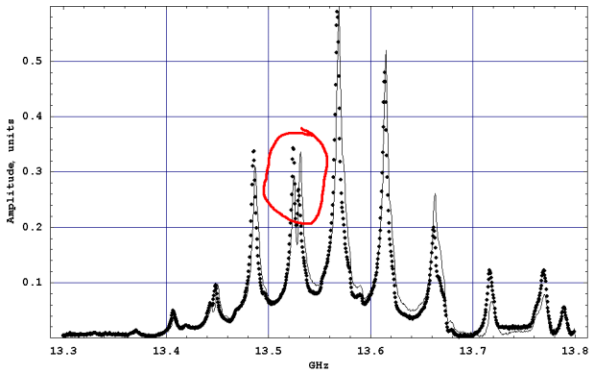

Figure 4: Large scale portions of reference spectra (solid line) and spectra taken with a bead in cell#2 (points). Comparison indicates that mode of 13.53 GHz has a field in cell #2.

We developed a special LabView program to automate the measurements – a PC controls the network analyzer and bead-pull system, and collects and preliminarily processes the stored data. Even so, the entire measurement process is still very time consuming. Depending on requirements, it takes 1-3 days to perform one run of measurements.

RESULTS

We have performed measurements for the following combination of loop positions (relative to input and output couplers): input-input, input-center, input-output, center-output, output-output. We covered the frequency range from 12.8 up to 18 GHz each run with a step of 0.5 MHz. The step for bead movement was one period of the structure for the first three trials, then reduced to ½ period for the next 5 trials. As a result, we obtained a very large amount of data and wrote several programs in Mathematica to process it.

A summarized result of the measurements is shown in Fig.5. Notice the sharp cut-off at frequencies close to the π-modes and the surprisingly long propagation of some modes along structure. The latter will probably disappear in traveling wave measurements.

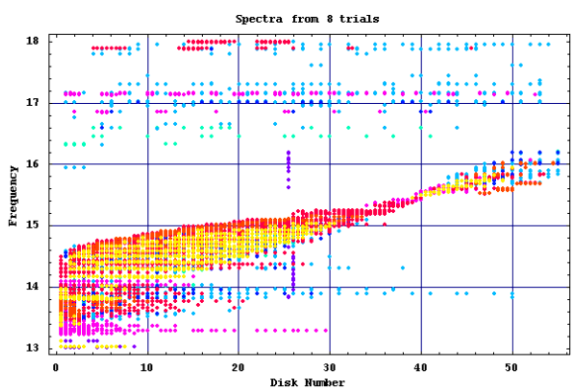

Figure 5: HOM locations in FXC-001. There are 8 separate colors in this graph, each color corresponds to a different magnetic loop positions within the manifolds.

We also conducted standard bead-pull measurements of the HOM field distribution to verify and complete the picture (see Fig.6). Detailed analysis confirmed good agreement between the two methods of measurements.

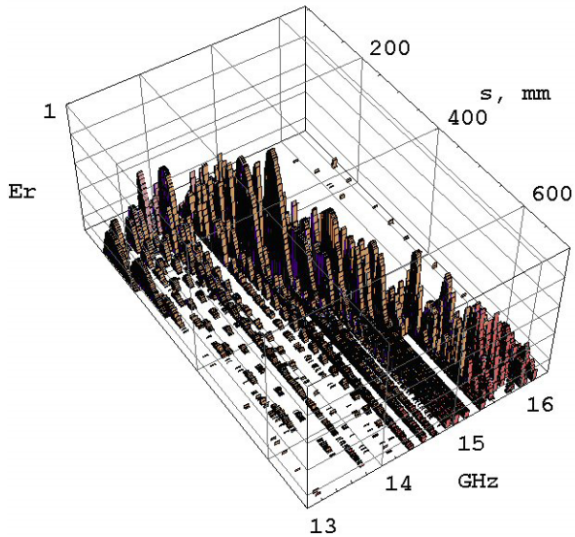

Figure 6: Distribution of E_r component of HOM field obtained with standard bead-pull measurements.

CONCLUSION

We developed bead-pull methods to measure high order modes using the HOM manifolds in a brazed HDDS-type structure. An essential part of this work was the significant expansion of the functions of our automated bead-pull system. We consider these first results very promising. We plan to modify the methods for the traveling wave case and to develop additional fast and effective QC procedures, which can be applied in industrial production flow to control HOM in completed structures.

REFERENCES

[1] "2001 Report on the Next Linear Collider", SLAC-R-571, June 2001.
[2] Z. Li et al. "Optimization of the X-band Structure for the JLC/NLC", PAC2003, Chicago, 2001.
[3] C. Adolphsen "Progress on X-band Accelerator Structure Development for NLC/GLC", EPAC04, Lucerne, Switzerland, 2004.
[4] H. Carter et al. "Automated Microwave Low Power Testing Techniques for NLC", Linac2002, Gyeongju, Korea, 2002.
[5] G Romanov et al. "Some Remarks on the Location of Higher Order Modes in Tapered Accelerating Structures with the use of a Coupled Oscillator Model", Proc. of PAC95, p.2345, 1995.

DESIGN OF A 300 GHZ BROADBAND TWT COUPLER AND RF-STRUCTURE*

Frank L. Krawczyk#, Bruce E. Carlsten, Lawrence M. Earley, Floyd E. Sigler, LANL, Los Alamos, NM 87545, USA, James M. Potter, JP Accelerator Works, Inc., Los Alamos, NM 87544, USA, Martin E. Schulze, General Atomics, Los Alamos, NM 87544, USA, Evgenya Smirnova, MIT, Cambridge, MA 02139, USA

Abstract

Recent LANL activities in millimeter wave structures focus on 95 and 300 GHz structures [1]. They aim at power generation from low power (100W-2kW) with a round electron beam (120kV, 0.1-1.0 A) to high power (2-100 kW) with a sheet beam structure (120 kV, 20 A). Applications cover basic research, radar and secure communications and remote sensing of biological and chemical agents. In this presentation the design of a 300-GHz RF structure with a broadband (> 6% bandwidth) power coupler is presented. The choice of two input/output waveguides, a special coupling region, and the structure parameters are presented. As a benchmark also a scaled up version at 10-GHz was designed and measured. These results will also be presented.

INTRODUCTION

We are investigating planar micro-fabricated traveling-wave tube amplifiers as sources for the generation of millimeter waves from 95 to 300 GHz. While for low energy applications narrow structures with pencil beams are proposed, for high-energy operation flat, thin sheet beams are required. For the latter, vane-loaded rectangular waveguides that operate in a slow-wave mode matched to the velocity of the electron beam are especially well suited. The 300-GHz effort initially is limited to narrow structures for pencil beams. The main emphases for this work are the study of fabrication issues and the understanding of features that allow a broadband operation (5-10% bandwidth.)

THE GEOMETRY

The design work is focused on the RF-structure. This structure is made up of the resonator, the power couplers to couple power to the structure, and the coupling regions between the RF-structure and the couplers.

The Base Geometry

The base geometry is a vane-loaded rectangular waveguide (see Fig. 1). We opted for a double-sided waveguide with vanes on the top and the bottom. The vane thickness, height and spacing are given by the desired phase velocity that has to match the energy of the electron beam. A second consideration is maximizing the achievable gain in the structure. The vane parameters that match these criteria, have been determined by simulations with the DETER code [2].

*Work supported by DOE/DOD

#fkrawczyk@lanl.gov

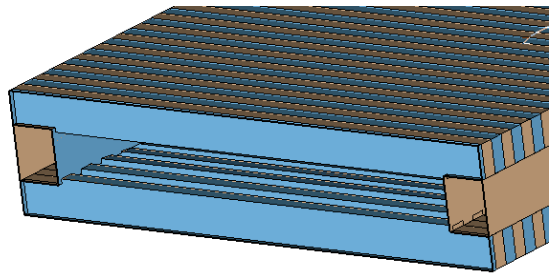

Figure 1: 3D model of the vane loaded waveguide. The top and bottom vanes can be seen inside the waveguide. The bars on the sides define the width and the proper spacing of the top and bottom halves of the resonator.

The Power Coupler

The power has to be fed to the structure off the central plane, away from the entrance path of the electron beam. We opted for two rectangular waveguides operated in a TE mode. These waves that are 180 degrees out of phase at the entrance into the structure combine into the operating TM mode. Figure 2 shows the arrangement of the couplers and the combination of the properly phased electric fields. In the central plane also the waveguide opening for the beam to enter the structure is included.

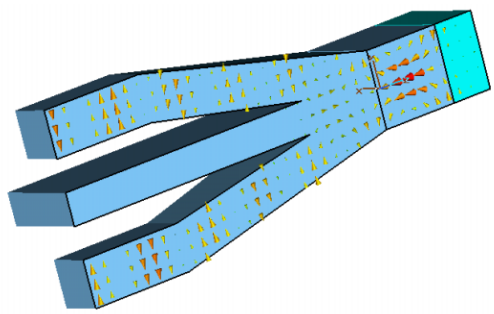

Figure 2: A cross-section through the input waveguides and their combination at the entrance of the RF-resonator are shown. For RF-considerations the inside volume, not the outside material is modeled. The cones indicate the amplitude and direction of the electric field.

The parameters for matching the coupler are the distance of the top and bottom waveguides, the length of the tapered section and a side taper that opens up the waveguide cross-sections towards the entry into the structure. An identical coupler is attached to the outlet of the structure as a load to remove the generated power.

The Coupling Region

As the vane-loaded waveguide presents a strong mismatch for the electromagnetic waves entering the RF-structure, a matching section has been incorporated into the cavity-coupler interface. The cavity starts with the unloaded dimensions of the rectangular waveguide. Tapered vanes are added with a height starting from zero and increasing to their nominal height over 14 cavity cells (see Fig. 3.) The number of coupling cells has been determined as part of the optimization of the coupler.

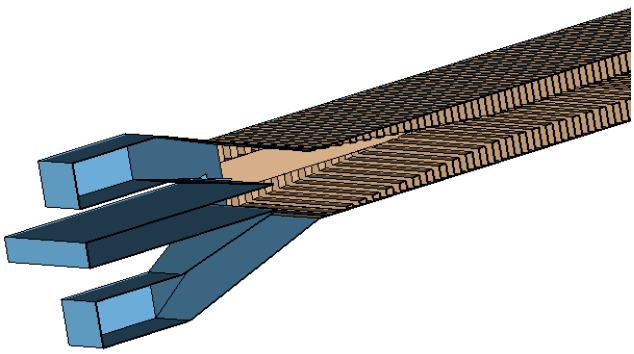

Figure 3: To reduce the mismatch from the coupler to the ridge-loaded waveguide, a matching section with increasing vane height is incorporated into the cavity/coupler arrangement.

THE OPTIMIZATION OF THE RF-PERFORMANCE

The design goal is to obtain a RF-structure wide enough to exhibit the wave propagation of an infinitely wide structure that at 300 GHz has very good RF-propagation over a bandwidth of more than 5%. While the inner dimensions are given from the previously mentioned DETER simulations, the coupling region and coupler dimensions to achieve this goal had to be found.

Figure 4: A snapshot of the traveling wave electric field fed to a structure with 30 inner cells is shown. The power is removed at the outlet by an identical coupler.

The RF-design has been done with the Microwave Studio (MWS) electromagnetic simulator [3]. Fields (Fig. 4), s-parameters (Fig. 5) and VWSR ratios (Fig. 6) have been evaluated for a wide range of parameters. The fact that no resonant peaks can be seen in the transmission curve indicates a good coupling between the couplers and the structure that provides the desired traveling wave operation. The bandwidth has been defined as the range of transmission, where the return loss is less than –10 dB. The frequency range of 294-313 GHz includes the 2π/3-mode operation mode.

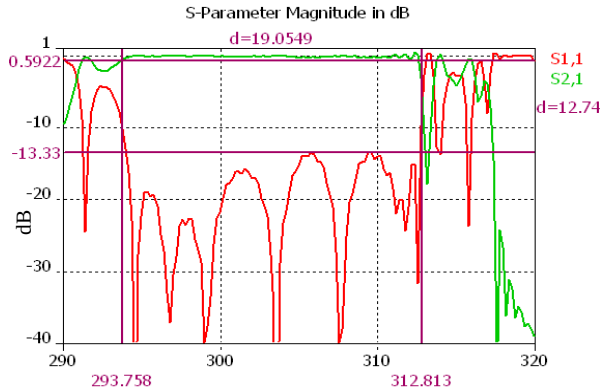

Figure 5: The s-parameters obtained by simulations with MWS show a good transmission over a range of 19 GHz, which corresponds to a bandwidth of 6.3%.

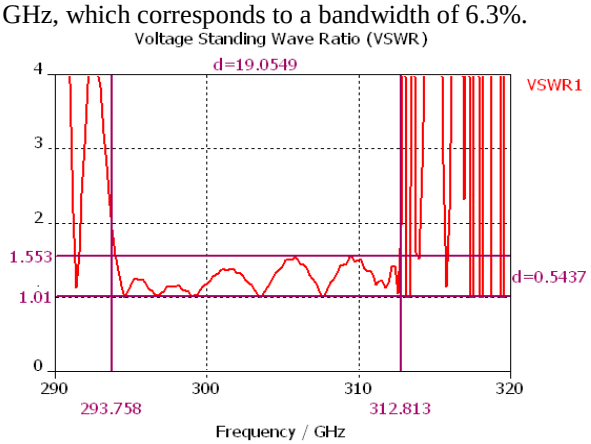

Figure 6: The VSWR ratio over the bandwidth is around 1.5 or better.

The final structure with input and output coupler is shown in figure 7. The dimensions are given in Table 1.

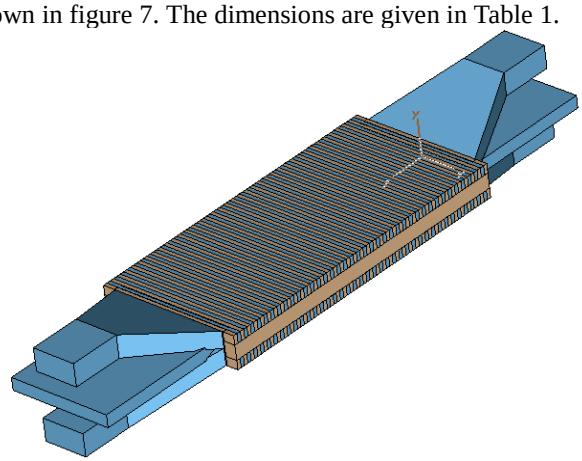

Figure 7: The final geometry of the optimized 300-GHz resonator with input and output couplers.

Table 1: Geometric parameters of the cavity and couplers

Quantity	**Value [mm]**	**Comments**
Waveguide height	0.6334	Resonator
Waveguide width	2.187342	Resonator
Vane height	0.1979	

Vane thickness	0.07765	
Aperture height	0.2376	
Cell length	0.07765	
Period	0.1553	
Waveguide width	0.864	Coupler (WR3)
Waveguide height	0.432	Coupler (WR3)
Waveguide separation	1.30	Coupler
Taper length	1.65	Coupler
Taper width	2.187342	Coupler
Beam guide height	0.2376	
Beam guide width	2.187342	
Coupling cells	14	14 at each end

ERROR STUDIES

As this was the first structure of its kind we have designed, we needed to study the effects of geometry variations. Discussions with industry indicated that over-tight tolerances would significantly increase the cost of fabrication. Too generous tolerances would significantly deteriorate the performance of the structure. Simulations showed that the overall performance was insensitive to achievable radii due to the wire EDM (electrical discharge machining) fabrication process. Surface positions required an accuracy of a few mils (0.03-0.07 mm). The most critical features were the coupling taper, whose volume is important to achieve the required bandwidth, and the orientation of the vanes perpendicular to the beam direction. The maximum RF-phase difference of 180±10 degrees between the two waveguides in each coupler is easily achievable.

10-GHZ COLD MODEL

As a proof-of-principle of the coupling scheme a 10 GHz cold model has been designed and built. A direct scaling from the 300 GHz model was not possible, as the WR90 waveguide available for 10-GHz operation has a different aspect ratio than the WR3 waveguide. The cold model has been designed for a bandwidth of > 6% around 10 GHz. It has been build by machining from aluminum. Figure 8 shows the two halves of this model. It has been built in two lengths with 11 and with 31 nominal inner cells. Both models have 14 coupling cells at each end. The measurements show that the coupling scheme with the two waveguides is working. The bandwidth of the coupling has been confirmed. However, the measured s-parameter curve is shifted lower by 500 MHz compared to the simulations and the transmission curve is not as flat as the simulated curve (see Fig. 9.) Tolerance studies show that only the overall height and tip-to-tip distance of the vanes can explain this shift. Measurements of the assembled structure are still under way.

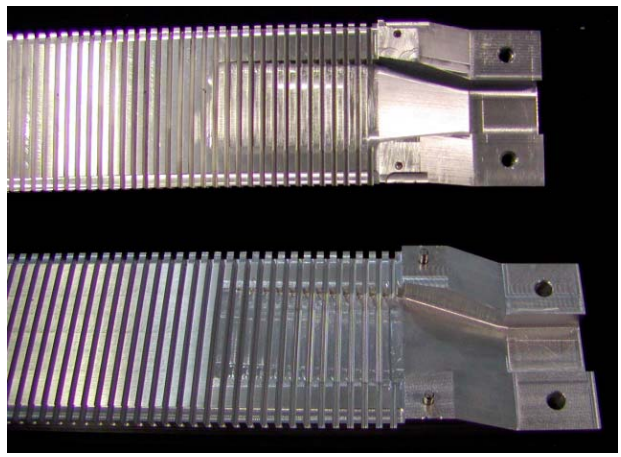

Figure 8: This photo shows the top and bottom half of the aluminum cold model. The material forming the coupler taper and the coupling cells can be seen.

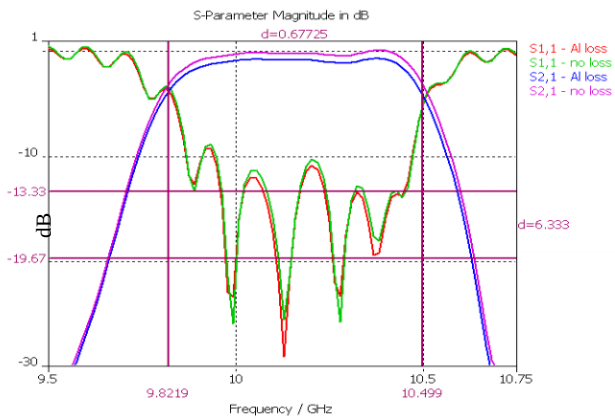

Figure 9: The s-parameter curves compare the simulated transmission and reflection for an ideal material and for aluminum. The measured reduction in transmission due to the losses in aluminum agrees very well with these simulations.

CONCLUSION

A cavity/coupler system for a 300-GHz TWT structure has been designed. The coupling principle for the broadband coupler has been confirmed in a cold model. Interaction with industry is under way to build and measure this structure.

REFERENCES

[1] B.E. Carlsten et al., ‘’MM-Wave Sheet-Beam Traveling-Wave Tube Development at Los Alamos’’, 31st IEEE International Conference on Plasma Science, Baltimore, MD, June 2004.

[2] B.E. Carlsten, ‘’Modal Analysis and Gain Calculations for a Sheet Electron Beam in a Ridged Waveguide Slow-Wave Structure’’, Physics of Plasmas, **9**, 5088 (2002).

[3] MWS Userguide, CST GmbH, Darmstadt, Germany, http://www.cst.de/

TEST RESULTS OF THE 3.9 GHz CAVITY AT FERMILAB*

N. Solyak, L. Bellantoni, T. Berenc, M. Foley, H. Edwards, I. Gonin, T. Khabiboulline, D.Mitchell, A.Rowe, FNAL, Batavia, IL 60510, USA

Abstract

Two types of 3.9GHz superconducting RF cavities are under development at FNAL for using in the upgraded A0 photo-injector facility. A TM_{010} mode cavity (3rd harmonic of 1.3GHz, frequency of accelerating capture cavity) will be used to linearize energy distribution in the bunch before compression for better emittance. A TM_{110} mode cavity (deflecting or "CKM" cavity) will provide streak capability for bunch slice diagnostics. In paper we present current status of both cavities and results of testing niobium and copper prototypes.

INTRODUCTION

Both cavities have strong motivation for development [1,2]. The design of cavities, infrastructure development and material study can be found in [3,4], R&D work on both cavities were presented at PAC'03 and SRF'03 conferences [2,5]. Here we discuss status and latest results of high gradient test and studies of the high order modes.

STATUS

Before building final design of each type of the cavity a few prototypes were produced and tested to finalize cavity design. Below we discuss current status of design work and production activity at Fermilab.

3rd Harmonic Cavity

Cavity is made of 9 cells with elliptical shape in iris and equator areas. End-cells have bigger iris (r=20mm) from the tube side, than the regular cells (r=15mm). It allows increased coupling with main coupler and facilitates HOM damping [3]. Two HOM couplers mounted in both ends of the cavity provide good damping. To study HOM performances of the cavity and RF properties for accelerating mode we have built two full-scale copper models, each equipped with main and HOM couplers. We also built short 3-cell niobium cavity for the low temperature high gradient tests. Briefly the current status of 3rd harmonic cavity is the following:

- Cavity design is finished, including helium vessel, magnetic shielding and frequency blade-tuner.
- 9-cell cavity in production, all components are ready and partly welded.
- Helium vessels and blade tuners for two cavities are placed an order, stepper motors with controllers are in hand.
- Main coupler and cryomodule for installation on photo-injector A0 are under design.

* Supported by the U.S. Department of Energy.
#solyak@fnal.gov

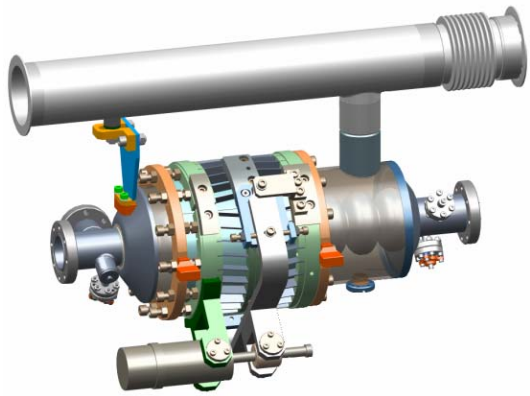

Figure 1: 3rd cavity, equipped with helium vessel and frequency tuner (design).

CKM Cavity

Eight TM_{110} mode cavities have been made, mostly shorter (3, 5 and 9 cells) structures, but there is one full 13-cell prototype. One more short structure is in production, and one more 13-cell is planned. First prototypes were made of 1.6mm niobium sheet, but cavity shape wasn't rigid enough. Last prototypes were built out of 2.2 mm niobium to improve mechanical properties. Helium vessel and frequency tuner are built, assembled and are under testing (see Fig.2). CKM cryomodule for two cavities are ready and will be tested soon. Small cryomodule (for single cavity) for A0 installation will be the same design as for 3rd harmonic cavity.

Figure 2: 13-cell CKM cavity, assembled with the helium vessel.

TEST RESULTS

Short niobium prototypes of both cavities were tested at helium temperature down to 1.6°K in a vertical dewar to investigate cavity performances and field limitations (fig.3). The results of cold tests are presented below.

Three Cell 3rd Harmonic Cavity

3rd harmonic cavity was tested several times. First test was done after production before any BCP etching. Second set of testing (2 thru 5) was done after cavity treatment at JLAB, which included ~20/140μm outside/inside BCP etching, high temperature treatment (10 hrs @ 600C) and 15min HPR at 1200psi. Visual inspection done after tests shown three "rust" spots on the iris in one of the end cells, which can explain high level of X-rays. Third set of the cold tests was done after additional 20μm BCP and 30min HPR.

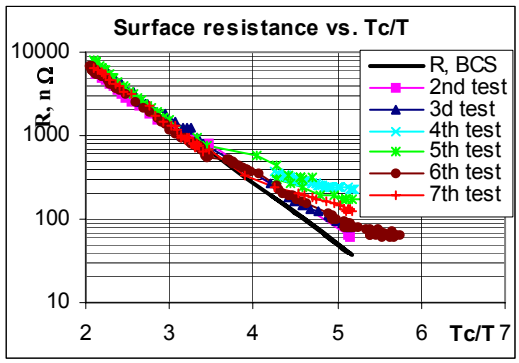

Figure 3: Surface resistance vs. T_c/T measured for few cold tests. T_c - critical temperature of niobium.

Fig.3 shows results of surface resistance measurements for all tests. In second test we have reached R_s~60 nΩ, not faraway from the theoretical limit. After working at high gradient with strong X-ray level, resistance dropped down on the following tests. After second BCP treatment surface resistance was restored again (test #6).
High gradient performances of 3-cell cavity measured at π-mode are shown in Fig.4. Achieved gradient ~12.5 MV/m was limited mostly by X-ray, not quench. The same set of measurements was done for 0 and π/2-modes in this cavity. For 0-mode fields in the mid-cell almost twice high than in end-cells, for π/2 mode mid-cell is empty, all fields are concentrated in end-cells.

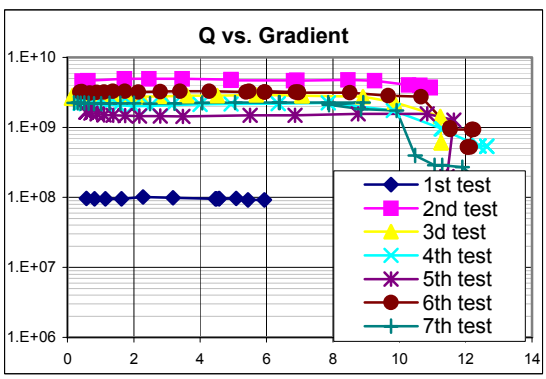

Figure 4: Q-value vs. Accelerating gradient in 3rd harmonic 3-cell cavity.

So, different cavity behaviour at these modes gives information, which cell causes problem. Measured surface magnetic fields before quench are 110;85;77mT for 0; π/2; π modes, which corresponds accelerating fields in 9-cell cavity E_{ACC} ~ 22;17;16MV/m (Design parameters: E=14 MV/m; B=68mT)

CKM TM_{110} Cavity

Few prototypes have been tested at helium temperature, most of them are short 3-cell cavities. In earlier tests done for cavities made of 1.6mm niobium we have reached $P_\perp$ ~ 5.4 MV/m, R_s=160nΩ in TM_{110} mode (R_s ~65nΩ in TM_{010}, 2.8GHz), but gradient has decreased to ~ 3.5MV/m with repeated tests. Last test, done for 3-cell cavity made of 2.2 mm niobium demonstrated good performances (Fig.5 and 6). Beam pipe in this cavity is 20mm longer, than in previous prototypes. Cavity treatment was done at JLAB.

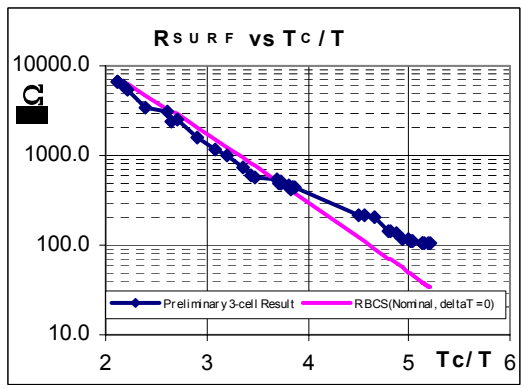

Figure 5: Surface resistance vs. T_c/T for CKM cavity.

In this test we measured surface resistance 100 nΩ @ 1.8°K. Fig.6 shows that we went up to 7.5MV/m kick, which is well above the 5MV/m goal. The second run shows that the performance remained after we ran up to the quench point in all the other cell coupled modes modes.

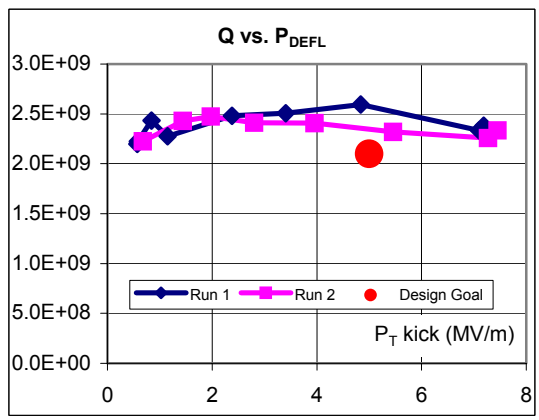

Figure 6: Q-value vs. kick gradient in CKM cavity.

We saw signs of multipacting in the other modes at high field levels. In all cases though it cleared up quickly. No X-rays. We never have seen them for deflecting modes. We do not see any sort of droop-off at high fields that one expects for a thermally loaded situation. Table 1 shows CKM design parameters compared to TESLA cavity parameters.

Table 1:

Cavity type	mode	Freq, GHz	Ea/ $P_{\perp}$ MV/m	Bmax mT	Emax MV/m
TESLA	TM010	1.3	25	105	50
CKM	TM110	3.9	5	80	18.5

HOM STUDIES

HOM studying and damping is a big issue for both accelerating and deflecting cavities. Each cavity has two HOM couplers with appropriate orientation to soak out both polarizations of the parasitic modes. Nevertheless calculations show that loaded Q-value for some of the modes is sensitive to the boundary conditions at the end of the tube[6]. In reality it means that the big reflection from the neighbour cavity can cause problems. To study HOM damping in 3rd harmonic cavity two copper models were built and tested (Fig.7). Rotatable flanges on HOM couplers and cavity to tube connection allow adjustment of coupler orientation to get maximum dissipations.

Figure 7: HOM studies of assembly of the two copper cavities on the bead-pull set-up in clean room.

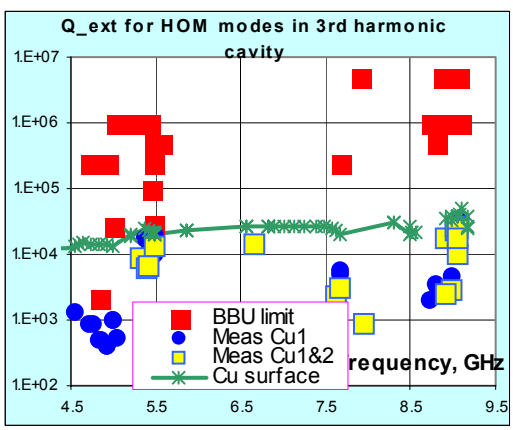

Figure 8: Q vs. frequency for HOM in TM_{010} cavity. Red-BBU limit, blue&yellow – measurements, green-Copper.

Fig.8 shows Q-value, measured in the single copper cavity and in chain of two assembled cavities. Red markers represent Beam Break Up (BBU) limits in photoinjector, calculated by P.Piot for more dangerous dipole modes with R/Q>1. Measured Q-values (blue and yellow) are well below limits for most of the modes up-to 10GHz. Green line shows Q for copper surface. As one can see from the plot, few modes from 2nd (f~5.5GHz) and 5th (f~9GHz) passbands have Q-value close to natural Q of the cavity. Calculation shows, that some modes from 5th passband might be trapped in cavity, but fortunately, they have low R/Q. Besides small perturbations in cell dimensions can easily disturb the field distribution for those modes. More precise measurements are needed to define the coupling of this mode to the HOM couplers.

Figure 9: HOM couplers.

HOM couplers developed for TM010 cavity are planned to use in deflecting cavity. The CKM cavity also needs a low mode coupler (LMC) to dump lowest accelerating mode at ~2.8GHz. Prototype of LMC is placed an on order. According to design, LMC will provide loaded Q~10^5 for the first monopole band and ~ 10^6 for 2nd and 3rd bands.

AKNOWLEDGEMENTS

We would like to thanks I.Terechkin, C.Boffo, P.Bauer from Fermilab and W-D. Moeller, R.Wanzenberg, J.Sekutowicz from DESY for help and discussions.

REFERENCES

[1] WE104, this conference; P. Piot and W. Decking, "A Modified Post-Damping Ring Bunch Compressor Beamline for the TESLA Linear Collider" FNAL TM-2235,

[2] L.Bellantoni et.al, Field flatness tunning of TM110 mode cavities with closely spaced modes. FERMI-LAB-CONF-03-353, Oct 2003. 4pp.

[3] N.Solyak et.al., "Development of the 3.9GHz, 3rd harmonic cavity at FNAL", proc. SRF-03, DESY, Germany, Sept. 2003.

[4] C. Boffo, D. Connolly, L. Elementi, Y. Terechkine, "Control System for BCP Processing Facility at FNAL", SRF-03, DESY, Germany, Sept. 2003.

[5] MOP82, this conference: SRF cavity and materials R&D at FERMILAB.

[6] FERMILAB-TM-2210/DESY-TESLA-FEL-2003-01, 2003,30 pp.

LOW POWER MEASUREMENTS ON A FINGER DRIFT TUBE LINAC*

K. Kühnel[1], A. Schempp, IAP Frankfurt, Germany
C. Welsch, MPI-K Heidelberg, Germany

Abstract

The efficiency of RFQs decreases at particle energies higher than a few MeV/u and thus typically DTL structures are used in this energy region. However, the rf field in the gap always has a defocusing influence on the beam. In order compensate this effect, fingers with quadrupole symmetry were added to the drift tubes. Driven by the same power supply as the spiral drift tubes, the focusing fingers do not need an additional power source or feedthrough.

Beam dynamics have been studied with the code RFQSIM . Detailed analysis of the field distribution was done and the geometry of the finger array has been optimized with respect to beam dynamics. A prototype cavity with finger drift tubes was built, and low power measurements were done. In this contribution, the results of the rf simulation with Microwave Studio are compared to bead perturbation measurements and the focusing effect on the beam is discussed.

INTRODUCTION

At low energies, RFQs are widely used to accelerate ions up to energies of a few MeV/u. Since they can capture relatively high current dc beams and convert them with a high efficiency into a bunched beam, they have found numerous applications [1-3]. However, at velocities above 0.1c, the efficiency of RFQ accelerators decreases.

Spiral loaded cavities have been developed over many years at IAP and are the ideal tool to further accelerate and bunch the beam [4, 5]. Their characteristic parameters can be calculated with high precision, and their compact design and large energy acceptance allows a usage in most beam lines.

A 4-gap spiral loaded cavity was planned as a booster after the 4 m RFQ of the COSY SCL upgrade, which consists of a room temperatur RFQ with a booster cavity to inject into a superconducting linac [6]. In order to accelerate deuterons from 2 MeV/u to 2.5 MeV/u an overall voltage of 1 MV is needed in the booster. A four gap structure was chosen in order to keep the required peak voltages in each section low. Table 1 gives an overview of the design parameters.

Table 1: Parameters of the booster cavity

Input Energy	2 MeV/u
Length	300 mm
Diameter	280 mm
Beam aperture radius	10 mm
Gap / total voltage	250 kV / 1 MV
Power consumption	150 KW
$\beta\lambda/2$	62 mm

While the desired energy gain can be realized with this structure, the rf-defocusing from the fields in the acceleration gaps would lead to a growth of the transverse dimensions of the beam. Therefore, fingers in quadrupole symmetry were added to the drift tubes in order to focus the ions. A prototype cavity, designed and built at IAP, is shown in fig. 1.

Figure 1: View of the spiral loaded cavity with finger drift tubes.

* Work supported by BMBF
[1] k.kuehnel@iap.uni-frankfurt.de

BEAM DYNAMICS

A detailed analysis of the particle motion was done with the code RFQSIM [7], developed at IAP. For that purpose, the original design of the COSY SCL Injector linac was chosen, which consists of a 4 m RFQ and a small booster cavity of only 0.3 m length.

The RFQ accelerates protons and deuterons to a final energy of 2 MeV/u where the booster takes over and increases the energy to 2.5 MeV/u.

The field distribution was calculated with an excel macro using the successive over-relaxation method. It allows the input of arbitrary geometrical structures and calculates a static 3D voltage distribution that can be imported into RFQSIM. The components of the electric field at the position of the particle are then calculated automatically. The simulation results for a beam passing through one cell of such a combined accelerating / focusing structure are shown in fig. 2. The beam is focused in the x-x' plane, while it is defocused in the y-y' plane. Modifications of the geometrical layout of the fingers and changes in the distances between the gaps can be combined to reach a compensation of the rf-defocusing and a match to the following accelerator stage.

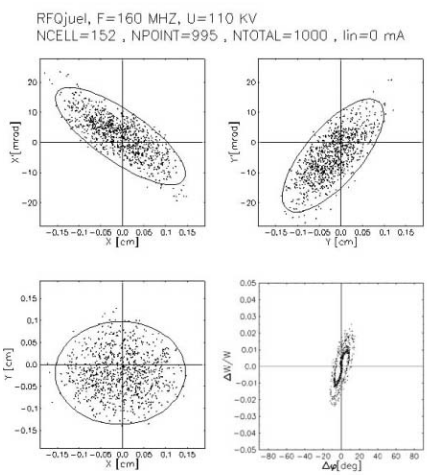

Figure 2: RFQSIM results with finger drift tubes.

SIMION SIMULATIONS

The simulations with RFQSIM were done with limited geometrical resolution and the assumption of an rf field based on a static potential distribution.

Therefore, the geometry was put into the program SimIon [8] and the effects on singly charged ions were analyzed. As a first test, the z-component of the electric field as shown in fig. 3 was calculated. It matches with earlier measurements [5]. In standard mode, SimIon is used for the analysis of static problems.. Thus a user program was written to fast adjust the voltage on the electrodes depending on the individual ion positions. This allows simulating the real field behaviour with high accuracy.

The resolution in the model was *1mm*, the ion parameters were chosen as given in table. 1. The geometrical parameters of the finger drift tubes as calculated are shown in table 2.

Table 2: Geometrical parameters of the finger drift tubes

Gap width	30 mm
Finger length	20 mm
Aperture radius	10 mm
Finger radius	7.5 mm

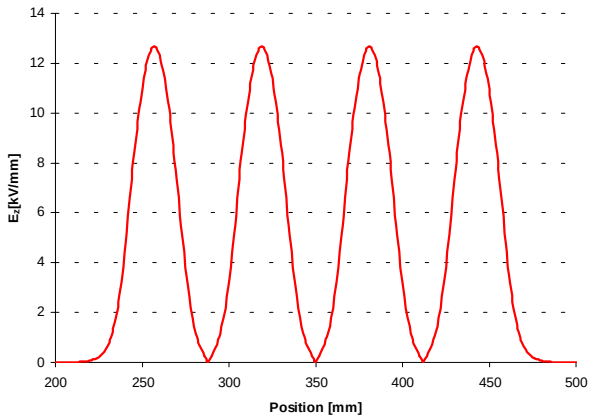

Figure 3: Z-component of the electric field as calculated with SimIon.

Individual ions were placed at radial positions from the central trajectory moving parallel to the beam axis. The strong focusing effect in one plane after passage of the whole structure is shown in fig. 4. While the ions are accelerated by the longitudinal field, a transverse focussing field component is superimposed. Like in a normal AG-beam-transport section, the beam is continuously focused and defocused.

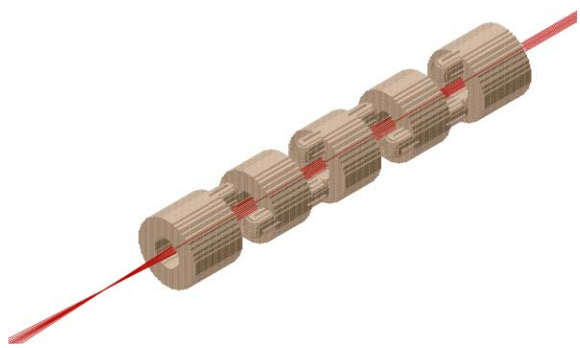

Figure 4: 3D view of the ion motion within the finger drift tube structure as calculated with SimIon.

The simulations of the particle motion show, that it is possible to optimize the design with respects to its focusing properties

BEAD PULL MEASUREMENTS

A prototype of a finger drift tube structure with the parameters given in table 1 was built up and tested at low power. These measurements show, that in the original design, the 0-mode and the π-mode are separated by a few MHz only, which would lead to unwanted effects and problems during operation.

Therefore, both spirals were first mounted in parallel orientation and in a successive step connected by a copper bridge to guarantee that they are on the same potential in 0-mode. Due to the bridge, the frequency of the π-mode was raised by about 90 MHz, which allows a very stable operation of the cavity. A comparison of the three designs is shown in table 2.

Table 2: Resonance frequency of different structures

	Original structure	parallel spirals	parallel spirals with bridge
0-mode	162.1 MHz	157.5 MHz	153.9 MHz
Q o	1680	1980	1880
π-mode	159.3 MHz	160.8 MHz	248.3 MHz
Q π	2200	1500	700

This configuration of the spirals and the short-circuit bridge between the two spirals resulted in a stronger coupling of the two spirals. Therefore the voltage on the drift tube is balanced and the operation is stable. Preliminary results of bead pull measurement on the above structure are shown in fig. 5.

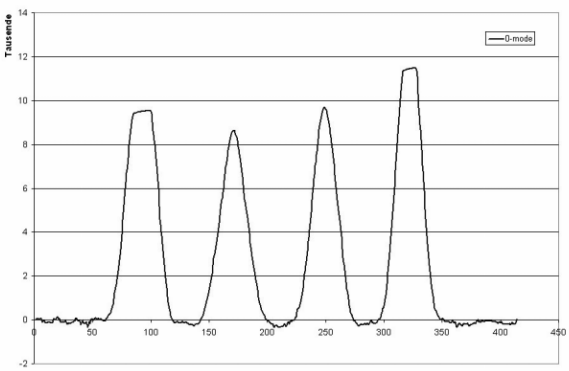

Figure 5: Measured field on the beam axis.

Besides errors due to small misalignment of the structure in the cavity, the field distribution matches nicely to the numerical simulation results obtained with Microwave Studio and SimIon.

The final layout of the inner structure with the stabilizing bridge between the spirals can be seen in Fig 6.

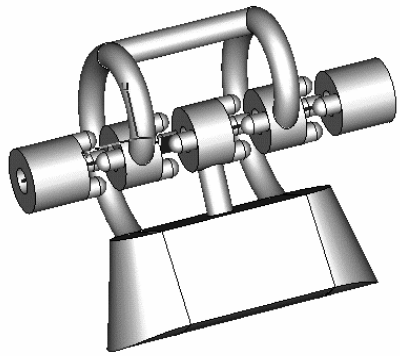

Figure 6: Spiral loaded cavity with stabilizing bridge.

CONCLUSION

The properties of this new spiral loaded cavity at higher energies were demonstrated. The field distribution measured with the bead pull method are in good agreement with the simulations. The beam dynamics calculations and the field simulations, done with RFQSIM, Microwave Studio and SimIon, allow a detailed optimization of the structure and show that such a combined focusing / accelerating structure could be used in future injectors.

REFERENCES

[1] A. Schempp, Design of Compact RFQ's", Proc. Linac 1996, Geneva, Switzerland, 1996

[2] O. Kester, et al, "Status of the REX-ISOLDE Linac" Proc. LINAC 1998, Chicago, USA, 1998

[3] A. Bechtold, C.P. Welsch, U. Ratzinger, A.Schempp, B. Schlitt, "The RFQ-Drifttube Combination for the Medicine Synchrotron in Heidelberg", Proc. LINAC 2002, South Korea, 2002

[4] A. Schempp, H. Klein, "Properties of Spiral Loaded Cavities", NIM A 126 (1976) 409

[5] K. Kühnel, A. Schempp, C.P. Welsch, "Development of Finger Drift Tube Linacs", Proc. EPAC 2004, Lucerne, Switzerland, 2004

[6] R. Tölle et al., "COSY-SCL, the Superconducting Injector Linac for COSY", Proc. PAC 2003

[7] A. Bechtold, "Eine integrierte RFQ-Driftröhrenkombination für ein Medizin-Synchrotron", Thesis, Univ. Frankfurt, 2003

[8] D. A. Dahl, „Simion 3D User Manual", Idaho National Engineering and Environmental Lab., 2000

ACCELERATOR STRUCTURE BEAD PULL MEASUREMENT AT SLAC*

J. R. Lewandowski, G. Bowden, R. H. Miller, J. W. Wang, SLAC, Menlo Park, Ca 94025, USA

Abstract

Microwave measurement and tuning of accelerator structures are important issues for the current and next generation of high energy physics machines. Application of these measurements both before and after high power processing can reveal information about the structure but may be misinterpreted if measurement conditions are not carefully controlled. For this reason extensive studies to characterize the microwave measurements have been made at SLAC. For the bead pull a reproducible measurement of less than 1 degree of phase accuracy in total phase drift is needed in order to resolve issues such as phase changes due to structure damage during high power testing. Factors contributing to measurement errors include temperature drift, mechanical vibration, and limitations of measurement equipment such as the network analyzer. Results of this continuing effort will be presented

INTRODUCTION

The measurement of an accelerator's internal electric field by the bead pull method is an established and trusted measurement. The bead pull measurement consists of pulling a small metallic bead attached to a string through the accelerator structure while a small amount of rf power is fed into the structure at the frequency of the mode you wish to investigate. Real and imaginary S_{11} data is acquired by a network analyzer as the bead moves through the accelerator structure. The electric field amplitude and phase is then calculated for each bead position in the structure.

At SLAC the measurement serves several roles: it is used to quantitatively judge engineering and fabrication issues, to tune newly fabricated accelerator structures and also to characterize any differences that might arise from high power processing by comparing pre and post processing bead pull measurements.

For the purpose of tuning the measurement is well established and its accuracy is trusted. When the measurement is used to investigate changes due to high power processing, which can be on the order of 1° degree of phase integrated across the structure, understanding errors with the measurement becomes essential. At this level there are many things that may contribute to the accuracy of the measurement including: temperature of the room and structure, stability of RF source in the network analyzer, data analysis techniques,[1] atmospheric pressure, and water vapor content of the air. This paper will address issues of temperature, mechanical vibration and network analyzer stability by using statistical analysis of multiple bead pull's with the goal of quantifying a phase measurement error that can be generalized for future measurements. Atmospheric pressure and humidity will not be addressed since a dry nitrogen purge is used during the measurements.

*Work supported by U.S. Department of Energy, contract DE-AC03-76F00515

TEMPERATURE CONSIDERATIONS

At SLAC we have introduced a commercial water temperature control system to stabilize the structure temperature during the measurement. The system consists of a Thermo Haake DC-30 circulator and temperature control unit along with the Themo Haake K-20 Chiller. The DC-30 is specified to control the water temperature to 0.1° Celcius.

The bead pull measurement is performed with the controller temperature set near the ambient room temperature typically around 20°C. Though the controller is specified to regulate the water temperature to $.1^{\circ}$C, temperature excursions during the measurement on this scale can occur due to the control algorithm of the DC-30. The consequence of the temperature control is a sawtooth variation in temperature data during the bead pull scan. S_{11} data for a non moving bead centered in the last cell of the structure is presented. Phase data is sampled at 5 Hz while temperature data is sampled at 1 Hz.

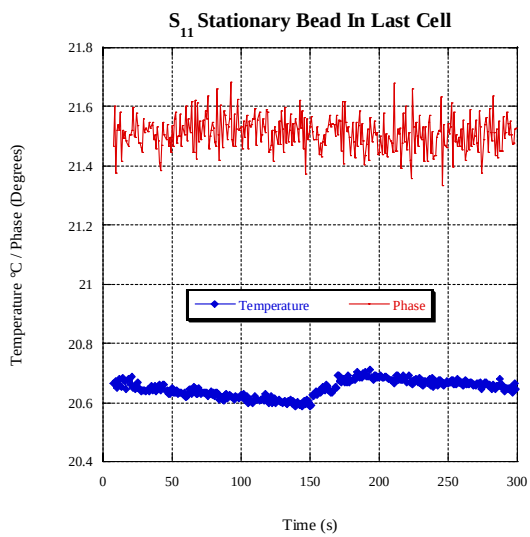

Figure 1:S_{11} phase measurement of a stationary bead in last cell for 5 minute scan.

The Figure 1 data address the phase stability of the bead measurement with the bead in the position where it is most sensitive to temperature and frequency variations. A

typical bead pull scan takes on the order of 3 minutes where the presented data scan is around 5 minutes. The small ramp in temperature is evidence of the control algorithm turning on the heater element. There seems to be no immediate reaction in the phase data.

Room Temperature

The ambient room temperature where the measurement is performed can also have an effect and is the reason for implementing the closed loop water circulation system. There may still be a correlation between the room air temperature and the structure temperature during the measurement even with the water regulation.

Though the room temperature is specified to be controlled to ±0.5°C larger fluctuations may occur. Figure 2 shows that the regulation system seems to adequately control the structure temperature.

The temperature measurement was performed with a J-type thermocouple attached midway in the structure at cell 27. Though Figure 1 suggests the phase does not immediately respond to the temperature changes, the phase of the sawtooth pattern a sequence of scans will not be constant with the measurement and may contribute to the random phase error in the measurement over many scans.

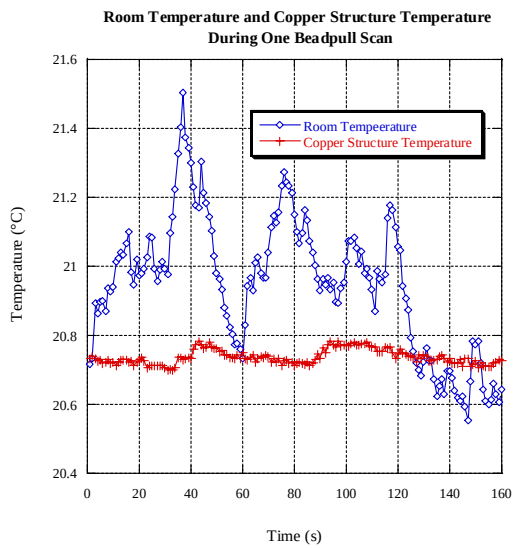

Figure 2: Room temperature vs. regulated structure temperature during bead pull scan.

Phase Sensitivity with Temperature

Structure damage due to high power processing and breakdown has been characterized by looking at pre and post processing bead pull scans. Data from the differences in these scans has been viewed as revealing an overall change to the structure due to the damage.

From a sampling of 20 bead pull scans, the data was grouped according to temperature. The phase is calculated from S_{11} data where the electric field peaks within each cell. The data from scans with two different temperature values might be misinterpreted as structure damage if careful temperature measurements are not taken during the scans.

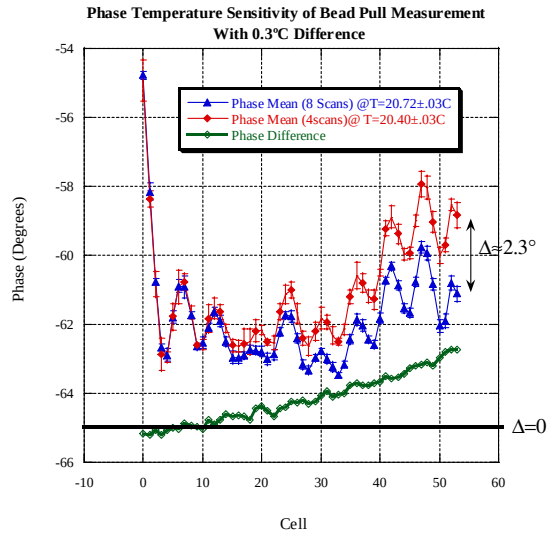

Figure 3: Phase sensitivity as a function of temperature. Error bars represent phase error for number of scans. Temperature standard deviation calculated from a sum of data for all scans in group.

The difference of 2.3° phase in Figure 3 agrees well with equation (1),

$$\Delta\phi = 2\pi\Delta T(df/dT)T_f\,. \qquad (1)$$

Where: ΔT is structure temperature difference of the scan, T_f is the fill time and $df/dT \approx 0.19$MHz/C°, a constant depending on the thermal expansion coefficient of copper and our working frequency of 11.424MHz.

NETWORK ANALYZER COMPARISON 8510 VS. 8720

A comparison of data taken with two different models of network analyzers, the HP 8510 NWA and the newer Agilent 8720 NWA, was performed. The 8510 is a modular system whose production began in the 1980's but is still a trusted instrument for its accuracy and stability, while the 8720 is a newer more compact and economical model. Bead pull measurements are made with the S_{11} parameter continuously as the bead moves through the structure. Data update rates vary between the 8510 and 8720 and methods of data collection can take two separate forms for the 8510. Both NWA's can acquire data in a mode that utilizes internal triggering, while the 8510 has an option to use an external trigger with varying trigger rates. The base internal trigger rate for the 8720 is much faster than that of the 8510 and more data can be collected during the same time period. The amount of data collected during a scan can have a significant effect on the measurement repeatability and accuracy due to data analysis techniques.

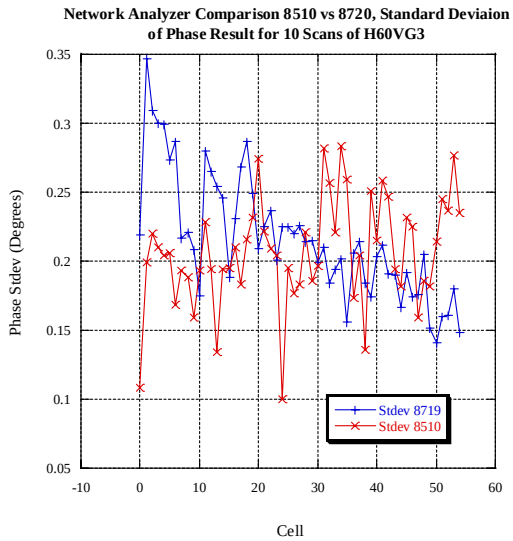

Figure 4: Standard Deviation of Phase for 10 Scans with different network analyzers.

A systematic error seems to dominate in the beginning cells for the 8720 network analyzer. This is most likely not due to the instrument but some unknown factor.

MECHANICAL AND MOTION CONSIDERATIONS

Since the measurement is made with a moving bead/string, motion related errors may be introduced into the data.

Vibration

One source of this motion is mechanical vibration transferred from the stepper motor system to the structure and bead/string system. Mechanically the structure strongback is separated from the bead pull tower that houses the stepper motor system. A considerable amount of noise can be transferred to the measurement if mechanical contact is established between the tower and accelerator structure.

The graph in Figure 5 compares the difference between having the input waveguide arms supported and unsupported during the scan with the previously mentioned tower contact eliminated. Measurement jitter that is visually observed on the network analyzer marker can be reduced by supporting the cable and input waveguide assembly. But when measured, figure 5 shows that this effect is only seen in the second and last cells. This should not lead one ignore the observed jitter, waveguide arms will continue to be supported to reduce observed noise.

String Position Reproducibility

Measurements performed after high power testing challenge us to mechanically reproduce the previous settings for the measurement. The string position within the structure should be accurately reproduced for a good comparison. This can be accomplished by visual inspection. Data for one such realignment is given in Figure 6 and gives confidence in the reproducibility of string alignment.

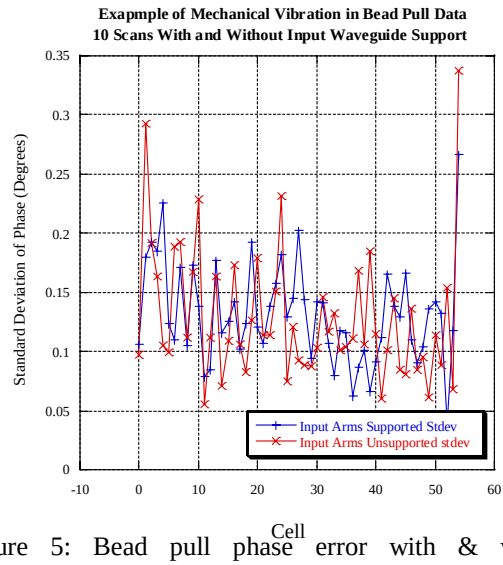

Figure 5: Bead pull phase error with & without mechanical vibration isolation.

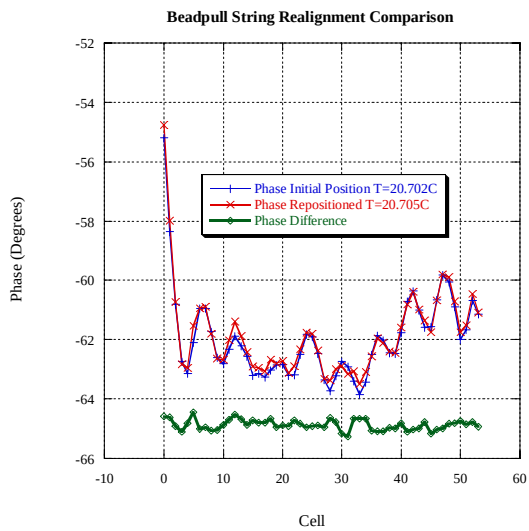

Figure 6: String replacement and realignment.

CONCLUSIONS

It seems we can trust the bead pull to produce an accurate measurement of internal structure fields. If we are to compare these measurements with previous results to extract meaningful information, close attention should be paid to the structure temperature during the scan and corrected with equation (1) if necessary. While investigations into vibrations and network analyzer model didn't reveal any great problems, a constant attention to detail is necessary for all aspects of the bead pull measurement to ensure consistent results.

REFERENCES

[1] T. Khabiboulline et al, "A New Tuning Method For Traveling Wave Structures," PAC 95

LONGITUDINAL BUNCH SHAPE MONITOR USING THE BEAM CHOPPER OF THE J-PARC

F. Naito*, KEK, Tsukuba, Japan

Abstract

We propose the longitudinal bunch shape monitor for the beam from the RFQ of the J-PARC linac. The monitor uses the beam chopper cavity installed in the MEBT line between the RFQ and the DTL of the J-PARC as a kind of the bunch rotator. Consequently the longitudinal bunch shape can be measured along the horizontal direction. If we can measure the energy distribution of the bunch also, the longitudinal emittance of the beam is derived. In the paper, the basic idea of the monitor is being discussed.

INTRODUCTION

The construction of Japan Proton Accelerator Research Complex (J-PARC) has been started in the Tokai campus of the JAERI. The injector linac consists of the radio-frequency quadrupole (RFQ) linac, the drift-tube linac (DTL), the separated DTL (SDTL) and several beam transport lines[1]. The beam from the linac is injected into the rapid cycle synchrotron (RCS) ring. For the beam injection into RCS without beam losses, the beam from the linac has to be chopped before the DTL by a chopper.

The measurement of the beam properties is quite important for the stable beam operation. In particular, the emittance of the beam is one of the most important parameters since the behavior of the beam in the phase space must be compared to the results of the beam dynamics calculation in order to improve the linac system of the J-PARC.

The shape of the 3-MeV beam, emitted from the RFQ, is tuned to be matched to the DTL by the Q-magnets and bunchers in the medium energy beam transport (MEBT) line between the RFQ and the DTL [2].

STRUCTURE OF THE CHOPPER

The chopper cavity is installed in the MEBT. As the chopper deflects the micro bunch in order to chop the beam by rf power, it is an rf deflector (RFD) [3]. The resonant frequency of the chopper cavity is 324 MHz which is the same frequency as that of RFQ and DTL. The chopper consists of two RFD both of which are coupled resonantly[4]. The each micro bunch of the beam is kicked horizontally by the crest of the rf electric field applied to the cavity. The performance of the chopper has been confirmed by using the beam from RFQ [5].

The photograph of the inside of the chopper cavity is shown in figure 1. The principle of the chopper is shown in figure 2. The deflected beam by the chopper is removed by the scraper. Figure 3 shows the layout of the MEBT components which include the chopper and the scraper.

* fujio.naito@kek.jp

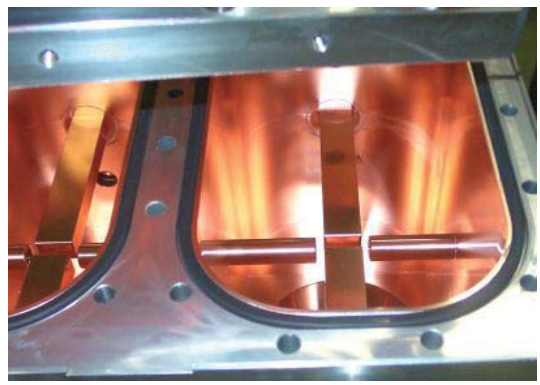

Figure 1: Inside of the chopper.

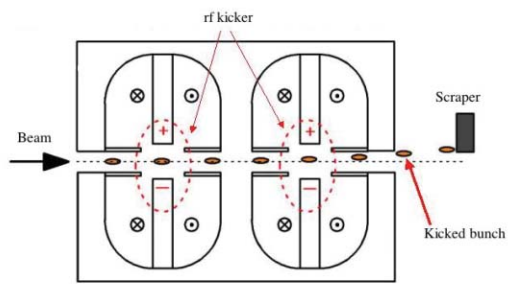

Figure 2: Principle of the chopper.

PRINCIPLE OF THE MONITOR

Measurement of the Longitudinal Bunch Shape

The chopper cavity is a main component of a longitudinal bunch shape monitor we proposed. Because the rf-system of the chopper is very flexible, we can easily use the cavity for another purpose by changing the rf phase. The principle of the bunch shape monitor is following:

1. Shift the rf-phase by $\pm\pi/2$ for the chopper cavity from the normal chopping mode as shown in figure 4. In this case the chopper cavity spreads the longitudinal distribution horizontally. Namely it woks as a kind of the bunch rotator. The middle part of the figure 5 shows the behavior of the bunch;

2. Measure the horizontal shape bunch at the down stream of the chopper by a wire scanner for instance. The measured width has the information about the longitudinal distribution of the micro bunch.

3. Set the slit which limits the bunch horizontal width before the chopper. It increases the spatial resolution for the longitudinal bunch distribution;

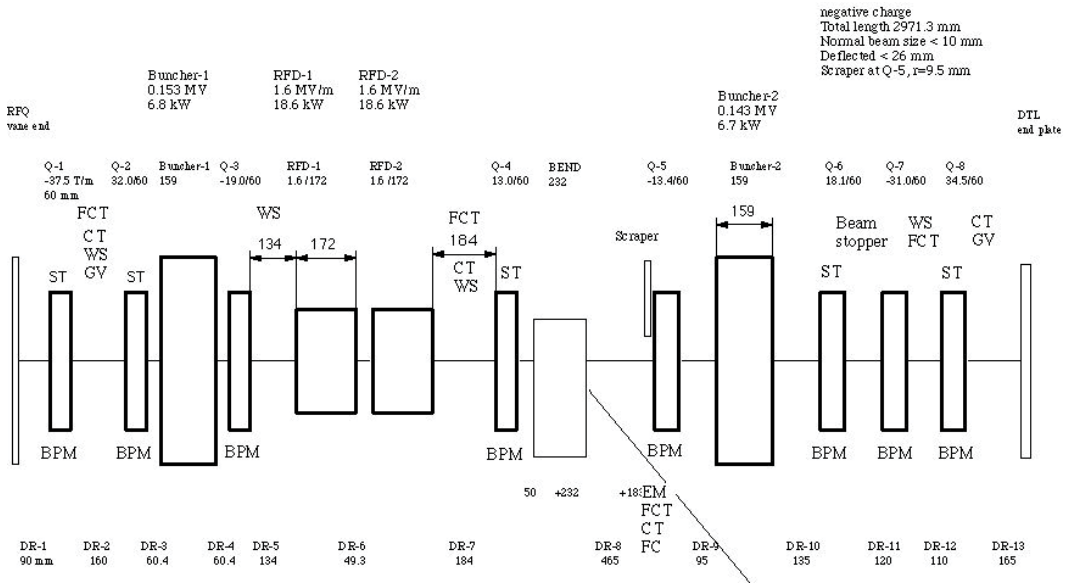

Figure 3: Layout of the MEBT components.

The principle of the monitor is very simple. We will be able to carry out the experiment for item 2 described above soon [6].

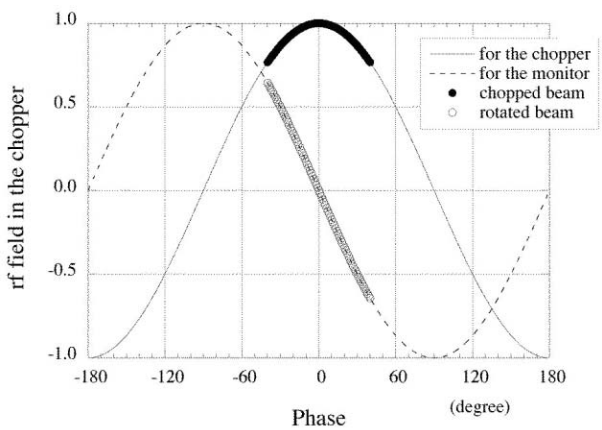

Figure 4: Phase relation between the beam bunch and rf in the chopper.
●: beam to be chopped and be removed
○: beam to be measured

Measurement of the Longitudinal Emittance

There is no longitudinal emittance monitor in the MEBT of J-PARC. However it is possible to construct the longitudinal emittance monitor in the MEBT if we can add the one more slit and momentum analyzer system at the down stream of the chopper. The principle of the system is shown in the figure 6. The desired phase is adjusted by moving the slit-2 or changing the rf phase of the chopper. Most difficult part of the monitor is the measurement of the energy of the cut beam since the energy spread of the beam from

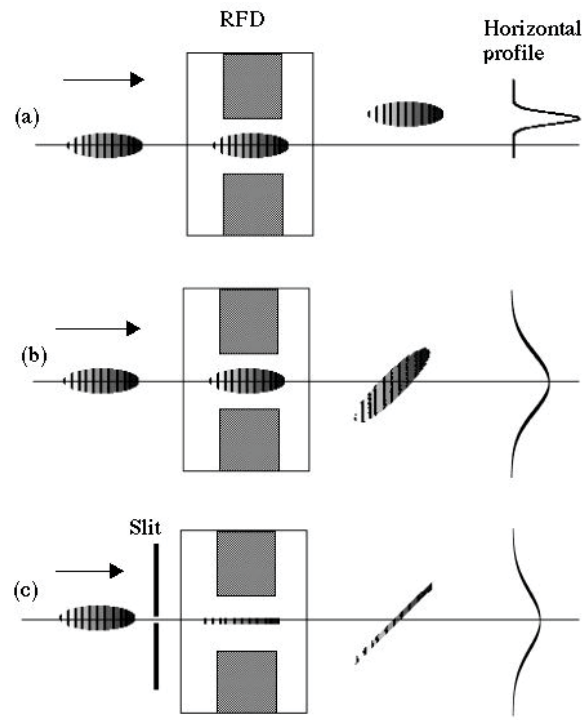

Figure 5: Schematic picture of the bunch behavior.
Beam comes from the left.
(a) chopper mode
(b) longitudinal beam shape monitor mode
(c) monitor mode with slit

RFQ is less than ±20 keV, which is described in the next section. Although the energy can be measured by an analyzer magnet or time of flight method in principle, it is hard

to put the detecting system which has such high energy resolution into practice.

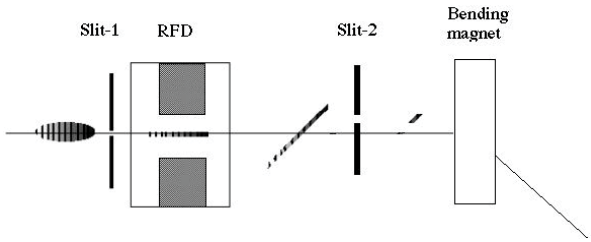

Figure 6: Principle of the longitudinal emittance monitor.

ESTIMATION OF THE SYSTEM PERFORMANCE

In this section, the practical performance of the longitudinal beam size monitor described above is estimated. The known beam parameters are follows:

1. the phase spread of the beam near the chopper is ± 20 degree in RMS[7].
2. the energy spread of the beam at the RFQ exit is about ± 20 keV [8]. (The value will be changed by the effect of the space charge and the tuning of the first buncher).
3. the transverse rms width of the beam for the horizontal direction in the chopper is about ± 1.8mm.
4. the expected maximum deflecting position of the beam at the scraper kicked by the chopper is 25 mm in the chopper mode[5].

From the item 1 and 4 described above the beam width is expected approximately $\pm$ 10 mm (= $\pm$ 25 mm * $\sin 25 / \sin 90$) for the longitudinal bunch size monitor mode at the scraper in the MEBT. It is enough for the measurement of the longitudinal shape of the bunch since the original horizontal width of the bunch is $\pm$ 2mm (item 3 described above). Because the beam scraper moves from -10 mm to + 25 mm for x-direction and it can measure the current of the irradiated beam, it is possible to confirm the principle of the monitor with the chopper. If we can add the slit just before the chopper, the wire scanner near the quadrupole 4 is usable for the measurement.

Although the phase difference between the two cells of the chopper is neglected for the rough estimation described above, it must be evaluated for the precise measurement.

For the longitudinal emittance monitor, it is not easy to measure the beam energy distribution since the energy spread of the beam from RFQ is small. The energy resolution must be less than 10 % of the beam energy spread. Thus the required energy resolution beam is less than 4 keV for 3 MeV.

It has been evaluated by a simulation that the energy spread can be measured by the bending magnet in the MEBT with slits. The simulation results show that the measured energy spread of the beam is bigger than the real one by the effect of the dispersion of the bending magnet. However the real energy spread can be estimated from the measured one by the comparison of the simulation results [9].

CONCLUSION

We proposed the longitudinal bunch shape monitor which can be set in the MEBT line for the J-PARC linac by using the beam chopper. The experiment of the proof of the principle for the longitudinal bunch shape monitor will be done in the beam test facility at KEK. Furthermore the possibility of the longitudinal emittance monitor with the chopper is also described. However the energy measurement of the beam with high accuracy is required.

ACKNOWLEDGMENTS

We would like to thank Prof. T. Kato for his valuable comments and discussions.

REFERENCES

[1] Y. Yamazaki, “The JAERI-KEK Joint Project for the High-Intensity Proton Accelerator, J-PARC”, Proc. of PAC 2003, Portland, Oregon, 576 (2003)

[2] T. Kato, S. Fu, “MEBT Design for the JHF 200-MeV Proton Linac”, Proc. of LAC 1998, Chicago, Illinois, 70 (1998)

[3] T. Kato, S. Fu, “RF-Chopper for JHF Linac”, Nucl. Instr. and Meth. in Phy. Res., 296 (2000) A440

[4] S. Wang, et al., “The Tuning Study of the Coupled Loaded Cavities for the RF Chopper System of J-PARC”, (THP69) in this conference.

[5] T. Kato, et al., “Beam Study with RF Choppers in the MEBT of the J-PARC Proton Linac”, Proc. of PAC 2003, Portland, Oregon, 1455 (2003)

[6] A few monitor in our MEBT have some troubles now. These will be fixed during this summer maintenance period. Thus we have a plan to perform the experiment for the bunch length monitoring in this autumn.

[7] M. Ikegami, et al., “Beam Commissioning of the J-PARC Medium Energy Beam Transport at KEK”, Proc. of PAC 2003, Portland, Oregon, 1509 (2003)

[8] JAERI/KEK Joint Project Team, “ACCELERATOR TECHNICAL DESIGN REPORT FOR J-PARC”, KEK Report 2002-13, 41 (2003)

[9] T. Kato, private communications.

MEASURED RF PROPERTIES OF THE DTL FOR THE J-PARC

H. Tanaka#, T. Kato, F. Naito, E. Takasaki, KEK, Tsukuba, Japan
H. Asano, T. Itou, T. Morishita, JAERI, Tokai, Japan

Abstract

RF properties of the second DTL tank for the J-PARC have been measured at KEK. The required flatness and stability of the accelerating field of the second tank have been obtained by the tuning of the post-couplers, whose shapes were modified to tune the resonant frequency to 324MHz. Consequently we have confirmed the following: (1) the achieved flatness of the field is 0.5% in maximum deviation, (2) the stabilized field can bear the perturbation of a 25% tilt of the field distribution.

INTRODUCTION

The J-PARC consists of a 181-MeV linac, a 3-GeV rapid cycle synchrotron and a 50-GeV synchrotron. The 181-MeV injection linac is comprised of an H^- ion source, a radio-frequency quadrupole (RFQ) linac, a drift-tube linac (DTL), a separated DTL (SDTL) and several beam transport lines. The linac will be extended to obtain a 400-MeV beam by adding the annular coupled structure (ACS) linac at the downstream of the SDTL in the next phase of the project.

The Alvarez-type DTL accelerates the H^- ion beam from 3 to 50 MeV. It consists of three independent tanks of which the length is about 9 m. Furthermore each tank is comprised of three short unit tanks (about 3 m in length). The inside diameter of the tank is 560 mm. The resonant frequency is 324 MHz. Each drift tube (DT) accommodates a tunable electromagnetic quadrupole magnet.

At this stage the assembling of all DTs for the DTL-2 and the DTL-3 has been completed. Moreover the first tank (DTL-1) already accelerates a 3 MeV beam from the RFQ up to an energy of 20 MeV at KEK [1]. Some RF properties were already described in the reference [2].

For the second DTL tank (DTL-2), which is designed to accelerate the beam from 20 to 37 MeV, some RF properties have been measured. A uniform accelerating field has been achieved by the fine adjustment of the post couplers and the fixed tuners. The field stabilization by the post-couplers against perturbations has been confirmed also. In order to achieve the stabilized-uniform distribution of the average field at the final target frequency of 324MHz, the following techniques have been applied for the post-coupler tuning: (1) non-uniform insertion length of the post-couplers from the tank wall; (2) increment of diameter of all post-couplers of the wall side.

Furthermore measurements of RF properties of the third tank (DTL-3) which will be used for beam acceleration from 37 MeV to 50 MeV, has been started.

#hirokazu.tanaka@kek.jp

STRUCTURE OF THE DTL-2 AND THE DTL-3

The second DTL tank consists of 42 full-size drift tubes, 42 post-couplers and 10 fixed tuners. Bore diameter of the DT is 22 mm. The third DTL tank consists of 26 full size drift tubes, 26 post-couplers and 8 fixed tuners. Bore diameter of the DT is 26 mm. Both tanks have two movable tuners and two half drift tubes. The layout of the tuners and the input couplers are shown in figure 1. The first and the third unit tanks for the DTL-2 and these for DTL-3 have four and three fixed tuners, respectively. The second unit tank has two fixed tuners and two movable ones. Diameter of the tuner is 90 mm. There are two ports for the input couplers in the tank in order to reduce the RF power per coupler. Each coupler is located at one fourth of the total length from the end plate in order to suppress the excitation of the TM_{011} mode.

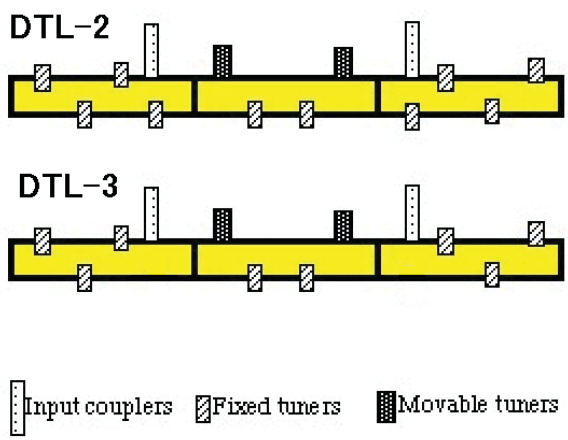

Figure 1: Layout of tuners.

TUNING OF THE DTL-2

Adjustment of the Tuners

The accelerating-field measurement for the DTL-2 has been done by using a bead-pull perturbation technique [3]. Initial field distribution of the TM010 mode without the tuners and the post-couplers is shown by the square marks in figure 2. The ordinate of figure 2 shows the normalized electric field of each gap. The DTL-2 tank has two movable tuners and 10 fixed ones as described above. The length of each fixed tuner was adjusted in order to tune the resonant frequency and to obtain the uniform accelerating field along the beam axis. (During the tuning, the ”fixed” tuners are replaced by the ”movable” model.)

The target frequency of tuner tuning is 323.650 MHz. The difference in the frequency from the operating point of 324 MHz is compensated by the effects of insertion of post-couplers, dielectric constant of the air, the deformation of the DT by the RF losses on the DT surface and the heat from the magnet in DTs. However, the measured resonant frequency is 323.105 MHz, which requires 80mm insertion in average of all tuners. It means that the effect of tuner is insufficient to tune the accelerating field. The reasons are as follows: (1) the maximum effective length of our tuner is about 100 mm, (2) however it was confirmed by the measurement that the maximum tuner length which is required to obtain the uniform field is approximately 40 mm longer than the average insertion length of the tuners.

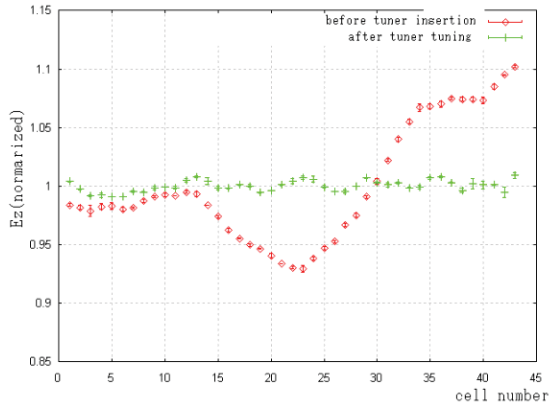

Figure 2: Field distribution (before and after tuning the tuners).

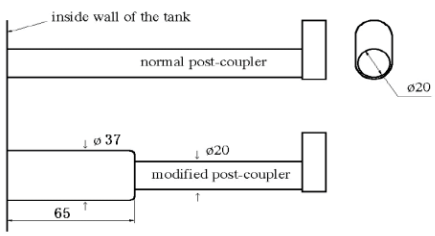

Figure 3: Shape of modified post-coupler.

Therefore, we modified the design of post-couplers in order to increase the resonant frequency. The designs of the post-coupler are shown in figure 3. The effect of the shape of the post-coupler (figure 3) on the resonant frequency was already confirmed by the tuning of the DTL-1. In the DTL-1 one third of the post-couplers were modified. However, all post-couplers had to be modified in the DTL-2, since the observed frequency difference for the DTL-2 was much larger than that for the DTL-1.

As a result, the resonant frequency became 323.653 MHz after tuning the tuners. The insertion length of the tuner is shown A in table 1. The accelerating field in this case is represented by the crosses (+) in figure 2.

After tuning the tuners, the measured unloaded Q (Q_0) value is 47000, which is about 84% of the calculated value. The Q_0 value is sufficiently high for the accelerating cavities.

Adjustment of the Post-Couplers

The length of the post-couplers has been adjusted by the measurement of the distribution of the average electric field for each gap along the beam axis with tuner perturbation. Two kinds of the tuner perturbation were applied. Both of tuner perturbations make a 25 % tilt of the field distribution without post-couplers. The perturbed field distributions without post-couplers are shown in figure 4.

The initial adjustment of the post-couplers has been done by keeping up the length of all post-couplers constant. The results are shown in figure 5 A). The ordinate of figure 5 is stability parameter which is defined as an RMS of difference between perturbed and non-perturbed electric fields of each cell.

$$\text{stability parameter} = \sqrt{\frac{\Sigma \Delta Ez_n}{N}}$$

ΔEz_n means difference of accelerating field between perturbed and non-perturbed at the n-th cell.

In order to obtain the best stabilization against the perturbations, the fine tuning of post-coupler length has been tried. The length of post-couplers was varied for each unit tank. Figure 5 B) shows the results of the stability parameter described above for the fine tuning of the post-coupler. A-G at abscissa in figure 5 means insertion patterns as shown in table 2. Thus, the best stabilization against perturbations is achieved by the pattern E.

The field distributions shown in figure 4 are changed to ones shown in figure 6 by the post-couplers with pattern E. In figure 6 the effect of perturbations shown in figure 4 has been suppressed.

Table 1: Insertion length of tuner

	F1	F2	F3	F4	F5	F6	F7	F8	F9	F10	A1	A2
A	60	48	83	75	14	43	65	86	75	85	46	39
B	65	53	88	80	14	43	60	81	70	80	46	39
C	55	43	78	70	14	43	75	95	85	94	46	39

A: uniform distribution [mm]
B: upward perturbation Fx: x-th fixed tuner
C: downward perturbation Ax: x-th movable tuner

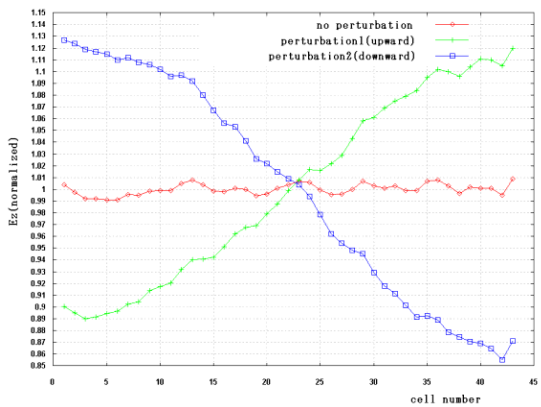

Figure 4: Field distribution without post-couplers.

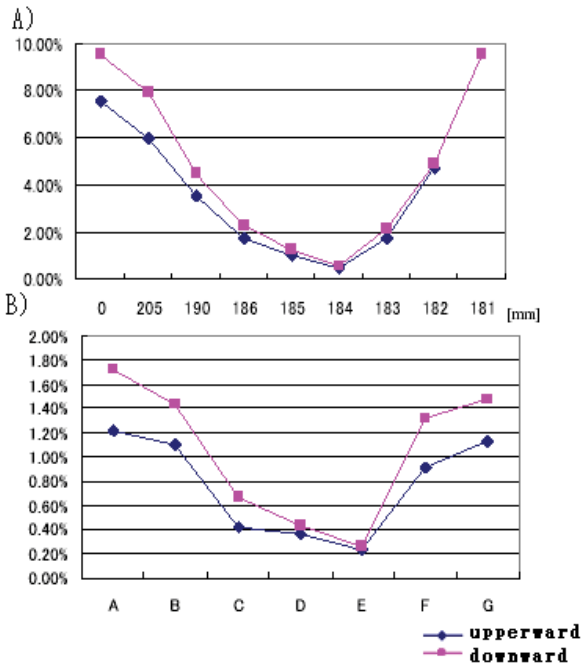

Figure 5: Stability parameter for each insertion pattern of post-couplers.

Table 2: Insertion patterns of post-couplers

	Insertion length of post-couplers(mm)		
	Unit tank 1 (1-16)	Unit tank2 (17-29)	Unit tank 3 (30-42)
A	186	185	184
B	186	185	183
C	186	184	183
D	185	184	183
E	185	184	182
F	185	183	182
G	184	183	182

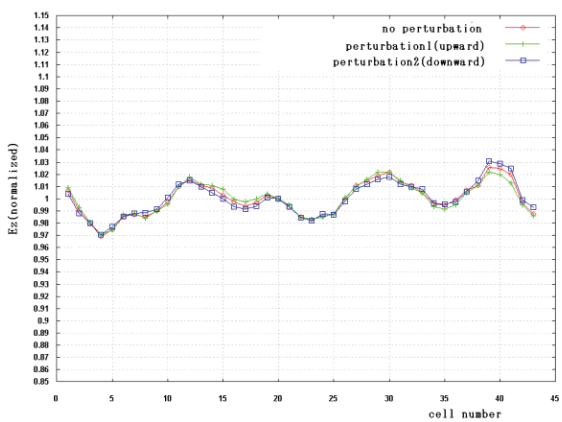

Figure 6: Field distribution with post-couplers.

After adjusting the post-coupler's length finely, the tabs of a part of post-couplers were tilted in order to improve the uniformity of the field distribution. Finally distribution of accelerating field without perturbation is achieved (figure 7). The maximum deviation and the standard deviation of the distribution are approximately 0.5% and 0.16%, respectively. The effect of perturbation on the field distribution is as small as (figure 6).

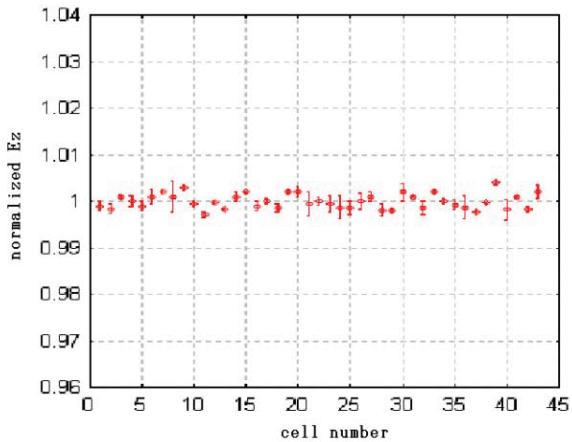

Figure 7: Field distribution after fine tuning (Error bar: 1 sigma).

CONCLUSION

The RF properties have been measured for DTL-2 of the J-PARC linac. As a result, sufficiently high Q_0 value of about 47000 has been confirmed. The value is more than 80% of the calculated one. The stabilized and uniform accelerating field has been achieved by the fine adjustment of post-coupler's length and rotation of tabs. The standard deviation of the field distribution is 0.16%.

The measurement of the RF properties for DTL-3 is in progress.

REFERENCES

[1] F. Naito, et al, "Results of the High-Power Conditioning and the First Beam Acceleration of the DTL-1 for J-Parc", Proc. of LINAC2004, Lubeck, GERMANY, to be published.

[2] F. Naito, et al, "Tuning of the RF field of the DTL for the J-PARC", PROC. OF PAC2003, Portland, OREGON, p2835 (2003)

[3] S. Okumura and A. Swenson, "Bead perturbation measurement for the KEK linac cavity", KEK-report, KEK-74-15(1975).

THE TECHNIQUE FOR THE NUMERICAL TOLERANCES ESTIMATIONS IN THE CONSTRUCTION OF COMPENSATED ACCELERATING STRUCTURES

V. V. Paramonov, A.K. Skassyrskaya, INR, 117312 Moscow, Russia

Abstract

The requirements to the cells manufacturing precision and tuning during multi-cells accelerating structures construction came from the required accelerating field uniformity, based on the beam dynamics demands. The standard deviation of the field distribution can be expressed in terms of accelerating and coupling cells frequencies deviations, stop-band width and coupling coefficient deviations. The deviations of the cells frequencies and coupling coefficient can be expressed from 3D fields distributions for accelerating and coupling modes and the cells surface displacements. With the modern software possibilities it can be done separately for every specified part of the cell surface. Finally, the surface displacements are expressed through characteristic cells dimensions deviations. This technique allows both qualitatively to define the critical regions and quantitative to optimize the tolerances definition.

INTRODUCTION

In the multi-cell accelerating structures all time exists the problem of cells identity - to realize the structure design parameters, the cells should be identical within the defined tolerances. The tolerances for cells parameters are directly related to tolerances for geometrical parameters. And the tolerances for cell geometry are directly related to the price (and possibility) of the cavity construction. The cavity mast realize design parameters, so, tolerances can not be too soft. But extremely rigid tolerances lead, at least, to the extra costs in the construction. The tolerances definition is all time the important part in the cavity development.

COUPLED CIRCUIT ANALYSIS

The original demands originate from the beam dynamics, which provides the requirements to the accelerating field distribution - the standard (rms) field deviations in accelerating gaps σ_E or field tilt along the cavity. The relation between σ_E value and deviations in cells rf parameters can be obtained by using well known coupled circuit model [1]. The rms value of the accelerating electric field deviation σ_E is [2]:

$$\sigma_E^2 = \sigma_{E_f}^2 + \sigma_{E_k}^2, \quad \sigma_{E_k}^2 = \sigma_{k_c}^2 \frac{N_p + 2}{3}, \qquad (1)$$

and

$$\sigma_{E_f}^2 \approx \frac{16\sigma_{f_a}^2}{k_c^4}(\sigma_{f_c}^2 \frac{N_p^2 + 3N_p}{12} + (\frac{\delta f}{f_a})^2 \frac{N_p^3 + 4N_p^2 + 6N_p}{3}), \qquad (2)$$

where σ_{f_a} and σ_{f_c} are the rms frequency deviations for the accelerating (f_a) and coupling (f_c) cells, $\delta_f = f_c - f_a$ is the stop-band width, N_p - number of structure periods in the cavity, σ_{k_c} is the rms deviation of coupling coefficient k_c. As it usually is supposed in coupled circuit approach, the influences of δk_c and $\delta f_{a,c}$ on the operating field distribution are independent.

Suppose the cell geometry (the shape and dimensions) are defined with the set of geometrical parameters x_i. Assuming the deviations of different parameters as independent, for relative rms deviations $\sigma_{f_{a,c}}, \sigma_{k_c}$ it is valid:

$$\sigma_{f_{a,c}} = \frac{\sqrt{\sum_i (\frac{\partial f_{a,c}}{\partial x_i})^2 \sigma_{x_i}^2}}{f_{a,c}}, \sigma_{k_c} = \frac{\sqrt{\sum_i (\frac{\partial k_c}{\partial x_i})^2 \sigma_{x_i}^2}}{k_c}, \quad (3)$$

where $\frac{\partial f_a}{\partial x_i}, \frac{\partial f_c}{\partial x_i}, \frac{\partial k_c}{\partial x_i}$ are the sensitivities of the cell parameters f_a, f_c, k_c with respect the small deviation in the geometrical cell parameter x_i, σ_{x_i} is the rms x_i deviation. The value σ_{x_i} corresponds to the tolerance $\pm 3\sigma_{x_i}$ for the parameter x_i.

To estimate values in numbers, we need in the sensitivities values.

Coupling Coefficient Deviations

Considering k_c deviations, we have to distinguish symmetrical and nonsymmetrical k_c distortions with respect coupling cells. Suppose k_c value of the j-th coupling cell with adjacent $j-1$-th and $j+1$-th accelerating cells has the same deviation δk_c^s. The total coupling between the coupling cell and adjacent accelerating cells remains equal. As it is easy to see from coupled equations, [1], the fields in $j-1$-th and $j+1$-th accelerating cells will be equal.

Estimating k_c deviations, we have to exclude from consideration the symmetrical (with respect coupling cells) parts.

3D NUMERICAL MODELS

The sensitivity values $\frac{\partial f_a}{\partial x_i}, \frac{\partial f_c}{\partial x_i}, \frac{\partial k_c}{\partial x_i}$ depend on the field distributions of both accelerating and coupling cells (modes).

Suppose the structure period has a length $d = 2l, -l \leq z \leq l$, z is the structure axis, and at least the accelerating cells has a plate of mirror symmetry. It means, at $z = \pm l$, in the middles of accelerating cells, one can apply boundary conditions of electric walls (to simulate accelerating mode) or magnetic ones (to simulate coupling mode).

3D fields distributions and frequencies can be calculates for accelerating ($\vec{E}_a, \vec{H}_a, f_a$) and coupling ($\vec{E}_c, \vec{H}_c, f_c$) modes

at one structure period, with appropriate boundary conditions at $z = \pm l$, can be calculated by using such software, as MAFIA and ANSYS.

Calculating and combining energy densities for electric $(\vec{E}_a, \vec{E}_c)$ and magnetic $(\vec{H}_a, \vec{H}_c)$ fields, one gets at the structure surface:

$$\frac{(\epsilon_0 E_{a,c}^2 - \mu_0 H_{a,c}^2)}{W_{a,c}} \sim \frac{\delta f_{a,c}^{(d)}}{f_{a,c}}, \qquad (4)$$

where W_a, W_c are the stored energies for accelerating and coupling modes.

At the case of confluence ($f_a = f_c$) in compensated structures exists the traveling wave $\vec{E}_{tr} = \vec{E}_a - i\vec{E}_c$ [3] with normalization conditions $W_a = W_c$ [4]. The relative group velocity of the traveling wave β_g, by definition, is:

$$\beta_g = \frac{dP_t}{cW_t} = \frac{\beta\lambda Re \int_{S_{z=l}} [\vec{E}_{tr}\vec{H}^*_{tr}]d\vec{S}}{2c(W_a + W_c)}, \qquad (5)$$

or,

$$|\frac{\beta_g}{\beta}| = |\frac{\lambda \int_{S_{z=0}} ([\vec{E}_a\vec{H}_c] - [\vec{E}_c\vec{H}_a])d\vec{S}}{4c\sqrt{W_a W_c}}|, \qquad (6)$$

where β is the particles relative velocity. The operating π mode is assumed. The ratio $\frac{\beta_g}{\beta}$ is related with coupling coefficient k_c as:

$$\frac{\beta_g}{\beta} = \frac{\pi k_c}{4}. \qquad (7)$$

The β_g reference value should be calculated according (6) - it is general expression and do not requires coupling cell mirror symmetry. The surface integral $I_{(z=0)} = \int_{S_{z=0}} ([\vec{E}_a\vec{H}_c] - [\vec{E}_c\vec{H}_a])\vec{z}_0 d\vec{S}$ in (6) can be calculated numerically, by using 3D software output. But β_g value doesn't depends on the reference plane coordinate and, remembering accelerating cell mirror symmetry, one has:

$$|\frac{\beta_g}{\beta}| = |\frac{\lambda \int_{S_{z=l}} [\vec{E}_c\vec{H}_a]d\vec{S}}{4c\sqrt{W_a W_c}}|, \qquad (8)$$

Let transform the integral $I_{(z=l)} = \int_{S_{z=l}} [\vec{E}_c\vec{H}_a]d\vec{S} = 2\pi f_0 \int_{V_0} (\epsilon_0\vec{E}_a\vec{E}_c - \mu_0\vec{H}_a\vec{H}_c) + \int_{S_{z=0}} [\vec{E}_c\vec{H}_a]d\vec{S}$. For β_g deviations one can neglect variations of the surface integral $\int_{S_{z=0}} [\vec{E}_c\vec{H}_a]d\vec{S}$, and, similar to (4):

$$\frac{(\epsilon_0\vec{E}_a\vec{E}_c - \mu_0\vec{H}_a\vec{H}_c)}{\sqrt{W_a W_c}} \sim \frac{\delta\beta_g^{(d)}}{\beta_g} = \frac{\delta k_c^{(d)}}{k_c}, \qquad (9)$$

The normalized scalar fields $(\epsilon_0 E_{a,c}^2 - \mu_0 H_{a,c}^2)$, $(\epsilon_0\vec{E}_a\vec{E}_c - \mu_0\vec{H}_a\vec{H}_c)$ (4), (9) represent at the structure surface the densities of sensitivity values $\frac{\partial f_a}{\partial x_i}, \frac{\partial f_c}{\partial x_i}, \frac{\partial k_c}{\partial x_i}$. The shift values are proportional to these densities and the volume of perturbation. We can estimate visually the relative influence of deviations in different structure elements on the cells parameters.

In Fig. 1 the Disk And Washer (DAW) structure [5] is shown (Fig. 1a) - the option for INR proton linac,

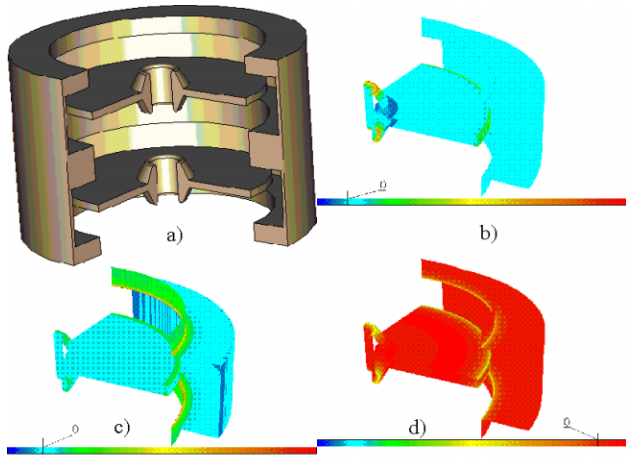

Figure 1: The DAW structure (a) and $\delta f_a^{(d)}$ (b), $\delta f_c^{(d)}$ (c), $\delta k_c^{(d)}$ (d) densities distribution at the structure surface.

$\frac{\beta_g}{\beta} = 0.512$. The scalar densities $\frac{\delta f_a^{(d)}}{f_a}, \frac{\delta f_c^{(d)}}{f_c}, \frac{\delta k_c^{(d)}}{k_c}$ are shown in Fig. 1 b,c,d, respectively. It is well known - the drift tube cone nose region has a strong influence on the frequency of accelerating mode f_a, Fig. 1b. As one can see from Fig. 1c, 1d, this region also has the influence on f_c and k_c values. In the DAW structure the field of coupling mode is distributed in the large part of the volume, providing strong $\vec{H}_a, \vec{H}_c$ overlapping and, as a sequence (see (9)), high β_g value . But for high $\beta \approx 1$ the fields $\vec{E}_c, \vec{H}_c$ penetrate to the drift tube region, leading to the influence on both k_c and f_c .

In Fig. 2 the CDS structure [6] is shown with two coupling windows, Fig. 2a, $\frac{\beta_g}{\beta} = 0.075$ and with four windows, Fig.2b, $\frac{\beta_g}{\beta} = 0.057$ [6]. The concept of k_c increasing without Z_e reduction in the CDS structure is described in [6] - for coupling mode $\vec{H}_c$ has no own space and trough coupling windows penetrate in accelerating cell. The windows opening angle has a large influence on f_a, f_c, k_c. Because the coupling windows are placed close to drift tubes, the drift tube nose surface has large $(\mu_0\vec{H}_a\vec{H}_c - \epsilon_0\vec{E}_a\vec{E}_c)$ density, mainly due to electric part in this combination.

The qualitative consideration shows - for the CDS structure the highest sensitivities for $\delta f_a, \delta f_c, \delta k_c$ deviations have the coupling windows and drift tubes dimensions.

Quantitative Estimations

For the values of $\delta f_a, \delta f_c, \delta k_c$ deviations both the sensitivity densities (4), (8) and surface areas are important. Basing on the FEM software (ANSYS) possibilities, the special procedure has been developed. The structure surface is described, (see Fig.3), in ANSYS as a set of numbered simple shapes. After rf problem solution, we have 3D distributions $\vec{E}_a, \vec{H}_a, \vec{E}_c, \vec{H}_c$ and can calculate deviations $\delta f_{ai}, \delta f_{ci}, \delta k_{ci}$, related to the fixed (say, $10\mu km$) normal displacement of the $i-th$ surface.

The cells geometry is described with parameters, or di-

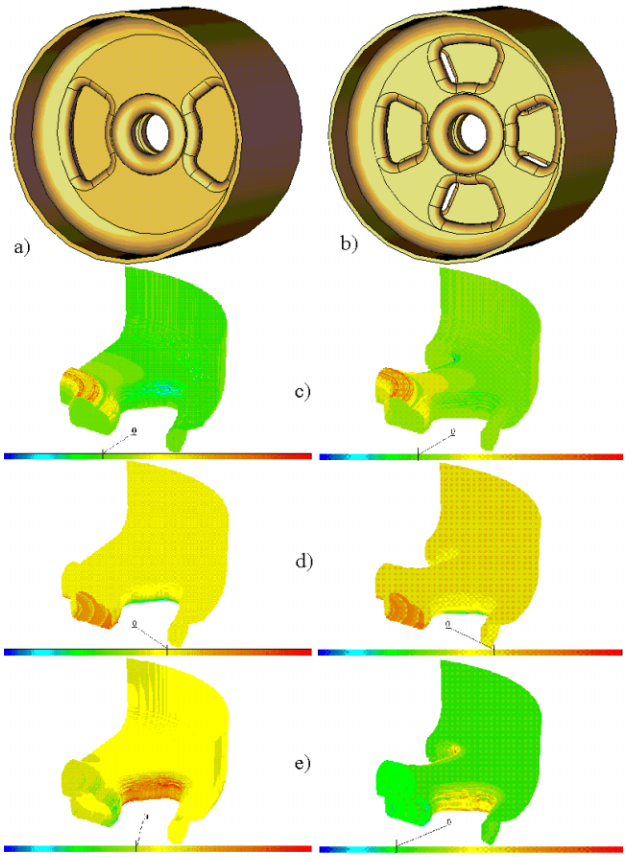

Figure 2: The CDS structure with two (a) and four (b) coupling windows and $\delta f_a^{(d)}$ (c),$\delta f_c^{(d)}$ (d), $\delta k_c^{(d)}$ (e) densities distribution at the structure surface for each CDS option (the left column - two windows, the right one - four windows).

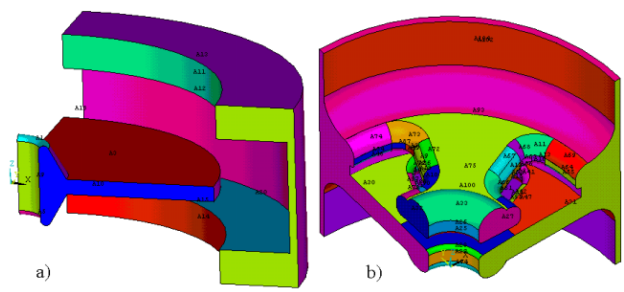

Figure 3: The surfaces of the DAW (a) and CDS (b) cells , divided in simple numbered shapes for deviations $\delta f_{ai}, \delta f_{ci}, \delta k_{ci}$ calculations.

mensions. The deviation in one parameter can lead to several simple shapes displacements. The relation between shape displacements and dimension deviations can be defined from geometry consideration.

EXAMPLES OF APPLICATIONS

In the DAW structure $10\mu km$ each surface displacements (due to simple shapes, see Fig. 3a, it is equivalent to dimensions deviations) lead to $\sigma_{f_a} = 7.3 \cdot 10^{-3}, \sigma_{f_c} = 1.3 \cdot 10^{-2}, \sigma_{k_c} = 2.7 \cdot 10^{-2}$. The main influence to k_c deviations provide the disk and the washer thickness, due to large surface area of these elements. For these dimensions the tolerances should be more rigid than $\pm 60\mu km$, which are considered in this example.

This technique was applied to determine the tolerances for the CDS booster cavity [7] construction. For the dimensions deviations, which correspond to $10\mu km$ simple shapes displacements, see Fig. 3b, we have $\sigma_{f_a} = 1.2 \cdot 10^{-4}, \sigma_{f_c} = 7.3 \cdot 10^{-4}, \sigma_{k_c} = 1.2 \cdot 10^{-3}$. The booster cavity is not too long, $N_p = 14$. For the reasonable stop-band width $\frac{\delta f}{f_a} = 3.0 \cdot 10^{-4}$ the first term (σ_{E_f} in (1), related to the $\delta f_{a,c}$ deviations, is two order less, as compared to the second one, related to the δk_c deviations influence. The coupling coefficient deviations determine σ_E value in the CDS booster cavity. Finally, reasonably comfortable tolerances for cells dimensions were chosen, taking into account technological reasons, to expect in the booster cavity $\sigma_E \leq 1\%$.

CONCLUSION

In this report the technique for numerical tolerances estimations in the construction of compensated accelerating is presented. The combination of different approaches provides the flexible, precise and visual method for problem understanding and well-grounded tolerances choice.

REFERENCES

[1] E.A. Knapp et al., Coupled resonator model for standing wave accelerators tanks. Rev. Sci. Instr., v.38, p. 22, 1967

[2] V.F. Vikulov, V.E. Kalyuzhny. The influence of manufacturing errors on parameters of standing wave accelerating structures, Soviet Journ. of techn. physics, V. 50, n4, p. 773, 1980.

[3] G. Dome. Review and survey of accelerating structures. in Linear Accelerators. /Ed. P. Lapostolle, A. Septier, North. Holland Pub. Co., 1970

[4] V. Paramonov. General relations for mode parameters of compensated structure in the vicinity pf operating point. Proc. of the 2000 Linac Conference, USA, p. 401, 2000

[5] V.G. Andreev et al., Study of high-energy proton linac structures. Proc. of the 1972 Linac Conference, p. 114

[6] V.V. Paramonov, The Cut Disk Structure for High Energy Linacs, Pros. 1997 PAC, v.3, p. 2962. 1998.

[7] V. Paramonov et al., Design parameters of the normal conducting booster cavity for the PITZ-2 test stand, MOP77, this Conference.

EFFECT OF THE TUNER ON THE FIELD FLATNESS OF SNS SUPERCONDUCTING RF CAVITIES

An Sun, Oak Ridge National Laboratory, Oak Ridge, TN 37830*
Haipeng Wang, Genfa Wu, Jefferson Lab, Newport News, VA 23606#

Abstract

The field flatness (FF) in a multi-cell superconducting cavity affects not only net accelerating voltage, but also peak surface field [1] and Lorentz detuning coefficient [2]. Our measurements indicate that the tuner's motion changes not only the cavity frequency but also its FF. This field amplitude change is a linear tilt and proportional to the distance between each cell center and the cavity's geometric center. This tilt also changes the coupling of the Fundamental Power Coupler (FPC) and Field Probe (FP) on either side of the cavity. The tilt has been measured and simulated, and is ~20%/MHz on the Spallation Neutron Source (SNS) medium β cavities. The FF change is not only due to the uneven volume change within the cell, but also due to the cell-to-cell coupling.

INTRODUCTION

The FF in a multi-cell cavity can be derived from its original definition [2].

$$\eta_{ff} = \frac{E_{cmax} - E_{cmin}}{\frac{1}{N}\sum_{i=1}^{N} E_{ci}} \times 100\% \quad (1)$$

Here E_{ci} is the peak axial electric field in the ith cell.

The FF specification for SNS production cavities is less than 8%. The FF was tuned after manufacture at ACCEL and qualified at JLab by the bead-pulling measurement during the cavity tuning. After final cavity etching and rinsing, there is no way to check or correct the FF.

The SNS cavity tuner uses a stepper motor to drive a tuner frame. The frame is seated on the one end of the helium tank to compress the cavity end dish [3]. The resulting frequency tuning range is ~±245kHz for an axial spring distance of 1.8mm.

From our cold (2K) cryomodule measurement, we found that when the tuner changes the cavity's frequency, it also changes the external Q of both fundamental power coupler (FPC) and field probe (FP). After excluding other causes, we concluded that it relates to the relative RF field change at each end cell or the FF has been altered. A later warm bead-pulling measurement and numerical simulations confirmed this speculation.

MEASUREMENT IN CRYOMODULE

The measurements were done on a medium β cryomodule in the Cryomodule Test Facility at JLab. The power transfer function from FPC to FP can be measured by the S21 parameter on a network analyzer. With a stable cryogenic system and a well matched circuit, a -3dB bandwidth of the |S21| resonance peak can lead to a relatively accurate measurement of the external Q of the FPC, (Q_{eFPC}) which is the lowest Q for the coupled superconducting cavity.

Only a relative measurement on S21 is needed [2] to get the external Q of FP Q_{eFP} in order to get the relative FF information.

$$\frac{Q_{eFP}}{Q_{eFP0}} = \frac{Q_{eFPC}}{Q_{eFPC0}} \cdot 10^{\frac{S21-S21_0}{10}} \quad (2)$$

Here subscript 0 corresponds to the values at the operation frequency of f_0=805MHz. Figure 1 shows this measurement data. It indicates that the field amplitude decreases at the FPC-end cell and increases at the FP-end cell, when the cavity frequency is increased by the tuner stretching the cavity. Supposing the cavity FF (η_{ff}) is perfect at f_0=805MHz (η_{ff}=0), and the electric field tilt is a linear function of frequency as the fits illustrate in Figure 1, then the FF can be expressed as:

$$\eta_{ff} = \frac{\left|\sqrt{Q_{eFPC0}/Q_{eFPC}} - \sqrt{Q_{eFP0}/Q_{eFP}}\right|}{\sqrt{Q_{eFPC0}/Q_{eFPC}} + \sqrt{Q_{eFP0}/Q_{eFP}}} \times 200\% \quad (3)$$

Figure 2 shows this calculation from Figure 1's data. The FF change can be estimated as ~20%/MHz.

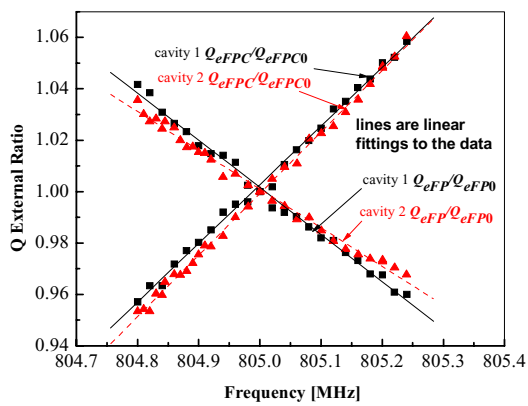

Figure 1: The relative external Q changes on FPC and FP measured on a medium beta cryomodule operated at 2K when tuner changes the cavity frequency.

BEAD-PULL MEASUREMENT

To verify the above result, we did a bead-pull experiment on cavity MB-19 with attached helium vessel to measure axial electric field profiles. To measure the helium vessel effect, we performed the bead-pull on

* Work supported in part by an appointment to the Oak Ridge National Laboratory Postdoctoral Research Associate Program.
# Work supported by the U.S. Department of Energy under contract DE-AC05-00OR22725

cavity MB-29 without the helium vessel. Tuner frames were then installed on both of them. A 3mm needle was used as a bead in all cases.

The phase angle change of S21 (*arg(S21)*) due to the needle's perturbation in the time domain were measured using a network analyzer. The coupling of input and pickup antennas was weak enough not to perturb the end-cell fields. A ~35dB gain preamplifier was needed for a signal strong enough to maintain phase lock. When the needle is short enough, the *arg(S21)* range can be controlled within a few degrees. Figure 3 shows this bead-pulling result. Then the FF can be approximated [2] by:

$$\eta_{ff} = \frac{\sqrt{-\arg(S21)_{max}} - \sqrt{-\arg(S21)_{min}}}{\frac{1}{N}\sum_{i=1}^{N}\sqrt{-\arg(S21)_i}} \times 100\% \qquad (4)$$

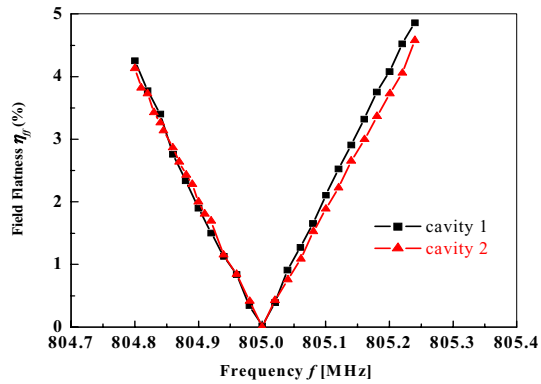

Figure 2: Measured FF changes calculated by Equation (3) from Figure 1's data.

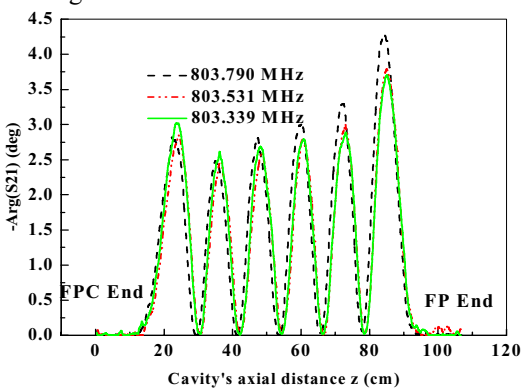

Figure 3: The bead pulling measurement on MB-19 cavity to measure the electric stored energy profile along the cavity beam axis.

As illustrated in Figure 4, the field tilt rate agrees with the cryomodule measurement The results on the MB-29 cavity were similar to those for the MB-19 cavity, but the FF change was ~17.2%/MHz.

NUMERICAL SIMULATIONS

To further understand the mechanism for the FF change, the ANSYS code was first used to calculate the cavity shape deformation when the tuner compressive force is applied. The actual displaced cavity shape and original shape were input into the SUPERFISH code. Using the option "MODT36=1" in the AUTOMESH program, SUPERFISH can calculate newly tuned cavity resonance frequency and field profile precisely.

The cavity frequency is a linear function of the cavity longitudinal deformation. The coefficient is 296 kHz/mm. The bead-pulling result is ~276 kHz/mm. Figure 5 shows the field profile from these simulations.

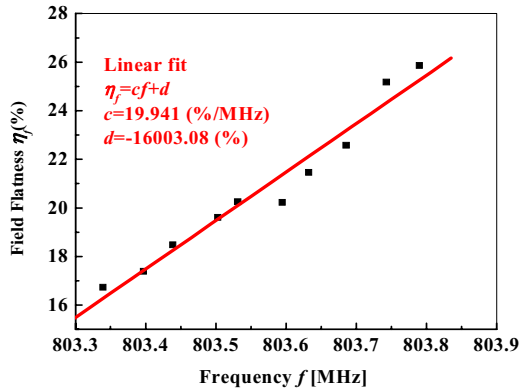

Figure 4: The MB-19 cavity's FF measured by the bead pull. The initial FF was 26% before the tuner compressed the cavity.

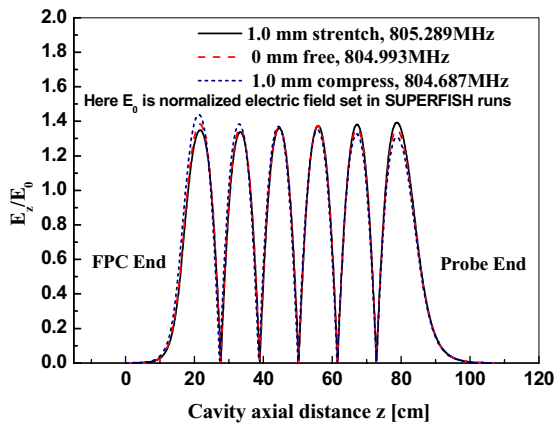

Figure 5: The cavity axial electric field profiles using ANSYS and SUPERFISH simulations.

To study the relative field amplitude change within each individual cell and the cell-to-cell coupling effect, we use the ratio of perturbed field amplitude E_c to its original value E_{c0} at a given frequency. Figure 6 shows the result. It can be seen that the end cells have a relatively larger change rates than the center cells. The E_{ci}/E_{ci0} ratio is nearly prefect (1.0) at f_0=805MHz.

From Figure 6, we can conclude and rewrite the E_{ci}/E_{ci0} as a linear function of frequency. The coefficient $\xi(i)$ is linear with cell number (i) as well. It is also the FF change rate.

$$E_{ci}/E_{ci0} = \xi(i)f + \eta_i , \qquad (5)$$

As depicted in Figure 7, the line pivot is at the structure center (including the beam pipe lengths) but not at any cell center. Interesting enough in the simulation is that Figure 8 would not be a symmetric "V" shape if the bottom of "V" was higher than 2% [2].

To study the cell-to-cell coupling effect on the FF, we used the ANSYS APDL (and Excel) to calculate the cavity volume deformation as a function of cavity axial

distance z (Figure 9). We found that the larger deformation in the iris area is the major cause to the frequency change. We integrated the cavity volume change with the energy densities on the wall from SUPERFISH (before compression). The relative stored energy changes in each cell can be obtained (Figure 10). Comparing the relative electric field amplitudes indicates that if we treat a multi-cell cavity as the individual uncoupled cavity cells, the relative stored energy changes by the volume deformation, both electric and magnetic, are not mainly responsible for the FF change of the cavity field. Instead the cell-to-cell coupling plays a major role.

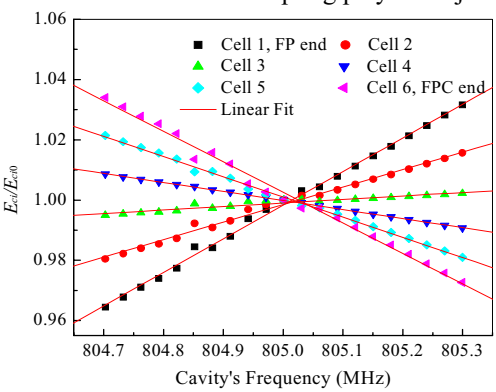

Figure 6: The relative field amplitude change within each individual cell simulated by the ANSYS and SUPERFISH.

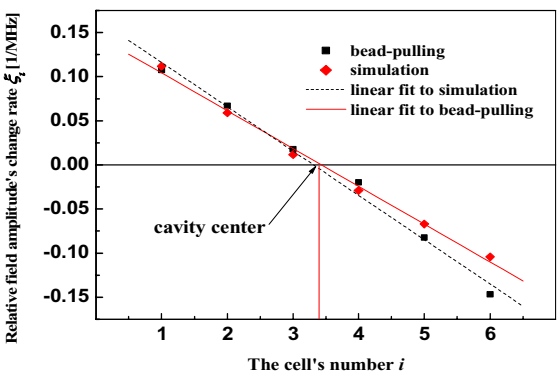

Figure 7: Linear relationship representation of Figure 6 and Equation 5.

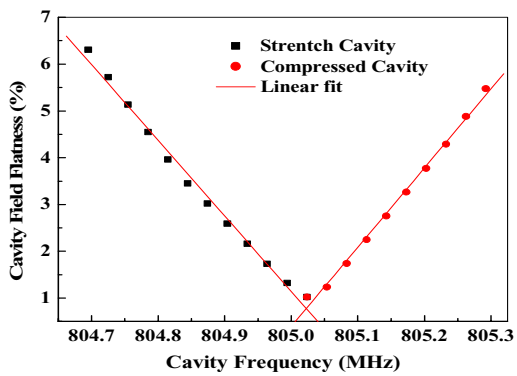

Figure 8: The simulation results of FF change with tuner-tuned frequency. The initial FF at free status is 1.32%.

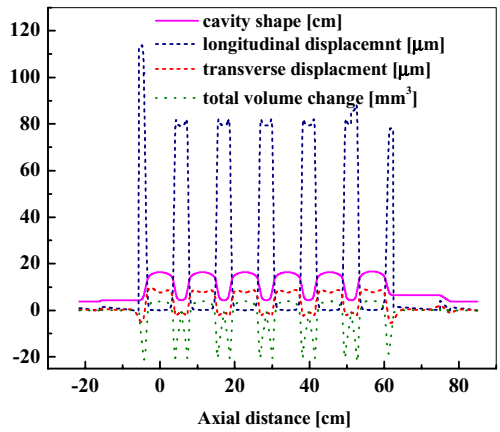

Figure 9: Cavity deformation calculated by ANSYS (and Excel) under a 1.0 mm longitudinal compression.

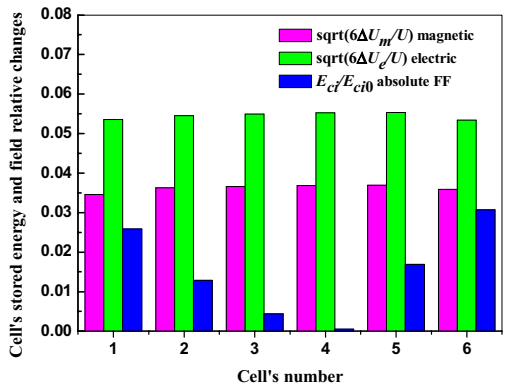

Figure 10: Cavity cell relative electric and magnetic stored energy changes by cavity deformation only after tuner compressed 1.0 mm.

GUIDE TO CAVITY TUNING PROCESS

Based on our analysis above, we can use Equation (5) to estimate the cavity FF change due to the tuner's preload and move into the operation position. We can intentionally over tune the field tilt in the cavity tuning procedure to compensate this later tuner effect.

ACKNOWLEDGEMENTS

The authors would to thank R. Overton for his help on the bead-pulling measurement setup. We also particularly acknowledge S. Kim for his early work on this subject.

REFERENCES

[1] H. Padamsee, et al., RF Superconductivity for Accelerators, John Wiley & Sons, INC. (1998), p. 129.

[2] A. Sun and H. Wang, "Tuner Effect on the FF of SNS Superconducting RF Cavity", JLAB-TN-03-043 or SNS-NOTE-AP119 (2003). http://it.sns.ornl.gov/asd/public/pdf/sns0119/sns0119.pdf

[3] J. Hogan, et al., "Design of SNS Cavity Support Structure", PAC2001, Chicago, IL, (2001), p. 1158.

A 3D SELF-CONSISTENT, ANALYTICAL MODEL FOR LONGITUDINAL PLASMA OSCILLATION IN A RELATIVISTIC ELECTRON BEAM

Gianluca Geloni, Evgeni Saldin, Evgeni Schneidmiller and Mikhail Yurkov
Deutsches Elektronen-Synchrotron (DESY), Notkestrasse 85,
22607 Hamburg, Germany

Abstract

Longitudinal plasma oscillations are becoming a subject of great interest for XFEL physics in connection with LSC microbunching instability [1] and certain pump-probe synchronization schemes [2]. In the present paper we developed the first exact analytical treatment for longitudinal oscillations within an axis-symmetric, (relativistic) electron beam, which can be used as a primary standard for benchmarking space-charge simulation codes. Also, this result is per se of obvious theoretical relevance as it constitutes one of the few exact solutions for the evolution of charged particles under the action of self-interactions.

INTRODUCTION

Longitudinal space-charge oscillations have been treated only from an electrodynamical viewpoint, or using limited one-dimensional models: in this paper we report a fully self-consistent solution to the initial value problem for the evolution of a relativistic electron beam under the action of its own fields in the (longitudinal) direction of motion. The beam is accounted for any given radial dependence of the particle distribution function. For a more detailed description of our work and references see [1]. An initial condition is set so that the beam, which is assumed infinitely long, is modulated in energy and density at a given wavelength. When the amplitude of the modulation is small enough the evolution equation can be linearized. An exact solution can be found in terms of an expansion in (self-reproducing) propagating eigenmodes.

Our theoretical findings constitute one of the few exact solutions known up to date to the problem of particles evolving under the action of their own fields. Yet, particle accelerator and FEL physics make large use of simulation codes to deal with space-charge fields, and these codes are benchmarked against exact solutions of Poisson equation only; recently partial attempts based on one-dimensional theory (which can only give some incomplete result) have been made to benchmark them against some analytical model accounting for the system evolution. We claim that our findings can be used as a standard benchmark for any space-charge code from now on. Our results are of relevance to an entire class of practical problems arising in state-of-the-art FEL technology when (optically) modulated electron beams are feed into an FEL (optical seeding or certain two-color pump-probe schemes): given the parameters of the system, plasma oscillations turn out to be an effect to be accounted for. It is also important to mention the relevance of plasma oscillation theory in the understanding of practical issues like longitudinal space-charge instabilities in high-brightness linear accelerators which may lead to beam microbunching and break up.

[1] E. Saldin et al. Longitudinal Spacs Charge Driven Michrobunching instability in TTF linac, TESLA-FEL-2003-02, May 2003

[2] J. Feldhaus et al. Two-color FEL amplifier for femtosecond-resolution pump-probe experiments with GW-scale X-ray and optical pulses DESY 03-091, July 2003

THEORY

We describe longitudinal plasma waves in a relativistic electron beam assuming that transverse coordinates enter as parameters in the description of fields and particle distribution. Our beam is initially modulated at some wavelength λ_m, in density and energy. It is natural to define the phase $\psi = \omega_m \left(z/v_z(\mathcal{E}_0) - t\right)$, where $v_z(\mathcal{E}_0) \sim c$ is the longitudinal electron velocity at the nominal beam kinetic energy $\mathcal{E}_0 = (\gamma - 1)mc^2$, $\omega_m = 2\pi v_z/\lambda_m$, t is the time and z the longitudinal abscissa. We operate in energy-phase variables (P, ψ), P being the deviation from the nominal energy.

A small energy deviation P is assumed; then the equations of motion for our system can be interpreted as Hamilton canonical equations corresponding to the Hamiltonian $H(\psi, P, z) = e\int d\psi E_z + \omega_m P^2/(2c\gamma_z^2\mathcal{E}_0)$. The bunch density distribution is then represented by $f = f(\psi, P, z; \boldsymbol{r}_\perp)$. Linearization of the evolution equation for f is possible when $f(\psi, P, z; \boldsymbol{r}_\perp)_{|z=0} = f_0(P; \boldsymbol{r}_\perp) + f_1(\psi, P, z; \boldsymbol{r}_\perp)_{|z=0}$, f_0 being the unperturbed solution of the evolution equation with $f_1 \ll f_0$ for any value of dynamical variables or parameters. Moreover we assume $f_0(P; \boldsymbol{r}_\perp) = n_0(\boldsymbol{r}_\perp)F(P)$, where the local energy spread function $F(P)$ is normalized to unity. The initial modulation can be written as a sum of density and energy modulation terms: $f_1(\psi, P, z; \boldsymbol{r}_\perp)_{|z=0} = f_{1d}(\psi, P; \boldsymbol{r}_\perp) + f_{1e}(\psi, P; \boldsymbol{r}_\perp)$ where $f_{1d}(\psi, P, z; \boldsymbol{r}_\perp) = a_{1d}(\boldsymbol{r}_\perp)F(P)\cos(\psi)$ and $f_{1e}(\psi, P, z; \boldsymbol{r}_\perp) = a_{1e}(\boldsymbol{r}_\perp)dF/dP\cos(\psi + \psi_0)$. Here ψ_0 is an initial (relative) phase between density and energy modulation. Finally it is convenient to define complex quantities $\tilde{f}_{1d} = a_{1d}F$, and $\tilde{f}_{1e} = a_{1e}(dF/dP)e^{i\psi_0}$ so that $f_{1_{|z=0}} = (\tilde{f}_{1d} + \tilde{f}_{1e})e^{i\psi} + CC$. Further definition of $\tilde{E}_z = \tilde{E}_z(z; \boldsymbol{r}_\perp)$ in such a way that $E_z = \tilde{E}_z e^{i\psi} + \tilde{E}_z^* e^{-i\psi}$ allows one to write the Vlasov equation linearized in $\tilde{f}_1$:

$$\frac{\partial \tilde{f}_1}{\partial z} + i\frac{\omega_m P}{c\gamma_z^2\mathcal{E}_0}\tilde{f}_1 - e\tilde{E}_z\frac{\partial f_0}{\partial P} = 0\,. \qquad (1)$$

Let us now introduce the longitudinal current density $j_z(z; \boldsymbol{r}_\perp) = -j_0(\boldsymbol{r}_\perp) + \tilde{j}_1 e^{i\psi} + \tilde{j}_1^* e^{-i\psi}$, where $j_0(\boldsymbol{r}_\perp) \simeq$

$ecn_0(\boldsymbol{r}_\perp)$ and $\tilde{j}_1 \simeq -ec\int_{-\infty}^{\infty} dP\tilde{f}_1$. From Eq. (1) follows

$$\tilde{j}_1 = -ec\int_{-\infty}^{\infty} dP\left(a_{1d}F + a_{1e}\frac{dF}{dP}e^{i\psi_0}\right)e^{-i\frac{\omega_m P z}{c\gamma_z^2\mathcal{E}_0}} - ej_0\int_0^z dz'\left[\tilde{E}_z\int_{-\infty}^{\infty} dP\frac{dF}{dP}e^{i\frac{\omega_m P}{c\gamma_z^2\mathcal{E}_0}(z'-z)}\right] . \quad (2)$$

Next we present the equation for the electric field $\tilde{E}_z$ which, coupled with Eq. (2), will describe the system evolution in a self-consistent way.

Starting with the inhomogeneous Maxwell equation for the z-component of the electric field, passing to complex quantities and assuming that the envelope of fields and currents vary slowly enough over the z coordinate (this simply means that we can neglect retardation effects) we have

$$\nabla_\perp^2\tilde{E}_z - \frac{\omega_m^2\tilde{E}_z}{\gamma_z^2c^2} = \frac{4\pi i\omega_m}{\gamma_z^2c^2}\tilde{j}_1 , \quad (3)$$

which forms, together with Eq. (2), a self-consistent description for our system.

Combining Eq. (2) with Eq. (3) and using properly normalized quantities we obtain an integro-differential equation for the field evolution:

$$\hat{\nabla}_\perp^2\hat{E}_z - q^2\hat{E}_z = iq^2\int_{-\infty}^{\infty} d\hat{P}\left(\hat{a}_{1d}\hat{F} + \hat{a}_{1e}\frac{d\hat{F}}{d\hat{P}}\right)e^{-i\hat{P}\hat{z}} - iq^2S_0\int_0^{\hat{z}} d\hat{z}'\left[\hat{E}_z\int_{-\infty}^{\infty} d\hat{P}\frac{d\hat{F}}{d\hat{P}}e^{i\hat{P}(\hat{z}'-\hat{z})}\right] . \quad (4)$$

Definitions of naturally normalized quantities in Eq. (4) are as follows: $\hat{\boldsymbol{r}} = \boldsymbol{r}_\perp/r_0$, $\hat{E}_z = \tilde{E}_z/E_0$, $q = k_m r_0/\gamma_z$, $\hat{P} = P/(\rho\mathcal{E}_0)$, $\hat{a}_{1d} = -eca_{1d}/J_0$, $\hat{a}_{1e} = -ece^{i\psi_0}a_{1e}/(J_0\rho\mathcal{E}_0)$, $\hat{z} = \Lambda_P z$; $\hat{F}(\hat{P})$ is normalized to unity and S_0, the transverse profile function of the beam, obeys $S_0(\mathbf{0}) = 1$. Parameters are the typical transverse size of the beam r_0 , $J_0 = I_0\left[\int S(\boldsymbol{r}_\perp/r_0)d\boldsymbol{r}_\perp\right]^{-1}$, $E_0 = 4\pi J_0/\omega_m$ (where I_0 is the beam current), the plasma wave number $\Lambda_P = \left[4I/(I_A r_0^2\gamma\gamma_z^2)\right]^{1/2}$ ($I_A = mc^3/e$ being the Alfven current), $\rho = \Lambda_p\gamma_z^2/k_m$. Moreover the rms energy spread $\langle(\Delta\mathcal{E})^2\rangle$ can be measured by the dimensionless parameter $\hat{\Lambda}_T^2 = \langle(\Delta\mathcal{E})^2\rangle/\rho^2\mathcal{E}_0^2$ and the dimensionless current densities can be written as $\hat{j}_0 = j_0/J_0 \equiv S_0(\boldsymbol{r}_\perp/r_0)$ and $\hat{j}_1 = \tilde{j}_1/J_0$.

An equivalent description of the system evolution in terms of $\hat{j}_1$ can be obtained using the following result:

$$\hat{E}_z = -\frac{iq^2}{2\pi}\int d\hat{\boldsymbol{r}}_\perp^{(s)}\hat{j}_1K_0\left(q \mid \hat{\boldsymbol{r}}_\perp - \hat{\boldsymbol{r}}_\perp^{(s)} \mid\right) , \quad (5)$$

where K_0 is the modified Bessel function of the second kind. Then, substitution in Eq. (2) and use of normalized quantities yield:

$$\hat{j}_1 = \int_{-\infty}^{\infty} d\hat{P}\left(\hat{a}_{1d}\hat{F} + \hat{a}_{1e}\frac{d\hat{F}}{d\hat{P}}\right)e^{-i\hat{P}\hat{z}} + \frac{iq^2}{2\pi}S_0\int_0^{\hat{z}} d\hat{z}'\left[\int d\hat{\boldsymbol{r}}_\perp^{(s)}\hat{j}_1K_0\left(q \mid \hat{\boldsymbol{r}}_\perp - \hat{\boldsymbol{r}}_\perp^{(s)} \mid\right)\times\int_{-\infty}^{\infty} d\hat{P}\frac{d\hat{F}}{d\hat{P}}e^{i\hat{P}(\hat{z}'-\hat{z})}\right] . \quad (6)$$

Eq. (4) is particularly suitable for analytical manipulations, while Eq. (6) can be used better in case of a numerical approach.

MAIN RESULT

After introduction of the Laplace transform of $\hat{E}_z$, $\bar{E}(p, \hat{\boldsymbol{r}}_\perp)$, with $Re(p) > 0$, it follows from Eq. (4) that

$$\mathcal{L}\bar{E} = f \quad \text{with :} \quad (7)$$

$$\mathcal{L} = \hat{\nabla}_\perp^2 + \hat{g}(\hat{\boldsymbol{r}}_\perp, p) , \quad (8)$$

$$f(\hat{\boldsymbol{r}}_\perp, p) = iq^2\left(\hat{D}_0\hat{a}_{1d} + \hat{D}\hat{a}_{1e}\right) , \quad (9)$$

$$\hat{g}(\hat{\boldsymbol{r}}_\perp, p) = -q^2(1 - i\hat{D}S_0) , \quad (10)$$

$$\hat{D}_0 = \int_{-\infty}^{\infty} d\hat{P}\frac{\hat{F}}{p + i\hat{P}} , \quad \hat{D} = \int_{-\infty}^{\infty} d\hat{P}\frac{d\hat{F}/d\hat{P}}{p + i\hat{P}} \quad (11)$$

with the boundary conditions $\bar{E} \longrightarrow 0$ for $|\hat{\boldsymbol{r}}_\perp| \longrightarrow \infty$ and $\partial\bar{E}/\partial\hat{\boldsymbol{r}}_\perp \longrightarrow 0$ for $|\hat{\boldsymbol{r}}_\perp| \longrightarrow \infty$. Solution is found when we find a Green function $\bar{G}$ such that $\bar{E} = \int d\hat{\boldsymbol{r}}'_\perp\bar{G}(\hat{\boldsymbol{r}}_\perp, \hat{\boldsymbol{r}}'_\perp)f(\hat{\boldsymbol{r}}'_\perp)$.

Assuming, without prove, completeness and discreteness of the spectrum of $\mathcal{L}$ (we ascribe to alternative theoretical approaches and numerical techniques the assessment of the validity region of this assumption) we can expand $\bar{G}$ using the eigenfunction of $\mathcal{L}$ defined by $\mathcal{L}\Psi_j = \Lambda_j\Psi_j$ thus getting

$$\bar{E} = \sum_j\frac{\Psi_j(\hat{\boldsymbol{r}}_\perp)}{\Lambda_j}\int d\hat{\boldsymbol{r}}'_\perp\Psi_j(\hat{\boldsymbol{r}}'_\perp)f(\hat{\boldsymbol{r}}'_\perp) . \quad (12)$$

To find $\hat{E}_z$ we use the inverse Laplace transformation and we perform the integration analytically with the help of Jordan lemma. We write results in a general form, but this method is straightforward only in the case of a cold beam $\hat{F} = \delta(\hat{P})$ that will be the only one considered here. Our final result is written as follows:

$$\hat{E}_z(\hat{z}, \hat{\boldsymbol{r}}_\perp) = \sum_j u_j\Phi_j(\hat{\boldsymbol{r}}_\perp)e^{\lambda_j\hat{z}} , \quad (13)$$

$$u_j = \frac{\int d\hat{\boldsymbol{r}}'_\perp\Phi_j(\hat{\boldsymbol{r}}'_\perp)f(\hat{\boldsymbol{r}}'_\perp, \lambda_j)}{\left[\int d\hat{\boldsymbol{r}}'_\perp\left(\frac{\partial g}{\partial p}\right)\Psi_j^2\right]_{p=\lambda_j}} . \quad (14)$$

The modes Φ_j are not orthogonal. Appropriate initial conditions can be chosen to obtain a single propagating mode at *fixed* values of j, namely:

$$\frac{\hat{a}_{1e}}{\hat{a}_{1d}} = -i\lambda_j \ , \quad \hat{a}_{1d} = (\hat{\nabla}_\perp^2 - q^2)\Phi_j . \quad (15)$$

From now on we will deal with case of an axis-symmetric beam described using a cylindrical coordinate system $(\hat{r}, \phi, \hat{z})$, with obvious meaning of symbols. It is convenient to discuss azimuthal harmonics of $\hat{j}_1$, $\hat{E}_z$ and f which will be indicated with $\hat{j}_1^{(n)}(z, \hat{r})$, $\hat{E}_z^{(n)}(\hat{z}; \hat{r})$ and $f^{(n)}(\hat{r}, p)$. Our results Eq. (13) and Eq. (14) take the simpler form:

$$\hat{E}_z^{(n)}(\hat{z}, \hat{r}) = \sum_j u_{nj}\Phi_{nj}(\hat{r})e^{\lambda_j^{(n)}\hat{z}} , \quad (16)$$

$$u_{nj}(\hat{r}) = \frac{\int_0^\infty d\hat{r}'\hat{r}'\Phi_{nj}f^{(n)}(\hat{r}',\lambda_j^{(n)})}{\left[\int_0^\infty d\hat{r}'\hat{r}'\left(\frac{\partial g}{\partial p}\right)\Psi_{nj}^2\right]_{p=\lambda_j^{(n)}}} . \quad (17)$$

We give here some explicit calculations for several profile cases.

Stepped profile - In this case $S_0 = 1$ for $\hat{r} < 1$ and $S_0 = 0$ for $\hat{r} \geq 1$. Putting $\alpha_j^2 = -q^2(1 + 1/{\lambda_j^{(n)}}^2)$ we obtain the eigenvalue equation:

$$\alpha_j J_{n+1}(\alpha_j)K_n(q) - qK_{n+1}(q)J_n(\alpha_j) = 0 . \quad (18)$$

It turns out that $\lambda_j^{(n)}$ are imaginary and such that $-1 < Im(\lambda_j^{(n)}) < 1$. The solution for the evolution equation is:

$$\hat{E}_z^{(n)}(\hat{z},\hat{r}) = \begin{cases} \sum_j u_{nj}J_n(\alpha_j\hat{r})e^{\lambda_j^{(n)}\hat{z}} & \hat{r} < 1 \\ \sum_j u_{nj}\frac{J_n(\alpha_j)}{K_n(q)}K_n(q\hat{r})e^{\lambda_j^{(n)}\hat{z}} & \hat{r} \geq 1 \end{cases} , \quad (19)$$

$$u_{nj} = \frac{K_n(q)\int_0^1 d\xi J_n(\alpha_j\xi)\xi f^{(n)}(\xi)}{J_n(\alpha_j)\frac{d}{dp}\left[\alpha J_{n+1}(\alpha)K_n(q) - qK_{n+1}(q)J_n(\alpha)\right]_{p=\lambda_j^{(n)}}} , \quad (20)$$

where $\alpha_j^2 = -q^2(1 + 1/p^2)$.

Parabolic profile - In this case $S_0(\hat{r}) = 1 - k_1^2\hat{r}^2$ for $\hat{r} < 1/k_1$ and $S_0 = 0$ for $\hat{r} \geq 1/k_1$. Solution for the homogeneous problem defined by $\mathcal{L}$ can be found in literature (see [1] for references). We can use that solution in order to solve our eigenvalue problem, and to write the expressions for the eigenfunctions Ψ_{nj} to be inserted in Eq. (13). Let us introduce the following notations: $\mu^2 = i\hat{D}q^2 - \Lambda_j^{(n)}$, $\delta^2 = i\hat{D}K_1^2$, $d^2 = \Lambda_j^{(n)}$, $\epsilon = (n+1)/2 - \mu^2/(4\delta)$. After some calculation we find:

$$\Psi_{nj}(\hat{r}) = \begin{cases} \hat{r}^n e^{-\delta\hat{r}^2/2}\ {}_1F_1(\epsilon, n+1, \delta\hat{r}^2) & \hat{r} < 1 \\ e^{-\delta/2}\ {}_1F_1(\epsilon, n+1, \delta)\frac{K_n(d\hat{r})}{K_n d} & \hat{r} \geq 1 \end{cases} . \quad (21)$$

where ${}_1F_1$ is the confluent hypergeometric function, and the eigenvalue equation analogous of Eq. (18) is now

$$\delta K_n(d)\left[2\epsilon(n+1)^{-1}\ {}_1F_1(\epsilon+1, n+2, \delta) - {}_1F_1(\epsilon, n+1, \delta)\right] + dK_{n+1}(d)\ {}_1F_1(\epsilon, n+1, \delta) = 0 . \quad (22)$$

Multilayer method approach - An arbitrary gradient axisymmetric profile can be approximated by means of a given number of stepped profiles, or layers, superimposed one to the other. Results for the stepped profile case can be then used to construct an algorithm to deal with any profile (see [1] for more details).

ALGORITHM FOR NUMERICAL CALCULATIONS

The linear regime assumption is not too restrictive but it would be interesting to provide a solution for the full problem. As a first step towards this goal we present here a numerical solution of the evolution equation in the case of an axis-symmetric beam, that we cross-checked with our main result, Eq. (13). In order to build a numerical solution it turns out convenient to make use of Eq. (6).

After some manipulations Eq. (6) yields:

$$\frac{d^2\hat{j}_1^{(n)}}{d\hat{z}^2} = -q^2 S_0 \int_0^1 d\hat{r}'\hat{r}' G^{(n)}\hat{j}_1^{(n)} , \quad (23)$$

where

$$G^{(n)}(\hat{r},\hat{r}') = \begin{cases} I_n(q\hat{r})K_n(q\hat{r}') & \hat{r} < \hat{r}' \\ I_n(q\hat{r}')K_n(q\hat{r}) & \hat{r} > \hat{r}' \end{cases} , \quad (24)$$

Eq. (23) is to be considered together with proper initial conditions for $\hat{j}_1$ and its z-derivative at $z = 0$. The interval $(0, 1)$ can be then divided into an arbitrary number of parts so that Eq. (23) is transformed in a system of the same number of 2nd order coupled differential equations to be solved numerically. This gave us the solution of the evolution problem in terms of the beam current. Then we calculated back $\hat{E}_z$ and we compared obtained results with Eq. (13) for different choices of transverse profiles. The real field E_z should be recovered but all relevant information is included in $Re(\hat{E}_z)$. We calculated $Re(\hat{E}_z)$ as a function of $\hat{z}$ and $\hat{r}$ in several cases (see [1]). Comparison with the Runge-Kutta integration program were performed (see [1]) and gave a perfect agreement. Finally we actually verified that selecting a single mode by fixing appropriate initial conditions as described in Eq. (15) is possible (see, again, [1]).

CONCLUSIONS

In this paper paper we presented one of the few self-consistent analytical solutions for a system of charged particles under the action of their own electromagnetic fields. Namely, we considered a relativistic electron beam under the action of space-charge at given initial conditions for energy and density modulation and we developed a fully analytical, three-dimensional theory of plasma oscillations in the direction of the beam motion in the linear regime. We specialized the general method to the important cases of stepped and parabolic transverse profiles, which are among the few analytically solvable situations. In particular, the stepped profile case could be used to develop a semi-analytical technique to solve the evolution problem for the field using an arbitrary transverse shape. We also developed an algorithm able to solve the evolution problem in terms of the beam currents. Numerical and analytical or semi-analytical solutions for the fields were then compared and gave a perfect agreement. Finally we showed how to build up initial conditions in such a way that a single mode is excited and propagates through and we checked our prescription by setting up particular initial conditions and looking at the propagation of various eigenmodes.

REFERENCES

[1] G. Geloni, E. Saldin, E. Schneidmiller and M. Yurkov, DESY 04-112, see http://xxx.lanl.gov/abs/physics/0407024

COLD TESTS OF A 160 MHZ HALF-WAVE RESONATOR

R.Stassen#, R.Eichhorn, F.M.Esser, B.Laatsch, R.Maier, G.Schug, H.Singer, FZ Juelich, Germany

Abstract

A new linac was projected based on superconductive half-wave resonators to fill the COoler SYnchrotron COSY Juelich up to the space charge limit.

The first prototype of a 160 MHz HWR has been built and tested. RF measurements in CW as well as in a pulsed operation will be presented. A second prototype with a slightly different way of fabrication will be completed soon.

All measurements have been performed using the 4 kW loop-coupler that was here developed especially for the HWR linac. The use of a cold window allows to change the coupling from $1*10^6$ to $1*10^{10}$ without any risk of contamination. The mechanical tuner consisting of a stepper-motor-driven coarse tuner and a fast piezo system has successfully integrated into the vertical test-cryostat. The piezos also allow to compensate for the Lorentz-force detuning.

HALF-WAVE RESONATORS

The design of the HWRs was dominated by the parameters of a linac concept to fill the synchrotron COSY at FZ-Juelich with polarized protons and deuterons up to the space charge limit [1].

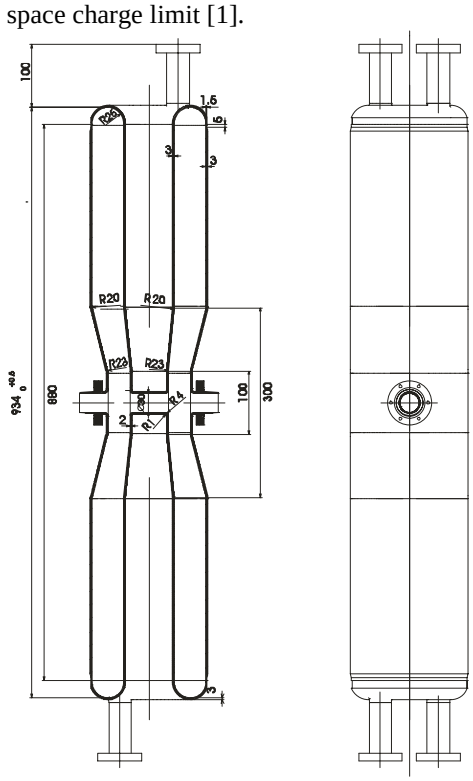

Figure 1: Layout of 160 MHz HWR.

Two prototypes had been ordered at different companies and show slight changes basically at the end-plates (fig. 2). These changes have no impact on the cavity parameters that are summarized in table 1.

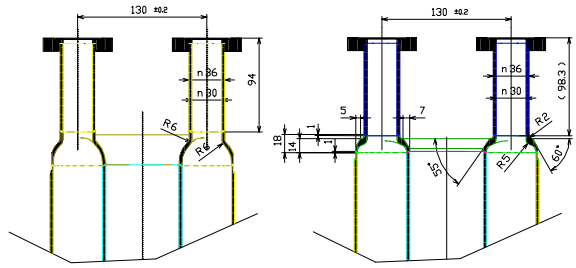

Figure 2: Different end-plate geometries of the HWRs.

Table 1: Main parameters of 160 MHz HWRs related to an accelerating length of $l = ß\lambda$

β	0.11
R/Q in Ohm	249
B_{peak}/E_{avg} in mT/MV/m	10.4
E_{peak}/E_{avg}	4.2
E_{avg} in MV/m peak	8

The first prototype of the 160 MHz HWRs was tested at room temperature prior to any chemical treatment. Figure 3 shows the good conformity of the field profiles measured and calculated by the simulation tool CST-MicroWaveStudio MWS [2].

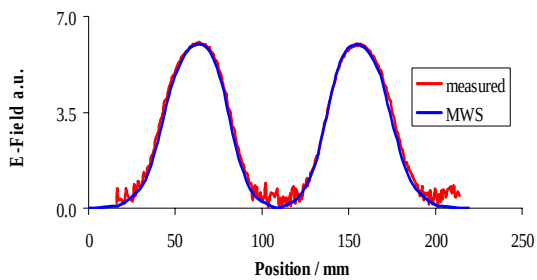

Figure 3: Field profiles, measured and calculated.

The measurements of the resonant frequency during the production process and each step towards operation (like pumping, cool-down and tuning-sensitivity) agree to the simulations [3].

Coupler

The coupler design differs from normally used concepts for superconducting cavities. One of the cavity access-ports, which are required for a good preparation of the cavity surface, has been chosen to hold the RF main coupler. The coupling is essentially magnetic via a current loop. It is variable and has been designed to match the beam-current as well as the unloaded cavity for an on-line

#r.stassen@fz-juelich.de

precise measurement of the unloaded Q_0. The coupling can be changed to give an external Q_{ext} ranging from $1*10^6$ to $1*10^{10}$ at a pulsed RF-power of at least 4 kW [4].

Cold Vase Window

A cold ceramic window is used in order to preserve the cavity from entering dust during the change of the coupling strength, which could spoil the superconducting surface [5]. This window (fig. 4) – installed in the clean room - separates the cavity vacuum from the insulation vacuum of the cryostat and splits up the coupler mechanism from the prepared cavity.

Figure 4: Cold window before (right) and after Ge plating.

The ceramic surface has been coated to protect the window from static discharges and to lower the multi-pacting effects on the ceramic surface. For this coating, undoped amorphous Ge has been chosen because of its very low secondary emission coefficient, the stability, the thermal match and the moderate energy gap. The basic parameters of the Ge film are summarized in tab. 2.

Table 2: Basic parameters of the cold window

Flange material	Ti 3.7035
Cearmic material	Aluminia F99,7 (HF)
Film material	Amorphous Ge
Film thickness	80nm
DC square resist. (300K)	50 MOhm
Estimated DC sq. resist. 4.2K, 1MV/m	1E18 Ohm
4.2K, 20MV/m	1E9 Ohm
Estimated RF sq. resist. 4.2K, 160MHz	3E8 Ohm

Tuner

The layout of the mechanical tuner is shown in fig. 5. The construction with a small horizontal dislocation allows an installation into the cryostat combining two cavities [5]. No additional length in longitudinal direction is required keeping the design of the cryomodule compact. The actuating mechanics of the tuner for each HWR consists of two parts: a stepper motor driving the coarse tuner and a piezo fine tuner, both mounted outside the cryostat allowing easy access for maintenance. The possible change in length of the piezos is about +120µm. A gear of 1:7 minimizes the microphonic effects of the long tuning rods and lowers the tuning forces. The resulting strain of the cavity is sufficient to compensate for the Lorentz-force detuning during the pulsed operation.

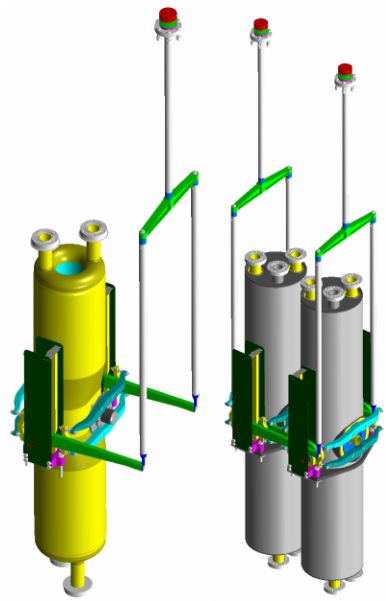

Figure 5: Tuning system and mounting position of a pair of cavities inside the cryostat.

The high sensitivity of the stepper motor system of about 1.2 Hz / step allows a frequency control based only on this stepper motor, corresponding to a frequency-change rate of 2.4 kHz / s.

The behaviour of the tuner mechanism shows a small hysteresis loop. This hysteresis does not affect the reaction of the resonant frequency control system, but can evoke a mechanical resonance when changing the direction of movement. Further investigations are undertaken to analyse this mechanical resonance in the final cryostat.

Cavity Preparation

A commercially available standard procedure has been used to get a chemical preparation of this prototype. The special high-pressure water-rinsing through the access ports at the bottom and top flanges of the HWR prototype guaranteed an optimized cleaning of the surfaces. Details of the preparation are summarized in the following list:

- 60µm BCP chemical etching in a temperature-controlled closed loop operation
- 60µm BCP after a 180° rotation of the cavity
- HPR through all of the four access-ports
- Drying by pumping
- Baking at 100° C for 4 hours
- Pumping to $1*10^{-5}$ mbar

The cavity, prepared in this manner, was cooled down to 4 K in a vertical bath cryostat without further pumping of the cavity vacuum.

CAVITY OPERATION

A first multi-pacting (MP) level occurred at the low RF level of about 2mW and a loaded Q_L of 1E7. This MP

barrier is located at the flat region near the beam ports. It needed at least about 2 weeks of different conditioning methods before the MP barrier was exceeded. Further multi-pacting has not been observed up to an accelerating gradient of more than 7 MV/m. The first measurement of the cavity performance, taken at CW operation is presented in fig. 6. The cavity quenched at 6.2 MV/m at CW operation, but reached up to 7.3 MV/m at pulsed mode.

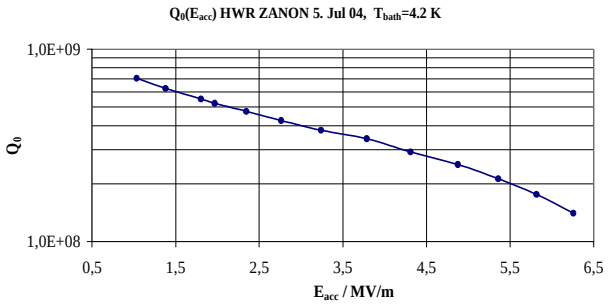

Figure 6: First Q_0- versus E_{acc} measurement.

While operating the cavity at high field, a huge dose of x-rays has been measured. The x-ray spectrum verifies the existence of high field-levels by an independent measurement. The center energy of 200 keV corresponds roughly to the accelerating fieldgradient of 6 MV/m.

Pulsed Operation

The concept of a new injector for COSY was based on a pulsed operation at a repetition rate of 2 Hz and a beam duration of 500 µs, having some impact on the cavity operation and control.

Fig. 7 shows the measurement of the Lorentz force-detuning (LFD) at a pulsed operation and the linear approximation. The resulting Lorentz-force constant of 6 Hz /(MV/m)² is about six times higher compared to the simulations [6].

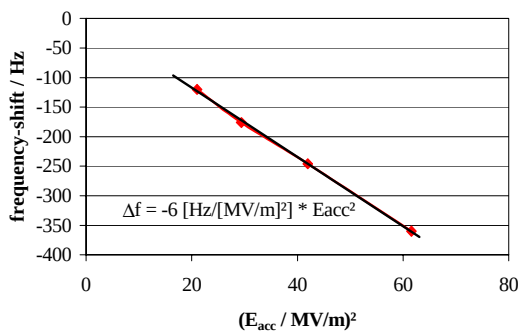

Figure 7: Measured Lorentz-force detuning.

The detuning itself stays within the operating range of the fast piezo-system, but the high rising time required for an overall compensation of the LFD limits the use of the piezos.

Mechanical resonances play an important role in the pulsed operation of a superconducting cavity, especially in the presented HWR. The most significant mechanical resonance has been found at 230 Hz (fig. 8).

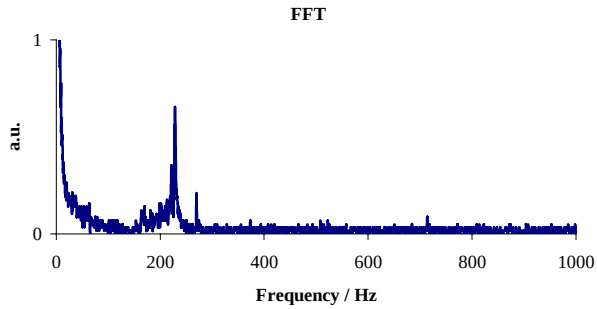

Figure 8: Fast Fourier Transformation of phase-detector signal as response to a 50V step function at the piezos.

This resonance is far away of the pulse repetition rate and 50Hz or 100Hz AC-ripple, but first measurements have shown that this resonance can easily be excited by subharmonics and fast frequency changes of the resonance-frequency control loop.

OUTLOOK

The results gained from the fist prototype cavity are very promising. The design gradient of 6 MV/m (goal 1) has been exceeded during the first test. Achieving the even more demanding goal 2 (8 MV/m in pulsed operation) seems to be within reach.

The final length of the second prototype cavity had been fixed and the last e-beam weldings have been done. The chemical preparation will start at beginning of September and testing will take place in fall. Comparable results, relating to the different behaviours of the slightly different geometries and fabrication processes will be available by the end of the year.

The first promising results of compensating the LFD by the piezo fine-tuner will be verified during the next month regarding the behaviour of the mechanical resonances in the pulsed operation foreseen for a possible new COSY-injector.

REFERENCES

[1] R. Toelle et al., A Superconducting Injector Linac for COSY, Proc. EPAC2002, Paris, 2002.

[2] http://www.cst.de , MicroWaveStudio, Simulation software.

[3] R. Stassen et al., First results of pulsed superconducting Half-Wave-Resonators, Proc. EPAC2004, Luzern, Switzerland, 2004.

[4] G. Schug, H. Singer, R. Stassen, The adjustable RF main coupler for the superconducting COSY Linac cavities, FZJ/IKP Annual Report 2002, Juelich, 2002.

[5] R. Eichhorn et al., Development of a pulsed Light Ion Accelerator Module based on Half-Wave Resonators, Proc. SRF2003, Luebeck, 2003.

[6] R. Maier et al., The superconducting injector linac for the cooler-synchrotron COSY at FZ-Juelich, Proc. LINAC2002, Korea, 2002.

Electro Polishing of Niobium Cavities at DESY

A.Matheisen, L. Lilje, H.Morales, M.Schmökel, B. Petersen, N. Steinhau-Kuehl,
Deutsches Elektronen Synchrotron DESY, Hamburg, Notkestraße 85, 22602 Hamburg, Germany

Abstract

At DESY a facility for electro polishing (EP) of the super conducting (s.c.) TESLA/TTF cavities has been built and is operational since summer 2003. The EP infrastructure is capable to handle single - cell structures and the standard TESLA/ TTF nine - cell cavities.

Several electro polishing processes have been made since and acceleration voltage up to 40 MV/m have been reached in nine cell structures. We report on measurements and experiences gained since 2003 as well as on handling procedures developed for the preparation of electro polished resonators. Specific data like heat production, variation of current density and bath aging will be presented. Another important point for reproducible results is the quality control of the electro polishing process.

INTRODUCTION

At DESY an electro-polishing stand (EPS) was built in 2003 [1;2;3]. According to the good experiences gained with electro polishing (EP) at KEK and CERN, constant voltages and a mixture of 9 volume parts of sulphuric acid (96%) and 1 part fluoric acid (48%) are chosen for the baseline parameters set of the EP process [3].

A total of 14 cavities are electro polished since summer of 2003. Voltages of 14 to 18 V have been tested. The well-established handling procedures for cavities processes with buffered chemical polishing (BCP) had to be changed to meet the needs of EP resonators. On three single cell and one 9-cell resonator acceleration voltages up to 40 MV/m are reached using the DESY EP set up and adapted handling procedures. During the EP processes all relevant parameters are monitored and stored for documentation. From these data set's a first analysis is made to find system parameters, gain online analysis of the process and find parameter sets for reproducible high gradient resonator preparation.

ELECTRO POLISHING INFRASTRUCTURE

The DESY EP set-up (EPS) is designed as a closed loop acid circuit with one acid supply barrel of about 150 –180 l storage volume, the cavity rotating horizontally on the EPS bench and a heat exchanger in line [1]. The acid is pumped into the resonators via the pure aluminium cathode and is distributed homogenously into the 9 cells via holes with adopted diameters. Main parameters to determine the EP process are the acid volume sent into the resonator (Q), the temperature at the inlet of the electrode (T3), the temperature at the cavity outlet (T4), the current (I) and the current oscillation (dI).

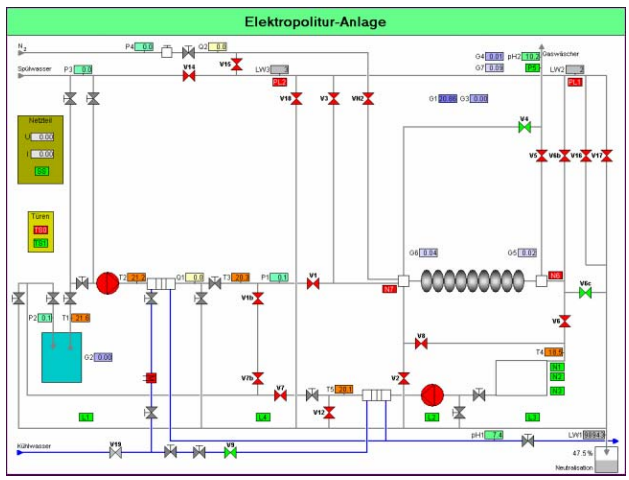

Figure 1: Flow chart of the DESY electro polishing infrastructure.

All other are Sensors are mainly installed to control the safety of the system and the automated process sequences [2] (Figure 1).

PROCEDURES

The procedures in use for processing the EP cavities are close to the once, which are well established for BCP cavities [6]. For safety reasons the EPS is located outside of the DESY TTF cleanroom. To enter the cleanroom after EP, the cavities have to under go an additional cleaning procedure by rough outside surface cleaning (solvent + DI water rinse at 80 bars pressure), ultrasonic cleaning and rinsing with ultra pure water (R=>18 Mohm cm, particle filtered to <= 0,2 µm). The number of high-pressure water (HP) rinses, following the assembly procedure, is increased from 2 to 6 rinses. Assembly and RF test at 2 K as well as heat treatment at 800 C resp. 1400 C (post purification) are identical to the standard BCP treatments. Up to now no technical solution for EP of cavities dressed with the helium vessel is available. The procedures for tank welding and tuning of cavities are modified and are still under investigation and optimization. The cavities, vented to normal pressure by argon gas are sealed inside the cleanroom and stay hermetically closed during electron beam welding (Nb cone to Ti connections) as well as during tuning of the field profile and tank welding by TIG weld. Major item developed for this process is a new flange system with

integrated bead pull and the RF antennas. This equipment stays with the cavity during all processes until the final HPR rinse before installation of the RF power coupler.

PARAMETERS OF THE EP PROCESS AT DESY

Until now a total of 14 cavities in about 163 hours have been electro polished in 6 runs (1 run = 1 barrel of 145 to 180 l of EP acid). Voltages of 16 to 18 V have been applied and tested. Average removal rates of 0.4 µm/min and current densities of 5,6 A/dm^2 have been measured.
For the DESY EPS 17 V as nominal voltage and a process temperature range of 28 to 34 C^o is established. At this work point the temperature of the acid can be controlled best and the available cooling power is reasonable. An extreme high out gassing of the hydro fluoride (hf) gases, starting when the cavity is rotating, is observed. A change in hf gas absorber lay out was necessary to handle the outgasing. Continuous runtimes of up to 4 hours for removal of niobium before oven treatments and 2 hours for the final preparation are established and can be handled in one shift.
Up to 13 gram of niobium can be dissolved in one liter of acid before the oscillation reduces and the system leaves the plateau of the EP polarogram [3].

RF TEST RESULTS

Three single- and 8 TTF multi-cell cavities have been EP processed and tested at 2 K in vertical tests (Table 1). The single cell cavities, pre-tested in the single-cell test program [4], reached acceleration gradients of 35 to 40 MV/m (Figure 2).

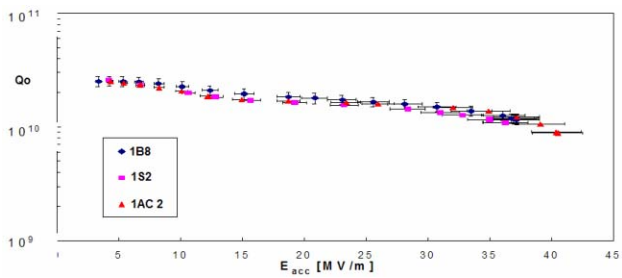

Figure 2: Test results (Qo vs. Eacc) of single cell cavities EP processed at DESY.

Four nine cell cavities (AC 70;71;74;78) that did not meet the high gradient goal of 35 MV/m in the KEK / DESY EP test sequences and were re-polished at DESY. Most cavities showed high quality factors and acceleration voltage improvement's. AC 71 and 74 were limited by field emission, origin from a defect filter cartridge in the HP rinse line. AC 71 improved its gradient from 19 MV/m (field emission loaded) to 38 MV/m after 23 µm EP and 120 C baking (Figure 3). This cavity was successfully welded into the He vessel and showed 38 MV/m acceleration gradient without field emission limitation in the horizontal test as well [5].

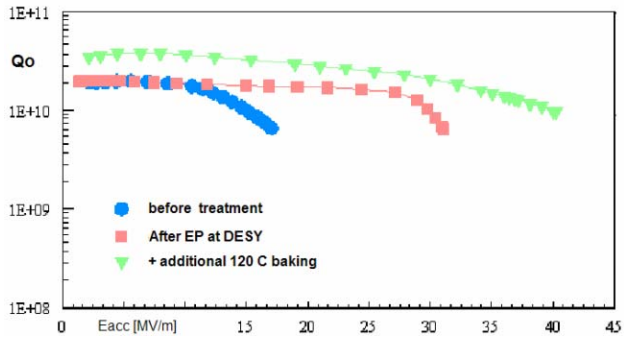

Figure 3: RF test results (Qo vs. Eacc) of AC 70.

Even after removal of about 40 µm the resonator AC 78 did not recover from a surface damage appearing during handling for tank welding. The resonator AC 80, made from hang over material of the last cavity production showed 28 MV/m acceleration gradient and is limited by quench. The prototype resonator p-1, in use since 10 years now, was recovered to 25 MV/m by electro polishing at DESY.

Table 1: RF test results of cavities EP processes at DESY

Cavity	Eacc [MV/m] before EP	Eacc [MV/m] after EP	+120 C baking	Q0 @23,5 mV/m	Limit
1b8	28	33,59	38	1,7E10	Breakdown
1s2	31,5	31,5	36,6	1,5E10	Breakdown
1ac 2	34,8	31,5	40,5	1,7 E10	Breakdown
ac 78	15,3	-	23,7	2,9E10	Breakdown
ac 78	20,7	15	-	1,7E10	Breakdown
p-1	0,5	10,6	-	7,6E8	Power
p-1	10,6	25,3	-	1,4E10	Breakdown
ac 70	19	30	39,4	1,7E10	Breakdown
ac 80	0,5	27,5	-	1,7E10	Breakdown
ac 80	27,5	28	-	1,6E10	Breakdown
ac 71	31,5	29		1,2E10	Field emission
ac 74	28	19,8		6E9	Field emission

OBSERVATIONS

The data analyzed from the EP data logging so far show a stronger relation ship between the current (I), establishing at the given voltage, the acid volume (Q) passing the cavity and the temperature measured at the cavity outlet

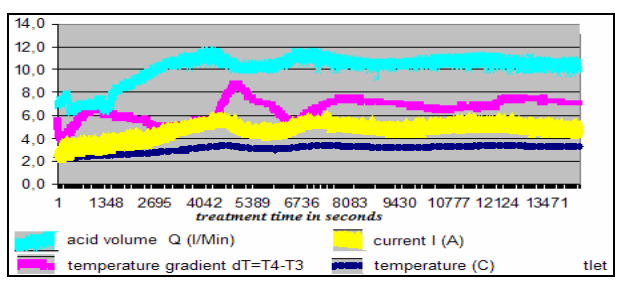

Figure 4: Example for correlation of I;T4; dT and Q.

(T4). The temperature gradient dT = T4 – T3 (T3= Temperature at Cavity inlet) seems to be of secondary order for the process (Figure 4). The linear relation

$$Y = \frac{I}{Q * T4} \qquad (1)$$

seems to be a good indicator for parameter settings of the EPS (Figures 5a-c). Wrong parameter setting and irregularities during the process show a non-linear behavior (Figure 5b). New acid shows higher temperatures

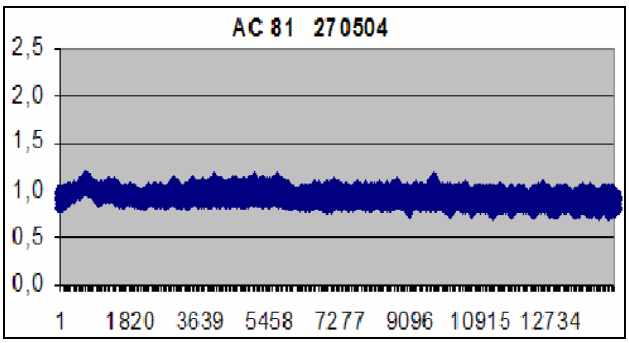

Figure 5a: Y parameter vs. time with correct settings.

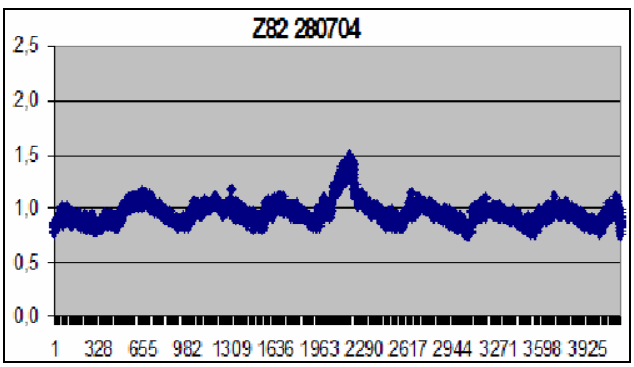

Figure 5b: Y parameter vs. time for wrong setting of N2 overflow.

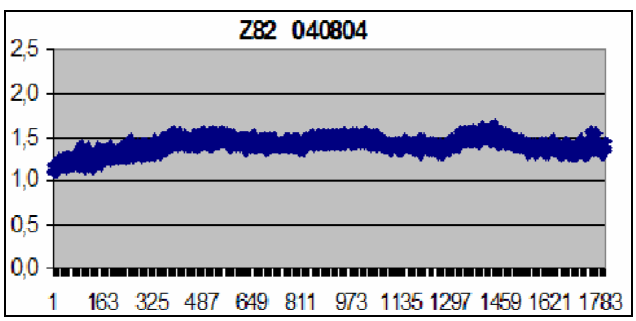

Figure 5c: Y parameter vs. time for correct setting and new acid.

resulting in a scaling factor Y of 1.2 to 1,5 (Figure 5c), while used acid shows, with same parameter setting, Y value of 0,8. The process parameters chosen for the EP are related to a plateau in the PE polarogram where current oscillation establishes [3]. Aging effects in the acid mixture may be indicated by the relation of the average current (I aver.[A]), the average of maximum current amplitude (Imax aver.[A]) and average of minimum current amplitude (Imin aver.[A]) during oscillation in a given time interval. This parameters show

$$Z\max(t1-t2) = \frac{I(\max.aver.)}{I(aver.)} \quad (2)$$

$$Z\min(t1-t2) = \frac{I(\min.aver.)}{I(aver.)} \quad (3)$$

a reduced oscillation with increasing use time and increasing amount of niobium dissolved in the acid (Figures 6a;b).

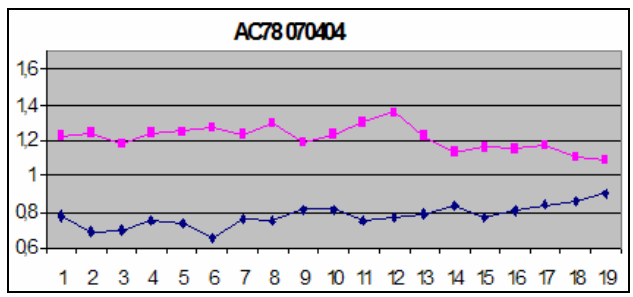

Figure 6a: Z max (red) and Z min (blue) parameter vs. time interval for new acid.

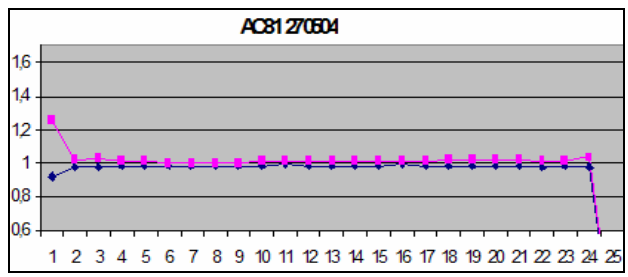

Figure 6b: Z max (red) and Z min (blue) parameter vs. time interval for used acid (10 gr. Nb dissolved per l acid).

REFERENCES

[1] K.Escherich et. al. “Electro-polishing at DESY, a set up for multi-cell resonator treatment” Proceedings of the SRF workshop 2001 Tsukuba , Japan

[2] H.Morales et. al. “Engineering solutions for the electro polishing of multi-cell superconducting accelerator structures” Proceedings of the SRF workshop 2001 Tsukuba , Japan

[3] N.Steinhau-Kühl et. al. “ Basic studies for the electro polishing facility at DESY” Proceedings of the SRF workshop 2001 Tsukuba , Japan

[4] D.Reschke DESY Hamburg priv. Communication

[5] L.Lilje this conference

[6] T.Ebeling et. al. “Processing of TTF cavities at DESY” Proceedings of the SRF workshop 2003 Travemünde, Germany

OVERVIEW OF LINEAR COLLIDER TEST FACILITIES AND RESULTS

H. Hayano, High Energy Accelerator research organization (KEK), Tsukuba, Japan

Abstract

In order to promote realization of Linear Collider (LC), the formation of international co-operation for unified LC design and efficient R&D share are thought to be necessary. As a first step of this co-operation, the International Technology Recommendation Panel (ITRP) will recommend a technology for the global LC design to the International Linear Collider Steering Committee (ILCSC). Towards this recommendation, many efforts of the developments and the output results of each technology have been made to satisfy the requirements of the technical review committee report (TRC)[1]. The test facilities of each LC design are the place of the key technology demonstration and realization. The summarized overview of the LC test facility activities and outputs of TTF, NLCTA, ATF&GLCTA and CTF will give information of LC technology direction.

INTRODUCTION

Major laboratories in the world began to start LC developments in late 1980s. LC workshop and many related workshop have been held from that time, having R&D information exchange and design review. After about 15 years R&D, LC designs of each laboratory became more realistic based on the demonstrations of technologies in their test facilities. The test facilities in this overview are the active facilities conducted by the leading laboratories. By the order of the main linac frequency, TTF (TESLA Test Facility) conducted by DESY, NLCTA (NLC Test Accelerator) conducted by SLAC, ATF (Accelerator Test Facility)&GLCTA (GLC Test Accelerator) conducted by KEK, and CTF (CLIC Test Facility) conducted by CERN, are briefly summarized in this text.

TESLA TEST FACILITY (TTF)

The TTF at DESY includes infrastructure labs and shops for superconducting cavity treatment, test stands and the accelerator module assembly and a test linac for an integrated system test of the TESLA[2] accelerator prototype with beam. The functions of this facility are development of accelerating module compatible to TESLA, integrated system test of the TESLA linac components with beam and application of SASE FEL in the VUV wavelength regime[3]. The performance of the TESLA superconducting cavities are well advanced by the electro-polishing (EP) processing as well as chemical etching of the inner surfaces, high temperature treatment at 1400degC, and high pressure rinsing with ultra-pure water. The design gradient 23.8 MV/m has been attained on average with cavities of the standard treatment. By application of new EP method to 9-cell cavities, another 6 cavities have reached gradients between 31 and 35 MV/m. Some of them are assembled into the TTF cryomodule. TTF linac is now in the phase 2 stage construction, which is planned for 2μm emittance, 1nC electron beam by upgraded laser-driven photocathode RF gun, 1 GeV acceleration by 6 cryomodules each containing 8 superconducting 9 cell cavities, and 50μm RMS bunch length by 2 stage bunch compressors. A 6.4nm wavelength FEL light will be generated by modified 27m undulator magnets, and will be transported to the downstream user experimental area. The photocathode RF gun injector is capable of delivering bunch trains with parameters very close to the TESLA linear collider specifications in terms of beam current and pulse length. It also delivers bunches with sufficiently low emittance for successful operation of the FEL. The TTF-I program is being concluded in autumn 2002. The last tests are devoted to one more accelerator module (named module 1*, because it is the original module 1 equipped with new cavities), which is expected to yield an average accelerating gradient of 25 MV/m, and to a beam test with a first version of the so-called superstructure concept. In a superstructure, two cavities are fed with RF power by a single coupler, which saves length (the fill factor is increased by 6% in comparison with the present TTF modules) and cost by reducing the number of couplers. First beam tests with two superstructures at a gradient of 15 MV/m have been performed successfully, proving the principle of this concept and confirming very satisfactory damping of higher order modes in the structures. After completion of that experimental program, the linac is lengthened by three more modules (two of which contain only cavities which have reached 25 MV/m or more on the test stand) in an already completed additional tunnel, and the FEL installations is modified to prepare for phase 2 (TTF-II) of the user facility, commissioning of which will begin in the second half of 2004[4].

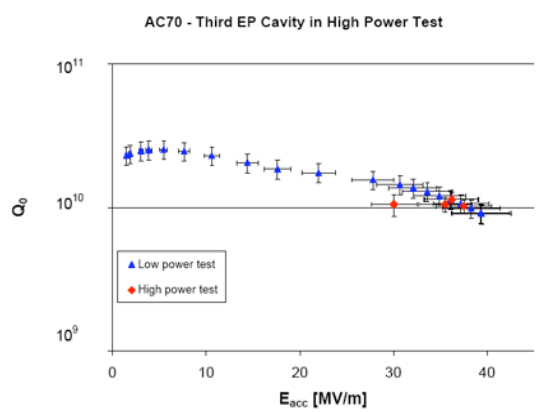

Figure 1: 35MV/m result of AC70 EP cavity.

For the start-up of TTF-II, emphasis is on achieving lasing and saturation at a wavelength of 30 nm, which requires beam energy of 461.5MeV. With a slice emittance of 2mmmrad, the saturation length will be less than 20m well within the undulator length of 27 m. Later, lasing at longer and shorter wavelengths and finally down to 6 nm will follow, where stronger requirements on the emittance apply.

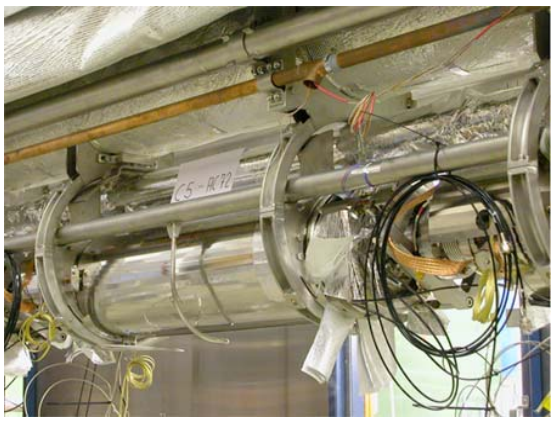

Figure 2: 35MV/m AC72 cavity installation.

NLC TEST ACCELERATOR (NLCTA)

The NLCTA of SLAC is a testing ground for the X-band RF system components and has been demonstrating the viability of the NLC RF system[5]. It has 4 RF stations and beam supply from the DC gun. The first RF station is used to power the injector, which was designed to generate beams with NLC-like currents (~1 A) by the thermionic DC gun and bunchers, except the bunch spacing of 88 ps. To improve the bunching efficiency, the first structure has a low beta section in its upstream end and is preceded by two pre-bunching cavities, all powered from the single 50MW solenoid focused klystron (1.5μs pulse length) and the SLED-II pulse (factor 4 gain in peak power). The structure testing for the gradient program has been done exclusively at NLCTA using the four accelerator slots in the two linac RF stations. To date, 12 structures have been tested in the two RF stations, which have been run in parallel for about 7000 hours at 60 Hz. As part of this testing, the SLED-II pulse compression systems have operated stably, producing up to 280 MW, 240 ns pulses. The fourth station is used for the 8-Pack system.

Designs for a future TeV scale electron-positron Xband linear collider (NLC/GLC) require main linac units, which produce and deliver 475 MW of RF power at 11.424 GHz to eight 60 cm accelerator structures. To demonstrate such high power RF, four 50 MW X-band klystrons, powered by a common 400 kV solid-state modulator, are used to drive a dualmoded SLED-II pulse compression system (the 8-Pack system). The three times compressed power is delivered to structures in the NLCTA beam line by an over-moded transmission and distribution system. Four 60 cm accelerator structures are currently installed and powered, with four additional structures and associated high power components available for installation late in 2004. Full GLC/NLC prototype structures with the short-range and long-range wake field control (HDDS1/HDDS2) are tested to verify the gradient performance 65MV/m. The system was run at 500-510 MW for 200 hours at 30 Hz and 100 hours at 60 Hz to measure RF breakdown rates in the system. During the 30 Hz operation, 11 RF breakdowns were observed in the SLED system and in the over-height high power waveguide, while none were measured during the 60 Hz running. The average rate of 0.06 breakdowns per hour (60 Hz equivalent) is better than the NLC/GLC requirement of < 0.16 per hour (for 475 MW operation), and the improvement during the last 100 hours indicates the breakdown rate was decreasing. Beam was then accelerated with the four accelerator structures powered by the 8-Pack system and the four previous structures on the NLCTA beam line. They have been operating at the NLC/GLC design accelerating gradient of 65 MV/m for 850 hours. The breakdown rate, averaged over the eight structures, during the most recent 150 hours of operation, is 0.085 per hour. This rate is better than the <0.1 breakdown per hour NLC/GLC goal.

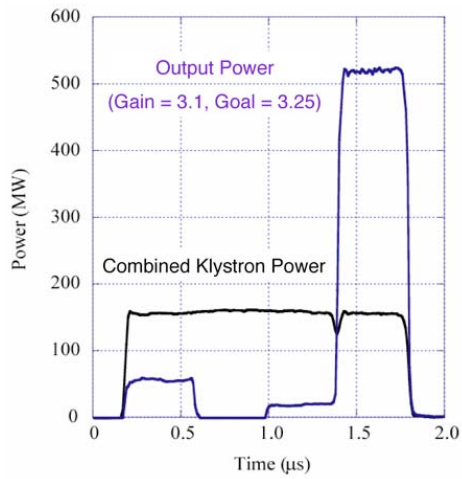

Figure 3: 510MW, 400ns power from 8-pack system.

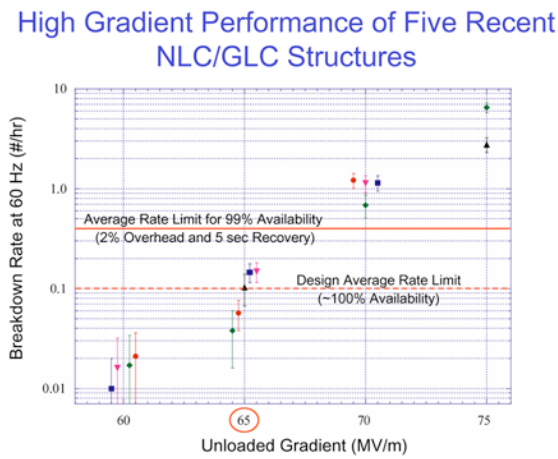

Figure 4: Structure breakdown rate at 65MV/m.

As for PPM (Periodic Permanent Magnet focused) klystron development[6], the XP3-3, which is the product of DFM (Design for Manufacture) strategy, was the first full-spec operational klystron operated at 75 MW, 120 Hz at 1.6μs pulse length. Due to the beam transmission, RF and thermal issues discovered with this DFM versions we decided to temporarily return to a design with pole pieces brazed directly to the drift tube. Next two tubes are currently under test. The first one, the XP3-4 was built and tested with air cooling rather than water cooling while the water cooling components were still under fabrication. The XP3-4 operated full spec at 120 Hz, 506 kV, 75 MW, 1.62μs RF, and 50 % efficiency with 60 dB gain. The beam transmission was 98.7 % during the full saturated RF pulse. The XP3-4 is currently under test at full power and has accumulated 60 hours at 120 Hz full-spec operation. The second one, XP3-5 is still processing up to the full pulse width and has reached 75 MW at 1μs and 120 Hz.

KEK ACCELERATOR TEST FACILITY (ATF) & GLC TEST ACCELERATOR (GLCTA)

ATF is the only LC facility devoted to the production of low emittance beams, a critical challenge in LC beam dynamics and technology. The ATF includes a 1.54 GeV S-band injection linac, a 138.6 m circumference damping ring and an extraction line for beam analysis. Technology development at ATF is centered on precision beam instrumentation, stabilization techniques and tuning methods. To achieve the low emittance goal, ATF operation has focused on the following investigations: (1) tuning techniques and error correction, (2) single bunch collective effects (e.g., intrabeam scattering), (3) wiggler performance, (4) damping ring acceptance, (5) extracted beam jitter, and (6) multibunch instabilities. The primary design goal of the ATF damping ring is to obtain a vertical normalized emittance less than 3×10^{-8} m.rad with a high intensity ($0.7\text{-}3.0\times10^{10}$ e-/bunch) multibunch beam. The ATF damping ring currently operates at 1.28 GeV beam energy at a repetition rate of 0.7 Hz with one bunch train of 20 bunches with 2.8 ns bunch spacing and 0.7x1010 particles/bunch. Extremely low emittance studies have been done in single bunch mode, resulting in the smallest single bunch, low current emittance recorded in the world, 1.6x10-8 m.rad (normalized)[7]. The tuning procedure to obtain low emittance involves the successive application of orbit, dispersion, and coupling corrections. Considerable work has been done to characterize the damping ring optics, resulting in high confidence in the present model. For instance, beam-based magnet field measurements (lattice diagnostics) uncovered quadrupole field-strength errors on the order of 1%. Correcting the optics model to account for these errors produced a model accurate to 0.01%. To correct residual alignment errors, beam-based alignment of focusing and sextupole magnets has begun. In late 2002, using new high-resolution ring BPMs, a quick, accurate beam-based alignment procedure has been developed to provide insight into the nature of the optics corrections that are presently used for emittance optimization. This should make it possible to identify sources of instability and quantify the physical limits on the minimum vertical emittance. This is one of the highest priority beam studies. With respect to intrabeam scattering, single bunch studies have shown a dependence of the measured emittance on both the bunch current and the longitudinal emittance, indicating strong intrabeam scattering (IBS). In October 2002, the thermionic gun and buncher system were replaced by a Cs_2Te photo-cathode RF gun in order to increase the injection efficiency into the ring to ~100% and to improve performance during multibunch operation. The stored charge of multibunch beam in the ring was increased to 7×10^9/bunch with 20 bunches without beam loss. After several days of scrubbing, observed instabilities at tail bunches of multibunch, which were seemed to come from fast ion effect, was disappeared. The measured emittance was still twice high compared to the single bunch by insufficient DR tuning at that time. The multibunch low emittance confirmation will be done in the next run. Additional studies at ATF have been aimed at developing the technology required to accurately measure very small beams. There are five wire scanners in the extraction line, a laser-wire monitor in the ring, SR interference monitor and X-ray imaging SR monitor in the ring, and Optical Transition and Diffraction Radiation (OTR and ODR) monitors under development in the extraction line. The ATF laser wire closely resembles a design, which is expected to be widely used in the LC. A laser beam with a very thin waist is generated in an optical cavity formed by nearly concentric mirrors. The laser intensity is amplified by adjusting the cavity length to meet the resonance condition. The cavity constructed for the ATF has produced a beam waist of 12 μm (2σ) and an effective power of 100 W, with good long-term stability. The laser wire is installed in the ring at a location with a transverse electron beam size of ~10 μm. It has been used over the last year to make accurate measurements of the vertical emittance of each bunch in the ring.

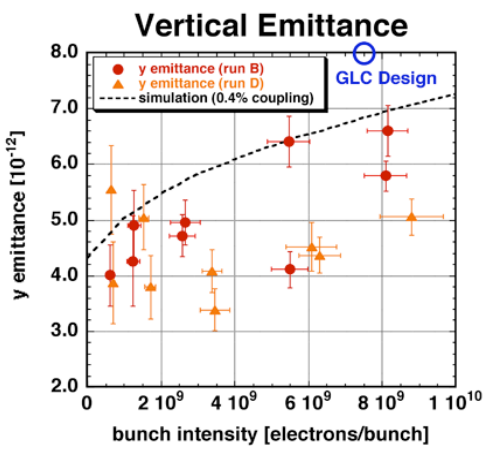

Figure 5: ATF vertical emittance in single bunch.

Since the LC design was similar between GLC and NLC, development of X-band technology has been done with close collaboration between KEK and SLAC from the beginning. The main collaboration area is the structure development and pulse compression component. They are installed and tested in NLCTA. In order to promote and demonstrate GLC main linac technology even in KEK, 3 years construction plan of GLCTA has been started from 2003. This is a realization of 1 main linac accelerator unit, which is the result of own GLC R&D and collaboration R&D with SLAC. For the beam acceleration demonstration, extracted ATF beam with additional bunch compression and/or additional photo-cathode RF gun beam with full GLC beam loading will be used. Construction is under way towards 2006 of beam acceleration demonstration.

CLIC TEST FACILITY (CTF)

CLIC[8] is a two beam-acceleration concept linear collider of a centre-of-mass energy of 3 TeV. It is based on the use of normal conducting accelerating structures operated at high gradient (150 MV/m), powered by 30 GHz high power RF pulses generated from a high current drive beam accelerator of low RF frequency. Since the overall efficiency is critical, the drive linac will be operated in the "full beam loading" condition, where the beam extracts almost all the power from the structures, expecting an overall transfer efficiency of about 98 %. A phase 3 of CLIC Test Facility (CTF3)[9] is being built at CERN in order to demonstrate this drive beam generation scheme and also to serve as a 30 GHz RF power source, necessary to develop CLIC RF components. CTF3 will consist of a 70 m long linac followed by two rings, where the bunch manipulations will be carried out by a 42 m long delay loop and an 84 m combiner ring. The 30 GHz high power test stand is also included for testing CLIC module and a test decelerator. The generation of 1.5 μs long drive beam pulse is done by a 140 kV thermionic gun and phase-coded bunching system followed by two travelling wave structures. It provides bunches spaced by 10 cm, at energy of 20 MeV. The CTF3 linac will be composed of 11 modules. The 3 GHz structure, have a total length of 1.22 m and operate at a loaded gradient (nominal current) of 6.5 MV/m. In order to suppress the transverse Higher Order Modes (HOMs) the structures (called SICA, for Slotted Iris Constant Aperture) use four radial slots in the iris to couple out the HOMs to SiC loads. The klystron RF power is compressed by a factor 2 with programmed phase ramp to provide rectangular 30MW over 1.5 μs pulses at each structure input. After the linac, a first stage of electron pulse compression and bunch frequency multiplication of the drive beam is obtained using a transverse RF deflector at 1.5 GHz and a 42 m long delay loop. The phase-coded 140 ns long sub pulses are first separated and then recombined by the deflector after half of them have been delayed in the loop. An 84 m long combiner ring is then used for a further stage of pulse compression and frequency multiplication by a factor of 5, through injection with 3 GHz transverse RF deflectors. The drive beam pulse is then transported to the 30 GHz test area. A 30 GHz decelerating structure, optimized for maximum power production, will be used in a high power test stand where CLIC prototype accelerator structures and RF components can be tested at nominal power and beyond. The probe beam is generated in a 3 GHz RF photo injector. It can be accelerated further to about 500 MeV in 30 GHz CLIC accelerator structures powered by the drive beam, operated at a maximum gradient of 150 MV/m.

In 2003 the injector and the first three linac modules were installed in CTF3. Beam commissioning started in June 2003[10]. The design beam current and pulse length were reached without beam break-up under full beam loading. The observation of the RF signals at the structures' output coupler allowed to adjust easily the beam-to-RF phase by maximizing the beam loading. When the beam is on, it extracts more than 90 % of the energy contained in the useful part of the RF pulse (1.5 μs). The RF signals were also used to assess the RF-to-beam efficiency. The RF-to-beam efficiency evaluated is 94 %. During the winter 2003 shutdown more modules were installed, bringing the total number of accelerating structures to 10. A dogleg transport line was installed after the instrumentation module, together with a new 30 GHz power test stand, where the drive beam can be used to generate 30 GHz RF power in a special Power Extraction and Transfer Structure (PETS). The commissioning of the newly installed hardware is presently under way, and the first 30 GHz RF pulses have already been produced, with moderate beam current. At present only a short PETS is installed, and preliminary measurements indicate a power above 100 kW, in accord to the expected value.

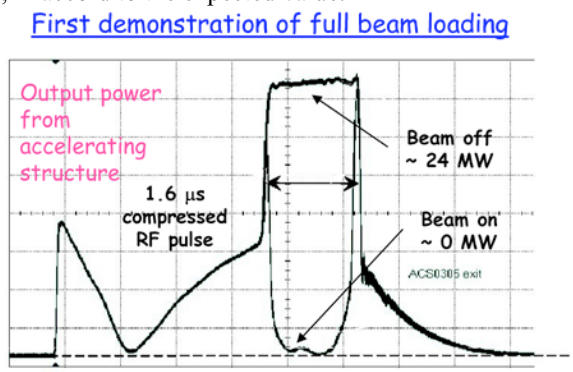

Figure 6: Beam loading of CTF3 injector structure.

As for CLIC structure development, CTF2 has provided 30 GHz RF pulses of up to 280 MW with a pulse-length variable from 3 to 15 ns. This pulse length was larger than the fill-time of the structures built so far, but was short compared to the nominal 130 ns pulse-length of CLIC. The constant impedance copper structures have reached mean accelerating gradients of 72 MV/m for a surface field of 317 MV/m. At these field levels, considerable surface damage is observed on the first iris.

The structure with an iris made of tungsten replaced the damaged region was tested applying a 160 MV/m gradient of 3ns long for 5x105 pulses, and no damage occurred on the tungsten iris.

The systematic comparison of the structure has been carried out during 2002 with reduced Esurf/Eacc ratio in the cells and in the coupler. The first structure made of tungsten with copper rings clamped in between showed that accelerating fields of 125 MV/m in average and of 152 MV/m in the first cell, were obtained in this structure without damage. The second structure entirely made from OFHC copper reached an average accelerating field of 102 MV/m and 114 MV/m in the first cell. This structure showed signs of surface damage on the first regular iris, where the surface E-field is highest. The third structure, with molybdenum irises, was reached to an average accelerating gradient of 150 MV/m, and 193 MV/m in the first cell without damage. Comparing results from these structures, importance of material rather than geometry effects should be stressed. The test facility CTF3 under construction will allow to produce 30 GHz RF power pulses of nominal length. 30 GHz structures testing with this new source will start in late 2004.

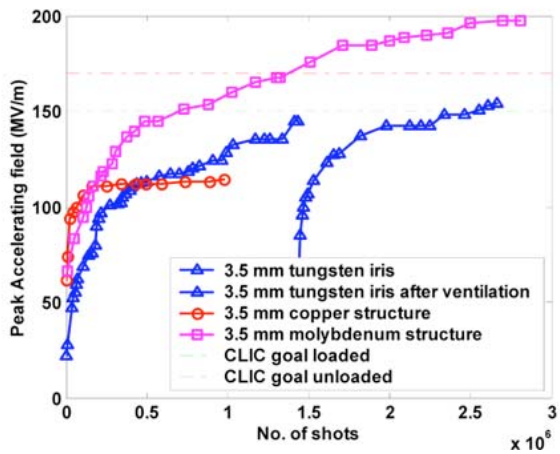

Figure 7: Peak accelerating field of Tungsten-iris and Molybdenum-iris in 30GHz structure.

SUMMARY

Major achievement and status of each test facilities are summarized briefly below;

TTF: Accelerating gradient of superconducting L-band cavity reached up to 35MV/m with applying EP method, cleared TESLA800 design goal. Acceleration demonstration with TESLA like beam loading was already done. SASE-FEL application using upgraded TTF is underway towards lasing at 30nm in September 2004.

NLCTA: RF power generation of 510MW, 400ns (design 475MW, 400ns) was achieved with 0.06 breakdowns per hour, better than the NLC/GLC requirement of < 0.16 per hour. The X-band structure also achieved 65 MV/m for 850 hours with 0.085 per hour breakdown, better than <0.1 breakdown per hour goal. The PPM klystron achieved the design rf output independent with test facility. The generated RF power by 8-pack will be delivered to 8 structures instead 4 in fall 2004.

ATF/GLCTA: The GLC vertical emittance goal of $2.0\text{x}10^{-8}$ rad.m was achieved in ATF damping ring with single bunch operation. Emittance of multibunch, which is suffered from ion effect, will be achieved in fall 2004. Beam instrumentation such as laser wire has been developed using very low emittance beam.

Complete RF unit demonstration of GLC is under construction at downstream of ATF towards 2006 commissioning.

CTF: More complete test facility for two-beam acceleration demonstration is under construction as CTF3. Delay loop and combiner ring for drive beam manipulation will be demonstrated in 2007. 94% RF-to-beam efficiency was demonstrated in CTF3 drive linac injector. 193MV/m gradient in 30GHz structure was reached using molybdenum irises in case of 16ns pulse length. CLIC nominal RF power will be available in 2007.

REFERENCES

[1] "International Linear Collider Technical Review Committee second report 2003" Edited by G.A. Loew, SLAC-R-606 (2003).
[2] "TESLA TDR," (2001).
[3] "SASE FEL at the TESLA Facility, Phase 2" TESLA-FEL 2002-01, June 2002.
[4] S. Schreiber, "commissioning of the VUV-FEL Injector at TTF," EPAC 2004.
[5] D. Schultz, et al. "Status of a Linac RF Unit demonstration for the NLC/GLC X-band Linear Collider," EPAC 2004.
[6] D. Sprehn, et al. "Current Status of the Next Linear Collider X-band Klystron Development Program," EPAC 2004.
[7] Y. Honda et al. "Achievement of Ultralow Emittance Beam in the Accelerator Test Facility Damping Ring", Phys. Rev. Lett. 92, 054802 (2004).
[8] "A 3 TeV e+ e- Linear Collider based on CLIC Technology," Edited by G. Guignard, CERN 2000-008 (2000).
[9] "CTF3 Design Report," Edited by G. Geschonke (CERN) and A. Ghigo (INFN), CERN/PS 2002-008(RF) and LNF-02/008(IR), (2002).
[10] R. Corsini et al. "First Full Beam Loading Operation with CTF3 Linac," EPAC 2004

MUON IONIZATION COOLING EXPERIMENT (MICE)*

M. S. Zisman†, LBNL, Berkeley, CA, 94720, USA, for the MICE Collaboration

Abstract

There is presently considerable activity worldwide on developing the technical capability for a "Neutrino Factory" based on a muon storage ring and, later, a muon collider. Muons are obtained from the decay of pions produced when an intense proton beam hits a high-Z target, so the initial muon beam has a large 6D phase space. To increase the muons' phase-space density (i.e., decrease the emittance), we use ionization cooling, which is based on energy loss in an absorber, followed by re-acceleration with high-gradient, normal-conducting RF cavities. A superimposed solenoidal focusing channel contains the muons. The international MICE collaboration will demonstrate ionization cooling in a short section of a realistic cooling channel, using a muon beam at Rutherford Appleton Laboratory (RAL). We will measure the cooling effects of various absorber materials at several initial emittance values using single-particle measurement techniques. The experiment layout and goals are discussed, as is the status of component R&D.

INTRODUCTION

It is now widely believed that a Neutrino Factory based on a muon storage ring will be the most effective tool to probe the physics of the neutrino sector. Depending on the values of presently unknown parameters, it may also offer the first means to observe charge-conjugation–parity (*CP*) violation in the lepton sector. Scientific results from a Neutrino Factory will test theories about neutrino masses and oscillation parameters, and thus provide important information for both particle physics and cosmology.

A high-performance Neutrino Factory—one capable of delivering roughly 4×10^{20} ν_e aimed at a remote detector in a 10^7 s "year"—depends on ionization cooling of the muon beam. As will be described below, this cooling process involves straightforward physics, but the technique has not been experimentally demonstrated. As a Neutrino Factory is expected to be an expensive facility, it is highly appropriate to carry out a demonstration of this key principle.

The cooling demonstration we propose aims to:

- design, engineer, and build a section of cooling channel capable of giving the desired performance for a Neutrino Factory
- place this apparatus in a muon beam and measure its performance in a variety of operating modes and beam conditions

*Work supported by U.S. Dept. of Energy, Office of High Energy Physics, under contract no. DE-AC03-76SF00098.

†mszisman@lbl.gov

The experiment will verify that our design tools (simulation codes) agree with observations. This will give confidence that we can optimize the design of an actual facility. No matter what configuration we test today, it is likely that there will be changes made before construction of a Neutrino Factory facility actually begins. Validating the design tools will permit their use in someday developing a full proposal for a Neutrino Factory. It is important to note, however, that this approach depends on both the equipment being tested and the simulation codes being as realistic as possible. Thus, full engineering details of all components must be included in the simulations—a nontrivial task.

The main challenge of MICE is that, for cost reasons, we use only a single cell of a cooling channel, which means that the expected cooling effect is small, about 10%. We therefore wish to measure the emittance reduction to a precision of about 10^{-3}. Other challenges include:

- operating high-gradient RF cavities in a solenoidal field and with field terminations (windows or grids)
- safely operating LH_2 absorbers with very thin windows
- integration of cooling channel components while maintaining functionality

Fortunately, these challenges are being worked on via R&D activities that fall outside of MICE, mainly carried out by the U.S. Neutrino Factory and Muon Collider Collaboration (MC).

NEUTRINO FACTORY INGREDIENTS

A Neutrino Factory is a relatively complex facility. It starts with a proton driver capable of providing a MW-level beam directed at a production target, such as a Hg-jet. Pions from the interaction are captured into a solenoidal decay channel, where they decay to muons. The muon beam is then bunched and "phase rotated" to reduce its energy spread (effectively exchanging energy spread for bunch length). Thereafter, an ionization cooling channel is used to reduce the transverse emittance of the beam. This is the aspect that is the focus of this paper. After cooling, the muon beam is rapidly accelerated to its final energy by means of Recirculating Linear Accelerators (RLAs) or Fixed-Field Alternating Gradient (FFAG) machines. Finally, the muon beam is injected into a storage ring where it circulates for about 500 turns. A long straight section of the ring is oriented toward a neutrino detector located several thousand kilometers from the accelerator site.

As should be obvious from this description, a Neutrino Factory is not an easy project, but no fundamental problems have been identified to date.

COOLING DESCRIPTION

Because the muon lifetime in its rest frame is quite short, 2.2 μs, it is necessary to cool the muons quickly. Standard cooling techniques, such as stochastic cooling, are far too slow to be useful. Instead we make use of ionization cooling, a technique tailor-made for the weakly interacting muons.

Ionization cooling is analogous to the familiar synchrotron radiation damping process in electron storage rings. In ionization cooling, the energy loss process corresponding to the synchrotron radiation energy loss is ionization energy loss, i.e., *dE/ds*, in an absorber medium, which reduces the momentum in all three planes (p_x, p_y, p_z). Energy gain is via RF cavities, which restore only the longitudinal momentum, p_z. Repeating this process many times reduces $p_{x,y}/p_z$, and thus transverse emittance.

Just as in the synchrotron radiation case, there is also a "heating" term. The equivalent to quantum excitation in our case is multiple scattering. There is a balance between heating and cooling that gives rise to an equilibrium emittance given approximately by:

$$\varepsilon_{x,N,equil.} = \frac{\beta_\perp (0.014\,\mathrm{GeV})^2}{2\beta\, m_\mu X_0 \left|\frac{dE_\mu}{ds}\right|} \qquad (1)$$

where $\beta = v/c$. We see from Eq. 1 that the best cooling results from low $\beta_\perp$ (strong focusing), large radiation length, X_0, and large *dE/ds*. With this in mind, Table 1 summarizes the merit factor for various candidate MICE absorber materials, defined as $[X_0(dE/ds)]^2$, relative to liquid hydrogen (LH_2). LH_2 is the optimal material choice. In practice, an LH_2 absorber is extended in size (sampling more than the minimum beta function) and has aluminum windows. Together, these aspects degrade the performance of the absorber by about 30%, but LH_2 remains the best absorber choice.

The cooling channel operates at a typical momentum of about 200 MeV/c. This momentum, which corresponds to the ionization minimum, is roughly optimal from the viewpoint of capturing muons from the production target. Running below the ionization minimum results in a substantial increase in longitudinal emittance, since in this regime particles of lower energy have increased *dE/ds*. Running above the ionization minimum is disadvantageous, as it is more demanding on RF and magnet performance and gives rise to more energy straggling. Considering transverse cooling alone, momenta below the ionization minimum are preferable to those above.

Table 1: Merit factors for candidate MICE absorbers.

Material	$(dE/ds)_{min}$ (MeV g^{-1} cm^2)	X_0 (g cm^{-2})	Rel. merit
H_2 gas	4.103	61.28	1.03
H_2 liq.	4.034	61.28	1
He	1.937	94.32	0.55
LiH	1.94	86.9	0.47
Li	1.639	82.76	0.30
CH_4	2.417	46.22	0.20
Be	1.594	65.19	0.18

BENEFITS OF COOLING

The need for cooling results from the fact that the initial muon beam emittance is quite large, making it difficult to transport and accelerate efficiently. To do so would require very large magnets and RF cavity apertures. Both are possible in principle, but are expected to be very costly. Cooling typically increases the phase space density within a given acceptance by a factor of 4–10, depending on the size of the acceptance. (The smaller the downstream acceptance, the larger the gain from cooling, and vice versa.)

MICE will calibrate the cost and performance of actual cooling hardware and permit a quantitative evaluation of the trade-offs between cooling and acceleration. This is very important, as the cost of a typical acceleration stage can be $500M.

For many particle physicists, the Holy Grail of muon beam R&D is to build a muon collider, for which cooling is a necessity both transversely and longitudinally. Successful construction of a muon collider would provide an energy-frontier facility that would fit easily onto the site of an existing laboratory.

MICE IMPLEMENTATION

The layout of the MICE components, based on a single cell of the U.S. Feasibility Study II configuration [1] is shown in Fig. 1. Note that, in effect, the cooling channel is simply a linac to which absorber material has been added.

Simulations of MICE performance have been done using ICOOL [2] and Geant4 [3]. The former code is used primarily for matching the beam optics of the cooling channel, whereas the latter code contains the information on the detectors and permits evaluation of anticipated backgrounds and systematic errors. Representative parameters used in the simulations are summarized in Table 2. Figure 2 shows the predicted transmission and predicted cooling effect of the configuration shown in Fig. 1. As can be seen, the transmission is essentially 100% for input emittance below 6 mm rad. Above this value, there is significant particle loss, and the curves in the lower part of Fig. 2 represent emittance reduction due to "scraping" as well as due to cooling.

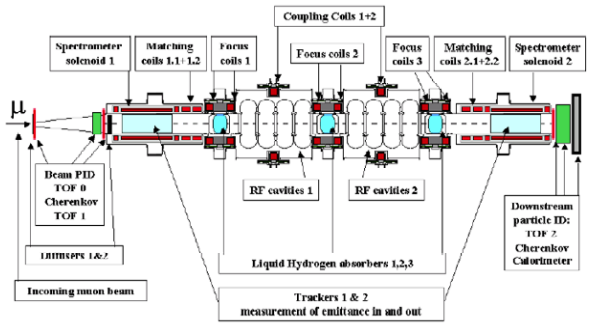

Figure 1: Layout of MICE, showing cooling channel components along with upstream and downstream spectrometers.

In addition to testing a baseline case corresponding to the Feasibility Study II optics, we plan to test alternative scenarios to verify that we can correctly scale our results using a simulation code. The variants to be studied will include some or all of the alternative absorber materials listed in Table 1, as well as different optics. Though our ability to produce a lower $\beta_\perp$ at the absorber is limited by the current density in the magnet coils, we expect to be able to reduce $\beta_\perp$ to about 250 mm at the nominal operating momentum of 200 MeV/c. Reducing the central momentum to 140 MeV/c should permit reaching $\beta_\perp \approx$ 60 mm. Other options to be studied include an optics configuration with no field flips at the absorbers and a configuration with higher RF gradients (by powering fewer cavities with the 8 MW of available RF power and/or by operating the cavities at liquid-nitrogen temperature to reduce the RF power dissipation).

COOLING HARDWARE

The basic ingredients of a cooling channel include:

- absorbers to give energy loss
- RF cavities to restore the lost energy
- solenoid magnets to contain and focus the muons as they traverse the channel

For MICE, we augment the cooling channel hardware with:

- a diffuser to create a large emittance muon sample
- an upstream diagnostics section including time-of-flight measurements, Cerenkov particle identification, and a tracker to measure incoming emittance

Table 2: Representative cooling simulation parameters.

Parameter	Value
Momentum (MeV/c)	200
Momentum spread (MeV/c)	±20
$\sigma_{x,y}$ [mm]	50
$\sigma_{x',y'}$ [mrad]	150
Solenoid field (T)	3
$\beta_\perp$ (mm)	420
RF phase (deg)	90 (on crest)

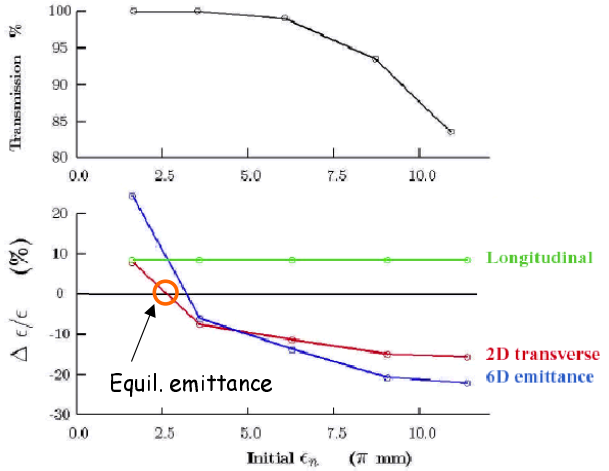

Figure 2: Result of "scan" over input emittance. The equilibrium emittance is given approximately by Eq. 1.

- a downstream diagnostics section having an electromagnetic calorimeter, another Cerenkov system, and an identical tracker to measure final emittance.

Two types of solenoid magnets are needed for the MICE cooling channel: focusing coils, which are integrated with the absorber and provide the low beta function at the absorber position, and coupling coils, which surround the RF cavities (see Fig. 1). In the baseline configuration, the focus coil modules have opposing polarities, resulting in the field profile shown in Fig. 3. For reasons of cost and simplicity, all magnets will use cryocoolers rather than conventional cryogens. As noted earlier, it is possible to power the focusing coils with the fields the same, referred to as a "non-flip" configuration.

The LH_2 absorber design makes use of internal convection cooling, as opposed to a more conventional forced-flow design with external heat exchanger. This choice is more than adequate for MICE, though the forced-flow approach might be preferred in a high-intensity Neutrino Factory. The absorber configuration, showing the surrounding focusing coils, is indicated in Fig. 4. This design, with a second set of thin windows for isolating the absorber from the rest of MICE, has been reviewed for safety by an international panel and found to be acceptable. The primary Al window has a 300 mm diameter and will be about 120 μm thick.

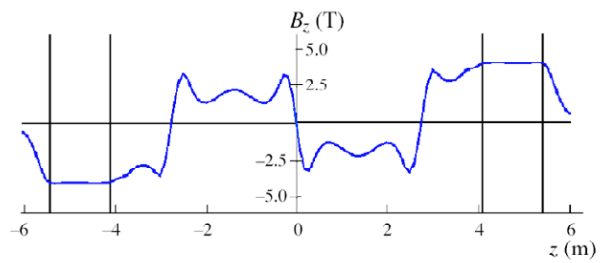

Figure 3: Baseline magnetic field configuration for MICE.

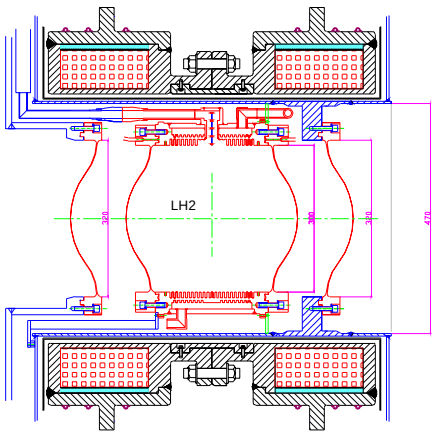

Figure 4: Liquid-hydrogen absorber assembly, showing inner absorber window, outer vacuum window, and surrounding focus coils.

The two RF modules for MICE each contain four separately powered 201 MHz cavities, 1.2 m diameter, with independent tuners. Each cavity iris is terminated with a pre-curved Be window of 420 mm diameter. The curvature makes the window resistant to thermal distortion. Furthermore, we orient the pair of windows for each cavity in a common direction, so any small deflection due to heating has only a minor effect on the cavity frequency.

MUCOOL R&D PROGRAM

The ability of MICE to achieve its goals is greatly enhanced by the hardware R&D programs under way worldwide. In particular, the MUCOOL R&D program [4] of the MC is developing prototypes of both the LH_2 absorber and the RF cavity needed for MICE. To promote this effort, a new facility, the MUCOOL Test Area (MTA), has been constructed by the MC at Fermilab to permit tests of the prototype components.

RF Cavity R&D

The main challenge for the RF cavity is to attain a high gradient in the presence of a strong magnetic field. In tests to date [5] using an 805 MHz pillbox cavity, we observed increased breakdown and dark currents as the magnetic field was increased. Continued R&D to test different materials and coatings to mitigate the observed effects will continue with the 805 MHz cavity, in preparation for the arrival of the prototype 201 MHz cavity later this year.

As shown in Fig. 5, the prototype 201 MHz cavity, being fabricated as a collaboration among LBNL, Jlab, and University of Mississippi, is now well along. In operation, the beam iris will be closed with a thin Be window.

LH_2 Absorber R&D

The absorber R&D program [6] is being carried out at KEK and at various Illinois universities near Fermilab. The university effort has focused on developing the thin Al windows for LH_2 containment, working with the University of Mississippi for fabrication and with Oxford University in the UK for engineering design and analysis. Windows as thin as 120 μm have been machined from solid aluminum blanks. The most recent window was destruction tested and found to fail at 9.8 bar. This is some 44% higher than needed for safety, but was not in good agreement with predictions from the FEA code. The discrepancy is believed to be partially due to different material properties in the actual window compared with what was assumed for the FEA model, and partially due to a different thickness of the window. Unfortunately, several measurements of the window gave conflicting results for its thickness and this needs to be resolved.

Figure 5: 201 MHz cavity being fabricated at Jlab. The beam aperture is 420 mm in diameter, and the cavity body is about 1.2 m in diameter. The small hole visible on the side is a pilot hole for extruding one of the four required equatorial ports.

The KEK effort is aimed at developing the absorber body, the required instrumentation for controlling the system, and the cryogenic seals. A prototype absorber (see Fig. 6), somewhat smaller than that specified for MICE, has been fabricated in Japan and—after meeting all of the appropriate safety requirements at Fermilab—was recently successfully test-filled with LH_2 at the MTA.

MICE INSTRUMENTATION

A parallel effort on the development and testing of the detectors for MICE is also under way [7], with much of the effort centered in Europe. Work on the upstream time-of-flight system, which aims for 70 ps resolution, is under way at Milan. This system will be used for particle identification, for timing with respect to the RF waveform, and for triggering the data acquisition system. The upstream Cerenkov detector, being developed by University of Mississippi, will be used for π/μ separation.

Figure 6: Prototype LH_2 absorber developed at KEK and successfully tested at the Fermilab MTA.

To provide downstream μ/e separation there will be an electromagnetic calorimeter (being developed by Rome III) and a Cerenkov detector (being developed by Louvain la Nueve). The tracker system, which will have identical units in both the upstream and downstream spectrometer solenoids, is based on a scintillating fiber detector. Five planar stations will be used to measure 6D emittance. This is a major effort for the particle physics members of the MICE Collaboration, involving groups from Bari, Brunel, CERN, Edinburgh, Fermilab, Geneva, IIT, Imperial College, KEK, Legnaro, Liverpool, Osaka, UCLA, and UC-Riverside. A prototype of the system has already been built and tested, and plans for a beam test at KEK are in progress.

Although not the baseline tracker option, considerable work, led by the Italian groups, has also been put into the development of a Time Projection Chamber with GEM readout, referred to as a "TPG." Assuming the R&D is completed successfully, this option could serve as a backup if major problems were to arise with the baseline tracker. (Given the present success with the baseline tracker, we do not anticipate the need for a fallback option, but prudence dictates extra caution on such a critical system.)

MICE STATUS

The MICE proposal [8] was submitted to RAL in January 2003. An international review panel, chaired by Alan Astbury, was convened in February 2003 and this group recommended to RAL management that the experiment be approved. Scientific approval from RAL was given in October 2003. As noted earlier, the absorber design concept has successfully undergone a preliminary safety review. A second review will be required before getting permission to operate the absorber at RAL, but there are no issues of principle remaining to be resolved.

We are now in the process of refining the cost estimate for the experiment and firming up funding commitments from the various countries involved. Our present estimate of the hardware costs for the experiment is £11M. The fully loaded cost, with effort, contingency, and tax included, is £25M. At present, we have commitments for more than half of the required funding and we are working diligently to find the remaining portion.

In the U.S., the technical advisory committee (MUTAC) and the oversight group (MCOG) for the MC program have both strongly endorsed our participation in MICE, deeming it a "crucially important demonstration." A proposal has been submitted to the NSF that is currently under review. Unfortunately, support for high-energy physics in the U.S. has been stagnant for some years, so new initiatives are finding it an uphill fight to secure funding.

SUMMARY

R&D on the various components required for MICE is already at an advanced stage. The first prototype absorber has been fabricated and filled with LH_2, and the fabrication of the prototype 201 MHz RF cavity is well along. A prototype tracker system has likewise been fabricated and tested with cosmic rays; a beam test at KEK is in the planning stages. MICE will assemble and test these components in a realistic beam environment and verify their operation. As new ideas mature, it is likely that MICE will be available to serve as a test-bed for additional cooling components. Clearly, MICE is a very challenging "linac R&D" program, and new collaborators would be most welcome to join.

The resultant demonstration of muon cooling will validate the key concept of a Neutrino Factory design, and will also put the idea of a muon collider closer to realization. The measured cooling performance will be compared quantitatively with our simulations, thus "calibrating" our design tools and permitting the optimization of both the cost and performance of a future Neutrino Factory. We strongly believe that there is no substitute to carrying out this program with an actual muon beam, which will be sensitive to all of the relevant physics issues—those we have included and those (if any) that we have forgotten.

REFERENCES

[1] S. Ozaki, R. Palmer, M. Zisman, and J. Gallardo; eds.; http://www.cap.bnl.gov/mumu/studyii/final_draft/The_Report.pdf.
[2] R. Fernow, http://pubweb.bnl.gov/users/fernow/www/icool/readme.html.
[3] Geant4 homepage, http://geant4.web.cern.ch/geant4/.
[4] D. Kaplan, J. Phys. G 29, 1585 (2003).
[5] D. Li, *et al.*, J. Phys. G 29, 1683 (2003).
[6] M. Cummings, *et al.*, J. Phys. G 29, 1689 (2003).
[7] R. Edgecock, J. Phys. G 29, 1601 (2003).
[8] See http://mice.iit.edu/mnp/MICE0021.pdf.

STATUS OF THE SNS* LINAC: AN OVERVIEW

N. Holtkamp, ORNL, Oak Ridge, TN 37831, USA

Abstract

The Spallation Neutron Source (SNS) is a second generation pulsed neutron source and under construction at Oak Ridge National Laboratory. The SNS is funded by the U.S. Department of Energyís Office of Basic Energy Sciences and is dedicated to the study of the structure and dynamics of materials by neutron scattering. A collaboration composed of six national laboratories (ANL, BNL, TJNAF, LANL, LBNL, ORNL) is responsible for the design and construction of the various subsystems. With the official start in October 1998, the operation of the facility will begin in 2006 and deliver a 1.0 GeV, 1.4 MW average power proton beam with a pulse length of approximately 700 nanoseconds on a liquid mercury target sixty times a second. The multi-lab collaboration allowed access to a large variety of expertise in order to enhance the beam power delivered by the accelerator by almost an order of magnitude compared to existing neutron facilities. The SNS linac consists of a combination of room temperature and superconducting structures and will be the first pulsed high power sc linac in the world. The challenges and the achievements will be described in the paper.

GENERAL PROJECT OVERVIEW

The Spallation Neutron Source (SNS) [1, 2], authorized for construction in fiscal year 1999, is 85% complete. The accelerator, Central Laboratory and Office Building (which includes the central control room) and the Center for Nanophase Material Sciences (CNMS), are shown in Figure 1. The Joint Institute for Neutron Sciences (JINS) will be operated in conjunction with the University of Tennessee in support of the users program. CNMS is one out of five nanophase science centers under construction in the United States.

Currently, all of the SNS accelerator-associated buildings and tunnels are completed with installation and staged commissioning of the accelerator components ongoing. The project goal for SNS is to deliver a proton beam of up to 1.4-MW beam power to a mercury target for neutron spallation. Longer term, higher beam power operation by increasing the beam energy and doubling the user access with a second target station is envisioned as summarized in DOEís 20 year outlook of science facilities for the future [3]. These upgrades are incorporated in the site layout with an identified area for the second target station. Also, empty spaces in the tunnel allow for installation of an additional nine cryomodules to increase the energy to more than 1.3 GeV. The accelerator systems, basically a full-energy injector linac and an accumulator ring, operate at a repetition rate of 60 Hz and an average current of 1.6 mA. The accelerator systems consist of a negative hydrogen (H-) RF volume source; a low-energy beam transport (LEBT) housing a first-stage beam chopper; a 4-vane RF quadrupole (RFQ) for acceleration up to 2.5 MeV; a medium-energy beam transport (MEBT) housing and a second-stage chopper; a 6-tank drift-tube linac (DTL) up to 87 MeV; a 4-module coupled-cavity linac (CCL) up to 186 MeV and a superconducting linac (SCL) with 11 medium-β cryomodules (up to 379 MeV) and 12 high-β cryomodules (up to 1000 MeV). The linac produces a 1 msec long, 38 mA peak, chopped beam pulse at 60 Hz for accumulation in the ring. A high-energy beam

Figure 1: The photograph shows the SNS site with the finished accelerator facilities in the upper left and the Target building, Central Laboratory Office and the Center for Nanophase Material sciences in the foreground, with civil construction still ongoing.

Table 1: Summary of SNS Facility Parameters

Proton beam energy on target	1.0	GeV
Proton beam current on target	1.4	mA
Proton beam power on target	1.4	MW
Pulse repetition rate	60	Hz
Beam macropulse duty factor	6	%
H- peak current from front end	>38	mA
Aver. current per macropulse	26	mA
Chopper beam-on duty factor	68	%
Linac length, incl. front end	335	m
Ring circumference	248	m
Ring fill time	1	ms
Ring extraction gap	250	ns
Protons per pulse on target	1.5×10^{14}	
Liquid mercury target	18 tons	1 m^3
Number of moderators	4	
Minimum initial instruments	8	

* SNS is managed by UT-Battelle, LLC, under contract DE-AC05-00OR22725 for the U.S. Department of Energy. SNS is a partnership of six national laboratories: Argonne, Brookhaven, Jefferson, Lawrence Berkeley, Los Alamos and Oak Ridge

transport line (HEBT) for diagnostics and collimation after the linac injects into an accumulator ring for compressing the 1-ms pulse to ~700 ns for delivery onto the target through a ring-to-target beam transport (RTBT) beam line. Neutrons are produced by spallation in the mercury target, and their energy is moderated to useable levels by supercritical hydrogen and water moderators. The basic parameters of the facility are summarized in Table 1.

The simultaneous performance goals of 1.4 MW of proton beam power and ultimately having more than 90% availability of the facility place significant operational-reliability demands on the technical and conventional systems. Hands-on maintenance capability, made possible by low activation in the accelerator, is key, and requires maintaining beam loss of < 1 W/m. Figure 2 is a schematic layout of the different linac structures as a function of beam energy.

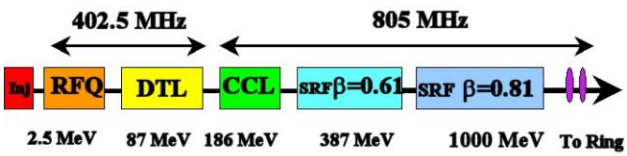

Figure 2: Schematic layout of the linac structures as a function of beam energy.

THE STATUS OF THE SNS LINAC

The Linac consists of four sections: It begins with the Front End System (FES), designed, built and originally commissioned at LBNL, followed by the DTL and the CCL. The DTL, CCL, as well as all the High-Power RF systems for the complete linac, were designed and procured by Los Alamos National Laboratory (LANL). Finally the SCL and the cryogenics support systems, which were largely designed by JLab with many contributions from LANL and ORNL. A separate talk was given during this conference on the Front End and DTL commissioning results [4].

The Front End Systems

Originally commissioned at LBNL in May 2002, the FES were re-assembled and re-commissioned at ORNL in late 2002. The front-end consists of a volume H- Ion source with 50 mA peak current, 6% duty factor and an electrostatic low-energy beam transport (LEBT) line to provide a properly matched, 65 keV beam for injection into the RFQ. Pre-chopping is performed by the LEBT chopper which deflects 32% of the beam onto the front face of the RFQ with a rise/fall time of 40 nsec. The RFQ is designed for 38 mA peak output current, operates at 402.5 MHz and provides 2.5 MeV output beam energy. Stable operation with excellent transmission has been demonstrated at a variety of currents between 15-40mA. The medium energy beam is transported to the drift tube linac via the MEBT, which contains four RF rebuncher cavities to properly match the beam longitudinally, a set of matching quadrupoles, and a fast chopper system with 10 nsec rise/fall time to remove the ìpartially choppedî beam from the LEBT chopper and further reduce the beam extinction ratio to below 10^{-4}.

A peak MEBT output current of 50mA was demonstrated, surpassing the design goal of 38 mA. In subsequent DTL commissioning, the Front-End Systems have operated at full 1 msec pulse length, and provided 1 mA average current (4% duty factor) beam for injection into the DTL. In parallel to operating the source on the linac, a hot spare stand is in operation to foster the development of more reliable, higher intensity sources. So far a variety of slightly modified sources have been tested at currents starting at 40 mA or higher and at nominal duty cycle. Typically after 7-10 days, currents reduced to below 20 mA and operation was interrupted to exchange the source.

The DTL Status and Commissioning Results

The Drift Tube Linac consists of six accelerating tanks with a final output energy of 87 MeV. Permanent magnet quadrupoles are distributed through the 210 drift tubes providing transverse focusing arranged in a FFODDO lattice. 24 steering dipoles as well as 10 BPM are integrated into otherwise empty drift tubes. The DTL operates at 402.5 MHz, the same bunch frequency as the RFQ. Tanks are individually powered with klystrons of 2.5 MW peak power and 8% duty factor capability. Some empty drift tubes contain beam position monitors and dipole correctors. The intertank sections contain toroidal beam current monitors, wire scanners and energy degrader/faraday cups.

To date, the entire DTL has been RF tuned and installed in the linac tunnel. DTL tank tuning has resulted in longitudinal fields within the specification of ±1% of design.

During Front End and DTL 1 commissioning, a peak current of 38 mA was accelerated and also 1mA average current beam with 100% beam transmission was demonstrated. Subsequently, DTL Tanks 1-3, with an output energy of 40 MeV, were commissioned during spring of 2004. Peak currents of 38 mA transported through all three tanks with 100% transmission were demonstrated as well. Beamstop and residual radiation considerations limited the beam pulse lengths to less than 50 microseconds, and repetition rates to 1 Hz maximum.

During commissioning availability of all subsystems was tracked in order to prepare early on for repairs that allow long term higher reliability operation, which is at this point ~ 60% of the time dedicated.

The Coupled Cavity Linac

The CCL, operating at 805 MHz and powered by four 5-MW (peak) klystrons, accelerates the beam to 186 MeV. The CCL has four modules with a total of 384 cells and is made of oxygen-free copper. The linac has been

designed at LANL and built in industry. It operates at 1.3 times the Klipatrick limit and includes 48 quadrupoles, 32 steering magnets, 10 beam position and phase monitors and seven carbon wire scanners.

The CCL is fully assembled in the SNS tunnel and has been tuned with final field values between ± 1% of design specification. The first 3 of the four modules are conditioned to full field, pulse length and 20 Hz rep rate. Conditioning went smoothly over a period of approximately 3-5 days per module.

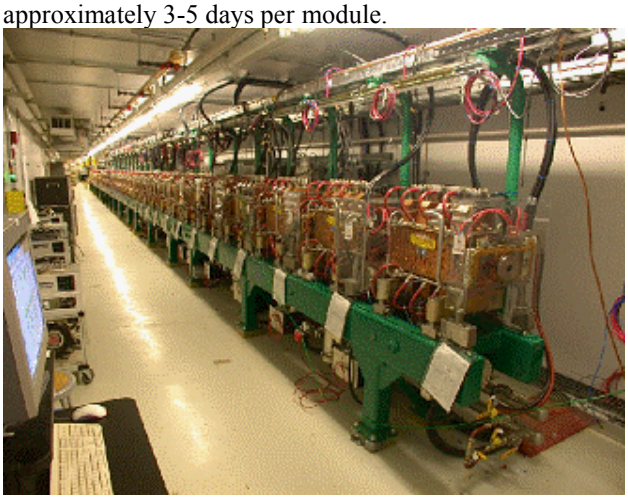

Figure 3: The CCL fully installed in the SNS linac tunnel.

The next beam commissioning begins in September 2004 and will include three out of the four modules and boost the beam energy to ~150 MeV. Average beam power generation will again be minimal to reduce residual contamination of the temporary beam stop within the tunnel.

The Superconducting Linac and the Cryogenic Support Systems

SNS will be the first large-scale superconducting proton linac that provides high beam power. The most prominent arguments for an SCL are large apertures, operational flexibility, high gradient, less real estate, lower operating costs, small wakefields, excellent vacuum, and very high electrical to beam power conversion efficiency.

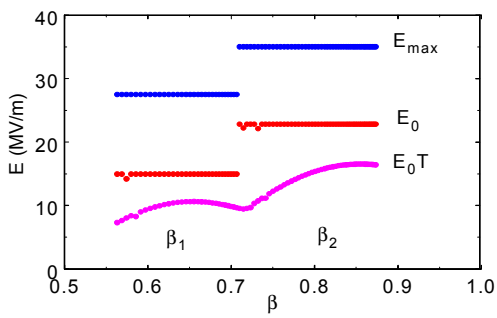

Figure 4: Surface, on-axis, and effective accelerating fields.

The velocity of the H^- ions within the SCL varies from β=0.55-0.87. The SNS approach (balancing the number of different types of cells to be used versus accelerating efficiency, compare figure 4) a two-cavity geometry with β=0.61 and β=0.81was chosen.

Table 2: Some Cavity Design Parameters

Parameter	β=0.61	β=0.81	Unit
No. of cells	6	6	
Epeak	27.5	35.0	MV/m
Epeak/Eacc	2.71	2.19	
Bpeak/Epeak	2.10	2.14	mT/(MV/m)
Cell:Cell cplng	1.61	1.61	%
Q at 2.1 K	>5 x 10^9	>5 x 10^9	
Active length	0.682	0.906	M

Some of the design parameters for both types are listed in Table 2. Beam is accelerated from 186 to 387 MeV by 11 cryomodules (CMs) with 3 medium-β (β = 0.61) cavities each and to 1 GeV by 12 CMs with 4 high-β (β = 0.81) cavities each, or a total of 81 cavities.

All 11 medium β CMs are built and 10 are located in the SNS tunnel. The production of the high β CMs is well advanced and nr 5 and 6 are nearing completion. One out of the 12 CMís is at the SNS site already. The overall schedule shows completion of CM construction in March 2005 and beginning commissioning of the linac shortly thereafter.

The SRF cavities are manufactured by industry out of high-purity RRR 7 250 niobium sheets. They are shipped to JLab for surface treatment, where they are subjected to standard cycles of buffered chemical polishing, high-pressure ultrapure water rinsing, and vacuum degassing, after which they are RF-power tested in a radiation-shielded vertical dewar. While Electro-polishing, a technique that has been demonstrated to further improve surface gradients, was originally foreseen, the performance of the cavities today is 25% above spec even without applying this technique. Some of the cavities over-perform by as much as 60%. While vertical single cavity tests are performed in continuous mode, cryomodule testing is done in a pulsed mode at nominal duty cycle, which allows even higher gradients for operation (Figure 5).

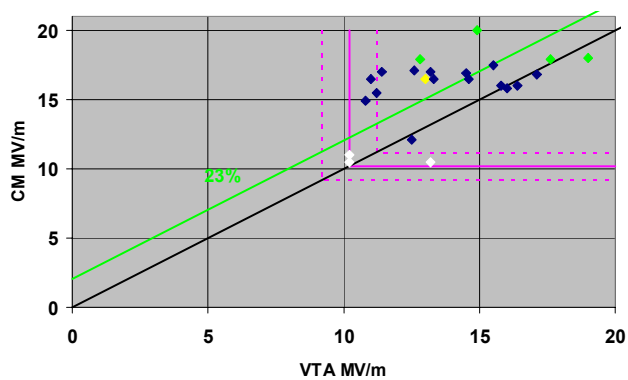

Figure 5: Comparison of single cavity test gradients (VTA, cw) with fully assembled cryomodule (CM) test results (6% duty cycle) for a variety of medium β cavities.

Three medium-β and four high-β cavities in their helium vessels are connected together per cryomodule. Figure 6 shows a picture of the 12 cryomodules in the SNS tunnel. One of the cryomodules is connected and the liquid helium transferline is cooled down to 4.5 K. RF testing at this temperature is ongoing until the 2 K cold box is operational.

Figure 6: Twelve out of 23 cryomodules are located in the SNS tunnel.

The Cryogenic System

Helium to cool the SRF linac is provided by the central helium liquefier (CHL), major parameters of which are listed in Table 3. Gas flows from two pairs of warm screw compressors, through oil removal, coalescer-demister, and charcoal filters. It is then piped to the 4.5K cold box where a standard liquefier cycle sends helium through cryogenic transfer lines to the cryomodules.

Joule Thomson valves on the cryomodules produce 2.1 K, 0.041 bar, liquid helium for cavity cooling, and 4.5 K helium for fundamental power coupler lead cooling. Cooling boil-off goes to four cold-compressors capable of 120 g/s steady state, recompressing the stream to 1.05 bar and 30 K for counter-flow cooling in the 4.5K cold box. Transfer line installation is complete and allows for a total of 32 cryomodules to be connected (23 are part of the present baseline design and 9 spots are available for future upgrades). CHL installation is largely finished with all three warm compressor streets as well as the 4.5 K cold box being commissioned. All baseline parameters have been verified up to this point. Slightly lower efficiency in the cold box has been observed so far and mitigation is underway. Operation of the 2 K cold box will start after final installation in September of 2004.

Table 3: Refrigeration Parameters

32 CMs	Primary	Secondary	Shield
Temp. (K)	2.10	5.0	35-55
Pressure (bar)	0.041,3	3.0	4.0-3.0
Static load	850 W	5.0 g/sec	6125 W
Dynamic load	600 W	2.5 g/sec	0 W
Capacity	2,850 W	15 g/sec	8300 W
Margin	100%	100%	35%

The RF Systems

The high-power RF systems are installed in a ~330 m long klystron gallery. They include 7+4 (installed + spares) 402.5-MHz, 2.5-MW; 4+5 805.0-MHz, 5-MW; and 81+20 805.0-MHz, 0.55-MW klystrons. The one cavity per klystron layout allows a lot of flexibility in operations but also leads to a very dense population of RF systems in the gallery (compare Figure 7).

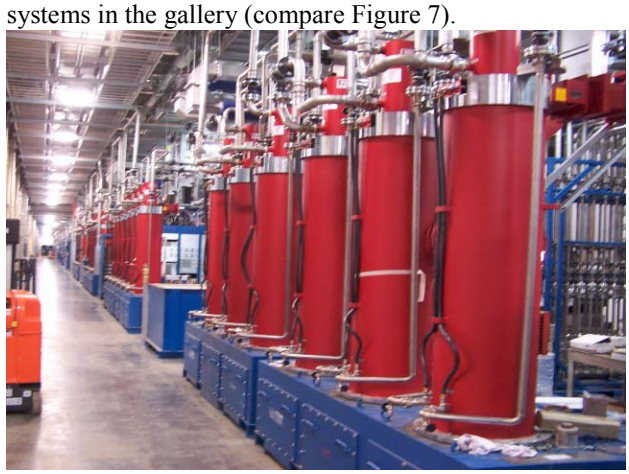

Figure 7: Klystron installation in the area of the superconducting linac. The one cavity per klystron layout requires a very dense population of rf equipment.

The klystrons are powered by 14 high-voltage converter modulators (HVCMs), which were specifically developed for SNS. Extremely high-power density and efficient AC-to-DC high-voltage conversion are the main features. High-frequency (20-kHz) switching using IGBT technology and newly developed boost transformers based on nanocrystalline transformer cores allow for a very compact design that saves investment cost as well as real estate. The HVCMs typically operate at 11-MW peak power and ~1-MW average power, feeding between 2 CCLs and 12 superconducting linac (SCL) klystrons. Integrated into the design are rectifiers and transformers, control racks, and SCR regulators. Between the nine HVCMs that are currently operating on the site, approximately 8000 h have been accumulated at a variety of power levels. 1500 hours were accumulated at design duty cycle of 7.5%. Weak spots of the design, like the switch design or the SCR units, are systematically identified and removed.

The low level rf system (LLRF) was designed and built within a collaboration at LBNL, LANL and ORNL. The very high external Q of the superconducting cavities (~$7x10^5$) requires very tight amplitude and phase control to within ±0.5% and ±0.5 degree in spite of deteriorating effects like Lorentz Force Detuning (LFD) and mechanical vibration. The recently deployed system thatís now delivered has demonstrated ±0.1% in amplitude and ±0.2 degree in phase on a superconducting cavity operating at design gradient. In addition the field control module incorporates a feed-forward loop that activates LFD piezo controllers. They reduce the frequency deviation during the pulse typically to 100 Hz and

therefore minimize the rf overhead required on the klystron output. All superconducting cavities are equipped with piezo controllers.

The klystrons as well as the HVCMs have a significant margin designed into them. To achieve the baseline beam power of 1.4 MW, many of the systems only have to operate at 50-70% of the design load which should increase the reliability substantially and later on allow for an upgrade in beam power quite easily.

Special Diagnostics Development for the Linac

Superconducting cavities are especially prone to contamination. At the same time it is very desirable to have non interceptive beam diagnostics available to monitor beam quality during normal operation. A Nd-Yag laser based transverse profile monitor system that would neutralize H^- ions fulfils both of these requirements, while traditional carbon wires would imply repetition rate as well as beam pulse length limitations when used. The number of electrons that are knocked off as a function of laser beam position can be measured with very high sensitivity into the 10^{-3}-10^{-4} range. Since the laser pulse is only ~ 10 nsec long, measurements can also be performed along the bunch train to see eventual changes of the beam emittance along the train. The laser beam is transported in an enclosed beam pipe in the linac tunnel over distance of approximately 200 meters. It can then be switched into each warm section between cryomodules. A typical measurement of a beam profile is shown in Figure 8. The laser transport pipe as well as the laser are fully installed and the first measurement stations in the superconducting linac are being assembled.

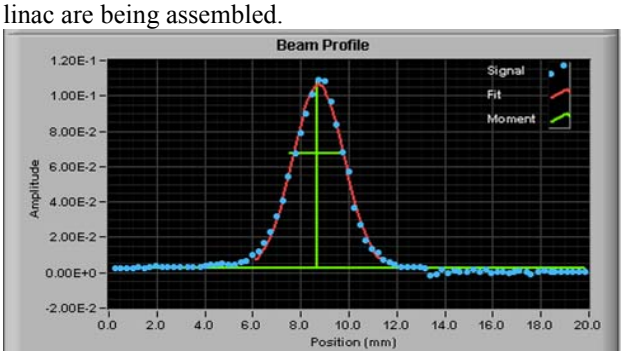

Figure 8: A beam profile measurement of a 2.5 MeV beam with a Gaussian fit plotted out to 2.5 sigma.

The High Energy Beam Transferline

The ring and all transferlines between the linac and ring and ring and target are designed and constructed by BNL and is 92% complete. Much of the hardware is installed in the tunnel and especially the HEBT with its collimation is completely in place. This allows beam transport from the linac to the dedicated commissioning beam dump straight ahead of the linac. In this beamline an experiment is prepared that will test the feasibility of highly efficient laser stripping of H- ions [5]

Summary

Over the last 5 years, the SNS collaboration has successfully met the project milestones and with the completion of the Front End Systems and the room temperature linac and rf systems two major contributors have transitioned out of the construction project. Major achievements were made during these years. In addition, an advanced technology, namely superconducting rf, as well as several other new ideas (laser profile monitors, highly efficient and compact high voltage converter modulators and advanced LLRF systems) were employed by the project and successfully further developed while in construction.

The SNS project at the time of this conference has another 22 months before completion and is well en route to achieve that goal. Future major commissioning steps include the superconducting linac in spring of 2005 and accumulator ring commissioning later that year finishing up with target commissioning in spring of 2006.

Acknowledgement

This paper is presented on behalf of the SNS collaboration and many people from different laboratories all over the world that have helped to make this a success so far. Without the enormous support from the community and the hard work of the collaborators it would have not been possible to be where SNS is today. I have not even attempted to make an accurate list of references since this would take a major fraction of the paper and I apologize. Much of the work reported here in general has been described in great detail over the past years in conferences likes this and can easily be accessed through the JACow web page at: http://www.jacow.org/

REFERENCES

[1] SNS web site: www.sns.gov.

[2] NSNS Collaboration, NSNS Conceptual Design Report, NSNS-CDR-2/V1, Martin Marietta Energy Systems, Inc., Oak Ridge Natl. Lab., Oak Ridge, Tenn., 1997.

[3] R.Orbach, ìFacilities for the Future of Science: A Twenty-Year Outlookî, DOE/SC-0078, December 2003.

[4] A.Aleksandrov, ìResults From The Initial Operations Of The SNS Front End And Drift Tube Linacî, this conference.

[5] V.Danilov et al, Oak Ridge Natl. Lab., ìThree-Step H- Charge Exchange Injection With A Narrow-Band Laserî, Phys.Rev.ST Accel.Beams 6:053501,2003

OVERVIEW OF HIGH-BRIGHTNESS ELECTRON GUNS*

J.W. Lewellen, Argonne National Laboratory, Argonne, IL, USA†

Abstract

In most electron linear accelerators, the beam brightness is set by the beam source. It is very difficult to improve the overall beam brightness after it has been produced; on the other hand, providing a brighter beam source can provide an "instant upgrade" to the performance of a brightness-limited electron-linac-based facility. The development and routine operation of high-brightness guns, therefore, is critical to the success of next-generation linac-based light sources. This includes sources already under construction, as well as proposed and as-yet completely theoretical machines.

In recent years, other potential applications of high-brightness electron beams have been identified, including high-average-power IR and UV free-electron lasers, and (relatively) high-energy electron microscopes.

The source requirements are discussed for these application areas, along with a description of some sources currently under development to meet those requirements.

AREAS OF INTEREST

High-brightness electron gun development can be broadly categorized into four distinct categories. Injectors for national facility-scale linac-based light sources represent one broad category. This includes both x-ray free-electron lasers and energy-recovery linacs; the main differences lie in the required beam repetition rates, as the desirable single-bunch characteristics are quite similar.

Second, there is presently strong interest in the use of small energy-recovery linacs to provide beams for high-power IR and UV free-electron lasers. The injectors for this category of device generally have (relatively) relaxed transverse emittance requirements, strong longitudinal emittance requirements, and very high (~ 1 A) average beam current requirements.

Third, a tantalizing possibility is the use of high-brightness injectors for use as electron microscope beam sources. Typical electron microscope beams have excellent emittance but very low (tens of keV) beam energies; among other things, this limits the depth of the sample that can be studied in transmission electron microscopes (TEMs). A high-energy (500 kV–5 MeV) electron gun, if transverse emittance and energy spread requirements can be met, represents a very interesting possible path towards dramatically expanding existing capabilities.

Finally, electron beam sources for next-generation linear colliders represent a combination of several fascinating challenges. The ability to produce a "flat" beam with a high transverse emittance ratio could at worst reduce the requirements on the e^- linac damping ring, and at best eliminate the need for one altogether. There is also a strong interest in developing photoinjectors capable of producing beams of polarized electrons.

* This work supported by the U.S. Department of Energy, Office of Basic Energy Sciences, under Contract No. W-31-109-ENG-38.

† Lewellen@aps.anl.gov

LINAC-BASED LIGHT SOURCES

The next generation of x-ray user facilities are widely seen as being driven by electron linacs, rather than storage rings. Thus, the electron beam source will be of critical importance to the performance of the facility.

In general, one can consider improving an x-ray source by increasing the flux (photons/s), the average or peak brightness, the coherence, or the temporal structure of the radiation pulse.

Linac-based light sources will probably offer the greatest potential enhancements in peak (and, to an extent, average) brightness, coherence, and temporal structure. They can be roughly categorized depending on whether the source provides spontaneous undulator radiation at a large number of photon beamlines, or uses a gain mechanism to provide coherent radiation at a relatively few number of photon beamlines. The former will be referred to as storage-ring replacements (SRRs), while the latter are known as x-ray free-electron lasers (X-FELs).

Although most future facilities will probably encompass combinations of these two basic categories of machines, the injector requirements can be derived separately. This is done more thoroughly in [1]; a synopsis is presented here.

For X-FEL injectors, we require the LCLS wavelength performance at the minimum practical electron beam energy, given present undulator technology. For storage-ring replacement injectors, we require a factor of at least 100 times peak brightness increase over existing third-generation storage rings such as the APS or ESRF.

X-ray Free-Electron Lasers

The equation relating the operational wavelength of a free-electron laser (FEL) to the electron beam energy and undulator parameters is

$$\lambda = \lambda_u \frac{1 + \tfrac{1}{2}K^2}{2\gamma^2}, \qquad (1)$$

where λ is the photon wavelength generated, λ_u is the undulator period, γ is the electron beam Lorentz factor, and K is the normalized undulator magnetic field strength. K scales with λ_u as well as the on-axis undulator field.

To minimize the overall length of the accelerator Eq. (1) implies that one should minimize λ_u and K; this results in the smallest possible electron Lorentz factor for a given wavelength. Given practical limits on undulator

technology [2], setting λ_u to 1.25 cm and K to 1 yields the smallest beam energy to obtain a given wavelength.

The Linac Coherent Light Source (LCLS), presently under construction at the Stanford Linear Accelerator Center (SLAC) is a prototypical SASE-based linac-based light source [3]. The LCLS will use a 14.35-GeV electron beam to generate 1.5-Å photons. The undulator will be approximately 90 m in length, with a K parameter of 3.7 and a period of 3.0 cm.

The LCLS is, in effect, emittance-limited. It requires large values for K and λ_u, along with strong bunch compression, to reduce the gain length to practical values given the design emittance of 1.2 μm (normalized). The LCLS saturation length as a function of emittance is shown in Figure 1, along with the relative importance of the emittance in determining the saturation length.

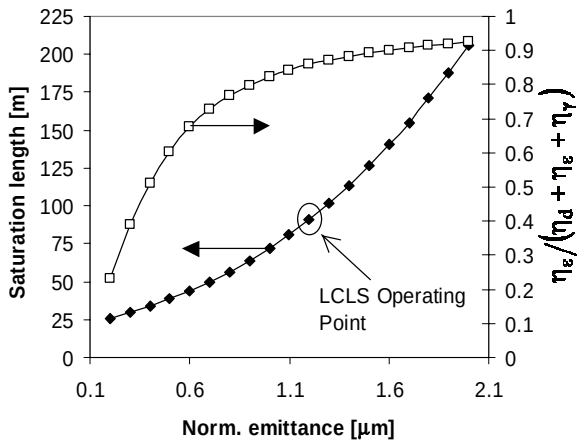

Figure 1: Saturation length (black dots) and the relative influence of emittance on saturation length (white squares) for the LCLS "High-Energy" case.

In order to reproduce the LCLS wavelength performance with a 4-GeV linac, a transverse emittance of about 0.1 μm and a peak current of 1 kA is required.

Storage Ring Replacements

Electron storage rings are typically very flexible in terms of the charge per bunch and bunch spacing within the ring, which allows the facility operator to make trade-offs between peak x-ray beam brightness, average brightness, and flux, depending on the needs of the local user community. For comparison purposes, "typical" operating figures from the Advanced Photon Source* (APS) will be used [4].

The spectral brightness of an x-ray beam from an undulator can be written as

$$B_{\Delta\omega/\omega} \propto \frac{\gamma^2 N^2 I}{\sigma_x \sigma_y \sqrt{\left(1+\frac{\sigma'^2_x}{\theta^2_{cen}}\right)\left(1+\frac{\sigma'^2_y}{\theta^2_{cen}}\right)}}, \qquad (2)$$

where γ is the electron beam Lorentz factor, N is the number of undulator periods, I is the beam current, $\sigma_{x(y)}$ is the horizontal (vertical) spot size of the electron beam, $\sigma'_{x(y)}$ is the horizontal (vertical) divergence of the electron beam, and θ_{cen} is the angular width of the radiation cone from a single electron. If $I = I_{peak}$, the peak electron beam current, Eq. (2) yields the peak photon beam brightness; if the average electron beam current is used instead, Eq. (2) provides the average x-ray beam brightness.

Of significant interest is the case of a small transverse emittance at modest charge and at a reduced repetition rate. Running in this fashion could theoretically improve the peak brightness significantly, without incurring a significant performance penalty on average brightness. (The flux, however, would of course be lowered considerably due to the lower beam current.) Several possible scenarios are given in Table 1.

There are two items of note regarding this table. First, there is an implicit assumption that the injectors can meet not only the single-bunch requirements but also the repetition rate and average current requirements. Second, unlike the X-FEL, which will either lase (e.g., saturate) or not, there is no single cutoff point at which an SRR can be said to either start or stop working. The desire for at least 100x brightness enhancement is fairly arbitrary, but is useful for showing the direction in which one might wish to proceed.

Common Considerations

It is interesting to note that X-FELs and SRRs have, at least in principle, similar single-bunch parameter requirements, in terms of emittance, bunch length, and charge. This strongly suggests that one driver linac could provide beam for both a storage ring replacement and an X-ray free-electron laser facility. Indeed, many proposed linac-based light source designs, such as LUX [5] and 4GLS [6], take just such an approach.

IR AND UV FREE-ELECTRON LASERS

In general, FELs are cost effective for applications only where conventional laser technology cannot be used due to wavelength or average power output considerations. This is the case in the hard x-ray regime, which was discussed in the previous section. It is also the case when average laser powers in the kW range and above are desired. At these power levels, removing heat from the optical medium can become problematic, and conventional lasers tend to grow large and expensive.

The Jefferson Laboratory FEL program, for instance, has proven to be a very impressive demonstration of a high-average-power FEL operating in the IR [7], with ongoing programs to increase the output power and to operate in the UV.

* Although some parameters are available on the Web, the APS has an ongoing program of storage ring performance improvements. The best way to obtain the most recent performance figures is to contact either the Accelerator Physics or Operations Analysis groups at APS.

Table 1: Brightness enhancement factors for several possible beam sources. The net brightness enhancement is normalized to the APS case, at 100-mA average beam current.

	Nominal parameters		Peak brightness enhancement factor		Net brightness enhancement	
Beam Source	Norm. emittance (hor. x vert.)	Peak current (assumed charge)	from ε_n decrease	from I_{peak} increase	peak	average
APS	40 μm × 0.5 μm	300 A	(n/a)	(n/a)	1	1
S-band gun	1 μm × 1 μm	3 kA (1 nC)	$\sqrt{20} \approx 4.5$	10	45	45(1)
new gun design	0.1 μm × 0.1 μm	1 kA (0.1 nC)	$\sqrt{400} \cdot \sqrt{5} \approx 45$	3	135	13.5(2)

(1) assumes 1 nC at 100 MHz for 100 mA average beam current
(2) assumes 0.1 nC at 100 MHz for 10 mA average beam current

In an FEL, the gain medium is the electron beam, and waste heat exits the cavity at just under the speed of light. Theoretically, the optical power output is limited only by the ability to extract energy from the electron beam and the ability of the mirrors to withstand the optical power.

The basic design of such a source is an energy-recovery linac, operating CW at high average beam currents with peak beam energies in the 100- to 500-MeV range. The emittance requirements are not particularly stringent compared to X-FELs, due both to the longer operating wavelengths and to the use of an optical cavity. Typical specifications would be 1-A average beam current, 5-μm (normalized) transverse emittance, and 100-keV·ps longitudinal emittance. Lower linac frequencies are preferred; the larger cavities allow for more stored energy, smaller wakefields, and lower cavity losses.

There are several complications to these designs not generally found in existing injector designs, centering around the high average currents. Beam breakup and transverse wakes are likely to be important in the injector. Further, a 1-A beam at 5 MeV delivers 5-MW beam power; limits on the ability to couple power into the cavities will thus limit available field gradients. An optimistic estimate is 2-MW power gain per cavity at 1-A average currents [8]. This will hold true whether the basic configuration is a dc gun "head" with rf booster cavities or a purely rf-based design.

Beam halo also becomes a significant concern, especially if the rf system is either partly or entirely superconducting. Consider that at 5 MeV, having 0.01% of a 1-A beam as halo corresponds to 500-W halo power. In an SRF system, this could exceed heat-leak and rf loss powers by an order of magnitude. Recent work on the subject implies that halo formation may be unavoidable [9]; further work is clearly needed on the subject.

ELECTRON MICROSCOPES

Electron microscopes are highly refined scientific instruments based around low-energy electron beam accelerator technology. To date, there has been remarkably (and depressingly) little information exchange and cross-fertilization between microscope designers and injector designers, perhaps due to the very different final goals for the electron beams.

This is unfortunate for both sides. From the injector side, the microscope designs present truly impressive electron beam transport optics, in terms of aberration corrections and beam control. On the other hand, the average currents are low, the beam is at extremely low energy (10–100 kV), and it is not bunched at all.

From the microscope side, injectors represent huge increases in beam voltage and, possibly, average power. The beam emittance, however, is about 10^3 greater than the best e-microscope beams, and the energy spread, at a few tenths of a percent, is huge.

A starting set of parameters for a "high-energy" electron microscope (from a high-brightness gun designer's standpoint) might be: average beam current, 0.1 mA; beam energy, 1-2 MeV (kinetic); normalized transverse emittance, 5 nm; rms energy spread, 10^{-5} or less. Clearly, these will be difficult parameters to meet; however, some initial work on the subject [10] is quite promising.

It is important to note that, with the exception of the beam energy, all of these parameters are mediocre at best from the electron microscope's perspective; they represent a starting point only. It is equally important to note, however, that the electron microscope community has spent the better part of a century refining their techniques and designs. An injector designer should not expect to meet all aspects of current microscope performance on the very first try, any more than an e-microscope designer should expect to be able to design the perfect 100-kW UV FEL injector on the first attempt.

It seems apparent that the electron microscope and high-brightness injector communities have much to offer each other in principle. The main hurdle, from the author's experience, appears to be a lack of willingness to consider accepting some sub-state-of-the-art parameters for the sake of initial investigations.

LINEAR COLLIDERS

The overall requirements for a linear collider gun are fairly similar to those of linac-based light sources, with two exceptions. First, the injector should be capable of

producing a beam of polarized electrons. Second, the injector should be capable of producing a "flat" beam so as to relax the requirements for, or ideally eliminate, the electron beam damping ring. These are, in effect, separable concerns. Most of the present development work in these areas focuses on rf photoinjector guns.

Polarized electron beams have been produced for some time using dc guns with strained GaAs cathodes [11]. The challenge in applying these techniques to rf photoinjectors lies in both the vacuum environment (generally worse in rf guns than in dc guns, all else being equal) and in the higher gradients typically found in rf guns. Initial attempts were interesting but inconclusive; additional work is ongoing at a number of places, including SLAC [12].

Flat-beam production from an rf gun is based around the transformation of a magnetized, symmetric electron beam [13]. Results to date [14] are quite promising, compared to the desired 100:1 aspect ratio.

The idea of a positron gun is interesting to contemplate. Typical positron-generation schemes, such as running a 200-MeV electron beam into a tungsten converter target, result in positron beams with large energy spreads and emittances. By using the target as a positron "cathode" one could consider designing a positron "gun" to effectively capture and damp the positron beam. Some initial studies on the idea apparently were not fruitful [15], and it appears from the dearth of publications on the subject that the idea has not been pursued further. More recent design tools, codes, and concepts, however, might permit both a more thorough and more successful exploration of the concept.

COMMON ELEMENTS

Electron injector design is in the process of branching out into several different areas, with applications ranging from the sole accelerator in an individual laboratory instrument (i.e., an electron microscope) to the beam source for a national facility (i.e., a linac-based light source or linear collider). There are elements common to most of these areas of application, however, which must be addressed regardless of the final application. These include:

- Increasing the duty factor, for higher average-performance figures;
- Improving the beam quality, for higher single-bunch performance figures;
- Improving the techniques used to build the guns, e.g., for improved symmetrization, cooling (for NC guns), or power-feed capabilities (for SRF guns);
- Increasing the operational reliability of the entire injector system, including drive laser and rf systems;
- Improving the fundamental electron source, e.g., cathodes and cathode research; and
- Improving the basic tools (theory and simulation) used to understand and design injectors.

Of these, perhaps the cathode research and development is the most critical common element. All of the injector categories require high-performance cathodes in one sense or another. Order-of-magnitude improvements in lifetime, robustness, quantum efficiency, and thermal emittance are known requirements. Electron beam emission uniformity is known to be a critical factor in determining final beam quality [16]; this is a topic that requires considerable further attention, both in terms of the type of cathode (especially high-quantum-efficiency materials) and in terms of uniformity evolution over time in an operational environment.

ONGOING INJECTOR DEVELOPMENT

There are several injector development projects worldwide that are addressing some or all of the performance aspects for these next-generation injector applications; most of the work, however, has tended to focus more on light source (including high-power FELs) and collider injectors.

Dr. Sinclair's group at Cornell has obtained good results with dc injectors; in particular, their simulations are predicting 0.7-μm emittances at 0.8 nC and 0.1-μm emittances at 0.08 nC, not including thermal emittance [17]. These results have been obtained in part through the use of large concurrent simulation runs for parameter optimization, a technique the author has long believed is underutilized in the high-brightness injector community.

In the past, rf guns for long-wavelength FELs have operated at up to 25% duty factor [18]. At present there is a development effort underway at Los Alamos National Laboratory (LANL) and Advanced Energy Systems, Inc. (AES) to develop a normal-conducting rf gun capable of true CW operation at high gradients [19].

The Drossel collaboration, centered at Rossendorf University, has made excellent progress in the construction and operation of a fully-superconducting rf gun [20]. Brookhaven National Laboratory (BNL), in collaboration with AES, has made significant progress in this area as well [19]. Recently, AES and BNL have begun working with Rossendorf on an improved overall design for high-power FEL applications.

The injector design for TESLA and the TESLA X-FEL, as well as for LUX, have taken somewhat different approaches. The LUX injector, a normal-conducting rf gun, is intended to produce single electron bunches per rf macropulse, at repetition rates at 1 kHz. The TESLA injector prototype, under study at the PITZ test facility at DESY-Zeuthen, has achieved a 1% rf duty factor operation at 1.3 GHz, producing ms-duration electron beam bunch trains at 10 Hz.

Linear collider injector development is also proceeding well. Flat-beam production tests at Fermi National Accelerator Laboratory (FNAL) have proven very successful to date and appear to be maturing. Development of rf gun cathodes for polarized beam production is an ongoing effort. The SLAC effort is considering the use of a plane-wave transformer (PWT) injector design [21] in order to improve vacuum pressure and pumping speed, and another effort at AES will be

comparing several different injector types in the light of cathode bombardment from both ions and field-emitted electrons.

There is also interesting work going on that is not as neatly categorized into one or more of the roles presented here, yet represents interesting developments in the field. This work includes the harmonic bandgap structures, x-band and higher frequency guns, on-axis coupling schemes, and multifrequency fields.

CONCLUSIONS

High-brightness electron beam source development will be critical to the success of upcoming projects, such as linac-based light sources and industrial-scale UV lasers, and offers the promise of extending capabilities of instruments such as electron microscopes.

Disparate needs are driving injector design in several different directions; for instance, high beam powers for IR and UV FELs, low transverse emittances for linac-based x-ray light sources, and emittance aspect-ratio control for linear colliders.

A number of common elements are identifiable, however. Almost all of these applications would benefit from higher duty-factor operation. Improvements to the cathode, encompassing uniformity, lifetime, and quantum efficiency, are likewise universally desirable.

Improvements to the software used to model injectors are also required. The specific needs vary widely depending on the application; however, common themes include multibunch effects, cavity-beam interactions (i.e., transverse and longitudinal wakefields), fine-structure resolution within the electron bunch, beam halo formation and evolution, and realistic cathode emission models.

High-energy, low-emittance electron guns are also being considered for use in novel (to the injector development community) applications such as electron microscopes. Doing so will require adaptation to a very different set of operational performance requirements and conditions; however, the potential benefits appear to be worth the effort.

REFERENCES

[1] J.W. Lewellen, "High-Brightness Electron Guns for Linac-Based Light Sources," to be published in the Proceedings of the 2004 SPIE Conference (Denver, CO).

[2] Private communication, Elizabeth Moog, Magnetic Devices Group Leader, Advanced Photon Source (2004).

[3] LCLS Conceptual Design Report, SLAC-R-593 (April 2002), available on the Web at http://www-ssrl.slac.stanford.edu/lcls/cdr.

[4] Private communication, Katherine Harkay, Advanced Photon Source Accelerator Physics Group Leader (2004).

[5] J.N. Corlett et al., "A Recirculating Linac-Based Facility for Ultrafast X-Ray Science," Proceedings of the 2003 Particle Accelerator Conference, Portland, OR, pp. 186-8 (2003).

[6] E.A. Seldon, "The 4GLS Project: update and technological challenges," presented at the 8th International Conference on Synchrotron Radiation Instrumentation, San Francisco, CA (2003).

[7] G.R. Neil et al., "Status of the Jefferson Lab IR/UV HIGH Average Power Light Source," Nucl. Instrum. Methods A **507**, II-5 (2003).

[8] Private communication, Alan Todd, Advanced Energy Systems (2004).

[9] C. Bohn, "Collective Modes and Colored Noise as Beam-Halo Amplifiers," presented at the 11th Advanced Accelerator Concepts Workshop, Stony Brook, NY (2004).

[10] U.S. Patent Application 10/887,142.

[11] D.T. Pierce et al., "The GaAs Spin Polarized Electron Source," Rev. Sci. Instrum. **51** (4), 478 (1980).

[12] J.E. Clendenin, "Polarized Electron Sources for Future Colliders: Present Status and Prospects for Improvement," presented at the ALCPG 2004 Winter Workshop, Palo Alto, CA (2004).

[13] R. Brinkmann et al., "A Low Emittance, Flat-Beam Electron Source for Linear Colliders," Proceedings of the 2000 European Particle Accelerator Conference, Vienna, Austria, pp. 453-5 (2000).

[14] Presentation by Philippe Piot, "Photo-injector production of flat beams," 17 May 2004; available online at http://www.fnal.gov/directorate/program_planning/all_experimenters_meetings/special_reports/Piot_Photoinjector%20Lab05_17_04.pdf.

[15] Private communication, Michael Borland, Operational Analysis Group Leader, Advanced Photon Source (1998).

[16] M.E. Hernandez et al., "Effects of Cathode Non-Uniformity on Emittance of an S-Band Photocathode rf Gun," SLAC-PUB-8307 & LCLS TN-99-13 (December 1999).

[17] Private communication, Charles Sinclair, Cornell University (2004).

[18] D.H. Dowell et al., "First Operation of a Photocathode Radio Frequenc Gun Injector at High Duty Factor," Appl. Phys. Lett. **63** (15), 2035 (1993).

[19] A.M.M. Todd et al., "Recent Advances in High-Brighntess Electron Guns at AES," Proceedings of the 2002 European Particle Accelerator Conference, Paris, France, pp. 1756-8 (2002).

[20] D. Janssen et al., "First operation of a superconducting RF-gun," Nucl. Instrum. Methods A **507**, 314 (2002).

[21] J.E. Clendenin et al., "Polarized Electrons Using the PWT RF Gun," SLAC-PUB-9550 (October 2002).

ACCELERATOR CONTROL AND GLOBAL NETWORKS – STATE OF THE ART*

D. Gurd, SNS, ORNL/LANL, Oak Ridge, TN, USA

Abstract

As accelerators increase in size and complexity, demands upon their control systems increase correspondingly. Machine complexity is reflected in complexity of control system hardware and software and careful configuration management is essential. Model-based procedures and fast feedback based upon even faster beam instrumentation are often required. Managing machine protection systems with tens of thousands of inputs is another significant challenge. Increased use of commodity hardware and software introduces new issues of security and control. Large new facilities will increasingly be built by national (e.g. SNS) or international (e.g. a linear collider) collaborations. Building an integrated control system for an accelerator whose development is geographically widespread presents particular problems, not all of them technical. Recent discussions of a "Global Accelerator Network" include the possibility of multiple remote control rooms and no more night shifts. Based upon current experience, observable trends and rampant speculation, this paper looks at the issues and solutions - some real, some probable, and some pie-in-the-sky.

INTRODUCTION

The phrase "state-of-the-art" can mean either of two quite different things. Whereas literally it describes current practice, it is also often used to describe "cutting edge" concepts, perhaps not yet quite ready for prime time. This paper will discuss some trends in accelerator controls which may be expected to lead from current practice to practical systems of the future.

Three main factors drive developments in accelerator control: the ever increasing scale and complexity of accelerators themselves; their ever more demanding reliability requirements and the fast pace of technology change in our discipline. Trends can be discerned by following the proceedings of the biennial accelerator controls conferences – The International Conference on Accelerator and Large Experimental Physics Controls Systems (ICALEPCS). Last year's conference was held in Gyeongju, Korea, and next year's is scheduled for Geneva, Switzerland. Many of the observations in this discussion are derived from those conferences. Although this conference is focused on linacs, the techniques and technology of linac control systems do not differ significantly from those applied to circular machines, and the following discussion applies equally to both.

* Work supported by the US Department of Energy under contract DE-AC05-00OR22725

THE CONTROLS "STANDARD MODEL"

For many years, the controls community has referred to a "Controls Standard Model." Although this three-layer distributed model has evolved in the details of its various implementations, it has remained surprisingly constant for over a decade. A good example, drawn from the LHC Design Report, is the architectural representation of the LHC control system shown below in figure 1. The three layers are known respectively as the "presentation" tier, the "application" or "server" tier and the "resource" tier.

Although well-established institutions (DESY, CERN, SLAC, BNL, Fermilab, etc) have built new facilities based upon this standard model but using legacy control system tools and technologies, it is not an exaggeration to suggest that the last decade has been dominated by the use of EPICS – the Experimental Physics and Industrial Control System [1] – developed jointly by Los Alamos National Laboratory and Argonne National Laboratory and embracing the contributions of many collaborators. The EPICS collaboration includes well over 100 licensees, and most "green-field" facilities started in the past ten years – including KEKB, SNS, ISAC at TRIUMF, SLS and Diamond – have opted to use EPICS, benefiting from a reliable, high-performance base and well-defined user interfaces that allow easy interfacing and widespread sharing of locally-developed applications and embellishments. As many as 50% of papers presented at recent ICALEPCS meetings come from the EPICS community, and the semi-annual EPICS collaboration meetings sometimes draw over one hundred participants. More recently, EPICS, which had been available free only to not-for-profit institutions and two competitively licensed companies, has been released as open software and distributed to industries and individuals, expanding its use even further. Several companies advertise products and instruments with EPICS drivers, and industry has been successfully contracted by SNS, SLS and others to develop EPICS-based subsystems for integration into otherwise home-built systems.

EPICS represents one possible approach to implementation of the standard model. Although EPICS users select from a variety of available tools, all implementations have two things in common – a communication protocol known as "Channel Access" and a common distributed database design. Without these it isn't EPICS; but after these almost anything goes. EPICS continues to be selected for new machines because its open architecture allows the use of modern (state-of-the-art) technology at all levels. Channel Access is layered upon the Ethernet TCP/IP protocol, and so EPICS has benefited from the ever-improving performance and cost

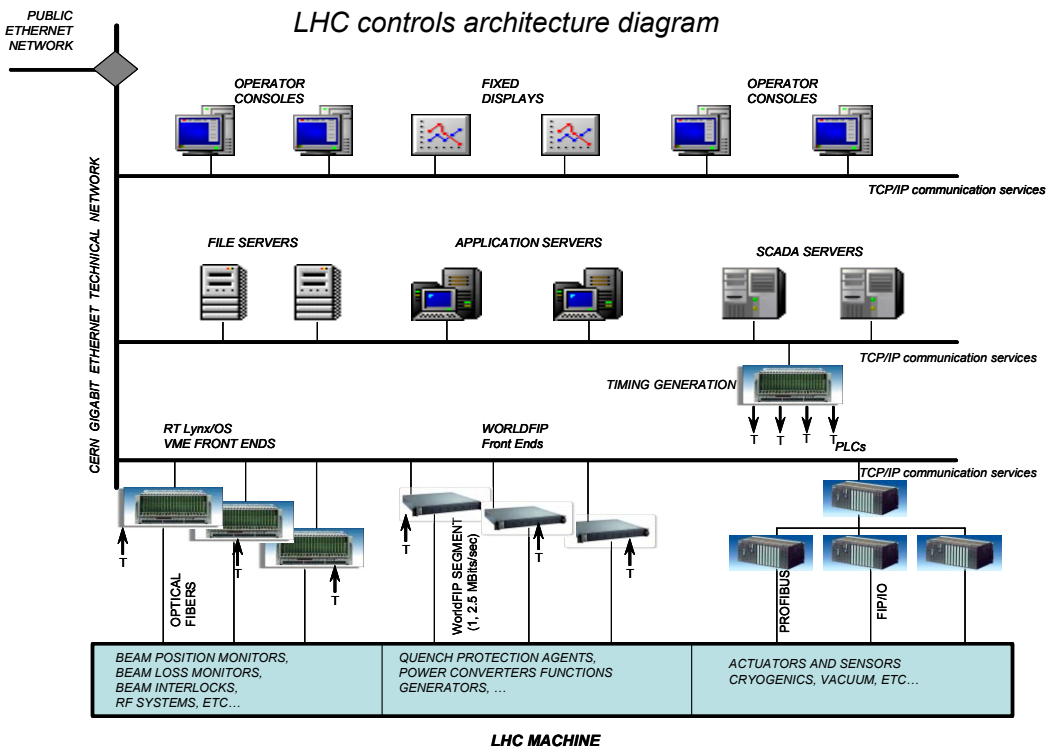

Figure 1: The LHC Control System Architecture as an example of the "Controls Standard Model" Ref. [2]

competitiveness of Ethernet hardware. New designs use off-the-shelf one-gigabyte backbone technology and fast switches. The well-defined channel access interface has also made it possible to incorporate modern fieldbuses and I/O devices as they become available. Most importantly, the EPICS open architecture has made it possible to incorporate commodity PC technology at all three layers of the standard model: Linux-based presentation layer operator interfaces; Linux-based application servers and Linux- or Windows-based I/O controllers. This openness is one of the most important features of the state-of-the-art in accelerator controls.

In a sense, then, (the sense in which it continues to be selected) EPICS *is* the "state-of-the-art" for accelerator control. Nonetheless the EPICS community is aware that it is working with technology and an architecture that is over fifteen years old. While "state-of-the-art" in one sense, it is most assuredly no longer "cutting edge." Moreover, it is clear that EPICS "out-of-the-box" will not be adequate to address the formidable challenges of potential new machines, such as the proposed linear collider. As a result the EPICS community has formed an international "EPICS 2010" committee to examine the requirements for a control system for the next decade, and to determine how EPICS might evolve to meet those requirements. Participants from outside the EPICS community have been included, and the underlying idea is that the outcome of these discussions might have nothing but the name in common with the EPICS of today.

The EPICS design sacrifices much on the altar of performance. The emphasis has been on optimizing the underlying infrastructure, and the application layer has been largely ignored. As suggested by the name of its protocol, all communication is at the level of a "channel," – a single process variable (PV) or signal – analog, binary or "soft." EPICS has no inherent concept of an accelerator model or of a group of related signals making up a "device." There have been various attempts to redress this deficiency, the most successful being the "cdev" protocol from JLab which found some acceptance both inside and beyond the EPICS community. EPICS purists, however, have seen the device concept to be unnecessary at the lower communication layers, and have been unwilling to pay even its rather small performance penalty. Physics users and application programs however think in terms of devices, and devices are "objects" with an appeal to computer science purists. At SNS accelerator objects and object-based application programs have been successfully grafted on to the control system at the top using the home-grown, Java-based XAL accelerator object library, toolkit and framework and a native Java Channel Access is under development. The desire for a more integrated object-oriented approach, however, has resulted in other, non-EPICS, implementations of the controls standard model. We use LHC as an example, although there are many others using similar concepts, such as the TANGO system developed at ESRF and recently adopted by Soleil. [3]

The similarities in technologies between the overall hardware architectures of the EPICS-based SNS control system and the non-EPICS LHC design illustrated in Figure 1 are striking. Besides the obligatory three layers, both are based upon a gigabit Ethernet communications backbone. At the "resource tier" both use VME and PC-based Front End Computers (FECs) running a standard real-time kernel as well as Programmable Logic

Controllers (PLCs) for slower or non-synchronized I/O. Both use a limited number of standard fieldbuses. (Specific PLCs and fieldbuses are different, reflecting different European and American preferences and availabilities.) In both cases the upper layers – application servers and operator consoles – are based upon PCs running the Linux operating system.

The differences are in the software architecture, and in particular in the use of an elaborate "Controls Middleware" which is the collection of protocols, frameworks and Application Programming Interfaces (APIs) that allow the various layers to communicate. For LHC, this software infrastructure is built around a standard Machine Control "Framework" (J2EE), which binds the three levels together and provides all the needed common services, freeing the applications programmer to concentrate on the applications. The LHC design is object-oriented and uses the widely-accepted higher-level, standardized "Common Object Request Broker Architecture" (CORBA) protocol. The concept of an accelerator device is inherent in the protocol, and an accelerator model is implicit in the implementation. "Wrapping" the communicated objects incurs a performance overhead cost, but the payback is in the more natural relationship between the accelerator model and applications on one hand and the common framework developed for the front end computers on the other. The LHC software design is surely state-of-the-art, and variations on this approach are widespread in the community. The most recent ICALEPCS featured a session devoted entirely to middleware and frameworks. At LHC, a similar framework (UNICOS) provides the unifying infrastructure and services for the PLC-based industrial controls.

COMPLEXITY

It is interesting that notwithstanding reduced hardware costs, substantially improved performance and the availability of free control system toolkits such as EPICS, the cost of accelerator control systems as a fraction of total facility costs has not changed significantly over the last three decades. The reason is that as these costs have gone down, machine complexity and corresponding demands on their control systems have increased equivalently. In big new machines, complexity manifests itself in sheer size and numbers. In smaller ones, often requiring control of very high power beams or having very demanding up-time requirements, the issue may be a need for complex automation, redundancy or complicated control and feedback algorithms. Increased accelerator complexity challenges control systems in several ways:

Scale:

The most obvious impact of big machines is big control systems. As the number of distributed processors goes up, the amount of data to be communicated and therefore network bandwidth requirements goes up correspondingly. Network technology has so far kept pace. Gigabit Ethernet is readily available with appropriately fast switches and routers and the switched architecture gives considerable flexibility in controlling traffic patterns. It is essential to consider the scalability of the software architecture. As an example, the EPICS Channel Access communication protocol does not assume a name service and uses network broadcasts to make connections. This approach does not scale well – the number of broadcasts could overwhelm slower devices on the network – and the introduction of name service (already developed at JLab) will be required for larger systems.

Configuration Management:

As numbers go up, managing the control system configuration becomes increasingly difficult. State-of-the art control systems use a number of computer-based tools to keep track of their control system configuration, including hardware and network configuration and software revision control. The more processors there are the more likely that multiple software versions require tracking. Hardware configuration is commonly maintained in a relational database – Oracle is the preferred product in the accelerator world – and software revision and release control is often managed by the Concurrent Version System (CVS) or a similar system. The APS at Argonne has developed a powerful on-line tool that populates a configuration database automatically whenever a front end processor is rebooted, assuring correctness by using the same files as were just loaded.

Data Management

Large machines produce large amounts of operational data that needs to be saved for subsequent analysis. The recent Au/Au run at RHIC archived about 6 Gbytes/day for the duration of that six month run in addition to 3 Gbytes/day of post-mortem data. Estimates for SNS are comparable (without, at present, the post-mortem), using a new EPICS archiver designed to log 10K process variables/sec. The LHC design document anticipates routine logging of $10^5 – 10^6$ variables with frequencies of up to 0.1 Hz, in addition to "several gigabytes" of post mortem data on events such as quenches. The data is inherently "bursty," so very high speed disk access is required. Here again we are saved by technology. For example, relatively "low-cost, entry-level" (advertiser's words) Fibre Channel-based storage arrays are available that achieve 320 Mbytes/sec data transfer rates and have a capacity of 6 Terabytes. Low demand systems can be built with commodity servers; high demand systems make use of "write-once" technology for improved throughput. Design of the archive files is particularly challenging. A compromise has to be reached between optimizing the rate of data acquisition and that of data retrieval. Acquiring these large amounts of data is challenging; managing the terabytes of accumulated data even more so. (A rough estimate based upon an early NLC design and – probably unrealistically – assuming 120Hz acquisition from 15,000 BPMs and 10,000 Klystrons and

as many other miscellaneous channels anticipated acquiring over 30 *petabytes* of data/year! [4]) Strategies for long-term storage and data decimation or compression are required. Happily, our problem is still relatively small in comparison with that of the high energy physics experimenter.

Fast Feedback and Automation

Modern accelerators are frequently loss-limited and too complex to operate safely manually. A high level of automation is required, as is fast feedback and/or feedforward. Model-based control requires the on-line availability of an accelerator model, leading to the widespread use of object-based programming languages and communication protocols to facilitate linking the model to the hardware. Fast feedback generally operates at speeds not achievable by the control system TCP/IP infrastructure, so separate point-to-point links (for example at SLC) or reflective memory (for example at APS) may be used. Algorithms typically execute in dedicated Digital Signal Processors (DSPs) or Field Programmable Gate Arrays (FPGAs), fortunately also keeping up in speed and memory size.

Reliability

State of the art control systems are expected to be reliable. Goals of 98.8% scheduled up-time are often set. Up-time requirements for the new machines demand it. Controls hardware is inherently more reliable than other accelerator components, and the less reliable components (power supplies, for example) can (with money) be made redundant. New facilities using VME have adopted the VME64 standard that permits "hot-swapping" for faster repair times, but software drivers need to be changed to take advantage of this feature. The widespread use of robust industrial controllers (see below) also contributes to improved reliability. Small accelerators – in hospitals, for example – perform reliably, in general by being very simple. (I recently asked a hospital technician operating a surgical robot how often he had to reboot. He didn't even understand the question!) It is harder to achieve reliability in large, complex systems. Reliability issues are most likely to occur in the software, and here configuration management is extremely important.

SOME COMMON APPROACHES

Open Systems

A trend in state-of-the-art accelerator control systems is the use of "open" or non-proprietary software systems. Until very recently, EPICS depended upon the proprietary VxWorks real-time kernel. That constraint has been removed, however, and some recent implementations of EPICS – notably the Canadian Light Source – have been successfully implemented with the open RTEMS kernel. Indeed, EPICS itself has become open and is available to anyone. The LHC J2EE framework described above is also a vendor-independent industrial standard which includes both the Java Message Service (JMS) and Enterprise Java Beans (EJB). Perhaps the most widely adopted open standard is the Linux operating system which is, at present, the system of choice for state-of-the art accelerator control systems.

Industrial Systems

What seems obvious now wasn't always so. Accelerators include many subsystems that do not differ in any important way from common industrial process control systems. These are the subsystems that do not require synchronization with the beam. Indeed beam synchronous systems – RF, Beam Instrumentation, ramping and/or kicker magnets and a few others – are in the minority. It makes sense to use industrial process control for industrial processes – vacuum, cooling, cryogenics, power, conventional facilities – and modern control systems do just that. All new facilities use PLCs and standard industrial fieldbuses for these systems, nonetheless integrating them at some level with beam synchronous subsystems so data can be correlated as required. CERN has carried the use of industrial controls to the limit, employing complete commercial SCADA systems for operator interaction and deploying the UNICOS framework as an infrastructure.

Ethernet as a Fieldbus

One aspect of the use of commercial controllers is an increasing number of devices connected directly to the Ethernet. Architecturally this is very attractive; however caution must be exercised. Commercial devices may on the one hand be putting unwanted traffic on the network; and on the other they may not be able to handle the high data rates already on the network. They may be confused by broadcast or multicast messages, or their processors may have no time for their own work while they make decisions about unsolicited traffic. The use of Ethernet controllers requires careful thought about network architecture and configuration in order to derive the benefit from these products without experiencing the potential problems. Nonetheless it is fair to say that new systems incorporate more and more Ethernet-based controllers.

PC-based Controllers

More and more devices come with "smart controllers," many of them PC-based. At the SNS, nearly all beam diagnostic devices are controlled individually by Windows-based "Network Attached Devices" (NADs). Hundreds of them. These devices run with a stripped-down version of Windows and EPICS core; have been configured with Labview© for initial front-end processing; use memory-mapping to transfer massaged data to EPICS and then talk to the control system transparently like any other IOC.[5] The deep integration of commercial software packages such as Labview© is another related and notable trend. The presence of hundreds of PCs on the control system network presents security and configuration management issues, but not

significantly different from those presented by (say) VME-based processors.

Timing

Timing system requirements are similar from accelerator to accelerator: some "events" for synchronization of RF and data acquisition, time-of-day for eventual data correlation and synchronous distribution of mode, magnet ramp information, etc. While the requirements are similar, specifications on resolution, stability (jitter), number of events or length of distributed messages become increasingly demanding. The jitter specification for LHC, for example, is 10^{-10}. The timing system at the SLS has achieved excellent performance using commercial Ethernet components to transmit 8 bit event codes at 50 MHz (20ns resolution) [6]. This system has proved very portable. The software was adapted from the APS, and the entire system is being imported by Diamond.

COLLABORATION

Perhaps the most significant development in new and planned large machines is not technical at all, but rather more sociological. As accelerators become larger and more expensive to build, it is clear that new projects can only be accomplished collaboratively. CERN has long provided one model for collaboration in accelerator building. SNS – a collaboration between six American National Laboratories – provides a different model, in which the control system itself was developed collaboratively by the partner laboratories. In anticipation of the international collaboration that will be required for a linear collider project, a series of international workshops has been held to discuss the idea of a "Global Accelerator Network" (GAN) [7]. The name refers both to a network of collaborating institutes, and to the communication networks that would be required to allow remote participation by distant laboratories in the commissioning and possibly operation of the facility itself. The technology for remote monitoring already exists, and remote access to modern control systems is generally implemented, subject to the security restrictions of individual institutions. One extreme idea was to have three complete control rooms, making extensive use of video-conferencing technology, one or more each in Europe, Asia and America, with machine control rotating around the world from continent to continent. Day shifts only! That concept requires video-conferencing technology well beyond the current state-of-the-art, and probably never usefully realizable. A remote Main Control Room is neither state-of-the-art nor cutting-edge. It is pie-in-the-sky. More practical is the ability for distant subsystem contributors to assist with the commissioning of their subsystems. This capability was found to be very useful for SNS, and existing networks can already meet most requirements. The principle obstacle, and likely show-stopper, will be meeting ever-more-stringent computer and network security requirements.

CONCLUSIONS

The "Controls Standard Model" has proven extremely adaptable and continues to be the model for new and yet-to-be-designed accelerators. Computer and communications technology has so far kept up with the requirements of ever larger and more complex systems. Commodity and industrial equipment play an increasing role. Notwithstanding its older software architecture, EPICS continues to be selected for many new machines under construction. The use of software "frameworks" and object-oriented techniques is increasing as more effort goes into applications and less into more routine tools. The biggest challenges for the very large accelerator control systems of the future include stringent reliability goals, large volumes of data and collaboration management. Accelerator Control is an exciting discipline; systems are built using rapidly-changing technologies and it is always tempting to use the "latest and greatest." It is wise, however to keep in mind that "better is the enemy of good enough," and to select mature technologies that can meet requirements when designing real machines. The true state-of-the-art isn't necessarily the sexiest or the most cutting edge – it is the one that really works.

ACKNOWLEDGEMENTS

This paper has been informed by discussions with many colleagues to whom I am very grateful. I would like particularly to acknowledge the contributions of Hamid Shoaee (LANL), Larry Hoff (BNL) and Bertrand Frammery (CERN).

REFERENCES

[1] Experimental Physics and Industrial Control System http://www.aps.anl.gov/epics
[2] LHC Design Report. Chapter 14. (B. Frammery et al)
[3] A. Götz et al. TANGO – "A CORBA-based Control System"
http://icalepcs2003.postech.ac.kr/db/proc_papers/MP705/MP705.pdf
[4] Hamid Shoaee. Private Communication
[5] D. Thompson and W. Blokland. "A Shared Memory Interface between Labview and EPICS"
http://icalepcs2003.postech.ac.kr/db/proc_papers/TU514/TU514.pdf
[6] Timo Korhonen and Martin Heiniger. "Timing System of the Swiss Light Source,"
http://arxiv.org/abs/physics/0111173
[7] Proceedings of the GoToGAN Workshop (Trieste, October 2003)
http://www.elettra.trieste.it/cotogan2003/contributions.html

STATUS OF HIGH-POWER TESTS OF DUAL MODE SLED-II SYSTEM FOR AN X-BAND LINEAR COLLIDER*

Sami G. Tantawi, Christopher D. Nantista, Valery A. Dolgashev, SLAC, Menlo Park, CA94025

Abstract

Future linear colliders and accelerators require rf systems and components that are capable of handling multi-hundred-megawatt peak power levels at X band frequencies and higher. We present a set of RF components capble of handling these levels of powers. We also present a system implementation that uses these components. We carry out all of the RF manipulations in more easily handled over-moded rectangular waveguide. We present a smooth transition from circuilar to rectangular waveguide. This transition is perfected for two modes simultaneously. We show a set of rectangular overmoded components that can handle the same two modes simultaneously. Using these sets of components we constructed a fully dual moded rf pulse compression system. The system has produced 400 ns flat-top rf pulses of greater than 500 MW at 11.424 GHz. The system ran for hundreds of hours. After 39 million pulses the system tripped only 14 times; indicating the high reliability of these sets of components.

INTRODUCTION

Recently, ultra-high-power rf systems at X-band and above have received a lot of attention in different laboratories around the world because of the desire to design and construct a future linear collier. For a review of these activities the reader is referred to [1-2]. These systems are required to generate and manipulate hundreds of megawatts. Standard rf components that have been in use for a long time such as waveguide bends, directional couplers and hybrids, cannot be used directly because of peak field considerations. Usually, these components are made with oxygen-free high-conductivity copper and the operation takes place under ultra-high vacuum conditions. Experimental work at X-band showed that peak electric fields should not exceed 500 kV/cm [3]. Peak magnetic field should be limited so that the pulsed surface heating does not exceed 30 C^o [4].

To reduce the losses and to enhance the power handling capabilities one must use overmoded waveguides. Manipulating rf signals in highly overmoded waveguide is not trivial. With even simple functions, such as bends, the designs are quite complicated in order to insure the propagation of a single mode without losses due to mode conversion to other modes.

Also, most proposed designs for future linear colliders contain long runs of waveguides. In X-band room temperature designs, these runs are on the order of 100 km or more. To reduce the length of these waveguides, we suggested multimoded systems [5]. In these systems the waveguide is utilized multiple times, carrying different modes simultaneously. At first glance, one might think that this would lead to extra complications in the design of most rf components. Indeed, one has to invent a whole new set of multimoded components. However, since simple manipulations such as bending an overmoded waveguide tend to couple the modes together anyway, it turns out that designs of multimoded components are not much more complex. This is also true from the mechanical design point of view; most of these components are compact.

Manipulation of multiple modes in a single component can be easier in rectangular waveguide than circular. The philosophy of our designs is to do all the manipulation in two dimensions, i.e. planar designs. We leave the height of the waveguide as a free parameter to reduce the fields. To transport the the rf signals we need to use the low-loss circular waveguides. To take advantage of this, we present an rf taper which maps modes in circular waveguide into modes in rectangular guide. The modes of choice are TE_{10} and TE_{20} in rectangular waveguides and TE_{11} and TE_{01} in circular waveguides.

We present the design methodologies for these components, which can handle these two modes simultaneously. These designs feature smooth transitions to minimize field enhancements and at the same time they are virtually losses. We also present a pulse compression system based on these components. This system produced a peak rf signal of about 580 MW. In a reliability test, it ran for hundreds of hours at a power level of about 500 MW with pulse energy of more than 200 joules. The repetition rate varied from 30 Hz to 60 Hz. This exceeds the previous state of the art [3] by increasing the pulse energy by more than a factor of 3 and the pulse power by more than 25%.

DUAL-MODED CIRCULAR-TO-RECTANGULAR TAPERS

We assumed that all these tapers will be built using wire electron discharge machining (EDM). When tapering from one shape, e.g. a circle, to another shape, e.g. a rectangle, the length of the taper, *l,* and the connecting points between the two shapes uniquely define the taper. In cylindrical coordinates a shape *i* placed with cylindrical symmetry around the z-axis can be described by a relation $r_i(\phi)$, which gives the radius as a function of the angle ϕ. The taper between two shapes $r_1(\phi)$, and $r_2(\phi)$ is then given by $r(\phi,z) = r_1(\phi) + (r_2(\phi) - r_1(\phi))/l\ z$.

*This work is supported by the US Department of Energy, Contract number DE-AC03-76SF00515

Such a taper is compatible with the process of wire EDM when the two heads of the machine are moving synchronously with the same angular speed. More complicated tapers are constructed from a set of tapers, each of them have the above form, and then, cascaded together. First, let us consider an adiabatic taper between a square waveguide and a circular waveguide. We chose the dimensions of both the square and circular waveguides to be as close as possible, so that they both support approximately the same number of modes. The S-matrix of the transition connects modes of the same symmetry class, and for a sufficiently adiabatic transition preserves their TE (or TM) character.

The modes of interest in our application are TE_{11} and TE_{01} in the circular waveguide. These map to the TE_{10} and both the TE_{20} and TE_{02} modes, respectively. Adiabaticity is sufficient to map the TE_{11} in circular guide to the TE_{10} in the square waveguide. However, one would want to convert the TE_{01} mode in the circular guide to a single polarization of the TE_{02} in the square guide. Modifying the square waveguide to a rectangular waveguide to break the degeneracy between the TE_{02} and TE_{20} modes could do this. However, in this case, the length of the taper required to achieve an adiabatic transition to a single mode in the rectangular guide is excessive. If one chooses the dimensions of the square waveguide and the circular waveguide such that the TE_{02} circular mode and the TE_{22} and TM_{22} rectangular modes do not propagate, the length of this taper is approximately 18 cm at 11.424 GHz, or about 7 wavelengths. Instead, we construct this taper from three sections. The middle section is a cylinder with the with the shape: $r_2(\phi) = r_0(1+0.1\cos 2\phi)$, where r_0 is the radius of the circular guide.

The taper from the circle to the intermediate shape scatters the TE_{01} mode into two modes M_1 and M_2 in the intermediate section. Also, the taper between the rectangular waveguide to the intermediate shape scatter the rectangular mode TE_{02} into the same M_1 and M_2 modes. The lengths of both tapers are adjusted such that the coefficients of the scattered modes M_1 and M_2 are the same from both sides. Since M_1 and M_2 propagate with different phase velocities in the intermediate section, the length of that section could be adjusted so that the circular TE_{01} mode gets completely converted into the rectangular TE_{02} mode.

The idea of this design was first reported by our group in [6], later it was implemented to split the output of a TE_{01} gyroklystron [7]. However, in both cases, no care was taken to insure the adiabatic propagation of the TE_{11} mode. Because of the odd shape in the middle of this taper, described by Eq (2). The taper tended to couple the rectangular TE_{01} to the circular TE_{31} mode. This is not surprising, since that shape essentially contains a second-order azimuthal deformation which couples modes that differ in azmithal index by 2. On the other hand, the circular TE_{11} mode is also coupled to TE_{12} in the rectangular guide.

The design of was the result of several iterations on the design, increasing the length until a perfect conversion between one polarization of the TE_{11} circular mode and the TE_{01} (not TE_{10}) rectangular mode was achieved. Each time the length was increased, the full design was repeated to insure perfect conversion between the TE_{02} rectangular mode and the TE_{01} circular mode. Then the TE_{11} circular to TE_{01} rectangular conversion was checked. Fig. 1 contains field plots for the simulated taper performance, showing the mode conversion for the two modes.

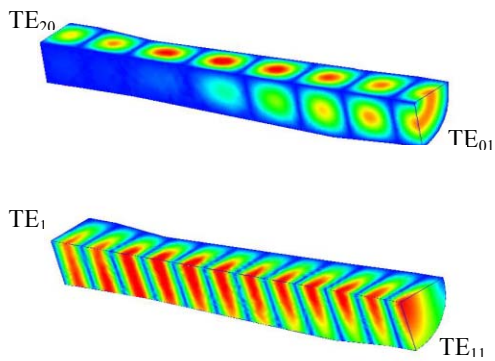

Figure 1: Simulated electric fields (HFSS) of the dual-moded circular-to-rectangular taper.

DUAL-MODED RECTANGULAR WAVEGUIDE SUPERHYBRID

The dual-moded rectangular super-hybrid, shown in Fig.2, is designed for our system using the overmoded rectangular waveguide planar design motif. The planar part of the device, is a four port device whose ports support the TE_{10} and the TE_{20} modes (actually TE_{01} and TE_{02} in this device, if one considers that the height is greater than the width). The cross-section tapers described above allow these ports to be connected to low-loss circular waveguide with one-to-one mode mapping. The planar design allows us to increase power-handling capability by building it overheight without having to take into account in our manipulations the additional propagating modes that this introduces, to which there should be no coupling.

The purpose of the super-hybrid is to pass the TE_{20} mode from the input port through two ports to a resonant delay lines pulse compressor [3], combining identical reflections from these ports out the fourth port, while also allowing the rectangular TE_{10} mode to be transmitted from input to output port by a different path, bypassing the pulse compressor. While the planar design allowed it to be machined out of a single block of copper, like a

circuit on a substrate, it is actually composed of several subcomponents, designed individually.

The input port leads directly into a mode mixer, a slight jog or dogleg that couples the two modes. This converts a pure input of either TE_{10} or TE_{20} into an equal mixture of the two. This is followed by a dual-moded splitter, a T-junction, matched for both modes, which divides power from either pure mode equally between two single-moded (single moded in the horizontal plane only) ports. Proper spacing from the mode mixer allows the fields from each of the orthogonal mode combinations to cancel in one arm and add in the other. In combination, these two subcomponents serve to direct the power of the two possible input modes along different paths.

The input port leads directly into a mode mixer, a slight jog or dogleg that couples the two modes. This converts a pure input of either TE_{10} or TE_{20} into an equal mixture of the two. This is followed by a dual-moded splitter, a T-junction, matched for both modes, which divides power from either pure mode equally between two single-moded (single moded in the horizontal plane only) ports. Proper spacing from the mode mixer allows the fields from each of the orthogonal mode combinations to cancel in one arm and add in the other. In combination, these two subcomponents serve to direct the power of the two possible input modes along different paths.

A pair of mitred bends connects the power input as TE_{10} into an arm of a mirror image of the splitter. The mixed output at its overmoded port is then converted back to pure TE_{10} at the output port of the super-hybrid by a mirror image of the mode mixer. Perforation holes in the outer wall of the short waveguide section between mitred bends allows vacuum pumping in the heart of the device.

Power input as TE_{20} follows a similar path on the opposite side of the device. Here, the section between mitred bends is occupied by a planar hybrid of the Magic-H type [10]. Its coupled ports lead to mitred bends, which turn perpendicular to the power flow of the super-hybrid at a spacing designed to accommodate parallel highly-overmoded circular waveguide delay lines. Short width tapers, optimized with blended arcs, return to overmoded waveguide. These are followed by jog converters, which completely couple power between the two modes. The TE_{10} which came from the Magic-H ports, is thus converted to TE_{20} at the delay line ports of the device. This allows the rectangular to circular tapers to couple these ports to low-loss circular TE_{01} mode delay lines.

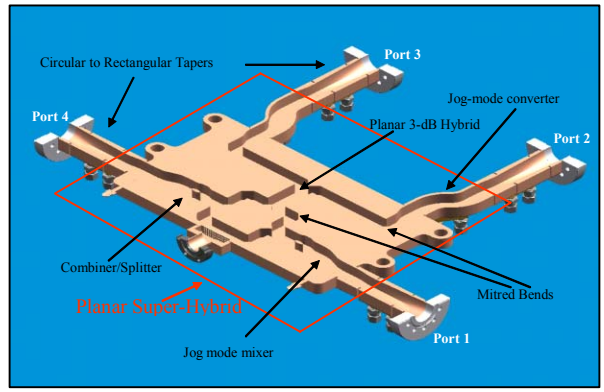

Figure 2: The design of the dual-moded superhybrid, a split view.

THE DUAL-MODED PULSE COMPRESSION SYSTEM

The Transfer Line Design

The components described above compose the heart of our dual-moded pulse compression system. The layout of our system is pictured in Fig. 3. WR90 waveguide carries the combined rf from each klystron pair to a port of a dual-mode combiner. This combiner is a three-port device, whose third port launches power from the single-moded inputs into overmoded circular waveguide in either the TE_{11} or TE_{01} mode, depending on the relative phase of the inputs.

The total combined power is fed into the super-hybrid described above. With the klystron pairs phased to launch TE_{01} into the system, power is directed through the resonant delay line [3,12,13]. These lines are also dual-moded. In the following subsection we give a brief description of this dual-moded pulse compressor. However, for a detailed design of the dual-moded delay lines, the reader is referred to reference [13].

By the opposite phasing, power is directed around an alternate path to the same dual-mode output port. Thus, the system can be run in compressed (TE_{01}) or uncompressed (TE_{11}) mode. Before and after the superhybrid are dual-mode directional couplers in circular waveguide for monitoring the power in each operating mode. The design of this coupler essentially follows the procedure outlined in [14].

A splitter similar to the combiner divides the output power from either operating mode between two arms, each of which further divides the power again in four, so that it can be sent into eight high-power loads.

The Pulse Compressor Delay Lines[13]

The pulse compressor consists of two highly-overmoded, iris-coupled, resonant delay lines, attached to two additional ports on a hybrid section of the super-hybrid. These delay lines, roughly 30 m long in 17 cm diameter circular waveguide, are also dual-moded. Here dual moding refers to the fact that they are designed to operate in both the circular TE_{01} mode and the circular TE_{02} mode, simultaneously. A mode converting reflector at the end of each line transfers power between these two modes. Since TE_{02} is cut off at the input taper of each line, it takes two round trips between each time the wave can impinge on the coupling iris. This effectively doubles the delay time for a line of given length, allowing the system to be considerably more compact than would be a standard delay lines for the desired compressed pulse width. The reflectors are mounted on accurately centered, stepping-motor driven vacuum feed-throughs for resonant tuning of the lines.

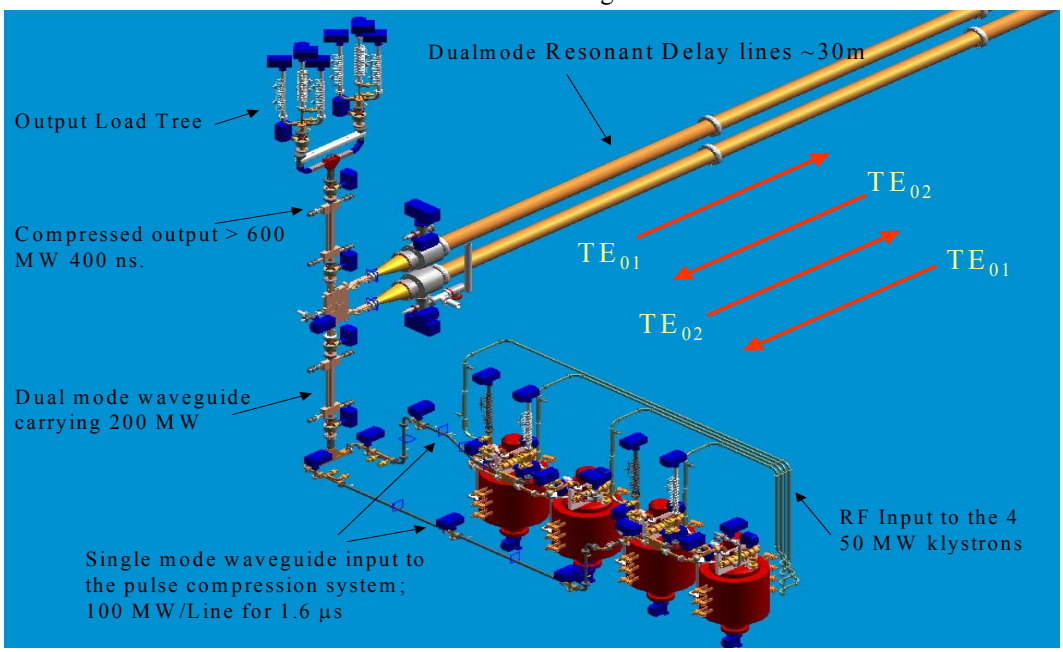

Figure 3: Isometric layout of the dual-moded RF system with dual-moded SLED-II pulse compressor.

TESTING AND OPERATION

Components were individually cold tested with a network analyzer. Results were quite satisfactory, with port matches and desired isolations typically somewhat better than -30 dB and losses on the order of a percent. The system itself was also cold tested at various stages of installation. Care was taken to avoid parasitic resonances, which can greatly degrade efficiency and can lead to dangerously high localized energy storage and field level

After completion of installation, the system was pumped down and carefully baked, after which vacuum levels on the order of 10^{-9} torr could be reached. Then high power operation commenced. While outgassing in the delay lines was a frequent cause of tripping our vacuum interlocks during processing, the main bottle neck was a faulty run of WR90 from the second pair of klystrons to the combiner.

Once this waveguide was replaced, processing progressed much more smoothly, and we soon reached our goal of more than 580 MW at full 400 ns pulse width. Further work on the the low-level rf drive system, incorporating arbitrary waveform generators and feedback optimization, allowed us to flatten the amplitude and phase of the pulse. Fig. 4 shows actual calibrated power meter measurements of the input and output pulses obtained.

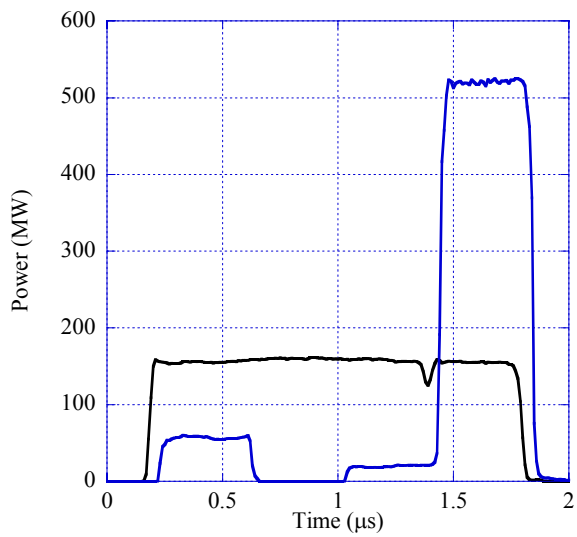

Figure 4: Power meter measurements of input (black) and output (blue) pulses during high power operation.

With this pulse shape and power level, slightly above 500 MW, we ran the system for more than 300 hours at a repetition rate that varied between 30Hz to 60 Hz. During this period the system produced more than 39 million

pulses. The system tripped only 14 times; indicating the high reliability of these sets of components.

CONCLUSION

We presented the design of a set of components suitable for ultra-high-power operations at X-Band. This set of components comprises a dual-moded circular to rectangular taper and a set of planar dual-moded rectangular components. Using this set of components we constructed an ultra-high-power rf pulse compressor, which produced compressed pulses with power levels above 580 MW and ran regularly slightly above 500 MW. The pulse energy exceeded 200 joules. This achievement represents a milestone in demonstrating an X-band rf system suitable for the Next Linear Collider. It also represents the state of the art in generating coherent ultra-high-power rf signals.

ACKNOWLEDGEMENT

The authors wish to thank and acknowledge the contributions of all those who helped to attain this important goal, including physicists, engineers, operators, and technicians. We specially thank Jose Chan, Dennis Atkinson, David Schultz and the NLC group for their efforts during the mechanical engineering and construction of the project. We thank Richard Cassel and the modulator team for their continuous effort and support during the high power testing phase of this experiment, which was going on for 24 hours a day. We also acknowledge the efforts of Marc Ross, Janice Nelson, and the NLCTA operation group for their support during the testing phase of this project.

REFERENCES

[1] Physics And Technology Of The Next Linear Collider: A Report Submitted To Snowmass '96. By NLC ZDR Design Group and NLC Physics Working Group (S. Kuhlman et al.). SLAC-R-0485, BNL-52502, FERMILAB-PUB-96-112, LBL-PUB-5425, LBNL-PUB-5425, UCRL-ID-124160, Jun 1996. 197pp. See also BOOKS subfile under call-number: QCD191:S861:1996. Presented at 1996 DPF / DPB Summer Study on New Directions for High-Energy Physics (Snowmass 96), Snowmass, Colorado, 25 Jun - 12 Jul 1996.

[2] Sami G. Tantawi "New Development in rf Pulse Compression," LINAC2000-WE203, Aug 2000. 5pp., Invited Talk at the 20th International Linac Conference (Linac 2000), Monterey, California, 21-25 Aug 2000.

[3] Sami G. Tantawi, et. al. "The Generation Of 400-MW RF Pulses At X Band Using Resonant Delay Lines,", IEEE Trans. on Microwave Theory and Techniques, Vol 47, No. 12, December, 1999, p. 2539-2546

[4] V.A. Dolgashev, "High Magnetic Fields in Couplers of X-Band Accelerating Structures Proceedings of the 2003 Particle Accelerator Conference, Portland, Oregon U.S.A., May 12-16, 2003, pp 1267-1269.

[5] S.G. Tantawi, *et al.*, "A Multimoded RF Delay Line Distribution System for the Next Linear Collider," Phys.Rev.ST Accel.Beams, vol. 5, March 2002.

[6] Tantawi, S.G.; Kroll, N.M.; Fant, K.; "RF components using over-moded rectangular waveguides for the Next Linear Collider multi-moded delay line RF distribution system," Proceedings of the 1999 Particle Accelerator Conference, 1999. , Volume: 2 , 27 March-2 April 1999 Pages:1435 – 1437.

[7] Spassovsky, I.; Gouveia, E.S.; Tantawi, S.G.; Hogan, B.P.; Lawson, W.; Granatstein, V.L., " Design and cold testing of a compact $TE_{01}{}^{o}$ to TE_{20} mode converter,", IEEE Transactions on Plasma Science, Volume: 30 , Issue: 3 , June 2002, Pages:787 – 793

[8] "HP High-Frequency Structure Simulator," HP EEsof, Hewalt Packard.

[9] AutoCAD, Copyright 1982-1998, Autodesk, Inc.

[10] Nantista, C.D.; Fowkes, W.R.; Kroll, N.M.; Tantawi, S.G.., "Planar Waveguide Hybrids for Very High Power RF," presented at the 1999 Particle Accelerator Conference, New York, NY, March 29—April 2, 1999; SLAC-PUB-8142.

[11] Sami G. Tantawi and A.E. Vlieks, "Compact X-Band High Power Load Using Magnetic Stainless," presented at the 1995 Particle Accelerator Conference, Dallas, TX, May 1-5, 1995; SLAC-PUB-6826.

[12] P.B. Wilson, Z.D. Farkas, and R.D. Ruth, "SLED-II: A New Method of RF Pulse Compression," presented at the Linear Accelerator Conf., Albuquerque, NM, September 10-14, 1990.

[13] S. G. Tantawi, "Multimoded reflective delay lines and their application to resonant delay line rf pulse compression systems," Phys. Rev. ST Accel. Beams 7, 032001 (2004)

[14] Tantawi, S.G.; "Mode selective directional coupler for NLC," Particle Accelerator Conference, 1993., Proceedings of the 1993 , 17-20 May 1993, Pages:1130 - 1132 vol.2.

The Science of Radioactive Ion Beams

B. Sherrill, NSCL, East Lansing, Michigan

Abstract

The primary intellectual challenge of nuclear physics is to understand the nature of strongly interacting matter and how the features of nuclear many-body systems derive from the fundamental forces and properties of their constituent parts. In nuclear science, interestingly, atomic nuclei present one of the most difficult problems to address. However, a comprehensive understanding of nuclear properties is essential to our ability to model the chemical evolution of the Universe, use nuclei for tests of the fundamental symmetries of nature and assess any number of nuclear technologies. Until recently, the fact that experiments had to be carried out with the limited range of stable isotopes found in nature has severely constrained our understanding. However, the current and next generation of radioactive ion beam facilities will remove this constraint. This talk will endeavor to summarize the most important opportunities made available with the next generation of radioactive ion beam facilities.

NO SUBMISSION RECEIVED

THE PHYSICS PERSPECTIVES AT THE FUTURE ACCELERATOR FACILITY FAIR

J. Stroth, GSI, Darmstadt, Germany*

Abstract

The future international accelerator Facility for Antiproton and Ion Research FAIR at Darmstadt, Germany will serve as research facility for a large community of scientists in Europe and around the world. It will expand on experiences made at GSI in combining synchrotrons with storage rings, and will open access to a broad spectrum of experimental approaches. The physics of strongly interacting systems is the main research field, but also aspects of atomic and plasma physics as well as material science will be addressed. The key features of the facility are high intensities, multi-user parallel operation and brilliant beams of secondary reaction products, i.e. exotic instable nuclei and anti-protons. The opportunities have attracted by now three large communities interested in nuclear structure studies using rare isotopes, hadron spectroscopy exploiting collisions of anti-protons with various targets and physics of ultra-dense nuclear matter created in central collisions of very heavy ions. Moreover, many smaller groups of scientists have proposed exiting experiments to investigate e.g. anti-matter, QED in strong fields and strongly correlated plasmas.

INTRODUCTION

At the end of the past decade the Gesellschaft für Schwerionenforschung (GSI), together with Universities and various international user groups, triggered an initiative aimed at providing the European and international science community with a new, world-wide unique accelerator complex. The Conceptual Design Report [1] was presented to the German Ministry for Education and Research in 2002 and was finally approved in 2003 after evaluation by an International Expert Committee put in charge by the German Science Council. The projected facility has been optimized to guarantee excellent conditions for future challenging experiments on open questions concerning - in broadest terms - many-body system governed by the strong interaction and also in related fields. The concept of the future facility founds on the positive experiences made at GSI with combining a synchrotron and a storage ring. Its layout is depicted in Fig. 1.

About 100 years after Rutherford's discovery of the atomic nucleus compelling information about the structure and reaction of nuclei has been collected. As of this, nuclear physics nowadays is concerned with a much broader scope of questions ranging from the dynamics of the elementary quarks and gluons to the evolution of super-nova explosions and the formation of neutron stars. Objects, which differ in size by almost 20 orders of magnitude,

* j.stroth@gsi.de

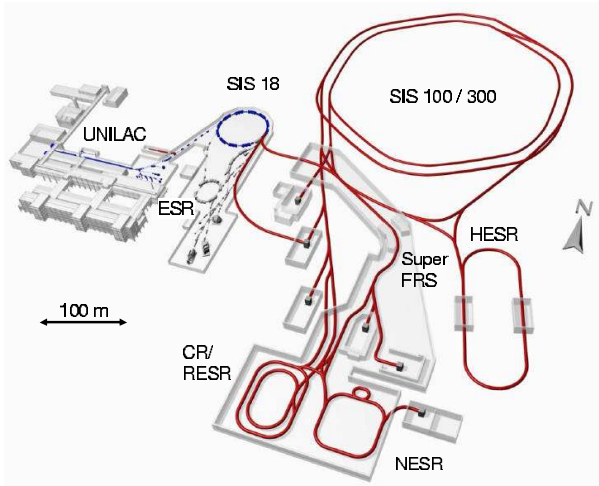

Figure 1: Projected layout of FAIR. The future facility (plotted in red) will be arranged around the old GSI accelerator complex (plotted in blue) comprising the Universal Linear Accelerator UNILAC, a 18 Tm synchrotron (SIS 18) and the Experimental Storage Ring (ESR). The new complex is composed of a rapid cycling 100 Tm synchrotron SIS 100 and a stretcher synchrotron SIS 300 for maximum beam energy and slow extraction. The new super fragment separator (Super FRS) will catch secondary reaction products after dissociation of stable beams of highest intensities. A set of three storage rings is used for collection and pre-cooling (CR), deceleration (RESR) and in-ring experiments with secondary beams in the New Experimental Storage Ring (NESR). The large high energy storage ring (HESR) will provide circulating brilliant beams of antiprotons.

but all essentially governed by the strong interaction. Recently, various national and international advisory committees have outlined the most important avenues for nuclear research in the next decade [2, 3, 4]. Among the top priority research direction are:

- Properties of hot and dense nuclear matter and new phases of matter.
- Non-perturbative effects of QCD and the formation of hadrons.
- Structure and reactions of short-lived, exotic isotopes.
- Symmetries and physics beyond the standard model.

Besides their importance in their own, these fields are intimately linked to the microscopic understanding of cosmological and astrophysical processes.

Although the larger part of the user community will work in nuclear and hadron physics, a still growing fraction of

the user community plans to exploit the possibilities of using ion and antiproton beams for probing the electromagnetic interaction in ultra-high fields and in systems built from anti-matter. In the next section the physics program of five mayor research activities will be outlined. The operating principle of the facility is presented in the subsequent section. The paper concludes with a short summary.

THE PHYSICS PROGRAM OF FAIR

Compressed Baryonic Matter

Nuclear matter accounts for more than 99 % of the mass of all directly observable matter around us. To most extend it occurs in the interior of atoms where it forms the nucleus. Filling only one trillionth of the volume of the atom it accounts for about all of the its mass. Independent of the size of the nucleus, its constituents, the nucleons, gather at a saturation density of 0.17 nucleons/fm^3 thus achieving a bulk mass density of 280 Million tons per cm^3. Yet nature provides much larger samples of nuclear matter with a few kilometers diameter, and core densities which outreach nuclear saturation density by factors: the neutron stars.

The exploration of the different phases of nuclear matter as temperature and density increases is the core subject of heavy ion reaction experiments at relativistic and ultra-relativistic energies. Once nuclear matter is heated, it converts from a liquid phase into a gas of hadrons. At yet higher temperatures the hadron gas again undergoes a phase transition into a gas of de-confined quarks and gluons. Collisions of heavy nuclei is the only tool to control the state variables of nuclear matter in the laboratory. The current knowledge is summarized in Fig. 2. In the past twenty years the phase diagram was mapped by analyzing the chemical composition of the reaction products of the decaying hot interaction volume. Meanwhile there are many indications that a de-confined state is reached at beam energies above 100 AGeV, or even somewhat below. This conjecture is evidenced by recent lattice QCD calculation which derive a phase boundary located at about 170 MeV temperature at small (net) baryon densities, exactly at the maximum freeze-out temperatures extracted from experiment.

The physics goal of the Compressed Matter Experiment CBM at FAIR is to map the phase diagram in the region of high baryon density (shown as hatched area in Fig. 2). In this region of the phase diagram the location of the phase boundary is much more uncertain. Moreover, at very high densities new exotic phases of nuclear matter are expected, like e.g. a color super-conducting phase. According to lattice calculations nuclear matter should also feature a critical point in the region accessible by the future accelerator. To identify this point experimentally would be a clear prove for the existence of a phase transition into the de-confined phase. CBM is designed to observe both, the bulk hadronic particles produced in the violent collisions but also products of rare decays out of the early phase of the collision zone. In order to be sensitive to such decays the spectrometer has to cope with high count rates and large integral luminosities. This experiment will typically use beam from the stretcher synchrotron SIS 300 in the slow-extraction mode and and will take data for different energies up to the highest possible (i.e. $\approx 35A$GeV for ^{238}U).

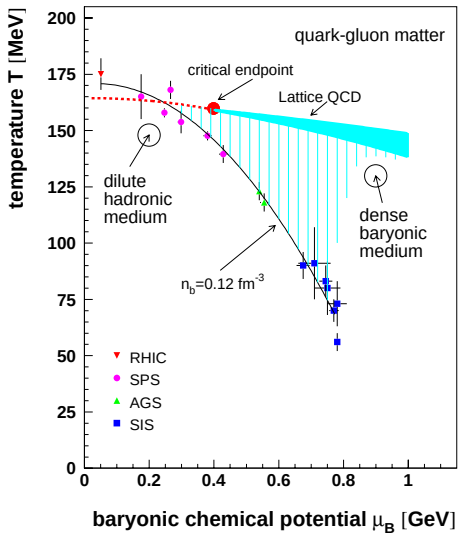

Figure 2: Location in the nuclear matter phase diagram of freeze-out configurations reached after collisions of heavy ions at center-of-mass energies per nucleon ranging from 2 - 200 GeV. The ordinate represent the temperature and the abscissae the baryonic chemical potential at the instant in time during the evolution of the nuclear fireball, when inelastic collisions between the constituents cease. The data points are derived from statistical model description of the hadronic final state recorded by the detectors. Their location can be described by a universal freeze-out condition defined by constant baryon number density n_b.

Research with Antiprotons

Although originally considered elementary particles, nowadays nucleons appear as rather complex realizations of QCD. Substantial research has been conducted over almost 50 years and many details have been unravelled. Yet a comprehensive theoretical description of nucleons, or more general hadrons, is not available. QCD is simple and well understood at short-distance scales, much shorter than the size of a nucleon ($\ll 10^{-15}$ m). In this regime, the basic quark-gluon interaction is sufficiently weak and one can apply perturbation theory. The perturbative approach, however, fails completely when the distance among quarks becomes comparable to the size of the nucleon. Under these conditions, the force among the quarks becomes so strong that they cannot be further separated, in contrast to the electromagnetic and gravitational forces, which fall off with increasing distance. This is the reason why freely propagating quarks have never been observed and why a tremendous energy density is necessary to create deconfined matter in heavy ion collisions.

The only known QCD objects are baryons and mesons, which are composed of three quarks and a quark anti-quark

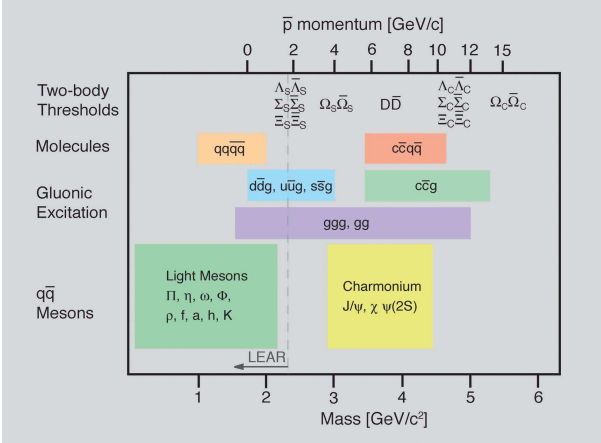

Figure 3: Mass range of hadrons accessible at the HESR with antiproton beams. The figure indicates the antiproton momenta required for charmonium spectroscopy, the search for charmed hybrids and glueballs, the production of D meson pairs and the production of Î baryon pairs for hypernuclear studies. The energy range covered by the former Low Energy Antiproton Ring (LEAR) at CERN is indicated by the arrow.

pair, respectively. QCD, however, also predicts objects composed entirely by gluons (glueballs) and mixtures of quarks, anti-quarks and gluons, so-called hybrids. To discover such states would mark an important milestone in the detailed understanding of the nature of matter. Another striking feature of non-perturbative QCD is the fact that the elementary light quarks, the up and down quarks, making up the nucleon have very small masses which amount to only a few percent of the total mass of the nucleon. Most of the nucleon mass, and therefore of the visible universe comes from the QCD interaction. This generation of mass is associated with the confinement of quarks and the spontaneous breaking of chiral symmetry, one of the fundamental symmetries of QCD in the limit of massless quarks. These phenomena, the confinement of quarks, the existence of glueballs and hybrids, and the origin of the mass of strongly interacting, composite systems related to confinement and the breaking of chiral symmetry are long-standing puzzles.

At the future facility, intense beams of cooled antiprotons will be used to address the issues presented above. Antiproton beams at momenta between 1 and 15 AGeV/c on fixed target will provide access to the heavier strange and charm quarks and to copious production of gluons, as is illustrated in Fig. 3. A dedicated high acceptance and high rate spectrometer $\bar{\mathrm{P}}$ANDA [5] is currently developed to cope with the high luminosities achievable in an HESR in-ring experiment. $\bar{\mathrm{P}}$ANDA aims at rates equivalent to 10 pb^{-1}/day. Cooled antiproton beams are ideally suited for spectroscopic experiments in the charm region. In formation experiments, the precision achievable in the determination of masses and widths of all charmonium states depends only on the quality of the antiproton beam and target, and not on any detector properties. Antiproton beams can be cooled (stochastic and/or electron cooling) to obtain a relative momentum resolution of better 10^{-5}. Thus, the beam energy resolution can be translated directly to mass resolution if very thin targets of hydrogen gas jet or hydrogen pellets are used in the stored circulating beam of antiprotons.

The Structure of Exotic Isotope

QCD explains the strong interaction by exchange of gluons. Compared to QED the strong force develops a rich structure as the gluons itself are carriers of the (color) charge. Already the interaction between nucleons has the character of a residual interaction, commonly described by exchange of virtual mesons. In nuclei the dynamics of the nucleons is essentially defined by three interactions: the strong, electromagnetic and weak forces. The first two interactions control the isotopic character of nuclei by balancing attraction and repulsion. The weak force transmutes unstable atomic nuclei into others and ultimately into stable nuclei. QCD, however, does not deliver a precise analytical form of the strong interaction at a length and energy scale relevant to nucleon-nucleon interactions in nuclei. To determine the emerging effective strong interaction represents a fundamental goal of nuclear physics. Probing nuclei under extreme conditions in various respects paves the way towards a more comprehensive understanding of nuclear matter.

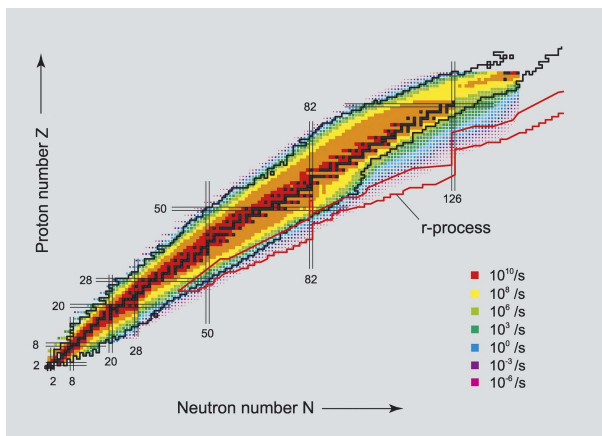

Figure 4: Expected production rates for unstable isotopes after fragmentation of primary stable beams at the FAIR facility. The production rates are indicated by a color code shown bottom right. Stable isotopes are printed in black. As yet unexplored parts of the presumed r-process path (hatched area) will become accessible, in particular around the closed neutron shells N=82, N=126 and even beyond.

All atomic nuclei in the universe beyond lithium have been and still are being created in stars. In various stellar environments this nucleosynthesis proceeds via the formation of transient nuclei that decay into stable ones, either directly or after several intermediate steps. A precise knowledge of the structure and reaction of exotic nuclei,

far off from the valley of stability is an essential ingredient to astrophysical model calculation simulating the evolution of explosive stellar processes.

Nuclei can also serve as test grounds for fundamental symmetries. Low-energy experiments addressing fundamental symmetries and their possible violations have been performed for a long time. Such studies comprise accurate tests of parity and time-reversal symmetry.

The new facility will open a qualitatively and quantitatively new era, since the considerably increased production yields for exotic nuclei together with novel beam manipulation techniques, such as beam cooling, deceleration to rest and storage in ion or atom traps, will increase the precision achievable in these studies by one order of magnitude and more. FAIR will provide primary beams of stable isotopes at intensities that are a factor of 100 higher than presently available at GSI. Secondary radioactive beam intensities will even increase by a factor of up to 10,000 through advanced concepts for beam separation and secondary beam phase-space handling. The maximum beam energies of the radioactive species will be unparalleled by any other existing or planned facility. Altogether, this will allow sensitive experiments with secondary beam species far away from stability (see Fig. 4). A large unser community (NUSTAR) [6] has proposed experiments using high energy reactions on fixed targets, in-beam scattering on internal targets as well as on colliding electron beams, decay spectroscopy at small energies or with stopped isotopes and finally ions stored in the NESR or in traps.

Atomic Physics in Strong Fields

FAIR has key features that offer a range of new opportunities in atomic physics and related fields. First, high charge-state ions, moving at velocities close to the speed of light, generate electric and magnetic fields of exceptional strength. Second, at those relativistic velocities, the energies of optical transitions, such as those of lasers, are boosted to the X-ray region. The strong fields carried by heavy, highly-charged ions are their outstanding attributes for atomic and applied physics research.

For the heaviest ions, Quantum Electrodynamics (QED), the Standard Model of electromagnetism and a basis of modern physics, will be probed near the critical field limit associated with the extreme conditions of high charge states and high velocities. The fields present in highly relativistic collisions are strong enough to produce real e+e- pairs directly out of the vacuum. Precision studies of QED in bound states will become possible through the large Doppler shifts of highly relativistic ions, which generate extreme energy shifts for photons in the ion rest frame. As a consequence, even the heaviest few-electron ions can now be studied in precision QED experiments by using state of the art laser systems.

By means of collinear laser spectroscopy the ground state hyperfine-splitting of very heavy, hydrogen-like atoms has been probed with high accuracy. Based on this experience, nuclear properties like radii, spins, magnetic dipole moments and higher electromagnetic moments of nuclei very far off stability will be addressed at the new facility by experimental techniques of atomic physics. Many of the research topics mentioned from collision studies to spectroscopy that were started successfully at the ESR, will be expanded into new regimes under much better and advanced experimental conditions at the NESR.

The Physics of Strongly Coupled Plasmas

A particularly interesting plasma region, the dense, strongly coupled plasma, is located at relatively low temperature and high density. The interior of the giant planets Saturn or Jupiter are interesting examples for this dense plasma region. The investigation of the properties of dense plasmas is at the focus of plasma physics research with the new facility. Of particular interest is the occurrence of phase transitions in cold compressed material, e.g. the insulator-to-metal transition of diamond expected at 10 Mbar, the insulator-to-metal transition of solid hydrogen predicted above 5 Mbar, or the plasma phase transitions at temperatures of about 1 eV. With the presently available beam pulses from the SIS18, a specific power deposition up to 50 GW/g is achieved resulting in a pressure inside the investigated solid-state target of only some 10 kbar.

The SIS 100 heavy-ion synchrotron combined with a bunch compression system for the generation of very intense short ion bunches below 50 ns pulse length will extend the available beam deposition power from the current level of 50 GW/g by more than two orders of magnitude up to 12,000 GW/g. This will open up unprecedented opportunities for the production of ion beam heated and/or compressed plasmas.

RUNNING IN PARALLEL

The different research programs outlined before require various running conditions. Plasma physics, i.e. is interested in receiving ultra short beam pulses at repetition rates in the order of minutes or longer. The high-energy antiproton program runs with one fill of the HESR for up to an hour. Such long repetition times are achieved by continuously cooling the beam to accommodate for the energy dissipation in the target. A major design criteria for the FAIR accelerator complex was the optimum use of the facility by allowing parallel operation of dedicated physics runs. In Fig. 5 we outline the scenario for three different experiments.

In the uppermost panel beam is produced for CBM. A preferably heavy beam is accelerated in three steps up to the maximum energy possible. After achieving maximum rigidity in SIS 300, the beam is slowly extracted onto the target station of the CBM spectrometer. During this extraction time - the goal is to achieve several tens of seconds - all facilities except SIS 300 are available to accelerate a different beam.

This time can be used e.g. for rare isotope studies using storage rings (middle panel). Primary beams are acceler-

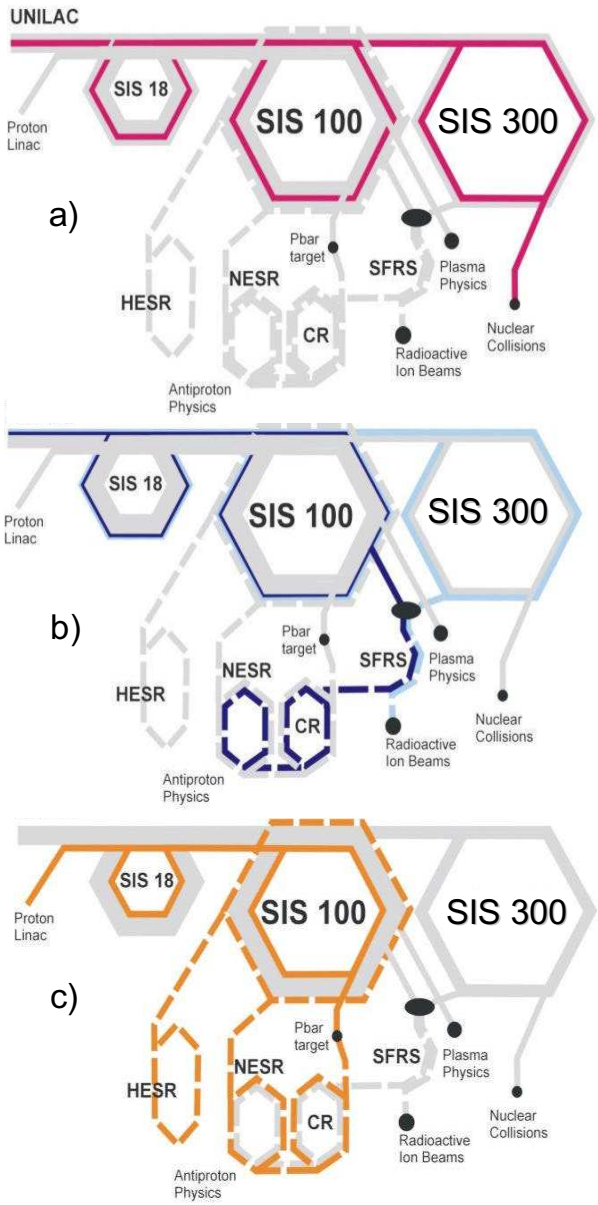

Figure 5: Pictorial representation of the beam transport through the elements of the facility for three different experimental runs. Case a) shows the acceleration of heavy ion the the highest beam energies as needed e.g. for the CBM experiment. Case b) depicts the production of rare isotopes which are cooled, decelerated and stored in the NESR. Case c) finally illustrates the production, cooling, re-acceleration and storage of antiprotons. For a detailed description see the text.

ated in SIS 100 up to typically 1 AGeV beam energy. The comparably high rigidity of the synchrotron is needed to accelerate low charge states, a measure to extend the space charge limit. Fast extraction is used to feed the secondary particle beam into the collector ring. After cooling and deceleration the beam is finally directed to the NESR. In case fixed target experiments are conducted, the beam is directed from SIS 100 to SIS 300 and slowly extracted into the respective target stations. In this case, the CBM experiment can not run in parallel.

An operational mode using most of the facility at once is shown in the lower panel. This mode is for production of antiproton beams. A primary proton beam is accelerated to 30 GeV/c momentum and directed on the antiproton production target. The antiprotons, which feature a wide momentum spread, are collected in the CR and pre-cooled in the NESR. After having collected sufficient antiprotons the particle beam is re-injected into the SIS 100, accelerated to the required energy and directed to the HESR.

SUMMARY

The future international accelerator facility FAIR will provide ideal conditions for next generation experiments dedicated to the exploration of strongly interacting (many-body) systems. It will establish a world-wide unique laboratory providing ion beams and antiprotons for experiments attracting also neighboring research communities. The expected user community comprises currently more than 1400 researchers. To achieve this goal advanced technologies have to be developed for high performance super conducting magnets and high energy beam cooling. The total project time until commissioning amounts to about 8 years. Part of the experimental program can begin at earlier times due to a sophisticated, staged construction schedule.

ACKNOWLEDGEMENT

Most of the material presented here is taken from the Conceptual Design Report to which more than 500 members of the science communities have contributed.

REFERENCES

[1] "An International Accelerator Facility for Beams of Ions and Antiprotons Conceptual Design Report", http://www.gsi.de/GSI-Future/cdr/

[2] "NuPECC Long Range Plan 2004: Perspectives for Nuclear Physics Research in Europe in the Coming Decade and Beyond", ESF Expert Committee, April 2004, http://www.nupecc.org/pub/lrp03/long_range_plan_2004.pdf

[3] "2002 NSAC Long-Range Plan: Opportunities in Nuclear Science, A Long-Range Plan for the Next Decade", DOE/NSF Nuclear Science Advisory Committee, April 2002, http://www.sc.doe.gov/henp/np/nsac/nsac.html

[4] "Hadron and Nuclear Physics in Germany: Status and Perspectives", BMBF Expert Committee, 2002 http://ikpp30.ikp.kfa-juelich.de/khuk/dokumente/nhpg2002.pdf

[5] The acronym stands for "antiProton ANihilation at DArmstadt"

[6] International Nuclear Structure and Astrophysics Community GSI. See http://www.gsi.de/forschung/kp/kp2/nustar.html and link to the Letter of Intend contained in there.

List of Authors

Italic papercodes indicate primary authors

— D —

— E —

— L —

— M —

— T —

Institutes List

ACCEL
Bergisch Gladbach
- Bauer, S.
- Dunkel, K.
- Manolitsas, J.
- Peiniger, M.
- Pekeler, M.
- Piel, C.
- Schwellenbach, J.
- Tradt, M.
- Trompetter, D.
- Vogel, H.
- vom Stein, P.

AEC
Chiba
- Fujimoto, T.

ANL
Argonne, Illinois
- Borland, M.
- Brumwell, F. R.
- Carwardine, J.
- Cours, A.
- Dimonte, N.
- Donley, L.
- Dooling, J.C.
- Kelly, M.
- Lewellen, J.W.
- McMichael, G.E.
- Nassiri, A.
- Norem, J.
- Smith, T.
- Stipp, V. F.

ANL/APS
Argonne, Illinois
- Arnold, N.D.
- Grelick, A.E.

ANL/Phys
Argonne, Illinois
- Aseev, N.
- Conway, Z.A.
- Fuerst, J.D.
- Kedzie, M.
- Nolen, J.A.
- Ostroumov, P.N.
- Sharamentov, I.
- Shepard, K.W.

BESSY GmbH
Berlin
- Jaeschke, E.
- Knobloch, J.
- Krämer, D.
- Richter, D.
- von Hartrott, M.

BIEVT
Beijing 100016
- Chen, B.
- Sun, B.
- Zou, Y.

BINP SB RAS
Protvino, Moscow Region
- Larionov, A.V.
- Teryaev, V.E.

BNL
Upton, Long Island, New York
- Alessi, J.
- Beebe Wang, J.
- Ben-Zvi, I.
- Calaga, R.
- Chang, X.Y.
- Jain, A.
- Kewisch, J.
- Kirk, H.
- Litvinenko, V.
- Montag, C.
- Raparia, D.
- Weng, W.-T.
- Yakimenko, V.

BNL/NSLS
Upton, Long Island, New York
- Wang, J.-M.

BUW
Wuppertal
- Müller, G.

CAEP/IAP
Mianyang, Sichuan
- Chen, H.
- Chen, Y.
- Jin, X.
- Li, M.
- Lu, H.
- Xu, Z.
- Yang, X.

CBMM
Tokyo
- Imagumbai, M.

CCLRC/DL/ASTeC
Daresbury, Warrington, Cheshire
- Gerth, C.K.M.
- Hannon, F.E.
- Holder, D.J.

CCLRC/RAL/ASTeC
Chilton, Didcot, Oxon
- Gerigk, F.

CEA DSM Grenoble
Grenoble
- Girard, A.

CEA
Pontfaverger-Moronvilliers
- Bombardier, F.
- Caron, M.
- Merle, E.
- Noël, C.
- Pierret, O.
- Rosol, R.
- Vermare, C.

CEA/DAM
Bruyères-le-Châtel
- Balleyguier, P.
- Binet, A.
- Lagniel, J.M.
- Le Flanchec, V.
- Lemaire, J.
- Pichoff, N.

CEA/DAPNIA-SACM
Gif-sur-Yvette Cedex
- Benmeziane, K.
- De Menezes, D.D.
- Delferriere, O.
- Devanz, G.
- Duperrier, R.
- Ferdinand, R.
- Gobin, R.
- Harrault, F.
- Paparella, R.

CEA/DIF/DPTA/SP2A
Bruyeres-le-Chatel
- Bailly-Salins, R.
- Millerioux, M.
- Quine, Chr.

CEA/DSM/DAPNIA
Gif-sur-Yvette
- Beauvais, P.-Y.
- Braud, D.
- Charrier, J.P.
- Charruau, G.
- Coadou, B.
- Gasser, Y.
- Gauthier, Y.
- Ismail, A.B.
- Napoly, O.
- Poupeau, J.P.
- Sahuquet, P.
- Uriot, U.D.
- Visentin, B.

CEA/PTN
Bruyères-le-Châtel
- Piquemal, A.

CEA/Saclay
Gif-sur-Yvette
- COMTE, N.

CERN
Geneva
- Ames, F.
- Assmann, R.W.
- Benedico Mora, E.
- Bossart, R.
- Bruno, L.
- Butler, P.
- Caspers, F.
- Chamings, J.A.
- Coco, V.
- Coosemans, W.
- Cuvet, Y.
- Delahaye, P.
- Garoby, R.
- Genest, J.
- Grudiev, A.
- Guignard, G.
- Hanke, K.
- Heikkinen, T.
- Herty, A.
- Hori, M.
- Kuchler, D.
- Lindroos, M.
- Lombardi, A.M.
- Magistris, M.
- Mathot, M. S.
- Millich, A.
- Mourier, J.
- Nonglaton, J.
- Paoluzzi, M.
- Redaelli, S.
- Rossi, C.
- Sargsyan, E.Zh.
- Schulte, D.
- Scrivens, R.
- Sieber, T.
- Silari, M.
- Steiner, T.
- Syratchev, I.

- Taborelli, T.
- Tanner, L.
- Vretenar, M.
- Völlinger, C.
- Wenander, F.J.C.
- Wilson, E. J. N.
- Wilson, I.
- Wuensch, W.
- Zimmermann, F.

CHEP Korea
Daegu
- Kim, Y.
- Son, D.

CIAE
Beijing
- Cui, B.
- Guan, X.
- Peng, Z.H.

CINEL
Vigonza (PD)
- Lamanna, G.

CLRC
Daresbury, Warrington, Cheshire
- Smith, R.J.

CPI
Palo Alto
- Balkcum, A.
- Cattelino, M.
- Cox, L.
- Cusick, M.
- Forrest, S.
- Friedlander, F.
- Staprans, A.
- Zitelli, L.
- Bohlen, H.P.
- Wright, E.

CPI/EIMAC
San Carlos, California
- Li, Y.
- Tornoe, R.N.

Chicago University
Chicago, Illinois
- Kim, K.-J.
- Sun, Y.-E.

DESY Zeuthen
Zeuthen
- Abrahamyan, K.
- Bohnet, I.
- Bähr, J.
- Donat, A.
- Gensch, U.
- Grabosch, H.-J.
- Han, J.H.
- Krasilnikov, M.
- Leich, H.
- Lipka, D.
- Miltchev, V.
- Oppelt, A.
- Petrosyan, B.
- Staykov, L.
- Stephan, F.
- Wenndorff, RW.

DESY
Hamburg
- Ayvazyan, V.
- Baboi, N.
- Balandin, V.
- Brandt, A.
- Brinkmann, A.
- Brinkmann, R.
- Carneiro, J.-P.
- Castro, P.
- Choroba, S.
- Desler, K.
- Dohlus, M.
- Duval, Ph.
- Flöttmann, K.
- Geloni, G.
- Golubeva, N.
- Grevsmühl, T.
- Hensler, O.
- Kahl, J.
- Kaiser, F.-R.
- Katalev, V.V.
- Kim, Y.
- Knaack, K.
- Kostin, D.
- Kreps, G.
- Kretzschmann, A.
- Lierl, H.
- Lilje, L.
- Limberg, T.
- Matheisen, A.
- Morales, H.
- Möller, W.-D.
- Nölle, D.
- Peters, J.
- Petersen, B.
- Prenting, J.
- Priebe, G.
- Proch, D.
- Rehlich, K.
- Reschke, D.
- Saldin, E.
- Schlösser, M.
- Schmoekel, M.
- Schneidmiller, E.

- Schreiber, S.
- Schwendicke, U.
- Sekutowicz, J.
- Simrock, S.
- Singer, W.
- Singer, X.
- Steinhau-Kühl, N.
- Weisse, S.
- Wendt, M.
- Werner, M.
- Wittenburg, K.
- Yurkov, M.V.
- Zolotov, A.

DIAMOND
Chilton, Didcot, Oxon
- Christou, C.
- Kempson, V.

DOE Nagoya
Nagoya-City
- Kobayakawa, H.
- Takashima, Y.
- Takeda, Y.
- Watanabe, O.

DOP Nagoya
Nagoya
- Furuta, F.
- Gotou, T.
- Kuwahara, M.
- Nakanishi, T.
- Naniwa, K.
- Nishitani, T.
- Okumi, S.
- Takeuchi, T.
- Yamamoto, M.
- Yamamoto, N.
- Yasui, K.

ELETTRA
Basovizza, Trieste
- Bocchetta, C.
- Danailov, M.
- Diviacco, B.
- Verzilov, V.

ENEA C.R. Frascati
Frascati (Roma)
- Picardi, L.
- Ronsivalle, C.

ETH
Zürich
- Candel, A.
- Li, K.

FKLAB
Fukui City
- Matsui, F.

FNAL
Batavia, Illinois
- Arkan, T.
- Bauer, P.
- Bellantoni, L.
- Berenc, T.
- Boffo, C.
- Carcagno, R.
- Carter, H.
- Chapman, C.
- Edwards, H.
- Elementi, L.
- Foley, M.
- Hahn, E.
- Hicks, D.
- Johnson, R. P.
- Khabiboulline, N.
- Mitchell, D.
- Piot, P.
- Popovic, M.
- Rowe, A.
- Santucci, J.
- Solyak, N.
- Terechkine, I.
- Wennerberg, J.

FSU
Jena
- Neubert, R.
- Nietzsche, S.
- Vodel, W.

FZ Karlsruhe
Karlsruhe
- Halbritter, J.

FZJ
Jülich
- Eichhorn, R.
- Esser, F. M.
- Laatsch, B.
- Schug, G.
- Singer, H.

FZJ/IKP
Jülich
- Maier, R.
- Stassen, R.

Fermilab
Batavia, Illinois
- Ankenbrandt, C. M.
- Bross, A.D.
- Finley, D.

- Geer, S.
- Gonin, I.
- Huening, M.
- Mishra, S.
- Moretti, A.
- Qian, Z.
- Romanov, G.
- Solyak, N.

GA
Los Alamos
- Schulze, M.E.

GANIL
Caen
- Lehérissier, P.
- Moscatello, M.-H.
- Pacquet, J.Y.

GSI
Darmstadt
- Barth, W.
- Beier, T.
- Dahl, L.
- Dermati, K.
- Forck, P.
- Glatz, J.
- Groening, L.
- Hollinger, R.
- Hutter, G.
- Klos, F.
- Lu, Y.R.
- Mühle, C.
- Peters, A.
- Richter, S.
- Schlitt, B.
- Spädtke, P.
- Stroth, J.
- Vinzenz, W.
- Will, C.
- Yaramishev, S.
- Zurkan, O.

GUAS/AS
Ibaraki
- Hozumi, Y.

IAP
Frankfurt-am-Main
- Bartz, U.
- Bechtold, A.
- Becker, R.
- Brendel, L.
- Clemente, G.
- Hofmann, B.
- Kitegi, C. A.
- Klein, H.
- Kühnel, K.-U.
- Li, Z.
- Liebermann, H.
- Meusel, O.
- Müller, N.
- Podlech, H.
- Pozimski, J.
- Ratzinger, U.
- Sauer, A.C.
- Schempp, A.
- Thibus, J.
- Tiede, R.
- Zhang, C.
- Zimmermann, H.
- Danilov, Y.Y.
- Denisov, G. G.
- Kuzikov, S.
- Paveliev, V. G.
- Shegol'kov, D. Yu.
- Shmelyov, M. Yu.
- Vikharev, A. A.

IHEP Beijing
Beijing
- Fang, S.X.
- Fu, S.
- Li, J.
- Ouyang, H.
- Qiao, J.
- Wang, S.
- Wang, S.H.
- Xu, X.
- Zhang, Z.
- Zhao, S.

IHEP Protvino
Protvino, Moscow Region
- Belyaev, O.K.
- Budanov, Yu.
- Ivanov, S.V.
- Kazakov, S.Y.
- Maltsev, A.P.
- Maltsev, I.G.
- Stepanov, V.B.
- Strekalovskyh, S.A.
- Teplyakov, V.A.
- Zenin, V.

IIT
Chicago, Illinois
- Kaplan, D. M.
- Torun, Y.
- Yonehara, K.

IKP
Mainz
- Euteneuer, H.
- Jankowiak, A.

- Schumann, S.
- Tchoubarov, O.

IMP
Lanzhou
- Li, Z.

INFN Milano
Milano
- Fagotti, E.
- Paparella, R.
- Puricelli, P.F.

INFN-Napoli
Napoli
- Masullo, M.R.

INFN/LASA
Segrate (MI)
- Bosotti, A.
- Giove, D.
- Michelato, P.
- Pagani, C.
- Sertore, D.

INFN/LNL
Legnaro, Padova
- Bassato, G.
- Bezzon, G.
- Bisoffi, G.
- Calore, A.
- Canella, S.
- Chiurlotto, F.
- Comunian, M.
- Esposito, J.
- Facco, A.
- Lombardi, A.
- Modanese, P.
- Palmieri, A.
- Pisent, A.
- Porcellato, A.M.
- Posocco, P.
- Stark, S.

INRNE
Sofia
- Tsakov, I.

IPA
Stuttgart
- Werner, D.

IPN
Orsay
- Biarrotte, J.-L.
- Blivet, S.
- Bousson, S.
- Fouaidy, M.
- Gassot, H.
- Junquera, T.
- Olry, G.
- Saugnac, H.
- Szott, P.

ISS
Rome
- Frullani, S.

ITEP
Moscow
- Kolomiets, A.
- Minaev, S.

J-PARC
Ibaraki-ken
- Kobayashi, T.
- Yamazaki, Y.

JAERI APRC
Ibaraki-ken
- Daido, H.

JAERI
Ibaraki-ken
- Asano, H.
- Chishiro, E.
- Hasegawa, K.
- Hiroki, F.
- Kishiro, J.
- Kobayashi, T.
- Kondo, Y.
- Morishita, T.
- Nakamura, N.
- Ohkawa, T.
- Sato, S.
- Suzuki, .H.
- Tanaka, M.
- Tomisawa, T.
- Ueno, A.
- Yoshikawa, H.

JAERI/ARTC
Gunma-ken
- Kashiwagi, H.

JAERI/FEL
Ibaraki-ken
- Yoshikawa, H.

JAERI/LINAC
Ibaraki-ken
- Akikawa, H.
- Ao, H.
- Itou, T.
- Yamazaki, Y.

JASRI-SPring-8
Hyogo
- Asaka, T.
- Dewa, H.
- Hanaki, H.
- Kobayashi, T.
- Mizuno, A.
- Suzuki, S.
- Taniuchi, T.
- Tomizawa, H.
- Yanagida, K.

JINR
Dubna, Moscow Region
- Alexandrov, V.
- Balalykin, N.
- Kazarinov, N.Y.
- Kobets, V.V.
- Meshkov, I.N.
- Seleznev, I.A.
- Shevtsov, V.F.
- Shirkov, G.
- Sumbaev, A.P.

JP Accelerator Works, Inc., 2245
Los Alamos, NM
- Potter, J.M.

Jefferson Lab
Newport News, Virginia
- Beard, K.
- Bogacz, A.
- Ciovati, G.
- Delayen, J. R.
- Derbenev, Y.S.
- Jordan, K.
- Kneisel, P.
- Mammosser, J.
- Myneni, G.
- Ozelis, O.
- Pozdeyev, E.
- Rimmer, R.A.
- Tennant, C.
- Wang, H.
- Wu, G.

KEK
Ibaraki
- Anami, S.
- Chiba, J.
- Chin, Y.H.
- Delerue, N.
- Enomoto, A.
- Fukuda, S.
- Fukui, Y.
- Furukawa, K.
- Hayano, H.
- Higashi, Y.
- Higo, T.
- Igarashi, Y.
- Igarashi, Z.
- Ikeda, M.
- Ikegami, K.
- Ikegami, M.
- Kadokura, E.
- Kakihara, K.
- Kamikubota, N.
- Kamitani, T.
- Kato, T.
- Kawamura, M.
- Kazakov, S.Y.
- Kobayashi, H.
- Kubota, C.
- Kumi, T.
- Kuriki, M.
- Lee, S.
- Matsumoto, H.
- Matsumoto, T.
- Michizono, S.
- Morozumi, Y.
- Naito, F.
- Nakao, K.
- Nigorikawa, K.
- Noguchi, S.
- Ohsawa, S.
- Oide, K.
- Oogoe, T.
- Sugimura, T.
- Takasaki, E.
- Takatomi, T.
- Takeda, S.
- Takenaka, T.
- Tanaka, H.
- Toge, N.
- Toyama, T.
- Ueno, K.
- Win, S.S.
- Yamaguchi, S.
- Yokoyama, K.
- Yoshida, M.
- Yoshino, K.
- Yoshioka, M.

Kyoto ICR
Kyoto
- Hashida, M.
- Iwashita, Y.
- Mihara, T.
- Nakamura, S.
- Noda, A.
- Sakabe, S.

- Shimizu, S.
- Shirai, T.
- Tongu, H.

LANL
Los Alamos, New Mexico
- Billen, J.
- Bultman, N.K.
- Carlsten, B.E.
- Chan, K. C. D.
- Dale, G.
- Earley, L.M.
- Ekdahl, C.
- Garnett, R.
- Kirbie, C.
- Krawczyk, F.L.
- McCrady, R.C.
- Merl, R.
- Moir, D.C.
- Power, J.
- Russell, S.J.
- Rybarcyk, L.
- Schrage, D.
- Shoee, H.
- Stovall, J.
- Wangler, T.P.

LANL/LANSCE
Los Alamos, New Mexico
- Gallegos, F. R.
- Krawczyk, F.L.
- Pillai, C.
- Schaller, S.
- Shelley, F. E.
- Sigler, F.E.
- Steck, A. I.

LBNL
Berkeley, California
- Doolittle, L.
- Lionberger, C.
- Monroy, M.
- Qiang, J.
- Ratti, A.
- Ryne, R.
- Zisman, M.S.

LBNL/AFR
Berkeley, California
- Li, D.
- Lidia, S.

LEBRA
Funabashi
- Hayakawa, K.
- Hayakawa, Y.
- Ishiwata, K.
- Kanno, K.
- Nakao, K.
- Sakai, T.
- Sato, I.
- Tanaka, T.

LEPP
Ithaca, New York
- Belomestnykh, S.A.
- Liepe, M.
- Medjidzade, V.
- Padamsee, H.
- Veshcherevich, V.

LLC
Albuquerque, New Mexico
- Starling, W.J.
- Swenson, D.A.

LLNL
Livermore
- Atkinson, D.P.
- Brooksby, C.
- Cook, E.
- Sullivan, J.

LMU
Garching
- Emhofer, S.
- Habs, D.
- Kester, O.K.
- Rudolph, K.

MBI
Berlin
- Sandner, W.
- Will, I.

MELCO
Hyogo
- Yoshida, K.

MEPhI
Moscow
- Masunov, E.S.
- Polozov, S.M.
- Sobenin, N.P.

MIT/PSFC
Cambridge, Massachusetts
- Smirnova, E.

MPI
Stuttgart
- Dosch, H.

MPI-K
Heidelberg
- Grieser, M.
- Repnow, R.
- Scheit, H.
- Schwalm, D.
- Welsch, C.P.
- von Hahn, R.

MRC
Albuquerque, NM
- Genoni, C.
- Hughes, P.

MSU
East Lansing, Michigan
- Radcliffe, C.

Mitsubishi Heavy Industries Ltd., Nagoya Aerospace Systems Works
Nagoya
- Ino, H.
- Kabeya, Z.
- Kakizaki, S.
- Kawasumi, T.

Muons, Inc.
Batavia
- Alsharo'a, M.M.
- Hartline, R.E.
- Kuchnir, M.
- Roberts, T.J.

NEOMAX
Osaka
- Sugiyama, E.

NIRS
Chiba-shi
- Evgeny, A.
- Fukumi, A.
- Iwata, Y.
- Kumada, M.
- Li, Z.
- Matsukado, K.
- Shibuya, S.
- Yamada, S.

NPC
Düsseldorf
- Klinkenberg, Chr.

NSCL
East Lansing, Michigan
- Andreev, V.
- Bricker, S.
- Compton, C.
- Doleans, M.
- Gorelov, D.
- Grimm, T.L.
- Hartung, W.
- Johnson, M.
- Kandil, T.H.
- Khalil, H.
- Marti, F.
- Popielarski, J.
- Schriber, S.O.
- Sherrill, B.
- Vincent, J.
- Wu, X.
- York, R.C.
- Zhao, Q.

Naples University Federico II
Napoli
- D'Elia, A.

Naples University Federico II, Mathematical, Physical and Natural Sciences Faculty
Napoli
- Falco, S.
- Vaccaro, V.G.

Northern Illinois University
DeKalb, Illinois
- Barov, N.
- Mihalcea, D.

OPU
Osaka
- Horinaka, H.
- Matsuyama, T.

ORNL
Oak Ridge
- Deibele, C.
- Gurd, D.P.
- Holtkamp, N.
- Jeon, D.-O.
- Johnson, G.

ORNL/SNS
Oak Ridge, Tennessee
- Aleksandrov, V.
- Assadi, S.
- Blokland, W.
- Champion, M.
- Crofford, M.
- Error, J.
- Gibson, P.
- Henderson, S.
- Kasemir, K.

- Ma, H.
- Piller, C.
- Sanchez, B. J.
- Sun, A.
- Tanke, E.P.

OXFORDphysics
Oxford, Oxon
- Green, J.
- Grzelak, G.
- Mitra, A.
- Perry, C.
- Reichold, A.

Omega-P, Inc.
New Haven, Connecticut
- Hirshfield, J.L.

PAL
Pohang
- Oh, J-O.

PKU/IHIP
Beijing
- Chen, J.
- Fang, J.
- Guo, Z.Y.
- Lu, Y.R.
- Peng, S.X.
- Song, Z.Z.
- Yu, J.X.
- Zhang, C.
- Zhu, K.

POSTECH
Pohang
- Oh, J-O.
- Namkung, W.

PPT
Dortmund
- Kaesler, W.

PSI
Villigen
- Dehler, M.
- Ganter, R.
- Gobrecht, J.
- Gough, C.
- Ingold, G.
- Leemann, S.
- Paraliev, M.
- Pedrozzi, M.
- Raguin, J.-Y.
- Rivkin, L.
- Schlott, V.
- Streun, A.
- Wrulich, A.

PTC LPI
Protvino, Moscow Region
- Avrakhov, P. V.
- Balakin, V.E.

Queen Mary University of London
London
- Burrows, P.
- Molloy, S.
- White, G.

RAS/INR
Moscow
- Brusova, N.I.
- Feschenko, A.
- Gaidash, A.
- Kisselev, Yu.
- Kravchuk, L.V.
- Kvasha, A.I.
- Liyu, A.
- Menshov, A.
- Mirzojan, A.N.
- Novikov-Borodin, A.V.
- Paramonov, V.V.
- Pronin, O.D.
- Skasyrskaya, A.K.
- Stepanov, A.A.
- Vasyuchenko, A.

RIKEN Spring-8 Harima
Hyogo
- Baba, H.
- Inagaki, T.
- Onoe, K.
- Shintake, T.
- Tanaka, T.
- Togawa, K.

RIKEN
Saitama
- Jameson, R.A.
- Okamura, M.
- Takano, J.
- Yamamoto, K.

RMC
Bridgeville
- Carneiro, T.

Rochester University
Rochester, New York
- Melissinos, A.C.
- Tikhoplav, R.

Rostock University, Faculty of Engineering
Rostock
- Hecht, D.
- Rothemund, K.
- van Rienen, U.

SAIC
Boston
- Eppley, K.

SLAC
Menlo Park, California
- Chang, A.
- Decker, V.
- Frisch, J.
- Hendrickson, L.
- Huang, Z.
- Krejcik, P.
- Li, Z.
- Markiewicz, T.
- Miller, R.
- Ruth, R.D.
- Schultz, D.C.
- Seryi, A.
- Spencer, C. M.
- Wilson, P.B.
- Wu, J.
- Xiao, L.
- Batygin, Y.K.
- Cassel, R.L.
- Döbert, S.
- Nguyen, M.
- Pappas, G.C.
- Partridge, R.
- Pearson, C.
- deLamare, J.E.

SLAC/ARDA
Menlo Park, California
- Bowden, G.
- Dolgashev, V.A.
- Emma, P.
- Jones, R.M.
- Lewandowski, J.
- Nantista, C.D.
- Tantawi, S.G.
- Wang, J.

SLAC/ARDB
Menlo Park, California
- Dolgashev, V.A.
- Nantista, C.D.
- Wang, J.

SLAC/NLC
Menlo Park, California
- Adolphsen, C.
- Burke, D.L.
- Chan, J.Q.
- Cornuelle, J.
- Döbert, S.
- Eric, D.
- Eric, E.
- Eriksson, L.
- Himel, T.
- Raubenheimer, T.O.
- Ross, M.C.
- Thomas, T.

SLAC/SSRL
Menlo Park, California
- Limborg, C.

SOREQ
Yavne
- Berkovits, D.
- Feinberg, G.
- Halfon, S.
- Shor, A.

Sincrotrone Trieste S.C.p.A.
Basovizza, Trieste
- Bakker, R.J.
- Craievich, P.
- D'Auria, G.
- De Ninno, G.
- Di Mitri, S.D.
- Ferianis, M.
- Pangon, P.G.
- Rumiz, R.L.
- Tosi, T.L.
- Zangrando, D.

TETD
Saitama
- Miyake, S.
- Yano, A.

TIT
Tokyo
- Hattori, T.
- Hayashizaki, N.

TJNAF
Newport News, Virginia
- Augustine, M.
- Delayen, J. R.
- Dong, H.
- Guerra, A.
- Hofler, A.
- Hovater, C.
- Lahti, G.
- Musson, J.
- Nelson, R.
- Plawski, T.
- Terrel, R.A.

- Tiefenback, M.
- Turlington, L.
- Wissmann, M.

TRIUMF
Vancouver
- Bylinskii, Y.
- Clark, G.S.
- Dutto, G.
- Fang, S.
- Fong, K.
- Harmer, P.
- Laverty, M.P.
- Laxdal, R.E.
- Mitra, A.K.
- Poirier, R. L.
- Rawnsley, B.
- Ries, T.
- Schmor, P.
- Sekatchev, I.
- Stanford, G.
- Waraich, B.
- Zvyagintsev, V.

TSINGHUA
Beijing
- Jin, Q.
- Lin, Y.
- Sun, X.
- Tao, X.
- Tong, D.

TU Berlin TET
Berlin
- Bruns, W.

TU Darmstadt
Darmstadt
- Ackermann, W.
- Araz, A.
- Bonnes, U.
- Brunken, M.
- Doliwa, B.
- Gräf, H.-D.
- Hertling, M.
- Karnaukhov, A.
- Kunze, M.
- Müller, W.F.O.
- Patalakha, O.
- Platz, M.
- Richter, A.
- Setzer, S.
- Steiner, B.
- Titze, O.
- Truckses, B.
- Weiland, T.

TUL
Lodz
- Cichalewski, W.
- Koseda, B.
- Napieralski, A.
- Sekalski, S. P.

TechSource
Santa Fe, NM
- Crandall, R.
- Young, L.

UCLA
Los Angeles, California
- Joshi, C.J.

USTC/NSRL
Hefei, Anhui
- Dong, S.
- Huang, G.
- Jia, D.
- Li, G.
- Wu, C.-F.
- Zhou, Y.G.

UTNL
Ibaraki
- Hosokai, T.
- Iijima, H.
- Kinoshita, K.
- Uesaka, M.
- Watanabe, T.
- Yoshii, K.

UW-Madison/ASC
Madison, Wisconsin
- Gurevich, A.
- Jewell, M.
- Larbalestier, D. C.
- Lee, P.
- Polyanskii, A.
- Squitieri, A.

Uni HH
Hamburg
- Rossbach, J.

Universita' degli Studi del Sannio
Benevento
- Davino, D.

University of Illinois at Urbana-Champaign
Urbana, Illinois
- Errede, D.M.
- Linder, G.

WUT
Warsaw
- Czarski, T.
- Jezynski, T.
- Pucyk, P.

Participants List

— A —

Alexander V. **Aleksandrov**
ORNL
sasha@ornl.gov
USA

James **Alessi**
Brookhaven National Laboratory
alessi@bnl.gov
USA

Lawrence **Allen**
Fermi National Accelerator Laboratory
allen@fnal.gov
USA

Wolfgang **Anders**
BESSY
anders@bessy.de
Germany

Norbert **Angert**
GSI
n.angert@gsi.de
Germany

Wolfgang **Arnold**
AFT GmbH
Arnold@AFTGmbH.de
Germany

Pavel **Avrakhov**
Physical Technical Center
avrakhov@vlepp.serpukhov.su
Russia

— B —

Nicoleta **Baboi**
DESY
nicoleta.baboi@desy.de
Germany

Vladimir **Balakin**
Physical Technical Center
balakin@vlepp.serpukhov.su
Russia

Adam **Balkcum**
CPI
adam.balkcum@cpii.com
Germany

Winfried **Barth**
GSI
w.barth@gsi.de
Germany

Yuri **Batygin**
SLAC
batygin@slac.stanford.edu
USA

Carl **Beard**
CLRC Daresbury Laboratory
c.d.beard@dl.ac.uk
Great Britain

Juergen **Bedau**
Bruker Biospin
marketing@bruker.fr
France

Sergey **Belomestnykh**
Cornell University
sab24@cornell.edu
USA

Ahmed **Benlsmail**
CEA Saclay
bismail@cea.fr
France

Dan **Berkovits**
Soreq Applied
Research Accelerator Facility
berkova@soreq.gov.il
Israel

Stephane **Bethuys**
Thales Electron Devices
stephane.bethuys@
thales-electrondevices.com
France

Wilhelm **Bialowons**
DESY
wilhelm.bialowons@desy.de
Germany

Jean-Luc **Biarotte**
IPN Orsay
biarrott@ipno.in2p3.fr
France

Giovanni **Bisoffi**
INFN - Laboratori Nazionali di Legnaro
giovanni.bisoffi@lnl.infn.it
Italy

Carlo **Bocchetta**
ELETTRA
carlo.bocchetta@elettra.trieste.
it
Italy

Franz **Boedker**
Danfysik
fb@danfysik.dk
Denmark

Heinz **Bohlen**
CPI
heinz.bohlen@cpii.com
Germany

Günter **Böhm**
Puls-Plasmatechnik
g.boehm@puls-plasmatechnik.de
Germany

Reinhard **Brinkmann**
DESY
reinhard.brinkmann@desy.de
Germany

Marco **Brunken**
TU-Darmstadt - Institut für Kernphysik
brunken@ikp.tu-darmstadt.de
Germany

Warner **Bruns**
Warner Bruns Feldberechnungen
bruns@gdfidl.de
Germany

Yury **Budanov**
IHEP
budanov51@mail.ru
Russia

Hartmut **Büttig**
FZ Rossendorf
buettig@fz-rossendorf.de
Germany

— C —

Michel **Caron**
CEA-Polygone d'experimentation
de Moronvilliers
michel.caron@cea.fr
France

Fritz **Caspers**
CERN
fritz.caspers@cern.ch
Switzerland

Richard **Cassel**
SLAC
rlc@slac.stanford.edu
USA

Pedro **Castro**
DESY
pedro.castro@desy.de
Germany

Kwok-Chi **Chan**
Los Alamos National Laboratory
kcchan@lanl.gov
USA

Yanglai **Cho**
Argonne National Laboratory
yc@aps.anl.gov
USA

Stefan **Choroba**
DESY
stefan.choroba@desy.de
Germany

Chris **Christou**
Diamond Light Source
chris.christou@diamond.ac.uk
Great Britain

Michele **Comunian**
INFN - Laboratori Nazionali di Legnaro
michele.comunian@lnl.infn.it
Italy

Alexander **Cours**
Argonne National Laboratory
cours@aps.anl.gov
USA

— D —

Gerardo **D Auria**
ELETTRA
dauria@elettra.trieste.it
Italy

Ludwig **Dahl**
GSI
L.Dahl@gsi.de
Germany

Winfried **Decking**
DESY
winfried.decking@desy.de
Germany

Craig **Deibele**
ORNL
deibele@sns.gov
USA

Horst **Deitinghoff**
J.W. Goethe-Universität
Deitinghoff@em.uni-frankfurt.de
Germany

Jean **Delayen**
Jefferson Laboratory
delayen@jlab.org
USA

Olivier **Delferrière**
CEA Saclay
olivier.delferriere@cea.fr
France

Marco **Di Giacomo**
CEA/GANIL
digiacomo@ganil.fr
France

Nicholas **Di Monte**
Argonne National Laboratory
npd@aps.anl.gov
USA

Steffen **Doebert**
SLAC
naomi@slac.stanford.edu
USA

Valery **Dolgashev**
SLAC
dolgash@slac.stanford.edu
USA

Burkhard **Doliwa**
TU-Darmstadt
doliwa@temf.tu-darmstadt.de
Germany

Sai **Dong**
NSRL, USTC
dongsai@ustc.edu.cn
China

Lawrence **Donley**
Argonne National Laboratory
lidonley@anl.gov
USA

Jeffrey **Dooling**
Argonne National Laboratory
jcdooling@anl.gov
USA

Helmut **Dosch**
MPI
dosch@mf.mpg.de
Germany

Per **Dost**
WTM
per.dost@desy.de
Germany

Mike **Dykes**
CLRC Daresbury Laboratory
d.m.dykes@dl.ac.uk
Great Britain

— E —

Marv **Eberhardt**
CPI
marvin.eberhardt@eimac.cpii.com
Germany

Jörg **Eckoldt**
DESY
hans-joerg.eckoldt@desy.de
Germany

Don **Edwards**
Fermi National Accelerator Laboratory
edwards@fnal.gov
USA

Helen **Edwards**
Fermi National Accelerator Laboratory
hedwards@fnal.gov
USA

Stephan **Emhofer**
Siemens Medical Solutions
stephan.emhofer@siemens.com
Germany

— F —

Enrico **Fagotti**
INFN - Laboratori Nazionali di Legnaro
enrico.fagotti@lnl.infn.it
Italy

Dan **Faircloth**
CCLRC Rutherford Appleton Laboratory
D.C.Faircloth@rl.ac.uk
Great Britain

Michael **Fazio**
Los Alamos National Laboratory
mfazio@lanl.gov
USA

Alexander **Feschenko**
Institute for Nuclear Research
feschenk@inr.troitsk.ru
Russia

Mark **Fitzgerald**
The Ferrite Company
markf@ferriteinc.com
USA

Klaus **Flöttmann**
DESY
klaus.floettmann@desy.de
Germany

Ken **Fong**
TRIUMF
Fong@triumf.ca
Canada

Friedrich **Frank**
Varian Deutschland GmbH
friedrich.frank@varianinc.com
Germany

Josef **Frisch**
SLAC
frisch@slac.stanford.edu
USA

Shinian **Fu**
IHEP, Beijing
fusn@mail.ihep.ac.cn
China

— G —

Robert **Garnett**
Los Alamos National Laboratory
rgarnett@lanl.gov
USA

Roland **Garoby**
CERN
roland.garoby@cern.ch
Switzerland

Terence **Garvey**
LAL Orsay
garvey@lal.in2p3.fr
France

Michael **Gehring**
Babcock Noell Nuclear GmbH
michael_gehring@bn-nuclear.de
Germany

Ulrich **Gensch**
DESY
ulrich.gensch@desy.de
Germany

Frank **Gerigk**
ASTEC RAL
frank.gerigk@rl.ac.uk
Great Britain

Raphael **Gobin**
CEA Saclay
rjgobin@cea.fr
France

Jürgen **Gothmann**
Globes Elektronik GmbH & Co. KG
juergen.gothmann@globes.de
Germany

Arthur **Grelick**
Argonne National Laboratory
grelick@aps.anl.gov
USA

Torsten **Grevsmühl**
DESY
torsten.grevsmuehl@desy.de
Germany

Terry **Grimm**
Michigan State University
grimm@nscl.msu.edu
USA

Lars **Groening**
GSI
La.Groening@gsi.de
Germany

Alexej **Grudiev**
CERN
alexej.grudiev@cern.ch
Switzerland

Zhiyu **Guo**
Peking University
zhyguo@pku.edu.cn
China

Dave **Gurd**
ORNL
gurd@sns.gov
USA

Frank **Guy**
Linac Systems
fglinac@azmail.net
USA

— H —

Klaus **Hanke**
CERN
klaus.hanke@cern.ch
Switzerland

Helmut **Haseroth**
CERN
helmut.haseroth@cern.ch
Switzerland

Ken **Hayakawa**
LEBRA, Institute of Quantum Science, Nihon University
hayakawa@lebra.nihon-u.ac.jp
Japan

Hitoshi **Hayano**
KEK
hitoshi.hayano@kek.jp
Japan

Dirk **Hecht**
Universität Rostock
dirk.hecht@etechnik.uni-rostock.de
Germany

Stephan **Heisen**
AFT GmbH
Heisen@AFTGmbH.de
Germany

Heino **Henke**
TU Berlin
henke@tu-berlin.de
Germany

Frank **Herbrand**
Forschungszentrum Rossendorf e.V.
herbrand@gmx.de
Germany

David **Holder**
Daresbury Laboratory
d.j.holder@dl.ac.uk
Great Britain

Doug **Holmes**
Advanced Energy Systems, Inc.
doug_holmes@mail.aesys.net
USA

Norbert **Holtkamp**
ORNL
holtkamp@ornl.gov
USA

Curt **Hovater**
Jefferson Laboratory
hovater@jlab.org
USA

Gerhard **Hüsken**
Thales Electron Devices GmbH
Gerhard.Huesken@de.thales-electrondevices.com
Germany

— I —

Masanori **Ikegami**
KEK
masanori.ikegami@kek.jp
Japan

Yoshihisa **Iwashita**
Institutute for Chemical Research, Kyoto University
Iwashita@kyticr.kuicr.kyoto-u.ac.jp
Japan

— J —

Andreas **Jankowiak**
Institut für Kernphysik, Universität Mainz
Janko@kph.uni-mainz.de
Germany

Jens-Peter **Jensen**
DESY
jens-peter.jensen@desy.de
Germany

Qingxiu **Jin**
Tsinghua University
qxjin@mail.tsinghua.edu.cn
China

Rolland **Johnson**
Muons, Inc.
roljohn@aol.com
USA

Roger **Jones**
SLAC
rmj@slac.stanford.edu
USA

Chan **Joshi**
UCLA
joshi@ee.ucla.edu
USA

— K —

Wolfgang **Kaesler**
Puls-Plasmatechnik
w.kaesler@puls-plasmatechnik.de
Germany

Tarek **Kandil**
Michigan State University
kandil@nscl.msu.edu
USA

Ulrich **Kappeller**
AFT GmbH
Kappeller@AFTGmbH.de
Germany

Valery **Katalev**
DESY
valery.katalev@desy.de
Germany

Takeshi **Kawano**
Hitachi High-Technologies Corporation
kawano-takeshi@nst.hitachi-hitec.com
Japan

Michael **Kelly**
Argonne National Laboratory
kelly@phy.anl.gov
USA

Michael **Kempkes**
Diversified Technologies, Inc.
kempkes@divtecs.com
USA

Oliver **Kester**
Ludwig Maximilian Universität
oliver.kester@physik.uni-muenchen.de
Germany

Avi **Keter**
Soreq Applied Research Accelerator Facility
AviKeter@hotmail.com
USA

Jorg **Kewisch**
Brookhaven National Laboratory
jorg@bnl.gov
USA

Yujong **Kim**
DESY
Yujong.Kim@desy.de
Germany

Harold **Kirk**
Brookhaven National Laboratory
kirk@bnl.gov
USA

Charles **Kitegi**
J.W. Goethe-Universität
kitegi@iap.uni-frankfurt.de
Germany

Horst **Klein**
J.W. Goethe-Universität
Horst.Klein@iap.uni-frankfurt.de
Germany

Christian **Klinkenberg**
Niobium Products Company GmbH
ck@niobium.de
Germany

Peter **Kneisel**
Jefferson Laboratory
kneisel@jlab.org
USA

Jens **Knobloch**
BESSY
jens.knobloch@bessy.de
Germany

Valery **Kobets**
JINR Dubna
kobets49@mail.ru
Russia

Yasuhiro **Kondo**
Japan Atomic Energy Research Institute
kondo@linac.tokai.jaeri.go.jp
Japan

Denis **Kostin**
DESY
dkostin@mail.desy.de
Germany

Bernward **Krause**
DESY
bernward.krause@desy.de
Germany

Leonid **Kravchuk**
Institute for Nuclear Research
kravchuk@inr.troitsk.ru
Russia

Frank **Krawczyk**
Los Alamos National Laboratory
fkrawczyk@lanl.gov
USA

Patrick **Krejcik**
SLAC
pkr@slac.stanford.edu
USA

Sergey **Kuzikov**
IAP, Russian Academy of Sciences
kuzikov@appl.sci-nnov.ru
Russia

Adolf **Kvasha**
Institute for Nuclear Research
kvasha@inr.ru
Russia

— L —

Lori **Lane**
ORNL / SNS
lanelj@ornl.gov
USA

Robert **Laxdal**
TRIUMF
lax@triumf.ca
Canada

Seishu **Lee**
KEK
seishu.lee@kek.jp
Japan

Jean-Louis **Lemaire**
CEA-Bruyères
jean-louis.lemaire@cea.fr
France

James **Lewandowski**
SLAC
jiml@slac.stanford.edu
USA

John **Lewellen**
Argonne National Laboratory
Lewellen@aps.anl.gov
USA

Zhihui **Li**
IMP
zhihui_li@yahoo.com
China

Holger **Liebermann**
Institut für Angewandte Physik
Liebermann@iap.uni-frankfurt.de
Germany

Lutz **Lilje**
DESY
lutz.lilje@desy.de
Germany

Torsten **Limberg**
DESY
torsten.limberg@desy.de
Germany

Augusto **Lombardi**
INFN - Laboratori Nazionali di Legnaro
augusto.lombardi@lnl.infn.it
Italy

Yuanrong **Lu**
J.W. Goethe-Universität
ylu@iap.uni-frankfurt.de
Germany

— M —

Jean **Marini**
LAL Orsay
marini@lal.in2p3.fr
France

Ronald **Martin**
Argonne National Laboratory
rmartin45@aol.com
USA

Eduard **Masunov**
MEPhI
masunov@dinus.mephi.ru
Russia

Axel **Matheisen**
DESY
axel.matheisen@desy.de
Germany

Hiroshi **Matsumoto**
KEK
hiroshi.matsumoto@kek.jp
Japan

Rodney **McCrady**
Los Alamos National Laboratory
mccrady@lanl.gov
USA

Elliott **McCrory**
Fermi National Accelerator Laboratory
McCrory@fnal.gov
USA

Gerald **McMichael**
Argonne National Laboratory
mcmichael@anl.gov
USA

Robert **Merl**
Los Alamos National Laboratory
merl@lanl.gov
USA

Oliver **Meusel**
J.W. Goethe-Universität
o.meusel@iap.uni-frankfurt.de
Germany

Shinichiro **Michizono**
KEK
shinichiro.michizono@kek.jp
Japan

Roger **Miller**
SLAC
rhm@slac.stanford.edu
USA

Tetsuji **Mitani**
Hitachi Ltd.
tetsuji_mitani@pis.hitachi.co.jp
Japan

Amiya **Mitra**
TRIUMF
Mitra@triumf.ca
Canada

Wolf-Dietrich **Möller**
DESY
wolf-dietrich.moeller@desy.de
Germany

Alfred **Moretti**
Fermi National Accelerator Laboratory
moretti@fnal.gov
USA

Karl **Morgen**
WTM
K.Morgen@wtm-hh.de
Germany

Marie-Hélène **Moscatello**
GANIL
moscatello@ganil.fr
France

Andrew **Moss**
CLRC Daresbury Laboratory
a.j.moss@dl.ac.uk
Great Britain

Jean **Mourier**
CERN
jean.mourier@cern.ch
Switzerland

Wolfgang **Müller**
TU-Darmstadt
mueller@temf.tu-darmstadt.de
Germany

— N —

Martin **Nagl**
DESY
martin.nagl@desy.de
Germany

Ami **Nagler**
Soreq Applied Research
Accelerator Facility
nagler@soreq.gov.il
Israel

Fujio **Naito**
KEK
fujio.naito@kek.jp
Japan

Tsutomu **Nakanishi**
Nagoya University
nakanisi@spin.phys.nagoya-u.ac.jp
Japan

Won **Namkung**
POSTECH
namkung@postech.ac.kr
Croatia

Christopher **Nantista**
SLAC
nantista@sla.stanford.edu
USA

Olivier **Napoly**
CEA Saclay
olivier.napoly@cea.fr
France

Tony **Nelson**
Wah Chang
Tony.Nelson@Wahchang.com
USA

Axel **Neumann**
BESSY
axel.neumann@bessy.de
Germany

Markus **Niedermaier**
The Ferrite Company
business@niedermaier.de
Germany

Akira **Noda**
Kyoto University
noda@kyticr.kuicr.kyoto-u.ac.jp
Japan

James **Norem**
Argonne National Laboratory
norem@anl.gov
USA

— O —

Jong-Seok **Oh**
POSTECH
jsoh@postech.ac.kr
Croatia

Satoshi **Ohsawa**
KEK
satoshi.ohsawa@kek.jp
Japan

Masahiro **Okamura**
RIKEN
mokamura@postman.riken.go.jp
Japan

Yoshihisa **Okubo**
Toshiba Electron Tubes & Devices Co., Ltd
yoshihisa.ookubo@toshiba.co.jp
Japan

Anne **Oppelt**
DESY
anne.oppelt@desy.de
Germany

Peter **Ostroumov**
Argonne National Laboratory
ostroumov@anlphy.phy.anl.gov
USA

— P —

Valentin **Paramonov**
Institute for Nuclear Research
paramono@inr.troitsk.ru
Russia

Marco **Pedrozzi**
Paul Scherrer Institut
marco.pedrozzi@psi.ch
Switzerland

Michael **Peiniger**
ACCEL GmbH
peiniger@accel.de
Germany

Michael **Pekeler**
ACCEL GmbH
pekeler@accel.de
Germany

Andreas **Peters**
GSI
a.peters@gsi.de
Germany

Jens **Peters**
DESY
jens.peters@desy.de
Germany

Bernd **Petersen**
DESY
bernd.petersen@desy.de
Germany

Luigi **Picardi**
ENEA
picardi@frascati.enea.it
Italy

Christian **Piel**
ACCEL GmbH
piel@accel.de
Germany

Raj **Pillay**
Dept. of Nuclear and Atomic Physics, Tata Institute of Fundamental Research
pillay@tifr.res.in
India

Philippe **Piot**
Fermi National Accelerator Laboratory
piot@fnal.gov
USA

Andrea **Pisent**
INFN - Laboratori Nazionali di Legnaro
andrea.pisent@lnl.infn.it
Italy

Markus **Platz**
TU Darmstadt, Institut für Kernphysik
platz@ikp.tu-darmstadt.de
Germany

Holger **Podlech**
J.W. Goethe-Universität
h.podlech@iap.uni-frankfurt.de
Germany

Roger **Poirier**
TRIUMF
Poirier@triumf.ca
Canada

Mike **Poole**
CCLRC Daresbury Laboratory
m.w.poole@dl.ac.uk
Great Britain

Joseph **Preble**
Jefferson Laboratory
preble@jlab.org
USA

Johannes **Prenting**
DESY
johannes.prenting@desy.de
Germany

Gunnar **Priebe**
DESY
gunnar.priebe@desy.de
Germany

Dieter **Proch**
DESY
dieter.proch@desy.de
Germany

— R —

Jean-Yves **Raguin**
Paul Scherrer Institut
jean-yves.raguin@psi.ch
Switzerland

Deepak **Raparia**
Brookhaven National Laboratory
raparia@bnl.gov
USA

John **Rathke**
Advanced Energy Systems
john_rathke@mail.aesys.net
USA

Alessandro **Ratti**
Lawrence Berkeley National Laboratory
aratti@lbl.gov
USA

Ulrich **Ratzinger**
J.W. Goethe-Universität
u.ratzinger@iap.uni-frankfurt.de
Germany

Bill **Rawnsley**
TRIUMF
Rawnsley@triumf.ca
Canada

Stefano **Redaelli**
CERN - AB Department
stefano.redaelli@cern.ch
Switzerland

Detlef **Reschke**
DESY
detlef.reschke@desy.de
Germany

Simone **Richter**
GSI
S.Richter@gsi.de
Germany

Claus **Rode**
Jefferson Laboratory
rode@jlab.org
Canada

Marc **Ross**
SLAC
mcrec@slac.stanford.edu
USA

Joerg **Rossbach**
DESY
joerg.rossbach@desy.de
Germany

— S —

Susumu **Sato**
Japan Atomic Energy Research Institute
ssato@linac.tokai.jaeri.go.jp
Japan

Herve **Saugnac**
IPN Orsay
saugnac@ipno.in2p3.fr
France

Volker RW **Schaa**
GSI
v.r.w.schaa@gsi.de
Germany

Alwin **Schempp**
J.W. Goethe-Universität
a.schempp@em.uni-frankfurt.de
Germany

Bernhard **Schlitt**
GSI
B.Schlitt@gsi.de
Germany

Charles **Schmidt**
Fermi National Accelerator Laboratory
cschmidt@fnal.gov
USA

Paul **Schmor**
TRIUMF
schmor@triumf.ca
Canada

Jochen **Schneider**
DESY
jochen.schneider@desy.de
Germany

Dale **Schrage**
Los Alamos National Laboratory
dls@lanl.gov
USA

Stan **Schriber**
Michigan State University
schriber@nscl.msu.edu
USA

Daniel **Schulte**
CERN
daniel.schulte@cern.ch
Switzerland

Dave **Schultz**
SLAC
dcs@slac.stanford.edu
USA

Jacek **Sekutowicz**
DESY
jacek.sekutowicz@desy.de
Germany

Bradley **Sherrill**
Michigan State University
sherrill@nscl.msu.edu
USA

Thomas **Sieber**
CERN
thomas.sieber@cern.ch
Switzerland

Stefan **Simrock**
DESY
stefan.simrock@desy.de
Germany

Henrik **Skov**
Danfysik
hs@danfysik.dk
Denmark

Guy **Stanford**
TRIUMF
Stanford@triumf.ca
Canada

Rolf **Stassen**
FZ Jülich
r.stassen@fz-juelich.de
Germany

Frank **Stephan**
DESY
frank.stephan@desy.de
Germany

Joachim **Stroth**
GSI - Kernphysik I
J.Stroth@gsi.de
Germany

Anatoly **Sumbaev**
JINR Dubna
sumbaev@nf.jinr.ru
Russia

Donald **Swenson**
Linac Systems
DASwenson@aol.com
USA

— T —

Eiji **Tanabe**
AET Japan, Inc.
etanabe@aetjapan.com
Japan

Sami **Tantawi**
SLAC
tantawi@slac.stanford.edu
USA

Xiaokui **Tao**
Tsinghua University
taoxk@mail.tsinghua.edu.cn
China

Jochen **Teichert**
FZ Rossendorf
j.teichert@fz-rossendorf.de
Germany

Rudolf **Tiede**
J.W. Goethe-Universität
Tiede@iap.uni-frankfurt.de
Germany

Kazuaki **Togawa**
RIKEN
togawa@spring8.or.jp
Japan

Hiromitsu **Tomizawa**
JASRI/SPring-8
hiro@spring8.or.jp
Japan

Dechun **Tong**
Tsinghua University
tongdc@mail.tsinghua.edu.cn
China

Dieter **Trines**
DESY
dieter.trines@desy.de
Germany

Wolfgang **Tschunke**
CPI
wolfgang.tschunke@cpii.de
Germany

— U —

Klaus **Unser**
Bergoz Instrumentation
unser@bergoz.com
Switzerland

— V —

Vittorio **Vaccaro**
Dip. di Scienze Fisiche,
INFN-Sezione di Napoli
vittorio.vaccaro@na.infn.it
Italy

Ursula **van Rienen**
Universität Rostock
ursula.van-rienen@etechnik.
uni-rostock.de
Germany

Wolfgang **Vinzenz**
GSI
W.Vinzenz@gsi.de
Germany

Bernard **Visentin**
CEA Saclay
bernard.visentin@cea.fr
France

Wolfgang **Vodel**
Friedrich-Schiller-Universität Jena
wolfgang.vodel@uni-jena.de
Germany

Hanspeter **Vogel**
ACCEL GmbH
vogel@accel.de
Germany

Jörg **Voigtländer**
FZ Rossendorf
j.voigtlaender@fz-rossendorf.de
Germany

Maurizio **Vretenar**
CERN
maurizio.vretenar@cern.ch
Switzerland

— W —

Nicholas **Walker**
DESY
nicholas.walker@desy.de
Germany

Wolfgang **Walter**
Babcock Noell Nuclear GmbH
wolfgang_walter@bn-nuclear.de
Germany

Juwen **Wang**
SLAC
jywap@slac.stanford.edu
USA

Shuhong **Wang**
IHEP, Beijing
wangsh@sun.ihep.ac.cn
China

Steffen **Watzlawik**
TU Darmstadt, Institut für Kernphysik
stwatz@ikp.tu-darmstadt.de
Germany

Thomas **Weiland**
TU Darmstadt
thomas.weiland@temf.
tu-darmstadt.de
Germany

Hans **Weise**
DESY
hans.weise@desy.de
Germany

Carsten **Welsch**
Max-Planck Institut für Kernphysik
carsten.welsch@mpi-hd.mpg.de
Germany

Manfred **Wendt**
DESY
manfred.wendt@desy.de
Germany

Marion **White**
Argonne National Laboratory - ASD Bldg
401
mwhite@aps.anl.gov
USA

Perry **Wilson**
SLAC
pwilson@slac.stanford.edu
USA

Xiaoyu **Wu**
Michigan State University
xwu@nscl.msu.edu
USA

Walter **Wuensch**
CERN
walter.wuensch@cern.ch
Switzerland

— Y —

Daisuke **Yamada**
Toshiba Electronics Europe GmbH
daisuke.yamada@toshiba.co.jp
Japan

Kazuo **Yamamoto**
RIKEN
k-yamamoto@riken.jp
Japan

Yoshishige **Yamazaki**
Japan Atomic Energy Research Institute
yoshishige.yamazaki@linac.tokai.jaeri.go.jp
Japan

Kenichi **Yanagida**
JASRI/SPring-8
ken@spring8.or.jp
Japan

Xingfan **Yang**
CAEP
xingfan_y@hotmail.com

Atsunori **Yano**
Toshiba Electron Tubes & Devices Co., Ltd
atsunori.yano@toshiba.co.jp
Japan

Stepan **Yaramishev**
GSI
S.Yaramishev@gsi.de
Germany

Masakazu **Yoshioka**
KEK
masakazu.yoshioka@kek.jp
Japan

Wei **Yu**
Elekta Ltd
Wei.Yu@elekta.com

Osamu **Yushiro**
Toshiba Electron Tubes & Devices Co., Ltd
osamu.yushiro@toshiba.co.jp
Japan

— Z —

Chuan **Zhang**
J.W. Goethe-Universität
Zhang@iap.uni-frankfurt.de
Germany

Michael **Zisman**
Lawrence Berkeley National Laboratory
MSZisman@lbl.gov
USA

Vladimir **Zvyagintsev**
TRIUMF
zvyagint@triumf.ca
Canada

AFT
Advanced Ferrite Technology

Germany

AFT GmbH
Spinnerei 44
D-71522 Backnang
Phone: +49 (0) 7191 9659 0
FAX: +49 (0) 7191 9659 20
info@AFTGmbH.de

Product Range / Components:

- Cathodes
- Guns
- Linac Structures
- UHV Components
- Beam Diagnostics
- Beam Dumps
- all you can think of

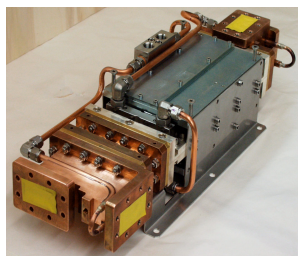

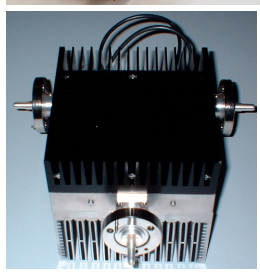
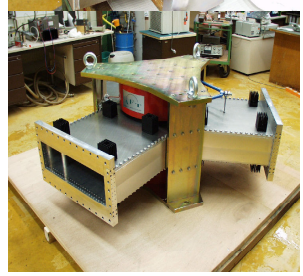

References:

- DESY
- GSI
- SLAC
- BESSY
- Los Alamos National Laboratory

Linac II, TESLA Test Facility
SNS, ATP, HPC, CLS, ALS

U.S.A

AFT Inc.
15200 Shady Grove Road - Suite 350
Rockville MD 20850 USA
Tel: 301-670-2833
Fax: 301-670-2831
E-mail: bobk4ew@aol.com

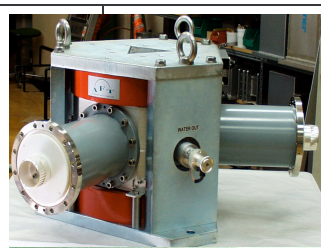
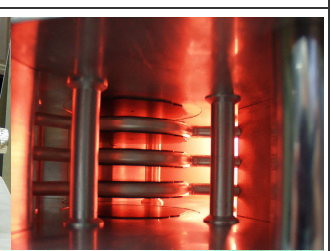
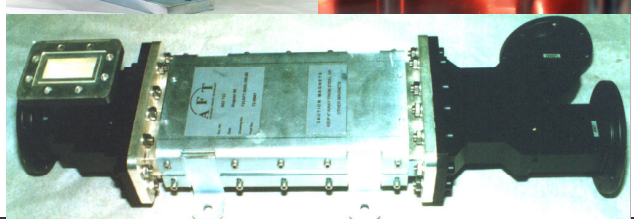

Communications & Power Industries

CPI International Inc.
Hohenadlstrasse 31
85737 Ismaning

☎ +49 (89) 458737-0
🖷 +49 (89) 458737-45
✉ contact@cpii.de

Product Range / Components:

We offer a comprehensive range of microwave and power grid vacuum electronic devices, e.g.

- Klystrons
- IOTs
- Triodes, Tetrodes, Pentodes etc.
- Gyrotrons
- TWTs
- Magnetrons
- etc.,

complete microwave amplifiers, modulators and various other power supply equipment and devices, e.g.

- Couplers
- RF-Windows
- etc.

References:

- DESY (TTF, HERA, PETRA)
- CNRS / LAL (TTF)
- GSI (Ion Source, Cancer Treatment)
- Max Plank Institut (W7X, W-AS etc.)

- Los Alamos National Lab (LAMPF, Lansce, AECL)
- Cornell University (CESR)
- Stanford University (FEL Research)
- SLAC (B-factory)
- Oakridge National Labs (SNS)
- NASA (Deep Space Network)
- Dutch Atomic Energy Commission (Particle Accelerator)
- Canal Plus (Satellite signals for TV transmission)
- MIT (Lincoln Lab Haystack Observatory, ICRH)
- Lawrence Berkeley National Lab (VENUS)
- Michigan State University (RIA)
- JAERI (ICRH, BTA-RFQ, JAERI FEL)
- Princeton University (Plasma Physics)
- Etc., etc., etc.

CPI International
Microwave Power
Products Division
811 Hansen Way
Palo Alto, CA 94303

☎ +1 (650) 846-3310
🖷 +1 (650) 856-0705
✉ marketing@cpii.com

CPI International
Eimac Division
301 Industrial Road
San Carlos, CA 94070

☎ +1 (650) 592-1221
🖷 +1 (650) 592-9988
✉ powergrid@eimac.cpii.com

CPI International
Beverly Microwave
Division
150 Sohier Road,
Beverly, MA 01915

☎ +1 (978) 922-6000
🖷 +1 (978) 922-2736
✉ marketing@bmd.cpii.com

For further locations in Europe or all over the world please contact us or visit www.cpii.com

GLOBES Elekronik GmbH & Co KG
Berliner Platz 12
74072 Heilbronn
Telefon: 07131 / 78100, Fax: 07131 7810-20

GLOBES Elektronik ist eine deutsche Vertriebsgesellschaft, die auf Hochfrequenz-, Mikrowellentechnik und verwandte Elektronik spezialisiert ist. Niederlassungen befinden sich in Heilbronn (nördlich **Stuttgart**), Norderstedt (**Hamburg)** und Germering (**München)**.

GLOBES vertritt hervorragende ausländische Hersteller, vornehmlich aus den USA, dem Fernen Osten, Europa und Israel und vertreibt deren HF-, Mikrowellen- und elektronische Komponenten, Superkomponenten, Subsysteme, Systeme und Instrumente; hauptsächlich in **Deutschland,** der **Schweiz** und **Österreich**.
GLOBES kann als Agent, Repräsentant oder Distributor handeln.

Unser Ziel ist es, ein umfassender und kompetenter Dienstleister für die Kunden zu sein und dabei nicht den kurzfristigen Gewinn, sondern die langfristige, für alle Beteiligten profitable Zusammenarbeit zu finden.

GLOBES Elektronik wurde Anfang des Jahres 1995 gegründet. Die Gesellschafter (alle im Unternehmen tätig) und Mitarbeiter repräsentieren mehr als **hundertfünfzig Jahre Erfahrung** im Spezialgebiet der Hochfrequenz-, Mikrowellen- und Kommunikationstechnik. Diese Erfahrung wurde im wesentlichen in den deutschsprachigen Ländern (Deutschland, Österreich und der Schweiz) erworben. Daraus resultiert ein fundiertes Wissen der Marktgegebenheiten, der Applikationen und der Produkte.
Die Vertriebsingenieure sind gewohnt mit Technologien wie **MMIC, Dünnfilm, Dickfilm, SMD, diskreten Elementen, MIC, (Micro-) Streifenleitung, Airline, Suspended Substrates, koaxial und Hohlleiter,** wie auch Kombinationen aus dem vorgenannten umzugehen. Die verwendeten **GaAs-, Si-** oder **SiC-Halbleiter** sind **Bipolar** oder in **UTSi-CMOS, MOS** oder **LDMOS** Technologie aufgebaut**.**

Die Märkte der **kommerziellen, militärischen und Raumfahrt- Applikationen** werden mit bewiesenem Erfolg und Erfahrung bedient, wobei die besonderen Erfordernisse jedes einzelnen Segmentes beachtet werden. Über das Tagesgeschäft hinaus können große OEM-Verträge und langfristige Programme abgewickelt werden. Die Distribution von HF- und Mikrowellenkomponenten oder auch Pufferlager und Logistikabkommen gehört zu den normalen Aufgaben.

All dies in Kombination mit der Erfahrung in allen kommerziellen Notwendigkeiten, ergibt eine hohe Sicherheit, das die Interessen von Kunden und vertretenen Herstellern bestens gewahrt sind. GLOBES‘ Aufgabe ist der verlängerte „Vertriebsarm“ der vertretenen Hersteller einerseits, und der „Anwalt“ der Kundeninteressen andererseits zu sein.
GLOBES ist finanziell sicher und unabhängig.

GLOBES stellt die Produkte über eigene Anzeigen, „Direkt Mail“ (mehr als **6000** aktive Adressen) und Ausstellungen wie **„electronica“, EEEfCOM** oder **„EuMW“** vor.

Die Kontakte mit unseren Partnern, sowohl technisch wie kommerziell, sind exzellent, wie auch das kombinierte Wissen über nahezu alle genannten Produkte. Die kompletten Import- und Exportprozeduren sind sehr gut organisiert. GLOBES fühlt sich von seinen Hauptkunden bestens akzeptiert. Die Reaktionen des Marktes sind positiv und zeigen den Willen zur Zusammenarbeit. Dies bildet eine weitere Grundlage des Erfolges.

GLOBES’ Verpflichtung ist Kompetenz und Qualität bei Produkten und Dienstleistungen.

PULS-PLASMATECHNIK GMBH
DORTMUND

Germany

Puls-Plasmatechnik GmbH
Feldstr. 56
D-44141 Dortmund
Phone: +49 (0)231 528833
FAX: +49 (0)231 553177
info@puls-plasmatechnik.de

Product Range / Components:

- Klystron Modulators
- Electron Source Pulsers
- Septum-/ Kicker Driver Systems
- Control-/Interlock Systems based on PLC or VME with Interface Standards CAN-, GPIB-, PROFIBUS, Ethernet
- EPICS implementation
- Pulsed Power Systems for Weather Radar Transmitters and Plasma Technology
- High Power Switch Assemblies based on thyratrons or solid state switches like thyristors, IGBTs, IGCTs
- High Voltage Capacitor Charging Units for scientific- / medical applications

Klystron Modulator cabinets for DIAMOND / UK

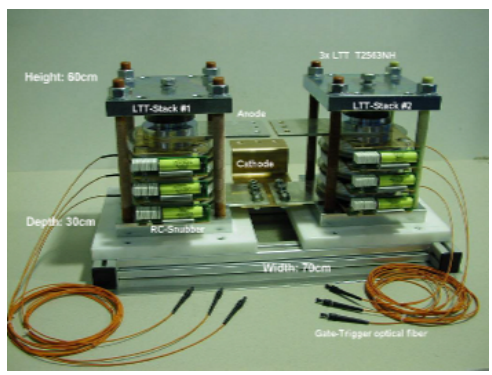

100-kA crowbar unit for TTF / DESY
Light-triggered thyristors as ignitron replacement

References:

- DESY Hamburg
- BESSY Berlin
- FZ Karlsruhe
- FZ Jülich
- University Dortmund
- MAXLab Lund / S
- Paul-Scherrer Institut / CH
- RAL / UK
- INFN Frascati / I

Projects:

- Linac II, TESLA Test Facility (TTF)
- Microtron
- ANKA
- COSY
- DELTA
- MAX -Linac
- SLS -Linac
- DIAMOND -Linac
- SPARC -Linac

WINDELS · TIMM · MORGEN
Partnerschaft

Beratende Ingenieure im Bauwesen

Windels · Timm · Morgen is an established engineering consultancy with more than 9000 completed projects to date.

Since its foundation in 1936, Windels · Timm · Morgen has been instrumental in making building history.

Today, the company is regarded as one of the top addresses in germany when it comes to engineering services for challenging, economically viable building projects.

Fields of Expertise

- Civil Engineering
- Structural Engineering
- Industrial Plants
- Traffic Facilities
- Marine and Harbour Engineering
- Environmental Protection

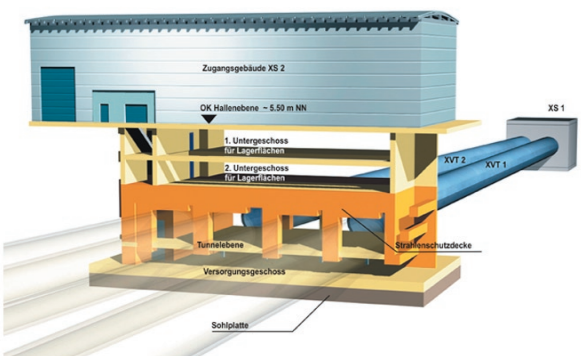

Scope of Service

- Preliminary and feasibility studies
- Project control
- Overall project planning including all applications for building and implementation permits etc.
- Project planning
- Supervision of execution
- Structural design and calculation including design of thermal insulation, fire protection and acoustical measures
- Checking of structural designs and calculations for all fields of civil engineering

Contact

Windels · Timm · Morgen Partnerschaft
Beratende Ingenieure im Bauwesen

Ballindamm 17
20099 Hamburg

Telefon	+49 40 35009 0
Fax	+40 40 35009 100
E-Mail	info@wtm-hh.de
Internet	www.wtm-ingenieure.de

Production Notes

The LINAC2004 proceedings were produced using a number of *Open Software* tools and newly developed scripts. The SPMS database (Scientific Program Management System, author: Matt Arena, FermiLab) of the JACoW Collaboration has been used for abstract and paper submission.

The contents of the database has been exported to XML, providing all data necessary for the batch production of the abstract booklet, proceedings and consistent conference web pages. The generated XML file consisted of 49 452 lines of meta data describing each paper contribution. A PERL script was developed to read this XML file and transform it to <html>, \ConTeXt, \LaTeX, and command files. A second PERL script transforms pdf-files submitted by the authors to text files, which then are scanned for keywords given by a reference list. The five top-most keywords are used for the keyword list.

A script run produces 1214 pages for the conference web site (http://bel.gsi.de/linac2004/). These pages consist of lists for *Sessions*, *Classification*, *Authors*, *Keywords*, and *Institutes* with all available cross links. All these pages are coded in UNICODE (UTF8), making greek characters and small math formulas in abstracts possible (see for example abstract MOP20, MOP84, or THP06), as well as showing the correct writing of names with accented characters. For alphabetic sorting of author names a rule based method is used honoring accented letters, umlauts, etc.

The script generated 282 pdfTeX wrappers for each single raw pdf-file, and one for the proceedings file. *Raw* pdf-files are papers conforming to the JACoW (Joint Accelerator Conferences on Web) editor's guideline without page numbers, running title, and session names (see http://www.jacow.org). A pdfTeX wrapper transforms the raw pdf-file into one that has all hidden fields (*Title*, *Subject*, *Author*, *Keywords*) filled, in addition to page numbering, classification names, and conference details.

The final printed proceedings required minimal manual intervention. Embedding of preface material, lists of authors, institutes, participants, papers, and affiliation details were controlled by means of a configuration file. The proceedings pdf-file, which can be downloaded from the proceedings web site (http://bel.gsi.de/dipac2004/papers/proceedings.pdf), features a completely cross-linked document including table of contents, list of authors, and list of institutes, as well as the papers themselves. The final version of the proceedings was made using pdfLaTeX (version 1.21a) with macro packages *pdfpages* (version v0.3e), *fancyhdr* (version v2.1), and *thumbpdf* (version v3.7).

The scripts are supported by the SPMS (Scientific Program Management System). They will be available from the JACoW site.

March 2005
Volker RW Schaa